Malaysian Journal of Analytical Sciences (MJAS)
Published by Malaysian Analytical Sciences Society

Vol 24 No 1 (2020)

Vol 24 No 2 (2020)

Vol 24 No 3 (2020)

Vol 24 No 4 (2020)

Vol 24 No 5 (2020)

Vol 24 No 6 (2020)

2020

Malaysian Journal of Analytical Sciences Vol 24 No 1 2020

Page

1. PREPARATION AND CHARACTERISATION OF pH PROBE MEMBRANE FOR DETERMINATION OF TOTAL ALKALINITY IN SEAWATER 1
(Penyediaan dan Pencirian Membran Prob pH bagi Penentuan Jumlah Kealkalian dalam Air Laut)
Noor Sheryna Jusoh, Azrilawani Ahmad, Marinah Mohd Ariffin, Hafiza Mohamed Zuki

2. SYNTHESIS AND SOLID-STATE STRUCTURAL ELUCIDATION OF RHENIUM(I) COMPLEX WITH 1-CINNAMOYL-3-(PYRIDIN-2-YL)PYRAZOLE 11
(Sintesis dan Penentuan Struktur Pepejal Kompleks Renium(I) dengan 1-Sinamoil-3-(Piridin-2-il)Pirazola)
Wun Fui Mark-Lee, Yan Yi Chong, Azizul Hakim Lahuri, Mohammad B. Kassim

3. STUDIES AND ABSORPTION ISOTHERMAL OF METHYLENE BLUE BY USING N,O-CARBOXYMETHYL CHITOSAN 21
(Kajian Kinetik dan Isoterma Serapan Metilena Biru Menggunakan N,O-Karboksimetil Kitosan)
Putri Amirah Solehin Sulizi and Nadhratun Naiim Mobarak

4. AGAROSE-CHITOSAN-INTERGRATED MULTIWALLED CARBON NANOTUBES FILM SOLID PHASE MICROEXTRACTION COMBINED WITH HIGH PERFORMANCE LIQUID CHROMATOGRAPHY FOR THE DETERMINATION OF TRICYCLIC ANTIDEPRESSANT DRUGS IN AQUEOUS SAMPLES 33
(Filem Agarosa-Kitosan Bersepadu Nanotiub Kabon Berbilang Dinding Pengestrakan Mikro Fasa Pepejal Digabungkan Dengan Kromatografi Cecair Prestasi Tinggi-Pengesanan Ultralembayung Untuk Penentuan Anti-Murung Trisiklik Di Dalam Sampel Akueus)
Wan Nazihah Wan Ibrahim, Mohd Marsin Sanagi, Nor Suhaila Mohammad Hanapi, Nursyamsyila Mat Hadzir, Noorfatimah Yahaya, Sazlinda Kamaruzaman

5. APPLICATION OF BOX-BEHNKEN DESIGN WITH RESPONSE SURFACE METHODOLOGY FOR OPTIMIZING OXYGEN COLOUR INDICATOR FOR ACTIVE PACKAGING 42
(Aplikasi Reka Bentuk Box-Behnken dengan Kaedah Gerak Balas Permukaan untuk Mengoptimumkan Penunjuk Oksigen Berwarna bagi Pembungkus Aktif)
Aishah Mohd Marsin and Ida Idayu Muhamad

6. APPLICATION OF MICROWAVE-ASSISTED EXTRACTION COUPLED WITH DISPERSIVE LIQUID-LIQUID MICROEXTRACTION FOR THE DETERMINATION OF POLYCYCLIC AROMATIC HYDROCARBONS IN VEGETABLES 53
(Aplikasi Pengekstrakan Berbantukan Mikrogelombang Gandingan dengan Pengekstrakan Mikro Cecair-Cecair Serakan bagi Penentukan Hidrokarbon Aromatik Polisiklik dalam Sayur-Sayuran)
Chai Mee Kin, Tan Yeong Hwang, Wong Ling Shing

7. CORROSION INHIBITION STUDY ON GLYCEROL AS SIMULTANEOUS GAS HYDRATE AND CORROSION INHIBITOR IN GAS PIPELINES 62
(Kajian Perencatan Kakisan oleh Gliserol sebagai Perencat Serentak untuk Hidrat Gas

dan Kakisan dalam Saluran Paip Gas)
Vinayagam Sivabalan, Belkhir Walid, Yoann Madec, Ali Qasim, Bhajan Lal

8. PHYTOCHEMICAL SCREENING AND FTIR SPECTROSCOPY ON CRUDE EXTRACT FROM *Enhalus acoroides* LEAVES 70
(Saringan Fitokimia dan Spektroskopi FTIR Ekstrak Mentah Daun *Enhalus acoroides*)
Made Pharmawati and Luh Putu Wrasiati

9. EFFECT OF BMIM-CHLORIDE ON PHYSIO CHEMICAL PROPERTIES OF NANOFIBER MEMBRANE FOR DOMESTIC WASTEWATER TREATMENT 78
(Kesan BMIM-Klorida ke atas Sifat-Sifat Fisio-Kimia Membran Nanogentian untuk Rawatan Sisa Air Domestik)
Ahmad Tarmizi Mohd, Nur Syakinah Abd Halim, Mohd Dzul Hakim Wirzal, Muhammad Roil Bilad, Nik Abdul Hadi Md Nordin, Zulfan Adi Putra, Abdull Rahim Mohd Yusoff

10. CHEMICAL COMPOSITION OF ESSENTIAL OILS FROM LEAF EXTRACT OF PANDAN, *Pandanus amaryllifolius* ROXB. 87
(Komposisi Kimia Minyak Pati daripada Ekstrak Daun Pandan, *Pandanus amaryllifolius* Roxb.)
Maisarah Mohamed Zakaria, Uswatun Hasanah Zaidan, Suhaili Shamsi, Siti Salwa Abd Gani

11. ELECTROCHEMICAL DETERMINATION OF DOPAMINE AND URIC ACID IN BLOOD SERUM USING ANIONIC SURFACTANTS AT CARBON PASTE ELECTRODES 97
(Penentuan Dopamin dan Asid Urik dalam Serum Darah Secara Elektrokimia Menggunakan Surfaktan Anionik pada Perekat Elektrod Karbon)
Liridon Berisha, Egzontina Shabani, Arsim Maloku, Granit Jashari, Tahir Arbneshi

12. MULTI-SPECTROSCOPIC AND CHEMOMETRICS ANALYSIS FOR FORENSIC DETERMINATION OF BLOOD SPECIES 107
(Multi-Spektroskopi dan Analisis Kemometrik untuk Penentuan Spesies Darah dalam Forensik)
Durga Devi Sandran, Yusmazura Zakaria, Noor Zuhartini Md Muslim, Nik Fakhuruddin Nik Hassan

13. MAGNETIC KAOLINITE COMPOSITE FOR LEAD REMOVAL IN AQUEOUS SOLUTION 115
(Komposit Kaolinit Bermagnetik Untuk Penyingkiran Plumbum Dari Larutan Akueus)
Izzan Salwana Izman, Siti Nor Atika Baharin, Ruhaida Rusmin

14. PENENTUAN KEPEKATAN LOGAM BERAT DALAM SEDIMEN DI MUARA SUNGAI KEMAMAN, TERENGGANU 125
(Determination of Heavy Metal Concentrations in Sediment of Kemaman River Estuary, Terengganu)
Ahmad Shamsuddin Ahmad, Suhaimi Suratman, Noor Azhar Mohamed Shazili, Ong Meng Chuan, Mohammed Faizal Abdul Rahim

15. INSIGHTS OF THE CHEMICAL CONSTITUENTS AND HYDROTHERMAL CARBONIZATION OF *Crescentia cujete* L. 134
(Pencirian Jujukan Kimia dan Pengkarbonan Hidroterma bagi *Crescentia cujete* L.)
Judith Clarisse Jose, Glenn Oyong, Michael Dominic Ajero, Irving Chiong, Esperanza Cabrera, Maria Carmen S. Tan

16. EXTRACTION OF 4-OCTYLPHENOL AND 4-NONYLPHENOL IN RIVER WATER USING SOLID-PHASE EXTRACTION AND HIGH-PERFORMANCE LIQUID CHROMATOGRAPHY (Pengekstrakan 4-Oktilfenol dan 4-Nonilfenol di dalam Air Sungai Menggunakan Pengekstrakan Fasa Pepejal dan Kromatografi Cecair Prestasi Tinggi) 146
Mohd Zahid Baharom, Nurulnadia Mohd Yusoff, Wan Mohd Afiq Wan Mohd Khalik, Marinah Mohd Ariffin, Jamilah Karim, Syazrin Syima Sharifuddin

Malaysian Journal of Analytical Sciences (MJAS)
Published by Malaysian Analytical Sciences Society

PREPARATION AND CHARACTERISATION OF pH PROBE MEMBRANE FOR DETERMINATION OF TOTAL ALKALINITY IN SEAWATER

(Penyediaan dan Pencirian Membran Prob pH bagi Penentuan Jumlah Kealkalian dalam Air Laut)

Noor Sheryna Jusoh, Azrilawani Ahmad*, Marinah Mohd Ariffin, Hafiza Mohamed Zuki

Faculty of Science and Marine Environment,
Universiti Malaysia Terengganu, 21030 Kuala Nerus, Terengganu, Malaysia

**Corresponding author: azrilawani.ahmad@umt.edu.my*

Received: 20 November 2019; Accepted: 16 January 2020

Abstract

A pH probe membrane was successfully synthesised using polyvinyl chloride (PVC), chromoionophore I (CI), different additives (KTFPB and ETH500), plasticiser 2-nitrophenyl octyl ether (NPOE) and tetrahydrofuran (THF). Membrane casting method was applied during the preparation of the membrane. In order to evaluate the performance of the functional PVC membrane, physical characterisation such as scanning electron microscopy (SEM), attenuated total reflectance-Fourier transform infrared spectroscopy (ATR-FTIR), ultraviolet-visible spectroscopy (UV-Vis), fluorescence spectroscopy and tensile strength were conducted. Electrochemical characterisation was carried out using glassy carbon (GC) and gold (Au) electrodes, in order to identify the presence of electroactive species and to examine the behaviour of the membrane under electrochemical environment. The voltammetric measurement was conducted in 2.5 mM ferricyanide/ferrocyanide in 0.1 M KCl redox probe, at potential range of -0.2 - +0.6 V with the scan rate of 50 mV/s. The performance of PVC membrane using different additives was compared and analysed.

Keywords: polymeric functional membrane, PVC, voltammetry, total alkalinity

Abstrak

Membran prob pH telah berjaya disintesis menggunakan polivinil klorida (PVC), kromoionofor I (CI), aditif yang berbeza (KTFPB dan ETH500), pemplastik 2-nitrofenil oktil eter (NPOE) dan tetrahidrofuran (THF). Kaedah penuangan membran telah diaplikasi semasa penyediaan membran. Bagi menilai prestasi membran PVC berfungsi, pencirian fizikal seperti mikroskopi elektron pengimbasan (SEM), pantulan keseluruhan dikecilkan-spektroskopi inframerah jelmaan Fourier (ATR-FTIR), spektroskopi ultralembayung-nampak (UV-Vis), spektroskopi pendafluoran dan kekuatan tensil telah dijalankan. Pencirian elektrokimia telah dilakukan menggunakan elektrod karbon berkaca (GC) dan emas (Au), untuk menentukan kehadiran spesis elektroaktif dan menguji tindakan membran di bawah persekitaran elektrokimia. Pengukuran voltametri telah dilakukan dalam 2.5 mM ferisianida/ferosianida dalam 0.1 M KCl prob redoks, pada julat keupayaan -0.2 V - +0.6 V dengan kadar imbasan 50 mV/s. Prestasi membran PVC menggunakan aditif yang berbeza telah dibandingkan dan dianalisa.

Kata kunci: membran polimerik berfungsi, PVC, voltametri, jumlah kealkalian

Introduction

Effect of seawater acidification in decreasing pH of oceans is an ongoing process that potentially threaten productivity of the ocean [1]. Measuring the degree of seawater acidification first requires understanding of carbonate chemistry in seawater and it is impossible to directly measure all carbon species in marine environment [2]. Carbon variables in ocean can be defined by measuring pH, dissolve inorganic carbon, partial CO_2 and total

alkalinity in seawater [3]. Recent development on the sensing system for total alkalinity determination has evolved with the usage of membrane as an alternative approach less prone to interferences involves the electrochemically driven transport of ions across ion-selective membranes [4]. However, little are reported on the more complex matrices such as in seawater. The important goal in membrane technology is to control the membrane structure, which affects its performance [5]. A comprehensive understanding between composition and the performance of the membranes is crucial for further development of membranes and optimisation of fabrication processes. The primary objective of this research is to study the behaviour of different composition of PVC pH probe membrane under physical, mechanical and electrochemical characterisation to measure total alkalinity in seawater.

Total alkalinity is an important parameter for describing the marine inorganic carbon system and the measurement of the total alkalinity in the surface seawater is particularly useful because it will give information with respect to water mass mixing and also advancing our understanding on the ocean carbon cycle and marine geochemistry [6]. However, the measurement of total alkalinity is limited, partly due to laborious processes of collecting and analysing samples [7]. Conventional titration method of analysing total alkalinity is time consuming and can only be applied for a single measurement at one time. Recently, polymeric membrane has been widely used in measurement of total alkalinity in lake and seawater due to its excellent chemical and mechanical properties [8]. However, the strong hydrophobicity contributed to the flux decline and frequent back-flushing operation resulting in the deterioration of membrane mechanical strength and cause the membrane to rupture. Therefore, it is very important to control the membrane structure, in the aspects of hydrophobicity, mechanical strength, and stability, which strongly influence its performance. For the preparation of polymeric membranes, the blending ratio, polymer concentration and the selection of solvent and non-solvent play a crucial role in influencing the thermodynamic and kinetic properties of the casting solution, which influence the morphology and properties of the final membranes [9]. However, in order to obtain the desired membrane pore structure, the application of different additives is essential, as well as the usage of suitable plasticiser and ionophore. Further improvement of existing membrane fabrication methods as well as the development of new fabrication techniques are essential, hence this study is necessary to get a better understanding on the synthesis and preparation of polymeric functional membranes for measurement of total alkalinity in seawater samples.

A membrane is an interphase between two adjacent phases acting as a selective barrier, regulating the transport of substances between the two compartments [10]. Membrane are generally classified by the nature of the materials, the membrane morphology, geometry, preparation method, separation regime and processes [11]. The role of plasticiser in the membrane preparation is to improve the characteristics of the polymers such as the elasticity and their mechanical properties [12-13]. The performance of plasticiser could be influenced by the lipophilicity of the plasticiser compound used, the amount of ionophore incorporated in the polymer membrane, type of support polymer and the inclusion of ion exchange sites in the form of lipophilic salts. By providing the properties as softening the polymeric membrane, solubilizes the ionophore and insoluble in water, it is considered as an ideal plasticiser. However, with the characteristics mentioned above, often does not prevent the loss of ionophore to the sample [14]. In order to obtain the desired membrane structure, the application of different additives is essential. An additive can function as a pore former, increase solution viscosity or accelerate the phase inversion process [15]. In the research conducted by Fadilah and Hassan, it was reported that by combining the surfactant to the polymeric solutions, the thickness of the prepared membranes significantly increases and hence, probably enhanced membrane performance for protein rejection [16]. Meanwhile, inorganic additives could accelerate the phase separation rate and contribute to a membrane structure with lots of interconnected pores, resulting the membrane exhibits excellent mechanical strength and thermal stability [17]. This research is important to study the optimum parameters required for the construction of a reliable and high performance polymeric functional membranes, hence would be of crucial information needed for further study for total alkalinity determination in ocean.

Materials and Methods

Chemicals and reagents

2-nitrophenyl octyl ether, potassium tetrakis[3,5-bis(trifluoromethyl)phenyl]borate, tetradodecylammonium tetrakis(4-chlorophenyl) borate and chromoionophore I were purchased from Sigma-Aldrich (Switzerland). Tetrahydrofuran, potassium ferricyanide, potassium ferrocyanide and potassium chloride were purchased from

Merck (Germany). Polyvinyl chloride (high molecular weight) and alumina slurry were purchased from Aldrich and Metrohm, respectively. All chemicals and reagents used were of analytical grade and better.

Preparation of pH probe membrane

1% CI, 30% PVC, 63% plasticiser (NPOE) and 7% additives (ETH500 and KTFPB) were dissolved in 1 mL THF. The mixture then was poured into glass ring. Filter paper and weight were placed on top of the glass ring. The solution was left to dry for 24 h. Control membrane was prepared without CI and additives in order to compare the performance of the ionophore and additives in the membrane.

Characterisation of pH probe membrane

ATR-FTIR was conducted using Fourier Transform Infrared Spectrophotometer IRTracer-100 (Shimadzu) equipped with Lab Solutions IR software. The membranes were scanned 40 times in the spectral range from 4000 cm^{-1} to 400 cm^{-1} with resolution of 4 cm^{-1} and Happ-Genzel apodisation *via* diamond attenuation total reflectance method.

UV-Vis measurement was carried out using dual beam UV-Vis Spectrophotometer UV-1800 (Shimadzu) equipped with UV Probe 2.43 software. Absorbance was measured at wavelength from 800 nm to 190 nm through 1 cm quartz cuvette. Concentration of sample used was 0.01 mM and THF was used as blank. Fluorescence was conducted using Cary Eclipse Fluorescence Spectrophotometer (Varian) equipped with Cary Eclipse software, through 1 cm quartz cuvette. Concentration of CI used was 0.01 mM.

Morphology of the membrane was investigated using Scanning Electron Microscope JSM-636OLA (JEOL) at various magnifications. SC7620 Mini Spurter coater was used to coat the membranes with gold. Mechanical measurement was carried out using Tensile Tester (Shimadzu) EZ500-NLX, equipped with TRAPEZIUMX software. Cross speed was set at 10 mm/min. Electrochemical measurement (CV) was conducted using AUTOLAB B.V. PGSTAT204 (AUT51243) (Metrohm). Membrane was deposited on electrodes (GC and Au) and measurement was conducted in 2.5 mM ferricyanide/ferrocyanide in 0.1 M KCl from potential of -0.2 V to 0.6 V at scan rate of 50 mV/s for five cycles. GC and Au electrodes were polished with alumina slurry prior to measurement.

Results and Discussion

ATR-FTIR spectroscopy

Spectral analysis was carried out on all prepared PVC membranes in order to identify the functional groups presence in the membranes. The result was shown in Figure 1. Control membrane was prepared with only PVC and NPOE, while ETH500 and KTFPB membranes were prepared with all reagents. All PVC membranes showed almost similar FTIR spectra, with the presence functional groups peaks at same wavenumber. An increase in transmittance was recorded for both ETH500 and KTFPB membranes at 3600–3000 cm^{-1}, which was not presence in the control spectrum. The peak was probably due to the presence of either CI (Figure 2) or additives (Figure 3) or both. KTFPB membrane displayed minor difference of peak transmittance from 1800-800 cm^{-1}. However, no significant presence of other functional group was detected in the range.

Recorded functional groups and respective wavenumbers were summarised in Table 1. Peaks at 2926-2856 cm^{-1} were assigned to alkane C-H stretching [18,19], which might come from NPOE (Figure 4) or ETH500 or both. Aromatic-related peaks were observed at 2000-1900 cm^{-1} and 987-744 cm^{-1}, which were assigned to C-H bending and benzene disubstituted, respectively. These peaks might come from all compounds since all the compounds has one or more benzene ring in the structure. Both nitro N-O stretching and aliphatic ether C-O stretching, which appeared at 1523 cm^{-1} and 1089 cm^{-1}, respectively, were from NPOE.

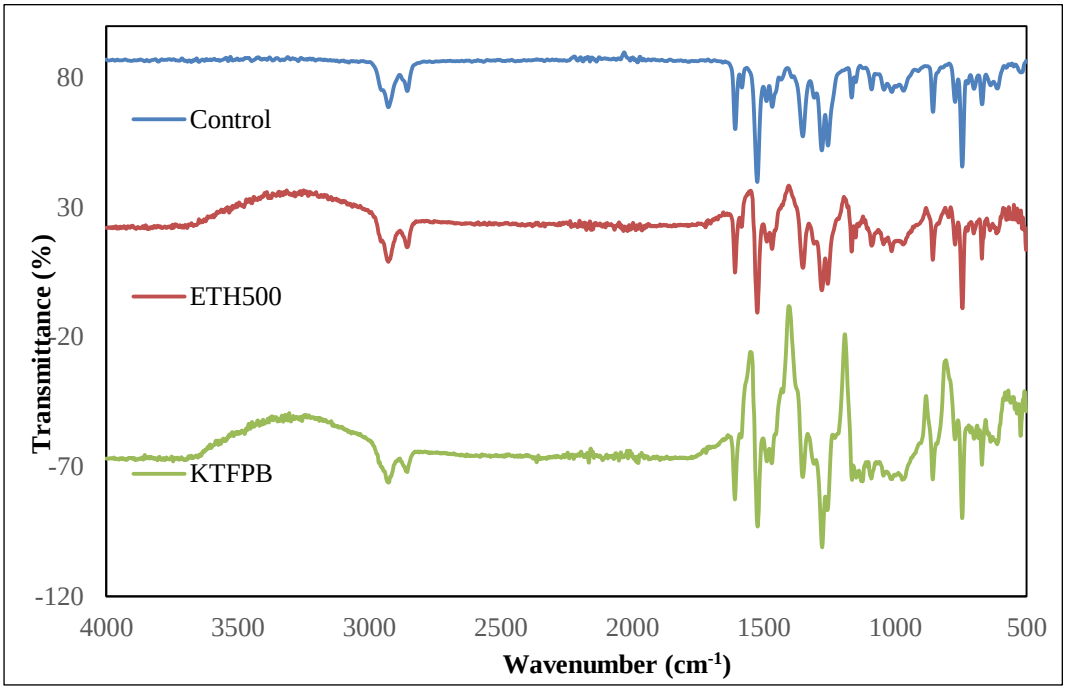


Figure 1. FTIR spectra of different composition of PVC membranes

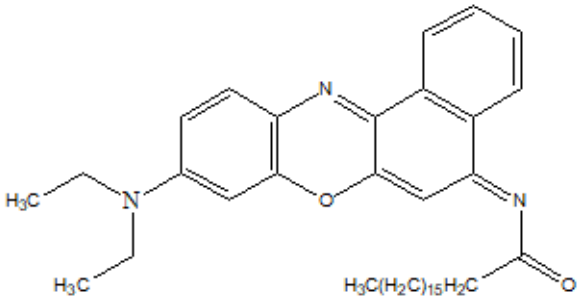


Figure 2. Chemical structure of CI (ionophore)

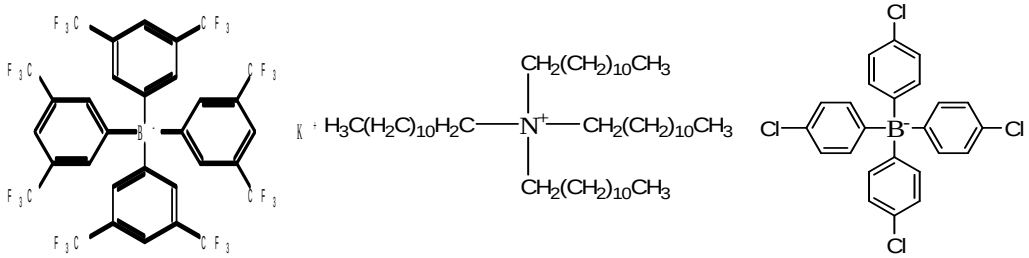


Figure 3. Chemical structure of additives; (a) KTFPB and (b) ETH500.

Table 1. List of functional groups of PVC membranes assigned to respective wavenumbers

Wavenumber (cm^{-1})	**Functional Group**	**Compound**
2926-2856	Alkane sp3 C-H stretching	NPOE, ETH500
2000-1900	Aromatic C-H bending (overtone)	All
1523	Nitro N-O stretching (asymmetric)	NPOE
1089	Aliphatic ether C-O stretching	NPOE
987-744	Aromatic disubstitute benzene (ortho, meta, para)	All

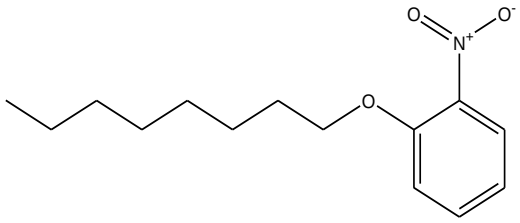


Figure 4. Chemical structure of NPOE (plasticiser).

UV-Vis spectroscopy

Absorption of PVC membranes was studied in UV-Vis region and the spectra were displayed in Figure 5. Two excitation peaks were observed at 318 nm and 526 nm, with the presence of CI. Membrane without CI did not present any noticeable peak. Thus, excitation was contributed by electrons in CI.

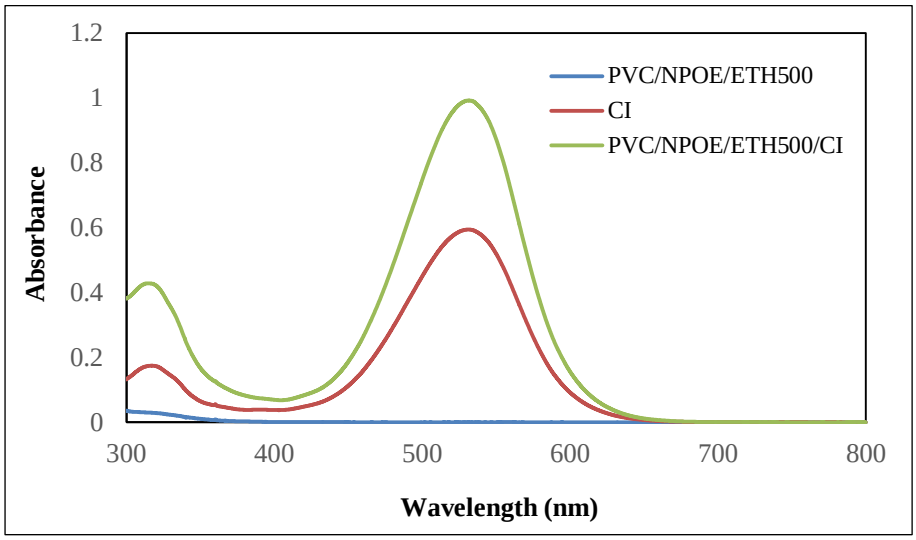


Figure 5. UV excitation peaks of CI in PVC membranes. Solvent: THF

Fluorescence spectroscopy

Further photophysical properties of CI has been performed using fluorescence spectroscopy. Figure 6 demonstrated that the maximum intensity of fluorescence emission at 528 nm was in corresponding with maximum excitation at 427 nm.

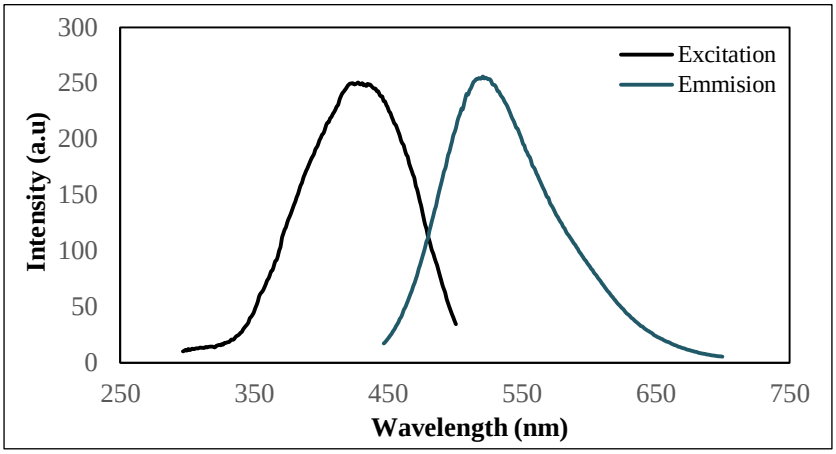
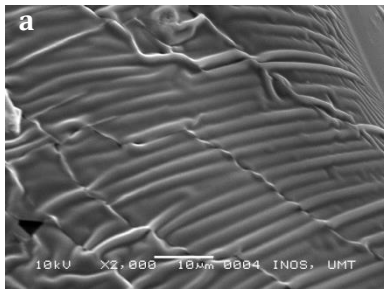
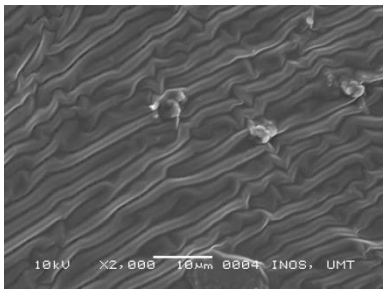
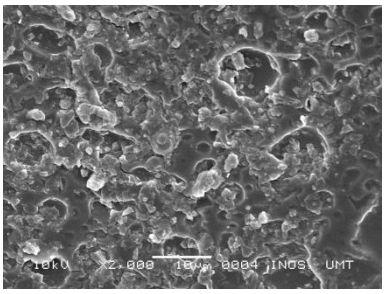
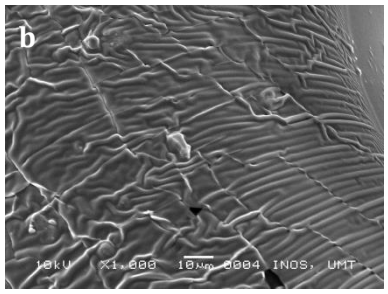
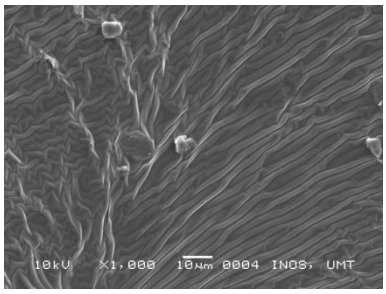
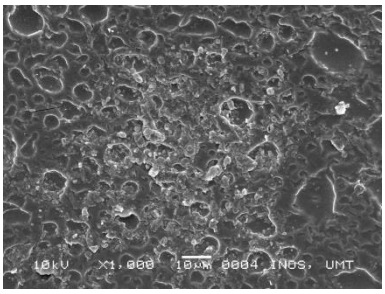


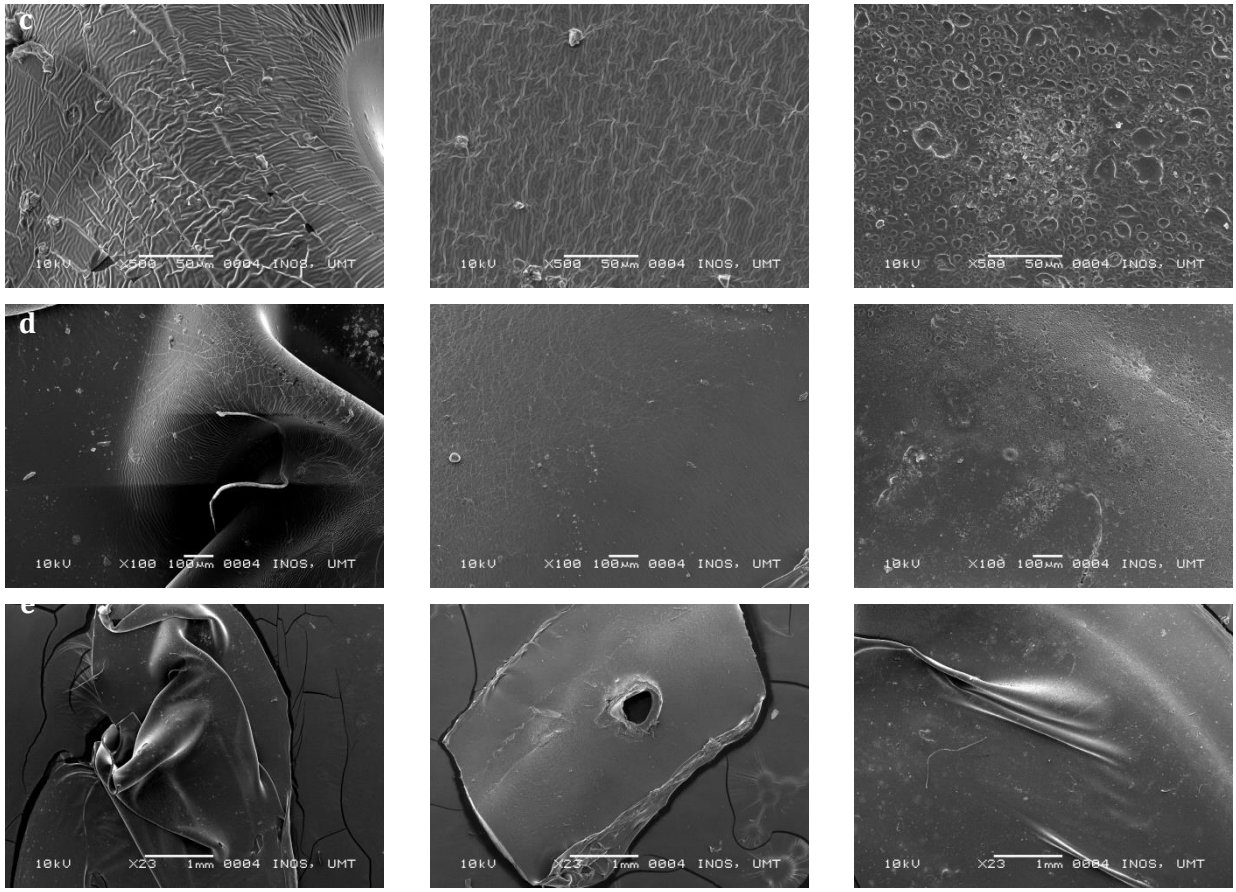
Figure 6. Excitation and emission peaks of CI in THF

Scanning electron microscopy

Surface morphology of PVC membranes was thoroughly studied using SEM at different magnifications. Table 2 displayed the micrographs of all PVC membranes. At x100 magnification, difference morphology of the membranes can be clearly seen, especially for KTFPB membrane. At closer view, both control and ETH500 membranes have similar surface morphology, with line-like structure. However, the position and arrangement of the line-like structure were different for both membranes. The lines in control membrane appeared to be more visible compared to ETH500 membrane. In contrast, the surface micrograph for KTFPB membrane showed the presence of crater-like structures, which were not observed in control and ETH500 membranes.

Table 2. Surface morphology of PVC membranes at different magnification (a) x 2000, (b) x 1000, (c) x 500, (d) x 100, (e) x 23

Control	ETH500	KTFPB
		
		



Tensile strength test

Mechanical strength of prepared PVC membranes was evaluated using tensile analysis. During measurement, each membrane was stretched at 10 mm/min. All results were tabulated in Table 3. Low initial force was recorded for all PVC membranes because the membranes was relatively thin. During elongation process, the membranes were easily stretched and broken, even at low force. Control membrane can be stretched up to 44 mm, which made it the longest among the PVC membranes, followed by KTFPB and ETH500 membranes. In addition, control membrane took the highest force to break the membrane at 38 mm. The toughness and flexibility of control membrane might be related to percentage of plasticiser used during the membrane preparation [20, 21]. The role of plasticiser is not only to increase elasticity, but also slightly contributes to the strength of the membrane. Even though KTFPB membrane can be stretched two times longer than ETH500 membrane, the force required to break the membranes were almost similar. Moreover, the length for both membranes during break was also similar.

Table 3. Parameters measured during tensile analysis for PVC membranes

Membrane	Maximum Displacement Force (N)	Maximum Displacement Stroke (mm)	Maximum Force at Break (N)	Maximum Displacement at Break (mm)
Control	-0.024	44.083	0.787	37.855
ETH500	0.062	21.147	0.308	18.736
KTFPB	0.103	42.044	0.430	17.798

Cyclic voltammetry

Electrochemical behaviour of PVC membranes was evaluated through CV measurement of GC and Au electrodes in 2.5 mM ferricyanide/ferrocyanide redox probe in 0.1 M KCl, from -0.2 V to +0.6V at 50 mV/s. As displayed in Figure 7a and Figure 8a, both bare GC and Au electrodes showed the highest current reading, with distinct presence of both oxidation and reduction peaks in the voltammogram. However, after the immobilisation of PVC membranes onto the electrode surface, current reading was significantly decreased (Figure 7b and Figure 8b). The values were excessively small, which implies that almost no current was recorded during the measurement. During the immobilisation, the membranes successfully occupied all the electrode surface, preventing any form of electron transfer to occur. Electrochemical measurement of PVC membranes was in complementary with SEM analysis, where there was no cavity or open area in the membrane that could exposed the electrode surface to the redox solution. In addition, there was no component in the membranes that can promote redox reaction.

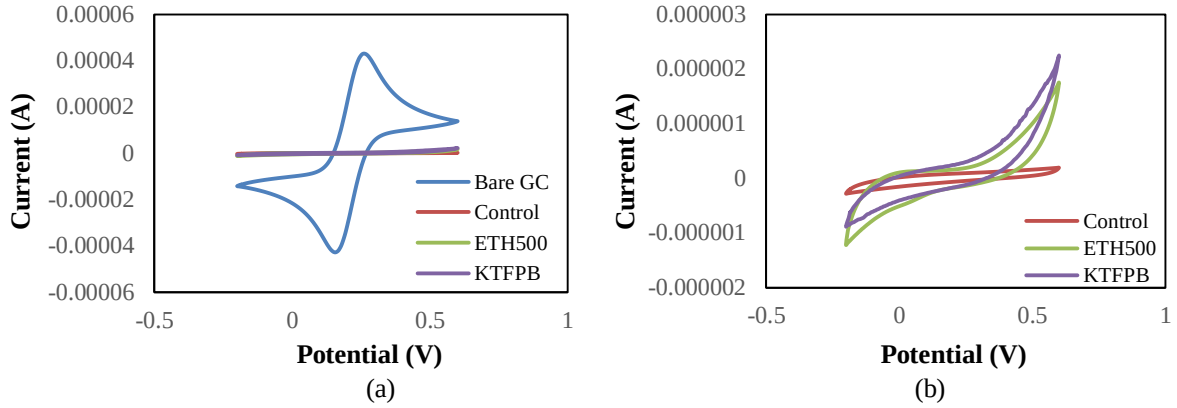


Figure 7. Electrochemical behaviour of PVC membranes using GC electrode; (a) Voltammograms of bare GC and GC with PVC membranes and (b) Closer view of voltammograms of GC with PVC membrane

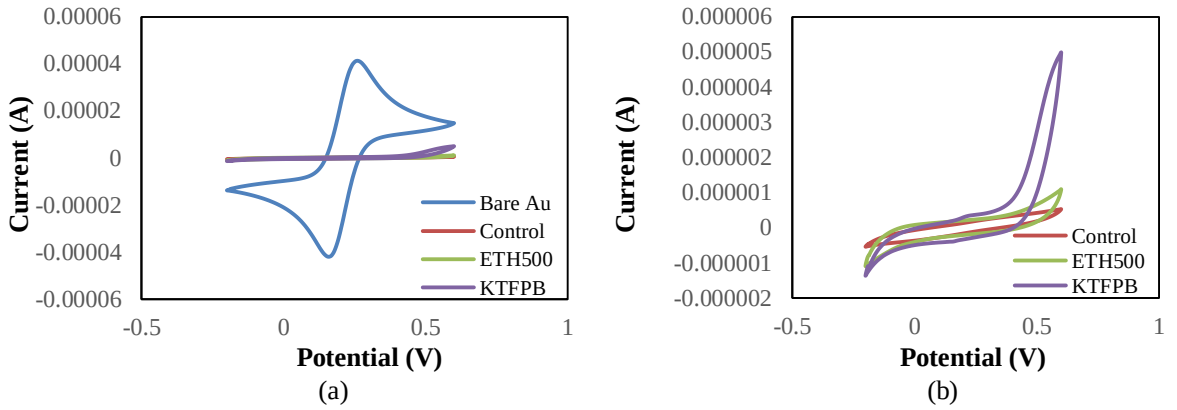


Figure 8. Electrochemical behaviour of PVC membranes using Au electrode; (a) Voltammograms of bare Au and Au with PVC membranes and (b) Closer view of voltammograms of Au with PVC membrane

Conclusion

PVC pH probe membranes with different compositions were successfully prepared and characterised. ATR-FTIR analysis showed no significant difference in functional groups presence in control, ETH500 and KTFPB membranes. However, main bands of the membranes were clearly observed in the spectra. Membranes with CI displayed positive results for UV-Vis and fluorescence, where active excitation and emission were recorded for both

measurements. Surface morphology investigation indicated major difference between ETH500 and KTFPB membranes, which might be contributed by the nature of the additives used in the membrane. During mechanical analysis, the force taken to break all the membranes was considerably low, but control membrane showed higher tensile property compared to ETH500 and KTFPB membranes. Electrochemical investigation concluded that all membranes completely hindered redox reaction, which contributed to low current reading. The successful developed membrane could be used as potential membrane for pH prob for total alkalinity measurement in seawater.

Acknowledgement

The authors would like to thank Ministry of Higher Education of Malaysia for the research grant FRGS/1/2017/WAB09/UMT/02/4 (FRGS59487). Special thanks goes to Central Laboratory and Faculty of Science and Marine Environment for providing research laboratories and analytical instruments.

References

1. Lohbeck, K. T., Riebesell, U. and Reusch T. B. H. (2012). Adaptive evolution of a key phytoplankton species to ocean acidification. *Nature Geoscience*, 5: 346-351.
2. Anthony, K. R. N., Kleypas, J. A. and Gattuso, J. P. (2011). Coral reefs modify their seawater carbon chemistry- implications for impacts of ocean acidification. *Global Change Biology*, 17(12): 3655-3666.
3. Dickson, A. G., Sabine, C. L. and Christian, J. R. (2007). Guide to best practices for ocean CO_2 measurement. North Pacific Marine Science Organization, Sidney, British Columbia: pp. 191.
4. Crespo, G. A., Afshar, M. G. and Bakker, E. (2012). Direct detection of acidity, alkalinity and pH with membrane electrodes. *Analytical Chemistry*, 84(23): 10165-10169.
5. Byrne, R. H. (2014). Measuring ocean acidification: New technology for a new era of ocean chemistry. *Environmental Science & Technology*, 48: 5352-5360.
6. Riebesell, U. F., Victoria, J., Hansson, L. and Gattuso, Jean-Pierre (2011). Guide to best practices for ocean acidification research and data reporting. Office for Official Publications of the European Communities, Luxembourg: pp 258.
7. Spaulding, R. S., DeGrandpre, M. D., Beck., J. C., Hart., R. D., Peterson, B., De Carlo, E. H., Drupp, P. S. and Hammar, T. R. (2014). Autonomous *in situ* measurements of seawater alkalinity. *Environmental Science and Technology*, 48(16): 9573-9581.
8. Afshar, M. G., Waeber, M. L. T., Wehrli, B. and Bakker, E. (2017). Direct sensing of total alkalinity profile in a stratified lake. *Geochemistry Perspectives Letters*, 3: 85-93.
9. Tan, X. M. and Rodrigue, D. (2019). A review on porous polymeric membrane preparation. Part 1: Production techniques with polysulfone and poly (vinylidene fluoride). *Polymers*, 11: 1-39.
10. Ulbricht, M. (2006). Advances functional polymer membranes. *Polymer*, 47(7): 2217-2262.
11. Ren, J. and Wang, R. (2010). Preparation of polymeric membranes. *Membrane and Desalination Technologies, Handbook of Environmental Engineering*, 13: 47-100.
12. Vihali, C. and Vaum, N. (2012). Use of plasticizers for electrochemical sensors: Recent advances in plasticisers. *Intech Open*: pp. 125-140.
13. Othman, M. A. F., Ahmad, A. and Zuki, H. M. (2016). Dithizone modified electrode for the determination of metals ion in aqueous solution. *Malaysian Journal of Analytical Sciences*, 20(1): 197-204.
14. Carey, C. (2015). Plasticizer effects in the PVC membrane of the dibasic phosphate selective electrode. *Chemosensors*, 3: 284-294.
15. Lalia, B. S., Kockodan, V., Hashaikeh, R. and Hilal, N. (2013). A review on membrane fabrication: Structure, properties and performance relationship. *Desalination*, 326: 77-95.
16. Fadilah, N. I. M. and Hassan, A. R. (2016). Preparation, characterization and performance studies of active PVDF ultrafiltration-surfactants membranes containing PVP as additive. *Malaysia Journal of Analytical Sciences*, 20(2): 335-341.
17. Zhang, Y.J., Lin, R., and Yuan, M.Y. (2013). Effects of Pore-Forming Additives on Structures and Properties of PVDF/Fe3+/Cu2+ Hollow Fiber Membranes. *Desalination. Water Treat*, 51: 3903–3908.
18. Tooma, M. A., Najim, T. S., Alsalhy, Q. S., Marino, T., Criscuoli, A., Giorno, L. and Figoli, A. (2015). Modification of polyvinyl chloride (PVC) membrane for vacuum membrane distillation (VMD) application. *Desalination*, 373: 58-70.

19. Ismayil, K. M. M., Manaf, O., Sujith, A. and Antony, R. (2019). Polymer thin films for chromatographic separation of plant pigments. *Materials Letters*, 252: 321-324.
20. Yu, Q. and Selvadurai, A. P. S. (2005). Mechanical behaviour of plasticized PVC subjected to ethanol exposure. *Polymer Degradation and Stability*, 89: 109-124.
21. Das, P. and Ray, S. K. (2016). Pervaporative recovery of tetrahydrofuran from water with plasticized and filled polyvinyl chloride membranes. *Journal of Industrial and Engineering Chemistry*, 34: 321-336.

Malaysian Journal of Analytical Sciences (MJAS)
Published by Malaysian Analytical Sciences Society

SYNTHESIS AND SOLID-STATE STRUCTURAL ELUCIDATION OF RHENIUM(I) COMPLEX WITH 1-CINNAMOYL-3-(PYRIDIN-2-YL) PYRAZOLE

(Sintesis dan Penentuan Struktur Pepejal Kompleks Renium(I) dengan 1-Sinamoil-3-(Piridin-2-il)Pirazola)

Wun Fui Mark-Lee[1], Yan Yi Chong[2], Azizul Hakim Lahuri[1], Mohammad B. Kassim[2]*

[1]*Department of Basic Science and Engineering, Faculty of Agriculture and Food Sciences, Universiti Putra Malaysia Bintulu, 97008 Sarawak, Malaysia*
[2]*Centre for Advanced Materials and Renewable Resources, Faculty of Science and Technology, Universiti Kebangsaan Malaysia, 43600 UKM Bangi, Selangor, Malaysia*

**Corresponding author: mb_kassim@ukm.edu.my*

Received: 20 November 2019; Accepted: 15 January 2020

Abstract

Re(I) complexes have been described as a promising tool for DNA probes. Rhenium(I) tricarbonyl complexes have favourable structural features suitable for DNA intercalation such as the new rhenium(I) tricarbonyl complex with polypyridyl ancillary ligand, namely, *fac*-[Re(CnPyPz)(CO)$_3$Cl] (CnPyPz = 1-cinnamoyl-3-(pyridin-2-yl)pyrazole). The complex was synthesised from the reaction of 1-cinnamoyl-3-(pyridin-2-yl)pyrazole and rhenium(I) pentacarbonyl chloride in toluene at refluxing temperature and characterised by infrared (IR), ultraviolet-visible (UV-Vis), ^{13}C and ^{1}H NMR spectroscopies and X-ray crystallography. The IR spectrum featured the three ν(C≡O) signal for the rhenium moiety at 1862-2019 cm^{-1} and other signals for the ligand namely ν(C=O), ν(C=N) and ν(C=C) at 1724, 1609 and 1497 cm^{-1}, respectively. The ^{13}C NMR spectra showed three C≡O (190.0 – 198.1 ppm) signals whereas the ^{1}H spectrum for Re(CO)$_3$(CnPyPz)Cl exhibited two pairs of doublets (7.81 and 8.18 ppm) for the vinylic H of the cinnamoyl group. The complex exhibited a broad band corresponding to the metal-to-ligand charge transfer (MLCT) in the region of 360-390 nm. The Re(CO)$_3$(CnPyPz)Cl complex underwent a ligand exchange during the crystallisation process, involving one of the tricarbonyl groups with a chlorine atom to form the Re(CO)$_2$(CnPyPz)Cl$_2$ complex. The corresponding, Re(CO)$_2$(CnPyPz)Cl$_2$ crystal adopts a triclinic crystal system with a *P*-1 space group. The implementation of flexible CnPyPz ligand contributes to a dynamic supramolecular arrangement that facilitates both a planar π-π stacking arrangement accompanied with an appreciable globularity character *via* C−H···π and C≡O···π interconnections.

Keywords: rhenium, carbonyl, π stacking, Hirshfeld, DNA probes

Abstrak

Kompleks Re(I) telah dikenali sebagai bahan yang berpotensi untuk prob DNA. Kompleks trikarbonil Re(I) mempunyai ciri struktur yang sesuai untuk interkalasi DNA seperti mana kompleks renium(I) trikarbonil dengan ligan ansilari polipiridina, *fac*-[Re(CnPyPz)(CO)$_3$Cl] (CnPyPz = 1-sinamoil-3-(piridin-2-il)pirazola). Kompleks ini telah disintesis daripada tindak balas 1-sinamoil-3-(piridin-2-il)pirazola dengan pentakarbonilklororenium(I) dalam toluena pada suhu refluks dan telah dicirikan dengan menggunakan spektroskopi inframerah (IR), ultralembahyung-cahaya nampak (UV-Vis), resonans magnet nukleus (NMR) ^{13}C dan ^{1}H dan kristalografi sinar-X. Spektrum IR menunjukkan tiga jalur ν(C≡O) untuk moieti logam renium pada 1862-2019 cm^{-1}, dan isyarat ligan seperti ν(C=O), ν(C=N) dan ν(C=C) masing-masing pada 1724, 1609 dan 1497 cm^{-1}. Spektrum NMR ^{13}C menunjukkan tiga isyarat C≡O pada julat 190.0 – 198.1 ppm manakala spektrum ^{1}H kompleks Re(CO)$_3$(CnPyPz)Cl menunjukkan proton vinil (CH=CH) kumpulan sinamoil sebagai dua pasangan dublet pada 7.81 dan 8.18 ppm. Kompleks Re(I) ini mempamerkan jalur yang lebar bagi pertukaran cas logam kepada ligan (MLCT) pada julat 360-390 nm. Kompleks Re(CO)$_3$(CnPyPz)Cl mengalami pertukaran ligan yang melibatkan pengoksidaan pusat logam Re(I) kepada Re(II) semasa proses

penghabluran yang melibatkan salah satu daripada kumpulan trikarbonil dengan satu atom klorin untuk membentuk kompleks $Re(CO)_2(CnPyPz)Cl_2$. Kompleks ini menghablur dalam sistem kristal triklinik dengan kumpulan ruang *P*-1. Penggunaan ligan CnPyPz yang fleksibel menyumbang kepada susunan supramolekul yang membawa kepada susunan *π-π* satah berserta dengan sifat globular yang ketara melalui ikatan C−H···π dan C≡O···π.

Kata kunci: renium, karbonil, susunan *π*, Hirshfeld, prob DNA

Introduction

The Re(I) metal ion has been widely explored as an intercalation agent [1-5] since its d^6 electron configuration promotes the formation of a low spin metal-ligand complex that prevents metal-DNA interaction, which is typically associated with heavy metal toxicity [6-7]. The Re(I) tricarbonyl complexes, $Re(CO)_3(N\text{^}N)X$ where the N^N chelating agent are conventionally polypyridine ligands and X = halide, pyridine, phosphine and alkyl, are known to efficaciously combat different kinds of cancerous cells but has a low toxicity towards normal cell [3]. In general, octahedral complexes such as $Re(CO)_3(N\text{^}N)X$ binds to the double-helical DNA in a three-dimension space through three types of interactions namely intercalation, groove binding and external electrostatic binding. The ancillary ligand can be used as a tool to modify or alter the DNA binding interactions and the complex molecule [8, 9] in such a way that an intercalation will spontaneously occur when ancillary ligands such as polypyridine with an almost planar geometry is employed. With regard to the molecular construction, this phenomenon will prompt the binding of rhenium complexes with the DNA interior hydrophobic pockets *via π-π* interactions [10-13]. At the same time, the corresponding hydrophilic exterior attracts the polar tricarbonyl ligands [14]. Therefore, it is imperative to design a molecule that can offer the characteristic features to facilitate such interaction and act as a potential DNA intercalation agent.

Herein, we present the synthesis and characterisation of the titled rhenium complex along with the description of the non-covalent intermolecular connections, geometry and solid-state architecture. This study discusses the fundamental structural characteristics of a novel rhenium complex and provides quintessential information for future biological application.

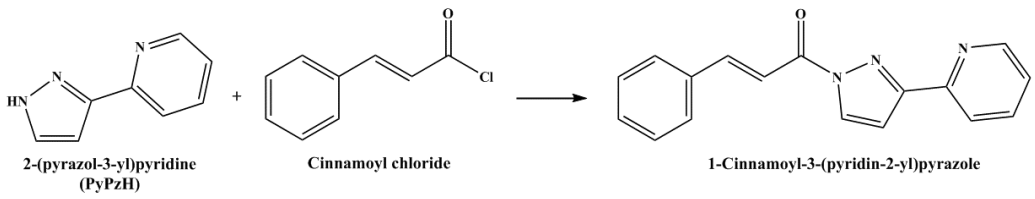
Materials and Methods

Instrumentations

The IR spectrum was recorded in the range of 4000-650 cm^{-1} using Agilent Cary 630 spectrophotometer. The NMR spectra were recorded by Bruker Ascend 400 spectrometer at 400 MHz and 100 MHz for ^1H and ^{13}C NMR, respectively by using tetramethylsilane (TMS) as internal standard. The UV-Vis spectrum was recorded in acetonitrile solution using UV-1650 Pc Shimadzu Fision spectrophotometer. The X-ray diffraction data of the single crystal were collected by using Bruker D8 Quest diffractometer using a molybdenum MoKα X-ray source (λ = 0.71073Å). The Hirshfeld surfaces and two-dimensional fingerprints (FPs) were generated using CrystalExplorer17 [15].

Synthesis of 1-cinnamoyl-3-(pyridin-2-yl)pyrazole

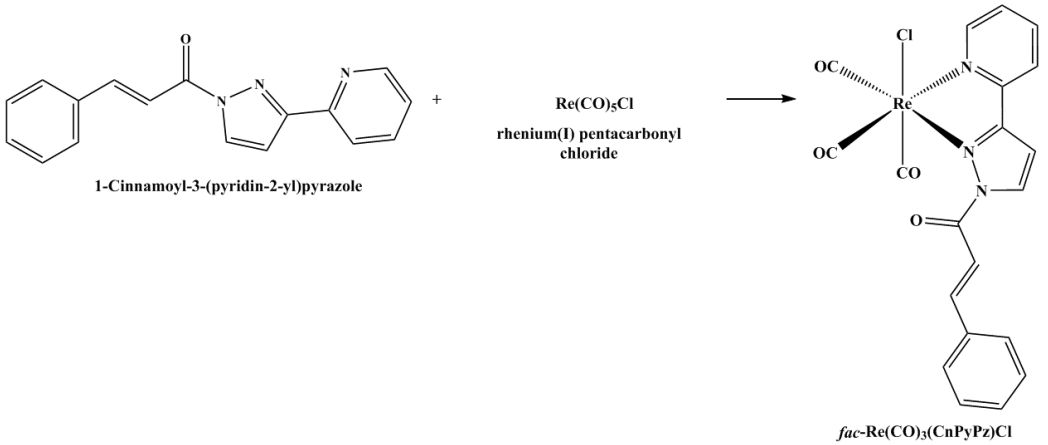
The 2-(pyrazol-3-yl)pyridine (PyPzH) ligand was synthesised according to a previous literature method [16]. Next, PyPzH was deprotonated by triethylamine in dichloromethane at room temperature. Then, cinnamoyl chloride was added slowly and the mixture was stirred for 3 hours (Scheme 1). The solvent was reduced under atmospheric pressure and the product was purified by column chromatography with dichloromethane as the eluent.



Scheme 1. Synthesis route of 1-cinnamoyl-3-(pyridin-2-yl)pyrazole (CnPyPz)

Synthesis of *fac*-Re(CO)$_3$(CnPyPz)Cl complex

The rhenium polypyridyl complex, *fac*-Re(CO)$_3$(CnPyPz)Cl was prepared from the reaction of rhenium(I) pentacarbonyl chloride with CnPyPz ligand in dry toluene at 120°C under nitrogen atmosphere for 5 hours (Scheme 2) [17, 18]. The desired product was obtained as a precipitate and washed with an excess volume of *n*-hexane.



Scheme 2. The reaction scheme for the synthesis of Re(CO)$_3$(CnPyPz)Cl complex

Results and Discussion

The IR spectra for CnPyPz ligand and Re(CO)$_3$(CnPyPz)Cl complex are compared as shown in Figure 1. A free CnPyPz ligand showed the characteristic featured signals of C=O, C=N and C=C at 1696, 1613 and 1541 cm^{-1}, respectively. Whereas the Re(CO)$_3$(CnPyPz)Cl complex showed three ν(C≡O) signals at 1862-2019 cm^{-1} which was defined in *Cs* symmetry for two A′ mode and one A″ mode [19] indicating the C≡O groups exist in the facial configuration [20]. The presence of the tricarbonyl peaks was further corroborated with ^{13}C NMR spectroscopy where the three C≡O signals were observed in the region of 190-198 ppm. In addition, the presence of the cinnamoyl group was also confirmed by the C=O signal at 168 ppm. Upon coordination of the free ligand to the Re(I) metal centre, the ^{1}H NMR spectrum of Re(CO)$_3$(CnPyPz)Cl complex showed the shifting of chemical signals corresponding to CnPyPz moiety at a lower field compared to the free ligand. This observation indicates that the ligand has successfully coordinated to the metal ion [21-22]. The vinylic hydrogens of the cinnamoyl group were observed as two pairs of doublets at 7.81 and 8.18 ppm with a coupling constant value of 15.6 Hz, indicating that the vinylic hydrogens were in a *trans*-configuration. The proton conformation was further supported by X-ray crystallography analysis. The complex showed two main absorption bands at around 330 nm (Figure 2) which was due to the intra ligand transition ($\pi \rightarrow \pi^*$) and a tapered low-lying broad band at 380nm (ε = 2723 L mol^{-1} cm^{-1}) was ascribed to the MLCT band [dπ(Re) $\rightarrow$ π^*]. This scarcely discernable band is known to overlap with the more stronger intra ligand transition [23].

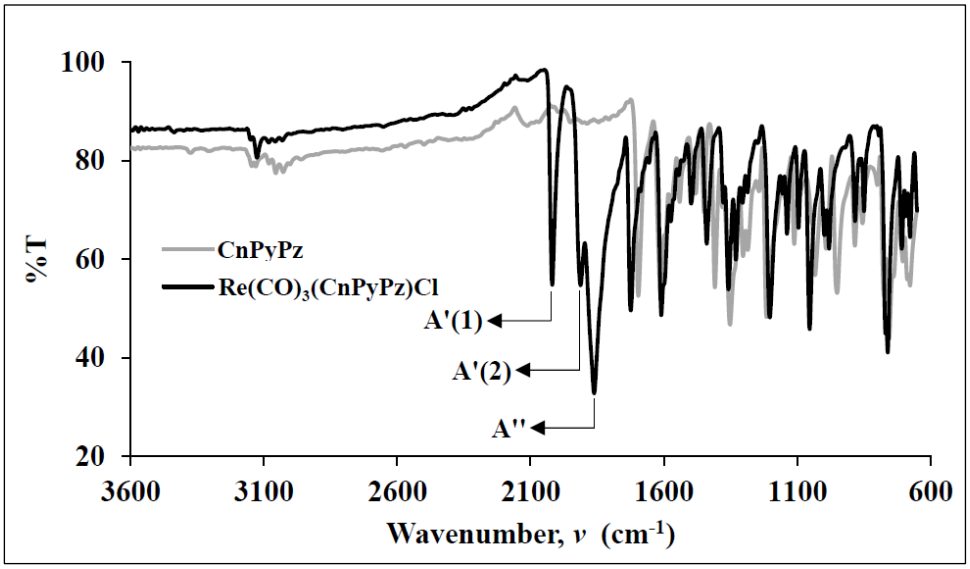


Figure 1. A comparison between the IR spectra of CnPyPz and $Re(CO)_3(CnPyPz)Cl$

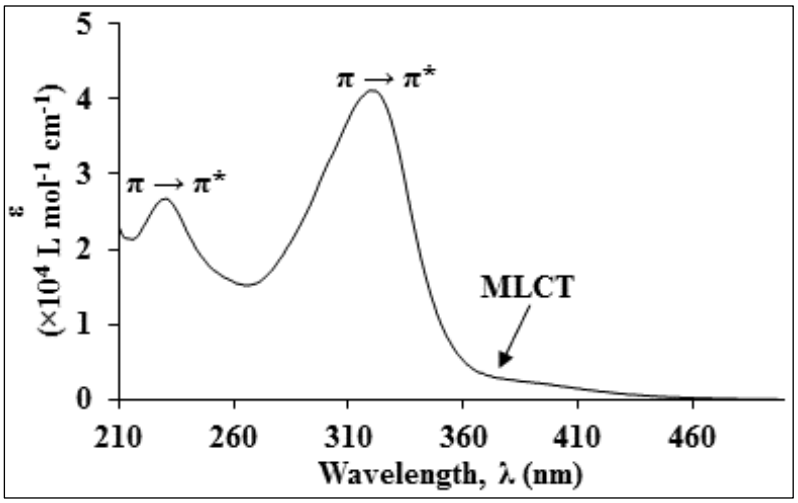


Figure 2. Electronic spectrum of $Re(CO)_3(CnPyPz)Cl$ complex measured in acetonitrile

The X-ray crystal structure of $Re(CO)_2(CnPyPz)Cl_2$ (Figure 3) adopts a triclinic system with a *P*-1 space group. Although the infrared spectrum of this complex initially revealed three ν(C≡O) signals, the metal centre Re(I) was oxidized to Re(II) in which the carbonyl group on the axial position was substituted by a chloro atom during the crystallisation process. Therefore, the three-dimensional complex possesses a distorted octahedral geometry at the metal centre, with two carbonyl and one chelating CnPyPz ligand in the equatorial planes; while, two chloro ligands situated at the axial positions. The bond lengths and angles around the rhenium centre (Table 1) resemble those of related structures, for example, *fac*-[ReCl(N^N)$(CO)_3$] (N^N is a polypyridine chelating ligand) [24-27]. The pyridine and pyrazole planes were essentially coplanar [9.0 (4)º] while the mean plane of the cinnamoyl fragment was distorted from the mean plane of the pyridylpyrazole fragment at an angle of 45.5 (3)º. Besides, the vinylic protons of the alkene group demonstrated a *trans*-configuration with the C11-C12=C13-C14 torsion angle of -176.3

(10)º and the observation agrees with the ^{1}H NMR spectrum of the complex. The crystal packing of this complex mainly exhibits C−H···O intermolecular hydrogen bonding in which the proton on pyridine (H1) and vinyl group (H8) formed a hydrogen bonding with O2 and O3, respectively, giving a one-dimensional chain viewed from *a*-axis (Figure 4).

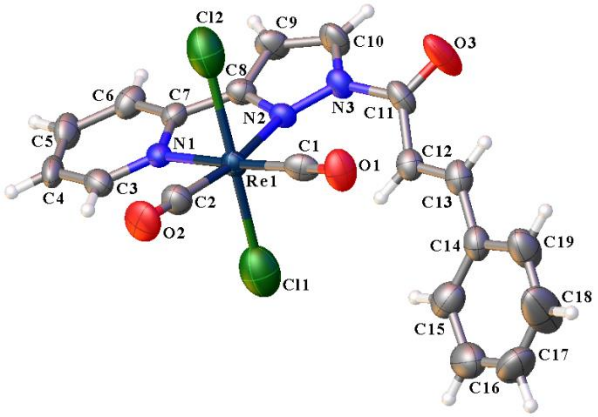


Figure 3. The X-ray crystallographic structure of $Re(CO)_2(CnPyPz)Cl_2$ complex with displacement ellipsoids drawn at the 50% probability level **CCDC Num. 1978548**

Table 1. Selected geometric parameters (Å, º) for $Re(CO)_2(CnPyPz)Cl_2$

Bond Length (Å)			**Bond Angle (º)**
Re1–C1	1.928(10)	N1–Re1–N2	73.9(3)
Re1–C2	1.903(11)	N1–Re1–C2	96.1(4)
Re1–N1	2.195(7)	C1–Re1–N2	103.4(3)
Re1–N2	2.223(7)	C1–Re1–C2	86.4(4)
Re1–Cl1	2.418(6)	N1–Re1–Cl2	87.2(2)
Re1–Cl2	2.432(6)	N2–Re1–Cl2	84.1(2)
C1–O1	1.147(13)	C2–Re1–Cl2	91.8(4)
C2–O2	1.146(14)	C1–Re1–Cl2	91.2(3)
		N1–Re1–Cl1	88.6(2)
		N2–Re1–Cl1	91.9(2)
		C2–Re1–Cl1	91.6(4)
		C1–Re1–Cl1	92.9(3)
		Cl1–Re1–Cl2	174.83(18)

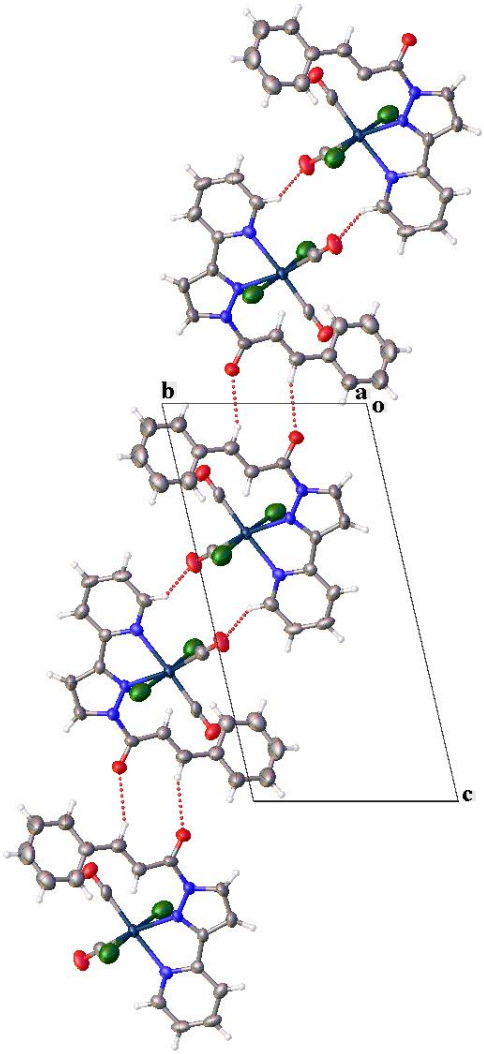


Figure 4. A partial view of the crystal packing of $Re(CO)_2(CnPyPz)Cl_2$ complex, illustrating one-dimensional chain viewed from *a*-axis

Further, the Hirshfeld surface analysis was performed on the Re(II) complex. The complex forms a centrosymmetric dimer with C–H···O intermolecular hydrogen bonding. The pair of dark-red spots in Figure 5, indicate that the sum of d_i and d_e is shorter than the sum of the respective individual vdW radii and this signifies stronger intermolecular interactions in these regions as compared to the ones with faint-red spots. The cinnamoyl ligands from adjacent complexes interconnects to construct the $R_2^2(10)$ loop [28].

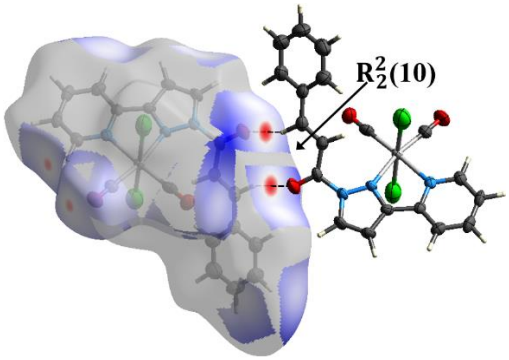


Figure 5. The centrosymmetric dimers of $Re(CO)_2(CnPyPz)Cl_2$ with C−H···O intermolecular contacts depicted by d_{norm} surface contours

The asymmetric unit of the complex is subjected to four intermolecular interactions that involves six-membered aromatic rings namely, *Cg*3 (centroid of the N1/C3-C7 pyridine ring) and *Cg*4 (centroid of the C14-C19 benzene ring) (Figure 6). Both sides of the *Cg*3 plane participates in *π*-*π* interaction involving neighbouring *Cg*3 rings with relatively similar centroid-to-centroid distances recorded at 3.851(6)Å [slippage = 1.454Å; symmetry code: -x,1-y,1-z] and 3.767(6)Å [slippage = 1.692Å, symmetry code: 1-x,1-y,1-z]. The coplanar conformation of pyridine and pyrazole moieties expedite close packing of the *π*-*π* stacking arrangement. Interestingly, the pendant cinnamoyl ring allows structural flexibility which elevates the overall globularity character (*G* = 0.746 a.u.). As a result, the benzene ring promotes C−H···*π* and C≡O···*π* interactions. This observations also correspond to rhenium complex analogue where the Re(I) complex with fluorine-substituted cinnamoyl ligand participates more in non *π*-*π* interactions i.e. C−H···*π* and C≡O···*π*. Moreover, these rhenium complexes can also accommodate a repertoire of non-covalent interactions with the appropriate utilisation of substituents [29].

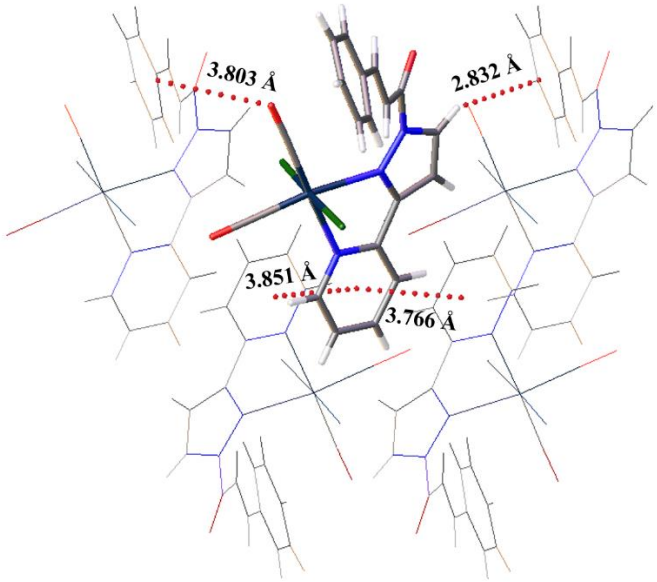


Figure 6. The intermolecular connections involving pyridine and benzene rings, namely *π*-*π*, C−H···*π* and C≡O···*π* interactions

In comparison to $Re(CO)_2(CnPyPz)Cl_2$, the reported Re(I) complex has a cinnamoyl fragment with a higher degree of distortion as a result of the substitution effect. Therefore, the Hirshfeld surface of $Re(CO)_2(CnPyPz)Cl_2$ exhibits an anisotropic quality in between that of Re(*p*-NO_2-CnPyPz)$(CO)_3Cl$ (Ω = 0.362 a.u.) and Re(*p*-F-CnPyPz)$(CO)_3Cl$ (Ω = 0.171 a.u.) with a measured asphericity value (Ω = 0.177 a.u.) [29]. The nature of the intermolecular interaction involves in the supramolecular scaffold along with their percentage contributions were studied with 2-D Hirshfeld surface FPs (Figure 7). Based on Figure 7(a), the two pairs of long sharp spikes labelled as '1' represents the C−H···O hydrogen bonds. The C−H···O hydrogen bonds project the largest contribution with a 27.9% from the overall non-covalent interactions [Figure 7(d)]. These spikes superimpose each other and appear to be complimentary in shape with (d_i, d_e) (1.3, 1.0Å). The sparsely distributed points located between the '1' spikes revealed that the internal H atoms from the Hirshfeld surface is in relative proximity to the external H atom with 16.9% contribution. The other two major contributors to the overall intermolecular interactions stemmed from the H···Cl (21.4%) and H···π (19.7%) connections [Figure 7(b) and (c)]. As per our earlier discussion, the flexible pendant provided by the cinnamoyl fragment played a significant role to the supramolecular formation. Whereby, the H···π and O···π interactions involving the benzene moiety of the cinnamoyl fragment collectively contributes to 23.3% to the overall interactions.

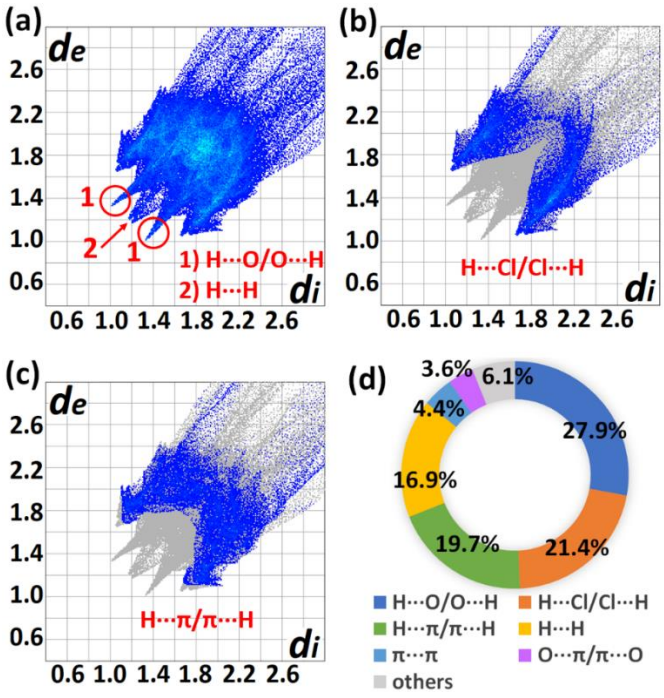


Figure 7. Fingerprint plots (a)-(c) of non-covalent interactions of $Re(CO)_2(CnPyPz)Cl_2$ where d_i (d_e) is the internal (external) distance (Å) from a point on the Hirshfeld surface and (d) represents the percentage contributions of the overall close contacts involving the generated Hirshfeld surface area of the complex

Conclusion

The Re(I) tricarbonyl complex, *fac*-[Re(CnPyPz)$(CO)_3Cl$] was successfully synthesised and characterised through spectroscopic methods. The presence of the characteristic tricarbonyl groups and the vinylic H of the cinnamoyl group were evident *via* IR stretching frequency responses and the NMR chemical shifts. These spectroscopic findings support the complexation of Re(I) tricarbonyl precursor with the CnPyPz ligand. The solid-state analysis demonstrated the occurrence of ligand-exchange phenomenon that produced and oxidised the Re(I) metal centre to Re(II) in the $Re(CO)_2(CnPyPz)Cl_2$ complex. Besides, the rhenium complex promotes structural synergistic properties through the pyridiylpyrazole moiety and the pendant cinnamoyl fragment that supports both the planar π-

π stacking alignment as well as C−H···π and C≡O···π arrangements, respectively. The favourable π-π stacking feature advocates future investigation on the propensity of the title complex towards DNA binding.

Acknowledgement

The authors would like to thank the Ministry of Higher Education, Malaysia for MyPhD support for CYY, Universiti Kebangsaan Malaysia for GGP-2017-091 and MI-2018-012 research grants and Universiti Putra Malaysia for GP-IPM-9657200 research grant. We are grateful to the Centre for Advanced Materials and Renewable Resources, Faculty of Science and Technology and Fuel Cell Institute (UKM) for their provision of experimental facilities.

References

1. Balakrishnan, G., Rajendran, T., Senthil Murugan, K., Sathish Kumar, M., Sivasubramanian, V.K., Ganesan, M., Mahesh, A., Thirunalasundari, T. and Rajagopal, S. (2015). Interaction of rhenium(I) complex carrying long alkyl chain with Calf Thymus DNA: Cytotoxic and cell imaging studies. *Inorganica Chimica Acta,* 434: 51-59.
2. Lo, K.K.-W. and Tsang, K.H.-K. (2004). Bifunctional luminescent rhenium(I) complexes containing an extended planar diimine ligand and a biotin moiety. *Organometallics*, 23(12): 3062-3070.
3. Medley, J., Payne, G., Banerjee, H.N., Giri, D., Winstead, A., Wachira, J.M., Krause, J.A., Shaw, R., Pramanik, S. K. and Mandal, S. K. (2015). DNA-binding and cytotoxic efficacy studies of organorhenium pentylcarbonate compounds. *Molecular and Cellular Biochemistry,* 398(1–2): 21-30.
4. Uma Maheswari, P. and Palaniandavar, M. (2004). DNA binding and cleavage properties of certain tetrammine ruthenium(II) complexes of modified 1,10-phenanthrolines - Effect of hydrogen-bonding on DNA-binding affinity. *Journal of Inorganic Biochemistry*, 98(2): 219-230.
5. Yam, V.W.-W., Lo, K.K.-W., Cheung, K.-K. and Kong, R.Y.-C. (1995). Synthesis, photophysical properties and DNA binding studies of novel luminescent rhenium(I) complexes. X-ray crystal structure of $[Re(ddpn)(CO)_3(py)](OTf)$. *Journal of the Chemical Society, Chemical Communications,* (11): 1191-1193.
6. Amoroso, A. J., Coogan, M. P., Dunne, J. E., Fernández-Moreira, V., Hess, J. B., Hayes, A. J., Lloyd, D., Millet, C., Pope, S. J. A. and Williams, C. (2007). Rhenium *fac* tricarbonyl bisimine complexes: Biologically useful fluorochromes for cell imaging applications. *Chemical Communications*, (29): 3066-3068.
7. Ranasinghe, K., Handunnetti, S., Perera, I. C. and Perera, T. (2016). Synthesis and characterization of novel rhenium(I) complexes towards potential biological imaging applications. *Chemistry Central Journal,* 10(1): 1-10.
8. Ma, D., Che, C., Siu, F., Yang, M. and Wong, K. (2007). DNA binding and cytotoxicity of ruthenium(II) and rhenium(I) complexes of 2-amino-4-phenylamino-6-(2-pyridyl)-1,3,5-triazine. *Inorganic Chemistry,* 46(3): 740-749.
9. Strekowski, L. and Wilson, B. (2007). Noncovalent interactions with DNA: An overview. *Mutation Research/Fundamental and Molecular Mechanisms of Mutagenesis*, 623 (1–2): 3-13.
10. Chan, C. Y., Noor, A., McLean, C. A., Donnelly, P. S. and Barnard, P. J. (2017). Rhenium(I) complexes of N-heterocyclic carbene ligands that bind to amyloid plaques of Alzheimer's disease. *Chemical Communications,* 53(15): 2311-2314.
11. Egli, M., Tereshko, V., Mushudov, G. N., Sanishvili, R., Liu, X. and Lewis, F. D. (2003). Face-to-face and edge-to-face π-π interactions in a synthetic DNA hairpin with a stilbene diether linker. *Journal of the American Chemical Society,*125 (36): 10842-10849.
12. Selamat, N., Yook Heng, L., Hassan, N. I. and Abd Karim, N. H. (2016). Synthesis and characterization of 6,6'-bis(2-hydroxyphenyl)-2,2'-bipyridyl ligand and its platinum complex for the interaction with CT-DNA. *Malaysian Journal of Analytical Science,* 20(1): 111-120.
13. Shamsuddin, R., Sahudin, M. A., Hassan, N. H. and Abdul Karim, N. H. (2017). Interaction of N,N'-bis[4-[1-(2-hydroxyethoxy)]salicylidene]-phenyldiamine-nickel(II) and copper(II) complexes with g-quadrupex DNA. *Malaysian Journal of Analytical Sciences*, 21(3): 544-551.
14. Ismail, M. B., Booysen, I. N., Hosten, E. and Akerman, M. P. (2017). Synthesis, characterization and DNA interaction studies of tricarbonyl rhenium(I) compounds containing terpyridine Schiff base chelates. *Journal of Organometallic Chemistry,* 833(1): 1-9.

15. Turner, M. J., McKinnon, J. J., Wolff, S. K., Grimwood, D. J., Spackman, P. R., Jayatilaka, D. and Spackman, M. A. (2017). CrystalExplorer17. University of Western Australia.
16. Lin, Y. and Lang, S. A. (1977). Novel two step synthesis of pyrazoles and isoxazoles from aryl methyl ketones. *Journal of Heterocyclic Chemistry*,14(2): 345-347.
17. Kianfar, E., Kaiser, M. and Knör, G. (2015). Synthesis, characterization and photoreactivity of rhenium and molybdenum carbonyl complexes with iminopyridine ligands. *Journal of Organometallic Chemistry*, 799–800: 13-18.
18. Mark-Lee, W. F., Chong, Y. Y., Law, K. P., Ahmad, I. B. and Kassim, M. B. (2018). Synthesis, structure and Density Functional Theory (DFT) study of a rhenium(I) pyridylpyrazol complex as a potential photocatalyst for CO_2 reduction. *Sains Malaysiana*, 47(7): 1491-1499.
19. Dattelbaum, D. M., Martin, R. L., Schoonover, J. R. and Meyer, T. J. (2004). Molecular and electronic structure in the metal-to-ligand charge transfer excited states of *fac*-[Re(4,4'-X_2bpy)$(CO)_3$(4-Etpy)] (X = CH_3, H, Co_2Et). Application of density functional theory and time-resolved infrared spectroscopy. *The Journal of Physical Chemistry A*,108(16): 3518-3526.
20. Brisdon, B. J., Edwards, D. A. and White, J. W. (1978). Anionic tricarbonyl derivatives of molybdenum and tungsten and their reactions with allyl halides. *Journal of Organometallic Chemistry*, 156: 427-437.
21. Piletska, K. O., Domasevitch, K. V., Gusev, A. N., Shul'Gin, V. F. and Shtemenko, A. V. (2015). *fac*-Tricarbonyl rhenium(I) complexes of triazole-based ligands: Synthesis, X-ray structure and luminescent properties. *Polyhedron*, 102 (I): 699-704.
22. Subasinghe, A., Perera, I. C., Pakhomova, S. and Perera, T. (2016). Synthesis, characterization, and biological studies of a piperidinyl appended dipicolylamine ligand and its rhenium tricarbonyl complex as potential therapeutic agents for human breast cancer. *Bioinorganic Chemistry and Applications*, 2016: 1–10.
23. Wu, P.-C., Yu, J.-K., Song, Y.-H., Chi, Y., Chou, P.-T., Peng, S.-M. and Lee, G.-H. (2003). Synthesis and characterization of metal complexes possessing the 5-(2-pyridyl) pyrazolate ligands: The observation of remarkable osmium-induced blue phosphorescence in solution at room temperature. *Organometallics*, 22 (24): 4938-4946.
24. Obata, M., Kitamura, A., Mori, A., Kameyama, C., Czaplewska, J. A., Tanaka, R., Kinoshita, I., Kusumoto, T., Hashimoto, H., Harada, M., Mikata, Y., Funabiki, T. and Yano, S. (2008). Syntheses, structural characterization and photophysical properties of 4-(2-pyridyl)-1,2,3-triazole rhenium(I) complexes. *Dalton Transactions*, 2008: 3292-3300.
25. Seridi, A., Wolff, M., Boulay, A., Saffon, N., Coulais, Y., Picard, C., Machura, B. and Benoist, E. (2011). Rhenium(I) and technetium(I) complexes of a novel pyridyltriazole-based ligand containing an arylpiperazine pharmacophore: Synthesis, crystal structures, computational studies and radiochemistry. *Inorganic Chemistry Communications*, 14(1): 238-242.
26. Wei, Q.-H., Xiao, F.-N., Han, L.-J., Zeng, S.-L., Duan, Y.-N. and Chen, G.-N. (2011). Synthesis, structure, photophysical and electrochemiluminescence properties of Re(I) tricarbonyl complexes incorporating pyrazolyl-pyridyl-based ligands. *Dalton Transactions*, 40(18): 5078-5085.
27. Zubaidi, Z. N., Metherell, A. J., Baggaley, E. and Ward, M. D. (2017). Ir(III) and Ir(III)/Re(I) complexes of a new bis(pyrazolyl-pyridine) bridging ligand containing a naphthalene-2,7-diyl spacer: Structural and photophysical properties. *Polyhedron*, 133: 68-74.
28. Etter, M. C., MacDonald, J. C. and Bernstein, J. (1990). Graph-set analysis of hydrogen-bond patterns in organic crystals. *Acta Crystallographica Section B*, 46(2): 256-262.
29. Mark-Lee, W. F., Chong, Y. Y. and Kassim, M. B. (2018). Supramolecular structures of rhenium(I) complexes mediated by ligand planarity via the interplay of substituents. *Acta Crystallographica Section C*, 74: 997-1006.

Malaysian Journal of Analytical Sciences (MJAS)
Published by Malaysian Analytical Sciences Society

KINETIC STUDIES AND ABSORPTION ISOTHERMAL OF METHYLENE BLUE BY USING N,O-CARBOXYMETHYL CHITOSAN

(Kajian Kinetik dan Isoterma Serapan Metilena Biru Menggunakan N,O-Karboksimetil Kitosan)

Putri Amirah Solehin Sulizi and Nadhratun Naiim Mobarak*

Department of Science Chemistry, Faculty of Science and Technology
Universiti Kebangsaan Malaysia, 43600 UKM Bangi, Selangor, Malaysia

**Corresponding author: nadhratunnaiim@ukm.edu.my*

Received: 11 June 2019; Accepted: 11 December 2019

Abstract

The potential of carboxymethyl chitosan as a low-cost and effective adsorbent for removal of methylene blue (MB) from aqueous solution has been investigated. N,O-carboxymethyl chitosan (N,O-CMCTS) was synthesized by reacting chitosan with monochloroacetic acid. The presence of a carboxymethyl group on carboxymethyl chitosan structure was demonstrated by Fourier Transform Infrared (FTIR) spectroscopy, with the presence of peaks at 1587 cm^{-1} and 1408 cm^{-1} assigned to the asymmetrical and symmetrical stretching vibrations of carboxylate anions ($-COO^-$). ^1H nuclear magnetic resonance (NMR) results confirm that *O*-, *N*- substituted carboxymethyl chitosan was synthesized, as the presence of peaks at 3.987 and 3.275 ppm that represent the substitution of carboxymethylation occurred at both hydroxyl and amino groups of chitosan. The influence of parameters such as initial dye concentration, sorbent dosage and sorption time on the sorption capacity were studied using the batch method. The results showed that maximum sorption capacity N,O-CMCTS was 0.549 mg/g. The concentration of methylene blue and the quantity of N,O-CMCTS were important in the absorption process, as the kinetic data followed pseudo second order. The sorption of methylene blue on N,O-CMCTS was via chemisorption, as in the isothermal studies, it followed Freundlich model.

Keywords: N,O-carboxymethyl chitosan, methylene blue, isotherms, kinetic

Abstrak

Potensi karboksimetil kitosan sebagai penjerap kos rendah dan efektif untuk menyingkirkan metilena biru (MB) dalam larutan akueus telah dikaji. N,O-karboksimetil kitosan (N,O-CMCTS) telah di sintesis melalui tindak balas kitosan dengan asid monokloroasetik. Kehadiran kumpulan karboksimetil pada struktur karboksimetil kitosan telah dibuktikkan dengan keputusan spektroskopi inframerah transformasi Fourier (FTIR) di mana kehadiran puncak pada 1587 cm^{-1} dan 1408 cm^{-1} yang menunjukkan getaran regangan asimetri dan simetri bagi anion karboksilat ($-COO^-$). Keputusan ^1H resonans magnet nukleus (NMR) mengesahkan penggantian *O*-, *N*- karboksimetil kitosan telah di sintesis dengan kehadiran puncak pada 3.987 dan 3.275 ppm yang menunjukkan penggantian pengkarboksimetil terjadi pada kedua-dua kumpulan hidroksil dan amino pada kitosan. Parameter yang mempengaruhi seperti kepekatan awal pewarna, dos penjerap dan masa erapan terhadap kapasiti erapan telah dikaji menggunakan kaedah kelompok. Keputusan menunjukkan kapasiti erapan maksima N,O-CMCTS adalah 0.549 mg/g. Dari kajian ini, kepekatan metilena biru dan kuantiti N,O-CMCTS adalah penting bagi proses serapan di mana data kinetik mengikut tertib pseudo kedua. Selain itu, erapan metilena biru pada N,O-CMCTS secara jerapan kimia serta ujian isoterma mengikut model Freundlich.

Kata kunci: N,O-karboksimetil kitosan, metilena biru, isoterma, kinetik

Introduction

It is estimated that over 10,000 different dyes and pigments are used industrially, while over 7 x 10^5 tons of synthetic dyes are annually produced worldwide [1]. In the textile industry, up to 200,000 tons of these dyes are lost to effluents every year. It is estimated that approximately 15% of dye stuffs are lost in industrial effluents during manufacturing and processing operations [2]. Unfortunately, most of these dyes escape conventional wastewater treatment processes and persist in the environment as a result of their high stability to light, temperature, water, detergents, chemicals, soap and other parameters such as bleach and perspiration [3]. The removal of dye pollutants from wastewater effluents is vital, because even a small quantity of dye in water is toxic and highly visible. Moreover, their degradation products may be mutagenic and carcinogenic. Methylene blue is widely used in the textile industry and may cause discoloration, coldness, redness or dryness when contact with skin if it exceeds World Health Organization (WHO) or United States Environmental Protection Agency (US-EPA) limits. Ingestion of methylene blue may result in gastrointestinal irritation, discoloration of oral mucosa, irritation of lips, mouth and throat, paleness of complexion, insufficient coordination or drowsiness [2]. International Organization of Standardization 16265 (ISO 16265) for the determination of the methylene blue active substances (MBAS) has an index which ranges from 0.05 mg/l to 0.5 mg/l and 0.5 mg/l to 5.0 mg/l in various water samples (e.g. ground water, drinking water, surface water, waste water and leachates) [4]. Major problems associated with colored effluent include lowering light penetration, photosynthesis and damages the aesthetic nature of the water surface [5]. It is challenging to treat the dye effluents, as they are mostly biologically non-degradable and stable to light and heat. Most dyes are of synthetic origin and have a complex aromatic structure.

Nowadays, there is great interest in finding inexpensive, biodegradable, non-toxic and an environment friendly material for the removal of dyes [6]. Many non-conventional low-cost adsorbents have been studied for the removal of methylene blue, including natural materials, biosorbents and waste materials from agriculture and industry [7]. Among the natural polymeric materials, chitosan is the most attractive polymer due its low cost and ready availability. Chitosan is a linear copolymer composed of (1-4)-linked D-glucosamine and N-acetyl-D-glucosamine and is obtained by alkaline hydrolysis of chitin (second abundant polymer in nature after cellulose) [8]. Chitin is obtained from crustaceans (crab, krill, crayfish) primarily because a large amount of crustacean exoskeletons is available as a by-product of food processing. Chitosan is widely used for removal of heavy metals, transition metals and dyes as a well-known sorbent. Chitosan based biosorbents show high affinity for various dyes and have wide range of applications in the biomedical, cosmetic, food and textile industries [9]. Even though chitosan can adsorb the anionic dyes, as it is cationic in nature, some chemical modifications of chitosan are necessary to enhance their properties and consequently their applications [10, 11]. Various modification on chitosan as adsorbents have been examined, such as grafting, cross-linking and functionalization for forming composite for adsorption of dyes in aqueous media [12]. Carboxymethylation of chitosan is a very attractive method as it introduces active carboxyl (-COOH) groups into the molecule. This is lead to an increase in the adsorption capacity of chitosan for dyes, transition and heavy metals [13].

The present work deals with a series of experiments that focus on higher concentrations of methylene blue, ranging from 1000-1800 mg/l [14]. In this study, we focused removal at low concentration of methylene blue on N,O-CMCTS. Therefore, the aim of this study was to investigate N,O-carboxymethyl chitosan as an effective sorbent for removal of methylene blue in detail. The effects of initial dye concentration at lower concentration, sorbent dosage and sorption time were investigated. The sorption kinetics and isotherms for methylene blue onto N,O-carboxymethyl chitosan have also been measured.

Materials and Methods

Materials

Chitosan was obtained from Chito-Chem Sdn. Bhd., Malaysia. Monochloroacetic acid was purchased from Sigma Aldrich. Other reagents used were of analytical grade and used without further purification.

Methylene blue stock solution

Methylene blue, also known as 3,7-bis (dimethylamino) phenazathionium chloride, λ_{max}= 664 nm is a basic dye. It was purchased from Sigma Aldrich. The molecular formula and molecular mass of methylene blue are $C_{16}H_{18}N_3SCl$

and 319 g mol^{-1}, respectively. Methylene blue stock solution of 1000 mg/L was prepared by dissolving 1 g of the dye into 1000 mL distilled water. The stock solution was used throughout the whole experiment by fresh dilution.

Preparation of N,O-carboxymethyl chitosan

N,O-carboxymethyl chitosan (N,O-CMCTS) was prepared according to the previous report [3] with slight modification. Briefly, 10 g of chitosan was swelled in 50 mL isopropanol and water mixture (1:1 v/v ratio) contained 10 g sodium hydroxide at a 25℃ for 1 hour. Then, 15 g monochloroacetic acid dissolved in 20 mL isopropanol was added drop-wise into the reaction mixture over the period of 30 min. The reaction was continued with constant stirring for another 4 hours at 55℃. Finally, the reaction was stop by adding 70% ethyl alcohol. The product was filtered and washed with 80% ethyl alcohol to remove salt and water. The N,O-CMCTS was dried in a desiccator overnight.

Characterization of N,O-carboxymethyl chitosan

N,O-CMCTS was characterized by Fourier transform infrared spectroscopy (FTIR) Perkin Elmer, USA. The infrared spectrum was recorded at the frequency range of 4000-800 cm^{-1}. The infrared spectrum analysis was done to determine the functional groups on chitosan and carboxymethyl chitosan. In order to confirm the structure of the products, analysis of ^{1}H NMR was performed using Bruker Avance 111 600 MHz. chitosan and carboxymethyl chitosan were dissolve in D_2O solvent.

Equilibrium adsorption and sorption isotherm studies

Batch adsorption experiments were performed in conical flask and stirring with a magnetic stirrer at a speed of 200 rpm. The effects of sorbent dosage on dye sorption were measured with different masses (0.05, 0.10, 0.15, 0.20 and 0.25 g) in 25 mL of dye solution (2 mg/L) at 25℃ for 30 minutes. For effect of initial dye concentrations, 50 mg of N,O-CMCTS was added to 25 mL of an aqueous solution of methylene blue at known concentrations in a 250 mL conical flask for 30 minutes. The adsorbent was separated by centrifuge and the dye content in the remaining aqueous was analyzed by using a UV-vis spectrophotometer at 664 nm corresponding to a maximum absorbency of methylene blue. The amount of absorption, q (mg/g) was calculated by the following equation:

$$q = \frac{(C_o - C_t)V}{W} \quad (1)$$

where C_o and C_t (mg/L) are the concentration of dye at initial and at time t, respectively. V is the volume of solution (L) and W is the mass of dry adsorbent used (g).

The experimental data were processed using two adsorption isotherm models, namely the Freundlich isotherm model and Langmuir isotherm model, in order to obtain information about the adsorption capacity, the degree of affinity and the surface characteristics of N,O-CMCTS, as well as to establish the equilibrium relationship and mechanism of methylene blue adsorption onto the N,O-CMCTS as adsorbent.

The sorption data were interpreted by Langmuir and Freundlich isotherm equations [15]. The Langmuir isotherm model estimates the maximum adsorption capacity corresponding to complete monolayer coverage on the sample surface. The linear form of Langmuir adsorption isotherm could be represented as:

$$\frac{C_e}{q_e} = \frac{1}{q_{max} K_L} + \frac{C_e}{q_{max}} \quad (2)$$

where K_L was constant of the sorption equilibrium (L/mg) and q_{max} was the maximum dye sorption capacity (mg/g). The values of q_{max} and b could be obtained from linear plot of C_e/q_e versus C_e.

The Freundlich isotherm model for sorption takes place in heterogenous systems and assumed that the sorption occurs on sites with different sorption energies. The model gives a representation of equilibrium between the amount of adsorbate in solution and that on the surface of the adsorbent. This involves the sorption occur in multilayer and the Freundlich isotherm equation as follows:

$$q_e = K_F C_e^{\frac{1}{n}} \quad (3)$$

This equation could be written in its linearized form:

$$\log q_e = \log K_F + \frac{1}{n}\log C_e \quad (4)$$

where K_F and n were the Freundlich constants, which represent sorption capacity and sorption intensity respectively. K_F and n were obtained from intercept and slope of a linear plot of log q_e against log C_e.

Kinetic adsorption studies

The influence of contact time on the adsorption of dye by N,O-CMCTS was studied in batch experiments, mixing 0.05 g of N,O-CMCTS and 25 mL of methylene blue (2mg/L) at a temperature of 25℃ for time intervals ranging from 30 to 300 minutes. Finally, the adsorbent was separated via centrifuge and the dye content in the remaining aqueous was analyzed using a similar procedure to that of the equilibrium studies.

To examine the kinetic mechanism of the absorption process of MB on N,O-CMCTS, the pseudo-first-order and the pseudo-second-order kinetics models were used for analyses. The pseudo-first-order rate equation of Lagergren model for the absorption of solid/liquid systems [3] as follows:

$$\log(q_e - q_t) = \log q_e - \frac{k_1 t}{2.303} \quad (5)$$

The pseudo-second-order rate equation was as below [3]:

$$\frac{t}{q_t} = \frac{1}{k_2 {q_e}^2} - \frac{t}{q_e} \quad (6)$$

where q_e and q_t were the absorption capacity (mg/g) at equilibrium and at time t (min), respectively. k_1 (min^{-1}) and k_2 ($g\ mg^{-1}\ min^{-1}$) the absorption rate constants of pseudo-first-order and pseudo-second-order absorption rates, respectively.

Results and Discussion

Characterization of carboxymethyl chitosan by FTIR

Figure 1 shows the FTIR spectra of chitosan and carboxymethyl chitosan (CMCTS). The chitosan spectra showed the basic characteristic peaks of chitosan at 3281 cm^{-1} (O-H stretch and N-H stretch), 2923 and 2883 cm^{-1} (C-H stretch), 1645 cm^{-1} (NH-CO stretch), 1576 cm^{-1} (N-H bend), 1152 cm^{-1} (bridge-O- stretch) and 1028 cm^{-1} (C-O stretch). It was observed that a broad absorption band and strong stretch was attributed to O-H, while N-H stretching vibrations were noticed for carboxymethyl chitosan at approximately 3350 cm^{-1} after carboxymethylation. A sharp and intense peak at 1587 cm^{-1} indicated the bending vibration of an amide for CMCTS [16]. The presence of absorption band at 1631 cm^{-1} assigned for carboxylic group of carboxymethyl chitosan. The bands at 1587 cm^{-1} and 1408 cm^{-1} were assigned to the asymmetrical and symmetrical stretching vibrations of carboxylate anions ($-COO^-$) while the bands at 1321 cm^{-1} was characteristic of CH_2 scissoring in the carboxymethyl group [17].

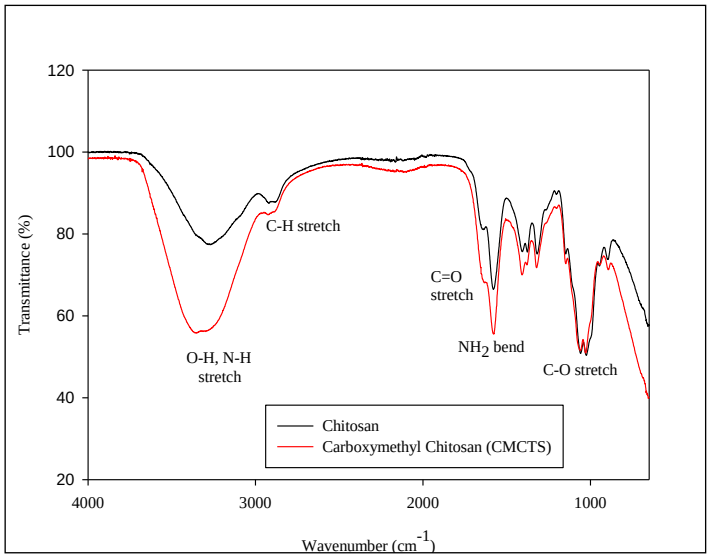


Figure 1. FTIR spectrum of chitosan and carboxymethyl chitosan (CMCTS)

Characterization of N,O-carboxymethyl chitosan by ^{1}H NMR

Figure 2 shows the ^{1}H NMR spectra of chitosan and carboxymethyl chitosan respectively (chemical shift ranging between δ = 1 and 5 ppm). The ^{1}H NMR chemical shifts of chitosan assigned as follows: ^{1}H NMR (D_2O): δ = 3.09 (H2) and δ = 3.64-3.84 (H3, H4, H5, H6). While the ^{1}H NMR chemical shifts of carboxymethyl chitosan could be assigned as follows ^{1}H NMR (D_2O): δ = 3.10-3.28 (H2) and δ = 3.65-4.00 (H3, H4, H5, H6) [17, 18]. The results confirmed that *O*-, *N*- substituted carboxymethyl chitosan was synthesized, as the presence of peaks at 3.99 and 3.28 ppm shows that the substitution of carboxymethylation occurred at both hydroxyl and amino groups of chitosan, respectively [16].

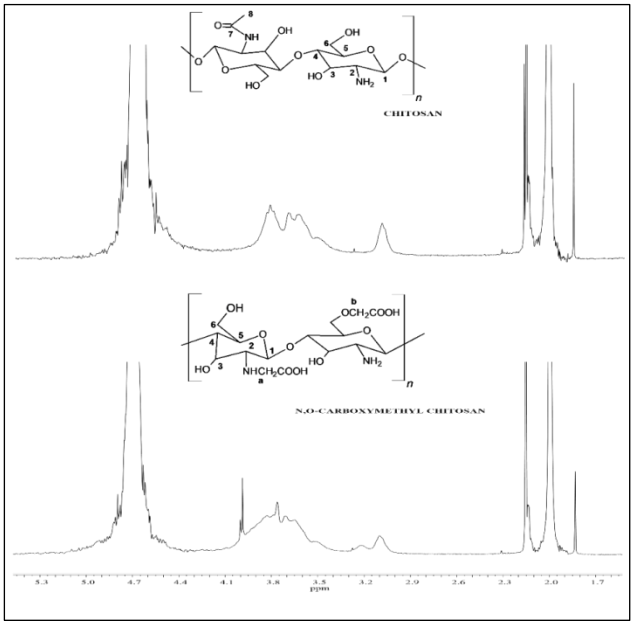


Figure 2. ^{1}H NMR spectra of chitosan and N,O-carboxymethyl chitosan

Effect of adsorbent dosage on methylene blue sorption

Previous literature had reported that chitosan was able to remove 99% of methylene blue from 10 ppm solution at dosage of 0.1 g; however, they do not clearly showed proof in terms of data [19]. Other literature has reported that chitosan cannot uptake cationic dye such as methylene blue and modification should be done to chitosan for adsorb cationic dyes [20]. It can be observed from Figure 3 0.05 g of N,O-CMCTS was able to remove 73% of methylene blue with a capacity sorption of methylene blue of 0.55 mg/g. However, that the sorption capacity sharply decreased as the mass of adsorbent increased due to the saturation of the system.

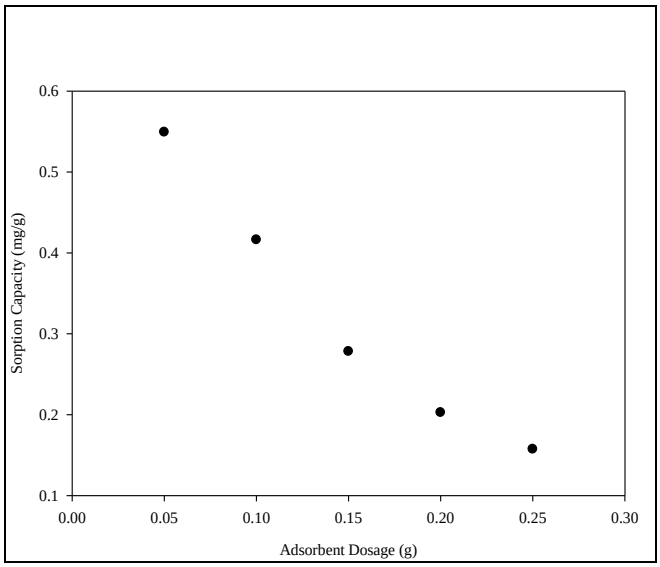


Figure 3. Effect of adsorbent dosage on methylene blue sorption by N,O-CMCTS

Effect of initial dye concentration on methylene blue sorption

Figure 4 shows that the sorption capacity of sample increased from 0.133 mg/g to 0.899 mg/g with an increase in initial dye concentration from 0.3 mg/L to 2.0 mg/L. The sorption capacity of MB on N,O-CMCTS was increased with increased concentrations of MB. This was due to presence of available active sites in N,O-CMCTS for the sorption of the MB [21]. The -OH, $-NH_2$ and -COOH groups of N,O-CMCTS were involve in sorption process between MB and N,O-CMCTS through chemical interaction and electrostatic attraction [14].

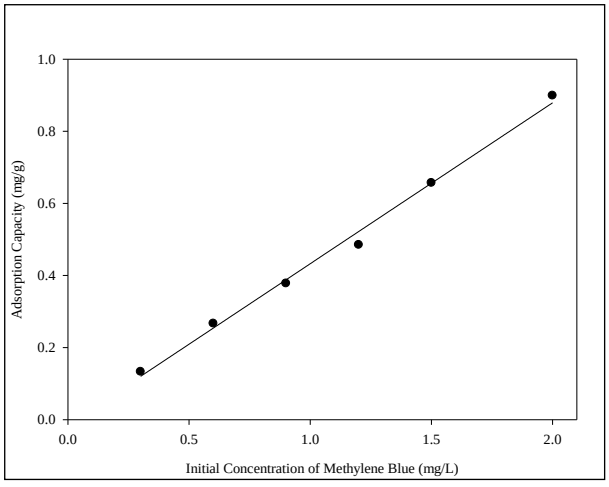


Figure 4. Effect of initial dye concentration on methylene blue sorption by N,O-CMCTS

Sorption Isotherm

Sorption isotherms were important to describe how molecules of methylene blue interact with the N,O-CMCTS surface. Hence, the correlation of equilibrium data using either a theoretical or empirical equation was essential for the sorption interpretation and prediction of the extent of sorption.

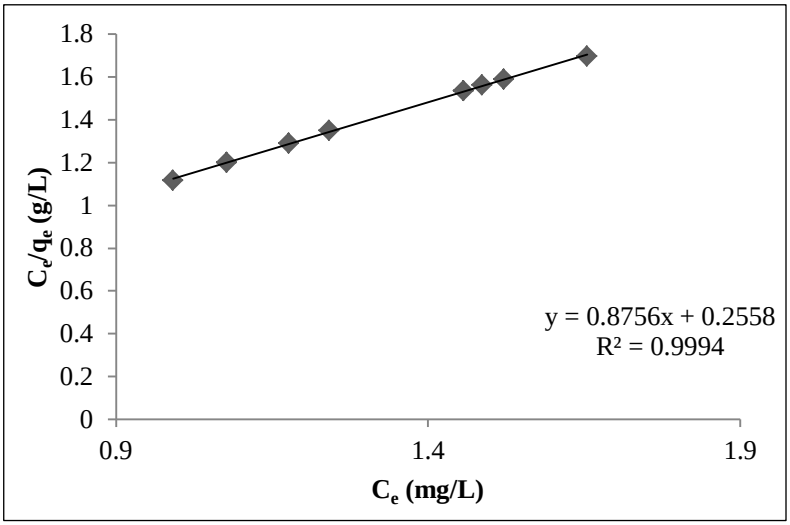


Figure 5. The linearized Langmuir adsorption isotherm for sorption of methylene blue on N,O-CMCTS

A linear plot of C_e/q_e versus C_e for the Langmuir model of sorption of methylene blue on N,O-CMCTS is shown in Figure 5 and corresponding parameters are listed in the Table 2. The affinity between the adsorbate and adsorbent could be obtained from the Langmuir parameter with the help of the dimensionless separation factor (R_L) as below [3]:

$$R_L = \frac{1}{1+a_L C_i} \tag{7}$$

According to the criteria of R_L in Table 1, R_L could be used to predict whether a sorption system was favorable or unfavorable. Based on Table 2 the R_L value for this sorption system was 0.1275, which was lower than 1 and higher than zero. These suggested that the sorption of methylene blue onto N,O-CMCTS was favorable at the range of concentration in these studies. The degree of favorability is generally related to the irreversibility of the system, giving a qualitative assessment of the N,O-CMCTS-MB interactions. The degrees tended toward zero (the completely ideal irreversible case) rather than unity (which represents a completely reversible case).

Table 1. Characteristics of the Langmuir adsorption isotherms

Separation Factor (R_L)	**Types of Isotherms**
$R_L > 1$	Unfavorable
$R_L = 1$	Linear
$0 > R_L < 1$	Favorable
$R_L = 0$	Irreversible

The Freundlich isotherm model the sorption takes place on heterogenous systems; the data are given in Table 2. When the value 1/n was between 0.1 less than equal to 0.5, the sorption process was favorable. If the value was between 0.5 and 1 the process is easy to adsorb and if value greater than 1 it was difficult to adsorb [22]. From our

study the value 1/n (1/n = 0.1316) which was between 0.1 less than equal to 0.5 and we can assume that the sorption was favorable or easy to adsorb. Moreover, the value of n was greater than 1 (n =7.5987), indicating that the sorption process was favorable in high and low concentration in the range of concentration being studied.

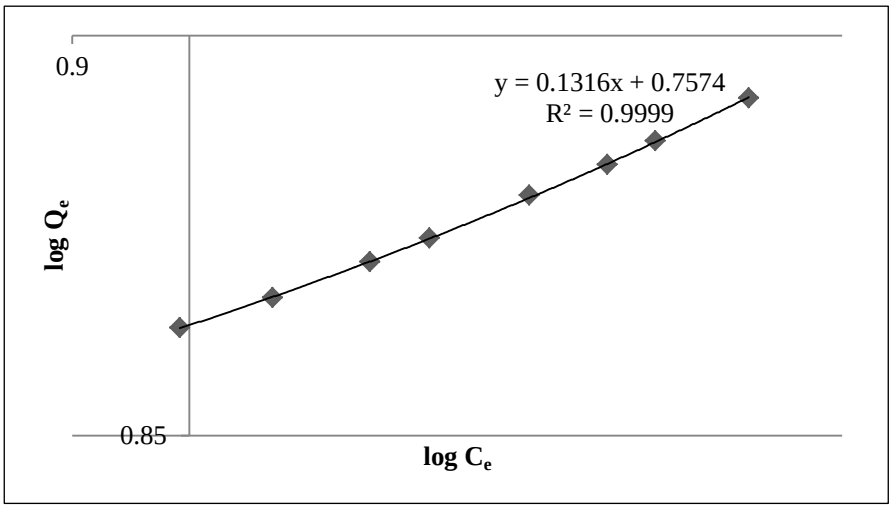


Figure 6. The linearized Freundlich absorption isotherm for sorption of methylene blue on N,O-CMCTS

Based on the correlation coefficient (R^2) values in Table 2 of the linearized form of Langmuir and Freundlich sorption equations indicated that sorption fitted to the Freundlich absorption model for the experimental equilibrium sorption data. From correlation coefficient (R^2) value for Freundlich model was close to 1 which was 0.9999 compared to correlation coefficient (R^2) value of Langmuir model. This suggests that sorption of methylene blue occur at multilayer on the N,O-CMCTS with non-uniform distribution of sorption heat and affinities over the heterogenous surface [23]. These proved that the sorption of methylene blue to N,O-CMCTS were through an absorption mechanism.

Table 2. The Langmuir and Freundlich isotherms model constants and their respectively correlation coefficients R^2 for the sorption of methylene blue by N,O-CMCTS

Experimental q (mg/g)	**Langmuir**				**Freundlich**		
	q_{max} (mg/g)	**K_L (L/mg)**	**R_L**	**R^2**	**K_F (g mg^{-1} min^{-1})**	**1/n**	**R^2**
0.975	1.1421	3.4229	0.1275	0.9994	5.7200	0.1316	0.9999

Absorption kinetics

The adsorption kinetic study was important in predicting the mechanisms (chemical reaction or mass-transport process) that control the rate of the pollutant removal and retention time of adsorbed species at the solid-liquid interface [24]. Figure 7 shown the absorption of MB onto N,O-CMCTS as a function of time. As observed in Figure 4, the absorption capacity of MB on N,O-CMCTS increased within 240 minutes, after that it decreased. The increase probably occurred due to the availability of more active sites on N,O-CMCTS, which acts as an absorbent. After that, the active sites were decreased by the occupancy of absorbent at 300 minutes. Under our experimental conditions, the assumption that the system reached the equilibrium time for absorption of methylene blue on N,O-CMCTS was 240 minutes.

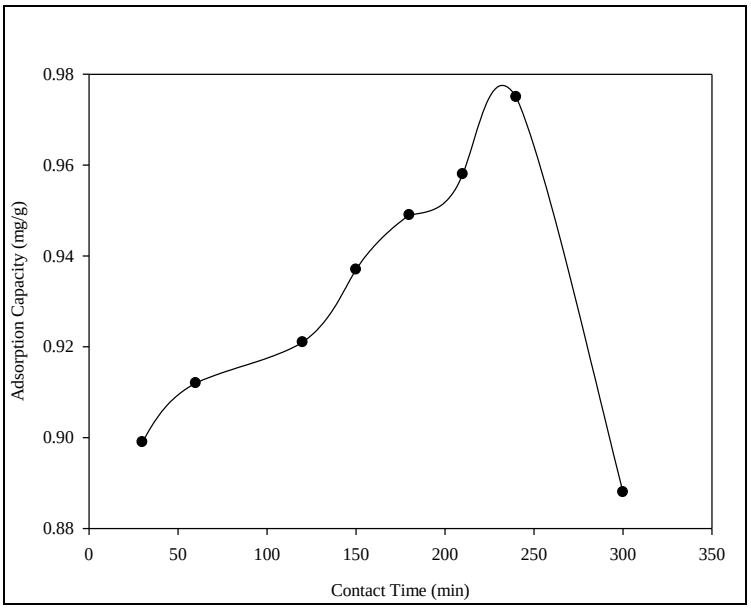


Figure 7. Absorption of methylene blue by N,O-CMCTS as a function of time

The linear plot of $\log(q_e-q_t)$ versus t for pseudo-first-order model in Figure 8 and that of (t/q_t) versus t for pseudo-second-order model in Figure 9 were shown. The values of q_e and the rate constants k_1 and k_2 could be obtained from the plot of experimental data.

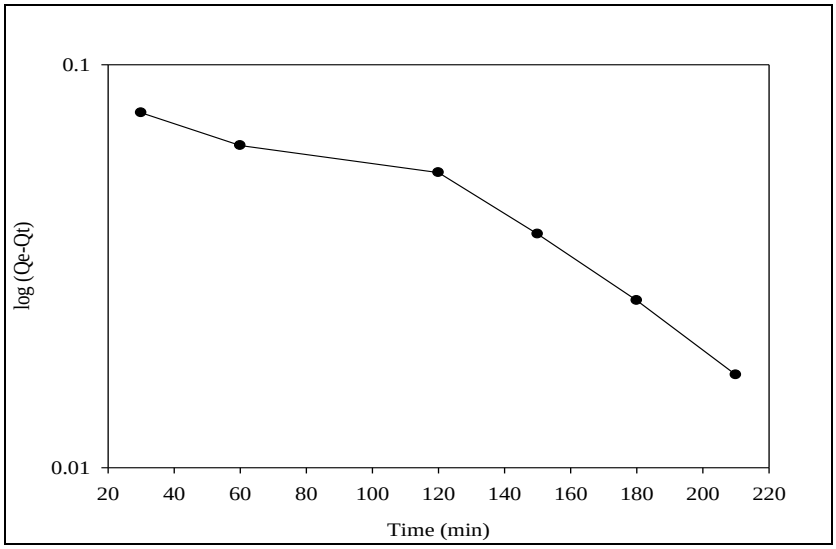


Figure 8. Linearized pseudo-first-order plot for absorption of methylene blue by N,O-CMCTS

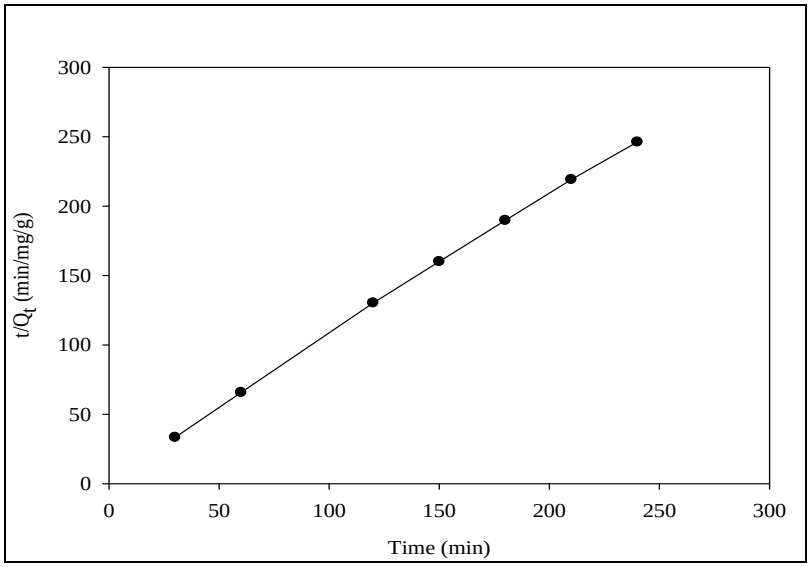


Figure 9. Linearized pseudo-second-order plot for absorption of methylene blue by N,O-CMCTS

Table 3. Theoretically determined constants of the pseudo-first-order and pseudo-second-order reaction kinetics based on the absorption of methylene blue

Experimental q (mg/g)	**Pseudo-first-order constants**			**Pseudo-second-order constants**		
	q_e (mg/g)	**k_1 (min^{-1})**	**R^2**	**q_e (mg/g)**	**k_2 (g mg^{-1} min^{-1})**	**R^2**
0.975	1.216	6.909×10^{-4}	0.9142	0.983	0.202	0.9993

The calculated q_e, the rate constants and the correlation coefficients for two kinetic models of N,O-CMCTS are shown in Table 3. The values of correlation coefficient (R^2) of pseudo-first-order and pseudo-second-order models were 0.9142 and 0.9993, respectively. The calculated q_e value of the pseudo-second-order model was 0.983 mg/g, which is close to the experimental data of 0.975 mg/g. Table 4 showed the comparison of maximum adsorption capacities for methylene blue by different adsorbents. The higher value of correlation coefficient (0.9993) and the close calculated q_e value indicated that these data was well fitted for pseudo-second-order model. Thus, it may be suggested that the absorption of methylene blue obeyed the pseudo-second-order kinetic, indicating that the absorption mechanism depended on the N,O-CMCTS and methylene blue [25].

Table 4. Comparison of maximum adsorption capacities for methylene blue by different adsorbents

Adsorbents	**Maximum Capacities (mg/g)**	**References**
Natural clay	15.40	[26]
Corncob based activated carbon	0.84	[27]
Fir wood activated carbon	1.21	[27]
Clay	6.30	[28]
Glass	2.24	[29]

Conclusion

Modified N,O-Carboxymethyl chitosan (N,O-CMCTS) has been prepared under heterogenous condition. The FTIR and NMR characterizations have shown that N,O-carboxymethyl chitosan was successfully synthesized. Sorption tests of Methylene Blue on N,O-CMCTS were carried out at various parameters including sorbent dosage, initial dye concentration and contact time, The results obtained showed that sorbent dosage 0.05 g exhibited the highest sorption capacity. The kinetics studies showed that the absorption process followed the second-order-kinetic model rather than the first-order-kinetic model. By comparing the correlation coefficient value of Langmuir and Freundlich model for each linear formed of isotherm analysis, Freundlich model properly described the absorption equilibrium of MB on N,O-CMCTS. Therefore, it may be concluded that N,O-CMCTS has shown strong potential in wastewater treatment in removal of dye. However, other parameters such as pH may be examined in order to enhance the potential of N,O-CMCTS as adsorbent for different type of dyes.

Acknowledgement

This research was subsidized with grants from GGPM-2017-093. We gratefully thank you our colleagues from Faculty Science and Technology who provided insight and expertise which greatly assisted the research.

References

1. Drumond Chequer, F. M., de Oliveira, G. A. R., Anastacio Ferraz, E. R., Carvalho, J., Boldrin Zanoni, M. V. and de Oliveir, D. P. (2013). Textile dyes: Dyeing process and environmental impact. *Eco-Friendly Text Dye Finishing*, pp. 151-173.
2. Zhu, X., Zhang, Z., and Yan, G. (2016). Methylene blue adsorption by novel magnetic chitosan nanoadsorbent. *Journal of Water Environment Technology*, 14: 96-105.
3. Mitra, P., Sarkar, K. and Kundu, P. P. (2014). Carboxymethyl chitosan modified montmorillonite for efficient removal of cationic dye from waste water. *Defence Science Journal*, 64: 198-208.
4. International, S. O. (2009). ISO 16265 Water Quality-Determination of the Methylene Blue Active Substances (MBAS) Index-Method using Continuous Flow Analysis (CFA).
5. Manish, K. S. (2012). Recyclable crosslinked O-carboxymethyl chitosan for removal of cationic dye from aqueous solutions. *Journal of Waste Water Treatment & Analysis*, 03(04).
6. Chang, M. Y. and Juang, R. S. (2004). Adsorption of tannic acid, humic acid, and dyes from water using the composite of chitosan and activated clay. *Journal of Colloid and Interface Science*, 278:18-25.
7. Rafatullah, M., Sulaiman, O., Hashim, R. and Ahmad, A. (2010). Adsorption of methylene blue on low-cost adsorbents: A review. *Journal Hazardous Material*, 177: 70-80.
8. Synowiecki, J. and Al-khateeb, N. A. (2003). Production, properties and some new applications of chitin and its derivatives. *Critical Reviews in Food Science and Nutrition*, 43(2): 145-171.
9. Vadivelan, V. and Vasanth Kumar, K. (2005). Equilibrium, kinetics, mechanism, and process design for the sorption of methylene blue onto rice husk. *Journal of Colloid and Interface Science*, 286: 90-100.
10. El-Sherbiny, I. M. (2009). Synthesis, characterization and metal uptake capacity of a new carboxymethyl chitosan derivative. *European Polymer Journal*, 45: 199-210.
11. Sridhari, T. R. and Dutta, P. K. (2000). Synthesis and characterization of maleilated chitosan for dye house effluent. *Indian Journal of Chemical Technology*, 7: 198-201.
12. Kyzas, G. Z. and Bikiaris, D. N. (2015). Recent modifications of chitosan for adsorption applications: A critical and systematic review. *Marine Drugs*, 13(1): 312-337.
13. Jeon, C. and Höll, W. H. (2003). Chemical modification of chitosan and equilibrium study for mercury ion removal. *Water Research*, 37: 4770–4780.
14. Wang, L., Li, Q. and Wang, A. (2010). Adsorption of cationic dye on N,O-carboxymethyl-chitosan from aqueous solutions: Equilibrium, kinetics, and adsorption mechanism. *Polymer Bulletin*, 65: 961-75.
15. Hamed, M. M., Ahmed, I. M. and Metwally, S. S. (2014). Adsorptive removal of methylene blue as organic pollutant by marble dust as eco-friendly sorbent. *Journal of Industrial Engineering Chemistry*, 20 (4): 2370-2377.
16. Jaidee, A., Rachtanapun, P. and Luangkamin, S. (2012). ^{1}H-NMR analysis of degree of substitution in N,O-carboxymethyl chitosans from various chitosan sources and types. *Advanced Materials Research*, 506: 158–161.

17. Chen, X. G. and Park, H. J. (2003). Chemical characteristics of O-carboxymethyl chitosans related to the preparation conditions. *Carbohydrate Polymer*, 53: 355–359.
18. de Abreu, F. R. and Campana-Filho, S. P. (2009). Characteristics and properties of carboxymethylchitosan. *Carbohydrate Polymer*, 75: 214–221.
19. Shashikala, M., Nagapadma, M., Lolita, P. and Sarath, N. N. (2013). Studies on the removal of methylene blue dye from water using chitosan. *International Journal of Development Research*, 3(8): 040-044.
20. Wang, J., Wang, L., Yu, H., Zain-ul-Abdin., Chen, Y., Chen, Q., Zhou, W., Zhang, H. and Chen, X. (2016). Recent progress on synthesis, property and application of modified chitosan: An overview. *International Journal of Biological Macromolecules*, 88: 333-344.
21. Rahman, M. A., Amin, S. M. R. and Alam, A. M. S. (2012). Removal of methylene blue from waste water using activated carbon prepared from rice husk. *Dhaka University Journal of Science*, 60: 185–189.
22. Dhananasekaran, S., Palanivel, R. and Pappu, S. (2016). Adsorption of methylene blue, bromophenol blue, and coomassie brilliant blue by α-chitin nanoparticles. *Journal of Advanced Research*, 7(1): 113-124.
23. Foo, K. Y. and Hameed, B. H. (2010). Insights into the modeling of adsorption isotherm systems. *Chemical Engineering Journal*, 156(1): 2–10.
24. Suteu, D. and Malutan, T. (2013). Industrial cellolignin wastes as adsorbent for removal of methylene blue dye from aqueous solutions. *BioResources*, 8(1): 427–446.
25. Meroufel, B., Benali, O., Benyahia, M., Benmoussa, Y. and Zenasni, M. A. (2013). Adsorptive removal of anionic dye from aqueous solutions by Algerian kaolin: Characteristics, isotherm, kinetic and thermodynamic studies. *Journal of Materials Environmental Science*, 4: 482-491.
26. Sahoo, S., Uma, Banerjee, S. and Sharma, Y. C. (2013). Application of natural clay as a potential adsorbent for the removal of a toxic dye from aqueous solutions. *Desalination and Water Treatment*, 52 (34-36): 6703-6711.
27. Tseng, R., Tseng, S. and Wu, F. (2006). Preparation of high surface area carbons from Corncob with KOH etching plus CO_2 gasification for the adsorption of dyes and phenols from water. *Colloids and Surfaces A: Physicochemical and Engineering Aspects*, 279(1-3): 69-78.
28. Gürses, A., Karaca, S., Do, Ç., Bayrak, R., Açıkyıldız, M. and Yalçın, M. (2004). Determination of adsorptive properties of clay/water system: methylene blue sorption. *Journal of Colloid and Interface Science*, 269(2): 310-314.
29. Chakrabarti, S. and Dutta, B. K. (2005). On the adsorption and diffusion of Methylene Blue in glass fibers. *Journal of Colloid and Interface Science*, 286(2): 807-811.

Malaysian Journal of Analytical Sciences (MJAS)
Published by Malaysian Analytical Sciences Society

AGAROSE-CHITOSAN-INTERGRATED MULTIWALLED CARBON NANOTUBES FILM SOLID PHASE MICROEXTRACTION COMBINED WITH HIGH PERFORMANCE LIQUID CHROMATOGRAPHY FOR THE DETERMINATION OF TRICYCLIC ANTIDEPRESSANT DRUGS IN AQUEOUS SAMPLES

(Filem Agarosa-Kitosan Bersepadu Nanotiub Kabon Berbilang Dinding Pengestrakan Mikro Fasa Pepejal Digabungkan Dengan Kromatografi Cecair Prestasi Tinggi-Pengesanan Ultralembayung Untuk Penentuan Anti-Murung Trisiklik Di Dalam Sampel Akueus)

Wan Nazihah Wan Ibrahim[1]*, Mohd Marsin Sanagi[2], Nor Suhaila Mohammad Hanapi[1], Nursyamsyila Mat Hadzir[1], Noorfatimah Yahaya[3], Sazlinda Kamaruzaman[4]

[1]Faculty of Applied Science,
Universiti Teknologi MARA, 40450 Shah Alam, Selangor, Malaysia
[2]Department of Chemistry, Faculty of Science,
Universiti Teknologi Malaysia, 81310 Johor Bahru, Johor, Malaysia
[3]Integrative Medicine Cluster, Advanced Medical and Dental Institute,
Universiti Sains Malaysia, 13200 Kepala Batas, Penang, Malaysia
[4]Department of Chemistry, Faculty of Science,
Universiti Putra Malaysia, 43400 Serdang, Selangor, Malaysia

**Corresponding author: wannazihah@uitm.edu.my*

Received: 20 November 2019; Accepted: 15 January 2020

Abstract

Agarose-chitosan-integrated multiwalled carbon nanotubes (Agr-Ch-MWCNTs) film solid phase microextraction (SPME) was developed and applied for the determination of tricyclic antidepressant drugs (TCAs) in aqueous samples using high performance liquid chromatography-ultraviolet detection (HPLC-UV). Integration of highly interconnected pores of MWCNTs in the agarose-chitosan matrix increases the hydrophobic sites, surface area and porosity of the materials and thus enhancing the extraction efficiency. The film of blended agarose and chitosan allows good dispersion of MWCNTs, prevents the leaching of MWCNTs during application and enhances the film mechanical stability. Optimized parameters for SPME parameters were obtained which no addition of salt included, sample pH = 11, 30 minutes extraction time, iso-propanol as desorption solvent and 0.4% w/v MWCNTs loading in agarose-chitosan matrix. The matrix match calibration curves demonstrated good linearity in the range of 10-500 ppb with excellent coefficients determination (r^2 = 0.9944-0.9961), good limits of detection (LODs) in the range of 3.13-3.60 ppb, high analyte recoveries (92.04-110.00%) and low relative standard deviations (RSD < 6.85).

Keywords: blended agarose/chitosan/multiwalled carbon nanotubes, solid phase microextraction, tricyclic antidepressant drugs

Abstrak

Filem agarosa-kitosan bersepadu nanotiub kabon berbilang dinding (Agr-Ch-MWCNTs) pengestrakan mikro fasa pepejal (SPME) telah dibangunkan dan diaplikasi untuk penentuan anti-murung trisiklik di dalam sampel akueus menggunakan kromatografi cecair prestasi tinggi-pengesanan ultralembayung (HPLC-UV). Persepaduan MWCNTs yang mempunyai liang yang saling berhubung di dalam matriks agarosa/kitosan menambahbaik tapak hidrofobik, luas permukaan dan keliangan bahan dan meningkatkan kecekapan pengestrakan. Filem campuran agarosa dan kitosan membenarkan penyerakan MWCNTs yang baik, menghalang pelunturan MWCNTs semasa aplikasi dan meningkatkan kestabilan mekanikal filem. Optimum parameter

untuk SPME telah diperolehi termasuk tiada penambahan garam, pH sampel = 11, masa pengestrakan 30 minit, iso-propanol sebagai pelarut desorpsi dan 0.4% w/v jumlah muatan MWCNTs di dalam matrik agarosa/kitosan. Lengkungan kalibrasi matrik menunjukkan kelinearan yang bagus di dalam skala 10-500 ppb dengan penentuan koefisien yang terbaik (r^2 = 0.9944-0.9961), had pengesanan yang bagus (LODs) di dalam skala 3.13-3.60 ppb, perolehan semula yang tinggi (92.04-110.00%) dan sisihan piawai relatif yang rendah (RSD < 6.85).

Kata kunci: campuran agarosa/kitosan/nanotiub karbon berbilang dinding, pengestrakan mikro fasa pepejal, anti-murung trisiklik

Introduction

Antidepressants are drugs commonly used by therapeutic patient as prescribed medication. However, uncontrolled intake dosage will cause clinical responses such as sleep problem, headache, eating disorder and other hormone mediated condition [1-3]. Low concentrations of existence of these residues, bring up the challenge of measuring trace levels of tricyclic antidepressants (TCAs) in aqueous matrices [4]. For these reasons, some effort has been devoted on the development of microextraction techniques such as dispersive liquid-liquid phase microextraction (DLLME) [5] and hollow fiber-liquid phase microextraction (HF-LPME) techniques [6] to improve the sensitivity and sufficient selectivity for analysis TCAs present at low concentration.

Previously, our research group was prepared new adsorbent agarose-chitosan-integrated multiwalled carbon nanotubes (MWCNTs) film (Agr-Ch-MWCNT) that has been used for the first time in solid phase microextraction (SPME) of acidic nonsteroidal anti-inflammatory drugs (NSAIDs) in water samples [7]. From the results, the Agr-Ch-MWCNT film offers hydrophobic, π-π and hydrogen bonding in acidic medium. The presence of -NH_2 and -OH group from backbone agarose and chitosan also serve as chelating and reaction sites [8]. These features are potentially beneficial in solid phase extraction as the higher the possible sorbent-sorbate interaction, the faster the sorption process reaches equilibrium. Therefore, it is of interest to investigate the performance of Agr-Ch-MWCNT film in alkaline medium. As the blending method overcomes the pH-sensitiveness of the polysaccharides, it is expected that the composite film would be stable over a wide pH range. Thus, this work was extended study of prepared adsorbent for determination of basic tricyclic antidepressant drugs (TCAs) in water samples. Two TCAs namely amitriptyline (AMIT) and chlorpromazine (CHLO) were selected as model analytes.

Materials and Methods

Chemical and materials

Amitriptyline hydrochloride (AMIT) was purchased from Sigma-Aldrich (St. Louis, USA) while chlorpromazine hydrochloride CHLO was purchased from Clearsynth (Mumbai, India). HPLC grade organic solvents acetonitrile (ACN), methanol (MeOH) and iso-propanol (IPA) were purchased from J.T. Baker (Pennsylvania, USA). Reagent grade sodium chloride was purchased from Bendosen (Selangor, Malaysia). Nylon membrane 0.45 μm (Gelman Sciences, Ann Arbor, MI, USA) was used to filter buffer solutions and samples.

HPLC-UV-Vis analysis

HPLC separations were carried out on a Zorbax Eclipes Plus C_{18} column (3.5 μm, 100 mm Length × 2.1 mm I.D.) (California, USA) with phosphate buffer (25 mM, pH 6)-acetonitrile-methanol (30:55:15, v/v) as the mobile phase at a flow rate 0.2 mL/min. The HPLC system consisted of a JASCO PU-980 pump (Hachioji, Japan), a Rheodyne 7725 valve with a 20-μL sample loop (Cotati, USA) for sample introduction and a Shimadzu UV-Visible detector (Tokyo, Japan). Both TCA Analytes were detected at 240 nm and were recorded on a Powerchrom data recording system (eDAQ, Australia).

SPME procedure

The SPME procedure is as describe in previous research [7]. Briefly, water sample (10 mL) was pipetted into a 15 mL sample vial and a magnetic stirrer was placed in the vial. A hypodermic needle was inserted through the Parafilm and pierced through four pieces of Agr-Ch-MWCNT film alternately separated by silicon septum. The films were conditioned by dipping in IPA for 2 minutes followed by 1 minute in deionized water before dipping it in the sample solution for extraction. The sample vial was sealed immediately with Parafilm and extraction was

carried out by stirring the solution at a speed of 600 rpm for 30 minutes. The films were then removed and sonicated with 100 µL of IPA for 5 minutes. A portion of the IPA (2 µL) was then directly injected for HPLC-UV analysis.

Preparation of standard solutions and water samples

Standard solutions of AMIT and CHLO (1000 µg/mL) were prepared separately in HPLC grade methanol. Fresh tap water sample was obtained from Separation Science Laboratory, Department of Chemistry, Universiti Teknologi Malaysia (Johor, Malaysia). The sample was filtered through a Whatman nylon membrane filter 0.45 µm (Gelman Sciences, Ann Arbor, MI, USA) to remove colloidal particles and stored in freezer at 4°C until analysis.

Validation of analytical method

The analytical parameters such as linearity, limit of detection (LOD), limit of quantification (LOQ), accuracy and precision were determined to ensure the result of the analysis is reliable and the procedure is fit for the intended purpose. The linearity of the method was determined by plotting a calibration curve at five different standard concentrations. The precisions of the method were determined by a triplicate reading of each analyte (n = 3) and for the accuracies, the values were obtained in terms of recoveries where the sample was spiked with minute volume of standard solutions. The LOD was determined based on the Signal (S) to Noise (N) ratio method as 3 × S/N in water samples. The method accuracies (expressed as percent relative recovery, RR%) were calculated by comparing the extracted amounts of TCAs from those samples with the corresponding spiking amounts on the calibration curves.

Results and Discussion

Optimization conditions for SPME procedure

Five parameters have been studied and optimized namely, sample pH, addition of salt, extraction time, desorption solvent and concentration of MWCNTs in composite film. Optimization was carried out using deionized water samples spiked with each TCAs to give concentration of 0.5 µg/mL for AMIT and CHLO. Each experiment was performed in triplicate (n = 3).

Addition of salt

The presence of salt in water sample can disrupt the diffusion rate of analytes from aqueous to solid phase and thus affecting the extraction efficiency. The effect of ionic strength on extraction efficiency was evaluated by increasing sodium chloride (NaCl) concentration in the sample solution in the range 0 to 3% (w/v). This range was chosen based on significant effect on extraction of drugs from previous research [7]. It was found that the addition of salt had a slightly negative effect on the extraction efficiency (Figure 1). This phenomenon might be due to the fact that the aqueous solution viscosity increases with the addition of salt, which results in more difficult mass transfer and low extraction efficiency. It could also be due to competition between the analytes and salt in solution to interact with the sorbent surface that resists the extraction efficiency [9, 10]. Thus, no salt was added in subsequent experiments.

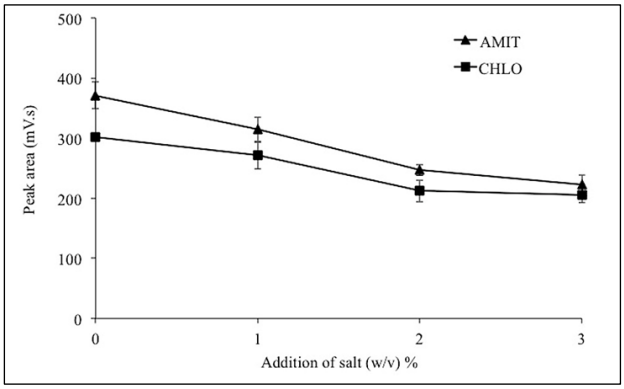


Figure 1. Effect of addition of salt on SPME of TCAs from aqueous samples

Sample pH

Sample pH plays an important role in determining the existing form of the analytes, and it affects the retention of analytes onto the sorbent bed. As the pK_a values of AMIT (9.42) and CHLO (9.30) show the basic characteristics, the pHs of the sample solutions were adjusted to pH 9-12 to reduce their water solubility. The results showed that, the peak areas of both analytes significantly increased with pH up to pH 11 (Figure 2). It may be explained as follows: at the beginning, the analytes were in the ionized form and gradually converted to molecular form with the addition of NaOH to the solution. However, at pH of > 11, further addition of NaOH caused the salting out effects due to simultaneous production of NaCl in the solution thus reducing the extraction efficiency [11]. This proved that at optimum pH, the extraction efficiency was governed by π-π and hydrophobic interactions between the MWCNTs and the analytes [12]. Therefore, the pH of sample solution was adjusted to 11 using 0.1 M NaOH in subsequent experiments in order to achieve the best extraction performance.

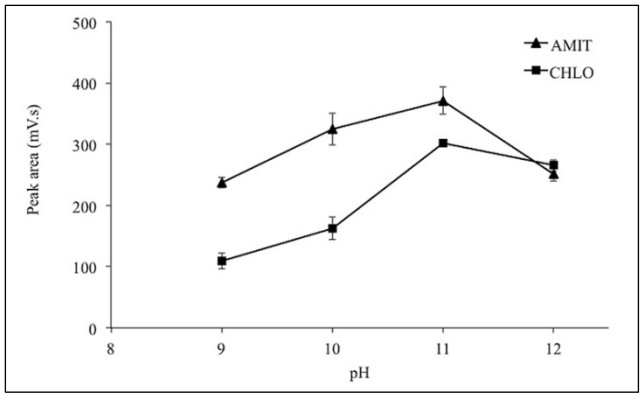


Figure 2. Effect of sample pH on SPME of TCAs from aqueous samples

Extraction time

Extraction times in the range of 10-40 minutes were studied. The result (Figure 3) indicated that the extraction efficiency was enhanced by increasing the extraction time from 10 to 30 minutes, and then a decreased at 40 min which might be due to desorption of analytes [13]. In addition, as SPME is an equilibrium process, 30 minutes is enough for sufficient sorption of analytes from sample solution onto sorbent surface [14]. Thus, 30 minutes was chosen as the optimized extraction time.

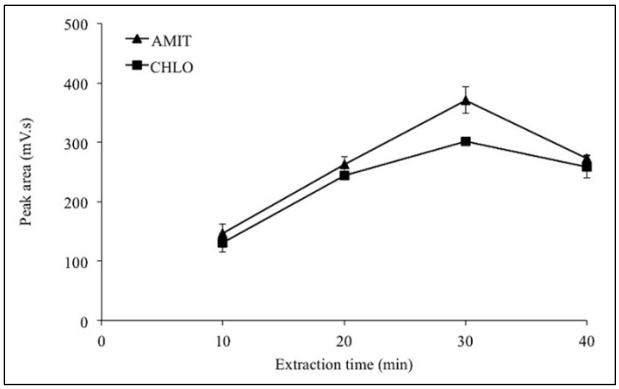


Figure 3. Effect of extraction time on SPME of TCAs from aqueous samples

Desorption solvent

Desorption solvent is one of the important parameters that affect the extraction efficiency in SPME. In this work, three organic solvents that are compatible with LC system namely isopropanol (IPA, polarity index 3.92), methanol (MeOH, polarity index 5.1) and acetonitrile (ACN, polarity index) were evaluated as desorption solvent. The volume of desorption solvent was fixed at 100 µL in all instances. Results showed that non-polar solvent (IPA) gave better desorption as compared to polar solvents (MeOH and ACN) (Figure 4). It proved that the TCAs were strongly sorbed on Agr-Ch-MWCNT film through hydrophobic interactions, thus only non-polar solvent can effectively disrupt the interactions and desorb the analytes [15].

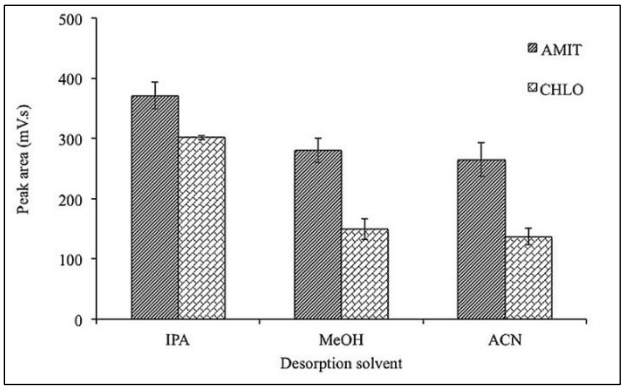


Figure 4. Effect of desorption solvent on SPME of TCAs from aqueous samples

MWCNTs concentration (% w/v) level in the film

To investigate the sorbent capacity in the SPME, different concentration levels of MWCNTs were investigated in the range of 0-0.5% w/v in the Agr-Ch-MWCNT composite film. The results demonstrated that the extraction performance improved considerably with the increasing concentration levels of MWCNTs up to 0.4% w/v. AMIT and CHLO are tricyclic basic molecules and therefore they are expected to be strongly sorbed *via* hydrophobic and π-π interactions with the MWCNTs in composite film as shown in Figure 5 [16].

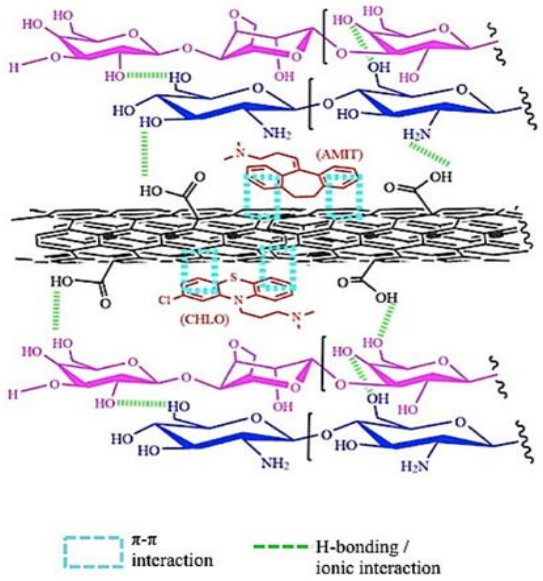


Figure 5. Proposed possible sorbent-sorbate interactions for SPME of TCAs

Method validation and analytical performances

The optimum extraction conditions obtained were as follows: 5 mL iso-propanol as an organic solvent for conditioning composite film, 10 mL of sample solution at pH 11 adjusted using 0.1 M NaCl, no addition of salt, 30 min extraction time at a stirring speed of 600 rpm, 100 µL of iso-propanol as desorption solvent, 5 minutes desorption time with ultrasonication and 0.4% (w/v) MWCNTs loading in composite film. In this study, experiments were carried out under the optimum conditions for the method validation. Matrix-match calibration method was constructed and plotted for laboratory tap water. Matrix-match calibration curves were plotted using water samples at spiked concentration of 10-500 ppb for AMIT and CHLO. The results showed good linearity for all the compounds with coefficients of determination $r^2 > 0.9944$ (Table 1). Extraction performances were measured based on recoveries of inter-day ($n = 3$) of the proposed methods by spiking analytes at two different concentration levels (30 and 400 ppb) into water samples. Good average relative recovery >92.30% and precision with RSDs <6.85% were obtained, indicating that Agr-Ch-MWCNT-SPME method proved high sensitivity, selectivity, and accurate sample preparation technique. Figure 6 illustrates HPLC-UV chromatograms of (i) unspiked and (ii) spiked with TCAs of tap water samples. All peaks in spiked water sample extracts were finely separated with good resolution in <12min. Thus, the overall results suggest that this method could be satisfactorily applied for therapeutic drug analysis and monitoring.

Table 1. Linear range, coefficient of determination (r^2), LOD, average relative recoveries (%), and inter-day method precisions (RSD%, $n = 3$) of the Agr-Ch-MWCNT-SPME-HPLC-UV of spiked tap water samples

Analytes	Linearity Range	r^2	LOD (ppb)	Average RR%, (RSD%) Spiking Level ($n = 3$)	
				30 ppb	400 ppb
AMIT	10-500	0.9944	3.13	92.04 (6.85)	110.00 (4.48)
CHLO	10-500	0.9961	3.60	97.08 (3.85)	102.66 (5.72)

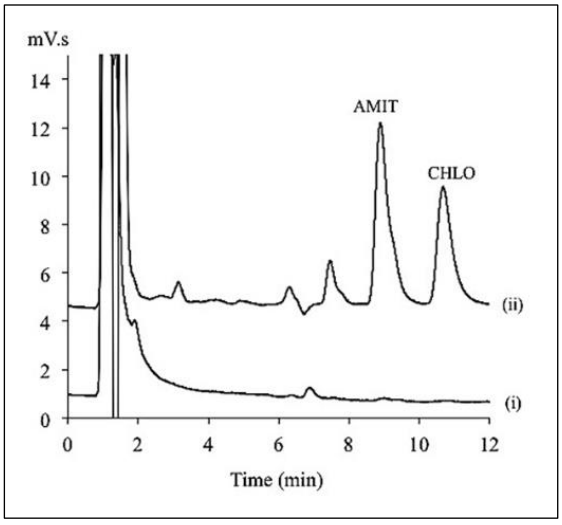


Figure 6. HPLC/UV chromatograms of (i) blank tap water and (ii) spiked tap water at a concentration level of 400 µg/L (AMIT and CHLO) respectively

Comparison with other reported methods

The performance of the proposed Agr-Ch-MWCNT-SPME-HPLC/UV method for the extraction and determination of TCAs was compared with other published methods (Table 2). Conventional SPE procedures with C_2-bond elute cartridges offered high selectivity and high extraction with LODs in the range 0.20-3.00 µg/L. However, it suffered from high amount of sorbent loading (50.0 mg) for each cartridge and involved multi-stage procedures with longer time [17]. The SPME has been successfully applied to the analysis of TCAs by liquid chromatography technique coupling to mass spectrometry. The method utilized PDMS/DVB as sorbent and it offered good detection limit (0.10 µg/L) as well as acceptable extraction efficiencies. However, SPME suffers from sample carry-over and fiber fragility [18]. The SBSE is a sample preparation technique based on the same principles as SPME, i.e. partitioning of the solutes between PDMS/DVB sorbent coated on the stir bar glass surface and the aqueous phase. This technique offers simple, rapid and solvent-free technique but it suffers from a long extraction time (60 minutes) and high limit of detection (40 µg/L) [19].

Meanwhile, membrane assisted micro solid phase extraction (MA-µ-SPE), is a technique where the sorbents are enclosed within a membrane bag that can minimize the loss of sorbent. The MA-µ-SPE with ureidopropyl-grafted silica (UPS) sorbent shows very good detection limit (0.66 µg/L). However, it suffers from long extraction time (60 minutes) probably due to gap between aqueous phases and sorbent that can prolonged the analytes transfer [20]. The Agr-Ch-MWCNT-SPME-HPLC/UV method shows comparable LODs as SPE and SBSE methods but with faster extraction time (30 min). Direct interactions between analytes and sorbent on the composite film increase the mass transfers and allows rapid equilibrium time.

Table 2. Comparison of proposed CFME-HPLC/UV method with other published methods for the analysis of TCAs in water samples

Method	Instruments	Adsorbent	Sorbent Loading (mg)	LOD (µg/L)	Extraction Time (min)	Ref.
SPE	HPLC/UV	C_2-catridges	50.0 mg	0.20-3.00	-	[17]
SPME	HPLC/MS	PDMS/DVB	-	0.10	30	[18]
SBSE	HPLC/UV	Twister-PDMS	-	10.0-40.0	60	[19]
MA-µ-SPE	HPLC/DAD	UPS	20.0 mg	0.66	60	[20]
SPME	HPLC/UV	Agr-Ch-MWCNT	0.6 mg	3.13-4.19	30	This work

SPE = solid phase extraction; SPME = solid phase microextraction; SBSE = stir bar sorptive extraction; MA-µ-SPE = membrane assisted micro-solid phase extraction; C_2 = silica dimethyl; PDMS/DVB = polydimethylsiloxane/divinylbenzene; PDMS = polydimethylsiloxane; UPS = ureidopropyl-grafted silica gel; Agr-Ch-MWCNT = agarose-chitosan incorporated multi-walled carbon nanotubes

Conclusion

The results demonstrate that this method is a simple technique that does not require successive clean up steps. The developed method provided simple procedures utilizing biodegradable polysaccharide materials, no analyte carryover (because of the single-use of the film), and required tiny amounts of organic solvents, thus favorable toward green chemistry. The Agr-Ch-MWCNT-SPME-HPLC-UV method may be used for effective monitoring of pharmaceutical residues in complex aqueous matrix. In addition, the sorbent showed their compatibility in wide range of pH with insignificant of MWCNT leaching during the application.

Acknowledgement

The authors wish to thank the Universiti Teknologi MARA for facilitations and the Ministry of Higher Education Malaysia for their financial support through vote numbers 600-IRMI/FRGS 5/3 (416/2019) [FRGS/1/2019/STG01/UITM/02/16].

References

1. Lindqvist, N., Tuhkanen, T. and Kronberg, L. (2005). Occurrence of acidic pharmaceuticals in raw and treated sewages and in receiving water. *Water Research*, 39: 2219-2228.
2. Tambosi, J. L., Yamanaka, L.Y. and Moreira, H. J. J. R. F. P. M. (2010), Recent data on the removal of pharmaceuticals from sewage treatment plants (STP). *Química Nova*, 33(2): 411-420.
3. Lin, A.Y-C., Yu, T-H. and Lateef, S.K. (2009). Removal of pharmaceuticals in secondary wastewater treatment processes in Taiwan. *Journal of Hazardous Materials*, 167:1163-1169.
4. Vas, G. and Vékey, K .J. (2004). Solid-phase microextraction: A powerful sample preparation tool prior to mass spectrometric analysis. *Mass Spectrometry*, 39: 233-254.
5. Pavlović, D. M., Babić, S., Horvat, A. J. M. and Kaštelan-Macan, M. (2007). Sample preparation in analysis of pharmaceuticals. *Trends in Analytica Chemistry*, 26(11): 1062-1075.
6. Jiménez, J. J. (2013). Simultaneous liquid–liquid extraction and dispersive solid-phase extraction as a sample preparation method to determine acidic contaminants in river water by gas chromatography/mass spectrometry. *Talanta*, 116: 678-687.
7. Wan Ibrahim, W. N., Sanagi, M. M., Hanapi, N. S. M, Kamaruzaman, S., Yahaya, N. and Wan Ibrahim, W. A. (2018). Solid-phase microextraction based on an agarose-chitosan-multiwalled carbon nanotube composite film combined with HPLC–UV for the determination of non-steroidal anti-inflammatory drugs in aqueous samples. *Journal of Separation Science*, 41: 2942-2951,
8. Sutirman, Z. A., Sanagi, M. M., Abd Karim, K. J., Abu Naim, A. and Wan Ibrahim, W. A. (2018). Chitosan-based adsorbent for the removal of metal ions from aqueous solutions. *Malaysian Journal of Analytical Sciences*, 22(5):839-850.
9. Dahane, S., Gil García, M. D., Martínez Bueno, M.J., Uclés Moreno, A., Martínez Galera, M. and Derdour, A. (2013). Determination of drugs in river and wastewaters using solid-phase extraction by packed multi-walled carbon nanotubes and liquid chromatography-quadrapole-linear ion trap-mass spectrometry. *Journal of Chromatography A*, 1297: 17-28.
10. Asgharinezhad, A. A., Mollazadeh, N., Ebrahimzadeh, H., Mirbabaei, F. and Shekari, N. (2014). Magnetic nanoparticles based dispersive micro-solid-phase extraction as a novel technique for coextraction of acidic and basic drugs from biological fluids and waste water. *Journal of Chromatography A*, 1338: 1-8.
11. Hamed Mosavian, M. T., Es'haghi, Z., Razavi, N., and Banihashem, S. (2012). Pre-concentration and determination of amitriptyline residues in wastewater by ionic liquid based immersed droplet microextraction and HPLC. *Journal Pharmaceutical. Analysis*. 2(5): 361-365.
12. Luo, Y-B., Zheng, H-B., Wang, J-X., Gao, Q., Yu, Q-W. and Feng, Y-Q. (2011). An anionic exchange stir rod sorptive extraction based on monolithic material for the extraction of non-steroidal anti-inflammatory drugs in environmental aqueous samples. *Talanta*. 86: 103-108.
13. Asgharinezhad, A. A., Karakami, S., Ebrahimzadeh, H., Shekari, N. and Jalilian, N. (2015). Polypyrrole/magnetic nanoparticles composite as an efficient sorbent for dispersive micro-solid phase extraction of antidepressant drugs from biological fluids. *International Journal of Pharmaceuticals*. 494: 102-112.
14. Sarafraz-Yazdi, A., Amiri, A., Rounaghi, G. and Estiagh-Hosseini, H. (2012). Determination of non-steroidal anti-inflammatory drugs in water samples by solid-phase microextraction based sol-gel technique using poly(ethylene glycol) grafted multi-walled carbon nanotubes coated fiber. *Analytical Chimica Acta*. 720: 134-141.
15. Loh, S. H., Sanagi, M. M., Wan Ibrahim, W. A., and Hassan, M. N. (2013). Multi-walled carbon nanotube-impregnated agarose film microextraction of polycylic aromatic hydrocarbons in green tea beverage. *Talanta*. 105: 200-205.
16. Zare, F., Ghaedi, M. and Daneshfar, A. (2015). Solid phase extraction of antidepressant drugs amitriptyline and nortiptyline from plasma samples using core-shell nanoparticles of the type Fe_3O_4@ZrO_2@N-cetylpryridinium, and their subsequent determination by HPLC with UV Detection. *Microchimica Acta*. 182: 1893-1902.
17. Mercolini, L., Mandrioli, R., Finizio, G., Boncompagni, G. and Raggi, M. A. (2010). Simultaneous HPLC determination of 14 tricyclic antidepressants and metabolites in human plasma. *Journal of Separation Science* 33: 23-30.

18. Alves, C., Santos-Neto, A. J., Fernandes, C., Rodrigues, J. C. and Lancas, F. M. (2007). Analysis of tricyclic antidepressant drugs in plasma by means of solid-phase microextraction-liquid chromatography-mass spectrometry. *Journal of Mass Spectrometry*. 42: 1342-1347.
19. Chaves, A. R., Silva, S. M., Queroz, R. H. C., Lanças, F. M. and Queroz, M. E. C. (2007). Stir bar sorptive extraction and liquid chromatography with UV detection for determination of antidepressants in plasma samples. *Journal of Chromatography B*, 850: 295-302.
20. Lim, T. H., Hu, L., Yang, C., He, C. and Lee, H. K. (2013). Membrane assisted micro-solid phase extraction of pharmaceuticals with amino and urea-grafted silica gel. *Journal of Chromatography A*, 1316: 8-14.

Malaysian Journal of Analytical Sciences (MJAS)
Published by Malaysian Analytical Sciences Society

APPLICATION OF BOX-BEHNKEN DESIGN WITH RESPONSE SURFACE METHODOLOGY FOR OPTIMIZING OXYGEN COLOUR INDICATOR FOR ACTIVE PACKAGING

(Aplikasi Reka Bentuk Box-Behnken dengan Kaedah Gerak Balas Permukaan untuk Mengoptimumkan Penunjuk Oksigen Berwarna bagi Pembungkus Aktif)

Aishah Mohd Marsin[1] and Ida Idayu Muhamad[1,2]*

[1]*Department of Bioprocess & Polymer Engineering, School of Chemical and Energy Engineering, Faculty of Engineering,*
[2]*Biomaterial Cluster, V01, IJN-UTM Cardiovasular Engineering Centre, Faculty of Engineering*
Universiti Teknologi Malaysia, 81310 UTM Johor Bahru, Johor, Malaysia

**Corresponding author: idaidayu@utm.my*

Received: 10 October 2019; Accepted: 7 January 2020

Abstract

The present work develops carrageenan-based oxygen colour indicator strip films using redox dye to improve the mechanical properties and efficiency of the strip in indicating the presence of oxygen. The optimized percentages of carrageenan (0.6-1.0%) as base medium, titanium dioxide (3.2-4.8%) as semiconductor photocatalyst, glycerol (3.6-4.8%) as sacrificial electron donor and methylene blue as redox dye were determined by applying Box-Behnken design and response surface methodology. It aims to achieve optimum film formulation with good mechanical properties and high colour change values after UV-activation compared to original colour. The indicator strip film formed whitish-light blue colour after activated with ultraviolet (UV) light and turned to original blue colour after exposure to oxygen. FTIR result shows higher peak on spectra curve in the range of 500 to 750 cm^{-1} and 2850 to 3750 cm^{-1} proving the disruption of H-bonds between glycerol and carrageenan after the glycerol molecules were oxidized by the photogenerated holes in TiO_2. Depending on the ratio of carrageenan, titanium dioxide and glycerol, the optimum formulation that indicates a protrude colour difference (73.9 ± 2.51) with improved tensile properties (3.39 ± 1.76) has the potential to be used as carrageenan-based oxygen indicator film for active packaging.

Keywords: oxygen colour indicator, redox dye, carrageenan, titanium dioxide, methylene blue

Abstrak

Kerja ini menghasilkan filem jalur penunjuk oksigen berwarna berasaskan karagenan menggunakan pewarna redoks untuk meningkatkan sifat mekanikal dan kecekapan filem jalur dalam menunjukkan perubahan warna dengan kehadiran oksigen. Peratusan optimum karagenan (0.6-1.0%) sebagai medium asas, titanium dioksida (3.2-4.8%) sebagai fotomangkin semikonduktor, gliserol (3.6-4.8%) sebagai penderma elektron karbon dan metilena biru sebagai pewarna redoks ditentukan dengan menggunakan reka bentuk Box-Behnken dan kaedah gerak belas permukaan. Ia bertujuan untuk mencapai perumusan filem optimum dengan ciri-ciri mekanikal yang baik dan nilai perubahan warna yang tinggi selepas UV diaktifkan berbanding warna asal. Penunjuk jalur filem bertukar ke warna putih kebiruan selepas diaktifkan dengan cahaya ultraungu (UV) dan bertukar kepada warna biru pekat asal selepas pendedahan kepada oksigen. Keputusan FTIR menunjukkan lengkung spektrum yang lebih tinggi dalam julat panjang gelombang 500 hingga 750 cm^{-1} dan 2850 hingga 3750 cm^{-1} yang membuktikan gangguan ikatan-H antara gliserol dan karagenan selepas gliserol terdioksida melalui lubang yang dihasilkan selepas pengaktifan UV di dalam TiO_2. Bergantung kepada nisbah karagenan, titanium dioksida dan gliserol, rumusan optimum yang menunjukkan perbezaan warna yang menonjol (73.9 ± 2.51) dengan sifat tegangan yang lebih baik (3.39 ± 1.76) berpotensi untuk digunakan sebagai penunjuk oksigen berwarna berasaskan karrageenan bagi pembungkus aktif.

Kata kunci: penunjuk warna oksigen, pewarna redoks, karagenan, titanium dioksida, metilena biru

Introduction

Oxygen indicator is one of the communications available through food packaging to notify the customer regarding the presence of oxygen in the packaging. Since oxygen indicator is mainly used in modified atmosphere packaging [1-4], it could monitor the integrity of the packaging due to physical impact, improper sealing or even insect inhibition. Various oxygen indicators have been studied in food packaging including redox reaction oxygen sensors [4-9]. The most common redox dye used as indicator is methylene blue which has the ability to turn into white colour in reduced state and blue in the oxidized state [5, 8, 10].

Previous works [6, 7, 9] have develop oxygen indicators using titanium dioxide (TiO_2) as the semiconductor photosensitizer, methylene blue (MB) as the redox dye and glycerol (Gly) as the sacrificial electron donor in a medium through UV-activation method. As stated by Mills and Hazafy [5], the intelligent system starts with electron-hole pairs created after TiO_2 absorbs UV light through activation step which reduces (bleach) the MB. In the presence of oxygen, Gly reacts rapidly towards the photo-generated holes, thus releasing photo-generated electrons to react with MB which turns into original blue colour [11]. Practically, this system could be used when the intelligent ink is casted and dried to develop UV-activated oxygen indicator film. Among various sources of TiO_2, Degussa P25 TiO_2 was chosen as a research standard due to its high photocatalytic activity compare to other TiO_2 [12]. Its small size (< 21 nm) helps to coordinate with other components to change from octahedral to pentahedral structure, which is more reactive [12]. Carrageenan (Carr) is selected as the medium in oxygen indicator film [7, 10, 14] due to its excellent properties to form gel and film. To develop an efficient indicating film with high mechanical strength, an optimization study was conducted to enhance the indication response.

The optimized formulation of oxygen colour indicator could increase the indication efficacy in detecting oxygen presence and clearly notify the observer. The optimized formulation could also identify the mechanical strength of the indicator to suit the conditions in locating and displaying the indicator in a food packaging. Thus far, no report has described the optimized formulation of carrageenan-based oxygen colour indicator to achieve good properties. Thus, this study investigates the optimization of the formulation of oxygen colour indicator consisting of Carr, TiO_2 and Gly with the highest total colour difference i.e. before and after detection of oxygen, with good mechanical properties by using Box-Behnken design. This formulation could be applied efficiently to the production of carrageenan-based oxygen indicator film in future active food packaging.

Materials and Methods

Materials

Carrageenan, Titanium dioxide (P25), Methylene Blue and Glycerol were purchased from R&M Chemicals (UK), Sigma-Aldrich (USA), Merck (Germany) and QRëC (Thailand) respectively.

Carrageenan-based oxygen indicator film preparation

Preliminary tests were performed using one factor at a time (OFAT) to determine the acceptable range of each component based on ideal colour of the film, film formability and recovery action after UV-activation (Table 1). All the materials was tested by reducing each to one third and two third of the initial formulation (Carr: 1.2%; TiO_2: 7.2%; MB: 0.12%; Gly: 7.2%) [10] for determining a lower usage of materials yet giving an efficient results compared to the existing formulation. Methylene blue was kept constant since the result of one third reduction from the initial formulation shows identical properties as the initial conditions. Despite initial formulation that shows ideal blue colour, film formability, and amount recovered after UV-activation, the one third reduction from the initial formulation was selected as the maximum range for Gly and TiO_2 materials in the formulation as it shows nearly identical properties as the initial formulation. Both materials Gly and TiO_2 minimum ranges were selected from a modified two third reduction from the initial formulation to obtain the applicability of indicator film by 3.6% and 3.2%, respectively. One third reduction of Carr was selected as the minimum range while the initial formulation was selected as the maximum range since lower usage of Carr do not exhibit film properties.

Table 1. Result of preliminary test in identifying the range of optimized formulation

Materials Ratio	**Carrageenan**			**Titanium dioxide**			**Glycerol**			**Methylene blue**		
w/v%	**0.3**	**0.6**	**1.2**	**3.2**	**4.8**	**7.2**	**3.6**	**4.8**	**7.2**	**0.04**	**0.08**	**0.12**
Hue *b angle	-17.3	-20.9	-14.5	-20	-15.1	-14.5	-21.2	-17.3	-14.5	-23.5	-19.4	-14.5
Film forming	Pass	Pass	Pass	Pass	Pass	Pass	Pass	Pass	Pass	Fail	Pass	Pass
UV-activation recovery	Fail	Pass	Pass	Pass	Pass	Pass	Pass	Pass	Pass	Fail	Pass	Pass
Selected range	-	Min	Max	Min	Max	-	Min	Max	-	-	Constant	-

The initial formulation and casting method followed the study reported by Deshwal et al. [10]. Meanwhile, the range of optimization formulations and conditions were conducted based on preliminary test to achieve film formability. The optimization formulations of Carr, TiO_2, and Gly were varied accordingly using Box-Behnken Design, as shown in Table 2. Selected percentage of Carr (0.6–1.0 w/v%), TiO_2 (3.2-4.8 w/v%) and Gly (3.6-4.8 w/v%) were mixed with 0.08% methylene blue (0.02 g) in 25 mL of distilled water using a magnetic stirrer (IKA C-Mag Hotplate, USA) at 75 - 80°C for 30 minutes. 10 mL of the solution was sieved before casting on 75-mm diameter glass plate and dried in an oven (Memmert Incubator Oven, Schwabach) at 55°C for 8 hours. The film was peeled and stored in desiccator to achieve equilibrium. Film thickness was measured using micrometre screw gauge (Digimatic Micrometer Mitutoyo IP 65, USA) randomly at five different regions of the film.

UV-activation and Colour Measurement

For comparison test, carrageenan-based indicator strip film was exposed to photo activation using UV-crosslinker (CL-1000 UV-Crosslinker, UK) equipped with 5 tubes of UVB lamp (8W) for 10 minutes [15].

Hunter CIE $*L*a*b$ values were determined using a colorimeter (Konica Minolta CR 10 Tristimulus, Tokyo) in constant light box. A total of 5 different measurements were taken in each test. The total colour difference, TCD (ΔE^*) between the photo-activated film compared to the colour of initial film (L_0*= 12.5, a_0*= + 8.05 and b_0* = -14.5) was calculated using Equation 1.

$$\Delta E* = \sqrt{(Lo* - L*)^2 + (ao* - a*)^2 + (bo* - b*)^2} \quad (1)$$

where in Equation 1, ΔE^* is TCD; L^* is the brightness of the test specimen; a^* is the greenness-redness of the test specimen; and b^* is the blueness-yellowness of the test specimen. Since the blue colour loses its colour during photobleaching and regains the colour during recovery, the blue colour, $-\Delta b^*$ change of the optimum formulation was calculated as Equation 2 [7].

$$-\Delta b^* = b_0^* - b_t^* \quad (2)$$

where b_0* is the initial b* value of film indicator and b_t* is the b* value at a specific time t over 80 min. The difference of the b* value was successfully used as one of the measures towards oxygen indicator film colour.

Mechanical properties

The film tensile strength was measured using Texture Analyzer (CT-3/10,000, Brookfield, USA) equipped with a 10 kg load cell in determination of the ultimate tensile strength (MPa) and elongation percentage (%) of the film. The films were cut into strip sizing dimension of 15 mm wide × 65 mm gauge length, based on the ASTM standard method D882-02 (ASTM D882, 2002). The grip separation was set at 30 mm, with 0.20 mm/s crosshead speed [16] and trigger load 0.05 N using a TA-DGA probe. Triplicate measurements were accomplished for each run test.

FTIR analysis

FTIR analysis was carried out to compare the chemical composition of the original film indicator and the UV-activated film. The chemical characterization was determined using Fourier transform infra-red (FTIR) (Perkin-Elmer Spectrum One FT-IR Spectrometer, USA) with a resolution of 4 cm^{-1} in the range of 400 – 4000 cm^{-1} and averaged over 30 scans. The film was cut to 20 × 20 mm sizing and dried overnight in an oven at 40 °C. The film was mounted directly in the sample holder for analysis.

Experimental design and statistical analysis

The response surface methodology was used to study the effect of three factors namely Carr, TiO_2 and Gly on the total colour difference and mechanical properties. An analysis of variance (ANOVA) and multiple comparison test were determined using Design Expert 6.0.4. The means that were statistically different from each other were compared using Tukey's comparison tests at 5% confidence level ($p < 0.05$) using IBM SPSS (version 21.0) software. The data were fitted to a second order equation (Equation 3) as a function of the independent variables.

$$Y = \beta_0 + \sum_{i=0}^{4} \beta_i X_i + \sum_{i=0}^{4} \beta_{ii} X_i^{\,2} + \sum_{i=0}^{4} \beta_{ij} X_i X_j \quad (3)$$

where β is constant regression coefficient, Y is response (TCD, elongation at break, tensile strength) and X is the coded process variables (factors).

Optimization of the process conditions and experimental validation

The optimization of the formulation was accomplished based on desirability generated by Design Expert 6.0.4 software. Desirability was gauged based on the objective with 1 is the closest to the objective set in the beginning and 0 being the most non desired results. Lastly, the carrageenan-based oxygen indicator films were prepared using the optimum formulation to validate the result in triplicate. The resulting films were characterized with respect to their total colour difference and mechanical properties.

Results and Discussion

Full experimental design

The results of Box-Behnken design are summarized in Table 2. Data regarding the dependent variables (total colour difference, elongation at break, tensile strength) were fitted to a second-order equation (Equation 2) as a function of the independent variables. The statistical analysis of these data was performed at 95% (p <0.05) confidence level and the regression coefficients of the generated data second-order models are listed in Table 3. High precision (R^2 close to 1) showed by all the models signifies that the variability in the data was explained by the model. Ratio of adequate precision which compares the range of the predicted values at the design points to the average prediction error is greater than 4 hence, proving that the model is in adequate discrimination.

Table 2. Box-Behnken design matrix with values of the factors and responses to colour difference, elongation at break and tensile strength

		Independent variables			Response		
Run	**Type**	**X1: Carrageenan (%)**	**X2: Titanium dioxide (%)**	**X3: Glycerol (%)**	**Y1: Colour Difference[a]**	**Y2: Elongation at Break (%)**	**Y3: Tensile Strength (MPa)**
1	Centre	3.6	0.8	4.2	66.61	16.51	1.33
2	IBFact	3.6	0.6	4.8	36.14	12.48	1.75
3	IBFact	3.2	0.8	3.6	66.14	10.26	1.73
4	IBFact	4	0.8	4.8	68.08	12.91	3.08
5	IBFact	3.2	0.6	4.2	51.66	10.23	1.43
6	IBFact	3.6	1	3.6	82.43	19.11	1.47
7	Centre	3.6	0.8	4.2	68.64	13.72	1.77
8	IBFact	4	0.6	4.2	59.44	11.23	2.49

Table 2 (cont'd). Box-Behnken design matrix with values of the factors and responses to colour difference, elongation at break and tensile strength

Run	Type	Independent variables			Response		
		X1: Carrageenan (%)	X2: Titanium dioxide (%)	X3: Glycerol (%)	Y1: Colour Difference[a]	Y2: Elongation at Break (%)	Y3: Tensile Strength (MPa)
9	IBFact	3.6	1	4.8	81.77	22.38	2.05
10	Centre	3.6	0.8	4.2	65.27	14.77	1.85
11	IBFact	4	0.8	3.6	71.14	12.26	2.87
12	Centre	3.6	0.8	4.2	64.09	12.72	1.67
13	IBFact	4	1	4.2	70.44	18.33	2.75
14	IBFact	3.2	0.8	4.8	61.41	16.91	1.33
15	IBFact	4	1	4.2	78.70	16.00	2.62
16	IBFact	3.6	0.6	3.6	35.69	7.88	1.35

[a] colour difference between initial colour and UV-activated film at minute 0

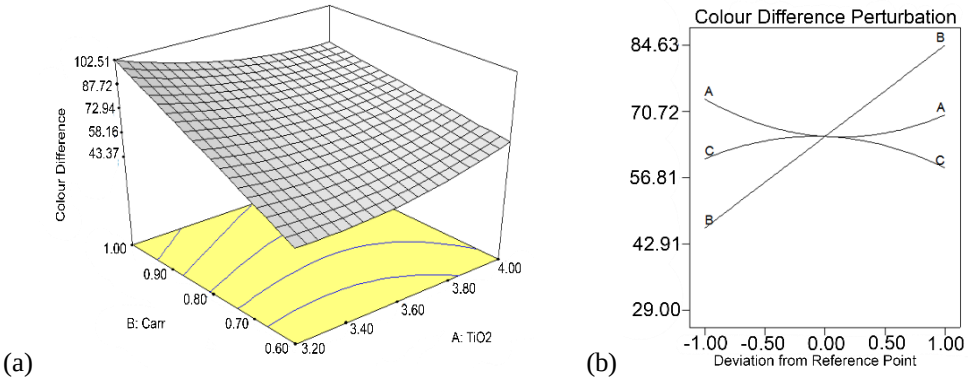
Table 3. Regression coefficients and analysis of variance for responses variables

Coefficients		Y1: Colour Difference		Y2: Elongation at Break (%)		Y3: Tensile Strength (MPa)	
Model		2452.29	(df:7)	202.68	(df:9)	4.92	(df:9)
Residual		303.77	(df:8)	12.60	(df:6)	0.37	(df:6)
Lack of fit (P)[a]		0.06	(df:4)	0.70	(df:2)	0.18	(df:2)
Pure error		45.59	(df:4)	10.58	(df:4)	0.16	(df:4)
Total		2756.06	(df:15)	215.28	(df:15)	5.34	(df:15)
Model P-value		0.0028		0.0046		0.0077	
Model F-value		9.23		10.72		8.82	
Critical F-value[b]		6.09		6.00		6.00	
R^2		0.89		0.94		0.93	
Adj R-squared		0.79		0.85		0.82	
Adeq Precision		9.25		11.88		9.39	
Regression coefficient							
	β	-137.55		-242.42		49.75	
	β_1	-181.77		76.32		-21.94	
Linear	β_2	560.92		50.75		1.25	
	β_3	-132.45		41.27		-5.97	
	β_{11}	38.66		-4.83		2.80	
Quadratic	β_{22}			40.12		-3.70	
	β_{33}	-15.69		-1.60		0.42	
	β_{12}	-125.81		-21.90		0.93	
Interactions	β_{13}			-6.25		0.64	
	β_{23}	-2.87		-2.76		0.37	

[a] (P) stands for P value lack of fit
[b] Tabulated for Fisher test using the significance level and degrees of freedom

Colour difference

All UV-activated films showed significantly different value of TCD compared to the initial colour film with high R^2 (0.85) that indicates significant model. The highest factors which influenced the TCD of the film was β_2 followed by β_{12}, β_1^2 and β_3^2 as shown by the 3D response surface graphs and trace plots in Figure 1(a) and Figure 1(b), respectively. Carr commonly forms into transparent and clear film through independent usage. However, higher Carr content could cause greater effect in bleaching process (high colour difference) due to the presence of larger medium of interactions between MB and TiO_2 towards UV crosslinking. Addition of carrageenan affected the colour properties of film based on a study by Pranoto et al. [17] with increasing Carr that darken the film. Factors β_{12} and β_1^2 have been eliminated in the total colour difference regression coefficient to improve the model by reducing the insignificant terms.

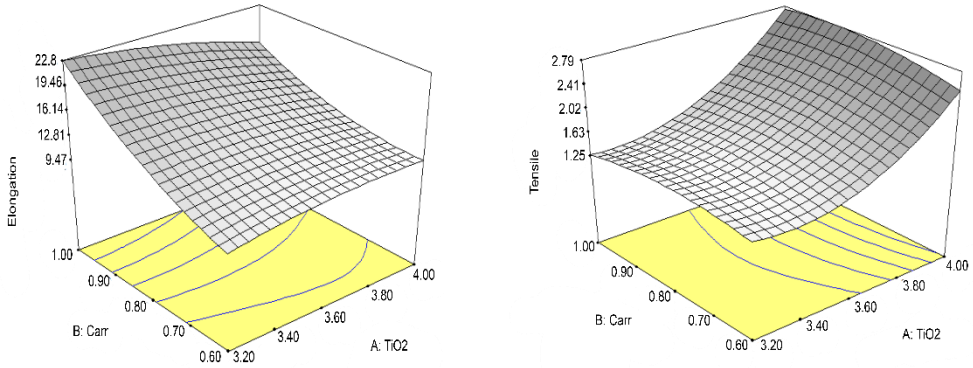


(a) (b)

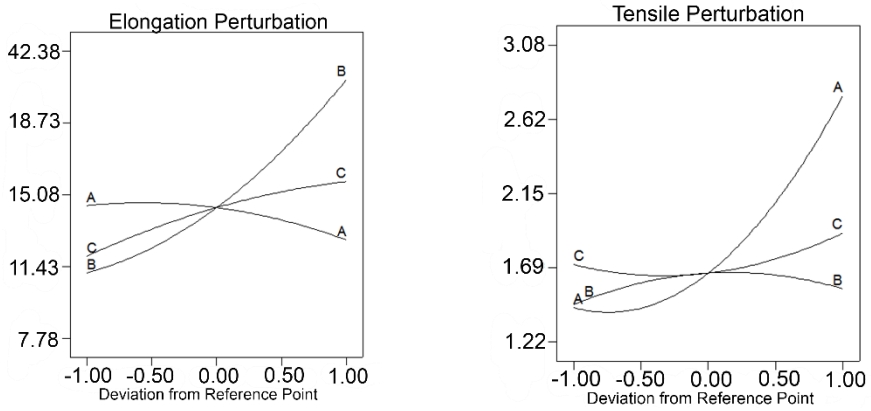
Figure 1. (a) 3D response surfaces for TCD that represent percentages of A: titanium dioxide and B: carrageenan at constant percentage of glycerol of 4.2%.and (b) trace plots showing the effects of each mixture component on TCD (A= TiO_2, B=Carr, C=Gly).

Mechanical properties

Mechanical properties of the strip film (oxygen indicator) involve tensile strength and elongation at break as shown in Figure 2. All the linear and quadratic parameters of both responses were statistically significant (p <0.05) and were considered in the second-order model (Table 3). High R^2 in elongation at break (94.15%) and tensile strength (92.97%) responses show that these data could be explained by the model.



(a) (b)



(c) (d)

Figure 2. 3D Response surfaces for (a) elongation at break and (b) tensile strength that represent percentage of A: titanium dioxide and B: carrageenan at constant percentage of glycerol of 4.2% and trace plots showing the effects of each mixture component on (c) elongation at break and (d) tensile strength (A= TiO_2, B=Carr, C=Gly).

Two studies on mechanical properties on carrageenan-based film incorporated with TiO_2 obtained elongation at break of 22 to 31% [18] and 19.5± 0.4% [19]. Therefore, this study (7% to 19% elongation at break) is in line with the previous report. Based on Figure 2 (c), the highest factor was shown by β_2 followed by β_3. Carr was previously studied as the main factor in influencing the flexibility and mechanical properties of film [1]. The current result is in agreement with a report by Abdou and Sorour [20] which mentioned the carrageenan consists of hygroscopic properties, hence water uptake could explain the plasticization behaviour (increase elongation at break) with higher carrageenan. TiO_2 factor also influencing the elongation at break due to its nanoparticle size that helps to fill in the smaller spaces in the medium, hence reduces the elongation percentage of the film as the film becomes more rigid. The presence of Gly also increases the flexibility by reducing the intermolecular force thus enhances the intermolecular mobility in the medium [17].

The tensile strength results (between 1.0 to 3.5 MPa) correlate with the study by Mohd Marsin and Muhamad [13] and Deshwal et al. [10] who formed a carrageenan-based film using casting method. However, in this study, the tensile strength of the film was mostly influenced by TiO_2 factors (β_1) and interactions between TiO_2 (β_1^2) as shown in Figure 2 (d). The presence of nanoparticle component increased the tensile strength of the film by forming a more compact structure. Higher tensile film helps to resist physical impact. The result was in line with Oun and Rhim [21] who reported that the presence of nanoparticle causes electrostatic interactions between the positive charges of nanoparticle and carrageenan biopolymer which increases biopolymer helical aggregation and forms a stronger film.

Optimization of formulation and experimental validation

Design expert 6.0.4 software generated the optimum formulation based on the desired properties, namely highest TCD of the initial film compared to UV-activated film, intermediate elongation at break, and high tensile strength. The optimum formulation consisting of 4.00% of TiO_2, 0.95% of Carr and 4.71% of Gly yielded highest TCD value of 75.17, 17.02% elongation and tensile strength of 3.08 MPa. The formulation was experimentally validated, and the results are presented in Table 4. Based on the percentage difference values achieved for each response variable, it can be deduced that the formulation employed for the optimization was satisfactory, and that the surface responses obtained by the full experimental design were suitably validated. Figure 3 shows the obviously colour-distinguishable resulted film using the optimum formulation (i) original and (ii) after UV-activation.

Table 4. Results of experimental validation of the optimal conditions for the development of carrageenan-based oxygen indicator strip film

Responses	Predicted value	Experimental value[a]	Difference (%)[b]
Total colour difference	74.32	73.9 ± 2.51	-3.02
Elongation (%)	17.20	17.40 ± 0.84	+1.15
Tensile strength (MPa)	3.08	3.39 ± 1.76	+9.14

[a] Values obtained at optimum formulation 4% of TiO_2, 1% of Carr and 4.69% of glycerol
[b] Percentage difference = [(experimental value-predicted value)/experimental value]

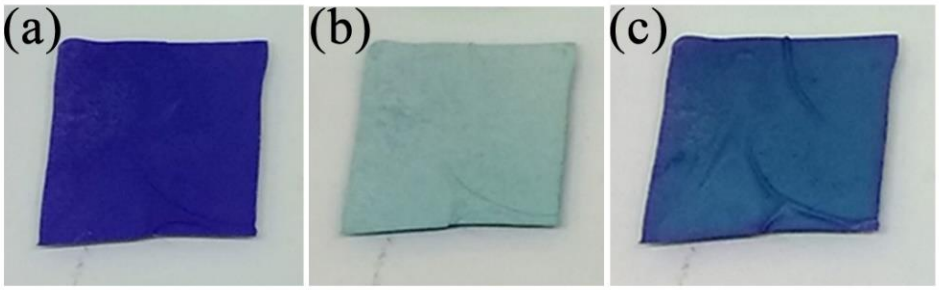


Figure 3. Photographs of carrageenan-based oxygen indicator films before (original) (a) and (b) after UV-activation at 55W for 10 minutes, and (c) recovery film after 80 minutes.

Figure 4 shows recovery behavior of carrageenan-based oxygen indicator strip film in air under ambient conditions in which -Δ*b** was plotted against recovery time. The carrageenan-based oxygen indicator strip film was recovered within 45 minutes. The bleached MB in the film was reoxidized by oxygen, and the original blue color of the indicator strip film was restored. This recovery is time is close to those reported recovery times of 20 minutes [22] and 60 minutes [10] and much faster than previously reported recovery rate of 5 days [23].

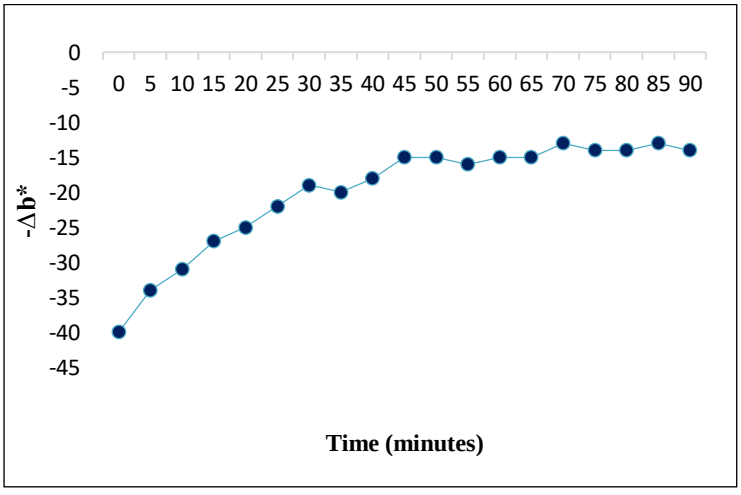


Figure 4. Recovery behavior of carrageenan-based oxygen indicator strip film in air under ambient conditions with a sampling time of 5 minutes.

FTIR analysis of optimum formulation

FTIR spectroscopy is a rapid technique with minimum sample preparation requirements that allows qualitative and quantitative determination of organic compounds in samples as intensities of spectrum bands are proportional to concentration [24]. Control original and UV-activated films were analyzed by FTIR spectroscopy to determine the difference in polymeric structure after UV crosslinking occurred in the indicator film. FTIR spectra for control original and UV-activated film ranging between 4000 and 400 cm^{-1} are shown in Figure 5. The control original and UV-activated curves were overlapped each other with differences in certain regions. The samples showed difference in absorbance spectra in the range of 500 to 750 cm^{-1} and 2850 to 3750 cm^{-1}. The result were in agreement with the study reported by Deshwal et al. [10] where the difference in spectra curve occurred between 3000 to 3600 cm^{-1}. An increased absorbance was observed at 992.47 cm^{-1} after UV-activation, which can be attributed to the stretching of carbonyl band (C=O) for aldehydes. In this case, glycerol which acted as the sacrificial electron donor was oxidized during UV irradiation to form glyceraldehyde, confirming the carbonyl stretching band [25]. The C-O-C vibration band in the film shifts from 3300.20 to 3344.57 cm^{-1} and from 555.50 to 563.23 cm^{-1} after UV activation could be due to the disruption of H bonds between glycerol and carrageenan as the glycerol molecules were oxidized by the photogenerated holes in TiO_2 [25]. The presence of titanium dioxide in nanocrystalline form also influenced the changes in spectra curves as penta-coordinated sites in TiO_2 interact with Carr resulting in decreased UV transmission, indicating high UV absorption ability of TiO_2 [26].

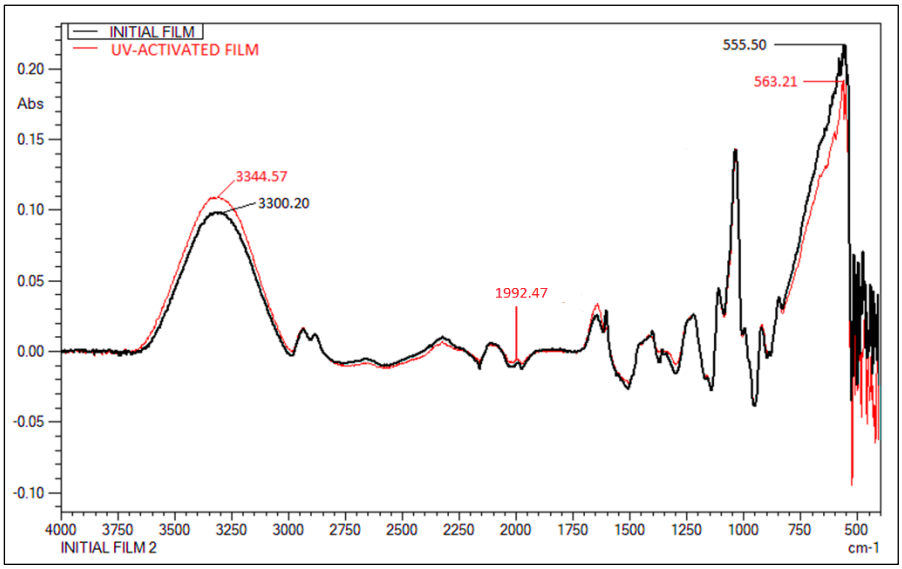


Figure 5. FTIR absorbance spectra of carrageenan-based oxygen indicator strip films; initial original film (bold black line) and UV-activated film (thin red line)

Conclusion

The optimal formulation for the development of carrageenan-based oxygen indicator strip film with enhanced colour difference and good mechanical properties was 4.00% (w/v) of titanium dioxide, 0.95% (w/v) of carrageenan and 4.71% (w/v) of glycerol. The film developed in this work show a significant colour difference between original and UV-activated film. The film could return to its original colour after exposure to oxygen and successfully work as an oxygen indicator. Good mechanical properties of high tensile strength and intermediate elongation at breaks enable the film to withstand physical impact and to be applied in active food packaging film. The data could be used for future reference in performing optimum oxygen indicator using the components proposed. This carrageenan-based oxygen indicator strip film could be used as biodegradable, safe and contemporary indicator in food packaging for future prospect.

Acknowledgment

This research was financially supported by the Project no. RJ130000.7851.4L868 of Research Management Centre, Universiti Teknologi Malaysia (UTM).

References

1. Mills, A. (2005). Oxygen indicators and intelligent inks for packaging food. *Chemical Society Reviews*, 34(12): 1003-1011.
2. Biji, K. B., Ravishanka, C. N. and Mohan, C. O. (2015). Smart packaging systems for food applications: a review. *Journal Food Science Technology*, 52(10):6125-6135.
3. Kelly, C., Yusufu, D., Okkelman, I., Banerjee, S., Kerry, J. P., Mills, A. and Papkovsky, D. B. (2020). Extruded phophorescence based oxygen sensors for large-scale packaging applications. *Sensors & Actuators: B. Chemicals*, 304:1-8.
4. Wen, J., Huang, S., Sun, Y., Chen, Z., Wang, Y., Li, H. and Liu, X. (2018). Titanium dioxide nanotube-based oxygen indicator for modified atmosphere packaging: efficiency and accuracy. *Materials*, 11(12): 1–10.
5. Mills, A. and Hazafy, D. (2009). Nanocrystalline SnO_2-based, UVB-activated, colourimetric oxygen indicator. *Sensors and Actuators, B: Chemical*, 136(2): 344-349.
6. Mills, A., Hazafy, D. and Lawrie, K. (2011). Novel photocatalyst-based colourimetric indicator for oxygen. *Catalysis Today*, 161(1): 59-63.
7. Vu, C. H. T. and Won, K. (2013). Novel water-resistant UV-activated oxygen indicator for intelligent food packaging. *Food Chemistry*, 140 (1-2): 52-56.
8. Lee, S. K., Mills, A. and Lepre, A. (2004). An intelligence ink for oxygen. *Chemical Communications*, 10(17): 1912-1913.
9. Lee, S. K., Sheridan, M. and Mills, A. (2005). Novel UV-activated colorimetric oxygen indicator. *Chemical Materials*, 17(10): 2744-2751.
10. Deshwal, G. K., Panjagari, N. R., Badola, R., Singh, A. K., Minz, P. S., Ganguly, S. and Alam, T. (2018). Characterization of biopolymer-based UV-activated intelligent oxygen indicator for food-packaging applications. *Journal of Packaging Technology and Research*, 2(1): 29-43.
11. Roberts, L., Lines, R., Reddy, S. and Hay, J. (2011). Investigation of polyviologens as oxygen indicators in food packaging. *Sensors and Actuators, B: Chemical*, 152(1): 63-67.
12. Bessergenev, V. G., Mateus, M. C., Rego, A. M. B., Hantusch, M. and Burkel, E. (2015). An improvement of photochatalytic activity of TiO_2 Degussa P25 powder. *Applied Catalysis A: General*, 500: 40-50.
13. Mohd Marsin, A. and Muhamad, I. I. (2016). Effects of kappa carrageenan and glycerol in purple sweet potato starch based edible film. *Jurnal Teknologi*, 78(6): 163-168.
14. Liu, J., Wang, H., Wang, P., Guo, M., Jiang, S., Li, X. and Jiang, S. (2018). Films based on K-carrageenan incorporated with curcumin for freshness monitoring. *Food Hydrocolloids*, 83: 134-142.
15. Vu, C. H. T. and Won, K. (2014). Leaching-resistant carrageenan-based colorimetric oxygen indicator films for intelligent food packaging. *Journal of Agricultural and Food Chemistry*, 62: 7263-7267.
16. Avachat, A. M., Gujar, K. N. and Wagh, K. V. (2013). Development and evaluation of tamarind seed xyloglucan-based mucoadhesive buccal films of rizatriptan benzoate. *Carbohydrate Polymers*, 91(2): 537-542.
17. Pranoto, Y., Lee, C. M. and Park, H. J. (2007). Characterizations of fish gelatin films added with gellan and k-carrageenan. *LWT - Food Science and Technology*, 40:766-774.
18. Rukmanikrishnan, B., Soo K., S., Lee, J. and Lee, J. (2019). Effect of TiO_2 on highly elastic, stretchable UV protective nanocomposite films formed by using a combination of k-Carrageenan, xanthan gum and gellan gum. *International Journal of Biological Macromolecules*, 123: 1020-1027.
19. Rhim, J. W. (2012). Physical-mechanical properties of agar/k-carrageenan blend film and derived clay nanocomposite film. *Journal of Food Science*, 77(12): 66-73.
20. Abdou, E. S. and Sorour, M. A. (2014). Preparation and characterization of starch/carrageenan edible films. *International Food Research Journal*, 21(1): 189-193.
21. Oun, A. A. and Rhim, J. W. (2017). Carrageenan-based hydrogels and films: Effect of ZnO and CuO nanoparticles on the physical, mechanical, and antimicrobial properties. *Food Hydrocolloids*, 67: 45-53.
22. Son, E. J., Lee, J. S., Lee, M., Vu, C. H. T., Lee, H., Won, K. and Park, C. B. (2015). Self-adhesive graphene oxide-wrapped TiO_2 nanoparticles for UV-activated colorimetric oxygen detection. *Sensors and Actuators, B: Chemical*, 213: 322-328.

23. Mills, A., Tommons, C., Bailey, R. T., Catriona Tedford, M. and Crilly, P. J. (2008). UV-activated luminescence/colourimetric O_2 indicator. *International Journal of Photoenergy*, 547301: 1-6.
24. Vlachos, N., Skopelitis, Y., Psaroudaki, M., Konstantinidou, V., Chatzilazarou, A. and Tegou, E. (2006). Applications of Fourier transform-infrared spectroscopy to edible oils. *Analytica Chimica Acta*, 573 (574): 459-465.
25. Mihindukularuriya, S. D. F. (2013). Oxygen detection using UV-activated electrospun poly(ethylene oxide) fibers encapsulated with TiO_2 nanoparticles. *Journal of Materials Science*, 48: 5489-5498.
26. Mihailović, D., Šaponjić, Z., Radoičić, M., Radetić, T., Jovančić, P., Nedeljković, J. and Radetić, M. (2010). Functionalization of polyester fabrics with alginates and TiO_2 nanoparticles. *Carbohydrate Polymers*, 79(3): 526-532.

Malaysian Journal of Analytical Sciences (MJAS)
Published by Malaysian Analytical Sciences Society

APPLICATION OF MICROWAVE-ASSISTED EXTRACTION COUPLED WITH DISPERSIVE LIQUID-LIQUID MICROEXTRACTION FOR THE DETERMINATION OF POLYCYCLIC AROMATIC HYDROCARBONS IN VEGETABLES

(Aplikasi Pengekstrakan Berbantukan Mikrogelombang Gandingan dengan Pengekstrakan Mikro Cecair-Cecair Serakan bagi Penentukan Hidrokarbon Aromatik Polisiklik dalam Sayur-Sayuran)

Chai Mee Kin[1]*, Tan Yeong Hwang[1], Wong Ling Shing[2]

[1]*College of Engineering,*
Universiti Tenaga Nasional, Jalan Ikram-Uniten, 43000 Kajang, Selangor, Malaysia
[2]*Faculty of Health and Life Science,*
INTI International University, Persiaran Perdana BBN, Putra Nilai, 71800 Nilai, Negeri Sembilan, Malaysia

**Corresponding author: mkchai@uniten.edu.my*

Received: 20 November 2019; Accepted: 21 January 2020

Abstract

Microwave-assisted extraction (MAE) coupled with dispersive liquid-liquid microextraction (DLLME) followed by gas-chromatography flame ionization detector (GC-FID) for the determination of 13 PAHs in vegetable samples was developed in this study. The analytical performances of the optimized DLLME and MAE-DLLME including limit of detection (LOD), limit of quantification (LOQ), precision, accuracy, relative extraction recovery and relative extraction factor were validated and compared. The LOD of DLLME and MAE-DLLME were in the range of 0.040-0.400 and 0.0200-0.080 µg/L, respectively. For DLLME, precision and accuracy were 1.22-7.50% (RSD) and 71.77% to 90.93%, respectively; while for MAE-DLLME, were 0.77%-3.07% (RSD) and 83.65-98.42%, respectively. The relative extraction recovery was improved from 70.81% – 85.41% in DLLME to 85.79% - 99.61% in MAE-DLLME. The relative enrichment factors were ranged from 126-156 and 165 to 202 for DLLME and MAE-DLLME, respectively. The volume of extraction solvent was reduced from 50 µL to 30 µL in MAE-DLLME. The overall analytical performances of MAE-DLLME is better than DLLME. The application of proposed MAE-DLLME in real samples was also investigated and discussed.

Keywords: dispersive liquid-liquid microextraction, microwave-assisted extraction, polycyclic aromatic hydrocarbons, extraction solvent

Abstrak

Pengekstrakan berbantukan mikrogelombang (MAE) gandingan dengan pengekstrakan mikro cecair-cecair serakan (DLLME) yang diikuti dengan gas kromatografi-pengesan nyalaan ion (GC-FID) bagi penentukan 13 jenis hidrokarbon aromatik polisiklik (PAHs) dalam sampel sayur-sayuran telah dibangunkan dalam kajian ini. Analisis prestasi optimum DLLME dan MAE-DLLME seperti had pengesanan (LODs), kepersisan, kejituan, perolehan semula pengekstrakan secara relatif dan faktor-faktor pengayaan secara relatif telah disahkan dan dibandingkan. Had pengesanan (LODs) bagi DLLME dan MAE-DLLME adalah dalam lingkungan 0.040-0.400 dan 0.0200-0.080 µg/L, masing-masing. Bagi DLLME, kepersisan dan kejituan adalah dalam lingkungan 1.22-7.50% dan 71.77-90.93%, masing-masing; manakala bagi MAE-DLLME, adalah dalam lingkungan 0.77-3.07% dan 83.65-98.42%, masing-masing. Perolehan semula pengekstrakan secara relatif telah ditingkatkan daripada 70.81-85.41% pada DLLME hingga 85.79 - 99.61% pada MAE-DLLME. Faktor-faktor pengayaan secara relatif adalah 126-156 dan 165-202 bagi DLLME dan MAE-DLLME, masing-masing. Jumlah pengekstrakan pelarut yang digunakan telah dikurangkan daripada

50 µL di DLLME kepada 30 µL di MAE-DLLME. Prestasi keseluruhan analisis MAE-DLLME adalah lebih baik daripada DLLME. Penggunaan MAE-DLLME dalam analisis sampel sebenar juga disiasat dan dibincangkan.

Kata kunci: pengekstrakan mikro cecair-cecair serakan, pengekstrakan berbantukan mikrogelombang, hidrokarbon aromatik polisiklik, pelarut pengekstrakan.

Introduction

Vegetables and fruits are essential elements of a healthy daily diet. They provide a large amount of vitamins, fibres and minerals. However, the occurrence of polycyclic aromatic hydrocarbons (PAHs) exposure on vegetables has been reported [1-3]. The contamination of PAHs on vegetables are primarily from human activities. Previous studies reported that the vegetables that grew in vicinity of contaminated sources were contaminated with high levels of PAHs sufficient to threaten human health [1, 2]. PAHs are a group of hydrocarbons with fused aromatic rings that form during the incomplete combustion of organic compounds. Numerous studies have confirmed their carcinogenicity. Therefore, PAHs have been declared as carcinogens and genotoxins by Scientific Committee on Food (SCF) [4] and the Joint FAO/WHO Expert Committee on Food Additives (JECFA) [5]. Since vegetables are an important part of human daily diets, it is necessary to ensure that vegetables are not exposed to high levels of PAHs.

Most analytical instruments are unable to handle analytes directly in food sample with complex matrices and usually trace levels of PAHs are found in food samples [6]. Therefore, before chromatographic analysis, well- designed sample preparation is necessary for the extraction and preconcentration of analytes from the food sample. There are several sample preparation methods available for extraction of PAHs from vegetable samples. Dispersive liquid-liquid microextraction (DLLME) is one of the successful sample preparation techniques developed by Rezaee et al. [7]. The DLLME technique showed several advantages such as miniaturized solvent consumption, simplicity, rapidity and high extraction efficiency [8]. However, DLLME has several drawbacks. Chlorinated solvents which are highly toxic usually chosen as extraction solvents due to their high efficiency [9]. Previous studies have employed DLLME for extraction of PAHs from vegetables and the presence of matrix interference was reported [9]. Even though dilution was used to reduce the effect of matrix interference, matrix components were still present and mixed with extraction solvent. This caused difficulty in transferring the clean extraction phase for chromatographic analysis and a high volume of extraction solvent was required to reduce this problem. In order to overcome the matrix interference of DLLME, it is imperative to introduce a clean-up step before chromatographic analysis of PAHs.

Recently, microwave-assisted extraction (MAE) has been developed for food samples preparation. MAE helps to isolate the organic analytes from food matrices. MAE gained noticeable attraction due to its extraction time minimization, low volumes of organic solvents consumption and increased extraction recovery [10]. MAE has been successfully used in previous studies to clean up food samples [11-13]. In the previous study [14], two extraction methods, which are DLLME and MAE coupled with DLLME (MAE-DLLME), have been used for the determination of 13 PAHs in vegetables followed by gas-chromatography-flame ionization detector (GC-FID). Various parameters such as extraction solvent, dispersion solvent, extraction time, microwave power and the irradiation time of MAE-DLLME have been studied and optimized. To overcome the limitations of using toxic chlorinated solvents as extraction solvents in conventional DLLME, the study selected low toxic brominated and alcohol solvents for extraction. The main objective of this study was to validate and compare analytical performances of DLLME and MAE-DLLME. The efficiency of both methods for extraction of 13 PAHs in different vegetable samples was also investigated.

Materials and Methods

Reagents and materials

Standard formulations of 13 PAHs (EPA 525 PAH Mix B, 500 µg/ml in acetone), containing acenaphthylene (ACY), phenanthrene (PHE), fluorine (FLU), anthracene (ANT), benzo[a]anthracene (BaA), pyrene (PYR), benzo[a]pyrene (BaP), chrysene (CHR), benzo[b]fluoranthene (BbF), benzo[k]fluoranthene (BkF), benzo[ghi]perylene (BghiP), dibenz[a,h]anthracene (DahA), indeno[1,2,3-cd]pyrene (IcP) and biphenyl solution (2000 µg/ml in methanol) were purchased from Sigma-Aldrich (USA). Acetone, hexane and acetonitrile were

purchased from Fisher Scientific (Loughborough, UK). Highest purity bromobenzene, 1-bromo-3-methylbutane, 1-bromobutane, 2-ethyl-1-hexanol, 2-heptanol, 2-bromo-2-methylbutane and 2-octanol were purchased from Merck (Darmstadt, Germany). All the reagents used were HPLC grade or analytical reagent grade.

Mixed working solutions (10 mg/L) of 13 PAHs and biphenyl as internal standard were prepared in acetone and methanol, respectively. Stock solutions were stored at 4°C in a refrigerator prior to use. Diluted solution was prepared daily for further studies.

Instrumentations

The mixture of PAHs was separated and identified using a gas chromatograph (GC, Agilent 7890A) with a split/splitless injector system, Agilent 7683B automatic liquid sampler and a flame ionization detector (FID). The SLB-5ms capillary column (30 m×0.25 mm ID, 0.25 µm film thickness) was used for PAHs separation. The carrier gas was high purity helium gas (99.9995%, Air products, UK), with a flow rate of 1.67 mL/min. It was passed through an Agilent Big Universal Trap-Helium purge (model RMSN-2) to remove water, oxygen and hydrocarbons. The injection port was kept at 290 °C and splitless mode was used. The PAHs separation was conducted with the following programmed temperatures: initial 70 °C held for 1 minute, 20 °C/min to 120 °C held for 1 minute; 120 to 258 at 10 °C/min held for 1 minute; 258 °C to 262 °C at 1 °C/min held for 2 minutes; and 262 °C to 280 °C at 5 °C/min and held for 5.1 minutes. The total time for one GC run was 36 minutes. The FID temperature was maintained at 300 °C, hydrogen gas (Air products, UK) and nitrogen gas (makeup flow) (Air products, UK) were regulated at a flow of 35 mL/min. The air flow (Air products, UK) for FID was at 350 mL/min. Agilent Chemstation (B.04.02 version) was used as an instrumental controller and for data analysis.

Sample preparation

The vegetable samples (cabbage) were purchased from a local hypermarket and washed with running tap water. The mass of 25 g vegetable was weighted, added with 300 mL distilled water, and homogenized using food processor (Philips, HR2001/70). Then, the homogenized sample was sieved using sift followed by filtration using Whatman filter paper (Grade 1, 110 mm). The filtered sample were then centrifuged using Spinplus Centrifuge (Topscien) at 4000 rpm for 5 minutes. After that, the supernatant was filtered using 0.22 µm pore size nylon membrane filters (Jinlong) and appropriate volume of filtered sample was transferred into glass bottle. The sample was spiked with appropriate concentrations of PAHs and biphenyl (internal standard) before extraction with DLLME or MAE-DLLME.

DLLME extraction

The parameters effecting the DLLME extraction such as extraction solvent, dispersion solvent, extraction time have been studied and optimized [14]. The mixture of extraction solvent (1-bromo-3-methylbutane), dispersive solvent (acetone) and internal standard (biphenyl) was rapidly injected into centrifuge tube containing spiked sample using a microvolume syringe in one minute extraction time. The mixture was gently shaken and centrifuged at 4000 rpm for 3 minutes. After centrifugation, organic phase was collected with syringe and sent for GC-FID analysis. The extraction was conducted in triplicate (n = 3).

MAE-DLLME extraction

Parameters such as microwave power, extraction solvent and irradiation time were optimized in the previous study [14]. The volume of 4 mL extraction solvent (acetone) was added into glass bottle containing 10 mL spiked sample. Then, it was closed with cap and microwaved at 200 W for 1.5 minutes. After it was cooling down to room temperature, the spiked sample was shifted into centrifuge tube and centrifuged at 4000 rpm for 5 minutes. Then, 5 mL aqueous phase was transferred into another centrifuge tube and immediately used for DLLME extraction process as described above.

Analytical Performances of DLLME and MAE-DLLME

Analytical parameters including sensitivity, limits of detection (LOD) and limits of quantification (LOQ), precision, accuracy, relative enrichment factor (EF) and relative extraction recovery (ER) were investigated and compared. The validation methods used were followed guideline set by International Conference on Harmonization (ICH) [15]. The validation was conducted in triplicate (n = 3). In this study, the calculation of LOD was performed by analyzing

blank samples which spiked with decreased concentration of PAHs until a peak height of three time higher than the noise level was achieved (S/N=3). For the calculation of LOQ, the blank samples which spiked with decreased concentration of PAHs were analyzed until a peak height of ten time higher than the noise level was achieved (S/N=10).

Accuracy was evaluated by spiking the vegetable sample with the standard solutions of PAHs at three different concentrations in triplicate. The results of spiked samples and spiked distilled water were compared. The precision was studied in terms of intra- and inter-day variability and evaluated at three concentration levels of PAHs. The precision was studied in triplicate (n = 3) during the same day (repeatability) and three different days (intermediate precision) in a week. The precision was expressed as the percentage of relative standard deviation (RSD%).

The extraction recovery (ER) was defined as the ratio of the amount of analyte in sedimented phase (n_{sed}) with the initial amount of analyte in the sample (n_0). The enrichment factor (EF) was defined as the ratio between the concentration of analytes in the sedimented phase (C_{sed}) with the initial concentration of analyte (C_0) within the sample [16]. The relative ERs (or EFs) were defined as ratio of ERs (or EFs) attained by spiking vegetable sample and spiked distilled water. Relative enrichment factor (EF) was defined as ratio of EF obtained by spiked vegetable sample and spiked distilled water within the working range [16].

Real sample analysis

To evaluate the feasibility of the proposed MAE-DLLME in real sample analysis, three types of popular salad organic vegetables, namely cabbage, tomato and carrot, purchased from a local market, were analyzed. The samples were prepared, extracted and analyzed using optimized MAE-DLLME-GC-FID. Relative ER was used to express the efficiency of proposed MAE-DLLME.

Results and Discussion

In this study, the one-at-a-time design has been employed to study the effects of parameters affecting the efficiency of MAE-DLLME. Relative extraction recovery (ER) and relative enrichment factor (EF) were used to express the extraction efficiency.

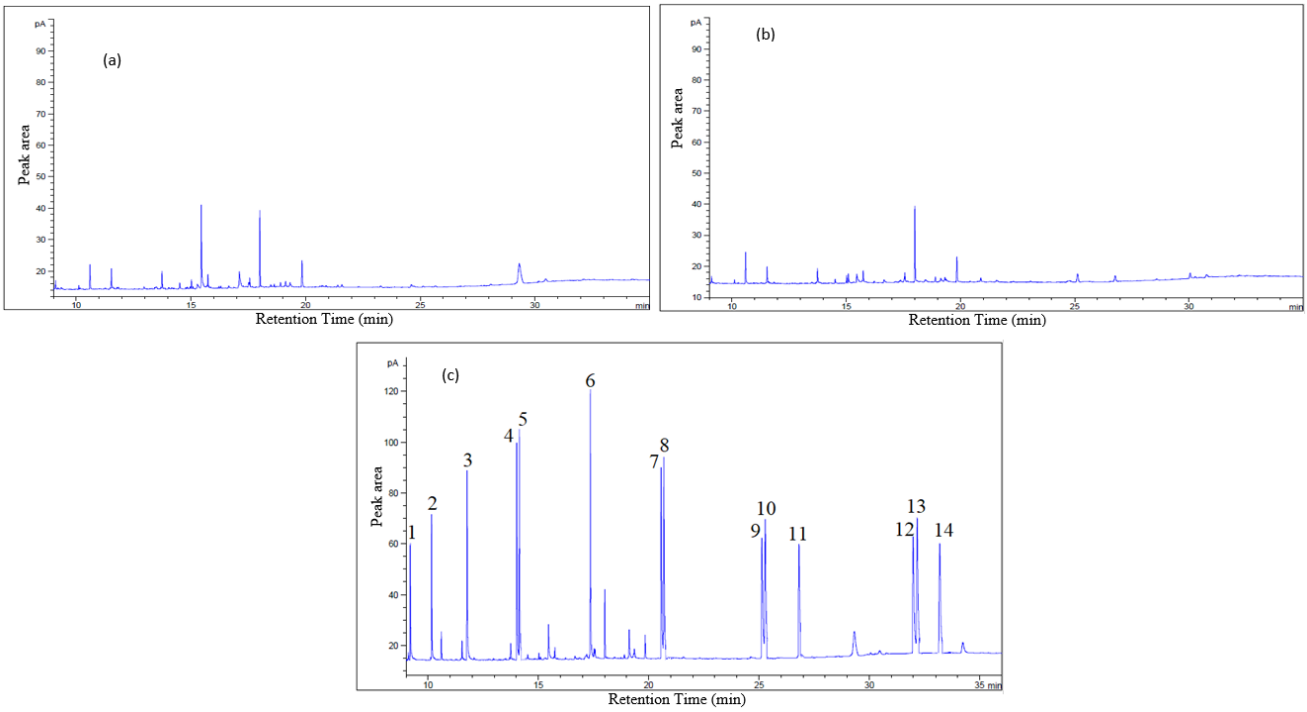
Optimization of DLLME and MAE-DLLME

The optimization of DLLME and MAE-DLLME extractions followed by a gas chromatography-flame ionization detector (GC-FID) for the determination of 13 PAHs in vegetables was discussed in a previous paper [14]. The extraction solvent of 1-bromo-3-methylbutane was found to be the most efficient in extracting the 13 investigated PAHs because of its nonpolar and water-insoluble nature which able to form nonpolar interaction with PAHs. Besides that, the solvent of 1-bromo-3-methylbutane is low toxic and less viscous than other extraction solvents. Low viscosity is more favorable for the extraction of PAHs because high viscosity would slow down the mass transfer thus reduce extraction efficiency [8, 17].

The optimum DLLME conditions were 5.0 mL of sample solution, 30 µL of 1-bromo-3-methylbutane (extraction solvent) and 800 µL of acetone (dispersive solvent) in one minute extraction time. In the MAE-DLLME, the sample was extracted by microwave power of 200 W in acetone for 1.5 minutes of irradiation time at room temperature followed by optimized DLLME [14].

Analytical performances of DLLME and MAE-DLLME

The sensitivity of DLLME and MAE-DLLME were evaluated by comparing chromatograms of blank sample obtained using optimized DLLME, optimized MAE-DLLME and chromatogram of spiked cabbage sample obtained using optimized MAE-DLLME. The results were illustrated in Figure 1. Based on Figure 1(a) and (b), some interferences were not fully abated in MAE-DLLME because there were some peaks still appear on the chromatogram (Figure 1b). However, their peak's number and height were lesser and lower than the interference peaks in DLLME (Figure 1a). Furthermore, no interference in MAE-DLLME was overlapped with the peak of PAHs. Therefore MAE-DLLME has better sensitivity than DLLME.



*Peak No. 1-Biphenyl (Internal Standard), 2-Acenaphthylene, 3-Fluorene, 4-Phenanthrene, 5-Anthracene, 6-Pyrene, 7-benzo[a]anthracene, 8-Chrysene, 9-benzo[b]fluoranthene, 10-benzo[k]fluoranthene, 11-benzo[a]pyrene, 12-Dibenz[a,h]anthracene, 13-Benzo[ghi]perylene, 14-Indeno[1,2,3-cd]pyrene.

Figure 1. Chromatograms of (a) blank cabbage sample using optimized DLLME (b) blank cabbage sample using optimized MAE-DLLME and (c) spiked cabbage sample using optimized MAE-DLLME.
No. 1-Biphenyl (Internal Standard), 2-Acenaphthylene, 3-Fluorene, 4-Phenanthrene, 5-Anthracene, 6-Pyrene, 7-benzo[a]anthracene, 8-Chrysene, 9-benzo[b]fluoranthene, 10-benzo[k]fluoranthene, 11-benzo[a]pyrene, 12-Dibenz[a,h]anthracene, 13-Benzo[ghi]perylene, 14-Indeno[1,2,3-cd]pyrene

The results of the analytical performance of DLLME and MAE-DLLME were summarized in Table 1 and 2. The LOD range was between 0.040 µg/L and 0.400 µg/L in DLLME and 0.020 µg/L and 0.080 µg/L in MAE-DLLME. For LOQ, the range was varied from 0.100 µg/L to 1.200 µg/L in DLLME and 0.080 µg/L to 0.250 µg/L in MAE-DLLME.

Table 1. Analytical performance of DLLME

Analytes	LOD[a]	LOQ[b]	Accuracy[c]	RSD[d]	Relative ER[e]	Relative EF[e]
ACY	8	20	88.16	2.94	88.16	192
FLU	8	20	90.93	4.59	90.93	202
PHE	10	80	82.99	2.79	82.99	195
ANT	10	30	89.40	7.19	89.40	182
PYR	15	100	79.28	4.93	79.28	168
BaA	4	10	77.08	4.89	77.08	179
CHR	4	10	78.52	4.66	78.52	174

Table 1 (cont'd). Analytical performance of DLLME

Analytes	LOD[a]	LOQ[b]	Accuracy[c]	RSD[d]	Relative ER[e]	Relative EF[e]
BbF	40	120	71.77	2.06	71.77	180
BkF	10	20	76.46	1.22	76.46	174
BaP	40	100	77.28	7.50	77.28	166
DahA	10	40	76.50	3.18	76.50	165
BghiP	10	30	80.22	2.84	80.22	166
IcP	10	40	78.56	2.40	78.56	167

[a]: LOD, limit of detection (S/N = 3), 10^{-2} µg/L
[b]: LOQ, limit of quantification (S/N = 10), 10^{-2} µg/L
[c]: Accuracy was obtained by calculating ratio of relative ER of cabbage sample and distilled water sample spiked with 120 µg/L in DLLME and 80 µg/L in MAE-DLLME respectively
[d]: Precision was obtained by calculating ratio of RSD of cabbage sample and distilled water sample spiked with 120 µg/L in DLLME and 80 µg/L in MAE-DLLME respectively
[e]: Relative ER and EF were obtained by calculating the ratio of EF obtained by spiked cabbage sample and spiked distilled water

Table 2. Analytical performance of MAE-DLLME

Analytes	LOD[a]	LOQ[b]	Accuracy[c]	RSD[d]	Relative ER[e]	Relative EF[e]
ACY	2	10	94.74	1.25	94.74	131
FLU	2	8	88.45	2.77	88.45	134
PHE	2	10	92.60	3.07	92.60	126
ANT	2	8	94.09	1.83	94.09	141
PYR	2	8	98.42	2.61	98.42	143
BaA	2	10	94.06	1.79	94.06	136
CHR	2	8	84.12	2.49	84.12	138
BbF	5	20	86.78	2.16	86.78	144
BkF	8	25	93.49	0.77	93.49	145
BaP	5	25	86.46	1.30	86.46	136
DahA	2	8	92.38	1.48	92.38	135
BghiP	4	10	87.46	1.43	87.46	142
IcP	2	8	83.65	1.86	83.65	156

The abbreviations are same as described in Table 1

The precision and the accuracy performances were attained by spiking cabbage sample at 80 µg/L of 13 PAHs in MAE-DLLME and 120 µg/L in DLLME. The precision and accuracy were ranged from 1.22% to 7.50% and 71.77% to 90.93% respectively in DLLME. For MAE-DLLME, the precision was ranged from 0.77% to 3.07% and accuracy was between 83.65% and 98.42%. These results demonstrated that MAE-DLLME is more accurate and repeatable than DLLME. Besides, the relative ERs and EFs of MAE-DLLME were higher than the relative ERs and EFs of DLLME. It may due to the low volume usage of extraction solvent and reduction of matrix interference in MAE-DLLME.

Based on the results in Table 1 and 2, the proposed MAE-DLLME showed better analytical performance than DLLME. This might due to the good sample preparation that eliminated the large matrix impurities from the sample. During the microwave process, the thermal labile matrix impurities would be degraded thus enable high

mass transfer of PAHs from samples into organic phase. Furthermore, the minimum volume of extraction solvent (50 µL) used in DLLME was higher than the minimum volume of extraction solvent (30 µL) used in MAE-DLLME. The reduction of extraction solvent minimized the exposure risk of organic solvent to operator and environment. MAE-DLLME is more cost-effective if large amounts of sample are required to be analysed.

Comparison of analytical performance of MAE-DLLME with other studies

The method performance of developed MAE-DLLME was compared with other methods from literature studies for the determination of PAHs in vegetables. Table 3 shows some analytical features and parameters of the previous studies and developed MAE-DLLME.

Table 3. Comparison of the developed MAE-DLLME with other methods for the determination of PAHs in vegetable samples

Method	Types of ES*	LD_{50} of Solvent (oral, mg/kg)	Organic Solvent Consumption (mL)	Extraction Time (min)	RSD %	Ref
CD-LLE-CC-HPLC-FLD[a]	Cyclohexane, N,N-dimethylformamide–water	>5000, 3000	> 150	>2	NA	[18]
CD-Soxhlet-HPLC-UVD[b]	Cyclohexane/acetone (2:1, v/v)	>5000, 5800	NA	480	4.5-11	[19]
CD-HOLLE-HPLC-FLD[c]	Tetrachloroethane	2629	< 10	0	1.1–8.5	[20]
MAE-DLLME-GC-FID	1-bromo-3-methylbutane	6150	4.83	1	0.77–3.07	This study

"NA" indicating no data; "ES" indicating extraction solvent; [a.] CC-HPLC-FLD: Chemical digestion-liquid-liquid extraction-column chromatography-high performance liquid chromatography-fluorescence detector; [b.] CD-Soxhlet-HPLC-UVD: Chemical digestion-Soxhlet extraction-column chromatography-high performance liquid chromatography-ultraviolet detector; [c.] CD-HOLLE-HPLC-FLD: Chemical digestion-homogeneous liquid-liquid extraction-high performance liquid chromatography-fluorescence detector

It is evident that the developed MAE-DLLME has numerous advantages. No hazardous chemicals were used in developed MAE-DLLME for sample preparation prior to extraction. The matrix interferences in vegetable samples can be minimized by microwave heating without chemical digestion. Low lethal dose (LD_{50}) indicating that the solvent is low toxic and safe to use. The extraction solvent employed in present study is less toxic than literature studies. In addition, MAE-DLLME required small volume of solvent to clean-up and extract the PAHs from one vegetable samples. Moreover, the extraction time is short and the RSD value was very low. Thereby, the developed MAE-DLLME-GC-FID used in this study is a fast, cost-effective and environmentally friendly method for the determination of PAHs in vegetable sample.

Real sample analysis

There are different organic nutrient levels and pollutants in organic vegetables were reported [21]. These organic contents such as nonpolar chlorophylls and carotenes might cause matrix effect in extraction of PAHs from vegetables [22]. Three types of popular salad organic vegetables, namely cabbage, tomato and carrot were analyzed in this study to evaluate the feasibility of the proposed MAE-DLLME in real sample analysis. Relative ER was used to express the efficiency of proposed MAE-DLLME.

The result of extraction of PAHs from real samples is tabulated in Table 4. The spiked blank sample was used as control sample and the analysis was conducted in triplicate. The proposed MAE-DLLME was able to extract 13

PAHs from organic vegetables. The samples of carrot were found to have high concentration of high molecular weight PAHs. This might because high molecular weight PAHs are more likely to adsorb to the soils, thus increase the chance of contamination [23]. Cabbages were found to have the highest concentration of total PAHs compared to tomato and carrot. The large surface area of air exchange in cabbage could facilitate the adsorption of PAHs [23]. According to the product label on the vegetables, the vegetable samples were planted in Johor and Negeri Sembilan of Malaysia. After harvested, these vegetables were transported to local market in Klang, Selangor of Malaysia. The distance between plantation and market is more than 100 kilometers. Therefore, the contamination of PAHs in these vegetables were mainly due to the long distance transportation.

Table 4. PAHs concentrations (µg/kg, fresh weight) in organic vegetables (n = 3)

Sample	Cabbage	Tomato	Carrot
ACY	0.049	0.044	0.161
FLU	0.113	0.139	n.d.
PHE	0.090	n.d.	n.d.
ANT	0.157	0.199	n.d.
PYR	0.368	0.402	0.184
BaA	0.223	0.167	0.231
CHR	0.195	n.d.	0.116
BbF	0.356	0.345	0.410
BkF	0.322	n.d.	n.d.
BaP	0.372	n.d.	0.278
DahA	0.560	0.192	0.196
BghiP	n.d.	n.d.	0.086
IcP	0.214	n.d.	0.621
Σ13PAH	2.969	1.488	2.283

n.d.: not detected

Conclusion

In the present study, an analytical method of MAE-DLLME coupled with GC-FID for clean-up and extraction of 13 PAHs from vegetable samples has been developed. The analytical performances of DLLME and MAE-DLLME were validated and compared. The results showed that both methods exhibited low limits of detection and limits of quantification, good precision, accuracy, extraction recovery and enrichment factor. Although MAE-DLLME required the consumption of organic solvents and processing time in microwave process, the overall performance of MAE-DLLME is better than DLLME due to the thermal degradation of matrix components. In conclusions, MAE coupled with DLLME successfully increased extraction efficiency by degrading matrix interference and reducing volume of extraction solvent. The developed MAE-DLLME is preferable for analysis of PAHs in food sample with complex matrices. With the recent development of automation technology, the automated MAE-DLLME procedure should be developed in the future.

References

1. Li, H., Zhu, D., Lu, X., Du, H., Guan, S. and Chen, Z. (2018). Determination and risk assessment of sixteen polycyclic aromatic hydrocarbons in vegetables. *Journal of Environmental Science and Health, Part A*, 53(2): 116-123.
2. Singh, L. and Agarwal, T. (2018). PAHs in Indian diet: Assessing the cancer risk. *Chemosphere*, 202: 366-376.
3. Soceanu, A., Dobrinas, S., Stanciu, G. and Popescu, V. (2014). Polycyclic aromatic hydrocarbons in vegetables grown in urban and rural areas. *Environmental Engineering and Management Journal*, 13(9): 2311-2315.

4. International Agency for research on cancer. (2017). IARC Monographs on the evaluation of carcinogenic risks to humans. http://monographs.iarc.fr/ENG/Classification/latest_classif.php. [Access online 18 April 2019].
5. European Commission (2002). Opinion of the scientific committee on food on the risks to human health of polycyclic aromatic hydrocarbons in food. https://ec.europa.eu/food/sites/food/files/safety/docs/sci-com_scf_out153_en.pdf. [Access online 19 April 2019].
6. Saraji, M., and Boroujeni, M. K. (2013). Recent developments in dispersive liquid-liquid microextraction microextraction techniques. *Analytical and Bioanalytical Chemistry*, 406: 2027-2066.
7. Rezaee, M., Assadi, Y., Milani Hosseini, M.R., Aghaee, E., Ahmadi, F. and Berijani, S. (2006). Determination of organic compounds in water using dispersive liquid-liquid microextraction. *Journal of Chromatography*. A, 1116 (1-2): 1-9.
8. Peng, G., Lu, Y., He, Q., Mmereki, D., Zhou, G., Chen, J. and Tang, X. (2016). Dispersive liquid–liquid microextraction using low-toxic solvent for the determination of heavy metals in water samples by inductively coupled plasma–mass spectrometry. *Journal of AOAC International*, 99 (1): 260-266.
9. Chai, M. K., Chander, P. D. and Wong, L. S. (2016). Modified dispersive liquid-liquid microextraction using green solvent for extraction of polycyclic aromatic hydrocarbosn (PAHs) in vegetable samples. *Malaysian Journal of Analytical Sciences*, 20(1): 14 – 20.
10. Wang, H., Ding, J. and Ren, N. (2016). Recent advances in microwave-assisted extraction of trace organic pollutants from food and environmental samples. *Trends in Analytical Chemistry*, 75: 197-208.
11. Campillo, N., Viñas, P., Martínez-Castillo, N. and Hernández-Córdoba, M. (2011). Determination of volatile nitrosamines in meat products by microwave-assisted extraction and dispersive liquid-liquid microextraction coupled to gas chromatography-mass spectrometry. *Journal of Chromatography A*, 1218: 1815-1221.
12. Mahmoudpour, M., Mohtadinia, J., Mousavi, M. M., Ansarin, M. and Nemati, M. (2016). Application of the microwave-assisted extraction and dispersive liquid–liquid microextraction for the analysis of PAHs in smoked rice. *Food Analytical Methods*, 10(1): 1-10.
13. Mari, A., Ahmadi-Jouibari, T. and Nazir, F. (2016). Application of microwave-assisted dispersive liquid– liquid microextraction and graphite furnace atomic absorption spectrometry for ultra-trace determination of lead and cadmium in cereals and agricultural. *International Journal of Environmental Analytical Chemistry*. 96: 271-283.
14. Tan, Y. H., Chai, M. K. and Wong, L. S. (2018). The effects of parameters on the efficiency of DLLME in extracting of PAHs from vegetable samples. *International Journal of Engineering and Technology*, 7 (4.35): 15-21.
15. ICH Expert Working Group. (2005). Validation of analytical procedures: text and methodology Q2 (R1).
16. Xu, F., Liu, L., Wei, W. and Xu, R. (2017). Determination of five endosulfan pesticides in the fish pond water by dispersive liquid-liquid microextraction combined with GC-MS. *Forensic Sciences Research*, 2(1): 1-6.
17. Wagner, I. and Stichlmair, J. (2001). The effect of viscosity on mass transfer in pulsed sieve-tray extraction columns. *Chemical Engineering and Technology*, 24 (6): 616-619.
18. Camargo, M. C. R., and Toledo, M. C. F. (2003). Polycyclic aromatic hydrocarbons in Brazilian vegetables and fruits. *Food Control*, 14(1): 49-53.
19. Ashraf, M. W. and Salam, A. (2012). Polycyclic aromatic hydrocarbons (PAHs) in vegetables and fruits produced in Saudi Arabia. *Bulletin of Environmental Contamination and Toxicology*, 88 (4): 543-547.
20. Zhao, X., Liu, X., Zhao, Z., Huang, C., Zhang, M., Wang, H. and Wang, X. (2009). Homogeneous liquid-liquid extraction combined with high performance liquid chromatography-fluorescence detection for determination of polycyclic aromatic hydrocarbons in vegetables. *Journal of Separation Science*, 32(12): 2051-2057.
21. Lima, G. P. P., and Vianello, F. (2011). Review on the main differences between organic and conventional plant-based foods. *International Journal of Food Science and Technology*, 46: 1-13.
22. Dugaya, A., Herrenknechtb , C., Czokc, M., Guyona, F and Pages, N. (2002). New procedure for selective extraction of polycyclic aromatic hydrocarbons in plants for gas chromatographic–mass spectrometric analysis. *Journal of Chromatography A*, 938: 1-7.
23. Paris, A., Ledauphin, J., Poinot, P. and Gaillard, J. (2018). Polycyclic aromatic hydrocarbons in fruits and vegetables: Origin, analysis, and occurrence. *Environmental Pollution*, 234: 96-106.

Malaysian Journal of Analytical Sciences (MJAS)
Published by Malaysian Analytical Sciences Society

CORROSION INHIBITION STUDY ON GLYCEROL AS SIMULTANEOUS GAS HYDRATE AND CORROSION INHIBITOR IN GAS PIPELINES

(Kajian Perencatan Kakisan oleh Gliserol sebagai Perencat Serentak untuk Hidrat Gas dan Kakisan dalam Saluran Paip Gas)

Vinayagam Sivabalan[1,2], Belkhir Walid[1,3], Yoann Madec[1,4], Ali Qasim[1,2], Bhajan Lal[1,2]*

[1]*Chemical Engineering Department,*
[2]*CO_2 Research Centre (CO_2RES),*
Universiti Teknologi PETRONAS, Bandar Seri Iskandar, 32610, Perak, Malaysia
[3]*Department of Science and Engineering of Materials,*
University Institute of Technology, 71100 Chalon-sur-Saône, France
[4]*Department of Process Engineering,*
National Superior Engineering School of Industrial Technologies (ENGSTI), 64000 Pau, France

**Corresponding author: bhajan.lal@utp.edu.my*

Received: 20 November 2019; Accepted: 23 January 2020

Abstract

Gas hydrate inhibitors (GHI) and Corrosion Inhibitors (CI) often tend to display antagonistic behaviour in flow assurance of oil and gas. Compatible GHI and CI that have no compromises are still under research and development. Latest researches are being done on multifunctional gas hydrate and corrosion inhibitor (GHCl). Glycerol has been tested for its inhibition performance for both hydrate and corrosion in various distinguished experiments. However, glycerol's corrosion inhibition on X52 mild steel in seawater environment has never been tested. In this work, the corrosion inhibitor property of glycerol on X52 mild steel in 3.5wt.% NaCl brine solution is investigated. The concentrations of glycerol used are 400, 600, 800, 1000, 5000, and 10000 ppm. The pH and conductivity of glycerol have been measured and the relationship between pH, conductivity and corrosion has been thoroughly discussed. The performance of glycerol has been studied further based on adsorption isotherms such as Langmuir, Frumkin, Temkin and Freundlich isotherm. The Temkin isotherm shows the best fit for adsorption isotherm with R^2 of 0.97.

Keywords: hydrate, corrosion, pH, conductivity, adsorption

Abstrak

Perencat hidrat gas (GHI) dan perencat kakisan (CI) sering menunjukkan kecenderungan antagonistik dalam penjaminan aliran minyak dan gas. GHI dan CI yang tidak mempunyai kompromi ialah masih dalam penyelidikan dan pembangunan. Penyelidikan terkini dilakukan pada perencat multifungsi (GHCl) yang boleh merencat hidrat dan kakisan. Gliserol telah diuji untuk prestasi perencatannya untuk hidrat dan kakisan dalam pelbagai eksperimen yang berbeza. Bagaimanapun, perencatan kakisan gliserol pada keluli lembut X52 dalam persekitaran air laut tidak pernah diuji. Dalam penyiasatan ini, sifat perencat kakisan gliserol pada keluli lembut X52 dalam larutan garam NaCl 3.5wt.% disiasat. Kepekatan gliserol yang digunakan ialah 400, 600, 800, 1000, 5000, dan 10000 ppm. Nilai pH dan konduktiviti gliserol telah diukur dan hubungan antara pH, konduktiviti dan kakisan telah dibincangkan dengan teliti. Prestasi gliserol telah dikaji lebih lanjut berdasarkan model isoterma penjerapan seperti model Langmuir, Frumkin, Temkin dan Freundlich. Model Temkin didapati paling sesuai untuk isoterma penjerapan dengan R^2, 0.97.

Kata kunci: hidrat, kakisan, pH, konduktiviti, penjerapan

Introduction

In the oil and gas industry, the term 'flow assurance' refers to the provision of the safe and economical delivery of hydrocarbon stream from the reservoir to the selling point through process facilities [1]. Flow assurance issues mainly involve the formation of hydrates, corrosion, asphaltenes, slugging, and emulsions [2]. Formation of gas hydrates and corrosion in pipelines are significant challenges in flow assurance [3-7]. These issues cause a considerable impact to the production in terms of the cost involved, the engineering effort and maintenance that have to be invested [8, 9]. To overcome these issues that lead to severe safety and economic losses, the industry is injecting different types of gas hydrate inhibitors (GHI) and corrosion inhibitors (CI). However, GHI and CI often tend to display antagonistic behaviour.

Along with the studies on hydrate inhibitors [10-13], and corrosion inhibitors [8, 14, 15], the researches on environmentally friendly dual functioning gas hydrate and corrosion inhibitor are ongoing as the presence of one hydrate inhibitor causes a negative impact on the corrosion inhibitor's performance and vice versa [16-19]. The understanding of the gas hydrate and corrosion phenomena is required to solve this incompatibility issue. While hydrate is an ice-like structure formed when water molecules entrap light gas molecules under high pressure and temperature, corrosion is the destructive chemical attack upon a metallic structure by its environment. Corrosion is a common electrochemical phenomenon experienced in oil and gas production [7, 20-22]. As the hydrate and corrosion inhibitors show antagonistic behaviour, it is well known that the hydrate inhibitors used in pipeline result in corrosion most of the time. Researchers have been working for decades to find a chemical that can inhibit both hydrate and corrosion in the oil and gas pipelines. Burgazli et al. [23] claimed that the corrosion inhibiting property of some gas hydrate inhibitors is an overlooked benefit to be looked upon [23, 24]. The purpose of this research is to find the dual functioning chemicals that can inhibit both hydrate and corrosion in oil and gas pipelines. In this work, glycerol showing good hydrate [25-28], and corrosion [29-31] inhibiting property in different conditions, is tested for its corrosion inhibition effect on Mild Steel X52 in 3.5wt.% sodium chloride (NaCl) solution.

Materials and Methods

Materials

Glycerol with 99.5% purity was purchased from MERCK (CAS 56-81-5) for this experiment. The 3.5wt.% NaCl brine solution, which is the corrosive medium for the corrosion study was prepared by using deionised water and reagent grade NaCl. Mild steel X52 samples with the dimensions of 10x10x5 mm have been used as the metal specimens. The composition of mild steel X52 is obtained from previous literature [32]. The metal specimen is abraded up to 800 grit, to eliminate the surface impurities. Mild steel X52 is then washed using distilled water, rinsed with Acetone to degrease, and dried. These metal samples are used for the weight loss method in the control solution of 3.5wt.% of NaCl, and the different concentrations of glycerol in the solution.

Evaluation of pH and electrical conductivity

Both pH and electrical conductivity meter are calibrated according to the user manual. SCHOTT Lab 860 probe has been used for the pH measurement. This equipment, which is used to measure the acidity or basicity of solutions has an electrode attached to the meter, and the corresponding reading can be taken from the screen. Meanwhile, for electrical conductivity, SCHOTT Lab 960 is used. This equipment has a probe with a 4-pole cell made of graphite, which enables quick and reliable conductivity measurement with an accuracy of ±0.5% using alternating current. The tests are done at room temperature, 298.15K. The temperature is essential for the reproducibility of the conductivity measurement. The probes are immersed directly into the beakers that contain the prepared solutions, and the results appearing on the screen are recorded once they are stabilised. The measurements are repeated to confirm reproducibility.

Weight loss method

The metal samples are accurately weighed with Mettler Toledo electronic digital weighing balance which has a sensitivity of 0.01mg and a standard deviation of ±0.02 mg. The weighed samples are dried before being inserted into the corrosive medium. The samples are submerged into the corrosive medium, and the beakers are covered with paraffin film to ensure the solution is not exposed to foreign compounds. After the 30 days of immersion, the metal specimen was removed, washed, dried and weighed again to obtain the final mass. The corrosion rate was calculated using Equation 1.

$$CR = 8.76 * 10^4 \left(\frac{m_F - m_o}{A\rho t}\right) * 100\% \quad (1)$$

where m_F is the final mass of the metal, m_0 is the initial mass of the metal; A is the exposed surface area of metal, ρ is the density of the metal and t is the immersion period. Meanwhile, the degree of surface coverage (θ) and inhibition efficiency (η %) can be determined using equations (2) and (3).

$$\theta = \frac{Cr1 - Cr0}{Cr1} \quad (2)$$

$$\eta\,\% = \theta * 100\% \quad (3)$$

where, Cr means corrosion rate (mm/year), θ stands for degree of surface coverage, η % means the inhibition efficiency while Cr_0 and Cr_1 mean Corrosion rate (cm/hr) without and with inhibitor.

Adsorption isotherm

Physical adsorption and chemisorption processes are the two main types of interaction in the adsorption of organic compounds onto solid surfaces. The processes are influenced by the nature and charge of the metal, the chemical structure of the inhibitor and the type of electrolyte. The experimental θ values were fitted to standard isotherms including that of Langmuir, Frumkin, Freundlich and Temkin. The value of correlation coefficient (R^2) was used to choose the best-fitting isotherm equation. The adsorption isotherm equations are shown below:

Langmuir isotherm: $$KC = \frac{\theta}{1-\theta} \quad (4)$$

Freundlich isotherm: $$\theta = KC^a \quad (5)$$

Temkin isotherm: $$KC = e^{a\theta} \quad (6)$$

Frumkin isotherm: $$KC = \frac{\theta}{1-\theta} * e^{-2a\theta} \quad (7)$$

K is the equilibrium constant of the inhibitor adsorption process, a is the parameter of interaction between inhibitor molecules adsorbed on the steel surface, and θ is the degree of surface coverage which can be calculated using equation (3).

The Langmuir adsorption model describes adsorption capacity for the coverage of surface sites by a monolayer quantitatively. The Langmuir isotherm is valid for monolayer adsorption onto a surface containing a finite number of identical sites. The model assumes uniform energies of adsorption onto the surface and no transmigration of adsorbate in the plane of the surface. Langmuir isotherm is applied to a perfectly uniform surface, and when there is no interaction between the adsorbed molecules. The Freundlich adsorption model is used in the case of the possible formation of more than one adsorption monolayer on the surface and the sites are heterogeneous. Frumkin isotherm considers the interaction between the adsorbed species, where 1 in the equation (7) represents the number of water molecules displaced by one surfactant molecule as previously described.

Results and Discussion

Values of pH and electrical conductivity

The pH and electrical conductivity values are measured at 298.15 K. The results are tabulated in Table 1. It is observed that there is an increment in electrical conductivity and decrement in pH values with the increase of concentration. Compared to pure water, Glycerol increased electrical conductivity significantly. The increase of electrical conductivity is due to the presence of more soluble ions in the water phase that increased the mobility of ion species. The literature review shows a similar trend [33]. For pH measurements, the decrement can be attributed to the fact that glycerol in water is a weak acid with a pKa value of 14.15 [34]. Though glycerol has three OH- ions in its structure, the -OH groups do not separate as an ion, making it not a base. This slightly acidic nature improves

the adsorption of Glycerol onto the mild steel X52. Both the pH and conductivity values are presented graphically in Figure 1.

Table 1. pH and electrical conductivity values of aqueous Glycerol at 298.15 K

Sample Concentration (ppm)	pH	Conductivity (mS/cm)
Deionised water	6.98	0.055
400	6.82	0.7944
600	6.84	0.8753
800	6.76	0.9933
1000	6.66	0.9802
5000	6.53	1.034
10000	6.35	1.235

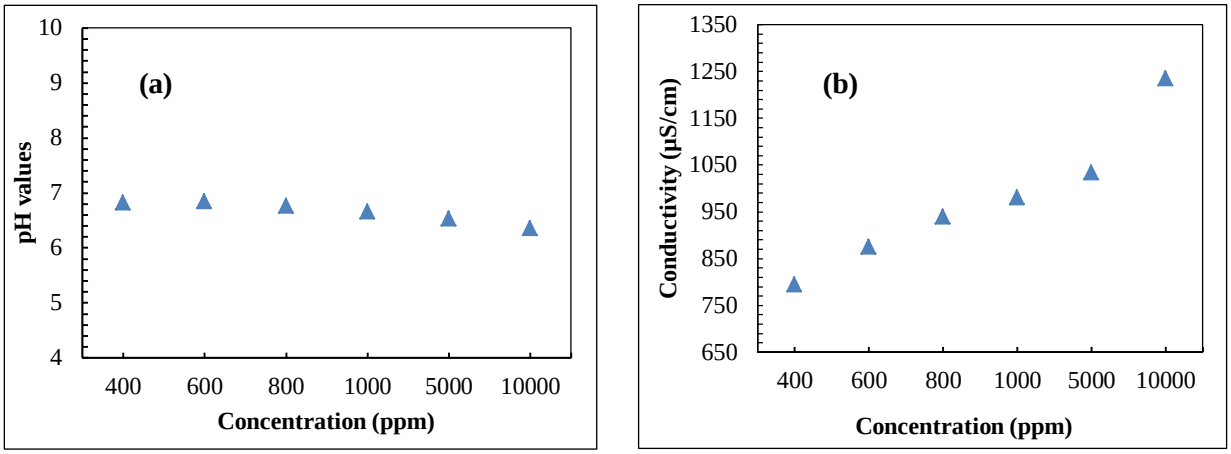


Figure 1. Results of (a) pH and (b) conductivity measurement of glycerol

Weight loss method

Based on the results from the weight-loss method, the corrosion rate and the corrosion inhibition efficiency are calculated. Table 2 tabulates the data of corrosion rate of Mild Steel X52 in the absence and presence of glycerol.

Table 2. Corrosion rate of sample and the corrosion inhibition efficiency of glycerol

Concentration (ppm)	Initial weight (g)	Final Weight (g)	Weight Loss (g)	Corrosion Rate (mm/year)	Inhibition Efficiency, %
Blank	3.6575	3.6416	0.0159	0.0661	0.00
400	3.6274	3.6130	0.0144	0.0604	8.68
600	3.7879	3.7730	0.0149	0.0598	9.52
800	3.7495	3.7350	0.0145	0.0588	11.04
1000	3.5634	3.5503	0.0131	0.0559	15.43
5000	3.9145	3.9064	0.0081	0.0315	52.40
10000	3.7612	3.7557	0.0055	0.0222	66.36

In the absence of glycerol, the corrosion rate of Mild steel X52 in 3.5wt.% NaCl is approximately 0.06mm/year. Addition of glycerol significantly reduces the corrosion rate and the inhibition efficiency increases with increasing concentration. From the addition of 400 ppm to 1000 ppm of glycerol to the corrosive medium, the corrosion rate reduces gradually. However, after adding 5000 ppm, there is a considerable leap in the corrosion inhibition efficiency. The increment of the inhibition efficiency might be due to the presence of optimum concentration glycerol at 5000 ppm, which is equivalent to 5wt.% the standard amount of chemical injection gas hydrate mitigation. Figure 2 clearly illustrates the effect of concentration of glycerol on the corrosion rate of the mild steel and the inhibition efficiency.

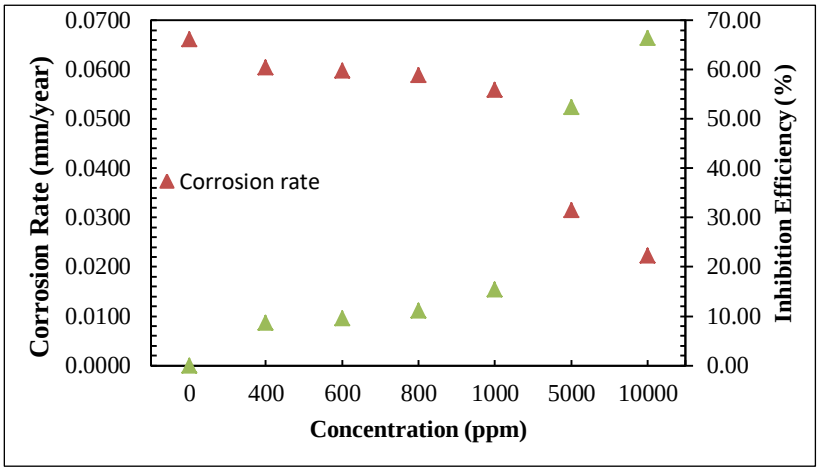
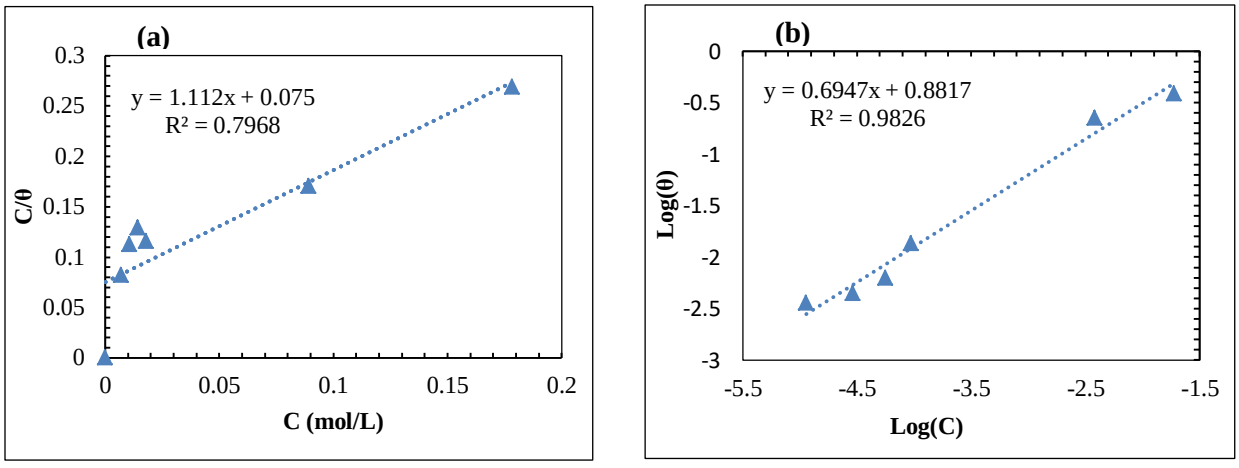


Figure 2. Effect of concentration (ppm) of corrosion rate(mm/year) and inhibition efficiency (%)

Adsorption isotherm

From the details obtained through the weight-loss method, adsorption isotherms are applied to the experimental data for further understanding of the corrosion inhibition mechanism of Glycerol. Figure 3 shows the adsorption isotherms compared with the experimental data.



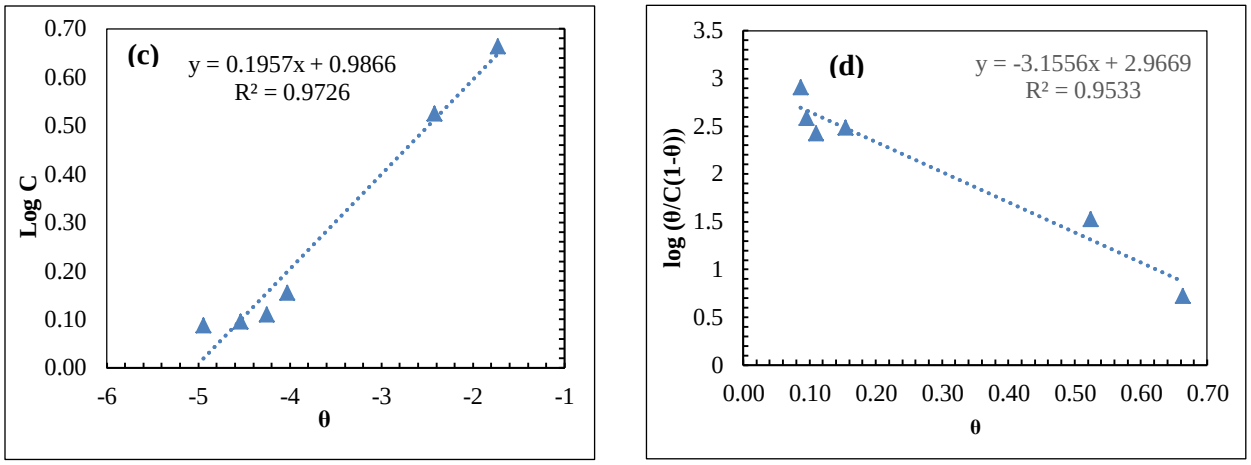


Figure 3. Adsorption isotherms fitted to experiment (a) Langmuir (b) Freundlich (c) Temkin and (d) Frumkin

All the adsorption isotherms give almost straight line to the experimental data. Based on the regression value, Freundlich Isotherm gives the best fit with R^2 equivalent to 0.97. The Freundlich isotherm equation (5) is modified to equation (8) as below to have the linear line.

$$\log \theta = \alpha \log C + \log K \quad (8)$$

From the graph plotted, it is found that the K and α values are 2.41 and 0.6947 respectively. Value of α is a measure of adsorption intensity or surface heterogeneity. If the value of α approaches zero, then it means that there is more surface heterogeneity. A value of α below unity implies chemisorption whereas α above one is an indication of cooperative adsorption[35]. The low values of K suggest that interaction between adsorbed molecules and the metal surface is not strong, indicating that the inhibitor molecules can be removed from the metal surface by any solvent molecules. Based on our results, a strong adsorption bond of chemisorptive nature could be implicated.

Conclusion

From this study, it can be concluded that glycerol has the potential to be a dual functioning gas hydrate and corrosion inhibitor. Glycerol is a common thermodynamic gas hydrate inhibitor in the oil and gas industry, and through this study, it has also been proven that glycerol has 66% corrosion inhibition efficiency at 10000 ppm (1wt%). The inhibition efficiency of glycerol shows the trend of proportionally increasing with the concentration. Although the glycerol has slightly acidic nature, the acidic nature enhances the adsorption process instead of promoting corrosion. Further researches with higher concentrations of glycerol should be done to validate the corrosion inhibition efficiency at higher concentrations of glycerol in 3.5 wt.% NaCl solution. Being an eco-friendly and cost-friendly chemical that has no adverse effect on the environment, glycerol holds vast potential towards greener application flow assurance in the oil and gas industry. It is recommended in subsequence study, influential factors of treatment temperature, CO_2 corrosion (in the absence of O_2 environment to better represent gas pipeline flowing conditions) and high-temperature high autoclave corrosion rate should be considered.

Acknowledgement

The authors would like to acknowledge YUTP Grant 015LCO-154 for supporting this work. Besides, the authors would like to thank everyone who contributed to the success of the Internship Project collaboration between IUT Chalon and ENGSTI, France, and Universiti Teknologi Petronas, Malaysia.

References

1. Sloan, Dendy; Koh, Carolyn; K.Sum, Amadeu; L.Ballard, Adam; Creek, Jefferson; Eaton, Michael; Lachance, Jason; McMullen, Norm; Palermo, Thierry; Shoup, George; Talley, L., Sloan, D., Koh, C., Sum, A., Windows, M., Corporation, M. and Sakajiri, A. (2011). Natural gas hydrates in flow assurance. In Elsevier Publisher.
2. Theyab, M. A. (2018). Fluid flow assurance issues: Literature review. *SciFed Journal of Petroleum*, *2*(1), 1-11.
3. Khan, M. S., Lal, B., Keong, L. K. and Sabil, K. M. (2018). Experimental evaluation and thermodynamic modelling of AILs alkyl chain elongation on methane riched gas hydrate system. *Fluid Phase Equilibria*, 473: 300-309.
4. Yaqub, S., Lal, B., Shariff, A. M., and Mellon, N. (2019). Unraveling the effect of sub-cooling temperatures on the kinetic performance of biopolymers for methane hydrate. *Journal of Natural Gas Science and Engineering*, 65(1): 68-81.
5. Qasim, A., Khan, M. S., Lal, B. and Shariff, A. M. (2019). Phase equilibrium measurement and modeling approach to quaternary ammonium salts with and without monoethylene glycol for carbon dioxide hydrates. *Journal of Molecular Liquids*, 282: 106-114.
6. Nashed, O., Dadebayev, D., Khan, M. S., Bavoh, C. B., Lal, B. and Shariff, A. M. (2018). Experimental and modelling studies on thermodynamic methane hydrate inhibition in the presence of ionic liquids. *Journal of Molecular Liquids*, 249(11): 886-891.
7. Asrar, N., MacKay, B., Birketveit, Ø., Stopanicev, M., Jackson, J. E., Jenkins, A. ad Vittonato, J. (2016). Corrosion- the longest war. *Oilfield Review*, 28(2): 34-49.
8. Yahya, S., Othman, N. K. and Ismail, M. C. (2019). Corrosion inhibition of steel in multiple flow loop under 3.5% NaCl in the presence of rice straw extracts, lignin and ethylene glycol. *Engineering Failure Analysis*, 100: 365-380.
9. Khan, M. S., Mellon, N. B. and Lal, B. (n.d.). Preliminary experimental evaluation for methane (CH_4) and carbon dioxide (CO_2) gas hydrate mitigation.
10. Nashed, O., Sabil, K. M., Ismail, L., Japper-Jaafar, A. and Lal, B. (2018). Mean induction time and isothermal kinetic analysis of methane hydrate formation in water and imidazolium based ionic liquid solutions. *The Journal of Chemical Thermodynamics*, 117: 147-154.
11. Bavoh, C. B., Lal, B., Osei, H., Sabil, K. M. and Mukhtar, H. (2019). A review on the role of amino acids in gas hydrate inhibition, CO_2 capture and sequestration, and natural gas storage. *Journal of Natural Gas Science and Engineering*, 64(1): 52-71.
12. Bavoh, C. B., Lal, B., Nashed, O., Khan, M. S., Lau, K. K. and Bustam, M. A. (2016). COSMO-RS: An ionic liquid prescreening tool for gas hydrate mitigation. *Chinese Journal of Chemical Engineering*, 24(11): 1619-1624.
13. Khan, M. S., Bavoh, C. B., Partoon, B., Lal, B., Bustam, M. A. and Shariff, A. M. (2017). Thermodynamic effect of ammonium based ionic liquids on CO_2 hydrates phase boundary. *Journal of Molecular Liquids*, 238(7): 533-539.
14. Nam, N. D., Hien, P. Van, Hoai, N. T. and Thu, V. T. H. (2018). A study on the mixed corrosion inhibitor with a dominant cathodic inhibitor for mild steel in aqueous chloride solution. *Journal of the Taiwan Institute of Chemical Engineers*, 91: 556-569.
15. Vu, N., Hien, P., Man, T., Hanh Thu, V., Tri, M. and Nam, N. (2017). A study on corrosion inhibitor for mild steel in ethanol fuel blend. *Materials*, 11(1): 59.
16. Menendez, C. M., Jardine, J., Mok, W. Y., Ramachandran, S., Jovancicevic, V., & Bhattacharya, A. (2014). New sour gas corrosion inhibitor compatible with kinetic hydrate inhibitor. *International Petroleum Technology Conference*, pp. 1-9.
17. Obanijesu, E. O., Gubner, R., Barifcani, A., Pareek, V. and Tade, M. O. (2014). The influence of corrosion inhibitors on hydrate formation temperature along the subsea natural gas pipelines. *Journal of Petroleum Science and Engineering*, 120: 239-252.
18. Sheng, Q., Silveira, K. C. Da, Tian, W., Fong, C., Maeda, N., Gubner, R. and Wood, C. D. (2017). Simultaneous hydrate and corrosion inhibition with modified poly(vinyl caprolactam) polymers. *Energy and Fuels*, 31(7): 6724-6731.
19. Moloney, J. J., Mok, W. Y. and Gamble, C. G. (2009). Compatible corrosion and kinetic hydrate inhibitors for wet sour gas transmission lines. *NACE International: Corrosion* 2009: pp. 09350.

20. Schütze, M. (2002). Corrosion books: Handbook of corrosion engineering. By Pierre R. Roberge - Materials and Corrosion 4/2002. *Materials and Corrosion*, 53(4): 284-284.
21. Dariva, G. C. and Galio, F. A. (2014). Corrosion inhibitors – principles, mechanisms and applications. In *Developments in Corrosion Protection*, 2014: pp. 365-379.
22. Macdonald, D. D., Lewis, M., McLafferty, J., Maya-Visuet, E. and Peek, R. (2018). Electromagnetic induction corrosion control technology (EICCT). *Materials and Corrosion*, 69(4): 436-446.
23. Burgazli, C. R., Navarrete, R. C. and Mead, S. L. (2005). New dual purpose chemistry for gas hydrate and corrosion inhibition. *Journal of Canadian Petroleum Technology*, 44(11): 47-50.
24. Leinweber, D. and Feustel, M. (2009). Patent No. US007615102B2. United States.
25. Chapoy, A., Burgass, R. and Tohidi, B. (2014). Hydrate inhibition in propylene glycol and glycerol systems. In 8th International Conference on Gas Hydrates, pp. 1-8.
26. Wu, H.-J. and Englezos, P. (2006). Inhibiting effect of triethylene glycol and glycerol on gas hydrate formation conditions. *Journal of Chemical & Engineering Data*, 51(5): 1811-1813.
27. Li, X.-S., Wu, H.-J. and Englezos, P. (2006). Prediction of gas hydrate formation conditions in the presence of methanol, glycerol, ethylene glycol, and triethylene glycol with the statistical associating fluid theory equation of state. *Industrial & Engineering Chemistry Research*, 45(6): 2131-2137.
28. Bavoh, C. B., Khan, M. S., Ting, V. J., Lal, B., Ofei, T. N., Ben-Awuah, J. and Shariff, A. B. M. (2018). The effect of acidic gases and thermodynamic inhibitors on the hydrates phase boundary of synthetic Malaysia natural gas. *IOP Conference Series: Materials Science and Engineering*, 458(1): 012016.
29. Chi-Ucán, S. L., Castillo-Atoche, A., Castro Borges, P., Manzanilla-Cano, J. A., González-García, G., Patiño, R. and Díaz-Ballote, L. (2014). Inhibition effect of glycerol on the corrosion of copper in NaCl solutions at different pH values. *Journal of Chemistry*, 2014: 1-10.
30. Zubaidi, I. Al, Ibrahim, H., Jones, R., Alzughaibi, M., Albayyadhi, M. and Darzi, F. (2016). Waste glycerol as new green inhibition for metal corrosion in acid medium. *Proceedings of the 3rd International Conference of Fluid Flow, Heat and Mass Transfer*, (162): 1-8.
31. Corrales-Luna, M., Le Manh, T., Romero-Romo, M., Palomar-Pardavé, M. and Arce-Estrada, E. M. (2019). 1-Ethyl 3-methylimidazolium thiocyanate ionic liquid as corrosion inhibitor of API 5L X52 steel in H_2SO_4 and HCl media. *Corrosion Science*, 2019: 85-99.
32. Nashed, O., Koh, J. C. H. and Lal, B. (2016). Physical-chemical properties of aqueous TBAOH solution for gas hydrates promotion. *Procedia Engineering*, 148: 1351-1356.
33. Bhattacharyya, L. and Rohrer, J. S. (Eds.). (2012). Applications of ion chromatography for pharmaceutical and biological products. John Wiley and Son Publisher.
34. Zhu, Y., Free, M. L., Woollam, R. and Durnie, W. (2017). A review of surfactants as corrosion inhibitors and associated modeling. *Progress in Materials Science*, 90: 159-223.

Malaysian Journal of Analytical Sciences (MJAS)
Published by Malaysian Analytical Sciences Society

PHYTOCHEMICAL SCREENING AND FTIR SPECTROSCOPY ON CRUDE EXTRACT FROM *Enhalus acoroides* LEAVES

(Saringan Fitokimia dan Spektroskopi FTIR Ekstrak Mentah Daun *Enhalus acoroides*)

Made Pharmawati[1]* and Luh Putu Wrasiati[2]

[1]*Biology Department, Faculty of Mathematics and Natural Sciences*
[2]*Department of Agro-Industrial Technology, Faculty of Agricultural Technology*
Udayana University, Kampus Bukit Jimbaran, Badung, 80361, Bali, Indonesia

**Corresponding author: made_pharmawati@unud.ac.id*

Received: 25 November 2019; Accepted: 9 January 2020

Abstract

Seagrass provides key ecological services in marine ecosystems, such as stabilising sediment, providing oxygen and acting as a nursery ground for marine biota. Seagrass has also been reported to have antioxidant activity that is useful for humans. One seagrass species, *Enhalus acoroides*, is widely distributed in Indonesia. This study aims to screen the phytochemical compounds, determine the functional groups and evaluate the profile of pigments present in *E. acoroides* leaf extract, which were collected from Semawang Beach, Sanur, Bali, Indonesia. The leaf extract was prepared using chloroform: ethanol (9:1) and tested for the presence of saponin, phenols, tannins and flavonoids. The functional groups and pigment profile were determined via Fourier-transform infrared spectroscopy (FTIR) and thin-layer chromatography (TLC), respectively. The results showed that the *E. acoroides* leaf extract contained phenols, tannins and flavonoids. The major functional groups found in the leaf extract were hydroxyl groups, lipids, alkanes, secondary amines, fatty acids, benzenoid compounds and phenols. The FTIR analysis also identified the presence of chlorophyll and carotenoids in the extract, which was further supported by the TLC analysis. This research shows that *E. acoroides* is a potential source of antioxidants and provides an opportunity for the development of natural products from *E. acoroides* in drug discovery.

Keywords: *Enhalus acoroides*, FTIR, chromatography, phytochemical compound, seagrass

Abstrak

Rumput laut memainkan peranan penting dalam ekosistem marin yang menstabilkan sedimen, membekalkan oksigen dan berfungsi sebagai halaman bagi biota marin. Rumput laut juga dilaporkan mengandungi aktiviti antioksidan yang bermanfaat bagi manusia. Spesis rumput laut, *Enhalus acoroides* di jumpai meluas di Indonesia. Kajian ini bertujuan menyaring sebatian fitokimia, penentuan kumpulan berfungsi dan menilai profil pigmen yang wujud di dalam ekstrak daun *E. acoroides*, yang diambil dari Pantai Semawang, Sanur, Bali, Indonesia. Ekstrak daun disediakan menggunakan klorofom: etanol (9:1) dan diuji untuk penentuan kehadiran saponin, fenol, tannin dan flavonoid. Kumpulan berfungsi dan profil pigmen telah ditentukan masing-masing melalui spektroskopi inframerah transformasi Fourier (FTIR) dan kromatografi lapisan nipis (TLC). Hasil kajian menunjukkan ekstrak daun *E. acoroides* mengandungi fenol, tannin dan flavonoids. Kumpulan berfungsi utama yang dijumpai dalam ekstrak daun adalah kumpulan hidroksil, lipid, alkana, amina sekunder, asid lemak, sebatian benzoid dan fenol. Analisis FTIR juga mengenalpasti kehadiran klorofil dan karotenoid di dalam ekstrak, yang mana ia juga disokong oleh hasil analisis TLC. This research shows that *E. acoroides* is a potential source of antioxidants and provides an opportunity for the development of natural products from *E. acoroides* in drug discovery. Hasil kajian mendapati *E. acoroides* berpotensi sebagai sumber antioksidan dan potensinya dalam pembangunan sumber semulajadi dalam penemuan ubat.

Kata kunci: *Enhalus acoroides*, FTIR, kromatografi, sebatian fitokimia, rumput laut

Introduction

Plant extracts have great potency and can be used for a variety of purposes. Approximately 80% of the world's population relies on traditional medicine for health care, and most therapies use plant extracts and their active compounds [1], suggesting that two-thirds of all plant species have medicinal value [2]. Research has shown that most medicinal plants contain antioxidant properties [3]. Nowadays, natural antioxidants are used in cosmetics, foods and pharmaceutical products due to the antioxidants' free radical scavenger activity. Exposure to environmental pollution, dietary xenobiotics and radiation leads to the generation of reactive oxygen species (ROS), which induce oxidative stress [4]. Antioxidants prevent the formation of ROS, neutralise ROS and repair the damage caused by ROS [5].

There are many plant species whose phytochemical content is unknown. One group of plants that has not yet been explored in depth is seagrass, which is the only flowering plant (Angiospermae) that grows in a marine environment. It can form a seagrass meadow that consists of one or a few dominant species [6]. In Indonesia, 13 seagrass species have been reported [7, 8], and nine species have been found in Bali alone [9]. One such species is *Enhalus acoroides* (L.f.) Royle, the largest tropical seagrass species in Southeast Asian waters [10]. A previous study on *E. acoroides* from India has reported that this species contains alkaloids, phenols, flavonoids, steroids, tannins and saponin. Furthermore, it has been shown that aqueous extracts of *E. acoroides* have a high radical scavenging activity [11]. Several studies on *E. acoroides* from Indonesia have shown that methanol extract of *E. acoroides* contains phenols, flavonoids and terpenes [12-14].

Several techniques are available to identify the phytochemical compounds in plant extracts. For example, Fourier-transform infrared spectroscopy (FTIR) is a method used to identify the functional groups in gaseous, liquid and solid materials via infrared radiation beams [15]. It has been used previously to identify the biomolecules present in plant extracts from *Erythrina variegata* [16], *Myristica dactyloides* [17] and *Urtica dioica* [18] among others. Thin-layer chromatography (TLC) is another method used to identify the compounds in a mixture via separating non-volatile mixtures. Many previous studies have employed TLC to analyse the bioactive compounds in medicinal plants [19, 20], plant pigments [21] and food additives and processing [22].

The objectives of this study were to screen the phytochemical compounds in the leaf extract of *E. acoroides* from Semawang Beach, Sanur, Bali, Indonesia, identify the pigments contained in the leaf extract and determine the functional groups present in the *E. acoroides* leaves before and after extraction with chloroform: ethanol (9:1).

Materials and Methods

Preparation of extract

The *E. acoroides* leaves were collected from Semawang Beach, Sanur, Bali, Indonesia, washed and air-dried for three days. The leaves were further dried in an oven at 50 ºC for one day until brittle. The dried leaves were disrupted using a blender and sieved with a 60-mesh sieve. The voucher specimen was deposited in the herbarium collection at Herbarium Biologi Udayana (HBU-MP10), Biology Department, Udayana University. The identification of *E. acoroides* based on morphological characteristics was conducted following the processes of den Hartog and Kuo [23] and McKenzie and Yoshida [24].

As much as 20 g of dried powder was extracted from 200 mL of chloroform: ethanol with a ratio of 9:1 (v/v). The extraction was performed using a Soxhlet extractor for three hours. The solvent was filtered using Whatman filter paper, and the filtrate was evaporated under a vacuum using a rotary evaporator at 40 ºC and 100 mbar (IKA®, RV10). The extraction was performed three times.

Yield and phytochemical screening

The yield was expressed as a percentage and calculated by dividing the weight of the *E. acoroides* extract by the weight of plant powder used and, then, multiplying by 100%. A preliminary phytochemical screening of the *E. acoroides* extract was performed in triplicate using various chemical tests following standard methods [25] to determine the presence of saponin, phenols, tannins and flavonoids. Saponin was tested via a foam test. As much as 2 ml of extract was added to water, and the mixture was shaken. The presence of saponin was indicated by the formation of foam. Phenols were determined by the ferric chloride test, in which ferric chloride was added to the

E. acoroides extract. A positive result was shown by the change of colour from green to black. The presence of tannins was tested by the addition of ferric chloride and sulphuric acid to diluted the extract, and a positive result was shown by black colouring and the formation of black deposits. Flavonoids were tested by adding ammonia and sulphuric acid to diluted extract; a yellow colour indicated the presence of flavonoids.

FTIR analysis

The FTIR analysis was conducted on non-extracted leaf powder and the chloroform: ethanol-extracted sample. The 50 ºC oven-dried *E. acoroides* leaves were blended into a fine powder. As much as 1 mg of the sample was mixed with 50 mg KBr (FTIR-grade); then, some of the mixture was placed into the sample holder. All investigations were performed with an IRPrestige-21 (Shimadzu). The chloroform: ethanol-extracted *E. acoroides* leaf paste was diluted with two drops of chloroform: ethanol (9:1). One drop of the diluted extract was then mixed with 50 mg KBr. The scanning absorption range was 400 to 4000 cm^{-1}.

TLC separation

The separation and identification of pigments were performed using TLC on a 20-cm x 20-cm cellulose plate (Merck). The solvent mixture consisted of petroleum ether, acetone and n-propanol at a ratio of 90:10:0.45 [26]. The TLC cellulose plate was first activated by drying the plate in an oven at 105 °C for at least 45 minutes. The extract was applied on the plate and allowed to dry. Then, the plate was placed in the TLC tank, and the spots were migrated.

Results and Discussion

The yield of the extract was 1.57% ± 0.23. The yield from this study, wherein chloroform: ethanol (9:1) was used, was higher than the yields of previous *E. acoroides* extracts from Wakatobi, Sulawesi, Indonesia, and Madura, East Java, Indonesia, wherein only chloroform was used as a solvent. The yield of the crude extract from Wakatobi was 0.55%, while that from Madura was 0.8% [27]. Chloroform is a non-polar solvent; therefore, it only extracts non-polar compounds. Ethanol is a polar solvent, so the addition of ethanol in the present study caused the extraction of more polar compounds in the leaf sample. Additionally, it is possible that the environmental growth conditions of *E. acoroides* affected the extraction yield.

The phytochemical compounds contained in the extract of *E. acoroides* are shown in Table 1. Saponin was not considered to be present in the extract because foam stability was not detected, i.e. the foam lasted less than five minutes. However, phenols, tannins and flavonoids were detected in the chloroform: ethanol (9:1) *E. acoroides* leaf extract. The presence of phenols and tannins in *E. acoroides* leaves from Indonesian coastal waters has been previously reported as well [13, 27]. A previous methanol extract of *E. acoroides* leaves from East Lombok, Nusa Tenggara Barat, Indonesia, was shown to contain phenols, tannins and terpenes, but flavonoids were not detected [13]. Another study tested a methanol extract of *E. acoroides* leaves from the coastal waters of Ambon, Indonesia, and found the presence of flavonoids [14]. Furthermore, a previous chloroform extract of *E. acoroides* leaves from India was reported to contain flavonoids [11]. The presence of phenols, tannins and flavonoids in *E. acoroides* indicates the seagrass species' potential as a source of antioxidants.

Table 1. Qualitative phytochemical composition of chloroform: ethanol (9:1) leaf extract of *E. acoroides*

Compounds	Colour Change	Results
Saponin	Unstable foam	-
Phenols	Dark green to black	+
Tannins	Dark green to black and black deposits formed	+
Flavonoids	Dark green to yellow	++

- = undetected, + = low, ++ = moderate

The chemical bonds or functional groups present in the dried leaf powder and leaf extract of *E. acoroides* were predicted using FTIR. The bonds were determined by interpreting the infrared absorption spectra. Figure 1 shows the FTIR spectrum of the dried leaf powder, while Table 2 shows the interpretation of the chemical bonds in the non-extracted leaf powder of *E. acoroides*. Strong bonds were found at 3552 cm^{-1}, 1654.92 cm^{-1} and 2054 cm^{-1}, while the others varied from weak to medium. These results demonstrated the presence of hydroxyl groups, lipids, alkanes, amino acids and phosphorus compounds.

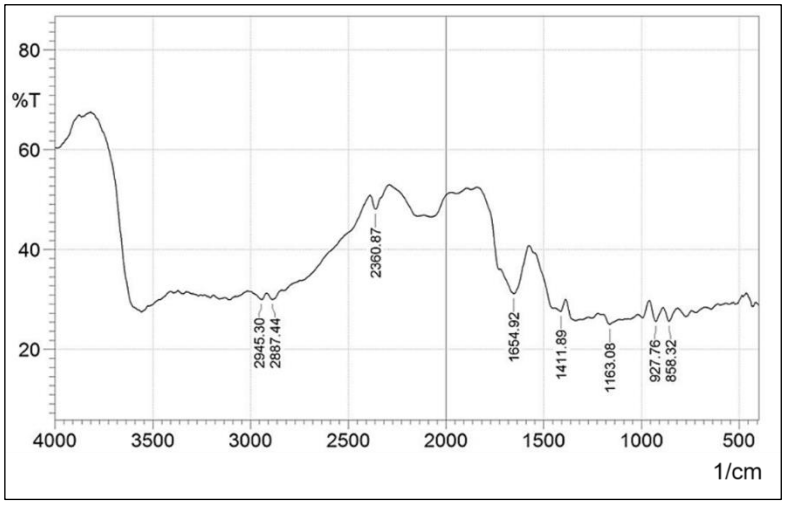


Figure 1. FTIR spectrum of dried leaf powder of *E. acoroides*

Table 2. FTIR spectral peak values and functional groups of dried leaf powder of *E. acoroides*

Spectrum No.	Wave Number cm^{-1}	Wave Number cm^{-1} [28, 29]	Functional Group Assignment	Predicted Compound
1	3552	3500–3650	v; O-H stretching vibration (free)	Hydroxyl group
2	2945.30	~2955	m; CH_3 asymmetry stretching	Lipid
3	2887.44	2880–2890	w; C-H stretching vibration	Alkane
4	2360.87	2250–2700	m; NH component	Amino acid, amino-related component
5	2054	2050–2140	m-w; symmetry -NH_3^+ stretching vibration; broad	Free amino acid and their hydrohalides
6	1654.92	1580–1660	s; C=C stretching vibration	C=C conjugated with C=O
7	1411.89	1350–1410	w; C-H deformation vibration	Secondary alcohol-free
8	1163.08	1155–1165	w-m; CH_3 rocking vibration	P-O-C_2H_5; Organic phosphorus compound
9	927.76	925–930	m; C-C skeletal vibration	Alkane
10	858.32	820–920	w-m; C-C skeletal vibration	Alkane

v = variable, m = medium, s = strong

Table 3 demonstrates the functional groups of the chloroform: ethanol leaf extract of *E. acoroides*. The FTIR spectra are shown in Figure 2. The peaks at 1743 cm^{-1}, 1219 cm^{-1} and 771 cm^{-1} were strong, while the others varied

from weak to medium. Various compounds were found, including hydroxyl groups, lipids, alkanes, secondary a mines, benzenoid compounds and phenols.

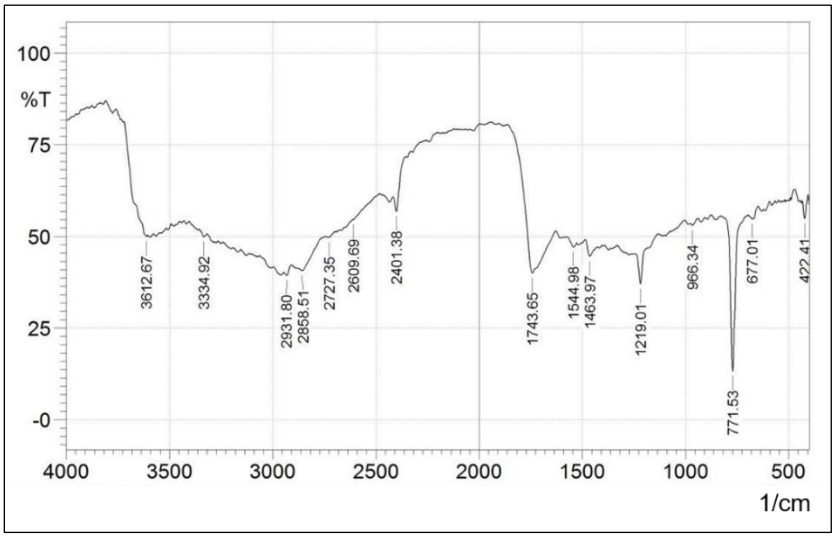


Figure 2. FTIR spectrum of *E. acoroides* leaf extract

Table 3. FTIR spectral peak values and functional groups of *E. acoroides* leaf extract

Spectrum No.	**Wave Number cm^{-1}**	**Wave Number cm^{-1} [28, 29]**	**Functional Group Assignment**	**Predicted Compound**
1	3612.67	3500–3650	v; O-H stretching vibration (free)	Hydroxyl group
2	2931.80	~2930	m; CH_2 asymmetry stretching	Lipid
3	2858.51	2800–2900	w; C-H stretching vibration	Alkane
4	2401.38	2400–2600	w-m; N-D stretching vibration	Imine
5	1743.65	1734–1745	v; C=O of esters	Membrane lipid, fatty acid
6	1544.98	1490–1580	w; N-H deformation vibrations	Secondary amine
7	1463.97	1440–1465	m; C-H deformation vibration	R-CH_3; Alkane
8	1219.01	1165–1225	C-C skeletal vibration	-$C(CH_3)_3$ Alkane
9	771.53	700–900	s; C-H out-of-plane bending (oop) vibration for substituted benzenes ring	Benzenoid
10	677.01	610–690	w; C-H wagging vibration	Vinyl hydrocarbon compounds
11	422.41	375–450	w; aromatic C-OH in-plane bending vibration	Phenol

v = variable, m = medium, s = strong

As can be seen in Tables 2 and 3, there were differences in the functional groups present between the dried leaf powder and the chloroform: ethanol (9:1) leaf extract of *E. acoroides*. The FTIR identified that the leaf extract contained strong C-H out-of-plane bending (oop bend) vibration for substituted benzene ring, indicating the

presence of phenols and flavonoids in the crude *E. acoroides* extract. Flavonoids are polyphenols characterised by two benzene rings joined by a linear carbon chain [30]. The identification of benzenoid compounds *via* FTIR spectrophotometry supported the findings from the phytochemical screening, which detected the presence of phenols and flavonoids. The amines, imines, alkanes and phenols present were considered the major functional groups of bioactive compounds [31].

The peak around 1734–1745 cm^{-1} was assigned as C=O ester [31], which may be related to pheophytin and chlorophyll [32]. In this study, the position of the peak was at 1743 cm^{-1} (Table 3). The carotenoids were predicted to be present in the dried leaf powder of *E. acoroides*. The FTIR spectrum at 1654 cm^{-1} (Table 2) was assigned as the C=O conjugate. The conjugated double bond in carotenoids has been reported as the structure responsible for light absorption [33]. A previous study stated that a peak at 1654 cm^{-1} is due to chlorophyll and protein content [34].

The separation of the *E. acoroides* extract via TLC is presented in Table 4. Eight spots were detected, and the Rf values ranged from 0.11 to 0.94. The colours were separated into bluish-green, dark green, yellow and yellowish-grey, and the predicted pigments included chlorophyll b, ethyl-chlorophyllide a, Mg-free chlorophyll b, lutein, Mg-free chlorophyll a, pheophytin and β-carotene.

Table 4. Identification of compounds based on Rf values and colour from TLC profiling

Fraction No.	Rf Value	Colour	Colour from Reference [26]	Identification	Maximum Spectra (nm)
1	0.11	Bluish-green	Blue-green	Chlorophyll a	655
2	0.21	Dark green	Green	Chlorophyll b	435 and 645
3	0.24	Bluish-green	Blue-green	Ethyl-chlorophyllide a	434 and 654
4	0.28	Yellow	Yellow	Mg-free chlorophyll b	654
5	0.33	Light yellow	Yellow	Lutein	649
6	0.39	Yellowish-grey	Grey	Mg-free chlorophyll a	630 and 656
7	0.53	Grey	Grey	Pheophytin	424 and 658
8	0.94	Orange	Yellow-orange	β-carotene	425

The maximum spectra for each spot of TLC for fractions one to eight are presented in Table 4. Based on a comparison to Lichtenthaler and Buschmann [35], fraction five with a maximum absorption at 654 nm was identified as chlorophyll b, and fraction eight with a maximum absorption at 425 nm was identified as β-carotene. The other fractions were unidentified. The presence of β-carotene was in agreement with the results from the FTIR analysis, which confirmed the presence of chlorophyll, pheophytin and carotenoids in the *E. acoroides* extract, wherein a functional group of C=O ester was identified (Table 3).

Based on the phytochemical compounds discovered in the FTIR and TLC analyses, *E. acoroides* has the potential to be used for biomedicinal applications, as phenolic compounds, tannins, flavonoids, chlorophyll and carotenoids are known to have antioxidant activities [36]. These findings provide an opportunity for the development of natural products from *E. acoroides* in drug discovery.

Conclusion

The phytochemical compounds present in the chloroform: ethanol (9:1) leaf extract of *E. acoroides* were phenols, tannins and flavonoids. The major functional groups identified were hydroxyl groups, lipids, alkanes, secondary amines, fatty acids, benzenoid compounds and phenols. The FTIR analysis also identified the presence of chlorophyll and carotenoids in the extract, which was then confirmed by TLC profiling. Further studies will focus on the fractionation and purification of potential bioactive compounds present in the extract.

Acknowledgement

This research was funded by Ministry of Research, Technology and Higher Education of the Republic of Indonesia with Grant Number 492.27/UN14.4.A/LT/2019

References

1. Winston, J. C. (1999). Health-promoting properties of common herbs. *The American Journal of Clinical Nutrition*, 70(3): 491s-499s.
2. Krishnaiah, D., Sarbatly, R. and Nithyanandam, R. (2011). A review of the antioxidant potential of medicinal plant species. *Food and Bioproducts Processing*, 89(3): 217-233.
3. Saeed, N., Khan, M. R. and Shabbir, M. (2012). Antioxidant activity, total phenolic and total flavonoid contents of whole plant extracts *Torilis leptophylla* L. *BMC Complementary and Alternative Medicine*, 12: 221.
4. Al-Gubory, K. H. (2014). Environmental pollutants and lifestyle factors induce oxidative stress and poor prenatal development. *Reproductive BioMedicine Online*, 29: 17-31.
5. Ighodaro, O. M. and Akinloye, O. A. (2018). First line defence antioxidants-superoxide dismutase (SOD), catalase (CAT) and glutathione peroxidase (GPX): Their fundamental role in the entire antioxidant defence grid. *Alexandria Journal of Medicine*, 54(4): 287-293.
6. Björk, M., Short, F., Mcleod, E. and Beer, S. (2008). Managing seagrasses for resilience to climate change. IUCN, Gland, Switzerland: pp. 8-18.
7. Kuriandewa, T. E., Kiswara, W., Hutomo, M. and Soemodihardjo, S. (2003). The seagrasses of Indonesia. In: Green, E. P. and Short, F. T., Eds., World Atlas of Seagrasses, University of California Press, Barkeley: pp. 172-182.
8. Kuo, J. (2007). New monoecious seagrass of *Halophila sulawesii* (Hydrocharitaceae) from Indonesia. *Aquatic Botany*, 87(2): 171-175.
9. Pharmawati, M., Nurkamila, U. S. and Stevanus. (2016). RAPD fingerprinting key and phylogenetic of nine seagrass species from Sanur coastal water, Bali, Indonesia using matK sequences. *Biodiversitas*, 17(2): 687-693.
10. Ogawa, H. and Namba, N. (2002). Ecological characteristics of tropical seagrasses, especially *Enhalus acoroides*. *Fisheries Science*, 68(sup2): 1767-1770.
11. Amudha, P., Vanitha, V., Mohanasundaram, S, Bharathi N. P. and Jayalakshmi, M. (2017). Phytochemical analysis and invitro antioxidant screening of seagrass *Enhalus acoroides*. *International Journal of Research and Pharmaceutical Science*, 8(2): 251-258.
12. Santoso, J., Anwariyah, S., Rumiantin, R. O., Putri, A. P., Ukhty, N. and Yoshie-Stark, Y. (2012). Phenol content, antioxidant activity and fiber profile of four tropical seagrasses from Indonesia. *Journal of Coastal Development*, 15(2): 189-196.
13. Windyaswari, A. S., Purba, J. P., Nurrahmah, S. S., Ayu, I. P., Imran, Z., Amin, A. A., Kurniawan, F., Pratiwi, N. T. M. and Iswantari, A. (2019). Phytochemical profile of seagrass extract (*Enhalus acoroides*): A new marine source from Ekas Bay, East Lombok. *IOP Conference Series: Earth and Environmental Science*, 278, 012081.
14. Tuapattinaya, P. M. J. and Rumahlatu, D. (2019). Analysis of flavonoid levels of *Enhalus acoroides* in different coastal waters in Ambon Island, Indonesia. *International Journal of Applied Biology*, 3(1): 70-80.
15. Khan, S. A., Khan, S., B., Khan, L. U., Farooq, A., Akhtar, K. and M. Asiri A. M. (2018). Fourier transform infrared spectroscopy: Fundamentals and application in functional groups and nanomaterials characterization. In: S. K. Sharma, S. K., Ed., Handbook of Materials Characterization. Springer International Publishing AG, Springer Nature, Switzerland: pp.317-344.
16. Hemmalakshmi, S., Priyanga, S. and Devaki, K. (2017). Fourier transform infra-red spectroscopy analysis of *Erythrina variegata* L. *Journal of Pharmaceutical Sciences and Research*, 9(11): 2062-2067.
17. Rajiv, P., Deepa, A., Vanathi, D. P. and Vidhya, D. (2017). Screening for phytochemicals and FTIR analysis of *Myristica dactyloids* fruit extract. *International Journal of Pharmacy and Pharmaceutical Sciences*, 9(1): 315-318.
18. Maobe, M. A. G. and Nyarango, R. M. (2013). Fourier transformer infra-red spectrophotometer analysis of *Urtica dioica* medicinal herb used for the treatment of diabetes, malaria and pneumonia in Kisii region, Southwest Kenya. *World Applied Sciences Journal*, 21(8): 1128-1135.

19. Kumar, S., Jyotirmayee, K. and Sarangi, M. (2013). Thin layer chromatography: A tool of biotechnology for isolation of bioactive compounds from medicinal plants. *International Journal of Pharmaceutical Science Review and Research*, 18(1): 126-132.
20. Porika, R., Poojari, S., Lunavath, V. and Mamidala, E. (2014). Preliminary phytochemical investigation and TLC analysis of *P. angulata* fruit extract. *IOSR Journal of Pharmacy and Biological Sciences*, 9(2): 11-14.
21. Forgacs, E. and Cserhati, T. (2002). Thin-layer chromatography of natural pigments: New advances. *Journal of Liquid Chromatography and Related Technologies*, 25(10-11): 1521-1541.
22. Zahra, N., Alim-un-Nisa, Fatima, Z., Kalim, I. and Saeed, K. (2015). Identification of synthetic food dyes in beverages by thin layer chromatography. *Pakistan Journal of Food Science*, 25(4): 178-181.
23. den Hartog, C. and Kuo, J. (2006). Taxonomy and biography of seagrasses. In Larkum, T., Orth, R. J. and Duarte, C. M., Eds. Seagrasses: Biology, ecology and conservation. Springer, The Netherlands: pp. 1-23.
24. McKenzie, L J. and Yoshida, R. L. (2009). Seagrass-watch. Proceeding of a workshop for monitoring seagrass habitats in Indonesia. The Nature Conservancy, Coral Triangle Center, Sanur, Bali: pp. 29-32.
25. Harborne, J. B. (1984). Phytochemical methods: A guide to modern technique of plant analysis. (2nd ed). Chapman and Hall. London. pp. 37-168.
26. Bacon, M. F. and Holden, M. (1967). Changes in chlorophylls resulting from various chemical and physical treatments of leaves and leaf extracts. *Phytochemistry*, 6: 193-210.
27. Dewi, C. S. U., Kasitowati, R. D. and Siagian, J. A. (2018). Phytochemical compounds of *Enhalus acoroides* from Wanci Island (Wakatobi) and Talango Island (Madura) Indonesia. *IOP Conference Series: Earth and Environmental Science*, 137: 012045.
28. Spectroscopic Tools. Access from http://www.science-and-fun.de/tools/. [Access online 21-25 October 2019]
29. Socrates, G. (2004). Infrared and Raman characteristic group frequencies tables and charts. John Wiley & Sons Ltd, Baffins Lane, Chichester, West Sussex PO19 IUD, England: pp. 1-340.
30. Corcoran, M. P., McKay, D. L. and Blumberg, J. B. (2012). Flavonoid basics: Chemistry, sources, mechanisms of action, and safety. *Journal of Nutrition in Gerontology and Geriatrics*, 31(3): 176-189.
31. Pratheeba, T., Ragavendran, C. and Natarajan, D. (2015). Larvicidal, pupicidal and adulticidal potential of *Ocimum gratissimum* plant leaf extracts against filariasis inducing vector. *International Journal of Mosquito Research*, 2 (2): 1-8.
32. Li, X., Zhou, R., Xu, K., Xu, J., Jin, J., Fang, H. and He, Y. (2018). Rapid determination of chlorophyll and pheophytin in green tea using Fourier transform infrared spectroscopy. *Molecules*, 23: 1010.
33. Mezzomo, N. and Ferreira, S. R. S. (2016). Carotenoids functionality, sources, and processing by supercritical technology: A review. *Journal of Chemistry*, 2016: 1-16.
34. Kushwaha, K., Saxena, J., Tripathi, B. K. and Agarwal, M. K. (2014). Detection of carotenoids in psychrotrophic bacteria by spectroscopic approach. *Journal of BioScience and Biotechnology*, 3(3): 253-260.
35. Lichtenthaler, H. K. and Buschmann, C. (2001). Chlorophylls and carotenoids: Measurement and characterization by UV-VIS spectroscopy. In: Wrolstad, R. E., Acree, T. E., An, H., Decker, E. A., Penner, M. H., Reid, D. S., Schwartz, S. J., Shoemaker, C. F. and Sporns, P., Eds., Current protocols in food analytical chemistry (CPFA), John Wiley and Sons, New York: pp. F4.3.1-F4.3.8.
36. Lachowicz, S., Oszmiański, J. and Wiśniewski, R. (2018). Determination of triterpenoids, carotenoids, chlorophylls, and antioxidant capacity in *Allium ursinum* L. at different times of harvesting and anatomical parts. *European Food Research Technology*, 244(7): 1269-1280.

Malaysian Journal of Analytical Sciences (MJAS)
Published by Malaysian Analytical Sciences Society

EFFECT OF BMIM-CHLORIDE ON PHYSIO CHEMICAL PROPERTIES OF NANOFIBER MEMBRANE FOR DOMESTIC WASTEWATER TREATMENT

(Kesan BMIM-Klorida ke atas Sifat-Sifat Fisio-Kimia Membran Nanogentian untuk Rawatan Sisa Air Domestik)

Ahmad Tarmizi Mohd [1], Nur Syakinah Abd Halim[1], Mohd Dzul Hakim Wirzal[1,4]*, Muhammad Roil Bilad[1], Nik Abdul Hadi Md Nordin[1], Zulfan Adi Putra[2], Abdull Rahim Mohd Yusoff[3]

[1]*Chemical Engineering Department,*
Universiti Teknologi PETRONAS, 32610 Seri Iskandar, Perak, Malaysia
[2]*PETRONAS Group Technical Solutions (GTS) Process Simulation and Optimization, 50450 Kuala Lumpur, Malaysia*
[3]*Faculty of Science,*
Universiti Teknologi Malaysia, 81310 Skudai, Johor, Malaysia
[4]*Center of Ionic Liquid Research (CORIL),*
Universiti Teknologi PETRONAS, 32610 Seri Iskandar, Perak, Malaysia

**Corresponding author: mdzulhakim.wirzal@utp.edu.my*

Received: 20 November 2019; Accepted: 21 January 2020

Abstract

Water is a vital source that is essential for all living things. With increasing demand towards water consumption, wastewater treatment is necessary. Nanofiber membrane (NFM) fabricated by electrospinning is suitable to be used as a filter especially for water treatment since it has huge surface area and high permeability compared to conventional membrane. However, fouling issue has always become a threat as it reduces membrane permeability over time. Therefore, surface modification methods are being applied to NFM where membrane surface property will be improved in order to reduce fouling. In this study, nylon 6,6 NFM was fabricated and soaked in 1-butyl-3-methylimidazolium chloride (BMIM-Cl). The coating layer of BMIM-Cl will reduce the effect of fouling while increasing membrane performance. This study also compares the ionic liquid concentration to nylon 6,6 NFM with respect to its performance and rejection. Based on the results, the coated layer of BMIM-Cl increases the permeability up to >400 L/m^2 .h.bar while having superior rejection of chemical oxygen demand (COD) and phosphorus content over 90%. Furthermore, the time taken to reach steady-state (relates to fouling effect) increased with ionic liquid concentration, signifying the increase of BMIM-chloride concentration will reduce the effect of cake formation.

Keywords: nanofiber membrane, BMIM-chloride, wastewater

Abstrak

Air adalah sumber penting yang diperlukan oleh semua hidupan. Dengan meningkatnya permintaan terhadap penggunaan air, rawatan sisa air diperlukan. Membran nanogentian (NFM) yang diperbuat oleh putaran elektrik sesuai digunakan sebagai penapis terutama untuk rawatan air kerana ia mempunyai permukaan yang luas dan kebolehtelapan tinggi berbanding dengan membran konvensional. Walau bagaimanapun, masalah kerosakan (kotoran) sentiasa menjadi ancaman kerana ia mengurangkan kebolehtelapan membran dari masa ke semasa. Oleh itu, kaedah pengubahsuaian permukaan digunakan untuk NFM di mana sifat permukaan membran akan dipertingkatkan untuk mengurangkan kerosakan. Dalam kajian ini, nilon 6,6 NFM dihasilkan dan direndam di dalam 1-butil-3-metilimidazolium klorida (BMIM-Cl). Lapisan BMIM-Cl akan mengurangkan kesan kerosakan di samping meningkatkan prestasi membran. Kajian ini juga membandingkan kepekatan cecair ionik ke atas nilon 6,6 NFM sesuai dengan prestasi dan penyingkirannya. Berdasarkan hasil kajian, lapisan BMIM-Cl meningkatkan kebolehtelapan hingga > 400 L/m^2. h.bar sementara mempunyai penyingkiran yang tinggi terhadap permintaan oksigen kimia (COD) dan kandungan fosforus lebih dari 90%. Tambahan pula, masa yang diambil untuk mencapai keadaan stabil (berkaitan dengan kesan kerosakan)

meningkat dengan kepekatan cecair ionik, menandakan peningkatan kepekatan BMIM-Klorida akan mengurangkan kesan pembentukan kek.

Kata kunci: membran nanogentian, BMIM-klorida, sisa air

Introduction

Nowadays, water shortages is a crisis that is encountered by most population in the world [1]. Change in climate, advance in industrial development and growth of world population increase the demand for clean and safe freshwater. In order to solve this problem, numerous water treatment technologies have been carried out and one of them would be membrane technology [2].

Membrane technology are currently being studied on its potential application on many fields including the separation process and selectivity of materials. Membrane technology proves to have low energy consumption, mild operating condition for separation, and optimization of membrane with diverse requirements [3]. The core application of membrane is to have high permeation rate for the targeted separation, selectivity, and versatility in different module, as well as the ability to tolerate against thermal excursion [4].

However, the major problem in membrane technology is membrane fouling. Fouling greatly affect the membrane's effectiveness and life span in industrial usage. Membranes fouling could occur in various unwanted events which cost the company through maintenance and replacement [5, 6]. The fouling occurs when deposition of particles and macromolecules from the feed stream forming a layer at the surface of the membrane and its pores causing the entering part to be partially blocked. This reduce the usage of membrane to perform separation and resulting in flux declination [7].

To address this issue, nanofiber membrane (NFM) has great potential to be used as a filter since it has high porosity, huge surface area to volume ratio [8], incredibly high flux [9] and is found to be more effective approach to reduce fouling [8, 10]. Nevertheless, membrane fouling will decrease the performance of the membrane throughout period of time. This problem can be solved by utilizing membrane surface modification where it will improve the membrane property by optimizing the surface morphology and chemical composition of the membrane [11, 12]. Apart from that, the characteristic of membrane surface has a huge role in most of the fluid separation during membrane filtration process [13]. Membrane surface modification can be categorized into two main processes; physical and chemical methods [14]. Physical surface modification includes blending, coating, plasma, heat and solvent vapor treatment [15,16] while chemical surface modification includes chemical coupling, free radical graft polymerization and atom transfer radical polymerization [17]. Choosing the best surface modification method is important since nanofibers require less harsh condition and controlled reaction. This to prevent deterioration of membrane morphology because of their nanoscale size [18, 19].

In this study, coating has been chosen as a post surface modification method for NFM. Park et al. [20] studied on the performance of polyvinylidene fluoride nanofiber support coated with polyvinyl alcohol for forward osmosis application. It is reported that the modified nanofiber support has higher hydrophilicity, porosity and mechanical strength with excellent flux performance at 34.2 $L/m^2/h$. As for the usage of ionic liquid as the coating layer of electrospun NFM, it does not usually be applied for treatment of wastewater.

In this study, direct immersion of electrospun nylon 6,6 NFM into 1-butyl-3-methylimidazolium chloride (BMIM-Cl) was applied for wastewater treatment. BMIM-Cl has great effect in NFM in the aspect of viscosity and conductivity of the membrane, as well as the morphology of membrane [21]. Nylon 6,6 polymer is chosen since it has great hydrophilicity [22,23] and great resistance to chemicals. Materials that have good hydrophilicity are more resistant to fouling problems [24]. To date, BMIM-Cl has never been used as a coating layer for electrospun nylon 6,6 NFM. Apart from that, characterization of membrane such as surface morphology, porosity and contact angle were studied together with wastewater permeability and its rejection performance.

Materials and Methods

Materials

Materials used for this research are formic acid (98-100%, MERCK, Kenilworth, NJ, USA), glacial acetic acid (99.85%, VWR Chemicals, Radnor, PA, USA), nylon 6,6 pellets (Sigma Aldrich, St. Louis, MO, USA), 1-Butyl-3-methylimidazolium chloride ≥98.0% (HPLC, MERCK, Kenilworth, NJ, USA), De-ionized water (PURELAB flex, ELGA LabWater, United Kingdom).

.

Preparation of nylon 6,6 solution

Nylon 6,6 solution was prepared by dissolving nylon 6,6 pellets (14.0 wt. %) in a mixture of glacial formic acid and acetic acid with ratio of 1:1. Nylon 6, 6 pellets was gradually added into the mixture of formic acid and acetic acid. The solution was then stirred at 180 rpm with temperature of 60 ^{o}C and left overnight for 12 hours until homogenous solution was formed.

Electrospinning of nylon 6,6 NFM

A 5 mL syringe was used as the solution container which was attached with capillary needle with tip of 0.8 mm inner diameter. The flowrate was set at 0.4 mL hr^{-1}. For the voltage, it was set at 20.0 kV and the distance from the tip of the needle to the collector was set at 15 cm. The collector was covered with aluminium foil and the rotation was set at 500 RPM. The setup of electrospinning is shown in Figure 1.

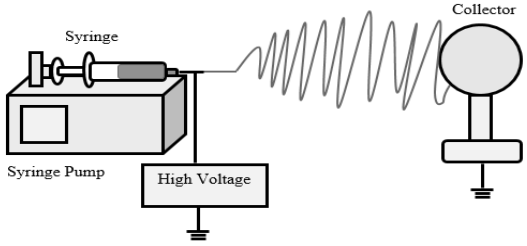


Figure 1. Setup of electrospinning

Coating of nylon 6,6 NFM with BMIM-chloride

BMIM-chloride was diluted into de-ionized water with concentration of 1%, 2%, 3%, 4%, and 5% as shown in Table 1. The membranes with same area size were immersed directly into each ionic liquid concentration for 12 hours. All of the membranes were then taken out and exposed to open air to dry for 3 hours.

Table 1. Preparation of BMIM-Cl based on concentration

Concentration (%)	Volume of Ionic Liquid (mL)	Volume of De-Ionized Water (mL)
1	1	99
2	2	98
3	3	97
4	4	96
5	5	95

Characterization

The membranes were characterized based on surface morphology, Fourier infrared spectra (FTIR), porosity and water contact angle. Field Emission Scanning Electron Microscope (FESEM, Model: VPFESEM, Zeiss Supra55 VP, Feldbach, Switzerland) was used to study the surface of the electrospun nylon 6,6. Fourier transform infrared spectroscopy (FTIR, Model: Thermo Scientific Nicolet, United State) was used to study the interaction between BMIM-chloride and nylon 6,6. Apart from that, dry-wet method was used to measure membrane porosity where the membrane weight and volume were measured. Goniometer was used to find the water contact angle of membrane by using interfacial tension method (IFT, Model: OCA 20, Data Physics, Filderstadt, Germany).

Permeability analysis for wastewater treatment

For this test, the wastewater was obtained from Universiti Teknologi PETRONAS wastewater treatment plant. The permeability test for membrane was measured by using Cross-flow Microfiltration Testing Unit (the model was made and provided by Engineering, Prototyping & Innovation Centre (EPIC), one of the Universiti Teknologi PETRONAS service centre) with pressure of 0.1 bar. The effective membrane filtration area was 9 cm^2. The membrane was put between the set-up casing and the feed was pumped through the membrane. Then, the permeate volume was measured each 10 minutes until it reaches steady-state.

Rejection analysis for wastewater treatment

Some permeate samples after permeability analysis were kept for rejection analysis. This analysis included turbidity, chemical oxygen demand (COD) and phosphorus analysis. They were measured by using turbidity meter (Hach 2100Q Turbidity Meter) and Hach-Lange kits for COD and phosphorus.

Results and Discussion

Membrane properties

Table 2 shows the summary of the membrane properties for NFM. From the table, it is found that, the pore size and porosity of the membrane decrease as the concentration of BMIM-Cl increases. This is due to the increase of fiber diameter when BMIM-Cl is added as shown in Figure 2. By using ImageJ software, the fiber diameter of the membrane is found to be in the range of 600 to 1300 nm.

Table 2. Summary of membrane properties

Membrane	BMIM-Cl concentration (%)	Fiber Diameter (µm)	Pore Size (µm)	Porosity (%)
M-0	0	600±80	0.07	85.6
M-1	1	800±60	0.06	82.3
M-2	2	1100±30	0.06	76.8
M-3	3	1100±70	0.05	77.4
M-4	4	1200±100	0.04	79.7
M-5	5	1200±100	0.04	65.2

Figure 2 shows the images of untreated nylon 6,6 NFM and treated nylon 6,6 NFM at 10.0 kx magnification. From the figures, it can be clearly seen that the diameter of fiber increases as the membranes were soaked with BMIM-Cl due to BMIM-Cl nanoparticles coated onto the fiber surface [25]. By increasing the concentration of BMIM-Cl, the fiber diameter will also increases. Apart from that, it can be observed that the number of coating layers which has a honeycomb structure increase as the concentration of BMIM-Cl increases (see the red arrows). From here, it indicates that the coating layer of BMIM-Cl has successfully attached to the surface of NFM.

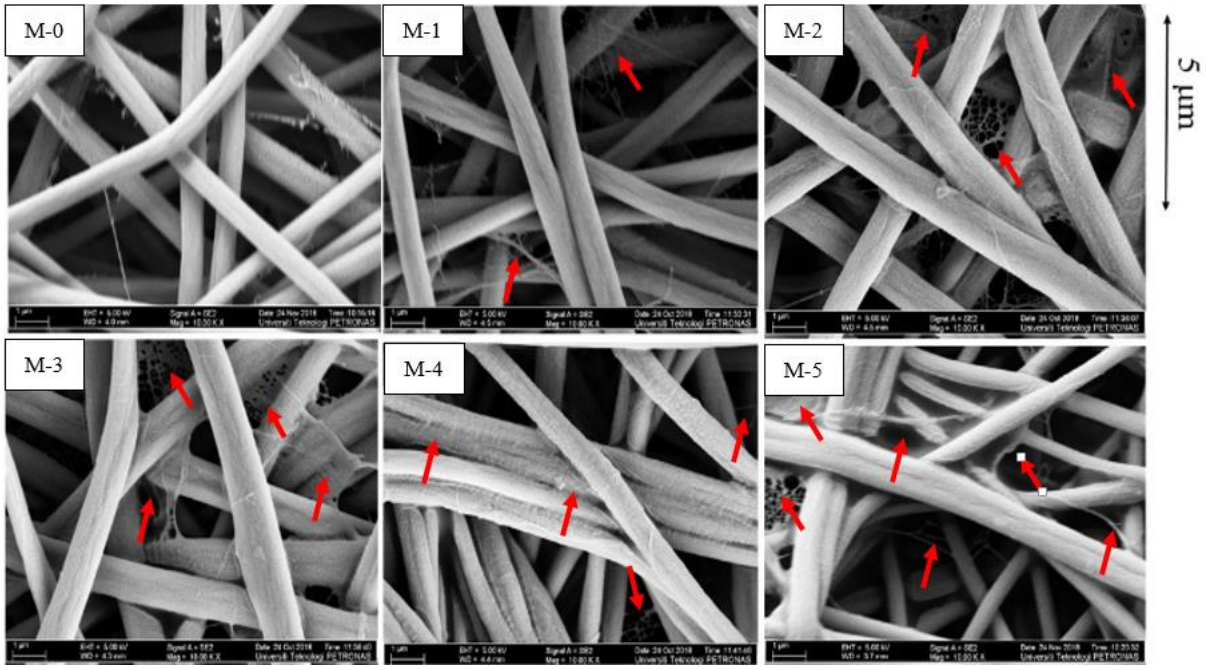


Figure 2. The FESEM images of untreated nylon 6,6 NFM and treated nylon 6,6

Figure 3 shows the graph of water contact angle *vs* time for untreated nylon 6,6 NFM and treated nylon 6,6 NFM. This is common for hydrophilic membrane as it will absorb the water over time. Based on the figure, the higher the concentration of BMIM-Cl, the faster the time taken for the membrane to reach 0°. In other words, the presence of BMIM-Cl improves the membrane hydrophilicity due to hydrophilic nature of BMIM-Cl [26]. Nevertheless, all of the membranes have contact angle of less than 90° which indicate that nylon 6,6 NFM exhibited good hydrophilic properties [27, 28].

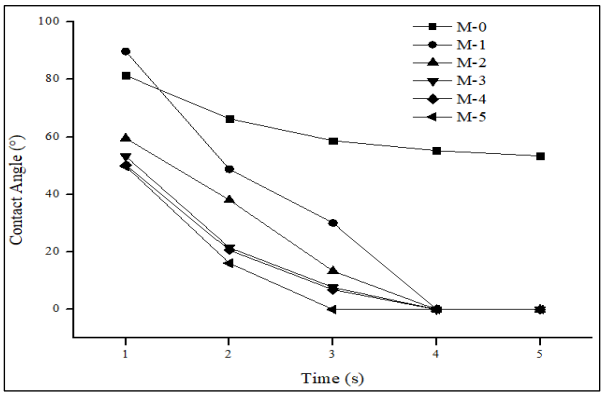


Figure 3. Water contact angle vs time for untreated nylon 6,6 NFM and treated nylon 6,6 NFM

Fourier-transform infrared spectroscopy (FTIR)

Figures 4 and 5 show the comparison of FT-IR graphs between M-0 and M-1 NFM. As can be observed from the figures, M-1 NFM has similar characteristics peaks as M-0 NFM. Based on both patterns, N-H stretching is indicated by the significant band at 3299 cm^{-1}. Same as CH_2 stretching, it can be observed at peaks 2933 cm^{-1} for both patterns. The peaks observed at 1634 cm^{-1} (M-0) and 1632 cm^{-1} (M-1) are attributed by the amide I band. For

amide II band, it can be observed at peak 1536 cm^{-1} (M-0) and 1535 cm^{-1} (M-1). From these patterns, it can be concluded that the addition of BMIM-Cl does not bring any significant difference in terms of chemical properties of nylon 6,6 NFM and only coat the outer layer of the membrane as can be observed in the increase number of web pattern on the surface of NFM in Figure 2.

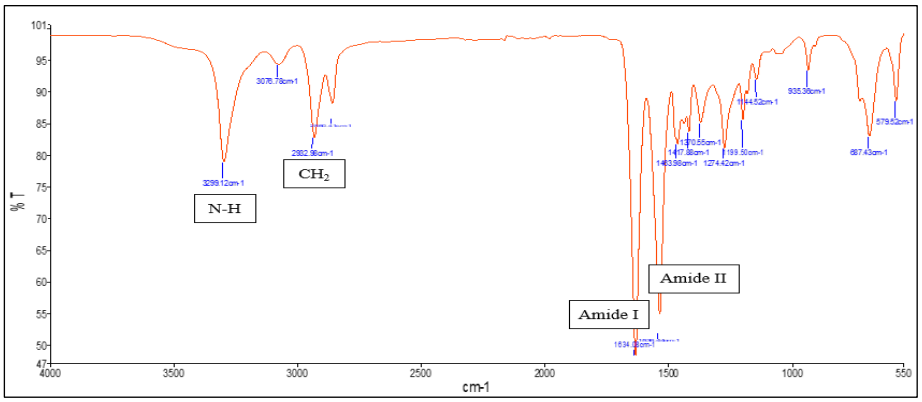


Figure 4. FT-IR pattern for M-0

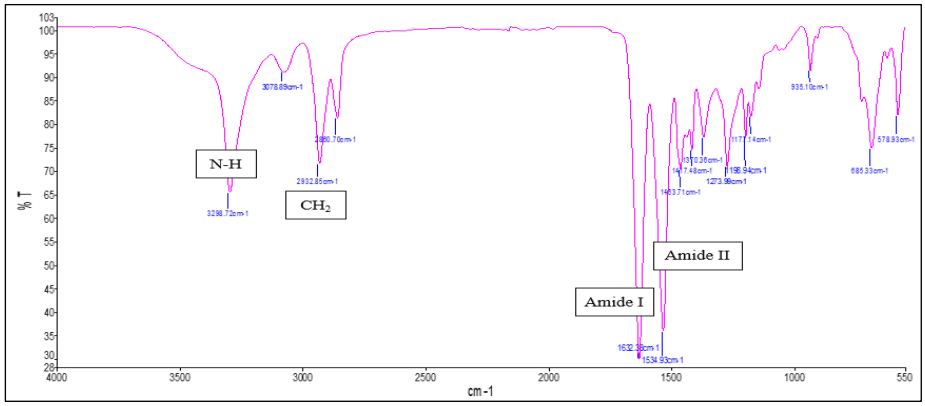


Figure 5. FT-IR pattern for M-1

Permeability test with wastewater

Figure 6 shows the wastewater permeability for untreated nylon 6,6 NFM and treated nylon 6,6 NFM. Based on the figure, the time taken for each membrane to reach steady-state varies where M-5 took the longest time to reach steady-state. This indicates that the soaking of BMIM-chloride prolongs the time taken for the membrane to get fouled. This is due to increase in membrane hydrophilicity where the waste particles unable to adsorb onto the membrane surface. As for the final permeability, all the membranes soaked with BMIM-chloride has the same value of permeability at 400 L/m^2.h.bar. As for M-0, it has the lowest final permeability of 333 L/m^2.h.bar. Note that the final permeability for all NFM coated with BMIM-Cl reached 400 L/m^2h.bar. Despite the small difference of final permeability between the membranes, the results significantly proved that soaking method affect the permeability of the membrane as there is large gap of time taken to reach steady state between M-0 and M-5.

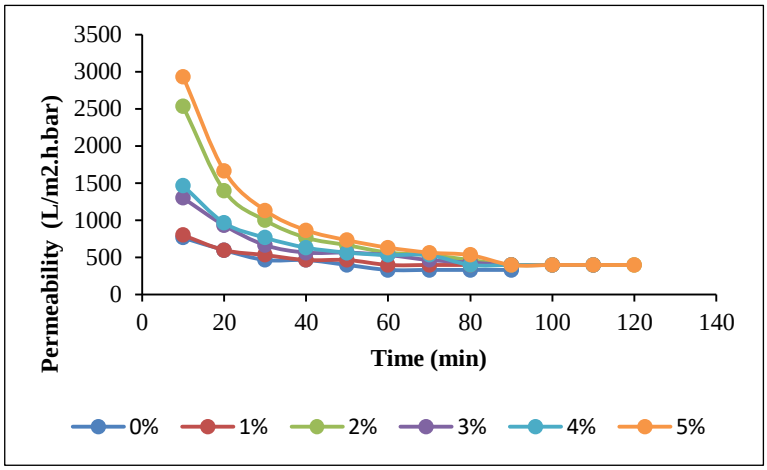


Figure 6. Wastewater permeability of nylon 6,6 with ranges of BMIM-Cl concentration from 0% to 5%

Rejection analysis

The permeate from the permeability test has been collected to be analysed for turbidity, COD and phosphorus test. The results in Table 3 show that more than 90% of rejection able to be achieved for turbidity, COD and phosphorus when nylon 6,6 NFM is coated with BMIM-chloride. This is due to the increase in fiber diameter and reduce in membrane pore size which enable the membranes to reject smaller particles inside the wastewater. From these results, it can be concluded that the soaking of BMIM-chloride onto the NFM is effective in treating wastewater as smaller particles inside the wastewater able to be rejected.

Table 3. Rejection analysis

Sample	Turbidity (NTU)	Rejection Analysis	
		COD Rejection (%)	Phosphorus Rejection (%)
Wastewater	2.72	-	-
Pure water	0.14	-	-
Permeate 0%	0.64	88.0	88.0
Permeate 1%	0.27	99.9	99.9
Permeate 2%	0.25	99.9	99.9
Permeate 3%	0.24	99.9	99.9
Permeate 4%	0.23	99.9	99.9
Permeate 5%	0.23	99.9	99.9

Conclusion

In this study, the soaking method by using BMIM-Cl has proven to be successfully influence the physio chemical of nylon 6,6 NFM. The soaking of BMIM-Cl increases the fibre diameter and hence reduce the pore size of the membrane. FT-IR results also concludes that the BMIM-chloride interaction only occur on the surface of nylon 6, 6 NFM. For the permeability analysis, M-5 NFM took the longest time to reach steady-state. The rejection test results also show that the soaked membrane able to achieve more than 90% of rejection for turbidity compared to absence of BMIM-Cl. As for COD and phosphorus test, all of the treated membranes able to achieve 100% of rejection. For further study, it is suggested to make other comparison with other surface modification methods such as solvent

vapour treatment and blending methods. As for example, for solvent vapor treatment, the time taken for the exposure of ionic liquid to the nanofiber membrane should be taken into consideration and on how it can affect the nanofiber membrane properties and characterization.

Acknowledgement

We would like to acknowledge Universiti Teknologi PETRONAS for providing grants (UTP grant number (YUTP): 0153AA-H29) for conducting the research activities.

References

1. Ibrahim, N. A., Wirzal, M. D. H., Nordin, N. A. H., and Halim, N. S. A. (2018). Development of polyvinylidene fluoride (PVDF)-ZIF-8 membrane for wastewater treatment. *IOP Conference Series: Earth and Environmental Science*, 140(1): 012021.
2. Bae, J., Baek, I. and Choi, H. (2016). Mechanically enhanced PES electrospun nanofiber membranes (ENMs) for microfiltration: The effects of ENM properties on membrane performance. *Water Research*, 105: 406-412.
3. Liao, Y., Loh, C., Tian, M., Wang, R., and Fane, A. G. (2018). Progress in electrospun nanofibrus membranes for water treatment: Fabrication, modification and applications. *Progress in Polymer Science*, 77: 69-94.
4. George, G., Bhoria, N., Alhallaq, S., Abdala, A. and Mittal, V. (2016). Polymer membranes for acid gas removal from natural gas. *Separation and Purification Technology*, 158: 333-356.
5. Singh, R. (2006). Hybrid membrane systems for water purification: Technology, systems design and operations. Elsevier.
6. Eliseus, A., Bilad, M. R., Nordin, N. A. H. M., Putra, Z. A. and Wirzal, M. D. H. (2017). Tilted membrane panel: a new module concept to maximize the impact of air bubbles for membrane fouling control in microalgae harvesting. *Bioresource Technology*, 241 (Supplement C): 661-668.
7. Chang, I. S., Le Clech, P., Jefferson, B., and Judd, S. (2002). Membrane fouling in membrane bioreactors for wastewater treatment. *Journal of Environmental Engineering*, 128(11): 1018-1029.
8. Foong, C. Y., Wirzal, M. D. H., and Bustam, M. A. (2020). A review on nanofibers membrane with amino-based ionic liquid for heavy metal removal. *Journal of Molecular Liquids*, 297: 111793.
9. Al-Husaini, I. S., Yusoff, A. R. M., Lau, W.J., Ismail, A. F., Al-Abri, M. Z., and Wirzal, M. D. H. (2019). Iron oxide nanoparticles incorporated polyethersulfone electrospun nanofibrous membranes for effective oil removal. *Chemical Engineering Research and Design*, 148: 142-154.
10. Bilad, M. R., Westbroek, P. and Vankelecom, I. F. J. (2011). Assessment and optimization of electrospun nanofiber-membranes in a membrane bioreactor (MBR). *Journal of Membrane Science*, 380(1): 181-191.
11. Qin, Y., Yang, H., Xu, Z, and Li, F. (2018). Surface modification of polyacrylonitrile membrane by chemical reaction and physical coating: comparison between static and pore-flowing procedures. *ACS Omega*, 3(4): 4231-4241.
12. Al-Husaini, I. S., Yusoff, A. R. M., Lau, W. J., Ismail, A. F., Al-Abri, M. Z., Al-Ghafri, B. N., and Wirzal, M. D. H. (2019). Fabrication of polyethersulfone electrospun nanofibrous membranes incorporated with hydrous manganese dioxide for enhanced ultrafiltration of oily solution. *Separation and Purification Technology*, 212: 205-214.
13. Kochkodan, V., Johnson, D. J., and Hilal, N. (2014). Polymeric membranes: Surface modification for minimizing (bio) colloidal fouling. *Advances in Colloid and Interface Science*, 206 (Supplement C): 116-140.
14. Kim, H.J., Park, S. J., Park, C. S., Le, T.-H., Hun Lee, S., Ha, T. H., Kim, H., Kim, J., Lee, C.S., Yoon, H., and Kwon, O. S. (2018). Surface-modified polymer nanofiber membrane for high-efficiency microdust capturing. *Chemical Engineering Journal*, 339: 204-213.
15. Vanangamudi, A., Yang, X., Duke, M. C., and Dumee, L. F. (2018). Nanofibers for membrane applications. In A. Barhoum, M. Bechelany, and A. Makhlouf (Eds.), *Handbook of Nanofibers* Springer International Publishing: pp. 1-24.
16. Nasreen, S. A. A. N., Sundarrajan, S., Nizarm, S. A. S., Balamurugan, R. and Ramakrishna, S. (2013). Advancement in electrospun nanofibrous membranes modification and their application in water treatment. *Membranes (Basel)*, 3 (4): 266-284.
17. Asadollahi M., Bastani, D., and Musavi, S. A. (2017). Enhancement of surface properties and performance of reverse osmosis membranes after surface modification: A review. *Desalination*, 420: 330-383.

18. Hilal, N., Khayet, M. and Wright, C. J. (2016). Membrane modification: Technology and applications. CRC Press.
19. Khayet, M. (2013). Polymeric nano-fibers and modified nano-fibers assembly in 3D network for different potential applications. *Journal of Materials Science & Nanotechnology*, 1 (1): 1-4.
20. Park, M. J., Gonzales, R. R., Abdel-Wahab, A., Phuntsho, S., and Shon, H. K. (2018). Hydrophilic polyvinyl alcohol coating on hydrophobic electrospun nanofiber membrane for high performance thin film composite forward osmosis membrane. *Desalination*, 426: pp. 50-59.
21. Javed, K., Krumme, A., Krasnou, I., Mikli, V., Viirsalu, M., Plamus, T., Mendez, J. D. (2017). Impact of 1-butyl-3-methylimidazolium chloride on the electrospinning of cellulose acetate nanofibers. *Journal of Mactomolecular Science, Part A: Pure and Applied Chemistry*, 2017: 1-6.
22. Abd Halim, N. S., Wirzal, M. D. H., Bilad, M. R., Md Nordin, N. A. H., Adi Putra, Z., Mohd Yusoff, A. R., Narkkun, T., and Faungnawakij, K. (2019). Electrospun nylon 6,6/ZIF-8 nanofiber membrane for produced water filtration. *Water*, 11(10): 2111.
23. Abd Halim, N. S., Wirzal, M. D. H., Bilad, M. R., Md Nordin, N. A. H., Adi Putra, Z., Sambudi, N. S., and Mohd Yusoff, A. R. (2019). Improving performance of electrospun nylon 6,6 nanofiber membrane for produced water filtration via solvent vapor treatment. *Polymers*, 11(12): 1-11.
24. Bilad, M. R., Azizo, A. S., Wirzal, M. D. H., Jia Jia, L., Putra, Z. A., Nordin, N. A. H. M. and Yusoff, A. R. M. (2018). Tackling membrane fouling in microalgae filtration using nylon 6,6 nanofiber membrane. *Journal of Environmental Management*, 223: 23-28.
25. Yang, J., He, F., Wu, H., Liang, Y., Wang, Y., and Sun, Z. (2018). Engineering surface and optical properties of TiO_2-coated electrospun PVDF nanofibers via controllable self-assembly. *Nanomaterials (Basel)*, 8(9): 794.
26. Shrotri, A., Kobayashi, H., and Fukuoka, A. (2017). Chapter Two - Catalytic Conversion of Structural Carbohydrates and Lignin to Chemicals, in Advances in Catalysis, vol. 60, C. Song, Ed. Academic Press: pp. 59–123.
27. Zhang, M., Liao, B., Zhou, X., He, Y., Hong, H., Lin, H. and Chen, J. (2015). Effects of hydrophilicity/hydrophobicity of membrane on membrane fouling in a submerged membrane bioreactor. *Bioresource Technology*, 175: 59-67.
28. Fujioka, T. and Nghiem, L. (2013). Modification of a polyamide reverse osmosis membrane by heat treatment for enhanced fouling resistance. *Water Science and Technology: Water Supply*, 13(6): 1553-1559.

Malaysian Journal of Analytical Sciences (MJAS)
Published by Malaysian Analytical Sciences Society

CHEMICAL COMPOSITION OF ESSENTIAL OILS FROM LEAF EXTRACT OF PANDAN, *Pandanus amaryllifolius* ROXB.

(Komposisi Kimia Minyak Pati daripada Ekstrak Daun Pandan, *Pandanus amaryllifolius* Roxb.)

Maisarah Mohamed Zakaria[1], Uswatun Hasanah Zaidan[1,2]*, Suhaili Shamsi[1], Siti Salwa Abd Gani[3]

[1]*Department of Biochemistry, Faculty of Biotechnology and Biomolecular Sciences*
[2]*Halal Products Research Institute*
[3]*Department of Agriculture Technology, Faculty of Agriculture*
Universiti Putra Malaysia, 43400 UPM Serdang, Selangor, Malaysia

**Corresponding author: uswatun@upm.edu.my*

Received: 28 April 2019; Accepted: 27 January 2020

Abstract

Pandan or *Pandanus amaryllifolius,* an aromatic tropical plant species, has gained much interest among researchers in the quest to develop further use of its essential oils beyond food flavoring, traditional medicines and limited food industries. There has been lack of comprehensive investigations on therapeutic activities of its essential oils (EOs) that may have potential use as therapeutic agents in the treatment of various health issues. The present investigation reports on the chemical composition of EOs from leaf extracts sourced from three different locations in Peninsular Malaysia. Leaf extracts of *P. amaryllifolius* were drawn out from leaves of plants grown in the states of Kedah, Selangor and Johor using Soxhlet extraction method with ethanol as the solvent resulting in extraction yields of 21.08%, 20.54%, and 15.87%, respectively. The leaf extracts were further analyzed by gas-chromatography-mass spectrometry (GC-MS) and Fourier transform-infrared spectroscopy (FTIR). A total of 57 chemical compounds were identified comprising of fatty acids, steroids, aromatic compounds and non-polar components making up 80.49-84.74% of total oils. A total of 11 common peaks were determined consisting of pyranone (0.78-1.74%); coumaran (1.12-5.31%); 1,4-di-tert-butylphenol (2.68-6.10%); pinane (0.80%-1.46%); ethyl palmitate (1.04%-1.66%); 3,6,6-trimethyl-1-(1-phtalazinyl)-1,5,6,7-tetrahydro-4H-indazol-4-one (0.75-1.69%); phytol (1.43-6.19%); purpurogallin (1.34-2.02%); squalene (14.14-33.83%); decamethyltetrasiloxane (0.27-0.52%); and vitamin E (2.58-3.66%) from the three different locations. Stigmasterol was not detected from plants sourced in Selangor but was detected in samples from Kedah and Johor with an amount of 6.73% and 9.05%, respectively. There were 16 common peaks observed in all IR spectra from the three plants' sources exhibiting functional groups. The findings from the study present useful additional information to existing literature on extractable EOs from pandan for potential use in pharmaceutical or nutraceutical applications in the production of functional food.

Keywords: *Pandanus amaryllifolius,* chemical composition, essential oils, functional group

Abstrak

Pandan atau *Pandanus amaryllifolius,* satu spesies tumbuhan aromatik tropika, telah mendapat perhatian di kalangan penyelidik dalam usaha membangunkan penggunaan minyak pati (EO) pandan selanjutnya melebihi kegunaan sebagai perasa makanan, perubatan tradisional dan dalam industri makanan yang terhad. Terdapat kekurangan penyelidikan yang menyeluruh mengenai aktiviti terapeutik EO yang mungkin mempunyai potensi sebagai ejen terapeutik dalam rawatan berbagai isu kesihatan. Penyelidikan ini melaporkan komposisi kimia EO daripada ekstrak daun dari tiga lokasi berbeza di Semenanjung Malaysia. Ekstrak daun *P. amaryllifolius* telah dihasilkan daripada pokok yang ditanam di negeri-negeri Kedah, Selangor dan Johor dengan menggunakan kaedah pengekstrakan Soxhlet bersama etanol sebagai pelarut dan menghasilkan masing-masing 21.08%, 20.54%, dan 15.87%. Selanjutnya, ekstrak daun telah dianalisis dengan menggunakan kromatografi gas-spektrometri jisim (GC-MS) dan spektroskopi inframerah transformasi Fourier (FTIR). Sejumlah 57 sebatian kimia telah dikenal pasti yang terdiri daripada asid

lemak, steroid, sebatian aromatik dan komponen bukan berkutub meliputi 80.49-84.74% minyak pati yang diperolehi. Terdapat sejumlah 11 puncak persamaan dan telah dikenal pasti sebagai mengandungi piranon (0.78-1.74%); koumaran (1.12-5.31%); 1,4-di-tert-butilfenol (2.68-6.10%); pinan (0.80-1.46%); etil palmitat (1.04-1.66%); 3,6,6-trimetil-1-(1-pitalazinill)-1,5,6,7-tetrahydro-4H-indazol-4-on (0.75-1.69%); fitol (1.43-6.19%); purpurogalin (1.34-2.02%); skualin (14.14-33.83%); dekamiltetrasiloxan (0.27-0.52%); dan vitamin E (2.58-3.66%) di kalangan tiga minyak pati pandan dari lokasi berbeza. Stigmasterol tidak dapat dikesan daripada pokok yang diperolehi dari Selangor tetapi di rekod diperolehi dari sampel Kedah dan Johor masing-masing dengan 6.73% dan 9.05%. Sebanyak 16 puncak persamaan diperolehi di semua spektrum IR daripada tiga sumber pokok dan mempamerkan kumpulan berfungsi. Keputusan daripada kajian mengemukakan informasi tambahan yang kepada penulisan sedia ada mengenai potensi EO yang boleh diekstrak dan yang mempunyai potensi dalam kegunaan farmaseutikal dan nutraseutikal dalam pengeluaran makanan.

Kata kunci: *Pandanus amaryllifolius,* komposisi kimia, minyak pati, kumpulan berfungsi

Introduction

Pandanus amaryllifolius or Pandan, belonging to the genus Pandanus, is a tropical plant species commonly used in South and Southeast Asian cooking as a flavoring. Its unique flavor and aroma are contributed by a compound, 2-acetyl-1-pyrroline (2AP) which enhances the sweet flavor of many Asian dishes [1]. The rice-aromatic compound can be also found in *Vallaris glabra* Ktze or Bread Flower, Kerak Nasi or Bunga Kesidang in Malay. Traditionally, pandan leaves have also been used to refresh body, reduce fever and relieves indigestion [2]. A study by Balinado and Chan [3] documented that the decoction of pandan leaves helped to cure urinary tract infection, hypertension, abdominal pain, and kidney problems. Traditionally, the Malays believe that pandan leaves can rid body odor for hygienic purposes as well as ward off mystical forces through post-partum bath among Malay women in the state of Kedah [4].

Pandan leaves have been widely used in medicinal applications using their aqueous extracts. However, the beneficial effects of the extracts containing essential oils (EOs) have not been thoroughly investigated. It is well-known that plants' EOs have been used in therapeutic treatments since the 15th century. EO is a concentrated hydrophobic aroma compound containing major active secondary metabolites including terpenes and oxygenated compounds which are known to be associated with sources of many therapeutic activities [5]. Various studies have reported that monoterpenes and sesquiterpenes are the predominant constituents of EOs from many plants [6-8] such as roses [9], cinnamon [10], lemon [11] and lavender [12]. Various tropical plants in Malaysia have gained the attention of researchers for being rich in these compounds and have prompted interests in the exploration of pharmaceutical properties of plants' EOs.

Extraction of plants' EOs is an essential procedure. The Soxhlet method is a popular extraction technique that has been proposed in 1879 by Franz Von Soxhlet. The method is a standard technique widely used to extract fats and oils to study and analyze bioactive compounds. The Soxhlet method has been reported to be a suitable technique as it takes shorter time for extraction and less solvent use [13] as well as its simplicity to handle and relatively safe [14]. This classical extraction method has proven to yield more phenolic content than the cold-pressed oils technique of Al Juhaimi and Özcan [15].

Gas chromatography-mass spectroscopy (GC-MS) is a tool capable of identifying active principles in plants' extractions. It identifies compounds such as fatty acids, steroids, aromatic compounds, and non-polar components with high separation efficiency and sensitivity to detect components in a mixture especially on volatiles compounds [16]. Gomathi et al. [17] added that GC-MS combines two analytical techniques into one method that analyzes mixtures of chemical compounds where the gas chromatography separates the components while the mass spectroscopy analyzes the components into individual constituent. Another analysis that is traditionally used in bioanalysis is Fourier Transform Infrared Spectroscopy (FT-IR) which is an adsorption spectroscopy that uses light to emit bright rays in the infra-red wavelength range to obtain an infrared spectrum that gives characteristics of the components in a mixture of solid, liquid or gas. Each compound has a specific infrared spectrum depending on its molecular structure.

In a study by Ghasemzadeh and Jaafar [18], leaf extract of *P. amaryllifolius* from Bachok in northern part of Peninsular Malaysia registered the highest total phenolic content, total flavonoid content, antioxidant activity, and anticancer activity compared to extracts from Pontian in southern part of Peninsular Malaysia. Ghasemzadeh et al. [19] recorded that bioactivities of leaf extracts and their bioactive components present from *Etlingera elatior* flower extracts were affected due to different geographical locations. The present study was conducted to evaluate chemical compositions of *P. amaryllifolius* EOs from different locations of north (Kedah), west (Selangor) and south (Johor) Malaysia representing the upper middle and bottom regions of the peninsular.

Materials and Methods

Sample preparation and essential oils extraction

Fresh leaves of *P. amaryllifolius* were obtained from plants originally planted in three states of Kedah, Selangor, and Johor. Harvested leaves were thoroughly washed with tap water to remove soil and dirt. The leaves were cut into small pieces to promote large surface area for rapid drying process. Subsequently, the leaf samples were frozen and dried for 48 hours using a freeze dryer. The cut leaves were ground into powder and kept in dark bottles. Samples of 5.0 g each of the ground leaves were weighted and placed in thimbles before inserting in the Soxhlet extractor chamber. A 250 mL of boiling flask was filled with 180 mL of ethanol as the extraction solvent which was heated to reflux for 10 hours. The product was collected and concentrated using a rotary evaporator at a temperature of 50 ºC. The samples were kept in airtight containers at under 4 ºC.

Gas chromatography-mass spectrometry analysis

GC-MS analysis was conducted using 7890A gas chromatography with 5975 Series mass spectrometer (Agilent, American). A fused silica capillary HP-5 ms column was used for separation. Electron ionization system with ionization energy of 70 eV was used and helium gas as the carrier gas at a constant flow rate of 1 mL/min. The injector and mass transfer line temperatures were set at 250 ºC and 300 ºC, respectively while the oven temperatures were set up from 50 ºC to 200 ºC at 8 ºC/min. Plant samples were kept at isothermal for 20 minutes and finally raised to 300 ºC at 10 ºC/min. Diluted samples (1/100 v/v, in ethanol) of 0.2 µL each were manually injected in split less mode. Identification of compounds of the EOs was based on GC retention times registered on the capillary column, with computer matching of mass spectra with those of standards. Other qualitative analyses was done upon mass spectra fragmentation patterns with similar compounds and principle (major) compounds with peak areas of more than 2% from the data base.

Fourier transform infrared spectroscopy analysis

FTIR spectrum of the EOs was analyzed using FTIR spectrometer (Nicolet 6700 from Thermo Scientific). The samples were run by using attenuated total reflection (ATR) method and measured with a number of 32 scans on the spectrum. The IR spectra were reported in percent transmittance in the range number regions of 500 to 4000 cm^{-1} with a resolution of 4 cm^{-1}. The functional groups were determined by IR correlation charts.

Results and Discussion

Oils extraction from *P. amaryllifolius*

Soxhlet extraction of all freeze-dried samples of *P. amaryllifolius* gave 21.08%, 20.54% and 15.87% of dark green wax oil yields (Figure 1) from Kedah, Selangor, and Johor, respectively, out of total dried leaves used. A study by Ghasemzadeh and Jaafar [18] found that samples of aqueous extracts of pandan leaves collected from state of Kelantan, the upper part of Peninsular Malaysia registered highest bioactivities compared to the lower parts of the Peninsular such as in states of Pahang and Johor. One possible factor affecting yields of EOs is the drying technique used. Freeze-drying of leaves using a freeze-dryer has the ability of maintaining and preserving plants' constituents as proven in a study by Yahya et al. [1] in which the highest extraction yield was obtained by freeze-drying followed by oven-drying.

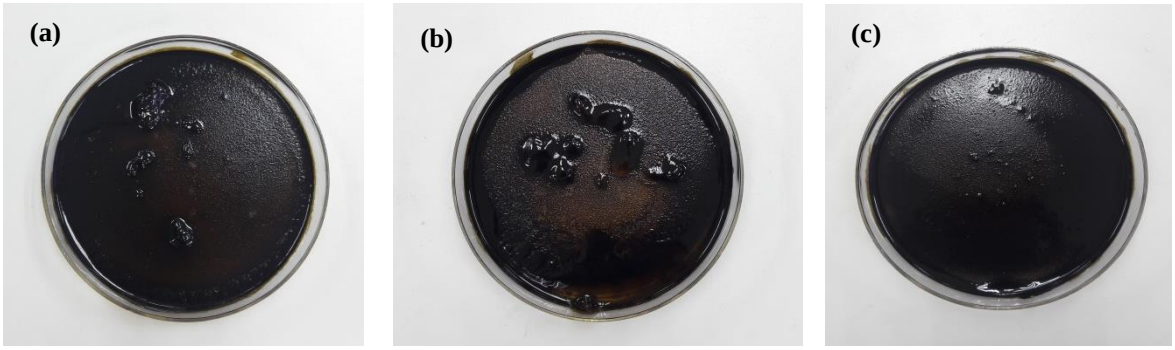


Figure 1. Dark-green-wax oil yields from (a) Kedah (21.08%), (b) Selangor (20.54%), and (c) Johor (15.87%)

Table 1. The main compounds identified in volatile oils extracted from *P. amaryllifolius* samples and the identified components of 11 common peaks from Kedah, Selangor and Johor

No.	Component	Common Peaks	RT*	Relative Peak Area (%)		
				Kedah	Selangor	Johor
1	Methoxyamine	-	4.320	0.17	1.18	ND
2	2-Cyclopentene-1,4-dione	-	5.014	0.11	0.25	ND
3	1,2-Cyclopentanedione	-	5.665	ND	1.50	ND
4	3-methylcyclopentanone	-	6.576	ND	ND	1.06
5	2-methyl-2pentenal	-	6.586	2.05	ND	ND
6	α-hydroxy-γ-butyrolactone	-	6.766	0.75	6.79	ND
7	Dimethylguanidine	-	8.678	ND	1.81	ND
8	Pyranone	1	9.583	1.74	1.06	0.78
8	Pyranone	1	9.583	1.74	1.06	0.78
9	Catechol	-	10.558	0.81	ND	0.33
10	Coumaran	2	10.881	5.31	1.12	2.42
11	Triethylene glycol	-	11.050	2.14	ND	ND
12	2-methoxy-4-vinylphenol	-	12.612	0.44	ND	0.40
13	Dimethyl lauramine	-	15.583	0.56	ND	0.71
14	1,4-di-tert-butylphenol	3	15.742	2.68	6.10	4.55
15	2,3,5,6-Tetrafluoroanisole	-	16.579	0.49	ND	0.51
16	Butyric acid silver	-	17.103	ND	ND	1.02
17	Ethyl (2-methylphenyl)carbamate	-	17.103	2.00	ND	ND
18	N-(Diethyl-λ-sulfanylidene)acetamide	-	17.701	ND	1.60	ND
19	3-(1-Ethoxyethoxy)butyl benzoate	-	17.833	1.99	ND	ND-
20	1-Nonadecene	-	19.676	0.27	ND	0.30
21	Ethyl coumarate	-	20.148	0.29	ND	0.20
22	Pinane	4	20.312	0.94	0.80	1.46
23	Methyl palmitic acid	-	21.678	0.27	ND	0.42
24	Ethyl palmitic acid	5	22.981	1.04	1.07	1.66

25	3,6,6-trimethyl-1-(1-phtalazinyl)-1,5,6,7-tetrahydro-4H-indazol-4-one	6	23.341	0.75	1.69	1.36
26	Phytol	7	26.025	4.35	1.43	6.19
27	Ethyl linolenate	-	27.884	0.92	ND	1.54
28	2,3,5-trimethylphenanthrene	-	44.326	0.30	ND	1.26
29	Purpurogallin	-	44.554	1.76	ND	1.56
30	4,5-diphenylimidazole	-	44.670	1.63	ND	ND
31	Purpurogallin	8	45.051	2.01	1.34	2.02
32	2,5-dipheylfuran	-	45.057	2.16	ND	ND
33	4,5-diphenylimidazole	-	45.126	ND	0.79	1.86
34	Purpurogallin	-	45.131	2.01	ND	ND
35	Hentriacontane	-	45.740	ND	1.76	ND
36	Purpurogallin	-	46.995	ND	ND	2.07
37	Flufylline	-	46.995	4.56	ND	ND
38	Icosane	-	47.090	ND	2.20	0.43
39	Octadecane	-	48.186	ND	1.72	ND
40	Squalene	9	48.488	14.14	33.83	16.92
41	1-Bromoicosane	-	49.124	ND	1.52	ND
42	Crotocin	-	49.452	0.92	2.26	ND
43	2,2,4-Trimethyl-3-(3,8,12,16-tetramethyl-heptadeca-3,7,11,15-tetraenyl)-cyclohexanol	-	49.452	ND	ND	1.27
44	Hexamethylcyclotrisiloxane	-	49.531	0.39	0.52	ND
45	2-(Adamantan-1-yl)-N-methylactamide	-	50.156	ND	1.15	0.79
46	Decamethyltetrasiloxane	10	50.087	0.27	0.48	0.52
47	β-tocopherol	-	50.474	1.07	ND	0.77
48	Vitamin E (α-tocopherol)	11	51.252	3.66	2.58	3.01
49	5-methyl-2-phenyl-1H-indole	-	52.290	2.37	ND	2.55
50	Stigmasterol	-	52.671	6.73	ND	9.05
51	Methyl trimethicone	-	52.677	ND	3.84	ND
52	2-Ethylacridine	-	53.386	ND	4.35	ND
53	Clionasterol	-	53.391	8.01	ND	9.10
54	4-decocyl 1,2-dimethyl 1,2,4-benzenecarboxylate	-	56.452	ND	ND	1.01
55	Methyl 2,2,6-trimethyl-1-[(1E)-3-oxo-1-buten-1-yl]-7-azabicyclo[4.1.0]heptane-7-carboxylate	-	56.532	1.08	ND	1.41
56	1,4-phenylenebis(trimethylsilane)	-	56.738	1.62	ND	ND
57	N-(4-methoxyphenyl)-2,2-dimethylpropanamide	-	56.749	ND	ND	2.32
			TOTAL	83.11	84.74	80.49

RT = Retention time, ND = Not detected

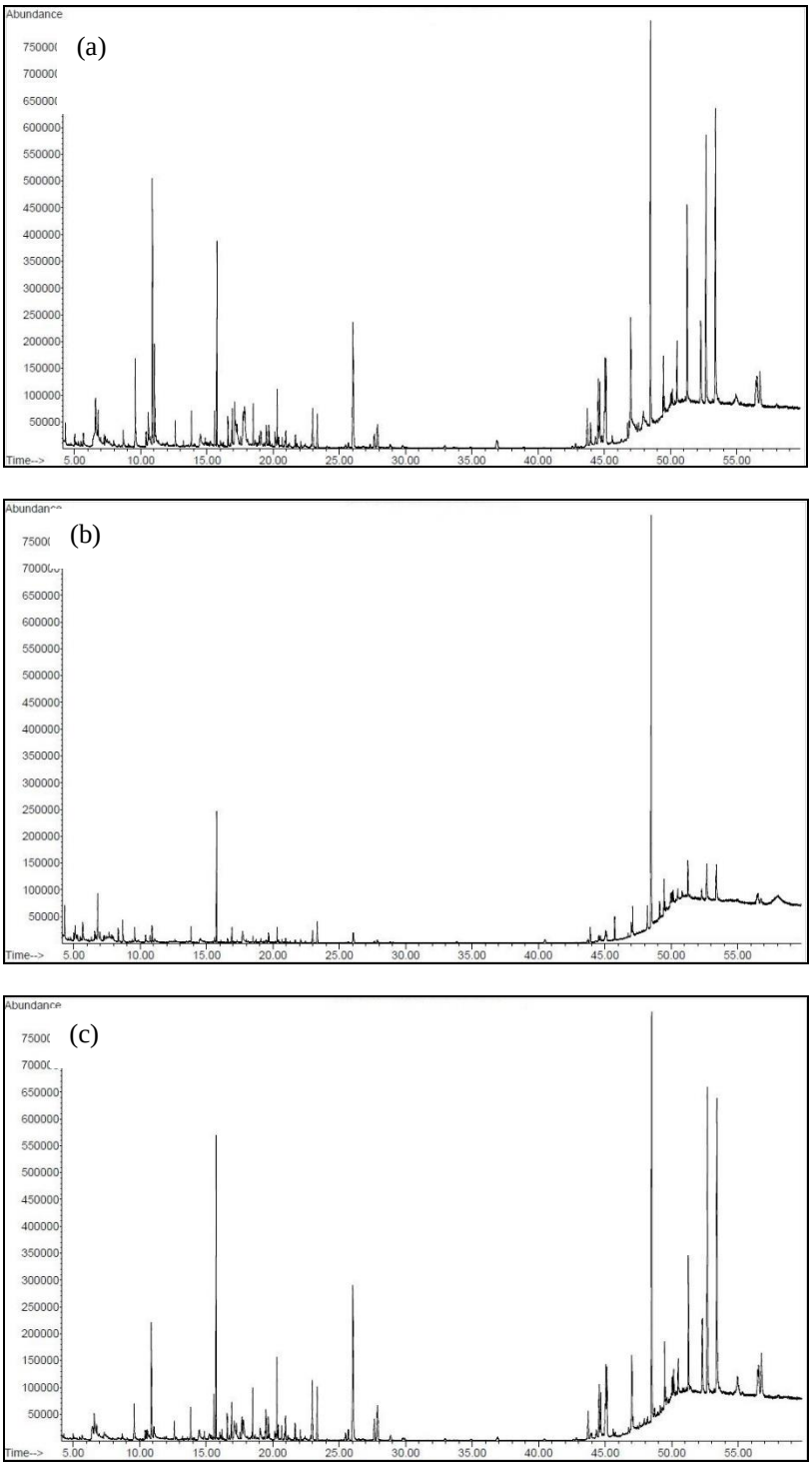


Figure 2. The GC-MS chromatograms of *P. amaryllifolius* essential oils from (a) Kedah, (b) Selangor, and (c) Johor

In the present study, volatile oils extracted from samples were analyzed by GC-MS and are shown in Table 1. A total of 57 components were identified in the samples from Kedah, Selangor, and Johor representing 83.11%, 84.74% and 80.49%, respectively. The total ion chromatograms of the samples are shown in Figure 2. The chromatograms demonstrate the chemical characteristics of the samples. The distributions of the peaks were distributed majority at retention time of 4.00 – 27.00 and 43.00 – 56.00. The EOs of the samples from the three states shared 11 similar peaks. These peaks were chosen as they existed in all chromatograms of all samples and named as "common peaks" which were pyranone (0.78-1.74%); coumaran (1.12-5.31%); 1,4-di-tert-butylphenol (2.68-6.10%); pinane (0.80-1.46%); ethyl palmitate (1.04-1.66%); 3,6,6-trimethyl-1-(1-phtalazinyl)-1,5,6,7-tetrahydro-4H-indazol-4-one (0.75-1.69%); phytol (1.43-6.19%); purpurogallin (1.34-2.02%); squalene (14.14-33.83%); decamethyltetrasiloxane (0.27-0.52%); and vitamin E (2.58-3.66%). Squalene and phytol were two components that were also identified in a study by Chen and Ge [20] with relative percentages of 16.81% and 42.15%, respectively.

The total of principal components of EOs of samples from Kedah, Selangor and Johor were 15, 8 and 11, respectively. In Kedah, the components were 2-methyl-2pentenal (2.05%), coumaran (5.31%), triethylene glycol (2.14%), 1,4-di-tert-butylphenol (2.68%), ethyl (2-methylphenyl)carbamate (2.00%), phytol (4.35%), purpurogallin (2.01%), 2,5-dipheylfuran (2.16%), flufylline (2.01%), purpurogallin (4.56%), squalene (14.14%), vitamin E (α-tocopherol) (3.66%), 5-methyl-2-phenyl-1H-indole (2.37%), stigmasterol (6.73%), and clionasterol (8.01%) while α-hydroxy-γ-butyrolactone (6.79%), 1,4-di-tert-butylphenol (6.10%), icosane (2.20%), squalene (33.83%), crotocin (2.26%), vitamin E (α-tocopherol) (2.58%), 2-ethylacridine (3.84%), methyl trimethicone (4.35%) are in Selangor. Furthermore, in Johor coumaran (2.42%), 1,4-di-tert-butylphenol (4.55%), phytol (6.19%), purpurogallin (2.02%), purpurogallin (2.07%), squalene (16.92%), vitamin E (α-tocopherol) (3.01%), 5-methyl-2-phenyl-1H-indole (2.55%), stigmasterol (9.05%), clionasterol (9.10%), and N-(4-methoxyphenyl)-2,2-dimethylpropanamide (2.32%). These components were mentioned as the principal compounds because of their peaks could be clearly observed from the chromatograms. These principal compounds gave significant difference as the dominant compounds which characterize the different origin of EOs.

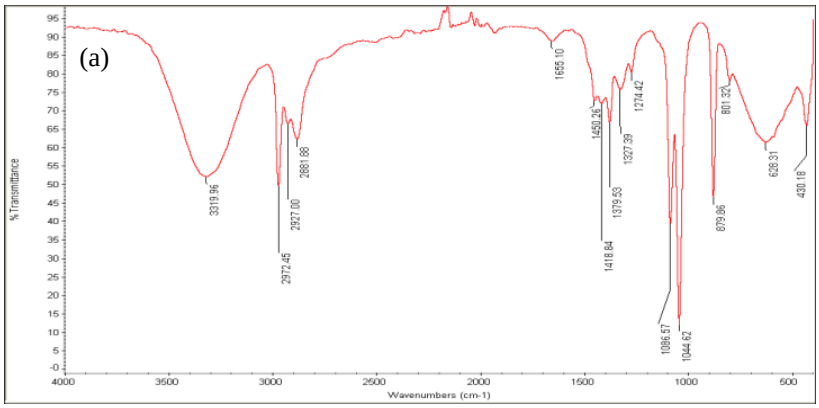
Squalene was identified as the major compound of EOs which contributed to the highest percentage area 14.14%, 33.83% and 16.92% of EOs from Kedah, Selangor, and Johor, respectively. Squalene is a compound similar to beta-carotene where it is an intermediate in the synthesis of cholesterol [21]. It is associated with very low density of lipoproteins and distributed in human tissue. At its greatest concentration, it has been documented to protect human skin from lipid peroxidation caused by ultraviolet exposures and other factors from ionizing radiation [21]. Phytol with 4.35%, 1.43% and 6.19% of EOs from Kedah, Selangor, and Johor, respectively was found as one of the components from the analysis done through GC-MS. Phytol ($C_{20}H_{40}O$) with a molecular weight of 296.539 g/mol has been reported by Zeb et al. [22] to have antibacterial, antimicrobial and insecticidal properties. One unique discovery proposed was that this terpene alcohol performs as a potential an anticancer candidate in pharmaceutical application [23]. The study was done on mice with DMBA-induced breast cancer where phytol showed its regulation on pro-carcinogen and apoptosis on cancer cells with the capacity to repair damaged cells. Other studies have shown that phytol is a precursor or limiting factor of Vitamin E ($C_{29}H_{50}O_2$) and Vitamin K1. Vitamin E, also known as tocopherol, was recorded in the EOs extracted from the plants under study with 3.66%, 2.58% and 3.01% content from Kedah, Selangor and Johor, respectively. It has been documented that this fat-soluble vitamin helps in maintaining skin moisture and restores the regular oil stability of the pores and skin [24]. The vitamin has been popular in treating minor sunburns where it heals damage caused by ultraviolet radiation [25]. Numerous brands of skincare products have included vitamin E as part of the ingredients to improve its sun protection properties when applied topically.

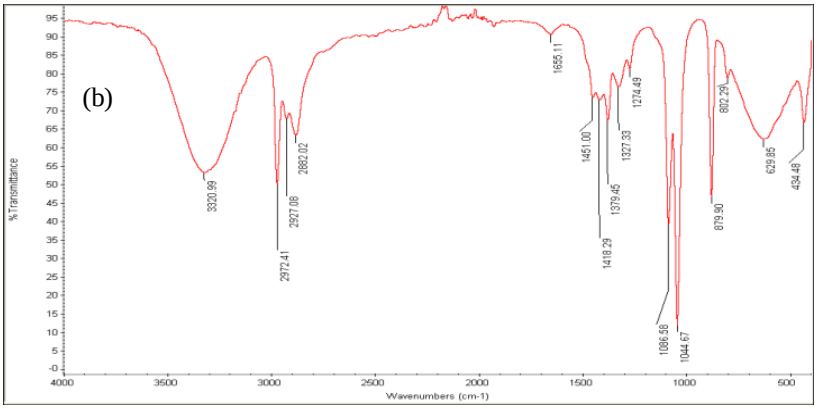
Steroids, recorded as stigmasterol and clionasterol, were present in plant samples at 6.73% and 8.01% in EOs from Kedah, and 9.05% and 9.10% in EOs from Johor respectively. Various studies have shown that environmental factors have strong influence on volatile components. Li et al. [16] reported that *Cinnamomum cassia* from nine different locations in China showed differences in bioactive compounds from plants of different geographical locations. *C. cassia* from Guangxi had higher content of trans-cinnamaldehyde by 73.56– 77.20% than Guangdong's by 66.28–71.22%. The study was conducted to identify the quality of cinnamon as part of the Chinese traditional herbal medicine to meet quality control requirements used throughout China. In another study in India,

methanolic extract of *Withania somnifera* from Uttarakhand had higher total phenolic content than in Rajasthan where the influence of environmental conditions, climate, edaphic factors and altitudes were said to be the cause of the differences [26]. The compounds listed in Table were according to their elution order on HP5-MS capillary column.

FT-IR Analysis of the EOs

IR spectroscopy (Figure 3) shows molecules that absorb frequencies which later stretched its characteristics of their structures by producing a wave spectrum. The IR fingerprints of the EOs of *P. amaryllifolius* were observed to be mostly in the range of 400-1700 cm^{-1} and 2800-3500 cm^{-1}. There were 16 common peaks that were observed in all the IR spectra from the samples under study. The peak at 3320 cm^{-1} was assigned to the stretching vibration of O-H. The peaks of 2972 cm^{-1}-2927 cm^{-1} and 2881 cm^{-1} were attributed to C-H stretching vibration and tertiary C-H group (CH_3). The spectra giving the characteristics of alcohol with C-OH deformation within the bending vibration absorption at 1450 cm^{-1} peak and aldehyde carbonyl C=O at 1655 cm^{-1} peak where the aromatic stretching bond occurred to absorb frequency. The peak at 1274 cm^{-1} corresponded to esters C-O stretching. The peaks at 1086 cm^{-1} and 1044 cm^{-1} were recognized for deformation of methoxyl group of C-O-C. In the fingerprint region, at peaks, 801 cm^{-1} and 879 cm^{-1} were assigned to benzene ring=CH vibration absorption with C-H deformation. Alkenes vibration absorption was identified at peak 630 cm^{-1}.





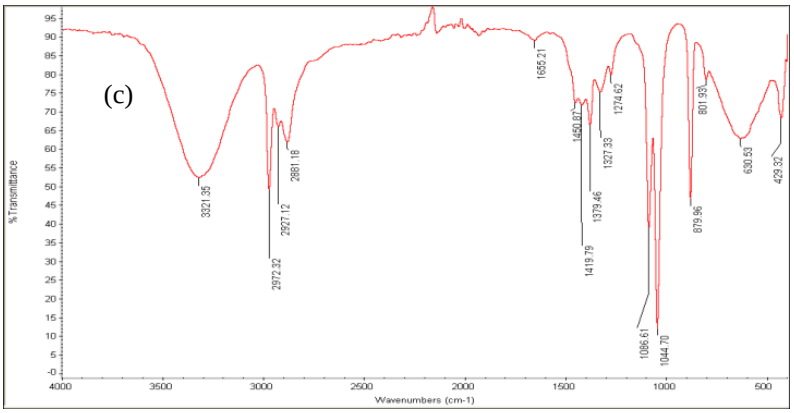


Figure 3. The IR spectrums of *P. amaryllifolius* essential oils from (a) Kedah, (b) Selangor, and (c) Johor.

Conclusion

The present study has presented a collection of important compounds putatively known for their therapeutic properties. Analyzed by gas chromatography-mass spectroscopy (GC-MS) and Fourier transform infrared spectroscopy (FT-IR) *P. amaryllifolius* appears to be a good source of compounds squalene, stigmasterol, alpha and beta tocopherol, coumaran and phytol which are known to be very important constituents in skin care products. Further study on genetic improvement of Pandan is suggested for higher concentration of EOs for better utilization of the plant beyond its use in culinary and traditional treatments.

Acknowledgment

The authors acknowledge Food and Microbiome Laboratory (FAMTech), Faculty of Biotechnology and Biomolecular Sciences and Halal Products Research Institute, Universiti Putra Malaysia for providing facilities and equipment. The study was supported by Putra Grant – Putra Graduate Initiative (GP-IPS 9651300) from Research Management Centre, Universiti Putra Malaysia.

References

1. Yahya, F., Lu, T., Santos, R. C. D., Fryer, P. J., and Bakalis, S. (2010). Supercritical carbon dioxide and solvent extraction of 2-acetyl-1-pyrroline from pandan leaf: the effect of pre-treatment. *The Journal of Supercritical Fluids*, 55(1): 200-207.
2. Nor, F. M., Mohamed, S., Idris, N. A., & Ismail, R. (2008). Antioxidative properties of *Pandanus amaryllifolius* leaf extracts in accelerated oxidation and deep frying studies. *Food Chemistry*, 110: 319-327.
3. Balinado, L., and Chan, M. (2017). An ethnomedicinal study of plants and traditional health care practices in District 7, Cavite, Philippines. *2017 International Conference on Chemical, Agricultural, Biological and Medical Sciences*, 10: 131-143.
4. Razak, N. I. A., Othman, R., and Pahang, J. T. (2018). Ethnobotanical study on plant materials used in Malay traditional post-partum bath (Mandi Serom) among Malay midwives in Kedah. *Proceedings of the Second International Conference on the Future of ASEAN*, 2: 891-897.
5. Aggarwal, N. (2011). A review of recent investigations on medicinal herbs possessing anti-diabetic properties. *Journal of Nutritional Disorder and Therapy*, 1: 102.
6. Courtois, E. A., Baraloto, C., Paine, C. T., Petronelli, P., Blandinieres, P. A., Stien, D., and Chave, J. (2012). Differences in volatile terpene composition between the bark and leaves of tropical tree species. *Phytochemistry*, 82: 81-88.
7. Elgendy, E. M., Ibrahim, H. S., Elmeherry, H. F., Sedki, A. G., and Mekhemer, F. U. (2017). Chemical and biological comparative *in vitro* studies of cinnamon bark and lemon peel essential oils. *Food Nutrition*, 8: 110-125.

8. Silvis, I. C. J., Luning, P. A., Klose, N., Jansen, M., and van Ruth, S. M. (2019). Similarities and differences of the volatile profiles of six spices explored by proton transfer reaction mass spectrometry. *Food Chemistry*, 271: 318-327.
9. Verma, R. S., Padalia, R. C., Chauhan, A., Singh, A., and Yadav, A. K. (2011). Volatile constituents of essential oil and rose water of damask rose (*Rosa damascena* Mill.) cultivars from north Indian Hills. *Natural Product Research*, 25(17): 1577-1584.
10. Singh, G., Maurya, S., and Catalan, C. A. (2007). A comparison of chemical, antioxidant and antimicrobial studies of cinnamon leaf and bark volatile oils, oleoresins and their constituents. *Food and Chemical Toxicology*, 45(9): 1650-1661.
11. Mehl, F., Marti, G., Boccard, J., Debrus, B., Merle, P., Delort, E., and Wolfender, J. L. (2014). Differentiation of lemon essential oil based on volatile and non-volatile fractions with various analytical techniques: A metabolomic approach. *Food Chemistry*, 143: 325-335.
12. Hui, L., He, L., Huan, L., XiaoLan, L., and AiGuo, Z. (2010). Chemical composition of lavender essential oil and its antioxidant activity and inhibition against rhinitis-related bacteria. *African Journal of Microbiology Research*, 4(4): 309-313.
13. Kodal, S. P., and Aksu, Z. (2017). Phenolic pigment extraction from orange peels: Kinetic modelling. *15th International Conference on Environmental Science and Technology*. *Rhodes, Greece*, 31: 798-803.
14. Ramluckan, K., Moodley, K. G., and Bux, F. (2014). An evaluation of the efficacy of using selected solvents for the extraction of lipids from algal biomass by the Soxhlet extraction method. *Fuel*, 116: 103-108.
15. Al Juhaimi, F., and Özcan, M. M. (2018). Effect of cold press and Soxhlet extraction systems on fatty acid, tocopherol contents, and phenolic compounds of various grape seed oils. *Journal of Food Processing and Preservation*, 42(1): 13417.
16. Li, Y. Q., Kong, D. X., and Wu, H. (2013). Analysis and evaluation of essential oil components of cinnamon barks using GC–MS and FTIR spectroscopy. *Industrial Crops and Products*, 41: 269-278.
17. Gomathi, D., Kalaiselvi, M., Ravikumar, G., Devaki, K., and Uma, C. (2015). GC-MS analysis of bioactive compounds from the whole plant ethanolic extract of *Evolvulus alsinoides* (L.) L. *Journal of Food Science and Technology*, 52(2): 1212-1217.
18. Ghasemzadeh, A., and Jaafar, H. Z. (2013). Profiling of phenolic compounds and their antioxidant and anticancer activities in Pandan (*Pandanus amaryllifolius* Roxb.) extracts from different locations of malaysia. *BMC Complementary and Alternative Medicine*, 13(1): 341.
19. Ghasemzadeh, A., Jaafar, H. Z., Rahmat, A., and Ashkani, S. (2015). Secondary metabolites constituents and antioxidant, anticancer and antibacterial activities of *Etlingera elatior* (Jack) RM grown in different locations of malaysia. *BMC Complementary and Alternative Medicine*, 15(1): 335.
20. Chen, X. K., and Ge, F. H. (2014). Chemical components from essential oil of *Pandanus amaryllifolius* leaves. *Journal of Chinese Medicinal Materials*, 37(4): 616-620.
21. Kelly, G. S. (1999). Squalene and its potential clinical uses. *Alternative Medicine Review: A Journal of Clinical Therapeutic* 4(1): 29-36.
22. Zeb, A., Ullah, F., Ayaz, M., Ahmad, S., and Sadiq, A. (2017). Demonstration of biological activities of extracts from *Isodon rugosus* wall. Ex benth: Separation and identification of bioactive phytoconstituents by GC-MS analysis in the ethyl acetate extract. *BMC Complementary and Alternative Medicine*, 17(1): 28.
23. de Alencar, M. V. O. B., Islam, M. T., de Lima, R. M. T., Paz, M. F. C. J., dos Reis, A. C., da Mata, A. M. O. F., and Mubarak, M. S. (2018). Phytol as an anticarcinogenic and antitumoral agent: An *in vivo* study in swiss mice with DMBA-induced breast cancer. *IUBMB Life*, 71(2): 200-121.
24. Driscoll, M. S., and Wagner, R. F. (2000). Clinical management of the acute sunburn reaction. *CUTIS-NEW YORK*, 66(1): 53-60.
25. Borel, P., and Desmarchelier, C. (2018). Bioavailability of fat-soluble vitamins and phytochemicals in humans: Effects of genetic variation. *Annual Review of Nutrition*, 38: 69-96.
26. Adhikari, L., Kotiyal, R., Pandey, M., Bharkatiya, M., Sematy, A., and Semalty, M. (2018). Effect of geographical location and type of extract on total phenol/flavon contents and antioxidant activity of different fruits extracts of *Withania somnifera*. *Current Drug Discovery Technologies*. 15:1.

Malaysian Journal of Analytical Sciences (MJAS)
Published by Malaysian Analytical Sciences Society

ELECTROCHEMICAL DETERMINATION OF DOPAMINE AND URIC ACID IN BLOOD SERUM USING ANIONIC SURFACTANTS AT CARBON PASTE ELECTRODES

(Penentuan Dopamin dan Asid Urik dalam Serum Darah Secara Elektrokimia Menggunakan Surfaktan Anionik pada Perekat Elektrod Karbon)

Liridon Berisha[1], Egzontina Shabani[1], Arsim Maloku[1]*, Granit Jashari[2], Tahir Arbneshi[1]

[1]*Department of Chemistry, Faculty of Mathematical and Natural Sciences, University of Prishtina, 10000 Prishtinë, Kosovo*
[2]*Department of Analytical Chemistry, Faculty of Chemical Technology, University of Pardubice, Studentská 573, 532 10 Pardubice, Czech Republic*

**Corresponding author: arsim.maloku@uni-pr.edu*

Received: 20 October 2019; Accepted: 9 December 2019

Abstract

A selective and sensitive method was developed for the simultaneous electrochemical determination of dopamine and uric acid by using a sodium dodecylbenzenesulfonate (SDBS) and sodium dodecyl sulfate (SDS) as a surface modifier of carbon paste electrodes (CPEs). At lower concentration of SDS and SDBS they form a negatively charged monolayer on CPE surface because of surfactants' hydrophobic chain interaction with paraffin of CPE. Optimized concentration of surfactants was 2 mM for SDS and 1 mM for SDBS in phosphate buffer solution (0.1 M, pH 7 and pH 6, respectively). Compared with plain CPE, CPE modified with SDS (CPE-SDS) and CPE modified with SDBS (CPE-SDBS) have shown the improved electrochemical response of dopamine (DA) at 0.230 V and uric acid (UA) at 0.345 V due to electrostatic interactions between positively charged analytes and surface negatively charged of SDBS and SDS. Under optimal experimental conditions, the designed electrodes exhibited a wide range of linear response to DA from 0.53 µM to 31.6 µM and UA from 5.95 µM to 118.97 µM. The detection limits for DA and UA were found to be 0.26 and 1.10 µM with CPE-SDS, whilst 0.22 and 0.38 µM with CPE-SDBS. The CPE-SDBS and CPE-SDS showed good reproducibility, repeatability, stability and high selectivity for determination of DA and UA in blood serum samples.

Keywords: dopamine, uric acid, carbon paste electrode, sodium dodecyl sulfate, sodium dodecylbenzenesulfonate

Abstrak

Kaedah sensitif dan selektif telah dibangun untuk penentuan serentak dopamin dan asid urik menggunakan sodium dodekilbenzenasolfonat (SDBS) dan sodium dodekil sulfat (SDS) sebagai perekat elektrod karbon yang diubah permukaan. Pada kepekatan rendah SDS dan SDBS membentuk cas negatif lapisan mono pada permukaan CPE disebabkan interaksi rantaian hidrofobik dengan paraffin CPE. Kepekatan optimum surfaktan ialah 2 mM SDS dan 1 mM SDBS dalam larutan penimbal fosfat (masing-masing 0.1 M, pH 7 dan pH 6). Berbanding CPE kosong, CPE yang terubahsuai dengan SDS (CPE-SDS) dan CPE terubahsuai dengan SDBS (CPE-SDBS) telah menunjukkan peningkatan respons elektrokimia bagi dopamin (DA) pada 0.230 V dan asid urik (UA) pada 0.345 V disebabkan oleh interaksi elektrostatik di antara cas positif analit dan cas negatif permukaan SDBS dan SDS. Pada keadaan optimum, elektrod yang dibangun menghasilkan julat respons kelinearan yang besar terhadap DA dari 0.53 µM to 31.6 µM hingga UA dari 5.95 µM hingga 118.97 µM. Had pengesanan DA dan UA didapati pada 0.26 dan 1.10 µM bagi CPE-SDS, manakala 0.22 and 0.38 µM bagi CPE- SDBS. CPE-SDBS dan CPE-SDS telah menghasilkan kebolehhasilan, kebolehulangan, kestabilan yang baik dan kepilihan yang tinggi bagi penentuan DA dan UA di dalam sampel serum darah.

Kata kunci: dopamin, asid urik, perekat elektrod karbon, sodium dodekil sulfat, sodium dodekilbenzenasolfonat

Introduction

Dopamine (DA) is an organic compound of catecholamine and phenethylamine families, as an important hormone and neurotransmitter have a crucial role in central nervous, renal, hormonal and cardiovascular systems [1]. Abnormal concentrations of DA may cause some neurodegenerative human diseases like Alzheimer's, Parkinson's and Schizophrenia [2, 3]. Uric acid (UA) is usually considered as the primary product of purine metabolism in the human body [4]. Its abnormal levels in human body fluids may lead to the occurrence of gout, hyperuricemia, Lesch-Nyhan syndrome or pneumonia [4, 5]. Due to those effects DA and UA are considered as crucial molecules for physiological processes in human metabolism. Therefore, the simultaneous determination of DA and UA is of great importance for analytical application and diagnostic research [6]. Several methods have been developed for the DA and AU determination, namely fluorometry [7], chemiluminescence [8], spectrophotometry [9], liquid chromatography [10], and electrochemical methods [11, 12].

Compared with other methods, the electrochemical methods are more accessible for dopamine and uric acid determination due to their low price, fast response, trouble-free operation, good stability, and convenient for in-situ detection [2, 13]. However, the major problem for simultaneous determination of DA and UA is the interference of ascorbic acid (AA) in high concentrations, because oxidation peak currents of ascorbic acid are overlapped with those of DA and UA at conventional electrodes [14]. To overcome this problem various electrodes have been developed, using different modification materials such as metal oxides [15], metal nanoparticles [14], nanosheets [16], polymers [17, 18], enzymes [19], and anionic or cationic surfactants as surface modifiers [3, 20].

This work describes simultaneous determination of DA and UA in presence of AA as an anionic interferent. using anionic surfactants (SDS and SDBS) as surface modifier of CPE. Anionic surfactants decreased electrode response to AA in neutral pH because of negatively charged electrode surface and give well defined peaks for dopamine and uric acid. New method was successfully applied on determination of DA and UA in blood serum. Surfactants are a special type of amphiphilic molecules that possess charged or polar head groups and long hydrocarbon end [21]. They have been widely used in electroanalysis to improve the properties of the electrode/solution interface and subsequently influence the electrochemical processes of other substances by charging electrode's surface i.e., cationic surfactant gives it positively charged and anionic surfactants make electrode surface negative charged [22 - 24]. Few studies reported the application of anionic surfactants as sensing materials only for quantification of dopamine, therefore it is necessary to develop a method which can quantify DA and UA in the same time in presence of ascorbic acid [20, 25]. Based on surfactants' properties, a selective and sensitive method was developed for the simultaneous electrochemical determination of dopamine and uric acid in the presence of ascorbic acid by using sodium dodecylbenzenesulfonate (SDBS) and sodium dodecyl sulfate (SDS) as surface modifiers of carbon paste electrodes.

Materials and Methods

Reagents and chemicals

Graphite powder (particle size < 20 µm, synthetic), sodium dodecylbenzenesulfonate ($C_{18}H_{29}NaO_3S$), sodium dodecyl sulfate ($NaC_{12}H_{25}SO_4$) and dopamine hydrochloride ($C_8H_{11}NO_2$•HCl) were obtained from Sigma-Aldrich. Uric acid ($C_5H_4N_4O_3$) and paraffin oil were from Merck. Ascorbic acid ($C_6H_8O_6$) was supplied by Lach-Ner. Phosphate buffer solution (PBS, 0.1 M) on a range of pH values from 3 to 9 used as supporting electrolyte was prepared by mixing aqueous solutions of 3.0 M NaOH and 0.1 M H_3PO_4. DA, UA, AA, SDS, and SDBS solutions were freshly prepared in supporting electrolyte solutions prior to use. All the aqueous solutions were prepared with deionized water (18.5 MΩ).

Apparatus

Cyclic voltammetry and differential pulse voltammetry were performed on potentiostat/galvanostat with multiplexer EmStatMUX8 controlled with PSTrace software. The conventional three-electrode system consists of an Ag/AgCl (KCl 3M) reference electrode, a platinum wire as the counter electrode and a bare or modified carbon paste

electrode (A= 12.57 mm^2) used as working electrode. A pH-Ion meter 301 HANNA Instruments was used for pH measurements. All electrochemical studies were performed at room temperature.

Preparation of working electrodes

Bare carbon paste was prepared by mixing 1.000 g of graphite powder with 360 µL paraffin oil in an agate mortar and gently mixing with a pestle until uniformity and proper compactness was obtained. Then carbon paste was transferred to glass vials (15 mL) and allowed to stand overnight in a refrigerator. Prepared pastes were packed into the cavity of a Teflon tube as an electrode holder. Modified electrodes, CPE-SDS and CPE-SDBS were prepared by adding a certain amount of SDS or SDBS in solution where measurements were conducted and stirring for optimal equilibration time.

Real samples preparation

Determination of dopamine and uric acid in blood serum was performed without sample pretreatment, 300 µL of blood serum was transferred into a 10 mL volumetric flask and diluted to the mark with PBS pH 6.0 and PBS 7.0. These diluted blood serum samples were analyzed with the standard addition method with the addition of 50 µL of 5.3 mM dopamine and five additions of 200 µL of 1.5 mM uric acid were used.

Results and Discussion

Cyclic voltammetry

Effects of SDS and SDBS in the detection of dopamine and uric acid were tested on cyclic voltammetry in phosphate buffer solution 0.1 M, pH 7.5. Surfactants as an electrode surface modifier were used to maintain dopamine and uric acid linkage on the electrode/solution interface, and also as electron exchange facilitators between them and the surface of the electrode. In Fig. 1. is shown the electrochemical response of dopamine (0.25 mM) and uric acid (0.30 mM) on bare carbon paste electrode (CPE), carbon paste electrode modified with SDS (CPE-SDS) and carbon paste electrode modified with SDBS (CPE-SDBS) where can be seen that modified carbon paste electrodes show well-defined peaks for DA and UA compared to unmodified electrode surface. Also, increased reversibility on dopamine and uric acid redox signals it is shown while using modified carbon paste electrode. SDS and SDBS critical micelle concentration (CMC) is around 1 and 2 mM and in the concentration higher than CMC hydrophobic chains of surfactant interacts and didn't make uniform layer adsorbed on CPE surface. In lower concentration than the critical micelle concentration surfactants form a monolayer with a high density of negative charges on the CPE surface *via* hydrophobic interaction of their hydrophobic chain and CPE [25]. Negatively charged electrode surface *via* electrostatic interaction with positive charge ions of analyte provide a more effective electron transfer channel for oxidation of dopamine and uric acid and currents are increased significantly.

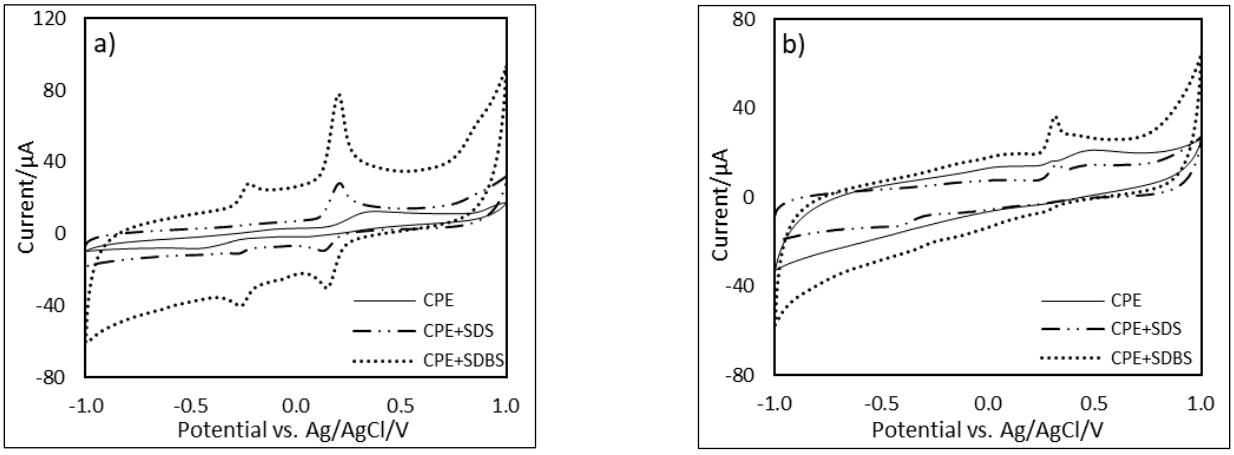


Figure 1. Cyclic voltammograms of (3rd scan) a) dopamine (0.25 mM) and b) uric acid (0.30 mM) gained at bare carbon paste electrode (CPE), carbon paste electrode modified with SDS (CPE-SDS) and carbon paste electrode modified with SDBS (CPE-SDBS) in pH 7.5 PBS. Scan rate: 50mV/s.

Figures 1a and b shows that CPE-SDBS versus CPE-SDS exhibits higher sensitivity to DA and UA, resulting from the phenyl ring in the SDBS structure which makes it more hydrophobic than SDS and enables stronger interaction with CPE. During the first scan in cyclic voltammetry dopamine gives the oxidation peak at 0.209 V, and in reverse scan appear two cathodic peaks at 0.154 V and -0.260 V. Electrochemical reaction of dopamine goes through several steps. First, involving two protons and two electrons DA is oxidized to o-dopaminequinone and after cyclation process (leucodopaminechrome) goes through oxidation to dopaminechrome. Further oxidation mechanism starts the polymerization process. Reduction of DA to dihydroxyzindole and aminochrome gives the cathodic peaks in Fig.1a involving two electrons for each reduction process [26].

Differential pulse voltammetry

It is known that AA coexists with DA and UA in real samples, hence AA electrochemical response was studied in our further work. The differential pulse voltammograms of dopamine, uric acid and ascorbic acid at the bare carbon paste electrode and in presence of surfactants are shown in Figure 2. At the bare CPE, the oxidation peak potentials of DA, UA, and AA appeared at 170 mV, 310 mV, and 330 mV respectively, indicating the possibility of simultaneous determination of DA and AU, but not in the presence of AA because of its broad oxidation peak. Compared to results obtained on bare CPE, CPE-SDS, and CPE-SDBS the anodic peaks potential of DA and UA were shifted negatively and two well-separated peaks were obtained with a difference of 115 mV in potentials between DA and UA peaks at CPE-SDS and 130 mV at CPE-SDBS (Figure 2). Voltammograms obtained at CPE-SDS and CPE-SDBS depict clear that AA has no electrochemical response according to the repulsion of ascorbate ion with a negatively charged electrode surface because at pH 7 ascorbic acid exists in its anionic form. These results mean that modified CPE-s can be used in order to the simultaneous determination of DA and UA in presence of ascorbic acid.

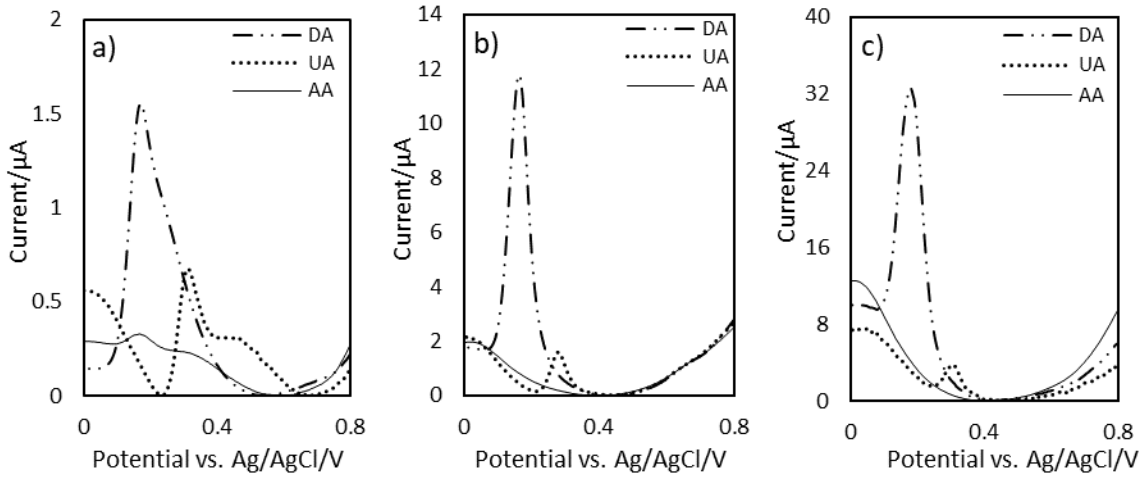


Figure 2. Differential pulse voltammograms of bare CPE (a), CPE-SDS (b), and CPE-SDBS (c) in 0.1 M PBS (pH 7.0) in presence of 50 µM DA (blue line), 60 µM AU (green line) and 60 µM AA (red line). Scan rate: 20 mV/s.

Effect of pH

The effect of pH value of 0.1 M PBS to an electrochemical response of 50 µM DA and 60 µM UA at CPE, CPE-SDS, and CPE-SDBS was investigated by DPV over pH range from 3 to 9. In Figure 3a and 3b can be seen the effect of pH value on the anodic peak current of DA and UA with three working electrodes (CPE, CPE-SDS, and CPE-SDBS). Comparing results obtained on three electrodes (Figure 3) depicts clearly that peak currents of DA and UA were the highest with CPE-SDBS. Due to better sensitivity and clearly peaks separation of DA and UA, pH 7 with CPE-SDS and pH 6 with CPE-SDBS were taken in our following investigation.

Due to linear relationships of anodic peak potentials of DA and UA as function of pH value, with increasing pH values on range from 3 to 9 the oxidation peak potentials of DA and UA with CPE-SDS were shifted to more negative potentials with a slope of 55.9 mV/pH and 55.5 mV/pH and with CPE-SDBS 54.1 mV/pH and 50.2 mV/pH. Slopes for DA and UA on both modified electrodes were closed to the theoretical value of 59 mV/pH, which indicated that an equal number of protons and electrons are involved in electrochemical reactions [4]. In further experiments the electrolyte pH was chosen to be 7 for CPE-SDS and pH 6 for CPE-SDBS, because the oxidation peaks of DA and UA are more separated and peak width were smaller compared to response in other pH values.

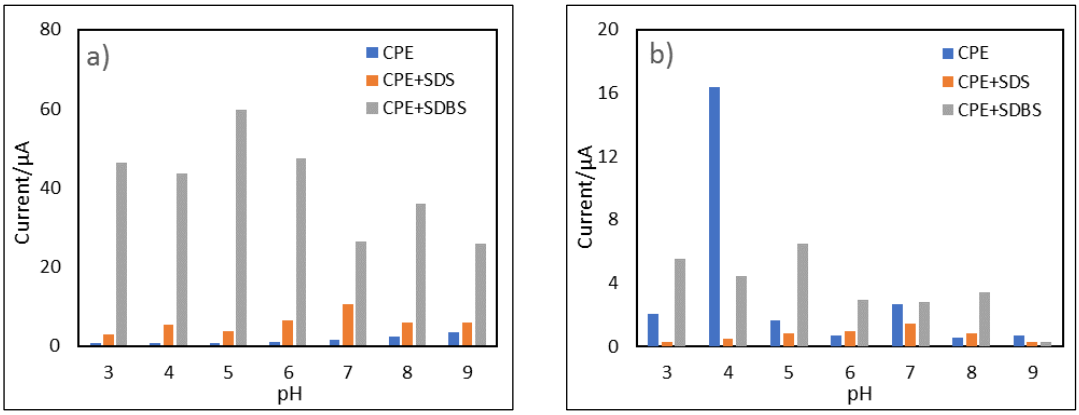


Figure 3. Effect of pH on the peak current (a) dopamine 50 µM, (b) uric acid 60 µM.

Optimization of surfactants' concentration and equilibration time

The concentration of surfactants was optimized by varying their concentration in the range of 0.05-5.00 mM in 0.1M PBS at pH 7.00 using CPE-SDS and pH 6 for CPE-SDBS as working electrodes. Figure 4 shows the effect of surfactants concentration on the peak current of 50 µM DA and 60 µM UA in differential pulse voltammetry. Using CPE-SDS as working electrode a linear relationship is established between SDS concentration versus DA and UA peaks current up to 2 mM of SDS, while at CPE-SDBS linearity is up to 1 mM of SDBS and they are chosen as optimal concentrations for certain cases of surfactants. The influence of equilibration time on electrochemical response of DA and UA was investigated by DPV in a range of equilibration time from 30 to 360 seconds. Considering the relationship between equilibration time and peaks current of DA (50 µM) and UA (60 µM), in following measurements was chosen 100 and 150 seconds equilibration time for CPE-SDS and CPE-SDBS, respectively.

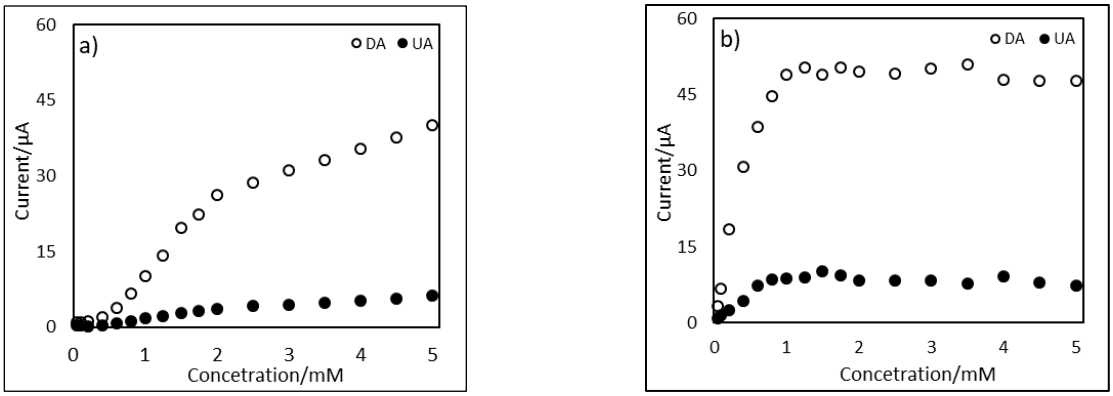
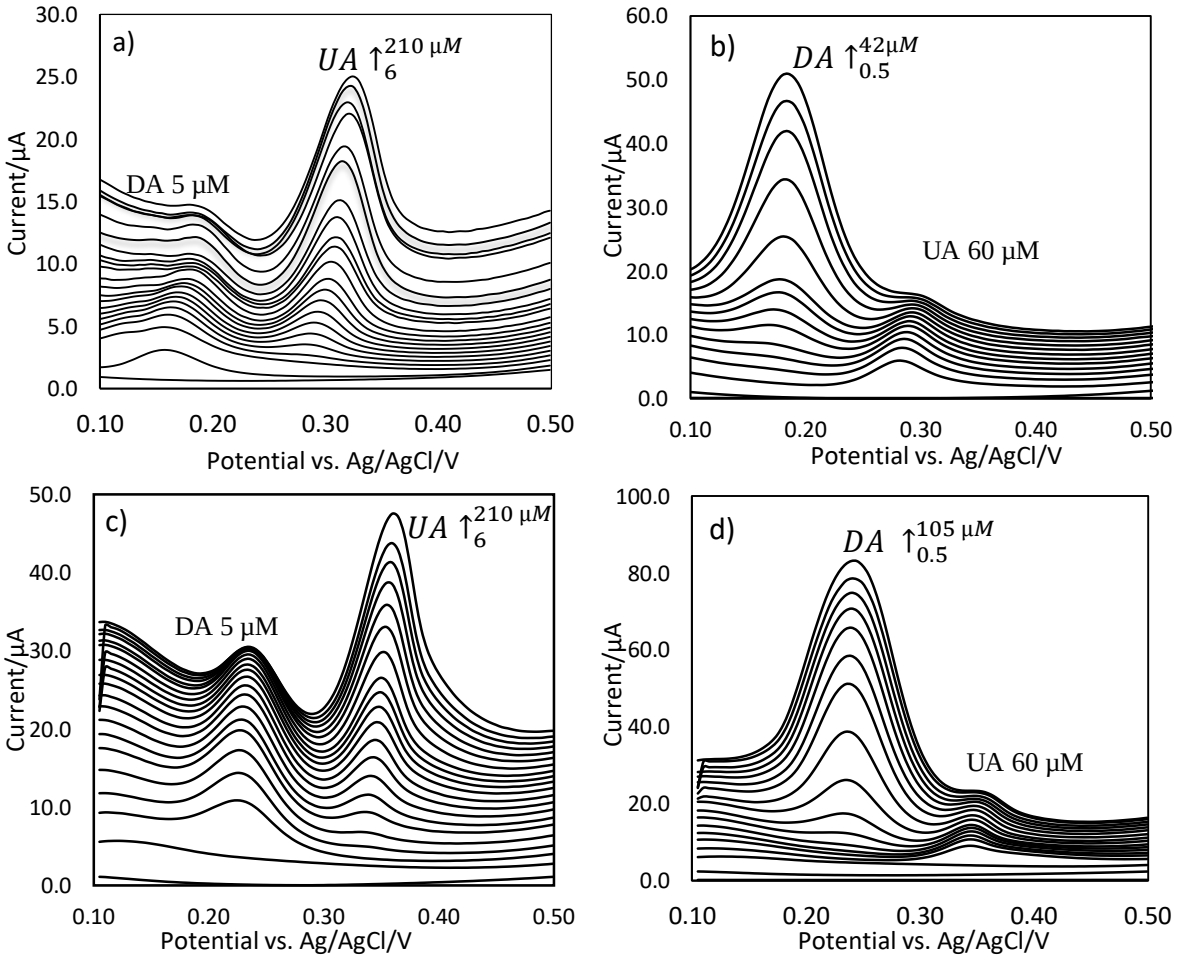


Figure 4. Effects of surfactants concentration a) SDS and b) SDBS on the peak current of DA 50 µM and AU 60 µM.

Concentration of AA was chosen 50 ppm based on CPE-SDBS electrode response to dopamine in different concentration of AA and for CPE-SDS concentration of AA was 25 ppm. In higher concentration of AA, electrode response was reduced significantly, and damaged electrode surface was observed.

Simultaneous determination of DA and UA in presence of AA

Simultaneous determination of DA and UA in presence of AA was performed by DPV in a range of potential from 0.10 V to 0.50 V, at a scan rate of 20 mV/s by keeping the constant concentration of one analyte and changing the concentration of the other. Figure 5 show voltammograms obtained with CPE-SDS (pH 7) with a difference on potentials about 105 mV between voltammetric responses of DA and UA, better results were obtained with CPE-SDBS (pH 6), where the peaks separation is about 115 mV. These voltammograms gained with CPE-SDS and CPE-SDBS depict clearly that high concentrations of AA have no influence on peaks potentials and currents of DA and UA. The linear response equations using CPE-SDS are I(µA) = 0.804·CDA[µM] + 0.9634 and I(µA) = 0.0716·CUA[µM] - 0.1116. While with CPE-SDBS was found higher sensitivity, better linearity and lower limit of detection for DA and UA, where regression equations are I(µA) = 1.0306·CDA[µM] -0.8492 and I(µA) = 0.1048·CUA[µM] - 0.6922. The detection limits for DA and UA were found to be 0.26 and 1.10 µM with CPE-SDS, whilst 0.22 and 0.38 µM with CPE-SDBS. CPE-SDS and CPE-SDBS can be applied for simultaneous determination of DA and UA in presence of AA with high sensitivity, good linearity and low limit of detection.



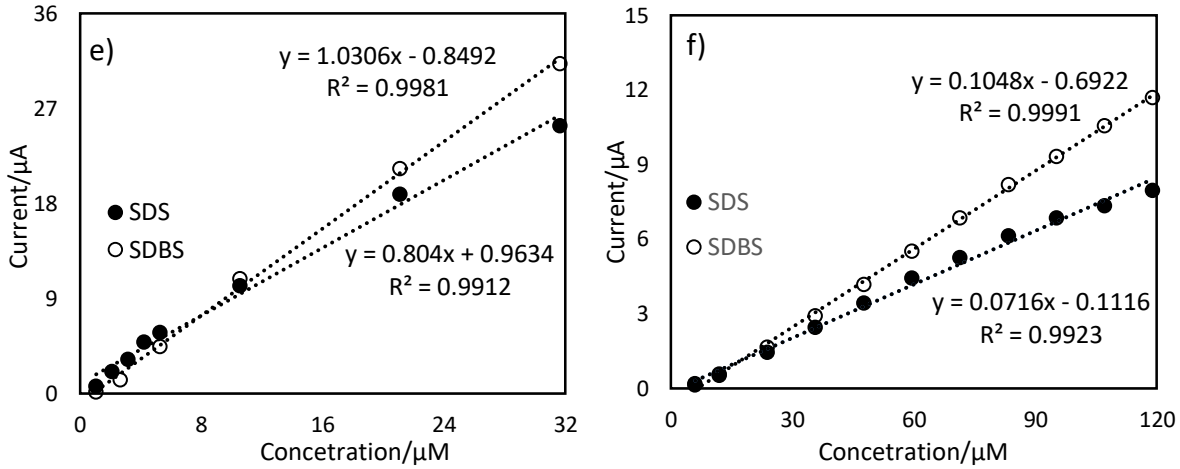


Figure 5. Differential pulse voltammograms at CPE-SDS a) 142 µM AA, 5 µM DA and 6-210 µM UA, b) 142 µM AA, 60 µM UA and 0.5-42 µM DA. Differential pulse voltammograms at CPE-SDBS c) 284 µM AA, 5 µM DA and 6-210 µM UA, d) 284 µM AA, 60 µM UA and 0.5-105 µM DA. Linear relationship of e) DA and f) UA concentration and current intensity in presence of ascorbic acid.

Recovery and real samples analysis

Under optimized conditions has been performed the recovery test for the mixture of dopamine and uric acid in the presence of ascorbic acid. Results of recovery tests presented in Table 1 shows the recovery result for DA and UA found in the range 96.5% to 102.1% for 5 replicated measurements. Hence, the obtained results show that the DPV method could be applied successfully for the determination of dopamine and uric acid simultaneously in presence of ascorbic acid. Further, the method was used for determination of DA and UA in blood serum using standard addition method. A sample was spiked with UA and recovery percentages for CPE-SDBS was 99.1% and CPE-SDS 82.9% (Figure 6). In the same sample was spiked DA which shows a clear peak (Figure 7) and we conclude that method in the quantification of them simultaneously is applicable.

Table 1. Determination of dopamine and uric acid in model samples using CPE-SDS and CPE-SDBS (n=5).

Electrode	Analyte	Added (µM)	Found (µM)	Recovery
CPE SDBS	Dopamine	0.53	0.54±0.01	102±1.9
	Uric acid	59.5	57.4±0.8	97±1.4
CPE SDS	Dopamine	5.27	5.18±0.03	98.3±0.6
	Uric acid	59.5	59±4.4	99±7.4

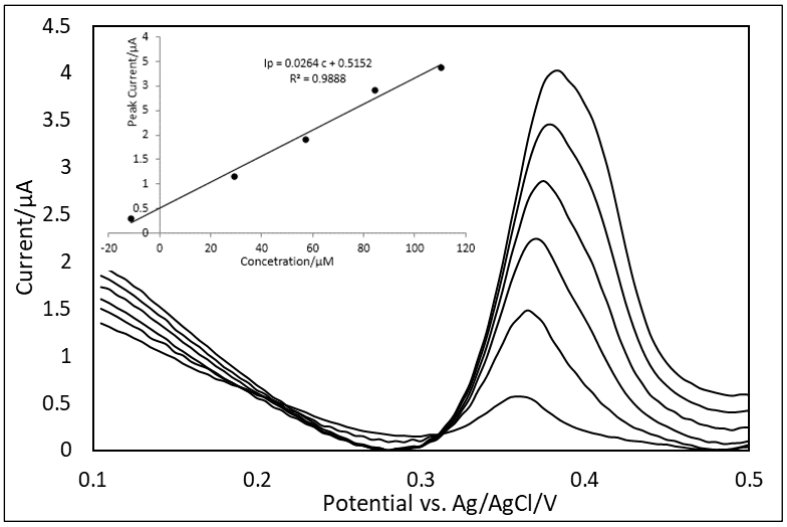


Figure 6. CPE-SDBS voltammograms of uric acid analyzed by standard addition method in blood serum.

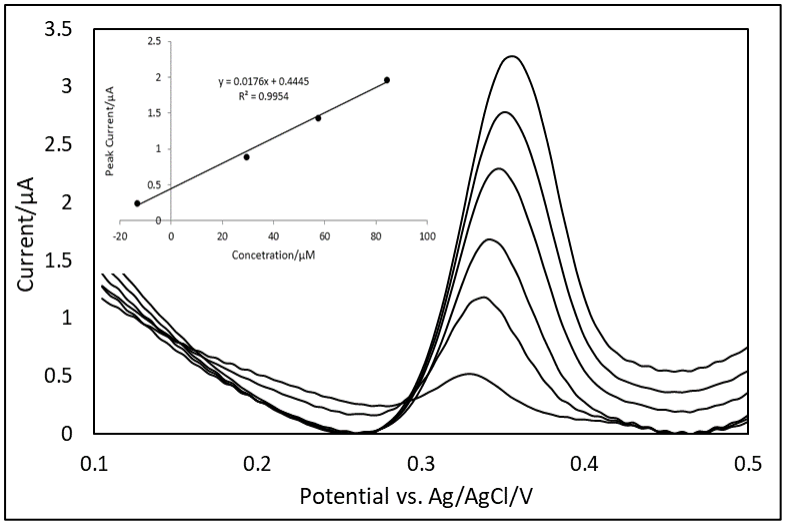


Figure 7. CPE-SDS voltammograms of uric acid analyzed by standard addition method in blood serum.

Conclusion

In this paper, is presented a voltammetric method developed for simultaneous determination of dopamine and uric acid in presence of ascorbic acid. Carbon paste electrode surface *via* hydrophobic interaction with a hydrophobic chain of anionic surfactant creates a high density of negatively charged monolayer. Electrostatic interaction of analytes' positive ions with electrode surface provide more effective electron transfer channel for electrochemical oxidation and make the method applicable for simultaneous determination. Due to the repulsion of negatively charged of ascorbic acid with electrode surface, it is possible to determinate dopamine and uric acid in his presence. The CPE-SDS and CPE-SDBS have shown good reproducibility, repeatability, and stability. Based on recovery test for mixture and real sample analysis we conclude that applied electrochemical method is practically applicable. Simple electrode surface modification makes it useful for determination of other dopamine and uric acid derivatives in different matrix media where almost interferents are anionic species. Modification of screen-printed carbon electrodes with surfactants will reduce sample volume for electrochemical determination of DA and UA.

References

1. Zhang, J., Song, X., Ma, S., Wang, X., Wang, W. and Chen, Z. (2017). A novel sodium dodecyl benzene sulfonate modified expanded graphite paste electrode for sensitive and selective determination of dopamine in the presence of ascorbic acid and uric acid. *Journal of Electroanalytical Chemistry*, 795: 10-16.
2. Zhang, K., Chen, X., Li, Z., Wang, Y., Sun, S., Wang, L., Guo, T., Zhang, D., Xue, Z., Zhou, X. and Lu, X. (2018). Au-Pt bimetallic nanoparticles decorated on sulfonated nitrogen sulfur co-doped graphene for simultaneous determination of dopamine and uric acid. *Talanta*, 178: 315-323.
3. Sharath, S., Swamy, B. E. K., Chandra, U., Manjunatha, J. G. and Sherigara, B. S. (2009). Simultaneous determination of dopamine, uric acid and ascorbic acid with CTAB modified carbon paste electrode. *International Journal of Electrochemical Science*, 4: 592-601.
4. Yang, L., Liu, D., Huang, J. and You, T. (2014). Simultaneous determination of dopamine, ascorbic acid and uric acid at electrochemically reduced graphene oxide modified electrode. *Sensors and Actuators, B: Chemical*, 193: 166-172.
5. Zhang, Y., Lei, W., Xu, Y., Xia, X. and Hao, Q. (2016). Simultaneous detection of dopamine and uric acid using a poly (L -lysine)/graphene oxide modified electrode. *Nanomaterials*, 178: 1-17.
6. Wu, D., Li, Y., Zhang, Y., Wang, P., Wei, Q. and Du, B. (2014). Sensitive electrochemical sensor for simultaneous determination of dopamine, ascorbic acid, and uric acid enhanced by amino group functionalized mesoporous Fe_3O_4@graphene sheets. *Electrochimica Acta*, 116: 244-249.
7. Wang, H. Y., Sun, Y. and Tang, B. (2002). Study on fluorescence property of dopamine and determination of dopamine by fluorimetry. *Talanta*, 57(5): 899-907.
8. Yu, J., Wang, S., Ge, L. and Ge, S. (2011). A novel chemiluminescence paper microfluidic biosensor based on enzymatic reaction for uric acid determination. *Biosensors and Bioelectronics*, 26(7): 3284-3289.
9. Guo, L., Zhang, Y. and Li, Q. (2009). Spectrophotometric determination of dopamine hydrochloride in pharmaceutical, banana, urine and serum samples by potassium ferricyanide-Fe(III). *Analytical Sciences*, 25 (12): 1451-1455.
10. Zhao, H.-X., Mu, H., Bai, Y.-H., Yu, H. and Hu, Y.-M. (2011). A rapid method for the determination of dopamine in porcine muscle by pre-column derivatization and HPLC with fluorescence detection. *Journal of Pharmaceutical Analysis*, 1(3): 208-212.
11. Han, D., Han, T., Shan, C., Ivaska, A. and Niu, L. (2010). Simultaneous determination of ascorbic acid, dopamine and uric acid with chitosan-graphene modified electrode. *Electroanalysis*, 22(17–18): 2001-2008.
12. Kang, G. and Lin, X. (2006). RNA modified electrodes for simultaneous determination of dopamine and uric acid in the presence of high amounts of ascorbic acid. *Electroanalysis*, 18(24): 2458-2466.
13. Khudaish, E. A., Al-Nofli, F., Rather, J. A., Al-Hinaai, M., Laxman, K., Kyaw, H. H. and Al-Harthy, S. (2016). Sensitive and selective dopamine sensor based on novel conjugated polymer decorated with gold nanoparticles. *Journal of Electroanalytical Chemistry*, 761: 80-88.
14. Xu, T.-Q., Zhang, Q.-L., Zheng, J.-N., Lv, Z.-Y., Wei, J., Wang, A.-J. and Feng, J.-J. (2014). Simultaneous determination of dopamine and uric acid in the presence of ascorbic acid using Pt nanoparticles supported on reduced graphene oxide. *Electrochimica Acta*, 115: 109-115.
15. Wang, G., Sun, J., Zhang, W., Jiao, S. and Fang, B. (2009). Simultaneous determination of dopamine, uric acid and ascorbic acid with $LaFeO_3$ nanoparticles modified electrode. *Microchimica Acta*, 164(3–4): 357-362.
16. Sun, H., Chao, J., Zuo, X., Su, S., Liu, X., Yuwen, L., Fan, C. and Wang, L. (2014). Gold nanoparticle-decorated MoS_2 nanosheets for simultaneous detection of ascorbic acid, dopamine and uric acid. *RSC Advances*, 4(52): 27625-27629.
17. Wang, S., Zhang, W., Zhong, X., Chai, Y. and Yuan, R. (2015). Simultaneous determination of dopamine, ascorbic acid and uric acid using a multi-walled carbon nanotube and reduced graphene oxide hybrid functionalized by PAMAM and Au nanoparticles. *Analytical Methods*, 7(4): 1471-1477.
18. Zheng, X., Zhou, X., Ji, X., Lin, R. and Lin, W. (2013). Simultaneous determination of ascorbic acid, dopamine and uric acid using poly(4-aminobutyric acid) modified glassy carbon electrode. *Sensors and Actuators, B: Chemical*, 178: 359-365.
19. Njagi, J., Chernov, M. M., Leiter, J. C. and Andreescu, S. (2010). Amperometric detection of dopamine in vivo with an enzyme-based carbon fiber microbiosensor. *Analytical Chemistry*, 82(3): 989-996.
20. Zheng, J. and Zhou, X. (2007). Sodium dodecyl sulfate-modified carbon paste electrodes for selective determination of dopamine in the presence of ascorbic acid. *Bioelectrochemistry*, 70 (2): 408-415.

21. Dang, X., Hu, C., Wei, Y., Chen, W. and Hu, S. (2004). Sensitivity improvement of the oxidation of tetracycline at acetylene black electrode in the presence of sodium dodecyl sulfate. *Electroanalysis*, 16 (23): 1949-1955.
22. Thomas, T., Mascarenhas, R. J., D'Souza, O. J., Detriche, S., Mekhalif, Z. and Martis, P. (2014). Pristine multi-walled carbon nanotubes/SDS modified carbon paste electrode as an amperometric sensor for epinephrine. *Talanta*, 125: 352-360.
23. Manjunatha, J. G., Kumara Swamy, B. E., Gilbert, O., Mamatha, G. P. and Sherigara, B. S. (2010). Sensitive voltammetric determination of dopamine at salicylic acid and TX-100, SDS, CTAB modified carbon paste electrode. *International Journal of Electrochemical Science*, 5(5): 682-695.
24. Teradale, A. B., Lamani, S. D., Ganesh, P. S., Kumara Swamy, B. E. and Das, S. N. (2017). CTAB immobilized carbon paste electrode for the determination of mesalazine: A cyclic voltammetric method. *Sensing and Bio-Sensing Research*, 15: 53-59.
25. Sancy, M., Francisco Silva, J., Pavez, J. and Zagal, J. H. (2013). Simultaneous electrochemical detection of dopamine, ascorbic acid and uric acid using copper-phthalocyanine functionalized MWCNTs. *Journal of the Chilean Chemical Society*, 58(4): 2117-2121.

Malaysian Journal of Analytical Sciences (MJAS)
Published by Malaysian Analytical Sciences Society

MULTI-SPECTROSCOPIC AND CHEMOMETRICS ANALYSIS FOR FORENSIC DETERMINATION OF BLOOD SPECIES

(Multi-Spektroskopi dan Analisis Kemometrik untuk Penentuan Spesies Darah dalam Forensik)

Durga Devi Sandran[1], Yusmazura Zakaria[2], Noor Zuhartini Md Muslim[1], Nik Fakhuruddin Nik Hassan[1]*

[1]*Forensic Science Program, School of Health Sciences*
[2]*Biomedicine Program, School of Health Sciences*
Universiti Sains Malaysia, Health Campus, 16150 Kubang Kerian, Kelantan, Malaysia

**Corresponding author: nikf@usm.my*

Received: 20 November 2019; Accepted: 21 January 2020

Abstract

Blood trace is commonly found biological evidence at crime scenes. The main issues forensic investigators encounter upon retrieving blood samples is determining their origin. There is no statistical probability in the current examination methodology of potential blood evidence, and it is deemed subjective. Another method, involving DNA analysis, lengthy to perform and restricted due to its degradation and lack of samples. The main aim of this study was to evaluate the potential and suitability of tandem analysis using ATR-FTIR and UV/Vis spectroscopy as means for the characterization of blood samples in the context of forensic science. Conventional visual examination is insufficient to differentiate and classify spectra between blood from different animal species. Hence, to aid classification in each group, chemometrics analysis of the IR and UV/Vis spectral dataset was employed using the combined techniques of principal component analysis and linear discriminant analysis (PCA-LDA). PCA-LDA results demonstrated that blood spectra of various animal species differed in the compositions of blood protein i.e. amide A, I and II. The multivariate analysis based on PCA-LDA models indicated that ATR-FTIR and UV/Vis spectroscopy coupled with chemometrics provided excellent discrimination (94% correct classification) for the classification of blood samples from animal species. The non-destructive nature of vibrational and optical spectroscopic techniques and the success of chemometrics analysis demonstrated in this work have indeed offered a new dimension for the rapid identification of biomaterials of forensic relevance and essentially warrants further research.

Keywords: spectroscopy, chemometrics, forensic, blood species

Abstrak

Kesan darah merupakan bahan bukti yang biasa dijumpai di tempat kejadian jenayah. Isu utama yang ditempuhi oleh para penyiasat forensik selepas menjumpai sampel darah ialah menentukan asal sumbernya. Kaedah baru iaitu pemeriksaan terhadap bahan bukti darah tidak memberi keputusan yang mempunyai kebarangkalian statistik serta ia dianggap sebagai subjektif. Kaedah lain iaitu analisis DNA, memakan masa yang agak lama untuk dijalankan dan terhad disebabkan degradasi dan kuantiti sampel yang kurang. Tujuan utama kajian ini adalah untuk menilai potensi dan kesesuaian spektroskopi ATR-FTIR dan UV-Vis sebagai satu cara untuk pencirian sampel darah dalam konteks sains forensik. Pemeriksaan visual konvensional tidak mencukupi untuk membezakan dan pengelasan spektrum antara darah spesies haiwan yang berlainan. Justeru, bagi membantu pengklasifikasian dalam setiap kumpulan, analisis kemometrik terhadap data spektrum IR dan UV-Vis telah diaplikasikan dengan menggunakan gabungan teknik analisis prinsip komponen dan analisis diskriminan linear (PCA-LDA). Hasil keputusan PCA-LDA menunjukkan bahawa spektrum darah pelbagai spesies haiwan mempunyai perbezaan dalam komposisi protein darah iaitu amida A, I dan II. Analisis multivariat berdasarkan model PCA-LDA menunjukkan bahawa gabungan spektroskopi ATR-FTIR dan UV-Vis bersamaan kemometrik menghasilkan diskriminasi yang cemerlang (94% klasifikasi yang tepat) bagi pengklasifikasian sampel darah spesies haiwan. Teknik getaran spektroskopi yang tidak memusnahkan sampel dan kejayaan analisis kemometrik yang didemonstrasikan di dalam kajian ini menawarkan dimensi baru bagi pengenalpastian bahan biologi dalam bidang forensik dengan lebih relevan dan memerlukan kajian yang lanjut.

Kata kunci: spektroskopi, kemometrik, forensik, spesies darah

Introduction

In a forensic examination, biological evidence has been essential in distinguishing a victim or perpetrator, and even in resolving a criminal investigation [1]. Biological evidence was originated from the human and non-human body. Blood has been the most known biological evidence found in a crime scene [2]. Blood identification has broadly been evaluated in three main stages: visual assessment, presumptive and confirmatory screening, and lastly species identification [3]. The presumptive and confirmatory tests often lead to potential false positives [4]. Determining the blood source has been fundamental throughout the forensic practice, as this could streamline the original inquiry by integrating or excluding non-human stains [5]. Besides, blood traces further assisted in crime scene reconstruction, as bloodstain patterns could provide information to the homicide, such as the suspect's locations during the blood splatter, the source of the blood traces, or the level of effect that the bloodspots were created [6].

DNA profiling is the primary goal for blood trace identification, which requires to extract DNA of blood specimen. Moreover, this method has been expensive, time-consuming and needs the reactants to activate a chemical reaction that results in DNA destruction of a blood specimen [7]. The vibrational spectroscopic study of blood trace is a non-destructive method that tends to be more suitable. The method involves distinguishing the blood samples from the unique spectral peak structure [8]. Attenuated total reflectance - Fourier-transform infrared (ATR-FTIR), Raman spectroscopy and Ultraviolet-visible (UV-Vis) spectroscopy were widely applied in scientific methods of biological fluid determination.

ATR-FTIR spectroscopy has been extensively applied in other research fields for the study of biochemical functions in biomedical, chemistry, forensic science, and pharmaceutical. The utilization of ATR-FTIR has been in demand for its well-known nature for being robust, zero or little usage of solvents, cost-effective and importantly time-saving as were been little or no sample preparation [9] was needed for the analysis. This nature allows the sample to be analyzed in the different forms either in solid, liquid or adsorbed upon a surface [10]. In addition, FTIR spectroscopy was also employed to analyze trace evidence that discovered in the scene of a crime, for examples, vehicle paints [11-12], fake currency [13-14], hair analysis [15-16], and questioned document examination [17-18]. Such a non-destructive characteristic enables multiple uses of the sample without creating no lasting disruption to the DNA biomolecules.

A comprehensive, robust and controlled research case of different human biological fluids involving breast milk, semen, saliva, and blood (menstrual and venous) were tested by ATR-FTIR spectroscopy on various materials such as fabrics, wood and paper. The diverse chemical functions namely immunoglobulins, proteins and, other micro-molecules of the biological fluids differ in spectral variations. The peak frequency relied on the porosity of the fabric substrates. This finding illustrated that the body fluid found at the crime scene can be determined and differentiated depending on the unique peaks variations that match a specific stain [19]. In liquid samples even on materials, the identification and detection of bodily fluids has proven how this method has been significant to forensic practice. Another study was conducted using UV-Vis and ATR-FTIR spectroscopy to estimate the post-mortem interval (PMI), which has been a significant role in a forensic application using blood plasma of male rabbit based on their varied spectral regions like amino acids, proteins, lactate and, fatty acids [20].

The use of Raman spectroscopy in species differentiation was also explored by Mclaughlin et al. [21, 22]. However, his work implied which the bloodstains of human and non-human could not be efficiently identified and differentiated by Raman's technique based on the spectral analysis. Thus, this allows the significance of vibrational spectroscopic methods to be further investigated using chemometrics, a method used to derive accurate data from a specific chemical spectral dataset [23]. This implication was supported by Kaminska et al. [24] in their study that showed by using principal component analysis (PCA), over 98% accuracy in the ABO blood classification can be achieved. Furthermore, ATR-FTIR coupled to chemometrics was proven to be an effective procedure to discriminate, predict and categories human and animal blood samples in species discrimination study [25].

Thus, in this study, ATR-FTIR and UV-Vis spectroscopy were utilized for blood species determination. Blood specimens of different species namely chicken, cow, deer, duck, fish, goat, and pig were analyzed. In order to improve the distinction of the spectral training dataset, the principal component analysis-linear discriminant analysis (PCA-LDA) of the statistical tool was established as predictive models. Accurate categorization and discrimination of different animal blood species were the primary aims of this research.

Materials and Methods

Materials / Solutions

EDTA tubes (BD Vacutainer® 367863, USA), test-tube racks (Thermo Scientific^{TM} 59700030, USA), disposable 5 mL plastic pipettes (Sigma-Aldrich Z740301, USA) gloves (CleanGuard, Malaysia), ice-packs (V-Cool, China), cooler bag (V-Cool, China) and cotton gauze cloth (McKesson,China) were used in this research. Distilled water and acetone (Sigma-Aldrich W332607, USA) were used as cleaning solvents. These materials and solvents were obtained from Unit Pengurusan Makmal Sains (UPMS), School of Health Science, USM, Kelantan.

Samples

Domestic animal bloods were chosen as samples for analysis in this study namely chicken, cow, deer, duck, fish, goat and pig. The total number of blood samples analyzed was 93.

Sample collection, storage and preservation

Fresh animal blood samples were obtained from the slaughterhouses and stored in 10 mL tubes with anti-coagulant ethylenediaminetetraacetic acid (EDTA) for preservation and stored at -20^{o}C in the freezer.

Instrumentation and sample analysis

ATR-FTIR spectrophotometer (Bruker Tensor 27, Germany) and UV-Vis spectrophotometer (Varian CARY 100 Bio UV-Vis, USA) were employed to collect the spectra of blood samples. For the FTIR analysis, the spectra were collected in the ranges from 4000 to 550 cm^{-1} with a 4 cm^{-1} resolution. For UV-VIS analysis, spectra were collected within 800 to 350 nm. Prior the analysis, all blood samples were thawed completely at a room temperature. A clean cotton gauze cloth with acetone were used to clean the ATR ZnSE crystal stage and for UV-Vis, a clean cuvette contained distilled water was used as blank sample. The cuvette was ensured to be cleaned from any fingerprints or dirt. All samples were analyzed in replicates (five times) for each animal species.

Spectral data pre-treatment and chemometric analysis

The spectral dataset was obtained from the both ATR-FTIR and UV-Vis analyses and the data were saved in Excel formats of .CSV as well as .XLS. The raw spectral data then imported into Minitab version 16 software (Minitab Incorporated, State College, USA) to perform chemometrics analysis; principal component analysis-discriminant analysis (PCA-DA). The scores for 20 principal components were extracted from the original spectral datasets which contributed the most to the total variance. These reduced spectral datasets were later included in the discriminant analysis (DA). The spectra data points were truncated in the range of 1900-1500 cm^{-1} (IR) and 600-400 nm (UV-Vis) for chemometrics analysis. Data pre-processing technique namely standardization was carried out on data set to minimize error due to larger variance by subtracting the mean and dividing standard deviation prior to PCA-DA.

Results and Discussion

Figures 1 and 2 illustrate the stacked plot of average ATR-FTIR and visible spectra of blood analyzed from various animal species. The overall ATR-FTIR and visible spectra were visually similar, but few differences can still be observed that related to the strength of peak intensity. The spectral peaks intensity can be sectioned into two regions, broad bands (wide and smoother) and narrow bands (smaller and sharp as dagger) [26]. In ATR-FTIR analysis, for instance, chicken, cow, deer and goat have an intense peak ranged from 1546 cm^{-1} to 1552 cm^{-1} while duck and fish spectra have lower peak intensity which contributed to a vital information about presence of secondary structures of protein known as parallel β-sheet of functional group. Güler et al. [27] described that allotting detail structural configuration to specific protein was challenging because of the functional groups number that lead to peak intensity. In addition, broader peaks were observed at wide range of wavenumbers from 3286 to 3302 cm^{-1} while narrower peaks can be seen at 1638 to 1464 cm^{-1}.

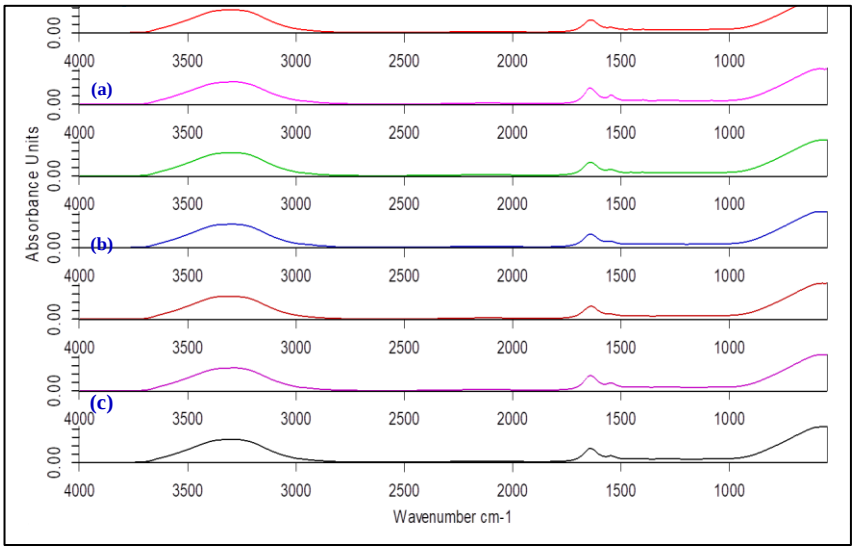


Figure 1. ATR-FTIR spectra of blood from a) chicken, b) cow, c) deer, d) duck, e) fish, f) goat and g) pig

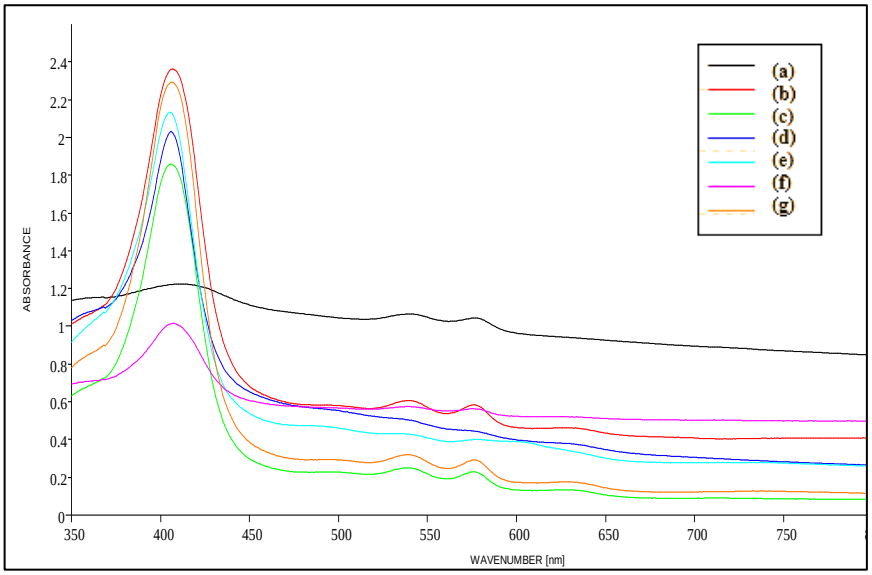


Figure 2. Visible spectra of blood from a) chicken, b) cow, c) deer, d) duck, e) fish, f) goat and g) pig

In visible spectral analysis, the narrower bands intensity of all blood species was predominantly ranged from 410 to 415 nm due to the maximum absorption rate by the samples. The broader bands were observed from 500 to 600 nm ranges. Bahrudeen et al. [28] reported that the stronger band intensity, the more or high specific wavelength being absorbed. Although, all the species showed similar absorption peaks that appeared at same location and same frequency or wavenumber in the both ATR-FTIR and visible spectra, the spectral peak intensity diverged around the spectra and can be classified as strong, medium and weak peaks as demonstrated by Coates [29]. Usually, a medium or weak peak intensity could be identified as smaller peaks with lower or minimal rate of absorption contrasted to strong peaks. Mistek and Lednev [30] reported that in their study, this may be since differences in blood

composition of these species come only from the quantitative changes within the same components, not deviations of components between species. De Wael et al. [31] also reported that visual distinction of these spectra was not possible. The difference between these species referred primarily to the composition of blood such as concentration of haemoglobin, glucose, ascorbic acid and various enzymes and hormones.

All the peaks in the ATR-FTIR spectra represented functional groups. A strong peak observed around 3319 cm^{-1} corresponded to amide-A band which is due to stretching vibration of N-H bond [32]. This amide-A band peak represented the component in the blood. It can be attributed to several possible components that were found in blood, including carbohydrates and lipids [33]. The two major intense band groups were focused at 1650 cm^{-1} and 1533 cm^{-1} within the FTIR range of blood. The Amide I and Amide II were correlating to them. Both groups represented secondary protein structures. Amide 1 group exhibited due to the formation of symmetry of C = O and stretching vibrations of hydrogen bonds. This group of Amide I provided the most information regarding the protein secondary structure. Whereas, Amide II was assigned to stretching of C-N as well as bending modes of NH and CH_2. The absorption regions Amide I and Amide II have also been affiliated with secondary subunit structures including α-helix, β-sheet, and protein coil. In Figure 2, the peaks characteristics of haemoglobin in visible spectra were observed at around 410, 539, and 577 nm.

Since a mere visual examination of spectra was insufficient to distinguish between them and hence the need for multivariate analysis was required. Despite having similar spectral features, the differences in relative intensities of the peaks/bands in bone spectra from different species exist. These variations can be interpreted using a chemometrics method. PCA was initially performed on the combined ATR-FTIR and visible spectral datasets after the standardization. The first twenty PCs explained most of the total variance in the spectral data and these were extracted to provide PC scores for the LDA input variables. Spectral datasets were analyzed by two common chemometric technique namely PCA and LDA. PCA known for data dimensionality reduction technique which extracted small number of data components from a larger training datasets also looks for pattern or cluster while LDA a computed linear combination of variables was used to determine direction of spectral space and to create models to classify the samples in classes [15].

The PCA score plot for the first two principal components (PC1 vs PC2) is shown in Figure 3. First and second principal components represents 43.3% and 24.0%, respectively of the total variance in the data (cumulatively 67.3%). The overlap between the animal groups was evident which resulted in no distinct cluster to distinguish them. Nevertheless, PCA was found not to be suitable technique in categorization problems as illustrated in Figure 3 because it cannot function well for class information of determining the spectral features extracted of a new dataset [34]. Hence, a supervised technique of PCA-LDA as predictive model to classify them. LDA has been renowned technique that observed a linear expression mode which spectral feature clusters have been most divisible later the transformation [28,35]. Figure 4 depicts the 3-dimensional discriminant function plot. Remarkably, results demonstrated 94% correct classification was achieved among animal species. This result was coherent with Efron's testimonial to employ 90% confidence intervals rather than 99% confidence intervals as the intervals work more best when they are less vivid coefficients [36]. The classification results are tabulated in Table 1. All bloods from duck and fish species were correctly classified to their respective groups. Meanwhile, correct classifications were achieved ranging between 84% to 97% for other animal species. The findings have proven that the combination of multi-spectroscopic analysis and PCA-LDA are effective and valid in species classification.

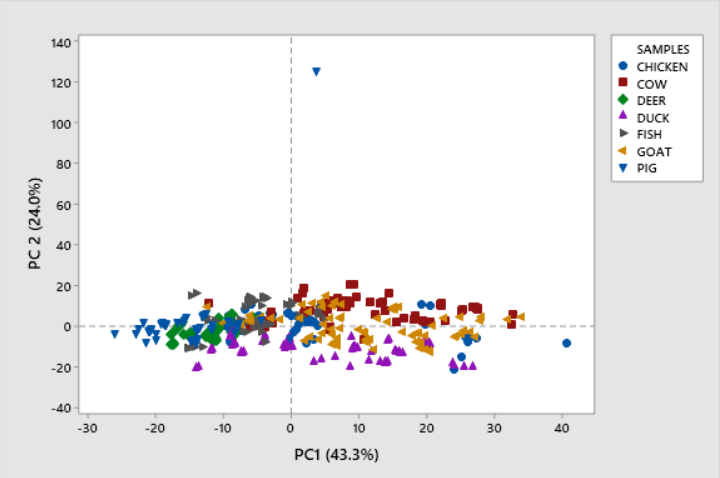


Figure 3. Score plot of PC1 and PC2 for animal blood samples

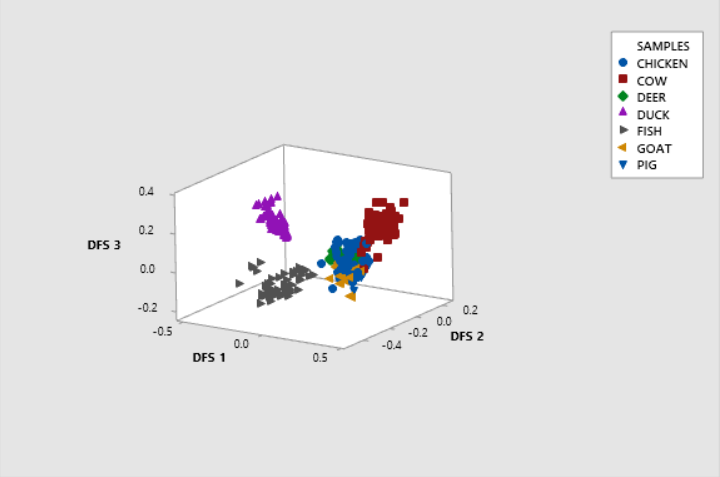


Figure 4. 3D discriminant function (DF) plot for animal blood samples

Table 1. Classification summary of blood species by PCA-LDA

	True Group						
Put into Group	**Chicken**	**Cow**	**Deer**	**Duck**	**Fish**	**Goat**	**Pig**
Chicken	57	0	0	0	0	4	0
Cow	0	68	0	0	0	0	0
Deer	0	0	57	0	0	5	7
Duck	0	0	0	70	0	0	0
Fish	0	0	0	0	60	0	0
Goat	3	2	0	0	0	67	0
Pig	0	0	3	0	0	4	58
Total N	60	70	60	70	60	80	65
N Correct	57	68	57	70	60	67	58
Proportion	0.950	0.971	0.950	1.000	1.000	0.838	0.892

N = Number of datasets, N = 465, N correct = 437, Total Proportion Correct (%) = 0.940

Conclusion

The primary objective of present study was to investigate the potential and application of multi-spectroscopic and chemometric analysis in forensic blood trace identification for different blood species. The results of this study have highlighted that multivariate analysis of PCA-LDA is an ideal and great tool of blood species identification and differentiation than PCA alone. This has been proven as the findings of PCA-LDA combination versus PCA alone were distinguished, the multivariate combination provides higher successful classification rate which was over 94% accuracy. In summary, the introduction of chemometrics to the vibrational multi-spectroscopic research study was an eminent way of extracting and gathering important records of spectral datasets. In chemometrics, the PCA-LDA technique has been shown to establish a successful classification rate for different animal blood species, although similarities in visual spectral comparison were noted in all spectra with reference to the peak position and pattern. The PCA-LDA models established in this research can be utilized to characterize spectra of unknown samples into a predicted group in forensic casework. Since, the current study has considered a limited number of blood species samples, therefore, further work should be conducted to represent a larger number of samples from various animal blood species and breeds as well as wildlife animals for larger database. In addition, human blood samples from different races and gender can be further investigated and explored for predictive classification model.

Acknowledgements

We would like to thank all staff at Forensic and Analytical Laboratories, School of Health Sciences of USM Health Campus for guidance and support towards this study.

1. An, J., Shin, K., Yang, W. and Lee, H. (2012). Body fluid identification in forensics. *Journal of Biochemistry a nd Molecular Biology*, 45(10): 545-553.
2. Magalhães, T., Dinis-Oliveira, R., Silva, B., Corte-Real, F. and Nuno Vieira, D. (2015). Biological Evidence M anagement for DNA analysis in cases of sexual assault. *The Scientific World Journal*, 2015: 1-11.
3. Kobilinsky, L. (2012). Forensic chemistry handbook. John Wiley & Sons, New Jersey: pp. 251-67.
4. Forensic Resources of Indigent Defense Services (2019). Serology - Blood and other Bodily Fluids. http://ww w.ncids.com/forensic/serology/serology.shtml. [Accessed: 14-May-2019].
5. Edelman, G. J. (2014). Spectral analysis of blood stains at the crime scene. Thesis of Doctoral Degree, Universi teit van Amsterdam, Netherlands.
6. Tobe, S. S., Watson, N. and Daéid, N. N. (2007). Evaluation of six presumptive tests for blood, their specificity , sensitivity, and effect on high molecular-weight DNA. *Journal of Forensic Sciences*, 52(1): 102-109.
7. Gefrides, L. and Welch, K. (2010). The forensic laboratory handbook procedures and practice. Humana Press. New Jersey: pp. 15-50.
8. Elkins, K. (2011). Rapid presumptive "Fingerprinting" of body fluids and materials by ATR-FTIR spectroscop y. *Journal of Forensic Sciences*, 56(6): 1580-1587.
9. Zapata, F., and Gregorio, I. (2016). Body fluids and spectroscopic techniques in forensics: A perfect match? *Jo urnal of Forensic Medicine*, 1 (1): 1-7.
10. Garidel P. and Schott H. (2006). Fourier-transform midinfrared spectroscopy for analysis and screening of liqui d protein formulations: Part 1, understanding infrared spectroscopy of proteins. *BioProcess International,* 4 (5): 40-46.
11. Milczarek, J., Zadora, G., Palus, J. and Kościelniak, P. (2008). Forensic examination of car paints. https://milcz arek.eu/wp-content/uploads/2012/10/IX.B-2-Milczarek.pdf. [Accessed: 17-May-2019].
12. Zhang, W., Liu, S., Chen, R. and Liu, Y. (2016). Analysis of 52 automotive coating samples for forensic purpos es with FTIR and Raman microscopy. *Journal of Environmental Forensics*, 17(1): 59-67.
13. Itrić, K., Vukoje, M., & Banić, D. (2018). FT-IR Spectroscopy as a discrimination method for establishing auth enticity of euro banknotes. *Journal for Printing Science and Graphic Communications*, 29(2): 27-30.
14. Itrić, K. and Modrić, D. (2017). Banknote characterization using the FTIR spectroscopy. *Technical Journal*, 11(3): 83-88.
15. Barton, P. (2011). A forensic investigation of single human hair fibres using FTIR-ATR spectroscopy and chem ometrics. Thesis of Doctoral Degree, Queensland University of Technology, Australia.

16. Kuwayama, K., Nariai, M., Miyaguchi, H., Iwata, Y., Kanamori, T. and Tsujikawa, K. (2018). Estimation of da y of death using micro-segmental hair analysis based on drug use history: A case of lidocaine use as a marker. *I nternational Journal of Legal Medicine*, 133(1): 117-122.
17. Ameh, P. and Ozovehe, M. (2018). Forensic examination of inks extracted from printed documents using Fouri er transform infrared spectroscopy. *Edelweiss Applied Science and Technology*, 2(1): 10-17.
18. Sharif, M., Batool, M., Chand, S., Farooqi, Z., Tirmazi, S., and Athar, M. (2019). Forensic discrimination poten tial of blue, black, green, and red colored fountain pen inks commercially used in Pakistan, by UV/Visible spect roscopy, thin layer chromatography, and Fourier transform infrared spectroscopy. *International Journal of Anal ytical Chemistry*, 2009: 1-10.
19. Quinn, A. and Elkins, K. (2016). The differentiation of menstrual from venous blood and other body fluids on v arious substrates by ATR-FTIR spectroscopy. *Journal of Forensic Sciences*, 62(1): 197-204.
20. Wang, Q., Li, B., Lin, H., Zhang, Y., Zhang, J. and Wang, Z. (2017). UV–Vis and ATR–FTIR spectroscopic in vestigations of postmortem interval based on the changes in rabbit plasma. *Plos One*,12 (7): E0182161.
21. Mclaughlin, G. and Lednev, I. K. (2014). A modified Raman multidimensional spectroscopic signature of bloo d to account for the effect of laser power. *Forensic Science International*, 240: 88-94.
22. Mclaughlin, G., Doty, K. C. and Lednev, I. K. (2014). Raman spectroscopy of blood for species identification . *Analytical Chemistry*, 86(23): 11628-11633.
23. Custers, D., Cauwenbergh, T., Bothy, J., Courselle, P. and Deconinck, E. (2015). ATR-FTIR spectroscopy and chemometrics: An interesting tool to discriminate and characterize counterfeit medicines. *Journal of Pharmace utical and Biomedical Analysis*, 112: 181-189.
24. Kamińska, A., Kowalska, A. and Waluk, J. (2016). ABO blood groups antigen–antibody interactions studied us ing SERS spectroscopy: Towards blood typing. *Analytical Methods*, 8(7): 1463-1472.
25. Lin, H., Zhang, Y., Wang, Q., Li, B. and Wang, Z. (2017). Species identification of bloodstains by ATR-FTIR s pectroscopy: The effects of bloodstain age and the deposition environment. *International Journal of Legal Medi cine*, 132(3): 667-674.
26. Cortes, S. (2010). Infrared Spectroscopy (IR) - Theory and Interpretation of IR spectra. https://personal.utdallas .edu/~scortes/ochem/OChem_Lab1/recit_notes/ir_presentation.pdf. [Accessed: 13-January-2020].
27. Güler, G., Vorob'ev, M., Vogel, V. and Mäntele, W. (2016). Proteolytically-induced changes of secondary struc tural protein conformation of bovine serum albumin monitored by Fourier transform infrared (FT-IR) and UV-c ircular dichroism spectroscopy. *Spectrochimica Acta Part A: Molecular and Biomolecular Spectroscopy*, 161(5): 8-18.
28. Hameed, B., Bhatt, C., Nagaraj, B. and Suresh, A. (2018). Chromatography as an efficient technique for the sep aration of diversified nanoparticles. *Nanomaterials in Chromatography*, 19(1): 503-518.
29. Coates, J. (2006). Interpretation of infrared spectra, a practical approach. *Encyclopedia of Analytical Chemistry*, 1(1): 10815-10837.
30. Mistek, E. and Lednev, I. (2015). Identification of species' blood by attenuated total reflection (ATR) Fourier tr ansform infrared (FT-IR) spectroscopy. *Analytical and Bioanalytical Chemistry*, 407(24): 7435-7442.
31. De Wael, K., Lepot, L., Gason, F. and Gilbert, B. (2008). In search of blood-detection of minute particles using spectroscopic methods. *Forensic Science International*, 180(1): 37-42.
32. Gunasekaran, S. and Uthra, D. (2008). Vibrational spectra and qualitative analysis of albendazole and mebenda zole. *Asian Journal of Chemistry*, 20(8): 6310.
33. Olsztynska-Janus, S., Szymborska-Malek, K., Gasior-Glogowska, M., Walski, T., Komorowska, M., Witkeiwic z, W., Pezowics, C., Kobielarz, M. and Szotek, S. (2012). Spectroscopic techniques in the study of human tissu es and their components. Part I: IR spectroscopy. *Acta of Bioengineering & Biomechanics*. 14(3): 101-115.
34. Lu, G., Zou, J. and Wang, Y. (2012). Incremental complete LDA for face recognition. *Pattern Recognition*, 45(7): 2510-2521.
35. Tan, Y., Yan, B., Xue, L., Li, Y., Luo, X. and Ji, P. (2019). Correction to: Surface-enhanced Raman spectrosco py of blood serum based on gold nanoparticles for the diagnosis of the oral squamous cell carcinoma. *Lipids in Health and Disease*, 18(1): 51.
36. Efron, B. and Tibshirani, R. (1993). Bootstrap methods for standard errors, confidence intervals, and other mea sures of statistical accuracy. *Statistical Science*, 1(1): 54-75.

Malaysian Journal of Analytical Sciences (MJAS)
Published by Malaysian Analytical Sciences Society

MAGNETIC KAOLINITE COMPOSITE FOR LEAD REMOVAL IN AQUEOUS SOLUTION

(Komposit Kaolinit Bermagnetik Untuk Penyingkiran Plumbum Dari Larutan Akueus)

Izzan Salwana Izman, Siti Nor Atika Baharin, Ruhaida Rusmin*

School of Chemistry and Environment, Faculty of Applied Sciences
Universiti Teknologi MARA, Negeri Sembilan Branch, Kuala Pilah Campus, 72000 Kuala Pilah, Negeri Sembilan, Malaysia

**Corresponding author: ruhaida@uitm.edu.my*

Received: 20 November 2019; Accepted: 21 January 2020

Abstract

Magnetic kaolinite composite was successfully synthesized using combination of kaolinite and iron oxide through co-precipitation method. The synthesized kaolinite-iron oxide (Kao-IO) and raw kaolinite (Kao) was characterized using X-ray diffractometer (XRD), scanning electron microscope (SEM), and Fourier-transform infrared spectroscopy (FTIR). The Kao-IO composite was used to remove Pb^{2+} ions from aqueous solution through adsorption studies under various experimental conditions (e.g. pH, contact time, and initial Pb concentration). Meanwhile the desorption studies of Pb loaded Kao-IO were performed with different desorbing agents. The optimum experimental condition was achieved at pH 6, reaction time of 120 min at initial concentration ranged from 10 to 70 mg/L. Kao-IO composite has a higher adsorption capacity (30.93 mg g^{-1}) compared to Kao (25.04 mg g^{-1}). Ethylenediaminetetraacetic acid (EDTA) was the best desorbing agent with the highest desorption efficiency (39.18%). Overall, Kao-IO composite demonstrated high potential as suitable adsorbent to treat Pb contaminated water.

Keywords: kaolinite, magnetic, iron oxide, lead, adsorption

Abstrak

Komposit kaolinit bermagnetik telah berjaya disintesis menggunakan gabungan kaolinit dan ferum oksida melalui kaedah pemendakan bersama. Kaolinit-ferum oksida (Kao-IO) dan kaolinit asli (Kao) dicirikan menggunakan pembelauan sinar-X (XRD), Mikroskop imbasan elektron (SEM) dan spektroskopi inframerah transformasi Fourier (FTIR). Komposit Kao-IO digunakan untuk menyingkirkan ion Pb^{2+} dari larutan akueus melalui kajian penjerapan dengan menggunakan pelbagai parameter eksperimen (contohnya pH, masa tindak balas dan kepekatan awal Pb). Sementara itu, kajian nyahjerapan Pb yang terjerap pada Kao-IO dilakukan menggunakan pelbagai ejen nyahjerapan. Parameter eksperimen yang optima dicapai pada pH 6, masa tindak balas 120 minit dan pada kepekatan awal antara 10 hingga 70 mg/L. Komposit Kao-IO menunjukkan kapasiti penjerapan yang lebih tinggi (30.93 mg g^{-1}) berbanding dengan Kao (25.04 mg g^{-1}). Asid etilinadiaminatetraasetik (EDTA) merupakan ejen nyahjerapan yang terbaik dengan kecekapan nyahjerapan tertinggi (39.18%). Secara keseluruhan, komposit Kao-IO menunjukkan potensi yang tinggi sebagai penjerap yang sesuai untuk merawat air yang tercemar dengan Pb.

Kata kunci: kaolinit, magnetik, ferum oksida, plumbum, penjerapan

Introduction

Uncontrolled release of heavy metals into environment from industries and domestic activities has become a serious global problem. Toxic heavy metal like lead (Pb) is categorized as one of the major pollutants in wastewater due to their non-biodegradable and persistence [1]. Lead poisoning is known to be hazardous and could cause severe health issues especially in children [2].

In order to remediate heavy metal contaminated water, treatments that are reliable, cost-effective and efficient are of great interest. Various methods have been used for this purpose, such as adsorption, solvent extraction, chemical precipitation, ion exchange, ultrafiltration, and reverse osmosis [3]. Adsorption technique has been reported as the most effective and economical way to remove heavy metals due to simplicity, ease of modification and regeneration potential. Adsorption using low cost adsorbents such as clays, fly ash, and agro-waste has been extensively reviewed and is continuously in demand to reduce the high cost of water treatment. Natural aluminosilicates like clay minerals have received much attention as an alternative adsorbent due to their efficiency, stability and high availability compared to other material like activated carbon [4].

Kaolinite (chemical composition of $Al_2Si_2O_5(OH)_4$) [5] is one of the natural clay minerals belong to a 1:1 (1 tetrahedral sheet and 1 octahedral sheet) with non-swelling properties. Kaolinite (Kao) has been previously used in water treatment industry with advantages such as large surface area, and good mechanical and chemical stability [6].To enhance the adsorption characteristics, Kao is usually chemically modified, this includes through the impregnation of clays with iron oxide particles nanoparticles forming a magnetic composite [4]. This magnetic modification has gained significant interest as the magnetic material is capable to address the difficult separation and recoveries of spent adsorbent from the reaction media. The centrifugation and sedimentation method commonly used to recover adsorbent is either costly, time or energy consuming hence is not practical in industries.

Due to the magnetism properties, magnetic materials like iron-based composites could be separated and collected easily by applying an external magnetic field [7]. Furthermore, iron oxide-based clay nanocomposite were reported to have a high surface area stable with low toxicity [8]. While several types of clay minerals like montmorillonite, bentonite and palygorskite has been used to prepare magnetic clays nanocomposite, little attention is given to kaolinite, especially those originated from Malaysia. Hence this research attempts to provide an insight on the potential industrial applications of locally available kaolinite as versatile adsorbent in treating contaminated water.

In this study, the magnetic kaolinite composite will be prepared, characterized and evaluated for its efficiency in removing Pb^{2+} ions from aqueous solution. Adsorption profile of composite and its nature of the interaction mechanism with Pb^{2+} will be deduced through the isothermal adsorption model and kinetic studies. In order to evaluate the potential of spent Kao-IO for regeneration, desorption test is being carried out using selected eluents.

Materials and Methods

Materials and reagents

Kaolinite (Kao) clay mineral purchased from MyLab Supplier (Johor, Malaysia) was used without further purification. Lead (II) nitrate ($Pb(NO_3)_2$) is supplied by R&M Chemicals (United Kingdom). Meanwhile the iron (III) chloride hexahydrate ($FeCl_3.6H_2O$) is from HmbG® Chemicals (Germany) and iron(II) sulphate heptahydrate ($FeSO_4.7H_2O$) is supplied by Bendosen (Malaysia). The ethylenediaminetetraacetic acid (EDTA) is obtained from Sigma-Aldrich (USA) while sodium hydroxide (NaOH, 96%) is by R&M Chemicals (United Kingdom). Ammonium hydroxide (NH_4OH, 25%) was from Systerm® (Malaysia) and nitric acid (HNO_3, 65%) were purchased from QReC (Malaysia). Other reagents (e.g. hydrochloric acid and ethanol are of analytical grade).

Preparation of kaolinite-iron oxide (Kao-IO) composite

Kao-IO composite was prepared according to previous proposed method [9 suspension through the co-precipitation method. Briefly, a 3.1 g of $FeCl_3.6H_2O$ and 2.4 g of $FeSO_4.7H_2O$ were respectively dissolved in 50 mL of deionized water. The Fe^{3+} solution was then mixed with a 4 g of raw kaolinite] using a one-pot synthesis route. In this approach, the iron oxide was directly synthesized in-situ in kaolinite (Kao) and the suspension was placed in ultrasonic bath at 40ºC for 15 min. Next, the mixture was transferred to water bath and the Fe^{2+} solution prepared earlier was then being added into the Fe^{3+}-Kao mixture. The Fe^{2+}- Fe^{3+}- Kao suspension were agitated (200 rpm) at 60 ºC in 30 minutes. The agitation speed was then increased (400 rpm) and a 10 mL of NH_4OH (25 %v/v) was added dropwise to the suspension for 60 min. Then, the suspension could react for another 120 minutes to produce black precipitation (known as Kao-IO composite). The precipitate was filtered and washed thoroughly with deionized water and ethanol (100 mL) until a neutral pH of supernatant was achieved. The Kao-IO was dried at 110 ºC for 3 hours, grind and kept in seal container for further use.

Material characterization

The surface morphology was examined using Scanning Electron Microscope (SEM) (Quanta 450 FEG). The powder X-ray Diffraction (XRD) patterns were collected using X-ray diffractometer in the 2θ range 10° to 80° using Bruker D8 Advance (Bruker AXS, Germany) operating at 40 kV under Cu Kα radiation (λ = 0.15406 nm). The Fourier Transform Infra-Red (FTIR) analysis was performed using Perkin-Elmer infrared spectrophotometer (ATR mode) with resolution of 4 cm^{-1} in the range of 4000-650 cm^{-1}.

Adsorption experiment

Aqueous solutions of Pb^{2+} were prepare by dissolving 100 mg/L of $Pb(NO_3)_2$ in deionized water followed by subsequent dilutions. A 0.05 g adsorbent immersed in 50 mL of Pb^{2+} at predetermined concentration was used as the adsorbent loading. Experiments were performed through batch method at 25°C at pH 4, 6, and 8 (adjusted using 0.01 M NaOH or HCl) to study the effect of pH. The contact time was varied from 10 to 240 minutes until equilibrium was reached. The kinetic study was performed at optimised condition at the initial concentration of 50 mg/L. After each completed adsorption reaction, the spent Kao-IO composite was separated from the reaction media through the magnetic separation process (using a magnet bar) followed by filtration. Meanwhile, for Kao, the spent adsorbent was collected through centrifugation (2500 rpm) up to 30 minutes until the solid was fully suspended. The initial and equilibrium concentrations of Pb^{2+} in the supernatant were determined using the atomic absorption spectroscopy (AAS) (Perkin Elmer).

The amount of Pb^{2+} adsorbed denoted as adsorption capacity, q (mg/g), onto raw kaolinite (Kao) and Kao-IO was calculated using the Equation 1,

$$\text{Adsorption capacity, } q_e = \frac{([Pb]_i - [Pb]_f)V}{m} \quad (1)$$

where the $[Pb]_i$ and $[Pb]_f$ are the concentration of Pb in the reaction solution before and after treatment (mg/L), respectively, m is the mass (g) of adsorbent, and V is the volume of the solution (L).

The adsorption data was fitted into selected adsorption isotherm model (Langmuir, Freundlich and Dubinin–Radushkevich). Chi- square test, x^2, (Equation 2) was used to evaluate the fitness of the isotherm data with the regression coefficient, r^2, determined from the linearized model.

$$\text{Chi - square, } x^2 = \frac{\sum_{i=1}^{n} (q_{e,meas} - q_{e,calc})^2}{q_{e,meas}} \quad (2)$$

where $q_{e,meas,}$ and $q_{e,\,calc}$ is the equilibrium adsorption capacity (mg/g) that is measured experimentally and calculated from the isotherm adsorption model, respectively, while n denotes the number of experimental observations.

Desorption experiment

The Pb^{2+} loaded Kao-IO retrieved from the adsorption experiment was washed thoroughly with deionized water. A deionized water with pH 4 and 8, 0.1 M NaCl and 0.1 M of EDTA were used as the desorption eluent. Desorption experiment was carried out identical to adsorption experiment described previously at an initial Pb concentration of 50 mg/L. The amount of Pb released in the supernatant was measured using the AAS. Desorption efficiency was calculated using equation 3, where $[Pb]_d$ is the concentration of Pb desorbed while $[Pb]_a$ is denoted as the amount of Pb^{2+} adsorbed initially.

$$\text{Desorption percentage (\%)} = \frac{[Pb]_d}{[Pb]_a} \times 100 \quad (3)$$

Results and Discussion

Physicochemical characteristics and surface morphology of Kao-IO

While the Kao is appeared as a white powder, the Kao-IO has a dark brown color (Figure 1a) due to iron oxide presence. From the physical observation, the impregnation of the iron particles in the Kao-IO composite was confirmed through its attraction towards the external magnetic field applied (i.e. magnetic bar) (Figure 1b and c). The surface morphology analysis through the SEM showed that the raw kaolinite (Kao) particles were closely-packed in platelet shape of sheets (Figure 2a). However, in the KaO-IO, the packed layers of Kao particles were loosening and more distributed (Figure 2b). The iron oxide particles appeared as agglomerates (Figure 2b) and their presence was further confirmed by the EDX analysis (Figure 2c) having an average of 17.10% wt. (Figure 2 c, inset).

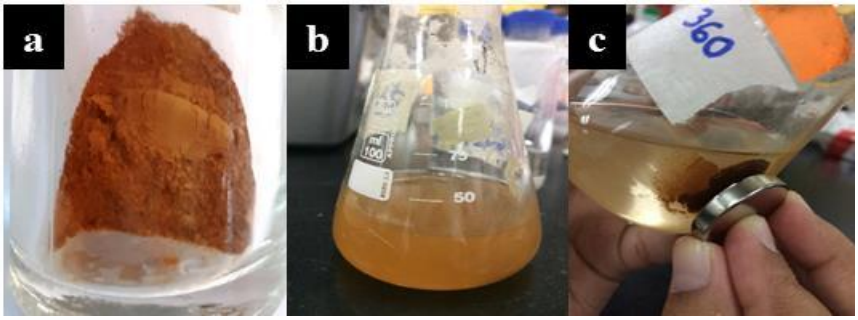
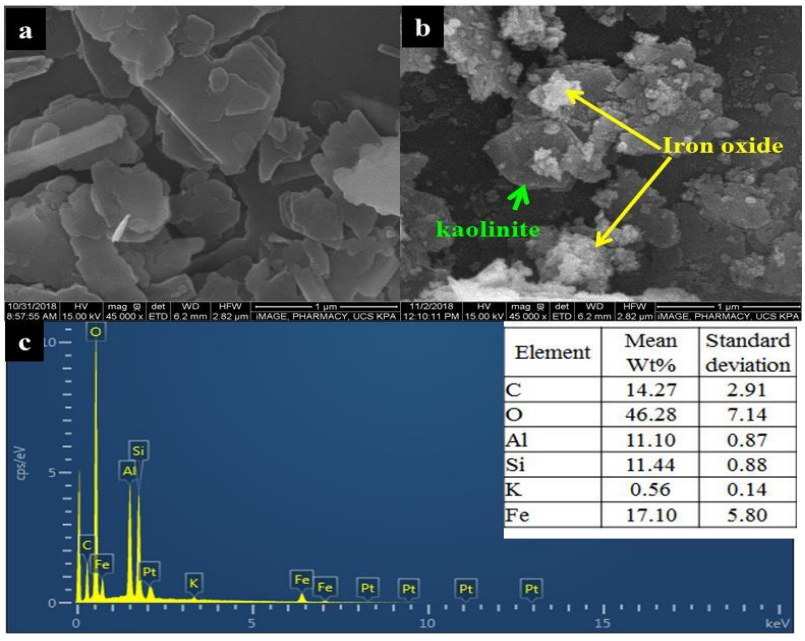


Figure 1. Image of (a) Kao-IO, (b) Kao-IO in Pb suspension, and (c) magnetic separation of spent Kao-IO from supernatant (after adsorption experiment)



Element	Mean Wt%	Standard deviation
C	14.27	2.91
O	46.28	7.14
Al	11.10	0.87
Si	11.44	0.88
K	0.56	0.14
Fe	17.10	5.80

Figure 2. SEM image of Kao (a), Kao-IO (b) and EDX analysis of KaO-IO (c)

Fourier transform-infrared (FTIR) analysis

Both the Kao and Kao-IO showed an almost similar FTIR spectra (Figure 3) with the presence of typical absorption bands of hydroxyl group in the range of 3700-3620 cm^{-1}associated with kaolinite [10]. The absorption band at 3692 and 3683 cm^{-1} (Figure 3a) represents the interlayer –OH stretching vibration of Al-OH whereas band at 3621 cm^{-1}

was assigned to inner hydroxyl group [4]. The spectral bands at around 1009, 1115, and 1030 cm^{-1} were assigned to the Si-O-Si/Al asymmetric bending vibrations, while the Si-O stretching was observed at 794 cm^{-1} [4] The bending of the inner and-surface hydroxyls groups of Al-OH were appeared at 911 cm^{-1} and 941 cm^{-1}. The Si-O-Al vibrations was observed at 751 cm^{-1} in Kao (Figure 3a) and has slightly shifted to 748 cm^{-1} in Kao-IO. Overall, it was observed that the Al-OH stretching mode (at 3695- 3620 cm^{-1}), Al-OH bending (941-911 cm^{-1}) and Si-O-Si/Al asymmetric (1115 & 1030 cm^{-1}) bands in Kao was much more intense as compared to those in Kao-IO (Figure 3b). These observation suggested the penetration of $Fe^{2+/}Fe^{3+}$ on the crystal structure of kaolinite [11].

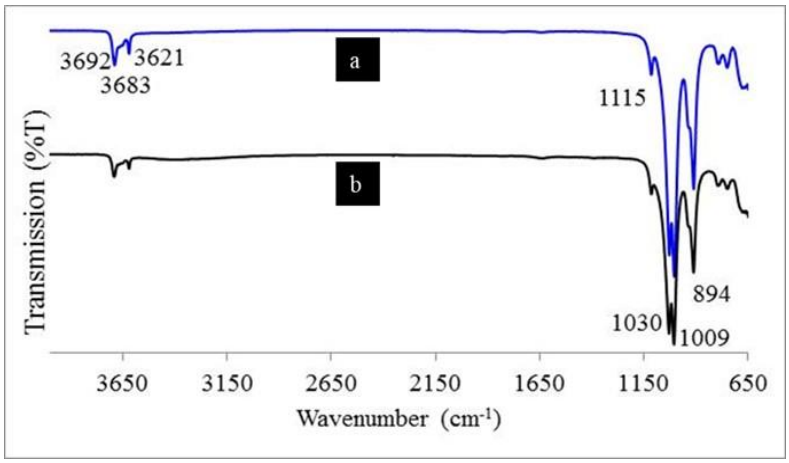


Figure 3. FTIR spectra of (a) Kao, and (b) Kao-IO

X-ray diffractometer (XRD) analysis

The sharp and intense peaks appeared at the 2θ = 12.3° and 26.6° in Kao (Figure 4a) represent the typical diffraction peak associated with kaolinite [12]. Those peaks were less intense (especially at the 26.6°) in the XRD patterns of Kao-IO (Figure 4b) implying a decrease in the clays' crystallinity. The diffraction peak for iron oxide (2θ around 35°, 57°, and 62°) [13] are difficult to trace probably due to only small quantity of iron oxide present. Furthermore, overlapping of those peaks with kaolinite peak was also possible, as being shown at the position around 2θ = 35°. No peak shifting or broadening was recorded for the composite since the kaolinite is a 1:1 layer type of clay minerals. The interaction between iron oxide and kaolinite was reported to occur only on the surface of kaolinite particles without involving the interlayer space.

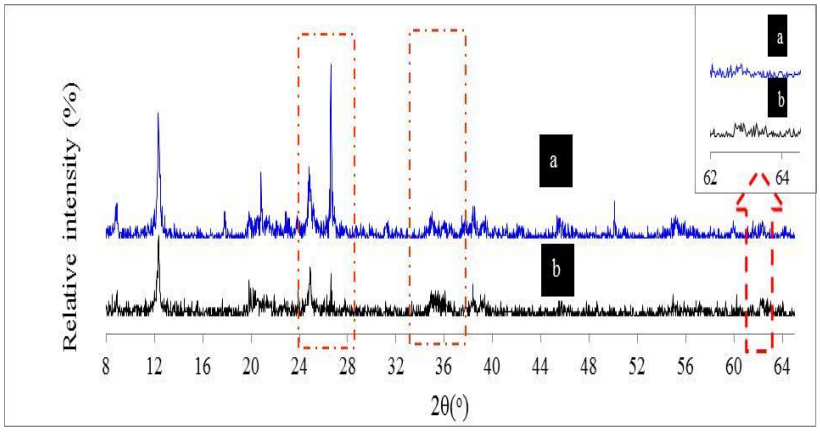


Figure 4. XRD spectrogram of (a) Kao and (b) Kao-IO

Optimization of experiment parameters: Effect of pH, contact time, and initial concentration

The adsorption of Pb^{2+} by Kao-IO was increased at pH 4 to 6, and then was dramatically decrease (Figure 5a). At a very acidic pH, the competition between H^+ and Pb^{2+} for active sites caused the adsorption capacity to be low [14]. In contrast, at high alkaline pH, changes in cationic metal speciation and ion precipitation could occur. The precipitation of metal hydroxide (such as $Pb(OH)_2$) would likely start to occur at pH above 6 [14]; causing a potential misleading result in the adsorption capacity calculation. Therefore, pH 6 was used as the optimum pH throughout this study.

The adsorption capacity was increase as the concentration was increased from 10 up to 50 mg/L for both Kao-IO and Kao (Figure 5b). An increase in initial concentration will allow more Pb^{2+} capable of being adsorbed to the adsorption sites [15]. At 60 mg/L, both Kao-IO and Kao reached a constant adsorption capacity, which implies saturation of their active sites [14]. Nevertheless, the equilibrium profile of Kao-IO demonstrated a lower C_e which yields a higher adsorption capacity, q_e (Figure 5c). This finding indicates that the KaO-IO has a higher affinity towards Pb^{2+} as compared to its pristine clay. The highest q_{max} achieved for Kao-IO and Kao was 30.93 and 25.04 mg g^{-1}, respectively (Figure 5c). The adsorption capacity of Kao-IO was fast and increases with the increment of adsorption time until equilibrium was reached at 120th minutes (Figure 5d).

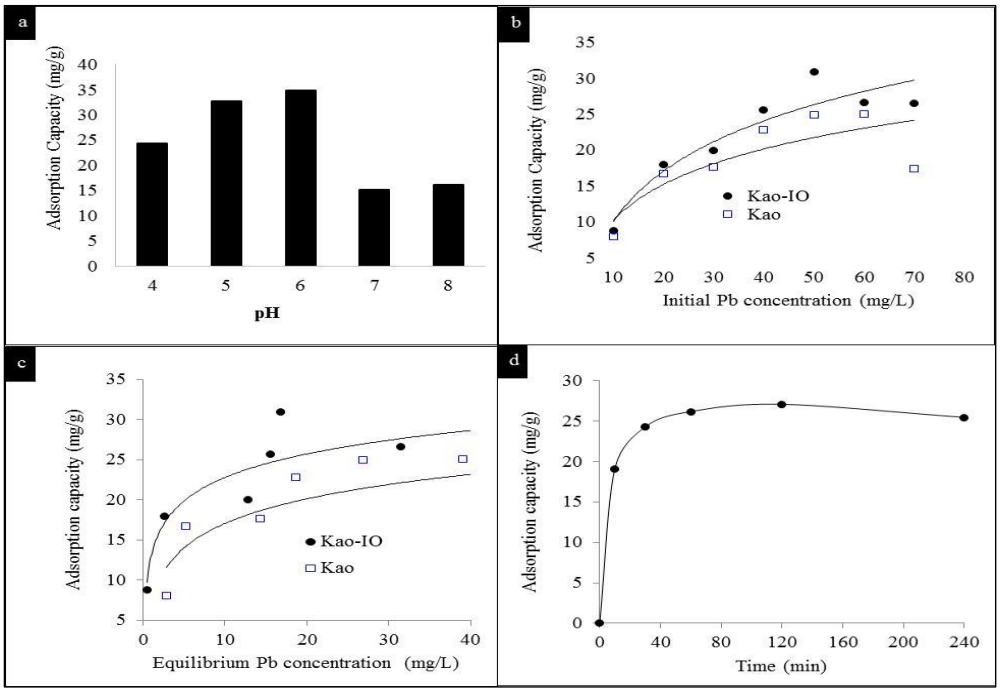


Figure 5. (a) Effect of pH values, (b) initial Pb concentration, (c) equilibrium adsorption isotherm and (d) reaction time on adsorption capacity of Kao-IO

Adsorption isotherm

The experimental adsorption data was fitted into three adsorption isotherms, namely the Langmuir, Freundlich and Dubinin–Radushkevich (D–R) model (Table 1). Based on the high regression coefficient (r^2, >0.95), satisfactory low chi-square (x^2) value and close agreement to experimental maximum adsorption capacity (q_{max}), the Langmuir isotherm model is considered the best fit model for both adsorbents (Table 1). The strong agreement of the experimental data with Langmuir model signifies a monolayer adsorption with homogenous adsorption sites. The Kao-IO has a larger K_L value showing a greater affinity of adsorbate (Pb) towards its active sites. A dimensionless constant called separation factor (R_L) to predict the adsorption favorability was calculated using the K_L value (L/mg) and was presented in the Table 1. A favorable adsorption is predicted if the R_L value is between 0 to 1 (0 <

R_L < 1); unfavorable if R_L > 1; linear if R_L=1; or irreversible when R_L = 0 [16]. The R_L value obtained from this experiment was in the range of 0 to 1 (Table 1) which confirms a favorable nature of Pb uptake by the adsorbents.

Table 1. Parameters adsorption isotherm model for all adsorbents

Isotherm model	**Equation**	**Parameters**	**Adsorbent**	
			Kao	**Kao-IO**
Langmuir	$\frac{C_e}{q_e} = \frac{1}{(q_{max} K_L)} + \frac{C_e}{q_{max}}$			
		q_{max}(mg/g)	29.59	28.09
		K_L (L/mg)	0.1538	0.6953
		r^2	0.9781	0.9638
	$R_L = \frac{1}{1 + K_L C_o}$	R_L value range (min – max)	0.0197 - 0.2150	0.0432 - 0.7591
		Chi-square (x^2)	1.3604	2.9294
Freundlich	$\log_{qe} = \log_{Kf} + \frac{1}{n} \log C_e$			
		1/n	0.3960	0.2684
		K_f (L/g)	6.571	11.92
		r^2	0.8390	0.8875
		Chi-square (x^2)	2.071	2.575
D–R	$\ln q_e = \ln q_{max} - \beta\varepsilon^2$			
	$\varepsilon = RT\ln(1 + \frac{1}{C_e})$	q_{max} (mg/g)	23.21	24.28
	$E=1/(2\beta)^{0.5}$	E (kJ/mol)	22.94	22.36
		r^2	0.9320	0.8453
		Chi-square (x^2)	1.411	4.212

* q_e = the adsorbed amount of Pb (mg/g), C_e = concentration of Pb (mg/L) at equilibrium, K_L = Langmuir constant, q_{max} = maximum adsorption capacity (mg/g), K_f = Freundlich constant (L/g), 1/n = adsorption intensity constant , β = coefficient related to the mean free energy of adsorption per mol of the adsorbate (mol^2/J^2), R = gas constant (J/mol K),T = the absolute temperature(K), and E = sorption energy (kJ/ mol).

The parameters of Freundlich isotherm model also give some beneficial information on the adsorption process. The value of 1/n obtained by the Kao-IO was approaching more closely towards the zero, in which indicates that the surface of Kao-IO was more heterogeneous than Kao. The higher K_f value also showed the tendency of Kao-IO to uptake more Pb that was portrayed through the slightly higher q_{max} obtained by this composite. The D-R isotherm model could be used to deduce the mechanism of adsorption. The E value (sorption energy) which is less than an 8 kJ/mol indicates physical adsorption; a value between 8 to16 kJ/mol is related to ion-exchange, whereas for E value in the range of 20-40 kJ/mol, chemisorption was predicted [17]. According to the analysis, Pb^{2+} adsorption towards Kao and Kao-IO was suggested as chemisorption with formation of specific chemical bonds like electrostatic bond and chemical bonding. Adsorption mechanism of Pb towards Kao-IO was deduced to occur *via* surface complexation between the Pb^{2+} and the hydroxyl group (silanol and aluminol) of clay minerals [18]. The Fe-OH functional group of iron oxide embedded on the clay's surface of Kao-IO may also likely participate in the

adsorption [8]. However further investigation is warranted to provide a precise understanding on the adsorption mechanism pathway.

Kinetic studies

The adsorption data was fitted into two common kinetic models; the pseudo first order and second order model. The adsorption data has strong agreement with the pseudo second order kinetic model (Table 2). This finding indicated that the adsorption mechanism is depended on the adsorbate-adsorbent interaction. Furthermore, pseudo second order model deduced chemisorption as the rate determining step, which agreed with the adsorption isotherm analysis described previously.

Table 2. Kinetic analysis on the Pb adsorption by Kao-IO (performed at initial [Pb] = 50 mg/L, at 0.1 g/mL loading, 25 ^{o}C)

Kinetic Model	**Equation****	**Parameters**	
Pseudo first order	$\log(q_e - q_t) = \log q_e - \frac{K_1 t}{2.303}$	q_e (mg/g)	5.4953
		k_1 (min^{-1})	0.0173
		r^2	0.6632
		Chi-square (x^2)	0.4798
Pseudo second order	$\frac{t}{q_t} = \frac{1}{h} + \frac{1}{q_e} t$	q_{ev}(mg/g)	28.16
		k_2 (g/mg.min)	0.0075
		r^2	0.9999
		Chi-square (x^2)	1.6160

** q_e = the adsorbed amount of Pb (mg/g) at equilibrium, q_t = the adsorbed amount of Pb (mg/g) at time t, K_1 is pseudo first order adsorption rate constant (min^{-1}), t = time (min), h = the initial sorption rate, (mg/g.min)

Desorption study

The desorption of Pb from spent Kao-IO using EDTA showed the highest percentage (39.18%) (Figure 6) compared to other eluents. EDTA solution can efficiently desorb Pb^{2+} due to the its ligand properties that capable to form chelation with metal cations [14]. A negligible percentage of Pb desorption was recorded in NaCl indicating that ion exchange between Pb and Na ions is less preferable. A slight Pb released in acidic water (pH 4) might be due to the protonation of the adsorbent's surface by H^+ that weakened the Pb-Kao interaction followed by Pb^{2+}desorption [8]. Hence it could be concluded that Pb^{2+} ions have a strong retention towards Kao-IO surface that prevent easy leaching of the adsorbed Pb back to the treated metal contaminated water.

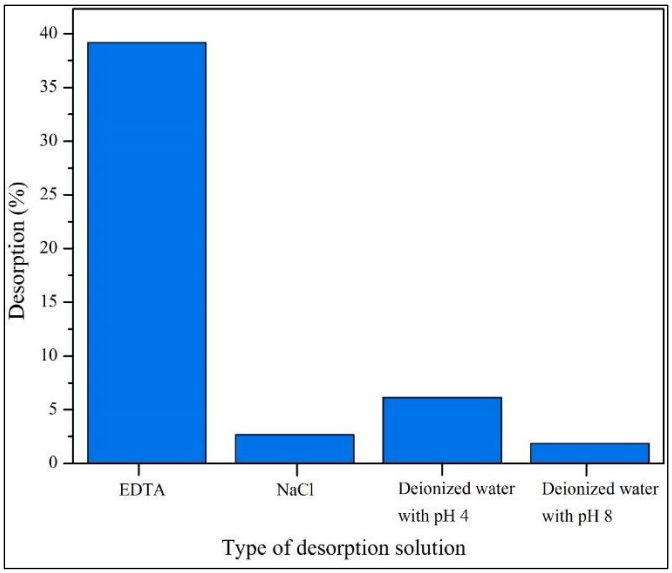


Figure 6. Desorption of Pb^{2+} from Kao-IO using various desorbing agent

Conclusion

The Kao-IO composite with magnetic properties was successfully prepared and characterized. Kao-IO showed a higher affinity in Pb^{2+} uptake and easy to be retrieved from the reaction media through the external magnetic separation. Pb retention on Kao-IO surface was stable thus require further optimization for desorption process to allow for possible regeneration of this material. Since raw kaolinite is abundance in Malaysia, the research findings will pave a way for more diversified application of the country's natural resources. Due to the simple synthesis route and high efficiencies towards Pb removal as demonstrated in this study, the Kao-IO hence has the potential to become a cost effective and environmental benign adsorbent to be used in water treatment.

Acknowledgement

The authors would like to thank Universiti Teknologi MARA, Negeri Sembilan branch, for technical facilities and financial support through internal training scheme. Partial funding from the research grant (FRGS/1/2019/STG07/UITM/02/15) sponsored by the Ministry of Education of Malaysia is greatly acknowledged.

References

1. Ali, R. M., Hamad, H. A., Hussein, M. M. and Malash, G. F. (2016). Potential of using green adsorbent of heavy metal removal from aqueous solutions: Adsorption kinetics, isotherm, thermodynamic, mechanism and economic analysis. *Ecological Engineering,* 91: 317-332.
2. Landrigan, P. J., Fuller, R., Fisher, S., Suk, W. A., Sly, P., Chiles, T. C. and Bose-O'Reilly, S. (2019). Pollution and children's health. *Science of the Total Environment,* 650: 2389-2394.
3. Sari, A. and Tuzen, M. (2014). Cd(II) adsorption from aqueous solution by raw and modified kaolinite. *Applied Clay Science,* 88: 63-72.
4. Tokarčíková, M., Tokarský, J., Kutláková, K.M. and Seidlerová, J. (2017). Testing the stability of magnetic iron oxides/kaolinite nanocomposite under various pH conditions. *Journal of Solid State Chemistry,* 253: 329-335.
5. Gao, W., Zhao, S., Wu, H., Deligeer, W. and Asuha, S. (2016). Direct acid activation of kaolinite and its effects on the adsorption of methylene blue. *Applied Clay Science,* 126: 98-106.
6. Duarte-Silva, R., Villa-García, M. A., Rendueles, M. and Díaz, M. (2014). Structural, textural and protein adsorption properties of kaolinite and surface modified kaolinite adsorbents. *Applied Clay Science,* 90: 73-80.

7. Yuan, P., Fan, M., Yang, D., He, H., Liu, D., Yuan, A., Zhu, J. X. and Chen, T. H. (2009). Montmorillonite-supported magnetite nanoparticles for the removal of hexavalent chromium [Cr(VI)] from aqueous solutions. *Journal of Hazardous Materials,* 166(2-3): 821-829.
8. Rusmin, R., Sarkar, B., Tsuzuki, T., Kawashima, N. and Naidu, R. (2017). Removal of lead from aqueous solution using superparamagnetic palygorskite nanocomposite: Material characterization and regeneration studies. *Chemosphere,* 186: 1006-1015.
9. Liu, H., Chen, W., Liu, C., Liu, Y. and Dong, C. (2014). Magnetic mesoporous clay adsorbent: Preparation, characterization and adsorption capacity for atrazine. *Microporous and Mesoporous Materials,* 194: 72-78.
10. Frost, R. L. (1997). The structure of the kaolinite minerals - a FT-Raman study. *Clay Minerals,* 32(1): 65-77.
11. Magdy, A., Fouad, Y. O., Abdel-Aziz, M. H. and Konsowa, A. H. (2017). Synthesis and characterization of Fe_3O_4/kaolin magnetic nanocomposite and its application in wastewater treatment. *Journal of Industrial Engineering Chemistry,* 56: 299-311.
12. Hu, P. and Yang, H. (2013). Insight into the physicochemical aspects of kaolins with different morphologies. *Applied Clay Science,* 74: 58-65.
13. Mirbagheri, N. S. and Sabbaghi, S. (2018). A natural kaolin/γ-Fe_2O_3 composite as an efficient nano-adsorbent for removal of phenol from aqueous solutions. *Microporous Mesoporous Materials,* 259: 134-141.
14. Rashidi, F., Sarabi, R. S., Ghasemi, Z. and Seif, A. (2010). Kinetic, equilibrium and thermodynamic studies for the removal of lead(II) and copper(II) ions from aqueous solutions by nanocrystalline TiO_2. *Superlattices and Microstructures,* 48 (6): 577-591.
15. Jiang, M., Jin, X., Lu, X.-Q. and Chen, Z. (2010). Adsorption of Pb(II), Cd(II), Ni(II) and Cu(II) onto natural kaolinite clay. *Desalination,* 252(1-3): 33-39.
16. Arias, F. and Sen, T. K. (2009). Removal of zinc metal ion (Zn^{2+}) from its aqueous solution by kaolin clay mineral: A kinetic and equilibrium study. *Colloids Surfaces A: Physicochemical and Engineering Aspects,* 348 (1-3): 100-108.
17. Desta, M. B. (2013) Batch sorption experiments: Langmuir and Freundlich Isotherm studies for the adsorption of textile metal ions onto teff straw (*Eragrostis tef*) agricultural waste. *Journal of Thermodynamics,* 2013: 1-6.
18. Liu, X., Lu, X., Sprik, M., Cheng, J., Meijer, E. J. and Wang, R. (2013). Acidity of edge surface sites of montmorillonite and kaolinite. *Geochimica et Cosmochimica Acta,* 117: 180-190.

Malaysian Journal of Analytical Sciences (MJAS)
Published by Malaysian Analytical Sciences Society

PENENTUAN KEPEKATAN LOGAM BERAT DALAM SEDIMEN DI MUARA SUNGAI KEMAMAN, TERENGGANU

(Determination of Heavy Metal Concentrations in Sediment of Kemaman River Estuary, Terengganu)

Ahmad Shamsuddin Ahmad[1]*, Suhaimi Suratman[2], Noor Azhar Mohamed Shazili[2], Ong Meng Chuan[1,2], Mohammed Faizal Abdul Rahim[1]

[1]Fakulti Sains dan Sekitaran Marin
[2]Institut Oseanografi dan Sekitaran
Universiti Malaysia Terengganu, 21030 Kuala Nerus, Terengganu, Malaysia

**Email pengarang utama: sham@umt.edu.my*

Received: 29 July 2019; Accepted: 28 December 2019

Abstrak

Penentuan kepekatan dan taburan beberapa logam berat terpilih seperti Al, Fe, Cr, Cu, Mn, Ni, Pb dan Zn di dalam sedimen dasar di muara Sungai Kemaman, Terengganu telah dijalankan menggunakan kaedah pencernaan basah. Selepas pencernaan, logam berat di dalam larutan ekstrak dianalisa menggunakan spektrofotometer serapan atom (AAS) dan spektrofotometer serapan atom relau grafit (GFAAS). Umumnya, keputusan menunjukkan bahawa kepekatan kebanyakan logam berat di kawasan kajian adalah lebih rendah atau setara jika dibandingkan dengan kawasan lain. Bagi pensampelan pertama, purata kepekatan logam adalah 4.44 ± 2.55% (Al), 2.36 ± 1.01% (Fe), 44.29 ± 23.82 $\mu g.g^{-1}$ (Cr), 12.13 ± 6.03 $\mu g.g^{-1}$ (Cu), 135 ± 83.08 $\mu g.g^{-1}$ (Mn), 27.08 ± 13.47 $\mu g.g^{-1}$ (Ni), 25.11 ± 10.34 $\mu g.g^{-1}$ (Pb) dan 69.85 ± 29.13 $\mu g.g^{-1}$ (Zn). Bagi pensampelan kedua pula purata kepekatan adalah 10.18 ± 6.64 % (Al), 1.78 ± 0.75 % (Fe), 27.00 ± 18.27 $\mu g.g^{-1}$ (Cr), 10.15 ± 6.75 $\mu g.g^{-1}$ (Cu), 120.71± 72.69 $\mu g.g^{-1}$ (Mn), 11.88 ± 5.18 $\mu g.g^{-1}$ (Ni), 20.49 ± 9.20 $\mu g.g^{-1}$ (Pb) dan 34.17 ± 29.97 $\mu g.g^{-1}$ (Zn). Analisis statistik ANOVA menunjukkan terdapatnya perbezaan bererti ($p<0.05$) di antara pensampelan pertama dan kedua. Penentuan faktor pengkayaan menunjukkan kepekatan Pb di kawasan kajian dipengaruhi oleh sumber-sumber antropogenik. Beberapa aktiviti di sekitar Sungai Kemaman telah dikenalpasti sebagai penyumbang sumber antropogenik iaitu aktiviti-aktiviti perikanan, perindustrian, aktiviti-aktiviti di dermaga dan dari kawasan perbandaran.

Kata kunci: logam berat, faktor pengkayaan, sedimen, Sungai Kemaman, Laut China Selatan

Abstract

The determination of the concentrations and distributions of selected heavy metals such as Al, Fe, Cr, Cu, Mn, Ni, Pb, and Zn in sediment of Kemaman River estuary, Terengganu has been carried out using the wet digestion method. After digestion, heavy metals in solution extracts were analysed by atomic absorption spectrophotometer (AAS) and graphite furnace atomic absorption spectrophotometer (GFAAS). In general, the results showed that most of heavy metals concentration in the study area are similar or lower compared to other areas. For the first sampling, mean concentration was 4.44 ± 2.55% (Al), 2.36 ± 1.01% (Fe), 44.29 ± 23.82 $\mu g.g^{-1}$ (Cr), 12.13 ± 6.03 $\mu g.g^{-1}$ (Cu), 135 ± 83.08 $\mu g.g^{-1}$ (Mn), 27.08 ± 13.47 $\mu g.g^{-1}$ (Ni), 25.11 ± 10.34 $\mu g.g^{-1}$ (Pb) and 69.85 ± 29.13 $\mu g.g^{-1}$ (Zn). In the second sampling, the mean concentration of Al was 10.18 ± 6.64 %, 1.78 ± 0.75 % (Fe), 27.00 ± 18.27 $\mu g.g^{-1}$ (Cr), 10.15 ± 6.75 $\mu g.g^{-1}$ (Cu), 120.71± 72.69 $\mu g.g^{-1}$ (Mn), 11.88 ± 5.18 $\mu g.g^{-1}$ (Ni), 20.49 ± 9.20 $\mu g.g^{-1}$ (Pb) and 34.17 ± 29.97 $\mu g.g^{-1}$ (Zn). The ANOVA statistical analysis showed that there was significant difference ($p<0.05$) between the first and second sampling. Enrichment factor determination showed that Pb concentration was influenced by anthropogenic sources. Several activities around the Sungai Kemaman have been identified as the contributors for anthropogenic sources such as fishing activities, industrial, shipyard activities and from urbanized area.

Keywords: heavy metals, enrichment factor, sediment, Kemaman River , South China Sea

Pendahuluan

Pencemaran laut dan sungai adalah satu isu yang amat sensitif untuk diperkatakan sama ada di Malaysia mahupun di serata dunia. Pada hari ini manusia mulai sedar akan kesan yang akan terjadi atau dihadapi apabila berlakunya sesuatu pencemaran. Bernt [1] dan Shamsuddin [2] telah mendapati terdapatnya bukti-bukti yang menunjukkan beberapa kawasan laut dan sungai di serata dunia ini dalam keadaan terancam. Sehubungan dengan itu, para saintis hari ini telah bersependapat bahawa pencemaran laut dan sungai memerlukan kajian yang segera kerana pada masa sekarang ini maklumat mengenai kesan negatif akibat daripada pencemaran masih lagi terbatas.

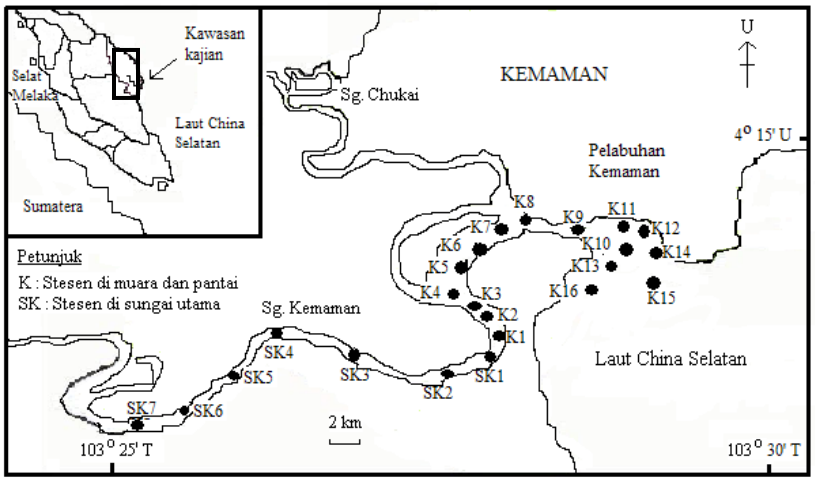
Sejak beberapa dekad yang lalu, penebusgunaan tanah di sepanjang sungai untuk pembinaan kawasan perindustrian telah dilakukan bagi meningkatkan ekonomi masyarakat setempat. Ini telah menyebabkan pertambahan penduduk, aktiviti yang semakin meluas dan yang paling penting sekali adalah pembuangan sisa-sisa perindustrian ke dalam sungai yang telah menyebabkan pengumpulan logam berat yang toksik sehingga pada tahap yang membimbangkan. Logam berat yang memasuki sungai ini akan tertinggal yang kemudiannya diserap oleh bahan terampai dan diangkut ke seluruh kawasan sungai mengikut pergerakan arah arus [3]. Semasa pengangkutan berlaku, ia akan bercampur dengan bahan-bahan enapan dan partikulat lain yang terdapat dalam sungai tersebut. Ini akan menyebabkan perubahan secara kimia dan pemendakan berlaku bersama dengan logam berat tersebut. Pada masa dahulu, sedimen sungai dikatakan dapat membantu membersihkan air dengan menyerap pencemaran. Tetapi sekarang, simpanan logam berat yang banyak di dalam sedimen telah digambarkan sebagai berbahaya dan bertoksik kerana boleh memberi kesan jangkamasa panjang kepada ekosistem sungai dan biota hidupan yang terdedah dengan bahan bertoksik ini [3].

Secara amnya, pencemaran sungai pada masa kini adalah pada tahap yang membimbangkan. Pembuangan sisa-sisa perindustrian daripada kilang-kilang yang dibina berhampiran telah menyebabkan sungai tercemar teruk. Begitu juga dengan pembuangan sisa-sisa domestik yang dilakukan oleh pihak yang tidak bertanggungjawab sehingga menyebabkan pencemaran berlaku. Berasaskan kepada keadaan ini maka satu kajian telah dijalankan di Sungai Kemaman untuk mengkaji faktor-faktor penyumbang kepada kepekatan logam berat dalam sedimen. Sungai Kemaman terletak di kawasan perindustrian Teluk Kalong, Kemaman, Terengganu.

Bahan dan Kaedah

Kawasan kajian dan persampelan

Kawasan kajian ditunjukkan dalam Rajah 1. Pensampelan enapan dasar daripada 23 stesen terpilih telah dijalankan sebanyak dua kali iaitu pada bulan Jun 2002 dan Oktober 2002 dengan menggunakan bot UNIPERTAMA III. Pensampelan sedimen dilakukan dengan menggunakan pencengkau Smith McIntyre. Sampel disimpan dalam bekas polietilena yang telah direndam di dalam larutan asid nitrik 20% selama satu minggu dan dibilas dengan air Milli-Q (18.2 MΩ) dan kemudiannya dibawa ke makmal.



Rajah 1. Kawasan kajian di muara Sungai Kemaman, Terengganu

Penyediaan sampel
Di dalam makmal, sampel dikeringkan sehingga mencapai berat yang tetap. Kemudian sampel diayak menggunakan penggoncang automatik Endecolls EFL2 mk3. Hanya sampel yang bersaiz di bawah 63 µm digunakan untuk analisis seterusnya.

Analisis logam berat
Kesemua peralatan kaca yang digunakan dalam analisis terlebih dahulu direndam di dalam larutan asid nitrik 10% untuk selama 24 jam dan dibilas dengan air Milli-Q (18.2 MΩ) untuk memastikan ia bebas daripada bahan-bahan pencemar. Kaedah pencernaan basah ke atas sampel telah dijalankan dengan menggunakan campuran asid nitrik (65%, GR, Merck), asid perklorik (70-72%, GR, Merck), asid hidroflorik (40%, GR, Merck) dan asid hidroklorik (37%, GR, Merck) [4]. Selepas pencernaan, analisis logam berat telah dijalankan dengan menggunakan spektrofotometer serapan atom (AAS) model Perkin Elmer 3100 dan spektrofotometer serapan atom relau grafit (GFAAS) model Hitachi Z–8270. Sampel rujukan NBS 1646a telah digunakan untuk memastikan ketepatan analisis yang dijalankan. Ketepatan analisis adalah di antara julat 92-104% (Jadual 1).

Jadual 1. Nilai ujian ketepatan analisis sampel dengan nilai rujukan NBS 1646a

Logam	Nilai Piawai ($\mu g.g^{-1}$ berat kering)	Nilai Diperolehi ($\mu g.g^{-1}$ berat kering)	Ketepatan (%)
Al %	2.29	2.35	103
Fe %	2.01	1.85	92
Cr	40.90	39.08	96
Cu	10.01	10.42	104
Mn	234.50	257.71	101
Ni	23.00	23.97	104
Pb	11.70	10.99	94
Zn	48.90	49.99	102

Penentuan Faktor Pengkayaan
Faktor pengkayaan merupakan salah satu kaedah yang boleh digunakan untuk menentukan samada sesuatu kawasan kajian tercemar dengan sumber antropogenik atau tidak. Nilai faktor pengkayaan diperolehi apabila nisbah kepekatan logam daripada data yang diperolehi dibahagikan dengan nisbah kepekatan logam daripada kerak bumi [5-8]. Dalam kajian ini, nilai kepekatan logam Al telah digunakan mengikut nilai yang dinyatakan oleh Mason dan Moore [9] sebagai nilai rujukan. Nilai faktor pengkayaan yang melebihi 1 menunjukkan terdapat kemasukan sumber-sumber antropogenik dalam sedimen kawasan yang dikaji [10, 11], manakala nilai faktor pengkayaan kurang daripada 1 menunjukkan logam tersebut berasal dari sumber semulajadi. Pengiraan faktor pengkayaan adalah berdasarkan formula berikut:

$$\text{Faktor pengkayaan (EF)} = \frac{\text{(kepekatan logam / Al) sampel}}{\text{(kepekatan logam / Al) kerak bumi}} \quad (1)$$

Keputusan dan Perbincangan

Kepekatan logam mengikut masa pensampelan
Kepekatan purata logam berat di kawasan kajian ditunjukkan dalam Jadual 2 dan perbandingan antara kajian dalam Jadual 3. Berdasarkan kepada analisis statistik ANOVA yang dijalankan didapati kepekatan logam menunjukkan perbezaan yang bererti (n=23, p <0.05) di antara pensampelan pertama dan kedua. Secara umumnya, didapati kepekatan logam pada pensampelan pertama adalah lebih tinggi berbanding dengan pensampelan kedua kecuali

logam Al. Keadaan ini adalah bersangkutan dengan perubahan musim [2, 11, 12]. Pensampelan pertama dilakukan sebelum musim tengkujuh manakala pensampelan kedua dijalankan ketika musim tengkujuh baru bermula. Akibat daripada itu, dicadangkan tekstur sedimen dasar kawasan kajian telah berubah yang mana min saiz enapan menjadi semakin kasar semasa permulaan musim tengkujuh (min saiz = 2.34∅±0.93) berbanding dengan sebelum tengkujuh (min saiz = 4.02∅±1.31). Menurut Kamaruzzaman [12], Donazzolo et al. [13], Nriagu et al. [14], Ong et al. [15] dan Ong et al. [16], saiz butiran yang halus mempunyai luas permukaan spesifik yang sangat tinggi untuk bersentuhan dengan logam dan seterusnya menjerap lebih banyak ion-ion logam berbanding dengan dengan partikel yang lebih besar. Ujian korelasi menunjukkan min saiz sedimen berkorelasi secara positif dan kuat dengan kepekatan ion-ion logam di dalam sedimen ($R^2 = 0.65$).

Jadual 2. Kepekatan purata untuk setiap logam dalam sedimen di kawasan kajian

Pensampelan	Al (%)	Fe (%)	Cr (μg.g^{-1})	Cu (μg.g^{-1})	Mn (μg.g^{-1})	Ni (μg.g^{-1})	Pb (μg.g^{-1})	Zn (μg.g^{-1})
Pertama	4.44±2.55 (1.36 – 10.50)	2.36±1.01 (0.97 – 3.90)	44.29±23.82 (6.00 – 78.17)	12.13±6.03 (2.88 – 20.27)	135.54±83.08 (31.47 – 444.7)	27.08±13.47 (10.98 – 70.42)	25.11±10.34 (9.47 – 40.29)	69.85±29.13 (12.0 – 164.01)
Kedua	10.18±6.64 (1.89 – 13.33)	1.78±0.75 (0.44 – 3.98)	27.00±18.27 (0.88 – 63.90)	10.15±6.75 (2.18 – 33.25)	120.71±72.69 (17.92 – 364.90)	11.88±5.18 (2.07 – 65.89)	20.49±9.20 (7.13 – 51.06)	34.17±29.97 (5.98 – 145.58)

( ) = julat nilai

Jadual 3. Kepekatan logam dalam sedimen di beberapa kawasan di Malaysia

Lokasi	Al (%)	Fe (%)	Cr (μg.g^{-1})	Cu (μg.g^{-1})	Mn (μg.g^{-1})	Ni (μg.g^{-1})	Pb (μg.g^{-1})	Zn (μg.g^{-1})
Muara K.Terengganu [a]	-	-	-	-	384 – 1744	25 – 53	30.6 – 638	47 – 159
Juru Penang [b]	2.6 –8.1	0.9 – 2.9	11.5 – 59.6	9.3 – 43	118 – 442	-	-	36.7 – 65
Luar Pantai Sabah[c]	2.4 –3.8	1.3 – 2.3	38 – 59	20 – 50	211 – 320	24 – 47	BDL – 41	34 – 55
Sungai Chukai[d]	6.0 – 15.2	1.3 – 3.4	33.4 –77.9	8.6 – 20.7	99.9 – 645.5		9.4 – 19.6	25.74 – 69.81
Laut China Selatan[c]	-	--	-	1.9 – 9.2	-	6.1 – 22.3	1.9 – 12.8	12.45 – 49.88
Sungai Rambai[e]	-	1.5 – 2.7	-	20 – 84	56 – 803	-	38 – 117	51 - 483

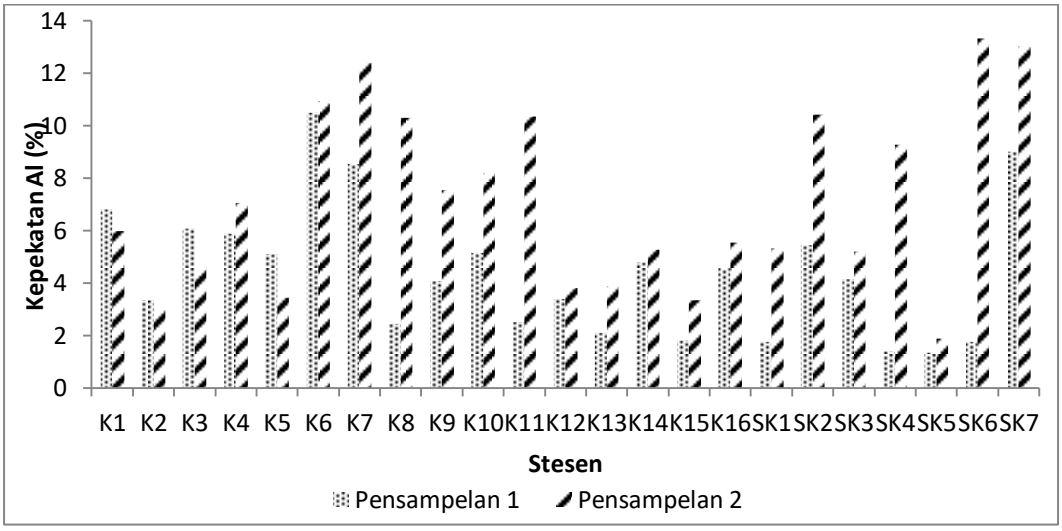
a) Nor [17], b) Khalik et al. [18], c) Shazili et al. [19], d) Shamsuddin et al. [20], e) Poh & Mun [21]

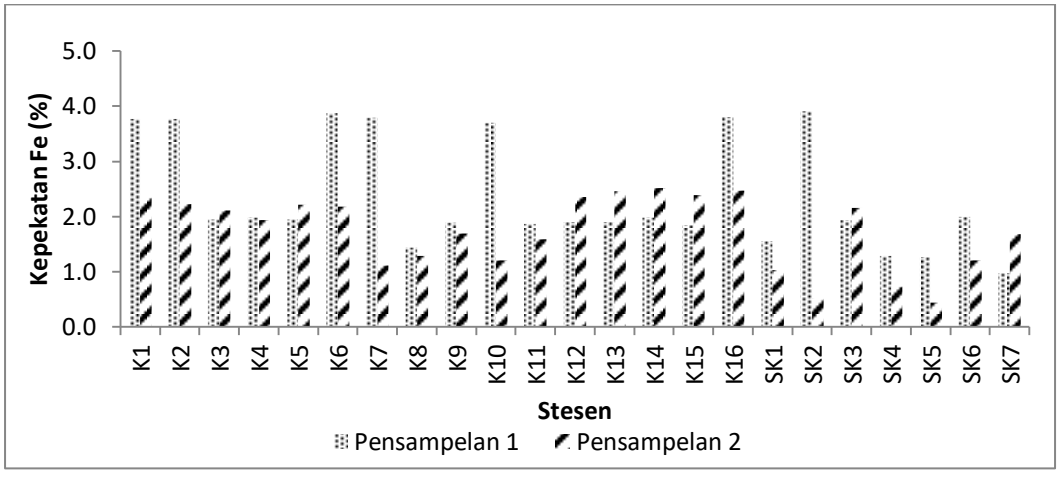
Perbandingan kepekatan logam kawasan kajian dengan beberapa kawasan di persisiran pantai di Malaysia

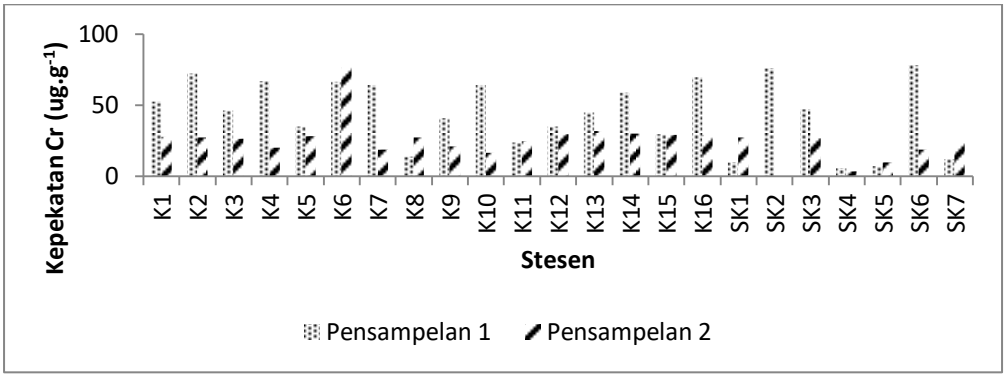
Jadual 3 menunjukkan perbandingan kepekatan logam di antara Sungai Kemaman dan sungai-sungai serta kawasan pesisiran pantai di Malaysia. Secara umumnya, melalui perbandingan didapati kepekatan logam Fe, Cr, Cu dan Mn di kawasan kajian berada dalam julat yang hampir sama dengan kepekatan logam dari Sungai Juru (Pulau Pinang), Luar Pantai Sabah, Sungai Chukai (Kemaman, Terengganu) dan Sungai Rambai (Melaka). Manakala julat kepekatan logam Ni, Pb dan Zn di kawasan kajian adalah berbeza dengan kepekatan logam di muara Kuala Terengganu, Sungai Chukai, Laut China Selatan dan Sungai Rambai. Perbezaan ini mungkin disebabkan oleh pengaruh aktiviti-aktiviti yang terdapat di persekitaran kawasan-kawasan kajian. Perbezaan kepekatan logam di sesuatu kawasan adalah disebabkan oleh pengaruh atau kemasukan logam dari berbagai-bagai sumber. Menurut Dryssen et al. [22] dan Bernhard [23], kepekatan logam boleh berubah secara terus melalui berbagai-bagai proses dan sumber pencemaran. Badri [24] telah menyatakan bahawa pencemaran logam berat mungkin masuk ke dalam persekitaran dalam bentuk pepejal atau bukan pepejal, di mana ianya boleh dirujuk kepada perlimpahan di dalam abiotik (seperti endapan, debu, tanah dan air) dan juga perlimpahan biotik (seperti tumbuhan, hidupan akuatik dan sebagainya).

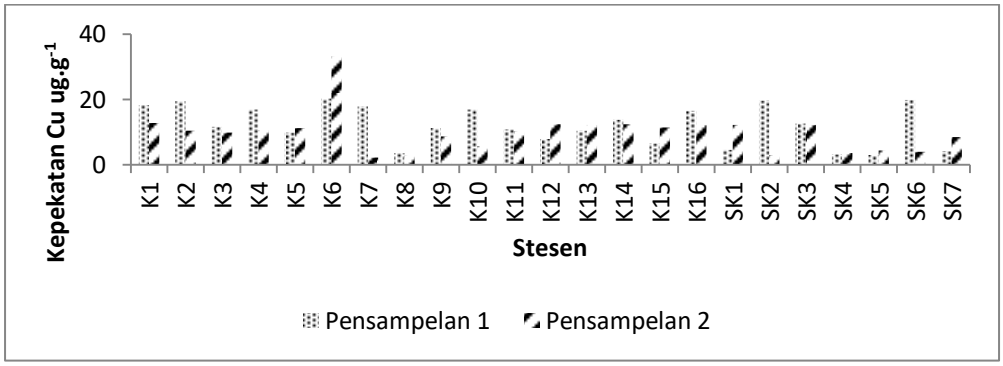
Kepekatan logam mengikut stesen kajian

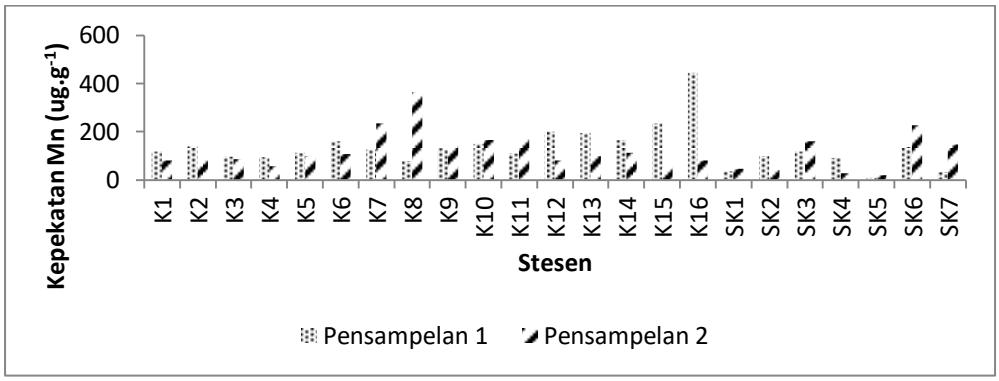
Rajah 2 menunjukkan kepekatan logam mengikut stesen kajian dan masa pensampelan. Berdasarkan kepada keputusan yang diperolehi, didapati beberapa stesen kajian mempunyai kepekatan logam yang lebih tinggi berbanding dengan stesen-stesen pensampelan yang lain. Ini mungkin disebabkan kedudukan geografi stesen pensampelan tersebut serta pengaruh daripada aktiviti-aktiviti manusia seperti perumahan, perindustrian dan perkapalan di sekitar kawasan sungai tersebut. Di samping itu, jenis tekstur sedimen dasar juga mempengaruhi kepekatan logam berat tersebut [2, 11, 25]. Umumnya, kepekatan beberapa logam di stesen K1, K2, K6 dan K7 adalah tinggi berbanding dengan kepekatan logam di stesen-stesen yang lain. Di stesen K1 dan K2 didapati kepekatan logam Fe, Cr, Cu dan Pb adalah tinggi disebabkan oleh kemasukan sumber logam dari aktiviti di limbungan kapal dan pusat perindustrian kecil yang menyalurkan bahan buangan ke dalam sungai tersebut. Manakala, kepekatan logam Fe, Cr, Cu, Ni, Pb dan Zn di stesen K6 dan K7 adalah tinggi akibat daripada bahan-bahan buangan dari aktiviti di pelabuhan perikanan, stesen minyak dan kawasan perbandaran. Hasil kajian saintis mendapati bahawa kandungan logam Cu dan Fe yang tinggi mungkin disebabkan oleh aktiviti perindustrian yang melepaskan sisa industri ke persekitaran akuatik berdekatan [2, 12, 26]. Shamsuddin [2], Kamaruzzaman [12] dan Donazzolo et al. [13] juga merumuskan bahawa kandungan logam Zn dan Pb yang tinggi di persekitaran akuatik seperti kawasan pelabuhan atau kawasan yang aktif dengan aktiviti perkapalan. Hasil dapatan sesetengah saintis juga menunjukkan bahan buangan manusia seperti dari perumahan, perbandaran dan automobil menyumbang kepada pencemaran Pb di persekitaran akuatik [2, 12, 20, 27, 28].

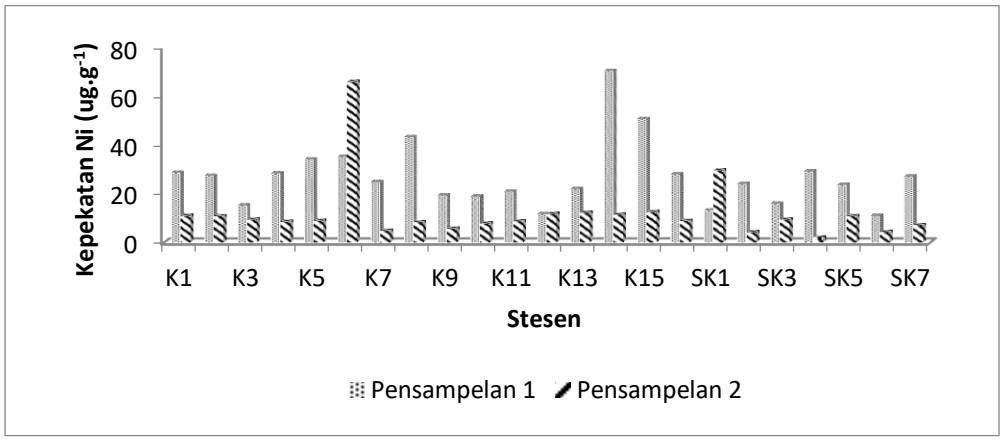


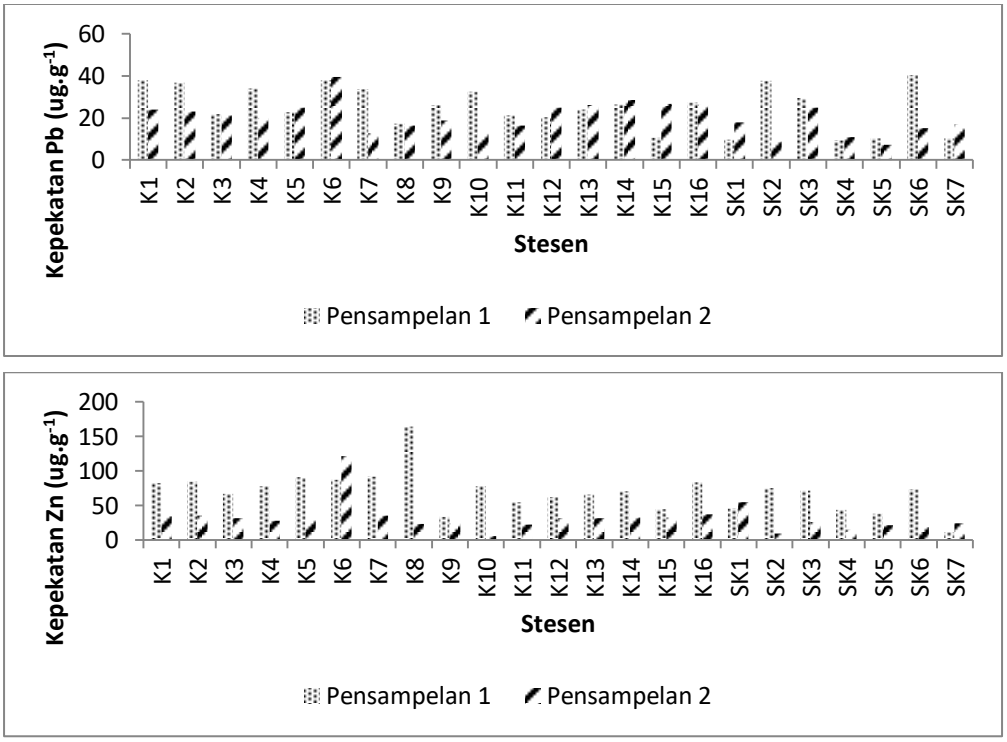



Kepekatan Cr (ug.g-1)
100
50
0
K1 K2 K3 K4 K5 K6 K7 K8 K9 K10 K11 K12 K13 K14 K15 K16 SK1 SK2 SK3 SK4 SK5 SK6 SK7
Stesen
Pensampelan 1
Pensampelan 2


Kepekatan Cu ug.g-1
40
20
0
K1 K2 K3 K4 K5 K6 K7 K8 K9 K10 K11 K12 K13 K14 K15 K16 SK1 SK2 SK3 SK4 SK5 SK6 SK7
Stesen
Pensampelan 1
Pensampelan 2


Kepekatan Mn (ug.g-1)
600
400
200
0
K1 K2 K3 K4 K5 K6 K7 K8 K9 K10 K11 K12 K13 K14 K15 K16 SK1 SK2 SK3 SK4 SK5 SK6 SK7
Stesen
Pensampelan 1
Pensampelan 2


Kepekatan Ni (ug.g-1)
80
60
40
20
0
K1 K3 K5 K7 K9 K11 K13 K15 SK1 SK3 SK5 SK7
Stesen
Pensampelan 1
Pensampelan 2



Rajah 2. Kepekatan logam berat bagi setiap stesen kajian muara Sungai Kemaman

Faktor pengkayaan

Nilai EF logam-logam yang dikaji ditunjukkan dalam Jadual 4. Kesemua logam yang dikaji menunjukkan nilai EF yang kurang daripada 1 bagi kedua-dua pensampelan kecuali logam Pb. Ini menggambarkan bahawa logam berat di kawasan kajian adalah berasal daripada proses semulajadi sama ada sebelum musim tengkujuh mahupun ketika musim tengkujuh [2, 10, 11]. Berdasarkan kepada nilai EF bagi Pb iaitu melebih 1, didapati kepekatan logam ini dipengaruhi oleh kemasukan logam daripada sumber antropogenik. Keputusan ini adalah selari dengan keputusan kajian yang diperolehi oleh Shamsuddin [2] dengan menggunakan kaedah penguraian berterusan ke atas enapan dasar muara Kuala Kemaman dan pesisiran pantai Kemaman. Daripada kajian Shamsuddin [2], didapati jumlah kepekatan logam Pb dalam pecahan bukan litogenik (fasa penguraian logam mudah bertukar, fasa penguraian ikatan karbonat, ikatan Fe-Mn oksida dan fasa ikatan bahan organik) adalah lebih tinggi jika dibandingkan dengan kepekatan logam Pb dalam pecahan litogenik (fasa hasil logam) dan ini menunjukkan kepekatan Pb di kawasan kajian adalah dipengaruhi oleh kemasukan sumber antropogenik. Kepekatan logam dalam sedimen sebenarnya boleh dibahagikan kepada pecahan yang tidak kekal (pecahan bukan litogenik) dan pecahan yang kekal (pecahan litogenik) [29-31]. Pecahan bukan litogenik adalah berpunca daripada bahan-bahan antropogenik iaitu bahan-bahan yang terhasil daripada aktiviti-aktiviti manusia manakala pecahan litogenik adalah logam yang terikat pada kekisi hablur atau sumber semulajadi [31]. Jika kepekatan logam dalam pecahan bukan litogenik tinggi bermakna terdapatnya kemasukan logam daripada sumber antropogenik dan begitu juga sebaliknya.

Jadual 4. Nilai faktor pengkayaan (EF) logam di kawasan kajian

Logam	Nilai EF (Pensampelan Pertama)	Nilai EF (Pensampelan Kedua)
Fe	0.80	0.46
Cr	0.31	0.13
Cu	0.55	0.27
Mn	0.26	0.10
Ni	0.46	0.29
Pb	2.25	1.56

Kesimpulan

Secara kesimpulannya, keputusan daripada kajian yang telah dijalankan di Sungai Kemaman menunjukkan kepekatan logam dalam sedimen dasar kawasan masih lagi berada dalam keadaan terkawal kecuali bagi logam Pb. Ini boleh dibuktikan dengan nilai faktor pengkayaan yang dikira dengan mengunakan logam Al sebagai rujukan. Hubungan kolerasi yang positif di antara kepekatan logam berat dan tekstur sedimen menunjukkan bahawa tekstur sedimen memainkan peranan dalam menentukan kepekatan logam berat di mana sedimen yang halus lebih mengikat ion-ion logam berat yang dikaji. Oleh yang demikian, berdasarkan data-data yang diperolehi, rumusan yang boleh dibuat adalah aktiviti-aktiviti persekitaran didapati memainkan peranan yang besar dalam memperkayakan kepekatan logam-logam di kawasan kajian.

Penghargaan

Penulis ingin merakamkan ucapan terima kasih kepada Universiti Malaysia Terengganu (UMT) di atas bantuan kewangan jangka pendek (no. vot 54064) yang telah diberikan.

Rujukan

1. Bernt, Z. (1978). Controlled environment experiments in pollution studies. *Ocean Management*, 4: 319-344.
2. Shamsuddin, A. A. (1996). Agihan beberapa logam berat di persisiran Pantai Kemaman, Terengganu. *Thesis of Master Degree*, Universiti Pertanian Malaysia.
3. Ouyang, Y., Higman, J., Thompson, J., O'Toole, T. and Campbell, D. (2002). Characterization and spatial distribution of heavy metals in sediment from Cedar and Ortega River subbasin. *Journal of Contaminant Hydrology*, 54: 19-35.
4. Windom, H. L., Schropp, S. J., Calder, F. D., Ryan, J. D., Smith, R. G. Jr., Burney, L. C., Lewis, F. G. and Rawlinson, C. H. (1989). Natural trace metal concentration in estuarine and coastal marine sediments of the southeastern United States. *Environmental Science & Technology*, 23: 314-320.
5. Fatima, M. D. A., Bernard, P. C. and Grieken, R. E. V. (1988). Heavy metal contamination in sediments from the Belgian Coast and Scheldt Estuary. *Marine Pollution Bulletin*, 19: 269-273.
6. Sinex, S. A. and Wright, D. A. (1988). Distribution of trace metals in the sediments and biota of Chesapeake Bay. *Marine Pollution Bulletin*, 19: 425-431.
7. Kamaruzzaman B. Y., Siti Waznah, A., Mohd Zahir, M. S., Ong, M. C., Shahbudin, S., Jalal, K. C. A., Rina Sharlinda, Z., Shuhada, A. T., Akbar, B. and Joseph, B. (2010). Spatial distribution of lead and copper in the bottom sediments of Pahang river estuary, Pahang, Malaysia. *Sains Malaysiana*, 39(4): 543–547
8. Kamaruzzaman, B. Y., Nurulnadia, M. Y., Noor Azhar, M. S., Ong, M. C. and Joseph, B. (2011). Heavy metal concentration in the surface sediment of Tanjung Lumpur mangrove forest, Kuantan, Pahang, Malaysia. *Sains Malaysiana* 40(2): 89–92
9. Mason, B. and Moore, C. B. (1982). Principles of geochemistry, 4th ed., John Wiley and Sons, New York.
10. Szefer, P., Glasby, G. P., Szefer, K., Pempkowiak, J. and Kaliszan, R. (1996). Heavy metal pollution in superficial sediments from the Southern Baltic Sea off Poland. *Journal of Environmental Science and Health*, 31: 2723-2754.

11. Soto-Jimenez, M. F. and Paez-Osuna, F. (2001). Distribution and normalization of heavy metal concentrations in mangrove and lagoonal sediments from Mazatlan Harbor (SE Gulf of California). *Estuarine, Coastal and Shelf Science*, 53: 259-274.
12. Kamaruzzaman, Y. (1994). Kajian beberapa aspek parameter fiziko-kimia di dalam sistem muara Sungai Chukai-Kemaman, Terengganu, Malaysia. *Thesis of Master Degree*, Universiti Pertanian Malaysia.
13. Donazzolo, R., Merlin, O. H., Vitturi, L. M., Orio, A. A., Pavoni, B., Perin, G. and Rabitti, S. (1981). Heavy metal contamination in surface sediments from the Gulf of Venice, Italy. *Marine Pollution Bulletin*, 12: 417-425.
14. Nriagu, J. O., Kemp, A. L. W., Wong, H. K. T. and Harper, N. (1979). Sedimentary record of heavy metal pollution in Lake Eric. *Geochimica et Cosmochimica Acta*, 43: 247-258.
15. Ong, M. C., Fok, F. M., Sultan, K. and Joseph, B. (2016). Distribution of heavy metals and rare earth elements in the surface sediments of Penang River estuary, Malaysia. *Open Journal of Marine Science*, 6: 79-92.
16. Ong, M. C., Joseph, B., Shazili, N. A. M., Ghazali, A. and Mohamad, M. N. (2015). Heavy metals concentration in surficial sediments of Bidong Island, South China Sea off the east coast of Peninsular Malaysia. *Asian Journal of Earth Sciences*, 8(3): 74-82.
17. Nor, M. A. (1993). Kajian ke atas penspesisan logam berat dalam enapan di muara Sungai Terengganu dan perairan pantai Kuala Terengganu. *Thesis of Bachelor Degree*, Universiti Pertanian Malaysia.
18. Khalik, W., Norzairuddin, M., Che Seman, M. and Zaharuddin, A. (1993). Persampelan 'corer' dan penggunaan teknik analisis pengaktifan neutron (APN) dalam penilaian rekod pencemaran unsur di Perairan Juru, Pulau Pinang. *Kertas Teknikal* 106: 124.
19. Shazili, N. A. M., Che, A. R. M. and Rosnan, Y. (1990). Trace element distribution in bottom sediments in the South China Sea off Sabah. *Ekspedisi Matahari `89*. Faculty of Fisheries and Marine Science, Occasional Publication No. 9: 75-80.
20. Shamsuddin, A. A., Nor Antonina, A., Shazili, N. A. M., Kamaruzzaman, Y., Suhaimi, S., Ridzuan, M. A. and Effendy, M. A. W. (2003). Distribution of some heavy metals in sediments of the Sungai Chukai, Kemaman, Terengganu. *Prosiding ke-2 KUSTEM*: 443-452.
21. Poh, E. L. and Mun, Y. K. (1995). Determination and speciation of heavy metals in sediments of the Juru River, Penang, Malaysia. *Environmental Monitoring and Assessment*, 35: 233-266.
22. Dryssen, D., Patterson, C., Ui, J. and Weichadt, G. F. (1972). Inorganic Chemicals. In: *A Guide to Marine Pollution Compiled*. By: Goldberg, E. D., Gordon and Breach, New York, London, Paris: 41-58.
23. Bernhard, M. (1981). Heavy metal and chlorinated hydro-carbons in the Mediterranean in marine environmental pollution 2. In: *Dumping and Mining*. Edited by Richard A. Geyer. 143-192.
24. Badri, M. A. (1988). Heavy metal pollution in the urban environment.: In. Sham Sani and M. Ahmad Badri (Eds.), *Environmental Monitoring and assessment Tropical Urban Application*.
25. Nor Antonina, A. (2001). Sedimentological and heavy metal studies of the Gulf of Thailand, East Coast Penisular Malaysia, Sabah and Sarawak continental shelf sediments. *Thesis of PhD*, Universiti Pertanian Malaysia.
26. Baffi, F., Dadone, A. and Frache, R. (1983). Heavy metals in inshore water near Genoa. *Marine Pollution Bulletin*, 14: 469-471.
27. Flegal, A. R. and Patterson, C. C. (1983). Vertical concentration profiles of lead in the Central Pacific at 15 ^{o}N and 20 ^{o}S. *Earth Planet Science Letter*, 64: 19-32.
28. Boyle, E. A., Chapnick, S. D. and Shen, G. T. (1986). Temporal variability of lead in the Western North Atlantic Ocean. *Journal of Geophysical Research*, 91: 8573-8593.
29. Pickering, W. F. (1986). Metal ion-speciation-soil and sediments (a review). *Ore Geology Reviews*, 1:83-146.
30. Kersten, M. and Forstner, U. (1987). Effect of sample pretreatment on the realiability of solid speciation data of heavy metals. Implications for the study of early diagenetic processes. *Marine Chemistry*, 22: 299-312.
31. Tuin, B. J. W and Tels, M. (1990). Distribution of six heavy metals in contaminated clay soils before and after extractive cleaning. *Journal Technology*, II: 935-948.

Malaysian Journal of Analytical Sciences (MJAS)
Published by Malaysian Analytical Sciences Society

INSIGHTS ON THE CHEMICAL CONSTITUENTS AND HYDROTHERMAL CARBONIZATION OF *Crescentia cujete* L.

(Pencirian Jujukan Kimia dan Pengkarbonan Hidrotermal bagi *Crescentia cujete* L.)

Judith Clarisse Jose[1], Glenn Oyong[2], Michael Dominic Ajero[3], Irving Chiong[3], Esperanza Cabrera[1,2], Maria Carmen S. Tan[3]*

[1]*Biology Department*
[2]*Molecular Science Unit Laboratory Center for Natural Sciences and Environmental Research*
[3]*Chemistry Department*
De La Salle University, 2401 Taft Avenue, Manila 0922, Philippines

**Corresponding author: maria.carmen.tan@dlsu.edu.ph*

Received: 12 December 2019; Accepted: 21 January 2020

Abstract

Crescentia cujete L. is an evergreen tree that presents several medicinal and industrial applications. This study primarily aimed to present preliminary characterization of the fruit extracts and fruit pulp of *Crescentia cujete* L. using several analytical techniques. Characterization of the crude MeOH extract and pure compound, *trans*-cinnamic acid, isolated from the fruit extract were performed using gas chromatography-electron ionization-mass spectrometry (GC-EI-MS). Lyophilized pulp was characterized by energy dispersive X-ray spectroscopy (EDX). Hydrochar samples resulting from hydrothermal carbonization (HTC) of fruit pulp were characterized using Fourier transform infrared spectroscopy (FTIR), scanning electron microscopy (SEM) and thermogravimetric analysis (TGA). Eight constituents were eluted from the crude MeOH extract which were mainly composed of furan (5-Hydroxymethylfurfural, 53.99%), a pyranone derivative (2,3-dihydro-3,5-dihydroxy-6-methyl-4H-pyran-4-one, 8.68%) and a carboxylic acid (3-phenyl-2-propenoic acid, 7.94% or compound **5)**. Other notable compounds of the extract include furaneol (0.78% and 1.56%), phenol, 2,4-bis(1,1-dimethylethyl)- (3.73%), benzenepropanoic acid, 3,5-bis(1,1-dimethylethyl)-4-hydroxy-, methyl ester (1.15%) and *n*-hexadecanoic acid (0.59%). GC-EI-MS confirmed the purity of the isolated compound *trans*-cinnamic acid (100%). EDX analysis showed high levels of K_2O (79.56%), P_2O_5 (9.925%), and SO_3 (9.131%) from the lyophilized pulp. Aliphatic compounds such as alkanes and alkenes were mostly present in both hydrochars as revealed by FTIR analyses. SEM and TGA analyses showed degradation of the lignin components of both hydrochars after the hydrothermal carbonization process. These results present the chemical characterization of the *C. cujete* fruit and the HTC of the pulp biomass which exhibited promising properties for applications as solid fuel or as an adsorbent.

Keywords: *Crescentia cujete* L., hydrothermal carbonization, hydrochar

Abstrak

Crescentia cujete L. ialah tumbuhan yang digunakan dalam perubatan dan aplikasi industri. Kajian ini dijalankan dengan tujuan melakukan saringan pencirian ekstrak buah dan pulpa *Crescentia cujete* L. menggunakan beberapa teknik analisis. Pencirian esktrak mentah MeOH dan sebatian tulen, *trans*-asid sinamik, dipencil dari ekstrak buah dilakukan menggunakan kromatografi gas-pengionan elektron-spektrometri jisim (GC-EI-MS). Pulpa liofili dicirikan melalui spektroskopi sinar-X tenaga serakan (EDX). Sampel hidrochar yang terhasil dari pengkarbonan hidrotermal (HTC) pulpa buah telah dicirikan menggunakan spektroskopi inframerah transformasi Fourier (FTIR), mikroskopi imbasan elektron (SEM) dan analisis termogravimetrik (TGA). Lapan jujukan kimia yang terelusi dari ekstrak mentah MeOH terdiri daripada furan (5-hidroksimetilfurfural, 55.99%), terbitan piranon (2,3-dihidro-3,4-dihidroksi-6-metil-4H-piran-4-on, 8.68%) dan asid karbosilik (3-fenil-2-asid propenoik, 7.94% atau sebatian 5). Sebatian lain yang dikenal pasti dari ekstrak termasuklah furaneol (0.78% dan 1.56%), fenol, 2,4-bis(1,1-dimetiletil)-(3.73%), asid benzenapropanoik, 3,5-bis(1,1-dimetiletil)-4-hidroksi-, metil ester (1.15%) dan asid *n*-heksadekanoik (0.59%). GC-EI-MS telah membantu mengesahkan ketulenan sebatia *trans*-asid sinamik yang dipencilkan (100%). Analisis EDX

menunjukkan aras tinggi bagi K_2O (79.56%), P_2O_5 (9.925%), dan SO_3 (9.131%) dari pulpa liofili. Sebatian alifatik seperti alkana dan alkena paling banyak dikesan dalam hidrochar seperti yang dibuktikan oleh analisis FTIR, Analisis SEM dan TGA menunjukkan degradasi komponen lignin bagi hidrochar selepas proses pengkarbonan hidrotermal. Hasil kajian ini menunjukkan pencirian kimia bagi *C. cujete* dan HTC bagi biojisim pulpa menjanjikan potensi aplikasi sebagai bahan bakar atau penjerap.

Kata kunci: *Crescentia cujete* L., pengkarbonan hidrotermal, hidrochar

Introduction

Hydrothermal carbonization is a thermochemical conversion process (wet pyrolysis) that can convert wet biomass into valuable products [1]. It is a process that utilizes high temperature to convert raw biomass into a solid coal-like product called hydrochar characterized by high carbon content and calorific value [2]. It is a carbonaceous solid organic material which can be potentially used as solid fuel, as precursor of activated carbon used in wastewater pollution, or in soil remediation [1, 3, 4].

Crescentia cujete L., also known as calabash (Family Bignoniaceae), is an evergreen tree originating from tropical America but is now widely distributed in tropical regions [5]. This plant is known as Miracle Tree in the Philippines due to its various medicinal properties as reported by several testimonies [6, 7]. Studies have shown the efficacy of the fruit and leaf extracts against cough, cold and other respiratory ailments [8, 9]. Other studies also indicate the potential use of the extracts of this plant against inflammation [10], tumors and cancer [11, 12].

Phytochemical screening of the leaf and fruit extracts obtained from solvent partitioning of this plant has been done through several detection tests. Studies showed presence of secondary metabolites such as flavonoids, alkaloids, glycosides, saponins, tannins and terpenoids [11,12]. However, results of another study showed presence of mostly benzene and its derivatives only. The analyzed extract also eluted other compounds including methyl salicylate and 3-phenyl-2-propenoic acid, also known as *trans*-cinnamic acid [13]. This *trans*-cinnamic acid is known for its potential use as an anti-inflammatory agent and in cancer treatment [14]. Despite the reported medicinal uses, the fruit pulp is not considered edible.

In this study, preliminary characterization of the fruit extracts and fruit pulp of *C. cujete* L. was determined. The crude methanolic (MeOH) extract and pure compound, *trans*-cinnamic acid isolated from the fruit pulp of *C. cujete* were characterized using gas chromatography- electron ionization- mass spectrometry (GC-EI-MS). Lyophilized fruit pulp was characterized by energy dispersive X-ray spectroscopy (EDX). The fruit pulp was subjected to hydrothermal carbonization (HTC) and the resultant hydrochars were analyzed using Fourier transform infrared spectroscopy (FTIR), scanning electron microscopy (SEM) and thermogravimetric analyzer (TGA). To the best of our knowledge, this is the first reported study to provide chemical characterization of the fruit pulp of *C. cujete* L. following these optimized analyses.

Materials and Methods

Materials

The *C. cujete* L. mature fruits (Figure 1) were gathered from Bocaue, Bulacan (14°48’02” N, 120°56’43” E). The plant identity was confirmed and authenticated by the Plants of the Philippines, De La Salle University Herbarium (DLSUH). A voucher specimen was deposited to the DLSUH with an accession number of DLSUH 6251.



Figure 1. Actual photos of *Crescentia cujete* L. tree from Bocaue, Bulacan

Preparation of sample

The mature fruit of *C. cujete* L. was carefully cut into half. The pulp was scraped out and seeds were separated. For the crude extract preparation, 20 g of fresh pulp was extracted using Soxhlet apparatus with 200 mL methanol. The extract was concentrated *in vacuo* using rotary evaporator (IKA® RV10) at 80 rpm. The collected extract was filtered into a vial using 0.45 µm syringe filter with a final volume of 0.5 mL and was subjected for gas chromatography-electron ionization- mass spectrometry (GC-EI-MS) for phytochemical profiling.

To isolate the pure compound, *trans*-cinnamic acid, fresh pulp (20 g) was incubated in dichloromethane for 3 hours. The extract was filtered using Whatman filter paper No. 1 (11 µm pore size) and dried by evaporating the solvent. The extract was diluted in methanol and purified by gravity column chromatography using an ExtraBond Cartridge (C_{18}, 500 mg, 6 mL). The eluted extract was purified again by diluting with ethyl acetate and petroleum ether. The extract was filtered into a vial using 0.45 µm syringe filter with a final volume of 0.5 mL and submitted for GC-EI-MS analysis to confirm the purity of the compound.

Gas chromatography – mass spectrometry analysis

Crude extracts from both solvents were scrutinized by GC−EI-MS. An Agilent GC MS7890B, equipped with a HP-5 ms (5% phenyl methylsiloxane) Ultra Inert column (30 m × 250 mm × 0.25 mm) with ultrapure helium gas as the mobile phase, was employed for the analysis of low-boiling-point components. Helium gas was delivered at 1 mL/min, while maintaining pressure at 8.2 psi, with a rate of 36.62 cm/s and holdup interval of 1.37 min. The splitless inlet was held at 250 °C, at 8.2 psi, and an overall stream of 24 mL/min, with a septum purge stream velocity of 3 mL/min. The temperature for the injector was stipulated at 250 °C. The temperature program started at 70 °C with a programmed linear ramp of 2 °C/min until 135 °C and was held at this temperature for 10 minutes. Another temperature increase was achieved at 4 °C/min until 220 °C and was maintained for 10 minutes. The temperature was then increased to 270 °C at a ramp of 3.5 °C/min and was held at 37 minutes. Compound identification was done using the NIST Archive 2.0, and percent peak area average was calculated from the subsequent total ion chromatograms (TIC). The consequential results were authenticated by the evaluation of the constituents corresponding to their elution succession with their comparative retention indices on an intermediate polar gas chromatograph column. The retention indices were computed for the entirety of the compounds using a homologous series of *n*-alkanes. The experiments were carried out in three replicates.

Energy dispersive X-ray spectroscopy
EDX-7000 (Shimadzu, Japan) was used for elemental analysis of the lyophilized sample of *C. cujete* fruit pulp prepared in a 3 mm Mylar cup. The collimator was set at 3 mm.

Hydrothermal carbonization
In this study, one gram of fresh pulp of *C. cujete* was placed inside a hydrothermal autoclave reactor (HAR) with PTFE Liner (Figure 2a) and inside a Parr Oxygen Combustion Vessel (POCV) (Figure 2b). The HAR was heated using a furnace set at 180 °C for two hours; whereas, the POCV was heated using an oven at 220 °C for two hours. The resulting hydrochars were used for thermogravimetric analysis and scanning electron microscopy for further analysis.



Figure 2. Images of the (a) HAR and (b) POCV used for hydrothermal carbonization

Fourier transform infrared spectroscopy
Characterization of the hydrochar samples was performed using a Thermo Scientific Nicolet 6700 FT-IR (Thermo Fisher Scientific, USA) using a DTGS KBr detector, Csl beamsplitter and transmission accessory. A total of 16 scans from 400-4000 cm^{-1} with spectral resolution of 4 cm^{-1} were taken for each sample. KBr was used to collect background to be subtracted by the sample. Analyses were performed using the Omnic Spectra software 8.0.342 (Thermo Fisher Scientific, USA).

Scanning electron microscopy
The morphology of the hydrochar was observed and examined using JSM 5310 Scanning Microscope (JEOL, Japan) which scans the surface of the material with a focused beam of electrons. A trace amount of each hydrochar was mounted to a metal stub, coated with gold ions for 60 seconds to make the sample conducting and be able to observe the morphology of the sample. SemAfore V. 5.2 was used to analyze the image produced.

Thermogravimetric analysis
TGA 55 (TA Instruments®, USA) was used to perform the thermal gravimetric analysis (TGA) of the produced hydrochar. TGA is an analytical technique that can provide analysis on the thermal stability of the sample. It measures the weight of the sample as it is exposed to gradually increasing temperature and records the mass loss over time and/or increase in temperature [15]. In this study, 3 mg of each of the hydrochar samples was placed and spread out evenly in a platinum HT pan of TGA 55. The analysis was performed at a flow rate of 25 mL/min under nitrogen gas with temperature set at 10 °C to 1000 °C, heating rate of 10 °C/min and scans starting at 30 °C. Analyses were done using the built-in TRIOS software V. 4.3.1.39215 TA Instruments-Waters LLC. Combustion behavior is indicated by the weight loss of the sample as a function of temperature.

Results and Discussion

Gas chromatography-mass spectrometry analysis

The plant extracts of *C. cujete* L. fruit were analyzed using GC-MS for phytochemical characterization. The identification of both extracts was verified and confirmed by the retention index through the NIST library v.2.0. The crude MeOH extract eluted a total of 8 volatile compounds listed in Table 1 and shown in Figure 3a. The GC-MS analysis revealed that the crude MeOH extract mainly composed of furan, 5-Hydroxymethylfurfural (53.99%), a pyranone derivative, 2,3-dihydro-3,5-dihydroxy-6-methyl-4H-pyran-4-one (8.68%) and a carboxylic acid, 3-phenyl-2-propenoic acid (7.94%) or compound **5**. Other notable compounds of the extract include furaneol (0.78% and 1.56%), phenol, 2,4-bis(1,1-dimethylethyl)- (3.73%), benzenepropanoic acid, 3,5-bis(1,1-dimethylethyl)-4-hydroxy-, methyl ester (1.15%) and *n*-hexadecanoic acid (0.59%). The presence of hydrocarbons may indicate the potential application of the fruit as fuels [16].

Table 1. Volatile constituents of the methanolic crude extract of *Crescentia cujete* L.

	Compound	RT (min)	RI[(a)]	% Peak Area	Functionality
1	2,5-Dimethyl-4-hydroxy-3(2H)-furanone	8.53	1082 ± 1	0.78 ± 0.1	furanone
2	2,5-Dimethyl-4-hydroxy-3(2H)-furanone	8.83	1090 ± 0	1.56 ± 0.93	furanone
3	4H-Pyran-4-one, 2,3-dihydro-3,5-dihydroxy-6-methyl-	12.09	1164 ± 1	8.68 ± 2.63	pyranone derivative
4	5-Hydroxymethylfurfural	18.53	1289 ± 1	53.99 ± 12.33	furan
5	2-Propenoic acid, 3-phenyl-	29.26	1476 ± 1	7.94 ± 0.47	unsaturated carboxylic acid
6	Phenol, 2,4-bis(1,1-dimethylethyl)-	31.44	1513 ± 0	3.73 ± 0.5	phenol
7	Benzenepropanoic acid, 3,5-bis(1,1-dimethylethyl)-4-hydroxy-, methyl ester	55.94	1941 ± 0	1.15 ± 0.02	diverse functional group
8	n-hexadecanoic acid	56.80	1969 ± 0	0.59 ± 0.08	fatty acid

[(a)] Retention Index (HP-5ms column)

Constituent **5** (Table 2; Figure 3b), with chemical formula $C_9H_8O_2$ and exact mass of 148.052429 (CAS#: 621-82-9 NIST#: 133307 ID#: 119939), was found in the dichloromethane fraction and purified using reverse phase column chromatography using a C_{18} column and methanol as the eluting solvent. The fraction found to have compound **5** was dried and reconstituted in ethyl acetate and finally with petroleum ether. The purity of the extract containing only the pure compound, *trans*-cinnamic acid, was confirmed by the GC-MS analysis percent report verifying that it was of high purity (100%).

Table 2. Phytochemical characterization of pure compound obtained from fruit extract of *Crescentia cujete* L.

	Compound	RT (min)	RI[(a)]	% Peak Area	Functionality
5	2-Propenoic acid, 3-phenyl-	27.854	1452	100.00%	unsaturated carboxylic acid

[(a)] Retention Index (HP-5ms column)

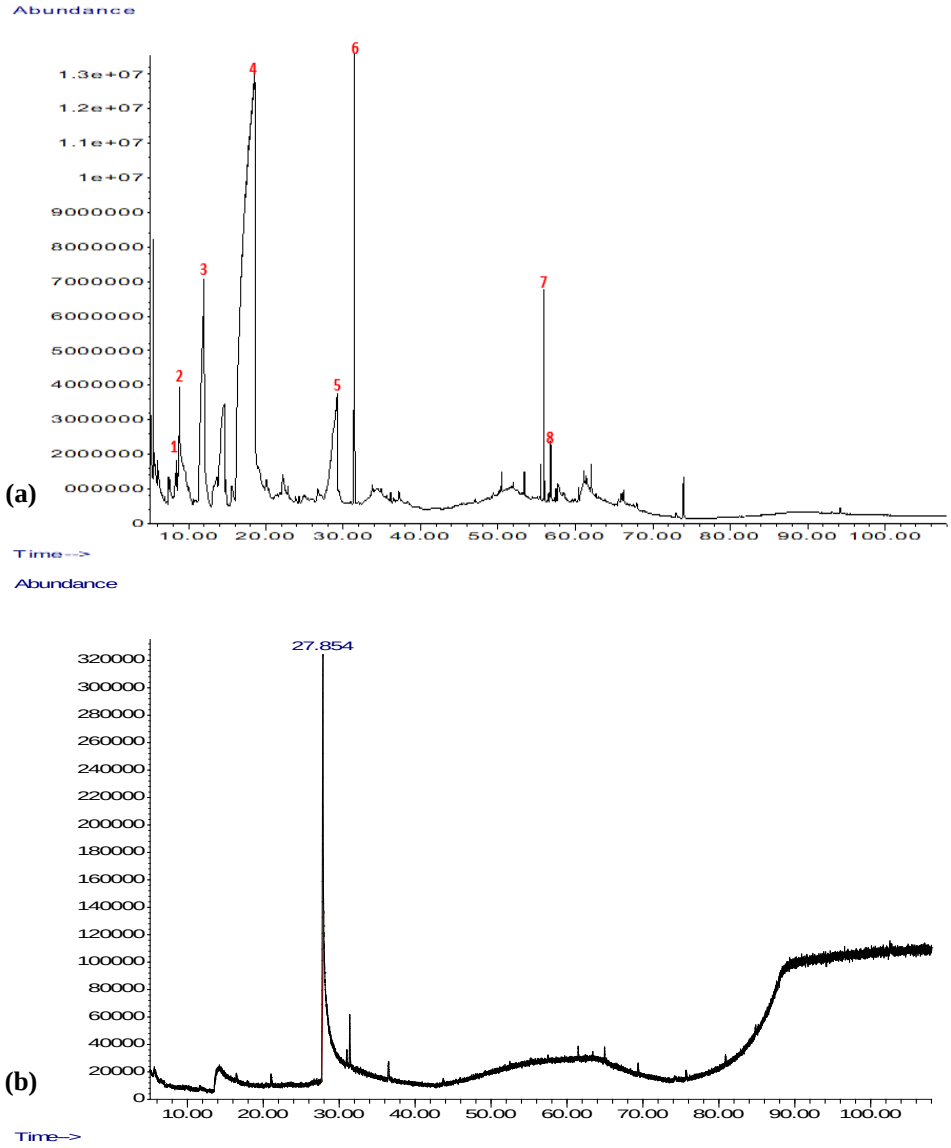


Figure 3. Total ion chromatogram of the volatile constituents of (a) crude methanolic extract and (b) pure compound, *trans*-cinnamic acid, from fruit pulp of *C. cujete* L.

Constituent **5** gave characteristic fragmentation paths of cinnamic acid as reported by Schaldach and Grützmacher [17]. Figure 4 shows the mass spectrum of **5** which shows a base peak of 147 m/z $(C_9H_7O_2)^+$ or $[M\text{-}H]^+$ from the loss of a hydrogen. The $[M\text{-}OH]^+$ fragment (131 m/z) was derived from the loss of OH from the molecular ion. After the loss of CO from $[M\text{-}OH]^+$, the fragment $(C_8H_7)^+$ was formed. The elimination of C_2H_2 produced $[C_6H_5]^+$, 77 m/z and another subsequent loss of C_2H_2 produced $[C_4H_3]^+$, 51 m/z. All of the aforementioned peaks were found in the mass spectrum of constituent **5**.

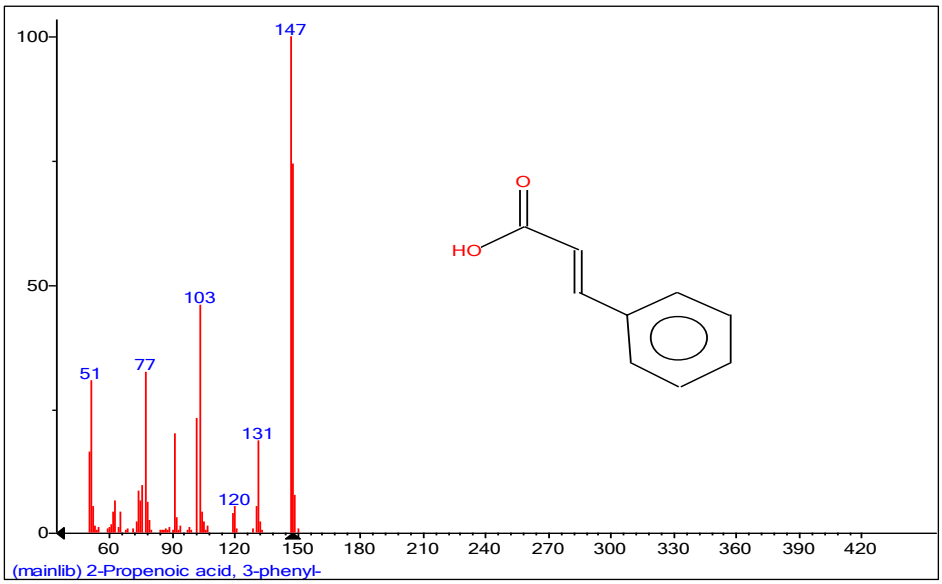


Figure 4. 70 eV mass spectrum of 5 from fruit pulp of *C. cujete* L.

EDX analysis

The elemental analysis of the lyophilized fruit pulp of *C. cujete* revealed high percentage composition of K_2O (79.56%), P_2O_5 (9.925%), and SO_3 (9.131%). Fe_2O_3 (0.624%), CuO (0.399%), ZnO (0.301%) and Rb_2O (0.059%) were also found to be present in the sample as shown in Figure 5. Studies revealed that potassium intake in diet is correlated with the reduction of blood pressure and reduces the risk of stroke and coronary heart diseases. Dietary potassium also induces protective effect on age-related bone loss and reduction of kidney stones [18,19]. Phosphorus intake is also necessary in human diet but high levels of phosphorus are associated with chronic kidney disease (CKD). Impaired renal function of CKD patients makes them unable to clear excess phosphorus. High level of serum phosphate is also associated with cardiovascular diseases and all-cause mortality [20]. Dietary supplements with sulfur containing compounds were used to treat diseases of the joints [21]. Copper is also observed to be present in the sample in minute quantities. Copper has been involved in numerous biological processes, including antioxidant defense neuropeptide synthesis and immunological processes. Copper deficiency *in utero* may lead to impairment in the development of the cardiovascular system, bone malformation and other immunologic and neurologic abnormalities, whereas modification in cholesterol metabolism may be the result of prolonged marginal copper deficiency in adulthood. However, high levels of copper may also induce toxicity resulting in oxidative cell damage and cell death [22].

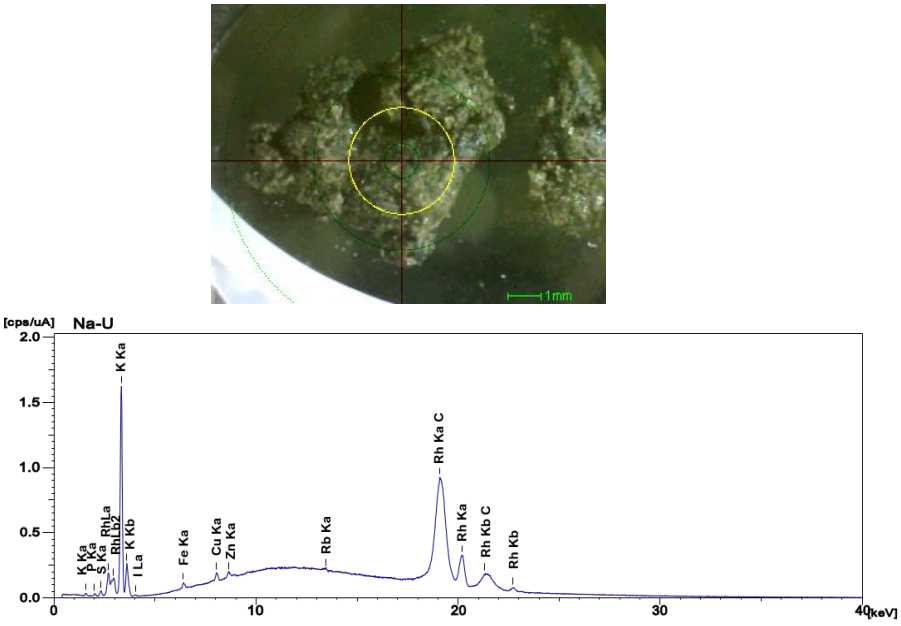


Figure 5. An EDX image and elemental analysis spectrum of lyophilized *C. cujete* L. fruit pulp

Fourier-transform Infrared Spectroscopy

The FTIR patterns of the hydrochars produced using HAR and POCV are presented in Figure 6. The results of the spectrum of hydrochar produced from HAR are listed on Table 3. The peaks obtained within 3300-2500 cm^{-1} can be attributed to the stretching of C-H with the presence of aliphatic compounds. The peak at 1711.59 cm^{-1} corresponds to C=O stretching from cellulose and lignin. Peaks within 1650-1566 cm^{-1} are attributed to C=C stretching representing cyclic alkenes. The peak at 1454.03 cm^{-1} corresponds to C-H bending of a methylene group while the peak at 1395.67 cm^{-1} is attributed to O-H bending of a carboxylic acid. The peak at 1254.65 cm^{-1} corresponds to C-O stretching vibrations of lignin. The peaks within 1210-1163 cm^{-1} are attributed to C-O stretching from the vibrations of ester compounds. Peak obtained at 1065.40 cm^{-1} is attributed to C-O stretching of primary alcohol.

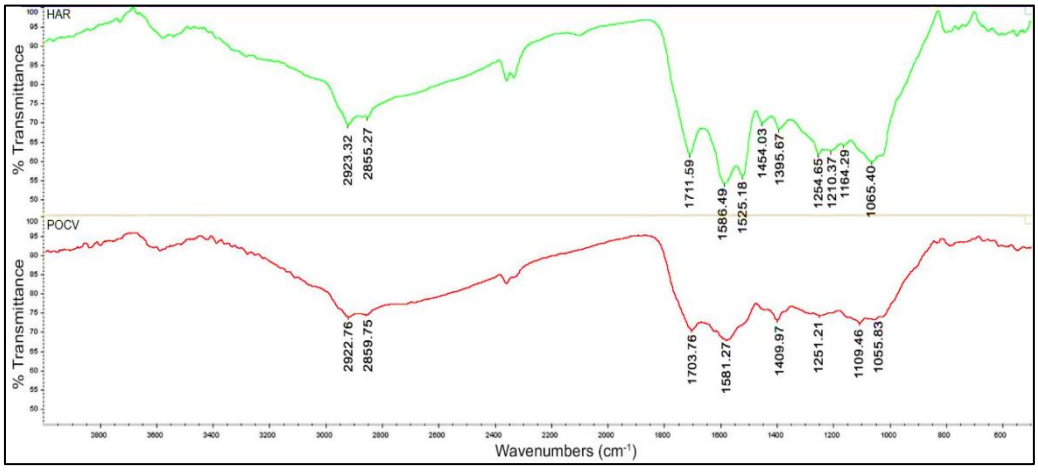


Figure 6. FTIR spectra of hydrochars produced from HAR (top) and POCV (bottom)

Table 3. Conditions of hydrochar produced using HAR

Wavenumber (cm^{-1})	Functional Group	Description
2923.32	C-H stretching	Aliphatic
2855.27	C-H stretching	Aliphatic
1711.59	C=O stretching	Carbonyl, ester or carboxyl from cellulose and lignin
1586.49	C=C stretching	Cyclic alkene
1525.18	C=C stretching	Cyclic alkene
1454.03	C-H bending	Methylene group
1395.67	O-H bending	Carboxylic acid
1254.65	C-O stretching	Vibrations in lignin
1210.37	C-O stretching	Ester
1164.29	C-O stretching	Ester
1065.40	C-O stretching	Primary alcohol

Table 4 presents the result of the spectrum of hydrochar produced from POCV. Peaks obtained around 3000-2840 cm^{-1} are attributed to aliphatic bands, C-H stretching vibrations. The peak at ~1700 cm^{-1} can be attributed to the stretching of C=O bonds from cellulose and lignin. Peak at ~1580 cm^{-1} is attributed to C=C stretching representing an aromatic compound. The peak at 1400 cm^{-1} corresponds to C-H bending. The peak at 1251.21 cm^{-1} is attributed to C-O stretching vibrations of lignin. The peak obtained around 1109 cm^{-1} is attributed to stretching of C-O from the vibrations of cellulose and hemicelluloses. After the HTC process, FTIR analysis of the hydrochar produced from both HAR and POCV revealed the possible presence of a complex mixture of aliphatic and olefinic hydrocarbons as seen by the aforementioned C-H stretching and methylene bending.

Table 4. Conditions of hydrochar produced using POCV

Wavenumber (cm^{-1})	Functional Group	Description
2922.76	C-H stretching	Aliphatic
2859.75	C-H stretching	Aliphatic
1703.76	C=O stretching	Carbonyl, ester or carboxyl from cellulose and lignin
1581.27	C=C stretching	Cyclic alkene
1400.97	C-H bending	Methylene group
1251.21	C-O stretching	Vibrations in lignin
1109.46	C-O stretching	Vibrations in cellulose and hemicelluloses
1055.83	C-O stretching	Primary alcohol

Scanning electron microscopy

Biomass morphology can be significantly altered by undergoing thermal pre-treatment, thereby reducing the fibrous nature of the sample. Cell walls degrade as a result of the decomposition of hemicellulose, depolymerization of cellulose, and softening of lignin components [1]. The morphologies of the fruit pulp of *C. cujete* subjected to thermal pre-treatment at 180 °C and 220 °C using HAR and POCV, respectively, were shown in Figure 7. The SEM results showed that the fruit pulp has been broken down considerably in both thermal pre-treatments. HTC might have caused the degradation of lignin appearing as small particles attached to the hemicellulose or fiber-like particles [23] observed in the SEM images (Figure 7). Several small particles like flakes can be observed on the surfaces of both hydrochars making them rough in appearance. Hydrochar produced using HAR was seen with small spherical particles measuring 3.84 ± 1.13 µm and flakes measured at 21.4 ± 10.33 µm attached on fiber-like

structures as observed on SEM (Figure 7a). On the other hand, the morphology of the hydrochar produced using a POCV was observed with smaller flakes (0.85 ± 0.11 µm) attached on fiber-like structures on the surface of the sample. Moreover, the surface of POCV hydrochar appeared to be smoother than the hydrochar produced by HAR (Figure 7b).

Research revealed that hydrochar produced under mild conditions (180-250 °C) of HTC is considered as a cost-effective novel material as an alternative adsorbent compared to other carbonaceous materials including activated carbon and biochar. Activated hydrochars have been widely utilized in environmental remediation such as on the adsorption of heavy metals and volatile organic compounds [24]. Thermochemical activation of hydrochar may result to a highly porous activated carbon [25]. This study showed both non-porous non-activated hydrochars produced by HTC under 180 °C and 200 °C similar to raw apple chip pomace and raw grape pomace fruit wastes [1].

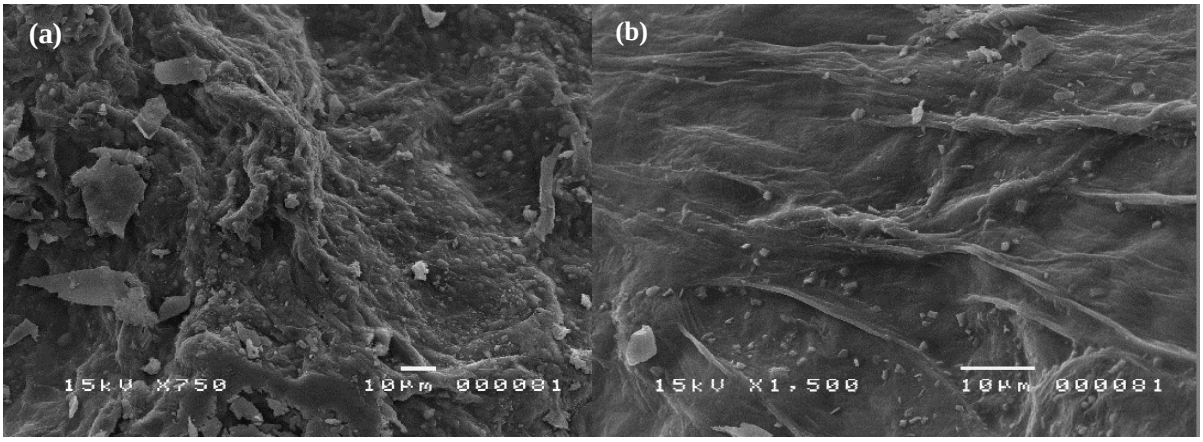


Figure 7. Scanning electron microscopy images of *Crescentia cujete* L. pulp after thermal pre-treatment at (a) 180 °C using HAR and (b) at 220 °C using a POCV

Thermogravimetric analysis

The TGA graphs of the pre-treated pulp samples are presented in Figure 8. It can be observed that the initial weight loss of both hydrochar samples occurred between 30 to 150 °C due to moisture loss. The main weight loss of hydrochar samples occurred in the second stage of TGA with the release of volatile matter content and combustion at temperatures between 290 to 430 °C wherein about 50% of the original weight was lost. This may be caused by the initial pre-treatment of the pulp samples heated at 180 and 220°C that might have reduced the volatile matter content present in the samples. The final stage of TGA analysis which is the fixed carbon content combustion occurred at around 540 °C and ended at 830 °C with inorganic residues collected weighing about 6-8% of the original mass. The results showed similarities in TGA graphs between hydrochar produced using hydrothermal autoclave reactor and hydrochar produced using the oxygen combustion vessel is indicative that the latter may be used as substitute for hydrothermal reactor.

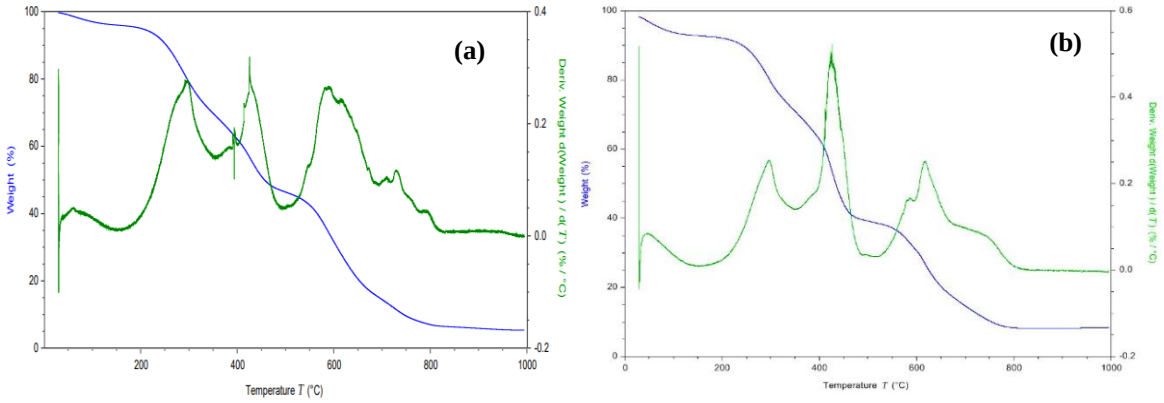


Figure 8. Thermogravimetric analysis graphs of the hydrochars produced from the hydrothermal carbonization of the fruit pulp of *Crescentia cujete* L using (a) HAR and (b) POCV

Conclusion

Crescentia cujete L. fruit presented several potential applications. The methanolic crude extract revealed volatile constituents consisting of mostly furans and unsaturated carboxylic acid, *trans*-cinnamic acid. The lyophilized pulp sample was found to have high levels of K_2O as revealed by the elemental analysis. Hydrochars produced by HTC under 180 °C and 220 °C showed degradation of cell walls by the decomposition of hemicellulose and lignin components of the samples. HAR and POCV can both be used in producing hydrochars as revealed by similarities between the hydrochar samples in all analyses. Moreover, further studies on these hydrochars are recommended as they may possibly be utilized as solid fuel as revealed by presence of hydrocarbons or as adsorbent of volatile organic compounds but further analyses must be performed.

References

1. Zhang, B., Heidari, M., Regmi, B., Salaudeen, S., Arku, P., Thimmannagari, M. and Dutta, A. (2018). Hydrothermal carbonization of fruit wastes: A promising technique for generating hydrochar. *Energies*, 11(8): 2022-2035.
2. Lucian, M. and Fiori, L. (2017). Hydrothermal carbonization of waste biomass: Process design, modeling, energy efficiency and cost analysis. *Energies*, 10(2): 211-228.
3. Kantakanit, P., Tippayawong, N., Koonaphapdeelert, S. and Pattiya, A. (2018). Hydrochar generation from hydrothermal carbonization of organic wastes. *IOP Conference Series: Earth and Environmental Science*, 159: 1-6.
4. Wang, T., Zhai, Y., Zhu, Y., Li, C. and Zeng, G. (2018). A review of the hydrothermal carbonization of biomass waste for hydrochar formation: Process conditions, fundamentals, and physicochemical properties. *Renewable and Sustainable Energy Reviews*, 90: 223-247.
5. Arango-Ulloa, J., Bohorquez, A., Duque, M. and Maass, B. (2009). Diversity of the calabash tree (*Crescentia cujete* L.) in Colombia. *Agroforestry Systems*, 76(3): 543-553.
6. Tacio, H. (2015). Calabash the miracle fruit. https://businessmirror.com.ph/2015/10/15/calabash-the-miracle-fruit/. [Access online 10 October 2019].
7. Agron, E. (2017). Calabash contains active ingredients potential for cancer treatment. http://www.pchrd.dost.gov.ph/index.php/14-r-d-updates/3132-calabash-contains-active-ingredients-potential-for-cancer-treatment. [Access online 10 October 2019].
8. Morton, J. (1968). The Calabash (Crescentia cujete) in folk medicine. *Economic Botany*, 22(3): 273- 280.
9. Parvin, M. S., Das, N., Jahan, N., Akhter, M. A., Nahar, L. and Islam, M. E. (2015). Evaluation of in vitro anti-inflammatory and antibacterial potential of *Crescentia cujete* leaves and stem bark. *BMC Research Notes*, 8(1): 412-418.

10. Jato, J. (2015). Anti-inflammatory, antimicrobial and antioxidant properties of *Margaritaria nobilis, Stylochiton lancifolius, Drypetes principum, Crescentia cujete* and *Albizia glaberrima*. Thesis of Master Degree, Kwame Nkrumah University of Science and Technology, Kumasi, Ghana.
11. Billacura, M. and Laciapag, G. C. (2017). Phytochemical screening, cytotoxicity, antioxidant, and anthelmintic property of the various extracts from *Crescentia cujete* Linn fruit. *Science International*, 29 (2): 31-35.
12. Billacura, M. and Pangcoga, K. K. (2017). Phytochemical screening, cytotoxicity, mutagenicity, antimutagenicity, and protective potentials of the different solvent extracts from the air-dried leaves of *Crescentia cujete* Linn. *International Journal of Advanced and Applied Sciences*, 4(4): 118-126.
13. Rellin, K. F. B., Dasmariñas, D. D. and Junio, H. A. (2018). Untargeted metabolite profiling of Philippine-grown *Crescentia cujete* and its commercial fruit juice using GC-MS and UPLC-HRMS. *Philippine Journal of Science*, 147(4): 647-658.
14. Liu, L., Hudgins, W., Shack, S., Yin, M. and Samid, D. (1995). Cinnamic acid: A natural product with potential use in cancer intervention. *International Journal of Cancer*, 62(3): 345-350.
15. Rajisha, K., Deepa, B., Pothan, L. and Thomas, S. (2011). Thermomechanical and spectroscopic characterization of natural fibre composites. *Interface Engineering of Natural Fibre Composites for Maximum Performance*: 241-274.
16. Hood, E. (2016). Plant-based biofuels. *F1000Research*, 5: pp. 1-9.
17. Schaldach, B. and Grützmacher, H.-Fr. (1980). The fragmentations of substituted cinnamic acids after electron impact. *Organic Mass Spectrometry*, 15(4): 175-181.
18. Lanham-New, S., Lambert, H. and Frassetto, L. (2012). Potassium. *Advances in Nutrition*, 3(6): 820- 821.
19. Weaver, C. (2013). Potassium and health. *Advances in Nutrition*, 4(3): 368S-377S.
20. Uribarri, J. and Calvo, M. (2013). Dietary phosphorus intake and health. *The American Journal of Clinical Nutrition*, 99(2): 247-248.
21. Nimni, M., Han, B. and Cordoba, F. (2007). Are we getting enough sulfur in our diet?. *Nutrition & Metabolism*, 4(1): 1-12.
22. Bost, M., Houdart, S., Oberli, M., Kalonji, E., Huneau, J. and Margaritis, I. (2016). Dietary copper and human health: Current evidence and unresolved issues. *Journal of Trace Elements in Medicine and Biology*, 35: 107-115.
23. Ghaffar, S. H. and Fan, M. (2013). Structural analysis for lignin characteristics in biomass straw. *Biomass and Bioenergy*, 57: 264-279.
24. Zhang, X., Gao, B., Fang, J., Zou, W., Dong, L. and Cao, C. (2019). Chemically activated hydrochar as an effective adsorbent for volatile organic compounds (VOCs). *Chemosphere*, 218: 680-686.
25. Plavniece, A., Zhurinsh, A., Dobele, G. and Locs, J. (2019). Chemically activated hydrochar flakes from birch wood. *Key Engineering Materials*, 800: 261-266.

Malaysian Journal of Analytical Sciences (MJAS)
Published by Malaysian Analytical Sciences Society

EXTRACTION OF 4-OCTYLPHENOL AND 4-NONYLPHENOL IN RIVER WATER USING SOLID-PHASE EXTRACTION AND HIGH-PERFORMANCE LIQUID CHROMATOGRAPHY

(Pengekstrakan 4-Oktilfenol dan 4-Nonilfenol di dalam Air Sungai Menggunakan Pengekstrakan Fasa Pepejal dan Kromatografi Cecair Prestasi Tinggi)

Mohd Zahid Baharom[1], Nurulnadia Mohd Yusoff[1,2]*, Wan Mohd Afiq Wan Mohd Khalik[1], Marinah Mohd Ariffin[1], Jamilah Karim[3], Syazrin Syima Sharifuddin[3]

[1]*Faculty of Science and Marine Environment*
[2]*Institute of Oceanography and Environment*
Universiti Malaysia Terengganu, 21030 Kuala Nerus, Terengganu, Malaysia
[3]*Water Quality Laboratory,*
National Hydraulic Research Institute of Malaysia, 43300 Seri Kembangan, Selangor, Malaysia

**Corresponding author: nurulnadia@umt.edu.my*

Received: 20 November 2019; Accepted: 2 February 2020

Abstract

An analytical method based on solid-phase extraction (SPE) combined with high performance liquid chromatography-photometric diode array (HPLC-PDA) was developed to determine 4-octylphenol (4-OP) and 4-nonylphenol (4-NP) in river water samples. The optimum SPE working conditions were secured with 200 mL sample loading and eluted with 10 mL of methanol and acetone (1:1, *v/v*) as re-constitute solvents. Acetonitrile and deionized water (80:20, *v/v*) were used as mobile phase with 225 nm set as the optimum wavelength. Good linearity for 4-OP and 4-NP were obtained in the range of 0.001–0.012 mg/L whereby the regression coefficient R^2 was 0.9988 and 0.9995, respectively. Limit of detections (LOD) and quantifications (LOQ) for 4-OP and 4-NP were calculated at LOD = 0.0006 and 0.0001 mg/L and LOQ = 0.0020 and 0.0005 mg/L, respectively. The recovery percentages obtained for three levels concentrations (0.005, 0.010 and 0.050 mg/L) were ranged from 41.0 to 114%. Repeatability for 4-OP and 4-NP has shown good performance with low relative standard deviation (< 2%). In the real sample, the measured concentrations of 4-OP and 4-NP were detected with 0.001 and 0.0003 mg/L, respectively. Liquid chromatography-mass tandem spectrometry (LC-MS/MS) equipped with Agilent Jet Stream Technology and electrospray ionization (AJS-ESI) was used to confirm the presence of 4-OP and 4-NP in the water sample. Overall, the method proposed can be accepted for further water sample analysis.

Keywords: endocrine-disrupting chemical, water quality, emerging pollutants, liquid chromatography-mass spectrometry

Abstrak

Kaedah analisis berdasarkan gabungan pengesktrakan fasa pepejal (SPE) dengan kromatografi cecair prestasi tinggi susunan diod fotometrik (HPLC-PDA) telah dibangunkan untuk penentuan 4-oktilfenol (4-OP) dan 4-nonilfenol (4-NP) di dalam sampel air sungai. Keadaan optimum SPE telah diperolehi dengan 200 mL sampel air dan dielusi dengan 10 mL metanol dan aseton (1:1, *v/v*) sebagai pelarut rekonstruksi. Asetonitril dan air suling (80:20, *v/v*) telah digunakan sebagai fasa gerak di mana panjang gelombang optimum ditetapkan pada 225 nm. Kelinearan yang baik untuk 4-OP dan 4-NP telah diperolehi pada julat 0.001–0.012 mg/L dan nilai pekali regresi R^2 iaitu masing-masing dengan 0.9988 dan 0.9995. Had pengesanan (LOD) dan kuantifikasi (LOQ) untuk 4-OP dan 4-NP telah dihitung masing-masing pada LOD = 0.0006 dan 0.0001 mg/L dan LOQ = 0.0020 dan 0.0005 mg/L. Peratusan pemulihan yang telah diperolehi pada tiga aras kepekatan (0.005, 0.010 and 0.050 mg/L) adalah pada julat antara 41.0 hingga 114%. Kebolehulangan untuk 4-OP dan 4-NP menunjukkan prestasi yang baik dengan nilai sisihan piawai relatif yang rendah (< 2%). Di dalam sampel sebenar, kepekatan yang diukur untuk 4-OP dan 4-NP adalah dikira masing-masing

dengan 0.001 dan 0.0003 mg/L. Spektrometri jisim cecair kromatografi (LC-MS/MS) bersama Teknologi Agilent Jet Aliran pengionan elektro-semburan (AJS-ESI) telah digunakan untuk mengesahkan kehadiran 4-OP dan 4-NP di dalam sampel air. Secara keseluruhannya, kaedah yang telah dibangunkan boleh diterima dan diguna pakai untuk analisis sampel air.

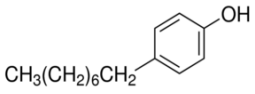
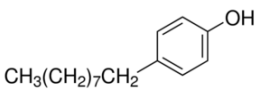
Kata kunci: kimia penganggu endokrin, kualiti air, pencemar memuncul, kromatografi cecair-jisim spektrometri

Introduction

The congeners, 4-octylphenol (4-OP) and 4-nonylphenol (4-NP) are biodegradation products from alkylphenol polyethoxylates which are persistently stable in water with higher bioaccumulative properties [1]. They are chemical substances that are widely used in domestic, industrial and agricultural applications (e.g. byproduct of surfactants in detergent and paint) [2, 3]. The structure and chemical characteristics of 4-OP and 4-NP are shown in Table 1. These chemical substances are known as endocrine-disrupting chemicals (EDCs) or endocrine disruptors (EDs) which are capable of causing adverse effects on the reproductive system of aquatic organisms such as fish [4]. EDCs could affect the organism *via* binding receptor or hormone-binding protein in the body by mimicking the effects of endogenous hormones [5]. The occurrence of 4-OP and 4-NP in river water comes from various sources such as effluents from sewage treatment plants, surface water run-off from settlements, direct discharge and leakage from septic tanks and landfill sites. The residue of these substances in the Malaysian river waters such as Tuaran River and Salut River in Sabah and Selangor Rivers were recorded at very low concentration level between ng/L to µg/L [6, 7]. Nevertheless, it is still deteriorative to the water quality, thus threatening aquatic organisms such as fish and bivalve [8-11]. Therefore, the determination of EDCs has been widely carried out in many countries.

Since target compound is usually detected low in river water, various water extraction methods such as liquid-liquid extraction [6, 12], steam distillation extraction [13] and solid-phase extraction [14-16] have been established to extract the compound effectively. However, SPE has been proven as the best and commonly used technique of extracting target analyte from water samples due to its ability to clean up interferences with low consumption of solvents and time [17]. Final analysis of EDC has been conducted using various instruments mainly by liquid chromatography [14, 18] and gas chromatography [15, 16, 19]. Nevertheless, the analysis of EDCs in Malaysian river water is mostly carried out using liquid-liquid extraction [6, 7] with high recovery percentage (50-120%). Unfortunately, the method is disadvantageous in terms of cost, time and sustainability of environment. Therefore, this study was aimed at modifying the SPE method towards creating a greener environment and validating the proposed method prior to application in real sample analysis.

Table 1. Structure and chemical characteristics of 4-OP and 4-NP

	4-octylphenol	**4-nonylphenol**
IUPAC name	4-octylphenol	4-(7-methyloctyl)phenol
	1806-26-4	26543-97-5
Molecular formula	$C_{14}H_{22}O$	$C_{15}H_{24}O$
Molecular weight (g/mol)	206.32	220.35
Structure		
Chemical properties		
Water solubility (mg/L)	12.6[a]	5.4[a]
Octanol-water partition coefficient, log K_{ow}	4.12[b]	4.48[b]

[a] Geyer et al. [5], [b] Ahel and Giger [20]

Materials and Methods

Analytical grade standards for 4-OP and 4-NP were purchased from Sigma Aldrich (USA). Acetonitrile, methanol and acetone (HPLC-grade solvents) were purchased from Elite Advance Materials (Malaysia). SPE cartridges, Resprep C_{18} 1 mL/100 mg were purchased from Restek (USA). GF/C filter membrane with a diameter of 47 mm and pore size of 1.2 microns were purchased from Whatman (UK). Milli-Q water was obtained from Q-POD remote dispenser Merck (Germany).

The stock solution of 4-OP and 4-NP were prepared separately in methanol at 100 mg/L each and stored at 2 °C. A series of dilutions ranged from (0.001-0.012 mg/L, n=5) were prepared to construct the external standard calibration curves. Repeatability test was validated at three concentration levels (0.005, 0.010 and 0.050 mg/L). Limit of detection (LOD) and limit of quantification (LOQ) of the mixture were performed based on 3:1 and 10:1 signal to noise ratios, respectively. The accuracy of the method was validated with recovery percentage (%) at three concentration levels (0.005, 0.010 and 0.050 mg/L) and expressed as relative standard deviation (% RSD).

SPE method

A comparison from previous studies was made to optimize the method [14-16] in order to produce less waste and trap target compounds effectively. The optimization of the method involved changes in volume sample, conditioning and elution volume. Lower volume of samples (100, 200 and 300 mL), different elution (6, 10 and 14 mL) and conditioning volumes (9, 15 and 21 mL) were validated in the present study to enhance the SPE adsorbent for maximum trapping of target analytes. The cartridge was initially conditioned with 15 mL of methanol (MeOH), acetone (ACE) and Milli-Q water (1:1:1, *v/v*) to activate the adsorbents for trapping the target analytes. Then 200 mL of filtered water sample was loaded into the cartridge at the flow rate of 1 mL/min. The cartridge was washed with 10 mL of Milli-Q water, followed by elution with 10 mL of MeOH and ACE (1:1, *v/v*). Extract (10 mL) of the extracted sample was pre-concentrated to 1 mL using a rotary evaporator prior to injection to HPLC-PDA. The spiking concentration levels used were 0.005, 0.010 and 0.050 mg/L for each optimization studies.

HPLC-PDA analysis

High performance liquid chromatography-Prominence (Shimadzu) with Phenomenex Luna 5µm C_{18} 100 A (250 mm x 4.6 mm, 5 µm) column equipped with photometric diode array (PDA) were used in the analysis of the 4-OP and 4-NP. The optimization of chromatographic performance included the peak area response (mAU) of different wavelengths and the mobile phase used was based on previous literature reviews [12, 20] with modification to obtain good separation of target compounds. The column temperature was set at room temperature (< 25 °C) with flow rate of 1.0 mL/min, 20 minutes running time and pressure of ≤ 100 bars. The injection volume used was 20 µL for each sample and tested for a minimum of three times to validate the precision of the data.

LC-MS/MS-AJS ESI analysis

Liquid chromatography-tandem mass spectrometry (LC-MS/MS) was carried out with an Agilent 6470 LC system (Agilent Technologies, USA)—a triple quadrupole mass spectrometer equipped with Agilent Jet Stream Technology and electrospray ionization (AJS-ESI) for the confirmation peaks of 4-OP and 4-NP in river water sample. The results were obtained based on the optimized conditions with the following settings: MS capillary voltages, 3500 V; gas temperature, 300 °C; gas flow rate, 5.0 L/min; nebulizer, 45 psi; charging voltage, 0/500 (PI/NI). The compounds were best shown in ESI (-) mode analysis. The mass-to-charge ratio (m/z) precursor and daughter ions of 4-OP (205, 106) and 4-NP (219, 147) were referred from a study conducted by Yusoff et al. [21].

Statistical analysis

The statistical analysis was carried out using IBM SPSS Statistics (Version 23.0). One-way ANOVA was derived to observe the significant difference using Tukey HSD ($p < 0.005$) with 95% confidence interval for sample volume, conditioning volume, elution volume and wavelength of 4-OP and 4-NP. The significant difference result will determine which aspect of optimization is best for further analysis.

Collection of water sample

The river water samples were collected from Kuala Terengganu River in selected areas to validate the method for the real sample analysis. Kuala Terengganu is known as the most populated town in Terengganu with new

infrastructures developing rapidly. The sampling was done in May 2018 whereby two stations were chosen during the period of the study. The sampling coordinates and physical water parameters are shown in Table 2. The physical water parameters such as temperature, salinity, pH, dissolved oxygen and depth were recorded using Hydrolab Quanta Multi-probe Meter (Sutron Corporation, USA). Water samples were collected using Niskin sampler (Silkeborg, Denmark) and stored in 1 L glass bottles. Then the water sample was placed into an ice chest filled with ice packs at approximately below 10 °C before immediately transferred to the laboratory for further analysis.

Table 2. The description and physical water parameters of sampling location

Station	Sampling Location	Coordinate	Temperature (°C)	Salinity (ppt)	pH	Dissolved Oxygen (mg/L)	Depth (m)	Remarks
S1	Upstream	N05°20'24.7" E103°09'26.0"	30.4	33.2	7.58	5.62	7.9	Nearby the breakwater
S2	Duyong Marina	N05°20'17.0" E103°07'48.4"	29.0	33.6	8.05	5.62	4.0	Pulau Duyong Port

Results and Discussion

The optimization of solid-phase extraction method: Effect of sample volume

The previous studies consumed a large sample volume (1000 mL) and various types of solvents for the water extraction method [14-16], and consequently produced substantial volume of wastes. Figure 1(a) shows that 200 mL of sample volume is sufficient to determine both 4-OP and 4-NP in a river water sample with higher peak area and good recovery percentage (%) in contrast to the analytical method proposed by Xu et al. [22] which required 1000 mL to determine the concentration of nonylphenol. However, the peak area decreased in 300 mL volume sample is mainly due to unsuitability of using large volume of sample in 1 mL (100 mg) size of cartridge. Al-Qaim et al. [23] also reported that lower size of the cartridge can effectively trap not more than 250 mL of sample volume with higher recovery percentage (> 80%). Therefore, 200 mL of volume sample in the study was considered for further analyses.

Effect of solvent type and volume

Solvents play important roles in extracting and separating specific matrix in order to determine the analytes of interests [24]. Previous methods [14-16] used various solvents (e.g. methanol, dichloromethane, hexane, acetone and ethyl acetate) for conditioning, elution or pre-concentrated processes. In the first trial, acetone was the only solvent used for the conditioning and elution processes but the results were inconsistent and only 4-NP was successfully eluted out from the cartridge. Previous studies [14-16] used methanol as their main solvent throughout the SPE processes. Methanol has the ability to efficiently extracting lower molecular weight compound, whereas acetone is good in extracting higher molecular weight compound [25]. In this case, 4-OP has lower molecular weight with 206.32 g/mol compared to 4-NP with 220.35 g/mol. The intermolecular forces in between solute-solvent molecules have strengthened the dipole-dipole forces. However, 4-OP and 4-NP are both insoluble in water thus, required polar solvents such as methanol and acetone to dissolve the compounds. In addition, methanol with polarity index and dielectric constant (*P*: 5.1 and ε: 32.7) acts as a polar molecule which helps to increase the solubility of the target analytes in water [27]. Meanwhile, acetone (*P*: 5.1 and ε: 20.7) acts as either polar or nonpolar molecules due to the two methyl groups presented in the chain which function relatively as elution solvent to effectively disrupt the nonpolar-nonpolar attractive forces (van der Waals forces) that secure the compounds in the sorbent.

Therefore, the combination of mixed solvent system, namely methanol and acetone obtained a synergistic effect in which the partition coefficient [25] mobilizes the hydrophobic compounds (4-octylphenol and 4-nonylphenol) in nonpolar sorbent (C_{18}) better in the present study. The combination of methanol and acetone was useful in conditioning the cartridge and eluting 4-OP and 4-NP consistently as shown in Figure 1 (b and c). Combination of

MeOH, ACE and Milli-Q water were tested for conditioning and elution processes [(9, 15 and 21 mL of MeOH, ACE and Milli-Q water, 1:1:1, *v/v*) and (6, 10 and 14 mL of MeOH and ACE, 1:1, *v/v*)]. The combination of 15 and 10 mL of MeOH, ACE and Milli-Q water showed good recovery percentages ranging between 80% and 110% compared to other volumes. Higher elution volume could cause the pre-concentrated process to take longer time than usual, thus leads to neither decomposition of target compounds nor loss through the evaporation process [25]. Therefore, the combination of volumes used for conditioning and elution processes were recommended for further analyses.

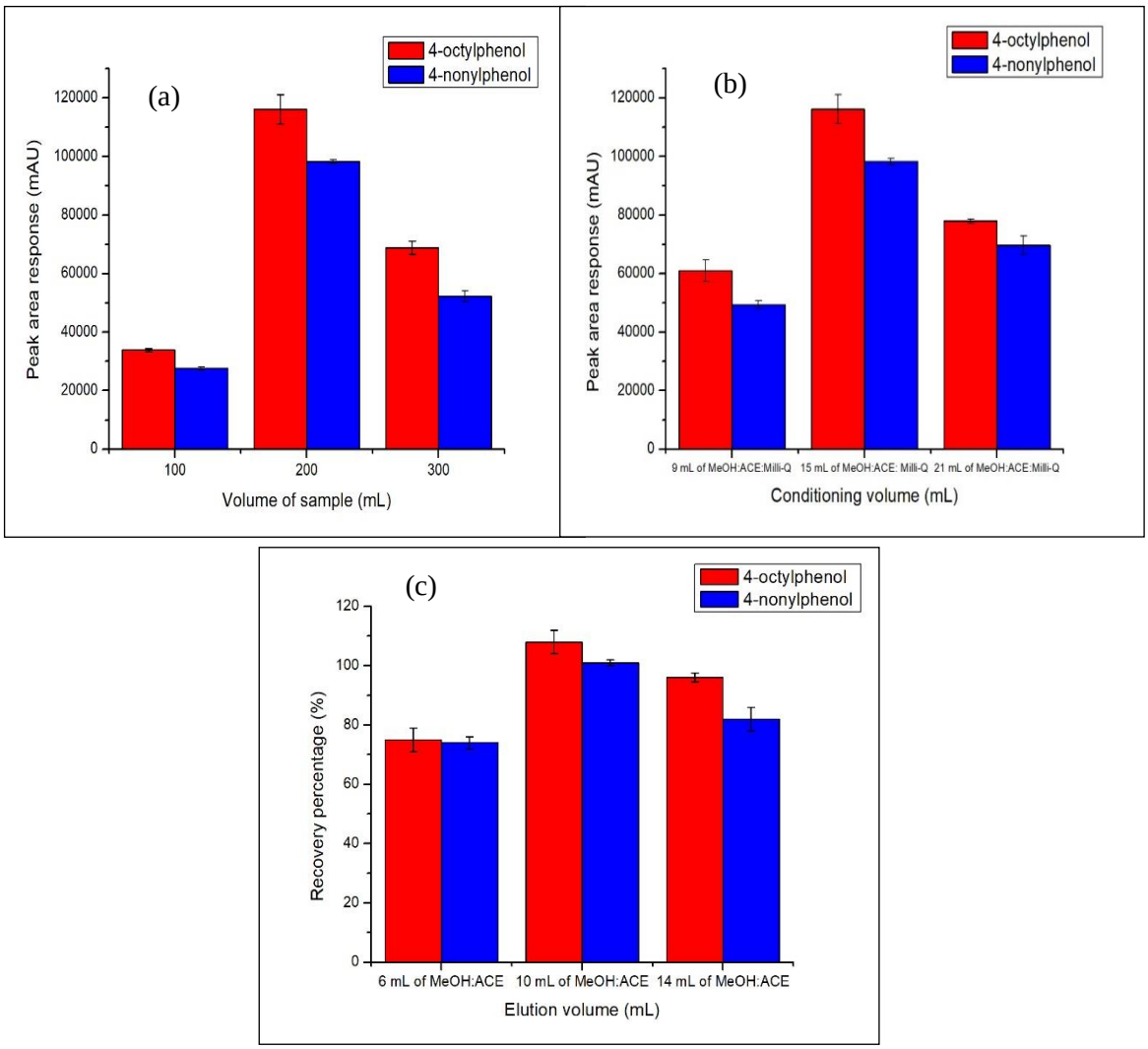


Figure 1. The effect of (a) sample volumes and (b) conditioning volumes and (c) elution volumes on the recovery of 4-OP and 4-NP analyses

In the present study, mobile phases with the composition of 20% water (A) and 80% acetonitrile (B) in an isocratic gradient elution were used based on the best peaks in both 4-OP and 4-NP. Following previous literature reviews [12, 20] with modification made, different wavelengths of 225, 230, 235, 265, 275, 280, 285 and 290 nanometers (nm) were considered and tested to find the highest intensities. By considering the best peak with the highest signal intensities and symmetries, 225 nm wavelength was chosen as optimum for the separation of 4-OP and 4-NP as shown in Figure 2. The peaks for 4-OP and 4-NP were identified based on the retention time of external standards in

a chromatogram. Figure 3 shows the chromatographic separation for 4-OP and 4-NP in a single analytical run (a) 5 mg/L pure standard of 4-OP and 4-NP without SPE and (b) 0.050 mg/L pure standard spiked in water with SPE.

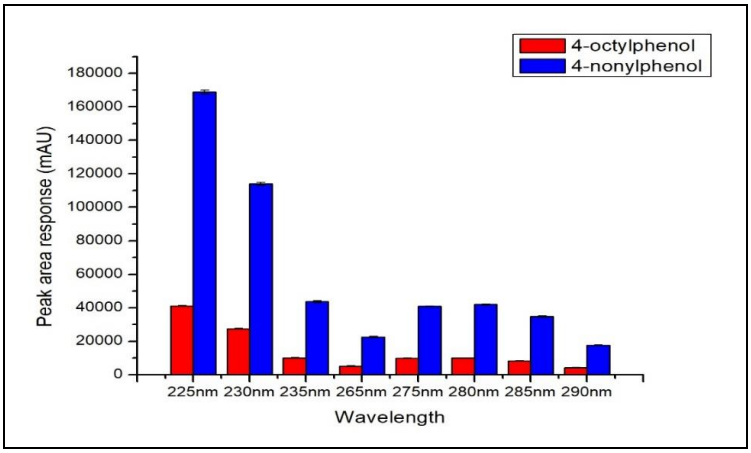


Figure 2. The sensitivity of 4-OP and 4-NP in different wavelengths

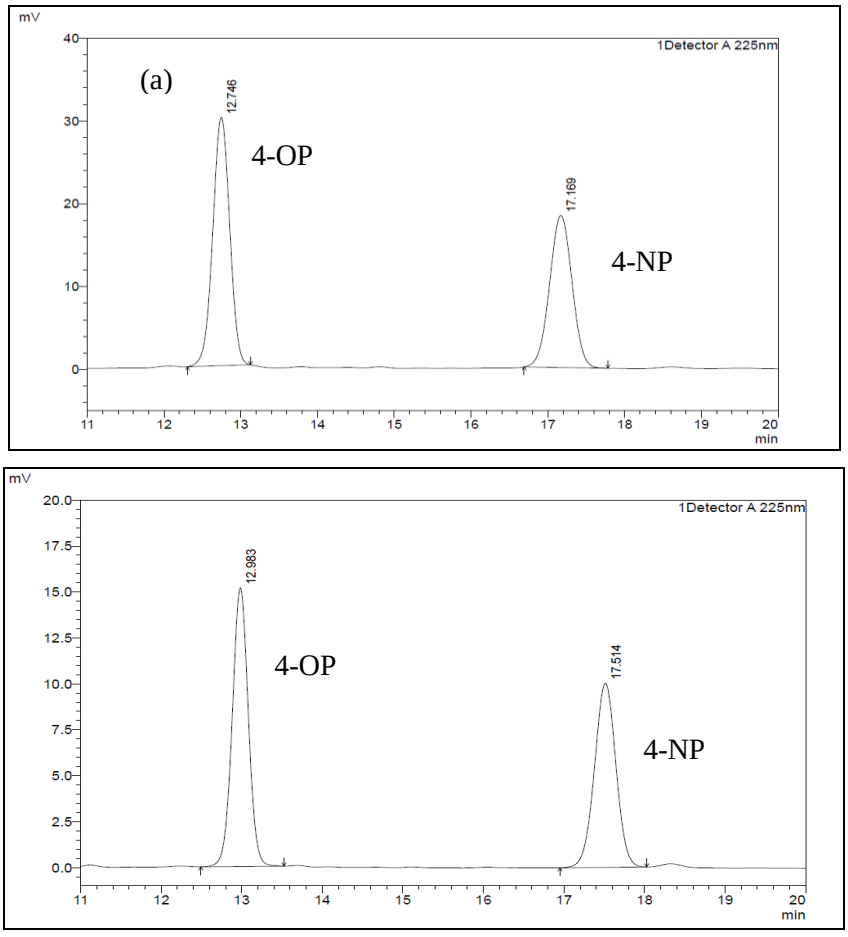


Figure 3. Chromatogram (a) 5 mg/L pure standard of 4-OP and 4-NP without SPE (b) 0.050 mg/L pure standard of 4-OP and 4-NP spiked in water with SPE

Statistical analysis

Statistical analysis was carried out to observe the significant difference among factor values (volume of sample, conditioning volume, elution volume and wavelength of 4-OP and 4-NP). The significant and insignificant values ($p < 0.005$, $p > 0.005$) are shown in Table 3 with the indicators such as 'A' and 'B' to prove the differences within the same group. The different volumes of sample (100, 200 and 300 mL) were significantly different for both 4-OP and 4-NP within the groups. This suggested that different volumes of sample influence the suitability of the size cartridge to trap the target analytes efficiently. In this case, 200 mL is the suitable volume sample to be used for 1 mL with 100 mg sorbent cartridge. The combination volume of conditioning and elution volume, 15 mL (MeOH, ACE and Milli-q water) and 10 mL (MeOH and ACE) were proven significantly different for both compounds. In fact, these combination volumes contribute to the highest peak area response. In addition, the wavelengths of 225, 230 and 285 nm (4-OP) were proven significantly different, likewise the wavelengths of 225, 230, 235, 265, 285 and 290 nm (4-NP) compared to the other wavelengths, as shown in Table 3. Based on higher peak area response, 225 nm of wavelength was chosen. Overall, the aspects chosen were statistically proven and considered for further analysis.

Table 3. Statistical analysis of one-way ANOVA using Tukey's with 95% interval confidence, ($p < 0.05$)

Volume of sample (mL)					
Factor value	**N**	**4-OP**	**4-NP**	**4-OP**	**4-NP**
		Mean Peak Area	**Mean Peak Area**	**Grouping**	
100	3	33868	27578	A	A
200	3	116143	98250	A	A
300	3	68846	52215	A	A
Volume of Conditioning (mL)					
Factor value	**N**	**Mean Peak Area**	**Mean Peak Area**	**Grouping**	
9	3	60906	49412	B	A
15	3	116143	98250	A	A
21	3	77954	69657	B	A
Volume of elution (mL)					
Factor value	**N**	**Mean Peak Area**	**Mean Peak Area**	**Grouping**	
6	3	60906	49412	B	A
10	3	116143	98250	A	A
14	3	77954	69657	B	A
Wavelength of 4-octylphenol and 4-nonylphenol					
Factor Value	**N**	**Mean Peak Area**	**Mean Peak Area**	**Grouping**	
225	3	41091	168802	A	A
230	3	27557	114067	A	A
235	3	10084	43563	B	B
265	3	4998	22523	B	A
275	3	9893	40852	B	B
280	3	9978	41989	B	B
285	3	8267	34762	A	A
290	3	4142	17645	B	A

'A' indicates significant with value $p < 0.005$, 'B' indicates insignificant with $p > 0.005$, N is the number of replicates

Method validation

The calibration curve for the mixed standard of 4-OP and 4-NP (n=5) were constructed at five different concentrations: 0.001, 0.0012, 0.006, 0.008 and 0.012 mg/L. These curves showed a strong positive and significant linearity for 4-OP and 4-NP (R^2 values at 0.9988 and 0.9995 with regression equation $y = 70000000x + 23021$ and $y = 10000000x + 1099$, respectively). The calibration curves for 4-OP and 4-NP are as shown in Figure 4.

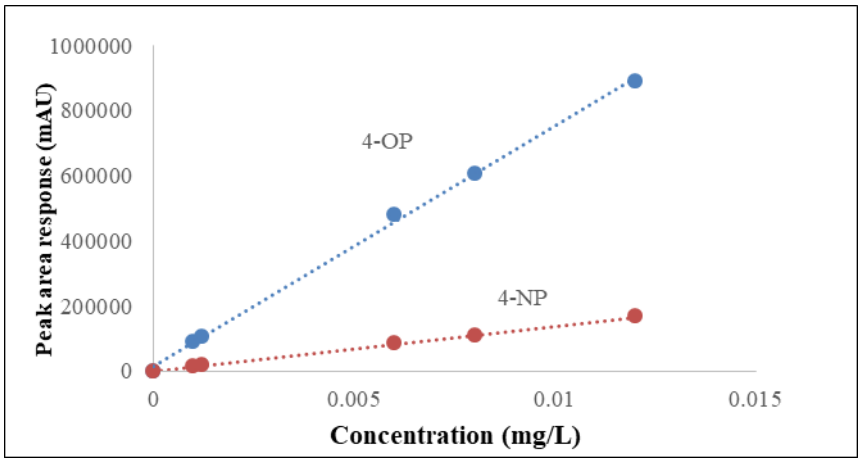


Figure 4. External standard calibration curves 4-octylphenol and 4-nonylphenol

The instrument detection limit (IDL) and method detection limit (MDL) were also validated in the present study. The IDL and MDL results showed low detection at 0.0012 and 0.0001 mg/L. The results were calculated for both limit of detection (LOD) and limit of quantification (LOQ) as shown in Table 4. LOD and LOQ were performed based on 3:1 and 10:1 signal to noise ratios. Compared with the MDL reported by Xu et al. [22] which achieved 0.01 mg/L for nonylphenol, the detection limit that can be achieved in this study is lower than that value.

Table 4. The instrument detection limit and method detection limit for SPE method optimization

Analytes	Instrument Detection Limit		Method Detection Limit	
	LOD (mg/L)	LOQ (mg/L)	LOD (mg/L)	LOQ (mg/L)
4-octylphenol	0.0013	0.0043	0.0006	0.0020
4-nonylphenol	0.0012	0.0041	0.0001	0.0005

A mixed standard (4-OP and 4-NP) was spiked into the water to validate the method recovery percentage (%). The recovery percentages (%) for 4-OP and 4-NP were spiked in three different concentrations (0.005, 0.010 and 0.050 mg/L) and the calculated results are as shown in Table 5. The recovery percentages are shown good for 4-OP and 4-NP ranged from 41.0 to 114% with lower RSD (< 2%). In the present study, the recovery percentage of 0.050 mg/L was lower for both compounds (< 50%) and this is due to its saturation capacity of sorbent (100 mg). This is supported by Baghdady and Schug [26] who found that the capacity of sorbent can be saturated with maximum number of sorbed analyte by the phase, thus the concentration of analyte passing through the sorbent can be similar with the ones exiting the cartridge. As a result, lower recovery would be achieved if higher concentration level (≥ 0.050 mg/L) was spiked into the sample to go through the SPE. However, lower RSD (< 20%) indicates good reproducibility and consistency [28]. Therefore, the method proposed is acceptable for real water sample analysis.

The precision of SPE method was validated using intra and inter-day reproducibility at 3 level concentrations (0.005, 0.010 and 0.050 mg/L) as shown in Table 6. Good reproducibility with lower RSD (< 2%) was shown between intra and inter-day for both compounds, 4-OP and 4-NP. Compared to previous study conducted by Wang et al. [15] in which the reproducibility in determining 4-OP and 4-NP was achieved with RSD (< 13%), the proposed method in this study can achieve better reproducibility with lower RSD.

Table 5. Mean recovery percentages (%) ± standard deviation and relative standard deviation in water (n = 3)

Analytes	**Spiked Concentration (mg/L)**	**Measured Concentration (mg/L)**	**Recovery Percentage ± SD**	**(%RSD)**
4-octylphenol	0.005	0.0048	96.7 ± 0.7	0.75
	0.010	0.011	114 ± 0.5	0.40
	0.050	0.023	46.0 ± 0.2	0.52
4-nonylphenol	0.005	0.0045	89.8 ± 0.7	0.75
	0.010	0.0104	104 ± 0.5	0.50
	0.050	0.021	41.0 ± 0.1	0.25

SD is standard deviation, RSD is relative standard deviation

Table 6. Precisions (intra and inter-day reproducibility) based on found concentrations and retention times (n=3)

Analytes	**Intra-day (n=3)**			**Inter-day (n=3)**	
	Spiked Concentration (mg/L)	**Measured Concentration ± SD (mg/L)**	**(%RSD)**	**Measured Concentration ± SD (mg/L)**	**(%RSD)**
4-octylphenol	0.005	0.0046 ± 0.00018	3.89	0.0048 ± 0.00004	0.75
	0.010	0.011 ± 0.00053	4.70	0.010 ± 0.00005	0.40
	0.050	0.025 ± 0.00474	19.17	0.020 ± 0.0001	0.52
4-nonylphenol	0.005	0.0046 ± 0.00024	5.13	0.0045 ± 0.00003	0.75
	0.010	0.011 ± 0.00099	8.76	0.010 ± 0.00005	0.50
	0.050	0.026 ± 0.00536	20.67	0.020 ± 0.00005	0.25

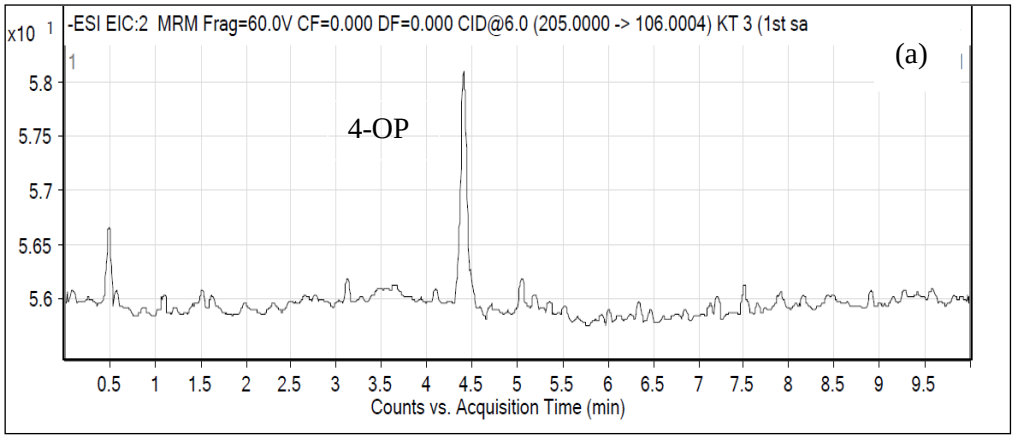
SD is standard deviation, RSD is relative standard deviation

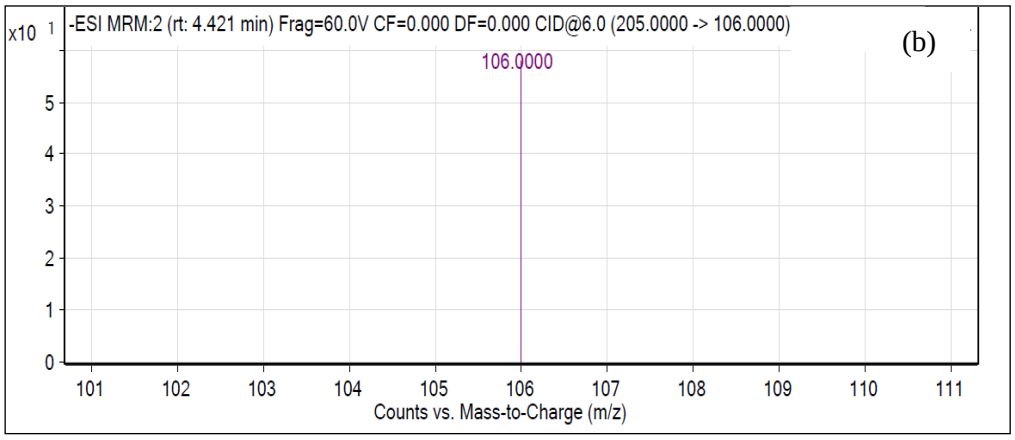
Analysis of water samples from Terengganu River

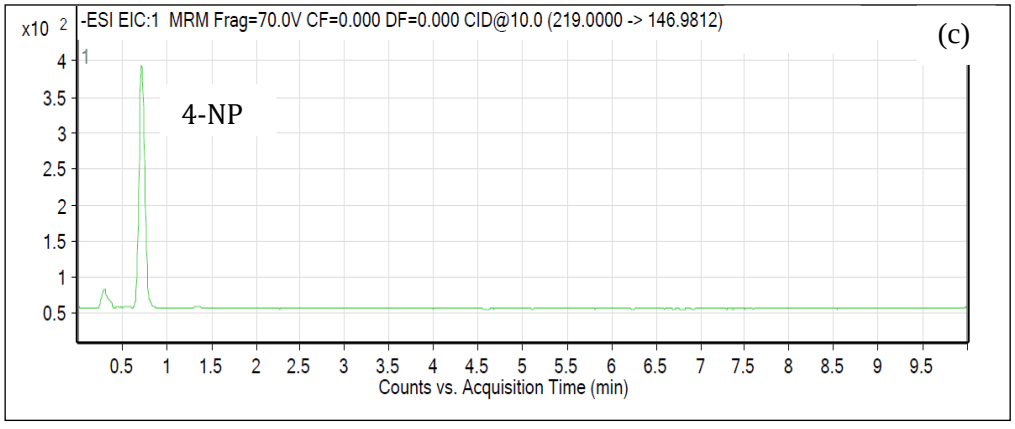
Analysis of 4-OP and 4-NP in river water was successfully carried out using the optimized method. Two samples (S1 and S2) were taken and extracted to detect the concentration of 4-OP and 4-NP. Both 4-OP and 4-NP were not detected in S1 but presented in S2 with 0.001 and 0.0003 mg/L. Station 2 is located in the combination of residential, recreational and port areas, thus the concentration of 4-OP and 4-NP could be contributed from the available sources. Residential (urban-rural districts) and recreational areas are linked to possible sources of target compounds as Wang et al. [29] stated that the compounds could come from untreated or non-biologically treated domestic wastewater which flows out into the river water without consent. In addition, the target pollutants could also come from port areas (boat and ship) due to the usage of detergents to clean the vessel as reported by Salqueiro-González et al. [30]. Overall, the method proposed is able to detect low level concentration of 4-OP and 4-NP in river water.

LC-MS/MS-ESI screening and confirmation

A mixture standard of 4-OP and 4-NP was first analyzed to optimize the condition of the instrument (mobile phase, gradient elution flow rate and injection volume). After the optimization was completed, one sample (St 2) was confirmed with the presence of 4-OP and 4-NP selected to be analyzed using LC-MS/MS. The compounds of 4-OP and 4-NP were determined using m/z based on a previous study [21]. Figure 5 (A, B, C, D) is the confirmation peak through extracted-ion chromatogram (EIC) and multiple reaction monitoring (MRM) for both 4-OP and 4-NP. The confirmation of 4-OP and 4-NP was further calculated with probability match between the sample and standard due to the unavailable library data installed in the system. The probability match (%) of 4-OP and 4-NP was calculated with 28 and 129%. Therefore, the peaks that appeared in the HPLC chromatogram were confirmed to be 4-OP and 4-NP based on the probability match with the standard.







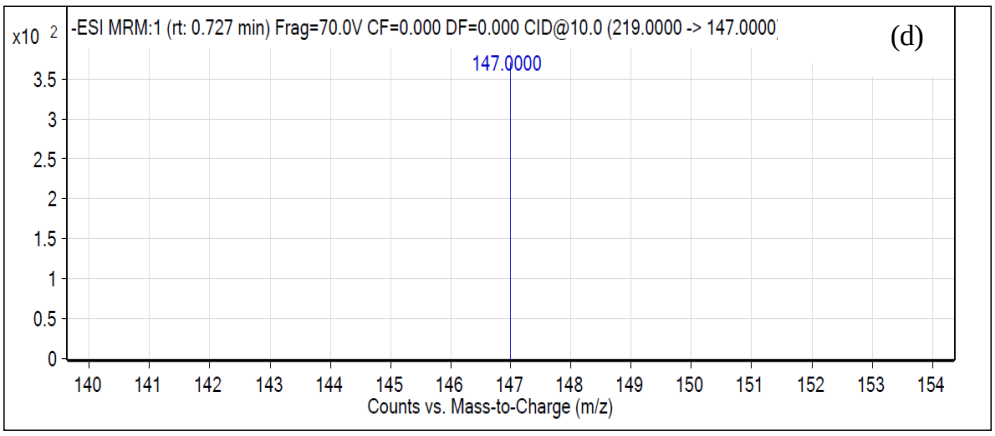


Figure 5. The confirmation peaks of 4-octylphenol and 4-nonylphenol in water sample through LC-MS/MS-ESI

Conclusion

The contribution of this study is apparent in terms of SPE method modification that emphasizes on using less volume of water sample and solvent for 4-octylphenol and 4-nonylphenol. Good validation results were obtained in terms of linearity, precision and sensitivity of the method extraction and HPLC-PDA performances. Trial analysis was proven using low level concentration (≤ 0.001 mg/L) of water sample from Terengganu River. However, further investigation on the other matrices such as sediment and biota need to be considered to report the occurrence and distribution of endocrine-disrupting compounds in the Malaysian river ecosystem.

Acknowledgement

This study has been funded by the Fundamental Research Grant Scheme (FRGS)-FRGS/1/2017/WAB09/UMT/03/3 and High Centre of Excellent (HICoE) in Marine Science, Ministry of Higher Education, Malaysia. Authors would like to acknowledge Centre of Research and Field Service (CRAFS, UMT) and National Hydraulic Research Institute of Malaysia (NAHRIM) staff for assisting this project.

References

1. Toor, J. S., & Sikka, S. C. (2017). Developmental and reproductive disorders-role of endocrine disruptors in testicular toxicity. reproductive and developmental toxicology. *Elsevier Inc*.
2. Tapiero, H., Nguyen, B. G. and Tew K. D. (2002). Estrogens and environmental estrogens. *Biomedicine & Pharmacotherapy*, 56: 36-44.
3. Imai, S., Koyama, J. and Fuiji, K. (2007). Effects of estrone on full life cycle of Java medaka, a new marine test fish. *Environmental Toxicology & Chemistry*, 26: 726-731.
4. Yusoff, N. M., Koyama, J. and Uno, S. (2017). Bioaccumulation of sedimentary endocrine disrupting chemicals (EDCs) by the benthic fish, *Pleuronectes yokohamae*. *Malaysian Journal of Analytical Science*, 21(3): 535-543.
5. Geyer, H. J., Rimkus, G. G., Scheunert, I., Kaune, A., Schramm., K.-W., Kettrup, A., Zeeman, M., Muir, D. C. G. and Mackay, D. (2005). Bioaccumulation and occurrence of endocrine-disrupting chemicals (EDCs), persistent organic pollutants (POPs), and other organic compounds in fish and other organisms including humans. Bioaccumulation – *New Aspects and Developments*, 2: pp. 1-166.
6. Duong, C. N., Ra, J. S., Cho, J., Kim, S. D., Choi, H. K., Park, J. H., Kim, K. W., Inam, E. and Kim, S. D. (2010). Estrogenic chemicals and estrogenicity in river waters of South Korea and seven Asian countries. *Chemosphere*, 78(3): 286-293.
7. Tan, B. L. L. and Mustafa, A. M. (2004). The monitoring of pesticides and alkylphenols in selected rivers in the State of Selangor, Malaysia. *Asia-Pacific Journal of Public Health*, 16(1): 54-63.
8. Jobling, S., Coey, S., Whitmore, J. G., Kime, D. E., Van Look, K. J. W., McAllister, B. G., Beresford, N., Henshaw, A. C., Brighty, G., Tyler, C. R. and Sumpter, J. P. (2002). Wild intersex roach (*Rutilus rutilus*) have reduced fertility, *Biology of Reproduction*, 67: 515-524.

9. Sumpter, J. P. and Johnson, A. C. (2005). Lessons from endocrine disruption and their application to other issues concerning trace organics in the aquatic environment. *Environmental Science & Technology*, 39(12): 4321-4332.
10. Burki, R., Vermeirssen, E. L. M., Körner, O., Joris, C., Burkhardt-Holm, P. and Segner, H. (2006). Assessment of estrogenic exposure in brown trout (*Salmo trutta*) in a Swiss midland river: Integrated analysis of passive samplers, wild and caged fish, and vitellogenin mRNA and protein. *Environmental Toxicology and Chemistry*, 25(8): 2077-2086.
11. Cheek, A. O. (2006). Subtle sabotage: endocrine disruption in wild populations, *Revista De Biologia Tropical*, 54: 1-19.
12. Cherniaev, A. P., Kondakova, A. S. and Zyk, E. N. (2016). Contents of 4-nonylphenol in surface sea water of Amur Bay (Japan/East Sea). *Achievements in the Life Sciences*, 10(1): 65-71.
13. Kannan, K., Keith, T. L., Naylor, C. G., Staples, C. A., Snyder, S. A. and Giesy, J. P. (2003). Nonylphenol and nonylphenol ethoxylates in fish, sediment, and Water from the Kalamazoo River, Michigan. *Achieve Environmental and Contamination Toxicology*, 44: 77-82.
14. Wang, W., Ndungu, A. W. and Wang, J. (2016). Monitoring of endocrine-disrupting compounds in surface water and sediments of the three Gorges reservoir region, China. *Archives of Environmental Contamination and Toxicology*, 71(4): 509–517.
15. Wang, B., Dong, F., Chen, S., Chen, M., Bai, Y., Tan, J., Li, F. and Wang, Q. (2016). Phenolic endocrine disrupting chemicals in an urban receiving river (Panlong River) of Yunnan-Guizhou plateau: Occurrence, bioaccumulation and sources. *Ecotoxicology and Environmental Safety*, 128: 133-142.
16. Cheng, J. R., Wang, K., Yu, J., Yu, Z. X. Y., Biao, X. and Zhang, Z. (2018). Distribution and fate modeling of 4-nonylphenol, 4-t-octylphenol, and bisphenol A in the Yong River of China. *Chemosphere*, 195: 594-605.
17. Oluseyi, T., Olayinka, K., Alo, B. and Smith, R. M. (2011). Improved analytical extraction and clean-up techniques for the determination of PAHs in contaminated soil samples. *International Journal of Environmental Research*, 5(3): 681-690.
18. Careri, M., Elviri, L. and Mangia, A. (2001). Development and validation of a method using on-line solid-phase extraction and liquid chromatography with ultraviolet detection for the determination of bisphenol A, octylphenol, and nonylphenol in groundwater. *Journal of AOAC International*, 84(5): 1383-1392.
19. Liu, R., Zhou, J. L. and Wilding, A. (2004). Simultaneous determination of endocrine disrupting phenolic compounds and steroids in water by solid-phase extraction-gas chromatography-mass spectrometry. *Journal of Chromatography A*, 1022(1-2): 179-189.
20. Ahel, M. and Giger, W. (1993). Partitioning of alkylphenols and alkylphenol polyethoxylates between water and organic solvents. *Chemosphere*, 26(8): 1471-1478.
21. Yusoff, N. M., Koyama, J., Uno, S., Kito, A., Kokushi, E., Bacolod, E. T., Ito, K. and Chuman, Y. (2014). Accumulation of endocrine disrupting chemicals (EDCs) in the polychaete *Paraprionospio* sp. from the Yodo River mouth, Osaka Bay, Japan. *Environmental Monitoring and Assessment*, 186(3): 1453-1463.
22. Xu, J., Wang, P., Guo, W., Dong, J., Wang, L. and Dai, S. (2006). Seasonal and spatial distribution of nonylphenol in Lanzhou Reach of Yellow River in China. *Chemosphere*, 65(9): 1445-1451.
23. Al Qaim, F. F., Jusof, S. H., Abdullah, M. P., Mussa, Z. H., Tahrim, N. A., Khalik, W. M. A. W. M. and Othman, M. R. (2017). Determination of caffeine in surface water using solid phase extraction and high performance liquid chromatography. *Malaysian Journal of Analytical Sciences*, 21(1): 95-104.
24. Moldoveanu, S. and David, V. (2015). Chapter 6 Solvent Extraction. Modern Sample Preparation for Chromatography. *Chromatography Elsevier*, 2015: pp 131-189
25. Dai, J. and Mumper, R. J. (2010). Plant phenolics: Extraction, analysis and their antioxidant and anticancer properties. *Molecules*, 15(10): 7313-7352.
26. Baghdady, Y. Z. and Schug, K. A. (2016). Evaluation of efficiency and trapping capacity of restricted access media trap columns for the online trapping of small molecules. *Journal of Separation Science*, 39(21): 4183-4191.
27. Ying, G. G., Kookana, R. S. and Chen, Z. (2002). On-line solid-phase extraction and fluorescence detection of selected endocrine disrupting chemicals in water by high-performance liquid chromatography. *Journal of Environmental Science and Health - Part B Pesticides, Food Contaminants, and Agricultural Wastes*, 37(3): 225-234.

Malaysian Journal of Analytical Sciences Vol 24 No 2 2020

Page

1. IONOTHERMAL SYNTHESIS OF Zn-BASED METAL ORGANIC FRAMEWORKS IN PYRIDINIUM IONIC LIQUID 159
(Sintesis Ionotermal Kerangka Logam-Organik Berasaskan Logam Zink Menggunakan Cecair Ionik Piridinium)
Haslina Ahmad, Nur Aininie Yusoh, Khairulazhar Jumbri, Mohd Basyaruddin Abdul Rahman

2. DEVELOPMENT AND VALIDATION OF HPLC METHOD FOR QUANTIFICATION OF DOCETAXEL IN PALM-BASED NANOEMULSION AEROSOLS 165
(Pembangunan dan Validasi Kaedah KCPT untuk Kuantifikasi Docetaxel di dalam Nanoemulsi Aerosol Berasaskan Sawit)
Azren Aida Asmawi, Norazlinaliza Salim, Emilia Abdulmalek, Mohd Basyaruddin Abdul Rahman

3. PHYTOCHEMICAL SCREENING AND ANTIOXIDANT ACTIVITY OF *Psidium guajava* 173
(Saringan Fitokimia dan Aktiviti Antioksidan terhadap *Psidium guajava*)
Nor Akmalazura Jani, Nurul Alia Ahmad Azizi, Nurul Iman Aminudin

4. DEVELOPMENT OF AN ENZYME-LINKED IMMUNOSORBENT ASSAY (ELISA) FOR DOMOIC ACID DETECTION IN SELECTED SHELLFISH SEAFOOD USING α-AMINO-3-HYDROXY-5-METHYL-4-ISOXAZOLEPROPIONIC ACID (AMPA) RECEPTOR 179
(Pembangunan Imunojerapan Berpaut Enzim Berpesaingan Tak Langsung (ELISA) bagi Pengesanan Domoik Asid dalam Makanan Laut Bercengkerang Terpilih menggunakan Reseptor α-Amino-3-Hidroksi-5-Metil-4-Isoksazolepropionik Asid (AMPA))
Hafiza Mohamed Zuki, Lai Yun Ru, Noor Sheryna Jusoh, Azrilawani Ahmad, Marinah Mohd Ariffin

5. ENZYME CATALYZED ESTERIFICATION OF SUGAR BY THERMOSTABLE T1 LIPASE FROM *Geobacillus zalihae* IN IONIC LIQUID 188
(Pengesteran Berenzim Gula oleh Lipase Termostabil T1 dari *Geobacillus zalihae* dalam Cecair Ionik)
Emilia Abdulmalek, Hanim Salami Mohd Saupi, Syarilaida Zulkefli, Raja Nor Zaliha Raja Abd Rahman, Mohd Basyaruddin Abdul Rahman

6. VORTEX-ASSISTED SUPRAMOLECULAR-BASED DISPERSIVE LIQUID PHASE MICROEXTRACTION FOR SPECTROPHOTOMETRIC DETERMINATION OF RHODAMINE B IN CHILI POWDER 197
(Supramolekul Berasaskan Serakan Cecair Fasa Pengekstrakan Mikro Berbantu-Vorteks untuk Penentuan Spektrofotometrik Rhodamin B dalam Serbuk Cili)
Renitha Harikrishnan, Kavisha Sundraraj, Boon Yih Hui, Nur Nadhirah Mohamad Zain, Noorfatimah Yahaya, Kavirajaa Pandian Sambasevam, Sharifah Mohamad, Yatimah Alias, Muggundha Raoov

7. CONTROLLED CONCENTRATION OF Mn SALT FOR THE SYNTHESIS OF MANGANESE OXIDE/MESOPOROUS CARBON FILM AS POTENTIAL ELECTRODES FOR 209

SUPERCAPACITOR
(Kepekatan Garam Mn Terkawal terhadap Sintesis Mangan Oksida/Karbon Filem Berliang Meso sebagai Elektrod Berpotensi bagi Superkapasitor)
Mahanim Sarif @ Mohd Ali, Zulkarnain Zainal, Mohd Zobir Hussein, Mohd Haniff Wahid, Noor Nazihah Bahrudin

8. DEACIDIFICATION OF NAPHTHENIC ACIDS FROM PETROLEUM CRUDE OILS USING 2-METHYLIMIDAZOLE IN PEG(400) WITH THE AID OF Ni/Ce/Al_2O_3 and Cu/Ce/Al_2O_3 CATALYSTS 218
(Deasidifikasi Asid Naftenik dari Minyak Mentah Petroleum menggunakan 2-Metilimidazola dalam PEG(400) dengan Bantuan Pemangkin Ni/Ce/Al_2O_3 dan Cu/Ce Al_2O_3)
Norshahidatul Akmar Mohd Shohaimi, Nor Shafira Hassan, Ahmad Zamani Ab Halim, Nurasmat Mohd Shukri, Nor Hakimin Abdullah

9. ELECTROBIOSYNTESIS OF NiO USING RAMBUTAN LEAVES FOR PHOTODEGRADATION OF REMAZOL BRILLIANT BLUE DYE 227
(Elektrobiosintesis NiO Menggunakan Ekstrak Daun Rambutan Untuk Fotodegradasi Pewarna Remazol Brilliant Biru)
Muhammad Farhan Hanafi, Noor Faizah Che Harun, Norzahir Sapawe, Azizzami Raidin

10. EFFICIENT REMOVAL OF LEAD FROM AQUEOUS USING HYBRID GRAPHITE NANOFLAKES/MESOPOROUS SILICA NANOPARTICLES, AMINE FUNCTIONALIZED MESOPOROUS SILICA AND GRAPHITE NANOFLAKES AS ADSORBENTS 236
(Penyingkiran Berkesan terhadap Plumbum dari Cecair Menggunakan Kepingan Nano Grafit Hibrid/ Silika Partikel Nano Berliang-Meso, Silika Partikel Nano Berliang-Meso Berfungsi Amin dan Kepingan Nano Grafit Sebagai Penyerap)
Haslina Ahmad, Vilander Vince Laini, Tan Zhi Qian, Radhiah Mohd Jelani, Fatin Ahza Rosli, Sazlinda Kamaruzaman

11. PREPARATION, CHARACTERIZATION AND SWELLING STUDIES OF CARBOXYMETHYL SAGO STARCH HYDROGEL 247
(Penyediaan, Pencirian dan Kajian Pengembangan Hidrogel Karboksimetil Kanji Sagu)
Normastura Sulta, Norhazlin Zainuddin, Mansor Ahmad, Mas Jaffri Masarudin

12. THE DEVELOPMENT OF *Acetobacter xylinum* GROWTH MEASUREMENT THROUGH TOTAL PROTEIN ANALYSIS 258
(Pembangunan Kaedah Pengukuran Pertumbuhan *Acetobacter xylinum* Melalui Analisis Jumlah Protein)
Sharifah Soplah Syed Abdullah, Jessica Harriette Supang Anak John, Mohd Azizan Mohd Noor

13. ELECTROSYNTHESIS OF SILVER OXIDE DEPOSITED ONTO HOT SPRING MUD WITH ENHANCED DEGRADATION OF CONGO RED 266
(Elektrosintesis Perak Oksida Disokong Pada Lumpur Air Panas Dengan Peningkatan Degradasi Congo Merah)
Muhammad Farhan Hanafi, Ahmad Norsyazwan Mustafa, Norzahir Sapawe

14. SOURCE DETERMINATION OF PSEUDOEPHEDRINE USING ATTENUATED TOTAL REFLECTANCE FOURIER TRANSFORM INFRARED SPECTROSCOPY COMBINED WITH CHEMOMETRIC ANALYSIS 276

(Penentuan Sumber Pseudoephederin Menggunakan Spektroskopi Atenuasi Pembalikan Transformasi Fourier Digabungkan Dengan Analisis Kemometrik)
Ainol Hayah Ahmad Nadzri, Saravana Kumar Jayaram, Puteri Nurul Hassanah Anuar, Noor Zuhartini Md Muslim, Dzulkiflee Ismail, Wan Nur Syuhaila Mat Desa

15. SCREENING OF NATURAL COLOURS FROM VARIOUS NATURAL RESOURCES AS POTENTIAL REUSABLE VISUAL INDICATORS FOR MONITORING FOOD FRESHNESS 288
(Saringan Pewarna Semula Jadi Daripada Pelbagai Sumber Semula Jadi Sebagai Indikator Visual Guna-Semula Untuk Pemantauan Kesegaran Makanan)
Mohd. Zulkhairi Abdul Rahim, Nurdiyana Husin, Mohd. Azizan Mohd Noor, Zaida Rahayu Yet, Mohammad Rashedi Ismail-Fitry

Malaysian Journal of Analytical Sciences (MJAS)
Published by Malaysian Analytical Sciences Society

IONOTHERMAL SYNTHESIS OF ZN-BASED METAL ORGANIC FRAMEWORKS IN PYRIDINIUM IONIC LIQUID

(Sintesis Ionotermal Kerangka Logam-Organik Berasaskan Logam Zink Menggunakan Cecair Ionik Piridinium)

Haslina Ahmad[1,2]*, Nur Aininie Yusoh[1], Khairulazhar Jumbri[3], Mohd Basyaruddin Abdul Rahman[1,2]

[1]*Chemistry Department, Faculty of Science*
[2]*Integrated Chemical Biophysics Research, Faculty of Science*
Universiti Putra Malaysia, 43400 UPM Serdang, Selangor, Malaysia
[3]*Department of Fundamental and Applied Sciences,*
Universiti Teknologi Petronas, Bandar Seri Iskandar, 32610, Perak, Malaysia

**Corresponding author: haslina_ahmad@upm.edu.my*

Received: 20 November 2019; Accepted: 24 February 2020

Abstract

Metal organic frameworks (MOFs) are crystalline porous frameworks which have been investigated as absorbent for removing dye, metal ion, drug contaminant, and organic solvent from water. However, the traditional synthesis of MOF involves the use of organic solvents and also requires high temperature; termed solvothermal reaction. This study aimed to synthesis MOF in a rather mild condition (room temperature) using ionic liquids (ILs) instead of organic solvents. Theoretically, high ionic conductivity of cetyl pyridinium bromide (C_{16}PyBr) ionic liquid can develop novel MOF compounds thus, this study also aimed to investigate the possible effects of using ionic liquid in MOF synthesis. Zinc nitrate hexahydrate ($Zn(NO_3)_2.6H_2O$) was used as the metal precursor and was reacted with the organic ligands, which is either benzene-1,3,5-tricarboxylic acid (H_3BTC) or benzene-1,4-dicarboxylate (H_2BDC), at 6:1 ratio in C_{16}PyBr ionic liquid at room temperature. We hope to fabricate Zn-BDC and Zn-BTC MOFs with the same compositions, and thus recognize the effects of ILs. The powder X-ray diffraction (PXRD) and Fourier Transform Infrared Spectroscopy (FTIR) spectra of both newly synthesized MOFs showed that both Zn-BDC and Zn-BTC MOFs can be reproduced with these conditions. ILs have also been found to significantly accelerate the formation of MOFs at room temperature as the reaction time is shortened to 6 hours in IL, meanwhile the organic solvent DMF needs at least 120 hours.

Keywords: metal organic frameworks, ionic liquids, zinc, pyridinium

Abstrak

Kerangka logam-organik (MOF) adalah kerangka kristal berliang yang telah disiasat sebagai penyerap untuk mengeluarkan perwarna, logam ion, bahan pencemar daripada ubat-ubatan, dan pelarut organik daripada air. Walau bagaimanapun, sintesis tradisional MOF melibatkan penggunaan pelarut organik dan juga memerlukan suhu yang tinggi; dipanggil tindak balas solvotermal. Kajian ini bertujuan untuk mensintesiskan MOF dalam keadaan yang agak ringan (suhu bilik) menggunakan cecair ionik (ILs) dan bukan pelarut organik. Secara teori, kekonduksian ionik yang tinggi di dalam cecair ionik piridinium bromida (C_{16}PyBr) boleh membangunkan perkembangan sebatian MOF yang baharu, oleh itu, kajian ini juga bertujuan untuk mengkaji kemungkinan pengaruh menggunakan cecair ionik dalam sintesis MOF. Zink nitrat heksahidrat ($Zn(NO_3)_2.6H_2O$) digunakan sebagai pelopor logam dan di campur dengan ligan organik, sama ada asid benzena-1,3,5-trikarbosilik (H_3BTC) atau benzena-1,4-dikarbosilat (H_2BDC), pada nisbah 6:1 menggunakan pelarut cecair ionik C_{16}PyBr pada suhu bilik. Kami berharap dapat menghasilkan MOF Zn-BDC dan Zn-BTC dengan komposisi yang sama, dan dengan itu dapat mengiktiraf pengaruh ILs. Pembelauan serbuk sinar-X (PXRD) dan spektroskopi inframerah transformasi Fourier (FTIR) daripada kedua-dua MOF yang di sintesis menunjukkan bahawa kedua-dua MOF Zn-BDC dan Zn-BTC boleh dihasilkan semula dengan keadaan ini. IL juga

didapati dengan ketara dapat mempercepat pembentukan MOF pada suhu bilik apabila masa tindak balas dipendekkan kepada 6 jam apabila menggunakan IL, di mana pelarut organik, DMF memerlukan sekurang-kurangnya 120 jam.

Kata kunci: kerangka logam-organik, cecair ionik, zink, piridinium

Introduction

Metal organic frameworks (MOFs) are porous materials that have been studied widely in the present days due to their possible applications in various fields such as in adsorption study, catalysis, sensors, and as drug delivery agents [1]. MOFs have been proven to have diverse and unique structures when synthesized under different reaction conditions, for example, changes in metal and ligand sources, temperature, and also solvents [2]. Ionothermal synthesis has been successfully applied since 2002, where ionic liquids (ILs) are used as the solvent instead of the conventional solvents (water or organic solvents). It is considered as an environmentally-friendly route and was used to get the desired structures and physiochemical properties in the design of MOFs [3]. The main reason for this is because ILs possessed many distinguished features and intriguing physicochemical properties compared to traditional solvents, i.e., negligible vapor pressure, high ionic conductivity, non-flammability, and tunable properties. The large temperature windows and high ionic conductivity of ILs make them a suitable solvent to provide different reaction environments involving reactions between metal ions and organic ligands, particularly in producing new MOF compounds [5]. It is also considered to be safer and has more advantages than the traditional solvothermal reactions which involves using traditional organic solvent, usually contains formamide functionality and involves heating the reaction mixture over 100°C for days. Solvothermal method is widely used in MOF synthesis as it can gives crystal product which is suitable for single crystal XRD analysis thus, its structure can be determined. However, this method is relatively slow, where the product takes hours to days to form [4].

In the present days, enormous effort has been devoted in applying this route, particularly to tailor the physical properties of MOFs by using various ILs with different structures. For example, using ILs with different alkyl group lengths with different anions [3]. In study done by others showed that the anions and cations of ILs play an important role in the structural development of MOF compounds in which the cations act as the template for the main structure, meanwhile the anionic parts determine the level of the deprotonation event of the ligands through their behaviors, particularly nucleophilicity. Therefore, tuning ILs properties becomes an important plan in designing MOF [2]. Furthermore, room temperature synthesis is more desirable and from previous studies done by others, ILs have also been found to significantly accelerate the formation of MOFs at room temperature [1]. Therefore, the main objective of this study is to develop a rapid, low energy and environmentally friendly method for MOFs synthesis.

We aimed to synthesis MOFs with a novel synthesis method which involves using ILs as the solvent at room temperature. The most commonly used IL in the MOF synthesis is the imidazolium-based IL, but here we tried to tackle this using IL which consists of pyridine group. The most interesting parts regarding ILs is different combination of cations and anions will change the ILs' properties. Therefore, by changing the cations from imidazolium to pyridinium, there is a possibility of obtaining MOFs with different morphologies. We have reported previously the utilization of 1-hexadecylpyridinium bromide ionic liquid (C_{16}PyBr) IL as a template for mesoporous silica nanoparticles (MSN) formation [6] thus, in this study, we are trying to see whether this particular IL can also be used as a template for MOF synthesis. This pyridinium-based IL consists of pyridinium cation; with long alkyl chain and a bromide anion. We have presented zinc-based MOF (Zn-MOF) systems to study the effects of IL on MOF synthesis. Zn-MOFs are one of the most widely studied systems in the field of synthesizing new MOF compounds, mainly because of its simple configuration which will eliminate the effect of the metal source and ligands. The metal source used is Zn^{2+} from zinc nitrate hexahydrate ($Zn(NO_3)_2.6H_2O$) and the ligands are H_3BTC (benzene-1,3,5-tricarboxylic acid) and H_2BDC (benzene-1,4-dicarboxylic acid) to produce Zn-BTC and Zn-BDC systems.

In this study, we hope to produce MOFs with the same composition and thus recognize the effect of IL. Zn-based MOFs that have been previously published are used as the marker to study the Zn-MOF system. We believe this system should be a promising strategy in order to study the effects of ILs as solvent [4]. Triethylamine (TEA) is added as a weak base to deprotonate the acidic ligand. These compounds were then characterized by powder X-ray

diffraction (PXRD) and Fourier Transform Infrared Spectroscopy (FTIR) [5]. Here, we found that when IL was used as solvent, the formation of Zn-MOFs at room temperature can be accelerated. The reaction duration was significantly shortened to 6 hours in IL, while the most widely used solvent system, dimethylformamide (DMF) needs at least 120 hours to complete [1].

Materials and Methods

Materials

All reagents and solvents were commercially purchased and used without further purification.

Synthesis of ILs

40 mmol of 1-bromohexadecane and 33 mmol of pyridine were mixed and the mixture was added into 10 mL of 95% ethanol. The mixture was then refluxed at 170°C for 24 hours. The resulting mixture was cooled below freezing point to allow precipitation and the precipitate was dissolved in a small amount of acetonitrile, before reforming again the solid by adding diethyl ether. The final product was filtered and dried at room temperature for several days. (Product = white solid, Yield = 96%)

Synthesis of Zn-BTC and Zn-BDC

Zinc nitrate hexahydrate ($Zn(NO_3)_2.6H_2O$) was mixed with benzene-1,3,5-tricarboxylic acid (H_3BTC) ligand, with and without the addition of TEA in 10 ml of 1-hexadecylpyridinium bromide IL media. The ratio used for the reaction mixture was 6:1 of metal to ligand ratio. The mixture was then stirred at room temperature for 6 hours and washed with methanol twice to remove the unreacted solvent and precursors. The white solid product was collected by centrifugation and dried at room temperature for several days.

For the synthesis of Zn-BDC

The organic ligand was changed to benzene-1,4-dicarboxylic acid (H_2BDC) and other experimental conditions were the same with those above. Table 1 shows the list of starting materials used in the synthesis and the metal: ligand ratio for all compounds.

Table 1. Starting materials and metal: ligand ratio for each compound

Compound	Metal Source	Ligand	Metal: Ligand Ratio	Addition of *TEA
1 (Zn-BDC)	$Zn(NO_3)_2.6H2O$	H_2BDC	6:1	Yes
2 (Zn-BDC)	$Zn(NO_3)_2.6H2O$	H_2BDC	6:1	No
3 (Zn-BTC)	$Zn(NO_3)_2.6H2O$	H_3BTC	6:1	Yes
4 (Zn-BTC)	$Zn(NO_3)_2.6H2O$	H_3BTC	6:1	No

For the synthesis of compounds 2 and 4 (without the addition of TEA), no solid product formed after washing with methanol, indicating the importance of TEA to facilitate the reaction. Yield for 1, 67%, and for 3, 75% (based on the organic ligand used).

Characterizations

Powder X-ray Diffraction (PXRD) data were recorded at ambient temperature on a Shimadzu-600 diffractometer with Cu Kα radiation (λ=15406Å, 30kV, and 40 mA) with a scan speed of 2° min^{-1} and a step size of 0.02° in 2theta. Fourier Transform Infrared Spectroscopy (FTIR) spectra were obtained using IRTracer-100 by Shimadzu FTIR spectrometer with sample powders in the range of 4000-400 cm^{-1}.

Results and Discussion

Ligands with simple configurations were used in this study to eliminate the effects on the structure and by fixing the experimental conditions of the starting materials, the reaction temperatures and time, we successfully synthesized Zn-BDC and Zn-BTC compounds. Both were obtained from the reactions between Zn^{2+}, and BTC^{3-} or BDC^{2-} in ILs.

A white precipitate was observed almost immediately when all of the materials were mixed and stirred rapidly at room temperature. They were synthesized through similar synthesis conditions at room temperature with the only differences were the ligands used and whether there is an addition of TEA. Figure 1 showed the organic ligands used in this study.

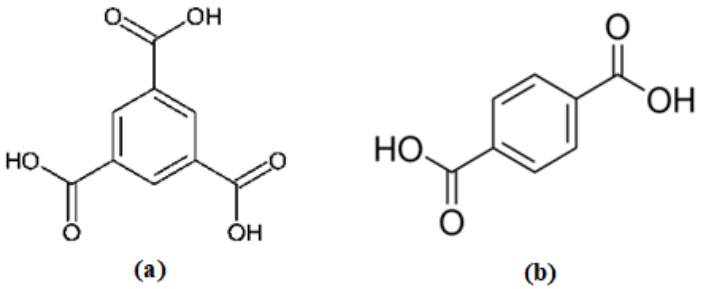


Figure 1. a) benzene-1,3,5-tricarboxylic acid (H_3BTC) and b) benzene-1,4-dicarboxylate (H_2BDC)

Fourier transform infrared spectroscopy spectra of Zn-BDC and Zn-BTC

Figure 2 shows the FT-IR spectra of both newly synthesized Zn-based MOFs. Two sharp peaks were obtained at 1551 cm^{-1} and 1360 cm^{-1} in sample Zn-BDC and 1602 cm^{-1} and 1370 cm^{-1} in sample Zn-BTC. Several small peaks were seen in the range of 1130-900 cm^{-1} and 570-850 cm^{-1} in both samples. A broad peak at around 3200 cm^{-1} in sample Zn-BDC and small peaks at 2917 and 2965 cm^{-1} in sample Zn-BTC were also seen. The characteristic absorption peaks of the main functional groups for these compounds are listed in Table 2.

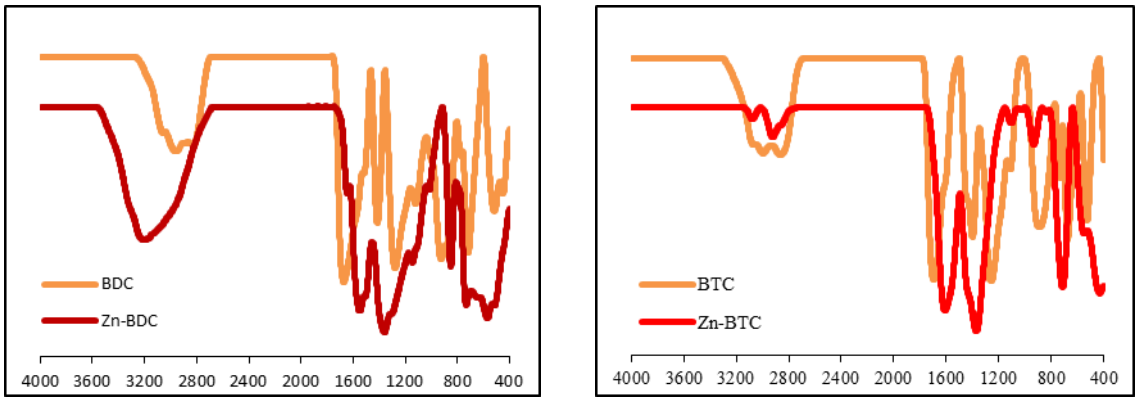


Figure 2. FTIR spectra a) the overlap between ligand BDC and Zn-BDC and b) the overlap between ligand BTC and Zn-BTC

The FTIR spectra (Figure 1) confirm the presence of all the functional groups present in Zn-BDC and ZN-BTC, respectively. The two sharp intense peaks at 1551 cm^{-1} and 1360 cm^{-1} are characteristic of the symmetric and asymmetric stretching of C-O bonded to benzene ring present in the ligand [4, 11]. The above stretching was shifted to lower wave numbers, compared to carbonyl frequencies of free BDC ligand (1680 cm^{-1}). The shifting of COO^- stretching was around 200 cm^{-1}, the characteristic for coordinated carboxylate groups. Several small peaks in the region of 570-850 cm^{-1} are because of the in-plane and out of the plane stretching of the aromatic C-H groups of the benzene ring present in BDC ligand [4,11]. The broad peak around 3200 cm^{-1} also are because of the adsorbed moisture content on the MOF structure, probably coming from the water used to dissolve IL. For Zn-BTC, the sharp

intense peaks at 1602 cm^{-1} and 1370 cm^{-1} are characteristic of the symmetric and asymmetric stretching of C-O bonded to benzene ring present in the ligand, corresponds to the characteristic of published Zn-BTC [4]. The above stretching was shifted to lower wave numbers, compared carbonyl frequencies of free BTC ligand (1636 cm^{-1}). The difference was around 200 cm^{-1}, which is the characteristic for coordinated carboxylate groups. Several small peaks in the region of 570-1000 cm^{-1} are because of the in-plane and out of the plane stretching of the aromatic C-H groups of the benzene ring present in BTC ligand.

Table 2. The main IR characteristic absorption peaks for both compounds

Compound	δ(C=O), cm^{-1}	δ(O-H), cm^{-1}	δ(C-H), cm^{-1}
Zn-BDC	1551,1360	3500-2700	980,519
Zn-BTC	1602,1370	3100-2700	950,514
BDC	1680	3200-2700	991,554
BTC	1636	3200-2600	899,584

Powder X-ray diffraction pattern of Zn-BDC and Zn-BTC

The X-ray diffractograms of the samples are shown in Figure 3. Zn-BDC product was observed as a single-phase, meanwhile Zn-BTC gave two phases under the conditions given in the experimental section as shown in the PXRD patterns in Figure 3. However, the experimental PXRD patterns of both compounds matched well with the simulated PXRD obtained from the single crystal structure data of published Zn-BDC and Zn-BTC, where the well-characterized peaks can be seen in the experimental pattern. Sample of the newly synthesized Zn-BDC and Zn-BTC showed a sharp intense peak at 8.94° and 9.89°, respectively. The spectra correspond with that of the pattern obtained by [11]. It is evident that both the samples are highly crystalline in nature thus, showed that in order to produce highly crystalline MOFs, heating is not required [4, 11].

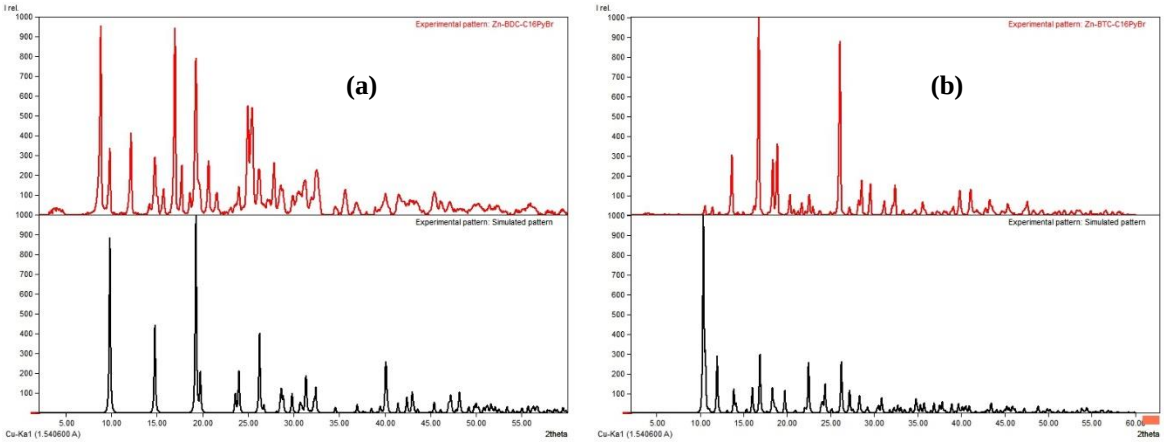


Figure 3. The comparison of the experimental PXRD patterns, in red of as-synthesized a) Zn-BDC and b) Zn-BTC to those simulated patterns, in black

Addition of the weak base, triethylamine (TEA) to deprotonate the organic ligands in order to precipitate MOF is required as without the addition of base, products were not formed. This showed that the use of TEA as a base is necessary when zinc nitrate is used as the metal source of Zn^{2+} in the Zn-MOF synthesis [4]. In this study, ILs have been found to significantly accelerate the MOFs formation at room temperature as the reaction duration is significantly reduced to 6 hours in IL for MOF formation, meanwhile the organic solvent DMF needs at least 120 hours [1]. Further nucleation and crystallization studies need to be done to understand how IL affects the reaction time.

Conclusion

In this study, we have explored another efficient method that respects the principle of green chemistry using a new solvent system to synthesis Zn-MOFs at room temperature. The FTIR and PXRD results demonstrate that Zn-BDC and Zn-BTC can be reproduced using this environmental-friendly method. This rapid, and low energy method was proven to provide a way of accelerating the formation of MOF. Further studies are currently undergoing to investigate whether this system of using IL has effects on the structure of MOFs or may even give new MOF compounds with desired structures and properties. Another study to produce MOF compounds with higher yields and better thermal stability can also be done to investigate its functions in various fields or applications.

Acknowledgement

The authors gratefully acknowledge the Putra Grant (UPM/700-2/1/GBP/2018/9598600) from Universiti Putra Malaysia (UPM).

References

1. Sang, X., Zhang, J., Xiang, J., Cui, J., Zheng, L. and Zhang, J. (2017). Ionic liquid accelerates the crystallization of Zr-based metal-organic framework. *Nature Communications*, 8(175): 1-7.
2. Zhang, Z. H., Liu, B., Xu, L. and Jiao, H. (2015). Combination effect of ionic liquid components on the structure and properties in 1,4-benzene-dicarboxylate based zinc metal-organic frameworks. *The Royal Society of Chemistry. Dalton Transactions*, 44: 17980-17989.
3. Xu, L., Choi, E. Y. and Kwon, Y. U. (2007). Ionothermal synthesis of six three-dimensional zinc metal-organic frameworks with 1-alkyl-3-methylimidazolium bromide ionic liquids as solvents. *Inorganic Chemistry*, 46(25): 10670-10680.
4. Tranchemontagne, D. J., Hunt, J. R. and Yaghi, O. M. (2008). Room temperature synthesis of metal-organic frameworks: MOF-5, MOF-74, MOF-177, MOF-199 and IRMOF-0. *Elsevier, Tetrahedron*, 64: 8553-8557.
5. Gao, J., Ye, K., Tang, L., Xiong, W. W., Ye, L., Wang, Y. and Zhang, Q. (2014). Growing crystalline zinc-1,3,5-benzenetricarboxylate metal-organic frameworks in different surfactants. *American Chemical Society. Inorganic Chemistry*, 53: 691-693.
6. Mohamed Isa, E. D., Abdul Rahman, M. B. and Ahmad, H. (2018). Monodispersed mesoporous silica nanoparticles based on pyridinium ionic liquids. *Journal of Porous Materials*, 25(5): 1439-1446.
7. Vaid, T. P., Kelley, S. P. and Rogers, R. D. (2017). Structure-directing effects of ionic liquids in the ionothermal synthesis of metal-organic frameworks. *Topical Reviews, IUCrJ*, 4: 380-392.
8. Sang, X., Zhang, J., Peng, L., Liu, C., Ma, X., Han, B. and Yang, G. (2015). Assembly of mesoporous metal-organic framework templated by an ionic liquid/ethylene glycol interface. *Wiley, ChemPhysChem Communications*, 16: 2317-2321.
9. Eddaoudi, M., Moler, D. B., Li, H., Chen, B., O'Keeffe, M. and Yaghi, O. M. (2000). Modular chemistry: Secondary building units as a basis for the design of highly porous and robust metal-organic carboxylate frameworks. *American Chemical Society, Accounts of Chemical Research*, 34(4): 319-330.
10. Chen, R., Zhang, J., Chelora, J., Xiong, Y., Kershaw, S. V., Li, K. F., Lo, P., Cheah, K. W., Rogach, A. L. Zapien, J. A. and Lee, C. (2017). Ruthenium(II) complex incorporated UiO-67 metal-organic framework nanoparticles for enhanced two-photon fluorescence imaging and photodynamic cancer therapy. *American Chemical Society, Applied Material and Interfaces*, 9: 5699-5708.
11. Iswarya, N., Kumar, M. G., Rajan, K. S. and Balaguru, R. J. B. (2012). Synthesis, characterization and adsorption capability of MOF-5. *Science Alert, Asian Journal of Scientific Research*, 5(4): 247-254.

Malaysian Journal of Analytical Sciences (MJAS)
Published by Malaysian Analytical Sciences Society

DEVELOPMENT AND VALIDATION OF HPLC METHOD FOR QUANTIFICATION OF DOCETAXEL IN PALM-BASED NANOEMULSION AEROSOLS

(Pembangunan dan Validasi Kaedah KCPT untuk Kuantifikasi Docetaxel di dalam Nanoemulsi Aerosol Berasaskan Sawit)

Azren Aida Asmawi[1], Norazlinaliza Salim[1,2], Emilia Abdulmalek[1,2], Mohd Basyaruddin Abdul Rahman[1,2]*

[1]*Integrated Chemical BioPhysics Research, Faculty of Science*
[2]*Department of Chemistry, Faculty of Science*
Universiti Putra Malaysia, 43400 UPM Serdang, Selangor, Malaysia

**Corresponding author: basya@upm.edu.my*

Received: 20 November 2019; Accepted: 3 March 2020

Abstract

Lung cancer is the leading cause of cancer-related deaths worldwide. Among the most potent of chemotherapeutic drugs used for lung cancer treatment are the taxanes, including docetaxel. However, the drugs' efficacy in combating the disease is reduced due to their poor solubility, low stability and high toxicity. Inhalation therapy of lipid-based carrier has great potential in direct target towards the respiratory diseases. Hence, application of aerosolized palm-based nanoemulsion system is one approach to alleviate the drawbacks. This study describes the development and validation of method that can quantitate the amount of docetaxel nanoemulsion formulation via high-performance liquid chromatography (HPLC). Chromatographic analysis was conducted using a reversed phase C_{18} column with a mixture of acetonitrile and water (50:50) adjusted to pH 3.0 as the mobile phase. The flow rate was 1.0 mL/min and the detection was carried out by ultraviolet-visible detector at 228 nm. The developed method was validated in terms of specificity, linearity, accuracy and precision accordance with the International Conference on Harmonization (ICH) guidelines. The calibration curve was linear (r^2 = 0.999) over the concentration range from 62.5 to 1000 µg/mL with lower limit of detection (LOD) of 9.88 µg/mL and lower limit of quantification (LOQ) of 29.93 µg/mL. The percentage relative standard deviation for both intra and inter-day precision was less than 2%, while percentage recovery was more than 90%, indicating the precision and accuracy of the study. The developed HPLC method was proved as suitable and reliable for its intended application.

Keywords: aerosols, docetaxel, high-performance liquid chromatography, nanoemulsion, lung cancer

Abstrak

Kanser paru-paru adalah punca utama kematian akibat kanser di seluruh dunia. Antara ubat kemoterapi yang berkesan digunakan untuk rawatan kanser paru-paru ialah taxane, termasuk docetaxel. Walau bagaimanapun, keberkesanan ubat dalam merawati penyakit ini berkurangan disebabkan oleh kelarutannya yang kurang baik, kestabilan yang rendah dan ketoksikan yang tinggi. Oleh itu, penggunaan sistem nanoemulsi berasaskan sawit adalah satu pendekatan untuk mengurangkan kelemahan tersebut. Kajian ini menerangkan pembangunan dan validasi yang boleh mengkuantifikasi jumlah docetaxel di dalam rumusan nanoemulsi melalui kaedah kromatografi cecair prestasi tinggi (KCPT). Analisis kromatografi dijalankan menggunakan turus fasa terbalik C_{18} dengan campuran asetonitril dan air (50:50) diselaraskan kepada pH 3.0 sebagai fasa bergerak. Kadar aliran adalah 1.0 mL/min dan pengesanan dilakukan oleh pengesan ultralembayung-nampak pada 228 nm. Kaedah yang dibangunkan telah disahkan dari segi kekhususan, kelinearan, kejituan, ketepatan dan kepersisan berdasarkan garis panduan persidangan pengharmonian antarabangsa (ICH). Plot tentukuran adalah linear (r^2 = 0.999) di atas kepekatan antara 62.5 hingga 1000 µg/mL dengan had pengesanan (LOD) iaitu 9.88 µg/mL dan had kuantifikasi (LOQ) sebanyak 29.93 µg/mL. Peratusan sisihan piawai relatif untuk kedua-dua kepersisan intra dan inter-hari adalah kurang daripada 2%, manakala purata kejituan adalah lebih

daripada 90%, menunjukkan kepersisan dan ketepatan kajian. Kaedah KCPT yang dibangunkan terbukti sesuai dan boleh digunakan untuk aplikasi yang dirancangkan.

Kata kunci: aerosol, docetaxel, kromatografi cecair prestasi tinggi, nanoemulsi, kanser paru-paru

Introduction

Docetaxel (DTX) is a chemotherapeutic drug derived from a natural inactive precursor of 10-deacetyl baccatin III, extracted from the Yew plant (Taxus genus). DTX is approved by the Food and Drug Administration (FDA) for the treatment of non-small-cell lung cancer (NSCLC) as a mitosis inhibitor in cell division *via* stabilization of the polymerization and de-polymerization of microtubules [1, 2]. However, poor water solubility, low stability and high toxicity of DTX has reduced its therapeutic index in combating the disease [3, 4]. Therefore, increasing the bioavailability and minimizing the side effects of DTX remain challenges in the lung cancer therapy.

Inhalation therapy of lipid-based carrier system has gained considerable attention for local non-invasive drug delivery. This system is a suitable alternative to deliver high local drug concentration to the desired region in the lungs, while significantly reduces the toxicity towards healthy cells [5–7]. Hence, research focus has shifted to the use of encapsulated DTX in palm-based nanoemulsion aerosols for pulmonary drug delivery to overcome the challenges. Investigations on aerosolization properties of the formulation using multistage cascade impactor was essential to quantitate the amount of DTX deposited and to predict the site of deposition in the lungs' region.

In this paper, the development and validation of a simple, precise and accurate reversed-phase high performance liquid chromatography-ultra violet (RP-HPLC-UV) analytical method to detect DTX in palm-based nanoemulsion aerosols was investigated. The validation method was accomplished according to the International Conference on Harmonisation (ICH) Q2 (R1) guidelines. Additionally, the method can be used for quantification of DTX in other type of nanoparticles.

Materials and Methods

Materials

Docetaxel (DTX) (98% purity) and trifluoroacetic acid (99% extra purity) were purchased from Acros Organics, UK. Lecithin Lipoid S75 was purchased from Lipoid via GmbH, Germany. Safflower seed oil, Tween® 85 and Span® 85 were purchased from Sigma-Aldrich, Germany. Palm kernel oil esters (PKOEs) was synthesized enzymatic alcoholysis of oleyl alcohol and palm kernel oil (3:1) catalysed by Lipozyme RM IM [8]. HPLC-grade acetonitrile and glycerol were purchased from J.T. Baker, USA while HPLC-grade methanol was purchased from Merck, Germany. Deionized water was generated using Milli-Q gradient water system (Billerica, USA).

Instrument and chromatographic conditions

Chromatographic analysis for detection of DTX was performed using the high-performance liquid chromatography (HPLC) (Waters, USA) equipped with Breeze software, dual GM150 gradient mixers in the 1525 pump, waters 2489 UV/Visible detector and C_{18} analytical column with particle size of 5 µm and dimension of 4.6 x 150 mm (Eclipse plus, Agilent Technologies, USA). The mobile phase was composed of filtered acetonitrile and deionized water (50:50, v/v) adjusted to pH 3.0 with trifluoroacetic acid. The analysis was performed at room temperature by isocratic elution at flow rate of 1.0 mL/min, with UV-vis detector set at 228 nm and injection volume of 10 µL. The sample solutions were filtered using polyvinylidene difluoride (PVDF) 0.45 µm prior to injection.

Preparation of nanoemulsion sample

A stable of DTX-loaded nanoemulsion was prepared with 0.1% DTX, 5.0 wt.% palm kernel oil esters (PKOEs) and safflower seed oil (9:1, w/w), 2.5 wt.% lecithin, 2.0 wt.% Tween® 85 and Span® 85 (9:1), 2.5 wt.% glycerol, and 87.9 wt.% water using high energy emulsification techniques. Lecithin was first dissolved in a mixture of PKOEs and safflower seed oil at 40 °C for 30 minutes before being mixed with DTX and mixture of Tween 85 and Span 85 for 30 minutes. The coarse emulsion was prepared by adding the oil phase dropwise into the aqueous phase containing deionized water and glycerol for 30 minutes at 350 rpm using overhead stirrer. The coarse emulsion was then further subjected to high shear homogenizer for 15 minutes at 12,000 rpm.

Preparation of standard solution
Stock solution of DTX was prepared by accurately weighed 10 mg of DTX and was added into a 5 mL volumetric flask. The flask was filled and dissolved with methanol to the mark to get a 2000 µg/mL stock concentration. The two-fold serial dilution factor in the range 62.5-1000 µg/mL was prepared by serially reducing the concentration by one half. The HPLC methods in quantification of DTX solutions were validated using specificity, linearity, sensitivity, repeatability and accuracy tests according to the guidelines from International Conference on Harmonisation.

Specificity and system suitability
Specificity is the ability of the developed method to distinguish and separate analyte and other component in the sample matrix [9]. A volume of 0.5 mL blank nanoemulsion formulation was spiked with 0.5 mL of DTX solution at concentration of 125 µg/mL. The mixture was vortexed vigorously and analysed using HPLC method as described above. The system suitability including asymmetric peak, tailing factor and number of theoretical plates were determined.

Linearity test
Five standard concentrations of 62.5, 125, 250, 500 and 1000 µg/mL were used in the preparation of standard plot of DTX. Three replicates (n = 3) at each concentration of DTX were analysed using HPLC method as described above. The slope and intercept of calibration plot was calculated for regression analysis in order to determine the linearity of the plot and the significance of linear regression was confirmed by one-way ANOVA test.

Sensitivity test
The sensitivity for detection of DTX was determined by evaluating the limit of detection (LOD) and limit of quantification (LOQ) of the analyte. According to ICH guidelines, the LOD of the analyte response is the lowest amount of analyte in the sample can be detected while the analyte response (signal) at the LOQ should be at least 10 times the response compared to blank response (noise) with suitable accuracy and precision. The LOD and LOQ of the response analyte were calculated using the following equations:

$$LOD = 3.3 \times \sigma/S \quad (1)$$

$$LOQ = 10 \times \sigma/S \quad (2)$$

where, σ is the standard deviation of intercept of calibration plot and S is the average of the slope of the corresponding calibration plot.

Precision and repeatability test
Intra-day (n = 3) and inter-day (n = 3) variation studies were determined by evaluating precision and repeatability over one and three days, respectively. Standard concentrations of DTX were prepared accordance with the method as described in preparation of standard solution section and were analysed using HPLC method as described above. The percentage of coefficient of variation (%CV) was calculated for each sample analysed in order to evaluate the closeness of the analytes response obtained from the same measurement procedures and conditions. The %CV was calculated using the following formula:

$$\%CV = (\sigma/\mu) \times 100 \quad (3)$$

where, σ is the standard deviation and μ is the sample mean.

Accuracy test
The recovery studies were carried out in triplicates by adding 62.5 µg/mL of analyte to four standard concentrations of 125, 250, 500 and 1000 µg/mL; thus, the final nominal concentrations were 93.75, 156.25, 281.25 and 531.25 µg/mL. The concentration of DTX in prepared solutions was analysed using HPLC method as described above and the mean percent recovery was then calculated. According to the ICH guidelines, accuracy is the closeness of agreement between the analyte of known concentration and the values found. The acceptance mean value should be within 15% of the nominal values.

Cascade impactor analysis

The evaluation of aerosolization performance of the palm-based nanoemulsion formulation was performed using eight –stage Andersen cascade impactor (ACI; Copley Scientific Ltd, UK). A sample of 3 mL was nebulized via OMRON MicroAIR nebulizer into the ACI that connected to vacuum pump with flow rate of 15 L/min on a continuous mode. The drug content on each stage of ACI including inlet cone, induction port, mouthpiece and adapter were quantitated using HPLC method as described above. The aerosolization properties including emitted dose (ED), deposited dose (DD) and fine particle dose less than 5 µm ($FPD_{<5\ \mu m}$) were calculated. The ED depicted as the cumulative percentage of DTX content collected from induction port, all stages (0 – 7) and the filter, while DD was the cumulative percentage of DTX content deposited on all stages (0 – 7) and the filter. The $FPD_{<5\ \mu m}$ was the percentage of DTX deposited on stage 3 to filter.

Results and Discussion

The HPLC method was developed to select chromatographic conditions including stationary phase, mobile phase and wavelength for detection. For this purpose, preliminary trials were performed by varying the conditions. After the optimization, the chromatographic conditions as described in previous section were used for the method validation. Specificity was indicated by the absence of any significant interfering peak in the chromatograms of blank sample and blank sample spiked with the analyte. From the chromatogram of blank palm-based nanoemulsion sample, selectivity was proved as no interfering endogenous peaks were found at the retention time of DTX, which was eluted at 3.12 minutes (Figure 1). The asymmetry (A_S) of DTX peak was found to be nearly symmetrical in shape with A_S value close to 1 and tailing factor value equal to 1 representing a Gaussian peak distribution [10]. Moreover, the number of theoretical plates which is used to measure column efficiency was higher than 1000. The results of system suitability are summarized in Table 1.

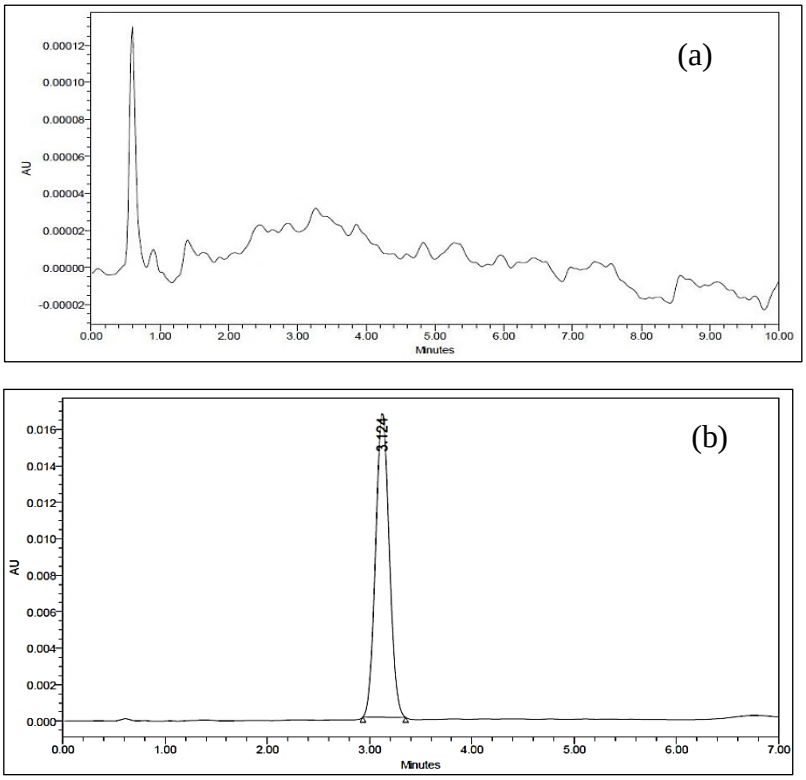


Figure 1. Chromatogram for (a) blank palm-based nanoemulsion sample and, (b) blank palm-based nanoemulsion sample spiked with DTX at 62.5 µg/mL

Table 1. Results of system suitability

Validation Parameter	
Retention time (min)	3.12
Asymmetry of peak	1.01
Tailing factor	1.00
Number of theoretical plates	1936

Calibration curve was constructed using the five-standard concentration of DTX in the range of 62.5 µg/mL and 1000 µg/mL against the mean peak area of DTX. A good linear relationship with equation of y = 624.94x – 341.33 was established between the peak area and DTX concentrations over the range tested (Figure 2). It was confirmed by the regression correlation coefficient value close to 1 (R^2 = 0.9999) indicating of strong positive linear correlation between the DTX concentration and the obtained peak area. ANOVA analysis also showed that the positive regression model is statistically significant ($p < 0.05$) to predict the response. The model *F* value also implies that the model is significant and less than 0.01% chance that the model *F*-value could occur due to noise (Table 2). The LOD and LOQ of DTX determined from the standard deviation of the regression line were found to be 9.88 µg/mL and 29.93 µg/mL, respectively.

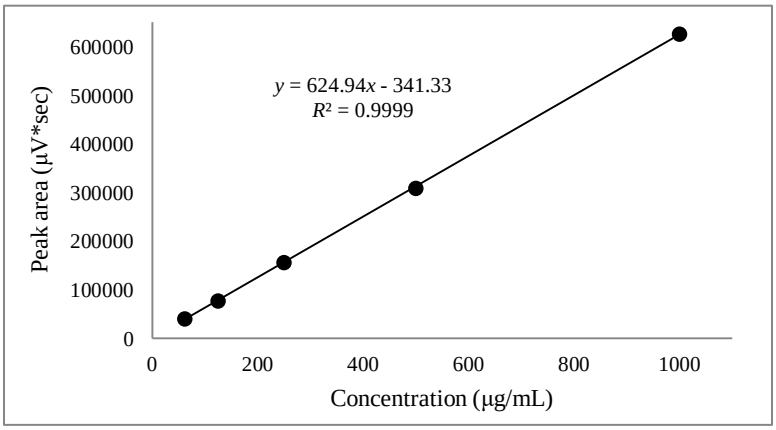


Figure 2. Calibration curve of DTX in concentration range of 62.5 – 1000 µg/mL

Table 2. Results of ANOVA analysis for calibration curve of DTX

ANOVA[b]	**Sum of squares**	**df**	**Mean square**	***F***	**Significance**
Regression	2.28*E*11	1	2.28*E*11	1.49*E*4	<0.0001[a]
Residual	4.58*E*6	3	*1.53E*6		
Total	2.28*E*11	4			

[a]Predictor: (constant), conc, [b]dependent variable: area

The intra-day and inter-day precision and repeatability for DTX were both found to be between 0.8-1.9%. In both cases, the percentage of CV values was found to be within the acceptable limits of ICH specification which is less than 2%. Therefore, the method is demonstrated to be precise and reproducible with less variation in the results regardless of whether the quantification of DTX (similar experiment) is perform several times within-day (intra-day) or between-day (inter-day). The percentage of CV value for precision and repeatability is summarized in Table

3. The results of accuracy study (Table 4) demonstrated of high rate of recovery from 93.3 to 99.9% over its therapeutic range. Furthermore, the CV value between the measurements in all concentrations did not exceed 5%. The method was proven to be accurate in quantitating DTX where the measured concentrations were close to the nominal concentrations.

Table 3. Results of precision and repeatability for determination of DTX

Concentration (µg/mL)	Intra-day (n = 3)			Inter-day (n = 3)		
	MC (µg/mL)	SD	CV (%)	MC (µg/mL)	SD	V (%)
62.50	64.31	0.97	1.5	62.67	1.20	1.9
125.00	124.67	0.94	0.8	124.07	1.84	1.5
250.00	252.38	4.88	1.9	252.81	3.92	1.6
500.00	494.44	4.66	0.9	490.13	4.12	0.8
1000.00	1008.33	15.65	1.6	1014.35	16.25	1.6

MC: mean concentration, SD: standard deviation, CV: coefficient of variation

Table 4. Results of accuracy for determination of DTX

Initial Concentration (µg/mL)	Added Concentration (µg/mL)	Nominal Concentration (µg/mL)	Recovery Concentration (µg/mL)	Accuracy (%)
62.50	62.50	62.50	59.77	95.6
125.00	62.50	93.75	87.45	93.3
250.00	62.50	156.25	156.44	99.9
500.00	62.50	281.25	266.17	94.6
1000.00	62.50	531.25	507.06	95.5

Successful drug delivery into the lungs *via* inhalation depends greatly on the aerosolization performance of its carrier system, which related directly to its aerodynamic properties. The use of ACI benefits the preliminary screening on DTX-loaded palm-based nanoemulsion formulations to possibly correlate the lung deposition based on mass of the deposited drug. In this study, most of DTX was deposited on stage 3 to 6 (Table 5), representing aerodynamic diameter cutoff of 4.53, 2.88, 1.51 and 0.96 µm, respectively [11]. Moreover, studies have demonstrated that, nanocarrier with aerodynamic diameter of less than 5 µm has a capability to deposit in the lower airways including alveolar region, where the tumors are normally found and absorption mainly occurred [7, 12, 13].

Table 6 summarized the aerosolization properties of nebulized DTX-loaded nanoemulsion calculated based on the amount of DTX deposited on stages of ACI. The aerosolized nanoemulsion emitted 85.4% of loaded drug while remaining drug might be trapped in the sampling apparatus including nebulizer. It was also found that, more than 75% of the loaded drug able to deposit on ACI stages (stage 0 – 7 and filter) which mimic the pulmonary region of human lungs. On top of that, a high deposition of drug in the lower stage of cascade impactor was obtained, as almost 71.8% of total drug deposited on stage 3 and below ($FPD_{<5\mu m}$).

Table 5. Amount of DTX deposited on stages of Anderson cascade impactor

Site of Deposition	Amount of DTX Deposited (µg)
Nebulizer	241.12 ± 36.80
Induction port	13.17 ± 6.74
Inlet cone	ND
Stage 0	34.74 ± 9.04
Stage 1	31.47 ± 16.41
Stage 2	86.73 ± 20.88
Stage 3	289.73 ± 27.71
Stage 4	757.91 ± 118.51
Stage 5	823.73 ± 59.60
Stage 6	212.70 ± 101.15
Stage 7	71.09 ± 22.60
Filter	ND

ND: not detected

Table 6. Aerosolization properties of nebulized DTX-loaded nanoemulsion

Parameter	
Emitted dose (DD), %	85.4 ± 3.8
Deposited dose (ED), %	75.8 ± 2.5
Fine particle dose ($FPD_{<5\mu m}$), %	71.8 ± 2.1

Conclusion

The proposed HPLC method was successfully developed and validated according to ICH guidelines and was found to fulfill the requirements and exhibited acceptable values of recovery. The method was found to be simple, fast, precise and highly accurate for analysis of DTX in palm-based nanoemulsion sample and can readily be used for quantitative analysis of DTX in many studies including stability, drug entrapment, and drug release.

Acknowledgement

This work was supported by the Universiti Putra Malaysia (UPM) and LRGS NanoMITe-Ministry of Higher Education, Malaysia (RU029-2014/5526306).

References

1. Gubens, M. A. and Wakelee, H. A. (2010). Docetaxel in the treatment of non-small cell lung carcinoma: an update and analysis. *Lung Cancer (Auckland)*, 1: 63-76.
2. Varshosaz, J., Taymouri, S., Hassanzadeh, F., Javanmard, S. H. and Rostami, M. (2015). Self-assembly micelles with lipid core of cholesterol for docetaxel delivery to B16F10 melanoma and Hepg2 cells. *Journal of Liposome Research*, 25(2): 157-165.
3. Zhang, L., Tan, L., Chen, L., Chen, X., Long, C., Peng, J. and Qian, Z. (2016). A simple method to improve the stability of docetaxel micelles. *Scientific Reports - Nature*, 6 (36957): 1-10.
4. Liu, Z., Liu, D., Wang, L., Zhang, J. and Zhang, N. (2011). Docetaxel-loaded Pluronic P123 polymeric micelles: in vitro and in vivo evaluation. *International Journal of Molecular Sciences*, 12(3): 1684- 1696.

5. Nesamony, J., Shah, I. S., Kalra, A. and Jung, R. (2014). Nebulized oil-in-water nanoemulsion mists for pulmonary delivery: Development, physico-chemical characterization and in vitro evaluation. *Drug Development and Industrial Pharmacy*, 40(9): 1253-1263.
6. Xia, D., Sun, W. K., Tan, M. M., Zhang, M., Ding, Y., Liu, Z. C., Su, X. and Shi, Y. (2015). Aerosolized amphotericin B as prophylaxis for invasive pulmonary aspergillosis: A meta-analysis. *International Journal of Infectious Diseases*, 30: 78-84.
7. Ngan C. L. and Asmawi, A. A. (2018). Lipid-based pulmonary delivery system: A review and future considerations of formulation strategies and limitations. *Drug Delivery and Translational Research*, 8 (5): 1527-1544.
8. Keng, P. S., Basri, M., Zakaria, M. R. S., Rahman, M. B. A., Ariff, A. B., Rahman, R. N. Z. A. and Salleh, A. B. (2009). Newly synthesized palm esters for cosmetics industry. *Industrial Crops and Products*, 29(1): 37-44.
9. Che, H. L., Tan, D. M. Y., Meganathan, P., Gan, Y. L., Abdul Razak, G. and Fu, J. Y. (2015). Validation of a HPLC/FLD method for quantification of tocotrienols in human plasma. *International Journal of Analytical Chemistry*, 2015: 1-7.
10. Le, T. H. H., Phung, T. H. and Le, D. C. (2019). Development and validation of an HPLC method for simultaneous assay of potassium guaiacolsulfonate and sodium benzoate in pediatric oral powder. *International Journal of Analytical Chemistry*, 2019: 1-9.
11. Shah, K., Chan, L. W. and Wong, T. W. (2017). Critical physicochemical and biological attributes of nanoemulsions for pulmonary delivery of rifampicin by nebulization technique in tuberculosis treatment. *Drug Delivery*, 24(1): 1631-1647.
12. Shin, S. W., Song, I. H. and Um, S. H. (2015). Role of physicochemical properties in nanoparticle toxicity. *Nanomaterials*, 5(3): 1351-1365.
13. Ezzati N. D. J., Hamishehkar, H. and Valizadeh, H. (2015). Development of dry powder inhaler formulation loaded with alendronate solid lipid nanoparticles: Solid-state characterization and aerosol dispersion performance. *Drug Development and Industrial Pharmacy*, 41(9): 1431-1437.

Malaysian Journal of Analytical Sciences (MJAS)
Published by Malaysian Analytical Sciences Society

PHYTOCHEMICAL SCREENING AND ANTIOXIDANT ACTIVITY OF *Psidium guajava*

(Saringan Fitokimia dan Aktiviti Antioksidan terhadap *Psidium guajava*)

Nor Akmalazura Jani[1]*, Nurul Alia Ahmad Azizi[1], Nurul Iman Aminudin[2]

[1]*Faculty of Applied Sciences,*
Universiti Teknologi MARA, Cawangan Negeri Sembilan, Kampus Kuala Pilah,72000 Kuala Pilah, Negeri Sembilan, Malaysia
[2]*Department of Chemistry, Kulliyyah of Science,*
International Islamic University Malaysia, Bandar Indera Mahkota, 25200 Kuantan, Pahang, Malaysia

**Corresponding author: NorAkmalazura@uitm.edu.my*

Received: 20 November 2019; Accepted: 11 February 2020

Abstract

Psidium guajava or commonly known as guava is useful to treat gastroenteritis, dysentery, stomach pain and indigestion. In this study, the leaves of this species were screened for its phytochemical and antioxidant activity. The phytochemicals were extracted by sequential maceration by using *n*-hexane, chloroform and methanol, while phytochemical screening was performed using various chemical tests. Meanwhile, its antioxidant activity was assessed by the 2,2-diphenyl-1-picrylhydrazyl (DPPH) assay. Steroids and terpenoids were found to be present in the *n*-hexane extract, while phenols and terpenoids were detected in the chloroform extract. The methanol extract contained flavonoids, steroids, saponins, phenols and terpenoids. Among the tested extracts, the methanolic extract demonstrated strong DPPH radical scavenging activity with an IC_{50} value of 45.52 µg/mL.

Keywords: *Psidium guajava*, phytochemical screening, antioxidant

Abstrak

Psidium guajava atau dikenali sebagai jambu batu berguna bagi mengubati gastroenteritis, disenteri, sakit perut dan masalah pencernaan. Dalam kajian ini, daun spesis ini telah disaring untuk fitokimia dan aktiviti antioksidan. Fitokimia telah diekstrak menggunakan rendaman berturutan menggunakan *n*-heksana, kloroform dan metanol, manakala saringan fitokimia telah dijalankan menggunakan pelbagai ujian kimia. Sementara itu, aktiviti antioksidan telah dinilai menggunakan kaedah 2,2-difenil-1-pikrilhidrazil (DPPH). Steroid and terpenoid telah didapati hadir di dalam ekstrak *n*-heksana, manakala fenol dan terpenoid telah dikesan di dalam ekstrak kloroform. Ekstrak metanol telah mengandungi flavonoid, steroid, saponin, fenol dan terpenoid. Di kalangan ekstrak yang diuji, ekstrak metanol menunjukkan aktiviti perencatan radikal DPPH yang kuat dengan nilai IC_{50} 45.52 µg/mL.

Kata kunci: *Psidium guajava*, saringan fitokimia, antioksidan

Introduction

Reactive oxygen species (ROS) such as superoxide ($O_2^{-\cdot}$), hydroxyl ($HO^{\cdot}$) and peroxide radicals ($ROO^{\cdot}$) are chemically reactive molecules that are produced from oxygen metabolism [1]. Their excessive production can cause severe damage to cells and tissues, loss of cellular function, oxidative stress, and ultimately, apoptosis or necrosis. Collectively, these damages are linked to many health issues, such as heart disease and carcinogenesis [2, 3]. In order to counteract the biomolecules against a ROS attack, antioxidants are needed to neutralise the excessive free radicals, protect the cells against their toxic effects and prevent diseases such as arthritis, stroke and chronic bronchitis [4]. In recent years, an intensive interest to search and identify natural and safe antioxidants, especially

those from a plant source has grown rapidly. These natural antioxidants may be either phenolic compounds (i.e. flavonoids, phenolic acids and tannins), nitrogen-containing compounds (i.e. alkaloids, amino acids, peptides and amines), carotenoids, tocopherols, or ascorbic acid and its derivatives [5].

Psidium guajava is commonly known as guave, goyave, or goyavier in France; guave, Guavenbaum, or Guayave in Germany; banjiro in Japan; goiaba or goiabeiro in Portugal; araçà-goiaba, araçà-guaçú, or guaiaba in Brazil; guayaba, or guayabo in Spain and guava in English [6]. This small tree is a native plant of tropical American regions, which is distributed throughout Southern Mexico, South America, European, Africa and Asia [6, 7]. Its leaves, barks, fruits, shoots and flower buds are applied for ethnomedicinal purposes, specifically in the treatment of several ailments such as gastroenteritis, dysentery, bacterial infection, diabetes, hypertension, caries and wounds, as well as a pain reliever and fever reducer. Meanwhile, this plant is also utilised commercially as food and in carpentry, house construction and toy manufacturing [6]. Biological investigations on *P. guajava* have revealed that its different extracts and isolated compounds exhibited antimicrobial, antihyperglycaemic, anti-inflammatory, analgesic, antipyretic, spasmolytic, central nervous system (CNS)–depressant, antidiarrhoeal, antimalarial, hepatoprotective, antigenotoxic, antimutagenic, antiallergic, antioxidant, anticancer, cardiovascular, hypotensive, antinociceptive and wound healing activities [6-8]. Furthermore, phytochemical studies undertaken by previous researchers have disclosed that this species can produce flavonoids, triterpenoids, tannins, phenolics, carotenoids and essential oils [6, 7, 9-14]. To date, there is only one study found detailing the phytochemical screening and antibacterial activity of *P. guajava* leaves extract, which have been collected from Selangor, Malaysia [14]. Accordingly, geographical distribution affects the chemical compositions of plants, while their biological activities are impacted conversely. In this study, the leaves of *P. guajava* were collected from Johor, Malaysia. The investigation was carried out to identify phytochemicals in the *P. guajava* leaves extracts and their relationship with the resulting antioxidant activity.

Materials and Methods

Plant material and preparation of extracts

The leaves of *P. guajava* were collected in February 2018 from Muar, Johor, Malaysia. The leaves were subjected to air-dried and ground into fine powder. The powdered leaves (200 g) were soaked sequentially with *n*-hexane (2 L), chloroform (2 L) and methanol (2 L) for three days each. The extracts were filtered using Whatman paper No. 1 and concentrated using a rotatory evaporator to afford *n*-hexane, chloroform and methanol extracts.

Phytochemical screening

The extracts were tested for the presence of alkaloids, flavonoids, phenolic compounds, terpenoids, steroids and saponins.

Test for alkaloids (Wagner's test)

Six drops of Wagner's reagent were added to 2 mL of crude extract. The Wagner's reagent was prepared by mixing iodine in potassium iodide solution. The formation of brown or reddish precipitate indicates the presence of alkaloids [15].

Test for flavonoids (Ferric chloride test)

Crude extract (2 mL) was treated with a few drops of ferric chloride solution. The intense green colour of the solution shows the presence of flavonoids [16].

Test for phenolics (Ferric chloride test)

A few drops of ferric chloride solution were added into each crude extract (2 mL). The appearance of a bluish black colour shows the presence of phenolic compounds [17].

Test for terpenoids (Salkowski test)

Each crude extract (1 mg) was mixed with chloroform (2 mL) and concentrated sulphuric acid (1 mL). The formation of reddish-brown colour at the interface indicates the presence of terpenoids [2].

Test for steroids (Salkowski test)
About 100 mg of dried crude extract was dissolved in 2 mL of chloroform. About 2-3 drops of sulphuric acid was carefully added to the extract to form a lower layer. A reddish-brown colour at the interface was indicative of the presence of steroidal ring [2, 18].

Test for saponins (Foam test)
Distilled water (2 mL) was added to 2 mL of crude extract. The mixture was shaken vigorously for 15 minutes period. The persistence of foam produced after 15 minutes indicates the presence of saponins [19].

Antioxidant assay
Antioxidant activity was performed using 2,2-diphenyl-1-picrylhydrazyl (DPPH) radical scavenging assay. The method was performed as described by the previous study with slight modifications [20]. Each sample (1.0 mg) was dissolved in methanol (1 mL) to obtain a stock concentration of 1000 µg/mL. The stock solution was further diluted to final concentrations of 500, 250, 125, 62.5, 31.3, 15.63 and 7.81 µg/mL in methanol. The DPPH solution was freshly prepared in MeOH to acquire final concentration of 50 µM. Then, 3.8 mL of DPPH solution was added to 0.2 mL of sample solution of different concentrations. The mixture was allowed to react at room temperature in the dark. After 30 minutes, the absorbance of the reaction mixture was recorded at 517 nm. Ascorbic acid was used as positive control, while the DPPH solution (3.8 mL DPPH and 0.2 mL methanol) was used as DPPH blank. The percentage inhibition (%) was calculated using the following formula [20]:

$$\text{Percentage Inhibition (\%)} = [A_{\text{DPPH blank}} - (A_{\text{Sample}} - A_{\text{blank sample}})] / A_{\text{DPPH blank}} \times 100 \quad (1)$$

where $A_{\text{DPPH blank}}$ is the absorbance of DPPH reagent and methanol, A_{sample} is the absorbance of sample solution with DPPH reagent and $A_{\text{blank sample}}$ is the absorbance of sample solution with methanol. The IC_{50} value was defined as the concentration of each sample required to scavenge 50% of the DPPH radical and was determined using GraphPad Prism 5. The assay was carried out in triplicate and the results were reported as means ± standard deviation. The Independent *t*-test was performed by using SPSS for Windows (version 22) software for comparison between samples and positive control. A value of $p < 0.05$ was considered significantly different.

Results and Discussion

Percentage yield of extracts
The removal of solvents under reduced pressure yielded *n*-hexane, chloroform and methanol extracts as shown in Table 1. The methanol extract gave the highest extraction yield of 9.65%, followed by chloroform (2.22%) and *n*-hexane (1.49%) extracts. These results indicate that the extraction yield increases alongside the increasing polarity of solvent utilized in the extraction process [21]. Therefore, the higher percentage yield shown by the methanol extract may be due to the high polarity of the methanolic solvent, which can extract abundant types of compounds [22].

Table 1. Yield of *P. guajava* leaves extracts

Extracts	Yield (g, %)
n-Hexane	2.98, 1.49
Chloroform	4.44, 2.22
Methanol	19.29, 9.65

Preliminary phytochemical screening
The results of qualitative phytochemical analysis for the *n*-hexane, chloroform and methanol extracts are presented in Table 2. From the findings, it was found that *n*-hexane extract contained steroids and terpenoids, while chloroform extract showed the presence of phenols and terpenoids. Flavonoids, steroids, saponins, phenols and terpenoids were detected in methanol extract. Furthermore, the current study revealed the existence of terpenoids in all extracts in which a reddish-brown colour was observed. However, these three extracts did not give brown or

reddish precipitate when treated with Wagner's reagent, thereby indicating the absence of alkaloids. The qualitative phytochemical analysis undertaken in this study showed identical findings for the existence of flavonoids and phenols compared to the reports by earlier researchers [11, 12, 14].

Table 2. Phytochemical screening of *P. guajava* leaves extracts

Phytochemicals	Extracts		
	***n*-Hexane**	**Chloroform**	**Methanol**
Alkaloids	-	-	-
Flavonoids	-	-	+
Steroids	+	-	+
Saponins	-	-	+
Phenols	-	+	+
Terpenoids	+	+	+

+ = present; - = absent

The phytochemicals detected in the leaves of *P. guajava* have been reported to offer countless benefits of medicinal importance. For examples, phenolics and flavonoids demonstrate many biological activities, such as antioxidant [23], antimicrobial [24], anticancer, anti-inflammatory and wound healing properties [25]. On the other hand, steroids are known to have antibacterial, insecticidal and cardiotonic properties [2], while saponins can treat diabetes [26]. Similarly, terpenoids have been used to alleviate human diseases such as cancer, malaria, inflammation and various infectious diseases [27].

DPPH radical scavenging activity

Data on the DPPH radical scavenging activity of *n*-hexane, chloroform and methanol extracts of *P. guajava* leaves along with the standard antioxidant, ascorbic acid is presented in Table 3. The samples that showed $p < 0.05$ were considered to have a statistically significant difference as compared to ascorbic acid as the positive control. Among the extracts, only methanol extract demonstrated radical scavenging activity with a percentage inhibition of 85.70% and an IC_{50} value of 45.52 µg/mL. However, the IC_{50} value was higher than that of ascorbic acid, which has an IC_{50} value of 25.32 µg/mL. The other extracts did not show radical scavenging activity since their respective percentage inhibitions were less than 50% at the concentration of 1000 µg/mL. The potent antioxidant activity of the methanol extract may be due to the existence of flavonoids and phenolics, which are known to be capable of donating their hydrogen atoms [23].

Table 3. DPPH radical scavenging activity of *P. guajava* leaves extracts

Samples	Inhibition at 1000 µg/mL (%)	IC_{50} (µg/mL)
n-Hexane extract	15.95 ± 0.92^{b}	ND
Chloroform extract	40.51 ± 1.25^{b}	ND
Methanol extract	85.70 ± 0.80^{b}	45.52 ± 3.71^{a}
Ascorbic acid	95.53 ± 0.10	25.32 ± 0.44

Data represent mean ± standard deviation of three replicate experiments; ND = not determined
a = $p < 0.01$, b = $p < 0.001$

Conclusion

The phytochemical screening revealed that the leaves extracts of *P. guajava* from Johor, Malaysia comprise of various beneficial phytochemicals such as flavonoids, steroids, saponins, phenols and terpenoids. This study also

disclosed that the methanol extract yielded the highest extraction yield and good DPPH radical scavenging activity. The present data may be useful as an initial step to determine the potential natural antioxidants that can be applied in pharmaceutical and therapeutic industries. In order to identify these antioxidants, further purification and characterization steps are suggested to be done in future study.

Acknowledgement

The authors would like to acknowledge the financial assistance and research facilities provided by Faculty of Applied Sciences, Universiti Teknologi MARA Negeri Sembilan, Malaysia.

References

1. Rahal, A., Kumar, A., Singh, V., Yadav, B., Tiwari, R., Chakraborty, S. and Dhama, K. (2014). Oxidative stress, prooxidants and antioxidants: The interplay. *BioMed Research International*, 2014: 1-19.
2. Iqbal, E., Salim, K. A. and Lim, L. B. L. (2015). Phytochemical screening, total phenolics and antioxidant activities of bark and leaf extracts of *Goniothalamus velutinus* (airy shaw) from Brunei Darussalam. *Journal of King Saud University – Science*, 27: 224-232.
3. Nordberg, J. and Arnér, E. S. J. (2001). Reactive oxygen species, antioxidants and the mammalian thioredoxin system. *Free Radical Biology and Medicine*, 31(11): 1287-1312.
4. Pham-Huy, L. A., He, H. and Pham-Huy, C. (2008). Free radicals, antioxidants in disease and health. *International Journal of Biomedical Science*, 4(2): 89-96.
5. Nićiforović, N., Mihailović, V., Mašković, P., Solujić, S., Stojković, A. and Pavlović Muratspahić, D. (2010). Antioxidant activity of selected plant species; potential new sources of natural antioxidants. *Food and Chemical Toxicology*, 48: 3125-3130.
6. Gutiérrez, R. M. P., Mitchell, S. and Solis, R. V. (2008). *Psidium guajava*: A review of its traditional uses, phytochemistry and pharmacology. *Journal of Ethnopharmacology*, 117(1): 1-27.
7. Sanches, N. R., Cortez, D. A. G., Schiavini, M. S., Nakamura, C. V., Prado, B. and Dias Filho, B. P. (2005). An evaluation of antibacterial activities of *Psidium guajava* (L.). *Brazilian Archives of Biology and Technology*, 48(3): 429-436.
8. Wan Nur Zahidah, W. Z., Noriham, A. and Zainon, M. N. (2013). Antioxidant and antimicrobial activities of pink guava leaves and seeds. *Journal of Tropical Agriculture and Food Science*, 41(1): 53-62.
9. Chen, K. C., Hseih, C. L., Huang, K. D., Ker, Y. B., Chyau, C. C. and Peng, R. Y. (2009). Anticancer activity of Rhamnoallosan against DU-145 cells is kinetically complementary to coexisting polyphenolics in *Psidium guajava* budding leaves. *Journal of Agriculture and Food Chemistry*, 57: 6114-6122.
10. Begum, S., Hassan, S. I., Ali, S. N. and Siddiqui, B. S. (2004). Chemical constituents from the leaves of *Psidium guajava*. *Natural Product Research*, 18(2): 135-140.
11. Gayathri, V. and Kiruba, D. (2014). Preliminary phytochemical analysis of leaf powder extracts of *Psidium guajava* L. *International Journal of Pharmacognosy and Phytochemical Research*, 6(2): 332-334.
12. Morais-Braga, M. F. B., Sales, D. L., Carneiro, J. N. P., Machado, A. J. T., dos Santos, A. T. L., de Freitas, M. A., Martins, G. M. A. B., Leite, N. F., de Matos, Y. M. L. S., Tintino, S. R., Souza, D. S. L., Menezes, I. R. A., Ribeiro-Filho, J., Costa, J. G. M. and Coutinho, H. D. M. (2016). *Psidium guajava* L. and *Psidium brownianum* Mart ex DC.: Chemical composition and anti-*candida* effect in association with fluconazole. *Microbial Pathogenesis*, 95: 200-207.
13. Rattanachaikunsopon, P. and Phumkhachorn, P. (2010). Contents and antibacterial activity of flavonoids extracted from leaves of *Psidium guajava*. *Journal of Medicinal Plants Research*, 4(5): 393-396.
14. Sarah, S. N., Sijam, K. and Omar, D. (2012). Antibacterial activity of *Psidium guajava* L. methanol leaf extract against plant pathogenic pacteria in the genera *Pectobacterium* and *Xanthomonas*. *International Journal of Applied Biology and Pharmaceutical Technology*, 3(1): 246-252.
15. Arya, V., Thakur, N. and Kashyap, C. P. (2012). Preliminary phytochemical analysis of the extracts of *Psidium* leaves. *Journal of Pharmacognosy and Phytochemistry*, 1(1): 1-5.
16. Pooja, S and Vidyasagar, G. M. (2016). Phytochemical screening for secondary metabolites of *Opuntia dillenii* haw. *Journal of Medicinal Plants Studies*, 4(5): 39-43.
17. Khanam, Z., Wen, C. S. and Bhat, I. U. H. (2015). Phytochemical screening and antimicrobial activity of root and stem extracts of wild *Eurycoma longifolia* jack (Tongkat Ali). *Journal of King Saud University – Science*, 27: 23-30.

18. Zulkifli, K. S., Abdullah, N., Abdullah, A., Aziman, N. and Wan Kamarudin, W. S. S. (2012). Phytochemical screening and activities of hydrophilic and lipophilic antioxidant of some fruit peels. *Malaysian Journal of Analytical Sciences*, 16(3): 309-317.
19. Rao, U. S. M., Abdurrazak, M. and Mohd, K. S. (2016). Phytochemical screening, total flavonoid and phenolic content assays of various solvent extracts of tepal of *Musa paradisiaca*. *Malaysian Journal of Analytical Sciences*, 20(5): 1181-1190.
20. Tagashira, M. and Ohtake, Y. A. (1998). New antioxidative 1,3-benzodioxole from *Melissa officinalis*. *Planta Medica*, 64: 555-558.
21. Markom, M., Hasan, M., Wan Daud, W. R., Singh, H. and Jahim, J. M. (2007). Extraction of hydrolysable tannins from *Phyllanthus niruri* linn.: Effects of solvents and extraction methods. *Separation and Purification Technology*, 52: 487-496.
22. Jamuna, S., Paulsamy, S. and Karthika, K. (2014). Phytochemical analysis and evaluation of leaf and root parts of the medicinal herb, *Hypochaeris radicata* L. for *In vitro* antioxidant activities. *Asian Pacific Journal of Tropical Biomedicine*, 4 (Suppl 1): S359-S367.
23. Bouaziz, A., Khennouf, S., Zarga, M. A., Abdalla, S., Baghiani, A. and Charef, N. (2015). Phytochemical analysis, hypotensive effect and antioxidant properties of *Myrtus communis* L. growing in Algeria. *Asian Pacific Journal of Tropical Biomedicine*, 5(1): 19-28.
24. Türkyılmaz, M., Tağı, Ş, Dereli, U. and Özkan, M. (2013). Effects of various pressing programs and yields on the antioxidant activity, antimicrobial activity, phenolic content and colour of pomegranate juices. *Food Chemistry*, 138: 1810-1818.
25. da Gama, R. M., Guimarães, M., de Abreu, L. C. and Armando-Junior, J. (2014). Phytochemical screening and antioxidant activity of ethanol extract of *Tithonia diversifolia* (Hemsl) A. gray dry flowers. *Asian Pacific Journal of Tropical Biomedicine*, 4(9): 740-742.
26. Keller, A. C., Ma, J., Kavalier, A., He, K., Brillantes, A. M. B. and Kennelly, E. J. (2011). Saponins from the traditional medicinal plant *Momordica charantia* stimulate insulin secretion *In vitro*. *Phytomedicine*, 19: 32-37.
27. Mbaveng, A. T., Hamm, R. and Kuete, V. (2014). Harmful and protective effects of terpenoids from African medicinal plants. in toxicological survey of African medicinal plants. Elsevier, London: pp. 557-576.

Malaysian Journal of Analytical Sciences (MJAS)
Published by Malaysian Analytical Sciences Society

DEVELOPMENT OF AN ENZYME-LINKED IMMUNOSORBENT ASSAY (ELISA) FOR DOMOIC ACID DETECTION IN SELECTED SHELLFISH SEAFOOD USING α-AMINO-3-HYDROXY-5-METHYL-4-ISOXAZOLEPROPIONIC ACID (AMPA) RECEPTOR

(Pembangunan Imunojerapan Berpaut Enzim Berpesaingan Tak Langsung (ELISA) bagi Pengesanan Domoik Asid dalam Makanan Laut Bercengkerang Terpilih menggunakan Reseptor α-Amino-3-Hidroksi-5-Metil-4-Isoksazolepropionik Asid (AMPA))

Hafiza Mohamed Zuki*, Lai Yun Ru, Noor Sheryna Jusoh, Azrilawani Ahmad, Marinah Mohd Ariffin

Faculty of Science and Marine Environment,
Universiti Malaysia Terengganu,
21030 Kuala Nerus, Terengganu, Malaysia

**Corresponding author: hafiza@umt.edu.my*

Received: 20 November 2019; Accepted: 12 March 2020

Abstract

In this study, a selective and sensitive enzyme-linked immunosorbent assay (ELISA) method using ionotropic glutamate receptor of amino-3-hydroxy-5-methyl-4-isoxazolepropionic acid (AMPA) was successfully developed in order to determine the presence of domoic acid (DA) in shellfish seafood. The optimum concentration of AMPA receptor and goat anti-mouse IgG alkaline phosphate (AP) were obtained at 1.3 ppm and 1.7 ppm, respectively. Absorbance response of the optimised assay towards DA recorded limit of detection (LOD) and limit of quantification (LOQ) at 0.72 ppm and 1.2 ppm, respectively. Cross-reaction with glutamic acid (GA) showed that the assay was less sensitive than DA, with cross-reactivity values of 12.96%. The competency of the immunoassay towards real samples analysis was studied using mussel and cockle. Detection of non-spiked samples recorded the presence of DA at 0.96 ppm for mussel and 0.56 ppm for cockle. Meanwhile, recovery of the spike samples with 3 ppm DA was found at 2.69 ppm for mussel and 2.60 ppm for cockle, with recovery percentages of 86.7% and 89.7%, respectively.

Keywords: enzyme-linked immunosorbent assay, α-amino-3-hydroxy-5-methyl-4-isoxazolepropionic acid, domoic acid, shellfish seafood

Abstrak

Dalam kajian ini, satu kaedah imunojerapan berpaut enzim berpesaingan tak langsung (ELISA) yang selektif dan sensitif dengan menggunakan reseptor glutamat ionotropik asid α-amino-3-hidroksi-5-metil-4-isoksazolepropionik (AMPA) telah berjaya dibangunkan untuk menentukan kehadiran asid domoik (DA) dalam makanan laut bercengkerang. Kepekatan optimum reseptor AMPA dan anti-tikus kambing IgG alkali fosfat (AP) masing-masing adalah didapati pada 1.3 ppm dan 1.7 ppm. Tindak balas penyerapan terhadap ujian optimum DA mencatatkan had pengesanan (LOD) dan had kuantifikasi (LOQ) masing-masing diperolehi sebanyak 0.72 ppm dan 1.2 ppm. Tindak balas silang dengan asid glutamat (GA) menunjukkan bahawa ujian GA adalah kurang sensitif daripada DA, dengan nilai tindak balas-silang 12.96%. Kecekapan imunoasai bagi analisis sampel sebenar telah dikaji menggunakan kupang dan kerang. Pengesanan sampel yang tidak dipaku mencatatkan kehadiran DA pada 0.96 ppm untuk kupang dan 0.56 ppm untuk kerang. Sementara itu, perolehan semula sampel yang dipaku dengan 3 ppm DA diperolehi pada 2.69 ppm bagi kupang dan 2.6 ppm bagi kerang, dengan peratusan pemulihan masing-masing sebanyak 86.7% dan 89.7%.

Kata kunci: ujian imunojerapan berpaut enzim berpesaingan tak langsung, asid α-mino-3-hidroksi-5-metil-4-isoksazolepropionik, asid domoik, makanan laut bercengkerang

Introduction

Domoic acid (DA) is frequently associated with Red Tide phenomenon, which occurs when certain phytoplankton species with reddish pigments bloom in the sea. Red tide usually occurs in marine, estuarine or fresh waters, where algae accumulate rapidly in the water columns. These algae, which are in the form of phytoplankton, can form visible and dense patches near the water surface [1]. DA is a toxin produced by marine diatoms that belongs to the members of the genus *Pseudo-nitzschia*, a tiny plant, in the form of microscopic algae, which lives in the sea and obtains energy from sunlight in the daytime [2]. A total of 22 species of the genus *Pseudo-nitzschia* have been identified, including 14 new records in Malaysia. Among these, nine species have been identified as the cause of amnesic shellfish poisoning (ASP) outbreak that has been documented worldwide [3].

The consumption of shellfish mollusks contaminated with DA can lead to ASP. Humans affected by ASP could experience nausea, vomiting, abdominal cramps, diarrhea, temporary memory loss as well as death [4]. DA poisoning was first detected in 1987 in Canada, with four casualties [5]. Since then, numerous DA-related incidents have been reported around the globe [6]. In Malaysia, DA screening in seafood has been carried out at two sites of cage cultures, in Tebrau Straits and in Johor in 2015, to evaluate the potential occurrence of DA [7]. Enforcement in the European Union (EU) of the regulatory limit for DA is 20 μg/kg (Regulation EC, 2074/2005), this implies that samples with DA levels below this value show no ill effects on human (tolerable daily intake (TDI) of DA for humans is 0.075 ppm) and would be released on the market [8].

α-amino-3-hydroxy-5-methyl-4-isoxazolepropionic acid (AMPA), is known as an ionotropic glutamate receptor, that was named after the activated agonists of α-amino-3-hydroxyl-5-methyl-4-isoxazole-propionate. AMPA is a nonselective cation channel that allows the passage of Na^+ and K^+, and in some cases small amounts of Ca^{2+} [9]. Figure 1 shows the ionotropic glutamate receptor of AMPA adapted from Chelsea & Shawn, 2017 [10].

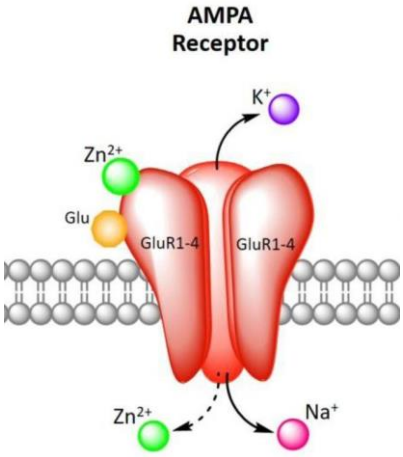


Figure 1. Ionotropic glutamate receptors AMPA

DA is an analogue to the neurotransmitter L-glutamate and excitatory amino acid. Occurrence of DA in the neurons subsequently activates AMPA. The activation causes an uncontrollable increasing level of intracellular Ca^{2+}, which then induces glutamate release [11]. Complementing the glutamic acid that is needed by the human body, DA will bind predominantly to the AMPA receptors in the central nervous system after the consumption of contaminated shellfish. This cause the depolarization of the neurons and the increase of intercellular Ca^{2+} concentration, resulting in sustained activation of calcium-sensitive enzymes, eventually leading to neuronal swelling, depletion of energy and cell death [12].

High performance liquid chromatography (HPLC) and liquid chromatography-mass spectrometry (LC-MS) are commonly used in the detection of DA [13]. Although these techniques have the advantages of high speed, high

resolution, high sensitivity and accuracy, they also possess some disadvantages such as bulky instrument, time consuming, large amounts of sample extract is needed which can lead to shortened column life, high maintenance and clean-up cost, and also require trained personnel to operate [14]. In order to overcome the limitations of these instruments, researchers have shifted to the development of a suitable bio-chemical sensors for DA detection.

An attempt of developing an AMPA as an immunoassay for the detection of DA in selected shellfish seafood was made using the enzyme-linked immunosorbent assay (ELISA) method. ELISA is a plate-based assay technique designed for quantifying and detecting substances such as proteins, hormones, peptides and antibodies. The main advantages of ELISA are that, it is sensitive, the equipment needed is relatively cheap and it has been formally validated in an interlaboratory study [15]. ELISA has the ability to selectively detect DA in shellfish samples with a detection limit in parts per trillion (ppt) [16]. Although the application of the ELISA method in determining DA is not new, researchers agree that ELISA is the best method for the regular monitoring of DA in shellfish samples due to its accurate quantification, high recovery and tolerable precision [17]. Therefore, in this study, the implementation of AMPA receptor as a sensing reagent that replace the use of antibodies in ELISA for DA detection was utilized, and the total performance of the assay towards DA was evaluated for the future development of the AMPA-ELISA immunosensor.

Materials and Methods

Chemicals and Reagents

Domoic acid, glutamic acid, α-amino-3-hydorxy-5-methyl-4-isoxazolepropionic acid, bovine serum albumin (BSA) and *para*-nitrophenylphosphate (*p*-NPP) were purchased from Sigma, USA. Sodium chloride, potassium chloride, disodium phosphate, monopotassium phosphate, sodium carbonate buffer and sodium bicarbonate buffer were purchased from Thermo Fisher, USA. Goat anti-mouse IgG alkaline phosphate (AP) was purchased from Santa Cruz Biotechnology, USA. Diethanolamine (DEA) was purchased from Merck, Germany. All reagents were of analytical grade.

Instrumentation

Mini incubator (VWR, China) was used to incubate samples at 37 °C. An Ascent Multiscan ELISA reader (Thermo Scientific) was used for optical characterization.

Preparation of buffer solutions and substrate

Buffer solutions and substrate were freshly prepared prior to assay. 0.1 M of sodium bicarbonate, sodium carbonate-bicarbonate and sodium carbonate buffer solutions were used as coating buffers. The washing buffer, phosphate buffer saline (PBS, pH 7.4) was prepared by dissolving 8 g of sodium chloride, 0.2 g of potassium chloride, 1.44 g of disodium phosphate and 0.24 g of monopotassium phosphate in deionized water. Mixture of 0.1 g (1%) BSA and PBS were used as blocking buffer (pH 7.4). AMPA was prepared in the coating buffer. DA and AP were diluted with PBS. 1 ml *para*-nitrophenylphosphate (*p*-NPP) substrate was diluted in 9 ml 1 M DEA buffer (pH 9.5).

Optimization of reagents and biomolecules:

Types of coating buffer

Three different types of coating buffer, which are carbonate buffer, bicarbonate buffer and carbonate-bicarbonate buffer, were applied in indirect ELISA. The performance of the assays using 50 µl of 0.1 M bicarbonate buffer, 50 µl of 0.1 M carbonate buffer and 50 µl of 0.1 M carbonate-bicarbonate buffer were compared.

Influence of blocking step

The effect of blocking step in ELISA was evaluated by comparing the performance of assays with and without a blocking buffer.

AMPA and AP concentration

50 µL of AMPA and 50 µL of AP in varying concentrations were used to determine the optimum condition and the optimum performance of the assays.

ELISA for DA Detection

50 µL of carbonate-bicarbonate buffer was added to each well. The wells were incubated for 1 hour at 37 °C. 200 µL PBS was used to wash the plate by inverting the plate frame over a sink and tapping against a pile of paper towels to remove the remaining liquid completely before proceeding to the next step. 50 µL AMPA was added to each well. The wells were incubated for 1 hour at 37 °C, and 200 µL PBS was used to remove the unbound receptors. 50 µL of serial dilutions of DA with different concentrations were added to each well. The wells were incubated for 1 hour at 37 °C, and 200 µL PBS was used to remove the unbound DA molecule. 50 µL AP was then added to the wells and the mixture was incubated for 1 hour at 37 °C. 200 µL PBS was used to remove the unbound AP. The reaction was initiated by the addition of 200 µL *p*-NPP to each well. A change of color was observed, and the plate was measured at 405 nm after 1 hour.

Control assays

Control assays were performed to evaluate the performance of optimized biomolecules and reagents. The procedures for the assays were similar to the procedures described in ELISA for DA detection, but with the exception of certain components. There were five types of control assays tested, namely, substrate (*p*-NPP) only, control 1 (no AMPA), control 2 (no DA), control 3 (no AP) and normal assay.

Cross-reactivity with glutamic acid

The ELISA procedure was repeated by replacing DA with GA for measuring a cross-reactivity of DA with GA.

Measurement with real samples

The ELISA procedure was repeated for DA measurement in real shellfish samples of cockle and mussel.

Results and Discussion

Optimization of Reagents and Biomolecules:

Types of coating buffer

In immunoassays, a coating step is basically conducted to allow the binding of biological elements (antibody or antigen) onto the solid support by passive adsorption [18]. This first step of immunoassay is very crucial, and thus a few considerations must be taken into account before the coating process, especially the selection of the coating buffer. Carbonate-type buffers are commonly used buffers in immunoassays. Figure 2 shows that, a carbonate-bicarbonate buffer had the most significant absorbance reading of 0.12 a.u. compared to bicarbonate buffer and carbonate buffer, which the absorbance obtained were 0.09 a.u. and 0.10 a.u. respectively. Carbonate-bicarbonate buffer provided better absorbance as it has a pH value of 9.6 which was proven efficient in coating step compared to bicarbonate and carbonate buffer with pH value of 8.3 and 11.0 respectively. Carbonate-bicarbonate buffer with pH 9.6 aids solubility of a variety of proteins, and makes sure that most proteins are unprotonated with an overall negative charge, which helps when binding to positively charged plate [19].

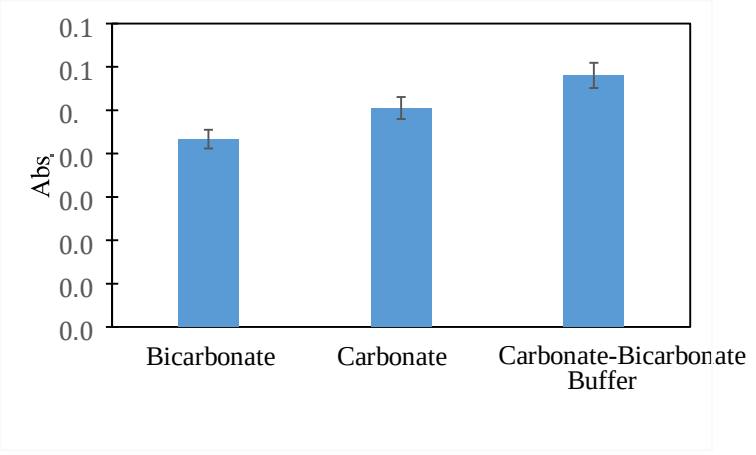


Figure 2. Absorbance reading of different coating buffers

Influence of blocking step

Blocking step is as important as coating step because it can improve the sensitivity of the assay by increasing the signal-to-noise ratio and reducing background interference. Blocking agents such as BSA, non-fat dry milk, and whole serum are commonly used to eliminate the residual binding capacity of the wells. Besides that, blocking agents can help in reducing non-specific interactions, and stabilize the biomolecules bound to the well surface [20]. Figure 3 shows that the assay with a blocking step is likely to have higher absorbance compared to the one without a blocking step. This study has proven that a blocking step was able to improve the sensitivity of the assay, as the remaining binding surface had been blocked to prevent the nonspecific binding of the antibodies. The blocker used in this study was 1% BSA in PBS buffer.

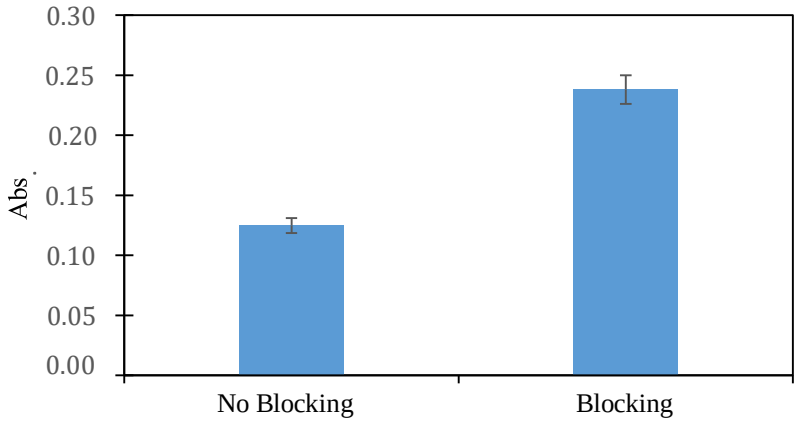


Figure 3. Influence of blocking step during assay

AMPA optimum concentration

The assay was conducted using different concentrations (0.2-2 ppm) of the AMPA receptor in order to find out the optimum condition for AMPA that will react with 1 ppm of DA in the assay. From Figure 4, it can be seen that the absorbance reading started to plateau at 1.3 ppm. As the concentration of AMPA increased, the absorbance reading did not differ much, and the absorbance was maintained at almost a similar value. Therefore at a concentration of 1.3 ppm of AMPA, the reaction between AMPA and DA was proven to be the most active.

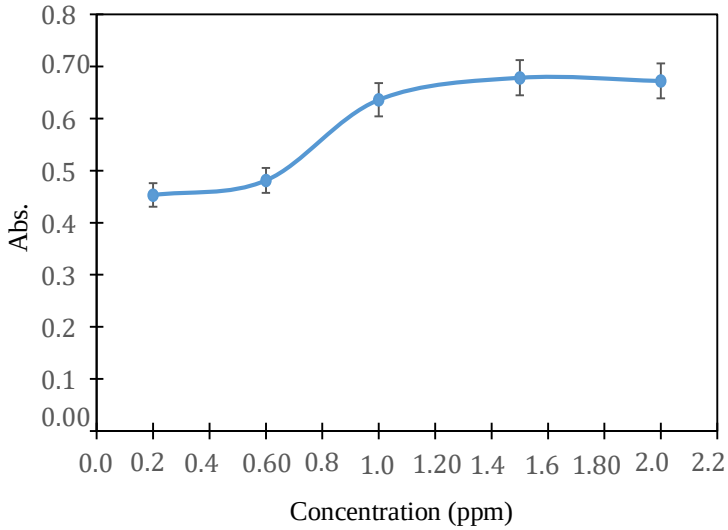


Figure 4. Absorbance reading for different concentrations of AMPA at 405 nm

AP optimum concentration

AP label antibody was used in ELISA for optical performance. The concentration of AP ranged from 1 ppm to 3 ppm. Color change was observed after one hour of *p*-NPP substrate addition, where it changed from colorless to yellow. The change in color implies that there are active formations of bio element complexes in the well. The plate was read at 405 nm and the absorbance reading observed is shown in Figure 5. From the graph, the absorbance started to plateau at 1.7 ppm. After that, the absorbance reading did not differ much and maintained almost similar value even when the concentration of AP had increased. Therefore, AP had been successfully optimized at 1.7 ppm.

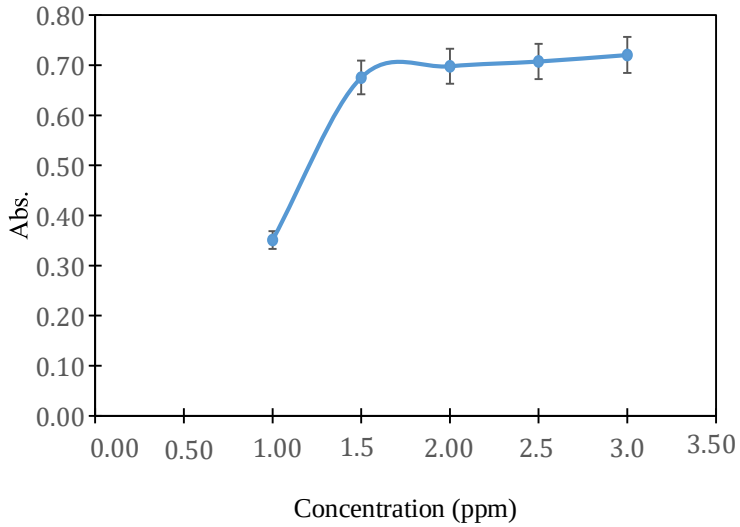


Figure 5. Absorbance for AP label antibody read at 405 nm

ELISA for DA detection

Responses of different concentrations of DA (0.2-2 ppm) in ELISA were examined and the result is shown in Figure 6. The developed ELISA method was verified by a series of experimental parameters including linear range, correlation coefficients (R^2), LOD and LOQ. Good linearity was recorded with R^2 of 0.9156. The calculated LOD and LOQ values for optical response of DA were 0.72 ppm and 1.20 ppm, respectively.

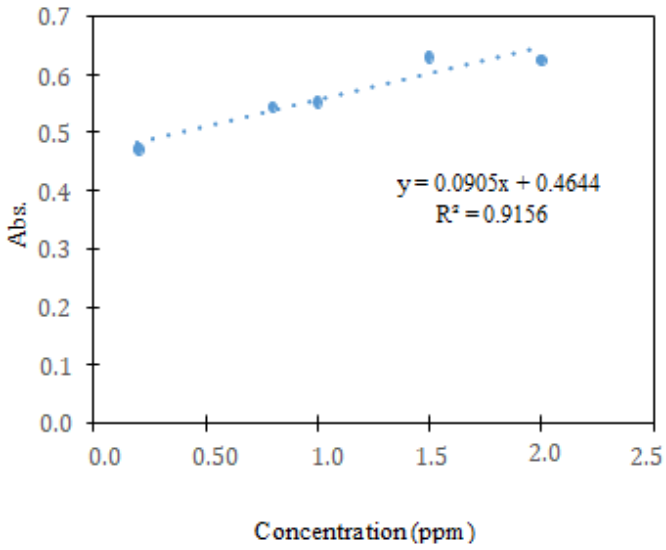


Figure 6. Calibration curve of absorbance against concentration of DA

Control assay

Control assays were conducted in order to assess the performance of each optimized bio element. The absorbance for all assays is shown in Figure 7. From the graph, it can be seen that the normal assay had the highest absorbance reading while the rest had almost similar absorbance readings. *p*-NPP acted as a blank assay. Control 1 had been performed without the addition of AMPA, while Control 2 was conducted without DA. Control 3 was performed without AP. In all the control assays, the absorbance reading was low, because there was no active interaction between the biomolecules. In ELISA, the performance of assay will be affected by any substance that adsorbs on the surface. By comparing control assays and normal assay, it was proven that all biomolecules must be present in order to obtain a better absorbance reading, in which the absorbance signals the formation of complex biomolecules in the assay.

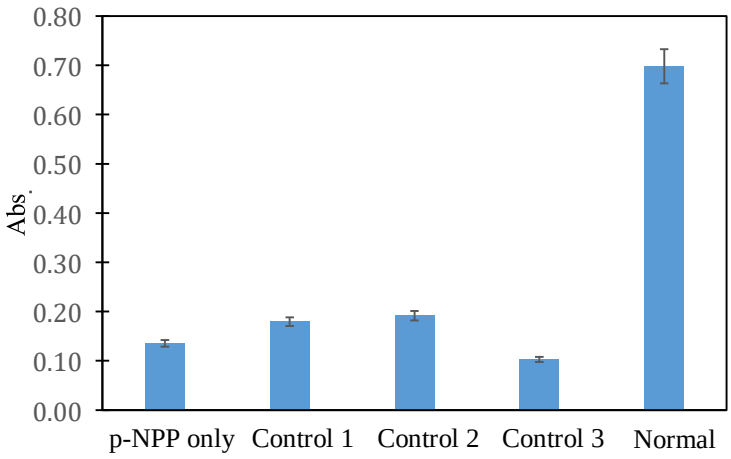


Figure 7. Control assays of biomolecules with indirect ELISA. All assays were read at 405 nm. (Control 1 without AMPA, Control 2 without DA and Control 3 without AP)

Cross-reactivity with GA

A cross-reactivity study was selected because in a real human body, AMPA normally reacts with GA to maintain the release of CA^{2+} ions. It was found that only with the presence of DA, the normal flow of CA^{2+} ions was distracted. Figure 8 shows the response carried out for GA in an indirect assay, in order to test the selectivity of the assay towards GA. GA was of GA towards ELISA. Good linearity was observed for the response between GA and the assay. The half maximal inhibitory concentration (IC_{50}) values for DA and GA calculated from Figure 6 and Figure 8 (equation 1) were 0.39 and 3.01, respectively. The low IC_{50} value indicates the high sensitivity of the assay towards the target analyte. Thus, this proves that the assay was evidently more sensitive towards DA than GA.

$$IC_{50} = \frac{(0.5-c)}{m} \quad (1)$$

where c is y-intercept and m is slope of the calibration plot.

Meanwhile, cross-reactivity value of DA with GA calculated using equation 2 was 12.96 %. The low cross-reactivity value obtained was due to the tendency of AMPA to also react with GA, even though it was more sensitive towards DA.

$$Cross-reactivity\ (\%) = \frac{IC_{50\ DA}}{IC_{50\ GA}}\ x\ 100 \quad (2)$$

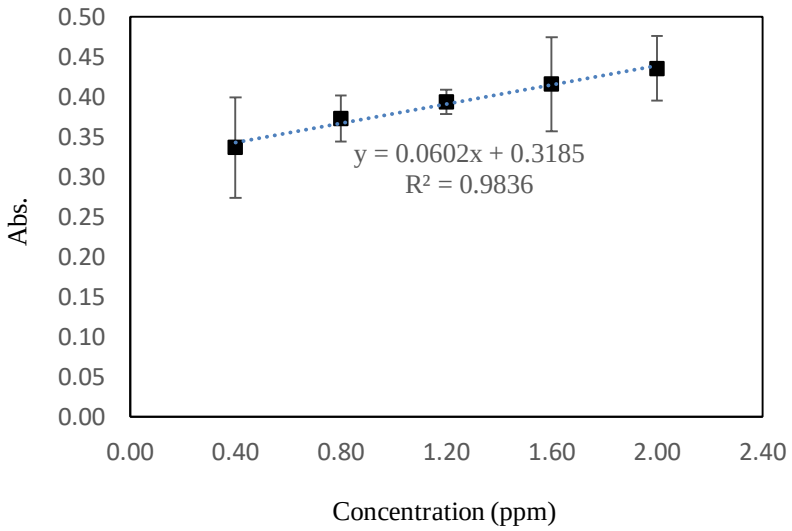


Figure 8. Absorbance reading of GA in indirect ELISA

Measurement with real samples

The sensitivity and selectivity of the developed assays were tested with spiked and non-spiked shellfish samples (mussel and cockle). The optical evaluation was recorded and is tabulated in Table 1. In non-spiked samples, 0.96 ppm and 0.56 ppm DA were found in mussel and cockle, respectively. Meanwhile, in spiked samples, 3 ppm of DA standard was injected into the samples. 2.69 ppm of DA in mussel and 2.60 ppm of DA in cockle samples were recovered with a recovery percentage of 89.7% and 86.7% for mussel and cockle samples, respectively. Low recovery from the spiked samples might be due to the interference of other substances in the samples. The interference might have caused the absorbance reading of DA to be hindered, causing low reading and recovery.

Table 1. Recovery of DA in cockle and mussel samples using optical measurement

Sample	Non-spiked	Spiked (3 ppm)	
	Found (ppm)	Found (ppm)	Recovery (%)
Mussel	0.96	2.69	89.7
Cockle	0.56	2.60	86.7

Conclusion

In this study, an approach of developing an ELISA immunoassay using an AMPA receptor as the recognition reagent for DA determination was successfully conducted. Since the glutamate receptors readily interact with DA in a normal human body, the concept of replacing antibodies with receptors in ELISA was derived out and experimented in the detection of DA in shellfish seafood. The immunoassay shows highly selective and sensitive responses toward DA, even in the case of real sample analysis. The achievements offer a great deal of potential for the future development of receptor-ELISA immunosensors for DA detection.

Acknowledgement

The authors would like to extend their gratitude towards the Ministry of Education Malaysia for Fundamental Research Grant Scheme of FRGS/1/2015/ST04/UMT/02/1 (FRGS 59409) and Universiti Malaysia Terengganu for providing support, laboratory facilities and instrumentation.

References

1. Botana, L.M., (2014), Seafood and freshwater toxins: Pharmacology, physiology, and detection, Third Edition. CRC Press, Boca Raton, Fl: pp 326-327.
2. Fehling, J., Green, D. H., Davidson, K., Bolch, C. J., and Bates, S. S. (2004). Domoic acid production by *Pseudo-Nitzschia Seriata* (Bacillariophyceae) in Scottish waters. *Journal of Phycology*, 40: 622-630.
3. Teng, S.T., Lim, P.T., Lim, H.C. and Leaw, C.P. (2014). *Pseudo-nitzschia* (Bacillariophyceae) in Malaysia: A record of taxa from field investigations. *15th International Conference on Harmful Algae (ICHA)*, 2014: pp. 1-4.
4. Zuki, H. M., Nasri, N. M., Muhammad, F. N., Jusoh, N. S., Ahmad, A., and Ariffin, M. M. (2019). Modification of gold screen printed electrode for the detection of toxic domoic acid. *Malaysian Journal of Analytical Sciences*, 23 (6): 991-1000.
5. Friedman, M. (2004). Applications of the ninhydrin reaction for analysis of amino acids, peptides, and proteins to agricultural and biomedical sciences. *Journal of Agriculture and Food Chemistry*, 52: 385-406.
6. Mos, L. (2001). Domoic acid: A fascinating marine toxin. *Environmental Toxicology and Pharmacology*, 9: 79-85.
7. Saeed, A. F., Awan, S. A., Ling, S., Wang, R. and Wang, S. (2017). Domoic acid: Attributes, exposure risks, innovative detection techniques and therapeutics. *Algal Research*, 24: 97-110.
8. Andjelkovic, M., Vandevijvere, S., Klaveren, J. V., Oyen, H. V., and Loco J. V. (2012). Exposure to domoic acid through shellfish consumption in Belgium. *Environment International*, 49: 115-119.
9. Purves, D., Augustine, G. J. Fitzpatrick, D., Katz, L. C., LaMantia, A. S., McNamara, J. O. and Williams, S. M. (2001). Neuroscience. https://www.ncbi.nlm.nih.gov/books/NBK10802/ [Accessed online 13 March 2018].
10. Chelsea, A. B. and Shawn, C. B. (2017). The zinc paradigm for metalloneurochemistry. *Essays in Biochemistry*, 61(2): 225-235.
11. Berman, F. W., Murray, T. F. and Lepage, K. T. (2002). Domoic acid neurotoxicity in cultured cerebellar granule neurons is controlled preferentially by the NMDA receptor Ca^{2+} influx pathway. *Brain Research*, 924(1): 20-29.
12. Berman, F. W. and Murray, T. F. (1997). Domoic acid neurotoxicity in cultured cerebellar granule neurons is mediated predominately by NMDA receptors that are activated as a consequence of excitatory amino acid release. *Journal of Neurochemistry*, 69(2): 693-703.
13. Suriyanti, S. N. and Usup, G. (2015). First report of the toxigenic *Nitzschia Navis-Varingica* (Bacillariophyceae) isolated from Tebrau Straits, Johor, Malaysia. *Toxicon*, 108: 257-263.
14. Aulakh, J. S., Malik, A. K., Varinder, K. and Philippe, S. K. (2005). A review on solid phase micro extraction-high performance liquid chromatography (SPME-HPLC) analysis of pesticides. *Critical Reviews in Analytical Chemistry*, 35: 71-85.
15. Alexander, J., Benford, D., Boobis, A., Ceccatelli, S., Cravedi, J. P., Domenico, A. D., Doerge, D., Dogliotti, E., Edler, L., Farmer, P., Filipic, M., Gremmels, J. F., Fürst, P., Guerin, T., Knutsen, H. K., Livesey, C. Machala, M., Mutti, A., Schlatter, J., Leeuwen, R. V. and Verger, P. (2009). Marine biotoxins in shellfish – domoic acid. *The EFSA Journal.* 1181: 1-61.
16. Yu, F. Y., Liu, B. H., Wu, T. S., Chi, T. F. and Su, M. C. (2004). Development of a sensitive enzyme-linked immunosorbent assay for the determination of domoic acid in shellfish. *Journal of Agricultural and Food Chemistry*, 52(17): 5334-5339.
17. Kleivdal, H., Kristiansen, S. I., Nilsen, M. V., Goksoyr, A., Briggs, l., Holland, P. and McNabb, P. (2007). Determination of domoic acid toxins in shellfish by biosense ASP ELISA – a direct competitive enzyme-linked immunosorbent assay: Collaborative study. *Journal of AOAC International*, 90(4): 1011-1027.
18. Crowther, J. R. (2009). The ELISA Guidebook (2nd Edition). Humana Press, New Jersey: pp 43-78.
19. Dmitriev, A. D., Tarakanova, J. N., Yakovleva, D. A., Dmitriev, D. A., Phartooshnaya, O. V., Kolyaskina, G. I., Massino, Y. S., Borisova, O. V., Segal, O. L., Smirnova, M. B., Ulanova, T. I. and Lavrov, V. F. (2013). Monoclonal antibodies requiring coating buffer with low pH for efficient antigen capture in sandwich ELISA: rarities or practically important phenomena? *Journal Immunoassay Immunochemistry*, 34(4): 414-437.
20. Xiao, Y. and Isaacs, S. N. (2012). Enzyme-linked immunosorbent assay (ELISA) and blocking with bovine serum albumin (BSA). *Journal of Immunology Methods*, 384(1-2): 148-151.

Malaysian Journal of Analytical Sciences (MJAS)
Published by Malaysian Analytical Sciences Society

ENZYME CATALYZED ESTERIFICATION OF SUGAR BY THERMOSTABLE T1 LIPASE FROM *Geobacillus zalihae* IN IONIC LIQUID

(Pengesteran Berenzim Gula oleh Lipase Termostabil T1 dari *Geobacillus zalihae* dalam Cecair Ionik)

Emilia Abdulmalek[1,2]*, Hanim Salami Mohd Saupi[1], Syarilaida Zulkefli[1], Raja Nor Zaliha Raja Abd Rahman[3], Mohd Basyaruddin Abdul Rahman[1,2]

[1]*Integrated Chemical BioPhysics Research, Faculty of Science*
[2]*Department of Chemistry, Faculty of Science*
[3]*Enzyme and Microbial Technology Research, Department of Microbiology, Faculty of Biotechnology and Biomolecular Science*
Universiti Putra Malaysia, 43400, UPM Serdang, Selangor, Malaysia

**Corresponding author: emilia@upm.edu.my*

Received: 20 November 2019; Accepted: 11 February 2020

Abstract

Thermostable T1 lipase from *Geobacillus zalihae* strain was utilized in esterification of various sugars with fatty acids to form fatty acid sugar esters. Fatty acid sugar esters (FASE) are an important class of non-ionic surfactant which possesses good emulsifying, stabilizing and conditioning properties. In this work the esterification reaction was done in [Bmim][BF_4] ionic liquid with dimethylsulfoxide (DMSO) as co-solvent. Esterification of galactose with oleic acid was initially screened by varying the conditions (temperature, time, enzyme loading and the fatty acid chain length). It was found that the reaction was optimum at the following conditions: temperature (65 °C), time (120 minutes) and enzyme loading (2% (w/w)) when carried out in mixture of DMSO: [Bmim][BF_4] (1:20). Interestingly, the percentage of conversion was not affected by the chain length of the acyl donor (C8 – C18) or the unsaturation degree. When the reaction was repeated with linoleic acid as acyl donor and different acyl acceptor (galactose, glucose, fructose, sucrose, maltose, trehalose and xylitol), sucrose gave the best conversion at 65%. In conclusion, TI lipase showed broad substrate specificity either for the acyl donor or acyl acceptor during the esterification of sugars in ionic liquid.

Keywords: T1 lipase, fatty acid sugar ester, ionic liquid, esterification, [Bmim][BF_4]

Abstrak

Lipase termostabil T1 dari strain *Geobacillus zalihae* telah digunakan dalam pengesteran pelbagai gula dengan asid lemak untuk membentuk ester gula asid lemak. Ester gula asid lemak (FASE) adalah kelas surfaktan bukan ionik yang penting yang mempunyai sifat pengemulsi, penstabilan dan penyesuaian yang baik. Dalam kerja ini tindak balas pengesteraan dilakukan dalam cecair ionik [Bmim][BF_4] dengan dimetilsulfoksida (DMSO) sebagai pelarut bersama. Pengesteran galaktosa dengan asid oleik pada mulanya disaring dengan mempelbagaikan keadaan (suhu, masa, muatan enzim dan panjang rantai asid lemak.) Ia didapati bahawa tindak balas adalah optimum pada keadaan berikut: suhu (65 °C), masa (120 minutes) dan muatan enzim (2% (w/w)) apabila dijalankan dalam campuran DMSO:[Bmim][BF_4] (1:20). Menariknya, peratusan penukaran tidak terjejas oleh panjang rantai asil dari C8 – C18 atau darjah ketaktepuan. Apabila tindak balas diulang dengan asid linoleik sebagai penderma asil dan penerima asil yang berbeza (galaktosa, glukosa, fruktosa, sukrosa, maltosa, trehalosa dan xilitol), sukrosa memberikan penukaran terbaik pada 65%. Kesimpulannya, lipase TI menunjukkan kekhususan substrat yang luas sama ada untuk penderma asil atau penerima asil semasa pengesteran gula dalam cecair ionik.

Kata kunci: lipase T1, ester gula asid lemak, cecair ionik, pengesteran, [Bmim][BF_4]

Introduction

Thermostable T1 lipase from *Geobacillus zalihae* sp. strain was first introduced and isolated by Leow and his co-workers [1, 2] with an aim to produce excellent thermostable lipase which can retain its activity and stability at higher temperature. Thermal stability is one of the important features of successful commercial biocatalyst as it would allow the reaction to be conducted at high temperature and in turn improve substrate solubility, increase conversion rates, reduce viscosity of reaction medium and lower microbial growth prospect [3]. Although, the thermostable T1 lipase has been discovered since 2004, to date there are still limited reports on the utilization of this enzyme in organic reactions that little is known about its substrate specificity and selectivity.

Fatty acid sugar ester (FASE) is widely known as non-toxic, odorless and biodegradable surfactant [4] which has good emulsifying, stabilizing, conditioning effect and antimicrobial properties [5]. This result in widespread usage of sugar ester in food, cosmetics, pharmaceutical and detergents [6]. Current commercial FASE is typically obtained via chemical synthesis but enzymatic synthesis of FASE catalyzed by free or immobilized lipase has become more prominent recently [7, 8]. The biocatalytic production of sugar ester is favored over the conventional process due to its advantages in term of mild reaction conditions, better regioselectivity and easy product separation to name a few [9, 10].

In large industrial scale organic solvent offers many advantages such as low price and viscosity. However, esterification of sugars in organic media suffers from low solubility of the highly polar sugars. Although polar solvent like dimethysulfoxide (DMSO) and dimethylformamide (DMF) can fully dissolve most sugars, their usage in enzymatic reaction is limited as they caused enzyme deactivation. Ionic liquid (IL) is a good alternative media for biocatalytic reactions and had been extensively studied for lipase-catalyzed esterification reaction of sugars [11]. It is an organic molten salt consists of pure ions that remains as liquid at room temperature [12]. Ionic liquid showed excellent potential in biocatalytic production of sugar ester due to higher sugar solubility, excellent enzymatic activity and selectivity [13]. Our previous work on the enzymatic esterification of galactose [14] and xylose [15] in ILs and organic solvents respectively, showed that small amount of DMSO for initial solubilization of the sugars was beneficial to get a good conversion. Other works have also demonstrated the utility of polar solvent like DMSO as co-solvent in sugar ester synthesis [16]. Similarly, super saturated sugar solution has been utilized for the same purpose [17, 18, 19].

In this work, we aim to investigate the utility of thermostable T1 lipase in esterification of sugars with fatty acids in order to further understand the lipase selectivity and specificity. The initial screening of the reaction conditions was done using the esterification of galactose with oleic acid in DMSO:[Bmim][BF_4] (1:20) mixture followed by reaction of galactose with various fatty acids to see the lipase preference, if any. The sugar preference of the lipase was also studied. This report is one of the earliest reports on T1 lipase as enzyme for biocatalysis reaction. This could be one of the main references for application of T1 lipase.

Materials and Methods

Materials

Crude free lipase from *Geobacillus zalihae strain* T1 was obtained from UPM, Selangor, Malaysia. 1-butyl-3-methylimidazolium tetrafluoroborate ([Bmim][BF_4]), DMSO, caprylic acid and lauric acid were purchased from Merck, Germany. Oleic acid was obtained from TCI Tokyo Kasei. All sugars (galactose, glucose, fructose, sucrose, maltose, trehalose and xylitol) and linoleic acid were purchased from Sigma Aldrich, USA.

Lipase-catalyzed esterification and parameter screening

The reactions were carried out in Eppendorf microcentrifuge tube (2 mL) and incubated in Eppendorf Thermomixer. Sugar (galactose, glucose, fructose, sucrose, maltose, trehalose or xylitol; 0.05 mmol) was dissolved in DMSO (50 µL) at 60 °C for 30 minutes until homogenous solution was observed by visual. Fatty acid (oleic, caprylic, lauric or linoleic acid; 0.10 mmol) and [Bmim][BF_4] (1.0 mL) were then added into homogeneous solution and stirred. The reaction was incubated after the addition of 2% (w/w) of total amount mixture except for enzyme loading study. The reaction was conducted at different temperature within a range of 50-80 °C for 2 hours and stirred at 250 rpm. Sample (20 µL) was taken after 2 hours for all experiments except for reaction profile experiment where sample was taken in 5 minutes interval. All reactions were conducted in triplicates. Determination of remaining fatty acid

by high performance liquid chromatography (HPLC) was then conducted on the sample and was used to calculate the percentage of conversion.

Analysis and characterization

Sample for HPLC analysis was prepared by dilution of 20 µL of reaction mixture into 40 µL of acetonitrile: methanol (1:1) and centrifuged at 4000 rpm for 15 minutes. The clear supernatant was filtered into micro volume vial inserts and injected to HPLC (Agilent 1200 series) equipped with an Evaporative Light Scattering Detector (ELSD) and an eclipsed XDB-C_{18}, 5 µm column (150 mm x 4.6 mm). The HPLC conditions were as follows: mobile phase (acetonitrile: water with ratio of 80:20 (v/v)), flow rate (0.5 mL/min) and injection volume (10 µL). The sample was analyzed for 25 minutes. Percentage of conversion was calculated by observing the concentration of remaining free fatty acid.

Results and Discussion

Effect of temperature

The effect of temperature on the activity of T1 lipase in the esterification reaction was studied at 50-80 °C. Initially, the percentage conversion increased as the temperature was raised and the highest conversion (67%) was recorded at 65 °C (Figure 1), the same optimum temperature that was reported for T1 lipase by Leow et al. [2]. However, the conversion began to slowly decrease when the temperature exceeded 65 °C which could be caused by thermal denaturation of T1 lipase. Temperature is crucial parameters in an enzymatic reaction as it can affect the stability and activity of enzyme used. In addition, the solubility of reactants and reaction rate will also be influenced [3]. *Candida antarctica* lipase B (CALB) immobilized within a macroporous resin (Novozyme 435) was reported to exhibit its highest conversion at 50 °C in the esterification of glucose with lauric acid in mixture of [Bmim][TfO] and [Omim][Tf_2N] (1:1) [19] and at 60 °C in the synthesis of propyl caffeate *via* transesterification reaction in ILs [20]. Immobilized *Thermomyces lanuginose* lipase (Immozyme TLL) was shown to be optimum at 50 °C during the synthesis of temsirolimus in methyl *ter*t-butyl ether [21]. This shows that at 65 °C optimum temperature, T1 lipase was able to surpass the thermal stability of commercial enzymes. Although T1 lipase can maintain its activity and stability at 65 °C, the rest of the parameter study were done at 60 °C for comparative purposes since most lipase catalyzed reaction rarely goes beyond 60 °C. It was also the same temperature used in our previous report using Lipozyme RMIM [14].

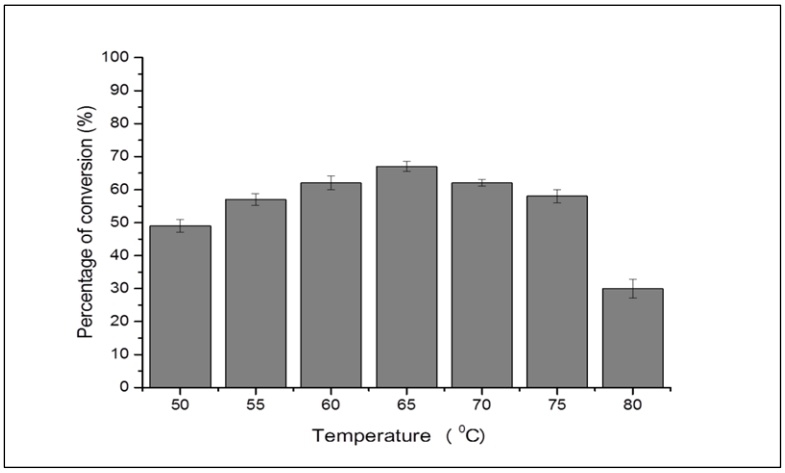


Figure 1. Effect of reaction temperature on percentage of conversion in esterification of galactose with oleic acid. Conditions: galactose (0.05 mmol), oleic acid (0.1 mmol), DMSO:[Bmim][BF_4] (1:20, 50 µL:1 mL), T1 lipase (2%, w/w), 2 hours.

The time profile of the esterification reaction

The time profile of the reaction was studied in the range of 0-240 minutes. Previously, we reported that for esterification of galactose in DMSO:[Bmim][BF_4] (1:20) mixture, the maximum conversion can be achieved within 2 hours and the reaction was followed for up to 4 hours only compared to the usual 72 hours when the reaction was carried out in organic solvent [14]. The percentage of conversion steadily increased as the reaction progress and achieved the maximum conversion at 120 minutes (Figure 2). After 2 hours the conversion started to decrease probably due to the deactivation of the lipase in the presence of very polar DMSO. Various factors affecting enzymes' activity in organic media have been previously reported such as loss of critical water, decrease flexibility, distortment of active site and disruption of quaternary structure of protein complexes, to name a few [22]. A short reaction time is not only advantageous in term of conserving the catalytic activity of the lipase but at the same time it would provide huge saving in production cost. At only 2 hours reaction time, these conversion rates are very promising as almost all reported enzymatic esterification of sugar ester were done at much longer period. Enzymatic transesterification of vinyl linoleate ester with trehalose was reported to give 64% yield of the sugar ester after 12 days using protease (Bioprase) enzyme in DMF [23] Whereas, glucose palmitate preparation using Novozyme 435 in [Bmim][PF_6] (with 0.1% water) achieved the best conversion of 77% after 48 h [24].

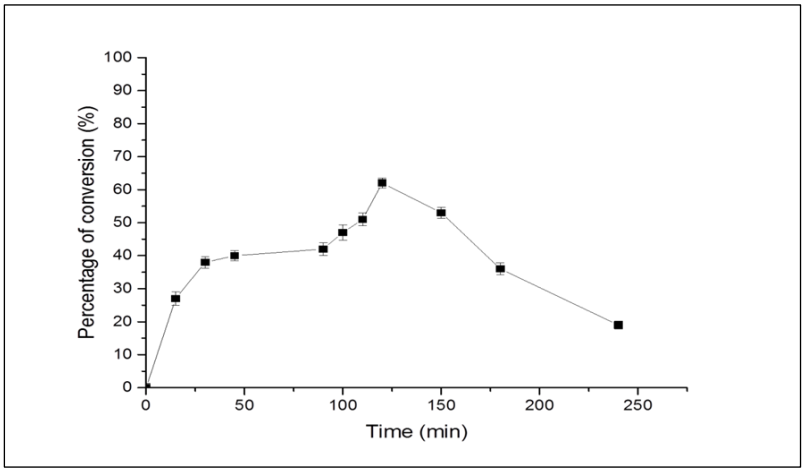


Figure 2. The time profile of esterification of galactose with oleic acid. Conditions: galactose (0.05 mmol), oleic acid (0.10 mmol), DMSO:[Bmim][BF_4] (1:20, 50 µL:1 mL), T1 lipase (2%, w/w), 60 °C.

The effect T1 lipase loading

The effect of T1 lipase loading amount was studied by varying the amount of T1 lipase from 1-5% (w/w). It was found that at low loading amount, 1-3% (w/w), the conversion was already optimum in the range of 60-63%. However, when the enzyme loading was increased to 4-5%, the conversion rapidly decreased. As the amount of enzyme is increased more active sites becomes available to accommodate the substrates which resulted in rate increase. However, above certain value, the number of active sites would exceed the number of available substrates. As a result, further increase in the amount of enzyme would not yield higher rate of conversion [25,26]. It has also been known that at high enzyme loading the reaction mixture can be quite viscous that enzyme tends to aggregate, and this will reduce the accessibility of the enzyme's catalytic site to the reactants. The mass transfer limit may have been reached at 3% enzyme loading. Thus, further increase resulted in the decrease of conversion [27]. For the rest of the study, the optimum enzyme loading of 2% (w/w) was used.

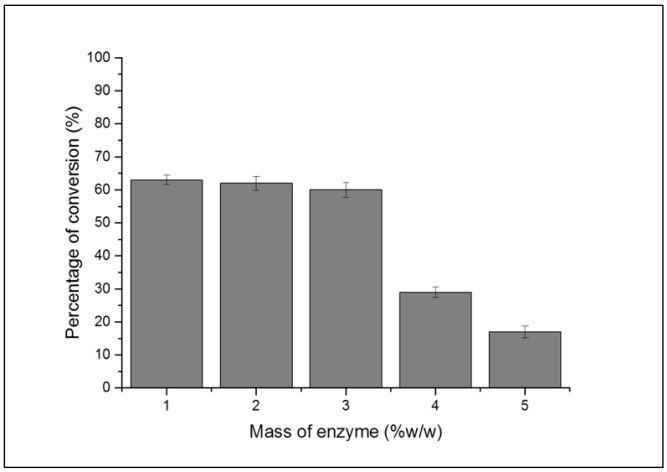


Figure 3. Effect of enzyme loading on percentage of conversion in esterification of galactose with oleic acid. Conditions: galactose (0.05 mmol), oleic acid (0.10 mmol), DMSO:[Bmim][BF_4] (1:20, 50 µL:1 mL), 60 °C, 2 hours.

The effect of fatty acids chain length

In the galactose esterification reaction, different aliphatic fatty acids with varying length and unsaturation level [levulinic acid (C5), caprylic (C8), lauric (C12), oleic (C18:1) and linoleic acid (C18:2)] were utilized to investigate the selectivity and specificity of T1 lipase. It was found that esterification with the shortest fatty acid, levulinic acid was the least favored at only 28% conversion (Figure 4). The conversions were more favorable for longer chain acids, C8 – C18 at 51 – 62%. However, lower conversion for lauric acid (C12) at 51% compared to caprylic (C8, 62%), oleic (C18:1, 62%) or linoleic acid (C18:2, 64%) was more likely due to high viscosity of the reaction mixture as lauric acid exist as solid at room temperature (m.p. 44-45°C) [28] while the other fatty acids are liquids. Higher viscosity may result in higher friction against enzymes molecule and decrease motion thus inhibiting catalysis [29]. Similarly, levulinic acid also exists as solid at room temperature which may also account for the low conversion. Previous work has reported that when comparing the activity of various lipases (Novozyme 435, Lipozyme TL IM, Lipozyme RM IM, and immobilized CRL) for esterification of levulinic acid in [Bmim][PF_6], only Novozyme 435 showed good activity [30]. This suggests that levulinic acid is not a favorable substrate for many lipases and not just T1 lipase. Although, levulinic acid as a keto acid, did not really fit well as substrate of choice to investigate the effect of acid's length, we were interested to see whether enzymatic esterification of levulinic acid can be done using T1 lipase in IL as part of our study on production of biofuel [31]. For its hydrolytic activity, T1 lipase has been shown previously favor medium to long chain fatty acids (C10 – C14) [32] and it seemed that for esterification the chain length can be extended further.

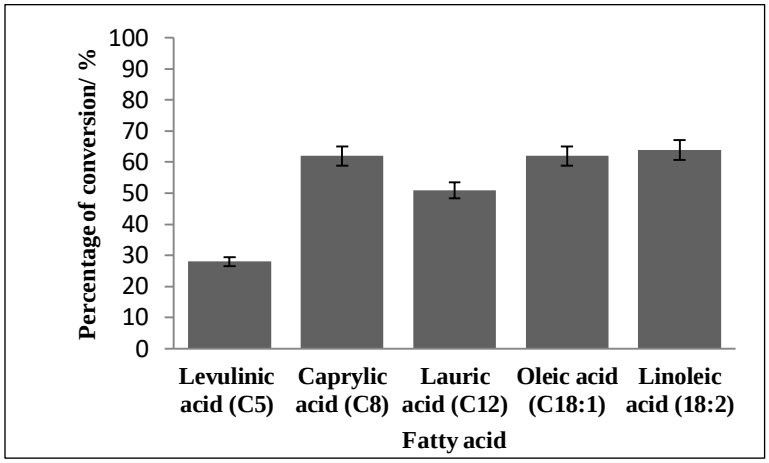


Figure 4. Effect of acyl donor on percentage of conversion in esterification of galactose with oleic acid. Conditions: (0.05 mmol), oleic acid (0.10 mmol), DMSO:[Bmim][BF_4] (1:20, 50 µL:1 mL), T1 lipase (2% (w/w), 60 °C, 2 hours.

The effect of acyl acceptor

In order to investigate the sugar preference of T1 lipase, esterification of linoleic acid with various sugars (glucose, fructose, sucrose, maltose, trehalose, xylitol and galactose) were carried out. Linoleic acid was chosen as the acyl donor in this study as it gave the best conversion in the study of the effect of fatty acid length previously. All monosaccharide's (glucose, fructose and galactose) gave moderate conversion at above 54% (Figure 5). The non-reducing disaccharides, sucrose and trehalose, gave better conversion than maltose (a reducing disaccharides), with sucrose exhibited the best conversion at 65%. Xylitol (a sugar alcohol) which would have better solubility in ILs than mono- and disaccharides, gave moderate conversion of 57%. These results showed that T1 lipase has no specificity for monosaccharides, disaccharides or sugar alcohol as the conversions were all above 45%. T1 lipase has also exhibited broad substrate specificity for its hydrolytic ability that it was able to degrade amorphous plastics as well as oils [33]. Only maltose gave slightly poorer conversion.

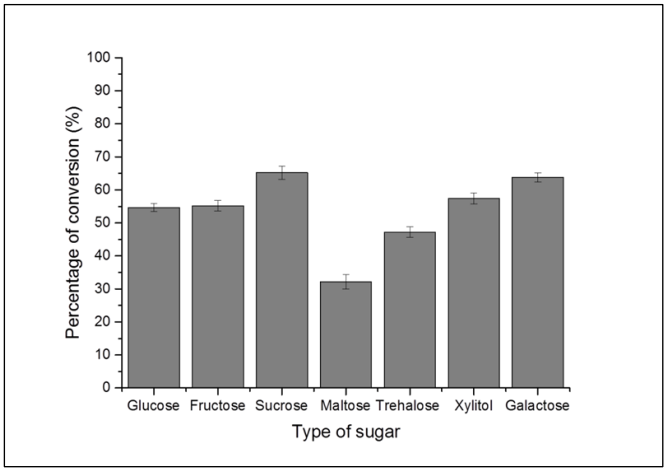


Figure 5. Effect of acyl donor on percentage of conversion in esterification of linoleic acid with various sugars. Conditions: sugar (0.05 mmol), oleic acid (0.10 mmol), DMSO:[Bmim][BF_4] (1:20, 50 µL:1 mL), T1 lipase (2% (w/w), 60 °C, 2 hours.

Enzymatic transesterification of maltose has previously been achieved in good yield in organic solvents and using various lipases; *tert*-butanol/DMSO, lipase from *Humicola lanuginosa* (immobilized on Celite) [34]; tert-butanol, *C. antarctica* lipase [35]; acetone/n-hexane, *C. antarctica lipase* B (Novozyme 435) [36]. Poorer yield for maltose esterification (21.9%) with acrylic acid in *tert*-butanol was reported by Tsukamoto et al. when glucose (80.3%) and fructose (64%) fared better using immobilized *C. antarctica lipase* B [37]. However, there is limited report on enzymatic esterification or transesterification of maltose in ILs. Most enzymatic preparation of sugar esters utilized immobilized lipase and it is useful to note that we are reporting the use of free lipase for similar work. This shows that T1 lipase has good stability for organic transformation on par with commercial immobilized lipase.

Conclusion

Successful enzymatic esterification of sugars in IL using thermostable T1 lipase with various fatty acid has been reported. Optimum temperature for T1 lipase in this work was like previous report. We can conclude that T1 lipase has the potential to synthesize sugar ester at or above 60 °C for short time incubation in ILs as reaction media, and T1 lipase exhibited broad specificity either for the sugars or fatty acids which is good for future commercial application of T1 lipase.

Acknowledgement

This project was supported by the Ministry of Science, Technology and Innovation, Malaysia under Exploratory Research Grant Scheme ERGS/1/11/STG/UPM/03/11 with Vot. number 5527054.

References

1. Leow, T. C., Rahman, R. N. Z. R. A., Basri, M. and Salleh, A. B. (2004). High level expression of thermostable lipase from *Geobacillus* sp. strain T1. *Bioscience, Biotechnology, and Biochemistry*, 68(1): 96-103
2. Rahman, R. N. Z. R. A., Leow, T. C., Salleh, A. B. and Basri, M. (2007). *Geobacillus zalihae* sp. nov., a thermophilic lipolytic bacterium isolated from palm oil mill effluent in Malaysia. *BMC Microbiology*, 7: 77.
3. Mozhaev, V. V., Berezin, I. V., and Martinek, K. (1988). Structure-stability relationship in proteins: Fundamental tasks and strategy for the development of stabilized enzyme catalyst for biotechnology. *CRC Critical Review in Biochemistry*, 173: 147-154.
4. Baker, I. J. A., Matthews, B., Suares, H., Krodkiewska, I., Furlong, D. N., Grieser, F. and Drummond, C. J. (2000). Sugar fatty acid ester surfactants: Structure and ultimate aerobic biodegradability. *Journal of Surfactants and Detergents*, 3(1): 1-11.
5. Staroń, J., Dąbrowski J. M., Cichoń, E. and Guzik, M. (2018) Lactose esters: synthesis and biotechnological applications. *Critical Reviews in Biotechnology*, 38(2): 245-258
6. Pyo, S.-H., Chen, J., Ye, R. and Hayes, D. G. (2019). Chapter 10 - Sugar Esters, Editors: Hayes, D. G., Solaiman, D. K. Y. and Ashby, R. D. Biobased Surfactants (Second Edition), AOCS Press, Urbana, USA: pp. 325-363.
7. Chang, S. W. and Shaw, J. F. (2009). Biocatalysis for the production of carbohydrate esters. *New Biotechnology*, 26(3–4): 109-116.
8. Yoo, I. S., Park, S. J. and Yoon, H. H. (2007). Enzymatic synthesis of sugar fatty acid esters. *Journal of Industrial and Engineering Chemistry*, 13(1): 1-6.
9. Gumel, A. M., Annuara, M. S. M., Heidelberg, T. and Chisti, Y. (2011). Lipase mediated synthesis of sugar fatty acid esters. *Process Biochemistry*, 46: 2079-2090.
10. Kennedy, J. F., Kumar, H., Panesar, P. S., Marwaha, S. S., Goyal, R., Parmar, A. and Kaur, S. (2006). Enzyme-catalyzed regioselective synthesis of sugar esters and related compounds. *Journal of Chemical Technology & Biotechnology*, 81: 866-876.
11. Kobayashi, T. (2011). Lipase-catalyzed syntheses of sugar esters in non-aqueous media, *Biotechnology Letters*, 33: 1911-1919.
12. Hallett, J. P. and Welton, T. (2011). Room-temperature ionic liquids: solvents for synthesis and catalysis. 2. *Chemical Reviews*, 111: 3508-3576.
13. Yang, Z. and Huang, Z. L. (2012). Enzymatic synthesis of sugar fatty acid esters in ionic liquids. *Catalysis Science & Technology*, 2: 1767-1775.

14. Abdulmalek, E., Mohd. Saupi, H. S., Tejo, B. A., Basri, M., Salleh, A. B., Rahman, R. N. Z. R. A. and Abdul Rahman, M. B. (2012). Improved enzymatic synthesis of galactose oleate ester in ionic liquid. *Journal of Molecular Catalysis B: Enzymatic*, 76: 37-43.
15. Abdulmalek, E., Hamidon, N. F. and Abdul Rahman, M. B. (2016) Optimization and characterization of lipase catalysed synthesis of xylose caproate ester in organic solvents. *Journal of Molecular Catalysis B: Enzymatic*, 132: 1-4.
16. Lee, K. P. and Kim, H. K. (2016). Antibacterial effect of fructose laurate synthesized by *Candida antarctica* B lipase-mediated transesterification. *Journal of Microbiology and Biotechnology*, 26(9): 1579-1585.
17. Shin, D. W., Mai, N. L., Bae, S.-W. and Koo, Y. (2019). Enhanced lipase-catalyzed synthesis of sugar fatty acid esters using supersaturated sugar solution in ionic liquids. *Enzyme and Microbial Technology*, 126: 18-23.
18. Sang, H. L., Dung, T. D., Sung, H. H., Chang, W.-J. and Koo, Y.-M. (2008). Lipase-catalyzed synthesis of fatty acid sugar ester using extremely supersaturated sugar solution in ionic liquids. *Biotechnology and Bioengineering*, 99(1): 1-8.
19. Ha, S. H., Hiep, N. M., Lee, S. H. and Koo, Y.-M. (2009). Optimization of lipase-catalyzed glucose ester synthesis in ionic liquids. *Bioprocess and Biosystems Engineering*, 33(1): 63-70.
20. Pang, N., Gu, S.-S, Wang, J., Cui, H.-S., Wang, F.-Q., Liu, X., Zhao, X.-Y. and Wu, F.-A. (2013). A novel chemoenzymatic synthesis of propyl caffeate using lipase-catalyzed transesterification in ionic liquid. *Bioresource Technology*, 139: 337-342.
21. Ju1, X., Li, J., Hou, M. and Tao, J. (2015). A lipase-catalyzed process for green synthesis of temsirolimus. *Engineering in Life Sciences*, 15: 229-233.
22. Kumar, A., Dhar, K., Kanwar, S. S., Arora, P. K. (2016), Lipase catalysis in organic solvents: Advantages and applications. *Biological Procedures Online*, 18: 1-11.
23. Raku, T., Kitagawa, M., Shimakawa, H. and Tokiwa, Y. (2003). Enzymatic synthesis of trehalose esters having lipophilicity. *Journal of Biotechnology*, 100(3): 203-208.
24. Findrik, Z., Megyeri, G., Gubicza, L., Bélafi-Bakó, K., Nemestóthy, N. and Sudar, M. (2016). Lipase catalyzed synthesis of glucose palmitate in ionic liquid. *Journal of Cleaner Production*, 112(1): 1106- 1111.
25. Wang, X., Li, D., Qu, M., Durrani, R., Yang, B. and Wang, Y. (2017). Immobilized MAS1 lipase showed high esterification activity in the production of triacylglycerols with n-3 polyunsaturated fatty acids. *Food Chemistry*, 216: 260-267.
26. Onoja, E., Chandren, S., Razak, F. I. A. and Wahab, R. A. (2018). Enzymatic synthesis of butyl butyrate by *Candida rugosa* lipase supported on magnetized-nanosilica from oil palm leaves: Process optimization, kinetic and thermodynamic study. *Journal of the Taiwan Institute of Chemical Engineers*, 91: 105-118.
27. Yadav, G. D. and Devendran, S. (2012). Lipase catalyzed synthesis of cinnamyl acetate via transesterification in non-aqueous medium. *Process Biochemistry*, 47(3): 496-502.
28. ChemSpider (Royal Society of Chemistry) http://www.chemspider.com/Chemical-Structure.3756.html [Access online 19th July 2019].
29. Uribe, S. and Sampedro, J. G. (2003). Measuring solution viscosity and its effect on enzyme activity. *Biological Procedures Online*, 5(1): 108-115.
30. Di, X., Zhang, Y., Fu, J., Yu, Q., Wang, Z. and Yuan, Z. (2019) Biocatalytic upgrading of levulinic acid to methyl levulinate in green solvents. *Process Biochemistry*, 81: 33 – 38
31. Lee, A., Chaibakhsh, N., Rahman, M. B. A., Basri, M. and Tejo, B. A. (2010). Optimized enzymatic synthesis of levulinate ester in solvent-free system. *Industrial Crops and Products*, 32(3): 246-251.
32. Leow, T. C., Rahman, R. N. Z. R. A., Basri, M. and Salleh, A. B. (2007) A thermoalkaliphilic lipase of *Geobacillus sp*. T1. *Extremophiles*, 11(3): 527-535.
33. Mohamed, R. A., Salleh, A. B., Leow, A. T. C., Yahaya, N. M. and Abdul Rahman, M. B. (2017). Ability of T1 lipase to degrade amorphous P(3HB): Structural and functional study. *Molecular Biotechnology*, 59: 284.
34. Ferrer, M., Cruces M. A., Plou, F. J., Bernabé, M. and Ballesteros, A. (2000). A simple procedure for the regioselective synthesis of fatty acid esters of maltose, leucrose, maltotriose and n-dodecyl maltosides. *Tetrahedron*, 56(24): 4053-4061
35. Woudenberg-van Oosterom, M., van Rantwijk, F. and Sheldon, R. A. (1996). Regioselective acylation of disaccharides in *tert*-butyl alcohol catalyzed by *Candida antarctica* lipase. *Biotechnology and Bioengineering*, 49: 328-333.

36. Jia, C., Zhao, J., Feng, B., Zhang, X. and Xia, W. (2010). A simple approach for the selective enzymatic synthesis of dilauroyl maltose in organic media. *Journal of Molecular Catalysis B: Enzymatic*, 62(3–4): 265-269.
37. Tsukamoto, J., Haebel, S., Valença, G. P., Peter, M. G. and Franco, T. T. (2008). Enzymatic direct synthesis of acrylic acid esters of mono- and disaccharides. *Journal of Chemical Technology and Biotechnology*, 83: 1486-1492.

Malaysian Journal of Analytical Sciences (MJAS)
Published by Malaysian Analytical Sciences Society

VORTEX-ASSISTED SUPRAMOLECULAR-BASED DISPERSIVE LIQUID PHASE MICROEXTRACTION FOR SPECTROPHOTOMETRIC DETERMINATION OF RHODAMINE B IN CHILI POWDER

(Supramolekul Berasaskan Serakan Cecair Fasa Pengekstrakan Mikro Berbantu-Vorteks untuk Penentuan Spektrofotometrik Rhodamin B dalam Serbuk Cili)

Renitha Harikrishnan[1], Kavisha Sundraraj[2], Boon Yih Hui[3], Nur Nadhirah Mohamad Zain[3], Noorfatimah Yahaya[3], Kavirajaa Pandian Sambasevam[4], Sharifah Mohamad[5,6], Yatimah Alias[5,6], Muggundha Raoov[5,6]*

[1] *School of Distance Education, Universiti Sains Malaysia, 11800, Pulau Pinang, Malaysia*
[2] *Department of Chemical Science, Faculty of Science, Universiti Tunku Abdul Rahman, Kampar 31900, Malaysia*
[3] *Integrative Medicine Cluster, Advanced Medical & Dental Institute, Universiti Sains Malaysia, Pulau Pinang 13200, Malaysia*
[4] *School of Chemistry and Environment, Universiti Teknologi MARA, Kuala Pilah, Negeri Sembilan, Malaysia*
[5] *Department of Chemistry, Faculty of Science*
[6] *Universiti Malaya Centre for Ionic Liquids (UMCiL), Department of Chemistry, Faculty of Science Universiti Malaya, Kuala Lumpur 50603, Malaysia*

**Corresponding author: muggundha@um.edu.my*

Received: 16 December 2019; Accepted: 8 March 2020

Abstract

A vortex-assisted supramolecular-based dispersive liquid phase microextraction technique was established to detect trace quantities of Rhodamine B (RhB) in chili powder prior to its determination by ultraviolet-visible spectrophotometry. The supramolecular solvent, which was made of reverse micelles of 1-pentanol created through self-assembly processes, was injected into the aqueous sample solution as fine droplets and assisted by vortexing, which accelerated the mass transfer of target analyte into the supramolecular solvent phase. Five important parameters (type and volume of the extraction solvent, extraction time, sample pH, and ionic strength) were investigated, and the optimum conditions were as follows: 400 µL of 1-pentanol as the supramolecular solvent; 30 min extraction time; pH 5; and 15% salt addition. Under optimum conditions, linearity was in the range of 0.1 to 2.5 mg kg^{-1}. The detection limit was 0.008 mg kg^{-1} with pre-concentration factor of 16, and the relative standard deviation (n = 5) was < 1.48%. The method was successfully applied to detect and measure RhB in selected chili powder samples, and good spiked recoveries in the range of 95.0 to 115.2% were obtained. This method has direct applications for monitoring the presence of potentially harmful dyes in processed foods.

Keywords: rhodamine B, UV-Vis spectrophotometry, supramolecular solvent, chili powder

Abstrak

Supramolekul berasaskan serakan fasa cecair pengekstrakan mikro berbantu vorteks (VASM-DLPME) telah dibangunkan untuk mengesan kuantiti Rhodamin B (RhB) dalam serbuk cili dengan menggunakan spektrofotometrik UV-Vis. Pelarut supramolekul adalah misel songsang yang dihasilkan daripada 1-pentanol melalui proses pemasangan kendiri dan disuntik ke dalam larutan sampel akueus sebagai titisan halus dibantu oleh vorteks, yang mempercepatkan masa pemindahan daripada analisis sasaran ke dalam fasa pelarut supramolekul. Lima parameter penting seperti jenis dan isipadu pelarut pengekstrakan, masa pengekstrakan, sampel pH dan kekuatan ionik telah dikaji dan keadaan optimum yang diperoleh adalah seperti berikut: 400 µL 1-pentanol

sebagai pelarut supramolekul, masa pengekstrakan selama 30 minit pada pH 5 dengan penambahan garam sebanyak 15%. Di bawah keadaan yang optimum, kelinearan didapati dalam julat 0.1 hingga 2.5 mg kg^{-1}. Had pengesanan yang diperolehi adalah 0.008 mg kg^{-1} dengan faktor pra-kepekatan 16 dan sisihan piawai relatif (RSD, n = 5) kurang daripada 1.48% telah dicapai. Kaedah ini telah berjaya diaplikasikan untuk penentuan RhB dalam sampel serbuk cili terpilih dan kadar pemulihan berada pada julat 95.0-115.2% diperolehi. Kaedah ini mempunyai aplikasi langsung untuk pemantauan pewarna berbahaya dalam makanan yang diproses.

Kata kunci: rhodamin B, spektrofotometri UV-Vis, pelarut supramolekul, serbuk cili

Introduction

Chili powder is a popular spice due to its beneficial health properties and the pungency and flavour it adds to dishes. Chili powder also is an ingredient utilized by the pabulum manufacturing industry in the formulation of a wide range of products, including oriental dishes, curries, sauces, and pickles. To meet the worldwide demand for chili powder, artificial food colorants are often added to it to preserve its natural colour during food processing and to create the desired coloured appearance [1].

Thus, the quality of chili powder is measured by the brightness and intensity of the spice's colour, and this affects its economic value. Colour additives are widely used in the food industry to make food more attractive, appealing, and appetizing [2]. Rhodamine B (RhB), which belongs to the class of synthetic azo dyes, was used commercially in chili powders to intensify their colour, but its use was prohibited more than 50 years ago. Nevertheless, spices from Vietnam and paprika and chimi churri from Argentina have been found to contain RhB [3].

RhB consists of xanthene rings and aromatic compounds that are an important source of environmental pollution. Their metabolites are considered to be carcinogenic and to have reproductive and developmental toxicity as well as neurotoxicity towards humans and animals [4, 5]. Consequently, most countries have banned and controlled its usage as a food additive. Therefore, monitoring of RhB, particularly in food samples, has become a great concern, and an improved, easy method for detection of RhB in various samples is needed.

Numerous analytical techniques to detect RhB have been developed, including ultraviolet spectrophotometry [6], fluorescence spectrophotometry [7], capillary electrophoresis, and high performance liquid chromatography [8]. Among these methods, ultraviolet-visible (UV-Vis) spectrophotometry is an attractive method due to its simplicity of operation and low cost. However, this method has two major limitations: (i) co-elution effects from samples influence the signal of analytes and (ii) low concentration of analytes likely leads to unsatisfactory quantitative results [9]. To overcome these issues, different sample preparation techniques can be used to isolate, clean-up, and pre-concentrate the target analytes before their measurement to increase the sensitivity and accuracy of the method. Different sample preparation methods used to preconcentrate different organic pollutants include dispersive liquid–liquid microextraction (DLLME) [10], solid-phase extraction (SPE) [11], magnetic solid phase extraction [12, 13], solid-phase microextraction [14, 15], and supramolecular based dispersive liquid phase microextraction (SM-DLPME) [16-18].

SM-DLPME uses supramolecular solvents (SUPRAS) as an extractant. Their principle is based on partitioning of an analyte between an alkyl-based nano-structured solvent and a bulk aqueous sample. SUPRAS are water-immiscible liquids widely used in extraction and pre-concentration techniques due to their excellent ability to extract various types of compounds, including organic and inorganic species [19]. SUPRAS can provide different types of interaction (e.g. hydrophobic, ionic, and hydrogen bonding) with the organic compounds and hydrophobic complexes of metals with ligands [20]. These interactions are important for extracting analytes from the water phase to the supramolecular solvent phase to increase the extraction efficiency [21-23].

The aim of this research was to develop a new and fast microextraction method using dispersion of SUPRAS as the extractant phase into the aqueous phase, yielding a mild emulsification procedure, under vortex conditions. The resulting methodology, called vortex-assisted supramolecular-based dispersive liquid-phase microextraction (VASM-DLPME), was used to extract trace amounts of RhB from chili powder samples. The fine droplets formed sped up the adsorption equilibrium process due to the shorter diffusion distance and larger specific surface area of

the SUPRAS. The developed method was successfully applied to assess the content of RhB in a variety of commercial chili powders available in Malaysia.

Materials and Methods

Instrumentation

A Shimadzu UV-1800 spectrophotometer (Torrance, CA, USA) with 3 mL quartz cuvettes and wavelength of 553 nm was used for all sample analyses. pH measurements were performed using a pH meter (Hanna Instruments, Woonsocket, RI, USA). A tabletop centrifuge (Kubota, 4200, Osaka, Japan) (16000 rpm) was applied during the phase separation, and a digital control ultrasonic bath with adjustable temperature (Thermo-10D, Thermoline Scientific, Wetherill Park, Australia) was used for the sample preparation.

Chemicals and reagents

RhB standard (molecular weight: 479.02 g mol^{-1}) with > 95% purity was purchased from Sigma Aldrich (Milwaukee, WI, USA). High performance liquid chromatography (HPLC) grade methanol was supplied by Merck (Darmstadt, Germany). Ultrapure water was produced using the Sartorius Milli-Q system (Aubagne, France). The sample supernatant was filtered through 0.45 µm membrane filters before analysis. A 1 mL syringe needle was used to collect the upper layer of the extractant. SUPRAS (i.e., 1-octanol, 1-undecanol, and 1-dodecanol) were purchased from Merck, and 1-pentanol, 1-hexanol, and 1-heptanol were purchased from Sigma-Aldrich (St. Louis, MO, USA). All other reagents were of analytical grade and used without further purification.

The stock solutions of 100 mg L^{-1} for RhB were made using methanol. Ultrapure water was used to prepare the working standard solutions by diluting them to desired concentrations. All standard solutions were stored in the refrigerator (4 °C) to avoid degradation.

Sample preparation

Chili powders used for this study were purchased from a local market in Kuala Lumpur, Malaysia. Briefly, 0.5 g of chili powder was precisely weighed and quantitatively transferred into a 15 mL centrifuge tube containing 10 mL of methanol. The mixture was sonicated for 30 minutes at room temperature to homogeneously agitate the chili powder. Thereafter, the sample mixture was centrifuged at 4000 rpm for 10 minutes. The supernatant was collected and filtered using a 0.45 µm membrane filter immediately to remove suspended particulate matter.

VASM-DLPME procedure

A 0.2 mL aliquot of sample solution containing the analyte was transferred into a centrifuge tube. Adjustment of the sample solution to pH 5 was carried out by dropwise addition of 0.1 M of HCl or NaOH solutions before subjecting the sample to the VASM-DLPME procedure. Next, 0.4 mL of SUPRAS as the extractant was injected into the sample solution, followed by addition of deionized water up to 5 mL. This contact with water is a crucial step that allows the formation of amphiphilic structures such as micelles. The solution was then vortexed for 30 s, followed by centrifugation for 5 minutes at 4000 rpm to facilitate phase separation.

Next, 0.3 mL of the extractant-rich phase was collected and diluted to 4 mL in methanol. This step was to ensure that the final volume was viable for transfer into the optical cell for UV measurement at the respective absorption wavelength and to reduce the viscosity of the extractant phase. Figure 1 illustrates the absorbance of the diluted extractant-rich phase measured at 553 nm, and Figure 2 shows the proposed VASM-DLPME procedure in schematic form.

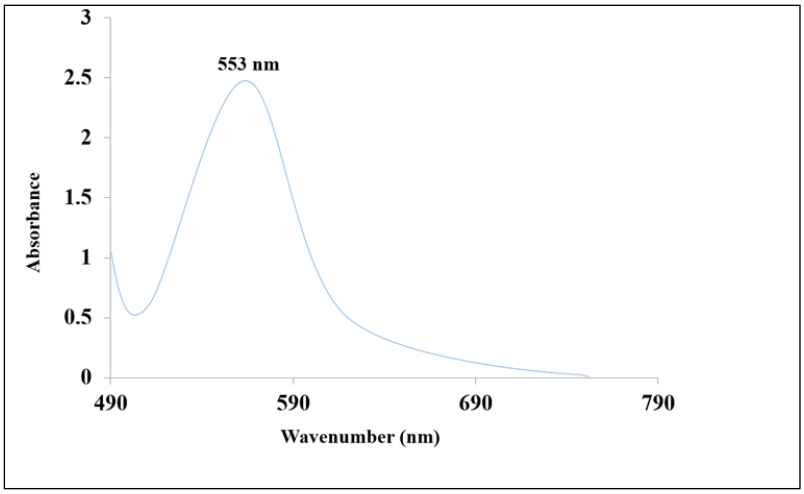


Figure 1. Absorbance of the diluted extractant-rich phase measured at 553 nm

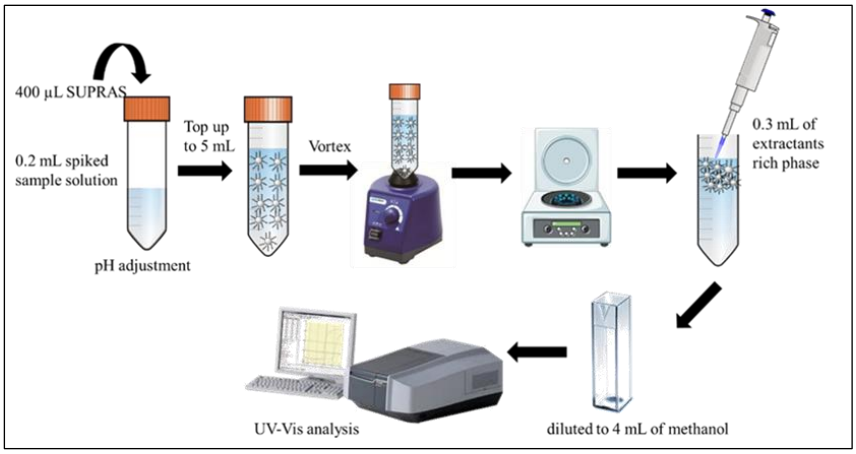


Figure 2. The proposed VASM-DLPME procedure

Optimization and validation of the VASM-DLPME procedure

One-variable-at-a-time analysis was employed for the optimization procedures (i.e. one variable was manipulated while the other variables were kept constant). For the optimization, 1.0 mg kg^{-1} of the spiked blank chili powder was used, and all measurements were conducted in triplicate using the UV-Vis spectrophotometer. The extraction efficiency, EE (expressed in %), was calculated using the following equation 1.

$$EE = \frac{V_f}{V_i} \text{ x } \frac{C_f \text{ x } D_f}{C_i} \text{ x } 100\ \% \quad (1)$$

where V_f is the final volume of the sample, V_i is the initial volume of the sample, C_f is the concentration in the spiked sample, C_i is the spiking concentration of RhB, and D_f is the dilution factor.

Validation to assess the viability of the method included measurement of linearity, repeatability, relative recovery, limit of detection (LOD), and limit of quantification (LOQ). The latter were calculated using the following formulas:

$$\text{LOD} = \frac{3\ x\ Sd}{b} \quad (2)$$

$$\text{LOQ} = \frac{10\ x\ Sd}{b} \quad (3)$$

where *Sd* is the standard deviation of 10 replicate measurements of blank samples and *b* is the slope of each calibration curve.

The enrichment factor (EF) was calculated as the ratio of the slope of the calibration curve of the RhB after pre-concentration to that prior to pre-concentration. The precision of the developed procedure was evaluated as intra- (repeatability) and inter- (reproducibility) day precision, which were analysed using five replicates (n =5) each.

Results and Discussion

Effect of type of SUPRAS

The extraction solvent should have several characteristics, such as low volatility, low toxicity, low solubility in water, and low amounts of interfering agent present in the sample matrix [24]. Furthermore, the desired analytes should have high solubility in the selected solvent for better extraction performance. Short-chain alkanols are better proton donors than longer ones, hence they are more capable of forming hydrogen bonding, whereas hydrophobic interactions dominate in the case of long-chain alkanols [25]. For this reason, six different types of alkanol-based SUPRAs (C5–C11) were studied. Figure 3 shows that extraction efficiency decreased with the increasing chain length of alkanols. This revealed that hydrogen bonding between the RhB and SUPRASs was the dominant interaction during the extraction. Subsequently, 1-pentanol with medium alkyl chain length was selected as the suitable SUPRAS for the developed technique, as it provided a compromise between the stability and polarity of RhB and the extractant.

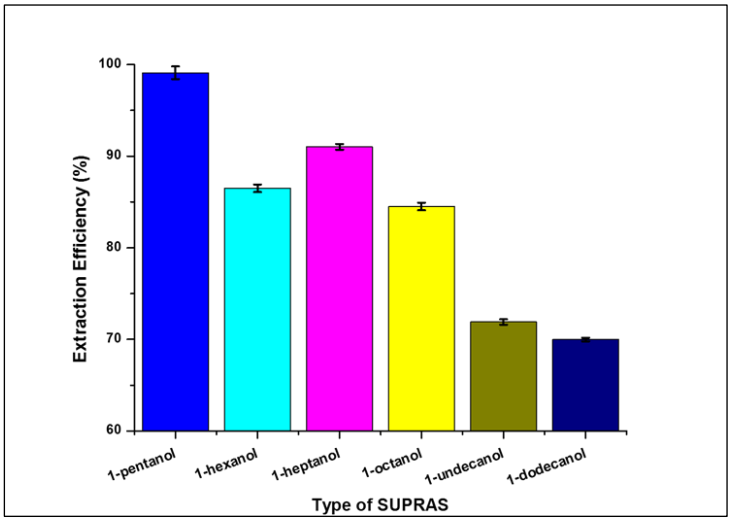


Figure 3. Effect of the type of SUPRAS on the extraction efficiency of RhB. Conditions: 5.0 mL of sample volume spiked with 1.0 mg kg^{-1} of RhB and 0.5 mL of SUPRAS

Effect of the volume of the SUPRAS

Selection of the optimum volume for the extraction solvent is another important factor in microextraction because it influences the extraction recovery [26]. To examine this effect, different volumes of SUPRAS from 200 to 750 µL at 50 µL intervals were investigated. As the extraction solvent volume increased, the final solvent volume collected after centrifugation also increased; however, this also led to reduction of the analyte signals. This result shows that it is essential to keep the volume of extraction solvent as low as possible to achieve maximum signals [27]. A larger volume of SUPRAS makes the collected final rich phase more dilute, and consequently decreases the extraction

efficiency [16]. Unfortunately, it is not always possible to reduce the solvent volume as desired because a sufficient volume of solvent is needed for the analysis. The obtained results (Figure 4) demonstrated that the extraction efficiency was high in the SUPRAS volume of 400 µL and decreased thereafter. Therefore, considering the high repeatability, 400 µL was selected as the optimum SUPRAS volume.

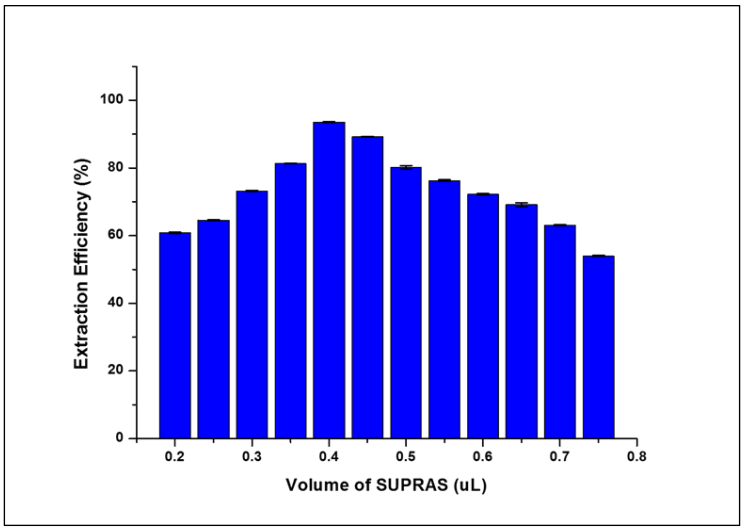


Figure 4. Effect of the volume of SUPRAS on the extraction efficiency of RhB. Conditions: 5.0 mL of sample volume spiked with 1.0 mg kg^{-1} of RhB and the SUPRAS 1-pentanol

Effect of extraction time

Sufficient extraction time is essential to ensure the formation of a homogeneous cloudy solution, which influences the complete transfer of analytes from the sample solution to the extractant phase [24]. The effect of extraction time on the extraction efficiency of RhB was evaluated from 10 to 30 minutes, and the results demonstrated that 30 minutes was adequate to reach the equilibrium between both phases (Figure 5). Hence, 30 minutes of extraction time was selected for subsequent analysis.

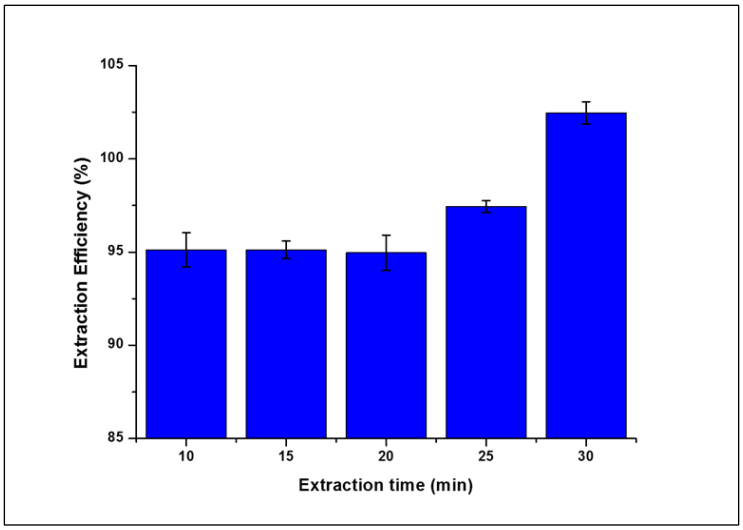


Figure 5. Effect of extraction time on the extraction efficiency of RhB. Conditions: 5.0 mL of sample volume spiked with 1.0 mg kg^{-1} of RhB and 0.4 mL of the SUPRAS 1-pentanol

Effect of pH

The sample pH can control the dissociation of target analytes with acid-base characteristics, thus it is another important factor that needs to be considered [16]. pH values ranging from 3 to 9 were evaluated, and the optimum analytical signal for RhB extraction was achieved at pH 5.0 (Figure 6). This can be explained by the molecular or ionic forms of RhB that were created during weak base protonation (or weak acid deprotonation), which usually interacted weakly with the SUPRAS micellar aggregate compared to the neutral form, thereby resulting in a lower extraction efficiency (Table 1). Therefore, pH 5.0 was selected as the optimum pH for the extraction of RhB in this study.

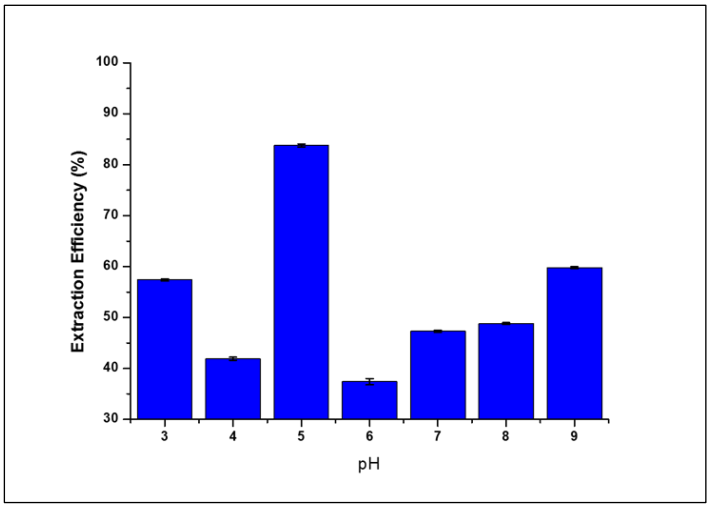
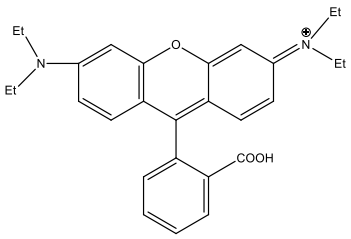
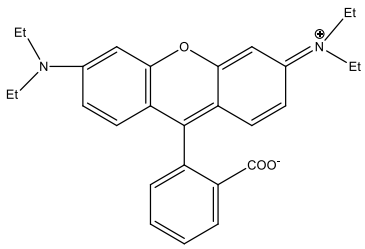
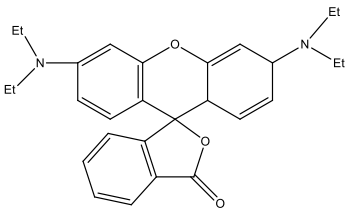


Figure 6. Effect of pH on the extraction efficiency of RhB. Conditions: 5.0 mL of sample volume spiked with 1.0 mg kg^{-1} of RhB and 0.4 mL of the SUPRAS 1-pentanol as SUPRAS and extraction time of 30 minutes

Table 1. Molecular structure of RhB under different pH conditions

pH < 5 **Protonated**	**pH 5** **Neutral**	**pH > 5** **Deprotonated**
		

Effect of ionic strength

Salt addition reduces the solubility of analytes in a sample solution, which can improve the extraction efficiency [24]. It also can increase the viscosity of the sample solution at higher concentrations, thereby affecting the physical properties of the extraction film and reducing the transfer of analytes towards the extractant phase [28]. To test the effect of ionic strength, 0–25% of NaCl was added to the sample solution. Extraction efficiency increased as salt concentration increased to 15% (w/v), but it decreased thereafter (Figure 7). This result can be explained by the fact

that higher ionic strength caused the sample solution to become more viscous, which likely restrained the transport of the analytes to the extractant phase, leading to lower extraction performance.

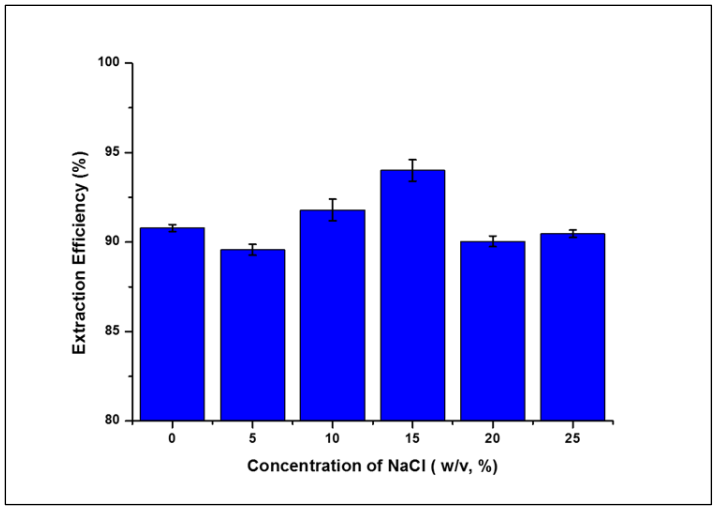


Figure 7. Effect of ionic strength on the extraction efficiency of RhB. Conditions: 5.0 mL at pH 5 of sample volume, spiked with 1.0 mg kg^{-1} of RhB and 0.4 mL of the SUPRAS 1-pentanol, and extraction time of 30 minutes

Analytical performance

Under optimum conditions, the calibration curve was linear over the range of 0.1 to 2.5 mg kg^{-1} with a coefficient of determination (R^2) of 0.9983. The precision of the method was evaluated by analysing 0.5 mg kg^{-1} of RhB five times continuously, and the RSD was 1.5%. The LOD and LOQ were 0.008 mg kg^{-1} and 0.03 mg kg^{-1}, respectively. The EF after pre-concentration was 16 at 1.0 mg kg^{-1}. The intra- (repeatability) and inter- (reproducibility) day precision were 0.82% and 1.05%, respectively (Table 2). To investigate the accuracy of the proposed method, blank chili powder was spiked with three different concentration of RhB (0.1, 0.5, and 1.0 mg kg^{-1}), and the recoveries of RhB ranged between 95.0% and 117% (Table 3).

Table 2. Validation parameters of the developed VASM-DLPME procedure

Validation Parameter	**Result**
Linearity range (mg kg^{-1})	0.1–2.5
Coefficient of determination (R^2)	0.9983
Regression equation	y = 0.4057x + 0.0245
LOD (mg kg^{-1})	0.008
LOQ (mg kg^{-1})	0.030
Enrichment factor at 1.0 mg kg^{-1}	16
Intra-day, RSD (%) at 0.5 mg kg^{-1}	0.82
Inter-day, RSD (%) at 0.5 mg kg^{-1}	1.05

Table 3. Recovery obtained from the measurement of RhB in spiked organic chili powder

Sample	Spiked Level (mg kg^{-1})	Found (mg kg^{-1})	Relative Recovery, RSD (%, n = 3)
Organic chili powder	0.1	0.095	95.00 ± 3.0
	0.5	0.587	117.47 ± 3.8
	1.0	1.152	115.23 ± 4.0

Analysis of real samples

To evaluate the feasibility of using the developed method to test real matrices, 10 different chili powders that are commercially available were purchased from a local market (Kuala Lumpur, Malaysia) to determine the contents of RhB. RhB was detected in several chili powder samples, which showed that the procedure was satisfactory for genuine food applications. Figure 8 shows the UV-Vis spectra of a real sample with detected RhB, and Table 4 tabulates the results of the detected RhB in real samples after analysis using the VASM-DLPME microextraction technique.

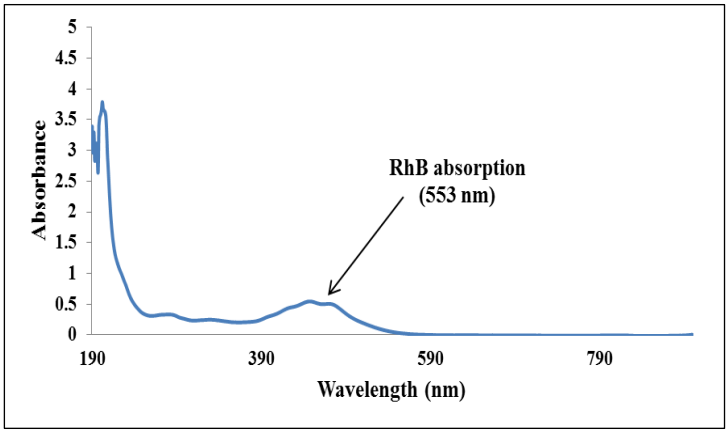


Figure 8. UV-Vis spectra of a real sample with detected RhB after analysis using the VASM-DLPME microextraction technique

Table 4. Results of the detected RhB in real samples after analysis using the VASM-DLPME procedure

Chili Powder	Concentration of RhB Residues (mg kg^{-1})
Sample 1	< LOQ
Sample 2	0.05
Sample 3	0.44
Sample 4	0.16
Sample 5	< LOQ
Sample 6	0.32
Sample 7	0.15
Sample 8	< LOQ
Sample 9	0.27
Sample 10	< LOQ

< LOQ = less than limit of quantification

Comparison with other reported methods

The analytical performance of the present method was compared with those reported in the literature for other methods, including SPE-UV spectrophotometry, SPE-HPLC, SPE-fluorescence spectrophotometry, liquid-liquid extraction-HPLC, and DSPE-HPLC (Table 5). Overall, the proposed VASM-DLPME produced results comparable to other methods in terms of LODs. It also is superior to the others because it uses SUPRAS that form micelle aggregates, and therefore it does not require the use of a dispersant solvent. Additionally, no heating is required during the extraction process, which greatly simplifies the operation.

Table 5. Comparison with results in the literature for RhB determination

Method	Limit of Detection ($mg\ kg^{-1}$)	Linear Range ($mg\ kg^{-1}$)	Reference
MIP-SPE-UV-Vis	2.57	0-12	[9]
SPE-UV	0.00746	0.02–51	[29]
HPLC-CL	0.0078	0.02–1.4	[30]
Fe_3O_4@ILs-β-CDCP	0.0052	0.1–9.0	[5]
VASM-DLPME/UV-Vis	8.0	0.1-2.5	This method

Conclusion

In the present study, a rapid and simple VASM-DLPME/UV-Vis spectrophotometric method for pre-concentration and measurement of RhB in chili powder samples was developed. The developed method is solvent minimized, cost-efficient, eco-friendly, and simple to operate. This study also successfully showed the great potential of SUPRAS as extractants for the determination of RhB in chili powder. Overall, the proposed SUPRAS-based microextraction is an attractive method that can be used as an alternative technique for extraction and off-line pre-concentration, and it is suitable for routine lab analysis and surveillance programs. This is important for the control of the presence of dyes in domestic and imported chili powders.

Acknowledgments

The authors would like to express their gratitude for a University Malaya Faculty Research Grant (GPF058B-2018). The authors acknowledge the Department of Chemistry, Faculty of Science, University of Malaya for the facilities provided.

References

1. Tsai, C.F., Kuo, C.H. and Shih, D.Y.C. (2015). Determination of 20 synthetic dyes in chili powders and syrup-preserved fruits by liquid chromatography/tandem mass spectrometry. *Journal of Food and Drug Analysis*, 23:453–462.
2. Vachirapatama, N., Mahajaroensiri, J. and Visessanguan, W. (2008). Identification and determination of seven synthetic dyes in foodstuffs and soft drinks on monolithic C_{18} column by high performance liquid chromatography. *Journal of Food & Drug Analysis*, 16:77–82.
3. Xu., X, Zhang, M., Wang, L., Zhang, S., Liu, M., Long, N., Qi, X., Cui, Z. and Zhang, L. (2016). Determination of rhodamine B in food using ionic liquid–coated multiwalled carbon nanotube–based ultrasound-assisted dispersive solid-phase microextraction followed by high-performance liquid chromatography. *Food Analytical Methods*, 9:1696–1705.
4. Jieping, C. and Zhu, X. (2016). Magnetic solid phase extraction using ionic liquid-coated core-shell magnetic nanoparticles followed by high-performance liquid chromatography for determination of rhodamine B in food samples. *Food Chemistry*, 200:10–15.
5. Ahmed Bakheet, A. A. and Zhu, X. S. (2017). Determination of Rhodamine B in food samples by Fe_3O_4@ionic liquids-β-cyclodextrin cross linked polymer solid phase extraction coupled with fluorescence spectrophotometry. *Journal of Fluorescene*, 27:1087–1094.

6. Sun, W. J., Li, J., Mele, G., Zhang, Z. Q. and Zhang, F. X. (2013). Enhanced photocatalytic degradation of rhodamine B by surface modification of ZnO with copper (II) porphyrin under both UV-Vis and visible light irradiation. *Journal of Molecular Catalysis A: Chemical*, 366: 84–91.
7. Ahmed Bakheet, A. A. and Zhu, X. S. (2017). Determination of rhodamine B pigment in food samples by ionic liquid coated magnetic core/shell Fe_3O_4@SiO_2 nanoparticles coupled with fluorescence spectrophotometry. *Science Journal of Chemistry*, 5:1–7.
8. Santiago Valverde, R., Sánchez Pérez, I., Franceschelli, F., Martínez Galera, M. and Gil García, M. D. (2007). Determination of photoirradiated tetracyclines in water by high-performance liquid chromatography with chemiluminescence detection based reaction of rhodamine B with cerium(IV). *Journal of Chromatography A*, 1167:85–94.
9. Liu, X., Zhang, X., Zhou, Q., Bai, B. and Ji, S. (2013). Spectrometric determination of rhodamine B in chili powder after molecularly imprinted solid phase extraction. *Bulletin of the Korean Chemical Society*, 34:3381–3386.
10. Souza, A. S., Siqueira, R.P., Prates, R. F., Bezerra, V. M., Rocha, D. da. S., Oliveira, M. V. and Santos, D. B. (2017). A dispersive liquid–liquid microextraction based on solidification of floating organic drop and spectrophotometric determination of uranium in breast milk after optimization using Box-Behnken design. *Microchemical Journal*, 134: 327–332.
11. Pichon, V. (2000). Solid-phase extraction for multiresidue analysis of organic contaminants in water. *Journal of Chromatography A*, 885: 195–215.
12. Tahmasebi, E., and Yamini, Y. (2012). Facile synthesis of new nano sorbent for magnetic solid-phase extraction by self assembling of bis-(2,4,4-trimethyl pentyl)-dithiophosphinic acid on Fe_3O_4@Ag core@shell nanoparticles: Characterization and application. *Analytical Chimica Acta*, 756: 13–22.
13. Zheng, H., Ding, J., Zheng, S., Zhu, G. and Yuan, B. (2016). Facile synthesis of magnetic carbon nitride nanosheets and its application in magnetic solid phase extraction for polycyclic aromatic hydrocarbons in edible oil samples. *Talanta*, 148: 46–53.
14. Rubio, L., Sanllorente, S., Sarabia, L. A. and Ortiz, M. C. (2014). Optimization of a headspace solid-phase microextraction and gas chromatography/mass spectrometry procedure for the determination of aromatic amines in water and in polyamide spoons. *Chemometrics and Intelligent Laboratory Systems*, 133: 121–135.
15. Trujillo-Rodríguez, M. J., Yu, H., Cole, W. T. S., Ho, T. D., Pino, V., Anderson, J. L. and Afonso, A. M. (2014). Polymeric ionic liquid coatings versus commercial solid-phase microextraction coatings for the determination of volatile compounds in cheeses. *Talanta*, 121: 153–162.
16. Scheel, G. L., and Tarley, C. R. T. (2017). Feasibility of supramolecular solvent-based microextraction for simultaneous preconcentration of herbicides from natural waters with posterior determination by HPLC-DAD. *Microchemical Journal*, 133: 650–657.
17. Ballesteros-Gómez, A., Sicilia, M. D. and Rubio, S. (2010). Supramolecular solvents in the extraction of organic compounds. A review. *Analytical Chimica Acta*, 677: 108–130.
18. Moradi, M., Kashanaki, R., Borhani, S., Bigdeli, H., Abbasi, N. and Kazemzadeh, A. (2017). Optimization of supramolecular solvent microextraction prior to graphite furnace atomic absorption spectrometry for total selenium determination in food and environmental samples. *Journal of Molecular Liquids*, 232: 243–250.
19. Seebunrueng, K., Dejchaiwatana, C., Santaladchaiyakit, Y., and Srijaranai, S. S. (2017). Development of supramolecular solvent based microextraction prior to high performance liquid chromatography for simultaneous determination of phenols in environmental water. *RSC Advances*, 7: 50143–50149.
20. Yilmaz, E. and Soylak, M. (2014). Development a novel supramolecular solvent microextraction procedure for copper in environmental samples and its determination by microsampling flame atomic absorption spectrometry. *Talanta*, 126: 191–195.
21. Shamsipur, M., Zohrabib, P., and Hashemi, M. (2015). Application of a supramolecular solvent as the carrier for ferrofluid based liquid-phase microextraction for spectro fluorimetric determination of levofloxacin in biological samples. *Analytical Methods*, 7: 9609–9614.
22. Ballesteros-Gomez, A., Rubio, S. and Perez-Bendito, D. (2009). Potential of supramolecular solvents for the extraction of contaminants in liquid foods. *Journal of Chromatography A*, 1216: 530–539.
23. Rezaei, F., Yamini, Y., Moradi, M. and Daraei, B. (2013). Supramolecular solvent-based hollow fiber liquid phase microextraction of benzodiazepines. *Analytical Chimica Acta*, 804: 135–142.

24. Ezoddin, M., Majidi, B. and Abdi, K. (2015). Ultrasound-assisted supramolecular dispersive liquid–liquid microextraction based on solidification of floating organic drops for preconcentration of palladium in water and road dust samples. *Journal of Molecular Liquids*, 209: 515–519.
25. López-Jiménez, F. J., Rosales-Marcano, M. and Rubio, S. (2013). Restricted access property supramolecular solvents for combined microextraction of endocrine disruptors in sediment and sample cleanup prior to their quantification by liquid chromatography – tandem mass spectrometry. *Journal of Chromatography A*, 1303: 1–8.
26. Yang, D., Li, X., Meng, D., Wang, M. and Yang, Y. (2017). Supramolecular solvents combined with layered double hydroxide-coated magnetic nanoparticles for extraction of bisphenols and 4-tert- octylphenol from fruit juices. *Food Chemistry*, 237: 870–876.
27. Dursun, G., Yildiz, E., and Cabuk, H. (2018). Supramolecular solvent-based microextraction of propachlor and prometryn herbicides in soil samples prior to liquid chromatographic analysis. *Cumhuriyet Science Journal*, 39:833–841.
28. Rezaei, F., Yamini, Y., Asiabi, H., and Moradi, M. (2015). Determination of diphenylamine residue in fruit samples by supercritical fluid extraction followed by vesicular based-supramolecular solvent microextraction. *Journal of Supercritical Fluids*, 100:79–85.
29. Soylak, M., Unsal, Y. E., Yilmaz, E. and Tuzen, M. (2011). Determination of rhodamine B in soft drink, waste water and lipstick samples after solid phase extraction. *Food Chemical Toxicology*, 49:1796–1799
30. Zhang, Q., Cui, H., Myint, A., Lian, M. and Liu, L. (2005). Sensitive determination of phenolic compounds using high-performance liquid chromatography with cerium (IV)-rhodamine 6G-phenolic compound chemiluminescence detection. *Journal of Chromatography A*, 1095: 94–101.

Malaysian Journal of Analytical Sciences (MJAS)
Published by Malaysian Analytical Sciences Society

CONTROLLED CONCENTRATION OF Mn SALT FOR THE SYNTHESIS OF MANGANESE OXIDE/MESOPOROUS CARBON FILM AS POTENTIAL ELECTRODES FOR SUPERCAPACITOR

(Kepekatan Garam Mn Terkawal terhadap Sintesis Mangan Oksida/Karbon Filem Berliang Meso sebagai Elektrod Berpotensi bagi Superkapasitor)

Mahanim Sarif @ Mohd Ali[1,3], Zulkarnain Zainal[1,2]*, Mohd Zobir Hussein[1], Mohd Haniff Wahid[2], Noor Nazihah Bahrudin[2]

[1]*Materials Synthesis and Characterization Laboratory, Institute of Advanced Technology*
[2]*Department of Chemistry, Faculty of Science*
Universiti Putra Malaysia, 43400 UPM Serdang, Selangor, Malaysia
[3]*Forest Product Division,*
Forest Research Institute Malaysia, 52109 Kepong, Selangor, Malaysia

**Corresponding author: zulkar@upm.edu.my*

Received: 15 December 2019; Accepted: 11 March 2020

Abstract

Manganese oxide (Mn_2O_3) mesoporous carbon (MPC) was synthesized by the incipient wetness of impregnation at room temperature and followed by calcination of 300 °C. The structure and morphology of Mn_2O_3/MPC were characterized by Fourier transform infrared (FTIR) spectrum, atomic force microscopy (AFM) and field emission scanning electron microscopy (FESEM). The electrochemical performance of synthesized composites was evaluated by cyclic voltammetry (CV), galvanostatic measurement of charge-discharge (GCD) as well as power and energy density characteristics. The specific capacitance of the composite electrode when 10 wt.% Mn salt was coated on the surface of MPC film could reach 53.59 mF cm^{-2} as compared to MPC film at only 15.23 mF cm^{-2}. These are in good agreement with the electrochemical performance improvement results of the energy and power density recorded for Mn_2O_3/MPC, which lead to higher specific capacitance as supported by the CV and GCD results in 1 M potassium chloride (KCl) of electrolyte. This enhanced capacitance was attributed to the outstanding electric properties of MPC film as well as the faradaic redox reactions of manganese oxide as proven by FESEM and EDX analysis. The results indicate the promising application of the fabricated Mn_2O_3/MPC composite as electrodes for supercapacitors.

Keywords: manganese oxide, mesoporous carbon, composite, specific capacitance, supercapacitor

Abstrak

Mangan oksida (Mn_2O_3) karbon filem berliang meso (MPC) telah disintesis melalui kaedah serapan basah pada suhu bilik dan diikuti oleh proses pengkalsinan pada suhu 300 °C. Struktur dan morfologi Mn_2O_3/MPC dicirikan oleh spektrum inframerah transformasi Fourier (FTIR), mikroskop kekuatan atom (AFM) dan mikroskop pengimbasan elektron serta pelepasan medan (FESEM). Prestasi elektrokimia komposit yang disintesis telah dinilai oleh kitaran voltammetri (CV), pengukuran pelepasan galvanostatik (GCD) juga ciri-ciri kuasa dan ketumpatan tenaga. Kapasitan khusus elektrod komposit apabila garam 10 wt.% Mn dilapisi pada permukaan MPC filem boleh mencapai 53.59 mF cm^{-2} berbanding dengan MPC filem hanya 15.23 mF cm^{-2}. Ini menyamai dengan peningkatan prestasi elektrokimia terhadap tenaga dan ketumpatan kuasa yang dicatatkan untuk Mn_2O_3/MPC, yang membawa kepada kapasitan khusus yang lebih tinggi, disokong oleh keputusan CV dan GCD dalam elektrolit 1 M kalium klorida (KCl). Peningkatan kapasitan ini adalah disebabkan oleh sifat-sifat elektrik yang cemerlang dari MPC filem serta tindak balas redoks faradaik dari mangan seperti yang dibuktikan juga dalam analisis FESEM dan EDX. Keputusan menunjukkan fabrikasi komposit Mn_2O_3/MPC mempunyai potensi aplikasi sebagai elektrod bagi superkapasitor.

Kata kunci: mangan oksida, karbon berliang meso, komposit, kapasitan khusus, superkapasitor

Introduction

Supercapacitors are widely used for electrochemical energy storage devices that are specifically tailored for rapid storage and energy release. Supercapacitors store energy using either electron/ electrolyte interface ion adsorption (electric double-layer capacitors) or rapid redox reactions in electrode materials (pseudocapacitors) [1-4]. Specific supercapacitors store energy much greater than conventional capacitors. A significant number of electrode materials have been widely used to create high-performance supercapacitors using different carbonaceous materials such as graphene [5], graphene oxide [6] and carbon nanotube [7].

In fact, transition metal oxide and conducting polymer were also used to improve the specific capacitance and power density of the supercapacitors by taking benefit of their pseudocapacitive behaviour [1-2]. Conventional carbon materials, including mesoporous carbon do not only have small electrical double layer capacitors (EDLC) surface area but also restricted power and energy density. Carbon material modification techniques have been suggested to solve these issues [4, 8-12]. A nanosized, high-capacitance MnO_x composite electrode embedded in an extremely conductive carbon material support would be advantageous in the design of supercapacitor electrodes. For instance, manganese oxide (MnO_2)/carbon aerogel [13], manganese oxide (Mn_2O_3)/mesoporous carbon [14-17], manganese oxide (MnO_2)/carbon nanotube, ruthenium oxide (RuO_2)/carbon nanotube and nickel oxode (NiO)/carbon nanotube [18] for the manufacturing of composite electrode materials, have been commonly used. The composites demonstrate enhanced capacitive behaviour due to their double-layer capacitance charge storage mechanisms [4, 9]. This has resulted in the development of composite materials for electrochemical condensers based on a mixture of carbon products and metal oxide.

Therefore, carbon material of MPC film through sol gel polymerization and self-assembly of resorcinol and formaldehyde under ambient conditions is developed in the present study. In order to combine outstanding electrochemical efficiency of MPC with pseudocapacitive properties of MnO, the latter was doped on the MPC film by incipient impregnation at different concentrations of Mn (0 – 15 wt.%). The composites were calcined at 300 °C for 2 hours under nitrogen atmosphere to become the Mn doped MPC films. These composite films were manufactured as electrodes for supercapacitors and their electrochemical performance was investigated.

Materials and Methods

Synthesis of Mn_2O_3/MPC composites film

The fabrication of MPC carbon film was carried out by polymerization of Resorcinol (R) and Formaldehyde (F) with triblock copolymer Pluronic F127 (F127) as a pore forming agent and hydrochloric acid (HCl) as a catalyst [16]. Prior to the incorporation of metal oxide by the incipient wetness impregnation method, the optimized carbon film MPC was prepared. A different concentration ranging from 0, 5, 10 and 15 wt.% of manganese (II) acetate tetrahydrate salt precursor was dissolved in deionized (DI) water and the titanium (Ti) foil was impregnated at room temperature for 150 minutes in the solution so that $(CH_3COO)_2Mn.4H_2O$ was completely adsorbed on the MPC surface. The resulting mixtures were dried for 12 hours at 80 °C and then calcined at 300 °C for 2 hours in the nitrogen atmosphere before the composite film Mn_2O_3/MPC was finally obtained.

Characterization

IR measurements of the samples were carried out with a Fourier transform infrared (FTIR) spectrometer (Perkin Elmer Spectrum 100) in the range of wave numbers from 4000 to 500 cm^{-1}. FESEM images were obtained using a field emission scanning electron microscope in combination with an energy dispersive X-ray (EDX) (FESEM-EDX, JEOL JSM-7600F) to analyse the morphology of the surface and the elemental composition of synthesised sample. The surface roughness of the prepared samples was investigated using an Atomic Force Microscopy (AFM). The AFM analysis was recorded using AFM unit, Brunker Crest, Dimension Edge. The data processing was performed using NanoDrive Dimension Edge software (version 8.06).

Electrochemical measurement

All electrochemical analyses were carried out using a three-electrode cell system. Tests consisting of cyclic voltammetry tests (CV), galvanostatic charge-discharge testing (GCD) and electrochemical impedance spectroscopy (EIS) were carried out using the Autolab PGSTAT204/FRA32 M module, Metrohm. The counter, reference and working electrode were used as a platinum wire, an electrode Ag/AgCl (3 M KCl) and the prepared samples, respectively. The prepared MPC film was measured with a potential range of -0.2 to 0.8 V. The specific capacitance of the supercapacitor can be calculated from the galvanostatic charge/discharge profile using Equation 1:

$$C_m = \frac{I\Delta t}{\Delta V \, x \, A} \tag{1}$$

where C_m is the specific capacitance in farads (F) per area (cm^2), I is the current of charge/discharge current, Δt is the discharging time, A is the area of the material of the electrode and V is the potential window. Using equations 2 and 3, the energy density and power density of the supercapacitor, respectively can be calculated:

$$E = \frac{1}{2} C(\Delta V)^2 \tag{2}$$

$$P = \frac{E}{\Delta t} \tag{3}$$

where E is the density of energy in Wh/kg, C is the specific capacitance of an electrode obtained from CV, V is the potential window, P is the density of power in W/kg, and Δt is the discharge time.

Results and Discussion

Figure 1 shows the FTIR spectrum of the sample at various concentrations of Mn salt. The large absorption band centred at 3160 - 3384 cm^{-1} corresponds to the stretching vibration of the adsorbed water in the samples. The absorption bands for all samples at 1391-1620 cm^{-1} can also be assigned to the bending vibrations of adsorbed water molecules that were linked to the aromatic ring structure that was replaced by the C-C bond. In the Mn_2O_3/MPC composites, a significant difference can be observed in comparison to the FTIR spectrum of 0 wt.% of Mn salt. Below 1400 cm^{-1}, the peaks attributed to the octahedral vibrations of basic MnO_6. Vibrations of Mn-O stretching and bending can be assigned to peaks from 630 cm^{-1} and 523 cm^{-1}. All the corresponding peaks seen on the Mn_2O_3/MPC spectra show that the composites were successfully prepared. Here, it should be noted that the stretching of aliphatic C-H at approximately 2900 cm^{-1} for composites and pure Mn_2O_3 can also be attributed to atmospheric CO_2 [4].

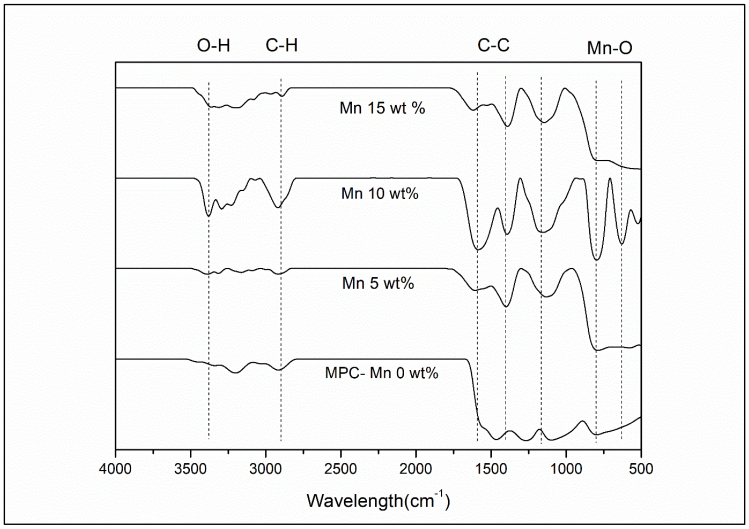


Figure 1. FTIR spectrum of composite film Mn_2O_3/MPC at different concentrations of Mn salt

Figure 2 (a)-(d) show the FESEM images of Mn_2O_3/MPC composite film samples at different concentrations of Mn salt. The FESEM images of 100,000 x magnification reveal that the concentration of Mn salt could increase the amount of deposited Mn_2O_3 nanoparticles. The EDX results in Figure 2 (e)-(g) and Table 1 show that the main composite elements are C, Mn, Ti and O. Mn can be considered to exist on the MPC surface in the form of Mn_2O_3 compared to FTIR results. According to the Mn salt content from 5 to 15 wt.%, the content of Mn_2O_3 in the Mn_2O_3/MPC composite film increased from 6.58 wt.% to 27.06 wt.%. It was believed that lower and optimized concentration contributed to better ion diffusion in the material leading to the formation of a uniform deposition and enhancement of the capacitive performance of the samples [4].

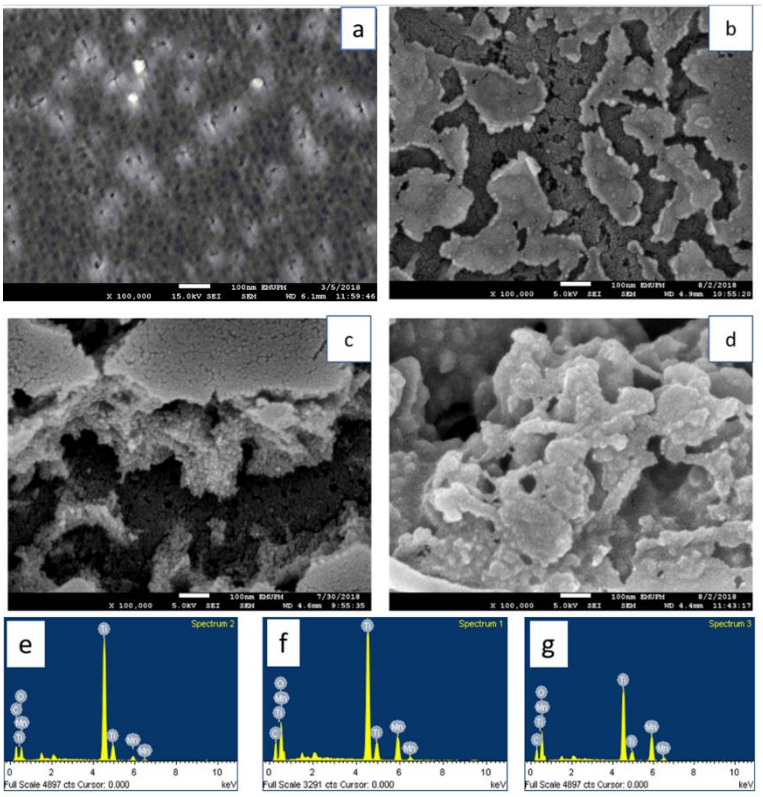


Figure 2. FESEM images of composite film samples of Mn_2O_3/MPC at different concentrations of Mn salt: (a) 0 wt.% (b) 5 wt.% (c) 10 wt.% (d) 15 wt.% (e-g) EDX of Mn_2O_3/MPC with Mn salt from 5 wt.% to 15 wt.%

Table 1. Elemental analysis (EDX) for composite film Mn_2O_3/MPC based on the concentration of Mn salt.

Mn Salt Concentration (wt.%)	**Weight %**				
	C	**O**	**Ti**	**Mn**	**Total**
5	25.95	36.18	35.58	2.29	100
10	20.23	46.01	26.13	7.63	100
15	18.95	50.53	21.11	9.42	100

The thickness was one of the beneficial properties for enhancing the surface contact and electrical conductivity of the film and the electrolyte ions at the electrode-electrolyte interface [19]. The surface profiler confirmed this results that the thickness increased when Mn_2O_3 was deposited at MPC samples (Table 2).

Table 2. Average thickness of MPC and Mn_2O_3/MPC composite film

Samples	**Average Thickness (nm)**
MPC	229.3
Mn_2O_3/MPC-300	2046

The surface morphology of the MPC and Mn_2O_3/MPC films was observed by atomic force microscopy (AFM) topographic as depicted in Figure 3(a) and 3(b), respectively. The MPC films are seen flat and uniform based on the analysis. The surface is also covered with open pores that are likely stripe pattern on the surface [20-22]. The surface topology of the composite film as observed clearly from AFM images shows that the mean square surface roughness is 2.36 which is higher compared with the MPC which is 1.22. The deposition of Mn_2O_3 on the MPC exhibited extra layer making the surface of the composite high in thickness as well as roughness. The specific surface morphologies and large surface areas of materials are necessary for potential applications in supercapacitors [19].

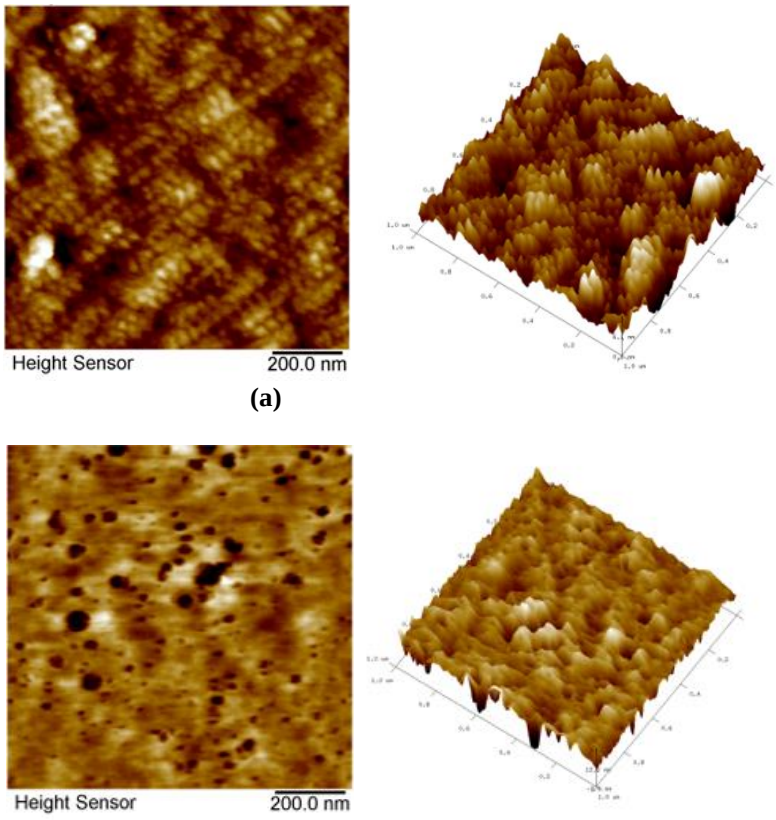
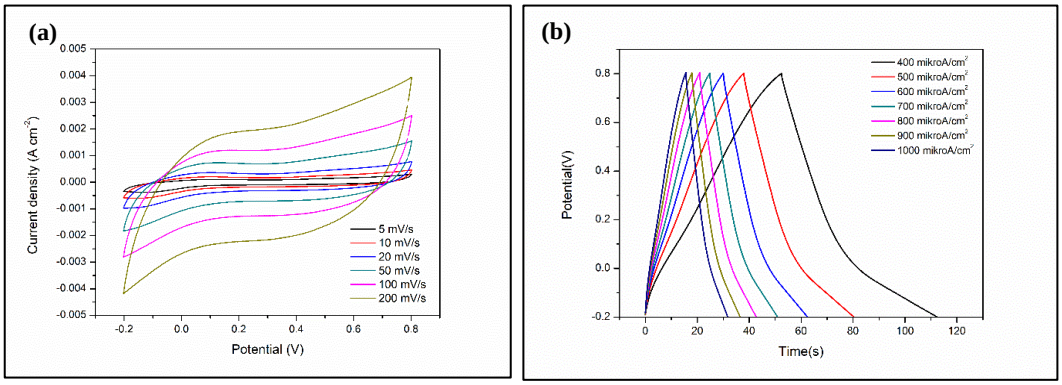


Figure 3. AFM images 2D and 3D of (a) MPC (b)Mn_2O_3/MPC composite film

Figure 4(a) shows the cyclic voltammetry (CV) curves for optimized Mn_2O_3/MPC composite film that was calcined for 2 hours at a temperature of 300 °C. This sample was observed in the potential range of 0.8 to-0.2 V at different scanning rates ranging from 5 mV s^{-1} to 200 mV s^{-1}. The CV curves for the composite electrodes showed significant redox peaks, indicating that there were Faradic reactions during the charge-discharge process. The composite materials of Mn_2O_3 had a combination of EDLC and pseudocapacitance [2, 9]. The specific capacitance decreased gradually from 53.59 mF cm^{-2} at 5 mV s^{-1} to 21.35 mF cm^{-2} when the scan rate increased. It was noted that the capacitance decreased as the potential scan rate increased, suggesting a diffusion limitation process in the porous structure of the composite. Figure 4(c) shows the CV plots at different Mn salt concentration 0, 5, 10 and 15 wt.%, showing the typical pseudocapacitive behaviour of the Mn_2O_3/MPC electrodes. Samples calcined at 300 °C, however, show the highest current response with changing scanning potential, indicating the highest electrochemical activity and the highest specific capacitance at the lowest scanning rate of 5 mV s^{-1}. The specific capacitance for the optimum sample was 53.59 mF cm^{-2}, compared with the values of 15.23, 20.1 and 30.24 mF cm^{-2} for the sample calcined at 0 wt.%, 5 wt.% and 15 wt.%, respectively.

Figures 4(b) and 4(d) show the galvanostatic charge-discharge (GCD) curves for optimal sample at different current densities and different concentrations of Mn salt at the lowest current density of 400 µA cm^{-2} in 1 M KCl, respectively. All samples show the charging and discharging curve. The basic symmetrical triangular shapes in the charge/discharge curve further validate the ideal pseudocapacitive behaviour of the Mn_2O_3 electrodes which correlates well to the CV discussions. The optimum sample showed a longer duration over the other six current densities due to a higher specific capacitance of 23.14 mF cm^{-2}, before the specific capacitance gradually reduced to 15.79 mF cm^{-2}. Highest electrochemical activity and specific capacitance is indicated by the longer charge/discharge process of the sample [19]. The specific capacitance calculated were 12.96 mF cm^{-2} and 17.13 mF cm^{-2} at 5 wt.% and 15 wt.%, respectively. As the concentration of Mn salt increased, the specific capacitance also decreased. Owing to the uniformity of pores and the larger pores at an optimal Mn salt concentration, a very good pathway can be set up for electrolyte to flow all over the samples. This led to a longer discharge time resulting in a higher specific capacitance. As compared to other samples, the calcined samples with a concentration of 10 wt.% Mn showed the highest specific capacitance value. This proved that lower Mn salt concentration could provide a larger area for effective ion diffusion in the samples, which could lead to greater capacitance of the prepared samples. It can be assumed that the superiority of the calcined sample at 10 wt.% of the Mn salt concentration was largely due to its optimal surface morphology. The large area of the composite surface can effectively enhance the pseudocapacitance due to the increase in the interface electroactive sites for the Faradaic reactions. The enhanced pseudocapacitance performance can be also achieved via a high mesoporosity composite since it can promote the penetration of the electrode/electrolyte interface [19].

Figure 4(e) and 4(f) show the correlation between the specific capacitance based on the scan rate and the current density, respectively. The results implied that the insufficient response time for electrolyte ions to diffuse at high scanning rates and current densities for samples calcined at 5, 10 and 15 wt.% of Mn salt concentration throughout the sample surface [9]. The specific capacitance was strongly influenced by the scanning rate and the current density applied, in which the capacitance decreased with increasing scanning rates and current densities.



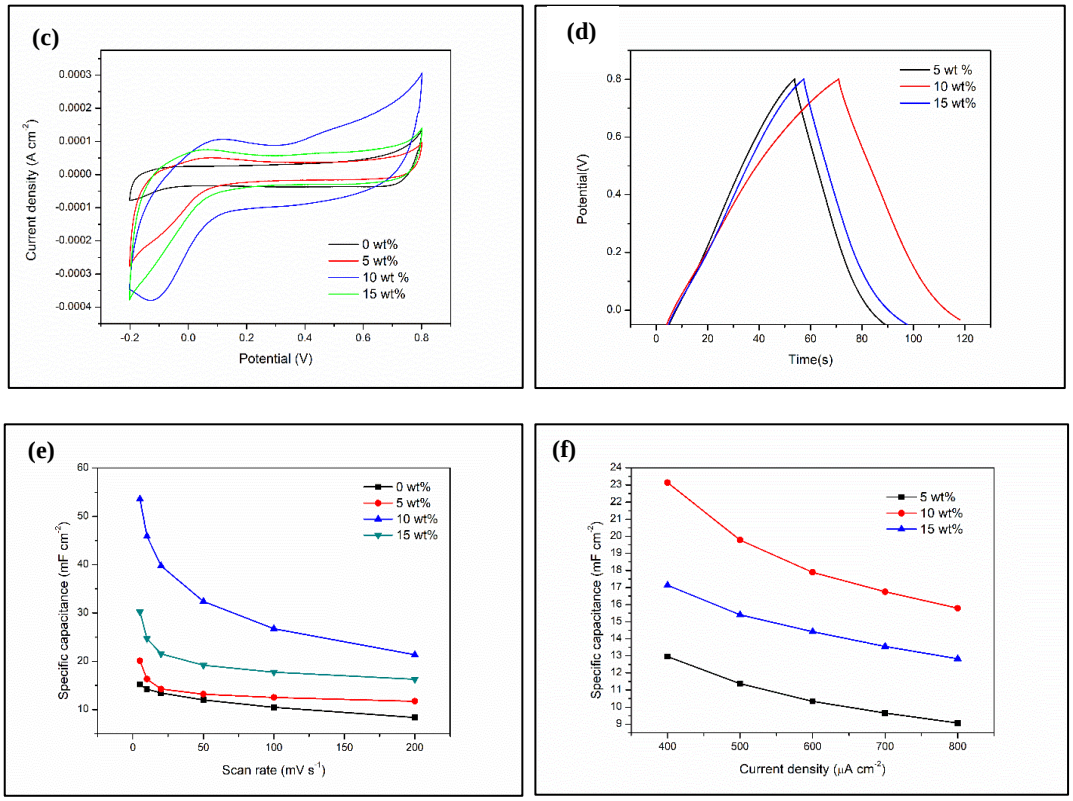


Figure 4. Optimum Mn_2O_3/MPC composite film prepared at 10wt% Mn (a) CV at different scan rates (b) GCD at various current densities (c) CV at different Mn salt concentration (d) GCD at different Mn salt concentration at lowest current density of 400 µA cm^{-2} (e) Specific capacitance as a function of scan rates (f) Specific capacitance as a function of current density

The efficiencies of the optimized samples MPC and Mn_2O_3/MPC supercapacitors were examined and predicted using equations 2 and 3, as shown in Figure 5. The Mn_2O_3/MPC supercapacitor initially has an energy density of 10.68 mWh cm^{-2} and 0.20 mW cm^{-2}, respectively, at 200 mV s^{-1} scanning rate. At a scan rate of 5 mV s^{-1} for the same material, the energy density and power density were 26.80 mWh cm^{-2} and 0.10 mW cm^{-2}, respectively that are in opposite to the 200 mV s^{-1} scan rate. The difference was probably due to internal losses of a higher scan rate [23]. After modification and incorporation of metal oxides, the Ragone plot clearly shows electrochemical performance improvement for Mn_2O_3/MPC which has higher energy and power density, 26.80 mWh cm^{-2} and 0.10 mW cm^{-2} as compared to MPC that has a very low energy density of 7.62 mWh cm^{-2} and 0.010 mW cm^{-2}. The significant improvement demonstrates the contribution of metal oxides to the MPC film. Based on the electrochemical performance, it can be confirmed that the Mn_2O_3/MPC composite film was more outstanding than MPC film in terms of power density and energy density characteristics.

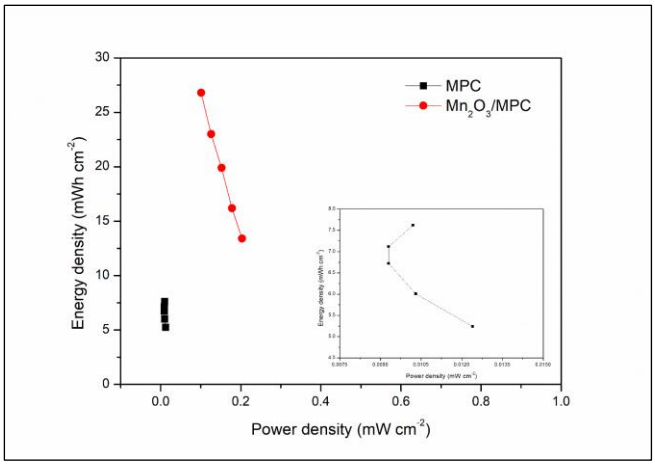


Figure 5. Ragone plot of optimised MPC and Mn_2O_3/MPC composite film at various current densities in 1.0 M KCl between -0.2 to 0.8 V. Inset shows the magnified version of the MPC plot

Conclusion

The Mn_2O_3/MPC composite film with different Mn content was successfully synthesized using a simple method based on the incipient wetness impregnation method followed by calcination to improve the supercapacitive behavior of the composites. It was impregnated with MPC film to purposely combine the excellent electrochemical performance of MPC film with the MnO pseudocapacitive properties. For the optimal sample of 10 wt.% Mn in composite, the specific capacitance was 53.59 mF cm^{-2}. Due to the excellent electrical properties of the MPC film and the faradaic redox reactions of Mn_2O_3, the specific capacitance was increased for the optimum sample. In this analysis, the Mn_2O_3/MPC composite film showed a relatively stable capacitance of approximately 71 % of the initial capacitance with an increase in cycle numbers up to 1000. Mn_2O_3/MPC has displayed the highest energy and power density characteristics of 26.80 mWh cm^{-2} and 0.10 mW cm^{-2}, respectively while MPC obtained lower energy density of 7.62 mWh cm^{-2} and 0.010 mW cm^{-2} at a scan rate of 5 mV s^{-1}. Therefore, incorporation of metal oxides in Mn_2O_3/MPC composite film is an effective way to increase the electrochemical performance in terms of specific capacitance, power density and energy density characteristics of carbon materials for supercapacitor application.

Acknowledgement

Universiti Putra Malaysia (UPM) supported this work under grant no.: GP/IPS/2017/9548000. JPA scholarship is recognized for the doctoral program for Mahanim Sarif @ Mohd Ali.

References

1. Li, Y. H., Li, Q. Y., Wang, H. Q., Huang, Y. G., Zhang, X. H., Wu, Q., Gao, H. Q. and Yang, J. H. (2015). Synthesis and electrochemical properties of nickel–manganese oxide on MWCNTs/CFP substrate as a supercapacitor electrode. *Applied Energy*, 153: 78-86.
2. Zhang, Y., Xuan, H., Xu, Y., Guo, B., Li, H., Kang, L., Han, P., Wang, D. and Du, Y. (2016). One-step large scale combustion synthesis mesoporous MnO_2/$MnCo_2O_4$ composite as electrode material for high-performance supercapacitors. *Electrochimica Acta*, 206: 278-290.
3. Lokhande, V. C., Lokhande, A. C., Lokhande, C. D., Hyeok, J. and Ji, T. (2016). Supercapacitive composite metal oxide electrodes formed with carbon, metal oxides and conducting polymers. *Journal of Alloys Compound*, 682: 381-403.
4. Wang, X., Liu, L., Wang, X., Yi, L., Hu, C. and Zhang, X. (2011). Mn_2O_3/carbon aerogel microbead composites synthesized by in situ coating method for supercapacitors. *Materials Science and Engineering: B*, 176(15): 1232-1238.

5. Worsley, M. A., Pauzauskie, P. J., Olson, T. Y., Biener, J., Satcher Jr, J. H. and Baumann, T. F. (2010). Synthes is of graphene aerogel with high electrical conductivity. *Journal of the American Chemical Society*, 132(40): 14 067-14069.
6. Liu, R. and Lee, S. B. (2008). MnO_2/poly (3, 4-ethylenedioxythiophene) coaxial nanowires by one-step coelectr odeposition for electrochemical energy storage. *Journal of the American Chemical Society*, 130 (10): 2942-294 3.
7. Yu, D. and Dai, L. (2009). Self-assembled graphene/carbon nanotube hybrid films for supercapacitors. *The Jou rnal of Physical Chemistry Letters*, 1(2): 467-470.
8. Yang, J., Yang, X., Zhong, Y. L. and Ying, J. Y. (2015). Porous MnO/Mn_3O_4 nanocomposites for electrochemi cal energy storage. *Nano Energy*, 13: 702–708.
9. Li, L., Wei, T., Wang, W. and Zhao, X. S. (2009). Manganese oxide–carbon composite as supercapacitor electr ode materials. *Microporous Mesoporous Material*, 123(1–3): 260–267.
10. Lee, Y. J., Park, H. W., Park, S. and Song, I. K. (2012). Electrochemical properties of Mn-doped activated carb on aerogel as electrode material for supercapacitor. *Current Applied Physics*, 12(1): 23-237.
11. Hu, C. C., Liu, M. J. and Chang, K. H. (2008). Anodic deposition of hydrous ruthenium oxide for supercapacito rs: Effects of the AcO−concentration, plating temperature, and oxide loading. *Electrochimica Acta*, 53 (6): 267 9-2687.
12. Gujar, T. P., Kim, W. Y., Puspitasari, I., Jung, K. D. and Joo, O. S. (2007). Electrochemically deposited nanogr ain ruthenium oxide as a pseudocapacitive electrode. *International Journal of Electrochemical Science*, 2: 666-673.
13. Li, G. R., Feng, Z. P., Ou, Y. N., Wu, D., Fu, R. and Tong, Y. X. (2010). Mesoporous MnO_2/carbon aerogel co mposites as promising electrode materials for high-performance supercapacitors. *Langmuir*, 26(4): 2209-2213.
14. Jiang, H., Yang, L., Li, C., Yan, C., Lee, P.S. and Ma, J. (2011). High–rate electrochemical capacitors from hig hly graphitic carbon–tipped manganese oxide/mesoporous carbon/manganese oxide hybrid nanowires. *Energy & Environmental Science*, 4 (5): 1813-1819.
15. Wang, T., Peng, Z., Wang, Y., Tang, J. and Zheng, G. (2013). MnO nanoparticle@ mesoporous carbon compos ites grown on conducting substrates featuring high-performance lithium-ion battery, supercapacitor and sensor. *Scientific Reports*, 3: 2693.
16. Mitome, T., Hirota, Y., Uchida, Y. and Nishiyama, N. (2016). Porous structure and pore size control of mesopo rous carbons using a combination of a soft-templating method and a solvent evaporation technique. *Colloids an d Surfaces A: Physicochemical and Engineering Aspects*, 494: 180-185.
17. Wang, Q., Zhang, W., Mu, Y., Zhong, L., Meng, Y. and Sun, Y. (2014). Synthesis of ordered mesoporous carb ons with tunable pore size by varying carbon precursors via soft-template method. *Microporous and Mesoporo us Materials*, 197: 109-115.
18. Fisher, R. A., Watt, M. R. and Ready, W. J. (2013). Functionalized carbon nanotube supercapacitor electrodes: a review on pseudocapacitive materials. *ECS Journal of Solid State Science and Technology* 2(10): 3170-3177.
19. Yang, J. and Zou, L. (2014). Graphene films of controllable thickness as binder-free electrodes for high perfor mance supercapacitors. *Electrochimica Acta*, 130: 791-799.
20. Li, H., Zhang, X., Ding, R., Qi, L. and Wang, H. (2013). Facile synthesis of mesoporous MnO_2 microspheres fo r high performance AC//MnO_2 aqueous hybrid supercapacitors. *Electrochimica Acta*, 108: 497-505.
21. Zhang, C, Zhen G. and Jianxin M. (2013). Self-assembly synthesis of ordered mesoporous carbon thin film by a dip-coating technique. *Microporous and Mesoporous Materials*, 170: 287-92.
22. Kataoka, S., Yamamoto, T., Endo, A., Nakaiwa, M. and Ohmori, T. (2009). Synthesis and characterization of m esoporous carbon thin films from phloroglucinol/surfactant self-assembly. *Colloids and Surfaces A: Physicoche mical and Engineering Aspects*, 347(1-3): 142-145.
23. Wang, Y. T., Lu, A. H. and Li, W. C. (2012). Mesoporous manganese dioxide prepared under acidic conditions as high performance electrode material for hybrid supercapacitors. *Microporous and Mesoporous Materials*, 15 3: 247-253.

Malaysian Journal of Analytical Sciences (MJAS)
Published by Malaysian Analytical Sciences Society

DEACIDIFICATION OF NAPHTHENIC ACIDS FROM PETROLEUM CRUDE OILS USING 2-METHYLIMIDAZOLE IN PEG(400) WITH THE AID OF Ni/Ce/Al_2O_3 and Cu/Ce/Al_2O_3 CATALYSTS

(Deasidifikasi Asid Naftenik dari Minyak Mentah Petroleum menggunakan 2-Metilimidazola dalam PEG(400) dengan Bantuan Pemangkin Ni/Ce/Al_2O_3 dan Cu/Ce Al_2O_3)

Norshahidatul Akmar Mohd Shohaimi[1]*, Nor Shafira Hassan[1], Ahmad Zamani Ab Halim[2], Nurasmat Mohd Shukri[3], Nor Hakimin Abdullah[4]

[1]*Faculty of Applied Sciences,*
Universiti Teknologi MARA Pahang, Bandar Tun Abdul Razak Jengka, Pahang, Malaysia
[2]*Faculty of Industrial Sciences & Technology,*
Universiti Malaysia Pahang, 26300 Gambang, Kuantan, Pahang, Malaysia
[3]*School of Health Sciences,*
Universiti Sains Malaysia, Health Campus, 16150 Kubang Kerian, Kelantan, Malaysia
[4]*Advanced Materials Research Centre (AMRC), Faculty of Bioengineering and Technology,*
Universiti Malaysia Kelantan, Locked Bag 100, 17600 Jeli, Kelantan, Malaysia

**Corresponding author: akmarshohaimi@uitm.edu.my*

Received: 20 November 2019; Accepted: 3 March 2020

Abstract

The presence of carboxylic acid derivative compound in crude oil adversely contributes to major corrosion in oil pipelines and distillation units installed in crude oil refineries. The acidity level in crude oil is measured based on the total acid number (TAN). Methods that are commonly used to remove naphthenic acid (NA) from crude oil, such as dilution and caustic washing, have several drawbacks, including emulsion formation, high temperature, and massive use of solvent. In order to overcome these shortcomings, catalytic deacidification method had been developed to reduce the TAN value in acidic crude oil by using basic chemical, along with the aid of metal oxide catalyst. In this study, crude oil from Petronas Penapisan Melaka was evaluated. The parameters studied were reagent concentration, reaction temperature, catalyst loading, calcination temperature, and reusability of potential catalyst. The basic chemical used was 2-methylimidazole in polyethylene glycol (PEG 400) with concentrations of 100, 500, 1000, and 1500 ppm. Next, Ce was used as base for the catalyst with both Ni and Cu serving as dopant. The potential catalysts were characterised *via* Fourier transform infrared spectroscopy (FTIR) and thermogravimetry analysis (TGA) to determine their physicochemical properties. The outcomes showed that the Cu/Ce catalyst met the Petronas requirement as the TAN value reduced to 0.93 mg KOH/g from the original TAN value of 3.93 mg KOH/g. As for Ni/Ce catalyst, the TAN value reduced to 1.03 mg KOH/g. The TGA results revealed the total weight loss of Cu/Ce = 23.40% and Ni/Ce = 25.22% due to complete removal of impurities from the catalysts. The reaction temperature was set at 27 °C, while the catalyst calcination temperature was fixed at 1000 °C, and seven beads of catalyst loading had been employed. It can be concluded that catalytic deacidification method with the aid of Cu/Ce was indeed efficient in removing NA from the acidic crude oil, thus lowering the TAN value to less than 1 mg KOH/g.

Keywords: deacidification, petroleum crude oil, naphthenic acid, catalyst

Abstrak

Kehadiran sebatian derivatif asid karboksilik dalam minyak mentah boleh menyumbang kepada hakisan utama dalam paip pemproses minyak dan unit penyulingan dalam kilang minyak mentah. Tahap keasidan dalam minyak mentah diukur dengan jumlah nombor asid (TAN). Kaedah-kaedah yang biasanya digunakan untuk mengeluarkan asid naftenik (NA) dari minyak

mentah seperti pencairan dan pencuci kaustik mempunyai kelemahan sendiri seperti pembentukan emulsi, suhu tinggi dan penggunaan pelarut yang banyak. Untuk mengatasi masalah ini, kaedah deasidifikasi pemangkin telah dicipta bagi mengurangkan nilai TAN dalam minyak mentah berasid dengan menggunakan bahan kimia asas dengan bantuan pemangkin logam oksida. Dalam kajian ini, minyak mentah dari Petronas Penapisan Melaka digunakan. Parameter yang dikaji adalah kepekatan reagen, suhu tindak balas, jumlah pemangkin, suhu pemangkin dan kebolehgunaan semula pemangkin yang berpotensi. Bahan kimia asas yang digunakan ialah 2-metilimidazola dalam polietilena glikol (PEG 400) dengan kepekatan 100, 500, 1000 dan 1500 ppm. Ce digunakan sebagai asas pemangkin dengan Ni dan Cu bertindak sebagai dopan. Pemangkin berpotensi menjalani kaedah pencirian seperti spekstroskopi inframerah transformasi Fourier (FTIR) dan analisis termogravimetri (TGA) untuk sifat fiziko-kimianya. Hasilnya menunjukkan bahawa pemangkin Cu/Ce memenuhi keperluan Petronas kerana nilai TAN dikurangkan kepada 0.93 mg KOH/g dari nilai TAN asal 3.93 mg KOH/g. Bagi pemangkin Ni/Ce, nilai TAN dikurangkan kepada 1.03 mg KOH/g. Keputusan TGA menunjukkan penurunan berat badan Cu/Ce = 23.40% dan Ni/Ce = 25.22% disebabkan oleh pembuangan lengkap bahan pencemar dalam mangkin. Suhu tindak balas yang digunakan adalah 27 °C dengan suhu pembakaran pemangkin 1000 °C dan 7 biji jumlah pemangkin. Dapat disimpulkan bahawa kaedah deasidifikasi pemangkin dengan bantuan Cu/Ce adalah cekap dalam menghilangkan NA dari minyak mentah berasid sehingga menurunkan nilai TAN kurang dari 1 mg KOH/g.

Kata kunci: deasidifikasi, minyak mentah petroleum, asid naftenik, pemangkin

Introduction

Petroleum crude oils have a complex hydrocarbon mixture that represents high concentrations of heteroatoms, for example sulphur and metals. These two heteroatoms are united by either covalent or non-covalent bond into molecules with high boiling points and high polarity. The compound that causes petroleum crude oils to become more acidic is naphthenic acid (NA). The minor acidic classes found in crude oil are aromatic, olefinic, hydroxyl, and dibasic acid, whereas NAs are composed of complicated and a variety of structure [1].

Total acid number (TAN) describes the amount of potassium hydroxide in milligrams required to neutralise the acid present in a gram of oil. According to Shah et al. [2], if the concentration of TAN is 1.5 mg KOH/g and above, corrosion can occur and lead to trouble, especially damages to oil and gas industry equipment, decrease in production quality, and frequent turn around, to name a few. The two methods that can effectively minimise TAN are destructive methods (thermal cracking and hydrogenation process) and non-destructive methods (adsorption and solvent extraction) [2]. Many studies have proposed a range of methods to discard NAs from petroleum crude oil, including neutralisation, adsorption, thermal decomposition, catalytic decarboxylation, esterification, and liquid-liquid extraction using organic solvents, whereby all the methods have some drawbacks.

The primary objective of this study is to overcome the weakness of previous method by introducing a combination of acid removal agent of 2-methylimidazole in polyethylene glycol, as well as heterogeneous catalysts of Ni/Ce and Cu/Ce with alumina beads as catalyst support.

Materials and Methods

Material and feedstock

Feedstock used for this study refers to high crude oil from the Petronas Penapisan Melaka with a TAN value of 3.93 mg KOH/g. A phenolphthalein solution 1% (w/v) was used as an indicator in the deacidification process. A 40 mL mixture of 2-propanol, toluene, and distilled water with ratio of (49.5:50:0.5) was used as titration solvent. Potassium hydroxide pellets and barium hydroxide were used as the titrants in this study.

Catalyst preparation

Cerium was used as a catalyst and supported with alumina beads using nickel and copper as dopants at a ratio of 90:10 (base:dopant). Five g of metal salt, $Ce(NO_3)_2$, was weighed in a beaker and dissolved in 5 mL of distilled water. The solution was mixed and stir continuously by using a magnetic bar for 10 minutes. After the solution had dissolved, 0.92 g dopants of $Ni(NO_3)_2$ based on the mol ratio was added. This solution was stirred again until it was fully dissolved. The process was performed at room temperature to homogenise the mixture [3].

The catalyst was prepared by using aqueous incipient wetness impregnation (IWI) method. The Al_2O_3 beads (diameter: 3-5 mm) were used as support material and dipped in the catalyst solution for 1 hour to allow good

coating of the catalyst solution on the surface of the alumina support. Next, the supported material was transferred onto an evaporating dish with glass wool placed on it. The solution was aged in an oven at 80-90 °C for 24 hours to eliminate excess water. The prepared catalyst was placed in furnace at 800 °C for 24 hours by using a ramp rate of 5 °C/min to discard impurities and metal precursor. The procedure was repeated by using different dopants with $Cu(NO_3)_2$ 0.82 g and the calcination temperatures of the catalysts were set at 900 °C and 1000 °C [3].

The potential catalysts were characterised by applying several techniques to study their chemical and physical properties. The characterisation techniques used in this research were thermogravimetry analysis (TGA) and Fourier transform infrared spectroscopy (FTIR).

Total acid number (TAN) determination

Approximately 0.2 g of crude oil sample was weighed in a 100 mL beaker and diluted with 40 mL of titration solvent mixture of 2-propanol, toluene, and distilled water with a ratio of (49.5:50:0.5) [4]. The 2-methylimidazole in PEG with a concentration of 100 ppm was added, along with the catalyst loading of three beads. Next, the mixture of the solution was stirred for 5 minutes until it dissolved. The TAN value was determined by using the semi-micro colour indicator titration method, where 0.1 mL of phenolphthalein solution was used as an indicator, whereby the end-point for the titration method was observed by a stable red colour. The titration method was repeated by using 2-methylimidazole in PEG concentrations of 500, 1000, and 1500 ppm, as well as catalyst loading of four, five, and seven beads. As for the titrant, potassium hydroxide solution (0.01 mol/L) and barium hydroxide were used in adherence to standard method of ASTM D664. The TAN value was calculated in milligrams of potassium hydroxide per gram of sample (mg KOH/g) by using the following equation:

$$TAN = 56.1 \times c \times (V_{KOH} - V_B)/m \quad (1)$$

where c is define as concentration in mole/L of standard volumetric KOH solution, V_{KOH} is volume in mL of titrant required for the determination, V_B is volume in mL of titrant required for the blank test, M is mass in grams of the test portion and 56.1 is molecular weight of KOH in g/mol.

Results and Discussion

Fourier transform infrared spectroscopy

Figure 1 illustrates the FTIR results of fresh and spent bimetallic catalyst of $Cu/Ce/Al_2O_3$ and $Ni/Ce/Al_2O_3$. The catalysts were tested with the best optimum parameter, whereby calcination temperature at 1000 °C was efficient in removing NA. The catalyst loading of seven beads had been added to the solution with 1000 ppm of reagent concentration. Both $Ni/Ce/Al_2O_3$ and $Cu/Ce/Al_2O_3$ catalysts underwent four catalytic cycles to obtain the optimum cycle for reusability testing. Comparison between both peaks was made to detect the presence of impurities at the catalyst surface after reaction.

The FTIR spectra for both catalysts prior to reaction (fresh) showed a peak at wavelength ranging at 820-563 cm^{-1}. The observed peak could be ascribed to the stretching mode of metal oxide group. According to Shohaimi et al. [5], the stretching mode of metal oxide group was present at 1029-563 cm^{-1} and this stretching mode served as an indicator for the formation of metal oxide catalyst, as all impurities were removed prior to heating at high temperature.

The FTIR band for Ni/Ce catalyst with support of Al_2O_3 after the reaction (spent) displayed emergence of new peaks ranging at 2920-2850 cm^{-1}, which represented the C-H (sp^3, stretching) of the alkane group that may derive from the NA chain or the component of the crude oil itself. The Cu/Ce also generated many peaks after the reaction, signifying that impurities from NA or reagent had bound to the catalyst surface. Catalyst offers a basic surface site for the reagent to react with NA in the catalytic reaction [6]. As NA was bound to the catalyst, the catalyst degenerated and deteriorated the efficiency of the catalysts in reducing the TAN value.

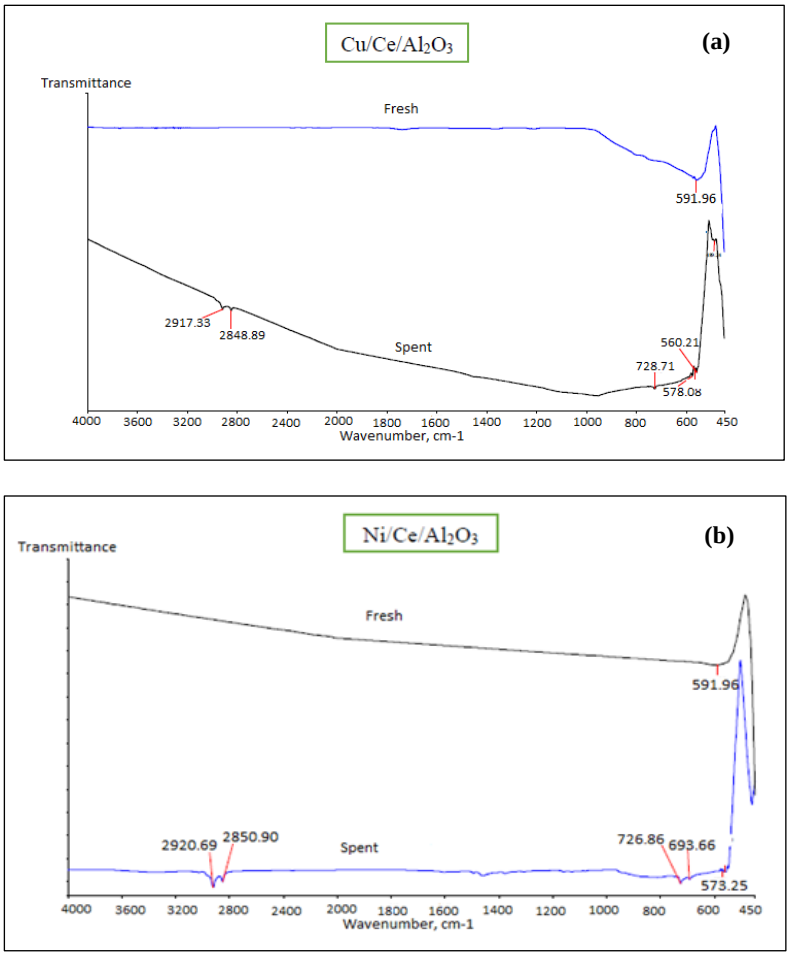


Figure 1. FTIR spectra of fresh and spent (a) $Cu/Ce/Al_2O_3$ and (b) $Ni/Ce/Al_2O_3$ catalysts at calcination temperature of 1000 °C (Spent condition: after 4 consecutive cycle, optimum condition for both catalyst: 1000 ppm of 2-methylimidaozle in PEG, reaction time of 5 minutes)

Thermogravimetry analysis

Thermogravimetric analysis was performed on the samples of both $Cu/Ce/Al_2O_3$ and $Ni/Ce/Al_2O_3$ catalysts, wherein Figure 2 displays their profiles. The total weight loss for $Cu/Ce/Al_2O_3$ catalyst was 23.40%, whereas 25.22% for $Ni/Ce/Al_2O_3$ catalyst. This stemmed from the complete removal of impurities from the catalysts at calcination temperature of 1000 °C. Based on the outcomes, the $Cu/Ce/Al_2O_3$ catalyst underwent three phases of thermal event. The first stage of thermal event was due to loss of surface water and crystal water molecule at temperatures ranging at 80-180 °C. As the temperature escalated from 180 to 430 °C, the complete removal of water led to 12.48% weight loss. The thermal third stage was continued until the temperature hit 1000 °C, while the result of weight loss was 4.98% due to loss of nitrate compound and surface of hydroxyl molecule. Loss of water molecules occurred mainly due to the hygroscopic property of the supported catalyst sample, as well as the preparation of the method employed.

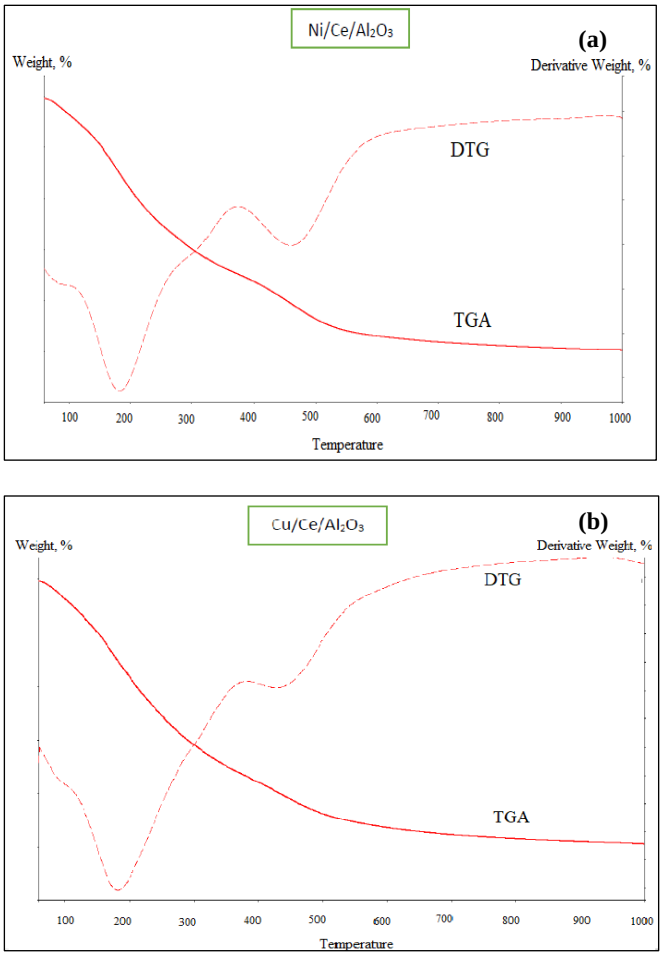


Figure 2. TGA-DTG thermogram of (a) $Ni/Ce/Al_2O_3$ and (b) $Cu/Ce/Al_2O_3$ catalysts after aging in oven for 24 hours at 80-90 °C (non-calcined catalyst before reaction)

As for the $Ni/Ce/Al_2O_3$ catalyst, four stages of thermal event had occurred. The first stage of weight loss took place at 80-180 °C due to loss of crystal water and surface water molecule. The second thermal treatment occurred at 180-320 °C due to complete removal of water. The next stage of thermal treatment happened at 320-450 °C, which could be attributed to decomposition of hydroxyl and carbonyl groups formation of pure metal oxide [7]. In the final stage, loss of nitrate compound and surface hydroxyl molecule had been detected.

Overall, the outcomes of thermogram for both TGA-DTG of $Ni/Ce/Al_2O_3$ and $Cu/Ce/Al_2O_3$ were completely obtained. It can be concluded that both impurities and water from the materials of weight loss in 14 mg for both catalysts were successfully removed by the thermal treatment and after heating until 700 °C, which yielded pure metal oxide. All nitrate compounds that originated from the metal precursor were discarded.

Total acid number for untreated crude oil

The untreated crude oil from Petronas Penapisan Melaka was analysed and the TAN value was found to be 3.93 mg KOH/g. This untreated crude oil was directly tested without any addition of reagent and catalyst by using the semi-micro colour titration method. The colour changed and the value was calculated to determine the original TAN value. The original TAN value is essential to serve as a reference in comparing with the value obtained for treated crude oil. This method was used to identify the effectiveness and the efficiency of both the reagents and catalysts used.

Effect of different reagent concentration

Figure 3 portrays various concentrations of 2-Methylimidazole in PEG (400) that had been used to further investigate the deacidification process, as well as to study the effectiveness of the reagent in reducing the TAN value. The concentrations of reagent added to the solution of crude oils were 100, 500, 1000, and 1500 ppm. Nevertheless, only a small amount of TAN value had been reduced. Despite the decrease in TAN value, it failed to meet the PETRONAS requirement, as the TAN value should be less than one [4]. According to Shohaimi et al. [8], the value of TAN reflects the amount of NA present in crude oils, whereby increment in TAN value signifies increased amount of NA.

Based on the figure above, the TAN value decreased with the increasing concentration of 2-methylimidazole in PEG. The most effective reagent concentration used was 1000 ppm at reaction temperature of 27 °C, whereby the TAN value could be lowered to 1.40 mg KOH/g. At 35 °C, the decreased TAN value did not differ much, but it could still lower the value of the original TAN. Upon hitting 40 °C with varying reagent concentrations, the TAN value turned constant after 500 ppm. Crude oils need an appropriate amount of dosing to react with NA, primarily because excessive reagent concentration could lead to stable emulsion. Hence, it could stabilise the NA in crude oils and automatically reduce the deacidification reaction. Therefore, the use of 1000 ppm of 2-methylimidazole concentration seemed adequate to reduce the NA in crude oils. If the reagent concentration of 2-methylimidazole in PEG used is too high, it could lead to operational constrictions [9]. The optimum reagent concentration, which is 1000 ppm at reaction temperature of 27 °C, was selected for further analysis since it could reduce the value of TAN to 1.40 mg KOH/g. The reagent concentration was deemed suitable for further investigation as it is cost efficient.

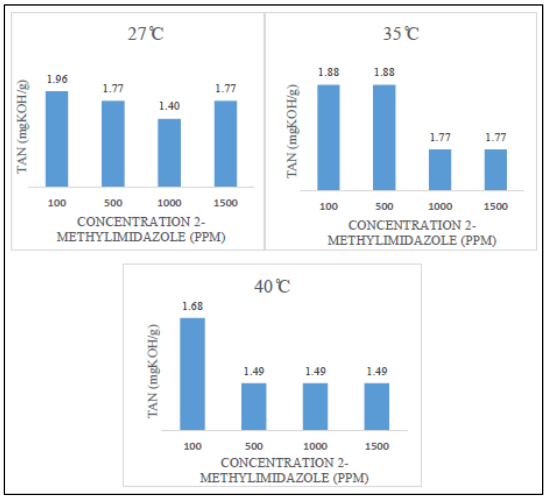


Figure 3. Effect of different reagent concentrations on TAN value without catalyst

Effect of $Ni/Ce/Al_2O_3$ and $Cu/Ce/Al_2O_3$ catalyst loading

This parameter was assessed to continue observing the efficiency of the catalysts, along with the reagents, on the TAN value. Monometallic of Ce/Al_2O_3 was used and $Cu(NO_3)_2$ and $Ni(NO_3)_2$, which served as a metal precursor due to its high solubility in water. According to Shukri et al. [4], cerium is a good metal to act as base catalyst for catalytic deacidification of NA in crude oil. This is because; cerium oxide is composed of a unique acid-base property and a strong metal-support interaction that can improve catalytic activity [7,10].

Figure 4 shows the three calcination temperatures used to obtain the best TAN value; 800, 900, and 1000 °C. Varied catalyst loading of three, four, five, and seven beads had been evaluated with different catalyst calcination temperatures. Inclusion of the catalyst into the crude of Petronas Penapisan Melaka had successfully reduced the

TAN value, in comparison to that without catalyst. The NA from the crude oils reacted with the reagent on the surface of the catalyst. The NA compound was bound on the surface of the catalyst, thus reducing the TAN value.

The purpose of adding catalyst into the crude oils solution is to obtain the optimum TAN value, which should be lower than 1, as required by PETRONAS. Based on the result of Ni/Ce catalyst calcined at 800 °C, increasing the amount of catalyst had slightly enhanced the reduction of TAN. The lowest TAN value obtained was 1.32 mg KOH/g by using seven beads of catalyst loading. For further reduction of TAN value, the calcination temperature was increase to 900 °C, along with the use of seven beads of catalyst loading. The TAN value slightly reduced from 1.32 mg KOH/g to 1.21 mg KOH/g. Upon increasing the calcination temperature to 1000 °C, the Ni/Ce/Al_2O_3 catalyst still failed to reduce the value of TAN to below 1, despite using the highest catalyst loading.

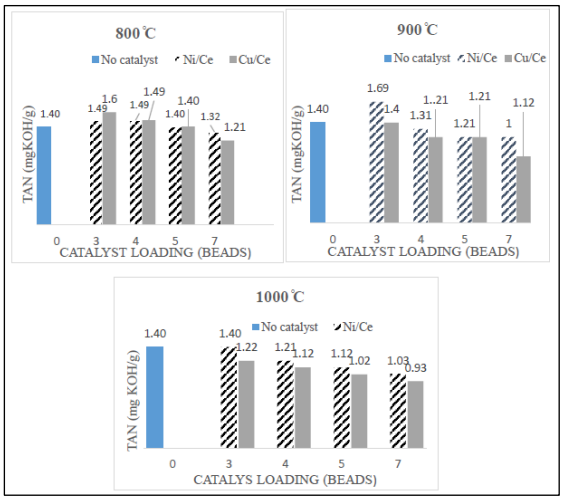


Figure 4. The effect of catalyst loading Ni/Ce/Al_2O_3 and Cu/Ce/Al_2O_3 on TAN value in crude oils

Nonetheless, the use of Cu/Ce catalyst with seven beads of catalyst loading at 1000 °C calcination temperature had successfully decreased the TAN value to 0.93 mg KOH/g. This was ascribed to the metal Cu that served as dopant in being the best promoter that increased the catalytic activity, as it increase the surface area of the active site [4]. The presence of Cu enhanced synergism between the metal and the cerium oxide, thus assisting in the cleavage of C-C bonds. Based on the outcomes, the trend of TAN value decreased as the catalyst loading of Cu/Ce/Al_2O_3 increased. Nevertheless, the results obtained by using Cu/Ce/Al_2O_3 catalyst calcined at 800 °C and 900 °C displayed a slight decrease with increment in catalyst loading. Here, cerium had been identified as amphoteric in nature. The addition of basic dopant led to the formation of basic catalyst, as it is superior to reduce NA in crude oils since NA is a weak acid [4].

As a conclusion, the optimum catalyst loading preferable for Cu/Ce/Al_2O_3 catalyst was seven beads as it had managed to reduce the TAN value to below 1. Upon comparing Ni/Ce/Al_2O_3 with Cu/Ce/Al_2O_3 catalysts, the Cu/Ce/Al_2O_3 catalyst appeared to be more effective and essential in discarding NA from crude oils, as it successfully reduced the original TAN value to 0.93 mg KOH/g with seven beads of catalyst loading at the calcination temperature of 1000 °C.

Catalyst reusability

Catalysts Ni/Ce/Al_2O_3 and Cu/Ce/Al_2O_3 calcined at 1000 °C were tested for several catalytic cycles under optimum reaction conditions. The primary aim of this study is to test the reusability of the potential catalysts. Hence, the catalysts were tested for their reusability until they were fully deactivated. Both catalysts of Ni/Ce/Al_2O_3 and Cu/Ce/Al_2O_3, along with the lower TAN value, had been analysed to determine the number of cycle(s) the catalysts could be used after reaction. The best TAN values of Ni/Ce/Al_2O_3 and Cu/Ce/Al_2O_3 catalysts from the previous

results were 1.03 mg KOH/g and 0.93 mg KOH/g, respectively. Catalyst loading of seven beads was applied along with the calcination temperature of 1000 °C at a reaction temperature of 27 °C.

Figure 5 illustrates the reusability of catalysts in light of TAN value with the constant temperature of 27 °C and the concentration of 2-methylimidazole at 1000 ppm. Based on the findings, the first catalytic cycle generated the TAN values of 0.93 KOH/g and 1.03 mg KOH/g for $Cu/Ce/Al_2O_3$ and $Ni/Ce/Al_2O_3$ catalysts, respectively. Upon completing the first catalytic cycle, the catalysts were rinsed with 2-propanol to release the adsorbed naphthenic compound, if any was present [9]. Next, the catalysts were dried in an oven at 80 °C and were reused for the next reaction. After the second catalytic cycle, the TAN values for both catalysts increased to 1.40 mg KOH/g and continued to increase until 1.68 mg KOH/g.

As the value of TAN increased at the second catalytic cycle, the catalyst had begun to deactivate. This indicates that the catalysts no longer can be used after the second cycle. Shukri et al. [9] claimed that as the catalyst starts to deactivate (spent catalyst), it produces higher TAN value as the catalyst slightly decreases in its activity. Studied that had assessed the $Ni/Ce/Al_2O_3$ catalysts displayed similar TAN values. Hence, both catalysts could only be used for a single reaction cycle. Upon continuation of use, the catalysts deactivated.

The catalysts used in the second catalytic cycle, which produced a TAN value of 1.40 mg KOH/g, were characterised *via* FTIR. Therefore, reduction of catalyst activity could be associated with the presence of impurities of C-H stretching that was noted in the spectra illustrated in Figure 1.

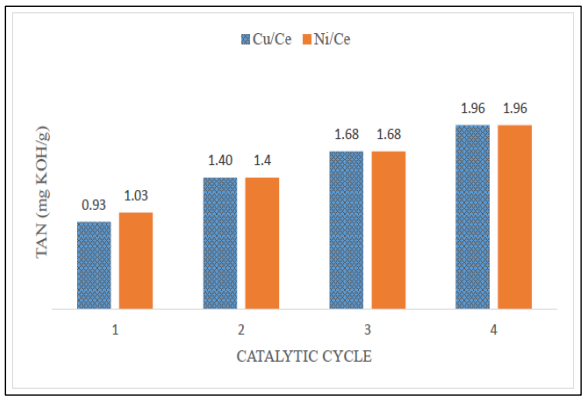


Figure 5. Catalysts reusability towards TAN value at constant temperature (27 °C) and concentration of 2-methylimidazole (1000 ppm)

Conclusion

This study reveals that $Cu/Ce/Al_2O_3$ catalyst had successfully reduced the TAN value to below 1; from 3.93 mg KOH/g to 0.93 mg KOH/g. The optimum parameter for calcination temperature used for both catalysts was 1000 °C with 1000 ppm reagent of 2-methylimidaozle in PEG. The reaction time used throughout this study was 5 minutes for both catalysts at room temperature. Upon using the $Ni/Ce/Al_2O_3$ catalyst, the value of TAN can only be reduced from the original TAN value of 3.93 mg KOH/g to 1.03 mg KOH/g. This signified that $Cu/Ce/Al_2O_3$ is more effective in reducing the TAN value.

Acknowledgement

We gratefully acknowledged the financial support by the Research Grant, FRGS with Grant No.: 011000190001 (File no.: 600 IRMI/FRGS 5/3 (108/2019)).

References

1. Najmuddin, R. A., Mutalib, M. A., Shah, S. N., Suleman, H., Lethesh, K. C., Pilus, R. B. M. and Maulud, A. S. (2016). Liquid-liquid extraction of naphthenic acid using thiocyanate based ionic liquids. *Procedia engineering*, 148: 662-670.
2. Shah, S. N., Chellappan, L. K., Gonfa, G., Mutalib, M. I. A., Pilus, R. B. M. and Bustam, M. A. (2016). Extraction of naphthenic acid from highly acidic oil using phenolate based ionic liquids. *Chemical Engineering Journal*, 284: 487-493.
3. Shohaimi, N. A. M., Bakar, W. A. W. A., Jaafar, J. and Shukri, N. M. (2013). Treatment of acidic petroleum crude oil utilizing catalytic neutralization technique of magnesium oxide catalyst. *Modern Chemistry & Applications*, 1(3): 1-5.
4. Shukri, N. M., Bakar, W. A. W. A., Jaafar, J. and Majid, Z. A. (2015). Removal of naphthenic acids from high acidity Korean crude oil utilizing catalytic deacidification method. *Journal of Industrial and Engineering Chemistry*, 28: 110-116.
5. Shohaimi, N. A. M., Bakar, W. A. W. A. and Jaafar, J. (2014). Catalytic neutralization of acidic crude oil utilizing ammonia in ethylene glycol basic solution. *Journal of Industrial and Engineering Chemistry*, 20(4): 2086-2094.
6. Shohaimi, N. A. M., Jaafar, J. and Bakar, W. A. W. A. (2015). Catalytic deacidification optimization of Korean crude oil based on response surface methodology. *Clean Technologies and Environmental Policy*, 17(6): 1513-1522.
7. Wang, Y., Chu, Z., Qiu, B., Liu, C. and Zhang, Y. (2010). Removal of naphthenic acids from a vacuum fraction oil with an ammonia solution of ethylene glycol. *Fuel*, 85(17-18): 2489-2493.
8. Shohaimi, N. A. M., Bakar, W. A. W. A. and Jaafar, J. (2017). The catalytic deacidification of acidic crude oil using Cu-doped alkaline earth metal oxide catalysts. *Petroleum Science and Technology*, 35(11): 1097-1103.
9. Shukri, N. M., Jaafar, J., Bakar, W. A. W. A., and Majid, Z. A. (2017). Characterization and deacidification of acidic petroleum crude oil utilizing metal oxide catalyst supported on alumina and ammoniated polyethylene glycol solution. *Malaysian Journal of Analytical Sciences*, 21(4): 830-838.
10. Toemen, S., Bakar, W. A. W. A., and Ali, R. (2014). Investigation of Ru/Mn/Ce/Al_2O_3 catalyst for carbon dioxide methanation: Catalytic optimization, physicochemical studies and RSM. *Journal of the Taiwan Institute of Chemical Engineers*, 45(5): 2370-2378.

Malaysian Journal of Analytical Sciences (MJAS)
Published by Malaysian Analytical Sciences Society

ELECTROBIOSYNTESIS OF NiO USING RAMBUTAN LEAVES FOR PHOTODEGRADATION OF REMAZOL BRILLIANT BLUE DYE

(Elektrobiosintesis NiO Menggunakan Ekstrak Daun Rambutan Untuk Fotodegradasi Pewarna Remazol Brilliant Biru)

Muhammad Farhan Hanafi, Noor Faizah Che Harun, Norzahir Sapawe*, Azizzami Raidin

Universiti Kuala Lumpur Branch Campus
Malaysian Institute of Chemical and Bioengineering Technology,
Lot 1988 Vendor City, Taboh Naning, 78000 Alor Gajah, Melaka, Malaysia

**Corresponding author: norzahir@unikl.edu.my*

Received: 28 April 2019; Accepted: 16 February 2020

Abstract

NiO catalyst was prepared through electrochemical method with rambutan (*Nephelium lappaceum*) leaves as an electrolyte. The effects of the preparation methods on the physical properties of the catalyst were studied *via* Fourier transform infrared spectroscopy (FTIR). The interaction between nickel species and bio-active compounds of rambutan leaves crude during the electrochemical was found to affect the NiO structure. An amount of 3.0 g L^{-1} of NiO was found to be the optimum dosage for 10 mg L^{-1} of Remazol Brilliant Blue (RBB) dye, which resulted in 83.7% of maximum degradation after 1 hour of contact time at pH 3 under fluorescent light. This study showed that the kinetics followed a pseudo-first order Langmuir–Hinshelwood model with the calculated values of K_r and K_{LH} at 1.38 mg L^{-1} h^{-1} and 0.03 L mg^{-1}, respectively. Measurements of the mineralization of RBB by COD and BOD_5 analysis were 66.6% and 73.4%, respectively, before and after reaction. Therefore, the effectiveness of synthesized NiO by the electrobiosynthesis method was established and confirmed through this study. The synthesized NiO has a great potential as a photocatalyst in photocatalytic reaction for wastewater treatment.

Keywords: electrobiosynthesis, nickel, remazol brilliant blue dye, degradation, light irradiation

Abstrak

Mangkin NiO disediakan melalui kaedah elektrokimia dengan ekstrak daun rambutan (*Nephelium lappaceum*) sebagai elektrolit. Kesan kaedah penyediaan ke atas sifat fizikal mangkin telah dikaji melalui spektroskopi inframerah transformasi Fourier (FTIR). Interaksi antara spesies nikel dan sebatian bio-aktif dari ekstrak daun rambutan semasa elektrokimia didapati mempengaruhi struktur NiO. Sejumlah 3.0 gL^{-1} NiO didapati sebagai dos optimum untuk 10 mgL^{-1} pewarna Remazol Brilliant Biru (RBB), yang menghasilkan 83.7% degradasi maksimum selepas 1 jam masa kontak di pH 3 di bawah lampu pendarfluor. Kajian ini juga menunjukkan bahawa kinetik mengikuti model Langmuir-Hinshelwood dengan pseudo pertama dengan nilai kiraan K_r dan K_{LH} masing-masing adalah 1.38 $mgL^{-1}h^{-1}$ dan 0.03 Lmg^{-1}. Pengukuran mineralisasi RBB oleh COD dan BOD_5 adalah 66.6% dan 73.4%, sebelum dan selepas tindak balas. Oleh itu, keberkesanan sintesis NiO dengan kaedah elektrobiosintesis telah ditubuhkan dan disahkan melalui kajian ini. NiO yang disintesis mempunyai potensi besar sebagai fotokatalis dalam tindak balas fotokatalitik untuk rawatan air sisa.

Kata kunci: elektrobiosintesis, nikel, pewarna remazol brilliant biru, degradasi, penyinaran cahaya

Introduction

Access to sufficient water sources is a noteworthy issue that concerns countries everywhere throughout the world. While the specific issue differs in every country, it is conceivable to classify the main issue as having either limited

access or substandard access to this indispensable asset. Moreover, this circumstance is foreseen to wind up being noticeably more extreme as environmental change and water shortage are happening around the world [1]. Wastewater treatment is thought to be a traditional way to deal with confronting deficient water supply [2]. In the last few decades, the structure of wastewater streams has changed because of the introduction of new chemicals. One of the examples is a synthetic dye. It is estimated that 90% of the total dyes produced will end up in fabrics, while the remaining portion will be used in leather, paper, plastic, and chemical industries. It is also estimated that 280,000 tons of textile dyes are discharged as industrial effluents every year worldwide [3].

Man-made textile fibre is a very popular industry in Malaysia, especially in the East Coast of Peninsular Malaysia. Recently, this industry has contributed to the economic growth, especially in the states of Kelantan and Terengganu. Malaysia has produced close to 400,000 tons of man-made fibres which consist of nylon, polyester filament and staple in 2008. Malaysia was the fifteenth largest producer of textile fibre in 2008 and ninth largest in the Asian region. Malaysia's textile industry had exports and imports valued at RM 10.8 billion (US$ 3.6 billion) and RM 6.6 billion (US$ 2.2 billion), respectively. At the same time, the huge amount of textile fibres produced by the textile industry in Malaysia has significantly affected the environmental quality, especially with respect to the liquid effluent [3]. Fortunately, a sustainable solution to this challenge is being developed in the form of photocatalytic reaction.

Photocatalytic is an advanced oxidation process (AOP) alternative that uses natural sunlight to activate a metal oxide catalyst which in turn generates oxidizing agents, able to degrade pollutants and inactivate pathogens typically resistant to traditional treatments [4]. This process is non-selective in regards to target pollutant, does not require the addition of extra chemicals (the catalyst can be reused and does not leave the system) and is expected to demand low operational costs; therefore, it has created high expectations among environmental scientists and engineers [4]. Many studies have attempted to use other semiconductors, such as nickel oxide (NiO) as a potential photocatalyst for synthetic dye degradation. NiO is the alternative semiconductor which is a transition metal oxide widely used as a catalyst with extraordinary electrical, thermal, catalytic and redox properties [5]. The most attractive features of NiO are excellent durability and electrochemical stability. Reported band gap energy value for the NiO is in the range of 3.4-3.8 eV. This suggests that the optical transition in NiO takes place through direct inter-band transition [6]. Also, NiO can act as a promoter for the generation of OH radicals [7].

In recent years, biological synthesis has emerged as an attractive alternative to traditional synthesis methods for producing nanoparticles of photocatalysts. Synthesizing nanoparticles *via* biological entities acting as biological factories offers a clean, nontoxic and environment-friendly method of synthesizing nanoparticles with a wide range of sizes, shapes, compositions and physicochemical properties [8]. Synthesizing nanoparticles *via* plants is a relatively straightforward and advantageous approach. The plant approach is more advantageous since it does not need any special, complex and multi-step procedures, such as isolation, culture preparation, and culture maintenance. Furthermore, synthesis in plants tends to be faster than microorganisms, is more cost-effective and is relatively easy to scale up for the production of large quantities of nanoparticles [9]. Therefore, in this study, the electrobiosynthesis of NiO using rambutan leaves extract as an alternative electrolyte was carried out and used for the removal of Remazol Brilliant Blue (RBB) dye in an aqueous solution.

Materials and Methods

Remazol Brilliant Blue (RBB) was purchased from Merck, Malaysia. Ethanol was purchased from RPE Reagent Pure Erba. Nickel and platinum plates with 99% purity were used as electrodes and were obtained from Nilaco, Japan. Tetraethylammonium perchlorate (TEAP), which was used as a supporting electrolyte in electrolysis, was prepared in accordance with the procedure reported in literatures [10-20]. In this study, the rambutan leaves were extracted using ethanol. The ratio of rambutan leaves to ethanol was 1:10. It was then left for 3 days to let the ethanol extract the bio-active compounds in the rambutan leaves completely. The mixture was filtered using a filter paper and the filtered solution was placed in the rotary evaporator to remove the ethanol and obtain the crude. Then the electrolysis was conducted at a constant current of 480 mA/cm^2 and at 0 ˚C with continuous stirring. The rambutan crude was used as an electrolyte. It was diluted with a certain amount of distilled water to get the concentration of 50 mgL^{-1} and 1000 mgL^{-1}, which were used to synthesize NiO_{50} and NiO_{1000}, respectively. After electrolysis, the mixture was dried at 100 ºC overnight and calcined for 3 hours at 550 ˚C to get a pure NiO catalyst.

FTIR spectroscopy was performed to identify the chemical functional groups present in the catalysts. IR absorbance data were obtained over a range of wavenumbers from 550 to 3500 cm^{-1}. The performance of the catalysts was tested for the degradation of RBB. It was conducted in a photoreactor where a florescent lamp (20W) as a light source was mounted 15 cm above the solution. A 50 ml Pyrex conical flask was placed on a magnetic stirrer to uniformly disperse the catalyst into solution. The initial pH of the solution was 5 and the reaction was carried out at 30 ˚C. The reaction of degradation of RBB was carried out for 2 hours under light irradiation and continuous stirring. The concentration of RBB dye in the solution prior to irradiation was used as the initial value for the RBB degradation measurements. Each set of experiments was performed three times. The adsorption band of RBB was taken at 600 nm and the degradation percentage was calculated using the following equation 1:

$$Decolorization(\%) = \frac{C_0 - C_t}{C_0} \times 100 \quad (1)$$

where C_0 and C_t are the initial concentration of RBB and the concentration at time t, respectively. The mineralization (BOD) was measured using a YSI model 3100 in which BOD bottles were incubated at 20 ˚C for 5 days; the difference in the dissolved oxygen was used to calculate BOD_5. A HACH DR4000 spectrometer was used for COD measurements.

Results and Discussion

Identification of functional group

The details of the functional groups involved in the catalyst structure prepared under varying electrolyte (rambutan leaves extract) concentrations were measured using FTIR, and the results are shown in Figure 1. The peak at 2360 cm^{-1} could be attributed to the hydroxyl groups [21]. The sharp peak at 668 cm^{-1} and 405 cm^{-1} might correspond to the Ni-O-H stretching bond and Ni-O bond vibration, respectively [21]. This peak decreased with increasing electrolyte concentration, possibly indicating the Ni groups [22].

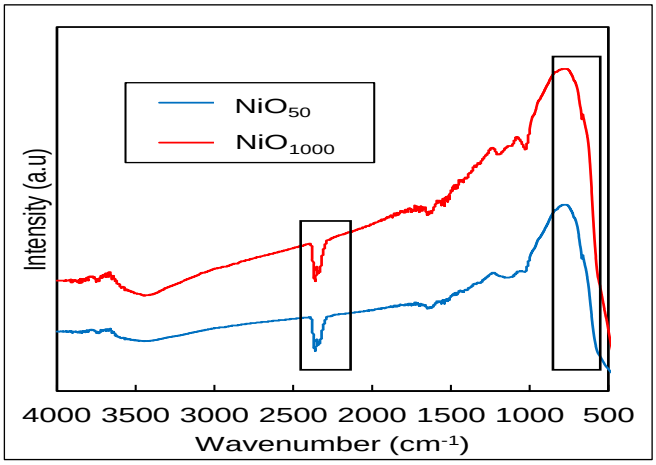


Figure 1. FTIR patterns of NiO catalysts synthesized using 50 mgL^{-1} (NiO_{50}) and 1000 mgL^{-1} (NiO_{1000}) of *Nephelium lappaceum* extract

Performance of the prepared catalysts

The performance of the prepared catalysts was examined by the degradation of RBB, and the results are shown in Figure 2. The results show that complete degradation of RBB was achieved within a very short contact time (2 hours) under visible light conditions when using NiO_{50} and NiO_{1000} at 480 mA cm^{-2}. By comparing the percentage of RBB degradation using both NiO, it is believed that the NiO_{1000} is more favourable to decolorize RBB in high percentage, which leads to high efficiency in treating dyes. It is attributed to the increasing amount of bio-active compound in the *Nephelium lappaceum* extract which will enhance the morphology of the synthesized NiO [22].

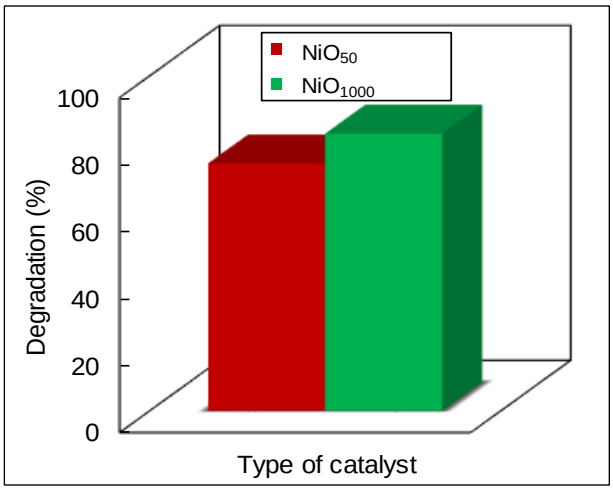


Figure 2. Performance of NiO on degradation of RBB [C = 10 mgL^{-1}, pH = 5, W = 1.0 gL^{-1}, t = 2 h, T = 303K]

Effect of pH

The pH value is one of the main factors influencing the rate of degradation of some organic compounds since it dictates the surface charge properties of the photocatalyst and the size of aggregates it forms [23]. In this study, the effect of pH on degradation of RBB was conducted with pH values of 3, 5, 7, 9 and 11, and illustrated in Figure 3. The highest performance of degradation of RBB was at pH 3 with an RBB degradation percentage of 89.1%. As the pH value increased, the percentage of RBB degradation decreased. Reactive dyes like RBB will release coloured negatively charged anions in the solution [24]. A metal oxide semiconductor usually exhibits an amphoteric behaviour, which influences the surface-charge properties of the photocatalyst when the reactions occur on the surface of the semiconductor [25]. Therefore, when the pH of the solution was low, more positively charged cations appeared on the surface of the NiO photocatalyst. Hence, it increased the electrostatic force of attraction between NiO photocatalyst and dye molecules of RBB, which consequently caused an increase in degradation of dye at low pH values.

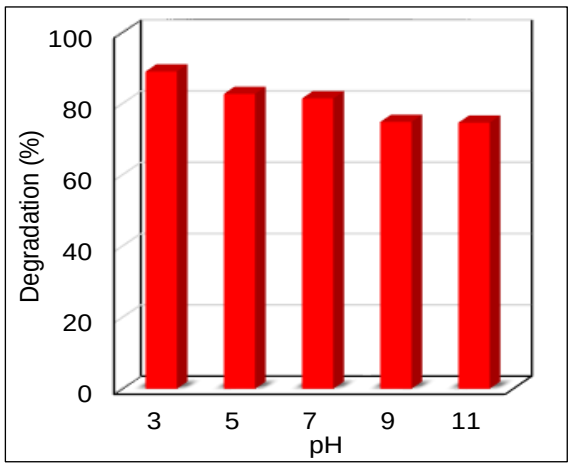


Figure 3. Effect of pH [W = 1.0 gL^{-1}, C = 10 mgL^{-1}, t = 2 h, T = 303K]

Effect of catalyst dosage

The effect of catalyst dosage on the degradation of RBB was carried out by varying the catalyst dosages (0.5, 1.0, 1.5, 3.0 and 5.0 gL^{-1}) to decolorize 10 mgL^{-1} of RBB. A plot of percentage degradation of RBB using different dosages of NiO is shown as in Figure 4. Increase in the dosage of NiO showed an increase in the degradation efficiency of RBB. This is because of the increase in the number of binding sites with increasing NiO dosage. About 3.0 gL^{-1} and 5.0 gL^{-1} of NiO showed the highest percentages of degradation of RBB, which were 83.7% and 83.8%, respectively. In addition, there was no drastic change between 3.0 gL^{-1} and 5.0 gL^{-1} of NiO as the increase in catalyst dosage may lead to higher turbidity of the suspension, hence reducing light penetration and inhibiting the degradation process. The increase in the catalyst dosage led to an increase in the active surface area and enhanced the photodegradation reaction [25]. Moreover, the increase in degradation was most likely due to the increase in the number of photons and dye molecules absorbed [24]. Increasing the number of photons will increase the number of free radical. These free radicals will attack the RBB dye molecule by breaking the structure of the RBB dye molecule and convert it into oxidative products and carbon dioxide gases.

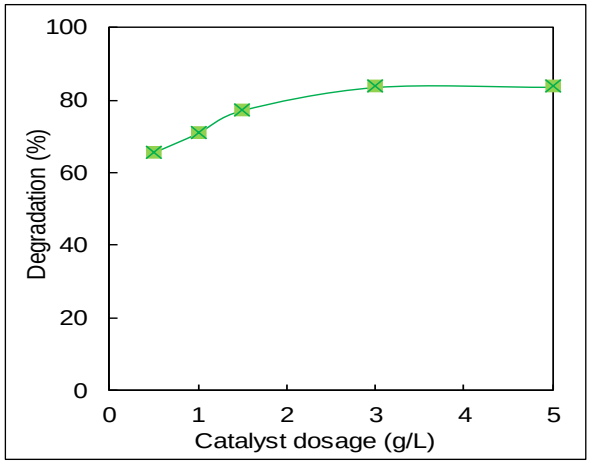


Figure 4. Effect of catalyst dosage [pH = 3, C = 10 mgL^{-1}, *t* = 1 h, T = 303K]

Effect of Initial Concentration

The effect of initial dye concentrations on degradation of RBB in this study was investigated by varying the RBB concentrations (10, 20, 30, 50, 70 and 100 mgL^{-1}). Figure 5 illustrates the changes in degradation of RBB as photodegradation has taken place. The degradation efficiency was decreased with increase in the initial concentration of RBB dyes. The initial concentration of 10 mgL^{-1} of RBB showed the highest percentage of degradation of RBB, which was at 83.7%. The decrease in degradation efficiency on increasing initial dye concentration may be due to the lack of available active sites required for the high initial concentration of dye [24]. At the same time, when the RBB dye concentration was increasing, higher particle concentration became present in the aqueous solution and led to a higher turbidity of the solution. Hence, it reduced the penetration of light to the photocatalyst. When a low amount of light intensity approached the surface of the photocatalyst, low amount of free radical is produced, therefore inhibiting the photodegradation process [25]. However, lowering the RBB dye molecule concentration will enhance the photocatalytic reaction because less RBB dye molecule will be degraded with enough active sites on the surface of the catalyst. At the same time, it will reduce the time of degradation of substrate molecule. The active sites of photocatalyst are probably completely exposed to the substrate ions [25] which will make the substrate molecule easier to degrade.

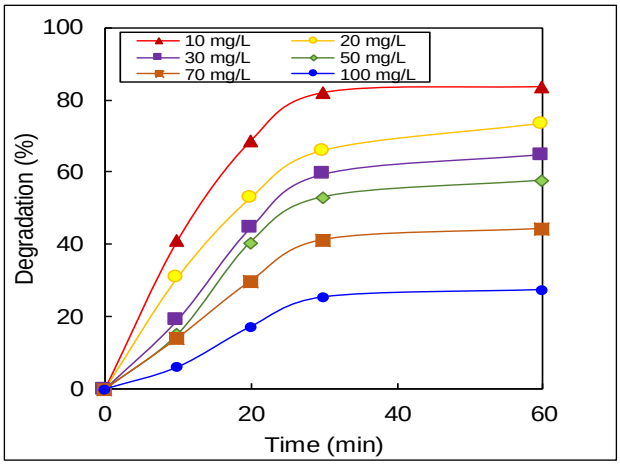


Figure 5. Effect of initial concentration [pH = 3, W = 3.0 gL^{-1}, t = 1 h, T = 303K]

Kinetic study

The kinetic degradation of RBB using NiO was studied by applying the Langmuir–Hinshelwood (L–H) kinetic model at different initial concentrations, and the results are shown in Figure 6. Higher concentrations showed lower efficiency of photocatalytic degradation due to the formation of several layers of adsorbed dye on the catalyst surface, which increased at higher dye concentrations. In addition, large amounts of adsorbed dye were found to inhibit the reaction with the dye molecules, since there was no direct contact of the catalyst with photogenerated holes or hydroxyl radicals [25]. The line with an intercept of $1/k_r$ and $1/k_rK_{LH}$ was obtained from the Langmuir–Hinshelwood (L–H) kinetic formula (equation 2):

$$\frac{1}{k_{app}} = \left[\frac{1}{K_r K_{LH}}\right] + \frac{C_0}{K_r} \qquad (2)$$

where K_r is the reaction rate constant (mg L^{-1} h^{-1}), K_{LH} is the Langmuir–Hinshelwood adsorption equilibrium constant (L mg^{-1}) and C_0 is the initial concentration of CR (mg L^{-1}). The calculated values of K_r and K_{LH} were 1.38 mg L^{-1} h^{-1} and 0.03 L mg^{-1}, respectively, for NiO_{1000}. The values of k_r were greater than those of K_{LH} for catalysts, indicating the dye adsorption was the controlling step of the process.

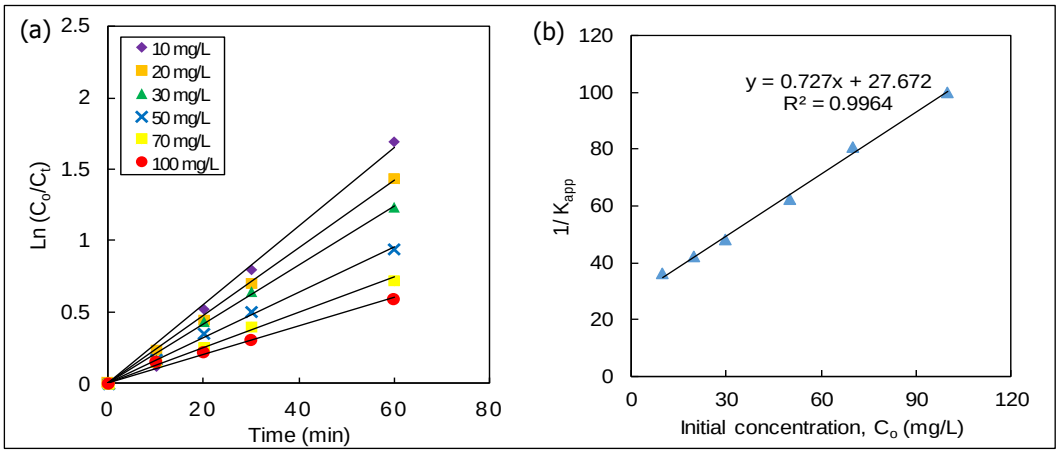


Figure 6. (a) Photodegradation kinetics of RBB by NiO at different RBB initial concentration; (b) the relationship between $1/K_{app}$ and $1/C_0$ at different initial concentrations of RBB

The values of k_{app} obtained from Fig. 6 are listed in Table 1. Higher values were obtained with lower concentrations of RBB, which illustrated the favourable system of low dye concentrations [25].

Table 1. Pseudo first-order apparent constant value for RBB degradation

Initial Concentration, C_0 (mgL^{-1})	**Reaction Rate Constant, K_{app} (min^{-1})**	**R^2**	**Initial Reaction Rate ($mgL^{-1}min^{-1}$)**	**Percentage of Degradation (%)**
10	0.0275	0.985	0.275	83.69
20	0.0238	0.999	0.476	73.53
30	0.0208	0.997	0.624	65.07
50	0.0160	0.997	0.800	57.69
70	0.0124	0.993	0.868	44.38
100	0.0100	0.983	1.000	39.75

Investigation on biodegradability

The biodegradability of RBB solution was conducted by performing the BOD_5 and COD analyses before and after the photocatalytic process. The purpose of this study is to determine the toxicity of final RBB solution produced after the process. Figure 7 shows the values of BOD_5 and COD of RBB solution before and after being treated *via* photocatalytic degradation, which were 66.7% and 73.4%, respectively. There was a significant change in BOD_5 and COD, where the biodegradability of the RBB solution can be enhanced by this photocatalytic process. By calculating the ratio of BOD_5 to COD before and after treatment, the value was 0.47 and 0.60, respectively. The ratio before being treated showed that the dye solution was non-biodegradable. However, it became biodegradable after undergoing the photocatalytic process by referring to the ratio value obtained after being treated. This stipulated that the final RBB solution can be treated because some non-organic components that had less biodegradability contained in the RBB molecule were decomposed during the photocatalytic process [25].

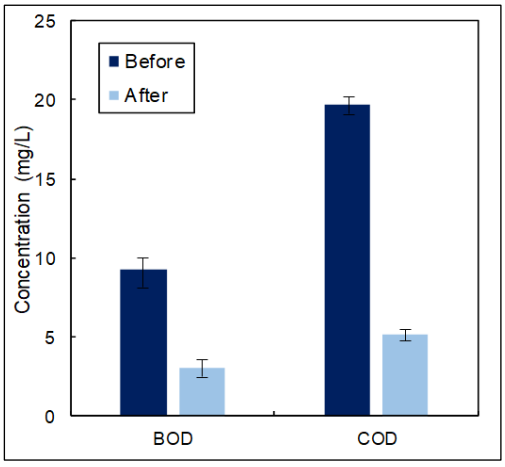


Figure 7. Concentrations of BOD_5 and COD levels before and after photocatalytic process [pH = 7, W = 1.0 gL^{-1}, C = 10 mgL^{-1}, t = 1 h, T = 303K]

Conclusion

The performance of NiO synthesized using 50 mgL^{-1} and 1000 mgL^{-1} of *Nephelium lappaceum* extracts were conducted to compare the performance of the photodegradation of RBB. NiO synthesized using 1000 mgL^{-1} of *Nephelium lappaceum* showed the highest percentage of RBB degradation which was 82.7%. The photocatalytic degradation of RBB was tested using several parameters, such as pH of solution, dosage of catalyst, and initial concentration of RBB dye solution. The degradation of RBB was more favourable in acidic conditions which was at pH of 3. A higher amount of catalyst dosage gave a higher degradation percentage of RBB. 10 mgL^{-1} of initial concentration of RBB is shown to be the most effective in photodegradation reaction due to high availability of active site on the surface of catalyst.

The photodegradation of RBB by NiO catalyst obeyed the pseudo first-order reaction because the apparent first-order rate constant (k_{app}) obtained from the graph of ln (C_o/C_t) with a function of time gave a higher value as the concentration of RBB decreased. There was a significant change in BOD_5 and COD at 66.5% and 73.3%, respectively, showing that the biodegradability of the RBB solution can be enhanced by the photocatalytic process. The ratio of BOD_5 to COD after being treated was 0.60. It stipulated the ability of the final RBB solution to be treated via the photocatalytic method. Furthermore, more instrument was needed in order to examine the pathway mechanism of catalyst synthesized using the electrolysis system and to explore new structural models of the catalyst. For the extension of this work, the system should be applied for degradation of other synthetic dyes and real wastewater should be employed.

Acknowledgements

The authors are grateful for the financial support by the Short Term Research Grant (STRG) from Universiti Kuala Lumpur (Grant No. 17004 & 17029), Majlis Amanah Rakyat Malaysia (MARA), the awards of Yayasan Tengku Abdullah Scholarship (YTAS-Muhammad Farhan bin Hanafi), and also the Malaysian Institute of Chemical and Bioengineering Technology, Universiti Kuala Lumpur for their support.

References

1. Li, X. K., Ji, W. J., Zhao, J., Wang, S. J. and Au, C. T. (2005). Ammonia decomposition over Ru and Ni catalysts supported on fumed SiO_2, MCM-41 and SBA-15. *Journal of Catalysis*, 236(2): 181-189.
2. Singh, A., Kumar, V. and Srivastava, J. N. (2013). Assessment of bioremediation of oil and phenol contents in refinery wastewater via bacterial consortium. *Journal Petroleum Environment Biotechnology*, 4: 145-151.
3. Sapawe, N., Jalil, A. A., Triwahyono, S., Sah, R. N. R. A., Jusoh, N. W. C. and Hairom, N. H. H. (2013). Electrochemical strategy for grown ZnO nanoparticles deposited onto HY zeolite with enhanced photodecolorization of methylene blue: Effect of the formation of Si-O-Zn bonds. *Applied Catalysis A: General*, 456: 144-158.
4. Sapawe, N., Jalil, A. A. and Triwahyono, S. (2013). One-pot electro-synthesis of ZrO_2-ZnO/HY nanocomposite for photocatalytic decolorization of various dye-contaminants. *Chemical Engineering Journal*, 225: 254-265.
5. Venu, G. D. and Sahle, E. E. (2008). Catalytic oxidation of dimethyl sulfide with ozone: effects of promoter and physico-chemical properties of metal oxide catalysts. *Applied Catalyst A: General*, 348(1): 86-93.
6. Bokare, A. D., Chikate, R. C., Rode, C. V. and Paknikar, K. M. (2008). Iron-nickel bimetallic nanopartilcles for reductive degradation of azo dye Orange G in aqueous solution. *Applied Catalysis B: Environmental*, 79: 270-278.
7. Petya, K., Naydenov, A., Christoskova, S. and Mehandjiev, D. (2006). Alumina-supported nickel oxide for ozone decomposition and catalytic ozonation of CO and VOCs. *Journal of Chemical & Engineering*, 122: 41-46.
8. Xinyu, Z., Li, X. and Qin, W. (2009). Investigation of the catalytic activity for ozonation on the surface of NiO nanoparticles. *Chemical Physics Letter*, 479(4): 310-315.
9. Swami, A., Selvakannan, P. R., Pasricha, R. and Sastry, M. (2004). One-step synthesis of ordered two-dimensional assemblies of silver nanoparticles by the spontaneous reduction of silver ions by pentadecylphenol Langmuir monolayers. *The Journal of Physical Chemistry B*, 108: 19269-19275.
10. Sapawe, N., Jalil, A. A., Triwahyono, S., Adam, S. H., Jaafar, N. F. and Satar, M. A. H. (2012). Isomorphous substitution of Zr in the framework of aluminosilicate HY by an electrochemical method: Evaluation by methylene blue degradation. *Applied Catalysis B: Environmental*, 125: 311-323.

11. Sapawe, N., Rustam, M. A., Mahadzir, M. H. H., Lani, M. K. E. M., Raidin, A. and Hanafi, M. F. (2019). A novel approach of *in-situ* electrobiosynthesis of metal oxide nanoparticles using crude plant extract as main medium for supporting electrolyte. *Materials Today: Proceedings*, 19(4): 1441-1445.
12. Hanafi, M. F., Sapawe, N., Rahim, M. Z. A., Rahman, N. N., Rahman, A. H. A. and Ahmad, A. A. (2016). Performance of $EGZrO_2$-$EGFe_2O_3$/HY as photocatalyst and its efficacy in decolorization of dye-contaminants. *Malaysian Journal of Analytical Sciences*, 20(5), 1052-1058.
13. Hanafi, M. F. and Sapawe, N. (2018). Remarkable degradation of methyl orange by tetragonal zirconia catalyst. *Materials Today: Proceedings*, 5(10), 21849-21852.
14. Hanafi, M.F. and Sapawe, N. (2019). The potential of ZrO_2 catalyst toward degradation of dyes and phenolic compound. *Materials Today: Proceedings*, 19(4): 1524-1528.
15. Hanafi, M. F. and Sapawe, N. (2019). Electrosynthesis of ZrO_2 nanoparticles with enhanced removal of phenolic compound. *Materials Today: Proceedings*, 19(4): 1529-1532.
16. Hanafi, M. F. and Sapawe, N. (2019). Effect of calcination temperature on the structure and catalytic performance of ZrO_2 catalyst in phenol degradation. *Materials Today: Proceedings*, 19(4): 1533-1536.
17. Hanafi, M. F. and Sapawe, N. (2019). Electrogenerated zirconia ($EGZrO_2$) nanoparticles as recyclable catalyst for effective photocatalytic degradation of phenol. *Materials Today: Proceedings*, 19(4): 1537-1540.
18. Sapawe, N. and Hanafi, M. F. (2015). Facile one-pot electrosynthesis of high photoreactive hexacoordinated Si with Zr and Zn catalyst. *RSC Advances*, 5(92): 75141-75144.
19. Sapawe, N. (2015). Hybridization of zirconia, zinc and iron supported on HY zeolite as a solar-based catalyst for the rapid decolorization of various dyes. *New Journal of Chemistry*, 39(6): 4526-4533.
20. Sapawe, N. (2015). Effective solar-based iron oxide supported HY zeolite catalyst for the decolorization of organic and simulated dyes. *New Journal of Chemistry*, 39(8): 6377-6387.
21. Rahdar, A., Aliahmad, M. and Azizi, Y. (2015). NiO nanoparticles: Synthesis and characterization. *Journal of Nanostructures*, 15: 145-151.
22. Yuvakumar, R., Suresh, J., Joseph, A. N., Sundrarajan, M. and Hong, S. I. (2014). Rambutan (*Nephelium lappaceum* L.) peel extract assisted biomimetic synthesis of nickel oxide nanocrystals. *Material Letters*, 128(1): 170-174.
23. Algubili, A. M., Alrobayi, E. M. and Alkaim, A. F. (2015). Photocatalytic degradation of remazol brilliant blue dye by ZnO/UV process. *International Journal Chemistry and Science*, 13(2): 911-921.
24. Das, D. P., Baliarsingh, N. and Parida, K.M. (2007). Photocatalytic decolorisation of methylene blue (MB) over titania pillared zirconium phosphate (ZrP) and titanium phosphate (TiP) under solar radiation. *Journal of Molecular Catalysis A: Chemical*, 261: 254-261.
25. Sapawe, N., Jalil, A. A., Triwahyono, S., Adam, S. H., Jaafar, N. F. and Satar, M. A. H. (2012). Isomorphous substitution of Zr in the framework of aluminosilicate HY by an electrochemical method: Evaluation by methylene blue degradation. *Applied Catalysis B: Environmental*, 125: 311-323.

Malaysian Journal of Analytical Sciences (MJAS)
Published by Malaysian Analytical Sciences Society

EFFICIENT REMOVAL OF LEAD FROM AQUEOUS USING HYBRID GRAPHITE NANOFLAKES/MESOPOROUS SILICA NANOPARTICLES, AMINE FUNCTIONALIZED MESOPOROUS SILICA AND GRAPHITE NANOFLAKES AS ADSORBENTS

(Penyingkiran Berkesan terhadap Plumbum dari Cecair Menggunakan Kepingan Nano Grafit Hibrid/ Silika Partikel Nano Berliang-Meso, Silika Partikel Nano Berliang-Meso Berfungsi Amin dan Kepingan Nano Grafit Sebagai Penyerap)

Haslina Ahmad[1,2]*, Vilander Vince Laini[1], Tan Zhi Qian[1], Radhiah Mohd Jelani[1], Fatin Ahza Rosli[1], Sazlinda Kamaruzaman[1]

[1]*Department of Chemistry, Faculty of Science*
[2]*Integrated Chemical Biophysics Research Centre, Faculty of Science*
Universiti Putra Malaysia, 43400 UPM Serdang, Selangor, Malaysia

**Corresponding author: haslina_ahmad@upm.edu.my*

Received: 20 November 2019; Accepted: 18 March 2020

Abstract

Noxious heavy metal ions contamination has become a serious environmental problem nowadays. Among all the toxic heavy metal ions, lead(II) ion, is the most commonly encountered in industrial and agricultural wastewater and in acidic wash-away from landfills site. Hence, the removal of lead traces from the environment has gained a special concern due to their persistence. In this study, batch experiments were conducted to study the capability of hybrid graphite nanoflakes/mesoporous silica nanoparticles (GNP-MSN), amine functionalized mesoporous silica (NH_2-MSN) and pristine graphite nanoflakes (GNP) as adsorbents for removal of lead from aqueous. The influence of several parameters such as pH of the aqueous sample, amount of adsorbent, initial concentration of the lead(II) ions and contact time were examined to optimize the adsorption efficiency of the adsorbents under study. Lead(II) ion can be extracted at pH 4 from sample volume of 10 mL with concentration of 10 ppm by utilizing 10 mg of each respective adsorbent. The analysis of the sample was done by using Flame Atomic Absorption Spectroscopy (FAAS). Furthermore, GNP-MSN also has greatly reduced the aggregation of pristine graphite in water in which GNP-MSN is more easily to be removed from tested sample by centrifugation process compared to pristine graphite. In term of consistency and selectivity of the lead(II) ions removal, GNP-MSN show the highest efficiency since it is able to remove lead(II) ions with higher adsorption capacity (23.940 mg/g) compared to NH_2-MSN (9.230 mg/g) and GNP (1.113 mg/g). Based on kinetic study, both GNP and NH_2-MSN were best-fitted with pseudo-second order while GNP-MSN fitted well with pseudo-first order.

Keywords: adsorption, mesoporous silica nanoparticles, graphite nanoflakes, lead, hybrid nanoparticles

Abstrak

Pencemaran ion logam berat secara tidak sengaja telah menjadi isu alam sekitar yang serius pada masa kini. Di antara semua ion logam berat toksik, ion plumbum(II), adalah yang paling biasa ditemui dalam air kumbahan perindustrian dan pertanian dan dalam cucian berasid dari tapak pelupusan. Oleh itu, penyingkiran plumbum dari alam sekitar telah mendapat keprihatinan khusus kerana masih berterusan. Dalam kajian ini, eksperimen berkumpulan dijalankan untuk mengkaji kemampuan kepingan nano grafit hibrid/ silika partikel nano berliang-meso (GNP-MSN) untuk penyingkiran plumbum, terhadap silika partikel nano berliang-meso berfungsi amin (NH_2-MSN) dan kepingan nano grafit asli (GNP) untuk penyingkiran plumbum dari akueus. Faktor beberapa parameter seperti pH sampel, jumlah penjerap, kepekatan awal ion plumbum(II) dan masa sentuhan telah dikaji

untuk mengoptimumkan kecekapan penjerapan untuk menyerap di dalam kajian. Ion plumbum(II) boleh disingkirkan pada pH 4 dari jumlah sampel 10 mL dengan kepekatan 10 ppm dengan menggunakan 10 mg bagi setiap penyerap. Analisis sampel dilakukan dengan menggunakan spektroskopi penyerapan atom bara (FAAS). Selain itu, GNP-MSN juga telah mengurangkan pengagregatan grafit asli di dalam air di mana GNP-MSN lebih mudah dikeluarkan daripada sampel yang diuji dengan proses sentrifugasi berbanding dengan grafit asli. Dari segi konsistensi dan pemilihan penyingkiran ion (II) ion, GNP-MSN menunjukkan kecekapan tertinggi kerana ia dapat menyingkirkan ion-ion plumbum (II) dengan kapasiti penjerapan yang lebih tinggi (23.940 mg/g) berbanding dengan NH_2-MSN (9.230 mg/g) dan GNP (1.113 mg/g). Berdasarkan kajian kinetik, kedua-dua GNP dan NH_2-MSN sangat sesuai dengan perintah pseudo-kedua manakala GNP-MSN sesuai dengan perintah pseudo-pertama.

Kata kunci: penjerapan, silika partikel nano berliang-meso, kepingan nano grafit, plumbum, partikel nano hibrid

Introduction

Due to the rapid growth of industrialization, discharge of untreated heavy metals into the water increased and caused a serious threat to the environment and living organisms. Unlike organic contaminants, heavy metals are not biodegradable and may bioaccumulate in living tissues in a similar way as other toxic heavy metal ion. Long-term consumption of water containing high level of lead ion would cause serious disorders, such as anemia, kidney disease, nausea, convulsions, coma, renal failure, and cancer, along with subtly negative effects on metabolism and intelligence. There are two main sources of heavy metals in wastewater effluents which are natural and anthropogenic [1]. Lead is a toxic metal, persistent, and it can bio-accumulate in the body over time. Once they enter the food chain, they may accumulate in the human body in high concentration which can cause serious health disorders [2]. The presence of excess lead in water may cause food poisoning, vomiting, diarrhea and stomach discomfort if it is being consumed.

There are several techniques used for heavy metal removal such as nanofiltration, osmosis, ion exchange, coagulation and flocculation, and adsorption. Adsorption is one of the effective methods to eliminate the metal ions especially when porous materials are being utilized [3, 4]. Due to the instability of the mesoporous silica shells under basic condition and its inability to adsorb heavy metal ions, hence this study was conducted to enhance its adsorption ability by hybridization with a low cost, high thermal stability and environmentally friendly material. Graphite nanoparticles was chosen to be hybridized with mesoporous silica nanoparticles due to its high surface area and high thermal stability which are excellent properties to withstand the high temperature during the hybridization process [5]. Moreover, the tendency of pristine graphite to aggregates in water also becomes one of the reasons for it to be hybridized with a material that able to provide good supporting framework to prevent the aggregation. Another approach is to functionalize the MSN by using the post-grafting method where the synthesized nanoparticles were grafted with organosilanes bearing amino group to produce NH_2-MSN. It is done under a basic condition.

In this study, three different nanoadsorbents; hybrid graphite nanoflakes/mesoporous silica (GNP-MSN) synthesized with ionic liquid template, NH_2-MSN and GNP were utilized as the adsorbent for the adsorption of lead (II) ions form an aqueous sample. The adsorption kinetic, isotherm and the effects of different adsorption conditions were studied: solution pH, initial concentration, adsorbent amount and contact time.

Materials and Methods

Chemicals and Materials

Lead nitrate, $Pb(NO_3)_2$ (99% purity) was purchased from BDH Chemicals Ltd, England. Graphene nanoplatelets (GNP-C750) were purchased from XG Sciences. Ionic liquid, hexadecylpyridinium bromide, $C_{16}PyBr$ was synthesized by using toluene that was purchased from Fischer Chemical with 1-bromohexadecane, $C_{16}Br$ (97%, Acros Organics) and pyridine (79.10 g/mol) which was supplied by Univar. Diethylether were purchased from Fischer Chemical and acetonitrile was purchased from J. Kollin Chemicals. Tetraethoxysilane, TEOS (99%, Merck KGaA, Germany) which is the source of silica; triethanolamine, TEA (98%, ChemPur®) as the catalyst; grade C graphite nanoplatelets (xGNP®, Inc) as the graphite coating; concentrated hydrochloric acid, HCl (37%, Fisher Chemical); ethanol, EtOH (99%, J. Kollin Chemicals).

Synthesis of Functionalized MSNs:

Synthesis of GNP-MSN

The synthesis of GNP-MSN was done by using the hydrothermal process [6]. Firstly, 0.50 g of ionic liquid (C_{16}PyBr) and 0.05 g of GNP was dissolved in 20.0 mL of distilled water then sonicated for 90 minutes. Then, it was heated at 90 °C and stirred at 750 rpm for one hour. This solution was denoted as solution A. In the meantime, preferred amount of TEA (0.05 mL) and TEOS (1.5 mL) were heated at 180 °C for 30 minutes. This second solution was denoted as solution B. After 30 minutes, the solution B premix was added in drop-wise manner into solution A. The solutions were mixed homogeneously with vigorous stirring at 90 °C for another 60 minutes. A black solution was formed. After sitting for a while, the cooled solution was then centrifuged and rinsed with ethanol twice to remove unreacted reagents. Black precipitates of GNP-MSN were observed. Finally, solvent-acid washing extraction method was employed to remove the template. The GNP-MSN precipitates were re-dispersed in 20.0 mL of 95% ethanol solution mixed with concentrated hydrochloric acid (2.0 mL) and refluxed at 90 °C with stirring at 750 rpm for overnight. Then, the solution containing GNP-MSN was centrifuged and rinsed twice with ethanol to obtain the purified products. The purified GNP-MSN precipitates were dried in oven at 55 °C.

Synthesis of NH_2-MSN

To enhance the adsorption of lead(II) ions, mesoporous silica nanoparticles (MSN) were functionalized with amine group using a post-grafting method [7]. 0.1 g of MSNs were grinded to get a fine form of MSN and then transferred to a 250 mL round-bottomed flask containing 20 mL of ethanol. 2 mL of (3-aminopropyl) triethoxysilane (APTES) was added dropwise into the mixture. A rubber stopper with needle was inserted. In a silicone oil bath, the mixture was stirred at 750 rpm for 6 hours at 70°C. The product was extracted using centrifuge with ethanol wash twice after being cooled to room temperature. Each extraction involved a sonication step of 2 to 3 minutes at room temperature before drying in oven. The dried white powder is the amine functionalized mesoporous silica nanoparticle (NH_2-MSN).

Characterization of the Nanoadsorbents

The chemical functional groups in the nanoadsorbents were determined by Fourier transform infrared (FTIR; IRTracer-100, SHIMADZU, Japan) spectroscopy. Approximately 0.10 mg of each of the nanoparticles was separately ground and placed into a KBr pellet. Then, the infrared spectra for each of the nanoparticles were measured in the range of 200 cm^{-1} to 4000 cm^{-1}. The surface area, pore volume and pore size distribution of nanoadsorbents were measured using Brunner-Emmett-Teller (BET) and Barrett-Joyner-Halenda (BJH) which the samples were degassed with nitrogen gas at about 50 °C with saturation pressure of approximately 756 mmHg overnight before analysis.

Batch Adsorption experiments and FAAS determination method

The adsorption process of lead(II) ions on nanoadsorbents were investigated by performing batch adsorption experiments as shown in Figure 1. 10.0 mg of nanoadsorbents were added to 10.0 mL of 10 mg/L lead solution while the pH of the solution was adjusted to 4.0 by adding 0.01 M HCl. The pH of the solution was measured with Eutech pH 5+ meter. The mixture was then stirred within 2 hours with magnetic stirrer at 600 rpm under normal room temperature. The flasks were plugged air-tight to avoid the pH fluctuation due to the gases exchange during the experiment. Then, the solid adsorbent was removed from each sample by centrifugation before the supernatant was collected and analyzed with Thermo Scientific iCE 3300FL Flame Atomic Absorption Spectrometer to determine the lead(II) ions residual. Then, the percentage removal of lead(II) ions was calculated using the equation (1):

$$\% \text{ Removal} = \frac{(\text{Co}-\text{Ce})}{\text{Co}} \times 100 \quad (1)$$

To be more precise, the amount of lead(II) ions adsorbed at equilibrium, q_e (mg/g) and amount of adsorbate at time t, q_t (mg/g) were calculated using the material balance of the adsorption system, by assuming the lead(II) ions, which has disappeared from the solution, must be in the adsorbent. The related equation used to calculate the amount of lead(II) ions was shown as follow:

$$q_e = \left(\frac{C_o - C_e}{m}\right) V \quad (2)$$

$$q_t = \left(\frac{C_o - C_t}{m}\right) V \quad (3)$$

where C_o (mg/L), C_e (mg/L) and C_t (mg/L) are the initial concentration, equilibrium concentration and equilibrium concentration at time t of adsorbate in solution, respectively. The dried mass of used adsorbent is denoted by m (g) and V (L) is the volume of the adsorbate solution.

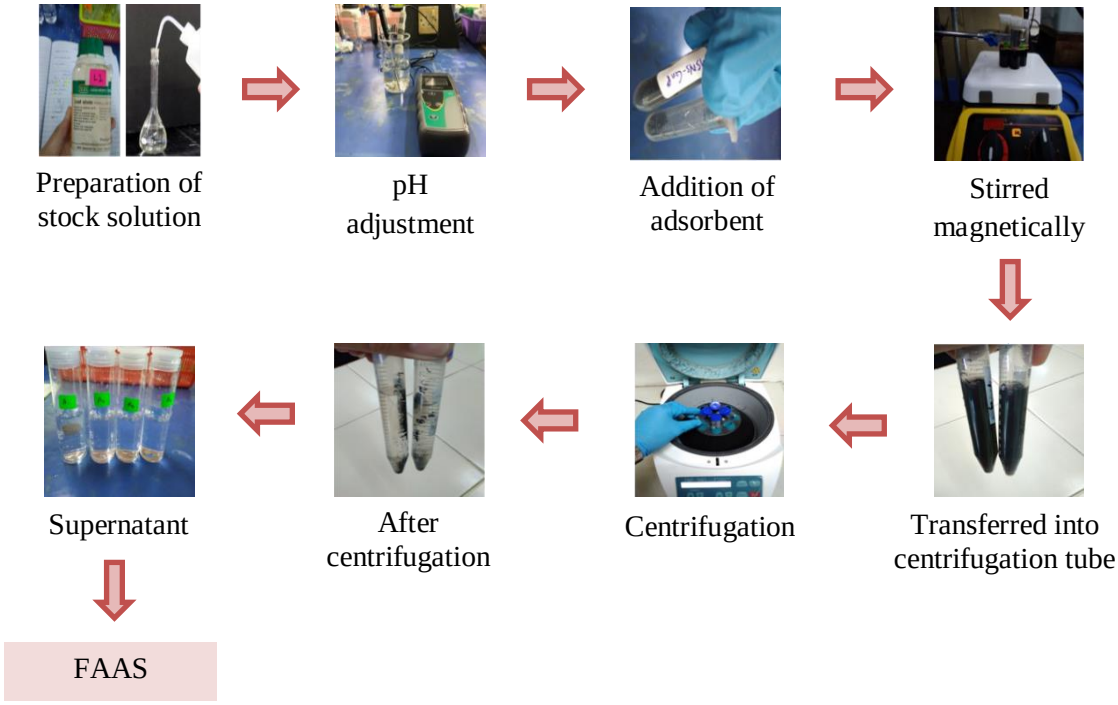


Figure 1. General procedures of batch adsorption study

Results and Discussion

Characterization of the nanoadsorbents

As shown in Figure 2, the chemical functional groups in MSN, GNP, NH_2-MSN and GNP-MSN were determined by FTIR. GNP spectrum has peaks at 3350 cm^{-1} (O-H stretch), 2800 to 3000 cm^{-1} (C-H characteristic band due to aliphatic vibrations) and 1710 cm^{-1} (C=O stretch), whereas aromatic C=C bending at 1540 cm^{-1}, and around 1000 to 1100 cm^{-1} (C-O stretch). Hence, the chemical functional groups present in GNP were hydroxyl, carboxyl and alkoxy groups. Based on the spectrum analysis shown, both MSN and NH_2-MSN showed peaks at 1060 cm^{-1} and at 793 cm^{-1} that indicates the asymmetric vibration and symmetric stretching for Si-O-Si group for both MSN and NH_2-MSN. At 2934 cm^{-1}, stretching vibration of CH_2 appeared due to introduction of methyl group between silylation [10]. Additional band for NH_2-MSN at 1638 cm^{-1} is the vibration of aliphatic NH_2 bending which indicates the presence of amine group.

According to Mehdinia et al. [8], the presence of amino groups in the adsorbent structure can also cause hydrophilic property of the adsorbent thus increase the removal efficiency. There are several peaks that represent the existence of silica and graphite components in GNP-MSN. The weak peak found on GNP-MSN line graph at 3300 to 3500 cm^{-1} (-OH antisymmetric stretching vibration) can be deduced that GNP is not reduced completely and still withhold

traces of hydroxyl during the hybridization process. Next, a small characteristic band in the range of 2800 to 3000 cm^{-1} due to (C-H aliphatic) vibrations was observed. The indicators that proved the successful attachment of graphite onto silica was the present of aromatic C=C stretch due to the carbon ring of graphite structure on the GNP-MSN line (1350 to 1550 cm^{-1}), the formation of C-H group in GNP-MSN was found after the bonding of Si-O group from SiO_2 with the epoxide group of the graphite. The breaking of the epoxide group creates a carbanion which was filled with H^+ ions produced from water molecules. The present of C-H group indicated that silica has effectively attached to graphite and the preparation of SiO_2-graphite through hydrothermal method was successful [9]. Moreover, the presence of a broad peak at approximately 1000 to 1250 cm^{-1} on the GNP-MSN line attributed to Si-O-C group proved the binding of graphite onto silica. Although this characteristic band also observed on the MSNs line, the band formed on GNP-MSN shows a shift toward the presence of C-O group which happen to be in the same wavelength range. Moreover, the presence of a broad peak at approximately 1000 to 1250 cm^{-1} on the GNP-MSN line attributed to Si-O-C group proved the binding of graphite onto silica.

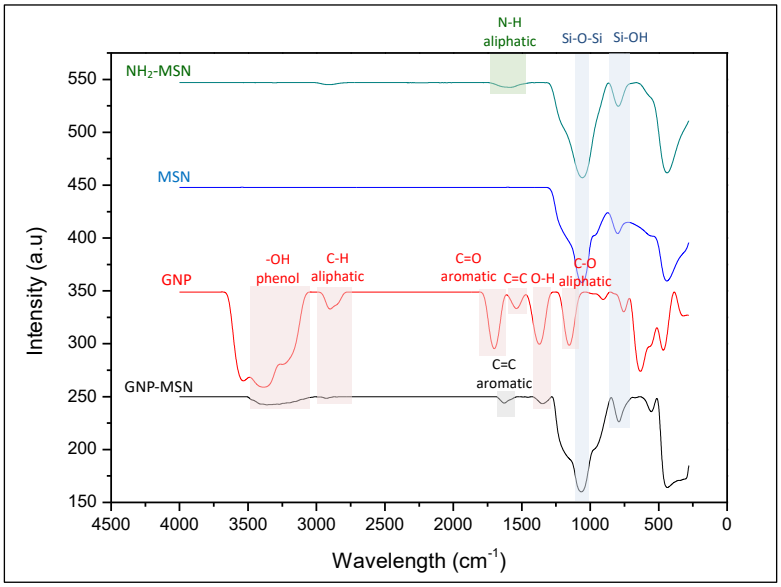


Figure 2. FTIR spectrums of NH2-MSN, MSN, GNP and GNP-MSN

By using Brunner-Emmett- Teller (BET), the surface area, pore size and pore volume of adsorbent was analyzed and summarized in the Table 1.

Table 1. Summary of BET analysis for MSN, NH2-MSN, GNP and GNP-MSN

	BET Surface Area (m^2/g)	**Pore Volume (cm^3/g)**	**Pore Size (Å)**
MSN	730.50	1.44	143.47
NH_2-MSN	258.00	0.85	78.00
GNP	741.31	1.03	67.80
GNP-MSN	128.41	0.19	88.12

The decrease in surface area of the hybridized GNP-MSN was probably due to the coating effect of silica onto GNP surface. Moreover, the pore size of GNP-MSN was slightly bigger than the pore size of GNP. This might be due to

the effect of MSNs which was able to preserve its pores size and structure due to the existence of the ionic template, C_{16}PyBr. In addition, the decreases in the surface area and pore volume of GNP-MSN also related to the larger particle size of GNP-MSN. The surface area of MSN decreased from 730 m²/g to 258 m²/g and the pore size also decreased from 131 Å to 78 Å after the functionalization on amine group onto the surface of the MSN. This also can be seen in the experiment conducted by He et al. [10] which found that, the surface area, pore size and pore volume of NH2-MSN were lower than that in MSN. This is due to integration of amine groups onto the surface of the pores making the pore size smaller and decrease in surface area [10, 11].

Batch adsorption experiments:

Effect of pH on the removal of lead(II) ions

Maximum adsorption was detected at pH 4 for all three nanoadsorbents; GNP, NH_2-MSN and GNP-MSN (Figure 3). At pH values of 1-3, adsorption was unfavorable. Mehdinia et al. [12] claimed that the surface of the GNP could be surrounded by the hydronium ions (H_3O^+) that hinder lead(II) ions from reaching the binding site on the surface of the GNP. Hence, there is competition between metal cations and hydronium ions (H_3O^+) or proton (H^+) on the surface of the adsorbent. As repulsive force present due to like charges, the mentioned ions will be hindered from achieving the adsorbent connection sites [13]. The high concentration of H^+ and H_3O^+ protonated from the hydroxyl and carbonyl could out-compete aqueous heavy metal ions for the available binding sites at low solution pH, resulting in little or no adsorption [14]. As for higher pH, the precipitation of metal cations in basic medium occur due to formation of metal hydroxides that reduces the adsorption efficiency [3]. For the pH values greater than 4 were not favorable until pH 8, it is because Pb species in water solution could be present in the forms of Pb^{2+}, $Pb(OH)^+$, $Pb(OH)^2$ and $Pb(OH)^{3-}$ which disturb the binding of lead species with GNP [15]. The possibility of precipitation of lead(II) ions as lead hydroxide would occur.

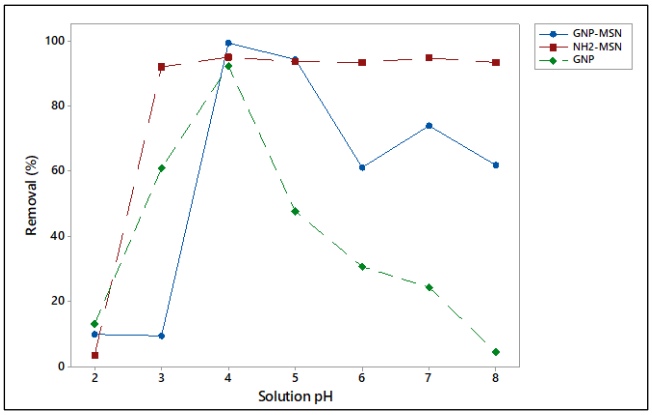


Figure 3. The effect of solution pH on the removal of lead(II) ions by different nanoadsorbents; GNP, GNP-MSN and NH_2-MSN

Effect of adsorbent amount on the removal of lead(II) ions

The adsorption studies of lead(II) ions was then further studied using different amount of adsorbent used with metal solution pH = 4.0. The amount of adsorbent used were 10 mg, 30 mg, 50 mg, 70 mg and 90 mg. According to the trend shown (Figure 4), the removal efficiency was higher and remained constant from 10.0 mg to 30.0 mg. However, the removal efficiency decreases when the amount of both GNP and GNP-MSN at range of 50.0 mg to 90.0 mg. This is due the strong repulsion of the negatively charged adsorbent surface which hindered the proper attachment of lead(II) ions on the active surface. Thus, it can be concluded that the most effective amount of GNP-MSN for the removal of lead(II) ions was in the range of 10.0 mg to 30.0 mg. Since the removal of lead is constant between 10.0 mg to 30.0 mg, therefore, 10.0 mg of GNP and GNP-MSN was further used to carry out the next parameters. The result shown as in Figure 5, the increase in adsorbent amount has increased the adsorption percentage of lead(II) ions for NH_2-MSN. As the adsorbent amount increased, the lead(II) ions removal increases. This is because of the increase of available binding site on the adsorbent. With the increase of amount of adsorbent,

available surface area that exposed to active sites for binding metal ions will increased [16]. This would enable more lead(II) ions to be adsorbed by adsorbent, hence resulting in a higher removal percentage. The maximum adsorption was detected which is 98.36% when 50 mg of adsorbent is used the removal of lead(II) ions and decreases gradually to 90 mg.

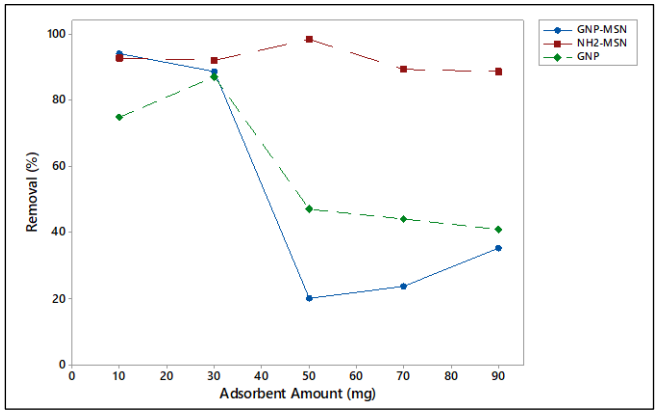


Figure 4. The effect of adsorbent amount on the removal of lead(II) ions by different nanoadsorbents; GNP, GNP-MSN and NH_2-MSN

Effect of initial lead concentration on the removal of lead(II) ions

To study the effects of initial heavy metal ions concentration on the removal efficiency of lead(II) ions, experiments were further carried out at different lead(II) ions concentration of 10, 30, 50, 70, and 90 mg/L under the previously determined optimum conditions. The outcome of the experiments was shown in Figure 7. It was observed that the removal efficiency of lead(II) ions gradually decreases with the increase of the initial concentration of lead(II) ions. At lower concentration of metal ions, the removal efficiency was higher due to the low interaction between ions present in the solution and on the nanoadsorbents surface. Furthermore, at low concentration of the metal ions, the ratio of the lead(II) ions initial mole for the available adsorbent surface area was large. However, at higher concentration, the available adsorption sites decrease. Hence, the ions removal efficiency becomes lesser. Another possible reason for the lower removal efficiency at high concentration of metal ions was the lead(II) ions form outer-sphere complexes with the adsorbent sites, which favor the adsorption when the concentration of the competing ions is decreased. This might indicate that adsorption between the adsorbent and the metal cations were mainly of ionic interaction nature [9]. Thus, the optimal initial concentration of lead(II) ions was selected as 10 mg/L for GNP and GNP-MSN while 30 mg/L for NH_2-MSN.

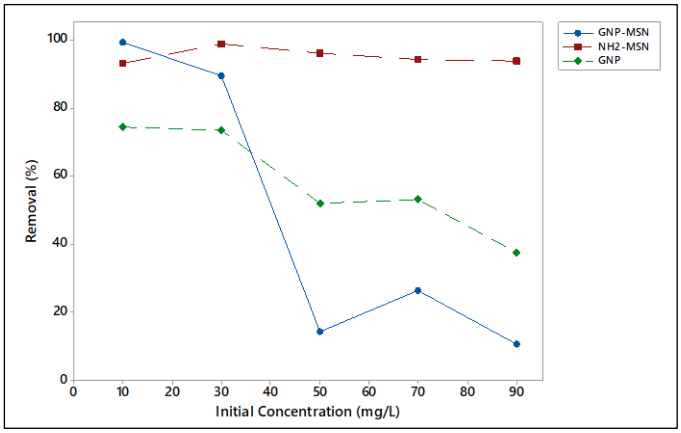


Figure 5. The effect of initial concentration on the removal of lead(II) ions by different nanoadsorbents; GNP, GNP-MSN and NH_2-MSN

Effect of contact time on the removal of lead(ii) ions

The effect of contact time between lead(II) ions and nanoadsorbents was studied with several set of batch adsorption experiment using the previously optimized condition at different time of 20 to 120 minutes. Figure 6 reveals that the percentage removal of lead(II) ion decreased when the contact time increased. The optimum contact time is 20 minutes as the removal was highest at 84.6% for GNP while NH_2-MSN have higher removal (98.74%). In the initial stages of removal efficiency of metal ion by nanoadsorbents increased rapidly due to the abundant availability of active binding sites on the adsorbent, and with gradual occupancy of these sites, the adsorption became less efficient in the later stages [12]. Hence, that means the equilibrium status can be achieved after 20 minutes. The rate of lead(II) ions removal was slow at the first 60 minutes of adsorption process for GNP-MSN. As the stirring time was increased, the removal efficiency of GNP-MSN significantly increases. After 80 min, the removal percentage of lead(II) ions decreased may be caused by desorption process.

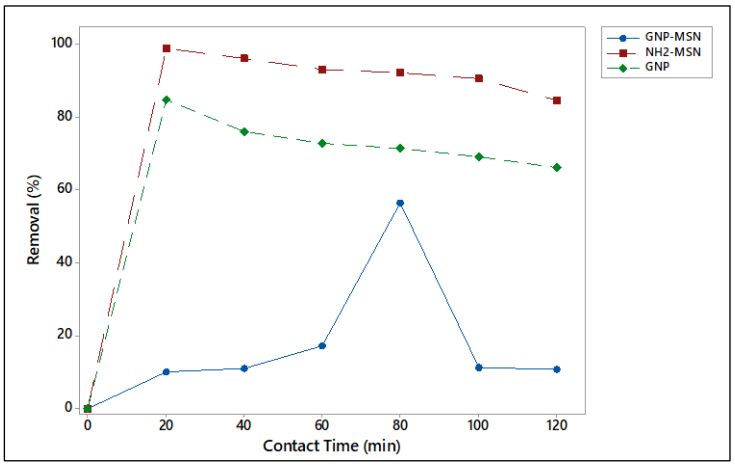


Figure 6. The effect of contact time on the removal of lead(II) ions by different nanoadsorbents; GNP, GNP-MSN and NH_2-MSN

Adsorption kinetic and isotherm studies:

Adsorption kinetics

Adsorption kinetic study determines the optimum condition of adsorption and quantify uptake. To determine the adsorption kinetic and rate limiting step, kinetic models which are pseudo-first kinetic order and pseudo-second kinetic order have been proposed to explain the mechanism of lead(II) ions adsorption from aqueous solution onto nanoadsorbents. The adsorption kinetics of lead(II) ions by GNP, NH_2-MSN and GNP-MSN are shown in Table 2. To better understand the adsorption mechanisms involved at different time intervals, pseudo-first-order (PFO) model and pseudo-second-order (PSO) model are used to fit kinetic data [17]. The non-linearized pseudo-first-order rate equation is defined by:

$$q_t = q_e(1 - e^{-k_1 t}) \quad (4)$$

and the non-linearized pseudo-second-order rate equation is:

$$q_t = \frac{q_e^2 k_2 t}{1 + k_2 q_e t} \quad (5)$$

where q_t and q_e are the equilibrium adsorption amounts of lead(II) ions adsorbed at time t and at equilibrium (mg g^{-1}) respectively. k_1 (min^{-1}) is the constant of PFO rate. Meanwhile, k_2 (g mg^{-1} min) represents the PSO rate constant for the kinetic model. Furthermore, the correlation coefficient, R^2 values were calculated by using equation (6) in order to determine the best-fitting of the data with the model.

$$R^2 = \frac{\sum(q_{e.cal} - q_{e.mean})^2}{\sum(q_{e,cal} - q_{e.mean})^2 + \sum(q_{e.cal} - q_{e.exp})^2} \quad (6)$$

where $q_{e.exp}$ (mg g^{-1}) is the amount of Pb^{2+} ions adsorbed at equilibrium obtained from Eq. (3). $q_{e.cal}$ (mg g^{-1}) is the amount of Pb^{2+} ions adsorbed determined from the model after using the Solver add-in, and $q_{e.mean}$ (mg g^{-1}) is the mean value of $q_{e.exp}$ values.

Based on Table 2, R^2 of pseudo-second order for both GNP and NH_2-MSN are 0.9978. Therefore, it can be concluded that the pseudo-second order was preferred to be chosen as the adsorption kinetic model for adsorption of lead(II) ions for both nanoadsorbents which proves that the adsorption occur is chemisorption rather than physisorption. Both PFO and PSO model show a calculated R^2 value of 0.5298 and 0.5264 for GNP-MSN respectively which suggest the adsorption could be controlled either by physical adsorption or chemical adsorption involving weak intermolecular forces or strong surface complexation of metal ions with oxygen-containing groups on the surface of GNP-MSN [18]. Besides, the rate of the reaction calculated by PFO model is slightly higher compared to the rate of the reaction calculated by PSO model. These outcomes suggest that the adsorption onto GNP-MSN occur through physisorption process rather than chemisorption.

Table 2. Pseudo-first order and pseudo-second order kinetic model for GNP, NH_2-MSN and GNP-MSN

	Pseudo-First Order			**Pseudo-Second Order**		
	q_e (mg g^{-1})	**K_1 (min^{-1})**	**R^2**	**q_e (mg g^{-1})**	**K_2 (min^{-1})**	**R^2**
GNP	0.3975	0.0068	0.8264	0.7306	0.1128	0.9978
NH_2-MSN	1.3478	0.0136	0.5956	0.2333	0.1247	0.9978
GNP-MSN	6.8100	0.9900	0.5298	7.2000	0.1900	0.5264

Adsorption isotherm

To determine the adsorption capacity of nanoadsorbents, a constant amount of the adsorbent was equilibrated with various concentrations of lead(II) ions until saturation was achieved. Adsorption isotherms were obtained at 25 °C using an adsorbent amount of 10.0 mg and initial concentration of lead ranging from 10 to 90 mg/L. Langmuir and Freundlich adsorption isotherms were applied to study the adsorption process of the adsorbent. Langmuir isotherm is an empirical model that assumes monolayer formation with adsorption can only occur at a finite number of definite localized site, that are identical and equivalent, with no lateral interaction and steric hindrance between the adsorbed molecules, even on adjacent sites [18]. The non-linear formula of the Langmuir model is defined as follow:

$$q_e = \frac{q_m K_L C_e}{1 + K_L C_e} \quad (7)$$

where q_m is the maximum monolayer adsorption capacity (mg/g), q_e is the equilibrium adsorption amount at heavy metal equilibrium concentration (mg/g), C_e is the equilibrium concentration of metals in the solution (mg/L), and K_L is the Langmuir adsorption constant (L/mg).

Next, to describe the equilibrium on the heterogeneous surfaces, Freundlich model was used. Freundlich assumed the multilayer adsorption where the non-linearized form of the Freundlich isotherm was calculated by the following equation:

$$q_e = K_F C_e^n \quad (8)$$

where C_e and q_e are calculated as above, n is the heterogeneity factor and K_F describes the Freundlich constant (L/mg). The values of n can indicate whether the adsorption process is favorable or unfavorable. According to the

Freundlich theory, the adsorption isotherm becomes linear when n = 1, favorable when n < 1, and unfavorable when n > 1.

Table 3. Langmuir and Freundlich adsorption isotherm for GNP, NH_2-MSN and GNP-MSN

	Langmuir Adsorption Isotherm			**Freundlich Adsorption Isotherm**		
	q_m (mg/g)	**K_L (mg/L)**	**R^2**	**K_F (mg/g)**	**1/n**	**R^2**
GNP	1.113	2.759	0.9995	2.718	1.739	0.9988
NH_2-MSN	9.230	0.116	0.9997	14.320	0.032	0.9532
GNP-MSN	33.300	3.360	0.5000	23.940	0.100	0.9800

As shown in Table 3, higher correlation coefficient, R^2 for Langmuir isotherm was observed, which reflect that Langmuir model was better represent the adsorption of lead(II) ions by GNP and NH_2-MSN over the entire solute concentration range as compared to Freundlich isotherm. Hence, suggesting that the lead(II) ion formed a monolayer coverage on the surface of GNP and NH_2-MSN. This probably due to a homogenous distribution of active site on the GNP, since Langmuir equation assumes that the surface is homogenous [12]. The monolayer coverage of lead(II) ions on the surface of NH_2-MSN increased with increasing lead(II) ions concentration. When the surface of NH_2-MSN was fully covered by lead(II) ions, maximum adsorption capacity was achieved. The correlation coefficient, R^2 is much higher for Freundlich model compared to Langmuir model which suggested the multilayer formation of the adsorbate on the surface of GNP-MSN. Hence, this result supported the pseudo-second-order kinetic model which suggested that the adsorption of lead(II) ion occur through physisorption process where the interaction between GNP-MSN and the adsorbate are held by Van der Waals forces or dipole-dipole forces. It was found that GNP-MSN performed better as the maximum adsorption capacity for GNP-MSN (23.940 mg/g) was higher compared to NH_2-MSN (9.230 mg/g) and GNP (1.113 mg/g).

Conclusion

Amine-functionalized mesoporous silica nanoparticle (NH_2-MSN) was successfully synthesized using ionic liquid template and post-grafting method while hybrid graphite nanoflakes/mesoporous silica nanoparticles (GNP-MSN) produced via hydrothermal process. GNP, NH_2-MSN and GNP-MSN were able to remove lead(II) ions from aqueous sample as nanoadsorbents. The crucial parameters such as; pH, adsorbent amount, initial concentration and contact time were optimized by batch adsorption study. From the adsorption study, adsorption kinetic and isotherm were then applied to understand the adsorption mechanism of GNP, NH_2-MSN and GNP-MSN. For further research, desorption study and application towards real water samples should be done to determine the reusability of the nanoadsorbents.

Acknowledgement

The authors gratefully acknowledge Universiti Putra Malaysia for the funding through the High Impact Putra Grant (UPM/700-2/1/GBP/2018/9598600).

References

1. Ali, I., Basheer, A. A., Mbianda, X. Y., Burakov, A., Galunin, E., Burakova, I. and Grachev, V. (2019). Graphene based adsorbents for remediation of noxious pollutants from wastewater. *Environment International*, 127(1): 160-180.
2. Barakat, M. A. (2011). New trends in removing heavy metals from industrial wastewater. *Arabian Journal of Chemistry*, 4(4): 361-377.
3. Burakov, A. E., Galunin, E. V, Burakova, I. V, Kucherova, A. E., Agarwal, S., Tkachev, A. G. and Gupta, V. K. (2018). Adsorption of heavy metals on conventional and nanostructured materials for wastewater treatment purposes: A review. *Ecotoxicology and Environmental Safety*. Elsevier Inc.
4. Cheah, W. K., Sim, Y. L. and Yeoh, F. Y. (2016). Amine-functionalized mesoporous silica for urea adsorption. *Materials Chemistry and Physics*, 175: 151-157.

5. Deliyanni, E. A., Kyzas, G. Z., Triantafyllidis, K. S. and Matis, K. A. (2015). Activated carbons for the removal of heavy metal ions: A systematic review of recent literature focused on lead and arsenic ions. *Open Chemistry*, 13(1): 699-708.
6. Firdaus, M., Rahman, A., Zaharudin, N. S., Ahmad, H. and Zulkepli, N. N. (2019). Synthesis of hybrid graphite-mesoporous silica nanoplatelet using 1-hexadecylpyridinium bromide ionic liquid as novel template, *Journal of Advanced Research in Materials Science*, 1(1): 6-14.
7. Hao, L., Song, H., Zhang, L., Wan, X., Tang, Y. and Lv, Y. (2012). SiO_2/graphene composite for highly selective adsorption of Pb(II) ion. *Journal of Colloid and Interface Science*, 369(1): 381-387.
8. He, Y., Luo, L., Liang, S., Long, M. and Xu, H. (2017). Amino-functionalized mesoporous silica nanoparticles as efficient carriers for anticancer drug delivery. *Journal of Biomaterials Applications*, 32(4), 524-532.
9. Isa, E. D. M., Ahmad, H. and Rahman, M. B. A. (2019). Optimization of synthesis parameters of mesoporous silica nanoparticles based on ionic liquid by experimental design and its application as a drug delivery agent. *Journal of Nanomaterials*, 2019: 1-8.
10. Karnib, M., Kabbani, A., Holail, H. and Olama, Z. (2014). Heavy metals removal using activated carbon, silica and silica activated carbon composite. *Energy Procedia*, 50: 113-120.
11. Mehdinia, A., Akbari, M., Baradaran Kayyal, T. and Azad, M. (2015). High-efficient mercury removal from environmental water samples using di-thio grafted on magnetic mesoporous silica nanoparticles. *Environmental Science and Pollution Research*, 22(3): 2155-2165.
12. Mehdinia, A., Shegefti, S. and Shemirani, F. (2015). Removal of lead(II), copper(II) and zinc(II) ions from aqueous solutions using magnetic amine-functionalized mesoporous silica nanocomposites. *Journal of the Brazilian Chemical Society*, 26(11): 2249-2257.
13. Mohan, S., Kumar, V., Singh, D. K. and Hasan, S. H. (2017). Effective removal of lead ions using graphene oxide-MgO nanohybrid from aqueous solution: Isotherm, kinetic and thermodynamic modeling of adsorption. *Journal of Environmental Chemical Engineering*, 5(3): 2259-2273.
14. Peng, W., Li, H., Liu, Y. and Song, S. (2017). A review on heavy metal ions adsorption from water by graphene oxide and its composites. *Journal of Molecular Liquids*, 230: 496-504.
15. Taman, R., Ossman, M. E., Mansour, M. S. and Faraj, H. A. (2015). Metal oxide nano-particles as an adsorbent for removal of heavy metals. *Journal of Advanced Chemical Engineering*, 5(3): 1-8.
16. Sheet, I., Kabbani, A. and Holail, H. (2014). Removal of heavy metals using nanostructured graphite oxide, silica nanoparticles and silica/graphite oxide composite. *Energy Procedia*, 50: 130-138.
17. Vojoudi, H., Badiei, A., Bahar, S., Mohammadi Ziarani, G., Faridbod, F. and Ganjali, M. R. (2017). A new nano-sorbent for fast and efficient removal of heavy metals from aqueous solutions based on modification of magnetic mesoporous silica nanospheres. *Journal of Magnetism and Magnetic Materials*, 441(5): 193-203.
18. Zhang, L., Luo, H., Liu, P., Fang, W. and Geng, J. (2016). A novel modified graphene oxide/chitosan composite used as an adsorbent for Cr(VI) in aqueous solutions. *International Journal of Biological Macromolecules*, 87: 586-596.

Malaysian Journal of Analytical Sciences (MJAS)
Published by Malaysian Analytical Sciences Society

PREPARATION, CHARACTERIZATION AND SWELLING STUDIES OF CARBOXYMETHYL SAGO STARCH HYDROGEL

(Penyediaan, Pencirian dan Kajian Pengembangan Hidrogel Karboksimetil Kanji Sagu)

Normastura Sulta[1], Norhazlin Zainuddin[1]*, Mansor Ahmad[1], Mas Jaffri Masarudin[2]

[1]*Chemistry Department, Faculty of Science*
[2]*Department of Cell and Molecular Biology, Faculty of Biotechnology and Biomolecular Sciences*
Universiti Putra Malaysia, 43400 UPM Serdang, Selangor, Malaysia.

**Corresponding author: norhazlin@upm.edu.my*

Received: 2 January 2020; Accepted: 26 March 2020

Abstract

Carboxymethyl sago starch (CMSS) hydrogel was prepared by dissolving CMSS in hydrochloric acid (HCl) solution under vigorous stirring to form a gel. The parameter studied were the effect of the percentage of CMSS, the concentration of the acid solution, reaction time and reaction temperature to identify the optimum condition of preparation of CMSS hydrogel. 60% of CMSS in 2.0M acid solution for 12 hours reaction time at room temperature were the optimum conditions for CMSS hydrogel. The hydrogel was characterized by using Fourier transform infrared (FT-IR), thermogravimetric analysis (TGA) and scanning electron microscopy (SEM). FTIR spectrum of CMSS showed an additional absorption band indicating the substitution of $CH_2COO^-Na^+$ group on the starch molecular chain during carboxymethylation, while the spectrum of CMSS hydrogel showed an additional sharp absorption band indicating that the Na in CMSS being exchanged to H from HCl solution. SEM image of CMSS hydrogel showed pores in structure and connected to form networks. TGA curve showed that the maximum rate of thermal decomposition of CMSS hydrogel was higher than CMSS which could be due to the presence of the cross-linkages in the CMSS hydrogel. CMSS hydrogel gave a high swelling degree in PBS solution at pH 7 and a low swelling degree in acidic medium.

Keywords: hydrogel, carboxymethyl sago starch, crosslinking, characterization,swelling

Abstrak

Hidrogel karboksimetil kanji sagu (CMSS) telah disediakan dengan melarutkan CMSS dalam larutan asid hidroklorik (HCl) di bawah pengadukan kuat untuk membentuk hidrogel. Parameter yang dikaji untuk mengoptimumkan penyediaan hidrogel CMSS, antaranya termasuklah kesan peratusan CMSS, kepekatan larutan asid, masa dan suhu tindak balas. 60% CMSS dalam larutan asid 2.0M dengan masa tindak balas 12 jam pada suhu bilik merupakan keadaan optimum untuk penyediaan hidrogel CMSS. Hidrogel dicirikan dengan menggunakan spektrometer infra-merah Fourier (FT-IR), analisis termogravimetrik (TGA) dan pengimbasan mikroskop elektron (SEM). Spektrum FTIR menunjukkan jalur penyerapan tambahan yang menunjukkan penggantian kumpulan CH_2COO^- Na^+ pada rantai molekul kanji semasa tindak balas karboksimetilasi, manakala spektrum hidrogel CMSS menunjukkan tambahan jalur penyerapan tajam yang menunjukkan bahawa Na dalam molekul CMSS ditukar kepada H dari larutan HCl. Imej SEM dari hidrogel CMSS menunjukkan liang-liang dalam struktur dan saling berhubungan untuk membentuk rangkaian. Lengkung analisis TGA menunjukkan bahawa kadar penguraian haba maksimum hidrogel CMSS lebih tinggi daripada CMSS pada 330.22 ºC dengan 60.22% penurunan berat utama. Ini mungkin disebabkan oleh adanya rangkai silang dalam hidrogel CMSS. Hidrogel CMSS memberikan tahap pengembangan yang tinggi dalam larutan PBS pada pH 7 dan tahap pengembangan yang rendah dalam medium berasid.

Kata kunci: hidrogel, karboksimetil kanji sagu, rangkai silang, pencirian, pengembangan

Introduction

Polysaccharides are polymeric carbohydrate molecules that can be subjected to a wide range of chemical and enzymatic reactions. They have biocompatible and biodegradable properties with low immunogenicity. Polysaccharides can be easily obtained and found in a living organism [1]. Examples of polysaccharides are starch, alginate, cellulose, hemicellulose which originate from plants. Sago starch which is isolated from sago palm is called *Metroxylon sagu* that can be found abundantly in marshy areas mostly in Sarawak state in Malaysia [2]. It has outstanding biological properties such as biocompatibility, biodegradable, and nontoxicity. However, in some applications, the usage of starch is confined due to deficiency in its solubility and has a tendency to retrograde. Retrogradation is a non-reversible process that occurs when cooked starch solutions are cooled and molecular interaction between amylose as well as other glucose units abound to form a double helix, resulting in the formation of colloidal crystallites [3].

Chemical modification is introduced to overcome the inherent defects and gain innovation in the utilization of starch. It involves the introduction of various functional groups into a starch structure including cationic and anionic group [4]. Sago starch undergoes the carboxymethylation process to produce carboxymethyl sago starch that has a variety of promising properties like high solubility, thermal stability, ion activity, and higher reaction efficiency [5].

Hydrogels are polymer networks that are able to absorb and retain a huge amount of water due to the presence of its hydrophilic group. The term "network" is implied indicating that cross-links must present for the prevention of the dissolution of the polymer chain before use [6]. Hydrogel has gained considerable attention in recent years due to its unique properties as a biocompatible smart material, which can be designed to achieve desirable properties [7]. It is widely used in various applications such as agriculture, wastewater treatment, food packaging, cosmetic, biotechnology, pharmaceutical, and biomedical including drug delivery applications [8, 9]. Carboxymethyl sago starch hydrogel can be prepared via a cross-linking technique. Crosslinking is a process of forming a network, where the polymers are linked together either by ionic and covalent bonds, van der Waals interaction, hydrogen bonding or physical entanglements [10]. Crosslinking can involve the exchange of sodium with a hydrogen ion, namely hydrogen bond formation. It is a rapid process but proceeds gradually with time [11].

This paper aims to prepare and characterize carboxymethyl sago starch hydrogel and study its swelling behavior. The finding may lead to potential drug and vaccine carriers in future studies. Currently, the use of biopolymers in drug delivery and vaccination has gained huge attention since these polymers can provide better materials due to its compatibility, degradation behavior and non-toxic administration [12].

Materials and Methods

Materials

Carboxymethyl Sago Starch (D.S 0.75) was prepared at Nuclear Malaysia Laboratory, Bangi Selangor. Sago starch was supplied by Song Ngeng Sago Ind. Sibu Sarawak. The CMSS had been synthesized and purified as described in Zainuddin [13]. The degree of substitution was determined as mentioned in Othman et al. [14]. Sodium monochloroacetate (SMCA) was purchased from Sigma-Aldrich. Phosphate buffer saline (PBS), phenolphthalein, diphenylamine reagent, sodium chloride, sodium hydroxide, acetic acid, solvents such as isopropanol, methanol (99%) and absolute ethanol were purchased from R & M Chemicals. Hydrochloric acid (HCl) (Fuming 37%) was purchased from Fisher Chemicals. All chemical reagents were of analytical grade. Deionized and distilled water were used throughout the experiment.

Preparation of CMSS hydrogel

CMSS hydrogel was prepared by dissolving the CMSS in HCl solution under vigorous stirring and left in a petri dish to allow the crosslinking process to complete. CMSS hydrogel was put into a tea bag and immersed in deionized water at room temperature to remove uncross-linked CMSS that were dissolved and extracted into the water. CMSS was also put in a tea bag and immersed in water as a control sample. The successful cross-linked hydrogel was kept inside the tea bag which was then collected out from the deionized water and oven-dried at 60 ºC to achieve constant weight. The effect of the percentage of CMSS (40-80% w/v), HCl concentration (0.5-2.5 M), reaction time (12-72 hours) and reaction temperature (RT-70 ºC) were studied to obtain the optimum condition in

which one variable at a time was used. The optimum condition of the CMSS hydrogel was determined based on its gel content.

Gel Content and Swelling of CMSS Hydrogel

The measurement of gel content was carried out in deionized water at room temperature. The insoluble part of the CMSS hydrogel after immersion was measured to estimate the content of the hydrogel. The swollen sample after immersion indicates the degree of swelling ability. Samples were removed from the water after immersion and weighed, then dried at 60ºC until a constant weight was achieved. Percentage of gel content was calculated by the following equation:

$$Percentage\ of\ Gel\ Content = \left(\frac{W2}{W1}\right) x\ 100 \quad (1)$$

where W_1 is the initial weight of the hydrogel before immersion and W_2 is the weight of the dried insoluble part of hydrogel after immersion.

Swelling studies in different media

A completely dried CMSS hydrogel was weighed and immersed in 150 mL deionized water at room temperature for 48 hours. And then, the CMSS hydrogel was removed, weighed and dried. The degree of swelling was calculated by the following equation:

$$Swelling\ =\ (Ws - Wd)/Wd \quad (2)$$

where Ws is the weight of swollen hydrogel and Wd is the initial weight of xerogel. The swelling studies were investigated by using different immersion media such as buffer solution at different pH levels, pH (4, 7, and 10), salt solution (NaCl), 1.0 M of HCl and NaOH solution. Data presented in this study were the mean values of triplicate measurements (n=3).

Characterization of CMSS hydrogel

The structures of sago, CMSS, and CMSS hydrogel were identified by FTIR analysis using a spectrometer (100 Series Perkin Elmer) with universal Attenuated Total Reflectance (UTAR) technique. All samples were analyzed in powder form, irradiated with infrared in the range of 4000-280 cm^{-1}. The thermal stability of sago, CMSS, and CMSS hydrogel was examined using TGA (Perkin Elmer TGA7). The samples were heated from 35 to 600 ºC with a rate of 5 ºC/min in the flow of inert nitrogen gas. The morphology of hydrogel was studied using scanning electron microscopy (FEI, Quanta 400). The hydrogel sample was soaked in 500 mL deionized water and then was freeze-dried to remove the water molecule. All samples were mounted on metal stubs and sputter-coated with gold.

Results and Discussion

Preparation of CMSS hydrogel:

The effect of percentage of CMSS

Figure 1 shows the percentage of gel content and degree of swelling of a various percentage of CMSS from 40 to 80% (w/v) in 1.0 M HCl solution. The percentage of gel content increased gradually with the increasing amount of CMSS from 40 to 60%. This indicates that by increasing amounts of CMSS, it provides more crosslinking points thus increasing the gel content. However, when it got higher than 60% (w/v), the gel content started to decrease slightly. The formation of the crosslinked CMSS hydrogel with an acid solution may reach its optimum at 60% (w/v) CMSS. In this experiment, the amount of HCl was fixed for all concentrations of CMSS. Therefore, when the percentage of CMSS was higher than 60% (w/v), there was a possibility that the amount of H^+ in the reaction was not sufficient to promote the crosslinking process through the formation of hydrogen bonding as the same volume of HCl was used. Thus, the gel content did not significantly increase when more than 60% (w/v) of CMSS was used.

Meanwhile, the degree of swelling is inversely proportional to the percentage of gel content. Increase in gel content caused a decrease in swelling capability. It may be due to the degree of crosslinking which affected the water uptake [15]. Higher CMSS concentration produced more crosslinked points in polymeric chains thus increasing

crosslinking network which resulted in less swelling when it was brought in water. An increased crosslinking network led to the formation of a tighter network. This caused difficulty for water to permeate and reduced the amount of water being trapped inside the hydrogel network thus resulted in a low degree of swelling [13, 15]. The highest gel content (62.05%) was obtained from 60% (w/v) of CMSS, which was chosen throughout the experiment to prepare hydrogel as a sorbent.

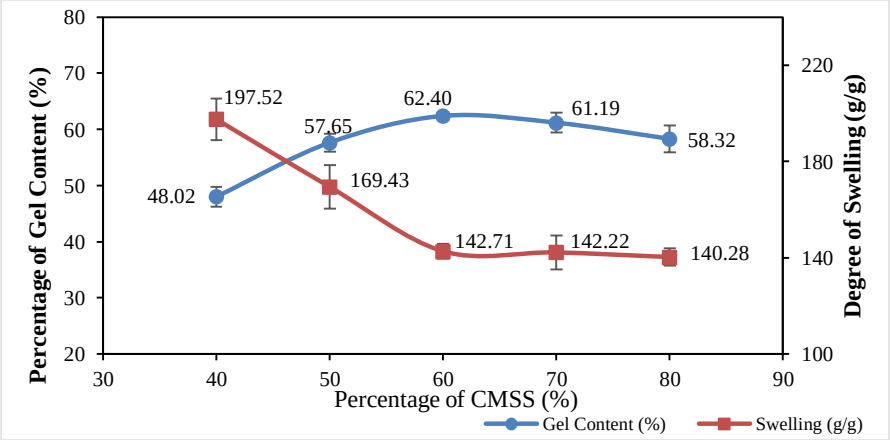


Figure 1. Effect of percentage amount of CMSS in 1.0M HCl on gel content and swelling of CMSS hydrogel at room temperature for 24 hours of reaction time

The effect of HCl concentration

The effect of different concentrations (0.5 to 2.5 M) of HCl solution on gel content and degree of swelling of CMSS hydrogel is shown in Figure 2. The percentage of gel content increased as the concentration of HCl increased. Similar results have been reported by Takigami et al. [11] where the number of crosslinks increased with the increase of acid concentration. However, the graph shows a slight decrease in gel content at 2.5 M that might be due to acid hydrolysis of the linkage at a high concentration of an acid solution. From the data obtained, 2.0 M of HCl gave the highest gel content and had been chosen as a suitable concentration of HCl in preparing the hydrogel in the next parameter. The swelling capability of CMSS hydrogel as expected, decreased as the concentration of the HCl increased. With the increase of the gel fraction, water absorption decreased significantly depending on the acid concentration [11]. A high swelling degree of hydrogel with 0.5M HCl indicates that it has high ability to absorb water.

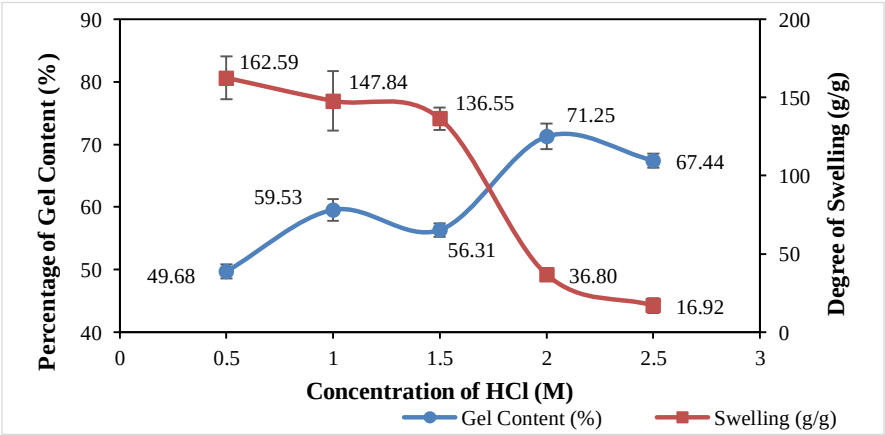


Figure 2. Effect of HCl concentration on gel content and swelling of 60% CMSS hydrogel at room temperature for 24 hours of reaction time

Pushpamalar et al. [16] reported in her study that hydrogels that are relatively weak and consist of a low number of intermolecular bonds can expand by absorbing water and holding it in their void. As the intermolecular bonds and the crosslink density increased, hydrogel becomes tightly packed, lessening the ability of the hydrogel to absorb water. This led to a decrease in the swelling degree of hydrogel with a high concentration of HCl. A similar finding was reported by Sadeghi et al. [17] which stated that higher crosslinker concentration diminished the free space between the polymer chain and subsequently resulted in highly crosslinked rigid structure that cannot be extended and held a vast amount of water.

The effect of reaction time

The third parameter investigated was the effect of reaction time from 12 to 72 hours. From the preliminary study, no gel was formed when the reaction time was less than 12 hours for a low concentration of CMSS. Figure 3 shows that there is no significant difference in gel content of CMSS hydrogel at 12, 24 and 36 hours, and it decreased slightly at 48 and 72 hours reaction time. A possible explanation may be the fact that the prolongation of the reaction time does not affect the gel content as the crosslinking process already achieved the maximum value in a short period. Although 36 hours reaction time gave 71.37% of gel content, 12 hours reaction time is preferable to avoid a waste of time. Usually, swelling capability decreases as the gel content of the hydrogel increases. However, in this parameter, the swelling capability decreased with the increased reaction time although the gel content did not show significant increment. As the reaction time increased, the structure of the hydrogel became stronger and denser. Prolong the reaction time could increase the crosslink density and caused the decreasing swelling capability of the hydrogel [18]. Kabiri et al. [19, 20] mentioned in their studies that there is a possibility of the additional linkage that increased the crosslink density, which resulted in reducing swelling capacity.

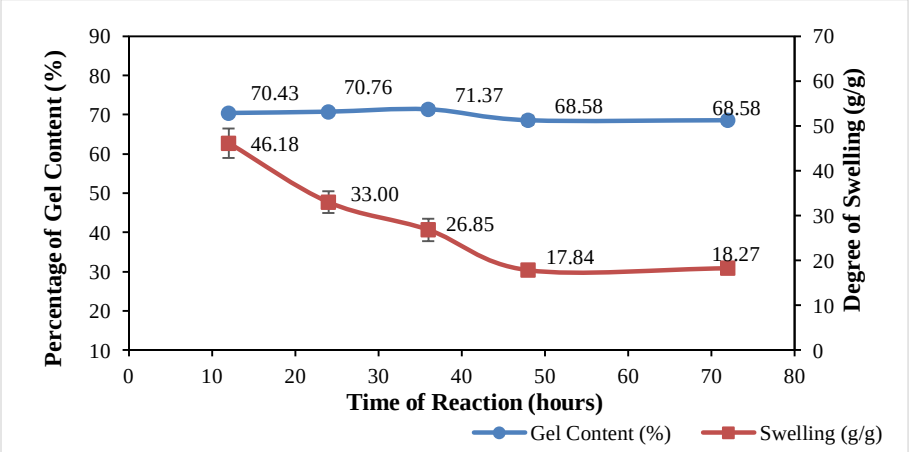


Figure 3. Effect of reaction time on gel content and swelling of 60% CMSS hydrogel in 2.0M HCl at room temperature

The effect of reaction temperature

The effect of the reaction temperature of 60% CMSS in 2.0M HCl at 12 hours of reaction time was examined from room temperature (24 ºC) to 70 ºC. Figure 4 shows a slight change in gel content as the temperature increased. This could be due to the degree of crosslinking of hydrogel decreased due to acid hydrolysis of CMSS at high temperature, thus reducing the number of long-chain polymers that were available for crosslinking resulting in decreased gel content of the hydrogel. A similar result reported by Takigami et al. [11] indicated that reaction at high temperature will cause starch hydrolysis and gives low gel formation. The swelling capability in this study was different than the expected trend as it decreased with the decrease of the gel content. When hydrogel comes in contact with any solvent molecules, the solvent tries to attack the hydrogel surface and penetrate within the polymeric network structure [21]. However, in this experiment, it was observed that the appearance of the gel prepared at high reaction temperature was hard and rigid. This could prevent the hydrogel to swell as the water found difficulty to pass through the surface of the hydrogel thus decreasing the swelling capability.

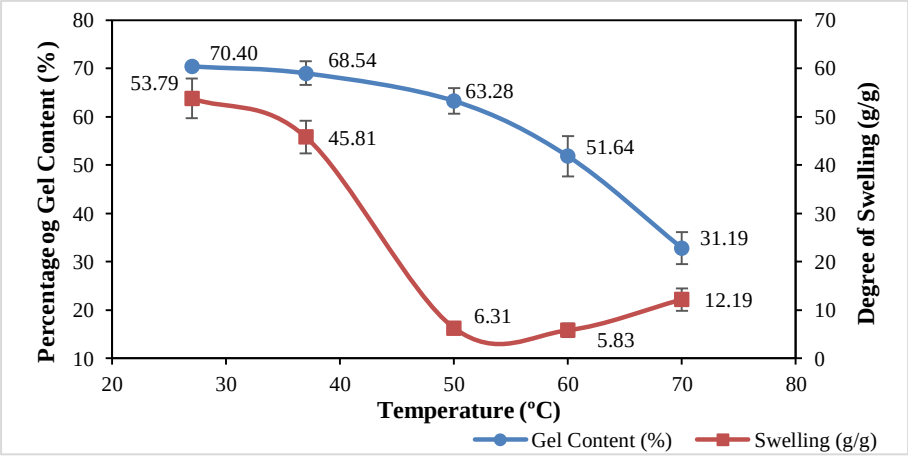


Figure 4. Effect of reaction temperature on gel content and swelling of 60% CMSS hydrogel in 2.0M HCl at 12 hours of reaction time

Swelling properties

A hydrogel is known for its ability to absorb and hold a huge amount of solvent in its network structure. This swelling property is a very crucial factor for its further application. The swelling studies would suggest a good prediction on the ability of the hydrogel to interact with the surrounding media, in which its smart behavior could be used in many applications especially in the controlled release of drug delivery [7]. Figure 5 shows the swelling degree for the CMSS hydrogel at different immersion media. PBS 7 gave a high swelling degree indicating that this CMSS hydrogel swelled well in PBS 7 solution. In acidic media (PBS 4), more –COOH groups were formed, which induced the formation of the hydrogen bond of –COOH with CMSS hydrogel, leading to a more compact network in CMSS hydrogel and caused a decrease in the swelling degree [7, 22]. Similarly, when CMSS hydrogel was immersed in HCl solution, the presence of H^+ ions in the surrounding induced the hydrogen bond formation, resulting in a low swelling degree. In salt solution (NaCl), the swelling ability of CMSS hydrogel significantly decreased compared to the swelling in deionized water. Gupta et al. [23] stated that the phenomenon can be explained on the basis of osmotic pressure developed due to the unequal distribution of ions in the medium and the polymer network. When the polymer immersed in NaCl solution, the development of osmotic pressure is much lower since the external solution contains Na^+ and Cl^-, the presence of Na^+ ions in the outer solution causes a decrease in the osmotic swelling pressure which operates due to the difference of counter ions in a gel phase and solution phase, therefore, reducing the swelling ability.

Sadeghi et al. [17] also reported that this behavior is often attributed to the charge screening effect and ionic crosslinking of monovalent cations. In alkaline solution (NaOH and PBS 10), it was observed that there was no swelling degree recorded as the CMSS hydrogel completely dissolved in the alkaline solution after 48 hours immersion time. This might be due to the degradation of the CMSS hydrogel crosslinked network at high concentration of alkaline solution present in the surrounding resulting in reformation of –COONa thus causing it to be dissolved in the media. These results indicated that CMSS hydrogel prepared in this study exhibited pH-sensitive characteristic and affected by its surrounding environment.

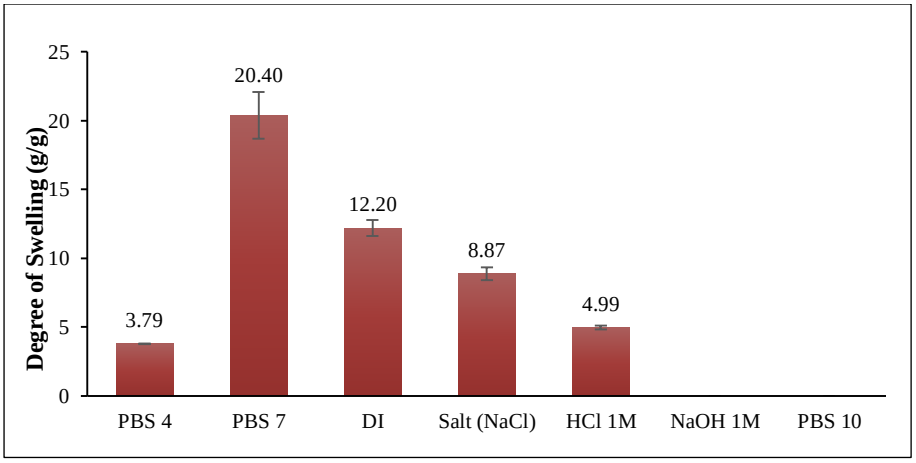


Figure 5. Swelling of CMSS hydrogel at different media at room temperature

Characterization of CMSS hydrogel:

Fourier transform infrared analysis

Figure 6 shows the FTIR spectra of sago starch, CMSS, and CMSS hydrogel. The spectrum of sago starch shows the absorption band at 3273 cm^{-1}, which is due to O-H stretching vibration, as well as intramolecular and intermolecular hydrogen bonds in glycosidic bond in the sago starch molecule [7]. The absorption band at 2910 cm^{-1} shows C-H stretching and 1643 cm^{-1} shows a tightly bound water presence in the starch molecule. The appearance of the absorption band at 1350 cm^{-1} belongs to -CH_2 symmetrical band, while the broad band at the range of 1100-990 cm^{-1} indicates the C-O stretching from C-O-C and C-O-H in a glycosidic ring of the starch molecule [24].

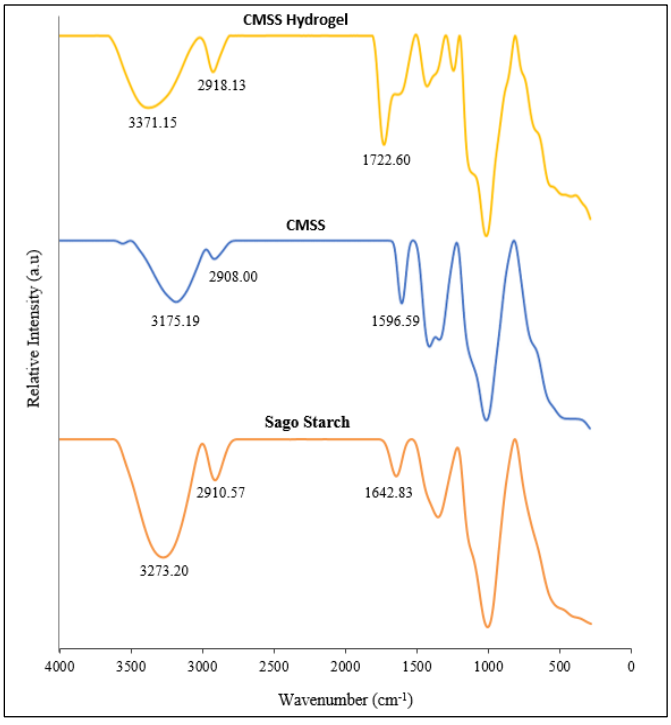


Figure 6. FTIR spectra for Sago Starch, CMSS and CMSS Hydrogel

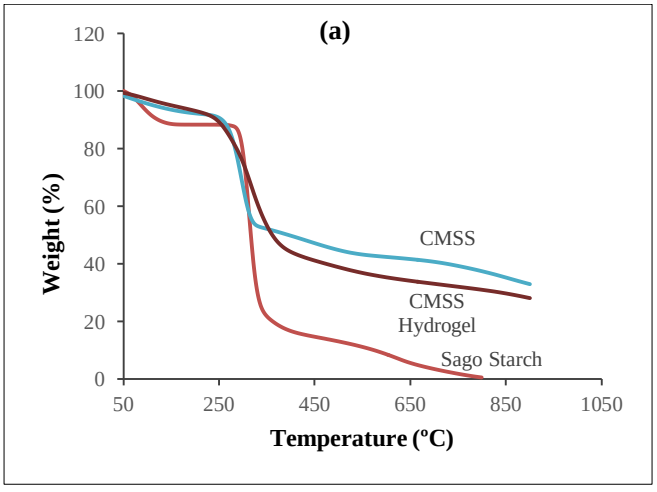
The FTIR spectrum of CMSS shows the shifting of O-H stretching band to lower wavenumber at 3175 cm^{-1}. This was probably due to the low intermolecular hydrogen bonds between the O-H group left in the glycosidic rings of CMSS prior to the substitution reaction take place during carboxymethylation process [13]. The additional absorption band at 1597 cm^{-1} indicates the substitution of the $CH_2COO^-Na^+$ group on the starch molecular chain during carboxymethylation.

CMSS hydrogel spectrum shows a new absorption band at 1723 cm^{-1} indicating the presence of the COOH group. This shows that the Na in CMSS was being exchanged to H from the HCl solution. The concentration of HCl solution used was 2.0 M, thus a sharp absorption at band can be observed indicating that most of the -COONa have been converted to COOH. The intensity of the absorption band depends on the concentration of the acid used, whereby low concentration of acid shows a weak absorption band of conversion of -COONa to COOH [24]. A similar result was reported previously where the replacement of Na in carboxymethyl group with hydrogen from acid occurred depending on the type of acid and concentration [11]. The absorption band at 1421 cm^{-1} and 1238 cm^{-1} are respectively due to $-CH_2$ scissoring and -OH bending vibration, while $OCH-O-CH_2$ stretching was represented by the absorption band at 1000 cm^{-1}.

Thermogravimetric analysis

TGA analysis is a convenient analysis to study the thermal decomposition and thermal stability of the polymer. It is a quantitative measurement of the weight change of a sample against the temperature applied. TGA thermograms of native sago starch, CMSS, and CMSS hydrogel are shown in Figure 7. Native sago starch, CMSS, and CMSS hydrogel have two steps of decomposition. The first step below 150 ºC corresponds to the removal of moisture from the surface and entrapped water in the sample. The second step occurred around 200 ºC to 500 ºC due to the decomposition of the starch backbone leaving a residue. Zhang et al. [25] stated that water was the main product decomposition at a temperature below 300 ºC and further heating up above 500 ºC resulted in carbonization and ash formation.

For CMSS, the maximum weight loss occurred at 295.33 ºC which is lower than native sago starch before carboxymethylation (309.57 ºC) with 49.71% of total CMSS decomposed and 42.37% residue due to the presence of ash and sodium salt in CMSS. It had been found that the carboxymethylation process decreased the thermal stability of starch materials [25]. The maximum thermal decomposition of CMSS hydrogel was 330.22 ºC with 60.22% major weight loss which indicates slight increase compared to native sago starch and CMSS. An increase in the maximum thermal decomposition of CMSS hydrogel could be due to the presence of cross-linkages in CMSS hydrogel [24]. High cross-linked structure and compact network improve the degree of stability of hydrogel resulted in higher temperature needed to decompose them [7].



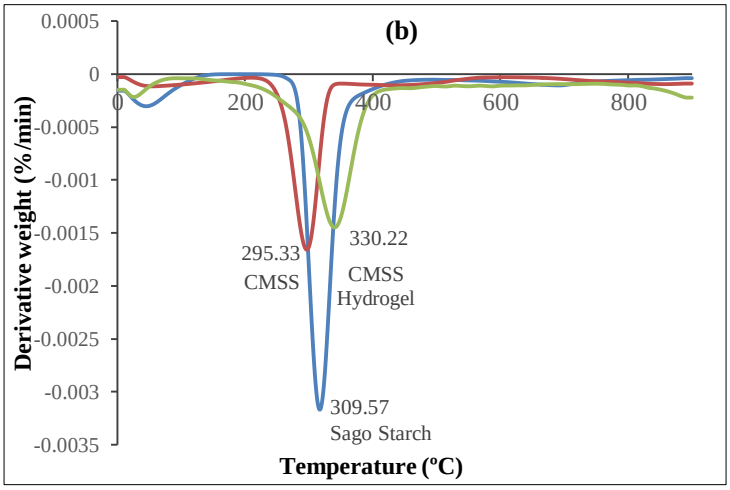
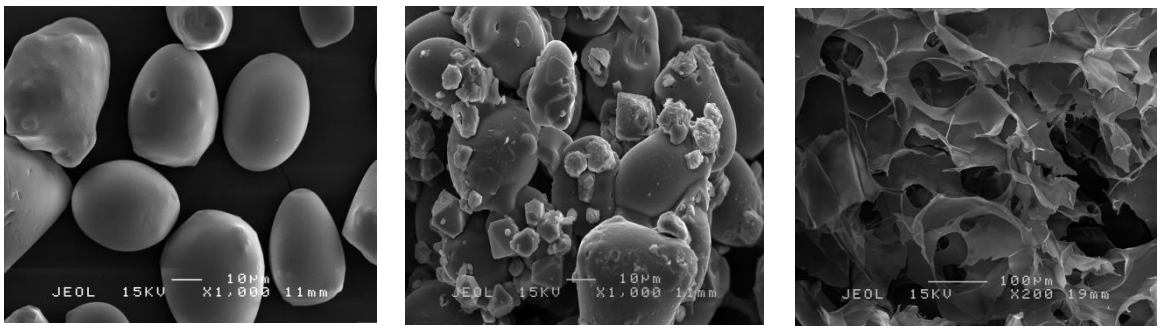


Figure 7. (a) TGA and (b) DTG thermograms of Sago Starch, CMSS and CMSS hydrogel

SEM analysis

Scanning Electron Microscopy (SEM) is an excellent technique in examining the surface morphology of a sample. Figure 8(a) shows a smooth surface and oval-shaped granules sago starch with a diameter in the range of 20-40 µm similar to the previous study reported by Ahmad et al. [26]. Figure 8(b) shows the massive distorted and irregular shape of carboxymethyl sago starch. In comparison with native starch, the surface of CMSS is rough where the groove indicates that the breakage of a chemical bond by a strongly alkaline environment during the carboxymethylation process. Thus, carboxymethylation is not only the reaction on the surface of starch granules but also from within [24]. The micrograph also shows that the CMSS remains intact and agglomerate after preparation with aqueous-alcoholic medium studied. Figure 8(c) shows that CMSS hydrogel has a spongy surface with space called pores in structure and connected to each other to form networks as a consequence of the crosslinking process [27].



(a) Sago starch (b) CMSS (c) CMSS hydrogel

Figure 8. SEM images of (a) Sago starch, (b) CMSS and (c) CMSS hydrogel

Conclusion

Carboxymethyl sago starch hydrogel was successfully prepared in the HCl solution. Carboxymethylation decreases the thermal stability of sago starch, but cross-linking increases the thermal stability of CMSS hydrogel. FTIR spectrum of CMSS hydrogel showed that the Na in CMSS is successfully exchanged to H from the HCl solution.

SEM image of CMSS hydrogel shows pores in the structure and connected to each other to form networks. Swelling studies of CMSS hydrogel prepared exhibited a smart behavior as it reacts depending on its surrounding environment and displays pH-sensitive characteristics. The finding of this study suggests that the CMSS hydrogel has potential in broad applications such as heavy metal removal in wastewater treatment and carrier in drug or vaccine delivery system.

Acknowledgment

The authors gratefully acknowledge the assistance of technical staff from the Chemistry Department, Universiti Putra Malaysia and Nuclear Agency Malaysia. Financial support from the Ministry of Higher Education, Trans-disciplinary Research Grant Scheme Fasa 2/2014 (Vot Number: 5535401) and Graduate Research Fellowship, UPM for the sponsorship were gratefully acknowledged.

References

1. Pushpamalar, J., Veeramachineni, A. K., Owh, C. and Loh, X. J. (2016). Biodegradable polysaccharides for controlled drug delivery. *ChemPlusChem*, 81: 1-12.
2. Pushpamalar, V, Langford, S. J., Ahmad, M. and Lim, Y. Y. (2006). Optimization of reaction conditions for preparing carboxymethyl cellulose from sago waste. *Carbohydrate Polymers*, 64: 312-318.
3. Alcázar-Alay, S. C. and Meireles, M. A. A. (2015). Physicochemical properties, modifications and applications of starches from different botanical sources. *Food Science and Technology (Campinas)*, 35(2): 215-236.
4. Chen, Q., Yu, H., Wang, L., Abdin, Z. U., Chen, Y., Wang, J., Zhou, W., Yang, X., Khan, R. U., Zhang, H. and Chen, X. (2015). Recent progress in chemical modification of starch and its applications. *RSC Advances*, 5: 67459-67474.
5. Kamel, S. and Jahangir, K. (2007). Optimization of carboxymethylation of starch in organic solvents. *International Journal of Polymeric Materials*, 56(5): 511-519.
6. Faheem A., M., Hanif, M. and Ranjha, N. M. (2016). Methods of synthesis of hydrogels: A review. *Saudi Pharmaceutical Journal*, 24: 554-559.
7. Jamingan, Z., Ahmad, M. B., Hashim, K. and Zainuddin, N. (2015). Sago starch based hydrogel prepared using electron beam irradiation technique for controlled release application. *Malaysian Journal of Analytical Sciences*, 19(3): 503-512.
8. Ullah, F., Bisyrul, M., Javed, F. and Akil, H. (2015). Classification, processing and application of hydrogels: A review. *Materials Science & Engineering C*, 57: 414-433.
9. Hoare, T. R. and Kohane, D. S. (2008). Hydrogels in drug delivery: Progress and challenges. *Polymer*, 49(8): 1993-2007.
10. Hamidi, M., Azadi, A. and Rafiei, P. (2008). Hydrogel nanoparticles in drug delivery. *Advanced Drug Delivery Reviews*, 60(15): 1638-1649.
11. Takigami, M., Nagasawa, N., Hiroki, A., Tagichi, M. and Takigami, S. (2012). Preparation of stable CMC-acid gel. *Gums and Stabilisers for the Food Industry*, 16: 175-182.
12. Nitta, S. and Numata, K. (2013). Biopolymer-based nanoparticles for drug/gene delivery and tissue engineering. *International Journal of Molecular Sciences*, 14(1): 1629-1654.
13. Zainuddin, N. B. (2003). Carboxymethylation of sago starch and sago waste and the formation of carboxymethyl starch-hydrogel via irradiation technique. Thesis Universiti Putra Malaysia.
14. Othman, Z., Hashim, K., Sabariah, K., Nasir, M. H. A. and Hassan, A. (2015). Synthesis and characterization of carboxymethyl derivatives of sago (*Metroxylon sagu*) starch. *Macromolecular Symposia*, 353(1): 139-146.
15. Nagasawa, N., Yagi, T., Kume, T. and Yoshii, F. (2004). Radiation crosslinking of carboxymethyl starch. *Carbohydrate Polymers*, 58: 109-113.
16. Pushpamalar, V., Langford, S. J., Ahmad, M., Hashim, K. and Lim, Y. Y. (2013). Preparation of carboxymethyl sago pulp hydrogel from sago waste by electron beam irradiation and swelling behavior in water and various pH media. *Journal Applied Polymer Science*, 128: 451-459.
17. Sadeghi, M. and Hosseinzadeh, H. (2010). Synthesis and super-swelling behavior of a novel low salt-sensitive protein-based superabsorbent hydrogel: collagen-g -poly(AMPS). *Turkish Journal of Chemistry*, 34: 739-752.
18. Budianto, E., Muthoharoh, S. P. and Nizardo, N. M. (2015). Effect of crosslinking agents, pH and temperature on swelling behavior of cross - linked chitosan hydrogel. *Asian Journal of Applied Sciences*, *3*(5): 2321-2893.

19. Kabiri, K, Omidian, H., Doroudiani, S., Mp, T. O. N. and Street, K. (2011). Superabsorbent hydrogel composites and nanocomposites: A review. *Polymer Composites*, 32(2): 277-289.
20. Kabiri, K. and Zohuriaan-Mehr, M. J. (2003). Superabsorbent hydrogel composites. *Polymers for Advance Technologies*, 444: 438–444.
21. Shah, R., Saha, N. and Saha, P. (2015). Influence of temperature, pH and simulated biological solutions on swelling and structural properties of biomineralized ($CaCO_3$) PVP–CMC hydrogel. *Progress in Biomaterials*, 4: 123-136.
22. Ping Zhao, S., Jie Cao, M., Yan Li, L. and Lin Xu, W. (2010). Synthesis and properties of biodegradable thermo-and pH-sensitive poly [(N-isopropylacrylamide)-co-(methacrylic acid)] hydrogels. *Polymer Degradation and Stability*, 95: 719-724.
23. Gupta, N. V. and Shivakumar, H. G. (2012). Investigation of swelling behavior and mechanical properties of a pH - sensitive superporous hydrogel composite. *Iranian Journal of Pharmaceutical Research*, 11(2): 1-10.
24. Basri, S. N., Zainuddin, N., Hashim, K. and Yusof, N. A. (2016). Preparation and characterization of irradiated carboxymethyl sago starch-acid hydrogel and its application as metal scavenger in aqueous solution. *Carbohydrate Polymers*, 138: 34-40.
25. Zhang, B., Tao, H., Wei, B., Jin, Z., Xu, X. and Tian, Y. (2014). Characterization of different substituted carboxymethyl starch microgels and their interactions with lysozyme. *PLoS ONE*, 2014: 1-13.
26. Ahmad, F. B., Williams, P. A., Doublier, J. L., Durand, S. and Buleon, A. (1999). Physico-chemical characterisation of sago starch. *Carbohydrate Polymers*, 38(4): 361-370.
27. Janarthanan, P., Zin Wan Yunus, W. M. and Ahmad, M. B. (2003). Thermal behavior and surface morphology studies on polystyrene grafted sago starch. *Journal of Applied Polymer Science*, 90(8): 2053-2058

Malaysian Journal of Analytical Sciences (MJAS)
Published by Malaysian Analytical Sciences Society

THE DEVELOPMENT OF *Acetobacter xylinum* GROWTH MEASUREMENT THROUGH TOTAL PROTEIN ANALYSIS

(Pembangunan Kaedah Pengukuran Pertumbuhan *Acetobacter xylinum* Melalui Analisis Jumlah Protein)

Sharifah Soplah Syed Abdullah*, Jessica Harriette Supang Anak John, Mohd Azizan Mohd Noor

Universiti Kuala Lumpur Branch Campus
Malaysian Institute of Chemical and Bioengineering Technology, Lot 1988 Vendor City Taboh Naning, 78000 Alor Gajah, Melaka, Malaysia

**Corresponding author: sharifahsoplah@unikl.edu.my*

Received: 20 November 2019; Accepted: 27 March 2020

Abstract

Acetobacter xylinum, an aerobic Gram-negative bacterium secretes ribbon-like cellulose polymer through the cell wall during growth. The information available on the growth determination of this organism was largely based on turbidimetric measurements which are inaccurate due to the presence of cellulose fragments in the growth medium. Therefore, this study was aimed at developing a rapid and more accurate method for the determination of *A. xylinum* growth through total protein analysis. The fermentation process was carried out at room temperature in static cultures using Hestrin-Schramm medium at pH 6.4 for 19 days. The methods used for the bacterial growth determination included the total protein content, cell dry weight, viable plate count, and turbidimetry. The total cellular protein content was determined based on the Lowry method after the cells were hydrolyzed in 3% (w/v) of potassium hydroxide (KOH) and boiled for 20 minutes. It was found that the growth profile obtained through the total protein analysis has similar pattern with other conventional methods. However, this method was found to be more accurate and less time-consuming compared to viable plate count and cell dry weight. The growth curve obtained showed four microbial growth phases, namely lag phase (day 0 – day 3), log phase (day 4 – day 12), stationary phase (day 13 – day 16), and finally death phase. The average total cellular protein content of *A. xylinum* was 27.1 ± 6.8% by weight percent.

Keywords: A*cetobacter xylinum*, growth profile, total protein assay, bacterial cellulose

Abstrak

Acetobacter xylinum merupakan bakteria aerobik Gram negatif yang mengeluarkan polimer pita selulosa melalui dinding sel ketika pertumbuhan. Sebahagian besar maklumat tentang kaedah penentuan pertumbuhan organisma ini adalah melalui kaedah turbidimetrik yang kurang tepat akibat kewujudan serpihan selulosa di dalam medium pertumbuhan. Oleh itu, kajian ini bertujuan untuk membangunkan kaedah yang cepat dan lebih tepat dalam menentukan pertumbuhan *A. xylinum* melalui analisis jumlah protein. Proses penapaian dijalankan pada suhu bilik dalam keadaan statik menggunakan medium Hestrin-Schramm pada pH 6.4 selama 19 hari. Kaedah yang digunakan untuk penentuan pertumbuhan bakteria termasuk jumlah kandungan protein, berat kering sel, bilangan sel hidup dan turbidimetri. Jumlah kandungan protein sel ditentukan melalui kaedah Lowry setelah sel-sel dihidrolisis dengan mendidihkannya di dalam 3% (w/v) KOH selama 20 minit. Profil pertumbuhan yang diperoleh melalui analisis jumlah protein mempunyai profil yang sama dengan kaedah konvensional yang lain. Walau bagaimanapun, kaedah ini didapati lebih tepat dan singkat berbanding kaedah bilangan sel hidup dan berat kering sel. Lekuk pertumbuhan yang diperolehi menunjukkan empat fasa pertumbuhan mikrob, iaitu fasa lag (hari 0 – hari ke 3), fasa log (hari ke 4 - hari ke 12), fasa pegun (hari ke 13 - hari ke 16) dan akhirnya fasa kematian. Kandungan protein selular keseluruhan *A. xylinum* adalah 27.1 ± 6.8% mengikut peratus berat sel.

Kata kunci: *Acetobacter xylinum*, profil pertumbuhan, penentuan jumlah protien, selulosa bakteria

Introduction

Acetobacter xylinum is an aerobic Gram-negative bacterium that produces extracellular cellulose when grown in the presence of sugars at pH 5 to 7 and at 25 to 30 °C [1]. This was first reported by Brown in 1886 that the resting cells of *Acetobacter* produce cellulose in the presence of oxygen and glucose [2]. *Acetobacter xylinum* has been extensively used as a model for fundamental and applied investigations on cellulose due to its capability to synthesize a relatively high number of polymers when grown on a range of carbon and nitrogen sources [3]. Microbial cellulose or usually known as bacterial cellulose is an exopolysaccharide that is branched, repeating units of sugars or sugar derivatives secreted extracellularly, mainly glucose, galactose, and rhamnose in different ratios [4].

The monitoring of bacterial cell growth is important to provide information on their nutritional and energetic requirements as well as an understanding of the survival and proliferation conditions of different species under different conditions [5]. The number of bacteria cells can be estimated using direct and indirect methods. Traditionally, the estimation of bacterial growth can be performed spectrophotometrically where the turbidity of the bacterial suspension is measured at a wavelength ranging from 540–600 nm. Turbidimetric measurement is an indirect method which is fast and mostly preferred when there are many culture samples to be counted. However, this measurement procedure does not reflect the actual cell numbers, as it is not able to differentiate between living and dead cells. To date, the growth of cellulose producing bacteria has been largely determined by turbidimetric [6] and cell dry weight [7] measurements. The adhesion of the cellulose to the cells will interfere with both turbidimetric and gravimetric measurements.

The viable count method estimates the cell numbers within the sample but the process is laborious and selective. This method counts the target bacteria through the colonies formed on the surface of agar plates where the environment is assumed to be suitable for the targeted bacteria. Even though the method can give accurate results of cell growth, the many dilutions needed prior to plating and the long incubation period makes this method unsuitable when working with a large number of samples.

Bacterial cellulose exists as structures known as microfibrils, which are composed of glucan chains interlocked by hydrogen bonds to produce a crystalline domain. It is preferred over plant cellulose as it can be obtained in high purity and exhibits a higher degree of polymerization and crystallinity index. It also has higher tensile strength and water holding capacity than plant cellulose, making it a more suitable raw material for producing high fidelity acoustic speakers, high quality paper, and dessert foods [4]. Since the produced cellulose is pure, the determination of cell growth can be relied on the protein content of the cells. Typically, 30-70% of the cell's dry weight is protein [8]. Based on this relationship, a more accurate result of *A. xylinum* growth can be determined through total protein assay. Therefore, this study was aimed to investigate the growth profile of *A. xylinum* through total protein analysis. Cell growth was also determined by conventional methods, which include turbidimetry, viable plate count, and cell dry weight as comparison. The findings from this study will provide an alternative and a more reliable method for the measurement of *A. xylinum* growth.

Materials and Methods

The preparation of inoculum

The *A. xylinum 0416* used in this study was purchased from the Malaysian Agriculture and Research Institute (MARDI), Serdang, Malaysia. Hestrin-Schramm (HS) medium was prepared as follows (% w/v): 4% glucose, 0.5% peptone, 0.5% granulated yeast extract, 0.27% Na_2HPO_4, and 0.115% citric acid in 100 mL of distilled water. The pH of the media was adjusted to 6.4 using either 0.1 M HCl or 0.1 M NaOH before being autoclaved at 121°C for 15 minutes at 15 psi. After the mixture was cooled to 28 ± 1°C, 10% (v/v) of *A. xylinum* 0416 seed culture was aseptically transferred into the sterile culture medium and incubated for 3 days at room temperature (±28 °C).

Fermentation process for growth profile studies

The HS medium was prepared accordingly as described in the inoculum preparation procedures. Then 10% (v/v) of the inoculum was aseptically transferred to the sterile HS medium. The static fermentation process was carried out

for 19 days at room temperature (±28 °C). The sampling was done at 24 hours intervals and analyzed for cell dry weight measurement, turbidimetric measurement, viable plate count, and total protein assay.

Cell dry weight measurement

A 1 mL sample of cell broth from 24 h sampling intervals was centrifuged at 4,000 rpm for 20 min at 4 ºC. The bacteria cell pellets were collected and the supernatants were kept for the determination of glucose consumption. The pellets were washed twice by adding 1 mL of sterile deionized water into the 1.5 mL tubes and were vigorously mixed by using a laboratory vortex mixer. The tubes were then centrifuged at 4,000 rpm for 20 minutes. The supernatants which consisted of the remaining medium and impurities were removed carefully, leaving the washed cell pellets in the tubes. These procedures were conducted twice to ensure the maximum removal of impurities. The cell pellets were then dried in an oven at 80 °C for 24 hours. The dried samples were placed in a desiccator for 20 minutes before being weighed using an analytical balance. The cell dry weight was calculated according to the formula given below.

$$Cell\ dry\ weight\ (mg/mL) = \frac{weight\ of\ dry\ sample\ in\ tube\ (mg) - weight\ of\ empty\ tube\ (mg)}{volume\ of\ sample\ (mL)} \quad (1)$$

Turbidimetry measurement

Similar to cell dry weight determination procedures, the cell pellets were rinsed before being suspended with 1 mL of sterile deionized water. A 100 µL samples of the cell suspension were pipetted into 96 well of microplate and the turbidity was measured at a wavelength of 600 nm by using microplate reader (ThermoFisher Scientific, model VLB000D0). The remaining cell suspensions were further used for viable plate count.

Viable plate count

HS agar was prepared by adding 1.5% technical agar to the HS medium. The mixture was boiled to solubilize the agar before being autoclaved at 121 °C for 15 minutes at 15 psi. The sterile medium was cooled to 45–50 °C before being poured into sterile petri dishes aseptically and left to solidify. The agar plates were stored in a refrigerator until further use. A total of 4 different dilutions were prepared for each bacteria suspension, which were 1:10, 1:100, 1:500, and 1:1000. The diluted samples were aseptically spread on agar plates by using the spread plate technique. The plates were incubated at room temperature for 5 days, and the colonies formed on the agar plates were counted. The colony forming unit (CFU/mL) was calculated by using the following formula.

$$\text{Colony Forming Unit (CFU/mL)} = \frac{colony\ forming\ unit\ (CFU)}{volume\ of\ sample\ (mL)} \times dilution\ factor \quad (2)$$

Total protein analysis: The preparation of bacterial suspension

The samples of 5 mL of cell broth from 24 hours sampling intervals were centrifuged at 4,000 rpm for 20 minutes at 4 ºC. The pellets were harvested by removing the supernatants from the microcentrifuge tubes. The pellets were washed twice by adding 5 mL of sterile deionized water into the tubes and were vigorously mixed by using a laboratory vortex mixer. The tubes were centrifuged at 4,000 rpm for 20 minutes. Then the supernatant which consisted of the remaining medium and impurities were removed carefully. Cell suspensions were prepared by adding 5 mL of sterile deionized water to the pellets which were then kept for further analysis.

Protein extraction

The extraction of proteins from *A. xylinum* cells was carried out through enzymatic and alkaline cell lyses prior to the quantification of the total protein content of the cells. The efficiency of protein extraction between the two methods was compared.

Alkaline cell lysis was carried out by boiling 5 mL of cell suspension that was mixed with 4 mL of 3% (w/v) KOH for 20 minutes to release all proteins and nucleic acids. The mixture was cooled down to room temperature, and 1 mL of the boiled sample was pipetted into a clean microcentrifuge tube and was further centrifuged at 10,000 rpm for 20 minutes. The supernatant which contained the cellular proteins was separated and kept for protein quantification.

Enzymatic cell lysis was carried out by using lysozyme from chicken egg white lyophilized powder, protein ≥ 40000 units/mg protein. The cell lysis buffer was prepared by adding 5 mL of 1 M Tris HCl, 0.8 mL 0.5 M MgCl, 0.1 mL of Triton X-100%, and 20 mg of lysozyme into 50 mL of distilled water. The solution was marked up to 100 mL with distilled water and stored in a refrigerator for further use. For cell lysis, 100 µL of bacterial suspension was mixed with 1 mL of cell lysis buffer and incubated for 40 minutes at room temperature before being centrifuged at 4000 rpm for 20 minutes. The supernatant was collected and kept for protein quantification by using the Lowry method.

Protein quantification

The protein quantification process was carried out using bovine serum albumin (BSA) at a concentration ranging from 1–1000µg/mL as the calibration standard as described by Lowry et al. [9]. Spectrophotometric measurements were done by using a microtiter plate reader at 750 nm.

Results and Discussion

The effect of alkaline and enzymatic cell lysis on total protein content

Figure 1 shows the effect of cell lysis method on the total protein extracted from *A. xylinum* cells using alkaline and enzymatic cell lysis. Overall, the total protein concentration profile during the entire fermentation period showed similar pattern in all samples obtained from the alkaline and enzymatic cell lysis, and without the cell lysis. However, the total protein obtained from the alkaline cell lysis was 1.7 fold higher than the enzymatic cell lysis. There was no significant difference of the total protein in the samples obtained from the enzymatic cell lysis and without the cell lysis. The cell lysis by 3% KOH is one of the most commonly used techniques due to its fast, reliable, and relatively clean way to obtain proteins from cells. KOH hydrolyses the cell wall and liberates the DNA, which is a very viscid compound [10]. The OH^- ion in alkaline cell lysis reacts with the cell membrane and breaks the fatty acid-glycerol ester bonds and subsequently makes the cell membrane permeable.

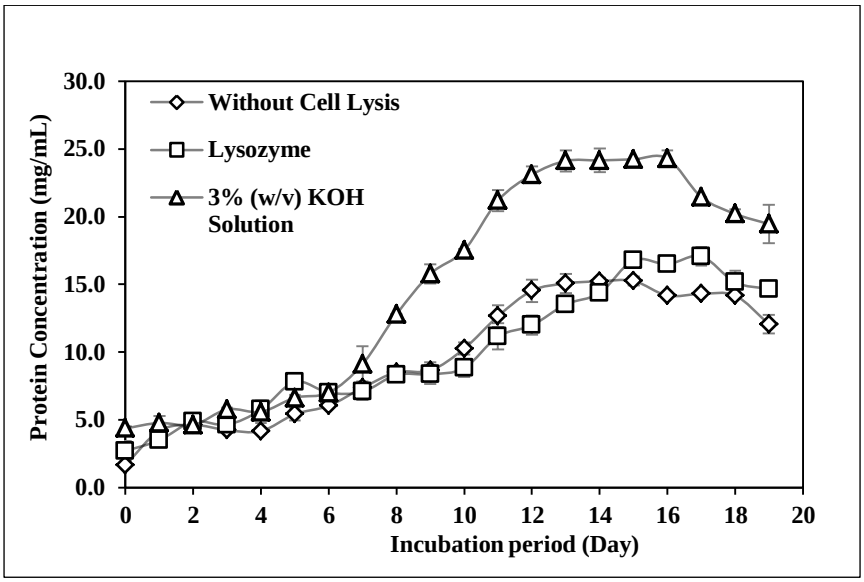


Figure 1. *Acetobacter xylinum* intracellular protein concentration profile during 19 days of fermentation period

On the other hand, lysozyme reacts with the peptidoglycan layer and breaks the glycosidic bonds. For that reason, Gram-positive bacteria can be directly attacked by lysozyme, but in Gram-negative bacteria, the outer membrane needs to be rem oved before exposing the peptidoglycan layer to the enzyme [11]. Accordingly, lysozyme is usually combined with detergent to break the cell wall and membrane, which later hydrolyses β-1-4-glucosidic bonds in the peptidoglycan of Gram-negative bacteria. However, the low concentration of total protein obtained from the

enzymatic lysis in this study suggested that the modification on the reaction condition, including incubation time, concentration of detergent, and lysozyme might be necessary. A combination of ultrasonication with detergent and lysozyme may also improve the extraction of intracellular protein from *A. xylinum*. The findings obtained from this study suggested that alkaline cell lysis is a good method to extract proteins from the cells.

The comparison of growth profile with conventional methods

Figure 2 shows the results of bacterial growth profile measured by turbidimetric method in comparison to the total intracellular protein concentration profile obtained through alkaline cell lysis. The static fermentation process took 19 days to get the complete phases of bacterial growth. The results obtained showed a typical bacterial growth curve with four distinct phases of growth, namely lag phase, exponential phase, stationary phase, and finally death phase. Both profiles showed similar patterns from the early stages of growth until stationary phase but the death phase was not clearly visible in the optical density profile. The cell debris from the non-viable cells present in the samples might have caused an increase in the optical density values. Moreover, the cellulose excreted might still be attached to the cells that contributed to the optical density values. On the contrary, the total protein content dropped after 16 days of static fermentation, indicating the onset of the death phase as the intracellular protein content also began to drop from day 16 onwards. Other studies have shown similar growth patterns of *A. xylinum* by using total viable count [12-14]. On the other hand, Lestari et al. have reported the growth pattern of *A. xylinum* in shake flask fermentation by the measurement of optical density where the whole fermentation process only took 5 days [6]. However, the bacterial cellulose produced had irregular shapes, which appeared in chunks and aggregate forms [12].

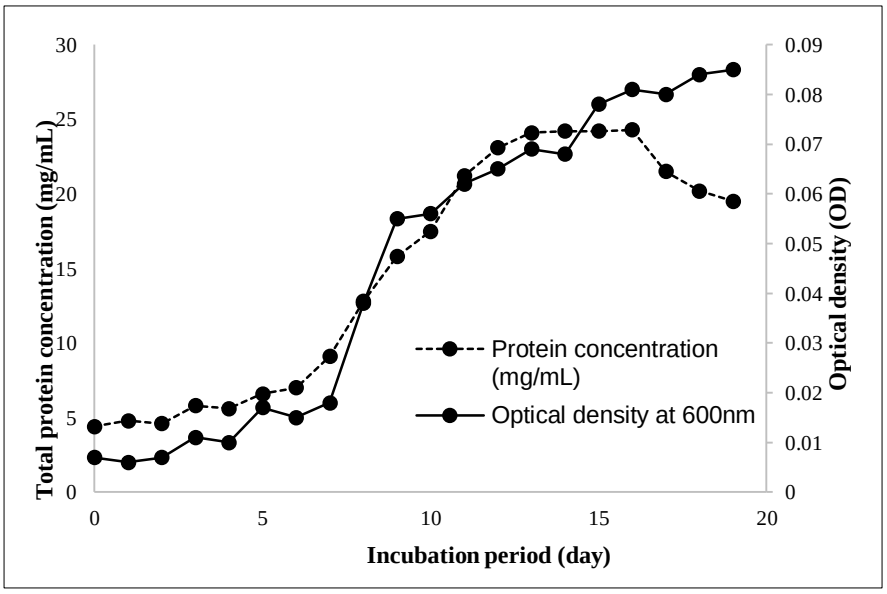


Figure 2. The time course profile of *Acetobacter xylinum* growth by turbidimetry measurement (OD 600) in comparison to the total intracellular protein concentration

In this study, the lag phase began on day 2 of the fermentation before entering the log phase. At this phase, the cellular metabolism started to be expressed and the bacteria cells began to increase in size. However, the cells were not competent to replicate and therefore no increment in cell mass was observed. The lag phase depended directly on the previous growth condition of the bacteria. Upon inoculation, the bacteria started to synthesize their necessary components, such as proteins, vitamins, and co-enzymes needed for growth.

The log phase began at day 3 until day 13 where *A. xylinum* grew rapidly based on the results of the total intracellular protein concentration. At this phase, the growth medium was consumed at a maximal rate and the number of bacteria cells increased logarithmically. All the nutrients in the HS medium were used up by the cells as

the population continued to grow. This resulted in the accumulation of toxic metabolites and waste materials in the medium. Therefore, this shifted log phase to stationary phase which can be seen on day 13 to day 16. Based on the total intracellular protein content, the death phase occurred from day 16 onwards. The depletion of nutrients and accumulation of toxic waste made the environment unsuitable for growth. Nevertheless, some bacteria cells were still viable even though they were starved of nutrients.

Figure 3 shows the results of bacterial growth profile measured by cell dry weight method in comparison to the total protein concentration profile obtained through alkaline cell lysis. Both profiles showed similar growth patterns, except that the death phase was not clearly seen in the cell dry weight method. The presence of dead cells in the biomass pellet may lead to the consistent values of cell dry weight until the end of fermentation period. Moreover, the cellulose excreted from the cells may still be attached to the cells, which therefore might contribute to the cell dry weight values. It can be concluded from this finding that the average protein content of *A. xylinum* is 27.1 ± 6.8% by weight. This result is closely correlated with the value reported by Kampen [8] who mentioned that typically 30–70% of the cell's dry weight is protein. This correlation can be used as a reference in the future study.

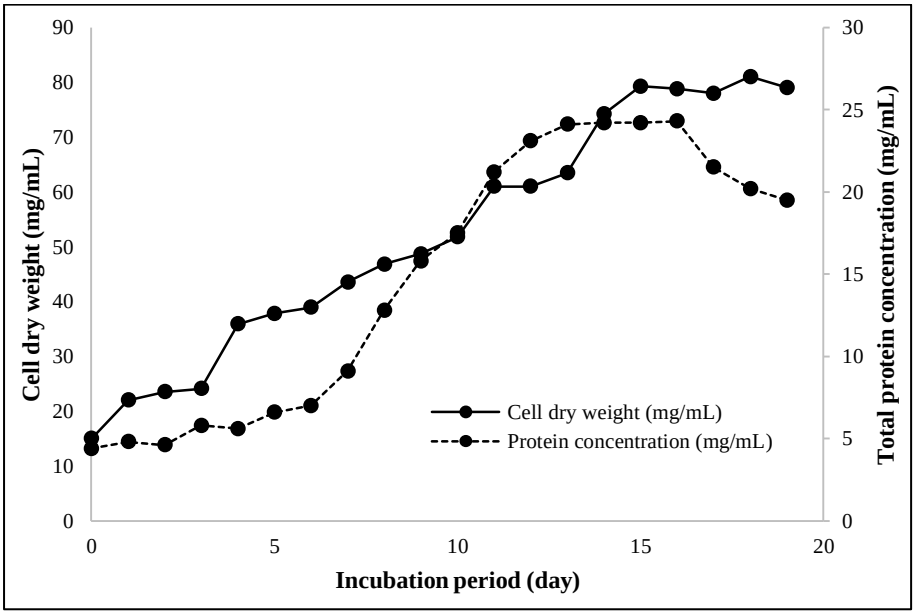


Figure 3. The time course profile of *Acetobacter xylinum* growth by cell dry weight measurement in comparison to the total intracellular protein concentration

Figure 4 shows the results of the bacterial growth profile measured by the viable plate count method in comparison to the total intracellular protein concentration profile obtained through alkaline cell lysis. The results from the viable plate count method showed that *A. xylinum* skipped the lag phase and directly entered the logarithmic phase until day 12 of fermentation. It later entered the stationary phase until the end of fermentation period but the death phase was not clearly seen.

The comparison between the conventional methods and the total protein analysis is summarized in Table 1. Of all the methods performed in this study, it was found that the total protein analysis is the best method to determine the growth of *A. xylinum*. The method can be considered rapid and reliable, as the estimated total protein obtained was solely from the cells. Moreover, it only took 1 hour and 30 minutes to get the final value of the protein.

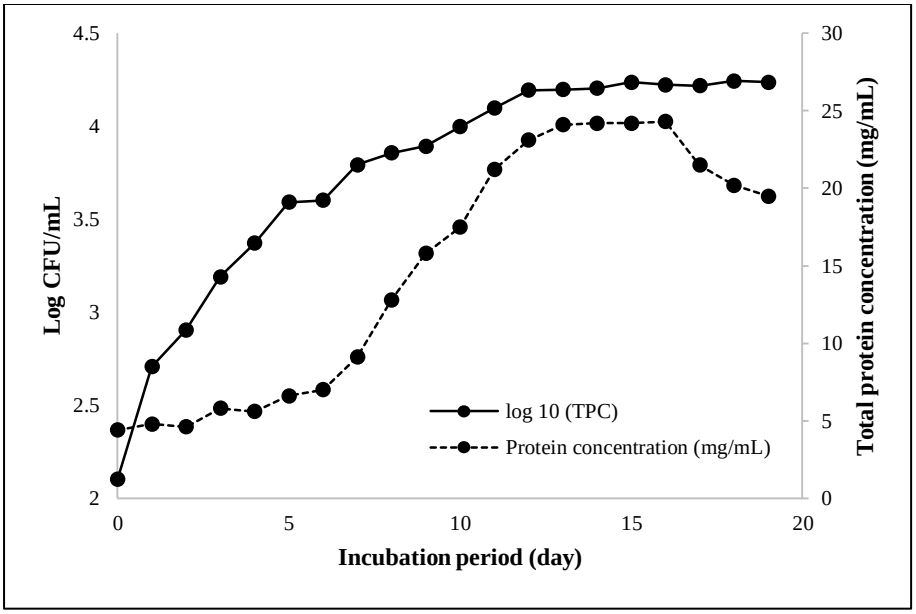


Figure 4. The time course profile of *Acetobacter xylinum* growth by viable plate count measurement in comparison to the total intracellular protein concentration.

Table 1. The comparison of all techniques used for *A. xylinum* growth in this study

	Cell Dry Weight	**Viable Plate Count**	**Turbidimetry Measurement**	**Total Protein Assay**
Procedures	Cell washing, dilution, weighing, drying, cooling, weighing	Cell dilution, agar plate preparation, spread plate, incubation, colony counting	Cell washing, Optical density measurement	Preparation of cell suspension, alkaline cell lysis, protein assay by Lowry method
Estimated time required	1 day 3 hours	3 days 10 hours	45 minutes	1 hour and 30 minutes.
Advantages	Simple steps Low cost	Distinguish between live and dead cells	Simple steps Rapid estimation of bacterial growth	Rapid and reliable method
Disadvantages	Tedious Does not differentiate live, dead cells and BC attached to the cells. Time consuming	Laborious High chance of contamination. Time consuming	Low cost Does not differentiate live, dead cells and BC attached to the cells.	Harsh cell lysis technique which may denature the protein.

Conclusion

The determination of the total protein content was shown to be a reliable and rapid method for the determination of the bacterial cellulose producer, *A. xylinum* growth. Unlike turbidimetric and dry weight measurements, the presence of contaminating cellulose attached to the cells did not cause interference, as only the protein content was measured. Therefore, the use of total protein content as the measurement for the growth of other polysaccharides producers, such as *Sarcina* and *Agrobacterium* can be further explored based on the recent findings. On average, *A. xylinum* contained 27.1 ± 6.8% protein by weight which may be used as a baseline data for future studies.

Acknowledgement

The authors are grateful for the research grant received from the Ministry of Higher Education through the Fundamental Research Grant Scheme (FRGS) FRGS/1/2017/TK10/UNIKL/02/6.

References

1. Castro, C., Zuluaga, R., Putaux, J. L., Caro, G., Mondragon, I. and Gañán, P. (2011). Structural characterization of bacterial cellulose produced by Gluconacetobacter swingsii sp. from Colombian agroindustrial wastes. *Carbohydrate Polymers,* 84(1): 96-102.
2. Brown, A. J. (1886). On an acetic ferment which forms cellulose. *Journal of Chemical Society Transaction,* (49); 432-439.
3. Moniri, M., Boroumand Moghaddam, A., Azizi, S., Abdul Rahim, R., Ariff, A., Zuhainis Saad, W., Navaderi, M. and Mohamad, R. (2017). Production and status of bacterial cellulose in biomedical engineering *Nanomaterials,* 7(9): 257.
4. Chawla, P. R., Bajaj, I. B., Survase, S. A. and Singhal, R. S. (2009). Microbial cellulose: Fermentative production and applications. *Food Technolgy and Biotechnology,* 47(2): 107-124.
5. Maia M. R. G., Marques, S., Cabrita, A. R., John Wallace, R., Thompson, G. and Fonseca, A. J. (2016). Simple and versatile turbidimetric monitoring of bacterial growth in liquid cultures using a customized 3D printed culture tube holder and a miniaturized spectrophotometer: application to facultative and strictly anaerobic bacteria. *Frontier Microbiology,* 7: 1381.
6. Lestari, P., Elfrida, N., Suryani, A. and Suryadi, Y. (2015). Study on the production of bacterial cellulose from *Acetobacter xylinum* using agro - waste. *Jordan Journal Biological Sciences,* 7(1): 75-80.
7. Zahan, K. A., Nordin, K., Mustapha, M. and Mohd Zairi, M. N. (2015). Effect of incubation temperature on growth of *Acetobacter xylinum* 0416 and bacterial cellulose production. *Applied Mechanics and Materials,* 815: 3-8.
8. Kampen, W. H. (1997). Nutritional requirements in fermentation processes. *Fermentation and Biochemical Engineering Handbook*. New Jersey: Noyes Publication, pp. 152.
9. Lowry, O. H., Rosebrough, N. J., Farr, A. L. and Randall, R. J. (1951). Protein measurement with the Folin phenol reagent. *Journal of Biological Chemistry,* 193: 265-275.
10. Gregersen, T. (1978). Rapid method for distinction of gram-negative from gram-positive bacteria. *European Journal Applied Microbiology Biotechnology,* 5: 123-127.
11. Islam, M. S., Aryasomayajula, A. and Selvaganapathy, P. R. (2017). A review on macroscale and microscale cell lysis methods. *Micromachines,* 8(83): 1- 27.
12. Kongruang, S. (2008). Bacterial cellulose production by *Acetobacter xylinum* strains from agricultural waste products. *Applied Biochemistry and Biotechnology,* 148(1-3): 245-256.
13. Aquary, I. D., Kawuri, R., Ramona, Y. and Cass, G. (2014). Optimization of the production of microbial cellulose by *Acetobacter xylinum* in *Aloe barbadensis* Mill. medium. *International Journal of Pure and Applied Bioscience,* 2(6): 215-222.
14. Esa. F., Rahman, N. A., Kalil, M. S. and Tasirin, S. M. (2017). Effects of agitation conditions on bacterial cellulose production by *Acetobacter xylinum* 0416 in fermentation of matured coconut water medium. *Malaysian Journal of Analytical Sciences,* 21(1): 261-266.

Malaysian Journal of Analytical Sciences (MJAS)
Published by Malaysian Analytical Sciences Society

ELECTROSYNTHESIS OF SILVER OXIDE DEPOSITED ONTO HOT SPRING MUD WITH ENHANCED DEGRADATION OF CONGO RED

(Elektrosintesis Perak Oksida Disokong Pada Lumpur Air Panas Dengan Peningkatan Degradasi Congo Merah)

Muhammad Farhan Hanafi, Ahmad Norsyazwan Mustafa, Norzahir Sapawe*

Universiti Kuala Lumpur Branch Campus
Malaysian Institute of Chemical and Bioengineering Technology, Lot 1988 Vendor City, Taboh Naning, 78000 Alor Gajah, Melaka, Malaysia.

**Corresponding author: norzahir@unikl.edu.my*

Received: 28 April 2019; Accepted: 18 February 2020

Abstract

AgO-supported hot spring mud (AgO-HSM) catalyst was prepared by introducing AgO onto HSM support through electrochemical method. The effect of preparation methods on the physical properties of the catalyst was studied. The interaction between silver species and HSM during the electrochemical process affected the AgO-HSM structure. The amount of 0.2 g L^{-1} of 11 wt.% AgO-HSM was the optimum dosage for 10 mg L^{-1} Congo red (CR), which resulted in 98.2% of maximum degradation after 2 hours of contact time at pH 5 under fluorescent light. This study showed that the kinetics followed a pseudo-first order Langmuir–Hinshelwood model with the calculated values of K_r and K_{LH} were 172.41 mg L^{-1} h^{-1} and 0.005 L mg^{-1}, respectively. The measurements of the mineralization of CR by COD and BOD_5 analysis were 38.4% and 61.1%, respectively, before and after reaction. Therefore, AgO-HSM could be a promising catalyst for the degradation of various dyes in wastewater.

Keywords: AgO-HSM, electrochemical, degradation, Congo red, light irradiation

Abstrak

Mangkin AgO yang disokong pada lumpur air panas (AgO-HSM) telah disediakan dengan memperkenalkan AgO ke atas sokongan HSM melalui kaedah elektrokimia. Kesan kaedah penyediaan sifat fizikal mangkin telah dikaji. Interaksi antara spesis perak dan HSM semasa elektrokimia didapati mempengaruhi struktur AgO-HSM. Sejumlah 0.2 gL^{-1} dari 11% berat AgO-HSM didapati sebagai dos optimum untuk 10 mgL^{-1} Congo merah (CR), yang mengakibatkan 98.2% degradasi maksimum selepas 2 jam masa sentuhan pada pH 5 di bawah cahaya pendarfluor. Kajian ini menunjukkan bahawa kesan kinetik mengikut model Langmuir-Hinshelwood dengan pseudo-pertama dengan nilai kiraan Kr dan K_{LH} masing-masing ialah 172.41 $mgL^{-1}h^{-1}$ dan 0.005 Lmg^{-1}. Pengukuran mineralisasi CR oleh COD dan BOD_5 adalah 38.4% dan 61.1%, sebelum dan selepas tindak balas. Oleh itu, AgO-HSM boleh menjadi mangkin yang menjanjikan degradasi pelbagai pewarna dalam air kumbahan.

Keywords: AgO-HSM, elektrokimia, degradasi, Congo merah, penyinaran cahaya

Introduction

Synthetic dyes are used almost in all branches of the consumer goods industry. About 10,000 tons of dyes are produced per year. Inevitably, there are dye losses (approximately 12% of used amount) during manufacturing and processing operations [1]. Azo dyes are characterized by the presence of N=N groups; methyl orange is a common water-soluble azo dye. The removals of these non-biodegradable organic chemicals from the environment are a crucial ecological problem and are suspected to be carcinogenic and mutagenic to humans, in addition to reducing light penetration in bodies of water, which is harmful to aquatic life.

Several methods for the removal of dyes have been reported, including adsorption, coagulation and flocculation, and membrane separation. However, these methods have their own limitations of being time consuming, expensive, and commercially unattractive, as well as resulting in the generation of secondary waste [2]. Photocatalysts have become important because advanced oxidation processes (AOPs) can convert a wide range of harmful dyes into non-toxic products, CO_2, and water at ambient temperature. The abundance of hydroxyl radicals generated by the AOPs plays an important role in oxidizing the organic species present in the wastewater into harmless species. Other than that, this reaction also has simple design and operation. It is also non-conventional, low cost, and a highly efficient method [3]. The photocatalytic detoxification of wastewater is a process that combines heterogeneous catalysis with solar technologies. Heterogeneous photocatalysis by semiconductor materials, such as TiO_2, ZnO, Fe_2O_3, CdS, GaP, and ZnS, has been widely used in photocatalytic degradation [2].

Hot spring mud is one of the clays that are widespread, easily available, and low-cost chemical substances. Both in their native state and in numerous modified forms, clays are versatile materials that catalyze a variety of chemical reactions. Clays are nanoparticles with layered structures that possess net negative charge neutralized by cations, such as Na^+, K^+, and Ca^{2+}, which occupy the interlamellar space. The amazing amenability of clays for modification lies in the fact that these interlamellar cations can be very easily replaced by other cations or molecules [4].

Most of the previous studies involving the degradation of dyes using Ag are outstanding with their unique optical, electrical, thermal, and electromagnetic properties [5]. For instance, silver nanoparticles have been investigated in fields such as high-density information storage, photoluminescence and electroluminescence devices, surface-enhanced Raman scattering, heterogeneous catalysis, photocatalysis, and disinfection [6]. Therefore, as an extension of the previous study, the present study intends to synthesize AgO supported on HSM by the electrochemical method and study the photoactivity in the decolorization of Congo red. The physical property of the catalyst was studied in detail *via* Fourier transform infrared spectroscopy (FTIR). Kinetic studies of photo decolorization and biodegradability of the catalysts were also discussed.

Materials and Methods

Congo red (CR) and *N*,*N*-dimethylformamide (DMF) were purchased from Merck, Malaysia. Naphthalene and tetraethylammonium bromide solution were purchased from Fluka Chemical whereas methanol was purchased from RPE Reagent Pure Erba. The hot spring mud was collected from Cherana Putih, Malacca. Silver and platinum plates of greater than 99% purity were used as electrodes and obtained from Nilaco, Japan. Tetraethylammonium perchlorate (TEAP) that was used as a supporting electrolyte in electrolysis was prepared in accordance with the procedure reported in the literature [2, 3, 7-16].

In this study, for the *in-situ* preparation technique, 10 ml of DMF solution was added to a one-compartment cell fitted with a platinum plate cathode (2 cm × 2 cm) and a silver plate anode (2 cm × 2 cm) containing TEAP, naphthalene, and HSM. Naphthalene was used as a mediator in the system to produce radical anions, which then reduced iron cations to give much smaller iron nanoparticles [2]. Then, the electrolysis was conducted at a constant current of 60 mA/cm^2 and 30 °C under N_2 atmosphere and continuous stirring (150 rpm). The required iron loading on the HSM support was calculated based on Faraday's law of electrolysis, as shown in the following equation 1:

$$n = \left(\frac{It}{F}\right)\left(\frac{1}{z}\right) \quad (1)$$

where n is the number of moles of Ag, I is constant current of electrolysis (A), t is the total time the constant current was applied (s), F is the Faraday constant (96,487 C mol^{-1}), and z is the valency number of ions of the substance (electron transferred per ion). The number of moles of Ag required was calculated based on the total time t of the electrolysis. For example, 5520 s is the time required to produce 11 wt.% of Ag in 15 g HSM. After electrolysis, the mixture was impregnated at 80 °C in an oil bath before being dried overnight at 100 °C and calcined for 3 hours at 550 °C to give a green-colored AgO-HSM catalyst.

UV-Vis was recorded at room temperature over a range of wavelengths from 400 to 850 nm using a UV-Vis spectrophotometer with an integrating sphere. FTIR spectroscopy was performed to identify the chemical functional

groups present in the catalysts. IR absorbance data were obtained over a range of wavenumbers from 650 to 3850 cm^{-1}. The photoactivity of the catalysts was tested for the decolorization of CR. The photocatalytic experiments were performed in batches consisting of 250 mL Pyrex conical flasks placed on a magnetic stirrer to uniformly disperse the catalyst into the solution. A fluorescent lamp (20 W) light source was mounted 10 cm above the solution. The initial pH of the solution was 5 and the reaction was carried out at room temperature. Then, the reaction was carried out for another 2 hours under light irradiation under continuous stirring. The concentration of CR dye in the solution prior to irradiation was used as the initial value for the CR decolorization measurements. Each set of experiments was performed three times. The adsorption band of CR was taken at 498 nm and the decolorization percentage was calculated using the following equation 2:

$$Decolorization(\%) = \frac{C_0 - C_t}{C_0} \times 100 \quad (2)$$

where C_0 and C_t are the initial concentration of CR and the concentration at time t, respectively. BOD was measured using a YSI model 3100 in which BOD bottles were incubated at 20 °C for 5 days, and the difference in the dissolved oxygen was used to calculate BOD_5. A HACH DR4000 spectrometer was used for COD measurements.

In addition, the kinetic study was determined using Langmuir–Hinshelwood model, which will fit by pseudo first-order kinetics. The line with an intercept of $1/k_r$ and $1/k_rK_{LH}$ was obtained from the Langmuir–Hinshelwood (L–H) kinetic formula (Eq. 3):

$$\frac{1}{k_{app}} = \left[\frac{1}{K_r K_{LH}}\right] + \frac{C_0}{K_r} \quad (3)$$

where K_r is the reaction rate constant (mg L^{-1} h^{-1}), K_{LH} is is the Langmuir–Hinshelwood adsorption equilibrium constant (L mg^{-1}) and C_0 is the initial concentration of CR (mg L^{-1}).

Results and Discussion

Functional group determination

The details of the functional groups involved in the catalyst structure under varying metal loading were measured *via* FTIR and the results are shown in Figure 1. The peak at 3745 cm^{-1} could be attributed to the hydroxyl groups of the terminal and internal framework defects of the SiOH groups [2]. The sharp peak at 1080 cm^{-1} might correspond to the asymmetric Si-O-Si vibration. This peak decreased with increasing silver loading, possibly indicating Ag with the silicon of the Si-O-Si groups [17].

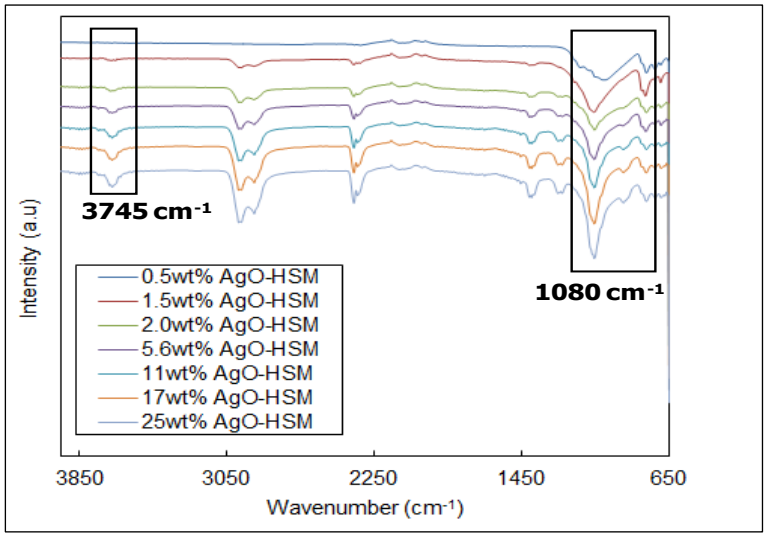


Figure 1. FTIR patterns of AgO catalysts with varying metal loading

Performance of the prepared catalysts

The performance of the prepared catalysts was examined by the decolorization of CR, and the results are shown in Figure 2. The result showed that complete decolorization of CR was achieved within a very short contact time (2 hours) under visible light conditions when using AgO-HSM at 480 mA cm^{-2}. It may be attributed to the narrower band gap of this catalyst, which facilitates excitation of electrons from the valence band to the conduction band, leading to the production of hydroxyl radicals. Therefore, the compatibility of AgO catalyst for the application in wastewater treatment of textile industry effluents is always at low concentration [18].

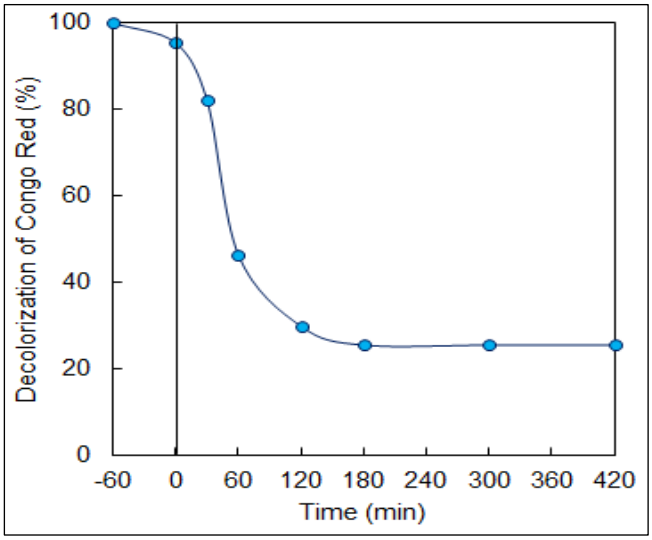


Figure 2. Performance of the AgO catalysts on the decolorization of CR (pH = 5, AgO loading = 2 wt.%, catalyst dosage = 0.3 g L^{-1}, temperature = 30 ºC, and initial concentration = 10 ppm)

Effect of pH

pH solution plays an important role in the photodecolorization of a dye as shown in Figure 3. Semiconductor oxides usually exhibit an amphoteric behavior, which influences the surface-charge properties of the photocatalysts when the reactions occur on the surface of the semiconductor [21]. In this study, the effect of pH on the removal of CR was examined over a pH range from 3 to 11 using AgO-HSM. The highest decolorization was obtained at pH 5 with decolorization of 70.2%. The activities of the catalysts may have been affected by the existence of a strong electrostatic field between the positively charged catalyst surface and the negatively charged CR, as well as the activity of Ag cations inside the framework of the mud [2]. The increase in the pH value did not seem to favor photodecolorization, which may be due to the reduction in the amount of positive charges on the surface of the catalyst, which in turn decreased the attraction of CR towards the surface. The reaction was not performed in alkaline conditions due to the competition between the hydroxyl ions and CR ions in the system. However, lowering the pH to acidic conditions made the surface of AgO-HSM became positively charged and this inhibited the dye cations from approaching the catalyst surface, thus reducing the efficiency of the reaction to 36.4% [19].

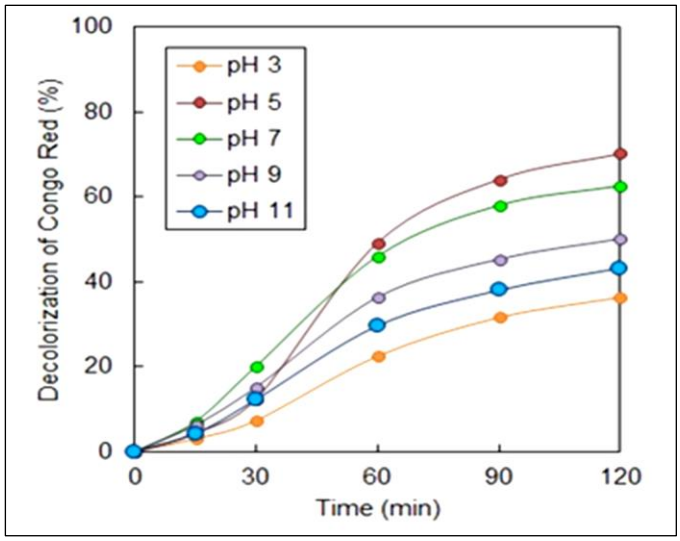


Figure 3. Effect of pH on the decolorization of CR (AgO loading = 2 wt.%, catalyst dosage = 0.3 g L^{-1}, temperature = 30 ºC, and initial concentration = 10 ppm)

Effect of metal loading

The effect of AgO content in HSM was studied for the decolorization of CR in the range of 0.5–25 wt.% loading using 0.2 g L^{-1} AgO-HSM for a 2 hours irradiation time and shown in Figure 4. The decolorization increased with the increasing silver loading up to 11 wt.%, yielding a maximum decolorization percentage of 77.1%. Further addition of AgO most probably resulted in more agglomeration of silver oxide on the surface of HSM, which then reduced the surface area for CR attraction and light penetration for an efficient photocatalytic reaction. A similar observation was reported on the photocatalytic degradation of C.I. basic violet 10 using TiO_2 catalysts supported on Y-zeolites [20].

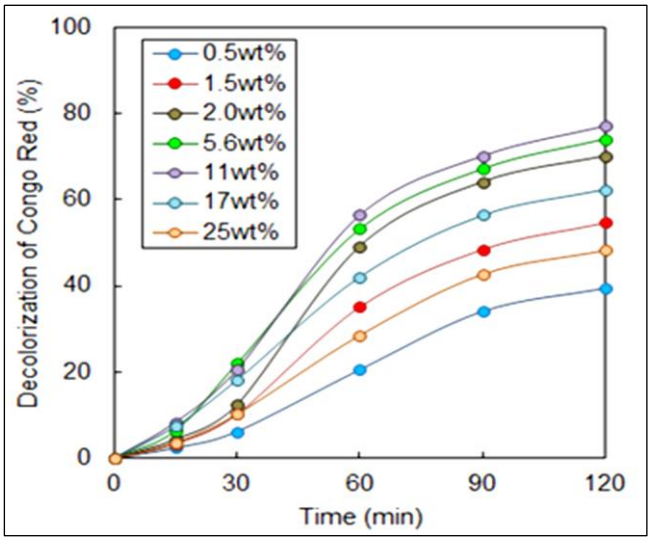


Figure 4. Effect of metal loading on the decolorization of CR (pH = 5, catalyst dosage = 0.3 g L^{-1}, temperature = 30 ºC, and initial concentration = 10 ppm)

Effect of catalyst dosage

In order to study the effect of catalyst dosage, a 10 mg L^{-1} CR solution was studied at pH 5 under various catalytic doses ranging from 0.1 to 0.5 g L^{-1}. Figure 5 shows a plot of the decolorization percentage of CR for AgO-HSM. The decolorization increased with increasing catalyst dosage up to 0.2 g L^{-1}, but further addition of the catalyst did not produce any significant effect on the decolorization. This result could be due to the increased turbidity of the suspension, which reduced light penetration and inhibited photodecolorization [8, 16]. The increase in the catalyst dosage led to an increase in the active surface area and enhanced the decolorization up to 80.2% for AgO-HSM [2].

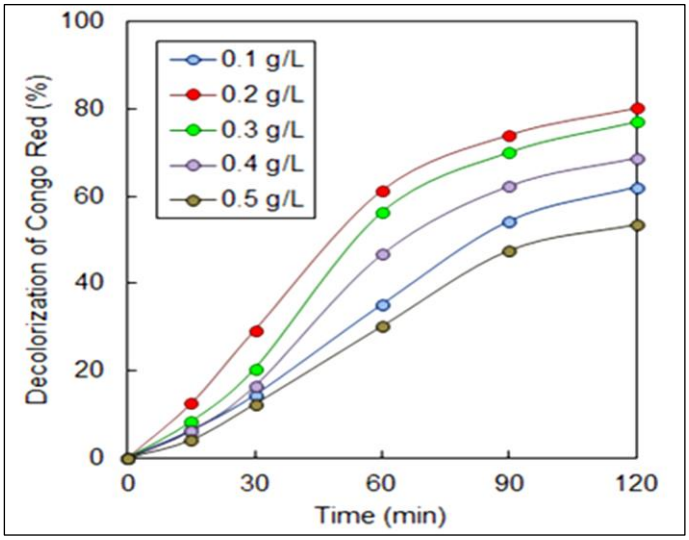


Figure 5. Effect of catalyst dosage on the decolorization of CR (pH = 5, AgO loading = 11 wt.%, temperature = 30 ºC, and initial concentration = 10 ppm)

Effect of initial concentration

Initial concentration is a very important aspect to be considered because the photocatalytic reaction rate depends on the substrate concentration. Figure 6 shows the effect of initial concentration, ranging from 10 to 100 mg L^{-1}, on the decolorization of CR using AgO-HSM. The catalyst demonstrated a decrease in the decolorization with the increase of the initial concentration. The increase in the concentration of CR caused the saturation of active sites on the catalyst surface with organic species, thus reducing light penetration and hydroxyl radical formation [2, 15, 16]. Lowering dye (pollutant in wastewater) concentration reduced the time of decomposition of the wastewater. This could be described when the concentration of the real industrial wastewater is less than its original concentration, then the catalyst active sites are probably completely exposed to dye ions. Further increase in dye concentration may also be responsible for screening the exposed light, so light intensity will be reduced [16].

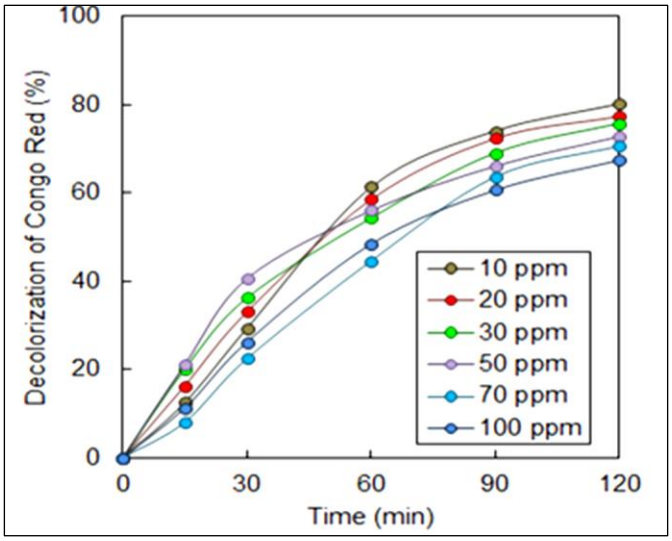


Figure 6. Effect of initial dye concentration on the decolorization of CR (pH = 5, AgO loading = 11 wt.%, catalyst dosage = 0.2 g L^{-1}, and temperature = 30 ºC)

Kinetic study

The kinetic decolorization of CR for 11 wt.% AgO-HSM was studied using the Langmuir–Hinshelwood (L–H) kinetic model at different initial concentrations, and the results are shown in Figure 7. Higher concentrations showed lower efficiency of photocatalytic decolorization due to the formation of several layers of adsorbed dye on the catalyst surface. In addition, large amounts of adsorbed dye were found to inhibit the reaction with the dye molecules, since there was no direct contact of the catalyst with photogenerated holes or hydroxyl radicals [11]. The calculated values of K_r and K_{LH} were 172.41 mg L^{-1} h^{-1} and 0.005 L mg^{-1}, respectively, for 11 wt.% AgO-HSM. The values of k_r were greater than those of K_{LH} for catalysts, indicating dye adsorption was the controlling step of the process. A similar phenomenon was reported on the degradation of Orange G using nano-sized Sn (IV)/TiO_2/AC as a photocatalyst [23].

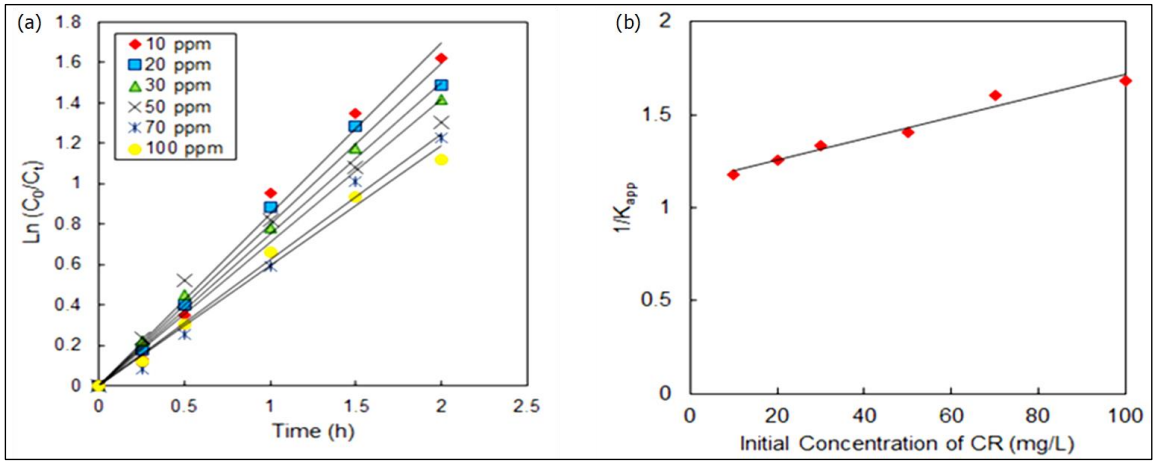


Figure 7. (a) Photodecolorization kinetics of CR using AgO-HSM at different CR concentrations; (b) Relationship between $1/K_{app}$ and $1/C_0$ at different initial concentrations of CR: 11 wt.% AgO-HSM

The values of k obtained from Figure 7 are listed in Table 1, which revealed a significant and favorable effect of catalysts on the photodecolorization of CR. A lower concentration of CR results in a higher first-order rate constant, demonstrating the suitability of the system for low dye concentrations. Indeed, the concentrations of dyes in the wastewater from textile industry effluents are always low, in the range of 10-50 mg L^{-1} [18].

Table 1. Pseudo first-order apparent constant value for CR decolorization

Initial Concentration, (mg L^{-1})	**Reaction Rate, k_{aqq} (h^{-1})**	**R^2**	**Initial Reaction Rate, r_0 (mg L^{-1} h^{-1})**	**Decolorization (%)**
10	0.8496	0.9848	8.496	80.23
20	0.7976	0.9853	15.952	77.41
30	0.7497	0.9888	22.491	75.84
50	0.7101	0.9539	35.505	72.82
70	0.6235	0.9876	43.645	70.70
100	0.5936	0.9886	59.36	67.45

Investigation on biodegradability

The degree of mineralization during photocatalytic decolorization was determined in order to confirm whether the final solution of CR was less toxic than the initial solution. COD and BOD_5 analysis were used to monitor the mineralization of the dyes. Figure 8 shows the COD and BOD_5 levels of CR solutions with 11 wt.% AgO-HSM. The results indicated that the COD and BOD_5 levels after reaction decreased to 38.4% and 61.1%, respectively. A significant change in BOD_5 proved that the biodegradability of the CR solution can be enhanced by this photo-oxidation system, by converting non-biodegradable organics into biodegradable forms. In addition, the BOD_5/COD ratio after reaction was 0.526, indicating that some non-biodegradable organic part of the CR molecule was destroyed, decomposed, and even mineralized in the photocatalytic process during the irradiation time [2, 15, 16].

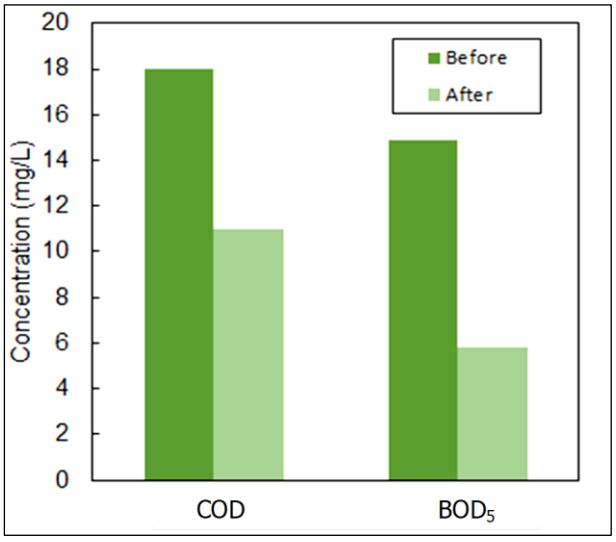


Figure 8. BOD_5 and COD levels before and after reaction (pH = 5, AgO loading = 11 wt.%, catalyst dosage = 0.2 gL^{-1}, initial concentration = 10 mgL^{-1}, and temperature = 30 ºC)

Conclusion

AgO supported hot spring mud (AgO-HSM) catalysts were prepared using electrochemical methods. The physical properties of the catalyst were studied *via* FTIR. The interaction between silver species and HSM support during the electrosynthesis was found to affect the AgO-HSM structure. The photodecolorization percentage of 80.2% in 10 mg L^{-1} CR was obtained for 11 wt. % AgO-HSM. The kinetic studies showed that the reaction rate was pseudo-first order as determined by the Langmuir–Hinshelwood model, where the value of K_r was higher compared to K_{LH}, indicating dye adsorption was the controlling step of the process. The COD and BOD_5 levels, used to determine the mineralization of CR, were 38.4% and 61.1%, respectively, before and after reaction. Moreover, the BOD_5/COD ratio after reaction was 0.526, indicating that some non-biodegradable organic parts of the CR molecules were destroyed, decomposed, and even mineralized in the photocatalytic process. Therefore, AgO has a great potential to be used as a catalyst for the photocatalytic decolorization of various dyes in wastewater.

Acknowledgements

The authors are grateful for the financial support by the Short Term Research Grant (STRG) from Universiti Kuala Lumpur (Grant No. 17004 & 17029), Majlis Amanah Rakyat Malaysia (MARA), the awards of Yayasan Tengku Abdullah Scholarship (YTAS-Muhammad Farhan bin Hanafi), and also the Malaysian Institute of Chemical and Bioengineering Technology, Universiti Kuala Lumpur for their support.

References

1. Sima, J. and Hasal, P. (2013). Photocatalytic degradation of textile dyes in a TiO_2/UV system. *Chemical Engineering Transactions*, 32: 79-84.
2. Sapawe, N., Jalil, A. A., Triwahyono, S., Adam, S. H., Jaafar, N. F. and Satar, M. A. H. (2012). Isomorphous substitution of Zr in the framework of aluminosilicate HY by an electrochemical method: Evaluation by methylene blue decolorization. *Applied Catalysis B: Environmental*, 125: 311-323.
3. Sapawe, N., Jalil, A. A., Triwahyono, S., Sah, R. N. R. A., Jusoh, N. W. C. and Hairom, N. H. H. (2013). Electrochemical strategy for grown ZnO nanoparticles deposited onto HY zeolite with enhanced photodecolorization of methylene blue: Effect of the formation of Si-O-Zn bonds. *Applied Catalysis A: General*, 456: 144-158.
4. Gopalpur, N. (2011). Organic synthesis using clay and clay-supported catalysts. *Applied Clay Science*, 53: 106-138.
5. Kumar, P., Govindaraju, M., Senthamilselvi, S. and Premkumar, K. (2013). Photocatalytic degradation of methyl orange dye using silver (Ag) nanoparticles synthesized from *Ulva lactuca*. *Colloids and Surfaces B: Biointerfaces*, 103: 658-661.
6. Albiter, E., Valenzuela, M. A., Alfaro, S., Valverde-Aguilar, G. and Martı´nez-Pallares, F. M. (2015). Photocatalytic deposition of Ag nanoparticles on TiO_2: Metal precursor effect on the structural and photoactivity properties. *Journal of Saudi Chemical Society*, 19: 563-573.
7. Sapawe, N., Rustam, M. A., Mahadzir, M. H. H., Lani, M. K. E. M., Raidin, A. and Hanafi, M. F. (2019). A novel approach of *in-situ* electrobiosynthesis of metal oxide nanoparticles using crude plant extract as main medium for supporting electrolyte. *Materials Today: Proceedings*, 19(4): 1441-1445.
8. Hanafi, M. F., Sapawe, N., Rahim, M. Z. A., Rahman, N. N., Rahman, A. H. A. and Ahmad, A. A. (2016). Performance of $EGZrO_2$-$EGFe_2O_3$/HY as photocatalyst and its efficacy in decolorization of dye-contaminants. *Malaysian Journal of Analytical Sciences*, 20(5): 1052-1058.
9. Hanafi, M. F. and Sapawe, N. (2018). Remarkable degradation of methyl orange by tetragonal zirconia catalyst. *Materials Today: Proceedings*, 5(10): 21849-21852.
10. Hanafi, M.F. and Sapawe, N. (2019). The potential of ZrO_2 catalyst toward degradation of dyes and phenolic compound. *Materials Today: Proceedings*, 19(4): 1524-1528.
11. Hanafi, M. F. and Sapawe, N. (2019). Electrosynthesis of ZrO_2 nanoparticles with enhanced removal of phenolic compound. *Materials Today: Proceedings*, 19(4), 1529-1532.
12. Hanafi, M. F. and Sapawe, N. (2019). Effect of calcination temperature on the structure and catalytic performance of ZrO_2 catalyst in phenol degradation. *Materials Today: Proceedings*, 19(4): 1533-1536.
13. Hanafi, M. F. and Sapawe, N. (2019). Electrogenerated zirconia ($EGZrO_2$) nanoparticles as recyclable catalyst for effective photocatalytic degradation of phenol. *Materials Today: Proceedings*, 19(4): 1537-1540.

14. Sapawe, N. and Hanafi, M. F. (2015). Facile one-pot electrosynthesis of high photoreactive hexacoordinated Si with Zr and Zn catalyst. *RSC Advances*, 5(92): 75141-75144.
15. Sapawe, N. (2015). Hybridization of zirconia, zinc and iron supported on HY zeolite as a solar-based catalyst for the rapid decolorization of various dyes. *New Journal of Chemistry*, 39(6): 4526-4533.
16. Sapawe, N. (2015). Effective solar-based iron oxide supported HY zeolite catalyst for the decolorization of organic and simulated dyes. *New Journal of Chemistry*, 39(8): 6377-6387.
17. Purkait, M. K., Maiti, A., Das Gupta, S. and De, S. (2007). Removal of Congo Red using activated carbon and its regeneration. *Journal Hazardous Materials*, 145: 287-295.
18. Grzechulska, J. and Morawski, A.W. (2002). Photocatalytic decomposition of azo-dye acid black 1 in water over modified titanium dioxide. *Applied Catalysis B: Environmental*, 36: 45-51.
19. Bokare, A. D., Chikate, R. C., Rode, C. V. and Paknikar, K. M. (2008). Iron-nickel bimetallic nanopartilcles for reductive degradation of azo dye Orange G in aqueous solution, *Applied Catalysis B: Environmental*, 79: 270-278.
20. Wang, C.C., Lee, C.K., Lyu, M.D., & Juang, L.C (2008). Photocatalytic degradation of C.I. basic violet 10 using TiO_2 catalysts supported by Y zeolite: an investigation of the effects of operational parameters. Dyes Pigments, 76, 817-824.
21. Sapawe, N., Jalil, A. A. and Triwahyono, S. (2013). One-pot electro-synthesis of ZrO_2–ZnO/HY nanocomposite for photocatalytic decolorization of various dye-contaminants. *Chemical Engineering Journal*, 225: 254-265.
22. Sun, J., Wang, X., Sun, J., Sun, R. and Qiao, L. (2006). Photocatalytic degradation and kinetic of Orange G using nano-sizes Sn(IV)/TiO_2/AC photocatalyst. *Journal Molecules Catalysis A: Chemical*, 260: 241-246.

Malaysian Journal of Analytical Sciences (MJAS)
Published by Malaysian Analytical Sciences Society

SOURCE DETERMINATION OF PSEUDOEPHEDRINE USING ATTENUATED TOTAL REFLECTANCE FOURIER TRANSFORM INFRARED SPECTROSCOPY COMBINED WITH CHEMOMETRIC ANALYSIS

(Penentuan Sumber Pseudoephederin Menggunakan Spektroskopi Atenuasi Pembalikan Transformasi Fourier Digabungkan Dengan Analisis Kemometrik)

Ainol Hayah Ahmad Nadzri[1], Saravana Kumar Jayaram[2], Puteri Nurul Hassanah Anuar[1], Noor Zuhartini Md Muslim[1], Dzulkiflee Ismail[1], Wan Nur Syuhaila Mat Desa[1]*

[1]*Forensic Science Programme, School of Health Sciences, Universiti Sains Malaysia, 16150 Kubang Kerian, Kelantan, Malaysia*
[2] *Narcotic Section, Forensic Science Unit, Chemistry Department, Jalan Sultan 46661 Petaling Jaya, Selangor*

**Corresponding author: wannurs@usm.my*

Received: 20 November 2019; Accepted: 27 March 2020

Abstract

Seizures of pseudoephedrine compound pertaining to clandestine drug laboratories were widely reported since it is abused for illicit amphetamine-type stimulant (ATS) production. In small scale clandestine laboratory, a commercial decongestant tablet is always encountered despite having properties claimed to deter pseudoephedrine extraction as pharmaceutical means to prevent the misuse of the compound. This study aims to investigate the feasibility of discriminating extracted pseudoephedrine powder based on its origin. In this study, five different types in varying strengths and sizes of pseudoephedrine-based tablets samples were extracted with direct and acid-base extraction methods. Identification of extracted pseudoephedrine was done by simple attenuated total reflection Fourier transform infrared spectroscopy (ATR-FTIR). In total, 90 spectra were obtained from 15 batches of samples at six repetitive scans. Spectral selection on characteristic fingerprint regions was performed and subsequently subjected to hierarchical cluster analysis (HCA) and principal component analysis (PCA). In HCA, discrimination among samples was evident at around 77-86% similarity while in PCA, discrimination is presented at 80-93% total variation. Groupings and linkages based on their origin were established. A simple and direct method for identification and source determination of chemically processed pseudoephedrine compounds is demonstrated. This information can be a valuable intelligent tool for forensics and law enforcers to understand precursor material sources hence would be beneficial to disrupt the supply of the compound intended for clandestine operations.

Keywords: pseudoephedrine, clandestine drug laboratory, forensic intelligence

Abstrak

Rampasan sebatian pseudoephedrin daripada makmal dadah haram semakin meluas dilaporkan kerana sebatian tersebut telah disalahgunakan dalam menghasilkan dadah perangsang jenis amfetamin (ATS). Dalam makmal dadah haram berskala kecil, pil dekongestan komersial yang mengandungi pseudoephedrin sering ditemui sebagai bahan prekursor alternatif walaupun formulasinya telah diubahsuai untuk menghalang proses pengekstrakan pseudoephedrin dan seterusnya mencegah daripada penyalahgunaan sebatian tersebut. Kajian ini bertujuan untuk menyiasat kebolehlaksanaan untuk mendiskriminasi serbuk pseudoephedrin yang diekstrak berdasarkan kepada sumbernya. Dalam kajian ini, lima jenis tablet yang mengandungi pseudoephedrin dengan pelbagai saiz dan kekuatan telah diekstrak melalui kaedah pengekstrakan secara langsung dan asid-bes. Pengenalpastian sebatian pseudoephedrin yang diekstrak telah dilakukan melalui spektroskopi atenuasi pembalikan dan

transformasi Fourier (ATR-FTIR). Secara keseluruhan, 90 spektra telah diperolehi daripada 15 kelompok sampel pada enam imbasan berulang. Pengujian spektra pada kawasan tertentu telah dilakukan dan spektra daripada kawasan terpilih kemudiannya tertakluk kepada analisis kluster hierarki (HCA) dan analisis komponen prinsipal (PCA). Dalam HCA, diskriminasi di antara sampel telah dibuktikan pada sekitar 77-86% persamaan manakala di PCA, diskriminasi dibentangkan pada 80-93% jumlah variasi. Kajian ini menunjukkan penggunaan kaedah secara langsung dan mudah dalam pengenalpastian dan penentuan asal-usul sebatian pseudoephedrin yang telah diproses secara kimia. Maklumat yang diperolehi melalui kajian ini adalah sangat bernilai sebagai alat perisikan kepada penguasa perundangan dan forensik untuk memahami sumber bahan prekursor dengan itu dapat memberi manfaat dalam mengganggu bekalan pseudoephedrine untuk operasi haram.

Kata kunci: pseudoephedrine, makmal dadah haram, perisikan forensik

Introduction

Ephedrine and its enantiomer, pseudoephedrine ($C_{10}H_{15}NO$, mwt. 165.23g/mol), are sympathomimetic drugs regulated for medical use [1]. This medication is a known nasal decongestant readily obtained over the counter for temporary relief of stuffy nose and sinus pain/pressure caused by infection (such as the common cold, flu) or other breathing illness such as allergies, bronchitis and hay fever [1]. Pseudoephedrine salts are common active pharmaceutical ingredients (APIs) in numerous cold medications, commonly sold in a fixed-dose combination with additional active ingredients such as acetaminophen, antihistamines, guaifenesin, dextromethorphan and/or ibuprofen [2].

Either in bulk form or chemical preparations, pseudoephedrine is strictly regulated for use in chemical, medical and pharmaceutical industries. Legitimate use, however, is diverted by drug trafficking organizations which utilize the compound as the main precursor for clandestine drug production, therefore has captured forensic investigation interest. This diversion has contributed to the continual increase in the use and seizures of a pharmaceutical preparation containing ephedrine/pseudoephedrine worldwide. Despite being listed under 1988 United Nations Convention Against Illicit Traffic in Narcotic Drugs and Psychotropic Substances [3] which enforces strict regulation in import, export, consumer purchase restriction and behind the counter safe-keeping of pseudoephedrine powder or products, illicit diversion of these precursors is extremely difficult to control. The compound is clandestinely isolated and purified from retail goods to improve batch sizes, yield and purity [4].

Over 65 million tablets were reported to have been seized around the world between to have been seized 2009-2013 [3]. Significant increase within South-East Asia countries is reported. Malaysia is among the countries within this region that have reported significant cases in Malaysia includes ephedrine and pseudoephedrine seizure of 287 kg raw material form originating from India, the seizure of 112 kg in clandestine methamphetamine laboratory in the form of pharmaceutical preparations of unknown origin and 33 kg of ephedrine preparations were also seized in another illicit laboratory [3]. As a precursor, the compound is highly coveted to produce some amphetamine-type stimulants (ATS) through reduction and/or oxidation reactions [5].

Applications of Fourier transform infrared spectroscopy (FTIR) for quality control and identification of solids samples has been established for pharmaceutical sample characterization but has limited application for illicit drug quantitative study [6, 7]. Nonetheless, rapid, direct, non-destructive and on-site detection of chemical evidence is highly warranted in forensic investigation and enforcement intelligence purposes. Several studies [8, 9] have reported the use of FTIR as a conventional approach for comparison and classification of illicit drug substances. Several works have utilized attenuated total reflection Fourier transform infrared spectroscopy (ATR-FTIR) and diffuse reflectance near infrared spectroscopy (NIRS) for quantitative analysis of imitated samples of methylamphetamine and diacetylmorphine (heroin), respectively [10, 11].

Additionally, works on the analysis of real seized samples also were done by applying the vibrational techniques jointly with chemometric analysis. While structural information is most useful for compound identification, spectral fingerprint information could be utilized for determination of sample origin although it may pose challenges for polymorph or mixed samples. Challenges were also observed for non–homogenous mixtures samples. Although FTIR is a very useful technique for extracting structural information from pure substances, IR spectra of complex real matrices that contain a wide range of contaminant/adulterants cannot be satisfactorily analyzed only by simple

spectral matching and univariate method. Hence, the use of multivariate chemometric technique is necessary [12, 13].

Chemometric techniques such as principal component analysis (PCA) and hierarchical component analysis (HCA) are powerful tools for compressing multidimensional chemical signal and data into a few variables and presenting them graphically for ease of classification especially when the work involves with high throughput workload. This approach is widely accepted for samples of forensic importance [14]. Despite its potential, application of chemometric methods for the analysis of drugs precursors particularly pseudoephedrine is limited although similar technique is widely applied to other samples of forensic interest [15, 16]. One related work used NIRS to perform analysis of real seized samples, with the aim of discriminating ecstasy tablets [17] while another work determined heroin by using this same analytical technique with partial least-squares (PLS) regression [18].

From a forensic intelligence perspective, investigation on the origin of the precursor used in the manufacturing process is useful to disrupt the diversion of precursors thus may help drug law enforcement authorities obtain other information of strategic relevance. Hence, this work was done to investigate the feasibility of combining non-destructive ATR-FTIR coupled to HCA and PCA as a facile and reliable approach to distinguish among pseudoephedrine samples obtained from different marketed formulations and brands. Specifically, this work presents the benefits originating from both techniques is combined for forensic source determination of precursors.

Materials and Methods

Materials

Sodium hydroxide pellets (NaOH) and 37% hydrochloric acid (HCl) were purchased from Friedman Schmidt, Germany. Diethyl ether, ethanol and sodium sulphate anhydrous were purchased from System, Malaysia. Distilled water was obtained from an in-house water purification system.

Samples collection

Decongestant tablets containing pseudoephedrine active compounds at varying strengths and from various manufacturer were purchased from registered pharmacies around Kota Bharu area in Kelantan, Malaysia. Decongestant tablet encountered in pseudoephedrine hydrochloride or sulfate form is a controlled medication. Both types were collected for the discrimination study before and after pseudoephedrine extraction. For security purposes regarding the clandestine operation, the samples were anonymously coded (Table 1). Other declared APIs and excipients of these tablets include loratadine, povidone, triprolidine, paracetamol, polyethylene glycol, wax, talc powder, magnesium stearate, corn starch and calcium phosphate to name a few. Physical descriptions of the samples were noted.

Samples preparation

All samples under study underwent simple preparative means prior to analytical measurement. For each brand, the tablets were divided into three equal portions. Size reduction was done by crushing the tablets using pestle and mortar and the powdered form was homogenized using square and cone technique. The homogenized sample was divided to three portions. The first portion was intended for direct analysis while the second and third portions were subjected to simple extraction and acid-base extraction respectively.

Simple and direct extraction was carried out by dissolving the homogenous sample in ethanol, covered, agitated for 10 minutes and filtered by gravity filtration. The pseudoephedrine–containing solvent was evaporated and the resultant solid was collected for subsequent analysis.

Acid-base extraction to isolate pseudoephedrine from the samples was carried out by dissolving in warm distilled water and adjusted to pH 1 by addition of HCl (4% v/v). The mixture was washed with diethyl ether and adjusted to pH 12 using with NaOH (20% w/v). Diethyl ether (20 mL) was added into the basified mixture and shaken for 10 minutes. This process was repeated for three times. The collected diethyl ether was washed with distilled water and dried using sodium sulfate anhydrous. The pseudoephedrine–containing organic solvent was left to evaporate and the resultant solid was then collected.

Six replicates were performed for each sample, therefore in total, 90 samples were subjected to subsequent analysis. For ease of identification, each prepared sample were given a reference code as displayed in Table 1.

Table 1. Decongestant samples understudy with their respective reference code

Tablets (API contents)	Physical Description	Preparations		
		Direct	Simple Extraction	Acid Base Extraction
A ($C_{10}H_{15}NO.SO_4$, 120 mg)	White, round, wax-coated	AP	AD	AS
B ($C_{10}H_{15}NO.HCl$, 60 mg)	White, round, wax-coated	BP	BD	BS
C ($C_{10}H_{15}NO.SO_4$, 120 mg)	White, round, not coated	CP	CD	CS
D ($C_{10}H_{15}NO.SO_4$, 240 mg)	White, oval, wax-coated	DP	DD	DS
E ($C_{10}H_{15}NO.HCl$, 30 mg)	Yellow, orange, oval, not coated	EP	ED	ES

ATR-FTIR analysis

All samples were analyzed using Bruker® TENSOR 27 FTIR spectrometer (Bruker, Germany) equipped with attenuated total reflection (ATR) sampling interface composed of a single reflection of a diamond crystal. Approximately 1 mg sample was mounted on ATR stage for spectra acquisition in absorbance mode that covers the spectral range of between 4000 cm^{-1} to 600 cm^{-1} wavenumbers with a resolution of 2 cm^{-1} and by averaging 16 scans. A reference spectrum of air was taken every time before sample measurements were made to ensure zero interference. The ATR stage was carefully cleaned with acetone before and after each sample was analyzed. Data acquisition and baseline correction were performed with OPUS software version 7.0.122 (Bruker, Germany). Interpretation and the resultant spectra were visually compared and characterized prior to chemometric analysis.

Chemometric analyses

A total of 90 spectra were subjected to HCA and PCA analysis to classify the differences among the sample. HCA and PCA were performed using MINITAB® software version 16.2.3 statistical software (Minitab Incorporated, State College, PA, USA). Prior to chemometrics analyses, the spectral data of all the samples were prepared in the Microsoft® Excel (Version 10, Microsoft, Inc.) spreadsheet. In this work, several IR regions were tested, including the entire spectral region, the functional group region and the fingerprint region.

Results and Discussion

Comparing the spectroscopic features

In forensic analysis, the conventional approach of a direct visual examination of FTIR spectra is often employed to ascertain congruency or correlation between samples or groups of samples. In the examination, the spectrum of the questioned sample is either placed side by side to the FTIR spectrum of reference sample or superimposition by placing the FTIR spectrum of reference sample on top of the questioned sample or vice versa. Differences in term of the chemical composition of the samples are readily noticeable or interpreted by the differences in the pattern of the FTIR spectra of the questioned and reference samples.

A representative ATR-FTIR spectrum of powdered homogenized samples containing pseudoephedrine from different brands is shown in Figure 1. Based on the figure, it is obvious that the spectrum of each brand of the tablet could be clearly discriminated from each other. For pseudoephedrine hydrochloride B and E samples, their FTIR spectra showed the presence of a small doublet band at 2435 and 2477 cm^{-1} due to excess HCl in the samples [19] while pseudoephedrine sulphate samples showed the presence of very strong characteristic band near 1000 cm^{-1} for sulfate anions. Sample C and D were from the same manufacturer thus, they can be discriminated from A by referring to the characteristic band between 2800-300 cm^{-1} which suggest the presence of starch, magnesium stearate and cellulose in its formulation (which is absent in C and D) [19].

It was also noted that spectrum of sample B (that contained the least number of excipients) closely resembled the spectrum of *d*-pseudoephedrine hydrochloride standard. The prominent N-H peak in the region about 3200-3600 cm^{-1} was present in all the samples except for sample E tablet which was noticeable as the tablet only contain 30 mg of pseudoephedrine. Presence of colorants in sample E explains the complexity of its spectra. It is important to reiterate that the presence of other active ingredients and excipients of varying quantities and types in the tablet formulations such as loratadine, triprolidine, paracetamol, povidone, talc powder, wax, starch, magnesium stearate and microcrystalline cellulose have contributed to the difference in their FTIR spectra. This is especially evident in the fingerprint region. It is important to note that clandestine settings hardly used raw unprocessed cold tablets as precursors, nonetheless, this result is useful as a reference material for comparison to the processed precursors.

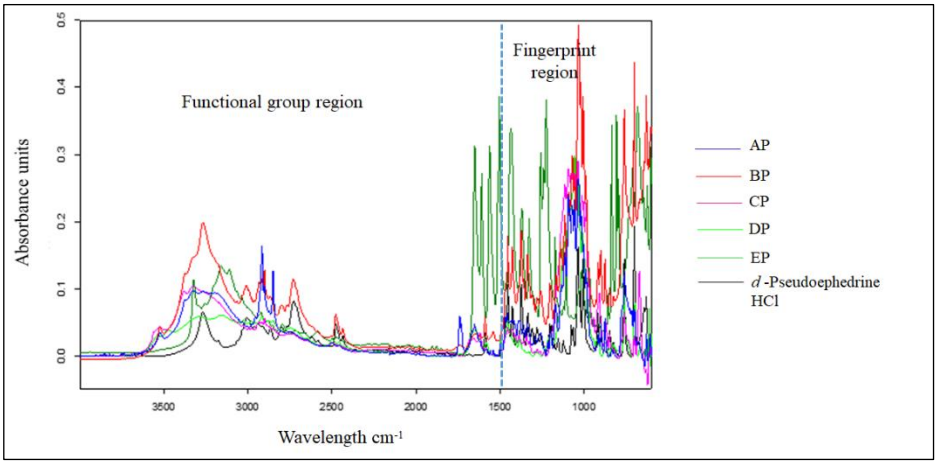


Figure 1. ATR-FTIR spectrum of powdered samples containing pseudoephedrine

The FTIR spectrum of the extracted samples via simple direct extraction method (Figure 2) revealed a slightly better spectra of most samples and the difference between pseudoephedrine sulfate and hydrochloride can be readily observed. Two regions of importance were found in the range of 2500-3000 cm^{-1}`that features the secondary amine hydrochloride and region 750-760 cm^{-1} that shows the characteristics of monoaromatic ring by simple direct extraction method [19]. Similar infrared spectrum was observed for sample B. This suggested that simple direct extraction would suffice to extract the precursor as sample B did not contain other APIs and has less excipient to begin with. Other samples, however, required a more extensive sample preparation to obtain a considerably 'cleaner' pseudoephedrine.

Figure 3 depicts the spectrum of extracted pseudoephedrine samples prepared by acid-based extraction method. Note that, the spectrum from pseudoephedrine acid-base extraction have improved and displayed identical spectra to freebase pseudoephedrine standard from the literature [21]. Similar signal characteristics were observed across all samples which suggested that the samples obtained were in a freebase form with a certain degree of purity. Therefore, results showed that acid-base solvent extraction technique could be used to successfully obtained good pseudoephedrine yield as it diminishes salts and isolates other APIs and excipients initial presence.

A broad O-H stretching at around 2700 cm^{-1} to 3320 cm^{-1} was noticeable but this band was not clearly seen because of overlapping with N-H stretching band within the same region. Perhaps, the most distinctive band was around 3317 cm^{-1}, which was attributed to the N-H stretching [19, 20]. The region which was associated to C-H stretching band at around 2950-2850 cm^{-1} was also evident. The peak attributable to the aromatic =CH band was detected within the region of 3100-3000 cm^{-1}[19, 20].

In fingerprint region, the characteristic peaks for freebase pseudoephedrine were distributed mainly at around 702 cm^{-1} and 760 cm^{-1} (torsion vibration of benzene rings), 1022 cm^{-1} (C-C stretching vibration), 1375 cm^{-1} (C-H bend

vibration), 1428 cm^{-1} (C-H bend vibration of CH^3) and 1453 cm^{-1} (O-H bend vibration) [21]. Bands at 1071, 1026 and 729 cm^{-1} represent mono-substituted benzene stretching and the last one an out-of-plane bending [21].

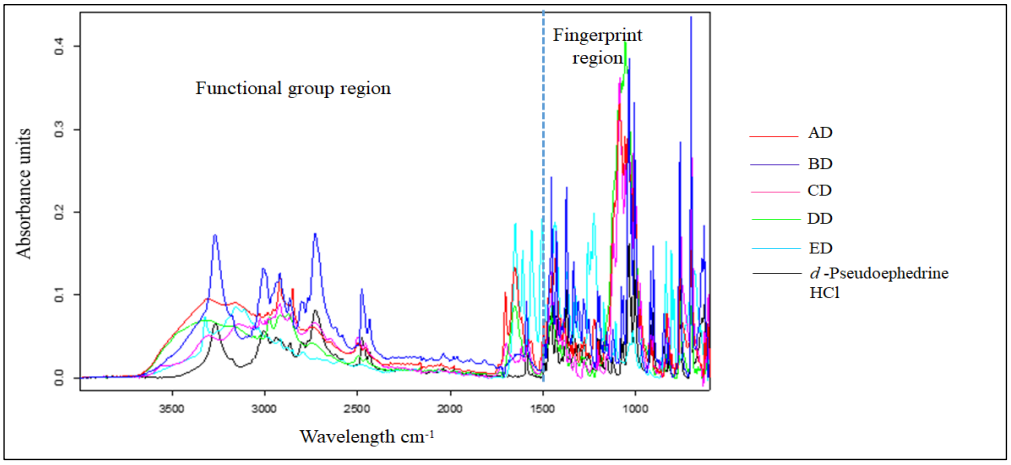


Figure 2. ATR-FTIR spectrum of the extracted sample *via* direct extraction method

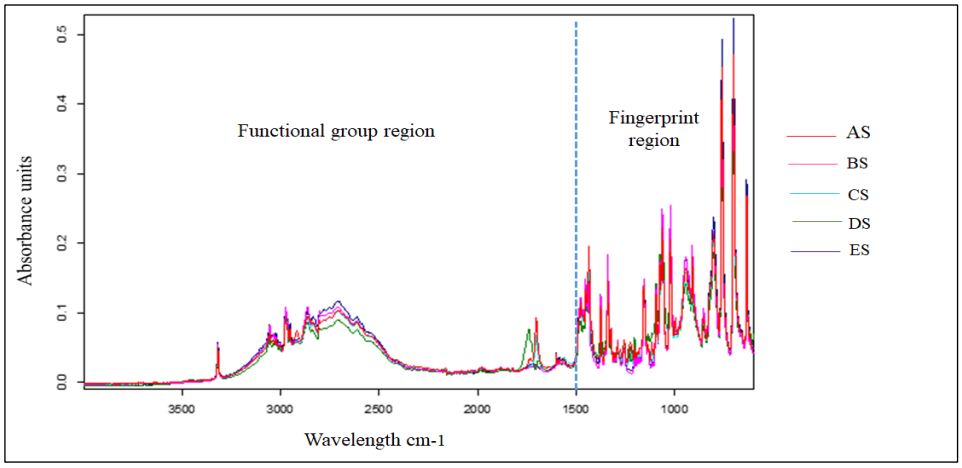


Figure 3. ATR-FTIR spectrum of the extracted sample *via* solvent extraction method

Statistical analysis

Direct visual examination for linking samples according to their origin using spectral pattern is difficult to carry out especially when dealing with a high number of samples having similar spectral pattern. Consequently, a discussion on the classification of sample from common origin using chemometrics approach is necessary. ATR-FTIR spectral data set showed in previous section (Figures 1-3) was subjected to HCA and PCA statistical package to reveal graphical linkages within and between samples for origin determination [22, 23]. The benefit obtained by performing HCA together with PCA is that they can reveal which clustering techniques could produce the most meaningful outcomes for a given dataset.

Hierarchical cluster analysis

Single linkage technique was utilized to link the clusters and Euclidean distance as the proximity measure between samples because they are among the most common algorithms used for clustering purpose [24, 25]. The resultant HCA dendrogram for each sample preparation type is displayed (Figures 4-6). For the powdered samples, HCA dendrogram in Figure 4 was unable to clearly distinguish the samples according to their brands. The formation of five clusters at around 83% of similarity revealed misclassification among all samples except for sample E. HCA dendrogram of the samples extracted using the simple direct extraction method shown in Figure 5 displays better linkages of samples from the same brands. Except for two misclassifications between sample D and A, other brands were clustered accordingly at approximately 86% similarity level. Meanwhile, for samples extracted using an acid-base method, five clusters were evident at approximately 77% similarity level. Only sample A and D were linked accordingly while sample B,C and E did not reveal any meaningful linkages. The first cluster (represented by the blue line) comprises of samples from a different brand while the other cluster (represented by grey, green and purple lines) were clustered separately as one group.

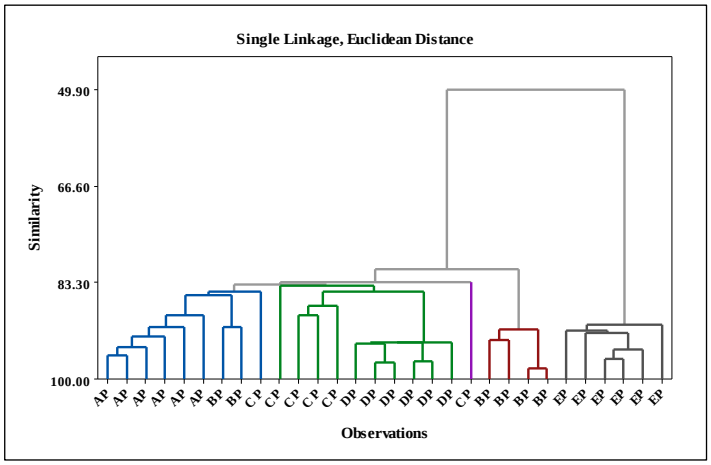


Figure 4. HCA dendrogram of the homogenized powdered samples

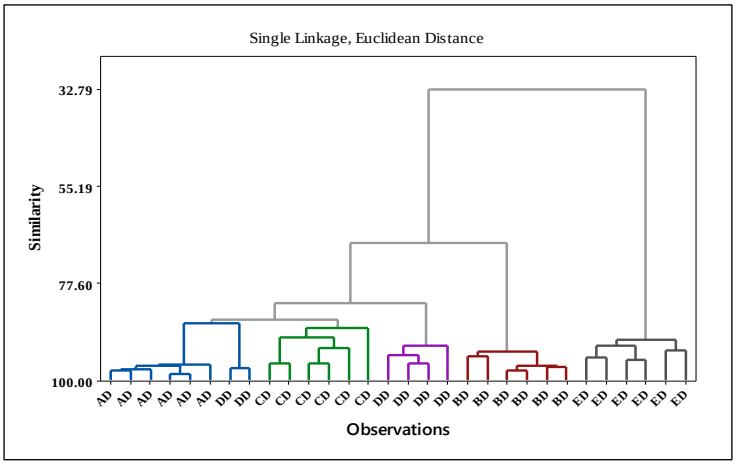


Figure 5. HCA dendrogram of the samples extracted by simple direct extraction method

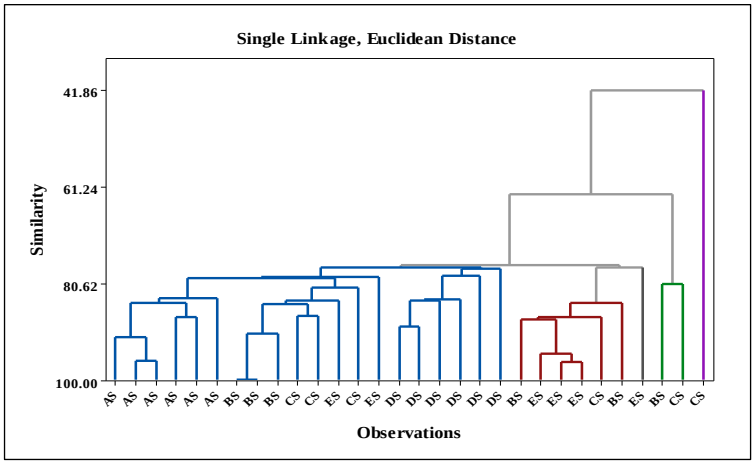


Figure 6. HCA dendrogram of samples extracted by acid-base extraction method

Principal component analysis

PCA was performed using correlation matrix and the clusters in the score plots were examined to reflect the actual information [24, 25]. Figure 7 shows three dimensional (3D) PCA score plot of the powdered samples. The first three PCs used to construct the score plot account for 92.5% of total variation (PC1 = 58.5%, PC2 = 19.9% and PC3 = 14.1%) in the dataset which signifies that PCA captured relevant information within the raw dataset. Contrary to the HCA result, all samples from different origin were well separated from each other in PCA. Despite having similar pseudoephedrine hydrochloride contents, discrimination between sample AP and AC from a different manufacturer is evident. Different pharmaceutical formulation unique to each tablet undoubtedly contribute significantly to the clustering of these samples [13].

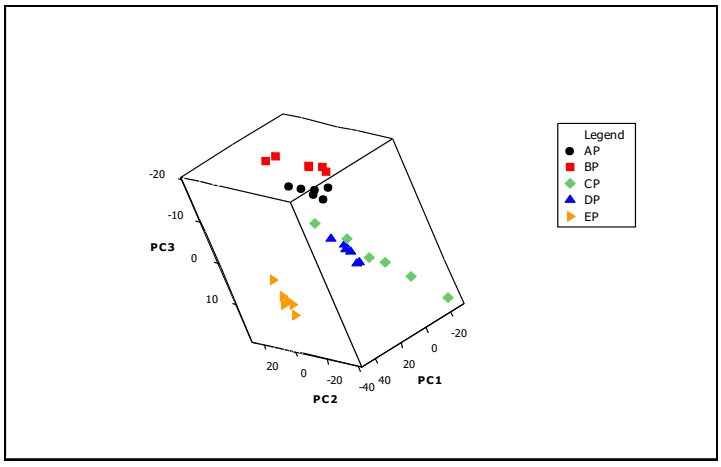


Figure 7. Three dimensional (3D) PCA scores plot for the powdered samples

When the samples were dissolved and filtered to obtain extract with considerably better pseudoephedrine purity, the clustering of the samples has improved tremendously. Dissolution and extraction using ethanol could have removed a substantial amount of bulking agents such as starch, waxes, binders and other excipients reducing redundant information across all samples, hence improving the PCA outcome. The corresponding 3D PCA score plot as shown

in Figure 8 represents 92.9% of the total variation (PC1 = 59.4%, PC2 = 24.6% and PC3 = 8.9%) in the dataset. This result has markedly improved in comparison to HCA of a similar dataset as all the samples are successfully grouped according to their brand without misclassification. Additionally, most of the clusters show tight clustering of the samples. Perhaps the presence of other existing APIs that were also soluble in ethanol could have contributed to definite discrimination of the samples. Loratadine, triprolidine, paracetamol or combinations were known to be present in sample A, B, C, D and E.

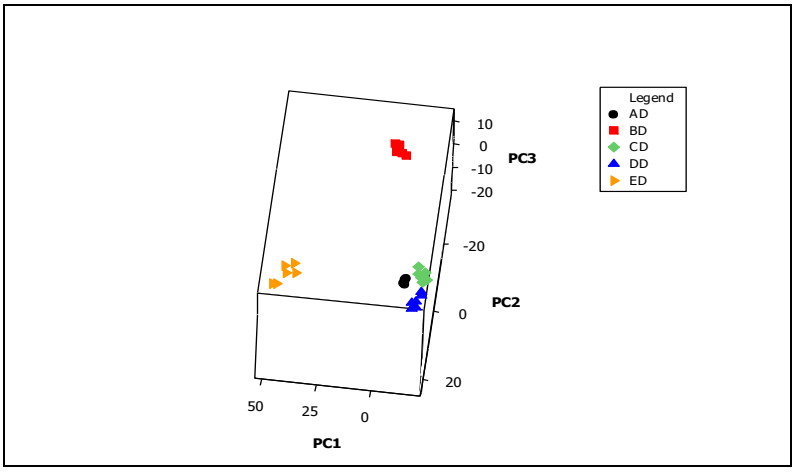


Figure 8. Three dimensional (3D) PCA scores plot for samples extracted by direct extraction method

Infield scenario seized pseudoephedrine from clandestine laboratory is usually of high purity which may suggest the precursor was obtained either from the commercial supplier or it might have undergone extensive chemical purification process such as acid-base extraction from originally innocent sources. The latter is the situation commonly encountered in the kitchen scale clandestine laboratory. PCA analysis for samples extracted by acid-base extraction method (Figure 9) provided a model that accounted for 84.7% of the total data variance (PC1 = 52%, PC2 = 19.3% and PC3 = 13.4%). Sample DS and AS formed two homogenous groups, however sample BS, CS and ES are closely convoluted in one area. To probe whether or not the samples in the convoluted group may be discriminated, further PC analysis was conducted involving only the three samples. The resultant 3D PCA score plot for the convoluted group is displayed in Figure 10.

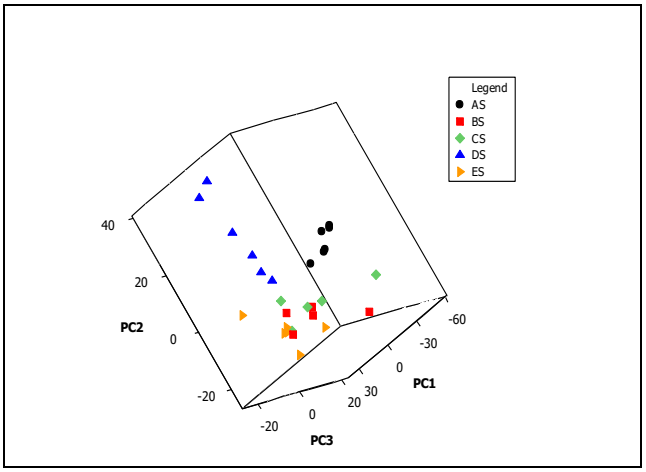


Figure 9. Three dimensional (3D) PCA score plot for samples extracted solvent extraction method

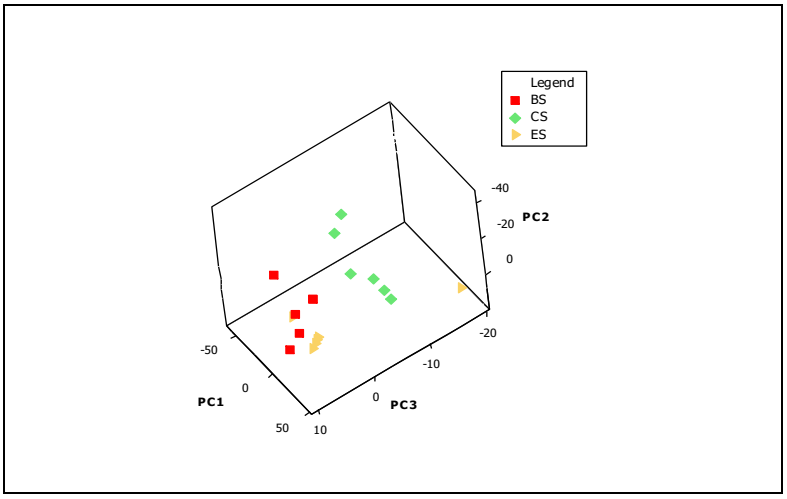


Figure 10. Three-dimensional (3D) score plot for the previously convoluted group comprising of BS, CS and ES samples

Combination of PC1, PC2 and PC3 described 92.4% of the total variation (PC1 = 69.9%, PC2 = 16.5.6% and PC3 = 6.0%) in the dataset. Predominantly, the samples from the three different brands can be separated into three homogenous groups despite the misclassification of one of the ES samples into the BS cluster. The detachment of one ES sample at the far right-hand side of the score plot from the ES cluster confirmed that the sample could be an outlier. Further scrutinization on the ES samples spectrum (Figure 11) confirmed that the sample is in fact an outlier due to sharp bending at around 1400 nm^{-1} and 1238 nm^{-1}.

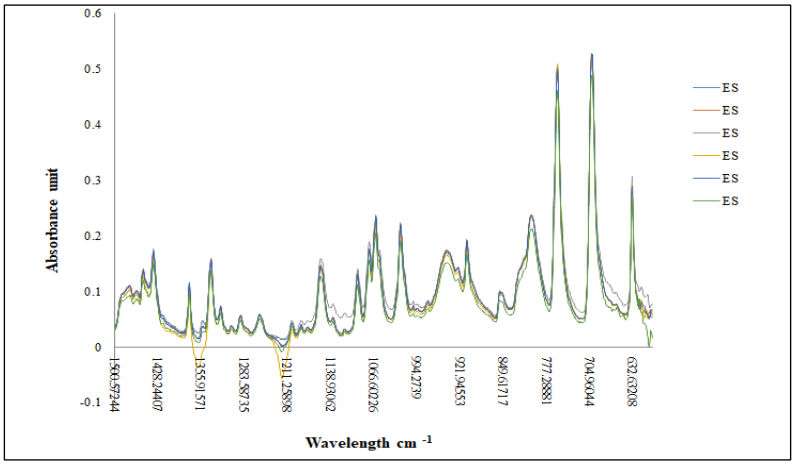


Figure 11. FTIR spectrum of the ES samples. The outlier which is represented by the purple line corresponds to ES sample detached from the ES cluster in the score plot

Conclusion

Clandestine operators can readily extract pseudoephedrine from over-the-counter cold medication tablet either by simple direct extraction or more complicated chemical purification techniques to use as a precursor for illicit drugs. Acid-base extraction can produce a precursor of considerably high purity when compared to pure standards which would make source determination for forensic intelligence challenging. The applicability of the ATR-FTIR

techniques to directly identify suspicious compound or sample is convenient. Interestingly, its use for origin or source profiling by combinatory chemometrics analysis such as PCA and HCA have enabled the extraction of relevant spectral data to give a meaningful association between and among the samples. Considering that these promising results were obtained using raw or untreated FTIR data, work using treated data is actively undergoing. Nonetheless, the output from this work has shown that the ATR-FTIR in combination with chemometrics techniques for chemically processed pseudoephedrine was able to provide a simple, rapid and more importantly non-destructive for linking precursor to their sources of origin.

Acknowledgement

The authors gratefully acknowledged Universiti Sains Malaysia (USM) for funding this study under the Bridging grant scheme (304.PPSK.6316202) and Ministry of Higher Education Malaysia (MOHE) for the MyBrain15 scholarship awarded to Ms. Ainol Hayah Ahmad Nadzri and also technical support provided by the Analytical Laboratory (MAL) staff of the School of Health Sciences, USM Kubang Kerian, Kelantan.

References

1. Bryan, J. (2012). Pseudoephedrine is a though product to challenge as a nasal decongestant. https://www.pharmaceutical-journal.com. [Access online 01 July 2019].
2. Silverman, B. (2018). Method and formulation for cold treatment in adults and children with increase safety. *US Patent App.* 10(046): 052.
3. International Narcotic Control Board (2015). Precursors and chemicals frequently used in the illicit manufacture of narcotic drugs and psychotropic substances. United Nation, New York: pp. 1-120.
4. Brzeczko, A. W., Leech, R. and Stark, J. G. (2013). The advent of a new pseudoephedrine product to combat methamphetamine abuse. *The American Journal of Drug and Alcohol Abuse*, 39(5): 284-290.
5. Maheux, C. R. and Copeland, C. R. (2010). Characterization of three methcathinone analogs: 4 methylmethcathinone, methylone, and bk-MBDB. *Microgram Journal*, 7(2): 42-49.
6. Roggo, Y., Chalus, P., Maurer, L., Lema-Martinez, C., Edmond, A. and Jent, N. (2007). A review of infrared spectroscopy and chemometrics in pharmaceutical technologies. *Journal of Pharmaceutical and Biomedical Analysis*, 44(3): 683-700.
7. Deisingh, A. K. (2005). Pharmaceutical counterfeiting. *Analyst*, 130(1): 271-279.
8. Hodges, C. M. and Akhavan, J. (1990). The use of Fourier transform Raman spectroscopy in the forensic identification of illicit drugs and explosives. *Spectrocimica Act*, 46(2): 303-307.
9. Baran, O. (2005). Determination of narcotic and psychotropic substance by using infrared spectroscopy. Thesis of Master of Science, Middle East Technical University, Turkey.
10. Goh, C. Y., Van Bronswijk, W. and Priddis, C. (2008). Rapid non-destructive on-site screening of methylamphetamine seizures by attenuated total reflection Fourier transform infrared spectroscopy. *Applied Spectroscopic*, 62(6): 640-648.
11. Melucci, D., Monti, D., D'Elia, M. and Luciano, G. (2012). Rapid in situ repeatable analysis of drugs in powder form using reflectance near-infrared spectroscopy and multivariate calibration. *Journal of Forensic Science*, 57(1): 86-92.
12. Rodrigues, N. V. S., Cardoso, E. M., Andrade, M. V. O., Donnici, C. L. and Sena, M. M. (2013). Analysis of seized cocaine samples by using chemometric method and FTIR spectroscopy. *Journal of the Brazilian Chemical Society*, 24(3): 507-517.
13. Pereira, L. S. A., Lisboa, F. L. C., Neto, J. C., Valladao, F. N. and Sena, M. M. (2017). Direct classification of new psychoactive substances in seized blotter papers by ATR-FTIR and multivariate discriminant analysis. *Microchemical Journal*, 133(1): 96-103.
14. Calvo, N. L., Kaufman, T. S. and Maggio, R. M. (2015). A PCA-based chemometrics-assisted ATR-FTIR approach for the classification of polymorphs of cimetidine: Application to physical mixtures and tablets. *Journal of Pharmaceutical and Biomedical Analysis*, 107(1): 419-425.
15. Mohamad Asri, M. N., Mat Desa, W. N. S. and Ismail, D. (2017). Raman spectroscopy of ballpoint-pen inks using chemometric techniques. *Australian Journal of Forensic Science*, 49(2): 175-185.
16. Ismail, D., Austada, Z. and Mat Desa, W. N. S. (2014). Ultra-violet and visible (UV-VIS) spectroscopy and chemometrics techniques for forensic analysis of ballpoint pen inks: A preliminary study. *Malaysian Journal of Forensic Science*, 5(1): 47-52.

17. Sondermann, N. and Kovar, K. A. (1999). Screening experiments of ecstasy street samples using near-infrared spectroscopy. *Forensic Science International*, 106(3): 147-156.
18. Moros, J., Galipienso, N., Vilches, R., Garrigues, M. and De La Guardia, S. (2008). Nondestructive direct determination of heroin in seized illicit street drugs by diffuse reflectance near-infrared spectroscopy. *Analytical Chemistry*, 80(19): 7257-7265.
19. Graf, W. F., Pearson, J. R., Appadoo, D. R.T., Robertson, E. G. and Ennis, C. (2020). The prediction of far-infrared spectra for molecular crystals of forensic interest- Phenylethylamine, ephedrine and pseudoephedrine. *Forensic Chemistry*, 17(1): 1-11.
20. Formula, C. and Weight, M. (2005). Scientific working group for the analysis of seized drugs (SWGDRUG. Access from http://forensics.org.my/pdf/fssmVol.6No.1/Article 04.pdf. [Access online 02 July 19].
21. Miao, L., Liu, Y., Li, H., Qi, Y. and Lu, F. (2017). Two-dimensional correlation infrared spectroscopy applied to the identification of ephedrine and pseudoephedrine in illegally adulterated slimming herbal products. *Drug Testing and Analysis*, 9 (2): 221-229.
22. Hughes, J., Ayoko, G., Collett, S. and Golding, G. (2013). Rapid quantification of methamphetamine: Using attenuated total reflectance Fourier transform infrared spectroscopy (ATR-FTIR) and Chemometrics. *PLoS ONE*, 8(7): e69609.
23. Nic Daeid, N. and Waddell, R. J. H. (2005). The analytical and chemometrics procedures used to profile illicit drug seizures. *Talanta* 67(2): 280-285.
24. Mat Desa, W. N. S., Nic Daeid, N., Dzulkiflee I. and Savage, K. (2020). Application of unsupervised chemometric analysis and self-organizing feature map (SOFM) for the classification of lighter fuels. *Analytical Chemistry* 82(1): 6395-6640.
25. Mat Desa, W. N. S., Ismail, D. and Nic Daeid, N. (2011). Classification and source determination of medium petroleum distillates by chemometric and artificial neural networks: A self-organizing feature approach. *Analytical Chemistry* 83(2): 7745-7754.

Malaysian Journal of Analytical Sciences (MJAS)
Published by Malaysian Analytical Sciences Society

SCREENING OF NATURAL COLOURS FROM VARIOUS NATURAL RESOURCES AS POTENTIAL REUSABLE VISUAL INDICATORS FOR MONITORING FOOD FRESHNESS

(Saringan Pewarna Semula Jadi Daripada Pelbagai Sumber Semula Jadi Sebagai Indikator Visual Guna-Semula Untuk Pemantauan Kesegaran Makanan)

Mohd. Zulkhairi Abdul Rahim[1]*, Nurdiyana Husin[2], Mohd. Azizan Mohd Noor[2], Zaida Rahayu Yet[1], Mohammad Rashedi Ismail-Fitry[3]

[1]*Section of Technical Foundation*
[2]*Section of Bioengineering Technology*
Universiti Kuala Lumpur Malaysian Institute of Chemical & Bioengineering Technology, Lot 1988, Bandar Vendor, 78000 Alor Gajah, Malacca, Malaysia
[3]*Faculty of Science and Food Technology,*
Universiti Putra Malaysia, Serdang, 43400 Seri Kembangan, Selangor, Malaysia

**Corresponding author: mohd.zulkhairi@unikl.edu.my*

Received: 20 November 2019; Accepted: 20 March 2020

Abstract

Natural colours have emerged as an alternative source of colours due to the high demand and public sensitivity towards the risk of using synthetic colours. Natural colours are non-hazardous and made from renewable resources, in which the supply is abundant and not harmful to the environment. This study aims to screen naturally-derived colours from butterfly pea, red cabbage, turmeric, and beetroot as visual indicators in monitoring food freshness. The study was carried out in three stages: the extraction of natural colours, the absorption of natural colours on the indicator paper, and the application of visual indicators on the real sample. The results showed that all visual indicators changed their colours towards the spoilage of meat in 24-h monitoring at room temperature. The most significant colour change was observed on the natural colour from butterfly pea compared to other natural resources. HS-SPME-GC-FID analysis confirmed the presence of methylamine as the main volatile compound from the spoiled meat, which contributed to the colour change of the visual indicators. FTIR analysis of useable indicators indicated the presence of amine compound (N-H) that aligned with the result of HS-SPME-GC-FID. The used visual indicators returned to their initial colours and characteristics, which provide the possibility for the fabrication of reusable visual indicators in the future.

Keywords: natural colour, visual indicator, meat freshness

Abstrak

Penggunaan warna semula jadi telah berkembang pesat disebabkan kesedaran pengguna terhadap bahaya pewarna sintetik. Pewarna semula jadi tidak berbahaya dan boleh diperbaharui selain sumber yang mudah didapati serta tidak membahayakan alam sekitar. Kajian ini bertujuan menyaring pewarna semula jadi daripada pelbagai sumber seperti bunga telang, kubis merah, kunyit, dan ubi bit untuk digunakan sebagai indikator visual bagi mengukur kesegaran makanan. Kajian dijalankan dalam tiga peringkat: pengekstrakan pewarna semula jadi, penyerapan pewarna semula jadi ke atas kertas penunjuk, dan penggunaan indikator visual ke atas sampel sebenar. Keputusan kajian menunjukkan kesemua indikator visual berubah warna apabila terdedah kepada daging yang rosak ketika dianalisis pada suhu bilik selama 24 jam. Perubahan warna indikator visual yang paling jelas adalah pada indikator visual yang menggunakan pewarna semula jadi bunga telang. Analisis HS-SPME-GC-FID yang dijalankan menunjukkan kehadiran metilamina yang terhasil ketika proses kerosakan daging. Metilamina menjadi penyebab utama terhadap perubahan warna indikator visual. Analisis FTIR ke atas indikator visual yang baru selesai digunakan

menunjukkan kehadiran sebatian amina yang mana selari dengan keputusan analisis HS-SPME-GC-FID. Indikator visual yang telah digunakan menunjukkan perubahan warna kepada warna asal membuktikan kemungkinan fabrikasi indikator visual secara guna-semula pada masa akan datang.

Kata kunci: pewarna semula jadi, indikator visual, kesegaran daging

Introduction

Nowadays, natural colour is important to enhance consumer acceptability as synthetic colour may cause serious health problems and hazardous effect. Natural colours are usually extracted from flowers, leaves, fruits and vegetables, seeds, insects, or algae. A few commonly used natural colours are annatto (seed), turmeric, beet juice (root), bell pepper, red cabbage (vegetable), spinach (leaf), and many more [1]. Other natural foods, such as carrots, pomegranates, grapes, mulberries, spinach, beets, parsley, and flowers are also used as food colouring agents.

The principal natural colours, most of which are used as additives, are carotenoids that give yellow to red colours, green pigment chlorophyll, and also anthocyanins, the pigments responsible for the shiny orange, pink, red, violet, and blue colours in flowers and fruits of some plants. Anthocyanins can be found in different chemical forms depending on the pH of the solution [2]. Beetroot pigments are collectively known as betalains and available in two classes: red betacyanins and yellow betaxanthins, in which both are very water soluble. Over thousands of years, natural colours (saffron, turmeric, and paprika) are used as traditional food colourants. Turmeric is a popular spice and until today it is still one of the principal ingredients in curry powder [1]. The principal colour present in the rhizome of the turmeric plant is curcumin, which is responsible for the yellow colour.

The incorporation of colours as changing indicators or sensing elements into food packaging materials is a new method to alert consumers to the conditions inside a food package. These indicators can facilitate the identification of products that are progressing towards spoilage or that have lost their quality and wholesomeness.

The quality and safety of a food product can be affected at various points during its distribution and transportation. Thus, any mishandling of the food product can have a significant impact on its safety and overall quality. For many consumers, the freshness and quality of a food is determined by the “use by” or “sell by” date that is printed on the package. The insertion of these indicators into packaged food products can help food regulatory bodies to identify the freshness of food products that are unsafe for consumption. Consumers are also beneficiaries of this technology since they will be alerted to the presence of an unsafe product.

Intelligent packaging systems can be helpful to communicate with consumers and provide information about the conditions of the food through a direct visual change. However, the usefulness of the device can be limited if the method of intelligent packaging used to communicate with consumers is not easily recognised. Time-temperature indicators, gas leakage indicators, toxin indicators, and spoilage detectors/freshness indicators are different types of intelligent packaging systems.

One method of communication that seems to work well with consumers is a change in colour in response to a change within the product itself. This change in colour should be sufficiently intense that it is easily recognised by consumers, processors, or government regulatory personnel.

In this study, naturally-derived colours from butterfly pea, red cabbage, turmeric, and beetroot were applied as the visual indicators in monitoring food freshness. Delphinidin, the major blue pigment extracted from butterfly pea, cyanidin from red cabbage, curcumin from turmeric, and betanin from beetroot were extracted using ultrasonic method. The natural colours were subjected for the screening study of the possibility for the fabrication of reusable visual indicators, which are promisingly indicating the freshness of a beef sample. This study used the pH of beef as the indication of freshness, in which the beef is considered fresh at pH 5.8 to 6.2. At pH above 6.5, the beef is considered spoiled, and this pH is a favourable growth condition for microorganisms to decompose the beef [3, 4].

Materials and Methods

Preparation of natural sources

Natural sources (i.e., butterfly pea, red cabbage, turmeric, and beetroot) were dried in an oven at 40 °C for 24 hours. Then, the sources were ground using a grinder and sieved. Powdered natural sources were stored in an air-tight container and kept in desiccators prior to the analysis [5].

Extraction of natural colours using ultrasonic method

10 g of powdered samples was added to 150 mL of water and placed in a beaker. The beaker was placed in an ultrasonic bath and sonicated for 30 minutes at 27–30 MHz and 160 V. After sonication, the contents of the beaker were filtered through a filter cloth to remove solid materials. Then, the filtered extract was centrifuged at 2,000 rpm for 10 minutes and at 4 °C [6]. The extract obtained was stored in a chiller at 4 °C for further analysis.

Analysis of pH on natural colour extracts

1 ml of each extract was added to 5 ml of buffer solutions of pH 1 to 14, and the colour change was observed [7] using a tintometer (Lovibond PFX880) to determine the CIE colour space coordinates, i.e. colour visible to the human eye, as specified by the International Commission on Illumination (Commission Internationale d'Eclairage, CIE) using L*, a*, and b* values. The values of L*, a*, and b* represent lightness, redness, and yellowness, respectively.

Ultraviolet-visible spectra measurement

The absorption spectra of the natural colours were studied using an ultraviolet-visible (UV-Vis) spectrophotometer (Varioskan LUX, ThermoFisher Scientific) for determining the wavelength and absorbance responsible for the difference in the colour of indicator solutions.

Fabrication of anthocyanin-based visual indicator

A visual indicator was made of filter paper (Whatman 42) with the dimension of 4.2 cm × 1.5 cm. The extracts from natural resources were immobilised on the indicator paper using spin-coated method. Seven strips of indicator paper were centrifuged with 15 mL of extracts at 3,000 rpm for 15 minutes and at 4 °C [8]. Then, the indicator was dried using a hair dryer for 15 minutes.

Fourier transform infrared analysis

The Fourier transform infrared (FTIR) spectra of the extracts were determined using the attenuated total reflection (ATR) method [6].

Preparation of beef sample

The semimembranosus muscle was taken from the top (inside) round of a cow carcass with insignificant fat content. The round portion obtained from the carcass was immediately kept in a cooler box and transported to the laboratory. Each portion obtained from the carcass was divided into 20 g of beef sample and placed in a sealed container.

Response of anthocyanin visual indicators towards beef

The visual indicators were placed inside the container of the beef sample, where the indicators were in direct contact with the atmosphere inside the container and then stored at room temperature (25 ± 1°C) for 24 hours. This method was used to make sure that there would be no effect from external atmospheric conditions. For the control, the visual indicator was placed inside a container without the beef sample. The distinct colour change of the indicator from the initial to the final stage was used as the measurable response of change. The colour changes on the indicator were checked using a hand-held colorimeter (Chroma Meter CR-10, Minolta Inc., Japan) to determine the CIE colour space coordinates (L*, a*, b*, and ΔE*). Here, ΔE* (i.e., colour change) was used as the indicator response for the colour changes of the visual indicator (in arbitrary units) that was calculated as [(a*2+b*2)0.5] [9].

Extraction of volatile compounds by headspace solid-phase microextraction-gas chromatography-flame ionisation detector

The volatile extraction by HS-SPME-GC-FID was carried out according to the modified method of Ma [10]. The volatile components in the beef sample were adsorbed onto a 50/30 μm layer of divinylbenzene-carboxen-

polydimethylsiloxane (Supelco Co., Bellefonte, USA) fibre that was exposed to the sample headspace for 30 minutes. After extraction, the SPME device was removed from the headspace vial and inserted directly into the injection port of the GC-FID. The SPME fibre was immediately thermally desorbed for 3 minutes at 250 °C in the SPME specific liner of the injector port of GC-FID and a HP-Innowax column. The oven temperature was held for 2 minutes at 40 °C, increased to 250 °C at 5°C/min, and held again for 3 minutes at this temperature, with nitrogen as the carrier gas.

Measurement of pH on beef sample

The pH of the beef sample was measured using a potable pH meter (LAQUAtwin, Horiba) with a flat sensor as the electrode. The beef sample was placed on the measuring electrode and the pH values were recorded.

Statistical analysis

The results from multiple samples were reported using analysis of variance (ANOVA) from Minitab software by means of the average values ± standard deviation. The data were analysed and the differences among mean values were processed by the Duncan's multiple range tests. The significance was defined at $p < 0.05$.

Results and Discussion

Extraction of natural colours

Figure 1 shows the colours of *Clitoria ternatea* (CT), *Brassica oleracea* (BO), *Curcuma longa* (CL), and *Beta vulgaris* (BV) extracted using water. The pH of the natural colours was observed at pH 5.93, 6.40, 7.55, and 4.85, respectively. The colour space value for each extract is tabulated in Table 1. The colour values of CT, BO, CL, and BV are different as shown by the L*, a*, and b* values. BV extract was the lightest among all extracts whereas CT extract was the most concentrated extract, as indicated by the L* value. The L* coordinate indicates the darkness or lightness of a colour and ranges from black (0) to white (100). The coordinates a* and b* indicate colour directions: +a* is the red direction, -a* is the green direction, +b* is the yellow direction, and -b* is the blue direction. Based on the values of a* and b*, the colours observed were purple, light purple, yellow, and light red for CT, BO, CL, and BV, respectively.

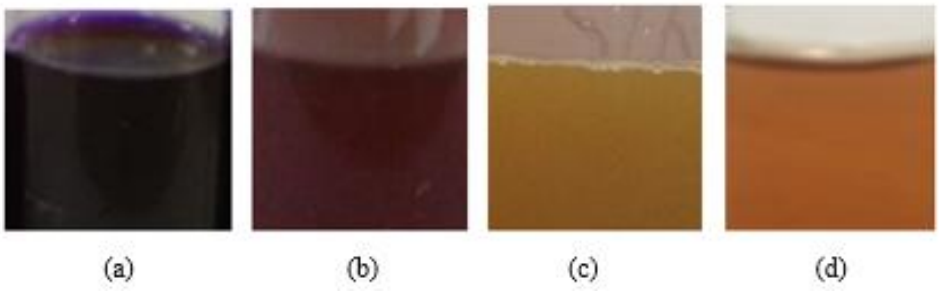


Figure 1. Natural colours for (a) CT, (b) BO, (c) CL, and (d) BV

Table 1. Values of colour space coordinates of the extracts

Extracts	Colour Value		
	L*	a*	b*
C. ternatea	17.78 ± 0.16	32.15 ± 0.16	-25.53 ± 0.11
B. oleracea	28.14 ± 0.01	42.58 ± 0.04	46.11 ± 0.13
C. longa	41.57 ± 1.44	13.82 ± 0.35	50.88 ± 0.28
B. vulgaris	43.13 ± 0.03	50.80 ± 0.06	40.12 ± 0.16

Characterisation study: pH analysis

Figure 2 shows the colour of CT, BO, CL, and BV extracts at distinct pH. The extracts from CT and BO showed a very significant colour change over the pH range. The trend of colour change was similar for CT and BO extracts; at pH 1–2, the colour was red, which then shifted to purple at pH 3–6, followed by blue at pH 7, turned to green at pH 8–10, and above pH 11, the colour changed to yellow. Specifically, for the CL extract, the colour maintained in yellow at acidotic pH and became brown at a higher degree of alkalinity. On the other hand, the BV extract showed colour change from brown at low pH and gradually turned to light yellow at alkaline pH. This pH analysis demonstrated the possibility of the extracts to respond towards beef freshness, which require detection towards pH changes.

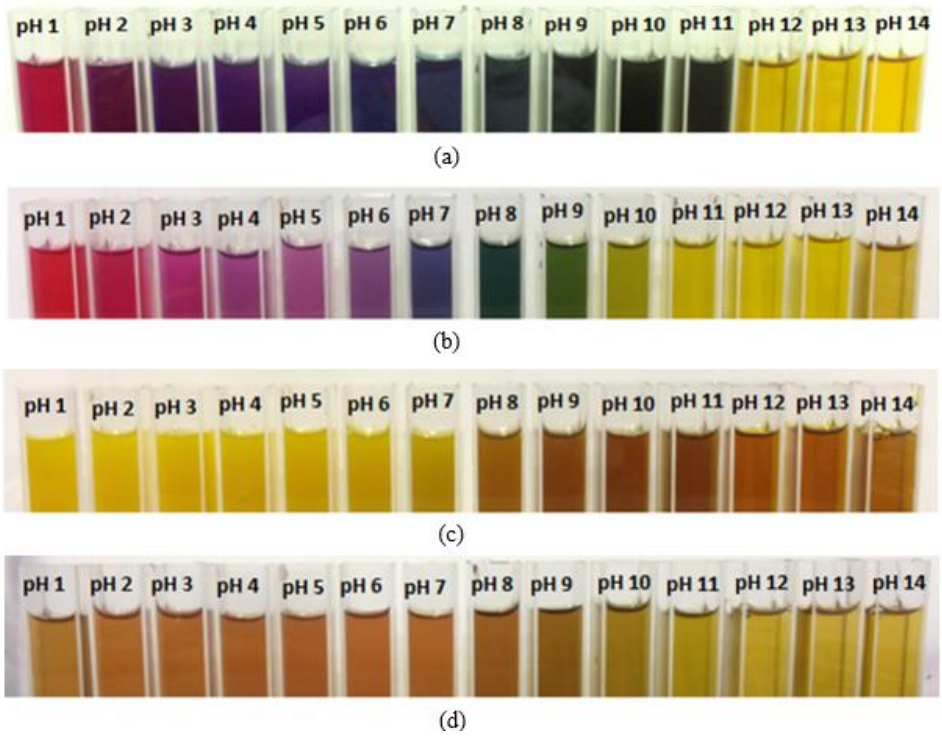


Figure 2. Natural colours of (a) CT, (b) BO, (c) CL, and (d) BV at different pH values

Characterisation study: UV-Vis analysis

The UV-Vis spectra of natural colours from CT, BO, CL, and BV are shown in Figure 3. Different levels of absorption are shown along the spectrum of wavelengths. The maximum wavelengths at the maximum absorbance (λ_{max}) obtained were at 568, 540, 419, and 540 nm for CT, BO, CL, and BV, respectively. The lambda maximum refers to the wavelength along the absorption spectrum where the substance has its strongest photon absorption. The wavelength at which the absorbance is highest is the wavelength in which the solution is most sensitive to concentration changes. The absorbance measurements are made at the lambda maximum because this is where the standard calibration is linear and where the element is identified.

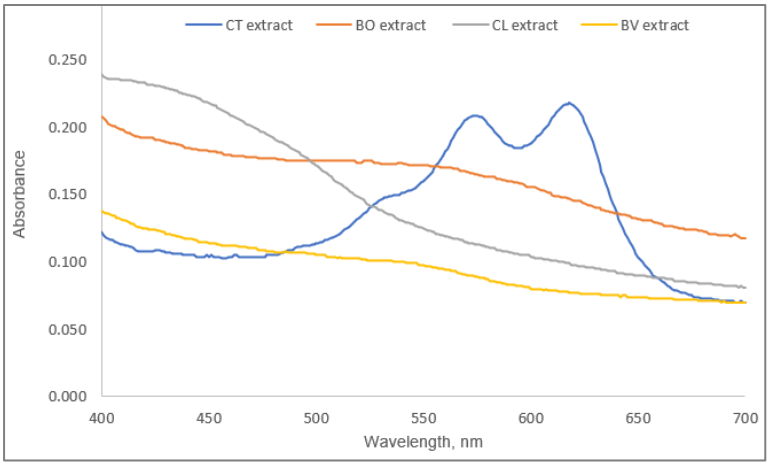
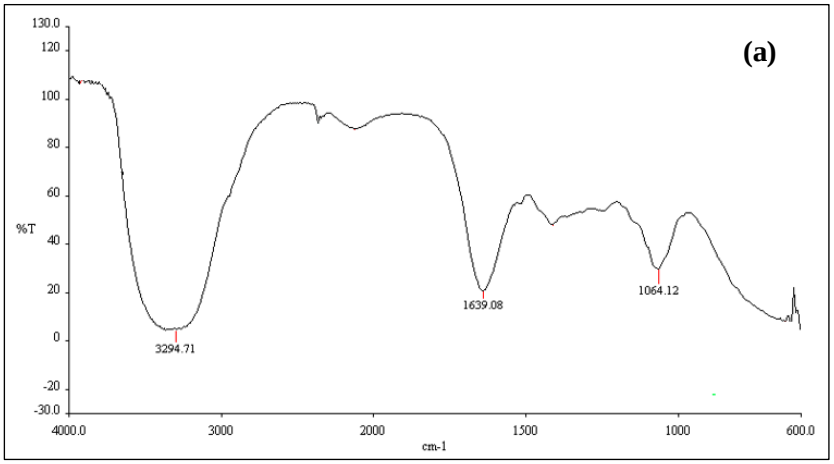


Figure 3. UV-Vis spectra of all extracts

Characterisation study: IR spectra of anthocyanin extracts

In the FTIR spectra of anthocyanin extracts (Figures 4 and 5), broad peaks appeared at 3100–3600 cm^{-1}, which are assigned to the fundamental stretching vibration of O-H hydroxyl groups. The absorption bands observed at 1640 cm^{-1} correspond to aromatic C=C. In the FTIR spectra of anthocyanin compounds (i.e. delphinidin and cyanidin), obvious peaks appeared at 1000–1300 cm^{-1}, which belong to ether C-O. The same trend of FTIR spectroscopy was described on the anthocyanin study by Wahyuningsih [11]. These FTIR peaks are indicative of anthocyanins like cyanidin and delphinidin [6, 11]. Besides, the FTIR spectrum of BV extract showed an amine peak at 1650–1580 cm^{-1} and carboxylic acid at 1440–1395 cm^{-1}, which reflect the compounds in betanin.



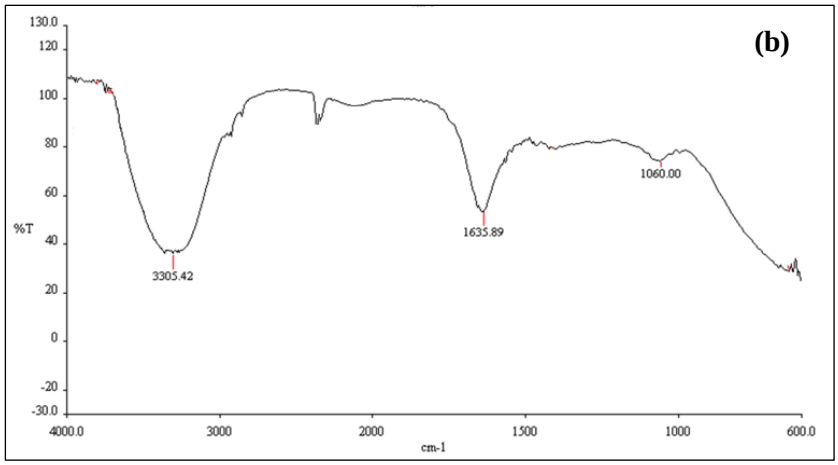
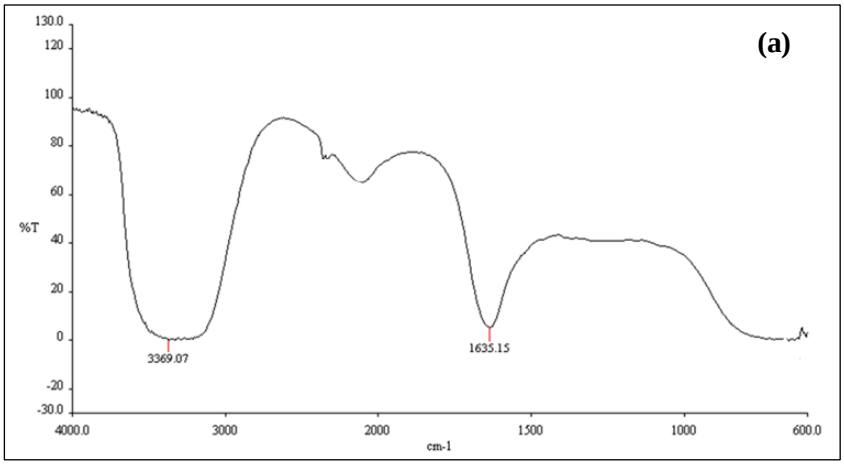


Figure 4. FTIR spectra of CT extract (a) and BO extract (b)



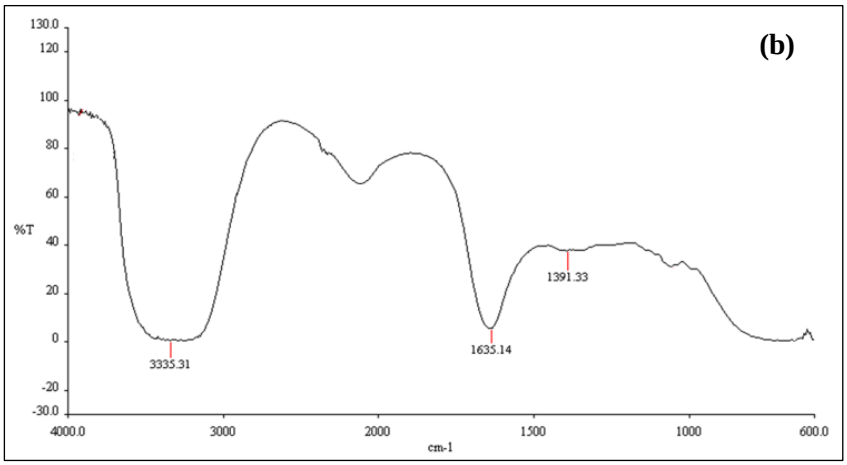


Figure 5. FTIR spectra of CL extract (a) and BV extract (b)

Response of visual indicators towards the freshness of beef sample

The response of the indicators towards a beef sample is shown in Figure 6. The results showed that at room temperature, the visual indicators changed their initial colour (purple for CT and light purple for BO) to green when the pH of the meat exceeded pH 6.5. Meanwhile, the visual indicators for CL and BV changed the initial colour from yellow and light pink to reddish orange and dark pink, respectively. The developed visual indicators were found sensitive to volatile compounds in the air since the indicators were not in direct contact with the beef sample and successfully indicated the freshness levels of the beef sample from the beginning (fresh) to spoiled beef. The change in colour is due to the increased concentration of volatile compounds released by the spoiled beef [9, 12]. The indicator response for CL followed a similar trend observed by Kuswandi [13] on a spoiling shrimp sample.

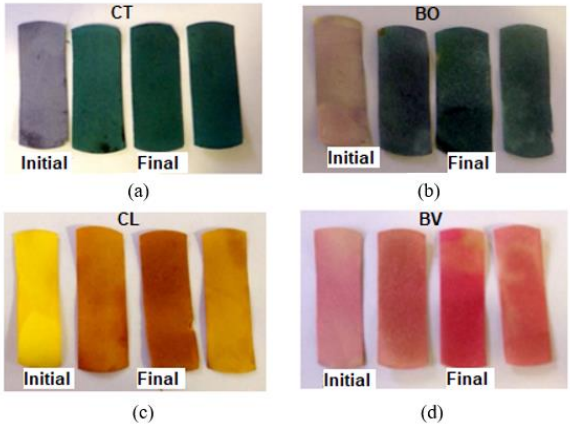


Figure 6. Initial and final indicator response towards beef spoilage: (a) CT indicator, (b) BO indicator, (c) CL indicator, and (d) BV indicator

Analysis on volatile compounds released from spoiled beef using HS-SPME-GC-FID

HS-SPME-GC-FID was successfully applied to extract the volatile compounds from a beef sample. A complete extraction was achieved after 30 minutes of exposure. Figure 7 shows a chromatogram of the volatile compounds of beef sample after 24 hours at room temperature. The compounds were identified by comparing their retention time with those of pure standards. Both results recorded a main peak at the same retention time (i.e. at 1.2 minutes), which indicated the presence of the same compound. The main volatile compound released by beef was detected as methylamine. Methylamine is produced by the microbial activity that contributes to beef spoilage [14].

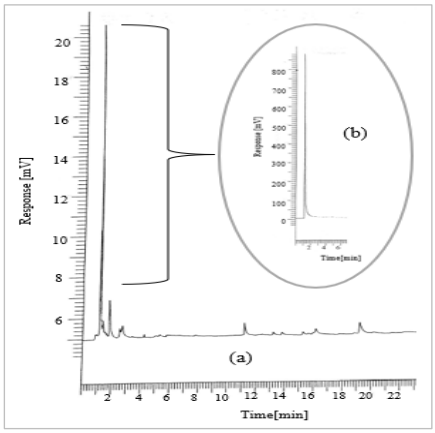


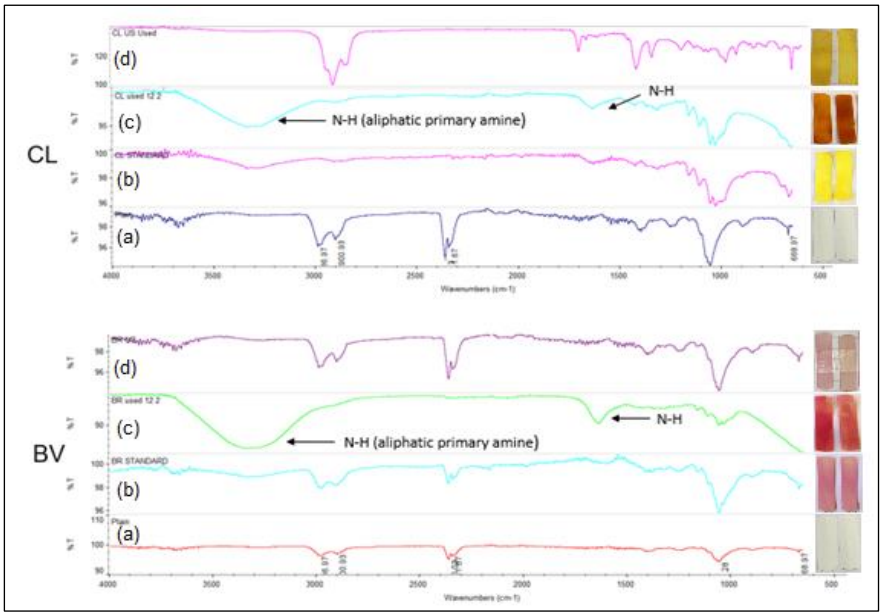
Figure 7. GC chromatogram of volatile compounds from (a) beef sample and (b) standard methylamine

IR spectra of visual indicators

Figure 8 presents the FTIR spectra of visual indicators for CT, BO, CL, and BV. The result was compared between (a) a plain indicator (i.e., without colour), (b) initial visual indicators (i.e. immobilised with colours), (c) final visual indicators after exposure on the beef sample (i.e. at room temperature), and (d) used visual indicators (i.e. after 24 hours removed from the beef container and exposed to air). It was found that all spectra (c) for CT, BO, CL, and BV showed the appearance of a broad peak at 3100–3600 cm^{-1}, which is assigned to the fundamental stretching vibration of O-H hydroxyl groups together with the N-H group. Besides, the spectra (c) for all types of indicators (CT, BO, CL, and BV) also showed another peak of the N-H group at 1633 cm^{-1}. These results are aligned with the HS-SPME-GC-FID analysis that detected the presence of methylamine as the volatile compound released from the beef sample. Subsequently, the used visual indicators (spectra (d) for all natural sources of CT, BO, CL, and BV) were observed without the presence of any N-H group and the indicators returned to their initial colour (dark purple, purple, yellow, and pink, respectively). These results indicate the possibility for the fabrication of reusable visual indicators in the future.

Overall colour values of visual indicators

The colour values for all visual indicators are tabulated in Table 2. The comparison of colour difference was done using Tukey's multiple comparison test, which is one of the several tests that can be used to determine which means amongst a set of means differ from the rest [15]. The Tukey's test showed that the initial colour values for all visual indicators were significantly different ($p < 0.05$) with the final colour values of the visual indicators. However, all colour values turned to insignificant difference ($p > 0.05$) after the indicators were removed from the container, except for BV. The visual indicator made of BV showed a significant difference ($p < 0.05$) with the initial visual indicator due to the faded colour of BV. These results provide the possibility for the visual indicators (CT, BO, and CL) to be reusable and can be recycled after the first use.



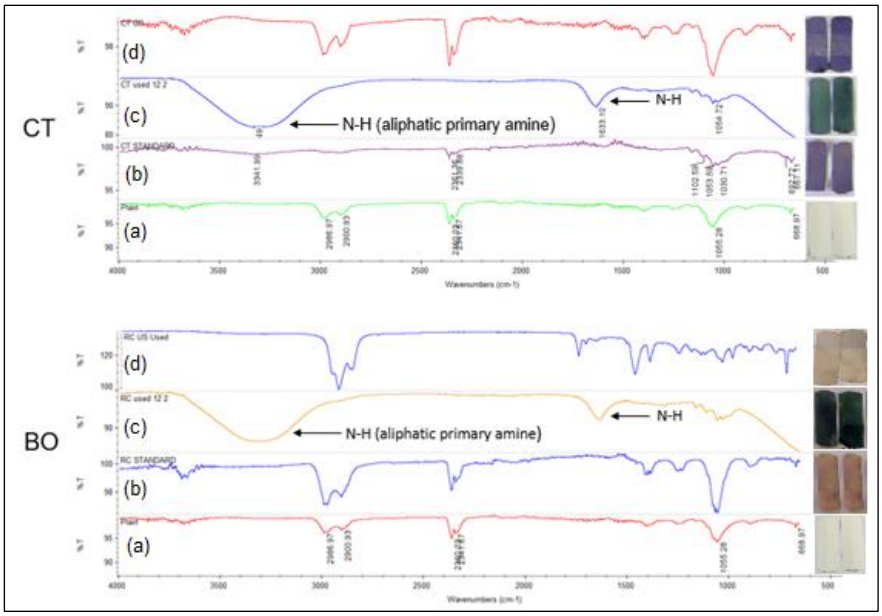


Figure 8. FTIR spectra of the visual indicators from CT, BO, CL, and BV. [(a) a plain indicator (i.e. without colour), (b) initial visual indicators (i.e. immobilised with colours), (c) final visual indicators after exposure on the beef sample (i.e. at room temperature), and (d) used visual indicators (i.e. after 24 hours removed from the beef container and exposed to air)]

Table 2. Colour values of the visual indicators of CT, BO, CL, and BV (Different superscripts in the same line indicate significant differences ($p < 0.05$) according to the Tukey's test)

Natural Colour	**Colour Value**		
	Initial Visual Indicator	**Final Visual Indicator**	**Used Visual Indicator**
CT	L* 47.99 ±1.30^{a} a* 16.15 ± 1.15^{a} b* -24.59 ± 0.44^{a}	L* 41.99 ± 1.69^{b} a* -9.52 ± 0.40^{b} b* -24.44 ±0.43^{a,b}	L* 53.32 ± 0.69^{a,c} a* 11.86 ± 1.19^{a,c} b* -22.18 ± 0.61^{a,c}
BO	L* 84.26 ± 0.58^{a} a* -4.87 ± 1.69^{a} b* 53.93 ± 1.05^{a}	L* 77.80 ± 0.28^{b} a* 1.1 ± 0.29^{b} b* 41.2 ± 0.59^{b}	L* 81.68 ± 1.69^{a,c} a* -6.29 ± 0.96^{a,c} b* 49.4 ± 1.15^{c}
CL	L* 65.00 ± 1.29^{a} a* 16.60 ± 0.64^{a} b* -13.08 ± 0.27^{a}	L* 41.59 ± 1.13^{b} a* 4.35 ± 0.31^{b} b* -12.75 ± 0.56^{b}	L* 70.00 ± 1.29^{a,c} a* 15.40 ± 0.40^{a,c} b* -10.75 ± 0.25^{a,c}
BV	L* 64.11 ± 0.68^{a} a* 27.33 ± 0.94^{a} b* 4.55 ± 0.43^{a}	L* 55.88 ± 1.09^{b} a* 20.84 ± 1.18^{b} b* 12.97 ± 0.46^{b}	L* 80.24 ± 0.24^{c} a* 30.35 ± 0.69^{a,c} b* 2.69 ± 0.87^{a,c}

Conclusion

This work employs natural colours from butterfly pea, red cabbage, turmeric, and beetroot as sensing elements for the detection of volatile compounds produced during the spoilage of beef sample. The natural colour visual indicators successfully displayed the progress of deterioration of beef sample in terms of colour changes. The visual indicators using CT and BO colours demonstrated the most significant colour change during spoilage detection. The amine compound released from the beef sample was detected on all visual indicators during spoilage detection and disappeared when the visual indicators were exposed to the environment without the amine compound. The disappearance of amine compound from the visual indicators made it possible for the indicators to be reusable as the colours of visual indicators returned to their initial colour. The proposed visual indicators could offer an extra analytical device to both meat industries and retailers that are interested in approaches and devices that are reusable, safe, low-cost, simple, rapid, disposable, non-destructive, and with real-time applications.

Acknowledgement

The authors gratefully thank Majlis Amanah Rakyat (MARA) for the funding under "Skim Geran Penyelidikan Inovasi MARA" and Universiti Kuala Lumpur Malaysian Institute of Chemical and Bioengineering Technology (UniKL Micet) for supporting this project.

References

1. Sharma, D. (2014). Understanding biocolour- A review. *International Journal of Scientific & Technology Research*, 3(1): 294-299.
2. Suppadit, T., Sunthorn, N. and Poungsuk, P. (2011). Use of anthocyanin extracted from natural plant materials to develop a pH test kit for measuring effluent from animal farms. *African Journal of Biotechnology*, 10(82): 19109-19118.
3. Kim, H. J., Kim, D., Kim, H. J., Song, S. O., Song, Y. H. and Jang, A. (2018). Evaluation of the microbiological status of raw beef in Korea: Considering the suitability of aerobic plate count guidelines. *Korean Journal for Food Science of Animal Resources*, 38(1): 43-51.
4. Meat & Livestock Australia (2011). Meat standards australia beef information kit. Access from https://www.mla.com.au/globalassets/mla-corporate/marketing-beef-and lamb/msa_tt_beefinfokit_jul13 _lr.pdf [Access online on 9 October 2017].
5. Rabeta, M. S. and Nabil, Z. A. (2013). Total phenolic compounds and scavenging activity in *Clitoria Ternatea* and *Vitex Negundo* Linn. *International Food Research Journal*, 20(1): 495-500.
6. Mishra, P. K., Singh, P., Gupta, K. K., Tiwari, H. and Srivastava, P. (2012). Extraction of natural dye from *Dhalia variabilis* using ultrasound. *Chemical Engineering*, 37: 1-18.
7. Saptarini, N. M., Suryasaputra, D. and Nurmalia, H. (2015). Application of butterfly bea (*Clitoria ternatea* Linn) extract as an indicator of acid-base titration. *Journal of Chemical and Pharmaceutical Research*, 7 (2): 275-280.
8. Shukla, V., Kandeepan, G. and Vishnuraj, M. R. (2015). Development of on-package indicator sensor for real-time monitoring of buffalo meat quality during refrigeration storage. *Food Analytical Methods*, 8(6): 1591-1597.
9. Kuswandi, B., Jember, U., Jayus, J. and Jember, U. (2015). Simple and low-cost on-package sticker sensor based on litmus paper for real-time monitoring of beef freshness. *Journal of Mathematical and Fundamental Sciences*, 47(1): 236-251.
10. Ma, Q. L., Hamid, N., Bekhit, A. E. D., Robertson, J. and Law, T. F. (2013). Optimization of headspace solid phase microextraction (HS-SPME) for gas chromatography mass spectrometry (GC-MS) analysis of aroma compounds in cooked beef using response surface methodology. *Microchemical Journal*, 111: 16- 24.
11. Wahyuningsih, S., Wulandari, L., Wartono, M. W., Munawaroh, H. and Ramelan, A. H. (2017). The effect of pH and color stability of anthocyanin on food colorant. *IOP Conference Series: Materials Science and Engineering*, 193(1): 012047.
12. Shukla, V., Kandeepan, G., Rajan, M. and Arvind, V. (2016). Anthocyanins based indicator sensor for intelligent packaging application. *Agricultural Research*, 5(2): 205-209.
13. Kuswandi, B., Jayus, Larasati, T. S., Abdullah, A. and Heng, L. Y. (2012). Real-time monitoring of shrimp spoilage using on-package sticker sensor based on natural dye of curcumin. *Food Analytical Methods*, 5 (4): 881-889.

14. Dave, D. and Ghaly, A. E. (2011). Meat spoilage mechanisms and preservation techniques: A critical review. *American Journal of Agricultural and Biological Science*, 6(4): 486-510.
15. Bland, J. M. and Altman, D. G. (1995). Tukey multiple comparison test. *British Medical Journal of Clinical Nursing*, 310(8): 299-304.

Malaysian Journal of Analytical Sciences Vol 24 No 3 2020

Page

1. A MINI REVIEW ON SPOROPOLLENIN-BASED MATERIALS FOR REMOVAL OF HEAVY METAL IONS FROM AQUEOUS SOLUTION 300
(Ulasan Mini Ke Atas Bahan Berasaskan Sporopollenin untuk Penyingkiran Ion Logam Berat dari Larutan Akueus)
Wan Aini Wan Ibrahim, Abdul-Aziz Mohd Hassan, Zetty Azalea Sutirman, Mohd Bakri Bakar

2. CYTOTOXIC ACTIVITY OF *Erythrina fusca* LOUR. LEAF, TWIG AND FLOWER EXTRACTS 313
(Aktiviti Sitotoksik Ekstrak Daun, Ranting, dan Bunga *Erythrina fusca* Lour.)
Adiez Sapura Azmi, Norina Abdul Rahim, Zuriati Zahari, Fatimah Salim

3. SYNTHESIS AND CHARACTERIZATION OF OXYGEN-DOPED MESOPOROUS GRAPHITIC CARBON NITRIDE USING NANODISC SILICA FROM RICE HUSK ASH AS HARD TEMPLATE 320
(Sintesis dan Pencirian Grafitik Karbon Nitrida Berliang Meso yang di Dop dengan Oksigen di Atas Nanocakera Silika dari Abu Sekam Padi Sebagai Templat Keras)
Shittu Fatimah Bukola, Mohammad Anwar Mohamed Iqbal, Farook Adam, Mohamad Nasir Mohamad Ibrahim, Nur Ruzaina Abdul Rahman, Srimala Sreekantan, Noor Hana Hanif Abu Bakar, Mohd Hazwan Hussain, Hariy Pauzi

4. SYNTHESIS AND CHARACTERIZATION OF CATALYTIC POLYMER- CLAY FILM FOR TREATMENT OF 17α-ETHINYLESTRADIOL 330
(Sintesis dan Pencirian Filem Polimer-Tanah Liat dengan Pemangkin untuk Rawatan 17α-Etinilestradiol)
Nur Khairunnisa Nazri, Nabilah Ismail, Mohd Aidil Adhha Abdullah, Fatimah Hashim, Leonard James Wright

5. LIPID DISTRIBUTIONS ASSOCIATED WITH CADAVER DECOMPOSITION IN MANGROVE AND OIL PALM PLANTATION SOILS UNDER TROPICAL CLIMATE 339
(Taburan Lipid Berkaitan dengan Pereputan Kadaver dalam Tanah Bakau dan Ladang Kelapa Sawit Di Bawah Iklim Tropika)
Siti Sofo Ismail, Xueer Chock, Mohamad Afdhali Kholidan, Ku Mohd. Kalkausar Ku Yusof, Siti Fathimah Putery Jemain

6. PERFORMANCE OF CERAMIC MEMBRANE COATED WITH GRAPHENE OXIDE AS ALTERNATIVE FOR OILY WASTEWATER TREATMENT 350
(Prestasi Selaput Seramik Grafin Oksida Sebagai Pilihan Untuk Rawatan Air Sisa Berminyak)
Nurdiyana Nabilah Kasim, Sharifah Abdullah, Nur Asmaliza Mohd Noor

7. PHASE BEHAVIOUR STUDY ON MEDIUM-CHAIN TRIGLYCERIDE/ SURFACTANT/WATER SYSTEMS CONTAINING GEMCITABINE USING PHASE INVERSION COMPOSITION TECHNIQUE 363
(Kajian Tingkah Laku Fasa Bagi Sistem Trigliserida Rantaian Sederhana/Surfaktan/Air yang Mengandungi Gemcitabine dengan Menggunakan Teknik Komposisi Penyongsangan Fasa)

Nadiatul Atiqah Wahgiman, Norazlinaliza Salim, Mohd Basyaruddin Abdul Rahman

8. HEADSPACE MEMBRANE-PROTECTED LIQUID PHASE MICROEXTRACTION OF PHENANTHRENE IN BEVERAGE AND WATER 373
(Pengekstrakan Mikro Fasa Cecair Dilindungi Membran Ruang Kepala bagi Fenantrena dalam Air Minuman dan Air)
Nor Hafiza Hassan, Wan Mohd Afiq Wan Mohd Khalik, Saw Hong Loh

9. IDENTIFICATION AND QUANTIFICATION OF FRUCTOSE, GLUCOSE AND SUCROSE IN WATERMELON PEEL JUICE 382
(Pengenalan dan Pengkuantitian Fruktosa, Glukosa dan Sukrosa di dalam Jus Kulit Tembikai)
Wan Mazlina Md. Saad, Nur Shafinaz Mohamad Salin, Ainza Suzila Ramzi, Fatimah Salim

10. OPTIMIZATION OF MONTMORILLONITE K10 ION-EXCHANGE WITH Fe^{3+} FOR THE APPLICATION OF BIODIESEL PRODUCTION 390
(Pengoptimuman Pertukaran Ion Montmorilonit K10 dengan Fe^{3+} untuk Aplikasi Penghasilan Biodiesel)
Syahirah Yahya and Farah Wahida Harun

11. THERMAL STABILITY AND POROSITY OF REDUCED GRAPHENE OXIDE/ZINC OXIDE NANOPARTICLES AND THEIR CAPACITY AS A POTENTIAL OXYGEN REDUCTION ELECTROCATALYST 405
(Kestabilan Haba dan Keliangan Partikel Nano Grafin Oksida Terturun/Zink Oksida dan Keupayaannya sebagai Pemangkin Elektro Tindakbalas Penurunan Oksigen)
Karthi Suresh and Farhanini Yusoff

12. STUDY OF CONDUCTIVITY AND THERMAL PROPERTIES OF POLYANILINE DOPED WITH *p*-TOLUENE SULFONIC ACID 413
(Kajian Pengaliran Elektrik dan Haba terhadap Polianilina di-Dopkan dengan Asid *p*-Toluena Sulfonik)
Muhammad Faiz Aizamddin, Nazreen Che Roslan, Muhammad Asyrap Kamarudin, Siti Nurzatul Ikma Omar, Muhd Fauzi Safian, Mohamed Izzharif Abdul Halim, Mohd Muzamir Mahat

13. EXPERIMENTAL AND DENSITY FUNCTIONAL THEORY INVESTIGATION ON IMINE FORMATION USING MICROWAVE IRRADIATION 422
(Penyiasatan Secara Eksperimen dan Teori Fungsi Ketumpatan ke atas Penghasilan Imina Menggunakan Penyinaran Gelombang Mikro)
Fatin Ilyani Nasir, Wun Fui Mark-Lee, Yan Yi Chong, Mohammad B. Kassim, Siti Aishah Hasbullah, Douglas Philp, Nurul Izzaty Hassan

14. GREEN SYNTHESIZED COPPER NANOPARTICLES FROM *Blumea balsamifera* LINN. LEAVES AND ITS BIOCIDAL ACTIVITIES AGAINST *Bactrocera dorsalis* (HENDEL) 436
(Sintesis Hijau Nanopartikel Kuprum dari Daun *Blumea balsamifera* Linn dan Aktiviti Biosida Melawan *Bactrocera dorsalis* (Hendel))
Danila S. Paragas, Kathlia D.C. Cruz, Elaida R. Fiegalan

15. STANDARIZATION BASED ON CHEMICAL MARKERS OF *Moringa oleifera* HERBAL PRODUCTS USING BIOAUTOGRAPHY ASSAY, THIN LAYER CHROMATOGRAPHY AND HIGH PERFORMANCE LIQUID CHROMATOGRAPHY-DIODE ARRAY DETECTOR 449
(Piawaian Berdasarkan Penanda Kimia bagi Produk Herba *Moringa oleifera*

Menggunakan Ujian Bioautografi, Kromatografi Lapisan Nipis dan Kromatografi Cecair Berprestasi Tinggi-Pengesan Susunan Diod)

Erick Sierra-Campos, Monica A. Valdez-Solana, Claudia I. Avitia-Dominguez, Alfredo Tellez-Valencia, Jorge A. Meza-Velazquez, Miguel Aguilera-Ortiz, Adelma Escobar-Ramirez

Malaysian Journal of Analytical Sciences (MJAS)
Published by Malaysian Analytical Sciences Society

A MINI REVIEW ON SPOROPOLLENIN-BASED MATERIALS FOR REMOVAL OF HEAVY METAL IONS FROM AQUEOUS SOLUTION

(Ulasan Mini Ke Atas Bahan Berasaskan Sporopollenin untuk Penyingkiran Ion Logam Berat dari Larutan Akueus)

Wan Aini Wan Ibrahim[1, 2]*, Abdul-Aziz Mohd Hassan[1, 3], Zetty Azalea Sutirman[1], Mohd Bakri Bakar[1]

[1]*Department of Chemistry, Faculty of Science*
[2]*Centre for Sustainable Nanomaterials, Ibnu Sina Institute for Scientific and Industrial Research*
Universiti Teknologi Malaysia, 81310 UTM Johor Bahru, Johor, Malaysia
[3]*Department of Pure and Applied Chemistry, Faculty of Science,*
Kebbi State University of Science and Technology Aliero, Nigeria

**Corresponding author: waini@utm.my; wanaini@kimia.fs.utm.my*

Received: 3 March 2020; Accepted: 8 April 2020; Published: 9 June 2020

Abstract

The use of sporopollenin-based materials as adsorbents in addressing environmental problems such as in removal of heavy metals from aqueous environment has received limited attention despite its remarkable physical and chemical properties that guaranteed its great potential for this application. This mini-review provides up-to-date information on the research and development of sporopollenin-based materials for the treatment of toxic heavy metals contaminated aqueous environments. Conventional techniques for heavy metals removal from aqueous environment are discussed; limitations and advantages of these techniques are highlighted. Sporopollenin-based materials were found to be good adsorbents in control and remediation of heavy metal ions in wastewater, but considering its characteristics, the full potentials of sporopollenin for this application is yet to be fully harnessed.

Keywords: sporopollenin, adsorbent, aqueous solution, heavy metals, environment

Abstrak

Penggunaan bahan berasaskan sporopollenin sebagai pengerap dalam menyelesaikan masaalah alam sekitar seperti penyingkiran logam berat dari larutan akueus telah mendapat perhatian terhad walaupun sifat fizikal dan kimianya yang luar biasa yang menjamin potensi yang besar untuk aplikasi ini. Ulasan mini ini memberikan maklumat terkini tentang penyelidikan dan pembangunan bahan berasaskan sporopollenin untuk merawat persekitaran akueus yang dicemari logam berat bertoksik. Teknik konvensional untuk penyingkiran logam berat dari persekitaran akueus dibincangkan; kelemahan serta kelebihan teknik ini diserlahkan. Bahan berasaskan sporopollenin didapati adalah penjerap yang baik dalam kawalan dan pemulihan ion logam berat dalam air kumbahan tetapi mempertimbangkan cirinya, potensi keseluruhan sporopollenin untuk aplikasi ini masih belum dimanfaatkan sepenuhnya.

Kata kunci: sporopollenin, penjerap, larutan akueus, logam berat, alam sekitar

Introduction

High level of heavy metals (HMs) contaminated water resource due to industrialization and human activities constitute a serious threat to the environment and public health [1]. Heavy metals like nickel, lead, chromium, arsenic, cadmium, mercury and copper, are hazardous to organisms even at very small concentrations. These metal ions accumulation in human system causes severe health problems such as cancers, bone softening, kidney failure, malfunction of nervous system and other serious illnesses [2]. Nowadays, adsorption technique through complexation or ion exchange mechanism is popularly used to mitigate metal ions toxicity in contaminated aqueous environment. Materials such as biomaterials, silica gel, activated carbon and resins [1] have been used for this purpose. However, the improvement of adsorbent's selectivity for heavy metals ions, involves the introduction of special functional groups with high affinity for metal ions onto the polymer matrix of the adsorbent [3]. In this case, the structure and chemical composition of the adsorbent as a supporting material plays significant role in the overall efficiency of the modified material or adsorbent.

One of such materials that can be used as adsorbent and excellent support is *Lycopodium clavatum* (sporopollenin, Sp). Sp is a highly resistant bio-macromolecule that occurs in nature as a component of the outer wall of spores and pollen which is resistant to attacks by mineral acids and alkalis. It can survive in geological strata over millions of years with full retention of its morphological characteristics, these suggest good stability of Sp at extreme conditions [4]. However, the detailed chemical structure of the Sp is yet unknown but it has stable cross-linked aromatic structure containing carbon, hydrogen, and oxygen in a stoichiometry of $C_{90}H_{144}O_{27}$ [5]. In addition, its main functional group is hydroxyl functional groups available for modification in large quantities. Thus, the hydroxyl group serves as anchoring sites for metal ion complexation as well as addition of desired surface functional groups and other materials with high affinity for metal ion [5]. However, literature search suggested that, studies on Sp-based materials for the removal of metal ions are quite few. The objective of this mini review is to report for the first time, the synthesis and application of different Sp-based materials so far being used for the removal of heavy metal ions from aqueous solution in order to provide insights of what need to be done to further harness its full potentials in removing heavy metal ions from contaminated aqueous environment.

Heavy metals

HMs naturally occur as part of the earth's crust, in rocks or soils, and are regarded as any dense metal with atomic weights of 63.5 - 200.6 Dalton, and a specific gravity above 5 g/mL [6, 7]. HMs includes cadmium, antimony, nickel, arsenic, lead, copper, cobalt, uranium, chromium, zinc, selenium, thallium and mercury [8]. Most of these heavy metals are discharged into the aquatic environment as domestic wastes or industrial effluents, causing water pollution [9]. Heavy metals are not degradable, thus tend to persist in environment, as a serious threat to public health once discharged.

Arsenic contaminated drinking water is a health risks to approximately 150 million people globally [10]. Cadmium has been identified as a potent carcinogen, its toxicity may also cause bone defects (osteomalacia and osteoporosis) [11]. Exposure to cadmium may also cause diseases of reproductive organs, lungs, kidneys and liver [12, 13]. Lead poisoning causes gastrointestinal diseases, central nervous system diseases, constipation and abdominal pains [14]. Mercury exposure may cause chest pain, impairment of pulmonary function, impairment of the kidney and dyspnoea [15]. Mercury accumulates in the brain, causing neurological and psychiatric effects [16, 17]. Chromium is found in the environment as Cr(III) and Cr(VI). Exposure to chromium causes lung cancers, skin irritation, kidney and liver damage [18, 19]. Considering the hazardous effects of these heavy metals, the World Health Organization (WHO) and the

United States Environmental Protection Agency (US EPA) have set maximum permissible limits (MPL) for metals in drinking water (Table 1). As a comparison, the MPL for Ministry of Health (MOH) Malaysia is also given.

Techniques for removing heavy metal ions from aqueous solution

Several methods are used for the removal of heavy metals ions from aqueous environments; the most widely used are chemical precipitation, ion exchange and adsorption [23].

Chemical precipitation

Precipitation is a chemical process in which soluble substances in a solution reacts chemically with certain suitable reagents to form insoluble solid precipitate. Metal precipitation can occur either through the addition of sodium hydroxide or lime (hydroxide precipitation) [24-26], addition of calcium or sodium carbonate (carbonate precipitation) [25, 26] or addition of sulfide ions (sulphide precipitation) [26].

Chemical precipitation is widely applied to remove heavy metals from industrial effluents [23, 27, 28]. However, it was observed that removing metal ions through sulphide precipitation is more efficient compared to hydroxide and carbonate precipitation [3].

Equations 1-3 presents the conceptual mechanism of heavy-metal removal using chemical precipitation.

$$M^{2+} + 2(OH)^{-} \rightarrow M(OH)_2 \quad (1)$$

$$M^{2+} + CO_3^{2-} \rightarrow MCO_3 \quad (2)$$

$$M^{2+} + S^{2-} \rightarrow MS \quad (3)$$

where M^{2+} is dissolved metal ions, OH^{-} is hydroxide, CO_3^{2-} is carbonate and S^2 is sulphide, while the precipitants are the insoluble metal hydroxide '$M(OH)_2$', carbonate 'MCO_3' and sulphide 'MS', respectively.

In chemical precipitation, the metal ions usually precipitated from solution in the form of insoluble hydroxides, carbonates and sulphides by pH adjustment of the solution to basic condition pH (9-11). Materials such as lime and limestone are often used as precipitants for pH adjustment to the basic range [29, 30]. Lime and limestone are cost effective and available. Recently, lime was use alongside milk casein for precipitation and form separation of heavy metals from mining wastewater. The milk casein functioned as a collector and a frother for foam separation in this system [31]. However, limitations of chemical precipitation involve the use of large volume of chemicals to reduce metals to an acceptable environmental limits for discharge, sludge production, environmental problems associated with sludge disposal and slow metal precipitation [30].

Table 1. Maximum permissible limit (MPL) of seven heavy metals in drinking water [20-22]

Heavy Metals	MPL (mg/L)		
	USEPA	WHO	MOH Malaysia
Lead	0.015	0.005	0.01
Cadmium	0.005	0.005	0.003
Mercury	0.002	0.001	0.001
Arsenic	0.01	0.01	0.01
Chromium	0.1	0.05	0.05
Nickel	0.04	-	0.02
Selenium	0.05	0.01	0.01

Ion exchange

Removing heavy metals through ion exchange involves the transfer of ions in the aqueous solution unto a solid matrix, which as a result, releases ions of a different type but of the same charge [32]. In addition to synthetic organic ion-exchange resins such as Purolite C100 [33], Lewatit TP207 [34] and Lewatit TP208 [34], 2,4- DHBEDF [35], Chelex-100 and Amberlite IRC748 [36] and C160-Purolite [37]. Other commonly used materials for ion exchange are zeolites, which have good cation-exchange ability [38, 39]. Alvarez et al. [40] studied the efficiency of natural zeolite (clinoptilolite) and synthetic zeolites (NaP1) to remove heavy metals from wastewater. It was found that synthetic zeolite has higher efficiency in removing heavy metals from wastewater compared to natural zeolite.

Natural zeolites effectively removed heavy metal from aqueous solution [41] and metal finishing wastewater [42]. Furthermore, modified natural zeolite such Fe(III)-zeolite [43, 44] and zeolite-alginate composite [45] have also been reported as ion-exchange materials for removal of heavy metals from industrial wastewater. On the other hand, synthetic zeolite prepared *via* alkali fusion of coal fly ash, followed by thermal treatment to improve the zeolite ion exchange ability to remove heavy metal from mineral and metal processing wastewater has been reported [46]. Recently, thermally treated zeolite showed good performance in removing heavy metal ions from wastewater with high thermal stability and retention of metal ions during ion exchange [47]. Thermal treatment is a promising technique to improve the performance of zeolites. The advantages of ion-exchange over chemical precipitation method are selectivity and less sludge volume are produced. However, its limitations are that the process cannot effectively treat concentrated solutions [23, 48] and incur high operational cost [48].

Adsorption

Adsorption is a promising and convenient technique for removing heavy metals ions from contaminated water. Adsorption involves the transfer of ions from solution to adsorbent surface then becomes bounded by either physical or chemical interactions [49]. Many materials have been reported as adsorbents for removal of metal ions from aqueous environments such as carbon nanomaterials (CNM) [50], multiwall carbon nanotubes (MWCNTs) [51], activated carbon (AC) [52], modified polypyrrole films [53], poly(-acrylamide) grafted on modified Fe_3O_4 [54], *Tinospora cordifolia* [55], algae waste biomass [56], modified sewage sludge[57], *Bauhini purpurea* pods [58], Chestnut buds [59], lignin/corncob biochar [60], activated carbon of *Typha angustifolia* [61], coal fly ash-nZVI [62], synthetic mineral [63], poly(methacrylamide) grafted crosslinked chitosan [64], silica-cyanopropyl magnetic GO (MGO/SiO_2-CN) [65], graphene oxide functionalized with dithiocarbamate [66], graphene oxide (GO) [67] and Sp [68]. Adsorption has several advantages over various methods of removing metal ions from aqueous solution such as the possibility to modify and improve the properties of adsorbent, selectivity, reusability and cost effectiveness. Furthermore, due to high adsorption capacities of adsorbents, this process is suitable for the treatments of high concentrated heavy metals contaminated aqueous environment.

Sporopollenin-based materials for metal ions removal from aqueous environment

Unmodified Sp was used as adsorbent to remove Cu(II), Pb(II) and Cd(II) from aqueous solution with adsorption capacities of 0.0195, 0.0411 and 0.0146 mmol/g for Cu(II), Pb(II) and Cd(II), respectively at optimum conditions [68]. Modification is necessary on the Sp, in order to improve its adsorption efficiency and harness its full potential in remediating heavy metals contaminated aqueous environments. In a related study, Murat et al. [69] used pretreated sporopollenin (PSp) biomass to remove Pb(II) and Cu(II) from water through batch biosorption technique and optimized using response surface methodology. Although this study reports only pretreatment not chemical modification with improved binding sites, Sp was pretreated using concentrated nitric acid in order to improve its metal affinity. However, Sp being a tough

biomaterial with physical, chemical stability and complex structure is likely to suffer from long diffusion path through solid particles. Thus, concentrated nitric acid was used to reduce the toughness and improve the porous nature of Sp for the metal ions to easily access the binding sites on Sp. The maximum adsorption capacity, q_{max} of PSp was 6.10 and 4.84 mg/g for Pb(II) and Cu(II), respectively.

Dithiocarbamated-Sp (DTC-Sp) was synthesised as adsorbent for removal of Cu(II), Pb(II) and Cd(II) from aqueous solution. The synthesis steps involved grafting of ethylenediamine (DAE) groups onto the Sp network. Furthermore, addition of carbon disulfide converted the amine groups to dithiocarbamates. The DTC-Sp attained q_{max} of 0.2734, 0.4572 and 0.0631 mmol/g for Cu(II), Pb(II) and Cd(II) metal ions, respectively [70]. DTC-Sp showed 1,320%, 1,012% and 332% improvements in sorption capacity for Cu(II), Pb(II) and Cd(II) respectively, compared to unmodified Sp, probably due to the presence of sulphur in dithiocarbamates, which improved the affinity of the adsorbent for these metal ions.

Sener el al. [71] reported magnetic nanoparticles modified Sp (Fe_3O_4-Sp) as biosorbent for removal of Pb(II) from aqueous solution with q_{max} of 22.7 mg/g. Modification of Sp with Fe_3O_4 was to facilitate separation after adsorption *via* the application of external magnet, without going through the tedious and time consuming filtration and centrifugation processes. However, Fe_3O_4-Sp showed superior q_{max} for Pb(II) (272% higher) compared to PSp. Recently, 1-(2-hydroxyethyl) piperazine magnetic nanoparticles-Sp (MNPs-Sp-HEP) was synthesized *via* modification of Sp spores with 3-cyanopropyltrimethoxysilane, then functionalized with 1-(2-hydroxyethyl) piperazine (Sp-HEP). The magnetic nanoparticles were then introduced, to modify the Sp-HEP to produce MNPs-Sp-HEP (Figure 1).

The MNPs-Sp-HEP was applied as adsorbent for the removal of Pb(II) and As(III) from aqueous solution. This adsorbent shows more selectivity for As(III) which attained q_{max} of 13.36 and 69.85 mg/g for Pb(II) and As(III), respectively in aqueous media [72], showing 119% increment in Pb(II) q_{max} compared to PSp, but 70% less Pb(II) q_{max} compared to Fe_3O_4-Sp. MNPs-Sp-HEP was easily separated from aqueous solution with the help of external magnet. This could be due to the competition of Pb(II) and As(III) for the limited active sites on MNPs-Sp-HEP. Thus, affecting its performance on Pb(II) adsorption.

Ersoz et al. [73] conducted a study to remove Zn(II), Cd(II) and As(III) from water using carboxylated-diaminoethyl modified Sp (DAEC-Sp) and bis-diaminoethyl-glyoxime Sp (bDAEG-Sp). These Sp-based materials possessing oxime and carboxylic acid functionality were synthesized *via* the reaction of diamino-Sp with bromoacetic acid and dichloro-antiglyoxime respectively. The q_{max} of DAEC-Sp was 1.801, 1.500 and 1.119 mmol/g for Zn(II), Cd(II) and As(III), respectively while bDAEG-Sp attained q_{max} of 1.855, 1.261 and 1.127 mmol/g for Zn(II), Cd(II) and As(III), respectively at solution pH of 6 and 50 °C. DAEC-Sp and bDAEG-Sp showed 2,277% and 1898% higher q_{max} for Cd(II) respectively, compared to DTC-Sp. However, 10.174% and 8.537% increment in Cd(II) q_{max} was achieved for DAEC-Sp and bDAEG-Sp compared to unmodified-Sp. Furthermore, there was not much difference (0.71%) in q_{max} of DAEC-Sp and bDAEG-Sp for As(III), this suggested that, the materials have almost similar sorption affinity for As(III).

Gode and Pehlivan [4] also employed b-DAEG-Sp and carboxylated epi-chlorohydrine-Sp (CEP-Sp) to remove Cr(III) from aqueous solution. b-DAEG-Sp attained a q_{max} of 1.23 mmol/g while CEP-Sp attained a high q_{max} of 133 mmol/g. Based on these findings, it can be deduced that, CEP is a better material to modify Sp compared to b-DAEG. Idris and Gulsin [74] reported chitosan modified Sp (chitosan-Sp) as hybrid bio-macromolecules adsorbent for metal ions. This material was prepared *via* cross-linking of chitosan with Sp. However, comparison was made on the sorption performance of chitosan-Sp and plain chitosan for Cu(II), Cd(II), Cr(III), Ni(II) and Zn(II) ions.

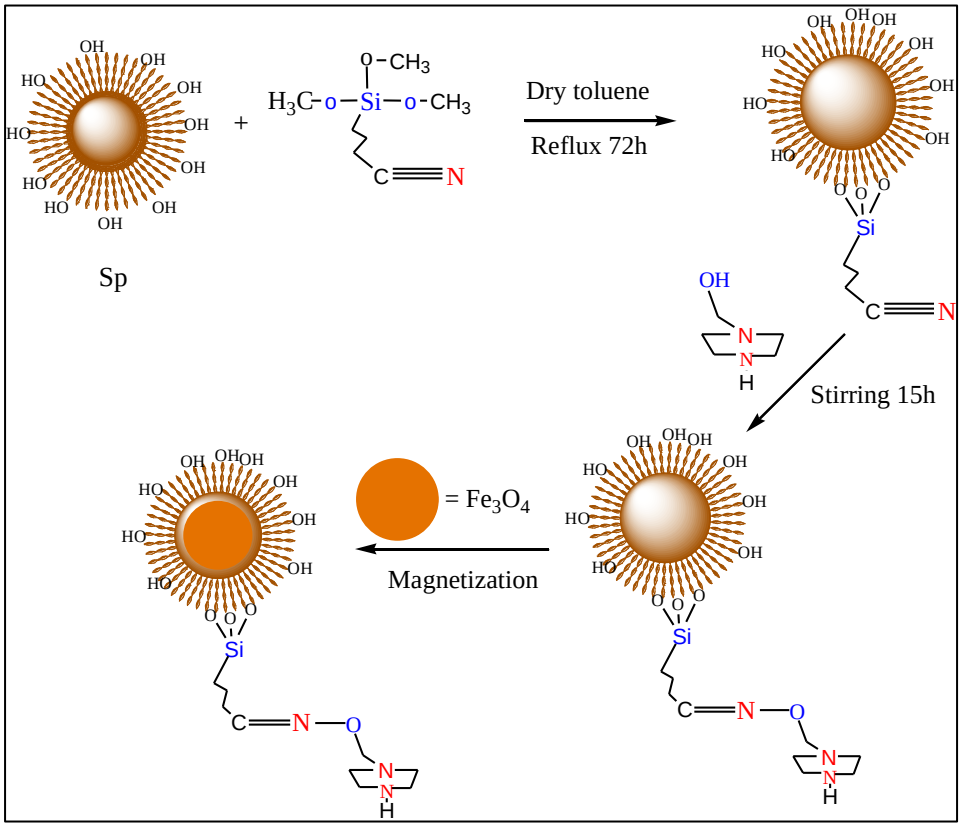


Figure 1. Schematic routes for the preparation of 1-(2-hydroxyethyl) piperazine-functionalized magnetic-Sp (MNPs-Sp-HEP)

Chitosan-Sp attained q_{max} of 1.34, 0.77, 0.99, 0.58 and 0.71 mmol/g for Cu(II), Cd(II), Cr(III), Ni(II), and Zn(II) ions, respectively. Plain chitosan attained q_{max} for Cu(II): 1.46, Cr(III): 1.16, Cd(II): 0.15, Ni(II): 0.81 and Zn(II): 0.25 mmol/g. This showed that, Sp enhanced the affinity and sorption capacity of the chitosan for Cd(II) and Zn(II) by 413% and 184% respectively. Thus, chitosan-Sp can be used in Cd(II) and Zn(II) ions removal. Furthermore, Sp immobilized E-4-((2-hydroxyphenylimino) methyl) benzoic acid (Sp-HPBA) adsorbent, attained q_{max} of only 0.043, 0.036 and 0.039 mmol/g for Cu(II), Ni(II) and Co(II), respectively, in aqueous solution [75]. In a related study, glutaraldehyde immobilized sporopollenin (GA-Sp) synthesized *via* sequential treatment of Sp with glutaraldehyde attained a q_{max} of 0.042, 0.143 and 0.130 mmol/g for Cu(II), Zn(II) and Co(II) respectively [76]. Sp-HPBA showed only 2.4% increment in Cu(II) q_{max} value compared to GA-Sp, but, the q_{max} of GA-Sp for Co(II) improved by 233% compared to Sp-HPBA.

Gode and Pehlivan [4] also employed b-DAEG-Sp and carboxylated epi-chlorohydrine-Sp (CEP-Sp) to remove Cr(III) from aqueous solution. b-DAEG-Sp attained a q_{max} of 1.23 mmol/g while CEP-Sp attained a high q_{max} of 133 mmol/g. Based on these findings, it can be deduced that, CEP is a better material to modify Sp compared to b-DAEG. Idris and Gulsin [74] reported chitosan modified Sp (chitosan-Sp) as hybrid bio-macromolecules adsorbent for metal ions. This material was prepared *via* cross-linking of chitosan with Sp. However, comparison was made on the

sorption performance of chitosan-Sp and plain chitosan for Cu(II), Cd(II), Cr(III), Ni(II) and Zn(II) ions.

p-tert-butylcalix[4]-aza-crown (CAC) immobilized Sp was used as a sorbent for the removal of selected heavy metals from aqueous media. Sp was initially functionalized with 3-chloropropyltrimethoxysilane (CPTS) to produce chloro-Sp (Sp-Cl). The Sp-Cl was further reacted with CAC to form the sorbent (Sp-Cl-CAC). The q_{max} of Sp-Cl-CAC for Zn(II), Pb(II) and Cu(II) were 0.14, 0.07, and 0.07 mmol/g, at pH 5.5 for Zn(II) and 5.0 for Cu(II) and Pb(II) [77]. Sp-Cl-CAC showed more affinity for Cu(II) compared to the earlier mentioned Sp-HPBA and GA-Sp adsorbents. Another calix[4]arene modified Sp, p-tert-butylcalix[4]arene-Sp (p-t-bCalix-Sp) was used for the removal of Cr(VI) from aqueous media. Calix-Sp was synthesised *via* the immobilization of dihydrazine amide derivative of p-tert-butylcalix[4]arene onto the Sp. Using batch adsorption technique, the sorption of Cr(VI) was pH dependent and optimum pH was 1.5. The q_{max} of Cr(IV) sorption onto Calix-Sp was found to be 0.54 mmol/g [78], *p-t*-bCalix-Sp appeared to be the only Sp-based sorbent so far used for the sorption of Cr(IV).

Recently, 3-aminopropyltrimethoxysilane functionalized Sp based silica coated GO (GO@SiO_2-MSp@SiO_2-NH_2) was used as hybrid adsorbent for removal of Pb(II) from aqueous environment, which attained qmax of 323.5 mg/g [79]. Figure 2 illustrates the synthesis of GO@SiO_2-MSp@SiO_2NH_2. The adsorbent showed significantly higher sorption capacity of 1,325% and 2,321% compared to Fe_3O_4-Sp and MNps-Sp-HEP respectively. This is probably due to the modification of the Sp with 3-aminopropyltrimethoxysilane and GO, which improved the sorption affinity of GO@SiO_2-MSp@SiO_2NH_2 towards Pb(II). Table 2 shows a summary of the reviewed Sp-based sorbents and their q_{max} values for metal ions.

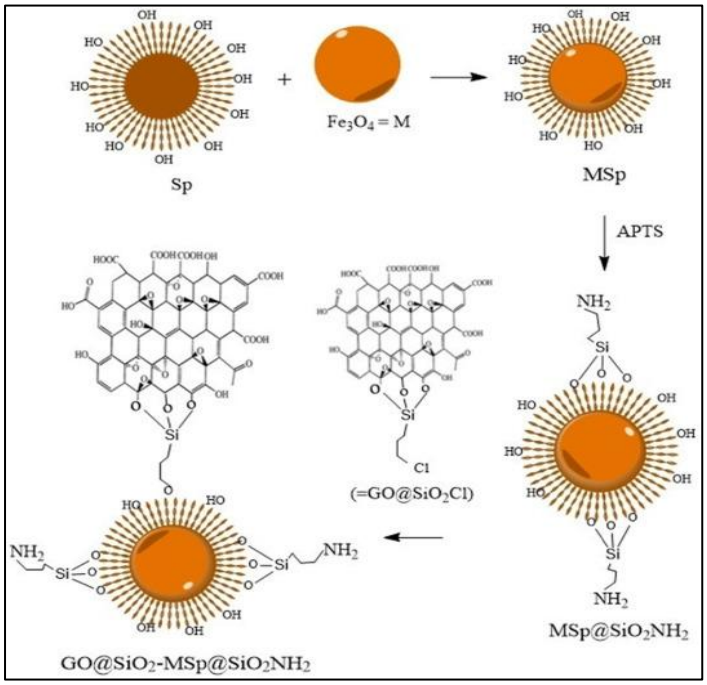


Figure 2. Schematic routes for the preparation of GO@SiO_2-MSp@SiO_2NH_2 [79]

Table 2. Summary of Sp-based sorbents for removal of metal ions

Sorbent	**Metal Ion**	**q_{max} (mmol/g)**	**References**
Sp	Cu(II)	0.0195	68
	Pb(II)	0.0411	
	Cd(II)	0.0146	
PSp	Pb(II)	6.10	69
	Cu(II)	4.84	
DTC-Sp	Cu(II)	0.2734	70
	Pb(II)	0.4572	
	Cd(II)	0.0631	
Fe_3O_4-Sp	Pb(II)	22	71
MNps-Sp-HEP	Pb(II)	13.36	72
	As(III)	69.85	
DAEC-Sp	Zn(II)	1.801	73
	Cd(II)	1.500	
	As(III)	1.119	
bDAEC-Sp	Zn(II)	1.855	73
	Cd(II)	1.261	
	As(III)	1.127	
	Cr(III)	1.23	
CEP-Sp	Cr(III)	133	4
Chitosan-Sp	Cd(II)	0.77	74
	Zn(III	0.71	
Sp-HPBA	Cu(II)	0.043	75
	Ni(II)	0.036	
	Co(II)	0.039	
GA-Sp	Cu(II)	0.042	76
	Ni(II)	0.143	
	Co(II)	0.130	
Sp-Cl-CAC	Zn(II)	0.14	77
	Pb(II)	0.07	
	Cu(II)	0.07	
p-t-bCalix-Sp	Cr(VI)	0.54	78
GO@SiO_2-MSp@SiO_2-NH_2	Pb(II)	323.5	79

Future prospective

Many research efforts have been devoted to developing efficient materials as adsorbents with suitable, physical properties, microstructures, chemical compositions and surface functionalities for the removal of both organic and inorganic contaminants from aqueous media. The prospects of Sp-based materials as sorbent in water treatment are promising, because of its endowed natural properties. The highly cross-linked polymer Sp is extraordinarily stable, both chemically and physically. It was found chemically intact in 500 million years old sedimentary rocks [80]. This shows that Sp-based materials can withstand extreme conditions, thus making Sp a suitable solid support for grafting materials with surface functionalities that have high sorption affinity for target pollutants. It can form hybrids with other material by physically incorporating materials into the Sp's microcapsules pores [81] and chemical grafting through the functional groups (OH, COOH, CO) on the Sp [72]. Furthermore, Sp is environmentally friendly, readily available and biocompatible [80]. Therefore, Sp-based materials can serve as sustainable sorbents in water treatment of heavy metals.

Conclusion

Different Sp-based materials have been successfully synthesized and the ability of these Sp-based materials for removal of metal ions depends on their chemical nature, and various physicochemical properties such as adsorbent dosage, temperature, solution pH, adsorbent dosage. To enhance the ability of these Sp-based materials to remove metal ions, more research is needed on materials with high affinity for metal ions that can be grafted onto Sp. Among the reported Sp-based materials, GO@SiO_2-MSp@SiO_2NH_2 showed the highest adsorption capacity with Pb(II) q_{max} of 323.5 mmol/g, followed by CEP-Sp with 133 mmol/g for Cr(III).

Acknowledgement

This work was supported by Universiti Teknologi Malaysia and the Ministry of Education (MOE), Malaysia under the Fundamental Research Grant Scheme (FRGS) vote number R.J130000.7826.4F735. and Universiti Teknologi Malaysia, GUP Grant number Q.J130000.2526.18H86**.**

References

1. Hatay, I., Gup, R. and Ersoz, M. (2008). Silica gel functionalized with 4-phenylacetophynone 4 aminobenzoylhydrazone: synthesis of a new chelating matrix and its application as metal ion collector. *Journal of Hazardous Materials*, 150: 546-553.
2. Wang, J., Zhang, D., Lawson, T. R. and Bartsch, R. A. (2009). Sorption of heavy metal ions by silica gel-immobilized, proton-ionizable calix[4] arenes. *Talanta*, 78: 477-483.
3. Kang, S. Y., Lee, J. U., Moon, S. H. and Kim, K. W. (2004). Competitive adsorption characteristics of Co^{2+}, Ni^{2+}, and Cr^{3+} by IRN-77 cation exchange resin in synthesized wastewater. *Chemosphere,* 56(2): 141-147.
4. Gode, F. and Pehlivan, E. (2007). Sorption of Cr(III) onto chelating b-DAEG–sporopollenin and CEP–sporopollenin resins. *Bioresource Technology*, 98: 904-911.
5. Gurten, A. A Ucan, M. Abdullah, M. I. and Ayar, A. (2006) Effect of the temperature and mobile phase composition on the retention behavior of nitro anilines on ligand exchange stationary phase. *Journal of Hazardous Materials,* B135: 53-57.
6. Jarup, L. (2003). Hazards of heavy metal contamination. *British Medical Bulletin*, 68: 167-182.
7. Hernández, M. V., Nava, R., Acosta-Silva, Y. J., Macías-Sánchez, S. A., Pérez-Bueno, J. J., Pawelec, B. (2012). Adsorption of lead(II) on SBA-15 mesoporous molecular sieve functionalized with−NH_2groups. *Microporous Mesoporous Materials,* 160: 133-142.
8. Akpor, O. B. (2014). Heavy metal pollutants in wastewater effluents: sources, effects and remediation. *Advances Bioscience and Bioengineering*, 2: 37.
9. Kyzas, G. Z. and Deliyanni, E. A. (2013). Mercury(II) removal with modified magnetic chitosan adsorbents. *Molecules,* 18: 6193-6214.

10. Singh, R., Singh, S., Parihar, P., Singh, V. P. and Prasad S. M. (2015). Arsenic contamination consequences and remediation techniques: a review. *Ecotoxicology and Environmental Safety*, 112: 247-270.
11. Sari, A., Mendil, D., Tuzen, M. and Soylak, M. (2008). Biosorption of Cd(II) and Cr(III) from aqueous solution by moss (*Hylocomium splendens*) biomass: equilibrium, kinetic and thermodynamic studies. *Chemical Engineering Journal*, 144: 1-9.
12. Waalkes, M. P. (2003). Cadmium carcinogenesis. *Mutation Research - Fundamental and Molecular Mechanisms of Mutagenesis,* 533: 107-120.
13. Filipiˇc, M. (2012). Mechanisms of cadmium induced genomic instability. *Mutation Research - Fundamental and Molecular Mechanisms of Mutagenesis,* 733: 69-77.
14. Anwar, J. Shafique, U. Salman, M. and Memoona, M. (2009). Adsorption study of cadmium(II) and lead(II) on radish peels. *Journal of Scientific Research*, 39: 29-34.
15. Naseem, R. and Tahir, S. S. (2001). Removal of Pb(II) from aqueous/acidic solutions by using bentonite as an adsorbent. *Water Research*, 35:3982-3986.
16. Wang, X. Qu, R. Wei, Z. Yang, X. and Wang, Z. (2014). Effect of water quality on mercury toxicity to *Photobacterium phosphoreum*: model development and its application in natural waters. *Ecotoxicology and Environmental Safety*, 104: 231-238.
17. Sieger, F. A. S., Silva, G. D., Ardila, G. P. and García, R. G. (2012). Mercury chronictoxicity might be associated to some cases of hydrocephalus in adult humans? *Medical Hypotheses.* 79: 13-16.
18. Selvi, K. (2001). Removal of Cr(VI) from aqueous solution by adsorption onto activated carbon, *Bioresource Technology*, 80: 87-89.
19. Kumar, P. A. Ray, M. and Chakraborty, S. (2007). Hexavalent chromium removal from wastewater using aniline formaldehyde condensate coated silica gel. *Journal of Hazardous Material,* 143: 24-32.
20. Mohod, C. V. and Dhote, J. (2013). Review of heavy metals in drinking water and their effect on human health. *The International Journal of Innovative Research in Science, Engineering and Technology*, 2: 2992-2996.
21. World Health Organization, WHO (2011). Guidelines for Drinking-water Quality-4th edition, 1–541.
22. Ministry of health Malaysia, Engineering Services Division. (2010). Drinking water quality surveillance program, drinking water quality standards. Access from http://kmam.moh.gov.my/public-user/drinking-water-quality-standard.html. [Accessed 21/04/2019].
23. Barakat, M. A. (2011). New trends in removing heavy metals from industrial wastewater. *Arabian Journal of Chemistry*, 4: 361-377.
24. Khraisheh, M. A., Al-degs, Y. S., and Mcminn, W. A. (2004). Remediation of wastewater containing heavy metals using raw and modified diatomite. *Chemical Engineering Journal*, 99(2): 177-184.
25. Ayodele, A. and Idris, A. (2018). Chemical precipitation approach to the removal of heavy hetals from wastewater for discharge into sanitary sewerage. *United Journal of Chemistry,* 1: 167-171.
26. Chen, Q., Yao, Y., Li, X., Lu, J., Zhou, J., and Huang, Z. (2018). Comparison of heavy metal removals from aqueous solutions by chemical precipitation and characteristics of precipitates. *Journal of Water Process Engineering,* 26: 289-300
27. Kurniawan, T. A., Chan, G. Y. S., Lo, W. H. and Babel, S. (2006). Physico-chemical treatment techniques for wastewater laden with heavy metals. *Chemical Engineering Journal*, 118: 83-98.
28. Ku, Y. and Jung, I. (2001). Photocatalytic reduction of Cr(VI) in aqueous solutions by UV irradiation with the presence of titanium dioxide. *Water Research*, 35: 135-142.
29. Mirbagheri, S. A. and Hosseini, S. N. (2005). Pilot plant investigation on petrochemical wastewater treatment for the removal of copper and chromium with the objective of reuse. *Desalination,* 171: 85-93.

30. Aziz, H. A., Adlan, M. N. and Ariffin, K. S. (2008). Heavy metals (Cd, Pb, Zn, Ni, Cu andCr(III)) removal from water in Malaysia: Post treatment by high quality limestone, *Bioresource Technology*, 99: 1578-1583.
31. Maralmaa, B., Erdenechimeg, D., Koichiro, S. and Yoshihiro, S. (2018). Removal and recovery of heavy metals from industrial wastewater by precipitation and foam separation using lime and casein. *Journal of Environmental Science and Technology*, 11 (1): 1-9.
32. Zewail, T. M. and Yousef, N. S. (2015). Kinetic study of heavy metal ions removal by ion exchange in batch conical air spouted bed. *Alexandria Engineering Journal*, 54: 83-90.
33. Abo-Farha, S. A., Abdel-Aal, A. Y., Ashour, I. A. and Garamon, S. E. (2009). Removal of some heavy metal cations by synthetic resin purolite C100. *Journal of Hazardous Materials*, 169: 190-194.
34. Rudnicki, P., Hubicki, Z. and Kołodyńska, D. (2014). Evaluation of heavy metal ions removal from acidic wastewater streams. *Chemical Engineering Journal*, 252: 362-373.
35. Gurnule, W. B. and Dhote, S. S. (2012). Preparation, characterization and chelating ion-exchange properties of copolymer resin derived from 2,4-dihydroxy benzoic acid, ethylene diamine and formaldehyde. *Der Pharma Chemica,* 4: 791-799.
36. Lin, L. and Juang, R. (2007). Ion-exchange kinetics of Cu(II) and Zn(II) from aqueous solutions with two chelating resins. *Chemical Engineering Journal*, 132: 205-213.
37. Agnieszka, B., Monika, O. N. and Stanisława, S. R. (2016). Removal of lead, cadmium and copper ions from aqueous solutions by using ion exchange resin C-160. *Mineral Resources Management,* 32(4): 129-140.
38. Ríos C. A., Williams C. D. and Roberts C. L. (2008). Removal of heavy metals from acid mine drainage (AMD) using coal fly ash, natural clinker and synthetic zeolites. *Journal of Hazardous Materials*, 156: 23–35.
39. Motsi, T. Rowson, N. A. and Simmons, M. J. H. (2009). Adsorption of heavy metals from acid mine drainage by natural zeolite. *International Journal of Mineral Processing*, 92: 42-48.
40. Alvarez, A. E., Garcıa, S. A. and Querol, X. (2003). Purification of metal electroplating wastewaters using zeolites. *Water Research*, 37:4855-4862.
41. Yazan, T. and Suhail, S. (2017). The removal of heavy metals from aqueous solution using natural Jordanian zeolite. *Applied Water Science*, 7:2021-2028.
42. Erdem, E., Karapinar, N. and Donat, R. (2004). The removal of heavy metal cations by natural zeolites. *Journal of Colloid and Interface Science*, 280: 309-314.
43. Kragovi´c, M., Dakovi´c, A., Markovi´c, M., Krsti´c, J., Gatta, G.D. and Rotiroti, N. (2013).Characterization of lead sorption by the natural and Fe(III)-modified zeolite. *Applied Surface Science*, 283: 764-774.
44. Kragovi´c, M., Dakovi´c, A., Sekuli´c, Ž., Trgo, M., Ugrina, M., Peri´c, J. and Gatta, G. D. (2012). Removal of lead from aqueous solutions by using the natural and Fe(III)-modified zeolite. *Applied Surface Science*, 258: 3667-3673.
45. Kragovi´c, M., Pašali´c, S., Markovi´c, M., Petrovi´c, M., Nedeljkovi´c, B., Momˇcilovi´c, M. and Stojmenovi´c, M. (2018). Natural and modified zeolite-alginate composites. Application for removal of heavy metal cations from contaminated water solutions. *Minerals,* 8(11): 2-16.
46. Parag, S., Vikal, G. and Ruchi, K. (2010). Synthesis of zeolite from fly ash and removal of heavy metal ions from newly synthesized zeolite. *E-Journal of Chemistry,* 7(4): 1200-1205
47. Lu, X., Wang, F., Li, X., Shih, K. and Zeng, E. Y. (2016). Adsorption and thermal stabilization of Pb^{2+} and Cu^{2+} by zeolite. *Industrial Engineering Chemistry Research*, 55: 8767-8773.
48. Farooq, U., Kozinski, J. A., Khan, M. A. and Athar, M. (2010). Biosorption of heavy metal ions using wheat based biosorbents − A review of the recent literature. *Bioresource Technology*, 101: 5043-5053

49. Sivarajasekar, N. and Baskar, R. (2019). Adsorption of basic magenta II onto H_2SO_4 activated immature *Gossypium hirsutum* seeds: kinetics, isotherms, mass transfer, thermodynamics and process design. *Arabian Journal of Chemistry*, 12(7): 1322-1337.
50. Ruparelia, J. P., Duttagupta, S. P., Chatterjee, A. K. and Mukherji, S. (2008). Potential of carbon nano materials for removal of heavy metals from water. *Desalination*, 232: 145-156.
51. Tawabini, B., Al-Khaldi, S., Atieh, M. and Khaled, M. (2010). Removal of mercury from water by multi-walled carbon nanotubes. *Water Science and Technology*, 61: 591-598.
52. Pyrzynska K. and Bystrzejewski M. (2010). Comparative study of heavy metal ions sorption onto activated carbon, carbon nanotubes, and carbon-encapsulated magnetic nanoparticles. *Colloids Surfaces* A, 362: 102-109.
53. Sall, M. L., Diaw, A. D., Sall, D. G., Biraud, A. C., Oturan, N., Oturan, M. A., Fourdrin, C., Huguenot, D. and Aaron, J. J. (2018). Removal of lead and cadmium from aqueous solutions by using 4-amino-3-hydroxynaphthalene sulfonic acid-doped polypyrrole films. *Environmental Science and Pollution Research*, 25: 8581-8591.
54. Moradi, A., Moghadam, P. N., Hasanzadeh, R., Sillanpaa, M. (2017). Chelating magnetic nano composite for the rapid removal of Pb(II) ions from aqueous solutions: characterization, kinetic, isotherm and thermodynamic studies. *RSC Advances*. 7: 433-448.
55. Sao, K., Pandey, M., Pandey, P. K. and Khan, F. (2017). Highly efficient biosorptive removal of lead from industrial effluent. *Environmental Science and Pollution Research*, 24: 18410-18420.
56. Bulgariu, D. and Bulgariu, L. (2016). Potential use of alkaline treated algae waste biomass as sustainable biosorbent for clean recovery of cadmium(II) from aqueous media: batch and column studies. *Journal of Cleaner Production,* 112: 4525-4533.
57. Zuo, W. Q. Chen, C. Cui, H. J. and Fu, M. L. (2017). Enhanced removal of Cd(II) from aqueous solution using $CaCO_3$ nanoparticle modified sewage sludge biochar. *RSC Advances*, 7: 16238-16243.
58. Sharma, R., Sarswat, A., Junior, C. U. P. and Mohan, D. (2017). Cadmium and lead remediation using magnetic and non-magnetic sustainable biosorbents derived from *Bauhinia purpurea* pods. *RSC Advances*, 7: 8606-8624.
59. Zha, R., Shi, T., Zhang, Z., Xu, D., Jianga, T. and Zhang, M. (2017). Quasi-reverse-emulsion-templated approach for a facile and sustainable environmental remediation for cadmium. *RSC Advances*, 7: 6345-6357.
60. Luo, M., Lina, H., Lia, B., Donga, Y., Hea, Y. and Wanga, L. (2018). A novel modification of lignin on corncob-based biochar to enhance removal of cadmium from water. *Bioresource Technol*ogy, 259: 312-318.
61. Tang, C. Shu, Y. Zhang, R. Li, X. Song, J. Li, B. Zhang, Y. Oua, D. (2017). Comparison of the removal and adsorption mechanisms of cadmium and lead from aqueous solution by activated carbons prepared from *Typha angustifolia* and *Salix matsudana*. *RSC Adv*ances, 7: 16092-16103.
62. Ma, L., Wei1, Q., Chen, Y., Song, Q. Sun, C. Z. and Wang, G. (2018). Removal of cadmium from aqueous solutions using industrial coal fly ash-nZVI. *Royal Society Open Sci*ence, 5: 171051.
63. Chen, G. and Shi, L. (2017). Removal of Cd(II) and Pb(II) ions from natural water using a low-cost synthetic mineral: Behavior and mechanisms, *RSC Advances,* 7: 43445-43454.
64. Sutirman, Z. A., Sanagi, M. M., Abd Karim, K. J. and Wan Ibrahim, W. A. (2016). Preparation of methacrylamide-functionalized crosslinked chitosan by free radical polymerization for the removal of lead ions. *Carbohydrate Polymer,* 151: 1091-1099.
65. Gabris, M. A., Jume, B. H., Rezaali, M., Syed, S. and Nodeh, H. R. (2018). Novel magnetic graphene oxide functionalized cyanopropyl nanocomposite as an adsorbent for the removal of Pb(II) ions from aqueous media: equilibrium and kinetic studies. *Environmental Science Pollution Research*, 25(27): 27122-27132.

66. Gao, T., Yu, J., Zhou, Y. and Jiang, X. (2017). The synthesis of graphene oxide functionalized with dithiocarbamate group and its prominent performance on adsorption of lead ions, *Journal of Taiwan Institute of Chemical Engineering,* 71: 426-432.
67. Tan, P., Sun, J., Hu, Y. Y., Fang, Z., Bi Q., Chen, Y. C. and Cheng, J. H. (2015). Adsorption of $Cu(^{2+})$, $Cd(^{2+})$ and $Ni(^{2+})$ from aqueous single metal solutions on graphene oxide membranes. *Journal of Hazardous Material*, 297: 251-260.
68. Nuri, U. and Mustafa E. (2006). Adsorption characteristics of heavy metal ions onto a low cost biopolymeric sorbent from aqueous solutions. *Journal of Hazardous Materials,* B136: 272-280.
69. Murat, S. D., Harikishore, K. R. and Berkant, K. (2014). Biosorption properties of pretreated sporopollenin biomass for lead(II) and copper(II): Application of response surface methodology. *Ecological Engineering,* 68: 200-208.
70. Nuri, U. and Mustafa E. (2007). Removal of heavy metal ions by using dithiocarbamated-sporopollenin. *Separation and Purification Technology*, 52: 461-469.
71. Sener, M., Kayana, B., Akaya, S., Zmenb, B. G. and Kalderisc D. (2016). Fe-modified sporopollenin as a composite biosorbent for the removal of Pb^{2+} from aqueous solutions. *Desalination and Water Treatment,* 57: 28294-28312.
72. Ahmad N. F., Kamboh M. A., Nodeh H. R., Abd Halim S. N. and Mohamad S. (2017). Synthesis of piperazine functionalized magnetic sporopollenin: A new organic-inorganic hybrid material for the removal of lead(II) and arsenic(III) from aqueous solution. *Environmental Science and Pollution Research*, 24: 21846 -21858.
73. Ersoz, M., Pehlivan, E., Dunkan, H.J., Yildiz, S. and Pehlivan, M. (1995). Ion exchange equilibria of heavy metals in aqueous solution in aqueous solution on new chelating resins of sporopollenin. *Reactive Polymers,* 24: 195-202.
74. Idris S. and Gulsin A. (2015) Chitosan/ sporopollenin microcapsules: Preparation, characterization and application in heavy metal removal. *International Journal of Biological Macromolecules,* 75: 230-238.
75. Çimen, A., Bilgiç, A., Kursunlu, A. N., Gübbük, I. H. and Uçan, H. I. (2014). Adsorptive removal of Co(II), Ni(II), and Cu(II) ions from aqueous media using chemically modified sporopollenin of *Lycopodium clavatum* as novel biosorbent. *Desalination and Water Treatment*, 52: 4837-4847.
76. Gubbuk, I. H. (2011). Isotherms and thermodynamics for the sorption of heavy metal ions onto functionalized sporopollenin. *Journal of Hazardous Materials,* 186: 416-422.
77. Gubbuk, I. H., Gürfidan, L., Serkan, E. and Yilmaz, M. (2012). Surface modification of sporopollenin with calixarene derivative, characterization and application for metal removal. *Water Air Soil Pollution*, 223: 2623-2632.
78. Sayin, S., Gubbuk, I. H. and Yilmaz, M. (2013). Preparation of calix[4]arene-based sporopollenin and examination of its dichromate sorption ability. *Journal of Inclusion Phenomena and Macrocyclic Chemistry,* 75:111-118.
79. Hassan, A. M, Wan Ibrahim, W. A., Bakar M. B, Sanagi, M. M., Sutirman, Z. A, Nodeh, H. R and Mokhter M. A. (2020). New effective 3-aminopropyltrimethoxysilane functionalized magnetic sporopollenin-based silica coated graphene oxide adsorbent for removal of Pb(II) from aqueous environment. *Journal of Environmental Management,* 253: 109658.
80. Grahame, M., Andrew, N. B., Alberto, D. T., Stephen L. A. and Thozhukat, S. (2015). Sporopollenin, the least known yet toughest natural biopolymer. *Frontiers in Materials*, 2: 66.
81. Amro, K. F. D., Elham, M. A., Salwa, A. A. and Mai, M. R. (2016). Fabrication and characterisation of novel natural *Lycopodium clavatum* sporopollenin microcapsules loaded *in-situ* with nano-magnetic humic acid-metal complexes. *Journal of Encapsulation and Adsorption Sciences,* 6: 109-131.

Malaysian Journal of Analytical Sciences (MJAS)
Published by Malaysian Analytical Sciences Society

CYTOTOXIC ACTIVITY OF *Erythrina fusca* LOUR. LEAF, TWIG AND FLOWER EXTRACTS

(Aktiviti Sitotoksik Ekstrak Daun, Ranting, dan Bunga *Erythrina fusca* Lour.)

Adiez Sapura Azmi[1], Norina Abdul Rahim[1], Zuriati Zahari[1], Fatimah Salim[2,3]*

[1]*Faculty of Applied Sciences,*
Universiti Teknologi MARA, Shah Alam, 40450, Selangor, Malaysia
[2]*Atta-ur-Rahman Institute for Natural Product Discovery (AuRIns),*
Universiti Teknologi MARA Selangor Branch, Puncak Alam Campus, 42300 Bandar Puncak Alam, Selangor, Malaysia.
[3]*Centre of Foundation Studies,*
Universiti Teknologi MARA Selangor Branch, Dengkil Campus, 43800 Dengkil, Selangor, Malaysia

**Corresponding author: fatimah2940@uitm.edu.my*

Received: 29 November 2019; Accepted: 2 April 2020; Published: 9 June 2020

Abstract

Erythrina fusca Lour. belongs to the legume family (Fabaceae) is a species of flowering tree, locally known as 'chengkering'. The plant is traditionally used for reducing inflammation, relieving migraine, reducing skin irritation and for dressing fresh wounds. This work reports on cytotoxic activities of the methanolic leaf, twig and flower extracts of *E. fusca* Lour. against human liver cancer cell line (HepG2) and monkey kidney normal cell line (Vero). The extracts were found to be nontoxic on both cell lines with IC_{50} values of more than 100 µg/mL and therapeutic index of less than 2. In order to obtain comparative information on the chemical composition and the complexity of the structure, the methanolic extracts were profiled on a reversed-phase ultrahigh-performance liquid chromatography (UHPLC).

Keywords: *Erythrina fusca* Lour., cytotoxic activities, HepG2, Vero, ultrahigh-performance liquid chromatography

Abstrak

Erythrina fusca Lour. berasal daripada famili legume (Fabaceae) merupakan spesies pokok berbunga dan nama tempatannya ialah chengkerng. Tumbuhan ini digunakan secara tradisional untuk mengurangkan keradangan, melegakan migrain, mengurangkan kegatalan kulit dan pembalut luka. Kajian ini melaporkan aktiviti sitotoksik ekstrak metanol daun, ranting dan bunga *E. fusca* Lour. terhadap sel tunggal kanser hati manusia (HepG2) dan sel tunggal buah pinggang monyet (Vero). Kesemua ekstrak didapati tidak toksik kepada kedua jenis sel tunggal yang diuji dengan nilai IC_{50} lebih daripada 100 µg/mL dengan indeks teraputik kurang daripada 2. Bagi memperolehi data perbandingan mengenai komposisi kimia dan kerumitan dalam struktur mereka, kesemua ekstrak metanol ini telah diprofilkan dalam fasa terbalik kromatografi cecair berprestasi tinggi ultra (UHPLC).

Keywords: *Erythrina fusca* Lour., aktiviti sitotoksik, HepG2, Vero, kromatografi cecair berprestasi tinggi ultra

Introduction

Erythrina is a genus belonging to the legume family, Fabaceae. The name "*Erythrina"* is derived from the Greek word "erythros" which means "red" referring to the flowers although some species exhibit pink, purple, orange, white, green, yellow and even coral colors [1-2]. Out of 290 species of the genus, 7 are available in Malaysia including *Erythrina fusca* Lour. and is locally known as 'chengkering' [3-5].

Erythrina fusca Lour. has been traditionally used in several countries including Malaysia. The bark of this plant is used to relieve migraines in Peru [6], while the bark and leaves are utilized to relieve inflammation in Thailand [7]. The seeds are used to cure skin irritation [8] while the inner bark is scraped for dressing fresh wounds in Indonesia [9]. The latter practice has also been observed among Malaysians population [10]. Moreover, the flowers are eaten as vegetables in Guatemala, and young leaves, in Java and Bali, Indonesia [11]. A thorough literature search revealed that most of the parts of the plant have been subjected to biological activities including anti-viral, anti-inflammatory, antitussive, rheumatism, hematuria, central nervous system depressor, hypotensive and as uterine stimulant [7-15]. Interestingly, none of the parts has been subjected to cytotoxic activity. Despite the traditional use and the biological activities reported thus far, there is no available data on the cytotoxic effect of the plant to our knowledge.

Thus in the present study, the methanolic crude extracts of the leaves, twigs and flowers of *E. fusca* Lour. were assessed for cytotoxic activity against human liver cancer cell line (HepG2) and on normal monkey kidney cell line (Vero). The extracts were also profiled on a reversed-phase ultrahigh-performance liquid chromatography (UHPLC) to obtain the comparative information on the chemical composition and their complexity in structure.

Materials and Methods

Chemical and reagents

Methanol (MeOH) analytical grade and acetonitrile (MeCN) HPLC grade were purchased from RCI Labscan (Bangkok, Thailand) and ultra-pure water (UPW) was from Sartorius. The leaves, twigs and flowers of *E. fusca* Lour. were collected from Bangi, Malaysia. A voucher specimen HTBP 5273 was identified by a certified botanist, Mr. Ahmad Zainudin Ibrahim, and deposited at the Herbarium of Atta-Ur-Rahman Institute for Natural Product Discovery (AuRIns).

Extraction procedure

The leaves, twigs and flowers of *E. fusca* Lour. were separately cut into small pieces, air-dried and ground into fine powder. The leaf (1.2 kg), twig (0.045 kg) and flower (0.060 kg) fine powder were subjected to exhaustive extraction using MeOH for 72 hours in room temperature. The extracts were filtered, and the solvent was evaporated under reduced pressure by using rotary evaporator yielding 60 g, 0.783 g, 2 g of leaf, twig and flower extracts, respectively. The crude extracts were stored at 4 °C prior to analysis.

Reversed-phase ultrahigh-performance liquid chromatography

The reversed-phase UHPLC analysis was performed using the DIONEX Ultimate 3000 HPLC system (Thermo-Fisher, USA) coupled with a diode array detector and equipped with an auto-sampler injector. The chromatography was performed on Hypersil GOLD C18 column (Thermo Scientific, Malaysia) with particle size 5 µm, height 250 mm and 4.6 mm internal diameter and pore size of 175 A. The control of the instrument and the data analyses were conducted by software Chromeleon version 7.2 provided by the supplier.

Sample preparation

Two mg/mL of each of the extracts were fully dissolved in MeCN and the samples were filtered with PTFE 0.45 µm filter (Agilent). Then the samples were subjected to a reversed phase UHPLC analyses. MeCN (acted as non-polar solvent) and ultra-pure water (acted as polar solvent) were used as solvent system.

UPHLC procedure

Chromatographic conditions were optimized in order to reach baseline separated peaks of the overall observable chemical components. For this purpose, different mobile phases with varying gradients were employed. The mobile phase consisting of MeCN/UPW with a gradient set up delivered good baseline separation of the overall observable components. The initial gradient was set at 5% MeCN: 95% UPW and gradually increased to 30% MeCN: 70% UPW at 12 minutes then increased to 95% MeCN: 5% UPW at duration of 33 minutes. The column conditioning and equilibrium were performed in 5 minutes attaining the initial condition. A 20 µL of the sample extracts were injected into the chromatographic column thermostatically maintained at 24.5 °C. The flow rate used was 1.00 mL/min and the detection of the eluted peaks was performed at 208 nm.

Cell Lines Culture

HepG2 cell was acquired from Dr. Normala at AuRIns, UiTM, while Vero cell was obtained from Malaysia Institute of Pharmaceutical & Nutraceuticals (IPharm). Both cell lines were cultured in growth medium containing Dulbecco Minimal Essential Media (Sigma) supplemented with 10% (v/v) Fetal Bovine Serum (Sigma) and 1% of 1000 µg/mL of Penicillin/Streptomycin (Nacalai Tesque). Incubation was carried out at 37 °C with an atmospheric 5% (v/v) CO_2 to allow the growth of the cells. Growth media were changed every 2 days and subculture was carried out when it reached 80% cell growth confluency.

MTT Assay

The cytotoxic activity on HepG2 and Vero cells were determined by the MTT assay described by Widianto et al. [7] with slight modifications. Briefly, 100 µL of 150,000 cells/mL suspension was added into 96-well-plate. The plates were incubated overnight in an incubator supplemented with 5% (v/v) CO_2 at 37 ºC to allow cells to be attached. The next day, the media was removed from the wells and 100 µL of fresh growth media were added into all wells except for the highest concentration wells. One hundred fifty µL of fresh growth media containing the highest concentration of drug was added into the highest concentration wells.

Serial dilutions of a 2-fold factor covering a range from 1000 – 15.625 µg/mL were then performed. Fifty µL were removed from the highest concentration wells into the next column and mixed appropriately. This step was repeated until the last column. The final 50 µL aspirated from the last column was discarded. Then, 100 µL of media with 1% (v/v) DMSO were added into the wells which served as a negative control while, other wells served as positive control without drugs. Plates were served in triplicate. The plates were placed in an incubator supplemented with 5% (v/v) CO_2 at 37 °C for 24 hours. After 24 hours of incubation, the test plates were inspected under an inverted microscope (Nikon, Japan) to observe the normal growth of both cells. Additional information was recorded, such as drug insolubility or contamination, etc. All media were discarded from the wells. Then 50 µl of MTT solution of 1 mg/mL was added to each well of test plates and incubated for 3 to 4 additional hours (until a subtle colour change was observed, but the maximum hour taken was not more than 4 hours).

The cell absorbance from the assay plate, illustrated in Figure 1, was measured by using a microplate reader (Tecan, USA) at a selected wavelength of 570 nm. The percentage growth inhibition was calculated using the formula (equation 1):

$$\text{Cell viability (\%)} = \frac{\text{Absorbance value of test compound}}{\text{Absorbance value of Negative Control}} \times 100\% \quad (1)$$

Statistical analysis was performed by SPSS 23.0 using one-way ANOVA. All results were presented as mean ± standard deviation.

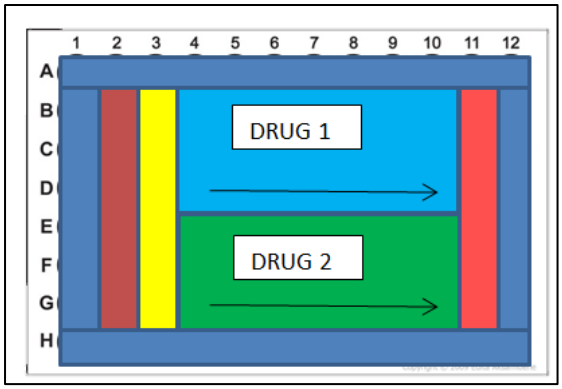


Figure 1. Illustration of assay plate

Results and Discussion

Cytotoxicity activities on HepG2 and Vero cell lines

According to the American National Cancer Institute guidelines [16], the limit of activity for crude extracts at 50% inhibition (IC_{50}) of proliferation was set less than 30 µg/mL after an exposure time of 24 hours [17]. As shown in Table 1, the IC_{50} values of the methanolic extracts of the leaves (MLE), twigs (MTE) and flowers (MFE) on HepG2 cancer cells were considered to be non-active due to their very high concentrations required to obtain 50 percent of cell viability. Similarly, a higher concentration of the extracts was required to achieve 50% cell viability (CC_{50}) on the normal cell Vero that considered them to be non-toxic. Despite this, the Vero cells still showed proliferation on those high concentrations. The pattern for inhibition for both cell lines by the extracts is shown in Figure 2 below. The therapeutic index for all the extracts are also less than 2, indicating they are not potent for the tested activities [17].

UHPLC Profiling

UHPLC chemical profiling exercises have been widely established in plant extracts. They are reputable practices for quality control and authentication. In this study, the purpose of UHPLC profiling on leaf, twig and flower extracts of *E. fusca* Lour. is to obtain comparative information on the chemical composition and the structure complexity that possibly exist in the extracts. By referring to Figure 3, based on the peak intensity and retention time, the three extracts produced different profiles of chemical constituents. The variety in the constituents is well distributed in the flower (c) extract compared to the leaf (a) and twig (b) extracts. The amount and the existence of major constituents (minutes 2.83, 15.92, 22.98 and 24.48) are also clearly different in the extracts. Notably, based on the elution time (14 - 25 minutes), most of the chemical constituents exhibited moderate polarity.

Table 1. IC_{50}, CC_{50} and therapeutic values of extracts

Sample	HepG2 (IC_{50}) (µg/ml)	Normal Vero (CC_{50}) (µg/ml)	Therapeutic Index (CC_{50}/ IC_{50}) CC_{50} Vero/ IC_{50}HepG2
MLE	771.76 ±15.85****	588.06±9.36****	0.76
MTE	315.07±6.98****	309.95±15.24****	0.98
MFE	182.09±11.62****	223.33±2.56****	1.23

*CC_{50} is the concentration at which 50% cells survive and IC_{50} is the concentration at which 50% cell death occurs with ± standard deviation. MLE refers to leaves methanolic crudes while MTE refers to twigs methanolic crudes and (MFE) refers to flower methanolic crudes. Statistical analysis was conducted using one-way ANOVA ($p<0.0001$) where **** denotes statistically significant difference between the MLE, MTE and MFE.

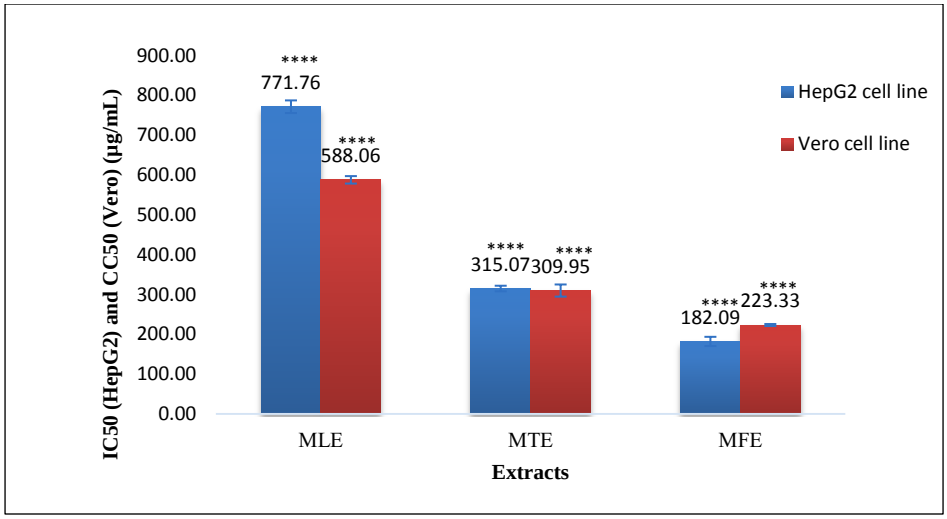


Figure 2. IC_{50} (µg/ml) and CC_{50} (µg/ml) of three extracts MLE, MTE and MFE against cancer liver cell line (HepG2) and compared with normal cell line (Vero), respectively, after 24 hours of incubation. Statistical analysis was conducted using one-way ANOVA ($p< 0.0001$) where **** denotes statistically significant difference between the MLE, MTE and MFE.

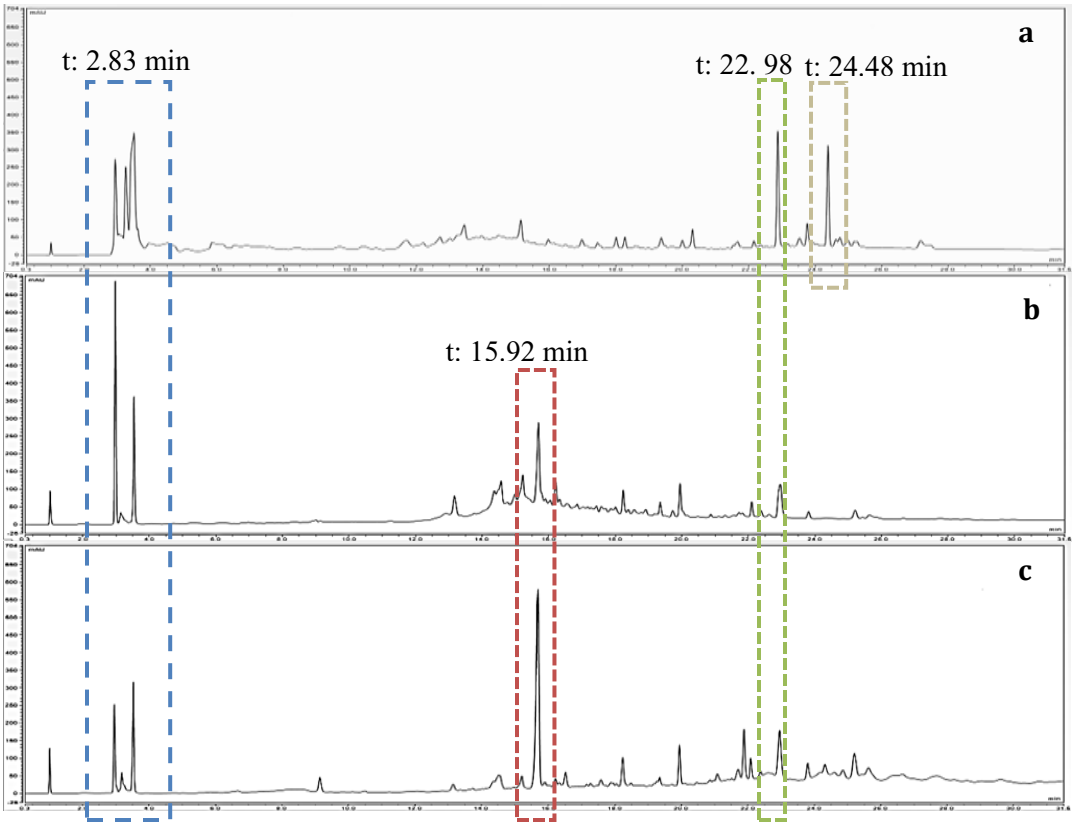


Figure 3. Chromatograms of methanolic extracts of the (a) leaves, (b) twigs and (c) flowers of *E. fusca* Lour. using gradient mode UHPLC and MeCN/UPW as the solvent system

The qualitative analysis on the chromatogram of the extracts is complemented with a thorough literature review on the classes of chemical composition reported for the species *E. fusca* Lour. and the genus *Erythrina*. Among the classes of compounds that have been reported in the *Erythrina* genus are alkaloids, flavonoids, pterocarpans and terpenoids as well as other miscellaneous [18]. Among those classes of compounds reported, the alkaloids are the major components where a total of 143 have been isolated from all plant parts [18-19]. However, for *E. fusca* Lour., very little has been reported. To date only 12 chemical components, which all are alkaloids, have been identified: erysodine, erysovine, erysopine, erysotrine, erythraline, erysothiovine, erysothiopine, epierythratidine, erythratinone, erythramine, erythratine and erythrinane [19].

All the alkaloids exhibit moderate polarity thus should be eluted in the middle of the chromatograms, supporting our early observation reported above. Furthermore, the detection was obtained at 208 nm where strong absorption for π-π^* and n-π^* electronic transitions usually observed for the alkaloid classes of compound [20]. This could be further supported by our preliminary qualitative phytochemical screening which revealed the presence of a high density of alkaloids in the flower, followed by the twig and the leaf extracts. Interestingly, since most of the biological activities reported for the *Erythrina* species were related to their alkaloids content [21], the pattern of extracts inhibition (Figure 2) in the cytotoxic activity on both tested cell lines also agreed with this claim. Nonetheless, this claim needs to be confirmed by further structural identification analysis on the extracts.

Conclusion

This work reports on the nontoxic property of the methanolic leaf, twig and flower extracts of *E. fusca* Lour. against human liver cancer cell line (HepG2) and monkey kidney normal cell line (Vero). Based on the peak intensity and retention time, the three extracts exhibited different UHPLC profile; the pattern of cytotoxic activities could be due to the alkaloid class of compounds. However, further studies are necessary to confirm and identify the chemical constituents that give rise to the peaks in the chromatogram and to strengthen the claim on the existence of alkaloids.

Acknowledgement

The authors would like to acknowledge Atta-ur-Rahman Institute for Natural Product Discovery (AuRIns) and Faculty of Applied Sciences (FSG), Universiti Teknologi MARA, for providing equipment and workplace to conduct the work. Appreciation also goes to Mr. Ahmad Zainudin Ibrahim for collecting and identifying the sample.

References

1. Stein, G. (2009). Introduction to the coral trees (*Erythrina* species). https://davesgarden.com/ guides/articles/ view/2594. [Access online 29 March 2020].
2. Salma, K., Gabr, R. O., Bakr, H. M., Elshishtawy, Ahlam, M. and Taha, S. E. (2017). Botanical and genetic characters of *Erythrina neillii* cultivated in Egypt. *Revista Brasileira de Farmacognosia,* 27(3): 273-281.
3. Atta-Ur-Rahman (2005). Studies in natural products chemistry. Elsevier B.V, Amsterdam: pp. 822.
4. Kumar, A., Lingadurai, S., Jain, A. and Barmanthat, N. R. (2010). *Erythrina variegata* Linn: A review on morphology, phytochemistry, and pharmacological aspects. *Pharmacognosy Review,* 4(8): 147-152.
5. Fazleen, I. A. B., Mohd, F. A. B., Norazlin, A., Susi, E. and Asmah, R. (2018). A review of Malaysian medicinal plants with potential anti-inflammatory activity. *Advances in Pharmacological Sciences,* 18: 13.
6. Valkenburg, J. L. C. H. and Bunyapraphatsara, N. (2001). Plant resources of South-East Asia: Medicinal and poisonous plants 2. Backhuys Publishers, Netherlands: pp. 252-532.
7. Widianto, M. B., Padmawinata, K. and Suhalim, H. (1980). An evaluation of the sedative effect of the seeds of *Erythrina fusca* Lour. 4th Asian Symposium on Medicinal Plants and Spices, Thailand: pp. 147.

8. Duke, J. A. (1994). Amazonian ethnobotanical dictionary. CRC Press, United States.
9. Singapore Botanic Gardens (2013). *Erythrina* fusca Lour. https://florafaunaweb.nparks.gov.sg/ specialpages /plant-detail.aspx?id=2879. [Access online 1st July 2019]
10. Wasuwat, S. (1967). A list of Thai medicinal plants. ASRCT, Bangkok: pp. 22.
11. Russo, R. O. and Baguinon N. T. (1997). *Erythrina fusca* Loureiro. http://www.proseanet.org. [Access online 29 March 2020].
12. Mc Kee, T. C., Bokesch, H. R., Mc Cormick, J. L., Rashid, A., Spielvogel, D., Gustafson, K. R., Alavanja, M. M., Cardelina, I. I. J. H. and Boyd, M. R. (1997). Isolation and characterization of new anti-HIV and cytotoxic leads from plants, marine and microbial organisms. *Journal of Natural Products,* 60(5): 431-438.
13. Perry, L. M. (1980). Medicinal plants of East and Southeast Asia. MIT Press, Cambridge.
14. Ross, S. A., Megalla, S. E., Bishay, D. W. and Awad, A. H. (1980). Studies for determining antibiotic substances in some egyptian plants. Part I. Screening for antimicrobial activity. *Fitoterapia,* 51: 303-308.
15. Ratnasooriya, W. D. and Dharmasiri, M. G. (1999). Aqueous extract of Sri Lankan *Erythrina indica* leaves had sedative but not analgesic activity. *Fitoterapia,* 7(3): 311-313.
16. Fadeyi, S. A., Fadeyi, O. O., Adejumo, A. A., Okoro, C. and Myles, E. L. (2013). *In vitro* anticancer screening of 24 locally used Nigerian medicinal plants. *BMC Complementary and Alternative Medicine,* 13: 79.
17. Suffness, M. and Pezzuto, J. M. (1990). Assays related to cancer drug discovery. In: Hostettmann K (ed). Methods in plant biochemistry: assays for bioactivity. Academic Press, London: pp. 71-133.
18. Hussain, M. M., Tuhin, Md. T. H., Akter, F., and Rashid, M. A. (2016). Constituents of *Erytrina* – A potential source of secondary Metabolites: *A Review. Bangladesh Pharmaceutical Journal,* 19(2): 237-253.
19. Fahmy, N., Alsayed, E., El-Shazly, M. and Singab, A. N. (2019). Alkaloids of genus *Erythrina*: An updated review. *Natural Product Research,* 2019: 1-22.
20. Challener, C. A. (2001). Overview of chirality: *In Chiral drug.* Aldershot, England: pp. 3-14.
21. Daniel, R. C., Thalita, B. R., Luis, G. P. F., Thais, G., Denise, B. S., Achyut, A., Shrestha, R.L., Lucas, M. M., Marques, M. D., Baruffi, João, L. C. L. and Norberto, P. L. (2014). Leishmanicidal evaluation of tetrahydro-protoberberine and spirocyclic *Erythrina*-alkaloids. *Molecules,* 19(5): 5692-5703.

Malaysian Journal of Analytical Sciences (MJAS)
Published by Malaysian Analytical Sciences Society

SYNTHESIS AND CHARACTERIZATION OF OXYGEN-DOPED MESOPOROUS GRAPHITIC CARBON NITRIDE USING NANODISC SILICA FROM RICE HUSK ASH AS HARD TEMPLATE

(Sintesis dan Pencirian Grafitik Karbon Nitrida Berliang Meso yang di Dop dengan Oksigen di Atas Nanocakera Silika dari Abu Sekam Padi Sebagai Templat Keras)

Shittu Fatimah Bukola[1], Mohammad Anwar Mohamed Iqbal[1]*, Farook Adam[1], Mohamad Nasir Mohamad Ibrahim[1], Nur Ruzaina Abdul Rahman[2], Srimala Sreekantan[2], Noor Hana Hanif Abu Bakar[1], Mohd Hazwan Hussin[1], Hariy Pauzi[3]

[1]*School of Chemical Sciences, Universiti Sains Malaysia, 11800, Minden, Penang, Malaysia*
[2]*School of Materials and Mineral Resources Engineering*
[3] *Science and Engineering Research Centre (SERC)*
Universiti Sains Malaysia, Engineering Campus, 14300 Nibong Tebal, Seberang Perai Selatan, Penang, Malaysia

**Corresponding author: anwariqbal@usm.my*

Received: 20 November 2019; Accepted: 5 April 2020; Published: 9 June 2020

Abstract

Oxygen-doped mesoporous carbon nitride (O-MCN) was successfully synthesized through a polymerization reaction between urea and glucose using nanodisc silica (NDS) from rice husk ash as a hard template. The presence of oxygen within the framework of the MCN was confirmed using X-ray photoelectron spectroscopy (XPS) and Fourier-transformed infrared (FTIR) analyses. The scanning electron microscope (SEM) analysis indicates the existence of irregular spherical pores on the surface of O-MCN mimicking the surface morphology of the NDS. The Brunauer–Emmett–Teller (BET) surface area of the O-MCN (145 m^2g^{-1}) was similar to NDS (152 m^2g^{-1}). However, the Barrett, Joyner, and Halenda (BJH) pore size distribution of the O-MCN (48- 84 Å) was smaller than the NDS (36-203 Å). The bandgap energy of the O-MCN was calculated to be 2.53 eV. The narrow bandgap energy suggests that the O-MCN has a high potential to be used as a photocatalyst under visible light irradiation.

Keywords: mesoporous carbon nitride, oxygen-doped mesoporous carbon nitride, rice husk, rice husk ash, photocatalyst

Abstrak

Karbon nitrida berliang meso mengandungi oksigen (O-MCN) berjaya disintesis melalui tindak balas pempolimeran antara urea dan glukosa menggunakan nanocakera silika (NDS) dari abu sekam padi sebagai templat keras. Kehadiran oksigen dalam kekisi MCN disahkan melalui analisis spektroskopi fotoelektron sinar-X (XPS) dan inframerah transformasi Fourier (FTIR). analisis mikroskop elektron imbasan (SEM) menunjukkan kewujudan liang sfera tidak sekata pada permukaan O-MCN yang menyerupai morfologi permukaan NDS. Luas permukaan Brunauer–Emmett–Teller (BET) O-MCN (145 m^2g^{-1}) sama dengan NDS (152 m^2g^{-1}). Walau bagaimanapun, taburan saiz liang Barrett, Joyner, and Halenda (BJH) O-MCN (48 - 84 Å) adalah lebih kecil berbanding NDS (36-203 Å). Tenaga sela jalur O-MCN dikira sebagai 2.53 eV. Tenaga sela jalur yang sempit mencadangkan O-MCN mempunyai potensi yang tinggi untuk digunakan sebagai fotokatalis dibawah iradiasi cahaya nampak.

Kata kunci: karbon nitrida berliang meso, karbon nitrida berliang meso mengandungi oksigen, sekam padi, abu sekam padi, fotopemangkin

Introduction

Carbon nitride (CN) is a polymeric material containing carbon and nitrogen atoms that has unique properties such as semi conductivity, basicity, high hardness, chemical robustness, high chemical and mechanical stability. These properties rely on the structure, composition, and crystallinity of the CN framework. So far, five different types of structures of CN have been reported. Namely, carbon nitrides C_3N_4 (g-C_3N_4), α-C_3N_4, β-C_3N_4, cubic-C_3N_4, and pseudocubic-C_3N_4. The former is a two-dimensional CN, whereas the latter is three-dimensional CNs. Among these CNs, g-C_3N_4 has gotten considerable attention because of its unique and combined properties such as extreme hardness, energy-storage capacity, semi conductivity, gas adsorption capacity, and low density [1]. However, low surface area (<10 m^2 g^{-1}) and porosity hamper the application of g-C_3N_4 in the area of adsorption and catalysis even though the presence of basic sites is considered beneficial [1].

Since the discovery of mesoporous carbon nitrides (MCN) by Vinu et al. in 2005, various types of MCN with large surface area, pore volume, and pore diameters have been synthesized. Larger surface area can support more active sites for reaction, whereas the porous structure can improve the light absorption [2, 3]. The MCNs have been synthesized using hard-templating (nanocasting or replication) and soft-templating (self-assembly) approaches. The MCNs synthesized *via* hard-templating approach indicate better control and replication of the morphology of the targeted product compared to the MCNs prepared *via* soft-templating approach [4].

Various types of oxygen doped mesoporous carbon nitrides (O-MCN) have been reported to be active as photocatalysts under visible light irradiation [5, 6]. Among the limitations concerning the synthesis strategies of O-MCN are the use of environmentally unfriendly C, N, and O precursors such as carbon tetrachloride, formaldehyde and ethylenediamine, and multiple synthesis steps. In addition, the silica precursors used in the synthesis of the hard template are from commercial sources such as tetraethyl orthosilicate (TEOS).

In this paper, O-MCN was synthesized *via* hard templating method in a single step by polymerizing urea and glucose as the C, O, and N sources. Nanodisc silica (NDS) prepared from rice husk ash (RHA) was used as the hard template. The NDS produced from RHA add value to agricultural waste, particularly rice husk, it's environmentally advantageous, low cost of production and abundantly available. The physicochemical characterizations indicate that the catalyst has potential to be used as a photocatalyst. To the best of our knowledge, no reports were found on the use of NDS from RHA as a template for the synthesis of O-MCN.

Materials and Methods

Raw materials

Nitric acid (HNO_3, 69%), sodium hydroxide (NaOH, , >99%), glucose ($C_6H_{12}O_6$, >99%), urea (CH_4N_2O, >99%) and hydrofluoric acid (HF, 49%, QREC). All chemicals were of analytical grade and used without further purification.

Synthesis of rice husk ash

The RHA was produced from rice husk (RH) according to the method reported by Adam et al [7]. The rice husk was washed with plenty of water and then rinsed with distilled water to remove all the soluble dirt and soil. The RH was dried at room temperature for 48 hours. The clean and dried RH was then stirred in 750 mL (1.0 M) HNO_3 for 24 hours to reduce the metallic impurities. It was further washed thoroughly with distilled water until the pH of the filtrate reached 7. The acid-treated RH was dried for 24 hours at 110 ^oC and then pyrolyzed at 600 ^{0} C for 6 hours to remove the organic components of the RH in a furnace. A white colored RHA was obtained at the end of the process.

Synthesis of NDS

A sodium silicate solution was prepared by dissolving 5.0 g of the RHA in 500 mL (0.5 M) aqueous NaOH solution [8]. The pH of the sodium silicate solution was reduced to pH 7 by adding 2.0 M HNO_3 under vigorous stirring at 1200 rpm. The silica gel started to form when the pH of the sodium silicate reached 7. The gel was aged in the mother liquor for 24 hours in a closed plastic container under vigorous stirring and then for 48 hours under static to allow the silica gel to slowly precipitate. After the aging process, the formed gel was filtered and washed with distilled water until the pH of the filtrate became constant. The washed silica gel was freeze-dried to remove water [9]. A fine white powder of NDS was obtained. The powder was kept in a desiccator for further use.

Synthesis of O-MCN

The O-MCN was prepared using the method reported by Hu et al. [10] with some modifications. In a typical synthesis process, glucose (0.5 g) and urea (10 g) were dissolved in 100 mL of distilled water and heated to 70 °C under stirring. Into the solution, 0.3 g of NDS was added as a hard template. The solution was stirred at 80 ^{0} C until the water evaporated. The catalyst was then transferred into a 50 mL crucible and dried in the oven at 80 °C for 24 hours. The catalyst was uniformly ground and calcined at 550 °C for 1 hour at a heating rate of 5 °C min^{-1}. A dark brown colored powder was obtained. The powder was then dispersed in 100 mL of an aqueous solution of HF overnight to remove the NDS [11]. The O-MCN powder was filtered and washed with 1000 mL distilled water, followed by drying at 80 °C overnight.

Catalyst characterization

The prepared samples were characterized by FT-IR spectroscopy (Perkin Elmer System 2000 FT-IR Spectrophotometer) using KBr pellets technique, N_2 adsorption porosimetry (Micromeritics Instrument Corporation model ASAP 2000, Norcross), powder X-ray diffraction (Siemens Diffractometer D5000 diffractometer Kristalloflex, equipped with CuK radiation,= 0.154 nm), scanning electron microscopy (Leica Cambridge S360), energy dispersive spectrometry (EDAX FALCON SYSTEM), UV–Vis diffuse reflectance spectroscopy (Perkin Elmer Lambda 35 UV–Vis spectrophotometer) and the XPS spectrum was recorded on AXIS Ultra DLD, Kratos, equipped with an AlK X-ray source = 1486.6 eV at 10 mA, 15 kV). All binding energies were calibrated using contaminant carbon (C 1 s = 284.6 eV) as reference. The C, N, and O content were determined using CHNO analyzer.

Results and Discussion

SEM analysis

Figures 1 (a) and (b) represent the SEM image of NDS and O-MCN, respectively. From Figure 1(a), it can be seen that the surface of NDS is constructed of irregular spherical shaped nanoparticles. The de-templating of NDS from the framework of O-MCN using aqueous HF had created a porous surface, as shown in Fig. 2(b). The pores on the surface of O-MCN were spherically shaped with various sizes similar to the surface of NDS.

HRTEM analysis

The HRTEM images of NDS and O-MCN are shown in Figures 2(a) and (b). The HRTEM of NDS revealed disc-like particles with sizes in the range of 58 to 63 nm. The HRTEM of O-MCN (Figure 2(b)) indicates the interconnected elongated rod-like nanoparticles with undefined pore channels. Often, the MCN will replicate the hard template used in the synthesis process. The O-MCN synthesized by Park et al. [12] replicated the morphology of the hard templates, SBA-15, and cubic meso-SiO_2 that they had used. Cha et al. [13] synthesized sulphur doped MCN (S-MCN) utilizing SBA-15 as the hard template, and they too observed that the S-MCN replicated the SBA-15 as well. Surprisingly, in this research, the synthesized O-MCN did not replicate the disc-like morphology of the NDS. The replication was not observed, possibly due to the physical properties of the NDS compared to SBA-15 and O-MCN synthesis procedure. However, further investigations are required to confirm these assumptions.

Nitrogen sorption analysis

The nitrogen adsorption-desorption isotherms of the NDS and O-MCN is shown in Figure 3. Both materials

exhibit type-IV isotherm with H3 hysteresis loop. The type-IV isotherm confirm the existence of mesopores, whereas the H3 hysteresis loop indicates the mesopores are slit-shaped with non-uniform size [14]. The BET surface area of O-MCN (145 m^2g^{-1}) is slightly lower compared to NDS (152 m^2g^{-1}). The BJH pore size distribution determined from the adsorption branch is given in inset of Figure 4. From the porogram of NDS, the mesopore distribution was predominantly in the range of 39-203 Å. The etching process using HF had created pores with broad diameter range. The pore size distribution in O-MCN was determined to be in the range of 48- 84 Å. The existence of pore sizes in a broad range is also visible, as in the SEM image of O-MCN (Figure 1(b). The pore volume of NDS was 0.30 cm^3g^{-1}, whereas the pore volume of O-MCN was 0.28 cm^3g^{-1}.

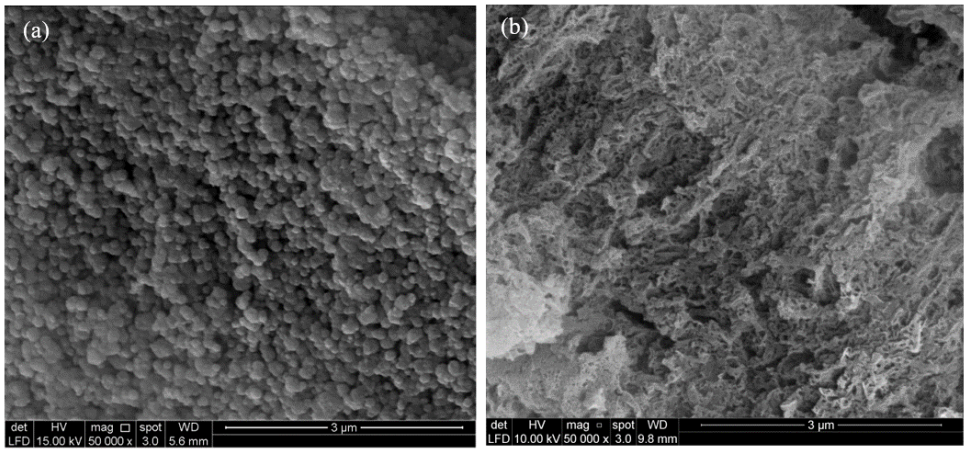


Figure 1. The SEM images of (a) NDS (magnification?) and (b) O-MCN

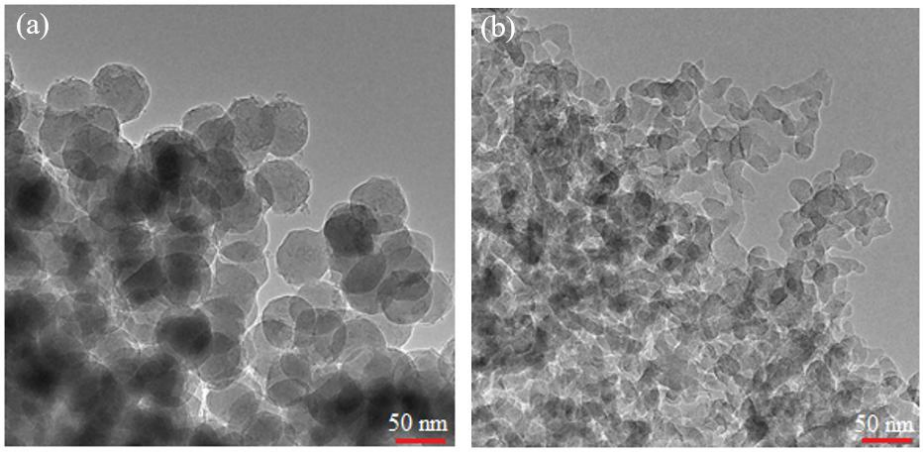


Figure 2. The HRTEM image of (a) NDS and (b) O-MCN

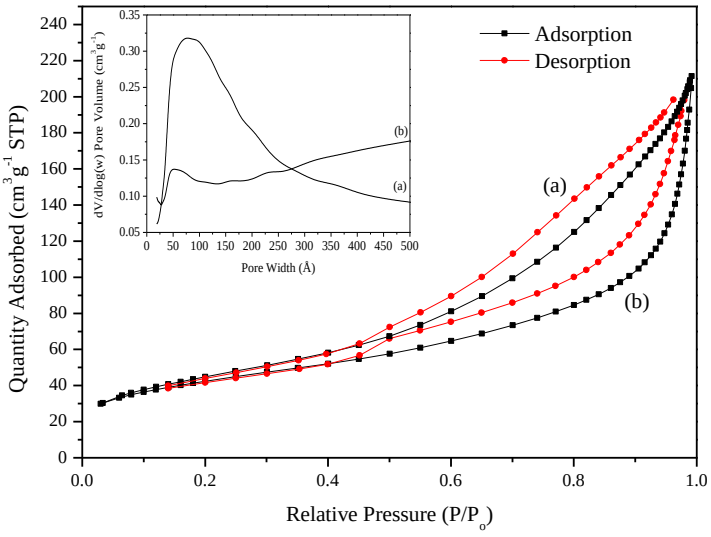


Figure 3. The nitrogen adsorption isotherms and BJH pore size distribution (inset) of (a) NDS and (b) O-MCN

FT-IR analysis

The FT-IR spectrum of O-MCN is shown in Figure 4. The sharp intense band observed at 810 cm^{-1} is assigned to the characteristic bending modes of triazine units [15]. The bands with weak intensity at 3159 and 3315 cm^{-1} are assigned to the stretching modes of secondary and primary amines and their intermolecular hydrogen bonding [16]. The collection of bands at 1200-1600 cm^{-1} is due to the stretching vibrations of heptazine-derived repeating units [17]. The absorption band at 2163 cm^{-1} is assigned to C≡N or N=C= N due to incomplete polymerization of the precursors [18]. The presence of the C-O bond is indicated by the presence of a weak shoulder at 1156 cm^{-1}. The IR bands related to the silica matrix could not be detected, indicating the successful removal of the template using aqueous HF.

X-ray diffraction analysis

The XRD pattern of the synthesized O-MCN is shown in Figure 5. A diffraction peak with a strong intensity at 2Θ = 27.2° in the diffractogram of the O-MCN is indexed to the (002) crystal plane. The plane is attributed to the lamellar packing of graphite in the π-conjugate plane [19]. The d_{002} value of O-MCN calculated from Bragg Equation was 0.329 nm. The value was relatively shorter compared to pure graphitic carbon (0.353 nm) [20]. The crystallite size of O-MCN determined from the Scherrer Equation was 3.00 nm. The peak associated with amorphous silica at 2Θ ~22° is also invisible [21], indicating the high purity of O-MCN.

CHNO analysis

The elemental analysis of O-MCN is summarized in Table 1. The chemical composition of the O-MCN shows a C/N ratio of 0.75 which is equivalent to the ideal or theoretical C/N value (0.75) of single-crystalline graphitic carbon nitride [22].

X-ray photoelectron analysis

The XPS of C 1s spectrum (Figure 6(a)) was fitted into five peaks at 283.2, 284.6, 285.9, 286.8 and 288.1 eV. These are attributed to sp^2 hybridized graphitic carbon, sp^3 hybridized graphitic carbon, N-C=C bond, C-O and C=N/C=O bonds, respectively [23, 24]. The deconvolution of O 1s spectrum resulted in two peaks at 529.2 and 531.3 eV (Fig. 6(b)). The former peak corresponds to the lattice oxygen, whereas the latter corresponds to the presence of C-O functional group [25]. The deconvolution of N 1s spectrum shown in Figure 6(c) shows the existence of three peaks. The

peak at 396.8 eV could be assigned to the sp^2 hybridized aromatic nitrogen bonded to carbon atoms (C-N=C) while the peak at 398.4 eV emerged from the tertiary nitrogen in the triazine units N-C_3 groups. Finally, the peak at 401.3 eV is derived from N atom of the amino-functional group with H-atom (C-N-H) in the aromatic CN heterocycles [26, 27].

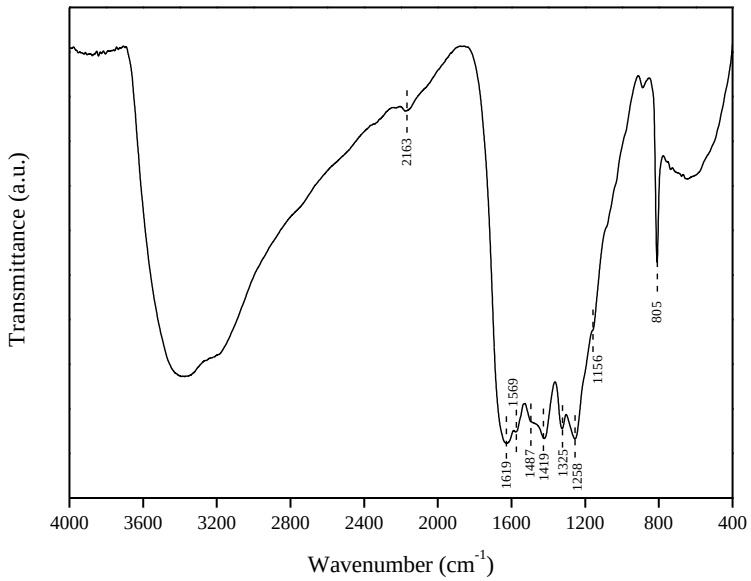


Figure 4. The FT-IR spectrum of O-MCN.

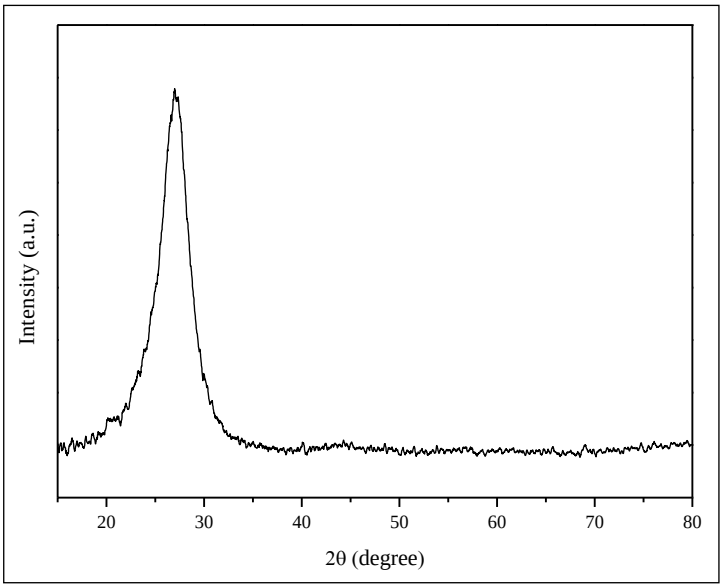


Figure 5. The XRD diffractogram of O-MC

Table 1. The elemental analysis of O-MCN

C (wt.%)	H (wt.%)	N (wt.%)	O (wt.%)
37.43	2.30	49.38	10.89

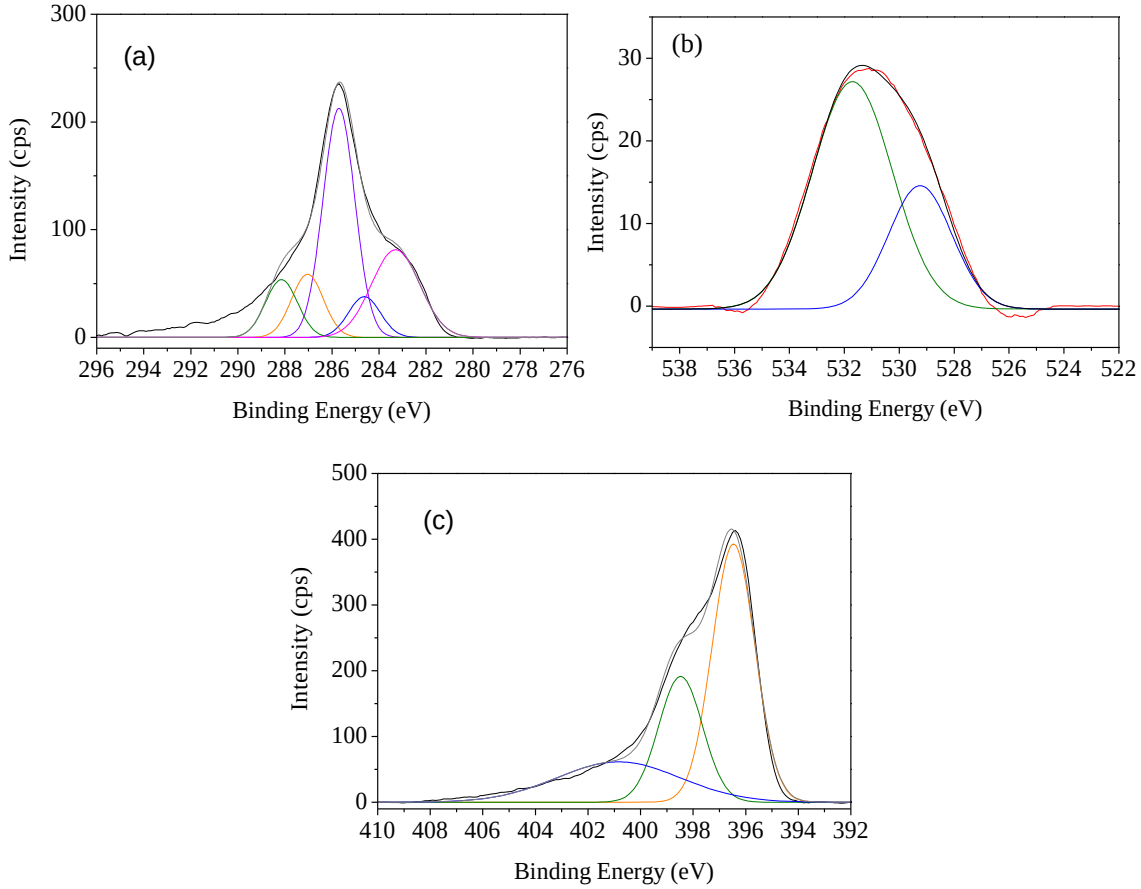


Figure 6. The XPS spectra for (a) C 1s, (b) O 1s, and (c) N 1s of -MCN

UV–Vis diffuse reflectance analysis

The UV-Vis diffuse reflectance spectrum of O-MCN is shown in Figure 7(a). The catalyst exhibits intrinsic absorption in the ultraviolet region attributed to the band-band transition [28]. The absorption edge around 460 nm is associated with the photocatalytic property in the visible region [29, 30]. The bandgap energy (E_g) of the composites was estimated from the intercept of a straight-line fitting to a plot of $[F(R)hv]^{0.5}$ against hv (Fig.7(b)), where $F(R)$ is the Kubelka-Munk function and hv is the incident photon energy. From Figure5(b), the calculated bandgap energy for O-MCN was 2.53 eV. The lower bandgap energy indicates that the O-MCN has potential to be used in photocatalysis under visible light irradiation.

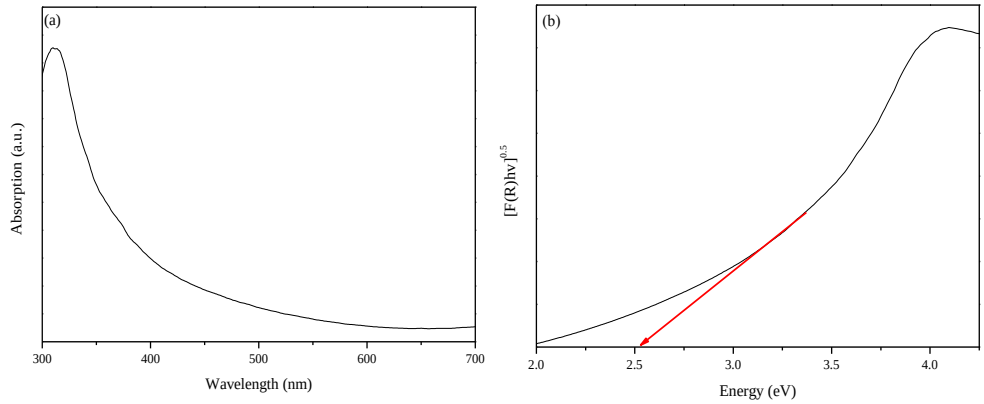


Figure 7. (a) The UV-Vis diffuse reflectance spectrum of O-MCN and (b) A plot of (F(R)hv) 0.5 vs photon energy

Conclusion

Oxygen doped mesoporous carbon nitride (O-MCN) with high purity was successfully synthesized *via a* hard-templating method. Urea and glucose were used as the carbon, oxygen and nitrogen source. The nano-disc silica (NDS) was used as a template. The O-MCN replicated the surface morphology of NDS; however, some changes were observed. The BET surface area of O-MCN (145 m^2g^{-1}) was slightly lower compared to NDS (152 m^2g^{-1}). The etching of NDS using aqueous HF had created pores with a broader diameter range (48- 84 Å) compared to NDS (39-203 Å). The UV–Vis diffuse reflectance analysis indicates that the O-MCN has the potential to be used in photocatalysis under visible light irradiation. However, further investigations are needed to be carried out to understand the morphogenesis of the O-MCN since the HRTEM indicate morphological change after NDS removal.

Acknowledgement

The authors would like to thank the Malaysia Government for the following RU Grant (Grant No: 203/PKIMIA/6769001) and the TRGS grant (Ac. No. 203/PKIMIA/6769001), which partly supported this work. We would also like to thank TETFUND through the Federal Polytechnique Offa Kwara State, Nigeria for a scholarship to Shittu Fatimah Bukola.

References

1. Ajayan, S., Lakhi, K. S, Dae-Hwan, Al-Bahily, K. Cha, W. Viswanathan, B. and Choy, J. H. (2017). Mesoporous carbon nitrides: synthesis, functionalization, and applications. *Chemical Society Reviews*, 46: 72-101.
2. Luo, L., Zhang, A., Janik, M. J., Li, K., Song, C. and Guo, X. (2017). Facile fabrication of ordered mesoporous graphitic carbon nitride for RhB photocatalytic degradation. *Applied Surface Science*, 396: 78-84.
3. Lee, S. C., Lintang, H. O. and Yuliati, L. (2012). A urea precursor to synthesize carbon nitride with mesoporosity for enhanced activity in the photocatalytic removal of phenol. *Chemistry-An Asian Journal*, 7(9): 2139-2144.
4. Zhao, Z., Dai, Y., Lin, J. and Wang, G. (2014). Highly-ordered mesoporous carbon nitride with ultrahigh surface area and pore volume as a superior dehydrogenation catalyst. *Chemistry of Materials*, 26(10): 3151-3161.
5. Dong, G., Ai, Z. and Zhang, L. (2014). Efficient anoxic pollutant removal with oxygen functionalized graphitic carbon nitride under visible light. *RCS Advances*, 4: 5553-5560.

6. Zhang, B., Li, X. J., Zhao, Y., Song, H. and Wang, H. (2019). Facile synthesis of oxygen doped mesoporous graphitic carbon nitride with high photocatalytic degradation efficiency under simulated solar irradiation. *Colloids and Surfaces: A*, 580: 123736.
7. Adam, F., Nelson, J. and Iqbal, A. (2012). The utilization of rice husk silica as a catalyst: Review and recent progress. *Catalysis Today*, 190(1): 2-14.
8. Lu, P. and Hsieh, Y. (2012). Highly pure amorphous silica nano-disks from rice straw. Powder Technology, 225: 149-155.
9. Ghorbani, F., Sanati, A. M. and Maleki, M. (2015). Production of silica nanoparticles from rice husk as agricultural waste by environmental friendly technique. *Environmental Studies of Persian Gulf*, 2(1): 56- 65.
10. Hu, J., Zhang, Z., Wang, F., Zheng, S., Cai, J., Qin, J., Liu, W., Liang, L. and Jiang, X (2016). A controllable synthesis of nitrogen-doped mesoporous carbon supported MoS_2 catalysts for hydrodesulfurization of thiophene. *RSC Advances*, 6(103): 101544-101551.
11. Deng, Q. F., Liu, L., Lin, X. Z., Du, G., Y Liu, Y. and Yuan, Z. Y. (2012). Synthesis and CO_2 capture properties of mesoporous carbon nitride materials. *Chemical Engineering Journal*, 203: 63-70.
12. Sung. S. P., Sang-Wook, C., Chunfeng, X., Dongyuan, Z., and Chang-Sik, H. (2011). Facile synthesis of mesoporous carbon nitrides using the incipient wetness method and the application as hydrogen adsorbent. *Journal of Materials Chemistry*, 21: 10801-10807.
13. Wangsoo, C., In, Y. K., Jang, M. L., Sungho, K., Kavitha, R., Kothandam, G., Selvarajan, P., Siva, U. and Ajayan, V. (2019). Sulfur-doped mesoporous carbon nitride with an ordered porous structure for sodium-ion batteries. *ACS Applied Materials & Interfaces*, 11: 27192-27199.
14. Chang, S., Clair, B., Ruelle,J., Beauchêne, J., Renzo, F. D., Quignard, F., Zhao, G., Yamamoto, H. and Gril, J. (2009). Mesoporosity as a new parameter for understanding tension stress generation in trees. *Journal of Experimental Botany*, 60(11): 3023-3030.
15. Mousavi, M., Habibi-Yangjeh, A. and Abitorabi, M. (2016). Fabrication of novel magnetically separable nanocomposites using graphitic carbon nitride, silver phosphate and silver chloride and their applications in photocatalytic removal of different pollutants using visible-light irradiation. *Journal of Colloid and Interface Science*, 480: 218-231.
16. Xu, H. Y., Wu, L. C., Zhao, H., Jin, L. G. and Qi, S. Y. (2015). Synergic effect between adsorption and photocatalysis of metal-free g-C_3N_4 derived from different precursors. *PLoS One*, 10(11): 1-20.
17. Liu, J., Zhang, T., Wang, Z., Dawson, G. and Chen, W. (2011). Simple pyrolysis of urea into graphitic carbon nitride with recyclable adsorption and photocatalytic activity. *Journal of Material Chemistry*, 21(38): 14398-14401.
18. Guo, Q., Xie, Y., Wang, X., Zhang, S., Hou, T. and Lv, S. (2004). Synthesis of carbon nitride nanotubes with the C_3N_4 stoichiometry via a benzene-thermal process at low temperatures. *Chemical Communications*, 1: 26-27.
19. Luo, J., Cui, Z. and Zang, G. (2013). Mesoporous metal-containing carbon nitrides for improved photocatalytic activities. *Journal of Chemistry*, 2013: 1-6.
20. Muniandy, L., Adam, F., Rahman, A., Iqbal, A., Ruzaina, N. and Rahman, A. (2017). Applied surface science from melamine for the liquid phase hydroxylation of benzene and VOCs. *Applied Surface Science*, 398: 43-55.
21. Nghiem, L., Tuan, A., Thi, L., Dung, K., Doan, L. and Ha, T. (2017). Preparation and characterization of nanosilica from rice husk ash by chemical treatment combined with calcination. *Vietnam Journal of Chemistry*, 55(4): 455-459.
22. Kwon, K., Sa, Y. J., Cheon, J. Y. and Joo, S. H. (2012). Ordered mesoporous carbon nitrides with graphitic frameworks as metal-free, highly durable, methanol-tolerant oxygen reduction catalysts in an acidic medium. *Langmuir*, 28(1): 991-996.

23. Mitra, A., Howli, P., Sen, D., Das, B. and Chattopadhyay, K. K. (2016). Cu_2O/g-C_3N_4 nanocomposites: An insight into the band structure tuning and catalytic efficiencies. *Nanoscale*, 8(45): 19099-19109.
24. Chena, Z., Wua, Y., Wanga, Q., Wang, Z., Heb, L. Lei, Y. and Wang, Z. (2017). Oxygen-rich carbonnitrogen quantum dots as cocatalysts for enhanced photocatalytic H_2 production activity of TiO_2 nano fibers. *Progress in Natural Science: Materials International*, 27(3): 333-337.
25. Seredych, M. and Bandosz, T. J. (2016). Nitrogen enrichment of S-doped nanoporous carbon by g-C_3N_4: Insight into photosensitivity enhancement. *Carbon*, 107: 895-906.
26. Wei, F., Liu, Y., Zhao, H., Ren, X., Liu, J., Hasan, T., Chen, L., Li, Y. and Su, B. (2018). Oxygen selfdoped g-C_3N_4 with tunable electronic band structure for unprecedentedly enhanced photocatalytic performance. *Nanoscale*, 4: 4515-4522.
27. Wang, K., Wang, X., Pan, H., Liu, Y., Xu, S. and Cao, S. (2018). In situ fabrication of CDs/g-C_3N_4 hybrids with enhanced interface connection via calcination of the precursors for photocatalytic H_2 evolution. *International Journal of Hydrogen Energy*, 43(1): 91-99.
28. Kautz, A. C., Kunz, P. C., Janiak, C. and Kautz, A. C. (2016). CO-releasing molecule (CORM) conjugate systems. *Dalton Transactions*,45(45): 18045-18063.
29. Li, J., Shen, B., Hong, Z. Lin, B. (2012). A facile approach to synthesize novel oxygen-doped g-C_3N_4 with superior visible-light photoreactivity. *Chemical Communications*, 98(48): 12017-12019.
30. Bandosz, T. J. (2016). Nitrogen-doped activated carbon-based ammonia sensors: Effect of specific surface functional groups on carbon electronic properties. *ACS Sensors*, 1(5): 591-599.

Malaysian Journal of Analytical Sciences (MJAS)
Published by Malaysian Analytical Sciences Society

SYNTHESIS AND CHARACTERIZATION OF CATALYTIC POLYMER-CLAY FILM FOR TREATMENT OF 17α-ETHINYLESTRADIOL

(Sintesis dan Pencirian Filem Polimer-Tanah Liat dengan Pemangkin untuk Rawatan 17α-Etinilestradiol)

Nur Khairunnisa Nazri, Nabilah Ismail[1]*, Mohd Aidil Adhha Abdullah[1], Fatimah Hashim[1], Leonard James Wright[2]

[1]*Faculty of Science and Marine Environment,*
Universiti Malaysia Terengganu, 21030 Kuala Nerus, Terengganu, Malaysia
[2]*Centre of Green Chemical Sciences,*
University of Auckland, 23 Symonds St, Private Bag 92019, Auckland, New Zealand

**Corresponding author: nabilah.i@umt.edu.my*

Received: 20 November 2019; Accepted: 5 April 2020; Published: 9 June 2020

Abstract

Synthetic estrogen such as 17α-ethinylestradiol (EE_2) is considered as one of the pharmaceuticals found in waterways worldwide usually due to human utilization and excretion into wastewater treatment system. In this study, catalytic polymer-clay film was used to treat EE_2 in the contaminated water by oxidizing the pollutant. Polychloromethylstyrene was synthesized along with the clay cloisite to form films that can anchor catalyst Iron-tetra amido microcylic ligand (Fe-TAML). Fe-TAML works efficiently with hydrogen peroxide to activate the iron to higher oxidation state for a film performance. Polymer-clay was then casted, cured, cross-linked and functionalized to form a film that can bind the catalyst into it. Characterization of the films was done using Fourier Transform Infrared (FTIR) to determine the presence of the functional group; preliminary analysis of oxidation study was carried out using UV-Vis Spectroscopy. Furthermore, the toxicity of the oxidized solution of EE_2 after undergoing oxidation with catalytic polymer-clay film was investigated using *Acanthamoeba* sp. to determine its toxicity towards the environment. The results of preliminary oxidation study showed the performance of film in oxidizing the contaminant and the result of toxicity study using MTT assay shows more than 70% of viability of *Acanthamoeba* sp. which indicated that the film was less toxic towards the environment. Hence, this film has high potential for solving the problems of contaminated water.

Keywords: ethinylestradiol, polychloromethylstyrene, Fe-TAML, cloisite, catalytic polymer-clay

Abstrak

Estrogen sintetik yang dikenali sebagai 17α-etinilestradiol (EE_2) adalah salah satu farmaseutikal yang terdapat dalam saluran air di seluruh dunia kebiasaannya disebabkan penggunaan oleh manusia dan perkumuhan ke dalam sistem rawatan air sisa. Dalam kajian ini, filem polimer-tanah liat pemangkin digunakan untuk merawat EE_2 dalam air yang tercemar dengan menumpukan bahan pencemar dan mengoksida bahan tersebut. Poliklorometilsterina di sintesis bersama dengan tanah liat cloisite untuk membentuk filem-filem yang boleh melekatkan pemangkin ferum ligan tetra amido mikrosiklik (Fe-TAML). Fe-TAML berfungsi cekap dengan hidrogen peroksida untuk mengaktifkan ferum kepada keadaan pengoksidaan yang lebih tinggi untuk prestasi filem. Polimer-tanah liat kemudian diacuankan, dirawat, disilangkan dan difungsikan untuk membentuk sebuah filem yang boleh mengikat pemangkin kepadanya. Pencirian filem dilakukan dengan menggunakan spektroskopi inframerah

transformasi Fourier (FTIR) untuk menentukan kehadiran kumpulan berfungsi. Tambahan lagi, kajian ketoksikan EE_2 yang teroksida setelah menjalani pengoksidaan dengan filem polimer-tanah liat pemangkin telah disiasat menggunakan *Acanthamoeba* sp. untuk menentukan ketoksikannya terhadap alam sekitar. Hasil kajian ketoksikan menggunakan pengujian MTT menunjukkan lebih dari 70% ia bertahan dan menujukkan filem tersebut kurang toksik terhadap alam sekitar. Oleh itu, filem ini mempunyai potensi yang tinggi untuk menyelesaikan masalah berkaitan air tercemar.

Kata kunci: ethinillestradiol, polikloro metilsterina, Fe-TAML, cloisite, pemangkin polimer-tanah liat

Introduction

Ethinylestradiol (EE_2), an artificial estrogen in oral contraceptives, can be found in inland waterways worldwide [1]. It mainly emerges in wastewater treatment system from human excretion [2] such as urine and through the disposal of wastes including pregnancy test [3-5]. To prevent pregnancy and stabilize menstrual cycle, most women use oral contraceptive. This is known as a huge contributor to synthetic EE_2 in the environment [6]. Based on several studies, human estrogens namely estradiol (E2) and estrone (E1) as well as the artificial estrogen (EE_2) are responsible for a significant part of the endocrine disrupting effects seen in the aquatic environment [7-9]. Compounds that adjust the endocrine system and because harmful effects are referred to as endocrine disrupting chemicals (EDCs) [10]. When EDCs pollute the aquatic environment, they will potentially disturb the endocrine system of animals by altering the natural balance of hormones [11]. EE_2 seems to be more harmful as it has a longer half-life compared to other natural estrogen [12]. Moreover, EE_2 has the possibility to accumulate in biota and sediment [13] where it has been shown that it is endocranially active [14]. The exposure effects of EE_2 in wastewater treatment bring the feminization of male fish based on most research [15]. As stated by Jobling et al. [16] and Harris et al. [17], EE_2 can reduce the reproductive success, leading to the feminization of wild male fish [18].

The method of using hydrogen peroxide with the presence of tetra amido microcyclic ligand (TAML) catalyst is one of the environmentally friendly, money saving and very effective way to help us overcome the unsuitable method of using ozone or activated carbon method to remove pharmaceutical ingredient from wastewater. Iron TAML are fully-functional, small molecule that imitate of peroxidase enzymes at nanomolar concentrations can decompose many micro pollutants. For example, in laboratory studies, TAML/peroxide has been shown to efficiently degrade the persistent drug sertraline via its oxidative metabolites [19], the recalcitrant pesticides trichlorophenol and pentachlorophenol [20], thiophosphate pesticides and many other micro pollutants [21]. TAML/peroxide has been reported to degrade a lot of pharmaceutical based on the preliminary studies on United Kingdom municipal wastewater [2].

The contraceptive pill hormone EE_2 causes serious impacts on aquatic life [22]; therefore, this study investigates the effectiveness of TAML/peroxide and polymer-clay in removing EE_2 and its biological effects. Preliminary studies at high pH (8-10) and high concentrations of hydrogen peroxide (4 mM, 136 ppm) indicate that the removal of EE_2 and other estrogens (estradiol (E2), estrone (E1) all at 80 μM) with TAML (83 nM**)** is possible [23]. In addition, *in vivo* toxicity tests using embryonic zebrafish suggest that TAML was not overtly toxic to fish [24] while *in vitro* tests also showed that TAML did not show inherent endocrine disrupting activity [25].

Taken together, these studies set the stage for the current multidisciplinary, cross-sector study to investigate the removal of EE_2 from laboratory waters and real wastewater, under more environmentally appropriate conditions. These include neutral pH, lower hydrogen peroxide concentrations and estrogen concentrations of more than a million-fold lower than previously tested, which are much more environmentally relevant and still ecotoxic to fish [2].

Organic-inorganic composite-based materials known as clay minerals have been widely used for water purification for decades. They have many

characteristics such as high surface area, easily to adsorb and unique chemical composition besides being small in size (nano). However, to make the clay effective in removing the micro pollutant from water, the developments of clay-polymer nanocomposite film have been introduced. The modified polymer or known as Cloisite has been use in this study. Cloisite 10A contains dimethyl, benzyl, hydrogenated tallow and quaternary ammonium and is used with polychloromethylstyrene. Several studies have reported enhanced performance and characteristic of polymeric films by adding clay-based nanomaterials into the film matrix [26-29]. The blending of polymer with clay improved the characteristic in term of optical [30-32], mechanical [33, 34] and barrier properties [35-37].

From this study, polymerization of chloromethyl styrene was used together with clay Cloisite 10A to treat the estrogen known as EE_2. Catalyst Fe-TAML/H_2O_2 helps in the process of heterogeneous catalytic oxidation reaction. In addition, the toxicity studies using MTT assay have been conducted.

Materials and Methods

4-vinylbenzyl chloride was purchase from Sigma Aldrich. N, N-dimethylhexadecylamine, 1,4-dioxane, 1,6-diaminohexane, diethanolamine, dimethyl-formamide and 17α-ethinylestradiol were purchased from Sigma Aldrich. Buffer solution were prepared by using sodium carbonate, sodium bicarbonate and 35% hydrogen peroxide from Merck.

Polymerization of chloromethylstyrene with clay

30 mL of 0.5% NaOH was added to 30 mL chloromethylstyrene (CMS) in separating funnel to remove inhibitor from chloromethylstyrene. This step was repeated for another two times. After that, the CMS were washed by using deionized water for three times until the water turned neutral. This step was followed by adding potassium carbonate to remove excess water. An amount 4% (w/v) of cloisite clay from the volume of CMS were added into flat bottom flask containing CMS and was heated in an oil bath with temperature of under 85 ^{o}C with stirring speed of 150 rpm in nitrogen condition. The CMS was heated until completely viscous. After viscous, methyl ethyl ketone was dropped in the viscous solution and the mixture was dropped added slowly to the volume of 20 mL in the beaker that contained methanol to obtain the polymer flakes. The flakes were then filtered using Buchner funnel and dried for 10 minutes in the oven.

Casting, curing and functionalization of polymer clay film

The flakes were dissolved in the dimethylformamide (DMF) and casted on the backing membrane (polypropylene) to obtain the film. After casted on the membrane and glass, the film was cured for 5 hours at the oven at 85 ^{o}C. Next, the film was heated for 5 hours at 85 ^{o}C in N, N-dimethylhexadecylamine in 1,4-dioxane with a ratio of (6:4). After functionalization, the polymer film was heated in 1,6-diaminohexane in 1,4-dioxane with ratio (6:4) for crosslinking the polymer. End capping step involved heating the polymer film with neat diethanolamine for 5 hours at 85 ^{o}C.

Anchoring of Fe-TAML

The film was immersed in the aqueous Fe-TAML solution (20.0 mL, 50 μM, 1.0 μmole Fe-TAML) until all the absorbed. After that, the film was removed from the solution, washed and immersed on a wire support in fresh carbonate buffer solution (20.0 mL 0.01 M, pH 9.5) and stirred for 15 to 20 minutes. The procedure was repeated for three times. The measurement of amount of Fe-TAML that was not adsorbed from the original solution of Fe-TAML and the amounts that leached into solution after immersion in the buffer solution was measured. To measure this, dye orange II together with hydrogen peroxide were catalyzed by small amount of Fe-TAML and used as a standard condition.

Characterization using attenuated total reflectance-Fourier-transform infrared and scanning electron microscope

ATR-FTIR spectra of the samples were analyzed on a Nicolet 380 FT-IR. The samples were put on the stage to analyzed their functional group. Further, SEM JEOL JSM-5800 was used to analyze the morphology of the film's surface.

Oxidation of EE_2 using catalyzed polymer-clay film

The oxidation of EE_2 was done in a beaker containing carbonate/bicarbonate buffer solution (8.5 mL, 0.01 M, pH 9.5). The EE_2 solution (11.4 mL, 11.83 μM) was added followed by H_2O_2 solution (0.1 mL, 0.2 M) and buffer solution was added until the total volume of the solution became 20 mL. The solution was stirred at 750 rpm and the film was added to the solution. The ratio of H_2O_2:EE_2:Fe-TAML was 200: 1.35: 40.5, while the resulting concentration for EE_2 was 2 ppm (6.76 μM), H_2O_2 (1.0 mM). After 30 minutes, the film was removed, and 1 mg catalase was added to the solution to destroy the H_2O_2 and stirred for another 30 minutes. Peroxide test strip was used to confirm that all H_2O_2 has been destroyed. The solution was then passed through the hydrophilic-lipophilic cartridge from Waters Corporation. The solution was collected for the MTT assay study.

MTT (2 3-[4,5-dimethylthiazol-2-yl]-2,5 diphenyl tetrazolium bromide) assay of oxidize solution on *Acanthamoeba* sp.

Acanthamoeba sp. (environmental isolate) used in the experiment was isolated from Setiu Wetlands, Terengganu and used in this experiment. The trophozoites were maintained in axenic conditions in 4% protease-yeast-glucose medium and were subculture for a week. MTT assay by Mossman [38] was used in this study to determine the toxicity of oxidized solution by catalytic polymer-clay film on *Acanthamoeba sp.* The first step was subculturing the cell in new flask for 4 days. After 4 days, the cells were ready to be used for the experiment. To start the experiment, all cells and media were transferred to centrifuge tube to sediment the cell. After centrifugation for 15 minutes, the media was removed and replaced with new media. The cell and media contained in the centrifuge tube were transferred in a 96-well plate, a process called cell seeding. After that, the 96-well plate was kept in the oven at 30 ^{o}C for 24 hours. After 24 hours, the treatment process was done. The media were removed, while oxidized solutions with different concentrations were put in the 96-well plate. There were five replicates with seven concentrations. This process was carried out for 24 hours. After that, the solutions were removed and rinsed with PBS solution. MTT was transferred into the 96-well plate and after 4 hours, MTT was suspended while DMSO was dropped into the 96-well plate. The readings of viability of the cell were analyzed by micro plate reader instrument.

Results and Discussion

Fourier-transform infrared analysis

The FTIR spectrum of polymer-clay film the characteristic absorption peaks due to stretching vibration of C–H in the region 3000-2850 cm^{-1} region which showed alkane functional group, whereas the band around 1645 cm^{-1} was due to stretching vibration of C–C stretch for alkane (Figure 1). The band around 1463 cm^{-1} showed the stretching vibration of C–C in ring or known as aromatic, 1043 cm^{-1} band was due to C–N stretching of functional group aliphatic amine and 808 cm^{-1} band was due to C–Cl stretching vibration and functional group of alkyl halide. These bands showed the stretching from the polychloromethylstyrene-clay films that were functionalized with N, N-dimethylhexadecylamine and 1,4-dioxane, 1,6-diaminohexane with 1,4-dioxane and neat diethanolamine.

Scanning electron microscope

SEM was used to investigate the surface morphology of prepared sample. The polychloromethylstyrene was synthesized with clay Cloisite 10A and casted. The image of SEM (Figure 2) showed that the film has no hole after casting and functionalization which can anchor any catalyst into it for further use. Polymer-clay film was treated with a long chain tertiary amine which reacts with chloromethyl groups converting them into quaternary ammonium functions and followed by crosslinking the polymer chain; end capping the remaining unreacted chloromethyl group. Therefore, Fe-TAML can be anchor to the film.

Viscosity of polymer-clay

Viscosity is the internal friction of a fluid to resist flow. Meanwhile, shear stress is stress component applied tangentially and commonly recognized by sigma (σ) symbol. It is equal to the force vector (a vector has magnitude and direction) divided by the area of application and is expressed in the unit of force per unit

area (Pa). Shear rate is the velocity gradient established in a fluid as a result of an applied shear stress and expressed in unit of reciprocal seconds, s^{-1}. Viscosity inconsistent and gives different results. Therefore, to ensure that we can produce the same viscosity of the film, this result can be referred.

$$\text{Viscosity} = \frac{\text{Shear Stress}}{\text{Shear Rate}} \quad (1)$$

Toxicity studies using MTT assay

MTT assay was conducted for studying the toxicity of the oxidize solution that was treated by the catalytic polymer-clay film. After the cells were treated with oxidized solution at varying concentrations for 24 hours at 30 ^{o}C in a 96-well plate, the medium in the plate was discarded. The plate was washed with PBS solution 3 times before loading the MTT solution. This was to ensure that the glucose content in the medium has been completely removed. The presence of glucose can be calculated as shear stress over shear rate. Based on the Figure 3, the shear stress increased as the shear rate increase. The viscosity of different polymers is in the medium will reduce the efficiency of MTT reaction. MTT specific activity can be reduced by cells that extensively metabolized D-glucose. Cytotoxicity of oxidized solution on *Acanthamoeba* sp. was determined based on the percentage of viable *Acanthamoeba* sp. after exposure to oxidized solution for 24 hours at 30 ^{o}C. In general, the viability of *Acanthamoeba* sp. decreased with increasing concentrations of oxidized solution. This shows that the growth of the cells was affected once exposed to oxidized solution. However, the percentage of viability of *Acanthamoeba* sp. as illustrated in Figure 4 showed that more than 70%. This means that the oxidize solution was not highly toxic to the cell and environment.

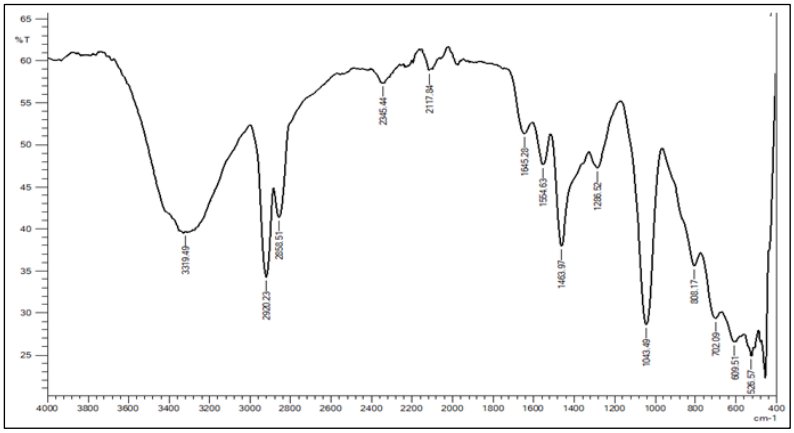


Figure 1. FTIR Spectrum of Polymer-Clay Films after functionalization

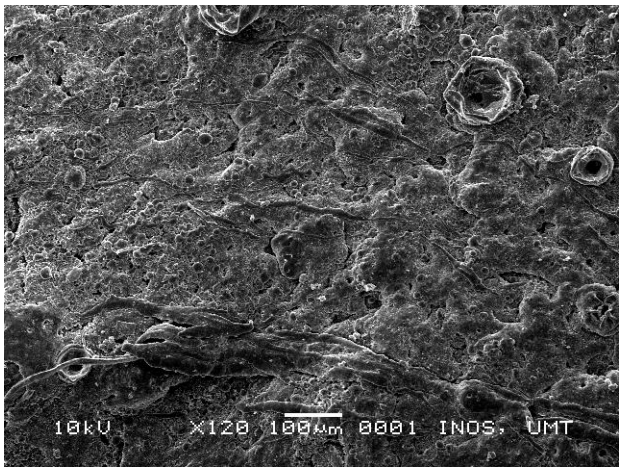


Figure 2. SEM image of functionalized polymer-clay film

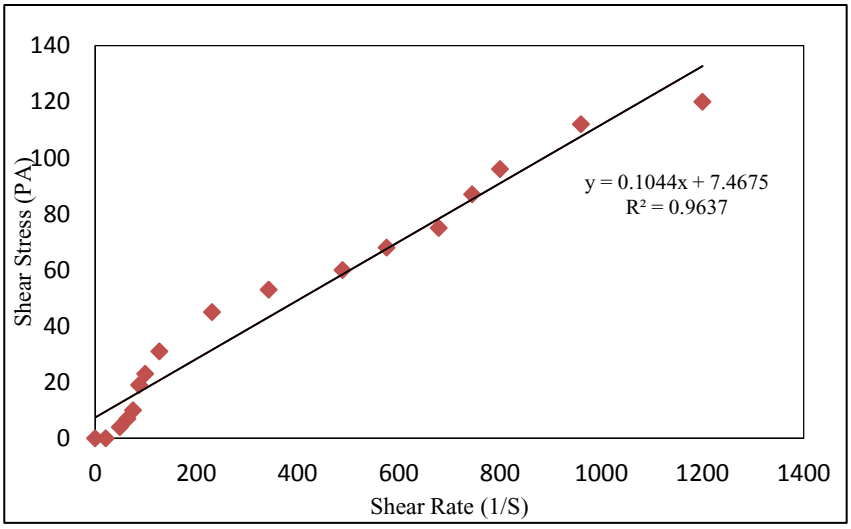


Figure 3. Shear rate against shear stress graph

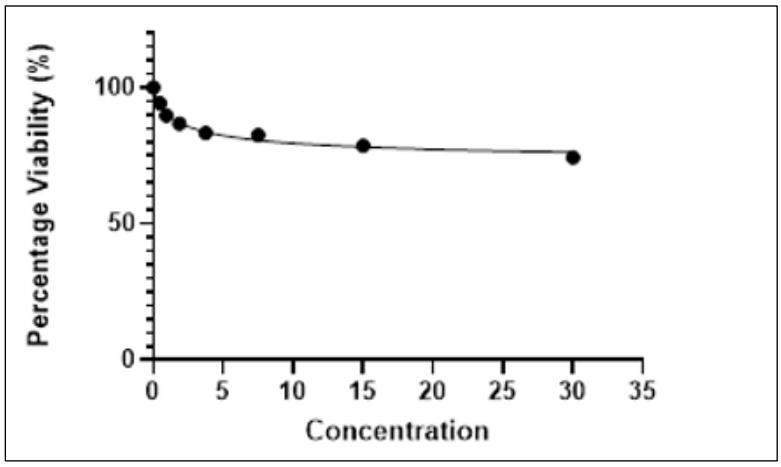


Figure 4. Graph of percentage of viability of *Acanthamoeba* sp. from MTT assay

Conclusion

The catalytic polymer-clay employed in this work in treating 17α-Ethinylestradiol has been successful. Characterization of the catalytic polymer-clay shows that the film contains functional group that helps the catalyst to oxidize EE_2. The results have showed that the production of film does not give harmful effects towards the environment based on the result of toxicity study obtained. Therefore, EE_2 can be treated using polymer and clay in the presence of catalyst.

Acknowledgement

The authors would like to acknowledge the Ministry of Education Malaysia for Fundamental Research Grant Scheme FRGS 59474 (FRGS/1/2017/ STG01/UMT/ 03/1) and Universiti Malaysia Terengganu for facilities and support.

References

1. Johnson, A. C., Dumont, E., Williams, R. J., Oldenkamp, R., Cisowska, I. and Sumpter, J. P. (2013). Do concentrations of ethinylestradiol, estradiol, and diclofenac in European rivers exceed proposed EU environmental quality standards? *Environmental Science & Technology*, 47(21): 12297-12304.
2. Mills, M. R., Arias-Salazar, K., Baynes, A., Shen, L. Q., Churchley, J., Beresford, N., Gayathri, C., Gil, R. R., Kanda, R., Jobling, S. and Collins, T. J. (2015). Removal of ecotoxicity of 17α-ethinylestradiol using TAML/peroxide water treatment. *Scientific Reports*, *5*: 10511.
3. Liu, Z. H., Lu, G. N., Yin, H., Dang, Z. and Rittmann, B. (2015). Removal of natural estrogens and their conjugates in municipal wastewater treatment plants: A critical review. *Environmental Science & Technology*, 49(9): 5288-5300.
4. Kostich, M., Flick, R. and Martinson, J. (2013). Comparing predicted estrogen concentrations with measurements in US waters. *Environmental Pollution*, 178: 271-277.
5. De Mes, T., Zeeman, G. and Lettinga, G. (2005). Occurrence and fate of estrone, 17β-estradiol and 17α-ethynylestradiol in STPs for domestic wastewater. *Reviews in Environmental Science and Biotechnology*, 4(4): 275.
6. Lim, Y. L., Morad, N., Lalung, J., Chan, S. Y. and Bakar, S. A. A. (2016). Isolation and identification of 17α-ethinylestradiol-degrading bacterial strains from POME and cow dung. *International Journal of Environmental Science and Development*, 7(12): 881.
7. Desbrow, C. E. J. R., Routledge, E. J., Brighty, G. C., Sumpter, J. P. and Waldock, M. (1998). Identification of estrogenic chemicals in STW effluent. 1. Chemical fractionation and *in vitro* biological screening. *Environmental Science & Technology*, 32(11): 1549-1558.

8. Körner, W., Spengler, P., Bolz, U., Schuller, W., Hanf, V. and Metzger, J. W. (2001). Substances with estrogenic activity in effluents of sewage treatment plants in southwestern Germany. 2. biological analysis. *Environmental Toxicology and Chemistry: An International Journal*, 20(10): 2142-2151.
9. Snyder, S. A., Villeneuve, D. L., Snyder, E. M. and Giesy, J. P. (2001). Identification and quantification of estrogen receptor agonists in wastewater effluents. *Environmental Science & Technology*, 35(18): 3620-3625.
10. Hultman, M. T., Song, Y. and Tollefsen, K. E. (2015). 17α-ethinylestradiol (EE2) effect on global gene expression in primary rainbow trout (*Oncorhynchus mykiss*) hepatocytes. *Aquatic Toxicology*, 169: 90-104.
11. Snyder, S. A., Westerhoff, P., Yoon, Y. and Sedlak, D. L. (2003). Pharmaceuticals, personal care products, and endocrine disruptors in water: Implications for the water industry. *Environmental Engineering Science*, 20(5): 449-469.
12. Scala-Benuzzi, M. L., Takara, E. A., Alderete, M., Soler-Illia, G. J., Schneider, R. J., Raba, J. and Messina, G. A. (2018). Ethinylestradiol quantification in drinking water sources using a fluorescent paper based immunosensor. *Microchemical Journal*, 141: 287-293.
13. De Wit, M., Keil, D., van der Ven, K., Vandamme, S., Witters, E. and De Coen, W. (2010). An integrated transcriptomic and proteomic approach characterizing estrogenic and metabolic effects of 17α-ethinylestradiol in zebrafish (*Danio rerio*). *General and Comparative Endocrinology*, 167(2): 190-201.
14. Bhandari, R. K., Deem, S. L., Holliday, D. K., Jandegian, C. M., Kassotis, C. D., Nagel, S. C., Tillitt, D. E., vom Saal, F. S. and Rosenfeld, C. S. (2015). Effects of the environmental estrogenic contaminants bisphenol a and 17α-ethinylestradiol on sexual development and adult behaviors in aquatic wildlife species. *General and Comparative Endocrinology*, 214: 195-219.
15. Caldwell, D. J., Mastrocco, F., Anderson, P. D., Länge, R. and Sumpter, J. P. (2012). Predicted- no- effect concentrations for the steroid estrogens estrone, 17β- estradiol, estriol, and 17α- ethinylestradiol. *Environmental Toxicology and Chemistry*, 31(6): 1396-1406.
16. Jobling, S., Coey, S., Whitmore, J. G., Kime, D. E., Van Look, K. J. W., McAllister, B. G., Beresford, N., Henshaw, A. C., Brighty, G., Tyler, C. R. and Sumpter, J. P. (2002). Wild intersex roach (*Rutilus rutilus*) have reduced fertility. *Biology of Reproduction*, 67(2): 515-524.
17. Harris, C. A., Hamilton, P. B., Runnalls, T. J., Vinciotti, V., Henshaw, A., Hodgson, D., Coe, T. S., Jobling, S., Tyler, C. R. and Sumpter, J. P. (2010). The consequences of feminization in breeding groups of wild fish. *Environmental Health Perspectives*, 119(3): 306-311.
18. Jobling, S., Williams, R., Johnson, A., Taylor, A., Gross-Sorokin, M., Nolan, M., Tyler, C.R., van Aerle, R., Santos, E. and Brighty, G. (2005). Predicted exposures to steroid estrogens in UK rivers correlate with widespread sexual disruption in wild fish populations. *Environmental Health Perspectives*, 114 (Suppl 1): 32-39.
19. Shen, L. Q., Beach, E. S., Xiang, Y., Tshudy, D. J., Khanina, N., Horwitz, C. P., Bier, M.E. and Collins, T. J. (2011). Rapid, biomimetic degradation in water of the persistent drug sertraline by TAML catalysts and hydrogen peroxide. *Environmental Science & Technology*, 45(18): 7882-7887.
20. Gupta, S. S., Stadler, M., Noser, C. A., Ghosh, A., Steinhoff, B., Lenoir, D., Horwitz, C. P., Schramm, K.W. and Collins, T. J. (2002). Rapid total destruction of chlorophenols by activated hydrogen peroxide. *Science*, 296(5566): 326-328.
21. Kundu, S., Chanda, A., Khetan, S. K., Ryabov, A. D. and Collins, T. J. (2013). TAML activator/peroxide-catalyzed facile oxidative degradation of the persistent explosives trinitrotoluene and trinitrobenzene in micellar solutions. *Environmental Science & Technology*, 47(10): 5319-5326.

22. Länge, R., Hutchinson, T. H., Croudace, C. P., Siegmund, F., Schweinfurth, H., Hampe, P., Panter, G.H. and Sumpter, J. P. (2001). Effects of the synthetic estrogen 17α- ethinylestradiol on the life- cycle of the fathead minnow (*Pimephales promelas*). *Environmental Toxicology and Chemistry: An International Journal*, 20(6): 1216-1227.
23. Shappell, N. W., Vrabel, M. A., Madsen, P. J., Harrington, G., Billey, L. O., Hakk, H., Larsen, G. L., Beach, E. S., Horwitz, C. P., Ro, K. and Hunt, P. G. (2008). Destruction of estrogens using Fe-TAML/peroxide catalysis. *Environmental Science & Technology*, *42*(4): 1296-1300.
24. George, P. (1953). The chemical nature of the second hydrogen peroxide compound formed by cytochrome C peroxidase and horseradish peroxidase. Titration with reducing agents. *Biochemical Journal*, 54(2): 267.
25. Ellis, W. C., Tran, C. T., Roy, R., Rusten, M., Fischer, A., Ryabov, A. D., Blumberg, B. and Collins, T. J. (2010). Designing green oxidation catalysts for purifying environmental waters. *Journal of the American Chemical Society*, 132(28): 9774-9781.
26. Alum, A., Yoon, Y., Westerhoff, P. and Abbaszadegan, M. (2004). Oxidation of bisphenol A, 17β- estradiol, and 17α- ethynyl estradiol and byproduct estrogenicity. *Environmental Toxicology: An International Journal*, 19(3): 257-264.
27. Balsiger, H. A., de la Torre, R., Lee, W.-Y. and Cox, M. B. (2010). A four-hour yeast bioassay for the direct measure of estrogenic activity in wastewater without sample extraction, concentration, or sterilization. *Science of The Total Environment.* 408(6): 1422-1429.
28. Barr, W. J., Yi, T., Aga, D., Acevedo, O. and Harper, W. F. (2011). Using electronic theory to identify metabolites present in 17α-ethinylestradiol biotransformation pathways. *Environmental Science & Technology,* 46(2): 760-768.
29. Boone, A. J., Chang, C. H., Greene, S. N., Herz, T. and Richards, N. G. J. (2003). Modeling the spin-dependent properties of open-shell Fe(III) - containing systems: towards a computational description of nitrile hydratase. *Coordination Chemistry Reviews 238*, 291-314.
30. Alexandre, M. and Dubois, P. (2000). Polymer-layered silicate nanocomposites: preparation, properties and uses of a new class of materials. *Materials Science and Engineering: Reports*, 28(1-2): 1-63.
31. Strawhecker, K. E. and Manias, E. (2000). Structure and properties of poly(vinyl alcohol)/Na^+ montmorillonite nanocomposites. *Chemistry of Materials*, 12(10): 2943-2949.
32. Koo, C. M., Ham, H. T., Choi, M. H., Kim, S. O. and Chung, I. J. (2003). Characteristics of polyvinylpyrrolidone-layered silicate nanocomposites prepared by attrition ball milling. *Polymer*, *44*(3): 681-689.
33. Giannelis, E. P. (1996). Polymer layered silicate nanocomposites. *Advanced Materials*, 8(1): 29-35.
34. LeBaron, P. C., Wang, Z. and Pinnavaia, T. J. (1999). Polymer-layered silicate nanocomposites: An overview. *Applied Clay Science*, 15(1-2): 11-29.
35. Messersmith, P. B. and Giannelis, E. P. (1995). Synthesis and barrier properties of poly (ε- caprolactone) - layered silicate nanocomposites. *Journal of Polymer Science Part A: Polymer Chemistry*, 33(7): 1047-1057.
36. Yano, K., Usuki, A. and Okada, A. (1997). Synthesis and properties of polyimide- clay hybrid films. *Journal of Polymer Science Part A: Polymer Chemistry*, 35(11): 2289-2294.
37. Ke, Z. and Yongping, B. (2005). Improve the gas barrier property of PET film with montmorillonite by *in situ* interlayer polymerization. *Materials Letters*, 59(27): 3348-3351.
38. Mosmann, T. (1983). Rapid colorimetric assay for cellular growth and survival: application to proliferation and cytotoxicity assays. *Journal of Immunological Methods*, 65(1-2): 55-63.

Malaysian Journal of Analytical Sciences (MJAS)
Published by Malaysian Analytical Sciences Society

LIPID DISTRIBUTIONS ASSOCIATED WITH CADAVER DECOMPOSITION IN MANGROVE AND OIL PALM PLANTATION SOILS UNDER TROPICAL CLIMATE

(Taburan Lipid Berkaitan dengan Pereputan Kadaver dalam Tanah Bakau dan Ladang Kelapa Sawit Di Bawah Iklim Tropika)

Siti Sofo Ismail[1]*, Xueer Chock[1], Mohamad Afdhali Kholidan[1], Ku Mohd. Kalkausar Ku Yusof[1], Siti Fathimah Putery Jemain[2]

[1]Faculty of Science and Marine Environment,
Universiti Malaysia Terengganu, 21030 Kuala Nerus, Terengganu, Malaysia
[2]Department of Chemistry, Centre for Foundation Studies,
International Islamic University Malaysia, 26300 Gambang, Pahang, Malaysia

**Corresponding author: sofo@umt.edu.my*

Received: 28 December 2019; Accepted: 8 April 2020; Published: 9 June 2020

Abstract

The burial environment has a significant effect on decomposition process. The most influential environmental factors that determine the fate of the process are temperature, moisture, pH, and partial pressure of oxygen. In this study, the decomposition of a cadaver buried in soils with contrasting pH under a tropical climate was investigated. Due to ethical issues, the fatty flesh of a commercial pig (*Sus scrofa*) was buried in mangrove (mild alkaline pH) and oil palm plantation (acidic pH) soils, which are amongst the most common body disposal sites encountered in forensic investigations. A controlled laboratory experiment was carried out. Soils were collected at different sampling points, corresponding to different decomposition stages. Modified Bligh-Dyer extraction method was used to extract soil lipids. Gas chromatography-flame ionisation detector (GC-FID) was used to identify the obtained lipids. A similar trend in the rate of decomposition was observed for both soils. The decomposition rate was higher at the initial and putrefaction stages. A sharp increase in the decomposition rate was observed between day 3 and day 5 of the burial interval. However, mangrove soil demonstrated a higher decomposition rate at all decomposition stages. Furthermore, the concentrations of palmitic ($C_{16:0}$), stearic ($C_{18:0}$), and oleic ($C_{18:1}$) acids were higher in mangrove soil compared to that of oil palm plantation soil. The significant differences observed between these contrasting pH soils may indicate that soil pH will eventually impose a different effect on decomposition.

Keywords: Cadaver decomposition, soil pH, clandestine grave, decomposition rate, fatty acids

Abstrak

Persekitaran pengebumian mempunyai kesan yang signifikan terhadap proses penguraian. Faktor persekitaran yang paling berpengaruh yang menentukan nasib proses adalah suhu, kelembapan, pH, dan tekanan separa oksigen. Dalam kajian ini, penguraian kadaver yang ditanam dalam tanah dengan pH yang berbeza di bawah iklim tropika telah disiasat. Disebabkan isu etika, daging lemak babi komersial (*Sus scrofa*) ditanam di ladang bakau (pH sedikit alkali) dan ladang kelapa sawit (pH berasid). Kedua-dua jenis kawasan ini adalah antara tapak pelupusan mayat yang paling biasa ditemui dalam siasatan forensik.

Eksperimen makmal terkawal telah dijalankan. Tanah dikumpulkan pada titik pensampelan yang berbeza, sepadan dengan peringkat penguraian yang berlainan. Kaedah pengekstrakan Bligh-Dyer yang telah diubah suai digunakan untuk mengekstrak lipid tanah. Kromatografi gas-pengesan nyalaan ion (GC-FID) digunakan untuk mengenal pasti lipid yang diperoleh. Corak yang sama dalam kadar penguraian telah diperhatikan untuk kedua-duanya. Kadar penguraian lebih tinggi pada peringkat awal dan pembusukan. Kadar penguraian meningkat mendadak telah diperhatikan antara hari 3 dan hari 5 selang pengebumian. Walau bagaimanapun, tanah bakau menunjukkan kadar penguraian yang lebih tinggi pada semua peringkat penguraian. Selain itu, kepekatan asid-asid palmitik ($C_{16:0}$), stearik ($C_{18:0}$), dan oleik ($C_{18:1}$) lebih tinggi di dalam tanah bakau berbanding dengan tanah ladang kelapa sawit. Perbezaan yang ketara antara pH tanah yang berlainan ini mungkin menunjukkan bahawa pH tanah akan akhirnya memberi kesan yang berbeza terhadap proses penguraian.

Kata kunci: pereputan kadaver, pH tanah, kubur rahsia, kadar pereputan, asid lemak

Introduction

Death under suspicious circumstances usually occurs without any witnesses, with no obvious clues of the cause, manner, and actual time of death. In most cases, inhumation is a common method to dispose of the body to hide the crime. It has been recognised that different burial environments will affect the decomposition process differently as each burial environment has its distinctive and complex system interrelated to the biological, chemical, and physical processes [1-5]. The four widely recognised factors influencing the rate of decomposition are temperature, moisture, pH, and partial pressure of oxygen [6]. Soil microorganisms take an important part in decomposition as they release enzymes that help in further breakdown of organic matters [7]. Besides, it also holds across a variety of spatial scales, i.e. continental scales, land-use types, small and sub-meter scales [8, 9]. It has been known that acidic and alkaline soils are dominated by fungi whereas neutral soil is dominated by bacterial communities [10].

The activity of recovering the body and estimating post-mortem interval (PMI) is crucial in forensic investigations to identify the criminals and/or the victim. Several conventional methods can be used to locate a body in a clandestine grave. Ground-penetrating radar and cadaver dog are commonly used during the search for clandestine graves [11, 12]. However, these methods have limitations, especially for the cases of longer burial interval [12]. The post-mortem investigations will be rather complicated for the body that is discovered long after it has been in contact with the surrounding soil. Hence, there is a crucial need for an alternative approach that can provide useful information for forensic investigations to find bodies in a terrestrial soil system. Recognising these deficiencies and the potential of belowground processes associated with cadaver decomposition will be useful, particularly for gathering important information to conduct criminal investigations. Locating clandestine graves and/or estimating PMI using information obtained from cadaveric materials, such as lipids extracted from the associated soil, may not be impossible and can be developed as one of the new approaches in forensic investigations [13].

The ability of forensic investigators to estimate PMI through analysis is important [14]. Hence, a simulated burial experiment was conducted to investigate the impact of different soil pH on cadaver decomposition as a burial study under tropical climate is not yet widely understood. The fatty flesh of a commercial pig (*Sus scrofa*) was used to replace human cadaver due to ethical issues. Furthermore, the pig was identified as the most reliable model due to similarities with humans in terms of organ morphology and lipid distribution [15]. The pig fatty flesh was buried in two types of soil with different acidity, i.e., mangrove (slightly alkaline, initial pH = 7.45) and oil palm plantation (acidic, initial pH = 3.74) soils. The soils were chosen for this experiment as they are known to be common disposal sites in Malaysia. Furthermore, these types of soil have different physical and chemical characteristics, including particle size and mineral content. Mangrove soil contains more sandy particles whereas oil palm plantation soil contains more clay particles.

Mangrove sandy loam soil was collected from Setiu Wetlands, Terengganu (5.6700° N, 102.7199° E),

which is a representation of most mangrove forests in the east coast region of Peninsular Malaysia. Setiu Wetland is the largest natural wetland in this region, combining various ecosystems including freshwater and seawater. This mangrove forest is much more under the influence of freshwater than seawater. This unique wetland is an area of high biodiversity with various types of flora and fauna, including *gelam* trees, coastal swamp, and freshwater swamp forest. Meanwhile, loam soil was sampled from an oil palm plantation owned by Sime Darby Industrial located in Kuala Berang, Terengganu (4.274520° N, 103.465652° E). Both mangrove and oil palm plantation sites are in isolated areas and away from villagers.

The changes in the decomposition rate and the quantity of the soil cadaveric derived lipids at different sampling points representing each decomposition stage were qualitatively and quantitatively analysed. The extent of particular soil lipid components was also analysed and evaluated. The unique characteristics that lipids possess, for example, the diagenetic pattern, are ubiquitously distributed in soil and chemically stable, making lipids an ideal marker [16]. Besides, the use of lipids as biomarkers provides higher accuracy in identifying multiple sources of organic materials [17, 18]. Furthermore, cadaveric fatty acids have demonstrated the potential to be used as burial biomarkers where the pattern and concentration of fatty acids in the soil at different decomposition stages can be used to locate a clandestine grave and estimate the PMI [17, 19]. Hence, the trend of decomposition rate and cadaveric derived lipids observed for each soil may provide preliminary data to further understand the decomposition in acidic and alkaline soils, especially for burial under tropical climate. Subsequently, the data may potentially be developed as a useful forensic tool to link the suspects with the crime.

Materials and Methods

Soil pH

The pre- and post-experimental pH of detritosphere soil were measured using a calibrated pH meter. Approximately 80 mL of distilled water was added into 20 g of the associated soil, creating a mixture of water and soil with a ratio of 4:1. The mixture was mixed well with a glass rod and allowed to settle for at least 5 minutes. The soil pH was measured three times for each soil under room temperature.

Simulated burial experiment

A laboratory-controlled simulated burial experiment was conducted to investigate and compare the decomposition of a cadaver buried in oil palm plantation and mangrove soils. Using a hoe and a shovel, the soils used in this experiment were taken from the depth of 50 cm from the surface to represent the soil of a shallow grave. Vessels were used to bury the abdominal fatty flesh of a commercial pig (*Sus scrofa*) that contained some muscles and skin. The pig fatty flesh was weighed accurately (± 20 g) and buried in a vessel, mimicking a burial in a shallow grave. Then, the fatty flesh was allowed to decompose for a burial period. The burial vessels of both mangrove and oil palm plantation soils were placed outside the laboratory to experience tropical climate ambient. The changes in the weather, such as the amount of precipitation, were obtained from the meteorological station located at the Sultan Mahmud International Airport, Kuala Terengganu, Terengganu. The associated soils were collected at eight different designated sampling points (i.e., days 0, 3, 5, 7, 15, 17, 21, and 28). These sampling points correspond to each decomposition stage. The remaining fatty flesh (if any) was removed from the vessel and weighed. Before the extraction and subsequent analyses, the associated soils were homogenised and stored in a freezer before being freeze-dried. The burial intervals were duplicated and the control soils without flesh were prepared with similar procedures, and then placed under a similar ambient environment similar to the vessels with fatty flesh.

Rate of decomposition

The rate of cadaver decomposition was calculated using the following equation 1:

$$Rate\ of\ decomposition = \frac{Difference\ in\ mass}{Days\ of\ decomposition} \quad (1)$$

Total lipid extracts

Lipid extraction was performed using a modified protocol of Bligh-Dyer extraction method [20]. Approximately 4 g of freeze-dried soil was transferred into vials. The soil was then mixed with 3 mL of DCM/methanol (2:1, v/v), and 100 µL of an internal standard (tetratriacontane) was added to quantify the lipid components extracted from the soils. The mixture was then sonicated (40 °C, 15 minutes) and centrifuged (~3,000 rpm, 5 minutes). The supernatant solution formed was transferred into a clean vial. This process was repeated three times with 2 mL of DCM/methanol (2:1, v/v), followed by 3 mL of Bligh-Dyer solution. The mixture was sonicated (40 °C, 15 minutes) and centrifuged (~3,000 rpm, 5 minutes). The supernatant solution formed was transferred to the same clean vial. The extraction was then repeated three times with 2 mL of Bligh-Dyer solution. About 2 mL of buffered water and chloroform were then added to the supernatant solution to break the organic phase and centrifuged (~ 3,000 rpm, 1 minute). The organic layer formed was transferred to a new clean vial. This process was repeated three times with 2 mL of chloroform. The excess solvent was removed with a gentle nitrogen flow. The total lipid extracted from the soil was weighed and kept in a freezer prior to further analysis.

Soil lipid analysis

Soil lipid extracts were analysed using gas chromatography-flame ionisation detector (GC-FID) (GC-6890N, Agilent). The samples were re-dissolved in hexane and injected (1 µL) *via* an on-column injector. The GC- FID was equipped with HP-5 5% phenyl methyl siloxane (30.0 m × 320 µm × 0.25 µm). The initial temperature for injection was 50 °C and the temperature was held constant for 2 minutes. The oven temperature then rose to 300 °C at a rate of 10 °C/min and kept constant for 20 minutes. Helium was used as the carrier gas. The generated peaks were identified by comparing them with an external standard. The external standard consists of several lipid components, including palmitic acid, stearic acid, methyl nonadecanoate, cholesterol, tetratriacontane, and tripalmitin.

Results and Discussion

Rate of decomposition

Figure 1 shows the decomposition rate for both types of soils throughout the experiment at different sampling points. Generally, a similar trend in the decomposition rate of pig fatty flesh was observed for both mangrove and oil palm plantation soils. The decomposition rate for both soils increased slightly between day 0 and day 3, corresponding to the initial stage of decomposition. Then, the decomposition rate increased rapidly after day 3 and reached the maximum decomposition rate on day 5, corresponding to the putrefaction stage. Between day 5 and day 7, a rapid decrease in the decomposition rate was observed. After day 7, the decomposition rate decelerated for both soils towards the completion of the experiment, with a slight increase on day 21 of the burial period for oil palm plantation soil. A similar trend was observed in a previous study where the decomposition rate was slow at the early stage, rapid at the intermediate stage, and slow again towards the end of the experiment [21].

Both mangrove and oil palm plantation soils demonstrated the highest decomposition rate on day 5 of the burial interval, i.e., 1.76 and 1.622 g/day, respectively. These findings observed during the putrefaction stage may be due to the occurrence of the autolysis process, accompanied by the release of nutrient-rich fluid. The substances in the released fluid, including sugars, amino acids, and fatty acids, serve as food and energy sources for the microbial community, thus promoting putrefaction [22, 23]. Meanwhile, another study found that the maximum microbial activity was observed within the first 10 days of the burial period [24]. The decomposition rate then decreased sharply after day 5 and continued to decrease to the end of the experiment. The decrease in the decomposition rate indicated the completion of decomposition as most of the fatty flesh decomposed, which was accompanied by the reduction in the mass of pig fatty flesh.

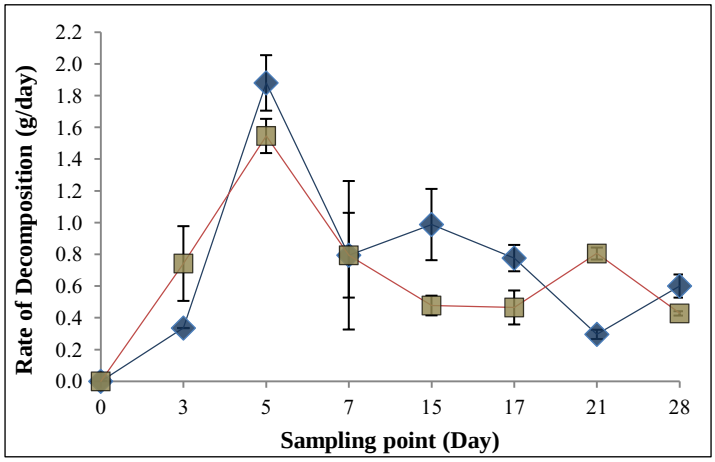


Figure 1. Plot of decomposition rate at different sampling points for 28 days of the burial period. The blue line represents the burial in mangrove soil whereas the red line represents the burial in oil palm plantation soil (n = 2)

Although a similar trend was observed for both soils, the decomposition rate of pig fatty flesh buried in mangrove soil occurred at a higher rate than that of oil palm plantation soil at most of the decomposition stages. This trend did not agree with previous studies as it is known that the rate of decomposition in the acidic soil was found to be two times faster than of the alkaline soil [25]. This observation may indicate the influence of other environmental factors on tends to occur in a mildly alkaline environment and can slow down the rate of decomposition [23, 28]. Adipocere is a decomposition product observable at the later stages of decay, usually following putrefaction [3, 29, 30]. The formation of adipocere results in unusual preservation, which also complicates the estimation of PMI [6, 31]. However, adipocere was not physically detected during sampling. Furthermore, the difference may also be due to the shift in microbial communities that is responsible for decomposition. It is well recognised that the decomposition of a cadaver will cause significant changes to the soil chemical properties and microbial communities [32]. It is also known that the changes in microbial communities across space are strongly associated with the differences in soil chemistry, particularly soil pH [33]. Besides, the introduction of cadaver decomposition materials will cause changes in many taxa contributing to the succession microbial community [34].

Total lipid extracts

Figure 2 shows the mass of total lipid extracts (TLEs) recorded at different sampling points for both soils throughout 28 days of the burial interval. The TLEs recovered from both soils showed an increasing trend in their masses throughout the experiment with minor fluctuation. The mass of TLEs extracted from the associated mangrove soil ranged between 0.076 and 0.5502 g g^{-1} soil dry weight. On the other hand, the mass of TLEs recovered from the oil palm plantation soil ranged between 0.2117 and 0.5423 g g^{-1} soil dry weight.

Even though both soils exhibited a similar trend in the decomposition rate, the mass of TLEs recovered from these soils was remarkably different. Between day 0 and day 7 of the burial interval, the mass of TLEs recovered from oil palm plantation soil was higher than that of mangrove soil. After day 7, the mass of TLEs extracted from mangrove soil was higher than that of oil palm plantation soil. The findings may be due to the shift in the soil microbial communities responsible for the decomposition of fatty flesh, as different microbial communities have a different need in nutrients and

energy [32, 35]. Thus, the response and adaptation of these microbial communities to the sudden increase in nutrient-rich fluid associated with decomposition may differ, resulting in varying mass of TLEs. These microbial communities may also involve in the mineralisation of the chemical components in the decomposition fluid into simpler components [10, 34].

A slower rate of decomposition for the burial in mangrove soil than that of oil palm plantation soil was evident by the decreasing mass of TLE between day 0 and day 3 of the burial period. After these days, the increase in the mass of TLEs recovered from this soil was observed, and a sharp increase in the mass of TLE was recorded between day 3 and day 5 of the burial interval. These observations may potentially be explained by the adaptation of microbial communities to the introduction of decomposing fatty flesh into the burial environment. The needs of nutrient sources may differ for different microbial communities; therefore, the shift in their communities can be observed towards the introduction of different cadaveric lipid components into the soil underneath [32, 36]. This shift due to the adaptation of the microbial communities to nutrient sources may lead to the decline in the degradation of fatty flesh between day 0 and day 3 of the burial period. The sharp increase in the TLE mass recorded after day 3 may be attributed to an enhanced adaptation of soil microbial communities towards the influx of cadaveric materials, which subsequently leads to the increase of decomposition. The rapid decrease and increase in the TLE mass may also be attributed to the slow and rapid mineralisation of cadaveric lipids into simpler components [32, 34, 36].

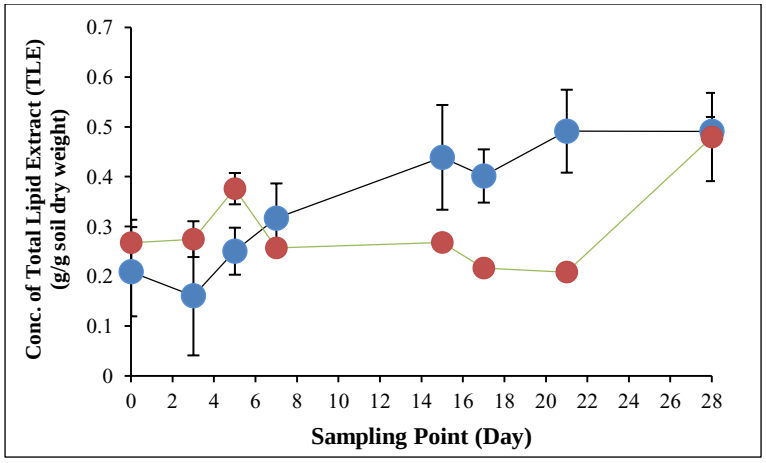


Figure 2. Mass of TLEs at different sampling points recovered from the associated mangrove and oil palm plantation soils for 28 days of the burial period. The black line represents the burial in mangrove soil whereas the green line represents the burial in oil palm plantation soil (n = 2)

For oil palm plantation soil, the mass of TLEs increased gradually from day 0 to day 3 and reached the maximum in the mass after 5 days of the burial period. The difference in the observation between that of mangrove and oil palm plantation soils at the initial decay and putrefaction stages can be regarded as an indication of different microbial responses towards the introduction of cadaveric materials. Furthermore, the findings agreed with the results from previous studies, which showed different burial soil environments have different influences on the cadaver decomposition rates [3, 4, 10]. After day 5 of the burial interval, the mass of TLEs decreased and the magnitudes in the mass were almost constant towards day 21. The observation was consistent with the decomposition rate shown in Figure 1, which may indicate less impact of cadaveric materials on the soil microbial communities after day 5 of the burial event. The results may also be an

indication of the rapid mineralisation of cadaveric materials into simpler compounds, resulting in a constant mass of TLEs. However, a rapid incline in the decomposition rate was observed after day 21, which contradicted the result of the decomposition rate; subsequently, it may explain a low mineralisation rate of cadaveric materials. Therefore, the mass of TLEs extracted from the burial associated soil will be higher compared to that of other burial days.

Free fatty acids

The GC results of TLEs for both mangrove and oil palm plantation soils revealed similar distributions of fatty acid components. Major free fatty acids (FFAs) recovered from both soils were saturated fatty acids of palmitic ($C_{16:0}$) and stearic ($C_{18:0}$) components, together with the unsaturated fatty acid of oleic ($C_{18:1}$) component. Relatively, the concentrations of these FFAs were higher in mangrove soil compared to that of oil palm plantation soil. This finding agrees with the finding of the higher decomposition rate of fatty flesh buried in mangrove soil compared to that of the oil palm plantation soil at most of the sampling points. It has been known that neutral fats of a decomposing cadaver will eventually be hydrolysed into a mixture of saturated and unsaturated fatty acids as the decomposition process involves the breaking down of larger compounds into smaller chemical components [23, 37, 38]. Furthermore, the fatty acids of oleic ($C_{18:1}$), linoleic ($C_{18:2}$), and palmitoleic ($C_{16:1}$) components have been identified to be the most abundant lipid components in the human body [38, 39].

Figure 3a shows that the concentration of FFAs recovered from the associated oil palm plantation soil varied with the burial interval. Remarkably, their concentrations were higher at the early stages of decomposition. The observations may suggest a massive introduction of cadaveric materials occurred at the early stages of decomposition for this type of soil. These early stages have been regarded as the active stages of decomposition [23, 38, 40]. The concentrations of $C_{16:0}$ ranged from 0.1808 to 61.0164 ppm g^{-1} soil dry weight. Meanwhile, the concentrations of $C_{18:0}$ were lower than that of $C_{16:0}$, ranging between 0.2548 and 21.6411 ppm g^{-1} soil dry weight. The fatty acid of the $C_{18:1}$ component exhibited the lowest concentration compared to that of $C_{16:0}$ and $C_{18:0}$, in the range between 0.0071 and 0.3839 ppm g^{-1} soil dry weight. It has been known that unsaturated fatty acids will be further hydrolysed and oxidised into simpler fatty acids shortly after death [39]. Furthermore, the mineralisation of $C_{18:1}$ is quicker in all the different soils [41]. The concentrations of these FFAs decreased towards the end of the experiment as the mass of decomposing fatty flesh will decrease with burial period.

Similarly, three major FFAs were extracted from the associated mangrove soil (Figure 3b). The $C_{18:0}$ component exhibited higher concentrations, ranging from 6.6374 to 3405.403 ppm g^{-1} soil dry weight, followed by $C_{18:1}$ with the concentration between 0.5949 and 2666.279 ppm g^{-1} soil dry weight. On the other hand, the $C_{16:0}$ component was found to have the lowest concentration, ranging from 0.00 to 36.0937 ppm g^{-1} soil dry weight. Remarkably, these FFAs demonstrated low concentration for the first 17 days of the burial period, contradicting to that of oil palm plantation soil. The concentrations of $C_{18:0}$ and $C_{18:1}$ increased rapidly after day 21 of the burial interval; however, the concentrations of $C_{16:0}$ were almost constant from the beginning of the burial event. The decomposition rate of pig fatty flesh in mangrove soil was almost similar to that of oil palm plantation soil (Figure 1); therefore, the finding may be an indication of rapid conversion of these FFAs into simpler compounds, such as carbon dioxide and water that occurred in mangrove soil. This rapid decomposition has been known to result in extensive hydrolysis and hydrogenation of fats, which eventually increases the mixture of saturated fatty acids, i.e., $C_{16:0}$ and $C_{18:0}$, and decreases the relative amount of unsaturated fatty acids, i.e., $C_{18:1}$ [39]. Subsequently, $C_{16:0}$ and $C_{18:0}$ dominated the oil palm plantation and mangrove soils for most of the sampling points. Previous studies identified that $C_{18:1}$ is the most abundant fatty acid found in adipose tissues, followed by $C_{18:2}$ and $C_{16:1}$, where the hydrogenation of unsaturated $C_{18:1}$, $C_{18:2}$, and $C_{16:1}$ will yield homologous saturated fatty acids, i.e., $C_{16:0}$ and $C_{18:0}$ [39, 42].

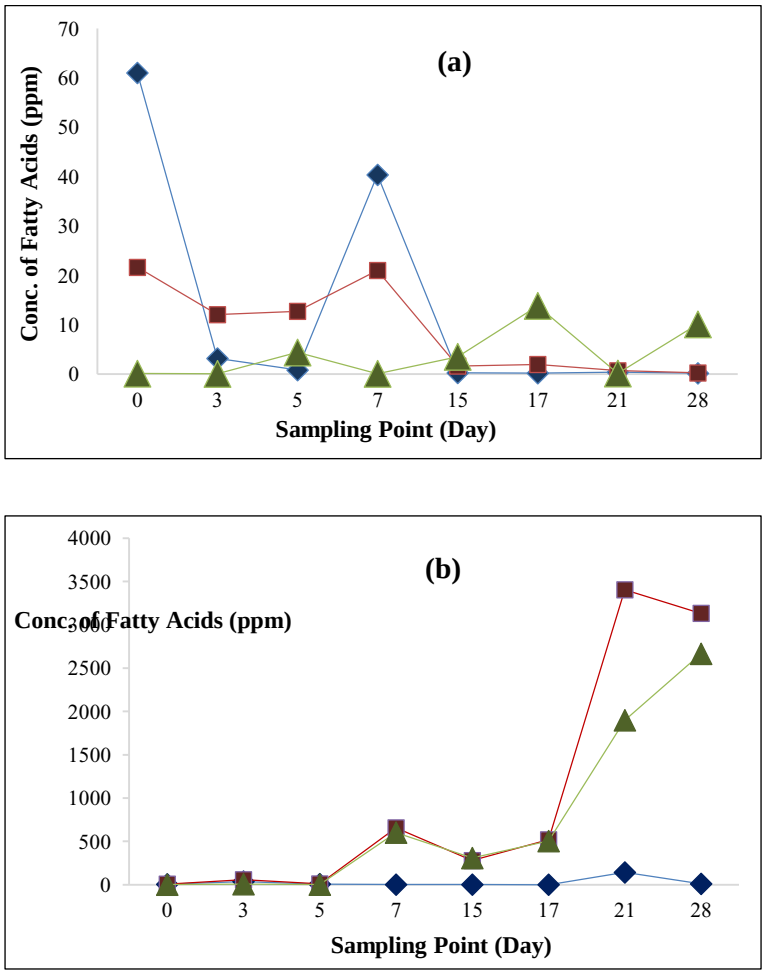


Figure 3. The concentration of fatty acids detected in oil palm plantation soil for 28 days of the burial interval. The blue line represents $C_{16:0}$, the red line represents $C_{18:0}$, and the green line represents $C_{18:1}$

Conclusion

In this study, three main parameters, namely decomposition rate, TLEs, and FFAs were the focus of discussion to describe the burial of a cadaver substituted by pig fatty flesh in mangrove and oil palm plantation soils. For a burial period of 28 days, a similar trend in the decomposition rate of pig fatty flesh was observed for both mangrove and oil palm plantation soil environments. However, the decomposition rate of the pig fatty flesh buried in mangrove (alkaline) soil was slightly higher compared to that of oil palm plantation (acidic) soil at sampling points of day 5, day 15, and day 17 of the burial period. Furthermore, both soils demonstrated a rapid increase in the decomposition rate after three days of the burial interval and reached maximum on day 5. Then, a rapid decline in the decomposition rate of both soils was observed between day 5 and day 7 of the burial period. The decomposition rate of both mangrove and oil palm soils continued to decrease towards the completion of the burial experiment as the mass of decomposing fatty flesh decreased with time. The mass of TLEs recovered from oil palm plantation soil was high at the first seven days of the burial period and low after this point.

Meanwhile, an opposite trend was observed for the mass of TLEs recovered from mangrove soil, i.e., the mass of TLEs was low at the first seven days of the burial period and high after this point. Both soils demonstrated a similar trend of decomposition rate; therefore, the different trends in the mass of TLEs may be an indication of different mineralisation rates occurring in both soils. Different responses of the microbial communities towards the introduction of different cadaveric materials at different decomposition stages may also lead to a different trend in the mass of TLEs recovered from the soils of different acidity. Even though both soils showed a similar trend of decomposition rate, the concentrations of FFAs recovered from mangrove soil were found to be higher than that of oil palm plantation soil. The findings may indicate different mineralisation rates and the response of microbial communities on the introduction of FFAs into the underneath of both soils. For oil palm plantation soil, the concentrations of FFAs were higher for the first 17 days of decomposing and lower after that point. In contrast, the concentrations of FFAs were low for the first 17 days and high after that point.

Remarkably, the introduction of decomposing fatty flesh in soils with different soil pH led to a significant difference in the decomposition rate for both soils, and subsequently resulted in a different mass of TLEs and other lipid components. Hence, the findings of this study may propose that the mass of TLEs and concentrations of FFAs can be developed as an alternative forensic tool to locate a clandestine grave and to estimate the PMI for different types of soils with different acidity.

Acknowledgement

The authors would like to thank the Ministry of Higher Education Malaysia (MOHE) for the research grant of the Fundamental Research Grant Scheme (Vot. 59405). We would also like to acknowledge the Royal Malaysia Police (RMP) for granting this study with ideas and soil samples from the crime scenes, as well as all staff at the Central Laboratory and School of Science and Marine Environment (FSME), Universiti Malaysia Terengganu.

References

1. Mann, R. W., Bass, W. M. and Meadows, L (1990). Time since death and decomposition of the human body: variables and observations in case and experimental field studies. *Journal of Forensic Science*, 35:103-11.
2. Janaway, R. C. (1997). The decay of buried human remains and their associated materials. studies in crime: an introduction to forensic archaeology. Routledge, London: pp. 58-85.
3. Forbes, S. L., Stuart, B. H. and Dent, B. B. (2005). The effect of soil type on adipocere formation. *Forensic Science International*, 154(1): 35-43.
4. Forbes, S. L., Stuart. B. H. and Dent, B. B. (2005b). The effect of the burial environment on adipocere formation. *Forensic Science International*, 154(1): 24-34.
5. Haslam, T. C. and Tibbett, M. (2009). Soils of contrasting pH affects the decomposition of buried mammalian (*Ovis aries*) skeletal muscle tissue. *Journal of Forensic Sciences*, 54(4): 900-904.
6. Vass, A. A. (2011). The elusive universal post-mortem interval formula. *Forensic Science International*, 204(1-3): 34-40.
7. Sullivan, T. S. (2017). Soil acidity impact beneficial soil microorganisms. Washington State University Extension: pp.1 - 6.
8. Lauber, C. L., Strickland, M. S., Bradford, M. A. and Fierer, N. (2008). The influence of soil properties on the structure of bacterial and fungal communities across land-use types. *Soil Biology and Biochemistry*, 40 (9): 2407-2415.
9. Lauber, C. L., Hamady, M., Knight, R. and Fierer, N. (2009). Pyrosequencing-based assessment of soil pH as a predictor of soil bacterial community structure at the continental scale. *Applied and Environmental Microbiology*, 75(15): 5111-5120.
10. Carter, D. O., Yellowlees, D. and Tibbett, M. (2006). Cadaver decomposition in terrestrial ecosystems. *Naturwissenschaften*, 94(1): 12-24.
11. Conyers, L, B. (2006). Ground penetrating radar techniques to discover and map historic graves. *Historical Archaeology*, 40(3): 64-73.

12. Larson, D., Vass, A. A. and Wise, M. (2011). Advanced Scientific Methods and Procedures in the Forensic Investigation of Clandestine Graves. *Journal of Contemporary Criminal Justice*, 27(2): 149 - 182.
13. Chock, X. and Ismail, S. S. (2017). Lipid distribution associated with a clandestine grave: A burial in mangrove soil. *Transaction on Science and Technology*, 4(4): 476-481.
14. Lowe, A. C., Beresford, D. O., Gaspari, F., O'rien, R. C., Stuart, B. H. and Forbes, S. L. (2013). The effect of soil texture on the degradation of textiles associated with buried bodies. *Forensic Science International*, 231(1-3): 331-339.
15. Notter, S. J., Stuart, B. H., Rowe, R. and Langlois, N. (2009). The initial changes of fat deposits during the decomposition of human and pig remains. *Journal of Forensic Sciences*, 54(1): 195-201.
16. Derrien, M., Cabrera, F. A., Tavera, N. L., Manzano, C. A. and Vizcaino, S. C. (2015). Sources and distribution of organic matter along the ring of cenotes, Yucatan, Mexico: Sterol markers and statistical approaches. *Science of the Total Environment*, 511: 223-229.
17. Bull, I. D., Berstan, R., Vass, A., and Evershed, R. P. (2009). Identification of a disinterred grave by molecular and stable isotope analysis. *Science & Justice*, 49(2): 142-149.
18. Derrien, M., Yang, L. and Hur, J. (2017). Lipid biomarkers and spectroscopic indices for identifying organic matter sources in aquatic environments: A review. *Water Research*, 112: 58-71.
19. Jin, J. F., Luo, G. H. and Gao, C. L. (2008). Study on the relationship between content of lipid in bone marrow of sternum and postmortem interval. *Shaanxi Medical Journal*, 37: 336-338.
20. Bligh, E. G. and Dyer, W. J. (1959). A rapid method of total lipid extraction and purification. *Canadian Journal of Biochemistry and Physiology*, 37(8): 911-917.
21. Carter, D. O. (2005). Forensic taphonomy: Processes associated with cadaver decomposition in soil. Thesis of Ph.D. Degree, James Cook University.
22. Zhou, C. and Byard, R. W. (2011). Factors and processes causing accelerated decomposition in human cadavers - an overview. *Journal of Forensic and Legal Medicine*, 18(1): 6-9.
23. Teo, C. H., Hamzah, N. H., Hing, H. L. and Hamzah, S. P. (2014). Decomposition process and postmortem changes: review. *Sains Malaysiana*, 43(12): 1873-1882.
24. Stokes, K. L., Forbes, S. L., Benninger, L. A., Carter, D. O. and Tibbett. M. (2009). Decomposition studies using animal models in contrasting environments: evidence from changes in soil chemistry and microbial activity. In: Ritz, K., Dawson, L. and Miller, D. (Eds.), *Criminal and Environmental Soil Forensics*. Springer Science & Business Media, Bradford: pp. 357-377.
25. Tibbett, M. and Carter, D. O. (2009). Research in forensic taphonomy: a soil-based perspective. In: Ritz, K., Dawson, L. and Miller, D. (Eds.), *Criminal and Environmental Soil Forensics*. Springer Science & Business Media: pp. 317-331.
26. Campobasso, C. P., Di Vella, G. and Introna, F. (2001). Factors affecting decomposition and diptera colonization. *Forensic Science International*, 120(1-2): 18-27.
27. Krishna, M. P. and Mohan, M. (2017). Litter decomposition in forest ecosystems: A review. *Energy, Ecology and Environment*, 2(4): 236-249.
28. Kibblewhite, M., Tóth, G. and Hermann, T. (2015). Predicting the preservation of cultural artefacts and buried materials in soil. *Science of the Total Environment*, 529: 249-263.
29. Mant, A. K. (1987). Knowledge acquired from post-war exhumation. In: Boddington, A., Garland, A. N. and Janaway, R.C: Death, decay and reconstruction-approaches to archaeological and forensic science. Manchester University Press, Manchester: pp. 65-78.
30. Takatori, T (1996). Investigations on the mechanism of adipocere formation and its relation to other biochemical reactions. *Forensic Science International*, 80(1-2): 49-61.
31. *Tsokos, M. and Byard, R. W. (2016). Postmortem changes: Overview. In:* encyclopedia of forensic and legal medicine. *2nd Edition, Academic Press Oxford: pp. 10-31.*

32. Benninger, L. A., Carter, D. O. and Forbes, S. L. (2008). The biochemical alteration of soil beneath a decomposing carcass. *Forensic Science International*, 180(2-3): 70-75.
33. Fierer, N. and Jackson, R. B. (2006). The diversity and biogeography of soil bacterial communities. *Proceedings of the National Academy of Sciences*, 103(3): 626-631.
34. Cobaugh, K. L., Schaeffer, S. M. and Debruyn, J. M. (2015). Functional and structural succession of soil microbial communities below decomposing human cadavers. *PloS One*, 10(6): e0130201.
35. Islam, R. and Wright, S. R. (2004). Soil microbial communities. Chapter in book: Encyclopedia of soil, Marcel Dekker, Inc. New York.
36. Cusack, D. F., Silver, W. L., Torn, M. S., Burton, S. D. and Firestone, M. K. (2011). Changes in microbial community characteristics and soil organic matter with nitrogen additions in two tropical forests. *Ecology*, 92(3): 621-632.
37. Vass, A. A., Barshick, S. A., Sega, G., Caton, J., Skeen, J. T., Love, J. C. and Synstelien, J. A. (2002). Decomposition chemistry of human remains: A new methodology for determining the postmortem interval. *Journal of Forensic Science*, 47(3): 542-553.
38. Janaway, R., Percival, S. and Wilson, A. (2009). Decomposition of human remains. In: microbiology and aging. Springer, New York: pp. 313-334.
39. Dent, B. B., Forbes, S. L. and Stuart, B. H. (2004). Review of human decomposition processes in soil. *Environmental Geology*, 45(4): 576-585.
40. Goff, M. L. (2009). Early post-mortem changes and sages of decomposition in exposed cadavers. *Experimental & Applied Acarology*, 49(1-2): 21-36.
41. Moucawi, J., Frustec, E. and Jacquesy, R. (1981). Decomposition of lipids soils: Free and esterified fatty acids, alcohol and ketones. *Soil Biology and Biochemistry,* 13 (6): 461-468.
42. Forbes, S. L. (2008). Decomposition chemistry in a burial environment. Soil analysis in forensic taphonomy. Taylor & Francis, New York: pp. 203-223.

Malaysian Journal of Analytical Sciences (MJAS)
Published by Malaysian Analytical Sciences Society

PERFORMANCE OF CERAMIC MEMBRANE COATED WITH GRAPHENE OXIDE AS ALTERNATIVE FOR OILY WASTEWATER TREATMENT

(Prestasi Selaput Seramik Grafin Oksida Sebagai Pilihan Untuk Rawatan Air Sisa Berminyak)

Nurdiyana Nabilah Kasim[1], Sharifah Abdullah[1], Nur Asmaliza Mohd Noor[2]*

[1]*Faculty of Civil Engineering,*
Universiti Teknologi MARA, 40450 Shah Alam, Selangor, Malaysia
[2]*Faculty of Civil Engineering,*
Universiti Teknologi MARA Pahang, Lintasan Semarak 26400 Jengka, Pahang, Malaysia

**Corresponding author: nurasmaliza@uitm.edu.my*

Received: 20 November 2019; Accepted: 5 April 2020; Published: 9 June 2020

Abstract

The high demand for liquefied natural gas (LNG) contributes to the increasing production of LNG thus leading to the increment of oily wastewater. The membrane technology shows a very promising alternative to replace the conventional method to treat oily wastewater. The objectives of this study are to synthesize graphene oxide (GO) as a modifier to graphitic carbon nitride (g-C_3N_4) for alumina ceramic membrane, to characterize the structure of nanosheet and bulk of graphitic carbon nitride, graphene oxide and g-C_3N_4/GO composite which leads to the study of the performance of g-C_3N_4/GO coated alumina ceramic photocatalytic membrane to degrade oil in oily wastewater. The methodology started with the material preparation, photocatalyse membrane preparation and the characterization of material using X-ray diffraction (XRD), Fourier Transformation Infrared (FTIR) analysis, Brunauer Emmet Teller (BET) surface area analyses and UV-Vis-NIR spectrophotometer analysis. The last method is the degradation of methylene blue (MB) dye and photocatalytic study degradation of oil in wastewater using synthesis oily wastewater. The results indicated the g- C_3N_4/GO reduced 73.79% of the MB dye compared to 38.85% and 62.71% for bulk g-C_3N_4 and g-C_3N_4 nanosheet respectively. The g-C_3N_4/GO composite photocatalyst showed remarkable photocatalytic efficiency rather than bulk g-C_3N_4 and g-C_3N_4 nanosheet. Thus, the introduction of GO into g-C_3N_4 has improved the charge separation efficiency of g-C_3N_4 and improving the organic degradation potential of g-C_3N_4.

Keywords: alumina, g-C_3N_4, graphene oxide, photocatalytic membrane, oily wastewater

Abstrak

Permintaan yang tinggi terhadap gas asli cecair (LNG) menyumbang kepada peningkatan pengeluaran LNG sehingga mengakibatkan pertambahan terhadap air sisa berminyak. Teknologi selaput menjadi pilihan yang menggantikan kaedah konvensional dalam merawat air sisa berminyak. Objektif kajian ini adalah untuk melakukan sintesis grafin oksida (GO) sebagai pengubahsuai karbon nitrida grafit (g-C_3N_4), untuk memperincikan struktur lapisan nano, karbon nitrida grafit, grafin oksida dan g-C_3N_4/GO komposit yang membawa kepada kajian prestasi selaput fotomangkin seramik alumina bersalut g-C_3N_4/GO untuk degradasi minyak dalam air sisa berminyak. Kaedah kajian bermula dengan penyediaan bahan, penyediaan selaput fotomangkin dan pencirian bahan menggunakan pembelauan sinar-X (XRD), analisis inframerah trasnformasi Fourier (FTIR), analisis kawasan permukaan Brunauer Emmet Teller (BET) dan analisis spektrofotometer UV-Vis-NIR. Kaedah terakhir adalah degradasi pewarna metilena biru (MB) dan kaedah fotomangkin dalam degradasi minyak dalam air sisa menggunakan jenis

tiruan. Keputusan kajian ini telah menunjukkan bahawa g-C_3N_4/GO berkurang kepada 73.79% daripada pewarna MB berbanding 38.85% untuk g-C_3N_4 dan 62.71% untuk g-C_3N_4 lapisan nano. Manakala kaedah fotomangkin bagi komposit g-C_3N_4/GO menunjukkan kecekapan fotomangkin yang luar biasa berbanding g-C_3N_4 dan g-C_3N_4 lapisan nano. Oleh itu, pengenalan GO ke dalam g-C_3N_4 telah meningkatkan kecekapan g-C_3N_4 sebagai agen pemisahan sekali gus meningkatkan potensi g-C_3N_4 sebagai degradasi organik.

Kata kunci: alumina, g-C_3N_4, grafin oksida, fotokatalik, selaput, air sisa berminyak

Introduction

Numerous processes and activities in various industries that have led to the production of wastewater are food processing, textile and oil and gas. In Malaysia, oil and gas industries are the major contribution in economy and thus a lot of activities related to these industries and causing major contribution to the production of wastewater. There are a few activities in oil and gas that produces wastewater such as raw natural gas that is fed into gas treating facilities such as acid gas removal unit (AGRU), mercury removal unit, and dehydration unit and then passed into the liquefaction unit to convert it into LNG. These units' associated facility leads to the generation of wastewater which can be divided into the conventional and non-conventional pollutants. The types of conventional pollutants which are also known as oily wastewater are oil and grease and suspended solids while the non-conventional pollutants which are known as chemically contaminated wastewater are phenolic compounds, sulphide and ammonia [1]. In this study, oily wastewater is emphasized due to the increase of its group therefore the proper and better oily wastewater treatment technology or strategies are needed to tackle these issues. It is necessary to purify the wastewater in order to meet the environment's discharge standards by the Department of Environment (DOE) Malaysia because oily wastewater can cause adverse effects to the environment especially marine life as shown in Table 1 [2].

New technology has been introduced to treat oily wastewater using the membrane [3] where it has a function to act as a selective barrier to separate the pollutants from water. Previously, most of the studies have been conducted to improve the efficiency of alumina ceramic membrane to separate and treat wastewater. However recently, the addition of the degradation capability to facilitate the membrane separation process using photocatalyst such as carbon nitride, g-C_3N_4 on the surface of the ceramic membrane as quite a promising method has been introduced. Despite the fact that the membrane presents great potential to be applied in the separating process, yet it has fouling problems [4]. The fouling is hard to be removed and it could weaken the permeation rate through the membrane and affect the quality of treated wastewater [3]. Thus, the introduction of photocatalyst on the surface of the membrane could contribute antifouling functions under light irradiation, sustain the clean membrane surface and improve the quality of treated wastewater. Therefore, the objectives of this study are to synthesize graphene oxide (GO) as a modifier to graphitic carbon nitride (g-C_3N_4) for alumina ceramic membrane, to characterize the structure of nanosheet and the bulk of graphitic carbon nitride, graphene oxide and g-C_3N_4 /GO composite and to study the performance of g-C_3N_4/GO coated alumina ceramic photocatalytic membrane to degrade oil in oily wastewater.

Table 1. Discharge of industrial effluent or mixed effluent of standard A and B [2]

Parameter	**Unit**	**Standard A**	**Standard B**
Temperature	^{0}C	40	40
pH Value	-	6.0-9.0	5.5-9.0
BOD_5 at 20^{0}C	mg/L	20	50
Suspended Solid	mg/L	50	100
Mercury	mg/L	0.005	0.05
Cadmium	mg/L	0.01	0.02
Chromium Hexavalent	mg/L	0.05	0.05
Chromium Trivalent	mg/L	0.20	1.0
Arsenic	mg/L	0.05	0.10
Cyanide	mg/L	0.05	0.10
Lead	mg/L	0.10	0.50
Copper	mg/l	0.20	1.00
Manganese	mg/L	0.20	1.00
Nickel	mg/L	0.20	1.00
Tin	mg/L	0.20	1.00
Zinc	mg/L	2.00	2.00
Boron	mg/L	1.00	4.00
Iron (Fe)	mg/L	1.00	5.00
Silver	mg/L	0.10	1.00
Aluminum	mg/L	10	15.0
Selenium	mg/L	0.02	0.50
Barium	mg/L	1.0	2.00
Fluoride	mg/L	2.0	5.00
Formaldehyde	mg/L	1.0	2.00
Phenol	mg/L	0.001	1.00
Free Chlorine	mg/L	1.0	2.00
Sulphide	mg/L	0.05	0.05
Oil and Grease	mg/L	1.0	10
Ammoniacal Nitrogen	mg/L	10	20
Color	ADMI	100	200

Materials and Methods

To achieve the objectives of this study, the methodology can be divided into 4 Parts. Part 1 covers the material preparation, that is, synthesis of bulk graphitic carbon nitride synthesis of bulk graphitic carbon nitrite (g-C_3N_4) nanosheet and synthesis of GO. Part 2 involves the photocatalyst membrane preparation, that is, synthesis alumina ceramic, disc membrane, preparation of ceramic dope solution, fabrication of alumina ceramic disc membrane and synthesis of g-C_3N_4/GO alumina ceramic membrane. The work on material characterization of materials is done in Part 3 utilizing analyzes *via* XRD, FTIR, BET and UV-Vis-NIR. The last part which is Part 4 involves related pre photocatalysis studies such as degradation measurement of methylene blue (MB) dye and photocatalytic studies on the degradation of oil in wastewater using synthetic oily wastewater. Details of each above-mentioned methodology parts are discussed as follows:

Material preparation

The facile temperature free method was used for preparation of g-C_3N_4 by using urea powder (HmbG Chemical Germany) and isopropanol alcohol (IPA, 99.7%, M = 60.10 g/mol) bought from Hypercube IT Solution as dispersion medium to exfoliate the bulk g-C_3N_4 into gC_3N_4 nanosheet. GO was prepared by Hummers' method by using graphite powder (Comak) and sodium nitrate (Systerm, $NaNO_3$, ChemAR). Sonochemical method was used to prepare gC_3N_4/GO composite.

Synthesis of bulk graphitic carbon nitride

The synthesis of bulk graphitic carbon nitride is achieved using the urea powder by applying facile template-free method [6]. An amount 20 g of urea powder purchased from HmbG Chemical was settled in a lidded alumina crucible and heated for 550 °C in a carbolite furnace for 4 hours using the heating rate of 15 °C/min.

Synthesis of bulk g-C_3N_4 nanosheet

Nanosheet form of g-C_3N_4 was synthesized using the liquid exfoliation method of g-C_3N_4 [7] in order to have improved photocatalytic effect. This method used organic solvent isopropanol alcohol (IPA, 99.7%, M = 60.10 g/mol) brought from Hypercube IT Solution as a dispersion medium where 0.3 g of bulk graphitic carbon nitride was dispersed into 100 mL of isopropanol alcohol. The dispersion was sonicated in room temperature for 8 hours to exfoliate the bulk g-CN then centrifuged at 3000 rpm for 30 minutes in order to give the homogenous dispersion of exfoliated g-C_3N_4 nanosheet. After that, the dispersion was dried at 50 °C for 6 hours in order to form and collect the final product which was a light-yellow powder of g-C_3N_4 nanosheet.

Synthesis of GO

GO was synthesized using the Hummers' method [8] where 5 g of graphite powder and 2.5 g of sodium nitrate was put in 1000 mL of concentrated sulphuric acid (H_2SO_4). Subsequently, the mixture was stirred for 1 hour and kept under low temperature by placing it in ice. After that, the 30 g of $KMnO_4$ was gradually added for 2 hours and continuously stirred for another 2 hours in room temperature and then heated with a temperature of 70 °C. Next, the 100 mL of water was gradually added to the mixture and stirred for another 1 hour. The 30 mL of H_2O_2 was added into the mixture to stop the reaction and the color of the suspension turned to bright yellow. In order to purify the suspension, 0.2M of HCI was added once and the 200 mL of distilled water, 3 times until pH 7 (neutral). Then the sample was dried in the furnace with a temperature of 80 °C for a day in order to form GO.

Synthesis of g-C_3N_4/GO composite photocatalyst

The synthesis followed the sonochemical method ([9]) where 0.2 g of GO of previous synthesis was added into 200 mL of high purity water, 0.2g of g-C_3N_4 nanosheet was added into the mixture, sonicated for 12 hours, furnace dried in a temperature of 80 °C for a day.

Photocatalyst membrane preparation

This part started with the synthesis of alumina ceramic disc membrane as it was used as the base membrane in

this study. The other steps for preparation for photocatalyst membrane are as follows:

Preparation of ceramic dope solution

The ceramic dope solution was prepared first for the process fabrication of the ceramic membrane. It consisted of the composition of ceramic particle, a polymeric binder, solvent, additive that acts as the dispersant [10]. The ceramic particle was used as Al_2O_3, alpha; 99.9% metal basis, surface area 6-8 m^2/g, <1.0-micron APS powder, Alfa Aesar for this research. Meanwhile dimethyl sulfoxide (HPLC grade, VWR), and polymeric binder polyethersulfone (PESf, Ameco Performance, USA) were used. Arlacel P135 (polyethylene glycol 30-dipolyhydroxystearate, Uniqema) was used as the additive. The process of preparation started with 55 wt.% of aluminum oxide powder, 0.38 wt.% of Arlacel weighed and added into 39.12 wt.% of the solvent, DMSO. Additionally, the mixture was rolled/milled with grinding balls for 48 hours. The ceramic dope solution was ready to be used to fabricate the ceramic disc membrane after adding 5.5 wt.% of PESf into the mixture and rolled for another 48 hours.

Fabrication of alumina ceramic disc membrane

The ceramic dope solution went through the inversion method where it needs to be poured into a stainless-steel mold with a diameter of 3 cm and placed in a water bath for 30 minutes and after it hardens, the precursor ceramic disk was removed. The next process was sintering the precursor ceramic disc calcite by using furnace CARBOLITE to obtain the final ceramic disc membrane. The temperature of the furnace was set at 600 °C at a rate of 2 °C/minute with a dwell time of 2 hours and has been increased to the targeted temperature of 1400 °C at a rate of 5 °C/minute with a dwell time of 4 hours. Then, the temperature was reduced to room temperature at a rate of 5 °C/minute and the alumina ceramic membrane was ready to be coated with the composite photocatalyst.

Synthesis of g-C_3N_4/GO alumina ceramic membrane

The 0.3 g of g-C_3N_4/GO composite was dissolved in 50 mL of distilled water and sonicated for 1 hour. Then, g-C_3N_4/GO solution was coated with alumina ceramic membrane by pouring the solution on the ceramic membrane surface and dried in the furnace at 50 °C for a day.

Characterization of material

Characterization of material for synthesized GO, bulk and nanosheet g-C_3N_4 and g-C_3N_4/GO composites used the XRD method which operated with 40 kV and 40 mA and the scanning rate was 2 °/minute. Besides, the FTIR was also used to characterize the material with the operation of wavelength around 800-3800 cm^{-1}. Other methods that used to characterize material was BET Surface Area Analysis where the specific surface area and pore size distribution of synthesized materials in powder was determined by the adsorption of nitrogen gas on the surface of the solid powder by calculating the amount of adsorbate gas on the layer of surface. It was done by using 3-Flex Micromeritics system. As for determination of degradation rate of MB dye and oily wastewater, the UV-Vis-NIR spectrophotometer (Perkin Elmer, LAMBDA 750) was used to obtain spectra.

Photocatalytic study: Degradation of MB dye

The preliminary photodegradation study was conducted on MB dye by using bulk g-C_3N_4, g-C_3N_4 nanosheet, and g-C_3N_4/GO composite powder under sunlight. An amount 0.1 g of each material added into a beaker that contained 50 mL of 25 mb/L MB dye. Then the solution was placed under sunlight for 2 hours and for every 30 minutes, 3 mL of solutions was extracted using a syringe and this was used to analyze and determine the degradation efficiency by using the UV-Vis-NIR Spectrophotometer at $\lambda > 400$ nm.

Photocatalytic study: Degradation of oil in wastewater

Photodegradation study on synthetic oily wastewater was conducted by using g-C_3N_4/GO composite powder. The synthetic oily wastewater was prepared by mixing 1 L of distilled water and of 1mL West Lutong light crude oil (SG 0.84, API 37.7) in room temperature but under sunlight. Then, an amount 0.1g of g-C_3N_4/GO composite was added into a beaker which contained 50 mL oily wastewater. The solutions were needed to be

placed under sunlight for 2 hours, 3 mL of solution was extracted using a syringe for every 30 minutes to determine the degradation efficiency using UV-Vis-NIR spectrophotometer.

Results and Discussion

Characterization of material: XRD analysis

Figure 1 shows the XRD pattern of fabricated bulk g-C_3N_4 and g-C_3N_4 nanosheet. Two peaks were identified for both g-C_3N_4 where for bulk g-C_3N_4, dominant (002) diffraction peak was identified at $2\theta = 27.2^o$. It was indicated in the interlayer stacking of conjugated aromatic CN unit with d = 3.27 µm. The improvement of (002) peak's intensity was found in g-C_3N_4 nanosheet due to the enhancement in crystallinity of g-C_3N_4 after liquid exfoliation [11].The small degree of shifting in (002) diffraction peak's point was identified from 27.2^o in bulk g-C_3N_4 to 27.4^o in g-C_3N_4 nanosheet. The same goes to the stacking distance from d= 3.27µm in bulk g-C_3N_4 to d= 3.25 µm. Both bulk g-C_3N_4 and g- C_3N_4 nanosheet indicated minor (100) diffraction peak around 13.0^o which corresponds to the in-plane structural packing of triazine units while the distance between pores of nitride in g-C_3N_4 are specified with planar distance of d = 6.79 µm for (100) diffraction peak. The diffraction peak at a lower angle of about 11.4^o GO implies the introduction of oxygen containing functional group of GO [12,13].

The XRD patterns of fabricated g-C_3N_4 nanosheet, GO and g-C_3N_4/GO composite are shown in Figure 2. GO shows intense (001) diffraction peak at $2\theta = 9.8^o$ which is typical for GO and the same pattern has been reported by Dutrow and Clark [11]. The factors that contributed to that pattern were the existence of oxygenated functional group and introduction of H_2O molecule. A study conducted by Olumurewa et al. [14] indicated that the introduction of diffraction peak at low angle furnace that the graphite was successfully oxidized to the GO. The XRD pattern for g-C_3N_4/GO composite showed the two diffraction peaks which was around 27.3^o and this was quite similar with the XRD pattern of g-C_3N_4 (002) peak thus indicating that the composite contains g-C_3N_4. This was consistent with the findings by Alam et al. [15] that introduction of GO into the g-C_3N_4 did not affect the structure of g-C_3N_4. The introduction of GO has caused the intensity of (002) diffraction peak of g-C_3N_4/GO to decrease and this proved that g-C_3N_4/GO has less layers than g-C_3N_4 and this is parallel with the report by Dutrow and Clark [11]. Besides that, the modification of GO into g-C_3N_4 also caused the widening of (002) diffraction peak and this condition was explained by authors, where it is caused by the wavelike motion of the layer of g-C_3N_4/GO composite.

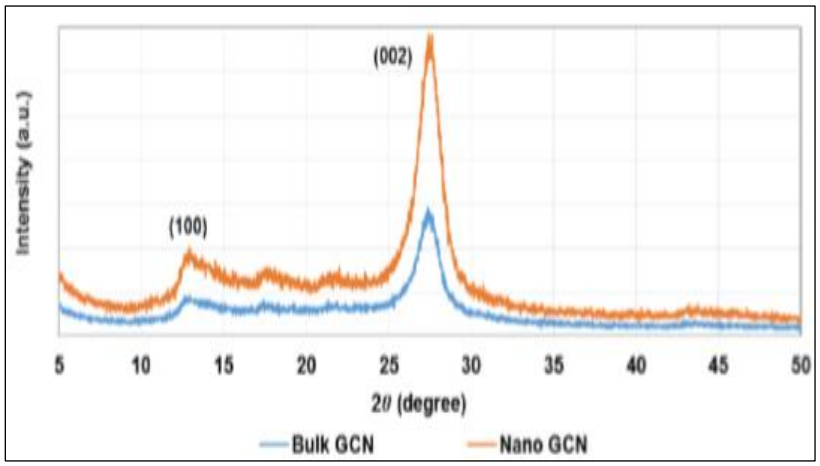


Figure 1. XRD pattern for bulk g-C_3N_4 and g-C_3N_4 nanosheet

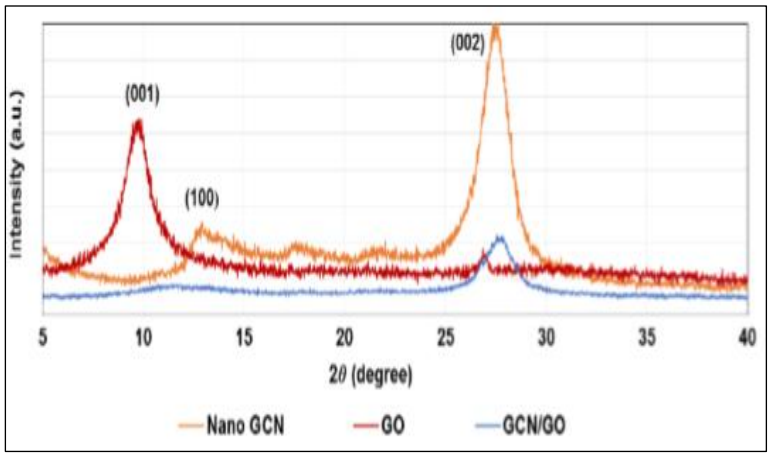


Figure 2. XRD patterns of g-C_3N_4 nanosheet, GO and g-C_3N_4/GO composite

FTIR analysis

Figure 3 shows FTIR spectrum of fabricated bulk g-C_3N_4 and g-C_3N_4 nanosheet with the wide absorption band at 3000 - 3400 cm^{-1}. According to Sheha [16], this is caused by the hydroxyl group due to the adsorption of H_2O molecule and uncondensed amine (-NH_2) or amine (-CH=NH). FTIR spectra of bulk g-C_3N_4 and g-C_3N_4 showed that at 1200 and 1220 cm^{-1} respectively due to the characteristics of the breathing mode of heptazine ring system [17]. FTIR spectrum of bulk g-C_3N_4 and g-C_3N_4 nanosheet in Figure 3 are clearly identified and can be concluded that the exfoliation of g-C_3N_4 still retain their chemical structure as bulk g-C_3N_4 and this is aligned with the study conducted by Raphael [18].

The FTIR spectrum of g-C_3N_4/GO composite shows the resemblance pattern to the FTIR spectrum of g-C_3N_4 but with a slight difference to the GO as shown in Figure 4 .The spectrum of GO shows the wider absorption band at a range of 3000-3500 cm^{-1} attributed by the stretching of OH group of water molecules. Meanwhile, the g-C_3N_4/GO composite shows the same pattern of absorption band as GO and this is contributed by the stretching of N-H group. The g-C_3N_4/GO composite exhibited the sharp peak at 804.19 cm^{-1} and the g-C_3N_4 nanosheet depicted the sharp peak at 1220 cm^{-1}. [19] conducted a study and found that the peak at 1039.31 cm^{-1} caused by the presence of the C-O functional group. Literature study [20] described that the peak at 1618.65 cm^{-1} was contributed by C=O stretching when at this stage the C=C bonds are still intact even after the oxidation process. Thus, this finding supports the justification for XRD analysis by introducing the GO into g-C_3N_4 and not altering the chemical structure of g-C_3N_4.

BET analysis

Table 1 shows the value of surface area and pore volume of bulk g-C_3N_4, g-C_3N_4 nanosheet, g-C_3N_4/GO composite and GO that was identified through the BET analysis.

The g-C_3N_4 nanosheet indicated the greater surface area and large pore volume compared to the other materials. The liquid exfoliation of bulk g-C_3N_4 has been minimized to the size of the nanometer thus the increase of specific areas for g-C_3N_4 was due to the bond cleavage of g-C_3N_4. BET surface area of g-C_3N_4 nanosheet was 94.08 m^2/g greater than bulk g-C_3N_4 that was 79.84 m^2/g as shown in Table 1. According to [21] the high surface area of g-C_3N_4 nanosheet would have the significant presence of active sites with nitrogen atom where it is very suitable to be used as a photocatalyst. Meanwhile, the BET surface area of GO and g-C_3N_4/GO composite were 2.01 m^2/g and 45.57 m^2/g respectively. These results have been agreed with the results produced by Vlachos et al. [22].

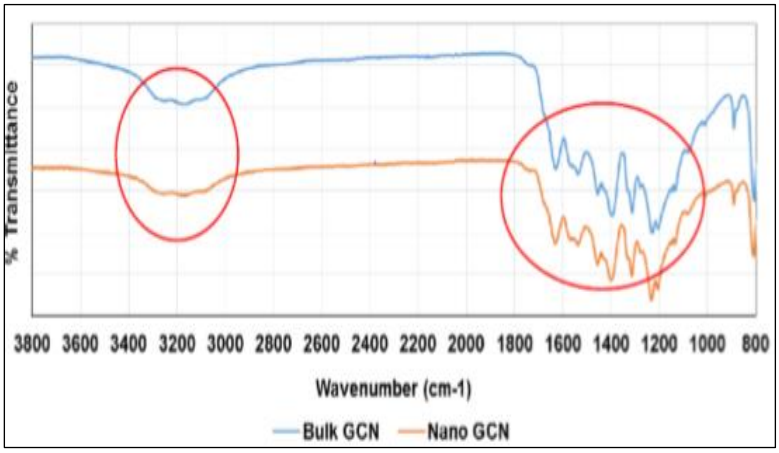


Figure 3. FTIR spectrum of bulk g-C_3N_4 and g-C_3N_4 nanosheet

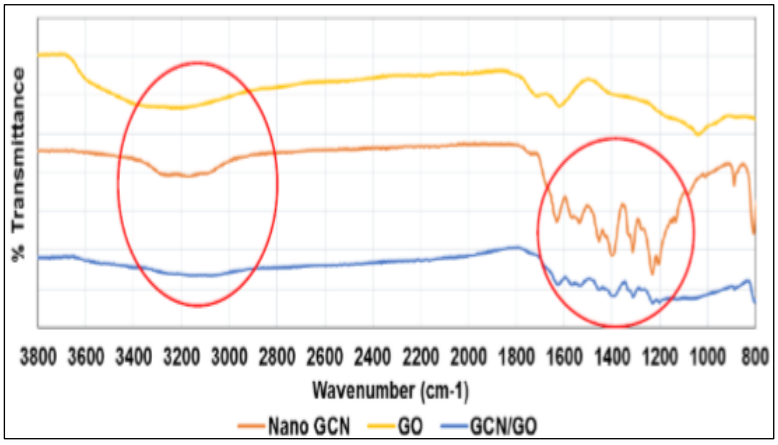


Figure 4. FTIR spectrum of g-C_3N_4 nanosheet, GO and g-C_3N_4/GO composite

Table 1. BET surface area and pore volume of material

Sample Name	**Sample Mass (g)**	**SBET (m^2/g)**	**Pore Volume (cm^2/g)**
Bulk g-C_3N_4	0.086	79.840	0.465
g-C_3N_4 nanosheet	0.048	94.079	0.639
g-C_3N_4/GO	0.224	45.572	0.057
GO	0.188	2.010	0.003

Photocatalytic study

Degradation of MB dye

Photocatalysis is the method to measure the acceleration of chemical conversion through the activation of a catalyst. The preliminary photo-degradation study under sunlight study was conducted on MB dye by using bulk g-C_3N_4, g-C_3N_4 nanosheet and g-C_3N_4/GO composite powder. Figure 5 shows the process of photocatalytic degradation of MB dye under sunlight for bulk g-C_3N_4, g-C_3N_4 nanosheet and g-C_3N_4/GO composite powder. The photocatalytic potential for different photocatalysts was evaluated by comparing the degradation efficiency for MB dye. The amount of MB dye degradation is 42.75% for g-C_3N_4/GO composite, 50.77% for g-C_3N_4 nanosheet and 31.29% for bulk g-C_3N_4 after 1 hour of exposure to sunlight can be seen through Figure 5. However, after 2 hours of exposure to sunlight, the amount of MB dye degradation has increased to 73.79% for g-C_3N_4/GO composite, 62.71% for g-C_3N_4 nanosheet and 38.85% for bulk g-C_3N_4. According to the findings, the bulk g-C_3N_4 and g-C_3 N_4 nanosheet depicted the reduction of degradation efficiency after 30 minutes and 90 minutes of exposure to sunlight. However, the g-C_3N_4/GO composite indicated the consistency of the degradation efficiency throughout 2 hours of exposure. The g-C_3N_4 is to be the potential photocatalysts for the degradation of numerous pollutants with photophysical potential of the parent nitride altered through doping with heteroatoms, heterojunction formation with other materials and textural enhancements to expand the surface area and porosity [23].

Thus, the finding showed that the g-C_3N_4/GO composite has a good degradation capability followed by g-C_3N_4 nanosheet and bulk g-C_3N_4.The photocatalyst potential of g-C_3N_4/GO composite was contributed by its characterization of chemical structure and properties. The introduction of GO has improved the charge of separation efficiency because when the visible light absorption capability g-C_3N_4 is combined with GO they act as electron sink [22] in helping the separation and storage to improve the photocatalytic capability of the composite. When g-C_3N_4 absorbed visible light, the electron is transferred to the GO layer where it reduces the chances of electron-hole recombination thus improving the separation efficiency. However, the left holes on the valence band of g-C_3N_4 contributed to the consistent degradation efficiency of g-C_3N_4/GO composite. The factor that bulk g-C_3N_4 is having the lowest degradation efficiency compared to g-C_3N_4 nanosheet due to the low surface area where active site is less thus a low number of MB dye molecule is interacted with the photoexcited carrier [24]. As for g-C_3N_4 nanosheet, it slightly contradicts where it had a greater surface area thus greater availability of active sites to react with MB dye molecule.

Degradation of oil in wastewater

The potential of bulk g-C_3N_4, g-C_3N_4 nanosheet and g-C_3N_4/GO composite to degrade organic pollutants were tested with the evaluation of the efficiency of photocatalyst to degrade oil in synthetic oily wastewater under sunlight. Figure 6 shows the photocatalytic degradation of oil in synthetic oily wastewater under sunlight with bulk g-C_3N_4, g-C_3N_4 nanosheet and g-C_3N_4/GO composite powder. The g-C_3N_4/GO composite shows the consistent degradation efficiency after 1 hour with 49.65% of oil degraded while the bulk g-C_3N_4 only degraded to 35.24% of oil. After 2 hours, the results indicated that the amount of oil degraded was 75.54%, 55.89% and 44.57% for g-C_3N_4/GO composite, g-C_3N_4 nanosheet and bulk g-C_3N_4 respectively. The samples also produced initially, strong aromatic smells however, after 2 hours, the g-C_3N_4/GO composite produced a less aromatic smell. [25,26] also conducted a study using low cost ceramic membrane to treat synthetic oily wastewater and it showed a capability to treat oily wastewater.

Performance of G-C_3N_4/GO alumina ceramic membrane

Figure 7 shows the process of separation and photocatalytic degradation of oil in synthetic oily wastewater in bare alumina ceramic membrane and g-C_3N_4/GO alumina ceramic membrane. From the results obtained, the g-C_3N_4/GO alumina ceramic membrane showed a greater percentage of oil adsorption compared to the bare alumina ceramic membrane with 47.65% and 27.66% respectively after 2 hours. After the degradation and separation process, permeate water of g-C_3N_4/GO alumina ceramic membrane looked

clearer compared to the permeated water of bare alumina ceramic membrane according to the clarity of red scale. Moreover, there was no change in the intensity of aromatic smell of wastewater for both samples thus indicating that the aromatic compound is mostly not degraded. The coating of g-C_3N_4/GO on alumina ceramic membrane also had a greater removal efficiency of oil in oily wastewater rather than the bare alumina ceramic membrane. This is due to the separation process of alumina ceramic membrane coupled with the degradation process of oil in the wastewater by gC_3N_4/GO [27]. In conclusion, g-C_3N_4/GO alumina ceramic membrane can be a potential candidate to treat the industrial oily wastewater.

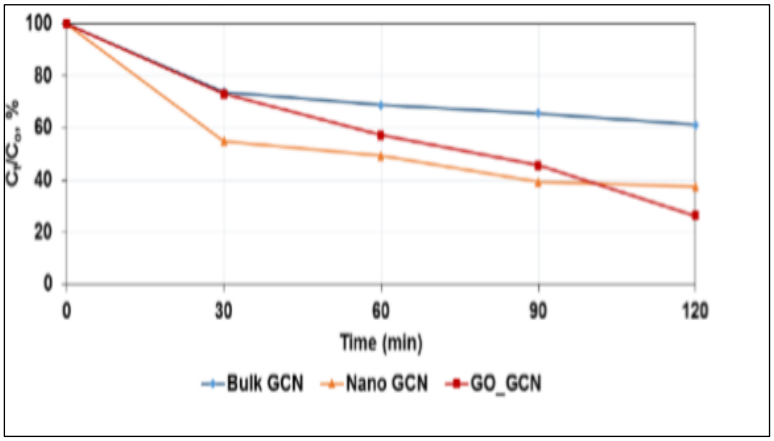


Figure 5. Photocatalytic degradation of MB dye under sunlight with bulk g-C_3N_4, g-C_3N_4 nanosheet, and g-C_3N_4/GO composite

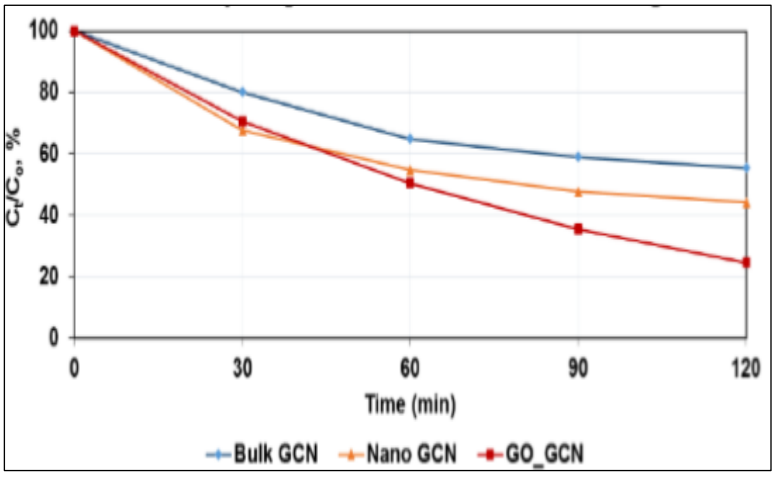


Figure 6. Photocatalytic degradation of oil in wastewater under sunlight with bulk g-C_3N_4, g-C_3N_4 nanosheet and g-C_3N_4/GO composite

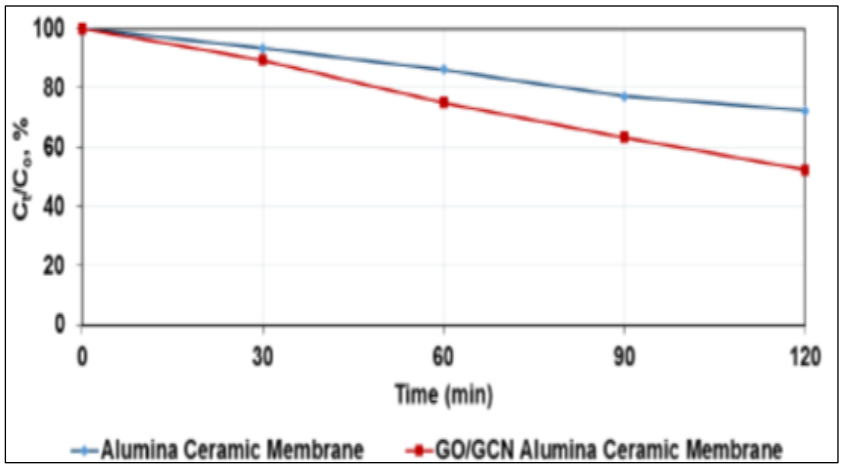


Figure 7. Separation and degradation of oil in synthetic oily wastewater with g-C_3N_4/GO alumina membrane and bare alumina membrane

Thus g-C_3N_4/GO alumina ceramic membrane shows good removal capability of oil in oily wastewater when compared to bare alumina ceramic membrane. The improvement of the performance of alumina ceramic membrane to remove oil in the wastewater was contributed by the introduction of photocatalyst g-C_3N_4/GO on the membrane surface. The additional g-C_3N_4/GO photocatalyst opened up a new process that the degradation facilitates the removal of the organic compound of oil hence improving the quality of the permeated water

Conclusion

GO, photocatalyst bulk g-C_3N_4, g-C_3N_4 nanosheet and g- C_3N_4/GO composites were successfully synthesized and a major enhancement of photocatalytic potential under sunlight was achieved through the g-C_3N_4/GO composite. According to the results of XRD analysis, bulk g-C_3N_4 and g-C_3N_4 nanosheet shows the dominant (002) diffraction peaks at $2\theta = 27.2^0$ and $2\theta = 27.4^0$ which validated that the materials prepared were correct. Besides, g-C_3N_4 shows improvement of (002) peak's intensity rather than bulk g-C_3N_4 due to the enhancement in crystallinity of g-C_3N_4 after liquid exfoliation. GO also successfully prepared and proved by results of XRD analysis where major (001) diffraction peak at $2\theta = 9.8^0$. For FTIR analysis, a wide absorption band at 3000 – 4000 cm^{-1} was identified for both bulk g-C_3N_4 and g-C_3N_4 nanosheet where it was indicated that both had hydroxyl groups in the structure. Both photocatalysts also indicated an absorption band at 1203 – 1628 cm^{-1} due to stretching of CN units in aromatic ring (RSC). FTIR spectrum of g-C_3N_4/GO showed the wide absorption band at 3000 – 3400 m^{-1} of FTIR spectrum which was close to the g-C_3N_4 which was attributed by stretching of the N-H group. This further strengthened the conclusion that introduction of GO into g-C_3N_4 did not alter the chemical structure of g-C_3N_4.

The BET analysis showed that g-C_3N_4 nanosheet has a greater surface area than bulk g-C_3N_4 and g-C_3N_4/GO where the results are 94.08 m^2/g, 79.84 m^2/g and 2.01 m^2/g respectively. The exfoliation of bulk g-C_3N_4 has minimized the size of the particle and improved the specific area of g-C_3N_4. This indicated that the exfoliation process was successful and the g-C_3N_4 bond was cleaved. The surface area of g-C_3N_4/GO was lower due to the stacking of layers on the structure of materials. The major enhancement of photocatalytic potential under sunlight was achieved by using g-C_3N_4/GO composite. The introduction of GO into g-C_3N_4 had improved the charge separation efficiency of g-C_3N_4 which enhanced the capability of g-C_3N_4 to MB and oil in oily wastewater. A g-C_3N_4/GO degraded 73.79% of MB dye rather than 38.85% and 62.71% for

bulk g-C_3N_4 and g-C_3N_4 nanosheet. g-C_3N_4/GO also degraded 75.54% of oil greater than bulk g-C_3N_4 and g-C_3N_4 nanosheet was 44.57% and 55.89% respectively. The exfoliation of g-C_3N_4 also showed a significant improvement in degradation capability of the g-C_3N_4 where, g-C_3N_4 nanosheet has a larger surface area with abundant active sites to react with photoexcited carriers compared to the bulk g-C_3N_4.

References

1. Jacobs, D. (2011).The global market for liquefied natural gas. *Reserve Bank Australian Bulletin*, 9: 17-28.
2. Department of Environment (2009). Discharge of industrial effluent or mixed effluent of standard A and B. Access from http://www.doe.gov.my/eia/wp-content/uploads/2012/03/A-Guide-For-Investors1.pdf. [Access online 20 March 2020].
3. Coca, J., Gutiérrez, G. and Benito, J. M. (2011). Treatment of oily wastewater. *NATO Science Peace and Security. Series C Environment Security,* 101: 1-55.
4. Won, W., Lee, S. K., Choi, K. and Kwon, Y. (2014). Current trends for the floating liquefied natural gas (FLNG) technologies. *Korean Journal of Chemical Engineering,* 31: 732-743.
5. De Angelis, L. and De Cortalezzi, M. M. F. (2013). Ceramic membrane filtration of organic compounds: Effect of concentration, pH, and mixtures interactions on fouling. *Separation and Purification Technology,* 118: 762-775.
6. Goettmann, F., Thomas, A. and Antonietti, M. (2007). Metal-free activation of CO_2 by mesoporous graphitic carbon nitride. *Angewandte Chemie - International Edition,* 46(15): 2717-2720.
7. Liu, J, Zhang, T., Wang, Z., Dawson, G. and Chen, W. (2011). Simple pyrolysis of urea into graphitic carbon nitride with recyclable adsorption and photocatalytic activity. *Journal of Materials Chemistry,* 21(38): 14398-14401.
8. Kang, J. H., Kim, T., Choi, J., Park, J., Kim, Y. S., Chang, M. S. and Park, C. R. (2016). Hidden second oxidation step of Hummers method. *Chemistry of Materials,* 28(3): 756-764.
9. Son, W.-J., Kim, J., Kim, J. and Ahn, W.-S. (2008). Sonochemical synthesis of MOF-5. *Chemical Communications,* 44(47): 6336-6338.
10. Kang, J. S., Won, J., Park, H. C., Kim, U. Y., Kang, Y. S. and Lee, Y. M. (2000). Morphology control of asymmetric membranes by UV irradiation on polyimide dope solution. *Journal of Membrane Science,* 169(2): 229-235.
11. Dutrow, B. and Clark, C. (2015). X-ray powder diffraction (XRD), geochemical instrumentation and analysis. Access from http://serc.carleton.edu/research_education/geochemsheets/techniques/XRD.html [Accessed online: 20 March 2020].
12. Hummers, W. S. and Offeman, R. E. (1958). Preparation of oxide. *Journal of the American Chemical Society,* 80(6): 1339-1339.
13. Guo, L. P., Wang, J., Fu, F. and Wu, Z (2015). Three dimensional Fe3O4-graphene macroscopic composites for arsenate removal. Journal of Hazardous Materials, 298: 28-35.
14. Olumurewa, K. O., Olofinjana, B., Fasakin, O., Eleruja, M. A. and Ajayi E. O. B. (2017). Characterization of high yield graphene oxide synthesized by simplified Hummers method. *Graphene*, 6(4): 85-98.
15. Alam, S. N., Sharma, N. and Kumar, L. (2017). Synthesis of graphene oxide (GO) by modified Hummers method and its thermal reduction to obtain reduced graphene oxide (rGO). *Graphene,* 6(1): 1-18.
16. Sheha, E. (2014). Studies on TiO_2/reduced graphene oxide composites as cathode materials for magnesium-ion battery. *Graphene*, 3(3): 36-43.
17. Bhargava, R., Wang, S. Q and Koenig, J. L. (2003). FTIR micro spectroscopy of polymeric systems. *Advances in Polymer Science*, 163: 137-191.
18. Raphael, L. (2011). Application of FTIR spectroscopy to agricultural soils analysis. *Fourier Transforms - New Analytical Approaches FTIR Strategies*: pp. 385-404.
19. Gao, W. (2015). The chemistry of graphene oxide in Graphene oxide: Reduction recipes, spectroscopy and applications: pp. 61-95.

20. Yang, K., Peng, H., Wen, Y. and Li, N. (2010). Re-examination of characteristic FTIR spectrum of secondary layer in bilayer oleic acid-coated Fe_3O_4 nanoparticles. *Applied Surface Science*, 256(10): 3093-3097.
21. Vlachos, N., Skopelitis, Y., Psaroudaki, M., Konstantinidou, V., Chatzilazarou, A. and Tegou, E. (2006). Applications of Fourier transform-infrared spectroscopy to edible oils. *Analytica Chimica Acta,* 573: 459-465.
22. Gulmine, J.V., Janissek, P. R. Heise, H. M. and Akcelrud, L. (2002). Polyethylene characterization by FTIR. *Polymer Testing,* 21(5): 557563.
23. Darkwah, K. W. and Ao, Y. (2018). Mini review on structure and properties (photocatalysis) and preparation techniques of graphitic carbon nitride nano-based particles and its application. *Nanoscale Research Letter,* 13(388): 3-15.
24. Huh, Y. S. and Chang, Y. K. (2015). Selective silver ion adsorption onto mesoporous graphitic carbon nitride. *Carbon,* 95: 58-64.
25. Nandi, B. K., Das B., Uppaluri R., Purkait M. K. (2010). Studies on submicron range microfiltration inorganic membranes: Preparation characterization. *Membrane Water Treatment*, 1(2): 121-137.
26. Ranfang, Z., Gaoxiang, D., Weiwei, Z., Lianhua, L., Yanming, L., Lefu, M. and Zhoahui, L.(2014). Photocatalytic degradation of methane blue using TiO_2 impregnated diatomite. *Advances in Materials Science and Engineering*, 2014: 1-7.
27. Nguyen, H. T. V., Ngo, T. H. A., Do, K. D., Nguyen, M. N., To Dang, N. T., Nong Yuen, T. T. and Anh Vu, V. T (2019). Preparation and characterization of hydrophilic polysulfide membrane using graphene oxide. *Hindawi Journal of Chemistry*, 2019: 1-10.

Malaysian Journal of Analytical Sciences (MJAS)
Published by Malaysian Analytical Sciences Society

PHASE BEHAVIOUR STUDY ON MEDIUM-CHAIN TRIGLYCERIDE/ SURFACTANT/WATER SYSTEMS CONTAINING GEMCITABINE USING PHASE INVERSION COMPOSITION TECHNIQUE

(Kajian Tingkah Laku Fasa Bagi Sistem Trigliserida Rantaian Sederhana/Surfaktan/Air yang Mengandungi Gemcitabine dengan Menggunakan Teknik Komposisi Penyongsangan Fasa)

Nadiatul Atiqah Wahgiman, Norazlinaliza Salim*, Mohd Basyaruddin Abdul Rahman

Integrated Chemical BioPhysics Research, Faculty of Science,
University Putra Malaysia, 43400 UPM Serdang, Selangor, Malaysia

**Corresponding author: azlinalizas@upm.edu.my*

Received: 20 November 2019; Accepted: 21 April 2020; Published: 9 June 2020

Abstract

In this study, the phase behavior of medium-chain triglyceride (MCT)/surfactant/water containing gemcitabine (GEM) was investigated. Ternary phase diagrams (TPD) were constructed with different surfactants (Span 20, Span 60, Span 80, Tween 80) and a mixture of surfactant (Tween 80:Span 80, at ratio 1:1). Two observations were recorded, isotropic and multilayer regions. The isotropic region was classified as a transparent, translucent or homogeneous mixture, while the multilayer region was classified as an opaque, milky or heterogeneous mixture. From the ternary phase diagrams constructed, it showed that MCT/(Tween 80: Span 80, ratio 1:1)/ GEM in deionized water system gave the largest isotropic region with the minimum usage of mixed surfactant, where 25% area of the isotropic region was formed with 1% of the usage of surfactant. The composition of F1 (selection based on the ternary phase diagram) was 0.02 % w/w of GEM, 19.98 % w/w of deionized water, 5.00 % w/w of Tween 80:Span 80 at ratio 1:1 and 75 % w/w of MCT. Nanoemulsion formulation was prepared by low energy emulsification method (i.e. phase inversion composition (PIC) technique). As the formulation was prepared in large scale with PIC technique, sodium chloride solution (0.1 M NaCl solution) was added to form a stable formulation as stabilizer. Effect of different volume of NaCl solution (0.5, 1.0 and 1.5 mL) added into formulation was investigated. The results showed that the particle size increased as the amount of NaCl increased, the effect of the amount of NaCl solution is significant towards particles size on F1. The F1 was stable in normal storage condition as it remained a homogeneous formulation against centrifugation test and it was also stable in storage stability test at different temperature (4, 25 and 45 °C) within three months.

Keywords: gemcitabine, nanoemulsion, ternary phase diagram

Abstrak

Dalam kajian ini, sifat fasa pada trigliserida rantaian sederhana (MCT)/surfaktan/air yang mengandungi GEM telah dikaji. Gambar rajah fasa ternari (TPD) telah dibina dengan surfaktan yang berbeza (Span 20, Span 60, Span 80, Tween 80) dan campuran surfaktan (Tween 80:Span 80, pada nisbah 1:1). Dua pemerhatian telah direkodkan, rantau isotropik dan pelbagai lapis. Rantau isotropik telah diklasifikasikan sebagai telus, lut atau campuran homogen, manakala rantau pelbagai lapisan telah diklasifikasikan sebagai legap, seperti susu atau campuran heterogen. Daripada gambar rajah fasa ternari yang telah dibina, ianya menunjukkan yang sistem MCT/(Tween 80: Span 80, pada nisbah 1:1)/ GEM dalam air ternyahion telah memberi rantau

isotropik yang paling tinggi dengan penggunaan campuran surfaktan yang minimum, di mana 25% keluasan rantau isotropik telah terhasil dengan 1% penggunaan surfaktan. Komposisi F1 (pilihan berdasarkan pada gambar rajah fasa ternari) ialah 0.02% w/w daripada GEM, 19.98% w/w daripada air ternyahion, 5.00% w/w daripada Tween 80:Span 80, pada nisbah 1:1 dan 75% w/w daripada MCT. Formulasi nanoemulsi telah dihasilkan dengan pengemulsi yang rendah tenaga (fasa penyongsangan (PIC). Formulasi yang dihasilkan dalam skala yang besar dengan teknik PIC, natrium klorida (0.1M larutan NaCl) telah ditambah untuk menghasilkan formulasi yang stabil sebagai penstabil. Kesan tiga isipadu larutan NaCl yang berbeza (0.5, 1.0 dan 1.5 mL) telah ditambah dalam formulasi dan dikaji. Keputusan menunjukkan peningkatan saiz zarah apabila jumlah NaCl meningkat, jumlah larutan NaCl memberi kesan yang signifikan terhadap saiz zarah F1. F1 adalah stabil di dalam penyimpanan keadaan biasa apabila ianya kekal homogen ketika diuji dengan ujian emparan dan stabil dalam ujian penyimpanan kestabilan pada suhu yang berbeza (4, 25 dan 45 °C) selama 3 bulan.

Kata kunci: gemcitabine, nanoemulsi, gambar rajah fasa ternari

Introduction

Gemcitabine (GEM) is an anti-metabolite drug which consists of two fluorine atoms substituted at 2' position of ribose ring [1, 2]. It is a hydrophilic drug due to the existence of a polar group (Fluorine, OH-group and NH_2 group) in the compound [3]. The high dosage was needed to achieve a therapeutic concentration in vivo, as it was hard to transport into the cancer cell by cross plasma membrane passively [4, 5]. The behavior of GEM in MCT/surfactant/water system was studied by constructing ternary phase diagram.

The ternary phase diagram is a mixture of surfactant-water-oil in various compositions and forms a variety of complex phases [6]. The observations of the ternary phase diagram were visualized by naked eyes and had several classifications such as microemulsions, liquid crystal, emulsion, emollient gel or cream and bi-continues phase [7]. For this study, the observation of the ternary phase diagram was categorized in two regions (isotropic region, Li and multilayer region, M). The isotropic region was identified by their transparent appearance [8] and this region has a high probability of forming nanoemulsion [6, 9].

Nanoemulsion is a colloidal system with high kinetic stability, low viscosity, optical transparency, and range particle size of 20 nm to 200 nm [10, 11] This colloidal system can solubilize hydrophilic and lipophilic drug either in their aqueous phase or oil phase [12]. From previous studies, nanoemulsion has provided a high drug loading such as 5 mg/mL of budesonide and 0.05% of quercetin in nanoemulsion [13, 14]. In this study, the composition of nanoemulsion containing GEM was determined from the ternary phase diagrams. Then nanoemulsion was formulated by the low energy emulsification method namely Phase Inversion Composition (PIC) and the findings was characterized.

Materials and Methods

Materials

Gemcitabine (GEM, purity >90%) was purchased from Sigma-Aldrich (USA). Polysorbate 80 (Tween 80), sorbitan mono-laurate 80 (Span 80) and sodium chloride (NaCl, purity 99.5%) were purchased from Merck (USA). Methanol (95%) and acetonitrile (HPLC grade, 99%) were purchased from J.T. Baker Chemical (USA). Isopropyl myristic (IPM) was purchased from Ak Scientific (USA). Medium-chain triglyceride (MCT) was purchased from Gattefosse Sas (France). The deionized water (DI water, 18.3 MΩcm, Millipore) was prepared using Milli-Q filtration system, EMD Millipore (Billerica, MA, USA).

Solubility of GEM

The solubility of GEM in deionized water, MCT and IPM were performed. The excess of GEM (10 mg) was dissolved in deionized water (0.5 mL) and centrifugated at 4000 rpm for 10 minutes. Then, the aqueous layer was injected to reserve phase high-performance liquid chromatography (RP-HPLC, Waters 1525, Waters Corporation, USA) which was equipped with a Phenomenex Luna C_{18} column (5µm, 250 x 4.6 mm, Phenomenex, USA) and UV-Vis detector (Waters 2489, Waters Corporation, USA) to measure the absorbance of GEM at a retention time of 3.5 minutes and wavelength of 269 nm. Then, the quantitative value of GEM dissolved in deionized

water was determined based on the standard curve of known GEM with concentration range of 20 to 1000 µg/mL (R^2 = 0.9995). The mobile phase used for HPLC measurement were deionized water and acetonitrile (DI: ACN, 90:10) with a flow rate of 1 mL/min and ambient temperature.

The solubility of GEM in MCT was performed used stirring, heating and centrifugation method [15]. GEM (1 mg) was added in MCT (50 mL), stirred (10 minutes) and heating while stirring (10 minutes, 40 °C). The mixture was then centrifuged at 4000 rpm for 15 minutes and observed by naked eyes. These methods were repeated using different mass of GEM until GEM did not dissolve. Then, these methods were repeated by replacing MCT with IPM.

The selection ratio of MCT: IPM

MCT and IPM were mixed (at ratio 1:1, total volume 1 mL) and sonicated for 2 mins. GEM (0.9 mg) was added to the mixture. The mixture was sonicated (2 minutes) and stirred while heating (30 minutes, 40 °C). The mixture was then centrifuged at 4000 rpm for 15 minutes and observed as if there were any precipitation and change of color by naked eyes [33]. These methods were repeated using different ratio of MCT: IPM (9:1, 8:2 and 7:3).

Construction ternary phase diagram

GEM (0.015 g) was dissolved in 14.985 g of deionized water. The Span 20 (with HLB value 8.60 respectively) and GEM mixture (dissolved in deionized water) (0.1 %, w/w) were weighed at various ratios ranging from 0:100 to 100:0. The mixture with a total weight of 0.500 g was placed into a 10 mL screw-cap glass tube (total of 11 tubes) and was vortexed using a vortex mixer (VM-300, Gemmy Industrial CORP-Taiwan). The mixture was centrifuged at 4000 rpm using a Hettich centrifuge (Model EBA, Germany) for 15 minutes at room temperature. Medium-chain triglyceride (MCT) was then added into the eleven test tubes separately and were vortexed to homogenize. The samples were centrifuged at 4000 rpm for 15 minutes and then physically observed by the naked eyes to determine the physical phase appearance [16]. The transparent or translucent appearance sample was considered as isotropic region, Li, while milky until separation layers formed was considered as multilayer region, M. The steps were repeated with the addition of 10, 20, 30, 40 until 90% w/w of MCT.

These methods were repeated by replacing surfactants (Span 60, Span 80, Tween 80 with HLB values 4.70, 4.30 and 15.00 respectively) and the mixed surfactant (Tween 80: Span 80, at ratio 1:1 with the HLB values were 9.65 respectively). Tween 80 and Span 80 were mixed well before the construction of ternary phase diagram.

Preparation of nanoemulsion containing gemcitabine

The low energy emulsification techniques were used to prepare nanoemulsion. GEM (0.002 g) was dissolved in deionized water (1.998 g) and 0.1 M NaCl solution (0.5 mL). The mixture was mixed with a mixed surfactant (Tween 80 and Span 80) at room temperature to form an aqueous phase. The oil phase was prepared by mixed MCT and IPM at a ratio of 9:1. Both phases were sonicated for 3 min at a medium level of sonification. The oil phase was added dropwise into a beaker containing an aqueous phase. The mixture was then homogenized at 391 rpm for 3 hours using an overhead stirrer (IKA@ RW 20 Digital, Nara, Japan). The mixture was then stirred by a magnetic stirrer for 1 hour while heated at 40 °C for 5 minutes, and this sample was labelled as F1a. These methods were repeated by replacing the volume of 0.1% NaCl solution (1.0 mL, 1.5 mL) and labelled as F1b and Flc.

Particle size and polydispersity index measurement

Zetasizer Nano ZS (Malvern Instrument Ltd., UK) was used to measure the particle size and polydispersity index (PDI) of the nanoemulsion at a temperature of 25 °C. A dynamic light scattering technique with the scattering angle of 173° was performed for measurement. The samples were diluted with MCT (1:500) and inserted into the sample cell. The intensity distribution was used for the measurement of the mean average (z-average) particle size. The measurement was repeated in triplicate.

Zeta potential measurement

Zetasizer Nano ZS (Malvern Instrument Ltd., UK) was used to measure the zeta potential of the nanoemulsion at a temperature of 25 °C. The calculation of their zeta potential was based on their electrophoretic mobility of dispersed particles in a charged field. The samples were diluted with MCT (1:500). The zeta potential with values higher than + 30.00 mV or lower than -30.00 mV improved the stability of nanoemulsion [17].

Stability study

Centrifugation test was used to predict the shelf life under normal storage condition [18], it was performed by centrifuging the fresh sample at 4000 rpm for 15 minutes, and any physical changes were observed. Besides, the storage stability to observe the physical appearance of samples was done at three different temperature (4, 25 and 45 °C) within three months.

Results and Discussion

The solubility of GEM and the selected ratio of MCT: IPM

The maximum GEM dissolved in deionized water was 10.09 mg/mL, which is slightly higher from reported value [19]. GEM did not dissolve in MCT, this is because GEM is a hydrophilic compound which consists of fluorine, OH-group and NH_2 group [3, 20]. GEM was dissolved at 0.20 mg/mL in IPM. Figure 1 shows the mixtures of MCT and IPM at ratio 1:1, 9:1 and 8:2 were performed where IPM acted as co-surfactant to dissolve GEM in MCT. Based on the result, ration 1:1, 9:1 and 8:2 were clear while 7:3 was cloudy and MCT:IPM with ratio 9:1 was selected to be used for constructing TPD. This is because it showed a clear mixture with less amount of IPM. The less amount of IPM used could decrease to the probability of irritation or allergy [21, 22]. Based on the solubility of GEM in deionized water, MCT and IPM, the amount of GEM used to construct TPD was 0.10 mg/mL of deionized water.

Phase behavior of MCT/surfactants/water system

Ternary phase diagrams were constructed based on different surfactant systems (Span 20, Span 60, Span 80 and Tween 80 and mixture surfactant (Tween 80: Span 80, 1:1) which were represented with different hydrophilic-lipophilic balance (HLB) values (8.60,4.70,4.30, 15.00 and 9.65 respectively).

Figure 2 indicates different surfactant system gives a different percentage area of isotropic regions. Span 20 formed 6% area of the isotropic region with 65% of the lowest usage of surfactant. Span 60 formed 2% area of the isotropic region with 72% of the lowest usage of surfactant. Span 80 formed 5% area of the isotropic region with 38% of the lowest usage of surfactant. Tween 80 formed 34% area of the isotropic region with 45% of the lowest usage of surfactant. While at ratio 1:1 of Tween 80: Span 80, 25% area of the isotropic region was formed with 1% of the lowest usage of surfactant. As HLB value of Span 20 is higher than Span 60, the isotropic region of Span 20 was higher than Span 60. This is due to their lipophilicity, as higher lipophilicity, they attribute to dissolve in oil (MCT) and vice versa. While for Tween 80, it had the highest isotropic region and dissolved in of GEM: water. This is due to having higher hydrophilicity, so it tends to dissolve in GEM: water. Ternary phase diagram of Tween 80: Span 80 at ratio 1:1 (Figure 2e) had the highest isotropic region among all of the samples with the lowest usage of surfactant to form it. This is due to the HLB of Tween 80: Span 80 at ratio 1:1 has higher lipophilicity compared to Span 20, Span 60 and Span 80, but lower hydrophilicity compared to Tween 80.

A point (F1) from ternary phase diagram of Tween 80: Span 80 at ratio 1:1 (Figure 2E) was selected for preparation and future studies as it is the highest amount of percentage area of isotropic region (25%) with the lowest amount of surfactant (1%). The F1 composition was used as it is in the isotropic region, which tends to obtain emulsion with nanoparticles size [6]. The higher use of surfactant could cause toxicity towards normal cell [23, 24]. Thus, lower amount of surfactant was used to prepare the nanoemulsions.

Physicochemical characterization of nanoemulsions

The composition of F1 shows separation as it was formulated in large scale (in double amount compared to during TPD studies). Thus, it was modified by adding 0.1 M NaCl solution as shown in Table 1. The reason of NaCl usage in large formulation scale is because it stabilizes the formulation as electrolytes decrease the attraction forces between the water droplets and the dielectric constant of aqueous phase which leads to a reduction of the collision frequency [25, 26]. The formulations show non separation condition after 0.1 M NaCl solution was added. The effect of different amount of NaCl solution (0.5 mL, 1.0 mL, 1.5 mL) towards particle size was investigated by adding different amount of NaCl during formulation.

The results show the particle size increased when the amount of NaCl increased as shown in Table 1. These might be due to the increment in the amount of electrolyte, the increment of the refractive index of the water phase leading to the increment of particles size, as well as decreasing the refractive index difference between oil and water phases and dielectric constant of the aqueous phase [27, 28]. Besides, the addition of NaCl into the aqueous phase decreased the attractive force between water droplets [29, 30], in turn causing particle size increment.

The particles size of nanoemulsions, F1a (137.77 ± 3.82), F1b (180.53 ± 1.76) and F1c (426.37 ± 5.40) were measured, F1a and F1b were considered as nanoemulsion as they were below 200 nm. The polydispersity index shows F1a and F1b nanoemulsions were monodisperse system as the values were less than 0.2. Based on Table 1, the zeta potential of F1a (- 36.40 mV), F1b (- 54.00 mV) and F1c (-37.80 mV) show stable nanoemulsions [16,31]. The negative value of zeta potential of samples is due to the presence of fatty acids and esters in the oil [32].

Stability analysis

The nanoemulsions had undergone centrifugation test for stability analysis to determine whether the nanoemulsion was stable under normal storage condition. The fresh nanoemulsions remained homogenous with no separation after being centrifuged at 4000 rpm for 15 minutes. The centrifugation is also known as accelerated ageing stability test where the nanoemulsions are subjected to gravitational stress and resistance as if there is any formation of cream or emulsion phase separation [34, 35]. The frequent collision between particles increases by centrifugal, which causes the decrease of colloidal stability [36]. As the nanoemulsion remained stable in centrifugation test which is the similar reported result of literature [3] for their accelerated stability analysis, it indicates the nanoemulsion is stable at the normal condition for up to 6 months [35].While for the storage stability test, it was done to determine their long-term stability by observing if there were any phase separation, sedimentation, flocculation, coalescence or creaming during storage [37]. Based on the results, the nanoemulsions mixture remained homogenous which indicates its stability for one day to 90 days against the temperature of 4, 25 and 45 °C, up to 3 months which are similar with the results reported [37] regarding their storage stability. Table 2 shows the observation of stability against centrifugation test and stability storage against different temperature (4, 25 and 45 °C).

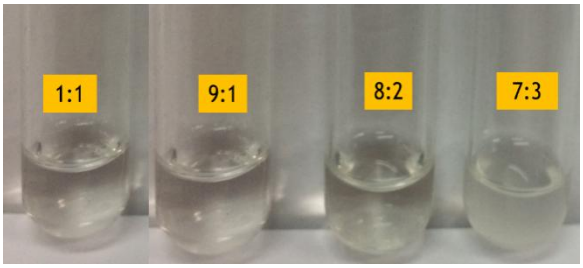
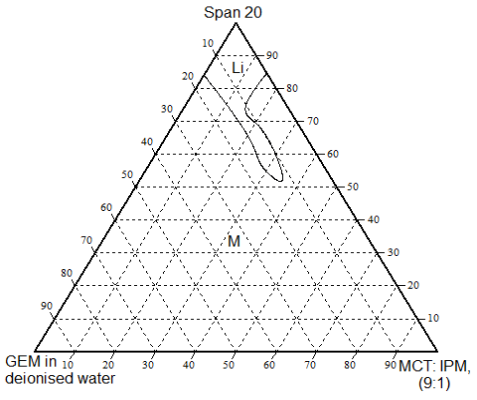
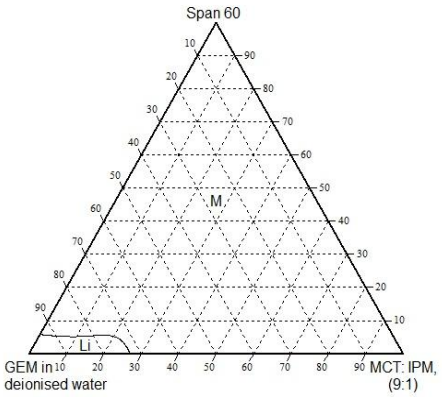


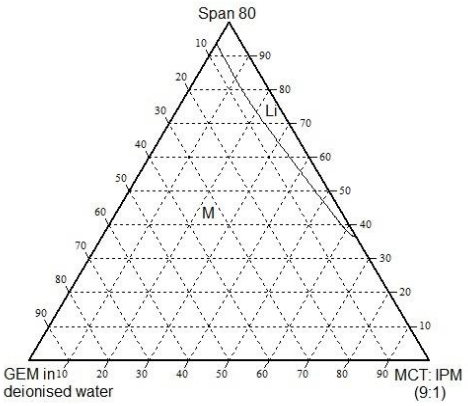
Figure 1. The physical appearance of the mixture ratio of MCT: IPM



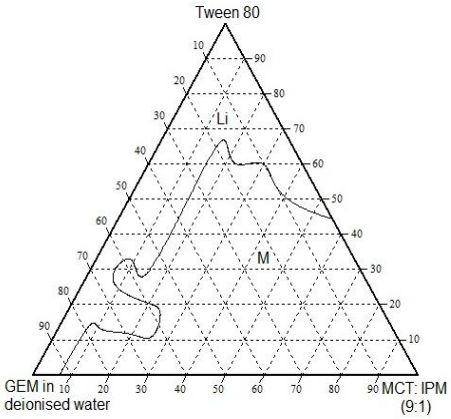
(a)



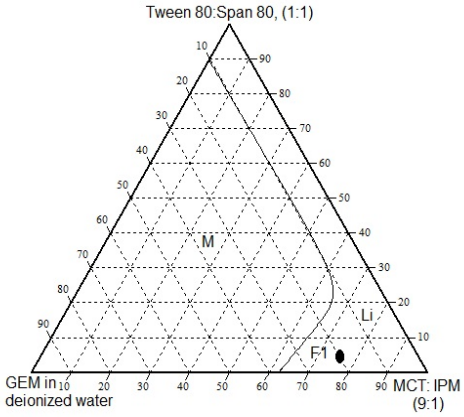
(b)



(c)



(d)



(e)

Figure 2. The ternary phase diagrams of MCT/surfactant/water systems at different surfactant and mixed surfactant (a) Span 20 (b) Span 60 (c) Span 80 (d) Tween 80 (e) T80: S80 at ratio 1:1 where, Li = Isotropic region and M = Multilayer region.

Table 1. Composition and characterization of nanoemulsions

Sample Name	Deionized Water, (%)	GEM, (%)	Tween 80: Span 80, (1:1, %)	NaCl Solution, (mL)	MCT: IPM (9:1, %)	Size, (nm)	PDI	Zeta Potential, (mV)
F1a	19.98	0.02	5.0	0.5	75.0	137.77 ± 3.82	0.12	-36.40
F1b	19.98	0.02	5.0	1.0	75.0	180.53 ± 1.76	0.42	-54.00
F1c	19.98	0.02	5.0	1.5	75.0	426.37± 5.40	0.31	-37.80

Table 2. Physical stability of nanoemulsions

Temperature (°C)	Stability storage (days)																	
	F1a						F1b						F1c					
	1	7	21	30	60	90	1	7	21	30	60	90	1	7	21	30	60	90
4	√	√	√	√	√	√	√	√	√	√	√	√	√	√	√	√	√	√
25	√	√	√	√	√	√	√	√	√	√	√	√	√	√	√	√	√	√
45	√	√	√	√	√	√	√	√	√	√	√	√	√	√	√	√	√	√
Centrifugation test																		
				√						√						√		

Conclusion

The ternary phase diagrams showed that the formation of the isotropic liquid region depended on the hydrophilicity and lipophilicity of surfactant. As higher lipophilicity, they attribute to dissolve in oil (MCT) and higher hydrophilicity attribute to dissolve in aqueous solution. The presence of NaCl as an electrolyte also leads to better stability and increases the particles size. Thus, future research on cytotoxicity study, *in-vitro* and *in-vivo* study to determine cytotoxicity level towards healthy and abnormal cell and also the efficiency of GEM released to the required area should be conducted. Besides, the research towards various applications such as tropical, oral, injection or aerosol administration should be performed in order to be used in medical industry.

Acknowledgement

The financial assistance provided by Graduate Research Fellowship (GRF) for Wahgiman N. A. by Universiti Putra Malaysia, and LRGS NanoMITe grant from the Ministry of Higher Education, Malaysia (RU029-2014/5526306) was gratefully acknowledged.

References

1. Hayashi, H., Kurata, T. and Nakagawa, K. (2011). Gemcitabine: Efficacy in the treatment of advanced stage nonsquamous non-small cell lung cancer. *Clinical Medicine Insights: Oncology,* 5: 177-184.
2. Alvarellos, M. L., Lamba, J., Sangkuhl, K., Thorn, C. F., Wang, L., Klein, D. J., and Klein T. E. (2014). PharmGKB summary. *Pharmacogenetics and Genomics*, 24(11): 564-574.
3. Toschi, L., and Cappuzzo, F. (2009). Gemcitabine for the treatment of advanced non-small cell lung cancer. *OncoTargets and Therapy*, 2: 209-217.
4. Wang, J., Zhang, X., Cen, Y., Lin, X., and Wu, Q. (2016). Biointerfaces antitumor gemcitabine conjugated micelles from amphiphilic comb-like random copolymers. *Colloids and Surfaces B*. 146: 707-715.
5. Parsian, M., Unsoy, G., Mutlu, P., Yalcin, S., and Tezcaner, A. (2016). Loading of gemcitabine on chitosan magnetic nanoparticles increases the anti-cancer efficacy of the drug. *European Journal of Pharmacology*, 784: 121-128.
6. Salim, N., Basri, M., Abdullah, D. K., and Basri, H. (2011). Phase behaviour, formation and characterization of palm-based esters nanoemulsion formulation containing ibuprofen. *Journal of Nanomedicine and Nanotechnology*, 2(4): 1-4.
7. Mahdi, E. and Sakeena, M. (2011). Effect of surfactant and surfactant blends on pseudoternary phase diagram behavior of newly synthesized palm kernel oil esters. *Drug Design, Development and Therapy*, 5:311-323.
8. Izquierdo, P., Esquena, J., Tadros, T. F., Dederen, J. C., Feng, J., Garcia-Celma, M. J. and Solans, C. (2004). Phase behavior and nano-emulsion formation by the phase inversion temperature method. *Langmuir,* 20(16): 6594-6598.
9. Jaiswal, M., Dudhe, R. and Sharma, P. K. (2015). Nanoemulsion: an advanced mode of drug delivery system. *3 Biotechnology*, 5(2):123-127.
10. Silva, H. D., Cerqueira, M. A., and Vicente, A. A. (2015). Influence of surfactant and processing conditions in the stability of oil-in-water nanoemulsions. *Journal of Food Engineering*, 167: 89-98.
11. Puglia, C., Rizza, L., Drechsler, M., and Bonina, F. (2010). Nanoemulsions as vehicles for topical administration of glycyrrhetic acid: Characterization and *in vitro* and *in vivo* evaluation. *Drug Delivery*, 17(3): 123-129.
12. Koroleva, M. Y., Nagovitsina, T. Y., Bidanov, D. A., and Gorbachevski, O. S. (2016). Nano- and microcapsules as drug-delivery systems. *Resource-Efficient Technologies*, 2(4):233-239.
13. Arbain N. H., Salim N., Masoumi H. R. F, Wong T.W., Basri M., and Rahman M. B. A. (2018). *In vitro* evaluation of the inhalable quercetin loaded nanoemulsion for pulmonary delivery. *Drug Delivery and Translational Research*, 67: 497-507.
14. Amani, A., York, P., Chrystyn, H., and Clark B. J. (2010). Evaluation of a nanoemulsion-based formulation for respiratory delivery of budesonide by nebulizers. *American Pharmaceutical Scientists PharmSciTech*, 11(3):1147-1151.

15. Samiun, W. S., Ashari, S. E., Salim, N. and Ahmad, S. (2020). Optimization of processing parameters of nanoemulsion containing aripiprazole using response surface methodology. *International Journal of Nanomedicine.* 15: 1585-1594.
16. Asmawi, A. A., Salim, N., Ngan, C. L., Ahmad, H., Malek, E. A., Mas, J. M. and Rahman, A. M. B. (2018). Excipient selection and aerodynamic characterisation of nebulised lipid-based nanoemulsion loaded with docetaxel for lung cancer treatment. *Drug Delivery and Translational Research*, 9(2):543-554.
17. Ribeiro, R. C., Barreto, S. M., Ostrosky, E. A., Da Rocho-Filho, P. A., Verissimo, L. M. and Ferrari, M. (2015). Production and characterisation of cosmetic nanoemulsions containing *Opuntia ficusindica* (L.) mill extract as moisturizing agent. *Molecules*, 20(2): 2492-2509.
18. Hadzir, N. M., Basri M., Rahman, M. B. A., Salleh, A. B., Rahman, R. N. Z. R. A., and Basri H. (2013). Phase behaviour and formation of fatty acid esters nanoemulsions containing piroxicam. *AAPS PharmSciTech*, 4:456-63.
19. Yılmaz, B., Kadıoğlu, Y. and Aksoy, Y. (2003). Simultaneous determination of gemcitabine and its metabolite in human plasma by high-performance liquid chromatography. *Journal of Chromatography B*, 791(1): 103-109.
20. Xu, H., Paxton, J., Lim, J., Li, Y., and Wu, Z. (2014). Development of a gradient high-performance liquid chromatography assay for simultaneous analysis of hydrophilic gemcitabine and lipophilic curcumin using a central composite design and its application in liposome development. *Journal of Pharmaceutical and Biomedical Analysis*, 98: 371-378.
21. Zidan, A. S., Kamal, N., Alayoubi, A., Seggel, M., Ibrahim, S., Cruz, C., and Ashraf, M. (2017). Effect of isopropyl myristate on transdermal permeation of testosterone from carbopol gel. *Journal of Pharmaceutical Sciences*, 106(7): 1805-1813.
22. Oliveira, J. S. L., Lange, S., Dobner, B., and Brezesinski, G. (2017). The effect of non-deuterated and deuterated isopropyl myristate on the thermodynamical and structural behavior of a 2D stratum corneum model with ceramide. *Chemistry and Physics of Lipids*, 204: 1-9.
23. Hwang, T. L, Fang, C. L, Chen, C. H, and Fang, J. Y. (2009). Permeation enhancer containing water-in-oil nanoemulsions as carriers for intravesical cisplatin delivery. *Pharmaceutical Research*, 26(10): 2314-2323.
24. Prajapati, H. N., Dalrymple, D. M., Serajuddin, A. T. M., Agu, R. U., Ugwoke, M. I., Armand, M., and Mehta, S. K. (2016). Formulation and physiochemical study of a-tocopherol based oil in water nanoemulsion stabilised with non-toxic, biodegradable surfactant: Sodium stearoyl lactate. *Ultrasonics Sonochemistry*, 29(1): 285-305.
25. Frasch-Melnik, S., Spyropoulos, F., and Norton, I. T. (2010). W1/O/W2 double emulsions stabilised by fat crystals: Formulation, stability and salt release. *Journal of Colloid and Interface Science.* 350(1): 178-185.
26. Matos, M., Gutierres. G., Coca, and J., Pazos, C. (2014). Preparation of water-in-oil-water (W/O/W) double emulsions containing trans-resveratrol. *Colloids and Surfaces A: Physicochemical and Engineering Aspects*, (442):69-79.
27. Park, C. I., Cho, W., and Lee, S. J. (2003). Emulsion stability of cosmetic creams based on water-in-oil high internal phase emulsions Emulsion stability of cosmetic creams based on water-in-oil high internal phase emulsions. *Korea-Australia Rheology Journal*, 15(3): 125-130.
28. Paunivic, M. and Schlesinger, M. (2006). Fundamentals of deposition (second edition). New Jersey: John Wiley & Sons, Inc.
29. Márquez, A. L., Medrano, A., Panizzolo, L. A. and Wagner, J. R. (2010). Effect of calcium salts and surfactant concentration on the stability of water-in-oil (w/o) emulsions prepared with polyglycerol polyricinoleate. *Journal of Colloid and Interface Science*, 341(1): 101-108.

30. Wahgiman, N. A., Salim, N., Abdul Rahman, M. B. and Ashari, S. E. (2019). Optimization of nanoemulsion containing gemcitabine and evaluation of its cytotoxicity towards human fetal lung fibroblast (MRC5) and human lung carcinoma (A549) cells. *International Journal of Nanomedicine*, 14: 7323-7338.
31. Sulaiman, I. S. C., Basri, M., Fard Masoumi, H. R., Ashari, S. E., Basri, H., and Ismail, M. (2017). Predicting the optimum compositions of a transdermal nanoemulsion system containing an extract of *Clinacanthus nutans* leaves (L.) for skin antiaging by artificial neural network model. *Journal of Chemometrics*, 31(7): 1-13.
32. Shakeel, F., Haq, N., Al-dhfyan, A., Alanazi, F. K. and Alsarra, I. A. (2014). Double w/o/w nanoemulsion of 5- fluorouracil for self-nanoemulsifying drug delivery system. *Journal of Molecular Liquids*, 200: 183-190.
33. Azhar, S. N. A. S., Ashari, S. E., and Salim, N. (2018). Development of a kojic monooleate-enriched oil-in-water nanoemulsion as a potential carrier for hyperpigmentation treatment. *International Journal of Nanomedicine*, 13: 6465-6479.
34. Xavier-Júnior, F. H., Silva, K. G. H., Farias, I. E. G., Morais, A. R. V. and Alencar, E. N. (2012). Prospective study for the development of emulsion systems containing natural oil products. *Journal Drug Delivery and Science Technology*, 22(4): 367-372.
35. Latreille, B., and Paquin, P. (1990). Evaluation of emulsion stability by centrifugation conductivity measurements. *Journal of Food Science*, 55(6): 1666-1669. Izadiyan, Z., Basri, M., Fard Masoumi, H. R., Abedi Karjiban, R., Salim, N. and Shameli, K. (2017). Modeling and optimization of nanoemulsion containing Sorafenib for cancer treatment by response surface methodology. *Chemistry Central Journal*, 11(1): 21.
36. Ramli, S., Zainuddin, N., Mohamad, S., and Rahman, I. A. (2017). Nanoemulsion based palm olein as vitamin E carrier. *Malaysian Journal of Analytical Sciences*, 12(6): 1399-1408.

Malaysian Journal of Analytical Sciences (MJAS)
Published by Malaysian Analytical Sciences Society

HEADSPACE MEMBRANE-PROTECTED LIQUID PHASE MICROEXTRACTION OF PHENANTHRENE IN BEVERAGE AND WATER

(Pengekstrakan Mikro Fasa Cecair Dilindungi Membran Ruang Kepala bagi Fenantrena dalam Air Minuman dan Air)

Nor Hafiza Hassan, Wan Mohd Afiq Wan Mohd Khalik, Saw Hong Loh*

Faculty of Science and Marine Environment,
Universiti Malaysia Terengganu, 21030 Kuala Nerus, Terengganu, Malaysia

**Corresponding author: lohsh@umt.edu.my*

Received: 30 March 2020; Accepted: 29 April 2020; Published: 9 June 2020

Abstract

Contamination of low molecular weights polycyclic aromatic hydrocarbons (PAHs) is common in beverage and water. This could pose a health risk to those beverage lovers when they consume the products. Phenanthrene (PHE) is one of the low molecular weights PAHs that consists of three benzene rings in the molecular structure. In this study, PHE was chosen as the model analyte due to its mid-volatility behavior. A headspace membrane-protected liquid phase microextraction (HS-MP-LPME) combined with high performance liquid chromatography-fluorescence detection (HPLC-FD) has been developed for the analysis of PHE in beverage and water samples. The nylon membrane containing 1-octanol as the extractant was exposed to the headspace of the sample vial containing 25 mL of sample solution. The extraction was performed at its optimal conditions with sample temperature fixed at 60 °C, agitation set at 700 rpm and extraction conducted for 30 minutes. Under these optimal extraction conditions, the HS-MP-LPME-HPLC-FD offered ultra-trace detection of PHE and insignificant matrix effects in beverages (green tea and coffee) and water (river, sea and tap) samples with average of relative recovery in the range of 83.7 to 116.1%. The HS-MP-LPME simplifies the routine analysis and resolves the extractant dissolution problem that commonly occurs in hollow fiber-protected LPME. The proposed technique consumes only minimal amounts of organic solvent (200 µL) and this indirectly supports our National Green Technology Policy: together we create a better tomorrow.

Keywords: beverage, water, headspace membrane-protected liquid phase microextraction, high performance liquid chromatography-fluorescence, phenanthrene

Abstrak

Kontaminasi hidrokarbons aromatik polisiklik (PAHs) berjisim molekul rendah dalam air minuman dan air adalah biasa. Ini akan menghasilkan risiko kesihatan kepada pencinta air minuman apabila mereka minum produk tersebut. Fenantrena (PHE) ialah salah satu PAHs berjisim molekul rendah yang mengandungi tiga cincin benzena dalam struktur molekulnya. Dalam kajian ini, PHE dipilih sebagai sebagai analit model kerana kemeruapannya yang sederhana. Satu pengekstrakan mikro fasa cecair dilindungi membran ruang kepala (HS-MP-LPME) bergabung dengan kromatografi cecair berprestasi tinggi-pengesanan pendarfluor (HPLC-FD) telah dibangunkan untuk menganalisis PHE dalam sampel air minuman dan air. Membran nilon yang mengandungi 1-oktanol sebagai pengekstrak didedahkan pada ruang depan botol sampel yang berisi 25 mL larutan sampel. Pengekstrakan dilaksanakan menggunakan keadaan optimum iaitu menetapkan suhu sampel pada 60 °C, mengacau sampel pada

kelajuan pengocakan 700 rpm dan mengekstrak selama 30 minit. Di bawah keadaan pengekstrakan optimum, HS-MP-LPME-HPLC-FD menawarkan pengesanan PHE pada tahap ultra-surihan dan memberi kesan matriks yang tidak signifikan dalam sampel air minuman (tea hijau dan kopi) dan air (sungai, laut dan paip) dengan perolehan semula secara relatif dalam lingkungan 83.7 hingga 116.1%. HS-MP-LPME memudahkan analisis rutin dan menyelesaikan masalah pelarutan pengekstrak yang biasa berlaku dalam LPME dilindungi fiber berongga. Teknik yang dicadangkan hanya menggunakan kuantiti pelarut organik yang minimum dan ini menyokong Polisi Hijau Nasional kita secara tidak langsung: bersama-sama kita membina keesokan yang lebih baik.

Kata kunci: air minuman, air, pengekstrakan mikro fasa cecair dilindungi membran pada ruang kepala, kromatografi cecair berprestasi tinggi-pendarfluor, fenantrena

Introduction

Polycyclic aromatic hydrocarbons (PAHs) are organic compounds consist of two or more aromatic benzene rings in one structure. Sources of PAHs can be found from natural and anthropogenic activities. For example, forest fires, volcanic eruptions and incomplete combustion. These pollutants tend to migrate through food chain and be transferred over long distances. PAHs are very toxic to human health because they have potential to cause cancer, affect male and female reproduction and cause obesity [1]. Contamination of low molecular weights polycyclic aromatic hydrocarbons (PAHs) is common in beverage and water. This could pose a health risk to those beverage lovers when they consume the products.

Microextraction techniques have been applied as alternatives to conventional sample preparation techniques since 1996, when the single drop microextraction (SDME) was first demonstrated [2, 3]. However, the application of SDME is less popular due to the dissolution of the hanging organic drop into the sample solution during extraction especially when the sample is agitated. Various membranes have been employed to address this limitation, with the aim to protect the organic extractant from losing into sample solution. Polypropylene hollow fiber protected liquid phase microextraction (PPHF-LPME) are the most employed membrane-protected LPME. This technique is reliable and proven to be sensitive and selective for the extraction of various organic and inorganic analytes in aqueous samples [4-8]. Other membrane-protected LPME techniques that utilized agarose film [9], agarose gel [10-12], nylon membrane [13, 14], polypropylene membrane bag [15] and silica monolith [16] were also successfully demonstrated to address the solvent dissolution problem.

This project offered an alternative method for the extraction of phenanthrene in beverage and water samples using headspace membrane-protected LPME coupled with high performance liquid chromatography and fluorescence detection. The extractant was doubled protected using a nylon membrane that was hung in the headspace of sample vial. This geometry design of this technique kept away the interruption the membrane from the agitation and thus freed the extractant from dissolution into sample solution.

Materials and Methods

Chemicals and reagents

Phenanthrene (PHE) reference standard was obtained from Dr. Ehrenstorfer (United Kingdom) and 1-octanol (analytical grade) were purchased from Sigma-Aldrich (Missouri, United States). HPLC grade reagents like acetonitrile (ACN), and methanol (MeOH) were purchased from Merck (New Jersey, United States).

Preparation of standard and samples

Standard stock solutions of PHE (500 mg/L) was prepared by dissolving 0.005 g of PHE in a 10 mL of volumetric flask and diluting to volume with acetonitrile. A series of working standard solutions were prepared by further diluting 500 mg/L of PHE standard stock solution with methanol. All of the standard solutions were stored at 0 ˚C in the refrigerator when not in use.

Different environmental water samples namely, river water, tap water and sea water were collected from area around Universiti Malaysia Terengganu whereas ready packed beverage samples (green tea and coffee) were purchased from local enterprise shops. The samples were kept in the fridge until analysis. The environmental water samples were filtered through Whatman filter paper No. 1 to exclude larger particles prior to extraction, whereas ready packed beverage samples were analyzed without any pre-treatment.

Preparation of nylon membrane

Round-shaped nylon membrane filters (I.D 47 mm, pore 0.2 μm) were purchased from Sartorius (Goettingen, Germany). The membrane filters were cut, folded and sealed according to Loh et al. [14]. The two edges of the membrane top were then poked and threaded through with a thread to enable the membrane hanging in the headspace of samples vial during extraction.

Headspace membrane-protected liquid phase microextraction procedure

The outer layer of the pre-sealed membrane was immersed into 1-octanol to impregnate the pores of the membrane wall. Then, the membrane was exposed to the headspace of a 40 mL of sample vial containing 25 mL of sample solution and a stir bar. The 1-octanol (200 μL) was then added into the membrane, this was followed by screwing the vial cap. Next the sample vial was placed in a 500 mL beaker containing pre-heated water at 60 °C on a hot plate. The sample solution was stirred at 700 rpm at 60 °C for 30 minutes. Later, 100 mL of the extract (1-octanol) was withdrawn with a micropipette and transferred into a 2.5 mL safe-lock tube prior to quantification using high performance liquid chromatography coupled with fluorescence detection (HPLC-FD). Figure 1 shows the schematic of headspace membrane-protected liquid phase microextraction (HS-MP-LPME).

Chromatographic conditions

Analyte quantification were performed using high performance liquid chromatography (Shimadzu, Kyoto, Japan) coupled with fluorescence detection (Shimadzu, Kyoto, Japan). The chromatographic separation of PHE was carried out on a reversed phase C_{18} column (4.6 × 150 mm, 5 μm). The separation was performed with isocratic elution utilizing mobile phase acetonitrile-water (70:30) (v/v) at column temperature of 30 °C. The flow rate, injection volume and detection wavelengths were fixed at 1.0 mL/min, 10 μL and 250/400 nm of excitation/emission wavelengths, respectively.

Optimization and validation of HS-MP-LPME-HPLC-FD

In this study, several extraction parameters were thoroughly investigated to enhance the analytes enrichment. Agitation speed (300-900 rpm), temperature (50-80 °C), and extraction time (20-40 minutes), were optimized before the application of the proposed method for the analysis of beverages and environmental water samples. Minimal validation were carried out to assess the viability of method and these included linearity, repeatability, relative recovery, limit of detection (LOD) and limit of quantification (LOQ). The relative recovery was calculated by comparing the peak area of spiked samples and the peak area of spiked deionized water. The LOD and LOQ were determined using linear regression approaches as the following (equation 1 and 2):

$$LOD = 3.3\ \sigma/S \quad (1)$$

$$LOQ = 10\ \sigma/S \quad (2)$$

where σ = the standard deviation of the y-intercept and S = the slope of the calibration curve.

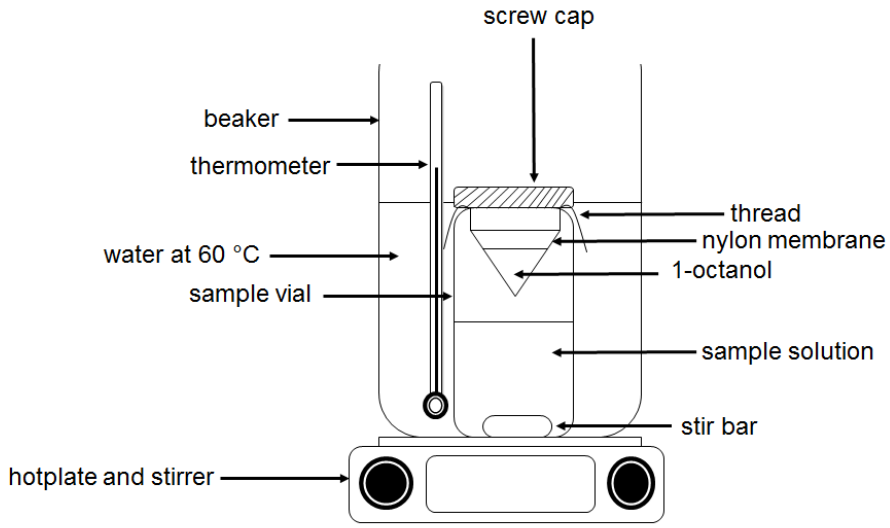


Figure 1. Schematic of headspace membrane-protected liquid phase microextraction

Results and Discussion

Optimization of HS-MP-LPME

There are several types of parameters that need to perform in this investigation to make sure optimum condition for the extraction of PHE in the beverages and environmental water samples are achieve using headspace membrane-protected liquid phase microextraction (HS-MP-LPME) technique. These parameters included extraction time, sample temperature and agitation speed. The condition for the optimization was carried out using deionized water samples spiked level with 200 ppb of PHE. The triplicate injection into HPLC-FD instrument were perform for each parameters to confirm the consistency of the results.

Extraction time is important to determine the time taken to reach equilibrium stage [17] because microextraction is non–exhaustive extraction technique. In this study, the extraction time for the analysis of PHE was carried out in the range 20 to 40 min whereas other parameters were kept constant. For instances, extraction temperature and agitation speed were both maintained at 60 °C and 700 rpm, respectively. Based on Figure 2(a), it was found that the peak area increased for more than 50% when extraction time was prolonged from 20 to 30 minutes. A decline in extraction efficiency was observed when the extraction time was extended to 40 min. The depletion of mid-volatile PHE was observed when the 1-octanol was evaporated due to the long exposing time at elevated temperature. Extraction time was then maintained at 30 minutes for the subsequent experiments.

PHE is a low molecular weight polycyclic aromatic hydrocarbon and it is classified as semi-volatile compound due to its low volatility [18]. Therefore, it was conveniently determined using headspace extraction, where the extractant was not contacted directly with the sample solution. This would prevent the extractant from dissolution into sample solution during extraction especially at high agitation speed. In this study, sample temperature ranging from 50 to 80 °C. The extraction was prolonged for 30 minutes as determined from previous experiments. Figure 2(b) shows, average peak area for the PHE gradually increased from 50 to 60 °C. No significant change in extraction efficiency indicated by peak area when the extraction temperature was fixed beyond 60 °C. Increased of sample temperature promoted an increase in PHE vapors in the headspace capacity [19]. The

recovery of PHE increased with temperature up to a certain level where the system achieved equilibrium and no more gain in peak area was observed. Therefore, the optimal sample temperature was fixed at 60 °C for the following experiments.

In this study, agitation speed was investigated in the range of 300 to 900 rpm. Figure 2(c) indicates that increase of agitation speed enhanced the convection in sample. The mass transfer of PHE was promoted from sample solution to headspace and finally reaching the extractant when the sample was agitated from 300 to 700 rpm. Above agitation at 700 rpm, the vortex formed in the sample solution disrupted the mass transfer rate and thus causing a drop in PHE recovery [11].

Validation of HS-MP-LPME-HPLC-FD method

Validation was performed to proof the HS-MP-LPME was acceptable for its application to extract PHE from water and beverage samples. The validation variables namely linearity range, accuracy, precision, limit of detection (LOD) and limit of quantification (LOQ) were carried out to ensure the HS-MP-LPME was viable in its intended application. Linearity regression was established using five deionized water spiked with PHE in the range of 25 to 500 ppb. A good linearity regression was obtained with correlation of determination (R^2), 0.9960. LOD and LOQ are normally used in an analytical analysis as a measurement to detect the limitation of the analytical method. LOD is defined as the lowest concentration of analyte that can be detected in a sample but not necessarily quantitated, whereas LOQ is defined as the lowest concentration of analyte that can be quantified with acceptable precision and accuracy [20]. The LOD and LOQ were calculated at concentration levels, 18 ppb and 25 ppb respectively. The technique was capable to offer ultra-trace detection and quantification of PHE in water. Both LOD and LOQ were lower than the maximum permissible concentration (MPC) of PHE proposed by National Institute for Public Health and the Environment, Netherlands for drinking water which is 0.14 ppm [21].

Accuracy of the HS-MP-LPME was investigated using relative recovery study. Relative recovery is defined as the initial concentration of the analyte after the extraction process acquired. The relative recovery was conducted by spiking each of the coffee, green tea, tap water, river water, and seawater samples with 25 and 100 ppb of PHE, respectively. Both sample blank and spiked samples were extracted using the optimized HS-MP-LPME. PHE was not detected in all of the sample blanks. Table 1 shows that the average of relative recovery of all samples exhibited acceptable recovery of PHE range from 83.7 to 116.1% with good precision indicated by relative standard deviations (RSDs) of three replicates $\leq$ 8.5%. Indeed, the HS-MP-LPME coupled with HPLC-FD was able to offer ultra-trace detection of PHE and provide negligible matrix effect for the analysis of PHE in beverage and environmental water samples.

The pros and cons of using HS-MP-LPME for the extraction of PHE

The comparison between HS-MP-LPME combined with HPLC-FD and previous methods was tabulated in Table 2. Overall, all of the previous reported methods offered much better sensitivity and wider linearity range as compared to HS-MP-LPME-HPLC-FD. However, all these methods involved several steps in extraction, whereas HS-MP-LPME combined extraction and pre-concentration in one step. Low density solvent based-dispersive liquid-liquid microextraction (LDSB-DLLME) coupled with HPLC-FD involved several steps which were, injection of solvents into sample solution, centrifugation for phase separation and withdrawal of extraction solvent prior to HPLC-FD analysis [22]. The extraction was completed in 6 minutes even though with multi-steps. This was because the extraction applied dispersive concept that accelerated the analytes mass transfer from the sample solution into the extraction solvent.

The micro solid phase extraction (μ-SPE) using C_{18} film as the adsorbents and combined with HPLC-FD incorporated simpler steps in the extraction of selected polycyclic aromatic hydrocarbons (PAHs) in coffee beverage, where analysts only needed to desorb the analytes from the film using a solvent and ultra-sonic

bath after the extraction [23]. The method offered slight lower and narrower of low concentration limit and linearity range, respectively as compared to HS-MP-LPME-HPLD-FD.

The magnetic solid phase extraction (MSPE) coupled with HPLC-FD were also reported for the analysis of PHE in coffee beverage [24]. The method simplified the collection of adsorbents after the extraction, where an external magnet was positioned outside of the sample vial to collect the adsorbent. This method has similar advantages as HS-MP-LPME, where both are environmentally friendly, inexpensive and easy to perform. Lastly, it is concluded that every method has its own pros and cons, where analysts can be based on their capability and convenience to choose their ideal method to achieve their analysis objectives.

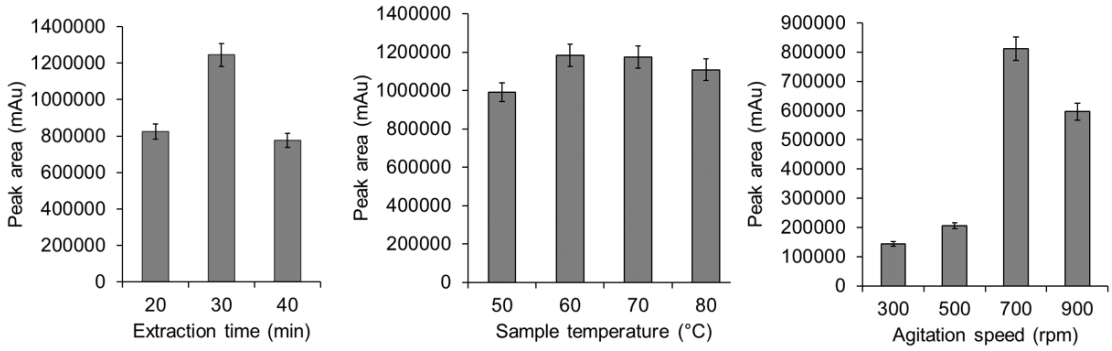


Figure 2. Effect of extraction time (a), sample temperature (b) and agitation speed (c) on the extraction efficiency of HS-MP-LPME for the extraction of PHE in spiked deionized water

Table 1. Relative recovery study using HS-MP-LPME-HPLC-FD for the analysis of PHE in beverage and water samples

Samples	**Average of Relative Recovery ± Relative Standard Deviation, % (n=3)**	
	Spiked at 25 ppb	**Spiked at 100 ppb**
Coffee	95.2 ± 3.2	97.7 ± 5.9
Green tea	112.4 ± 7.4	83.7 ± 8.4
Tap water	96.8 ± 3.8	97.0 ± 3.6
River water	107.9 ± 8.5	86.1 ± 5.0
Sea water	116.1 ± 6.8	98.0 ± 4.4

Table 2. Comparison between HS-MP-LPME and other published methods for the analysis of PHE in beverage and environmental water samples

Analysis Method	Matrix	Linear Range (ppb)	LOD (ppb)	Extraction Time (minutes)	Reference
LDSB-DLLME-HPLC-FD	Beverage	0.005-50 and 0.01-50	0.001 and 0.008	6	[22]
μ-SPE-HPLC-FD	Beverage	5-200	0.1	20	[23]
MSPE-HPLC-FD	Beverage	0.1-200	0.005	12	[24]
HS-MP-LPME-HPLC-FD	Beverage	25-500	18	30	This work

Conclusion

The HS-MP-LPME is proven as a green analysis method because only a small amount of organic solvent is consumed, and no harmful by-product is generated after extraction. This method is easy to perform for the extraction of PHE and the cost is inexpensive as compared to other extraction methods. For future research, the size and shape of the membrane can be further minimized to maximize the nylon membrane usage. Increase of sample temperature causes an increase of analytes in headspace capacity which then increases the extraction rate and shortens the extraction time. Therefore, we suggest that the sample temperature can be decreased to lower than 50 °C to increase the analyte recovery with prolong extraction time.

Acknowledgement

The authors would like to thank Universiti Malaysia Terengganu for laboratory facilities and the Ministry of Education Malaysia for financial support through research grant with vote numbers 59508 (FRGS/1/2018/STG01/UMT/02/4).

References

1. Ramesh, A., Archibong, A., Hood, D., Guo, Z. and Loganathan, B. (2011). Global environmental distribution and human health effects of polycyclic aromatic hydrocarbons. *Global Contamination Trends of Persistent Organic Chemicals*: pp. 97-126.
2. Liu, H. and Dasgupta, P. L. (1996). Analytical chemistry in a drop. solvent extraction in a microdrop. *Analytical Chemistry*, 68(11): 1817-1821.
3. Jeannot, M. A. and Cantwell, F. F. (1996). Solvent microextraction into a single drop. *Analytical Chemistry*, 68(13): 2236-2240.
4. Thordarson, E., Pálmarsdóttir, S., Mathiasson, L. and Jönsson, J. A. (1996). Sample preparation using a miniaturized supported liquid membrane device connected on-line to packed capillary liquid chromatography. *Analytical Chemistry*, 68(15): 2559-2563.
5. Pedersen-Bjergaard, S. and Rasmussen, K. E. (1999). Liquid−liquid−liquid microextraction for sample preparation of biological fluids prior to capillary electrophoresis. *Analytical Chemistry*, 71(14): 2650-2656.
6. Wang, J., Huang, S., Wang, P. and Yang, Y. (2016). Method development for the analysis of phthalate esters in tea beverages by ionic liquid hollow fibre liquid-phase microextraction and liquid chromatographic detection. *Food Control*, 67: 278-284.
7. Ali, W., Arain, M. B., Yamini, Y., Shah, N., Gul Kazi, T., Pedersen-Bjergaard, S. and Tajik, M. (2019). Hollow fiber-based liquid phase microextraction followed by analytical 2 instrumental techniques for quantitative analysis of heavy metal ions and 3 pharmaceuticals. *Journal of Pharmaceutical Analysis*, In press.

8. Peng, J. F., Liu, R., Liu, J. F., He, B., Hu, X. L. and Jiang, G. B. (2007). Ultrasensitive determination of cadmium in seawater by hollow fiber supported liquid membrane extraction coupled with graphite furnace atomic absorption spectrometry. *Spectrochimica Acta Part B: Atomic Spectroscopy*, 62(5): 499-503.
9. Sanagi, M. M., Loh, S. H., Wan Ibrahim, W. A. and Hasan, M. N. (2012). Agarose film liquid phase microextraction combined with gas chromatography–mass spectrometry for the determination of polycyclic aromatic hydrocarbons in water. *Journal of Chromatography A*, 1262: 43-48.
10. Loh, S. H., Sanagi, M. M., Wan Ibrahim, W. A. and Hasan, M. N. (2013). Solvent-impregnated agarose gel liquid phase microextraction of polycyclic aromatic hydrocarbons in water. *Journal of Chromatography A*, 1302: 14-19.
11. Chong, Y. T., Mohd Ariffin, M., Mohd Tahir, N. and Loh, S. H. (2018). A green solvent holder in electro-mediated microextraction for the extraction of phenols in water. *Talanta*, 176: 558-564.
12. Sedehi, S., Tabani, H. and Nojavan, S. (2018). Electro-driven extraction of polar compounds using agarose gel as a new membrane: determination of amino acids in fruit juice and human plasma samples. *Talanta*, 179: 318-325.
13. Sanagi, M. M., See, H. H., Wan Ibrahim, W. A. and Abu Naim, A. (2007). Determination of pesticides in water by cone shaped membrane protected liquid phase microextraction prior to micro-liquid chromatography. *Journal of Chromatography A*, 1152: 215-219.
14. Loh, T. Y., Khalik, W. M. A. W. M. and Loh, S. H. (2020). Simple extraction of bisphenol A in beverages and water by membrane-protected liquid phase microextraction. *Sains Malaysiana*, 49(1): 49-55.
15. Goh, S. X. L., Goh, H. A. and Lee, H. K. (2018). Automation of ionic liquid enhanced membrane bag-assisted-liquid-phase microextraction with liquid chromatography-tandem mass spectrometry for determination of glucocorticoids in water. *Analytica Chimica Acta*, 1035: 77-86.
16. Xu, L. and Lee, H. K. (2009). Solvent-bar microextraction - using a silica monolith as the extractant phase holder. *Journal of Chromatography A*, 1216: 5483-5488.
17. Ng, N. T., Sanagi, M. M., Wan Ibrahim, W. N. and Wan Ibrahim, W. A. (2017). Agarose-chitosan-C_{18} film micro-solid phase extraction combined with high performance liquid chromatography for the determination of phenanthrene and pyrene in chrysanthemum tea samples. *Food Chemistry*, 222: 28-34.
18. Kumar, B., Verma, V. K., Gaur, R., Kumar, S., Sharma, C. S. and Akolkar, A. B. (2014). Validation of HPLC method for determination of priority polycyclic aromatic hydrocarbons (PAHs) in wastewater and sediments. *Advances in Applied Science Research*, 5 (1): 201-209.
19. Thorvaldsson, K. and Janestad, H. (1999). A model for simultaneous heat, water and vapour diffusion. *Journal of Food Engineering*, 40(3): 167-172.
20. Vial, J. and Jardy, A. (1999). Experimental comparison of the different approaches to estimate LOD and LOQ of an HPLC method. *Analytical Chemistry,* 71(14): 2672-2677.
21. Verbruggen, E. M. J. and van Herwijnen, R. (2011). Environmental risk limits for phenanthrene. National Institute for Public Health and the Environment, Ministry of Health, Welfare and Sport, Netherlands.

22. Loh, S. H., Chong, Y. T., Nor Afindi, K. N. and Abdullah Kamaruddin, N. (2016). Determination of Polycyclic aromatic hydrocarbons in beverage by low density solvent based-dispersive liquid-liquid microextraction-high performance liquid chromatography-fluorescence detection. *Sains Malaysiana*, 45 (10): 1453-1459.
23. Loh, S. H., Neoh, P. E., Tai, C. T. and Kamaruzaman, S. (2018). Simple μ-solid phase extraction using C_{18} film for the extraction of polycyclic aromatic hydrocarbons in coffee beverage. *Malaysian Journal of Analytical Sciences*, 22(1): 1-7.
24. Shi, Y., Wu, H., Wang, C., Guo, X., Du, J. and Du, L. (2016). Determination of polycyclic aromatic hydrocarbons in coffee and tea samples by magnetic solid-phase extraction coupled with HPLC–FLD. *Food Chemistry*, 199: 75- 80.

Malaysian Journal of Analytical Sciences (MJAS)
Published by Malaysian Analytical Sciences Society

IDENTIFICATION AND QUANTIFICATION OF FRUCTOSE, GLUCOSE AND SUCROSE IN WATERMELON PEEL JUICE

(Pengenalan dan Pengkuantitian Fruktosa, Glukosa dan Sukrosa di dalam Jus Kulit Tembikai)

Wan Mazlina Md. Saad[1]*, Nur Shafinaz Mohamad Salin[1], Ainza Suzila Ramzi[1], Fatimah Salim[2,3]

[1]Centre of Medical Laboratory Technology, Faculty of Health Sciences
[2]Atta-ur-Rahman Institute for Natural Product Discovery
Universiti Teknologi MARA, Selangor Branch, 42300 Puncak Alam, Selangor, Malaysia
[3]Centre of Foundation Studies,
Universiti Teknologi MARA, Selangor Branch, Dengkil Campus, 43800 Dengkil, Selangor, Malaysia

**Corresponding author:*

Received: 20 November 2019; Accepted: 12 April 2020; Published: 9 June 2020

Abstract

Watermelon (*Citrullus lanatus*) contains various chemical components with sugar rating the highest. Sugar content in watermelon usually reflects the fruit quality and sweetness. Watermelon sugar is mainly distributed into three types; fructose, glucose and sucrose. This study was conducted to identify and quantify fructose, glucose and sucrose in watermelon peel juice by using a reversed-phase high-performance liquid chromatography (RP-HPLC) method coupled with refractive index detector (RID). The separation of sugars was carried out on NH_2 column thermostatically maintained at 23°C. The flow rate used was 1.00 mL/min on 20 µL sample injection. An isocratic elution mode of mobile phase acetonitrile and water (75:25) was used for duration of 20 minutes. Fructose and glucose were eluted at minutes 8.88 and 10.00, respectively while sucrose was not detected. The amount of quantified fructose (0.60 mg/mL) and glucose (0.50 mg/mL) indicated that fructose was the highest sugar content in the watermelon peel juice, followed by glucose. This study described the ability of HPLC-RID method which is suitable for profiling major sugars content in watermelon peel juice. The analytical method was validated, and the results showed good precision, accuracy, and linearity.

Keywords: watermelon peel, *Citrullus lanatus*, peel, fructose, glucose, sucrose

Abstrak

Tembikai (*Citrullus lanatus)* mengandungi pelbagai komponen kimia di mana kandungan gula adalah yang paling tinggi. Kandungan gula di dalam tembikai biasanya menjadi penentu kepada kualiti dan kemanisan buah. Gula di dalam tembikai terbahagi kepada tiga jenis; fruktosa, glukosa dan sukrosa. Kajian ini dijalankan untuk mengenalpasti dan pengkuantitian kandungan fruktosa, glukosa dan sukrosa di dalam jus kulit tembikai dengan menggunakan kaedah fasa terbalik kromatografi cecair berprestasi tinggi (RP-HPLC) digandingkan dengan pengesan indeks biasan (RID). Pemisahan kandungan gula tersebut dilakukan dalam turus NH_2 dengan pengawalan suhu 23°C. Kadar aliran yang digunakan ialah 1.00 mL/min pada muatan sampel 20 µL. Mod elusi isokratik dengan gabungan pelarut asetonitril dan air (75:25) digunakan dalam durasi 20 minit. Fruktosa dan glukosa dielusi masing-masing pada minit ke 8.88 dan 10.00, manakala tiada sukrosa dikesan. Jumlah pengkuantitian fruktosa (0.60 mg/mL) dan glukosa (0.50 mg/mL) dalam jus kulit tembikai menunjukkan bahawa fruktosa adalah gula yang paling banyak di dalam jus kulit tembikai, diikuti oleh glukosa. Dapatan kajian ini menerangkan keupayaan kaedah HPLC-RID dalam

memprofil jenis gula utama di dalam jus kulit tembikai. Kaedah analitikal yang digunakan di sini telah divalidasi dan dapatan kajian menunjukkan kejituan, ketepatan dan kelinearan.

Kata kunci: kulit tembikai, *Citrullus lanatus*, kulit, fruktosa, glukosa dan sukrosa

Introduction

Watermelon or scientifically known as *Citrullus lanatus* belongs to Cucurbitaceous family. It has been widely cultivated by approximately 7% of the world's total vegetable production in warm and subtropical countries [1]. Watermelon is also known as "the king of fruits in summer" and contains about 93% of water. Hence the name 'water' while melon refers to the large, round, sweet and pulpy flesh [2]. Watermelon beneficial to human health as it contains phytochemicals including lycopene, phytofluene, phytoene, beta-carotene and lutein [3] besides minerals, proteins and fibres [4]. Typically a watermelon weighs from 1.5 to 15 kilogrammes and is elongated, oval or round. Hannah and Krishnakumari supported that an average watermelon contains about 30% peel (also known as rind), 68% flesh and 2% seed [3]. The peel stripes appear from light to dark green with various patterns. The flesh commonly found in yellow, red, orange or white [5], with the flesh colour represents its sweetness [6].

Malaysians usually prefer watermelon as a dessert due to its delicious, sweet and refreshing taste. In addition, it is an affordable fruit that is readily available in the market. The main soluble sugars in watermelon include fructose, glucose and sucrose with the sugar ratio determining the fruit sweetness [7]. Among these sugars, fructose contributes the highest taste of sweetness in the fruit. In the early stage of its growth, a higher concentration of glucose and fructose are found with only sucrose detected when the fruit reaches maturity [4]. In a mature watermelon, sucrose and glucose concentration ranges from 20-40% while fructose concentration is approximately 30-50% [8].

Currently, many types of new instruments and methods are available for sugar analysis [9]. The common method used for determination and separation of fructose, glucose and sucrose is high-performance liquid chromatography (HPLC) with ideal detectors and columns [10, 11]. Columns that are widely used for sugar separation are carbohydrate and amino bonded columns [12]. The most common detectors that could be used for quantification of sugars are pulsed amperometric detector (PAD), evaporative light scattering detector (ELSD) and refractive index detector (RID). In this study, isocratic mode reversed-phase high-performance liquid chromatography (RP-HPLC) method was chosen with ZORBAX NH_2 column and refractive index detector (RID) were used in identifying and quantifying fructose, glucose and sucrose in watermelon juice peel.

Materials and Methods

Chemicals and reagents

Analytical grade powder of D-(-)-Fructose (≥ 99%), D-(+)-Glucose (≥ 99.5%) and sucrose (≥ 99.5%) standards were purchased from Sigma-Aldrich (St. Louis, MO, USA). Acetonitrile (MeCN) and methanol (MeOH) of HPLC grade were purchased from Merck (Germany).

Instrument

The isocratic-mode RP-HPLC was carried out using Agilent 1200 (Agilent Technology, 1200 Series) equipped with an auto-sampler injector (G1330B), column oven and refractive index detector (RID) for detection of fructose, glucose and sucrose. The column used was ZORBAX (Agilent) NH_2 column, 5µm (4.5 x 250mm).

Sample preparation

Four watermelons ranging from 2.0 to 2.8 kg (*Citrullus lanatus*) were obtained from Selangor Fruit Valley, Selangor, Malaysia and were identified by Forest Research Institute Malaysia (FRIM) with reference no. FRIM394/490/5/17(650). The watermelons were washed and wiped with tissue papers. Then, the watermelon was peeled and weighed before juicing, and filtered with Whatman Filter paper to clarify the sample.

Preparation of standard solution

10 mg of each fructose, glucose and sucrose standard were dissolved in 1.5 mL of MeCN and water solution (2:1), and then filtered through 0.45-µm polyvinylidene fluoride (PVDF) syringe filter. A series of working solutions were prepared by diluting stock solution two-folds in ranges 0.31-5.00 mg/mL.

Sample preparation procedure

150 µL peel juice was filtered using 0.45- µm polyvinylidene fluoride (PVDF) syringe filter into 2 mL HPLC vial prior for injecting into RP-HPLC.

Isocratic mode reverse-phase high-performance liquid chromatography

Identification and quantification of fructose, glucose and sucrose were performed according to a study performed by Sabeetha et al. with slight modification [4]. The isocratic mode of RP-HPLC was conducted using NH_2 column 5 µm (4.5 x 250 mm) (ZORBAX, Agilent) at temperature (23 °C) with flow rate of 1 mL/min of mobile phase MeCN and water (75:25). Separation and detection of fructose, glucose and sucrose was carried out by injecting 20 µL of standard and sample of watermelon peel juice triplicate into NH_2 column coupled with refractive index detector (RID) at 35°C. After each analysis, the column was washed with isopropanol.

Method validation

The validation of this study was achieved by determining the linearity of calibration curve, limit of detection (LOD), limit of quantification (LOQ) and % recovery. The linearity of isocratic-mode RP-HPLC method for fructose, glucose and sucrose detection in watermelon peel juice was determined by injecting triplicate of 20 µL of 5 different concentrations of standards at 0.31, 0.63, 1.25, 2.50, 5.00 mg/mL. Calibration curve of peak area against each standard concentration was constructed to obtain linear equation and regression coefficient (R^2). LOD is the lowest amount of sugar that could be detected in the sample while LOQ is the lowest amount of sugar that could be quantitatively determined with suitable precision and accuracy by using statistical calculation [13]. Three different concentration of 5.00, 2.50 and 1.25 mg/mL for each standard solution were injected triplicate to evaluate the accuracy and % recovery of method used as referred to Kayesh et al. [14] .The LOD, LOQ and recovery were calculated using the formula in equations 1-3:

$$\text{LOD} : \frac{3 \times \text{Standard deviation of response}}{\text{Slope of calibration curve}} \quad (1)$$

$$\text{LOQ} : \frac{10 \times \text{Standard deviation of response}}{\text{Slope of calibration curve}} \quad (2)$$

$$\%\ \text{Recovery} : \frac{Recovered\ concentration}{\text{Injected concentration}}\ x100 \quad (3)$$

Statistical analysis

The result of analyses were presented as mean ± standard deviation based on three replicates. Microsoft Excel 2007 (Microsoft Corporation, Redmond, WA, USA) was used for data analysis.

Results and Discussion

Identification of fructose, glucose and sucrose in watermelon juice peel

This study demonstrated the analytical isocratic mode RP-HPLC method for separation of sugars in watermelon peel juice. The representative chromatograms for standards and sample by using RP-HPLC are shown in Figure 1. The chromatographic peaks were identified by comparing the retention time of the injected fructose, glucose and sucrose standards solution against watermelon peel juice. In order to obtain a good analysis of fructose, glucose and sucrose, method was adapted from Veena et al. with slight modification [12]. Triplicated injection of 20 µL standards and sample using isocratic mode RP-HPLC with thermostatic NH_2 column coupled with RID showed the best results with noise eliminated. A flow rate of 1 mL/min pre-mixture of MeCN and water (75:25, v/v) as mobile phase showed the optimum ratio composition that is able to improve the separation and resolution of targeted fructose, glucose and sucrose component as performed by Sabeetha et al. and Karkacier et al. [4,14].

In Figure 1, a good peak separation was presented with the first elution peak detected is fructose followed by glucose and sucrose, which is in line with study by

Sabeetha et al. [4]. Figure 1(a) shows RP-HPLC chromatogram of fructose, glucose and sucrose mixed standards were detected at retention time of 8.41, 9.46 and 13.74 minutes, respectively. Figure 1(b) shows RP-HPLC chromatogram peaks of watermelon peel juice with fructose and glucose detected at retention time of 8.88 minutes and 10.00 minutes respectively with no detection of sucrose as tabulated in Table 1. Chromatogram peaks in Figures 1(a) and 1(b) with retention time 3.193 and 3.167 minutes show the mobile peak of MeCN and water solution. The instability of the detector used may possibly cause slight changes in the chromatographic retention time of standards and sample. RID is sensitive to changes in many conditions including optical property of sugar molecule, temperature, pressure and flow rate which can affect chromatogram [15]. To overcome this limitation, an ELSD detector is strongly suggested.

Method validation

The validity of optimized method used in term of linearity, LOD, LOQ and accuracy was evaluated. In Table 2, the regression equations, LOD and LOQ for fructose, glucose and sucrose are shown. Linear equation for fructose, glucose and sucrose were y = 614063x + 152854, y = 135258x +386377 and y = 265249x +35564, respectively. Regression coefficient (R_2) values from this study were compared with data from Zhang et al. where R_2 value for fructose, glucose and sucrose were 0.9997, 0.9997, and 0.9990 respectively. Thus, it indicated that present data is reproducible as R_2 value (≥0.99) [16]. The linear regression in this study reflected a linear relationship between sugars concentration against chromatographic response [17]. The LOD of fructose, glucose and sucrose were found at 0.124, 0.054 and 0.00002 mg/mL with LOQ 0.414, 0.180 and 0.00007 mg/mL, respectively. LOD and LOQ is the lowest concentration detected and quantitatively measured reflecting the precision and accuracy of method used [13]. The lowest LOD and LOQ values in this study indicated that the method used was efficiently sensitive [18].

In Table 3, the data of accuracy for fructose, glucose and sucrose are tabulated. Accuracy was evaluated and expressed in recovery between the mean concentration and the added standard concentration found [19]. Triplicate injection of 5.00, 2.50 and 1.25 mg/mL were analysed before and after the injection of watermelon peel juice. The percentage of recovery for fructose, glucose and sucrose was found ranging from 91 to 99.4%, which is within the range reported by Uney et al. [20]. Kayesh et al. supported that more than 97% recovery demonstrated the accuracy of optimized method used [19]. Hence, the linearity, LOD, LOQ and recovery values showed that the isocratic mode RP-HPLC method used in this study was sensitive and precise in quantification of fructose, glucose and sucrose.

Quantification of fructose, glucose and sucrose in watermelon juice peel

European guidelines advises that 45-60% of our daily energy intake should come from carbohydrates including sugars [21]. The optimized method of NH_2 column and RID were applied to analyse sugar types in watermelon peel juice. In Table 4, the concentration of fructose, glucose and sucrose calculated from the linear equation obtained by calibration curve were tabulated This study reported that watermelon peel juice had the highest concentration of fructose at 0.60 mg/mL followed by glucose 0.50 mg/mL and not detected for sucrose. The result obtained agrees with Sabeetha et al. that reported the sequence of sugar type concentration found in watermelon are fructose, glucose and sucrose [4]. Yau et al. demonstrated that watermelon containing the highest concentration of fructose is in excellent condition since the degree of sweetness for fructose is 1.5-2.0 times higher than sucrose [22]. No detection of sucrose in this study may possibly be due to the negligible concentration of sucrose in the watermelon peel juice which was below the LOD and LOQ limits [4].

In addition, sucrose concentration in watermelon could only be detected after 4 weeks of maturity [4]. Thus, this study found that watermelon used had not attained a full maturity stage due to the absence of sucrose content, and suggests that the consumption of immature watermelon peel could be beneficial due to the low fructose glycaemic index properties. Through this study, the quality and value of Malaysian's local fruits specifically watermelon, could be highlighted. Not only the flesh, but the peel also has added-value due to its low glycaemic index properties.

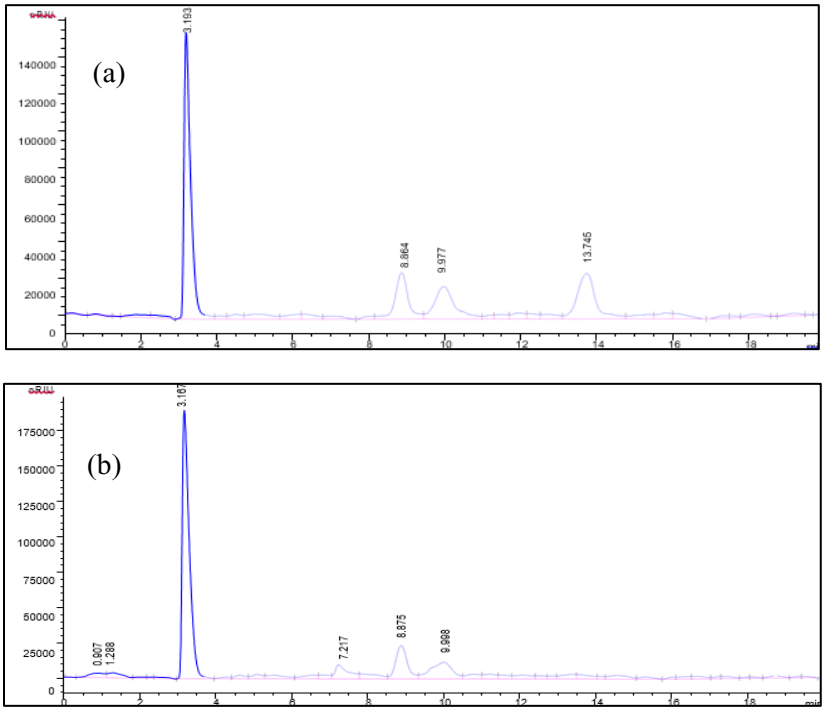


Figure 1. Comparative chromatogram of fructose, glucose and sucrose. (a) Standard of fructose, glucose and sucrose, and (b) Watermelon juice peel of fructose and glucose peak at 8.88 and 10.00 minutes, respectively with no sucrose peak mode RP-HPLC

Table 1. Retention time (min) of sugar content in standards and sample detected using isocratic

Sample	**Retention time (minutes)**		
	Fructose	**Glucose**	**Sucrose**
Standard	8.41	9.46	13.74
Watermelon juice peel	8.88±0.05	10.00±0.21	0.00

Table 2. Regression parameters, LOD and LOQ for fructose, glucose and sucrose

Compound	Linear Equation	Regression Coefficient	Linear Range (mg/mL)	LOD (mg/mL)	LOQ (mg/mL)
Fructose	y=614063x + 152854	0.9961	0.3-5.0	0.124	0.414
Glucose	y=135258x +386377	0.9938	0.3-5.0	0.054	0.180
Sucrose	y=265249x +35564	0.9993	0.3-5.0	0.00002	0.00007

Table 3. Recovery data for separation of fructose, glucose and sucrose using isocratic mode RP-HPLC

Sugar	Spiked Concentration (mg/mL)	Measured Concentration (mg/mL)	Recovery (%)
Fructose	5.00	4.97	99.4
	2.50	2.40	96.0
	1.25	1.14	91.0
Glucose	5.00	4.90	98.0
	2.50	2.37	94.8
	1.25	1.18	94.4
Sucrose	5.00	4.96	99.2
	2.50	2.48	99.2
	1.25	1.22	97.6

Conclusion

The RP-HPLC isocratic mode analysis was successfully identified and quantified the respective sugar content in watermelon peel juice in less than 15 minutes. The results showed that this method is accurate and reproducible with an excellent linearity of standards (≥0.99), low LOD and LOQ values in range of 0.00002 and 0.414 as well as accuracy of 91% to 99.4%. Fructose content is the highest in watermelon peel juice followed by glucose and no detection of sucrose. This study shows that watermelon peel has an added-value as it contains significant amount of fructose, which is a potential low glycaemic index energy source. The quality of watermelon peel can thus be highlighted not is just the flesh that is edible. This study also serves as a base reference for future plans to turn local fruit waste into wealth. However, the limitation lies on the slight instability of the RI detector used in this study which could be overcome with ELS detector.

Acknowledgement

The authors would like to acknowledge (1) Ministry of Higher Education, Malaysia, through Lestari Grant Scheme and Institute of Research Management and Innovation (IRMI), Universiti Teknologi MARA for funding the study (IRMI grant no. 600-IRMI5/3/LESTARI.(047/2019); (2) Centre of Medical Laboratory Technology, Centre of Postgraduate Study, Faculty of Health Sciences, Universiti Teknologi MARA, Puncak Alam campus, for providing facilities throughout this study; (3) Atta-ur-Rahman Institute for Natural Product Discovery (AuRIns), Universiti Teknologi MARA Puncak Alam, for workplace, (4) Instrument Laboratory of Faculty of Pharmacy for the HPLC-RID usage, and (5) Prof Dr Mohd Ilham Adenan from Universiti Teknologi MARA, Jengka Campus, Pahang Branch and En. Effendy from Selangor Fruit Valley, Selangor for providing watermelon samples.

References

1. Zhang, H. and Ge, Y. U. (2016). Dynamics of sugar-metabolic enzymes and sugars accumulation during watermelon (*Citrullus lanatus*) fruit development. *Pakistan Journal of Botany*, 48(6): 2535-2538.
2. Kumawat, G., Goyal, M., Mathur, K. and Yadav, S. K. (2017). *Citrullus lanatus*: An overview on pharmacological activities. *International Journal of Pharmaceutical & Biological Archives*, 8(1): 6-9.
3. Angeline, C. H. M. and Krishnakumari, S. (2015). Qualitative phtochemistry profile of watermelon (*Citrullus vulgaris* schrad) rind extracts with different solvent. *Asian Journal of Pharmaceutical and Clinical Research,* 8(4): 62-65.
4. Sabeetha, S., Amin, I. and Nisak, M. Y. B. (2017). Physico-chemical characteristics of watermelon in Malaysia. *International Food Research Journal*, 45(2): 209-223.
5. Kyriacou, M. C., Leskovar, D. I., Colla, G. and Rouphael, Y. (2018). Watermelon and melon fruit quality: The genotypic and agro-environmental factors implicated. *Scientia Horticulturae*, 234: 393-408.
6. Naz, A., Butt, M. S., Sultan, M. T., Qayyum, M. M. N. and Niaz, R. S. (2014). Watermelon lycopene and allied health claims. *EXCLI Journal*, 13: 650-666.
7. Brown, A. C. and Summers, W. L. (1985). Carbohydrate accumulation and colour development in watermelon. *Journal American Social Horticulture Science*, 10: 683.
8. Yativ, M., Hanary, I. and Wolf, S. (2010). Sucrose accumulation in watermelon fruits: genetic variation and biochemical analysis. *Journal of Plant Physiology,* 167:589-596.
9. Brokl, M., Hernández-Hernández, O., Soria, A. C. and Sanz, M. L. (2011). Evaluation of different operation modes of high-performance liquid chromatography for the analysis of complex mixtures of neutral oligosaccharides. *Journal of Chromatography A,* 1218: 7697-7703.
10. Ma, C., Sun, Z., Chen, C., Zhang, L. and Zhu, S. (2014). Simultaneous separation and determination of fructose, sorbitol, glucose and sucrose in fruits by HPLC-ELSD. *Food Chemistry*, 145: 784-788.
11. Magwaza, L. S. and Opara, U. L. (2015). Analytical methods for determination of sugars and sweetness of horticultural products-A review. *Scientia Horticulturea*, 184: 179-192.
12. Veena, K. S., Sameena, M. T., Padmakumari, A. K. P., Srinivasa, G. T. K., Nishanth, K. S. and Reshma, M. V. (2018). Development and validation of HPLC method for determination of sugars in palm sap, palm syrup, sugarcane jaggery and palm jaggery. *International Food Research Journal*, 25(2): 649654.
13. Md Saad, W. M., Ridwan, R., Md, Lasim. N. S., Rapi, N. L. and Salim, F (2019). Determination and quantification of p-coumaric acid in pineapples (*Ananas comosus*) extracts using gradient mode RP-HPLC. *Pharmacognosy Research*, 2019(11): 78-82.
14. Karkacier, M., Erbas, M., Uslu, M. K. and Aksu, M. (2003). Comparison of different extraction and detection methods for sugars using amino-bonded phase HPLC. *Journal of Chromatography Science,* 41: 331-333.
15. Wilson, I. D. (2009). Handbook of methods and instrumentation in separation science. Academic press, London.
16. Zhang, C-R., Aldosari, S. A., Vidyasagar, P. S., Shukla, P. and Nair, M. G. (2016). Determination of the variability of sugars in date fruit varieties. *Journal of Plantation Crops*, 43(1): 53-61.
17. Montesano, D., Cossignani, L., Giua, L., Urbani, E., Simonetti, M. S. and Blasi, F. (2016). A simple HPLC-ELSD method for sugar analysis in goji berry. *Journal of Chemisry,* 2016: 5.
18. Ridwan, R., Rashmizal, H., Razak, A., Adenan, M. I. and Saad, W. M. (2018). Development of isocratic RP-HPLC method for separation and quantification of L-citrulline and L-arginine in Watermelons. *International Journal of Analytical Chemistry,* 2018: 9.

19. Kayesh, R., Sultan, M. Z., Rahman, A., Uddin, M. G., Aktar, F. and Rashid, M. A. (2013). 19.Development and validation of a RP-HPLC method for the quantification of omeprazole in pharmaceutical dosage form. *Journal of Scientific Research*, 5(2): 335-342.
20. Uney, K., Altan, F. and Elmas, M. (2011). Development and validation of a high-performance liquid chromatography method for determination of cefquinome concentrations in sheep plasma and its application to pharmacokinetic studies. *Antimicrobial Agents and Chemotherapy*, 55(2): 854-859.
21. EFSA Panel on Dietetic Products, Nutrition, and Allergies (2010). Scientific opinion on dietary reference values of carbohydrates and dietary fibre. *EFSA Journal* 8(3): 1462.
22. Yau, E. W., Rosnah, S., Noraziah, M., Chin, N. L. and Osman, H. (2010). Physio-chemical composition of red seedless watermelons (*Citrullus lanatus*). *International Food Research Journal,* 17: 327-33.

Malaysian Journal of Analytical Sciences (MJAS)
Published by Malaysian Analytical Sciences Society

OPTIMIZATION OF MONTMORILLONITE K10 ION-EXCHANGE WITH Fe^{3+} FOR THE APPLICATION OF BIODIESEL PRODUCTION

(Pengoptimuman Pertukaran Ion Montmorilonit K10 dengan Fe^{3+} untuk Aplikasi Penghasilan Biodiesel)

Syahirah Yahya[1] and Farah Wahida Harun[2, 3]*

[1]*Department of Chemistry and Food Technology,*
Politeknik Tun Syed Nasir Syed Ismail,
Hab Pendidikan Tinggi Pagoh, KM1 Jalan Panchor, 84600 Pagoh, Johor, Malaysia
[2]*Faculty of Science and Technology*
[3]*Frontier Materials Research Group*
Universiti Sains Islam Malaysia, Bandar Baru Nilai, 71800 Nilai, Negeri Sembilan, Malaysia

**Corresponding author: farahw@usim.edu.my*

Received: 20 November 2019; Accepted: 17 April 2020; Published: 9 June 2020

Abstract

The modification of montmorillonite K10 with Fe^{3+} was investigated to study the optimum ion-exchange occurred in the interlayers of clays. Montmorillonite K10 was modified to be applied as a catalyst in biodiesel production from waste cooking oil (WCO). Three methods to optimize the ion-exchange process were investigated. For method 1 and method 2, respective 14% and 27% by mass of Fe in montmorillonite K10 were stirred in a closed cap system for 7 hours while method 3 applied 20% of Fe stirred with montmorillonite K10 for 24 hours until it became mold and slurry. The ability of ion-exchange was tested using SEM/EDX. It was found that 1.21% Fe composition increased by using method 1 while 2.66% Fe increased using method 2. The highest Fe exchange was detected using method 3 with 5.23% increment. For more accurate result, 20% Fe-MMT K10 from method 3 was characterized using XRF and it was found that the ion exchange occurred with interchangeable Ca^{2+}. In correlation, the effect of Fe increment on acidity was studied by using TPD-NH_3. Naturally, montmorillonite K10 possessed 0.232 mmol/g of acidity. The results found that the highest acidity was detected for 20% Fe-MMT K10 (14.261 mmol/g). The application of montmorillonite K10 on biodiesel production increased the yield up to 38.39% compared to the reaction without catalyst (26.80%). With the aid of modified montmorillonite K10, 66.54% and 69.32% biodiesel were produced using catalyst from method 1 and 2 respectively. Amazingly, an outstanding yield was produced by using catalyst from method 3 (84.58%). Therefore, 20% Fe-MMT K10 catalyst was selected for further biodiesel optimization via conventional method. It was found that 96.49% biodiesel was successfully produced with 28.65% acid conversion at 150 °C, 6 h, 12:1 methanol: oil and 4 wt.% mass of catalyst. The investigations on acid conversion and biodiesel yield proved that the modification of montmorillonite K10 with 20% Fe is the optimum and the catalyst can undergo both esterification and transesterification reactions simultaneously to produce optimum biodiesel yield.

Keywords: Montmorillonite K10, Fe^{3+} ion-exchange, simultaneous esterification-transesterification, biodiesel, waste cooking oil

Abstrak

Pengubahsuaian montmorilonit K10 dengan Fe^{3+} telah dijalankan untuk mengkaji pertukaran ion yang optimum pada lapisan tanah liat. Montmorilonit K10 diubahsuai untuk dijadikan sebagai pemangkin dalam pengeluaran biodiesel dari minyak masak terpakai (WCO). Tiga kaedah untuk mengoptimumkan proses pertukaran ion telah dikaji. Untuk kaedah 1 dan kaedah 2, masing-masing 14% dan 27% jisim Fe dalam montmorilonit K10 telah dicampur dalam sistem tertutup selama 7 jam. Manakala kaedah 3 menggunakan 20% Fe dikacau dengan montmorilonit K10 selama 24 jam sehingga pekat seperti tanah liat. Keupayaan penukaran ion telah diuji menggunakan SEM/EDX. Hasil kajian mendapati bahawa komposisi Fe meningkat sebanyak 1.21% dengan menggunakan kaedah 1 manakala 2.66% Fe meningkat dengan menggunakan kaedah 2. Pertukaran Fe tertinggi telah dikesan menggunakan kaedah 3 dengan kenaikan Fe sebanyak 5.23%. Untuk hasil yang lebih tepat, 20% Fe-MMT K10 dari kaedah 3 dicirikan dengan menggunakan XRF dan didapati ion Ca^{2+} bertukar dengan Fe^{3+}. Kesan kenaikan Fe terhadap tahap keasidan dikaji dengan menggunakan TPD-NH_3. Pada asalnya, montmorilonit K10 mempunyai tahap keasidan 0.232 mmol/g. Setelah diubahsuai, keasidan tertinggi dikesan pada sampel 20% Fe-MMT K10 (14.261 mmol / g). Penggunaan montmorilonit K10 dalam pengeluaran biodiesel menghasilkan 38.39% produk berbanding tindak balas tanpa pemangkin (26.80%). Dengan bantuan montmorilonit K10 yang diubahsuai, masing-masing 66.54% dan 69.32% biodiesel dihasilkan menggunakan pemangkin yang diubahsuai dari kaedah 1 dan 2. Namun, biodiesel yang paling tinggi dihasilkan dengan menggunakan pemangkin daripada kaedah 3 (84.58%). Oleh itu, pemangkin 20% Fe-MMT K10 telah dipilih untuk pengoptimuman biodiesel melalui kaedah konvensional. Hasil kajian mendapati bahawa 96.49% biodiesel berjaya dihasilkan dengan penukaran asid sebanyak 28.65% pada 150 °C, 6 jam, 12: 1 metanol: minyak dan 4% berat masa pemangkin. Kajian penukaran asid dan hasil biodiesel telah membuktikan bahawa pengubahsuaian montmorilonit K10 dengan 20% Fe adalah optimum dan 20% Fe-MMT K10 boleh menjalani tindak balas esterifikasi dan transesterifikasi secara serentak untuk menghasilkan biodiesel yang optimum.

Kata kunci: Montmorilonit K10, pertukaran ion Fe^{3+}, esterifikasi-transesterifikasi serentak, biodiesel, minyak masak terpakai

Introduction

The application of heterogeneous catalyst in many reactions is important in recent time. Many natural catalysts were investigated on selective organic transformations as synthetic techniques under green chemistry. Currently, the natural catalyst under investigation includes natural clay like montmorillonite. It can work under mild condition and the catalyst can be recovered by simple filtration and evaporation, and then can be regenerated and reused. In nature, montmorillonite possessed Lewis and Brønsted acidity [1] that enable the clay to function in esterification and transesterification reactions simultaneously. The Lewis acidity mainly originates from the metal atoms at the edge sites while the Brønsted acidity is from the interlamellar water coordinated to exchangeable cations.

Montmorillonite was used in biodiesel production, however the production was low with around 60% yield and required a long reaction time and a large amount of catalyst loading to achieve the yield [2, 3]. Hence, some modification is required to be done on montmorillonite to improve the acidity. There are two modification methods to improve the acidity which are pillaring method [4] and ion-exchange method [5]. The pillaring method was successful in laboratory synthesis. However, it is not an ideal preparation technique for large-scale production because of the long preparation period as well as waste water and chemical [4, 6]. Therefore, ion-exchange method is considered as a relevant technique to modify the montmorillonite as it involves simple stirring method in short duration.

In biodiesel production, iron (Fe) was considered as efficient Lewis metal when the single metal can act as a catalyst and produced up to 94% biodiesel from waste cooking oil (WCO) [7]. The collaboration of Fe with montmorillonite can reduce the metal consumption in biodiesel production as it is able to improve the acidic sites of montmorillonite. However, the review from literature noticed that the ion exchange of montmorillonite with Fe could only achieve 70% conversion [8, 9]. Some modification in the preparation technique is required to optimize the ion exchange.

In this study, we employed a simple technique, modified from the previous methods [10, 11] to optimize the ion exchange and acidity of montmorillonite K10. The montmorillonite interchangeable cations were exchanged with iron (III) ion (Fe^{3+}) and the ion exchange and acidity were tested using scanning electron microscope with energy dispersive X-ray (SEM/EDX) and temperature programmed desorption with ammonia (TPD-NH_3). The ion exchange method was confirmed by X-ray fluorescence (XRF) analysis. The performance was evaluated based on biodiesel production from WCO to study the effect of metal concentrations on the catalyst efficiency. The optimum condition for the catalytic activity was also investigated for the maximum biodiesel production.

Materials and Methods

Materials

WCO sample was collected from restaurants near USIM and was previously characterized [12] with free fatty acid content (%FFA) of 3.97% ± 0.01. Another purchased materials like montmorillonite K10 powder (CAS Number: 318-93-0) and FAME Mix C8 – C24 (CAS Number: CRM18918) were purchased form Sigma-Aldrich, iron(III) chloride, 98%, pure, anhydrous (CAS Number: 7705-08-0) was purchased from Acros Organics™, Methanol anhydrous (CAS Number: 67-56-1) was purchased from SupraSolv and silver nitrate ($AgNO_3$) (CAS Number: 7761-88-8) was purchased from Fischer Scientific.

Modification of catalyst

Method 1

The modification steps of montmorillonite K10 by using ion-exchange method were modified from Almadani et al. [10] and Sabri et al. [11]. 14% Fe in montmorillonite K10 was weighed by using $FeCl_3$. The mass of Fe was calculated using equation 1.

$$\text{mass of MClx} = (14\% \times 5\text{g of montmorillonite K10}) \times \frac{\text{molecular mass of MClx}}{\text{Atomic mass of M}} \quad (1)$$

Then, $FeCl_3$ was dissolved in 80 mL distilled water and mixed with 5 g of montmorillonite K10 clay. The mixture was let in stirring condition at 300 rpm for 7 hours at 80 °C with loose closed cap to avoid evaporation. After that, it was filtered and rinsed for a few times until no Cl^- ion was detected by $AgNO_3$ drop. This is to ensure the excessive ions were removed. The residue was collected and dried in the oven at 105 °C for overnight before allowed to be calcined at 500 °C for 4 hours.

Method 2

The same steps as in Method 1 were repeated by using 27% $FeCl_3$ and denoted as 27% Fe-MMT K10.

Method 3

The modification method was improved by weighing 20% Fe in montmorillonite K10 clay and left in stirring condition at a slightly lower temperature i.e. 40 °C as compared to method 1 and 2. The mixture was stirred until it became montmorillonite K10 by mass and dissolved in 25 mL of distilled water. The $FeCl_3$ solution was mixed with 5 g of slurry to allow the optimum ions exchange [14, 15]. It took 24 h to let the mixture became slurry. The purpose of slurry condition was to ensure the Fe rich environment surrounded the montmorillonite K10, hence promoted the ion exchange to occur. After that, the slurry mixture was washed with distilled water to remove excessive ions followed by dryng and calcination steps as in Method 1. The catalyst was labeled as 20% Fe-MMT K10. Figure 1 shows the steps of ion-exchange method.

Characterization of catalyst

X-ray diffractometers (XRD)

The diffraction patterns of montmorillonite K10 and the modified montmorillonite K10 were identified by using SHIMADZU X-ray Diffractometers (Lab X, XRD-6000). The XRD was calibrated with zero diffraction plate which was made up of silica. After that, dry sample was pressed compactly on the plate. The method of analyzing was set-up at continuous mode with the scan axis 2Theta/Theta, with the scan condition range 5 – 80°, step 0.02°, speed 2°/min and the preset time 0.6 sec while the voltage used was 30 kV and current 30 mA.

Scanning electron microscope with energy dispersive X-ray (SEM-EDX)

The morphology of catalysts was analyzed using Hitachi SU 1510 SEM. It was analyzed with magnification 1500x at 15 kV with 8.0 mm distance of laser tip to dental surface. Temperature-programmed desorption with ammonia desorption (TPD-NH_3): The Lewis and Brønsted acid sites were analyzed using Thermo Scientific TPDRO 1100. About 0.05 g of sample was placed in the reactor, treated under 150 °C.

Catalytic screening

The prepared solid acid catalysts were evaluated for the synthesis of biodiesel from WCO under identical reaction conditions; 6 hours reaction period, 12:1 methanol to oil molar ratio and 4% w/w catalyst at 130 °C *via* reflux system connected to circulatory chiller (Figure 2). Prior to the reaction, WCO was filtered to remove insoluble impurities and further heating above 105 °C for overnight to remove the moisture. This was to ensure no strange particle that may inhibit the reaction. The efficiency of catalyst was studied based on the acid conversion (Equation 2) and fatty acid methyl ester (FAME) yield (Equation 3).

$$\% \text{ Acid Conversion} = \frac{AV_i - AV_f}{AV_i} \times 100 \quad (2)$$

$$\% \text{ yield} = \frac{\text{mass of FAME}}{\text{mass of fed WCO}} \text{ X } 100 \quad (3)$$

Optimization of biodiesel production

From the catalytic screening, the most efficient catalyst capable of producing the highest FAME yield was considered to optimize the biodiesel production conventionally. Four parameters at three levels were studied and the conditions were varied at temperature of 100, 150 and 200 ºC; reaction time of 3, 6 and 9 hours; methanol to WCO ratio 10:1, 12:1 and 14:1 and catalyst loading 2, 4 and 6 wt.% [14, 16]. The acid conversion and FAME yield were calculated according to equation 2 and 3.

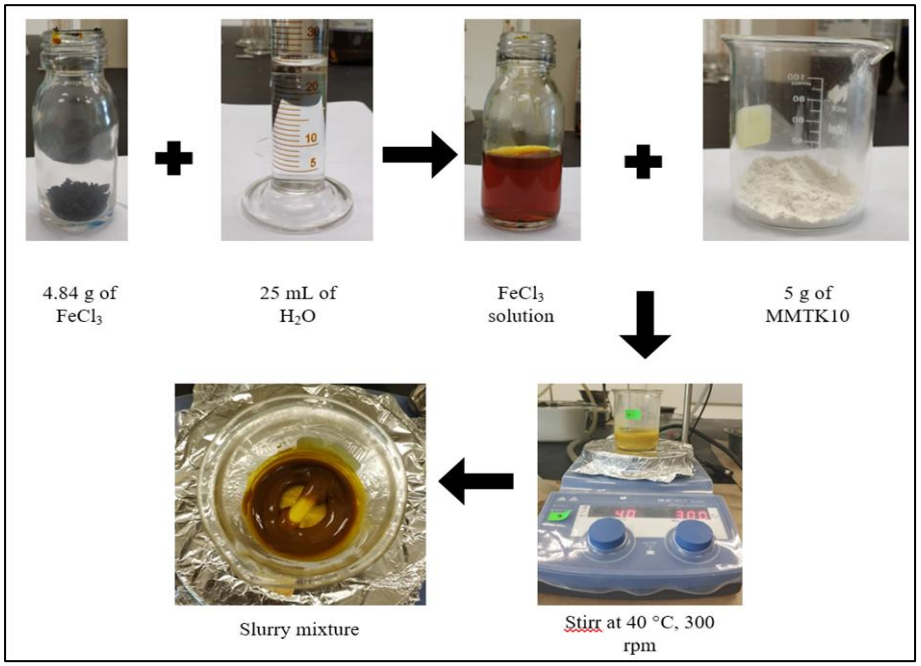


Figure 1. Catalyst modification steps

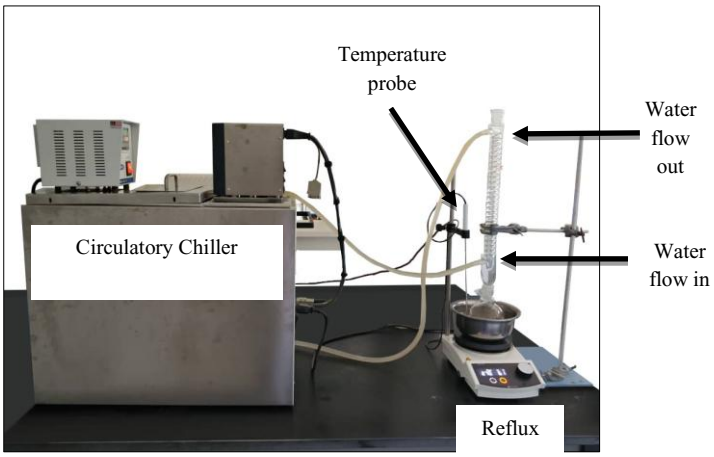


Figure 2. Reflux system to produce biodiesel

Results and Discussion

Characterization of catalyst

XRD patterns

XRD patterns of the samples are shown in Figure 3. The X-ray patterns reveal that the modified samples have structural characteristics nearly identical to the unmodified montmorillonite K10. This refers to the interlayer clay that was not affected by Fe^{3+} exchange reaction and the clay structure was retained during the exchange processes. The basal spacing of d001 observed for all samples at 8.8° (ca. 10.01 Å) indicated the presence of 2:1 (T:O:T) structure [17, 18]. This can perceive maintenance of reflection characteristic of this clay mineral. According to Michelle et al. [19], this is an important point, since the preservation of the crystal structure is essential for the material to maintain its thermal stability when applied in catalytic processes. Figure 3 shows that the montmorillonite K10 is composed of mixed phases and this result is in good agreement with previously reported data [20–22].

The treatment of the montmorillonite K10 with Fe^{3+} did not have a marked effect on its phase structure. The intensity of the diffraction peaks at 25.6° decreased when the samples were modified using method 3. It could be due to the leaching of existing cations from the octahedral layers of the montmorillonite K10 to exchange with new loaded metal [22] and crystallinity reduction. However, no diffraction peaks resulted from the metal compounds were observed, indicating that the metal cations were highly dispersed throughout the catalysts by the displacement of small cations [22]. Fe^{3+} gradually occupied the interlayer vacancies by the exchangeable metal ions in the montmorillonite K10 clay interlayers, thus retained the clay structure during the exchange processes. The findings of consistent structure after modification have been studied previously in the case of Cu^{2+}, Zn^{2+} and Fe^{3+} ions exchanged montmorillonite clay [10, 13].

SEM morphology

The SEM images of montmorillonite K10 and modified samples with 1500x magnification are depicted in Figure 4. From the morphology images, the montmorillonite K10 consisted of large particles. After modifications, the modified catalysts were found to be more compact compared to the original montmorillonite K10. This was due to the grinding steps that reduced the size of the particles. It can be clearly seen that the clay surface after exchanged process has non-aggregated morphology. Similar result was obtained by Almadani et al. in the modification of montmorillonite K10 with Fe [5]. In addition, the morphology of 20% Fe-MMT K10 seems to have

shinier particles compared to 14% and 27% Fe-MMT K10. This was probably contributed by the metal properties with higher composition.

EDX analysis

For screening purpose, all catalyst samples were characterized using EDX. Table 1 shows the elemental composition of montmorillonite K10 and modified samples from the EDX analysis, while Table 2 shows the change of Fe after the modification with Fe^{3+}. The result shows that the composition of Fe increased with the increase of metal concentration during modification. In method 3, the concentration of Fe increased by stirring period until it became slurry. It can be concluded that, the longer the stirring period during modification step, the higher the opportunity for the montmorillonite K10 to be exposed with the environment that possessed high Fe concentration.

XRF analysis

According to the EDX results, method 3 shows the highest Fe compositions in the catalyst. However, due to the large error of EDX, a confirmatory test using XRF was done on 20% Fe-MMT K10 for more accurate result. From Table 3, montmorillonite K10 primarily consisted of octahedral Al^{3+} and tetrahedral Si^{4+} with Na^{+}, K^{+}, Mg^{2+} and Ca^{2+} as exchangeable interlayer cations [14]. The decrease in Ca^{2+} and increase in Fe^{3+} compositions confirmed the occurrence of ion-exchange in the MMT clay. Similar result was found in the modification of montmorillonite K10 with erbium ion [22]. The decrease of other elements concentrations indicate that the erbium ions gradually occupied the interlayer vacancies by replacing H^{+} and exchangeable metal ions in the montmorillonite K10 clay interlayers.

TPD-NH_3 analysis

TPD of adsorbed ammonia is a reliable method to feature the acidity strength but not the nature (Brønsted or Lewis) of surface acid sites in solid acid catalysts [23]. Liu et al. revealed the definition of acidic sites as weak, medium and strong at desorption temperatures of 150-250 °C, 250-500 °C and >500 °C respectively [24]. Figure 5 and Table 4 show that montmorillonite K10 was readily consisted of small ammonia desorption band corresponding to the weak and strong acidic sites with total NH_3 desorption of 0.232 mmol/g. The result obtained was similar to Phukan et al., who obtained 0.20 mmol/g NH_3 desorption for montmorillonite K10 [25]. The trend of acidity increased from 14% Fe-MMT K10, followed by 27% and 20% Fe-MMT K10 was in line with the increasing Fe composition as shown in Table 2. Figure 5 shows that the most obvious NH_3 peak elevated by 20% Fe-MMT K10 with 14.261 mmol/g desorption. The modification of montmorillonite K10 with 20% Fe^{3+} was found to be better compared to the Fe-pillared montmorillonite done by Bharate et al. [26] with total acidity of 7.91 mmol/g. The maximum acidity possessed by method 3 correlated to the elemental compositions in Table 2 indicates the optimum cation exchange has occurred.

Catalytic screening

In order to determine the catalytic activity, esterification and transesterification reactions were done simultaneously on WCO by reflux system connected to rotatory chiller at 8 °C. An optimum condition of 130 °C, 6 h, 12:1 methanol to oil ratio and 4 wt.% catalyst loading were selected according to Munir et al. [27] and Olutoye et al. [16], to study the activity of montmorillonite K10 and its modified samples. As a control, a reaction without catalyst was carried out. The efficiency of the catalysts was summarized and compared in Figure 6 and Figure 7. From the results, it was proven that montmorillonite K10 has the potential to undergo simultaneous esterification and transesterification reactions to produce biodiesel compared to the reaction without catalyst as the biodiesel yield increased from 26.80 to 38.39% and the acid conversion increased from 13.15 to 18.22%. Among the reactions, 20% Fe-MMT K10 shows the highest biodiesel yield (84.58%) and acid conversion (37.56%) compared to 14% Fe-MMT K10 (yield: 66.54%; acid conversion: 24.86%) and 27% Fe-MMT K10 (yield: 69.32%; acid conversion: 25.02%). The results obtained show the correlation between metal cation concentration, elemental composition and acidity as the yield and acid conversion increased from 14% to 20% modifications accordingly. In conclusion, the modification of montmorillonite K10 with 20% Fe

concentration shows the optimum ion exchange which contributed to the most efficient catalyst with highest biodiesel yield and acid conversion, and eventually was selected for further investigation.

Optimization of biodiesel production

From the catalytic screening, 20% Fe-MMT K10 was selected as the most efficient catalyst to produce high biodiesel yield. The biodiesel production was optimized by varying four parameters; temperature (100 – 200 °C), reaction time (3 – 9 hours), catalyst loading (2-8 wt.%) and methanol to oil ratio (8 to 16:1) [14, 16]. The ability on esterification was examined (Figure 8) to ensure that the catalyst can convert the free fatty acid content as shown in Table 1 into FAME. 28.65% acid was converted at optimum condition of maximum biodiesel production. However, the optimization of esterification was not considered since the optimum condition for acid and triglyceride seemed to be different. In addition, it was quite difficult to find the optimum condition since WCO consisted of different types of FFA, which favor different conditions [27]. The benefit of selecting raw material with small amount of FFA content (3.97%) was it would give insignificant effect to produce high FAME yield. Furthermore, high FFA content would lead to the incomplete conversion of WCO due to the FFA conversion limitation. The esterification of FFA also produced water by product that would significantly decrease the ester production by hydrolysis [29]. In this case, since triglyceride is the main composition of WCO, more attention was given on the percentage yield of biodiesel compared to acid conversion.

The effect of temperature on the activity of 20% Fe-MMT K10 was investigated within the range from 100 °C to 200 °C, at fixed reaction time 6 hours, methanol to oil ratio 12:1 and catalyst loading 6 wt.%. From the results in Figure 9, it seems that the optimum temperature was 150 °C with yield 96.49%. At low temperature (100 °C), only 46.35% biodiesel yield was produced. The catalyst could not complete the conversion of WCO within 6 hours because less heat energy was supplied to the endothermic reaction, which is inadequate to activate the total sites of 4 wt.% catalyst [30]. Therefore, more reaction period is required. This situation was observed when Jung et al. optimized the reaction within 2 hours at 360 ºC [2]. However, when Olutoye et al. and Munir et al. used lower temperature between 120 – 150 ºC, 5 hours was taken to optimize the reaction [16, 27]. Beyond the optimum temperature, the yield decreased to 65.36% because reflux system did not really work to condense the vigorous vaporized methanol. Hence, the methanol took a very short time to contact with oil-catalyst phase before reverted. Thus, little contact between methanol and WCO restricted the complete conversion of WCO. In this case, a closed reactor is required.

The effect of reaction time on the activity of 20% Fe-MMT K10 was investigated within range 3 to 6 hours at fixed reaction temperature 150 °C, methanol to oil ratio 12:1 and catalyst loading 6 wt.%. At 3 hours reaction time, the biodiesel yield was low (60.24%) due to the incomplete reaction. As the reaction time increased to 6 hours, more contact time between reactants and catalyst became available, which led to more frequent collision and reached the optimum period. A further increase in reaction time beyond optimum condition (6 hours) decreased the biodiesel yield to 74.52%. It was probably due to the reverse transesterification [16].

The concentration of catalyst loading was studied between 2 and 6 wt.% at fixed reaction temperature of 150 °C, reaction time of 6 hours and methanol to oil ratio at 12:1. The results proved that the presence of 4 wt.% catalyst optimized the catalytic activity with 96.49% FAME yield. Below than 4 wt.%, the result showed a partial conversion of WCO by producing only 58.59% biodiesel due to the insufficient amount of catalyst [16]. The increasing amount of catalyst increased the surface contact between the catalyst and the reactants [31]. The excess catalyst led to a marked reduction in the product yield (65.20%) due to the viscous reaction medium [32]. It decreased the interaction between the catalyst and reaction components [33, 34].

The effect of methanol concentration was investigated by varying the methanol to oil ratio from 8:1 to 16:1 at fixed reaction temperature 150 °C, reaction period 6 hours and catalyst loading 4 wt.%. Methanol to oil ratio of 12:1 showed the optimum amount for the reaction with WCO. Below than 12:1 led to incomplete conversion even after 6 hours of reaction as part of methanol was dissolved by glycerol by product [35], thus produced lower biodiesel (59.51%) compared to the optimum condition. Meanwhile, beyond the limit, the biodiesel yield reduced to 66.13%. This is because the catalyst started to degrade due to the leaching of active components from the catalyst [36]. The absence of active components on the catalyst caused the catalyst inactivation to complete the reaction. However, the problem could be overcome by increasing the amount of catalyst, so it would be sufficient enough to enhance the activity of excess methanol with WCO towards biodiesel production [37].

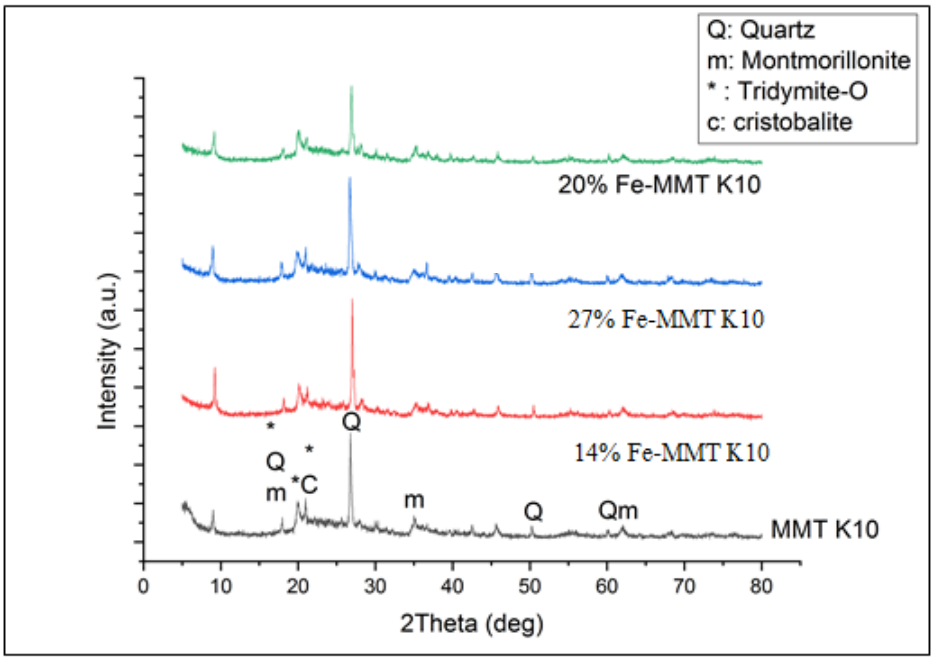


Figure 3. XRD patterns of montmorillonite K10 and its modified samples

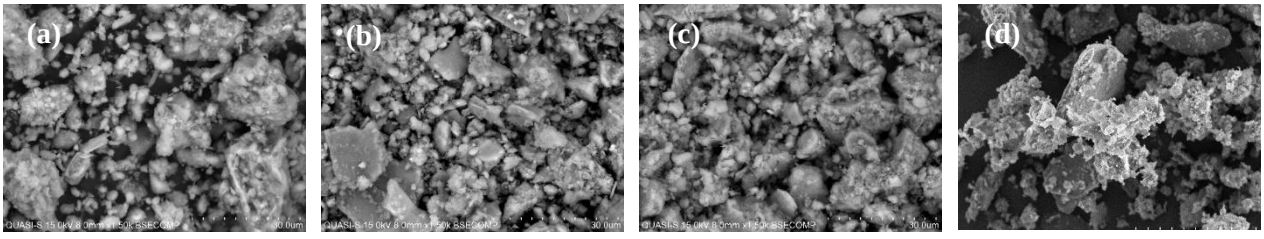


Figure 4. SEM morphology of montmorillonite K10 and its modifications with (b) 14% Fe^{3+}, (c) 27% Fe^{3+} and (d) 20% Fe^{3+}

Table 1. Elemental compositions of montmorillonite K10 and its modified samples

Type of catalyst	C	O	Mg	Al	Si	K	Fe
Montmorillonite K10	28.97 ± 3.03	53.52 ± 3.09	0.58 ± 0.08	2.97 ± 1.66	13.64 ± 1.52	0.39 ± 0.11	0.45 ± 0.13
14% Fe-MMT K10	26.30 ± 1.58	53.63 ± 0.80	0.41 ± 0.09	3.35 ± 1.06	14.51 ± 1.40	0.30 ± 0.03	1.66 ± 0.60
27% Fe-MMT K10	15.30 ± 1.35	54.69 ± 3.61	0.58 ± 0.10	3.32 ± 0.48	23.61 ± 2.59	0.31 ± 0.14	3.11 ± 0.66
20% Fe-MMT K10	26.13 ± 1.99	40.26 ± 2.50	0.94 ± 0.09	3.70 ± 1.07	22.72 ± 1.84	0.57 ± 0.09	5.68 ± 0.46

Table 2. Change of Fe composition in montmorillonite K10 after modification

Type of Catalyst	Change of Fe Composition (%)
Montmorillonite K10	0
14% Fe-MMT K10	1.21
27% Fe-MMT K10	2.66
20% Fe-MMT K10	5.23

Table 3. The elemental compositions of catalysts as determined by XRF

Elements	Mass Compositions (%)	
	Montmorillonite K10	20% Fe-MMT K10
Na	0.0992	0.156
Mg	0.739	0.705
Al	5.88	6.05
Si	28.0	30.0
K	1.04	1.30
Ca	0.211	0.0685
Fe	1.69	3.46
Zn	0.0026	0.0031

Table 4. Ammonia desorption of montmorillonite K10 and its modified samples

Type of Catalysts	NH_3 Desorption (mmol/g)		
	Weak Acidic Site	Strong Acidic Site	Total Acidity
MMT K10	0.090	0.142	0.232
14% Fe-MMT K10	1.350	0.220	1.57
27% Fe-MMT K10	1.494	-	1.494
20% Fe-MMT K10	-	14.261	14.261

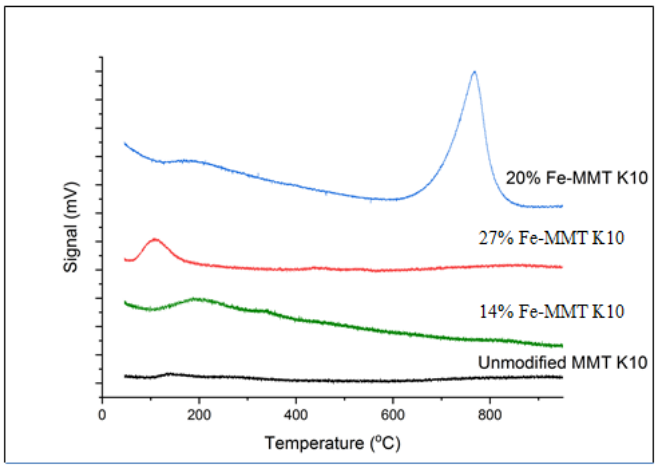


Figure 5. Peak of acidity of montmorillonite K10 and its modifications from TPD-NH_3 analysis

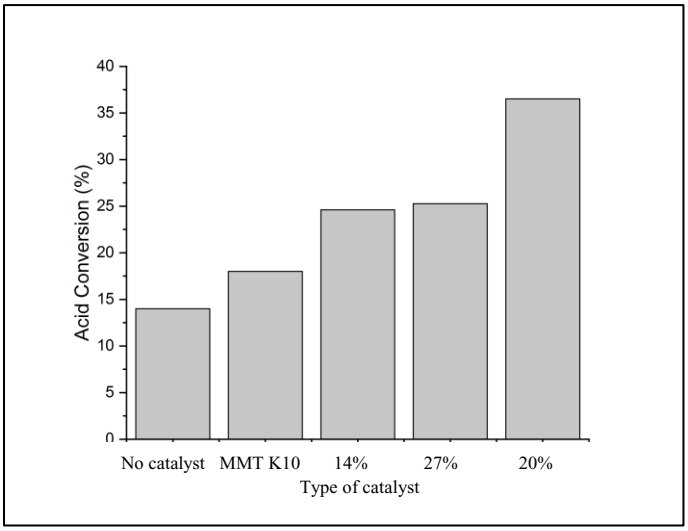


Figure 6. Acid conversion of WCO at 6 hours reaction period, 12:1 methanol to l molar ratio and 4% w/w catalyst at 130 °C

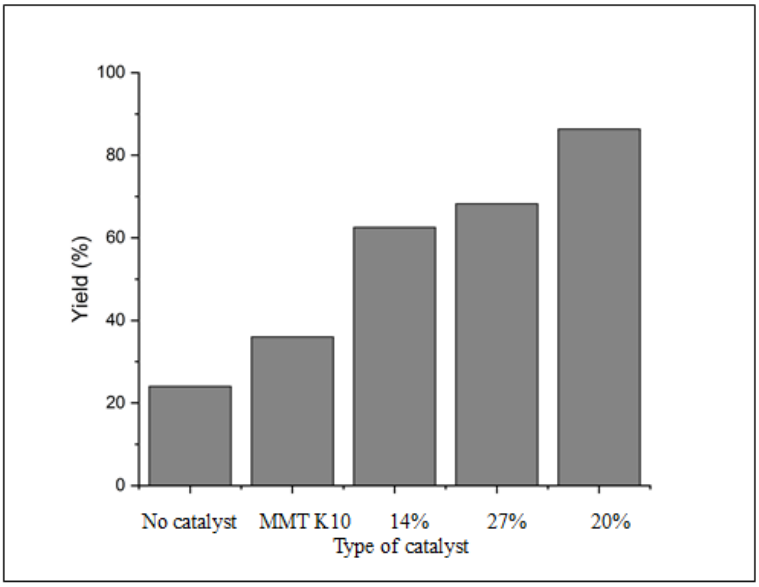


Figure 7. Percentage of FAME yield at 6 hours reaction period, 12:1 methanol to oil molar ratio and 4% w/w catalysts at 130 ^{o}C

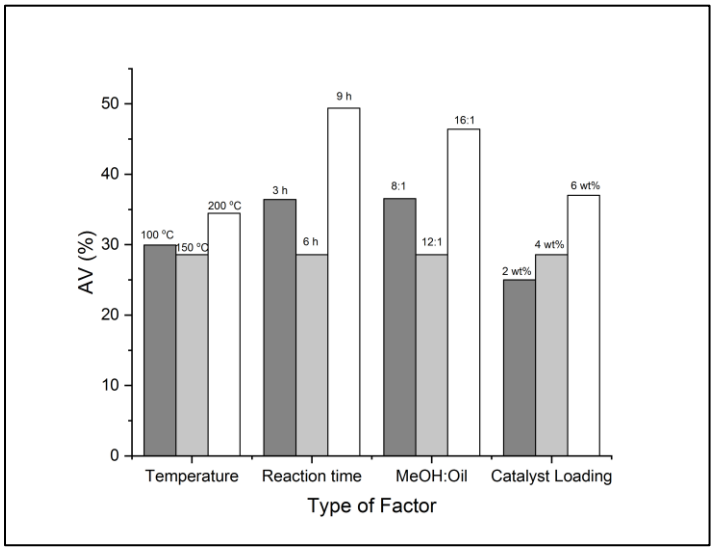


Figure 8. Effect of parameters in acid conversion

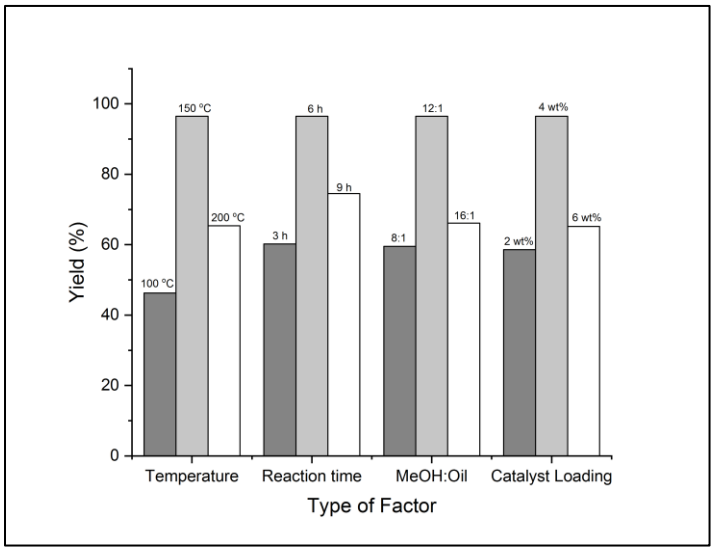


Figure 9. Effect of parameters in FAME yield

Conclusion

From the investigations, it was proven that the optimum ion exchange occurred with high concentration of Fe^{3+} within long stirring duration. It gave chance to the montmorillonite K10 interchange layer in contact with high concentration metal to exchange the ion. In this study, 20% Fe^{3+} to the mass of montmorillonite K10 optimize the ion exchange up to 5.68% with the highest acidity contribution up to 14.261 mmol NH_3/g compared to 14% and 27%. The catalytic improvement was proven by the catalytic screening in the application of biodiesel production. 20% Fe-MMT K10 produced the highest biodiesel of 84.58% with 37.56% acid conversion compared to the other two catalysts. After optimization, it was found that the optimum conditions for the activity of 20% Fe-MMT K10 in the biodiesel production was 150 °C, 6 hours, 12:1 methanol: oil and 4 wt.% catalyst loading with 96.49% biodiesel production. It proved that the modification of montmorillonite K10 with 20% Fe^{3+} successfully optimized the ion exchange capacity to enhance the acidity property, which was responsible in the esterification and transesterification reaction simultaneously.

Acknowledgement

The author acknowledges the Ministry of Education Malaysia (MOE) for the financial support through Grant USIM/FRGS/FST/055002/51417 and facilities provided by Faculty of Science and Technology, Universiti Sains Islam Malaysia (USIM) and Centre of Excellence for Catalysis Science and Technology (PutraCAT), Universiti Putra Malaysia (UPM).

References

1. Reddy, C. R., Nagendrappa, G. and Prakash, B. J. (2007). Surface acidity study of Mn^{+}-montmorillonite clay catalysts by FT-IR spectroscopy: Correlation with esterification activity. *Catalysis Communications*, 8(3): 241-246.
2. Jung, J. M., Oh, J. I., Park, Y. K., Lee, J. and Kwon, E. E. (2019). Biodiesel synthesis from fish waste via thermally-induced transesterification using clay as porous material. *Journal of Hazardous Materials*, 371: 27-32.

3. Bouguerra Neji, S., Trabelsi, M. and Frikha, M. H. (2009). Esterification of fatty acids with short-chain alcohols over commercial acid clays in a semi-continuous reactor. *Energies*, 2(4): 1107-1117.
4. Fatimah, I., Hidayat, A. and Setiawan, K. H. (2010). Preparation of aluminium pillared clay from Indonesian montmorillonite and its catalytic activity in bio-oil cracking. *Asian Journal of Chemistry*, 22(5): 3793.
5. Almadani, E. A., Radzi, S. M. and Harun, F. W. (2016). Stearic acid esters synthesized using iron exchanged montmorillonite K10 clay catalysts. *International Journal of Applied Chemistry*, 12(1): 62-67.
6. Kloprogge, J. T., Duong, L. V. and Frost, R. L. (2005). A review of the synthesis and characterisation of pillared clays and related porous materials for cracking of vegetable oils to produce biofuels. *Environmental Geology*, 47(7): 967-981.
7. Ma, Y., Wang, Q., Sun, X., Wu, C. and Gao, Z. (2017). Kinetics studies of biodiesel production from waste cooking oil using $FeCl_3$-modified resin as heterogeneous catalyst. *Renewable Energy*, 107: 522-530.
8. Harun, F. W., Almadni, E. A. and Ali, E. S. (2017). M-MMT K10 (M: Cu, Al and Fe) as catalysts for the esterification of acetic acid and stearic acid with methanol. In *Proceedings of the World Congress on Engineering and Computer Science,* 2: 606-609.
9. Liu, J., Yun, Z. and Gui, X. (2018). Ce/kaolin clay as an active catalyst for fatty acid methyl esters production from cottonseed oil in a new integrated apparatus. *Brazilian Journal of Chemical Engineering*, 35(1): 147-154.
10. Almadani, E. A., Harun, F. W., Radzi, S. M. and Muhamad, S. K. (2018). Cu^{2+} montmorillonite k10 clay catalyst as a green catalyst for production of stearic acid methyl ester: optimization using response surface methodology (RSM). *Bulletin of Chemical Reaction Engineering & Catalysis*, 13(1): 187-195.
11. Sabri, S. M. M., Yahya, S., Razali, F. H. and Harun, F. W. (2019). Modification of montmorillonite K10 with Al^{3+} and its potential in biodiesel production. *Malaysian Journal of Science Health & Technology,* 4: 30-34.
12. Yahya, S., Razali, F. H. and Harun, F. W. (2019). Physicochemical properties of refined palm cooking oil and used palm cooking oil. *Materials Today: Proceedings*, 19: 1166-1172.
13. Jha, A., Garade, A. C., Shirai, M. and Rode, C. V. (2013). Metal cation-exchanged montmorillonite clay as catalysts for hydroxyalkylation reaction. *Applied Clay Science*, 74: 141-146.
14. Liu, J., Wang, X. Q., Yang, B. B., Liu, C. L., Xu, C. L. and Dong, W. S. (2018). Highly efficient conversion of glucose into methyl levulinate catalyzed by tin-exchanged montmorillonite. *Renewable Energy*, 120: 231-240.
15. Ramesh, S., Prakash, B. J. and Bhat, Y. S. (2010). Enhancing Brønsted acid site activity of ion exchanged montmorillonite by microwave irradiation for ester synthesis. *Applied Clay Science*, 48(1-2): 159-163.
16. Olutoye, M. A., Wong, S. W., Chin, L. H., Amani, H., Asif, M. and Hameed, B. H. (2016). Synthesis of fatty acid methyl esters via the transesterification of waste cooking oil by methanol with a barium-modified montmorillonite K10 catalyst. *Renewable Energy*, 86: 392-398.
17. Dharne, S. and Bokade, V. V. (2011). Esterification of levulinic acid to n-butyl levulinate over heteropolyacid supported on acid-treated clay. *Journal of Natural Gas Chemistry*, 20(1): 18-24.
18. Harun, F. W., Almadani, E. A. and Radzi, S. M. (2016). Metal cation exchanged montmorillonite K10 (MMT K10): surface properties and catalytic activity. *Journal of Scientific Research and Development*, 3(3): 90-96.
19. Nascimento, A. R. D., Alves, J. A. B. L. R., Melo, M. A. D. F., Melo, D. M. D. A., Souza, M. J. B. D. and Pedrosa, A. M. G. (2015). Effect of the acid treatment of montmorillonite clay in the oleic acid esterification reaction. *Materials Research*, 18(2): 283-287.

20. Shimizu, K. I., Higuchi, T., Takasugi, E., Hatamachi, T., Kodama, T. and Satsuma, A. (2008). Characterization of Lewis acidity of cation-exchanged montmorillonite K-10 clay as effective heterogeneous catalyst for acetylation of alcohol. *Journal of Molecular Catalysis A: Chemical*, 284(1-2): 89-96.
21. Varadwaj, G. B. B. and Parida, K. M. (2013). Montmorillonite supported metal nanoparticles: an update on syntheses and applications. *RSC Advances*, 3(33): 13583-13593.
22. Wang, F. F., Liu, J., Li, H., Liu, C. L., Yang, R. Z. and Dong, W. S. (2015). Conversion of cellulose to lactic acid catalyzed by erbium-exchanged montmorillonite K10. *Green Chemistry*, 17(4): 2455-2463.
23. Wen, K., Zhu, J., Chen, H., Ma, L., Liu, H., Zhu, R., Xi, Y. and He, H. (2018). Arrangement models of Keggin-Al30 and Keggin-Al13 in the interlayer of montmorillonite and the impacts of pillaring on surface acidity: A comparative study on catalytic oxidation of toluene. *Langmuir*, 35(2): 382-390.
24. Liu, D., Yuan, P., Liu, H., Cai, J., Tan, D., He, H., Zhu, J. and Chen, T. (2013). Quantitative characterization of the solid acidity of montmorillonite using combined FTIR and TPD based on the NH_3 adsorption system. *Applied Clay Science*, 80: 407-412.
25. Phukan, A., Bhorodwaj, S. K., Sharma, P. P. and Dutta, D. K. (2018). Mesoporous aluminosilicate: Efficient and reusable catalysts for esterification of sec-butanol with acetic acid. *Journal of Porous Materials*, 25(1): 129-136.
26. Bharate, J. B., Sharma, R., Aravinda, S., Gupta, V. K., Singh, B., Bharate, S. B. and Vishwakarma, R. A. (2013). Montmorillonite clay catalyzed synthesis of functionalized pyrroles through domino four-component coupling of amines, aldehydes, 1, 3-dicarbonyl compounds and nitroalkanes. *RSC Advances*, 3(44): 21736-21742.
27. Munir, M., Ahmad, M., Saeed, M., Waseem, A., Rehan, M., Nizami, A.S., Zafar, M., Arshad, M. and Sultana, S. (2019). Sustainable production of bioenergy from novel non-edible seed oil (*Prunus cerasoides*) using bimetallic impregnated montmorillonite clay catalyst. *Renewable and Sustainable Energy Reviews*, 109: 321-332.
28. Olutoye, M. A., Wong, S. W., Chin, L. H., Amani, H., Asif, M. and Hameed, B. H. (2016). Synthesis of fatty acid methyl esters via the transesterification of waste cooking oil by methanol with a barium-modified montmorillonite K10 catalyst. *Renewable Energy*, 86, 392-398.
29. Babaki, M., Yousefi, M., Habibi, Z., Mohammadi, M., Yousefi, P., Mohammadi, J. and Brask, J. (2016). Enzymatic production of biodiesel using lipases immobilized on silica nanoparticles as highly reusable biocatalysts: effect of water, t-butanol and blue silica gel contents. *Renewable Energy*, 91: 196-206.
30. Ayoub, M., Ullah, S., Inayat, A., Bhat, A. H. and Hailegiorgis, S. M. (2016). Process optimization for biodiesel production from waste frying oil over montmorillonite clay k-30. *Procedia Engineering*, 148: 742-749.
31. Tan, Y. H., Abdullah, M. O., Nolasco-Hipolito, C. and Taufiq-Yap, Y. H. (2015). Waste ostrich-and chicken-eggshells as heterogeneous base catalyst for biodiesel production from used cooking oil: Catalyst characterization and biodiesel yield performance. *Applied Energy*, 160: 58-70.
32. Maneerung, T., Kawi, S., Dai, Y. and Wang, C. H. (2016). Sustainable biodiesel production via transesterification of waste cooking oil by using CaO catalysts prepared from chicken manure. *Energy Conversion and Management*, 123: 487-497.
33. Liu, H., shuang Guo, H., jing Wang, X., zhong Jiang, J., Lin, H., Han, S. and Peng Pei, S. (2016). Mixed and ground KBr-impregnated calcined snail shell and kaolin as solid base catalysts for biodiesel production. *Renewable Energy*, 93: 648-657.
34. Negm, N. A., Sayed, G. H., Yehia, F. Z., Habib, O. I. and Mohamed, E. A. (2017). Biodiesel production from one-step heterogeneous catalyzed process of Castor oil and Jatropha oil using novel sulphonated phenyl silane montmorillonite catalyst. *Journal of Molecular Liquids*, 234: 157-163.

35. Ghoreishi, S. M. and Moein, P. (2013). Biodiesel synthesis from waste vegetable oil via transesterification reaction in supercritical methanol. *The Journal of Supercritical Fluids*, 76: 24-31.
36. Refaat, A. A. (2011). Biodiesel production using solid metal oxide catalysts. *International Journal of Environmental Science & Technology*, 8(1): 203-221.
37. Liu, X., He, H., Wang, Y., Zhu, S. and Piao, X. (2008). Transesterification of soybean oil to biodiesel using CaO as a solid base catalyst. *Fuel*, 87(2): 216-221.

Malaysian Journal of Analytical Sciences (MJAS)
Published by Malaysian Analytical Sciences Society

THERMAL STABILITY AND POROSITY OF REDUCED GRAPHENE OXIDE/ZINC OXIDE NANOPARTICLES AND THEIR CAPACITY AS A POTENTIAL OXYGEN REDUCTION ELECTROCATALYST

(Kestabilan Haba dan Keliangan Partikel Nano Grafin Oksida Terturun/Zink Oksida dan Keupayaannya sebagai Pemangkin Elektro Tindakbalas Penurunan Oksigen)

Karthi Suresh and Farhanini Yusoff*

Faculty of Science and Marine Environment,
Universiti Malaysia Terengganu, 21030 Kuala Nerus, Terengganu, Malaysia

**Corresponding author: farhanini@umt.edu.my*

Received: 30 March 2020; Accepted: 2 May 2020; Published: 9 June 2020

Abstract

Zinc oxide/reduced graphene oxide (ZnO/rGO) nanoparticle were synthesized through a facile one-pot method. The use of rGO was initiated due to presence of more active sites compared to graphene oxide (GO). Physical characterization such as Fourier transform infrared spectroscopy (FTIR) confirmed the presence of ZnO stretching peak in the spectrum of rGO, suggesting that nanoparticles coexisted as a component. Thermo-gravimetric analysis (TGA) confirmed the stability of nanoparticles as 68.91% of the nanoparticles remained after exposure to high temperature of 900 $^{\circ}$C. The nanoparticles were under mesopore region when studied using Brunauer-Emmett-Teller (BET), with the pore volume of 10.4 nm. Drops of ZnO/rGO were drop-casted onto a bare glassy carbon electrode (GCE) to study the electrochemical behavior of the nanoparticles using cyclic voltammetry (CV) and electrochemical impedance spectroscopy (EIS) as well as oxygen reduction reaction (ORR). Electrochemical studies on the modified electrode of ZnO/rGO/GCE exhibited greater current responses, stable electron transfer and also lower charge transfer resistance compared to a bare GCE. The nanoparticles demonstrated the potential application as an electrocatalyst with high yield rate in (ORR). Hence, the nanoparticles could be used as a substitute for precious metal usage, such as platinum, in current production and overcoming high costs.

Keywords: electrochemistry, nanoparticle, electrolyte, graphene, zinc oxide

Abstrak

Nanopartikel zink oksida/grafin oksida terturun (ZnO/rGO) disintesis dengan cara satu pot. rGO digunakan kerana mempunyai tapak aktif yang banyak berbanding grafin oksida (GO). Pencirian fizikal yang dilaksanakan menggunakan spektroskopi inframerah transformasi Fourier (FTIR) mengesahkan kehadiran ZnO di spektrum rGO, yang mencadangkan kedua partikel ini wujud sebagai satu komponen sebati. Analisa gravimetrik terma (TGA) mencatatkan kestabilan nanokomposit dengan lebihan 68.91% di penghujung analisa 900 ^{o}C, dan nanokomposit disahkan sebagai komposit liang meso melalui keputusan analisa BET, dengan saiz liang 10.4 nm. Elektrod karbon berkaca (GCE) digunakan dan diubahsuai menggunakan ZnO/rGO dengan teknik salutan titisan kemudiannya dikaji pencirian elektrokimia menggunakan kitaran voltametri (CV), spektroskopi elektrokimia impedans (EIS) dan tindak balas penurunan oksigen (ORR) yang menunjukkan respon elektrik yang bagus dan pemindahan

elektron yang stabil serta kurang rintangan pemindahan kuasa apabila dibandingkan dengan GCE. Komposit nano menunjukkan keupayaan pengganti sebagai pemangkin elektro dan kadar hasil tinggi di ORR yang berkemungkinan menjadi pengganti logam berharga seperti platinum dan dapat mengurangkan kos penghasilan.

Kata kunci: elektrokimia, nanopartikel, elektrolit, grafin, zink oksida

Introduction

The demand of energy for essential consumption increases tremendously in response to uncontrolled growth of the human population in the world. By focusing on renewable energy, fuel cells have been invented with platinum as the common material [1]. Despite its optimal energy yield, platinum is far more expensive compared to other precious metals. In addition, the electrode used in the production of fuel cells cannot be recovered completely and the amount of platinum used is extensive to reach the desired power densities, and this contributes to major economic issues [2]. Moreover, pollution occurs when using a platinum electrode, which releases carbon dioxide (CO_2) during the reaction.

Therefore, the idea of producing a relatively inexpensive electrocatalyst that can be used as a substitute or an even better conductor than platinum, and with better stability and porosity has been put forward [3]. The synthesized nanoparticles consist of zinc oxide (ZnO) and reduced graphene oxide (rGO). Graphene is a two-dimensional carbon allotrope that has been considered as a research interest due to its unique structure and physicochemical properties. In this research, rGO was prioritized by reducing the synthesized graphene oxide (GO) using hydrazine hydrate through a one-pot method. The reduction of GO causes loss in the hydroxide (-OH) functional group, hence creating more active sites in the structure [4].

The unification of nanoparticles with graphene-related materials, in this case ZnO and rGO as nanoparticles have recently become a trend in research due to their enhanced functionalities that cannot be achieved by either component alone. Previous research on fabricating metal oxide/graphene nanoparticle enhanced the electrocatalytic activity [5].

The porosity and thermal stability of nanoparticles have been studied thoroughly as these criteria affect the electrochemical capacitance of nanoparticles. A pore volume that fits perfectly into the mesopore region of 2-50 nm is said to be optimal as energy density will be higher and applicable in electrochemistry. Thermal stability examines the strength if the nanoparticles can be used at higher temperature during energy production. These three aspects play a major role in the nanoparticles, especially when dealing with energy and electrochemistry as these properties affect the kinetics of ionic diffusion within the matrix, electron transfer, and capacitance of the nanoparticles [6]. Mesoporosity is preferred for better energy capacitance and electron transfer as a larger (macroporosity) or smaller (microporosity) size of particle directly affect energy density.

Materials and Methods

Chemicals and reagents

Graphite powder was used to synthesize GO using modified Hummers' method [7]. Zinc nitrate ($Zn[NO_3]_2$) and hydrazine hydrate were purchased from Sigma Aldrich to synthesize of nanoparticles using a one-pot method. All the chemicals purchased were of analytical grade reagents and no further purification was required. Deionized water of 18.2 MΩcm was used for the purpose of diluting and washing the substances.

Physical characterization

The powder form of ZnO/rGO was characterized using several instruments to determine the purity of the obtained powder. The characterization was done using Fourier transform infrared spectroscopy (FTIR) to identify the functional groups available in the nanoparticles, scanning electron microscope (SEM) to study the morphological structure, thermal gravimetric analysis (TGA) to study the rate of mass loss in samples and thermal stability, and also Brunauer-

Emmett-Teller (BET) analysis to study the surface area and porosity of the synthesized nanoparticles.

Electrochemical characterization

To determine the electrocatalytic activity of the synthesized nanoparticles, cyclic voltammetry (CV), electrochemical impedance spectroscopy (EIS) and oxygen reduction reaction (ORR) were studied using a potentiostat galvanostat (PG) instrument. A glassy carbon electrode (GCE) was used as the modified electrode in this method. The electrode was polished using alumina oxide to ensure its purity. About 1 mg of ZnO/rGO powder was sonicated with 10 ml of deionized water for 30 minutes. Then, 10 µL of the solution was dropped onto the GCE and allowed to dry. After that, the electrocatalytic activity was studied with 5.0 mM of potassium ferricyanide ($K_3[Fe(CN)_6]$) in 0.1 M of potassium chloride (KCl) electrolyte solution using the modified electrode with potential window of -0.2 to 0.8 V. For ORR, the electrolyte was purged with oxygen (O_2) for 10 minutes for oxygen saturation condition.

Synthesis of graphene oxide

Graphene oxide (GO) was synthesized using modified Hummers' method [7, 8]. Graphite powder was added to 0.5 g of sodium nitrate ($NaNO_3$) and concentrated sulfuric acid (H_2SO_4) in a volumetric flask that was kept under ice bath under continuous stirring for 30 minutes. Potassium permanganate ($KMnO_4$) was gradually added into the solution and stirred for 2 hours. Next, the paste was slowly diluted with 45 mL of deionized water and the reaction temperature increased to 98 $^{\circ}$C. The stirring was continued and further dilution with deionized water was done. Hydrogen peroxide (H_2O_2) was used to stop the reaction. About 5% of hydrochloric acid (HCl) and deionized water were used to rinse the solution and then centrifuged for purification. After centrifugation, the solution was filtered and dried under vacuum at room temperature [4].

Facile one-pot synthesis of ZnO/rGO

Zinc nitrate was added into a beaker containing 50 mL of deionized water and stirred in an ice bath for 1 hour. Later, 0.1 g of GO was mixed with 100 mL of deionized water and stirred for 30 minutes. After that, 0.5 g of sodium hydroxide (in pallets) and 0.3 mL of hydrazine hydrate were added into the beaker and stirred vigorously for another 30 minutes. Hydrazine hydrate was added into the solution for further reduction of GO's hydroxyl functional group. The mixture was left overnight for precipitation. Then, the precipitate was filtered using a vacuum pump and washed with deionized water to adjust the pH to neutral. Finally, the precipitate was dried in an oven for 12 hours at 60 $^{\circ}$C for further use.

Results and Discussion

The functional groups of all synthesized materials were studied using FTIR. The spectra of graphite, GO and ZnO/rGO are shown in Figure 1. Graphite (1a) possessed a tiny, almost unidentified peak at 1610 cm^{-1} of C=C in its spectrum, describing its carbon characteristics. Other peaks were not identified in the spectrum (1a), possibly due to the miniscule width of the peak [9]. A broad peak of 3400 cm^{-1} was observed in the spectra of GO in Figure 1(b) indicating the presence of hydroxyl (-OH) functional group, which later shrank in the spectrum of ZnO/rGO (1c). This proved that reduction occurred as well as the elimination of functional groups. The peaks at 1718 cm^{-1} and 1623 cm^{-1}, and also 1225 cm^{-1} and 1054 cm^{-1} in the spectrum of GO represent the functional groups of C=O (amide), aromatic C=C, and stretching vibration of C–OH groups, respectively [8]. Meanwhile in the ZnO/rGO spectrum, there were only peak at 1589 cm^{-1} for C=O (amide) and 1384 cm^{-1} for aromatic C=C originated from GO. Other functional groups mainly C-OH groups were reduced during reduction process. The peak at 476 cm^{-1} in Figure 1(c) shows the presence of ZnO in the spectra of ZnO/rGO, indicating the co-existence of nanoparticles. The spectra of FTIR was further supported by the data of X-ray diffraction (XRD) presented in previous articles [5].

Scanning electron microscope (SEM) explains the morphological structure of the nanoparticles produced. Figure 2(a) shows the image of graphite, which can be seen as flaky layers, and later changed its structure into a rough and wrinkled surface (Figure 2b) when synthesized into GO. The microscopic image of

ZnO/rGO shown in 2(c) consist of a sharp tentacle-star-like structure observed coating the GO sheet which now exists as rGO [5]. From these morphological images, it can be concluded that the desired product is achieved with a larger surface area and more active sites are produced, which are useful for increased catalytic activity [10].

In TGA, the nanoparticles were exposed at 30 °C and heated constantly at the range of 10 °C/min in N_2 atmosphere until the maximum stop temperature of 900 °C. As observed in Figure 3(a), first degradation occurred consistently up to about 100 °C for all graphite, GO, and ZnO/rGO with the percentage loss of mass of 4.55%, 17.88%, and 8.21%, respectively. This indicates the loss of water vapors, hydroxyl (-OH) groups and residuals in the nanoparticles [11]. Graphite showed a steady decrease until 620 °C, and a rapid degradation was later observed until complete combustion at 850 °C. This might be due to the combustion of carbon-carbon skeletons [12]. A significant drop of GO mass, (approximately 49.60%) was observed at 670 °C which might be resulted from further loss of hydroxyl groups attached to the graphene layer [13]. Meanwhile, ZnO/rGO was stable throughout the end temperature with a loss of mass about 31.09%. Therefore, it is proved that the stability of ZnO/rGO nanoparticles is better compared to GO and the reduction of GO gives better thermal stability [5, 14, 15].

The BET analysis measures the specific surface area of nanoparticles by studying the physical adsorption of N_2 of the material. In this analysis, the bath temperature used was 78 K. The result of the analysis (as tabulated in Table 1) show that the surface area for GO is the greatest amongst other materials, with a surface area of 304.43 m^2/g, whereas ZnO/rGO has a surface area of 35.62 m^2/g. Lower surface area could be linked with the drastic reduction of hydroxyl functional group when one-pot synthesis was carried out. However, GO is categorized as macropores with pore volume of 1.425 cm^3/g, which is about 143 nm when the Barrett-Joyner-Halenda (BJH) pore volume was studied. ZnO/rGO recorded the pore volume of 0.104 cm^3/g, which is in the mesopore region of the analysis. Macropores are not suitable in the study of electrochemistry as it may disrupt electron transfer due to larger pore size. Mesoporosity is the optimal condition in the aspect of energy and capacitance, as well as electron transfer [16]. The condition is applicable in quick energy transfer and storage. Based on the physisorption isotherm plotted in Figure 3(b), the hysteresis loop of H2 is for GO and the hysteresis loop for H1 is for ZnO/rGO.

CV explains the electrochemical efficiency of the nanoparticles in Figure 4(a). A bare GCE was used which was later modified into a nanoparticle-deposited modified electrode by drop-casting GO and ZnO/rGO. The current used in this study was 50 mV standard for all three experiments. The analysis showed that ZnO/rGO possessed greater current responses compared to the bare GCE and GO. The peak potential separation ($\Delta E_P = E_{\text{Anodic peak}} - E_{\text{Cathodic peak}}$) of ZnO/rGO is identical to GO and bare GCE at the value of $\Delta E_P = 150$ mV, suggesting that the electron transfer is stable and rapid with a reversible process [5, 17].

EIS is conducted to determine the electron mass transfer between the electrolyte and electrode surface. Charge transfer resistance (R_{ct}) represents the kinetic resistance of charge transfer in the redox reaction between the electrode and the electrolyte [18]. As seen in Figure 4(b), the R_{ct} that is represented the semicircle in the Nyquist plot becomes smaller. ZnO/rGO modified electrode possessed discrete and incomplete semicircle compared to the bare GCE electrode, hence providing data that the R_{ct} is higher in the bare GCE compared to the modified electrode Table 2 tabulates the data of R_{CT} obtained from the software based on the Nyquist plots of experimented modified electrodes. The R_{ct} decreased as the bare GCE electrode was modified to GO and then to ZnO/rGO. Lower R_{CT} indicates less resistance in electron transfer between the electrode surfaces [19, 20].

Figure 5 portrays the cyclic voltammogram of the modified electrode ZnO/rGO/GCE in ORR studied under condition of 0.1 M of potassium hydroxide (KOH) solution as the electrolyte. The study of ORR is important in electrochemical analysis as it provides

information on catalytic activity in reduction process [6, 21]. Two electrolyte bases were prepared; one was purged with N_2 and another base was purged with O_2, for 10 minutes. The voltammograms plotted in Figure 5(b) do not show any peak in nitrogen saturated electrolyte, indicating no redox reaction occurred in that condition. A single cathode reduction peak was observed in oxygen saturated electrolyte, indicating an irreversible process of O_2 reduction at the electrocatalyst [3]. The ZnO/rGO/GCE modified electrode (Figure 5a) shows better electrocatalytic performance compared to the GO/GCE modified electrode. The cathode peak observed indicates higher and better current density of the ZnO/rGO/GCE electrode compared to the GO/GCE electrode. This shows the high affinity of the electrode towards O_2 saturated condition [16].

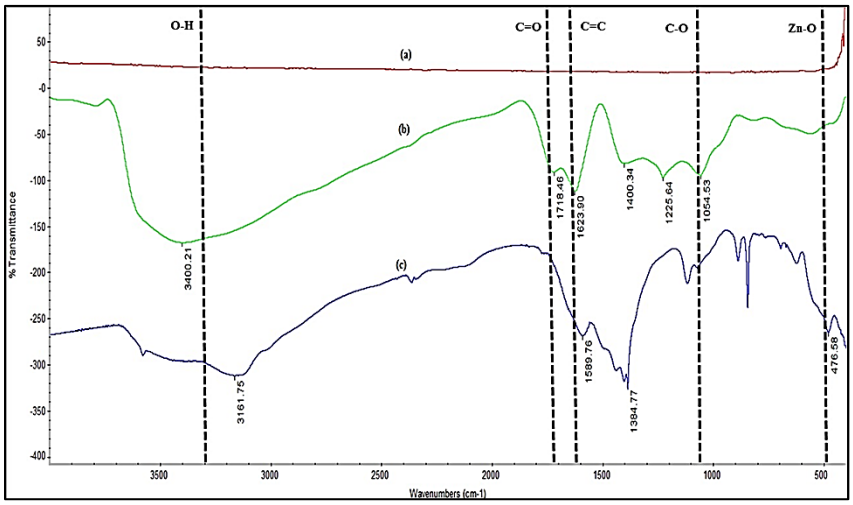


Figure 1. FTIR spectra of (a) graphite, (b) GO, and (c) ZnO/rGO

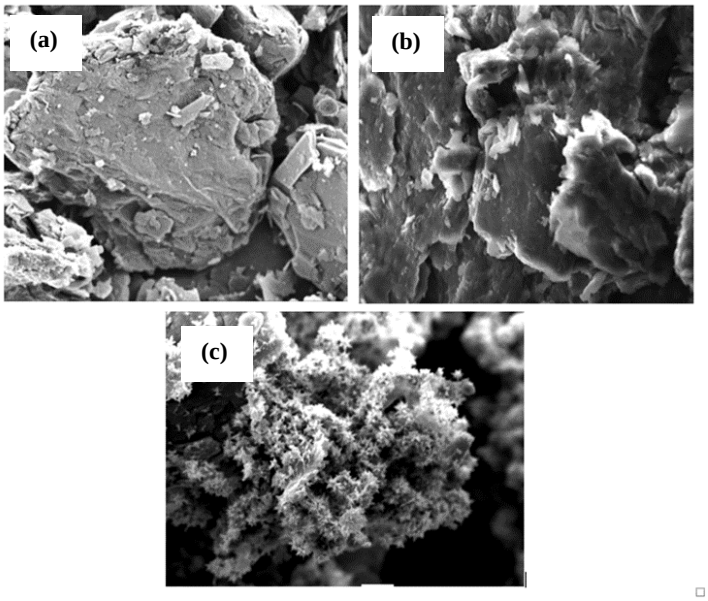


Figure 2. SEM images of (a) graphite, (b) GO, and (c) ZnO/rGO

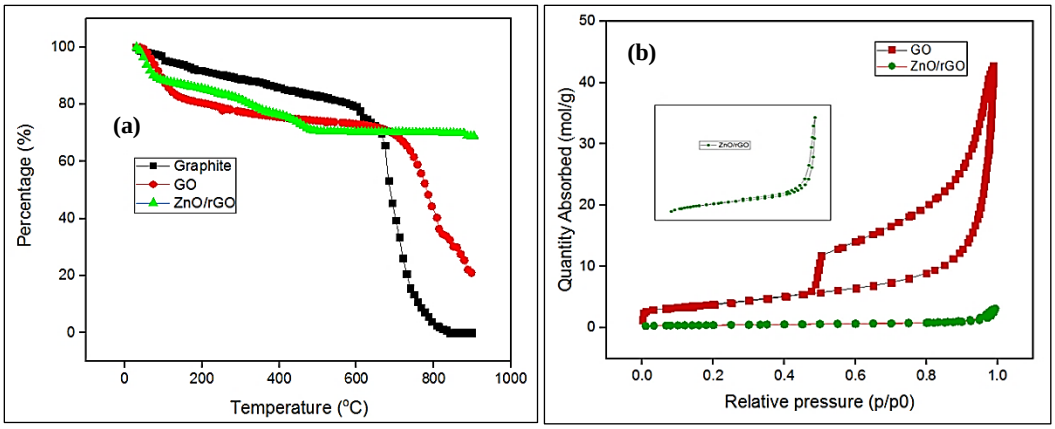


Figure 3. (a) TGA comparison between GO and ZnO/rGO and (b) BET isotherm graph, (Inset) a clearer graph of ZnO/rGO

Table 1. BET and BJH analyses for surface area, pore volume, and pore adsorption diameter

Sample	BET Surface Area (m^2/g)	BJH Pore Volume (cm^3/g)	Average Adsorption Pore Diameter (4V/A)
GO	304.43	1.425	194.91
ZnO/rGO	35.62	0.104	121.51

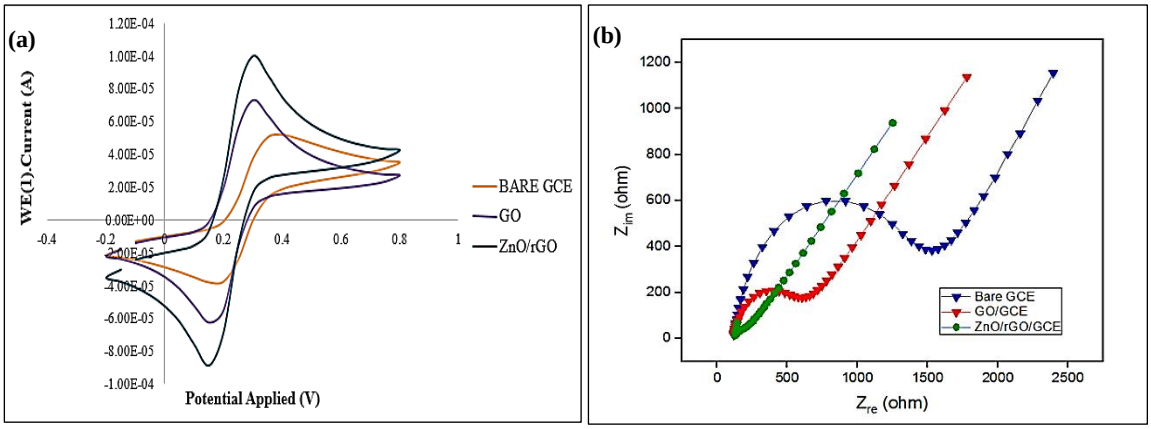


Figure 4. (a) CV comparison between bare GCE, GO, and ZnO/rGO and (b) EIS comparison between bare GCE, GO, and ZnO/rGO

Table 2. R_{ct} values of bare GCE, GO/GCE, and ZnO/rGO/GCE

Electrodes	Charge Transfer Resistance, R_{CT} ($\Omega cm^{2)}$
Bare GCE	1586.03
GO/GCE	698.58
ZnO/rGO/GCE	160.18

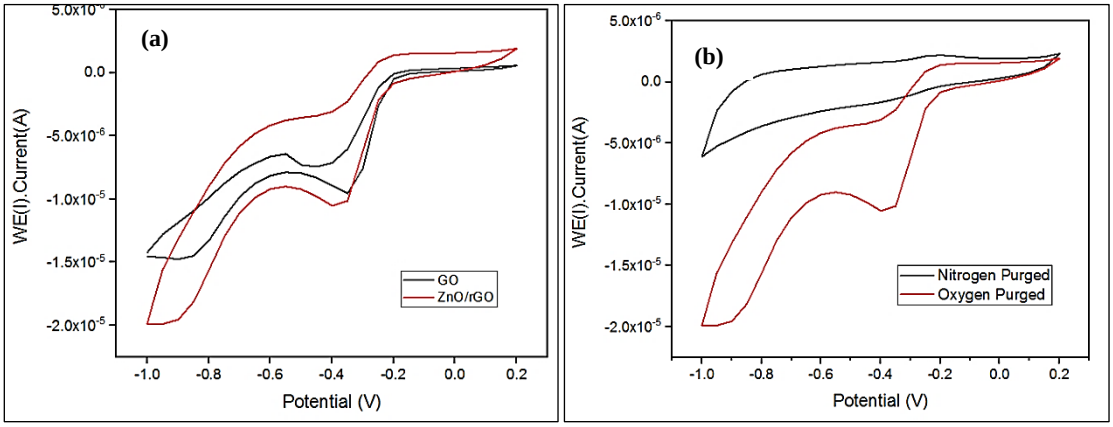


Figure 5. a) CV of ORR of GO with ZnO/rGO and (b) comparison of ZnO/rGO voltammetry with both N_2 and O_2 purged into the electrolytes

Conclusion

The synthesis of ZnO/rGO powder was carried out through a facile one-pot synthesis method. The analysis of FTIR, SEM, TGA, and BET showed that the desired product was successfully synthesized. The FTIR spectra of ZnO/rGO show a great reduction in the broad peak of 3400 cm^{-1} compared to the spectra of GO, proving that reduction occurred by the elimination of hydroxyl (-OH) functional groups due to the addition of $Zn(NO_3)_2$ and hydrazine hydrate. The TGA analysis showed that ZnO/rGO is thermally stable and suitable for use at high temperature condition. The acquired results of CV show greater current responses with rapid and stable electron transfer with the value of ΔE_P obtained and smaller R_{CT} value for the modified electrode, indicating lower resistance during electron transfer. The ORR analysis portrayed an increase at the cathode peak of ZnO/rGO ascribing optimum surface area to volume ratio and possessing high affinity toward oxygen. The nanoparticles are believed to be a better option to be used as a potential electrocatalyst with better stability as proven in this study.

Acknowledgement

Authors wish to thank the Ministry of Education Malaysia for the Fundamental Research Grant Scheme (FRGS Vot: 59472) provided as financial support in conducting the research. Authors also acknowledge the Faculty of Science and Marine Environment, University Malaysia Terengganu for the research facilities and instrumentation provided.

References

1. Abdalla, A. M., Hossain, S., Azad, A. T. and Petra, P. M. I. (2018). Nanomaterials for solid oxide fuel cells: A review. *Renewable and Sustainable Energy Reviews*, 82: 353-368.
2. Wang, Y., Leung, D. Y. C., Xuan, J. and Wang, H. (2017). A review on unitized regenerative fuel cell technologies, Part B: Unitized regenerative alkaline fuel cell, solid oxide fuel cell, and micro fluidic fuel cell. *Renewable and Sustainable Energy Reviews*, 75: 775-795.
3. Muhamad, N. B., Khairul, W. M. and Yusoff, F. (2019). Synthesis and characterization of poly(3,4-ethylenedioxythiophene) functionalized graphene with gold nanoparticles as a potential oxygen reduction electrocatalyst. *Journal of Solid State Chemistry*, 275: 30-37.
4. Stankovich, S., Dikin, D. A., Piner, R. D., Kohlhaas, K. A., Kleinhammes, A., Jia, Y. and Wu, Y. (2007). Synthesis of graphene-based nanosheets via chemical reduction of exfoliated graphite oxide, *Carbon,* 45: 1558-1565.
5. Yusoff, F., Khing, N. T., Hao, C. C., Sang, L. P., Basyirah, N. A. and Saleh, N. M. (2018). The electrochemical behavior of zinc oxide/reduced graphene oxidecomposite electrode in dopamine. *Malaysian Journal of Analytical Sciences*, 22(2): 227-237.

6. Chen, Y. L., Hu, Z. A., Wang, H. W., Zhang, Z, Y., Yang, Y. Y. and Wu, H. Y. (2011). Zinc oxide/reduced graphene oxide composites and electrochemical capacitance enhanced by homogeneous incorporation of reduced graphene oxide sheets in zinc oxide matrix. *The Journal of Physical Chemistry*, 115(5): 2563-2571.
7. Hummers, W. S. and Offeman, R. E. (1958). Preparation of graphitic oxide. *Journal of the American Chemical Society*, 80(6): 1339.
8. Teymourian, H., Salimi, A. and Khezrian, S. (2013). Fe_3O_4 magnetic nanoparticles/reduced graphene oxide nanosheets as a novel electrochemical and bioeletrochemical sensing platform. *Biosensors and Bioelectronic*, 49: 1-8.
9. Du, W., Lu, J., Sun, P., Zhu, Y. and Jiang, X. (2013). Organic salt-assisted liquid-phase exfoliation of graphite to produce high-quality graphene. *Chemical Physics Letters*, 568-569: 198-201.
10. Deemer, E. M., Kumar, P., Manciu, F. S., Botez, C. E., Hodges, D. R., Landis, Z. and Chianelli, R. R. (2017). Consequence of oxidation method on graphene oxide produced with different size graphite precursors. *Materials Science & Engineering B*, 224: 150-157.
11. Papageorgiou, D. G., Kinloch, I. A. and Young, R. J. (2017). Mechanical properties of graphene and graphene-based nanoparticles. *Progress in Materials Science*, 90: 75-127.
12. Zaghib, K., Song, X. and Kinoshita, K. (2001). Thermal analysis of the oxidation of natural graphite: Isothermal kinetic studies. *Thermochimica Acta*, 371(1-2): 57-64.
13. Ryu, S. H. and Shanmugharaj, A. M. (2014). Influence of hexamethylene diamine functionalized graphene oxide on the melt crystallization and properties of polypropylene nanoparticles. *Materials Chemistry and Physics*, 146(3): 478-486.
14. Tiwari, A. and Hihara, L. H. (2009). Thermal stability and thermokinetics studies on silicone ceramer coatings: Part 1-inert atmosphere parameters. *Polymer Degradation and Stability*, 94(10): 1754-1771.
15. Huang, S. and Sheng, J. J. (2017). An innovative method to build a comprehensive kinetic model for air injection using TGA/DSC experiments. *Fuel,* 210: 98-106.
16. Yusoff, F., Mohamed, N., Aziz, A. and Ghani, S. A. (2014). Electrocatalytic reduction of oxygen at perovskite (BSCF)-MWCNT composite electrodes. *Materials Sciences and Applications*, 5(04): 199-211.
17. Nicholson, R. S. (1965). Theory and application of cyclic voltammetry for measurement of electrode reaction kinetics. *Analytical Chemistry*, 37(11):1351-1355.
18. Palanisamy, S., Ezhil Vilian, A. T. and Chen, S. M. (2012). Direct electrochemistry of glucose oxidase at reduced graphene oxide/zinc oxide composite modified electrode for glucose sensor. *International Journal of Electrochemical Science,* 7(3): 2153-2163.
19. Tehrani, R. M. A., Ghadimi, H. and Ab Ghani, S. (2013). Electrochemical studies of two diphenols isomers at graphene nanosheet-poly(4-vinyl pyridine) composite modified electrode. *Sensors and Actuators, B: Chemical,* 177: 612-619.
20. Yusoff, F., Aziz, A., Mohamed, N. and Ghani, S. A. (2013). Synthesis and characterizations of BSCF at different pH as future cathode materials for fuel cell. *International Journal of Electrochemical Science,* 8: 10672-10687.
21. Yu, J., Liu, Z., Zhai, L. and Huang, T. (2016). Reduced graphene oxide supported TiO_2 as high performance catalysts for oxygen reduction reaction. *International Journal of Hydrogen Energy*, 41(5): 3436–3445.

Malaysian Journal of Analytical Sciences (MJAS)
Published by Malaysian Analytical Sciences Society

STUDY OF CONDUCTIVITY AND THERMAL PROPERTIES OF POLYANILINE DOPED WITH *p*-TOLUENE SULFONIC ACID

(Kajian Pengaliran Elektrik dan Haba terhadap Polianilina di-Dopkan dengan Asid *p*-Toluena Sulfonik)

Muhammad Faiz Aizamddin[1], Nazreen Che Roslan[1], Muhammad Asyrap Kamarudin[1], Siti Nurzatul Ikma Omar[1], Muhd Fauzi Safian[2], Mohamed Izzharif Abdul Halim[2], Mohd Muzamir Mahat[1]*

[1]*School of Physics and Materials Studies, Faculty of Applied Sciences*
[2]*School of Chemistry and Environmental Studies, Faculty of Applied Sciences*
Universiti Teknologi MARA, 40450 Shah Alam, Selangor, Malaysia

**Corresponding author: mmuzamir@uitm.edu.my*

Received: 20 November 2019; Accepted: 31 March 2020; Published: 9 June 2020

Abstract

In this study, polyaniline (PANI) was prepared by oxidative polymerization method with aniline salt. *p*-toluene sulfonic acid (*p*TSA) acted as the dopant to impart conductive properties. The doping process changed the color of PANI from blue PANI emeraldine base (EB) to green PANI emeraldine salt (ES). The thermal characteristic of the doped PANI was analyzed with thermogravimetric analysis (TGA) and differential scanning calorimetry (DSC). TGA results illustrated two major stages of weight loss of PANI-EB, which were the loss of moisture content and polymer degradation. PANI-ES displayed three stages of degradation, which were the removal of dopant, moisture content and the breakdown of polymer backbone. PANI-ES began to degrade at a higher temperature around 170 to 173 ˚C due to the crosslinking of PANI and *p*TSA. This result suggested that PANI ES had higher thermal stability compared to PANI-EB, which started deteriorating at a lower temperature range of 160 to 163 ˚C. DSC analysis revealed that PANI with 0.9 wt.% of *p*TSA portrayed a range of broad peaks in its thermograms which suggested a higher rate of heat transformation (155.35 ˚C) and enthalpy than PANI with different concentrations of *p*TSA. Furthermore, PANI with 0.9 wt.% of *p*TSA exhibited the highest thermal stability at 125 ˚C. The prepared PANI was utilised to fabricate conductive fabric by applying the facile immersion technique. Cotton fabric was immersed in PANI-*p*TSA solution in three different concentrations (0.3, 0.6 and 0.9 wt.%). Based on the findings of electro impedance spectroscopy (EIS) analysis, it can be concluded that PANI with 0.9 wt.% of *p*TSA demonstrated better conductivity (3.30 x 10^{-3} S/m) when compared to PANI with 0.3 wt.% of *p*TSA (1.06 x 10^{-7} S/m).

Keywords: polyaniline, conductive polymer, thermogravimetric analysis, differential scanning calorimetry, electro impedance spectroscopy

Abstrak

Dalam kajian ini, polianilina (PANI) disediakan menggunakan kaedah pempolimeran oksidatif daripada anilina. Asid *p*-toluena sulfonik (*p*TSA) bertindak sebagai dopan yang menyebabkan sifat pengaliran elektrik terhadap polianilina. Proses dop PANI dengan *p*TSA telah mengubah warna PANI dari PANI emeraldin bes (EB) biru ke warna hijau, PANI garam emeraldin (ES).

Analisis-analisis termogravimetrik (TGA) dan kalorimetri pengimbasan berbeza (DSC) digunakan untuk menganalisis ciri-ciri PANI yang didopkan dengan *p*TSA. Hasil TGA menggambarkan bahawa terdapat dua peringkat utama kehilangan berat pada PANI-EB iaitu kandungan kelembapan air dan rantaian utama polimer. Dari sudut berbeza, PANI-ES menunjukkan tiga peringkat kehilangan berat iaitu penyingkiran kandungan dopan, kandungan kelembapan air dan rantaian utama polimer. Kajian ini mendapati bahawa kehilangan berat PANI-ES bermula pada suhu lebih tinggi sekitar 170 hingga 173 ˚C disebabkan oleh ikatan molekul PANI dan *p*TSA. Ini menunjukkan bahawa PANI-ES mempunyai kestabilan haba yang lebih tinggi berbanding dengan PANI-EB yang bermula sekitar 160 hingga 163 ˚C. Analisis DSC mendedahkan bahawa 0.9% kepekatan *p*TSA menggambarkan puncak yang lebar dalam termogram yang menunjukkan bahawa transformasi haba yang tinggi (155.35 ˚C) dan entalpi yang tinggi daripada kepekatan lain. Analisis DSC ini mendapati bahawa PANI pada kepekatan 0.9 wt.% mempunyai kestabilan yang tinggi iaitu pada 125 ˚C. Selepas itu, kain PANI yang bersifat konduktif dibuat menggunakan teknik rendaman yang mudah. Kain kapas direndam dalam larutan PANI-*p*TSA dalam kepekatan yang berbeza (0.3, 0.6 dan 0.9 wt.%). Elektro impedans spektroskopi (EIS) digunakan untuk menganalisis kajian pengaliran elektrik pada kain kapas PANI. Berdasarkan keputusan EIS, dapat disimpulkan bahawa PANI dop dengan 0.9 wt.% *p*TSA (3.30 x 10^{-3} S/m) memperlihatkan pengaliran elektrik yang sangat baik berbanding dengan kepekatan 0.3 wt.% (1.06 x 10^{-7} S/m).

Kata kunci: polianilina, polimer pengalir elektrik, analisis termogravimetrik, kalorimetri pengimbasan berbeza, elektro impedans spektroskopi

Introduction

The conductivity of the eponymous conducting polymers (CPs) makes it a common base material for advanced materials [1]. CPs have found their way into a wide range of applications such as electromagnetic interference (EMI) shielding [2], batteries [3], biosensors [4] and electronic devices [5, 6]. Since the discovery of conjugated polymers, research in the field of CPs has been intensified [7]. Researchers have also discovered that certain polymers with an extended π-conjugation along its backbone such as polyaniline, polyethylene or polypropylene exhibit semiconducting behavior [8]. This process requires mobility of charges that originates from the polymer backbone (by the process of doping) which renders the polymer to be able to conduct electricity. Mahat et al. [9] reported that the doping of PANI is a reversible process that is dependent on environmental conditions such as pH and temperature. Conductivity, flexibility, non-toxic and environmental stability [10] would be the compulsory properties of PANI if it were to be a part of biomedical devices [11].

Furthermore, the versatility of PANI processing is the primary driver in the research of its potential applications. Fabric is one of the viable candidates to impart flexibility and non-toxic properties to CPs. These additional properties can be achieved by incorporating CPs into a fabric. Previously, Zahid et al. [12] reported that the interlacement structure of cotton fabric could exhibit high conductivity after the incorporation of CPs. Thermal properties are equally important as they determine the thermal stability of fabrics. It is also critical to fabricate the conductive PANI at a compatible elevated temperature. The stability at high temperature is crucial since fabrics are easily burnt at low temperature [13]. In their study, Jinsong et al. [14] described the thermal properties of nylon fabric has been prepared using immersion method. They found that the degradation temperature of nylon fabric can reach up to 408 °C. TGA analysis can be used to study the degradation of fabrics by monitoring changes in the weight of the fabric.

In this study, the conductive fabric was created with the immersion technique. PANI was employed as the conductive agent to impart conductivity to the fabrics. *p*TSA was used as the dopant during the synthesis of PANI. Cotton was immersed in a PANI solution which was followed by drying. The fabricated fabric and powder were characterized with thermogravimetric analysis (TGA), differential scanning calorimetry (DSC) and electro impedance spectroscopy (EIS) to analyze their thermal stability and conductivity.

Materials and Methods

Materials

Cotton fabric (50 cm x 60 cm) were purchased from textile company, Kamdar Sdn. Bhd. Aniline water base was purchased from Sigma-Aldrich. Hydrochloric acid (HCl), *p*-toluene sulfonic acid (*p*TSA), sodium hydroxide (NaOH), ammonium persulfate $(NH_4)_2S_2O_8$, sulfuric acid (H_2SO_4) and dimethylformamide (DMF) were sourced from ACROS, United Kingdom.

Synthesis of PANI

An amount 10 mL of aniline was mixed with 100 mL of HCl. The mixture was stirred at room temperature. An amount 22 g of ammonium persulfate (APS) was dissolved in distilled water. The APS solution was added into the aniline solution drop by drop at room temperature and stirred for 4 hours until the mixture turned green. The green solution was filtered with filter paper to separate the solution and precipitate. The precipitate was rinsed with HCl, acetone and distilled water before it was dried for 24 hours. The precipitate was mixed with 1M NaOH, followed by a 4-hour stirring. The solution was dried in a furnace at 60 °C to form the blue-colored polyaniline emeraldine base (PANI-EB) powder. This process was repeated twice.

Preparation of doped and undoped PANI-EB with *p*TSA

PANI-EB powder was dissolved in 60 mL of dimethylformamide (DMF). 0.0154 g of *p*TSA was added into the solution. The solution was labelled as a conductive doped solution once its color changed from blue to green. A similar step was repeated for two concentrations of *p*TSA (0.6 wt.% and 0.9 wt.%). The undoped PANI without the acid served as the control solution. The PANI solutions were centrifuged for 30 minutes at 400 rpm.

Immersion of cotton fabric in doped and undoped PANI

The dimension of the cotton fabric in this study was 5 cm x 5 cm. The cotton fabrics were immersed in the PANI solution for 15 minutes, followed by drying for 24 hours at room temperature. The dried cotton fabrics were kept in the dark before they were characterized with TGA, DSC and EIS.

Thermogravimetric analysis (TGA)

Thermogravimetric analysis (TGA; SETARAM model) measured the weight loss of the sample. An amount 10 mg sample in powder form was measured and alumina pan was used. The temperature was fixed from 27 °C to 300 °C at a heating rate of 20 °C/min. The result of the thermal reaction was reflected as the percentage of weight loss versus temperature or time.

Differential scanning calorimetry (DSC)

DSC (PerkinElmer: PYRIS 1 DSC) measures the heat flow rate of a reference and a sample as a function of temperature. The initial weight of the sample powder was 10 mg. Alumina pans acted as the sample and reference which can conduct heat in the temperature range of 30 to 300 °C with 20 °C/min heating rate. Heat flow of the samples was monitored over course of temperature fluctuations.

Electrochemical impedance spectroscopy (EIS)

HIOKI 3532-50LCR Hi Tester Electrochemical Impedance Spectroscopy was operated at constant room temperature with a frequency range of 100 Hz to 1000 kHz. Two stainless steel disc electrode with a diameter of 2.0 cm were used as the clipper for the 5.0 cm x 5.0 cm PANI fabrics. The impedance and conductivity of the PANI Fabrics were then measured.

Results and Discussion

Synthesis of PANI

Synthesis of PANI by chemical polymerisation changed its chemical composition by modifying the polymer's backbone chain. Chemical polymerisation also inevitably introduced conductivity into PANI. An amount 60 mL of dimethylformamide (DMF) was poured into PANI-EB powder which was followed by the addition of 0.3 wt.% of *p*TSA into the solution. The change in the color of the solution from deprotonated blue emeraldine base to protonated green emeraldine salt verified its conductivity. Another two variants of doped solution were prepared with the addition of 0.6 wt.% and 0.9 wt.% *p*TSA. The undoped solution acted as the control and was defined by the absence of acid. Figure 1 distinguishes the chemical structure and the polymer's backbone chain that were modified by the synthesis of PANI.

The green emeraldine salt displayed conductivity due to its oxidised iminium and reduced amine nitrogen [15]. The immersion process transferred the PANI into the cotton fabric (Figure 1c and d). Figure 2 distinguishes the surfaces of bare cotton fabric and cotton fabric that was doped with 0.9 wt.% of PANI-*p*TSA.

These FESEM micrographs are evidence that precipitates were uniformly distributed on the fibre's surface. It can be said with certainty that the PANI powder was successfully embedded in the fabrics (Figure 2b). This result is in line with the findings of Bhat et al. [16], who reported that PANI was substantially absorbed within the fibres and had rough with non-uniform surface after fabricated with fabric.

Thermal properties of PANI

Thermogravimetric analysis (TGA)

Thermogravimetric analysis was performed in an atmosphere of nitrogen and air at a heating rate of 20 °C min^{-1} up to the point of degradation. Figure 3 shows the TGA thermograms of PANI emeraldine base (EB) to PANI emeraldine salt (ES) powder.

Three stages of weight loss were observed in PANI-ES. Meanwhile, PANI-EB exhibited two stages of weight loss. PANI-ES started to lose weight at 38 °C due to the loss of the dopant (*p*TSA) which 20%. The weight loss of PANI-ES at 75 °C and PANI-EB at 74 °C occurred due to the loss of volatile component, moisture or solvent content. The temperature decomposition of elements in the polymeric (carbon, nitrogen and hydrogen) were recorded at the temperature range of 170 to 173 °C for PANI ES and 160 to 163 °C for PANI-EB with observed weight loss of 42% and 67%, respectively. These phenomena could be credited to inter-chain crosslinking and breakdown of PANI backbone. From the results, there was a direct correlation between the presence of dopant resulting lower weight loss as shown from the TGA study of PANI-ES. Therefore, it was evident that cross-linked of PANI displays better thermal stability in PANI-ES compared to PANI-EB powder [17].

Differential scanning calorimetry (DSC)

DSC thermogram provided information regarding the changes in enthalpy of polyaniline (PANI) emeraldine base (EB) and emeraldine salt (ES) powder. The heat transition of PANI was observed by monitoring the plot of heat flow against temperature. The DSC plot also can be used to interpret changes in physical phase, elimination of moisture and other components. The chemical changes like decomposition depending on the temperature that have been set. Figure 4 represents the DSC analysis of PANI emeraldine base (EB) and emeraldine salt (ES) powder.

PANI-EB displayed peaks at 114 °C and 137 °C and their respective delta enthalpy were 3.969 J/g and 8.701 J/g. These distinct endotherm peaks reflected the loss of some components. The first peak could be attributed to the vaporisation of water. This finding suggested that PANI-EB powder had discernible moisture content [18, 19]. The second, broader peak signalled the presence of lower enthalpy and a lower rate of transformation, which implied the presence of a eutectic impurity in PANI-EB. In contrast, PANI-ES displayed a single broad peak at 107 °C with a delta enthalpy of 67.403 J/g. From the results, PANI-ES needed less heat to transform which resulting the higher thermal stability than PANI-EB [20].

Further analysis was performed on doped PANI by varying concentrations of *p*TSA with the outcome of broad peaks, as shown in Figure 5.

Results from Table 1 shows that as the concentration of *p*TSA in PANI-ES increased, the rate of transformation and enthalpy of PANI-ES increased as well. The small endotherm (0.3 wt.%) starts at around 80.65 °C and ends at around 135.55 °C at peak 110.67 °C. The second endotherm (0.6 wt.%) starts at around 77.71 °C and ends at around 142.37 °C with a broad peak at around 115.67 °C. Finally, third endotherm (0.9 wt.%) starts at around 81.45 °C and ends at around 155.35 °C with a peak at around 125 °C. According to Corcione [21], broad peaks are an indication of a partially crystalline polymer. Increasing the concentration of

acid in PANI will promote the excellent crystallinity of PANI.

Conductivity measurements

Electro impedance spectroscopy (EIS) measured the conductivity of all fabricated fabrics. Table 2 shows the conductivity of *p*TSA-doped PANI-cotton fabric.

The conductive fabrics were fabricated with various value within the acceptable range of conductive state. Yao et al. in 2019 [22] found that the conductivity of doped polymer fell between 10^{-5} to 10^{2} S/cm while insulator exhibited conductivities below 10^{-12} S/cm. Bare and undoped PANI cotton fabric displayed no significant voltage and slight electrical current, respectively. This observation could be attributed to the absence of acids that act as a dopant to alter conductivity. 0.9 wt.% PANI-*p*TSA showed a relatively higher conductivity compared to 0.3 wt.% PANI-*p*TSA. Figure 6 shows a bar chart of conductivity against different concentrations of *p*TSA. For instance, 0.9 wt.% PANI-*p*TSA had a conductivity value of 3.30 x 10^{-3} S/m compared to that of 0.3 wt.%, which was 2.35 x 10^{-6} S/m. Therefore, the conductivity of doped PANI was proportional to the concentration of acid. This outcome showed that the proportion of doped acid in the fabric has an impact on the fabric's characteristic. Additionally, 0.9 wt.% of PANI-*p*TSA showed that the majority of the polymer chain was connected to the cotton fabric through hydrogen bonds [23, 24]. It was also discovered that a high fraction of PANI chain was chemically grafted onto the surface of the cotton fabric.

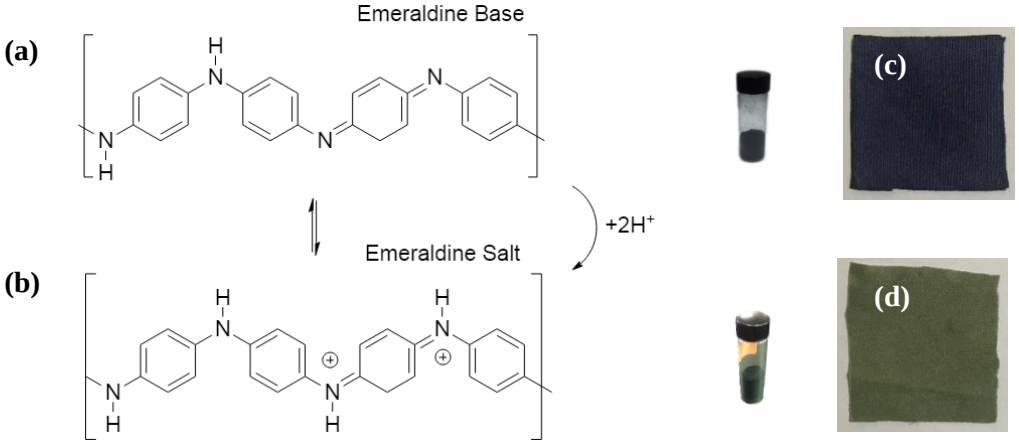


Figure 1. Chemical structure of PANI (a) PANI-EB (b) PANI-ES (c) PANI-EB fabric (blue colour) and (d) PANI-ES fabric (green colour)

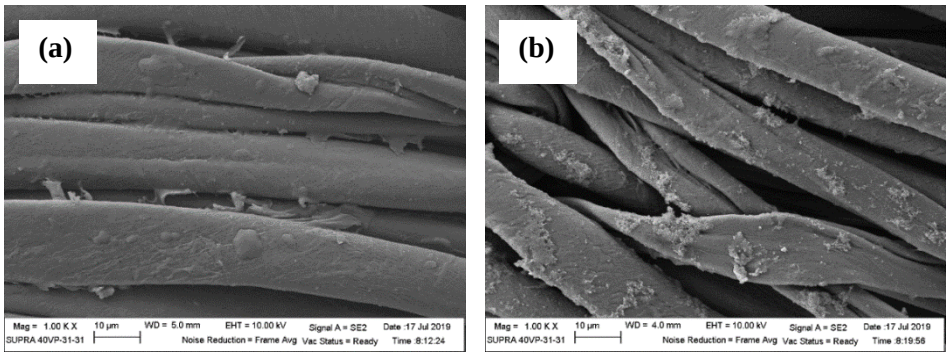


Figure 2. Field emission scanning electron microscope (FESEM) micrographs of (a) bare cotton fabric (b) cotton fabric doped with 0.9 wt% of PANI-*p*TSA

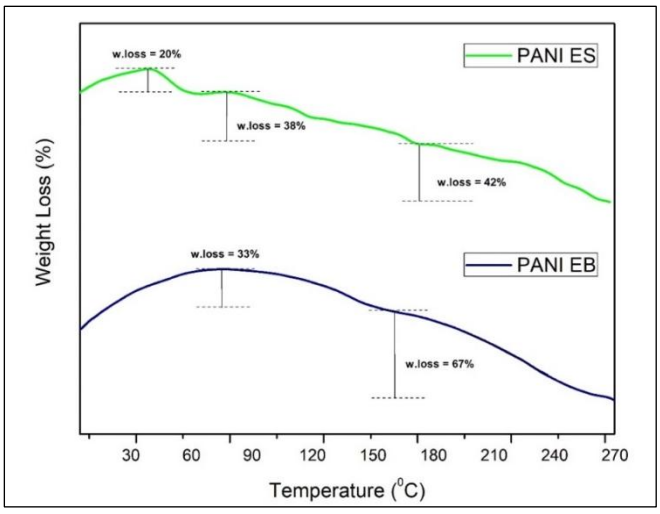


Figure 3. TGA thermograms of PANI-EB and PANI-ES powder

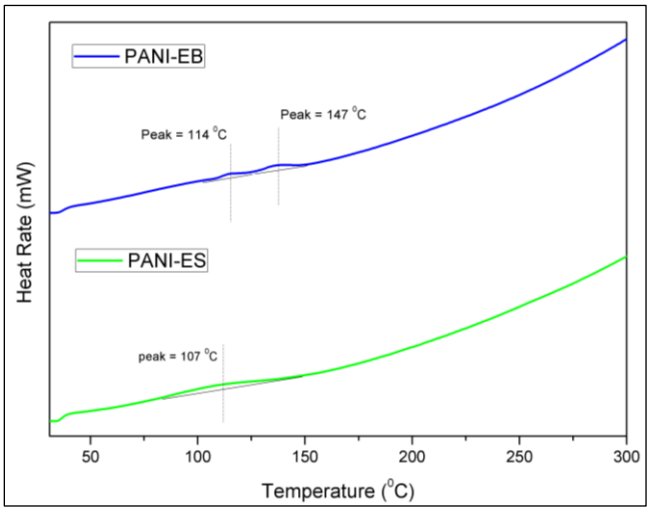


Figure 4. DSC thermogram of PANI-EB and PANI-ES powder

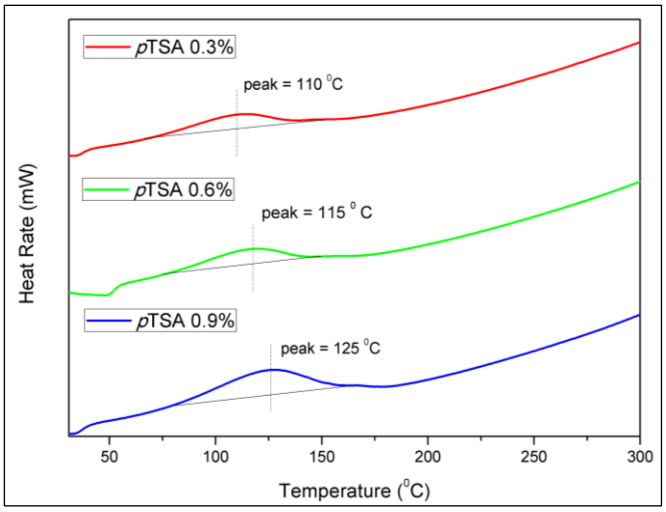


Figure 5. DSC thermogram of doped PANI-ES powder with varying concentrations of *p*TSA (0.3, 0.6, and 0.9 wt.%)

Table 1. The endotherm temperature for doped PANI with *p*TSA concentrations of 0.3, 0.6 and 0.9 wt.%

Concentration of *p*TSA (wt.%)	**Temperature of Endotherm (°C)**		
	Beginning	**Peak**	**Final**
0.3	80.65	110.67	135.55
0.6	77.71	115.67	142.37
0.9	81.45	125	155.35

Table 2. Conductivity of PANI-cotton fabric doped with different concentrations of *p*TSA

Doping Condition	**Weight %**	**Conductivity (S/m)**
Bare	-	NIL
Undoped	-	$1.06 \times 10^{-7} \pm 6.38 \times 10^{-8}$
Doped PANI with *p*TSA	0.3	$2.35 \times 10^{-6} \pm 7.26 \times 10^{-7}$
	0.6	$1.62 \times 10^{-5} \pm 3.13 \times 10^{-6}$
	0.9	$3.30 \times 10^{-3} \pm 1.00 \times 10^{-3}$

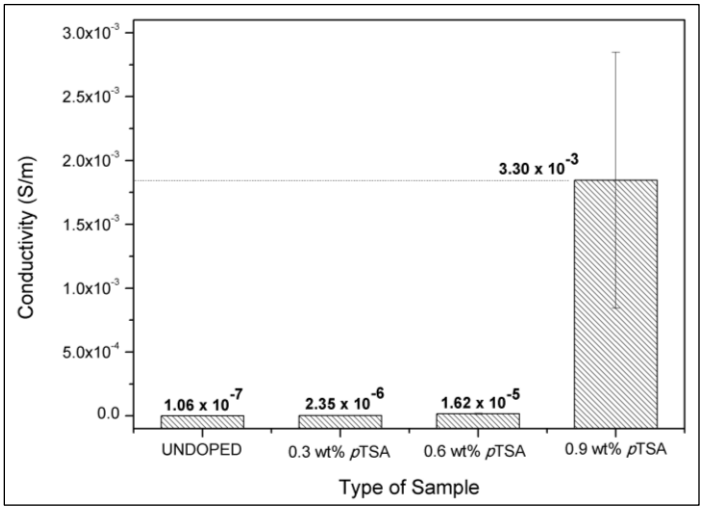


Figure 6. Conductivity of PANI cotton fabrics at different weight percentage of *p*TSA

Conclusion

PANI was synthesized with the chemical oxidation method. Successful doping of *p*TSA in PANI was confirmed by the change in the color of PANI solution from blue to green. Thermal analysis by TGA illustrated two major stages of weight loss in PANI-EB powder due to the changes in moisture content and breakdown of the polymer backbone. In contrast, PANI-ES had three major stages of weight loss due to the removal of dopant, moisture content and the breakdown of polymer chain. The degradation temperature of PANI-ES began at a higher temperature range of 170 to 173 °C due to the crosslinking between PANI and *p*TSA. This finding indicated that PANI-ES had higher thermal stability compared to PANI-EB, which began to degrade in the temperature range of 160 to 163 °C. DSC analysis expressed broad peaks for 0.9 wt.%. This result suggested that PANI with this specific concentration of *p*TSA had a higher rate of heat transformation and enthalpy than PANI with lesser concentrations of *p*TSA. Furthermore, PANI with 0.9 wt.% concentration displayed the highest thermal stability. Conductive fabrics were fabricated with the prepared PANI by applying facile immersion technique. Cotton fabric was immersed in PANI with varying concentrations of *p*TSA (0.3, 0.6 and 0.9 wt.%). Based on the EIS results, it can be concluded that PANI with 0.9 wt.% *p*TSA (3.30 x 10^{-3} S/m) exhibited superior conductivity compared to PANI with 0.3 wt.% *p*TSA (1.06 x 10^{-7} S/m).

Acknowledgement

The authors are grateful for the funding from Research Management Center UiTM under GIP grant (600-IRMI 5/3/GIP(010/2019)).

References

1. Mishra, A. K. (2018). Conducting polymers: Concepts and applications. *Journal of Atomic, Molecular, Condensate and Nano Physics,* 5(1): 159-193.
2. Shacklette, L. W., Colaneri, N. F., Kulkarni, V. G. and Wessling, B. (1992). EMI shielding of intrinsically conductive polymers. *Journal of Vinyl and Additive Technology*, 14(2): 118-122.
3. Rochliadi, A., Akbar S. A. and Suendo. V. (2015). Polyaniline/Zn as secondary battery for electric vehicle base on energy return factor. *Proceedings of the Joint International Conference on Electric Vehicular Technology and Industrial, Mechanical, Electrical and Chemical Engineering, Surakarta*, 1(13): 353-358.
4. Sengupta, P. P., Barik, S. and Adhikari, B. (2006). Polyaniline as a gas-sensor material. *Materials and Manufacturing Processes*, 21(3): 263-270.

5. Wei, R., Hua, X. and Xiong, Z. (2018). Polymers and polymeric composites with electronic applications. *International Journal of Polymer Science*, 2018: 1.
6. Heng Teo, C., Karode, N. S., Abid, K. and Rahman, F. (2011). Interfacial behaviour of polyaniline as an organic electronic material. *Journal of Physics and Chemistry of Solids*, 72(7): 886-890.
7. Ramakrishnan, S. (1997). Conducting polymers. *Inorganic and Physical Chemistry* 2(11): 48-58.
8. Srinivas, C. H., Srinivani, D., Kavitha, B., Narsimlu, N. and Siva Kumar, K. (2012). Synthesis and characterization of nano size conducting polyaniline. *IOSR Journal of Applied Physics,* 1(1): 12-15.
9. Mahat, M. M., Mawad, D., Nelson, G. W., Fearn, S., Palgrave, R. G., Payne, D. J. and Stevens, M. M. (2015). Elucidating the deprotonation of polyaniline films by X-ray photoelectron spectroscopy. *Journal of Materials Chemistry C*, 3(27): 7180-7186.
10. Wang, H., Lin, J. and Shen, Z. X. (2016). Polyaniline (PANI) based electrode materials for energy storage and conversion. *Journal of Science: Advanced Materials and Devices*, 1(3): 225-255.
11. Olad, A. and Azhar, F. F. (2013). Trends in polyaniline research e-book. Hauppauge, New York: pp. 361- 384.
12. Zahid, M., Papadopoulou, E., Athanassiou, A. and Bayer, I. (2017). Strain-responsive mercerized conductive cotton fabrics based on PEDOT: PSS/graphene. *Materials and Design,* 1(2): 135.
13. Gorji, M. and Ali J. (2018). The study of burning behavior of cotton/glass woven fabrics. *Trends in Textile Engineering & Fashion Technology,* 3(5): 2578.
14. Jinsong, H., Li, R. and Gu, F. (2012). Preparation of polyaniline/nylon conducting fabric by layer-by-layer assembly method. *Journal of Applied Polymer Science,* 3(1): 12-19.
15. Zaki, M. R., Anuar, K., Jelas, M. H. and Faiz, M. (2001). Electrical properties and thermal stabilities studies of conducting polyaniline doped with different sulphonic acids. *Malaysian Journal of Analytical Sciences*, 7(2): 445-451.
16. Bhat, N. V., Seshadri, D. T. and Radhakrishnan, S. (2004). Preparation, characterization, and performance of conductive fabrics: Cotton and PANI. *Textile Research Journal*, 74(2): 155-166.
17. Wang, X., Liu, D., Deng, J., Duan, X., Guo, J. and Liu, P. (2015). Improving cyclic stability of polyaniline by thermal crosslinking as electrode material for supercapacitors. *RSC Advances*, 5(96): 78545-78552.
18. Yılmaz, F. and Küçükyavuz, Z. (2009). The influence of polymerization temperature on structure and properties of polyaniline. *e-Polymers*, **16**(3): 225-233.
19. Chauhan, N., Ametab, R., Ametac, R. and Ameta, S. (2011). Thermal and conducting behavior of emeraldine base (EB) form of polyaniline (PANI). *Indian Journal of Chemical Technology*, 18(1): 118-122.
20. Chen, C. H. (2003). Thermal and morphological studies of chemically prepared emeraldine- base- form polyaniline powder. *Journal of Applied Polymer Science*, 89(1): 2142-2148.
21. Corcione, C. and Frigione, M. (2012). Characterization of nanocomposites by thermal analysis. *Materials*, 5(12): 2960-2980.
22. Yao, C. J., Zhang, H. L. and Zhang, Q. (2019). Recent progress in thermoelectric materials based on conjugated polymers. *Journal of Polymers*, 11(1): 107.
23. David, N. C., Anavi, D., Milanovich, M., Popowski, Y., Frid, L. and Amir, E. (2017). Preparation and properties of electro-conductive fabrics based on polypyrrole: covalent vs. non-covalent attachment. *IOP Conference Series: Materials Science and Engineering*, 254: 032002.
24. Wei, Y., Jang, G. W., Hsueh, K. F., Scherr, E. M., MacDiarmid, A. G. and Epstein, A. J. (1992). Thermal transitions and mechanical properties of films of chemically prepared polyaniline. *Journal of Materials Polymer*, 1(33): 314.

Malaysian Journal of Analytical Sciences (MJAS)
Published by Malaysian Analytical Sciences Society

EXPERIMENTAL AND DENSITY FUNCTIONAL THEORY INVESTIGATION ON IMINE FORMATION USING MICROWAVE IRRADIATION

(Penyiasatan Secara Eksperimen dan Teori Fungsi Ketumpatan ke atas Penghasilan Imina Menggunakan Penyinaran Gelombang Mikro)

Fatin Ilyani Nasir[1,2], Wun Fui Mark-Lee[3], Yan Yi Chong[1], Mohammad B. Kassim[1], Siti Aishah Hasbullah[1], Douglas Philp[4], Nurul Izzaty Hassan[1]*

[1]*Department of Chemical Sciences, Faculty of Science and Technology, Universiti Kebangsaan Malaysia, 43600 UKM Bangi, Selangor, Malaysia*
[2]*Analytical Biochemistry Research Centre, Universiti Sains Malaysia, 11800 Penang, Malaysia*
[3]*Department of Basic Science and Engineering, Faculty of Agriculture and Food Sciences, Universiti Putra Malaysia, 97008 Bintulu, Sarawak, Malaysia*
[4]*Department of Chemistry, Northwestern University, 2145 Sheridan Road, Evanston, IL 60208-3113, USA*

**Corresponding author: drizz@ukm.edu.my*

Received: 3 April 2020; Accepted: 10 May 2020; Published: 9 June 2020

Abstract

Four starting materials comprising of *N*-(4,6-dimethylpyridin-2-yl)-4-formylbenzamide **1,** 4-amino-*N*-(4,6-dimethylpyridin-2-yl)benzamide **2**, 4-amino-2-methylbenzoic acid **3** and 4-formylbenzoic acid **4** react in a pairwise manner through the condensation reaction to give four imine derivatives, **Imine 5**, **6**, **7** and **8**. A simple method has been developed for the synthesis of these imine derivatives under microwave irradiation. In addition, these compounds were synthesised also by conventional heating procedures for comparison. All the compounds synthesised were characterised by melting point, infrared, mass spectrometry, ^{1}H and ^{13}C NMR spectroscopy. Comparison between conventional and microwave irradiation was done by comparing total reaction time and percentage yield. The results suggest that microwave-irradiation lead to higher yields within very short reaction times. Compounds **1** and **2** crystallised in the orthorhombic ($P2_12_12_1$ space group) and monoclinic ($P2_1/c$ space group) crystal systems, respectively. The nature of minimal replicator of imine **6** *via* autocatalytic reaction was calculated using density functional theory (DFT) with the combination of hybrid functional B3LYP and 6-311G(d,p) basis set. The reaction pathway facilitated with the addition of imine **6** or imine **5** equipped with complementary recognition sites of two carboxylic acids and two 4,6-dimethylamidopyridines were predicted to be thermodynamically favourable.

Keywords: imine, condensation, conventional heating, microwave irradiation, density functional theory

Abstrak

Empat bahan bermula terdiri daripada *N*-(4,6-dimetilpiridin-2-il)-4-formilbenzamida **1**, 4-amino-*N*-(4,6-dimetilpiridin-2-il)benzamida **2**, asid 4-amino-2-metilbenzoik **3** dan asid 4-formilbenzoik **4** bertindak balas secara berpasangan melalui tindak balas kondensasi untuk menghasilkan empat terbitan imina, imina **5**, **6**, **7** dan **8**. Satu kaedah mudah telah dibangunkan untuk menghasilkan terbitan imina di bawah penyinaran gelombang mikro. Di samping itu, terbitan imina ini turut dihasilkan melalui kaedah pemanasan konvensional sebagai perbandingan. Semua sebatian yang di sintesis dicirikan melalui analisis takat lebur, inframerah, spektrometri jisim, spektroskopi ^{1}H dan ^{13}C RMN. Perbandingan antara kaedah konvensional dan penyinaran gelombang mikro dilakukan dengan membandingkan masa tindak balas dan hasil peratusan. Keputusan ini mencadangkan kaedah penyinaran gelombang mikro memberikan peratusan hasil yang lebih tinggi dalam masa tindak balas yang singkat. Sebatian **1** dan **2** masing-masing menghablur dalam sistem ortorombik (kumpulan ruang $P2_12_12_1$) dan monoklinik (kumpulan ruang $P2_1/c$). Sifat replikator minimal imina **6** melalui tindak balas autokatalitik telah dikira menggunakan teori fungsi ketumpatan (DFT) dengan menggunakan gabungan asas fungsi hibrid B3LYP dan set asas 6-311G(d,p). Laluan tindak balas dibantu dengan penambahan sebatian imina **6** atau imina **5** yang dilengkapi dengan tapak pengecaman, terdiri daripada dua moieti asid karboksilik dan dua moieti 4,6-dimetilpiridina yang dijangka berada di bawah kawalan termodinamik.

Kata kunci: imina, kondensasi, pemanasan konvensional, penyinaran gelombang mikro, teori fungsi ketumpatan

Introduction

Imine derivatives typically formed through condensation between an amine and an aldehyde are an essential precursor in the pharmaceutical industry to produce dyes [1], catalysts [2], and pigments [3]. Imine represents a class of biological reactive intermediates that have been the focus of intensive toxicological research in recent years. Hence, these derivatives play a role in various biological activities such as antiviral [4], antibacterial [5], antimicrobial [6], antitumor [7], anti-inflammatory agents [8], antituberculosis [9] and anticonvulsant activity [10]. The standard method for the preparation of imine is the conventional reflux technique, which is carried out in ethanol with or without the presence of a catalyst. The molecular sieves are utilised to remove the water molecules formed in the reaction before tetramethyl orthosilicate [11] or trimethyl orthoformate are introduced as an *in-situ* method to remove the water [12]. The main drawbacks are that it involves large amounts of flammable solvents and relatively time-consuming.

Since 1996, microwave technology has been implemented in many organic synthesis explorations. Microwave irradiation significantly reduces the use of toxic solvents, as well as, the reaction time, ensuring high yields and clean product formations [13]. The ease of preparation also helps to encourage more research in preparing the imine derivatives. Souza et al. used ethanol to synthesise thiazol-2-imines *via* a one-pot reaction [14], while others used water as the solvent [15]. Additionally, a new one-pot acid-catalysed to furnish aromatic imines using a minimum amount of methanol as solvent under microwave irradiation. The reaction yields a substantial amount of imine derivatives and can also be extended to include various substrates [16]. This technique allows the condensation reactions such as imine synthesis to complete the reaction by heating the water generated [17]. The formation of imine derivatives that consists of two aromatic aldehydes and amines incorporating a recognition site of 4,6-dimethylamidopyridines and carboxylic acid has been carried out previously in our research group [18-20] utilising the classical heating, which resulted in longer reaction time and excessive use of organic solvents.

In this approach, the formation of imine derivatives was carried out under microwave irradiation in a minimum amount of organic solvents and compared with conventional synthesis based on the percentage yield and time of reaction. **Imine 5** were formed when aldehyde **1** reacted with amine **3** while **Imine 6** were obtained through condensation reaction between amine

2 and aldehyde **4** as shown in Figure 1. On the other hand, **Imine 7** utilised the condensation between aldehyde **1** and amine **2**. Similarly, aldehyde **4** was reacted with similar amine **3** to furnish **Imine 8**. Subsequently, we validated the minimal replication capability [20] of **Imine 5** and **6** using density functional theory calculation with the combination of hybrid functional B3LYP at 6-311G(d,p) basis set.

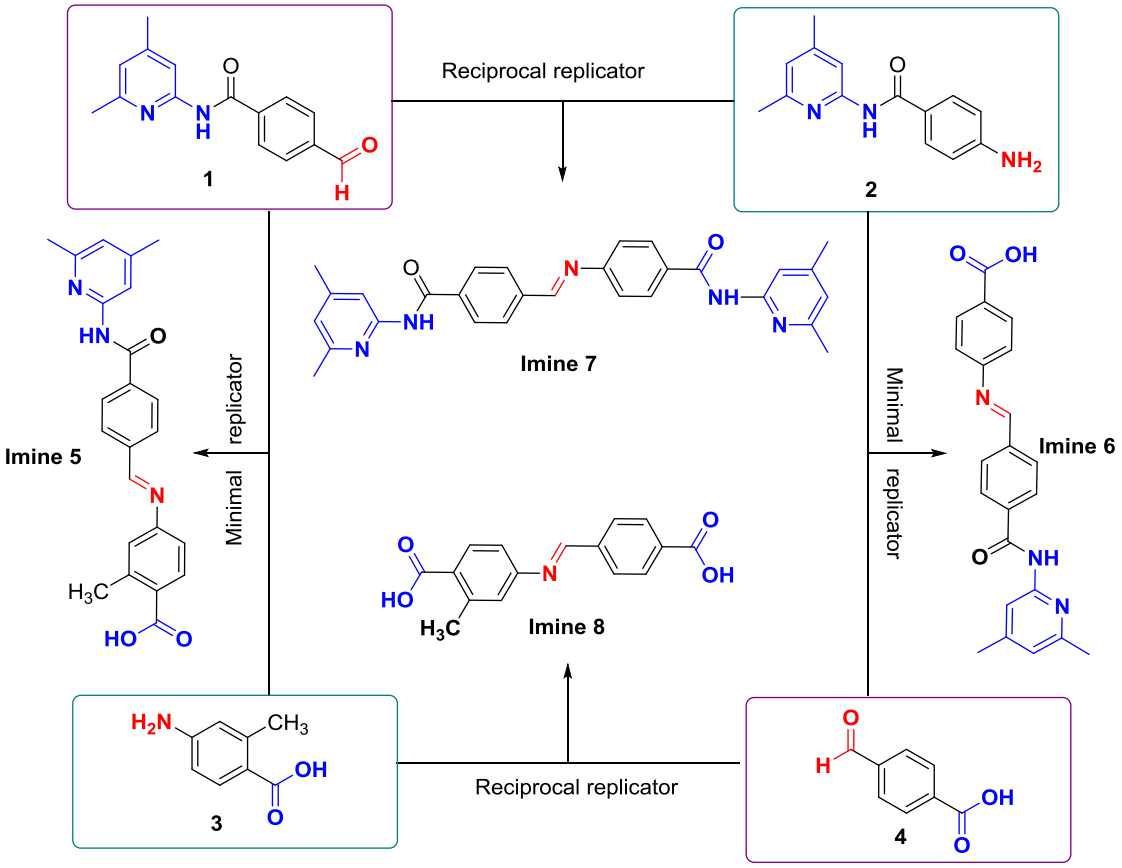


Figure 1. The schematic reaction consists of two aldehydes (**1** and **4** – purple boxes) and two amines (**2** and **3** – emerald boxes) to obtain four imine derivatives, namely Imine **5** and **6** (minimal replicator) and Imine **7** and **8** (reciprocal replicator)

Materials and Methods

All solvents and reagents used for synthesis were of general reagent grade and used as received or otherwise purified by standard techniques. 4-amino-2-methylbenzoic acid (**3**), 4-formylbenzoic acid (**4**), 2-amino-4,6-dimethylpyridine, 4-nitrobenzoyl chloride, $Ni(OAc)_2 \cdot 4H_2O$, triethylamine, sodium borohydride ($NaBH_4$), toluene, cyclohexane, ethyl acetate, acetonitrile, dichloromethane, acetone, ethanol, hydrochloric acid, sodium hydrogen bicarbonate, magnesium sulphate, and thionyl chloride were purchased from Sigma Aldrich, Bodensen and Merck. Anhydrous dichloromethane was prepared in the presence of calcium hydride at 40 °C for 6 h before undergoing distillation under inert condition. Synthesis

was carried out using modified reported procedures for microwave-assisted synthesis [21].

For comparison, conventional synthesis was also carried out using the reported procedures [19, 20]. The reactions were monitored by thin layer chromatography (TLC) with precoated silica plates (POLYGRAM® SIL G/UV254). Column chromatography was carried out on silica gel (230-400 mesh) eluting with solvents as supplied under positive pressure or compressed air. Melting points were recorded in open capillaries tube apparatus and are uncorrected. Infrared (IR) was recorded (KBr disc method) on Perkin-Elmer spectrum GX spectrophotometer. ^{1}H and ^{13}C NMR spectra were recorded on a Bruker Avance 400 MHz spectrometer at 400 MHz and 100 MHz, respectively. Chemical shifts were reported in ppm downfield from tetramethylsilane (TMS), which was used as the internal standard. Mass spectra were recorded on a Bruker MICROTOF-Q 86 spectrometer equipped with electrospray ionization (ESI) module in the positive ion mode. Single crystal X-ray experiments were performed on a Bruker D8 QUEST diffractometer with MoK α radiation. Microwave-assisted reactions were carried out in a domestic microwave oven (Electrolux, EMM2017X) at 360 W.

Computational methods

The quantum chemical calculations carried out in the present work were performed with the Gaussian09 program package. The molecular structure of the imine compounds as well as their duplex and ternary complex structures were fully optimised using the combination of hybrid functional B3LYP with 6-311G(d,p) basis set [22-26]. The vibrational frequency calculations were performed to ensure that the optimised structures represent the local minima where only positive real number force constants (eigen values) were present [27, 28]. The enthalpy of reaction (ΔH) and thermal energy corrections were obtained with the consideration of the vibrational mode calculation [29]. Gaussian09 program provides the sum of internal electronic energy (ε_0) and thermal enthalpies, H_{corr} (H_{corr} = E_{tot} + k_BT; k_B = Boltzmann constant = 1.380662 × 10^{-23} J/K). The E_{tot} expression gives the internal thermal energy due to translation (E_t), rotational (E_r), vibrational (E_v) and electronic (E_e) motions. Thus, the ΔH is simply the difference of the sums of ε_0 and H_{corr} for the reactants and the product, as given in Equation 1.

$$\Delta H\,(298\ \mathrm{K}) = \sum(\varepsilon_0 + H_{corr})\mathrm{products} - \sum(\varepsilon_0 + H_{corr})\mathrm{reactants} \quad (1)$$

Synthesis of N-(4,6-dimethylpyridin-2-yl)-4-formylbenzamide - 1

4-formylbenzoic acid (**4**) (4.0 g, 26.6 mmol, 1.0 eq) and thionyl chloride (3.0 mL, 40.0 mmol, 1.5 eq) were added at 110 °C for 24 hours in toluene (100 mL) to obtain brownish precipitate. The precipitate was subsequently washed with toluene for three times to remove the remaining chloride before dried under vacuum to yield brownish solid, 4-formylbenzoyl chloride (4.4 g, 97%). The 4-formylbenzoyl chloride (1.0 g, 5.9 mmol, 1.0 eq) obtained was then used without any purification to react with 2-amino-4,6-dimethylpyridine (0.7 g, 5.9 mmol, 1.0 eq) in the presence of Et_3N (900 µL, 6.53 mmol, 1.1 eq) at 0 °C. The reaction was then left stirred at room temperature for 48 hours in anhydrous CH_2Cl_2 (14 mL) under N_2 gas. The resulting brownish solution obtained was then quenched with distilled water. The organic layer was then extracted with 1 M HCl and saturated $NaHCO_3$ solution before dried with anhydrous $MgSO_4$, filtered and dried under vacuum before purified using column chromatography (CHex:EtOAc, 3:2) to obtain colourless powder, *N*-(4,6-dimethylpyridin-2-yl)-4-formylbenzamide **1** (67%). Colourless solid; m.p.: 109 - 110 °C; FT-IR (KBr, cm^{-1}) 3331, 2920, 2857, 1678, 1543, 1425 cm^{-1}; ^{1}H NMR (400 MHz, $CDCl_3$) δ_H 10.13 (1H, s, C*H*O), 8.67 (1H, br s, CON*H*), 8.11 (2H, d, $^{3}J_{HH}$ 8.0 Hz, 2×Ar*H*), 8.06 (1H, s, Ar*H*), 8.03 (2H, d, $^{3}J_{HH}$ 8.0 Hz, 2×Ar*H*), 6.83 (1H, s, Ar*H*), 2.45 (3H, s, CH_3), 2.40 (3H, s, CH_3); ^{13}C NMR (100 MHz, $CDCl_3$) δ_C 191.5 (*C*HO), 164.5 (*C*=O), 156.4 (Ar*C*), 150.6 (Ar*C*), 150.4 (Ar*C*), 139.5 (Ar*C*), 138.6 (Ar*C*), 130.0 (Ar*C*H), 127.9 (Ar*C*H), 121.1 (Ar*C*H), 111.8 (Ar*C*H), 23.8 (*C*H_3), 21.4 (*C*H_3); MS (ESI) m/z calculated for $C_{15}H_{14}N_2O_2$ $[M + Na]^+$ 277.1055, found 277.1022.

Synthesis of 4-amino-N-(4,6-dimethylpyridin-2-yl)benzamide - 2

2-amino-4,6-dimethylpyridine reacted with 4-nitrobenzoyl chloride (3.0 g, 16.2 mmol) to yield *N*-(4,6-dimethylpyridin-2-yl)-4-nitrobenzamide (4.2 g, 15.5 mmol, 97 %) as intermediate compound. Subsequently, the nitro compound obtained (0.3 g, 1 mmol, 1.0 eq) was then dissolved in wet acetonitrile (CH_3CN:H_2O ; 3.0 mL:0.3 mL) before the addition of $Ni(OAc)_2 \cdot 4H_2O$ (0.049 g, 0.2 mmol, 0.2 eq). The reaction was stirred for 5 minutes before further reduced using $NaBH_4$ (0.151 g, 4.0 mmol). The black precipitate was immediately deposited and left stirred for 20 minutes while being monitored using thin layer chromatography (TLC) before quenched with distilled water. The reaction mixture extracted with CH_2Cl_2 (8 mL × 3), dried using anhydrous $MgSO_4$ and purified using column chromatography (CHex:EtOAc; 3:2) to yield 4-amino-*N*-(4,6-dimethylpyridin-2-yl)benzamide **2** (54%). Yellowish solid; m.p.: 132 - 133°C; FT-IR (KBr, cm^{-1}) 3461, 3350, 1606, 1446, 1283 cm^{-1}; ^{1}H NMR (400 MHz, $CDCl_3$) δ_H 8.43 (1H, s; CON*H*), 8.05 (1H, s; Ar*H*), 7.78 (2H, d, $^3J_{HH}$ 8.4 Hz; 2×Ar*H*), 6.76 (1H, s; Ar*H*), 6.72 (2H, d, $^3J_{HH}$ 8.4 Hz; 2×Ar*H*), 4.09 (2H, s; NH_2), 2.44 (3H, s; CH_3), 2.36 (3H, s; CH_3); ^{13}C NMR (100 MHz, $CDCl_3$) δ_C 165.3 (*C*=O), 155.9 (Ar*C*), 151.2 (Ar*C*), 150.4 (Ar*C*), 150.3 (Ar*C*), 129.2 (Ar*C*H), 123.5 (Ar*C*), 120.2 (Ar*C*H), 114.2 (Ar*C*H), 111.6 (Ar*C*H), 23.7 (*C*H_3), 21.4 (*C*H_3); MS (ESI) m/z calculated for $C_{14}H_{15}N_3O$ $[M + Na]^+$ 264.1215, found 264.1169.

Synthesis of (E)-4-((4-((4,6-dimethylpyridin-2-yl)carbamoyl)benzylidene)amino)-2-methylbenzoic acid - Imine 5

N-(4,6-dimethylpyridin-2-yl)-4-formylbenzamide (**1**) (0.05 mmol) and 4-amino-2-methylbenzoic acid (**3**) (0.05 mmol) were sonicated in acetone (1 mL) for 1 minute to mix the mixture well in a reaction vial before it was placed in a microwave oven. The mixture was then irradiated at 360 W for 5 minutes. After the reaction was completed, chilled ethanol (2 mL) was added into the reaction mixture. The resulting precipitate was filtered off and dried under vacuum. Likewise, *N*-(4,6-dimethylpyridin-2-yl)-4-formyl-benzamide (**1**) (0.5 mmol) and 4-amino-2-methylbenzoic acid (**3**) (0.5 mmol) were dissolved in acetone (5 mL) and refluxed for 5 hours. The reaction mixture was then evaporated to approximately half its original volume, and the resulting imine **5** was filtered, washed with chilled ethanol and dried under vacuum. The compound was obtained as yellowish powder in 94% yield (microwave irradiation), 93% yield (conventional method); m.p.: 284 - 285 °C; FT-IR (KBr, cm^{-1}) 3273, 2491, 1679, 1629, 1581, 1447 cm^{-1}; ^{1}H NMR (400 MHz, d_6-DMSO) δ_H 12.68 (1H, br s; COO*H*), 10.81 (1H, s; CON*H*), 8.73 (1H, s; C*H*=N), 8.15 (2H, d, $^3J_{HH}$ 8.4 Hz; 2×Ar*H*), 8.05 (2H, d, $^3J_{HH}$ 8.4 Hz; 2×Ar*H*), 7.92 (1H, d, $^3J_{HH}$ 8.0 Hz; Ar*H*), 7.90 (1H, s; Ar*H*), 7.20 (1H, s; Ar*H*), 7.18 (1H, d, $^3J_{HH}$ 8.4 Hz; Ar*H*), 6.90 (1H, s; Ar*H*), 2.58 (3H, s; CH_3), 2.42 (3H, s; CH_3), 2.32 (3H, s; CH_3); ^{13}C NMR (100 MHz, d_6-DMSO) δ_C 168.7 (*C*OOH), 165.6 (*C*ONH), 161.8 (*C*=N), 156.7 (Ar*C*), 152.8 (Ar*C*), 149.6 (Ar*C*), 142.4 (Ar*C*), 141.5 (Ar*C*), 139.7 (Ar*C*), 138.5 (Ar*C*), 133.5 (Ar*C*H), 129.7 (Ar*C*H), 129.2 (Ar*C*H), 124.4 (Ar*C*), 120.8 (Ar*C*H), 116.2 (Ar*C*H), 112.7 (Ar*C*H), 110.9 (Ar*C*H), 23.8 (*C*H_3), 22.8 (*C*H_3), 21.3 (*C*H_3); MS (ESI) m/z calculated for $C_{23}H_{21}N_3O_3$ $[M + H]^+$ 388.1583, found 388.1492.

Synthesis of (E)-4-((4-((4,6-dimethylpyridin-2-yl)carbamoyl)benzylidene)amino)benzoic acid - Imine 6

A mixture of 4-amino-*N*-(4,6-dimethylpyridin-2-yl)benzamide (**2**) (0.05 mmol) and 4-formylbenzoic acid (**4**) (0.05 mmol) was sonicated in acetone (1 mL) for 1 minute to mix it well in a reaction vial before it was placed in a microwave oven. The mixture was then irradiated at 360 W for 5 minutes. After the reaction was completed, chilled ethanol (2 mL) was added into the reaction mixture. The resulting precipitate was filtered off and dried under vacuum. Likewise, 4-amino-*N*-(4,6-dimethylpyridin-2-yl)benzamide (**2**) (0.5 mmol) and 4-formylbenzoic acid (**4**) (0.5 mmol) were dissolved in acetone (5 mL) and refluxed for 5 hours. The reaction mixture was then evaporated to approximately half its original volume, and the resulting imine **6** was filtered, washed with chilled ethanol and dried under vacuum. The compound was obtained as yellowish powder in 93% yield (microwave irradiation), 82% yield (conventional method); m.p.:

294 - 296 °C; FT-IR (KBr, cm^{-1}) 3280, 2457, 1688, 1630, 1602, 1453 cm^{-1}; ^{1}H NMR (400 MHz, d_6-DMSO) δ_H 13.32 (1H, br s; COO*H*), 10.63 (1H, s; CON*H*), 8.78 (1H, s; C*H*=N), 8.13 (2H, d, $^3J_{HH}$ 8.0 Hz; 2×Ar*H*), 8.10 (4H, m; 4×Ar*H*), 7.91 (1H, s; Ar*H*), 7.38 (2H, d, $^3J_{HH}$ 8.0 Hz; 2xAr*H*), 6.87 (1H, s; Ar*H*), 2.41 (3H, s; CH_3), 2.32 (3H, s; CH_3); ^{13}C NMR (100 MHz, d_6-DMSO) δ_C 167.1 (*C*OOH), 165.9 (*C*ONH), 161.9 (*C*=N), 156.4 (Ar*C*), 152.9 (Ar*C*), 152.5 (Ar*C*), 149.1 (Ar*C*), 139.3 (Ar*C*), 136.2 (Ar*C*), 132.2 (Ar*C*), 130.4 (Ar*C*H), 130.1 (Ar*C*H), 130.0 (Ar*C*H), 121.4 (Ar*C*), 113.0 (Ar*C*H), 112.3 (Ar*C*H), 23.9 (*C*H_3), 21.3 (*C*H_3).

Synthesis of (E)-N-(4,6-dimethylpyridin-2-yl)-4-((4-((4,6-dimethylpyridin-2-yl)carbamoyl)benzylidene) amino)benzamide - Imine 7

N-(4,6-dimethylpyridin-2-yl)-4-formylbenzamide (**1**) (0.05 mmol) and 4-amino-*N*-(4,6-dimethylpyridin-2-yl)benzamide (**2**) (0.05 mmol) were sonicated in acetone (1 mL) for 1 minute to mix the mixture well in a reaction vial before it was placed in a microwave oven. The mixture was then irradiated at 360 W for 5 minutes. After the reaction was completed, chilled ethanol (2 mL) was added into the reaction mixture. The resulting precipitate was filtered off and dried under vacuum. Likewise, a mixture of 4-amino-*N*-(4,6-dimethylpyridin-2-yl)benzamide (**2**) (0.5 mmol) and *N*-(4,6-dimethylpyridin-2-yl)-4-formylbenzamide **1** (0.5 mmol) was dissolved in acetone (5 mL) and refluxed for 5 hours. The reaction mixture was then evaporated to approximately half its original volume, and the resulting imine **7** was filtered, washed with chilled ethanol and dried under vacuum. The compound was obtained as yellowish powder in 71% yield (microwave irradiation), 64% yield (conventional method); m.p.: 211 - 212 °C; FT-IR (KBr, cm^{-1}) 3413, 1686, 1680, 1575, 1449 cm^{-1}; ^{1}H NMR (400 MHz, d_6-DMSO) δ_H 10.83 (1H, s; CON*H*), 10.66 (1H, s; CON*H*), 8.77 (1H, s; C*H*=N), 8.16 (2H, d, $^3J_{HH}$ 8.0 Hz; 2×Ar*H*), 8.13 (1H, s; Ar*H*), 8.11 (1H, s; Ar*H*), 8.07 (2H, d, $^3J_{HH}$ 8.0 Hz; 2×Ar*H*), 7.90 (2H, m), 7.39 (2H, d, $^3J_{HH}$ 8.0 Hz; 2×Ar*H*), 6.89 (1H, s; Ar*H*), 6.88 (1H, s; Ar*H*), 2.41 (3H, s; CH_3), 2.31 (3H, s; CH_3); ^{13}C NMR (100.6 MHz, d_6-DMSO): δ_C 165.8 (*C*=O), 165.7 (*C*=O), 161.9 (*C*=N), 156.7 (Ar*C*), 156.6 (Ar*C*), 154.6 (Ar*C*), 152.1 (Ar*C*), 151.9 (Ar*C*), 149.5 (Ar*C*), 149.4 (Ar*C*), 138.9 (Ar*C*), 137.2 (Ar*C*), 132.1 (Ar*C*H), 129.8 (Ar*C*H), 129.1 (Ar*C*H), 128.9 (Ar*C*H), 121.4 (Ar*C*H), 120.7 (Ar*C*H), 120.5 (Ar*C*H), 112.7 (Ar*C*H), 23.9 (*C*H_3), 21.3 (*C*H_3); MS (ESI) m/z calculated for $C_{29}H_{27}N_5O_2$ $[M + Na]^+$ 500.2165, found 500.1868.

Synthesis of (E)-4-(((4-carboxyphenyl)imino)-methyl)-2-methylbenzoic acid - Imine 8

A mixture of 4-amino-2-methylbenzoic acid **3** (0.05 mmol) and 4-formylbenzoic acid (**4**) (0.05 mmol) was sonicated in acetone (1 mL) for 1 minute to mix it well in a reaction vial before it was placed in a microwave oven. The mixture was then irradiated at 360 W for 5 minutes. After the reaction was completed, chilled ethanol (2 mL) was added into the reaction mixture. The resulting precipitate was filtered off and dried under vacuum. Likewise, a mixture of 4-amino-2-methylbenzoic acid **3** (0.5 mmol) and 4-formylbenzoic acid (**4**) (0.5 mmol) was dissolved in acetone (5 mL) and refluxed for 5 hours. The reaction mixture was then evaporated to approximately half its original volume, and the resulting imine **5** was filtered, washed with chilled ethanol and dried under vacuum. The compound was obtained as yellowish powder in 93% yield (microwave irradiation), 80% yield (conventional method); m.p.: 334 - 337 °C; FT-IR (KBr, cm^{-1}) 2667, 1693, 1645, 1584, 1455 cm^{-1}; ^{1}H NMR (400 MHz, d_6-DMSO) δ_H 12.93 (2H, br s; 2×COO*H*), 8.73 (1H, s; C*H*=N), 8.08 – 8.07 (4H, m; 4×Ar*H*), 7.91 (1H, d, $^3J_{HH}$ 8.0 Hz; Ar*H*), 7.20 (1H, s; Ar*H*), 7.18 (1H, d, $^3J_{HH}$ 8.4 Hz; Ar*H*), 2.58 (3H, s; CH_3); ^{13}C NMR (100 MHz, d_6-DMSO) δ_C 167.3 (*C*OOH), 167.0 (*C*OOH), 161.8 (*C*=N), 152.8 (Ar*C*), 141.5 (Ar*C*), 133.5 (Ar*C*H), 132.3 (Ar*C*), 130.4 (Ar*C*H), 130.2 (Ar*C*H), 130.0 (Ar*C*H), 129.4 (Ar*C*H), 124.4 (Ar*C*), 118.8 (Ar*C*H), 21.9 (*C*H_3); MS (ESI) m/z calculated for $C_{16}H_{13}NO_4$ $[M + H]^+$ 284.0845, found 284.0809.

Results and Discussion

Four imine derivatives were prepared under microwave irradiation and the percentage yield was compared with conventional heating methods as indicated in Table 1. The yields of the synthesised imine **5**, **6** and **8** have been increased nearly 10% under microwave irradiation within 5 min of reaction time. However, the percentage yield of imine **7** gave the lowest yield,

presumably due to steric factors [30]. From the ^{1}H NMR data for all of the imine derivatives, there was a characteristic proton signal at around 8.73 to 8.78 ppm indicated the imine group's proton (*H*C=N), while ^{13}C NMR showed the presence of the carbon signal at 161.2 ppm from the imine group (C=N).

Compounds **1** and **2** have been described earlier [19], though no information on the crystal structure has been reported so far. The molecular structure of *N*-(4,6-dimethylpyridin-2-yl)-4-formylbenzamide **1** and 4-amino-*N*-(4,6-dimethylpyridin-2-yl)benzamide **2** with the atomic numbering schemes are shown in Figure 2(a) and 2(b), respectively. The asymmetric unit of **1** contains a water solvent molecule, which was omitted for clarity purposes. The crystals were crystallised separately from CH_2Cl_2 through a slow evaporation technique. Compound **1** and **2** crystallised in the orthorhombic ($P2_12_12_1$ space group) and monoclinic ($P2_1/c$ space group) crystal system, respectively. The crystal data and parameter of structure refinement for **1** and **2** are given in Table 2.

In the molecular structure of **1**, the plane of pyridine (N2/C9/C10/C11/C12/C13) and the benzene moieties (C1/C2/C3/C4/C5/C6) are substantially planar and slightly twisted to each other by a minor deviation angle of 2.9 (2)º. The former aromatic ring adopted a *cis* configuration for the carbonyl, O atom, across the N1−C8 bond. Besides, both the aromatic rings are positioned *trans* against each other along with the same reference bond, N1−C8. The *co*-planar situation with regards to both of the aromatic rings was likely attributed to the presence of intramolecular hydrogen bond formation *via* C10−H10···O2, which led to the construction of a pseudo-six-membered ring (C10/H10/O2/C8/N1/C9). Concurrently, an inter-molecular hydrogen bonding connecting **1** with a water molecule, was also observed in the crystal lattice, N1−H1A···O1W, forming a one-dimensional column viewed along the *a*-axis [Figure 2(a)]. The presence of water adducts was due to the loose packing arrangement of the molecules [31].

Based on Figure 2(b), the asymmetric unit consists of two **2** molecules and two water solvent molecules (omitted for clarity). Similar to compound **1**, the two molecules of **2** possessed both the pyridine and benzene rings. However, the mean plane angles of both aromatic rings for molecule A [17.8268 (6)°] and B [16.6744 (7)°] are deviated much more compared to that of compound **1**. Congruently, the bond length of intramolecular connections *via* C1A-H1A···O1A [2.307 Å (molecule A)] and C1B-H1B···O1B [2.347 Å (molecule B)] are also much longer compared to C10-H10···O2 (2.264 Å) of compound **1**. Nevertheless, both the aromatic rings are still positioned *trans* against each other along the N2A-C8A and N2B-C8B bond for molecule A and B, respectively. Water molecules are involved in the construction of the supramolecular structure **2** that propagates in a network viewed along the *b*-axis [Figure 3(b)]. The bond lengths and angles corresponding to the secondary amide linkage in compounds **1** and **2** agree with related structures, for example, *R*-fluoro-*N*-(pyridyl)benzamide (*R* = *para*-/*meta*-/*ortho*-) [32].

It has been shown that similar imine compounds bearing both amidopyridine and carboxylic acid active sites tend to self-generate *via* a series of dynamic replication cycle [20]. Besides, such a reaction mechanism was also shown to be kinetically favourable compared to the direct bimolecular formation of imine [19, 33]. Herein, we explore the enthalpies and geometrical characteristics involved through the quantum chemical calculation to validate the replicating pathways. Figure 4 demonstrates a typical autocatalytic reaction cycle, which involves the self-replication of imine **6** *via* its own-template or the use of imine **5**-template.

Table 1. The comparison in yield and reaction time between conventional heating method and microwave irradiation

Imine	Conventional Method		Microwave Irradiation		
	Time (hours)	Yield (%)[a]	Time (minutes)	Power (W)	Yield (%)
5	5	93	5	360	94
6	5	82	5	360	93
7	5	64	5	360	71
8	5	80	5	360	93

[a]the yield of the reflux method is comparable to the previous literature [19-20]

Table 2. Crystal data and parameter of structure refinement for compounds **1** and **2**

Parameter	1	2
Empirical formula	$C_{15}H_{16}N_2O_3$	$C_{28}H_{33}N_6O_4$
Molar mass	272.30	517.60
Temperature, T	302(2)K	303(2)K
Crystal system	Orthorhombic	Monoclinic
Space group	$P2_12_12_1$	$P2_1/c$
Unit cell dimension	a = 4.548(2) Å	a = 21.2704(9) Å
	b = 12.012(6) Å	b = 7.6084(3) Å, β = 103.871(2) °
	c = 25.347(11) Å	c = 17.4597(7) Å
Volume	1384.8(11) $Å^3$	2743.17(19) $Å^3$
Density, Z	1.306 g/cm^3, 4	1.253 g/cm^3, 4
Absorption coefficient	0.092 mm^{-1}	0.086 mm^{-1}
F(000)	584	1100
Theta range for data collection	2.95 to 25.49 °	2.85 to 28.33°
Index ranges	-5<=h=<4, -9<=k=<14, -19<=l=<30	-26<=h=<-28, -10<=k=<10, -23<=l=<23
Refinement method	Full-matrix least-squares on F^2	Full-matrix least-squares on F^2
Data / restraints / parameters	1550 / 2 / 195	6780 / 4 / 363
Final R indices [I>2sigma(I)]	R1 = 0.0600, wR2 = 0.1563	R1 = 0.0633, wR2 = 0.1332

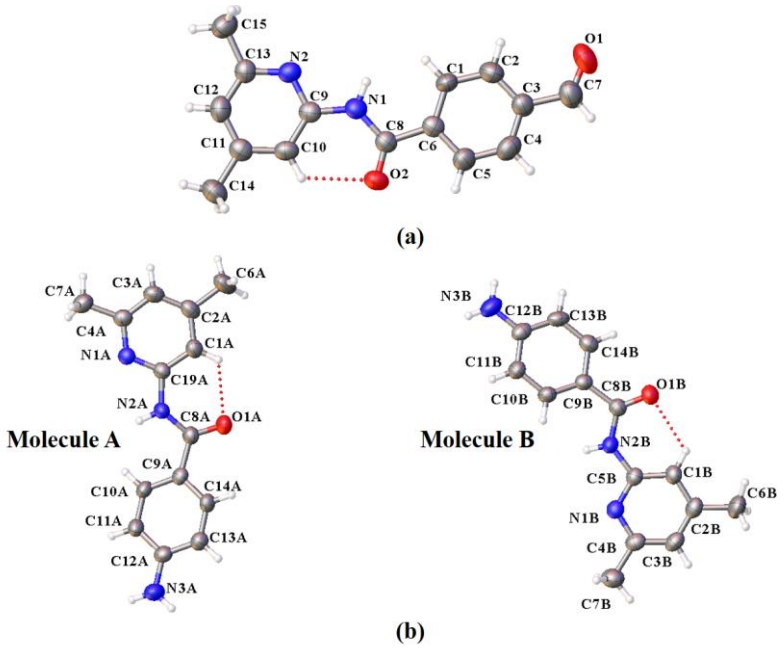


Figure 2. The asymmetric unit of compound (a) **1** and (b) **2**, showing the atom-labelling scheme. Displacement ellipsoids are drawn at 50 % probability level. Intramolecular interactions are shown as dotted lines.

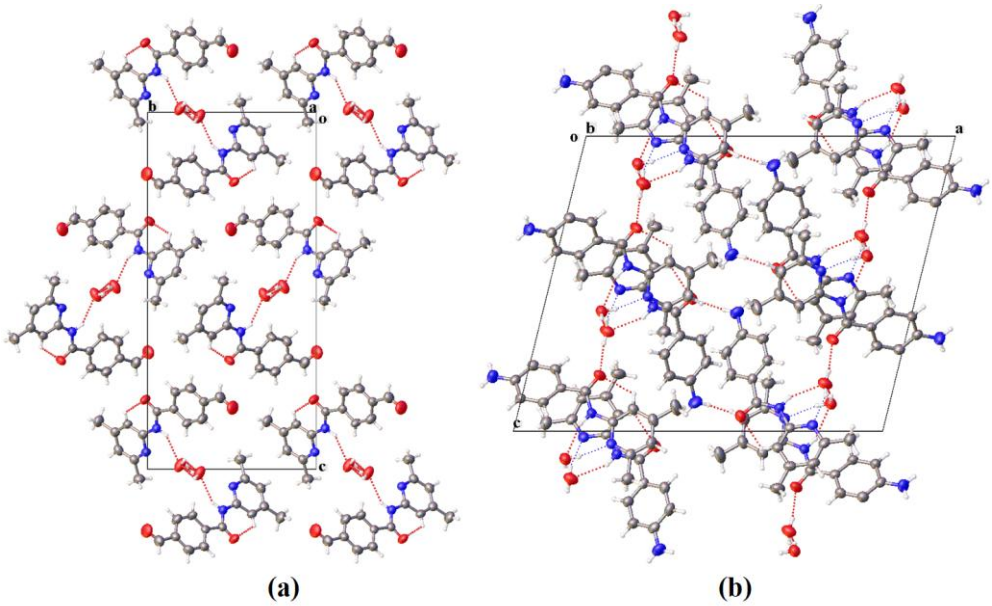


Figure 3. A partial view of the crystal packing of compound (a) **1** and (b) **2**, displaying the crystal packing, viewed along with the *a*- and *b*-axis, respectively. The hydrogen-bonding interactions are shown as dotted lines

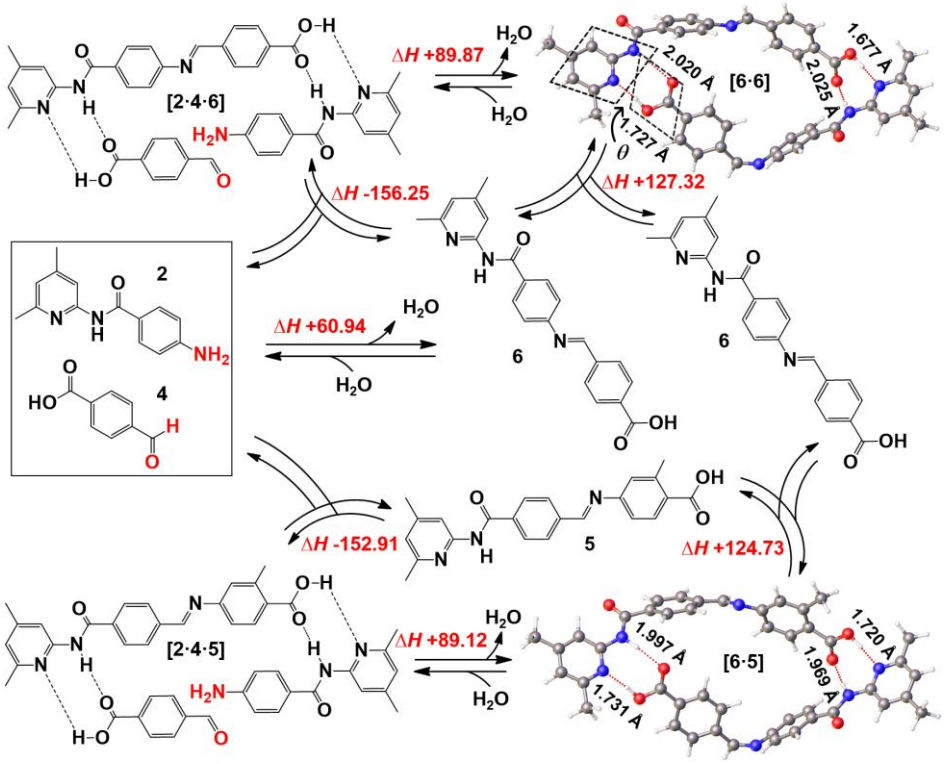


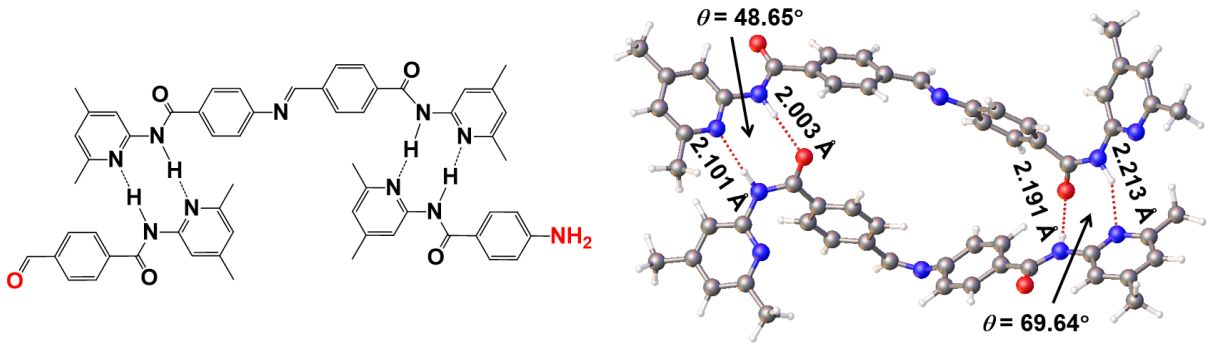
Figure 4. The formation of imine **6** *via* direct condensation of **2** and **4**, as well as through thermodynamically [Δ*H* (kJ/mol)] favourable autocatalytic cycles mediated by ternary complexes **[2·4·6]** or **[2·4·5]**. The optimised [B3LYP/6-311G(d,p)] duplex complexes **[6·6]** and **[6·5]** are shown along with the measured intermolecular hydrogen bond (red dotted lines) lengths. The angle, θ represents the degree of deviation between the mean planes of the amidopyridines and carboxylic acids

Conventionally, compounds **2** and **4** can undergo a reversible reaction to form imine **6,** and it is deemed to have taken place at the initial stages of the reaction. Our theoretical investigation on the condensation process suggests that such a pathway entails an endothermic process with the enthalpy of reaction (Δ*H* = +60.94 kJ/mol). Then, the synthesised imine **6** can act as a template for its subsequent formation. The scouring and binding of compounds **2** and **4** *via* the reciprocal sites on the imine **6** engender the formation of a ternary complex **[2·4·6]** (Δ*H* = -156.25 kJ/mol) with less net energy than the reactants did at the start of the process.

It has been reported that the lowest energy geometry is related to the *co*-planar arrangement of the two binding fragments (θ = 0°), which creates a strong intermolecular hydrogen bonding between the recognition sites [23]. Based on the **[6·6]** complex structure, the mean plane angles of the two associated binding sites involving the amidopyridines and carboxylic acids are not planar and are twisted by an average angle of (θ = 47.06°). The distorted duplex complex ultimately dissociates itself from the steric conformation and completes the autocatalytic cycle.

We also envisaged that imine **5** might act as a similar template for the autocatalytic formation of amine 6 shown in Figure **4**. The optimised geometry of the imine **5** compound revealed that both recognition sites, amidopyridine, and carboxylic acid are placed within the suitable spacer length as of imine **6**, to enable the interaction between the two recognition sites through intermolecular hydrogen bonding and facilitate the formation of imine **6**. In this case, the formation of a ternary complex **[2·4·5]** is also feasible, and the exothermic reaction accounts for ΔH = -152.91 kJ/mol. The eventual condensation step (ΔH = +89.12 kJ/mol) develops into a duplex complex **[6·5]**. Likewise, the mean plane angles of the corresponding recognition fragments are also similarly twisted with the average angle (θ = 46.37°). Noteworthily, the net enthalpy involved in the template-mediated pathway, either with imine **6** or **5** as the template, adds up to the same with the direct bimolecular mechanism, which is an endothermic process. The strong intermolecular hydrogen bond interactions observed in the duplex complexes following the hydrogen bond criterion [34]. Nevertheless, the use of a catalytic template-**5** in the synthesis of imine **6** is considered redundant since the latter can undertake a self-replicating route and catalyses its formation, corroborated by a high percentage yield (82-93%) for the reaction.

Imine **7** is devoid of the carboxylic group, which can complement and attract an amidopyridine group. Interestingly, the synthesis of imine **7** reflects the lowest percentage yield (64-71%) compared to the rest, regardless of the synthetic methods used. To access the likelihood of imine **7** adapting a self-replicating mechanism for its formation, we have performed DFT calculation to identify the possible binding modes. We found that the first possible binding mode involves only the N-H···N, hydrogen bond of amidopyridine (Figure 5a), while the other feasible mode is *via* the amide [C(O)NH] linkage (Figure 5b). Unfortunately, the former mode promotes a counter-positioned aldehyde and amine group of the reactants that impede the condensation process to form imine **7**. The second mode of binding is also undesirable since the intermolecular hydrogen bonds are elongated, and the distances are extended further as compared to the situation involving imine **6**. Moreover, the mean planes of similar binding sites are severely twisted, 48.65-69.64° suggesting that the autocatalytic mechanism is not preferably viable for an efficient self-replicating reaction.



(a) **(b)**

Figure 5. The chemical structure of the ternary complex (a) and the DFT optimised [B3LYP/6-311G(d,p)] duplex complex (b) involving the formation of imine **7**. The former assumes only the N-H···N intermolecular hydrogen bonding, while the latter participates in a reciprocal interaction *via* N-H···N and N-H···O

Conclusion

In summary, we have demonstrated the synthesis of four imine derivatives utilising both microwave irradiation and conventional heating procedure. The microwave irradiation method is proven to increase the yield by approximately 10% higher than conventional synthesis within very short reaction times. The improvement in yield is significant considering acceleration of the chemical reaction can be accelerated from hours to minutes, thus providing quick results. Besides, the molecular structures of compounds **1** and **2**, possessing an orthorhombic and monoclinic system, respectively, were successfully described with the X-ray crystallographic method. Based on the DFT studies, the capability of imine **5** and **6** to establish an autocatalytic reaction with the participation of recognition sites involving the aminopyridine and carboxylic acid is corroborated. On the contrary, imine **7** has a low percentage yield, which is justified by the lack of reciprocal recognition sides for an efficient self-replicating reaction.

Acknowledgement

The authors express their gratitude to the Faculty of Science and Technology and Centre for Research and Instrumentation, Universiti Kebangsaan Malaysia, for laboratory and instrumental facilities. This work received financial assistance from the Ministry of Higher Education, (FRGS/1/2019/STG01/UKM/02/3). We also like to thank Professor Hideaki Kasai, Professor Wilson Agerico Diño, and Osaka University (Japan) for supporting us with quantum computational facilities.

References

1. Hawaiz, F. E., Raheem, D. J. and Samad, M. K. (2016). Synthesis and characterization of some new azo-imine dyes and their application. *Journal of Zankoy Sulaimani, Part A*, 201(1): 18-23.
2. Sharghi, H. and Nasseri, M. A. (2003). Schiff-base metal(II) complexes as new catalysts in the efficient, mild and regioselective conversion of 1,2- epoxyethanes to 2-hydroxyethyl thiocyanates with ammonium thiocyanate. *Bulletin of the Chemical Society of Japan*, 76(1): 137-142.
3. Kovacic, P. and Somanathan, R. (2014). Toxicity of imine-iminium dyes and pigments: electron transfer, radicals, oxidative stress and other physiological effects. *Journal of Applied Toxicology*, 34(8): 825-834.
4. Ke, S., Wei, Y., Yang, Z., Wang, K., Liang, Y. and Shi, L. (2013). Novel cycloalkylthiophene–imine derivatives bearing benzothiazole scaffold: Synthesis, characterization, and antiviral activity evaluation. *Bioorganic & Medicinal Chemistry Letters,* 23(18): 5131-5134.
5. Hania, M. M. (2009). Synthesis of some imines and investigation of their biological activity. *European Journal of Chemistry* 6(3): 629-632.
6. Silva, C. M., Silva, D. L., Modolo, L. V., Alves, R. B., Resende, M. A., Martins, C. V. B. and Fátima, Â. (2011). Schiff bases: A short review of their antimicrobial activities. *Journal of Advanced Research,* 2(1): 1-8.
7. Mohamaed, S. S., Tamer, A. R., Bensaber, S. M., Jaeda, M. I., Ermeli, N. B., Allafi, A. A., Mrema, I. A., Erhuma, M. Hermann, A. and Gbaj, A. M. (2013). Design, synthesis, molecular modeling and biological evaluation of sulfanilamide-imines derivatives as potential anticancer agents. *Naunyn-Schmiedeberg's Archives of Pharmacology*, 386(9):813-822.
8. Vazzana, A., Terranova, E., Mattioli, F. and Sparatore, F. (2004). Aromatic Schiff bases and 2,3-disubstituted-1,3-thiazolidin4-one derivatives as anti-inflammatory agents. *ARKIVOC*, 5: 364-374.
9. Sager, A. A., Abood, Z. S., El-Amary, W. M., Bensaber, S. M., Al-Sadawe, I. A., Ermeli, N. B., Mohamed, A. B., Al-Forgany, M., Mrema, I. A., Erhuma, M., Hermann, A. and Gbaj, A. M. (2018). Design, synthesis and biological evaluation of some triazole schiff's base derivatives as potential antitubercular agents. *The Open Medicinal Chemistry Journal,* 12: 48-59.

10. Yu, H., Shao, L. and Fang, J. (2007). Synthesis and biological activity research of novel ferrocenyl-containing thiazole imine derivatives. *Journal of Organometallic Chemistry,* 692(5): 991-996.
11. Love, B. E. and Ren, J. (1993). Synthesis of sterically hindered imines. *The Journal of Organic Chemistry,* 58(20): 5556-5557.
12. Look, G. C., Murphy, M. M., Campbell, D. A. and Gallop, M. A. (1995). Trimethyl orthoformate: a mild and effective dehydrating reagent for solution and solid phase imine formation. *Tetrahedron Letters* 36(17): 2937-2940.
13. Flitsch, W. (1996). 8.09 – Bicyclic 5-6 systems with one ring junction nitrogen atom: No extra heteroatom. *Comprehensive Heterocyclic Chemistry II,* 8: 237-248
14. Souza, F. B., Pimenta, D. C. and Stefani, H. A. (2016). Microwave-assisted one-pot three-component synthesis of imines 1,2,3-triazoles. *Tetrahedron,* 57(14): 1592-1596.
15. Dallinger, D. and Kappe, C. O. (2007). Microwave-assisted synthesis in water as solvent. *Chemical Reviews,* 107(6): 2563-2591.
16. Baruah, S., Fisyuk, A., Kulakov, I.V. and Puzari, A. (2017). An atom economic acid-catalyzed synthetic method for aromatic imines. *Asian Journal of Chemistry and Pharmaceutical Sciences,* 2(1): 6-9.
17. Caddick, S. and Fitzmaurice, R. (2009). Microwave enhanced synthesis. *Tetrahedron,* 65: 3325-3355.
18. Del Amo, V. and Philip, D. (2010). Integrating replication-based selection strategies in dynamic covalent systems. *Chemistry-A European Journal,* 16(45): 13304-13318.
19. Del Amo, V., Slawin, A. M. Z. and Philp, D. (2008). Manipulating replication processes within a dynamic covalent framework. *Organic Letters,* 10(20): 4589-4592.
20. Robertson, C. C., Mackenzie, H. W., Kosikova, T. and Philp, D. (2018). An environmentally responsive reciprocal replicating network. *Journal of the American Chemical Society,* 140(22): 6832-6841.
21. Bekdemir, Y. and Efil, K. (2014). Microwave-assisted solvent-free synthesis of some imine derivatives. *Organic Chemistry International,* 2014: 1-5.
22. Becke, A. D. (1988). Density-functional exchange-energy approximation with correct asymptotic behavior. *Physical Review A,* 38(6): 3098-3100.
23. Becke, A. D. (1993). Density functional thermochemistry III the role of exact exchange. *Journal of Chemical Physics,* 98: 5648-5652.
24. Davidson, E. R. and Feller, D. (1986). Basis set selection for molecular calculations. *Chemical Reviews,* 86(4): 681-696.
25. Hehre, W. J., Radom, L., Schleyer, P. V. R. and Pople, J. A. (1986). Ab initio molecular orbital theory. *Accounts of Chemical Research,* 9: 399-406.
26. Lee, C., Yang, W. and Parr, R. (1988). Development of the ColleSalvetti correlation energy formula into a functional of the electron density. *Physical Review B,* 37(2): 785-789.
27. Mark-Lee, W. F., Chong, Y. Y., Law, K. P., Ahmad, I. B. and Kassim, M. B. (2018). Synthesis, structure and density functional theory (DFT) study of a rhenium(I) pyridylpyrazol complex as a potential photocatalyst for CO2 reduction. *Sains Malaysiana,* 47(7): 1491-1499.
28. Mark-Lee, W. F., Rusydi, F., Minggu, L. J. and Kassim, M. B. (2017). Bis(Bipyridyl)-Ru(II)-1-benzoyl-3-(pyridine-2-yl)-1H-pyrazole as potential photosensitiser: Experimental and density functional theory study. *Jurnal Teknologi,* 79(5-3): 117-123.
29. Ochterski, J. W. (2000). Thermochemistry in Gaussian. Gaussian, Inc.: Wallingford, CT: pp 1-19.
30. Tauber, J., Imbri, D. and Opatz, T. (2014). Radical addition to iminium ions and cationic heterocycles. *Molecules,* 19(10): 16190-16222.
31. Mark-Lee, W. F., Chong, Y. Y. and Kassim, M. B. (2018). Supramolecular structures of rhenium(I) complexes mediated by ligand planarity via the interplay of substituents. *Acta Crystallographica Section C,* 74: 997-1006.

32. Mocilac, P., Donnelly, K. and Gallagher, J. F. (2012). Structural systematics and conformational analyses of a 3×3 isomer grid of fluoro-N-(pyridyl)benzamides: Physicochemical correlations, polymorphism, and isomorphous relationships. *Acta Crystallographica Section B: Structural Science,* 68(2): 189-203.
33. Sadownik, J. W., Kosikova, T. and Philp, D. (2017). Generating system-level responses from a network of simple synthetic replicators. *Journal of the American Chemical Society,* 139(48): 17565-17573.
34. Arunan, E., Desiraju, G. R., Klein, R. A., Sadlej, J., Scheiner, S., Alkorta, I., Clary, D. C., Crabtree, R. H., Dannenberg, J. J., Hobza, P., Kjaergaard, H. G., Legon, A. C., Mennucci, B. and Nesbitt, D. J. (2011). Definition of the hydrogen bond (IUPAC Recommendations 2011). *Pure and Applied Chemistry* 83(8): 1637-1641.

Malaysian Journal of Analytical Sciences (MJAS)
Published by Malaysian Analytical Sciences Society

GREEN SYNTHESIZED COPPER NANOPARTICLES FROM *Blumea balsamifera* LINN. LEAVES AND ITS BIOCIDAL ACTIVITIES AGAINST *Bactrocera dorsalis* (HENDEL)

(Sintesis Hijau Nanopartikel Kuprum dari Daun *Blumea balsamifera* Linn dan Aktiviti Biosida Melawan *Bactrocera dorsalis* (Hendel))

Danila S. Paragas [1,2]*, Kathlia D.C. Cruz[1], and Elaida R. Fiegalan[3]

[1]*School of Chemical, Biological and Materials Engineering and Sciences, Mapua University, Intramuros, Manila, Philippines*
[2]*Department of Chemistry, College of Arts and Sciences, Central Luzon State University, Science City of Muñoz, Nueva Ecija, Philippines*
[3]*Department of Crop Protection, College of Agriculture, Central Luzon State University, Science City of Muñoz, Nueva Ecija, Philippines*

**Corresponding author: danilaparagas1010@clsu.edu.ph*

Received: 20 November 2019; Accepted: 16 April 2020; Published: 9 June 2020

Abstract

The biocidal components of sambong (*Blumea balsamifera*) leaves against oriental fruit fly, *Bactrocera dorsalis* (Hendel) (Diptera: Tephritidae), were extracted using four green solvents, namely rice wine, rice wash, apple cider vinegar, and distilled water employing hot infusion, maceration, fermentation, and Soxhlet methods. These extracts were used in the synthesis of copper nanoparticles (CuNPs). The suspensions of nanoparticles were centrifuged, and the aggregates were separated and dried. The dried aggregates and colloidal suspensions of copper nanoparticles were tested on male adult oriental fruit flies. Improvised olfactometer was used to determine the adulticidal activities of the nanoparticles. Both dried aggregates and colloidal suspensions had varying effects on the mortality rates of fruit flies, which ranged from 25-100% within 12 hours exposure. However, dried aggregates yielded higher mortality rates than those of the colloidal suspensions. The researchers concluded that sambong can be used in the preparation of nanoparticle-enhanced biocide either as suspension concentrate or dust or powder with suitable sorption material. Ultimately, sambong can be considered as an alternative in managing the oriental fruit fly.

Keywords: biocide, *Blumea balsamifera*, nanoparticle, nanosuspension, oriental fruit fly

Abstrak

Komponen biosida bagi daun sambong (*Blumea balsamifera*) melawan lalat buat oriental, *Bactrocera dorsalis* (Hendel) (Diptera: Tephritidae), telah diekstrak menggunakan empat pelarut hijau iaitu wain beras, basuhan beras, cuka epal, dan air suling berdasarkan keadah infusi panas, maserasi, penapaian dan Soxhlet. Pengestrakan ini digunakan dalam sistesis nanopartikel kuprum (CuNPs). Nanopartikel terampai telah diempar, dan gumpalan telah diasing dan dikeringkan. Gumpalan kering dan ampaian koloid bagi nanopartikel kuprum telah diuji terhadap lalat buah oriental jantan dewasa. Olfactometer telah digunapakai dalam penentuan aktiviti pendewasaan lalat terhadap nanopartikel. Gumpalan kering dan ampaian koloid, keduanya

menghasilkan kesan yang berbeza terhadap kadar kematian lalat buah, iaitu julat 25-100% dalam tempoh 12 jam pendedahan. Walau bagaimanapun, gumpalan kering menghasilkan kadar kematian yang lebih tinggi berbanding ampaian koloid. Penyelidik membuat kesimpulan bahawa sambong boleh diguna dalam penyediaan nanopartikel-yang diperkaya biosida sama ada ampaian pekat, debu atau serbuk dengan bahan jerapan yang sesuai. Sambong boleh dipertimbangkan sebagai alternatif dalam pengawalan lalat buat oriental.

Kata kunci: biosida, *Blumea balsamifera*, nanopartikel, nanoampaian, lalat buah oriental

Introduction

Biocides are pesticides derived from natural materials, such as plants, animals, bacteria, and certain minerals. The use of biocides as pest management tools in various cropping systems is becoming increasingly important due to the adverse effects of chemical pesticides on human health causing diseases including cancer [1] and to the environment [2-4]. In addition, the use of chemical pesticides promotes the destruction of beneficial predators of pests, which, in effect, increases virulence in many species of several agricultural pests [5]. Target-specific on pests, biocides are presumed to be relatively safe to nontarget organisms including humans [6]. Therefore, biocides provide a strategic option toward sustainable pest management [7, 8].

Blumea balsamifera, locally known as sambong, was reported to contain more than hundreds of active components [9] that contribute to antibacterial, antiviral, antitumor, anthracycline [10], antioxidation, [11] and wound healing activity in mice [12]. Only a few studies on pesticidal activities of sambong were reported in the late 1980s. Rejesus et al. [13] reported that sambong was toxic to stored grain pests, corn weevil, lesser grain borer, and red flour beetle based on LD_{50} values. Sambong extract also showed activity against green leaf hopper and was comparable to monocrotophos insecticide activity [14]. Another study conducted on the pesticidal action of botanical plants, including sambong, against Fusarium rot of garlic showed that high concentrations of these botanical extracts are comparable with the activities of benomyl [15]. Moreover, sambong leaves extract was reported as toxic against golden snails [16, 17].

Based on the reports above, no information was published about the effects of *B. balsamifera* on adult oriental fruit fly. This study aimed to extract the bioactive components of sambong using green solvents and four extraction methods. The extracted insecticidal components of sambong were used in the synthesis of copper nanoparticles, then tested for insecticidal activities against *B. dorsalis*.

Materials and Methods

Collection, preparation, and extraction of plant materials

Blumea balsamifera, leaves were collected in a hilly place at Balloc, San Clemente, Tarlac, Philippines. Branches were gathered in the morning. The sample was washed thoroughly with tap water and was hung for five days under the shade. Then, the clean leaves were detached from the branches and were ground using a blender. The sample was stored in a tightly covered container until further use.

Four different methods of extractions were performed, namely hot infusion, maceration, Soxhlet (hot continuous extraction), and fermentation. Rice wine, rice wash, apple cider vinegar, and distilled water were then used as green solvents. Hot infusion was conducted by adding 10 g of previously weighed ground leaves into a 100 mL boiling solvent. The mixture was set aside for 15 minutes. Second, maceration was employed by placing 10 g of the plant material into 100 mL of the solvent. Then, the mixture was set aside for 1 hour, and filtered. The Soxhlet method was performed as follows: the ground plant material was loaded into the cellulose thimble, which was placed inside the Soxhlet extractor afterward. Afterward, the solvent was heated using the heating mantle, causing it to evaporate and move through the apparatus to the condenser. The condensation was then allowed to drip into the reservoir containing the thimble. The level of solvent poured back into the flask

upon reaching the siphon, repeating the cycle. This process ran for a total of 8 hour. Fermentation was carried out by soaking 10 g of the plant material into 100 mL of the solvent. The container was wrapped with aluminum foil, stored inside the locker, and set aside for five days. Filter paper was used to filter the extracts. Furthermore, the filtrates were placed in an amber bottle, and stored in the refrigerator until used for nanoparticles preparation.

Preparation of copper nanoparticles using sambong leaves extracts

The method described by Harne et al. [18] was used with some modifications. Copper nanoparticles (CuNPs) were prepared using 1 mM $CuSO_4$ solution. Volume ratios (extract: $CuSO_4$) of 1:99, 5:95, 10:90, and 20:80 were tested. The initial pH of each solution was recorded. Then, the mixture was placed in an Erlenmeyer flask, stirred, and heated gradually in a hotplate up to 100 °C. Drop by drop addition of 0.1 M NaOH was done every 10 minutes. When the color of the solution changed from dark to greenish brown, the pH of the mixture was measured. The formation of metal nanoparticles was monitored using UV-Vis spectrophotometer scanning from 800 to 300 nm. Absorption peaks were observed at 500–600 nm for CuNPs at the optimum temperature. The nanoparticle suspension was centrifuged once the peak was observed to be constant, while the aggregates were separated from the colloidal suspension by decantation. Then, the test tubes containing the aggregates were covered with parafilm that was pricked with a needle to allow passage of air. They were stored in a locker and allowed to dry. Moreover, the colloidal suspensions were covered with parafilm and stored in the refrigerator for the insecticidal activity test. The CuNPs were further analyzed using Fourier transform infrared spectroscopy (FTIR) and scanning electron microscopic techniques.

Collection of test insects (male fruit flies)

Male fruit flies were trapped inside a canister with cotton wet with 10 drops of methyl eugenol. The trap was placed under a mango or guava tree before sunrise as more fruit flies are trapped during this time. Then, the canister was covered when there were enough fruit flies inside. Balls of cotton dipped in sugar solution placed on the net covering of the canister served as food for the fruit flies.

Insecticidal effect of extracts

The insecticidal activities of sambong-copper nanoparticles (sambong-CuNPs) were tested in an improvised olfactometer (Figure 1). The olfactometer was made with a transparent plastic food container with the following measurements: 4 in top diameter, 3 in bottom diameter, and 4 in high. Then, the cover was cut, forming a 2 in diameter hole that was replaced with silk fabric to prevent the fruit flies from suffocating during the test.

Male fruit flies were introduced into the plastic container using a transparent tube (acetate). A small cotton ball was doused with ten drops of the colloidal suspension. For the dried nanoparticle aggregates, the cotton ball was dipped into the test tube itself. Then, the cotton ball was placed at the top center of the container 5–10 minutes after the male fruit flies were introduced. The container was covered, and the fruit flies were observed after 6, 12, and 24 hours. The effect of the pure solvents on the mortality of fruit flies, as well as the flies' reaction toward the nanoparticles, were determined. Moreover, a fruit fly was considered dead when it falls ventral side-up, and no more movement can be observed.

Treatment applications were tabulated below. E stands for extraction; and S, for solvent. The process involved a total of 16 extraction x solvent combinations, as presented in Table 1.

Percent mortality was computed by subtracting the number of dead flies in control from the number of dead fruit flies as affected by the treatment and dividing the difference by the total number of flies inside the plastic container [19]. This was done with sambong-copper nanosuspensions. However, correction using Abbott's was not applicable to the dried copper nanoparticles. Mortality rates were recorded after 6, 12, and 24 hours exposure to different treatments.

Data analysis

The percent mortality of adult fruit flies in CuNP nanosuspensions and nanopowders were compared per treatment using Analysis of Variance and post hoc using Duncan Multiple Range Test at a 95% level of confidence. Then, the plant that showed the highest mortality rates was further investigated by applying the procedure below. Moreover, those that showed the highest mortality at an earlier exposure time were subjected to efficacy test. The same cotton ball with the extract was moistened with 10 drops of distilled water, and mortality rates were read again after 6, 12, and 24 hours. This process was repeated twice. The plant extract that gave higher mortality rates was subjected to further investigation employing the four solvents and extraction methods.

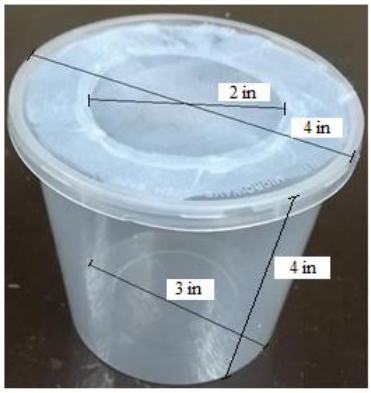


Figure 1. Improvised olfactometer

Table 1. Assignment of treatment application

Method of Extraction	Extracting Solvent			
	Rice Wine (S_1)	**Rice Wash (S_2)**	**Apple Cider (S_3)**	**Distilled Water (S_4)**
Hot infusion (E_1)	T1 = E_1S_1	T5 = E_1S_2	T9 = E_1S_3	T13 = E_1S_4
Maceration (E_2)	T2 = E_2S_1	T6 = E_2S_2	T10 = E_2S_3	T14 = E_2S_4
Hot reflux (E_3)	T3 = E_3S_1	T7 = E_3S_2	T11 = E_3S_3	T15 = E_3S_4
Fermentation (E_4)	T4 = E_4S_1	T8 = E_4S_2	T12 = E_4S_3	T16 = E_4S_4

Results and Discussion

Sixteen extracts from the extraction x solvent combinations were obtained. The colour, odour, and other characteristics of the extracts are described in Table 2.

Green synthesis of copper nanoparticles

The method described by Harne et al. [18] in the green synthesis of copper nanoparticles (CuNPs) uses 1 mM copper sulfate solution and extracts. Optimum conditions for the CuNP synthesis in each treatment are indicated in Table 3. The optimum pH ranges from 4-11.8, while the optimum temperature falls around 60-100°C. On the other hand, the optimum volume ratio is 20:80, except for E3S1, which is 10:90.

Insecticidal activity

The potential insecticidal activity of the different treatments (Table 4) was performed in three replicated procedures. Test for mortality was observed after 6, 12, and 24 hours after treatment application. Mortality rates were corrected using Abbot's formula. Analysis of variance revealed that the treatments are significantly different. Post hoc analysis using Duncan multiple range test (DMRT) further revealed which treatment is the most effective. T9 (E_1S_3), which used hot infusion–apple cider vinegar extract copper nanosuspension, produced the highest mortality rate against adult male oriental fruit fly at 91.67% with only 6 hours exposure. Other treatments that showed activity were T2, T3, T13, and T14, but with low percent mortality of 8.33%, 25.00%, 33.33%, and 8.33%, respectively. Rice wine was used as the solvent in treatments T2 and T3; while distilled water, in T13 and T14. The treatments that utilized rice wash as solvents (T5-T8) did not show any activity at 6 hours of exposure.

At 12 hours exposure, the percent mortality of the different treatments ranged from 0% to 91.67%, with T9 showing the highest mortality (91.67%), followed by T4 (41.67%), T13, and T14 (33.33%). Other treatments yielded around 0–25% mortality only.

At 24 hours exposure, only T5 and T11 showed no activity to Oriental fruit fly, while only T4, T9, T14, and T15 yielded mortality rates of 50% and above. Analysis of Variance of the different treatments showed significant differences measured at a level of 5%. Post hoc analysis further identified which treatments produced the highest mortality rates. Table 4 shows the differences in treatments. T15 and T9 were effective against oriental fruit fly. T15 utilized distilled water as solvent and employed continuous reflux for 8 hours. Meanwhile, apple cider vinegar was used in T9 and extracted through hot infusion.

Insecticidal activities of the sambong-CuNP (dried powder) (Table 5) revealed that the mortality rate was at 87.50% at 6 hours exposure, and 100% at 12 hours. Only a few treatments resulted in a mortality of less than 100% after 24 hours exposure. These were T4, T5, T10, T12, and T16. The effectiveness of T9 (apple cider vinegar-sambong extract by hot infusion) may be due to the chemicals released by the apple cider, such as acetic acid, acetone, ethanol, and methanol. These chemicals are key olfactory signals for fruit flies, while related metabolites are specific gene disruptors. In addition to these chemicals, the bioactive components in sambong that were extracted may have had a synergistic effect that caused the mortality of the fruit flies within 6 hours exposure.

T9 still showed the highest mortality rate at 6 hours exposure to the dried nanopowder, but not significantly different from T1, T3, and T14. At 12 hours exposure, T1, T2, T3, T7, and T14 were the most effective treatments resulting in 100% mortality each. T9's mortality, which yielded the highest within 6 hours exposure only, increased to 100% at 24 hours.

Table 2. Description of different extracts

Method of Extraction	**Extracting Solvent**			
	Rice Wine (S_1)	**Rice Wash (S_2)**	**Apple Cider (S_3)**	**Distilled Water (S_4)**
Hot infusion (E_1)	Dark brown with aromatic, sweet odor	Dark brown with aromatic odor	Dark brown with aromatic but sour odor	Brown with aromatic odor
Maceration (E_2)	Brown with sweet odor	Brown with sweet odor	Brown with sour odor	Brown with aromatic odor
Hot reflux (E_3)	Blackish brown, sweet caramel odor	Dark brown with aromatic odor	Dark brown with aromatic and sour odor	Dark brown with aromatic odor
Fermentation (E_4)	Brown with sweet odor	Light brown with a little off odor	Brown with sour odor	Brown with strong off odor

Table 3. Optimum conditions for the green synthesis of copper nanoparticles and the corresponding λ_{max} and absorbance

Treatments	pH	Temperature	Volume Ratio	λ_{max}, nm	Abs
T1 = E_1S_1	11	97	20:80	545	3.793
T2 = E_2S_1	7.81	60	20:80	543	3.715
T3 = E_3S_1	10	80	10:90	460	3.486
T4 = E_4S_1	10	100	20:80	591	3.769
T5 = E_1S_2	11	100	20:80	546	3.744
T6 = E_2S_2	11.8	60	20:80	530	3.597
T7 = E_3S_2	10	90	20:80	537	3.735
T8 = E_4S_2	8.94	60	20:80	526	3.663
T9 = E_1S_3	11	100	20:80	554	3.685
T10 = E_2S_3	6.25	60	20:80	534	3.772
T11 = E_3S_3	4	60	20:80	544	4.173
T12 = E_4S_3	11.69	60	20:80	483	3.475
T13 = E_1S_4	11	90	20:80	592	3.669
T14 = E_2S_4	10.74	70	20:80	539	3.785
T15 = E_3S_4	10.69	80	20:80	563	3.728
T16 = E_4S_4	5.36	60	20:80	528	3.627

Table 4. Percent mortality of adult male fruit flies observed under different treatments and exposure times (sambong-copper nanosuspension)

Treatment	Mean Percent Mortality*		
	6 hours	12 hours	24 hours
T1 = E_1S_1	0.00^{c}	0.00^{d}	41.67^{bc}
T2 = E_2S_1	8.33^{c}	25.00^{bc}	41.67^{bc}
T3 = E_3S_1	25.00^{b}	25.00^{bc}	41.67^{bc}
T4 = E_4S_1	0.00^{c}	41.67^{b}	50.00^{b}
T5 = E_1S_2	0.00^{c}	0.00^{d}	0.00^{e}
T6 = E_2S_2	0.00^{c}	25.00^{bc}	41.67^{bc}
T7 = E_3S_2	0.00^{c}	8.33^{cd}	25.00^{cd}
T8 = E_4S_2	0.00^{c}	0.00^{d}	16.67^{de}
T9 = E_1S_3	91.67^{a}	91.67^{a}	91.67^{a}
T10 = E_2S_3	0.00^{c}	0.00^{d}	16.67^{de}
T11 = E_3S_3	0.00^{c}	0.00^{d}	0.00^{e}
T12 = E_4S_3	0.00^{c}	0.00^{d}	16.67^{de}
T13 = E_1S_4	33.33^{b}	33.33^{b}	33.33^{cd}
T14 = E_2S_4	8.33^{c}	33.33^{b}	50.00^{b}
T15 = E_3S_4	0.00^{c}	8.33^{cd}	75.00^{a}
T16 = E_4S_4	0.00^{c}	8.33^{cd}	8.33^{de}

*Means with the same letter superscript in a column are not significantly different at 5% level using DMRT

Table 5. Percent mortality of adult male fruit flies observed under different treatments and exposure times (sambong-CuNP powder)

Treatment	Mean Percent Mortality*		
	6 hours	12 hours	24 hours
T1 = E_1S_1	75.00^{a}	100.00^{a}	100.00^{a}
T2 = E_2S_1	62.50^{ab}	100.00^{a}	100.00^{a}
T3 = E_3S_1	75.00^{a}	100.00^{a}	100.00^{a}
T4 = E_4S_1	0.00^{b}	50.00^{abc}	50.00^{b}
T5 = E_1S_2	0.00^{b}	37.50^{bc}	62.50^{b}
T6 = E_2S_2	50.00^{ab}	62.50^{ab}	100.00^{a}
T7 = E_3S_2	25.00^{ab}	100.00^{a}	100.00^{a}
T8 = E_4S_2	50.00^{ab}	75.00^{ab}	100.00^{a}
T9 = E_1S_3	87.50^{a}	87.50^{ab}	100.00^{a}
T10 = E_2S_3	0.00^{b}	12.50^{c}	62.50^{b}
T11 = E_3S_3	0.00^{b}	37.50^{bc}	100.00^{a}
T12 = E_4S_3	25.00^{ab}	62.50^{ab}	62.50^{b}
T13 = E_1S_4	37.50^{ab}	75.00^{ab}	100.00^{a}
T14 = E_2S_4	75.00^{a}	100.00^{a}	100.00^{a}
T15 = E_3S_4	0.00^{b}	50.00^{abc}	100.00^{a}
T16 = E_4S_4	25.00^{ab}	50.00^{abc}	50.00^{b}

*Means with the same letter superscript in a column are not significantly different at 5% level using DMRT

The sambong-CuNP powder was more effective in eradicating oriental fruit flies compared with the sambong-copper nanosuspension. This result may be due to the higher diffusivity of the powder to the fruit fly than the nanosuspension. The most common means of contact between a toxicant and a living organism is through accidental or deliberate application to the integument (e.g., insect cuticle or vertebrate skin), or ingestion with food followed by absorption through the walls of the alimentary tract. After ingestion, the toxicant enters the hemolymph where it may be carried to all parts of the organism as a dissolved solution, a particle bound to protein, or one dissolved in lipid particles [21]. As the sambong-copper nanosuspension or nanopowder was placed on top of the olfactometer where the fruit flies tended to stay, there was a high possibility that the insects flew near the bait, causing the nanosuspension to accumulate on the wings (Figure 2a), dried nanoparticles gathered on the different parts of the fruit fly's body (Figure 2b), and on the compound eye (Figure 2c).

Fourier transform infrared (FTIR) spectroscopic and scanning electron microscopic (SEM) analyses

The FTIR spectra of the four solvents are presented in Figure 3. The broad band of the O-H stretching in all the solvents are evident. This band (3000–3500 cm^{-1}) is due to the OH group present in all the solvents. However, the OH for apple cider vinegar and rice wine, respectively, have lower intensities. This can be the alcohol group for the rice wine and the polyphenolics in the apple cider vinegar. The water used to prepare the rice wash was distilled water; hence, there are similarities between the peaks for rice wash and distilled water.

There were changes in the bands at 3300 cm^{-1} and 1600 cm^{-1} corresponding to O-H stretching of alcohols and phenols, and carbonyl stretching (Figure 4). These

changes in the IR spectra suggested that the CuNPs are being surrounded by different organic molecules present in the different extracts [18]. The spectra also justified the differences among the mortality rates of the nanoparticles against *B. dorsalis*.

Moreover, mortality may be related to the shape or size of the nanoparticles. The surface morphology of the nanoparticles produced using the different extracts analyzed with SEM is presented in Figure 5.

Based on the insecticidal activities of the extracts and the diameter of the synthesized CuNPs, larger CuNPs resulted in lower insecticidal activities. Among the CuNPs produced, only T9 (E_1S_3) yielded the highest mortality at 91.67%. The CuNP diameters range from 49 to 96 nm, which fall under the range of nanomaterials. Other treatments yielded copper nanoparticles greater than 100 nm. The formation of aggregates can be one explanation for this large particle size, as copper nanoparticles aggregate rapidly in water suspension [22]. Considering the diameter of the nanoparticles above, there were more particles with a diameter greater than 100 nm than those with less than 100 nm.

Studies have also shown that the size of nanoparticles found on the insect's wings may vary from 200 to 1000 nm. The structures have a rounded shape at the apex and protrude some 150–350 nm out of the surface plane. These wing nanoparticles help with the insect's aerodynamic efficiency [23].

The nanoparticles produced from different extracts have diverse shapes. Irregular shapes can be observed in E_1S_1, while spherical shapes and flakes can be distinguished in E_1S_3 and E_1S_4, respectively. These three treatments were extracted by hot infusion. Spherical and irregularly shaped nanoparticles were also observed in E_2S_2 and E_2S_4, respectively. Both were prepared by maceration. E_3S_1 and E_3S_2 seemed to have produced blocks or rectangular shapes. Nanoparticles prepared using fermentation had different shapes as well. E_4S_1 produced irregular-shaped particles, while E4S4 had mostly spherical.

Energy dispersive spectroscopic (EDS) analysis

The energy of the characteristic radiation within a given series of lines varies monotonically with the atomic number. This is Moseley's Law:

$$E = C_1 (Z - C_2)^2$$

where E is defined as energy of the emission line for a given X-ray series, Z is atomic number of the emitter C_1 and C_2 are constants.

Moseley's Law is the basis for elemental analysis with EDS. If the energy of a given K, L, or M line is measured, then the atomic number of the element producing that line can be determined. The K, L, and M series X-rays increase in energy with increasing atomic number. The following figures present the EDS analyses of four samples showing the differences in their copper content as affected by the synthesized nanoparticles.

Based on the EDS analysis of the four representative sambong-CuNP (Figure 6), the copper nanoparticles emitted X-rays of the K and L series. The peaks observed at 8 and 9 keV were X-rays from the K series, while the peaks at 1 keV were from the L series. Copper is an intermediate element characterized by these X-ray emissions. X-ray emissions for C and O in the L series indicated that the active components were with the nanoparticle, which means the copper nanoparticle is being capped by the organic components.

The occurrence of small amounts of P, S, Cl, Fe, and Ca (Figure 7) was likely due to some of the macro- and micro-elements needed by the plants, which may have been extracted together with the active components of the sambong leaves. E_1S_1, E_2S_4, E_3S_1, and E_4S_1 have percent Cu of 27.11%, 31.57%, 1.26%, and 17.72%, respectively. E_2S_4 contained the highest amount of Cu but corresponded only to 8.33%, 33.33%, and 50.00% mortality in the nanosuspension. However, the extract rated higher in the powdered nanoparticles, with 75%, 100%, and 100% mortality at 6, 12, and 24 hours, respectively. These were the lumps or aggregates, as

seen in Figure 5e. Moreover, E_3S_1 contained the lowest amount of Cu, but had the highest amount of C. Figure 5f displays the Cu nanoparticles embedded in the organic moieties. This means that the copper nanoparticles formed from rice wine extract by Soxhlet method did not form aggregates or were well-dispersed in the suspension. This may be the reason behind the high percent mortality (75% in 6 hours exposure, and 100% in 12 hours exposure) that was registered in the dried nanoparticles of E_3S_1. In the case of E_3S_1 nanosuspension, lower percent mortality was observed compared with the dried nanoparticles. This contrasts with Singh's [24] findings that chemicals in solution were more effectively absorbed than chemical powder. Nevertheless, the results conform to Fick's law of diffusion. The kinetics of penetration into insect cuticle appear to be predictable from this law, which lead to a first-order form in which the rate of penetration at any time is proportional to the amount on the "outside" at that time [21]. As the nanoparticles were attached to the different parts of the fruit fly's body (Figure 2), penetration into the cuticle most likely occurred, triggering the death of the fly.

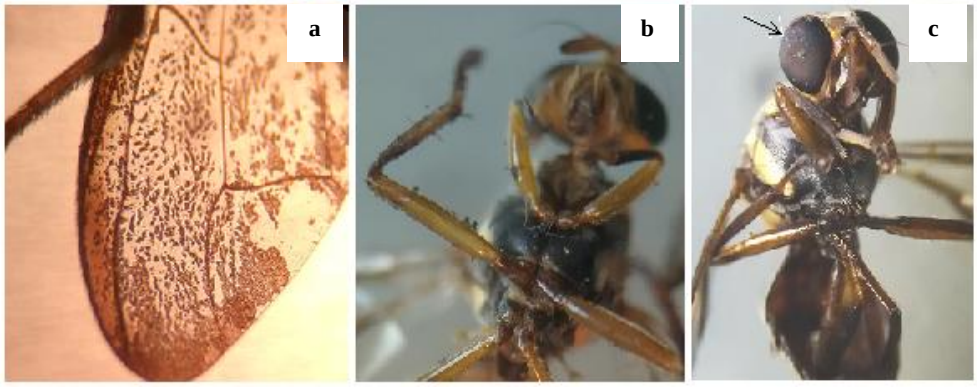


Figure 2. Accumulation of (a) nanosuspension on the wings; nanopowder on the (b) legs; and (c) compound eye

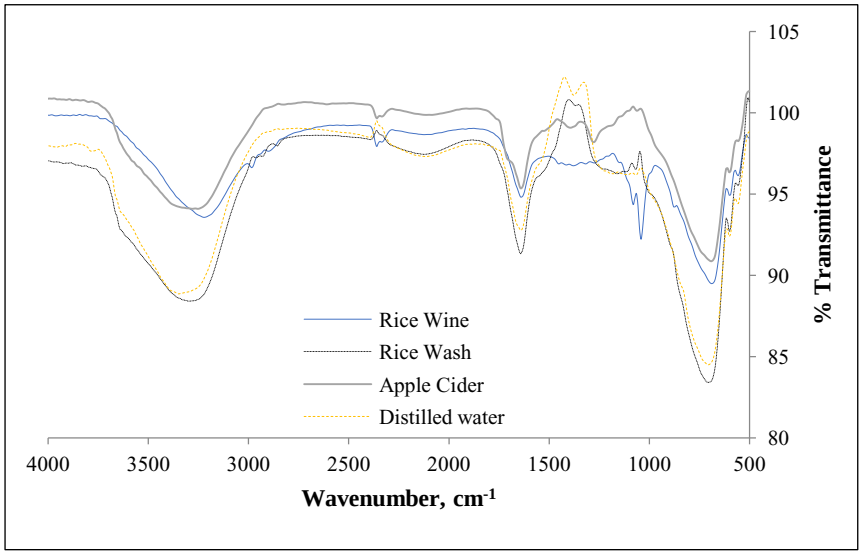


Figure 3. FTIR spectra of the four solvents

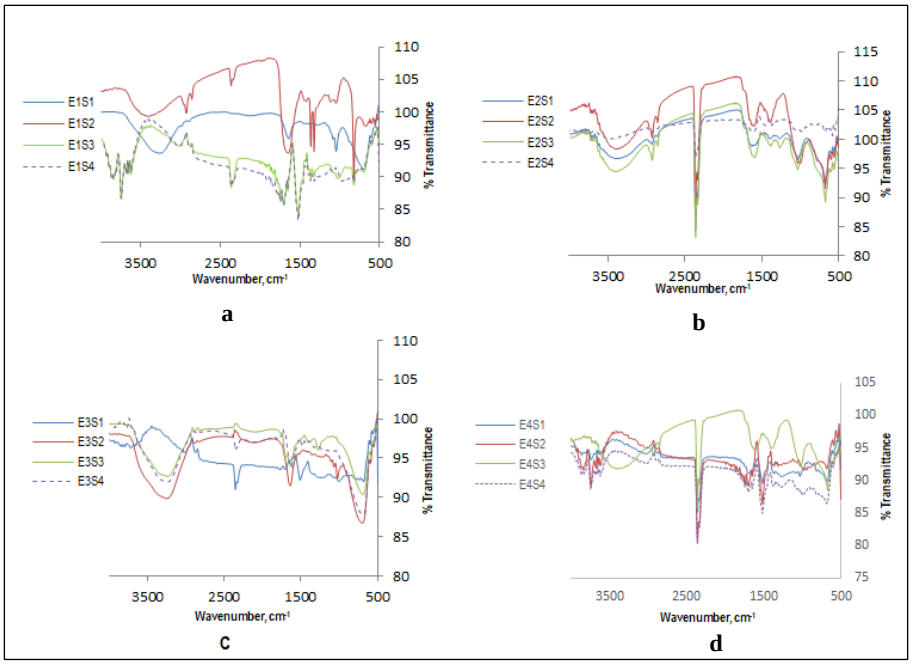


Figure 4. FTIR spectra of the CuNPs as affected by the solvents used in the four methods of extraction: (a) hot infusion; (b) maceration; (c) hot reflux; and (d) fermentation (S1 = rice wine; S2 = rice wash; S3 = apple cider vinegar; S4 = distilled water)

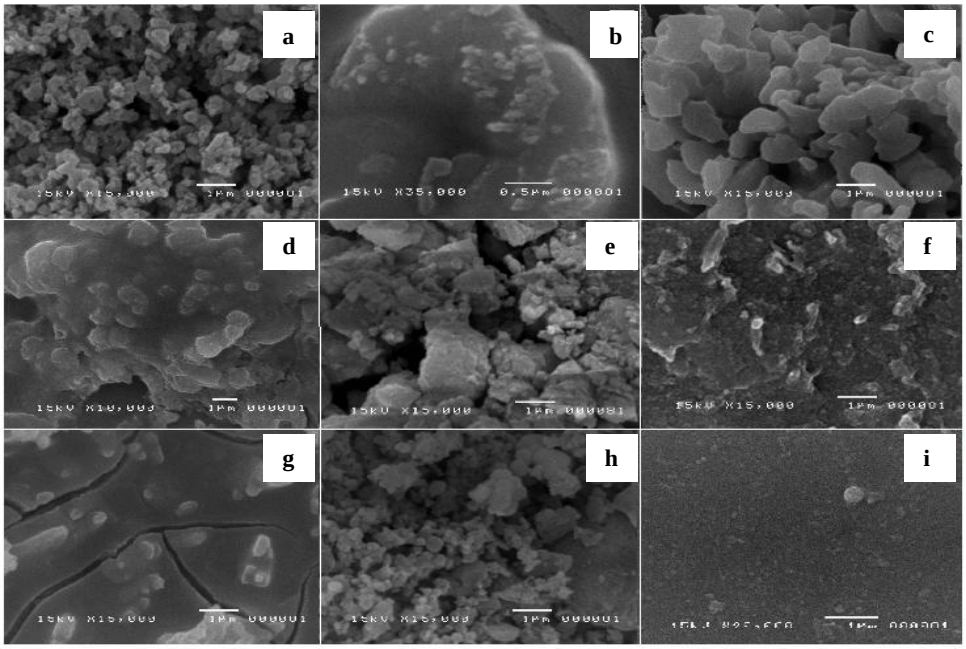


Figure 5. SEM photomicrograph of green synthesized CuNPs using (a) rice wine-hot infusion (E_1S_1); (b) apple cider vinegar-hot infusion (E_1S_3); (c) distilled water-by hot infusion (E_1S_4); (d) rice wash-maceration (E_2S_2); (e) distilled water-maceration (E_2S_4); (f) rice wine-hot reflux (E_3S_1); (g) rice wash-hot reflux (E_3S_2); (h) rice wine-fermentation (E_4S_1); and (i) distilled water-fermentation (E_4S_4)

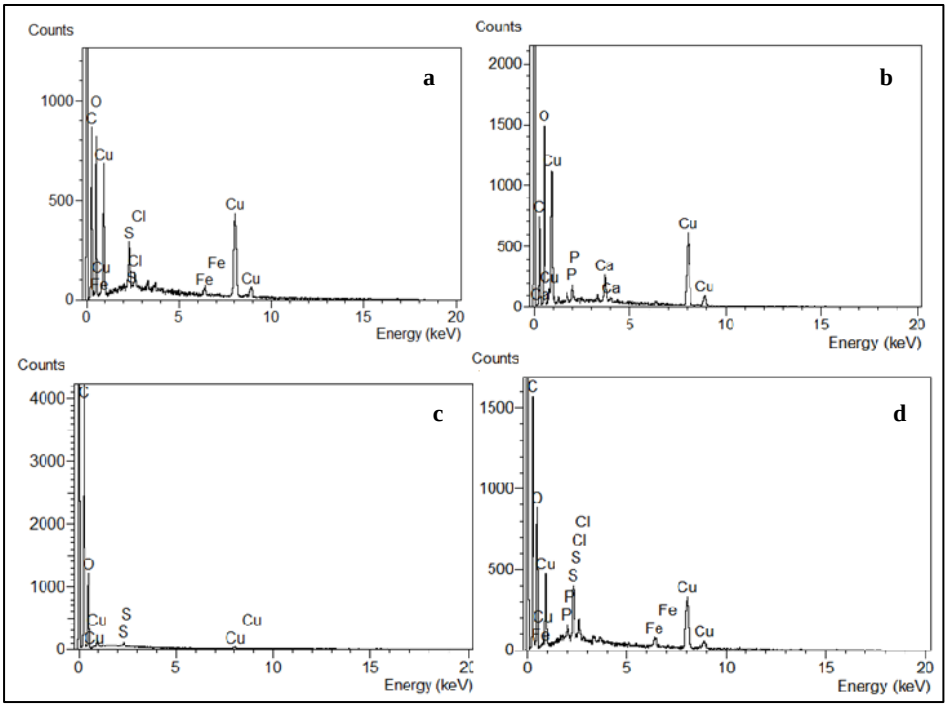


Figure 6. EDS analysis for some representative sample (a) E_1S_1; (b) E_2S_4; (c) E_3S_1; and (d) E_4S_1

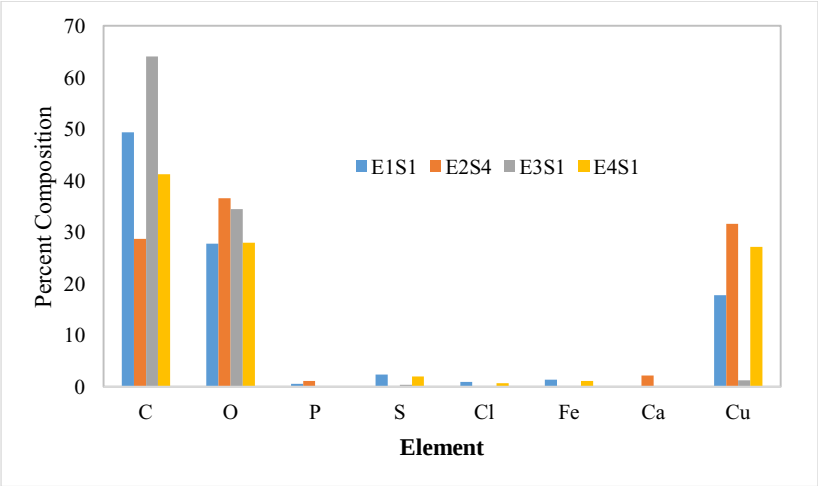


Figure 7. Elemental percent composition of the four extracts

Conclusion

The insecticidal components of sambong (*Blumea balsamifera*) leaves against oriental fruit fly, *Bactrocera dorsalis* (Hendel), were extracted using four green solvents, namely rice wine, rice wash, apple cider vinegar, and distilled water, employing hot infusion, maceration, fermentation, and Soxhlet extraction methods. These extracts were used in the synthesis of copper nanoparticles (CuNPs). The suspensions of nanoparticles were centrifuged, and the aggregates were separated and dried. Then, the dried aggregates and the colloidal suspensions of copper

nanoparticles were tested against male adult Oriental fruit flies. Both dried aggregates and nanosuspensions had effects on the fruit flies, with mortality rates ranging from 25% to 100% within 12 hours exposure. However, the dried aggregates yielded higher mortality rates than the nanosuspensions. Thus, sambong can be used in the preparation of nanoparticle-enhanced biocide either as suspension concentrate, or dust or powder with suitable sorption material, and as an alternative method in the management of oriental fruit fly as well.

Acknowledgment

The authors wish to acknowledge Mr. and Mrs. Juanito Palaganas and Dr. Luzviminda S. Quitos for their assistance in the collection of samples. Due appreciation also goes to Dr. Adelina P. Valdez, Dr. Glenn V. Alea, Dr. Marita S. Labe, Ms. Rhanney L. Gonzales, and Ms. Ella Joyce S. Paragas for the assistance they extended in the improvement of this study.

References

1. Sharpe, R. M. and Irvine, D. S. (2004). How strong is the evidence of a link between environmental chemicals and adverse effects on human reproductive health?. *British Medical Journal*, 328(7437): 447.
2. Pingali, P. L. and Roger, P. A. (2012). Impact of pesticides on farmer health and the rice environment (Vol. 7). Springer Science & Business Media.
3. Mahmood, I., Imadi, S. R., Shazadi, K., Gul, A. and Hakeem, K. R. (2016). Effects of pesticides on environment. In Plant, soil, and microbes. Springer: pp. 253-269.
4. Tubbs, C. W. and McDonough, C. E. (2018). Reproductive impacts of endocrine-disrupting chemicals on wildlife species: implications for conservation of endangered species. *Annual Review of Animal Biosciences*, 6: 287-304.
5. Ndakidemi, B., Mtei, K. and Ndakidemi, P. A. (2016). Impacts of synthetic and botanical pesticides on beneficial insects. *Agricultural Sciences*, 7(06): 364.
6. Gupta, S. and Dikshit, A. K. (2010). Biopesticides: an ecofriendly approach for pest control. *Journal of Biopesticides*, 3(1): 186-188.
7. Thakore, Y. (2006). The biopesticide market for global agricultural use. *Industrial Biotechnology*, 2(3):194-208.
8. Lichtfouse, E. (2013). Sustainable agriculture reviews (Vol. 13). Springer Science & Business Media.
9. Pang, Y., Wang, D., Fan, Z., Chen, X., Yu, F., Hu, X., and Yuan, L. (2014). *Blumea balsamifera* - A phytochemical and pharmacological review. *Molecules*, 19(7): 9453-9477.
10. Yuan, N. N., Hou, H. Y., Wang, J., Chen, Y. Z. and Xie, P. B. (2012). The research status of chemical constituents and activities of Blumea DC. [J]. *Guangzhou Chemical Industry*, 24: 015.
11. Nessa, F., Ismail, Z., Mohamed, N. and Haris, M. R. H. M. (2004). Free radical-scavenging activity of organic extracts and of pure flavonoids of *Blumea balsamifera* DC leaves. *Food Chemistry*, 88(2): 243-252.
12. Pang, Y., Wang, D., Hu, X., Wang, H., Fu, W., Fan, Z. and Yu, F. (2014). Effect of volatile oil from *Blumea balsamifera* (L.) DC. leaves on wound healing in mice. *Journal of Traditional Chinese Medicine*, 34(6): 716-724.
13. Sivapragasam, A. (2009). Biopesticides from Malaysian flora–resources for sustainable pest management. In Discovering opportunities, expanding the economic horizon. Proceedings of the National Conference on New Crops and Bioresources, Seremban, Malaysia, 15–17 December 2009: pp. 125-132.
14. Glova III, F. and Ines, M. C. (1989). Evaluation of selected botanical pesticides against rice green leafhopper *Nephotettix virescens*. In Pest Control Council of the Philippines, Baguio City (Philippines), 9–12 May 1989.
15. Ines, M. C. and Baga, L. P. N. (1990). Evaluation of botanical pesticides against Fusarium rot of garlic. In 21. Pest Control Council of the Philippines Annual Convention, Bacolod City (Philippines), 7–10 May 1990.

16. Suharto, H. (2002). Golden apple snail, *Pomacea canaliculata* (Lamarck) in Indonesia. Los Banos, Laguna, SEAMEO Regional Center for Graduate Study and Research in Agriculture (SEARCA), Philippines, 69–73.
17. Sebastian, L. S. (2003). Management options for the golden apple snail. Access from http://issg.org/database/species/reference_files/pomcan/pest_management.pdf. [Access online 05 December 2017].
18. Harne, S., Sharma, A., Dhaygude, M., Joglekar, S., Kodam, K. and Hudlikar, M. (2012). Novel route for rapid biosynthesis of copper nanoparticles using aqueous extract of *Calotropis procera* L. latex and their cytotoxicity on tumor cells. *Colloids and Surfaces B: Biointerfaces*, 95: 284-288.
19. Abbott, W. S. (1978). A method of computing the effectiveness of an insecticide. *Journal of the American Mosquito Control Association*, 3(2):302-303.
20. Cha, D. H., Adams, T., Werle, C. T., Sampson, B. J., Adamczyk, J. J., Jr., Rogg, H. and Landolt, P. J. (2014). A four-component synthetic attractant for *Drosophila suzukii* (Diptera: Drosophilidae) isolated from fermented bait headspace. *Pest Management Science,* 70: 324-331.
21. Wilkinson, C. F. (1976). Insecticide biochemistry and physiology. Plenum Press.
22. Griffitt, R. J., Weil, R., Hyndman, K. A., Denslow, N. D., Powers, K., Taylor, D. and Barber, D. S. (2007). Exposure to copper nanoparticles causes gill injury and acute lethality in zebrafish (*Danio rerio*). *Environmental Science & Technology*, 41(23): 8178-8186.
23. Ragaei, M. and Sabry, A. K. H. (2014). Nanotechnology for insect pest control. *International Journal of Science, Environment And Technology*, 3(2): 528-545.
24. Singh, A. K. (2015). Engineered nanoparticles: Structure, properties, and mechanisms of toxicity. Academic Press.

Malaysian Journal of Analytical Sciences (MJAS)
Published by Malaysian Analytical Sciences Society

STANDARIZATION BASED ON CHEMICAL MARKERS OF *Moringa oleifera* HERBAL PRODUCTS USING BIOAUTOGRAPHY ASSAY, THIN LAYER CHROMATOGRAPHY AND HIGH PERFORMANCE LIQUID CHROMATOGRAPHY-DIODE ARRAY DETECTOR

(Piawaian Berdasarkan Penanda Kimia bagi Produk Herba *Moringa oleifera* Menggunakan Ujian Bioautografi, Kromatografi Lapisan Nipis dan Kromatografi Cecair Berprestasi Tinggi-Pengesan Susunan Diod)

Erick Sierra-Campos[1]*, Mónica A. Valdez-Solana[1], Claudia I. Avitia-Domínguez[2], Alfredo Téllez-Valencia[2], Jorge A. Meza-Velázquez[1], Miguel Aguilera-Ortiz[1], Adelma Escobar-Ramírez[3]

[1]*Facultad de Ciencias Químicas GP, Universidad Juárez del Estado de Durango, Av. Artículo 123 S/N Fracc. Filadelfia. Gómez Palacio, Durango. México*
[2]*Facultad de Medicina y Nutrición, Universidad Juárez del Estado de Durango, Av. Universidad y Fanny Anitúa S/N, 34000 Durango. México*
[3]*División Académica de Ciencias Básicas, Universidad Juárez Autónoma de Tabasco, Av. Universidad S/N, Zona de la Cultura, Col. Magisterial, Vhsa, Centro, Tabasco, México*

**Corresponding author: ericksier@ujed.mx*

Received: 29 December 2019; Accepted: 25 April 2020; Published: 9 June 2020

Abstract

The present study investigated the variation of phytochemical composition, antioxidant activity and chemometric thin layer chromatography (TLC) and high performance liquid chromatography (HPLC) fingerprinting profiles of five *Moringa oleifera* herbal products. TLC and HPLC along with the PCA and K-mean can adequately discriminate different herbal products. The content of total bioactive compounds of the samples were ranged from 591.5 to 966.1 mg/100 g dried weight. The total antioxidant activity of *M. oleifera* samples was in the following order: Mas lait > De Font Quer > Akuanandi > Infusionate > Terbal. Wavelength at 352 nm, 75 components were detected in all herbal products; among these, 10 potential biomarkers with higher contents enabled differentiation between each sample and foreign organic matter. HPLC-DAD analysis of the extracts showed a decline in the quality of components in the five commercial products. Thus, this study presents the TLC and HPLC profiles of the Mexican *M. oleifera* extracts that may serve as a reference for the proper identification, standardization and quality control of this plant. These methods can be used for routine quality control of herbal products and formulations containing this medicinal plant.

Keywords: *Moringa oleifera* leaves, chemical markers

Abstrak

Kajian ini menyiasat variasi komposisi fitokimia, aktiviti antioksidan dan kemometrik kromatografi lapisan nipis (TLC) dan kromatografi cecair berprestasi tinggi (HPLC) bagi profil pencapjarian lima produk herba berasaskan *Moringa oleifera.* TLC dan HPLC bersama PCA dan K-min boleh membezalayan secara tepat bagi produk berbeza. Jumlah kandungan sebatian bioaktif bagi sampel berada di dalam julat 591.5 to 966.1 mg/100 g berat kering. Jumlah aktiviti antioksidan bagi sampel *M. oleifera* seperti tertib berikut: Mas lait > De Font Quer > Akuanandi > Infusionate > Terbal. Para panjang gelombang 352 nm, 75 komponen ditemui dalam semua produk herba; antaranya 10 potensi penanda bio dengan kadungannya yang tinggi membantu membezakan setiap sampel dengan jirim organik asing. Analisis HPLC-DAD terhadap ekstrak menunjukkan penurunan dalam kualiti komponen di dalam lima produk komersial. Kajian ini membentangkan profil TLC dan HPLC bagi ekstrak *M. oleifera* tulen dari Mexico yang boleh digunakan sebagai rujukan bagi tujuan pengenalpastian, paiwaian dan kawalan kualiti tumbuhan ini. Keadah ini boleh digunakan bagi rutin kawalan kualiti produk herba dan formulasi yang mengandungi tumbuhan perubatan ini.

Kata kunci: daun *Moringa oleifera*, penanda kimia

Introduction

Plants have primary and secondary metabolite factories for their survival and that play a vital role in the management of human health. Of an estimated 250,000 to 350,000 plant species identified, about 35,000 are used worldwide for medicinal purposes. The World Health Organization (WHO) has confirmed that herbal medicines serve the health needs of about 80% of the world´s population; especially for millions of people in the vast rural areas of developing countries [1]. Additionally, plants and their metabolites are necessary for food supplement and nutrition, and for all type of medicines including traditional, herbal, complementary, natural products related and semi-synthetics [2].

Moringa is a genus of medicinal plants that has traditionally been used to heal wounds and various diseases such as colds and diabetes. The genus consists of 13 species that have been widely cultivated mainly throughout Asia and Africa for their multiple uses. Moringa species are well-known for their antioxidant, anti-inflammatory, anti-cancer, and anti-hyperglycemic activities [3]. *Moringa oleifera* has been used as a source of medicine to treat different diseases and ailments including wound healing, hypertension, diabetes, obesity and cancer [4]. However, the chemical composition of *M. oleifera* vary greatly since it has varieties and an extensive distribution. Different chemical composition may lead to significant differences in the effectiveness of the health problems and the safety related to intake. Additionally, only few extracts were evaluated for their chemical constituents and mechanism-based pharmacological activities.

In order to profit from the beneficial therapeutic properties of *M. oleifera*, Mexican markets are full of various medicinal, dietary, and cosmetic preparations, available to the public. Most of these *M. oleifera* based products are available in our country as capsules or tea for daily drinking that contain simple powdered leaves. Moreover, there is a huge demand for pharmaceutical, cosmetic, and food products in local and global markets, which create a cutthroat competition between suppliers and manufacturers. However, manufacturers sometimes do not follow the right way to achieve the quality products and some do not have quality control facilities [5, 6]. The proportion of adulterated herbal products varies significantly among continents, higher in Australia (79%) and South America (67%), lower in Europe (47%), North America (33%), Africa (27%) and Asia (23%) [7]. However, adulteration is not necessarily intentional and herbal products may be altered due to accidental adulteration, misidentification and confusion resulting from vernacular names [8, 9].

Moringa oleifera contains a range of polyphenolic compounds that are especially abundant in leaves. These contribute to its high antioxidant activity. Therefore, an evaluation of the diversity of antioxidant

compounds from different sources is desirable to ensure the quality of *M. oleifera* and its derived edible products. Therefore, interest in the antioxidant activity of *M. oleifera* leaves is growing. Several investigations have shown that *M. oleifera* contains strong antioxidant capacity [10-12]. Antioxidants play an important role in inhibiting and scavenging free radicals, thus providing protection to humans against infections and degenerative diseases. Various antioxidant compounds were reported in leaves extract of *M. oleifera* as gallic acid, chlorogenic acid, kaempferol, quercetin, caffeic acid, luteolin, epicatechin, and others [13-15]. However, it is unknown which is the most important in the antioxidant activity.

The fingerprinting approach has been recently recognized and accepted for quality assessment of traditional medicines. The thin layer chromatography (TLC) fingerprint profile is an important tool that serves as a guideline to the phytochemical profile of the antioxidant compounds in ensuring quality. It provides quantitative and semi-quantitative information of the resolved compounds [16]. The concept of phyto-equivalence was developed to ensure consistency of herbal products. According to this concept, a chemical profile, such as chromatographic fingerprinting, for herbal products, should be constructed and compared with the profile of a clinically proven reference product [17].

TLC is an easy, inexpensive, rapid, and the most widely used method for the analysis and isolation of small organic natural and synthetic products [18,19]. In the screening of antioxidants, the stable free radical 2,2-diphenyl-1-picrylhydrazyl (DPPH) was often used as a derivatization reagent for this purpose [20]. High performance liquid chromatography (HPLC) fingerprinting has been widely used in some studies of natural products [21, 22].

Taken together, the purposes of the present study included: (1) to evaluate the antioxidant potential of different commercial products of *Moringa oleifera* , with the results compared to standard antioxidants such as quercetin, gallic acid and rutin; (2) to characterize the polyphenols to provide biomarkers using TLC and HPLC-DAD.

Materials and Methods

Reagents

TLC with various solvent systems by using TLC aluminum sheet pre-coated with silica gel 60 F254-Merck. All the solvents (Trichloroacetic acid, ethyl acetate and methanol) used for extraction and isolation of analytic grade or HPLC grade and purchased from Sigma-Merck.

Raw material

Moringa oleifera powder leaves based commercial products were obtained from naturist stores from Mexico; Akuanandi® capsules (Lombardia, Mich); Terbal tea® (Mexico City), Infusionate tea® (Monterrey, NL), De Font Quer® capsules (Zapopan, Jal), and Mas lait® powdered leaves (Monterrey, NL).

Preparation of *M. oleifera* leaves extract and polyphenolic standards

At first, 0.5 g of powder of dried leaves of *M. oleifera* was extracted by Ultrasonication assisted extraction with methanol/water (80:20, v/v) for 30 minutes at 30 °C. The extract was filtered through a 0.22 µm nylon filter. The solvent was removed under reduced pressure at 40 °C (rotary evaporator Büchi R-215). The crude extract was kept separately in sterile sample tubes and stored at 4°C. Extracts were performed in triplicate. Each appropriate amount of standard compound was accurately weighed and dissolved in 70% methanol as stock solutions, which were stable for at one week under 4 °C. Linearity range of chlorogenic acid (0.6-23.1 µg/mL), isoquercetin (0.99-3.0 µg/mL), luteolin (0.5-4.0 µg/mL), and apigenin (0.66-3.3 µg/mL).

Phytochemical screening by TLC

The extracts were dissolved in methanol to achieve a concentration of 5 mg/mL. The hydromethanolic extracts of *M. oleifera* were applied in a concentration of 5 µL using a Hamilton syringe on aluminum sheets pre-coated with silica gel 60 F_{254} of 0.2 mm thick, 5 cm x 7.5 cm used as a stationary phase. The plates were developed in the mobile phase, TCA-ethyl acetate-methanol (1:7.5:1.5 v/v) for the hydromethanolic

extract to a distance of 120 mm trough glass chamber saturated with ternary solvent system consisting of TCA-ethyl acetate-methanol (1:7.5:1.5) at room temperature (25 °C). Daylight, UV 254 nm, UV 366 nm and DPPH stain were used as visualization techniques. To qualitatively screen, it was dipped upside down for 10 seconds in a 0.4 mM DPPH solution. Additionally, standards were used to assist the identification of compounds present in the extract when known compounds were present in the sample. The identification of known polyphenolics was performed by comparison of respective standards through Rf calculation.

The retention factor (Rf) values of the different spots were then calculated using the equation 1:

$$Rf = \frac{Distance\ of\ spot\ from\ origin}{Distance\ of\ solvent\ front\ from\ origin} \quad (1)$$

The documented pictures were saved in jpg mode and processed by the digitally enhanced thin-layer chromatography by means of the ImageJ. MATLAB and TLC analyzer – Science Buddies. First, color images were turned into 8-bit type images (Image/type/8-bit). The images obtained were denoised by applying the following steps: Process/Filters/Median/Radius -5 pixels, with the baseline drift then removed (Process/FFT/Bandpass Filter/Filter large structures down to -40 pixels; filter small structures up to -0 pixels).

HPLC-DAD analysis

Seven phenolic standards and samples were dissolved in the mobile phase, yielding concentrations of 25 µg/mL. The solutions were filtered through a 0.45 µm membrane filter, and the evaluation of each calibration curve was fitted by linear regression. An Agilent 1200 HPLC Series (Agilent, Palo Alto, Calif.) was operated at 30 °C, equipped with a degasser, a diode array detector (DAD), a quaternary gradient pump, and a Polaris 5 C_{18} analytical column of 150 mm × 4.6 mm and a 3.5 µm particle (Agilent, USA). The mobile phase was a binary gradient: methanol and buffer solution. The buffer contained TCA 0.1% solution in water, with its pH adjusted to 2.1. The linear gradient began with 20 to 50% methanol over the first 30 minutes, followed by 70% methanol over the next 30 minutes. The flow rate was 0.8 mL/min. Data were collected at 352 nm. The injection volume was 20 µL. Data acquisition, peak integration, and calibrations were performed with Agilent 1200 Chemstation software. The results are reported as means ± standard deviations of triplicate independent analyses.

Data analysis

The data were expressed as means ± SD, and the correlation of entire chromatographic patterns among the samples were calculated. Principal component analysis (PCA) was performed using XLSTAT software and Past (folk.uio.no/ohammer/past). Additionally, K-mean cluster distribution was applied for raw data to categorize the samples into proper clusters based on the amount and number of main components in the collected samples.

Results and Discussion

Recently, it was described a direct TLC quantitative analysis for some flavonoids as crypto-chlorogenic acid, isoquercetin, and astragalin contents in *Moringa oleifera* leaf extracts [23]. However, this reported method requires expensive equipment (CAMAG Linomat 5) and resource intensive calibrations. Therefore, attempts were made in this work to develop a fast, sensitive, robust, and cost-effective TLC-densitometric method suitable for semi-quantitative analysis of main flavonoids in the commercial products of *M. oleifera*.

To develop the TLC-densitometry method for the estimation of flavonoids of *M. oleifera*, a selection of the mobile phase was carried out based on polarity. Initially, a combination of various proportions of solvents including methanol, acetonitrile, ethyl acetate, hexane and ether of petroleum were tried as mobile phase, but diffusion of the spots and tailing was observed. To avoid this problem trichloroacetic acid (TCA) was added to solvent system. Finally, a mobile phase composed of TCA-ethyl acetate-methanol (1:7.5:1.5 v/v/v) was established as observed with Rf values of 0.75, 0.58, 0.51, 0.48, 0.42, 0.36, 0.14 and 0.07 when plate was developed and scanned at 366 nm

and visible light (Figure 1). At 254 nm, we observed only seven well defined spots, while that at 366 nm, we observed up to 15 spots. Moreover, evaluation of linearity for the TLC assay was done by preparing four dilutions from a stock extract, i.e., 14.2% (1:7), 20% (1:5), 33.3% (1:3) and 50% (1:2). Spots were applied for each concentration starting with lowest concentration to avoid a carryover effect. The results show that the intensity of each compound depends on the amount of sample tested. The best separation and resolution were obtained with the 1:5 dilution, which corresponds to a concentration of 20 µg/spot (Figure 1, left panel). Therefore, this concentration was applied to the follow assays.

Later, five products of *M. oleifera* from different regions of Mexico were analyzed to develop a standard fingerprint under the established TLC conditions. Seven common peaks were selected as characteristic peaks. Figure 2a shows the suitability of the TLC method to detect and semi-quantify flavonoids presented by different products. TLC clearly revealed that Mas lait (S4) presented high amounts of antioxidant compounds, whereas Terbal (S2) exhibited low amounts of antioxidants. S4 extract exhibited the best DPPH radical scavenging activity, followed by De Font Quer (S5) and Akuanandi (S3) extracts. These results are agrees with that the major antioxidant constituents of *M. oleifera* include vitamins, micronutrients, polyphenols and isothiocyanates, which are a potent mixture of direct and indirect antioxidants that can explain its various health-promoting effects [24].

The content of total bioactive compounds (TBCC) in the evaluated extracts were as follows, the lower TBCC value of 591.5 ± 1.14 mg/100 g DW for S2 and a higher value of 966.1 ± 2.19 mg/100 g DW for S3, followed by S5, S4 and S1. Depending on fingerprint profile showed the prevalence of different bioactive classes in chemical composition of all samples, with the most quantitatively important classes were flavonols (40%), cinnamic acids (20.5%) and flavones (7.5%). In Table 1, it can be seen that peak 8 was not found in S1, while S1 extract did not contain peak 1.

Although the classical fingerprinting by TLC is done visually and mainly in a non-chemometric way. Several peaks can be proposed as markers, known as substances responsible for differences between discriminated classes. However, the main disadvantage of classical fingerprinting is its subjectivity. Therefore, the chemometric fingerprinting treats the chromatogram as a unique signal, without a need to identify and interpret the peaks [25], for which, we decided to use and validate the chemometric method with the previous results and compare them with other commercial herbal products.

The image processing procedure was based on previously published methods [25-27]. The typical order of preprocessing includes normalization, denoising, and baseline removal, followed by warping/registering. The chromatographic peaks area shown as signals (Figure 2b), and the integration of all peaks was done automatically by TLC analyzer and MATLAB (with Image Processing Toolbox) (Table 1) to characterize their presence in a given sample. The intensity and area of these main peaks in the different samples showed significant changes; however, their peak positions remained unaltered.

A multivariate analysis, the principal component analysis (PCA) is based on the generation of a new set of variables, called principal components to explain the variability of results, besides showing the correlation between the different variables. PCA has been used as an unsupervised technique to evaluate whether the approach TLC/chemometrics may differentiate samples according to different phytochemicals, thus discriminating the original *Moringa oleifera* leaf products.

The scree plot gave two principal components, where the contribution of variance for individual components was: component 1 explaining 83.75%, and component 2 explaining 13.14%. Furthermore, the total contribution of variance from the two components was 96.99%. In terms of major contribution, compounds 1, 5 and 8 made the greatest contribution towards F1 whereas compounds 4 and 6 were the contributors for F2. It was found that F1 has no associated with peak 9.

Whereas F2 was found to be positively associated with peak 4. In the first quadrant we have the samples of Mas Lait and De Fort Quer that are characterized by compound 6. In contrast, in the fourth quadrant, we have the Infusionate, Terbal and Akanandi samples that are characterized by the compounds 2 and 7 (Figure 4). The results indicated that the chemical composition and content in the *M. oleifera* herbal products significantly varied.

Additionally, we use the distance metric to measure the similarity or dissimilarities between points. The K-mean cluster showed distribution of data into three clusters: 1 (3), 2 (1) and 3 (1). Cluster 1 shows three samples (Infusionate, Terbal and Akanandi) with minimum distance to centroid of 2,228.76. Cluster 2 shows one sample (Mas lait) with minimum distance to centroid of 2472.88; Cluster 3 shows one sample (De Font Quer) with minimum distance to centroid of 1816.44. According to the inter-cluster distances, it was observed that Mas lait and De Fort Quer, characterized by high values of phytochemicals, differs significantly to the samples from Cluster 1. K-mean analysis clusters *M. oleifera* samples into different groups, clearly showing that this method can adequately discriminate different products using TLC.

Based on the comparison of the Rfs with standard compounds, the spots obtained in all the tracks were analyzed and the Rf values were compared to the standard. If Rf value of pure compound is matching to any Rf value of extract shows the presence of that standard in the extract. The presence of specific peaks for quercetin, gallic acid and rutin at Rfs around 0.8, 0.5, and 0.32 were recorded and considered a positive result for polyphenols (Figure 4). The spots observed under UV light and DPPH stain indicate the absence or few abundances of these compounds in the De Font Quer sample extract. Natural products are extremely complex, containing many components of various composition, size, and acid-base properties. Additionally, Rf values are affect by several factors such as depth of mobile phase, nature of the TLC plate, and solvent parameters. Therefore, these results indicating that TLC has low resolution and its necessity the confirmation of extract by HPLC-DAD.

When developing a new analytical method, it is desirable to compare the results from the new method with those from an accepted method. The HPLC-DAD chromatogram of the hydroalcoholic extract of *M. oleifera* revealed the presence of various compounds with corresponding peaks at different times (Figure 5). The compounds identified in the extracts are shown in Table 2. Based on a comparison of the retention times with those of the standards, peaks 1, 2, 4, 5, 7 and 9 were identified as chlorogenic acid, syringic acid, luteolin, rutin, isoquercetin and astragalin, respectively. The most abundant flavonoids in all samples were chlorogenic acid and isoquercetin, while luteolin was found at lower concentration. Among the main detected peaks 3, 4, 7, 8 and 10, did not match any compounds previously identified in our laboratory [14]. However, kaempferol and quercetin derivatives were the most predominant flavonoids in *M. oleifera* leaves [28, 29]. Therefore, additional mass-spectrometry studies are required to know the identity of the unknown compounds.

The HPLC-DAD fingerprints of herbal products were obtained and are shown in Figure 5. It was found that all samples (S1-S5) had similar spectra which indicated the similar chemical composition of these products. There were 10 main common peaks, which were marked (1-10) in each chromatogram. Peak 7 (TR = 28.49±0.8 min) was selected as the reference peak because it was the maximum peak in each sample.

Statistically significant differences were observed among the different samples for all single bioactive compounds: the most important differences were observed in the concentration of syringic acid, isoquercetin and astragalin. All were previously described in *M. oleifera* leaves. However, the values are extremely variable across the five samples, most likely because both *M. oleifera* variety and industrial product manufacturing affect the amount of flavonoids eventually present in the final product.

The major constituents of the extract were:

Peak 1 was found to be chlorogenic acid which is an ester of caffeic acid and quinic acid and is made up of 20.5% of the S1 extract. The chlorogenic acid content did not drastically vary, although S2 and S4 contained slightly lower concentration and it agreed with Vergara-Jimenez [30] which reported higher concentration of cinnamic acids in *M. oleifera*. This compound is a potent antioxidant that protects plants from lipid peroxidation [31]. Peak 2 was identified as syringic acid a dimethoxybenzene that is 3, 5 dimethyl ether derivatives of gallic acid and it made up 5.37% of the S4 extract. The level of syringic acid was 3.3-times higher in S4 versus S1. Leaves of *M. oleifera* are a good source of syringic acid and an excellent compound to be used as a therapeutic agent in various diseases [32, 33].

Peak 3 was not identified and made up 6.11% of the 6.49% of the S3 extract. Peak 4 was identified as luteolin, 3′,4′,5,7-tetrahydroxy flavone and it made up 2.31% of the S5 extract. Luteolin (3′,4′,5,7-tetrahydroxyflavone) possesses antioxidant activity [34]. Peak 5 was found to be rutin, a dietary flavonoid and it made up 2.79% of the S5 extract. It has demonstrated that rutin has strong antioxidant properties [35]. Peak 6 was not identified and made up 21.6% of the S3 extract.

Peak 7 was identified as isoquercetin, a flavonoid that makes up 42.15% of the S3 extract. The S3 showed the high amount of isoquercetin. It is well established that one of the mechanisms for cancer development is oxidative stress, therefore the chemopreventive effects of isoquercetin could be attributed to its antioxidant and oxidative damage preventive activities [36]. Peak 8 was not identified and made up 19.26% of the S5 extract. This compound can be tentatively identified as quercetin derivative.

Peak 9 was characterized as astragalin is a 3-O-glucoside of kaempferol and it made up 7.24% of the S5 extract. It has been reported to exhibit multiple pharmacological properties including antioxidant, anti-inflammatory, anticancer, neuroprotective, and cardioprotective property [37]. Peak 10 was not identified and made up 5.97% of the S3 extract. This compound can be tentatively identified as Kaempferol derivative. The peaks remained unidentified: they likely represent other bioactive markers with potential therapeutically important effects on human health.

As expected, the predominant group of phenolic compounds in all samples was flavonols. In recent years, they have been studied primarily for their antioxidant activity, free radical scavenging capacity, coronary heart disease prevention, hepatoprotective anti-inflammatory, anticancer and potential antiviral activities [38].

The scree plot gave two principal components, where the contribution of variance for individual components was: component 1 explaining 59.18%, and component 2 explaining 31.42%. Furthermore, the total contribution of variance from the two components was 90.6%. In terms of major contribution, compounds 2-6 and 9 made the greatest contribution toward F1 whereas compounds 1, 7, 8, and 10 were the contributors for F2. Through PCA, it can be seen that, in plot, the five samples are discernibly separated.

In the first quadrant, we have the samples of Akuanandi and De Fort Quer that are characterized by the compounds 1, 2, 3, 4, 5, 6, 9 and 10. In contrast, Terbal sample is located in the third quadrant, but not it is characterized by some compounds. In the second quadrant we have the Infusionate sample that is characterized by compounds 7 and 8 (Figure 6). The results indicated that the internal qualities of five *M. oleifera* herbal samples from different sources had market chemical variations. Therefore, this comparative study indicates that Akuanandi, Mas lait, and De Font Quer can be considered appropriate sources of bioactive phytochemicals.

The K-mean cluster showed distribution of data into two clusters: 1 (3) and 2 (2). Cluster 1 shows three samples (Infusionate, Terbal and Akanandi) with minimum distance to centroid of 597.359, 558.341 and 1080.808, respectively. Cluster 2 shows two sample

(Mas lait and De Fort Quer) with minimum distance to centroid of 388.422. According to the inter-cluster distances, it was observed that the Infusionate and Terbal from cluster 1 differ significantly to the samples from cluster 2 except for the Akanandi of Cluster 1, which agrees with the biplot.

In contrast to the allopathic formulations that contain defined amounts of therapeutically active chemistry principles, herbal medicinal products usually comprise a defined amount of plant material but seldom mention the concentration of bioactive principles therein. Similarly, variation of bioactive metabolites in plant material obtained from a different geographical origin eventually incurs great difficulties in determination of potency, purity, consistency, and safety of medicinal plants and herbal products [39].

According to Karlund et al. [40], and Zuhrotum et al. [41] the most common parameters that influence the composition of flavonoids include: variety, growing area, the degree of maturity of leaves, harvesting method, storage conditions, and others. Thus, phyto-equivalence is required due to the following reasons: 1) each product has variation in active constituents; 2) to meet same compendia or other standards; 3) it is necessary to match the products and doses in clinical trials; 4) to achieve the same efficacy in disease management; and 5) extracts of similar drug should demonstrate similar pharmacological and physiological activity [42].

To date, little has been done to study phytochemical profile of *M. oleifera*. Several variables are important in the formulation of natural products like uniformity of plant material, harvest time, temperature, purity, and identity. Additionally, the market of *M. oleifera* has grown extensively due to an increased awareness of the potential health benefits of bioactive polyphenols present in leaves. Thus, results obtained from the present study provide important information to the industry and consumers concerning polyphenols, antioxidant capacity and flavonoids composition.

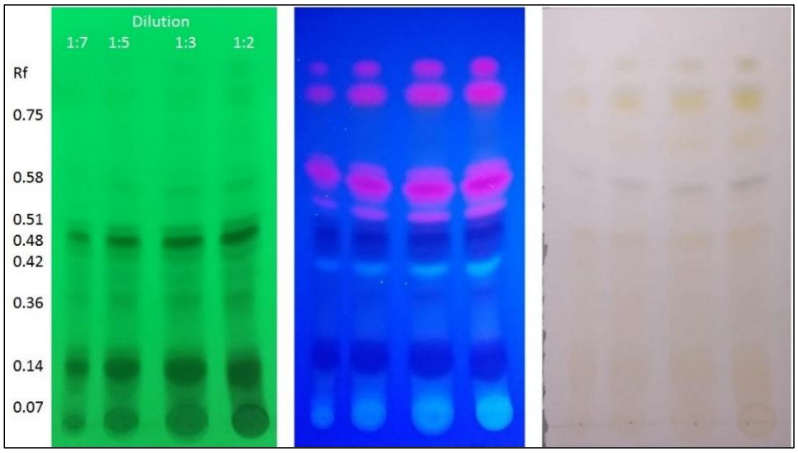


Figure 1. TLC plates of different amounts of *Moringa oleifera* leaves extracts (Akuanandi) under UV 254 nm (green panel), 366 nm (blue panel) and visible (gray panel) without derivatization.

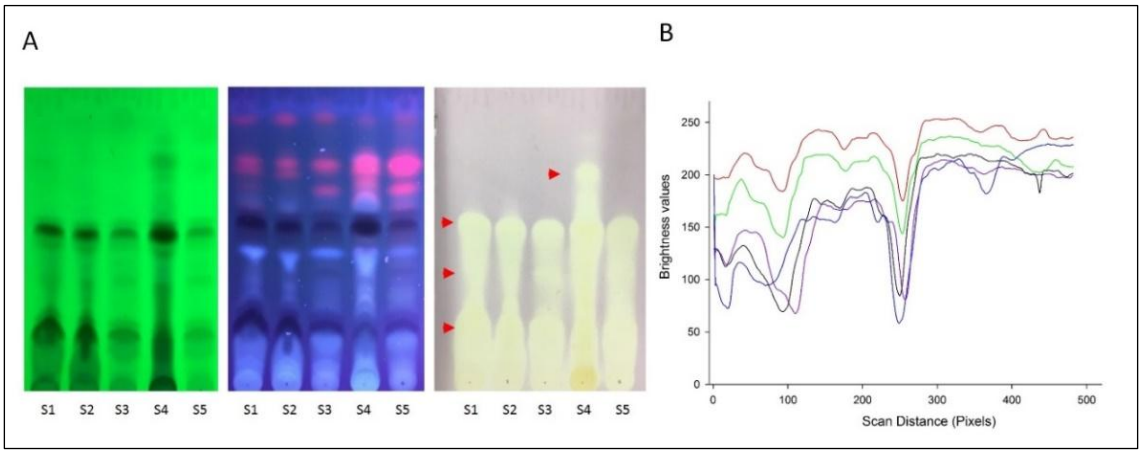


Figure 2. a) Comparative plate of the hydromethanolic extracts of five commercial products of *Moringa oleifera* revealed with UV 254 nm (green), UV 366 nm (blue), respectively. S1) Infusionate, S2) Terbal, S3) Akuanandi, S4) Mas lait and S5) De Font Quer. Left panel represents staining with DPPH. b) An example of a raw univariate densitogram extracted from image before denoising.

Table 1. Target compounds from different *M. oleifera* leaves extracts by TLC (254 nm). The retention factor and relative peak are of nine common peaks of different herbal samples

Peak No.	**Retention Factor (Rf)**	**Relative Peak Area**				
		S1	**S2**	**S3**	**S4**	**S5**
1	0.07	14.82	0	23.82	490.96	27.39
2	0.14	1,329.85	1,007.19	1,394.96	308.41	1,384.61
3	0.36	36.36	30.62	33.42	11.24	475.4
4	0.42	199.98	17.37	679.65	483.92	538.97
5	0.48	119.47	169.72	287.34	91.79	288.08
6	0.51	875.58	999.53	2,284.11	1,324.93	2,982.01
7	0.58	2,554.42	2,666.08	3,133.23	899.02	2,108.75
8	0.65	0	41.28	117.06	289.88	159.46
9	0.75	465.38	393.26	641.98	49.17	557.79

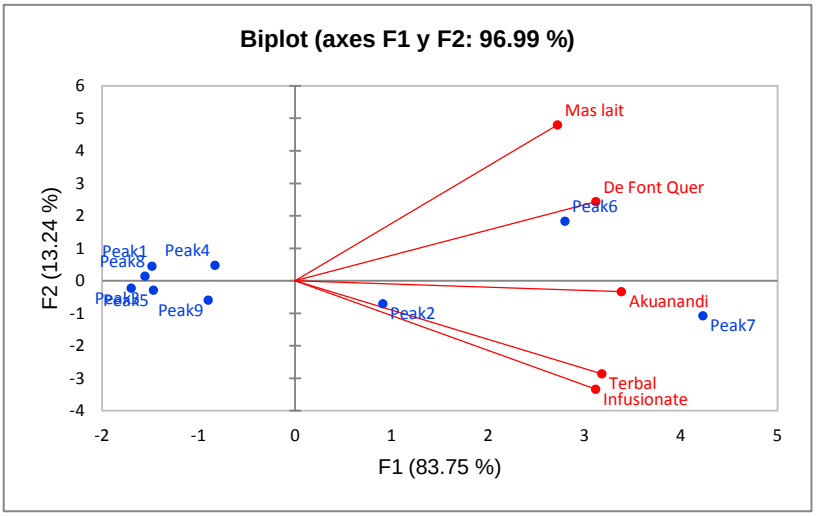


Figure 3. Two-dimensional scatter plots of the loadings of the first two factors. Biplot (axes F1 y F2: 96.9%)

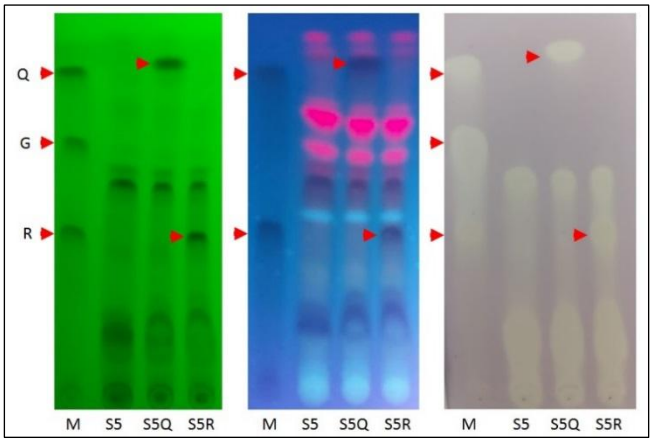


Figure 4. Hydromethanolic extract plate of *Moringa oleifera* (S5, De Font Quer) revealed with UV 254 nm (green), UV 366 nm (blue) and DPPH (gray), respectively. The red arrow heads indicate the band of each standard (Q, Quercetin; G, Gallic acid and R, Rutin). M, reference antioxidants; S5, De Font Quer; S5Q, sample plus quercetin and S4R, sample plus rutin

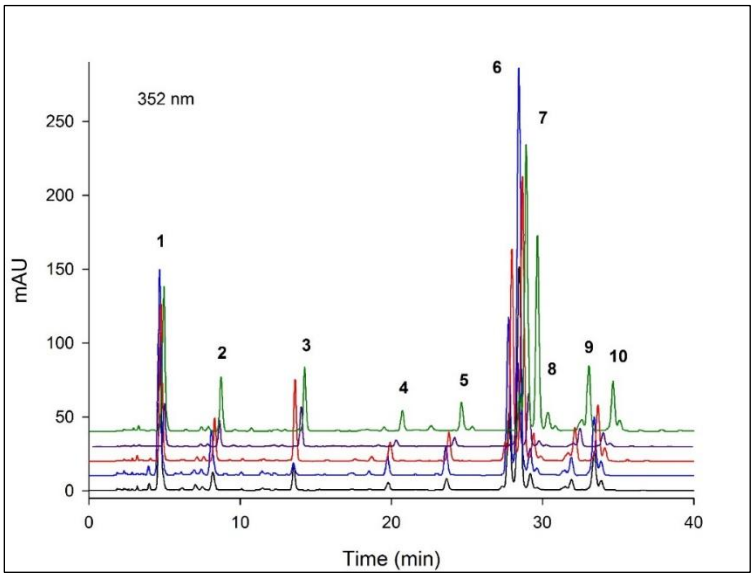


Figure 5. Characterization of gradient HPLC analysis of different *M. oleifera* leaves extracts. S1) Infusionate (purple), S2) Terbal (black), S3) Akuanandi (green), S4) Mas lait (blue), and S5) De Font Quer (red).

Table 2. Target compounds from different *M. oleifera* leaves extracts by HPLC-DAD (352 nm). The retention time and relative peak are of 10 common peaks of *M. oleifera* samples

Biomarkers	**Retention time (min)**	**Relative Peak Area**				
		S1	**S2**	**S3**	**S4**	**S5**
1 (chlorogenic acid)	4.79±0.2	1329.8	1007.2	1394.9	981.9	1384.6
2 (syringic acid)	8.33±0.3	185.2	253.8	346.7	616.8	475.4
3 (unknown)	13.64±0.5	199.9	58.78	679.6	967.84	538.9
4 (luteolin)	19.92±1.0	77.0	110.5	186.2	185.8	193.6
5 (rutin)	23.81±0.7	119.4	169.7	287.3	307.2	288.0
6 (unknown)	27.96±1.2	875.6	999.5	2284.1	2649.8	2982.0
7 (isoquercetin)	28.66±0.8	2554.4	2666.0	3133.2	1798.0	2108.7
8 (unknown)	29.39±1.9	205.3	145.3	312.7	134.9	159.4
9 (astragalin)	32.13±1.5	118.8	110.6	394.6	579.76	713.6
10 (unknown)	33.65±1.1	465.38	393.26	642.0	450.56	557.8

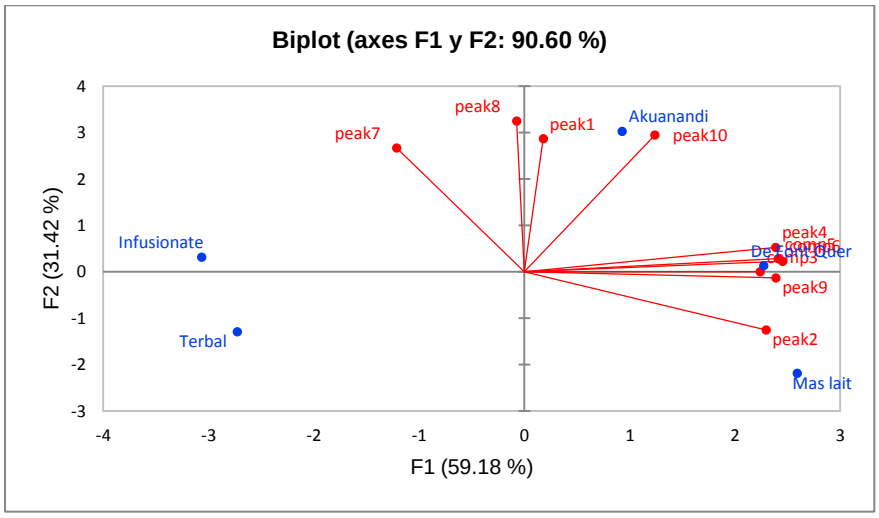


Figure 6. Two-dimensional scatter plots of the loadings of the first two factors. Biplot (axes F1 y F2: 90.6%)

Conclusion

This study indicated that TLC and HPLC-DAD fingerprint analysis can be readily utilized as a quality control method for *M. oleifera* herbal products. The advantages of using TLC to construct the fingerprints of *Moringa oleifera* based products are its simplicity, versatility, specific, sensitivity and simple sample preparation. Quantitative data generated by means of an image processing program enabled comparison of phytochemical composition. Furthermore, the clear discrimination of compounds of herbal products in PCA analysis indicated that the internal qualities of five *M. oleifera* herbal samples from different sources had market chemical variations. Additional researches are required to obtain more detailed identification of unknown peaks by HPLC-MS/MS. Akuanandi, Mas lait, and De Font Quer samples can be considered as appropriate sources of antioxidants. Thus, the proposed TLC and HPLC-DAD screening methods could be an easy way to evaluate the phytochemicals screening and determine the quality and possible adulteration of *M. oleifera* products.

Acknowledgements

A special acknowledgement is due to Guadalupe Arely Suárez-Adame for his technical assistance in the course of this research. The authors are also grateful to the Mexican Moringa producers for the supply of samples used in this study. They thank Ilse Andrea Marcial-Martínez for her technical support. We thanks to Iván Artemio Corral-Guerrero for helpful discussions and critical reading of this paper.

References

1. World Health Organization (2008). Herbal medicine research and global health: an ethical analysis access from https://www.who.int/bulletin/volumes/86/8/07-042820/en/ [Date access April 2020].
2. Zhang, J., Onakpoya, I. J., Posadzki, P. and Eddouks, M. (2015). The safety of herbal medicine: From prejudice to evidence. *Evidence-Based Complementary and Alternative Medicine*, 2015: 1-3.
3. Cimpoiu, C. (2006). Analysis of some natural antioxidants by thin-layer chromatography and high performance thin-layer chromatography. *Journal of Liquid Chromatography and Related Technologies*, 29: 1125-1142.
4. Abd Rani, N.Z., Husain, K. and Kumolosasi, E. (2018). Moringa genus: A review of phytochemistry and pharmacology. *Frontiers in Pharmacology*. 2018(9: 108.

5. Leone, A., Fiorillo, G., Criscuoli, F., Ravasenghi, S., Santagostini, L., Fico, G., Spadafranca A., Battezzati, A., Schiraldi, A., Pozzi, F., di Lello, S., Filippini, S. and Bertoli S. (2015). Nutritional characterization and phenolic profiling of moringa oleifera leaves grown in Chad, Sahrawi refugee camps, and Haiti. *International Journal of Molecular Sciences*, 16(8): 18923-18937.
6. Srirama, R., Kumar, J. U. S., Seethapathy, G. S., Newmaster, S. G., Ragupathy, S., Ganeshaiah, K. N., Uma, S. and Gudasalami, R. (2017). Species adulteration in the herbal trade: Causes, consequences and mitigation. *Drug Safety*, 40(8): 651-661.
7. Ichim, M. C. (2019). The DNA-based authentication of commercial herbal products reveals their globally widespread adulteration. *Frontiers in Pharmacology*, 10: 1227.
8. Saslis-Lagoudakis, C. H., Bruun-Lund, S., Iwanycki, N. E., Seberg, O., Petersen, G., Jäger, A. K. and Rønsted, N. (2015). Identification of common horsetail (*Equisetum arvense* L.; Equisetaceae) using thin layer chromatography versus DNA barcoding. *Scientific Reports*, 5: 11942.
9. Farah, M. H., Olsson, S., Bate, J., Lindquist, M., Edwards, R., Simmonds, M. S. J., Christine, L., Hugo, J. d. B. and Mats, T. (2006). Botanical nomenclature in pharmacovigilance and a recommendation for standardisation. *Drug Safety*, 29(11): 1023-1029.
10. Wright, R. J., Lee, K. S., Hyacinth, H. I., Hibbert, J. M., Reid, M. E., Wheatley, A. O. and Asemota, H. N. (2017). An investigation of the antioxidant capacity in extracts from *Moringa oleifera* plants grown in Jamaica. *Plants*, 6(4): 48.
11. Vongsak, B., Mangmool, S. and Gritsanapan, W. (2015). Antioxidant activity and induction of mRNA expressions of antioxidant enzymes in HEK-293 cells of *Moringa oleifera* leaf extract. *Planta Medica*, 81 (12–13): 1084-1089.
12. Sreelatha, S. and Padma, P. R. (2009). Antioxidant activity and total phenolic content of *Moringa oleifera* leaves in two stages of maturity. *Plant Foods for Human Nutrition*, 64(4): 303-311.
13. Falowo, A. B., Mukumbo, F. E., Idamokoro, E. M., Lorenzo, J. M., Afolayan, A. J. and Muchenje, V. (2018). Multi-functional application of *Moringa oleifera* Lam. in nutrition and animal food products: A review. *Food Research International*, 106: 317–334.
14. Valdez-Solana, M. A., Mejía-García, V.Y., Téllez-Valencia, A., García-Arenas, G., Salas-Pacheco, J., Alba-Romero, J. J. and Sierra-Campos, E. (2015). Nutritional content and elemental and phytochemical analyses of *Moringa oleifera* grown in Mexico. *Journal of Chemistry*, 2015: 1-9.
15. Mao, Q.-Q., Xu, X.-Y., Cao, S.-Y., Gan, R.-Y., Corke, H. and Beta, T. (2019). Bioactive compounds and bioactivities of ginger (*Zingiber officinale* roscoe). *Foods*, 8(6): 185.
16. Rajani, M. and Kanaki, N. S. (2008). Phytochemical standardization of herbal drugs and polyherbal formulations. Bioactive Molecule and Medicinal Plants: pp. 349-369.
17. Hiremath, R., Jalalpure, S. S. and Pethakar, S. (2016). Chromatographic fingerprint analysis of hydroalcoholic extract of medicinally important plant *Elephantopus scaber* L. using HPTLC technique. *Indian Journal of Pharmaceutical Education and Research*, 50(4): 689-694.
18. Gibbons, S. (2012). An introduction to planar chromatography and its application to natural products isolation. *Methods in Molecular Biology*, 864: 117-153.
19. Marston, A. (2011). Thin-layer chromatography with biological detection in phytochemistry. *Journal of Chromatography A*, 1218(19): 2676-2683.
20. Sarkar, R. and Mandal, N. (2012). Hydroalcoholic extracts of Indian medicinal plants can help in amelioration from oxidative stress through antioxidant properties. *Journal of Complementary & Integrative Medicine*, 9: 1-9.
21. Cieśla, Ł. (2012). Biological fingerprinting of herbal samples by means of liquid chromatography. *Chromatography Research International*, 2012: 1-9.

22. 22. Wang, C., Zhang, C.-X., Shao, C.-F., Li, C.-W., Liu, S.-H., Peng, X.-P. and Xu, Y. Q. (2016). Chemical fingerprint analysis for the quality evaluation of deepure instant pu-erh tea by HPLC combined with chemometrics. *Food Analytical Methods*, 9(12): 3298-3309.
23. 23. Vongsak, B., Sithisarn, P. and Gritsanapan, W. (2013). Simultaneous determination of crypto-chlorogenic acid, isoquercetin, and astragalin contents in *Moringa oleifera* leaf extracts by TLC-densitometric method. *Evidence-Based Complementary and Alternative Medicine*, 2013: 1-7.
24. 24. Tumer, T. B., Rojas-Silva, P., Poulev, A., Raskin, I. and Waterman, C. (2015). Direct and indirect antioxidant activity of polyphenol- and isothiocyanate-enriched fractions from *Moringa oleifera*. *Journal of Agricultural and Food Chemistry*, 63(5): 1505-1513.
25. 25. Komsta, Ł. (2012). Chemometrics in fingerprinting by means of thin layer chromatography. *Chromatography Research International*, 2012: 1-5.
26. 26. Olech, M., Komsta, Ł., Nowak, R., Cieśla, Ł. and Waksmundzka-Hajnos, M. (2012). Investigation of antiradical activity of plant material by thin-layer chromatography with image processing. *Food Chemistry*, 132(1): 549-553.
27. 27. Kupski, L. and Badiale-Furlong, E. (2015). Principal components analysis: An innovative approach to establish interferences in ochratoxin A detection. *Food Chemistry*, 177: 354-360.
28. 28. Lin, H., Zhu, H., Tan, J., Wang, H., Wang, Z., Li, P., Zhao, C. and Liu, J. (2019). Comparative analysis of chemical constituents of *Moringa oleifera* leaves from China and India by ultra-performance liquid chromatography coupled with quadrupole-time-of-flight mass spectrometry. *Molecules*, 24(5): 942.
29. 29. Rodríguez-Pérez, C., Quirantes-Piné, R., Fernández-Gutiérrez, A. and Segura-Carretero, A. (2015). Optimization of extraction method to obtain a phenolic compounds-rich extract from *Moringa oleifera* Lam leaves. *Industrial Crops and Products*, 66: 246-254.
30. Vergara-Jimenez, M., Almatrafi, M. M. and Fernandez, M. L. (2017). Bioactive components in *Moringa oleifera* leaves protect against chronic disease. *Antioxidants*, 6(4): 91.
31. 31. Kasai, H., Fukada, S., Yamaizumi, Z., Sugie, S. and Mori, H. (2000). Action of chlorogenic acid in vegetables and fruits as an inhibitor of 8-hydroxydeoxyguanosine formation in vitro and in a rat carcinogenesis model. *Food and Chemical Toxicology*, 38(5): 467-471.
32. 32. Manguro, L. O. A. and Lemmen, P. (2007). Phenolics of *Moringa oleifera* leaves. *Natural Product Research*, 21(1): 56-68.
33. 33. Srinivasulu, C., Ramgopal, M., Ramanjaneyulu, G., Anuradha, C. M., and Kumar, C. S. (2018). Syringic acid (SA)–a review of its occurrence, biosynthesis, pharmacological and industrial importance. *Biomedicine & Pharmacotherapy*, 108: 547-557.
34. 34. Wang, H., Yang, L., Zu, Y. and Zhao, X. (2014). Microwave-assisted simultaneous extraction of luteolin and apigenin from tree peony pod and evaluation of its antioxidant activity. *Scientific World Journal*, 2014: 1-12.
35. 35. Ganeshpurkar, A. and Saluja, A. K. (2017). The pharmacological potential of rutin. *Saudi Pharmaceutical Journal*, 25(2): 149-164.
36. 36. di Camillo Orfali, G., Duarte, A. C., Bonadio, V., Martinez, N. P., De Araújo, M. E. M. B., Priviero, F. B. M., Calvalho, P. O. and Priolli, D. G. (2016). Review of anticancer mechanisms of isoquercitin. *World Journal of Clinical Oncology*, 7(2): 189.
37. 37. Riaz, A., Rasul, A., Hussain, G., Zahoor, M. K., Jabeen, F., Subhani, Z., Younis, T., Ali, M., Sarfraz, I. and Selamoglu, Z. (2018). Astragalin: a bioactive phytochemical with potential therapeutic activities. *Advances in Pharmacological Sciences*, 2018: 1-15.
38. 38. Kumar, S. and Pandey, A. K. (2013). Chemistry and biological activities of flavonoids: an overview. *The Scientific World Journal*, 2013: 1-17.

39. Sidhu, O. P., Annarao, S., Chatterjee, S., Tuli, R., Roy, R. and Khetrapal, C. L. (2011). Metabolic alterations of *Withania somnifera* (L.) dunal fruits at different developmental stages by NMR spectroscopy. *Phytochemical Analysis*, 22(6): 492-502.
40. Kårlund, A., Moor, U., Sandell, M. and Karjalainen, R. O. (2014). The impact of harvesting, storage and processing factors on health-promoting phytochemicals in berries and fruits. *Processes*, 2(3): 596-624.
41. Nisa, F. Z., Astuti, M., Haryana, S. M. and Murdiati, A. (2019). Antioxidant activity and total flavonoid of *Carica papaya* L. leaves with different varieties, maturity and solvent. *AgriTECH*, 39(1): 54-59.
42. Anju, D. (2017). Phytoeq uivalence: A balanced perspective. *Annals of Pharmacology and Pharmaceutics*, 2(6): 2-6.

Malaysian Journal of Analytical Sciences Vol 24 No 4 2020

		Page
1.	A REVIEW ON APPLICATIONS OF GOLD AND SILVER-BASED SORBENTS IN SOLID PHASE EXTRACTION AND SOLID PHASE MICROEXTRACTION (Satu Ulasan Penggunaan Pengerap Berasaskan Aurum dan Argentum dalam Pengekstrakan Fasa Pepejal dan Pengekstrakan Mikro Fasa Pepejal) *Wan Aini Wan Ibrahim, Zetty Azalea Sutirman, Jawed Qaderi, Kasimu Abu Bakar, Siti Hajar Md Basir, Imad Eddine Aouissi*	464
2.	LIGNIN FROM OIL PALM FROND UNDER SUBCRITICAL PHENOL CONDITIONS AS A PRECURSOR FOR CARBON FIBER PRODUCTION (Lignin daripada Pelepah Kelapa Sawit dibawah keadaan Subgenting Fenol sebagai Produk Perantaraan bagi Penghasilan Serat Karbon) *Khalidatul Athirah Khalid, Vijayaletchumy Karunakaran, Asimi Ana Ahmad, Khairul Faizal Pa'ee, Norfahana Abd-Talib, Tau Len-Kelly Yong*	484
3.	ACETYLCHOLINESTERASE INHIBITORY ACTIVITY OF THE METHANOL EXTRACT AND PHYTOCHEMICAL STUDY OF THE LEAVES OF *Macaranga gigantea* (Rchb.f. & Zoll.) (Aktiviti Perencatan Asetilkolinesterase Terhadap Ekstrak Methanol dan Kajian Fitokimia ke atas Daun *Macaranga gigantea* (Rchb.f. & Zoll) *Muhammad Sulaiman Mohd Johari, Norizan Ahmat, Aisyah Salihah Kamarozaman, Zetty Zulikha Hafiz*	495
4.	ANTIOXIDANT AND XANTHINE OXIDASE INHIBITORY ACTIVITY OF *Euphorbia hirta* LEAVES CRUDE EXTRACT (Antioksidan dan Aktiviti Perencatan Xantina Oksidase Bagi Ekstrak Mentah Daun *Euphorbia hirta*) *Ahmad Anas Nagoor Gunny, Thum Carmen, Mohd Hishamuddin Che Mat, Ahmad Azudin Nordin, Azalina Mohamed Nasir*	503
5.	UNCERTAINTY OF IODINE VALUE DETERMINATION IN PALM OLEIN (Ketidakpastian Penentuan Nilai Iodin dalam Minyak Sawit Olein) *Mohd. Azmil Mohd. Noor, Hajar Musa, Razmah Ghazali*	511
6.	EFFECT OF PROCESS PARAMETERS ON GELLING TIME OF SOL-GEL SILICA AND KENAF-SOL-GEL SILICA SYSTEMS (Kesan Parameter Proses pada Masa Penggelan dalam Sistem Sol-Gel Silika dan Kenaf-Silika Sol-Gel) *Fahmi Asyadi Md Yusof, Zulhafiz Tajudin, Ong Siew Kooi, Azanam Shah Hashim*	519
7.	IRIDOID GLYCOSIDES AND PHENYLPROPANOIDS FROM *Asystasia gangetica* (L) T. ANDERSON VAR. *Micrantha* (ACANTHACEAE) (Iridoid Glikosida dan Fenilpropanoid daripada *Asystasia gangetica* (L) T. Anderson Var. *Micrantha* (Acanthaceae)) *Isna Athirah Othman, Norizan Ahmat, Amjad Ayad Qatran Al-Khdhairawi*	530
8.	EVALUATION ON THE EFFICACY OF DIFFERENT DISRUPTION METHOD OF OIL PALM ROOTS AND Ganoderma boninense CELL WALL	538

(Penilaian ke atas Keberkesanan Kaedah Pemusnahan yang Berbeza pada Dinding Sel Akar Kelapa Sawit dan Ganoderma boninense)
Arnnyitte Alexander, Jedol Dayou, Coswald Stephen Sipaut, Khim Phin-Chong

9. LEVEL OF HEAVY METALS IN BAMBOO SHARKS (*Chiloscyllium* sp.) IN STRAITS OF MALACCA, MALAYSIA 546
(Kepekatan Logam Berat di dalam Yu Cicak (*Chiloscyllium* sp.) di Selat Melaka, Malaysia)
Jun-Han Poong, Lian-Sheng Tee, Evonne Tan, Tiam-Hing Yip, Muhammad Hasbi Ramli, Abd Rahman Ali Hassan, Ahmad Ali, Chen Meng-Hsien, James Lam Chung Wah, Ong Meng Chuan

10. REAL-TIME MONITORING OF FOOD FRESHNESS USING DELPHINIDIN-BASED VISUAL INDICATOR 558
(Pemantauan Kesegaran Masa Nyata Makanan dengan Menggunakan Indikator Visual Berasaskan Delphinidin)
Nurdiyana Husin, Mohd. Zulkhairi Abdul Rahim, Mohd. Azizan Mohd. Noor, Ismail Fitry Mohammad Rashedi, Nazatulshima Hassan

11. EVALUATION OF PHYSICOCHEMICAL CHARACTERISTICS AND PHYTOCHEMICAL PROPERTIES OF TOMATO (*Lycopersicon esculentum* L.) DURING DIFFERENT MATURITY STAGES 570
Md. Ashikur Rahman, Md. Parvez Hasan, Rakibul Hasan

12. STABILISATION OF PEAT SOIL USING MAGNESIUM OXIDE: A PRELIMINARY STUDY 578
(Penstabilan Tanah Gambut Menggunakan Magnesium Oksida: Satu Kajian Awal)
Lily Suhaila Yacob and Amelia Md Som

13. IMPACTS OF CITRIC ACID ON THE PHYTOEXTRACTION OF ZINC (Zn) USING SORGHUM (*Sorghum bicolor (L.)* Moench) PLANTS 587
(Kesan Asid Sitrik Terhadap Pengekstrakan Fito Zink (Zn) Mengunakan Tumbuhan Sorghum (*Sorghum bicolor (L.)* Moench))
Hamza Badamasi, Muhammad Saminu Dagari, Isyaku Sale

14. A FEASIBILITY STUDY ON VOLATILE ORGANIC COMPOUNDS PROFILING OF OIL PALM-*Ganoderma* INFECTED WOOD FOR BASAL STEM ROT DETECTION 599
(Kajian Kebolehlaksanaan Pemprofilan Sebatian Organik Meruap daripada Kayu Sawit yang Dijangkiti *Ganoderma* bagi Mengesan Penyakit Reput Pangkal Batang)
Zainol Hilmi Nur Hailini, Idris Abu Seman, Mohd Azmil Mohd Noor, Shariffah-Muzaimah Syed Aripin

15. SCREENING OF PLANTS FOR INSECTICIDAL ACTIVITIES AGAINST ORIENTAL FRUIT FLY *Bactrocera dorsalis* (HENDEL) FOR PEST MANAGEMENT OF MANGO *Mangifera indica* 615
(Saringan Tumbuhan bagi Aktiviti Serangga Perosak Terhadap Lalat Buah Oriental *Bactrocera dorsalis* (Hendel) untuk Pengurusan Serangga Perosak Mangga *Mangifera indica*)
Danila S. Paragas, Kathlia D. C. Cruz, Elaida R. Fiegalan

Malaysian Journal of Analytical Sciences (MJAS)
Published by Malaysian Analytical Sciences Society

A REVIEW ON APPLICATIONS OF GOLD AND SILVER-BASED SORBENTS IN SOLID PHASE EXTRACTION AND SOLID PHASE MICROEXTRACTION

(Satu Ulasan Penggunaan Pengerap Berasaskan Aurum dan Argentum dalam Pengekstrakan Fasa Pepejal dan Pengekstrakan Mikro Fasa Pepejal)

Wan Aini Wan Ibrahim[1, 2]*, Zetty Azalea Sutirman[1], Jawed Qaderi[1,3], Kasimu Abu Bakar[1,4], Siti Hajar Md Basir[1], Imad Eddine Aouissi[1]

[1]Department of Chemistry, Faculty of Science
[2]Centre for Sustainable Nanomaterials, Ibnu Sina Institute for Scientific and Industrial Research
Universiti Teknologi Malaysia, 81310 UTM Johor Bahru, Johor, Malaysia
[3]Department of Physical Chemistry, Faculty of Chemistry,
Kabul University, Jamal Mina 1001 Kabul, Afghanistan
[4]Department of Chemistry, Faculty of Science,
Sokoto State University, Sokoto, Nigeria

**Corresponding author: waini@utm.my, wanaini@kimia.fs.utm.my*

Received: 5 April 2020; Accepted: 7 June 2020; Published: 11 August 2020

Abstract

Organic and inorganic pollutants and contaminants are considered harmful to ecosystem, even at low or trace-level concentrations. Several studies have been performed to degrade or remove these contaminants from environmental matrices and the use of pre-concentration approaches such as solid phase extraction (SPE) and solid phase microextraction (SPME) for their quantitation has been developed and showed great demand as an essential module to upgrade both practical efficiency and analytical sensitivity. Gold nanoparticles (Au NPs) and silver nanoparticles (Ag NPs) could be used as a sorbents prior to the combined high efficient separation or extraction methods with different detection techniques. Along with the rapid development of nanotechnology in material science, numerous nanomaterials include Au NPs and Ag NPs have been developed with particularly useful applications in analytical chemistry. Au NPs and Ag NPs are attracting a great deal of attention for their use in various technologies, including catalysis, optical and electronic devices, and separation science. In this review, recent progress of Ag NPs applied in SPE and SPME have been summarized and discussed. Au NPs and Ag NPs materials are evaluated for their unusual performance in various applications from environmental trace sample analysis to clinical investigations. Such great variety of uses makes nanomaterials kind of versatile tools in sample preparation for almost all categories of analytes.

Keywords: silver nanoparticles, gold nanoparticles, pre-concentration, solid phase extraction, solid phase microextraction

Abstrak

Bahan pencemar organik dan tak organik dianggap berbahaya kepada ekosistem, walaupun, pada kepekatan tahap rendah atau surih. Beberapa kajian telah dilakukan untuk nyahdegradasi atau penyingkiran bahan pencemar ini dari matriks sekitaran dan penggunaan pendekatan pra-pemekatan seperti pengekstrakan fasa pepejal (SPE) dan pengekstrakan mikro fasa pepejal (SPME)

untuk penentuan kuantitatif telah dibangunkan dan menunjukkan permintaan yang besar sebagai modul penting untuk meningkatkan kecekapan praktik dan sensitiviti analisis. Zarah nano emas (Au NPs) dan perak (Ag NPs) boleh digunakan sebagai pengerap sebelum gabungan pemisahan kecekapan tinggi atau kaedah pengekstrakan dengan teknik pengesanan yang berbeza. Seiring dengan perkembangan nanoteknologi yang pesat dalam sains bahan, banyak bahan nano termasuk Au NPs dan Ag NPs telah dibangunkan terutama aplikasi berguna dalam kimia analisis. Au NPs dan Au NPs menarik banyak perhatian untuk penggunaannya dalam pelbagai teknologi termasuklah pemangkinan, alat optik dan elektronik, dan sains pemisahan. Dalam ulasan ini, kemajuan terkini Au NPs dan Ag NPs dalam SPE dan SPME dirumus dan dibincangkan. Bahan Au NPs dan Ag NPs dinilai untuk prestasi luar biasanya dalam pelbagai aplikasi dari analisis sampel surih alam sekitar kepada penyiasatan klinikal. Kepelbagaian penggunaan bahan nano menjadikannya sebagai peranti serba boleh dalam penyediaan sampel untuk hampir semua kategori analit.

.

Kata kunci: zarah-nano aurum, zarah-nano argentum, pra-pemekatan, pengekstrakan fasa pepejal, pengekstrakan mikro fasa pepejal

Introduction

Nanomaterials are a special kind of materials with nanometric scales in at least one dimension of their particles or pore structures, typically in the range of 1-100 nm [1]. Compared with conventional materials with micrometric or larger sizes, such limited scales endow nanomaterials with some exceptional and unprecedented properties in many aspects. Among them, the ultrahigh specific areas [2] and increasing surface activities facilitate the application of nanomaterials in sample preparation. In addition, tunable compositions, various morphologies and flexible functionalization offer a great number of opportunities in the development of novel nanomaterials for more efficient and versatile sample preparation. The qualitative and quantitative identification techniques of a large variety of complex and low volume samples based on using nanoparticles (NPs) as sorbents in various branches of analytical chemistry have been studied. Generally, NPs synthesis is conducted by either top-down or bottom-up procedures, which containing physical, chemical and biological methods (Figure 1). Their potential for sensing and biosensing has also been studied in depth for the detection of proteins, drugs, pesticides, and explosives. As such, the NPs have become desirable options for the development of pre-concentration techniques for trace-level chemical compounds from environmental matrices. The selectivity and sensitivity of analytical techniques have tremendously improved by using NPs as sorbents because of their advantageous properties (e.g. large surface area and specific affinity towards ultra-trace-level target analytes). At present, a large number of NPs (e.g. metallic and metal oxides, polymer-based nanocomposites, and silicon- and carbon-based NPs) have been incorporated in several sample preparation techniques for the proficient extraction and preconcentration of ultra-trace level chemical species before their determination by different analytical techniques. NPs have thus gained significant interest in the field of environmental science and technology, which includes the sampling and analysis of various organic pollutants. For soil and sediment samples, polymer-based nanosorbents have commonly been used for the determination of parabens, benzene homologues, and imidazolinones. For water samples, NPs such as metallic and mixed oxide NPs, have been introduced for a diverse of organic pollutants [3].

Gold nanoparticles (Au NPs) are gradually attracting a great deal of attention for their use in technologies, including catalysis, optical materials, electronic devices, biosensors, drug carriers, and high contrast cell imaging. On the other hand, Au NPs have been widely used in analytical procedures because of their size dependent electrical properties, high electrocatalytic activity, and functional compatibility with molecules and polymers. Besides, biomolecules containing thiol (SH) or amino (NH_2) groups can be adsorbed spontaneously on to gold surfaces to generate well-organized, self-assembled monolayers. Although Au NPs provide a large surface area to interact with column surface and analyte, very little research has been dedicated to understanding their impact in separation science. Additionally, Au NPs are

characterized by a high surface-to-volume ratio, long-term stability, easy synthesis and favourable chemical modification [4].

The application of silver nanoparticles (Ag NPs) has been gradually increasing in nano-functionalised consumer products. Ag NPs are among the most commonly used in the fields of textiles, medical devices, dentistry, wound healing, cosmetics, water filters, water disinfection, paints, food industries and electrical appliances due to its antimicrobial activities, the unique physicochemical properties and high surface-to-volume ratio [5]. The rapid development and increase use of Ag NPs has given rise to their release into the environment and has possible toxic effects on living organisms such as plants, fish and humans [6]. The toxicity of Ag NPs is generally believed to be related with their release of Ag ions, which have toxic effects on many pathogens.

Nowadays there are various analytical options available for the extraction and pre-concentration of trace levels of organic pollutants based on the integration between different kinds of nanomaterials and various types of extraction techniques which includes solid phase extraction (SPE), magnetic solid phase extraction (MSPE), solid phase microextraction (SPME), and stir bar sorptive extraction (SBSE). These techniques are being used for the quantitative analysis on different forms of analytes in environmental samples such as volatile organic compounds (VOCs), polycyclic aromatic hydrocarbons (PAHs), phthalates, alkylphenols, pesticides, polybrominated diphenyl ethers, pharmaceuticals, and other endocrine disrupting chemicals. As a result, the use of these innovative pre-treatment approaches has become crucial for the identification and quantitation of many pollutants [3].

The challenge in speciation analysis of organic and inorganic pollutants and contaminants deals with sample preparation techniques for separation prior to determination. Solid phase extraction (SPE) and solid phase microextraction (SPME) are promising approaches for the separation of these pollutants based on gold nanoparticles (Au NPs) and silver nanoparticles (Ag NPs) [7]. SPE and SPME are also widely-used sample preparation technique for the extraction of pesticides and ions due to their high extraction efficiency, little consumption of organic solvent, low cost and easy operation. According to Zhao et al. [6], in view of the low concentration of target species and complex sample matrix in the real-world samples, the novel non-chromatographic separation techniques such as cloud point extraction, liquid phase microextraction and SPE and LPME methods are good choices for real sample analysis, which can not only separate analytes of interest, but also remove sample matrix and pre-concentrate target species. To date, there are numbers of publications on applications of Au and Ag NPs, but only few of them reported on their application, individually in separation and extraction area [8-11]. Therefore, the present review specifically describes the application of both Au and Ag NPs as well as their derivatives in extraction techniques for analysis of various analytes. It also summarizes the published works from the year of 2011 to 2019.

Sorptive extraction techniques

Solid-phase extraction (SPE) is progressively a suitable sample preparation technique. It is used either to pre-concentrate or to purify analytes of interest from a great variety of sample matrices [12]. SPE is used for extracting and pre-concentrating trace-level organic impurities from environmental matrices. This technique developed in the 1980s and ever since then, it has confirmed to be the most dominant tool for the isolation and purification of target analysis [13]. The advantages of SPE include simplicity, flexibility, high selectivity, automation, rapidity, higher enrichment factors, and the absence of emulsion and use of different sorbents [14]. The extraction efficiency of SPE has been significantly improved by the combination of NPs, which provided more trapping sites than previous sorbents. Compared with other liquid extraction techniques for organic pollutants, NPs-based SPE provides lower detection limits for a wide variety of organic pollutants with minimal sample and solvent volumes [3].

SPME was introduced for the first time as sample separation technique by Belardi and Pawlizyn [15].

SPME consists of fused silica coated with a polymeric stationary phase where the partition equilibrium between the analytes and the stationary phase occurs. This solvent free method has undergone a rapid development [16] owing to the fact that SPME is environmentally friendly and able to do multiple operations in a single step (sampling, extraction, pre-concentration and sample introduction) [17]. SPME has been applied in various research areas, from environmental chemistry [18] to biomedical analysis [19, 20]. Besides being solvent free, this method is rapid and selective [21]. It can also be coupled with various separation techniques and analytical technologies such as gas chromatography (GC), gas chromatography-mass spectrometry (GC-MS) [22], high performance liquid chromatography (HPLC) [23], HPLC-mass spectrometry (HPLC-MS) [24] and capillary electrophoresis (CE) [25]. Although the SPME technique has various advantages; the fiber that is available in the market has serious drawbacks such as does not chemically bond well with the coating material, the fibers are quite thick and lack stability at high temperatures [26]. In recent years, these problems are being solved by developing a new coating protocol [3]. In the literature there are examples of sorbent particles that lower the accumulated amount of analyte [27], which achieve large errors if analyte concentrations are determined on the basis of calibration with non-complexing standards. To evaluate the utility of SPME for the analyte, it will be necessary to develop a thorough understanding of how the sample components can influence the SPME measurement of a specific target molecule or species.

The rather high cost of SPME coatings does not allow their use for many applications. Moreover, the available commercial coatings are not suitable for a wide range of analytes. Some features such as the ease of coating procedure, ability to extract the specific target analyte(s), cost and (chemical, mechanical and thermal) stability must be taken into account for the applied materials as SPME coatings. Recently, nanomaterials have attracted a great importance as new fiber coatings because of their excellent properties better than conventional polymeric coatings used in SPME [28]. Au NPs possess several interesting properties such as long-term stability, high surface-to-volume ratio, ease of chemical modification and compatibility with biomolecules [29]. In addition, molecules with functional group such as thiol (–SH) or amino ($–NH_2$) groups can be adsorbed onto the Au surface to form a well-organized self-assembled monolayer (SAM), and this flexibility has attracted great attentions and has been widely used in sample pre-concentration and separation science [30]. The overview of the whole procedures to determine various pollutants from different samples is shown in Figure 2.

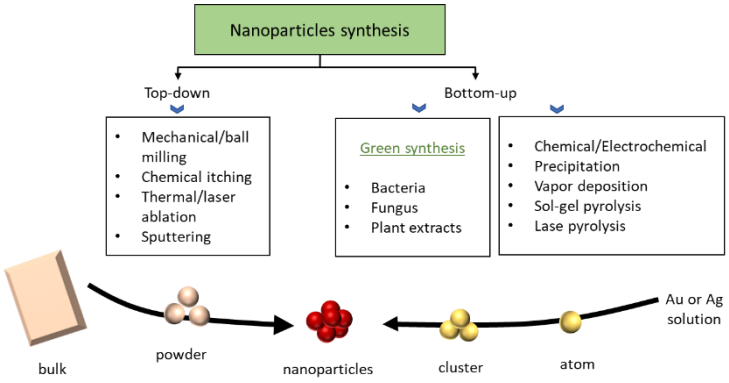


Figure 1. Different approaches for nanoparticles synthesis

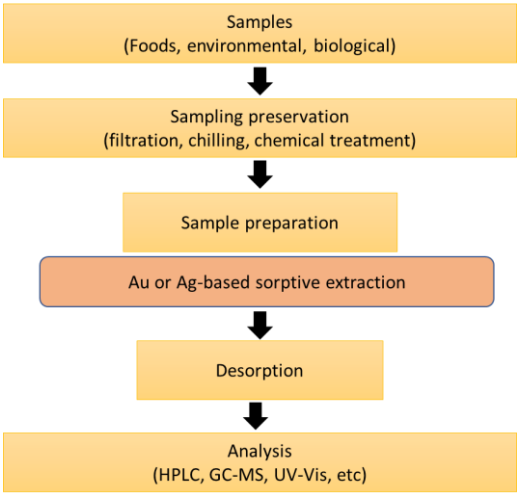


Figure 2. General procedures for determination of various pollutants in different samples using Ag or Au-based extraction techniques

Gold nanoparticles

In ancient times, gold was still considered a way to improve health. In fact, Chinese and Indian cultures have used many gold compounds in the form of "Swarna Bhasma" to treat various health problems, such as improving the vital power and male ineffectiveness [29]. The exceptional properties of this element, such as inertness, nontoxic nature towards cell and biocompatibility, make it an attractive material for many researchers in biological and medical applications. It is also considered an important material for use in therapy and imaging [31]. Au NPs have unique optoelectronic properties and the way that they interact with the light produces vibrant colors which have been used for centuries by artists, and have been further developed into advanced applications like organic photovoltaics, sensory probes, therapeutic agents, drug delivery in biological and medical applications, electronic conductors and catalysis [29, 31]. It is worth noting that by varying the size, shape and surface textures, or aggregation state of Au NPs, we can adjust different optical and electronic properties. Besides to these applications, in earlier 1978s, scientists found that it can also be used as an antitumor agent which can open a new investigation gate to be deeply explored [32]. Au NPs tend to resonantly absorb and scatter visible light and infrared light during the excitation of surface plasmon oscillation. By studying the distance dependent scattering properties of the Au NPs, it has been found that it is possible to detect biological events at the single molecular level. This finding was used for bio-sensing [33]. Au NPs publications has magnificently increased in various fields including biological fields which according to Chen et al., this development is related to the increase in nanotechnology field that increased the governmental awareness and funding, and fast evolution in synthetic chemistry molecular biology. On the one hand to recent developments in the field of nanotechnology, which has increased government awareness and funding, and on the other hand to the rapid evolution in synthetic molecular biology chemistry [34].

Au NPs can be synthesized by reduction of gold salts in the presence of stabilizing agents which act to prevent their agglomeration. They can be prepared by using physical, chemical, and supercritical fluid technology methods. The tendency of Au NPs to absorb and scatter visible and near infrared light resonantly, facilitate the production of Au NPs by physical methods like microwave irradiation, sonochemical method, ultraviolet radiation, laser ablation, thermolytic process and photochemical

process [32]. These methods have proved a good adaptation for the production of nanoparticles. As for the chemical methods, they are based on the production of Au NPs using chemical reactions such as the synthesis of Au NPs in an aqueous medium using citrate or sodium borohydride as the reducing agent. It has been reported in the literature that the synthesis of small and uniform size of Au NPs can be achieved by controlling the concentration of citrate [35]. One of the most important advantages of Au NPs, is that they can be effectively altered by functionalizing their monolayers by thiol linkers. The modification can be performed by proteins, nucleic acids, oligosaccharides, and peptides [36-38]. Another way to produce Au NPs is using an inorganic matrix as a support or host. In fact, Mukherjee et al. have used silica supported surface which contains silanol groups. These allow the reduction of chloroaurate ion to Au NPs [39].

Au NPs have unique properties such as special stability, multiple surface functionalities, and great biocompatibility [8]. The physical properties of Au NPs are inertness, nontoxicity and the tendency to absorb and scatter visible and near infrared (NIR) light resonantly. Au NPs are versatile materials for a broad range of applications with well characterized electronic and physical properties due to well-developed synthetic procedures. In addition, their surface chemistry is easy to modify. These features have made Au NPs one of the most widely used nanomaterials for academic research and an integral component in point-of-care medical devices and industrial products worldwide [32].

Silver nanoparticles

Ag NPs play an important role in nanoscience and nanotechnology and their application have been gradually increased in nano-functionalized consumer products. Ag NPs are among the most commonly used in the fields of textiles, medical devices, dentistry, wound healing, cosmetics, water filters, water disinfection, paints, food industries and electrical appliances due to its antimicrobial activities, the unique physicochemical properties and high surface-to-volume ratio [5].

Peculiar properties of Ag NPs, they have been used for several applications, including as antibacterial agents, in industrial, household, and healthcare-related products, in consumer products, medical device coatings, optical sensors, and cosmetics, in the pharmaceutical industry, the food industry, in diagnostics, orthopedics, drug delivery, as anticancer agents, and have ultimately enhanced the tumor-killing effects of anticancer drugs. Nano-sized metallic particles of Ag NPs are unique and can considerably change physical and chemical properties which include optical, electrical, and thermal, high electrical conductivity, and biological properties due to their surface-to-volume ratio; therefore, these nanoparticles have been exploited for various purposes [40, 41].

The determination of heavy metals at trace levels is one of the most important targets of analytical chemists because of their roles in our life. Although some trace metals such as cobalt are essential to human whose daily requirement is only a few milligrams, however, it can be harmful to human health if ingested in high level. Therefore, the elemental composition of trace metals is important to ensure the water and food quality. Furthermore, the metal content in water, sediment, plants and animals can also provide essential information on the levels of contamination in the environment [42].

Physical and chemical properties of Ag NPs including surface chemistry, size, size distribution, shape, particle morphology, particle composition, coating/capping, agglomeration, dissolution rate, particle reactivity in solution, efficiency of ion release, cell type, and finally type of reducing agents used for synthesis are crucial factors for determination of cytotoxicity [43]. The smaller size particles of Ag NPs could cause more toxicity, because they have larger surface area. Shape is equally important to the determination of toxicity. Ag NPs toxicity mainly depends on the availability of chemical and or biological coatings on the nanoparticle surface [41].

In the past decade, nano-scale solid materials including Ag NPs have become very important due to their unique chemical and physical properties including high

chemical activity and adsorption capacity to many element ions onto the surface of the nanomaterials. The surface atoms are unsaturated and subjected to combination with other element ions by static electricity for which the nanoparticles can adsorb element ions with good adsorption speed. Ag NPs have been utilized as sorbent due to their improved intrinsic properties such as chemical activity and fine grain size compared with the macro-scaled classical substances such as normal scale titanium dioxide, alumina, etc. Nanoparticles were chemically modified by a reagent to obtain a new selective solid phase extractant for the pre-concentration of metal ions [42].

Sample preparation based on gold nanoparticles

Gold nanoparticles in solid phase extraction technique

Au NPs are the main metal nanomaterials for bio-separation and analysis of pesticides and organic contaminants due to their excellent physical and chemical properties, providing an excellent surface for recognizing target molecules. Gong *et al*. developed a sensitive enzymeless Au NPs decorated graphene nanosheets (GNs) sensor to separate organophosphate pesticides (OPPs) in solid phase extraction (SPE) [43]. Such a nanostructured composite film, combining the advantages of Au NPs with two dimensional GNs, intensely enabled the enrichment of nitroaromatic OPPs onto the surface and recognized their stripping voltammetric exposure of OPPs by choosing methyl parathion (MP) as the model analyte. The stripping voltammetric routines of seized MP were assessed by cyclic voltammetric and square-wave voltammetric analysis. The combination of the nanoassembly of Au NPs-GNs, SPE, and stripping voltammetry provided a fast, simple, and sensitive electrochemical method for detecting nitroaromatic OPPs. The stripping analysis is highly linear over the MP concentration ranges of 0.001 - 0.1 μg/L and 0.2 - 1.0 μg/L, with a detection limit of 0.6 μg/mL. This designed enzymeless sensor exhibited good reproducibility and acceptable stability [43].

Photo luminescent amino functionalized graphene quantum dots (GQDs-amino) associated with Au NPs was made in the determination of kanamycin sulfate where the Au NPs were produced by the reduction of $AuCl_4$ with $NaBH_4$ in an aqueous dispersion of graphene quantum dots (GQDs-amino) containing the cationic surfactant cetyltrimethylammonium bromide (CTAB). The Au NPs-GQDs-amino-CTAB system showed a suppressed photoluminescence that was amplified in the presence of kanamycin. Under optimized experimental conditions, the photoluminescence amplification of the nanomaterial system showed a linear response as a function of kanamycin concentration, covering three orders of magnitude (10^{-7} to 10^{-5} mol/L). The use of SPE with a cartridge packed with aminoglycoside selective molecularly imprinted polymer ensured selectivity in determination of yellow-fever vaccine and veterinary pharmaceutical formulations. The analytical results were statistically similar to those obtained with an HPLC based fluorescence method. The proposed method was a simple, sensitive and selective approach that did not involve the use of toxic reagents employed for chemical derivatization of aminoglycoside antibiotics [44].

Gold/polypyrrole (Au-PPy) nanocomposite coated silica is a novel sorbent described for the efficient SPE of common microcystins (MCs) well below the recommended United States EPA and World Health Organization (WHO) guidelines. With the optimized SPE protocol, samples spiked with MCs were determined at ng/L concentrations by liquid chromatography mass spectrometry (LC–MS) in different aqueous sample matrices, including HPLC-grade, tap, and lake water which indicated excellent extraction efficiency and reproducibility. The Au-PPy nanocomposite coated sorbent material was reusable for at least three independent MC extractions with a single SPE cartridge in the concentration range of 10 - 500 ng/L. Therefore, the Au-PPy nanocomposite coated silica sorbent is a promising new material for the quantification of MC variants in water samples [45].

Silver (Ag) and gold (Au) NPs impregnated in nylon membrane filters were capable of being used as a new sorbent for SPE of small amounts of Hg from natural waters [47]. This sorbent had a large surface area of

NPs and thus contributed to high efficiency of adsorption of Hg from aqueous phase to membrane filters. A Zeeman mercury analyzer RA–915+ helped in thermal desorption of Hg from membrane filters which eliminated the sample preparation step sharply reducing the risk of contamination. The LOD for the determination of Hg in water using Ag-Au NPs impregnated in nylon membrane filters was around 0.4 ng/L which was much lower than 200 ng/L achieved by cold vapour generation technique. This convenient sorbent obviously showed the potential which could be applied to remove Hg in water samples with appropriate results. Additionally, water samples could be sampled directly to the impregnated filters from water forms thus decreasing contamination during transport and storage [46].

Nowadays Au NPs coated silica sorbent with ionic liquid (Au NPs-IL-silica sorbent) has been productively prepared and applied for the pre-concentration of sulfonylurea herbicides (SUHs) in water samples [4]. Different factors that influenced pre-concentration efficiency, such as pH of the sample and elution conditions, were optimized. It was confirmed that pH was a critical variable in the adsorption process of the SUHs onto the prepared sorbent. On the other hand, this sorbent helped to achieve good recoveries and precisions in terms of repeatability and reproducibility by SPE. Better recoveries and lower LODs and LOQs were obtained when the Au-NP–IL–silica sorbent was used, although its synthesis time was longer due to the addition of the IL. In addition to this, the use of the Au-NP–IL-functionalized silica sorbent as SPE material is in some cases, a better option than the use of conventional SPE materials such as C18 sorbents. The use of these types of materials could be expanded to the extraction of other compounds for clean-up/pre-concentration processes prior to a chromatographic or electrophoretic separation method [4].

In addition, gold nanoclusters (Au NCs) immobilized paper has been developed for the detection and determination of zinc (Zn) in whole blood and cells. A headspace (HS)-SPE method was used for the separation of Zn and a visible fluorescence from the Au NCs coated paper was quenched by ZnH_2 produced from hydride generation (HG). By using X-ray photoelectron spectroscopy (XPS) and density functional theory (DFT), the potential mechanism for the detection of zinc was studied. This new sorbent increased selectivity of the HS-SPE method because the zinc hydride was effectively separated from sample matrices by hydride generation. A limit of detection of 3 μg/L Zn^{2+} and a relative standard deviation (RSD, n = 7) of 2% were obtained using a commercial fluorescence spectrophotometer as the detector. In visual detection, a very low amount of Zn^{2+} in biological sample was simply distinguished from the blank with the bare eye. The above mentioned sorbent had several unique benefits, which contributed in straight forward, rapid, affordable and equipment-free HS-SPE technique for visual detection [47]. Table 1 lists some of the applications of Au NPs-based SPE for extracting organic pollutants prior to analysis.

Gold nanoparticles in solid phase microextraction technique

Organic hydrophobic compounds are present in water in low concentrations, and they can be analyzed by means of a pre-concentration method using sorptive extraction techniques such as SPME. In the last decades, organic-inorganic hybrid materials have received considerable attention because they can combine the advantages of organic and inorganic materials to some extent [52]. Some hybrid materials, especially hybrid nanomaterials, are considered to be high-efficiency sorbents due to their high specific surface area, and excellent thermal and mechanical stability [47]. For instance, a novel poly(3,4-ethylenedioxythiophene)@Au nanoparticles (PEDOT@AuNPs) hybrid coatings were prepared and characterized.

First, the monomer 3,4-ethylenedioxythiophene was self-assembled on AuNPs, and then electropolymerized on a stainless steel wire by cyclic voltammetry. The obtained PEDOT@AuNPs coating was rough and presented micro-structure with thickness of ~40 μm. It displayed high thermal (up to 330 ℃) and mechanical stability and could be used more than 160 times in SPME without losing extraction performance. The

coating showed high extraction capacity for many pollutants such as naphthalene, 2-methylnaphthalene, acenaphthene, fluorene and phenanthrene, due to the hydrophobic interaction between the analytes and PEDOT and the additional physicochemical affinity between polycyclic aromatic hydrocarbons and Au NPs. The SPME-GC method was successfully applied for the determination of three real samples, and the recoveries for standards added were 89.9 - 106% for lake water, 95.7 - 112% for rainwater and 93.2 - 109% for soil saturated water [53].

In order to improve the SPME performance, a novel SPME fiber coating was fabricated by direct hydrothermal growth of titanium (Ti) and nickel oxide composite nanosheets (NiOCNS) on a NiTi wire (NiTi–TiO_2/NiOCNSs). Modification of the TiO_2/NiOCNSs coating was carried out by electrodeposition of Au NPs with potentiostatic technology. The extraction performance of the Au NPs modified TiO_2/NiOCNSs coated NiTi (NiTi–TiO_2/NiOCNSs-Au NPs) fiber was evaluated using polycyclic aromatic hydrocarbons (PAHs), phthalate acid esters (PAEs) and chlorophenols (CPs). The results obtained indicated that the novel fiber exhibited excellent extraction efficiency and good selectivity for PAHs. Relative recoveries varied from 86.3% to 104%. Furthermore, the novel fiber could be fabricated in a highly reproducible manner and had a high stability and long life span [28].

In a similar report, a novel fiber coating based on electrodeposition of Au NPs onto stainless steel followed by self-assembled 1, 8-octanedithiol coating were developed. This novel fiber resulted in high surface area with floccular structure and was found to be capable and selective towards some polychlorinated biphenyls (PCBs), UV filters, CPs and PAHs. The different selectivity for all UV filters was due to the weak polarity for alkyl chain on the coating surface. Furthermore, the fiber was more stable and durable than the commercially available PDMS and PA coated fibers by being able to maintain its performance when getting immersed into organic solvents and can be used up to 200 times [54].

The excellent physical and chemical properties of carbon nanomaterials have made them promising materials to be used as SPME fiber coatings. Among them, graphene oxide (GO) has some properties such as long term stability and a huge surface area, and thus has great potential as a sorbent material in SPME [55]. Several graphene-coated SPME fibers have been reported [56]. However, the stable structure of graphene has limited potential application as a fiber coating. Au NPs decorated GO coating was studied intensively and the nanomaterials of GO and Au NPs were successfully used as fiber coating absorbents. The novel Au NPs decorated GO-coated SPME fiber was prepared through layer by layer (LBL) self-assembly process of GO and a self-assembled monolayer process between the thiol (–SH) and Au NPs. Effects of the adsorption and desorption factors were investigated systematically. The single fiber repeatability (RSDs = 1.9 - 6.5%) and fiber-to-fiber reproducibility (RSDs = 4.3 - 9.2%) were both satisfactory.

The analysis of ten aromatic hydrophobic organic compounds (HOCs) in two real water samples (running water and snow water) showed satisfactory results using Au NPs/GO SPME fiber. The inherent chemical stability of Au and GO makes the novel Au NPs/GO SPME fiber having high stability and durability towards acid, alkali and organic solutions, and high temperature. A novel SPME fiber based on a stainless steel wire coated with Au nanoparticle decorated GO was reported [1]. The extraction performance of the fiber was tested with aromatic hydrophobic organic chemicals as the model analytes. The fiber showed excellent extraction efficiency, good mechanical strength, and good stability in acid, alkali and organic solutions, and under high temperature. The relative standard deviations for the single fiber repeatability and fiber-to-fiber reproducibility were less than 6.90 and 16.87%, respectively. Compared with GO SPME fibers and Au nanoparticle SPME fibers, the Au NPs/GO fiber has lower detection limits (≤ 60 ng/L) and a better linear range for all analytes. Correlation coefficient values were between 0.9958 and 0.9993. The as-established SPME-GC-FID method was successfully used for two real natural samples, and

recovery of the analytes ranged from 82.65% to 126.06%.

Table 2 lists some of the applications of Au NPs-based SPME for extracting organic pollutants prior to analysis. Comparing the work of Zare et al. [16] and Liu et al. [59] on PAHs using HPLC-UV for water samples showed that the work by Zare et al using SAM of Au-NPs gives a much lower LOD compared to the use of gold-coated fiber.

Table 1. Summary of different Au NPs-composite sorbent employed in SPE techniques for extraction of organic and inorganic pollutants in environmental samples

Sorbent	Analyte	Matrix	Linear Range	RSD (%)	LOD	Recovery (%)	Detection Technique	Ref.
Au NPs-GNs	Organophosphates (Ops)	Methyl parathion (MP)	0.001 - 1.0 µg/L	5.6 (n=10)	0.6 ng/L	96.2 - 105.0	UV-Vis	[43]
Au NPs-GQDs-amino-CTAB	Kanamycin sulphate	Yellow fever vaccine	2.5×10^{-7} – 1.0×10^{-5} mol/L	1.2 - 1.7	6.0×10^{-8} mol/L	96.7 ± 2.1	HPLC-FLD	[44]
rGO/Au composite	Microcystins (MCs)	Milk	0.05 - 200 ng/L	2.0 - 14.9	≤1.5 ng/L	94.1 - 103.2	UHPLC-MS/MS	[48]
Ag/AuNPs-impregnated in nylon membrane filters	Hg	Water	5 - 500 ng/L	-	0.4 ng/L	100± 2	Zeeman Mercury analyzer RA–915+	[46]
AuNPs-PPy nanocomposite	Microcystins (MCs)	Water	2.5 - 80.0 ng/L	1.6 - 5.4 (n=3)	≤1.5 ng/L	94.1 - 103.2	LC-ESI–MS	[45]
Au-NP–IL–silica	Sulfonylurea herbicides (SUHs)	Water	0.05 - 1.00 mg/L	4.5 (n=10)	0.002 - 0.009 µg/L	83.9 - 105.0	CLC–DAD	[4]
Au NPs-PDMS	Hg(II)	Environmental water	0.2 - 1.0 µg/L	2.24 - 6.21	70 µg/L	97.5 - 101.7	ICP-MS	[49]
(SPCE/PEDOT:PSS/Au NPs/1-m-4-MP)	Tyramine (4-hydroxyphenethyl amine)	Spiked serum	5 - 100 nM	2.73 (n=3)	2.31 nM	93.6 - 102.4	CE-NMR	[50]

Table 1 (cont'd). Summary of different Au NPs-composite sorbent employed in SPE techniques for extraction of organic and inorganic pollutants in environmental samples

Sorbent	Analyte	Matrix	Linear Range	RSD (%)	LOD	Recovery (%)	Detection Technique	Ref.
Au@Ag nanostructure based SERS substrate	Acetamiprid (AC)	Matcha tea	1.0 x 10^{-5} - 1.0 x 10^{3} µg/L	<4.85 (n=5)	2.63 $\times 10^{-5}$ µg/g	99.85 - 115.60	GA-PLS-DFT	[51]
Paper immobilized BSA–Au NCs	Zinc, Zn^{2+}	Whole blood and cells	1 - 200 µg/L	2 (n=7)	3 µg/L	95 - 102	ICP-MS	[47]

GNs, graphene nanosheets; GQDs, graphene quantum dots; CTAB, cetyltrimethylammonium bromide; PPy, polypyrrole; PDMS, polydimethylsiloxane; SPCE/PEDOT: PSS/Au NPs/1-m-4-MP, poly(3,4-ethylenedioxythiophene) polystyrene sulfonate gold nanoparticles 1-methyl-4- mercaptopyridine modified screen-printed carbon electrode; BSA, bovine serum albumin; SERS, surface-enhanced Raman scattering

Table 2. Summary of different Au NPs-composite sorbent employed in SPME techniques for extraction of organic and inorganic pollutants in environmental samples

Sorbent	Analyte	Matrix	Linear Range	RSD (%)	LODs	Recovery (%)	Detection Techniques	Ref
Poly (3,4-ethylenedioxythiophene) @Au nanoparticles (PEDOT@AuNPs)	Naphthalene, 2-methyl-naphthalene, acenaphthene, fluorene and phenathrene)	Lake water (LW), rainwater (RW) and soil saturated water (SSW)	0.01-100 µg/L	1.1 - 4.0 and 5.8 - 9.9	2.5 - 25 ng/L	89.9 - 106 (LW) 95.7 - 112 (RW) 93.2 - 109 (SSW)	GC-FID	[53]
SAM of 1,8 - octanedithiol onto AuNPs coating via Au-S bonding (C8–S–AuNPs/SS fibers)	UV filters	Environment-al water	0.10 - 400 µg/L	3 - 9.4	0.025 - 0.056 µg/L	92.0 - 106.0	HPLC-UV	[54]
Cedar-like AuNPs (AuNPs/SS)	Phthalate esters and aromatic hydrocarbons	River water under Bapanxia bridge	0.05 - 300 µg/L	03.82 - 5.19	0.008-0.037 µg/L	97.00	HPLC-UV	[57]

Table 2 (cont'd). Summary of different Au NPs-composite sorbent employed in SPME techniques for extraction of organic and inorganic pollutants in environmental samples

Sorbent	**Analyte**	**Matrix**	**Linear Range**	**RSD (%)**	**LODs**	**Recovery (%)**	**Detection Techniques**	**Ref**
Porous Ag@Au)	Nitrofurazone and (NFZ) Semicarbazide (SCA)	Aqueous solution	0.1- 5.0 nmol/L (NFZ) and 0.1- 7.0 nmol/L (SCA)	4.4 (NFZ) and 5.3 (SCA)	2.7 nmol/L 6.4 nmol/L		Surface enhanced Raman spectroscopy	[58]
AuNPs Modified TiO_2/NiOCNSs coated NiTi fiber (NiTi–TiO_2/NiOCNSs-AuNPs)	Organic solvents (methanol, tetrahydrofuran, Chloroform and dimethylsulfoxide)	River water, rainwater, Wastewater	0.05 - 350 µg/L	5.2- 7.5	0.012- 0.053 µg/L	95.4–103	HPLC-UV	[28]
SAM of Au-NPs	Polycyclic aromatic hydrocarbons (PAHs)	Environmental water	1 - 500 ng/mL	<5.1	0.10- 0.89 ng/mL	84- 106	HPLC/UV	[16]
Au NPs/ GO/SPME fiber	Aromatic Hydrophobic organic chemicals (HOCs)	Ultrapure water	0.05 - 300 µg/L	16.87	10- 50	82.65- 126.06	GC-FID	[1]
Gold-coated fiber	PAHs	Water	0.20 - 500 µg/L	2.03- 11.7	0.016 - 0.22 µg/L	86.0- 112.9	HPLC-UV	[59]
AuNPs coated fiber	2-hydroxy-4-ethoxybenzophenone (BP-3) 2-ethylhexyl-4-methoxycinnamate (EHMC), 2-ethylhexyl-4-(*N*,*N*-dimethylamino) benzoate (OD-PABA) and 2-ethylhexyl salicylate (EHS)	River water	0.004 - 200 µg/L	1.91 - 4.20	0.43 - 570 ng/L	77.9 and 108	HPLC-UV	[60]
AuNPs	organochlorine pesticides (OCPs)	Water	100 - 500 µg/L	8.67- 21.3.	0.04- 0.41 µg/L	85.0- 97.1	GC–ECD	[61]

SAM, self-assembled monolayer; NiOCNs, nickel oxide composite nanosheets; OD-PABA, octyl-dimethyl-para-aminobenzoic acid

Table 3. Summary of different Ag NPs-composite sorbent employed in SPE techniques for extraction of organic and inorganic pollutants in environmental samples

Sorbent	**Matrix**	**Analyte**	**LOD**	**RSD (%)**	**Coefficient of Determination (R^2)**	**Detection Technique**	**Ref.**
Impregnated nylon membrane filter AgNPs	Natural water	Mercury, Hg	0.4 ng/L	7.9	0.9989	ETAAS	[46]
AgNPs coated silica gel-ammonium pyrrolidine-dithiocarbamate (APDC)	Tap and sea water	Lead, Pb	0.36 ng/mL	<10.0	0.95	FAAS	[66]
1-(2-pyridylazo)-2-naphthol (PAN)-AgNPs	Natural water	Co(II)	0.78 µg/L	3.1	0.992	AAS	[42]
CS-AgNPs	Lake water	Al(III), Cd(II), Cu(II), Co(II), Fe(III), Ni(II), Pb(II), Zn(II)	0.001 - 0.1 µg/L	7.0 -12.0	0.92 - 0.98	ICP-MS	[63]
Ag-SiO_2-PDPA	Pesticides	Lindane, Diazinon, Fenthion, Ethion, Piperonyl-butoxide, Fenoxaprop-*p*-ethyl	0.02 - 0.05 µg/L	6.0-10.0	0.983-0.999	GC-MS	[64]
AzS@AgNDs	Water	HEX, DES, DIS, BPA	0.1 - 5.0 pg/mL	2.8 - 6.0	0.991-0.995	UPLC-MS/MS	[65]

PVIM-MNPs, poly(1-vinylimidazole) functionalized magnetic nanoparticles; UMPs, unmodified magnetic particles; GMPs, glutathione-functionalized magnetic particles; DMPs, dopamine-functionalized magnetic particles; Mix D–G, mixture of GMPs and DMPs; Ag-SiO_2-PDPA, silver nanoparticles-doped silica-polydiphenylamine; HEX, hexestrol; DES, diethylstilbestrol; DIS, dienestrol; BPA, bisphenol

Table 4. Summary of different Ag NPs-composite sorbent employed in SPME techniques for extraction of organic and inorganic pollutants in

Sorbent	Analyte	Matrix	Linearity	RSD (%)	LOD	Recovery (%)	Detection Technique	Ref.
Ag nanocomposite	Parabens	Water/Beverages	0.05−200 µg/L	2.4 - 3.1 and 3.4 - 4.2 (n=3)	0.01 µg/L	25−28	HPLC/UV	[73]
Ag nanodendrites and PDMS/PEG	Volatile Aldehydes	Edible Oils	−	7.5 - 11.2 (n=3)	0.5 - 0.2 µg/L	56.7−86.3	GC-MS	[75]
Ag NPS decorated graphene oxide	PAHs	Water Sample	0.02 - 50 µg/L	8.6 - 17.5	2 - 10 ng/L	84.4−116.3	GC-FID	[76]
Porous Ag fiber	Organotin compounds	Textile	1.0 - 5.0 nmol/L	−	0.2 ppb	−	Raman Spec.	[77]
Dendritic AgN structure	UV filters	Water Sample	0.3 - 400 µg/L	5.7 - 8.7	0.05 - 0.12 µg/L	85.5−105.5	HPLC-UV	[68]
Graphene coated Ag NPs	Bisphenol A	Water Sample	2 - 100 µg/L	14 and 13	1 µgL	97-110	Raman Spec.	[78]
Ag NPs aggregate	PAHs	Water sample	−	3.85 - 96.98	7.56 x 10^{-10} M	95-115	Raman Spec.	[69]
Ag NPs	MUFAMES	Food sample	0.2 - 0.9 mg/kg	< 5.2	< 5.2 µg/kg	86.6−96.1	HPLC	[72]
Ag NPs	PAHs	Water Sample	−	< 25	0.6 ng/L	86.3−105	GC-FID	[71]
AgNPs@MCM-14	Capecitabine	Plasma Sample	25 - 1000 µg/L	1.3 and 13.3	−	87 - 105	CE−UV	[79]

PDMS, polydimethylsiloxane; PEG, polyethylene glycol; MUFAMEs, monounsaturated fatty acid methyl ester

Conclusion

Au and Ag NPs and their functionalized forms are attracting a great deal of interest because of their wide applications in sorptive SPE and SPME techniques for the analysis of trace-level organic pollutants from various environmental matrices. The integration of Au NPs, Ag NPs, polymers, and nanocomposite materials with SPE and SPME has produced tremendous improvements in analytical performance. Analytical merits such as sensitivity, reproducibility, repeatability, and reusability were greatly improved by integrating Au NPs and Ag NPs and its functionalized form with SPE and SPME for trace level analytes. The Au NPs an Ag NPs themselves have recently emerged as powerful separation materials when their surfaces are modified with appropriate chemical species because Au NPs and Ag NPs-based separation materials are easy to produce and modify. Thus, we believe that analytical systems incorporating Au NPs and Ag NPs will be an important part of future investigations into the applications of nanotechnology in separation science. Functionalization of gold and silver nanoparticle is an effective strategy for the generation of highly selective and sensitive sorbent materials for many kinds of targets. There is great demand for the design and development of new functionalized Ag and Au nanomaterials with better specificity and selectivity for the various applications possible in analytical chemistry in food, drugs, and as sensors.

Acknowledgment

We would like to express our thanks to the Ministry of Education (MoE) and Universiti Teknologi Malaysia (UTM) for the award of the Professional Development Research Grant (PDRU grant number Q.J130000.21A2.04E12)) to ZAS. JQ is grateful for the scholarship awarded by the Higher Education Development Program (HEDP), Ministry of Higher Education and Kabul University, Afghanistan and KAB would like to thank the Petroleum Technology Development Fund, Nigeria for the postgraduate scholarship.

References

1. Xu, L., Qi, X., Li, X., Bai, Y. and Liu, H. (2016). Recent advances in applications of nanomaterials for sample preparation. *Talanta*, 146: 714-726.
2. Wu, W., Zhang, C. and Yang, S. (2017). Controllable synthesis of sandwich-like graphene-supported structures for energy storage and conversion. *New Carbon Materials*, 32(1): 1-14.
3. Azzouz, A., Kailasa, S. K., Lee, S. S., Rasc, A. J., Ballesteros, E., Zhang, M. and Kim, K. (2018). Review of nanomaterials as sorbents in solid-phase extraction for environmental samples, *Trends in Analytical Chemistry,* 108: 347-369.
4. Simo, E. F. and Zougagh, M. (2013). Use of gold nanoparticle-coated sorbent materials for the selective preconcentration of sulfonylurea herbicides in water samples and determination by capillary liquid chromatography, *Talanta,* 105: 372-378.
5. Anekthirakun, P. and Imyim, A. (2019). Separation of silver ions and silver nanoparticles by silica based-solid phase extraction prior to ICP-OES determination. *Microchemical Journal*, 145: 470-475.
6. Zhao, B., He, M., Chen, B., and Bin, H. (2018). Ligand-assisted magnetic solid phase extraction for fast speciation of silver nanoparticles and silver ions in environmental water. *Talanta*, 183: 268-275.
7. Mwilu, S. K., Siska, E., Baig, R. B. N., Varma, R. S., Heithmar, E. and Rogers, K. R. (2014). Separation and measurement of silver nanoparticles and silver ions using magnetic particles. *Science of the Total Environment,* 472: 316-323.
8. Liu, F. K. (2009). Analysis and applications of nanoparticles in the separation sciences: A case of gold nanoparticles. *Journal of Chromatography A*, 1216: 9034-9047.
9. Lin, J. H. and Tseng, W. L. (2012). Gold nanoparticles for specific extraction and enrichment of biomolecules and environmental pollutants. *Reviews in Analytical Chemistry*, 31: 153-162.

10. Dastafkan, K., Khajeh, M., Ghaffari-Moghaddam, M. and Bohlooli, M. (2015). Silver nanoparticles for separation and preconcentration processes. *TrAC-Trends in Analytical Chemistry*, 64: 118-126.
11. Oliveira, E., Núnez, C., Santos, H. M., Fernández-lodeiro, J., Fernández-lodeiro, A., Capelo, J. L. and Lodeiro, C. (2015). Revisiting the use of gold and silver functionalised nanoparticles as colorimetric and fluorometric chemosensors for metal ions. *Sensors & Actuators: B. Chemical*, 212: 297-328.
12. Ten-Doménech, I., Martínez-Pérez-Cejuela, H., Lerma-García, M. J., Simó-Alfonso, E. F. and Herrero-Martínez, J. M. (2017). Molecularly imprinted polymers for selective solid-phase extraction of phospholipids from human milk samples. *Microchimica Acta*, 184(9): 3389-3397.
13. Erger, C., and Schmidt, T. C. (2014). Disk-based solid-phase extraction analysis of organic substances in water. *Trends in Analytical Chemistry*, 61: 74-82.
14. Dimpe, K. M., and Nomngongo, P. N. (2016). Current sample preparation methodologies for analysis of emerging pollutants in different environmental matrices. *Trends in Analytical Chemistry,* 82: 199-207.
15. Belardi, R. and Pawliszyn, J. (1989). The application of chemically modified fused silica fibers in the extraction of organics from water matrix samples and their rapid transfer to capillary columns. *Water Quality Research Journal*, 24(1): 179-191.
16. Zare, F., Ghaedi, M., and Daneshfar, A. (2015). The headspace solid-phase microextraction of polycyclic aromatic hydrocarbons in environmental water samples using silica fiber modified by self-assembled gold nanoparticles. *Analytical Methods*, 7(19): 8086-8093.
17. Arthur, C. L., and Pawliszyn, J. (1990). Solid phase microextraction with thermal desorption using fused silica optical fibers. *Analytical Chemistry*, 62(19): 2145-2148.
18. Sadowska-Rociek, A., Surma, M. and Cieślik, E. (2014). Determination of polycyclic aromatic hydrocarbons in coffee and coffee substitutes using dispersive SPE and gas chromatography-mass spectrometry. *Food Analytical Methods*, 8(1): 109-121.
19. Pincemaille, J., Schummer, C., Heinen, E. and Moris, G. (2014). Determination of polycyclic aromatic hydrocarbons in smoked and non-smoked black teas and tea infusions. *Food Chemistry*, 145: 807-813.
20. Serrano, M., Bartolome, M., Gallego-Pico, A., Garcinuno, R. M., Bravo, J. C. and Fernandez, P. (2015). Synthesis of a molecularly imprinted polymer for the isolation of 1-hydroxypyrene in human urine. *Talanta*, 143: 71-76.
21. Li, L. and Leopold, K. (2012). Ligand-assisted extraction for separation and preconcentration of gold nanoparticles from waters. *Analytical Chemistry*, 84: 4340-4349.
22. BorFuh, C., Yang, Y. C., Tsai, H. Y. and Ho, L. S. (2003). Solid-phase microextraction coupled with gas chromatography and gas chromatography-mass spectrometry for public health pesticides analysis. *Chromatographia*, 57(7): 525-528.
23. Eisert, R., and Pawliszyn, J. (1997). Automated in-tube solid-phase microextraction coupled to high-performance liquid chromatography. *Analytical Chemistry*, 69(16): 3140-3147.
24. Wu, J., Tragas, C., Lord, H. and Pawliszyn, J. (2002). Analysis of polar pesticides in water and wine samples by automated in-tube solid-phase microextraction coupled with high-performance liquid chromatography-mass spectrometry. *Journal of Chromatography A,* 976 (1-2): 357-367.
25. Fang, H., Liu, M. and Zeng, Z. (2006). Solid-phase microextraction coupled with capillary electrophoresis to determine ephedrine derivatives in water and urine using a sol-gel derived butyl methacrylate/silicone fiber. *Talanta*, 68(3): 979-986.
26. Lashgari, M. and Yamini, Y. (2019). An overview of the most common lab-made coating materials in solid phase microextraction. *Talanta*, 191: 283-306.

27. Guo, M., Gong, Z., Allinson, G., Tai, P., Miao, R., Li, X. and Zhuang, J. (2016). Variations in the bioavailability of polycyclic aromatic hydrocarbons in industrial and agricultural soils after bioremediation. *Chemosphere*, 144: 1513-1520.
28. Wang, H., Zhang, Y., Zhang, M., Zhen, Q., Wang, X. and Du, X. (2016). Gold nanoparticle modified NiTi composite nanosheet coating for efficient and selective solid phase microextraction of polycyclic aromatic hydrocarbons. *Analytical Methods*, 8(31): 6064-6073.
29. Daniel M. C. and Astruc, D. (2004). Gold nanoparticles: Assembly, supramolecular chemistry, quantum-size-related properties, and applications toward biology, catalysis, and nanotechnology. *Chemical Review*, 104: 293-346.
30. Sykora, D., Kasicka, V., Miksik, I., Rezanka, P., Zaruba, K., Matejka, P. and Kral, V. (2010). Application of gold nanoparticles in separation sciences *Journal of Separation Science*, 33(3): 372-87.
31. Boisselier, E. and Astruc, D. (2009). Gold nanoparticles in nanomedicine: preparations, imaging, diagnostics, therapies and toxicity. *Chemical Society Reviews,* 38(6): 1759-1782.
32. Khan, M. S., Vishakante, G. D., and Siddaramaiah, H. (2013). Gold nanoparticles: A paradigm shift in biomedical applications. *Advances in Colloid and Interface Science*, 199-200: 44-58.
33. Sönnichsen, C., Franzl, T., Wilk, T., von Plessen, G., Feldmann, J., Wilson, O. and Mulvaney, P. (2002). Drastic reduction of plasmon damping in gold nanorods. *Physical Review Letters*, 88(7): 077402.
34. Chen, H., Roco, M., Li, X. and Lin, Y. (2008). Trends in nanotechnology patents. *Nature Nanotechnology*, 3(3): 123-125.
35. Mandal, T., Fleming, M. and Walt, D. (2002). Preparation of polymer coated gold nanoparticles by surface-confined living radical polymerization at ambient temperature. *Nano Letters*, 2(1), 3-7.
36. Lévy, R., Thanh, N. T. , Doty, R. C., Hussain, I., Nichols, R. J., Schiffrin, D. J., Brust, M., and Fernig, D. G. (2004). Rational and combinatorial design of peptide capping ligands for gold nanoparticles. *Journal of American Chemical Society,* 126(32): 10076-10084.
37. Schofield, C. L., Haines, A. H., Field, R. A. and Russell, D. A. (2006). Silver and gold glyconanoparticles for colorimetric bioassays. *Langmuir,* 22(15): 6707-6711.
38. Skidmore, M. A., Patey, S. J., Thanh, N. T. K., Fernig, D. G., Turnbull, J. E. and Yates, E. A. (2004). Attachment of glycosaminoglycan oligosaccharides to thiol-derivatised gold surfaces. *Chemical Communications,* (23): 2700-2701.
39. Mukherjee, P., Patra, C. R., Ghosh, A., Kumar, R. and Sastry, M. (2002). Characterization and catalytic activity of gold nanoparticles synthesized by autoreduction of aqueous chloroaurate ions with fumed silica. *Chemistry of Materials,* 14(4): 1678-1684.
40. Chernousova, S. and Epple, M. (2013). Silver as antibacterial agent: Ion, nanoparticle, and metal. *Angewandte Chemie International Edition*, 52: 1636-1653.
41. Zhang, X. F., Liu, Z. G., Shen, W. and Gurunathan, S. (2016). Silver nanoparticles: Synthesis, characterization, properties, applications, and therapeutic approaches. *International Journal of Molecular Sciences*, 17(9): 1534-1568.
42. Khajeh, M. and Sanchooli, E. (2011). Synthesis and evaluation of silver nanoparticles material for solid phase extraction of cobalt from water samples. *Applied Nanoscience,* 1: 205-209.
43. Gong, J., Miao, X., Zhou, T. and Zhang, L. (2011). An enzymeless organophosphate pesticide sensor using Au nanoparticle-decorated graphene hybrid nanosheet as solid-phase extraction. *Talanta*, 85: 1344-1349.
44. Toloza, C. A. T., Almeida, J. M. S., Khan, S., Yasmin, G., Andrea, R., Romani, E. C. and Aucélio, R. Q. (2018). Gold nanoparticles coupled with graphene quantum dots in organized medium to quantify aminoglycoside anti-biotics in yellow fever vaccine after solid phase extraction using a selective imprinted polymer. *Journal Pharmaceutical and Biomedical Analysis,* 158: 480-493.

45. Devasurendra, A. M., Palagama, D. S. W., Rohanifar, A., Isailovic, D., Kirchhoff, J. R. and Anderson, J. L. (2018). Solid-phase extraction, quantification, and selective determination of microcystins in water with a gold-polypyrrole nanocomposite sorbent material. *Journal of Chromatography A*, 1560: 1-9.
46. Panichev, N., Kalumba, M. M. and Mandiwana, K. L. (2014). Solid phase extraction of trace amount of mercury from natural waters on silver and gold nanoparticles. *Analytica Chimica Acta*, 813: 56-62.
47. Huang, K., Dai, R., Deng, W., Guo, S., Deng, H. and Wei, Y. (2018). Gold nanoclusters immobilized paper for visual detection of zinc in whole blood and cells by coupling hydride generation with headspace solid phase extraction. *Sensors And Actuators B: Chemical*, 255: 1631-1639.
48. Jiang, K., Huang, Q., Fan, K., Wu, L., Nie, D. and Guo, W. (2018). Reduced graphene oxide and gold nanoparticle composite-based solid-phase extraction coupled with ultra-high-performance liquid chromatography-tandem mass spectrometry for the determination of 9 mycotoxins in milk. *Food Chemistry,* 264: 218-225.
49. Hsu, K., Lee, C., Tseng, W., Chao, Y. and Huang, Y. (2014). Selective and eco-friendly method for determination of mercury(II) ions in aqueous samples using an on-line AuNPs-PDMS composite microfluidic device/ICP-MS system, *Talanta*. 128: 408-413.
50. Li, Y., Hsieh, C., Lai, C., Chang, Y., Chan, H., Tsai, C., and Wu, L. (2017). Biosensors and Bioelectronics Tyramine detection using PEDOT: PSS/AuNPs/1-methyl-4- mercaptopyridine modified screen-printed carbon electrode with molecularly imprinted polymer solid phase extraction. *Biosensors and Bioelectronic*, 87: 142-149.
51. Hassan, M. M., Li, H., Ahmad, W., Zareef, M., Wang, J., Xie, S., Wang, P., Ouyang, Q., Wang, S. and Chen, Q. (2019). Au@Ag nanostructure based SERS substrate for simultaneous determination of pesticides residue in tea via solid phase extraction coupled multivariate calibration. *LWT Food Science and Technology*, 105: 290-297.
52. Chen, C., Liang, X., Wang, J., Shaolei, Y., Yan, Z., Cai, Q. and Yao, S. (2013). Development of a highly robust solid phase microextraction fiber based on cross-linked methyl methacrylate-polyhedral oligomeric silsesquioxane hybrid polymeric coating. *Analytica Chimica Acta,* 792: 45-51.
53. Yang, L., Zhang, J., Zhao, F., and Zeng, B. (2016). Electrodeposition of self-assembled poly(3,4-ethylenedioxythiophene) @gold nanoparticles on stainless steel wires for the headspace solid-phase microextraction and gas chromatographic determination of several polycyclic aromatic hydrocarbons. *Journal of Chromatography A*, 1471: 80-86.
54. Yang, Y., Li, Y., Liu, H., Wang, X., & Du, X. (2014). Electrodeposition of gold nanoparticles onto an etched stainless steel wire followed by a self-assembled monolayer of octanedithiol as a fiber coating for selective solid-phase microextraction. *Journal of Chromatography A*, 1372: 25-33.
55. Xiao, C., Han, S., Wang, Z., Xing, J., Wu, C. (2001) Application of the polysilicone fullerene coating for solid-phase microextraction in the determination of semi-volatile compounds. *Journal of Chromatography A*, 927: 121-130.
56. Chen, J. M., Zou, J., B., J., Zeng, X. H., Song, J. J., Ji, Y. R., Wang, Chen, J. and Ha X., (2010) Preparation and evaluation of graphene-coated solid-phase microextraction fiber. *Analytica Chimica Acta*, 678: 44-49.
57. Zhang, Y., Yang, Y., Li, Y., Zhang, M., Wang, X. and Du, X. (2015). Growth of cedar-like Au nanoparticles coating on an etched stainless steel wire and its application for selective solid-phase microextraction. *Analytica Chimica Acta*, 876: 55-62.
58. Bian, W., Liu, Z., Lian, G., Wang, L., Wang, Q. and Zhan, J. (2017). High reliable and robust ultrathin-layer gold coating porous silver substrate via galvanic-free deposition for solid phase microextraction coupled with surface enhanced Raman spectroscopy. *Analytica Chimica Acta*, 994: 56-64.

59. Liu, H., Liu, L., Li, Y., Wang, X. and Du, X. (2014). Preparation of a robust and sensitive gold-coated fiber for solid-phase microextraction of polycyclic aromatic hydrocarbons in environmental waters. *Analytical Letters*, 47(10): 1759-1771.
60. Liu, H.-X., Yang, Y.-X., Ma, M. G., Wang, X.-M. and Du, X.-Z. (2015). Self-assembled gold nanoparticles coating for solid-phase microextraction of ultraviolet filters in environmental water. *Chinese Journal Analytical Chemistry*, 43(2): 207-211.
61. Gutierrez-Serpa, A., Rocio-Bautista, P., Pino, V., Jimenez-Moreno, F. and Jimenez-Abizanda, A. I. (2017). Gold nanoparticles based solid-phase microextraction coatings for determining organochlorine pesticides in aqueous environmental samples. *Journal of Separation Science*, 40(9): 2009-2021.
62. Tran, Q. H., Nguyen, V. Q. and Le, A. T. (2013). Silver nanoparticles: synthesis, properties, toxicology, applications and perspectives. *Nanoscience and Nanotechnology*, 4: 033001.
63. Djerahov, L., Vasileva, P., Karadjova, I., Kurakalva, R. M. and Aradhi, K. K. (2016). Chitosan film loaded with silver nanoparticles-sorbent for solid phase extraction of Al(III), Cd(II), Cu(II), Co(II), Fe(III), Ni(II), Pb(II) and Zn(II). *Carbohydrate Polymer*, 147: 45-52.
64. Bagheri, H. and Banihashemi, S. (2015). Sol-gel-based silver nanoparticles-doped silica-polydiphenylamine nanocomposite for micro-solid-phase extraction. *Analytica Chimica Acta*, 886: 56-65.
65. Gao, Y., Xia, B., Liu, J., Ji, B., Ma, F., Ding, L., Li, B. and Zhou, Y. (2015). Development and characterization of a nanodendritic silver-based solid-phase extraction sorbent for selective enrichment of endocrine disrupting chemicals in water and milk samples. *Analytica Chimica Acta*, 900: 76-82.
66. Baysal, A., Kahraman, M. and Akman, S. (2009). The solid phase extraction of lead using silver nanoparticles – attached to silica gel prior to its determination by FAAS. *Current Analytical Chemistry,* 5: 352-357.
67. Gopidas, K. R., Whitesell, J. K. and Fox, M. A. (2003). Synthesis, characterization, and catalytic applications of a palladium-nanoparticle-cored dendrimer. *Nano Letters*, 3(12): 1757-1760.
68. Yang, Y., Guo, M., Zhang, Y., Song, W., Li, Y., Wang, X. and Du, X. (2015). Self-assembly of alkyldithiols on a novel dendritic silver nanostructure electrodeposited on a stainless steel wire as a fiber coating for solid-phase microextraction. *RSC Advances*, 5(88): 71859-71867.
69. Liu, C., Zhang, X., Li, L., Cui, J., Shi, Y. E., Wang, L. and Zhan, J. (2015). Silver nanoparticle aggregates on metal fibers for solid phase microextraction–surface enhanced Raman spectroscopy detection of polycyclic aromatic hydrocarbons. *Analyst*, 140(13): 4668-4675.
70. White, R. J., Luque, R., Budarin, V. L., Clark, J. H. and Macquarrie, D. J. (2009). Supported metal nanoparticles on porous materials. Methods and applications. *Chemical Society Reviews,* 38(2): 481-494.
71. Gutiérrez-Serpa, A., Napolitano-Tabares, P. I., Pino, V., Jiménez-Moreno, F., and Jiménez-Abizanda, A. I. (2018). Silver nanoparticles supported onto a stainless steel wire for direct-immersion solid-phase microextraction of polycyclic aromatic hydrocarbons prior to their determination by GC-FID. *Microchimica Acta*, 185(7): 341.
72. Jiang, N., Wang, J., Li, W., Xiao, J., Li, J., Lin, X., Xie, Z., You, L. and Zhang, Q. (2019). Silver nanoparticles-coated monolithic column for in-tube solid-phase microextraction of monounsaturated fatty acid methyl esters. *Journal of Chromatography A*, 1585: 19-26.
73. Yazdi, M. N., Yamini, Y. and Asiabi, H. (2018). Fabrication of polypyrrole-silver nanocomposite for hollow fiber solid phase microextraction followed by HPLC/UV analysis for determination of parabens in water and beverages samples. *Journal of Food Composition Analysis*, 74: 18-26.

74. Feng, J., Sun, M., Li, J., Liu, X. and Jiang, S. (2011). A novel silver-coated solid-phase microextraction metal fiber based on electroless plating technique. *Analytica Chimica Acta*, 701(2): 174-180.
75. Hasanli, F., Mohammadiazar, S., Bahmaei, M. and Sharif, A. A. M. (2018). Coating of sol–gel film on silver nanodendrite as a novel solid-phase microextraction fiber for determination of volatile aldehydes in edible oils. *Food Analytical Methods*, 11: 2149-2157.
76. Wang, L., Hou, X., Li, J., Liu, S. and Guo, Y. (2015). Graphene oxide decorated with silver nanoparticles as a coating on a stainless steel fiber for solid phase microextraction. *Journal of Separation Science*, 38(14): 2439-2446.
77. Liu, Z., Wang, L., Bian, W., Zhang, M. and Zhan, J. (2017). Porous silver coating fiber for rapidly screening organotin compounds by solid phase microextraction coupled with surface enhanced Raman spectroscopy. *RSC Advances*, 7(6): 3117-3124.
78. Qiu, L., Liu, Q., Zeng, X., Liu, Q., Hou, X., Tian, Y., and Wu, L. (2018). Sensitive detection of bisphenol A by coupling solid phase microextraction based on monolayer graphene-coated Ag nanoparticles on Si fibers to surface enhanced Raman spectroscopy. *Talanta*, 187: 13-18.
79. Forough, M., Farhadi, K., Molaei, R., Khalili, H., Shakeri, R., Zamani, A., and Matin, A. A. (2017). Capillary electrophoresis with online stacking in combination with AgNPs@ MCM-41 reinforced hollow fiber solid-liquid phase microextraction for quantitative analysis of Capecitabine and its main metabolite 5-Fluorouracil in plasma samples isolated from cancer patients. *Journal of Chromatography B*, 1040: 22-37.

Malaysian Journal of Analytical Sciences (MJAS)
Published by Malaysian Analytical Sciences Society

LIGNIN FROM OIL PALM FROND UNDER SUBCRITICAL PHENOL CONDITIONS AS A PRECURSOR FOR CARBON FIBER PRODUCTION

(Lignin daripada Pelepah Kelapa Sawit dibawah keadaan Subgenting Fenol sebagai Produk Perantaraan bagi Penghasilan Serat Karbon)

Khalidatul Athirah Khalid, Vijayaletchumy Karunakaran, Asimi Ana Ahmad, Khairul Faizal Pa'ee, Norfahana Abd-Talib, Tau Len-Kelly Yong*

Universiti Kuala Lumpur,
Branch Campus Malaysian Institute of Chemical and Engineering Technology,
78000 Alor Gajah, Melaka, Malaysia

**Corresponding author: kytlen@unikl.edu.my*

Received: 20 November 2019; Accepted: 16 June 2020; Published: 11 August 2020

Abstract

The market price of carbon fiber which is considerably high, has limited its application as a value-added material. Lignin, a natural source that can be obtained from oil palm frond (OPF) is a promising precursor for carbon fiber production. This study aims to determine the feasibility of OPF lignin extracted under subcritical phenol conditions as a precursor for carbon fiber. The focus of this study is to determine the fundamental properties (ash content and volatile content) of the produced lignophenol produced based on the effect of reaction parameters such as temperature (260–300 °C), reaction time (5–30 minutes), and solid loading (6 and 10 g). The results indicate that the lowest ash content and volatile content of 9.87% and 6.45% was obtained at 260 °C, 5 minutes, and 6 g solid loading respectively. It can be further concluded that low reaction temperature as well as time and higher solid loading produced lignophenol with low ash and volatile content under subcritical phenol conditions.

Keywords: lignin, carbon fiber, subcritical fluid, oil palm frond, lignophenol

Abstrak

Harga pasaran serat karbon yang tinggi telah menghadkan penggunaannya sebagai bahan nilai tambahan. Lignin merupakan sumber asli yang boleh dihasilkan daripada pelepah kelapa sawit dan mempunyai potensi sebagai bahan pengantaraan untuk penghasilan serat karbon. Tujuan kajian ini dijalankan adalah untuk menentukan kebolehgunaan lignin yang diekstrak daripada pelepah kelapa sawit dibawah keadaan subgenting fenol sebagai bahan pengantaraan untuk serat karbon. Tumpuan kajian ini adalah untuk menentukan sifat-sifat asas (kandungan abu dan kandungan meruap) lignophenol yang dihasilkan berdasarkan kesan parameter tindak balas seperti suhu (260–300 °C), masa (5–30 minit) dan kandungan pepejal (6 dan 10 g). Hasil kajian menunjukkan bahawa kandungan abu dan kandungan meruap terendah sebanyak 9.87% dan 6.45% didapati pada suhu 260 °C, 5 minit dan 6 g kandungan pepejal. Kesimpulan dari kajian ini mendapati bahawa suhu tindak balas, masa, dan muatan pepejal yang sederhana mampu menghasilkan lignophenol dengan kandungan abu and kandungan meruap yang rendah dibawah keadaan subgenting fenol.

Kata kunci: lignin, serat karbon, cecair subgenting, pelepah kelapa sawit, lignofenol

Introduction

Carbon fiber is a corrosion-resistant material consisting of at least 92% carbon content, with applications in various industries such as aviation, construction, automobiles, and sporting goods. Unfortunately, the utilization of carbon fiber is restricted by its high purchasing price due to the high cost of feedstock and manufacturing. Polyacrylonitrile (PAN) and pitch are the conventional feedstock for carbon fiber production. Currently, about 96% of carbon fiber's precursors in the market is dominated by PAN due to its effectiveness, and the quality of the fiber produced [1]. However, PAN and pitch are derived from fossil fuels, a known non-renewable resource. Thus, there is a great concern to find sustainable and environmentally friendly alternative resources. Biomass can be an alternative and can be used and as a substitution to fossil fuels as raw material to produce carbon fiber due to its availability, renewability, and sustainability. There are several types of biomass, including animal and plant waste. Cellulose, hemicellulose, and lignin are the major polymeric compounds present in lignocellulosic biomass. These compounds can be depolymerized and decomposed into lower molecular weight compounds, which are the platform chemicals used to produce numerous intermediates and end chemicals for various industries and applications.

The exponential growth of palm oil production over the past few decades has resulted in the expansion of the oil palm plantation area especially in Indonesia and Malaysia since both countries possess optimum conditions for oil palm growth and production such as humid tropical climate, sufficient sunlight, and uniformly distributed annual rainfall. In 2015, the Malaysian Palm Oil Board (MPOB) highlighted that about 5.64 million hectares of plantation areas are dedicated to palm oil which is equivalent to about 23% of Malaysia's total land area [2]. However, the increasing demand for palm oil globally resulted in copious amount of oil palm waste. Oil palm biomass is divided into two types, namely solid and liquid biomass. Solid biomass consists of empty fruit bunch (EFB), oil palm frond (OPF), oil palm trunk (OPT), mesocarp fiber (MF), and palm kernel shells (PKS).

Meanwhile, palm oil mill effluents (POME) are the only liquid biomass produced by the oil palm plantation. Severe environmental problems are often associated with oil palm biomass. The slow decomposition rate of the biomass causes the breeding of mouse and mosquitoes, which may lead to epidemics. Meanwhile, burning the waste to produce steam for energy in the oil palm plantation releases CO_2, which is harmful to the environment. It is estimated that about 231.5 kg dry weight of oil palm biomass are produced yearly, of which 70% is OPF, 10% EFB, and 5% OPT [3]. Therefore, the oil palm industry must be ready to take advantage of these circumstances and exploit these abundant resources in the best possible way. The massive annual generation of OPF has attracted researchers' interest to study its potential as a bio-based chemical and material. All lignocellulosic biomass, such as OPF, consists of three important natural polymers, i.e., cellulose, hemicellulose, and lignin. Lignin has the potential to be a feasible precursor for carbon fiber production.

Lignin is a three-dimensional complex biopolymer, that is amorphous and cross-linked consisting primarily of three monolignols as the building blocks, i.e., *p*-coumaryl (H), coniferyl (G), and sinapyl (S) alcohol. Lignin is categorized as softwood, hardwood, or grass lignin based on the relative amounts of its monolignols where softwood lignin is mainly coniferyl (about 90%), hardwood lignin consists of coniferyl and sinapyl, while grass lignin contains *p*-coumaryl monolignols [4]. Lignin contains numerous functional groups such as phenolic compounds, hydroxyl, carbonyl groups, ether, and ester bonds. Due to the numerous functional groups, it can be used to produce various bio-based chemicals, including as a precursor for carbon fiber [5]. However, the biggest concern of lignin as a precursor for carbon fiber is yielding an equal or better precursor that possesses properties similar to the conventional carbon fiber precursors available in the market. To produce lignin as a commercial precursor for carbon fiber, the presence of contaminants in the lignin should be minimal as contaminants may decrease the quality of carbon fiber [6]. The Oak Ridge National Laboratory (ORNL) has actively investigated the potential of lignin

as carbon fiber precursor and introduced a set of specifications as reference for lignin suitability as a carbon fiber precursor (Table 1) [7].

The decomposition of lignin into low molecular weight compounds are divided into three fractions: liquid product (primarily phenolic compounds) [8, 9], gaseous product mainly CO_2, CO, H_2, CH_4, and trace amounts of C_2 and C_3 hydrocarbons [10] and solid residue (condensed and unconverted lignin) [11]. This study aims to determine the feasibility of OPF lignin extracted under subcritical phenol conditions as a precursor for carbon fiber. The separation of lignin from other biomass constituents (cellulose, hemicellulose, and ash) is the primary focus in this study, which aims to obtain high purity and low contaminants (ash and volatile content). Being an essential part of the plant fiber cell wall, the separation of lignin cannot be done without any significant alterations to its native structural properties. Unfortunately, the alteration may affect the quality and purity of the lignin [12]. This problem was a challenge and prevented the application of lignin as a carbon fiber precursor in large-scale applications. Therefore, finding a new method that permits the extraction of high-purity lignin from biomass with minimal chemical modifications may provide a breakthrough pathway for the high value propositions of lignin.

The focus on biomass conversion using sub and supercritical fluids has increased due to its varying fluid properties as a result of manipulating the temperature and pressure. Solvents such as water, methanol, and ethanol at ambient conditions possess hydrogen-bonded structures that change with the increase in temperature. This condition causes a decrease in polarity and low dielectric permittivity, which subsequently facilitates the dissolution and breakage of the linkages of non-polar substances such as cellulose, hemicellulose, and lignin [13].

Extraction of lignin using sub and supercritical water have been extensively studied previously due to its clean reaction [14, 15]. Unfortunately, several studies reported that subcritical water caused repolymerization of monomers, producing char (an undesirable solid product), which decreased the potential of lignin as a precursor for carbon fiber. Therefore, this study proposes a new method using phenol under its subcritical condition (421.1 °C and 6.13 MPa). Few studies have shown the ability of sub and supercritical phenol in reducing the formation of char [16, 17]. Subcritical phenol functioned as a capping agent to cap active sites, preventing reactions with the decomposing lignin fragments; hence, it suppressed char formation. Hence, this study will focus on the effect of temperature (260–300°C), time (5–30 min) and solid loading (6–10 g) toward lignin properties (ash and volatile content) to determine its suitability as a precursor of carbon fiber production.

Table 1. Lignin specification as carbon fiber precursor

Criteria	**Value (wt.%)**
Lignin purity	99%
Ash content	<0.1
Volatile matter	<5.0
Particulate matter	100% removal for matter >1 μm in diameter

Materials and Methods

Raw material and chemicals

OPF was obtained from the Federal Land Development Authority (FELDA) plantation in Negeri Sembilan, Malaysia. Sample preparation followed standard procedures [18]. The samples were ground and sieved to obtain particles in the size range of 210–500 µm. Subsequently, the samples were subjected to an extraction process using methanol and a Soxhlet extractor to remove any oil residues and extractives. After 6 hours, the extracted samples were washed with water and dried in the oven for 48 hours at 45 °C. The chemical composition of OPF was determined based on the standard methods by the Technical Association of the Pulp and Paper Industry (TAPPI). The ultimate analysis of OPF was determined using CHNS/O elemental Analyzer, Perkin Elmer, Series II 2400, USA.

Experimental procedure

The reaction was conducted in an autoclave batch reactor with a working volume of 100 mL. Weighed OPF (6 or 10 g) and 70 mL of phenol were mixed and loaded into the autoclave reactor and subjected to various experimental conditions (temperature, reaction time and solid loading). The amount of phenol was chosen with the aim of maintaining the reaction pressure under subcritical phenol conditions (6.13 MPa). The reaction time was recorded once the temperature inside the vessel reached the target temperature. When the reaction was completed, the reactor was immersed in a water bath to quench the reaction. The solid residue was separated from the liquid residue using vacuum filtration. Subsequently, the solid residue was washed with methanol until the refractive index (RI) reached 1.33141 to ensure the removal of phenol. The solid residue was subsequently dried in an oven at 70 °C for 12 hours. The oven-dry weight (ODW) of the recovered solid residue was measured. The experimental conditions are shown in Table 2.

Table 2. Experimental conditions

Condition	Experimental Range
Reaction temperature (°C)	260, 280, and 300
Reaction time (min)	5, 10, and 30
Solid loading (g)	6 and 10

Lignin recovery and purification

Lignin recovery and purification were conducted according to National Renewable Energy Laboratory (NREL) specifications (determination of structural carbohydrates and lignin in biomass) [19]. An amount 3 mL of 72% sulfuric acid was added in a 50 mL test tube loaded with 300 mg of solid residue. The sample was incubated for 60 ±5 minutes inside a water batch shaker at 30 ± 3 °C. The sample was transferred to a 250 mL volumetric flask, and the acid was diluted to 4% concentration by adding 84.00 ± 0.04 mL deionized water. The sample was subsequently autoclaved at 121°C for another 60 ± 5 minutes. Upon completion, the purified lignin sample, known as an acid-insoluble residue (AIR), was collected by filtering the sample from the aliquot using Whatman™ filter paper with a pore size of 11µm. The AIR was washed with hot water and dried in an oven at 105 °C for 12 hours.

Analysis

Ash content

Ash content was determined according to the TAPPI Standard Test Method T 413 om-93 [20]. The AIR sample was combusted in a muffle furnace at 900 °C. The ash content percentage was calculated by dividing

the weight fraction of residual ash to the weight of the original sample, as shown in equation 1.

Volatile content

The volatile content in the recovered lignin sample was determined by following the standard proposed by ORNL and Luo (2010) [21]. The AIR sample was heated in the muffle furnace at 250 °C for 6 hours. The percentage of volatile content was determined on the basis of the weight loss of the sample to the weight of the original sample (equation 2).

$$\text{Ash content (\%)} = \frac{\text{Weight of the residual ash (g)}}{\text{Weight of the original sample (g)}} \times 100\% \quad (1)$$

$$\text{Volatile Matter Content (\%)} = \frac{\text{Initial weight of the sample (g) - Final weight of the sample (g)}}{\text{Initial weight of the sample (g)}} \times 100 \quad (2)$$

Results and Discussion

Characterization of OPF

The chemical and physical properties of biomass are different due to its origin and types. The high content of ash and extractives present in biomass result in the formation of slag, which reduces the efficiency of the process [22]. Therefore, the characterization of biomass is essential for determining how it may influence the quality of the precursor for carbon fiber production. Generally, biomass consisted of cellulose (30–50 wt.%), hemicellulose (20–35 wt.%), and lignin (15–30 wt.%), respectively [23]. Table 3 shows the chemical composition of OPF used in this study and compares it to other studies.

It can be observed that the lignin content in the OPF is consistent with other reported studies [24–26]. The minor difference in the OPF composition, especially lignin and cellulose, are based on its location, variety and agricultural practice [27–28]. The low amount of ash in OPF is favorable to prevent excessive generation of biochar at high temperatures [24]. Furthermore, the main composition of ash is inorganic salts. The high amount of inorganic salts may result in volatile release and the formation of pores in the fibers due to the catalytic effect of lignin thermal decomposition. Meanwhile, the high content of extractives remaining in carbon fiber resulted in mechanical defects [29]. Although the amount of lignin in OPF is lower than in other oil palm biomass, the high amount of OPF generated annually is certainly an essential consideration in its possibility as a raw material for this study [30–33]. Table 4 shows the analysis of OPF on a dry basis and its comparison with other types of oil palm biomass.

The carbon content (36.2%) of the OPF is lower than other types of oil palm biomass, with trace contents of nitrogen (0.4%) and sulfur (0.2%). Biomass decomposition resulted in the conversion of nitrogen to ammonia and hydrogen cyanide, while sulfur is converted to hydrogen sulfide [24, 36]. Therefore, a minimal amount of both elemental compositions is essential to minimize the formation of hazardous gases.

Ash content

Inorganic residues are commonly referred to as ash. Ash is defined as the residue left after combustion at high temperature (900 °C). Minimum inorganic content matter in lignin is desirable as a precursor for carbon fiber production. The ash content should be <0.1 wt.% to ensure minimal inclusions and defects of the carbon fiber [7, 37].

Figures 1 and 2 show the effect of temperature (260–300 °C), reaction time (5–30 minutes), and solid loading (6 and 10 g) on the ash content in the lignin. From the results, the lowest ash content of 9.87% and 10.10% were obtained at low temperature (260 °C) and short reaction time (5 minutes) for both solid loading. However, as observed in both figures, the ash content increased with higher temperature (280–300 °C) and longer reaction time (10–30 minutes) for both 6 and 10 g solid loading.

Table 3. Chemical composition of OPF (dry basis)

Compounds	This study	Omar et al. [24]	Tan et al. [25]	Kumneadklang et al. [26]
Cellulose	28.4	47.3 ± 1.1	42.8 ± 3.1	41.9
Hemicellulose	39.9	27.3 ± 1.9	14.8 ± 2.5	36.1
Lignin	18.9	20.1 ± 2.4	19.7 ± 2.7	22
Ash	3.6	3.4 ± 0.02	5.8 ± 0.4	NA
Extractives	9.2	NA	20.6 ± 4.1	NA

NA – no data available

Table 4. Ultimate analysis of OPF (dry basis)

Types of Biomass	Ultimate Analysis (wt.%)					Ref.
	C	H	N	S	O	
OPF	36.2	5.9	0.4	0.2	57.3	This study
MF	45.4	10.6	1.3	0. 7	42.0	[34]
OPT	41.6	6.8	0.4	0.9	50.4	[35]

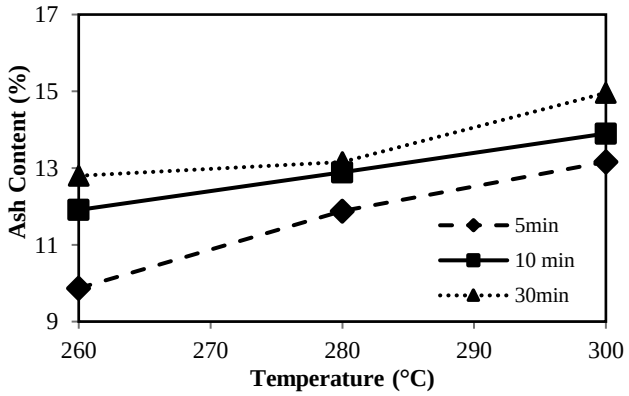


Figure 1. Ash content (%) at various temperatures (260–300 °C), reaction time (5–30 minutes) and 6 g solid loading

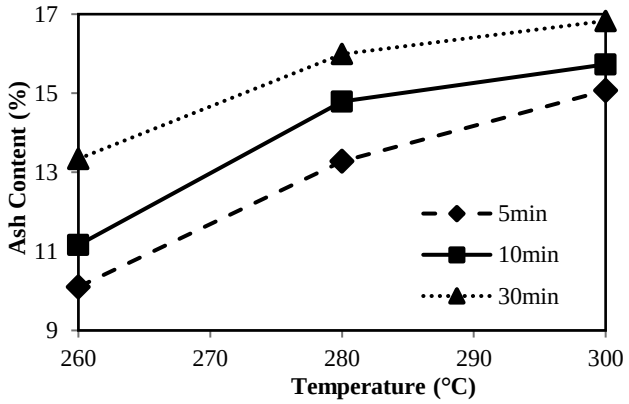


Figure 2. Ash content (%) at various temperatures (260–300 °C), reaction time (5–30 min) and 10 g solid loading

It can be concluded from Figures 1 and 2 that lower temperature and shorter reaction time produced lignin with low ash content under subcritical phenol conditions. Calcium, potassium, and magnesium are the main elements present in wood ash, while sodium and silicon existed relatively in small amounts [38]. The higher amount of ash with the increase in temperature and reaction time could be attributed to the increased condensation rate of the degraded ash with other intermediates. This finding is in line with Mäkelä et al. [40], who reported the increase in ash content from 48% to 67% for hydrothermal carbonization of biomass at 180–260 °C and 1–6.25 hours of reaction time. Shakya et al. [41] observed a similar trend, where they observed the increase in ash content from 6.07% (250 °C) to 43.29% (350 °C) at 60 minutes reaction time. On the other hand, Mäkelä et al. [42] concluded that solid loading is not a significant parameter in the ash content.

Based on the results, the ash content reported in this study did not meet the ORNL specifications (Table 1), which requires it to be less than 0.1% to be considered a suitable precursor for carbon fiber production. This might be due to the presence of sulfur from sulfuric acid in the sample before purification. Sameni et al. [38] obtained a higher ash content of 4.25% for lignin from pine species that had undergone acid hydrolysis compared to samples purified with other methods. Moreover, the incomplete removal of ash and extractives with methanol using Soxhlet extractor in this experimental work may contribute to the high ash content. Furthermore, the removal of ash might decrease due to the recycled solvent. This result is in line with Qu et al. [29].

Volatile content

Volatile content in the extracted lignin needs to be determined since these fragments can cause changes in the carbon fiber structures due to evaporation, especially during carbonization at high heating rate. The volatile content was determined by measuring the change in sample mass before and after heating in an oven at 250 °C for 6 hours. The volatile content must be less than 5% as specified by ORNL for it to be considered a suitable precursor for carbon fiber production (Table 1). The presence of low molecular weight fragments may cause defects in the structure of carbon fiber during lignin carbonization due to the rapid heating rate and evaporation [43]. Figures 3 and 4 show the effect of temperature (260–300 °C), reaction time (5–30 minutes) and solid loading (6 and 10 g) on volatile content.

The lowest volatile content of 6.45% and 8.47% were obtained at 260 °C and 5 minutes at 6 and 10 g solid loading, respectively. The result indicated that the volatile content is minimal at low temperature (260 °C) and reaction time (5 minutes) but increases with an increase in temperature (280–300 °C) and reaction time (10–30 minutes) for both solid loadings. It is also

observed that higher solid loading produced higher volatile content.

The degradation of lignin occurred over a wide range of temperature, between 140–600 °C [44]. The increase in volatile content could be attributed to the reduction of bond strengths in the chemical structure of lignin to form macromolecules volatiles during the reaction and subsequently volatilized. This is in agreement with Zhao et al. [11], who observed higher volatile gas formation at 300–700 °C and 20 minutes. Another study by Zhu et al. [9] shows that the volatile content obtained at 220 °C and 2 minutes is 60.5%. Meanwhile, Nanda et al. [45] obtained 35.5% volatile content at 550°C and 60 minutes with supercritical water. Thus, it can be concluded that lower volatile content can be obtained at low temperature and short reaction time under subcritical phenol conditions.

The results also indicate that the volatile content does not meet the specifications of ORNL (Table 1). One of the drawbacks of biomass is its high volatile content [46,47]; several studies reported that OPF has a high volatile content (82.70–85.10%) [30, 48, 49]. This study was conducted with a batch reactor without agitator. The high amount of solid loading formed a compacted mixture, resulting in a difficulty to mix thoroughly, resulting in challenges to obtaining homogenous reactions. This is in agreement with Meilany et al. [50].

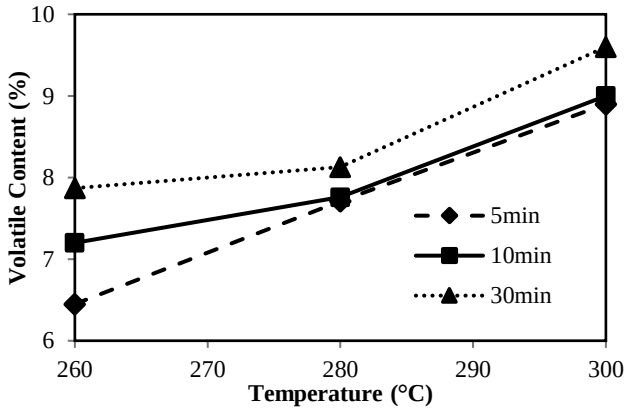


Figure 3. Volatile content (%) at various temperatures (260–300 °C), reaction time (5–30 minutes) and 6 g solid loading

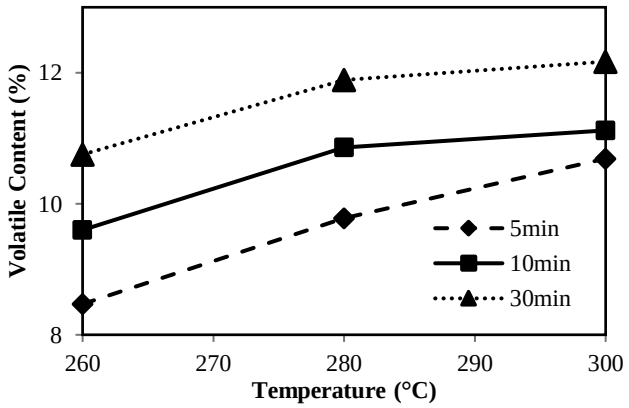


Figure 4. Volatile content (%) at various temperatures (260–300 °C), reaction time (5–30 minutes) and 10 g solid loading

Conclusion

Lignin as a precursor for carbon fiber can be commercially utilized if the impurities are reduced to a minimum. Low ash and volatile content are crucial to producing high-quality carbon fiber. As shown in this study, temperature, reaction time, and solid loading under subcritical phenol conditions have a significant effect on ash and volatile content. Although the results in this study did not meet ORNL specifications, it can be used as a reference for the future development of lignin as a precursor for carbon fiber production. On the other hand, this study has proven the feasibility of obtaining lignin under subcritical phenol conditions as a precursor for carbon fiber production. In this study, the extraction of lignin was focused on solid residues. Further analysis of the liquid residues should be considered as the solubilized lignin may possess the properties needed as a precursor. Additionally, this study could be further expanded by including other parameters such as pressure or pH value. This is because any changes in the reaction condition will alter the properties of the solvent, which would subsequently affect the properties of the lignin.

Acknowledgement

This research was funded by the Malaysia Ministry of Higher Education through the Fundamental Research Grant Scheme (FRGS).

References

1. Das, S., Warren, J., West, D. and Schexnayder, S. M. (2016). Global carbon fiber composites supply chain competitiveness analysis. Access from http://www.nrel.gov/docs/fy16osti/66071.pdf. [Access online 23 January 2019].
2. Malaysian Palm Oil Board (2019). Economics & industrial development division (area). Access from http://www.bepi.mpob.gov.my. [Access online 1 February 2019].
3. Barros, A. J., Ferrara, L. and Martinelli, E. (2017). Recent advances on green concrete for structural purposes. Springer, Cham: pp 197-331.
4. Graglia, M., Kanna, N. and Esposito, D. (2015). Lignin refinery: Towards the preparation of renewable aromatic building blocks. *ChemBioEng Reviews*, 2(6): 377-392.
5. Neata, G., Campeanu, G., Popescu, M. I., Popa, O., Babeanu, N., Basaraba, A. and Popescu, D. (2015). Lignin extraction from corn biomass using supercritical extraction. *Romanian Biotechnological Letters*, 20(3): 10406-10412.
6. Li, Q., Woodhead, A. L., Church, J. S. and Naebe, M. (2018). On the detection of carbon fibre storage contamination and its effect on the fibre–matrix interface. *Scientific Reports*, 8(1): 16446.
7. Baker, F. S., Griffith, W. L. and Compere, A. L. (2005). Low-cost carbon fibers from renewable resources. Access from http://roussev.net/sdhash/tutorial-data/files/853.pdf. [Access online 3 March 2019].
8. Nguyen, T. D. H., Maschietti, M., Åmand, L. E., Vamling, L., Olausson, L., Andersson, S. I. and Theliander, H. (2014). The effect of temperature on the catalytic conversion of kraft lignin using near-critical water. *Bioresource Technology*, 170: 196-203.
9. Zhu, G., Zhu, X., Xiao, Z., Zhou, R., Zhu, Y. and Wan, X. (2014). Kinetics of peanut shell pyrolysis and hydrolysis in subcritical water. *Journal of Material Cycles and Waste Management*, 16(3): 546-556.
10. Sun, P., Heng, M., Sun, S. and Chen, J. (2010). Direct liquefaction of paulownia in hot compressed water: Influence of catalysts. *Energy*, 35(12): 5421-5429.
11. Zhao, C., Jiang, E. and Chen, A. (2017). Volatile production from pyrolysis of cellulose, hemicellulose and lignin. *Journal of the Energy Institute*, 90(6): 902-913.
12. Alvarez-Vasco, C., Ma, R., Quintero, M., Guo, M., Geleynse, S., Ramasamy, K. K. and Zhang, X. (2016). Unique low-molecular-weight lignin with high purity extracted from wood by deep eutectic solvents (DES): A source of lignin for valorization. *Green Chemistry*, 18(19): 5133-5141.
13. Marcus, Y. (2018). Extraction by subcritical and supercritical water, methanol, ethanol and their mixtures. *Separations*, 5(1): 4.
14. Ko, J. K., Kim, Y., Ximenes, E. and Ladisch, M. R. (2015). Effect of liquid hot water pretreatment severity on properties of hardwood lignin and enzymatic hydrolysis of cellulose. *Biotechnology and Bioengineering*, 112(2): 252-262.
15. Machmudah, S., Wahyudiono, W., Kanda, H., Sasaki, M. and Goto, M. (2015). Hot compressed water extraction of lignin by using a flow-through reactor. *Engineering Journal*, 19(4): 25-44.

16. Saisu, M., Sato, T., Watanabe, M., Adschiri, T. and Arai, K. (2003). Conversion of lignin with supercritical water-phenol mixtures. *Energy & Fuels*, 17(4): 922-928.
17. Takada, M., Tanaka, Y., Minami, E. and Saka, S. (2016). Comparative study of the topochemistry on delignification of Japanese beech (*Fagus crenata*) in subcritical phenol and subcritical water. *Holzforschung*, 70(11): 1047-1053.
18. Hames, B., Ruiz, R., Scarlata, C., Sluiter, A., Sluiter, J. and Templeton, D. (2008). Preparation of samples for compositional analysis. Access from http://citeseerx.ist.psu.edu/ viewdoc/download?doi=10.1. 1.693.6586&rep=rep1&ty pe=pdf. [Access online 12 June 2018].
19. Sluiter, A., Hames, B., Ruiz, R., Scarlata, C., Sluiter, J., Templeton, D. and Crocker, D. (2008). Determination of structural carbohydrates and lignin in biomass. Access from http://www.academia.edu/download/34289991/ Determination-Structural-Carbohydrates-L....pdf. [Access online 12 June 2018].
20. TAPPI (1993). Ash in Wood, Pulp, Paper and Paperboard: Combustion at 900 °C (T 413 om-93). Access from http://grayhall.co.uk/BeloitResearch/tappi/t413.pdf . [Access online 2 February 2019].
21. Luo, J. (2010). Lignin-based carbon fiber. Thesis of Doctoral Degree, University of Maine, United State of America.
22. Braz, C. E. M. and Crnkovic, P. C. G. M. (2014). Physical-chemical characterization of biomass samples for application in pyrolysis process. *Chemical Engineering Transactions*, 37: 523-528.
23. Lu, Y., Lu, Y. C., Hu, H. Q., Xie, F. J., Wei, X. Y. and Fan, X. (2017). Structural characterization of lignin and its degradation products with spectroscopic methods. *Journal of Spectroscopy*, 2017: 1-15.
24. Omar, N., N, Abdullah, N, Mustafa, I., S. and Sulaiman, F. (2018). Characterization of oil palm frond for bio-oil production. *ASM Science Journal,* 11(1): 9-22.
25. Tan, J. P., Jahim, J. M., Harun, S., Wu, T. Y. and Mumtaz, T. (2016). Utilization of oil palm fronds as a sustainable carbon source in biorefineries. *International Journal of Hydrogen Energy*, 41(8): 4896-4906.
26. Kumneadklang, S., Larpkiattaworn, S., Niyasom, C. and Sompong, O. (2015). Bioethanol production from oil palm frond by simultaneous saccharification and fermentation. *Energy Procedia*, 79: 784-790.
27. Wunna, K., Nakasaki, K., Auresenia, J. L., Abella, L. C. and Gaspillo, P. D. (2017). Effect of alkali pretreatment on removal of lignin from sugarcane bagasse. *Chemical Engineering Transactions*, 56: 1831–1836.
28. Canilha, L., Santos, V. T., Rocha, G. J., e Silva, J. B. A., Giulietti, M., Silva, S. S. and Carvalho, W. (2011). A study on the pretreatment of a sugarcane bagasse sample with dilute sulfuric acid. *Journal of Industrial Microbiology & Biotechnology*, 38(9): 1467-1475.
29. Qu, W., Liu, J., Xue, Y., Wang, X. and Bai, X. (2018). Potential of producing carbon fiber from biorefinery corn stover lignin with high ash content. *Journal of Applied Polymer Science*, 135(4): 45736.
30. Loh, S. K. (2017). The potential of the malaysian oil palm biomass as a renewable energy source. *Energy Conversion and Management*, 141: 285-298.
31. Kong, S. H., Loh, S. K., Bachmann, R. T., Rahim, S. A. and Salimon, J. (2014). Biochar from oil palm biomass: A review of its potential and challenges. *Renewable and Sustainable Energy Reviews*, 39: 729-739.
32. EU-Malaysia Chamber of Commerce and Industry (EUMCCI). (2017). Oil palm biomass & biogas in Malaysia, 2017 potentials for European SMES. Access https://businessmalaysia.eu [Access online 3 January 2019].
33. Malaysian Industry-Government Group for High Technology (MIGHT). (2013). Malaysian biomass industry action plan 2020 driving SMEs towards sustainable future. Access from http://www.biomass.org.my [Access online 3 January 2019]
34. Kabir, G., Din, A. M. and Hameed, B. H. (2017). Pyrolysis of oil palm mesocarp fiber and palm frond in a slow-heating fixed-bed reactor: A comparative study. *Bioresource Technology*, 241: 563-572.
35. Alias, N. B., Ibrahim, N., Hamid, M. K. A., Hasbullah, H., Ali, R. R. and Kasmani, R. M. (2015). Investigation of oil palm wastes' pyrolysis by thermo-gravimetric analyzer for potential biofuel production. *Energy Procedia,* 75: 78-83.

36. García, R., Pizarro, C., Lavín, A. G. and Bueno, J. L. (2012). Characterization of Spanish biomass wastes for energy use. *Bioresource Technology*, 103(1): 249-258.
37. Aldaeus, F., Olsson, A. M. and Stevanic, J. S. (2017). Miniaturized determination of ash content in kraft lignin samples using oxidative thermogravimetric analysis. *Nordic Pulp & Paper Research Journal*, 32(2): 280-282.
38. Sameni, J., Krigstin, S., dos Santos Rosa, D., Leao, A. and Sain, M. (2013). Thermal characteristics of lignin residue from industrial processes. *BioResources*, 9(1): 725-737.
39. Attwenger, A. (2014). Value-added lignin-based carbon fiber from organosolv fractionation of poplar and switchgrass. Thesis of Master Degree, University of Tennessee, United State of America.
40. Mäkelä, M., Benavente, V. and Fullana, A. (2015). Hydrothermal carbonization of lignocellulosic biomass: Effect of process conditions on hydrochar properties. *Applied Energy*, 155: 576–584.
41. Shakya, R., Whelen, J., Adhikari, S., Mahadevan, R. and Neupane, S. (2015). Effect of temperature and Na_2CO_3 catalyst on hydrothermal liquefaction of algae. *Algal Research*, 12: 80-90.
42. Mäkelä, M., Fullana, A. and Yoshikawa, K. (2016). Ash behavior during hydrothermal treatment for solid fuel applications. Part 1: Overview of different feedstock. *Energy Conversion and Management*, 121: 402-408.
43. Luo, J., Genco, J., Cole, B. J. and Fort, R. C. (2011). Lignin recovered from the near-neutral hemicellulose extraction process as a precursor for carbon fiber. *BioResources*, 6(4): 4566-4593.
44. Stefanidis, S. D., Kalogiannis, K. G., Iliopoulou, E. F., Michailof, C. M., Pilavachi, P. A. and Lappas, A. A. (2014). A study of lignocellulosic biomass pyrolysis via the pyrolysis of cellulose, hemicellulose and lignin. *Journal of Analytical and Applied Pyrolysis*, 105: 143-150.
45. Nanda, S., Reddy, S. N., Vo, D. V. N., Sahoo, B. N. and Kozinski, J. A. (2018). Catalytic gasification of wheat straw in hot compressed (subcritical and supercritical) water for hydrogen production. *Energy Science & Engineering*, 6(5): 448-459.
46. Sulaiman, S. A., Balamohan, S., Moni, M. N. Z., Atnaw, S. M. and Mohamed, A. O. (2015). Feasibility study of gasification of oil palm fronds. *Journal of Mechanical Engineering and Sciences*, 9:1744-1757.
47. Yang, W. (2015). Degradation mechanism of biomass in subcritical water and applications of the remained solid char. Thesis of Bachelor Degree, Okayama University, Japan.
48. Subramaniam, V., Chow, M. C. and Ma, A. N. (2004). Energy database of the oil palm. *Palm Oil Engineering Bulletin,* 70(94): 29-42.
49. Abnisa, F., Arami-Niya, A., Daud, W. W., Sahu, J. N. and Noor, I. M. (2013). Utilization of oil palm tree residues to produce bio-oil and bio-char via pyrolysis. *Energy Conversion and Management*, 76: 1073-1082.
50. Meilany, D., Kresnowati, M. T. A. P. and Setiadi, T. (2018). Temperature, solid loading and time effects on recovery of sugar from OPEFB. *MATEC Web of Conferences*, 156: 03022.

Malaysian Journal of Analytical Sciences (MJAS)
Published by Malaysian Analytical Sciences Society

ACETYLCHOLINESTERASE INHIBITORY ACTIVITY OF THE METHANOL EXTRACT AND PHYTOCHEMICAL STUDY OF THE LEAVES OF *Macaranga gigantea* (Rchb.f. & Zoll.)

(Aktiviti Perencatan Asetilkolinesterase Terhadap Ekstrak Methanol dan Kajian Fitokimia ke atas Daun *Macaranga gigantea* (Rchb.f. & Zoll)

Muhammad Sulaiman Mohd Johari[1, 2], Norizan Ahmat[1, 2]*, Aisyah Salihah Kamarozaman[1, 3], Zetty Zulikha Hafiz[1, 2]

[1]Faculty of Applied Sciences,
Universiti Teknologi MARA, 40450 Shah Alam, Selangor, Malaysia
[2]Atta-Ur-Rahman, Institute of Natural Product,
Universiti Teknologi MARA, Kampus Puncak Alam, 42300 Bandar Puncak Alam, Selangor, Malaysia
[3]Centre of Foundation Studies,
Universiti Teknologi MARA Kampus Dengkil, 43800 Dengkil, Selangor, Malaysia

**Corresponding author: noriz118@uitm.edu.my*

Received: 20 November 2019; Accepted: 18 June 2020; Published: 11 August 2020

Abstract

Genus *Macaranga* belongs to Euphorbiaceae family and is known for their mutualistic associations with ants. This plant is widely distributed in the tropics of Africa, South-East Asia, Australia and the South Pacific region. In folk medicine, traditional healers use fresh or dried leaves of *Macaranga* species to treat swellings, cuts, sores, boils and bruises. In this study, 20 µL methanol crude extract from the leaves of *Macaranga gigantea* was assayed for its *in-vitro* acetylcholinesterase inhibitory activity. The crude extract displayed a good acetylcholinesterase (AChE) inhibition activity at IC_{50} at 39.89 ± 4.57 ug/mL. Phytochemical study on the crude leaf extract lead to the isolation and purification of two pure compounds *via* radial chromatographic techniques. Based on the ^{1}H NMR and ^{13}C NMR analysis, the structure of the pure compounds was found to have a prenylated substituent which could be recognized through the presence of methyl, methylene, and a vinyl group. Based on the analysis of spectral data and comparison with literature, the compounds were elucidated as a geranylated stilbene, schweinfurthin C **(1)** and a farnesylated flavonol, macagigantin **(2)**.

Keywords: acetylcholinesterase, Euphorbiaceae, *Macaranga gigantea*, schweinfurthin C, macagigantin

Abstrak

Genus *Macaranga* tergolong di dalam famili Euphorbiaceae dan dikenali sebagai tumbuhan yang mempunyai hubungan mutual dengan semut. Tumbuhan ini boleh ditemui di kawasan tropika seperti Afrika, Selatan-Timur Asia, Australia dan di kawasan Selatan Pasifik. Menurut ilmu perubatan lama, pengamal perubatan mengunakan daun segar atau kering dari spesies *Macaranga* untuk mengubati bengkak, luka, sengal, lecur dan lebam. Melalui kajian ini, ekstrak mentah yang telah dilarutkan di dalam metanol telah diuji dengan aktiviti perencatan asetikolinesterase. Sebanyak 20 µL larutan ekstrak telah digunakan dan menunjukkan keputusan yang baik sebagai perencat asetilkolinesterase di IC_{50} 39.89 ± 4.57 ug/mL. Kajian fitokimia yang dijalankan telah

berjaya memisah dan menulenkan dua sebatian tulen menggunakan kromatografi radial. Bersandarkan pada data ^{1}H NMR and ^{13}C NMR, struktur sebatian tulen yang diperoleh mempunyai kumpulan prenil yang terdiri daripada metil, metilina dan vinil. Berdasarkan analisis data spektra ini dan perbandingan dengan literatur, sebatian-sebatian tulen tersebut dicirikan sebagai geranil stilbena, schweinfurthin C **(1)** dan farnesil flavonol, macagigantin **(2)**.

Kata kunci: asetilkolinesterase, Euphorbiaceae, *Macaranga gigantea*, schweinfurthin C, macagigantin

Introduction

Macaranga (known as Mahang) comes from the family of Euphorbiaceae which comprises 300 species [1, 2]. In Malaysia, this genus is commonly found in the village areas, wastelands, and swampy forests [3]. This genus is also widely distributed around the globe such as Africa, South-East Asia, Australia, South Pacific region, Burma, Indo China, China and India [4]. With a lot of sunlight in secondary forests, the plants can grow up to 20 m tall [5]. Species from this genus are well-known for their mutualistic association with the genus *Crematogaster* (Myrmicinae) ants [6]. *Macaranga* species is closely related to *Mallotus*, but several characteristics may differentiate the two such as the presence of red latex, the *Macaranga* myrmecophytic habit and the anatomy of the leaves [7]. The use of some *Macaranga* species in traditional medicine have led many researchers to carry out extensive studies on the bioactive compounds of the genus, thus validating the use of this genus as a therapeutic remedy. Numerous biological activities such as cytotoxicity, antioxidant, antiplasmodial, antimicrobial, anti-inflammatory and other types of activities have been reported from the extracts as well as individual compounds [8]. The leaves of *Macaranga gigantea* were selected as part of our current research on bioactive compounds in Malaysia. Two known compounds namely, schweinfurthin C **(1)**, a geranylated stilbene and macagigantin **(2)**, a farnesylated flavonol were isolated and purified. We herein report the isolation and elucidation of the compounds as well as assay of the crude methanol extract.

Materials and Methods

Instrumentation

The structure of the isolated compound was analyzed by 1D & 2D NMR. The ^{1}H NMR and ^{13}C NMR were analyzed in acetone-d_6 on Bruker 600 Ultrashield NMR spectroscopy measured at 600MHz and 150MHz respectively. The vacuum liquid chromatography technique (VLC) used Silica gel 60, 70-230 ASTM (MERCK 1.07747); aluminum supported silica gel 60 F254 was used for thin-layer chromatography (TLC) and the radial chromatography technique (RC) used the Si-gel 60 PF (Merck catalogue 254 number: 1.07749). The TLC plates were spotted using a fine glass capillary tube and were developed in a chromatographic chamber with various solvent systems at room temperature. The spots were then visualized under UV light (254 and 356 nm). The solvent used were *n*-hexane, chloroform, ethyl acetate, methanol, and acetone from RCI Labscan Limited, Thailand (AR grade solvent, 2.5L).

Plant material

A total of 7 kg *M. gigantea* leaves were collected from the forest area at Universiti Teknologi MARA, Puncak Alam. A voucher specimen (UKMB40430) consisting leaves, stems and fruit were submitted and deposited in UKM Herbarium.

Extraction and Isolation

Standard procedures for extraction and isolation of pure compounds from plant materials were applied in this research [9]. The 7 kg of *M. gigantea* leaves were rinsed carefully with tap water to remove dirt and were dried at room temperature for two weeks. The dried leaves were cut into small pieces and ground to powder using a grinder which resulted in 3 kg dried powder. The solvent used for extraction was methanol (AR grade solvent). The 3 kg of the sample were macerated in 30 liters of methanol for 72 hours at room temperature. The methanol extract was filtered using No 1 Whatman filter paper with a diameter circle of 25 mm. The extracts were then evaporated under reduced pressure at 20 mbar/ 50 °C using a rotary evaporator which resulted in the concentrated methanol extracts (270 g). The extracts were stored at 5 °C until further use. About 100 g of crude methanol extract was fractionated by using VLC

with solvent system *n*-hexane: ethyl acetate in 100 mL (100:0 to 50:50) four-time for each solvent system to give six (6) major fractions 1-6. Fraction 2 (1 g) was separated by RC eluted with chloroform: ethyl acetate (100 to 70:30) to afford compound **1,** schweinfurthin C (2 mg) and compound **2,** macagigantin (2 mg).

Acetylcholinesterase inhibitory activity assay

The spectroscopic method of Ellman et al. [10] was used as reference method as described by Salles et al. [11], in which thiocholine produced by the action of acetylcholinesterase forms a yellow color with 5, 5`-dithiobis(2-nitrobenzoic acid). Eserine was used as a positive control. A 96-well plate was designed by adding 190 µL DTNB solution, 20 µL samples and 20 µL enzyme solution, were mixed and incubated for 10 minutes at 37 °C. Then, 20 µL substrates were added to the wells. Measurement of the intensity of the product color was completed by reading the microplate reader kinetically at 412 nm, runtime 15 minutes and interval 1 minute, which is proportionate to the enzyme activity in the sample. The control contained all components except the tested sample. The percentage of AChE inhibitory activity (%IA) was calculated by using the following equation 1:

$$\%IA = \frac{\text{Negative control absorbance} - (\text{Sample absorbance} - \text{Blank absorbance})}{\text{Negative control absorbance}} \times 100 \quad (1)$$

Results and Discussion

The phytochemical screening (Table 1) on the crude methanol extract of *M. gigantea* showed the presence of flavonoid, tannin and terpene as illustrated by the red, green and reddish-brown solution form from Shinoda, tannin and terpenoid test respectively. This screening procedure was performed in triplicate and was repeated three times with similar results.

Spectral data of isolated compound

Compound **1**: A yellow solid. ^{1}H NMR (acetone-d_6, 600 MHz) spectral data: δ_H 6.93 (d,2.0, H-3), 6.81 (d, 2.0,H-5), 3.38 (t, 7.0,H-7), 5.37 (m,H-8), 1.75 (s,H-10), 1.98 (m,H-11), 2.11 (m, H-12), 5.14 (m, H-13), 1.59 (s, H-15), 1.74 (s, H-16), 6.83 (d, 16,H-1'), 6.74 (d, 16,H-2'), 6.58 (s, H-4'), 6.58 (s, H-8'), 3.35 (t, 7.2, H-"'), 5.34 (m, H-2"), 1.80 (s, H-4"). 1.94 (t, 7.4,H-5"), 1.98 (m, H-6"), 5.11 (m,H-7"), 1.59 (s, H-9"), 1.66 (s,H-10"). ^{13}C NMR (acetone-d_6, 150 MHz) spectral data: δ_C 143.0 (C-1), 144.6 (C-2), 110.2 (C-3), 131.4 (C-4), 119.8 (C-5), 130.6 (C-6), 28.1 (C-7), 122.9 (C-8), 136.4 (C-9), 15.3 (C-10), 39.6 (C-11), 29.4 (C-12), 124.2 (C-13), 133.6 (C-14), 16.8 (C-15), 24.9 (C-16), 129.7 (C-1'), 127.7 (C-2'), 137.2 (C-3'), 104.8 (C-4'), 156.1 (C-5'), 115.5 (C-6'), 156.1 (C-7'), 104.8 (C-8'), 22.1 (C-1"), 123.3 (C-2"), 134.5 (C-3"), 15.4 (C-4"), 39.7 (C-5"), 26.5 (C-6"), 124.3 (C-7"), 132.4 (C-8"), 17.0 (C-9"), 25.0 (C-10").

Compound **2**: A yellow solid. ^{1}H NMR (acetone-d_6, 600 MHz) spectral data: δ_H 6.62 (s, H-8), 8.15 (dd, 9.0, 2.4,H-2'/6'), 7.03 (dd, 7.0, 2.4, H-3'/5'), 3.40 (d, 7.2,H-1"), 5.32 (m, H-2"), 1.83 (s, H-4"), 1.98 (s, H-5"), 5.10 (m, H-6"), 1.77 (d, H-8"), 1.83 (s, H-9"), 5.04 (m, H-10"), 1.59 (s, H-12"), 1.54 (s, H-13"), 1.57 (s, H-14"), 1.60 (s, H-15"), 12.44 (s, 5-OH), 9.71 (br s, 7-OH), 7.98 (br s, 3-OH), 9.04 (br s,4'-OH).

Elucidation of compound 1 as schweinfurthin C

Compound **1** was obtained as a yellow solid. The ^{1}H NMR spectrum (Table 2) showed two *meta*-couple aromatic proton signals at δ_H 6.93 (H-3), δ_H 6.81 (H-5) and δ_H 6.58 (H-4'/8') indicating that the compound contained two aromatic rings with AB spin system. A stilbene skeletal was shown by two doublet signals at δ_H 6.83 (H-1') and δ_H 6.74 (H-2') representing the vinyl proton that connected the two phenolic rings. The substitution of two geranyl group in the structure was shown through the presence of six methyl singlets at δ_H 1.75 (H-10), 1.59 (H-15), 1.74 (H-16), 1.80 (H-4"), 1.59 (H-9"), 1.66 (H-10"), six methylene signals at δ_H 3.38 (H-7), 1.59 (H-15), 1.74 (H-16), 3.35 (H-1"), 1.94 (H-5"), 1.98 (H-6") and four vinyl signals at δ_H 5.37 (H-8),

5.14 (H-13), 5.34 (H-2"), 5.11 (H-7"). ^{1}H-^{13}C long-range HMBC correlation showed that H-1" correlated with C-5', C-6', C-7' and H-7 with C-1, C-5, C-6 which confirmed the attachment of geranyl substituent in the structure. Based on the analysis of spectroscopic data and comparison with the literature [12], compound **1** was assigned as schweinfurthin C (Figure 1).

Table 1. Phytochemical screening from crude methanol extract of *M. gigantea.*

Type of Compound	**Crude Methanol Extract**
Flavonoid	+++
Alkaloid	---
Saponin	---
Tannin	+++
Terpene	+++

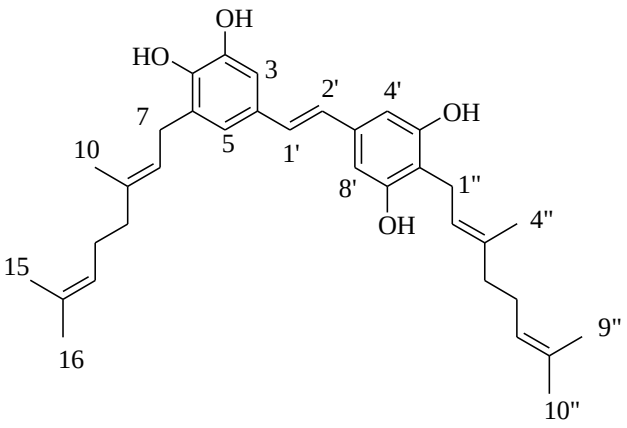


Figure 1. Structure of schweinfurthin C

Table 2. NMR Spectroscopy of Compound **1**

Position	**δ_H (multi, *J* (Hz))**		**δ_C**		**^{1}H-^{13}C HMBC**
	Compound 1	***Schweinfurthin C**	**Compound 1**	***Schweinfurthin C**	
1	-	-	143.0	144.2	-
2	-	-	144.6	146.1	-
3	6.93 (d, 2.0)	6.81 (d, 2.0)	110.2	111.0	C-1, C-5, C-2'
4	-	-	131.4	130.3	-
5	6.81 (d, 2.0)	6.67 (d, 2.0)	119.8	120.6	C-5, C-3, C-2', C-1
6	-	-	130.6	129.6	-
7	3.38 (t, 7.0)	3.34 (t, 7.0)	28.1	29.1	C-6, C-1, C-5
8	5.37 (m)	5.33 (t, 7.4)	122.9	124.1	C-8

Table 2 (cont'd). NMR Spectroscopy of Compound **1**

Position	δ_H (multi, *J* (Hz))		δ_C		^1H-^{13}C HMBC
	Compound 1	***Schweinfurthin C**	**Compound 1**	***Schweinfurthin C**	
9	-	-	136.4	136.6	-
10	1.75 (s)	1.72 (s)	15.3	16.2	-
11	1.98 (m)	2.04 (t, 7.8)	39.6	40.9	C-15, C-12, C-13, C-7, C-14
12	2.11 (m)	2.11 (t, 7.8)	29.4	27.7	C-12, C-11
13	5.14 (m)	5.14 (t, 7.2)	124.2	125.3	C-15
14	-	-	133.6	132.2	-
15	1.59 (s)	1.58 (s)	16.8	17.7	C-14
16	1.74 (s)	1.64 (s)	24.9	25.8	C-15, C-13
1'	6.83 (d, 16)	6.77 (d, 16)	129.7	129.0	C-3, C-5
2'	6.74 (d, 16)	6.63 (d, 16)	127.7	127.0	C-4'/8', C-2', C-1'
3'	-	-	137.2	137.7	
4'	6.58 (s)	6.43 (s)	104.8	105.7	C-4'/8', C-5', C-7'
5'	-	-	156.1	157.2	-
6'	-	-	115.5	115.8	-
7'	-	-	156.1	157.2	-
8'	6.58 (s)	6.43 (s)	104.8	105.7	C-4'/8', C-5', C-7'
1"	3.35 (t, 7.2)	3.27	22.1	23.2	C-6', C-5', C-7', C-2"
2"	5.34 (m)	5.24 (t, 7.4)	123.3	124.6	C-5"
3"	-	-	134.5	134.8	-
4"	1.80 (s)	1.75 (s)	15.4	16.3	C-5", C-7", C-3"
5"	1.94 (t, 7.4)	1.93 (t, 7.2)	39.7	41.0	-
6"	1.98 (m)	2.04 (t. 7.8)	26.5	27.8	C-5"
7"	5.11 (m)	5.07 (t, 7.0)	124.3	125.5	C-9"
8"	-	-	132.4	132.0	-
9"	1.59 (s)	1.56 (s)	17.0	17.8	C-10", C-5"
10"	1.66 (s)	1.62 (s)	25.0	25.9	-

Compound **1** NMR Spectra recorded at 600 MHz (^1H) and 150 MHz (^{13}C-APT) in acetone-d_6
Schweinfurthin C NMR Spectra recorded at 500 MHz (^1H) and 125 MHz (^{13}C-APT) in CD_3OD [12]

Elucidation of compound 2 as macagigantin

Compound **2** (Figure 2) was obtained as a yellow solid. The ^1H NMR spectrum displayed a chelated hydroxyl signal that appeared to be at the most deshielded at δ_H 12.44 (br s, 5-OH), δ_H 7.98 (s, 3-OH), δ_H 9.71 (s, 7-OH) and δ_H 9.04 (s, 4'-OH) showed that this compound is a flavonol from kaempferol derivative. Two proton signals, which is a pair of doublet for AA"BB" system at aromatic region δ_H 8.15 (dd, 9.0, 2.4, H-2'/6') and δ_H 7.03 (dd, 7.0, 2.4, H-3'/5') corresponds to the hydroxyphenyl group that attaches to C-4' at ring B. A singlet at δ_H 6.62 (H-8) in the aromatic region of ^1H NMR spectrum suggested there is a farnesyl group attached to ring A of flavonol group. This can be observed through the presence of four methyl's at δ_H 1.59 (s, H-12"), 1.54 (s, H-13"), 1.57 (s, H-14") and 1.60

(s, H-15”), five methylene at δ_H 3.40 (d, 7.2, H-1”), 1.83 (s, H-4”), 1.98 (s, H-5”), 1.77 (d, H-8”) and 1.83 (s, H-9”) and three methine vinyl protons at δ_H 5.32 (m, H-2”), 5.10 (m, H-6”) and 5.04 (m, H-10”). Based on the ^{1}H NMR data (Table 3), compound **2** was confirmed as macagigantin. The spectral data were identical to that reported by Tanjung et al. [13].

The crude methanol extract was assayed for its *in-vitro* acetylcholinesterase inhibitory activity. Eserine was used as a positive control. The crude extract displayed a good acetylcholinesterase (AChE) inhibition activity at IC_{50} 39.89 ± 4.57 ug/mL. It is believed that the abundance of secondary metabolite compounds were responsible for this activity. A study by Howes & Perry stated that several flavonoids and stilbenoids inhibited AChE [14]. The catechol moiety on ring B of flavonoid compound formed a binding interaction with the active site of AChE enzyme which is the main cause factor of the activity [15].

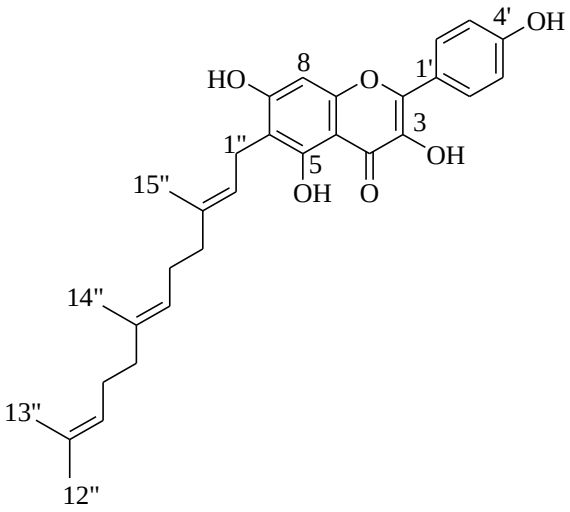


Figure 2. Structure of macagigantin **(2)**

Table 3. NMR Spectroscopic Data of Compound **2**

Position	**Compound 2** δ_H **(multi, *J* (Hz))**	**Macagigantin*** δ_H **(multi, *J* (Hz))**
8	6.62 (s)	6.59 (s)
2’/6’	8.15 (dd, 9.0, 2.4)	8.12 (d, 9.0)
3’/5’	7.03 (dd, 7.0, 2.4)	7.00 (d, 9.0)
1”	3.40 (d, 7.2)	3.37 (d, 6.7)
2”	5.32 (m)	5.29 (tm, 6.7)
4”	1.83 (s)	1.97 (t, 7.3)
5”	1.98 (s)	2.06 (br q, 7.3)
6”	5.10 (m)	5.06 (br t, 7.3)
8”	1.77 (d)	1.85 (br t, 7.3)
9”	1.83 (s)	1.93 (br q, 7.3)

Table 3 (cont'd). NMR Spectroscopic Data of Compound **2**

Position	**Compound 2** δ_H **(multi, *J* (Hz))**	**Macagigantin*** δ_H **(multi, *J* (Hz))**
10"	5.04 (m)	5.00 (br t, 7.3)
12"	1.59 (s)	1.57 (br s)
13"	1.54 (s)	1.51 (br s)
14"	1.57 (s)	1.54 (br s)
15"	1.60 (s)	1.79 (br s)
5-OH	12.44 (s)	12.41 (s)
7-OH	9.71 (br s)	-
3-OH	7.98 (br s)	-
4'-OH	9.04 (br s)	-

Compound **2** NMR Spectra recorded at 600 MHz (^{1}H) in acetone-d_6

*Macagigantin NMR Spectra recorded at 500 MHz (^{1}H) in methanol-*d* [13]

Conclusion

The crude methanol extracts of *M. gigantea* showed a good acetylcholinesterase inhibitory activity. Phytochemical screening of the crude extracts showed a potential secondary metabolite which leads to the isolation and purification of schweinfurthin C **(1)** and macagigantin **(2).** This suggests that this plant could be used as a potential treatment for Alzheimer's disease. However, further studies on the pharmacology of the isolated compounds are needed to find which bioactive compound is responsible for the acetylcholinesterase inhibitory activity of this species.

Acknowledgement

The authors would like to thank Universiti Teknologi MARA for the research grant 600-RMC/LESTARI SDG-T 5/3 (162/2019), Faculty of Applied Sciences and Atta-ur-Rahman Institute for Natural Product Discovery, UiTM for the equipment's and facilities as well as Dr. Shamsul Khamis, a botanist from Universiti Kebangsaan Malaysia for plant identification.

References

1. Yang, D. S., Peng, W. B., Yang, Y. P., Liu, K. C., Li, X. L. and Xiao, W. L. (2015). Cytotoxic prenylated flavonoids from *Macaranga indica*. *Fitoterapia*, 103: 187-191.
2. Johari, M. S. M., Ahmat, N., Kamarozaman, A. S. and Isa, M. H. M. (2019). Prenylated flavonols from the leaves of *Macaranga gigantea* (Rchb. F. & Zoll.). *Scientific Research Journal*, 16(1): 29-40.
3. Kamarozaman, A. S., Ahmat, N., Rahman, N. F. A. and Yen, K. H. (2018). Prenylated dihydrostilbenes from *Macaranga heynei* (Euphorbiaceae). *Malaysian Journal of Analytical Sciences*, 22(2): 258-263.
4. Lim, T. Y., Lim, Y. Y. and Yule, C. M. (2014). Bioactivity of leaves of *Macaranga* species in tropical peat swamp and non-peat swamp environments. *Journal of Tropical Forest Science*, 2014: 134-141.
5. Aminah, N. S., Kristanti, A. N. and Tanjung, M. (2014). Antioxidant activity of flavonoid compounds from the leaves of *Macaranga gigantea*. *Journal of Chemical and Pharmaceutical Research*, 6(6): 688-692.

6. Heckroth, H. P., Fiala, B. and Maschwitz, U. (2016). Integration of scale insects (Hemiptera: Coccidae) in the south-east Asian ant-plant (*Crematogaster* (Formicidae)-*Macaranga* (Euphorbiaceae)) System. *Entomologica*, 33: 287-295.
7. Norfaizal, G. M., Khalijah, H. and Ruzi, A. M. (2012). Leaf anatomical study of five *Macaranga* species (Euphorbiaceae). *Journal of Tropical Agriculture & Food Science*, 40(2): 289-296.
8. Magadula, J. J. (2014). Phytochemistry and pharmacology of the genus *Macaranga*: A review. *Journal of Medicinal Plants Research*, 8(12): 489-503.
9. Pandey, A. and Tripathi, S. (2014). Concept of standardization, extraction and pre phytochemical screening strategies for herbal drug. *Journal of Pharmacognosy and Phytochemistry*, 2(5): 115-119.
10. Ellman, G. L., Courtney, K. D., Andres Jr, V. and Featherstone, R. M. (1961). A new and rapid colourimetric determination of acetylcholinesterase activity. *Biochemical pharmacology*, 7(2): 88-95.
11. Salles, M. T., Viana, F. V., Van De Meent, M., Rhee, I. K. and Verpoorte, R. (2003). Screening for acetylcholinesterase inhibitors from plants to treat Alzheimer disease. *Química Nova*, 26: 1-7.
12. Beutler, J. A., Shoemaker, R. H., Johnson, T. and Boyd, M. R. (1998). Cytotoxic geranyl stilbenes from *Macaranga schweinfurthii*. *Journal of Natural Product,* 61: 1509-1512.
13. Tanjung, M., Hakim, E. H., Mujahidin, D., Hanafi, M. and Syah, Y. M. (2009). Macagigantin, a farnesylated flavonol from *Macaranga gigantea*. *Journal of Asian natural products research*, 11(11): 929-932.
14. Howes, M. J. R. and Perry, E. (2011). The role of phytochemicals in the treatment and prevention of dementia. *Drugs & Aging*, 28(6): 439-468.
15. Kamarozaman, A. S., Ahmat, N., Isa, S. N. M., Hafiz, Z. Z., Adenan, M. I., Yusof, M. I. M. and Latip, J. (2019). New dihydrostilbenes from *Macaranga heynei* IM Johnson, biological activities and structure-activity relationship. *Phytochemistry Letters*, 30: 174-180.

Malaysian Journal of Analytical Sciences (MJAS)
Published by Malaysian Analytical Sciences Society

ANTIOXIDANT AND XANTHINE OXIDASE INHIBITORY ACTIVITY OF *Euphorbia hirta* LEAVES CRUDE EXTRACT

(Antioksidan dan Aktiviti Perencatan Xantina Oksidase Bagi Ekstrak Mentah Daun *Euphorbia hirta*)

Ahmad Anas Nagoor Gunny[1]*, Thum Carmen[1], Mohd Hishamuddin Che Mat[2], Ahmad Azudin Nordin[2], Azalina Mohamed Nasir[1]

[1]Department of Chemical Engineering Technology,
Universiti Malaysia Perlis, Uniciti ALAM Campus, 02100 Padang Besar, Perlis, Malaysia
[2]Institute of Sustainable Agrotechnology,
Universiti Malaysia Perlis, Sg. Chuchuh Campus, 02100 Padang Besar, Perlis, Malaysia

**Corresponding author: ahmadanas@unimap.edu.my*

Received: 20 November 2019; Accepted: 30 May 2020; Published: 11 August 2020

Abstract

Today, exposure to free radicals and gout cases have been a concern, showing several health effects from synthetic medications and clinical drugs for antioxidant effect and xanthine oxidase inhibition effect, respectively; all of which lead to the discovery of natural inhibitors from medicinal plants. In this study, a green solvent known as the deep eutectic solvent is synthesised to replace conventional solvents for the extraction of free radical inhibitors and xanthine oxidase inhibitors from a medicinal plant that has shown many health benefits and is widely used in traditional medicine, the *Euphorbia hirta.* The leaves extract from *Euphorbia hirta* showed the highest inhibition (87.95 ± 0.0061%) on free radical assays. The IC_{50} for free radical inhibition of the leaves extract is 10.56 ± 0.58 µg/mL. The IC_{50} value for xanthine oxidase inhibition of allopurinol was the lowest, which was at 6.94 ± 0.32 µg/mL; while the leaves extract of *Euphorbia hirta* exhibited value at 9.40 ± 0.13 µg/mL. The correlation value between the antioxidant effect and the xanthine oxidase inhibition of the leaves extract was 0.960, which indicated that there is a strong relationship between the two said parameters. From the Lineweaver-Burk plot and solver function analysis, the mode of enzyme inhibition was a non-competitive inhibition.

Keywords: antioxidant, deep eutectic solvent, *Euphorbia hirta*, gout treatment, xanthine inhibitor

Abstrak

Pendedahan kepada radikal bebas dan kes-kes gaut telah menjadi kebimbangan pada hari ini di mana ubat sintetik untuk kesan antioksidan dan kesan perencatan xantina oksidase dari ubat klinikal telah menunjukkan beberapa kesan dalam kesihatan yang membawa kepada penemuan perencatan semulajadi dari tumbuhan perubatan. Dalam kajian ini, pelarut hijau yang dikenali sebagai pelarut eutektik dalam telah disintesis untuk menggantikan pelarut konvensional untuk pengekstrakan perencatan radikal bebas dan perencatan xantina oksidase dari tumbuhan perubatan yang telah menunjukkan banyak manfaat kesihatan dan digunakan secara meluas dalam ubat tradisional, *Euphorbia hirta*. Ekstrak daun dari *Euphorbia hirta* menunjukkan perencatan tertinggi (87.95 ± 0.0061%) pada asai radikal bebas. Nilai IC_{50} untuk perencatan radikal bebas daripada ekstrak daun ialah 10.56 ± 0.58 µg/mL. Nilai IC_{50} untuk perencatan xantina oksidase terhadap alopurinol adalah paling rendah pada 6.94 ± 0.32 µg/mL manakala ekstrak daun

Euphorbia hirta menunjukkan nilai dekat pada 9.40 ± 0.13 μg/mL. Nilai korelasi antara kesan antioksidan dan perencatan xantina oksidase bagi ekstrak daun terbukti pada nilai 0.960 yang menunjukkan hubungan yang kuat. Dari plot Line-weaver Burk dan analisis fungsi penyelesai, mod perencatan enzim adalah perencatan yang tidak kompetitif.

Kata kunci: antioksidan, larutan eutektik dalam, *Euphorbia hirta*, rawatan gaut, perencat xantina

Introduction

Our unhealthy lifestyle and constant exposure to harmful sources, such as pollution, smoking, and radiation, have gradually increased the rate of gout occurrence and free radical exposure. Studies have shown that the occurrence of gout has been rising over the past 50 years worldwide [1]. Gout is a type of disease caused by the accumulation of uric acid crystal deposits in the joints as a result of the high level of uric acid. Meanwhile, aging and other diseases are triggered by high exposure of free radicals that severely damages the cells, DNA, and proteins in the body, resulting in the malfunctioning of cells and molecules in their respective roles [2, 3]. In order to treat gout and other diseases that are resulted by free radical exposure, synthetic antioxidants and synthetic xanthine oxidase inhibitor are usually advocated. In the case of gout, allopurinol is commonly prescribed to suppress gout attacks, but there are several side effects to its long-term intake, such as fever, nausea, rashes, renal impairment, and hepatic dysfunction, among others [4]. Xanthine oxidase is an enzyme in a form of xanthine oxidoreductase, which catalyses the oxidation of hypoxanthine and xanthine to uric acid. Its high expression will cause an increased production of uric acid, thus leading to gout [5]. In the case of free radicals, synthetic antioxidants, such as butylated hydroxyanisole (BHA), butylated hydroxytoluene (BHT), propyl gallate (PG), and tert-Butylhydroquinone (TBHQ), are commonly recommended although with little effectiveness [6, 7].

A locally available herb, *Euphorbia hirta* (locally known as *ara tanah* or *pokok susu nabi*) was introduced as a new and potential natural source of gout medication, in which it is deemed a promising substitute for synthetic xanthine oxidase inhibitors as well as for antioxidant effect. This herb has been used traditionally for the treatment of gout and other diseases. However, there has yet to be a scientific report on the application of this plant extract as a xanthine oxidase inhibitor.

Conventional methods of extracting bioactive compounds using organic solvents, such as methanol and ethanol, have been indicative of several adverse health and environmental effects [8]. As such, a green solvent known as the deep eutectic solvent (DES) has been chosen to be used in the study of natural inhibitor, *Euphorbia hirta via* green extraction method. Deep eutectic solvent is produced from the mixing of two or more components, where one acts as a hydrogen bond donor and the other a hydrogen bond acceptor. This solvent has several advantages, such as low in cost and toxicity, is biodegradable, and requires simple preparation [9].

Materials and Methods

Preparation of choline chloride-glucose (ChCl-Glu)-based deep eutectic solvent (DES)

A choline chloride with D-glucose (ChCl-Glu) solvent was prepared with a molar ratio of 2:1. The choline chloride and D-glucose used in the DES were dried in a vacuum oven at 80 °C overnight to eliminate moisture from the powder [8]. Then, the mixture was heated and stirred at 80 °C in a conical flask wrapped with aluminium foil until a homogenous, colourless liquid was formed. Next, the DES solution was stored in a vacuum desiccator containing silica gels to prevent humidity [10,11].

Extraction of *Euphorbia hirta* using ChCl-Glu-based deep eutectic solvent

An amount of 0.5 g of the plant leaves crude extract was weighed and subsequently mixed with 10 mL of DES. The mixture was stirred using a magnetic stirrer for 2 hours at 60 °C, and then centrifuged at the speed of 3000 rpm for 30 minutes. Centrifugation was repeated twice to ensure the layers were evenly separated. Then, the supernatant and pellet were collected [11, 12].

1,1-Diphenyl-2-Picrylhydrazyl (DPPH) radical scavenging assay

Methanol with a concentration of 0.2 mM of DPPH was prepared by adding 2 mL of the solution into 200 µL of extracts and subsequently mixed with 800 µL of methanol. Next, the mixture was left at room temperature for 30 minutes. A corresponding blank sample was prepared using only methanol. Then, a control solution was prepared by mixing 2 mL of methanolic solution of DPPH radical scavenging assay and 800 µL of methanol. In this case, gallic acid was used as reference. The whole process was carried out in a dark environment, and an absorbance was measured at 517 nm after 30 minutes [13, 14].

Inhibitory activity assay of xanthine oxidase (XO)

An amount of one millilitre (100–500 µg/mL) of sample solution from *Euphorbia hirta* pellet extract of leaves was mixed with 2.9 mL of 0.05 M of sodium phosphate buffer (with a pH of 7.5), where the solution was further added with 0.1 mL of XO. The assay had then undergone preincubation at 25 °C for 15 minutes, where 2 mL of 150 mM of xanthine solution was then added into the assay mixture and further incubated for 30 minutes at 25 °C. Using the water bath, the solution was heated to 90 °C for 5 minutes, and the enzymatic reaction halted. The absorbance was measured at 295 nm by using UV-Vis spectrophotometer. Allopurinol was used as reference and positive control by through similar preparation method and concentration. Dimethyl sulfoxide (DMSO) was used to replace the test sample in order to obtain the maximum formation of uric acid. The activity of XO inhibitory was calculated as equation 1:

$$\% \text{ XO Inhibition} = (1-\beta/\alpha) \times 100\% \quad (1)$$

where α is the activity of XO without any sample extract, and β is the activity of XO with a sample extract [11, 15, 16].

Inhibitory concentration of 50% (IC_{50}) of XO analysis

The IC_{50} for the inhibition of XO can be calculated by transforming it to probit analysis using Microsoft Excel and probit table. Equation from the graph obtained via the regression method in probit analysis was used to determine the IC_{50} values for allopurinol and *Euphorbia hirta* [17].

Correlation study of xanthine oxidase inhibition (XOI) and free radical inhibition

A correlation study between the antioxidant and XOI activities was done by plotting a graph of correlation for a range of concentration: 100, 200, 300, 400, and 500 µg/mL of sample extracts to assess the antioxidant and XOI activities. A correlation between the two independent variables was obtained using correlation and regression analysis in Microsoft Excel to relate antioxidant activity with xanthine oxidase inhibitory activity of the leaves pellet of *Euphorbia hirta* extract.

Kinetic study of enzyme

The Lineweaver-Burk plot analysis was adopted to perform a kinetic study of the enzyme. This assay was carried out with the presence or absence of the sample extract from *Euphorbia hirta*, with varying substrate concentrations of xanthine at 10, 20, 40, 60, 80, 100, and 120 µM; while the tested sample was set at 500 µg/mL by using the xanthine oxidase assay methodology [11, 12].

Results and Discussion

Antioxidant test on different parts of *Euphorbia hirta* extracts using deep eutectic solvent (DES)

Figure 1 shows the comparison made between the percentage of inhibition for each sample and the positive control, which was gallic acid, demonstrated that the flower pellet of *Euphorbia hirta* extract recorded the highest percentage inhibition at 88.61%, followed closely by the leaves pellet extract at 87.95%. In view of this result, the leaves pellet had been chosen throughout the conduction of this work, as it had the second nearest percentage inhibition to flower pellet; this is because the flowers of *Euphorbia hirta* are difficult to harvest due to its scarcity. The high antioxidant activity of the plant pellet might be due to the existence of flavonoids, where the phytochemical analysis of the plant had revealed the presence of two types of flavonoids: quercetin and myricitrin. They are deemed to have a reliable role of having strong anti-oxidative activity with either their reducing capabilities or their influence on intracellular redox status [18].

Xanthine oxidase inhibitory assay

Both allopurinol and leaves pellet extracts showed a gradual increase in their percentage inhibition when the concentration of the sample was increased from 100 to 500 µg/mL (Figure 2). The higher the concentration of the extract, the higher the inhibition activity of XO. This could be due to the increasing presence of flavonoids in the extracts. A strong inhibition activity of XO exhibited by allopurinol proved its effective usage on the clinical treatment of gout [15].

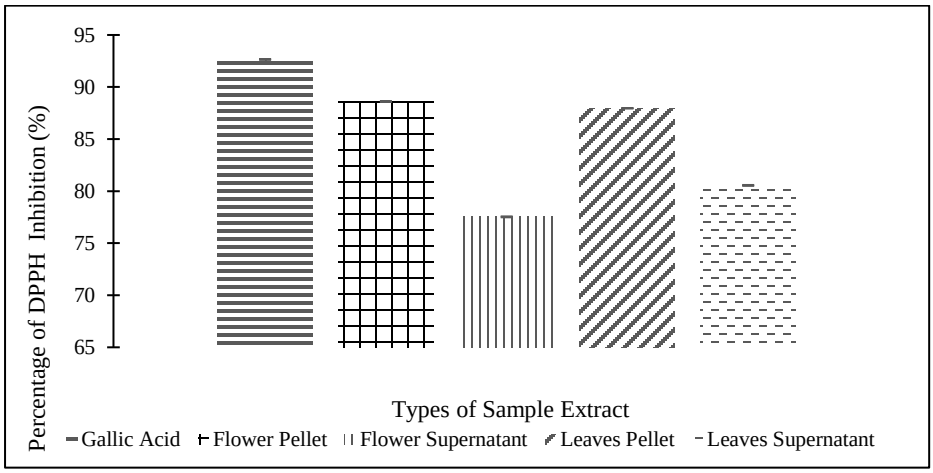


Figure 1. The percentage inhibition of DPPH radical scavenging activity by leaves and flowers crude extract of *Euphorbia hirta*

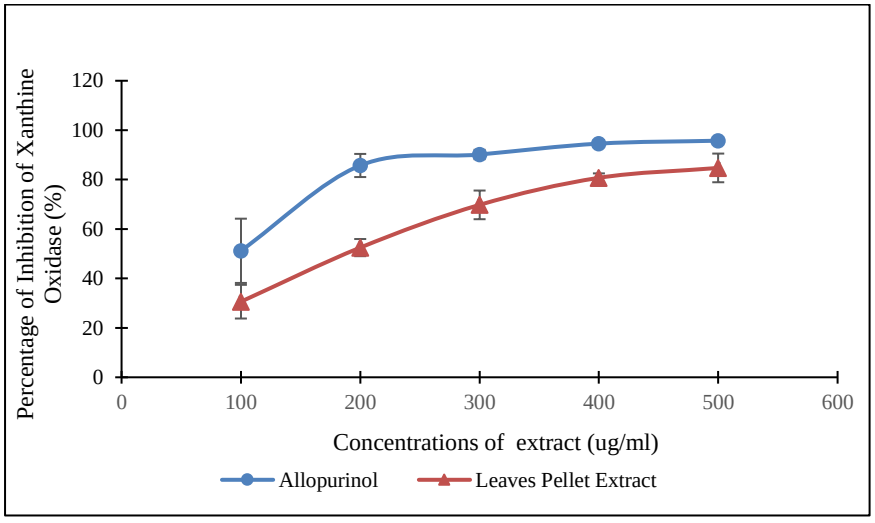


Figure 2. Xanthine oxidase inhibition by *Euphorbia hirta* extract

The IC_{50} of xanthine oxidase inhibition (XOI) and DPPH free radical inhibition

For the IC_{50} of XOI (Figure 3), the concentration of allopurinol needed to inhibit XO at 50% was 6.94 ± 0.32 µg/mL, while that of leaves pellet of *Euphorbia hirta* was 9.40 ± 0.15 µg/mL. This indicated that allopurinol required lesser dose than the leaves pellet extract do to inhibit XO at 50% inhibition response, which was expected because allopurinol has a structure similar to that of purines and pyrimidines. This means that it has to compete with xanthine for the metabolism process, hence, leading to a decrease in uric acid production [19]. The low dose of leaves pellet needed for half-maximal inhibitory on XO also ascertained that the leaves pellet may have contained compounds that were capable of inhibiting XO. The structure of flavonoids and its role as an XO inhibitor was studied, revealing that the hydroxyl groups at C-5 and C-7, as well as the presence of double bond between the C-2 and C-3 structures, had contributed to the high inhibitory activity of XO [5].

For the IC_{50} of DPPH free radical inhibition (Figure 4), the IC_{50} of gallic acid (3.47 ± 0.47 µg/ml) was lower than that of the leaves pellet (10.56 ± 0.58 µg/mL). This confirmed that only a small concentration of gallic acid required in order to inhibit the free radicals at 50%. However, gallic acid, which is known to be a pure synthetic antioxidant, usually displays lower IC_{50} values compared with that of other extracts. The small value of IC_{50} required by the leaves pellet also substantiated its anti-oxidative effect. Previous research has established that *Euphorbia hirta* has an antioxidant effect by demonstrating its dose-dependent reducing power due to the presence of phenolic compounds, such as flavonoids [18, 20].

Correlation study

The coefficient correlation between xanthine oxidase inhibition and DPPH free radical inhibition activities was determined at 0.9212, which indicated a strong correlation due to the value being very close to 1.000 (indicative of positively correlated). This confirmed that when the antioxidant activity increased, the XO inhibitory activity also increased as shown in Figure 5. The presence of flavonoids, such as quercetin and myricetin, is known to have effects on XO, as well as on the additional superoxide scavenging activity, which could have resulted in the antioxidant effect [21].

Kinetic study of enzyme

DMSO was used as the negative control, in which its V_{max} in the assay demonstrated the highest maximum reaction rate at 0.063 abs/min; whereas allopurinol as the positive control in this assay displayed the lowest maximum reaction rate, V_{max}, at 0.020 abs/min (Table 1 and Figure 6). This is followed by the leaves pellet of *Euphorbia hirta* at 0.050 abs/min. The high V_{max} value of DMSO indicated a higher content of uric acid in comparison to that of allopurinol and the leaves pellet of *Euphorbia hirta* extract; while the low V_{max} value of allopurinol indicated a low formation of uric acid and low detection of its content via the UV-Vis spectrophotometer. The low formation of uric acid by allopurinol and leaves pellet of *Euphorbia hirta* extract ascertained that there was an inhibition mechanism by the compounds that prevented XO from forming the uric acid. The K_m values of allopurinol, leaves pellet of *Euphorbia hirta*, and DMSO were 11.618, 11.618, and 11.614 µM, respectively. This shows that there were no changes in the K_m values of the extracts. The screening of kinetic parameters of the extracts exhibited a mixed-inhibition mode by the leaves pellet of *Euphorbia hirta* extract, as the non-competitiveness of inhibition mode will only lower the V_{max} values but with no influence on the K_m values [22].

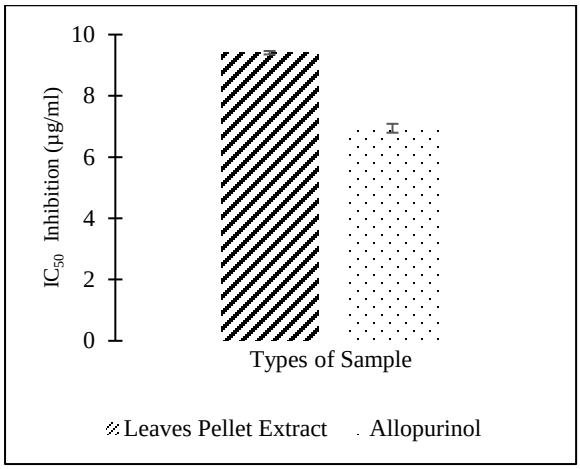


Figure 3. IC_{50} of xanthine oxidase

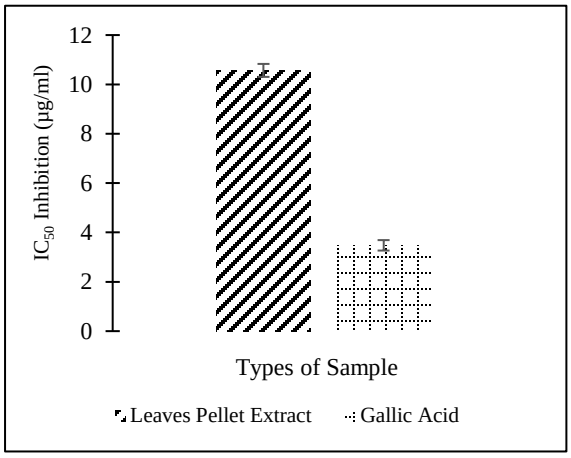


Figure 4. IC_{50} of DPPH

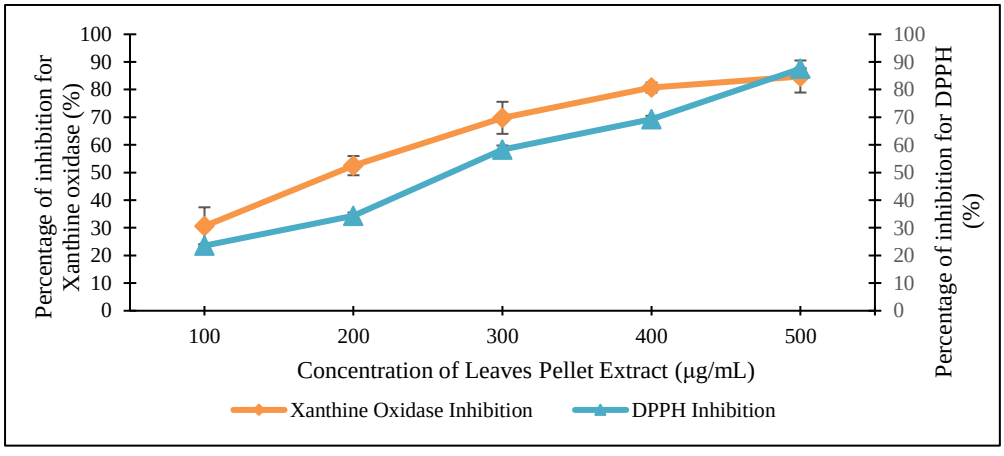


Figure 5. Correlation graph between xanthine oxidase inhibition (XOI) and free radical inhibition of the leaves pellet extract

Table 1. Enzyme Kinetic Parameters

Sample	V_{max} (abs/min)	K_m (µM)
Leaves pellet of *Euphorbia hirta* extract	0.0503	11.6182
Allopurinol (positive control)	0.0207	11.6187
Dimethyl sulfoxide (negative control)	0.0631	11.6140

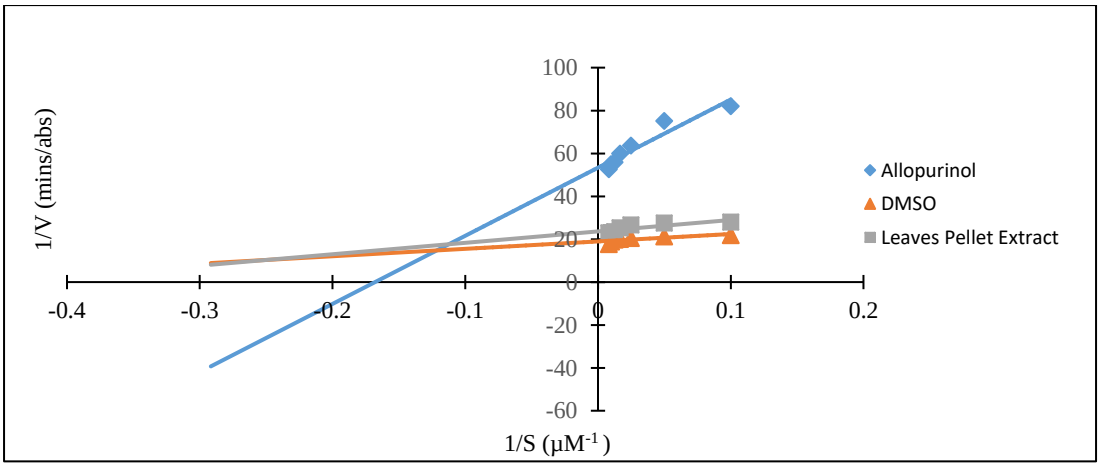


Figure 6. Lineweaver-Burk Plot

Conclusion

This study reveals that the leaves pellet of *Euphorbia hirta* indicated the highest free radical inhibition (87.95 ± 0.006%) and IC_{50} of the leaves pellet. The IC_{50} of the leaves pellet was 10.56 ± 0.58 µg/mL, while that of the gallic acid was 3.4779 ± 0.4736 µg/mL. Meanwhile, the IC_{50} values of the leaves pellet with allopurinol and gallic acid were 9.40 ± 0.13 and 6.94 ± 0.32 µg/mL, respectively. The close values between both assays showed great ability of the extract in inhibiting XO. The correlation value between both effects was 0.921, which is very close to 1.0; thus, this proved the direct relationship of both effects. From the Lineweaver-Burk plot and enzyme kinetic parameters obtained, the leaves pellet of *Euphorbia hirta* also signified a mixed-inhibition mode by comparing allopurinol and the absence of inhibitors. These results have substantiated the potential application of the *Euphorbia hirta* plant as both a xanthine oxidase inhibitor and a free radical inhibitor.

Acknowledgement

The authors would like to express their gratitude to the Faculty of Engineering Technology and Universiti Malaysia Perlis for their support.

References

1. Thiagarajan, K. (2017). Gear up to deal with gout. Access from http://www.livemint.com/Leisure/AORFz4K5pS2sapQ8F5WJrM/Gear-up-to-deal-with-gout.html. [Access online 04 March 2018].
2. Lobo, V., Patil, A., Phatak, A. and Chandra, N. (2010). Free radicals, antioxidants and functional foods: Impact on human health. *Pharmacognosy Reviews*, 4(8): 418.
3. Szalay, J. (2016). What are free radicals?. Access from https://www.livescience.com/54901-free-radicals.html. [Access online 04 March 2018].

4. Ying, P. W., Ruey, C. N., Shu, P. C. and Rhun, Y. K. (2014). Antioxidant and xanthine oxidase inhibitory activities of *Swietenia macrophylla* and *Punica granatum*. *International Conference Biology Environment Food Engineering,* August 4-5.
5. Mehta, S. K. and Akmal, N. N. (2014). Natural xanthine oxidase inhibitors for management of gout: A Review. *Journal of Medical and Health Sciences*, 3(3): 4-11.
6. Shahidi, F. and Zhong, Y. (2005). Antioxidants: Regulatory Status. *Bailey's Industrial Oil and Fat Products:* pp. 1-21.
7. Poljsak, B., Šuput, D. and Milisav, I. (2013). Achieving the balance between ROS and antioxidants: When to Use the Synthetic Antioxidants. *Oxidative Medicine Cell. Longevity*, 2013: 956792.
8. Altemimi, A., Lakhssassi, N., Baharlouei, A., Watson, D. and Lightfoot, D. (2017). Phytochemicals: Extraction, isolation, and identification of bioactive compounds from plant extracts. *Plants*, 6(4): 42.
9. Wan, Y. L. and Mun, Y. J. (2018). Assessment of natural deep eutectic solvent pretreatment on sugar production from lignocellulosic biomass. *MATEC Web of Conferences*, 152: 01014.
10. Gunny, A. A. N., Arbain, D., Nashef, E. M. and Jamal, P. (2015). Applicability evaluation of deep eutectic solvents-cellulase system for lignocellulose hydrolysis. *Bioresource Technology*, 18: 297-302.
11. Jia, L. W. (2017). Synthesis of deep eutectic solvents for xanthine oxidase inhibitors extracted from medicinal plant, *Coleus aromaticus*. Thesis of Bachelor's Degree, Universiti Malaysia Perlis.
12. Huo, L. N., Wang, W., Zhang, C. Y., Shi, H. B., Liu, Y., Liu, X. H. and Gao, H. (2015). Bioassay-guided isolation and identification of xanthine oxidase inhibitory constituents from the leaves of *Perilla frutescens*. *Molecules*, 20(10):17848-17859.
13. Sahu, R. K., Kar, M. and Routray, R. (2013). DPPH free radical scavenging activity of some leafy vegetables used by tribals of Odisha, India. *Journal of Medicine Plants Studies*, 1(4): 21-27.
14. Wee, X. T. (2017). Synthesis of deep eutectic solvent for natural antioxidants extracted from medicinal plant, *Coleus aromaticus*. Thesis of Bachelor's Degree, Universiti Malaysia Perlis.
15. Azmi, S. M. N., Jamal and Amid, P. (2012). Xanthine oxidase inhibitory activity from potential Malaysian medicinal plant as remedies for gout. *International Food Research Journal*, 19(1): 159-165.
16. Nessa, F. and Khan, S. (2014). Evaluation of antioxidant and xanthine oxidase inhibitory activity of different solvent extracts of leaves of *Citrullus colocynthis*. *Pharmacognosy Research*, 6(3): 218.
17. Vincent, K (2018) "Probit Analysis. Access from http://userwww.sfsu.edu/efc/classes/biol710/ probit /Probit Analysis.pdf. [Access online 15 March 2018].
18. Shih, M., Cherng, J., Fen, M. and Yuh, J. (2012). Potential applications of *Euphorbia hirta* in pharmacology. *Drug Discovery Research Pharmacognosy, 2012:* 165-180.
19. Herrington, J. D. (2015). The differences in the mechanisms of action betweem allopurinol and febuxostat. Access from https://www.ebmconsult.com/articles/allopurinol-febuxostat-zyloprim-uloric-uric-acid-gout-mechanism. [Access online 13 March 2018].
20. Kumar, S., Malhotra, R. and Kumar, D. (2010). Euphorbia hirta: Its chemistry, traditional and medicinal uses, and pharmacological activities. *Pharmacognosy Reviews*, 4(7): 58.
21. Hendriani, R., Sukandar, E. Y. and Sukrasno (2014). In vitro evaluation of xanthine oxidase inhibitory activity of sonchus arvensis leaves. *International Journal Pharmacy and Pharmaceutical Sciences*, 6(2): 501-503.
22. Sharma, R. (2012). Enzyme inhibition: Mechanisms and scope, enzyme inhibition and bioapplications. Access from https://www.intechopen.com/books/enzyme-inhibition-and-bioapplications/enzyme-inhibition- mechanisms-and-scope. [Access online 04 March 2018].

Malaysian Journal of Analytical Sciences (MJAS)
Published by Malaysian Analytical Sciences Society

UNCERTAINTY OF IODINE VALUE DETERMINATION IN PALM OLEIN

(Ketidakpastian Penentuan Nilai Iodin dalam Minyak Sawit Olein)

Mohd Azmil Mohd. Noor*, Hajar Musa, Razmah Ghazali

Quality and Environmental Assessment Unit,
Advanced Oleochemical Technologies Division,
Malaysian Palm Oil Board, No. 6, Persiaran Institusi, Bandar Baru Bangi, 43000 Kajang, Selangor, Malaysia

**Corresponding author: mohd.azmil@mpob.gov.my*

Received: 1 January 2020; Accepted: 18 June 2020; Published: 11 August 2020

Abstract

The uncertainty of the iodine value determination in refined, bleached, and deodorised palm olein was investigated and calculated. The major sources of measurement uncertainty were identified as the mass of the sample, the molarity of sodium thiosulfate ($Na_2S_2O_3$) solution, the volume of the titrant, the repeatability, and the recovery of the method. The uncertainty sources were quantified according to the law of propagation of errors, standardised, and then combined. The expanded uncertainty calculated was 56.8 ± 1.2 (2.2%). The measurement uncertainty was compared to the precision data of the method, i.e. the repeatability limit. Good agreement was found, which indicated that the major uncertainty sources had been identified. The study also showed that the major sources of uncertainties were contributed by the repeatability component, which will be the main focus in reducing the uncertainty of the iodine value determination.

Keywords: iodine value, palm oil, measurement uncertainty, precision, repeatability limit

Abstrak

Ketidakpastian dalam penentuan nilai iodin di dalam minyak sawit olein yang ditapis, diluntur, dan dinyah bau telah dikaji dan dikira. Sumber utama bagi ketidakpastian penentuan ini adalah berat sampel, kepekatan larutan natrium tiosulfat ($Na_2S_2O_3$), jumlah titran, kebolehulangan dan perolehan semula. Sumber-sumber ketidakpastian telah dikira mengikut hukum penyebaran ralat, dipiawaikan dan kemudian digabungkan. Ketidakpastian terkembang yang dikira adalah 56.8 ± 1.2 (2.2%). Ketidakpastian pengukuran telah dibandingkan dengan data ketepatan kaedah, iaitu had kebolehulangan. Nilai ketidakpastian dan had kebolehulangan bagi kedua-dua data adalah setara dan ini menunjukkan bahawa sumber-sumber utama ketidakpastian telah dikenalpasti. Kajian ini juga menunjukkan bahawa sumber utama ketidakpastian disumbangkan oleh komponen kebolehulangan, yang akan menjadi fokus utama dalam mengurangkan ketidaktentuan untuk penentuan nilai iodin.

Kata kunci: nilai iodin, minyak sawit, ketidakpastian penentuan, ketepatan, had kebolehulangan

Introduction

Iodine value (IV) is one of the most widely used parameters to determine the quality of vegetable oils 1. IV is often used to assess the unsaturation level of oils, which is contributed by fatty acid chains. This unsaturation is represented by double bonds that react with iodine compounds. Consequently, the amount of double bonds present in the oil is proportionate to the iodine number [1]. It can also serve as an indication of the type of oil and its purity with reference to the chemical characteristics of the oil. Saturated vegetable oils, e.g., coconut oil and palm kernel oil, have low IV, whereas unsaturated oils, e.g., olive oil and soybean oil, have higher IV.

In the palm oil industry, IV is used as one of the trading specifications worldwide. Palm Oil Refiners Association of Malaysia (PORAM) established the quality specifications for refined palm oil products, and these formed the normal specifications for refined oil trade based on the Federation of Oils, Seeds, and Feeds Association (FOSFA) free-on-board (FOB) contract for bulk oils. These normal specifications are generally referred to as the PORAM specifications, which are accepted for international trading of refined palm oil products in bulk. The minimum specification of IV for refined, bleached, and deodorised palm olein (RBDPOo) is 56 [2]. The specifications of palm olein are also given in the Malaysian Standard, where the standard palm olein has an IV of 56.0-59.1 [3].

When reporting the result of an analysis, it is important to give some quantitative indications of its uncertainty. The evaluation of measurement uncertainty enables analytical laboratories to measure the quality and to compare analytical results. The measurement uncertainty is defined by ISO as a parameter associated with the result of a measurement that characterises the dispersion of the result that could reasonably be attributed to the measurand [4]. The ISO Guide to the Expression of Uncertainty in Measurement (GUM) recommends uncertainty to be estimated from its components and by applying the law of propagation of errors to combine uncertainties into the total uncertainty. EURACHEM has subsequently interpreted this ISO guide for analytical chemistry [5].

In this work, the uncertainty components and the combined uncertainty of a standard method for the determination of IV in RBDPOo were evaluated. The objectives are to determine the major sources of uncertainty and to subsequently reduce the overall measurement uncertainty of the result.

Materials and Methods

Chemicals and standards

The samples used in this work were RBDPOo (Sime Darby Jomalina, Malaysia). The reagent for diluting the samples was prepared by mixing cyclohexane and acetic acid at 1:1 ratio. Wijs solution was purchased from Merck (USA) and used without further modification. Potassium iodide (KI) solution was prepared by dissolving 100 g of reagent-grade KI in 1000 mL of deionised water to produce a 10% solution. 0.1 M sodium thiosulfate ($Na_2S_2O_3$) solution was prepared from reagent-grade $Na_2S_2O_3 \cdot 5H_2O$. Starch indicator solution was prepared by initially making a paste with 1 g of natural, soluble starch and a small amount of cold distilled water. Boiling water was then added to make up to 100 mL. A reagent-grade potassium dichromate ($K_2Cr_2O_7$) was dried at 110 °C for 2 hours prior to use.

Procedures

The evaluation of the uncertainty of IV determination was done by describing the method, specifying the measurand, identifying uncertainty sources, quantifying the uncertainty components, and calculating combined and expanded uncertainty.

Description of the method

IV was determined according to the standard method AOCS Cd 1d-92 [6]. A molten sample was filtered and weighed into an iodine flask. A mixture of cyclohexane and acetic acid was added to dilute the sample. After the addition of Wijs solution, the iodine flask was stored in the dark for 1 hour. After the required reaction time, 20 mL of 10% KI solution was added, followed by distilled water. The sample was then titrated with 0.1 M $Na_2S_2O_3$ solution until the yellow colour almost disappeared. The

starch indicator solution was added, and the titration was continued until the blue colour disappeared. A blank determination was conducted where no molten sample was added.

An amount 0.1 M $Na_2S_2O_3$ solution was also standardised according to the method AOCS Cd 1d-92. Dried $K_2Cr_2O_7$ was dissolved in distilled water before 5 mL of concentrated hydrochloric acid (HCl) and 20 mL of 10% KI solution were added. The solution was then titrated with the prepared $Na_2S_2O_3$ solution until the yellow colour almost disappeared. The starch indicator solution was added, and the titration was continued until the blue colour just disappeared.

Specification of the measurand

IV was calculated as:

$$\text{Iodine Value} = \frac{(B-S)\times M\times 12.69}{m} \quad (1)$$

where B is the volume of titrant of blank (ml), S is the volume of titrant of sample (ml), M is the molarity of $Na_2S_2O_3$ solution, and m is the mass of sample (g).

The molarity of $Na_2S_2O_3$ solution was calculated as:

$$\text{Molarity of } Na_2S_2O_3 = \frac{W\times 20.394}{V} \quad (2)$$

where W is the mass (g) of $K_2Cr_2O_7$ and V is the volume of titrant (mL).

Identification of uncertainty sources

One of the common tools for the determination of uncertainty sources is the Ishikawa diagram, which is also known as the fishbone diagram or causes and effects diagrams. Therefore, the Ishikawa diagram was created (Figure 1) in order to identify measurement uncertainty components. The figure presents a simplified review of all registered measurement uncertainty causes and shows other potential uncertainty sources that need to be investigated.

The main sources of uncertainty in the measurements were identified as the mass of sample (m), the molarity of $Na_2S_2O_3$ solution (M), the volume of titrant of blank (B), the volume of titrant of sample (S), the repeatability (rep), and the recovery (rec). Uncertainty due to sampling was not considered because the samples in the laboratory were received from the customer who requested the analyses.

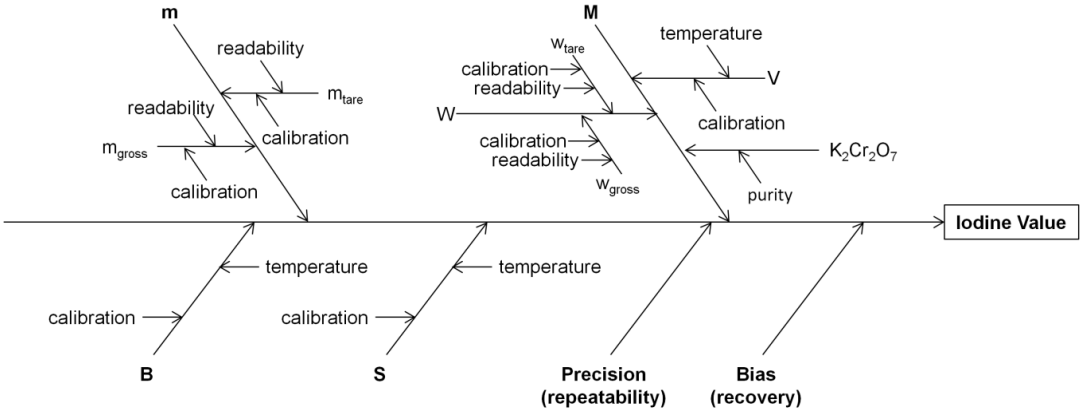


Figure 1. Ishikawa diagram for the determination of iodine value

Quantification of uncertainty components:
Uncertainty associated with weighing operations, u_m
The usual identified uncertainty sources for weighing operations are linearity, readability, sensitivity, and repeatability of a balance [5, 7]. In this work, the linearity and readability (i.e., digital resolution) of the balance used are two potential uncertainty sources. The linearity was obtained from the manufacturer's certificate, where it was reported with a 95% confidence level and converted to a standard deviation by dividing it with a factor of 2. The readability is assumed as a rectangular distribution and its standard uncertainty is obtained by dividing the value given by 2 and √3. The repeatability component is included in the precision estimation whereas the sensibility is neglected because the mass was weighed using the same balance over a very narrow range [5, 8]. The uncertainties should be counted twice because two successive weighing were used, and they are combined as given by Eq. (3).

Uncertainty associated with volumetric operations, u_v
The uncertainty of volumetric operations is associated with the calibration of burette, the use of burette at a temperature different from the one in the calibration, and the repeatability of volumetric deliveries [5, 7]. The limits of accuracy of the burette used (i.e., tolerance) are given by the manufacturer. Since no data on the distribution is reported, a rectangular distribution was assumed as the values are expected to be more likely in the centre than near bounds. The standard uncertainty is obtained by dividing the value given by √3. According to the manufacturer, the burette used has been calibrated at 20 °C, although the temperature in the laboratory varies around 20 ± 4 °C. The uncertainty associated with the temperature can be estimated from the temperature range and the volume expansion coefficient. The volume expansion of water is considerably larger than glass. Therefore, the water volume expansion coefficient is considered as 2.1×10^{-4} °C^{-1}. The repeatability component is included in the precision estimation. In these conditions, the uncertainty associated with the volumetric operations is given by Eq. (4).

Uncertainty associated with reagent purity, u_{pur}
The uncertainty of $K_2Cr_2O_7$ purity was determined from the manufacturer's indications. Since there were no data on distribution, a rectangular distribution was assumed and therefore, u_{pur} is given by Eq. (5).

Uncertainty associated with precision (repeatability)
The method for IV determination is applicable to all normal fats and oils with IV in the range of 18-165 which do not contain conjugated double bonds [6]. The method's precision, in terms of repeatability, may constitute an important source of uncertainty, and hence needs to be studied comprehensively to avoid overestimation or underestimation of the combined uncertainty. The uncertainty associated with the repeatability of IV determination, expressed as a standard deviation, was determined by analysing 23 RBDPOo samples.

Uncertainty associated with bias (recovery)
The method for IV determination is an empirical method where the measurand is defined by the method. The bias of the method is zero by definition when it is used within its defined scope of application [4, 5]. The bias was estimated by the verification of the laboratory implementation of the method according to the parameters influencing the result. The laboratory performance of the method was verified by analysing a certified reference material (CRM) and by performing significance *t*-test. The significance *t*-test indicated that the result of the measurement was not significantly different from the certified value.

$$u_m = \sqrt{2\left({u_{m,linearity}}^2 + {u_{m,readability}}^2\right)} = \sqrt{2\left(\left(\frac{unc}{2}\right)^2 + \left(\frac{R}{2\sqrt{3}}\right)^2\right)} \quad (3)$$

$$u_v = \sqrt{u_{v,calibration}{}^2 + u_{v,temperature}{}^2} = \sqrt{\left(\frac{tolerance}{\sqrt{3}}\right)^2 + \left(\frac{4\times2.1\times10^{-4}\times V}{\sqrt{3}}\right)^2} \quad (4)$$

$$u_{pur} = \frac{100-purity}{2\sqrt{3}} \quad (5)$$

Calculation of combined and expanded uncertainty

The result of a measurement is generally determined from other quantities and the relationship between the result Y and the values of the input parameters can be expressed by Eq. (6).

The uncertainty of the result (u(Y)) depends on the uncertainty of the input parameters and is described by Eq. (7) following the law of propagation of errors.

The sensitivity coefficient describes how the measurement result varies with changes in the value of input estimates. Eq. (7) is valid for measurements where there is no correlation between input parameters.

The relationship between the uncertainty of IV (u(IV)) and the uncertainty of the independent input quantities, which is not correlated, is expressed by Eq. (8).

An expanded uncertainty at 95% confidence level is obtained by multiplying the combined uncertainty with a coverage factor (k) of 1.96. The standard uncertainties, i.e., u(M), u(m), and u(B-S) constituted various uncertainty contributions obtained from uncertainty budgets.

Relative uncertainty variance contributions were used to show the relative impact of different uncertainty components. The relative uncertainty variance contribution (r_i) of an uncertainty component X_i to the combined standard uncertainty, expressed in %, is defined in Eq. (9).

$$Y = f(X_1, X_2, \dots\dots\dots, X_i, \dots\dots\dots, X_N) \quad (6)$$

where X_1,....., X_i,...., X_N represent the model input parameters.

$$u(Y) = \sqrt{\sum_{i=1}^{N}\left(\left(\frac{\partial Y}{\partial X_i}\right)^2 . u(X_i)^2\right)} \quad (7)$$

where $u(X_i)$ are the standard uncertainties of the input parameters and $\delta Y/\delta X_i$ is a sensitivity coefficient.

$$u(IV) = \sqrt{\begin{matrix}\left(\frac{(B-S)\times12.69}{m}\right)^2 . u(M)^2 + \left(-\frac{(B-S)\times M\times12.69}{m^2}\right)^2 . u(m)^2 + \\ \left(\frac{M\times12.69}{m}\right)^2 . u(B-S)^2 + \left(\frac{(B-S)\times M\times12.69}{m}\right)^2 . u(rep)^2 + \\ \left(\frac{(B-S)\times M\times12.69}{m}\right)^2 . u(rec)^2\end{matrix}} \quad (8)$$

$$r_i = \frac{\left(\frac{\partial Y}{\partial X_i}\right)^2 . u(X_i)^2}{u(Y)^2} . 100 \quad (9)$$

where Y is the model equation (($Y=f(X_1, X_2, ..., X_i, ..., X_N)$), X_i are the input parameters of the model, and u(Y) is the combined uncertainty calculated according to Eq. (7).

Results and Discussion

The values of the input quantities, i.e., M, m, B-S, rep, and rec, as well as their respective standard uncertainty are listed in Table 1. Standard uncertainties of the model input quantities were also based on uncertainty budgets and calculated according to Eq. (7). The details for M are presented in Table 2.

The result of IV determination was 56.8 g I_2/100 g sample and the evaluated combined uncertainty was 0.6 g I_2/100 g sample, which corresponded to a relative standard uncertainty of 1.1%. An expanded uncertainty at 95% confidence level was obtained by multiplying the combined uncertainty with a coverage factor (k) of 1.96. As a result, the expanded uncertainty of the result of measurement was 56.8 ± 1.2 g I_2/100 g sample (2.2%). The calculated measurement uncertainty was very close to the repeatability limit of the method, i.e., 0.8 g I_2/100 g sample.

The relative variance contributions (r_i) from single input quantities, i.e., u(M), u(m), u(B-S), u(rep), and u(rec) are presented in Figure 2. The largest contribution came from u(rep), which contributed 86.8% to the combined standard uncertainty variance. The volumes of $Na_2S_2O_3$ for the titration of the blank and the sample (B-S) contributed 10.8%. Uncertainty contributions from other input quantities, such as the mass of the sample (m), the molarity of $Na_2S_2O_3$ (M), and recovery are of minor importance.

The development of the measurement uncertainty budget can be a useful tool to reduce uncertainties. In this study, the uncertainty associated with the repeatability component accounted for more than 80% of the uncertainty of IV determination. Several reports have shown that the most effective way to reduce uncertainty contributed by repeatability component is by expanding the number of replicates [10, 11].

The calculation of combined measurement uncertainty reported here considered all uncertainty sources to assess the contribution of each of the uncertainty components and their influence on the final result. Studies on metrological evaluation of IV determination which had been previously reported elsewhere, have not identified the biggest contributor to the measurement uncertainty [12, 13]. Finally, the knowledge of the measurement procedure is as important as the result of the measurement uncertainty calculation.

Table 1. Uncertainty components (u_{xi}) of IV, their standard uncertainty, sensitivity coefficient, and relative variance contribution

Component (X_i)	**Symbol**	**Value (X_i)**	**Standard Uncertainty (u_{xi})**	**Sensitivity Coefficient ($\delta Y/\delta X_i$)**	**Relative Variance Contribution (r_i, %)**
Molarity of $Na_2S_2O_3$ (mol L^{-1})	M	0.1	8.5×10^{-5}	568	0.6
Mass of sample (g)	m	0.2079	7.1×10^{-5}	273	0.1
Volume of titrant (ml)	B-S	9.3	0.0331	6.11	10.8
Precision (repeatability)	rep	1	0.0101	56.80	86.8
Bias (recovery)	rec	0.9995	0.00142	56.83	1.7

IV = 56.8, u(IV) = 0.6

Table 2. Uncertainty components (u_{xi}) of M, their standard uncertainty, sensitivity coefficient, and relative variance contribution

Component (X_i)	**Symbol**	**Value (X_i)**	**Standard Uncertainty (u_{xi})**	**Sensitivity Coefficient ($\delta Y/\delta X_i$)**	**Relative Variance Contribution (r_i, %)**
Purity of $K_2Cr_2O_7$	pur	0.999	2.9×10^{-4}	0.1	11.5
Mass of $K_2Cr_2O_7$ (g)	W	0.1794	8.2×10^{-5}	0.56	28.4
Volume of titrant (ml)	V	36.6	0.024	0.0027	60.1

M = 0.1 mol L^{-1}, u(M) = 0.000085 mol L^{-1}

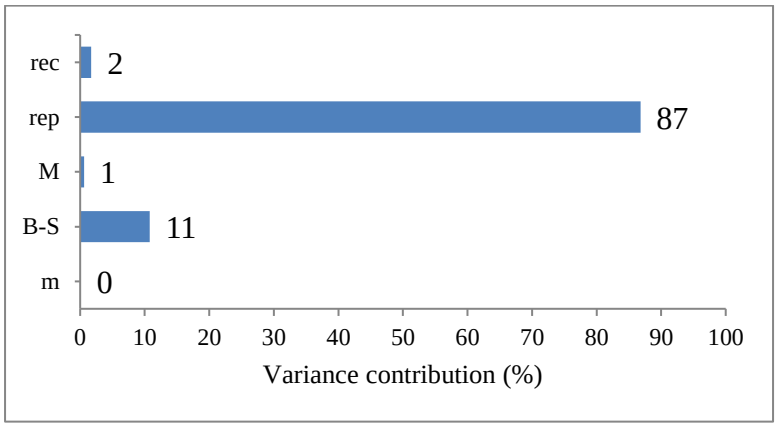


Figure 2. Relative variance contributions from single input quantities to the uncertainty of IV determination

Conclusion

The measurement uncertainty of IV determination of RBDPOo was investigated. The employment of the Ishikawa diagram has allowed the identification of the major uncertainty components and offered a tool for improving the method performance. The uncertainty components were organised in tables, which subsequently facilitated the quantification and estimation processes. Systematic uncertainty budgets have allowed an easy uncertainty evaluation process and enabled a straightforward comparison of the contributions of uncertainty components to the total uncertainty budget. The results revealed that repeatability is the prevailing source of uncertainty. The estimation of measurement uncertainty will be done with a larger number of samples and other palm oil products, e.g. crude palm oil and palm stearin. The IV determination can also be carried out using secondary NIR spectroscopy method and metrological evaluation of the method can be investigated further.

Acknowledgements

The authors would like to thank the Director-General of MPOB and the Director of AOTD for the permission to publish this article. The authors would like to acknowledge all personnel of the ATS Laboratory (Abdul Halim Abdul Jalal, Bahriah Bilal, Makmor Abd Wahab, Rosilah Muin, Nur Hazariah Mohamed, Mariana Kasmuin, Sharipah Samsiah Rahman, Mohd. Ridzuan Zakaria and Zamiah Hasman) for their technical contribution in producing this article.

References

1. Thomas, A., Matthäus, B. and Fiebig, H.-J. (2015). Fats and fatty oils. In Ullmann's encyclopaedia of industrial chemistry. Wiley-VCH, Weinheim: pp. 66-68.
2. The Palm Oil Refiners Association of Malaysia (2012). PORAM handbook 7th edition. PORAM, Selangor: pp. 7-8.
3. Department of Standards Malaysia. (2007). MS 816:2007 Palm olein - Specification (Second revision). Department of Standards Malaysia, Selangor: pp. 2-3.
4. International Organization for Standardization (1995). GUM: Guide to the expression of uncertainty in measurement. ISO, Geneva: pp. 15-17.
5. Ellison, S. L. R. and Williams, A. (2012). Quantifying uncertainty in analytical measurement. EURA-CHEM/CITAC, Teddington: pp. 3-4.
6. American Oil Chemists' Society. (2017). AOCS Official method Cd 1d-92 (Reapproved 2017). Iodine value of fats and oils cyclohexane-acetic acid method. AOCS, Illinois: pp. 1-2.
7. Drolc, A., Cotman, M. and Ross, M. (2003). Uncertainty of chemical oxygen demand determination in wastewater samples. *Journal of Accreditation and Quality Assurance*, 8: 138-145.
8. Sousa, A. R. and Trancoso, M. A. (2005). Uncertainty of measurement for the determination of fluoride in water and wastewater by direct selective electrode potentiometry. *Journal of Accreditation and Quality Assurance*, 10: 430-438.
9. Miller, J. N. and Miller, J. C. (2000). Statistics and chemometrics for analytical chemistry, 4th edition. Prentice Hall, Harlow: pp. 12-14.
10. Tomic, T., Nasipak, N. U. and Babic, S. (2012). Estimating measurement uncertainty in high-performance liquid chromatography methods. *Journal of Accreditation and Quality Assurance*, 17: 291-300.
11. Choi, J. O., Hwang, E., So, H. and Kim, B. (2003). An uncertainty evaluation for multiple measurements by GUM. *Journal of Accreditation and Quality Assurance*, 8: 13-15.
12. Leal, R. V. P., Borges, P. P. and Seidl P. R. (2008). Metrological evaluation of titration techniques for the determination of the iodine value in biodiesel. *International Conference on Metrology of Environmental, Food and Nutritional Measurements*, 10-12 September 2008.
13. Meena, A. K., Rao, M. M., Panda, P., Padhi, M. M. and Babu, R. (2010). Evaluation and expression of uncertainty in the measurement of iodine value in mustard oil. *International Journal of Chemical and Analytical Science*, 1(7): 136-140.

Malaysian Journal of Analytical Sciences (MJAS)
Published by Malaysian Analytical Sciences Society

EFFECT OF PROCESS PARAMETERS ON GELLING TIME OF SOL-GEL SILICA AND KENAF-SOL-GEL SILICA SYSTEMS

(Kesan Parameter Proses pada Masa Penggelan dalam Sistem Sol-Gel Silika dan Kenaf-Silika Sol-Gel)

Fahmi Asyadi Md Yusof[1]*, Zulhafiz Tajudin[2], Ong Siew Kooi[1], Azanam Shah Hashim[1]

[1]Polymer Department
[2]Process Department
Malaysian Institute of Chemical & Bioengineering Technology,
Universiti Kuala Lumpur, 78000 Alor Gajah, Melaka, Malaysia

**Corresponding author: fahmiasyadi@unikl.edu.my*

Received: 20 November 2019; Accepted: 6 July 2020; Published: 11 August 2020

Abstract

The gelation process of sol-gel silica and kenaf-sol-gel silica were rheologically investigated. The correlation between gelling time and process parameters (i.e., the catalyst ratios: 0.03, 0.05, 0.07, water ratios: 2, 4, 6 and temperatures: 30, 40, 50 ^{o}C) were elucidated. The gelling time was determined from crossing over of storage moduli (G′) and loss moduli (G″). The effect of the process parameters on gelling time was analysed by using response surface methodology (RSM) based on a three-factorial design. Response surface methodology (RSM) based on 3-level factorial design. Analysis of variance (ANOVA) depicted that all examined parameters had a profound effect on the gelling time for both sol-gel silica and kenaf-sol-gel silica systems. In the sol-gel silica system, RSM predicted that the interaction between catalyst ratio and water ratio influenced the gelling time response. Interestingly, in the kenaf-sol-gel silica system, the interaction between catalyst ratio and temperature contributed to the gelling time response. In particular, gelling time for the kenaf-sol-gel silica system was faster as compared to the sol-gel silica system.

Keywords: kenaf, sol-gel silica, gelling time, response surface methodology

Abstrak

Proses gelasi silika sol-gel dan kenaf-silika sol-gel disiasat secara rheologi. Korelasi antara masa gelasi dan parameter proses (iaitu nisbah pemangkin: 0.03, 0.05, 0.07, nisbah air: 2, 4, 6 dan suhu: 30, 40, 50 ^{o}C) telah dijelaskan. Masa gelasi ditentukan daripada penyilangan moduli penyimpanan (G') dan moduli kehilangan (G"). Kesan parameter proses pada masa gelasi dianalisis menggunakan kaedah gerakbalas permukaan (RSM) berdasarkan rekabentuk tiga faktor. Analisis varians (ANOVA) menggambarkan bahawa semua parameter yang diperiksa mempunyai kesan yang mendalam terhadap masa gelasi untuk kedua-dua sistem silika sol-gel dan kenaf-silika sol-gel. Dalam sistem sol-gel silika, RSM meramalkan bahawa interaksi antara nisbah pemangkin dan nisbah air mempengaruhi tindak balas masa gelasi. Menariknya, dalam sistem kenaf-silika sol-gel, interaksi antara nisbah pemangkin dan suhu menyumbang kepada tindak balas masa gelasi. Khususnya, masa gelasi untuk sistem kenaf-silika sol-gel lebih cepat berbanding siste. silika sol-gel.

Kata kunci: kenaf, silika sol-gel, masa penggelan, kaedah gerakbalas permukaan

Introduction

Major efforts were made on kenaf fibers instead of synthetic fibers. The main advantages of kenaf fiber are abundance, biodegradable, cost-effective, and low density as compared to synthetic fibers. Despite its benefits, kenaf fibers suffer from several major drawbacks, such as low strength, low moisture resistance, low durability, and low compatibility with polymer matrix [1-3]. To address these issues, organic-inorganic hybrid technology was widely studied as it can design the product with specific surface properties and multiple functionalities in a single material. Sol-gel silica method is one of the most promising techniques for producing organic-inorganic mixtures. It is a low-temperature solution process to produce inorganic materials and thus the decomposition of organic components can be minimised.

$$\mathrm{Si-OR + H_2O \xrightarrow{k_h} Si-OH + ROH} \quad (1)$$

$$\mathrm{Si-OH + ROH \xrightarrow{k_{h'}} Si-OR + H_2O} \quad (2)$$

$$\mathrm{Si-OH + HO-Si \xrightarrow{k_{cw}} Si-O-Si + H_2O} \quad (3)$$

$$\mathrm{Si-OH + RO-Si \xrightarrow{k_{ca}} Si-O-Si + ROH} \quad (4)$$

The sol-gel silica synthesis involves two major reactions (equations 1-4) namely hydrolysis of alkoxysilane groups to form silanol and condensation between silanol groups of products and/or between these groups to form siloxane networks. The most commonly used precursor for sol-gel silica synthesis is tetraethyl orthosilicate (TEOS), with a solvent for homogenisation of water-alkoxysilane mixture. Typically, a basic or acidic catalyst is added to increase the rate of hydrolysis reaction [4-6]. In this case, hybridisation is achieved whereby the kenaf fibers were added during the *in-situ* synthesis of sol-gel silica.

The investigation of sol-gel silica processes has great significance, in particular, the gel point, to illustrate the development of the system structure responsible for the potential use of the material. In relation to the gel point, gelling time is a critical parameter in assessing their suitability because gelation cannot be too fast, to encourage its use (penetration into voids or surface coatings) on kenaf fibers or too slow, to avoid evaporation of volatile molecules [7]. One of the best ways to test gelling time is to perform dynamic viscoelastic experiments. The small-amplitude friction motion technique can measure the viscoelastic reaction of the gel as a function of shear rate.

This study provides an important opportunity to advance the understanding of kenaf-sol-gel silica nanocomposites vis-a-vis organic-inorganic hybrids. The influence of sol-gel process parameters (i.e. catalyst ratio, water ratio, and temperature) in two systems, namely sol-gel silica and kenaf-sol-gel silica system was successfully determined. The RSM based on three-factorial design was used to derive gelling time behaviour for both systems. The effects and relations of the synthesised parameters during the gelation time of both systems were investigated.

Materials and Methods

Materials

Kenaf (KF, 300-400µm, 500g) was obtained from the National Kenaf and Tobacco Board (LKTN, Malaysia). Tetraethyl orthosilicate (TEOS, 98%) was purchased from Acros Organics. Ethanol (99.5%) was supplied by Fisher Scientific and n-butylamine (99.5%) was obtained from Merck. All reagents were used as received.

Synthesis of kenaf-sol-gel silica

Kenaf fibers (2 g) were added to 1M TEOS (22.83 mL) and ethanol (80 mL) in a water bath at different temperatures (30, 40, 50 ^{o}C). The amount of catalyst (n-butylamine) and water was added based on the molar ratio with TEOS. All reactions were performed in a 250 mL reactor with a mixing speed of 300 rpm. After 2 minutes, the sample was measured with a rheometer to analyse the gelling time.

Design of experiment

Gelling time was determined as the optimisation response (results) performed by using the three-factorial design in the RSM method (Design-Expert® ver.10, Stat-Ease, Inc.). Gelling time was calculated from crossing over the storage module (G ') and loss module (G ") by using a rheometer (MC 302, Anton Paar). The

independent variables were the catalyst ratio (0.03, 0.05, and 0.07), temperature (30, 40, 50 ºC) and water ratios (2, 4, and 6). The range values set for the independent variables (Table 1) were created as low (-1), middle (0), and high (+1). The three-factorial design generated 32 different conditions of sol-gel silica and kenaf-sol-gel silica systems as shown in Table 2. Analysis of variance (ANOVA) was used to calculate the statistical relation of independent variables.

Table 1. Levels of the variables by using three-factorial design

Variables	Code	Unit	Level		
			-1	0	1
Catalyst Ratio	A		0.03	0.05	0.07
Temperature	B	ºC	30	40	50
Water Ratio	C		2	4	6

Results and Discussion

RSM modelling of gelling time with respect to silica sol-gel processing parameters

The results of each experimental run are tabulated in Table 2. The gelling time for the sol-gel silica system is in the range of between 185 and 2089 s. The determination of the appropriate polynomial equation to represent the relationship between the input parameters and output response (gelling time) was performed by carrying out sequential model sum of squares (SMSS) and Lack of Fit tests. Both analyses suggested that the relation between input parameters and resultant gelling time can be modelled by using a 2FI equation. The equation in terms of coded factors used to predict the response for given levels of each factor is indicated below:

$$\text{Gelling Time} = 988.75 - 525.5A + 290.22B - 140.28C - 111.75AB + 33.99AC + 94.67BC \quad (5)$$

Table 2. Design of experiments and results by using three-level factorial for sol-gel silica system

Run	Catalyst Ratio	Water Ratio	Temperature (°C)	Gelling Time (s)
1	0.05	2	30	958
2	0.07	4	30	468
3	0.03	4	50	1198
4	0.07	2	50	185
5	0.05	6	30	1403
6	0.07	6	50	619
7	0.05	4	30	978
8	0.03	6	50	2089
9	0.03	4	40	1459
10	0.07	4	50	349
11	0.05	4	40	959
12	0.03	2	50	680
13	0.03	6	30	1930
14	0.07	2	40	319

Table 2 (cont'd). Design of experiments and results by using three-level factorial for sol-gel silica system

Run	Catalyst Ratio	Water Ratio	Temperature (°C)	Gelling Time (s)
15	0.05	6	50	1239
16	0.05	2	40	902
17	0.05	6	40	1438
18	0.07	4	40	496
19	0.07	6	40	542
20	0.07	2	30	450
21	0.05	4	40	962
22	0.05	2	50	539
23	0.05	4	40	990
24	0.05	4	50	750
25	0.05	4	40	501
26	0.03	2	40	1409
27	0.05	4	40	961
28	0.05	4	40	957
29	0.03	4	30	1680
30	0.07	6	30	894
31	0.03	2	30	1412
32	0.03	6	40	1924

The ANOVA analysis for the 2FI model of the sol-gel silica system is shown in Table 3. The model F-value of 45.44 implied that the model was significant. There is only a 0.01% chance that an F-value this large could occur due to noise. Values of "Prob > F" of less than 0.001 indicated that the model terms were significant. In this study, factors such as catalyst ratio, water ratio, temperature, and interaction between catalyst ratio and water ratio were considered as significant model terms. The "Lack of Fit F-value" of 0.65 implied the Lack of Fit was not significant relative to the pure error. There was a 77.59% chance that a "Lack of Fit F-value" this large could occur due to noise.

The behaviour of the gelling time in response to variations in catalyst ratio, water ratio, and temperature in the sol-gel silica system is shown in Figure 1. The main effects plot indicated that the catalyst ratio was the most influential factor, followed by water ratio and temperature. It was expected that by increasing the catalyst concentration the gelling time will increase. As the concentration of catalyst (n-butylamine) increased, the rate of hydrolysis and condensation increased in all studied scales. This occurred when the intermediates reached the supersaturation region. The intermediate speed also increased, most likely to shorten the nucleation time. Therefore, the total number of nuclei formed will be less, and the gelation time will be faster [8, 9].

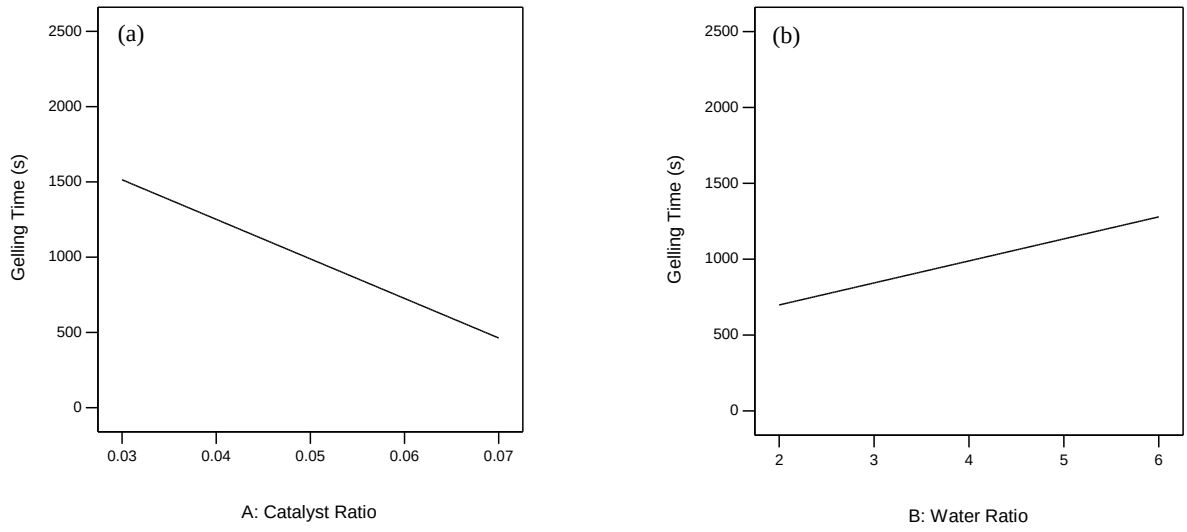
Further analysis of the main effects revealed that the gelling time was highest when the water ratio was kept at high level. The increase in gelling time with the increased water ratio was because as more water was added, the amount of solvent was constant, and the silicate concentration was reduced [10]. This dilution effect will change the rate of hydrolysis and condensation which eventually led to higher gelling time. It is interesting to note that temperature had the least influence on the gelling time whereby it can be kept

within 30-50ºC. As this factor did not appear to be the most important, it can be safely kept at a low-level setting (30 ºC).

The interaction effect of catalyst ratio and water ratio on gelling time is shown in Figure 2. The non-parallel lines indicated that there was a strong interaction between the process variables catalyst ratio and water ratio. As it can be observed from the plot, the effect of catalyst ratio on gelling time was different at low and high water ratios levels. The minimum variability of gelling time was observed at the low water ratio level. On the other hand, the gelling time was higher at the low catalyst ratio (0.03) level and the high water ratio (6) level.

Table 3. Analysis of variance for sol-gel silica system

Source	**Sum of Squares**	**df**	**Mean Square**	**F Value**	***p*-value Prob > F**	
Model	7.11E+06	6	1.19E+06	45.44	< 0.0001	significant
A-Catalyst Ratio	4.97E+06	1	4.97E+06	190.57	< 0.0001	significant
B-Water Ratio	1.52E+06	1	1.52E+06	58.12	< 0.0001	significant
C-Temperature	3.54E+05	1	3.54E+05	13.58	0.0011	significant
AB	1.50E+05	1	1.50E+05	5.75	0.0243	significant
AC	13068	1	13068	0.50	0.4856	not significant
BC	1.08E+05	1	1.08E+05	4.12	0.0531	not significant
Residual	6.52E+05	25	26083.81			
Lack of Fit	4.71E+05	20	23565.79	0.65	0.7759	not significant
Pure Error	1.81E+05	5	36155.87			
Cor Total	7.76E+06	31				



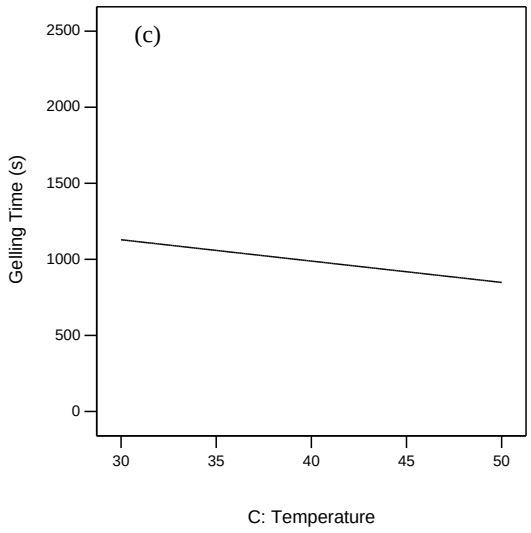


Figure 1. Behaviour of gelling time in response to variation of (a) catalyst ratio, (b) water ratio, and (c) temperature in sol-gel silica system

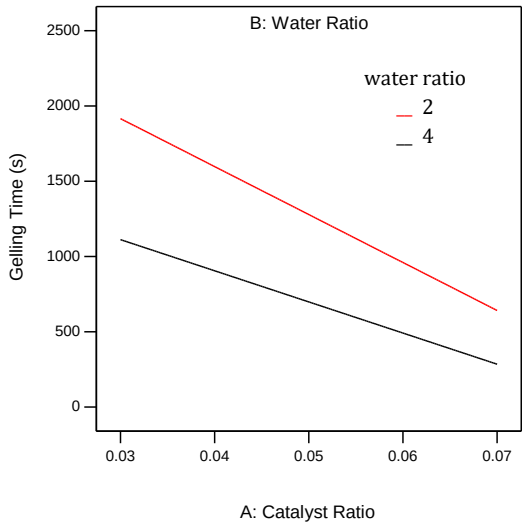


Figure 2. Behaviour of gelling time in response to interaction between catalyst ratio and water ratio in sol-gel silica system

RSM modelling of gelling time with respect to kenaf-sol-gel silica processing parameters

The results of each experimental run are tabulated in Table 4. The gelling time for the kenaf-sol-gel silica system is in the range of 157 and 1173s. Similar to the sol-gel silica system, the determination of appropriate polynomial equation to represent the relation between the input parameters and the output response (gelling time) was performed by carrying out the sequential model sum of squares (SMSS) and the Lack of Fit tests. The relation between input parameters and resultant gelling time was modelled by using a 2FI equation. The equation in terms of coded factors used to make predictions about the response for the given levels of each factor is indicated below:

$$\text{Gelling Time} = 462.16 - 209.94A\ 126.94B\ -73.11C\ -39.00AB\ +48.83AC\ -51.42BC \quad (6)$$

Table 4. Design of experiments and results by using three-level factorial for kenaf-sol-gel silica

Run	Catalyst Ratio	Water Ratio	Temperature (°C)	Gelling Time (s)
1	0.05	4	40	431
2	0.05	4	40	433
3	0.05	6	30	679
4	0.05	4	40	502
5	0.05	4	30	439
6	0.05	4	40	438
7	0.07	6	30	404
8	0.05	2	40	289
9	0.07	2	40	198
10	0.03	6	30	1173
11	0.05	2	30	350
12	0.03	6	40	700
13	0.07	6	40	352
14	0.03	2	40	509
15	0.07	4	40	239
16	0.07	2	30	219
17	0.07	4	50	223
18	0.03	4	50	600
19	0.03	4	40	609
20	0.03	2	50	509
21	0.03	4	30	819
22	0.05	4	50	369
23	0.05	2	50	274
24	0.05	6	40	588
25	0.07	6	50	275
26	0.05	6	50	549
27	0.03	2	30	558
28	0.05	4	40	429
29	0.03	6	50	628
30	0.07	2	50	157
31	0.07	4	30	259
32	0.05	4	40	588

The ANOVA analysis for the 2FI model of the kenaf-sol-gel silica system is shown in Table 5. The model F-value of 46.84 implied that the model was significant. There was only a 0.01% chance that an F-value this large could occur due to noise. Values of "Prob>F" of less than 0.001 indicated that model terms were significant. In this study, parameters A, B, C, AC, and BC were considered as significant model terms. The "Lack of Fit

F-value" of 1.11 implied that the Lack of Fit was not significant relative to the pure error. There was a 49.92% chance that a "Lack of Fit F-value" this large could occur due to noise. In this study, catalyst ratio, water ratio, temperature, the interaction between catalyst ratio-temperature and interaction between water ratio-temperature were as considered significant model terms.

It can be seen from Figure 3 that the catalyst ratio has a significant impact on gelling time, while the water ratio has a lower impact on whatever gelling time. It is interesting to note that temperature had the lowest sensitivity to variability in gelling time as compared to other variables. The behaviour of the main effects on gelling time in the kenaf-sol-gel silica system was similar to the sol-gel silica system. However, there was a clear trend of decreasing gelling time in the kenaf-sol-gel silica system as compared to the sol-gel silica system for all variables, whereby reduction was almost half. This result may be explained by the fact that the addition of kenaf fibers had changed the hydrolysis rate of sol-gel silica process. It was postulated that the hydrolysis reaction followed a second-order mechanism and could be described as a bimolecular nucleophilic substitution (S_n2-type), forming the silanol groups. The hydrolysis proceeds by nucleophilic attack of a hydroxide ion (^-OH) at the silicon atom, with an alkoxy group (RO^-) as the leaving group [11]. Therefore, the gelling time for sol-gel silica hydrolysis was faster with additional hydroxyl groups derived from the kenaf fibers. It is noteworthy that changes in gelling times affected the size and distribution of silica formed at the end of the reaction.

The non-parallel lines in the graph of Figure 4 (a) indicated that there was an interaction effect, in which the significant p-value (Table 5) for the catalyst ratio and temperature term confirmed. Figure 4 (a) shows that the highest gelling time for the catalyst ratio was 0.03 and temperature was 50 ^oC. In contrast, the gelling time was low when the parameter settings for the catalyst and temperature ratios were 0.07 and 30 ^oC, respectively. Figure 4(b) shows the interaction between water ratio and temperature in the kenaf-sol-gel silica system. The interaction lines showed that the ratio of water at different temperatures was non-paralleled. This indicated that there was a strong interaction between these two factors. The graph also shows that the highest gelling time was achieved when the water ratio was kept at 6 and the temperature at 50 ^oC.

Table 5. Analysis of variance table for kenaf-sol-gel silica

Source	Sum of Squares	df	Mean Square	F Value	*p*-value Prob > F	
Model	1.26E+06	6	209709.13	46.84	2.1E-12	significant
A-Catalyst Ratio	7.93E+05	1	793380.06	177.20	7.5E-13	significant
B-Water Ratio	2.90E+05	1	290068.06	64.79	2.1E-08	significant
C-Temperature	9.62E+04	1	96214.222	21.50	9.6E-05	significant
AB	1.83E+04	1	18252	4.08	0.05433	not significant
AC	2.86E+04	1	28616.333	6.40	0.01816	significant
BC	3.17E+04	1	31724.083	7.09	0.01339	significant
Residual	1.12E+05	25	4477.4188			
Lack of Fit	9.14E+04	20	4569.6318	1.11	0.49924	not significant
Pure Error	2.05E+04	5	4108.5667			
Cor Total	1.37E+06	31				

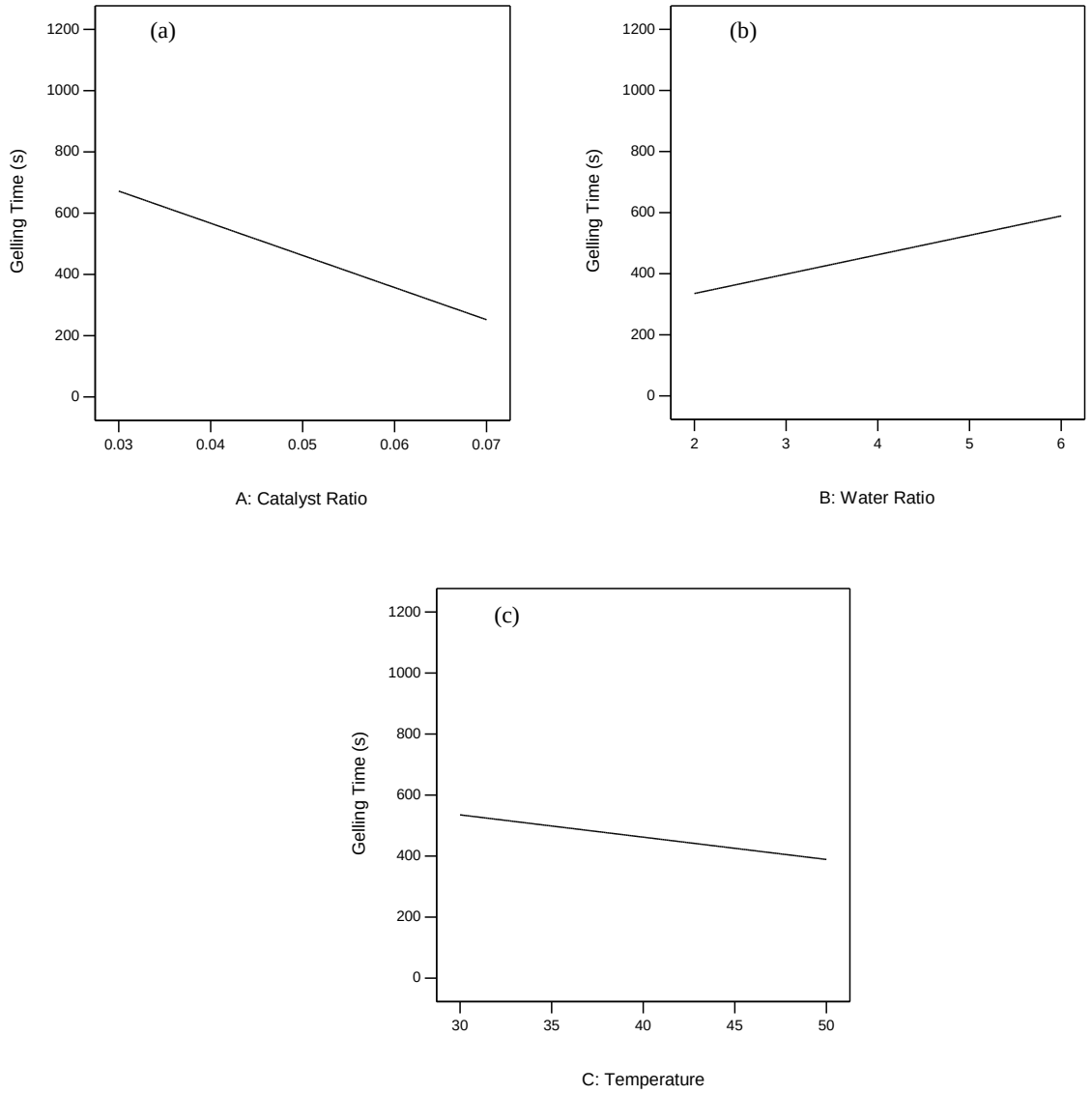


Figure 3. Behaviour of gelling time in response to variation of (a) catalyst ratio, (b) water ratio, and (c) temperature in kenaf-sol-gel silica system

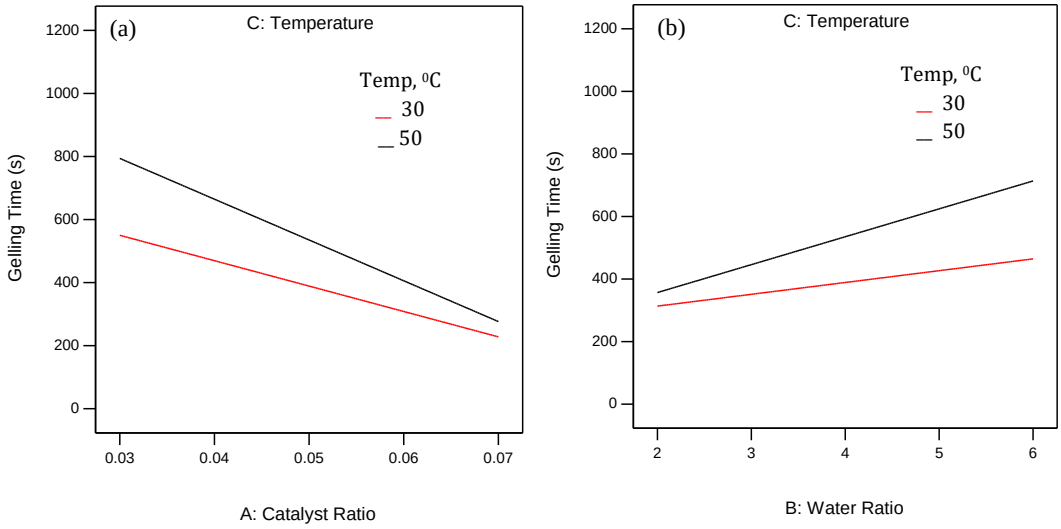


Figure 4. Behaviour of gelling time in response to the interaction between (a) catalyst ratio and temperature and (b)water ratio and temperature in kenaf-sol-gel silica system

Conclusion

The gelling time of sol-gel silica and kenaf-sol-gel silica systems was successfully measured as a function of catalyst ratio, water ratio and temperature, and their interaction by using RSM-based on three-factorial design. Among these factors, the catalyst ratio was the most significant factor which influenced the gelling time as compared to the water ratio and temperature in both sol-gel silica and kenaf-sol-gel silica systems. The findings from the ANOVA also revealed that by increasing the catalyst ratio and temperature and lowering the water ratio, individually, the gelling time decreased in both systems. In the sol-gel silica system, there was a strong interaction between the catalyst ratio and water ratio. Interestingly, in the kenaf-sol-gel silica system, the interactions which influenced the gelling time were between catalyst ratio and temperature as well as the water ratio and temperature. It is concluded that RSM can be a successful technique to identify the significant factors and their interactions that influence the gelling time of sol-gel silica and kenaf-sol-gel silica systems. This method can provide a framework for further research on other cellulosic fibers.

Acknowledgement

The authors gratefully acknowledge the financial support for this work through the *Skim Geran Penyelidikan & Inovasi Mara* (SGPIM) for the project number 1/33/19/18(1).

References

1. Guerrero-Martínez, A., Pérez-Juste, J. and Liz-Marzán, L. M. (2010). Recent progress on silica coating of nanoparticles and related nanomaterials. *Advanced Materials,* 22(11): 1182-1195.
2. Wang, J., Shah, Z. H., Zhang, S. and Lu, R. (2014). Silica-based nanocomposites via reverse microemulsions: Classifications, preparations, and applications. *Nanoscale,* 6(9): 4418-4437.
3. Kim, T. G., An, G. S., Han, J. S., Hur, J. U., Park, B. G. and Choi, S. C. (2017). Synthesis of size controlled spherical silica nanoparticles via sol-gel process within hydrophilic solvent. *Journal of the Korean Ceramic Society,* 54(1): 49-54.
4. Bogush, G. H., Tracy, M. A. and Zukoski IV, C. F. (1988). Preparation of monodisperse silica particles: Control of size and mass fraction. *Journal of Non-Crystalline Solids,* 104(1): 95-106.
5. Rao, K. S., El-Hami, K., Kodaki, T., Matsushige, K. and Makino, K. (2005). A novel method for synthesis of silica nanoparticles. *Journal of Colloid and Interface Science,* 289(1): 125-131.

6. Rahman, I. A. and Padavettan, V. (2012). Synthesis of silica nanoparticles by sol-gel: Size-dependent properties, surface modification, and applications in silica-polymer nanocomposites. A review. *Journal of Nanomaterials,* 2012: 1155-1170.
7. Mika, J., Györvary, E. and Rosenholm, J. B. (1998). Viscoelastic characterization of three different sol-gel derived silica gels. *Colloids and Surfaces*, 141: 205-216.
8. Greasley, S. L., Page, S. J., Sirovica, S., Chen, S., Martin, R. A., Riveiro, A. and Jones, J. R. (2016). Controlling particle size in the Stöber process and incorporation of calcium. *Journal of Colloid and Interface Science,* 469: 213-223.
9. Zulkifli, M., Hossain, M. S., Khalil, N. A., Yahaya, A. N. A., Yusof, F. A. M. and Hashim, A. S. (2018). Preparation and characterization of sol-gel silica modified kenaf bast microfiber/polypropylene composites. *BioResources,* 13(1): 1977-1992.
10. Shekarriz, M., Khadivi, R., Taghipoor, S. and Eslamian, M. (2014). Systematic synthesis of high surface area silica nanoparticles in the sol-gel condition by using the central composite design (CCD) method. *The Canadian Journal of Chemical Engineering,* 92(5): 828-834.
11. Arantes, T. M., Pinto, A. H., Leite, E. R., Longo, E. and Camargo, E. R. (2012). Synthesis and optimization of colloidal silica nanoparticles and their functionalization with methacrylic acid. *Colloids and Surfaces A: Physicochemical and Engineering Aspects,* 415: 209-217.

Malaysian Journal of Analytical Sciences (MJAS)
Published by Malaysian Analytical Sciences Society

IRIDOID GLYCOSIDES AND PHENYLPROPANOIDS FROM *Asystasia gangetica* (L) T. ANDERSON VAR. *Micrantha* (ACANTHACEAE)

(Iridoid Glikosida dan Fenilpropanoid daripada *Asystasia gangetica* (L) T. Anderson Var. *Micrantha* (Acanthaceae))

Isna Athirah Othman[1, 2], Norizan Ahmat[1, 2]*, Amjad Ayad Qatran Al-Khdhairawi[2]

[1]Faculty of Applied Sciences,
Universiti Teknologi MARA, 40450 Shah Alam, Selangor, Malaysia
[2]Atta-ur-Rahman Institute for Natural Product Discovery,
Universiti Teknologi MARA, Puncak Alam Campus, 42300 Bandar Puncak Alam, Selangor, Malaysia

**Corresponding author: noriz118@uitm.edu.my*

Received: 20 November 2019; Accepted: 29 June 2020; Published: 11 August 2020

Abstract

Asystasia gangetica (L) T. Anderson var. *micrantha* (Acanthaceae) or commonly known as "Chinese Violet" or "*rumput Israel"* in Malaysia is a rapidly growing herb usually found among short grasses and along pathways. This plant is used traditionally to treat diabetes mellitus, ear disease and gonorrhea. Its anthelmintic activity helps to treat swelling and rheumatism. The present study was designed to isolate and elucidate chemical constituents from *A. gangetica*. The methanolic extract of the *A. gangetica* leaves was fractionated by using vacuum liquid chromatography (VLC) and preparative high-performance liquid chromatography (HPLC). Selected fractions were purified by recycling HPLC and monitored by using ultra high-performance liquid chromatography (UHPLC). The structures of isolated compounds were characterized by using various spectroscopic methods, mainly nuclear magnetic resonance (NMR) and comparisons with previously reported data. Five phytochemical constituents namely, salidroside **(1)**, verbascoside **(2)**, forsythiaside **(3)**, 3''-*O*-caffeoyl-6-*O*-rhamnopyranosyl catalpol **(4)**, and 4''-*O*-caffeoyl-6-*O*-rhamnopyranosyl catalpol **(5)** were purified using recycling HPLC. Compounds **2**, **3** and **5** were identified for the first time from *A. gangetica*.

Keywords: acanthaceae**,** *Asystasia gangetica*, iridoid glycosides, phenylpropanoid, high-performance liquid chromatography, nuclear magnetic resonance

Abstrak

Asystasia gangetica (L) T. Anderson var. *micrantha* (Acanthaceae) yang juga dikenali sebagai "Chinese Violet" atau "rumput Israel" di Malaysia adalah herba yang mudah membiak, biasanya ditemui di kalangan rumput pendek dan sepanjang jalan. Tumbuhan ini secara traditionalnya digunakan untuk merawat diabetes mellitus, sakit telinga dan gonorea. Keupayaan antihemintiknya membantu merawat bengkak dan reumatik. Kajian ini diolah untuk memencilkan dan mengenalpasti sebatian aktif daripada *A. Gangetica.* Ekstrak metanol daripada daun *A. Gangetica* difraksi menggunakan kromatografi cecair vakum (VLC) dan penyediaan kromatografi cecair bertekanan tinggi (HPLC). Fraksi terpilih telah ditulenkan menggunakan HPLC kitar semula dan dipantau menggunakan kromatografi cecair bertekanan tinggi ultra (UHPLC). Struktur sebatian yang dipencilkan dikenalpasti menggunakan pelbagai teknik spektroskopi terutamanya resonan magnetik nuklear (NMR) dan perbandingan dengan data yang

telah dilaporkan sebelumnya. Lima sebation kimia iaitu salidrosida **(1)**, verbascosida **(2)**, forsithiasida **(3)**, 3''-*O*-kafeoil-6-*O*-rhamnopiranosil katalpol **(4)** dan 4''-*O*-kafeoil-6-*O*-rhamnopiranosil katalpol **(5)** telah dipencilkan menggunakan HPLC pengitaran semula. Sebatian **2**, **3** dan **5** adalah dilaporkan buat pertama kali dari *A. gangetica*.

Kata kunci: acanthaceae**,** *Asystasia gangetica*, iridoid glikosida, fenilpropanoid, kromatografi cecair bertekanan tinggi, resonan magnetik nuklear

Introduction

In the present study, the leaves of *A. gangetica* were investigated for compounds in tropical plants of Malaysia. The preliminary phytochemical screening of this plant showed the presence of flavonoids, alkaloids, glycosides, coumarins, tannins, steroids, terpenoids and saponins [1]. Previous studies on this plant have led to the isolation of some iridoid glycosides and flavonoids [1-3]. Several studies have reported the bioactivities of this plant such as antidiabetic, antiasthmatic, anti-inflammatory activity and antioxidant [4]. In this study, our research group attempt to isolated five compounds, namely salidroside **(1)**, verbascoside **(2)**, forsythiaside **(3)**, 3''-*O*-caffeoyl-6-*O*-rhamnopyranosyl catalpol **(4)**, and 4''-*O*-caffeoyl-6-*O*-rhamnopyranosyl catalpol **(5)** from the methanol extract of the leaves of *A. gangetica*. The structures of the isolated compounds were characterized by using several spectroscopic methods including NMR and comparisons with previously reported data.

Materials and Methods

Chemicals and raw materials

All the chemicals used were of analytical and HPLC grade and purchased from Sigma Chemical Co. (St Louis, Missouri). The leaves of *A. gangetica* were collected in Kapar, Klang, Selangor and were identified by Dr Shamsul Khamis, a botanist from Universiti Kebangsaan Malaysia (UKM), and the voucher specimens were deposited in the Herbarium, School of Environmental and Natural Resource Sciences, Faculty of Science and Technology, Universiti Kebangsaan Malaysia, Bangi, Selangor with the voucher number UKMB40431.

Extraction and isolation

Standard procedures for extraction and isolation of pure compounds from plant materials were used in this research [2]. The leaves were air-dried and ground to obtain a powdered sample (2.3 kg) and were macerated in methanol for 24 h to extract the constituents. The solvent was filtered and concentrated under reduced pressure to obtain crude extract (294.2 g). The crude extract was dissolved in 90% aqueous methanol and subjected to liquid-liquid partition by using hexane and ethyl acetate (EA) to obtain three major fractions. The EA partition (62 g) and aqueous residual partition (83 g) were further fractionated by preparative liquid chromatography (PLC) to obtain nine smaller fraction each. Fraction 2 of EA partition was subjected to recycling HPLC to obtain compounds **1** (3.6 mg) and **2** (126.3 mg). Purification on fraction 3 of the residual aqueous partition produced compounds **3**, **4** and **5** (1.7, 10.2 and 6.7 mg respectively).

Purification and structure elucidation

The structural elucidation of the isolated compounds was done by utilizing several spectroscopic methods. IR spectra were performed on Bruker Tensor II FT-IR, while UV spectra were recorded on Gen-5 Microplate Reader (Synergy HT). The ^{1}H NMR and ^{13}C NMR were recorded in methanol-d_4 on Bruker 600 Ultrashield NMR spectrometer measured at 600 MHz for ^{1}H NMR and 151 MHz for ^{13}C NMR. Peak multiplicities were presented in *H*z and chemical values were shown in ppm (δ). Various chromatographic techniques were used to purify the chemical constituents. For fractionation, liquid chromatography (VLC) was applied by using silica gel 60, 70 – 230 mesh ASTM (Merck 1.07747). Further fractionation was done by using semi-preparative HPLC, while recycling HPLC was applied for the final purification process.

Results and Discussion

Five constituents, namely, salidroside **(1)**, verbascoside **(2)**, forsythiaside **(3)**, 3''-*O*-caffeoyl-6-*O*-rhamnopyranosyl catalpol **(4)**, and 4''-*O*-caffeoyl-6-*O*-rhamnopyranosyl catalpol **(5)** were successfully isolated from the leaves of *A. gangetica*. Compounds were elucidated based on ^{1}H and ^{13}C NMR spectroscopy as well as comparison with the spectroscopic data with values obtained from related literature. The ^{13}C and ^{1}H NMR data are presented in Table 1 and 2 respectively. Salidroside (**1**) [5], a naturally occurring tyroside, was obtained as a white amorphous powder. The ^{1}H NMR showed the presence of an AA''XX'' aromatic ring system, where two pairs of symmetrical protons overlapped at 7.09 (*d*, *J*=8.4, 2H, H-2, 4) and 6.72 (*d*, *J*=8.4, 2H, H-1, 5), followed by the signals at δ_H 4.06 (*td*, *J*=8.9, 6.7, 1H, H-7), 3.75 – 3.71 (*m*, 1H, H-7) and δ_H 2.90 – 2.82 (*m*, 1H, H-8) which corresponded to the 5-hydroxyphenylethyl moiety. The spectrum also displayed signals of a typical glycoside moiety at δ_H 4.31 (*d*, *J*=7.8, 1H, H-1''), 3.20 (*dd*, *J*=9.1, 7.9, 1H, H-2''), 3.37 (*t*, *J*=8.6, 1H, H-3''), 3.32 – 3.26 (*m*, 2H, H-4'',5''), 3.88 (*dd*, *J*=11.9, 2.0, 1H, H-6'') and 3.69 (*dd*, *J*=11.9, 5.2, 1H, H-6''). Salidroside was previously purified from the heartwood of *Acer tegmentosum* and it was shown to possess analgesic and anti-gastropathy properties [6].

Verbascoside **(2)** [7] was isolated as an amorphous powder. ^{1}H NMR showed resonances at δ_H 6.72 (*d*, *J*=2.1, 1H, H-2), 6.70 (*d*, *J*=8.0, 1H, H-5), 6.59 (*dd*, *J* = 8.0, 2.0 Hz, 1H, H-6), 3.77 – 3.71 (*m*, 1H, H-7), 4.10 – 4.03 (*m*, 1H, H-7) and 2.87 – 2.75 (*m*, 2H, H-8) which corresponded to the 3,4-dihydroxyphenylethyl moiety. The signals of two trans-olefinic protons at δ_H 6.30 (*d*, *J* = 15.8 Hz, 1H, H-7') and 7.62 (*d*, *J* = 15.9 Hz, 1H, H-8') as well as the ABX system signals at 7.09 (*d*, *J* = 2.0 Hz, 1H, H-2'), 6.81 (*d*, *J* =8.1, 1H, H-5'), 6.98 (*dd*, *J* = 8.2, 2.1 Hz, 1H, H-6') clearly showed the presence of a *trans*-caffeoyl unit. A glucose unit was observed at δ_H 4.40 (*d*, *J* = 7.9 Hz, 1H, H-1''), 4.95 (*m*, 1H, H-2''), 3.84 (*t*, *J* = 9.2 Hz, 1H, H-3''), 4.95 (*m*, 1H, H-4''), 3.60 – 3.52 (*m*, 2H, H-5'', 6'') and 3.67 – 3.60 (*m*, 1H, H-6''), while the signals at 5.21 (*d*, *J* = 1.8 Hz, 1H, H-1'''), 3.96 – 3.94 (*m*, 1H, H-2'''), 3.60 – 3.52 (*m*, 1H, H-3'''), 3.36 – 2.32 (*m*, 1H, H-4'''), 3.67 – 3.60 (*m*, 1H, H-5''') and 1.11 (*d*, 6.1, 3H, H-6''') belonged to rhamnose. The site of acylation was determined by HMBC correlation at between C=O/ H-4'', which indicated that the caffeoyl unit was attached to C-4'' of the glucose, while a correlation of C-1''/H-8 confirmed the attachment of 3,4-dihydroxyphenylethyl moiety at the anomeric carbon. As for the rhamnose, the correlation found at C-3''/H-1''' confirmed the attachment at the C-3'' of the glucose. This compound was previously isolated from *Buddleja globosa* leaves and was reported to possess antimicrobial properties [8].

Forsythiaside (**3**) [9-10] was obtained as an orange sticky solid. The ^{1}H NMR signals were comparable to those of **2**. The signals for the 3,4-dihydroxyphenylethyl were exhibited at δ_H 6.70 (*d*, *J* = 2.1 Hz, 1H, H-2), 6.79 (*d*, *J* = 8.2 Hz, 1H, H-5), 6.56 (*dd*, *J* = 8.1, 2.1 Hz, 1H, H-6) and 2.83 – 2.78 (*m*, 2H, H-7). The presence of *trans*-caffeoyl moiety was observed at 7.06 (*d*, *J* = 2.1 Hz, 1H, H-2'), 6.66 (*d*, *J* = 8.0 Hz, 1H, H-5'), 6.92 (*dd*, *J* = 8.2, 2.0 Hz, 1H, H-6'), 6.32 (*d*, *J* = 15.9 Hz, 1H, H-7') and 7.59 (*d*, *J* = 15.8 Hz, 1H, H-8'). The signals at δ_H 4.36 (*d*, *J* = 7.8 Hz, 1H, H-1''), 3.36 (*d*, *J* = 11.3 Hz, 1H, H-2''), 3.57 – 3.53 (*m*, 1H, H-3''), 4.03 (*dd*, *J* = 9.6, 6.3 Hz, 1H, H-4''), 3.60 – 3.57 (*m*, 1H, H-5''), 4.40 – 4.37 (*m*, 1H, H-6'') and 4.52 (*dd*, *J* = 11.8, 2.1 Hz, 1H, H-6'') belonged to the glucose moiety, while the signals at 5.20 (*d*, *J* = 1.8 Hz, 1H, H-1'''), 3.97 (*dd*, *J* = 3.4, 1.9 Hz, 1H, H-2'''), 3.75 – 3.72 (*m*, 1H, H-3'''), 3.46 – 3.43 (*m*, 1H, H-4'''), 3.43 – 3.40 (*m*, 1H, H-5'''), 1.27 (*d*, *J* = 6.2 Hz, 3H, H-6''') indicated the presence of rhamnose. By comparing the ^{1}H NMR data to those of compound **2**, compound **3,** however, showed a significant change at H-4'' and H-6'' signals which shifted downfield by 0.92 and 0.87 ppm respectively. The signal for C-3'' also became more shielded by 6.27 ppm which indicated the loss of a glycosyl bond at this site. The long-range correlation observed at C-5''/H-1''' confirmedd the attachment of rhamnose at C-6'' position of glucose. This compound was first isolated from *Forsythia suspensa* [9] and was found to possess strong antioxidant and antibacterial activity [11].

3''-*O*-caffeoyl-6-*O*-rhamnopyranosyl catalpol (**4**) [12] was isolated as orange sticky solid. The signals observed at δ_H 5.11 (*d*, *J* = 9.6, 1H, H-1), 6.40 (*dd, J* = 6.0, 1.9 Hz, 1H, H-3), 5.10 (*d, J* = 10.5, 1H, H-4), 2.47 – 2.39 (*m*, 1H, H-5), 4.05 (*dd*, *J* = 8.2, 1.1 Hz, 1H, H-6), 3.67 (*s*, 1H, H-7), 2.59 (*dd, J* = 9.7, 7.6 Hz, 1H, H-9), 3.82 (*d, J* = 13.1 Hz, 1H, H-10) and 4.18 (*d, J* = 13.2 Hz, 1H, H-10) indicated the presence of cyclopentan-pyran structure ring system with a double bond between C-3 and C-4. The ^{1}H NMR resonance at δ_H 4.80 (*d*, *J* = 7.9 Hz, 1H, H-1'') was assigned to the anomeric proton and their *J* coupling indicated β–glucopyranose structure as a sugar unit. The complete assignment for glucose and rhamnose moiety is presented in Table 2. Additionally, long-range correlations observed at C-1''/H-1 and C-1'''/H-6 showed the attachment site for the sugars. After the complete interpretation of the NMR data and comparison of the data with those reported in the literature were carried out, the core skeleton of **4** was determined to be 6-*O*-rhamnopyranosyl catalpol (**4a**) [11]. The presence of caffeoyl moiety was determined from the presence of the signals at δ_H 7.09 (*t, J* = 2.0 Hz, 1H, H-2'), 6.81 (*d*, *J* = 8.2 Hz, 1H, H-5'), 6.99 (*dd*, *J* = 8.2, 2.1 Hz, 1H, H-6'), 7.62 (*d*, *J* = 15.8 Hz, 1H, H-7') and 6.36 (*d*, *J* = 15.8 Hz, 1H, H-8'). ^{1}H NMR chemical shifts of the rhamnose moiety of **4** were compared to those of **4a** where the H-3" signal was seen to significantly shift downfield by 1.49 ppm. The other signals were comparable to those in literature. This pattern established that the position of the caffeoyl ester of compound **4** is at C-3" of rhamnose. Table 2 shows the spectroscopic data (^{1}H NMR) for compounds **4** – **5**. This compound was previously isolated from *Veronica hookeri* [12] and was shown to exhibit antioxidant properties [2].

4''-*O*-caffeoyl-6-*O*-rhamnopyranosyl catalpol (**5**) [15] was isolated as orange sticky solid. The NMR signals showed a very close similarity to those of **4** [16]. However, in compound **5**, a significant downfield shift by 1.79 ppm was observed at H-4", followed by upfield shifts for H-3" and H-5", which established that caffeoyl esterification happened at C-4". Signals for catalpol iridoid was shown at δ_H 5.13 (*d*, *J* = 9.8, 1H, H-1), 6.41 (*dd*, *J* = 6.0, 1.8, 1H, H-3), 5.17 – 5.09 (*m*, 1H, H-4), 2.51 – 2.45 (*m*, 1H, H-5), 4.07 (*dd*, *J* = 8.2, 1.1 Hz, 1H, H-6), 3.68 (*s*, 1H, H-7), 2.60 (*dd*, *J* = 9.7, 7.6, 1H, H-9), 3.84 (*d*, *J* = 13.0 Hz, 1H, H-10) and 4.18 (*d*, *J* = 13.2 Hz, 1H, H-10). Signals for the caffeoyl moieties roused at δ_H 7.09 (*d*, *J* = 2.1, 1H, H-2'), 6.81 (*d*, *J* = 8.2, 1H, H-5'), 6.99 (*dd*, *J* = 8.2, 2.2, 1H, H-6'), 7.66 (*d*, *J* = 15.8, 1H, H-7') and 6.38 (*d*, *J* = 15.9, 1H, H-8'). The signals for glucose and rhamnose moiety as well as the comparison of ^{1}H NMR data for compounds **4** – **5** are presented in Table 2. This compound has been previously purified from *Verbascum thapsus* [15]. To date, no literature has been found to describe the bioactivity of the compound, however, catalpol derivatives have been proven to possess laxative, diuretic, hypoglycemic, antihyperglycemic and immunomodulatory properties [13, 14]. The comparison of the ^{13}C NMR for compounds **1** – **5** is tabulated in Table 1. Figure 1 shows the structure of the compounds.

Table 1. Spectroscopic data (^{13}C NMR) for compounds **1** – **5**

No. of Carbon	**Compound**				
	1 δ_c	**2** δ_c	**3** δ_c	**4** δ_c	**5** δ_c
Aglycone					
1	114.7	130.14	130.02	93.80	93.80
2	129.5	115.78	115.69		
3	155.4	144.72	144.74	140.89	140.85
4	129.5	143.27	143.26	102.05	102.19
5	114.7	114.98	114.98	35.88	35.88
6	129.4	119.93	119.87	82.98	82.40

Table 1 (cont'd). Spectroscopic data (^{13}C NMR) for compounds **1** – **5**

No. of Carbon	Compound				
	1 δ_c	**2** δ_c	**3** δ_c	**4** δ_c	**5** δ_c
7	70.7	70.87	71.02	58.13	57.92
8	35.0	35.17	35.28	65.16	65.18
9				41.91	41.89
10				60.09	60.08
Caffeoyl					
1'		126.30	126.30	126.36	126.47
2'		113.92	113.71	115.15	115.12
3'		145.42	145.39	148.31	148.17
4'		148.38	148.24	145.43	145.76
5'		115.19	115.16	113.87	113.95
6'		121.86	121.75	121.71	121.54
7'		113.35	145.86	146.21	145.43
8'		146.66	113.45	113.46	113.79
C=O		166.96	167.75	167.33	167.51
Glucose					
1''	103.0	102.80	103.00	98.34	98.86
2''	73.7	74.80	74.29	73.45	73.90
3''	76.7	80.30	74.03	76.31	76.30
4''	76.6	69.23	69.01	70.39	70.40
5''	70.3	74.62	74.02	77.23	77.24
6''	61.4	63.05	63.24	61.54	61.55
Rhamnose					
1'''		101.64	101.32	96.38	98.33
2'''		70.96	70.95	69.13	69.96
3'''		70.69	68.65	68.91	69.86
4'''		72.42	72.61	72.81	73.45
5'''		69.04	70.87	68.90	68.97
6'''		17.08	16.47	16.63	16.60

Table 2. Comparison of ^{1}H NMR data for compounds **4** – **5**

No. of proton	Compound		
	4	**4a**	**5**
Aglycone			
1	5.11 (*d*, 9.6, 1H)	5.07 (*d*, 10, 1H)	5.13 (*d*, 9.8, 1H)
3	6.40 (*dd*, 6.0, 1.9, 1H)	6.35 (*dd*, 6, 2, 1H)	6.41 (*dd*, 6.0, 1.8, 1H)
4	5.10 (*d*, 10.5, 1H)	5.05 (*dd*, 6, 5, 1H)	5.17 – 5.09 (*m*, overlapped)
5	2.47 – 2.39 (*m*, 1H)	2.38 (*m*, 1H)	2.51 – 2.45 (*m*, 1H)

Table 2 (cont'd). Comparison of ^{1}H NMR data for compounds **4** – **5**

No. of proton	Compound		
	4	**4a**	**5**
6	4.05 (*d*, 8.2, 1H)	3.99 (*dd*, 8, 2, 1H)	4.07 (*dd*, 8.2, 1.1, 1H)
7	3.67 (*s*, 1H)	3.62 (d, 2, 1H)	3.68 (*s*, 1H)
8			
9	2.59 (*dd*, 9.7, 7.6, 1H)	2.54 (*dd*, 10, 8, 1H)	2.60 (*dd*, 9.7, 7.6, 1H)
10	3.82 (*d*, 13.1, 1H) 4.18 (*d*, 13.2, 1H)	3.81 (*d,* 13, 1H) 4.13 (*d*, 13, 1H)	3.84 (*d*, 13.0, 1H) 4.18 (*d*, 13.2, 1H)
Caffeoyl			
1'			
2'	7.09 (*d,* 2.0, 1H)		7.09 (*d*, 2.1, 1H)
3'			
4'			
5'	6.81 (*d*, 8.2, 1H)		6.81 (*d*, 8.2, 1H)
6'	6.99 (*dd*, 8.2, 2.1, 1H)		6.99 (*dd*, 8.2, 2.2, 1H)
7'	7.62 (*d*, 15.8, 1H)		7.66 (*d*, 15.8, 1H)
8'	6.36 (*d*, 15.8, 1H)		6.38 (*d*, 15.9, 1H)
C=O			
Glucose			
1''	4.80 (*d*, 7.9, 1H)	4.77 (*d*, 8, 1H)	4.80 (*d*, 7.9, 1H)
2''	3.32 – 3.21 (*m*, overlapped)	3.25 (*dd*, 8, 9, 1H)	3.32 – 3.22 (*m*, overlapped)
3''	3.42 (*t*, 9.0, 1H)	3.38 (*t*, 9, 1H)	3.43 (*t*, 9.1, 1H)
4''	3.32 – 3.21 (*m*, overlapped)	3.24 (*dd*, 8, 10, 1H)	3.32 – 3.22 (*m*, overlapped)
5''	3.32 – 3.21 (*m*, overlapped)	3.30 (*m*, 1H)	3.32 – 3.22 (*m*, overlapped)
6''	3.95 (*dd, J* = 8.9, 2.7 Hz, 1H) 3.64 (*dd*, *J* = 12.0, 6.7 Hz, 1H)	3.61 (*dd*, 12, 6, 1H) 3.91 (*dd*, 12, 2, 1H)	3.65 (*dd*, 12.0, 6.7, 1H) 3.95 (*dd*, 12.0, 2.1, 1H)
Rhamnose			
1'''	5.04 (*d,* 1.8, 1H)	4.92 (*d*, 2, 1H)	4.99 (*d*, 1.8, 1H)
2'''	3.93 – 3.91 (*m*, 1H)	3.84 (*dd*, 2, 3, 1H)	3.74 – 3.68 (*m*, overlapped)
3'''	5.16 (*dd*, 3.5, 1.7, 1H)	3.67 (*dd*, 9, 3, 1H)	3.74 – 3.68 (*m*, overlapped)
4'''	3.51 (*t*, 9.5, 1H)	3.38 (*t*, 9, 1H)	5.17 – 5.09 (*m*, overlapped)
5'''	3.79 – 3.75 (*m*, 1H)	3.63-3.69 (*m*, 1H)	3.87 – 3.81 (*m*, overlapped)
6'''	1.33 (*d*, 6.3, 3H)	1.25 (*d*, 6, 3H)	1.33 (*d,* 6.2, 3H)

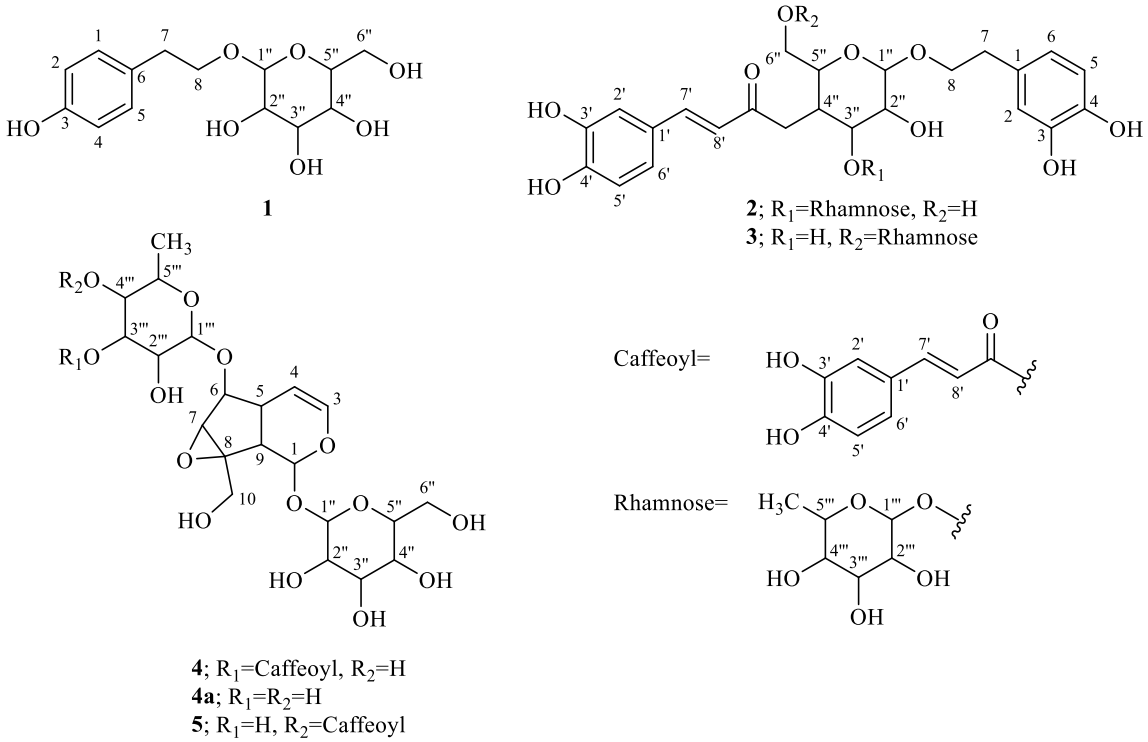


Figure 1. Structure of compounds **1** – **5**

Conclusion

Five known compounds, including a tyrosol derivative, two iridoid glycosides and two phenylpropanoids have been isolated and characterized from the methanol extract of the leaves of *A. gangetica*. These compounds include salidroside **(1)**, verbascoside **(2)**, forsythiaside **(3)**, 3''-*O*-caffeoyl-6-*O*-rhamnopyranosyl catalpol **(4)**, and 4''-*O*-caffeoyl-6-*O*-rhamnopyranosyl catalpol **(5)**. Compounds **2**, **3**, and **5** were identified for the first time in *A. gangetica*. As previous reports found that these types of phenolic compounds displayed diverse pharmacological properties, further detailed investigation of their biological activities is recommended.

Acknowledgements

The authors would like to thank the Ministry of Higher Education, Malaysia for the financial support under MyPhD Scholarship and the Fundamental Research Grant Scheme [600-RMIFRGS 5/3 (0064/2016)].

References

1. Gopal, T., K., Megha, G., Chamundeeswari, D. and Reddy, C., U. (2013). Phytochemical and pharmacological studies on the whole plant of *Asystasia gangetica*. *Indian Journal of Research in Pharmacy and Biotechnology*, 1(3): 365-370.
2. Worawittayanon, P., Ruadreo, J., Disadee, W., Sahakitpichan, P., Sitthimonchai, S., Thasana, N., Ruchirawat, S. and Kanchanapoom, T. (2012). Iridoid and flavone glycosides from *Asystasia gangetica* subsp. *micrantha* and *Asystasia salicifolia* and their antioxidant activities. *Biochemical Systematics and Ecology,* 40:38-42.
3. Senthamilselvi, M. M., Kesavan, D. and Sulochana, N. (2011). A new biflavone glycoside from flowers of *Asystasia gangetica. Chemistry of Natural Compounds,* 47(3):360-362.
4. Tilloo, S., K., Pande, V. B., Rasala, T., M. and Kale V., V. (2012). *Asystasia gangetica*: Review on multipotential application. *International Research Journal of Pharmacy*, 3(4):18-20.

5. Mastihubová, M. and Poláková, M. (2016). A selective and mild glycosylation method of natural phenolic alcohols. *Beilstein Journal of Organic Chemistry,* 12: 524-530.
6. Yoo, Y. M., Nam, J. H., Kim, M. Y., Choi, J., Lee, K. T. and Park, H. J., 2009. Analgesic and anti-gastropathic effects of salidroside isolated from *Acer tegmentosum* heartwood. *The Open Bioactive Compounds Journal*, 2: 1-7.
7. López-Rodríguez, R., Herrera-Ruiz M., Trejo-Tapia, G., Domínguez-Mendoza, B. E., González-Cortazar M. and Zamilpa, A. (2019). *In vivo* gastroprotective and antidepressant effects of iridoids, verbascoside and tenuifloroside from *Castilleja tenuiflora* Benth. *Molecules*, 24: 1292.
8. Pardo, F., Perich, F., Villarroel, L. and Torres, R., 1993. Isolation of verbascoside, an antimicrobial constituent of *Buddleja globosa leaves*. *Journal of Ethnopharmacology*, 39(3): 221-222.
9. Nishibe, S., Okabe, K., Tsukamoto H., Sakushima A. and Hisada S. (1982). The structure of forsythiaside isolated from *Forsythia suspensa. Chemical and Pharmaceutical Bulletin*, 30(3): 1048-1050.
10. Jia, J., Zhang, F., Li, Z., Qin, X. and Zhang, L. (2015). Comparison of fruit of *Forsythia suspensa* at two different maturation stages by NMR-based metabolomics. *Molecules,* 20: 10065-10081.
11. Qu, H., Zhang, Y., Wang, Y., Li, B. and Sun, W., 2008. Antioxidant and antibacterial activity of two compounds (forsythiaside and forsythin) isolated from *Forsythia suspensa*. *Journal of Pharmacy and Pharmacology*, 60(2): 261-266.
12. Kroll-Møller, P., Pedersen, K. D., Gousiadou C., Kokubun, T., Albach D., Taskova, R., Garnock-Jones. P. J., Gotfredsen C. H. and Jensen S. R. (2017). Iridoid glucosides in the genus *Veronica* (Plantaginaceae) from New Zealand. *Phytochemistry,* 140: 174-180.
13. Kupeli, E., Harput, U. S., Varel, M., Yesilada, E., Saracoglu, I. (2005). Bioassay-guided isolation of iridoid glucosides with antinociceptive and anti-inflammatory activities from *Veronica anagallis-aquatica* L. *Journal of Ethnopharmacology,* 102: 170-176.
14. Oh, H., Pae, H. O., Oh, G. S., Lee, S. Y., Chai, K. Y., Song, C. E., Kwon, T. O., Chung, H. T., Lee, H. S. (2002). Inhibition of inducible nitric oxide synthesis by catalposide from *Catalpa ovata. Planta Medica,* 68: 685-689.
15. Warashina, T., Miyase, T. and Ueno, A. (1991). Iridoid glycosides from *Verbascum thapsus* L. *Chemical and Pharmaceutical Bulletin*, 39(12): 3261-3264.
16. Helfrich, E. and Rimpler, H., 1999. Iridoid glycosides and phenolic glycosides from *Holmskioldia sanguinea*. *Phytochemistry*, 50(4): 619-627.

Malaysian Journal of Analytical Sciences (MJAS)
Published by Malaysian Analytical Sciences Society

EVALUATION ON THE EFFICACY OF DIFFERENT DISRUPTION METHOD OF OIL PALM ROOTS AND *Ganoderma boninense* CELL WALL

(Penilaian ke atas Keberkesanan Kaedah Pemusnahan yang Berbeza pada Dinding Sel Akar Kelapa Sawit dan *Ganoderma boninense*)

Arnnyitte Alexander[1], Jedol Dayou[2], Coswald Stephen Sipaut[3], Khim Phin-Chong[1]*

[1]*Biotechnology Programme, Faculty of Science and Natural Resources*
[2]*Vibration and Sound Research Group (e-VIBS), Faculty of Science and Natural Resources*
[3]*Chemical Engineering Programme, Faculty of Engineering*
Universiti Malaysia Sabah, 88400 Jalan UMS, Kota Kinabalu, Sabah, Malaysia

**Corresponding author: chongkp@ums.edu.my*

Received: 31 May 2020; Accepted: 7 July 2020; Published: 11 August 2020

Abstract

The cell wall is the outermost layer of cell encountered by pathogens, determining the infection fate. However, the chemical composition involves during host-pathogen interaction has not been fully elucidated. Prior to determining the composition in the cell walls, the walls must be isolated first from the intercellular component. Selected methods for oil palm roots and *G. boninense* cell disruption were evaluated for their suitability for cell wall isolation and presented in this paper. The effect of selected disruption methods on the content of crude proteins and DNA absorbance under 260 and 280 nm wavelengths in the produced cell wall materials was established on the basis of their solubilized materials. The investigated methods were; i) homogenization with sonication; ii) grinding with liquid nitrogen and; iii) lyophilization with homogenization. The cell wall materials with the highest degree of cytoplasmic component released were produced using lyophilization with homogenization. This was confirmed with the highest DNA absorbance at 260/280 nm of 2.25/1.95 for *G. boninense* and 2.47/2.35 for oil palm roots in their solubilized materials. The thus-produced preparation also released 4.5 and 10.1 µg/g of crude proteins for *G. boninense* and oil palm roots respectively. The degree of cell wall purification from intracellular components was validated using Fourier Transform Infrared Spectroscopy (FTIR). Isolated cell wall can be further utilized in cell wall composition analysis.

Keywords: cell wall, disruption methods, lyophilization with homogenization

Abstrak

Dinding sel merupakan lapisan sel paling luar yang ditentang oleh patogen dan menentukan nasib jangkitan. Walau bagaimanapun, komposisi kimia yang terlibat semasa interaksi perumah-patogen masih lagi belum dijelaskan secara terperinci. Sebelum kajian ke atas komposisi dinding sel, dinding tersebut harus dipisahkan daripada komponen sel dalaman terlebih dahulu. Kesesuaian beberapa kaedah terpilih untuk memusnahkan sel akar kelapa sawit dan *G. boninense* telah dinilai untuk memisahkan dinding sel. Kesan kaedah pemusnahan sel terhadap kandungan protin dan penyerapan asid deoksiribonukleik di bawah panjang gelombang 260 dan 280 nm berdasarkan kepada bahan terlarut di dalam hasil bahan dinding sel telah dinilai. Kaedah pemusnahan yang dikaji adalah; i) homogenisasi dan sonikasi, ii) pengisaran dengan cecair nitrogen, iii) liofilisasi dan homogenisasi. Kaedah liofilisasi dan homogenisasi menghasilkan bahan dinding sel yang mempunyai komponen sitoplasma terbebas tertinggi. Keputusan ini disahkan

dengan serapan asid deoksiribonukleik yang tinggi pada 260/280 nm di dalam bahan terlarut iaitu sebanyak 2.25/1.95 untuk *G. boninense* dan 2.47/2.35 untuk akar kelapa sawit. Selain itu, hasil dinding sel melalui keadah yang sama juga membebaskan 4.5 dan 10.1 µg/g protin masing-masing untuk *G. boninense* dan akar kelapa sawit. Tingkat kebersihan dinding sel daripada komponen dalaman telah disahkan dengan menggunakan spektrofotometer inframerah transformasi Fourier. Dinding sel yang terpisah seterusnya boleh digunakan di dalam analisa komposisi dinding sel.

Kata kunci: dinding sel, kaedah gangguan, liofilisasi dan homogenisasi

Introduction

Ganoderma boninense infection causes basal stem rot (BSR), a destructive disease that is responsible for considerable decrease in oil palm yield. However, to date there is no adequate control measure to control BSR disease. An improvement of the oil palm defense system against *G. boninense* is the alternative option, thus requires in-depth understanding on the pathogenesis of *G. boninense* in oil palm. Plants use various defense mechanisms during their interactions with the pathogens; this includes strengthening of physical barriers which is the cell walls. Living plant cell walls respond to fungal penetration rapidly through the deposition of cell wall components directly onto the inner layer of cellulose (papillae), a process known as cell wall apposition [1]. It has been suggested that cell wall-metabolites are involved in plant-pathogen interaction including communication between host pathogen, activation and implementation of plant defenses in response to pathogen attack [2, 3]. However, until today little is known about the specific component of metabolites in the cell walls. The location of metabolites in the cell wall structure requires disruption to enable the production of cell wall preparations then the metabolite isolation. Efficient breakage of cell wall strength-providing components is necessary to effectively remove intracellular compounds [4]. To date, very little literature has been reported on the evaluation of the suitability of different methodologies for the preparation of plant roots and fungal cell walls for metabolite isolation purpose. Therefore, in this current study we explore the efficacy of different selected methods for oil palm roots and *G. boninense* cell wall disruption. This includes thorough investigation on the effects of homogenization with sonication, grinding with liquid nitrogen and lyophilization with homogenization on the purity of the produced cell wall materials.

Materials and Methods

Sample preparation

For oil palm root sample preparation, root tissues from eight month-old oil palm seedlings (D x P purchased from Saplantco Sdn. Bhd.) were harvested and washed under running tap water to remove attached dirt. Then roots were soaked in 99% ethanol for 30 seconds and air-dried to remove ethanol and proceeded for further analysis. For *G. boninense* sample preparation, the pathogen culture was prepared in Potato Dextrose Broth (PDB).6 mm diameter mycelial plug was taken from the edge of a 14 days-old *G. boninense* culture (obtained from Universiti Malaysia Sabah microbial stock culture) using a cork borer and sub-cultured into PDB and incubated at 28 ºC in an orbital shaker at 150 rpm for 14 days to obtain bulky mycelia. The culture was filtered with muslin cloth to collect the fungal mycelia and rinsed with sterile distilled water thrice. Finally, the mycelia were filtered using Whatman® No.3 filter paper to remove excessive water and kept in sterile falcon tube at -80 °C until further use.

Procedures for cell disruption

The methods employed for physical disruption were selected based on the method's feasibility, cost, and size of samples.

Grinding under liquid nitrogen

Oil palm roots (100 g fresh weight) were freeze in -80 ˚C overnight. The frozen samples were transferred into a sterile pre-cooled mortar and ground with adequate amount of liquid nitrogen with a pestle. The fine ground samples were then kept in a zip lock plastic bag until further use. *G. boninense* materials (5 g) were also prepared using similar steps as mentioned above.

Homogenization and sonication

Oil palm roots (100 g fresh weight) were cut into 1.5 cm in size and freshly blended with sterile deionized water using a commercial blender (Waring®, USA). The materials were sonicated using water bath sonicator (Branson, USA). Disruption includes four cycles consisting of 5 minutes of sonication and a 2 minutes break in-between each cycle. The ultrasound frequency was 20 kHz. The resulted materials were washed with distilled water twice, air-dried overnight and kept in zip lock plastic bag at -80 ˚C until further use. *G. boninense* materials (5 g) were also prepared using similar methods.

Lyophilization and Homogenization

Oil palm root (100 g fresh weight) were lyophilized for 48 hours. Then, the lyophilized materials were homogenized using commercial blender until fine powder and kept in zip lock plastic bag under room temperature ±25 °C until further use. *G. boninense* materials (5 g) were also prepared using similar methods.

The influence of the disruption methods on solubilized materials

The effectiveness of cell disruption methods was evaluated based on the DNA absorbance (260 and 280 nm) and protein content in their solubilized material.

Determination of UV absorption

The method was based on previous study [4] with some modifications. Solubilization of the studied roots and fungal intracellular materials was determined on the basis of the increase of sample absorbance read at 260 and 280 nm after tissue disruption. For that purpose, 1 g/mL of cell suspension in deionized water was prepared after cell disruption. Samples were centrifuged at 5,000 rpm for 5 minutes and the obtained supernatants were diluted eight times using sterile deionized water before measurements. Absorbance was read at 260 and 280 nm using microplate reader against water. The increase of absorbance of samples at each wavelength was calculated as a difference between the absorbance of samples after a particular disruption method.

Determination of Protein Content

The protein content in solubilized material after cell disruption was analyzed as described previously [5] with some modification. For that purpose, 1 g/mL of cell suspension in deionized water was prepared. Samples were centrifugated at 5,000 rpm for 5 minutes and supernatants were harvested. Four volumes of methanol (Merck, Germany) were added to one volume of the sample and the mixture was vortexed. Later, one volume of chloroform (Merck, Germany) was then added to the mixture, vortexed and centrifuged at 10,000 rpm for 5 minutes. The aqueous methanol layer was removed from the top of the sample. Extracted proteins remained at the boundary phase between the aqueous methanol layer and the chloroform layer. Four volumes of methanol were added, vortexed and centrifuged at 10,000 rpm for 15 minutes. The supernatant was removed and the pellet was air-dried. Then, protein pellets were re-solubilized in 50 µL Milli-Q water and the concentration was determined using Bradford assay (Bradford, 1976). A serial of Bovine serum albumin (99% pure, Sigma-Aldrich) standard ranging from 10-500 mg/mL was prepared for protein quantification.

Isolation and purification of cell walls (CW) material

The resultant CW preparations were pre-purified from cytosol components before further analyses. Only the best disruption method was used for CW isolation as described previously [6] with slight modification. The procedures were conducted at 4 ˚C unless mentioned otherwise. Disrupted cell tissues (3 g) were washed overnight in 50 mL of pre-cooled extraction buffer (5 mM acetate, 0.4 M sucrose, (Sigma-Aldrich, USA) pH 4.6) added with 1% of polyvinylpolypyrrolidone on an orbital shaker. CW were separated from soluble cystoplasmic fluid by centrifuging at 1,000 rpm for 15 minutes. The pellet was re-suspended in 50 mL of 5 mM acetate buffer at pH 4.6 with 0.6 M sucrose followed by centrifugation at 1,000 rpm for 15 minutes. The pellet was further washed in 50 mL of 5 mM acetate buffer at pH 4.6 with 1 M sucrose and centrifuged at 1,000 rpm for 15 minutes. The residue was washed extensively with 50 mL of 5mM acetate buffer at pH 4.6 and centrifuged at 1,000 rpm for 15 minutes, thrice. The supernatant was discarded and the final pellet was lyophilized overnight. Most intercellular components

were removed from the CW given the advantage of sucrose gradients and extensive washing with low ionic strength of acidic buffer.

Characteristics of produced cell walls (CW) material

The purity of produced CW was evaluated based on the DNA absorbance (260 and 280 nm) and protein content in the CW material as mentioned previously. In addition, the CW components were also validated using FTIR spectroscopy. FTIR based analysis was preferable due to its sensitivity, high throughput means to access carbon allocation change and less time consuming.

Validation of cell walls (CW) extract using Fourier transform infrared spectroscopy (FTIR) analysis

The chemical composition of isolated CW from oil palm roots seedling and *G. boninense* were studied using FTIR (Fourier transform infrared) spectroscopy. Raw materials (disrupted cells) were compared with extracted CW. The analysis was performed using FTIR spectrometer (Perkin Elmer, USA) with an attached unit to measure attenuated total reflectance (ATR unit). FTIR spectra were recorded for the wave number range of 4000 to 450 cm^{-1} with a spectral resolution of 4 cm^{-1}. 32 spectra per sample were added and averaged to improve the signal-to-noise ratio. Spectra were baseline corrected, smoothed and used to compare differences in the spectra. Five replicates were analyzed per sample and data were reported as representative spectra per sample.

Statistical analysis

Statistical differences between methods were determined using one-way ANOVA with Post-Hoc test *via* Tukey testing with significant value at $p = 0.05$ using Statistical Package for the Social Sciences (SPSS) software, ver. 21 (SPSS Inc., Rochester, NY).

Results and Discussion

Cell disruption enhances the release of intercellular components, thus improving extraction efficiency and higher CW purity. Extraction of CW metabolite involves three major stages including tissue disruption, isolation, purification of CW materials and finally extraction of CW metabolite. The current study prompted to verify suitable methods to be selected for both oil palm and *G. boninense* CW isolation at the highest purity to ensure optimum metabolite extraction.

The influence of the tested disruption methods on DNA and proteins contents

The effectiveness of the selected cell disruption's methods in producing cytoplasm-free CW preparation procedures was determined. The investigated methods included: homogenization with sonication, grinding with liquid nitrogen, and lyophilization with homogenization. According to the study assumptions, CW preparations should be characterized by the highest release of possible content of impurities like proteins and genetic material which served as indicators of complete cell disruption. Effectiveness of the disruption methods on the purity of extracted cell wall of oil palm root and *G. boninense* are shown in Table 1. The effect of different disruption methods on DNA and proteins contents in the produced solubilized materials was analyzed. Low percentage of protein content and UV absorbance at 260 nm and 280 nm indicated the poorest effectiveness of cells disruption. The highest level of protein release was noted after cell disruption using lyophilization and homogenization for both oil palm roots and *G. boninense* with 10.1 and 4.5 μg/g respectively. Protein release is one of the key characteristic of microbial cell disruption [7]. The absorbance values at the mentioned wavelengths correspond to absorption by nucleic acid and proteins, respectively, which are the main intracellular constituents of biological cells [8]. The results of absorbance at 260 nm and 280 nm (8-fold diluted samples) presented in Table 1 confirmed the release of intracellular genetic material and proteins during the tested disruption processes.

The highest absorbance values of 260 nm were observed in lyophilization with homogenization method for both oil palm and *G. boninense*. Homogenization with sonication method was characterized by the lowest efficiency of nucleic acids release (based on absorbance values of 260 nm) applied on oil palm roots. Meanwhile no significant difference observed between the latter method compared to grinding with liquid nitrogen method on *G. boninense*. In the case of homogenization with buffer followed with sonication, the method is not

sufficient enough to disrupt the sample tissues. Homogenization of hard materials and indirect sonication apparently does not lyse all cells equally, as plant and fungi CW are far more resistant to cell lysis sonication compared to cell membranes, thus making them difficult to rupture. Middleberg [7] explained that mild heat treatment during the sonication primarily kills the cells which may lead to smaller and toughened cells, thus making subsequent mechanical disruption less efficient. A similar result was also observed for the cells subjected to direct grinding with liquid nitrogen. Interestingly, this result contradicts with the findings [9] which reported this method facilitated higher level of CW disruption in *Chlorella vulgaris*. However, due to the differences in CW structure, not all samples respond the same to similar pre-treatment. Furthermore, this method was not applicable to larger sample volumes as it is quite costly. Both *G. boninense* and oil palm CW preparations with the highest degree of cytosol component release were produced with lyophilization followed with homogenization. Therefore, this method was selected for the next CW isolation work.

Previous researcher [10] produced *Populus tremoloides* CW preparations as a result of grinding freeze-dried materials. In effective cell disruption for oil palm roots and *G. boninense* tissue, lyophilization with homogenization method showed higher released of intercellular components. Apart from providing a complete destruction of the root and fungal cells, this method is apparently simple and consumes less energy. Removal of water molecules from the cells through lyophilization makes the walls structure fragile upon disruption. This allows hypothesizing that the shear forces during homogenization in a blender more easily damaged these cells whose walls were already losing its rigidity producing powder materials. Samples in powder prior to solvent extraction produce a more homogeneous sample and increase the surface area of CW metabolites exposed to the solvent.

Table 1. Effect of different disruption methods of cell disruption on the DNA and total soluble protein content in oil palm and *Ganoderma* cell wall

Method	Protein (µg/g)		DNA Absorbance			
	GB	OP	GB		OP	
			260 nm	280 nm	260 nm	280 nm
M1	3.11 ± 0.22^{b}	2.9 ± 0.2^{c}	1.62 ± 0.2^{b}	0.75 ± 0.1^{b}	1.81 ± 0.2^{b}	1.60 ± 0.3^{b}
M2	3.13 ± 0.3^{b}	5.03 ± 0.5^{b}	1.7 ± 0.3^{b}	0.84 ± 0.6^{b}	1.71 ± 0.2^{c}	1.52 ± 0.1^{c}
M3	4.5 ± 0.21^{a}	10.1 ± 0.4^{a}	2.25 ± 0.2^{a}	1.95 ± 0.4^{a}	2.47 ± 0.6^{a}	2.35 ± 0.7^{a}

Notes; * M1 = Homogenization with sonication; M2 = Grinding with liquid nitrogen; M3 = Lyophilization with homogenization; GB = *Ganoderma boninense*; OP = oil palm; same letter in columns are not significantly different (Tukey's test, $p = 0.05$). Each sample consists of three replicates in each disruption methods.

Effectiveness of lyophilization with homogenization method in CW isolation

Lypophilization with homogenization method turned out to be the most effective cell disruption method for both OP roots and *G. boninense*. Disrupted materials resulted from this method were preceded to CW isolation and purification. Based on Table 2, protein content in the isolated CW of *G. boninense* and oil palm decreased to 0.001 and 0.005 µg/g respectively. Similarly, lower absorbance at 260 nm and 280 nm in solubilized material after CW purification observed in both *G. boninense* and oil palm.

The method was proven to be the most effective method for cell disruption and purification from cytosol components for both OP roots and *G. boninense* based

on the lowest reading of protein content and absorbance at 260 nm and 280 nm in solubilized material after CW purification. Lower content of protein and DNA absorbance in CW solubilized material also demonstrated the effectiveness of washing steps in CW purification stage. Plant and fungal cell walls are mainly build with highly dense polysaccharides [11], therefore, purification of their CW materials from cytoplasmic fraction were conducted through density gradients by centrifugation. Low centrifugation and extensive washing with cold buffer were able to wash CW materials free from intercellular contaminants [12]. It is often necessary to dry purified CW materials prior to solvent extraction because many organic solvents cannot penetrate into CW with water content, and therefore extraction would be inefficient. Dried samples that were ground finely prior to solvent extraction would produce a more homogenous sample and increase the surface area of metabolites exposed to the solvent.

Spectral analysis of CW extracts using FTIR

Purity of the produced CW was validated using infrared spectroscopy. Figure 1 shows the IR spectrum of *G. boninense* disrupted cells and its purified CW. The purified CW exhibited weak intensities at 3280 cm^{-1}, 1630 cm^{-1}, 1550 cm^{-1} and 1370 cm^{-1} corresponding to proteins components of amide A, amide I, amide II and amide III respectively [13]. These were correlated with the total protein content as mentioned previously in Table 2. Bands at 1050 cm^{-1} and 550 cm^{-1} are characteristic of polysaccharides (α- and β-glucans, α-mannan) [14]. Band absorption at 1230 cm^{-1} influenced by PO3 groups from nucleic acid residues was absent in purified CW. The absorption band in the spectral region at 2900 cm^{-1} confirmed the presence of lipid residues (CH3 and CH2 groups) in the studied CW, similarly, absorption band at 2160 cm^{-1} (C ≡ C group) derived from fatty acid in lipids [15].

Figure 2 shows the IR spectrum of disrupted OP roots and its purified CW *via* lyophilization and homogenization method. Bands at 3340 cm^{-1}, 1250 cm^{-1}, 1030 cm^{-1} and 550 cm^{-1} are characteristics of polysaccharides. Absorption bands located in the spectral region at approximately between 775 cm^{-1} to 1030 cm^{-1} in disrupted root cells could be a consequence of genetic material residue and the presence of glycogen in the analyzed sample [16]. For example, guanine and cytosine absorption bands occur at 775 cm^{-1} while the bands at 820 cm^{-1}, 867 cm^{-1} and 1030 cm^{-1} could result from deoxyribose and phosphodiester backbones. Subsequently these bands were not observed in purified CW, thus showing the effectiveness of the washing stage in CW purification stage which is also correlated to the DNA absorbance result as shown in Table 2. Therefore, CW materials are considered to be cytoplasmic free. Meanwhile, absorption bands at 2930 cm^{-1} (C-H group) and 1645 cm^{-1} (C-O group) confirmed the presence of lipid residues [15]. Bands at 1425 cm^{-1} and 1370 cm^{-1} attributed to methyl and amine group from protein are absence in purified CW.

Table 2. Effect of lyophilization with homogenization method in cell wall isolation and purification

Protein (µg/g)		**DNA Absorbance (260/280 nm)**			
		GB		**OP**	
GB	**OP**	**260 nm**	**280 nm**	**260 nm**	**280 nm**
0.001 ± 0.9	0.005 ± 1.3	0.002 ± 1.5	0.001 ± 0.3	0.002 ± 0.6	0.003 ± 0.4

Notes: GB = *Ganoderma boninense*; OP = oil palm. Each sample consists of three replicate

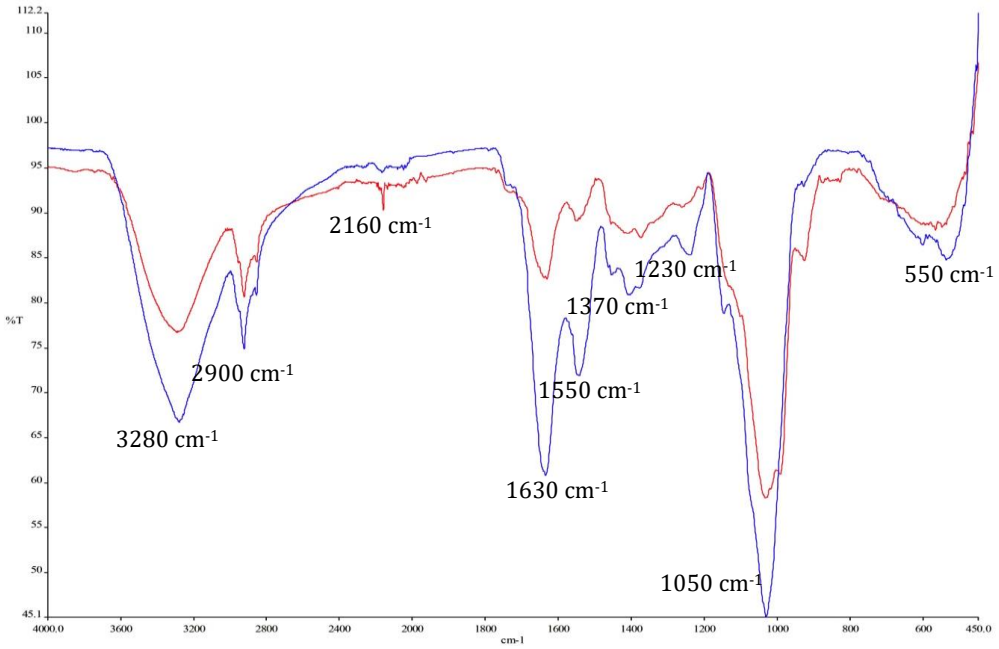


Figure 1. Infra-red spectrum of disrupted cells and purified cell wall of *G. boninense via* lyophilization with homogenization disruption method. Notes: Red line indicates purified cell wall; Blue line indicates disrupted cells before cell wall purification

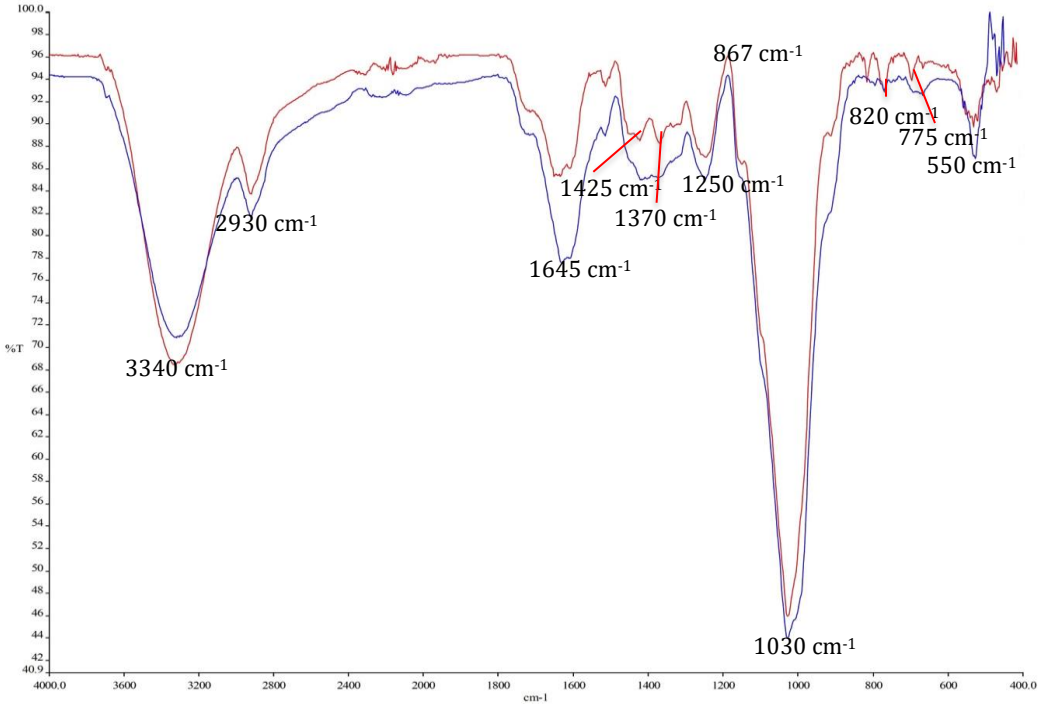


Figure 2. Infra-red spectrum of oil palm roots cell wall preparation after disruption with lyophilization with homogenization. Notes: Red line indicates disrupted roots; Blue line indicates purified cell wall

Conclusion

The use of different methods for oil palm and *G. boninense* cell disruption had a significant effect in the resulting cell wall outcome. Among the analyzed methods, the most promising result was achieved by using lyophilization followed by homogenization disruption method. Cell wall preparation produced with this method was characterized by the lowest proteins content and DNA absorbance under 260 and 280 nm. Isolation of CW at the highest purity will ensure optimum metabolites extraction.

References

1. Underwood, U. (2012). The plant cell wall: A dynamic barrier against pathogen invasion. *Frontier Plant Science*, 3: 85.
2. Shah, J. and Chaturvedi, R. (2009). Lipid signals in plant-pathogen interactions. *Annual Plant Reviews*, 34: 292-333.
3. Siebers, M., Brands, M., Wewer, V., Duan, Y., Georg, H. and Peter, P. (2016). Lipids in plant-microbe interactions. *Biochimica et Biophysica Acta*, 1861(9): 1379-1395.
4. Liu, D. Zeng, Z. A. Sun, D. W. and Han, Z. (2013). Disruption and proteins release by ultrasonication of yeast cells. *Innovative Food Science and Emerging Technologies*, 18: 132-137.
5. Fic, E., Krok, S. K., Jankowska, U., Pirog, A. and Wasylewska, M. D. (2010). Comparison of protein precipitation methods for various rat brain structures prior to proteomic analysis. *Electrophoresis*, 31: 3573-3579.
6. Canut, H., Albenne, C. and Jamet, E. (2016). Isolation of the cell wall. *Methods in Molecular Biology*, 1511: 171-185.
7. Middleberg, A. J. (1995). Process-scale disruption of microorganisms. *Biotechnology Advance*, 113: 491-551.
8. Cheung, M. C., LaCroix, R. and McKenna, B. K. (2013). Intercellular protein and nucleic acid measured in eight cell types using deep-ultraviolet mass mapping. *Cytometry*, 83(6): 540-551.
9. Zheng, H., Yin, J., Gao, Z., Huang, H., Ji, X. and Dou, C. (2011). Disruption of *Chlorella vulgaris* cells for the release of biodiesel-producing lipids: A comparison of grinding, ultrasonication, bead milling, enzymatic lysis, and microwaves. *Applied Biochemistry and Biotechnology*, 164: 1215-1224.
10. Siebers, M., Brands, M., Wewer, V., Duan, Y., Georg, H. and Peter, P. (2016). Lipids in plant-microbe interactions. *Biochimica et Biophysica Acta*, 1861(9): 1379-1395.
11. Cooper, G. M. (2000). The cell: A molecular approach (2nd edition). Sinauer associates: Sunderland, Massachusetts.
12. Dallies, N., Jean, F. and Veranique, P. (1998). A new method for quantitative determination of polysaccharides in the yeast cell wall. Application to cell wall defective mutants of *Saccharomyces cerevisiae. Yeast*, 14: 1297-1306.
13. Tatulian, S. A. (2013). Structural characterization of membrane proteins and peptides by FTIR and ATR-FTIR spectroscopy. *Methods in Molecular Biology*, 974: 117-218.
14. Galichet, A., Sockalingum, G. D., Belarbi, A. and Manfait, M. (2001). FTIR spectroscopic analysis of *Saccharomyces cerevisiae* cell walls: Study of an anomalous strain exhibiting a pink-colored cell phenotype. *FEMS Microbiology Letters*, 197: 179-186.
15. Adt, I., Toubas, D., Pinon, J. M., Manfait, M. and Sockalingum, G. D. (2006). FTIR spectroscopy as a potential tool to analyse structural modifications during morphogenesis of *Candida albicans*. *Archeology Microbiology*, 185: 277-285.
16. Tajmir-Rhiai, H. A., N'soukpoé-Kossi, C. N. and Joly, D. (2009). Structural analysis of protein-DNA and protein-RNA interactions by FTIR, UV-visible and CD spectroscopic methods. *Spectroscopy*, 23: 81-101.

Malaysian Journal of Analytical Sciences (MJAS)
Published by Malaysian Analytical Sciences Society

LEVEL OF HEAVY METALS IN BAMBOO SHARKS (*Chiloscyllium* sp.) IN STRAITS OF MALACCA, MALAYSIA

(Kepekatan Logam Berat di dalam Yu Cicak (*Chiloscyllium* sp.) di Selat Melaka, Malaysia)

Jun-Han Poong[1], Lian-Sheng Tee[1], Evonne Tan[1], Tiam-Hing Yip[1], Muhammad Hasbi Ramli[1], Abd Rahman Ali Hassan[2], Ahmad Ali[3], Chen Meng-Hsien[4], James Lam Chung Wah[5], Ong Meng Chuan[1,6,7]*

[1]*Faculty of Science and Marine Environment,*
Universiti Malaysia Terengganu, 21030 Kuala Nerus, Terengganu, Malaysia
[2]*Pejabat Perikanan Daerah Larut Matang dan Selama, 34000 Taiping, Perak, Malaysia*
[3]*Marine Fishery Resources Development and Management Department,*
Southeast Asian Fisheries Development Center (SEAFDEC), 21080 Chendering, Terengganu, Malaysia
[4]*Department of Oceanography,*
National Sun Yat-sen University, 70 Lian-Hai Road, Kaohsiung 80424, Taiwan
[5]*Department of Science and Environmental Studies,*
The Education University of Hong Kong, 10 Lo Ping Road, Tai Po, New Territories, Hong Kong
[6]*Institute of Oceanography and Environment*
[7]*Ocean Pollution and Ecotoxicology (OPEC) Research Group*
Universiti Malaysia Terengganu, 21030 Kuala Nerus, Terengganu, Malaysia

**Corresponding author: ong@umt.edu.my*

Received: 20 November 2019; Accepted: 11 June 2020; Published: 11 August 2020

Abstract

Sharks which are the top predators in the ocean food chain are still high in demand as delicacies (shark meat) in restaurants despite the efforts to protect them. Anyhow, sharks accumulate a significant amount of metals in their bodies. Hence, a study was carried out to examine the presence and concentration of heavy metals (Cd, Cu, Pb and Zn) in bamboo sharks (*Chiloscyllium*), the most commonly landed species. A total of 43 *Chiloscyllium* samples were collected from the local fishermen in Lumut, Perak. In this study, the two edible tissue samples, namely the muscle and fins were dissected and analysed using inductively coupled plasma – mass spectrometry (ICP-MS) following a Teflon bomb closed digestion with HNO_3 acid. Based on the results, the concentration of heavy metals in muscle tissues arranged in a diminution order is Zn > Cu > Pb > Cd. Meanwhile, the concentration pattern of metals in fin tissues followed the Zn > Pb > Cu > Cd sequence. The average concentration of metals in the fin tissues was higher than that of muscle tissues. All metals examined were associated with the sharks' length and weight, whereby the findings also indicated that all metals exhibited positive correlation except for Pb concentration in muscle and Zn concentration in fin tissues. The Pollution Load Index (PLI) was used as the predictor to assess the contamination status in the tissue samples. The average PLI value calculated for the muscle and fin tissues ranged between 3.2 and 12.4, respectively. These values also indicated that the level of contamination is very much under control, hence, no monitoring is needed. Therefore, all findings from this study may be used as a reference for future studies, especially on the west coast of Peninsular Malaysia waters.

Keywords: Straits of Malacca, sharks, heavy metals, pollution load index

Abstrak

Ikan yu adalah pemangsa teratas dalam rantaian makanan dan boleh mengakumulasi sejumlah besar logam berat dalam badan mereka. Terdapat juga permintaan tinggi daging ikan yu sebagai makanan istimewa di restoran. Oleh itu, kajian ini bertujuan untuk menentukan kepekatan logam berat (Cd, Cu, Pb, dan Zn) dalam tisu yu cicak (*Chiloscyllium*) yang paling banyak didaratkan. Sebanyak 43 sampel *Chiloscyllium* telah dikumpulkan daripada nelayan tempatan di Lumut, Perak. Dalam kajian ini, dua tisu iaitu daging dan sirip ikan yu telah dipilih untuk dianalisa dengan menggunakan spektrometri jisim-gadingan aruhan plasma (ICP-MS) selepas proses pencernaan tertutup bom Teflon dengan asid HNO_3. Corak kepekatan logam dalam tisu daging dalam urutan Zn > Cu > Pb > Cd. Manakala kepekatan logam dalam tisu sirip ikan menurun dalam urutan Zn > Pb > Cu > Cd. Pada umumnya, kepekatan logam dalam tisu sirip adalah lebih tinggi berbanding tisu daging. Kandungan logam dalam setiap organ dikaitkan dengan panjang dan berat ikan yu dan semua logam dalam tisu daging menunjukkan korelasi positif, manakala Pb dalam tisu daging dan Zn dalam tisu sirip menunjukkan korelasi negatif kepada panjang dan berat ikan yu. Status pencemaran ikan yu cicak juga dinilai menggunakan Indeks Beban Pencemaran (PLI) sebagai petunjuk pencemaran. Purata nilai PLI untuk tisu daging adalah 3.2, dan untuk tisu sirip adalah 12.4 dan ini menunjukkan tahap pencemaran berada di bawah kawalan dan pemantauan tidak diperlukan. Hasil dapatan kajian ini boleh digunakan sebagai rujukan pada kajian akan datang terutamanya di perairan barat Semenanjung Malaysia.

Kata kunci: Selat Melaka, ikan yu, logam berat, indeks bebanan pencemaran

Introduction

Heavy metal pollution in the marine ecosystem is deemed as a significant environmental problem. The concern, however, is regarding the toxic accumulation of heavy metals in the organism's body and within the ecosystem [1]. These toxic heavy metals are introduced into the estuarine and aquatic environments through anthropogenic activities such as the development of coastal areas. Moreover, the urban, municipal and industrial wastes discharged into the aquatic environment contain a substantial amount of heavy metals contaminating the marine environment [2].

Having said that, the heavy metals input into water easily accumulate in aquatic organisms like sharks. Lopez et al. [3] stated that sharks readily accumulate these elements in their tissues due to their diet as they prey on various trophic organisms. The level of heavy metal accumulation in each organism may differ depending on its diet and habit. Hence, sharks being the top predator consuming most of the organisms would be taking in a higher level of heavy metal concentration into their system [4], especially muscle and fin tissues [5]. Therefore, sharks are suitable bio-indicators of heavy metal contamination in the aquatic environment [6].

In this study, the bamboo shark (*Chiloscyllium*) was chosen as the study sample to determine the level of heavy metals. Based on our survey together with an officer from Department of Fisheries Malaysia located in Lumut, Perak and their statistical data [7], *Chiloscyllium* is the most landed sharks which can be found at the study area. The statistics [7] also documented that the Perak state landed the most number of sharks species, 530 metric tonnes or 58% of the total catch compared to other states along the Straits of Malacca. According to our survey, *Chiloscyllium* is one of the species most fishmongers seek as it is one of the most popular fish among the public at several landing points.

Materials and Methods

Sample collection and preparation

A total of 43 *Chiloscyllium* samples were collected from the local fishermen at Lumut, Perak, Malaysia (Figure 1) in October 2018 which are usually collected as trawl bycatch. Once collected, the samples were labelled and stored in an icebox at low temperature before dissection and analysis in the laboratory [7]. Prior to the dissection, the samples were defrosted at room temperature. The total body length and weight of samples were measured. The sex of the shark was also determined by checking for the presence of clasper. Only the muscle tissues and fin samples were dissected using a ceramic knife. For

each shark, a total of 50g muscle and fin tissues were transferred to a clean sample container. The samples were then rinsed with distilled water to avoid contamination. Next, the muscle and fin samples were dried in an oven at 60 °C until a desired constant dry weight was obtained. Once the samples were dried, pestle and mortar were used to homogenise the sample into powder form. All the apparatus used in sample preparation were cleaned using ethanol after every sample.

Analytical procedures

The Teflon bomb digestion method for biological samples was suggested by Okamoto and Fuwa [8]. This method determines the metal concentration of biota samples in liquid form. Hence, this study employed the modified procedures as described by Kamaruzzaman et al. [9] and Ong et al. [10]. Firstly, 0.05g of the homogenised sample was weighed and transferred into 25 mL Teflon beaker. Then, 1.5 mL of Suprapur 65% nitric acid (HNO_3) was added into the Teflon beaker. Since HNO_3 is a strong acid, this step was performed in a perchloric fume hood. Then, the Teflon beaker was sealed tight to prevent acid leakage during the acid digestion process.

Blank and certified reference material (DOLT-4 Dogfish liver) samples were processed simultaneously to test the accuracy of the procedure. All the Teflon bombs were heated in an oven at 100 °C for 8 hours to aid the digestion process. After 8 hours of heating, the Teflon bombs were let to cool down to room temperature, where the acid-digested solution in the Teflon bombs was transferred into separate centrifuge tubes. Deionized water was added to a 10mL mark. Finally, the concentrations of heavy metals namely Cadmium (Cd), Copper (Cu), Lead (Pb) and Zinc (Zn) were obtained using inductively coupled plasma mass spectrometry (ICP-MS) model Elan 6000. Table 1 lists the detection and quantification limits for the ICP-MS instrument used in the sample detection.

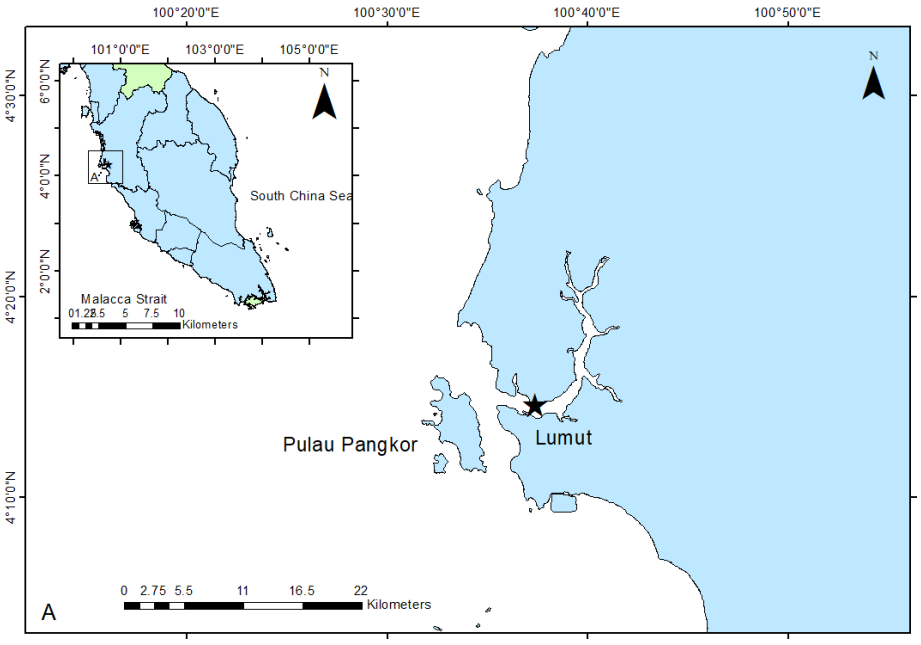


Figure 1. Map showing the location of the sampling area at Lumut, Perak

Table 1. Detection and quantification limits for the ICP-MS Elan 9000 instrument

Element	Mass	Detection Limit (µg/L)	Quantification Limit (µg/L)
Cd	114	0.003	0.01
Cu	63	0.21	0.69
Pb	208	0.02	0.05
Zn	64	0.26	0.85

Results and Discussion

Table 2 illustrates the biological data of the 43 *Chiloscyllium* samples collected in this study, including the length and weight. The average length and weight were estimated at 54.5cm and 758g, respectively. The length of the largest *Chiloscyllium* in this study was 82.0 cm, while the smallest recorded was 38.3 cm. Meanwhile, the weight ranged from 213 to 2483g. The length and weight of each *Chiloscyllium* were recorded to determine the correlation with the studied metals.

Table 3 indicates the result of the recovery test for the selected heavy metals using 1946 DOLT-4 Dogfish liver as the Standard Reference Material (SRM). The recovery test is used to control the accuracy of the methodology. The recovery percentage of the selected metals namely Cd, Cu, Pb and Zn ranged between 87.2% and 112.5%. According to Yohannes et al. [11], recovery percentage ranging between 80% - 115% indicate good accuracy and that the data obtained is acceptable.

The concentration of heavy metals in the edible tissues of *Chiloscyllium* are tabulated in Table 4 and Table 5, respectively. Based on the results, muscle samples indicated a decreasing trend of Zn > Cu > Pb > Cd, whereby this metal concentration trend in muscle tissue was in agreement with previous studies [12, 13, 14]. The fin samples, on the other hand, demonstrated a trend of Zn > Pb > Cu > Cd. Of the four heavy metals, Zn and Cu appeared to be present in high concentrations because they are essential metals [15]. These heavy metals are fundamentally necessary for fish growth development [14] and as micronutrients to fishes that is obtained through water and diet [16].

However, the non-essential metals such as Pb and Cd were present in low concentrations as they do not have any biological importance and are not needed by an organism [17]. The concentration of Pb was higher than that of Cu in the fin samples possibly due to the ambient Pb concentration in the sampling location, Lumut. Lumut is a coastal town with notable ship activities for fisheries and tourism. Hence, the accumulation of such metals in the waters at a reasonably high concentration in a developed coastal area indicates the impacts of human activities. Additionally, several researchers have also mentioned the accumulation of heavy metals in marine ecosystems were associated with urban runoff, water treatment systems, industrial effluents and waste, shipping and agricultural runoff [18-22].

Compared to the concentrations of metals (Zn, Cu, Pb and Cd) between the samples, fin tissues contained higher concentrations of metal than that of the muscle. This observation could probably be because fin is the final destination where all metals accumulate [7]. However, the concentration of metals can vary in shark tissues due to several factors, including the size of the shark, sex, species, feeding habit and habitat [23, 24].

Table 2. Size of *Chiloscyllium* sp. collected in this study

	Length (cm)	**Weight (g)**
Average	54.5±9.3	758±469
Min	38.3	213
Max	82.0	2483

Table 3. Recovery test using Standard Reference Material (SRM) 1946 DOLT-4 Dogfish liver

Metals	**Measured Value (µg/g dry wt.)**	**Certified Value (µg/g dry wt.)**	**Recovery (%)**
Copper (Cu)	28.8±1.5	31.2±1.1	92.3
Zinc (Zn)	110±8.0	116±6.0	94.8
Cadmium (Cd)	21.2±1.2	24.3±0.8	87.2
Lead (Pb)	0.18±0.07	0.16±0.04	112.5

Table 4. Concentration of metals in bamboo shark muscle

Samples	**Concentration of Metals in Muscle (µg/g dry wt.)**			
	Cu	**Zn**	**Cd**	**Pb**
Average	0.75 ± 0.33	28.30 ± 16.20	0.07 ± 0.04	0.72 ± 0.35
Min	0.31	9.50	0.02	0.31
Max	1.65	110.40	0.16	2.33

Table 5. Concentration of metals in bamboo shark fins

Samples	**Concentration of Metals in Fins (µg/g dry wt.)**			
	Cu	**Zn**	**Cd**	**Pb**
Average	4.16 ± 3.74	62.20 ± 25.00	0.31 ± 0.33	9.53 ± 12.90
Min	0.75	24.50	0.02	0.26
Max	20.61	138.80	1.45	63.54

Figure 2 to Figure 5 represent the correlation graphs between the concentrations of selected metals (Cu, Zn, Cd and Pb) in edible shark tissues against shark size. The correlation of Zn and Pb against shark size varied between muscle and fin sample. Kamaruzzaman et al. [13] also published similar findings that there was no or weak relationship between Zn and Pb against the size of the shark.

According to Adel et al. [15] and Endo et al. [25], the concentration of accumulated Cu and Cd in shark muscle were related to shark body length. However, Cd concentration pattern in *Chiloscyllium* from the Straits of Malacca indicated a weak positive correlation between shark size and edible tissue of shark, which might be associated with the shark's feeding preference and habits. Generally, *Chiloscyllium* species feed extensively on molluscs and cephalopods, which contains a high concentration of Cd in their body [15].

On the other hand, the positive correlation between Cu with shark size and a comparatively higher Cu level in their body might be due to the diet of bamboo sharks [26]. Ong & Gan [7] mentioned that *Chiloscyllium* is a demersal shark species that consume a higher proportion of crustaceans and molluscs in their diet [26]. According to Vas [27], crustacean and molluscs usually contain high Cu content due to the presence of haemocyanin in their tissues. Hence, the crustaceans and molluscs dependent diet may be accounted for the high level of Cu in *Chiloscyllium* sp.

As previously reported by Mendoza-Carranza et al. [28], the primary transfer route of heavy metals in the aquatic environment is through the diet of an organism, which is mainly through vertical (between different trophic levels) and horizontal (within the same tropical level) transfer [29]. Similar observations can also be concluded for the bamboo sharks as the aforementioned literature [12, 15, 26, 27]. Moreover, molluscs are also deemed as good bioindicators for metal pollution in seawater as they easily absorb heavy metals in the aquatic environment [30]. Since molluscs are identified as ecologically important organisms and are preyed upon by bamboo sharks [12], bamboo sharks end up as ecological basin accumulating much of the heavy metals in the aquatic environment.

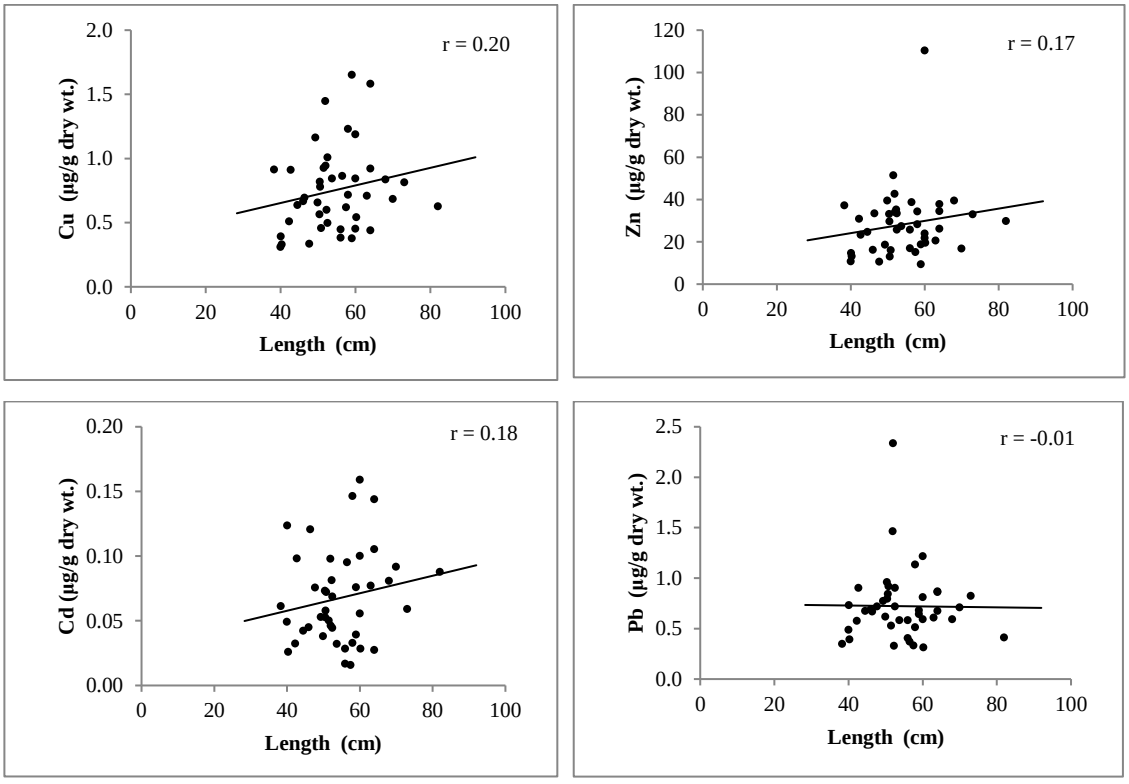


Figure 2. Correlation graph between concentration of selected metals (Cu, Zn, Cd, and Pb) in shark muscle and length of shark

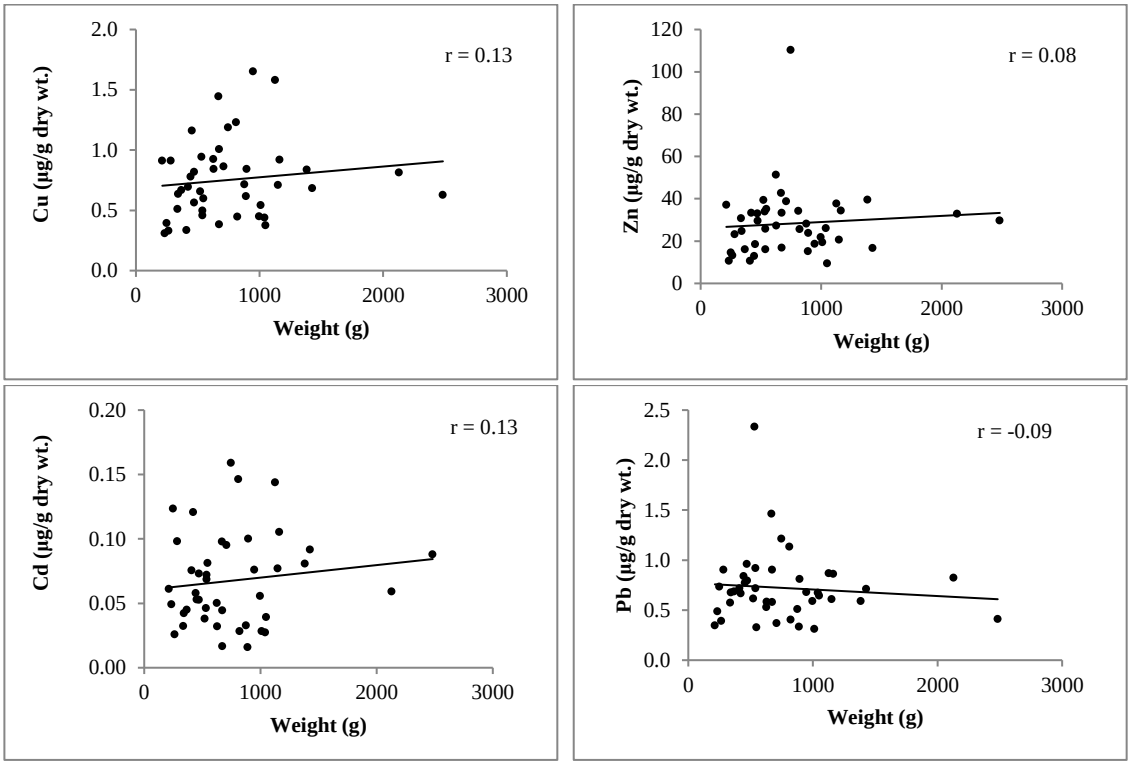
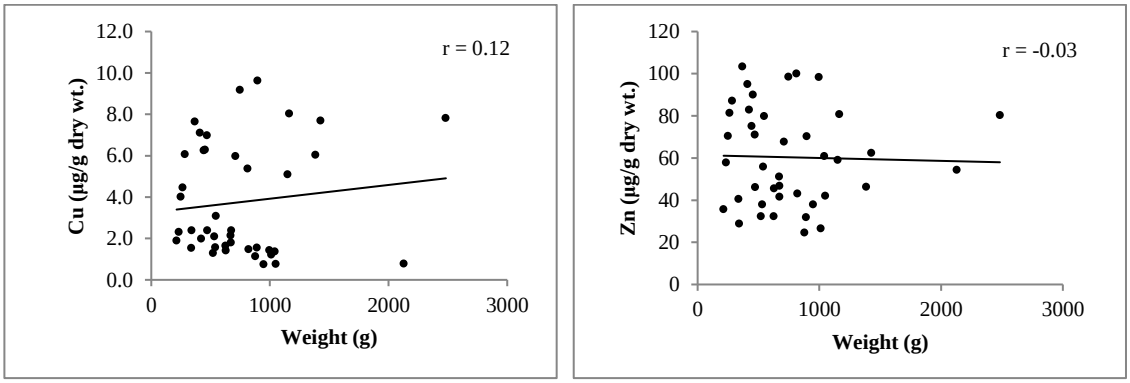


Figure 3. Correlation graph between concentration of selected metals (Cu, Zn, Cd, and Pb) in shark muscle and weight of shark



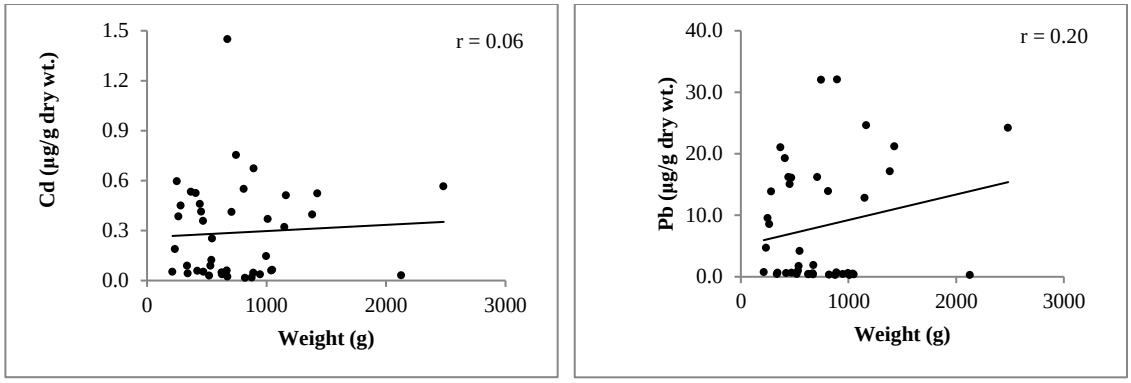


Figure 4. Correlation graph between concentration of selected metals (Cu, Zn, Cd, and Pb) in shark fin and length of shark

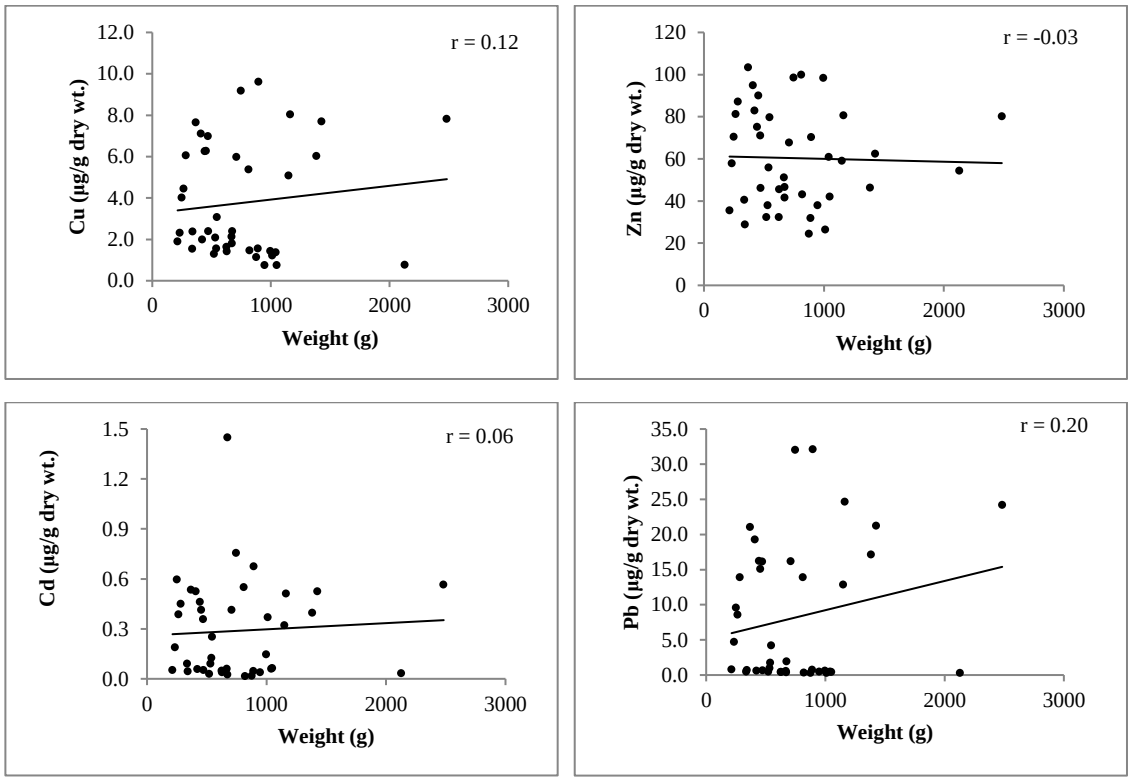


Figure 5. Correlation graph between concentration of selected metals (Cu, Zn, Cd, and Pb) in shark fin and weight of shark

Table 6 presents the correlation between heavy metals in muscle and fin samples, respectively. According to the table, all four metals exhibited a positive correlation among them, indicating a common source of the metals [31]. Among the metals, Cu-Pb demonstrated a strong correlation value of 0.70, further suggesting that these two metals might originate from the same source. According to Yap et al. [32], Cu and Pb might have originated from anthropogenic sources, such as industrial activities and sewage systems.

Table 6. Correlation values between heavy metals in *Chiloscyllium* sample

	Cu	**Zn**	**Cd**
Zn	0.56		
Cd	0.57	0.47	
Pb	0.70	0.48	0.47

The Pollution Load Index (PLI) compares the pollution levels among different sites or at different times [33]. The index provides a general and clear view of the levels of total heavy metal pollution. PLI values below 50 indicate that no action is required, values of 50 and above suggest the requirement of monitoring, while values of 100 and above indicate extreme pollution [34]. PLI was determined using the method described by Angulo [35] based on the Equation 1 and 2.

The calculated PLI values from the *Chiloscyllium* samples are provided in Table 7. Generally, the PLI values of the fins were higher than that of the muscle samples. However, according to the overall PLI values, no action is required in this study area as the average values were far below 50.

$$Pollution\ Load\ Index\ (PLI) = \sqrt[n]{CF_1 \times CF_2 \times CF_3 \times \ \dots \ \times \ CF_n} \quad (1)$$

where, n = number of metals

$$Contamination\ factor\ (CF) = \frac{Concentration\ of\ metal}{Concentration\ of\ background} \quad (2)$$

Table 7. The Pollution Load Index (PLI) of edible tissue of *Chiloscyllium* sp.

	PLI	
	Muscle	**Fin**
Average	3.2 ± 0.9	12.4 ± 10.4
Min	2.6	1.7
Max	4.7	35.0

Conclusion

Based on the findings, *Chiloscyllium* samples obtained from Lumut, Perak, Malaysia, demonstrated a concentration of heavy metals in the muscle and fin samples with a descending order of Zn > Cu > Pb > Cd and Zn > Pb > Cu > Cd, respectively. The concentrations of heavy metals in the fins were higher than that was accumulated in the muscle. Moreover, the uptake of heavy metals is size-dependent and accumulates in the fins at a higher rate. Nevertheless, some previous studies indicated that shark size is not the only factor influencing the heavy metal content in sharks. Other variables such as the shark biological, environmental factors and dietary preferences need to be taken into account to assess the accumulation of heavy metals in sharks. However, based on the PLI values recorded in

this study, no monitoring is required currently in the study area. Nevertheless, frequent research could ensure that the degree of pollution in well under control in marine environments. The findings from this study can also be used to estimate the intake of heavy metals by a human *via* the consumption of bamboo shark meat since it is a delicacy for the public.

Acknowledgment

This research was conducted with the funding from the Faculty of Science and Marine Environment and INOS under Higher Institution Centre of Excellence (HICoE, 66928), Universiti Malaysia Terengganu. First of all, the authors wish to acknowledge their gratitude to the anonymous reviewers who gave freely time and effort, constructive recommendations that enhanced the value of this manuscript. The authors also wish to express their gratitude to Oceanography Laboratory, Faculty of Science and Marine Environment staff for their invaluable assistance and providing the facilities to carry out the research. The authors also would like to thank Mr. Joseph Bidai for his assistant in detecting heavy metals using ICPMS at the Institute of Oceanography and Environment.

References

1. Kotze, P., Du Preez, H. H. and Van Vuren, J. H. J. (1999). Bioaccumulation of copper and zinc in *Oreochromis mossambicus* and *Clarias gariepinus*, from the Olifants River, Mpumalanga, South Africa. *Water SA*, 25(1): 99-110.
2. Guthrie, R. K., Davis, E. M., Cherry, D. S. and Murray, H. E. (1979). Biomagnification of heavy metals by organisms in a marine microcosm. *Bulletin of Environmental Contamination and Toxicology*, 21(1): 53-61.
3. Lopez, S. A., Abarca, N. L. and Meléndez, R. C. (2013). Heavy metal concentrations of two highly migratory sharks (*Prionace glauca* and *Isurus oxyrinchus*) in the Southeastern Pacific Waters: Comments on public health and conservation. *Tropical Conservation Science*, 6(1): 126-137.
4. Stevens, J. D., Bonfil, R., Dulvy, N. K. and Walker, P. A. (2000). The effects of fishing on sharks, rays, and chimaeras (*chondrichthyans*), and the implications for marine ecosystems. *ICES Journal of Marine Science*, 57(3): 476-494.
5. Bengil, F. and Mavruk, S. (2019). Warming in Turkish Seas : Comparative multidecadal assessment. *Turkish Journal of Fisheries and Aquatic Sciences*: 1-10.
6. Storelli, M. M., Giacominelli-Stuffler, R. and Marcotrigiano, G. (2002). Mercury accumulation and speciation in muscle tissue of different species of sharks from Mediterranean Sea, Italy. *Bulletin of Environmental Contamination and Toxicology*, 68(2): 201-210.
7. Ong, M. C. and Gan, S. L. (2017). Assessment of metallic trace elements in the muscles and fins of four landed elasmobranchs from Kuala Terengganu waters, Malaysia. *Marine Pollution Bulletin*, 124(2): 1001-1005.
8. Okamoto, K. and Fuwa, K. (1984). Low-contamination digestion bomb method using a teflon double vessel for biological materials. *Analytical Chemistry*, 56(9): 1758-1760.
9. Kamaruzzaman, B. Y., Rina, Z., Akbar John, B. and Jalal, K. C. A. (2011). Heavy metal accumulation in commercially important fishes of south west Malaysian coast. *Research Journal of Environmental Sciences*: 1-8.
10. Ong, M. C., Yong, J. C., Khoo, X. Y., Tan, Y. F. and Joseph, B. (2014). Selected heavy metals and polycyclic aromatic hydrocarbon in commercial fishes caught from UMT enclosed lagoon, Terengganu, Malaysia. *Advances in Environmental Biology*, 8(14): 91-98.
11. Yohannes, Y. B., Ikenaka, Y., Nakayama, S. M. M., Saengtienchai, A., Watanabe, K. and Ishizuka, M. (2013). Organochlorine pesticides and heavy metals in fish from Lake Awassa, Ethiopia: Insights from stable isotope analysis. *Chemosphere*, 91(6): 857-863.
12. Adel, M., Copat, C., Saeidi, M. R., Conti, G. O., Babazadeh, M. and Ferrante, M. (2018). Bioaccumulation of trace metals in banded persian bamboo shark (*Chiloscyllium arabicum*) from the Persian Gulf: A food safety issue. *Food and Chemical Toxicology*, 113: 198-203.

13. Kamaruzzaman, B. Y., Ong, M. C. and Rina, S. Z. (2010). Concentration of Zn, Cu and Pb in some selected marine fishes of the Pahang coastal waters, Malaysia. *American Journal of Applied Sciences*, 7(3): 309-314.
14. Ong, M. C. and Gan, S. L. (2016). Heavy metals concentration in four landed elasmobranchs from Kuala Terengganu waters, Malaysia. *International Journal of Applied Chemistry*, 12(4): 761-772.
15. Adel, M., Oliveri Conti, G., Dadar, M., Mahjoub, M., Copat, C. and Ferrante, M. (2016). Heavy metal concentrations in edible muscle of whitecheek shark, *Carcharhinus dussumieri* from the Persian Gulf: A food safety issue. *Food and Chemical Toxicology*, 97: 135-140.
16. Clearwater, S. J., Farag, A. M. and Meyer, J. S. (2002). Bioavailability and toxicity of dietborne copper and zinc to fish. *Comparative Biochemistry and Physiology - C Toxicology and Pharmacology*, 132(3): 269-313.
17. Mohammed, A. and Mohammed, T. (2017). Mercury, arsenic, cadmium and lead in two commercial shark species (*Sphyrna lewini* and *Caraharinus porosus*) in Trinidad and Tobago. *Marine Pollution Bulletin*, 119(2): 214-218.
18. Chow, T. J., Earl, J. L. and Bennett, C. F. (1969). Lead aerosols in marine atmosphere. *Environmental Science and Technology*, 3(8): 737-740.
19. Järup, L. (2003). Hazards of heavy metal contamination. *British Medical Bulletin*, 68: 167-182.
20. Tong, S., von Schirnding, Y. E. and Prapamontol, T. (2000). Environmental lead exposure: A public health problem of global dimensions. *Bulletin of the World Health Organization*, 78(9): 1068-1077.
21. Alemdaroglu, T., Onur, E. and Erkakan, F. (2003). Trace metal levels in surface sediments of Lake Manyas, Turkey and tributary river. *International Journal of Environmental Studies*, 60: 287-298.
22. Alina, M., Azrina, A., Mohd Yunus, A. S., Mohd Zakiuddin, S., Mohd Izuan Effendi, H. and Muhammad Rizal, R. (2012). Heavy metals (mercury, arsenic, cadmium, plumbum) in selected marine fish and shellfish along the Straits of Malacca. *International Food Research Journal*, 19(1): 135-140.
23. Al-Yousuf, M. H., El-Shahawi, M. S. and Al-Ghais, S. M. (2000). Trace metals in liver, skin and muscle of *Lethrinus lentjan* fish species in relation to body length and sex. *Science of the Total Environment*, 256(2–3): 87-94.
24. Canli, M. and Atli, G. (2003). The relationships between heavy metal (Cd, Cr, Cu, Fe, Pb, Zn) levels and the size of six mediterranean fish species. *Environmental Pollution*, 121(1): 129-136.
25. Endo, T., Kimura, O., Ohta, C., Koga, N., Kato, Y., Fujii, Y. and Haraguchi, K. (2016). Metal concentrations in the liver and stable isotope ratios of carbon and nitrogen in the muscle of silvertip shark (*Carcharhinus albimarginatus*) culled off Ishigaki Island, Japan: Changes with growth. *PLoS ONE*, 11(2): 1–18.
26. Cornish, A. S., Ng, W. C., Ho, V. C. M., Wong, H. L., Lam, J. C. W., Lam, P. K. S. and Leung, K. M. Y. (2007). Trace metals and organochlorines in the bamboo shark *Chiloscyllium plagiosum* from the southern waters of Hong Kong, China. *Science of the Total Environment*, 376(1–3): 335-345.
27. Vas, P. (1991). Trace metal levels in sharks from British and Atlantic waters. *Marine Pollution Bulletin*, 22(2): 67-72.
28. Mendoza-Carranza, M., Sepúlveda-Lozada, A., Dias-Ferreira, C. and Geissen, V. (2016). Distribution and bioconcentration of heavy metals in a tropical aquatic food web: A case study of a tropical estuarine lagoon in SE Mexico. *Environmental Pollution*, 210: 155-165.
29. Jara-Marini, M. E., Soto-Jiménez, M. F. and Páez-Osuna, F. (2009). Trophic relationships and transference of cadmium, copper, lead and zinc in a subtropical coastal lagoon food web from SE Gulf of California. *Chemosphere*, 77(10): 1366-1373.
30. Conti, M. E., Stripeikis, J., Finoia, M. G. and Tudino, M. B. (2012). Baseline trace metals in gastropod mollusks from the Beagle Channel, Tierra del Fuego (Patagonia, Argentina). *Ecotoxicology*, 21(4): 1112-1125.

31. Nyangababo, J. T., Henry, L. and Omutange, E. (2005). Lead, cadmium, copper, manganese, and zinc in wetland waters of Victoria Lake Basin, East Africa. *Bulletin of Environmental Contamination and Toxicology*, 74(5): 1003-1010.
32. Yap, C. K., Ismail, A., Tan, S. G. and Omar, H. (2002). Concentrations of Cu and Pb in the offshore and intertidal sediments of the west coast of Peninsular Malaysia. *Environment International*, 28: 467-479.
33. Wuana, R. A. and Okieimen, F. E. (2011). Heavy metals in contaminated soils : A review of sources, chemistry, risks and best available strategies for remediation. *ISRN Ecology,* 2011: 402647.
34. Goher, M. E., Farhat, H. I., Abdo, M. H. and Salem, S. G. (2014). Metal pollution assessment in the surface sediment of Lake Nasser, Egypt. *Egyptian Journal of Aquatic Research*, 40(3): 213-224.
35. Angulo, E. (1996). The Tomlinson Pollution Load Index applied to heavy metal, "Mussel- Watch" data: A useful index to assess coastal pollution. *Science of the Total Environment*, 187(1): 19-56.

Malaysian Journal of Analytical Sciences (MJAS)
Published by Malaysian Analytical Sciences Society

REAL-TIME MONITORING OF FOOD FRESHNESS USING DELPHINIDIN-BASED VISUAL INDICATOR

(Pemantauan Kesegaran Masa Nyata Makanan dengan Menggunakan Indikator Visual Berasaskan Delphinidin)

Nurdiyana Husin[1]*, Mohd. Zulkhairi Abdul Rahim[2], Mohd. Azizan Mohd. Noor[1], Ismail Fitry Mohammad Rashedi[3], Nazatulshima Hassan[2]

[1]*Section of Bioengineering Technology*
[2]*Section of Technical Foundation*
Universiti Kuala Lumpur Malaysian Institute of Chemical & Bioengineering Technology, Lot 1988, Bandar Vendor, 78000 Alor Gajah, Malacca, Malaysia
[3]*Faculty of Science and Food Technology, Universiti Putra Malaysia, Serdang, 43400 Seri Kembangan, Selangor, Malaysia*

**Corresponding author: mohd.zulkhairi@unikl.edu.my*

Received: 20 November 2019; Accepted: 18 June 2020; Published: 11 August 2020

Abstract

Nowadays, there is an increasing demand from consumers for better quality and hygienic food products, particularly for vulnerable foods that are easily infected by microorganisms. At present, consumers only depend on the expiry date, but this information does not always portray the real indication of the actual progress of food spoilage. The use of a colorimetric freshness indicator can provide direct and real-time visual quality information, but most of the previous works focused on synthetic colours. In this project, a natural colour (anthocyanin-delphinidin derivative) from *Clitoria ternatea* (butterfly pea) flower was extracted using an ultrasonic processor, followed by immobilisation on indicator strips, and finally applied as a freshness indicator for the qualitative detection of beef freshness. The extracted colour changed obviously at different pH values, from dark blue (pH 5.93) to green (pH 8) and yellow at pH 12. The delphinidin-based visual indicator was also able to detect the spoilage of beef at hour 18 (pH 6.76 ± 0.29 and point of rejection at 25.67 ΔE*) at room temperature (25 ± 1 °C) and on day 6 (pH 6.71 ± 0.05 and point of rejection at 27.09 ΔE*) in chiller storage (4 ± 1 °C). The tested visual indicators at room and chiller temperature responded to the changes of pH as volatile compounds were gradually produced from the spoiled product. The colour of the indicators subsequently changed from dark blue to green and was easily visible to the naked eye. This study provides a foundation for developing a new visual indicator for monitoring real-time beef freshness and may also be used for intelligent packaging.

Keywords: beef freshness, butterfly pea, visual indicator, intelligent packaging

Abstrak

Kebelakangan ini, keinginan pengguna terhadap produk makanan yang bersih dan berkualiti semakin meningkat, terutama bagi produk makanan yang mudah dijangkiti mikroorganisma. Sehingga kini, pengguna hanya bergantung kepada tarikh luput untuk menentukan kualiti produk makanan, yang mana ia tidak menggambarkan keadaan sebenar makanan tersebut. Penggunaan indikator visual kesegaran berdasarkan warna akan membolehkan kesegaran makanan dapat dikenal pasti secara terus, akan tetapi

kebanyakan kajian tersebut adalah lebih kepada menggunakan bahan pewarna sintetik. Dalam kajian ini, pewarna natural diekstrak daripada bunga telang dengan menggunakan kaedah ultrasonik, diserap ke atas kertas indikator, dan akhir sekali digunakan sebagai pengukur kesegaran bagi mengukur tahap kesegaran daging. Hasil kajian menunjukkan berlaku perubahan warna yang ketara pada pH yang berbeza; bermula daripada warna biru gelap pada pH 5.93 dan bertukar kepada warna hijau pada pH 8–9 dan berubah ke warna kuning pada pH 12. Pada suhu bilik (25 ± 1 °C), indikator visual berjaya mengesan kerosakan daging pada jam ke 18, pada pH 6.76 ± 0.29 dan titik penolakan pada 25.67 ΔE*. Manakala pada suhu penyejuk (4 ± 1 °C), kerosakan daging dapat dikesan pada hari ke 6, pada pH 6.71 ± 0.05 dan pada titik penolakan 27.09 ΔE*. Indikator visual yang diuji pada suhu bilik dan penyejuk telah menunjukkan tindak balas terhadap perubahan pH yang disebabkan oleh gas yang terhasil daripada daging yang rosak. Warna indikator visual kemudiannya telah bertukar daripada biru gelap ke hijau dan ia mudah dilihat dengan mata kasar. Kajian ini menyediakan asas kepada pembangunan indikator visual bagi mengukur kesegaran daging secara terus dan boleh juga digunakan untuk kegunaan pembungkusan pintar.

Kata kunci: kesegaran daging, bunga telang, visual indikator, pembungkusan pintar

Introduction

At present, the monitoring of superior quality and hygienic food products becomes a great concern due to the increasing awareness of consumers. Vulnerable foods like seafood, chicken, fish, and meat are products that are easily infected by microorganisms at ambient conditions (~ 25 °C). Poultry meat is a highly perishable food and usually deteriorates within one week of slaughter, regardless of the chilled storage system [1].

Commonly, the meat quality is checked through sensory evaluation and chemical experiments that involved the evaluation of microbial growth. Sensory evaluation is usually based on flavour, stickiness, elasticity, and colour of its texture. This so-called traditional method is sometimes rejected due to human errors that may come from the expert panels [2]. Furthermore, this method is inefficient and has low precision. Moreover, the microbiological test including bacterial counts is very time consuming and very far from real-time monitoring. These characteristics contradict with consumers' interest that would like to know the quality of food products. Therefore, in order to satisfy consumers and assist food manufacturers, a real-time quality control and safety system should be introduced for food products.

Meat, specifically beef, is considered fresh at pH 5.8 to 6.2. At pH above 6.5, the beef is considered spoiled, and it is a favourable growth condition for microorganisms to decompose the beef [3, 4]. As the pH of meat increases, the pH of volatile compounds gradually increases [5]. During the decomposition of meat by microorganisms, meat usually releases volatile compounds, such as methylamine, dimethylamine, trimethylamine, fatty acids, ketones, alcohols, hydrogen sulphide, methyl sulphide, and dimethyl sulphide to the air [6].

The pH of meat is measured at pH 7.1 and after being slaughtered, the pH becomes acidic (pH 5.4-5.7) within 18-24 hours due to the conversion of glycogen to lactic acid (Figure 1). After reaching the lowest point of acidic pH, the pH value will gradually increase to a neutral pH and known as the pH of fresh meat [5]. During the aging period of beef, muscle proteins are partially hydrolysed into ammonia, amines, and other alkaline substances by cathepsins, and thus the pH values of beef increased during this period [7, 8].

Several studies have demonstrated that colours can be used as sensing elements for a real-time freshness indicator on different food samples, but most of the researchers focused on synthetic colours rather than natural colours [1, 5, 9, 10, 11]. Natural colours are more favourable compared to chemical or synthetic colours (or dyes), which are harmful to human life, can cause lung diseases, and trigger skin infection. Natural colours have the merits obtained from renewable resources and are also non-hazardous and eco-friendly. Common natural colours are bell pepper, red cabbage (vegetable), spinach (leaf), annatto (seed), turmeric, beet juice (root), and many more [12, 13].

Clitoria ternatea (butterfly pea) is a perennial twining herb found abundantly in Malaysia, and the most outstanding feature is its intense deep blue flowers [14].

Traditionally, the blue dye aqueous extract from the petal is used to cover grey hair as a cosmetic for hair dying. It is also used in the pharmaceutical industry as a pH indicator, as well as confectionery colouring substances in the food industry [15]. Butterfly pea is originally from Southeast Asia and its petals store ternatins, a group of (poly)acylated anthocyanins. All anthocyanins in butterfly pea petals originated from delphinidin, which is responsible for the blue colour [15, 16]. Purified delphinidin from butterfly pea suffers from colour instability and bleaching, whereas non-purified delphinidin retains its original colour for months [17].

Saptarini et al. [18] revealed that the delphinidin derivative in butterfly pea contained flaviliumcation, which likely changed the colour of butterfly pea extract in different pH solutions. Thus, this indicates that the butterfly pea colour has a good potential to be used as an indicator in food quality measurement and at the same time, this indicator provides an inexpensive value-added approach for intelligent packaging, which acts as analytical instrument [19].

In this research, the natural colour from *C. ternatea* flower was extracted using an ultrasonic processor, followed by immobilisation on indicator paper, and finally applied as a freshness indicator for the qualitative detection of beef freshness. The idea of freshness indicators is that they monitor the quality of the packed beef by reacting in one way or another to changes occurring in the fresh food product due to microbial growth or metabolism. The employment of natural colour in the colorimetric indicator is advantageous because this indicator does not have any chemical effect on packed beef. Besides, this study provides a foundation for developing a new visual indicator in monitoring real-time meat freshness and may also be used in intelligent packaging.

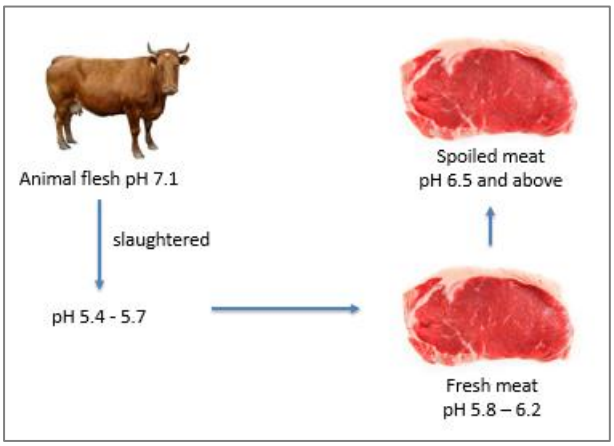


Figure 1. Chronology of pH in meat, from animal flesh until it becomes spoiled meat

Materials and Methods

Preparation of butterfly pea

Butterfly pea petals were collected from a private plantation based in Serdang, Selangor. The area of cultivation is free of fungicide and pesticide. The sampling was done by hand picking method and only the flowers with no visible symptoms of any diseases were collected. The collected materials were stored in zip-lock plastic bags and processed within 24 hours after the collection. In the laboratory, the samples were cleaned under running tap water and proceeded with the sample preparation method. Butterfly pea was dried in an oven at 40 °C for 24 hours. It was ground using a commercial grinder and sieved using sieve number 60 (250 µm) to achieve a constant particle size [20]. Powdered butterfly pea was stored in an air-tight container and kept in desiccators prior to analysis [21].

Extraction of natural colour from butterfly pea using water extraction assisted by ultrasonic irradiation

Water (100 mL) was added in powdered butterfly pea (15 g) and placed in a 250 mL beaker. The beaker was placed in an ultrasonic bath and sonicated for 5-30 minutes at 27-30 MHz and 160 V. After sonication, the content of the beaker was filtered through a filter cloth to remove solid particles. Then, the filtered extract was centrifuged at 2,000 rpm, 10 minutes, and 4 °C [22]. The delphinidin solution obtained was stored in a chiller at 4 °C for further analysis.

Total anthocyanin content

The determination of the total amount of anthocyanins (TAC) was adapted from the reported spectrophotometric method [23]. Absorbance was measured after centrifugation (at 3,000 ×g for 15 minutes) at 568 nm against a reagent blank. Delphinidin-3-glucoside-chloride (Cayman Chemical, USA) was used as a standard pigment, and TAC was expressed as mg delphinidin 3-glucoside equivalent per 100 mL of extract.

Analysis of pH on delphinidin solution

Butterfly pea extract was added to a 5 ml buffer solution of pH 1 to pH 14, and then the colour change was observed [18]. Colour changes were checked using a tintometer (Lovibond PFX880) to determine the CIE colour space coordinates, i.e. colour visible to the human eye, as specified by the International Commission on Illumination (Commission Internationale d'Eclairage, CIE) using L*, a*, and b* values. The values of L*, a*, and b* represent lightness, redness, and yellowness, respectively.

Ultraviolet-visible spectra measurement

The absorption spectra of butterfly pea extract were analysed using an ultraviolet-visible (UV-Vis) spectrophotometer (Varioskan Lux, ThermoFisher Scientific) for determining the wavelength and absorbance. UV-Vis spectrum of the extract was obtained at a wavelength of 400 to 700 nm. The absorption spectra of the extracted solutions were correlated with the standard, delphinidin glucoside, to validate the extraction process.

Fabrication of delphinidin-based visual indicator

A visual indicator was made of filter paper (Whatman 42) with the dimension of 4.2 cm × 1.5 cm (Figure 2). Butterfly pea extract was immobilised on the indicator paper using spin-coated method. Seven strips of indicator paper were centrifuged with 15 mL of butterfly pea extract at 3,000 rpm, 15 minutes, and 4 °C [24]. Then, the indicator was dried using a hair dryer for 15 minutes for uniform drying on both sides of the indicator.

Preparation of beef sample

Semimembranosus muscle was extracted from the top (inside) round of a cow carcass with insignificant fat content. The round portion obtained from the carcass (12 hours after slaughtered) was immediately kept in a cooler box and transported to the laboratory. Each portion obtained from the carcass was divided into 20 g of beef sample and placed in a sealed container.

Measurement of the response of delphinidin-based visual indicator

To evaluate the applicability of the developed visual indicator in monitoring the spoilage of beef, the delphinidin-based visual indicator was placed inside the package of the beef sample. The indicator was in direct contact with the atmosphere inside the container and stored at room temperature (25 ± 1 °C) and chiller temperature (4 ± 1 °C). This method was used to make sure that there would be no effect from external atmospheric conditions. For the control, the visual indicator was placed inside a container without beef sample. The distinct colour change of the indicator from the initial to the final stage was used as the measurable response of change, ΔE*. The colour changes on the indicator were checked using a hand-held colorimeter (Chroma Meter CR-10, Minolta Inc., Japan) to determine the CIE colour space coordinates (L*, a*, b*, and ΔE*). Here, ΔE* (i.e. colour change) was used as the indicator response for the colour changes of the visual indicator (in arbitrary units) that was calculated as [(a*2+b*2)0.5] [5].

Measurement of pH on meat

The pH of the beef sample was measured using a portable pH meter (LAQUAtwin, Horiba) with a flat

sensor as the electrode. The beef sample was placed on the measuring electrode and the pH values were recorded with the accuracy of ± 0.1 pH.

Statistical analysis

The results from multiple samples were reported using analysis of variance (ANOVA) from Minitab version 18 (companion by Minitab®) by means of the average values ± standard deviation. The significance was defined at $p < 0.05$.

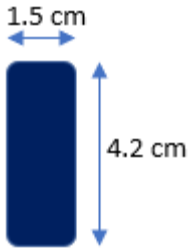


Figure 2. Delphinidin-based visual indicator

Results and Discussion

Extraction of natural colour from butterfly pea

The total anthocyanin concentration was calculated at 1.3 mg of delphinidin 3-glucoside equivalent per 100 mL of extract. The original colour of butterfly pea extract was dark blue at pH 5.93. The analysis of pH on butterfly pea extract showed that at pH 1-2, the colour was red, which then shifted to purple at pH 3-5, followed by blue at pH 6-7, changed to green at pH 8-11, and at pH above 11, the colour became yellow (Figure 3). The values of colours at each pH is presented in Table 1. The changes of colour are due to the presence of flaviliumcation in butterfly pea extract, which is unstable with the change of pH solution [18]. This result confirmed the potential of butterfly pea extract as a pH indicator.

The maximum absorption of the extract was recorded at two different wavelengths at maximum absorbance (λ_{max}), 568 and 618 nm, as shown in Figure 4 (appeared as a red line, pH 5.93). The difference between both wavelengths was on the bands at 568 (K-band) and 618 nm (R-band) [13, 16, 25]. Based on the standard (delphinidin 3-glucoside), the absorption maxima at the wavelength of 568 nm was selected for further analysis. The UV-Vis analysis done by Saptarini et al. [18] showed absorption at the maximum wavelength of 572 and 614 nm. As the pH changed, the absorption maxima shift was observed between 548 and 627 nm [25]. Figure 4 shows the UV-Vis spectra of butterfly pea extract at different pH. The wavelength showed a similar trend from pH 1 until 11; however, the peaks almost disappeared when the solution was at pH 13. The extract indicated a slight spectral shift in the spectrum due to the interaction between the extract and its microenvironment [26].

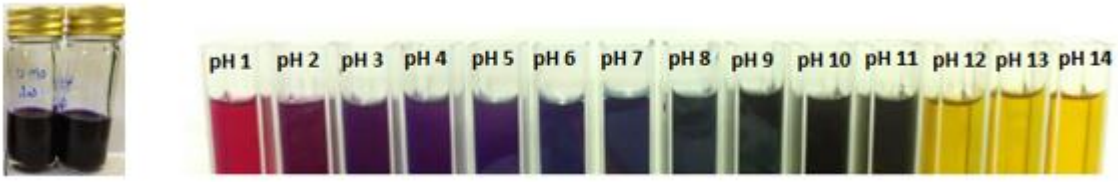


Figure 3. Butterfly pea extract (left) and butterfly pea extracts in different pH buffer solutions (right) [12]

Table 1: L*, a*, and b* values of delphinidin extract at different pH values

pH	L*	a*	b*
1	33.98 ± 0.12	60.01 ± 0.10	36.65 ± 0.34
2	15.62 ± 0.28	41.51 ± 0.36	4.21 ± 0.01
3	8.30 ± 0.23	32.15 ± 0.55	-7.21 ± 0.44
4	8.51 ± 0.11	31.32 ± 0.14	-11.77 ± 0.06
5	7.84 ± 0.16	26.18 ± 0.06	-15.10 ± 0.11
6	8.69 ± 0.27	14.61 ± 0.06	-14.71 ± 0.16
7	9.53 ± 0.16	7.85± 0.06	-10.71 ± 0.10
8	5.41 ± 0.37	9.56 ± 0.37	-0.64 ± 0.08
9	5.71 ± 0.21	10.96 ± 0.12	4.25 ± 0.03
10	5.69 ± 0.19	11.93 ± 0.21	6.44 ± 0.07
11	10.94 ± 0.16	14.45 ± 0.09	11.17 ± 0.09
12	65.81 ± 0.13	10.74 ± 0.03	83.88 ± 0.08
13	68.61 ± 0.05	11.74 ± 0.00	87.96 ± 0.29
14	70.03 ± 0.04	17.71 ± 0.24	97.07 ± 2.09
5.93	17.78 ± 0.16	32.15 ± 0.16	-25.53 ± 0.11

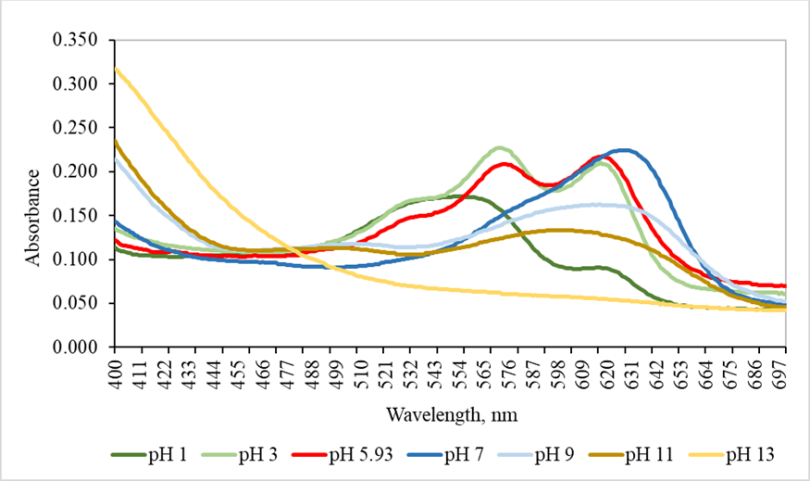


Figure 4. UV-Vis spectra of butterfly pea extract at different pH

Response of delphinidin-based visual indicator towards the beef sample

The delphinidin-based visual indicator was placed in a sealed container with a beef sample. The visual indicator was left unattached to the beef sample for the visual indicator to respond to the increasing volatile amines generated by beef spoilage. The visual indicators were monitored periodically until no further colour change was observed. The colour changes in the indicators were

due to the reaction of the indicators with volatile bases produced during the storage of the beef [24].

Figures 5 and 6 show the changes in the visual indicators before and after the analysis of the beef sample. These visual indicators portrayed real-time freshness of the beef sample during storage by sensing volatile compounds or gases released by the sample. The chemical changes occurring in meat during storage are indicators of the freshness of muscle-based food products [27]. As reported by Mohebi and Marques [2], the characteristics of volatile compounds in each meat product are different; therefore, each beef might spoil at different time.

The indicators tested at different storage temperatures respond to the changes of pH in the package headspace. The pH increased due to the volatile compounds produced gradually by the beef sample during spoilage. This situation was subsequently reflected by the colour of the indicators, which changed from dark blue to green for spoilage indication and easily visible to the naked eye. These results showed that the delphinidin-based visual indicators reacted with the volatile compounds released by the beef sample inside the package. On the other hand, the control delphinidin visual indicator was tested inside an empty package without beef, where the colour of the indicator remained unchanged throughout the storage duration, as shown in Figure 7.

The colour values for indicators at room temperature and chiller temperature are tabulated in Table 2. The comparison of colour difference was done using Tukey's multiple comparison test, which is one of the tests that can be used to determine which means (μ) amongst a set of means differ from the rest [28]. The Tukey's test showed that for both storage temperatures, the initial colour value was significantly different ($p < 0.005$) with the colour value at the point of rejection at hour 18 (room temperature) and day 6 (chiller temperature), where the visual indicators changed its colour from dark blue to green. The difference was observed in a* and b* values, which referred to the redness and yellowness of the visual indicator, respectively. However, the L* value might remain same or different, as it only represents the lightness of the colour. This result proved that the delphinidin-based visual indicator is able to indicate the freshness of beef based on the significant colour change.

Figure 8 shows the indicator response (ΔE*) towards spoiling beef at room temperature. The indicator responded significantly at hour 18 as the indicator colour changed from dark blue to green, and the beef was found at pH 6.76 ± 0.29. The initial pH of the beef was at pH 6.01 ± 0.07, and it was considered spoiled at pH above 6.5. The colour indicator response was similar to the deterioration of the beef sample as stated by Kuswandi and Nurfawaidi [8].

A study by Kuswandi and Nurfawaidi [8] showed that beef (specifically at the flank part) spoiled at hour 8 at room temperature, whereas in this study, the beef (specifically at the top (inside) round part) spoiled at hour 18. The difference indicates that different parts of beef spoiled at different rates and this contributes to different real-time detection of beef freshness. Even if the beef spoiled at different rates, the freshness is still measurable based on the colour change. The rate of colour change at chiller temperature is shown in Figure 10. Initially, the pH value of the beef sample was at pH 6.01 ± 0.07 and increased to pH > 6.0 starting from day 4 of storage. At day 6, the pH of beef turned to pH 6.71 ± 0.05, which indicated that the beef was already spoiled. A study by Maggiolino et al. [29] showed that the highest volatile nitrogen released from aging beef was observed on day 6, which was similar with the point of rejection in this study.

During the spoilage period, many microorganisms started to reproduce and decompose proteins, which contributed to the rise of pH in beef [7]. Throughout the storage of beef, the proteins of muscle are decomposed by either enzymatic hydrolysis or microbial action, which leads to changes in the pH value [7]. Kuswandi and Nurfawaidi [8] stated that beef samples with a similar degree of freshness produced a similar amount of volatile compounds, which changed the pH to the similar pH inside the headspace of beef package. The result obtained in Figure 10 has a similar trend as in Figure 9, which means that the indicators responded well to the increase of pH value in the container headspace as the colour of the visual indicators is related

to the pH level in the beef sample. The error values for both results are smaller than 5%, which demonstrated high precision of the indicator response related to the reproducibility of the measurement.

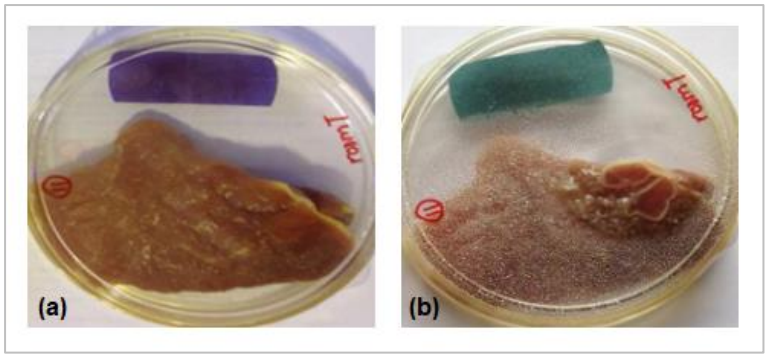


Figure 5. Changes in colour of the visual indicator in the closed container containing beef at room temperature (a) at 0 hour and (b) at hour 24

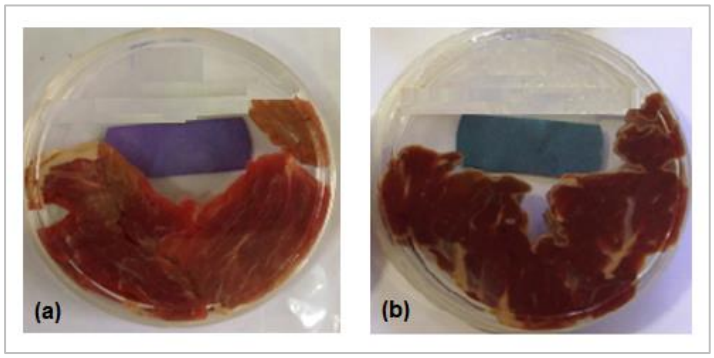


Figure 6. Changes in colour of the visual indicator in the closed container containing beef at chiller temperature (a) at day 0 and (b) at day 10

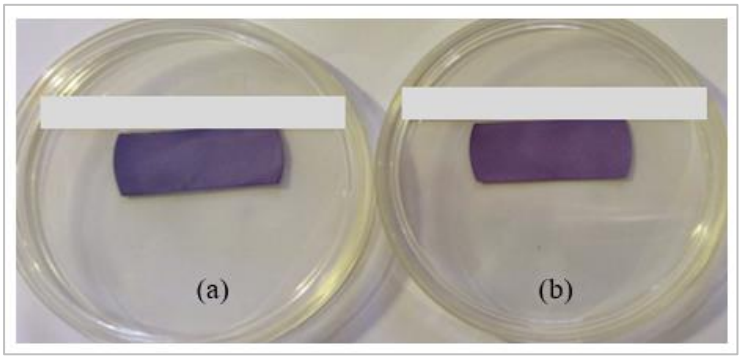


Figure 7. Control analysis of visual indicators throughout the storage duration (a) stored at room temperature and (b) stored at chiller temperature

Table 2. Colour space coordinate values of the visual indicators at (a) room temperature and (b) chiller temperature (Different superscripts in the same line indicate significant differences ($p < 0.05$) according to Tukey's test)

Colour Value	(a) Room Temperature		
	Hour 0	**Hour 18**	**Hour 24**
L*	47.99 ± 1.30^{a}	$41.99 \pm 1.69^{a,b}$	37.60 ± 1.70^{b}
a*	16.15 ± 1.15^{c}	-9.52 ± 0.40^{d}	-13.39 ± 2.18^{e}
b*	-24.59 ± 0.44^{f}	$-24.44 \pm 0.43^{g,h}$	-19.59 ± 1.12^{h}

Colour Value	(b) Chiller Temperature		
	Day 0	**Day 6**	**Day 10**
L*	47.99 ± 1.30^{i}	41.93 ± 0.48^{j}	35.79 ± 0.63^{k}
a*	16.15 ± 1.15^{l}	-9.03 ± 0.97^{m}	-17.52 ± 0.47^{n}
b*	-24.59 ± 0.44^{o}	$-14.58 \pm 1.79^{p,q}$	-14.32 ± 1.14^{q}

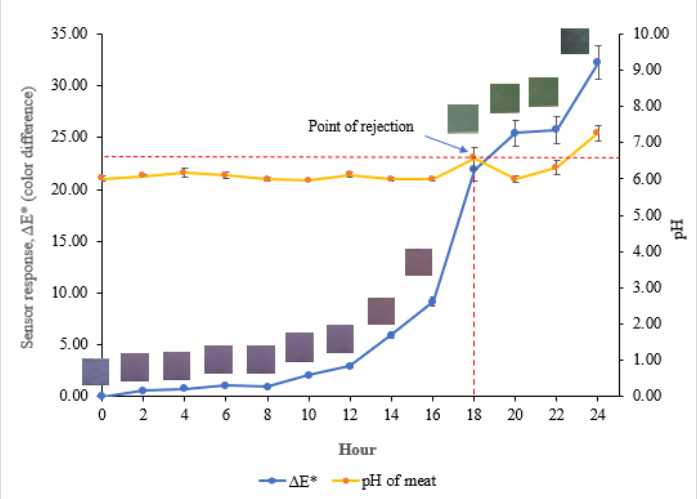


Figure 8. Rate of colour change of delphinidin visual indicators as sensor response (c*) towards beef spoilage at room temperature (29 ± 1 °C) (The yellow line referred to the pH of meat and the blue line referred to ΔE* compared to the initial colour of the indicator)

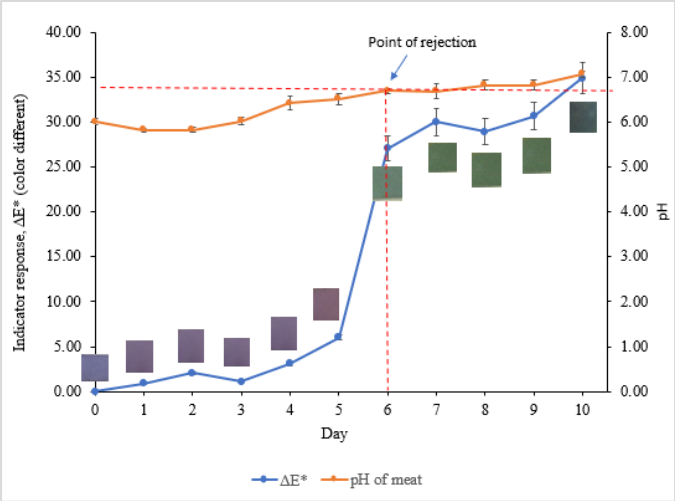


Figure 9. Rate of colour change of delphinidin visual indicators as sensor response (c*) towards beef spoilage at chiller temperature (4 ± 1 °C) (The yellow line referred to the pH of meat and the blue line referred to ΔE* compared to the initial colour of the indicator)

Conclusion

Delphinidin-based visual indicator was successfully developed and used for monitoring beef freshness. The produced visual indicator could be used for detecting the beef freshness quality as the colour changes of the visual indicators had a similar trend with the deterioration of the beef sample (i.e. when the delphinidin-based visual indicator changed to green). The visual indicator demonstrated accurate response to the beef freshness and intense colour changes (green) due to the spoilage of the meat sample. Thus, the developed visual indicator has a potential to be used as an attractive and effective tool for monitoring the microbial quality of packaged fresh beef and may serve as active shelf-life labelling devices to optimise distribution control, management of the stock rotation system, and most importantly, to reduce food waste.

Acknowledgement

The authors would like to thank Majlis Amanah Rakyat (MARA) for the funding “Skim Geran Penyelidikan Inovasi MARA” and also Universiti Kuala Lumpur Malaysian Institute of Chemical and Bioengineering Technology (UniKL MICET) for supporting this project.

References

1. Rukchon, C., Nopwinyuwong, A. and Trevanich, S. (2014). Development of a food spoilage indicator for monitoring freshness of skinless chicken breast. *Talanta,* 130: 547-554.
2. Mohebi, E. and Marquez, L. (2015). Intelligent packaging in meat industry: An overview of existing solutions. *Journal of Food Science Technology,* 52: 3947-3964.
3. Kim, H. J., Kim, D., Kim, H. J., Song, S. O., Song, Y. H. and Jang, A. (2018). Evaluation of the microbiological status of raw beef in Korea: Considering the suitability of aerobic plate count guidelines. *Korean Journal Food Science Animal Resource*, 38(1): 43-51.
4. Meat & Livestock Australia (2011). Meat standards Australia beef information kit. Access from https://www.mla.com.au/globalassets/mla-corporate/marketing-beef-and-lamb/msa_tt_beefinfokit_jul13_lr.pdf. [Access online on 9 October 2017].
5. Kuswandi, B., Jember, U., Jayus, J. and Jember, U. (2015). Simple and low-cost on-package sticker sensor based on litmus paper for real-time monitoring of beef freshness. *Journal of Mathematical and Fundamental Sciences*, 47: 236-251.

6. Dave, D. and Ghaly, A. E. (2011). Meat spoilage mechanisms and preservation techniques: A critical review. *American Journal of Agricultural and Biological Sciences*, 6(4): 486-510.
7. Liu, H., Saito, Y., Dimas, F. A. R., Kondo, N., Yang, X. and Han, D. (2019). Rapid evaluation of quality deterioration and freshness of beef during low temperature storage using three-dimensional fluorescence spectroscopy. *Food Chemistry*, 287: 369-374.
8. Kuswandi, B. and Nurfawaidi, A. (2017). On-package dual sensors label based on pH indicators for real-time monitoring of beef freshness. *Food Control*, 82: 91-100.
9. Kuswandi, B., Anggi, R., Aminah, A., Lee, Y. H. and Musa, A. (2012). A novel colorimetric food package label for fish spoilage based on polyaniline film. *Food Control*, 25: 184-189.
10. Kuswandi, B., Chrysnanda, M., Jayus, A. A and Lee, Y. H. (2013). Real time on-package freshness indicator for guavas packaging. *Food Measure*, 7: 29-39.
11. Pacquit, A., Frisby, J., Diamond, D., Lau, K. T., Farrell, A., Quilty, B. and Diamond, D. (2007). Development of a smart packaging for the monitoring of fish spoilage. *Food Chemistry*, 102: 466-470.
12. Mohd Zulkhairi, A. R., Nurdiyana, H., Mohd Azizan, M. N., Zaida Rahayu, Y. and Ismail-Fitry, M. R (2020). Screening of natural colours from various natural resources as potential reusable visual indicators for monitoring food freshness. *Malaysian Journal of Analytical Sciences*, 24(2): 288-299.
13. Sharma, D. (2014). Understanding biocolour- a review. *International Journal of Scientific & Technology Research*, 3(1): 294-211.
14. Pahune, B. (2013). Antimicrobial activity of *Clitoria Ternatea* L. flower extract and use as a natural indicator in acid base titration. *Journal of Natural Product and Plant Resource*, 3: 48-51.
15. Tantituvanont, A., Werawatganone, P., Jiamchaisri, P. and Manopakdee, K. (2008). Preparation and stability of butterfly pea color extract loaded in microparticles prepared by spray drying. *Thai Journal of Pharmaceutical Sciences*, 32: 59-69.
16. Wongs - Aree, C., Giusti, M. M. and Schwartz, S. J. (2016). Anthocyanins derived only from delphinidin in the blue petals of *Clitoria ternatea*. *Acta Horticulturae*, 712: 437-442.
17. Dudnyk, I., Jane, E. R., Joanne, V. J. and Stellacci, F. (2018). Edible sensors for meat and seafood freshness. *Sensors and Actuators B*, 259: 1108-1112.
18. Saptarini, N. M., Suryasaputra, D. and Nurmalia, H. (2015). Application of butterfly pea (*Clitoria ternatea Linn*) extract as an indicator of acid-base titration. *Journal of Chemical and Pharmaceutical Research*, 7: 275-280.
19. Yoshida, C. M. P., Maciel, V. B. V., Mendonça, M. E. D. and Franco, T. T. (2014). Chitosan biobased and intelligent films: Monitoring pH variations. *LWT - Food Sci Technology*, 55: 83-89.
20. Anuar, N., Mohd Adnan, A. F., Saat, N., Aziz, N., and Mat Taha, R. (2013). Optimization of extraction parameters by using response surface methodology, purification, and identification of anthocyanin pigments in *Melastoma malabathricum* fruit. *The Scientific World Journal*, 2013: 810547.
21. Rabeta, M. S. and Nabil, Z. A. (2013). Total phenolic compounds and scavenging activity in *Clitoria ternatea* and *Vitex negundo linn*. *International Food Research Journal*, 20: 495-500.
22. Mishra, P. K., Singh, P. and Gupta, K. K. (2012). Extraction of natural dye from *Dhalia Variabilis* using ultrasound. *Chem Engineering*, 37: 1-18.
23. Kungsuwan, K., Singh, K., Phetkao, S. and Utama-ang, N. (2014). Effects of pH and anthocyanin concentration on color and antioxidant activity of *Clitoria ternatea* extract. *Food and Applied Bioscience Journal*, 2(1): 31-46.
24. Shukla, V., Gurunathan, K. and Mangalathu, R. V. (2015). Development of on-package indicator sensor for real-time monitoring of buffalo meat quality during refrigeration storage. *Food Analytical Methods,* 8: 1591-1597.
25. Kamat, S. S., Khairnar, B. S. and Patil, V. D. (2016). Investigation on new natural colour - acid violet from *Clitoria ternatea Linn*. *Journal of Academia and Industrial Research*, 5(1): 14-16.

26. Mohammad, R. and Ahmad, M. (2019). Sol-gel/chitosan hybrid thin film immobilised with curcumin as pH indicator for pH sensor fabrication. *Malaysian Journal of Analytical Sciences*, 23(2): 204-211.
27. Realini, C. E. and Marcos, B. (2014). Active and intelligent packaging systems for a modern society. *Meat Science*, 98: 404-419.
28. Olleveant, N.A. (1999). Tukey multiple comparison test. *Journal of Clinical Nursing*, 8: 299-304.
29. Maggiolino, A., Lorenzo, J. M., Marino, R., Malva, A. D., Centoducati, P. and Palo, P. D. (2019). Foal meat volatile compounds: Effect of vacuum ageing on semimembranosus muscle. *Journal of Science Food Agriculture*, 99(4): 1660-1667.

Malaysian Journal of Analytical Sciences (MJAS)
Published by Malaysian Analytical Sciences Society

EVALUATION OF PHYSICOCHEMICAL CHARACTERISTICS AND PHYTOCHEMICAL PROPERTIES OF TOMATO (*Lycopersicon esculentum* L.) DURING DIFFERENT MATURITY STAGES

(Penilaian Ciri Fizikokimia dan Sifat Fitokimia Tomato (*Lycopersicon esculentum* L.) pada Tahap Kematangan yang Berbeza)

Md. Ashikur Rahman[1]*, Md. Parvez Hasan[2], Rakibul Hasan[2]

[1]*Food Safety and Quality Analysis Division, Institute of Food and Radiation Biology, Bangladesh Atomic Energy Commission, Dhaka, Bangladesh*
[2]*Regional agriculture research center, Bangladesh Agriculture Research Institute, Ishwardi, Pabna, Bangladesh*

[*]*Corresponding author: ashikur07038@gmail.com*

Received: 8 June 2020; Accepted: 5 July 2020; Published: 11 August 2020

Abstract

Tomato is an indispensable constituent of the daily food consumed in Bangladesh. The present study evaluated the physicochemical characteristics and phytochemicals present in tomato during different maturity stages, showing that pH and total soluble solids gradually increased with the decreased titratable acidity during different maturity stages of tomato. Chlorophyll content also decreased with the maturation of the tomato. Also, the anti-nutritional factors, tannin, phytate, and cyanogenic glycoside as well as antioxidants, such as vitamin C, were quantified, showing the highest amount of tannin, (2.61 ± 0.02 mg/100 g), phytate (4.28 ± 0.02 mg/100 g), and cyanogenic glycoside (7.81 ± 0.02 mg/100 g) in the green mature (unripe) stage, with the lowest values (1.16 ± 0.02 mg/100 g, 3.08 ± 0.01 mg/100 and 5.91 ± 0.02 mg/100 g, respectively) in the red (ripen) stage. In contrast, the maximum amount of vitamin C (25.07 ± 0.05 mg/100 g) was found in the red (ripen) stage, with the lowest amount (22.15± 0.22 mg/100 g) in the green mature stage. Overconsumption, that is, more than the daily recommended intake, of tomatoes may harm health but the concentration of anti-nutritional factors present in tomato was found to below toxic levels. Furthermore, vitamin C is a positive indicator of health and was in a high concentration in all maturity stages of tomato. In conclusion, this study revealed that the red ripened tomato is the best for human consumption compared to those green-yellow and green mature stages in terms of the physicochemical characteristics and phytochemical properties.

Keywords: tomato, maturity, tannin, phytate, cyanogenic glycoside

Abstrak

Tomato merupakan bahan utama yang diguna secara harian di Bangladesh. Kajian ini menilai ciri fiziko-kimia dan fitokimia yang hadir di dalam tomato semasa peringkat kematangan yang berbeza, menunjukkan nilai pH dan jumlah pepejal terlarut meningkat dengan pengurangan keasidan yang boleh dititrat semasa peringkat kematangan tomato yang berbeza. Kandungan klorofil juga berkurangan pada kematangan tomato. Juga, faktor anti-nutrisi, tannin, fitat, dan glikosida sinogenik bersama antioksidan, seperti vitamic C, telah dikuantifikasi, menunjukkan kandungan yang tinggi bagi tannin (2.61 ± 0.02 mg/100 g), fitat (4.28 ± 0.02 mg/100

g), dan glikosida sinogenik (7.81 ± 0.02 mg/100 g) pada peringkat belum matang (hijau) dengan nilai paling rendah telah ditemui (masing-masing 1.16 ± 0.02 mg/100 g, 3.08 ± 0.01 mg/100 dan 5.91 ± 0.02 mg/100 g) pada peringkat matang (merah), Sebaliknya, jumlah maksimum vitamin C (25.07 ± 0.05 mg/100 g) dijumpai pada peringkat matang (merah) dengan kandungan paling rendah (22.15± 0.22 mg/100 g) pada peringkat belum matang, hijau. Pengambilan secara lebihan melebihi cadangan harian, tomato mungkin membahayakan kesihatan tetapi kepekatan factor anti-nutrisi hadir di dalam tomato dijumpai lebih rendah dari aras toksik. Selanjutnya, vitamin C ialah indikator positif kesihatan dan ia mempunyai kepekatan yang tinggi pada semua peringkat kematangan tomato. Kesimpulan, kajian ini membuktikan bahawa tomato pada kematangan merah adalah terbaik bagi pengambilan oleh manusia berbanding kematangan hijai kekuningan dan hijau dari aspek ciri fizikokimia dan sifat fitokimia.

Kata kunci: tomato, kematangan, tannin, fitat, glikosida sinogenik

Introduction

Fruits and vegetables are important sources of nutrients for humans but in some lower-middle-income countries like Bangladesh, their production is periodic [1]. The tomato (*Lycopersicon esculentum* L.) is commonly consumed in Bangladesh as well as globally in garden-fresh or processed form [2]. Tomato farming in Bangladesh is of economic importance, accounting for approximately 68,366 acres with the production of 388,725 metric tons [3]. The tomato is a good source of nutrients and phytochemicals such as vitamin C, chlorophyll, phytate, tannins, cyanogenic glycoside that impact health [4]. Indeed, the tomato is a rich source of vitamin C, whose synergistic effects on wound healing are beneficial to health preventing scurvy [5]. Vitamin C is often used as a food additive due to its oxidation-reduction characteristics, reducing harmful agents present in food and to stabilize the color of food [6]. The maturation and superiority of tomato are predominantly based on color, with unripe tomatoes being green due to the high chlorophyll content, which degrades to yellow constituents, such as β-carotene and xanthophyll as the tomato matures, finally becoming red due to lycopene [7, 8]. Consumer and market demands influence the harvesting stage of the tomato [9]. Generally, the tomato is harvested during the mature green stage to full ripened stage until post-harvest damage considering various factors, for instance, cultivation time, growing environment, and market value [8, 10].

Furthermore, phytate, tannins, cyanogenic glycoside are present in the tomato in varying amounts. Excessive consumption of tannin in tomato reduces the digestion of several nutrients and prevents the body from captivating advantageous bioavailable elements [11]. Digestive enzymes, for example, amylase, pepsin, and trypsin are hindered by the consumption of a high amount of phytate in tomato [12]. Mono- and divalent cations K^+, Mg^{2+}, and Ca^{2+} are phytate salts and stored in tomato seeds at different harvesting times. The high pH favorable for phytate has adverse effects on the bioavailability of divalent and trivalent mineral ions, such as Zn^{2+}, $Fe^{2+/3+}$, Ca^{2+}, Mg^{2+}, Mn^{2+}, and Cu^{2+}, resulting in mineral deficiency when large amounts of phytate in tomato are consumed [13]. Most of the people in Bangladesh are not aware of the presence of anti-nutritional factors in tomatoes and their effect on health due to lack of information. Indeed, to the best of our knowledge, this is the first study of the anti-nutritional factors in tomatoes in Bangladesh. The present study aimed to quantitatively assess the anti-nutritional factors, physicochemical characteristics, and other phytochemicals present in tomato during different maturation stages.

Materials and Methods

Samples and Chemicals

Tomatoes were collected from the field during the three maturity stages, with spotless, uniform tomatoes collected randomly for analysis. The collected samples were washed and stored at 4 °C for analysis. Chemicals used in this research were analytical grade.

Determination of pH

The pH of samples was determined using a pH meter (Model PCE-PH20M) at room temperature. An amount 10 g of sample were placed taken into 250 mL beaker, then homogenized with 100 mL distilled water (pH 7.00) in a blender. Finally, the pH electrode was put into

the suspension and allowed to stand until a constant pH was recorded.

Measurement of total soluble solids

The total soluble solids in the blended samples were measured using a digital refractometer (DR 6000T, Germany).

Estimation of titratable acidity

Titratable acidity was estimated according to the method described by Srivastavata and Sanjeev [14]. An amount 5 g of sample was blended with 15 mL distilled water for 3 minutes, then 3 mL of the sample was taken for titration against 0.1N sodium hydroxide using phenolphthalein as an indicator, with the presence of the pink color indicating the endpoint. The results were expressed as a percentage of citric acid.

Calculation of maturity

The maturity index was calculated using the formula given by Navez et al. [15] and Nielsen et al. [16]. The formula was used as shown in Equation 1:

$$\text{Maturity index} = [(\text{Total soluble solid}/20*\text{titratable acidity}) + \text{titratable acidity}] \quad (1)$$

Spectrophotometric measurement of chlorophyll

Chlorophyll a and Chlorophyll b were measured using the method described by Srivastavata and Sanjeev [14]. An amount 20 g of the sample was homogenized in 120 mL of distilled water using GEA lab homogenizer panda plus 1000 for 5 minutes. After filtration, the solution was centrifuged (Model: Rotina 380/380 R) at 6000 rpm for 5 minutes. After extraction of the pigments, 5 mL aliquot was placed in 25 mL of 90% acetone in a centrifuge tube and centrifuged at 2000 rpm for 3 minutes. The supernatant was removed and the optical density was recorded at 645 and 663nm respectively (Model: GENESYS 150 UV-visible spectrophotometer).

Measurement of vitamin C

The vitamin C content was measured using a 2,4-dinitrophenyl hydrazine (DNPH) method as described by Rahman et al. [17]. Briefly, 10 gm of sample was blended (Barum MR 404 plus), homogenized in 60 mL of 5% meta phosphoric acid-10% acetic acid solution, and transferred into a 100-mL volumetric flask and shaken lightly. The suspension was diluted up to the mark using a 5% meta phosphoric acid-10% acetic acid solution and filtered for the estimation of vitamin C. Bromine water was added to the solution until the solution becomes colored, excess bromine was removed by adding thiourea to give a clear solution. The standard solution of ascorbic acid was made from the stock solution as per the required dilution, before the addition of 1.5 mL of DNPH solution to all standards and samples to oxidize the ascorbic acid. All standards, samples, and blank samples (without sample) were kept in a water bath at 37 °C for 4 hours to complete the reaction, then placed in an ice bath with the addition of 85% sulfuric acid before the optical density was measured at 521 nm.

Determination of phytate

Phytic acid was determined by the method described by Lucas and Markakas [18]. The sample (2 g) was dissolved in 100 mL of 2% concentrated hydrochloric acid for 4 hours and filtrated. Then, 50 mL of the filtrate was placed in a 250-mL beaker and 100 mL of distilled water was added to ensure adequate acidity. As an indicator, 10 mL of 0.3% ammonium thiocyanate solution was added and the solution was titrated using 0.00195 g iron/mL containing standard iron (III) chloride. The yellow-brownish color indicated the endpoint of the titration.

Measurement of cyanogenic glycoside

The alkaline picrate method of Onwuka [19] was used to measure cyanogenic glycoside. An amount 6 g of the samples were dissolved in 50 mL of distilled water and the cyanide was extracted overnight. Then, 4 mL of alkaline picrate was added to 1 mL filtrate sample and standard cyanide solution (different concentration) separately, before incubation in a water bath for 10 minutes and the optical density was recorded at 490 nm.

Measurement of tannin

Two gm of the sample was dissolved in 25 mL distilled water and stirred for 1 hour at room temperature. Then, the sample was centrifuged at 2500 rpm for 4 minutes and 5 mL of the supernatant was transferred to a 50-mL volumetric flask. An amount 5 mL standard tannic acid solution was prepared in another 50-mL flask. An amount 4 mL of saturated sodium carbonate solution and 2 mL folin dennis reagent were added to the sample solution and the standard solution respectively. The solution mixture was diluted to 100 mL and incubated for 90 minutes at room temperature before the optical density was measured at 250 nm. The percentage of tannin was calculated based on the formula of Jaffe [20].

Statistical analysis

The data are presented as the mean and standard deviation of three replicates using Microsoft Excel (2016 version) software.

Results and Discussion

Physicochemical properties play a vital role in the selection of tomatoes by the consumer. Consumer acceptance mostly depends on maturation which determines the physical quality of the tomato. Tomato maturation is influenced by acidity and total soluble substances as presented in Table 1.

The ratio of acidity and the total soluble solids was lowest in mature green tomatoes, indicating a minimum maturity index (6.096), whereas the red (ripen) tomatoes had the highest ratio of acidity and total soluble solids, indicating a maximum maturity index (9.263). The highest pH was found in red (ripen) tomatoes (4.93 ± 0.014), with the lowest pH observed in the green-yellow stage (3.10 ± 0.01). The pH value obtained from mature green (unripe) (3.42 ± 0.41) and green-yellow (half ripen) was below the value (3.7 to 4.1) as previously reported by Fagbohoun and Kiki [21].

A low pH (below 4.00) in tomatoes is unfavorable for the growth of pathogenic organisms as stated by Foolad [22]. Red (ripen) tomatoes was more perishable due to the high pH. The present study indicated that acidity gradually decreases with increased tomato maturation. The acidity ranged from 0.57 ± 0.02% to 0.36 ± 0.26% in line with a previous report by Fagbohoun and Kiki [21]. Sensory properties, for example, the essence of tomato is linked to the level of acidity [23], with the lowest acidity of tomato in the red (ripen) stage having the best flavor.

The quantity of soluble solids (Brix) is also a major parameter for evaluating tomato quality. The core soluble part of the tomatoes is the reducing sugar (fructose and glucose) according to Malundo et al. [24]. The present study recorded the lowest amount of soluble solids (5.92 ± 0.04) in mature green (unripe), with the highest amount (9.1 ± 0.17) in the red (ripen) stage. The highest quality tomatoes contained total soluble solids ranging from 4.8 to 8.8 as stated by Duma et al. [8]. The data presented in Table 1 showed that the acidity content decreases with the increase of soluble solids and the maturation stage of tomato. Significantly, low acidity and a high soluble solid content specify a high-quality tomato. The high pH is not a good quality marker due to the initiation of spoilage by pathogenic organisms, therefore, maturation (ripen) of the tomato is better determined in terms of physical quality.

Chlorophyll is responsible for the green color of a tomato, hence, the content of chlorophyll a and chlorophyll b was high in the green tomato, as shown in Figure 1. As expected, the chlorophyll content decreased in the green-yellow (half ripen) tomato and the tomatoes became more yellow as the chlorophyll was reduced as the tomato matured. The enzymes peroxidase and lipoxygenase are responsible for the degradation of chlorophyll, thereby enhancing the yellow color of the tomato [25].

The phytochemical properties of the tomato at different maturity stages are presented in Table 2. The highest amount of tannin was found in the mature green stage (2.61 ± 0.02 mg/100 g), gradually decreasing as the tomato ripened (1.16 ± 0.02 mg/100 g). A previous study revealed that a low amount (0.15 - 0.2 mg/100 g) of tannin present in food is advantageous to health [26] but excessive consumption of tannin acts as an anti-nutrient. The high level of tannins present in tomato may impede the actions of trypsin, chymotrypsin, amylase, and

lipase, thereby making the protein inferior quality as well as delaying iron absorption [27].

Tomato is a source of phytate, which prevents heart disease by reducing blood clots and cholesterol, as well as averting stone development in kidneys by removing heavy metal ions [28]. In the present study, the phytate content of tomatoes ranged from 4.28 ± 0.02 mg/100 g to 3.08 ± 0.01 mg/100 g. The daily intake recommended in developing countries is 2000 - 2600 mg for vegetarians and 150 - 1400 mg for mixed diets [29]. The consumption of excessive phytate may cause mineral deficiency due to a lack of the digestive phytase enzyme that is required for the absorption of iron, zinc, and calcium [30]. The level of cyanogenic glycoside was higher in all mature stages compared to tannin and phytate presented in Table 2. Phytate and tannin are heat resistant, whereas cyanogenic glycoside vanished at an extreme temperature [31]. Tomato contains a high amount of vitamin C at different maturity stages, assisting in the deactivating effect of tannin on iron absorption [32]. The maximum amount of vitamin C was found in the red (ripen) stage (25.07 ± 0.05 mg/100 g), while the minimum amount was found in the mature green stage (22.15 ± 0.22 mg/100 g), which agrees with the previous observation of Ilahy et al. [33] and is in line with Dumas et al. [34] and Gautier et al. [35], who reported that the vitamin C content increases on ripening. In the ripening stage of tomato, a high amount of oxygen is absorbed by the cell as a consequence of the increased rate of respiration due to the anti-oxidative function of vitamin C.

Table 1. Physicochemical properties during different maturity stages of tomato

	pH	Acidity% (Citric Acid Equivalent)	Total Soluble Solids (Brix)	Maturity Index
Mature green (Unripe)	3.42 ± 0.41	0.57 ± 0.02	5.92 ± 0.04	6.096
Green-yellow (Half ripen)	3.10 ± 0.01	0.50 ± 0.02	7.34 ± 0.03	7.525
Red (Ripen)	4.93 ± 0.014	0.36 ± 0.26	9.1 ± 0.17	9.263

Data presented as mean ± standard deviation of three replicates

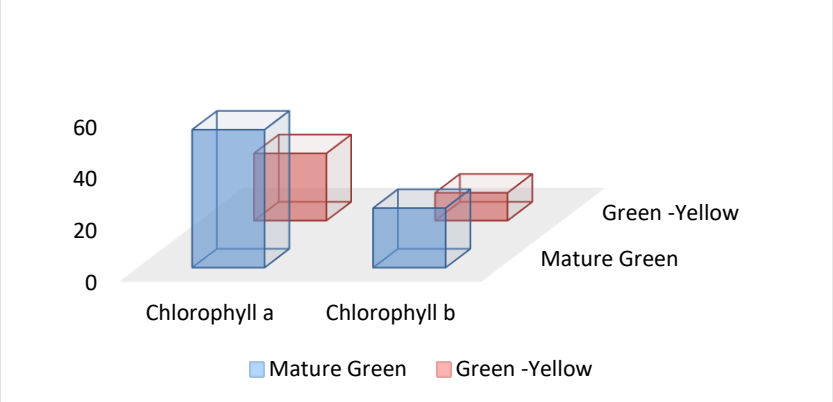


Figure 1. Comparison of chlorophyll a and chlorophyll b at different maturity stages of the tomato

Table 2. Phytochemical properties of tomato at different maturity stages

Sample	Tannin (mg/100 g)	Phytate (mg/100 g)	Cyanogenic Glycoside (mg/100 g)	Vitamin C (mg/100 g)
Mature green (Unripe)	2.61 ± 0.02	4.28 ± 0.02	7.81 ± 0.02	22.15 ± 0.22
Green-yellow (Half ripen)	2.06 ± 0.02	3.86 ± 0.02	6.2 ± 0.05	24.81 ± 0.02
Red (Ripen)	1.16 ± 0.02	3.08 ± 0.01	5.91 ± 0.02	25.07 ± 0.05

Data presented as mean ± standard deviation of three replicates

Conclusion

Tomato quality is highly influenced by the maturity stage, with mature tomatoes having a high soluble solid content and low titratable acidity. Furthermore, the chlorophyll content decreases with maturity, consequently, the tomatoes become less green as the chlorophyll degrades. Tomatoes contain anti-nutritional factors, tannin, phytate, and cyanogenic glycoside, the amount of which decreases as the tomatoes ripen, thereby confirming that consumers should select the best quality tomatoes for consumption. Future studies should identify and quantify other anti-nutritional factors present in tomatoes.

Acknowledgment

The authors express their gratitude to their colleagues and laboratory members for the encouragement to complete the work. The authors would like to thank the field workers for cultivating and supplying the research samples. The authors express immense gratitude to the Ministry of Agriculture for funding this research.

References

1. Beckles, D.M. (2012). Factors affecting the postharvest soluble solids and sugar content of tomato (*Solanum lycopersicum L.*) fruit. *Postharvest Biology and Technology*, 63: 129-140.
2. FAOSTAT (2017). Access from http://faostat.fao.org/site/339/default.aspx [Accessed June 10, 2018].
3. Bangladesh Bureau of Statistics (2019). Yearbook of Agricultural Statistics-2017, 29th Series: access from http://www.bbs.gov.bd/bbs report. [Access online 17 April 2018].
4. Giovanelli, G. and Paradise, A., (2002). Stability of dried and intermediate moisture tomato pulp during storage. *Journal of Agriculture and Food Chemistry*, 50: 7277-7281.
5. Willcox, J. K., Catignani, G. L. and Lazarus, S. (2003). Tomatoes and cardiovascular health. *Critical Review in Food Science and Nutrition,* 43: 1-18.
6. Eitenmiller, R. R., Ye, L. and Landen, W. O. (2008). Vitamin analysis for the health and food sciences (2nd edition). CRC Press, Taylor & Francis Group, UK: pp. 307.
7. Ilahy R., Hdider C., Lenucci M.S., Tlili I. and Dalessandro G. (2011). Antioxidant activity and bioactive compound changes during fruit ripening of high lycopene tomato cultivars. *Journal of Food Composition and Analysis*, 24: 588-595.
8. Duma M., Alsin I., Dubova L. and Erdberga I. (2015). Chemical composition of tomatoes depending on the stage of ripening. *Cheminė Technologija*, 1: 24-28.
9. Leonardi C., Ambrosino P., Esposito F. and Fogliano V. (2000). Anti-oxidative activity and carotenoid and tomatine contents in different typologies of fresh consumption tomatoes. *Journal of Agricultural and Food Chemistry*, 48: 4723-4727.

10. Moneruzzaman K. M. Hossain A. B. M. S., Sain W. and Saifuddin N. (2008). Effect of stages of maturity and ripening conditions on the biochemical characteristics of tomato. *American Journal of Biochemistry and Biotechnology*, 4: 329-335.
11. Hendek, E. M. and Bektaş, M. (2018). Enhancement of bioavailable micronutrients and reduction of antinutrients in foods with some processes. *Food Health*, 4(3): 159–165.
12. Kumar, V., Sinha, A. K. and Makkar, H. P. S. (2010). Dietary roles of phytate and phytase in human nutrition: A review. *Food Chemistry*, 120: 945–959.
13. Mueller I. (2001). Analysis of hydrolyzable tannins. *Animal Feed Science and Technology*, 91: 3-20.
14. Srivastava, R. P., and Sanjeev, K. (2003). Fruit and vegetable preservation principles and practices: Important methods for the analysis of fruits and vegetables and their products (3rd edition). International Book Distribution Co. Lucknow: pp. 354-359.
15. Navez B., Letard M., Graselly D., Jost J. (1999): Les crit.resde qualit. de la tomate Infos Ctifl, 155: 41-47.
16. Nielsen S. (2003): Food analysis. (3rd edition) Kluwer Academic, New York: pp. 557.
17. Rahman Khan, M. M., Rahman M. M., Islam M. S. and Begum S. A. (2006). A simple UV-spectrophotometric method for the determination of vitamin C content in various fruits and vegetables at the Sylhet area in Bangladesh. *Journal of Biological Sciences*, 6: 388-392.
18. Lucas, G. M. and Markakas (1975). Phytic acid and other phosphorus compounds of bean (*Phaseolus vulgaris*). *Journal of Agriculture Educational Chemistry*, 23: 13-15.
19. Onwuka, G. (2005). Food Analysis and Instrumentation. Naphohla Prints. (3rd edition), A division of HG support Nigeria Ltd.: pp. 133-161.
20. Jaffe, C.S. (2003). Analytical chemistry of food. Blackie Academic and Professional, New York: pp. 200.
21. Fagbohoun, O. and Kiki, D. (1999) Aper.u sur les principales vari.t.s de tomate locale cultiv.es dans le sud du Benin. *Bulletin de la Recherche Agronomique du Benin*, 24: 10-21.
22. Foolad, M. R. (2007). Genome mapping and molecular breeding of tomato. *International Journal of Plant Genomics*, 2007 :1-52.
23. Aoun, A. B., Lechiheb, B., Benyahya, L. and Ferchichi, A. (2013). Evaluation of fruit quality traits of traditional varieties of tomato (*Solanum lycopersicum*) grown in Tunisia. *African Journal of Food Science*, 7(10): 350-354.
24. Malundo, M. M., Shewfelt, R.L. and Scott, J.W. (1995). Flavor quality of fresh tomato (*Lycopersicon esculentum Mill*.) as affected by sugar and acid levels. *Postharvest Biology and Technology*, 6:103-110.
25. Murcia, M. A., López-Ayerra, B., Martinez-Tomé, M. and Garcia-Carmona, F. (2000). Effect of industrial processing on chlorophyll content of broccoli. *Journal of the Science of Food and Agriculture*, 80: 1447-1451.
26. Schiavone, A., Guo, K. and Tassone, S. (2008). Effect of a natural extract of chestnut wood on digestibility, performance traits, and nitrogen balance. *Sciences,* 87(3): 521–527.
27. Felix, J. P. and Mello, D. (2000). Farm animal metabolism and nutrition. CABI, United Kingdom: pp. 163.
28. Selvam, R. (2002). Calcium oxalate stone disease: Role of lipid peroxidation and antioxidants. *Urological Research,* 30(1): 35-47.
29. Golden, M. (2009). Nutrient requirements of moderately malnourished populations of children. *Food and Nutrition Bulletin*, 30: 267-342.
30. Masum-Akond, A. S. M. G., Crawford, H., Berthold, J., Talukder, Z. I. and Hossain, K. (2011). Minerals (Zn, Fe, Ca, and Mg) and antinutrient (Phytic acid) constituents in common bean. *American Journal Food Technology*, 6(3): 235-243.
31. Kyriazakis, I. and Whittenmore, C.T. (2006). Whittemore's science and practice of pig production. Oxford: Wiley- Blackwell, United Kingdom: pp. 103.
32. Osada, K. and Ogino, Y. (2004). Effect of dietary apple polyphenol on metabolic disorder of lipid in rats given oxidized cholesterol. *Proceeding Japan Conference Biochemistry Lipid*, 39: 317-320.

33. Ilahy, R., Siddiqui, M. W., Tlili, I., Piro, G., Lenucci, M. S. and Hdider, C. (2016). Functional quality and color attributes of two high-lycopene tomato breeding lines grown under greenhouse conditions. *Turkish Journal of Agriculture Food Science and Technology*, 4(5): 365-373.
34. Dumas, Y., Dadomo, M., Di Lucca, G. and Grolier, P. (2003). Effects of environmental factors and agricultural techniques on the antioxidant content of tomatoes. *Journal of the Science of Food and Agriculture*, 83: 369-382.
35. Gautier, H., Diakou-Verdin, V., Benard, C., Reich, M., Buret, M., Bourgaud, F., Poessel, J. L., Caris-Veyrat, C. and Genard, M. (2008). How does tomato quality (sugar, acid, and nutritional quality) vary with ripening stage, temperature, and irradiance? *Journal of Agricultural and Food Chemistry*, 56: 1241-1250.

Malaysian Journal of Analytical Sciences (MJAS)
Published by Malaysian Analytical Sciences Society

STABILISATION OF PEAT SOIL USING MAGNESIUM OXIDE: A PRELIMINARY STUDY

(Penstabilan Tanah Gambut Menggunakan Magnesium Oksida: Satu Kajian Awal)

Lily Suhaila Yacob* and Amelia Md Som

Green Chemistry & Sustainable Technology Cluster,
Universiti Kuala Lumpur-Malaysian Institute Chemical & Bioengineering Technology, 78000 Alor Gajah, Malacca, Malaysia

**Corresponding author: lilysuhaila@unikl.edu.my*

Received: 20 November 2019; Accepted: 30 June 2020; Published: 11 August 2020

Abstract

This is a preliminary study for the stabilisation of peat soil from Teluk Kerang, Pontian, Johor using ordinary Portland cement (OPC) and magnesium oxide (MgO) as binders. Spent garnet and sand were used as fillers. In Malaysia, peat soil has been identified as one of the major groups of soils with low shear strength and high compressibility. Peatlands are used as an alternative option for future development due to lack of suitable lands and expensive cost. The presence of soft or peaty soil is a major problem in construction. The properties of peat soil used in this study were analysed and it was found to be acidic with the pH value of 4.15. According to von Post classification, peat soil can be classified as H3. In this research, various ratios of mix design for binders (OPC and MgO) and fillers (spent garnet and sand) were studied. Peat soil and binders (70:30) were inserted into a PVC pipe with the diameter of 50 mm and length of 200 mm. Unconfined compressive strength (UCS) test was conducted to determine the strength gained after 28 days of curing period. The relationships between the UCS and binder of the specimen after curing were investigated to determine the effect of binder changes on the strength of stabilised peat. The results showed that the samples without MgO could not maintain their form even when the samples were assisted with fillers. For the OPC:MgO ratio of 50:50, the samples achieved the UCS value of 32.97 kPa. The findings showed the potential contribution of MgO in peat stabilisation, and the addition of OPC alone is insufficient to stabilise the peat. The pH values varied from 9.0 to 10.1. Overall, the UCS test results showed that peat soil stabilisation using MgO and spent garnet improved the strength of stabilised peat

Keywords: peat soil, magnesium oxide, unconfined compressive strength test, pH, moisture content

Abstrak

Ini adalah kajian awal untuk penstabilan tanah gambut dari Teluk Kerang, Pontian, Johor dengan menggunakan simen Portland biasa (OPC) dan magnesium oksida (MgO) sebagai pengikat. Garnet dan pasir yang digunakan sebagai pengisi. Di Malaysia, tanah gambut telah dikenalpasti sebagai salah satu daripada kumpulan utama tanah yang mempunyai kekuatan ricih yang rendah dan kebolehmampuan tinggi. Tanah gambut akan menjadi pilihan alternatif untuk pembangunan masa depan disebabkan kekurangan tanah yang sesuai dan harga mahal. Kehadiran tanah lembut atau tanah gambut adalah masalah utama dalam pembinaan. Sifat-sifat tanah gambut yang digunakan dalam kajian ini dianalisis dan didapati berasid dengan nilai pH 4.15. Mengikut klasifikasi von Post, tanah gambut dapat diklasifikasikan di antara H3. Dalam kajian ini, pelbagai nisbah reka bentuk campuran untuk pengikat (OPC dan MgO) dan pengisi (garnet dan pasir) dikaji. Tanah gambut dan pengikat (70:30) diletakkan di dalam PVC paip berukuran 50 mm diameter dan 200 mm panjang. Ujian kekuatan mampatan tak terkurung (UCS) telah dijalankan untuk menentukan kekuatan

selepas 28 hari tempoh pengawetan. Hubungan antara UCS dan pengikat spesimen selepas pengawetan disiasat untuk menentukan kesan pengikat pada kekuatan gambut yang stabil. Keputusan menunjukkan bahawa sampel tanpa MgO tidak dapat mengekalkan bentuknya walaupun dibantu dengan pengisi dan nisbah OPC: MgO 50:50, sampel dapat mencapai nilai UCS sebanyak 32.97 kPa. Penemuan menunjukkan potensi sumbangan MgO dalam penstabilan gambut dan apabila penambahan OPC sahaja tidak mencukupi untuk menstabilkan gambut. Nilai pH berbeza dari 9.0 hingga 10.1. Secara keseluruhannya, keputusan ujian UCS menunjukkan bahawa penstabilan tanah gambut menggunakan MgO dan garnet menghasilkan peningkatan kekuatan gambut yang stabil.

Kata kunci: tanah gambut, magnesium oksida, kekuatan mampatan tak terkurung, pH, kelembapan

Introduction

Peat covers a substantial land area of many countries, including Malaysia. It consists of more than 75% organic substances and is well known for its low shear strength and high compressibility. There are four types of organic matters in peat soils, which are humin, humic acids, fulvic acids, and yellow organic acids [1]. However, the components of peat may vary by location, fibre origin, humidity, and temperature. These materials may also change chemically and biologically over time.

Land use activities increase intensely due to population and economic growth. To support the growing population, suitable lands for infrastructure development have decreased and may become a drawback in the near future. Many techniques have been carried out to support construction over peat. The soil stabilisation approach, especially for peat, is used to improve its stability, reduce settlement, lateral deformation, and increase bearing capacity [2]. Soil stabilisation can be defined as a method of soil improvement by blending and mixing with other materials [3]. This research focused on using chemical stabilisation for improving peat soil using a combination of magnesium oxide (MgO) and ordinary Portland cement (OPC), which is also known as magnesia cement or magnesia as binders, and spent garnet with sand as fillers.

Magnesia is a non-hydraulic cement produced by Stanislas Sorel in 1867. It has the potential to be used as a sustainable alternative to OPC [4]. The cement is an alkaline earth metal oxide that consists of a magnesium ion and an oxygen ion held together by an ionic bond. Magnesia is also known as a refractory binder, which has fast hardening properties, and several refractory and general repair applications [5]. Nowadays, magnesia is widely applied, such as in cement, steel, and super alloy industries. In the cement industry, magnesia is widely used as a curing agent at room temperature for phosphate cements. Meanwhile, magnesia is used in the steel industry to give optimum properties for corrosion resistance.

The variability nature of peat requires a trial-and-error approach to find the best mix design. In this preliminary study, the potential of using magnesia as a binder and industrial spent garnet as a filler is evaluated. The use of magnesia as an alternative binder and recycled industrial waste as a filler will reduce the carbon footprint and assist in the stabilization process into a more sustainable construction. To achieve this aim, several mix designs were prepared and tested for their unconfined compressive strength. The pH values of the mix design were also analysed.

Materials and Methods

Sampling and materials: Soil

A total 10 kg of peat samples were collected from Teluk Kerang, Pontian, Johor, Malaysia (1.419885° N, 103.440528° E). The peat samples were collected from 0.5-1.0 m depth below the surface. From initial investigation and observation, the soil colour was light brown with some roots and leaves on the surface. The sample transported to the laboratory were kept in a sealed plastic bag and screened through a sieve to remove larger objects (> 0.06 mm).

Binder

Ordinary Portland cement (OPC) and magnesium oxide (MgO) act as binders that hold peat, sand, and spent

garnet. The presence of MgO will increase the capability of OPC.

Spent garnet and sand

In this research, spent garnet and sand were added for soil stabilisation and as fillers to increase the number of solid particles in soil. The recycled spent garnet was collected from a dockyard in Pasir Gudang Johor. The sand was bought from a local hardware. It was well-graded and its particle size distribution was in accordance with ASTM F2396-11 [6].

Mould preparation. A polyvinyl chloride (PVC) pipe was used as a split mould to determine the unconfined compressive strength (UCS) of the specimens. The PVC pipe was cut into 50 mm diameter and 100 mm length, as shown in Figure 1. The end of the PVC pipe was covered with a cotton cloth to prevent peat sample leakage. The top of the PVC pipe was covered with a zinc plate with the diameter of 50 mm. A steel bar weighed 3.6 kg was used to stimulate 18 kPa pressure on top of the peat.

Physical and chemical properties

Von Post method

The physical properties tests carried out were von Post classification (degree of decomposition). The von Post classification test was done at the sampling site on peat. One-third of the peat soil was passed between the fingers and the colour of the water released from the fingers was determined. Table 1 shows 10 degrees of humification (H1 to H10) in the von Post classification [2].

Moisture content

Water is naturally present in a peat sample. Moisture content is defined as the ratio of the mass of water in a sample to the mass of solids in the sample. It is expressed as a percentage. The moisture content of the collected peat soil sample was determined by weighing 20 g of the sample and dried in an oven at 90 °C for 16 hours as per ASTM D2974-71 [8]. The moisture content was calculated according to

$$\text{Moisture Content, \%} = \frac{A - B}{A} \times 100 \quad (1)$$

where A is mass of the as-received test specimen in gram (g) and B is mass of the oven-dried specimen, gram (g).

pH

The acidity or pH value was determined using ASTM D2976-71 [9]. 50 mL of deionised water was poured into 3 g of peat soil samples in a small container and left overnight. The samples were then tested using a pH meter.

Specific gravity

Specific gravity is defined as the ratio of the density of a substance to the density of a reference substance (water). The specific gravity test of the peat soil samples was carried out using a 50 mL density bottle. The test specimen for specific gravity was ground to smaller size and sieved through a 425 μm sieve.

Ash content

Ash content was determined according to ASTM D2974 [8] standard test methods for moisture, ash, and organic matter of peat and other organic soils. The ash content of the peat was determined by igniting the oven-dried (100 °C) sample in a muffle furnace at 550 °C according to Method C in ASTM standards.

Organic content

Organic matter content test is a very important test in the classification of peat soil and other organic soils. Organic matter influences the physical and chemical properties of soil, such as compressibility, structure, and shear strength. Organic matter also affects water holding capacity. It is expressed as the percentage of the mass of organic matter in each mass of soil to the mass of dry soil solids. The peat samples from the moisture content test were oven-dried. The samples were weighed and placed in a muffle furnace at 440 °C for 24 hours.

Bulk density

The bulk density of peat soil was determined by collecting an undisturbed sample using a cylindrical corer with the dimensions of 100 mm diameter and 130 mm high. Bulk density was calculated using Equation 2:

$$\text{Bulk Density (g/cm}^3\text{)} = \frac{\text{dry soil (g)}}{\text{soil volume (cm}^3\text{)}} \quad (2)$$

FTIR analysis

Fourier transform infrared (FTIR) was carried out using KBr pellets. In this study, KBr was mixed with powdered samples and pressed into disks. Three samples were compressed at 7000 kPa to obtain transparent pellets. Analysis was carried out in the frequency range of 400-4000 cm^{-1} with 4.0 cm^{-1} resolution.

Stabilization and water curing: Design mix

The design mix containing various ratios of peat, OPC, MgO, sand, and spent garnet are shown in Table 2. Triplicate samples were prepared for each varied condition. Peat, binders, and fillers were weighed according to the mix design and mixed well. The mixture was put inside the mould, as shown in Figure 1. After the mould had been covered, the water curing process was carried out for 28 days.

Unconfined compressive strength test

UCS test was conducted for the peat specimens after 28 days curing in water according to ASTM D2166 [10]. The specimens were loaded axially using UCS testing equipment at the rate 0.5% to 2% per minute. The samples were tested until the load values decreased, the sample failed, or the strain reached 15%.

Table 1. Degree of decomposition according to Von Post [7]

Condition of Peat Before Squeezing				**Condition of Peat on Squeezing**		
Degree of Humification	**Soil Colour**	**Degree of Decomposition**	**Plan Structure**	**Squeezed Solution**	**Material Extruded Between Fingers**	**Nature of Residue**
H1	white or yellow	none	easily identified	clear, colourless		
H2	very pale brown	insignificant		Yellowish/ pale brown yellow	nothing	not pasty
H3	pale brown	very slight	still identified	dark brown, muddy		
H4		slight	not easily identified		some peat	somewhat pasty
H5	brown	moderate	recognizable but indistinct	very dark brown, muddy		strongly pasty
H6		moderately strong	indistinct (clearer after squeezing)		about one-third of the peat	
H7	dark brown	strong	faintly recognizable		about one-half of the peat	very strongly pasty
H8		very strong	very indistinct	very dark brown, pasty	about two-thirds of the peat	
H9	very dark brown	nearly complete	almost unrecognizable	very dark brown, muddy	Nearly all peat as fairly uniform paste	
H10	black	complete	no discernible	very dark brown, muddy	all the peat; no free water visible	n/a

n/a is no data available

Table 2. Additive and filler dosage for peat samples of various ratios

	OPC	MgO	Garnet	Sand	Peat
1	300	0	0	0	700
2	300	0	150	0	700
3	300	0	0	150	700
4	300	0	75	75	700
5	150	150	0	0	700
6	150	150	150	0	700
7	150	150	0	150	700
8	150	150	150	150	700
9	150	150	200	100	700
10	150	150	300	0	700
11	150	150	0	300	700
12	100	200	0	0	700
13	100	200	150	0	700
14	100	200	0	150	700
15	100	200	75	75	700

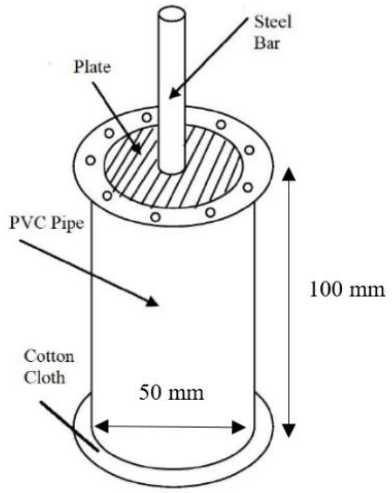


Figure 1. Molding design

Results and Discussion

Physical and chemical properties of unstabilized peat

The results for the von Post scale, natural moisture content, pH, specific gravity, ash, organic content, and bulk density for unstabilized peat are shown in Table 3. When crushing and squeezing the peat between fingers, more than two-thirds of its original amount remained in hand [2]. Based on the characteristic, the soil can be classified as H3 according to the von Post scale of humification. In this study, the moisture content of the peat soil is 230.8%, which shows that the water content in the peat soils is about 230.8% of the total mass of the

peat soil. The lower pH value of 4.15 implies that the soil is acidic. The average value of the specific gravity obtained is 0.60 Gs. It shows that the peat soil is less dense than the water density, which has the potential to float on water. High organic content of 90% shows that the soil can be categorized as highly organic fibrous peat [2]. High organic content and very low ash content of 5.34% indicate that the peat soil has unique geotechnical properties and different from inorganic soils.

Unconfined compressive strength and binder

UCS test was performed on the cured peat soil samples after 28 days. Referring to Table 2, the peat soil was treated with various masses of MgO and OPC as binders, and sand with spent garnet as fillers. The results presented in Figure 2 show the relationship between the measured UCS with the binders and fillers ratio. These values are the averages of three specimens for each condition. Sample 1 to 4 are without MgO and 5 to 11 with 50:50 ratio of OPC: MgO but with a variable amount of fillers. The amount of MgO was doubled for Sample 12 to 15. The results show that without MgO, the samples (Sample 1 to 4) are unable to maintain their form even when assisted with fillers (sand and spent garnet). The reasons may have been that OPC does not have enough alkalinity to neutralize the humic acid in peat and the acids strongly retard hydration [11]. The cementing properties of cement come from its hydration products, such as calcium silicate hydrate (CSH) gel, portlandite, ettringite, and monosulfoaluminate. The functional groups OH, C=O, and COOH present in humic acid has strong affinity to Ca^{2+} [12]. The complex inhibits crystallization of calcium to form CSH.

However, the pH of the samples (Sample 1 to 4) varies from 9.4 to 10.1, which indicate that even though ettringite and monosulfoaluminate may have decomposed at this pH [13], CSH gel should be present for strength contribution. The comparison between Sample 5 and 12 shows that when the amount of MgO was doubled, the peat could achieve 30.18 kPa UCS even without the addition of any fillers. Sample 5 that has half the amount of MgO could not even maintain its form. The findings show the potential contribution of MgO in peat stabilization, and the addition of OPC alone is insufficient to stabilize the peat. The chemical reaction between MgO and water will lead to the formation of hydrate compound, $Mg(OH)_2$ or brucite, as shown in Equation 3.

In the presence of carbon dioxide (CO_2) as those in a peaty environment, the reaction may continue to form more carbonation products. The result of brucite reacting with CO_2 and additional water will produce hydrated magnesium carbonates (HMCs) that can form strength in stabilized peat. HMCs are mainly form nesquehonite ($MgCO_3 \cdot 3H_2O$), hydromagnesite ($4MgCO_3 \cdot Mg(OH)_2 \cdot 4H_2O$), and dypingite ($4MgCO_3 \cdot Mg(OH)_2 \cdot 5H_2O$). The chemical reaction of brucite to form HMCs were shown in Equation 4 -6 [14].

MgO in carbonated concrete formulation is capable of leading the strength of stabilised peat due to the permanent sequestration of CO_2. The carbonation of magnesium oxide, followed by hydration reaction, can lead give strength and act as a permanent storage of CO_2 in the form of stable carbonates [15]. MgO hydration and brucite carbonation are expansive reactions that can increase MgO solid volume by 3.8-6.7 times and fill available pores [16]. Furthermore, humic acid has the potential to precipitate on the surface of MgO or MgO hydration and carbonation products [17].

In the presence of sand as a filler, the binder OPC: MgO with the ratio of 50:50 (Sample 7) has better UCS value of 32.97 kPa in comparison to 25.25 kPa for 33:67 ratio (Sample 14), with the pH values of 9.4 and 10.0, respectively. The formation of Mg $(OH)_2$ may also reduce the quantity of available C_2S and C_3S and consequently CSH phases to bind with the filler [18]. The effect of filler ratios was evaluated in Sample 7 to 11. Spent garnet, which is a chemically inert material, does not take part in hydration but acts as a filler that reduces the void ratio in stabilised peat. The highest result was recorded for the design mix containing well-graded sand only. Even though garnet has higher density than sand, it is not well graded, and when garnet is combined with sand, the combination becomes poorly graded and similar to a previous study, which found that poor graded gravels did not produce better results than those of well-graded sand [19]. The pH of unstabilized peat soil sample is 4.15, whereas the pH of stabilised

peat sample is from 9.0 to 10.2, meaning that the acidic nature of peat soil is effectively neutralised by OPC and MgO.

Fourier transform infrared spectroscopy

Fourier transform infrared (FTIR) spectroscopy is an established and simple equipment that can be used to identify and characterise soil organic matter. This is because FTIR spectroscopy can show direct information of functional groups in the soil organic matter fraction analysed. The FTIR spectra of hydrated MgO, hydrated OPC, and stabilised peat soil are displayed in Figure 4. The bands at 800 cm–1000 cm^{-1} belong to tricalcium silicate (C_3S, alite) or Ca_3SiO_5. The bands at 1100–1200 cm^{-1} are due to CSH_2. The bands between 3000 and 3600 cm^{-1} and at 1650 cm^{-1} are the results of H_2O molecules. These bands underwent changes with the evolution of hydration. The peaks appeared at 900–1200 cm^{-1} and 1350 cm^{-1} represent the formation of CSH or $3CaO.2SiO_2.3H_2O$. The bands at 3650 cm^{-1} are due to the OH groups of calcium hydroxide ($Ca(OH)_2$). The bands at around 1400 cm^{-1} in both dry and hydrated samples are carbonates, which arose from raw materials of cement and the reactions of atmospheric CO_2 with CH during storage and operation.

Table 3. Basic Properties of the unstabilized peat

Basic Soil Property	Average Value
Von Post scale	H_3
Natural moisture content (%)	230.8
pH	4.15
Specific gravity (G_s)	0.60
Ash Content (%)	5.34
Organic content (%)	90.0
Bulk density (g/m^3)	890.17

$$MgO + H_2O \rightarrow Mg^{2+} + 2OH^- \rightarrow Mg(OH)_2 \text{ (Brucite)} \quad (3)$$

$$Mg(OH)_2 + CO_2 + 2H_2O \rightarrow MgCO_3.3H_2O \text{ (nesquehonite)} \quad (4)$$

$$5Mg(OH)_2 + 4CO_2 \rightarrow 4MgCO_3.\ Mg(OH)_2.4H_2O \text{ (hydromagnesite)} \quad (5)$$

$$5Mg(OH)_2 + 4CO_2 + H_2O \rightarrow 4MgCO_3.Mg(OH)_2.5H_2O \text{ (dypingite)} \quad (6)$$

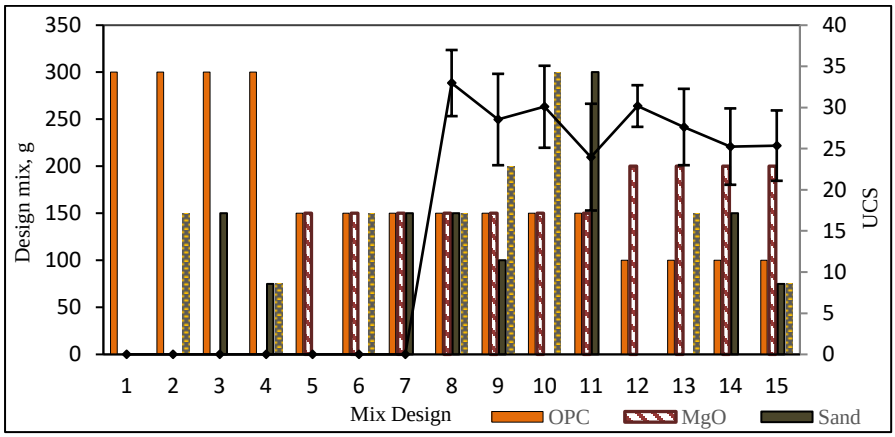


Figure 2. Unconfined compressive strength for stabilizer mixes of stabilized peat

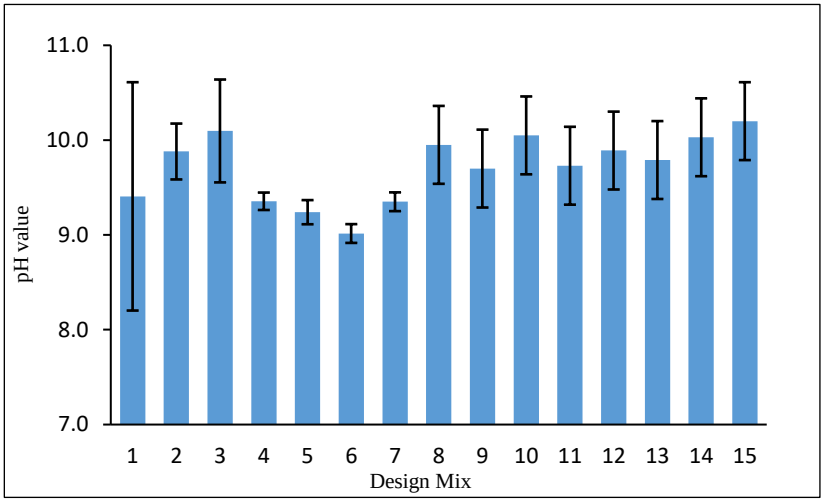


Figure 3. pH value of design mix

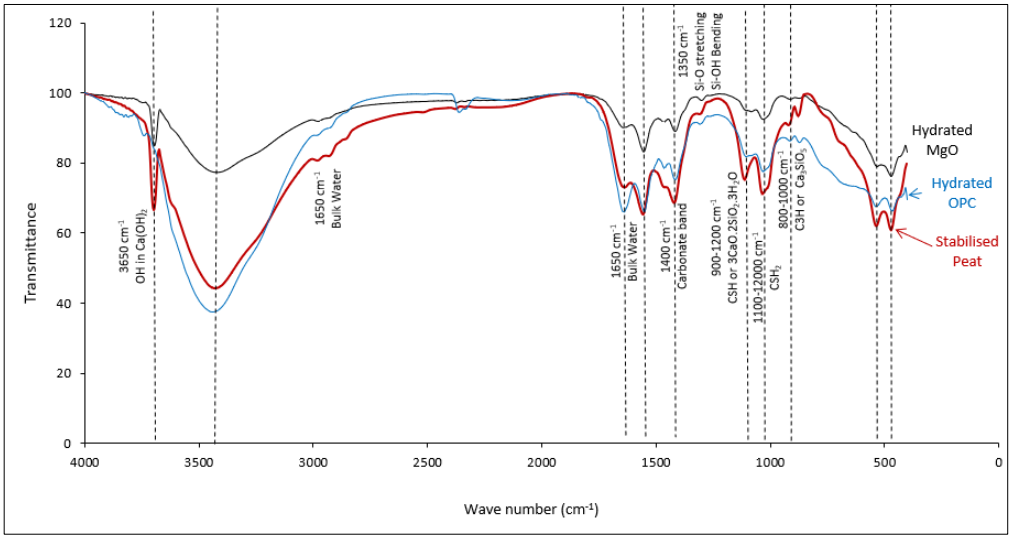


Figure 4. FTIR spectra of hydrated MgO, hydrated OPC and stabilized peat

Conclusion

In this research, a preliminary laboratory investigation using MgO and recycled spent garnet for the stabilisation of peat soil was carried out. Overall, the UCS test results show that peat soil stabilisation using MgO resulted in the improvement of strength of the stabilised peat. The addition of spent garnet as the filler altered the engineering properties of peat soils. Spent garnet has been proven as materials that have the potential to stabilise the road shoulder. This research will introduce recycled spent garnet to be partially added into peat soil. Alternatively, the industrial waste can be reused and reduced to prevent environmental issues. This preliminary research gives an idea about peat soils stabilisation using magnesium oxide and highlights their

properties and importance in chemical and geotechnical engineering.

Acknowledgement

The authors would like to express deep gratitude for the financial support provided by Dana Penyelidikan Inovasi MARA (DPIM) and Universiti Kuala Lumpur (Malaysian Institute Chemical & Bioengineering Technology) for providing facilities to conduct the study.

References

1. Nikookar, M., Arabani, M., Mirmoa'Zen, S. M. and Pashaki, M. K. (2016). Experimental evaluation of the strength of peat stabilized with hydrated lime. *Periodica Polytechnica Civil Engineering*, 60(4): 491-502.
2. Wong, L. S., Hashim, R. and Ali, F. (2013). Improved strength and reduced permeability of stabilized peat: Focus on application of kaolin as a pozzolanic additive. *Construction and Building Materials*, 40: 783-792.
3. Firoozi, A. A., Guney Olgun, C., Firoozi, A. A. and Baghini, M. S. (2017). Fundamentals of soil stabilization. *International Journal of Geo-Engineering*, 8(1): 26.
4. Imbabi, M. S., Carrigan, C. and McKenna, S. (2012). Trends and developments in green cement and concrete technology. *International Journal of Sustainable Built Environment*, 1(2): 194-216.
5. Walling, S. A. and Provis, J. L. (2016). Magnesia-based cements : A journey of 150 years, and cements for the future.
6. ASTM (2000). Annual book of ASTM standards, section four: Construction. American Society of Testing Materials, USA.
7. Landva, A. O. and Pheeney, P. E. (1980). Peat fabric and structure. *Canadian Geotechnical Journal*, 17(3): 416-435.
8. ASTM D 2974 (2000). Standard test method for moisture, ash, and organic matter of peat and other organic soils. Annual book of ASTM Standards, ASTM, Philadelphia, USA.
9. ASTM D2976-71(2004). Standard test method for pH of peat materials. ASTM International, Philadelphia, USA.
10. ASTM D 2166 (2000). Standard test method for unconfined compressive strength of cohesive soil. Annual book of ASTM standards, ASTM, Philadelphia, USA.
11. Wong, L. S., Hashim, R. and Ali, F. H. (2008). Strength and permeability of stabilized peat soil. *Journal of Applied Sciences*, 8(21): 3986-3990.
12. Saride, S., Puppala, A. J. and Chikyala, S. R. (2013). Swell-shrink and strength behaviors of lime and cement stabilized expansive organic clays. *Applied Clay Science*, 85(1): 39-45.
13. Lagerblad, B. (2005). Carbon dioxide uptake during concrete life cycle – State of the art. Stockholm.
14. Unluer, C. and Al-tabbaa, A. (2014). Cement and concrete research enhancing the carbonation of MgO cement porous blocks through improved curing conditions. *Cement and Concrete Research*, 59: 55-65.
15. Unluer, C. and Al-Tabbaa, A. (2013). Impact of hydrated magnesium carbonate additives on the carbonation of reactive MgO cements. *Cement and Concrete Research*, 54: 87-97.
16. Yi, Y., Liska, M., Unluer, C. and Al-tabbaa, A. (2013). Carbonating magnesia for soil stabilization, 905: 899-905.
17. Wall, N. A. and Mathews, S. A. (2005). Sustainability of humic acids in the presence of magnesium oxide. *Applied Geochemistry*, 20(9): 1704-1713.
18. Gonçalves, T., Silva, R. V, Brito, J. De, Fern, J. M. and Esquinas, A. R. (2019). Hydration of reactive MgO as partial cement replacement and its influence on the macroperformance of cementitious mortars. *Advances in Materials Science and Engineering,* 2019: 1-12.
19. Dehghanbanadaki, A., Ahmad, K. and Ali, N. (2013). Influence of natural fillers on shear strength of cement treated peat. *Journal of the Croatian Association of Civil Engineers*, 65(7): 633-640.

Malaysian Journal of Analytical Sciences (MJAS)
Published by Malaysian Analytical Sciences Society

IMPACTS OF CITRIC ACID ON THE PHYTOEXTRACTION OF ZINC (Zn) USING SORGHUM (*Sorghum bicolor (L.)* Moench) PLANTS

(Kesan Asid Sitrik Terhadap Pengekstrakan Fito Zink (Zn) Mengunakan Tumbuhan Sorghum (*Sorghum bicolor (L.)* Moench))

Hamza Badamasi[1]*, Muhammad Saminu Dagari [2], Isyaku Sale[3]

[1]*Department of Chemistry,*
Federal University Dutse, Jigawa State, Nigeria
[2]*Department of Chemistry,*
Federal University Gashua, Yobe State, Nigeria
[3]*Department of Polymer Technology,*
Husaini Adamu Federal Polytechnic Kazaure, Jigawa State, Nigeria

**Corresponding author: hamza.badamasi@fud.edu.ng*

Received: 20 November 2019; Accepted: 21 June 2020; Published: 11 August 2020

Abstract

Greenhouse hydroponic experiments were carried out to examine the impacts of citric acid on Zn uptake and phytoextraction potentials of sorghum (S*orghum bicolor (L.)* Moench). Two-week-old seedlings transplanted in hydroponic solutions were treated with different doses of Zn in the concentration range of 5, 25, 50, 100, and 200 mg/L alone or in combination with 10 mM citric acid. After 21 days of culture, the plants were harvested, separated into roots and shoots, and then dried. Fresh and dry weights were measured using Sartorius balance, Zn uptakes in the roots and shoots were determined by atomic absorption spectrometry. Translocation factor (TF) was determined by dividing Zn concentrations in roots by Zn concentration in the shoots, bioconcentration factor (BCF) was determined as a ratio of Zn concentration in the roots to Zn concentration in the hydroponic solution. Proline, pigments, protein, and ascorbate content were measured spectrophotometrically using acid ninhydrin, acetone, Lowry assay, and dinitrophenyl hydrazine methods respectively. The results indicate that Zn uptake, fresh and dry weights, TF, BCF, proline, and ascorbate contents were concentration dependent with a more significant increase ($p < 0.05$) after the application of citric acid. Pigments and protein contents were, however severely decreased with increasing Zn concentrations and appreciated gradually with the addition of citric acid. Thus, citric acid efficiently increased phytoextractability of Zn and reduced Zn-induced toxicity; *Sorghum bicolor LM* was non-hyperaccumulator of Zn but may be used for phytoremediation of Zn contaminated environments with assistance of citric acid.

Keywords: citric acid, hydroponic, phytoextraction, *Sorghum bicolor (L)* Moench, Zn

Abstrak

Kajian hidroponik rumah hijau telah dijalankan untuk menkaji kesan asid sitrik terhadap pengambilan Zn dan potensi pengekstrakan fito bagi sorghum (S*orghum bicolor (L.)* Moench). Pembenihan selama 2 minggu di dalam larutan hidroponik telah dirawat mengunakan dos Zn yang berbeza di dalam julat kepekatan 5, 25, 50, 100, dan 200 mg/L tunggal atau gabungan bersama 10 mM asid sitrik. Selepas 21 hari dikultur, tumhuban dituai, diasingkan kepada bahagian pucuk dan akar, dan kemudian dikeringkan. Berat asal dan kering telah diukur mengunakan penimbang Sartorius, manakala pengambilan Zn pada bahagian akar

dan pucuk telah ditentukan mengunakan spektrometri serapan atom. Faktor translokasi (TF) telah ditentukan dengan membahagi kepekatan Zn di dalam akar dengan kepekatan Zn pada bahagian pucuk, manakala factor biokepekatan (BCF) telah ditentukan dengan nisbah kepekatan Zn di dalam akar kepada kepekatan Zn di dalam larutan hidroponik. Prolin, pigmen, protein, dan kandungan askorbat telah diukur mengunakan spektrofoto masing-masing mengunakan kaedah asid ninhydrin, aseton, ujian Lowry, dan dinitrofenil hidrazin. Keputusan menunjukan pengambilan Zn, berat asal dan kering, TF, BCF, prolin, dan kandungan askorbat mempunyai kepekatan berbeza dengan peningkatan signifikan ($p < 0.05$) selepas aplikasi asid sitrik. Kandungan pigmen dan protein walaubagaimana pun merosot dengan peningkatan kepekatan Zn dan meningkat dengan penambahan asid sitrik. Maka, asid sitrik berkesan meningkatkan kebolehupayaan fito bagi Zn dan mengurangkan ransangan ketoksikan Zn; *Sorghum bicolor LM* tak berfungsi penumpukan hiper bagi Zn tetapi boleh digunakan bagi pemulihan fito bagi persekitaran yang tercemar dengan Zn dengan bantuan asid sitrik.

Kata kunci: asid sitrik, hidroponik, pengesktrakan fito, *Sorghum bicolor (L)* Moench, Zn

Introduction

Pollution through heavy metals is an issue of worldwide concern due to their negative effects on public and environmental health [1]. Zinc (Zn) is a heavy metal essential for optimal growth and development; however, at elevated concentrations, it is highly toxic to plants and animals leading to impaired growth [2]. Contamination of soils by Zn had become one of the major environmental problems due to frequent Zn related anthropogenic activities such as mining, fertilization, etc. [3]. Higher Zn levels often lead to the production of reactive oxygen species (ROS) resulting in the stimulation of oxidative damage to plants [4]. This will result in stunted growth, reduced chlorophyll, and overall illness [5].

Phytoextraction is a cost-effective and green method of de-contamination for an environment polluted by heavy metals; it involves the use of plants to remove heavy metals from the soil, water, or any other substrate by extracting the metals from the roots and translocating them to the above-ground portions [6, 7]. Phytoextraction is a method of choice and substituted the traditional physicochemical methods because of their high cost and adverse effects on the environment [6]. Many researches had proven the effectiveness of chelating agents, such as citric acids in enhancing and assisting the phytoextraction of metals in plants [8]. Citric acid is a low molecular weight organic acid that belongs to the carboxylic acid group. It is weakly acid and usually found in citrus and in the vacuoles of many plants [9]. Besides it cost-effectiveness, citric acid is reported to have a low affinity to group I and II metals; this unique feature makes it to easily complex Zn forming strong and stable Zn-citrate complex [10]. Citric acid also increases the solubility and availability of Zn for plant uptake [10, 11].

Sorghum bicolor (L.) Moench belongs to the family poacea, rapogeneae and subtribe sorghastrae. It has been ranked fourth in importance among the cereal crops [12]. The crop is environmentally friendly as it is resistant to drought, water-efficient, and requires little or no fertilizer. It is an excellent material for heavy metal stress studies especially Zn because of its higher biomass production, vascular nature, heavy metal tolerance as well as the accumulation of a large quantity of Zn in shoot [13]. The widespread Zn contamination in the environment as a result frequent use of Zn related anthropogenic activities request for an urgent cost-effective and environmentally friendly response [2]. For this reason, this work is was aimed to examine the potential use of *Sorghum bicolor (L.)* Moench for phytoextraction of Zn and to evaluate the impact of citric acid on the *Sorghum bicolor (L.)* Moench growth, Zn uptake, and accumulation.

Materials and Methods

Plant material

Two hundred (200) seeds of *Sorghum bicolor (L.)* Moench were obtained from the Institute of Tropical Agriculture (IITA), Tarauni station, Kano state. The variety is an early maturing one, which has been adopted by many farmers of West Africa [13].

Soil sampling and analysis

Six different sampling points were used to bring together five soil samples as recommended by Patterson

[14]. Parameters namely: total Zn content, soil texture, pH, total organic matter, CEC were determined using atomic absorption spectrometer, hydrometer, pH meter, Walkley and Black wet oxidation and ammonium acetate methods respectively [15, 16].

Field experiment

The experiment was conducted at the Faculty of Agronomy Experimental Farm, Bayero University. The seeds of *Sorghum bicolor (L.)* Moench were raised on the farm for 2 weeks. Seedlings of equal height and strength were selected for control and hydroponic culture experiments.

Hydroponic experiment

The experiment took place in a greenhouse of the department of plant biology's botanical garden, Bayero University, Kano. After 2 weeks of harvest, uniform seedlings were cautiously removed from the soil and transferred immediately to a 1L good plastic containers containing the hydroponic solution of various treatment. Three seedlings were chosen per treatment with one seedling in each container. The hydroponic solution was prepared based on a modified Hoagland solution as described by Taiz and Zeiger [17].

Three treatments were designed in a completely randomized manner which composed of:

i. A hydroponic solution only (control)
ii. Hydroponic solution + Zn supplied as $ZnSO_4 .5H_2O$ at 5, 25, 100 and 200 mg/L.
iii. Hydroponic solution + Zn supplied as $ZnSO_4 .5H_2O$ at 5, 25, 100, and 200 mg/L + 10 mM citric acid added as citrate ($C_6H_5Na_3O_7$).

Measurement of growth parameters

After 6 weeks of treatment, the plants were harvested; cleaned with tap water, and then distilled water. The plants were cut and divided into shoots and roots. Fresh weight was immediately recorded using Sartorius balance (ENTRIS64-1S). The plants were subsequently dried and weight. The roots and shoots were placed in different dark polyethylene bags for further analysis.

Determination of Zn concentration

The dried samples were ground, weighed based on availability, and burned in a furnace at 450 °C for 4 hours. The ash obtained was dissolved in 0.10M HNO_3 and then filtered into a 50 cm^3 volumetric flask. Zn contents in the roots and shoots were analysed using atomic absorption Spectrometer. Zn concentration in the samples was obtained from a calibration curve prepared from the Zn stock solution. Blank determinations were carried out in the same way.

Determination of Translocation factor (TF) and Bioconcentration Factor (BCF)

TF and BCF were estimated using the following relations [18]:

$$TF = \frac{\text{Zn Conc. in the Shoot}}{\text{Zn Conc. in the Root}} \quad (1)$$

$$BCF = \frac{\text{Zn Conc. in the Root}}{\text{Zn Conc. in the Hydroponic Solution}} \quad (2)$$

Determination of proline Contents

The proline contents were measured based on the method described by Bates et al. [19]. A proline standard curve was used to estimate the concentrations of proline and computed using Equation 3.

Estimation of pigment contents

The estimation of pigments content in control and treated plants were carried as per the method of Arnon [20]. The amount Chl a, Chl b and CR were calculated using Equations 4 - 6 [21].

Protein estimation

Protein contents were based on the method of Lowry et al. [22]. An amount 1 g of treated and control plants were milled with 5 ml of $K_2(SO_4)_3$ buffer and centrifuged at 12000 for 15 minutes. About 0.5 ml of the supernatant were mixed with 1 ml of complex-developing reagent (solution A: 2% Na_2CO_3 in distilled water, solution B: 1% $CuSO_4 \cdot 5H_2O$ in distilled water and solution C: 2 % sodium potassium tartrate in distilled water) and then cooled for 15 minutes. A 0.1 ml of diluted Folin reagent was added, cooled for 1 hour and the absorbance was read at 550 nm using a spectrophotometer. The unknown concentration of

protein was determined by plotting a standard curve of absorbance as a function of initial protein concentration.

Analysis of ascorbic acid

Ascorbic acid estimation was accomplished using the method described by Mukherjee and Choudhari [23]. An amount 2 g of control and treated plants were ground in 6% trichloroacetic acid and the extract was filtered and centrifuged at 1000 rpm for 20 minutes and the filtered was made up to 15 mL with trichloroacetic acid. Five mL of extract was mixed with 3 ml of 2% dinitrophenyl hydrazine followed by an addition of 10% thiourea. The mixture was boiled for 20 minutes in a water bath. A 5 mL of 80% H_2SO_4 was added to the mixture in an ice bath. The absorbance was recorded at 530 nm using a spectrophotometer. The concentration of ascorbic acid was calculated from a standard curve plotted with a known concentration of ascorbic acid.

Statistical analysis

The data were analysed in triplets and expressed as mean and standard deviation. The mean of all treatments was subjected to a One-way analysis of variance (ANOVA) using IBM SPSS Statistics 23 software and mean differences were performed using the Tukey test. All graphs were plotted using Microsoft® Excel 2013.

$$\text{Proline}\left(\frac{\mu g}{g}\right) FW = \frac{\text{Proline}\left(\frac{\mu g}{ml}\right) \times \text{Vol. of toluene} \times \text{Vol. of salicylic acid}}{\text{Weight of plant} \times \text{Molecular weight of proline}} \quad (3)$$

$$\text{Chl a (mg g}^{-1}) = \frac{12.7 \times (A663) - 2.69 \times (A645) X\ V}{1000 \times W} \quad (4)$$

$$\text{Chl b (mg g}^{-1}) = \frac{22.9 \times (A645) - 4.68 \times (A663)\ X\ V}{1000 \times W} \quad (5)$$

$$\text{CR (mg g}^{-1}) = \frac{1000A470 \times 1.90\text{Chl a} - 63.14\text{Chl b}}{214} \quad (6)$$

Results and Discussion

The suitability of the *Sorghum bicolor (L.)* Moench optimal growth and development was evaluated by analysing the soil parameters in the studied farm soil (Table 1). The pH value of 7.4±0.133 was in the range (4.0-8.5) suitable for *Sorghum bicolor (L.)* Moench cultivation. The pH value obtained is indicating that Zn was not readily available in soluble form in the soil. The background Zn concentration in the soil was 15.698±0.34 mg/kg. This was within the range of 10-300 mg/kg of uncontaminated soil [24]. Cation exchange capacity (CEC) of 40.12 cmolc/kg±0.10 is demonstrating that Zn is readily be adsorbed by soil and thus leaching will be minimized. High organic matter content (27.49±0.38 g/kg) is signifying the fertility of the soil.

Effects of Zn and citric acid on fresh weight (FW) and dry weight (DW)

A dose-dependent decrease in FW and DW of both roots and shoots was observed after the application of Zn (Table 2). There were maximum reductions of 60% and 46% in FW of root and shoot respectively after 200 mg/L Zn exposure compared to control. The minimum reductions were 25% and 4% at 5 mg/L Zn level respectively. Several authors had reported that higher reduction of FW in the roots and shoots at elevated concentrations might be due to the interference with photosystem alteration which subsequently resulted in stunted growth and chlorosis [24]. A 58% and 71% decrease in root and shoot DW were respectively recorded at maximum Zn dosage. At a minimum dose, 10 % and 18% decline in root and shoot DW were observed in that order. Hasan et al. [25] detected the same pattern in *Sorghum bicolor (L.)* Moench and *Chenopodium album* when treated with Zn.

Manivasagaperuma et al. [26] also witnessed related decline after the application of high Zn concentrations. The reduction is more obvious in roots. This might be because roots are the first tissue in contact with Zn and perhaps the tolerance of *Sorghum bicolor (L.)* Moench to Zn stress [27]. The reduction in weight is reported to be associated with a deficiency of other micronutrients [28]. However, the addition of 10 mM citric acid significantly ($p < 0.05$) improved FW and DW of both root and shoots. There were 11% and 10 % increase in root and shoot FW at maximum Zn dosage. At a minimum, 18% and 2% improvement in root and shoot FW were noted respectively compared to control treatments. Root and shoot DW also followed the same pattern. Since a fixed amount of citric was used across all concentration levels, a citric acid-induced increment is Zn concentration-dependent.

Table 1. Properties of soil

Parameter	**Value**
Texture (%)	Clay (%) 0.46 ±0.07
	Sand (%) 86.50±0.81
	Silt (%) 5.15±0.62^{a}
pH (%)	7.4±0.13^{a}
Organic matter(g/kg)	27.49±0.38^{b}
CEC ($cmol_c$/kg)	40.12±0.10^{d}
Background Zn Conc. (mg/kg)	11.698±0.28^{c}

The result is expressed as mean ± SD. Different letters above denote significant different at P < 0.05 according Tukey test

Table 2. Effects of Zn and citric acid on roots and shoots FW and DW

Treatments	**Parameters**			
	Root FW (mg)	**Shoot FW (mg)**	**Root DW (mg)**	**Shoot DW (mg)**
Control	57.54 ± 0.32^{cd}	122.54 ± 0.62^{c}	15.6 ± 0.21^{a}	38.14 ±0.13^{da}
Zn 5	42.83 ± 0.43^{a}	117.19 ± 0.43^{ab}	14.1 ± 0.41^{b}	31.22 ± 0.23^{c}
Zn 25	33.21 ± 0.51^{b}	97.73 ± 0.51^{d}	11.65 ± 0.51^{d}	17.10 ± 0.11^{b}
Zn 100	27.89 ± 0.32^{a}	72.19 ± 0.32^{a}	8.12 ± 0.13^{c}	14.76 ± 0.32^{a}
Zn200	22.77 ± 0.63^{cb}	65.95 ± 0.63^{a}	6.5 ± 0.12^{ab}	11.11 ± 0.13^{d}
Zn 5 + 10 mM CA	53.70 ± 0.70^{c}	120.39 ± 0.70^{c}	14.76 ± 0.24^{c}	22.76 ± 0.20^{c}
Zn 25 + 10 mM CA	37.23 ± 0.43^{ab}	92.09 ± 0.43^{bd}	13.71 ± 0.13^{d}	18.71 ± 0.32^{a}
Zn 100 + 10 mM CA	31.93 ± 0.53^{b}	81.11 ± 0.53^{b}	12.03 ± 0.32^{b}	17.98± 0.25^{b}
Zn 200 + 10 mM CA	29.45 ± 0.61^{d}	78.15 ± 0.61^{d}	11.81 ± 0.41^{a}	15.05 ± 0.21^{d}

The result is expressed as mean ± SD. Different letters above denote significant different at P < 0.05 according Tukey test

Effects of Zn and citric acid on Zn uptake

The uptake of Zn in the roots and shoots of *Sorghum bicolor (L.)* moench on the addition of different levels of Zn (5, 25, 100, and 200 mg/L) and 10 mM of citric acid are shown in Figure 1.

The addition of Zn to hydroponics enhanced the metal uptake considerably in both roots and shoots ($p < 0.05$). The uptakes increased with increasing Zn levels and roots accumulated more Zn than the shoots. Davis and Parker [29] made similar observations that uptake of Zn increased with increasing application of Zn in peanut plants. The maximum uptakes at 200 mg/L Zn were 2711.83±0.27 and 1068.21±0.31 mg/kg for the root and shoot respectively. The minimum uptakes for root and shoot were 329.09±0.23 and 79.14±0.21 mg/kg. This is in line with the work reported by literature [30, 31]. The addition of citric increased the uptake further. At a minimum Zn level, there was 16% and 13% increase in root and shoot Zn accumulation respectively. At maximum Zn level, the root and shoot uptakes were accelerated to 40% and 69% respectively. Turgut et al. [32] studied the impact of citric acid on metals uptake and accumulation in *Helianthus annus*. Their results indicated that citric acid had considerably increased the metal bioavailability and enhanced the metal uptake in the plant. This study followed the same pattern with the above study. Tandy *et al.* [33] also found that citric acid enhanced the solubility of Zn in the soils and thus increase their bioavailability for plant uptake.

Effects of Zn and citric acid on TF and BCF

TF and BCF were respectively used to estimate the hyperaccumulating and phytoremediation potential of *Sorghum bicolor (L.)* Moench TF increased significantly ($p < 0.05$) from 0.059±0.09 in control to 0.414±0.06 when the concentration of Zn reached a maximum of 200 mg/L (Figure 2). The TF was less than one (TF<1) in all treatments indicating the non-hyperaccumulation capacity of *sorghum bicolor (L.)* Moench TF appreciated further with increased Zn application. The increase might be due to the accumulation of more Zn in the shoots with increasing Zn concentrations [29]. BCF however, decreased gradually with increasing Zn concentration (Figure 3). The decrease may be due to the resistance of metal transfer from roots to the above parts [34]. There was a significant increase ($p < 0.05$) when citric acid was added. The highest increase was observed at 200 mg/L + 10 mM concentrations and the lowest at control. Han *et al.* [35] reported a similar pattern that BCF of Cd significantly reduced with increasing metal concentrations levels. BCF was greater than one in all treatments. For viable phytoextraction, the BCF ought to be greater than one [36, 37]. This is suggesting that *Sorghum bicolor (L.)* Moench is a potential candidate for phytoextraction of Zn contaminated environment.

Effects of Zn and citric acid on proline and ascorbic acid contents

Proline and ascorbic acid are dominant antioxidants that play an important role in the plant's defence mechanism against heavy metals stress. *Sorghum bicolor (L.)* Moench under Zn stress shows a significant upsurge in proline levels. Proline which is considered as a protective mechanism against heavy metal stress increased considerably ($p < 0.05$) from 0.23± 0.01 µg/g in control to a maximum of 3.66±0.02 µg/g at 200 mg/L Zn application (Figure 4). The elevated levels of proline suggest induction of osmotic stress under Zn stress [37]. Addition of citric acid generally lower proline value especially at lower Zn levels. The lowering of proline values may be due to the reaction of Zn with citric acid; forming stable Zn-citrate complex that reduces Zn stress [38]. Proline accumulation in plants assists in preserving the integrity of proteins cytoplasm, functions as carbon and nitrogen sources, and prevents denaturation of enzymes [37]. Kishor et al. [39] proposed that enhanced proline accumulation in plants could be owing to the protection of feedback inhibition of all biosynthetic enzymes by sequestrating proline out of its direction. Bohnet and Jersen [40] stated that proline protects plants from stress by removing the toxic reactive oxygen species and safeguarding of membrane and protein. Ascorbic acid plays an essential role in chlorophyll formation and functions as a substrate for the enzyme, the ascorbate peroxidase. A rise in ascorbic acid is signaling heavy metal stress and consequently the toxicity in plants [41]. The findings of this study indicate a significant elevation (50%) of ascorbic acid at

maximum Zn level; while at minimum Zn concentration, there was a 10% increment. Kandziora-Ciupa et al. [41] had documented that ascorbic acid content was positively correlated with the Zn level. Olkhovych et al. [42] also made similar observations. Hydroponic experiments conducted by Dolatabadian and Jouneghani [43] reveals that ascorbic acid detoxified the damaging effects of reactive oxygen species (ROS). However, after the addition of citric acid, a significant ($p < 0.05$) decrease in ascorbic acid was noted. The study conducted by Chen et al. [44] revealed that citric acid is capable of reducing the toxicity of heavy metals.

Effects of Zn and citric acid on pigments and protein contents

Table 3 shows the changes in the pigments and protein contents with respect to an increase in the concentration of Zn and 10 mM citric acid.

The changes in pigments are associated with visual symptoms of plant disorder and photosynthesis [45]. The amounts Chl a, Chl b, and Car were severely affected by Zn treatments, especially at higher Zn dosages. The addition of citric acid however, increased significantly ($p < 0.05$) the pigment contents compared to free Zn treatments. The reduction of pigments in plants with increasing Zn concentration might be due to the exchange of central Mg^{2+} in chlorophyll by Zn^{2+} [46]. Fikrye and Omer [47] reported that the generation of reactive oxygen species which later caused oxidative damage might lead to reduction in pigment levels. Formation Zn-citrate complex after citric acid addition led to decreased pigment levels and reduced Zn toxicity [48]. Zn application had significantly ($p < 0.05$) affected the protein contents. 36%, 57%, 65%, and 78% decline in protein contents were observed when 5, 25, 100, and 200 mg/L Zn concentration levels were respectively applied. This is in line with the investigation performed by Alia et al. [49]. Previous research indicated that the decline in protein is linked to a decrease in pigment contents and impairment of nitrogen absorption [50]. However, there was considerable improvement in the value of protein when 10 mM Citric acid was applied. There were only 2%, 9%, 21%, and 42% decrease in protein level at 5, 25, 100, and 200 mg/L Zn levels respectively compared to when Zn was used alone.

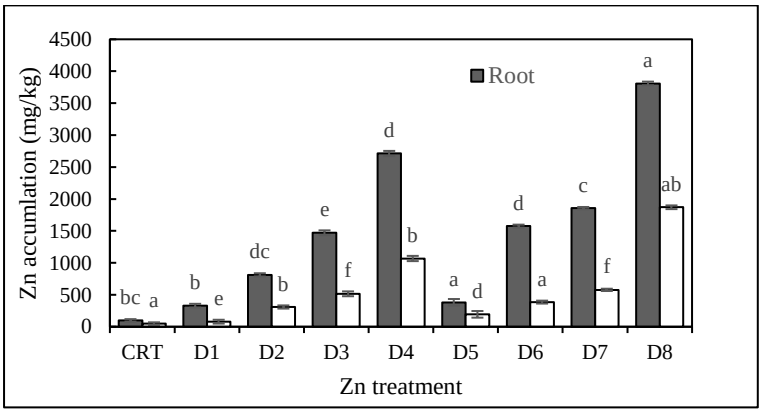


Figure 1. Effect of added Zn and 10 mM citric acid on Zn uptake in the roots and shoots of *sorghum bicolor L.M*. **CRT** = Control, **D**1 = Zn 5**, D2** = Zn 25, **D3** = Zn 100, **D4** = Zn 200, **D5** = Zn 5 + 10 mM CA, **D6** = Zn 25 + 10 mM CA, **D7** = Zn 100 + 10 mM CA, **D8** = Zn 200 + 10 mM CA

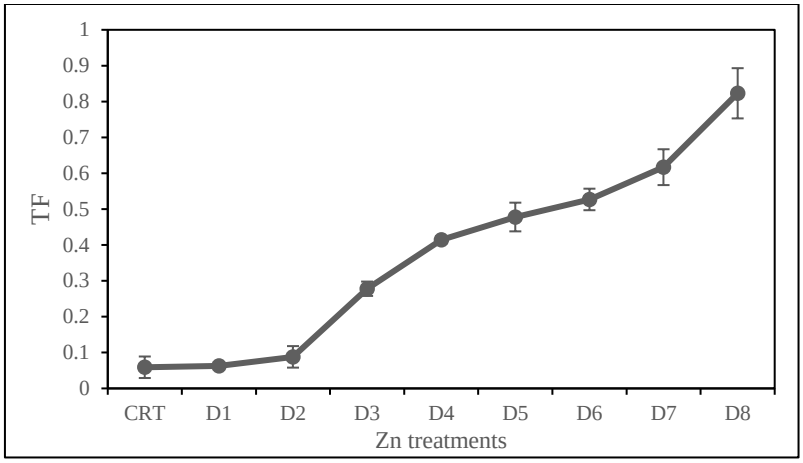


Figure 2. Effects of Zn and 10 mM citric acid on TF. **CRT** = Control, **D**1 = Zn 5**, D2** = Zn 25, **D3** = Zn 100, **D4** = Zn 200, **D5** = Zn 5 + 10 mM CA, **D6** = Zn 25 + 10 mM CA, **D7** = Zn 100 + 10 mM CA, **D8** = Zn 200 + 10 mM CA

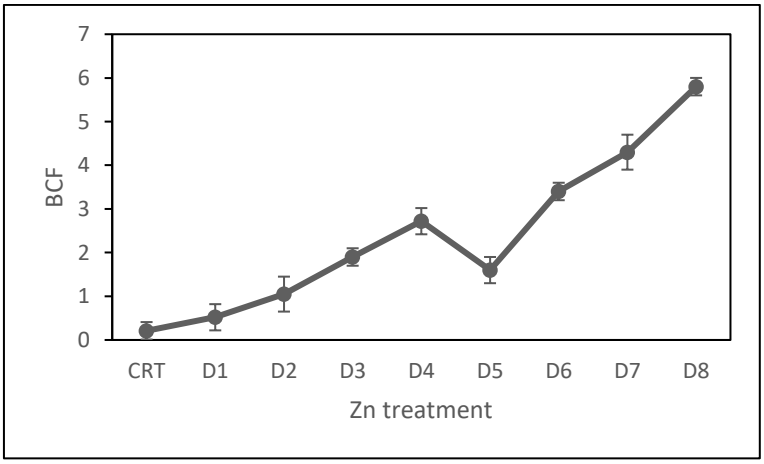


Figure 3. Effects of Zn and 10 mM citric acid on BCF. **CRT** = Control, **D**1 = Zn 5**, D2** = Zn 25, **D3** = Zn 100, **D4** = Zn 200, **D5** = Zn 5 + 10 mM CA, **D6** = Zn 25 + 10 mM CA, **D7** = Zn 100 + 10 mM CA, **D8** = Zn 200 + 10 mM CA

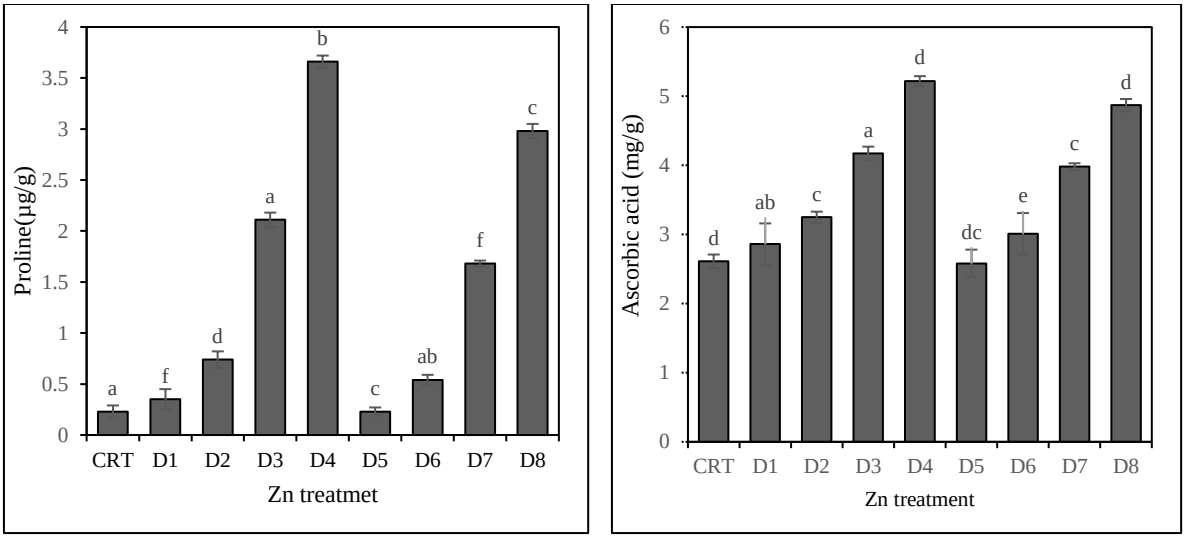


Figure 4. Effects of added Zn levels and citric acid on accumulation of proline and ascorbic acid contents. **CRT** = Control, **D**1 = Zn 5**, D2** = Zn 25, **D3** = Zn 100, **D4** = Zn 200, **D5** = Zn 5 + 10 mM CA, **D6** = Zn 25 + 10 mM CA, **D7** = Zn 100 + 10 mM CA, **D8** = Zn 200 + 10 mM CA

Table 3. Effects of Zn and citric acid on pigment and protein content

Treatments	**Parameters**			
	Chl a (mg/g)	**Chl b (mg/g)**	**CR (mg/g)**	**Protein (mg/g)**
Control	79.39 ± 0.45^{a}	126.86 ± 0.71^{c}	330.05 ± 0.31^{a}	6.05 ± 0.11^{da}
Zn 5	76.28 ± 0.32^{ab}	121.21 ± 0.44^{b}	325.78 ± 0.45^{bc}	3.78 ± 0.21^{c}
Zn 25	70.31 ± 0.51^{c}	17.77 ± 0.31^{b}	316.14 ± 0.85^{a}	2.62 ± 0.15^{b}
Zn 100	63.98 ± 0.32^{a}	102.52 ± 0.35^{a}	210.79 ± 0.72^{c}	2.11 ± 0.12^{a}
Zn200	48.36 ± 0.77^{d}	87.57 ± 0.42^{a}	156.71 ± 0.92^{c}	1.34 ± 0.13^{d}
Zn 5 + 10 mM CA	72.59 ± 0.62^{a}	115.61 ± 0.60^{ab}	320.17 ± 0.76^{b}	5.91 ± 0.30^{c}
Zn 25 + 10 mM CA	69.03 ± 0.45^{dc}	94.07 ± 0.23^{cd}	300.14 ± 0.65^{a}	5.52 ± 0.32^{a}
Zn 100 + 10 mM CA	51.23 ± 0.53^{b}	86.12 ± 0.46^{b}	240.13 ± 0.42^{d}	4.76 ± 0.35^{b}
Zn 200 + 10 mM CA	49.87 ± 0.74^{c}	74.81 ± 0.33^{a}	187.67 ± 0.45^{a}	3.53 ± 0.21^{d}

The result is expressed as mean ± SD. Different letters above denote significant different at $P < 0.05$ according to Tukey test

Conclusion

Results of this study indicated that addition Zn to different hydroponic treatments significantly affect the various parameters such as pigments, proline, protein contents of *Sorghum bicolor (L.)* Moench by inducing the toxicity symptoms. The effects were more pronounced with increasing Zn level. However, the addition of citric acid significantly alleviated these effects. The TF was less than one (TF<1) in all treatments but the BCF was greater than one in all treatment (BCF > 1). This is suggesting that citric acid efficiently increased phytoextractability of Zn and

Sorghum bicolor (L.) Moench was not hyperaccumulator of Zn but it may successfully be used in the phytoextraction of Zn contaminated environment with the assistance of citric acid. This study provides recommendation for future use of *Sorghum bicolor (L.)* Moench and its related species for large scale phytoremediation of Zn and other metals contaminated areas in a cheap and environmentally friendly techniques.

Acknowledgement

The authors are grateful to the Head of Departments, Biochemistry, and Plant Biology, Bayero University Kano for their invaluable support in providing research facilities. Our sincere appreciation also goes to TET fund for providing a grant to support this work.

References

1. Blaylock, M. J. and Huang, J. W. (2000). Phytoremediation of toxic metals using plants to clean up the environment. John Wiley & Sons Inc., New York: pp. 53-70.
2. Alloway, B. J. (2004). Zinc in soils and crop nutrition. IZA Publications, International Zinc Association, Brussels: pp. 135-150.
3. Chaney, R. L. (1993). Plant uptake of inorganic waste constituents. Park Ridge, Noyes Data Corporation, New Jersey, USA: pp. 50-76.
4. Sharma. P. and Dubey, R. S. (2007). Involvement of oxidative stress and role of antioxidative defense system in growing rice seedlings exposed to toxic concentrations of aluminum. *Plant Cell Reports,* 26(1): 2027-2038.
5. Lo'pez-Mosquera, M.E., Moiro'n, C. and Carral, E. (2000). Use of dairy-industry sludge as fertilizer for grasslands in northwest Spain: heavy metal levels in the soil and plants. *Resources, Conservation and Recycling,* 30(1): 95-109.
6. Islam, E., Yang, X. E., He, Z. L. and Mahmood, Q. (2007). Assessing potential dietary toxicity of heavy metals in selected vegetables and food crops. *Journal of Zhejiang University of Science B,* 20(1): 1-13.
7. Achakzai, A. K. K., Bazai, Z. A. and Kayani, S. A. (2011). Accumulation of heavy metals by lettuce (*Lactuca sativa L.)* irrigated with different levels of wastewater of Quetta city. *Pakistan Journal of Botany,* 43: 2953-2960.
8. Zhao, Z., Xi, M., Liang, G., Liu, X., Bai, Z. and Huang, Y. (2010). Effects of IDSA, EDDS and EDTA on heavy metals accumulation in hydroponically grown maize (*Zea mays, L.*). *Journal of Hazardous Materials*, 181(2): 455-459.
9. Gunawardana, B., Singhal, N. and Johnson, A. (2010). Amendments and their combined application for enhanced copper, cadmium, lead uptake by *Lolium perenne*. *Plant and Soil*, 329 (3):283-294.
10. Bassi, R., Prasher, S. O. and Simpson, B. K (2000). Extraction of metals from a contaminated sandy soil using citric acid. *Environmental Progress,* 19(4): 275-282.
11. Irannajad, M., Meshkini, M. and Azadmehr, A. R. (2013). Leaching of zinc from low grade oxide ore using citric acid. *Physicochemical problems of Mineral Processing*. 49(5):547-555.
12. Aba, D. A., Marley, P. S. and Maigida, D. N. (2008). Cereals crops of Nigeria; principles production and utilization. Ade-commercial press, Zaria, Nigeria: pp. 40-53.
13. Obilana, A. T. (1981). International Symposium on Sorghum grain quality, ICRISAT, Patancheru: pp.40-45.
14. Patterson, J. J. and Olson, J. J. (1983). Effects of heavy metals on radicle growth of selected woody species germinated on filter paper, mineral and organic soil substrates. *Canadian Journal of Forest Research,* 13 (1): 233-238.
15. IITA (1979). Laboratory manual on basic soil and plant analyses, 3rd edition, Longman London, UK: pp. 3-12.
16. Juo, A. S. B. (1988). Selected methods for soil and plant analysis, Manual Series No.1 International Institute of Tropical Agriculture (IITA), Ibadan, Nigeria: pp. 10-30.
17. Taiz, L. and Zeiger, E. (2002). Plant physiology, Sinauer Associates, (eds.). Sunderland, U.S.A: pp. 67-86.
18. Shrikrishna, R. S. and Singh. S. (2012). Effect of zinc on yield, nutrient uptake and quality of Indian mustard. *Journal of Indian Society of soil Science*, 40(3): 321-325.

19. Bates, L. S., Waldren, R. P. and Teare, I. D. (1973). Rapid determination of free proline for water stress studies. *Plant and Soil,* 39(1):205-207.
20. Arnon, D. I. (1949). Copper enzymes in isolated chloroplast, polyphenoloxidase in *Beta vulgaris*. *Plant Physiolology*, 24(5): 1-15.
21. Lichtenthaler, H. and Wellburn, A. (1983). Determination of total carotenoids and chlorophylls a and b of leaf extract in different solvent. *Biochemical Society Transaction*, 11(1): 591-592.
22. Lowry, O.H., Rosembrough, N. J., Farr, A. L and Randall, R. J. (1951). Protein measurement with the Folin phenol reagent. *Journal of Biological Chem*istry, 193(1): 267-275.
23. Mukherjee, S. P. and Choudhari, M. A. (1983). Implication of water stress induced changes in the levels of endogenous ascorbic acid and hydrogen perioxide in *Vigna* seedlings. *Physiology Plant Journal*, 58: 166-170.
24. Hafeez, B., Khanif, Y. M. and Saleem, M. (2013). Role of zinc in plant nutrition-A review. *American Journal of Experimental Agriculture,* 3(2):374-391.
25. Hasan, M. H., Reza, A. and Habib K. (20120. Effect of zinc toxicity on plant productivity, chlorophyll and Zn contents of Sorghum (*Sorghum bicolor*) and common lambsquarter (*Chenopodium album*). *International Journal of Agricultural Research and Review,* 2(1): 247-254.
26. Manivasagaperuma, R., Vijayarengan, P., Balamurugan, S. and Thiyagarajan G. (2012). Effect of zinc on growth, dry matter yield and nutrient content of *Vigna Radiata (L.) Wilczek*. *International Journal of Recent Scientific Research,* 3(3):687-692.
27. Anamika, S., Eaparn, S. and Fulekar, M. (2009). Phytoremediation of Cd, Pb and Zn by *Brassica juncea L*, Czern. *Cross Journal of Applied Biosciences,* 13(1): 726-736.
28. Wang, C., Zhang, S. H., Wang, P. F., Hou, J., Zhang, W. J., Li, W. and Lin, Z. P. (2009). The effect of excess Zn on mineral nutrition and ant oxidative response in rapeseed seedlings. *Chemosphere*, 75:1468-1476.
29. Davis, J. G. and Parker, M. B. (1993). Zinc toxicity symptom development and partitioning of biomass and Zn in peanut plants. *Journal of plant Nutrition,* 16(2): 2353-2369.
30. Wong, M. H., Li, W. C. and Zhang, Y. C. (2009). Effect of bacteria on enhanced metal uptake of the Cd/Zn hyperaccumulating plant *Sedum alferedii*. *Journal of Experimental Botany,* 58(1): 4173-4182.
31. Carl, E. S., Heather, D. T., Timothy, W. C. and Williams, M. R. (2013). Zn availability in hydroponics culture influences Glucosinolate concentration in *Brassica rapa. Horticultural Science,* 39: 84-86.
32. Turgut, C., Pepe, M. K. and Culright, T. J. (2008). Effects of EDTA and citric acid on phytoremediation of Cd, Cr, and Ni from soil using *Helianthus annus*. *Environmental Pollution*, 131:147-154.
33. Tandy, S., Schulin, R. and Norwaek (2008). Uptake of metals and Chelant-assisted phytoextraction with EDDS related to the solubilized metal concentration. *Environmental Science and Technology,* 40(1): 2753-2758.
34. Justin, V., Majid, N., Islam, M. M. and Abdu A, (2011). Assessment of heavy metal uptake and translocation in *Acacia mangium* for phytoremediation of cadmium contaminated soil. *Journal of Food Agriculture and Environ*ment, 9(2): 588-592.
35. Han, F., Shan, X. Q., Zhang, S. Z., Wen, B. and Owens, B. (2011). Enhanced cadmium accumulation in maize roots: the impact of organic acids. *Plant and Soil*, 289: 355-368.
36. Ma, L.Q., Komar, K. M., Zhang, T. U. C., Caiv, W. and Kenmelley E. D. (2012). A fern that hyperacumulates arsenic. *Nature*, 11(1): 409-579.
37. Sharma, S. S., Schat, H. and Vooijs, R. (1998). In vitro alleviation of heavy metal-induced enzyme inhibition by proline. *Phytochemistry,* 49:1531-1535.
38. Siripornadulsil, S., Traina, S., Verma, D. P. S. and Sayre, R. T. (2014). Molecular mechanisms of proline–mediated tolerance to heavy metals in transgenic microalgae, *Plant Cell,* 14:2837-2947.

39. Kishor, P. B. K, Sangam, S., Amrutha, R. N., Laxmip, S. N., Naidu, K. R., Rao, K. R. S. S., Rao, S., Reddy, K. S., Theriappan, P. and Screenivasule, N. (1995). Regulation of proline synthesis, degradation, uptake and transport in higher plants; its implication in plant growth and abiotic stress tolerance. *Current Science*, 88: 424-438.
40. Bohnet, H. J. and Jersen, R. J. (1993). Strategies for engineering water–stress tolerance in plants. *Trends in Biotechnology,* 14(1): 89-97.
41. Kandziora-Ciupa, M., Nadgórska-Soch, A., Barczyk, G. and Ciepa, R. (2017). Bioaccumulation of heavy metals and ecophysiological responses to heavy metal stress in selected populations of *Vaccinium myrtillus L*. and *Vaccinium vitis-idaea L*. *Ecotoxicology,* 26(1): 966-980.
42. Olkhovych, O., Volkogon. M., Taran. N., Batsmanova, L. and Kravchenko, I. (2016). The effect of copper and zinc nanoparticles on the growth parameters, contents of ascorbic acid, and qualitative composition of amino acids and acylcarnitines in *Pistia stratiotes L. (Araceae)*. *Nanoscale Research Letters*, 11:218-228.
43. Dolatabadian, A. and Jouneghani, S. (2009). Impact of exogenous ascorbic acid on antioxidant activity and some physiological traits of common bean subjected to salinity stress. *Notulae Botanicae Horti Agrobotanici Cluj-Napoca,* 37(2): 165-172.
44. Chen, Y. X., Lin, Q., Luo, Y. M., He, Y. J., Zhen, S., Yu, Y. L., Tian, W. and Ming G. M. (2003). The role of citric acid on the phytoremediation of heavy metal contaminated soil. *Chemosphere*, 50(1): 807-811.
45. Küpper, H. F. and Spiller, M. (1996). Environmental relevance of heavy metal substituted chlorophyll using the example of water plant. *Journal of Experimental Bio*logy, 47:259-266.
46. Balashouri, P. (2009). Effects of zinc on germination, growth, pigment content and phytomass of *Vignia Radiata* and sorghum. *Journal of Ecobiology*, 7:109-114.
47. Fikriye, K. Z. and Omer, M. (2008). Effects of some heavy metals on concentration of chlorophyll, proline and antioxidant chemicals in beans (*Phaseoley Vulgarus. L*) seedlings. *Biological Craco-Viensia.* 47:157-164.
48. Doncheva, S. and Stoyanova, Z. (2010). The effect of Zinc supply and succinate treatment on plant growth and mineral uptake in pea plant. *Brazilian Journal of Plant Physio*logy, 14(1):1871-1880.
49. Alia, N., Sarda, K., Said, M., Salma, K., Sadia, A., Sadaf, S., Toqeer, A. and Miklas, S. (2015). Toxicity and bioaccumulation of heavy metals in spinach (*Spinacia oleracea*) grown in a controlled environment. *International Journal of Environmental Resources and Public Health,* 12(2):74-84.
50. Lin, R. Z., Wang, X. R., Luo, Y., Du, W. C., Guo, H. Y., Yin, D. Q. (2007). Effects of soil cadmium on growth, oxidative stress and antioxidant system in wheat seedlings (*Triticum aestivum* L.). *Chemosphere,* 69(2): 89-98.

Malaysian Journal of Analytical Sciences (MJAS)
Published by Malaysian Analytical Sciences Society

A FEASIBILITY STUDY ON VOLATILE ORGANIC COMPOUNDS PROFILING OF OIL PALM-*Ganoderma* INFECTED WOOD FOR BASAL STEM ROT DETECTION

(Kajian Kebolehlaksanaan Pemprofilan Sebatian Organik Meruap daripada Kayu Sawit yang Dijangkiti *Ganoderma* bagi Mengesan Penyakit Reput Pangkal Batang)

Zainol Hilmi Nur Hailini*, Idris Abu Seman, Mohd Azmil Mohd Noor, Shariffah-Muzaimah Syed Aripin

Malaysian Palm Oil Board,
6, Persiaran Institusi, Bandar Baru Bangi, 43000 Kajang, Selangor, Malaysia

**Corresponding author: hailini@mpob.gov.my*

Received: 11 March 2020; Accepted: 28 May 2020; Published: 11 August 2020

Abstract

Volatile organic compounds (VOCs) are commonly released during plant-pathogen interactions due to pathogenicity or plant defence responses. Basal stem rot (BSR) disease caused by *Ganoderma boninense* fungus remains a serious threat to oil palm cultivation. This study aimed to investigate the feasibility of detecting VOCs released from oil palm wood tissue infected by *G. boninense* using headspace solid-phase microextraction (HS-SPME) method combined with gas-chromatography mass-spectrometry (GC-MS). Several factors affecting the HS-SPME extraction efficacy were investigated; 0.25 g of sample homogenised in liquid nitrogen was shown to be the most useful preparation procedure, while fibre divinylbenzene/carboxen/polydimethylsiloxane (DVB/Car/PDMS) was shown as the optimum extraction phase. The optimised method was capable of sampling VOCs with high reproducibility with a balanced VOCs profile of various chemical classes. The most abundant VOCs detected were the aliphatic compounds with eight-carbon atoms, 1-octen-3-ol (69.43%) and 3-octanone (10.34%). This preliminarily study reveals that the detected VOCs could also be used as biomarker candidates for basal stem rot disease detection. However, further study is required.

Keywords: basal stem rot, *Ganoderma*, oil palm, 1-octen-3-ol, 3-octanone

Abstrak

Sebatian-sebatian organik meruap (VOCs) biasanya dibebaskan semasa interaksi tumbuhan-patogen kesan kepatogenan atau tindak balas pertahanan tumbuhan. Penyakit reput pangkal batang (BSR) yang disebabkan oleh kulat *Ganoderma boninense* masih lagi menjadi ancaman serius terhadap penanaman sawit. Kajian ini dijalankan bertujuan menyelidik kebolehlaksanaan pengesanan VOC yang terbebas dari tisu kayu kelapa sawit yang dijangkiti oleh *G. boninense* menggunakan kaedah mikroekstraksi fasa pepejal-ruang tutupan (HS-SPME) yang digabung bersama kromatografi gas-spektrometri jisim (GC-MS). Beberapa faktor yang mempengaruhi keberkesanan pengambilan HS-SPME telah dikaji; 0.25 g sampel yang dihomogenkan dalam nitrogen cair terbukti sebagai prosedur penyediaan yang paling sesuai, sementara gentian divinilbenzena/karboksena/polidimetilsikloheksana (DVB/Car/PDMS) dibuktikan sebagai fasa pengekstrakan yang optimum. Kaedah yang optimum ini mampu mengekstrak VOCs dengan kebolehulangan yang tinggi dengan profil VOCs yang seimbang dari pelbagai kelas kimia. VOCs yang paling banyak

dikesan adalah sebatian-sebatian alifatik dengan atom-atom lapan-karbon, 1-okten-3-ol (69.43%) dan 3-oktanon (10.34%). Kajian awal ini mendedahkan bahawa VOCs yang dikesan juga berpotensi digunakan sebagai penanda biologi bagi pengesanan penyakit reput pangkal batang. Walau bagaimanapun, kajian lanjutan adalah diperlukan.

Kata kunci: reput pangkal batang, *Ganoderma*, sawit, 1-okten-3-ol, 3-oktanon

Introduction

Oil palm (*Elaeis guineensis* Jacq.) is one of the major economic crops feeding the world. In 2018, the main palm oil producing countries, Indonesia and Malaysia, contributed 85% of the palm oil supply worldwide, accounted for 34% of the global vegetable oils consumption [1]. Oil palm as a monoculture plantation crop is exposed to serious threats by pests and diseases. In Southeast Asia, the basal stem rot (BSR) disease due to *Ganoderma boninense* is a major disease of oil palm plantation. BSR infection starts with the penetration of mycelia into oil palm roots and slowly spread to the stem bole [2]. The BSR infection can only be recognised at a very late stage with severe foliar chlorosis and breakage at older fronds, presence of decayed tissues at palm base and production of fruiting bodies [3]. BSR disease has caused severe economic losses due to reduction in oil yield, number of stands, and replanting cycle of new palms [4]. Therefore, rapid and accurate detection of *Ganoderma* fungus at the early stage of infections is desired to assist more efficient management practices for the reduction of disease spread.

Volatile organic compounds (VOCs) have gained attention for their application in both plant disease detection and discrimination. VOCs analysis for recognition of infected plant materials has been achieved on several economically important crops species such as apple and pear plants [5], grapevine plants [6], strawberries [7] and also potato tubers [8-10]. VOCs are carbon compounds with low molecular weight and high vapour pressure, making them easily evaporate at room temperature [11].

Detection of BSR disease in oil palm has been previously reported through the use of an electronic nose; but the VOCs identity has not yet been examined [12]. The determination of VOCs is claimed to be crucial in the development of electronic sensor systems, as shown in the studies of soft rot diseases [13, 14]. Therefore, the profiling of VOCs from oil palm infected with *G. boninense* is necessary to produce more effective electronic noses for BSR disease detection so that the disease spread can be reduced and suitable control management can be carried out. Sampling of VOCs is challenging as the VOCs profiles are highly dependent on the extraction method chosen, particularly when high temperature application is involved, pyrolysis and thermal rearrangement of VOCs may take place [15]. Because of that, solid phase microextraction (SPME) has been the most favourable method in the analysis of VOCs due to its simple preparation technique, particularly the ability to pre-concentrate analytes in the absence of solvent, and rapid detection. SPME is generally employed together with headspace analysis of VOCs because it is the most useful method to obtain a true volatile species at a given time. Thus, headspace-SPME (HS-SPME) are often demonstrated as the method of choice for VOCs detection from fungi and plants [6-8, 15-18]. However, optimisation of HS-SPME is required to ensure its extraction efficiency, which includes the sample preparation method, the sample weight and the type of SPME fibre.

The present work demonstrates VOCs released from *in vitro* infection of *Ganoderma* on oil palm wood tissues that were extracted through HS-SPME and profiled by gas chromatography-mass spectrometry (GC-MS). The main objective was to conduct preliminary assessment on the sampling method to obtain VOCs profile from the oil palm-*Ganoderma* infected wood tissues.

Materials and Methods

Preparation of oil palm-*Ganoderma* infected samples

Ganoderma boninense strain PER71 was obtained from the internal culture collection of Malaysian Palm Oil Board (MPOB). *G. boninense* (PER71) was grown on a sterilised cellophane membrane on top of potato dextrose agar (PDA) of pH 5.5 in 145 mm petri plate and

incubated at 28±2 ºC for 7 days. Oil palm wood shavings were collected from areas in MPOB Kluang Research Station, Johor plantation with no *Ganoderma* incidence and autoclaved at 121 ºC, 103.4 kPa for 15 min. *In vitro* infection of oil palm wood was attained by placing the sterilised oil palm wood shavings on PDA with 7-day-old *G. boninense* and further incubated at 28±2 ºC for one week (Figure 1). For headspace analysis of VOCs, after 14 days of incubation, samples of oil palm-*Ganoderma* infected were collected and subjected to two types of sample preparation methods. The first sample preparation method was without any mechanical force, while the other preparation method was with mechanical force application where oil palm-*Ganoderma* infected sample was crushed into fine powder in the presence of liquid nitrogen. Each sample type was distributed into 0.25 g, 0.50 g and 1.00 g in 20 ml headspace vials. Headspace vials were sealed with PTFE/silicone-coated septa and aluminium crimp cap. Blank headspace vials were set up as controls. All samples were stored at -80 ºC until required.

Extraction of fungal VOCs

An SPME manual holder and four types of fibres *i.e.* 100 µm polydimethylsiloxane (PDMS), 85 µm carboxen/polydimethylsiloxane (CAR/PDMS), 65 µm polydimethylsiloxane/divinylbenzene (PDMS/DVB) and 50/30 µm divinylbenzene/carboxen/polydimethyl siloxane (DVB/Car/PDMS) were purchased from Supelco (Bellefonte, PA, USA). All the SPME fibres were conditioned according to manufacturer's specification before VOCs sampling. SPME fibres were directly thermally desorbed in a GC inlet heated to 250 ºC for 30 min to eliminate contaminants. For analysis of headspace VOCs, *in vitro* oil palm-*Ganoderma* infected sample was preincubated for 30 min at 40 ºC before being exposed to SPME fibres (Figure 2). After 15 min of exposure, the SPME fibre was immediately desorbed into GC heated injection port, heated to 250 ºC in splitless mode. HS-SPME analyses were repeated four times.

GC-MS analysis

GC analysis was performed on an Agilent Technologies (CA, USA) GC 7890A, equipped with an inert MS Triple-Axis detector model 5975C. VOCs were separated on a fused-silica bonded-phase capillary column Zebron^{TM} ZB-5HT Inferno, 30 m in length by 0.25 mm in internal diameter, with 0.25 µm of film thickness (5% phenyl 95% dimethylpolysiloxane). Helium was used as the carrier gas and the flow rate was 1 mL/min. The following three-step heating oven programme was applied: (1) 45 ºC for 1 minute; (2) 10 ºC min^{-1} temperature increased to 260 ºC; (3) 260 ºC for 30 minutes. The transfer line temperature was 280 ºC. A mass range from 20–400 m/z was scanned in full scan mode at 70 eV ionisation energy. The chromatograms were analysed using Agilent Enhanced MSD ChemStation (Version E.02.00.493) and tentative identification of VOCs was performed by comparing their mass spectra and retention indices with the NIST data library.

Statistical analysis

Raw data generated from GC-MS analyses were extracted and imported into Microsoft Excel to create a data matrix. The differences between VOCs concentrations were examined using analysis of variance (ANOVA) at significant level of $p < 0.05$ (IBM SPSS Statistics version 20.0).

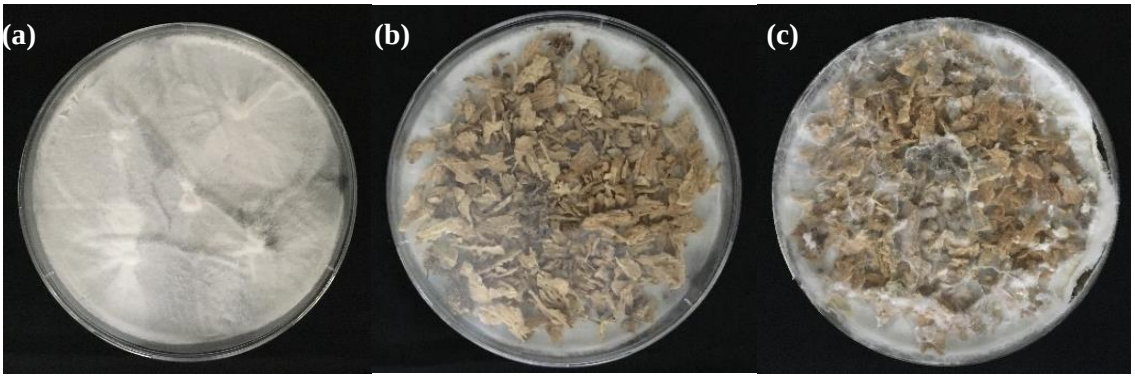


Figure 1. Preparation of artificial infection of oil palm wood tissues by *Ganoderma boninense*. Pure culture of *G. boninense* after 7 days of incubation at 28±2 ºC (a), sterilised oil palm wood on top of fully grown *G. boninense* (b), and oil palm wood colonised by *G. boninense* after 14 days (c)

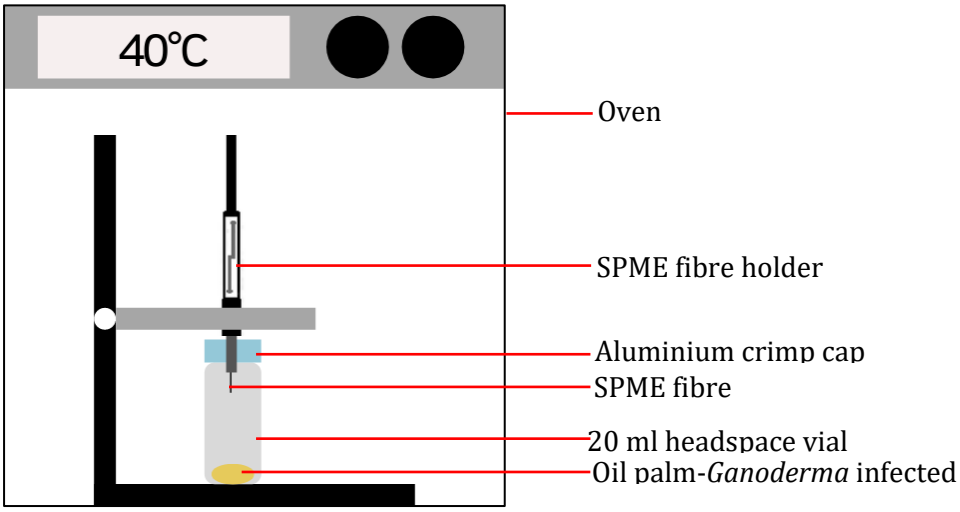


Figure 2. Schematic diagram of experimental setup for headspace VOCs extraction from oil palm-*Ganoderma* infected tissues using SPME in an oven at 40 ºC.

Results and Discussion

Optimisation of HS-SPME sampling protocol

The performance of a given SPME application was highly dependent on the selected extraction phase which determined the selectivity and the reliability of the method. However, analysis of VOCs using SPME in biological studies should also examine sample stability and integrity to obtain a consistent profile because of their dynamic nature due to enzymatic and non-enzymatic reactions. Therefore, preliminary studies were conducted to analyse the experimental conditions that may influence the VOCs profiles generated.

Sample preparation method

The first factor investigated was the method of sample preparation, either with or without the application of mechanical force with the use of liquid nitrogen. Results showed that higher and well-balanced GC profile with wider range of chemical classes were obtained when biological tissues were disrupted at ultra-low

temperature. In addition, the chromatograms of all replicates demonstrated consistent sequence of VOCs, which were hexanal, benzaldehyde, 3-octanone, 2-pentylfuran, octanal, (E)-2-octenal, 1-octanol, nonanal, naphthalene, dodecane, tetradecane and α-cardinene, eluted from the column (Figure 3). Constant chromatogram profiles indicated the sample was stable, and therefore, was used for further analyses.

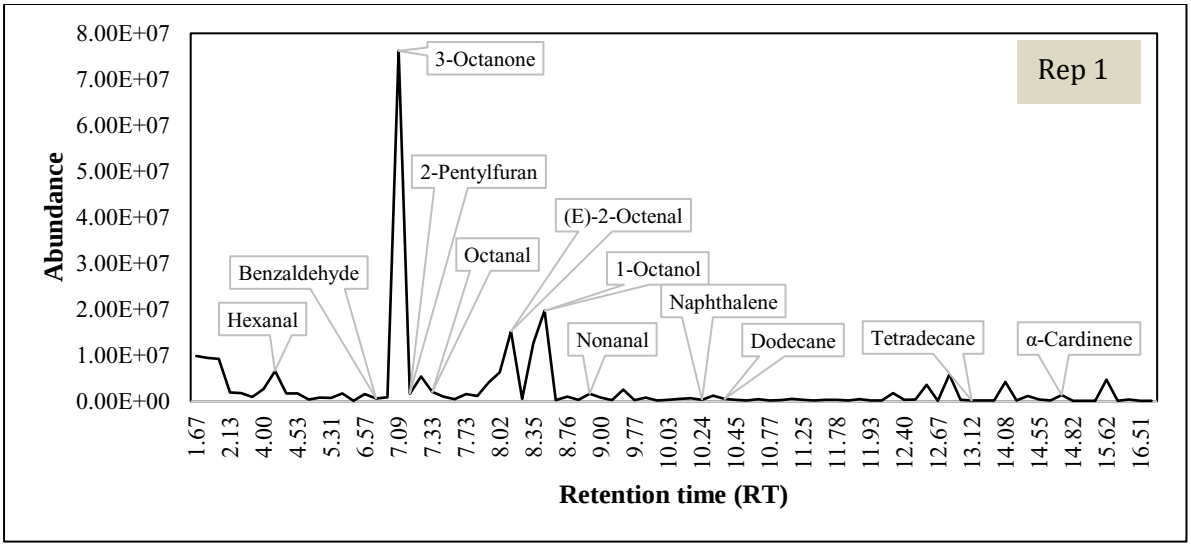
This study reveals oil palm-*Ganoderma* infected samples crushed in the presence of liquid nitrogen were more stable and produced wider range of GC profile with various chemical classes compared to samples that were not given any pre-treatment. Similar observations were reported in the development of HS-SPME-GCMS protocol for herbivore-induced volatiles in *Myrcia splendens* [19]. This is due to the use of liquid nitrogen that has allowed tissue disruption to take place at very low temperature, minimising the loss of highly volatile compounds, and thus, providing higher exposure of biological cells that gives higher volatile emission. More importantly, processing samples at ultra-low temperature also limited the activities of the enzymes by quenching, subsequently reducing changes in compound composition due to internal and external environmental effects.

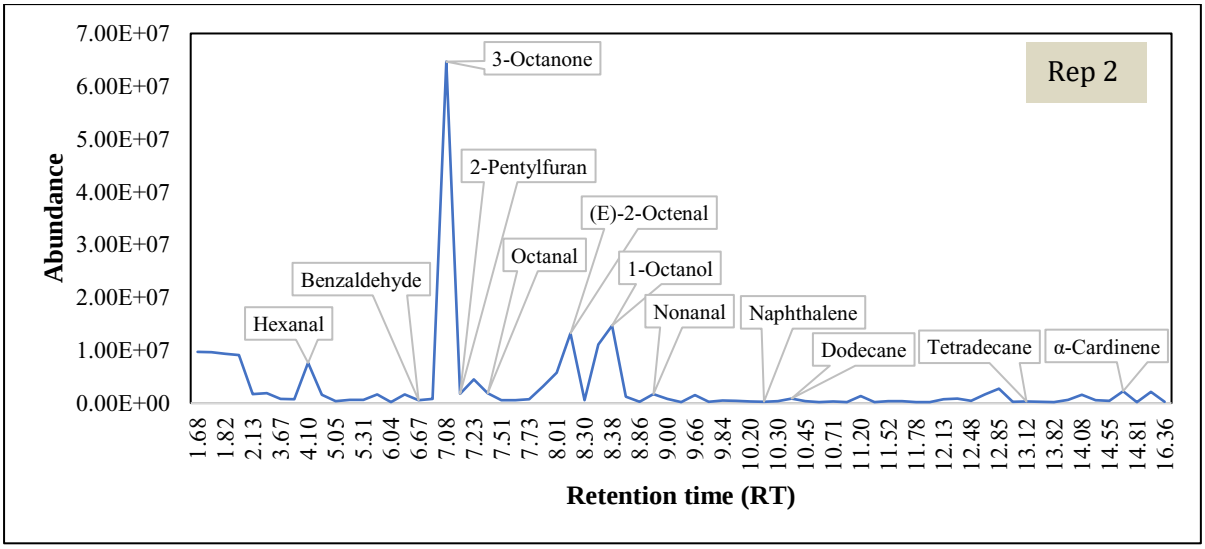
Sample weight

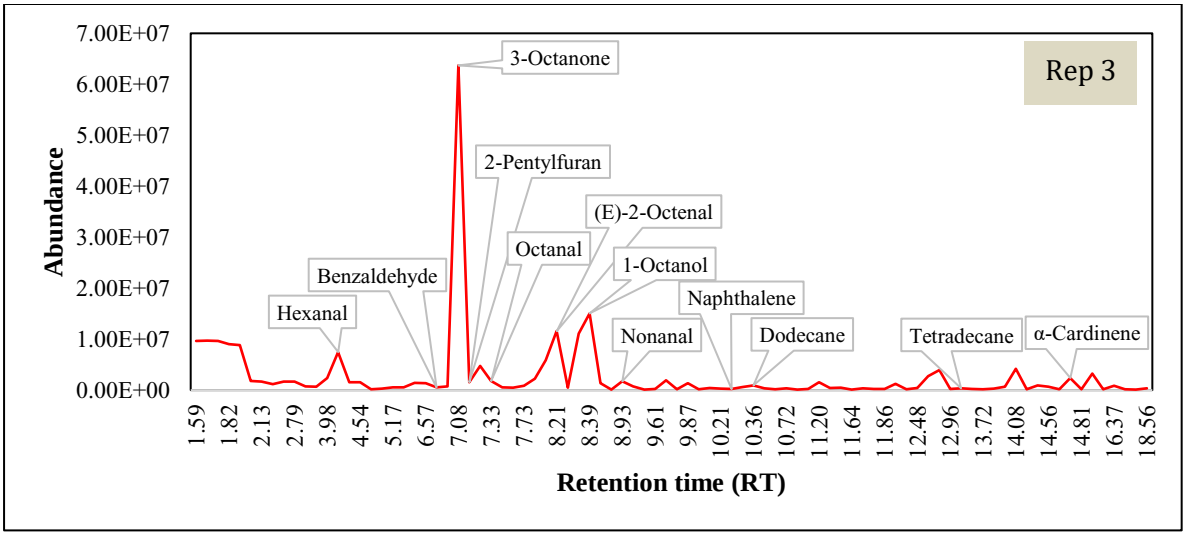
Sixteen commonly reported VOCs from fungi, i.e. hexanal, benzaldehyde, 1-octen-3-ol, 2-pentylfuran, (E)-2-octenal, 1-octanol, undecane, nonanal, naphthalene, dodecane, tridecane, butyl butanoate, tetradecane, 2,4-di-tert-butylphenol, α-cardinene and β-cardinene were chosen to perform HS-SPME optimisation using different sample weight [15, 17, 19-27]. VOCs were selected based on the highest total average peak area of the gas chromatogram with minimal variation between samples. The effect of sample weight is presented in Figure 4, where results were the average response of quadruplicate of extractions and normalised to the response obtained for 0.25 g.

The concentration or amount of sample injected into GC was generally increased to obtain better signal, thereby increasing the signal strength. However, in headspace analysis, increasing sample weight did not necessarily resulted in increased peak areas as greater sample weight caused reduction in the actual headspace volume [28, 29].

The oil palm-*Ganoderma* infected tissues released various compounds with different chemical and physical properties which explained the different responses observed across the headspace volumes tested (Figure 4). This work demonstrates the small sample weight that implied higher headspace volume in 20 mL headspace vial, making 0.25 g the most appropriate weight since the signal intensities observed was sufficient to achieve the satisfactory peak areas for the diverse chemical natures of the selected compounds. Thus, 0.25 g was chosen as the sample weight for subsequent experiments.


Rep 1
Abundance
8.00E+07
7.00E+07
6.00E+07
5.00E+07
4.00E+07
3.00E+07
2.00E+07
1.00E+07
0.00E+00
3-Octanone
2-Pentylfuran
(E)-2-Octenal
Octanal
Benzaldehyde
1-Octanol
Naphthalene
Hexanal
Nonanal
Dodecane
Tetradecane
α-Cardinene
1.67 2.13 4.00 4.53 5.31 6.57 7.09 7.33 7.73 8.02 8.35 8.76 9.00 9.77 10.03 10.24 10.45 10.77 11.25 11.78 11.93 12.40 12.67 13.12 14.08 14.55 14.82 15.62 16.51
Retention time (RT)


Rep 2
Abundance
7.00E+07
6.00E+07
5.00E+07
4.00E+07
3.00E+07
2.00E+07
1.00E+07
0.00E+00
3-Octanone
2-Pentylfuran
(E)-2-Octenal
Octanal
Benzaldehyde
1-Octanol
Nonanal
Naphthalene
Hexanal
Dodecane
Tetradecane
α-Cardinene
1.68 1.82 2.13 3.67 4.10 5.05 5.31 6.04 6.67 7.08 7.23 7.51 7.73 8.01 8.30 8.38 8.86 9.00 9.66 9.84 10.20 10.30 10.45 10.71 11.20 11.52 11.78 12.13 12.48 12.85 13.12 13.82 14.08 14.55 14.81 16.36
Retention time (RT)



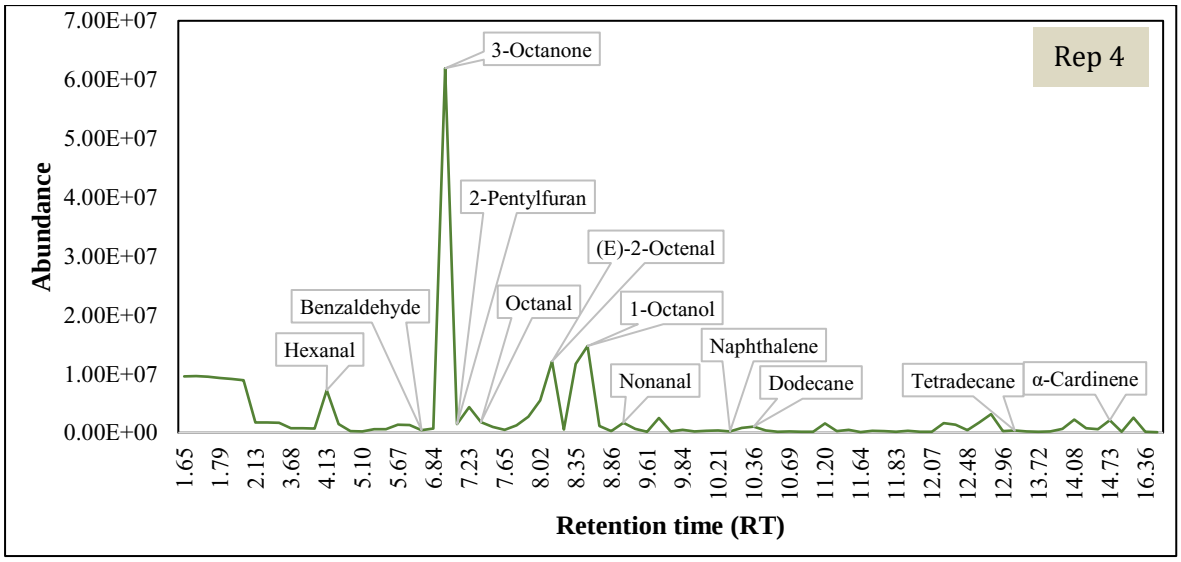


Figure 3. Consistent total ion current chromatograms across HS-SPME extraction replicates using 100 µm PDMS extraction phase from 0.25 g of oil palm-*Ganoderma* infected tissues homogenised to fine powder using liquid nitrogen

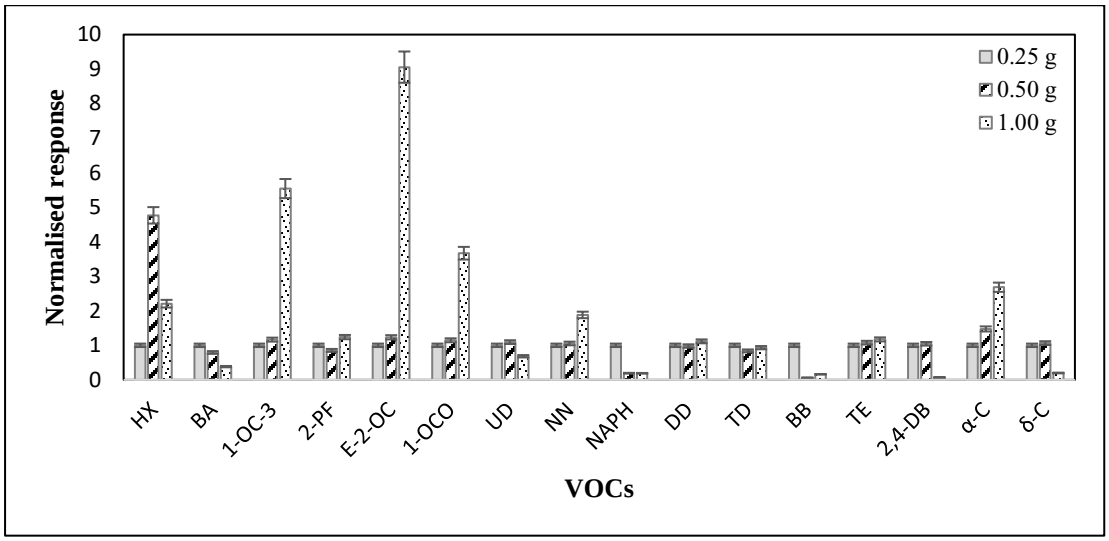


Figure 4. Effect of sample weight for selected compounds (HX = hexanal; BA = benzaldehyde; 1-OC-3 = 1-octen-3-ol; 2-FP = 2-pentylfuran; E-2-OC = (E)-2-octenal; 1-OCO = 1-octanol; UD = undecane; NN = nonanal; NAPH = naphthalene; DD = dodecane; TD = tridecane; BB = butyl butanoate; TE = tetradecane; 2,4-DB = 2,4-di-tert-butylphenol; α-C = α-cardinene and β-C = β-cardinene) obtained by HS-SPME-GCMS analysis of oil palm-*Ganoderma* infected tissues using 100 µm PDMS extraction phase. Response shown as normalised to response obtained for 0.25 g. Error bars represent standard deviation for four replicate ran of each weight.

Selection of SPME fibre extraction phase

Figure 5 summarises the average normalised areas of the total selected compounds obtained from different SPME fibre extraction phases. Higher absorption was generally observed in combined extraction phases in comparison to PDMS. ANOVA test showed significant differences between the SPME fibre extraction phases tested. No significant difference was observed between the responses obtained between CAR/PDMS and PDMS/DVB (p >0.05). The average normalised areas of total selected compounds of CAR/PDMS and PDMS/DVB were almost six times higher than PDMS, while extraction using DVB/Car/PDMS had shown nearly seven times higher than PDMS. Therefore, the composite DVB/Car/PDMS extraction phase exhibited superior extraction efficiency compared to other fibre extraction phases tested (Figure 5).

Fibre coating selection was the most important factor in any development of SPME method. Assorted kinds of SPME fibres were introduced commercially with different extraction phase polarity and thickness to favour the adsorption of analytes for various classes and molecular weights during extraction. Unlike absorbents, in the solid coating, analytes were extracted via adsorption where analytes moved into the pores of the absorbent and got physically trapped or chemically bonded with the surface of the absorbent. Being a porous material, it is important to note on the degree of pore distribution and pore size since their ability to retain an analyte was dependent on the pore size diameter [30]. For instance, carboxen was generally developed for the adsorption of analytes with a molecular weight of less than 90 m/z due to its micropores with an opening diameter of 2 to 20 Å, making it less efficient for adsorption and desorption of large molecular weight analytes. In comparison, DVB was designed for the entrapment of larger analytes with high degree of mesopores (20 to 500 Å) and therefore, did not suitable for low molecular weight analytes extraction. Thus, the

combination of both adsorbents' properties coating in DVB/Car/PDMS has enabled excellent fibre coating for wide range molecular weight analytes during a single extraction [31].

Figure 5 presents the average normalised areas of total selected compounds of CAR/PDMS and PDMS/DVB that is almost six times higher than PDMS. In contrast, composite coating DVB/Car/PDMS exhibited superior extraction efficiency compared to other fibre coating extraction phase. This difference might be due to monoterpenes being compounds with molecular weights closed to the upper limit of the carboxen adsorbent, and thus were extracted by the fibre containing carboxen and/or DVB coating. Compounds such as 2-pentylfuran, naphthalene, α-terpinol, N,N-dibutylformamide, chloroxylenol, and dibutylhydroxytoluene were only detected if DVB-containing fibre was used. In DVB/Car/PDMS fibre, the layers were assembled with carboxen layer located on the inside and DVB layer on the outside of the coating, which means that molecules of both high and low molecular weight might be successfully adsorbed as DVB layer was efficient for large molecules but less efficient in the entrapment of smaller molecules [31]. The small molecules could then migrate to the inner part of the coating and be fully adsorbed by the carboxen layer [30]. Similar studies on fibre extraction phase selection in the development of SPME methods have demonstrated DVB/Car/PDMS as the most efficient extraction fibre [19, 32]. Based on these results, DVB/Car/PDMS was selected as the most efficient fibre extraction phase to extract VOCs from the oil palm-*Ganoderma* infected tissues.

Tentative VOCs profile

The optimised HS-SPME-GCMS condition was employed for the analysis of VOCs released from *in vitro* oil palm-*Ganoderma* infected tissues. The composition of VOCs released was expressed in percentage of the total ion count (TIC) and presented in Table 1. A total of 39 compounds were found in the headspace of oil palm-*Ganoderma* infected tissues. They belong to alcohols, alkanes, volatile acids, ketones, aldehydes, esters, sesquiterpenes and polycyclic aromatic hydrocarbon groups. Figure 6 shows the molecular structures of the compounds.

Qualitatively, the largest absorption of VOCs was with DVB/Car/PDMS fibre: chromatograms demonstrated that VOCs with low molecular mass were eluted first with short retention times, followed by long chain alcohols, aldehydes and ketones, then long chain hydrocarbons and acids, then terpenes and sesquiterpenes, and finally organic esters at long retention times (Table 1).

Some of the VOCs found in the oil palm-*Ganoderma* infected tissues were the aliphatic C_8-complex that were found ubiquitous in truffle species and fungi, i.e. 1-octen-3-ol, 3-octanone and 1-octanol. They had been described as the key contributors to mushroom flavour and fungal aroma giving the scent or the odour ranging from sweet, fruity, musty, lavender, detergent and soap to orange like [23]. The most abundant VOC detected, 1-octen-3-ol (sometimes referred to as "mushroom alcohol"), was reported to emit by decomposers and wood-rotting fungi, and the alcohol biosynthesis from 10-hydroperoxide isomer of linoleic acid was well discussed in several literature [15, 23, 33-35]. The detection of volatile compound 1-octen-3-ol in this study is expected considering *G. boninense* is a basidiomycete and a white rot fungi.

Similar findings on the detection of hexanal is shown in the study of VOCs emitted from wood-rotting fungi *Serpula lacrymans* on the shavings of *Pinus sylvestris* (pine) timber [15]. The aromatic compound benzaldehyde was released in the study of volatile constituents of wood-rotting basidiomycetes *Piptoporus betulinus,* while in *Fomitopsis pinicola* and *Trametes suaveolens*, another aromatic compound, 2-pentylfuran, was also detected [20]. A preliminary head-space gas chromatographic analysis of volatile flavour compounds released from *Ganoderma sinense* (a medicinal mushroom) emitted octanoic acid and 2,4-di-tert-butylphenol in the mushroom broth while in the mycelium, only the latter compound was found [25, 26]. Among the VOCs detected in this study was the two-ring polycyclic aromatic hydrocarbon naphthalene which is known as effective insect repellent. Endophytic fungus, *Muscodor vitigenus* is also claimed to produce naphthalene almost exclusively [36]. Naphthalene derivatives, α-cadinene and δ-cadinene, are released in

the *in vitro* oil palm-*Ganoderma* infected tissues. The same volatile compounds are released when *Myrcia splendens* is attacked by gall-inducing insects, as a signal of plant-insect interaction [19]. Therefore, the same VOCs released in this study could be due to the metabolic changes that take place in oil palm (host plant) when it is under attack by *G. boninense* (plant pathogen).

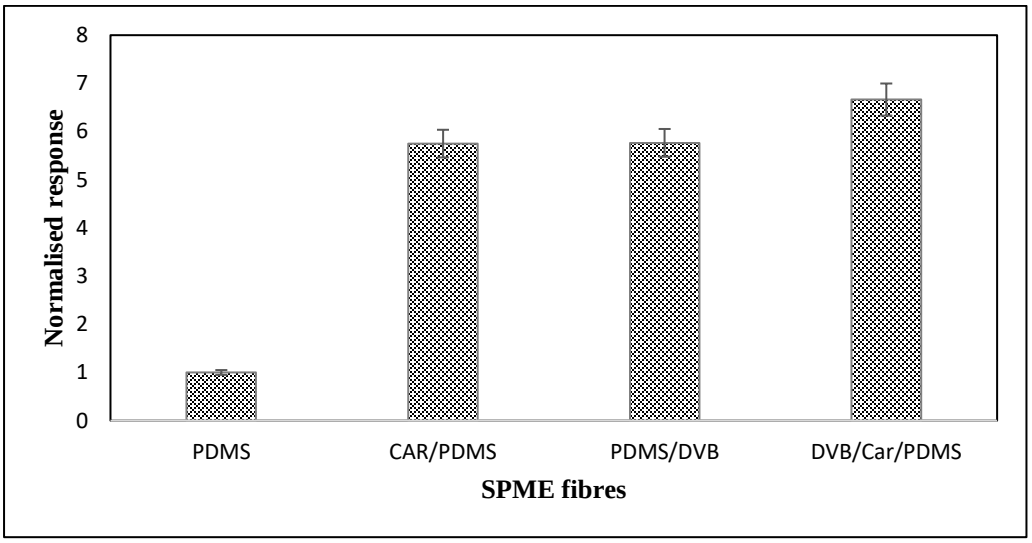


Figure 5. Effect of SPME fibre extraction phases (PDMS = polydimethylsiloxane; CAR/PDMS carboxen/polydimethylsiloxane; PDMS/DVB = polydimethylsiloxane/divinylbenzene and DVB/Car/PDMS = divinylbenzene/carboxen/polydimethylsiloxane) on extraction efficiency of headspace VOCs released from oil palm-*Ganoderma* infected tissues. Average areas of compounds obtained were normalised to response obtained for PDMS. Error bars represent standard deviation of four replicate ran for each SPME fibre.

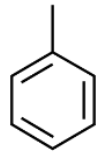
Table 1. Overview of tentative VOCS emitted by oil palm-*Ganoderma* infected tissues using the optimised HS-SPME-GCMS protocol

#	RT*	Compound Name	Molecular Formula	CAS	m/z	Percentage of Total Ion Current‡
1	3.72	Toluene	C_7H_8	108-88-3	92	0.580
2	4.12	Hexanal	$C_6H_{12}O$	66-25-1	100	7.162
3	5.17	m-Xylene	C_8H_{10}	108-38-3	106	0.321
4	5.30	p-Xylene	C_8H_{10}	106-42-3	106	0.362
5	5.84	Methyl (Z)-N-hydroxybenzene-carboximidate	$C_8H_9NO_2$	1000222-86-6	151	1.006
6	6.68	Benzaldehyde	C_7H_6O	100-52-7	106	0.181
7	6.97	1-Octen-3-ol	$C_8H_{16}O$	3391-86-4	128	69.43
8	7.08	3-Octanone	$C_8H_{16}O$	106-68-3	128	10.34
9	7.16	2-Pentylfuran	$C_9H_{14}O$	3777-69-3	138	0.270

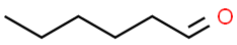
Table 1 (cont'd). Overview of tentative VOCS emitted by oil palm-*Ganoderma* infected tissues using the optimised HS-SPME-GCMS protocol

#	RT*	Compound Name	Molecular Formula	CAS	m/z	Percentage of Total Ion Current‡
10	7.33	Octanal	$C_8H_{16}O$	124-13-0	128	0.554
11	7.65	4-Methyldecane	$C_{11}H_{24}$	2847-72-5	156	0.148
12	7.83	1,3-Hexadiene, 3-ethyl-2-methyl	C_9H_{16}	61142-36-7	124	0.770
13	8.21	(E)-2-Octenal	$C_8H_{14}O$	2548-87-0	126	2.100
14	8.30	Eicosane	$C_{20}H_{42}$	112-95-8	282	0.047
15	8.35	2-Octen-1-ol	$C_8H_{16}O$	22104-78-5	128	1.457
16	8.39	1-Octanol	$C_8H_{18}O$	111-87-5	130	2.520
17	8.76	4-Octanyl butyrate	$C_{12}H_{24}O_2$	20286-46-8	200	0.231
18	8.86	Undecane	$C_{11}H_{24}$	1120-21-4	156	0.042
19	8.93	Nonanal	$C_9H_{18}O$	124-19-6	142	0.293
20	9.77	(E)-2-Nonenal	$C_9H_{16}O$	18829-56-6	140	0.033
21	9.85	Octanoic acid	$C_8H_{16}O$	124-07-2	144	0.136
22	10.20	1-(2-Butoxyethoxy)ethanol	$C_8H_{18}O$	54446-78-5	162	0.063
23	10.24	Naphthalene	$C_{10}H_8$	91-20-3	128	0.038
24	10.30	α-Terpineol	$C_{10}H_{18}$	98-55-5	154	0.100
25	10.36	Dodecane	$C_{12}H_{26}$	112-40-3	170	0.113
26	11.20	1,3-Ditert-butylbenzene	$C_{14}H_{22}$	1014-60-4	190	0.151
27	11.25	UNK§ *m/z* 314	-	-	314	0.064
28	11.52	7-Hexylicosane	$C_{26}H_{54}$	55333-99-8	366	0.047
29	11.71	2-Undecanone	$C_{11}H_{22}$	112-12-9	170	0.070
30	11.86	N,N-dibutylformamide	$C_9H_{19}NO$	761-65-9	157	0.050
31	12.85	Butyl butanoate	$C_8H_{16}O_2$	109-21-7	144	0.460
32	12.95	Chloroxylenol	C_8H_9ClO	88-04-0	156	0.046
33	13.12	Tetradecane	$C_{14}H_{30}$	629-59-4	198	0.039
34	14.55	2,4-Di-tert-butylphenol	$C_{14}H_{22}O$	96-76-4	206	0.079
35	14.63	Dibutylhydroxytoluene	$C_{15}H_{24}O$	128-37-0	220	0.013
36	14.73	α-Cardinene	$C_{15}H_{24}$	483-75-0	204	0.239
37	14.81	δ-Cardinene	$C_{15}H_{24}$	483-76-1	204	0.032
38	15.62	UNK§ *m/z* 286	-	-	286	0.395
39	15.63	Propanoic acid, 2-methyl-, 1-(1,1-dimethylethyl)-2-methyl-1,3-propanediyl ester	$C_{16}H_{30}O_4$	74381-40-1	286	0.020

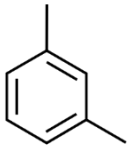
*RT, retention time; ‡The percentages were calculated using the peak area for each VOC relative to the total average normalised areas of the total ion current recorded; §UNK, unknown.



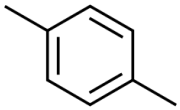
Toluene



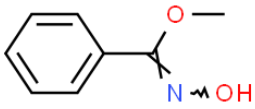
Hexanal



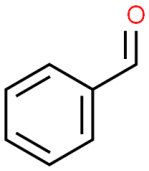
m-Xylene



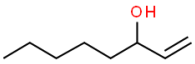
p-Xylene



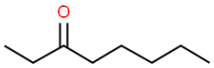
Methyl (Z)-N-hydroxybenzene-carboximidate



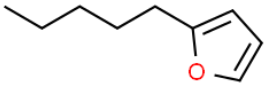
Benzaldehyde



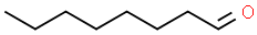
1-Octen-3-ol



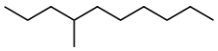
3-Octanone



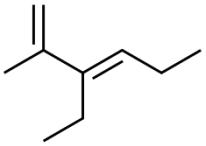
2-Pentylfuran



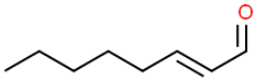
Octanal



4-Methyldecane

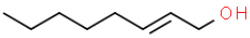


1,3-Hexadiene, 3-ethyl-2-methyl



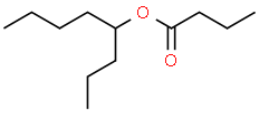
(E)-2-Octenal

Eicosane

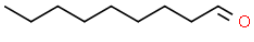


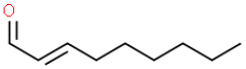
2-Octen-1-ol

1-Octanol

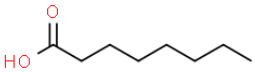






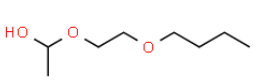


4-Octanyl butyrate



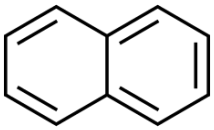
Octanoic acid

Undecane



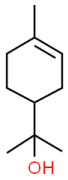
1-(2-Butoxyethoxy)ethanol

Nonanal

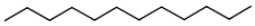


Naphthalene

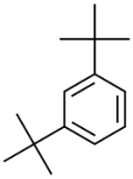
(E)-2-Nonenal



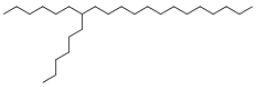
α-Terpineol



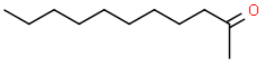
Dodecane



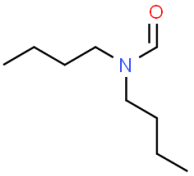
1,3-Ditert-butylbenzene



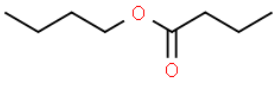
7-Hexylicosane



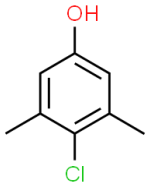
2-Undecanone



N,N-dibutylformamide

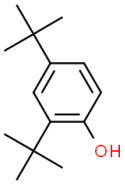


Butyl butanoate

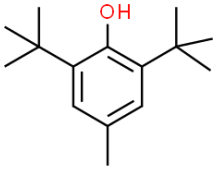


Chloroxylenol

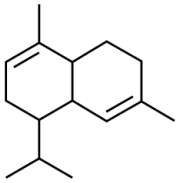
Tetradecane



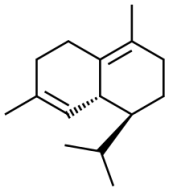
2,4-Di-tert-butylphenol



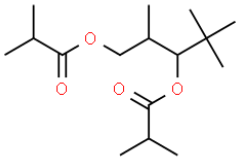
Dibutylhydroxytoluene



α-Cardinene



δ-Cardinene



Propanoic acid, 2-methyl-,
1-(1,1-dimethylethyl)-2-methyl-1,3-propanediyl ester

Figure 6. Molecular structures of tentative VOCs emitted

Conclusion

The results showed the initial feasibility application of HS-SPME extraction method for VOCs profiling of *in vitro* oil palm-*Ganoderma* infected tissues. The HS-SPME-GCMS protocol developed here is capable of detecting a diverse volatile chemical profile with high reproducibility. Future research should focus on the VOC profiles of *G. boninense* culture and oil palm wood to complement the current study for the VOCs to be developed as biomarker candidates for BSR disease detection. Coupled with the available electronic tools such as handheld electronic noses or any portable air monitoring systems, it could raise the possibility for the on-site detection of BSR disease.

Acknowledgement

We acknowledge the Director-General of MPOB for approving the publication of this paper. We would also like to extend our appreciation to Mrs Bahariah Bilal from the Advanced Oleochemical Technology Division (AOTD) and all research personnel in the Plant Pathology and Biosecurity unit of Biological and Sustainability Research Division who have contributed to this work either directly or indirectly.

References

1. Khusairi, A., Ong-Abdullah, M., Nambiappan, B., Hishamuddin, E., Mohd Noor Izzuddin, Z. B., Razmah, G., Subramaniam, V., Sundram, S. and Ahmad Parveez, G. K. (2019). Oil palm economic performance in Malaysia and R&D progress in 2018. *Journal of Oil Palm Research,* 31(2): 165-194.
2. Rees, R. W., Flood, J., Hasan, Y., Potter, U. and Cooper, R. M. (2009). Basal stem rot of oil palm (*Elaeis guineensis*); Mode of root infection and lower stem invasion by *Ganoderma boninense*. *Plant Pathology,* 58: 982-989.
3. Idris, A. S., NurRashyeda, R., Rusli, M. H., Sundram, S. and Norman, K. (2016). Standard operating procedures (SOP) guidelines for managing *Ganoderma* disease in oil palm. Malaysian Palm Oil Board, Malaysia: pp. 1-5.
4. Ariffin, D., Idris, A. S. and Singh, G. (2000). Status of *Ganoderma* in oil palm, in: *Ganoderma diseases of perennial crops* (eds) Flood, J., Bridge, P. D. and Holderness, M. CABI Publishing, London: pp. 49-68.
5. Spinelli, F., Costa, G., Rondelli, E., Busi, S., Vanneste, J. L., Rodriguez, E. M. T., Savioli, S. and Cristescu, S. M. (2011). Volatile compounds produced by *Erwinia amylovora* and their potential exploitation for bacterial identification. *Acta Horticulturae,* 896: 77-84.
6. Blasioli, S., Biondi, E., Braschi, I., Mazzucchi, U., Bazzi, C. and Gessa, C. E. (2010). Electronic nose as an innovative tool for the diagnosis of grapevine crown gall. *Analytica Chimica Acta,* 672: 20-24.
7. Pan, L., Zhang, W., Zhu, N., Mao, S. and Tu, K. (2014). Early detection and classification of pathogenic fungal disease in post-harvest strawberry fruit by electronic nose and gas chromatography–mass spectrometry. *Food Research International,* 62: 162-168.
8. Kushalappa, A. C., Lui, L. H., Chen, C. R. and Lee, B. (2002). Volatile fingerprinting (SPME-GC-FID) to detect and discriminate diseases of potato tubers. *Plant Disease,* 86: 131-137.
9. Biondi, E., Blasioli, S., Galeone, A., Spinelli, F., Cellini, A., Lucchese, C. and Braschi, I. (2014). Detection of potato brown rot and ring rot by electronic nose: from laboratory to real scale. *Talanta*, 129: 422-430.
10. Blasioli, S., Biondi, E., Samudrala, D., Spinelli, F., Cellini, A., Bertaccini, A., Cristescu, S. M. and Braschi, I. (2014). Identification of volatile markers in potato brown rot and ring rot by combined GC–MS and PTR–MS techniques: study on *in vitro* and *in vivo* samples. *Journal of Agricultural and Food Chemistry,* 62: 337-347.
11. Bennett, J. W. and Inamdar, A. A. (2015). Are some fungal volatile organic compounds (VOCs) mycotoxins?. *Toxins,* 7: 3785-3804.
12. Markom, M. A., Shakaff, A. Y. M., Adom, A. H., Ahmad, M. N., Hidayat, W., Abdullah, A. H. and Fikri, N. A. (2009). Intelligent electronic nose system for basal stem rot disease detection. *Computers and Electronics in Agriculture,* 66: 140-146.

13. de Lacy Costello, B. P. J., Ewen, R. J., Gunson, H. E., Ratcliffe, N. M. and Spencer-Phillips, P. T. N. (2000). The development of a sensor system for the early detection of soft rot in stored potato tubers. *Measurement Science and Technology,* 11: 1685-1691.
14. de Lacy Costello, B. P. J., Ewen, R. J., Gunson, H., Ratcliffe, N. M., Sivanand, P. S. and Spencer-Phillips, P. T. N. (2003). A prototype sensor system for the early detection of microbially linked spoilage in stored wheat grain. *Measurement Science and Technology,* 14: 397-409.
15. Ewen, R. J., Jones, P. R. H., Ratcliffe, N. M. and Spencer-Phillips, P. T. N. (2004). Identification by gas chromatography-mass spectrometry of the volatile organic compounds emitted from the wood-rotting fungi *Serpula lacrymans* and *Coniophora puteana*, and from *Pinus sylvestris* timber. *Mycological Research*, 108(7): 806-814.
16. Müller, A., Faubert, P., Hagen, M., zuCastell, W., Polle, A., Schnitzler, J. and Rosenkranz, M. (2013). Volatile profiles of fungi – Chemotyping of species and ecological functions. *Fungal Genetics and Biology,* 54: 25-33.
17. Sawoszczuk, T., Syguła-Cholewi´nska, J. and del Hoyo-Meléndez, J. M. (2015). Optimization of headspace solid phase microextraction for the analysis of microbial volatile organic compounds emitted by fungi: Application to historical objects. *Journal of Chromatography A,* 1409: 30-45.
18. Cellini, A., Biondi, E., Buriani, G., Farneti, B., Rodriguez-Estrada, M. T., Braschi, I., Savioli, S., Blasioli, S., Rocchi, L., Biasioli, F., Costa, G. and Spinelli, F. (2016). Characterization of volatile organic compounds emitted by kiwifruit plants infected with *Pseudomonas syringae* pv. *actinidiae* and their effects on host defences. *Trees,* 30 (3): 795-806.
19. Souza Silva, E. A., Saboia, G., Jorge, N. C., Hoffmann, C., dos Santos Isaias, R. M., Soares, G. L. G. and Zini, C. A. (2017). Development of a HS-SPME-GC/MS protocol assisted by chemometric tools to study herbivore induced volatiles in *Myrcia splendens. Talanta,* 175: 9-20.
20. Rösecke, J., Pietsch, M. and König, W. A. (2000). Volatile constituents of wood-rotting basidiomycetes. *Phytochemistry*, 54: 747-750.
21. Magan, N. and Evans, P. (2000). Volatiles as an indicator of fungal activity and differentiation between species, and the potential use of electronic nose technology for early detection of grain spoilage. *Journal of Stored Products Research*, 36: 319-340.
22. Wheatley, R. E. (2002). The consequences of volatile organic compound mediated bacterial and fungal interactions. *Antonie van Leeuwenhoek*, 81: 357-364.
23. Combet, E., Henderson, J., Eastwood, D. C. and Burton, K. S. (2006). Eight-carbon volatiles in mushrooms and fungi: properties, analysis, and biosynthesis. *Mycoscience*, 47: 317-326.
24. Matysik, S., Herbarth, O. and Mueller, A. (2008). Determination of volatile metabolites originating from mould growth on wall paper and synthetic media. *Journal of Microbiological Methods*, 75: 182-187.
25. Liu, G. Q., Wang, X. L. and Jin, X. C. (2009). Head-space gas chromatographic analysis for the volatile flavor compounds from submerged culture broth of *Ganoderma sinense* (a medicinal fungus). *3rd International Conference on Bioinformatics and Biomedical Engineering*, pp. 1-3.
26. Wang, X. L., Han, W. J. and Zhou, G. Y. (2009). Analysis of volatile flavor compounds in submerged cultured *Ganoderma sinense* mycelium by headspace gas chromatography. *2nd International Conference on Biomedical Engineering and Informatics*, pp. 1-4.
27. Morath, S. U., Hung, R. and Bennett, J. W. (2012). Fungal volatile organic compounds: A review with emphasis on their biotechnological potential. *Fungal Biology Reviews*, 26: 73-83.
28. Kolb, B. and Ettre, L. S. (2006). Static headspace-gas chromatography: Theory and practice 2nd edition. JohnWiley and Sons, New York: pp. 73-80.
29. Sithersingh, M. J. and Snow, N. H. (2012). Chapter 9 - Headspace-Gas Chromatography, In: Gas Chromatography. Elsevier, Amsterdam: pp. 221-233.

30. Górecki, T., Yu, X. and Pawliszyn, J. (1999). Theory of analyte extraction by selected porous polymer SPME fibres. *Analyst,* 124: 643-649.
31. Pawliszyn, J. (1999). Applications of solid phase microextraction. Royal Society of Chemistry, Cambridge: pp. 39-40.
32. Cortina, P. R., Asis, R., Peralta, I. E., Asprellid, P. D. and Santiago, A. N. (2017). Determination of volatile organic compounds in andean tomato landraces by headspace solid phase microextraction-gas chromatography-mass spectrometry. *Journal of the Brazilian Chemical Society,* 28(1): 30-41.
33. Tressl, R., Bahri, D. and Engel, K. H. (1982). Formation of eight-carbon and ten-carbon components in mushrooms (*Agaricus campestris*). *Journal of Agricultural and Food Chemistry,* 30: 89-93.
34. Wurzenberger, M. and Grosch, W. (1983). Determination of 1 octen-3-ol in mushrooms and in products containing mushrooms. *Z Lebensm-Unters-Forsch,* 176: 16-19.
35. Wurzenberger, M. and Grosch, W. (1984). The formation of 1-octen-3-ol from the 10-hydroperoxide isomer of linoleic-acid by a hydroperoxide lyase in mushrooms *Psalliotta bispora*. *Biochimica et Biophysica Acta,* 794: 25-30.
36. Daisy, B. H., Strobel, G. A. Castillo, U., Ezra, D., Sears, J., Weaver, D. K. and Runyon, J. B. (2002). Naphthalene, an insect repellent, is produced by *Muscodor vitigenus*, a novel endophytic fungus. *Microbiology*, 148: 3737-3741.

Malaysian Journal of Analytical Sciences (MJAS)
Published by Malaysian Analytical Sciences Society

SCREENING OF PLANTS FOR INSECTICIDAL ACTIVITIES AGAINST ORIENTAL FRUIT FLY *Bactrocera dorsalis* (HENDEL) FOR PEST MANAGEMENT OF MANGO *Mangifera indica*

(Saringan Tumbuhan bagi Aktiviti Serangga Perosak Terhadap Lalat Buah Oriental *Bactrocera dorsalis* (Hendel) untuk Pengurusan Serangga Perosak Mangga *Mangifera indica*)

Danila S. Paragas[1,2*], Kathlia D. C. Cruz[1], Elaida R. Fiegalan[3]

[1]*School of Chemical, Biological and Materials Engineering and Sciences, Mapua University, Intramuros, Manila, Philippines*
[2]*Department of Chemistry, College of Arts and Sciences*
[3]*Department of Crop Protection, College of Agriculture*
Central Luzon State University, Science City of Muñoz, Nueva Ecija, Philippines

[*]*Corresponding author: danilaparagas1010@clsu.edu.ph*

Received: 20 November 2019; Accepted: 13 June 2020; Published: 11 August 2020

Abstract

The mango, *Mangifera indica*, is one of the many fruits exported by the Philippines. However, the oriental fruit fly, *Bactrocera dorsalis* (Hendel) (Diptera: Tephritidae), is becoming a threat to its production; thus, its control and management are now imperative. This research conducted a preliminary screening of different plants with insecticidal properties that could be used for the development of potential biocides. Twenty plants were screened for their insecticidal activities against *B. dorsalis*. The plant that showed the highest mortality was further investigated using various extraction methods such as hot infusion, maceration, hot continuous reflux (Soxhlet), and fermentation. Several solvents were also considered in the extraction, including rice wine, rice wash, vinegar, and distilled water. The extracts were tested in terms of mortality against *B. dorsalis* after 6, 12, and 24 hours of exposure using an improvised olfactometer. *Azadirachta indica, Andrographis paniculata, Indigofera zollingeriana*, and *Lantana camara* gave 100% mortality at 24 hours exposure, but *A. indica* was the most effective, having 46.67%, 91.67%, and 100% mortality at 6, 12, and 24 hours, respectively. Further investigations employing different extraction–solvent combinations revealed that fermentation of *A. indica* leaves using rice wash is the most economical method for extracting the active components against *B. dorsalis* and can be utilized in the development of biocide for mango pest management.

Keywords: neem, biocide, fermentation, mangoes, pest management

Abstrak

Mangga, *Mangifera indica* adalah satu dari buah-buahan yang dieksport oleh Filipina. Namun, lalat buah oriental, *Bactrocera dorsalis* (Hendel) (Diptera: Tephritidae) menjadi ancaman bagi penghasilannya. Oleh itu, pengawalan dan pengurusan mestilah dimulakan. Kajian ini dijalankan melalui saringan awal bagi tumbuhan yang mempunyai sifat aktiviti serangga perosak yang boleh digunakan bagi pembangunan potensi biosida. Dua puluh tumbuhan telah disaring bagi mengkaji aktiviti serangga perosak terhadap *B. dorsalis.* Tumbuhan yang menunjukan kematian tertinggi telah dikaji lebih terperinci mengunakan pelbagai kaedah pengekstrakan seperti seduhan panas, maserasi, refluks berterusan panas (Soxhlet), dan fementasi. Pelarut berbeza juga

dipertimbang semasa pengekstrakan termasuklah wain beras, basuhan beras, cuka dan air suling. Ekstrak yang diuji bagi kematian terhadap B. dorsalis selepas 6, 12 dan 24 jam pendedahan mengunakan olfaktometer yang telah ditambahbaik. *Azadirachta indica, Andrographis paniculata, Indigofera zollingeriana*, dan *Lantana camara* memberikan 100% kematian pada masa 24 jam pendedahan, tetapi *A. Indica* adalah paling efektif mempunyai 46.67%, 91.67%, dan 100% kematian masing-masing pada 6, 12 dan 24 jam. Kajian selanjutnya dijalankan dengan kombinasi pelarut pengekstrakan berbeza mendedahkan bahawa fementasi daun *A. Indica* mengunakan basuhan beras adalah kaedah paling ekonomikal bagi pengekstrakan komponen aktif melawan *B. dorsalis* dan boleh di manfaat bagi pembangunan biosida terhadap pengurusan serangga manga.

Kata kunci: margosa, biosida, fementasi, manga, pengurusan serangga

Introduction

The fruit fly species *Bactrocera dorsalis* (Hendel) (Diptera: Tephritidae), also known as the oriental fruit fly, has been one of the most serious economic pests affecting agricultural fruits in India, East Asia, and the Pacific [1]. These fruit flies deposit their eggs into fruits and vegetables, whose flesh is subsequently consumed by developing larvae [2]. The fruit flies' invasive action has caused major economic losses in horticultural crop production [3]. Oriental fruit flies attack more than 150 kinds of fruits and vegetables, including avocadoes, bananas, citrus, coffee, figs, guavas, mangoes, papayas, passion fruit, pineapples, and tomatoes. *B. dorsalis* has been identified as the principal pest of mangoes in the Philippines [4], having caused a decrease in production of 34.36 and 33.13 thousand metric tons in 2014 and 2015, respectively [5]. As the mango is of valuable importance in both domestic and international markets, control and management of *B. dorsalis* is necessary to prevent significant losses in fruit production. This research conducted a preliminary screening of different plants reported to possess insecticidal properties, followed by screening of extraction procedures and solvents that could be employed for the development of potential biocides against *B. dorsalis*.

Three criteria were used in the selection of plants for the screening. The first was that the plants were reported to possess insecticidal properties. The second was their availability in the locality, and the last was that the plants were indigenous or endemic. Twenty plants were screened for their activities against *B. dorsalis.* Most of these plants were reported to possess insecticidal properties. These are *Andrographis paniculata* (Burm f.) Wall. ex Nees (whole plant ethanolic extract has larvicidal, pupicidal, adulticidal, and ovicidal properties against the malarial vector *Anopheles stephensi* Liston [6], and adulticidal against cowpea [7]; contains andrographolide, a diterpene against *Aegis egypti* [8]); *Annona muricata* L. (antiparasitic [9] and has mosquitocidal activities [10]); *Annona squamosa* Linn. (seeds extract contains antifeedant activity against lepidopteran pests [11,12]).

Azadirachta indica (effective against malarial vector *Anopheles stephensi* [13]); *Blumea balsamifera* (Linn.) DC. (used in livestock healthcare as poultice for abscesses in swine and ruminants [14]); *Cassia alata* L. (Roxb.) and *Chromolaena odorata* Linn. (weeds with a strong aromatic odor sometimes used to drive away insects in stored products [15]; *Chrysophyllum cainito* and *Tabernaemontana pandacaqui* (repellents against hematophagous insects [16]); *Cymbopogon citratus* (insecticidal properties against the house fly, *Musca domestica* [17]); *Cyperus rotondus* (tuber with toxicity to the diamondback moth [18]); *Euphorbia tithymaloides* (with high toxicity to the oriental fruit fly [19]), *Garcinia vidalii* (no reported properties but represents an endemic species); *Gliricidia sepium* (rodenticide [20]); *Indigofera zolligeriana* (used as feed for goats and sheep; contains flavanols, glycosides, and megastigmane glucosides [21]); *Lantana camara* (contains pentacyclic triterpenes called lantadene [22]), *Moringa oleifera* (bioinsecticide with mechanism of action involving carbohydrate–lectin interactions on the surface of the digestive tract, with glycoproteins and other glycosylated structures in the midgut and resistance to enzymatic digestion [23]); *Ocimum sanctum* (with larvicidal effect on *Aedes aegypti* and *Culex quinquefasciatus* [24]); *Tridax procumbens* (exhibits activity against scale insects (*Phenacoccus solenopsis*) of *Psidium guajava* [25]); and *Zamioculcas zamiifolia* (in combination with *C. odorata* exhibits insecticidal properties against the harlequin cockroach

[26]). *Euphorbia tithymaloides* was the only plant in this study reported to have insecticidal effects on the oriental fruit fly [19].

The extraction methods and the solvents used are crucial in the evaluation of plants' secondary metabolites. Numerous studies have been conducted in search of the best technique and solvent to extract plants' secondary metabolites [27]. Among these techniques are the use of liquid, steam, and supercritical extractions [28]. The conventional methods like hot infusion, maceration, decoction, Soxhlet extraction, etc. are being modified, and pretreatments of samples like microwave and ultrasound processes are adopted [29]. Soxhlet is a conventional extraction method still considered as one of the reference methods in comparing the success of a newly developed methodology [30]. Rice wine, rice wash, and vinegar have been employed in the extraction of phytochemicals as substitutes for methanol, ethanol, hexane, ether, etc., which are conventionally used in the extraction process. Rice wine contains 15-20% ethanol and 120-440 mg/mL glucose levels [31, 32]. Rice wash contains para-aminobenzoic acid (PABA), ferulic acid and allantoin [33], and volatile fatty acids [34]. Vinegar, on the other hand, contains not less than 3% but no more than 5% acetic acid, 0.5% ethanol and other polyphenols [35]. This study aimed at employing a "green approach" using household chemicals in the preparation of biocide for *B. dorsalis*.

Materials and Methods

Plant materials collection, preparation, and extraction

The leaves of the different plants were detached from the stems and washed thoroughly with tap water. The clean leaves were air dried for 3-5 days in the shade during the summer season. Drying for more than 5 days is not advisable, since molds will grow during this period. The sample was considered to be dry when it was easily crushed by the hand. The dried leaves were ground in a blender and stored in a tightly covered container until further use. Hot infusion was done by boiling 150 mL of distilled water, then adding 15 grams of the previously ground leaves. The mixture was set aside for 15 minutes. The extract was filtered using Whatman No. 42 filter paper, and the filtrate was placed in an amber bottle and stored in the refrigerator until it was used for analysis. This was to prevent reaction with light or degradation at room temperature.

Trapping of male fruit flies

Male fruit flies were trapped inside a canister with cotton wet with 10 drops of methyl eugenol. The trap was placed under a mango or guava tree from 6:00 to 8:00 in the morning, as this is the time when the most fruit flies are trapped. The canister was covered when there were enough fruit flies inside. Cotton dipped in sugar solution placed on the net covering of the canister served as food for the fruit flies.

Mortality test

The mortality test was done using an improvised olfactometer adopting the method of Chang and co-workers [36] with some modifications. The olfactometer was a transparent plastic food container measuring 4.5 in. in top diameter, 3.5 in. in bottom diameter, and 4 in. high. The cover was cut, forming a 2-in.-diameter hole, which was covered with silk fabric to prevent the fruit flies from suffocating during the test.

Male fruit flies were introduced into the improvised olfactometer after 30-60 minutes using a transparent tube made of acetate. A small cotton ball was wet with 10 drops of the crude extract and placed at the top center of the container 5-10 minutes after the male fruit flies were introduced. The container was covered, and the flies were observed after 6, 12, and 24 hours for the screening study and 3, 6, 12, 18, 22, and 24 hours for further investigations of the most effective plant. The fruit flies' reaction to the extract was noted. A fruit fly was considered dead when no more movement was observed. Percent mortality was computed by dividing the number of dead fruit flies by the total number of flies inside the plastic container.

Data analysis part A

Adult fruit flies' percent mortality was compared per plant extract using analysis of variance and post hoc using the Duncan multiple range test. The plant extract that showed the highest mortality rates at 6, 12, and 24 hours and the plant extract that showed the highest mortality at 6 hours exposure time were further

subjected to efficacy tests applying the following procedure. For the first cycle, male fruit flies were introduced into the improvised olfactometer after 30-60 minutes using a transparent tube made of acetate. A small cotton ball was wet with 10 drops of the crude extract and placed at the top center of the container 5-10 minutes after the male fruit flies were introduced. The container was covered, and the flies were observed after 6, 12, and 24 hours.

Mortality rates were recorded, after which the dead fruit flies were transferred into vials and stored in the refrigerator. For the second cycle, the same olfactometer and cotton ball were used. The olfactometer was cleaned by wiping it with tissue paper wet with 70% ethanol to remove the remaining particles from the dead flies. The same cotton ball with extract (no addition of fresh extract) was moistened with 10 drops of distilled water, a new set of fruit flies were introduced into the olfactometer, and the mortality rates were read after 6, 12, and 24 hours. Mortality rates were recorded, the dead fruit flies were placed into vials and stored in the refrigerator, the olfactometer was cleaned with ethanol, and the cotton ball was wet with distilled water. The third cycle used the same procedure as the second cycle. The plant extract that gave higher mortality rates was subjected to further investigations employing the four solvents and four extraction methods.

Effects of solvent and extraction method on insecticidal properties

Four different extraction methods were tested: Soxhlet or hot continuous extraction, hot infusion, fermentation, and maceration. The Soxhlet method was done as follows: The ground plant material (15 g) was loaded into the cellulose thimble, which was then placed inside the Soxhlet extractor. The solvent (150 mL) was heated using the heating mantle, and the solvent began to evaporate, moving through the apparatus into the condenser. The condensate then dripped into the reservoir containing the thimble. When the level of solvent reached the siphon, it poured back into the flask, and the cycle began again. The process ran for a total of 8 h to ensure that the sample was in contact with the solvent long enough; thus, extraction of the active components was more efficient.

Hot infusion was done by adding 15 g of previously weighed ground leaves into 150 mL of boiling solvent. The mixture was set aside for 15 minutes. The extract was then filtered using Whatman No. 42 filter paper, and the filtrate was placed in an amber bottle and stored in the refrigerator until it was used for analysis. The fermentation method was carried out by soaking 15 g of the plant material in 150 mL of the solvent. The container was wrapped with aluminum foil and stored inside a locker. The mixture was set aside for 5 days, after which the mixture was filtered, and the filtrate was placed in an amber bottle and stored in the refrigerator until it was used for analysis. Maceration was done by placing 15 g of the plant material in 150 mL of the solvent. The mixture was set aside for 1 hour, then filtered, and the filtrate was placed in an amber bottle and stored in the refrigerator until it was used for analysis.

Four green solvents were used in this experiment primarily to test the effect of household chemicals and waste in rice cooking. These are readily available in a Filipino household in the provinces where mango production is usually located. These are rice wine, rice wash, vinegar, and distilled water. These materials contain polar substances that can extract the insecticidal components of the plant under study. The rice wine was produced in Panupdupan, Lamut, Ifugao, Philippines. The rice wash was prepared by washing 100 g of bungkitan glutinous rice with 100 mL of distilled water. The rice-washing water was then drained into a beaker. Another 100 mL of distilled water was added to the glutinous rice, which was then washed, and the second washing was added to the first washing. The combined rice wash was filtered to remove the suspended solids. The vinegar, called '*sukang basi*' is a byproduct of sugar production.

Data analysis part B

The adult fruit flies' percent mortalities were compared per solvent–extraction method combination using analysis of variance and post hoc using the Duncan multiple range test. The solvent–extraction combinations that showed high mortality rates were evaluated for their economic value by subjecting them to probit analysis to determine the lethal dose (LD_{50}).

This is the concentration of the extract that is lethal to 50% of the insect population tested.

Results and Discussion

The percent mortalities of the different aqueous extracts against *Bactrocera dorsalis* (Hendel) were observed after 6, 12, and 24 hours (Table 1). There were two plant extracts that showed mortality of >20% after 6 hours exposure; 11 plants after 12 hours, the highest of which was *A. indica* (91.67%); and 16 plants after 24 hours, of which *A. paniculata*, *A. indica*, *I. zollingeriana*, and *L. camara* showed mortality of 100%.

Analysis of variance and post-hoc analysis (Duncan multiple range test at the 5% level) of the activity of the extracts at 6-hour exposure indicate that *A. indica* leaf extract is the most effective, with 46.67% mortality, followed by *O. sanctum* (40.00%) and *C. alata* (33.33%). However, the mortality rates of *L. camara* (20.00%), *B.* balsamifera, *G. sepium*, and *I. zollingeriana* (13.33%) cannot be ignored when compared to those plants with 0% mortality. Effectivity may increase at a longer time of exposure, as seen in their activities at 12 and 24 hours. These extracts may contain smaller amounts of the active components; thus, diffusion into the olfactometer is slower. But at longer periods, the concentration of extract inhaled or ingested by the fruit flies increases, leading to mortality.

At 12-hour exposure, *A. indica* still gave the highest mortality (91.67%), but this was not significantly different from the activities of *L. camara* (73.33%), *O. sanctum, G. sepium*, and *A. paniculata* (66.67%). This could mean that these five plants' components namely, azadirachtin, lantadane, eugenol, oxytroside and andrographolide, respectively, possess insecticidal effect against *B. dorsalis*.

At 24-hour exposure, four extracts gave 100% mortality: *A. paniculata*, *A. indica*, *I. zollingeriana*, and *L. camara*. Those extracts with mortality ranging from 53.33% to 93.33% are not significantly different from the four extracts with 100% mortality at 5% level of significance using the Duncan multiple range test (Table 1). The plants with mortality rates of 53.33–93.33% after 24 hours are *G. sepium*, *T. pandacaqui, O. sanctum*, *M. oleifera*, *A. squamosa*, *A. muricata*, *B. balsamifera*, *C. alata*, *E. tithymaloides*, *C. rotondus*, and *Z. zamiifolia*. All these plants were reported to possess insecticidal properties against different pests. The mode of action of the different plant extracts against the oriental fruit fly cannot be explained further at this point. Neurotoxicity may be one of the reasons [33]. Of the 20 plants screened in this study, only *C. odorata*, *C. cainito*, *C. citratus*, *G. vidalii*, and *T. procumbens* did not show promising results using water as the extracting solvent. This may be because the insecticidal properties reported in the literatures cited above were extracted using organic solvents [15–17, 25].

Two extracts were chosen for the efficacy test: *A. indica*, which had the highest mortality at 12 hours, and *A. paniculata*, which did not show activity at 6 hours but gave 100% mortality at 24 hours. The dried cotton balls with extract used in the test in Table 1 were wetted with 10 drops of distilled water, the improvised olfactometers were cleaned and loaded again with fruit flies for the second and third cycles, and mortality rates were again recorded (Table 2).

Post-hoc analysis denotes that the *A. indica* and *A. paniculata* aqueous extracts are still effective up to the third cycle. However, a decrease in activity was observed at 6 and 12 hours for *A. indica* and at 12 hours for *A. paniculata*. Moreover, at 24 hours, there was a slight decrease in the activities in the third cycle for *A. indica* and in the second and third cycles for *A. paniculata*, but still no significant differences from the first cycle. This result implies that the extracts can be used against *B. dorsalis* not only once but up to three times or maybe more. The significant decrease in the activity of both plant extracts in the second and third cycles at 12 hours may be due to the decrease in concentration of the active components as a result of inhalation or consumption by the first batch of fruit flies. This part of the study further implies that *A. indica* (also known as neem) is the most effective plant in the management of *B. dorsalis.* This result conforms with the report that the azadirachtin present in the neem has antifeedant and growth inhibition effects against insects [31].

Table 1. Percent mortality of the different aqueous plant extracts against fruit fly *Bactrocera dorsalis* (Hendel)

Scientific Name	Percent Mortality*		
	6 hours	12 hours	24 hours
A. paniculata	0.00^{d}	66.67^{abc}	100.00^{a}
A. muricata	6.67^{cd}	20.00^{efg}	66.67^{abc}
A. squamosa	0.00^{d}	33.33^{def}	73.33^{ab}
A. indica	46.67^{a}	91.67^{a}	100.00^{a}
B. balsamifera	13.33^{bcd}	33.33^{def}	66.67^{abc}
C. alata	33.33^{abc}	60.00^{bcd}	66.67^{abc}
C. odorata	0.00^{d}	0.00^{g}	6.67^{ef}
C. cainito	0.00^{d}	0.00^{g}	0.00^{f}
C. citratus	0.00^{d}	6.67^{fg}	26.67^{bcdef}
C. rotondus	0.00^{d}	6.67^{fg}	53.33^{abcde}
E. tithymaloides	6.67^{cd}	26.67^{efg}	60.00^{abcd}
G. vidalii	0.00^{d}	0.00^{g}	20.00^{cdef}
G. sepium	13.33^{bcd}	66.67^{abc}	93.33^{a}
I. zollingeriana	13.33^{bcd}	40.00^{cde}	100.00^{a}
L. camara	20.00^{bcd}	73.33^{ab}	100.00^{a}
M. oleifera	0.00^{d}	0.00^{g}	75.00^{ab}
O. sanctum	40.00^{ab}	66.67^{abc}	80.00^{a}
T. procumbens	0.00^{d}	6.67^{fg}	13.33^{def}
T. pandacaqui	6.67^{cd}	26.67^{efg}	86.67^{a}
Z. zamiifolia	6.67^{cd}	20.00^{efg}	60.00^{abcd}

*: In a column, values with the same letter superscript are not significantly different at a 5% level using the Duncan multiple range test

Table 2. Mean percent mortality of fruit flies using the cotton balls with extracts from first to third cycle

Plant Extract	Mean Percent Mortality		
	6 hours	12 hours	24 hours^{ns}
A. indica			
1st cycle	46.67^{a}	91.67^{a}	100.00^{a}
2nd cycle	16.67^{b}	58.33^{b}	100.00^{a}
3rd cycle	18.92^{b}	65.19^{b}	93.64^{a}
A. paniculata			
1st cycle	0.00	66.67^{a}	100.00^{a}
2nd cycle	0.00	33.33^{b}	91.67^{a}
3rd cycle	0.00	22.29^{b}	91.17^{a}

*: In a column, values with the same letter superscript are not significantly different at a 5% level using the Duncan multiple range test

Effect of method of extraction

Mortality of fruit flies treated with the leaf extracts prepared by four extraction methods and four extracting solvents was recorded and is presented in Figure 1. The insecticidal experiments were replicated thrice. Observations were done at 3, 6, 12, 18, 22, and 24 hours to determine which of the extraction methods and solvents would be the best in extracting the insecticidal properties of *A. indica* against the fruit fly, *B. dorsalis*.

It was observed that Soxhlet extraction yielded the highest mortality at 3- and 6-hour exposure times irrespective of what solvent was used (Figure 1). This effect may be due to the higher amount of bioactive components extracted in this method. The total phenolic content and antioxidant activity of *Quercus infectoria* galls was reported to be higher with the Soxhlet technique than with supercritical carbon dioxide extraction [38]. A similar study on the total phenolic and anti-radical capacity of extracts from *Pinus radiata* bark showed that total phenols and tannin content were highest with the Soxhlet technique compared to microwave-assisted and ultrasound-assisted extractions [29]. Soxhlet extraction causes a more rapid rupture of cells, facilitating the release of their contents [28]. This may explain why the neem leaf extract via Soxhlet extraction showed higher fruit fly mortality at 6 hours than those from hot infusion, maceration, and fermentation. Based on the study of Subramanian et al. [39], a binary extraction approach using a Soxhlet extraction device with a 50:50 solvent mixture (hexane: ethanol) resulted in a yield of 720 $mg_{azadirachtin}/kg_{leaves}$ at 6 hours extraction.

At 12, 18, and 22 hours exposure, on the other hand, hot infusion gave the lowest mortality, while Soxhlet, fermentation, and maceration had no significant differences. Hot infusion was done by adding 15 g of ground leaves into 150 mL of boiling solvent. The mixture was set aside for 15 minutes and filtered. The duration of solvent–sample interactions in the hot infusion process may not be long enough to extract a significant amount of azadirachtin, resulting in low fruit fly mortality at 12–22 hours. According to the study of Ramirez-Rodrigues et al. [40], hot infusion resulted in higher amounts of aldehydes, while cold infusion or maceration yielded higher amounts of alcohols. Azadirachtin has more affinity to polar solvents. Alcohols are more polar than aldehydes, and this may explain why hot infusion extracts yielded lower fruit fly mortality.

At 24 hours, the extraction method has no significant effect on mortality. This result suggests that a small amount of active component in the extract (toxicant) can also lead to death in fruit flies when they are exposed to it for 24 hours or longer.

Effect of solvent on percent mortality

The effect of the green solvents used in the extraction of the insecticidal properties of neem leaves is revealed in Figure 2. Mortality rate was observed to be comparable at 3- and 6-hour exposure of the fruit flies to the different extracts. At 12, 18, 22, and 24 hours, rice wash, vinegar, and distilled water had no significant differences in terms of mortality, though it can be observed in the graph that vinegar gave the highest percent mortality from 12 to 24 hours exposure. Rice wine gave the lowest mortality from 3 to 24 hours. This can be attributed to the volatiles in rice wine, such as ethanol and acetic acid. Fruit flies are attracted to some volatile wine and vinegar compounds. The fruit flies that did not die immediately thrived on the wine components. In contrast to rice wine, vinegar, which also has undergone fermentation and might contain some volatile compounds that attract fruit flies, was able to register the highest mortality. Vinegar contains polyphenols that have antioxidant properties [41]. The polyphenols in vinegar (amounting to approximately 0.30-32.67 GAE) [42], in addition to the bioactive components extracted from the neem leaves, might have a synergistic effect on the anti-fruit fly activities, causing the highest mortality after 22 and 24 hours. The following effects of the extracts on the oriental fruit fly (Figure 4) are more to do with primary antifeedancy, which targets mouthparts and other chemoreceptors, and whose mode of action is deterrent cell stimulation and sugar cell inhibition [43]. An observable effect was darkened and damaged proboscises. The other effect was cellular processes targeting the muscles, whose mode of action was loss of

muscle tone. Torn wings and damaged legs were the documented effects on the fruit flies.

The effect of rice wash as an extracting solvent cannot be disregarded in this study. It was not significantly different from vinegar and distilled water from 12 to 24 hours exposure time. In fact, it yielded higher mortality than the distilled water extract. The use of rice wash in the extraction of phytochemicals has not been given attention by natural product chemists who practice green chemistry. This rice byproduct (also called rice broth or rice water) is used by Filipinos in the preparation of '*burong mustasa*' [44] or pickled flat mustard green. Rice wash provides a small amount of lactic acid bacteria (LAB) that produce lactic acid as they act on the sugars from the mustard. Acetic acid may also be produced in the pickled product due to the presence of acetobacter [45]. The results of this experiment reveal the potential of rice wash in extraction of neem's insecticidal components. The polar substances present in rice wash may have extracted the insecticidal components against fruit flies, which is why neem leaf rice wash extract was as effective as vinegar. Higher concentration of azadirachtin is extracted by polar solvents than nonpolar solvents [39].

Solvent and extraction method combinations

Analysis of variance of the solvent and extraction method combinations showed significant differences at the 5% level (Table 3). There were 16 extraction × solvent combinations in this study. Of these, there were seven effective combinations with insecticidal effects on *B. dorsalis*, namely, Soxhlet–vinegar (S-V), Soxhlet–rice wash (S-RWa), Soxhlet–distilled water (S-D), fermentation–rice wash (F-RWa), fermentation–vinegar (F-V), fermentation–distilled water (F-D), and maceration–vinegar (M-V). The use of hot infusion combined with all four solvents and the use of rice wine in the four extraction methods were not effective.

The above statistics were calculated to determine which method is most economical in terms of utilization of materials. Fermentation using rice wash was found to be the most economical way of extracting the insecticidal components of neem leaves. Rice wash is a household waste material generated every day among Filipino families. Meanwhile, fermentation is done without the use of electricity. The rice wash and the organisms in the neem leaves will ferment even without the addition of commercial yeast; thus, no additional cost will be incurred in the production of the biocide from neem leaves.

Lethal concentration of the extracts (with high mortality rates)

The lethal concentrations of the fermentation–rice wash extract (F-RWa) (Figure 3a) and Soxhlet–vinegar (S-V) extract (Figure 3b) were calculated using probit analysis. This was done to compare the lethality of the two extracts, S-V being the one with the highest interaction effect and F-RWa being the most economical among the 16 extraction × solvent methods defined in this study. The lethal dose for F-RWa extract was found to be 2.7% v/v (mL extract per 100 mL solution), versus 1.9% for the S-V extract. These lethal doses for F-RWa and S-V extracts mean that 50% of the fruit flies will die if the toxicant is introduced into the olfactometer. This result shows that neem extracts prepared by fermentation using rice wash and Soxhlet extraction using vinegar are effective biocides against *B. dorsalis* when the extracts are introduced via inhalation, as was done in this experiment. Rice wash when fermented contains small amounts of alcohol and acetic acid, while vinegar contains acetic acid and small amounts of alcohol. These are polar substances and may contribute to the extraction of azadirachtin from neem leaves.

The above results conform to the reports that neem leaf extracts have insecticidal properties. In the first few hours after the fruit flies were exposed to the neem extracts, hyperactivity was observed, and after about 4–6 hours, the fruit flies' mobility was observed to be depleted. This may be attributed most probably to the plant's azadirachtin, a triterpenoid [46]. Triterpenoids cause loss of tyrosine hydroxylase which can lead to a depletion of dopamine and norepinephrine in the brain due to the lack of precursor L-3,4-dihydroxy-phenylalanine (L-DOPA), which then results in inhibition of locomotor activity and death [47]. Saponins have the same effect as triterpenoids on tyrosine hydroxylase [48]. Hyperactivity may have been due to neuroexcitation, and the slow mobility could have

been due to energy depletion, neuromuscular fatigue, and neuroinhibition by possible oxygen deprivation and/or reduced respiratory capacity, which may lead to mortality.

The manifestations of the observed effects on the fruit flies exposed to the neem extracts were damaged wings, legs, proboscises, and antennae and empty abdomens (Figure 4). Damaged wings and legs might be due to the flies' hyperactivity after a few hours of exposure to the neem extracts. Ceaseless movement of the legs, rubbing against each other to remove the substances attached to the legs and other parts, was observed. This may have been the effect of cellular processes targeting the muscles, resulting in loss of muscle tone. The flies' death may also have been due to the inhibition of protein synthesis in various tissues. Since the extracts were introduced into the cap of the improvised olfactometer, the flies either inhaled or tasted the extract. The taste organs of fruit flies are widely distributed in the adult body, legs, and wings and the proboscis's labellum, the external gustatory centers. All these taste organs detect tastants through the gustatory receptor neurons (GRNs) [49]. The biocide is the tastant to which the fly's initial reaction was movement of the legs and spreading of the wings without body movement, as if it sensed something. But after a few hours, this behavior manifested as movement of legs and suppressed proboscis extension [50], as shown in Figure 4b. Disappearance of the sensory hairs, called sensilla, was observed. These sensilla are usually made of odor-binding proteins (OBP) and can react to the active components, causing the proboscis to darken.

One behavior that was documented in this study when the fruit flies were exposed to the plant extracts is the manner of courtship. The flies were all males, as they were trapped using methyl eugenol, a male sex pheromone. There were flies that showed courting behaviors, such as movement around one fly as if guarding it from other flies. Attempting copulation with another male fly was also observed. In the study conducted by Liu's research group [51], dopamine level reduction in *Drosophila melanogaster* enhanced the attractiveness of male *Drosophila* to other males. Dopamine is an important neuromodulator in animals, and it plays an important role in mammalian behavior associated with sexual encounters. When the dopamine level decreases due to inhibition of tyrosine hydroxylase, male–male courtship behavior is enhanced.

The empty abdomens among the dead flies can be associated with the behavior of the living fruit flies recorded by the researcher. The living flies were attracted to the dead flies and fed on the pheromone reservoir near the anus. Methyl eugenol is a pheromone of *B. dorsalis* which is ingested and metabolized into *E*-coniferyl alcohol (ECF) and 2-allyl-4,5-dimethoxy phenol (DMP). ECF and DMP are stored in the rectal gland and eventually released as sex pheromone during courtship at dusk [52, 53].

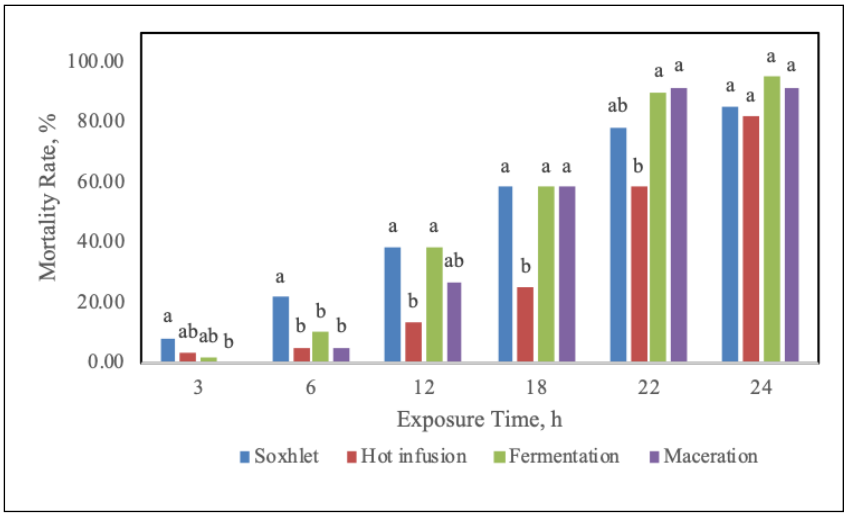


Figure 1. Effect of methods of extraction on the anti-fruit fly properties of neem leaf extract

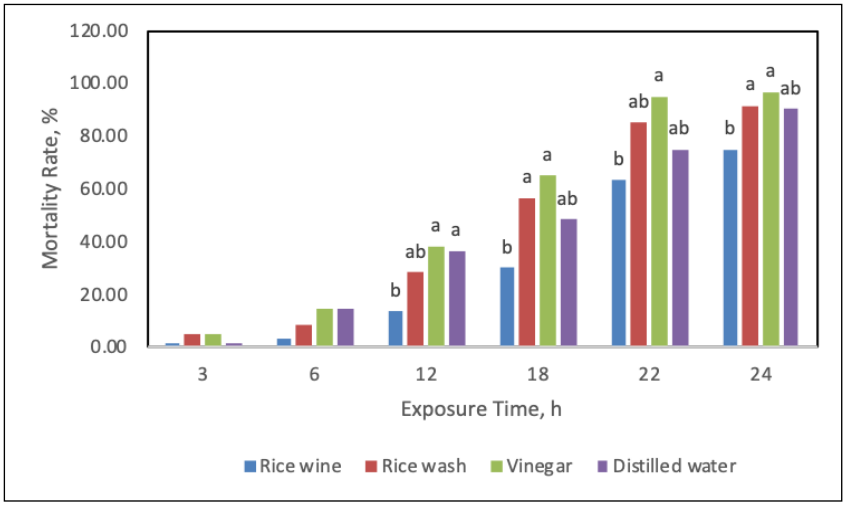


Figure 2. Effect of green solvents on the anti-fruit fly properties of neem leaf extract

Table 3. Effect of extraction method–solvent combinations on the percent mortality of *B. dorsalis*

Extraction Method	**Mean % Mortality (Extraction × Solvent Combinations)***			
	Rice Wine (RW)	**Rice Wash (RWa)**	**Vinegar (V)**	**Distilled Water (D)**
Soxhlet (S)	27.78^{g}	54.44^{ab}	61.11^{a}	50.00^{abcd}
Hot infusion (HI)	15.56^{h}	37.78^{defg}	40.00^{cdefg}	31.11^{fg}
Fermentation (F)	35.56^{efg}	51.11^{abcd}	56.67^{ab}	52.22^{abc}
Maceration (M)	45.56^{bcde}	40.00^{cdefg}	52.22^{abc}	44.44^{bcdef}

*: Means with the same letter superscript are not significantly different at the 5% level using Duncan's multiple range test

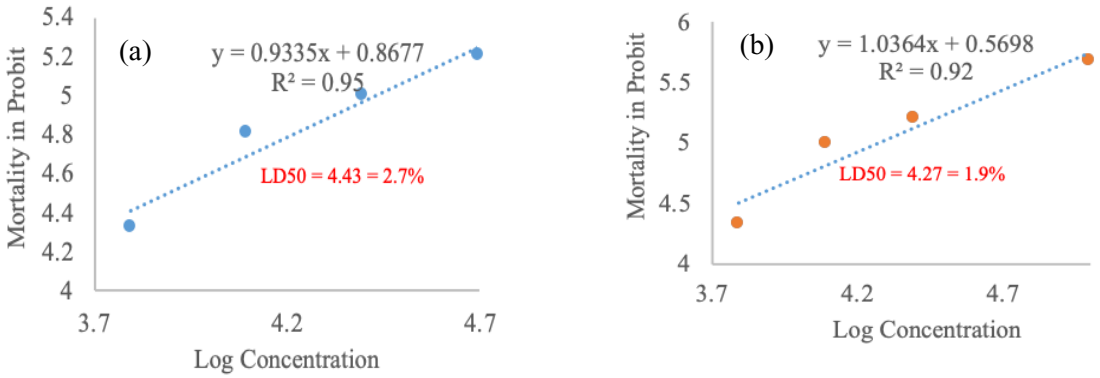


Figure 3. Graphical presentation of the lethal dose for (a) F-RWa and (b) S-V extracts using probit analysis

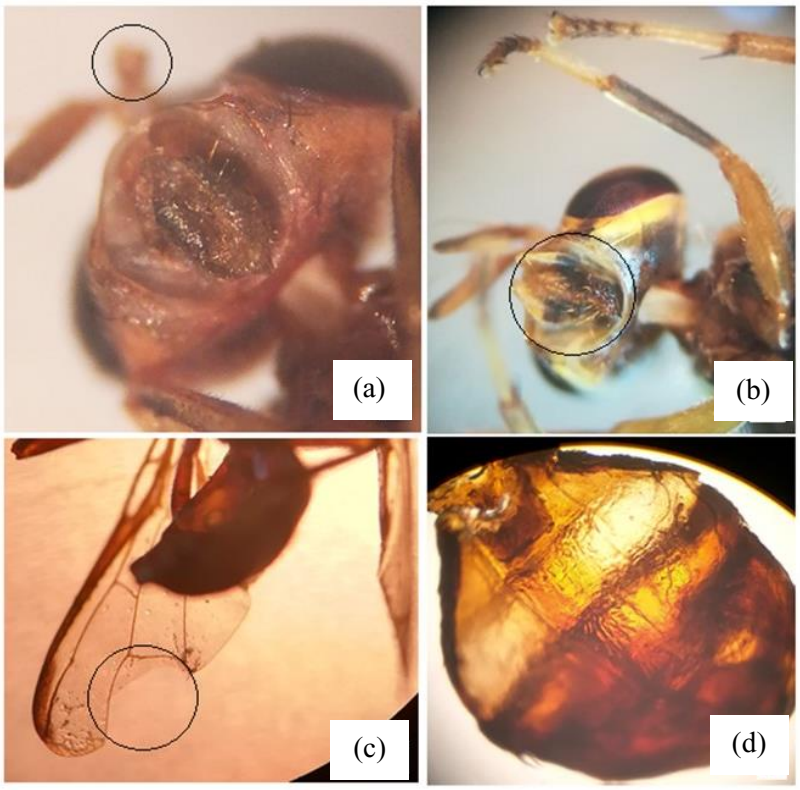


Figure 4. Observed effects of the plant extracts on oriental fruit flies (a–damaged antennae; b–darkened and retracted proboscis; c–torn wings; d–empty abdomen).

Conclusion

The findings cited above suggest that there are plants that showed activities against *Bactrocera dorsalis* and can be used in the formulation of biocide for the management of oriental fruit flies. These are the following: *Azadirachta. indica, Andrographis paniculata*, *Indigofera zollingeriana*, and *Lantana camara* with 100% mortality; *Glericidia sepium*,

Tabernaemontana. pandacaqui, Ocimum sanctum, *Mangifera oleifera*, *Annona squamosa*, *Annona muricata*, *Blumea balsamifera*, *Casia alata*, *Euphorbia tithymaloides*, *Cyperus rotondus*, and *Zamioculcas zamiifolia* with 60–93% mortality after 24 hours. *A. indica* (neem) leaf extract was the most effective against *B. dorsalis* and was used for the screening of extraction methods and solvent. Fermentation using rice wash was the most economical method but was found to be effective in the preparation of biocide from neem leaves against *B. dorsalis.*

Acknowledgement

The authors wish to acknowledge Mr. and Mrs. Juanito Palaganas, Mary Ann Gabriel, John Paul Maximo, Orly Neuda, and Luzviminda Quitos for their assistance in the collection of plant samples. Acknowledgment is also due to Ms. Ella Joyce S. Paragas for the statistical analyses.

References

1. Tharanathan, R. N., Yashoda, H. M., and Prabha, T. N. (2006). Mango (*Mangifera indica* L.), The king of fruits–an overview. *Food Reviews International*, 22(2): 95-123.
2. Briones, R. M. (2013). Market structure and distribution of benefits from agricultural exports: The case of the Philippine mango industry (No. 2013–16). PIDS Discussion Paper Series.
3. Hamamoto K. and Nago H. (2002). Integrated management of fruit fly and its impact on yield of crops with effective microorganisms (a case study). In proceeding 7th *International Conference on Kyusei Nature Farming*. Christchurch, New Zealand. pp. 15-18.
4. Weems, H. V., Heppner, J. B., Nation, J. L. and Fasulo, T. R. (2012). Oriental fruit fly, *Bactrocera dorsalis* (Hendel) (Insecta: Diptera: Tephritidae). *Featured Creatures: Entomology and Nematology. Entomology Circulars*, 21: 1-6.
5. Philippine Statistics Authority (2016). Major fruit crops quarterly bulletin. Access from https://psa.gov.ph/sites/default/files/fruits_q4_2015.
6. Kuppusamy, C. and Murgan, K. (2009). Mosquitocidal effect of *Andrographis paniculata* nees against the malaria vector, *Anopheles stephensi* Liston (Diptera: culicidae). *International Journal of Integrative Biology*, 5(2): 75-81.
7. Bright, A. A., Babu, A., Ignacimuthu, S. and Dorn, S. (2001). Efficacy of crude extracts of *Andrographis paniculata* nees. on *Callosobruchus chinensis* L. during post harvest storage of cowpea. *Indian Journal of Experimental Biology*, 39(7): 715-718.
8. Edwin, E. S., Vasantha-Srinivasan, P., Senthil-Nathan, S., Thanigaivel, A., Ponsankar, A., Pradeepa, V. and Duraipandiyan, V. (2016). Anti-dengue efficacy of bioactive andrographolide from *Andrographis paniculata* (Lamiales: Acanthaceae) against the primary dengue vector *Aedes aegypti* (Diptera: Culicidae). *Acta tropica*, 163: 167-178.
9. Patel, S., Patel, J. K. and Sejal Patel, C. (2016). A review on a miracle fruits of *Annona muricata*. *Journal of Pharmacognosy and Phytochemistry*, 5(1): 137-148.
10. Komansilan, A., Abadi, A. L., Yanuwiadi, B. and Kaligis, D. A. (2012). Isolation and identification of biolarvicide from soursop (*Annona muricata* Linn.) seeds to mosquito (*Aedes aegypti*) larvae. *International Journal of Engineering & Technology*, 12(3): 28-32.
11. Kotkar, H. M., Mendki, P. S., Sadan, S. V. G. S., Jha, S. R., Upasani, S. M. and Maheshwari, V. L. (2002). Antimicrobial and pesticidal activity of partially purified flavonoids of *Annona squamosa*. *Pest Management Science*, 58(1): 33-37.
12. Jaswanth, A., Ramanathan, P. and Ruckmani, K. (2002). Evaluation of mosquitocidal activity of *Annona squamosa* leaves against filarial vector mosquito, *Culex quinquefasciatus* say. *Indian Journal of Experimental Biology*, 40(3): 363-365.
13. Nathan, S. S., Kalaivani, K. and Murugan, K. (2005). Effects of neem limonoids on the malaria vector *Anopheles stephensi* liston (Diptera: Culicidae). *Acta Tropica*, 96(1): 47-55.
14. Sabaldica, A. C. (2011). A primer on medicinal plants for livestock healthcare. Western Sustainable Agriculture Research & Education. Access from https://cdn.sare.org/wp-content/uploads/20171204135421/954566nmc-wsare-plant-herbal-medicine-for-livestock-booklet-all.pdf.

15. Gbeassor, M., Kedjagni, A. Y., Koumaglo, K., De Souza, C., Agbo, K., Aklikokou, K. and Amegbo, K. A. (1990). *In Vitro* antimalarial activity of six medicinal plants. *Phytotherapy Research*, 4(3): 115-117.
16. Obico, J. J. A. and Ragragio, E. M. (2014). A survey of plants used as repellents against hematophagous insects by the Ayta people of Porac, Pampanga Province, Philippines. *Philippine Science Letters*, 7(1): 179-186.
17. Pinto, Z. T., Sánchez, F. F., Santos, A. R. D., Amaral, A. C. F., Ferreira, J. L. P., Escalona-Arranz, J. C. and Queiroz, M. M. D. C. (2015). Chemical composition and insecticidal activity of *Cymbopogon citratus* essential oil from Cuba and Brazil against housefly. *Revista Brasileira de Parasitologia Veterinária*, 24(1): 36-44.
18. Visetson, S., Milne, M. and Milne, J. (2001). Toxicity of 4, 11-Selinnadien-3-one from nutsedge (*Cyperus rotundus* L.) tuber extracts to diamondback moth larvae (*Plutella xylostella* L.), detoxification mechanisms and toxicity to non target species. *Kasetsart Journal (Natural Science)*, 35(3): 284-292.
19. Areekul, S., Sinchaisri, P. and Tigvatananon, S. (1987). Effects of thai plant extracts on the oriental fruit fly. *Kasetsart Journal (Natural Science)*, 21(4): 395-407.
20. Simons, A. and Stewart, J. (1994). 2.2 *Gliricidia sepium*–A multipurpose forage tree legume. Access from https://pdfs.semanticscholar.org/e330/4eb3340bdeabd1af4a3322d6162602e16780.pdf.
21. Hisaeda, A., Matsunami, K., Otsuka, H. and Takeda, Y. (2011). Flavonol glycosides from the leaves of *Indigofera zollingeriana*. *Journal of Natural Medicines*, 65(2): 360-363.
22. De Oliveira, C. F. R., Luz, L. A., Paiva, P. M. G., Coelho, L. C. B. B., Marangoni, S. and Macedo, M. L. R. (2011). Evaluation of seed coagulant *Moringa oleifera* lectin (cMoL) as a bioinsecticidal tool with potential for the control of insects. *Process Biochemistry*, 46(2): 498-504.
23. Prabhu, K., Murugan, K., Nareshkumar, A., Ramasubramanian, N. and Bragadeeswaran, S. (2011). Larvicidal and repellent potential of *Moringa oleifera* against malarial vector, *Anopheles stephensi* Liston (Insecta: Diptera: Culicidae). *Asian Pacific Journal of Tropical Biomedicine*, 1(2):124-129.
24. Anees, A. M. (2008). Larvicidal activity of *Ocimum sanctum* Linn. (Labiatae) against *Aedes aegypti* (L.) and *Culex quinquefasciatus* (Say). *Parasitology Research*, 103(6): 1451-1453.
25. Banu, K. A. and Devaraj, A. (2012). Formulation of herbal pesticide towards effective biological control of scale insects in *Psidium guajava* L. *International Journal of Pharmaceutical Research and Allied Sciences.* 2: 2-13.
26. Galvez, D. B. P. and Landrito, R. F. G. (2017). Insecticidal efficacy of hagonoy plant (*Chromolaena odorata* (L.) RM King & H. Rob.) and ZZ Plant (*Zamioculcas zamiifolia* (Lodd.) Engl.) against harlequin cockroach (*Neostylopyga rhombifolia* (Stoll, 1813)). In 52nd BIOTA Annual National Convention and Scientific Sessions, Philippine Normal University, Manila, Philippines. Access from https://biotaph.org/conferences/index.php/conventions/52/paper/view/795
27. Azmir, J., Zaidul, I. S. M., Rahman, M. M., Sharif, K. M., Mohamed, A. and Sahena, F. (2013). Techniques for extraction of bioactive compounds from plant materials: A review. *Journal of Food Engineering* 117(4): 426-436.
28. Hasmida, M., Liza, M., Nur Syukriah, A., Harisun, Y., Mohd Azizi, C. and Fadzilah Adibah, A. (2015). Total phenolic content and antioxidant activity of *Quercus infectoria* galls using supercritical CO_2 extraction technique and its comparison with soxhlet extraction. *Pertanika Journal of Science & Technology,* 23 (2): 287-295.
29. Zhang, H. F., Yang, X. H. and Wang, Y. (2011). Microwave assisted extraction of secondary metabolites from plants: Current status and future directions. *Trends in Food Science & Technolnology,* 22(12): 672-688.
30. Chemat, A, Lagha, A, AitAmar, H., Bartels, P. V. and Chemat, F. (2004). Comparison of conventional and ultrasound-assisted extraction of carvone and limonene from caraway seeds. *Flavour and Fragrance Journal*, 19(3): 188-195.

31. Tamang, J. P. and Kailasapathy, K. (2010). Fermented foods and beverages of the world. CRC Press.
32. Palaniveloo, K. and Vairappan, C. S. (2013). Biochemical properties of rice wine produced from three different starter cultures. *Journal of Tropical Biology & Conservation*, 10: 31-41.
33. Lin, F. H., Lin, J. Y., Gupta, R. D., Tournas, J. A., Burch, J. A., Selim, M. A. and Pinnell, S. R. (2005). Ferulic acid stabilizes a solution of vitamins C and E and doubles its photoprotection of skin. *Journal of Investigative Dermatology*, 125(4): 826-832.
34. Fang, Q., He, S., Xiao, Y. and Huang, Z. (2018). Effect of pH on volatile fatty acids (VFAs) in rice wash. *Desalination and Water Treatment*, 112: 303-309.
35. Ho, C. W., Lazim, A. M., Fazry, S., Zaki, U. K. H. H. and Lim, S. J. (2017). Varieties, production, composition and health benefits of vinegars: A review. *Food Chemistry*, 221: 1621-1630.
36. Chang, C. L., Cho, I. K., Li, Q. X., Manoukis, N. C., Vargas, R. I. (2013). A potential field suppression system for *Bactrocera dorsalis* (Hendel). *Journal of Asia-Pacific Entomology* 2013(4): 513-519.
37. Mehlhorn, H., Al-Rasheid, K. A. and Abdel-Ghaffar, F. (2011). The neem tree story: Extracts that really work. Springer, Berlin, Heidelberg: pp. 77-108.
38. Hasmida, M. N., Nur Syukriah, A. R., Liza, M. S. and Mohd Azizi, C. Y. (2014). Effect of different extraction techniques on total phenolic content and antioxidant activity of *Quercus infectoria* Galls. *International Food Research Journal*, 21(3): 1039-1043.
39. Subramanian, S., Salleh, A. S., Bachmann, R. T., & Hossain, M. (2019). Simultaneous extraction and separation of oil and azadirachtin from seeds and leaves of *Azadirachta indica* using binary solvent extraction. *Natural Product Sciences*, 25(2): 150-156.
40. Ramírez-Rodrigues, M. M., Balaban, M. O., Marshall, M. R. and Rouseff, R. L. (2011). Hot and cold water infusion aroma profiles of *Hibiscus sabdariffa*: Fresh compared with dried. *Journal of Food Science*, 76(2): C212–C217.
41. Verzelloni, E., Tagliazucchi, D. and Conte, A. (2007). Relationship between the antioxidant properties and the phenolic and flavonoid content in traditional balsamic vinegar. *Food Chemistry*. 105(2): 564-571.
42. Liu, Q., Tang, G. Y., Zhao, C. N., Gan, R. Y. and Li, H. B. (2019). Antioxidant activities, phenolic profiles, and organic acid contents of fruit vinegars. *Antioxidants*, 8(4): 78-89.
43. Nisbet, A. J. (2000). Azadirachtin from the neem tree *Azadirachta indica*: Its action against insects. *Anais da Sociedade Entomológica do Brasil*, 29(4): 615-632.
44. Sanchez, P. C. (2008). Philippine fermented foods: Principles and technology. UP Press. pp. 105-111.
45. Larcia II, L. L., Estacio, R. and Dalmacio, L. M. (2011). Bacterial diversity in Philippine fermented mustard (burong mustasa) as revealed by 16S rRNA gene analysis. *Beneficial Microbes*, 2(4): 263-271.
46. Ogbuewu, I. P., Odoemenam, V. U., Obikaonu, H. O., Opara, M. N., Emenalom, O. O., Uchegbu, M. C., Okoli, I. C., Esonu, B. O. and Iloeje, M. U. (2011). The growing importance of neem. *Research Journal of Medicinal Plants*, 5(3): 230-245.
47. Liby, K. T. and Sporn, M. B. (2012). Synthetic oleanane triterpenoids: Multifunctional drugs with a broad range of applications for prevention and treatment of chronic disease. *Pharmacological Reviews*, 64(4): 972-1003.
48. Kim, H. S., Zhang, Y. H., Fang, L. H. and Lee, M. K. (1999). Effects of ginsenosides on bovine adrenal tyrosine hydroxylase. *Journal of Ethnopharmacology*, 66(1): 107-111.
49. Depetris-Chauvin, A., Galagovsky, D. and Grosjean, Y. (2015). Chemicals and chemoreceptors: Ecologically relevant signals driving behavior in drosophila. *Frontiers in Ecolology and Evolution*, 3(41): 1-21.
50. Thoma, V., Kobayashi, K. and Tanimoto, H. (2017). The role of the gustatory system in the coordination of feeding. *Eneuro*, 4(6): 1-7.

51. Liu, T., Dartevelle, L., Yuan, C., Wei, H., Wang, Y., Ferveur, J. F. and Guo, A. (2008). Increased dopamine level enhances male-male courtship in drosophila. *Journal of Neuroscience*, 28(21): 5539-5546.
52. Tan, K. H., Nishida, R., Jang, E. B. and Shelly, T. E. (2014). Pheromones, male lures, and trapping of tephritid fruit flies. In *Trapping and the Detection, Control, and Regulation of Tephritid Fruit Flies*. Springer, Dordrecht: pp. 15-74.
53. Hee, A. K. W. and Tan, K. H. (2004). Male sex pheromonal components derived from methyl eugenol in the hemolymph of the fruit fly *Bactrocera papayae*. *Journal of Chemical Ecology*, 30(11): 2127-2138.

Malaysian Journal of Analytical Sciences Vol 24 No 5 2020

Articles 9 - 19 are selected papers from the "7th International Conference on Solid State Science and Technology 2019 (7th ICSSST 2019), 11th - 13th November 2019, Everly Hotel, Putrajaya, Malaysia; organized by Centre for Defence Foundation Studies, National Defence University of Malaysia and the Malaysian Solid State Science and Technology Society"
Guest Editor: Nor Laili-Azua Jamari

		Page
1.	SYNTHESIS OF SEMISYNTHETIC TRYPSIN-1,10-PHENANTHROLINE COMPLEXES WITH DIVALENT METAL IONS FOR HYDROLYSIS OF AZOCASEIN (Sintesis Kompleks Separa Sintetik Tripsin-1,10-Fenantrolin dengan Ion Logam Divalen untuk Hidrolisis Azokasin) *Mohd Basyaruddin Abdul Rahman, Azizah Misran, Muhammad Alif Mohammad Latif, Emilia Abdulmalek*	630
2.	LINKING OF SHOOTER AND SHOOTING: DETECTION OF GUNSHOT RESIDUE ON SHOOTER'S HANDS USING MICROSCOPY AND SCANNING ELECTRON MICROSCOPE-ENERGY DISPERSIVE X-RAY METHODS (Perkaitan Antara Penembak dan Penembakan: Pengesanan Sisa Tembakan pada Tangan Penembak Menggunakan Kaedah Mikroskop dan Kaedah Mikroskop Pengimbas Elektron-Sebaran Sinaran-X Bertenaga) *Farah Ad-din Nordin, Ahmad Fahmi Lim Abdullah, Kah Haw Chang*	636
3.	ANALYSES ON TOXICITY OF Pb^{2+} TOWARDS CHLOROPHYLL A, TOTAL SOLUBLE PROTEIN AND CASPASE-3-LIKE ENZYME ACTIVITY OF *Scenedesmus regularis* (Analisa Kesan Ketoksikan Pb^{2+} Terhadap Klorofil A, Jumlah Protein Terlarut dan Aktiviti Enzim Bak Kaspase-3 *Scenedesmus regularis*) *Hazlina Ahamad Zakeri, Nakisah Mat Amin, Nur Hidayah Kamilia Rassman, Wan Bayani Wan Omar*	649
4.	STORAGE STABILITY OF KUINI POWDER IN TWO PACKAGING ALUMINUM LAMINATED POLYETHYLENE AND POLYETHYLENE TEREPHTHALATE (Kestabilan Penyimpanan Serbuk Kuini dalam Dua Pembungkusan Polietilena Berlapis Aluminum dan Polietilena Tereftalat) *Loo Yian Yian and Pui Liew Phing*	657
5.	DETERMINATION OF SELECTED HEAVY METAL CONCENTRATIONS IN UNREGISTERED FACE WHITENING CREAMS SOLD IN JOHOR BAHRU, JOHOR, MALAYSIA BY USING INDUCTIVELY COUPLED PLASMA OPTICAL EMISSION SPECTROSCOPY AND THEIR HEALTH RISK ASSESSMENT (Penentuan Kepekatan Logam Berat Terpilih dalam Krim Pemutih Muka yang Tidak Berdaftar Dijual di Johor Bahru, Johor, Malaysia dengan Menggunakan Spektrofotometer Pancaran Optik Plasma Gandingan Aruhan dan Penilaian Risiko Kesihatan) *Anusia Selvaraju, Anis Nur Shasha Abdul Halim, Aemi Syazwani Abdul Keyon*	670
6.	ELECTRICAL AND INFRARED SPECTROSCOPIC ANALYSIS OF SOLID POLYMER ELECTROLYTE BASED ON POLYETHYLENE OXIDE AND GRAPHENE OXIDE BLEND (Kajian Elektrik dan Spektroskopik Inframerah kepada Elektrolit Polimer Pepejal Campuran Polietilena Oksida dan Grafena Oksida)	682

Ahmad Syafiq Fauzan Mohd Asnawi, Alyaa Amalina Mohd Azli, Muhamad Hafiz Hamsan, Mohd Fakhrul Zamani Abdul Kadir,Yuhanees Mohamed Yusof

7. MORPHOLOGICAL AND CONDUCTIVITY STUDIES OF POLYANILINE FABRIC DOPED PHOSPHORIC ACID 698
(Kajian Morfologi dan Kekonduksian Fabrik Polianilina yang telah Terdop oleh Asid Fosforik)
Nazreen Che Roslan, Muhammad Faiz Aizamddin, Siti Nurzatul Ikma Omar, Nur Aimi Jani, Mohamed Izzharif Abdul Halim, Zaidah Zainal Ariffin, Mohd Muzamir Mahat

8. ANTIMICROBIAL EFFICACY, ANTIOXIDANT PROFILE AND NINE ALTERNATIVE ACTIVE CONSTITUENTS FROM PETROLEUM ETHER AND ETHYL ACETATE EXTRACT OF *Entada spiralis* 707
(Keberkesanan Antimikrob, Profil Antioksida dan Sembilan Komponen Alternatif Aktif dari Ekstrak Petroleum Eter dan Etil Asetat dari Pokok *Entada spiralis*)
Aiza Harun, Norshilawati Abdul Aziz, Nor Shazleen Mohd Azenan, Nurfarah Farini Muhammad Kamarazzaman, Siti Zaiton Mat So'ad

9. COMPUTATIONAL STUDIES ON NONLINEAR OPTICAL PROPERTIES OF METAL COMPLEXES CONTAINING AZOBENZENE 719
(Kajian Pengkomputeran Sifat Optik Tidak Linear Terhadap Sebatian Komplek Logam yang Mengandungi Azobenzena)
Pang Siew Woon, Suhaila Sapari, Juan Matmin, Fazira Ilyana Abdul Razak

10. THE INFLUENCE OF Pd NANOPARTICLE SIZE ON Pd/TiO_2 CATALYSTS FOR CINNAMALDEHYDE HYDROGENATION REACTION 727
(Pengaruh Saiz Nanopartikel Pd pada Pemangkin Pd/TiO_2 untuk Tindak Balas Hidrogenasi Sinnamaldehid)
Norli Abdullah, Hasliza Bahruji, Fadhlina Che Ros, Imran Syakir Mohamad

11. FOURIER TRANSFORM INFRARED SPECTROSCOPY AND OPTICAL PROPERTIES OF SAMARIUM DOPED ZINC BOROTELLURITE GLASSES 736
(Inframerah Transformasi Fourier dan Sifat Optik Kaca Samarium didop dengan Zink Borotelurit)
Siti Nasuha Mohd Rafien, Azman Kasim, Azhan Hashim, Wan Aizuddin Wan Razali, Norihan Yahya

12. CARBOXYMETHYL CHITOSAN-BASED BIOPOLYMER ELECTROLYTE WITH IMIDAZOLIUM IONIC LIQUID 744
(Elektrolit Biopolimer Berasaskan Karboksimetil Kitosan Dengan Cecair Ionik Imidazolium)
Intan Juliana Shamsudin, Norsyabila Shrgawi, Hussein Hanibah, Nur Hasyareeda Hassan, Azizan Ahmad

13. EQUIVALENT CIRCUIT ANALYSIS OF $LaZrTa_3O_{11}$ CERAMIC SYNTHESISED BY USING THE CONVENTIONAL SOLID-STATE METHOD 757
(Analisis Litar Sepadan Seramik $LaZrTa_3O_{11}$ Disintesis dengan Menggunakan Kaedah Keadaan Pepejal Konvensional)
Fadhlina Che Ros and Jumiah Hassan

14. EFFECT OF Cr_2O_3 ON THE TRANSITION TEMPERATURE AND PHASE FORMATION OF $Tl_{2-x}Cr_xBa_2CaCu_2O_{8-\delta}$ SUPERCONDUCTOR 766
(Kesan Cr_2O_3 Terhadap Suhu Peralihan dan Pembentukan Fasa Superkonduktor Tl_{2-}

$_{x}Cr_{x}Ba_{2}CaCu_{2}O_{8-\delta}$)
Syahrul Humaidi and Roslan Abd-Shukor

15. A BRIEF REVIEW ON THE DESIGN AND SYNTHESIS OF NEW ANTIDOTES IN THE TREATMENT OF ORGANOPHOSPHORUS POISONINGS 772
(Ulasan Ringkas pada Reka Bentuk dan Sintesis Antidot Baru untuk Merawat Keracunan Organofosforus)
Mas Amira Idayu Abdul Razak, Mohd Nor Faiz Norrrahim, Ong Keat Khim, Siti Aminah Mohd Noor, Norhana Abd Halim, Noor Aisyah Ahmad Shah, Victor Feizal Knight, Wan Md. Zin Wan Yunus, Noor Azilah Mohd Kasim

16. STRUCTURAL AND OPTICAL PROPERTIES OF DYSPROSIUM AND EUROPIUM CO-DOPED WITH YTTRIUM ALUMINIUM GARNET NANOCRYSTALLINE POWDERS PREPARED BY COMBUSTION SYNTHESIS 783
(Sifat-sifat Struktural dan Optikal daripada Serbuk Nanokristal Dysprosium dan Europium Di-ko-dopkan dengan Yattrium Aluminium Garnet yang Disediakan Secara Sintesis Pembakaran)
Abd Rahman Tamuri, Nor Ezzaty Ahmad, Nurliyana Nabilah Ghazali, Rosli Husin

17. GREEN SYNTHESIS OF SILVER PARTICLES USING *Citrus microcarpa* PEEL EXTRACT 791
(Sintesis Partikel Perak Menggunakan Ekstrak kulit *Citrus microcarpa*)
Gong Wee Jie, Masrina Mohd Nadzir, Kalaivani Rangasamy

18. EFFECT OF TIME AND TEMPERATURE ON REDUCED GRAPHENE OXIDE (rGO) LAYER STABILITY AND CYCLIC VOLTAMMETRIC BEHAVIOUR OF MODIFIED SCREEN-PRINTED CARBON ELECTRODE (mSPCE) FOR BIOSENSING PURPOSES 800
(Kesan Masa dan Suhu Pengeraman terhadap Kestabilan Lapisan rGO dan Perlakuan Voltametri Berkitar Elektrod Karbon Tercetak Terubahsuai (mSPCE) bagi Tujuan Penderiaan Bio)
Ahmad Farid Mohd Azmi, Vayithiswary Kannan, Nur Sabila Yasin, Jahwarhar Izuan Abdul Rashid, Ainsah Omar, Emee Marina Salleh

19. INFLUENCE OF HYDROXYMETHYLATED LIGNIN ON MECHANICAL PROPERTIES AND PAYNE EFFECT OF NR/BR COMPOUNDS 810
(Kesan Lignin Hidroksimetilasi Terhadap Sifat Mekanik dan Kesan Payne dalam Sebatian Campuran NR/BR)
Nor Anizah Mohamad Aini, Nadras Othman, M. Hazwan Hussin, Kannika Sahakaro, Nabil Hayeemasae

Malaysian Journal of Analytical Sciences (MJAS)
Published by Malaysian Analytical Sciences Society

SYNTHESIS OF SEMISYNTHETIC TRYPSIN-1,10-PHENANTHROLINE COMPLEXES WITH DIVALENT METAL IONS FOR HYDROLYSIS OF AZOCASEIN

(Sintesis Kompleks Separa Sintetik Tripsin-1,10-Fenantrolin dengan Ion Logam Divalen untuk Hidrolisis Azokasin)

Mohd Basyaruddin Abdul Rahman[1,2]*, Azizah Misran[2], Muhammad Alif Mohammad Latif[1,2], Emilia Abdulmalek[1,2]

[1]*Integrated Chemical BioPhysics Research*
[2]*Department of Chemistry, Faculty of Science*
Universiti Putra Malaysia, 43400 UPM, Serdang, Selangor, Malaysia

**Corresponding author: basya@upm.edu.my*

Received: 30 March 2020; Accepted: 2 September 2020; Published: 12 October 2020

Abstract

Modification of trypsin from bovine pancreas was studied to understand the biomolecular interactions between the protein and ligand, toward metal ion. A semisynthetic complex of trypsin-1,10-phenanthroline (trypsin-PHN) was prepared and investigated for its role in the hydrolysis of azocasein. Predicted results from molecular docking studies aid in the comprehension of the protein-ligand system. PHN ligand demonstrated the ability to provide more sites for interactions with metal ions and contribute extensively to the development of a new generation of industrial biocatalysts. The trypsin-PHN complex had an increment of 40% activity in the hydrolysis of azocasein. In the presence of 5 μM Ca^{2+} ions the activity was higher than native enzyme but decreased in the presence of Mg^{2+}, Zn^{2+} and Fe^{2+} ions, thus, providing additional insight into potential inhibitors of the rational enzyme design.

Keywords: metalloenzyme, semisynthetic, trypsin, biocatalyst, hydrolysis

Abstrak

Modifikasi tripsin daripada pankreas anak lembu telah dikaji untuk mengetahui interaksi biomolekul di antara protein dan ligan, dan ion logam. Satu kompleks separa sintetik tripsin-1,10-fenantrolin (trypsin-PHN) telah disediakan dan aktiviti terhadap hidrolisis azokasin telah dikaji. Hasil jangkaan daripada kajian pendokkan molekul turut membantu dalam kajian sistem protein-ligan ini. Ligan PHN menunjukkan kebolehan untuk memberikan lebih tapak interaksi dengan ion logam yang berkeupayaan mencetus pembangunan dalam generasi baru industi biomangkin. Kompleks tripsin-PHN menunjukkan peningkatan aktiviti sebanyak 40% dalam hidrolisis azokasin. Kehadiran sebanyak 5 μM ion Ca^{2+} turut meningkatkan aktiviti berbanding enzim asal tetapi menurun dengan kehadiran ion Mg^{2+}, Zn^{2+} dan Fe^{2+}. Maklumat ini dapat membantu penghasilan perencat dalam rekabentuk enzim secara rasional.

Kata kunci: metaloenzim, separa sintetik, tripsin, biomangkin, hidrolisis

Introduction

In the design of semisynthetic catalysts, enzyme function can be improved for practical use by introducing cofactors or other reactive moieties into proteins that provide enormous flexibility which could be employed for a variety of purposes [1]. The outcomes of such structuring may include altered substrate specificity of an enzyme or increased stability of a protein for specific applications [2]. Protein engineering and chemical modification has become a successful valuable tool for creating or improving protein function for practical uses. This topic is becoming an important one in bioorganic chemistry due to the availability of direct information on the unique interactions of metal cofactors with adjacent amino acids using X-ray analysis [3].

Examination of the protein pocket or cavity would be a good start for the creation of an artificial catalyst [4]. Despite of protein structure being completely organized; a protein has regions on its surface where small molecules (ligands) or ions can bind. It is possible that there are many binding sites on the surface of enzymes and each binding site has only limited range of the ligands. Selected binding sites of thermostable lipase from *Geobacillus zalihae* strain T1 exemplified how the characteristics of interactions like hydrogen bonds, electrostatic interactions, van der Waals and hydrophobic contacts played very important roles in the protein-ligand interaction studies [5]. The design and development of semisynthetic enzyme was based on the use of protein pockets that can accommodate ligand as an intermediate between the pockets at the surface of the enzyme with metal. A thermostable thermolysin-phosphoethanolamine-Ca^{2+} protein complex suggested metal ions can add new functionality to proteins and help catalyse some of the most difficult biological reactions [6].

In this work, trypsin from bovine pancreas was selected as the backbone due to its high precision information regarding its experimental kinetic data on the enzyme reaction. Furthermore, it has well-defined mechanisms that are consistent with many structural and kinetic studies. It has also been extensively used in research in developing methods for structural stabilizations and catalytic improvements that increased global attention on enzyme engineering [6]. The protein-ligand complex of trypsin also provides a well-defined second coordination sphere that induces the selectivity of the reaction [7]. For advance systematic use of the trypsin, attention should be paid to the fine-tuning of its artificial metalloproteins, design of metal drugs, and electron transfer systems. The objective of this work is to study the structural interactions within the complexes of semisynthetic metalloenzymes through computational-aided molecular modelling and to analyse the effect of ligands and metal ions in the system through experimental work.

Materials and Methods

Materials

Trypsin from bovine pancreas was purchased from Fluka, Switzerland. All metal complexes ($MgSO_4.7H_2O$, $CaCl_2$, $ZnSO_4$ and $FeSO_4$) were purchased from Merck, Germany. All other chemicals and solvents used in this study were of analytical grade.

Protein preparation and assay

A solution of trypsin was prepared by dissolving trypsin (1 mg/mL) in a 20 mM Tris-HCl buffer, pH 7.6, 10 mM NaCl. It was then purified on a pre-packed Hi-Trap Benzamidine column. The protein content was determined by the Bradford method [8] and trypsin activity was measured by the Tomarelli method using azocasein as a substrate [9].

Synthesis of the trypsin-PHN

A 100 μM solution of PHN in dimethylformamide (DMF) (10 mM, 5 mL) was added to purified trypsin in Tris-HCl (20 mM, pH 7.6, 5 mL), and the mixture was allowed to react at room temperature, for approximately one hour. Later, the solution was purified by gel filtration (Sephadex 25, Desalting Column, Amersham) to remove excess PHN. The activity of the trypsin-PHN was determined by azocasein assay.

Synthesis of trypsin-PHN-metal ion

Each of the following $MgSO_4.7H_2O$, $CaCl_2$, $ZnSO_4$ and $FeSO_4$ was dissolved in 20 mM of Tris-HCl at pH 7.6 to

a final concentration of 5, 10, 15, 20, 25, 30 μM. The solutions were added to a solution of trypsin-PHN (1 mL, 100 μM) in the same buffer and allowed to react for an hour at ambient temperature. Unbound metal ions were removed using gel filtration (Sephadex 25, Desalting Column, Amersham) in a 20 mM, pH 7.6 Tris-HCl buffer. The activity of the resulting protein complex was determined by azocasein assay.

Molecular docking

The AutoDock programme 3.0.5 was employed to perform docking using Lamarckian genetic algorithm (LGA) [10]. Pocket cavities were computed using the CASTp (Computed Atlas of Surface Topography of proteins) web server. The four letter PDB name of trypsin structure (1AUJ) was used for querying on the CASTp server. The hydrogen bonds and hydrophobic contacts were represented using the LigPlot software. BIOVIA Discovery Studio Visualizer was used to visualize the semisynthetic metallotrypsin complexes.

Results and Discussion

Nitrogen-containing ligand PHN is highly stable and rigid which makes it promising for the development of a biocatalyst when incorporated into enzymes. A study of ligand concentration showed that at 100 μM and pH 7.6, the rate of azocasein hydrolysis increased by more than 40% when compared to native enzyme. This increment may due to effects such as high electronegativity of PHN, which increases the charge distribution at the pocket cavity or the active site. The binding of PHN to trypsin (ratio 1:1) was evaluated by UV-visible and fluorescence spectroscopy (results not shown). Instead of increasing the charge distribution in the pocket, PHN would increase the charge of the neighbouring surface area. Consequently, it was hypothesized that more substrates can enter the active site to allow trypsin to efficiently catalyse the reaction.

In this study, the effects of different metal ions in a trypsin-PHN complex were evaluated as shown in Figure 1. The results obtained can be divided into two parts; first, the effect of different metal ions in the complex trypsin-PHN and second, the effect of different concentration of the metal ions. In general, the activity of trypsin-PHN complex was reduced by the presence of metal ions except for Ca^{2+} at 5 μM. In the case of Mg^{2+} and Zn^{2+}, trypsin activity was slightly decreased with the increase of metal ion concentrations. However, in the presence of Fe^{2+} inhibited the activity of the trypsin-PHN at all concentration which may due to PHN complexing to iron [11]. It has been suggested that divalent Ca^{2+} is involved with intermolecular protein Ca^{2+}-protein cross-linking, intra-molecular electrostatic shielding and induced protein conformational changes [12].

It was well-established that in many cases, metal ions can accelerate the reaction rate and as well retarding the activity of the enzyme. Gradual increase of metal ion concentration from 5 to 30 μM seemed to inhibit the trypsin-PHN complex. Excess metal ions increase the charge distribution at the active site which may lock the geometry of the active site so that only certain substrates could be accommodated. Furthermore, higher concentrations of metal ions might also denature the structure of trypsin-PHN due to imbalance of ionic strength. The presence of Ca^{2+} in low quantities is needed to stabilize the conformation of the trypsin-PHN and to accomplish its function. Other studies of Ca^{2+} binding to protein demonstrated that large amounts of Ca^{2+} (2.4 mM) bound to trypsinogen, significantly changing the conformation of trypsinogen to produce Ca^{2+}-trypsinogen conjugates [12]. The formation of multiple conjugates between Ca^{2+} and trypsinogen demonstrated that trypsinogen has multiple sites for the Ca^{2+} binding.

The bidentate PHN ligand can interact with several pockets of the protein. Predicted results from molecular docking may help to explain the protein-ligand system. Based from a previous report [13], a docked complex of pocket 24-PHN showed that 9 residues were involved in hydrophobic contact with PHN; Asp189, Ser190, Cys191, Gln192, Ser195, Trp215, Gly216, Gly219, and Gly226. The detailed preference for pocket 24 might be due to the charge distribution on the pocket itself as illustrated in Figure 2. The rigid ligand of PHN has the most favourable value for the final docked energy (-8.74 kcal/mol) at pocket 24 of trypsin (1AUJ.pdb). The coordinated structure of Ser195 at the active site would promote the attraction of PHN, its highly

electronegative nitrogen atom into the pocket. As the PHN contacts the pocket, it may induce conformational changes at the binding site to make the active site of trypsin (His57, Asp102, Ser195) capable of facilitating azocasein as the substrate (Figure 3). It was found that the N-ring was oriented towards the interior of the pocket. Experimental data observed by Ananthanarayanan and Kerman [14] indicated that either the carbonyl or hydroxyl of the ligands could participate in the chelation of a metal ion in conjugation with polar or acidic groups in the ligand binding pocket of the respective receptor.

Since Ca^{2+} is highly charged, it seeks the possibility of sharing electron pairs with other atoms so that a bond or charge-charge interaction can be formed. Katz et al. [15] proposed that Ca^{2+} could accommodate several coordination numbers from 4-10. Electrostatic interactions provided by Ca^{2+} could contribute to the structural effect by inducing conformational changes at the active site to accommodate the substrate [16]. It is interesting to note that pocket cavity 24 provided the site for PHN interaction as it affords the site for hydrophobic interactions for PHN and metal ions attraction due to the electrostatic environment (Figure 4). Despite the stability of trypsin, the binding of Ca^{2+} to protein was suggested to provide the electrostatic environment to orient and attract the substrates to the active site.

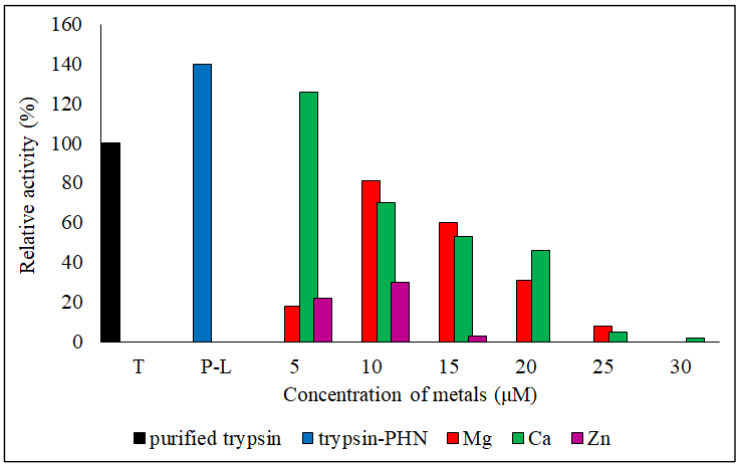
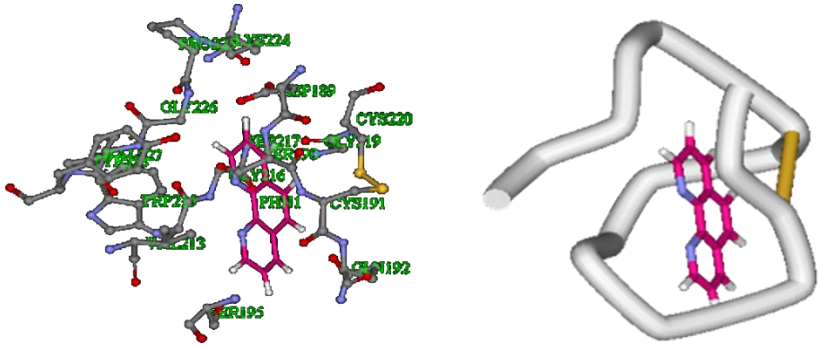


Figure 1. Effect of Mg^{2+}, Ca^{2+} and Zn^{2+} metal ions at different concentrations (5 to 30μM) of the trypsin-PHN complex. Fe^{2+} inhibited activity at all concentrations (P-L denoted as Protein-Ligand)



(a) (b)

Figure 2. Orientation of PHN at its lowest docked energy at pocket 24 (-8.74 kcal/mol) [13]. The presentation of interaction trypsin-PHN complex using (a) scaled ball and stick and (b) tube

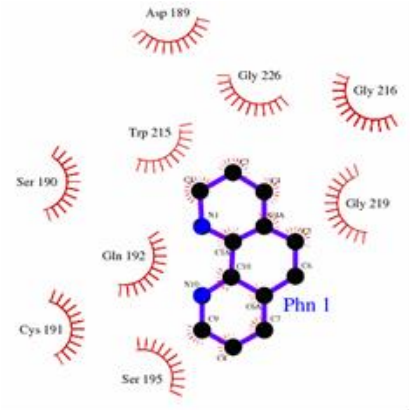


Figure 3. Interactions of PHN at pocket 24 of pancreatic bovine trypsin. Hydrophobic interactions of the lowest docked energy of PHN with pocket 24 of pancreatic bovine trypsin represented by LigPlot. The comb-like arrangements indicate the hydrophobic contacts

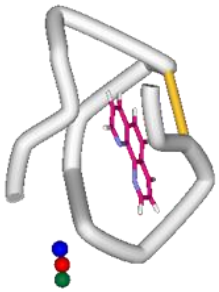


Figure 4. Result of the orientation of 24-PHN-metal complex at its lowest docked energy. The docked metal ions were rendered by CPK structure. The blue ball represents Ca^{2+} (-5.56 kcal/mol), the green ball represents Mg^{2+} (-6.99 kcal/mol), and the red ball represents Fe^{2+} (-9.33 kcal/mol)

Conclusion

It can be deduced that the complex trypsin-PHN-Ca^{2+} was probably the best complex to create semisynthetic metalloenzyme model, as it was capable to increase the activity of the complex in term of designing catalyst. Nevertheless, the association of Mg^{2+}, Zn^{2+} and Fe^{2+} into complex trypsin-PHN would provide additional insight of potential inhibitor to the rational enzyme design.

Acknowledgement

This project was supported by the Ministry of Science, Technology and Innovation, Malaysia research grant (Vot. No. 5450618).

References

1. Qi, D., Tann, C. M, Haring, D. and Distefano, M. D. (2001). Generation of new enzymes via covalent modification of existing proteins. *Chemical Reviews*, 101: 3081-3111.
2. Mayer, C., Gillingham, D. G., Ward, T. R. and Hilvert, D. (2011). An artificial metalloenzyme for olefin metathesis, *Chemical Communications*, 47: 12068-12070.
3. Heinisch, T. and Ward, T. R. (2010). Design strategies for the creation of artificial metalloenzymes, *Current Opinion in Chemical Biology*, 14(2), 184-199.

4. Lu, Y., Yeung, N., Sieracki, N. and Marshall, N. M. (2009). Design of functional metalloproteins. *Nature*, 460, 855-862.
5. Abdul Rahman, M. B. and Latif, M. A. M. (2019). Interaction studies of putative chemical ligands in binding sites of thermostable lipase from *Geobacillus zalihae* strain T1. *Malaysian Journal of Analytical Sciences*, 23(4): 613-624.
6. Abdul Rahman, M. B., Jaafar A. H, Basri, M., Raja Abdul Rahman, R. N. Z. and Salleh, A. B. (2014). Biomolecular design and receptor-ligand interaction of a potential industrial biocatalyst: A thermostable thermolysin-phosphoeth-anolamine-Ca^{2+} protein complex. *Journal of Advanced Catalysis Science and Technology*, 1: 1-5.
7. Villalonga, R., Villalonga M. R. and Gomez L. (2000). Preparation and functional properties of trypsin modified by carboxymethylcellulase. *Journal of Molecular Catalysis B: Enzymatic*, 10: 483-490.
8. Bradford, M. M. (1976). A rapid and sensitive method for the quantitation of microgram quantities of protein utilizing the principle of protein-dye binding. *Analytical Biochemistry*, 72: 248-254.
9. Tomarelli, R. M., Charney, J. and Harding, M. L. (1949). The use of azoalbumin as a substrate in the colorimetric determination of peptic and tryptic activity. *Journal of Laboratory and Clinical Medicine*, 34: 428-433.
10. Morris, G. M., Goodsell, D. S., Halliday, R. S., Huey, R., Hart, W. E., Belew, R. K. and Olson, A. J. (1998). Automated docking using a Lamarckian genetic algorithm and an empirical binding free energy function, *Journal of Computational Chemistry*, 19: 1639-1662.
11. Walczak, M. M. and Flynn, N. T. (1998) Spectroelectrochemical study of the generation of tris-(1,10-phenanthroline)iron(II/III) from μ-oxo-bis[aquabis(1,10-phenanthroline)iron(III)]. *Journal of Electro-analytical Chemistry*, 441(1–2): 43-49.
12. Bao, T. and Pawlyszyn, J. (2006). Role of calcium binding in protein structural changes and phospholipid–protein interactions studied by capillary isoelectric focusing with whole column imaging detection, *Analytica Chimica Acta*, 559(1): 1-8.
13. Abdul Rahman, M. B., Misran, A., Basri, M., Raja Abdul Rahman, R. N. Z., Salleh, A. B. and Abdul Wahab, H. (2005). Screening and docking chemical ligands onto pocket cavities of a protease for designing a biocatalyst. *Biocatalysis and Biotransformation*, 23: 211-216.
14. Ananthanarayanan, V. S. and Kerman, A. (2006). Role of metal ions in ligand-receptor interaction: insights from structural studies. *Molecular and Cellular Endocrinology*, 246: 53-59.
15. Katz, A. K., Glusker, J. P., Beebe, S. A. and Bock C. W. (1996). Calcium ion coordination: A comparison with that of beryllium, magnesium, and zinc. *Journal of American Chemical Society*, 118(24): 5752-5763.
16. Steinreiber, J. and Ward, T. R. (2008). Artificial metalloenzymes as selective catalysts in aqueous media. *Coordination Chemistry Reviews*, 252: 751-766.

Malaysian Journal of Analytical Sciences (MJAS)
Published by Malaysian Analytical Sciences Society

LINKING OF SHOOTER AND SHOOTING: DETECTION OF GUNSHOT RESIDUE ON SHOOTER'S HANDS USING MICROSCOPY AND SCANNING ELECTRON MICROSCOPE-ENERGY DISPERSIVE X-RAY METHODS

(Perkaitan Antara Penembak dan Penembakan: Pengesanan Sisa Tembakan pada Tangan Penembak Menggunakan Kaedah Mikroskop dan Kaedah Mikroskop Pengimbas Elektron-Sebaran Sinaran-X Bertenaga)

Farah Ad-din Nordin[1, 2], Ahmad Fahmi Lim Abdullah[1], Kah Haw Chang[1]*

[1]Forensic Science Programme, School of Health Sciences,
Universiti Sains Malaysia, 16150 Kubang Kerian, Kelantan, Malaysia
[2]Criminalistic Section, Forensic Division,
Department of Chemistry, Jalan Sultan, 46661 Petaling Jaya, Kuala Lumpur, Malaysia

**Corresponding author: changkh@usm.my*

Received: 10 March 2020; Accepted: 5 August 2020; Published: 12 October 2020

Abstract

One important link in the chain of proof during investigation of shooting cases is the evidence to prove a person had fired a firearm, or somehow was connected with the firing activity. Gunshot residues (GSR), particularly on shooter's hand, could provide significant aid in such investigation. Therefore, this study was aimed to investigate the detection of GSR particles recovered from the hands of shooter using two sampling methods, namely stubbing and swabbing, on the basis of the types of firearms and ammunitions, as well as the varying sampling sites. By considering lead, barium and antimony as the criterion to definitely confirm the presence of GSR, the experimental results revealed that greater number of GSR particles were shown in those samples subjected to firing by using revolver with .38 SPL ammunition compared to semi-automatic pistol with 9 mm ammunition ($p = 0.034$). Based on Kruskal-Wallis test, there was no statistically significant association shown between the sampling sites and number of GSR particles detected ($p= 0.545$ for semi-automatic pistol; $p = 0.218$ for revolver). All stub samples demonstrated positive detection of GSR particles, but only one single characteristic GSR particle was detected on swab samples. Further examination on the collection efficiency of respective sampling methods demonstrated with no significant association between the types of firearms and number of GSR particles detected from the respective cartridge cases ($p = 0.568$). The number of swabbing from spent cartridge case gave almost similar testing result ($p = 0.561$). This study has successfully detected the presence of GSR particles, which could serve as a supporting evidence to relate a suspect to a shooting case. Although swabbing has limited ability in recovering GSR samples from the hands of shooter, it is useful whenever a stub is not available or to recover GSR particle from a place where could not be reached by a stub to avoid the loss of trace particles.

Keywords: forensic science, firearm, gunshot residue, stub, swab, shooter

Abstrak

Satu perkaitan penting dalam rantaian bukti ketika penyiasatan kes penembakan adalah bahan bukti yang dapat membuktikan seseorang individu telah melepaskan suatu tembakan atau dikaitkan dengan aktiviti penembakan tersebut. Sisa tembakan (GSR) yang lazimnya pada tangan penembak boleh memberikan bantuan bererti dalam penyiasatan kes-kes sedemikian. Justeru, kajian ini bertujuan menyiasat pengesanan zarah GSR yang dipulihkan daripada tangan penembak menggunakan dua kaedah pensampelan, iaitu dengan puntung dan kesatan, berdasarkan jenis senjata api dan amunisi serta pelbagai tapak pensampelan. Dengan mengambil kira plumbum, barium dan antimoni sebagai kriteria untuk mengesahkan kehadiran GSR secara jelas, keputusan eksperimen telah menunjukkan bahawa bilangan zarah GSR yang lebih banyak telah ditunjukkan pada sampel-sampel yang ditembak menggunakan revolver bersama dengan amunisi .38 SPL berbanding pistol semi-automatik dengan amunisi 9 mm (p = 0.034). Berdasarkan ujian Kruskal-Wallis, tiada perkaitan statistik bererti yang terbukti antara tapak-tapak pensampelan dan bilangan zarah GSR yang dikesan (p = 0.545 bagi pistol semi-automatik; p= 0.218 bagi revolver). Kesemua sampel puntung menunjukkan pengesanan positif bagi zarah GSR tetapi hanya satu zarah berciri GSR sahaja yang dikesan pada sampel kesatan. Pemeriksaan seterusnya pada keberkesanan pengumpulan bagi kedua-dua kaedah pensampelan tidak menunjukkan perkaitan yang bererti antara jenis senjata api dan bilangan zarah GSR yang dikesan daripada kelongsong peluru masing-masing (p = 0.568). Bilangan kesatan daripada kelongsong peluru tertembak memberikan keputusan yang lebih kurang sama (p = 0.561). Kajian ini telah berjaya mengesan kehadiran zarah-zarah GSR yang boleh berfungsi sebagai bahan bukti sokongan dalam mengaitkan seseorang suspek kepada suatu kes penembakan. Sungguhpun kaedah kesatan mempunyai kekangan dalam memulihkan sampel GSR daripada tangan penembak, kaedah ini adalah berguna apabila suatu puntung tidak tersedia atau untuk memulihkan zarah GSR daripada sesuatu tempat tidak dapat dicapai oleh sesuatu puntung demi mengelakkan kehilangan zarah-zarah surih.

Kata kunci: sains forensik, senjata api, sisa tembakan, puntung, kesatan, penembak

Introduction

Locard's Principle of Exchange is the underlying principle during crime scene investigation, which could be summarised as "every contact leaves a trace". In firearm related cases, therefore, one important link in the chain of proof during its investigation is gunshot residue (GSR) evidence to prove that a person had fired a firearm, or somehow was connected to the firing activity. Traces of GSR particles, following the discharge of firearm are deposited onto various parts of body surfaces, particularly on the hands of a shooter [1-3]. Hence, based on the principle, the detection of GSR on a suspect apprehended after a shooting can be used as an associative evidence to link the suspect in cases of armed assaults, murders, poaching and other violations involving the possible use of firearms [2-5]. Additionally, GSR can also serve as reconstructive evidence for the investigator to gain better understanding whether an individual is definitely involved in the shooting, merely being in the nearest vicinity of a firing weapon, or just getting in contact with an object contaminated with GSR [2, 3]. As a result, forensic investigator must be able to recover and determine the presence of GSR or exclude its presence, mainly looking at the morphology of the particles, and more importantly, its elemental composition.

GSR analysis by scanning electron microscope-energy dispersive X-ray (SEM-EDX) detector on the basis of their morphology and characteristic elemental composition has become the preferred method until today [1, 6]. The standard for GSR analysis used in the forensic community was set forth by the American Society for Testing and Materials (ASTM), with acceptable criteria for morphological features and respective elemental profiles to definitely confirm GSR identities, to allow the questioned samples to be said as "characteristic of" or "consistent with" GSR [6]. ASTM E1588 states that particles which are the characteristic of GSR must contain lead, antimony and barium. The presence of only one or two of these three elements could only be considered as indicative or merely consistent with GSR [6-8].

A suspect in shooting related case shall be sampled as soon as possible, particularly from the hands, since the time elapsed between an incident and sampling [4, 9-13], washing of hand by a suspect [4, 9, 10, 13] and concealment of body surfaces by the suspect [14] could

contribute to potential sample loss. Under controlled condition, GSR particle count drops rapidly in the first two to four hours after firing [12]. Unnecessary delayed sampling should not be tolerated due to foreseeable sample loss or introduction of contaminants [3]. Several GSR collecting techniques for GSR have been developed, including swabbing, glue-lifting, vacuuming, tape-lifting and direct stubbing [3, 13]. For SEM-EDX analysis, direct stub collection method involves the dabbing of an adhesive coated aluminium stub over the sampling area [1, 4, 6, 15, 16]. Swabbing using cotton swab as collection media has been used for inorganic GSR analyses by atomic absorption spectroscopy and SEM-EDX analysis [16, 17]. As a non-adhesive surface, GSR could be lost during handling, packaging and transporting, and this explains why swabbing gave much poorer recovery [16]. Nonetheless, when stub kits are not available, swabbing should be attempted.

Common small firearms found in forensic cases are revolver and semi-automatic pistols. Ammunition could be loaded in a revolver and upon firing; the cartridge has to be extracted out manually. In semi-automatic pistol, the cartridge is ejected from the firearm after each round of firing. The two mechanisms also led to the deposition of GSR onto the different parts of hands of a shooter [3, 18-20]. In this study, samples were collected from the hands of shooter using two different firearms to establish if there was significant difference on the total GSR count. Samples were collected using stubs and swabs on different parts of hands to compare sampling efficiency using both the methods, as well as to establish the distribution of GSR on different parts of the hands of shooter. The determination of suitable sampling method is crucial for investigative team in maximising the chance for the detection of GSR particles, and subsequently aid in linking a suspect to a shooting incident.

Materials and Methods

Shooting and sampling

A semi-automatic pistol P-99 Walther® and a Smith & Wesson® .38 Special police revolver were used in firing the ammunitions, namely SME 9 mm and SME .38 SPL, SME Ordnance, Selangor, Malaysia supplied by Royal Malaysia Police, in an open shooting range in Police Training Centre, Kuala Lumpur. Shooting was performed by a trained police officer. Prior to shooting, both hands of the shooter were washed thoroughly. Two-hand shooting was performed and GSR was generated from single shot with the respective firearm in three replicates. Immediately after each shot, samples were collected from the hand surface of the shooter at four different sites, namely right palm, right back, left palm and left back, using four different stubs (Electron Microscopy Sciences, Hatfield, PA). Stubs with samples were packed into their respective containers and labelled accordingly. The same procedure was also carried out using cotton buds (Puritan Medical Products, Guilford, ME) and packed into separate paper bags after each sampling. Between each shooting, the shooter was asked to wash both hands with tap water thoroughly and dry on disposal paper towels. The washing procedure was aimed to remove any residual GSR particles from hand surface to avoid carrying over. Positive control was collected by swabbing the inner compartment of spent cartridges while negative control was sampled from shooter's hand surface before shooting and after each washing procedure.

Physical examination

Samples on stubs and swabs were examined visually and under microscope (digital microscope KH-7700, Hirox Co. Ltd., Japan) equipped with a digital camera and supported by the operating system integrated into one unit. Magnification factors for image display were ranged from 50× to 200×. Any foreign particles on the stubs and swabs were carefully observed and photographed.

Sample preparation prior to SEM/EDX analysis

No preparation procedure was performed on stub samples since they were directly placed on the stage of the microscope for analysis. Swab samples were placed into a small test tube and added with 1 mL of GC grade hexane of purity ≥ 96.0% (Merck, Kenilworth, NJ). The solution was then sonicated for 30 minutes and transferred onto individual evaporating dish, allowing for evaporation until it dried. Then, the surface was tape-lifted using individual SEM collection kit. Positive controls were also prepared using the same procedure

after swabbing of the inner compartment of cartridge cases. A clean unused cotton bud was used as negative control.

SEM-EDX analysis

All samples were analysed using a Zeiss Evo 50 SEM (Zeiss, Germany) with Oxford EDS system (Oxford Instrument Analytical Limited, United Kingdom). The system was supported by INCA GSR-analysis Software (Oxford Instrument Analytical Limited, United Kingdom), allowing detection, analysing and classifying of particles into a pre-determined classification scheme. The analysis was performed by means of an automated INCA Feature/GSR programme, searching for particles of defined characteristics through analysis of specimen surface divided into small rectangular fields. Size of the field depends on the applied magnification and scanning resolution. In this study, two magnification settings, namely 100× and 200×, were used according to the standard of procedure in Department of Chemistry Malaysia. An accelerating voltage of 20 kV and working distance of 8.5 mm were used throughout the scanning process. On completion of each run, any particles that classified under unique and characteristic category was relocated and reanalysed for reconfirmation.

Statistical analysis

Statistical analyses were carried out using IBM Statistical Package for the Social Sciences (SPSS) Statistics Version 24.0 (IBM Corporation, NY). Data cleaning and descriptive analysis were performed to ensure there were no errors. Independent t-test or Mann Whitney statistical tests were carried out when there were two categorical groups. One-way ANOVA or Kruskal Wallis test was used for more than two groups of independent variables for parametric and non-parametric tests, respectively. These statistical tests determined an association between the tested variable (*i.e.* types of firearm, sampling sites, sampling methods, and efficiency of extraction techniques) and the number of GSR particle detected. Two-way ANOVA compared the mean differences between groups of two independent variables (*i.e.* types of firearm and number of swabbing procedure) to establish if there are an interaction between the two variables on the number of GSR detected from the SEM-EDX analysis. In this study, a p-value of <0.05 was considered as statistically significant.

Results and Discussion

Physical examination

Using microscope, foreign particles were observed on the surface of cotton swab stick, appearing as irregular shape of varying sizes (Figure 1a). Smaller particles appeared in dust form were also shown (Figure 1b). Besides being black in colours, they were also brown coloured particles on the surface (Figure 1c). On the contrary, negative control samples showed no evidence of such particles, suggesting that these particles could be deposited upon the combustion of ammunition after a firing activity [2]. The observations were similar to those observed on gloves in a previous study [14]. Note that these particles were only observed on cotton swab stick with white background. On carbon adhesive tape attached on stubs, such particles were not readily visible due to poor background contrast. Besides particles originating from the combustion process, foreign materials such as fibre were also observed on the surface of carbon tape and cotton swab stick, shown in Figure 1d and Figure 1e.

SEM-EDX analysis

The presence of GSR was confirmed through the detection of particles by SEM-EDX on the examined surfaces, specifically stubs in this study. Negative control samples gave negative result with no detection of GSR particle. In other word, samples taken from the shooter prior to contact with firearm did not contain particle to be identified as GSR. Under view using SEM, GSR appeared as spheroidal or irregular shaped particles, as illustrated in Figure 2.

Overall, the sizes of GSR particles detected, focusing on stub samples, were ranged from 1.8 to 53 μm. Spheroidal particles were also found to be smaller in size as compared to those irregular ones, as stated by ASTM that the former particles usually found with a diameter between 0.5 and 5.0 μm while the latter could be varied from 1 μm up to more than 100 μm [6]. Therefore, the size of a GSR particle was not definite, especially after the combustion of the primer and smokeless powders

contained in ammunition. In term of the percentage of spheroidal and irregular particles detected on stubs, the latter was reported with high percentage as tabulated in Table 1, regardless of the types of ammunition.

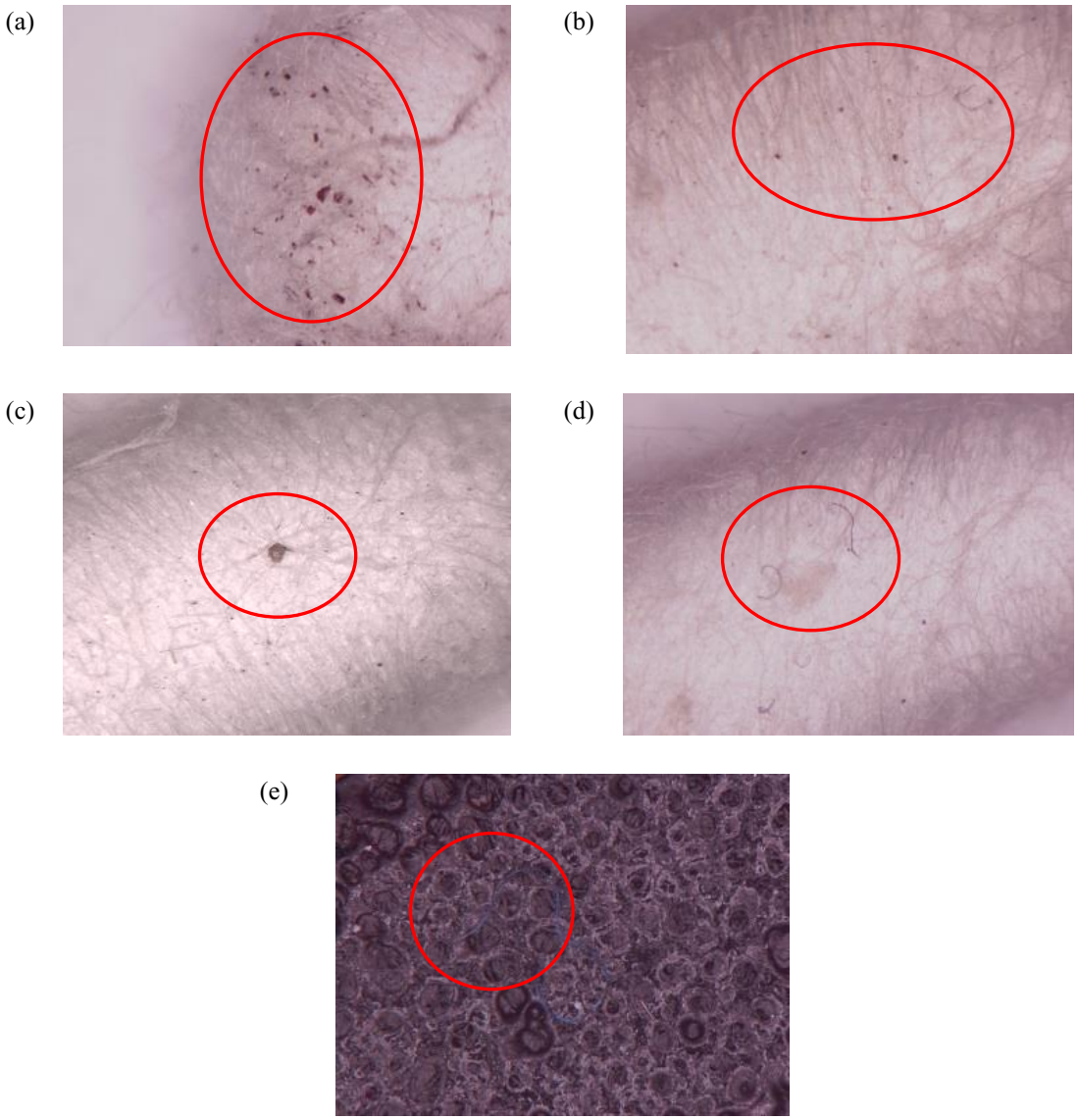
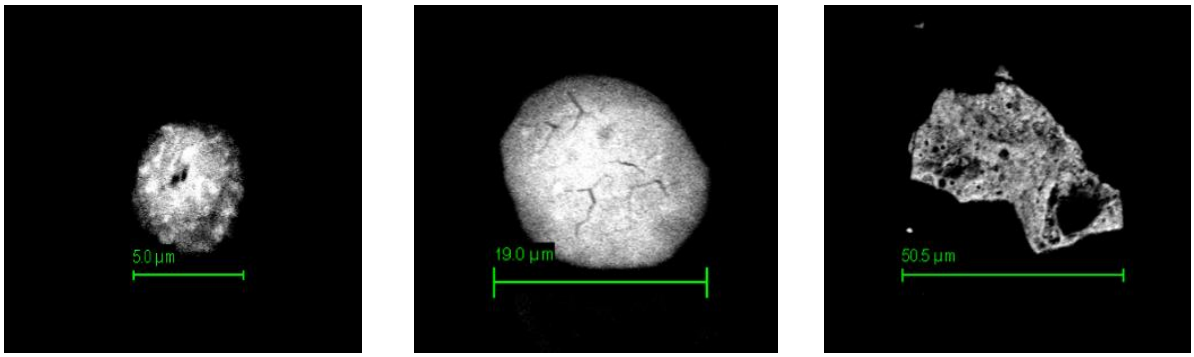


Figure 1. Illustration of (a) irregular-shaped flakes, (b) dust form particles and (c) brown coloured particle, (d)-(e) foreign materials found on the surfaces of cotton swab sticks after sampling from the hands of surface



(a) (b) (c)

Figure 2. Illustration of spherical and irregular shaped GSR particles (100× magnification)

Table 1. The percentage of frequencies for spheroidal and irregular particles on stubs

Ammunition	Shape	Frequency (Percentage)
9 mm	Spheroidal	27 (48.2%)
	Irregular	29 (51.8%)
0.38 SPL	Spheroidal	41 (33.1%)
	Irregular	83 (66.9%)

Previous study found that GSR particles were mostly in spheroidal shape [21]. In this study, irregular shaped particles were slightly greater in their percentages. Since both spheroidal and irregular particles could indicate the presence of GSR particles, morphological feature alone should never be considered as the only criterion for GSR identification [6]. As such, elemental analysis is used in the forensic investigation for the presence of GSR particles. In this study, only characteristic GSR particles were taken into consideration according to the classification scheme by ASTM [6], as in Table 2. A representative EDX spectrum of a particle recovered from shooter's hand is shown in Figure 3.

During a firing, striking of firing pin of a firearm hits the primer cup, causing the ignition of shock-sensitive chemicals, and subsequently channels a tiny flame through a flash hole into the powder charge, which is the smokeless powder. The ignition of smokeless powder gives off heat and creates gases to develop very high pressure inside the cartridge case to force the projectile out of it and accelerate at high speed towards a target. Due to the firing mechanism, the gunshot residues could consist of burnt, partially burnt or unburned products originated from the smokeless powder, primer, bullet, cartridge case and/or traces from the firearm itself [2, 3]. Table 3 summarised the elements detected from the EDX analysis on the GSR samples collected from the hands of the shooter in this study, as well as their possible sources.

The elements detection from the GSR particles could be derived from the constitution of the bullet, a jacket over the bullet, as well as the ingredients of the primer and smokeless powders. The results suggest that the ammunition used in this study were typical type of primer, containing initiating explosive (*i.e.* lead styphnate), an oxidiser (*i.e.* barium nitrate) and a fuel (*i.e.* antimony sulphide) as the main composition [4, 22-25]. The presence of these materials or so-called "tri-

components unique particles" making up the primer also enabled the definite confirmation of GSR particles whenever Pb, Ba and Sb exist in one single particle analysed by SEM-EDX [6, 25]. This rarely occurring set of trio-elements in other settings is the foundation criterion for the identification of GSR particle when the molten metals in the expanding plume rapidly cooled upon firing.

In addition to above trio-elements, the primer composition among ammunition manufacturers could be varied as a result of product formulation of other compounds to achieve the desired ballistic performance [26]. Aluminium in the powder form and silicon as powdered glass, were also commonly found in primer mixture, acting as a friction material in ammunition [13, 22]. The presence of both sulphur and antimony indicate the usage of antimony sulphide as fuel, reacts together with oxidiser through rapid burning upon ignition has contributed to the profiles of both ammunitions [24]. Calcium silicide in the primer mixture also aids the passage of incendiary sparks to the smokeless powder to ignite the charge, as indicated by calcium and silicon seen in the GSR profiles [24, 27].

Table 2. Classification scheme for GSR particles by ASTM

Characteristic GSR particle	• Pb, Sb and Ba
Consistent with GSR particle[a]	• Ba, Ca and Si (with or without trace of S) • Ba and Sb (with no more than a trace of either Fe/S) • Pb and Sb • Ba and Al (with or without trace of S) • Pb and Ba • Pb[b] • Sb[b] • Ba (with or without trace of S)

[a] May contain one or more of the elements: Al, Si, P, S (trace), Cl, K, Ca, Fe (trace), Ni, Cu, Zn, Zr and Sn
[b] Only in the presence of particles with compositions mentioned in characteristic and consistent of GSR

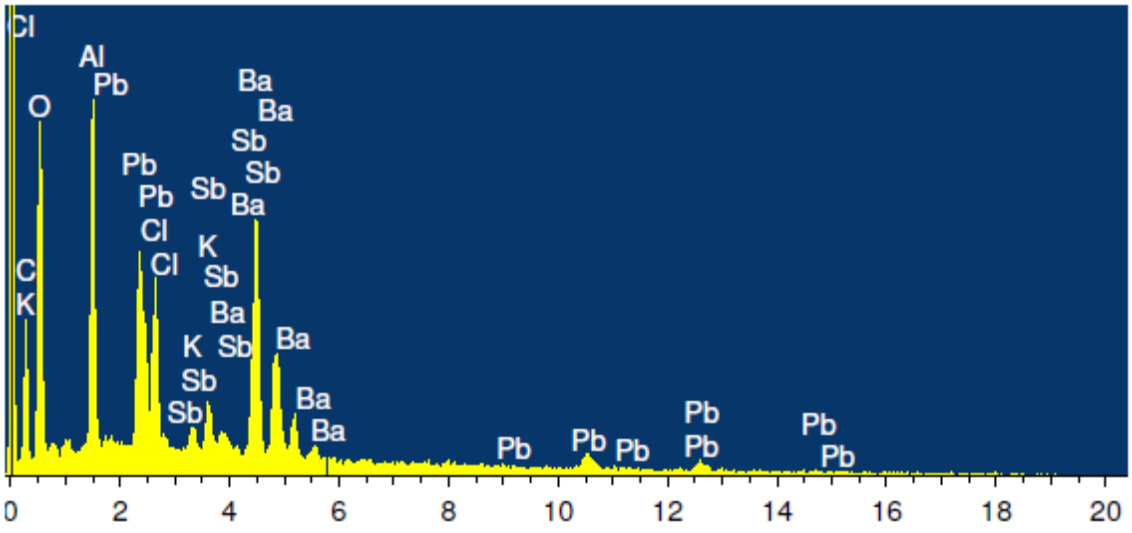


Figure 3. EDX spectrum of a unique GSR particle, showing the detection Pb, Ba and S

Table 3. Elements detected in this study and their respective sources

Element	Ammunition		Possible Sources
	9 mm	.38 SPL	
Aluminium (Al)	+	+	Primer mix
Antimony (Sb)*	+	+	Primer mix/Bullet
Arsenic (As)	+	+	Case
Barium (Ba)*	+	+	Primer mix
Calcium (Ca)	+	+	Primer mix/Propellant powder
Chloride (Cl)	+	+	Propellant powder
Copper (Cu)	+	+	Primer cup/Bullet jacket/Case
Iron (Fe)	-	+	Rust inside barrel/Erosion of internal bore/Case
Molybdenum (Mb)	+	+	Barrel
Lead (Pb)*	+	+	Primer mix/Bullet/Case
Potassium (K)	+	+	Propellant powder
Silicon (Si)	+	+	Primer mix
Sulphur (S)	+	+	Primer mix
Tin (Sn)	+	+	Primer cup/Bullet jacket
Zinc (Zn)	+	+	Primer cup/Bullet jacket/Case

* Elements of characteristic GSR particle; + Detected; - Not detected

Noteworthy to mention that lead could also be contributed by the lead core that made up of the projectile, and usually with a small amount of antimony [4, 13, 22]. Jacketed bullets, where softer lead core is encased by a thin layer of harder metals, provide substantially lead-copper-zinc particles [13, 21, 22]. In addition, a small amount of Sn could also be added to the composition of bullet jacket [13, 22].

Cartridge case is usually made up of brass, a combination of copper and zinc, and may contain traces of lead and iron [22-26]. Copper and zinc are also two main ingredients in manufacturing primer cup with very small amount of other elemental impurities [25]. These two elements could vaporise from the primer cup upon discharging of a projectile down the barrel [24]. In certain instances, a small amount of arsenic was added into the composition of brass in the manufacturing process of cartridge case and primer cup [25]. Tin detected in this study might be originated from the sealing of the primer cup in the bottom of the cartridge case [1].

The presence of iron, only observed in the profile of .38 SPL ammunition, could probably arise due to the erosion of the internal bore of the weapon [22, 24]. Molybdenum alloy steels were reported in barrels of modern firearm and could contribute to the composition of gunshot residue [1, 25]. It was observed that potassium and chlorine were also found in the GSR samples. They were possibly not contributed by the primer mixtures, but from the propellant powders [22, 24, 25]. Besides being an ingredient in primer mixture in the form of calcium silicate, the presence of calcium in the GSR profile could also be contributed by the modern smokeless powders, appearing as calcium carbonate [22, 25]. Literature has reported that titanium and zinc could be seen in lead-free ammunition [28]. However, titanium was not observed in our analysis, and this observation is in-line with the traditional ammunition used in our experiment.

Based on the elemental profiles, Al, Ca, Cl, Cu, Fe, K, Si, S, Sn and Zn were detected alongside with characteristic GSR with Pb, Sb and Ba, in agreement with the definition by ASTM [6]. In general, the elemental compositions of the two GSR produced from two locally manufactured ammunitions by two types of firearms were very similar, with exceptions on iron, probably due to the makeup of the firearm. Though it is not the aim of this study to investigate the elemental profiles of various ammunitions by different firings, it is possible to compare the profiles of the two firing incidents; nonetheless, further collation of analytical information with different combination of ammunition and firearm are necessary for forensic intelligence.

Comparison of GSR particles recovered from firing a pistol and a revolver

When comparing two different firearms, the Mann-Whitney statistical test shows that the median number of characteristic GSR particles detected when firing with a revolver is not equal to those detected when firing with a semi-automatic pistol (p= 0.034) (Table 4). Revolver produced greater number of GSR particles (7.50, IqR 12) as compared to a semi-automatic pistol (2.50, IqR 7).

GSR could be detected from various surfaces in the proximity of shooters, specifically on hands, face and the clothes they worn [2, 29]. Upon firing, the gaseous GSR exits all openings of a firearm [18]. Literature reported that the design of a weapon and its firing mechanism affect the escape of GSR away from that particular firearm [3, 13, 20]. The presence of gap between the revolving drum and barrel allow a substantial amount of GSR to be escaped and subsequently deposited on any surface in close proximity areas, especially hands [13, 20]. The formation of plume could be observed from the gap for revolvers on which intense condensation, particle formation and deposition process take place [3, 20]. On the contrary, a semi-automatic pistol ejects the spent cartridge from one side of the pistol and reloads a new round from within the magazine. The smoke and particles are mainly emitted through the opening of ejection port in a more compact flume, restricting the spread of GSR resulting in the detection of lesser GSR particles upon firing by using semi-automatic pistol [18, 20]. Additionally, larger calibre ammunition used in revolver could also give rise to possibility of larger amount of GSR that to be deposited onto the hands of shooter, as opposed to semi-automatic pistol [3, 13].

Comparison of GSR particles recovered from different sampling sites

Upon firing, GSR particles escape from a firearm, move outward and away from a firearm, and finally deposit onto nearby surfaces. Due to the non-normal distributed data by Shapiro-Wilk test (p <0.05), a Kruskal Wallis test was used in our study to determine association between the sampling sites and the detection of GSR particles for pistol, as showed in Table 5. On the other hand, with the normal distributed data (Shapiro-Wilk test with p >0.05) in relation to firing using revolver, one-way ANOVA was used to compare the mean of the four sampling sites on the number of GSR particles detected, and the statistical output was demonstrated in Table 6.

Our experimental results supported the finding by Jalanti et al. [12] and Ditrich [20], in which GSR particles could be detected in both hands if the other hand was used as support during a shooting event. In our study, the shooter was a right handed person. His left hand that was below the grip overlapped the right hand which was positioned above the grip while holding the grip. For GSR samples recovered from pistol, the Kruskal Wallis test showed that there was no statistically significant association between the sampling sites with the detection of GSR on hands (p = 0.545) (Table 5). The medians on the number of GSR particles detected for the four sampling sites were not significantly different. There was also no significant different among the sampling sites where GSR particle were recovered after firing using revolver (p = 0.218) (Table 6). All the sampling sites showed the detection of GSR.

Deposition of GSR was random and varied with each firearm discharge. The GSR particles were found on both the firing hands, and both “back” and “palm” sites [12, 14, 29]. Generally, dorsum of the hand holding the weapon would be exposed to deposition of GSR

particles, thus giving more chances for the detection of GSR particles as compared to the palm surface that used to grab the pistol. GSR found on the "palm" surface could be due to the transfer of previously deposited GSR from the grip of the pistol or revolver, which was termed as "memory effect" [12, 20, 30]. Since there is possibility to find GSR particles on all the four different sites allowable for sampling, it is advisable to collect GSR samples from more sampling sites whenever a suspect is apprehended for forensic examination to maximise the chance for positive identification.

Table 4. Comparison of GSR particles recovered from firing a pistol and a revolver

Variable	Median (IqR)		Z stat[a]	*p*-value
	Pistol	Revolver		
Number of unique GSR particle	2.50 (7)	7.50 (12)	-2.120	0.034

*Mann-Whitney test was used

Table 5. Association between the sampling sites and the detection of GSR particles from firing using pistol.

Sampling Site	Median	$\chi 2$ stat* (df)	*p*-value
Right back	4	2.133 (3)	0.545
Right palm	1		
Left back	1		
Left palm	2		

*Kruskal Wallis test was used

Table 6. Means and standard deviations in the number of GSR particles detected on different sampling sites.

Sampling Site	Mean	SD	F-statistics (df)	*p*-value
Right back	4.67	3.512	1.843 (3, 8)	0.218
Right palm	16.00	8.544		
Left back	13.67	8.083		
Left palm	7.00	6.083		

Comparison of collection efficiency of swabs and stubs from shooter's hands

SEM-EDX analysis utilised automated search for GSR particles at a magnification of 100×. All the stub samples demonstrated positive detection of GSR particles. On the contrary, only one characteristic GSR particle was detected on swabs through SEM-EDX analysis, even though a higher magnification of 200× was used. It showed that stub shall be the preferred collection method to recover GSR particles from the hands of shooter, especially in cases where only one shot was being released by the suspect as seen in our experimental conditions. The adhesive strength of the tape attached on the aluminium stub allows the collection of GSR particles from a large surface area, although the stickiness tends to loss with repeated dabs [4, 16, 31]. Besides, the packaging step where the placements of cotton swab stick into the paper bag could also potentially remove some of the collected particulates from the hand surface of the shooter [16].

Our experimental continued to test the efficiency of GSR particle recovery from swab stick samples. The internal part of spent cartridge was swabbed using

cotton stick and proceeded with extraction procedure as described in swab stick samples from shooter's hand. Both types of spent cartridges were swabbed by circling the inner compartment of cartridge case once, thrice and five times, separately. After the extraction procedure, all the swab samples from the cartridge cases revealed the presence of GSR particles. A two-way ANOVA statistical test (Table 7) shows that there was no significant difference on the number of GSR particles recovered from the spent cartridges of 9 mm and .38 SPL after firing (p = 0.568). Apart from that, the detection of GSR particles on the swabs has also no significant association with the number swabbing carried on a single cartridge case (p = 0.561).

The successful detection of GSR particles from swab stick samples suggested the possibility of recovering the particles from the surface of the swab stick through the extraction procedure. It also proved that the residues for a surface could be transferred onto the cotton bud during swabbing. The failure in recovering GSR particles from the hand surfaces, in our case, could be due to the limited number of GSR particles that successfully deposited onto the sampling surfaces upon firing of only a single shot as demonstrated in our experimental condition. This was also explained by a previous study where three shots were used in the experimental design [21]. Still, approximately half of the total samples were tested negative using an alcohol-moistened swab of much larger collecting surface area as compared to cotton bud used in our experiment. In fact, the deposition of GSR particles onto proximate surfaces was influenced by a number of factors, including retention mechanism or collection issue, the type and condition of the weapons, the number of shots, the direction and force of air currents, and the amount of oil, moisture or perspiration on a skin surface [4, 13, 32].

In general, stubbing technique is preferable to collect GSR particles from the hands of a shooter, providing higher probability to successfully determine a shooting activity. In some scenarios, the use of cotton sticks was also important and could not be ruled out, especially for surfaces which could not be reached by a stub such as nose [1] or bullet hole [17, 33] when sampling of suspected GSR samples become necessary.

Table 7. Adjusted mean and 95% confidence interval of the main effects of ammunition types and number of swabbing on the detection of GSR particles

Factors		**Adjusted Mean (95% CI)**	**F Statistic (df)**	***p*-value**
Ammunition type	9 mm	11.33 (8.41, 14.26)	0.341	0.568
	.38 SPL	9.22 (1.64, 16.80)		
Number of Swabbing	1	8.00 (2.90, 13.10)	0.602	0.561
	2	10.00 (3.33, 16.67)		
	3	12.83 (2.10, 23.56)		

Conclusion

This study shows that the detection of GSR particles from the hands of a shooter is important to offer an investigative clue on shooting related cases. Using stubs, GSR particles were detected with the presence of Pb, Ba and Sb as the criteria for positive determination. The experimental results revealed that the types of firearms and ammunitions show significant association with the number of GSR particles detected from the stub samples, where greater number was seen in revolver with .38 SPL as compared to semi-automatic pistol with 9 mm ammunition. When two-hand shooting was performed, the four sampling sites equally allow for the detection of GSR. In this study, all stub samples demonstrated positive detection of GSR particles, but only one swab sample showed the presence of such particles under the experimental conditions, indicating the limitation of letter in a single shot case scenario.

Further testing on the collection efficiency suggested that neither revolver nor semi-automatic pistol showed significant association with the number of GSR particles detected from respective cartridge cases. Additionally, no statistically significant association was also shown among the three different swabbing procedures from cartridge cases. Since GSR particles could be varied unpredictably between each firing, it is advisable to collect suspected GSR samples from various surfaces of a suspect. Whenever a stub is not available or a place could not be reached by a stub, swabbing procedure should still be carried out to avoid the loss of trace particles at a larger skin surface area. To conclude, this study has successfully detected the presence of GSR particles, which could serve as a supporting evidence to relate a suspect to a shooting case. For future study, the factors such as the influence of the number shots, single-handed shooting as well as the time elapsed between the firing activity and the sampling, which could affect the detection of GSR, should be investigated.

Acknowledgement

Special thanks to the personnel in Royal Malaysia Police for the technical advice and supplying the ammunition samples. The authors also thank to Universiti Sains Malaysia for the financial support *via* the USM Short Term grant (304/PPSK/6315250).

References

1. SWGGSR (2011). Guide for primer gunshot residue analysis by scanning electron microscopy/energy dispersive X-ray spectrometry. Scientific Working Group for Gunshot Residue, Cincinnati.
2. Chang, K. H., Jayaprakash, P. T., Yew, C. H. and Abdullah, A. F. L. (2013). Gunshot residue analysis and its evidential values: A review. *Australian Journal of Forensic Sciences*, 45 (1): 3-23.
3. Blakey, L. S., Sharples, G. P., Chana, K. and Birkett, J. W. (2018). Fate and behavior of gunshot residue-A review. *Journal of Forensic Sciences*, 63(1): 9-19.
4. Dalby, O., Butler, D. and Birkett, J. W. (2010). Analysis of gunshot residue and associated materials – a review. *Journal of Forensic Sciences*, 55(4): 924-943.
5. Costa, R. A., Motta, L. C., Destefani, C. A., Rodrigues, R. R. T., do Espirito Santo, K. S., Aquije, G. M. F. V., Boldrini, R., Athayde, G. P. B., Carneiro, M. T. W. D. and Ramao, W. (2016). Gunshot residue (GSR) analysis of clean range ammunition using SEM/EDX, colorimetric test and ICP-MS: A comparative approach between the analytical techniques. *Microchemical Journal*, 129: 339-347.
6. ASTM (2016). Standard guide for gunshot residue analysis by scanning electron microscopy/energy dispersive X-ray spectrometry E1588-16. American Society for Testing and Materials International, Pennsylvania.
7. Wolten, G. M., Nesbitt, R. S., Calloway, A. R., Loper, G. L. and Jones, P. F. (1979). Particle analysis for the detection of gunshot residue I: Scanning electron microscopy/energy dispersive X-ray characterization of hand deposits from firing. *Journal of Forensic Sciences*, 24(2): 409-422.
8. Wallace, J. S. and McQuillain, J. (1984). Discharge residues from cartridge-operated industrial tools. *Journal of the Forensic Science Society*, 24(5): 495-508.
9. Kilty, J. W. (1975). Activity after shooting and its effects on the retention of primer residue. *Journal of Forensic Sciences*, 20(2): 219-230.
10. Krishnan, S. S. (1977). Detection of gunshot residue on the hands by trace element analysis. *Journal of Forensic Sciences*, 22(2): 304-324.
11. Mastruko, V. (2003). Detection of GSR particles on clothing of suspects. *Forensic Science International*, 136 (Suppl. 1): 153-154.
12. Jalanti, T., Henchoz, P., Gallusser, A. and Bonfanti, M. S. (1999). The persistence of gunshot residue on shooters' hands. *Science & Justice*, 39(1): 48-52.
13. Meng, H-H. and Caddy, B. (1997). Gunshot residue analysis—A review. *Journal of Forensic Sciences*, 42 (4): 553-570.
14. Mohd Rafae, A. A., Mohd Ali, S. F., Abdullah, A. F. L. and Chang, K. H. (2019). Colourimetric based detection of gunshot residue on gloves worn during shooting. *Malaysian Journal of Analytical Sciences*, 23(2): 229-236.

15. Zeichner A. and Eldar B. (2004). A novel method for extraction and analysis of gunpowder residues on double-side adhesive coated stubs. *Journal of Forensic Sciences*, 49(6): 1194-1206.
16. Reid, L., Chana, K., Bond, J. W., Almond, M. J. and Black, S. (2010). Stubs versus swabs? A comparison of gunshot residue collection techniques. *Journal of Forensic Sciences*, 55(3): 753-756.
17. Koons, R., Havekost, D. and Peters, C. (1987). Analysis of gunshot primer residue collection swabs using flameless atomic absorption spectrophotometry: A re-examination of extraction and instrument procedures. *Journal of Forensic Sciences*, 32(4): 846-865.
18. Schwoeble, A. J. and Exline, D. L. (2000). Current methods in forensic gunshot residue analysis. CRC Press, Boca Raton.
19. Brozek-Mucha, Z. (2009). Distribution and properties of gunshot residue originating from a Luger 9 mm ammunition in the vicinity of the shooting gun. *Forensic Science International*, 183(1-3): 33-44.
20. Ditrich, H. (2012). Distribution of gunshot residue – the influence of weapon type. *Forensic Science International*, 220: 85-90.
21. Kara, I., Sarikavak, Y., Lisesivdin, S. B. and Kasap, M. (2016). Evaluation of morphological and chemical differences of gunshot residues in different ammunitions using SEM/EDS technique. *Environmental Forensics*, 17(1): 68-79.
22. Wolten, G. M., Nesbitt, R. S., Calloway, A. R., Loper, G. L. and Jones, P. F. (1977). Final report on particle analysis for gunshot residue detection. The Aerospace Corp, Segundo.
23. Wallace, J. S. (1990) Chemical aspects of firearms ammunition. *AFTE Journal*, 22(4): 364-389.
24. Warlow, T. A. (1996). Firearms, the laws and forensic ballistics. Routledge, United Kingdom.
25. Wallace, J. S. (2008). Chemical analysis of firearm, ammunition, and gunshot residue. CRC Press, Boca Raton.
26. Zeichner, A. (2009). Firearm discharge residue: Analysis of. In: Wiley encyclopedia of forensic science. John Wiley & Sons, Ltd., New York.
27. Meng, H-H. and Lee, H-C. (2007). Elemental analysis of primer mixtures and gunshot residues from handgun cartridges commonly encountered in Taiwan. *Forensic Science Journal*, 6 (1): 39-54.
28. Gunaratnam, L. and Himberg, K. (1994). The identification of gunshot residue particles from lead-free Sintox ammunition. *Journal of Forensic Sciences*, 39(2): 532-536.
29. Zeichner, A. and Levin, N. (1995). Casework experience of GSR detection in Israel, on samples from hands, hair, and clothing using an Autosearch SEM-EDX System. *Journal of Forensic Sciences*, 22(2): 288-322.
30. Rijnders, M. R., Stamouli, A. and Bolck, A. (2010). Comparison of GSR composition occurring at different locations around the firing position. *Journal of Forensic Sciences*, 55(3): 616-623.
31. Wrobel, H. A., Millar, J. J. and Kijek, M. (1998). Comparison of properties of adhesive tapes, tabs and liquids used for the collection of gunshot residue and other trace materials for SEM analysis. *Journal of Forensic Sciences*, 43(1): 178-181.
32. Kara, I. (2017). The influence of different skin types on GSR sampling by tape lifting for SEM analysis. *Microscopy Research and Technique*, 80(12): 1-5.
33. Merli, D., Amadasi, A., Mazzarelli, D., Cappella, A., Castoldi, E., Ripa, S., Cucca, L., Cattaneo, C. and Profumo, A. (2019). Comparison of different swabs for sampling inorganic gunshot residue from gunshot wounds: applicability and reliability for the determination of firing distance. *Journal of Forensic Sciences*, 64(2): 558-564.

Malaysian Journal of Analytical Sciences (MJAS)
Published by Malaysian Analytical Sciences Society

ANALYSES ON TOXICITY OF Pb^{2+} TOWARDS CHLOROPHYLL A, TOTAL SOLUBLE PROTEIN AND CASPASE-3-LIKE ENZYME ACTIVITY OF *Scenedesmus regularis*

(Analisa Kesan Ketoksikan Pb^{2+} Terhadap Klorofil A, Jumlah Protein Terlarut dan Aktiviti Enzim Bak Kaspase-3 *Scenedesmus regularis*)

Hazlina Ahamad Zakeri[1, 3], Nakisah Mat Amin[1], Nur Hidayah Kamilia Rassman[1], Wan Bayani Wan Omar[1, 2]*

[1]*Faculty of Science and Marine Environment,*
[2]*Institute of Marine Biotechnology,*
[3]*Biological Security and Sustainability (BioSeS) Research Group,*
Faculty of Science and Marine Environment,
Universiti Malaysia Terengganu, 21030 Kuala Nerus, Terengganu, Malaysia

**Corresponding author: bayani@umt.edu.my*

Received: 24 December 2019; Accepted: 28 July 2020; Published: 12 October 2020

Abstract

Heavy metal pollutions, including lead (Pb), has become an increasing concern to humans due to their adverse effects and the fact that they are not easily degraded or destroyed. Microalgae are aquatic organisms that can be used in metal bioremediation since they can accumulate and detoxify metals. This study reported on the responses of a freshwater microalga, which was *Scenedesmus regularis*, when exposed to the inhibitory concentrations (IC) of Pb^{2+} at 25%, 50% and 75%. The tolerance level of *S. regularis* against Pb^{2+} at IC_{25}, IC_{50} and IC_{75} was determined to be 3.5 mg/L, 7.2 mg/L and 10.9 mg/L, respectively. Then, the microalga was treated with these inhibitory concentrations. The concentration of Chlorophyll A (Chl A) and total soluble protein (TSP), as well as caspase-3-like enzyme activity of the alga were analysed. It was observed that Chl A concentration of the alga significantly decreased as more cells were inhibited by Pb^{2+}. The highest concentration of Pb^{2+} significantly reduced the TSP concentration of the alga. However, no changes were observed amongst the concentrations of Pb^{2+}, which inhibited 25% and 50% of the alga population. Activity of caspase-3-like enzyme was significantly induced by more than 3-fold of control in IC_{25} of Pb^{2+}, while the activity of this enzyme was observed to be supressed in both the IC_{50} and IC_{75}. In conclusion, the alga has the potential to be a good indicator for Pb^{2+} toxicity and the Chl A concentration and caspase-3-like enzyme activity can be applied as biomarkers.

Keywords: lead(II) ion, metal toxicity, microalgae, biochemical analyses, inhibitory concentration

Abstrak

Pencemaran logam berat termasuk plumbum menjadi semakin menarik perhatian manusia akibat kesan buruknya dan hakikat bahawa ia tidak mudah diurai atau dimusnah. Mikroalga ialah organisma akuatik yang boleh digunakan dalam bioremediasi logam kerana ia boleh mengumpul dan menyahtoksik logam. Kajian ini melaporkan tentang tindak balas mikroalga air tawar, iaitu *Scenedesmus regularis* apabila didedahkan kepada ujian toksik Pb^{2+} pada kepekatan rencatan (IC) 25%, 50% dan 75%. Tahap toleransi *S. regularis* terhadap Pb^{2+} pada IC_{25}, IC_{50} dan IC_{75} ialah masing-masing pada 3.5 mg/L, 7.2 mg/L dan 10.9 mg/L. Kemudian mikroalga dirawat dengan kepekatan ini dan kepekatan Klorofil A. Jumlah protein terlarut (TSP) serta aktiviti enzim

bak kaspase-3 dianalisis. Didapati bahawa kepekatan Klorofil A alga berkurangan apabila sel-sel lebih banyak direncat oleh Pb^{2+}. Kepekatan tertinggi Pb^{2+} mengurangkan kepekatan TSP alga dengan ketara. Namun, tiada perubahan diperhatikan antara kepekatan Pb^{2+} yang merencat 25% dan 50% populasi alga. Aktiviti enzim bak kaspase-3 telah meningkat lebih daripada tiga kali ganda dalam IC_{25} Pb^{2+} berbanding kawalan, manakala aktiviti enzim ini berkurangan pada IC_{50} dan IC_{75}. Kesimpulannya, alga mempunyai potensi untuk menjadi petunjuk yang baik untuk ketoksikan Pb^{2+} manakala kepekatan Klorofil A dan aktiviti enzim bak kaspase-3 boleh digunakan sebagai biopenanda.

Kata kunci: ion plumbum(II), ketoksikan logam, mikroalga, analisa biokimia, kepekatan rencatan

Introduction

Heavy metals, such as copper (Cu), zinc (Zn), cadmium (Cd), chromium (Cr), mercury (Hg) and lead (Pb), are major environmental pollutants particularly in industrial areas. When discharged into the aquatic ecosystem, they will pose threats to organisms that live in the ecosystem. This will become a serious concern since the metals can accumulate in organisms and eventually reach the primary consumers, which are humans. The metals are toxic to all organisms since they can exert adverse effects. They are not easily degraded nor destroyed. However, they can be removed from polluted areas through phytoremediation which include the application of microalgae [1].

Microalgae are ubiquitous organisms that can be found anywhere, whether in the terrestrial or aquatic ecosystems. Due to their photoautotrophic nature, microalgae are able to uptake metals into their cells and detoxify them. Therefore, they can be used as bioremediation tools to clean up metal contaminants. However, since some metals are non-essential and are not useful to them, these metals can exert toxicity effects to the algae. In fact Pb^{2+}, as one the non-essential and most toxic metals, was proven to affect amongst others, the cell growth [2, 3], photosynthetic rate [4, 5], pigment contents [6] and cell morphology [7] in algae. The non-redox active metal Pb^{2+} can also induce the generation of reactive oxygen species (ROS) which can lead to damages to important biomolecules such as proteins [8]. In addition, the metals may trigger some sort of intercellular defense mechanisms which can help the algae to protect themselves from the toxicity effect for survival [2, 3, 9].

This includes the trigger of cellular signalling pathways that can either be death or survival signals, leading to the programmed cell death (PCD) modes which are 'self-suicidal' apoptosis, 'self-eating' autophagy and necrosis [10]. Studies by many researchers have found several species of microalgae, for example, *Micrasterias denticulata* [11], *Dunaliella tertiolecta* [12] and *Karenia brevis* [13], which can undergo PCD coordinated by caspases, a family of cysteine proteases. According to Segovia and Berges [12], there is a link between cell death and ROS which involve caspase-like enzymes, as observed in the microalga, *Dunaliela tertiolecta*. All the above-mentioned responses may be used as biomarkers for Pb^{2+} contamination.

In this study, *Scenedesmus regularis* which is a freshwater microalga was treated with Pb^{2+} to determine the inhibitory concentration (IC) at 25%, 50% and 75% of the algae cell populations. *Scenedesmus* algae are known to have high biomass productivity and strong tolerability amongst green algae. Therefore, this genus of algae is a suitable material for toxicity test. The findings from this study can be cross-referenced against other experiments, whereby different species of *Scenedesmus* have been used as test algae. This study aims to assess the responses of the algae towards these three concentrations of Pb^{2+} in terms of its Chlorophyll A and total soluble protein (TSP) concentrations as well as the activity of caspase-3-like enzyme. From these observations, it can be concluded if the alga was suitable to be used as a bioindication tool for Pb^{2+} contamination in an aquatic ecosystem or not.

Materials and Methods

Culture of microalga sample

The algae stock culture of *Scenedesmus regularis* was provided by the Institute of Marine Biotechnology, Universiti Malaysia Terengganu. The algae were cultured in f/2 medium in filtered seawater at 5 ppt. The

algae were aerated at 25 °C and under the light intensity of 17 µmol photon m^{-2} s^{-1} until it reached the middle of the exponential growth phase, whereby they were harvested by centrifugation for treatment.

Inhibitory concentrations and treatments of Pb^{2+} on *S. regularis*

Tolerance assay was done to determine the inhibitory concentration (IC) based on number of cells response for *S.regularis* against Pb^{2+} in the form of lead(II) nitrate, $Pb(NO_3)_2$ toxification. A 24-well plate was filled with f/2 medium at initial cell density of 10^6 and six different $Pb(NO_3)_2$ concentrations (i.e. ranging from 0 mg/L to 30 mg/L). Treatment was done for 24 hours under light intensity of 17 µmol photon m^{-2} s^{-1} and 25°C, and the number of live cells were counted at 0, 12 and 24 hours by using a haemocytometer. To differentiate between live and dead cells, trypan blue was used to stain the dead cells. The concentrations of Pb^{2+} which inhibited 25% (IC_{25}), 50% (IC_{50}) and 75% (IC_{75}) of *S. regularis* cells were then calculated based on probit analysis [14].

S. regularis was then treated with the $IC_{25,}$ $IC_{50,}$ and IC_{75} of Pb^{2+}, as determined above. Treatments were done for 24h at an initial cell density of 10^6 in similar conditions as the tolerance assay. The number of cells was counted at the end of treatment by using a haemocytometer (Merck, BLAUBRAND® Neubauer). The treated algae aliquots were pelleted in falcon tubes via centrifugation at 15000 xg and 4°C for 15 min. The pellets were then stored at -80 °C before further analyses.

Parameters analysed

After treatments, the algae Chlorophyll A (Chl A) concentration, total soluble protein (TSP) concentrations and activity of caspase-3-like enzyme were studied. The Chl A was extracted following a method by Ritchie [15] with some modifications. The pellet obtained earlier was suspended in acetone and homogenised for 10 s. The mixture was then left overnight in the dark at -20 °C. Prior to the absorbance reading, the extract was centrifuged at 15000 xg and 4 °C for 10 minutes. Absorbance was then read at 630 nm, 647 nm, 664 nm, and 691 nm by using a UV-Vis spectrophotometer (Shimadzu, UV-1800)) and the content of Chl A was calculated by using this formula (Equation 1) [15]:

$$\text{Chl A content (mg/mL)} = [(-0.3319*A_{630nm}) - (1.7485*A_{647nm}) + (11.9442*A_{664nm}) - (1.4306*A_{691nm})] \quad (1)$$

Extraction of proteins was done according to a method described by Faurobert et al. [16] with some modifications. The pellet obtained earlier was ground with liquid nitrogen into fine powder. The powder was added to a cold extraction buffer (i.e. stored at 4 °C), which contained 500 mM Tris-HCl, 50 mM EDTA, 700 mM sucrose, 100 mM KCl, 2% β-mercaptoethanol, 1 mM phenylmethylsulfonyl fluoride and 0.001 mg/mL protease inhibitor cocktail at pH 8.5. The extract was then vortexed and incubated on ice for 10 minutes. Next, an equal volume of Tris-saturated phenol was added. Samples were vortexed for 10 minutes at room temperature and then centrifuged at 13000 xg and 4 °C for 20 minutes. The phenolic phase was recovered and reextracted with the same volume of extraction buffer. Subsequently, centrifugation was repeated and acetone was added to the recovered phenolic phase. Proteins were allowed to precipitate overnight. After centrifugating for 20 minutes at 13000 xg and 4 °C, the pellet was washed three times with the precipitation solution and once with acetone. Each washing step was followed by 5 minutes of centrifugation, as described above. After being dried under vacuum, the pellet was resuspended in lysis buffer which contained 7 M urea, 2 M thiourea, 2% CHAPS, 2% Triton X, 1% DTT and 0.001 mg/ml of protease inhibitor cocktail at pH 8.0. Total soluble protein (TSP) content of the extract was then determined by using the method reported by Bradford [17].

To quantify the caspase-3-like activity, Enzchek® Caspase-3 Assay Kit #2 (Invitrogen, USA) was used

following the method by Bouchard and Yamasaki [18]. The protein extract obtained above was mixed with 2x reaction buffer (Caspase 3 Assay Kit #2, Invitrogen) and Z-DEVD-R110 substrate. Sample was then incubated in the dark at room temperature for 4 hours. The fluorescence was detected by using Varioskan™ Flash Multimode Reader (Thermo Scientific). The excitation and detection wavelength used were 496 nm and 520 nm, respectively. Rhodamine 110 (R110) was used to generate a standard curve in the range of 0.002 μM to 0.01 μM to quantify the caspase activity.

Mean values and standard errors were determined from three replicates of each treatment. The statistically significant differences between treatments were analyzed by using a one-way ANOVA followed by Tukey HSD post-hoc test at probability level of 0.05. The statistical software used was Daniel's XL Toolbox v. 6.60 Add-in for Microsoft Excel.

Results and Discussion

From Figure 1, it was determined that the concentrations of Pb^{2+} needed to inhibit 25%, 50% and 75% of *S. regularis* populations were 3.5 mg/L, 7.2 mg/L and 10.9 mg/L, respectively. Inhibitory concentration (IC) value is often used to determine the effectiveness of any substance in inhibiting a specific biological or biochemical function. It also can also indicate how well the organism can tolerate any foreign substances that they encounter in their cells. In this study, presence of Pb^{2+} in the form of $Pb(NO_3)_2$ interfered with the survivality of *S. regularis* and low level of Pb^{2+} indeed can become toxic to this alga as 10.9 mg/L was needed to reduce the population of the alga by 75%. This was expected as Pb^{2+} is known to inhibit the growth of many organisms, including three green unicellular algae, namely *Cladophora* [2], *Acutodesmus obliquus* [3] and *Chlorella sorokiniana* [7].

Presence of Pb^{2+} did not only affect the growth of *S. regularis*, but also significantly reduced the algae Chl A concentration when the concentration of Pb^{2+} increased the reduction was found to be the highest in IC_{75} by about 70% (Figure 2a). Chl A is the primary pigment found mainly in Photosystem I and Photosystems II of the photosynthetic machinery. Therefore, the reduction in Chl A concentration of *S. regularis* after Pb^{2+} exposure can suggests that there are detrimental effects on the core complexes of the photosystems. This will lead to the inhibition of photosynthetic processes and eventually affects the growth and development of the alga. Pb^{2+} can also affect the synthesis and degradation of chlorophylls through various mechanisms. For example, Pb^{2+} affects the synthesis of chlorophylls by inhibiting the activity of essential enzymes involved in the pathway [19] or through the substitution of the central Mg ion [20]. In addition, metals affect chlorophylls degradation via the synthesis of reactive oxygen species (ROS) [21] or by enhancing activity of the enzyme chlorophyllase which triggers the breakdown of chlorophylls [22]. Furthermore, the colour of the algae culture was observed to change from bright green in the control to colourless in IC_{75} Pb^{2+}. This phenomenon is normal to metal-stressed photosynthetic organisms, whereby metals can cause chlorosis in them [23].

Total soluble protein (TSP) content of *S. regularis* was also observed to be significantly reduced in Pb^{2+} (Figure 2b). However, the impact was in smaller scale as compared to Chl A. While IC_{75} Pb^{2+} decreased the TSP content to 85%, there was a 10-11% reduction in IC_{25} and IC_{50} with no significant changes observed among these two concentrations. The reduction in TSP observed in the alga may be explained by several factors. Firstly, exposure to heavy metals stress, including that of non redox active metal Pb^{2+}, can induce the generation of cellular ROS [8]. According to Villiers et al. [24], excess ROS level alters the protein structure by inducing oxidation of both protein backbone and amino acid side chain residues. Secondly, Pb^{2+} has the ability to react with the N and S elements in amino acids [5] and can render the proteins dysfunction. Thirdly, Pb can also inhibit the activity of proteins at cellular level by reacting with their sulfhydryl groups [23]. Lastly, to ensure cell growth during the metal-stress, the alga used the proteins as emergency sources of N and S and to supply carbon skeletons which resulted from the low photosynthetic rate [27].

In this study, activity of caspase-3-like enzyme was observed to be highly induced in alga treated with IC_{25}

of Pb^{2+} (Figure 2c). The activity significantly rose to more than 3-fold of that from the control, which indicated that apoptosis was triggered by Pb^{2+} in the alga since caspase-3 enzyme played a central role in mediating the progress of apoptosis [25]. In fact, Pb was proven to trigger the activation of caspase-3, which led to the induction of apoptosis in a study by Wan Bayani et al. [26] in *Chlorella vulgaris* and Yedjou et al. [27] on human leukemia cells. However, the activity of this enzyme suddenly slowed down to below that of the control in algae treated with IC_{50} and IC_{75} of Pb^{2+} (Figure 2c). Caspases can inhibit the non-apoptotic signaling events such as autophagy by cleaving and destroying pro-autophagic activity of pro-autophagy related proteins [28]. Both apoptosis and autophagy are two important catabolic processes which contribute to the maintenance of cellular and tissue homeostasis and they are highly interconnected [28]. When one is activated, the other will be inhibited. Several studies have also indicated that autophagy itself may be a mechanism of caspase- independent and apoptosis-independent cell death [29, 30].

Furthermore, Sui et al. [9] stated that cells protect themselves from Pb toxicity by promoting cellular autophagy. Autophagy can prevent cells from undergoing apoptosis,and thus ensure their survivality [31]. Therefore, from this study it can be suggested that at IC_{25} Pb^{2+} level, the algae cells triggered the cell death through apoptosis by inducing the production of caspase-3-like enzyme but at the IC_{50} and IC_{75} levels, the algae protected the remaining cells from death by inducing autophagy. Following either apoptosis or autophagy, necrosis may occur as the secondary events of cell death [32]. However, further analyses are needed to prove this theory.

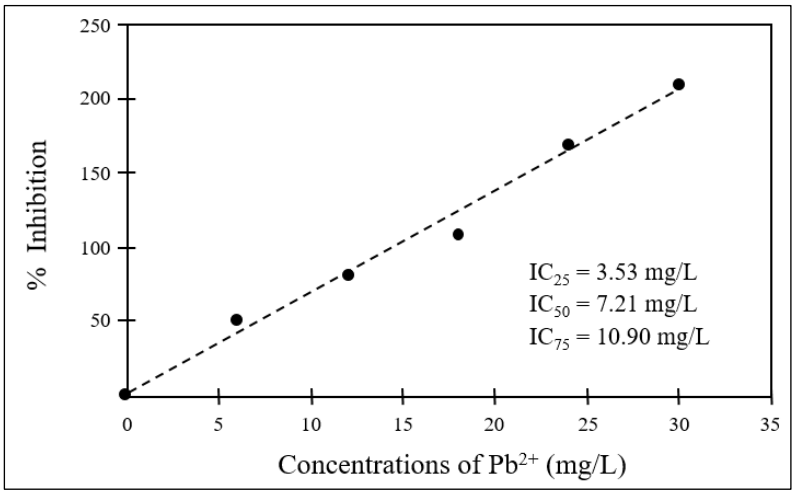


Figure 1. Percentage of *S. regularis* cells inhibited by Pb^{2+} to determine the inhibitory concentration

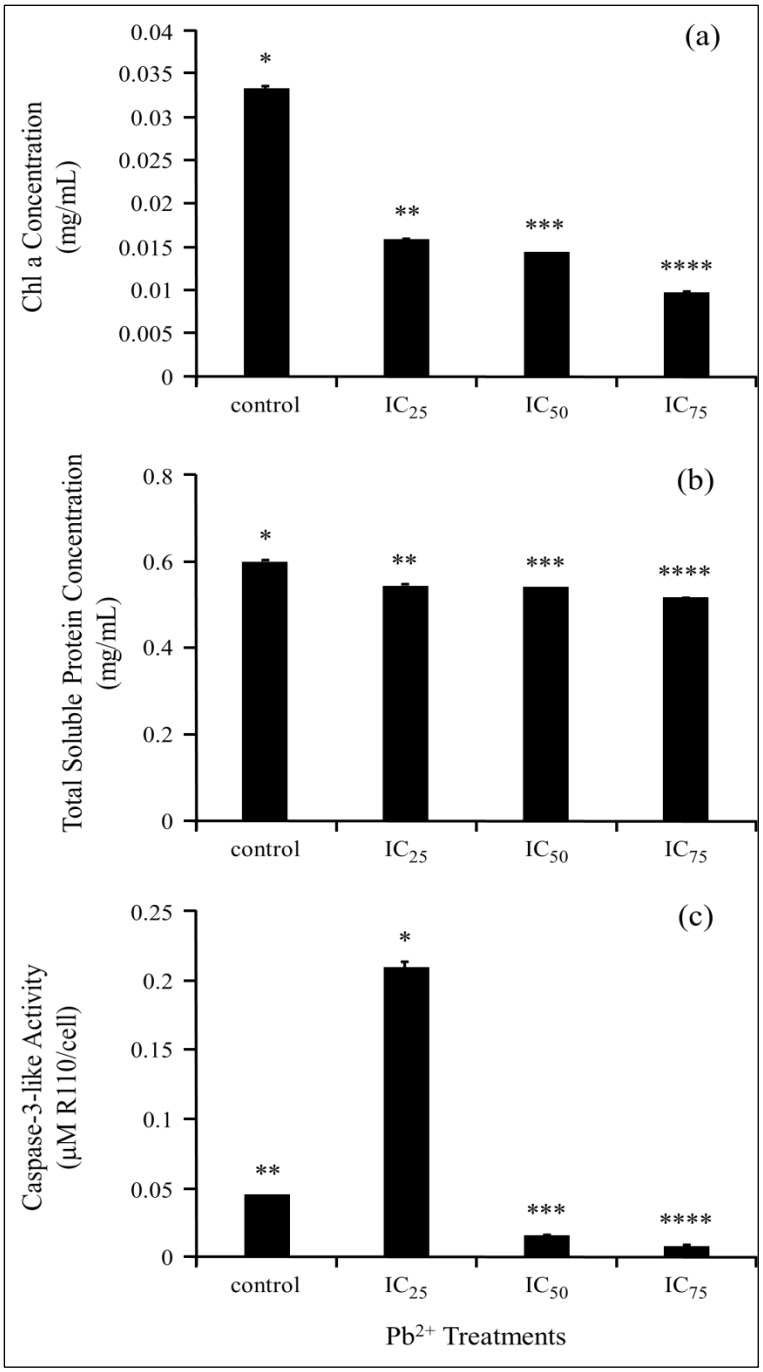


Figure 2. (a) Chlorophyll a concentration, (b) total soluble protein concentration and, (c)caspase-3-like activityof *S. regularis* after 24 h in IC_{25}, IC_{50} and IC_{75} of Pb^{2+} as compared to the control. Asterisks above barsindicate statistically significant differences at $p < 0.05$

Conclusion

Pb^{2+} exerts toxic effects on *Scenedesmus regularis* by reducing the algae Chlorophyll A (Chl A) and TSP content. At low level of Pb^{2+}, the algae induced apoptosis, whereas at high level of Pb^{2+}, the algae induced autophagy as mode of cell death. This is shown by the high activity of caspase-3-like enzyme observed at low Pb^{2+}, but a reduction below the control was seen in cells at high Pb^{2+}. In general, changes observed in this alga, as shown by its Chl A content and caspase-3-like enzyme activity, can be used as biomarkers for Pb^{2+} toxicity. However, further analyses should be done in other areas of toxicity to fully explore the potential of *S. regularis* as heavy metals bioremediation and bioindication tools.

Acknowledgement

The authors acknowledged the Malaysian Ministry of Higher Education for funding the research under the Fundamental Research Grant Scheme, and managed by the Research Management Centre, University Malaysia Terengganu (vot. no. 59311).

References

1. Kumar, K. S., Dahms, H-U., Won, E. J., Lee, J. S. and Shin, K-H. (2015). Microalgae - a promising tool for heavy metal remediation. *Ecotoxicology and Environmental Safety,* 113: 329-352.
2. Cao, D.J., Shi, X.D., Li, H., Xie, P.P., Zhang, H.M., Deng, J.W. and Liang, Y.G. (2015). Effects of lead on tolerance, bioaccumulation, and antioxidative defense system of green algae, *Cladophora*. *Ecotoxicology and Environmental Safety,* 112: 231-237.
3. Piotrowska-Niczyporuk, A., Bajguz, A., Talarek, M., Bralska, M. and Zambrzycka, E. (2015). The effect of lead on the growth, content of primary metabolites, and antioxidant response of green alga *Acutodesmus obliquus* (Chlorophyceae). *Environmental Science and Pollution Research,* 22: 19112-19123.
4. Luqman, A. B. and Hazlina, A. Z. (2015). Accumulation of Cu(II) and Pb(II) in three rhodophytes of the genus *Gracilaria* and the impact of the metals on the algae physiology. *Bioscience and Bioengineering,* 1: 106-111.
5. Dao, L. H. and Beardall, J. (2016). Effects of lead on growth, photosynthetic characteristics and production of reactive oxygen species of two freshwater green algae. *Chemosphere,* 147: 420-429.
6. Saleh, B. (2016). Lead (Pb) heavy metal impacts in the green *Ulva lactuca* (Chlorophyceae) marine algae. *Journal of Stress Physiology and Biochemistry,* 12: 62-71.
7. Carfagna, S., Giovanna, N. L., Adriana, S., Sorbo, B. S. and Vona, V. (2013). Physiological and morphological responses of lead or cadmium exposed *Chlorella sorokiniana* 211-8K (Chlorophyceae). *SpingerPlus,* 2: 147-152.
8. Szivák, I., Behra, R. and Sigg, L. (2009). Metal-induced reactive oxygen species production in C*hlamydomonas reinhardtii* (Chlorophyceae). *Journal of Phycology,* 45: 427-435.
9. Sui, L., Zhang, R-H., Zhang, P., Yun, K-L., Zhang, H-C., Liu, L. and Hu, M-X. (2015). Lead toxicity induces autophagy to protect against cell death through mTORC1 pathway in cardiofibroblasts. *Bioscience Reports,* 35: 1-9.
10. Chatterjee, S., Sarkar, S. and Bhattacharya, S. (2014). Toxic metals and autophagy. *Chemical Research in Toxicology,* 27: 1887-1900.
11. Darehshouri, A., Affenzeller, M. and Lütz-Meindl, U. (2008). Cell death in unicellular green alga *Micrasterias* upon H_2O_2 induction. *Plant Biology,* 10: 732-745.
12. Segovia, M. and Berges, J. A. (2009). Inhibition of caspase-like activities prevents the appearance of reactive oxygen species and dark-induced apoptosis in the unicellular chlorophyte *Dunaliella tertiolecta*. *Journal of Phycology,* 45: 1-11.
13. Johnson, J. G., Janech, M. G. and Van Dolah, F. M. (2014). Caspase-like activity during aging and cell death in the toxic dinoflagellate *Karenia brevis. Harmful Algae,* 31: 41-53.
14. Hii, Y. S., Shia, K. L., Chuah, T. S. and Hing, L. S. (2009). Physiological responses of *Chaetoceros* sp. and *Nannochloropsis* sp. to short-term 2,4-D, Dimethylamine and Endosulfan exposure. *Aquatic Ecosystem & Health Management,* 12: 375-389.

15. Ritchie, R. J. (2008). Universal chlorophyll equations for estimating chlorophylls a, b, c, and d and total chlorophylls in natural assemblages of photosynthetic organisms using acetone, methanol, or ethanol solvents. *Photosynthetica,* 46: 115-126.
16. Faurobert, M., Mihr, C., Bertin, N., Pawlowski, T., Negroni, L., Sommerer, N. and Causse, M. (2007). Major proteome variations associated with cherry tomato pericarp development and ripening. *Plant Physiology,* 143: 1327-1346.
17. Bradford, M. M. (1976). A rapid and sensitive method for the quantitation of microgram quantities of protein utilizing the principle of protein-dye binding. *Analytical Biochemistry,* 72: 248-254.
18. Bouchard, J. N. and Yamasaki, H. (2009). Implication of nitric oxide in the heat-stress-induced cell death of the symbiotic alga *Symbiodinium microadriaticum. Marine Biology,* 156: 2209-2220.
19. Cenkci, S., Cigerci, I. H., YildIz, M., Ozay, C., Bozdag, A. and Terzi, H. (2010). Lead contamination reduces chlorophyll biosynthesis and genomic template stability in *Brassica rapa* L. *Environmental and Experimental Botany,* 67: 467-473.
20. Pourraut, B., Shahid, M., Dumat, C., Winterton, P. and Pinelli, E. (2011). Lead uptake, toxicity and detoxification in plants. *Reviews of Environmental Contamination and Toxicology,* 213: 113-136.
21. Shakya, K., Chettri, M. K. and Sawidis, T. (2008). Impact of heavy metals (copper, zinc and lead) on the chlorophyll content of some mosses. *Environmental Contamination and Toxicology,* 54: 412-421.
22. Drazkiewicz, M. (1994). Chlorophyllase: occurrence, functions, mechanism of action, effects of external and internal factors. *Photosynthetica,* 30: 321-331.
23. Gill, M. (2014). Heavy metal stress in plants: A review. *International Journal of Advanced Research,* 2: 1043-1055.
24. Villiers, F., Ducruix, C., Hugouvieux, V., Jarno, N., Ezan, E. and Garin, J. (2011). Investigating the plant response to cadmium exposure by proteomic and metabolomic approaches. *Proteomics,* 11: 1650-1663.
25. Cryns, V. and Yuan, J. (1998). Proteases to die for. *Genes & Development,* 12: 1551-1570.
26. Wan Bayani, W. O., Hazlina, A. Z., Nakisah, M. A. and Nur Hidayah, K. R. (2017). Responses of a freshwater microalga, *Scenedesmus regularis* exposed to 50% inhibition concentration of Pb^{2+} and $Hg^{2+.}$ *Malaysian Applied Biology*, 46(4):213-220.
27. Yedjou, C. G., Milner, J. N., Howard, C. B. and Tchounwou, P. B. (2010). Basic apoptotic mechanisms of lead toxicity in human leukemia (HL-60) cells. International Journal of Environmental Research and Public Health, 7: 2008-2017.
28. Wu, H., Che, X., Zheng, Q., Wu, A., Pan, K., Shao, A., Wu, Q., Zhang, J. and Hong, Y. (2014). Caspases: a molecular switch node in the crosstalk between autophagy and apoptosis. *International Journal of Biological Sciences,* 10: 1072-1083.
29. Yu, L., Wan, F., Dutta, S., Welsh, S., Liu, Z. H., Freundt, E., Baehrecke, E. H. and Lenardo, M. (2006). Autophagic programmed cell death by selective catalase degradation. *Proceedings of the National Academy of Sciences of the United States of America,* 103: 4952-4957.
30. Kroemer, G. and Levine, B. (2008). Autophagic cell death: the story of a misnomer. *Nature Reviews Molecular Cell Biology,* 9: 1004-1010.
31. Thorburn, A. (2008). Apoptosis and autophagy: regulatory connections between two supposedly different processes. *Apoptosis,* 13: 1-9.
32. Majno, G.and Joris, I. (1995). Apotosis, oncosis and necrosis: an overview of cell death. *American Journal of Pathology,* 146: 3-15.

Malaysian Journal of Analytical Sciences (MJAS)
Published by Malaysian Analytical Sciences Society

STORAGE STABILITY OF KUINI POWDER IN TWO PACKAGING ALUMINUM LAMINATED POLYETHYLENE AND POLYETHYLENE TEREPHTHALATE

(Kestabilan Penyimpanan Serbuk Kuini dalam Dua Pembungkusan Polietilena Berlapis Aluminum dan Polietilena Tereftalat)

Loo Yian Yian and Pui Liew Phing*

Department of Food Science and Nutrition, Faculty of Applied Sciences
UCSI University, 56000 Cheras, Kuala Lumpur, Malaysia

**Corresponding author: puilp@ucsiuniversity.edu.my*

Received: 15 June 2020; Accepted: 13 August 2020; Published: 12 October 2020

Abstract

Kuini fruit is a type of tropical mango with a strong aroma. It has yellow-orange colored pulp with a green peel. Due to its short life and seasonal harvest, kuini can be converted into powder, which is more stable and versatile to be added later as a food ingredient. The powder needs to be stable during storage prior to consumption or usage. In this study, the storage stability of spray-dried kuini powder is investigated. The kuini powder was placed in two different packaging materials: aluminum laminated polyethylene (ALP) and polyethylene terephthalate (PET). Then, it was stored under accelerated conditions (48±1 °C, 90±1% RH). The physicochemical properties of packaged powder were evaluated each week for a total of 7 weeks and included color, hygroscopicity, moisture content, water activity, degree of caking, flowability, water solubility index, and carotenoid. Our results show that after 7 weeks in storage, kuini packaged in ALP pouches has better properties such as lower moisture content (13.33), water activity (0.43), and hygroscopicity (23.37), when compared to PET packaging (24.77 moisture content, 0.50 water activity, and 28.00 hygroscopicity. These properties have also influenced an increase in caking and presented difficulties in solubilization when packaged in PET. In addition, the stored kuini powder packaged in PET pouches showed a greater color difference (9.40) and lower carotenoid content (16.90 μg/g), when compared to what was stored in ALP, i.e. it was more stable. From its physicochemical properties, it can be concluded that ALP is better than PET in protecting the stored powder from degradation. Hence, when compared to PET, ALP is more suitable as a packaging material for kuini powder.

Keywords: packaging; powder, storage stability, physicochemical properties, kuini

Abstrak

Buah kuini adalah sejenis mangga tropika dengan aroma yang kuat. Ia mempunyai pulpa berwarna kuning-oren dengan kulit hijau. Oleh kerana jangka hayatnya yang pendek dan ianya buah bermusim, kuini boleh diubah menjadi serbuk, yang lebih stabil dan serbaguna untuk ditambahkan sebagai bahan makanan. Serbuk perlu stabil semasa penyimpanan sebelum penggunaan atau penggunaan. Dalam kajian ini, kestabilan penyimpanan serbuk kuini kering semburan disiasat. Serbuk kuini diletakkan dalam dua bahan pembungkusan yang berbeza: polietilena berlapis aluminium (ALP) dan terefthalat polietilena (PET). Kemudian, ia disimpan dalam keadaan dipercepat (48 ± 1 °C, 90 ± 1% RH). Sifat fizikokimia serbuk yang dibungkus dinilai setiap minggu selama 7 minggu dan termasuk warna, higroskopian, kandungan kelembapan, aktiviti air, tahap kek, aliran, indeks kelarutan air,

dan karotenoid. Hasil kajian kami menunjukkan bahawa setelah penyimpanan selama 7 minggu, kuini yang dibungkus dalam bungkusan ALP mempunyai sifat yang lebih baik seperti kandungan lembapan yang lebih rendah (13.33), aktiviti air (0.43), dan higroskopian (23.37), jika dibandingkan dengan pembungkusan PET (kandungan air 24.77, 0.50 aktiviti air, dan 28.00 higroskopian. Sifat-sifat ini juga mempengaruhi peningkatan kek dan menunjukkan kesukaran dalam larutan ketika dibungkus dalam PET. Di samping itu, serbuk kuini yang disimpan dalam bungkusan PET menunjukkan perbezaan warna yang lebih besar (9.40) dan kandungan karotenoid yang lebih rendah (16.90 μg/g), jika dibandingkan dengan apa yang disimpan di ALP, iaitu lebih stabil. Dari sifat fizikokimia, dapat disimpulkan bahawa ALP lebih baik daripada PET dalam melindungi serbuk yang tersimpan dari degradasi. Oleh itu, jika dibandingkan dengan PET, ALP lebih sesuai sebagai bahan pembungkus untuk serbuk kuini.

Kata kunci: pembungkusan, serbuk, kestabilan simpanan, sifat fizikokimia, kuini

Introduction

Kuini fruit is a type of tropical mango with a unique aroma and a green outer part. It is rich in nutrients and it provides about 83 kcal per 100 g of water, with 23 mg per 100 g of vitamin c, and with about 1888 g of carotenes content [1, 2]. Kuini is an excellent source of vitamins c and a [3]. It has been reported to contain the following isoflavones: daidzein and genistein [4]. Low-temperature storage is a common way to extend storage life as well as lowering the respiration rate and production of ethylene, which makes for the fresh consumption of kuini fruit [5]. Kuini is currently an underutilized fruit in Malaysia. The bioactivity of its flesh and peel were investigated to better assess its economic potential [6]. It can also be fermented [7] and added with probiotics as a functional juice drink [8].

Due to its seasonal nature and short shelf life, it can be converted into powder to have a longer shelf life from spray-drying, which is a common method [9]. Spray-drying transforms feed from a liquid into powder form [10, 11]. Spray-drying has been employed in the conversion of many high-sugar rich fruits into various types of fruit powder. Spray-drying with maltodextrin, which acts as carrier to prevent stickiness, which can be seen in production of *terung asam*, Sarawak pineapple, *cempedak,* and papaya fruit powder [12–15]. It was reported that maltodextrin enhances the properties of powders be developing the following characteristics: lower hygroscopicity and better flow ability [16].

Packaging materials for powders are essential, because they protect it during handling and storage. Pua et al. [17] reported that accelerated storage involving high humidity and temperatures such as 90% relative humidity (RH) and 38±1 °C can be used to determine moisture ingress and storage time quicker. Kumar and Mishra [18] conducted a storage study of mango soy fortified yogurt powder in aluminum laminated polyethylene (ALP) and high-density polypropylene (HDPP) pouches. ALP is considered as a laminate and metallized film. The lamination of aluminum films binds aluminum foil together with paper or plastic such as polyethylene or polypropylene to improve its barrier properties [19]. Lamination of aluminum to plastic or paper enables heat sealability, provides an excellent barrier for light, and reduces the permeability of oxygen [20]. The individual components of ALP are recyclable. PET is a type of polyesters formed by the reaction between dimethyl terephthalate and ethylene glycol [19]. PET provides a good barrier against gases, moisture, heat, mineral oils, solvents, and acids [23]. ALP has a water vapor transmission rate (WVTR) of 1.21 10^6 kg/m^2 /day at 38 °C, 90% RH; whereas, the water vapor transmission rate of PET packaging material of 17 μm was approximately 2.0 x 10^{-6} kg/m^2 /day at 38 °C and 90% RH.

This study determines the storage stability of kuini powder using two different packaging materials: ALP and PET, which were used to determine the physicochemical properties under accelerated storage for a total of 7 weeks. The physicochemical properties of stored powder were analyzed and included color, hygroscopicity, moisture content, water activity, degree of caking, water solubility index, and carotenoid content.

Materials and Methods

Materials: Fruit samples

The kuini fruit (*Mangifera Odorata*) was purchased from a local market located in Selayang, Malaysia (Figure 1). The fruit samples were selected based on roundness and each with length of 9-12 cm, diameter of 5-9 cm, no bruising, and a strong odor. The kuini was vacuum-packed and placed in a freezer at -20 °C prior to usage. It was then transferred to a 4 °C refrigerator and thawed at room temperature for 2 hours before the juice was extracted.



Figure 1. Fresh kuini fruit

Preparation of kuini juice

The kuini fruit were peeled and deseeded. The kuini pulp were blended in a high-speed blender (Warring, USA), and then diluted with a water 1:2 to a total soluble solids (TSS) content of 12°Brix. The kuini juices were then filtered using filter cloth.

Spray-drying of kuini juice

Before spray-drying, 20% (w/w) maltodextrin was added into kuini juice (300 g), and the mixture was homogenized using prepared spray-drier feed (Ika, Germany). A mini spray-dryer (B-290, Büchi, Switzerland) was employed for spray-drying the kuini juice. The aspirator setting was set at 100%, nozzle speed at 5, and the air compressor was set at 40 nm. The spray-dryer was set with an inlet temperature of 160 °C [15]. After the temperature was achieved, the spray-dryer feed was pumped into the spray-dryer drying chamber where it is atomized and dried. The kuini powder produced was then gathered in a collection vessel attached to the spray-dryer.

Accelerated storage of kuini powder

The kuini powders were separately packaged in ALP and PET pouches (80 mm x 70 mm). They were sealed using heat before being placed in a desiccator (90±1% RH with saturated solution of ammonium sulfate) at 38±1°C. The of kuini powder were then analyzed at 7 days intervals for up to 49 days [18].

Physicochemical analysis of kuini powder

Color

The color of the kuini powder was measured using a colorimeter (Hunter Associates Laboratory Inc, USA)[21] that was utilized via EasyMatch QV-ER. After calibration with the white and black tile, the sample cup with kuini powder was placed on the sample port, and L*, a*, b* values were recorded. Total color difference was determined shown in the Equation 1 [17].

Hygroscopicity (HG)

Two grams of kuini powder was placed in a desiccator, which was pre-filled with a saturated solution of ammonium sulfate. After 1 week, the aluminum cups were weighed, and the hygroscopicity of powder was then calculated by as g of moisture per 100 g of dry solids, as in the Equation 2 [12].

Moisture content (MC)

Kuini powder was then weighed and dried in an oven (Memmert, Germany) at 105 °C for 24 hours; after which, the sample powder was weighed [22]. The moisture content was calculated as in thr Equation 3.

Water activity (a_w)

A LabMaster Water Activity Meter was used to measure the water activity of the spray-dried powder [13].

Degree of caking (DC)

Kuini powder (3 g) was transferred into a sieve and shaken for 5 min. The weight of the powder remaining in the sieve was then measured [23]. The degree of caking (DC) was calculated using Equation 4.

Flowability (F)

A plastic funnel with a narrow stem was mounted exactly 2 cm above a piece of paper. Kuini powder, which flowed through the funnel and formed a powder

heap. The radius of the powder heap (circle) was then calculated, and the angle of repose was estimated, as in Equation 5 [24].

Water solubility index (WSI)

Kuini powder (1 g) was added with 10 mL of distilled water and then placed in a water bath at 37 °C for 30 minutes. It was then centrifuged for 10 minutes (Eppendorf, Germany) and the remaining supernatant collected and oven-dried for 5 hours at 105 °C. The water solubility index was calculated with Equation 6 [25].

Carotenoid content

Kuini powder (3 g) was added to 10 mL of distilled water. The mixture was held for 30 minutes, then another 20 mL of cold acetone was added before holding for another 15 minutes. It was then poured into a Büchner flask and filter in a vacuum. The extraction and filtration was repeated twice. Petroleum ethylene (20 mL) and one-third of the solution was poured into a separatory funnel. Distilled water (300 mL) was added and then the colorless layer was discarded. This was repeated twice before being filtered through 15 g of sodium sulfate. The collected yellow pigment was next subjected to a rotary evaporator at 35 °C and then measured with a spectrophotometer at 450 nm [21]. The standard curve was plotted along the beta-carotene standard and with the following equation: y= 0.0666x +0.0752, R^2 = 0.985.

Statistical analysis

All analyses were done in triplicate (n = 3). All results were put into a table. Mean and the standard deviation was determined for each analysis and analyzed using PASW Statistics 18 (ANOVA). Differences were considered statistically significant at $p \leq 0.05$.

$$\text{Total color difference} = \sqrt{(L_0^* - L^*)^2 + (a_0^* - a^*)^2 + (b_0^* - b^*)^2} \quad (1)$$

where L_0^* , a_0^* , b_0^* are lightness, redness, and yellowness values of week zero kuini powder and L^*, a^*, and b^* are the lightness, redness, and yellowness values for each week.

$$Hygroscopicity\ (\tfrac{g}{100g}) = \frac{Final\ weight\ of\ sample\ (g) - Initial\ weight\ of\ sample\ (g)}{Intial\ weight\ of\ sample\ (g)} \times 100\text{g} \quad (2)$$

$$Moisture\ content\ (\%) = \frac{weight\ of\ initial\ powder\ (g) - weight\ of\ dry\ powder\ (g)}{weight\ of\ initial\ powder\ (g)} \times 100\% \quad (3)$$

$$Degree\ of\ caking = \frac{powder\ collected\ from\ the\ sieve}{initial\ weight\ of\ powder} \times 100\% \quad (4)$$

$$Tan\ \theta = h/(r - \tfrac{1}{2\alpha}) \quad (5)$$

where, θ is defined as angle of repose, h is height of stem base (2cm), r is radius of the base of powder heap, and α is diameter of funnel stem.

$$Water\ solubility\ index = \frac{weight\ of\ dried\ powder}{weight\ of\ original\ powder} \times 100\% \quad (6)$$

Results and Discussion

Color

Color of food is a critical sensory attribute for product acceptance because it influences purchase intent and taste perception [26]. According to HunterLab [27], the higher the L* value, the brighter or whiter the sample is, and it is from black (0) to white (100). Figure 2a shows that the lightness (L*) value of kuini powder packaged in ALP and PET pouches under accelerated storage conditions for 7 weeks. Figure 2a also shows that the lightness (L*) value of kuini powder packed in ALP was reduced from 88.52±0.36 (week 0) to 84.89±0.94 (week 7), indicating that kuini powder on week 7 had a darker color when compared to week 0. Whereas for the PET packaging, the results showed that the degree of lightness (L*) of kuini powder was reduced steadily (week 6 = 85.26±0.64), and then followed by a larger reduction at week 7 (83.46±1.54). Color change with storage time was significantly affected by packaging material and storage time [18], where the ALP packaging had a better color based on L* value when compared to PET packaging. Hunter L, a, b values of mango soy fortified yoghurt powder decreased during accelerated storage and were significantly ($p < 0.01$) affected by packaging material and storage time. After storage for 49 days, a greater color change occurred in MSFY powder packaged in HDPP when compared to ALP [28].

Figure 2b shows the variation in a* value of kuini powder packaged in ALP and PET pouches under accelerated storage conditions for 7 weeks. According to HunterLab [27], if a* value increased, which shows that the color will be more reddish. For ALP packaging at week 1, a* value were 0.47±0.12, and then increased to 0.65±0.12 at week 2; while the increase from week 2 to week 4, and week 4 to week 7 were insignificant ($p > 0.05$). PET packaging followed a similar trend as ALP, except for a major increase at week 7. This result agrees with Kumar et al. [18], who reported that mango soy fortified yogurt powder in ALP pouches have a significantly higher a* value when compared to HDPP packaging, indicating that ALP better maintains the color of powder after 7 weeks of accelerated storage. According to Chauhan et al. [24], powder that was stored in an oven at temperature 40°C and with a relative humidity of 90% RH will have a higher a* value and a lower b* value.

Conversely, the b* value of kuini powders decreased (Figure 2c) and total color difference increased (Figure 2d) with storage time. These tables show that there is almost no difference between the packaging types. Wong and Lim [29] also reported that after storage of 7 weeks, there was a greater color change (56.30) in papaya powder stored under accelerated condition (38 ºC, 90% RH) in PET when compared to ALP (16.22). This can be explained by the permeability of the packaging material to water vapor and oxygen. Moreover, residual air remaining in the package may cause oxidation, which led to color changes during storage.

Hygroscopicity (HG), moisture content (MC) and water activity (aw)

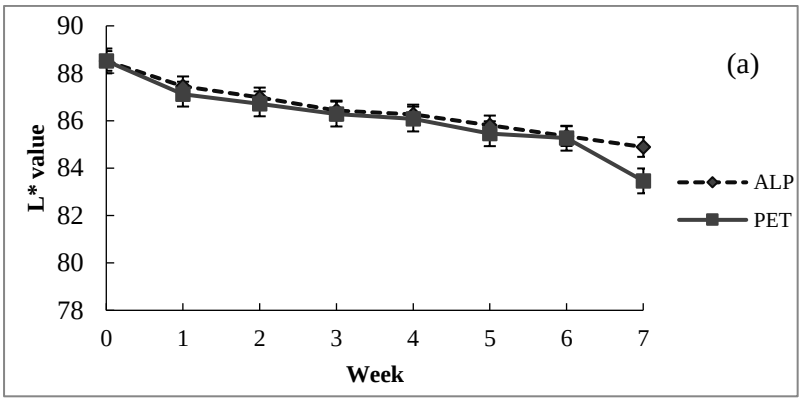
In this study, ammonium sulfate was used to create a high relative humidity for the kuini powder. The purpose of creating a high humidity environment for kuini powders is to test the ability of powder to absorb water [28]. Figure 3a describes the storage stability of hygroscopicity (HG) of kuini powder packaged in ALP and PET under accelerated storage conditions for 7 weeks. The hygroscopic percentages for kuini powder packaged in ALP pouches (22.37±1.16 g/100g) were increased but not as much as in PET pouches (28.00±1.60g/100g). This result agrees with Yu et al. [31], whereby spray-dried bovine colostrum powder had a higher degree of caking when packaged in ALP when compared to PET. This was probably due to ALP pouches providing a better barrier to water vapor and temperature [20]. Additionally, powder with high HG has a tendency to absorb moisture easily, which results in the stickiness of powder and eventually causes the powder to cake.

The kuini powder packed moisture content was 2.81±0.74 at week 0. It was packed in ALP and PET and showed an increase in moisture content with an increase in storage time with the moisture content at 11.44% higher than ALP pouches after 7 weeks of storage (Figure 3b). The moisture uptake depends on the water vapor permeability of the packaging film [17]. ALP packaging had a better barrier for water permeability and the kuini powder were not high in moisture content.

The moisture gained by powders packaged in PET pouches was higher than in ALP pouches during the 90-day storage period, mainly due to the higher water vapor permeability of PET pouches, indicating that ALP pouches provided a better barrier to water vapor for SDBC powders [29] while Mridula et al. [32] also reported the moisture gained by two sattu samples in laminated aluminum foil pouches was lower than in low density polyethylene pouches. This was probably due to the packaging used (PET) and it may not have provided an effective barrier against oxygen and water vapor [29].

The higher value of water vapor transmission rates for PET packaging showed that it had a greater permeability against moisture gained during storage. Wong and Lim [29] noted the moisture content of powder packaged in PET was double (13.28%) those packaged in ALP (6.38%) by the end of 7 weeks storage for papaya powder. Aluminum foil thicker than 17 μm could be considered a total barrier against gases, moisture, and light. Aluminum foil with a thickness between 6-9 μm could not be regarded a total barrier and was also superior to other polymeric materials such as PET [17]. Further, the results obtained showed that papaya powder packaged in ALP with a thickness of 10 μm showed a tempered increase in water activity when compared to powder packaged in PET with a thickness of 17 μm.

Kumar et al. [18] have reported that the moisture gain by powder packed in the HDPP pouches was greater than for ALP pouches. Figure 3c illustrates the change in water activity (a_w) for ALP and PET pouches under accelerated storage conditions for 7 weeks. Although powder packaged in either packaging showed an increase in water activity, the increase was greater for kuini powder in packaged in PET. At week 0, the water activity (a_w) in kuini powder was 0.24±0.003. After 7 weeks, the powder in ALP and PET packaging were 0.43±0.00 and 0.50±0.02, respectively. Hence, they are each considered microbiologically stable [23]. Dak et al. [33] and Wong and Lim. [29] also reported that ALP showed a lessened increase in water activity when compared to HDPP and PET. Thus, ALP could be a more effective packaging material in the prevention of increases in water activity.



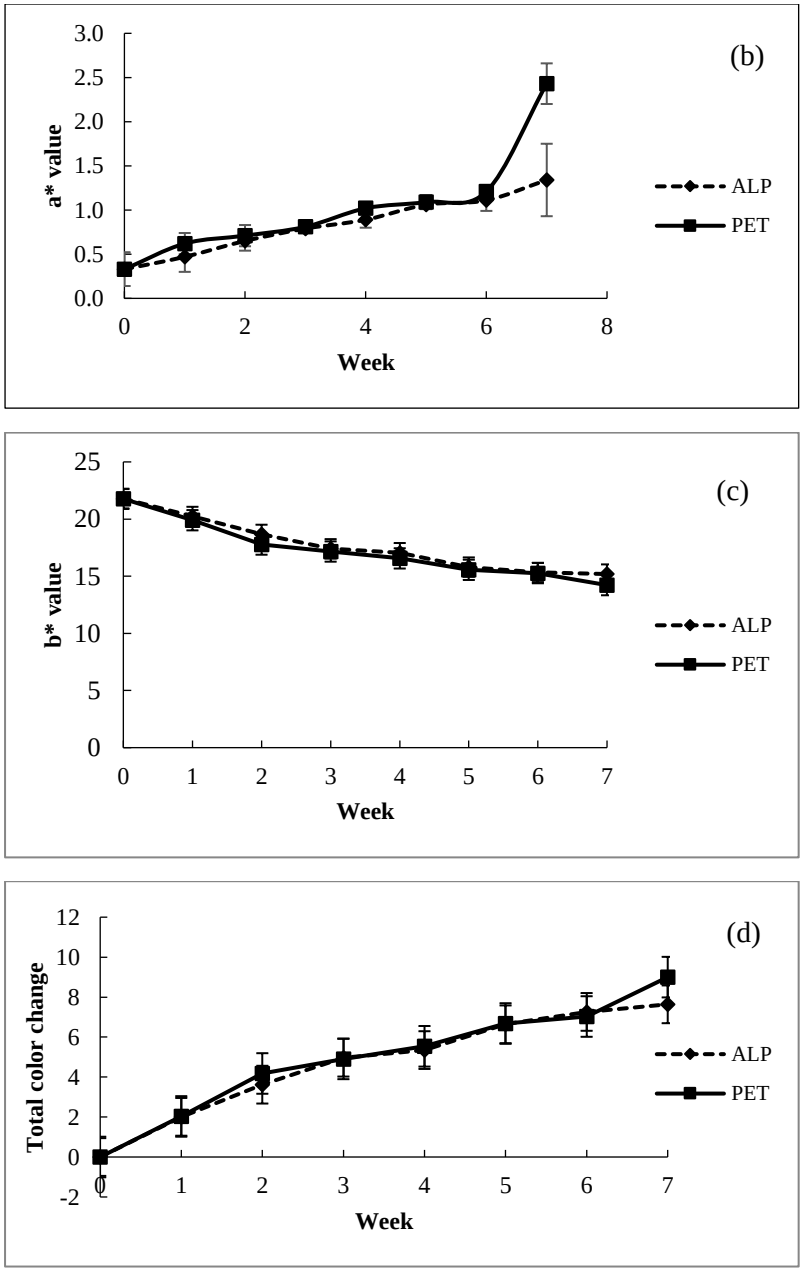


Figure 2. (a) L* value, (b) a* value, (c) b* value, and (d) Total color different of kuini powder packaged in ALP and PET pouches under accelerated storage conditions for 7 weeks

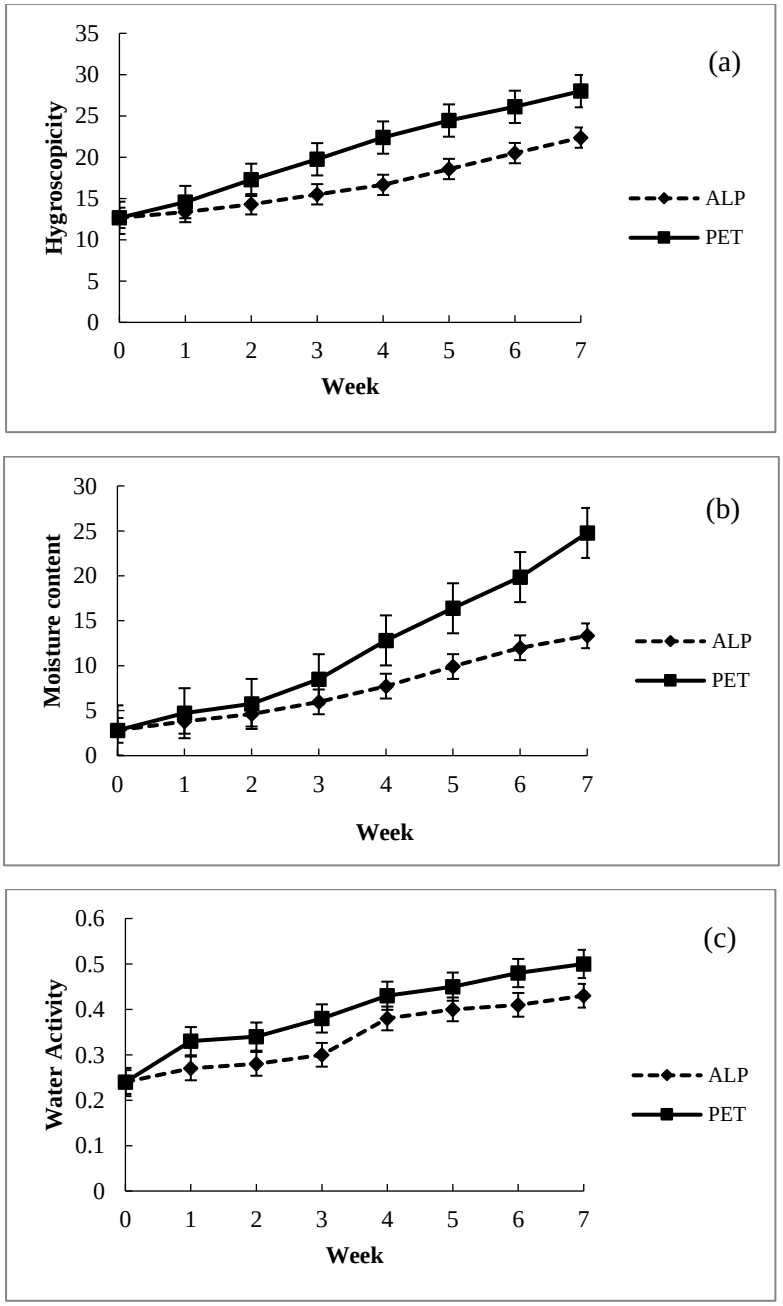


Figure 3. (a) Hygroscopicity, (b) moisture content, and (c) water activity (a_w) of kuini powder packaged in ALP and PET pouches under accelerated storage conditions for 7 weeks

Degree of caking, flowability, and water solubility index (WSI)

Figure 4a shows the variation in the degree of caking of kuini powder packaged in ALP and PET pouches under accelerated storage conditions for 7 weeks. The difference between the initial week and the first week was not significant (p >0.05); followed by a gradual increase and with the degree of caking increasing in ALP when compared to PET. After week 7, the degree of caking for ALP packaging was 9.95% and PET

packaging was 28.89%. ALP pouches had a greater barrier of moisture, which helps to prevent clumps from forming. According to Hui [34], the caking of powder may occur due to moisture absorption, crystallization of sugar components, and softening of the surface by heat.

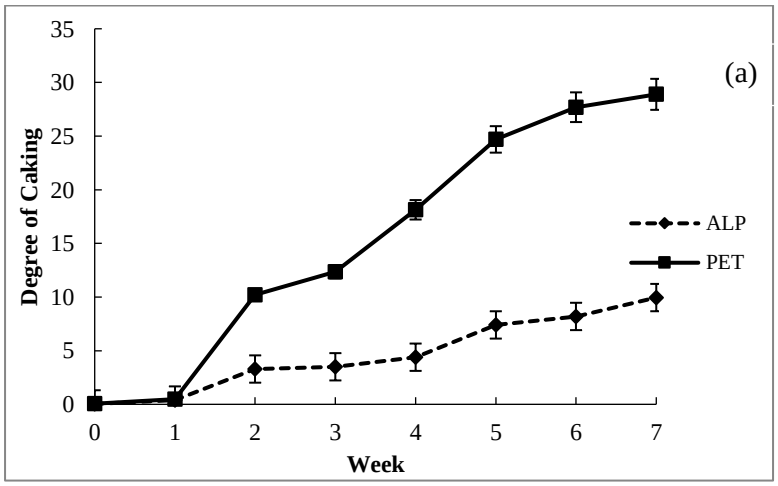
The angle of repose measures the angle of the heap's slope and indicates its flowability [35, 36]. Figure 4b describes the variation in flowability of kuini powder packaged in ALP and PET pouches under accelerated storage conditions for 7 weeks. Figure 4b shows that the angle of repose for ALP packaging had a lower value compared to PET packaging at week 7. The change in particle structure is attributed to moisture absorption during storage, because it increases the powder's cohesiveness and leads to a reduction in flowability [24]. Lai et al. [37] showed that the larger the mean particle size, the more difficult for the powder to flow, and the higher angle of repose.

Figure 4c shows the change in water solubility index (WSI) of kuini powder packaged in ALP and PET pouches under accelerated storage conditions for 7 weeks. Further, Figure 4c shows that the WSI for kuini powder packaged in ALP pouches was 73.33±1.72 at week 0. ALP packaging showed that on week 7 that the WSI of the powder was 11.66% higher than the powder packaged in PET.

Carotenoid content

The β-carotene is a major dietary precursor of vitamin A [38]. Figure 5 describes the variation in carotenoid content for kuini powder packaged in ALP and PET pouches under accelerated storage conditions for 7 weeks. Generally, a decrease of carotenoid content was observed when the storage time increased. The carotenoid content of kuini powder in each packaging showed no significant difference (p >0.05) from week 0 to week 5. However, after week 5, the carotenoid reduction was found be more prominent in kuini powder packaged in PET. At the end of storage (week 7), the kuini powder in ALP and PET were 76.9% and 65.5%, respectively. Kołakowska and Sikorski [39] showed that temperature can cause faster decomposition of alpha- and beta-forms than other carotenoids. In our study, the powders were stored at 38 °C, which is also the main influence on carotenoid loss.

Hymavathi and Khader [40] reported significant differences between metallized polyester/polyethylene (MPP) and polyester poly (PP) packaging in the loss of b-carotene in mango powder during storage. The percent loss of b-carotene was higher in powder packaged in PP pouches compared to MPP pouches throughout the storage period due to higher oxygen permeability of PP pouches compared to MPP. Wong and Lim reported [27] that β-carotene was degraded from an initial of 1.83 µg/g to 0.95 µg/g and 0.16µg/g for powder stored in ALP and PET, respectively.



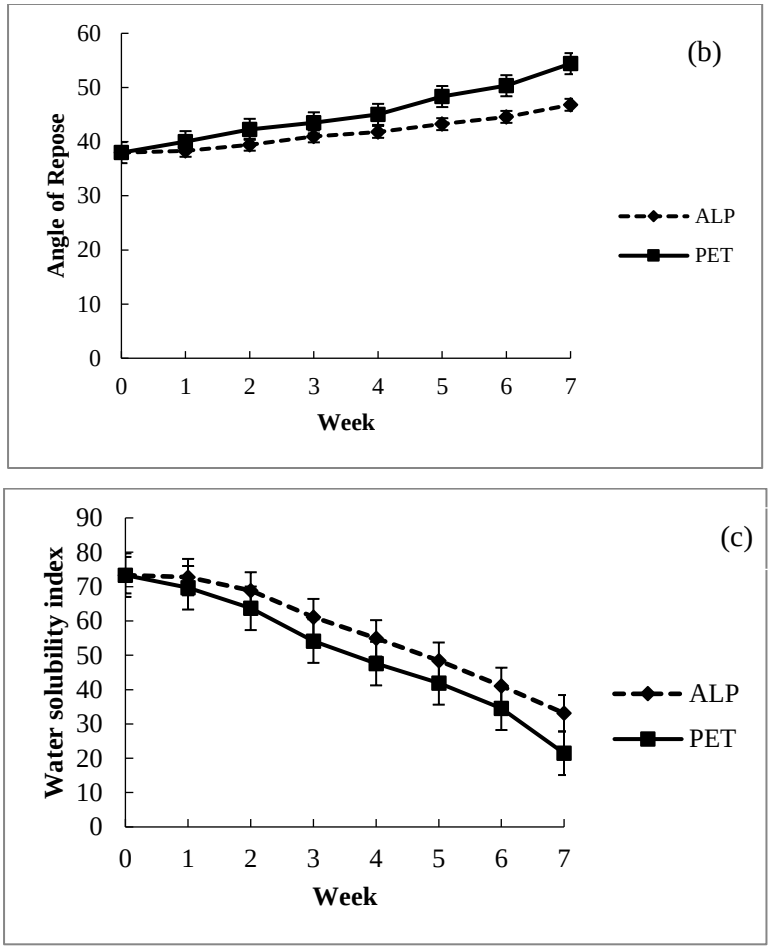


Figure 4. (a) Degree of caking, (b) flowability, and (c) water solubility index (WSI) of kuini powder packaged in ALP and PET pouches under accelerated storage conditions for 7 weeks

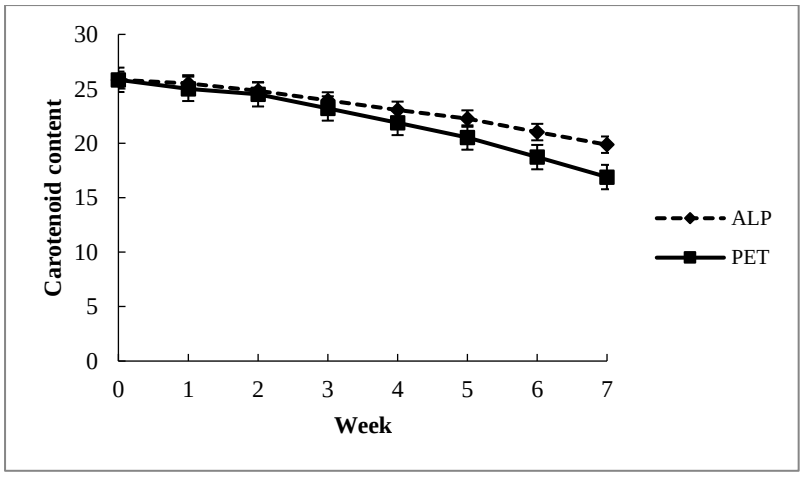


Figure 5. Variation in carotenoid content of kuini powder packaged in ALP and PET pouches under accelerated storage conditions for 7 weeks.

Conclusion

Kuini fruit (*Mangifera odorata*) is an aromatic tropical fruit that is yellow in color in its pulp and has a green peel. In this research, the storage stability of kuini powder in ALP and PET under accelerated storage conditions at temperature 38±1 °C and relative humidity 90% RH for 7 weeks. The physicochemical analyses were carried out to determine the packaging material properties. With accelerated storage, powder in both packaging types had increases in water activity, moisture content, flowability, degree of caking, and hygroscopicity; while showing decreases in WSI and carotenoid content. ALP is better than PET in retaining moisture content, WSI, water activity, carotenoid content, flowability, degree of caking, and hygroscopicity. This study has shown that ALP packaging has better protection in terms of stability. The comparison can serve as guidance in packaging selection for fruit powder.

References

1. Kim, Y., Brecht, J. K. and Talcott, S. T. (2007). Antioxidant phytochemical and fruit quality changes in mango (*Mangifera indica* L.) following hot water immersion and controlled atmosphere storage. *Food Chemistry*, 105(5): 1327-1334.
2. Lim, T. K. (2012). Edible medicinal and non-medicinal plants: Volume 1, Fruits. Springer Science & Business Media, London: pp. 127-130.
3. Siddiq, M. (2012). Tropical and subtropical fruit: Postharvest physiology, processing and packaging. John Wiley & Sons, Oxford: pp. 292-295.
4. Khoo, H. E. and Ismail, A. (2008). Determination of daidzein and genistein contents in Mangifera fruit. *Malaysian Journal of Nutrition*, 14(2): 189-198.
5. Salunkhe, D. K. and Kadam, S. S. (1995). Handbook of fruit science and technology: Production, composition, storage, and processing. Marcel Decker, Inc. New York: pp.123-157.
6. Adnan, H., Ali, M. S. M., Hassan, H., Manan, M. A., Ghazali, M. N. and Ramli, N. S. N. (2018). Bioassay-guided of fresh and fermented kuini (*Mangifera odorata*) extracts against bacterial activity. *International Journal of Agriculture, Forestry and Plantation*, 7: 27-32.
7. Adnan, H., Ali, M. S. M, Manan, M. A., Hassan, H., Ghazalli, M. N. and Ramli, N.S.N. (2018). Acetic acid fermentation of kuini (Mangifera odorata) and its potential substrate for human health. 7th International Conference on Biotechnology for the Wellness Industry: Bioresources for Human Wellness, University of Technology Malaysia, pp. 27-28.
8. Lai, J. T., Lai, K. W., Zhu, L. Y., Nyam, K. L. and Pui, L. P. (2020). Microencapsulation of *Lactobacillus plantarum* 299v and its storage in kuini juice. *Malaysian Journal of Microbiology*, 16(4): 235-244.
9. Shishir, M. R. I., Taip, F. S., Aziz, N. A. and Talib, R. A. (2014). Physical properties of spray-dried pink guava (*Psidium guajava)* powder. *Agriculture and Agricultural Science Procedia*, 2: 74-81.
10. Goula, A. M. and Adamopoulos. K. G. (2010). A new technique for spray drying orange juice concentrate. *Innovative Food Science and Emerging Technologies*, 11: 342-351.
11. Chew, S., Tan, C., Pui, L., Chong, P., Gunasekaran, B. and Nyam, K. (2019). Encapsulation technologies: A tool for functional foods development. *International Journal of Innovative Technology and Exploring Engineering*, 8(5): 154-162.
12. Chang, L. S., Yong, S. M. E. and Pui, L.P. (2020). Production of spray-dried "Terung Asam" (*Solanum lasiocarpum* Dunal) powder. *Walailak Journal of Science and Technology*, 18(1): In press.
13. Wong, C. W., Pui, L. P. and Ng, J. M. L. (2015). Production of spray-dried Sarawak pineapple (*Ananas comosus*) powder from enzyme liquefied puree. *International Food Research Journal*, 22(4): 1631-1636.
14. Pui, L. P., Karim, R., Yusof, Y. A., Wong, C. W. and Ghazali, H. M. (2020). Optimization of spray-drying parameters for the production of 'Cempedak' (*Artocarpus integer*) fruit powder. *Journal of Food Measurement and Characterization*, 2020: In press.
15. Chang, L. S., Tan, Y. L. and Pui, L. P. (2020). Production of spray-dried enzyme-liquefied papaya (*Carica papaya* L.) powder. *Brazilian Journal of Food Technology*, 23: e2019181.

16. Goula, A. M. and Adamopoulos, K. G. (2008). Effect of maltodextrin addition during spray drying of tomato pulp in dehumidified air: II. Powder properties. *Drying Technology,* 26(6): 726-737.
17. Pua, C. K., Sheikh, A. H., Tan, C. P., Mirhosseini, H., Rahman, R. A. and Rusul, G. (2008). Storage stability of jackfruit (*Artocarpus heterophyllus*) powder packaged in aluminum laminated polyethylene and metallized co-extruded biaxially oriented polypropylene during storage. *Journal of Food Engineering,* 89(4): 419-428.
18. Kumar, V., Sukumar, D. and Muruganantham, M. (2015). Microbial quality of frozen squid (*Sepioteuthis lessoniana*, Lesson 1830) treated with food grade commercial chemicals. *Indian Journal of Animal Research*, 49(5): 736-741.
19. Marsh, K. and Bugusu, B. (2007). Food packaging—roles, materials, and environmental issues. *Journal of Food Science*, 72(3): 39-55.
20. Abdel-Bary, E. M. (2003). Handbook of plastic films. Smithers Rapra Publishing, Shawbury.
21. Pui, L. P., Karim, R., Yusof, Y. A., Wong, C. W. and Ghazali, H. M. (2018). Physicochemical and sensory properties of selected 'cempedak' (*Artocarpus integer* L.) fruit varieties. *International Food Research Journal*, 25(2): 861-869.
22. AOAC (Association of Analytical Chemists) (2000). Official Methods Of Analysis, Rockwill.
23. Bhusari, S. N., Muzaffar, K. and Kumar, P. (2014). Effect of carrier agents on physical and microstructural properties of spray dried tamarind pulp powder. *Powder Technology*, 266: 354-364.
24. Chauhan, A.K. and Patil, V. (2013). Effect of packaging material on storage ability of mango milk powder and the quality of reconstituted mango milk drink. *Powder Techonology*, 239: 86-93.
25. Santhalakshmy, S., Bosco, S. J. D., Francis, S. and Sabeena, M. (2015). Effect of inlet temperature on physicochemical properties of spray dried jamun fruit juice powder. *Powder Technology*, 274: 37-43.
26. Sun, D. W. (2011). Handbook of frozen food processing and packaging, 2nd Ed. CRC Press, pg 552-553.
27. Hunter Lab (2008). CIE L* a* b* color scale. Hunter Lab Application note, Boca Raton: pp. 1-4.
28. Kumar, P. and Mishra, H. N. (2004). Mango soy fortified set yoghurt: effect of stabilizer addition on physicochemical, sensory and textural properties. *Food Chemistry*, 87(4): 501-507.
29. Wong, C. W. and Lim, W. T. (2016). Storage stability of spray-dried papaya (*Carica papaya* L.) powder packaged in aluminium laminated polyethylene (ALP) and polyethylene terephthalate (PET*). International Food Research Journal*, 23(5): 1887-1894.
30. Senka, S. V., Jelena, Z. V., Zuzana, G. V., Zoran, P. Z. and Ljiljana, M. P. (2014). Maltodextrin as a carrier of health benefit compounds in *Satureja Montana* dry powder extract obtained by spray drying technique. *Powder Techonology*, 258: 209-215.
31. Yu, H., Zheng, Y. and Li, Y. (2015). Shelf life and storage stability of spray-dried bovine colostrum powders under different storage conditions. *Journal of Food Science and Technology*, 52(2), 944-951.
32. Mridula, D., Jain, R. and Singh, K. K. (2010). Effect of storage on quality of fortified Bengal gram sattu. *Journal of Food Science and Technology*, 47(1): 119-123.
33. Dak, M., Sagar, V. R. and Jha, S. K. (2014). Shelf-life and kinetics of quality change of dried pomegranate arils in flexible packaging. *Food Packaging and Shelf Life,* 2(1): 1-6.
34. Hui, Y. H. (2008). Food drying science and technology: Microbiology, chemistry, applications. DEStech Publication, Inc, Pennsylvania: pp. 244-245.
35. Enrique, O. R., Pablo, J., and Hong, Y. (2006). Food powders: Physical properties, processing and functionality. Kluwer Academic/Plenum Publisher: New York: pp. 52-55.
36. Ganesan, V., Rosentrater, K. A., and Muthukumarappan, K. (2008). Flowability and handling characteristics of bulk solids and powders–a review with implications for DDGS. *Biosystems Engineering*, 101(4): 425-435.
37. Lai, P. Z., Yusof, Y. A., Aziz, M. G., Chin, N. L. and Amin, M. A. (2013). Compressibility and dissolution characteristics of mixed fruit tablets made from guava and pitaya fruit powder. *Powder Technology*, 247: 112-119.

38. Igual, M., Garcia-Martinez, E., Camacho, M. M. and Martínez-Navarrete, N. (2013). Jam processing and storage effects on β-carotene and flavonoids content in grapefruit. *Journal of Functional Foods*, 5(2): 736-744.
39. Kołakowska, A. and Sikorski, Z. E. (2010). Lipids and food quality. chemical, biological, and functional aspects of food lipids. CRC press, Boca Raton: pp. 71-72.
40. Hymavathi, T. V. and Khader, V. (2005). Carotene, ascorbic acid and sugar content of vacuum dehydrated ripe mango powders stored in flexible packaging material. *Journal of Food Composition and Analysis*, 18(2-3): 181-192.

Malaysian Journal of Analytical Sciences (MJAS)
Published by Malaysian Analytical Sciences Society

DETERMINATION OF SELECTED HEAVY METAL CONCENTRATIONS IN UNREGISTERED FACE WHITENING CREAMS SOLD IN JOHOR BAHRU, JOHOR, MALAYSIA BY USING INDUCTIVELY COUPLED PLASMA OPTICAL EMISSION SPECTROSCOPY AND THEIR HEALTH RISK ASSESSMENT

(Penentuan Kepekatan Logam Berat Terpilih dalam Krim Pemutih Muka yang Tidak Berdaftar Dijual di Johor Bahru, Johor, Malaysia dengan Menggunakan Spektrofotometer Pancaran Optik Plasma Gandingan Aruhan dan Penilaian Risiko Kesihatan)

Anusia Selvaraju[1], Anis Nur Shasha Abdul Halim[1], Aemi Syazwani Abdul Keyon[1,2]*

[1]*Department of Chemistry, Faculty of Science*
[2]*Centre for Sustainable Nanomaterials, Ibnu Sina Institute for Scientific and Industrial Research*
Universiti Teknologi Malaysia, 81310 UTM, Johor Bahru Johor, Malaysia

**Corresponding author: aemi@kimia.fs.utm.my*

Received: 25 June 2020; Accepted: 5 August 2020; Published: 12 October 2020

Abstract

This study determined the concentrations of arsenic (As), cadmium (Cd), mercury (Hg) and lead (Pb) in unregistered face whitening creams that are commonly accessible in Johor Bahru (Johor, Malaysia) local markets. Three separate brands (marked as Brand X, Brand Y and Brand Z) of unregistered face whitening creams were chosen. Each brand was purchased with five replicates. A total of 15 samples were purchased from five different locations. Microwave digestion process was used to digest the heavy metals out from the cream matrices, and later analysed by using inductively coupled plasma-optical emission spectroscopy (ICP-OES) method. Results showed slightly higher Hg concentrations in Brand X (6.5 ppm), whereas Pb concentration in the whitening creams were below the acceptable limit (ranged 0.1–0.4 ppm) as set by the Malaysia National Pharmaceutical Regulation Act (NPRA). Nevertheless, the Pb concentration exceeded the limit set by the World Health Organisation (WHO) for daily use, which is 0.05 ppm. Besides, As and Cd were not detected significantly in all brands. Health risk assessment for all samples identified with heavy metals, in consideration of the excessive mercury concentration and based on HRI results, could not ignore the fact that Brand X holds possible harmful effects on human health, following its use.

Keywords: face whitening creams, heavy metals, mercury, microwave digestion, inductively coupled plasma-optical emission spectroscopy

Abstrak

Kajian ini menentukan kepekatan arsenik (As), kadmium (Cd), merkuri (Hg) dan plumbum (Pb) dalam krim pemutihan wajah yang tidak dikawal selia yang biasanya dapat diakses di pasaran tempatan wilayah Johor Bahru. Tiga jenama berasingan (bertanda X, Y dan Z) krim pemutihan wajah yang tidak didaftarkan telah dipilih. Setiap jenama dibeli dengan lima replikat. Sebanyak 15

sampel telah dibeli dari lima lokasi berbeza. Proses penghadaman gelombang mikro digunakan untuk mencerna logam berat dari matriks krim dan kemudian dianalisis menggunakan kaedah spektrofotometer pancaran optik plasma gandingan aruhan (ICP-OES). Hasil menunjukkan kepekatan merkuri pada jenama 'X' ialah sedikit lebih tinggi (6,5 ppm), manakala kepekatan plumbum dalam krim pemutihan berada di bawah had (berjulat 0.1–0.4 ppm) yang dapat diterima seperti yang ditetapkan oleh Akta Peraturan Farmasi Nasional (NPRA). Walau bagaimanapun, kepekatan Hg melebihi had yang ditetapkan oleh Pertubuhan Kesihatan Sedunia (WHO) untuk kegunaan harian iaitu 0.05 ppm. Selain itu, As dan Cd tidak dapat dikesan secara signifikan dalam ketiga-tiga jenama. Penilaian risiko kesihatan untuk semua sampel yang dikenal pasti dengan logam berat melalui penimbangan kepekatan merkuri berlebihan dan berdasarkan hasil HRI tidak dapat diabaikan hakikat bahawa Jenama 'X' mempunyai kemungkinan kesan berbahaya terhadap kesihatan manusia berikutan penggunaan produk tersebut.

Kata kunci: krim pemutihan wajah yang tidak dikawal selia, penghadaman gelombang, logam berat, spektrofotometer pancaran optik plasma gandingan aruhan

Introduction

Cosmetics industry is one of Asia's fast-growing industries [1]. The Asia Pacific's market value improves to over USD 70 billion, making it the second highest after Western European market. Different beauty products are distributed in local market and believed to originate from China, the Philippines and Thailand. Excessive amounts of hazardous heavy metals, such as cadmium (Cd), chromium (Cr), lead (Pb) and arsenic (As) are found in these cosmetic products [2]. According to the World Health Organisation, of all potentially toxic elements, these four heavy metals have generated the most public health concern [3]. The heavy metals in cosmetic products that are applied to the skin (including face) can accumulate locally, and some metals such as Hg, Pb, Cd and Al can pass through the skin barrier and enter the blood vessels [3]. Complications such as extreme swelling, redness and thinning of the skin, ochronosis, dermatitis, severe kidney damage, anxiety, depression, psychosis and peripheral neuropathy were reported in patients. Skin whitening, which is one of the famous beauty products in Malaysia, are usually creams, gels or soaps [4]. The trend of using skin whitening products usually starts as a treatment for skin darkening caused by acne vulgaris, atopic dermatitis, eczema or even a condition that is being identified as darker skin due to social media stress [4]. Skin whitening products work by interfering with melanogenesis pathway, melanin transfer, or desquamation at any stage. The disruption of these processes will result in pigmentation reduction [4]. It is not surprising that toxic substance such as Hg is added into whitening creams, as it inactivates the enzyme responsible for melanin production [5].

Many aspects can cause skin pigmentation, the most common of which is ultraviolet (UV) radiation, which induces tanning reaction. The diverse kinetics of skin reaction towards UV radiation may result in skin tanning for several weeks [6]. Ultra-radiation is the most important factor in altering pigmentation of human skin. Instant skin darkening happens within minutes as a direct result of UV treatment (ultraviolet long wave (UVA)), followed by permanent skin darkening within a few hours, lasting for a few days [7]. On top of that, hormonal changes in the body can also stimulate pigmentation. Increases in oestrogens hormones that arise during pregnancy appear to have melanocyte inhibitory effects and contribute to hyperpigmentation. Darkening of skin is also clinically observed in response to inflammation [6].

Heavy metals can be defined as any chemical element that has at least five times a specified gravity than that of water [8]. Heavy metals turn out to be toxic when the body fails to digest them, and heavy metal accumulation occurs in the soft tissues. The most hazardous heavy metals to human health are As, Cd, Pb, Hg and tin (Sb) [9,10,11]. Increasing levels of Pb and Cd in the human body can cause skeletal muscle damage, cancer cell activation, reproductive deficiencies, brain impairment and kidney impairment. Hg is recognised as the most hazardous heavy metal that threatens the brain and central nervous system [12, 13, 14]. On the same note, As induces haematological disturbance, dermal

disruption, gastrointestinal disorder, respiratory changes, neurological abnormalities, cardiovascular weakness, genotoxic effects, reproductive abnormalities and cancer irregular differences in genetic material [15, 16, 17]. Long-term inhalation exposure to As is a leading cause of many serious conditions, such as skin disorders, central and peripheral nervous disorders, potential lung cancer risk and increased risk of gastrointestinal tract and urinary system cancer [18]. It was reported that Hg in skin whitening creams and other personal care products causes birth defects [19]. Abnormal placenta size leads to complications at birth as such, low cortisol levels, resulting in higher birth defect rates [19].

In addition, a woman with complication of erythema and itchy papulovesicular lesions on her face, neck, trunk sides and antecubital fossa prior (5h–6 h) was documented by using a skin whitening cream on her cheek and upper lip. The patient had a positive patch test for ammoniated mercury, thimerosal and metallic Hg [19]. Studies have reported many health effects related to Pb toxicity, including hypertension and renal failure [18], malformation of cognitive abilities and behaviour [20], Cd and its salts used in the manufacture of nickel-cadmium batteries, pigments and alloys are associated with emphysema, proximal renal tubular necrosis and deformities of the skeleton [20]. Latest studies show that Pb does not have a safe exposure level on its own, because even in trace amounts this element affects the foetus and causes abnormality to the central nervous system of children. [21, 22]. Considering the unfavourable adverse effects associated with high exposure of As, Cd, Hg and Pb to human health, many countries and organisations have prescribed specific maximum permissible limits for such heavy metals, covering the various types of personal care products. Face whitening creams are usually associated with Hg poisoning, whereby adverse reactions that range from dermatitis to exogenous ochronosis and steroidal acne can happen. Nephrotic syndrome is also associated with Hg and other elements such as corticosteroids and hydroquinone [23].

Considering the potential health issues that may arise when these chemicals are used, they are globally regulated by different regulatory bodies. For example, the National Pharmaceutical Control Bureau (NPCB) classifies all health and pharmaceutical nutrition products [24]. Under the Dangerous Drugs Act 1952, Control of Drugs and Cosmetics Regulations 1984, NPCB will determine whether the health or medicinal food products require registration [24]. Aligned with the need of a regulating amount of heavy metals in different matrices (including cosmetics), several organisations have set the acceptable amounts for As, Cd, Pb and Hg. For instance, the guidelines for control of cosmetic products in Malaysia (1st Revision) by the National Pharmaceutical Regulatory Agency (NPRA) set these limits based on factors such as in what amount should heavy metals be used in cosmetics; As ≤5.0 ppm, Cd ≤ 5.0 ppm, Pb ≤ 20.0 ppm and Hg ≤ 1.0 ppm [25]. The U.S. Food and Drug Administration (USFDA) has set the limit for heavy metals of As (≤ 3.0 ppm), Cd (≤ 4.0 ppm), Pb (≤ 10.0 ppm) and Hg (≤ 1.0 ppm) [26]. Furthermore, Malaysia's Food Act 1983 and Food Regulations 1985 have set the limits for As (≤ 1.0 ppm), Cd (≤ 1.0 ppm), Pb (≤ 2.0 ppm) and Hg (≤ 0.05 ppm) [26].

In Malaysia, there is no precise definition of counterfeit drugs in Malaysian law, but in The Sale of Drug Act (SODA) 1952 there are specific provisions under Regulation 7(1) (a), Regulation 7(1A) (a-g) Control of Drugs and Cosmetics Regulations (CDCR) 1984, which require all medical products to be licensed with the Ministry of Health (MOH) National Pharmaceutical Control Bureau (NPCB) before they reach the market. Moreover, they must meet a procedure which requires thorough review and final approval by the Drug Control Authorities (DCA) [27]. When the drugs go through all the criteria they are known as registered drugs or registered products [27]. Increase in market reports, cases and incidents is a bad sign for the public. They may consume health products which have been adulterated with poison or unsafe or unclean products because all unregistered drugs do not meet the requirements of Good Manufacturing Practices (GMP) [27].

Several studies were conducted to determine heavy metal concentrations in different personal care products,

including cosmetics [28, 9, 29]. Inductively coupled plasma-optical emission spectroscopy (ICP-OES) is a common technique to determine metal concentrations [30]. In 2015, impurities of heavy metals in lipsticks and their related risk of adverse impact to lipstick consumers were analysed by using ICP-OES [31]. Other included techniques used for such a determination by previous researchers were the atomic absorption spectrophotometer (AAS) [32, 33]. The use of solid-state techniques, such as laser-induced breakdown spectroscopy (LIBS) and X-ray fluorescence spectrometry (XRF), are other options for cosmetic analysis [33]. AAS, ICP-mass spectrometry (ICP-MS), ICP-atomic emission spectrometry (ICP-AES), and X-ray fluorescence spectroscopy (XFS) are the most widely used techniques for analysis of trace and heavy metals [34]. In Malaysia, the use of cosmetic products, particularly unregistered face whitening creams is increasingly in growth. The quantities of contaminants, including heavy metals, used in cosmetics as additives cannot be ignored as they pose health risks to consumers. In the future, this condition could lead to serious health effects on consumers as a hazardous chemical being accidentally introduced to consumers through the derma.

Therefore, this paper presents the output found when Hg, As, Pb and Cd concentrations were determined in several unregistered face whitening cream samples sold in Johor Bahru, Johor, Malaysia. ICP-OES was used and the most harmful brand whitening cream was classified by using statistical comparative method. Health risk assessment was also presented.

Materials and Methods

Chemicals and instrumentation

The chemical analyses were conducted in a government-certified (MS ISO/IEC 17025:2017) commercial laboratory in Johor Bahru. The methodology employed for this study was adapted from the respective commercial laboratory in-house method, which were based on AOAC 999.11, 20th Edition (for Pb and Cd) and AOAC 971.21, 20th Edition (for Hg and As). Nitric acid, hydrochloric acid, hydrogen peroxide 30% v/v, 1.1% w/v stannous chloride in 3%v/v hydrochloric acid or 0.2% w/v sodium borohydride in 0.05% sodium hydroxide, 50% w/v magnesium nitrate and deionised water were used for sample preparation. All glassware was soaked with sulphuric acid (H_2SO_4) 5-10%. Later, these apparatuses were deeply cleaned with detergents and then rinsed with deionised water and air dried before use. Sample digestion was conducted by using analytical grade nitric acid (Sigma Aldrich, Malaysia) and perchloric acid (70%, Sigma Aldrich, Malaysia). Custom calibration solutions for As, Cd, Pb, and Hg were prepared from a common stock solution of 1000 mg/L. All solutions were prepared by using deionised water.

The stock solutions were diluted in series to provide the desired concentrations of 0 mg/L, 0.05 mg/L, 0.10 mg/L and 0.20 mg/L for As, Cd and Hg, and 0 mg/L, 0.1 mg/L, 0.5 mg/L and 1.2 mg/L for Pb, with regard to the calibration curves. When needed, the face whitening cream samples with concentrated metals were diluted appropriately to fit the linearity of the calibration curves. The dilution factor was then then factored in during final calculation. For this study, inductively coupled plasma-optical emission spectrometer (Thermo Scientific ICAP 600 SERIES) was used for the heavy metal's determination. The calibration curves were constructed by using the absorbance values versus the analyte concentrations applied, with the determination coefficient (R^2) which exceeded 0.995. Wavelengths used to identify targeted heavy metals were as follows; Hg (185.0 nm), As (193.8 nm), Pb (220.4 nm) and Cd (226.5 nm).

Sampling and sample preparation

In March 2018, three different brands of face whitening creams (Brand X, Brand Y, and Brand Z) were collected from five different shops in Johor Bahru, Johor, Malaysia. Each brand had five respective replicates (marked as X_1, X_2, X_3, X_4, X_5, Y_1, Y_2, Y_3, Y_4, Y_5, Z_1, Z_2, Z_3, Z_4 and Z_5). The cream samples were uniformly combined by using a sterile stirrer. Samples of whitening cream (1.5 g) were weighed into a 20 mL Teflon tube and added to each concentrated acid samples of 6 mL nitric acid (HNO_3, 65%), 3 mL hydrochloric acid (HCl, 37%) and 0.25 mL hydrogen

peroxide (H_2O_2). Samples were then placed for 30 minutes in an ETHOS 900 microwave digester, and the solution was allowed to cool to room temperature. Approximately 5 mL of distilled water was applied to each sample and then filtered into 20 mL Teflon tube through a funnel with a Whatman No. 41 filter paper. By using distilled water, the solution was then filtered to 20 mL. The liquid extract was then used under the recommended instrument parameters for the determination of As, Pb, Cd and Hg by using ICP-OES.

Estimation of daily intake of toxic metals and health risk index assessment

An adult's daily absorption rate for As, Cd, Hg and Pb was calculated by consumption of the unregistered face whitening cream following an Equation 1 suggested by Omenka et al. [35].

$$EDI = (C \times D) \div W \quad (1)$$

where, estimated daily intake (EDI) is the estimated daily intake, C is the concentration of the metals obtained in this study, D is the estimated daily amount of whitening cream being used in g/kg/day (1.54g) and W is the average body weight of an adult [35]. Body weight of an adult was reported in the Malaysian Adult Nutrition Survey as 63 kg as the average weight [35]. The potential health risks to consumers due to heavy metal exposure through the unregistered face whitening creams in this study were estimated by using the Health Risk Index (HRI), obtained by dividing the estimated daily intake by the metal dermal reference doses (Equation 2). Dermal reference dose for As is 3×10^{-4}, Cd is 2.5×10^{-3}, Hg is 1.6×10^{-4} and Pb is 1.4×10^{-4}.

$$HRI = Calulated\ EDI \div dermal\ reference\ dose\ for\ each\ metal \quad (2)$$

The hazard index collected must be less than 1 so that there are no health risks. If the hazard index values surpass 1, there could be worries about the correlation amongst possible health risks over exposure.

Statistical analysis

Data analyses were carried out in this research by using the IBM SPSS Version 22.0, and the normality of the data was checked by using the Kolmogorov-Smirnov and Shapiro-Wilk tests prior to the hypothesis test. It was given that the small number of samples used in this research, and the indication provided by the Shapiro-Wilk test prevailed over the Kolmogorov-Smirnov. Therefore, when the Shapiro-Wilk test values were found to be less than 0.05 ($p<0.05$), the data could be interpreted as not normally distributed. The analysed details included quantities of As, Cd, Pb and Hg within the three different brands. Based on the analysis, it was found that the data breached the assumption of normality. Statistical inference was used to compare the median between groups by using the non-parametric Mann-Whitney U test. The level of significance (*) was set at 0.05 for inferring the importance of the result [36].

Results and Discussion

ICP-OES method validation

For all the four heavy metals, linear range, coefficient of determination (R^2), limit of detection (LOD) and limit of quantification (LOQ) are shown in Table 1. The three-point calibration curve shows excellent linearity over the concentration range from 0.01 ppm to 0.25 ppm, whereby R^2 ranged from 0.9996 to 1.000. Given that all the calibration curves obtained followed the standard requirements, it could be explained that the responses were linear. Therefore, the detection of these analytes in all samples proved to be acceptable. LOD was the lowest analyte concentration reported with a signal-to-noise ratio (S/N) of at least 3:1, while LOQ corresponded to the lowest analyte concentration in a calibration curve with an S/N of at least 10:1. The LODs and LOQs for Pb, Cd, Cu and Hg were determined with the aid of the data from the calibration curves.

Concentration of heavy metals in face whitening creams

This work focused mainly on the determination of four heavy metals, namely As, Cd, Hg, and Pb in unregistered face whitening products, which are often associated with side effects to human health. The Guidelines for Control of Cosmetic Products in Malaysia (1st Revision) published by the NPRA, Ministry of Health Malaysia [20] stated that the limits for As, Cd, Pb and methyl-Hg are 5 ppm, 5 ppm, 20 ppm, 1 ppm, respectively. The concentrations of heavy metals determined in all 15 samples are tabulated in Table 2.

No Cd was detected for all brands (Brand X, Brand Y and Brand Z). As was detected in samples of Brand Y, which was 0.2 ppm for two out of five replicates. According to the *Guidelines for Control of Cosmetic Products in Malaysia* (1st Revision) released by NPRA, the volume of As found in both samples was within the permitted range [20]. However, As was not found in the other three samples of Brand Y, which might be because they belong to separate processing batches. Even though the determined concentration of As in Brand Y was within the permitted limit, repeated use of this product may lead to critical skin disease and chronic effects on health [37]. As enters the body through inhalation, ingestion, and skin penetration. Hyperpigmentation, palmar and solar keratosis, diarrhoea and vomiting, skin changes and neuropathy, ischemic heart disease, confusion and memory loss, respiratory disease and a higher risk of diabetes are other symptoms that are associated with As poisoning [38].

Pb was detected in two brands, which were three samples of Brand Y (range 0.1-0.4 ppm) and five samples of Brand Z (range 0.2-0.4 ppm). The concentrations were found within the allowed Malaysian standard range. Pb in the form of organic compounds is very much easily absorbed by skin barrier as compared to its inorganic form because of its tendency to bind to proteins [39]. It was reported that, the absorption of lead took place more through the sweat gland ducts as compared to through epidermis. Furthermore, because of the poor affinity for red blood cells, Pb which has penetrated through the skin would be distributed almost completely in the intercellular fluid [39]. Due to its high affinity for protein, lead tended to attach itself to haemoglobin and plasma protein of blood cell. These prevented the production of red blood cells, and thus caused inadequate supply of oxygen to vital organs. Moreover, as the capacity bonding of Pb and protein increased, the tendency to pass through the bone marrow may increase as well. Such intoxication can cause damage to sexual organs, renal impairment, liver damage and encephalopathy in the central nervous system [39].

The amount of Hg detected for Brand X (ranged from 4.3-6.5 ppm) and Y (ranged from 0-0.05 ppm), in which the detected Hg concentrations were higher than the permitted level set by the Malaysian standard for Brand X. Typically, Hg is found in two forms of cosmetics, which is organic or inorganic. Organic mercury is used in cosmetic preservatives, while inorganic mercury is commonly used as an agent for skin whitening. Inorganic compounds are generally a combination of Hg with chlorine, sulphur and oxygen. Meanwhile mercury (II) chloride and ammonised mercury (II) are most common in skin creams [38]. Small amounts of Hg and its compounds are dangerous to human health, and these are cumulative toxins. An adult skin could consume up to 450 µg Hg from a single treatment of a product, carrying 10,000 ppm of mercury [40, 41].

Table 1. The method validation data for the ICP-OES of As, Cd, Pb and Hg

Heavy Metals	Linear Range (ppm)	Calibration Curve		
		R^2	LOD (ppm)	LOQ (ppm)
As	0.01 - 0.25	1.0000	0.03	0.1
Cd	0.01 - 0.25	0.9990	0.03	0.1
Hg	0.01 - 0.25	0.9996	0.003	0.01
Pb	0.01 - 1.2	0.9996	0.03	0.1

Table 2. Concentrations of As, Cd, Hg and Pb in face whitening cream samples

Unregistered Whitening Products Analyzed	Heavy Metals Concentration (ppm)			
	As	Cd	Hg	Pb
X_1	N.D	N.D	4.7	N.D
X_2	N.D	N.D	6.5	N.D
X_3	N.D	N.D	4.3	N.D
X_4	N.D	N.D	4.6	N.D
X_5	N.D	N.D	5.8	N.D
Y_1	N.D	N.D	0.05	N.D
Y_2	N.D	N.D	0.05	N.D
Y_3	N.D	N.D	0.03	0.1
Y_4	0.2	N.D	N.D	0.4
Y_5	0.2	N.D	N.D	0.4
Z_1	N.D	N.D	N.D	0.4
Z_2	N.D	N.D	N.D	0.4
Z_3	N.D	N.D	N.D	0.4
Z_4	N.D	N.D	N.D	0.4
Z_5	N.D	N.D	0.02	0.2

N.D = Not Detected

Table 3. Range of As, Cd, Hg and Pb detected in whitening cream samples

Heavy Metals	Unregistered Face Whitening Products Analyzed		
	Brand X Median (Range)	Brand Y Median (Range)	Brand Z Median (Range)
As	0.2 (N.D-0.2)	N.D	N.D
Cd	N.D	N.D	N.D
Pb	N.D	0.1(0.1-0.4)	0.4 (0.2-0.4)*
Hg	5.8 (4.3-6.5)*	0.03 (0-0.05)	N.D

N.D = Not Detected

Table 4. Estimated daily intake and health risk index of As, Hg and Pb *via* dermal exposure from whitening creams commonly found in local market of Johor Bahru

Sample	Heavy Metals (g/kg/day)			Heavy Metals (HRI)		
	As	Hg	Pb	As	Hg	Pb
X_1		0.1149			3.8296	
X_2		0.1589			52.9630	
X_3		0.1051			35.0370	
X_4		0.1124			37.4815	
X_5		0.1418			47.2593	
Y_1						
Y_2						
Y_3			0.0024			17.4603
Y_4	0.0005	0.0012	0.0098	0.1630	0.4074	69.8413
Y_5	0.0005	0.0012	0.0098	0.1630	0.4074	69.8413
Z_1			0.0098			69.8413
Z_2			0.0098			69.8413
Z_3			0.0098			69.8413
Z_4			0.0098			69.8413
Z_5			0.0049			34.9206

Statistical analysis

Statistical analysis was carried out on the study data to determine which of the selected whitening cream brands is the most hazardous to health. To determine the normality of data distribution, Kolmogorov–Smirnov and Shapiro-Wilk tests were used.

The cross-sectional sampling of products took place on March 2018, and here the values were expressed as median (range). Considering that the results violated normality assumption, the Mann-Whitney U test was used to compare the median between classes. Significance level of 0.05 was used to determine the significant differences between groups.

Symbol (*) represents the significantly higher concentration of an analyte in a group as compared to another ($p < 0.05$). Comparison by using Mann Whitney U test with a significance level of 0.05 was used to determine the significant concentration differences between brands (Table 3). The data are presented as a median ± interquartile range. Mann Whitney U test was performed for concentrations of Brand X and Brand Y for Hg, and concentrations of Brand Y and Brand Z for Pb. The concentration of Hg in Brand X was statistically higher than in Brand Y. The concentration of Pb in Brand Z was higher than in Brand Y, but statistically it was not significant. As compared to the other two products, Brand Y was comparatively safer, but repeated use of this product may result in Hg and Pb accumulation and ultimately acquired the side effects of the respective heavy metals.

Estimation of daily intake of toxic metals and health risk assessment

Table 4 provides the estimated daily intake (EDI) of metals (As, Hg, and Pb) from the use of unregistered face whitening creams which were included in this work. Cd was not counted for EDI because Cd was not observed in the samples. The EDI obtained were 0.00049 mg/day for As, 0.0012 mg/day to 0.16 mg/day for Hg, and 0.0024 mg/day to 0.0098 mg/day for Pb. The EDI order of metals in unregistered face whitening creams was Hg>Pb>As. The hazard risk indices (HRI) were determined by using the EDI and the values are also shown in Table 4. The HRI value must be less than 1 to avoid any health hazards to consumers. If the gained HRI values were more than 1, there may be concerns about the potential health risk [42]. HRI obtained for As was 0.1629 while for Hg the values ranged from 0.4074 to 52.69, and Pb was ranged from 17.64 to 69.84 respectively. Since the HRI values obtained for Hg and Pb were greater than 1, this means that such products will no longer be safe for use and may have side effects to consumers' health.

Conclusion

Three different brands of unregistered face whitening creams obtained from local markets in Johor Bahru had been analysed for heavy metals concentrations. Cd was not detected in all brands while very high concentration of Hg was found in Brand X. From direct comparison, Brand X could be categorised as the most harmful face whitening cream relative to the other two brands because it contained the highest Hg concentration, which was 6.5 ppm; higher than the NPBC limit set. Small amount of Pb was detected in Brand Y and Brand Z with variation of Pb concentration in Brand Y. There was no substantial concentration of As detected for Brand Y and Brand Z, but some amount of Hg and Pb were detected. Meanwhile the amount of As and Pb were below the limit for Brand Y and Brand Z, the results of the risk assessment suggested that the brands could cause a risk to human health upon prolonged use. The HRI values obtained for Hg and Pb in Brand X and Brand Z were > 1. Therefore, it could be concluded that these brands have high potential to be harmful to humans and the long-term use of these substances could cause a public health issue.

Acknowledgement

The financial support by Universiti Teknologi Malaysia via UTMShine grant (Q.J130000.2454.09G30) is gratefully appreciated.

References

1. Hassali, M. A. and Al-Tamimi, S. K. (2015). Malaysian cosmetic market: current and future prospects. *Pharmaceutical Regulatory Affairs: Open Access,04*(04): 1-3.
2. Farrah N. K., and Aliza. S. (2016). Toxic cosmetics killing Malaysians. Access from https://www.nst.com.my/news/2016/12/198864/exclusive-toxic-cosmetics-killing-malaysians-video. [Access on January 2018].
3. Saadatzadeh, A., Afzalan, S., Zadehdabagh, R., Tishezan, L., Najafi, N., Seyedtabib, M. and Noori, S. M. A. (2019). Determination of heavy metals (lead, cadmium, arsenic, and mercury) in authorized and unauthorized cosmetics. *Cutaneous and Ocular Toxicology,* 38(3): 207-211.
4. Adebajo, S. B. (2002). An epidemiological survey of the use of cosmetic skin lightening cosmetics among traders in Lagos, Nigeria. *Mercury*, 5(7): 43-48.

5. Arbab, A. and Eltahir, M. M. (2010). Review on skin whitening agents. *Khartoum Pharmaceutical Journal*, 13(1): 5-9.
6. Yamaguchi, Y., Morita, A., Maeda, A. and Hearing, V. J. (2009). Regulation of skin pigmentation and thickness by Dickkopf 1 (DKK1). *Journal of Investigative Dermatology Symposium Proceedings,*14(1): 73-75.
7. Young, A. R. (2006). Acute effects of UVR on human eyes and skin. *Progress in Biophysics and Molecular Biology,* 92(1): 80-85.
8. Williams, H. (1992). Skin lightening creams containing hydroquinone. *BMJ: British Medical Journal*, 305(6859): 903-904.
9. Zainy, F. M. (2017). Heavy metals in lipstick products marketed in Saudi Arabia. *Journal of Cosmetics, Dermatological Sciences and Applications,*07(04): 336-348.
10. Hadiani, M. R., Dezfooli-Manesh, S., Shoeibi, S., Ziarati, P. and Mousavi Khaneghah, A (2015). Trace elements and heavy metals in mineral and bottled drinking waters on the Iranian market. *Journal Food Additives and Contaminants: Part B,* 8: 18-24.
11. Shahsavani, A., Fakhri, Y., Ferrante, M., Keramati, H., Zandsalimi, Y., Bay, A., Hosseini Pouya, S. R., Moradi, B., Bahmani, Z. and Mousavi Khaneghah, A. (2017). Risk assessment of heavy metals bioaccumulation: fished shrimps from the Persian Gulf. *Toxin Review*, 36: 322-330.
12. Adegbola, R. A., Adekanmbi, A. I., Abiona, D. L. and Atere, A. A. (2015). Evaluation of some heavy metal contaminants in biscuits, fruit drinks, concentrates, candy, milk products and carbonated drinks sold in Ibadan, Nigeria. *International Journal of Brain and Cognitive Sciences*, 9: 1691-1696.
13. Ahmadi, A. and Ziarati, P. (2015). Chemical composition profile of canned and frozen sweetcorn (*Zea mays* L.) in Iran. *Oriental Journal of Chemistry*. 31: 1065-1070.
14. Akan, J., Kolo, B., Yikala, B. and Ogugbuaja, V. (2013). Determination of some heavy metals in vegetable samples from biu local government area, Borno State, North Eastern Nigeria. *International Journal of Environmental Monitoring and Analysis*, 1: 40-46.
15. Ali, M. H. and Al-Qahtani, K. M. (2012). Assessment of some heavy metals in vegetables, cereals and fruits in Saudi Arabian markets. *The Egyptian Journal of Aquatic Research,* 38: 31-37.
16. Anwar, A., Mahmood, T., Khan, M. Z., Kiswar, F., Perveen, R. and Ikram, S. (2014). Heavy metals in fruit juices in different packing material. *FUUAST Journal of Biology*. 4: 191-194.
17. Eleboudy, A. A., Amer, A., Abo El-Makarem, H., Hadour, H. and Abo, H. (2016). Heavy metals residues in some dairy products. *The Alexandria Journal of Veterinary Sciences*, 51(2): 334-346.
18. Agency for Toxic Substances and Disease. (2017). ATSDR's substance priority list. Access from https://www.atsdr.cdc.gov/SPL/. [Access online June 2020].
19. Nurmi, P., Özkaya, B., Kaksonen, A. H., Tuovinen, O. H. and Puhakka, J. A. (2009). Inhibition kinetics of iron oxidation by *Leptospirillum ferriphilum* in the presence of ferric, nickel and zinc ions. *Hydrometallurgy*. 97(3-4): 137-145.
20. Flanagan, P. R., McLellan, J. S, Haist, J., Cherian, G., Chamberlain, M. J. and Valberg L. S. (2008). Increased dietary cadmium absorption in mice and human subjects with iron deficiency. *Gastroenterology,* 74: 841-846.
21. Bellinger, D. C. (2008). Neurological and behavioral consequences of childhood lead exposure. *PLoS Medicine, 5*(5): 115.
22. Sanders, A. P., Claus Henn, B. and Wright, R. O. (2015). Perinatal and childhood exposure to cadmium, manganese, and metal mixtures and effects on cognition and behavior: A review of recent literature. *Current Environmental Health Reports,* 2: 284-294.
23. Benn, E. K. T., Alexis, A., Mohamed, N., Wang, Y.-H., Khan, I. A. and Liu, B. (2016). Skin bleaching and dermatologic health of african and afro-caribbean populations in the US: New directions for methodologically rigorous, multidisciplinary, and culturally sensitive research. *Dermatology and Therapy*, 6(4): 453-459.

24. Hassali, M. A. A., Shafie, A. A., See, O. G. and Wong, Z. Y. (2016). Pharmacy practice in Malaysia in. Pharmacy practice in developing countries edited by Fathelrahman, A. I., Mohamed Ibrahim, M. I. and Wertheimer, A. I., Academic Press: pp. 23-40.
25. National pharmaceutical regulatory agency (2017). Guidelines for control of cosmetic products in malaysia-1st revision. https://www.npra.gov.my/images/Guidelines_Central/Guidelines_on_Cosmetic/2017/feb2017/Annex_I_part_14heavy_metal_and_microbiological_test_limit_for_cosmetic_ product.pdf. [Access online June 2020].
26. Centre for food safety and applied nutrition. (2019). Arsenic, cadmium, chromium, cobalt, lead, mercury, and nickel content. https://www.fda.gov/cosmetics/potential-contaminants-cosmetics/fdas-testing-cosmetics-arsenic-cadmium-chromium-cobalt-lead-mercury-and-nickel-content [Access online June, 2020].
27. Zulkifli, N. W., Aziz, N. A., Hassan, Y., Hassali, M. A., Bahrin, N. L. Z. and Ahmad, A. (2016). Are we on the right track?: overview of unregistered drugs in Malaysia. *Journal of Pharmacy Practice and Community Medicine, 2*(4): 107-115.
28. Ababneh, F. A. and Al-Momani, I. F. (2018). Assessments of toxic heavy metals contamination in cosmetic products. *Environmental Forensics*, 19(2): 134-142.
29. Eltegani, S. E., Ali, H. M., and Hammad, A. Y. (2013). The hazards of hidden heavy metals in face make-ups. *British Journal of Pharmacology and Toxicology*, 4(5): 188-193.
30. Lech, T. (2014). ICP OES And CV AAS in determination of mercury in an unusual fatal case of long-term exposure to elemental mercury in a teenager. *Forensic Science International*, 237: 1-5.
31. Zakaria, A. and Ho, Y. B. (2015). Heavy metals contamination in lipsticks and their associated health risks to lipstick consumers. *Regulatory Toxicology and Pharmacology*,73(1): 191-195.
32. Ayenimo, J. G., Yusuf, A. M., Adekunle, A. S. and Makinde, O. W. (2009). Heavy metal exposure from personal care products. *Bulletin of Environmental Contamination and Toxicology*, 84(1): 8-14.
33. Marguí, E., Dalipi, R., Borgese, L., Depero, L. E. and Queralt, L. (2019). Possibilities and drawbacks of total reflection x-ray fluorescence spectrometry as a fast, simple and cost-effective technique for multielement analyses of cosmetics. *Analytica Chimica Acta*, 1075: 27-37.
34. Chakraborty, K. and Chaudhary, S. (2019). Estimation the presence of heavy metals and trace elements in indian herbal cosmetics by atomic absorption spectrophotometer. *Asian Journal of Pharmaceutical Research and Development*, *7*(5): 59-64.
35. Omenka, S. S., and Adeyi, A. A. (2016). Heavy metal content of selected personal care products (PCPs) available in Ibadan, Nigeria and their toxic effects. *Toxicology Reports*, 3: 628-635.
36. Munro, B. H. and Jacobsen, B. S. (2005). Key principle of statistical inference in statistical methods for health care research edited by Duffy, M. E. Philadelphia: Lippincott Williams and Wilkins, Lippincott-Raven Publishers: pp. 83-84.
37. World Health Organisation (2018). Arsenic. https://www.who.int/news-room/fact-sheets/detail/arsenic. [Access online June 2020].
38. Mohammed, T., Mohammed, E. and Bascombe, S. (2017). The evaluation of total mercury and arsenic in skin bleaching creams commonly used in Trinidad and Tobago and their potential risk to the people of the Caribbean. *Journal of Public Health Research*, 6(3): 1097.
39. Lu, H., Sun, G., Hu, W., Yuan, Z. and Zhang, B. (2017). Characteristics of mercury intoxication induced by skin-lightening products. *Chinese Medical Journal*, 130(24): 3003-3004.
40. Dórea, J. G. (2016). Additional comments to "Potential health consequences of applying mercury-containing skin-lightening creams during pregnancy and lactation periods. *International Journal of Hygiene and Environmental Health,* 219(8): 920-921.
41. Azevedo, B. F., Furieri, L. B., Peçanha, F. M., Wiggers, G. A., Vassallo, P. F., Simões, M. R. and Vassallo, D. V. (2012). Toxic effects of mercury on the cardiovascular and central nervous systems. *Journal of Biomedicine and Biotechnology*, 2012: 1-11.

42. Khalid, S., Shahid, M., Dumat, C., Niazi, N. K., Bibi, I., Gul Bakhat, H. F. S. and Javeed, H. M. R. (2017). Influence of groundwater and wastewater irrigation on lead accumulation in soil and vegetables: implications for health risk assessment and phytoremediation. *International Journal of Phytoremediation,* 19(11): 1037-1046.

Malaysian Journal of Analytical Sciences (MJAS)
Published by Malaysian Analytical Sciences Society

ELECTRICAL AND INFRARED SPECTROSCOPIC ANALYSIS OF SOLID POLYMER ELECTROLYTE BASED ON POLYETHYLENE OXIDE AND GRAPHENE OXIDE BLEND

(Kajian Elektrik dan Spektroskopik Inframerah kepada Elektrolit Polimer Pepejal Campuran Polietilena Oksida dan Grafena Oksida)

Ahmad Syafiq Fauzan Mohd Asnawi[1], Alyaa Amalina Mohd Azli[2], Muhamad Hafiz Hamsan[2], Mohd Fakhrul Zamani Abdul Kadir[3], Yuhanees Mohamed Yusof[1]*

[1]Chemical Engineering Section,
Universiti Kuala Lumpur, Malaysian Institute of Chemical & Bioengineering Technology, 78000 Alor Gajah, Malacca, Malaysia
[2]Institute of Graduate Studies
[3]Centre for Foundation Studies in Science
University of Malaya, 50603 Kuala Lumpur, Malaysia

**Corresponding author: yuhanees@unikl.edu.my*

Received: 30 March 2020; Accepted: 21 August 2020; Published: 12 October 2020

Abstract

Poly(ethylene oxide) (PEO), polyvinyl alcohol (PVA), and poly(ethylene carbonate) are synthetic polymers that have been widely used as polymer host in solid polymer electrolyte (SPE). A proton source, for example, lithium triflate ($LiCF_3SO_3$), ammonium bromide (NH_4Br), and ammonium fluoride (NH_4F) are doped in the polymer blend to provide the mobile Li^+ or H^+ ions. Polymer blending has been introduced to improve the properties of SPEs due to the easy preparation and excellent physical properties. In the present work, SPEs hosted by poly(ethylene oxide) (PEO) - graphene oxide (GO) blend doped with ammonium triflate ($NH_4CF_3SO_3$) has been prepared *via* solution casting technique. The highest room temperature conductivity of the PEO-GO polymer electrolytes containing 35 wt.% $NH_4CF_3SO_3$ was found to be $(2.48 \pm 0.83) \times 10^{-6}$ S cm^{-1}. This conductivity is comparable to our previous work for the system of PEO-GO-$LiCF_3SO_3$ at $(3.84 \pm 0.83) \times 10^{-6}$ S cm^{-1}. Fourier transmission infrared (FTIR) analysis exhibits the complexation between ammonium salt and polymer host. The FTIR spectra have been deconvoluted in the wavenumber region between 1010 and 1100 cm^{-1} to determine the percentage of free triflate ion and ion aggregations. The results show that the number of free ions increases and attains maximum at 35 wt.% $NH_4CF_3SO_3$. The relaxation time of the electrolytes was found to decrease as the ionic conductivity at room temperature increased. Dielectric studies show that all electrolytes obeyed non-Debye behavior.

Keywords: polymer electrolyte, PEO-GO blend, ammonium triflate, ionic conductivity, dielectric constant

Abstrak

Poli (etilena oksida) (PEO), polivinil alkohol (PVA), dan poli (etilena karbonat) merupakan polimer sintetik yang banyak digunakan sebagai polimer asas dalam elektrolit polimer pepejal (SPE). Sebagai sumber proton seperti litium triflate ($LiCF_3SO_3$), amonium bromida (NH_4Br), dan amonium fluorida (NH_4F) ditambah ke dalam campuran polimer untuk memberi ion Li^+ atau H^+.

Pengadun polimer telah diperkenalkan untuk meningkatkan sifat-sifat SPE kerana penyediaannya yang mudah dan sifat fizikal yang sangat baik. Dalam kajian ini, SPE yang berasaskan campuran poli (etilena oksida) (PEO) - grafena oksida (GO) yang dengan tambahan amonium triflate ($NH_4CF_3SO_3$) telah disediakan melalui teknik pengacuan larutan. Kekonduksian pada suhu bilik tertinggi ialah bagi elektrolit polimer PEO-GO yang mengandungi 35% berat $NH_4CF_3SO_3$ iaitu pada $(2.48 \pm 0.83) \times 10^{-6}$ S cm^{-1}. Kekonduksian ini adalah setanding dengan kajian kami sebelum ini bagi sistem PEO-GO-$LiCF_3SO_3$ pada $(3.84 \pm 0.83) \times 10^{-6}$ S cm^{-1}. Analisis spektrometer inframerah (FTIR) mempamerkan kompleks antara garam ammonium dan polimer asas. Spektrum FTIR telah didikonvolutkan di antara 1010 dan 1100 cm^{-1} untuk menentukan peratusan agregat ion dan ion triflat bebas. Keputusan menunjukkan bahawa bilangan ion bebas meningkat dan mencapai maksimum pada 35% berat $NH_4CF_3SO_3$. Masa kelonggaran elektrolit didapati berkurangan apabila kekonduksian ionik meningkat pada suhu bilik. Kajian dielektrik menunjukkan bahawa semua elektrolit mematuhi tingkah laku bukan Debye.

Kata kunci: elektrolit polimer, campuran PEO-GO, amonium triflate, kekonduksian ionik, pemalar dielektrik

Introduction

Polymer electrolyte is a vital component that is used in electrochemical devices such as proton batteries and electrochemical double layer capacitors (EDLCs). The development of solid polymer electrolyte (SPE) first began in 1979 by applying lithium batteries [1]. Liquid electrolytes are well known due to their high performance in various energy devices [2, 3]. However, liquid electrolytes are easy to evaporate and damage the equipment due to leaking and corrosive problems [4]. SPEs have good potential to replace liquid electrolyte due to their safe and easy fabrication as well as having long shelf life [5]. Lithium batteries provide high conductivity and overall good performance. However, their characteristics which include not being able to naturally degrade may lead to environmental pollutions [6]. Hence, researchers have started to replacing Li-ion provider with other alternatives to replace the H^+ ion including Mg^{2+} ion and NH_4^+ ion [2, 7].

Blending two or more different polymers in producing a polymer electrolyte system is a technique that can assist in increasing the sites availability for ion hopping and exchange [8]. Rather than a single polymer, a mixture of polymers can enhance the thermal stability and mechanical strength [9]. Polymer electrolyte hosted by poly(ethylene oxide) (PEO) has the potential for the development of ion conduction because it is naturally semi crystalline, has high tensile strength, and flexible due to non-hazardous and easy preparation of electrolyte [10, 11]. The high molecular weight of PEO based polymer electrolytes shows the movement of ions *via* their amorphous phase [12]. Thus, the selection of PEO as polymer host for the designing of SPE is significant due to their ability to form complexation with other components as well as improving the transport mechanism [13]. Meanwhile, graphene oxide (GO) has the ability to be used as an active nanofiller [14]. Mohanta et al. stated that GO has high surface area, able to disperse in organic solvents, and is stable thermally and chemically. Polymer nanocomposites of GO based have better mechanical and electrical properties compared to other clay or carbon filler based [15]. GO can be modified and functionalized for the preparation of polymer host, and it is also a pioneer material for the preparation of large quantities of graphene nanosheets for various functions such as sensors and transparent conductive films [16, 17].

The addition of salt into polymer blend has been proven to increase the ionic conductivity. Anuar et al. reported that addition of ammonium triflate ($NH_4CF_3SO_3$) salt into poly(ethyl methacrylate) (PEMA) based polymer electrolyte had increased the conductivity from 8.60×10^{-11} S cm^{-1} to 1.02×10^{-5} S cm^{-1} [18]. The incorporation of ammonium salt was more cost-effective and had been reported as a suitable proton donor to the polymer electrolyte salted system which was comparable with a lithium salt-doped system [19, 20]. Rodi et al. reported that the incorporation of 20 wt.% $LiCF_3SO_3$ in PEMA based electrolyte had obtained an ionic conductivity of 7.20×10^{-8} S cm^{-1} at room temperature [21].

Our previous work showed that the X-ray diffraction (XRD) analysis of 90 wt.% PEO - 10 wt.% GO blend was suitable to act as polymer host since it exhibited the

most amorphous blend [22]. In the present work, attention was given to develop the same ratio of PEO-GO blend polymer host with the incorporation of $NH_4CF_3SO_3$ salt as proton provider for the system. The effect of salt concentration on the ionic conductivity at room temperature was studied based on the electrical properties via electrical impedance spectroscopy (EIS) and Fourier transform infrared (FTIR) spectroscopy. The transport and dielectric properties of the electrolytes are further discussed.

Materials and Methods

Preparation of graphene oxide (GO)

GO nanosheets were prepared by a modified Hummers method [23]. The impurities such as sulfuric acid and phosphoric acid traces from the Hummers method were removed through the washing process by using distilled water. Mild sonication was applied to the suspension for about 10 minutes to exfoliate graphite oxide that remained in the GO suspension. Finally, GO suspension was put into the oven for 48 hours at 60°C to discard water present, thus obtaining dark brown GO nanosheets.

Preparation of PEO-GO-$NH_4CF_3SO_3$ (salted) system

The polymer blend electrolyte system was prepared by homogenizing 10 wt.% of GO nanosheets in 50 mL distilled water from a total of 0.5 g polymer blend by using ultrasonicator XO-650D (Nanjing Xianou Instruments Co. Ltd.) for about 15 minutes at 50% crusher capacity. After the solution was cooled to room temperature, 90 wt.% of PEO (Aldrich Chemistry) was then added to the GO solutions and stirred until a homogeneous solution was obtained. Before the preparation of salted electrolytes, $NH_4CF_3SO_3$ (Aldrich Chemistry) was dried at 100 °C for 1 hour to eliminate trace amounts water. Different amount of $NH_4CF_3SO_3$ between 5 to 45 wt.% was added to the PEO-GO solutions and stirred until complete dissolution. The composition and designation of various PEO-GO-$NH_4CF_3SO_3$ blends are listed in Table 1. All homogeneous solutions were cast onto plastic Petri dishes and left to dry at room temperature for 4 to 5 days to form a film. The dry films were then kept in desiccators filled with silica gel desiccants for 2 to 3 hours before being characterized to avoid any trace of moisture.

Characterization of electrolytes

Impedance measurements were conducted using HIOKI 3532-50 LCR HiTESTER at room temperature in the frequency range of 50 Hz to 5 MHz. The electrolyte films were sandwiched between two stainless steel electrodes of a conductivity holder with a diameter of 1.9 cm. The value of bulk resistance (R_b) determined from the Cole-Cole plots. Conductivity (σ) was calculated using the equation below;

$$\sigma = \frac{d}{R_b A} \quad (1)$$

where d is the thickness of the electrolyte samples, and A is the electrode-electrolyte contact area. A digital thickness gauge (Mitutoyo Corp.) was employed to measure the thickness of the electrolytes.

The Fourier transform infrared spectroscopy (FTIR) studies were performed using attenuated total reflection infrared spectroscopy (ATR-IR) Perkin Elmer Spectrum 400 GladiATR in the wavenumber range of 600 - 4000 cm^{-1}. The purpose of FTIR analysis was to confirm the complexation between polymer and salt. Deconvolution technique was used to extract any overlapping peaks. Correction of baseline and fitting curve was implemented via Gaussian-Lorentzian function. From FTIR deconvolution, number density (n), ionic mobility (μ), and diffusion coefficient (D) of charges carriers were calculated the following Eq. 2 to Eq. 4.

$$n = \frac{M \times N_A}{V_{Total}} \times (free\ ion\%) \quad (2)$$

$$\mu = \frac{\sigma}{ne} \quad (3)$$

$$D = \frac{\mu kT}{e} \quad (4)$$

In Eq. 2, M is the number of moles of $NH_4CF_3SO_3$ salt used, N_A is Avogadro's number (6.02×10^{23} mol^{-1}), and V_{Total} is the total volume (cm^3) of polymer electrolyte. In Eq. 3, e is the elementary charge (1.602×10^{-19} C) while k and t in Eq. 4, is a Boltzmann constant (1.38×10^{-23} JK^{-1}) and absolute temperature, respectively.

Table 1. The composition and designation of electrolytes in salted system

Poly(ethylene oxide) : Graphene oxide : $NH_4CF_3SO_3$ composition (wt.%)	Designation
90 wt.% PEO - 10 wt.% GO	PG9
90 wt.% PEO - 10 wt.% GO - 5 wt.% $NH_4CF_3SO_3$	S5
90 wt.% PEO - 10 wt.% GO - 15 wt.% $NH_4CF_3SO_3$	S15
90 wt.% PEO - 10 wt.% GO - 25 wt.% $NH_4CF_3SO_3$	S25
90 wt.% PEO - 10 wt.% GO - 35 wt.% $NH_4CF_3SO_3$	S35
90 wt.% PEO - 10 wt.% GO - 45 wt.% $NH_4CF_3SO_3$	S45

Results and Discussion

Figure 1 shows the ionic conductivity of the polymer electrolyte with different concentration of $NH_4CF_3SO_3$ at room temperature. The conductivity for an un-doped sample (PG9) is $(4.10 \pm 1.12) \times 10^{-11}$ S cm^{-1}, which is relatively low since there is no mobile ions presence within the film. However, the conductivity increases to $(1.30 \pm 0.32) \times 10^{-8}$ S cm^{-1} for S5. Anuar et al. also reported that addition of $NH_4CF_3SO_3$ salt into PEMA would increase the conductivity of the polymer electrolyte. On the addition of 35 wt.% of $NH_4CF_3SO_3$ into PEO-GO polymer blend, the conductivity is further increased to $(2.48 \pm 0.83) \times 10^{-6}$ S cm^{-1}. The conductivity with the order of $\sim 10^{-6}$ S cm^{-1} is comparable with other reports on polymer host containing triflate salt [24, 25]. The conductivity is then decreased to $(3.64 \pm 3.67) \times 10^{-7}$ S cm^{-1} with the addition of 45 wt.% of $NH_4CF_3SO_3$. It clearly explains that the addition of $NH_4CF_3SO_3$ more than 35 wt.% will reduce the ionic conductivity due to the formation of overcrowded ions in the system. Samsudin et al. had reported a 35 wt.% of dodecyltrimethyl ammonium bromide salt in carboxymethylcellulose-based electrolyte resulted the highest ionic conductivity which also proved that the ion mobility is lower at higher salt concentration due to the aggregation of ion clusters [26].

In this work, the focus has been given to study the interaction of the polymer blend with ammonium salt based on the FTIR analysis. The band assignments for the polymer electrolyte system are listed in Table 2. Figure 2 shows the FTIR spectra for regions at 600 - 4000 cm^{-1}.

The appearance of a peak at (i) 638 cm^{-1} for S5 could be assigned to asymmetric SO_3 bending due to the incorporation of $NH_4CF_3SO_3$ salt into the PEO-GO polymer host. Besides, the peak at (v) 1031 cm^{-1} and (ix) 1242 cm^{-1} are assigned to symmetric SO_3, $\upsilon_s(SO_3)$ and asymmetric SO_3, $\upsilon_{as}(SO_3)$ vibrations of $NH_4CF_3SO_3$ for S5 respectively. The peaks are then shifted to 1024 cm^{-1} and 1252 cm^{-1} as the salt concentration rises to 45 wt.%. Asmara et al. mentioned that free triflate ion should peak at 1032 cm^{-1} [31]. However, according to Wendsjö et al., the peak may shift to 1020 - 1026 cm^{-1} for higher salt concentration [32]. The triflate ion peaks may produce various FTIR active bands when the salt concentration is increased due to sensitive vibrational spectrum to the coordination state [39].

Peaks located at (iii) 843 cm^{-1} and (iv) 960 cm^{-1} are recognized to CH_2 rocking and twisting, respectively. These peaks are shifted to 840 cm^{-1} and 952 cm^{-1} as the concentration of salt increases to 45 wt.%. Moreover, for CH_2 wagging and scissoring bands, the peaks are located at 1344 cm^{-1} and 1471 cm^{-1} and then shifted consequently to (x) 1360 cm^{-1} and (xi) 1446 cm^{-1}. Hence, this indicates that there is an interaction of salt in

PEO/GO polymer blend [40]. The peak at (vi) 1100 cm^{-1} fits for the C-O-C stretching band and is relocated to 1090 cm^{-1} upon the addition of salt. Since the cation of $NH_4CF_3SO_3$ is coordinated with the ether oxygen of PEO, the spectral changes are believed to be due to the influence of salt or the C-O-C stretching mode and deformation [34].

Another band is observed at lower wavenumbers that is symmetric CF_3 deformation at (ii) 760 cm^{-1}. The appearance of this peak indicates the complexation of salt addition into the polymer host has occurred and the intensity of the peak increases as the concentration of salt increases. The CF_3 deformation has appeared at 755 - 765 cm^{-1} in the system of propylene carbonate (PC) with $NH_4CF_3SO_3$ salt [41]. Other transmittance bands were also reported by Kumar et al. that are for symmetric and asymmetric CH stretching vibrations at 2700 - 3800 cm^{-1} and 2962 - 2695 cm^{-1}, respectively. Symmetric and asymmetric CH stretching bands are located at (xii) 2897 cm^{-1} and (xiii) 3102 cm^{-1} for S45 [29].

The FTIR spectroscopy is also an analytical technique that can further be used to analyze the transport properties of an electrolyte. This study was performed for further understanding of the ionic conductivity (σ) and its relationship with the number density of mobile ion (n), ionic mobility (μ) and diffusion coefficient (D) [42]. The overlapping bands can be solved through FTIR deconvolution by compensating the essential line widths of a particular band. This technique yields spectra that have much narrower bands and can distinguish space features closely.

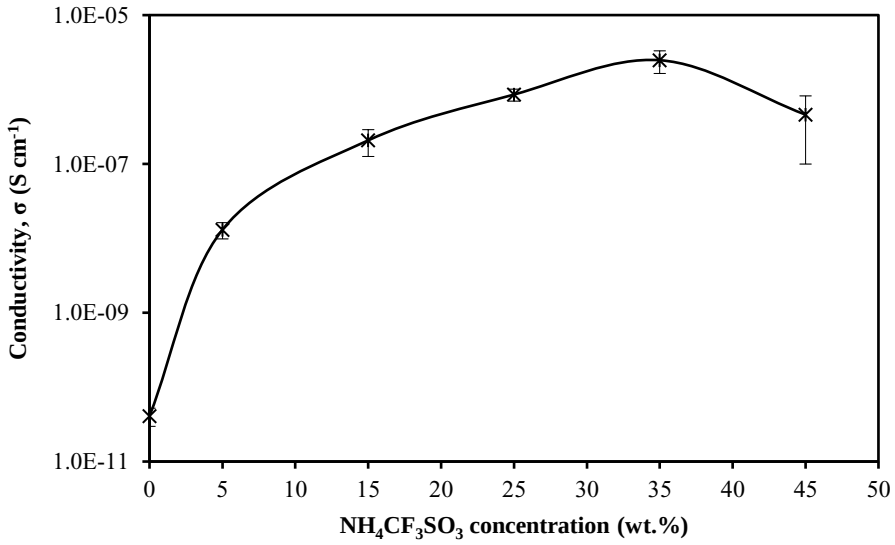


Figure 1. Ionic conductivity at room temperature for PEO-GO-$NH_4CF_3SO_3$ system

Table 2. Vibrational assignments of salted system for PEO-GO-$NH_4CF_3SO_3$ system

Wavenumber (cm^{-1})		Assignments	Reference
(i)	638	Asymmetric SO_3 bending	[27]
(ii)	760	Symmetric CF_3 deformation	[25, 28]
(iii)	843	CH_2 rocking	[27–30]
(iv)	960	CH_2 twisting	[28, 30]
(v)	1031	Symmetric SO_3 stretching	[27, 30–33]
(vi)	1100	C-O-C stretching	[34]
(vii)	1152	Asymmetric CF_3 stretching	[28, 35, 36]
(viii)	1225	Symmetric CF_3 stretching	[36, 37]
(ix)	1242	Asymmetric SO_3 stretching	[27, 30, 33]
(x)	1360	CH_2 wagging	[29, 38]
(xi)	1446	CH_2 scissoring	[27, 28, 30]
(xii)	2897	Symmetric CH stretching	[29, 30, 38]
(xiii)	3102	Asymmetric CH stretching	[29]

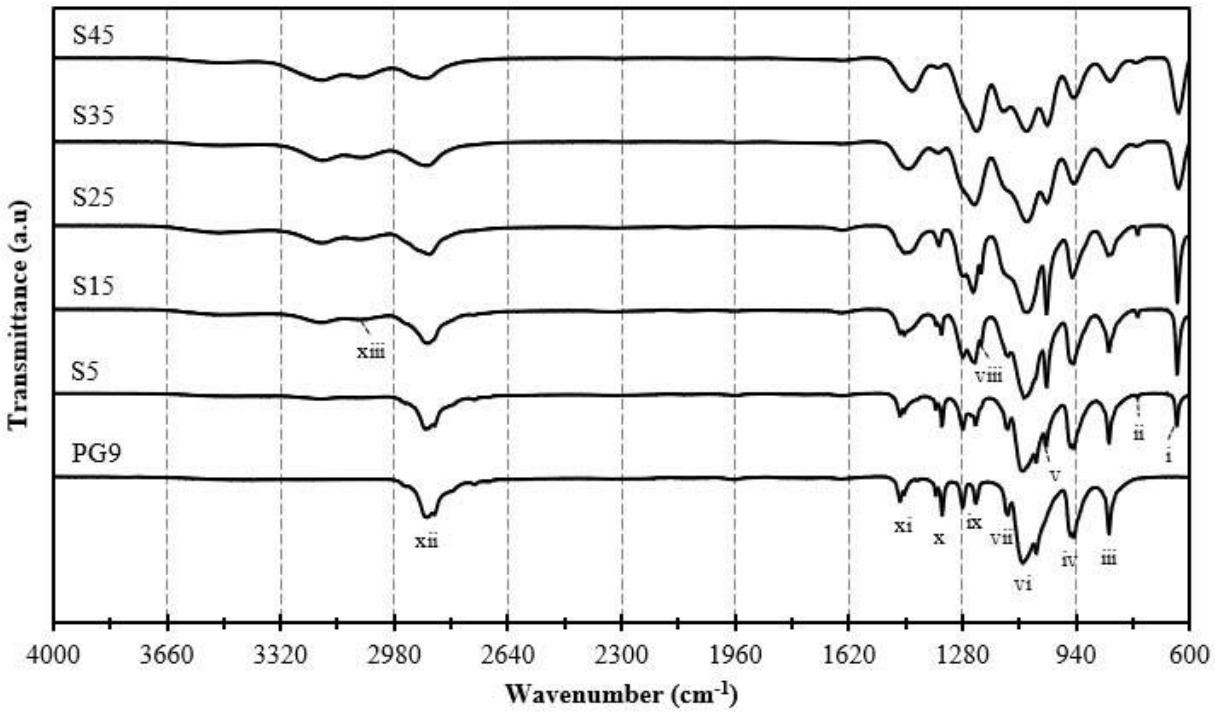


Figure 2. FTIR spectra for PEO-GO-$NH_4CF_3SO_3$ system

In this study, FTIR spectra of 1010 cm^{-1} to 1100 cm^{-1} was deconvoluted by using Gaussian-Lorentzian function, as shown in Figure 3 where the significant interaction of several peaks can be spotted. The deconvoluted area of FTIR peak will show the transport parameters. According to Asmara et al., a study on the poly(methyl methacrylate) (PMMA) gel polymer electrolytes with magnesium triflate ($Mg(CF_3SO_3)_2$), free triflate ion should peak at 1032 cm^{-1} due to decomposition of the SO_3 bands; and bands due to ion pairs and large ion aggregates should peak at 1051 cm^{-1} and 1062 cm^{-1} respectively. The peak of free triflate ion at 1032 cm^{-1} is agreeable to the previous literatures stated in Table 2. However, the free triflate ion peak may shift to 1020 - 1026 cm^{-1} for the higher salt concentration [32]. The bands that peak at 1070 cm^{-1} and 1080 cm^{-1} were also mentioned by Asmara et al. that is corresponding to ring breathing and skeletal stretching of the carbonate compound.

From Figure 3, two main peaks of free triflate ion (1026 - 1033 cm^{-1}) and ion aggregates (1058 - 1064 cm^{-1}) can be observed. Besides, ring breathing and skeletal stretching peaks from carbonate compound are located respectively between 1074 to 1079 cm^{-1} and 1087 to 1093 cm^{-1}. Meanwhile, a peak is found between 1018 to 1023 cm^{-1} which is ascribed to band of $\upsilon_s(SO_3)$. Bergstroem & Frech reported that the additional band of $\upsilon_s(SO_3)$ could be detected at wavenumber 1020 cm^{-1} to 1026 cm^{-1} [35].

The percentage of free triflate ion and ion aggregate was calculated and plotted in Figure 4. The percentage of free triflate ion increases as the $NH_4CF_3SO_3$ concentration increases but the trend is vice versa with the ion aggregates. Highest conducting electrolyte has the highest free triflate ion percentage (93.34%) that can be related to the hypothesis that the ionic conductivity of a polymer electrolyte will increase as the percentage of free ions increases. This trend of results is similar to the study by Aniskari & Mohd Isa that had 95.45% of free ion for the highest conducting sample of the 2-hydroxyethyl cellulose doped with glycolic acid polymer electrolyte system [37]. However, further addition of $NH_4CF_3SO_3$ reduces the intensity of the free triflate ion peaks which caused the ions to recombine. The recombination of ions may lead to the formation of ion pairs and caused the number of movable ions to reduce. The intensity of $\upsilon_s(SO_3)$ band is found to increase in S45 electrolyte that explains the reduction of mobile charge carriers hence decreasing the conductivity [43].

The calculated ionic transport parameters based on the percentage of free triflate ion (Eq. 2-Eq. 4) for PEO-GO polymer electrolyte with different $NH_4CF_3SO_3$ concentration are tabulated in Table 3 and plotted in Figure 5. The graphs follow the trend of ionic conductivity at room temperature are plotted in Figure 1. From the graphs, the addition of salt into the system causes the number density of mobile ion in the polymer electrolytes increases. It is believed that doping the parental host polymer leads to the increment of free ions that can contribute to the rise of ionic conductivity [37]. This is proven when the highest conducting electrolyte (S35) resulted on the highest n, μ and D values compared to other electrolytes as shown in Figure 5(a) to (c). It can be seen that after the addition of 35 wt.% $NH_4CF_3SO_3$, the ionic mobility and diffusion coefficient have decreased, which explains that the optimum value of number density was obtained at the highest conducting sample. Higher composition of salt form ion clouds where the overcrowding situation blocks most of the free ions present in the sample hence the ionic mobility and diffusion coefficient have decreased [44].

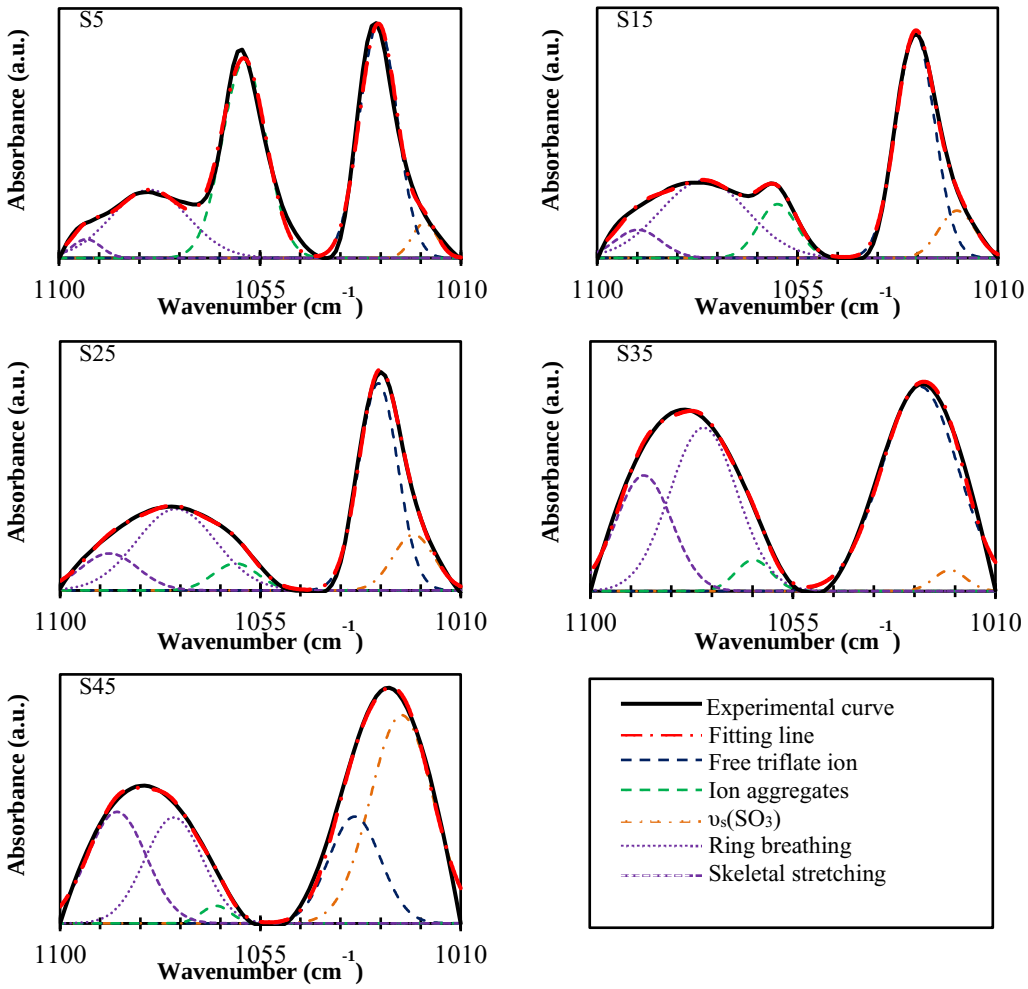


Figure 3. FTIR deconvolution for PEO-GO-$NH_4CF_3SO_3$ salted system between 1010 to 1100 cm^{-1}

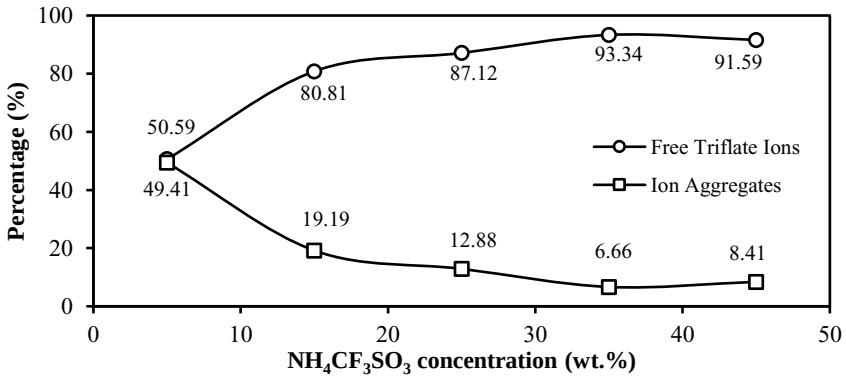


Figure 4. Percentage of free triflate ion and ion aggregates of PEO-GO-$NH_4CF_3SO_3$ salted system

Table 3. Transport parameters for PEO-GO-$NH_4CF_3SO_3$ salted system

Sample	Ionic Conductivity, σ (S cm^{-1})	Number of Density, n (cm^{-3})	Ionic Mobility, μ (cm^{2}V^{-1}s^{-1})	Diffusion Coefficient, D (cm^{2}s^{-1})
S5	$(1.30 \pm 0.32) \times 10^{-8}$	4.50×10^{23}	1.81×10^{-13}	4.64×10^{-15}
S15	$(2.07 \pm 0.81) \times 10^{-7}$	2.00×10^{24}	6.48×10^{-13}	1.66×10^{-14}
S25	$(8.56 \pm 1.57) \times 10^{-7}$	3.67×10^{24}	1.46×10^{-12}	3.74×10^{-14}
S35	$(2.48 \pm 0.83) \times 10^{-6}$	5.06×10^{24}	3.05×10^{-12}	7.84×10^{-14}
S45	$(4.60 \pm 3.60) \times 10^{-7}$	4.63×10^{24}	6.20×10^{-13}	1.59×10^{-14}

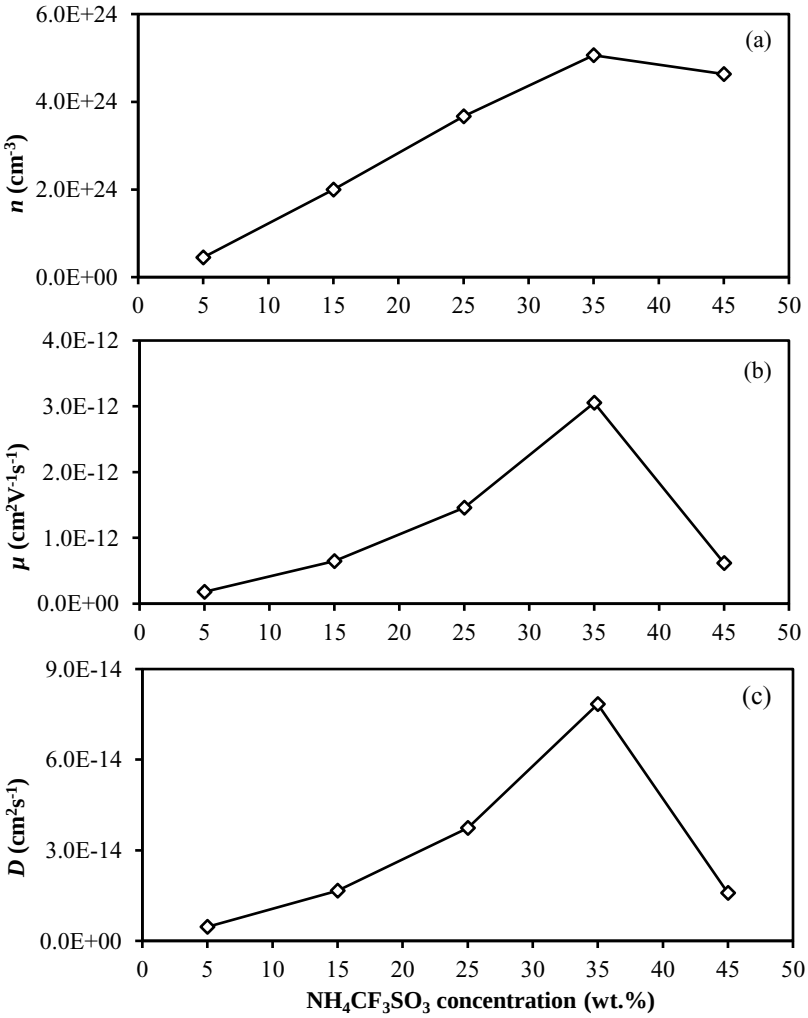


Figure 5. The transport parameter of (a) number of densities, (b) ion mobility and (c) diffusion coefficient for PEO-GO-$NH_4CF_3SO_3$ salted system

Dielectric study is useful to further verify the conductivity trend of PEO-GO polymer electrolyte with the addition of $NH_4CF_3SO_3$. The dielectric constant (ε_r) represents the charges stored in materials and dielectric loss (ε_i) stands for the loss of energy to move ions and align dipoles when the electric field polarity reverses rapidly [45]. Studies on dielectric properties help to understand the behavior of conductivity and also further support the hypothesis that the increase in the charge or the number of free mobile ions will increase the conductivity. Moreover, a detailed study of polarization and relaxation phenomena is conducted because the transport mechanism in the electrolyte is strongly correlated to the properties of the polymer matrix [46]. Both ε_r and ε_i can be expressed as in the equation below;

$$\varepsilon_r = \frac{Z_i}{\omega C_o (Z_r^2 + Z_i^2)} \quad (5)$$

$$\varepsilon_i = \frac{Z_r}{\omega C_o (Z_r^2 + Z_i^2)} \quad (6)$$

From Eq. 5 and Eq. 6, the Z_i is the imaginary part of impedance, Z_r is the real part of impedance, ω stands for the angular frequency and C_o representing the vacuum capacitance. Figure 6 shows the dependence of dielectric properties on $NH_4CF_3SO_3$ salt content. It can be observed that the highest conducting electrolyte has a higher value of ε_r and ε_i, especially at lower frequency. The increasing charge stored in the electrolyte shows that the number density of mobile ions has increased, hence increasing the conductivity [47]. Shukur et al. reported that the dielectric constant result is agreeable with the conductivity [48]. Besides, both ε_r and ε_i rise towards lower frequencies due to the electrode polarization and space charge effects, therefore obey the non-Debye behavior [7]. However, the ε_r and ε_i have decreased and become almost constant values towards higher frequencies due to the rapid periodic reversal of the electric field where there is no excess ion diffusion following the direction of the field. The polarization from the decrease of charge accumulation will lead to the a decrease in the value of ε_r and ε_i [49]. Figure 7 exhibits the $NH_4CF_3SO_3$ salt dependence of ε_r and ε_i at selected frequencies to support the trend.

The loss tangent (tan δ) graph is plotted to determine the relaxation behavior in the polymer electrolytes. It is a ratio of energy loss to energy stored in a periodical field which is also called as dissipation factor [50]. The value of tan δ can be calculated using the Eq. 7 below;

$$\tan \delta = \frac{\varepsilon_i}{\varepsilon_r} \quad (7)$$

The frequency dependence of tan δ for PEO-GO with different concentration of $NH_4CF_3SO_3$ salt at room temperature is shown in Figure 8. It illustrates that the tan δ consists of a well-defined curve at a characteristic frequency. At low frequency, tan δ increases with frequency due to the active component (ohmic) presence is more dominant than the reactive component (capacitive) while tan δ decreases at higher frequency because the amount of active component is frequency independent and the reactive component rises proportionally to the frequency [51]. The maximum of tan δ (tan δ_{max}) represents the relaxation peak that is located at a higher frequency for higher conducting electrolyte. The relaxation time (t_r) for each electrolyte can be obtained from the Eq. 8.

$$t_r \, \omega_{peak} = 1 \quad (8)$$

where ω_{peak} is the angular frequency of the relaxation peak. The values of t_r are tabulated in Table 4. The highest conducting electrolyte with the incorporation of 35 wt.% of $NH_4CF_3SO_3$ exhibits the lowest t_r value of 1.22×10^{-5} s while the lowest conducting electrolyte with 5 wt.% of $NH_4CF_3SO_3$ shows the highest value of relaxation time. The reduction in the value indicates that the polymer chain can easily orient through the increased amorphous region and/or empty room by incorporating more concentration of salts [52]. Idris et al. also reported that the lowest relaxation time possessed by the highest conducting electrolyte [53].

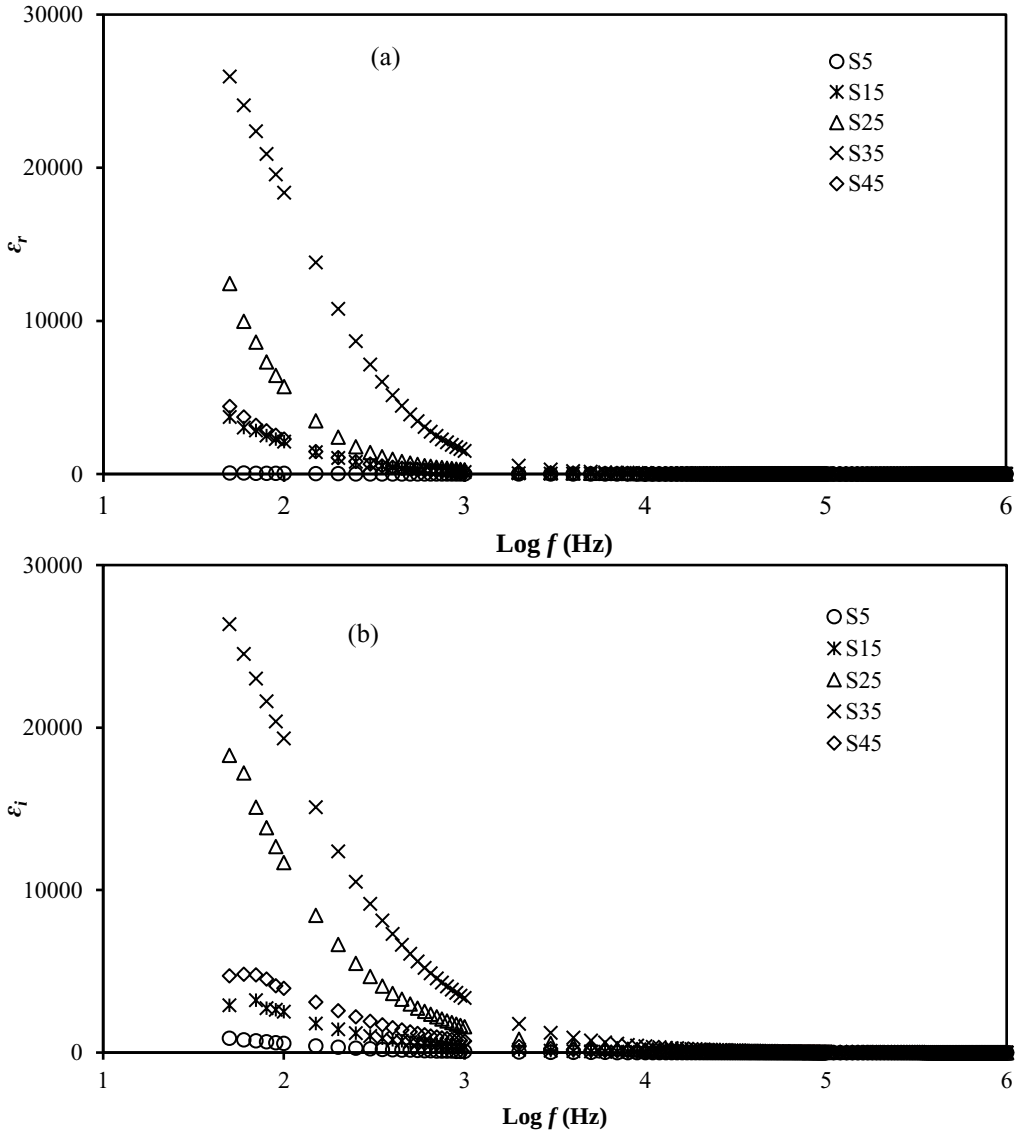


Figure 6. Frequency dependence of (a) ε_r and (b) ε_i for PEO-GO-$NH_4CF_3SO_3$ salted system at room temperature

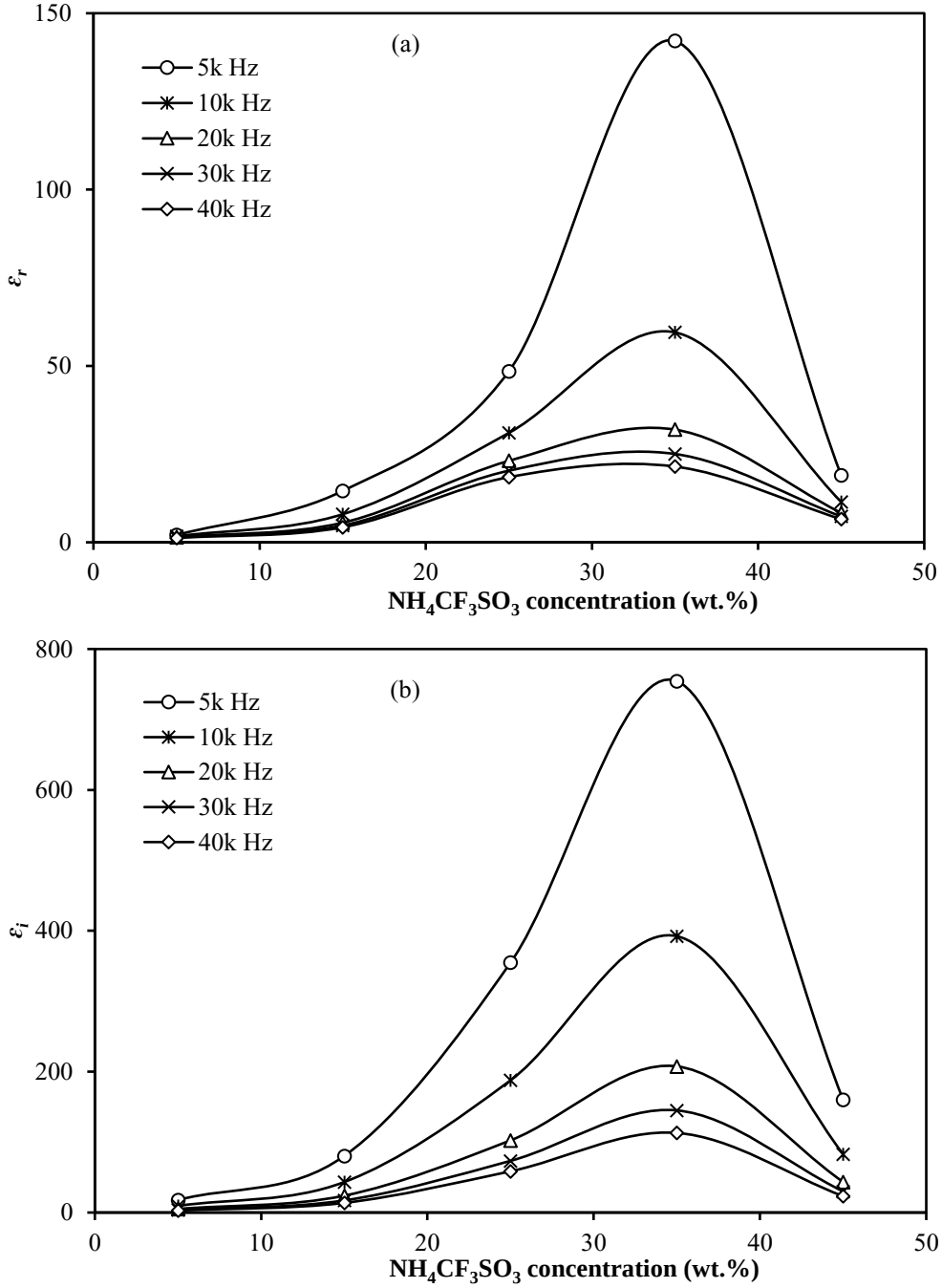


Figure 7. $NH_4CF_3SO_3$ salt dependence of (a) ε_r and (b) ε_i at room temperature for selected frequencies

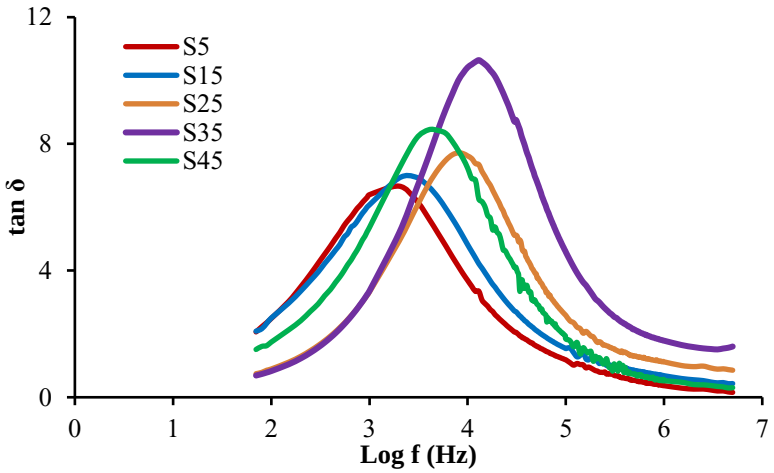


Figure 8. The frequency dependence of tan δ for PEO-GO-$NH_4CF_3SO_3$ salted system at room temperature

Table 4. Relaxation time (t_r) for PEO-GO-$NH_4CF_3SO_3$ salted system

Concentration of $NH_4CF_3SO_3$ (wt.%)	**t_r (s)**
5	$7.96. \times 10^{-5}$
15	$5.31. \times 10^{-5}$
25	$1.99. \times 10^{-5}$
35	1.22×10^{-5}
45	$3.98. \times 10^{-5}$

Conclusion

Solid polymer electrolytes hosted by PEO-GO polymer blend with varied composition of $NH_4CF_3SO_3$ salt were successfully prepared *via* solution casting technique. The conductivity studies at room temperature showed that there is an increment of ionic conductivity from $(4.10 \pm 1.12) \times 10^{-11}$ S cm^{-1} for an un-doped PEO-GO polymer blend to $(2.48 \pm 0.83) \times 10^{-6}$ S cm^{-1} with the incorporation of 35 wt.% of $NH_4CF_3SO_3$. FTIR study showed the interactions between PEO-GO polymer host blend with the addition of ammonium salt into the system occurring at certain observed peaks. FTIR deconvolution in the wavenumber region between 1010 and 1100 cm^{-1} was carried out to determine the percentage of free triflate ion and confirmed the dependence of ionic conductivity on the number density of mobile ion (n), ionic mobility (μ) and diffusion coefficient (D) of the solid polymer electrolyte. The relaxation time of the electrolytes is found to decrease as the ionic conductivity at room temperature increases. Dielectric studies show that all the electrolytes obey non-Debye behavior. The characteristics exhibited by the electrolyte in this study shows that this system has a great potential to be applied in the application of low-energy density devices such as electrical double layer capacitors (EDLCs) and proton batteries.

Acknowledgment

The authors would like to thank the Ministry of Higher Education (MOHE) for FRGS grant (FRGS/1/2018/STG07/UNIKL/02/8) and also University of Malaya and University of Kuala Lumpur for all their support for this project to be completed.

References

1. Syzdek, J., Armand, M., Marcinek, M., Zalewska, A., Zukowska, G. and Wieczorek, W. (2010). Detailed studies on the fillers modification and their influence on composite, poly(oxyethylene)-based polymeric electrolytes. *Electrochima Acta,* 55 (4): 1314-1322.
2. Zainol, N. H., Osman, Z., Othman, L. and Md. Isa, K. B. (2013). Transport and morphological properties of gel polymer electrolytes containing $Mg(CF_3SO_3)_2$. *Advanced Material Research*, 686: 137-144.
3. Isa, K. B. M. (2013). Magnesium ion-based gel polymer electrolytes: Ionic conduction and infrared spectroscopy studies. *International Journal of Electrochemical Science*, 8(3): 3602-3614.
4. Buraidah, M. H., Shah, S., Teo, L. P., Chowdhury, F. I., Careem, M. A., Albinsson, I., Mellander, B. E. and Arof, A. K. (2017). High efficient dye sensitized solar cells using phthaloylchitosan based gel polymer electrolytes. *Electrochima Acta,* 245: 846-853.
5. Riess, I. (2000). Polymeric mixed ionic electronic conductors. *Solid State Ionics,* 136-137: 1119-1130.
6. Gong, S. D., Huang, Y., Cao, H. J., Lin, Y. H., Li, Y., Tang, S. H., Wang, M. S. and Li, X. (2016). A green and environment-friendly gel polymer electrolyte with higher performances based on the natural matrix of lignin. *Journal of Power Sources,* 307: 624-633.
7. Yusof, Y. M., Shukur, M. F., Illias, H. A. and Kadir, M. F. Z. (2014). Conductivity and electrical properties of corn starch-chitosan blend biopolymer electrolyte incorporated with ammonium iodide. *Physica Scripta,* 89(3): 1-10.
8. Parameswaran, V., Nallamuthu, N., Devendran, P., Nagarajan, E. R. and Manikandan, A. (2017). Electrical conductivity studies on ammonium bromide incorporated with zwitterionic polymer blend electrolyte for battery application. *Physica B: Condensed Matter,* 515: 89-98.
9. Bakar, N. Y. A., Muhamaruesa, N. H. M., Aniskari, N. A. B. and Isa, M. I. N. M. (2015). Electrical studies of carboxy methycellulose-chitosan blend biopolymer doped dodecyltrimethyl ammonium bromide solid electrolytes. *American Journal of Applied Science,* 12(1): 40-46.
10. MacGlashan, G. S. and Andreev, Y. G. (1999). Structure of the polymer electrolyte poly(ethylene oxide)$_6$: $LiAsF_6$. *Nature*, 398: 792-794.
11. Karan, N. K., Pradhan, O. K., Thomas, R., Natesan, B. and Katiyar, R. S. (2008). Solid polymer electrolytes based on polyethylene oxide and lithium trifluoro-methane sulfonate (PEO-$LiCF_3SO_3$): Ionic conductivity and dielectric relaxation. *Solid State Ionics*, 179 (19-20): 689-696.
12. Utpalla, P., Sharma, S. K., Sudarshan, K., Sahu, M. and Pujari, P. K. (2019). Investigation of the free volume characteristics of PEO based solid state polymer electrolyte by means of positron annihilation spectroscopy. *Solid State Ionics,* 339(May): 114990.
13. Pitawala, H. M. J. C., Dissanayake, M. A. K. L. and Seneviratne, V. A. (2007). Combined effect of Al_2O_3 nano-fillers and EC plasticizer on ionic conductivity enhancement in the solid polymer electrolyte (PEO)$_9$LiTf. *Solid State Ionics,* 178 (13-14): 885-888.
14. Mohanta, J., Padhi, D. K. and Si, S. (2018). Li-ion conductivity in PEO-graphene oxide nanocomposite polymer electrolytes: A study on effect of the counter anion. *Journal of Applied Polymer Science,* 135 (22): 1-10.
15. Mahmoud, W. E. (2011). Morphology and physical properties of poly(ethylene oxide) loaded graphene nanocomposites prepared by two different techniques. *European Polymer Journal,* 47(8): 1534-1540.
16. Cano, M., Khan, U., Sainsbury, T., O'Neill, A., Wang, Z., McGovern, I. T., Maser, W. K., Benito, A. M. and Coleman, J. N. (2013). Improving the mechanical properties of graphene oxide based materials by covalent attachment of polymer chains. *Carbon,* 52: 363-371.
17. Zhu, Y., Murali, S., Cai, W., Li, X., Suk, J. W., Potts, J. R. And Ruoff, R. S. (2010). Graphene and graphene oxide: synthesis, properties, and applications. *Advanced Materials,* 22(35): 3906-3924.

18. Anuar, N. K., Subban, R. H. Y. and Mohamed, N. S. (2012). Properties of PEMA-$NH_4CF_3SO_3$ added to BMATSFI ionic liquid. *Materials,* 5(12): 2609-2620.
19. Kadir, M. F. Z., Majid, S. R. and Arof, A. K. (2010). Plasticized chitosan-PVA blend polymer electrolyte based proton battery. *Electrochima Acta,* 55(4): 1475-1482.
20. Sohaimy, M. I. H. and Isa, M. I. N. (2015). Conductivity and dielectric analysis of cellulose based solid polymer electrolytes doped with ammonium carbonate (NH_4CO_3). *Applied Mechanics and Materials,* 719-720: 67-72.
21. Rodi, I., Saaid, F. and Winie, T. (2017). PEMA-$LiCF_3SO_3$ Polymer electrolytes: Assessment of conductivity and transport properties. *AIP Conference Proceedings,* 1877 (September): 060003.
22. Azli, A. A., Manan, N. S. A. and Kadir, M. F. Z. (2015). Conductivity and dielectric studies of lithium trifluoromethanesulfonate doped polyethylene oxide-graphene oxide blend based electrolytes. *Advanced in Materials Science and Engineering,* 2015: 1-10.
23. Hummers, W. S. and Offeman, R. E. (1958). Preparation of graphitic oxide. *Journal of the American Chemical Society,* 80(6): 1339.
24. Hamdan, K. Z. and Khiar, A. S. A. (2013). Conductivity and dielectric studies of methylcellulose/chitosan-$NH_4CF_3SO_3$ polymer electrolyte. *Key Engineering Materials,* 594-595(3): 818-822.
25. Mobarak, N. N., Ramli, N., Abdullah, M. P. and Ahmad, A. (2013). Spectroscopic Studies of carboxymethyl chitosan-ammonium triflate ($NH_4CF_3SO_3$) based solid polymer electrolytes. *AIP Conference Proceedings,* 1571 (December 2013): 843-849.
26. Samsudin, A. S., Khairul, W. M. and Isa, M. I. N. (2012). Characterization on the potential of carboxy methylcellulose for application as proton conducting biopolymer electrolytes. *Journal of Non-Crystalline Solids,* 358(8): 1104-1112.
27. Rathika, R., Padmaraj, O. and Suthanthiraraj, S. A. (2018). Electrical conductivity and dielectric relaxation behaviour of PEO/PVdF-based solid polymer blend electrolytes for zinc battery applications. *Ionics,* 24(1): 243-255.
28. Karan, S., Sahu, T. B., Sahu, M., Mahipal, Y. K. and Agrawal, R. C. (2017). Characterization of ion transport property in hot-press cast solid polymer electrolyte (SPE) films: [PEO: $Zn(CF_3SO_3)_2$]. *Ionics,* 23 (10): 2721-2726.
29. Kumar, K. K., Ravi, M., Pavani, Y., Bhavani, S. Sharma, A. K. and Narasimha Rao, V. V. R. (2014). Investigations on PEO/PVP/NaBr complexed polymer blend electrolytes for electrochemical cell applications. *Journal of Membrane Science,* 454: 200-211.
30. Ramesh, S., Yuen, T. F. and Shen, C. J. (2008). Conductivity and FTIR Studies on PEO-LiX [X: $CF_3SO_3^-$, SO_4^{2-}] polymer electrolytes. *Spectrochimica Acta - Part A: Molecular and Biomolecular Spectroscopy*, 69 (2): 670-675.
31. Asmara, S. N., Kufian, M. Z., Majid, S.R. and Arof, A. K. (2011). Preparation and characterization of magnesium ion gel polymer electrolytes for application in electrical double layer capacitors. *Electrochimica Acta,* 57(1): 91-97.
32. Wendsjö, Å., Thomas, J. O. and Lindgren, J. (1993). Infra-red and X-ray diffraction study of the hydration process in the polymer electrolyte system $M(CF_3SO_3)_2PEO_n$ for *M*=Pb, Zn and Ni. *Polymer,* 34 (11): 2243-2249.
33. Navaratnam, S., Ramesh, K., Ramesh, S., Sanusi, A., Basirun, W. J. and Arof, A. K. (2015). Transport mechanism studies of chitosan electrolyte systems. *Electrochimica Acta,* 175: 68-73.
34. Johan, M. R., Shy, O. H., Ibrahim, S., Yassin, S. M. M. and Hui, T. Y. (2011). Effects of Al_2O_3 nanofiller and EC plasticizer on the ionic conductivity enhancement of solid PEO-$LiCF_3SO_3$ solid polymer electrolyte. *Solid State Ionics,* 196 (1): 41-47.
35. Bergstroem, P. A. and Frech, R. (2005). Raman and infrared study of the polymer electrolytes formed by poly(propylene oxide) with $Sn(CF_3SO_3)_2$ and $Pb(CF_3SO_3)_2$. *Journal of Physical Chemistry,* 99(33): 12603-12611.
36. Bernson, A. and Llndgren, J. (1993). Free ions and ion pairing/clustering in the system $LiCF_3SO_3$-PPO. *Solid State Ionics,* 60: 37-41

37. Aniskari, N. A. B. and Mohd Isa, M. I. N. (2017). The effect of ionic charge carriers in 2-hydroxyethyl cellulose solid biopolymer electrolytes doped glycolic acid *via* FTIR-deconvolution technique. *Journal of Sustainability Science and Management,* 12(2): 71-79.
38. Ahmed, H. T. and Abdullah, O. G. (2019). Preparation and composition optimization of PEO: MC polymer blend films to enhance electrical conductivity. *Polymers,* 11 (5): 1-18.
39. MacFarlane, D. R., Meakin, P., Bishop, A., McNaughton, D., Rosalie, J. M. and Forsyth, M. (1995). FTIR study of ion-pairing effects in plasticized polymer electrolytes. *Electrochimica Acta,* 40 (13-14): 2333-2337.
40. Karan, S., Sahu, M., Sahu, T. B., Mahipal, Y. K., Sahu, D. K. and Agrawal R. C. (2017). Investigations on materials and ion transport properties of Zn^{2+} conducting nano-composite polymer electrolytes (NCPEs): [(90 PEO: 10 $Zn(CF_3SO_3)_2$)+ x ZnO]. *Materials Today Communications,* 13: 269-274.
41. Kamisan, A. S., Kudin, T. I. T., Ali, A. M. M. and Yahya, M. Z. A. (2011). Polymer gel electrolytes based on 49% methyl-grafted natural rubber. *Sains Malaysiana,* 40 (1): 49-54.
42. Arof, A. K., Amirudin, S., Yusof, S. Z. and Noor, I. M. (2014). A method based on impedance spectroscopy to determine transport properties of polymer electrolytes. *Physical Chemistry Chemical Physics,* 16 (5): 1856-1867.
43. Woo, H. J., Majid, S. R. and Arof, A. K. (2011). Conduction and thermal properties of a proton conducting polymer electrolyte based on poly(ε-caprolactone). *Solid State Ionics,* 199-200 (1): 14-20.
44. Ramlli, M. A. and Isa, M. I. N. (2016). Structural and ionic transport properties of protonic conducting solid biopolymer electrolytes based on carboxymethyl cellulose doped with ammonium fluoride. *Journal of Physical Chemistry B,* 120(44): 11567-11573.
45. Kadir, M. F. Z. and Hamsan, M. H. (2018). Green electrolytes based on dextran-chitosan blend and the effect of NH_4SCN as proton provider on the electrical response studies. *Ionics,* 24 (8): 2379-2398.
46. Marzantowicz, M., Dygas, J. R., Krok, F., Florjańczyk, Z. and Zygadło-Monikowska, E. (2006). Influence of crystallization on dielectric properties of PEO:LiTFSI polymer electrolyte. *Journal of Non-Crystalline Solids,* 352(42-49): 5216-5223.
47. Khiar, A. S. A. and Arof, A. K. (2011). Electrical properties of starch/chitosan-NH_4NO_3 polymer electrolyte. *International Journal of Physical and Mathematical Sciences,* 5 (11): 23-27.
48. Shukur, M. F., Ithnin, R. and Kadir, M. F. Z. (2016). Ionic conductivity and dielectric properties of potato starch-magnesium acetate biopolymer electrolytes: The effect of glycerol and 1-butyl-3-methylimidazolium chloride. *Ionics,* 22 (7): 1113-1123.
49. Ramly, K., Isa, M. I. N. and Khiar, A. S. A. (2011). Conductivity and dielectric behaviour studies of starch/PEO + x wt-% NH_4NO_3 polymer electrolyte. *Materials Research Innovations,* 15(2): 82-85.
50. Pawlicka, A., Tavares, F. C., Dörr, D. S., Cholant, C. M., Ely, F., Santos, M. J. L. and Avellaneda, C. O. (2019). Dielectric behavior and FTIR Studies of xanthan gum-based solid polymer electrolytes. *Electrochimica Acta,* 305: 232-239.
51. Woo, H. J., Majid, S. R. and Arof, A. K. (2012). Dielectric properties and morphology of polymer electrolyte based on poly(ε-caprolactone) and ammonium thiocyanate. *Materials Chemistry and Physics,* 134 (2-3): 755-761.
52. Gohel, K. and Kanchan, D. K. (2018). Ionic conductivity and relaxation studies in PVDF-HFP:PMMA-based gel polymer blend electrolyte with $LiClO_4$ salt. *Journal of Advanced Dielectrics,* 8(1): 1850005.
53. Idris, N. H., Senin, H. B. and Arof, A. K. (2007). Dielectric spectra of LiTFSI-doped chitosan/PEO blends. *Ionics,* 13(4): 213-217.

Malaysian Journal of Analytical Sciences (MJAS)
Published by Malaysian Analytical Sciences Society

MORPHOLOGICAL AND CONDUCTIVITY STUDIES OF POLYANILINE FABRIC DOPED PHOSPHORIC ACID

(Kajian Morfologi dan Kekonduksian Fabrik Polianilina yang telah Terdop oleh Asid Fosforik)

Nazreen Che Roslan[1], Muhammad Faiz Aizamddin[1], Siti Nurzatul Ikma Omar[1], Nur Aimi Jani[1,2], Mohamed Izzharif Abdul Halim[3], Zaidah Zainal Ariffin[4], Mohd Muzamir Mahat[1]*

[1]School of Physics and Materials Studies, Faculty of Applied Sciences
[2]Centre of Functional Materials and Nanotechnology, Institute of Science
[3]School of Chemistry and Environmental Studies, Faculty of Applied Sciences
[4]School of Biology, Faculty of Applied Sciences
Universiti Teknologi MARA, 40450 Shah Alam, Selangor, Malaysia

**Corresponding author: mmuzamir@uitm.edu.my*

Received: 30 March 2020; Accepted: 9 September 2020; Published: 12 October 2020

Abstract

Polyaniline doped phosphoric acid was synthesised through chemical oxidation. The morphology and conductivity properties of the materials were characterised with field emission scanning electron and electrochemical impedance spectroscopy. UV-Vis analysis confirmed the presence of polyaniline through the observation of benzenoid and quinoid structure. The protonation of polyaniline emeraldine base (PANI-EB) into PANI-ES was confirmed when the solution changed from blue to green. The addition of hydrochloric acid (HCl) in the protonation supplied H^+ ion to the polymer backbone. Three batches of PANI solutions were treated with 10% v/v, 20% v/v and 30% v/v phosphoric acid as the dopant. Conductive polyaniline was fabricated by immersing bare cotton fabric into PANI solutions of different concentrations, followed by drying. Conductivity studies with EIS revealed that doped sample had higher conductivity compared to undoped sample, with the highest recorded conductivity of $3.37 \times 10^{-6} \pm 8.89 \times 10^{-7}$ S/m at a concentration of 30% v/v. This result was supported by FESEM analysis which showed a homogenous distribution of PANI on the cotton, which reflected optimum incorporation of PANI into the fabric. Furthermore, the amount of deposited precipitate increased as the concentration of dopant acid increased. This observation was in line with the results from EIS analysis that showed higher conductivity of fabric in tandem with increasing concentration of dopant.

Keywords: polyaniline, conductive fabrics, cotton, electro impedance spectroscopy, field emission scanning electron microscope

Abstrak

Polianilina, suatu bentuk polimer pengalir elektrik telah disintesis melalui kaedah pengoksidaan kimia menggunakan asid fosforik sebagai dopan. UV-Vis telah menunjukkan kehadiran struktur benzenoid dan quinoid dalam sampel selari dengan struktur polianilina. PANI-EB yang pada mulanya berwarna biru berubah menjadi hijau apabila melalui protonasi (PANI-ES). Protonasi ini berlaku disebabkan oleh penambahan asid hidroklorik (HCl) yang membekalkan caj H^+ terhadap rantaian utama polimer. Fabrik konduktif polianilina dihasilkan melalui kaedah perendaman. Proses ini dilakukan dengan merendamkan kain kapas kosong ke dalam larutan PANI yang dirawat dengan asid fosforik sebagai dopan pada kepekatan yang berbeza, iaitu 10% v/v, 20% v/v dan 30% v/v diikuti dengan proses pengeringan. Kajian konduktiviti menggunakan EIS menunjukan bahawa sampel

yang terdop dengan asid mempunyai kekonduksian yang lebih tinggi berbanding sampel tidak terdop. Kekonduksian tertinggi didapati pada 30% v/v ($3.37 \times 10^{-6} \pm 8.89 \times 10^{-7}$ S/m). Analisis morfologi menggunakan FESEM menunjukkan pengedaran PANI yang sekata pada permukaan kapas. Ini membuktikan penyerapan PANI yang baik ke dalam kain. Selain itu, lebih banyak mendakan PANI didapati pada permukaan kain apabila kepekatan asid dopan bertambah. Ini adalah selari dengan hasil bacaan tahap kekonduksian elektrik.

Kata kunci: polianilina, fabrik konduktif, fabrik, spektroskopi impedansi elektrokimia, mikroskop pengimbasan pelepasan medan

Introduction

Conducting polymers (CPs) can conduct electricity due to the existence of conjugated double bonds. Such polymers exhibit unusual chemical, optical and electronic properties. CPs have found their way in various applications such as antistatic coating material to avoid electrical discharge exposure on primary and secondary batteries [1], antistatic coatings [2] and biosensors [3]. Mawad et al. stated that the conductivity of CPs could be induced by doping. In this process, the polymer is introduced to oxidising (p-type) dopant or reducing (n-type) dopant. These dopants can remove or add electrons to the backbone of a polymer which will modify its conductivity [4]. In addition, Mahat et al. also claimed any modification in the polymeric backbone will influence the electrical conductivity and disparity in oxidation state [5].

Among the CPs, polyaniline (PANI) is favoured in research due to its simple synthesis, unique electrochemical properties and chemical stability [6]. The conductivity of PANI can be achieved by treatment with acids [7]. The conductivity and thermal properties of PANI are highly dependent on the dopant acid and filler. This characteristic opens the possibility to study the various effects that come from the combination of different dopant acids [8]. Conductive nature of PANI is a complex phenomenon that can be attributed to polaron charge carriers due to the protonation of acids [9]. PANI can be prepared through a facile method of electro-polymerisation [10] or chemical oxidative polymerisation [11]. Both methods allow the electron valence of PANI to be controlled to achieve various colours of PANI with specific properties [12]. However, chemical oxidation polymerisation is highly favoured since the technique is easier to be performed with higher yield in sample production.

PANI could be integrated with other elements to be composite materials [13, 14] to enhance its properties such as mechanical [15], conductivity [16] and biocompatibility [17]. In biomedical applications, fabrics are highly sought after due to its flexibility and non-toxic properties to CPs. [18]. The integration of CPs into fabric can impart electrical conductivity to the material. The hydrophilic properties of cotton make them an ideal substrate to study the deposition of CPs [19]. The polymerisation of these materials on textiles can produce flexible conductive materials with a wide range of conductivity, structure, mechanical and electromagnetic properties. The field of intelligent textiles and wearable sensors are driven by the progress in conductive materials [20]. For instance, PANI was incorporated within the textile to fit these properties [21]. Despite its potential for future bioelectronic material, its application is hindered due to its low conductivity and more works are necessary to be conducted to find the ideal conductivity.

This study analysed the variation in the conductivity of PANI when phosphoric acid of different concentrations was used as the dopant. PANI was first synthesised via chemical oxidation. A few fabrics was immersed in PANI doped phosphoric acid. These fabrics were then characterised with electrochemical impedance spectroscopy (EIS) and field emission scanning electron microscope (FESEM) to investigate their conductivity and morphology, respectively.

Materials and Methods

Materials

Aniline solution (99.5%) and phosphoric acid (H_3PO_4, 85%) were purchased from Sigma-Aldrich. Hydrochloric acid (HCl, 37%), ammonium persulphate (APS), sodium hydroxide (NaOH) pellets and dimethyl sulfoxide (DMSO) were sourced from ACROS, United

Kingdom. Cotton fabrics (100 gsm) were purchased from a local fabric retailer. All reagents were in analytical reagent grade and used without further purification.

Synthesis of polyaniline

10 mL of aniline was dissolved in 100 mL of 6 M HCl. 22 g of ammonium persulphate (APS) was dissolved in 10 mL of distilled water. The aniline and APS solution were cooled to room temperature. This step was followed by the addition of APS to aniline solution drop by drop and the mixture was stirred for 4 hours to promote the polymerisation process. A green solution was produced when it passed through a filter paper (Whatman, 2.5 μm). The filtrate was rinsed with hydrochloric acid, acetone and distilled water in this particular order. Next, the sample was dried in an oven at 60 °C for 24 hours. Polyaniline emeraldine base (PANI-EB) was acquired with the addition of 200 mL of sodium hydroxide (NaOH) to the precipitate.

Synthesis of polyaniline-doped phosphoric acid

The undoped PANI was subjected to doping with phosphoric acid. 0.3 wt.% PANI-EB (0.18 g) was diluted with DMSO solvent followed by protonating with phosphoric acid. The solutions were centrifuged for 30 minutes at 2000 rpm to separate them from precipitates. In this study, there are only three different volume percentage of dopant were used which are 10% v/v, 20% v/v and 30% v/v. The percentage of dopant was designed to be at minimum as possible, in order to in line with concentration the prepared PANI. 30%, is the highest condition that can be fitted with the synthesized PANI as reported by Omar et al. [22]. The colour of the solution changed from blue to green. This change of colour signalled the permutation of emeraldine base (PANI-EB) to emeraldine salt (PANI-ES). As for the control solution, an undoped solution was prepared by dissolving 0.3 wt.% PANI-EB (0.18 g) with dimethyl sulfoxide (DMSO) solvent without the addition of phosphoric acid. Cotton fabrics with a dimension of 5 cm x 5 cm were immersed in the PANI solution for 30 minutes. The solutions were removed after 30 minutes, and the samples were dried in a dark room before they were subjected to testing.

Material characterisation: **UV-Visible spectroscopy (UV-Vis)**

UV-Vis was used to study the molecular structure of PANI-ES and PANI-EB with DMSO solvent as the reference. The energy absorbed by the sample was measured and compared. The percentage of absorption was measured by scanning the sample in the UV-Visible range (250-800 nm).

Electrochemical impedance spectroscopy (EIS)

Electrochemical impedance spectroscopy (HIOKI 3520 LCR Hi-Tester) was employed to determine the conductivity of the sample. The range of frequency was 100 Hz to 1000 kHz at room temperature. Two stainless steel disc electrodes with a diameter of 2 cm were used to clip the PANI-infused fabric sample. EIS works by applying a small sinusoidal potential or time-varying potential across the sample, and the resulting current through the sample is measured. The impedance was recorded for each operating frequency. The value of conductivity was derived from the impedance.

Field emission scanning electron microscope (FESEM)

The morphology of doped and undoped PANI was examined with Oxford Instruments: IncaPentaFETx3 field emission scanning electron microscope (FESEM). The undoped and doped fabric were coated with gold to impart electrical conductivity. FESEM analysis was performed with 200x and 500x magnifications. EDX analysis followed suit to analyse the elemental composition of sulphur (S) and phosphate (PO_4^{3-}) in the sample.

Results and Discussion

Synthesis of polyaniline

A green solution of polyaniline emeraldine salt (PANI-ES) was obtained upon rinsing with HCl. This process is known as protonation, where HCl, contributed an H^+ ion to the existing aniline at the amine group (-NH-). This protonation activated the conjugation of the electron along the backbone. Undoped PANI was obtained through deprotonation. Deprotonation was achieved by adding NaOH solution to PANI-ES. The change in the colour of the solution from blue to green indicated a successful protonation (Figure 1b).

UV-Vis analysis was performed to determine the changes in molecular structure. Both PANI-EB and PANI-ES solutions were diluted with DMSO solvent. As shown in Figure 1c, PANI-ES showed three absorption peaks at 256 nm, 329 nm and 439 nm. The absorption of the first peak, 255 nm and 328 nm represented π - π* benzene ring [23] which pointed to conjugation between adjacent phenyl rings in the copolymer chain [24]. The π-π* interactions are typical behaviour of CP. Peaks of 256 nm and 329 nm both shifted by 1 nm to 255 nm and 328 nm when they were in deprotonated state (PANI-EB). The band at 439 nm implied the occurrence of polaron absorption from the doping process and the conductivity of PANI-ES. Electron absorption in the backbone of the polymer is evidence of successful doping of acids as displayed by the green solution. According to Karaoğlan and Bindal [25], the decreasing of the absorption band in region 615 nm of PANI-EB illustrates the conversion of imine nitrogen atoms of the quinonoid rings to benzenoid rings. However, this peak disappeared after successful doping. This is in line with study conducted by Wang et al. where peak at 630 nm disappeared upon doping which is due to quinone ring being ruptured from the doping. [25]. Table 1 is a summary of absorption values in the UV-Vis spectrum of PANI-ES and PANI-EB.

Immersion of fabrics

The colour of the fabric changed when they were immersed in undoped and doped PANI solutions. The pre-immersion fabric was white (Figure 2a). FESEM image of bare cotton fabric showed a fibrous structure, as seen in Figure 2b. The colour of the fabric changed to blue and green upon immersion in undoped and doped PANI solutions, respectively (Figure 2c and Figure 2d). The blue fabric represented PANI-EB, while the green fabric represented PANI-ES. The differences in the colour of pre and post-immersion fabric proved the successful preparation of PANI fabric.

Electrochemical impedance spectroscopy (EIS)

Fabrics were tested using EIS to measure the electrical conductivities. This analysis was repeated three times for each sample to draw an average value. The undoped fabric was also subjected to similar EIS analysis. Table 2 shows the average conductivity for each fabric sample.

EIS analysis proved that the conductivity of fabric increased when they were assimilated with PANI solutions. Undoped PANI had a conductivity of $6.36 \times 10^{-8} \pm 2.38 \times 10^{-8}$ S/m, which was the lowest among the samples due to the absence of dopant that is essential to impart conductivity [27]. On the contrary, doped sample ranges $1.25 \times 10^{-7} \pm 2.81 \times 10^{-8}$ S/m to $3.37 \times 10^{-6} \pm 8.89 \times 10^{-7}$ S/m which suggests that the incorporation of PANI may potentially inflate number of electrical pathways across the sample [28]. This is supported by Omar et al. that indicate the increase of conductivity is contributed by the presence of polaron in the backbone of PANI upon addition of dopant. The dopant promotes mobility of charge transfer throughout the polymer chain [29].

Figure 3a illustrates the conductivity of fabrics under different conditions. It was found that there are differences of conductivity value for the various concentration of dopant used. The highest conductivity value was recorded at 30% v/v that suggest the optimum concentration of dopant for phosphoric acid is at 30% v/v. These conductivity value substantiate that dopant acid increases the conductivity of PANI-EB [30]. This is due to presence of polarons in the backbone of PANI, attributed from the protonation by dopant. The electrochemical impedance spectrum for PANI at different condition is shown in Figure 3b. Doped samples showed higher real impedance value (Zr), correspond to the value of charge-transfer resistance of the fabrics, which is depending on the ionic diffusion of the fabric [31]. Bare fabrics illustrate relatively straight line in the low frequency region, which indicates the limiting diffusion of electron migration. On the contrary, doped fabrics are in higher frequency region as they have higher ionic diffusion.

Morphological analysis using FESEM

FESEM images were captured to study the surface morphology of the PANI fabrics at two different magnification (200x and 500x) (See Figure 4).

FESEM analysis shows the micrograph of all fabrics, compromised of fibrils and bundles. These structures were contributed from the natural structure of cotton fabrics. We observe that the fibres of the fabric were finely- covered by polyaniline particles, similar to a previous study by Wu et al. [32]. In addition, doped samples showed more distribution of granules structure as compared to undoped sample indicating PANI is well absorbed into the fabric during the immersion process. Based on previous studies, the conductivity may be influenced by the significant amount of polyaniline particle present throughout the fabric. Thus, with higher deposition of precipitate, the higher conductivity values are expected. As illustrated in Figure 4 (e-f), PANI doped-PA 10% v/v cotton sample has relatively smooth surface which indicates PANI are well incorporated into the fibres. On contrary, PANI doped-PA 20% v/v cotton and PANI doped-PA 30% v/v cotton illustrated rough and uneven surface. This result is in line with the conductivity values obtained using EIS, in which the more concentration of dopant incorporated, the higher the conductivity of the fabrics.

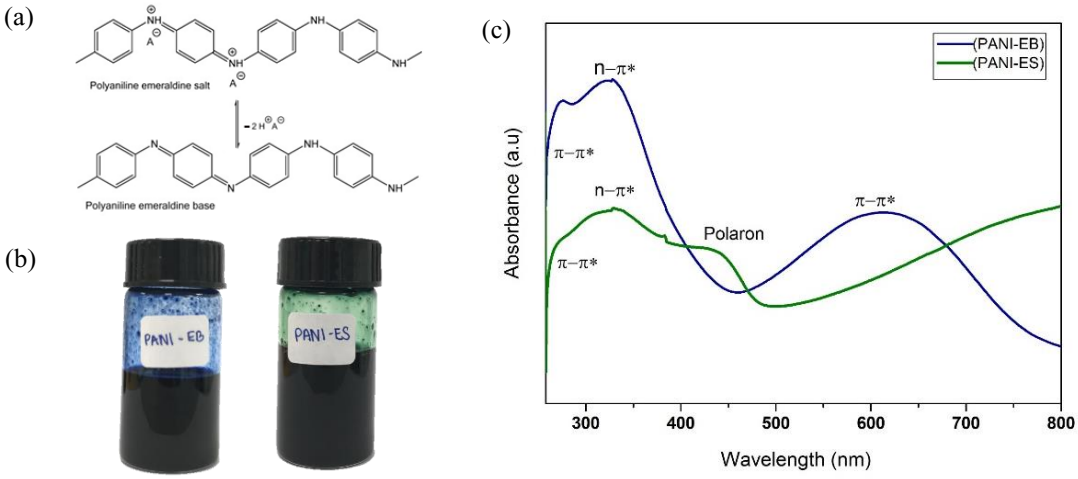


Figure 1. (a) Chemical structure of PANI-ES and PANI-EB, (b) Image of PANI-EB and PANI-ES, and (c) UV-Vis spectrum of PANI-EB and PANI-ES

Table 1. Summary of absorption bands of PANI-ES and PANI-EB with UV-Vis

	Reference (nm)	**PANI-ES (nm)**	**Reference (nm)**	**PANI-EB (nm)**
$\pi \rightarrow \pi^*$ (Benzene Ring)	286 [24]	256	285 [26]	255
$\pi \rightarrow \pi^*$ (Benzene Ring)	350 [24]	329	345 [24]	328
$\pi \rightarrow \pi^*$ (Quinoid Ring)	450[25]	439	592[25]	615

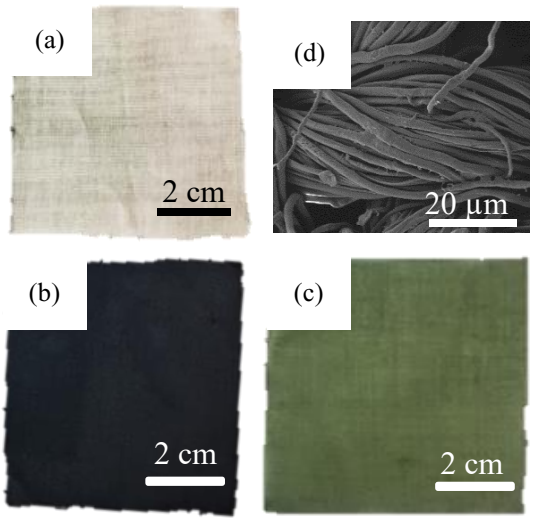


Figure 2. Photograph of (a) bare cotton fabric, (b) undoped PANI fabric, (c) doped PANI fabric and d) FESEM image of bare cotton fabric at 200x magnification

Table 2. Average conductivity for each fabric sample

	Volume % of Dopant (v/v)	Conductivity (S/m)
Bare Cotton	-	NIL
Undoped PANI	-	$6.36 \times 10^{-8} \pm 2.38 \times 10^{-8}$
PANI doped with phosphoric acid	10%	$1.25 \times 10^{-7} \pm 2.81 \times 10^{-8}$
	20%	$2.50 \times 10^{-6} \pm 2.41 \times 10^{-7}$
	30%	$3.37 \times 10^{-6} \pm 8.89 \times 10^{-7}$

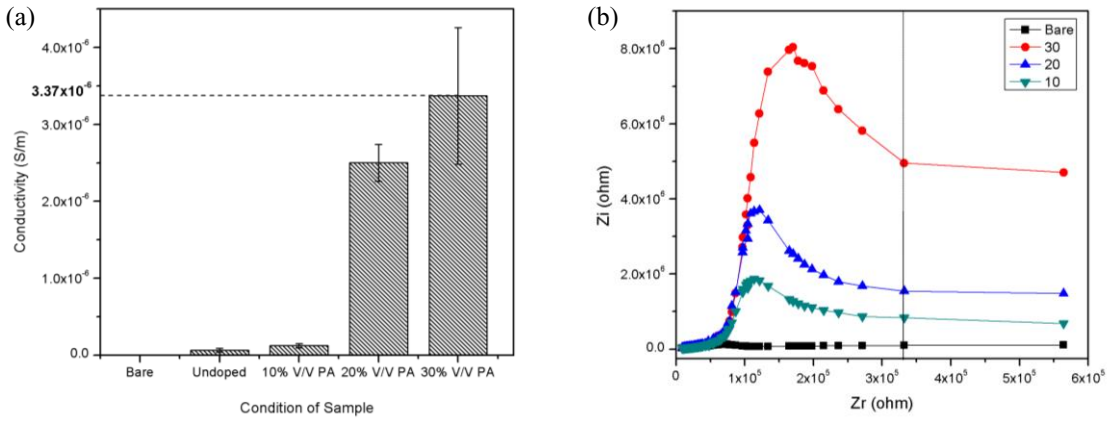


Figure 3. (a) Conductivity of various condition of fabric and (b) EIS spectrum for PANI at different v/v% of dopant

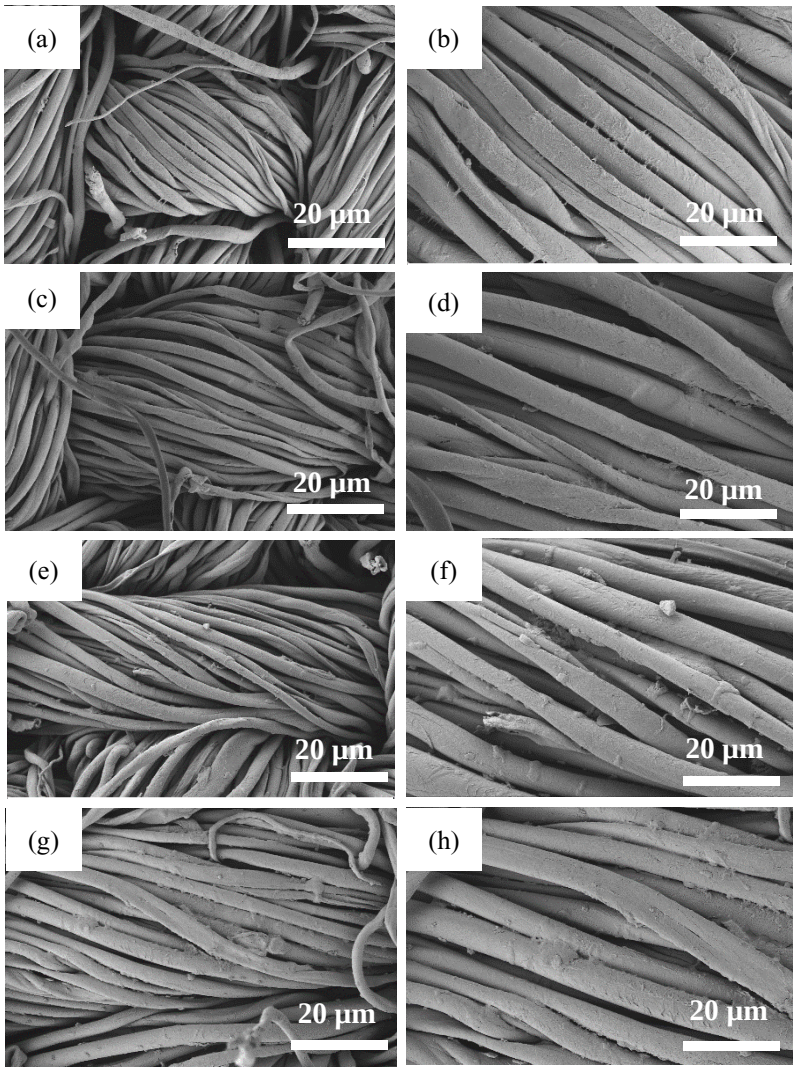


Figure 4. FESEM images of (a-b) undoped cotton, (c-d) PANI doped PA 10% v/v, (e-f) PANI doped PA 20% v/v and (g-h) PANI doped PA 30% v/v at 200x and 500x magnification, respectively

Conclusion

Polyaniline-doped with phosphoric acid using chemical oxidation method was successfully synthesized. This is proven by UV-Vis analysis that identified the presence of benzenoid and quinoid structures, corresponded to the structure of polyaniline. PANI was incorporated into the fabric by immersion method. Conductivity measurement using Electrochemical Impedance Spectroscopy (EIS) has shown that conductivity of PANI increased with addition of dopant since doped fabrics showed distinct different in conductivity as compared to bare and undoped fabric. The highest conductivity of conductive fabric was found at 3.37 x 10^{-6} ± 8.89 x 10^{-7} S/m, for the 30% v/v sample. Morphological study using FESEM showed homogenous distribution of precipitate on the surface of sample. Also, more precipitate was found as the higher volume concentration of acid dopant used. Overall, this study reinforces the correlation between higher amounts of PANI precipitate on the fabric surface with higher

conductivity values. In the near future, the durability of PANI fabrics when exposed to real environment such as humidity, pH and washing condition can be further explored. This is highly important to ensure the stability and extended functionality of the fabrics when in used. Alternatively, researchers may also venture a study on the effect of other types of dopant from natural sources (citric acid, acetic acid, and nitric acid) that can best fit for various applications.

Acknowledgement

Authors are grateful for the funding from Research Management Center UiTM under 600-IRMI 5/3/LESTARI (029/2019).

References

1. Ahmad, S., Sultan, A., Raza, W., Muneer, M. and Mohammad, F. (2016). Preparation, characterization and application of polyaniline/silk fibroin composite. *Polymers and Polymer Composites*, 24(8): 633-642.
2. Mirmohseni, A., Azizi, M. and Dorraji, M. S. (2020). Cationic graphene oxide nanosheets intercalated with polyaniline nanofibers: A promising candidate for simultaneous anticorrosion, antistatic, and antibacterial applications. *Progress in Organic Coatings,* 139: 105419.
3. Ma, Z., Shi, W., Yan, K., Pan, L. and Yu, G. (2019). Doping engineering of conductive polymer hydrogels and their application in advanced sensor technologies. *Chemical Science*, 10(25): 6232-6244.
4. Mawad, D., Mansfield, C., Lauto, A., Perbellini, F., Nelson, G. W., Tonkin, J. and Stevens, M. M. (2016). A conducting polymer with enhanced electronic stability applied in cardiac models. *Science Advances*, 2(11): e1601007.
5. Mahat, M. M., Mawad, D., Nelson, G. W., Fearn, S., Palgrave, R. G., Payne, D. J. and Stevens, M. M. (2015). Elucidating the deprotonation of polyaniline films by X-ray photoelectron spectroscopy. *Journal of Materials Chemistry C,* 3(27): 7180-7186.
6. Yang, Y., Chen, S. and Xu, L. (2011). Enhanced conductivity of polyaniline by conjugated crosslinking. *Macromolecular Rapid Communications*, 32(7): 593-597.
7. Noby, H., El-Shazly, A., Elkady, M. and Ohshima, M. (2019). Strong acid doping for the preparation of conductive polyaniline nanoflowers, nanotubes, and nanofibers. *Polymer,* 182: 121848.
8. Ansari, M. O., Khan, M. M., Ansari, S. A., Amal, I., Lee, J. and Cho, M. H. (2014). *p*TSA doped conducting graphene/polyaniline nanocomposite fibers: Thermoelectric behavior and electrode analysis. *Chemical Engineering Journal*, 242: 155-161.
9. Price, A. D. and Naguib, H. E. (2008). Synthesis and characterization of porous polyaniline conductive polymers. *Cellular Polymers*, 27(3): 201-212.
10. Aggadi, S. E., Loudiyi, N., Chadil, A., Abbassi, Z. E. and Hourch, A. E. (2020). Electropolymerization of aniline monomer and effects of synthesis conditions on the characteristics of synthesized polyaniline thin films. *Mediterranean Journal of Chemistry,* 10(2): 138-145.
11. Taş, R., Can, M. and Sarı, H. (2019). The chemical synthesis and characterizations of silver-doped polyaniline: Role of silver–solvent interactions. *Polymer Bulletin,* 77(4): 1913-1928.
12. Boeva, Z. A. and Sergeyev, V. G. (2014). Polyaniline: Synthesis, properties, and application. *Polymer Science Series C*, 56(1): 144-153.
13. Ramli, R., Arawi, A. Z., Mahat, M. M., Mohd., A. F. and Yahya, M. F. (2011). Effect of silver (Ag) substitution nano-hydroxyapatite synthesis by microwave processing. *2011 International Conference on Business, Engineering and Industrial Applications, Kuala Lumpur*: pp. 180-183
14. Ramli, J., Jeefferie, A. R. and Mahat, M. M. (2011). Effects of UV curing exposure time to the mechanical and physical properties of the epoxy and vinyl ester fiber glass laminates composites, *ARPN Journal of Engineering and Applied Sciences*, 6(4): 104-109.

15. Sharma, S., Kumar, V., Pathak, A. K., Yokozeki, T., Yadav, S. K., Singh, V. N. and Singh, B. P. (2018). Design of MWCNT bucky paper reinforced PANI–DBSA–DVB composites with superior electrical and mechanical properties. *Journal of Materials Chemistry C*, 6(45): 12396.
16. Wu, L., Ge, Y., Zhang, L., Yu, D., Wu, M. and Ni, H. (2018). Enhanced electrical conductivity and competent mechanical properties of polyaniline/polyacrylate (PANI/PA) composites for antistatic finishing prepared at the aid of polymeric stabilizer. *Progress in Organic Coatings*, 125: 99-108.
17. Humpolíček, P., Radaszkiewicz, K. A., Capáková, Z., Pacherník, J., Bober, P., Kašpárková, V. and Stejskal, J. (2018). Polyaniline cryogels: Biocompatibility of novel conducting macroporous material. *Scientific Reports,* 8(1): 135.
18. Aizamddin, M. F., Roslan, N. C., Kamaruddin, M. A., Omar, S. N., Safian, M. F., Abdul Halim, M. I. and Mahat, M. M. (2020). Study of conductivity and thermal properties of polyaniline doped with *p*-toluene sulfonic acid. *Malaysian Journal of Analytical Sciences*, 24(3): 413-421.
19. Hao, L., Wang, R., Fang, K. and Cai, Y. (2017). The modification of cotton substrate using chitosan for improving its dyeability towards anionic microencapsulated nano-pigment particles. *Industrial Crops and Products,* 95: 348-356.
20. Liu, Y., Zhao, X., Tuo, X. (2016). Preparation of polypyrrole coated cotton conductive fabrics. *The Journal of the Textile Institute*, 108(5): 829-834.
21. Cruz-Pacheco, A. F., Paredes-Madrid, L., Orozco, J., Gómez-Cuaspud, J. A., Batista-Rodríguez, C. R. and Gómez, C. A. (2020). Assessing the influence of the sourcing voltage on polyaniline composites for stress sensing applications. *Polymers,* 12(5): 1164.
22. Omar, S. N., Ariffin, Z. Z., Zakaria, A., Safian, M. F., Halim, M. I., Ramli, R., Mahat, M. M. (2020). Electrically conductive fabric coated with polyaniline: Physicochemical characterisation and antibacterial assessment. *Emergent Materials,* 3: 469-477.
23. Tang, S. J., Wang, A. T., Lin, S. Y., Huang, K. Y., Yang, C. C., Yeh, J. M. and Chiu, K. C. (2011). Polymerization of aniline under various concentrations of APS and HCl. *Polymer Journal*, 43(8): 667-675.
24. Paschoalin, R. T., Steffens, C., Manzoli, A., Paris, E. C. and Herrmann, P. S. (2012). PANI conductivity: A dependence of the chemical synthesis temperature. *Macromolecular Symposia*, 319(1): 48-53.
25. Karaoğlan, N. and Bindal, C. (2018). Synthesis and optical characterization of benzene sulfonic acid doped polyaniline. *Engineering Science and Technology, an International Journal*, 21(6): 1152-1158.
26. Wang, Y., Chen, K., Li, T. and Li, H. (2015). One-step and template-free synthesis of itaconic acid–doped polyaniline nanorods in aqueous solution. *High Performance Polymers*, 28(3): 322-330.
27. Ziadan, K. (2016). Study of the electrical characteristics of polyaniline prepared by electrochemical polymerization. *Energy Procedia*, 19(2012): 71-79.
28. Alamer, F. A. (2018). Structural and electrical properties of conductive cotton fabrics coated with the composite polyaniline/carbon black. *Cellulose*, 25(3): 2075–2082.
29. Omar, S., Ariffin, Z., Akhir, R., Shri, D., Halim, M., Safian, M. and Mahat, M. (2019). Polyaniline (PANI) fabric doped *p*-toluene sulfonic acid (pTSA) with anti-infection properties. *Materials Today: Proceedings*, 16: 1994-2002.
30. Mostafaei, A. and Zolriasatein, A. (2012). Materials international synthesis and characterization of conducting polyaniline nanocomposites containing ZnO nanorods. *Progress in Natural Science: Materials International,* 22(4): 273-280.
31. Perumalraj, R. (2015). Electrical surface resistivity of polyaniline coated woven fabrics. *Journal of Textile Science & Engineering*. 5(3): 1-5.
32. Wu, B., Zhang, B., Wu, J., Wang, Z., Ma, H. and Yu, M. (2015). Electrical switchability and dry-wash durability of conductive textiles. *Scientific Report,* 5: 11255.

Malaysian Journal of Analytical Sciences (MJAS)
Published by Malaysian Analytical Sciences Society

ANTIMICROBIAL EFFICACY, ANTIOXIDANT PROFILE AND NINE ALTERNATIVE ACTIVE CONSTITUENTS FROM PETROLEUM ETHER AND ETHYL ACETATE EXTRACT OF *Entada spiralis*

(Keberkesanan Antimikrob, Profil Antioksida dan Sembilan Komponen Alternatif Aktif dari Ekstrak Petroleum Eter dan Etil Asetat dari Pokok *Entada spiralis*)

Aiza Harun[1]*, Noorshilawati Abdul Aziz[2], Nor Shazleen Mohd Azenan[1], Nurfarah Farini Muhammad Kamarazzaman[1], Siti Zaiton Mat So'ad[3]

[1]*Faculty of Applied Science*
[2] *Faculty of Plantation and Agrotechnology*
Universiti Teknologi MARA Pahang, 26400 Bandar Tun Razak Jengka, Pahang, Malaysia
[3]*Kulliyyah of Pharmacy,*
International Islamic University Malaysia, 25200 Bandar Indera Mahkota, Pahang, Malaysia

**Corresponding author: aizaharun@.uitm.edu.my*

Received: 9 March 2020; Accepted: 25 June 2020; Published: 12 October 2020

Abstract

This study aimed to investigate the antimicrobial activity of petroleum ether extracts and the identification of alternative antimicrobial and antioxidative constituents from petroleum ether extract and ethyl acetate extract of *Entada spiralis* stem. Antimicrobial activity was evaluated through disc diffusion method on five human superficial skin disease-caused microbes such as *Staphylococcus aureus, Staphylococcus epidermidis*, *Microsporum gypseum*, *Trichophyton mentagrophytes, Trychophyton tonsurans* and one plant pathogen namely *Erwinia chrysanthemi*. The presence of antioxidants was determined from thin layer chromatography (TLC) sprayed with 2,2-diphenyl-1-picrylhydrazyl. The isolation of antioxidant and antimicrobial compounds was performed through preparative TLC. The structure of isolated compounds was determined from gas chromatography mass spectrometry (GCMS) and liquid chromatography mass spectrometry (LCMS) equipped with Wiley Library matching individually. The petroleum ether extract successfully inhibited the growth of all bacteria and dermatophytes in a concentration dependent manner whereby *S. epidermis* was highly susceptible towards the extract with inhibition zone of 16.0 mm at concentration of 400 mg/mL as well as *M. gypseum*. Most of the components from petroleum ether extract and ethyl acetate extract developed on TLC were antioxidative which was seen as yellow spots against purple background after spraying with DPPH reagent. Four antioxidative constituents were successfully isolated and tentatively identified as 18,19-Secoyohimban-19-oic acid,16,17,20,21-tetradehydro-16-(hydroxymethyl)-methylester **(1**), Oxiraneoctanoic acid **(2),** 9,12-Octadecadienoic acid **(3),** and 11-O-p- Coumarylnepeticin **(4)**. Five antimicrobial constituents were successfully isolated and tentatively identified as 4-benzyloxy-4-[2,2,-dimethyl-4-dioxolanyl]Butylaldehyde, **(5),** Isobutyl octadecyl benzoate ester **(6),** 3',8,8'-Trimethoxy-3-piperidyl-2,2'-binaphthalene-1,1',4,4'-tetrone **(7)**, 1,2,4,5-tetramethylbenzene **(8)** and Hordatine B **(9)**. Thus, *E. spiralis* is seen to be a promising source of bioactive ingredients which is very important as the basis of scientific information for the development of natural antimicrobial and antioxidant agents.

Keywords: Leguminoceae, *Entada spiralis*, antioxidant, antibacterial activity

Abstrak

Kajian ini memfokuskan kepada kajian sifat antimikrob ekstrak petroleum eter dan pencarian komponen aktif antimikrob dan antioksida dari ekstrak petroleum eter dan etil asetat dari batang pokok *Entada spiralis*. Aktiviti antimikrob dinilai menggunakan kaedah penyerakan cakera terhadap lima jenis mikrob penyakit kulit iaitu *Staphylococcus aureus*, *Staphylococcus epidermis*, *Microsporum gypseum*, *Trichophyton mentagrophytes*, *Trychophyton tonsurans* dan satu jenis mikrob tumbuhan iaitu *Erwinia chrysanthemi*. Ciri antioksidan ekstrak komponen yang telah dipisahkan di atas kromatografi lapisan nipis (KLN) telah dianalisa menggunakan kaedah penyemburan dengan bahan 2,2-difenil-1-pikrilhidrazil (DPPH) di atas KLN. Pemisahan komponen aktif antioksida dan antimikrob telah dijalankan dengan menggunakan KLN. Spektrometer jisim kromatografi gas dan spektrometer jisim kromatografi cecair dengan data Wiley telah digunakan untuk menganalisa dan mengenalpasti struktur bahan aktif. Ekstrak petroleum eter berkesan dalam menyekat pertumbuhan bakteria dan kulat di mana bakteria *S. epidermis* dan kulat *M. gypseum* paling kuat disekat pertumbuhannya oleh ekstrak dengan zon perencatan 16.0 mm pada kepekatan 400 mg/mL. Kebanyakan komponen dalam ekstrak petroleum eter dan etil asetat yg telah dipisahkan di atas KLN bersifat antioksida dengan memberikan kesan tompokan kuning setelah disembur dengan larutan DPPH. Sebanyak empat komponen antioksida berjaya dipisahkan dan dikenalpasti sebagai Asid 18,19-Sekoyohimban-19,16,17,20,21-tetradihidro-16-(hidroksimetil)-metilester **(1**), Asid okzairanoktanoik **(2),** Asid 9,12-Oktadekadienoik **(3),** dan 11-O-p- Koumarilnepetisin **(4).** Sebanyak lima jenis komponen antimikrob berjaya dipisahkan dan dikenali sebagai, 4-benziloksi-4-[2,2,-dimetil-4-dioksolanil]Butilaldehid**(5),** Isobutil oktadesil benzoat ester**(6),** 3',8,8'-Trimetoksi-3-piperidil-2,2'-binaftalin-1,1',4,4'-tetron **(7)**, 1,2,4,5-tetramethylbenzene **(8)** dan Hordatin B **(9)**. Maka, *E. spiralis* dilihat sebagai pokok yang berpotensi untuk mendapatkan bahan bioaktif semulajadi di mana bahan ini penting sebagai maklumat asas bagi kajian penghasilan bahan antioksida dan antimikrob semulajadi.

Kata kunci: Leguminosae, *Entada spiralis*, antioksida, aktiviti antibakteria

Introduction

Free radical which is usually known as a disease source can possibly come into contact with our body either directly or indirectly by damaging internal cell *via* oxidation process and this may cause several diseases. Thus, to combat free radicals, an antioxidant is a good alternative to consume externally or internally. It is a molecule that restrains the oxidation of other molecules. Generally, oxidation is a chemical reaction that can produce free radicals which lead to chain reactions that could destroy cells. Antioxidants such as thiols or ascorbic acid (vitamin C) stop these chain reactions by preventing some degeneration of certain diseases such as cancer by inhibiting the reaction of radical. Antioxidant of phytochemicals from plant such as flavonoids and terpenoids are able to block the reaction of free radical and in the same way, protect human body from suffering due to a disease [1]. The antifungal efficacy of *E. spiralis* against human pathogens has been well-documented [2] in which methanol extract was declared as the most active extract as well as its fractions [3]. The antibacterial activity of stem and leaves of *E. spiralis* against *E. chrysanthemi* has recently been reported [4] in which ethyl acetate extract was claimed as the most active extract.

The isolation and structure elucidation of compounds from seed kernels of *E. rheedii* showed the presence of two triterpenoid saponins [5] but unfortunately, they were not antioxidative. For the past few years, the antibacterial and antidermatophytic constituents from methanol extracts of *E. spiralis* have previously been isolated and identified [6, 7, 8], however, there was lack of identification of antioxidative and antimicrobial compounds from other *E. spiralis* extracts. Currently, antioxidative constituents from methanol extract of the stem bark of *E. spiralis* have been successfully determined and they were reported as tetrahydroxyflavone [9], ferulic ester such as (E)-hexyl 3-(4-hydroxy-3-methoxyphenyl) acrylate and five known phenolic constituents identified as kaempferol, 5,4'-dihydroxy-3,7,3'-trimethoxyflavone, gallic acid, (+)-catechin, as well as (-)-epicatechin, with gallic acid being the most antioxidative [10].

Therefore, we embarked our investigation upon antimicrobial activity, antioxidant profile and

identification of alternative antioxidative and antimicrobial compounds from petroleum ether and ethyl acetate extracts from *E. spiralis* stem.

Material and Methods

Sample preparation

About 1 kg stem of *E. spiralis* was obtained from Pahang's Tasik Chini forest and authenticated by a botanist with voucher specimen given as KMS-2558. It was ground into powdered form and soaked for three consecutive times with 3L of petroleum ether, dichloromethane and methanol. The maceration was filtered and evaporated under vacuum to obtain crude extracts. All extracts were kept in refrigerator before use.

Fourier transform infrared (FTIR) analysis

A small amount of stem extract was mixed with ethanol. Then, it was placed onto sample detector of Attenuated Total Reflectance FTIR (ATR-FTIR) Perkin-Elmer SPECTRUM 100 FTIR to generate an infrared spectrum. The interpretation of infrared spectrum was conducted by means of determining functional groups in the stem extract of *E. spiralis.*

Preparation of spraying reagents for thin layer chromatography (TLC) screening: $FeCl_3$ reagent

An amount 1 g of ferric chloride was dissolved in mixture of 50 mL of methanol and 50 mL of distilled water. Dark blue spot appearing on TLC sprayed with $FeCl_3$ solution was the indication of the presence of phenolic compound.

Vanillin/ H_2SO_4 reagent

An amount 1.5 mL of concentrated sulfuric acid was added to a mixture of 1% vanillin in absolute ethanol. The grey, pink, blue and purple spots appearing on TLC which was sprayed and heated on hot plate was the indication of terpenoid compounds.

Dragendorff's reagent

Solution A: 0.85 g basic bismuth nitrate was added in mixture of 100 mL acetic acid and 40 mL of water. Solution B: 8g of potassium iodide was mixed with 20 mL of water. The spraying reagent was prepared by mixing 5 mL of solution A and 5 mL of solution B with a mixture of 20 mL of acetic acid and 70 mL of water. Orange spot against yellow background appearing on the sprayed TLC was the indication of alkaloid compound.

DPPH reagent

This reagent was prepared by mixing suitable amount of DPPH solid in methanol to obtain DPPH solution with concentration of 0.6% (w/v). The yellow spot against purple background that appeared on TLC of extracts sprayed with DPPH revealed the presence of antioxidative compounds.

TLC screening for phytochemicals

The petroleum crude extract was applied on a TLC plate as 1 cm fine bands with capillary tube. Then, the TLC plate was developed with suitable developing solvent in the chromatographic chamber until solvent front is reached. The plate was taken out and was dried for a few minutes. After completely dried, the plate was sprayed with chemical reagents. For terpenoid screening, the plate was heated directly on hot plate just after spraying with vanillin/H_2SO_4 reagent to visualize the terpenoid spots. The TLC screening process was repeated with other reagents such as $FeCl_3$, Dragendorff's and DPPH reagent to screen phenolic, alkaloid and antioxidative spots respectively.

Isolation of active compounds from preparative thin layer chromatography (pTLC)

The stem extract was applied on 10 cm x 10 cm TLC plate and was subjected to chromatographic separation. The bands of active components were marked, and desired bands were scraped off. The isolated compound was separated from silica gel through filtration and then was re-subjected to thin layer chromatographic separation to screen the purity of active components.

Gas chromatography (GC-MS)

The GC-MS analysis of isolated constituents was performed using Agilent Technologies GCMS 5977A MSD. The isolated compounds from petroleum ether extract were introduced using splitless injection of 1.0 µL in hexane fitted with cross linked of 5% phenyl methyl siloxane capillary column. The oven temperature

was at 60 - 290 °C with the rate of 5 °C min^{-1}. The injector temperature was about 220 °C.

Liquid chromatography mass spectrometer (LCMS)

The LCMS spectrum of isolated compounds from ethyl acetate extract were obtained using Vion IMS QTOF MS. Chromatographic separation was performed using Column Temperature at 40°C. The mobile phase for solvent A contained water and 0.1% formic acid, whereas for solvent B, it contained acetonitrile. The spectral data were collected at 254 nm. The high mass analysis performed was at 1000 m/z and low mass at 50 m/z under positive ion mode. The capillary voltage was set at 3.0 kV using a desolvation gas at 800 L/h. The voltage offset was at 0 mV and the full-scale voltage was at 2000 mV.

***In vitro* antimicrobial activity assay of petroleum ether extract**

The antifungal activity and antibacterial activity assay of petroleum ether extract were evaluated through disc diffusion method as previously reported [2, 3]. In antibacterial assay, the disc diffusion method was repeated in the same manner as in antifungal assay, whereby extract impregnated discs were aseptically transferred on the inoculated agar plate of muller hinton agar (MHA) and incubated for 24 hours.

Results and Discussion

FTIR analysis

FTIR spectra of petroleum ether extract which depicted in Figure 1 is used to determine types of functional groups present in petroleum ether extract. The figure reveals absorption peak at 2917.63 cm^{-1} which indicated the sp^2 C-H stretching vibration and absorption peak of sp^3 C-H stretching at 2850.16 cm^{-1}. The visibility of C=C stretching vibration was traced at absorption peak 1462.33 cm^{-1} and the adsorption peak at 1709.49 cm^{-1} was for carbonyl group, C=O stretching. The absorption peak at 1364.80 cm^{-1} belonged to absorption peak of N-H bending and the C-O functional group was determined at absorption peak of 1121.65 cm^{-1}. Since the petroleum ether extract contains C=O,C-O, C=C, C-H and N-H functional groups, we suggest that such constituents like alkaloid, ester derivatives and carboxylic acid derivatives are probably present in petroleum ether extract.

The types of functional groups present in ethyl acetate extract is illustrated in Figure 2 in which the presence of C=O stretching vibration was observed at 1709.49 cm^{-1}, C-O stretching at 1165.07 cm^{-1}, C-N stretching at 1242.86 cm^{-1} and sp^3 C-H stretching at 2917.65 cm^{-1}. The O-H stretching was found at 3240.45 cm^{-1} and the absorption peak at 1606.13 cm^{-1} and 1459.40 cm^{-1} belonged to C=C aromatic. In both extracts, all the functional groups provided basic information to determine the structure of the compounds. As far as we are concerned, some compounds bearing OH and N-H groups are able to display antioxidant behavior [9] and compounds with aromatic ring and COOH linkage have revealed remarkable antimicrobial properties[11].

TLC analysis of petroleum ether extract and ethyl acetate extract

The spots on TLC were visualized under UV short wave (TLC a), long wave (TLC b) and also sprayed with certain chemical reagents (TLC c, d, e). According to Figure 3, TLC a and b illustrated that certain spots demonstrated aromatic character since black spots on TLC a and fluorescence spot on TLC b were visualized. Thus, we suggest that the structure of compounds from desired spots may contain benzenoid ring. TLC **c** indicated an obvious spot of an alkaloid (dark orange) after being sprayed with Dragendorff's reagent, and it displayed its antioxidant properties since the spot was nearly in the same R_f with one of antioxidative spots from TLC d. Referring to TLC d, most of the compounds were antioxidative which were signaled by yellowish spot against purple background when sprayed with DPPH reagent.

Generally, the mechanism was based on the reduction of DPPH, a stable nitrogen-cantered and violet-coloured free radical, that upon reduction, was converted to yellow colour by electron or hydrogen donating ability of the antioxidant compound found in the extract [9]. The degree of discoloration indicated the scavenging potential of antioxidant compounds of extract in terms of hydrogen ability. The more the decolonization of purple colour, the greater the reduction ability was. TLC e illustrated various kinds of terpenoid compounds

(colour range of blue, purple, pink) and several of them were also antioxidative. Thus, the results of TLC analysis suggested that petroleum ether extract was antioxidative which was caused from the presence of alkaloid and terpenoid.

TLC screening method using DPPH spraying reagents is a convenient and the simplest way to detect antioxidant in extract sample because only a small amount of extract and reagent are needed, and it reveals a fast result. As depicted in Table 1, the antioxidant behaviour of ethyl acetate extract was caused by the emergence of terpenoid, alkaloid and phenolic compounds while in petroleum ether extract, only terpenoid and alkaloid were responsible for its antioxidant properties. The antioxidant properties of *E. spiralis* from methanol extract has been previously reported [10] but there is still no report of antioxidants being recorded from petroleum ether and ethyl acetate extract. Thus, this is the first report of antioxidant screening for petroleum ether extract and ethyl acetate extract from *E. spiralis* stem as well as the antimicrobial activity.

Antioxidative constituents from petroleum ether extract and ethyl acetate extract of *E. spiralis* stem

Figure 4 demonstrated three antioxidative constituents from petroleum ether extract labelled as **(1), (2)** and **(3)** and one constituent labelled as **(4)** from ethyl acetate extract of *E spiralis* stem. The structures of antioxidative constituents from petroleum ether extract were identified via GCMS with the assistance of Wiley Library matching individually and LCMS with Library Data was utilized for structure identification of constituent from ethyl acetate extract. Generally, the presence of functional groups in the structures are consistent with FTIR analysis of petroleum ether and ethyl acetate extract. FTIR analysis of petroleum ether extract has recorded the existence of C=O group, C=C for aromatic ring and nitrogen linkage. These data agreed with compound **(1)** as the structure showed the functional group of C=O, C=C, C-N and N-H linkage. Compound **(2)** and **(3)** revealed the appearance of C=O, C-O and C=C group which are still in the range of FTIR analysis data. The structure of compound **(4)** revealed the presence of OH, C=O group, C=C, C-O linkage and aromatic linkage and they were consistent with FTIR analysis of ethyl acetate extract.

According to all antioxidative structures, the hydroxyl group OH or NH group possibly functions as the main part for antioxidant effect towards DPPH radical. Theoretically, hydrogen atom from OH or NH group reacts with free radical species of DPPH through Hydrogen Atom Transfer (HAT) or Single Electron Transfer (SET). During radical scavenging process, the electron of hydrogen from NH or OH group is donated to nitrogen radical of DPPH which contains single electron through reduction reaction, which can be seen from the reduction of dark purple colour to yellow colour of DPPH [12]. After reduction process completes, the radical nitrogen has no more single electron as it has bonded with hydrogen from OH group.

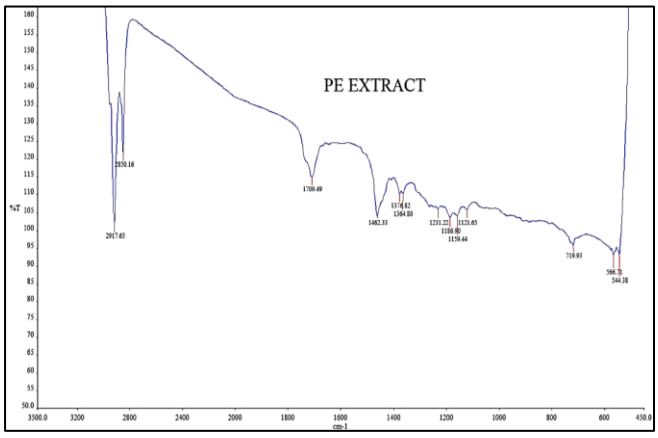


Figure 1. FTIR spectra of petroleum ether extract of *E. spiralis*

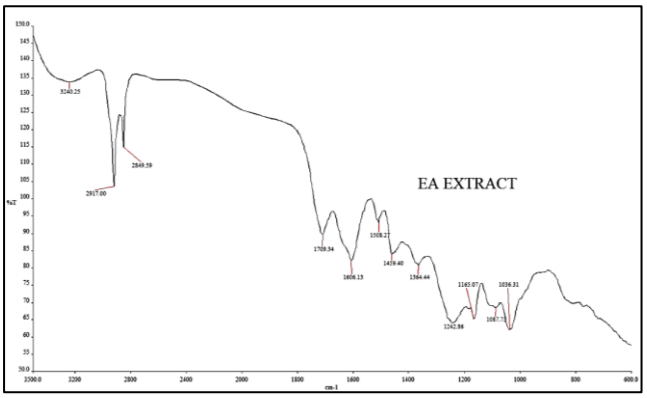
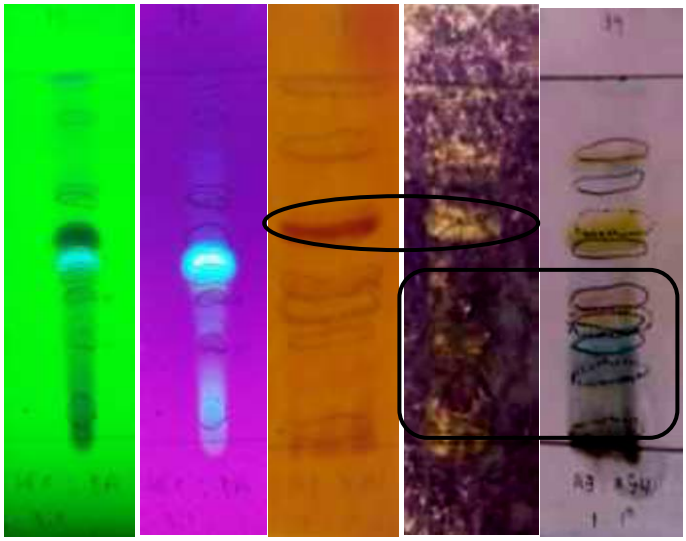


Figure 2. FTIR spectra of ethyl acetate extract of *E. spiralis*



Antioxidative spots (TLC d) is an alkaloid (TLC c)

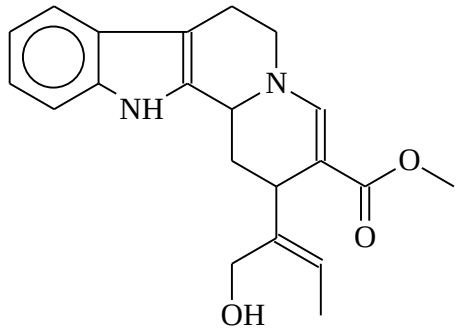
Antioxidative spots (TLC d) are terpenoids (TLC e)

Figure 3. TLC analysis of petroleum ether extract (a) UV_{254} (b) UV_{366} (c) After spraying with Dragendorff's reagent to visualize orange spot of alkaloid (d) After spraying with 2, 2 – Diphenyl – 1 – picryl – hydrazyl (DPPH) solution to visualize yellowish antioxidative spots against purple background and (e) After sprayed with Vanilin/ H_2SO_4 reagent and heated at 110ºC to visualize terpenoid spots

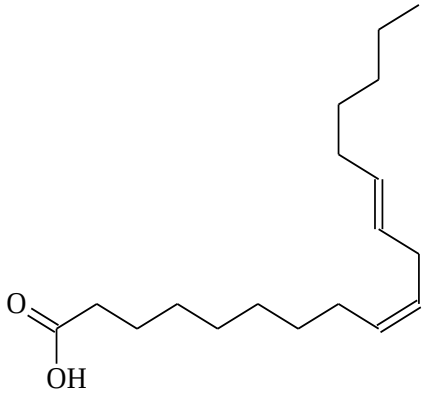
Table 1. Selected phytochemicals screened from petroleum ether and ethyl acetate extract

Extract	**Terpenoid**	**alkaloid**	**phenolic**
Petroleum ether	√*	√*	x
Ethyl acetate	√*	√*	√*

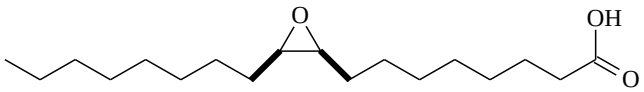
* Antioxidative ; √ = present; x = absent



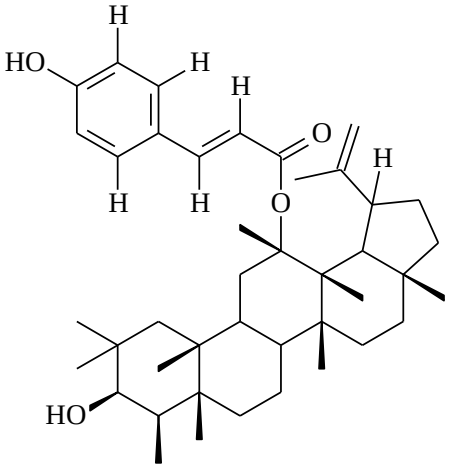
18,19-Secoyohimban-19-oic acid,16,17,20,21-tetradehydro-16-(hydroxymethyl)-, methyl ester **(1)**



Oxiraneoctanoic acid **(2)**



9,12-Octadecadienoic acid **(3)**



11-O-p- Coumarylnepeticin **(4)**

Figure 4. Antioxidative compounds from pet ether extract and ethyl acetate extract of *E. spiralis* stem

***In vitro* Antimicrobial activity of petroleum ether extract of *E. spiralis* stem**

Table 2 and Table 3 depicted the result of antibacterial and antifungal activity of petroleum ether extracts against *S. aureus*, *S. epidermidis*, *T. tonsurans*, *T. mentagrophytes* and *M. gypseum* strains by means of the size of inhibition zone. In Kirby-Bauer disc diffusion method, the size of inhibition zone measures the compound's effectiveness in which the greater the zone of inhibition is, the more effective the compound becomes. The petroleum ether extract was strongly inhibited the growth of *S. epidermidis* with inhibition zone of 16 mm compared to *S.aureus*. Among all bacteria, *S. epidermidis* (ATCC 12228) was found to be the one that is most susceptible toward petroleum ether extract, whereas *S. epidermidis* (ATCC 13518) was found to be resistant towards petroleum ether extract. All bacteria were sensitive towards positive control ampicillin.

The petroleum ether extract of *E. spiralis* stem also inhibited the growth of all dermatophytes in a concentration dependent manner as presented in Table 2. The extract strongly inhibited the growth of *M.*

gypseum with inhibition zone of 16 mm at 400 g/mL. Thus, *M.gypseum* was recognized as the one that is most susceptible to petroleum ether extract compared to other dermatophytes. The results obtained could be generally explained in terms of the effect of the active principles in the extracts once they get into contact with cell wall of microconidia of dermatophytes. As a result, the microconidia lost its rigidity and became ruined and the growth of microconidia was no longer sustained. According to previous study [10], the sensitivity of all dermatophytes towards extracts could be due to the synergistic action of different group of active constituents comprised in the extracts, such as benzenoid compounds. These active constituents may interact with each other to enhance the antimicrobial activity of the extracts. Therefore, this action could possibly be one of the factors for our present results of antimicrobial activity of *E. spiralis* stem.

The inhibition effect in antibacterial activity was also most probably due to the interference by active sources existed in the extracts, which lead to the disruption of cell wall of bacteria and as a result, the cell wall lost its rigidity and caused cell death and consequently the growth of bacteria was no longer emerged.

Figure 5 illustrated the structures of five antimicrobial constituents from petroleum ether extract and ethyl acetate extracts of *E.spiralis* stem that may involve in inhibiting the growth of bacteria and dermatophytes. Compound **(5),(6), (7)** and **(8)** were identified from petroleum ether extract and compound **(9)** was identified from ethyl acetate extract. We had previously reported the data of antibacterial effect of ethyl acetate extract against plant pathogen [4]. Compounds **(5), (6), (7)** and **(8)** can be regarded as new antimicrobial constituents since no investigation to identify antimicrobial constituents from petroleum ether extract of *E. spiralis* has been reported. Meanwhile, compound **(9)** Hordatine B is not a new compound in other plant species, but it can be suggested as a new antimicrobial compound since it was identified for the first time from ethyl acetate of *E. spiralis* stem.

Theoretically, the action of antimicrobial activity starts when the constituent attacks the cell wall of bacteria to prevent them from keeping on synthesizing a peptidoglycan; a molecule that provides the strength of cell wall in order to survive in human body. Attacking cell wall may disrupt membrane potential through depolarization and this leads to the death of cell wall of bacteria. Antifungal agent works by affecting a substance in the cell membrane of fungi, causing the contents of the fungal cells to leak out and the cells to die, thus preventing the fungal cells from growing and reproducing. The antifungal agent such as azoles is a five-membered heterocylic compound containing nitrogen (N) atom. Since structure **(7)** and **(9)** are also compound containing nitrogen atom, it is possible for the structures to have same the function as antifungal agent just like azoles. Another antimicrobial agent is Echinocandin B [13]. The C=O(NH) linkage in Hordatine B **(9)** is quite consistent with the C=O(NH) linkage in Echinocandin B and benzene-OH group linkage. Thus, this similarity may explain the antimicrobial properties of **(9).**

Table 2. *In vitro* antibacterial activity of petroleum ether extract of *E. spiralis* stem

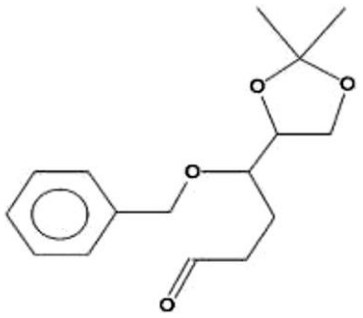
Extracts Concentration (mg/mL)		**Inhibition Zone (mm)[a]**			
		SA 33591	**SA 33592**	**SE 12228**	**SE 13518**
Petroleum ether extract	50	14.0 ± 0.71	14.50 ± 0.71	12.0 ± 0	-
	100	15.0 ± 0	15.0 ± 0	15.0 ± 0	-
	200	15.0 ± 0	15.0 ± 0	15.5 ± 0	-
	400	15.0 ± 0	15.33±0.58	16.0 ± 1.61	-
Standard Ampicillin		9.0 ± 0	10.0 ± 0	19.0 ± 1.0	23.0 ± 1.4

- No activity; SA, *Staphylococcus aureus*; SE, *Staphylococcus epidermidis*; ±, Standard deviation (S.D); [a] Mean of three replicates. Statistical significance was determined using ANNOVA. Differences were considered significant at (p <0.05). 16 mm above: highly inhibited; 11-15 mm: moderately inhibited; 6-10 mm: weakly inhibited.

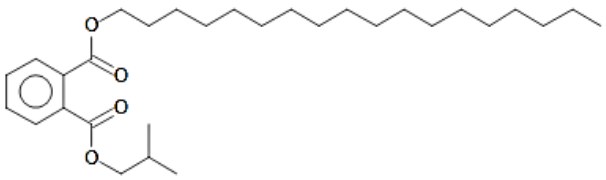
Table 3. *In vitro* antifungal activity of petroleum ether extract of *E. spiralis* stem

Extracts Concentration (mg/mL)		**Inhibition Zone (mm)[a]**		
		TM	**TT**	**MG**
Petroleum ether extract	50	-	8.67±0.58	9.50±0.71
	100	8.33±0.58	10.3±0.58	10.0±0
	200	9.0±0.00	9.00±1.0	13.0±0
	400	10.67±0.58	13.0±1.73	16.0±0
Standard Nystatin		21.33±0.58	40.33±0.58	24.0±0

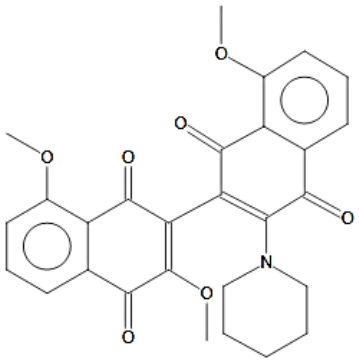
- No activity; TM, *Trichophyton mentagrophytes*; TT, *Trichophyton tonsurans*; MG, *Microsporum gypseum*; CG, *Candida glabrata*; ±, Standard deviation (S.D); [a] Mean of three replicates. Statistical significance was determined using ANNOVA. Differences were considered significant at (p <0.05). 16 mm above: highly inhibited; 11-15 mm: moderately inhibited; 6-10 mm: weakly inhibited



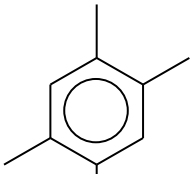
4-benzyloxy-4-[2,2,-dimethyl-4-dioxolanyl] Butylaldehyde **(5)**



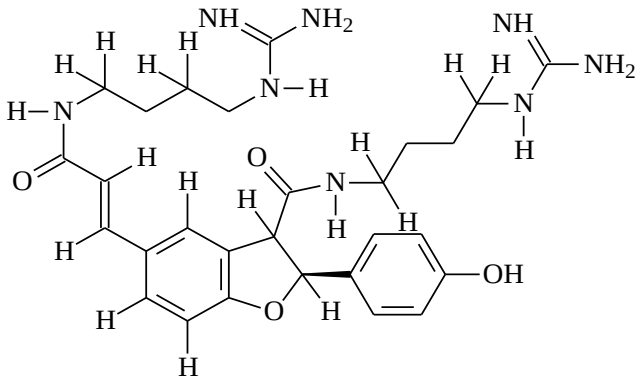
Isobutyl octadecyl benzoate ester **(6)**



3',8,8'-Trimethoxy-3-piperidyl-2,2'-binaphthalene-1,1',4,4'-tetrone **(7)**



1,2,4,5-tetramethylbenzene **(8)**



Hordatine B **(9)**

Figure 5. Antimicrobial active constituents from petroleum ether extract of *E. spiralis* stem

Conclusion

The petroleum ether extract and ethyl acetate extract from stem of *E. spiralis* displayed antioxidant properties and potent antimicrobial activity. Four antioxidative constituents were successfully isolated and tentatively recognized as 18,19-Secoyohimban-19-oic acid,16,17,20,21-tetradehydro-16-(hydroxymethyl)-methylester **(1**), Oxiraneoctanoic acid **(2),** 9,12-Octadecadienoic acid **(3),** and 11-O-p-Coumarylnepeticin **(4)**. Five antimicrobial constituents were isolated and tentatively identified as 4-benzyloxy-4-[2,2,-dimethyl-4-dioxolanyl]Butylaldehyde, **(5),** Isobutyl octadecyl benzoate ester **(6),** 3',8,8'-Trimethoxy-3-piperidyl-2,2'-binaphthalene-1,1',4,4'-tetrone **(7)**, 1,2,4,5-tetramethylbenzene **(8)** and Hordatine B **(9).** All active constituents may be regarded as new compounds since no investigation from petroleum ether extract and acetate extract of *E. spiralis* were used and reported. Thus, this plant appears to be a good source of antimicrobial and antioxidant agents as well. However, further spectroscopic analysis study such as 1D and 2D NMR need to be carried out for structure confirmation.

Acknowledgement

We would like to express our gratitude to all science laboratory staff especially from Chemistry and Agrotechnology laboratories of UiTM Jengka, Pahang, for their contribution throughout the journey of completing this research work.

References

1. Harun, A., Mat So'ad, S. Z., Mohd Hassan, N. and Che Mohd Ramli, N. K. (2011). *In-vitro* antifungal activity of *Entada spiralis* Ridl. crude extract against dermatophytes of superficial skin disease. *Revelation and Science,* 1(1): 57-61.
2. Chandel, M., Sharma, U., Kumar, N., Singh, B. and Kaur, S. (2012). Antioxidant activity and identification of bioactive compounds from leaves of *Anthocephalus cadamba* by ultra-performance liquid chromatography/electrospray ionization quadrupole time of flight mass spectrometry. *Asian Pacific Journal of Tropical Medicine*, 5(12): 977-985.
3. Nzowa, L. K., Barboni, L., Teponno, R. B., Ricciutelli, M., Lupidi, G., Quassinti, L., Bramucci, M. and Tapondjou, L. A. (2010). Rheediinosides A and B, two antiproliferative and antioxidant triterpene saponin from *Entada rheedii*. *Phytochemistry* 71(2): 254-261.
4. Maha Yudden, N. K., Nordin, N. N., Harun, A., Mohd Rosli, N. H., Abdul Aziz, N. and Daud, S. (2019). Comparative study of antioxidant activity of stem and leaves of *Entada spiralis* and their antibacterial properties against *Erwinia Chrysanthemi*. *Science Letters,* 13(2): 37-47.
5. Harun, A., Mat So'ad, S. Z., Mohd Hassan, N. and Che Mohd Ramli, N. K. (2014a). Bioactive terpenoids from the stem bark of *Entada spiralis* Ridl. (sintok). Proceeding of the International Conference on Science Technology and Social Science (ICSTSS) 2012. Chapter in Book Springer Science+Business Media Singapore: pp. 605-615.
6. Harun, A., Mat So'ad, S. Z. and Mohd Hassan, N. (2015). Bioassay guided isolation of an antidermatophytic active constituent from the stem bark of *Entada spiralis* Ridl. *Malaysian Journal of Analytical Sciences* 19(4):752-759.
7. Harun, A., Mat So'ad, S. Z., Mohd Hassan, N. and Che Mohd Ramli, N. K (2016). Two isolated crystalline solids from the stem of *Entada spiralis* Ridl. *Malaysian Journal of Analytical Sciences,* 20 (2):752-759.
8. Harun, A., Mat So'ad, S. Z., Mohd Hassan, N. and Che Mohd Ramli, N. K. (2014). *In-vitro* Antidermatophytic activity of methanolic fractions from *Entada spiralis* Ridl. stem bark and its bioautographic profile. *Pertanika Journal Science & Technology*, 22(1): 113-121.
9. Kedare, S. B. and Singh, R. P. (2011). Genesis and development of DPPH method of antioxidant assay. *Journal of Food Science and Technology*, 48(4): 412-422.
10. Kuiate, J. R., Bessiere, J. M., Zollo, P. H. A. and Kuate, S.P., (2006). Chemical composition and antidermatophytic properties of volatile fractions of hexanic extract from leaves of *Cupressus lusitanica* Mill. from Cameroon. *Journal of Ethnopharmacology,* 103: 160-165.

11. Dzoyem, J. P., Melong, R., Tsamo, A. T., Maffo, T., Kapche, D. G. W. F., Ngadjui, B. T., McGaw, L. J. and Eloff, J. N.(2013). Cytoxicity, antioxidant and antibacterial activity of four compounds produced by endophytic fungus *Epicoccum nigrum* associated with *Entada Abyssinica*. *Brazillian Journal of Pharmacognosy*, 27: 251-252.
12. Opeyemi, R. F., Mat So'ad, S. Z., Ahmed, Q. U., and Mohd Hassan, N. (2019). α-glucosidase inhibitory and antioxidant activities of *Entada spiralis* Ridl. (Sintok) stem bark extracts. *Pertanika Journal Tropical Agriculture Science,* 42(1): 139-153.
13. Shao, L., Li, J., Liu., A., Chang, Q., Lin, H. and Chen, D. (2013). Efficient bioconversion of echinocandin B to its nucleus by overexpression of deacylase genes in different host strains. *Applied and Environmental Microbiology*, 79(4): 1126-1133.

Malaysian Journal of Analytical Sciences (MJAS)
Published by Malaysian Analytical Sciences Society

COMPUTATIONAL STUDIES ON NONLINEAR OPTICAL PROPERTIES OF METAL COMPLEXES CONTAINING AZOBENZENE

(Kajian Pengkomputeran Sifat Optik Tidak Linear Terhadap Sebatian Komplek Logam yang Mengandungi Azobenzena)

Pang Siew Woon[1], Suhaila Sapari[2], Juan Matmin[1], Fazira Ilyana Abdul Razak[1]*

[1] *Faculty of Science,*
Universiti Teknologi Malaysia, 81200 Skudai, Johor Bahru, Malaysia
[2]*Centre for Advanced Materials and Renewable Resources, Faculty of Science and Technology,*
Universiti Kebangsaan Malaysia, 43600 UKM Bangi, Selangor, Malaysia

**Corresponding author: fazirailyana@utm.my*

Received: 13 November 2019; Accepted: 3 September 2020; Published: 12 October 2020

Abstract

Ruthenium complexes containing different azobenzene derivatives with different substituents provide different nonlinear optical (NLO) properties. A computational study through the Hartree-Fock (HF) method based on a 3-21G level and the density functional theory (DFT) methods based on LANL2DZ/6-31G level were used in the investigation to reduce cost and time of the experimental investigation. It was discovered that DFT-based calculations were more accurate than the HF method based on the result of bond length and bond angle obtained after the geometry optimization of three ruthenium-azobenzene complexes; complex A, complex B, and complex C. The investigation through the DFT method revealed that the three complexes possess a high NLO property based on the value of total frequency-dependent first hyperpolarizability, β_{tot} obtained at the wavelength of 1064 nm contributed by the electron delocalization effect, due to the presence of a strong electron donating and withdrawing group in the azobenzene derivatives. It was revealed that Complex C possessed the highest NLO property with a β_{tot} value of 12414.87 $x10^{-30}$ esu followed by complex A (11828.63$x10^{-30}$ esu) and Complex B (3372.10 $x10^{-30}$ esu). The influence of the different structures of azobenzene containing metal to enhance the strength of nonlinear optical properties through NLO calculation has been successfully performed by the DFT method. The high NLO property of complex C was contributed by the -O(C=O)R group, which is a moderate electron-donating group (EDG) and an amine group, which is a strong EDG especially when its hydrogen group is replaced by the alkyl group.

Keywords: nonlinear optic property, ruthenium complex, azobenzene, Hartree Fock, density functional theory

Abstrak

Komplek ruthenium yang mengandungi terbitan azobenzena pada kumpulan pembolehubah yang pelbagai memberikan sifatoptik tidak linear yang berbeza. Kajian pengkomputeran menggunakan kaedah Hartee-Fock (HF) dengan set asas 3-21G dan teori fungsi ketumpatan (DFT) dengan set asas LANL2DZ/6-31G telah dijalankan bagi mengurangkan kos dan masa yang digunakan dalam kaedah experimen. Hasil pengiraan menunjukkan pengiraan menggunakan kaedah DFT adalah lebih tepat berbanding menggunakan kaedah HF, berdasarkan nilai panjang ikatan dan sudut ikatan yang diperolehi untuk tiga sebatian komplek ruthenium-azobenzena; komplek A, B, dan C. Pengiraan menggunakan DFT menunjukkan ketiga-tiga sebatian ini memberikan sifat optik tidak linear (NLO) yang tinggi berdasarkan nilai jumlah dinamik kebergantungan frekuensi pertama, β_{tot} pada panjang

gelombang 1064 nm yang berpunca daripada kesan penyahsetempatan elektron dengan kehadiran kumpulan penderma yang kuat dan kumpulan penarik yang kuat pada terbitan azobenzena. Sebatian komplek C memberikan nilai β_{tot} tertinggi iaitu 12414.87x10^{-30} esu diikuti dengan sebatian A (11828.63x10^{-30} esu) dan B (3372.10 x10^{-30} esu). Perubahan pada perbezaan struktur terbitan azobenzene yang mengandungi logam dapat dilihat meningkatkan sifat optik tidak linear sebatian berdasarkan pengiraan NLO yang telah dijalankan menggunakan kaedah DFT. Dapat dilihat sebatian komplek C menunjukkan sifat optik tidak linear (NLO) yang tinggi disebabkan kehadiran kumpulan -O(C=O)R yang merupakan kumpulan penderma elektron dan kumpulan amina sebagai kumpulan penderma eletron yang kuat terutamanya setelah kumpulan hidrogen digantikan dengan kumpulan alkil.

Kata kunci: sifat optik tidak linear, komplek ruthinium, azobenzena, Hartree Fock, teori fungi ketumpatan

Introduction

In a nonlinear optic material (NLO), the oscillation of electrons will eventually become anharmonic as an intense light source travels through the material, thus causing changes in the properties of light, such as frequency, amplitude, or polarization [1]. This situation is due to the distortion of the spatial distribution between the electrons and the nucleus in the materials [2]. NLO materials are widely used in various types of applications, such as data storage, processing of information, and medical diagnostics such as the use of second harmonic imaging microscopy (SHIM) [3]. Second harmonic generation (SHG) is based on the second order NLO effect, which can be related to the frequency-dependent first hyperpolarizability, β. It is also called frequency doubling, a nonlinear optical process, in which photons interacting with a nonlinear material are effectively combined to form new photons having twice the frequency of the initial photons [4].

Hyperpolarizability is normally shown by the compound with a high charge transfer and strong electron delocalization effect, such as azobenzene with an electron-donating or accepting substituent. Although organic materials have fast and large non-linear responses over a broad frequency range, inherent synthetic flexibility, and large optical damage threshold, they have weaknesses such as volatility and low thermal stability [2]. Inorganic materials with a good chemical and mechanical property usually show a lower NLO efficiency; hence, metal complexation is needed to overcome this weakness. Ruthenium complex has been studied widely in NLO investigations due to its strengths, such as synthetic accessibility, chemical and thermal stability, and the reversibility of the Ru(II)/Ru(III) redox couple [5]. The electron-rich d^6 of Ru(II) centers are especially well-suited to be used as NLO materials due to the high polarizable d orbitals and effective π-electron-donating properties [6]. This study shows the medium that can convert new photons at an excitation wavelength of 532 nm as NLO materials.

Materials and Methods

The experiment was divided into two stages. The first step was the determination of the potential of Hartree-Fock (HF) and density functional theory (DFT) method for computational investigation. The software GaussView5 was used to draw and visualize the complexes, while Gaussian16 was used to perform calculations. Geometry optimization was done on the three surveyed azobenzene-ruthenium complexes by using the unrestricted HF method at the basis set of 3-21G, and unrestricted DFT method at the level of B3LYP/LANL2DZ/6-31G (B3LYP/GENECP) with the keyword “OPT”. The three complexes were formed through the combination of Ru complex, L with three azobenzene derivatives, and X (Figure 1). For the DFT method, the LANL2DZ basis set was used for ruthenium metal, while 6-31G was used for the other atoms in the complex.

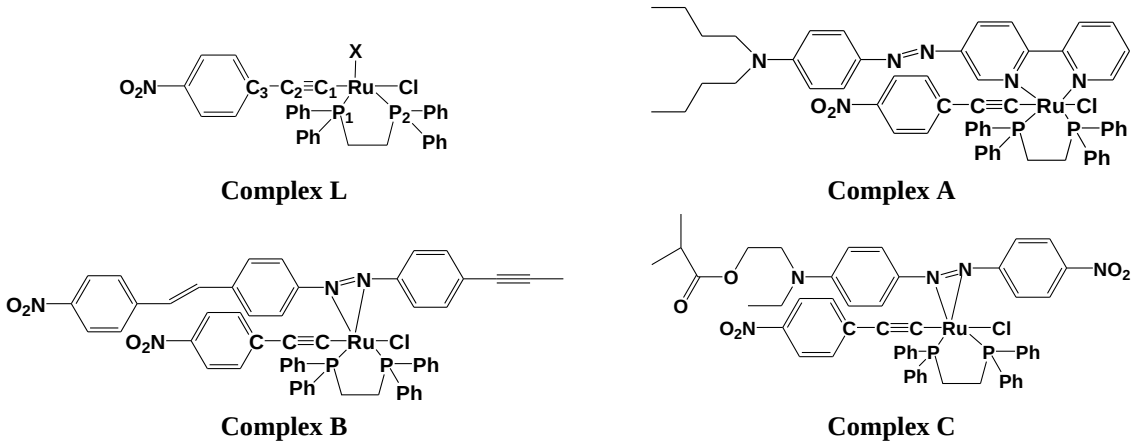


Figure 1. Studied Complexes

After geometry optimization, the bond length, bond angle, and bond energy of the complexes were analysed. The second stage was determining the influence of the different structures of azobenzene containing metal to enhance the strength of NLO properties through NLO calculation. All three optimized complexes obtained through the method that could provide a more accurate geometry structure were used to perform the first hyperpolarizability calculation at 1064 nm with the level of B3LYP/LANL2DZ/6-31G. This step was done by using the keyword "polar=gamma" with the combination of "CPHF=RdFreq" in the job tab [7]. After the calculation, information such as dipole moment (μ), total frequency-dependent first hyperpolarizability, β_{tot} for SHG (2ω; ω, ω) at the wavelength of 1064 nm, and energy for HOMO and LUMO were extracted. The β_{tot} was calculated by using the following equations [8]:

$$\beta_{tot} = (\beta_x^2 + \beta_y^2 + \beta_z^2)^{0.5} \quad (1)$$

$$\beta_{tot} = [(\beta_{xxx} + \beta_{xyy} + \beta_{xzz})^2 + (\beta_{yyy} + \beta_{yxx} + \beta_{yzz})^2 + (\beta_{xxx} + \beta_{xyy} + \beta_{xzz})^2 + (\beta_{zxx} + \beta_{zyy} + \beta_{zzz})^2]^{0.5} \quad (2)$$

Results and Discussion

Geometry Optimization

The selected bond length (Table 1) and bond angle (Table 2) for the optimized ruthenium complexes were elucidated by using numbering, and the label of the atom is shown in Figure 1. From this study, all the bond length calculated by the HF method had a percentage deviation of 0.21% to 11.18%, and for those calculated by the DFT method, the percentage deviation was between 0.37% and 7.48%. From the average percentage deviation calculated using Equation 3, it was found that the DFT (2.42%) method provided a more accurate bond length as compared to HF (4.07%). The average percentage deviation of bond angle obtained after the optimization process done by the HF method (2.26%) was slightly lower than the DFT method (2.34%). The percentage deviation of bond angle obtained through the HF method was between 0.01% and 4.68%, whereas for the DFT method, the percentage deviation was between 0.23% and 7.46%. The higher deviation of bond angle calculated by DFT method from the experimental value mainly presented by the Cl-Ru-C_1 angle in Complex B was presumably due to the steric effect of the large molecular azobenzene derivative. The accuracy of the bond angle obtained from HF and DFT methods were in agreement with literature study, and further calculations for non-linear optic (NLO) properties were performed using the DFT method at a wavelength of 1064 nm [9].

$$\text{Percentage deviation} = \frac{\text{Calculated value - Experimental value}}{\text{Experimental value}} \times 100\% \quad (3)$$

Table 1. Selected bond length (Å)

Bond	Complex A		Complex B		Complex C		Exp [10]
	HF	DFT	HF	DFT	HF	DFT	
Ru-Cl	2.622	2.619	2.601	2.556	2.627	2.607	2.500
Ru-C_1	2.100	1.993	2.085	1.993	2.088	1.995	1.986
C_1-C_2	1.211	1.242	1.209	1.240	1.209	1.240	1.206
C_2-C_3	1.423	1.416	1.424	1.418	1.424	1.417	1.442
Ru-P_1	2.612	2.488	2.490	2.455	2.563	2.468	-
Ru-P_2	2.650	2.501	2.594	2.359	2.524	2.404	-
Ru-P_{ave}[a]	2.631	2.495	2.542	2.407	2.544	2.436	2.367

[a]Ru-P_{ave} is the average value of angle of Ru-P_1 and Ru-P_2

Table 2. Selected bond angle (°)

Bond	Complex A		Complex B		Complex C		Exp [8]
	HF	DFT	HF	DFT	HF	DFT	
Cl-Ru-C_1	171.22	169.71	167.96	163.05	169.08	170.17	176.20
Ru-C_1-C_2	173.84	172.80	176.03	173.97	175.27	174.84	175.30
C_1-C_2-C_3	178.41	178.74	179.85	179.48	179.52	178.45	174.40
P_1-Ru-P_2	79.17	81.22	82.68	83.79	81.87	83.10	82.91
P_1-Ru-C_1	87.65	87.36	86.17	85.62	86.83	86.94	-
P_2-Ru-C_1	89.00	89.09	88.10	89.17	88.22	87.28	-
P_{ave}-Ru-C_1[a]	88.32	88.23	87.14	87.40	87.52	87.11	89.63

[a]P_{ave}-Ru -C_1 is the average value of angle of P_1-Ru -$C_1$and P_2-Ru -C_1.

For both HF and DFT methods, the molecular energy of complex B (-8242.67 a.u for HF method and -3954.84 a.u for DFT method) was the highest, followed by complex A (-8246.97 a.u and -3959.45 a.u) and complex C (-8336.86 a.u and -4049.93 a.u.). The huge difference obtained between DFT and HF was due to the DFT method provide a greater number of Gaussian functions that were used to describe the inner shell orbital [11]. Besides that, the ability of DFT to include a large part of the dynamic electron correlation function allowed the processing of an accurate result in the evaluation of molecular properties [12]. Generally, a higher-energy molecule is a molecule with a high number of atoms. However, complex B that had a smaller number of atoms, which was 114, had a higher energy value than complex A (127) and complex C (121). This was presumably due to the presence of three benzene rings in the azobenzene derivative of complex A and complex B that resulted in both compounds having a similar value of molecular energy as compared to complex C, which had only 2. The higher energy of complex B may also be due to its smaller angle of N-Ru-N' (26.82° for HF method; 28.42° for DFT method) as compared to complex C (30.47°; 34.52°) and A (76.72°; 78.20°).

The higher molecular energy calculated by the DFT method was due to the principle of DFT theory where the total energy of a molecule is a function of an electron density surrounding the nuclei. Also, the contribution of total energy is based on five properties, which are kinetic and potential energy, the Coulomb repulsion among the electrons, exchange energy due to the Pauli exclusion principle, and correlation energy [13].The higher accuracy based on the result of bond length and bond angle was also due to the inclusion of correlation energy in the DFT method and the use of a higher basis set.

NLO calculation

The complexes used in this calculation were chosen from those optimized by the DFT method since it was able to provide a more accurate geometry structure. Based on the result as shown in Table 3, the higher the dipole moment of the complexes, the higher the total frequency-dependent first hyperpolarizability, which indicates a higher NLO property. This is because a molecule with a higher dipole moment has a higher redistribution of electron density, which leads to a greater charge transfer [14]. Dipole moment in a molecule is generally due to the separation of charge and the difference of electronegativities in the structure; hence, a molecule with a high dipole moment has a higher redistribution of electron density and greater charge transfer. From the result, all three complexes can be predicted as possessing a high NLO property when compared to other ruthenium complexes in which study by Karakas et al. (2013) provided the value of β_{tot} is 957 x 10^{-30} esu. [15]. Complex C had the highest NLO property and an almost similar NLO property as complex A, while complex B had the lowest NLO property. However, this property can be related to the HOMO-LUMO energy gap and the dipole moment of the molecules.

It is hypothesized that the high NLO property calculated for the three complexes can be contributed by the presence of phosphine ligand and carbon-carbon triple bond in the ruthenium complex. The presence of this ligand has caused the formation of back donation of the ruthenium metal and metal-to-ligand charge transfer effect (MLCT). The presence of azobenzene further enhanced the NLO property of the complex. The remaining valence electrons from the σ orbital of nitrogen can be donated to the metal to form a σ bond, whereas the non-bonding d-orbitals of the metal can be donated to the π* orbitals of the nitrogen molecules in the azobenzene group to form π bond [16]. The electron delocalization and resonance effect in the aromatic system of the azobenzene is high, and it can be strengthened by the introduction of a suitable group inside the system.

Complex C with a high NLO property consisted of -O(C=O) R group, a moderate electron-donating group (EDG), and an amine group, which is a strong EDG, especially when its hydrogen group is replaced by the alkyl group. Another benzene ring of the azobenzene group was bonded to a strong electron-withdrawing group (EWG), which is the nitro group. Hence, the pull- and push electron effect in this azobenzene is very high. For complex A, there was a strong EDG bonded to one side of the azobenzene, which was a tertiary amine that consisted of two linear butyl substituents, whereas another side was a bipyridine group. The benzene group

usually serves as the weak EDG group. The nitrogen atom in the aromatic system also induced an electron-withdrawing effect. This smaller NLO property of complex B was presumably due to the presence of two alkyl groups, which was a weak EDG on each side of the azobenzene derivatives. Although there was a strong presence of EWG of nitro group in one of the benzene groups, the effect on electron delocalization of the azobenzene group was small as it was too far from the azobenzene.

Figure 2 shows the HOMO (highest occupied molecular orbital) and LUMO (lowest unoccupied molecular orbital) energy level of the complexes. The LUMO and HOMO energy of complex A (-0.09827 and -0.17047), complex B (-0.11408 and -0.19018), and complex C (-0.12662 and -0.18347) obtained was used to calculate the HOMO-LUMO energy by calculating their difference. Based on the results, as the value of energy gap (E_{gap}) decreases, the NLO properties increases. This is because a smaller HOMO-LUMO energy gap (E_{gap}) enables a higher charge transfer within the electron delocalization system. Besides, the frontier molecular analysis shows that the charge transfer of the complexes happened from the push azobenzene derivatives to pull the ruthenium linear fragment. This is indicated by the higher electron density at the donor part in HOMO and the acceptor part in LUMO. The electron density is higher at the azobenzene derivatives in HOMO distribution and at the linear fragment of Cl-Ru-aryl alkynyl in LUMO distribution.

Table 3. The dipole moment and the value of first hyperpolarizability

Property	**Complex**		
	A	**B**	**C**
Dipole moment, μ (D)	11.39	6.37	16.34
First hyperpolarisability, β (x10^{-30}esu)			
β_{xxx}	-13.76	-255.84	699.28
β_{xyy}	-44.43	-68.62	-4422.28
β_{xzz}	-294.53	-77.27	235.86
β_{yyy}	-38.07	200.05	326.25
β_{yxx}	32.01	142.72	-38.32
β_{yzz}	5.99	259.95	-17.66
β_{zxx}	-982.07	-520.69	540.44
β_{zyy}	-472.28	82.74	-6280.57
β_{zzz}	-2777.19	-641.68	-1165.16
β_{x}	-807.38	-1695.73	-3931.73
β_{y}	-355.05	2371.33	-2116.38
β_{z}	-11795.70	-1694.80	-11584.10
β_{tot}	11828.63	3372.10	12414.87

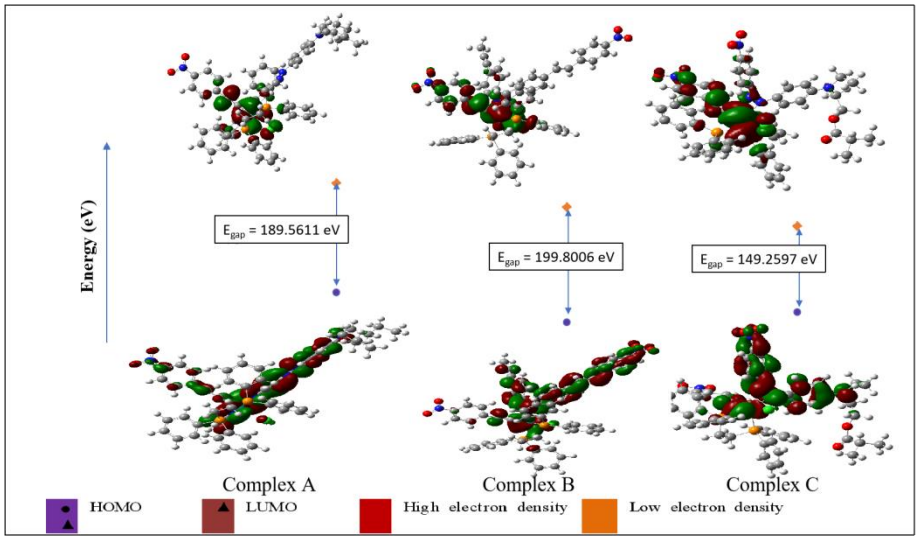


Figure 2. The HOMO and LUMO energy level of the studied complex

Conclusion

The geometry optimization of the studied complexes was successfully done for both methods. It is found that the DFT method provided a more accurate result based on the result of bond length and bond angle as compared to the HF method, as the DFT method includes electron correlation in the calculation. Through the DFT method, it is found that complex C had the highest NLO property, followed by complex A and complex B. This property can be related to the HUMO-LUMO energy gap and the dipole moment of the molecules. The formation of MLCT effect in the complexes and the presence of EDG and EWG in the azobenzene derivative enhance the NLO property of the complex.

Acknowledgement

The authors acknowledge the Faculty of Science, UTM, and the Centre for Information and Communication Technology (CICT), UTM for supporting and providing facilities and services of high-performance computing to reduce the investigation time. Funding from Universiti Teknologi Malaysia under the grant of Tier 1 (Vot Q.J130000.2526.20H08) and the Fundamental Research Grant Scheme (FRGS, Vot R.J130000.7826.4F957) from the Ministry of Higher Education, Malaysia supported this work. We also would like to acknowledge the valuable help and suggestions provided by our colleagues.

References

1. Lind, P. (2007). Organic and organometallic compounds for nonlinear absorption of light. Phd Thesis, Umeå University, Sweden.
2. Suresh, S., Ramanand, A., Jayaraman, D. and Mani, P. (2012). Review on theoretical aspect of nonlinear optics. *Review Advance Material Sciences,* 30: 175-183.
3. Adur, J., Carvalho, H. F., Cesar, C. L., and Casco, V. H. (2014). Nonlinear optical microscopy signal processing strategies in cancer. *Cancer Informatic,*13: 67-76.
4. Li, A. D. and Liu, W. C (2010). Optical properties of ferroelectric nanocrystal/polymer composites. *Physical Properties and Applications of Polymer Nanocomposites,* 108-158.
5. Sahraoui, B., Luc, J., Meghea, A., Czaplicki, R., Fillaut, J. L. and Migalska-Zalas, A. (2009). Nonlinear optics and surface relief gratings in alkynyl–ruthenium complexes. *Journal of Optics A: Pure and Applied Optics,* 11(2) :1-26.
6. Papadopoulos, M. G., Sadlej, A. J. and Leszczynski, J. (2006). Non-linear optical properties of matter. Springer, Dordrecht.
7. Foresman, J. B. and Frisch Æ. (2015). Exploring chemistry with electronic structure methods. Gaussian Inc., Wallingford, CT.

8. Baseia, B., Osório, F., Lima, L., and Valverde, C. (2017). Effects of changing substituents on the non-linear optical properties of two coumarin derivatives. *Crystals,* 7(6): 158-172.
9. Jamaludin, R. (2018). Nonlinear optical properties investigation of ruthenium arylalkynyl complexes via Hartree-Fock and density functional theory methods. PhD Thesis, Universiti Teknologi Malaysia, Skudai.
10. Younus, M., Long, N. J., Raithby, P. R., Lewis, J., Page, N. A., White, A. J., Williams, D. J., Colbert, M. C.B., Hodge A. J., Khan, M. S. and Parker, D. J. (1999). Synthesis and characterisation of mono-acetylide and unsymmetrical bis-acetylide complexes of ruthenium and osmium: X-ray structure determinations on $[(dppe)_2Ru(Cl)(C{\equiv}C–C_6H_4\text{-}p\text{-}NO_2)]$,$[(dppe)_2Ru(Cl)(C{\equiv}C–C_6H_3\text{-}o\text{-}CH_3\text{-}p\text{-}NO_2)]$ and $[(dppm)_2Os\ (C{\equiv}C–C_6H_4\text{-}p\text{-}CH_3)(C{\equiv}C–C_6H_4\text{-}p\text{-}NO_2)]$. *Journal of Organometallic Chemistry,* 578(1-2) :198-209.
11. Lewars, E. G. (2010). Computational chemistry: Introduction to the theory and applications of molecular and quantum mechanics. New York: Springer Science & Business Media.
12. Oprea, C. I. (2007). Density functional response theory with applications to electron and nuclear magnetic resonance. Doctoral dissertation. KTH Royal Institute of Technology, Sweden.
13. Chachiyo, T. and Chachiyo, H. (2017). Simple and accurate exchange energy for density functional theory. Cornell University, New York.
14. Bartashevich, E. and Tsirelson, V. (2013). Atomic dipole polarization in charge-transfer complexes with halogen bonding. *Physical Chemistry Chemical Physics,* 15(7): 2530-2538.
15. Karakas, A., Dag, T., Taser, M., Fillaut, J., Migalska-Zalas, A. and Sahraoui, B. (2013). Second-order hyperpolarizability and susceptibility calculations of a series of ruthenium complexes. 15th International Conference on Transparent Optical Networks (ICTON). 23-27 June. Cartagena, Spain: ICTON, pp. 1-4.
16. Chatt, J. (1969). Nitrogen complexes of the platinum metals. *Platinum Metals Review,*13: 9-14.

Malaysian Journal of Analytical Sciences (MJAS)
Published by Malaysian Analytical Sciences Society

THE INFLUENCE OF Pd NANOPARTICLE SIZE ON Pd/TiO_2 CATALYSTS FOR CINNAMALDEHYDE HYDROGENATION REACTION

(Pengaruh Saiz Nanopartikel Pd pada Pemangkin Pd/TiO_2 untuk Tindak Balas Hidrogenasi Sinnamaldehid)

Norli Abdullah[1]*, Hasliza Bahruji[2], Fadhlina Che Ros[3], Imran Syakir Mohamad[4]

[1]Department of Chemistry and Biology, Centre for Defence Foundation Studies,
National Defence University of Malaysia, Sungai Besi Camp, 57000 Kuala Lumpur, Malaysia
[2]Centre of Advanced Material and Energy Sciences,
Universiti Brunei Darussalam, Jalan Tungku Link, BE 1410, Brunei Darussalam
[3]Department of Physics, Centre for Defence Foundation Studies,
National Defence University of Malaysia, Sungai Besi Camp, 57000 Kuala Lumpur, Malaysia
[4]Faculty of Mechanical Engineering,
Universiti Teknikal Malaysia Melaka, Hang Tuah Jaya, 76100 Durian Tunggal, Melaka, Malaysia

**Corresponding author: norli.abdullah@upnm.edu.my*

Received: 13 November 2019; Accepted: 3 September 2020; Published: 12 October 2020

Abstract

Palladium nanoparticles (PdNP) supported onto the anatase phase of TiO_2 were successfully synthesised using a colloidal method. This synthesis method involved the reduction of K_2PdCl_4 solution by $NaBH_4$ at different temperatures (1, 25, 50, 75 ^oC) and stabilised with PVA ligand. Transmission electron microscope (TEM) was used to determine the particle size of PdNP on the TiO_2. Colloidal synthesis at 1 ^oC and 25 ^oC produced PdNP with less than a 3 nm diameter, whereas when the synthesis temperatures were higher than 25 ^oC, PdNP were produced with a size larger than 4 nm. The catalytic activity of Pd/TiO_2 was significantly improved when palladium (Pd) was produced at 1 ^oC with high selectivity towards the hydrogenation of cinnamaldehyde to hydrocinnamaldehyde. The conversion and selectivity trends from the cinnamaldehyde hydrogenation reaction demonstrated the influence of Pd nanoparticle size to provide active sites for the reduction of C=C and C=O bonds. Pd with a diameter of 2.58 nm favoured hydrogenation of C=C bond to produce high selectivity towards hydrocinnamaldehyde, meanwhile a large Pd diameter > 4 nm allowed simultaneaous reduction of C=C and C=O bonds to give comparable selectivity between hydrocinnamaldehyde and hydrocinnamylalcohol.

Keywords: palladium nanoparticles, cinnamaldehyde hydrogenation

Abstrak

Nanopartikel palladium (PdNP) yang disokong pada fasa anatase TiO_2 telah berjaya disintesis dengan kaedah koloidal. Kaedah sintesis ini melibatkan penurunan larutan K_2PdCl_4 oleh $NaBH_4$ pada kumpulan suhu yang berbeza (1, 25, 50, 75 ^oC) dan distabilkan menggunakan ligan PVA. Mikroskop elektron transmisi (TEM) digunakan untuk mengukur saiz partikel PdNP di atas pemangkin. Sintesis koloid pada suhu 1 ^oC dan 25 ^oC menghasilan PdNP kurang daripada 3 nm, manakala suhu lebih tinggi dari 25 ^oC menghasilkan PdNP lebih besar daripada 4 nm. Aktiviti pemangkinan Pd/TiO_2 meningkat dengan ketara apabila palladium (Pd)

dihasilkan pada 1 ºC dengan pemilihan yang tinggi terhadap hidrogenasi sinamaldehid ke hidrosinamaldehid. Trend penukaran dan pemilihan dalam tindak balas hidrogenasi sinamaldehid menunjukkan pengaruh diameter saiz nanopartikel dalam menyediakan tapak aktif untuk penurunan ikatan C=C dan C=O. Pd dengan diameter 2.58 nm lebih menyukai hidrogenasi ikatan C=C untuk menghasilkan pemilihan tinggi terhadap hidrosinamaldehid, manakala saiz Pd berdiameter > 4nm membenarkan penurunan ikatan C=C dan C=O secara serentak untuk memberikan persamaan pemilihan antara hidrosinamaldehid dan hidrosinamilalkohol.

Kata kunci: palladium nanopartikel, hydrogenasi sinamaldehid

Introduction

Noble metal nanoparticles deposited on metal oxide support (TiO_2, Al_2O_3, ZrO_2, CeO_2) exhibit a huge role as heterogenous catalysts for various industrial applications. Heterogeneous catalysts based on metal nanoparticles contribute towards the production of commercially valuable products such as environmental remediation, synthesis of fine chemicals, hydrogen gas production, and biomass processing [1, 2]. Palladium (Pd) metal nanoparticles show high catalytic ability towards hydrogenation reaction, whereas TiO_2 is widely utilised as heterogenous support due to its pysical and chemical stability in acidic and oxidative environments [3]. TiO_2 exists in three different phases, namely anatase, rutile, and brookite. With anatase, TiO_2 has been frequently utilised as a catalyst support due to strong interaction with metal nanoparticles [4]. Supported metal nanoparticles (NPs) have attracted huge interests in the field of heterogeneous catalysis due to their unique optical, electronic, and catalytic properties in comparison with their larger counterparts. Tailoring metal NPs allow the optimisation of catalytic performance for a given process, with the metal particle size, shape, and structure dictating the overall catalytic performances [5].

A colloidal method for the preparation of NPs provides a reliable pathway to control the nanoparticles' growth and improve the dispersions of nanoparticles.The colloidal method involves metal reduction using reduction agents such as hydrazinem sodium borohydride and sodium citrate with the addition of stabilisers to avoid particle agglomeration [6, 7]. Polyvinylpyrrolidone (PVP) is used to stabilise palladium (Pd) nanoparticles to form different shapes and sizes; for example, the octahedrons (24 nm), tetrahedrons (22 nm), and cubes (20 nm) nanoparticles are obtained by reducing Pd in ethanol with the addition of hydrochloric acid. High concentration of inorganic ligand stabliser to control the size and shape of Pd nanoparticles leads to the appearance of various irregular sizes and shapes of Pd [8]. Many attempts have been made to develop suitable catalysts for selective hydrogenation of α, β-unsaturated aldehydes and the challenge is not only faced by the industrial sector but also the scientific communities.

Hydrogenation of cinnamaldehyde (CAL) produces variations of products resulting from the hydrogenation of olefin bond (C=C) and/or aldehyde functionality (C=O). Hydrogenation at the C=C bond leads to the formation of hydrocinnamaldehyde (HCALD), meanwhile hydrogenation at the C=O site produces cinnamyl alcohol (COL). Further hydrogenation of these two partially hydrogenated products produces hydrocinnamyl alcohol (HCALC) [9]. Small Pd particles shows high selectivity towards C=C hydrogenation reaction to HCALD, while large Pd particles catalyse the reduction of C=O to produce HCALC [10]. In the early work by Xu Yang et al. [11], they successfully obtained nearly 100% conversion with 80% selectivity towards HCALD using Pd nanoparticles entrapped in titanate nano-tubes. On the other hand, Arai et al. [12] obtained 87% HCA selectivity and 100% CA conversion using Pd/C catalyst. The small diameter of Pd granules over the multiwalled carbon nanotubes (MWCNTs) leads to a high catalyst activity, and results in a better hydrogenation performance for C═O bonds than that for C═C bonds.

In this study, the influence of Pd nanoparticles supported on the anatase phase of TiO_2 was investigated as catalysts for the hydrogenation reaction of cinnamaldehyde. PdNP were prepared using the

colloidal method with in-situ reduction of Pd carried out at different reaction temperatures. The effect of temperature variation on the distribution of nanoparticles was correlated with the catalytic activity of cinnamaldehyde hydrogenation.

Materials and Methods

Potassium tetrachloropalladate (II) K_2PdCl_4 (99.99% purity) was purchased from Johnson Matthey. Cinnamaldehyde C_9H_8O (>99% purity), Sodium borohydrate $NaBH_4$ (>96% purity), Polyvinylalcohol (80% hydrolysed), and TiO_2 anatase phase were supplied by Sigma-Aldrich. Toluene as solvent for the catalytic reaction was purchased from MERCK. Deionised water was used in all of the experiments. Supported Pd/TiO_2 were prepared using a modified colloidal method with various reduction temperatures in order to tune the Pd particle size diameter. In a beaker, a 500 mL aqueous solution of K_2PdCl_4 of the desired concentration was stirred for 15 minutes at different temperatures (1, 25, 50, 75 ^oC). Then, freshly prepared aqueous solutions of PVA were added into the beaker and continued to be stirred for 10 minutes. This was followed by adding drop-wise freshly prepared 0.1 M aqueous solutions of $NaBH_4$. The reduction of Pd occured when the solution turned dark brown upon 30 minutes of stirring. After completion of reduction, TiO_2 powder was added to the above mixture under vigorous stirring at 900 rpm. The amount of support TiO_2 required was calculated to achieve final metal loadings of 1 wt.%. The mixtures were acidified to pH 1-2 by sulphuric acid before they were stirred for 60 minutes to accomplish immobilisation of the PdNP onto the Titania support. The colloid was washed with distilled water and dried overnight prior to analysis and catalytic reaction.

Catalysts characterisation

Formation of the colloidal-reduced Pd was analysed by a UV-Vis spectroscopy. UV-Vis spectra (200-800 nm, Shimadzu UV-1800 spectrometer) of the Pd precursor and corresponding reduced Pd solution were recorded in a quartz cuvette after 15 and 30 minutes of process generation. Samples for examination by a transmission electron microscope (TEM) were prepared by first dispersing the catalyst powder in ethanol using ultra-sonication for 30 minutes before dropped on to a holey carbon film supported by a 300 mesh copper TEM grid where the solvent was allowed to evaporate. The samples for TEM were then examined using a JEOL JEM 2100 TEM model operating at 200 kV.

Catalytic activity

Catalytic hydrogenation of cinnamalydehyde was carried out in 50 ml autoclave. The reactor pot was added with 50 mg of catalyst, 5 mg of trans-cinnamalydehyde (purity >98%, Aldrich), and 20 mL toluene used as solvent. The reactor was flushed three times with He gas and repeated using pure H_2 gas before it was pressurised to the desired pressure of 9 bars. The reaction time was taken once the reactor reached 323 K. The reaction was allowed for 2 hours. Product analysis was performed using a Shimadzu gas chromatography (GC) equipped with a flame ionisation detector. The calculation of cinnamaldehyde conversion and the product selectivity are defined respectively in the following equations:

$$Conversion\ (\%) = \frac{[Cal]_0 - [Cal]_t}{[Cal]_o} \times 100 \quad (1)$$

$$Selectivity\ of\ product\ X\ (\%) = \frac{[X]_t}{\Sigma[X]_t} \times 100 \quad (2)$$

Table 1. Experimental conditions for the synthesis of Pd/TiO_2 catalysts

Temperature (°C)	Solvent	Theoretical wt.% Pd loading	Sample Coding
1	H_2O	1	PdA1
30	H_2O	1	PdA2
50	H_2O	1	PdA3
75	H_2O	1	PdA4

Results and Discussion

The UV-Vis spectrometer was used to monitor the transition of metal precursor salt, K_2PdCl_4 to Pd metal nanoparticles during the colloidal synthesis with $NaBH_4$ as the reduction agent. Figures 1(a)-(b) show the UV-Vis spectra of the aqueous solution of K_2PdCl_4 as well as the Pd colloidal suspension after reduction with $NaBH_4$ at 1, 25, 50, and 75 ^oC. Figure 1 (a) presents the UV-Vis spectra of Pd aqeuous solution prepared at 1^oC and 25 ^oC that exhibited absorption band at 208 nm (peak) and 236 nm (shoulder). This indicates the adsorption of ligand to the metal *via* charge transfer between the halide-metal and the metal halide in $[PdCl_4]^{2-}$, respectively [13,14]. The disappearance of these two bands in the colloidal solution specified the reduction of Pd^{2+} precursor to Pd^0. The K_2PdCl_4 solution prepared at 50 ^oC and 75 ^oC showed the formation of broad adsorption band at low energies, 286 nm corresponded to *d-d* transition. After 30 minutes of stirring with $NaBH_4$, PVA-stabilised Pd nanoparticles were formed, and the total reduction of the Pd metal precursor was confirmed by the disappearance of the band, as illustrated in Figure 1(b).

TEM analysis was performed on the Pd/TiO_2 catalysts to determine the particle size distribution of PdNP. The representative TEM images and the derived histograms of the Pd catalysts are presented in Figures 2 and 3, respectively. It is apparent that increasing the reduction temperatures during the syntehsis of colloidal Pd increased the average diameter of Pd nanoparticles. Pd produced using water as solvent formed the smallest average of Pd particle diameter at 2.66 nm with a very narrow particle size distribution. The catalyst also showed a very homogenous Pd distribution on the anatase support as indicated in Figures 2(a-b) and 3(a). As the temperature was increased to 25 ^oC, the particle size of Pd was slightly increased to 2.88 nm as shown in Figures 2(c-d). Pd with large particle sizes of 4.1 nm and <5.5 nm were observed when the synthesis temperatures were increased at 50 ^oC and 75 ^oC, respectively. Reduction of Pd^{2+} to form Pd nanoparticles during the colloidal synthesis was significantly influenced by the temperatures of the solution [15]. High temperatures accelerated the nucleation process and strengthened the interaction between Pd nanoparticles, resulting in agglomeration and non-uniformed distribution of Pd nanoparticles [16] as shown in Figure 3(c). Analysis on the particle size distribution of Pd when the synthesis was carried out at 75 ^oC was unable to be performed due to the agglomeration of the particles. Reducing the synthesis temperature below room temperature formed colloidal PdNP that was stable towards agglomeration.

Figure 4 presents the variations of Pd/TiO_2 activity as catalysts for cinnamaldehyde hydrogenation reaction using toluene as solvent at 50 ^oC under 9 bars of hydrogen gas pressure. The liquid product was analysed using gas chromatography and the two main products observed were HCALD and HCALC. There were no products detected from selective hydrogenation to cynnamalalcohol, which were consistent with the results reported by others [17, 18]. The catalytic activity of PdA1 that contained the smallest Pd particle size exhibited high conversion (48%) of cinnamaldehyde with the selectivity of 60%, 27%, and 13% towards HCALD, HCALC, and other products, respectively. Pd/TiO2 catalyst with a slightly bigger particle size (PdA2) resulted in 43% conversion with the selectivity to HCALD that was reduced to 51%. However, the catalysts produced at 25 ^oC showed enhanced selectivity of HCALC at 41%. As the particle size of PdNP became larger >4.0 nm (PdA3 and PdA4), the conversion of cinnamaldehyde was significantly reduced to give less than 5% conversion. Apparently, the selectivity to HCALD was similar in comparison to the PdA2 catalyst. The distribution of products from α, β-unsaturated aldehydes hydrogenation was influenced by several factors such as the dispersion of metal on the support, the metal particle size, and also the type of support [19, 20].

Therefore, in the current case, there was a trend in the product distribution from the hydrogenation of cinnamaldehyde, in which Pd/TiO2 catalyts with narrow Pd size distribution showed the domination of CAL hydrogenation to HCALD as compared to the hydrogenation of HCALC, to give high selectivity ratios

between HCALD/HCALH. However, the ratio between the selectivity of HCALD/HCALC was reduced as the PdNP particle size increased. Pd with larger particles favoured hydrogenation to both HCALD and HCALC. Linear reduction of conversion was also contributed from the enlargement of Pd particle size and the reduction of homogenous distribution of PdNP on the anatase support. Small PdNP provided more available sites for the hydrogenation of C=C that led to high selectivity towards HCALD. Fast hydrogenation reaction promoted further hydrogenation of HCALD to HCALC at C=O sites [21]. The finding was consistent with the results from other researchers that showed Pd nanoparticles were prone to catalyse hydrogenation reaction of C=C bond in cinnamaldehyde [22]. Increasing the temperature of the synthesis of Pd colloidal exhibited agglomeration of Pd nanoparticles to form larger particles, which consequently reduced the available actives sites for hydrogenation reaction. Small Pd also allowed simultaneous adsorption at both C=C and C=O sites on the metal surface and therefore enhanced the selectivity for both HCALD and HCALC products. The suggested schematic reaction of cinnamaldehyde hydrogenation on Pd is presented in Figure 5. This schematic reaction was based on the reaction graph for all samples.

The schematic reaction herein was formed by two types of pathways. Hydrogenation at C=C bond that led to HCALD and futher hydrogenation to form HCALC occurred on smaller particle size as seen in Figure 5(a). Meanwhile, for bigger particle size, both C=C and C=O bonds were preferred, leading to the production of HCALC and HCALD.

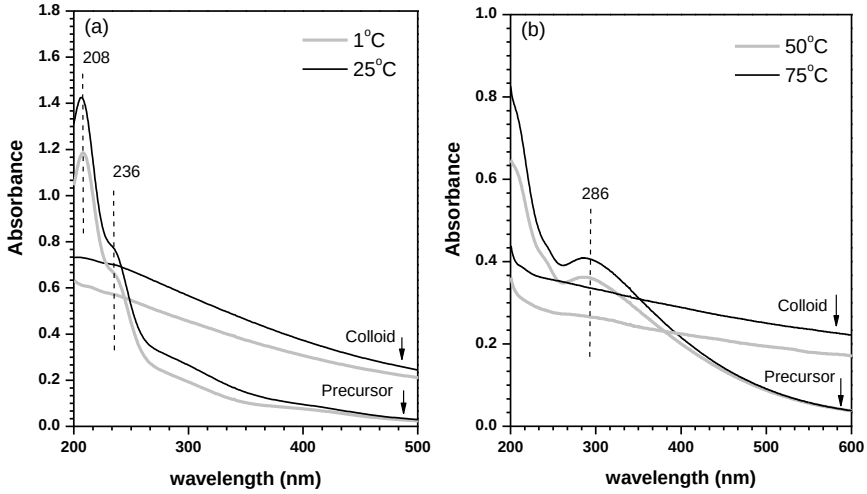


Figure 1. UV-Vis spectra of precursor and colloidal Pd nanoparticles on anatase prepared at different tenperatures

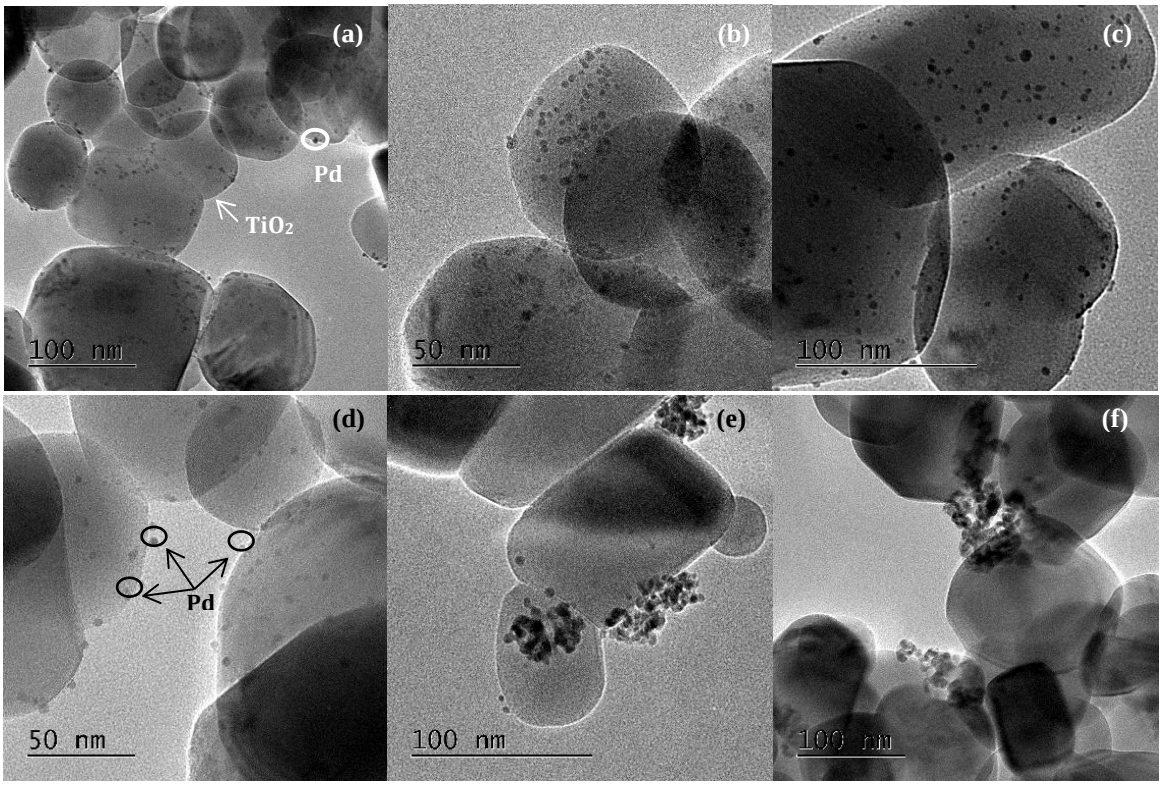


Figure 2. TEM images for the Pd/TiO_2 catalysts prepared at different temperatures; (a)-(b) 1 °C, (c)-(d) 25 °C, (e) 50 °C, (f) 75 °C

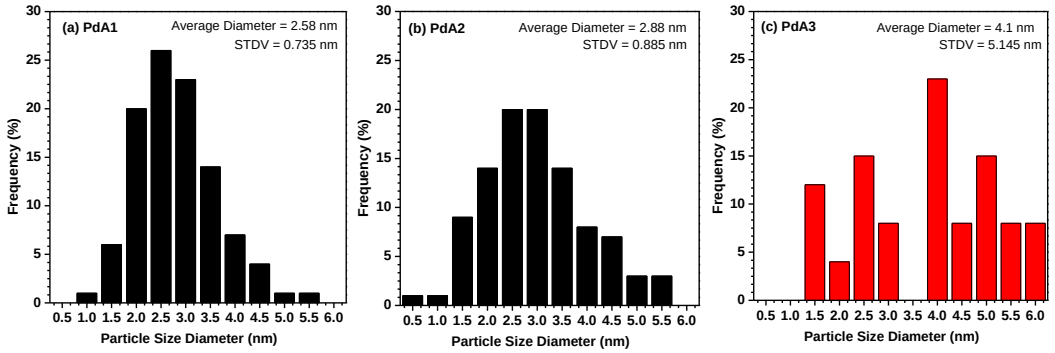


Figure 3. Particle size histogram for the Pd/TiO_2 catalysts prepared at different temperatures; a) 1 °C, b) 25 °C, and c) 50 °C

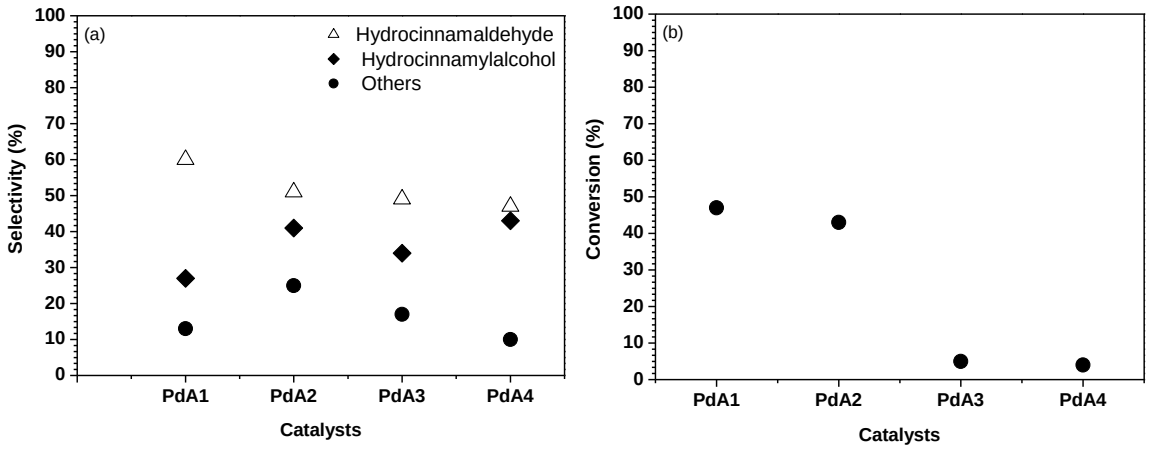


Figure 4. Plot of selectivity to hydrocinnamaldehyde and hydrocinnamyl alcohol (a) as a function of conversion (b) of Pd/TiO_2 prepared at 1°C

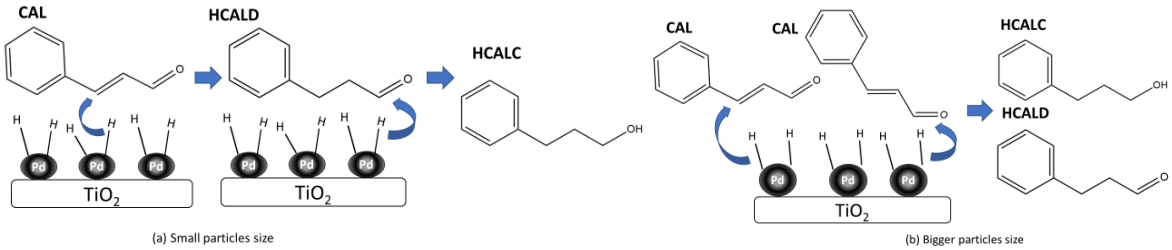


Figure 5. Schematic process of cinnamaldehyde hydrogenation on Pd/TiO_2 catalysts

Conclusion

The colloidal method for the synthesis of Pd nanoparticles on TiO_2 anatase with the various reduction temperatures produced Pd nanoparticles with tailored particle sizes in the range of 2.5 nm to 6 nm. Reducing the synthesis temperatures to 1 °C produced a narrow size of Pd nanoparticles, which exhibited high cinnamaldehyde conversion towards hydrocinnamaldehyde. Significant Pd particles agglomeration occurred when the synthesis was carried out at elevated temperatures. The enlargement of PdNP on TiO_2 reduced the conversion of cinnamaldehyde and the selectivity towards hydrocinnamaldehyde. Tailored synthesis of Pd nanoparticles controlled the active sites of Pd that allowed selective hydrogenation of cinnamaldehyde.

Acknowledgement

This work is supported by the National Defence University of Malaysia under the internal research grant SF0067-UPNM/2019/SF/SG/4. The authors are particularly grateful to the Ministry of Education Malaysia (MOE) for the financial support given in the form of a post-doctoral award to Norli Abdullah. The authors would also like to thank Prof C. Richard A. Catlow and Dr. Scott. M. Rogers from University College London, UK, Dr. Peter P. Wells from Southampton University, UK, and Dr. Nikolaus Dimitratos from University of Cardiff, UK for their fruitful discussions. Additional appreciation is given to the Research Complex at Harwell (RCaH), UK for the research facilities and assistance.

References

1. Lichen, L. and Avelino, C. (2018). Metal catalysts for heterogeneous catalysis: From single atoms to nanoclusters and nanoparticles. *Chemical Reviews*, 118(10): 4981-5079.
2. Solsona, B. E., Edwards, J. K. and P. Landon. (2006). Direct synthesis of hydrogen peroxide from H2 and O_2 using Al_2O_3 supported Au-Pd catalysts. *Chemistry of Materials*, 18(11): 2689-2695.
3. Tapin, B., Epron, F., Especel, C., Ly, B. K. and Pinel, C. (2013). Study of monometallic Pd/TiO2 catalysts for the hydrogenation of succinic acid in aqueous phase. *American Chemical Society*, 3(10): 2327-2335.
4. Bagheri, S., Julkapli, M., Nurhidayatullaili, and Abd Hamid, S. B. (2014). Titanium dioxide as a catalyst support in heterogeneous catalysis. *The Scientific World Journal*, 2014: 727496.
5. Kaden, W. E., Kunkel, W. E., Roberts, F. S., Kane, M., and Anderson, S. L. (2014). Thermal and adsorbate effects on the activity and morphology of size-selected Pdn/TiO_2 model catalysts. *Surface Science*, 621; 40-50.
6. Kim, B. H., Hackett, M. J., Park, J. and Hyeon, T. (2014). Synthesis, characterization, and application of ultrasmall nanoparticles. *Chemistry of Materials*, 26(1): 59-71.
7. Cao, A.-M., Cao, A.-M., Lu, R., Veser, G. and Veser, G. (2010). Stabilizing metal nanoparticles for heterogeneous catalysis. *Physical Chemistry Chemical Physics*, 12(41): 13499-13510.
8. Long, N. T., Nguyen, C., Hirata, H., Ohtaki, M., Hayakawa, T. and Nogami, M. (2010). Chemical synthesis and characterization of palladium nanoparticles. *Advances in Natural Sciences: Nanoscience and Nanotechnology*, 1(035012): 1-5.
9. Espro, C., Donato, A. and Galvagno, S. (2016). On the formation of cinnamyl alcohol during the hydrogenation of cinnamaldehyde under mild conditions on supported palladium catalysts. *Reaction Kinetic, Mechanisms and Catalysis*, 118: 223-233.
10. Feng, J., Jian, C., Bing, L., Yuebing, X. and Xiaohao, L. (2016). Particle size effects in the selective hydrogenation of cinnamaldehyde over supported palladium catalysts. *Royal Society of Chemistry Advanced*, 6: 75541-75551.
11. Yang, L. W., Longlong, M., Xinjun, L., Tiejun W. and Shijun, Liao. (2015). Pd nano-particles (NPs) confined in titanate nanotubes (TNTs) for hydrogenation of cinnamaldehyde. *Catalysis Communications*, 59: 184-188.
12. Zhao, B. N., Chen, J. G., Liu, X., Liu, W., Hao, Z., Xiao, J. and Liu Z, T. (2012). Selective hydrogenation of cinnamaldehyde over Pt and Pd supported on multiwalled carbon nanotubes in a CO_2-expanded alcoholic medium. *Industrial & Engineering Chemistry Research.*, 51(34): 11112-11121.
13. Mehri A, Kochkar H, Daniele S, Mendez V., Ghorbel A. and Berhault G. (2012). One-pot deposition of palladium on hybrid TiO_2 nanoparticles and catalytic applications in hydrogenation. *Journal of Colloidal Interface Science,* 369(1): 309-316.
14. Ansari, P., Kizhakoottu, K. J., Sanchita, Sil. and Nallaperumal, S. K. (2018). A facile green tea assisted synthesis of palladium nanoparticles using tecovered palladium from dpent palladium impregnated carbon. *Johnson Matthey Technology Rev*iew, 62(1):60-73.
15. Norli, A., Hasliza, B., Michael, B., Scott M. R., Peter P. W. and C. Richard A. C. (2019). Efficient electronic transfer on palladium/TiO_2 for hydrogen production from photocatalytic reforming of methanol. *Physical Chemistry Chemical Physic*, 21:16154-16160.
16. Nguyen T. K., Thanh, N., Maclean. and Mahiddine, S. (2014). Mechanisms of nucleation and growth of nanoparticles in solution. *Chemical Reviews*, 114(15):7610-7630.
17. Kahsar, K. R., Johnson, S. and Schwartz, D. K. (2014). Hydrogenation of cinnamaldehyde over Pd/Al_2O_3 catalysts modified with thiol monolayers. *Topic in Catalysis*, 57: 1505-1511.
18. Cabiac, A., Cacciaguerra, T., Trens, P., Durand, R., Delahay, G., Medevielle, A., Plee, D. and Coq. B. (2008). Influence of textural properties of activated carbons on Pd/carbon catalysts synthesis for cinnamaldehyde hydrogenation. *Applied Catalysis A*: *General*, 340: 229-235.

19. Gallezot, P. and Richard, D. (1998). Selective hydrogenation of α,β-unsaturated aldehydes. *Catalysis Reviews-Science and Engineering*, 40: 81-126.
20. Ma, Y., Feng, Lu., Guo, Z., Deng, J., Pham-Huu, C., and Liu, Y. (2019). Palladium supported on calcium decorated carbon nanotube hybrids for chemoselective hydrogenation of cinnamaldehyde. *Frontiers in Chemistry*, 7(751):1-10.
21. Maki-Arvela, P., Hajek, J., Salmi, T. and Yu, M. (2005). Chemoselective hydrogenation of carbonyl compounds over heterogeneous catalysts. *Applied Catalysis A: General,* 292:1-49.
22. Kołodziej, M., Drelinkiewicz, A., Lalik, E., Gurgul, J., Duraczyńska, D., and Kosydar, R. (2016). Activity/selectivity control in Pd/$HxMoO_3$ catalyzed cinnamaldehyde hydrogenation. *Applied Catalysis A: General,* 515: 60-71.

Malaysian Journal of Analytical Sciences (MJAS)
Published by Malaysian Analytical Sciences Society

FOURIER TRANSFORM INFRARED SPECTROSCOPY AND OPTICAL PROPERTIES OF SAMARIUM DOPED ZINC BOROTELLURITE GLASSES

(Inframerah Transformasi Fourier dan Sifat Optik Kaca Samarium didop dengan Zink Borotelurit)

Siti Nasuha Mohd Rafien[1]*, Azman Kasim[2], Azhan Hashim[2], Wan Aizuddin Wan Razali[2], Norihan Yahya[2]

[1]Faculty of Applied Sciences,
Universiti Teknologi MARA, 40450 Shah Alam, Selangor, Malaysia
[5]Faculty of Applied Sciences,
Universiti Teknologi MARA Pahang, 26400 Jengka, Pahang, Malaysia

**Corresponding author: nasuharafien1@gmail.com*

Received: 13 November 2019; Accepted: 3 September 2020; Published: 12 October 2020

Abstract

Zinc borotellurite glasses doped with Sm^{3+} ions of the (70-x)TeO_2-20B_2O_3-10ZnO-xSm_2O_3 system were prepared by a melt-quenching technique. The values of x varied from 0.0 mol% to 2.5 mol%. The studies on structural and optical characterisation of Sm^{3+} ions were carried out through Fourier transform infrared spectroscopy (FTIR), absorption spectra, optical band gap (E_{opt}) and Urbach energy (ΔE) analysis were presented for Sm^{3+} ions in zinc borotellurite glasses. From the FTIR analysis, the presence of BO_3, BO_4, TeO_3, TeO_4 and B – O $^-$ structural units in the prepared glasses was investigated. Three strong absorption peaks in the ultraviolet and visible regions were observed from absorption spectra due to transition between the ground state and various excited state of Sm^{3+} ions. The value of optical band gap, E_{opt} laid between 2.605 eV to 2.982 eV for the direct transition, and 2.768 eV to 3.198 eV for indirect transition, respectively. Meanwhile, the Urbach energy (ΔE) was observed in the range of 0.112 eV to 0.694 eV, respectively. Some other results were analysed and discussed in details.

Keywords: optical properties, zinc, borotellurite, absorption spectra

Abstrak

Kaca zink borotelurit didop dengan ion Sm^{3+} dalam sistem (70-x)TeO_2-20B_2O_3-10ZnO-xSm_2O_3 telah disediakan melalui kaedah konvensional sepuh lindap. Nilai x bervariasi dari 0.0 mol% hingga 2.5 mol%. Kajian terhadap pencirian struktur dan optik ion Sm^{3+} telah dilakukan melalui analisis spektroskopi inframerah transformasi Fourier (FTIR), spektrum penyerapan, jurang jalur optik (E_{opt}) dan tenaga Urbach (ΔE) telah dibentangkan untuk ion Sm^{3+} dalam kaca zink borotelurit. Dari analisis FTIR, kehadiran struktur unit BO_3, BO_4, TeO_3, TeO_4 dan B - O- dalam kaca yang disediakan telah dikaji. Tiga puncak penyerapan yang kuat pada ultraungu dan rantau terlihat telah diamati dari spektra penyerapan kerana transisi antara keadaan dasar dan pelbagai keadaan teruja ion Sm^{3+}. Nilai jurang jalur optik terletak antara 2,605 eV hingga 2,982 eV untuk transisi langsung dan 2,768 eV hingga 3,198 eV untuk transisi tidak langsung. Sementara itu, tenaga Urbach (ΔE) diperhatikan dalam lingkungan 0.112 eV hingga 0.694 eV, masing-masing. Beberapa keputusan lain telah dianalisis dan dibincang secara terperinci.

Kata kunci: sifat optik, zink, borotelurit, spektra penyerapan

Introduction

Rare earth (RE) ions incorporated with various glass oxides have attracted a great deal of interest due to their important role in the development of many optical devices, such as solid-state laser, light converters, sensor and optical communication fibres [1]. The RE ions doped in various glass hosts, such as zinc borotellurite [2], zinc tellurite [3], borotellurite [4] and zinc sodium phosphate [5] have received considerable attention. Amongst these glass hosts, zinc borotellurite glass systems are found suitable to be used as an excellent candidate for laser material due to their low phonon energy, high mechanical strength, high refractive index, large corrosion resistance, extended infrared transmittance (0.35 μm – 6.0 μm) and relatively high thermal stability [6,7]. Sailaja et al. reported that the RE ions, Sm^{3+}, can be used as a dopant in different glass hosts and crystal hosts for their high intense fluorescence in the visible region [8] since the absorption and emission spectra possess broad band region from ultraviolet to infrared [9]. This glass host is very interesting to analyse since the energy transfer process has relatively high quantum efficiency by means of their large energy gap (less non-radiative decay) between the lowest emitting level and next lower lying energy level. However, this glass also shows different quenching mechanisms [10].

In this paper, the effects of Sm^{3+} ions on the structural and optical properties of zinc borotellurite glass were investigated. This study is done to provide more data on the effect of Sm^{3+} ions on zinc borotellurite glass, which are suitable to be used for laser and optical devices. It is expected that the addition of Sm^{3+} ions in the glass network will enhance the optical properties of glass by lowering the optical band gap [11]. Their structural properties by means of FTIR spectroscopy, as well as their optical properties will be analysed and presented.

Materials and Methods

Sm^{3+} ions doped zinc borotellurite glasses with the chemical composition of $(70\text{-}x)TeO_2\text{-}20B_2O_3\text{-}10ZnO\text{-}xSm_2O_3$ ($0.0 \leq x \leq 2.5$ mol%) were prepared by following the melt-quenching technique. Each batch had chemical composition of about 10 g. The chemical compositions were firstly milled together for about 1 hour by using a milling machine to obtain homogeneous mixtures. Then, the mixtures were transferred into an alumina crucible and melted in an electric box furnace at 1000 ℃ for 30 min. The molten mixture was poured onto a stainless-steel plate, followed by an annealing process at 400 ℃ for 5 hours before it was allowed to cool down to room temperature gradually. Then, glass sample was polished before being used for any structural and optical studies.

The FTIR spectra of the glass samples were recorded by using Perkin - Elmer Spectrum 100 FT-IR Spectrometer system in the wavelength region 650–4000 cm^{-1} to identify the local structure and presence of fundamental functional groups. The absorption spectra were measured by using Perkin - Elmer Lambda 35 UV/VIS Spectroscopy in the range of 380-600 nm. By these absorption spectra, the optical absorption coefficient ($\alpha(\omega)$) can be calculated by using the equation as in [12]:

$$\alpha(\omega) = 2.303\frac{A}{d} \quad (1)$$

where, A is the absorbance and d is the thickness of sample in cm^{-1}. The optical band gap, E_{opt}, of the glass samples can be calculated by using the known Mott – Davis equation [13]:

$$\alpha = \frac{B(\hbar\omega - E_{opt})^r}{\hbar\omega} \quad (2)$$

where, B is the band tailing parameter, E_{opt} is the optical band gap, $\hbar\omega$ is the incident photon energy while r is the index number used to decide the nature of the interband electronic transition causing the absorption (r=1/2 for direct allowed transition and r=2 for indirect allowed transition) [14]. Based on this equation, the graph of $(\alpha\hbar\omega)^2$ and $(\alpha\hbar\omega)^{1/2}$ versus $\hbar\omega$ can be plotted and the value of optical band gap is the extrapolation of the linear region in these two graphs.

In addition, Urbach energy is another optical parameter that can be attained from the absorption spectra.

Referring to the equation from Urbach rule, it is obtained by calculating the reciprocal of slope in the graph of natural logarithm of α(ω) as a function of photon energy, ħω:

$$\alpha(\omega) = \alpha_{\circ} exp\left(\frac{\hbar\omega}{\Delta E}\right) \quad (3)$$

where, $\alpha_{\circ}$ is a constant and ΔE is the Urbach energy [15].

Results and Discussion

Figure 1 shows the FTIR spectra of zinc borotellurite glasses with respect to Sm^{3+} ions content. The spectra band around 714-735 cm^{-1} were assigned with the stretching vibrations of the Te-O bonds in trigonal bipyramid (TeO_4) with bridging oxygen and trigonal pyramid (TeO_3) with non-bridging oxygen (NBO) [16, 17]. The bands at 839-855 cm^{-1} and 1215-1218 cm^{-1} belonged to asymmetric stretching vibrations of B-O bonds in BO_4 tetrahedral and BO_3 trigonal units [18, 19]. Meanwhile, the peaks positioned at 1362-1367 cm^{-1} were due to the asymmetric stretching vibrations in trigonal BO_3 and trigonal $B - 0^-$ bond. Whereas the bands present at 2993-3003 cm^{-1} were attributed to the characteristic of the hydrogen bond in the glasses [20]. Finally, the absorption bands located around 3618-3748 cm^{-1} were due to fundamental stretching of molecular water groups, OH, as reported by Elbatal et al. [21].

Figure 2 shows the absorption intensity as a function of wavelength, normalised by the sample thickness of the glass with 0 mol% to 2.5 mol% Sm_2O_3. These were three absorption peaks centred at 403 nm, 422 nm and 480 nm, that corresponded to the $^6H_{5/2} \rightarrow {}^4L_{13/2}$, $^6H_{5/2} \rightarrow {}^4M_{19/2}$ and $^6H_{5/2} \rightarrow {}^4I_{11/2}$ transitions observed. Similar trend of results was also reported by Yaru et al., Som & Karmakar and Selvaraju & Marimuthu in their works, respectively [22-24].

Figure 3(a) and Figure 3(b) show the graph of direct and indirect optical band gaps. The variations of indirect and direct optical band gaps are shown in Table 1. Indirect and direct optical band gaps of the glass samples were found to be varied with the Sm_2O_3 content. These changes may be due to the variations in the amount of bridging oxygen (BOs) and non-bridging oxygen (NBOs) in the glass system. According to Fares et al., the decrement of NBOs caused a reduction in glass polarizability and increment of the optical band gap [25]. This was due to the fact that NBOs bound an excited electron less tightly as compared to BOs. Therefore, NBOs tends to be more polarisable than the BOs. Decrement of E_{opt} might be caused by weaker bond strength of Sm_2O_3 as compared to other chemical oxide in the glass. As a result, it was easier for the electrons to jump into the conduction band. The existence of trivalent electrons, Sm^{3+} ions caused the increment in the number of free electrons in the glass network. This will cause electrons to localise in deep energy levels and contributed to the declining of E_{opt} [26]. Table 1 also shows the results of Urbach energy (ΔE). Urbach energy gives information regarding to defects and disorderness of the glass network [27]. As tabulated in Table 1 as well as in the plotted graph of ln α versus photon energy, ħω is shown in Figure 4, the values of the Urbach energy were found to lay between 0.112 eV to 0.694 eV for the glass samples which were in agreement with the results found with other oxide glass, such as P_2O_5-TeO_2, Bi_2O_3-P_2O_5-TeO_2 (0.17-0.67 eV) and TeO_2-MgO-Na_2O-Nd_2O_3 (0.12-0.21 eV), depending on glass composition [28, 29]. The Urbach energy, ΔE, was measured from the reciprocal of the linear region slope (in lower photon energy) of the curves.

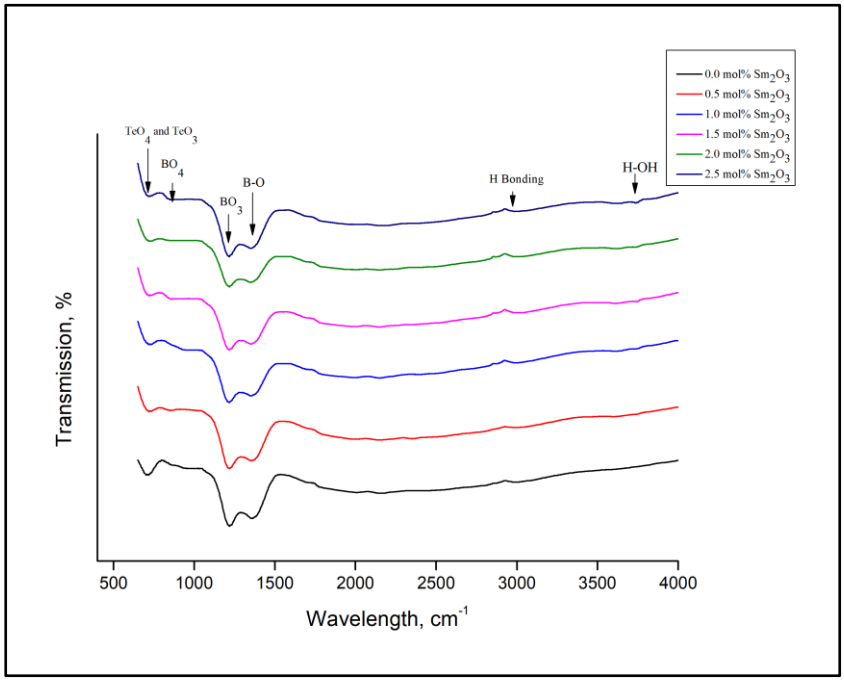


Figure 1. FTIR spectra of the Sm^{3+} doped zinc borotellurite glasses

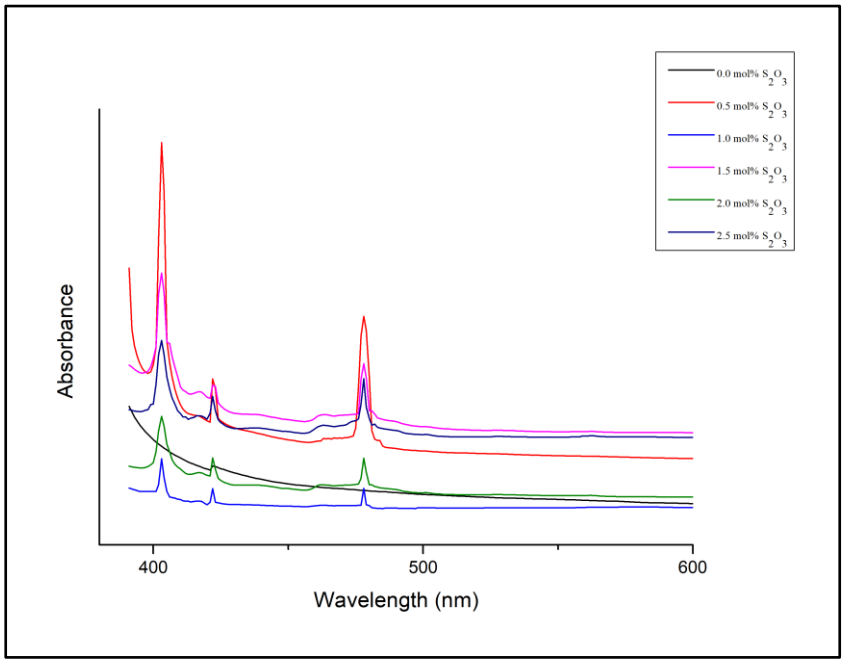


Figure 2. Normalised optical absorption spectra of glasses with different mol% Sm_2O_3

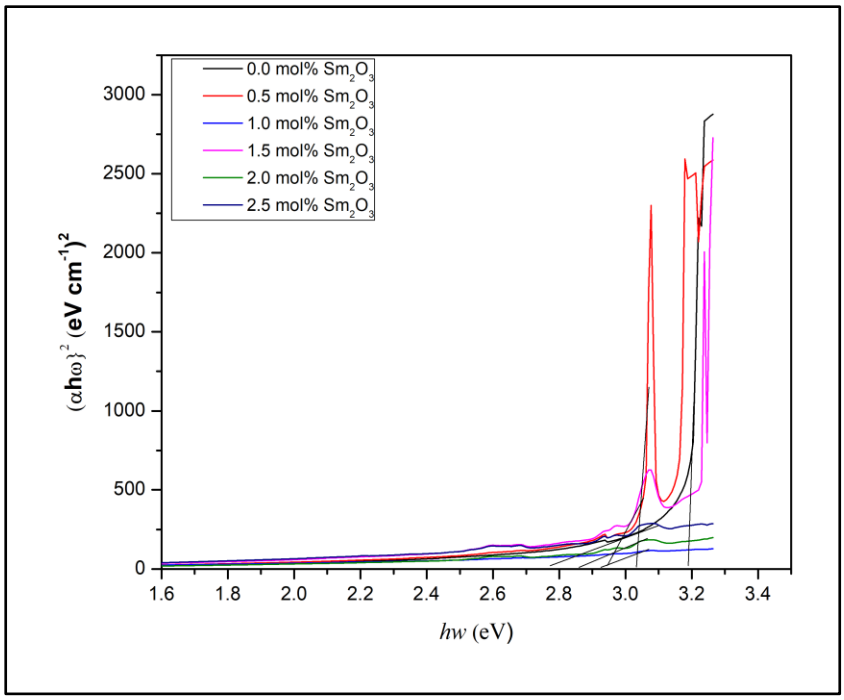


Figure 3(a). Plot of $(\alpha\hbar\omega)^2$ versus $\hbar\omega$ for direct band gap of $(70\text{-}x)TeO_2\text{-}20B_2O_3\text{-}10ZnO\text{-}xSm_2O_3$ glass system

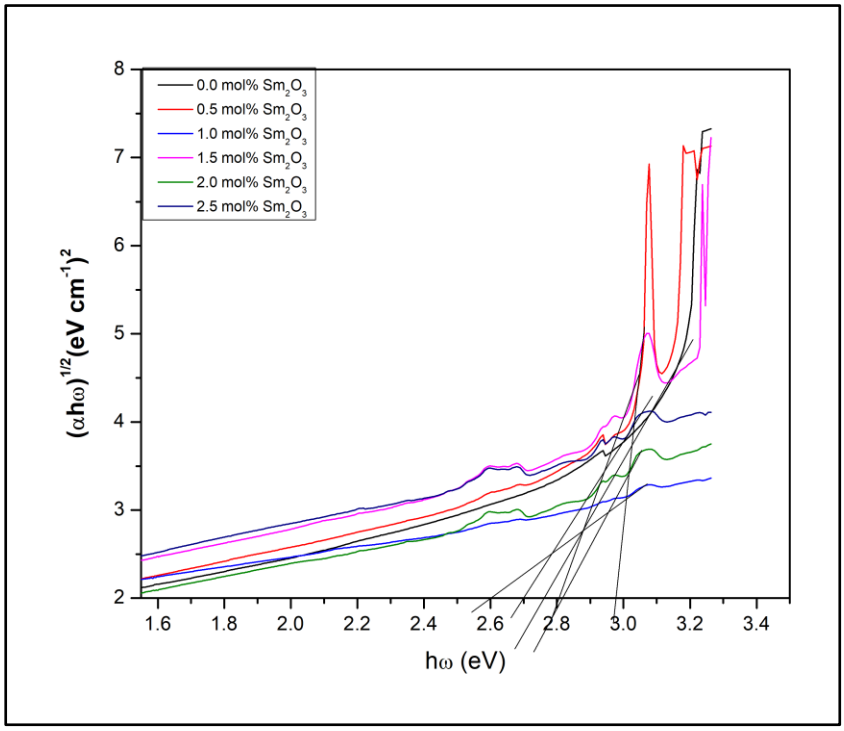


Figure 3(b). Plot of $(\alpha\hbar\omega)^{1/2}$ versus $\hbar\omega$ for indirect band gap of $(70\text{-}x)TeO_2\text{-}20B_2O_3\text{-}10ZnO\text{-}xSm_2O_3$ glass system

Table 1. Indirect E_{opt}, direct E_{opt} and Urbach energy (ΔE) of the glass samples

Samples No.	Indirect E_{opt} (eV)	Direct E_{opt} (eV)	Urbach Energy, ΔE (eV)
S1	3.198	2.815	0.644
S2	3.036	2.982	0.440
S3	2.768	2.605	0.112
S4	2.946	2.812	0.488
S5	2.868	2.755	0.694
S6	2.938	2.714	0.618

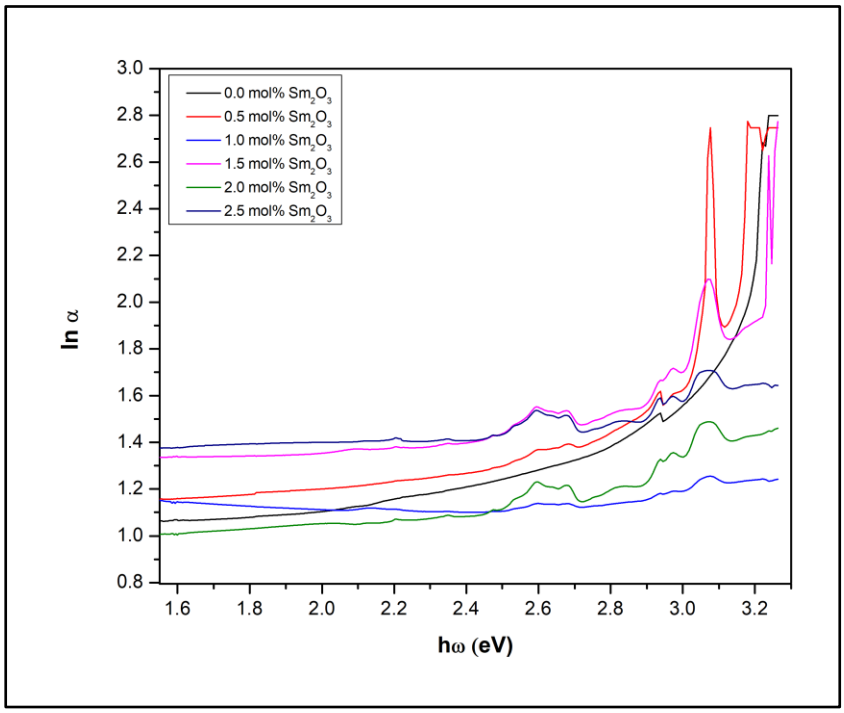


Figure 4. Plot of ln α versus ħω for Urbach energy of (70-x)TeO_2-20B_2O_3-10ZnO-xSm_2O_3 glass system

Conclusion

Sm^{3+} ions doped zinc borotellurite glasses were prepared and their structural and optical properties were studied and reported. The FTIR revealed the presence of asymmetric stretching vibrations of B-O bonds in BO_3 trigonal, BO_4 tetrahedral units and $B-0^-$ trigonal, Te-O bonds in trigonal pyramid (TeO_3) and trigonal bipyramid (TeO_4) units and the hydroxyl groups in the prepared glasses. The absorption spectra showed that the strongest absorption occurred at 480 nm. The direct and indirect optical band gaps were found to vary independently with Sm_2O_3 contents.

Acknowledgement

The author would like to thank UiTM for the encouragement and financial support.

References

1. Selvi, S., Venkataiah, G., Arunkumar, S., Muralidharan, G. and Marimuthu, K. (2014). Structural and luminescence studies on Dy^{3+} doped lead boro- telluro-phosphate glasses. *Physica B: Condensed Matter,* 454: 72-8.
2. Hasnimulyati, L., Halimah, M. K., Zakaria, V., Halim, S.A., Ishak, M. and Eevon, C. (2016). Structural and optical properties of Tm_2O_3-doped zinc borotellurite glass system. *Journal of Ovonic Research*, 12(6): 291-299.
3. Dousti, M. R., Sahar, M. R., Ghoshal, S. K., Amjad, R. J. and. Samavati, A. R. (2013). Effect of AgCl on spectroscopic properties of erbium doped zinc tellurite glass. *Journal of Molecular Structure,* 1035: 6-12.
4. Nasuha, M. R. S., Azman, K., Azhan, H., Senawi, S. A. and Mardhiah. A. (2016). The physical characteristic of Sm^{3+} doped borotellurite glass. *Material Science Forum*, 846: 69-74.
5. Biju, P. R., Jose, G., Thomas, V., Nampoori, V. P. N. and Unnikrishnan, N. V. (2004). Energy transfer in Sm^{3+}, Eu^{3+} system in zinc sodium phosphate glasses. *Optical Materials,* 24(4):671-677.
6. Selvaraju, K. and Marimuthu, K. (2012). Structural and spectroscopic studies on Er^{3+} doped boro-tellurite glasses. *Physica B: Condensed Matter,* 407 (7): 1086-1093.
7. Sasikala, T., Moorthy, L. R. and. Babu, A. M. (2013). Molecular and biomolecular spectroscopy optical and luminescent properties of Sm^{3+} doped tellurite glasses. *Spectrochimica Acta Part A*: *Molecular and Biomolecular Spectroscopy*, 104: 445-450.
8. Sailaja, S., Raju, C. N., Reddy, C. A., Prasad, B. D., Jho, Y. and Reddy, B. S. (2013). Optical properties of Sm^{3+} doped cadmium bismuth borate glasses. *Journal of Molecular Structure,* 1038: 29-34.
9. Ravi, O., Reddy, C. M., Manoj, L. and Prasad, B. D. (2012). Structural and optical studies of Sm^{3+} ions doped niobium borotellurite glasses. *Journal of Molecular Structure,* 1029: 53-59.
10. Hager, I. Z., El-mallawany, R. and Bulou, A. (2011). Luminescence spectra and optical properties of TeO_2 – WO_3 – Li_2O glasses doped with Nd, Sm and Er rare earth ions. *Physica B: Physics of Condensed Matter,* 406(4): 972–980.
11. Auwalu, I. A., Hotoro, M. A. Y., Jamo, U. H. and Diso, D.G. (2018). Effect of samarium oxide on structural and optical properties of zinc silicate glass ceramics from waste material. *Nano Hybrids and Composites.* 22: 35-46.
12. Ghribi, N., Dutreilh-Colas, M., Duclere, J. R., Hayakawa, T., Carreaud, J., Karray, R., Kabadou, A. and Thomas, P. (2015). Thermal, optical and structural properties of glasses within the TeO_2TiO_2ZnO system. *Journal of Alloys and Compounds,* 622: 333-340.
13. Eraiah, B. (2010). Optical properties of lead–tellurite glasses doped with samarium trioxide. *Indian Academy of Sciences,* 33(4): 391.
14. Kundu, R. S., Dhankhar, S., Punia, R., Nanda, K. and Kishore, N. (2014). Bismuth modified physical, structural and optical properties of mid-IR transparent zinc boro-tellurite glasses. *Journal of Alloys and Compounds,* 587: 66-73.
15. Halimah, M. K., Daud, W. M., Sidek, H. A. A., Zainal, A. S., Zainul, A. H. and Jumiah, H. (2007). Structural analysis of borotellurite glass. *American Journal of Applied Sciences,* 4(5):323-327.
16. Maheshvaran, K., Veeran, P. K. and Marimuthu, K. (2013). Structural and optical studies on Eu^{3+} doped boro-tellurite glasses. *Journal of Solis State Sciences,* 17: 54-62.
17. Ghribi, N., Hayakawa, T., Carreaud, J., Kabadou, A., Thomas, P. and Karray, R. (2014). Thermal, optical and structural properties of glasses within the TeO_2-TiO_2-ZnO system. *Journal of Alloys and Compounds,* 622: 333-340.
18. Noorazlan, A. M., Kamari, H. M., Zulkefly, S. S. and Mohamad, D. W. (2013). Effect of erbium nanoparticles on optical properties of zinc borotellurite glass system. *Journal of Nanomaterials,* 2013: 1-8.
19. Kaur, N. and Khanna, A. (2014). Structural characterization of borotellurite and alumino-borotellurite glasses. *Journal of Non-Crystalline Solids,* 404: 116-123.

20. Nawaz, F., Sahar, M. R., Ghoshal, S. K., Awang, A. and Ahmed, I. (2014). Concentration dependent structural and spectroscopic properties of Sm^{3+}/Yb^{3+} co-doped sodium tellurite glass. *Physica B: Condensed Matter,* 433: 89-95.
21. ElBatal, H. A., Abdelghany, A. M. and Ali, I. S. (2012). Optical and FTIR studies of CuO-doped lead borate glasses and effect of gamma irradiation. *Journal of Non-Crystalline Solids,* 358(4): 820-825.
22. Yaru N. and Chunhua, L. (2007). Study on optical properties and structure of Sm_2O_3 doped boron-aluminosilicate glass. *Journal of Rare Earth,* 25: 94-98.
23. Som Tirtha, B. K. (2008). Infrared-to-red upconversion luminescence in samarium-doped antimony glasses. *Journal of Luminescence,* 128(12): 1989-1996.
24. Selvaraju, K. and Marimuthu, K. (2013). Structural and spectroscopic studies on concentration dependent Sm^{3+} doped boro-tellurite glasses. *Journal of Alloys and Compounds,* 553: 273-281.
25. Fares, H., Jlassi, I., Hraiech, S., Elhouichet H. and Férid, M. (2014). Radiative parameters of Nd^{3+} doped titanium and tungsten modified tellurite glasses for 1.06 µm laser materials. *Journal of Quantitatives*
Spectroscopy and Radiatice Transfer, 147: 224-232.
26. Azlan, M. N., Halimah, M. K., Shafinas, S. Z. and Daud, W. M. (2014). Polarizability and optical basicity of Er^{3+} ions doped tellurite glass. *National Institute of Materials Physics,* 11(7): 319-335.
27. Hajer, S. S., Halimah, M. K., Azmi, Z. and Azlan, M. N. (2014). Optical properties of zinc-borotellurite doped samarium. *Chalcogenide Letter,* 11(11): 553-566.
28. Rajendran, V., Palanivelu, N., Chaudhuri, B. K. and Goswami, K. (2003). Characterisation of semiconducting V_2O_5-Bi_2O_3-TeO_2 glasses through ultrasonic measurements. *Journal Non-Crystal Solids,* 320(1): 195-209.
29. Mat Jan, N. A., Sahar, M. R., Ghoshal, S. K., Ariffin, R., Rohani, M. S. and Hamzah, K. (2014). Absorption spectra of neodymium doped tellurite glass. *Advanced Materials Research,* 895: 395-399.

Malaysian Journal of Analytical Sciences (MJAS)
Published by Malaysian Analytical Sciences Society

CARBOXYMETHYL CHITOSAN-BASED BIOPOLYMER ELECTROLYTE WITH IMIDAZOLIUM IONIC LIQUID

(Elektrolit Biopolimer Berasaskan Karboksimetil Kitosan Dengan Cecair Ionik Imidazolium)

Intan Juliana Shamsudin[1]*, Norsyabila Shrgawi[1], Hussein Hanibah[2], Nur Hasyareeda Hassan[3], Azizan Ahmad[3]

[1] Chemistry & Biology Department, Centre for Defence Foundation Studies,
National Defence University of Malaysia, 57000 Kuala Lumpur, Malaysia
[2] Centre of Foundation Studies,
Universiti Teknologi MARA, Selangor Branch, Dengkil Campus, 43800 Dengkil, Selangor Darul Ehsan, Malaysia
[3] School of Chemical Sciences and Food Technology, Faculty of Science and Technology,
Universiti Kebangsaan Malaysia, 43600, Bangi, Selangor Darul Ehsan, Malaysia

** Corresponding author: intanjuliana@upnm.edu.my*

Received: 13 November 2019; Accepted: 3 September 2020; Published: 12 October 2020

Abstract

Solid biopolymer electrolyte based on carboxymethyl chitosan has been successfully prepared with ionic liquid 1-butyl-3-methylimidazolium acetate, [Bmim][OAc] as the charge carrier. The strong interactions of the ionic liquid with the biopolymer host were detected by several changes in the FTIR spectra. The decreased percentage of the crystallinity index derived from the XRD diffractograms suggested the amorphous nature of the film prepared. SEM observations showed formation of the linkages due to the plasticising effect of [Bmim][OAc]. Higher amount of [Bmim][OAc] led to the enhancement in the ionic conductivity, σ. The highest σ achieved was $(3.05 \pm 0.35) \times 10^{-3}$ S cm^{-1} measured at ambient temperature. The highest conducting electrolyte achieved high electrochemical stability up to ±2.8 V measured by linear sweep voltammetry (LSV). Transference number measurement confirmed that ions were the major contributor in the conduction of electrolyte with ±0.980 ion transference number.

Keywords: carboxymethyl chitosan, ionic liquid, imidazolium, biopolymer electrolytes, ionic conductivity

Abstrak

Elektrolit biopolimer pepejal berasaskan karboksimetil kitosan telah berjaya disediakan dengan cecair ionik 1-butil-3-metillimidazolium asetat, [Bmim][OAc] sebagai pembawa cas. Interaksi yang kuat di antara cecair ionik dengan perumah biopolimer dikesan oleh beberapa perubahan dalam spektrum FTIR. Peratusan penurunan indeks penghabluran yang diperolehi daripada difraktogram XRD mencadangkan sifat amorfus filem yang disediakan. Pemerhatian SEM menunjukkan pembentukan jaringan kerana kesan pemplastikan [Bmim][OAc]. Lebih banyak jumlah [Bmim][OAc] membawa kepada peningkatan dalam kekonduksian ionik, σ. Kadar tertinggi σ dicapai $(3.05 \pm 0.35) \times 10^{-3}$ S cm^{-1} yang diukur pada suhu ambien. Elektrolit berkonduksian tertinggi mencapai kestabilan elektrokimia yang tinggi sehingga ± 2.8 V diukur dengan voltammetri sapuan linear (LSV). Pengukuran nombor pemindahan mengesahkan bahawa ion adalah penyumbang utama dalam pengaliran elektrolit dengan nombor pemindahan ion sebanyak ± 0.980.

Kata kunci: karboksimetil kitosan, cecair ionik, imidazolium, elektrolit biopolimer, konduktiviti ionik

Introduction

Chitosan is the second most abundant polysaccharide after cellulose and has a wide number of applications due to its biocompatibility, biodegradability, and abundance in nature. However, chitosan has very low ionic conductivity, σ (~10^{-9} S cm^{-1}) due to the strong intermolecular and intramolecular hydrogen bonding in the chitosan matrix [1]. Previous studies have reported the chemical modification (carboxymethylation) on chitosan, where a carboxyl group (COO^-) is substituted into the biopolymer matrix [2-4]. Based on the findings, carboxymethyl chitosan showed a lower degree of crystallinity due to the presence of carboxymethyl residue, which hindered the inter and intramolecular hydrogen bonding in the modified chitosan. The σ of carboxymethyl chitosan was also enhanced by three orders of magnitude to ~10^{-6} S cm^{-1} compared to pristine chitosan. Figure 1 shows the chemical structure of carboxymethyl chitosan.

Ionic liquids are a group of organic salts in which the ions are poorly coordinated, which results in these solvents being liquid at relatively low temperatures (below 100 °C). Ionic liquids have attracted the interest of many researchers due to the green solvent properties such as low toxicity, thermal stability, and negligible vapour pressure [5]. 1-butyl-3-methylimidazolium acetate, [Bmim][OAc] have been extensively used as dissolution media for polysaccharide such as cellulose and chitosan. The dissolution mechanism of chitosan in [Bmim][OAc] were reported by Tian and co-workers, whereby a strong interaction between chitosan and [Bmim]OAc was identified, which interrupted the initial hydrogen bonds in chitosan due to the formation of new hydrogen bonds in the complexes. The high basicity value of the anion, CH_3COO^- reflected the strong tendency of the anion to accept hydrogen bond [6].

Our previous work discussed the bi-function effect of [Bmim][OAc] in solid polymer electrolyte based on chitosan [7]. Hence, this paper described the effects of [Bmim][OAc] on the biopolymer derivative, carboxymethyl chitosan. The chemical interactions, crystallinity, and electrochemical studies will be discussed, in order to investigate the ability and effectiveness of carboxymethyl chitosan as a polymer host in an electrolyte system.

Materials and Methods

The carboxymethylation of chitosan was done by employing Williamson's ether synthesis process; a consecutive two-step reaction [2]. Chitosan was used as the starting material. 1-butyl-3-methylimidazolium acetate [Bmim][OAc] was purchased from Sigma-Aldrich. All materials were used without further purification.

Preparation of thin film

Mixtures of carboxymethyl chitosan with different concentrations of ionic liquid were prepared *via* the solution casting method. Carboxymethyl chitosan was dissolved in 1% solution of acetic acid and stirred overnight in order to obtain complete dissolution of carboxymethyl chitosan. Different concentrations of ionic liquid [Bmim][OAc] (10, 20, 20, 40, 50, and 60 wt.%) were dried under vacuum for 2 hours with vigorous stirring. The dissolved chitosan solution was then added to the dried [Bmim][OAc] under nitrogen gas. The mixed solution was further stirred for 24 hours under nitrogen gas. After complete dissolution, the solution was poured into a Teflon petri dish and left to dry for several days. The resulting thin film was then peeled and stored in a desiccator to prevent any moisture contact. Seven thin film samples have been successfully prepared which were CMChi-0 (pure carboxymethyl chitosan), CMChi-10 (added with 10 wt.% [Bmim][OAc]), CMChi-20 (added with 20 wt.% [Bmim][OAc]), CMChi-30 (added with 30 wt.% [Bmim][OAc]), CMChi-40 (added with 40 wt.% [Bmim][OAc]), CMChi-50 (added with 50 wt.% [Bmim][OAc]), and CMChi-60 (added with 60 wt.% [Bmim][OAc]).

Characterisation

ATR-FTIR analyses were performed using Perkin-Elmer Spectrum 2000, USA in the range of 4000-650

cm^{-1}. The scanning resolution was 4 cm^{-1}. The analyses were carried out to observe any changes and shifts of the characteristic band due to the chemical interactions of chitosan with the charge carrier. X-ray diffraction (XRD) measurements were performed using model D5000 Siemens, Germany. The data were collected from a range of diffraction angle 2θ from 3° to 60° at rate 0.05° s^{-1} to determine whether the sample was crystalline, semi-crystalline, or amorphous. Investigation on the morphologies of the polymer electrolytes was examined by FESEM Supra 55VP, UK model at 10,000 magnifications. The measurement of the bulk resistance (R_b) of the sample was carried out by using Electrical impedance spectroscopy (EIS) model HIOKI 3522 LCR Hi-Tester, Japan, with the frequency range between 50 Hz to 5 MHz. The sample was sandwiched between the blocking stainless steel under spring pressure with a contact area of 5.13 cm^2. The conductivity values, (σ) of electrolyte have been calculated from equation (1):

$$\sigma = tR_b^{-1}A^{-1} \quad (1)$$

where t is the thickness of the sample, R_b is the bulk resistance, and A is the contact area. A complex impedance plot was used to calculate the R_b. The effect of temperature on the conductivity was measured within the temperature range of 30 to 70 ºC at approximately 5 ºC intervals. Linear sweep voltammetry (LSV) technique was used to determine the electrochemical stability window of the polymer electrolyte. The sample was placed between two stainless steel blocking electrodes using 1 mVs^{-1} scan rate from 0 to 5.0 V. Transference number measurement was carried out in order to investigate the main conducting element in the polymer electrolyte system using the dc polarisation method. The ions transference number t_{ion} in the electrolyte was determined by monitoring the current as a function of time. Fixed 1.0 V dc voltage was applied across the sample sandwiched between the two stainless steel electrodes. By applying Wagner's Polarisation technique, the value of t_{ion} was calculated from the normalised polarisation current versus time plot using equation (2) where i_T and i_e are the total and residual current, respectively.

$$t_{ion} = (i_T - i_e)/i_T \quad (2)$$

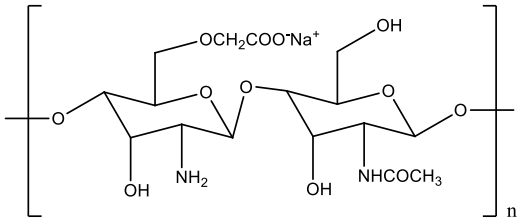


Figure 1. The chemical structure of carboxymethyl chitosan

Results and Discussion

ATR-FTIR

FTIR spectra of pure CMChi film (CMChi-0) and CMChi with various wt.% of [Bmim][OAc] (10-60 wt.%) in the wavenumber region 4000-2500 cm^{-1} are depicted in Figure 2. This region shows the characteristic peaks for polar groups such as hydroxyl (-OH) and amino ($-NH_2$) which were anticipated to be altered with the inclusion of [Bmim][OAc]. Significant changes in the FTIR spectra with the addition of ionic liquid are observed in the figure. Upon the inclusion of [Bmim][OAc], the presence of a new peak at 2962 cm^{-1} was observed which belonged to the -C-H stretching of methyl group in the ionic liquid [8]. Hence, the appearance of these new peaks and the increase in the intensities indicated the complexation between CMChi matrix with [Bmim][OAc].

The appearance of peaks at 3353 cm^{-1} in the CMChi/[Bmim][OAc] films indicated the presence of NH_3^+ that has been protonated by the acetic acid [4]. The O-H band in the CMChi/[Bmim][OAc] films was suggested to be protonated as well, as evidenced by the shift of the band towards lower wavenumber at 3292 cm^{-1} to 3281 cm^{-1}. Thus, these protonated O-H suggested the formation of OH_2^+. The broadening of the O-H stretching peaks also might be due to the presence of water molecules in the CMChi films as polysaccharide is hydrophilic in nature [9].

There are also several displacements in the wavenumbers of certain characteristic peaks in CMChi/[Bmim][OAc] films depicted in Figure 3(a). The peak at 1572 cm^{-1} which belonged to the overlapping of amine (N-H) in the polymer chain was displaced to about 10 cm^{-1} of wavenumbers to 1562 cm^{-1} [10]. The C-O-C stretching bridge in CMChi at 1152 cm^{-1} was observed to shift to higher wavenumbers to 1166 cm^{-1} and peak at 1058 $cm^{-1,}$ which attributed to the C-O-H stretching of CMChi and acetate ion was shifted to 1066 cm^{-1} [11, 12]. The shift of the band toward lower wavenumber indicated the particular bonds have been lengthened and thus required less energy to vibrate the particular bond. Meanwhile, the shift towards higher wavenumbers showed that the particular bonds' length has been shortened which resulted in more energy needed to vibrate the bonds [13]. Scheme 1 shows the proposed interaction mechanism between CMChi and [Bmim][Oac]. In addition, there were two interesting changes in terms of the intensity noted upon the inclusion of [Bmim][OAc] in the CMChi matrix in Figure 3(b). The intensity of C-C(=O)-C stretching in the carboxyl in CMChi at 1323 cm^{-1} and the C-O stretching in the CMChi backbone around 1060-1025 cm^{-1} was reduced with the increasing wt.% of [Bmim][OAc]. These changes suggested the strong interaction of the ionic liquid with the biopolymer hosts. Table 1 lists the assigned bands and wavelengths of the CMChi films at different wt.% of [Bmim][OAc].

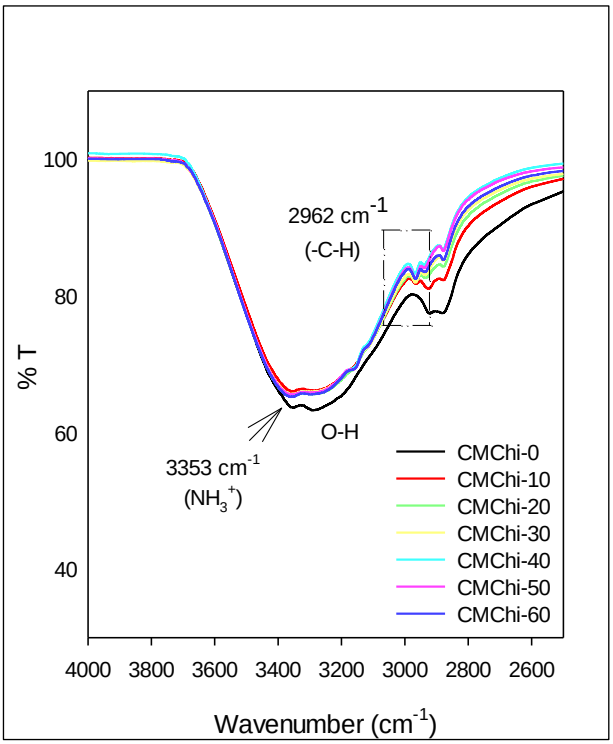


Figure 2. FTIR spectra CMChi with various wt.% of [Bmim][OAc] in the wavenumber region 4000-2500 cm^{-1}

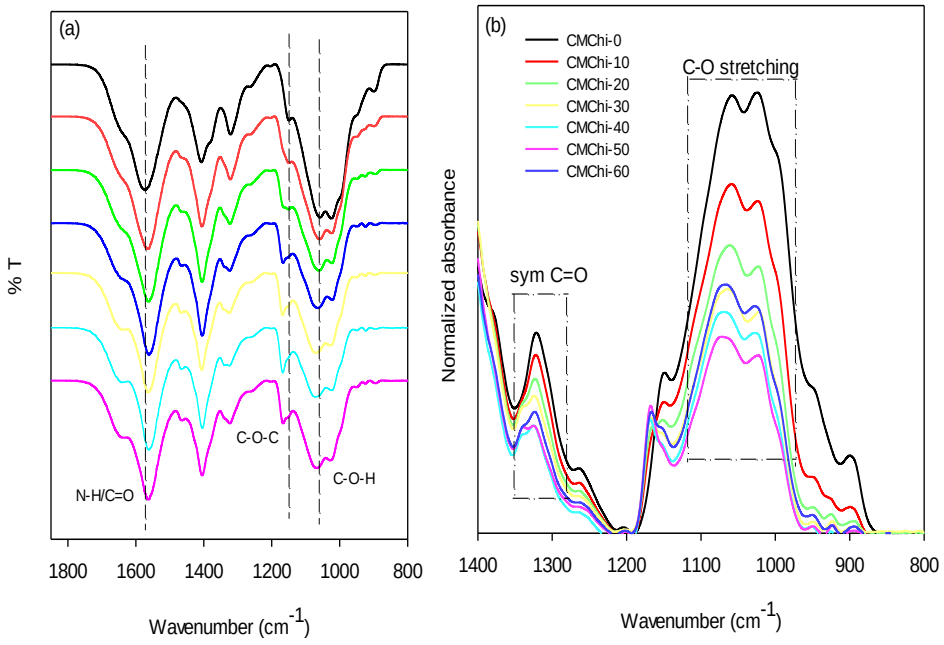
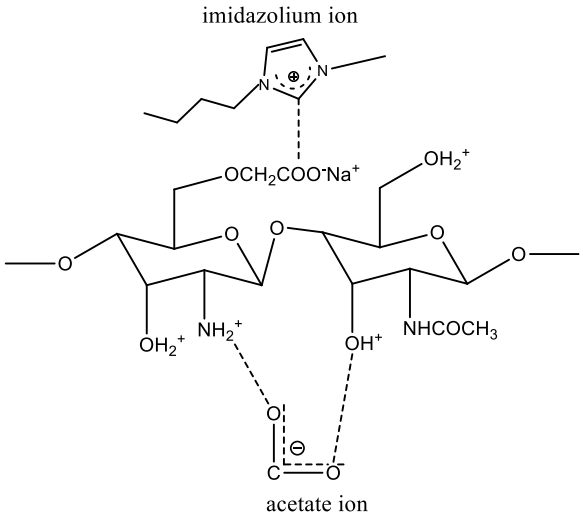


Figure 3. (a) FTIR spectra and (b) normalised absorbance of CMChi with various wt.% of [Bmim][OAc] in the wavenumber range 1850-800 cm^{-1} and 1400-800 cm^{-1} respectively.

Table 1. The assigned bands and wavelength of the CMChi films at different wt.% of [Bmim][OAc]

Assignments of Bands	**Wavelength (cm^{-1})**						
	CMChi-0	**CMChi-10**	**CMChi-20**	**CMChi-30**	**CMChi-40**	**CMChi-50**	**CMChi-60**
O-H	3292	3280	3281	3282	3281	3281	3281
N-H	1572	1563	1561	1560	1561	1561	1562
C-O	1152	1156	1160	1167	1166	1167	1166
C-O	1058	1061	1061	1064	1067	1071	1066



Scheme 1. Proposed interaction between CMChi and [Bmim][OAc]

X-ray diffraction (XRD)

XRD diffractogram in Figure 4 shows pure CMChi film (CMChi-0) and CMChi with various wt.% of [Bmim][OAc]. The pure CMChi film showed a semicrystalline peak at 2θ of 21.0°, comparable to the previous reports [14, 15]. The crystallinity peak of CMChi was lower than other polysaccharide such as pristine chitosan and cellulose, thus implying lower degree of crystallinity [16, 17]. It was noticeable that, as the wt.% of [Bmim][OAc] increased, the intensity of the peak reduced. At low loading of [Bmim][OAc], (CMChi-10), the intensity and broadness of the peak has not been greatly changed. However, at 20 wt.% of [Bmim][OAc], the intensity of the peak was observed to reduce which indicated that the addition of [Bmim][OAc] has taken impact on the crystalline nature of CMChi. Higher concentration of [Bmim][OAc] has further reduced the intensity, which indicated the development of amorphous phase in the biopolymer. It was noted that in the CMChi-50 and CMChi-60 diffractograms, only a very small peak appeared, reflecting the great disruption of the crystalline phase in CMChi. Moreover, although the amount of [Bmim[OAc] added was rather high, there was no sign of ion multiple peak formation observed, suggesting the miscibility of the ionic liquid in the biopolymer matrix. The plasticising effect of [Bmim][OAc] might have assisted in the reduction of the crystallinity as ionic liquid has been previously reported as an effective plasticiser for polysaccharide [18-20]. In this case, [Bmim][OAc] might have broken the inter and intra-molecular hydrogen bonds of CMChi and destroyed the original crystalline form. As a result, the polymer chain structures have been rearranged whereby the new arrangement has led to the formation of amorphous phase in CMChi [7]. Table 2 depicts the crystallinity index of CMChi/[Bmim][OAc] films. Decreased value in the crystallinity index was observed with higher inclusion of [Bmim][OAc] into the CMChi matrix.

Morphology

SEM micrographs of pure CMChi film (CMChi-0), and CMChi with 20 wt.%, 40 wt.% and 60 wt.% of [Bmim][OAc] (CMChi-20, CMChi-40 and CMChi-60) are depicted in Figure 5. The morphology of CMChi-0 in Fig. 5(a) shows a smooth and homogenous surface indicating the low degree of crystallinity of the pure film. Addition of 20 wt.% of [Bmim][OAc] as can be seen in Fig. 5(b) has slightly altered the morphology as the film showed signs of agglomeration. Nevertheless, no phase separation was observed, suggesting the miscibility of [Bmim][OAc] in the CMChi matrix and the persisted amorphousness of the film. Higher addition of ionic liquid in CMChi-40 film as can be observed in Fig. 5(c) has greatly changed the morphology as the appearance of linkage-like structures can be observed. A

similar observation was previously reported whereby the formation of the linkages was identified due to the plasticising effect of glycerol in the blend of chitosan and starch [21]. The plasticiser was believed to act as a spacer between the polymer chains by creating links that functioned as an alternative pathway for ionic conduction. A similar explanation was proposed for the change in the morphology in CMChi-40 film. The [Bmim][OAc] was proposed to function as a plasticiser and form linkages in the CMChi matrix, thus favouring the ionic conduction in the film. However, at the maximum loading of ionic liquid in CMChi-60 film as depicted in Fig. 5(d), the linkages formation was reduced. The co-solvent function of [Bmim][OAc] might have enhanced the miscibility and compatibility of the CMChi matrix and the ionic liquid, which resulted in more homogenous structure in the film. Although the film appeared to agglomerate, no phase separation was observed, suggesting the miscibility of [Bmim][OAc] in the biopolymer. The permanent dark region in the surface micrograph indicates the amorphous phase of the film [21, 22] thus suggesting that the amorphousity of the film was not changed even at high loading of [Bmim][OAc].

Ionic conductivity

Figure 6 depicts the ionic conductivity of Chi and CMChi films as a function of [Bmim][OAc] wt.% at ambient temperature (298 K). Apparently, as reported in our previous work [7], the pure Chi exhibited very low σ, which was $(2.93 \pm 0.62) \times 10^{-9}$ S cm^{-1}. However, the derivative of Chi, CMChi showed improvement in the σ. The σ enhanced by almost two orders of magnitude to $(2.20 \pm 0.45) \times 10^{-7}$ S cm^{-1}. The low crystallinity phase of CMChi as has been identified in the XRD and SEM studies might have assisted the ion conduction and a low crystallinity phase favoured the movement of ions in the system thus resulting in more interactions with the polymer chain.

In the CMChi/[Bmim][OAc] system, the strong conducting effect of [Bmim][OAc] has been observed with only 10 wt.% addition of the ionic liquid. The σ was enhanced by two orders of magnitude to $(4.66 \pm 0.35) \times 10^{-5}$ S cm^{-1}. Further inclusion of [Bmim][OAc] has improved the σ to $(2.50 \pm 0.30) \times 10^{-5}$ S cm^{-1}. The maximum addition at 60 wt.% of [Bmim][OAc] has resulted in the highest σ of $(3.05 \pm 0.35) \times 10^{-3}$ S cm^{-1}. This has resulted in the total enhancement of four orders of magnitude compared to the σ of the pure CMChi film. A few investigations have been reported that utilised carboxymethyl chitosan as a polymer host in an electrolyte system. However, Mobarak reported that the addition of 20 wt.% of ammonium triflate salt has improved the σ of CMChi to 8.90×10^{-6} S cm^{-1}. Further addition of ammonium triflate has reduced the σ and was attributed to the formation of ion pairs and ion aggregates, which reduced the number of mobile charge carriers [4]. Thus, this has also shown that [Bmim][OAc] is an efficient charge carrier and suitable to be applied in the CMChi matrix.

The significant σ increase in the systems might also be due to the strong plasticising effect of the ionic liquid. [Bmim][OAc] might have broken the inter and intramolecular hydrogen bonding in CMChi matrixes and thus softened the polymer backbone and enhanced the flexibility of the polymer chains [23]. This is supported by the XRD data. As the flexibility increased, the free volume of the polymer system increased as well. Thus, greater dissociation of the charge carriers was experienced. The increase in number of charge carriers then contributed to higher ionic conductivity in the systems. In addition, the amorphous phase with the higher content of [Bmim][OAc] as shown by the SEM in the CMChi/[Bmim][OAc] system contributed to higher flexibility of the electrolyte chain. As a result, the movement of the conducting ions was easier in the electrolyte and thus increased the ions mobility [24]. Since ionic conductivity is proportional to ion mobility, the enhancement in the ionic conductivity was perceived.

Linear sweep voltammetry analysis

Linear sweep voltammetry analysis has been performed in order to investigate the stability of the polymer electrolyte by measuring the electrochemical stability window. The working cell potential range of electrolytes is an essential factor to be evaluated as it shows the ability of the electrolyte to endure operating voltage of electrochemical devices such as batteries or other electrochemical devices. In this regard, the

electrochemical stability window of pure biopolymer film (CMChi-0) and the highest conducting polymer electrolytes CMChi-60 have been studied and the corresponding voltammograms are shown in Figure 7. Based on Figure 7(a), the pure CMChi films showed no electrochemical stability as it underwent immediate oxidation as the cell potential exceeded 0 V. On the other hand, the films with the inclusion of [Bmim][OAc], depicted in Figure 7(b), showed improved electrochemical stability up to ± 2.0 V, and experienced oxidation above the potential. The decomposition voltage of the electrolyte was detected at ±2.8 V. The results revealed that the presence of ionic liquid [Bmim][OAc] in the CMChi biopolymer matrix has increased the electrochemical stability. An investigation reported that addition of ionic liquid improved the oxidative stability of electrolyte, which made the tighter polymer electrolyte [25]. Thus, this result showed that CMChi/[Bmim][OAc] has potential to be applied in electrochemical devices.

Transference number study

The information about the contribution of the particular charge species, whether ions or electrons present in the polymer electrolyte to the overall charge transport can be determined by measuring the transference number. The plots of polarised current versus time for the highest conducting films CMChi-60 are shown in Figure 8. The depletion of the charge carriers or ionic species in the electrolyte caused the initial total current to decrease with time. In the completely depleted condition, the current became constant. Based on Figure 8, high ionic transference number ±0.980 was observed in CMChi-60 film. The high ion transference number in CMChi-60 might be due to the low crystallinity phase of CMChi-60 which eased the mobility of ions in the polymer matrix. The electron transference number in CMChi-60 was only ±0.02 and can be neglected [26]. Thus, this suggested that ions were predominantly responsible in the conduction of CMChi-60 electrolytes film.

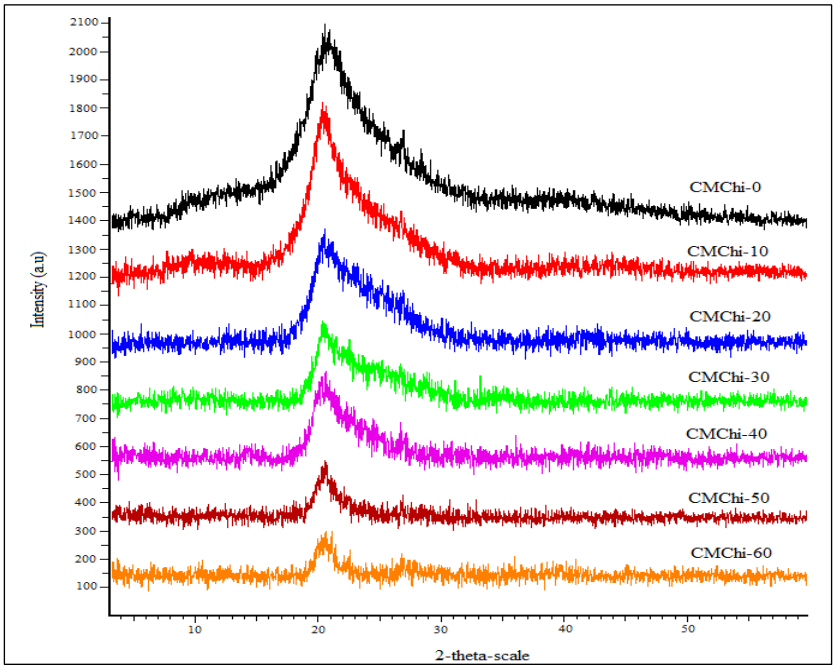


Figure 4. XRD diffractograms of CMChi with various wt.% of [Bmim][OAc]

Table 2. Crystallinity index of pure CMChi film (CMChi-0) and CMChi with 10-60 wt.% of [Bmim][OAc] films

Sample	**Crystallinity index, X_{CI} (%)**
CMChi-0	34.2
CMChi-10	32.3
CMChi-20	30.0
CMChi-30	28.5
CMChi-40	25.2
CMChi-50	22.5
CMChi-60	18.3

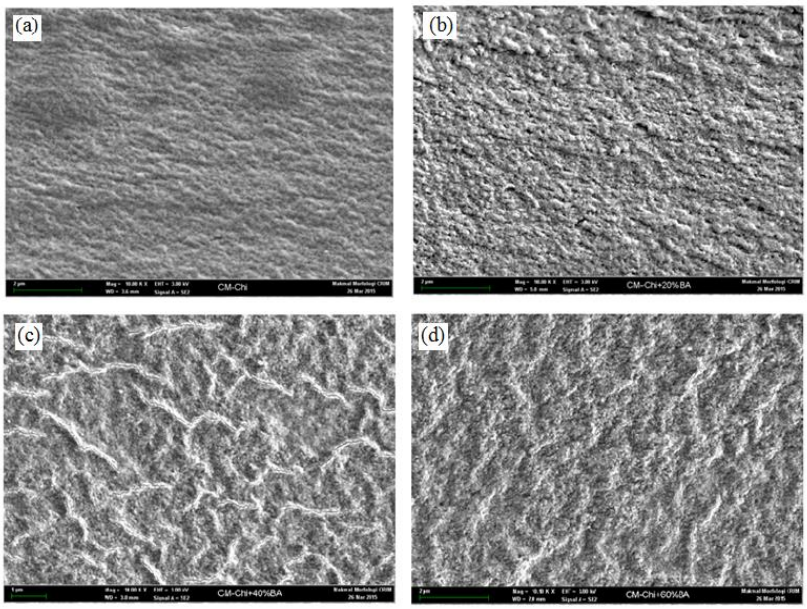


Figure 5. SEM micrographs of (a) CMChi-0, (b) CMChi-20, (c) CMChi-40 and (d) CMChi-60

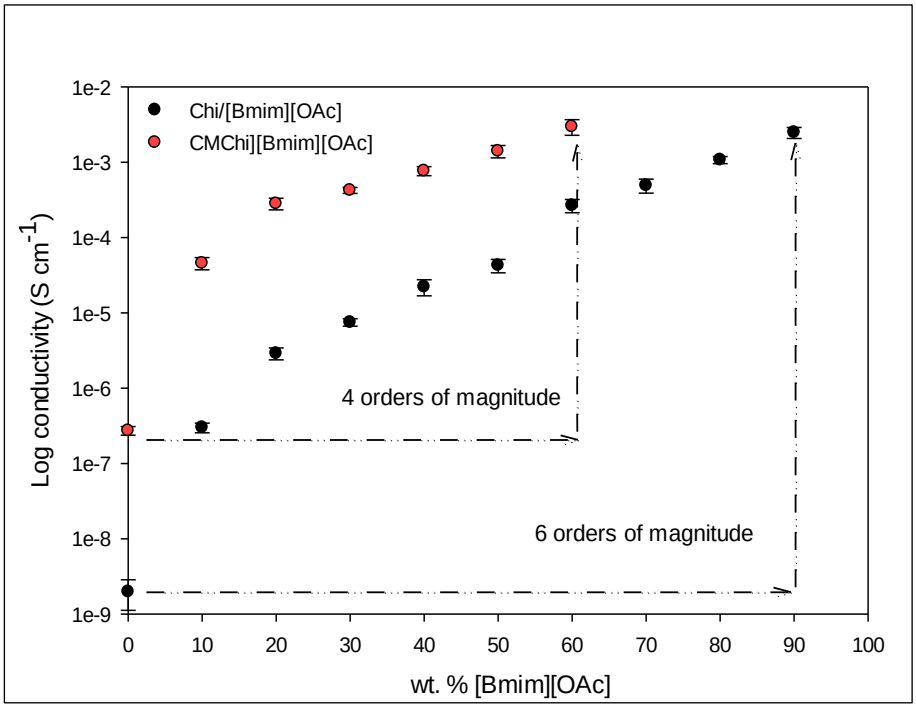
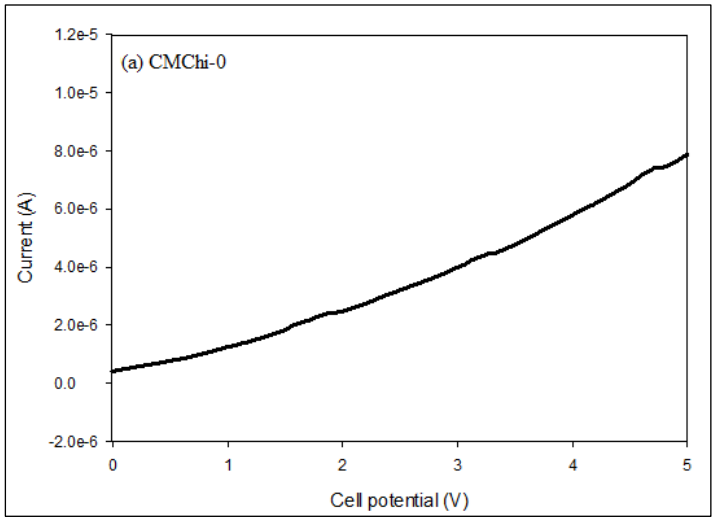


Figure 6. Ionic conductivity (σ) of Chi and CMChi films as a function of [Bmim][OAc]



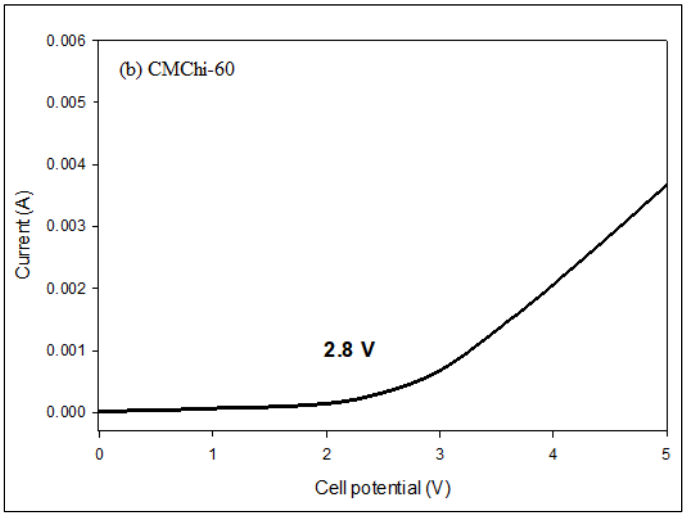


Figure 7. Linear sweep voltammetry of (a) CMChi-0 and (b) CMChi-60 electrolyte films

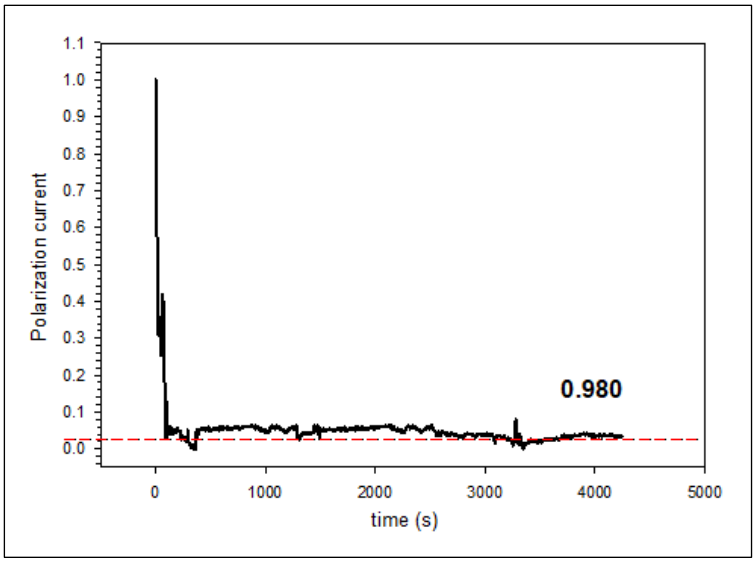


Figure 8. Polarisation current versus time of CMChi-60 films

Conclusion

Solid biopolymer electrolytes based on CM-chitosan with ionic liquid [Bmim][OAc] were prepared and characterised. ATR-FTIR analysis has proven the complexation and interaction between CM-chitosan and ionic liquid while XRD analysis has confirmed the plasticising effect of ionic liquid in the polymer matrix by the disruption of the crystalline phase of the polymer matrix. The SEM morphologies of the biopolymer electrolytes showed a smoother surface as the quantity of ionic liquid increased, thus reinforcing the function of [Bmim][OAc] as a plasticiser in the system. EIS results

revealed that the ionic liquid enhanced the ionic conductivity of the electrolyte up to $(3.05 \pm 0.35) \times 10^{-3}$ S cm^{-1}. The ion transference number was found to be ±0.980 and electrochemical stability up to ±2.8 V was achieved. These results verified that CMChi/[Bmim][OAc] electrolyte system shows potential to be applied in electrochemical devices.

Acknowledgement

The authors are pleased to acknowledge UPNM for the provision of grant RACER/1/2019/STG01/UPNM//2.

References

1. Zhang, M., Li, X. H., Gong, Y. D., Zhao, N. M. and Zhang, X. F. (2002). Properties and biocompatibility of chitosan films modified by blending with PEG. *Biomaterials*, 23(13): 2641-2648.
2. Sun, G. Z., Chen, X. G., Li, Y. Y., Zheng, B., Gong, Z. H., Sun, J. J., and Lin, W. X. (2008). Preparation of H-oleoyl-carboxymethyl-chitosan and the function as a coagulation agent for residual oil in aqueous system. *Frontiers of Materials Science in China*, 2(1): 105-112.
3. Ge, H. C., and Luo, D. K. (2005). Preparation of carboxymethyl chitosan in aqueous solution under microwave irradiation. *Carbohydrate Research*, 340(7): 1351-1356.
4. Mobarak, N. N., Ramli, N., Abdullah, M. P. and Ahmad, A. (2013). Spectroscopic studies of carboxymethyl chitosan-ammonium triflate ($NH_4CF_3SO_3$) based solid polymer electrolytes. *AIP Conference Proceedings*, 1571(1): 843-849.
5. Mallakpour, S. and Dinari, M. (2012). Ionic liquids as green solvents: progress and prospects. In Green Solvents II, Springer, Dordrecht: pp. 1-32
6. Cláudio, A. F. M., Swift, L., Hallett, J. P., Welton, T., Coutinho, J. A. and Freire, M. G. (2014). Extended scale for the hydrogen-bond basicity of ionic liquids. *Physical Chemistry Chemical Physics*, 16(14): 6593-6601.
7. Shamsudin, I. J., Ahmad, A., Hassan, N. H. and Kaddami, H. (2015). Bifunctional ionic liquid in conductive biopolymer based on chitosan for electrochemical devices application. *Solid State Ionics*, 278: 11-19.
8. Leones, R., Sentanin, F., Rodrigues, L. C., Marrucho, I. M., Esperança, J. M. S. S., Pawlicka, A. and Silva, M. M. (2012). Investigation of polymer electrolytes based on agar and ionic liquids. *Express Polymer Letters*, 6(12): 1007-1016.
9. Rueda, D. R., Secall, T. and Bayer, R. K. (1999). Differences in the interaction of water with starch and chitosan films as revealed by infrared spectroscopy and differential scanning calorimetry. *Carbohydrate polymers*, 40(1), 49-56.
10. Stefanescu, C., Daly, W. H. and Negulescu, I. I. (2012). Biocomposite films prepared from ionic liquid solutions of chitosan and cellulose. *Carbohydrate Polymers*, 87(1): 435-443.
11. Chen, X. G, and Park, H. J. (2003). Chemical characteristics of O-carboxymethyl chitosans related to the preparation conditions. *Carbohydrate Polymers*, 53(4): 355-359.
12. Mourya, V. K., Inamdar, N. N. and Tiwari, A. (2010). Carboxymethyl chitosan and its applications. *Advanced Materials Letters*, 1(1): 11-33.
13. Shamsudin, I. J., Ahmad, A., Hassan, N. H. and Kaddami, H. (2016). Biopolymer electrolytes based on carboxymethyl κ-carrageenan and imidazolium ionic liquid. *Ionics*, 22(6): 841-851.
14. Lu, G., Kong, L., Sheng, B., Wang, G., Gong, Y. and Zhang, X. (2007). Degradation of covalently cross-linked carboxymethyl chitosan and its potential application for peripheral nerve regeneration. *European Polymer Journal*, 43(9): 3807-3818.
15. Mobarak, N. N., Ahmad, A., Abdullah, M. P., Ramli, N. and Rahman, M. Y. A. (2013). Conductivity enhancement via chemical modification of chitosan based green polymer electrolyte. *Electrochimica Acta*, 92: 161-167.
16. Ju, X., Bowden, M., Brown, E. E. and Zhang, X. (2015). An improved X-ray diffraction method for cellulose crystallinity measurement. *Carbohydrate polymers*, 123: 476-481.
17. Ioelovich, M. (2014). Crystallinity and hydrophility of chitin and chitosan. *Journal of Chemistry,* 3(3): 7-14.

18. Domene-López, D., Delgado-Marín, J. J., García-Quesada, J. C., Martín-Gullón, I. and Montalbán, M. G. (2020). Electroconductive starch/multi-walled carbon nanotube films plasticized by 1-ethyl-3-methylimidazolium acetate. *Carbohydrate Polymers*, 229: 115545.
19. Ismail, S., Mansor, N., Majeed, Z. and Man, Z. (2016). Effect of water and [Emim][OAc] as plasticizer on gelatinization of starch. *Procedia Engineering*, 148: 524-529.
20. Ismail, S., Mansor, N. and Man, Z. (2017). A study on thermal behaviour of thermoplastic starch plasticized by [Emim] Ac and by [Emim] Cl. *Procedia Engineering*, 184: 567-572.
21. Shukur, M. F. and Kadir, M. F. Z. (2015). Hydrogen ion conducting starch-chitosan blend based electrolyte for application in electrochemical devices. *Electrochimica Acta*, 158: 152-165.
22. Su'ait, M. S., Ahmad, A., Hamzah, H. and Rahman, M. Y. A. (2011). Effect of lithium salt concentrations on blended 49% poly (methyl methacrylate) grafted natural rubber and poly (methyl methacrylate) based solid polymer electrolyte. *Electrochimica Acta*, 57: 123-131.
23. Liew, C. W. and Ramesh, S. (2013). Studies on ionic liquid-based corn starch biopolymer electrolytes coupling with high ionic transport number. *Cellulose*, 20(6): 3227-3237.
24. Yap, Y. L., You, A. H., Teo, L. L. and Hanapei, H. (2013). Inorganic filler sizes effect on ionic conductivity in polyethylene oxide (PEO) composite polymer electrolyte. *International Journal of Electrochemical Sciences*, 8: 2154-2163.
25. Bai, J., Lu, H., Cao, Y., Li, X. and Wang, J. (2017). A novel ionic liquid polymer electrolyte for quasi-solid state lithium air batteries. *RSC advances*, 7(49): 30603-30609.
26. Deraman, S. K., Mohamed, N. S. and Subban, R. H. Y. (2013). Conductivity and electrochemical studies on polymer electrolytes based on poly vinyl (chloride)-ammonium triflate-ionic liquid for proton battery. *International Journal of Electrochemical Science*, 8(1): 1459-68.

Malaysian Journal of Analytical Sciences (MJAS)
Published by Malaysian Analytical Sciences Society

EQUIVALENT CIRCUIT ANALYSIS OF $LaZrTa_3O_{11}$ CERAMIC SYNTHESISED BY USING THE CONVENTIONAL SOLID-STATE METHOD

(Analisis Litar Sepadan Seramik $LaZrTa_3O_{11}$ Disintesis dengan Menggunakan Kaedah Keadaan Pepejal Konvensional)

Fadhlina Che Ros* and Jumiah Hassan

Physics Department, Centre for Defence Foundation Studies,
Universiti Pertahanan Nasional Malaysia, Kem Sungai Besi 57000, Kuala Lumpur, Malaysia

**Corresponding author: fadhlina@upnm.edu.my*

Received: 13 November 2019; Accepted: 3 September 2020; Published: 12 October 2020

Abstract

$LaZrTa_3O_{11}$ ceramic with α-U_3O_8-type structure has been prepared by using the conventional solid state-route and studied by using powder X-ray diffraction for phase analysis and impedance spectroscopy for electrical measurements. It has hexagonal unit cell with space group $P6_322$ at room temperature. $LaZrTa_3O_{11}$ is reported to be isostructural with $CaTa_4O_{11}$ and $Ag_2Nb_4O_{11}$; the structure is related to U_3O_8-structure, where it consists of single layers of edge-sharing pentagonal Ta-O bipyramids alternating with layers of edge-sharing octahedra. The impedance spectroscopy response showed that $LaZrTa_3O_{11}$ exhibited a typical insulating behaviour at room temperature, with permittivity, $\varepsilon \sim 19$. It was a highly resistive material with $R >> 10^9\ \Omega$ at temperature below 500° C and as the temperature increased, frequency-dependence of alternating current conductivities at high frequency was clearly visible. The electrical properties of $LaZrTa_3O_{11}$ is best modelled by using non-Debye response circuit that consists of a parallel combination of a resistor, capacitor, and a constant phase element.

Keywords: $LaZrTa_3O_{11}$, dielectrics, high-temperature ceramics, lanthanide-oxide, non-Debye circuit

Abstrak

Seramik $LaZrTa_3O_{11}$ dengan struktur jenis α-U_3O_8 telah disediakan melalui kaedah keadaan pepejal konvensional dan dikaji dengan menggunakan pembelauan sinar-X untuk analisis fasa dan spektroskopi impedans untuk kajian sifat keelektrikan. Ia mempunyai sel unit heksagonal dengan kumpulan ruang $P6_322$ pada suhu bilik. $LaZrTa_3O_{11}$ dilaporkan mempunyai sama struktur dengan $CaTa_4O_{11}$ dan $Ag_2Nb_4O_{11}$; struktur tersebut adalah berkait dengan struktur U_3O_8 di mana ia terdiri daripada satu lapisan pentagonal bypiramid Ta-O berkongsi-sisi, berselang-seli dengan lapisan-lapisan oktahedra yang berkongsi-sisi. Tindak-balas spektroskopi impedans menunjukkan bahawa seramik $LaZrTa_3O_{11}$ mempamerkan sifat penebat yang tipikal pada suhu bilik, dengan kebolehtelapan, $\varepsilon \sim 19$. Ia adalah bahan berkerintangan tinggi dengan $R >> 10^9\ \Omega$ pada suhu di bawah 500° C dan apabila suhu meningkat, kebergantungan frekuensi konduktiviti arus ulang alik pada frekuensi tinggi jelas kelihatan. Model terbaik sifat keelektrikan bagi seramik $LaZrTa_3O_{11}$ adalah menggunakan litar non-Debye yang terdiri daripada kombinasi selari perintang, kapasitor dan elemen fasa pemalar.

Kata kunci: $LaZrTa_3O_{11}$, dielektrik, seramik bersuhu tinggi, oksida lanthanid, litar non-Debye

Introduction

Lanthanum zirconium tritantalum hendecaoxide ($LaZrTa_3O_{11}$) exhibits layers of edge-sharing pentagonal (Ta, Zr)-O_7 bipyramids that alternate with layers of edge-sharing LaO_8 polyhedra and (Ta,Zr)-O_6 octahedra. Many researchers have reported on its structure, namely Zheng and West reported $LaZrTa_3O_{11}$ ceramic as orthorhombic, a face-centred cell that belongs to one of the three possible space groups, *Fmmm*, *Fmm2*, or *F222*, a = 10.890(3), b = 12.450(3), and c = 6.282(2) Å, but later in 1992, Grins and Nygren reported the true symmetry of $LaZrTa_3O_{11}$ as the hexagonal space group $P6_322$, a = 62824(2), c = 12.4469(7) Å. Literature have also reported that $LaZrTa_3O_{11}$ is isostructural with $CaTa_4O_{11}$ and the newly-discovered ferroelectric material silver niobate, $Ag_2Nb_4O_{11}$ [1,2]. The nature of $LaZrTa_3O_{11}$ is shown in Figure 1.

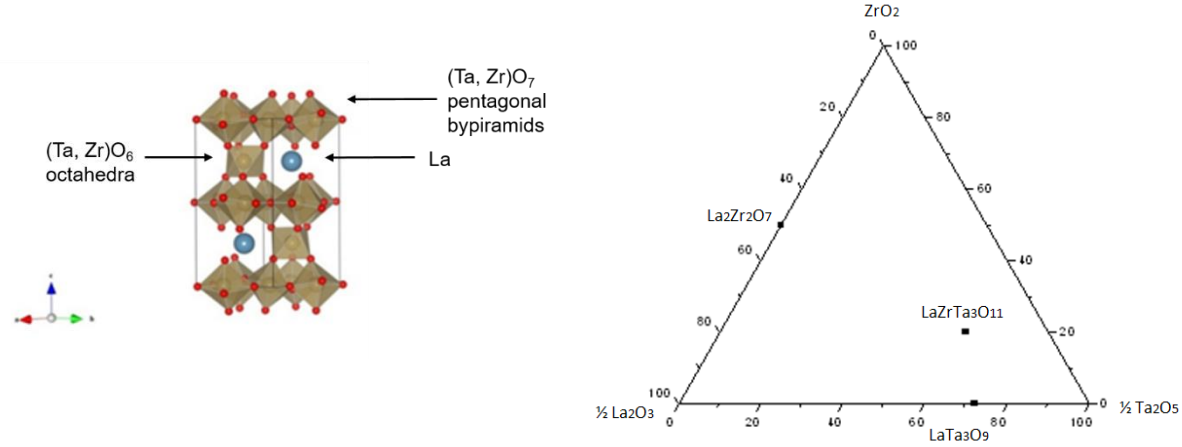
The unique structure of $LaZrTa_3O_{11}$ has attracted much interest among researchers except for its electrical properties of which even at the highest temperature, $LaZrTa_3O_{11}$ is very poor in electrical conductivity due to its extremely large amount of resistance [3–6]. No detailed studies on its electrical properties have been published so far. Recently, the researchers have reported eight new phases of similar structure to $LaZrTa_3O_{11}$ with the general formula $REMY_3O_{11}$, namely LaHfTa, LaHfNb, LaZrNb, PrHfTa, NdHfTa, NdHfNb, SmHfTa, and GdHfTa, where all phases had highly insulated permittivities in the range of 17 to 50 [4]. Insulators like $LaZrTa_3O_{11}$ have possible applications as substrate or plastic-based laminates due to their low conductivity even at a high temperature. Laminates are dominant in a relatively low technology application, such as casings for radios and televisions, whereas substrates are extensively used for demanding application in communications, military, space technologies, and automotive control [7]. In this study, the electrical properties and equivalent circuit analysis of $LaZrTa_3O_{11}$ at different temperatures were reported by using impedance spectroscopy (IS) method as a function of frequency. The analysis and modelling of IS data provided useful information about physical processes that occurred within the samples, which can be represented by a capacitor, *C*, resistor, *R*, and constant phase element (CPE) components of the proposed equivalent circuit.

Materials and Methods

$LaZrTa_3O_{11}$ was synthesized by using conventional solid-state routes, namely La_2O_3, Ta_2O_5 and ZrO_2 (99.9% pure Stanford Materials), which were dried overnight and stored under vacuum prior to being used. Mixtures totaling 5 g were weighed, mixed, and ground with acetone by using an agate mortar and pestle and were subsequently dried, pressed into pellets, and fired in a platinum (Pt) crucible in an electric muffle furnace at 1500 ^oC for 12 hours with plenty of air. The sample was removed from the furnace, crushed into a fine powder, repelleted, and returned to the furnace for another 12 h reaction at 1500^o C intermittently for up to 3 days to obtain a single-phase product.

STOE STADI P diffractometer, Cu $K\alpha_1$ radiation (λ = 1.54056 Å) was used in X-ray diffraction (XRD). External silicon standard, NIST 640d Si was used for line position calibration in which data were managed and compared against reference data in the ICDD's PDF-2 database by using STOE $WinX^{POW}$ software package. Data were collected for ~ 4 hours and corrected for absorption.

For electrical measurement, Pt paste electrodes were fabricated on the opposite pellet faces of cylindrical sintered pellets and hardened by gradually heating in the air at 800 ^oC for 2 hours. The samples with electrodes attached were placed into a conductivity jig and heated in a small tube furnace within the temperature range of room temperature to 800 ^oC. Electrical data were recorded by using a Hewlett Packard 4192A Impedance Analyser over the frequency range of 10 Hz to 1 MHz, with an alternating current (AC) voltage of 100 mV. The impedance raw data were corrected for the overall geometric factor of ceramic and data analysis was performed by using the software program, ZView.



(a) (b)

Figure 1. (a) Local coordination environments in $LaZrTa_3O_{11}$; two TaO_6 octahedra with three edge-sharing pentagonal bipyramids above and below near La positions, (b) $LaZrTa_3O_{11}$ within the ternary diagram ½ La_2O_3 - ½ Ta_2O_5 – ZrO_2

Results and Discussion

Phase analysis

The relative peak intensities of $LaZrTa_3O_{11}$ corresponded well with the calculated pattern reported in the ICDD - PDF card 81, 1935. The XRD data were indexed on the hexagonal space group, $P6_322$ and the data were collected over a 2θ-range from 10° to 70°. The sample was not in a single-phase due to the existence of impurities even at 72 hours of firing. The lattice parameters of the obtained $LaZrTa_3O_{11}$ were slightly bigger: a = 6.28724(4), c = 12.4525(1) Å as compared to the literature [2]: a = 6.2824, c = 12.4469 Å, which may be due to the presence of impurities. By matching the impurities' reflection with those of known phases, the sample contained a small amount of $LaTa_3O_9$ observed at 11°, 23°, 25°, and 57° and unreacted ZrO_2 at 30°, with 2.82% total weight fraction of $LaTa_3O_9$ at 72 hours heating duration. However, the intensity of $LaTa_3O_9$ and ZrO_2 reflections decreased gradually in time. The difficulty to decompose $LaTa_3O_9$ even when the sample was reheated longer is due to its high thermal stability, where the literature reported that $LaTa_3O_9$ melts congruently at 1850 ± 20 °C [6]. The low reactivity level of ZrO_2 towards Ta_2O_5 and La_2O_3 raw materials contributed to the formation of $LaTa_3O_9$, since $LaTa_3O_9$ formation temperature was also at 1500 °C. Figure 2 shows the XRD profile of $LaZrTa_3O_{11}$ at different firing hours.

Electrical properties

$LaZrTa_3O_{11}$ pellets were characterised by IS using data collected from room temperature to high temperature in air. The pellet density calculated from the pellet mass and dimension was ~ 91% of the value expected for a fully dense pellet that was calculated from the unit cell dimensions and contents. The data were analysed as a function of frequency at fixed temperatures. Permittivity, ε at room temperature was low, ~ 19, of which from room temperature to 400 °C, the capacitance at high frequency plateau was ~ 1.7 pF/cm (Figure 3(a)), and within these temperatures, the sample was highly insulated, $R >> 10^9$ Ω. Indeed, the conductivity, Y' data were too small to measure since the values were outside the machine limit. At a higher temperature range of 500 to 800 °C (Figure 3(b)), the data exhibited dispersion at a low frequency. The magnitude of C' increased from 10^{-11} to 10^{-10} F/cm with decreasing frequency, suggesting that the response originated from either i) an interfacial or grain boundary capacitance, ii) the

impurity phase, $LaTa_3O_9$, or iii) a bulk of CPE. The onset of dispersion to give a low capacitance plateau should be associated with any bulk response, which is observable at a higher frequency.

The admittance spectra, *Y'* of $LaZrTa_3O_{11}$ can only be measured above 600 °C, which showed a temperature-dependent behaviour in which *Y'* showed a power law response (Figure 4(a)). In the temperature range of 600 to 700 °C, the data set did not show a frequency-independent admittance plateau at lower frequencies, however, at temperatures ≤ 700 °C, *Y'* decreased with decreasing frequency and tended to become independent of frequencies below a certain value. With increasing temperatures, there was evidence of lower frequency of direct current (DC) plateau that changed to a power law at higher frequencies. At 800 °C, a crossover between low-frequency *dc* plateau and high-frequency power law was clearly visible. Such behaviour is observed in many materials and is based on Jonscher's universal power law relation [8]:

$$\sigma_\omega = \sigma_o + A\omega^n \quad (1)$$

where, σ_o corresponds to bulk conductivity, σ_{dc}, σ_ω is the *ac* conductivity, *A* is a constant, ω is the angular frequency, and *n* is the power law exponent, where $0 < n < 1$. The σ_{dc} value for $LaZrTa_3O_{11}$ was estimated and the Arrhenius law with the activation energy ~ 1.1(2) eV was followed, as shown in Figure 4(b).

All the temperature data of *C*' against log *f* spectrum showed a similar trend of capacitance frequency-independent at a high frequency. The low conductivity of 6×10^{-7} Ω^{-1} cm^{-1} at 800° C and the increasing capacitance from 10^{-12} Fcm^{-1} at room temperature to 10^{-11} Fcm^{-1} at 800° C were due to the nonideality of the bulk response that can be represented by a CPE element. At a low temperature, the electrons were localised and possessed relatively very small thermal vibration and as the temperature increased to 700 °C, these charges were capable of traversing the sample and therefore gave rise to direct current conduction. At higher temperatures, hopping conduction was easier since ions have a greater thermal energy and vibrate more vigorously, and also, defect concentrations are higher. The activation energy, E_a of the total conduction process was high, with the value of 1.1(2) eV whereby usually, a high activation energy is required for the occurrence of a thermally hopping type electronic mechanism.

Equivalent circuit analysis

In order to recognize which parameters contributed to the data shown in Figure 3 and Figure 4, it was essential to find an equivalent circuit that accurately represented the electrical response of $LaZrTa_3O_{11}$. The impedance data were modelled by using fitting programme, ZView Equivalent Circuit 2.9 Software. Appropriate frequency range data was selected, as some data may be seen unreliable due to instrument's limit at low frequencies and resonance effect for data above 1 MHz. The model started with a low temperature data which is usually related to bulk response in which some of the bulk parameters may be fixed to enable the modelling of higher temperature data which increasingly featured lower frequency phenomena, such as grain boundary. It is evident from Figure 3(b) and Figure 4(a) that $LaZrTa_3O_{11}$ ceramic sample showed a non-ideal Debye response, where it was usually described by adding a CPE to the parallel *RC* circuit element. Even though the specific meaning of CPE behaviour was not known, it was often used to describe the electrical behaviour of ionically conducting materials. CPE can be described by the relationship as follows:

$$Y^* = a(j\omega)^n = a\cos\left(n\frac{\pi}{2}\right) + j\ a\ sin\left(n\frac{\pi}{2}\right) = A\omega^n + jB\omega^n \quad (2)$$

where, $j = \sqrt{-1}$, *A* and *B* are interrelated by the admittance complex relationship, where $A = a \cos n(\pi/2)$, unit: $Scm^{-1}rad^{-(n)}$, and $B = a \sin n (\pi/2)$, unit: $Fcm^{-1}rad^{-(n-1)}$. The value of the power law parameter, *n* was between 0 and 1 of which the capacitive or resistive behaviour of a material depended on the *n* value.

A summary of equivalent circuits used to fit data at different temperatures is shown in Figure 5. The impedance data collected from room temperature to 400° C can be represented by a simple, ideal, temperature-independent capacitor of magnitude ~ 1.7 pF/cm. At these temperature ranges, the *Y'* data cannot

be measured at any frequency, which indicated that the resistance, *R* was simply too large to measure. At temperatures ≥ 500 °C, the capacitance data showed a power law dependence on frequency, that the inclusion of a CPE may be required to fit the data. Therefore, a parallel combination of capacitor, *C* and CPE was used to fit the dispersions for the temperature range of 500 to 650 °C (Figure 5(b)). As the temperature reached ≥ 650 °C, the *Y'* data showed frequency-dependent values at high frequencies, corresponding to AC conduction as well as the *C'* data showed a power law response at low frequencies of slope (n-1), which levelled off to a frequency-independent value at high frequencies. Therefore, for temperatures in the range of 675 to 800 °C, the dispersions may be fitted by using a parallel combination of *RC* circuit and CPE, as shown in Figure 5(c). The obtained values of the circuit parameters *C*, *R*, *A*, and *n* from the fits are summarized in Table 1. The *R* components of $LaZrTa_3O_{11}$ can only be measured at 675 °C and above. Its magnitude decreased with increasing temperature and magnitude of $A\omega^n$, and thus this represented that the frequency-dependent conductive component of the *Y'* data gradually increased in temperature. The magnitudes of bulk capacitance, *C* were fixed at high temperatures so as to enable the high temperature data to be fitted without unreasonable value of *C*, *A*, and *n* parameters.

It was possible to model the data accurately in terms of equivalent circuits by using the circuit that was frequently used to model the electrical properties of ionically conducting materials, which had a parallel combination of resistor, capacitor, and CPE. An associated capacitance of 1.663×10^{-12} Fcm^{-1} obtained at 651°C corresponded to C_b of the material. The CPE parameters, *n* and *A* showed changes in temperature. The *n* value showed intermediate low values from $n \sim 0.4$ to 0.27, which corresponded to intermediate behaviour between a frequency-dependent capacitor and resistor. The AC conductivity parameter, *A* showed an increase in temperature, which indicated a thermal activation. Since most of the data showed no measurable DC conductivity, the conductivity was just limited to localized AC conductivity represented by parameter *A*, which was attributed to small atomic/electronic vibrations. These vibrations may be associated with the polarizable nature of the crystal structure from either A-site cation La, B-site cations Zr or Ta, or some oxygen. Like other insulators, these atomic displacements occurred only at high temperatures, with the activation energy of 1.1(2) eV. The resistivity, *R* was too large to be measured below the temperature of 675 °C of which the values fell from 9.8×10^7 to 2.3×10^6 Ω·cm as the temperature increased. This could be associated with the increase in thermally activated drift mobility of electronic charge carriers by a hopping conduction mechanism. The circuit that is deduced in Figure 5(c) may be regarded as an extension of the ideal dielectric relaxation circuit in which the introduction of CPE added frequency-dependent elements to the single-value components, *R* and *C*. By excluding the CPE element, the circuit was often used to represent dielectric relaxation processes within an insulating system, which were composed of ideal, frequency-independent circuit elements.

The ε value of a compound was closely related to the stability of material's crystal structure, and thus oxides crystallized in the hexagonal structure should exhibit higher ε values than the oxides crystallized in the cubic and monoclinic ones. In this study, the capacitance value, $C' \sim 1.663 \times 10^{-12}$ Fcm^{-1}, ($\varepsilon \sim 19$) exhibited by $LaZrTa_3O_{11}$ was what the researchers expected from lanthanide oxides-based materials in which the value was comparable to the literature which reported that early rare-earth materials possessed intermediate dielectric constants ($\varepsilon \sim$ 12-20) with large band gaps of ~ 5.4 eV [9].

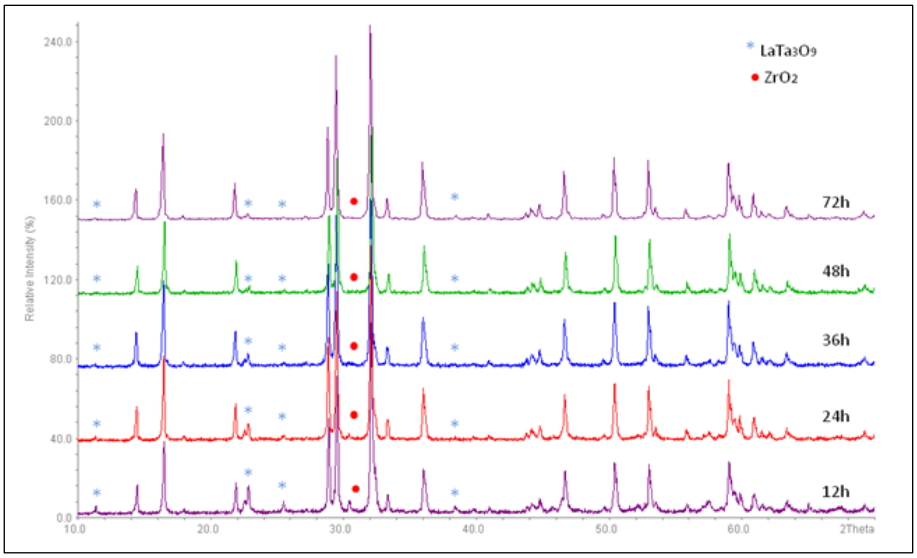


Figure 2. XRD profiles for $LaZrTa_3O_{11}$ using La_2O_3, Ta_2O_5 and ZrO_2 as starting reagents. The sample was heated from 12 to 72 hours at 1500 ^oC

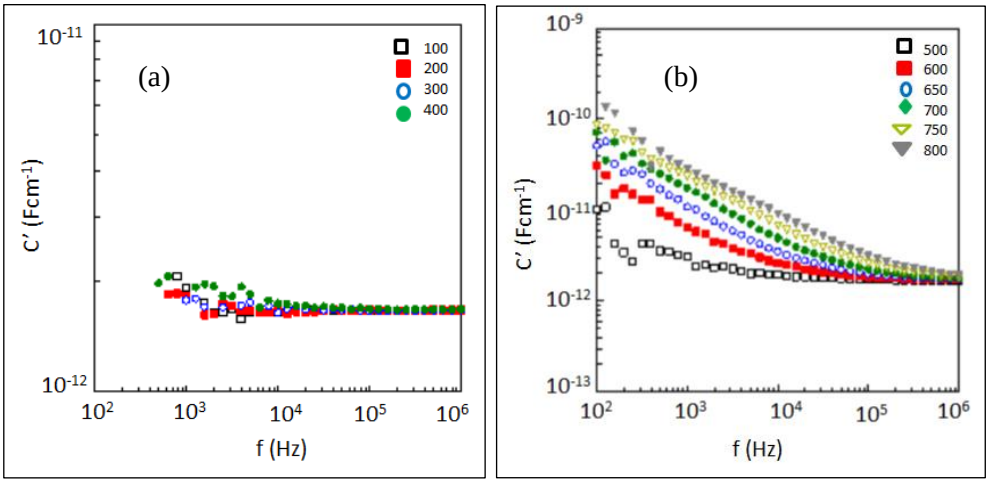


Figure 3. Capacitance, *C'* versus frequency for temperatures (a) 100 to 400 ^oC (b) 500 to 800^o C

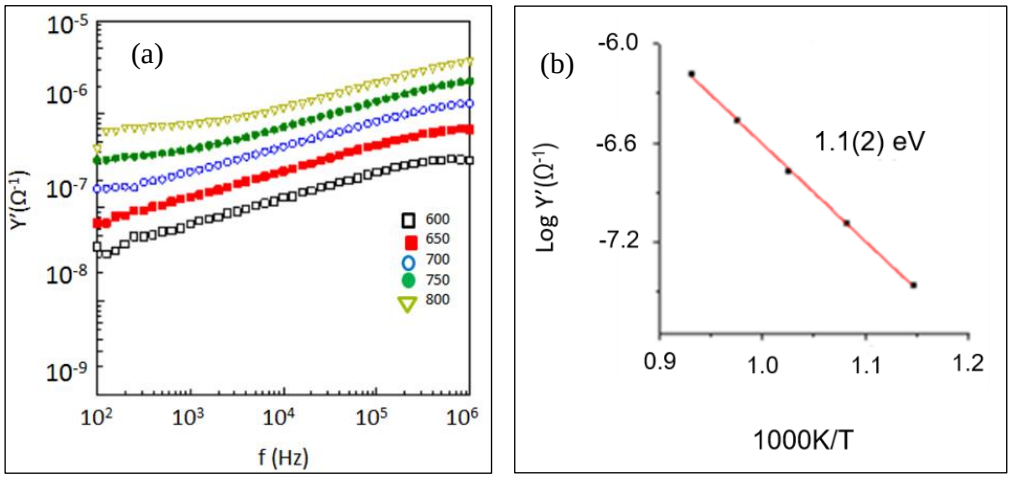


Figure 4. (a) Admittance, *Y'* versus frequency for 500 to 800 °C (b) Arrhenius plot of the total admittance, *Y'*

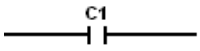
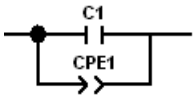
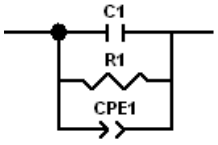
Temperature (° C)		**Circuit**
Room temperature – 400	(a)	
500 – 650	(b)	
675 – 800	(c)	

Figure 5. Equivalent circuits used at different temperatures, (a) simple capacitor from room temperature to 400 °C, (b) parallel combination of a capacitor and a CPE at temperature range of 500 to 650 °C, and (c) non-ideal Debye circuit for temperatures from 675 to 800 °C

Table 1. Fitting parameters data of *C*, *A*, *n*, and *R* from room temperature to 800 °C

T (°C)	*C* (Fcm^{-1})	*A* (Scm^{-1}rad^{-n})	*n*	*R* (Ωcm)
23	$1.68(1) \times 10^{-12}$	-	-	-
100	$1.67(1) \times 10^{-12}$	-	-	-
200	$1.672(9) \times 10^{-12}$	-	-	-
300	$1.70(1) \times 10^{-12}$	-	-	-
400	$1.66(2) \times 10^{-12}$	$1.0(4) \times 10^{-10}$	0.41(4)	-
500	$1.67(9) \times 10^{-12}$	$8.9(7) \times 10^{-10}$	0.323(8)	-
600	$1.673(5) \times 10^{-12}$	$6.5(1) \times 10^{-9}$	0.277(1)	-
625	$1.667(4) \times 10^{-12}$	$9.3(1) \times 10^{-9}$	0.277(1)	-
651	$1.663(4) \times 10^{-12}$	$1.27(2) \times 10^{-8}$	0.276(1)	-
676	1.663×10^{-12}	$1.5(2) \times 10^{-8}$	0.28(1)	$9.8(8) \times 10^{7}$
702	1.663×10^{-12}	$1.6(1) \times 10^{-8}$	0.294(5)	$2.2(3) \times 10^{7}$
726	1.663×10^{-12}	$1.6(1) \times 10^{-8}$	0.311(5)	$9.8(7) \times 10^{6}$
751	1.663×10^{-12}	$1.7(1) \times 10^{-8}$	0.321(5)	$5.5(3) \times 10^{6}$
775	1.663×10^{-12}	$2.0(2) \times 10^{-8}$	0.324(7)	$3.5(2) \times 10^{6}$
800	1.663×10^{-12}	2.3×10^{-8}	0.32(1)	$2.3(2) \times 10^{6}$

Conclusion

$LaZrTa_3O_{11}$ was prepared by using the conventional solid-state route and studied by using XRD and IS electrical measurements. It had a hexagonal space group, $P6_322$ of a larger unit cell, a ≈ 6.28 and $c \approx 12.45$ Å as compared to the literature. The structure consisted of layers of edge-sharing pentagonal Ta-O bipyramids, which alternated with layers of edge-sharing octahedral. The IS response showed that $LaZrTa_3O_{11}$ exhibited a typical insulating behaviour, i.e., low permittivity, $\varepsilon \sim 19$ with a large value of activation energy, $E_a \sim 1.1(2)$ eV; dispersion of capacitance at low frequencies and frequency-independent capacitance at high frequencies were also observed. $LaZrTa_3O_{11}$ sample showed a highly resistive material of $R >> 10^9$ Ω at temperatures below 500 °C. As the temperatures went higher than 675 °C, frequency-dependence of AC conductivities at high frequency was observed; DC conductivities were observed as the temperature increased further. The electrical properties may be accurately modelled by using the non-ideal Debye response circuit, which consisted of a parallel combination of resistor, capacitor, and CPE elements. The introduction of CPE into the equivalent circuit may be an indication of nonideality in the bulk conduction mechanism for $LaZrTa_3O_{11}$, which was electrically homogeneous in terms of its electrical microstructure. The insulating behaviour as well as the interesting structure of $LaZrTa_3O_{11}$ were noted in the literature [1, 2], and thus this type of material could potentially be used for dielectric applications.

Acknowledgement

The researchers would like to thank Universiti Pertahanan Nasional Malaysia (UPNM) and the Ministry of Higher Education Malaysia (MOHE) for their financial support through the Fundamental Research Grant Scheme (FRGS/1/2017/STG07/ UPNM/02/2) as well as the Engineering and Physical Sciences Research Council (EPSRC) for funding this research.

References

1. Masó, N., Woodward, D. I., Thomas, P. A., Várez, A. and West, A. R. (2011). Structural characterisation of ferroelectric $Ag_2Nb_4O_{11}$ and dielectric $Ag_2Ta_4O_{11}$. *Journal of Materials Chemistry,* 21: 2715-2722.
2. Grins, J. and Nygren, M. (1992). Structure of $LaZrTa_3O_{11}$, a $CaTa_4O_{11}$ isotype. *Materials Research Bulletin*, 27: 141-145.
3. Masó, N., Woodward, D. I., Thomas, P. A., Várez, A. and West, A. R. (2011). Polymorphism, structural characterisation and electrical properties of $Na_2Nb_4O_{11}$. *Journal of Materials Chemistry,* 21: 12096-12102.
4. Fadhlina Che Ros, Mclaren, N. R., Masó, N. and West, A. R. (2018). Synthesis, structure and dielectric properties of a new family of phases, ABC_3O_{11}: A = La, Pr, Nd, Sm, Gd; B = Zr, Hf; C = Ta, Nb. *Journal of Australian Ceramic Society*, 54: 1-10.
5. Jahnberg, L. (1970). Crystal structures of $Na_2Nb_4O_{11}$ and $CaTa_4O_{11}$. *Journal of Solid State Chemistry*, 1: 454-462.
6. Zheng, C. and West, A. R. (1991). Compound and solid-solution formation, phase equilibria and electrical properties in the ceramic system ZrO_2-La_2O_3-Ta_2O_5. *Journal of Materials Chemistry,* 1(2): 163-167.
7. Moulson, A. J. and Herbert, J. M. (2008) Electroceramics. John Wiley & Sons: pp. 285.
8. Joncher, A. K. (1983). Dielectric relaxation in solids. chelsea dielectric press. London: pp. 209.
9. Scarel, G., Svane, A. and Fanciulli, M., (2007). Scientific and technological issue related to rare–earth oxides: An introduction. *Journal of Applied Physics*, 106: 1-14.

Malaysian Journal of Analytical Sciences (MJAS)
Published by Malaysian Analytical Sciences Society

EFFECT OF Cr_2O_3 ON THE TRANSITION TEMPERATURE AND PHASE FORMATION OF $Tl_{2-x}Cr_xBa_2CaCu_2O_{8-\delta}$ SUPERCONDUCTOR

(Kesan Cr_2O_3 Terhadap Suhu Peralihan dan Pembentukan Fasa Superkonduktor $Tl_{2-x}Cr_xBa_2CaCu_2O_{8-\delta}$)

Syahrul Humaidi[1]* and Roslan Abd-Shukor[2]

[1]*Department of Physics,*
FMIPA-Universitas Sumatera Utara, Jln Bioteknologi 1, Medan 20155, Indonesia
[2]*Department of Applied Physics,*
Universiti Kebangsaan Malaysia, 43600 UKM Bangi, Selangor, Malaysia

**Corresponding author: syahrul1@usu.ac.id*

Received: 13 November 2019; Accepted: 3 September 2020; Published: 12 October 2020

Abstract

The Tl-based high T_c superconductors, $Tl_{2-x}Cr_xBa_2CaCu_2O_{8-\delta}$ (Tl2212) have been prepared *via* the solid-state reaction method. The substitution of Cr into the Tl-site was aimed to investigate the role of Cr on the transition temperature and phase stability of the Tl2212 phase. $Ba_2CaCu_2O_y$ precursor material was synthesized using $BaCO_3$ (99.9%, Aldrich), CaO (99.99%, Alfa Aesar), and CuO (99.9%, Alfa Aesar) powder as the starting compound. The powders were mixed and sintered at 900 ^oC for 24 hours before cooled to room temperature. The precursor was mixed with Tl_2O_3 (99.9%, Alfa Aesar) and Cr_2O_3 (99.9%, Merck) powders before being pressed to obtain $Tl_{2-x}Cr_xBa_2CaCu_2O_8$ pellet. The pellets were heated at 900 ^oC with oxygen flow for 4 minutes. The transition temperature, T_c was determined using the standard four-point probe electrical resistance measurements from 50 K to 300 K with a constant current of 20 mA. The phases were determined by powder X-ray diffraction (XRD) method using CuK_α source with λ= 1.5418 Å. Based on XRD analysis, the x = 0, 0.2, and 0.6 showed unit cell belonging to the 14/mmm space group. In the x = 0.4, the space group changed to P4/mmm which is the Tl1212 phase. It was found that the optimum composition was $Tl_{1.8}Cr_{0.2}Ba_2CaCu_2O_{8-\delta}$ and the maximum zero-resistance temperature, $T_{c\text{-}zero}$ was 96 K, and the onset temperature, $T_{c\text{-}onset}$ was 116 K. It was observed that the transition temperatures decreased with increasing Cr_2O_3. The volume fraction of the Tl2212 phase in this composition was 88% with the *c*-lattice parameter equals to 29.388Å. Superconductivity was destroyed in the x = 1.0 samples.

Keywords: transition temperature, structure, Tl2212 phase

Abstrak

Superkonduktor suhu tinggi berasaskan Tl iaitu, $Tl_{2-x}Cr_xBa_2CaCu_2O_{8-\delta}$ (Tl2212) telah disediakan melalui kaedah tindak balas pepejal. Penggantian Cr pada kedudukan Tl dilakukan untuk menyelidik peranan Cr terhadap suhu genting dan kestabilan fasa superkonduktor Tl2212. Bahan pelopor $Ba_2CaCu_2O_y$ disintesis dengan menggunakan serbuk $BaCO_3$(99.9%, Aldrich), CaO(99.99%, Alfa Aesar) dan CuO(99.9%, Alfa Aesar) sebagai campuran awal. Serbuk ini kemudiannya disinter pada 900 ^oC selama 24 jam dan dibiarkan sejuk sehingga suhu bilik. Bahan pelopor ini kemudianmya dicampurkan dengan serbuk Tl_2O_3 (99.9%, Alfa Aesar) dan serbuk Cr_2O_3(99.9%, Merck) untuk menghasilkan pelet $Tl_{2-x}Cr_xBa_2CaCu_2O_8$. Pelet kemudiannya disinter

pada 900 °C dengan aliran gas oksigen selama 4 minit. Suhu peralihan, T_c ditentukan dengan pengukuran rintangan elektrik menggunakan kaedah piawai empat titik dalam suhu 50 K hingga 300K dengan bekalan arus malar 20 mA. Pecahan fasa diperolehi daripada kaedah pembelauan serbuk sinar-X (XRD) menggunakan sinar CuKα dengan panjang gelombang λ= 1.5418Å. Berdasarkan analisis XRD, sampel x = 0, 0,2, dan 0.6 adalah pada kumpulan ruang 14/mmm. Untuk sampel x = 0.4 kumpulan ruang berubah menjadi P4/mmm iaitu fasa yang berlainan (Tl1212). Didapati bahawa suhu peralihan sifar maksimum, $T_{c\ sifar}$ adalah 96 K dan suhu perlalihan mula, $T_{c\ mula}$ adalah 116 K bagi komposisi $Tl_{1.8}Cr_{0.2}Ba_2CaCu_2O_{8-\delta}$. Pecahan isipadu daripada fasa Tl2212 dalam sampel ini adalah 88% dengan parameter kekisi c bersamaan 29.388 Å. Sifat superkonduktor hilang pada komposisi x = 1.0.

Kata kunci: suhu peralihan, struktur, fasa Tl2212

Introduction

High temperature superconductor (HTSC) based on copper oxides have critical temperature greater than 77 K (above liquid nitrogen temperature). Some of the common types of HTSCs include YBaCuO (YBCO), BiSrCaCuO (BSSCO), TlBaCaCuO (TBCCO), HgBaCaCuO, and HgTlBaCaCuO. Many efforts are being made to enhance the transition temperature of HTSCs. Some researchers modified the fabrication techniques of the materials [1-4]. Most of the research works [5-9] deal with doping and atomic substitution. The thallium-based copper oxide superconductor consists of several phases with a different number of copper oxide layers. Previous works on thallium-based high temperature superconductor concentrated on several phases of Tl-based HTSCs. T_c of $TlBa_2CaCu_2O_{7-\delta}$ (Tl1201) was around 70 K [10], whereas $Tl_2Ba_2CaCu_2O_{8-\delta}$ (Tl1212) had T_c of 110 K [11]. The $TlBa_2Ca_3Cu_4O_{11-\delta}$ (Tl1234) was reported with T_c of around 114 K [12].

The role of Cr at the Tl-sites in Tl-based superconductor has been widely studied. Chromium is an effective element for substitution in Tl-Sr-Ca-Cu-O systems [13]. There have been several reports on the effect of Cr on the superconductivity of Tl-1212 phase. The substitution of Cr for Tl or Ca site improves the superconducting behavior [11, 14, 15]. Cr substitution improves the critical temperature up to 110 K [16]. The $Tl_2Ba_2CaCu_2O_{8-\delta}$ samples with high purity were reported to have T_c of 106 K [17, 18]. The samples were prepared from metal oxides with a starting composition Tl2212 and heated at 900 °C for 24 hours followed by adding appropriate amounts of Tl_2O_3 and heated again at 915-920 °C for 4-5 minutes. In a previous report, it has been observed that the volume fraction of Tl2212 phase increased as Te content was increased [19]. It is interesting to investigate the effects of Cr in other phases of the Tl-based superconductor. In this paper, we report the effects of Cr on the superconducting properties and phase formation of the Tl-2212 phase.

Materials and Methods

Samples with the nominal starting composition $(Tl_{2-x}Cr_x)Ba_2CaCu_2O_8$ with x = 0.0, 0.2, 0.4, 0.6, and 0.8 were prepared by the solid state reaction method. Appropriate amounts of high purity (>99.99%) $BaCO_3$, CaO, and CuO were mixed completely using an agate mortar to obtain a homogeneous mixture. The precursor powders were heated at 900 °C for 24 hours with several intermittent grinding. Appropriate amounts of Tl_2O_3 and Cr_2O_3 with appropriate mole% were then added to the precursor and completely mixed before being pressed into pellets with 1.3 cm diameter and 0.2 cm thickness under 7 ton/cm^2 of pressure. The pellets were heated at 900 °C in flowing oxygen for 4 minutes. This was followed by furnace cooling to room temperature. An excess of 10% Tl_2O_3 was added to compensate for the thallium lost during heating.

The dc electrical resistance measurements were performed between 50 K and 300 K. The four-point method with silver paste contact was used for the measurement. A closed cycle refrigerator from CTI Cryogenic Model 22 cryostat and a temperature controller from Lake Shore Temperature Controller Model 340 was employed. A constant current source between 1 mA and 100 mA was used throughout the measurements. The powder X-ray diffraction (XRD) method was used to identify the phases. A Bruker model

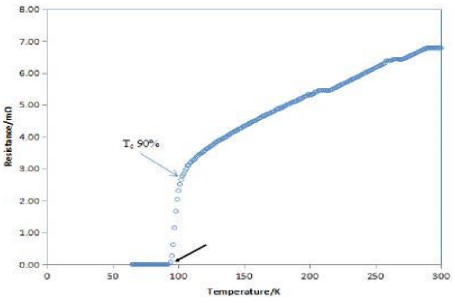
D8 Advance diffractometer with CuKα radiation source with λ=1.5418Å was used. A software from Eva program was used to analyze the XRD patterns.

Results and Discussion

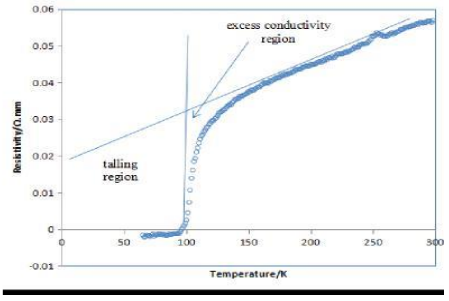
The curves of electrical resistance as a temperature function are shown in Figures 1(a) to 1(d). Samples with x = 0.0- 0.6 showed metal-like behaviour above the transition temperature. For x = 0 the resistance dropped abruptly at 105 K, where it is defined as $T_{c\ onset}$. The zero resistance occurs at 93 K and is denoted as $T_{c\text{-}zero}$. A narrow transition width ΔT_c of 12 K was observed. For samples with x = 0.2, $T_{c\text{-}onset}$ was observed to increase to 116 K and $T_{c\text{-}zero}$ was 96 K. However, ΔT_c increased to 20 K. When the content of Cr was increased to x = 0.4, $T_{c\text{-}onset}$ decreased to 105 K. A drastic decrease of $T_{c\text{-}onset}$ occurred for x = 0.6 with $T_{c\text{-}onset}$ of 84 K and a narrower ΔT_c of 13 K. Samples with x = 0.8 showed a high $T_{c\text{-}onset}$, but $T_{c\text{-}zero}$ decreased to 60 K. This is due to the high resistivity in the normal state (Table 1). It is interesting to note that superconductivity was not observed in the x = 1.0 sample. The transition temperatures and room temperature resistivity of $Tl_{2-x}Cr_xBa_2CaCu_2O_{8-\delta}$ is presented in Table 1.

A previous finding on the Tl-1212 phase using Cr_2S_3 as a source of Cr [18] reported that $T_{c\text{-}onset}$ is between 90 K and 105 K. This is due to the high resistivity in the normal state. In this work the highest $T_{c\text{-}onset}$ as well as $T_{c\text{-}zero}$ was observed in the x = 0.2 samples indicating an optimal doping level was achieved. This also coincided with the lowest normal state resistivity at 297 K, which indicates the optimization of hole concentration as a result of Cr substitution [20]. Using XRD patterns and analysis by EVA programme, the lattice parameters were calculated and presented in Table 2.

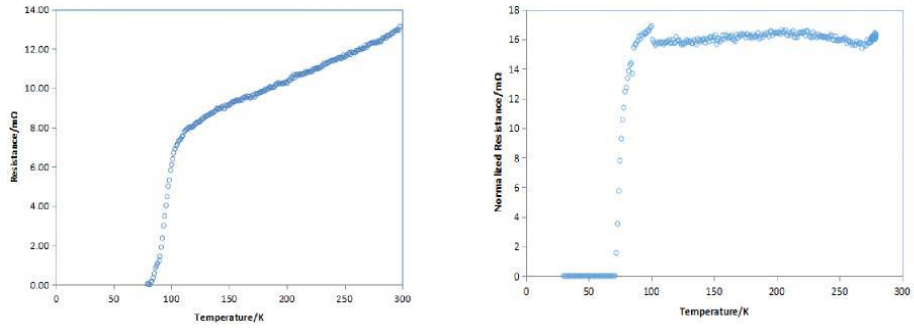
Table 2 shows the phases in the samples which consist of the Tl1212, Tl2223, Tl1223, Tl2234, and Tl1234 phases. It is noted that the Tl2212 phase was present with a volume fraction between 50% and 88%. The occurrence of multi phases in the x = 0.8 sample resulted in the reduction of $T_{c\text{-}zero}$ to 60 K. The samples were in 14/mmm and P4/mmm space group for x = 0.0 and x = 0.6. In the x = 1.0 samples, superconductivity was completely suppressed and the sample became insulating. This was due to the presence of unknown phases.



(a)



(b)



(c) (d)

Figure 1. Electrical resistance as a function of temperature for $Tl_{2-x}Cr_xBa_2CaCu_2O_{8-\delta}$ with (a) $x = 0$, (b) $x = 0.2$, (c) x 0.4 and (d) $x = 0.6$

Table 1. Transition temperatures and electrical resistivity at 297 K of $Tl_{2-x}Cr_xBa_2CaCu_2O_{8-\delta}$

x	$T_{c\text{-zero}}$ (± 1 K)	$T_{c\text{-onset}}$ (±1 K)	ΔT_c (± 1 K)	$\rho_{297\ K}$(Ωcm)
0	93	105	12	0.1562
0.2	96	116	20	0.1249
0.4	84	105	21	0.5966
0.6	71	84	13	0.5220
0.8	60	104	64	0.6072
1.0	-	-	-	-

Table 2. Phases occurrence, volume fraction, and space group of the samples

Sample	Tl-2212 Phase (%)	Tl-1212 Phase (%)	Tl-1223 Phase (%)	Tl-2223 Phase (%)	Tl-2201 Phase (%)	Tl-2234 Phase (%)	Other Phase (%)	Space group
$x = 0.0$	50	8	0	0	27	0	0	14/mmm (139)
$x = 0.2$	83	6	0	6	0	6	0	14/mmm (139)
$x = 0.4$	88	6	0	0		6	0	P4/mmm
$x = 0.6$	68	4	4	12	0	4	Tl-1234 (4)	14/mmm (139)
$x = 0.8$	46	4	4	4	0	15	Tl-1234 (15)	Pnma (60)
$x = 1.0$	40	0	0	20	6	8	Tl-1234 (2) Unknown/ 22	-

Conclusion

We have prepared Tl2212 superconductor *via* the solid-state reaction method. The addition of Cr into ($Tl_{2-x}Cr_x$)$Ba_2CaCu_2O_8$) has significantly affected the transition temperature. The volume fraction of the Tl2212 phase should be considered in the enhancement of transition temperature. Based on our experiments, it was found that the $Tl_{1.8}Cr_{0.2}Ba_2CaCu_2O_{8-\delta}$ sample can be used as a starting composition for further investigation.

Acknowledgement

This research was supported by the Ministry of Higher Education of Malaysia under grant no. FRGS/1/2017/STG02/UKM/01/1.

References

1. Ahmad, K. Y. and Abd-Shukor, R. (2003). Synthesis and formation of Tl-1223 and Tl-2223 high-Tc superconductors. *Pertanika Journal Science & Technology,* 11(1): 1-7.
2. Ji, L., Yan, S. L., Zhao, X. J., Fang, L., Li, Y. G., He, M., Zhou, T. G., Chai, C., Eickmeye, J. and Holzapfel, B. (2006). Preparation and characterization of $Tl_2Ba_2CaCu_2O_8$. *Superconductor Science Technology*, 19: 338-341.
3. Cheng, Z. X., Wang, X. L., Keshavarzi, S., Qin, M. J., Silver, T. M., Liu, H. K., Kimura, H. and Dou, S. X. (2004). The morphology, periodical modulation structure and effects of heat treatment on the superconductivity of (Tl,Pb)(Sr,Ba)-1223 single crystal. *Superconductor Science Technology,* 17: 696-700.
4. Dark, C. J., Speller, S. C. and Grovenor, C. R. M. (2006). The development of bi-epitaxial texture and high grain boundary J_c values in Tl-2212 films on MgO substrate. *Superconductor Science Technology,* 19: 484-492.
5. Pu, M. H., Cao, Z. S., Wang, Q. Y. and Zhao, Y. (2006). The influence of Cr-ions on the flux creep in Bi-2223/Ag tapes. *Superconductor Science Technology,* 19: 462-465.
6. Kong, W. and Abd-Shukor, R. (2007). Effect of nano Cr_2O_3 addition on (Bi,Pb)-Sr-Ca-Cu-O superconductor. *Solid State Science and Technology,* 15(1): 1-5.
7. Ihara, H. and Sekita, Y. (2001). United States Patent, US006300284B1 (10) Patent No:(45) Patent:US 6,300,284 B1.
8. Jorda, J. L., Hopfinger, Th., Couach, M., Pugnat, P., Bertrand, C and Galezl, Ph. (1998). Formation of thallium-1223 superconductors. *Journal of Superconductivity,* 11(1): 87-89.
9. Faizah, M. S., Yahya, A. K., Hamadneh, I. and Abd-Shukor, R. (2002). Effects of Ag addition and properties of Tl-2212 superconductors. *Solid State Science and Technology,* 10(1 & 2): 30-36.
10. Kikuchi, M., Ohshima, E., Ohninshi, N., Muraoka, Y., Nakajima, S., Aoyagi, E., Ogawa, M., Akimitsu, J., Oku, T., Hiraga, K. and Syono, Y. (1994) Synthesis and superconductivity of oxycarbonates of the Tl-1201 phase. *Physica C*, 219(1-2):200-204.
11. Abd-Shukor, R., Baharuddin, Y. and Lau, R. S. L. (1997). Formation of Tl-1212 phase in ($Tl_{0.8}M_{0.2}$)Sr_2(Ca,Cr)Cu_2O_7 (M:Cd, and Sc) High-Tc superconductor, *Journal of Materials Science Letters,* 16: 818-820.
12. Ogborne, D. M. and Weller, M. T. (1994). Oxygen non-stoichiometry in the (Tl,Pb)-Sr-Ca-Cu-O 1212 system. *Physica C,* 220: 389-395.
13. Ranjbar, M. G. and Abd-Shukor, R. (2016). Excess conductivity and superconducting fluctuation analysis of Cr-substituted Tl-1223 type phase Tl1−xCrx)Ba2Ca2Cu3O9−δ (x = 0.4–0.8). *Journal of Superconductor and Novel Magnetism,* 29: 2235-2240.
14. Abd-Shukor, R. and Quah, C. T. (1994) Superconductivity of 1212-type phase TlSr2(Ca,Cr)Cu2O7 and TlSr2(Sr,Tm)Cu2O7. *Journal of Materials Science and Engineering B*, 23: 54-57.
15. Li, Y. F., Chmaissem, O., and Sheng, Z. Z. (1995). Crystal structure and Tc of 1212-type cuprate (Tl,Cr)Sr2(Ca,Tl) Cu_2O_7. *Physica C,* 248: 42-48.
16. Sheng, Z. Z., Gu, D. X., Xin, Y. and Pederson. (1991). A new 1212-type phase Cr-substituted $TlSr_2CaCu_2O_7$ with Tc up to about 110K. *Modern Physics Letters B,* 9:635-642.
17. Abd-Shukor, R.(2002). The ubiquitous superconductor: Materials and mechanism. *Solid State Science and Technology,* 10(1&2): 14-21.

18. Al-Sharabi, A., and Abd-Shukor, R. (2013) Formation of $(Tl_{1-x}\ Cr_x)\ Sr_2CaCu_2O_{7-\delta}$ (Tl-1212) Superconducting Phase Using Cr_2S_3. *International Journal Electrochemical Sciences,* 8: 7825-7830.
19. Humaidi, S., Marlianto, E., Marhaposan, S. and Abd-Shukor, R. (2019). Superconducting properties of Te-substituted $(Tl_{2-x}Te_x)Ba_2CaCu_2O_{8-\delta}$. *Solid State Phenomena*, 290: 239-244.
20. Yusuf, A. A., Yahya, A. K., Khan, N. A., Salleh, F. M. D., Marsom, E and Huda, N. (2011). Effect of Ge^{4+} and Mg^{2+} doping on superconductivity, fluctuation induced conductivity and interplanar coupling of $TlSr_2CaCu_2O_{7-\delta}$ superconductors. *Physica C,* 471:363-372.

Malaysian Journal of Analytical Sciences (MJAS)
Published by Malaysian Analytical Sciences Society

A BRIEF REVIEW ON THE DESIGN AND SYNTHESIS OF NEW ANTIDOTES IN THE TREATMENT OF ORGANOPHOSPHORUS POISONINGS

(Ulasan Ringkas pada Reka Bentuk dan Sintesis Antidot Baru untuk Merawat Keracunan Organofosforus)

Mas Amira Idayu Abdul Razak[1,2], Mohd Nor Faiz Norrrahim[2], Ong Keat Khim[2,3], Siti Aminah Mohd Noor[3], Norhana Abd Halim[3], Noor Aisyah Ahmad Shah[3], Victor Feizal Knight[2], Wan Md. Zin Wan Yunus[2,3], Noor Azilah Mohd Kasim[2,3]*

[1]Faculty of Defence Science and Technology
[2]Centre for Chemical Defence
[3]Centre for Defence Foundation Studies
Universiti Pertahanan Nasional Malaysia, Kem Perdana Sungai Besi, 57000 Kuala Lumpur, Malaysia

**Corresponding author: azilah@upnm.edu.my*

Received: 13 November 2019; Accepted: 3 September 2020; Published: 12 October 2020

Abstract

Organophosphorus (OP) are highly toxic compounds commonly used as pesticides and chemical warfare nerve agents. Exposure to OP compounds can lead to death due to respiratory failure. OP compounds function to inhibit the enzyme acetylcholinesterase (AChE) which controls the transmission of nervous impulses and accumulation of acetylcholine (Ach) at cholinergic receptor sites. The inhibition of AChE by OP compounds can cause motor convulsions and epileptic seizures. There are several drugs used to treat OP poisonings, such as atropine, diazepam, and oximes. However, none of them are considered to be effective in treating OP poisonings. Recently, several new researches have been done to introduce strategies on designing oximes to treat OP poisonings. Therefore, this brief review summarizes several recent findings on the design and synthesis of new oximes that can reactivate the inhibited AChE.

Keywords: organophosphorus, nerve agents, acetylcholinesterase, acetylcholine, oximes

Abstrak

Peranti agen saraf organofosforus (OP) sering digunakan sebagai agen racun perosak dan agen saraf dalam peperangan kimia. Pendedahan kepada OP boleh menyebabkan kematian akibat kegagalan sistem pernafasan. OP menghalang enzim asetilkolinesterase (AchE) yang berfungsi untuk mengawal penghantaran impuls saraf dan pengumpulan asetilkolin (Ach) di tapak reseptor kolinergik yang boleh menyebabkan sawan motor dan sawan epilepsi. Terdapat beberapa kaedah yang digunakan untuk merawat keracunan organofosforus seperti atropin, diazepam, dan oksim. Walaubagaimanapun, tidak ada satu pun yang berkesan untuk merawat keracunan OP. Baru-baru ini, beberapa penyelidikan telah dijalankan untuk memperkenalkan strategi baru dalam rek bentuk penawar atau antidot yang boleh merawat agen saraf OP. Oleh itu, tinjauan semula ini meringkaskan beberapa strategi baru dalam reka bentuk dan sintesis penawar atau antidot baru yang dapat mengaktifkan semula AchE yang terhalang.

Kata kunci: sebatian organofosforus, agen saraf, asetilkolinesterase, asetilkolin, antidot

Introduction

Organophosphorus (OP) are highly toxic compounds which are usually used as chemical warfare nerve agents, such as tabun, soman, sarin, and VX [1,2,3,4]. Figure 1 shows several examples of chemical warfare agents.

The OP compounds show their toxic effects by phosphorylating the active site of serine in acetylcholinesterase (AChE) [5]. It hydrolyses acetylcholine (ACh) to choline, thus terminating cholinergic neurotransmissions [6]. The subsequent irreversible inhibition of AChE results from the accumulation of ACh in both central and peripheral synapses [7], which causes several side effects, such as cholinergic crisis, respiratory distress, convulsive seizures, respiratory failure, and fatality [8].

Decades ago, the action mechanism of oximes was investigated [9]. Several indications showed that the oximes have the potency to reactivate the inhibited AChE. The inhibited AChE is reactivated by transferring the phosphoryl group from the AChE due to their large affinity and strong nucleophilicity [10,11]. During reactivation, phosphorylated oximes are formed. Some of the phosphorylated oximes appeared to be potent inhibitors of AChE [12,13]. Figure 2 shows the phosphorylated oximes which are commercially used in researches of OP treatments.

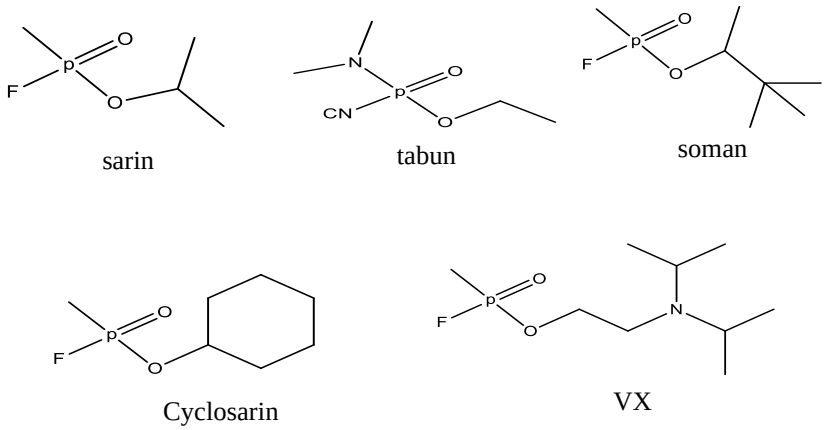
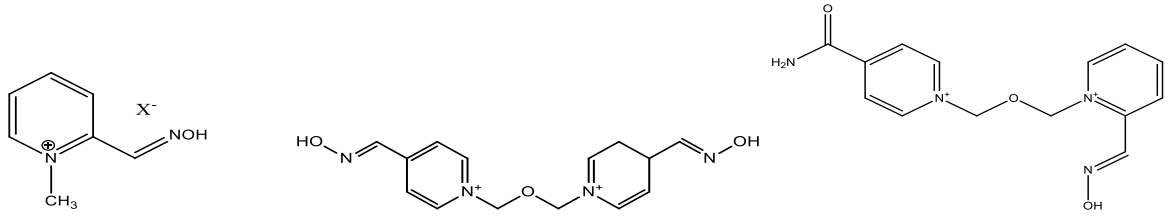
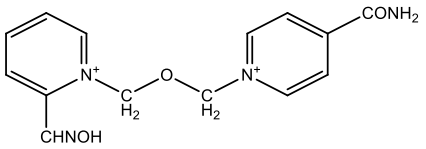
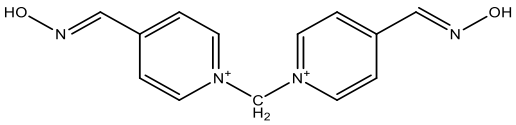


Figure 1. OP nerve agents

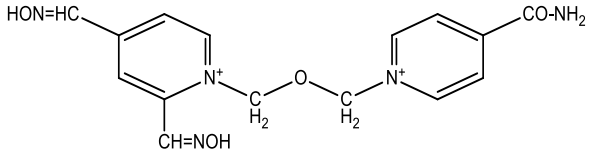




HI-6



Methoxime (MMB-4)



HLö-7

Figure 2. Structures of oximes used in the treatment of OP poisoning

Design and Synthesis of New Antidotes (Reactivators)

In this paper, several recent strategies related to the development of new oximes are discussed.

Musilek et al. [14] has prepared a new series of 26 monooxime-monocarbamoyl bispyridinium xylene-linked compounds. The compounds were evaluated on tabun-inhibited and paraoxon-inhibited AChE. The result showed that these oximes were able to reactivate the paraoxon-inhibited AChE, but not the tabun-inhibited AChE. The molecular features of K107(1), K108(2), and K203(3) shown in Figure 3 were combined to design the monooxime-monocarbamoyl xylene-linked compounds 4-29, as shown in Table 1. Firstly, based on the in-vitro study, the symmetrical xylene-linked bispyridinium bisoximes K107 and K108 have showed promising reactivation of chlorpyrifos-inhibited and tabun-inhibited AChE [15]. Though they were selected by in-vitro screening, they showed an increase in-vivo toxicity (lower LD_{50} values) compared to all commercial oximes. However, the xylene linker was still considered as a valuable molecular tool in the design of new oximes.

In 2011, Musilek et al. developed the mono-oxime bisquaternary, as shown in Figure 4a. These developed oximes consist of prop-1,3-diyl as a linker and have different moieties on a non-oxime aromatic ring. The compounds were evaluated on tabun-inhibited and paraoxon-inhibited AChE. Results revealed that these developed oximes showed promising in-vitro results, which are as good or better than existing oximes [16]. In this study, some developed oximes were found to possess better reactivation ability at a lower concentration (10 µM) than at a higher concentration (100 µM). The authors determined the inhibition data (IC_{50}) for the main compounds of interest based on suggestion by Pohanka et al. [17]. The developed oxime, as shown in Figure 4b (IC_{50}, 105 µM) was the best inhibitor. Poor inhibition on human acetylcholinesterase (hAChE) was observed at concentration of 100 µM (11%) and 10 µM (31%.). It produced 50% hAChE inhibition at the 100 µM concentration (screening concentration, 100 µM ~ IC_{50}, 105 µM). At 10 µM, the inhibition ability of this developed oxime was decreased 10-fold, had a better reactivation rate of (31%).

In the same year, Koning et al. [18] presented a concept linkage of peripheral site ligand (PSL) through a spacer to a reactivation moiety. The designed dual binding site mode of AChE contained two moieties with are A-site and P-site. The P-site contained benzhydryl-piperidine derivatives which acted as the PSL. Meanwhile, the A-site contained oxime. These two sites was conjugated via N-alkylation. The biological evaluation of the non-quaternary conjugates in Figures 5a and 5b not only demonstrate higher affinity of AChE, but also show

enhanced reactivation potency as compared to neat oxime. Besides, the conjugates were able to reactivate sarin-inhibited and VX-inhibited AChE. It was revealed that the linkage of PSL resulted in increased reactivation potency of the non-quaternary conjugates. Moreover, the obtained non-quaternary conjugates were still inefficient as compared to the current pyridinium oximes.

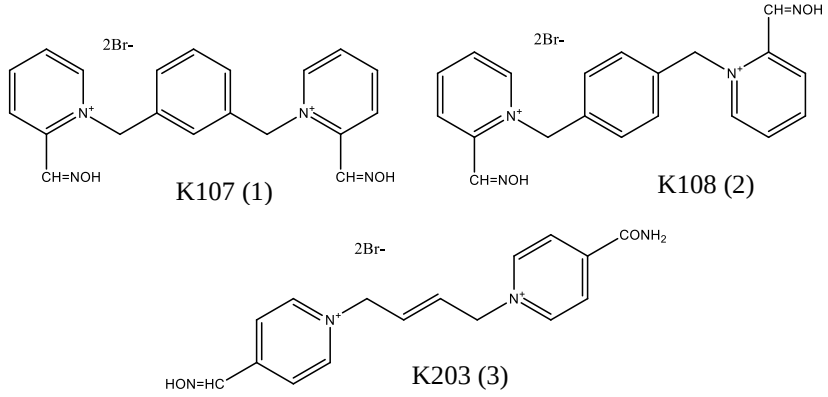


Figure 3. The molecular features of K107(1), K108(2), and K203(3)

Table 1. Structure of newly prepared compounds

Compound	A	Oxime	Carbamoyl	Compound	A	Oxime	Carbamoyl
4	O	2’	2	17	m	3’	4
5	O	2’	3	18	m	4’	2
6	O	2’	4	19	m	4’	3
7	O	3’	3	20	m	4’	4
8	O	3’	4	21	p	2’	2
9	M	4’	2	22	p	2’	3
10	M	4’	3	23	p	2’	4
11	M	4’	4	24	p	3’	2
12	M	2’	2	25	p	3’	3
13	M	2’	3	26	p	3’	4
14	M	2’	4	27	p	4’	2
15	M	3’	2	28	p	4’	3
16	M	3’	3	29	p	4’	4

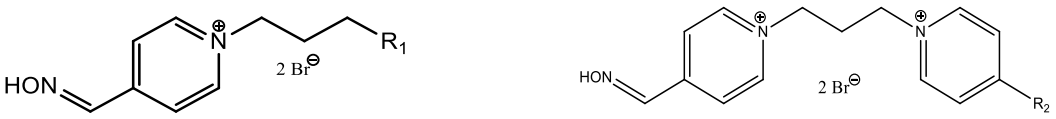


Figure 4a. Structure of the newly developed mono-oxime-bisquaternary oxime

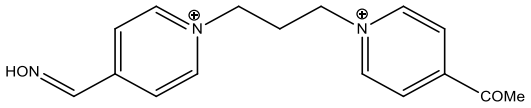
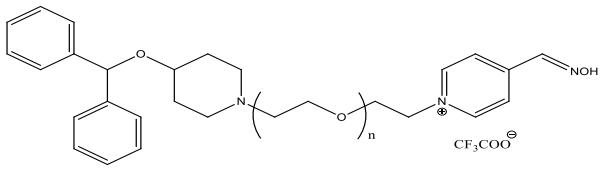
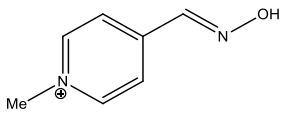


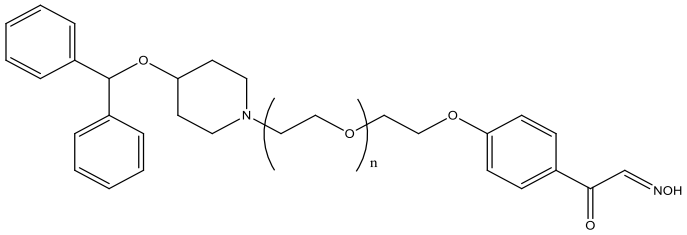
Figure 4b. Structure of the best inhibitor among the prepared mono-oxime-bisquaternary oxime





1a: n=1 (14%)
1b: n=2 (15%)
1c: n=3 (14%)

Figure 5a. Compound structure of PSL conjugates with varying spacer length and neat oxime



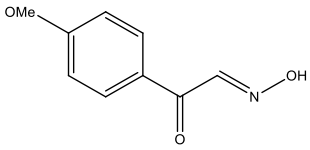


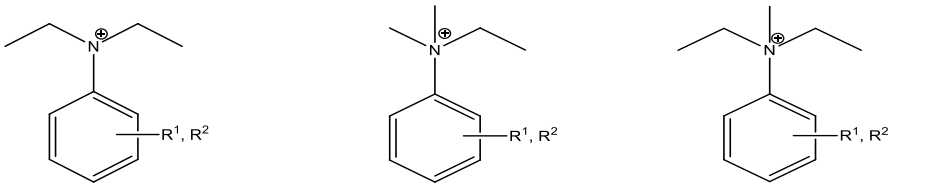
Figure 5b. Compound structure of PSL conjugates with varying spacer length and non-quaternary and neat oxime

Sit et al. [19] prepared pyridinium and non-pyridinium oximes derived from pralidoxime and edrophonium, respectively, as shown in Figure 6. The developed oximes were tested on cyclosarin-inhibited, VX-inhibited, and paraoxon-inhibited AChE. The reactivation rate was compared with pralidoxime and asoxime. These developed oximes were found to showed better reactivation potency than pralidoxime. However, none of them had better reactivation than asoxime.

A series of nine non-quaternary phenyltetra-hydroisoquinoline-pyridinaldoxime conjugates were prepared by Gillon and Renard [20]. The highest reactivation efficiency was obtained with a linker length of four or five carbon atoms attached on position 6 of the pyridine ring, as shown in Figure 7. These compounds showed difficulty to reactivate tabun-inhibited and VX-inhibited AChE, which is in contrast to that of 2-PAM. Some of them were reported to have similar or more efficiency than TMB-4. Moreover, these compounds were efficient as obidoxime and TMB-4 towards paraoxon-inhibited AChE [21]. Therefore, the compounds were evaluated in-vivo because of their general efficiency and broad-spectrum. Ideally, oximes must not be strong inhibitors of hAChE at their practical reactivation concentration. The measured IC_{50} of the eight developed oximes for hAChE are as shown in Table 2. All of these developed oximes had $IC_{50} > 100$ μM, indicating that their affinity towards hAChE is lower than their affinity towards OP-inhibited AChE. Moreover, these developed oximes did not significantly inhibit the hAChE once reactivated.

McHardy et al. [22] recognized two new chemical series of non-quaternary pyridinium oximes of cyclosarin-

inhibited AChE. The developed compounds shown in Figure 8 retained substantial reactivation activity, low affinity, and favorable physicochemical properties. These developed compounds also improved blood-brain barrier permeability and showed a good in-vivo reactivation of inhibited AChE.

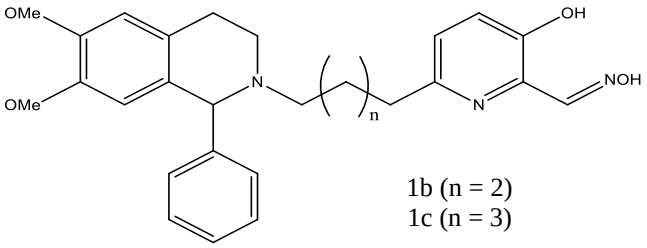


R^1 = H, OH
R^2 = CH=NOH

R^1 = H, OH, CH_2OH
R^2 = CH=NOH

R^1 = H, OH, CH_2OH
R^2 = CH=NOH

Figure 6. Structures derived from pralidoxime and endrophonium

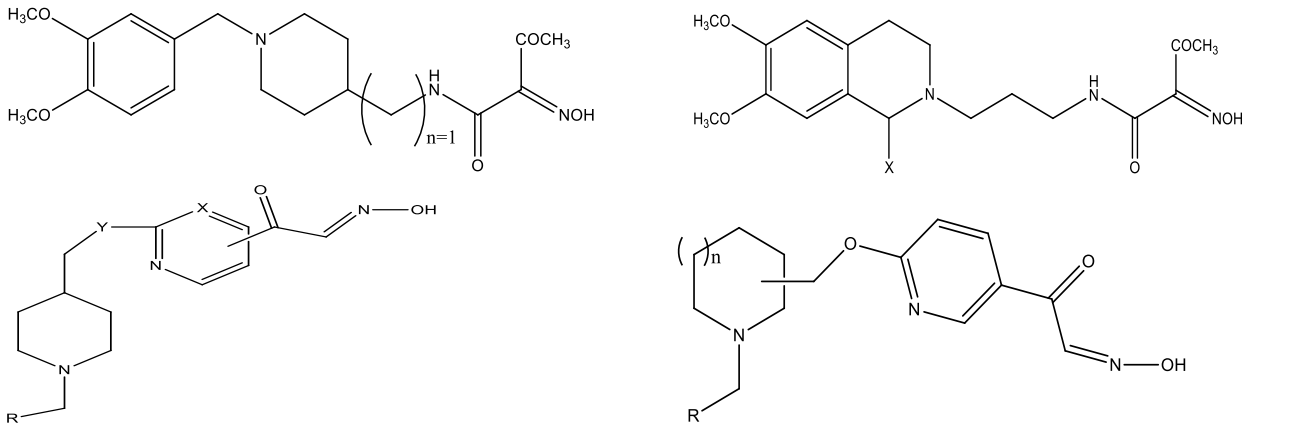


1b (n = 2)
1c (n = 3)

Figure 7. The most efficient compound of non-quaternary phenyltetrahydroisoquinoline-pyridinaldoxime conjugates

Table 2. Inhibitory activity (IC_{50}) of uncharged reactivators towards native human AChE

Reactivator	**IC_{50} (μM)**
1a	260
1b	>100
1c	>100
1d	>400
1f	>200
1h	320
1j	300
1k	>500



R = phenyl, Y = O, X = CH, 2,3-pyridine/2,5-pyridine

n = 1, R = 3,4-dimethoxyphenyl, (+/1)2-piperidine

Figure 8. New chemical series of non-quaternary pyridinium oximes of cyclosarin-inhibited AChE

In 2016, the non-quaternary oximes that are efficiently used to treat soman poisoning were designed. Dual site inhibitors strategy was used to enhance the properties of non-quaternary oximes [23]. Ortho-hydroxyl-benzaldoximes were preferred as reactivation ligands of AChE to inhibit the secondary poisoning of AChE. This developed compound was similarly linked to the oximes found in HI-6. The *in-vitro* study demonstrated that some of the resulting conjugates shown in Figure 9 have potent activity against soman-inhibited AChE. The reactivation potency of these compounds was not as good as HI-6, but showed potential for the development of more efficient centrally acting reactivators for soman poisoning due to their novel non-quaternary structures, which were forecasted to be able to cross the blood-brain barrier. IC_{50} was determined, as shown in Figure 9. It was found that these newly developed oximes were moderate or weak inhibitors of hAChE with IC_{50} greater than 100 μM, thus allowed a proper affinity to hAChE for the reactivation of inhibited AChE.

In 2017, a new family of non-quaternary oximes for inhibited hAChE was developed, as shown in Figure 10. It introduced a different PSL of AChE to achieve extra affinity. The in-vitro reactivation experiments revealed that some of the compliant conjugates presented the same or even higher ability to reactivate sarin-, VX-, or tabun-inhibited AChE, in comparison with the mono- and bis-pyridinium aldoximes. It was found that oxime **(d**) was the most efficient reactivator [24]. Besides that, these newly synthesized oximes were either moderate or weak inhibitors of hAChE with IC_{50} greater than 100 μM. This might allow a proper affinity to hAChE for the reactivation of inhibited AChE. Based on previous studies by [25-27], it was confirmed that the oxime concentration of 100 μM suitable for in-vitro reactivation experiments.

Recently, Wei et al. found that the substitution of salicylaldehyde conjugate with aminobenzamide piperidine as PSL, such as **L6M1R3**, **L6M1R5** to **L6M1R7**, **L4M1R5** to **L4M1R7** shown in Figure 11 can efficiently reactivate the sarin, VX-, and tabun-inhibited AChE. The in-vitro reactivation study of these newly developed oximes was conducted [28]. Even though they were less efficient than obidoxime, some of them showed an equal or a higher reactivation efficiency as compared to 2-PAM. In most cases, it can be concluded that the introduction of PSL could increase the oximes binding affinity towards the inhibited AChE, which results in greater reactivation potency. Most of these newly developed oximes are weak inhibitors of hAChE with IC_{50} greater than 200 μM, which might allow a proper affinity to hAChE for the reactivation of inhibited hAChE [29, 30]. Oximes **L4M1R2** displayed adequate inhibition potency against hAChE. A similar phenomenon was observed in a previous study [24], where the phenol para-linked conjugates presented higher inhibition ability of hAChE than the corresponding ortho-linked conjugates.

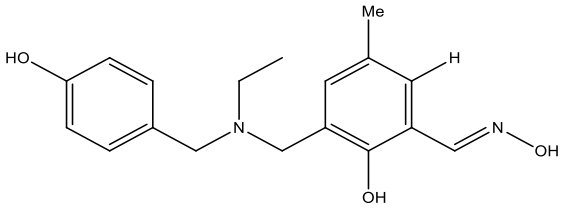
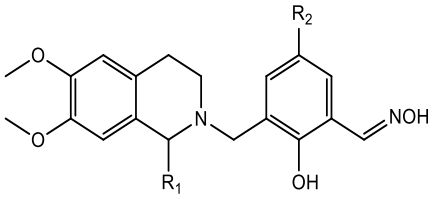
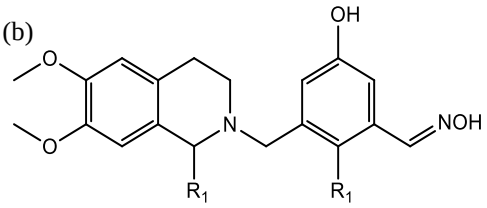


Figure 9. The most efficient structure of non-quaternary oximes to treat soman poisoning

(a)



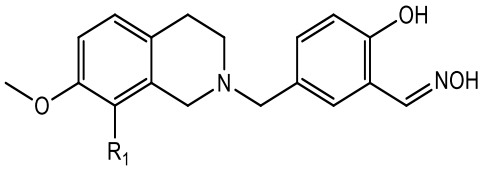
(b)



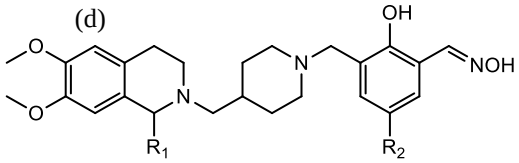
1a: R_1 = H, R_2 = H, 1b: R_1 = Ph, R_2 = H;
3a: R_1 = H, R_2 = Me, 3b: R_1 = Ph, R_2 = Me;
4a: R_1 = H, R_2 = Cl, 4b: R_1 = Ph, R_2 = Cl;
5a: R_1 = H, R_2 = Br, 5b: R_1 = Ph, R_2 = Br;
6a: R_1 = H, R_2 = F, 6b: R_1 = Ph, R_2 = F;
7a: R_1 = H, R_2 = OMe, 7b: R_1 = Ph, R_2 = OMe;

1c: R_1 = H, R_2 = H, 1d: R_1 = Ph, R_2 = H;
3c: R_1 = H, R_2 = Me, 3d: R_1 = Ph, R_2 = Me;
4c: R_1 = H, R_2 = Cl, 4d: R_1 = Ph, R_2 = Cl;
5c: R_1 = H, R_2 = Br, 5d: R_1 = Ph, R_2 = Br;
6c: R_1 = H, R_2 = F, 6d: R_1 = Ph, R_2 = F;
7c: R_1 = H, R_2 = OMe, 7d: R_1 = Ph, R_2 = OMe;

(c)



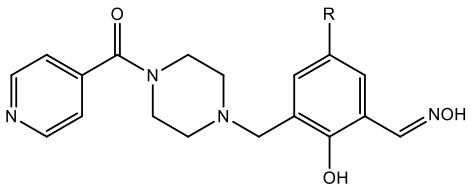
(d)



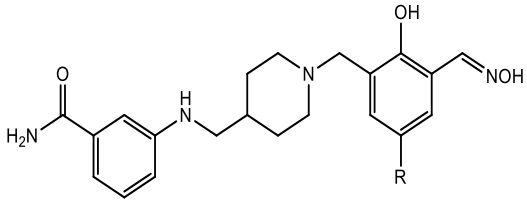
2a: R_1 = H;
2b: R_1 = Ph

2c: R_1 = H;
2d: R_1 = Ph

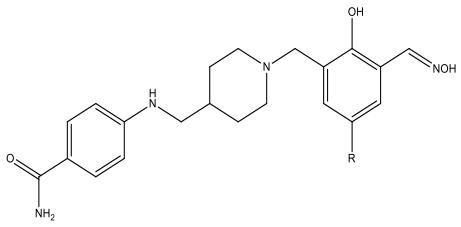
Figure 10. Family of non-quaternary developed oximes for inhibited hAChE [24]



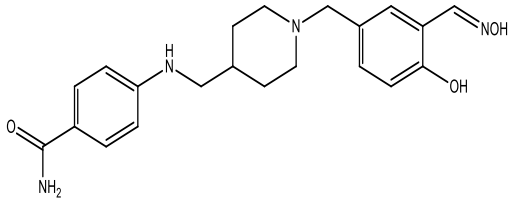
L3M2R3: R = Me, L3M2R5: R = Cl,
L2M2R6: R = Br



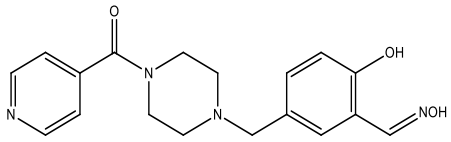
L6M1R1: R = H, L6M1R3: R = Me,
L6M1R5: R = Cl, L6M1R6: R = Br,
L6M1R7: R = F, L6M1R8: R = OMe



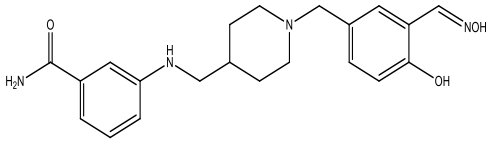
L4M1R3: R = Me, L4M1R5: R = Cl,
L4M1R6: R = Br, L4M1R7: R = F,
L4M1R8: R = OMe



L3M2R2



L6M1R2



L4M1R2

Figure 11. The designed structures of novel non-quaternary oximes

Conclusion

Regardless of the number of efforts done for the development of new oximes to treat OP poisonings, there is still no specific oxime that can be an efficient reactivator of inhibited AChE. However, several researches had reported that the introduction of PSL not only increased the affinity of oxime towards AChE, but also enhanced the reactivation potency of inhibited AChE. Throughout the year, newly developed oximes have showed different efficiencies in treating OP poisonings. Until now, scientists are continuously working to design new oximes for the treatment of OP poisonings.

Acknowledgement

The research was supported by CHEMDEF research grant (grant code: UPNM/2018/CHEMDEF/ST4).

References

1. Sharma, R., Gupta, B., Singh, N., Acharya, J. R. and Musilek, K. (2014). Development and structural modifications of cholinesterase reactivators against chemical warfare agents in last decade: A review. *Mini Reviews in Medicinal Chemistry,* 15(1): 58-72.
2. Jokanović, M. and Stojiljković, M. P. (2006). Current understanding of the application of pyridinium oximes as cholinesterase reactivators in treatment of organophosphate poisoning. *European Journal of Pharmacology*, 553 (1–3): 10-17.
3. Jokanović, M. (2012). Structure-activity relationship and efficacy of pyridinium oximes in the treatment of poisoning with organophosphorus compounds: A review of recent data. *Current Topics in Medicinal Chemistry*, 12(16): 1775-1789.
4. Faiz Norrrahim, M. N., Idayu Abdul Razak, M. A., Ahmad Shah, N. A., Kasim, H., Wan Yusoff, W. Y., Halim, N. A., and Mohd Kasim, N. A. (2020). Recent developments on oximes to improve the blood brain barrier penetration for the treatment of organophosphorus poisoning: A review. *RSC Advances*, 10(8): 4465–4489.
5. Digiovanni, C. (2017). The spectrum of human reactions to terrorist attacks with weapons of mass destruction: Early management considerations. *Prehospital Disaster Medicine,* 18(13): 253-257.
6. Luo, C., Tong, M., Maxwell, D. M. and Saxena, A. (2008). Comparison of oxime reactivation and aging of nerve agent-inhibited monkey and human acetylcholinesterases. *Chemico-Biological Interactions*, 175 (1–3): 261-266.

7. Soukup, O., Krusek, J. and Oz, M. (2011). Oxime reactivators and their *in vivo* and *in vitro* effects on nicotinic receptors. *Physiological Research,* 60(4): 679-86.
8. Marrs, T. C. (1993). Organophosphate poisoning. *Pharmacology and Therapeutics,* 58: 51-66.
9. Musilek, K., Dolezal, M., Gunn-moore, F. and Kuca, K. (2009). Design, evaluation and structure-activity relationship studies of the AChE reactivators against organophosphorus pesticides. *Medicinal Research Reviews*, 31 (4): 548-575.
10. Worek, F., Thiermann, H. and Wille, T. (2016). Oximes in organophosphate poisoning: 60 years of hope and despair. *Chemico-Biological Interactions*, 259: 93-98.
11. Maxwell, D. M., Koplovitz, I., Worek, F. and Sweeney, R. E. (2008). A structure-activity analysis of the variation in oxime efficacy against nerve agents. *Toxicology and Applied Pharmacology*, 231(2): 157-164.
12. Ashani, Y., Bhattacharjee, A. K., Leader, H., Saxena, A. and Doctor, B. P. (2003). Inhibition of cholinesterases with cationic phosphonyl oximes highlights distinctive properties of the charged pyridine groups of quaternary oxime reactivators. *Biochemical Pharmacology*, 66(2): 191-202.
13. Worek, F., Eyer, P., Aurbek, N., Szinicz, L. and Thiermann, H. (2007). Recent advances in evaluation of oxime efficacy in nerve agent poisoning by *in vitro* analysis. *Toxicology and Applied Pharmacology*, 219 (2–3): 226-234.
14. Musilek, K., Holas, O., Misik, J., Pohanka, M. and Novotny, L. (2010). Monooxime-monocarbamoyl bispyridinium xylene-linked reactivators of acetylcholinesterase-synthesis, *in vitro* and toxicity evaluation and docking studies. *ChemMedChem,* 5: 247-254.
15. Kuca, K., Karasova, J. and Musilek, K. (2007). Development of new reactivators of tabun inhibited acetylcholinesterase and the evaluation of their efficacy by in vitro and in vivo methods. In Defence against the Effects of Chemical Hazards: Toxicology, Diagnosis and Medical Countermeasures, 17: pp. 1-12.
16. Musilek, K., Komloova, M., Holas, O., Horova, A., Pohanka, M., Gunn-Moore, F. and Kuca, K. (2011). Mono-oxime bisquaternary acetylcholinesterase reactivators with prop-1,3-diyl linkage-Preparation, *in vitro* screening and molecular docking. *Bioorganic and Medicinal Chemistry*, 19 (2): 754-762.
17. Pohanka, M., Jun, D. and Kuca, K. (2008). Improvement of acetylcholinesterase-based assay for organophosphates in way of identification by reactivators. *Talanta*, 77 (1): 451-454.
18. Koning, M. C., Joosen, M. J. A., Noort, D., van Zuylen, A., and Tromp, M. C. (2011). Peripheral site ligand–oxime conjugates: A novel concept towards reactivation of nerve agent-inhibited human acetylcholinesterase. *Bioorganic & Medicinal Chemistry*, 19(1): 588-594.
19. Sit, R. K., Radić, Z., Gerardi, V., Garcia, E., Zhang, L., Katalinic, M., Amitai, G., Kovarik, Z., Fokin, V. V., Sharpless, K. B. and Taylor, P. (2011). New structural scaffolds for centrally acting oxime reactivators of phosphylated cholinesterases. *The Journal of Biological Chemistry.* 286(22): 19422-19430.
20. Gillon, E. and Renard, P. (2012). Phenyltetrahydroisoquinoline-pyridinaldoxime conjugates as efficient uncharged reactivators for the dephosphylation of inhibited human acetylcholinesterase. *Journal of Medicinal Chemistry,* 55: 10791-10795.
21. Worek, F., Wille, T., Koller, M. and Thiermann, H. (2012). Reactivation kinetics of a series of related bispyridinium oximes with organophosphate-inhibited human acetylcholinesterase Structure-activity relationships. *Biochemical Pharmacology*, 83(12): 1700-1706.
22. McHardy, S. F., Bohmann, J. A., Corbett, M. R., Campos, B., Tidwell, M. W., Thompson, P. M. and McDonough, J. (2014). Design, synthesis, and characterization of novel, nonquaternary reactivators of GF-inhibited human acetylcholinesterase. *Bioorganic and Medicinal Chemistry Letters*, 24(7): 1711-1714.
23. Wei, Z., Liu, Y., Wang, Y., Li, W., Zhou, X., Zhao, J. and Li, S. (2016). Novel nonquaternary reactivators showing reactivation efficiency for soman-inhibited human acetylcholinesterase. *Toxicology Letters*, 246: 1-6.

24. Wei, Z., Liu, Y. Q, Wang, S. zheng, Yao, L., Nie, H. F., Wang, Y. and Li, S. (2017). Conjugates of salicylaldoximes and peripheral site ligands: Novel efficient nonquaternary reactivators for nerve agent-inhibited acetylcholinesterase. *Bioorganic and Medicinal Chemistry*, 25(16): 4497-4505.
25. Ralph, E. C., Zhang, J. and Cashman, J. R. (2011). Amidine-oximes: Reactivators for organophosphate exposure. *Journal of Medicinal Chemistry,* 54: 3319-3330.
26. Kalisiak, J., Ralph, E. C. and Cashman, J. R. (2012). Nonquaternary reactivators for organophosphate-inhibited cholinesterases. *Journal of Medicinal Chemistry*, 55(1): 465-474.
27. Koning, M. C., Grol, M. Van. and Noort, D. (2011). Peripheral site ligand conjugation to a non-quaternary oxime enhances reactivation of nerve agent-inhibited human acetylcholinesterase. *Toxicology Letters*, 206 (1): 54-59.
28. Wei, Z., Bi, H., Liu, Y., Nie, H., Yao, L. and Wang, S. (2018). Bioorganic chemistry design, synthesis and evaluation of new classes of nonquaternary reactivators for acetylcholinesterase inhibited by organophosphates. *Bioorganic Chemistry*, 81: 681-688.
29. Mercey, G., Verdelet, T., Saint-André, G., Gillon, E., Wagner, A., Baati, R. and Renard, P. Y. (2011). First efficient uncharged reactivators for the dephosphylation of poisoned human acetylcholinesterase. *Chemical Communications*, 47(18): 5295–5297.
30. Mercey, G., Verdelet, T., Renou, J., Kliachyna, M., Baati, R., Nachon, F. and Renard, P. Y. (2012). Reactivators of acetylcholinesterase inhibited by organophosphorus nerve agents. *Accounts of Chemical Research*, 45(5): 756-766.

Malaysian Journal of Analytical Sciences (MJAS)
Published by Malaysian Analytical Sciences Society

STRUCTURAL AND OPTICAL PROPERTIES OF DYSPROSIUM AND EUROPIUM CO-DOPED WITH YTTRIUM ALUMINIUM GARNET NANOCRYSTALLINE POWDERS PREPARED BY COMBUSTION SYNTHESIS

(Sifat-sifat Struktural dan Optikal daripada Serbuk Nanokristal Dysprosium dan Europium Di-ko-dopkan dengan Yattrium Aluminium Garnet yang Disediakan Secara Sintesis Pembakaran)

Abd Rahman Tamuri*, Nor Ezzaty Ahmad, Nurliyana Nabilah Ghazali, Rosli Husin

Physics Department, Faculty of Science,
Universiti Teknologi Malaysia, 81310 Johor Bahru, Malaysia.

**Corresponding author: rahmantamuri@utm.my*

Received: 13 November 2019; Accepted: 3 September 2020; Published: 12 October 2020

Abstract

This paper presents the study on synthesized yttrium aluminum garnet (YAG), europium-doped YAG (YAG: Eu), and europium and dysprosium co-doped YAG (YAG: Eu, Dy) phosphors prepared by combustion synthesis (CS) using a mixture of fuel (urea). The effects of Eu^{3+} and Dy^{3+} ions concentration and annealing temperature were analysed using by X-ray diffraction (XRD) and photoluminescence (PL). YAG nano-crystalline powders were calcined at a temperature range of 900 ℃ to 1200 ℃ for 4 hours. Europium and dysprosium were added in different concentrations in the range of 0.1 at.% to 1.0 at.% to the coarsened pure YAG particles to understand its influences on the optical properties and sintered microstructures. The doping of YAG: Eu and co-doped YAG: Eu, Dy was calcined at 1100 ℃ for 4 hours. X-ray diffraction results showed the phosphors are single-phase YAG with crystalline sizes ranging from 30 to 40 nm. The room temperature photoluminescence results confirmed the introduction of the ion in the host lattice and its optical activation for all the Eu3+ and Dy^{3+} ions concentrations. The CIE1931 color coordinates showed the sample's emission laid in the near red region for Eu^{3+} ion concentration and near white region for the addition of Eu^{3+} and Dy^{3+} ion concentration. Eu^{3+} ion concentration of 1.0 at.% achieved the highest emission spectra intensity while the highest emission spectra was achieved at 0.5 at.% for Dy^{3+} ion concentration and the ion luminescence were preferentially excited with 395 nm for YAG: Eu while, 353 nm for YAG: Eu, Dy wavelength photons.

Keywords: YAG: Eu, Dy, europium, dysprosium, combustion synthesis, emission, urea

Abstrak

Kertas kerja ini membentangkan kajian hasil sintesis yttrium aluminium garnet (YAG), YAG Europium-doped (YAG: Eu) dan europium dan dysprosium bersama-sama doped YAG (YAG: Eu, Dy) fosfor yang disediakan oleh sintesis pembakaran (CS) menggunakan campuran bahan api (urea). Kesan kepekatan Eu^{3+} dan Dy^{3+} ion dan suhu kalsinasi telah dikaji oleh belauan sinar-X (XRD) dan fotoluminesens (PL). Serbuk YAG nano-kristal telah dikalsinasi dalam julat suhu 900 ℃ hingga 1200 ℃ selama 4 jam. Europium dan dysprosium ditambah dengan kepekatan yang berlainan dalam julat 0.1% hingga 1.0% kepada zarah YAG tulen untuk memahami pengaruhnya terhadap sifat optikal dan mikrostruktur sintered. Dop YAG: Eu dan ko-dop YAG: Eu, Dy telah dikalsinasi pada suhu 1100 ℃ untuk 4 jam. Keputusan belauan sinar-X menunjukkan bahawa fosfor adalah berfasa tunggal

YAG dengan saiz kristal antara 30 nm hingga 40 nm. Hasil fotoluminensi pada suhu bilik mengesahkan pengenalan ion dalam kekisi tuan rumah dan pengaktifan optikal untuk semua kepekatan Eu^{3+} dan Dy^{3+} ions. Koordinat warna CIE1931 menunjukkan bahawa spektrum pancaran sampel terletak di kawasan merah berhampiran untuk kepekatan Eu^{3+} ion dan berhampiran kawasan putih untuk penambahan kepekatan Eu^{3+} dan Dy^{3+} ion. Keamatan spektrum pancaran tertinggi dicapai untuk kepekatan Eu^{3+} ion pada 1.0 % sementara kepekatan 0.5% pada ion Dy^{3+} dan pengujaan lebih sesuai pada panjang gelombang 395 nm untuk YAG: Eu manakala, 353 nm untuk YAG: Eu, Dy.

Kata kunci: YAG: Eu, Dy, europium, dysprosium, sintesis pembakaran, pancaran, urea

Introduction

Yttrium aluminum garnet, $Y_3Al_5O_{12}$ (YAG) materials have received huge interest in research for their wide range of applications found in fluorescent and solid-state lasers [1]. A conventional route has been introduced in obtaining YAG by combustion via self-propagating high temperature (SHS) for a fast and efficient productivity in various materials [2]. Good conductivity, high purity of products, reduced cost and increased materials size are some of the advantages that are contributed by SHS. Recently, attention has shifted to conventional light sources by using a white light-emitting diode (w-LED) for its high luminescent efficiency and energy-saving characteristics where the Dy^{3+} transition bands emit white light with small red emission [3]. Thus, the Eu^{3+} acts as efficient activators that contribute to red emission when occupied with the host. Previously, the solid-state method and the use of high temperature was used to synthesize pure yttrium aluminum garnets. Heat treatment below 1600°C was required to distinguish between YAP and YAM phases [4]. Furthermore, other various conventional routes were used such as sol-gel, co-precipitation, hydrothermal synthesis, and combustion synthesis [5-11].

The particle size and irregular morphology were produced with high temperatures that reduce its luminescent properties. Thus, by reducing particle sizes, it will increase the resolution of the material. The combustion synthesis also helps in good crystallinity and enhances the efficiency of luminescence with evading absorbed ligands. During the past decades, the novel and enhanced properties of nanostructured materials have attracted considerable attention because of their interesting chemical and physical properties. The nanostructure materials may have applications in the development of a novel type of luminescent material for display applications. In particular, the Mn-doped ZnS nanocrystal can yield both high luminescent efficiencies and lifetime shortening [12-17]. This greatly promotes the development of rare-earth-doped nano-phosphors. YAG: Eu^{3+} is a red phosphor widely used in optical display and lighting applications. Furthermore, YAG: Eu^{3+} can be used in fluorescence thermometry because its fluorescence properties vary with temperature [16].

Hence, the purpose of this paper is to report on the formation of YAG phosphors by low-temperature combustion synthesis and the influence of concentration in $Eu^{3+}$and Dy^{3+} doping ions on the YAG. In this work, europium doped YAG that exhibited orange-red emission was synthesized and the effect of Dy^{3+} co-doping on structural and luminescent properties will be studied. The results revealed that this technological approach enables us to achieve a stable single-phase structure of garnet and orange-red emission of YAG: Eu can be efficiently improved by incorporating a small amount of Dy^{3+} ions.

Materials and Methods

Study area

The starting material, Y_2O_3(99.99%), $Al(NO_3)_3.9H2O$, and CH_4N_2O (urea) used as a fuel by Sigma Aldrich and europium were added with a concentration between 0.1 to 1.0 mol%, while dysprosium, used as a co-dopant, was added with a concentration between 0.1 to 0.5 mol% using redox mixtures of strict stoichiometric amounts of metal oxides and urea, and initiates the combustion at 500 °C. The Y_2O_3, Eu_2O_3, Dy_2O_3 powders were converted into the corresponding nitrate by dissolving in 2.5 M of nitric acid. 15 g of aluminum nitrate,

$Al(NO_3)_3.9H_2O$, 9.6 g of urea, CH_4N_2O, $Y(NO_3)_3.6H_2O$, $Eu(NO_3)_3.6H_2O$, $Dy(NO_3)_3.6H_2O$, and 30 mL distilled water were mixed using a magnetic stirrer for 30 minutes until a colorless aqueous solution was formed. The solution was transferred into a 200 mL alumina crucible and kept in a furnace that has been pre-heated at 500 °C. The removal of water took place before combustion initiated until it formed a voluminous fluffy mass and taken out immediately. The fluffy mass was cooled for 30 minutes at room temperature, then transferred into a mortar. The fine powder was obtained from grinding and sieving. 2 g for each sample powders were transferred into a 10 mL alumina crucible and kept at 1100 °C for 4 hours for the calcination process. The powders were taken out and left for the cooling process for 30 minutes before grinding the powders that were then weighed and kept in zipped packaging plastic bags.

The phase of the samples was determined by using X-ray Diffraction (XRD) and the photoluminescence measurement was recorded by a Horiba FluoroMax-4 Spectroflourometer of which offered extended performance with detection of emission spectra of up to 1700 nm. X-ray profile analysis is a simple and powerful tool to estimate the crystallite size and lattice strain [18]. Among the available methods to estimate the crystallite size and lattice strain are the pseudoVoigt functions, Rietveld refinement, and Warren-Averbach analysis [19-22]. Williamson-Hall (W-H) analysis is a simplified integral breadth method where both size-induced and strain-induced broadening are deconvoluted by considering the peak width as a function of 2θ [23].

The International Commission on Illumination (CIE) parameters such as color coordinates (x, y) were calculated to know the photometric characteristics of the prepared samples [24, 25]. The CIE coordinates were estimated using a PL emission spectrum. The value of CIE parameter of the phosphor is highly useful for the production of artificial white light which is similar to the natural white light owing to its better spectral overlap in white LEDs and solid-state display applications.

Results and Discussion

X-ray analysis

Figure 1 represents the XRD diffraction patterns of YAG, YAG: Eu and YAG: Eu, Dy calcined at 1100 °C for 4 hours. It can be observed that all the diffraction peaks were matched well with the JCPDS No. 33-0040, the XRD maximum was observed at 2θ ~ 33.33°. There is a slight shift in the diffraction pattern for YAG: Eu and YAG: Eu, Dy towards a high angle compared to pure YAG. The lattice parameter was calculated as YAG (12.0183 Å), YAG: Eu (11.976 Å), and YAG: Eu, Dy (12.0148 Å) using the combined formula of Bragg and the interplanar distance of the cubic structure. The lattice parameter of the europium doped YAG and dysprosium co-doped YAG was higher than the pure YAG crystal. The radius of Eu^{3+} ion (0.950 Å) and Dy^{3+} ion (0.908 Å) is higher than Y^{3+} ion (0.893 Å) ions. Factors that cause a decrease in lattice parameter are due to the contribution of the stress, strain, dislocation and defects or irradiation effects that alter the lattice parameter [24]. But, Eu^{3+} and Dy^{3+} ions are successfully substituted Y^{3+} ion that contain small amounts of Eu^{3+} and Dy^{3+} ions that did not change the crystalline structure but broadened by increasing of the crystallite size. As the dopants were introduced to pure YAG phosphor, the size increased thus forming a diffraction pattern comparable to pure YAG.

To simplify the method of studying the changes of the strain and size the W-H plot and size strain plot method can be used. This is where the size-induced and strain-induced broadening contributes to the peak as a function of 2θ. The peak width derived from crystallite size varies as 1/cos θ, whereas the strain varies as tan θ. Figure 2 shows the W-H plots drawn with 4 sin θ along the x-axis and β cos θ along the y-axis for sample YAG pure, YAG:Eu and YAG:Eu,Dy. The value of the slope and the y-intercept of the fitted line represent the strain and the crystallite size of the samples as shown in Table 1. It was found that the crystallize size is bigger compared to the crystallite size calculated from Scherrer's equation. The strain was assumed to be uniform in all crystallographic directions, which takes into consideration the isotropic nature of the crystal, where the material properties are independent of the direction

along which they are measured. The Scherrer's equation and W-H analysis were in agreement for this report.

Photoluminescence

Figure 3 presents the emission spectrum of the nanopowders YAG: Eu with 0.1, 0.5, 1.0 at.%. The spectrum consists of bands that belong to the characteristic emission of Eu^{3+} bands that correspond to the transitions from the excited state $^5D_0$ at 395 nm. The stark component of the $^5D_0 \rightarrow {}^7F_1$ transition is observed at (590, 595 nm). The peaks corresponding to the $^5D_0 \rightarrow {}^7F_4$ (695, 709 nm), $^5D_0 \rightarrow {}^7F_3$ (649, 655 nm), and $^5D_0 \rightarrow {}^7F_2$ (609, 629 nm) transition are weaker. It is worth mentioning that all the above-listed transitions are the characteristics of a well in YAG: Eu that is in agreement with Kumar, M et al. [4]. According to the selection rules, magnetic dipole transition $^5D_0 \rightarrow {}^7F_1$ is allowed while electric dipole transition $^5D_0 \rightarrow {}^7F_2$ (609, 629 nm) is forbidden. Thus, the emission intensity of the transition $^5D_0 \rightarrow {}^7F_1$ is higher than the transition $^5D_0 \rightarrow {}^7F_2$. The spectral intensity increased proportionally to the concentration of Eu^{3+}.

Figure 4 shows the luminescence spectra and transition energy levels of YAG:Eu phosphors co-doped with Dy^{3+} ions ranging from 450 nm to 680 nm and excitation wavelength of 353 nm. The prominent emission peaks were observed at blue emission (483 nm) and yellow emission (582 nm) [4]. The transition corresponded to $^4D_{9/2} \rightarrow {}^6H_{15/2}$ (483 nm), $^4D_{9/2} \rightarrow {}^6H_{15/2}$ (582 nm), $^4D_{9/2} \rightarrow {}^7F_1$ (589 nm) and $^4D_{9/2} \rightarrow {}^7F_2$ (608 and 629 nm). Six emission bands were observed from the results such as 596 nm, 610 nm, 630 nm, 649 nm and 710 nm which corresponds to the emission bands and transition of Eu^{3+} in Figure 3(a). Due to the strong influence of the environment, Dy^{3+} ions contributed to the blue and yellow emission while Eu^{3+} enhanced the red emission of the phosphors. The spectral intensity of 1.0 mol at % Dy^{3+} is the highest compared to 0.5 and 0.1 mol at.% thus, these characteristics satisfy the requirement for YAG phosphors for white light-emitting diode (w-LED) applications.

The chromaticity coordinates for ideal white light is located at (0.313, 0.329) [9]. Figure 5(a) shows the Commission International de I'Echairage (CIE)1931 chromaticity coordinates for the YAG:Eu, *y*Dy (y = 0.1, 0.3 and 0.5 mol%) phosphors excited at 353 nm and Figure 5(b) the colour coordinates of 0.1 at.% YAG:Eu,Dy phosphor (x,y) = (0.310, 0.353) are close to the ideal white emission colour. This result satisfies the requirement for YAG phosphors for white light-emitting diode (w-LED) applications.

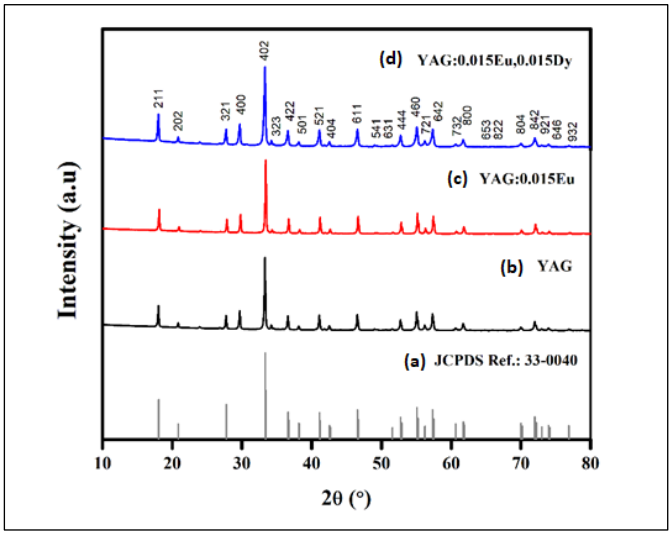


Figure 1. XRD pattern of selected (a) JCPDS Ref.:33-0040, (b) YAG pure, (c) YAG:0.015Eu and (d) YAG:0.015Eu, 0.015Dy. As dopants are introduced, pattern is comparable to pure YAG

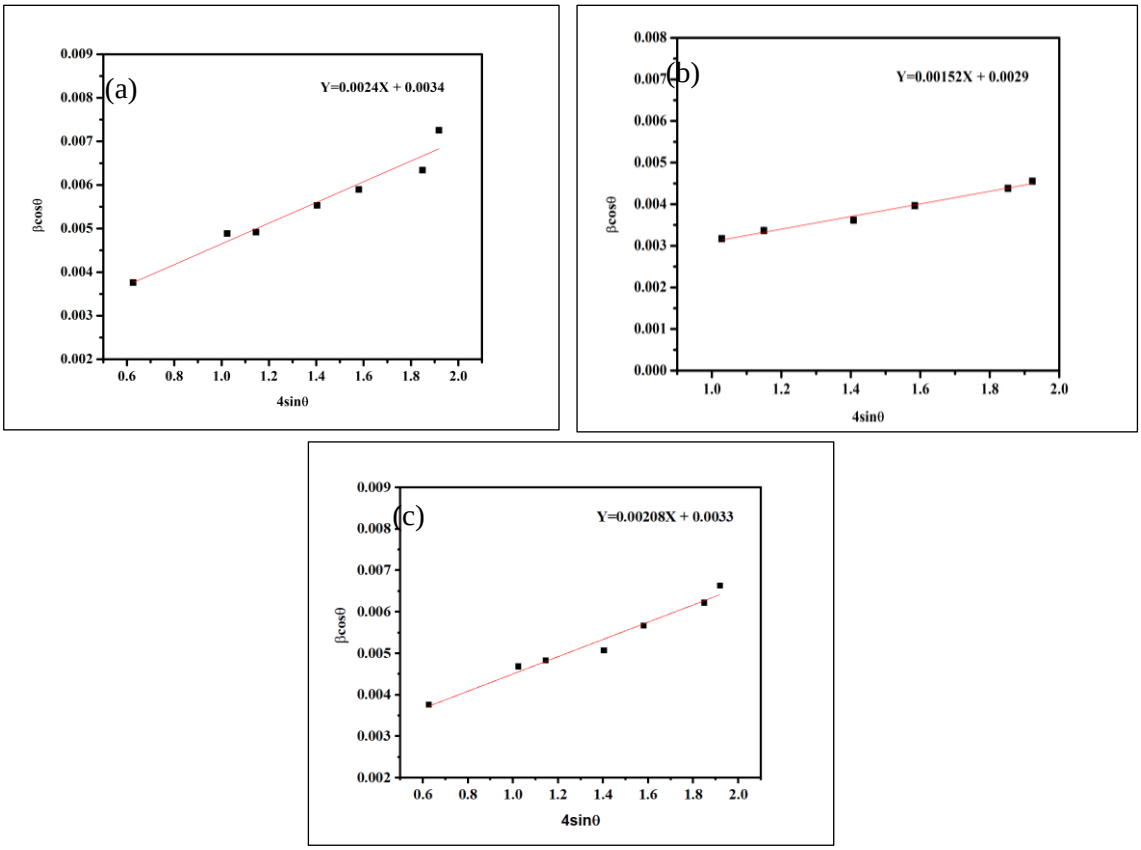
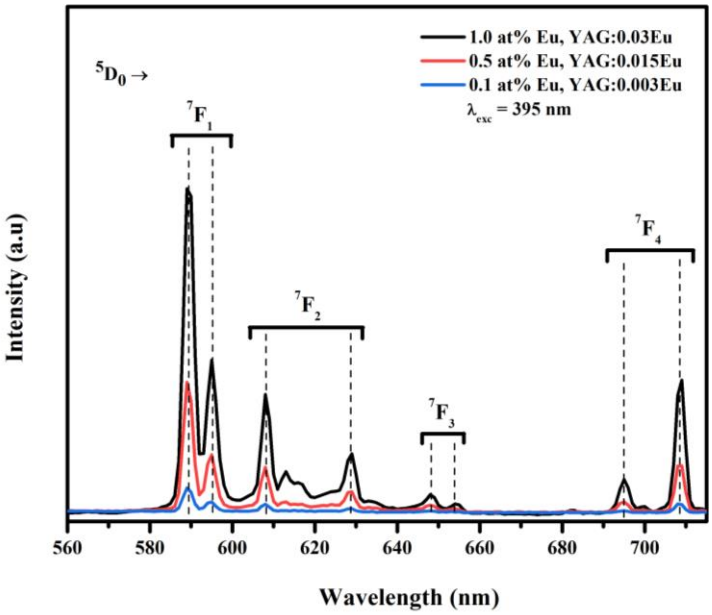


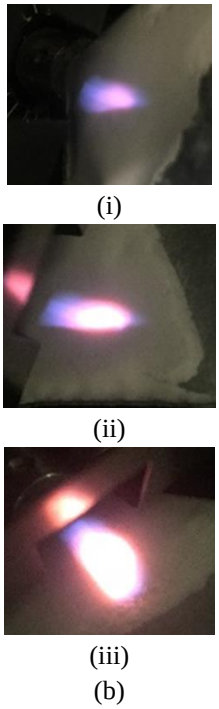
Figure 2. The Williamson Hall plot (a) YAG phosphors, (b) 0.5 mol % for YAG: Eu (c) 0.5 mol% for YAG: Eu, Dy

Table 1. Crystallite size of YAG, YAG: Eu and YAG: Eu, Dy

Crystallite size* (nm) (Scherrer's method)	**Compound**	**Crystallite size* (nm) (W-H method)**	**Microstrain ε**
38	YAG	40.3	2.40
40	YAG:0.015Eu	47.3	1.52
30	YAG:0.015Eu,0.015Dy	41.5	2.08



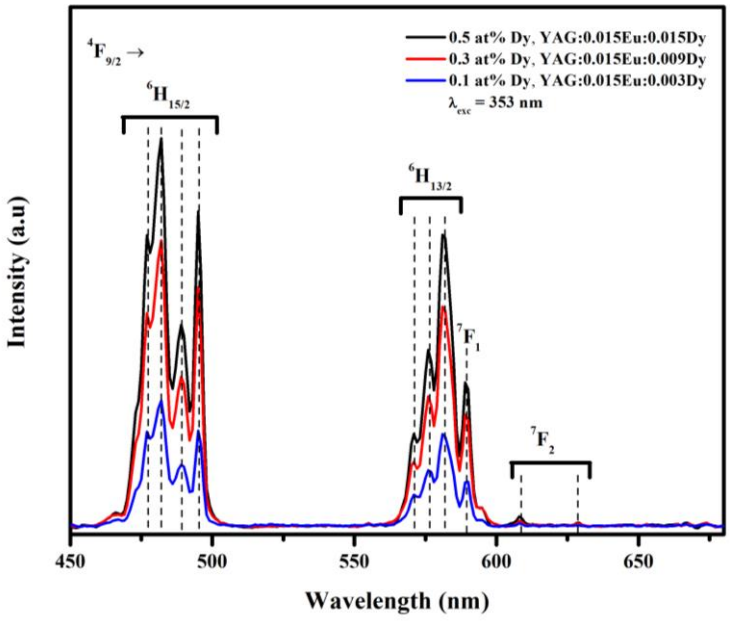
(a)



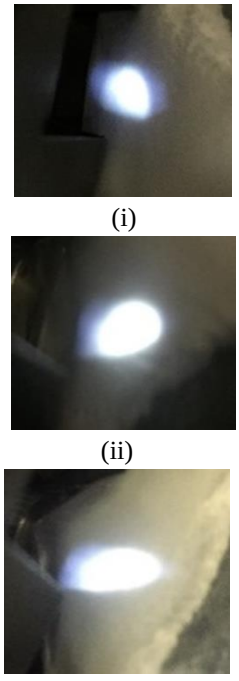
(i) (ii) (iii)

(b)

Figure 3. (a) The PL emission spectra of samples YAG:Eu with 0.1,0.5,1.0 mol % concentration excited at 395 nm. (b) The colour emitted by the YAG:Eu sample of (i) 0.1 %, (ii) 0.5 % and (iii) 1.0 % respectively



(a)



(i) (ii) (iii)

(b)

Figure 4. (a) YAG:Eu,Dy with 0.5 mol % of europium and 0.1, 0.3, 0.5% concentration of dysprosium, excited at 353 nm. (b) The colour emitted by the YAG:Eu,Dy sample of (i) 0.1 %, (ii) 0.3 %, and (iii) 0.5 % respectively

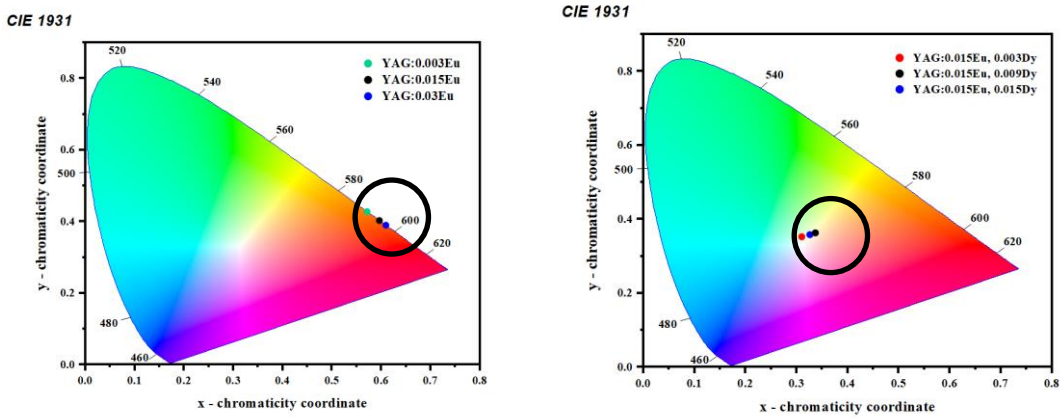


Figure 5. The CIE coordinates of (a) YAG: Eu with 0.1, 0.5, 1.0 mol% concentration excited at 395 nm (b) YAG: Eu, Dy with 0.5 mol% of europium and 0.1, 0.3, 0.5% concentration of dysprosium, excited at 353 nm

Conclusion

The pure YAG and doped YAG: Eu and YAG: Eu, Dy with different concentrations have been successfully synthesised by using the combustion synthesis method. The sample size of 40 nm was confirmed using Scherrer's method and W-H method. The Eu^{3+} emitted red light, thus proving the fact that Eu^{3+} ions show promising red light emission. However, a combination of Eu^{3+} and Dy^{3+} in YAG gave white emission. From the chromaticity diagram of YAG: Eu, 1.0 mol% of Eu^{3+} ions were located at the reddest region (0.60916, 0.39032) while for Dy^{3+} ions, 0.1, 0.3, and 0.5 mol% concentrations were used. The emission spectra and transition energy were observed within the range of 450 nm and 680 nm. The excitation wavelength was set to 353 nm. Moreover, the chromaticity shows that 0.1 mol% of Dy^{3+} ions were nearest to the ideal white light value which is (0.31002, 0.35291).

Acknowledgment

The authors gratefully acknowledge the Ministry of Education (MOE) of Malaysia and Universiti Teknologi Malaysia for providing financial support under Grant No. Q.J1300000.2526.10H20. We would also like to extend our gratitude to the Faculty of Science, Universiti Teknologi Malaysia for providing experimental facilities for this research.

References

1. Pan, Y. X., Wang, W., Liu, G. K., Skanthakumar, S., Rosenberg, R. A., Guo, X. Z. and Li, K. K. (2009). Correlation between structure variation and luminescence redshift in YAG:Ce. *Journal of Alloys and Compounds,* 488(2): 638-642.
2. Jiang, J., Wang, P., He, W., Chen, W., Zhuang, H., Cheng, Y. and Yan, D. (2004). Self-propagating high-temperature synthesis of α-SiAlON doped by RE (RE=Eu,Pr,Ce) and codoped by RE and Yttrium. *Journal of American Ceramic Society*, 87(4): 703-705.
3. Chong, J. Y., Zhang, Y., Wagner, B. K. and Kang, Z. (2013). Co-precipitation synthesis of YAG:Dy nanophosphor and its thermometric properties. *Journal of Alloys and Compounds*, 581: 484-487.
4. Kumar, K. S., Lou, C., Xie, Y., Hu, L., Gowri, A.M., Xiao, D., Ye, H., Tang, L., and Didier, P. (2017). Energy transfer in co- and tri- doped $Y_3Al_5O_{12}$ phosphors. *Journal of Rare Earths*, 35(8): 775-782.
5. Mithlesh, K., Mohapatra, M., and Natarajan, V. (2014). Luminescence characteristics of blue emitting $ZnAl_2O_4$:Ce nanophosphors. *Journal of Luminescence*, 149: 118-124.

6. Kurrey, M. S., Tiwari, A., Khokhar, M. S. K., Kher, R. S. and Dhoble, S.J. (2015). Thermoluminescence investigations of sol–gel derived and -irradiated rare earth (Eu and Nd) doped YAG nanophosphors. *Journal of Luminescence*, 164: 94-98.
7. Ya-Wei, L. and Su-Hsen, W. (2018). Fabrication and performance assessment of coprecipitation-based YAG:Ce nanopowders for white LEDs. *Microelectronic Engineering,* 199: 24-30.
8. Hora, D. A., Andrade, A. B., Ferreira, N. S., Teixeira, V. C., and dos S. Rezende, M.V. (2016). X-ray excited optical luminescence of Eu-doped YAG nanophosphors produced via glucose sol–gel route. *Ceramics International,* 42: 10516-10519.
9. Raju, G. S. R., Park, J. Y., Jung, H. C., Hyun, K, Y., Byung, K. M., Jung, H. J., and Jung, H. K. (2009). Synthesis and luminescent properties of low concentration Dy^{3+}:GAP nanophosphors. *Optical Materials,* 31: 1210-1214.
10. Kolesnikov, I. E., Tolstikova, D. V., Kurochkin, A. V., Manshina, A. A. and Mikhailov, M. D. (2014). Eu^{3+} concentration effect on luminescence properties of YAG:Eu^{3+} nanoparticles. *Optical Materials,* 37: 306-310.
11. Guodong, X., Shengming, Z., Junji, Z., Sumei, W., Yanmei, L. and Jun, X. (2015). Sol–gel combustion synthesis and luminescent properties of nanocrystalline YAG:Eu^{3+} phosphors. *Journal of Crystal Growth,* 283: 257-262.
12. Bhargava, R. N., Gallagher, D., Hong, X. and Nurmikko, A. (1994). Optical properties of manganese-doped nanocrystals of ZnS. *Physics Review Letters,* 72(3): 416-419.
13. Zhang, W. P., Xi, P. B., Duan, C. K., Yan, K., Yi, M., Lou, L. R., Xia, S. D. and Krupa, J. C. (1998). Preparation and size effect on concentration quenching of nanocrystalline Y_2SiO_5: Eu. *Chemistry Physics Letters*, 292(1-2):133-136.
14. Allison, S. W. and Gillie, G. T. (1997). Remote thermometry with thermographic phosphors. *Review of Scientific Instruments,* 68(7): 2615-2650.
15. Mu, Z., Hu, Y., Wang, Yi., Wu, H., Fu, C., and Kang, F. (2011). Effect of substitution of Dy^{3+} on structure and luminescence properties of $Y_3Al_5O_{12}$:Ce^{3+}. *Acta Optica Sinica*, 31(2): 0216007.
16. Lojpur, V., Egelja, A., Pantić, J., Dordević, V., Matović, B. and Dramićanin, M. D. (2014). $Y_3Al_5O_{12}$:Re^{3+} (Re=Ce, Eu, and Sm) nanocrystalline powders prepared by modified glycine combustion method. *Science of Sintering*, 46(1): 75-82.
17. Mote, V. D., Purushotham, Y. and Dole, B. N. (2012). Williamson-Hall analysis in estimation of lattice strain in nanometer-sized ZnO particles. *Journal of Theoretical and Applied Physics*, 6(6):1-8.
18. Cullity, B. D., and Stock, S. R. (2001). Elements of X-ray diffraction, 3rd edition. Prentice Hall Publication, India.
19. Rietveld, H. M. (1967). Line profiles of neutron powder-diffraction peaks for structure refinement. *Acta Crystallographica,* 22(1): 151-152.
20. Balzar, D. and Ledbetter, H. (1993). Voigt-function modeling in Fourier analysis of size- and strain-broadened X-ray diffraction peaks. *Journal of Applied Crystallography*, 26: 97-103.
21. Warren, B. E. and Averbach, B. L. (1950). The effect of cold-work distortion on X-ray patterns. *Journal of Applied Physics,* 21(6): 595-599.
22. Suryanarayana, C. and Grant Norton, M. (1998). X-ray diffraction: A practical approach. Springer, New York.
23. Anitha, S. N., and Jayakumari, I. (2015). Synthesis and analysis of nanocrystalline $Fe_2Mn_2Ni_{0.5}Zn_{1.5}O_9$ at different treating temperatures. *Journal of Nanoscience and Technology*, 1(1): 26-31.
24. Chowdhury, M. and Sharma, S. K. (2015). Spectroscopic behavior of Eu^{3+} in SnO_2 for tunable red emission in solid state lighting devices. *RSC Advances*, 5: 51102-51109.
25. Ashwini, K. R., Premkumar, H. B., Darshan, G. P., Nagabhushana, H., Sharma, S., Prashantha, S. and Nagaswarupag, H. P. (2017). Synthesis and photometric properties of $SrAl_2O_4$: Gd^{3+} nanophosphors via solution combustion method. *Materials Today: Proceedings,* 4: 12168-12173.

Malaysian Journal of Analytical Sciences (MJAS)
Published by Malaysian Analytical Sciences Society

GREEN SYNTHESIS OF SILVER PARTICLES USING *Citrus microcarpa* PEEL EXTRACT

(Sintesis Partikel Perak Menggunakan Ekstrak kulit *Citrus Microcarpa*)

Gong Wee Jie, Masrina Mohd Nadzir*, Kalaivani Rangasamy

School of Chemical Engineering, Engineering Campus
Universiti Sains Malaysia, 14300 Nibong Tebal, Penang, Malaysia

**Corresponding author: chmasrina@usm.my*

Received: 13 November 2019; Accepted: 3 September 2020; Published: 12 October 2020

Abstract

Green synthesis of particles involves the use of safe biological agents as an eco-friendly and cost-effective alternative to chemical synthesis. In this study, silver particles were biosynthesised by using silver nitrate and aqueous *Citrus microcarpa* peel extract as the reducing and stabilising agent. The synthesised silver particles were confirmed and characterised by UV-Vis spectroscopy, scanning electron microscopy (SEM), energy dispersive X-ray spectroscopy (EDX), and dynamic light scattering (DLS). The UV-Vis spectrum showed surface plasmon resonance (SPR) with maximum peak intensity around 450 nm. The DLS studies show that silver particles have an average Z-diameter value of 235 nm with a polydispersity index of 0.363, which indicates the presence of agglomeration. The reaction parameters have a significant effect on the formation of silver particles. The highest absorbance recorded was 1.42 obtained under conditions of 72 hours reaction time, using 5 wt.% peel extract that reacted with 8 mM silver nitrate solution, while the ratio of solution of peel extract to silver nitrate was fixed at 1:5. Silver particles were successfully synthesised by *Citrus microcarpa* peel extract, which has the potential to replace the chemical method.

Keywords: silver particles, *Citrus microcarpa*, green synthesis

Abstrak

Sintesis hijau partikel melibatkan penggunaan agen biologi yang selamat sebagai alternatif yang mesra alam dan keberkesanan kos dibandingkan dengan kaedah sintesis kimia. Dalam kajian ini, partikel perak disintesis dengan menggunakan nitrat perak dan ekstrak kulit *Citrus microcarpa* berair sebagai ejen penurunan dan penstabilan. Partikel perak yang disintesis telah dikaji dan dicirikan dengan menggunakan analisis spektoskopi UV-Vis, mikroskop imbasan elektron (SEM), spektroskopi tenaga sinar-X (EDX), dan penyerakan cahaya dinamik (DLS). Spektrum UV-Vis menunjukkan permukaan resonan plasma (SPR) pada panjang gelombang maksimum sekitar 450 nm. Kajian PCD menunjukkan bahawa purata saiz bagi partikel ialah 235 nm dan indeks poliserakan adalah 0.363 yang membuktikan pengaglomeratan partikel. Parameter reaksi mempunyai kesan yang signifikan terhadap pembentukan partikel perak. Panjang gelombang tertinggi yang direkodkan adalah 1.42 yang diperolehi dalam keadaan masa 72 jam dengan menggunakan ekstrak 5 wt.% yang bertindak balas dengan larutan perak nitrat 8 mM, manakala nisbah larutan kulit ekstrak ke nitrat perak ditetapkan pada 1:5. Partikel perak boleh disintesis dengan menggunakan ekstrak kulit *Citrus microcarpa* yang mempunyai potensi untuk menggantikan kaedah sintesis kimia.

Kata kunci: partikel perak, *Citrus microcarpa*, sintesis hijau

Introduction

Silver particles are among the most utilised particles in therapeutic gadgets, medicinal service items, and material coatings. Since silver particles can disrupt the membrane and enzymatic activities of pathogenic microorganisms, it is widely applied in numerous biomedical applications such as surgical instruments, wound dressings, and antiseptic sprays [1]. Various preparation techniques can be used for the synthesis of silver particles, notably the chemical reduction method, thermal decomposition, and laser ablation [2]. In most cases, these methods include the utilisation of toxic chemicals especially the use of organic solvents as stabilising and reducing agents that are hazardous to living organisms, not to mention cause environmental pollution [3].

Biological methods are suitable alternatives to overcome the drawbacks of the chemical methods as it is straightforward, cost-effective, dependable, and environmentally friendly. Much consideration has been given to the high yield production of silver particles obtained from different biological medium including bacteria, fungi, algae, plant extract, and waste materials [4]. Green synthesis of silver particles utilising plants has been widely reported in literature due to their wide range of applications [5].

The green synthesis method that uses plant extracts stems from green chemistry principles since the overall synthesis of particles is environmentally friendly [6]. This method is generally utilised for the synthesis of metallic particles such as silver, iron, platinum, and gold. This strategy is a practical method for producing particles and offers flexibility with regards to the morphology, size, and nature of the separated particles [7]. Green synthesis of silver particles is one of the viable alternatives for acquiring size-controlled silver particles with antibacterial activity [8]. Smaller-sized silver particles have a significantly larger surface area that is in contact with the bacteria, thus making them more effective as antibacterial agents [9].

It is believed that the genus Citrus originated from Southeast Asia. Advances in natural or artificial crossbreeding has produced several hundreds of varieties and different hybrids [10]. *Citrus microcarpa (C. microcarpa)* is a natural hybrid from the crossbreed of a mandarin and an oval kumquat. It has been cultivated throughout tropical countries such as Southeast Asia countries, India, Hawaii, and West Indies. The health benefits of this citrus fruit have been attributed to their high content of phenolic compounds, including coumarins, flavonoids, lignin's, phenolic acids, and tannins [11]. Phenolic acids such as caffeic, p-coumaric, ferulic, and sinapic acids were found in *C. microcarpa* peel [12]. These acids were reported to exhibit high antioxidant activity [13].

In this paper, silver particles were synthesised by using *C. microcarpa* peel extract as a reducing and stabilising agent. The reduction of silver ion to silver particles was observed through colour change of samples during incubation. The peel extract concentration, silver nitrate concentration and incubation time were varied to determine the highest absorbance spectra. The silver particles formed were characterised by using UV-Vis spectrophotometer, SEM, EDX, and DLS. These characterisations were conducted to observe and study their formation, surface morphology, and size distribution of the silver particles.

Materials and Methods

Materials

Citrus Microcarpa fruits were purchased from Nibong Tebal, Pulau Pinang. Silver nitrate ($AgNO_3$, 99.8% purity) was purchased from Bendosen Laboratory Chemical. Distilled water was used for all preparations of aqueous solutions.

Preparation of *C. microcarpa* peel extract

Fresh *C. microcarpa* fruits were washed thoroughly with distilled water and the peel was separated from the flesh. Then, the peels were finely blended into powder and dried in the oven. The mass of the sample was weighed and the drying process was continued until a constant mass of the sample was reached whereby all moisture was removed. Aqueous extract of (2 wt.%) *C. microcarpa* peels were prepared by weighing 2 g of powdered peels and added to 100 mL of distilled water

in a beaker. The beaker was then placed on a hot plate magnetic stirrer at 750 rpm and heated at a temperature of 80 °C for 10 minutes. The solution was then removed from the heat source and left at room temperature to be cooled down. The aqueous extract was filtered with muslin cloth followed by filtration using Whatman no.1 filter paper (Whatman Limited, England) and finally using a 0.45 µm syringe filter.

Synthesis of silver particles using *C. microcarpa* peel extract

Silver nitrate was weighed and then placed in a 250 ml volumetric flask filled with distilled water to obtain a concentration of 8 mM silver nitrate. Aqueous extract of 2 wt.% *C. microcarpa* peel was slowly added to the silver nitrate solution while stirring. The mixture was incubated at room temperature for 48 hours. A series of experiments were performed to investigate the effect of incubation time, concentration of plant extract and concentration of silver nitrate. The effect of incubation time (0, 1, 5, 24, 48 and 72 hours) was studied at room temperature. The amount of plant extract was varied at 2, 5, and 10 wt.% while maintaining the concentration of silver nitrate at 8 mM. The effect of silver nitrate was determined by varying the concentration at (2, 4, 6, and 8 mM). The ratio of solution of peel extract to silver nitrate was fixed at 1:5.

Characterisation of silver nanoparticles

UV-Vis absorption spectra were measured using Agilent Cary 60 UV-Vis spectrophotometer at different time intervals in the absorption wavelength of 400-800 nm. The average size of silver particles was determined by using Dynamic light scattering (DLS). For DLS analysis, the sample was dispersed in distilled water followed by ultrasonication for 5 minutes, then centrifuged for 40 minutes at 4,400 rpm. The supernatant was collected and diluted with distilled water and analysed by using a computer-controlled particle size analyser (Malvern Instrument, UK). The morphological features of synthesised silver particles from the peel extract were studied by using Quanta FEG 450 scanning electron microscopy (SEM). The sample was centrifuged, and the sample was placed on a stub and analysed at an accelerating voltage of 20 KV. Elemental composition of the sample was tested using energy dispersive X-ray spectroscopy, EDX (Quanta FEG 450).

Results and Discussion

Effect of peel extract concentration

As seen in Figure 1, the colour of the solutions changed from pale yellow to yellowish brown and deep brown for solution mixture containing 2, 5, and 10 wt.% peel extract respectively. The colour change is because of the excitation of SPR in the silver particles that indicates the formation of silver particles [14]. The increase in colour intensity of reaction mixture is caused by the increase in number of particles formed due to the reduction of silver ions in the aqueous solution. Solution containing silver particles will appear yellowish-brown in colour when the surface plasmon vibrations are excited [15].

Figure 2 shows the maximum absorption that was obtained at 450 nm for 5 wt.% peel extract concentration. The SPR phenomenon occurs when metal particles emit strong electromagnetic fields on the particle surface, leading to strong absorption band in the range of 400-500 nm in UV-Vis spectra [16]. The absorption peak was more intense at around 450 nm with increasing concentration of the peel extract from 2 to 5 wt.%. When the concentration of biomolecules involved in the metal reductive process increases, more Ag^{+} are reduced to Ag^{0}, thus resulting in higher peak absorbance [17]. However, the absorbance decreases significantly when the concentration was further increased to 10 wt.% peel extract. An excess in peel extract concentration will cause the silver particle size to agglomerate which leads to larger particle size. The absorbance decreases with increasing silver particle size due the decrease in particle density [18]. This phenomena has also been reported by Kokila et al. [19] for the green synthesis of silver nanoparticles from cavendish banana peel extract, where the absorbance of 50 wt.% cavendish banana peel extract decreases when the volume was increased from 4 to 5 mL.

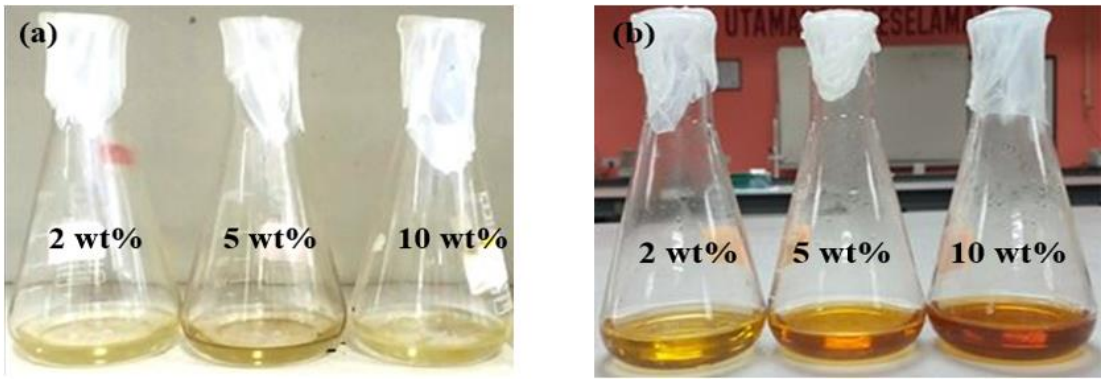


Figure 1. Silver particles prepared at different peel extract concentration for (a) 0 hour (b) 48 hours.

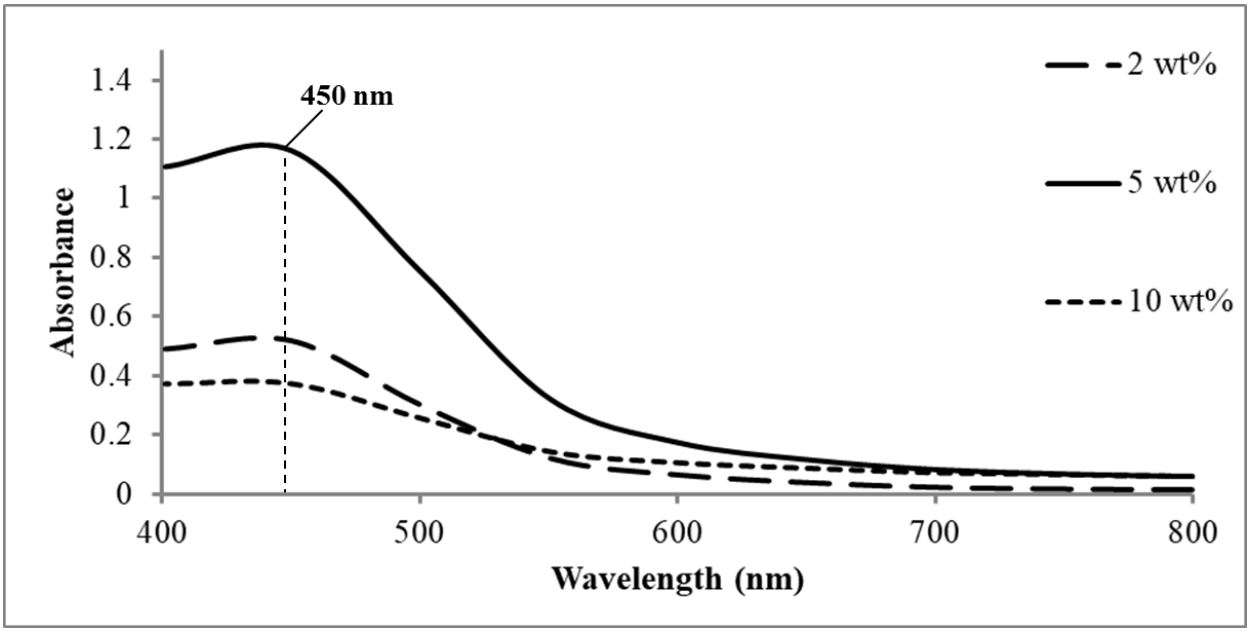


Figure 2. UV-Vis absorption spectra of silver particles observed for different peel extract concentration (wt.%) after 48 hours of incubation process

Effect of silver nitrate solution

Peel extract at 5 wt.% was chosen as a constant variable to evaluate the optimum concentration of the silver nitrate solution. Figure 3 shows that the sample colour with 2, 4, and 6 mM are yellowish brown while the sample with the highest concentration of silver nitrate solution at 8 mM is dark brown. As concentration of the silver nitrate solution increases, the intensity of colour changes will be more significant due to the presence of more silver particles than the reducing agent [20].

The highest peak of absorbance was recorded for 8 mM of silver nitrate solution at a wavelength around 450 nm (Figure 4). The graph depicts that as the concentration of the silver nitrate solution increases, the peak of absorbance also increases. Yang and Li [21] who synthesised silver particles from mango peels also reported that the peak of absorbance increases and shifts to higher wavelength with an increase of silver nitrate concentration. The slight increase in wavelength could

be due to excess silver ions aggregates on the surface of preformed nuclei, by which the secondary reduction process occurs which leads to the formation of larger particles.

Effect of incubation time

The effect of different reaction times was investigated for the synthesis of silver particles using 5 wt.% of peel extract and 8 mM of silver nitrate solution. Figure 5 shows the result of UV-Vis analysis at incubation time of 0, 1, 5, 24, 48, 72 hours. No absorbance peak was obtained during 0 and 1 h, indicating few or no particles formed in the solution. For the following hours, the absorbance intensity increases with time. The highest peak of absorbance was obtained after 72 hours of incubation time at a wavelength around 450 nm. Longer reaction time allows for more chemical interaction between the bio-reducing agents to reduce the silver ion into silver particles in the medium [20]. Based on previous literature, the incubation time required for the reduction of silver ions to silver particles varies significantly, from 90 minutes to [21] and up to one week [22].

Scanning electron microscopy (SEM)

Scanning electron microscopy was conducted to observe the morphology of silver particles produced. The analysis was performed with proportions of 5 wt.% of plant extract concentration, 8 mM of $AgNO_3$ solution after incubation time of 72 hours. Figure 6 shows the image of the silver particles (white clusters) formed with different magnification scales. The silver particle observed are polydisperse. The morphology of the silver particles was observed to be dense silver particles which were highly aggregated.

Energy-disperse X-ray analysis

Energy-disperse X-ray (EDX) analysis was used to observe the chemical compositions of the silver particles produced at 5 wt.% of the plant extract concentration, 8 mM of $AgNO_3$ solution after incubation time of 72 hours. The analysis confirmed the presence of elemental silver signal of the silver particles. The result in Figure 7 revealed strong carbon signal along with a weaker oxygen and silver peak (silver element of 19.38% weight) that could have originated from silver particles with bound biomolecules on the surface of the silver particles [23]. The highest peak that was obtained from the EDX could have been from carbon that was released by the pectin that was present in the *C. microcarpa* peel. The intracellular layer of plant cells especially fruits contains high amounts of pectin which is a type of structural fibre. The peels of citrus fruits contain 0.5%-3.5% pectin [24]. Hence, weaker signal of silver is obtained as the carbon from the pectin is difficult to be separated from the peel extract because of its high gelling capacity. The strong signal for silver particles at 3.0 keV in the EDX profile corresponds to the absorption of metallic silver due to SPR of silver particles [25].

Size distribution of silver particles

The distribution of silver particle size in the solution was determined using the DLS method. Figure 8 shows the size range of synthesised silver particles was between 100 nm to 500 nm with low polydispersity index (PDI) of 0.363. Anandalakshmi et al. [26] who used *Pedalium murex* leaf extract to bio-synthesise silver particles found that the size distribution of silver particles ranges from 10 to 150 nm. The average diameter determined by DLS is approximately 235 nm. This could be due to the measured particles size which includes biomolecules that surrounds the surface of the silver particles. In addition, the large particle size could be explained by the different interactive forces in the solution such as Van der Waals forces that allows agglomeration of particles [27]. Kokila et al. [19] also reported large silver particle size of 297 nm obtained from DLS using cavendish banana peel extract to biosynthesise silver particles.

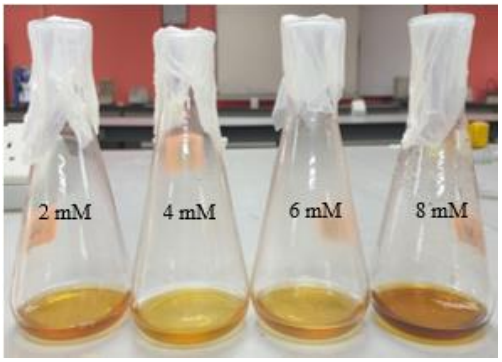


Figure 3. Silver particles prepared at different silver nitrate concentration at 48 hours

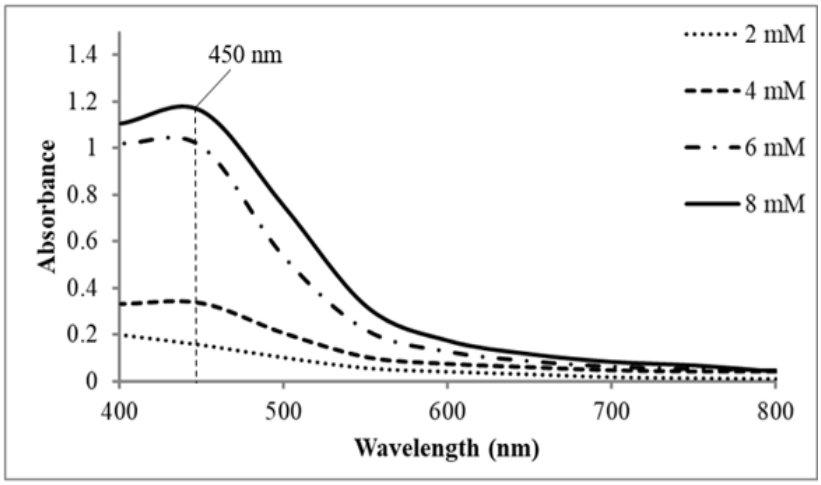


Figure 4. UV-Vis absorption spectra of silver particles observed using different silver nitrate concentration after 48 hours

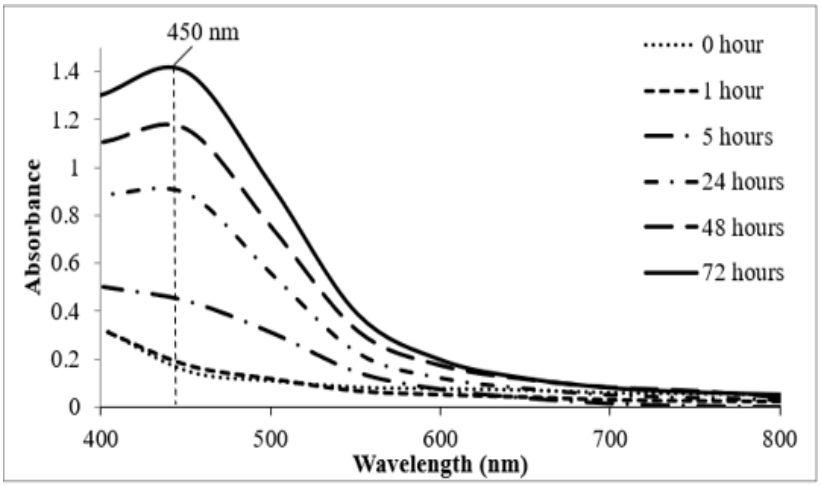


Figure 5. UV-Vis absorption spectra of silver particles observed for the incubation time of 0, 1, 5, 24, 48, and 72 hours

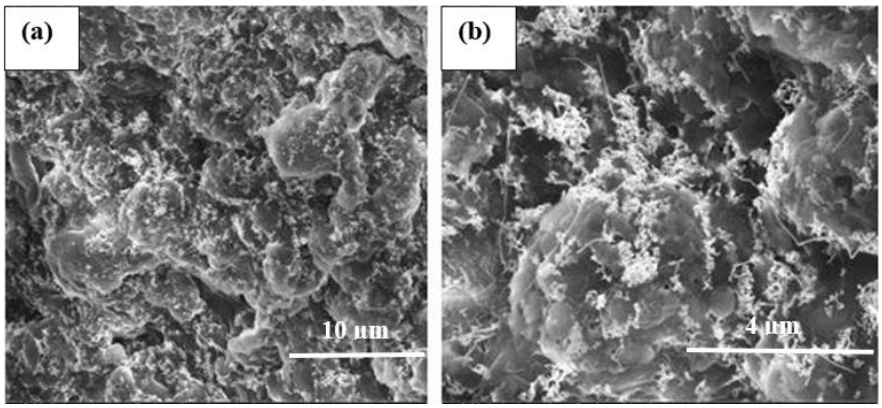


Figure 6. Scanning electron micrographs of the prepared silver particles of sample at (a) 10 000× magnification and (b) 30 000× magnification

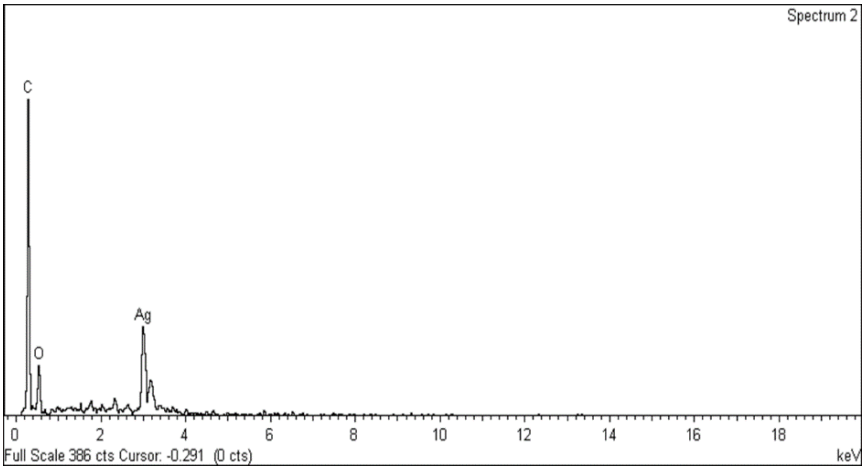


Figure 7. Energy disperse X-ray analysis spectra of silver particles

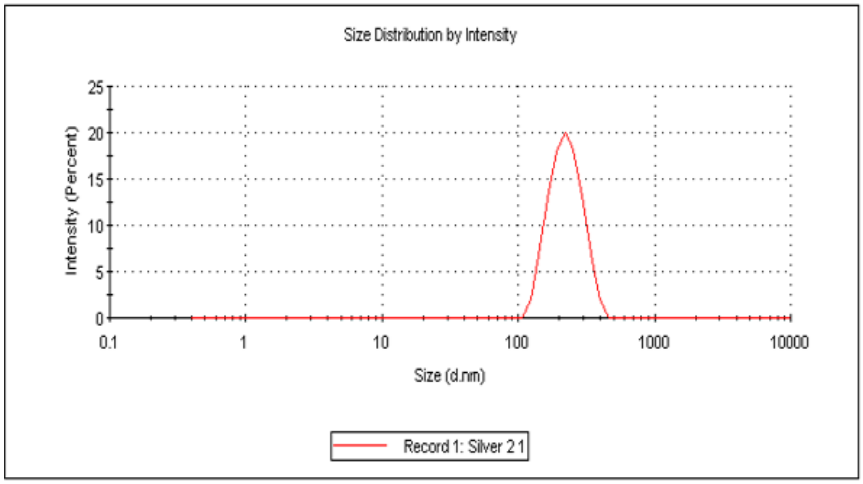


Figure 8. Size distribution of synthesised silver particles

Conclusion

The polydisperse silver particles with an average diameter of 235 nm were successfully synthesised using *C. microcarpa* peel extract as the reducing agent. The optimum condition to obtain the maximum peak absorbance is when the concentration of peel extract is 5 wt.% which reacts with 8 mM of silver nitrate solution for 72 hours. *Citrus microcarpa* peel extract provides an environmentally friendly and cost-effective method that could potentially be used for the biosynthesis of silver particles.

Acknowledgement

This study was funded by the Fundamental Research Grant Scheme (203/PJKIMIA/6071379) from the Ministry of Higher Education, Malaysia.

References

1. Franci, G., Falanga, A., Galdiero, S., Palomba, L., Rai, M., Morelli, G. and Galdiero, M. (2005). Silver nanoparticles as potential antibacterial agents. *Molecule*s, 20(5): 8856-8874.
2. Ranoszek-Soliwoda, K., Tomaszewska, E., Socha, E., Krzyczmonik, P., Ignaczak, A., Orlowski, P., Krzyzowska, M., Celichowski, G. and Grobelny, J. (2017). The role of tannic acid and sodium citrate in the synthesis of silver nanoparticles. *Journal of Nanoparticle Research*, 19: 1-15.
3. Bar, H., Bhui, D. K., Sahoo, G. P., Sarkar, P., De, S. P. and Misra, A. (2009). Green synthesis of silver nanoparticles using latex of *Jatropha curcas*. *Colloids and Surfaces A*, 339: 134-139.
4. Zhang, X. F., Liu, Z. G., Shen, W. and Gurunathan, S. (2016). Silver nanoparticles: Synthesis, characterization, properties, applications, and therapeutic approaches. *International Journal of Molecular Sciences,* 17(2016): 1-34.
5. Rafique, M., Sadaf, I., Rafique, M. S. and Tahir, M. B. (2017). A review on green synthesis of silver nanoparticles and their applications. Artificial cells. *Nanomedicine and Biotechnology*, 45(7): 1272-1291.
6. Nakhjavani, M., Nikkhah, V., Sarafraz, M. M., Shoja, S. and Sarafraz, M. (2017). Green synthesis of silver nanoparticles using green tea leaves: Experimental study on the morphological, rheological and antibacterial behavior. *Heat Mass Transfer*, 53: 3201-3209.
7. Thuc, D. T., Huy, T. Q., Hoang, L. H., Tien, B. C., Van Chung, P., Thuy, N. T. and Le, A. T. (2016). Green synthesis of colloidal silver nanoparticles through electrochemical method and their antibacterial activity. *Materials Letters*, 181: 173-177.
8. Roy P., Das, B., Mohanty, A. and Mohapatra, S. (2017). Green synthesis of silver nanoparticles using *Azadirachta indica* leaf extract and its antimicrobial study. *Applied Nanoscience,* 7: 843-850.
9. Raza, M. A., Kanwal, Z., Rauf, A., Sabri, A. N., Riaz, S. and Naseem, S. (2016). Size- and shape-dependent antibacterial studies of silver nanoparticles synthesized by wet chemical routes. *Nanomaterials,* 6(4): 1-15.
10. Dugo, G. and Mondello, L. (2010). Citrus oils: Composition, advanced analytical techniques, contaminants, and biological activity. Illustrate CRC Press, pp. 60-61.
11. Xu, G., Ye, X., Liu, D., Ma, Y. and Chen, J. (2008). Composition and distribution of phenolic acids in Ponkan and Huyou during maturity. *Journal of Food Composition and Analysis,* 21(5): 382-389.
12. Cheong, M. W., Chong, Z. S, Liu, S. Q., Zhou, W., Curran, P. and Yu, B. (2012). Characterization of calamansi (*Citrus microcarpa*). Part I: Volatiles, aromatic profiles and phenolic acids in the peel. *Food Chemistry*, 134 (2): 686-695.
13. Rice-Evans, C. A., Miller, N. J. and Paganga, G. (1997). Antioxidant properties of phenolic compounds. *Trends in Plant Science,* 2 (4): 152-159.
14. Khalil, M. M. H., Ismail, E. H., El-Baghdady, K. Z. and Mohamed, D. (2014). Green synthesis of silver nanoparticles using olive leaf extract and its antibacterial activity. *Arabian Journal of Chemistry,* 7(6): 1131-1139.
15. Vasireddy, R., Paul, R. and Krishna, A. (2012). Green synthesis of silver nanoparticles and the study of optical properties. *Nanomaterials and Nanotechnology*, 2: 1-6.

16. Senthamilselvi, S., Kumar, P., Prabha, A. L. and Govindaraju, M. (2013). Green simplistic biosynthesis of anti-bacterial silver nanoparticles using *Annona squamosa* leaf extract. *Nano Biomedicine and Engineering*, 5(2): 102-106.
17. Satishkumar, M., Sneha, K., Won, S., Cho, C., Kim, S. and Yun, Y. (2009). Cinnamon zeylanicum bark extract and powder mediated green synthesis of nano-crystalline silver particles and its antibacterial activity. *Colloids and Surfaces B: Biointerfaces,* 73(2): 332-338.
18. Goh, E. G., Xu, X. and McCormick, P. G. (2014). Effect of particle size on the UV absorbance of zinc oxide nanoparticles. *Scripta Materialia,* 78-79: 49-52.
19. Kokila, T., Ramesh, P. S. and Geetha, D. (2015). Biosynthesis of silver nanoparticles from Cavendish banana peel extract and its antibacterial and free radical scavenging assay: A novel biological approach. *Applied Nanoscience*, 5: 911-920.
20. Veerasamy, R., Xin, T. Z., Gunasagaran, S., Xiang, T. F. W., Yang, E. F. C., Jeyakumar, N. and Dhanaraj, S. A. (2011). Biosynthesis of silver nanoparticles using mangosteen leaf extract and evaluation of their antimicrobial activities. *Journal of Saudi Chemical Society,* 15(2): 113-120.
21. Yang, N. and Li, W. H. (2013). Mango peel extract mediated novel route for synthesis of silver nanoparticles and antibacterial application of silver nanoparticles loaded onto non-woven fabrics. *Industrial Crops and Products,* 48: 81-88.
22. Dipankar, C. and Murugan, S. (2012). The green synthesis, characterization and evaluation of the biological activities of silver nanoparticles synthesized from *Iresine herbstii* leaf aqueous extracts. *Colloids and Surfaces B: Biointerfaces,* 98(1): 112-119.
23. Subba Rao, Y., Kotakadi, V. S., Prasad, T. N., Reddy, A.V. and Sai Gopal, D.V. (2013). Green synthesis and spectral characterization of silver nanoparticles from Lakshmi tulasi (*Ocimum sanctum*) leaf extract. *Spectrochimica Acta Part A: Molecular and Biomolecular Spectroscopy,* 103:156-159.
24. Mudgul, D. (2017). The interaction between insoluble and soluble fiber. dietary fiber for the prevention of cardiovascular disease. Academic press, pp. 35-39.
25. Jagtap, U. B. and Bapat, V. A. (2013). Green synthesis of silver nanoparticles using *Artocarpus heterophyllus* Lam. seed extract and its antibacterial activity. *Industrial Crops and Products,* 46: 132-137.
26. Anandalakshmi, K., Venugobal, J. and Ramasamy, V. (2016). Characterization of silver nanoparticles by green synthesis method using *Pedalium murex* leaf extract and their antibacterial activity. *Applied Nanoscience*, 6: 399-408.
27. Prathna, T. C., Chandrasekaran, N., Raichur, M. and Mukherjee, A. (2011). Biomimetic synthesis of silver nanoparticles by *Citrus limon* (lemon) aqueous extract and theoretical prediction of particle size. *Colloids and Surfaces B: Biointerfaces*, 82(1): 152-159.

Malaysian Journal of Analytical Sciences (MJAS)
Published by Malaysian Analytical Sciences Society

EFFECT OF TIME AND TEMPERATURE ON REDUCED GRAPHENE OXIDE (rGO) LAYER STABILITY AND CYCLIC VOLTAMMETRIC BEHAVIOUR OF MODIFIED SCREEN-PRINTED CARBON ELECTRODE (mSPCE) FOR BIOSENSING PURPOSES

(Kesan Masa dan Suhu Pengeraman terhadap Kestabilan Lapisan rGO dan Perlakuan Voltametri Berkitar Elektrod Karbon Tercetak Terubahsuai (mSPCE) bagi Tujuan Penderiaan Bio)

Ahmad Farid Mohd Azmi[1]*, Vayithiswary Kannan[2,3], Nur Sabila Yasin[2], Jahwarhar Izuan Abdul Rashid[1], Ainsah Omar[4], Emee Marina Salleh[2]

[1]*Centre for Defence Foundation Studies*
[2]*Centre for Research Management and Innovation*
[3]*Faculty of Defence Science and Technology*
[4]*Faculty of Medicine and Defence Health*
Universiti Pertahanan Nasional Malaysia, Sungai Besi Camp, 57000 Kuala Lumpur, Malaysia.

**Corresponding author:* ahmad.farid@upnm.edu.my

Received: 13 November 2019; Accepted: 3 September 2020; Published: 12 October 2020

Abstract

In recent times, electrochemical immunosensing has emerged as a promising technique for a simple, portable, cost-effective, and efficient detection of cortisol in biofluids. The 2D graphene nanosheet is widely considered as a 'wonder material', attributing to its numerous incredible qualities which are commonly used as nanomaterial in today's biosensing technology. In this study, the working condition of biosensor for layer stability and cyclic voltammetric behaviour of modified screen-printed carbon electrode (mSPCE) integrated with reduced graphene oxide (rGO) was optimized. Two main parameters, i.e., incubation time and incubation temperature were investigated to assess the stability of rGO layer on the surface of modified electrode. After the modification of SPCE with rGO, the anodic and cathodic peak currents were remarkably enhanced at peak potentials 0.04 V and 0.22 V for incubation time and 0 V and 0.23 V for incubation temperature, respectively. The optimum condition of layer stability for the developed rGO-mSPCE was achieved by incubating the rGO on the electrode surface for 24 hours at 25 °C.

Keywords: biosensor, graphene oxide, electrochemical, screen printed carbon electrode, incubation

Abstrak

Sejak kebelakangan ini, teknik pengesanan penderiaan imuno elektrokimia telah muncul sebagai teknik yang berpotensi dalam mengesan kortisol secara ringkas, mudah alih dan cekap. Lapisan nano grafin 2D adalah terkenal sebagai bahan yang menakjubkan yang merujuk kepada kepelbagaian kualitinya yang luar biasa yang menjadikannya sebagai nanomaterial yang kini selalu digunakan dalam teknologi penderiaan bio. Dalam kajian ini, kestabilan lapisan grafin teroksida yang terturun (rGO) dan tindak balas voltametri berkitar di atas permukaan elektrod karbon tercetak terubahsuai (mSPCE) telah dioptimumkan. Dua parameter utama iaitu tempoh pengeraman masa dan tempoh pengeraman suhu telah dikaji untuk menilai kestabilan lapisan rGO di atas

permukaan elektrod tersebut. Selepas pengubahsuaian SPCE dengan rGO, arus puncak katod dan anod telah dipertingkatkan pada potensi puncak bernilai 0.04 V dan 0.22 V bagi tempoh pengeraman masa serta pada potensi puncak 0 V dan 0.23 V bagi tempoh pengeraman suhu. Keadaan optimum untuk kestabilan lapisan rGO-mSPCE yang telah diubahsuai dicapai melalui pengeraman lapisan rGO pada permukaan elektrod selama 24 jam pada suhu 25 °C.

Kata kunci: biosensor, grafin oxida, elektrokimia, elektrod karbon tercetak terubahsuai, pengeraman

Introduction

The development of analytical devices to measure bodily analytes as a biomarker for certain health conditions has been reported to be challenging. In recent times, electrochemical immunosensing has emerged as a promising technique for a simple, portable, cost-effective, and efficient detection of cortisol in biofluids. It is according to the principle of measuring the changes in the electrical properties of a conductive substrate due to the adsorption of an analyte on the surface functionalized with antibodies, which is sensitive and selective to the analyte [1, 2, 3]. In enhancing the sensitivity and selectivity of analyte detection, numerous explorations of nanomaterials and metallic nanoparticles composites have shown great promises. Reduced graphene oxide- (rGO) modified electrodes are desirable due to the fact that they are the most economical way of obtaining graphene-like structures, and graphene is recognized for its unique conductivity due to its large surface area and high chemical stability [4, 5].

Towards the development of high performance, lightweight and reliable electronic devices, attention has been drawn to the production of flexible supercapacitors that possess high electrochemical capacitance even under high mechanical stretch. Owing to its two-dimensional (2D) monolayer of carbon nanosheet, graphene may offer fascinating characteristics, including a large specific surface area (up to 2675 m^2/g), great electron mobility (230,000 cm^2/Vs), high thermal conductivity (3000 W/mK), high electrical conductivity (10^3–10^4 S/m), high strength (130 GPa), and outstanding elasticity and stiffness, which have attracted attention for the application as a supercapacitor [6, 7, 8]. Graphene consists of a thin layer pure carbon that is tightly packed and bonded together in a hexagonal honeycomb lattice with sp^2 bonds. Graphene and its various derivatives are widely considered as a ‘wonder material’, attributing to its numerous incredible qualities which are commonly used as nanomaterial in today’s biosensing technology [9-13].

Physical parameters such as incubation time and temperature are one of the factors that would potentially influence the stability and integrity of a material or substance in biosensors or in this case; a self-assembled monolayer [14, 15, 16]. Therefore, this current work investigates the effect of incubation time and temperature of rGO layer (post electro-reduction), mainly on its electrical behaviour through cyclic voltammetric analysis.

Materials and Methods

The stock solution of graphene oxide dispersed in water (4 mg/mL) was purchased from Sigma Aldrich (St. Louis, MO) and further diluted in distilled water to a desired concentration of 2 mg/mL upon 10 minutes sonication. C110 Screen Printed Carbon Electrode (SPCE) consisting of a 4 mm diameter carbon working electrode, carbon auxiliary electrode, and silver reference electrode was purchased from Metrohm DropSens. The SPCE was drop-casted onto 10 µL of 2 mg/mL graphene oxide (GO) solution and electrochemically reduced at applied potentials of -1.5 V to 0 V by using Metrohm Autolab B.V. (PGSTAT204) (Netherlands).

Figure 1 shows the appearance of the SPCEs pre- and post-modifications. The functionalized rGO on the electrode is denoted as rGO-mSPCE and its physical appearance perceived by the naked eyes is shown in Figure 1b. After electro-reduction, the rGO-mSPCE were incubated according to their respective incubation period of 1, 8, 18, 24, and 48 hours initially at room temperature and to their respective temperatures -24, 4, 25, 37, and 45 °C at a selected incubation period. Cyclic voltammetry (CV) test was carried out in 100 µL of 5

mM potassium ferricyanide, $K_3Fe(CN)_6$ in 0.1 M of potassium chloride (KCl) at the potentials of -0.4 V to 0.6 V, and 0.05 V/s scan rate, as referred from Omar et al. [17]. Both tests were carried out in duplicates. The average cathodic peak current from the cyclic voltammogram was recorded for each set of data. The condition of rGO layer on each mSPCE is observed through electrode photography (naked eye view) and Field Emission Scanning Electron Microscope (FESEM).

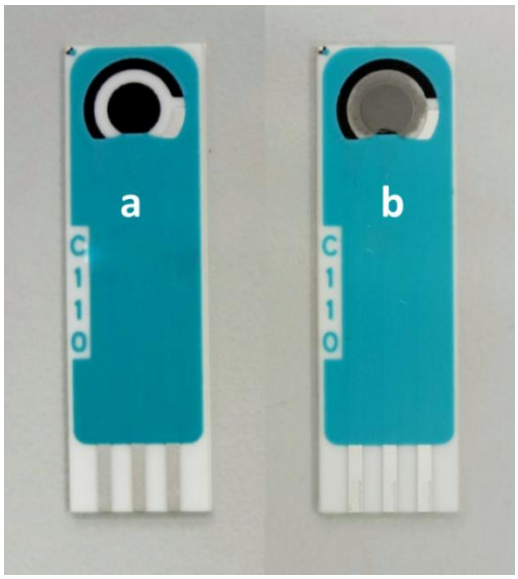


Figure 1. (a) Bare SPCE and (b) rGO-modified SPCE (rGO-mSPCE)

Results and Discussion

Morphological characterization of rGO-mSPCE

The morphology of rGO layer on the modified electrode (rGO-mSPCE) was characterized by using Field Emission Scanning Electron Microscope (FESEM). Figure 2 shows the FESEM image of the layer, with a distinctive crumpled surface. This depicts a high surface area ratio of rGO. The rGO monolayer was also seen to be uniformly distributed across the working electrode surface.

Effect of incubation time

Figure 3 shows the effect of incubation time on the average peak currents of the modified SPCE at room temperature. The peak current was reduced from 143 to 137.6 µA with the time increased from 1 to 18 hours. This shows that the incubation time was insufficient in enhancing the electrical sensitivity of the electrode within this duration of incubation. After 24 hours of incubation, the peak current was increased to 172.1 µA, but was then considerably reduced to 130.1 µA beyond 24 hours. This finding was also recorded as the highest peak current. However, prolonged duration of incubation up to 48 hours has resulted in a significant reduction of the peak current, as low as 130.1 µA. In brief, the optimum incubation time in enhancing the performance of rGO-mSPCE was achieved at 24 hours; being the adequate time for the freshly electro-reduced rGO layer to set on the working electrode of rGO-mSPCE prior to application with other chemicals or solutions. The readings obtained from this parameter study were significantly higher than the peak current recorded from a bare, unmodified SPCE with a peak current of 67.14 µA. From Table 1, the rGO layer appearance was seen to be intact and there was no noticeable difference from the pre-incubation and post-incubation time prior to the CV test, suggesting that the integrity of the layer remained unchanged.

Effect of incubation temperature

The incubation was performed at various temperatures for 24 hours to determine the optimum condition for the electrochemical detection of analytes, apart from assessing the rGO layer stability and morphology on the mSPCE. Five sets of temperature were chosen, which signified a random storage temperature for the rGO-mSPCE whereby the lowest temperature was of a freezer (-24 °C), chiller (4 °C), room temperature at 25 °C, and incubator at 37 °C and 45 °C as the normal human body temperature and the highest ambient temperature, respectively. Figure 4 shows that the average peak current of rGO-mSPCE was decreased slightly from 127.5 µA at -24 °C to 124.6 µA at 4 °C. The current response was increased at 25 °C and 37 °C with the current difference of 1.34 µA at 139.86 µA and 138.52 µA, respectively. The increment of electrical current explained that the electrochemical activity of the modified electrode was affected by the temperature. However, the electrical current dropped to 127.14 µA when the temperature was increased to 45 °C, which was almost the same current range seen at lower temperature settings. The reduction in the electrochemical behaviour of the mSPCE might be due to the deterioration of rGO layer that has been exposed to a considerably high temperature, which affected the redox reaction.

This scenario advocated that the optimum incubation temperature in attaining a high electrical performance of the rGO-mSPCE for analyte detection was achieved at 25 °C and stable at 37 °C, which demonstrated a maximal current conductivity, thus providing an improved electrochemical activity of the carbon working electrode. Furthermore, through naked eye observation, small 'bulge-like' appearances are shown by the white arrows (Table 2) on the rGO layer incubated at lower and higher temperatures than 25 °C and 37 °C, which suggest that changes that occurred in the integrity of rGO layer might have affected its current conductivity [18]. The room temperature and normal human body temperature were seen to be ideal as a working environment and storage temperature for the rGO-mSPCE. Extreme temperature, however, is not ideal for analyte detection that uses rGO-mSPCE with certain heat-labile sensing materials, i.e., antibodies, as they are subjected to degradation [19].

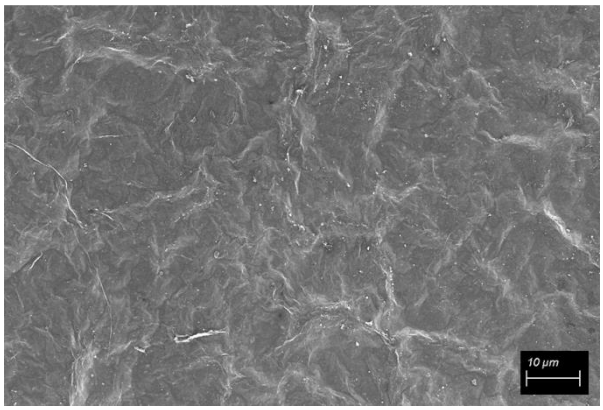


Figure 2. FESEM image of rGO-mSPCE at 1000X magnification

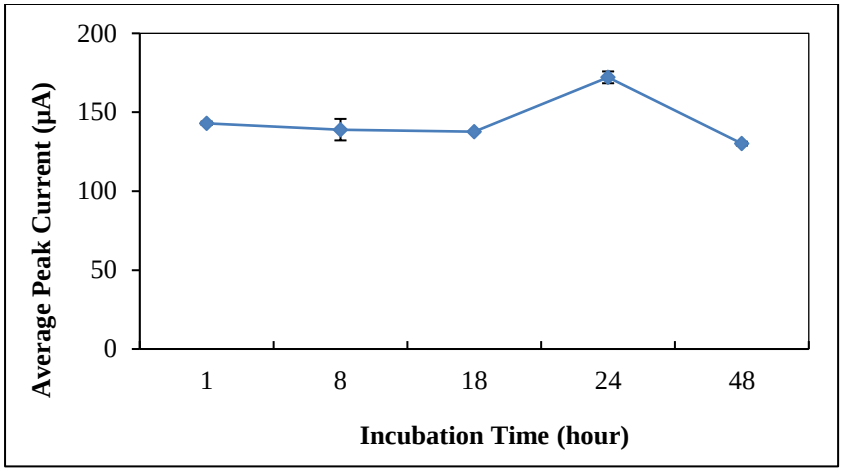


Figure 3. Average peak currents of rGO-mSPCE for various incubation time

Table 1. rGO layer appearance on mSPCE at different incubation durations

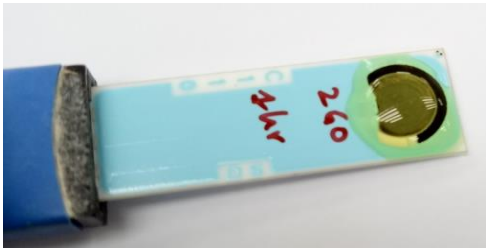
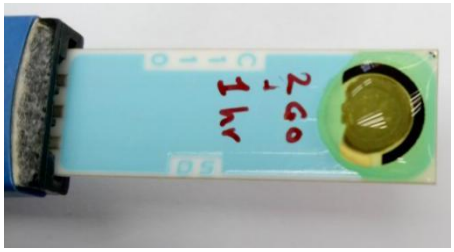
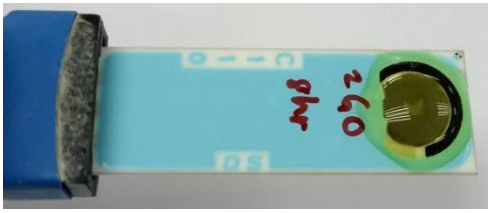
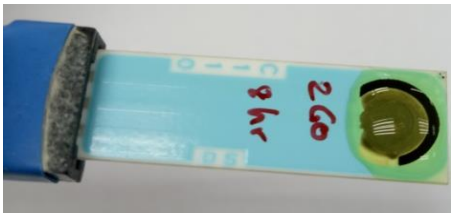
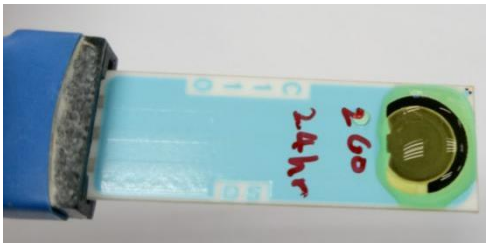
Incubation Time (h)	**Test 1**	**Test 2**
1		
8		
18		

Table 1 (cont'd). rGO layer appearance on mSPCE at different incubation durations

Incubation Time (h)	Test 1	Test 2
24		
48		

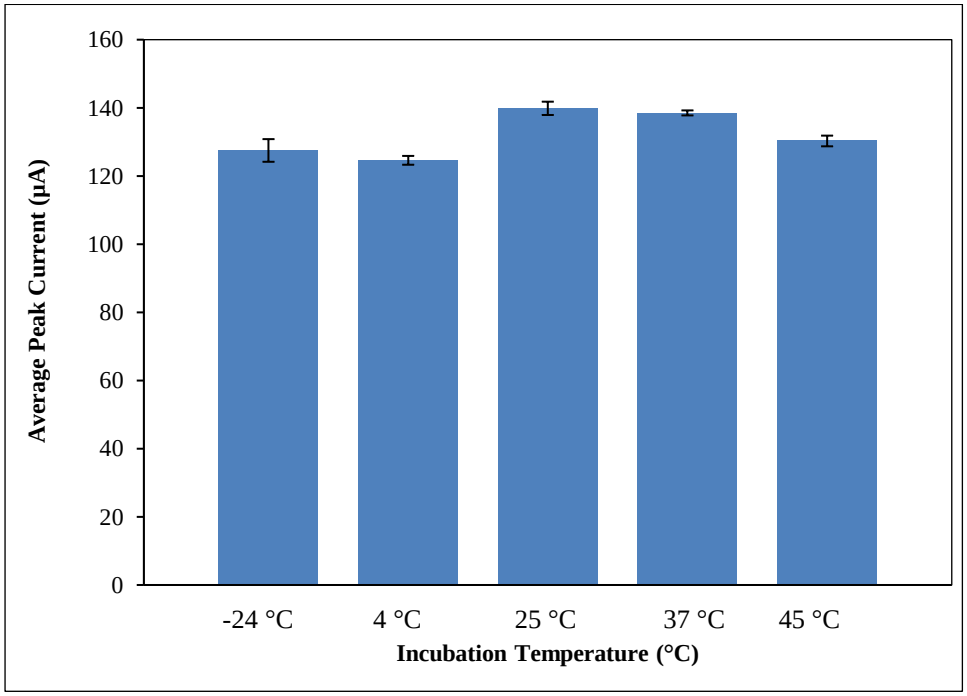
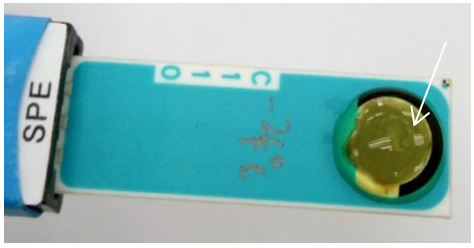
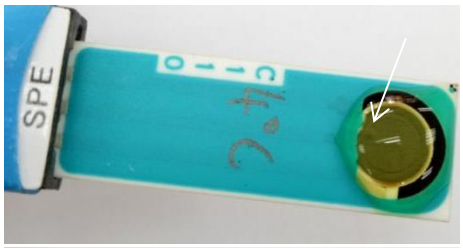
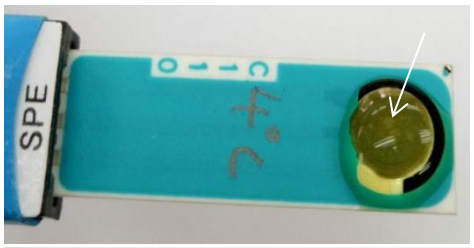
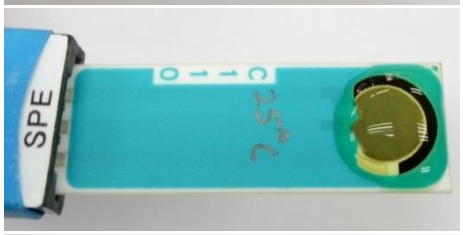
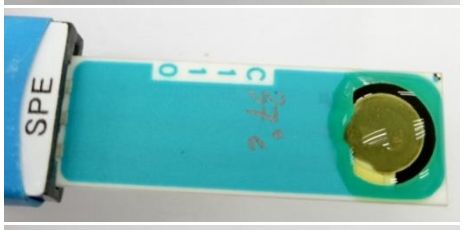
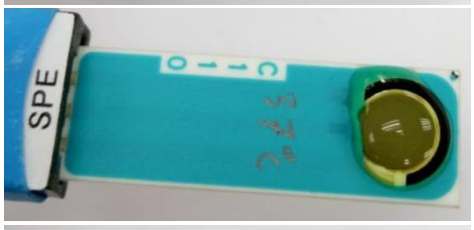


Figure 4. Average peak currents of rGO-mSPCE for various incubation temperatures

Table 2. rGO layer appearance on mSPCE at different incubation temperatures

Incubation Temperature (ºC)	**Test 1**	**Test 2**
-24 (freezer)		
4 (chiller)		
25 (room temperature)		
37 (human body temperature)		
45 (highest ambient temperature)		

Cyclic voltammetric behaviour

Cyclic Voltammetry (CV) is a potentio-electrochemical technique for acquiring qualitative information about electrochemical reactions that take place within the electrode-electrolyte interface. CV was performed to study the electrochemical properties of an analyte in a solution, particularly to measure the current that develops in an electrochemical cell for a voltage range. Figure 5 and Figure 6 show that the cyclic voltammogram of incubation times and incubation

temperatures were both consistent of which each was depicted by quasi-rectangular curve shape. This phenomenon implied that both studied parameters slightly affected the oxidation-reduction process of the rGO-mSPCE as there were only a slight difference of electrical conductivity in terms of their current responses towards time and temperature incubation [20, 21].

Figure 5 displays the large CV curve of mSPCE which was due to its relatively high redox activity. However, within the incubation duration of 1 to 18 hours, the electrochemical reactions decreased in their current responses. The eenhancement of peak currents was observed after 24 h of incubation whereby the anodic and cathodic peak currents were increased at peak potentials 0.04 V and 0.22 V, respectively. The increasing incubation time resulted in a smaller CV and the redox process was not very well defined, which might be attributed to low capacitive currents and surface area of the working electrode [11, 22].

Figure 6 shows the cyclic voltammograms generated at incubation temperatures -24, 4, 25, 37, and 45 °C. The CV curves of all temperature settings were almost similar to each other in terms of their shape, with two distinctive anodic and cathodic peaks. However, the CV curve of rGO-mSPCE incubated at 25 °C and 37 °C exhibited slightly higher anodic and cathodic peak currents at peak potentials 0 V and 0.23 V, respectively than other temperatures. Further increase in incubation temperatures resulted in a slight decrease of the current responses, which was almost to its initial range during the first two incubation temperatures. This phenomenon suggested that the redox reaction of the mSPCE was affected by the incubation temperature [20]. It was evident that at 25 °C and 37 °C, the rGO layer was seen to be stable, which correlated to the observations in Table 2, thus proving a suitable working temperature or condition for analyte detection using biosensor with the rGO-mSPCE.

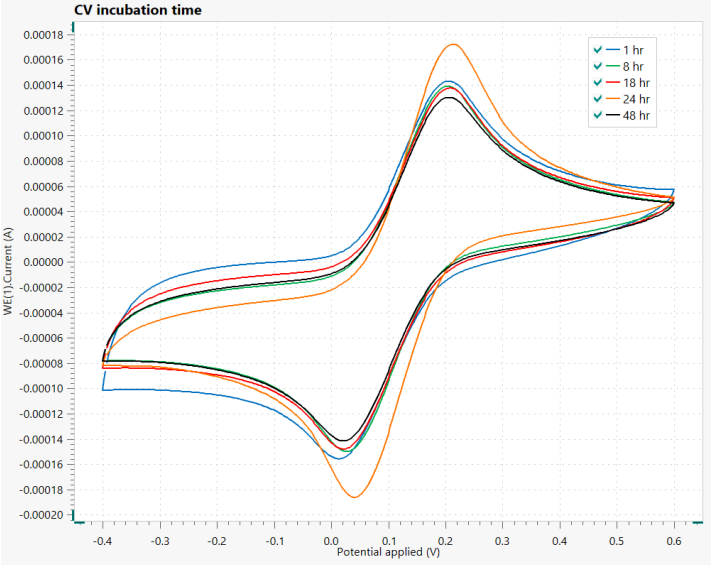


Figure 5. CV of rGO-mSPCE for various incubation time

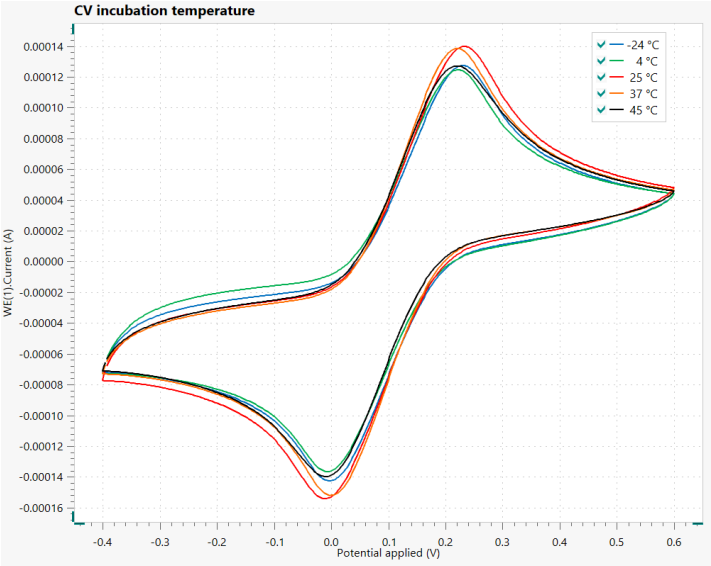


Figure 6. CV of rGO-mSPCE for various incubation temperatures

Conclusion

The optimum incubation time and temperature for the rGO-mSPCE were achieved after 24 hours at 25 °C, which exhibited an adequately high current conductivity, thus demonstrated an improved electrochemical activity of the carbon working electrode. The cyclic voltammogram of both studied parameters was in a consistent curved shape. At 24 hours of incubation, the anodic and cathodic peak currents were increased at the peak potentials 0.04 V and 0.22 V, respectively. The largest CV was obtained at 25 °C whereby the anodic and cathodic currents peaked at the peak potentials 0 V and 0.23 V, respectively. The optimum condition of layer stability for the developed rGO-mSPCE was achieved by incubating the rGO on the electrode surface for 24 hours at 25 °C.

Acknowledgement

The authors would like to acknowledge the financial support provided by the Ministry of Higher Education Malaysia under the Niche Research Grant Scheme (NRGS/2013/UPNM/PK/P4). The funding for the publication of this article was provided by the Centre for Defence Foundation Studies, Universiti Pertahanan Nasional Malaysia (UPNM).

References

1. Kidd, T., Carvalho, L. A. and Steptoe, A. (2014). The relationship between cortisol responses to laboratory stress and cortisol profiles in daily life. *Biological Psychology,* 99: 34-40.
2. Walter, E. E., Fernandez, F., Snelling, M. and Barkus, E. (2018). Stress induced cortisol release and schizotypy. *Psychoneuroendocrinology,* 89: 209-215.
3. Wichmann, S., Kirschbaum, C., Böhme, C. and Petrowski, K. (2017). Cortisol stress response in post-traumatic stress disorder, panic disorder, and major depressive disorder patients. *Psychoneuroendocrinology,* 83: 135-141.
4. Linninge, C., Jönsson, P., Bolinsson, H., Önning, G., Eriksson, J., Johansson, G. and Ahrné, S. (2018). Effects of acute stress provocation on cortisol levels, zonulin and inflammatory markers in low-and high-stressed men. *Biological Psychology,* 138: 48-55.
5. Wichmann, S., Kirschbaum, C., Lorenz, T. and Petrowski, K. (2017). Effects of the cortisol stress response on the psychotherapy outcome of panic disorder patients. *Psychoneuroendocrinology,* 77: 9-17.

6. Cruz, A. F. D., Norena, N., Kaushik, A. and Bhansali, S. (2014). A low-cost miniaturized potentiostat for point-of-care diagnosis. *Biosensors and Bioelectronics,* 62: 249-254.
7. Herrera, A. Y., Nielsen, S. E. and Mather, M. (2016). Stress-induced increases in progesterone and cortisol in naturally cycling women. *Neurobiology of Stress,* 3: 96-104.
8. Koh, W. C. A., Son, J. I., Choe, E. S. and Shim, Y.-B. (2010). Electrochemical detection of peroxynitrite using a biosensor based on a conducting polymer− manganese ion complex. *Analytical Chemistry,* 82(24): 10075-10082.
9. Malhotra, B. D., Chaubey, A. and Singh, S. (2006). Prospects of conducting polymers in biosensors. *Analytica Chimica Acta,* 578(1): 59-74.
10. Sun, W., Zhang, Y., Hu, A., Lu, Y., Shi, F., Lei, B. and Sun, Z. (2013). Electrochemical DNA biosensor based on partially reduced graphene oxide modified carbon ionic liquid electrode for the detection of transgenic soybean A2704-12 gene sequence. *Electroanalysis,* 25(6): 1417-1424.
11. Bollella, P., Fusco, G., Tortolini, C., Sanzò, G., Favero, G., Gorton, L. and Antiochia, R. (2017). Beyond graphene: electrochemical sensors and biosensors for biomarkers detection. *Biosensors and Bioelectronics,* 89: 152-166.
12. Liu, C.-Y., Chou, Y.-C., Tsai, J.-H., Huang, T.-M., Chen, J.-Z. and Yeh, Y.-C. (2019). Tyrosinase/Chitosan/Reduced graphene oxide modified screen-printed carbon electrode for sensitive and interference-free detection of dopamine. *Applied Sciences,* 9(4): 622.
13. Patri, S. B., Adarakatti, P. S. and Malingappa, P. (2019). Silver nanoparticles-chitosan composite embedded graphite screen-printed electrodes as a novel electrochemical platform in the measurement of trace level nitrite: application to milk powder samples. *Current Analytical Chemistry,* 15(1): 56-65.
14. Hanifah, M. F. R., Jaafar, J., Aziz, M., Ismail, A., Othman, M. and Rahman, M. A. (2015). Effects of reduction time on the structural, electrical and thermal properties of synthesized reduced graphene oxide nanosheets. *Bulletin of Materials Science,* 38(6): 1569-1576.
15. Kimiagar, S., Rashidi, N. and Ghadim, E. E. (2015). Investigation of the effects of temperature and time on reduction of graphene oxide by microwave hydrothermal reactor. *Bulletin of Materials Science,* 38(7): 1699-1704.
16. Timofeeva, T., Evseev, Z., Vinokurov, P., Alexandrov, G. and Smagulova, S. (2018). The effect of temperature conditions during graphene oxide synthesis on humidity dependence of conductivity in thermally reduced graphene oxide. *Journal of Structural Chemistry,* 59(4): 799-805.
17. Omar, A., Rashid, J. I. A., Latif, A. A. A., Karim, K. A., Bakar, O. C., Bakar, M. A. and Yunus, W. (2017). Development of cortisol immunosensor based reduced graphene oxide (rGO) for future application in monitoring stress levels among military personnel. *Science & Technology Research Institute for Defence (STRIDE),* 10(2): 142-149.
18. Colonna, S., Monticelli, O., Gomez, J., Novara, C., Saracco, G. and Fina, A. (2016). Effect of morphology and defectiveness of graphene-related materials on the electrical and thermal conductivity of their polymer nanocomposites. *Polymer,* 102: 292-300.
19. Le Basle, Y., Chennell, P., Tokhadze, N., Astier, A. and Sautou, V. (2020). Physicochemical Stability of Monoclonal Antibodies: A Review. *Journal of Pharmaceutical Sciences,* 109(1): 169-190.
20. Rahman, M. S., Anower, M. S., Bashar, L. B. and Rikta, K. A. (2017). Sensitivity analysis of graphene coated surface plasmon resonance biosensors for biosensing applications. *Sensing and Bio-Sensing Research,* 16: 41-45.
21. Settu, K., Liu, J.-T., Chen, C.-J. and Tsai, J.-Z. (2017). Development of carbon-graphene-based aptamer biosensor for EN2 protein detection. *Analytical Biochemistry,* 534: 99-107.
22. Song, H. S., Kwon, O. S., Kim, J.-H., Conde, J. and Artzi, N. (2017). 3D hydrogel scaffold doped with 2D graphene materials for biosensors and bioelectronics. *Biosensors and Bioelectronics,* 89: 187-200.

Malaysian Journal of Analytical Sciences (MJAS)
Published by Malaysian Analytical Sciences Society

INFLUENCE OF HYDROXYMETHYLATED LIGNIN ON MECHANICAL PROPERTIES AND PAYNE EFFECT OF NR/BR COMPOUNDS

(Kesan Lignin Hidroksimetilasi Terhadap Sifat Mekanik dan Kesan Payne dalam Sebatian Campuran NR/BR)

Nor Anizah Mohamad Aini[1], Nadras Othman[1]*, M. Hazwan Hussin[2], Kannika Sahakaro[3], Nabil Hayeemasae[3]

[1]School of Materials and Mineral Resources Engineering, Engineering Campus, Universiti Sains Malaysia, 14300 Nibong Tebal, Penang, Malaysia
[2]School of Chemical Sciences, Universiti Sains Malaysia, 11800 Minden, Penang, Malaysia
[3]Department of Rubber Technology and Polymer Science, Faculty of Science and Technology, Prince of Songkla University, Pattani Campus, Pattani, 94000 Thailand

[*]Corresponding author: srnadras@usm.my

Received: 13 November 2019; Accepted: 3 September 2020; Published: 12 October 2020

Abstract

This work investigates the correlation between hydroxymethylated lignin and its performance in natural rubber (NR)/ butadiene rubber (BR) blend compounds, focusing on Payne effect and mechanical properties. Two types of lignin from kenaf biomass, organosolv lignin (OL) and soda lignin (SL) are modified by using hydroxymethylation modification process and named as hydroxymethylated organosolv lignin (HMOL) and hydroxymethylated soda lignin (HMSL). Every structural characteristic of lignin's is characterized using Fourier Transform Infrared (FTIR). Then, the modified and unmodified lignin's are utilized as a filler in NR/BR blends by conventional approach method viz., dry-mixing. Payne effect by rubber process analyzer (RPA) and mechanical properties (tensile properties and hardness) of lignin–filled NR/BR blends are investigated in both masterbatches and vulcanized compounds respectively. Based on the results obtained, it is revealed that alterations in the structural characteristics of hydroxymethylated lignin influence its filler-filler interaction and reinforcement capability. Therefore, a significant improvement has been observed in mechanical properties especially at low loading up to 10 phr. Comparing between two modified lignin, HMSL contributes higher enhancement than HMOL in rubber composites which increase the tensile strength from 15.78 to 17.20 MPa, modulus at 100% strain (1.09 to 1.93 MPa), modulus at 300% strain (3.22 to 7.06 MPa) and hardness (52 to 61.5 Shore A). In conclusion, the inclusion of modified lignin to rubber compounds improves the rubber compounds performance.

Keywords: lignin, hydroxymethylation, bio-filler, structural characteristic, Payne effect

Abstrak

Kajian ini menyiasat korelasi antara lignin hidroksimetilasi dan prestasinya dalam sebatian campuran getah asli (NR)/ butadiena getah (BR), memberi tumpuan kepada kesan Payne dan sifat mekanik. Dua jenis lignin daripada tumbuhan kenaf, organosolv lignin (OL) dan soda lignin (SL) diubahsuai menggunakan kaedah pengubahsuaian hidroksimetilasi dan dinamakan sebagai organosolv lignin hidroksimetilat (HMOL) dan soda lignin hidroksimetilat (HMSL). Ciri-ciri struktur lignin dicirikan menggunakan spektroskopi inframerah transformasi Fourier (FTIR). Kemudian, lignin yang diubahsuai telah digunakan sebagai pengisi dalam

campuran NR/BR oleh kaedah pendekatan konvensional iaitu pencampuran kering. Kesan Payne menggunakan penganalisis process getah (RPA) dan sifat mekanik (sifat tegangan dan kekerasan) campuran NR/BR yang diisi dengan lignin diselidiki dalam kedua-dua kelompok induk dan sebatian tervulkan. Berdasarkan hasil yang diperoleh daripada ujian menunjukkan bahawa perubahan dalam ciri-ciri struktur lignin hidroksimetilasi mempengaruhi interaksi antara pengisi dan keupayaan pengukuhan. Oleh itu, penambahbaikan yang ketara telah dilihat dalam sifat mekanik terutama dalam kandungan rendah sehingga 10 phr. Perbandingan antara dua lignin yang diubahsuai, HMSL menyumbang peningkatan yang lebih tinggi daripada HMOL dalam komposit getah yang meningkatkan kekuatan tegangan dari 15.78 kepada 17.20 MPa, modulus pada 100% terikan (1.09 kepada 1.93 MPa), modulus pada 300% terikan (3.22 kepada 7.06 MPa) dan kekerasan (52 kepada 61.5 Shore A). Kesimpulannya, penggunaan lignin yang diubahsuai kepada sebatian getah meningkatkan prestasi sebatian getah.

Kata kunci: lignin, hidroksimetilasi, bio-pengisi, ciri struktur, kesan Payne

Introduction

In recent years, 'green' rubber composites containing natural materials have received particular attention due to the awareness towards environmental protection and utilization of biodegradable and sustainable resources. Many natural fillers have been utilized as filler in rubber composites to increase the mechanical properties of rubber product [1, 2, 3]. Among natural sources, lignin is a cheaper and abundant natural polymer obtained from non-food resources, making it suitable and has high potential to be used as reinforcing filler in the rubber compound.

Lignin possesses a unique complex structure. It consists of *p*-hydroxyphenyl (H), guaiacyl (G) and syringyl (S) with the presence of various of functional groups attached on the lignin's structure: methoxyl, hydroxyl (alcoholic and phenolic) and the side propanoic chain. The propanoic units bound to each other through various of bonds, i.e., β-O-4, β-5, β-β, and etc. [4]. The functional group and reactivity of lignin depend on the species of origin and isolation methods. However, the functional group on the lignin structure makes polar and incompatible with non-polar rubber matrix. This is the main reason for the lack of utilization in a value-added application. Therefore, structural modifications of the lignin are required [5]. It becomes the pursued directions of researchers to improve the properties of lignin through reactions that may lead to increase functionality and diverse lignin applications. From this perspective, the hydroxymethylation reaction compromises high potentials of increasing the functionality of lignin and porosity which is a key element in rubber systems. Additionally, the addition of hybrid filler into rubber composites is successfully improving its properties and enhances overall mechanical properties in comparison with the solely conventional filler [6,7,8].

This work demonstrates the outcomes of a comparative study on the reactivity of two lignin's isolated from kenaf biomass with different pulping methods, *viz*. organosolv and soda method. Both types of lignin have been modified with formaldehyde, as well as characterized structural characteristic by FTIR technique. Furthermore, the obtained modified lignin have been added to natural rubber/polybutadiene rubber (NR/BR) blend composites to partially substitute carbon black (CB) in varying loading content (5, 10, 15, 20 phr) with the total filler at 50 phr. The rubber composites have been further investigated to study the effectiveness of utilization of modified lignin in term of the Payne effect and mechanical properties.

Materials and Methods

Materials

Natural rubber (SMR10) and polybutadiene rubber (BR9000) are supplied by the Rubber Research Institute of Malaysia (RRIM) and Zarm Scientific (M) Sdn Bhd respectively. Two types of lignin are in-house isolated from kenaf biomass through different delignification process, organosolv and soda process. The particle size of both lignin is prepared in the average size less than 250 μm. Sodium hydroxide (NaOH), sodium sulfide (Na_2S), ammonium hydroxide (NH_4OH), formaldehyde, acetic anhydride, pyridine, sulphuric acid (H_2SO_4), and hydrochloric acid (HCl) are purchased from Merck (Petaling Jaya, Malaysia). The N220-grade carbon black (CB) is supplied by Cabot Corporation. Other rubber

compounding ingredients are purchased from Bayer (M) Ltd. All the ingredients have been used once received.

Hydroxymethylation procedures

Hydroxymethylation process is performed on both lignin (OL and SL) to alter their structure by substitution of hydroxymethyl groups as outlined by Popa et al. [9]. This modification is expected to develop the interaction between phases of lignin and the rubber matrix. The complete procedure has been elaborated elsewhere [10]. The resultant formaldehyde-modified lignin is called hydroxymethylated organosolv lignin (HMOL) and hydroxymethylated soda lignin (HMSL).

Specimen preparation

Subsequently, modified lignin-containing NR/BR composites blends are prepared based on the formulation listed in Table 1 by using laboratory-scale open two-roll. It is further been hot-pressed into a 2 mm thick sheet at 150 °C after 24 hours of mixing. Moreover, the MDR 2000 moving die rheometer (Alpha Technologies, Akron, OH, USA) is used to determine the optimum cure time, t_{90}. The rubber composites are labeled as NR/BR/OL, NR/BR/SL, NR/BR/HMOL or NR/BR/HMSL, where OL and SL indicate unmodified lignin. The NR/BR/OL, NR/BR/SL and NR/BR/CB50 (no lignin) composites as control samples are prepared in a similar technique to the NR/BR/HMOL and NR/BR/HMSL composites.

Testing and characterization

FTIR spectra are recorded with a Thermo-Nicolet IR 200 Fourier transform infrared (FTIR) with attenuated total reflection (ATR). The range used is 600 - 4000 cm^{-1} at a resolution of ±4cm^{-1} with 32 scans. The filler-filler interaction of the uncured compounds is studied by strain sweep test in the range of 0.6-100% strain at 100 °C and a frequency of 0.50 Hz by a Montech D-RPA 3000, rubber process analyzer (RPA) instrument (Werkstoffprüfmaschinen Gmbh, Buchen, Germany). The differences in the storage shear moduli (G') at low strain (0.6%) and high strain (100%) are reported. Tensile tests are carried out by using H10KS tensiometer (Hounsfield Test Equipment Co., Ltd., Croydon, UK) following guideline from the ASTM D412 method. The crosshead speed of 500 mm/min is applied to the die type C dumbbell-shaped specimen. Wallace Shore A durometer (Cambridge, UK) is used to determine the hardness of the rubber compounds following the ASTM D2240 method.

Table 1. Formulations of NR/BR and modified or unmodified lignin used in this work

Ingredients	Amount (phr)					
	NR/BR/ CB50 (No Lignin)	NR/BR/ Unmodified Lignin	NR/BR/ HM-5	NR/BR/ HM-10	NR/BR/ HM-15	NR/BR/ HM-20
NR (SMR10)[1]	50	50	50	50	50	50
BR (BR9000)[2]	50	50	50	50	50	50
Zinc Oxide	5	5	5	5	5	5
Stearic Acid	2	2	2	2	2	2
Carbon Black (N220)	50	40	45	40	35	30
Unmodified Lignin[3]	-	10	-	-	-	-
Hydroxymethylated Lignin (HM)[4]	-	-	5	10	15	20
TDAE[5]	5	5	5	5	5	5
6PPD[6]	2	2	2	2	2	2
TMQ[7]	1	1	1	1	1	1

Results and Discussion

Structural analysis

Both lignin from kenaf biomass, OL and SL have been altered by hydroxymethylation method in the alkaline atmosphere known as HMOL and HMSL. In order to evaluate the differences in term of functional level between modified and unmodified lignin, the comparative spectral data are analyzed and displayed in Figure 1. Based on spectra presentations, absorption bands specific to C-H aromatic bonds, aliphatic bonds and hydroxyphenyl groups appeared in the 3000 – 2850 cm^{-1} range. It is proven that the containing of hydroxylic groups and the introduction of hydroxymethyl groups in the lignin structure through the hydroxymethylation reaction. The 1710-1600 cm^{-1} range corresponds to carbonylic groups bound by the aromatic nucleus. From the peak observed, the shifted C=O bands in the modified lignin's spectra are due to interaction with the aromatic nucleus. Furthermore, the etheric bond and hydroxyphenolic peak appear in the range of ~1200 cm^{-1} displays the peak for hydroxymethylated lignin samples increases because of the introduction of substitution. Lignin structure possesses G and S unit which have a free C5 position for G units and methoxy groups attached on the C3 and C5 positions for S units in the aromatic ring. The reactive G units can react and linked with hydroxymethyl groups which convert from formaldehyde, while the S units demonstrate no reactivity with formaldehyde [11].

The absorptions of G and S structural units appear in the region of 1600 – 900 cm^{-1}. However, when compared to unmodified lignin, the peak intensity of the modified lignin decreases. The 1400 – 1460 cm^{-1} range is affected by the excitation of the C-H asymmetric aromatic nucleus, which reacts with formaldehyde. The methylene chains or known as methylene bridge in this study which formed by further condensations shows stronger vibrations, thus increment of absorption bands intensity may occur. The presence of absorption bands in the 1360 - 835 cm^{-1} range presents a higher content of C-H bonds. The lignin displays both G and S characteristics absorption at 1219, 1324 and 1120 cm^{-1}. On the other hand, the band, the increasing of peak C-O stretching vibration for primary alcohol and ether (~1100 cm^{-1}) and peak of out-of-plane (820-835 cm^{-1}) deformation vibration of C2, C5 and C6 positions in G units become weaker. This proposes the presence of hydroxymethyl groups into lignin structure and connection of these hydroxymethyl lignin molecules through formation of methylene bridge. These data confirmed that the hydroxymethylation reaction occurred in the structure of lignin.

Payne effect

The strain sweep analysis is conducted for NR/BR/HMOL and NR/BR/HMSL containing various loading of modified lignin at 100 °C. The results of storage modulus (G') as function of strain are shown in Figure 2a. The G' value of all rubber compounds has decreased rapidly when the amplitude of strain reached above ~5% strain amplitude. This is due to the breakdown of the entangled chains in rubber compound [12], which is related to the dissociation of the hydrogen bonds and filler networks. Therefore, deformation contributes to changes in microstructure [13]. This phenomenon is well known as the "Payne effect". The effect sharply reduces with increasing lignin content as shown in Figure 2b, which indicates the reduction of filler-filler interaction. The storage modulus of NR/BR containing hydroxymethylated lignin at low strains is higher than NR/BR containing unmodified lignin, demonstrating the development of strong hydroxymethylated linkages in the NR/BR blends matrix. The values of G' of NR/BR with hydroxymethylated lignin composites decline with the upturn of the lignin contents. Nonetheless, lignin networks are relatively weaker than carbon black. The inclusion of lignin's breaks the carbon black network, hence lead to a reduction of the interaction between carbon particles. Consequently the decreasing of Payne effect is due to the substitution of carbon black by lignin.

Curing characteristics

Cure characteristics of NR/BR compound with different content of modified lignin as compared to NR/BR with unmodified lignin and 50 phr of carbon black without lignin are shown in Figure 3. The scorch and cure times reduce with increasing modified lignin content up to 15 phr compared to unmodified lignin-filled as shown in

Figure 3a before it rapidly increased when lignin content is above 15 phr. These trends result in increasing cure rate index (CRI) especially for NR/BR/HMSL than control samples as displayed in Figure 3c. The retardation effect at high lignin contents is due to the increment of the polar surface that absorbs more rubber additives in rubber system [14]. Moreover, hindered phenols in lignin structure also affect the vulcanization of rubber due to its radical scavenging effect. The maximum cure torque (M_H) and torque difference (M_H-M_L) are gradually decreased with increasing modified lignin contents (Figure 3b).This is due to the descent of crosslink density with the inclusion of lignin. However, the values are enhanced compared to unmodified lignin filled especially with the utilization of HMSL due to the presence of more solid filler that leads to contributions from hydrodynamic effect, filler-rubber and filler-filler interactions. The minimum torque (M_L) is similar with unmodified lignin-filled NR/BR composites at same lignin content. The reduction trend with increasing lignin content proposes greater flowability of the rubber composites, demonstrating the substitution of CB by lignin possibly will improve the process-ability behavior [7].

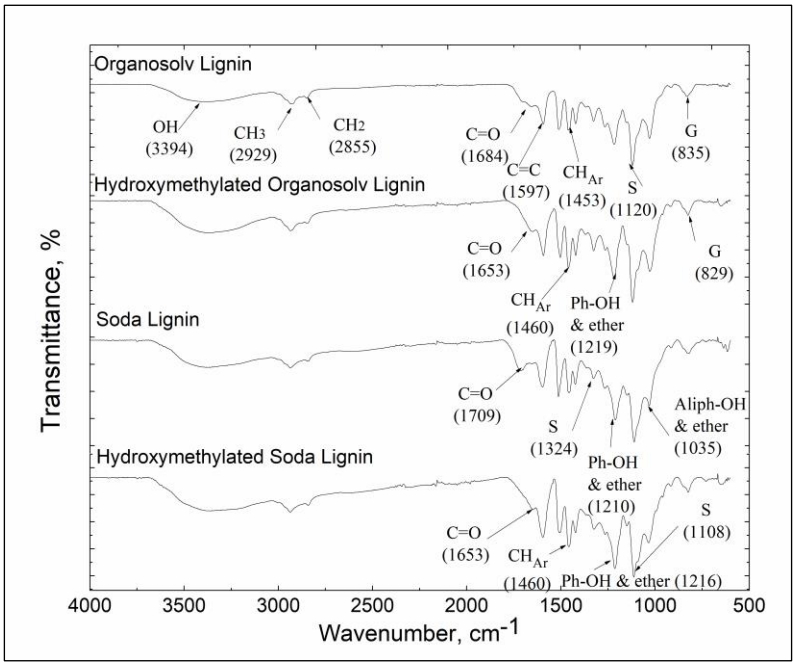


Figure 1. The Fourier transform infrared (FTIR) spectra of unmodified lignin (OL and SL) and hydroxymethylated lignin (HMOL and HMSL)

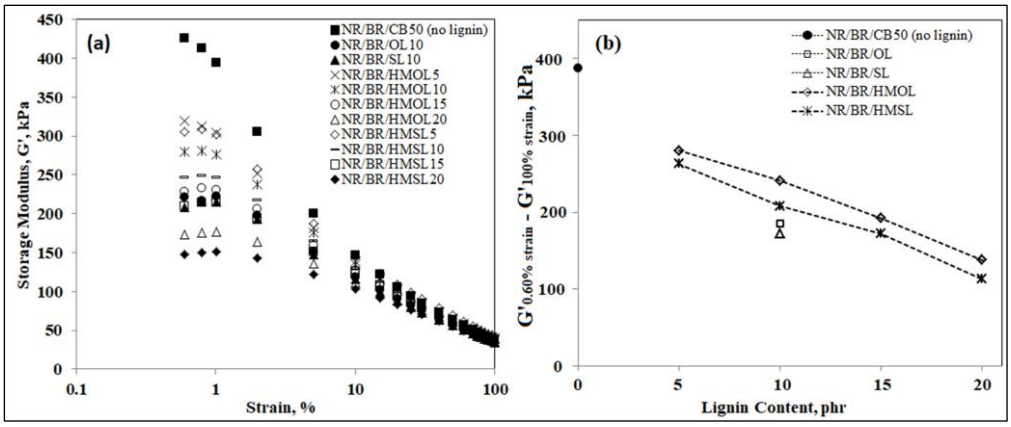


Figure 2. Storage modulus versus strain (a) and Payne effect (b) of NR/BR with unmodified and hydroxymethylated lignin with different loading

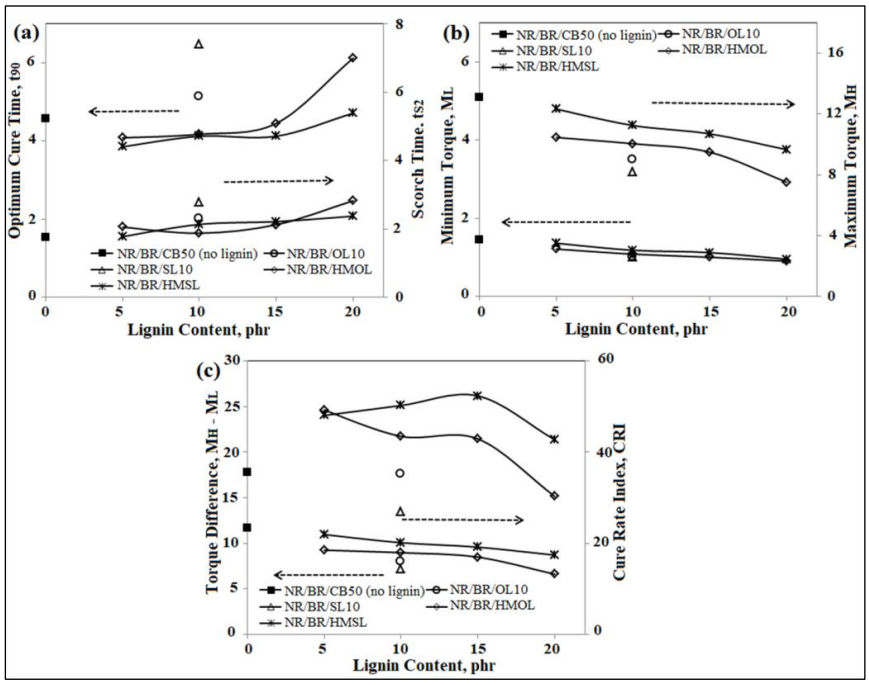


Figure 3. Cure characteristics of NR/BR with different hydroxymethlated lignin content, scorch time, cure time (a) and cure torque (b)

Mechanical properties

Theoretically, the utilization of fillers in the rubber compound may enhance the performance of unfilled rubber such as mechanical properties. This is because all main loads and obstructive deformation encouraged by external stress are hindered by the fillers. Therefore, several factors may improve the rubber performance, i.e. level of filler dispersion and filler-rubber interfacial adhesion. Figure 4 displays the stress-strain graph of the NR/BR composites containing unmodified (OL and SL) and modified lignin (HMOL and HMSL). The tensile properties and hardness of the composites with

increasing lignin content are been summarized in Table 2. It shows that when comparing with unmodified and modified lignin-containing rubber composites, the improvement of hardness is demonstrated only by the inclusion of 5 phr HMOL in the NR/BR compounds, which increase the value from 57.0 (NR/BR/OL) to 60.5 Shore A (NR/BR/HMOL5). It contradicts to the hardness values during incorporation of HMSL in NR/BR compounds, in which 7 – 18% enhancement is observed for all HMSL loading. Meanwhile, the modulus 100% and 300% strain for both HMOL and HMSL increases with lignin loading up to 15 phr when compares to unmodified lignin. This is possibly due to stronger filler-rubber interaction in the modified lignin-filled NR/BR composites. This significant improvement can be ascribed to the hydroxymethyl groups of modified lignin which reacts with rubber molecules especially with the inclusion of HMSL in NR/BR composites at low contents (up to 15 phr). The values are comparable with NR/BR/CB50 (no lignin). This proposes the strongest interaction at rubber-filler interface and the rigid elastomeric network structure as observed in SEM micrograph in Figure 5d [15]. Moreover, it probably due to an effective surface modification towards SL filler originates from the alkaline extraction process. Thus, it is confirmed that hydroxymethylated lignin at low content contributes to the enhancement of interaction between lignin and rubber molecule.

The tensile strength of NR/BR with unmodified lignin, OL and SL are only 15.07 and 15.78 MPa respectively. However, utilization of 10 phr modified lignin improved the tensile strength for both HMOL and HMSL to be 16.72 and 17.20 respectively, which is better or comparable to NR/BR with 50 phr of solely CB. The strength of modified lignin-filled NR/BR composites increased significantly by approximately 10.9% and 8.9% for HMOL and HMSL respectively. This shows that hydroxymethylated lignin at low loading possesses a remarkable reinforcing effect on NR/BR. However, further addition of lignin to more than 10 phr constantly reduces the strength of the NR/BR composites. Nevertheless, HMSL-filled NR/BR composite shows better tensile strength with low content of lignin (up to 10 phr) compared to its HMOL counterpart. The former demonstrates better wetting effect than the latter with unmodified lignin, as evident from SEM micrograph in Figure 5.

Figure 5a and 5c display the fractured surface of rubber composite containing unmodified OL and SL respectively. The surface with OL and SL shows a smooth surface with lignin particles observed on the surface. Lignin distribution for SL seems to be more homogenous compared to OL, which correlates with low Payne effect value shown in Figure 2b and exhibit higher value of tensile strength compared to rubber containing OL. However, after modification, the fractured surface of HMOL- and HMSL-filled with 10 phr loadings becomes rougher compared to unmodified lignin as evident in Figure 5b and 5d respectively. Surface roughness indicates higher modulus and rigid surface with the presence of lignin particle. Moreover, better compatibility and better dispersion (Figure 5d) is observed for HMSL-filled, as its strength is higher than that of HMOL-filled composite. But, the effectiveness in term of the strength of the NR/BR composites is constantly declined with the addition of more than 10 phr of both modified lignin. This deteriorating trend is caused by poor dispersibility and modified filler-rubber interfacial, which is probably due to network formation between lignin particle.

Furthermore, the introduction of the hydroxymethylated group on the lignin structure leads to less elongation at break of the modified lignin-filled rubber composites compared to composite with unmodified lignin. This suggests that the bridge formation between lignin and rubber molecules through “methylene bridge” increases the rigidity of the rubber network structure. Additionally, the short chains bridging neighboring filler particles restrict the chain extensibility, as well as restriction of the slippage of rubber molecular chains on the surfaces fillers, contributed by the good chemical bonding between the filler and rubber matrix at low lignin content [15]. Moreover, the uniform dispersion contributes to strong interaction with the rubber matrix. However, incorporation of modified lignin higher than 10 phr deteriorates the properties due to the potential of filler agglomeration in the rubber matrix.

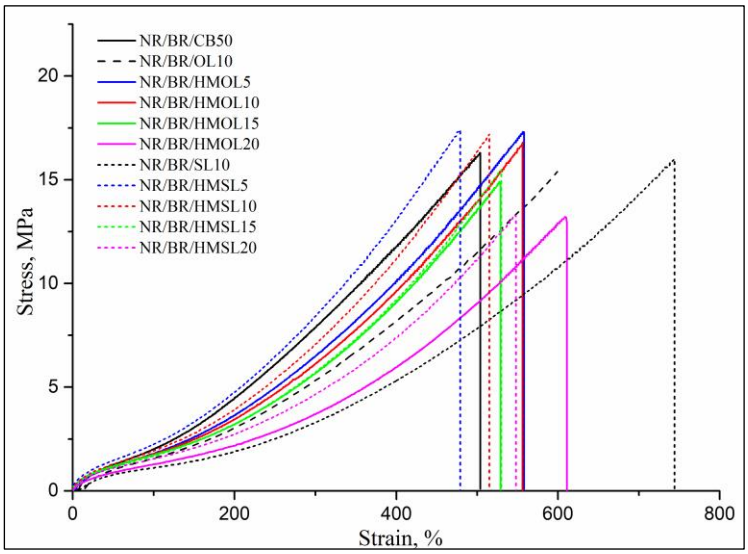


Figure 4. Stress-strain behavior of NR/BR with different hydroxymethlated lignin content

Table 2. Mechanical properties NR/BR compounds with incorporation of hydroxymethylated and unmodified lignin

Sample	**Hardness (Shore A)**	**Modulus at 100% Strain, M100 (MPa)**	**Modulus at 300% Strain, M300 (MPa)**	**Tensile Strength (MPa)**	**Elongation at Break (%)**
NR/BR/CB50	61.0±0.40	2.01±0.02	8.02±0.13	16.72±0.45	501±5.72
NR/BR/OL10	57.0±0.70	1.61±0.12	5.40±0.78	15.07±0.26	599±31.26
NR/BR/HMOL5	60.5±0.24	1.77±0.09	6.58±0.53	17.31±0.17	563±31.26
NR/BR/HMOL10	56.5±0.24	1.76±0.06	6.13±0.36	16.72±0.38	557±28.18
NR/BR/HMOL15	56.5±0.41	1.74±0.02	5.68±0.11	14.84±0.70	530±19.75
NR/BR/HMOL20	51.2±0.24	1.33±0.08	3.72±0.40	13.41±0.15	617±35.49
NR/BR/SL10	52.0±0.30	1.09±0.05	3.22±0.28	15.78±0.15	748±34.41
NR/BR/HMSL5	61.7±0.62	2.19±0.08	8.42±0.16	17.56±0.13	480±5.79
NR/BR/HMSL10	61.5±0.82	1.93±0.03	7.06±0.22	17.20±0.32	510±9.18
NR/BR/HMSL15	60.7±0.47	1.72±0.06	5.82±0.25	15.50±0.23	530±9.46
NR/BR/HMSL20	56.0±0.71	1.55±0.05	4.73±0.15	13.47±0.19	538±8.16

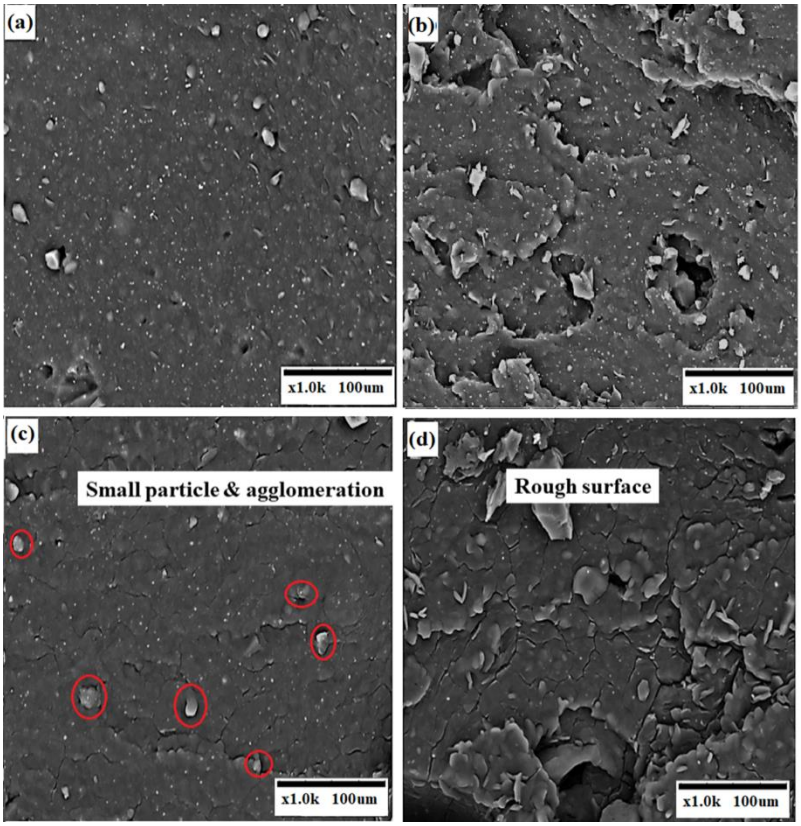


Figure 5. Scanning electronic microscopy (SEM) of NR/BR with 10 phr of (a) unmodified OL, (b) HMOL, (c) unmodified SL and (d) HMSL

Conclusion

A comprehensive characterization of structural organosolv and soda lignin, both unmodified and modified lignin by hydroxymethylation method has been accomplished. This treatment reveals the formation of methylene bridges which connect with the macromolecular lignin. Based on the Payne effect, it can be concluded that the presence of HMOL and HMSL in rubber composite weakens the filler-filler interaction and enhance the rubber's processability as lignin content increases. As the consequences, the optimum cure time, t_{90} and scorch time, t_{S2} reduced by 18% to 36% which contributes to shorter production period. Generally, the most important factors that lead to better reinforcement of rubber composite are filler dispersion and filler-rubber interaction. Unmodified lignin is poorly spread throughout the NR/BR matrix as well as poor interaction between phases. As opposed to unmodified lignin, the incorporation of hydroxymethylated lignin improves the performance of rubber composite contributed by the construction of crosslinking points between filler and rubber matrix. This interaction is advantageous to transmit the external stress from the rubber matrix to hydroxymethylated lignin particles. Low lignin content can endure much more stress than high lignin content thus producing better reinforcing ability on NR/BR composite since the latter has a high tendency of agglomeration. Subsequent enhancement of the mechanical properties of rubber composite at low hydroxymethylated lignin content of up to 10 phr is evident especially for HMSL filler. The hardness of NR/BR/HMSL has been enhanced 7 – 18% with an increment of lignin loading, while tensile strength is improved by almost 10% compared to unmodified lignin up to 10 phr. However, for compounds with HMOL, the hardness enhancement can only be observed for NR/BR/HMOL5. Furthermore, modulus at 100% and 300% strain is improving with the presence of lignin.

Based on the results, replacing CB with HMSL up to 10 phr loading reduces the Payne effect and improves the curing and mechanical performance of rubber composite. This opened up an opportunity for safe manufacturing and green rubber tires.

Acknowledgement

The authors acknowledge School of Materials and Mineral Resources Engineering (SMMRE), Universiti Sains Malaysia (USM), and Prince of Songkla University, Pattani Campus (PSU), Ministry of High Education (MoHE) of Malaysia and Postgraduate Research Attachment (PGRA) Fund, Institute of Postgraduate Studies, USM for funding this research.

References

1. Rajisha, K. R., Maria, H. J., Pothan, L.A., Ahmad, Z. and Thomas, S. (2014). Preparation and characterization of potato starch nanocrystal reinforced natural rubber nanocomposites. *International Journal Biology Macromolecules*, 67: 147-153.
2. Abraham, E., Deepa, B., Pothan, L.A., John, M., Narine, S.S., Thomas, S. and Anandjiwala, R. (2013). Physicomechanical properties of nanocomposites based on cellulose nanofiber and natural rubber latex, *Cellulose,* 20: 417-427.
3. Jong, L. (2014). Modulus enhancement of natural rubber through the dispersion size reduction of protein/fiber aggregates. *Indian Crops Production*, 55: 25-32.
4. Upton, B. M., and Kasko, A. M. (2016). Strategies of the conversion of lignin to high-value polymeric materials: review and perspective. *Chemical Reviews*, 116: 2275-2306.
5. Stewart, D. (2008). Lignin as a base material for material for materials applications, chemistry, application and economics. *Indian Crops Production,* 27: 202-207.
6. Wang, M.-J., Kutsovsky, Y., Zhnag, P., Murphy, L. J., Laube, S. and Mahmud, K. (2002). New generation carbon-silica dual phase filler part 1. Characterization and application to passenger tire. *Rubber Chemistry and Technology*, 75: 247-263.
7. Yu, P., He, H., Jia, Y., Tian, S., Chen, J., Jia, D. and Luo, Y. (2016). A comprehensive study on lignin as a green alternative of silica in natural rubber composites. *Polymer. Testing*, 54: 176-185.
8. Bahl, K., Miyoshi, T. and Jana, S. C. (2014). Hybrid fillers of lignin and carbon black for lowering of viscoelastic loss in rubber compounds. *Polymer,* 55: 3825-3835.
9. Popa, V. I., Căpraru, A. M., Grama, S. and Măluțan, T. (2011). Nanoparticles based on modified lignins with biocide properties. *Cellulose Chemistry Technology*, 45: 221-226.
10. Mohamad Aini, N. A., Othman, N., Hussin, M. H., Sahakora, K. and Hayeemasae, N. (2019). Hydroxymethylation-modified lignin and its effectiveness as a filler in rubber composites. *Processes,* 7: 315.
11. Tejado, A., Pena, C., Labidi, J. and Echeverria, J. M. (2007). Physico-chemical characterization of lignins from different sources for use in phenol-formaldehyde resin synthesis. *Bioresource Technology,* 98: 1655.
12. He, S., Xue, Y., Lin, J., Zhang, L., Du, X. and Chen, L. (2016). Effect of silane coupling agent on the structure and mechanical properties of nano-dispersed clay filled styrene butadiene rubber. *Polymer Composite,* 37: 890-896.
13. Jia, Q.-X., Wu, Y.-P., Wang, Y.-Q., Lu, M., Yang, J. and Zhang, L.-Q. (2007). Organic interfacial tailoring of styrene butadiene rubber-clay nanocomposites prepared by latex compounding method. *Journal Applied Polymer Science*, 103: 1826-1833.
14. Zheng, H., Zhang, Y., Peng, Z. and Zhang, Y. (2004). Influence of clay modification on the structure and mechanical properties of EPDM/montmorillonite nanocomposites. *Polymer Testing*, 23: 217-223.
15. Jiang, C., He, H., Yao, X., Yu, P., Zhou, L. and Jia, D. (2017). The aggregation structure regulation of lignin by chemical modification and its effect on the property of lignin/styrene-butadiene rubber composites. *Journal Applied Polymer Sciences,* 135: 45759.

Malaysian Journal of Analytical Sciences Vol 24 No 6 2020

Articles 15 - 22 are selected papers from the "7th International Conference and Workshop on Basic and Applied Sciences (ICOWOBAS 2019), 16th - 17th July 2019, KSL Resorts, Johor Bahru, Malaysia; organized by the Faculty of Science, Universiti Teknologi Malaysia (Johor, Malaysia), Faculty of Science and Technology, Universitas Airlangga (Surabaya, Indonesia), and Salahaddin University-Erbil (Erbil, Kurdistan, Iraq)."

Guest Editor: Nik Ahmad Nizam Nik Malek

		Page
1.	FIELD-AMPLIFIED SAMPLE INJECTION-CAPILLARY ZONE ELECTROPHORESIS METHOD FOR THE ANALYSIS OF 5-FLUOROURACIL ANTICANCER DRUG (Kaedah Suntikan Sampel Medan Dipertingkat-Elektroforesis Zon Kapilari untuk Analisa Ubat Antikanser 5-Fluorouracil) *Nur Shahz Ereena Zulkifli, Khairil Juhanni Abd Karim, Noorfatimah Yahaya, Wan Aini Wan Ibrahim, Sazlinda Kamaruzaman, Nur Idayu Mat Ghani, Aemi Syazwani Abdul Keyon*	820
2.	STUDY ON THE OXIDATION AND PROPERTIES OF DIHYDROXYL CELLULOSE USING DIFFERENT AMOUNTS OF SODIUM PERIODATE (Kajian ke atas Pengoksidaan dan Pencirian bagi Dihidroksil Selulosa Menggunakan Kuatiti Natrium Periodat yang Berbeza) *Nur Nadia Dzulkifli, Nur Wahibah Mohd Zaki, Ahmad Husaini Mohamed, Nor Monica Ahmad, Sheikh Ahmad Izaddin Sheikh Mohd Ghazali*	830
3.	VALIDATION AND DETERMINATION OF ASCORBIC ACID IN MULTIVITAMIN TABLETS BY DIFFERENTIAL PULSE ANODIC STRIPPING VOLTAMMETRIC TECHNIQUE AT A BARE GLASSY CARBON ELECTRODE (Validasi dan Penentuan Asid Askorbik dalam Tablet Multivitamin Menggunakan Teknik Voltammetrik Perlucutan Anodik Denyutan Pembezaan pada Elektrod Karbon Berkaca) *Nur Syamimi Zainudin, Siti Norbaitina Shaari, Megat Ahmad Kamal Megat Hanafiah*	838
4.	PHYSICOCHEMICAL COMPOSITION OF SPENT OYSTER MUSHROOM SUBSTRATE (Komposisi Fizikokimia bagi Sisa Substrat Cendawan Tiram) *Aina Nasuha Mortada, Mohamad Hasnul Bolhassan, Rafeah Wahi*	848
5.	A SNAPSHOT ON THE IRON CONTENT IN MALAYSIAN CRUDE PALM OIL (Tinjauan Mengenai Kandungan Ferum dalam Minyak Sawit Mentah Malaysia) *Farah Khuwailah Ahmad Bustamam, Najwa Sulaiman, Yeoh Chee Beng, Nik Sasha Khatrina Khairuddin*	855
6.	CHARACTERIZATION OF INCLUSION COMPLEX OF β-CYCLODEXTRIN/ISONIAZID USING SPECTROSCOPIC METHOD (Pencirian Kompleks Kemasukan β-Siklodektrin/Isoniazid Menggunakan Kaedah Spektroskopi) *Nurul Yani Rahim and Nurul Ain Elmira Elleas*	862
7.	PHYSICOCHEMICAL AND SENSORY PROPERTIES OF BREAD ADDED WITH CHICKEN EGGSHELL POWDER	873

	(Fizikokimia dan Sifat Sensori Roti Ditambah dengan Serbuk Kulit Telur Ayam) *Wafiqah Zulkeflee, Pavalee Chompoorat, Raseetha Siva*	
8.	DETERMINATION OF PHENANTHRENE AND FLUORANTHENE IN RICE SAMPLES BY ACTIVATED CARBON-BASED DISPERSIVE SOLID PHASE MICRO-EXTRACTION COUPLED WITH GAS CHROMATOGRAPHY-FLAME IONIZATION DETECTOR ANALYSIS (Penentuan Phenantrena dan Fluorantena dalam Sampel Beras Menggunakan Pengekstrakan Mikro Fasa Pepejal Berserak Berasaskan Karbon Diaktifkan Bersama Analisis Pengesan Pengionan Nyalaan-Kromatografi Gas) *Nurul Nadjwa Nahrowi, Boon Yih Hui, Mohamad Shariff Shahriman, Noorfatimah Yahaya, Nur Nadhirah Mohd Zain, Saliza Asman, Md Firoz Khan, Kavirajaa Pandian Sambasevam, Vuanghao Lim, Muggundha Raoov*	882
9.	DEVELOPMENT OF DISPERSIVE MICRO-SOLID PHASE EXTRACTION FOR THE ANALYSIS OF OFLOXACIN AND SPARFLOXACIN IN HUMAN PLASMA (Pembangunan Pengekstrakan Fasa Pepejal-Mikro Disesarkan untuk Analisis Oflosaksin dan Sparflosaksin dalam Plasma Manusia) *Sohaib Jumaah Owaid, Noorfatimah Yahaya, Nurul Yani Rahim, Rania Adam Edrees Mohammad, Maizatul Najwa Jajuli, Mazidatulakmam Miskam*	893
10.	BIO-BASED CONTENT OF OLIGOMERS DERIVED FROM PALM OIL: SAMPLE COMBUSTION AND LIQUID SCINTILLATION COUNTING TECHNIQUE (Kandungan Berasaskan Bio dalam Oligomer daripada Minyak Sawit: Teknik Pembakaran Sampel dan Penghitungan Sintilasi Cecair) *Mohd Azmil Mohd Noor, Tuan Noor Maznee Tuan Ismail, Razmah Ghazali*	906
11.	A USE OF AN EVERYDAY LIFE CAMERA WITH IMAGE PROCESSING AS ALTERNATIVE DETECTION FOR A FLAME PHOTOMETER (Penggunaan Kamera Harian Dengan Pemprosesan Imej Sebagai Alternatif Pengesanan Fotometer Nyalaan) *Narong Kotchabhakdi and Kate Grudpan*	918
12.	OPTIMISATION AND VALIDATION OF ULTRAHIGH PERFORMANCE LIQUID CHROMATOGRAPHY METHOD FOR QUANTIFICATION OF 25-HYDROXYVITAMIN D IN MATERNAL PLASMA (Pengoptimuman dan Pengesahan Kaedah Kromatografi Cecair Berprestasi Ultra Tinggi untuk Kuantifikasi 25-hidroksivitamin D dalam Plasma Ibu Mengandung) *Siew Siew Lee and Su Peng Loh*	927
13.	STABILITY AND ANTIBACTERIAL PROPERTIES OF GREEN SYNTHESIS SILVER NANOPARTICLES USING *Nephelium lappaceum* PEEL EXTRACT (Kestabilan dan Ciri Antibakteria bagi Sintesis Hijau Nanopartikel Perak Menggunakan Ekstrak Kulit *Nephelium lappaceum*) *Nur Syazwanie Mohd Saidi, Hanis Mohd Yusoff, Irshad Ul Haq Bhat, Suganthi Appalasamy, Alia Diyana Mohamed Hassim, Farhanini Yusoff, Asnuzilawati Asari, Nurul Huda Abdul Wahab*	940
14.	CORROSION BEHAVIOR OF LOW-CARBON STEEL AND STAINLESS STEEL 304 UNDER TWO SOIL CONDITIONS AT PANTAI MENGABANG TELIPOT, TERENGGANU, MALAYSIA (Kelakuan Kakisan dan Penyusutan Bahan Logam Rendah Karbon dan Keluli Tahan Karat 304 di dalam Dua Keadaan Tanih di Pantai Mengabang Telipot, Terengganu, Malaysia) *Suriani Mat Jusoh, Wan Mohd Norsani Wan Nik, Nor Azila Azman, Mohammad Fakhratul Ridwan Zulkifli*	954

15.	PHYTOCHEMICAL ANALYSIS AND ISOLATION OF SECONDARY METABOLITES FROM Persea declinata (Analisis Fitokimia dan Pengasingan Metabolit Sekunder Daripada Persea declinata) *Sani Aliyu, Norazah Basar, Yakubu Rufai, Shamsul Khamis*	970
16.	REMOVAL OF COPPER IONS FROM AQUEOUS SOLUTIONS USING POLY(VINYLBENZYL CHLORIDE) (Penyingkiran Ion Kuprum dari Larutan Akueus Menggunakan Poli(vinilbenzil klorida)) *Hamzah Gamal Abdo Allozy and Khairil Juhanni Abd Karim*	978
17.	SYNTHESIS OF ORDERED NANOARRAYS ACTIVATED CARBON USING SBA-15 AS HARD TEMPLATE FOR ADSORPTION OF IBUPROFEN (Sintesis Karbon Aktif Nano Berketeraturan Menggunakan SBA-15 Sebagai Templat Keras untuk Penjerapan Ibuprofen) *Maria Ulfa, Didik Prasetyoko, Hasliza Bahruji, Wega Trisunaryanti, Yatim Lailun Nimah*	992
18.	EFFECT OF AUXIN AND METHYL JASMONATE ON TOTAL PHENOLIC CONTENT AND TOTAL FLAVONOID CONTENT IN ADVENTITIOUS ROOTS OF *Justicia gendarussa* (Kesan Auksin dan Metil Jasmonat ke atas Jumlah Kandungan Fenolik dan Flavonoid dalam Akar Adventitius *Justicia gendarussa*) *Noor Khaleeda Arsad and Azman Abd Samad*	1002
19.	CELLULOSE ACETATE-TiO2 PHOTOCATALYTIC HOLLOW FIBRE MEMBRANE FOR DEGRADATION OF METHYLENE BLUE (Membran Fiber Berongga Fotomangkin Selulosa Asetat-TiO2 bagi Degradasi Metilena Biru) *Siti Wafiroh, Miriam R. Prananda, Linda Yuliana, Pratiwi Pudjiastuti, Abdulloh*	1013
20.	INDUCTION AND IDENTIFICATION OF BIOACTIVE COMPOUNDS FROM CALLUS EXTRACT OF *Piper betle* L. var. Nigra (Induksi Dan Pengenalpastian Sebatian Bioaktif dari Ekstrak Kalus *Piper betle* L. var. Nigra) *Junairiah, Rizka Kusuma Rahmawati, Yosephine Sri Wulan Manuhara, Ni'matuzahroh, Manikya Pramudya, Lilis Sulistyorini*	1024
21.	FLAVONOIDS WITH MONOAMINE OXIDASE A AND B INHIBITORY AND ANTI-INFLAMMATORY EFFECTS FROM *Vitex grandifolia* (Flavonoid Bersama Perencat Moniamin Oksidase A dan B dan Kesan Anti-Radang dari *Vitex grandifolia*) *Tijjani Ali, Bello Oluwasesan Michael, Abiodun B. Ogbesejana*	1035
22.	ROLE OF VANADIA AND TITANIA PHASES IN THE REMOVAL OF METHYLENE BLUE BY ADSORPTION AND PHOTOCATALYTIC DEGRADATION (Peranan Fasa Vanadia dan Titania dalam Penyingkiran Metilena Biru Melalui Penjerapan dan Degradasi Fotokatalisis) *Pei Wen Koh, Cheng Yee Leong, Leny Yuliati, Hadi Nur, Siew Ling Lee*	1045

Malaysian Journal of Analytical Sciences (MJAS)
Published by Malaysian Analytical Sciences Society

FIELD-AMPLIFIED SAMPLE INJECTION-CAPILLARY ZONE ELECTROPHORESIS METHOD FOR THE ANALYSIS OF 5-FLUOROURACIL ANTICANCER DRUG

(Kaedah Suntikan Sampel Medan Dipertingkat-Elektroforesis Zon Kapilari untuk Analisa Ubat Antikanser 5-Fluorouracil)

Nur Shahz Ereena Zulkifli[1], Khairil Juhanni Abd Karim[1], Noorfatimah Yahaya[3], Wan Aini Wan Ibrahim[1, 2], Sazlinda Kamaruzaman[4], Nur Idayu Mat Ghani[1], Aemi Syazwani Abdul Keyon [1, 2]*

[1]*Department of Chemistry, Faculty of Science*
[2]*Centre for Sustainable Nanomaterials, Ibnu Sina Institute for Scientific and Industrial Research*
Universiti Teknologi Malaysia, 81310 UTM, Johor, Malaysia
[3]*Integrative Medicine Clusters, Advanced Medical and Dental Institute (AMDI),*
Universiti Sains Malaysia, 13200 Kepala Batas, Penang, Malaysia
[4]*Department of Chemistry, Faculty of Science,*
Universiti Putra Malaysia, 43400 UPM Serdang, Selangor, Malaysia

**Corresponding author: aemi@utm.my*

Received: 20 July 2020; Accepted: 11 September 2020; Published: 10 December 2020

Abstract

Field-amplified sample injection-capillary zone electrophoresis (FASI-CZE) method was developed to enhance the detection sensitivity of anticancer drug 5-fluorouracil (5-FU). The analyte was introduced electrokinetically for 5 s into a capillary loaded with highly conductive background electrolyte (BGE). The injected analyte migrated in negative polarity, reducing separation time to 5 minutes as compared to positive polarity in hydrodynamic injection-CZE (18 minutes). FASI-CZE was optimized based on three parameters: Sample injection time (5 s, 10 s, and 40 s), BGE concentration in sample (3 mM, 5 mM, and 10 mM) and BGE concentration (15 mM and 25 mM). Optimization of FASI-CZE was conducted to achieve optimal conditions as followed: 15 mM borate BGE containing 0.1% w/v hexadimethrine bromide (HDMB), 5-FU and 5-BrU (IS) prepared in 5 mM diluted BGE, 20% v/v organic modifier in mixture sample was injected at -5 kV for 5 s. The separation was conducted using -25 kV and detected at the wavelength of 234 nm in diode array detection (DAD). The precision was reasonable; %RSD 4.43% at low concentration levels (5 mg/L). The LOD value was 0.24 mg/L when applied with FASI as compared to 0.58 mg/L using HDI-CZE. The sensitivity enhancement factor (SEF) was almost 3 times higher than HDI-CZE at positive polarity, showing that the proposed of FASI-CZE approach is appropriate for the study of 5-FU at trace level.

Keywords: 5-fluorouracil, field-amplified sample injection, capillary electrophoresis, anticancer drug

Abstrak

Kaedah suntikan sampel medan dipertingkat-elektroforesis zon kapilari (FASI-CZE) dibangunkan untuk pertama kalinya bagi meningkatkan kepekaan pengesanan ubat antikanser 5-fluorouracil (5-FU). Analit diperkenal secara elektrokinetik selama 5 s ke

dalam kapilari yang dimuatkan dengan elektrolit latar belakang yang sangat konduktif (BGE). Analit yang disuntik berpindah dalam medan kutub negatif, mengurangkan masa pemisahan kepada 5 minit berbanding dengan medan kutub positif dalam suntikan hidrodinamik-CZE (18 minit). FASI-CZE dioptimumkan berdasarkan tiga parameter: masa suntikan sampel (5s, 10s, dan 40s), kepekatan BGE dalam sampel (3 mM, 5 mM, dan 10 mM), dan kepekatan BGE (15 mM dan 25 mM). Pengoptimuman FASI-CZE dilakukan untuk mencapai keadaan yang optimum. Keadaan optimum untuk FASI-CZE adalah seperti berikut: 15 mM BGE borat yang mengandungi 0.1% w/v heksadimetrin bromida (HDMB), 5-FU dan 5-BrU (IS) yang disiapkan dalam 5 mM BGE cair, 20% v/v pengubah organik dalam campuran sampel disuntik pada voltan -5 kV selama 5 s. Pemisahan dilakukan dengan menggunakan -25 kV voltan dan dikesan pada panjang gelombang 234 nm dalam pengesanan susunan diod (DAD). Ketepatannya wajar; %RSD 4.43% pada tahap kepekatan rendah (5 mg/L). Nilai LOD adalah 0.24 mg/L ketika diterapkan dengan FASI berbanding 0.58 mg/L menggunakan HDI-CZE. Faktor peningkatan kepekaan (SEF) hampir 3 kali lebih tinggi daripada HDI-CZE pada medan kutub positif, menunjukkan bahawa pendekatan FASI-CZE yang dicadangkan sesuai untuk kajian 5-FU pada tahap kepekatan surih.

Kata kunci: 5-fluorouracil, suntikan sampel medan dipertingkat, elektroforesis zon kapilari, elektroforesis kapilari, ubat antikanser

Introduction

Cancer is considered as one of the world's most serious causes of death. Different types of chemotherapy drugs are used to effectively treat various cancers [1]. But patients are more likely to receive chemotherapy along with surgery, radiotherapy, targeted therapy or immunotherapy [2]. There are about 178 drugs used to combat various types of human cancers [3]. The most widely prescribed cancer treatment includes 5-fluorouracil (5-FU), cyclophosphamide, and hydroxyurea [4]. Fluoropyrimidine 5-FU drug has been used for almost 50 years in routine clinical oncology [5]. 5-FU primarily acts as an inhibitor of thymidylate synthase, disrupting the action of enzyme, that is a nucleoside required for DNA replication [6]. The durability and the effectiveness of the drug in cancer chemotherapy is due to the fact that 5-FU is the only anticancer agent on the market that demonstrates compatibility with most combinations of anticancer drugs [7]. Most anticancer drugs contain compounds that are highly toxic due to low therapeutic index and may have strong pharmacological properties from their degradation products that can often lead to an increase in toxicity [8]. Therefore, reliable and sensitive analytical approaches are certainly necessary for determination of 5-FU.

Since capillary electrophoresis (CE) works with any form of ionizable material regardless of polarity, CE-ultraviolet (CE-UV) method has been developed for the analysis of 5-FU [9] and cytarabine [10]. CE is a highly efficient separation technique that provides rapid, inexpensive, low detection limits. Therefore, CE might be a strong alternative for anticancer drugs determination. It was found that due to the above advantages, CE is becoming more common among oncologists [3]. Given the high performance of CE approaches, the issue of relatively low sensitivity cannot be avoided due to limited volume of sample injected (2-10 nL) and short optical pathlength (25-100 um) in spectroscopy-based detectors [11]. The use of sensitive detection techniques such as laser-induced fluorescence, mass spectrometry, and electrochemical detection. is able to improve CE sensitivity [12, 13]. Besides, sensitivity improvement of CE can be achieved by employing a special design of detection cells such as bubble cells [14] and Z-shaped cells [15], due to the extended optical path. The applicability of such approaches is however constrained by time-consuming or expensive setups. Most CE systems; on-line sample preconcentration or stacking techniques, have been commonly employed for the enhancement of concentration sensitivity in CE [13]. These techniques are focused on specific mechanism of preconcentration, which depends on variations in the properties of sample solution and a running buffer [11], and developed dependent on the physico-chemical characteristics of electrophoresis [16]. The three mechanisms that are frequently used are field-amplified sample injection, transient isotachophoresis (t-ITP) [17], and dynamic pH junction stacking and sweeping [16]. FASI-CZE is the simplest and most effective preconcentration technique[18].

FASI, which is established based on the difference in conductivity between the sample and buffer zones, remains as one of the most sought-after stacking techniques due to its simplicity. The analyte from the sample solution (prepared in a diluted BGE) electrokinetically enters the capillary filled with high conductivity BGE. Theoretically, the stacking occurs in the boundary region between high resistivity solvent and BGE, and the separation was performed [19]. Hence, at the point when the sample ions cross the boundary between the analyte and the BGE with high voltage, the ions may undergo a large decrease in velocity owing to a drastic drop in the local electric field, thus causes stacking at the boundary [16]. FASI offers a simpler process and relatively short enrichment time, as well as allows for a greater amount of analyte addition. The present paper reports the development and validation of FASI-CZE for 5-FU. The optimization of the experimental conditions was conducted and the validity of FASI was assessed. FASI-CZE was optimized based on three parameters: Sample injection time (5 s, 10 s, and 40 s), BGE concentration in sample (3 mM, 5 mM, and 10 mM) and BGE concentration (15 mM and 25 mM). The optimal conditions were as follow: -5 kV for 5 s, 20 mg/L standard mixture prepared in 5 mM diluted BGE containing 20% v/v organic solvent and 15 mM borate BGE only (pH 9.3).

Materials and Methods

All chemical materials such as 5-fluorouracil (5-FU ≥ *99%* HPLC), and 5-bromouracil (5-BrU, 98%) were purchased with highest grade of purity from Nano Life Quest Sdn Bhd and supplied by Sigma Aldrich from Shah Alam, Selangor. Boric acid and hexadimethrine bromide (HDMB) were also purchased from Sigma Aldrich, while sodium hydroxide pellets were purchased from Qrec (ASIA) Sdn Bhd. Other chemicals such as methanol (MeOH) of HPLC grade and di-sodium tetraborate decahydrate were obtained from Merck from Masai, Johor by VNK Supply and Service company.

HDI-CZE and FASI-CZE experiments were conducted using Agilent CE (7100, Agilent Technologies, Waldbronn, Germany) coupled with diode array detector (DAD). Electrophoretic separations were accomplished using 64.5 cm polyimide coated fused-silica capillary with an effective length of 56.0 cm. The capillary was placed at a temperature of 25 °C. For normal polarity HDI-CZE, pressure–assisted hydrodynamic injection (HDI) was used to load the sample (10 s, 3.5 kPa) with +25 kV separation voltage. BGE consisted of a buffer solution with 25 mM of di-sodium tetraborate decahydrate (pH 9.3). Two wavelengths of 234 nm and 270 nm were performed on the analytes for the detection of UV absorption using UV-DAD. From the two wavelengths, the 234 nm wavelength was the best detection wavelength for the analytes. On the other hand, FASI was performed by introducing the sample into the capillary using electrokinetic injection (EKI) at -5 kV for 5 s, using -25 kV separation voltage and BGE (borate buffer with pH 9.3). The standard solutions were prepared in a 10x diluted borate BGE buffer solution containing 20% v/v of organic modifier used as a sample matrix to ensure the ionization of 5-FU (the chemical structure of 5-FU as in Figure 1) and its internal standard of 5-bromouracil (5-BrU). For instrumental quality parameters, 5-fluorouracil was prepared in five different concentrations (0.5 ppm, 5 ppm, 10 ppm, 20 ppm, and 25 ppm) and each concentration were mixed constantly with 20 ppm of internal standard (IS) 5-BrU.

Intra-day (all concentrations) and inter-day (three consecutive days with two different concentrations) analyses were fully validated by performing external calibration curve, calculating LODs and LOQs, precision and %RSD. Prior to use, the new capillary was pretreated with 1 M NaOH at 950 mbar for 60 minutes, Milli-Q water for 20 minutes, and borate buffer (pH 9.3) only as BGE for 10 minutes. The capillary was conditioned with Milli-Q water for 5 minutes at the start of the day to ensure the electrodes for both inlet and outlet were clean. The capillary was further conditioned with NaOH (0.1M) for 10 minutes, again with water (10 minutes), with 1% w/v HDMB (20 minutes), and lastly with 20 minutes BGE (added with diluted HDMB [0.1% w/v]). Between each run, the capillary was rinsed with BGE (added with 0.1% w/v HDMB) for 5 minutes to ensure that the capillary wall was still coated with HDMB surfactant before sample injection. The electropherograms were controlled by Agilent ChemStation software.

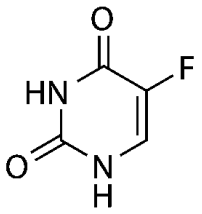


Figure 1. Chemical structure of 5-FU

Results and Discussion

Separation of analytes using CZE

5-FU is an acidic compound (with p*K*a= 7.93) that can be negatively charged when in an alkaline medium [20, 21]. Separation at positive (normal) polarity +25 kV voltage using di-sodium tetraborate decahydrate buffer at pH 9.3 as BGE was able to separate 5-FU and 5-BrU, having resolution (Rs) just above 1.5. Even though both negatively charged compounds could arrive at the detector end due to the electroosmotic flow (EOF), they were also strongly attracted towards the anode, resulting in poor peak shape (wide and tailing) and long analysis time (18 minutes), as shown in Figure 2. In this case, effective separation was accomplished by conducting the separation in negative polarity with the aid of HDMB, which is a polycationic polymer that acts as a cationic surfactant for EOF reversal. The positively charged HDMB attached to the negatively charged double layer within the fused silica capillary, was attracted towards the anode, thus reversing the EOF. The separation in negative polarity HDI-CZE condition gave a good resolution (Rs > 1.5) and shorter analysis time (< 5 minutes) as compared to the separation using positive polarity HDI-CZE (< 18 minutes) (Figure 2).

Field-amplified sample injection-CZE (FASI-CZE)

Having the optimized criteria for the separation, the sensitivity enhancement is important for analyte trace analysis. FASI was chosen as a quick online preconcentration method prior to CZE. The analytes entered the capillary through EKI, and they stacked up between low conductive sample (analyte prepared in low concentration BGE) and BGE in the boundary region dependent on the velocity changes of the analytes, and then separation started to occur. FASI helps improve sensitivity by introducing more ions from the sample vial. Moreover, FASI has been reported to enhance sensitivity up to 1000x [22]. FASI-CZE of 5-FU and 5-BrU were optimized systematically to enhance sensitivity as well as to reduce analysis time.

Effect of sample injection time

Electrokinetic sample injection times of 5 s, 10 s, and 40 s were tested. Theoretically, the higher the injection time, the greater the signal. Increasing the injection time improved the signal but caused some loss in resolution and peak symmetry. It was found to be more acceptable when sample injected for 5 s even though signal gradually increased from 5 s to 40 s (as electropherograms depicted in Figure 3), where 40 s injection time showed highest signal. This was because of the difference in conductivity between the injected sample plug and separation BGE inside capillary. Nevertheless, the peaks became less symmetrical and peak width increased (dispersion effect). Better repeatability was observed for 5 s injection time (RSD 0.62%), and the resolution between 5-FU and the IS was much higher. Therefore, 5 s injection time was selected in subsequent FASI optimization.

Effect of concentration of BGE in sample

The rationale to optimize BGE concentration in sample was to enhance the sensitivity of the analyte, as FASI helps to stack the analyte (increasing the peak signal). Borate buffer in BGE was diluted and added with 20% v/v MeOH as an organic modifier in the sample. The organic solvent was used to increase solubilization, minimize conductivity, and enhance FASI [22]. For this

study, the conductivity of the sample must be at least ten times less than the electrolyte, which is one of the stacking criteria. The sample was prepared by diluting in a diluted buffer (at least 10 times dilution) to allow stacking due to extreme difference in conductance. Three different concentrations (3 mM, 5 mM, and 10 mM) of diluted BGE were tested. The signals increased when the concentration of diluted BGE decreased (as shown in Figure 4). The resolutions for the three different diluted BGE concentrations were observed with Rs values of 2.67, 2.64, and 2.56, respectively. Therefore, 5 mM was chosen as the optimum concentration.

Effect of separation of BGE concentration

The effect of increasing the electrolyte concentration will increase the current and the migration of EOF, and sometimes the current will suddenly drop due to instability of the buffer system. Thus, inorganic electrolytes such as borate and phosphate must be optimized appropriately and used in low concentrations because of their high conductivities. The separation BGE concentrations (15 mM and 25 mM) were tested, while the other conditions were made constant; sample injection at -5 kV for 5 s (sample injection voltage × time: -25 kV.s), and the standard mixture (20 mg/L) contained 5 mM BGE. Although the signal for 25 mM concentration was better, 15 mM was still preferred for separation BGE. This was because the peak tailing and width were minimized, which gave the peak width ratio value 1.25 using 15 mM borate BGE as compared to 25 mM borate BGE (1.32), giving a better separation of the compounds.

Accordingly, FASI-CZE optimum conditions were 15 mM separation BGE concentration, 5 s sample injection time, and sample should contain 5 mM diluted BGE with 20% MeOH as the organic modifier. The electropherogram of 5-FU and 5-BrU at optimum conditions is shown in Figure 5.

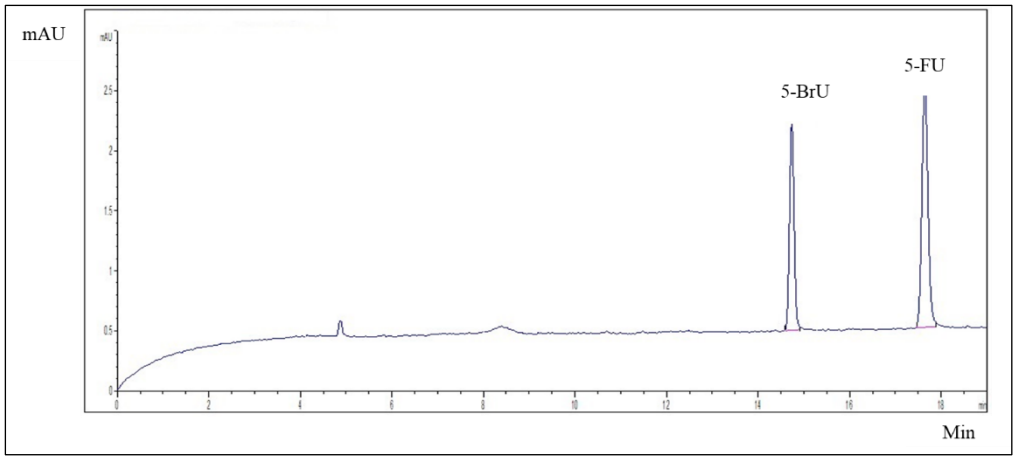


Figure 2. Electropherogram showing separation of 5-BrU and 5-FU using positive polarity HDI-CZE at 25 kV CE conditions: polyimide coated fused-silica capillary (i.d.= 50 μm, l= 56 cm, L= 64.5 cm); 25 mM borate BGE (pH 9.3); separation at 25 ^{o}C. Experiment was performed on standards mixture (20 mg/L); UV detection at 234 nm.

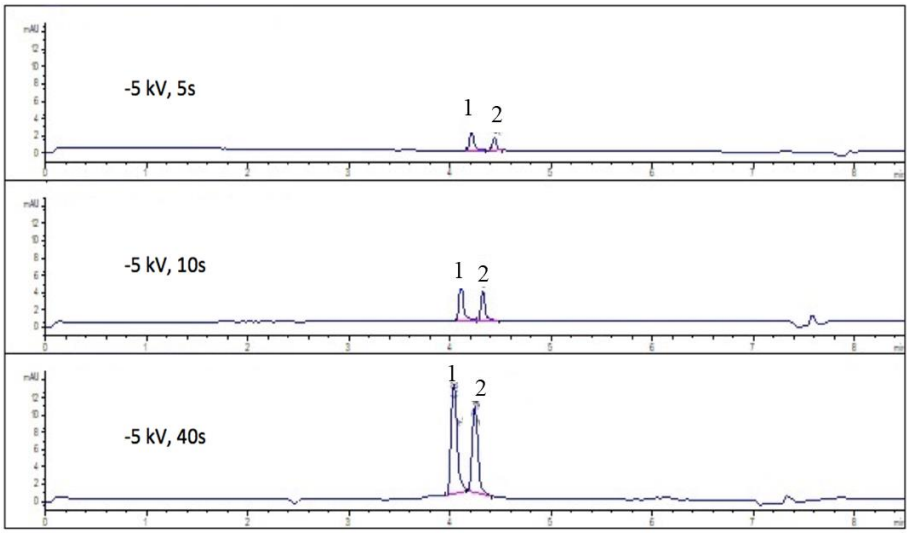


Figure 3. Electropherograms showing separation of 5-FU and 5-BrU using negative polarity FASI-CZE. Effect of the sample injection time. CE conditions: polyimide coated fused-silica capillary (i.d.= 50 μm, *l*= 56 cm, L= 64.5 cm); 25 mM borate BGE (pH 9.3) (added with 0.1% HDMB); separation at 25 ^{o}C and -25 kV. Peak 1 = 5-FU, peak 2 = 5-BrU. Experiment was performed on standards mixture (20 mg/L); UV detection at 234 nm.

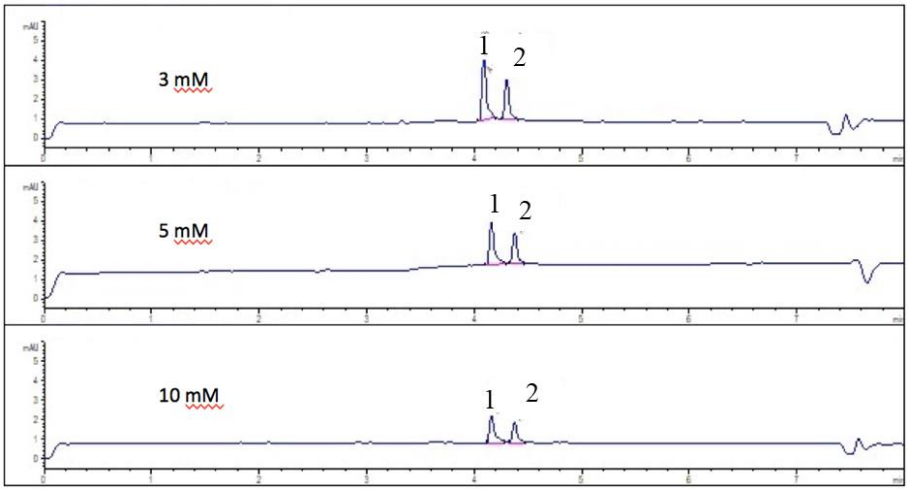


Figure 4. Electropherograms showing separation of 5-FU and 5-BrU using negative polarity FASI-CZE. Effect of BGE concentration in sample. CE conditions: polyimide coated fused-silica capillary (i.d.= 50 μm, *l*= 56 cm, L= 64.5 cm); 25 mM borate BGE (pH 9.3) (added with 0.1% HDMB); separation at 25 ^{o}C and -25 kV. Other experimental conditions as in Figure 3.

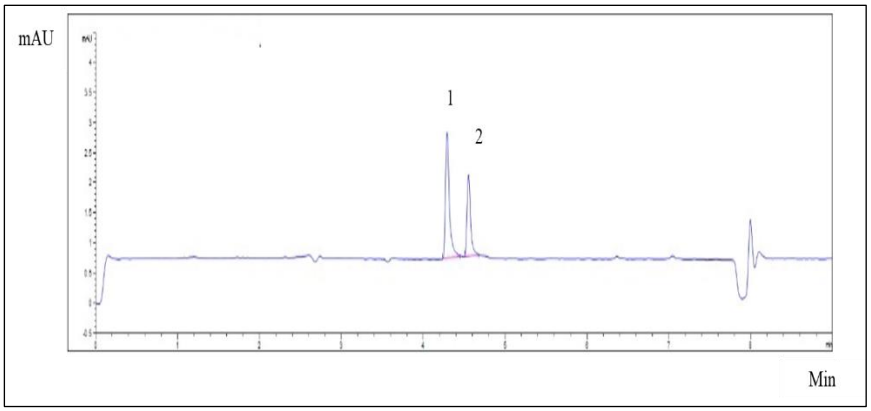


Figure 5. Electropherogram showing separation of 5-FU and 5-BrU using optimized negative polarity FASI-CZE conditions. CE conditions: polyimide coated fused-silica capillary (i.d.= 50 µm, *l*= 56 cm, L= 64.5 cm); 15 mM borate BGE (pH 9.3) (added with 0.1% HDMB); separation at 25 °C and -25 kV; Experiment was performed on standards mixture (20 mg/L) prepared in diluted BGE (5 mM) containing 20% v/v of MeOH; standards mixture was injected by EKI at -5 kV for 5 s. Other experimental conditions as in Figure 3.

Method validation

The method validation for HDI-CZE and FASI-CZE were conducted under optimum conditions. An external calibration curve was plotted from 0.5 mg/L to 25 mg/L, whereby good coefficient of regression was achieved with $R^2 > 0.997$. The limit of detection (LOD) for both methods were obtained based on a signal to noise ratio (S/N) of 3. As summarized in Table 1, HDI-CZE method provided a LOD value of 0.58 mg/L. With the pre-concentration technique of FASI, the LOD value reduced to a value of 0.24 mg/L, indicating improvement of sensitivity. The limit of quantification values (LOQ) obtained based on S/N of 10; 1.97 mg/L and 0.82 mg/L for HDI-CZE and FASI-CZE methods, respectively. The SEF obtained was almost 3 times higher than HDI-CZE method at positive polarity. Intraday and interday precisions were calculated for the signal (peak to height ratio, PHR). The RSD% values obtained for intraday and interday were 6.69% (5 mg/L) and 4.43% (5 mg/L), respectively. Table 2 summarizes current FASI-CZE method performance with other reported methods. Table 2 summarizes comparative data from our work against other reported CZE methods. The negative polarity FASI-CZE method compares well with other methods. The present LOD value for 5-FU was comparable or superior with most of the other methods. Most importantly, the total separation time achieved in our work was the shortest among all (due to the negative polarity used during separation of anionic analytes in a coated capillary).

Table 1. The analytical figure of merits for both analytes using HDI-CZE and FASI-CZE methods

Compound	Method	LODs (mg/L)	(SEF_c)[a]	Intraday %RSD (*n* = 3)	Interday %RSD (*n* = 3)
				Signal (PHR)[b]	Signal (PHR)[b]
5-FU	HDI-CZE	0.58	-		
5-FU	FASI-CZE	0.24	3	6.69	4.43

[a] SEF_c = LOD (HDI-CZE)/ LOD (FASI-CZE)

[b] Peak height ratio (PHR) = Height (5-FU)/ Height (IS)

Table 2. FASI-CZE method performance with other reported methods

Analyte	Separation Mode	Total Separation Time	LODs	Regression Coefficient	Intraday %RSD	Interday %RSD	Ref.
5-FU	HDI-CZE	<6 min	1.72 μg/mL	0.999	<7.6%	<8.8%	[23]
5-FU	HDI-CZE	10 min	2.60 mg/L	0.994	NA	NA	[24]
5-FU	HDI-CZE	<15 min	NA	0.999	<2.9%	<2.9%	[25]
5-FU	HDI-CZE	15 min	1.04 μM	0.999	2.0%	3.3%	[26]
5-FU	HDI-CZE	21 min	1.7 μg/L	0.9992	0.7-8.9%	2.2-9.5%	[27]
5-FU	FASI-CZE	4.4 min	0.24 mg/L	0.997	6.69%	4.43%	Current work

NA = Not available

Conclusion

A new negative polarity FASI-CZE method was developed for the analysis of 5-FU. With FASI, LOD of 0.24 mg/L was obtained as compared to positive polarity HDI-CZE with 0.58 mg/L, indicating that FASI could be an effective alternative method to increase sensitivity. A BGE solution of 15 mM sodium tetraborate buffer was recommended as the optimal solution for CZE separation of 5-FU. HDMB surfactant was used as co-EOF to reverse the EOF, giving the capillary wall a net positive charge. The migration time of analytes was significantly reduced by the assistance of FASI, thus allowed the analytes to be separated within 5 min using 15 mM borate BGE at pH 9.3 added with 0.1% w/v HDMB. Further application of this online sample preconcentration system through increased speed and sensitivity will render CE a great instrument in the routine monitoring in healthcare and pharmaceutical industry, as well as environmental analysis (soil and water bodies polluted with 5-FU residuals).

Acknowledgement

A.S.A.K is grateful for the financial support of the work by the Ministry of Higher Education Malaysia (MOHE) and Universiti Teknologi Malaysia via Fundamental Research Grant Scheme (R.J130000.7854.5F010) and Universiti Teknologi Malaysia Fundamental Research grant (UTMFR, Q.J130000.2554.20H98). N.Y thanked financial support from Universiti Sains Malaysia through Research University Grant (1001.CIPPT.8011052).

References

1. Abdollahi, Z., Taheri-Kafrani, A., Bahrani, S. A. and Kajani, A. A. (2019). Pegaylated graphene oxide/superparamagnetic nanocomposite as a high-efficiency loading nanocarrier for controlled delivery of methotrexate. *Journal of Biotechnology*, 298: 88-97.
2. National Cancer Institute (2018). Chemotherapy and you. National Cancer Institute, U.S.: pp. 1-55.
3. Ali, I., Haque, A., Wani, W. A., Saleem, K., and Al Za'abi, M. (2013). Analyses of anticancer drugs by capillary electrophoresis: A review. *Biomedical Chromatography*, 27(10): 1296-1311.
4. Usawanuwat, J., Boontanon, N. and Boontanon, S. K. (2014). Analysis of three anticancer drugs (5-fluorouracil, cyclophosphamide and hydroxyurea) in water samples by HPLC-MS/MS. *International Journal of Advances in Agricultural & Environmental Engineering*, 1: 72-76.
5. Saif, M. W., Choma, A., Salamone, S. J. and Chu, E. (2009). Pharmacokinetically guided dose adjustment of 5-fluorouracil: A rational approach to improving therapeutic outcomes. *JNCI: Journal of the National Cancer Institute*, 101(22): 1543-1552.

6. Kosjek, T. and Heath, E. (2011). Occurrence, fate and determination of cytostatic pharmaceuticals in the environment. *TrAC Trends in Analytical Chemistry*, 30(7): 1065-1087.
7. Cirillo, G., Iemma, F., Puoci, F., Parisi, O. I., Curcio, M., Spizzirri, U. G. and Picci, N. (2009). Imprinted hydrophilic nanospheres as drug delivery systems for 5-fluorouracil sustained release. *Journal of Drug Targeting*, 17(1): 72-77.
8. Zalewska, M., Wilk, K., and Milnerowicz, H. (2013). Capillary electrophoresis application in the analysis of the anti-cancer drugs impurities. *Acta Poloniae Pharmaceutica*, 70(2): 17180.
9. Sun, H., Wu, Y., He, P., Zuo, Y. and Lv, Y. (2012). Characterization of interaction between antitumor drug 5-fluorouracil and human serum albumin by affinity capillary electrophoresis. *Asian Journal of Pharmaceutical Sciences*, *7*(1): 75-79.
10. Guichard, N., Guillarme, D., Bonnabry, P. and Fleury-Souverain, S. (2017). Antineoplastic drugs and their analysis: A state of the art review. *Analyst*, 142(13): 2273-2321.
11. Forough, M., Farhadi, K., Molaei, R., Khalili, H., Shakeri, R., Zamani, A. and Matin, A. A. (2017). Capillary electrophoresis with online stacking in combination with AgNPs@ MCM-41 reinforced hollow fiber solid-liquid phase microextraction for quantitative analysis of capecitabine and its main metabolite 5-fluorouracil in plasma samples isolated from cancer patients. *Journal of Chromatography B*, 1040: 22- 37.
12. Zhang, Z., Zhang, F. and Liu, Y. (2013). Recent advances in enhancing the sensitivity and resolution of capillary electrophoresis. *Journal of Chromatographic Science*, 51(7): 666-683.
13. Kitagawa, F. and Otsuka, K. (2014). Recent applications of on-line sample preconcentration techniques in capillary electrophoresis. *Journal of Chromatography A*, 1335: 43-60.
14. Xue, Y. and Yeung, E. S. (1994). Characterization of band broadening in capillary electrophoresis due to nonuniform capillary geometries. *Analytical Chemistry*, 66(21): 3575-3580.
15. Bruin, G. J. M., Stegeman, G., Van Asten, A. C., Xu, X., Kraak, J. C. and Poppe, H. (1991). Optimization and evaluation of the performance of arrangements for uv detection in high-resolution separations using fused-silica capillaries. *Journal of Chromatography A*, 559(1-2): 163-181.
16. Chen, X., Tang, Y., Wang, S., Song, Y., Tang, F. and Wu, X. (2015). Field-amplified sample injection in capillary electrophoresis with amperometric detection for the ultratrace analysis of diastereomeric ephedrine alkaloids. *Electrophoresis*, 36(16): 1953-1961.
17. Rabanes, H. R., Aranas, A. T., Benbow, N. L. and Quirino, J. P. (2012). Synergistic effect of field enhanced sample injection on micelle to solvent stacking in capillary electrophoresis. *Journal of Chromatography A*, 1267: 74-79.
18. Purrà, M., Cinca, R., Legaz, J. and Núñez, O. (2014). Solid-phase extraction and field-amplified sample injection–capillary zone electrophoresis for the analysis of benzophenone UV filters in environmental water samples. *Analytical and Bioanalytical Chemistry*, 406(25): 6189-6202.
19. Hou, X., Deng, D., Wu, X., Lv, Y. and Zhang, J. (2010). Simultaneous stacking of cationic and anionic compounds in single run capillary zone electrophoresis by two-end field amplified sample injection. *Journal of Chromatography A*, 1217(35): 5622-5627.
20. Diasio, R. B. and Harris, B. E. (1989). Clinical pharmacology of 5-fluorouracil. *Clinical Pharmacokinetics*, 16(4): 215-237.
21. Wielińska, J., Nowacki, A. and Liberek, B. (2019). 5-fluorouracil—complete insight into its neutral and ionised forms. *Molecules*, 24(20): 3683.
22. Breadmore, M. C. (2007). Recent advances in enhancing the sensitivity of electrophoresis and electrochromatography in capillaries and microchips. *Electrophoresis*, 28(1-2): 254-281.
23. Prochazkova, A., Liu, S., Friess, H., Aebi, S., and Thormann, W. (2001). Determination of 5-fluorouracil and 5-fluoro-2'-deoxyuridine-5'-monophosphate in pancreatic cancer cell line and other biological materials using capillary electrophoresis. *Journal of Chromatography A,* 916: 215-224.

24. Flores, J. R., Nevado, J. J. B., Penalvo, G. C., and Caceres, M. I. R. (2003). Direct capillary electrophoretic determination of three chemotherapeutic drugs in human urine. *Journal of Chromatographia,* 57: 493-496.
25. Lu, H.-j., Guo., Y.-l., Zhang, H. and Ou, Q.-y. (2003). Rapid determination of 5-fluorouracil in plasma using capillary electrophoresis. *Journal of Chromatography B,* 788(2): 291-296.
26. Liu, Y., Zhu, P., Huang, Z., Zhou, Li. and Shi, P. (2018). Simultaneous detection of 5-fluorocytosine and 5-fluorouracil in human cells carrying CD/5-FC suicide gene system by using capillary zone electrophoresis. *Journal of Chromatography B,* 1076: 1-7.
27. Mahnik, S. N., Rizovski, B., Fuerhacker, M., and Mader, R. M. (2004). Determination of 5-fluorouracil in hospital effluents. *Analytical and Bioanalytical Chemistry,* 380(1): 31-35.

Malaysian Journal of Analytical Sciences (MJAS)
Published by Malaysian Analytical Sciences Society

STUDY ON THE OXIDATION AND PROPERTIES OF DIHYDROXYL CELLULOSE USING DIFFERENT AMOUNTS OF SODIUM PERIODATE

(Kajian ke atas Pengoksidaan dan Pencirian bagi Dihidroksil Selulosa Menggunakan Kuatiti Natrium Periodat yang Berbeza)

Nur Nadia Dzulkifli*, Nur Wahibah Mohd Zaki, Ahmad Husaini Mohamed, Nor Monica Ahmad, Sheikh Ahmad Izaddin Sheikh Mohd Ghazali

School of Chemistry and Environment, Faculty of Applied Sciences,
Universiti Teknologi MARA Negeri Sembilan Branch, Kuala Pilah Campus,
Pekan Parit Tinggi 72000 Kuala Pilah, Negeri Sembilan

**Corresponding author: nurnadia@uitm.edu.my*

Received: 23 July 2020; Accepted: 23 September; Published: 10 December 2020

Abstract

Sodium periodate is as an oxidizing agent that breaks the cellulose ring at the C2-C3 bond of the anhydroglucose units (AGU) by creating two vicinal hydroxyl groups which have the potential to form a Schiff base for further reactions. The objective of this study was to evaluate the effects of different amounts of sodium periodate on the formation and arrangement of hydroxyl groups at the C2-C3 bond of the anhydroglucose units (AGU), which is so-called dihydroxyl cellulose (DHC). Firstly, microcrystalline cellulose (MCC) was sonicated to break down the intermolecular and intramolecular interactions. Then, MCC was oxidized with 3 g and 5 g of sodium periodate to prepare the DHC compounds. The DHC and MCC were characterized by FTIR-ATR, FESEM, TGA, and XRD techniques. The numbers of hydroxyl group of DHC increased with the addition of sodium periodate. Besides, the thermal stability and crystallinity of DHC was found to be higher with the increasing amount of sodium periodate. Lastly, the morphology of DHC was found to be smooth, needle- (1:3) and leaf-like (1:5) structure as compared to the irregular forms of MCC. Difference of thermal stability, crystallinity, and morphological structure of DHC compounds concluded that different amounts of sodium periodate could modify the physicochemical properties of MCC.

Keywords: microcrystalline cellulose, dihydroxyl cellulose, sodium periodate, oxidation

Abstrak

Sodium periodat adalah agen pengoksidaan yang membuka gegelang selulosa di ikatan C2-C3 pada unit anhidroglukosa (AGU) dengan mewujudkan dua kumpulan visinal hidroksi yang berpotensi untuk membentuk Bes Schiff bagi tindak balas selanjutnya. Objektif kajian ini ialah untuk menilai kesan perbezaan kuantiti natrium periodat ke atas pembentukan dan susunan kumpulan hidroksil di ikatan C2-C3 pada unit anhidroglukosa (AGU), yang dikenali sebagai dihidroksi selulosa (DHC). Pertamanya, mikrohablur selulosa (MCC) telah disonikasi untuk memutuskan interaksi intermolekul dan intramolekul, Kemudian, MCC dioksidakan dengan 3g dan 5g natrium periodat untuk menyediakan sebatian DHC. DHC dan MCC dicirikan dengan teknik FTIR-ATR, FESEM, TGA, dan XRD. Bilangan kumpulan hidroksil bagi DHC meningkat dengan penambahan kuantiti natrium periodat. Disamping itu, kestabilan haba dan kehabluran DHC dikenalpasti adalah tinggi dengan peningkatan kuantiti natrium periodat. Terakhir, morfologi DHC dikenalpasti adalah licin, struktur yang menyerupai jejarum (1:3) dan dedaun (1:5) berbanding dengan bentuk yang tidak teratur bagi MCC. Perbezaan kestabilan haba, kehabluran dan struktur morfologi sebatian DHC dapat disimpulkan bahawa perbezaan kuantiti natrium periodat berupaya mengubah sifat fizik-kimia MCC.

Kata kunci: mikrohablur selulosa, dihidroksi selulosa, natrium periodat, pengoksidaan

Introduction

Cellulose is categorized as a biopolymer which is biocompatible, hydrophilic, and biodegradable by nature [1]. Each cellulose moiety is composed of multiple (1,4)-linked *ß-D*-glucan linear chains [2]. Hydrogen bonds are formed between hydroxyl (OH) groups from a chain with a nearby oxygen atom to build up stable and rigid cellulose structures, protecting them from being dissolved by common solvents. Various processes have been suggested to improve the solubility of cellulose as well as to expand its application in the industry [3,4]. The process can be made by introducing functional groups, particularly carboxylic acid and aldehyde at C2-C3 bond in the position of anhydroglucose units (AGU), as shown in Figure 1. On the other hand, in this study, hydroxyl groups have been produced at C2-C3 of AGU by opening the ring structure of the compound using sodium periodate as an oxidizing agent [5]. The sodium periodate oxidation of cellulose has the potential to break down the C2-C3 bond and form dialdehyde groups [6]. Then, dialdehyde compounds can be further oxidized to form a new functional group, carboxylic acid, or imine after it reacts with the amine group [7]. The effects of different amounts of sodium periodate added into the MCC was investigated under controlled conditions of pH, temperature, and time of reaction. Fourier-transform infrared-attenuated total reflectance spectroscopy (FTIR-ATR), power X-ray diffraction (PXRD), thermogravimetric analysis (TGA), and field-emission scanning electron microscopy (FESEM) techniques were applied to characterize and investigate the effects of oxidation on the chemical structure of MCC and its crystallinity. Figure 2 shows the proposed mechanism on the formation of DHC.

Material and Methods

The chemical reagents used to prepare DHC are MCC, sodium periodate, and ethylene glycol, which were purchased from Aldrich. All the reagents were used without purification. The MCC is light brown microcrystalline powder. The particle size and density of MCC were 51 μm and 0.6 g mL^{-1}, respectively. The samples were analyzed using FTIR-ATR Perkin Elmer GX spectrophotometer. The transmittance of the samples was detected with a resolution of 4 cm^{-1} in the range of 4000–650 cm^{-1}. The morphology of the samples was observed using a ZEISS MERLIN compact microscope equipped with a field emission gun. The samples were mounted in aluminium stubs on double-sided carbon tape and coated with iridium to reduce the effects of charging. Powder X-ray Diffraction pattern (PXRD) of the samples was recorded on Shidmazu D600 diffractometer (Shidmazu Kyoto Jaya, Japan) in the 2θ range of 5º to 70º using Cu-Kα radiation (λ = 0.15415) at 40 kV and 20 mA with 0.17˚min^{-1}. Powder X-ray diffraction analysis was performed on the sample to determine the phase of MCC and DHC crystallinity.

The ultrasonication of MCC

One hundred mL of deionized water and 2 g of MCC were added into a flask. The ultrasonication was performed for 30 minutes to break the intermolecular and intramolecular interactions of chemicals in MCC. Then, the treated MCC was filtered and washed with deionized water. The MCC was dried in the oven at 45 ºC for 24 hours.

The oxidation of MCC by using sodium periodate

Firstly, 30 mL of deionized water was added into a 100 mL flask. Then, 1 g of sonicated MCC and 3 g of sodium periodate were added into the flask and continuously stirred in water bath at 48 ºC for 4 hours. The flask was kept in dark condition by wrapping it using aluminium foil. After 4 hours of incubation, the ethylene glycol was added into the mixture and left for 1 hour. The oxidized product was filtered and washed with methanol. The product was dried in the oven at 45 °C for 24 hours. The process was repeated using 5 g of sodium periodate to study the effects of different amounts of sodium periodate on the oxidation of MCC.

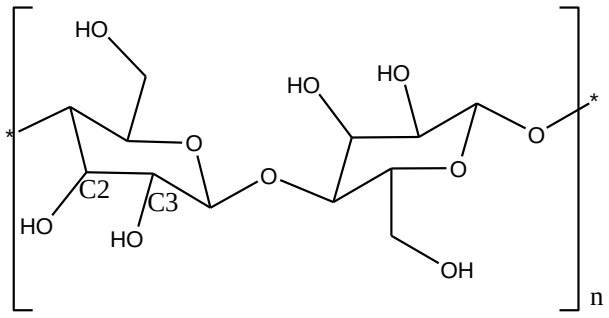


Figure 1. The structure of the AGU in cellulose

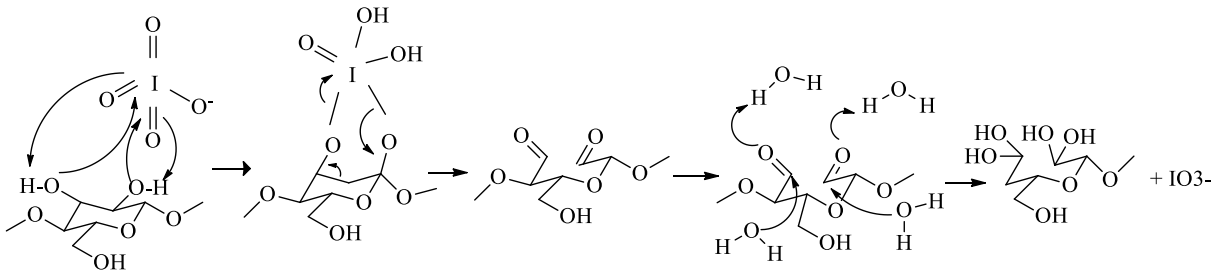


Figure 2. The mechanism of DHC formation

Results and Discussion

FTIR-ATR

FTIR-ATR spectroscopy is an important and easy technique to obtain a detailed information on the changes of chemical structure of cellulose after it was treated with different amounts of sodium periodate, as shown in Figure 4. The wide range of absorption band was attributed to the hydroxyl group, υ(OH) that was displayed at 3341 cm^{-1} (MCC), 3468 cm^{-1} (DHC 1:3), and 3338 cm^{-1} (DHC 1:5), respectively. The intensity of υ(OH) increased when the amount of sodium periodate was increased. It can be inferred that the DHC consisted of more OH in its structure as compared to that of MCC, as shown in Figure 3. The stretching bond of υ(C-H) was displayed at 2900 cm^{-1} (MCC), 2945 cm^{-1} (DHC 1:3), and 2939 cm^{-1} (DHC 1:5). This finding was contradicted with those performed by Liming et. al, which has reported that the stretching bond of CH and CH_2 groups were found to be at the range of 2800-2900 cm^{-1} [8]. Furthermore, the absorption band ranging from 1633 to 1649 cm^{-1} might be attributed to the deformation of OH vibration induced by absorbing the moisture of samples [9]. The vibration band at 897 cm^{-1} was correlated with υ(C-O-C) vibration, portraying the *β*-glycosidic linkages ring presented in MCC. Meanwhile, the vibration bands of DHC (1:3) and DHC (1:5) at 883 cm^{-1} and 880 cm^{-1}, respectively could be due to the presence of υ(C-OH) structure in the compound [10].

TGA

The TGA analysis can be used to figure out the thermal stability of MCC, DHC (1:3), and DHC (1:5). The initial degradation process at 100-130 ºC was attributed to the deterioration of intermolecular and intramolecular hydrogen bonding as well as the evaporation of a small amount of moisture from the sample [11]. Mahendra et al. proclaimed that a pyrolysis process will occur during the degradation process of cellulose and oxidation of cellulose in the range of 200-400 ºC [12]. In this study, it was found that the pyrolysis process of DHC

celluloses was lower than MCC, as shown in Figure 5. Meanwhile, Sofla et al. reported that the reduction of DHC dimension after oxidation will reduce the pyrolysis process temperature [13]. Besides, it was suggested that the hemicellulose and cellulose were decomposed between 200-400 ºC, which will decrease the thermal stability of DHC after the oxidation process [14]. It was reported that the temperature in the range of 200-400 ºC facilitated the decomposition of volatile and dehydrated compounds as well as the breakdown of glycosidic in compounds [15]. In this study, the decomposition of DHC compounds could only be detected when the temperature exceeded 400 ºC. This phenomenon could be attributed to the carbonization process, resulting in complete degradation and decomposition process. The finding suggests that the thermal stability of DHC was higher than MCC after surface modification with sodium periodate. It is conceivably due to the increase in number of hydroxyl groups in the cellulose ring after the cleavage of C2-C3 bond of the AGU, which promotes the crystallinity of DHC.

PXRD

The PXRD findings on the patterns of MCC and DHC are presented in Figure 6. It was found that DHC (1:3) and DHC (1:5) possessed different patterns from MCC, whereby the degree of crystallinity of DHC increased from 50.1% (MCC) to 99.8% (DHC 1:3) and 99.5% (DHC 1:5) after the oxidation process. Anuj et al. proclaimed that the cellulose structure displayed three main peaks close to 16º (110), 23º (200), and 35º (004) in MCC [16]. After the oxidation process, the crystallinity of MCC increased when the amount of sodium periodate had increased. It is deduced that the lignin and hemicelluloses, which are amorphous, were successfully removed with the addition of sodium periodate. This process facilitated the formation of hydroxyl groups in DHC which led to the rearrangements of crystalline cellulose structure. This was due to the development of intermolecular and intramolecular H bonding in DHC. The finding obtained from the PXRD analysis on MCC, DHC (1:3) and DHC (1:5) was further supported by the analysis on the surface morphological characteristics of the compound using field-emission scanning electron microscopy (FESEM) techniques.

FESEM

The photomicrograph of FESEM analysis showed the changes on surface morphology of MCC (A), DHC (1:3) (B) and DHC (1:5) (C) following the reaction with different amounts of sodium periodate (Figure 7). The surface roughness of the MCC seems uneven and irregular, indicating the absence of cementing materials such as lignin and hemicellulose components in MCC as shown in Figure 7(a) [17-19]. DHC (1:3) showed a clear, smooth, and needle-shaped like morphology of the cellulose after 3 g of sodium periodate was added. The findings demonstrated a complete defibrillation of MCC structure, which promotes the micronization of fibers into its constituent due to the increment of repulsion between the structure of fibers [20]. With the addition of 5 g of sodium periodate, the cellulose staked up or clustered together and the texture became more compact, resembling a thick leaf-like shape, in which the amorphous area was obviously destroyed as shown in Figure 7(c) [2]. The surface morphology of DHC (1:3) and DHC (1:5) were found to be smooth as compared to MCC, whereby it showed that the crystallinity of DHC increased with the increasing amount of sodium periodate added. It can be deduced that the cellulose chain exfoliation process was developed during the oxidation of sodium periodate. However, further addition of sodium periodate concentration will reduce the structure diameter and cause aggregation of the structure by hydrogen bonding and less steric hindrance between the neighboring hydroxyl group of DHC [22-23].

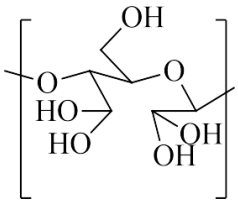


Figure 3. The structure of hydrated aldehyde (DHC) that was proposed in this study

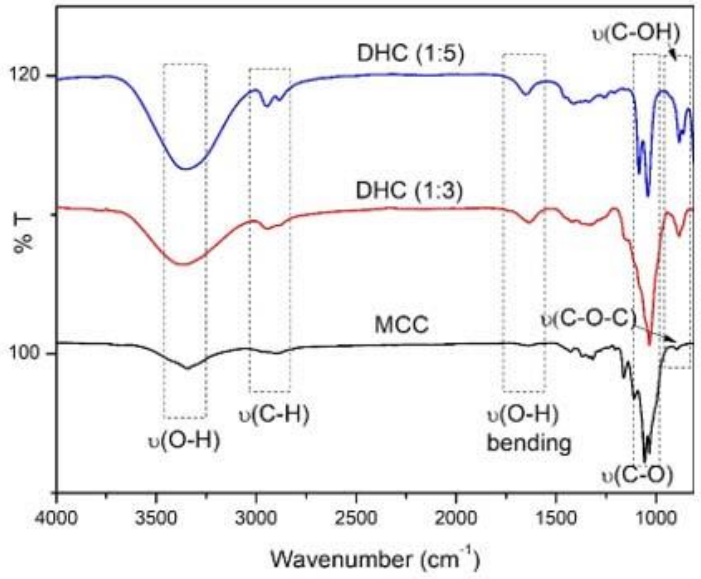


Figure 4. The FTIR-ATR spectra of MCC, DHC (1:3) and DHC (1:5)

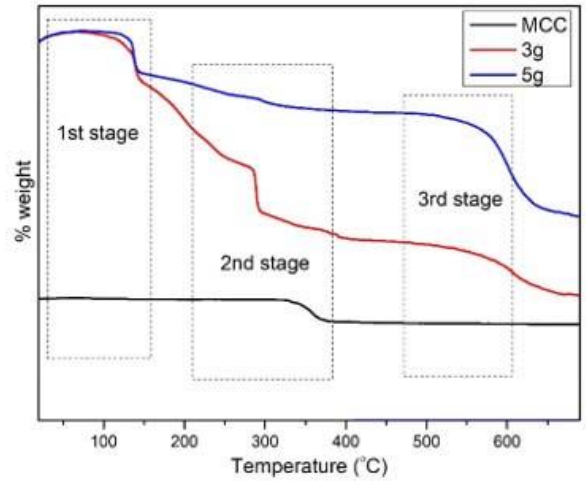


Figure 5. The TGA curves of MCC and DHC compounds

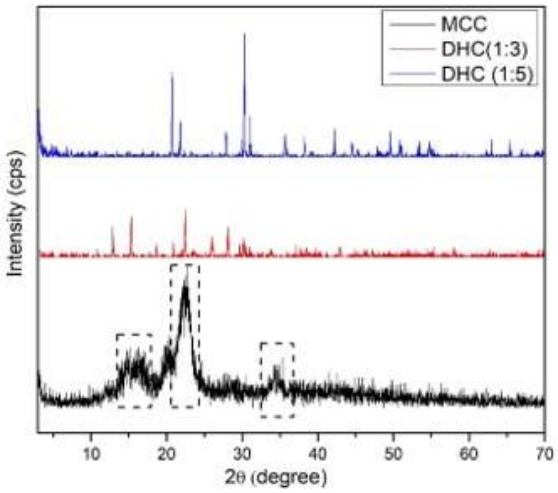


Figure 6. The PXRD diffractograms of MCC, DHC (1:3), and DHC (1:5)

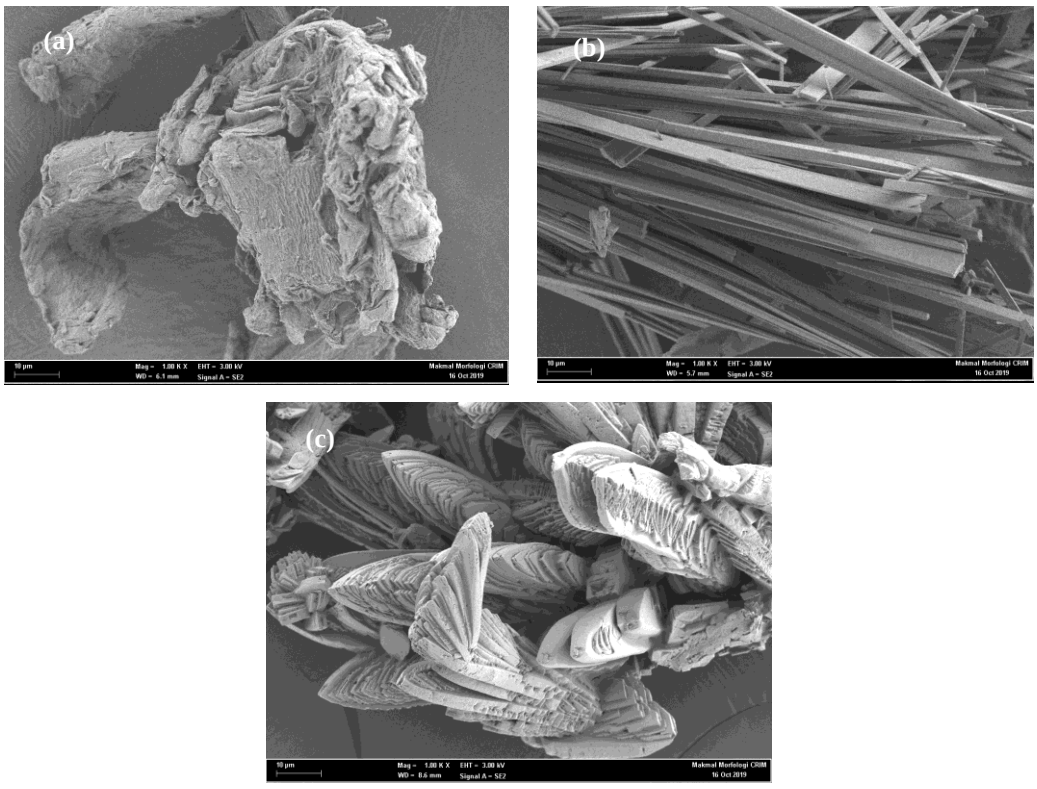


Figure 7. The morphology screening of MCC (a), DHC (1:3) (b), and DHC (1:5) (c)

Conclusion

In this study, DHC was successfully oxidized with different amount of sodium periodate on MCC in a concentration-dependent manner. The addition of sodium periodate on MCC increased the intensity of υ(OH) stretching band and the stability of DHC. The DHC also showed crystal-like structure with the increasing amount of sodium periodate, suggesting the possible occurrence of crystallinity of DHC during the oxidation process. The recent findings concluded that the DHC possessed more OH groups compared to that of MCC.

Acknowledgement

The authors would like to thank the Faculty of Applied Sciences, Universiti Teknologi MARA (UiTM), Negeri Sembilan Branch, Kuala Pilah Campus and the Centre of Research and Instrumentation Management (CRIM), Universiti Kebangsaan Malaysia for providing the facilities and instrumentation in this study.

References

1. Cunzhen, G., Zhihui, Z., Zhixin, X., Peilong, X. and Yanzhi, Xia. (2019). Preparation of ion-exchanged TEMPO-oxidized celluloses as flame retardant products. *Molecules*, 24:1-10.
2. Zuwu, T.,Wenyan, L., Xinxing, L., He, X., Qingxian, M., Liulian, H., Lihui, C. and Hui, W. (2017). TEMPO-oxidized cellulose with high degree of oxidation. *Polymers*, 9(9): 421.
3. Lin, X., Ma, W., Wu, H., Huang, L., Chen, L. and Takahara, A. (2017). Fabrication of cellulose based super hydrophobic microspheres for the production of magnetically actuatable smart liquid marbles. *Journal of Bioresources and Bioproducts*, 2:110-115.
4. Weng, R., Chen, L., Lin, S., Zhang, H., Wu, H., Liu, K., Cao, S. and Huang, L. (2017). Preparation and characterization of antibacterial cellulose/chitosan nanofiltration membranes. *Polymers*, 9(116):1-13.
5. Luo, C. C.,Wang, H. and Chen, Y. (2015). Progress in modification of cellulose and application. *Chemical Industry and Engineering Progress*, 34(3):767-773.
6. Liu, P., Pang, B., Tian, L., Schafer, T., Gutmann, T., Liu, H., Volkert, C. A., Buntkowsky, G. and Zhang, K. (2018). Efficient, self-terminating isolation of cellulose nanocrystals through periodate oxidation in pickering emulsions. *ChemSusChem*, 11(20): 3581-3585.
7. Ruan, C. Q., Stromme, M. and Lindh, J. (2018). Preparation of porous 2,3-dialdehyde cellulose beads crosslinked with chitosan and their application in adsorption of Congo red dye. *Carbohydrate Polymers*, 181:200-207.
8. Liming, Z., Huanhuan, G., Meng, X., Jie, C. and Yujie, D. (2017). Physicochemical properties, antioxidant and antibacterial activities of dialdehyde microcrystalline cellulose. *Cellulose*, 24: 2287-2298.
9. Zaman, M., Xiao, H., Chibante, F. and Ni, Y. (2012). Synthesis and characterization of cationically modified nanocrystalline cellulose. *Carbohydrate Polymers*, 89:163-170.
10. Anjali, T. (2012). Modification of carboxymethyl cellulose through oxidation *Carbohydrate polymers,* 87(1): 457-460.
11. Xiuzhi, T. and Xue, J. (2017). Preparing water-soluble 2,3-dialdehyde cellulose as a bio-origin cross-linker of chitosan. *Cellulose*, 25:987-998.
12. Mahendra, I. P., Wirjosentono, B., Tamrin, I. H. and Mendez, J. A. (2019). Thermal and morphology properties of cellulose nanofiber from TEMPO-oxidized lower part of empty fruit bunches (LEFB). *Open Chemistry*, 17: 526-536.
13. Sofla, M. R. K., Brown, R. J., Tsuzuki, T. and Rainey, T. J. (2016). A comparison of cellulose nanocrystals and cellulose nanofibres extracted from bagasse using acid and ball milling methods. *Advances in Natural Sciences: Nanoscience and Nanotechnology*, 7(3):1-9.
14. Horseman, T., Tajvidi, M., Diop, C. I. K. and Gardner, D. J. (2017). Preparation and property assessment of neat lignocellulose nanofibrils (LCNF) and their composite films. *Cellulose*, 24(6): 2455-2468.

15. Marina, D. C. E. P., Demetrius, D. D. S., Ana, L. A. G., Victor, D. S. A. L., Allan, R. F., Moraes, R. F. D. N., Jairo, T. and Frederico, G. P. (2019). Film based on magnesium impregnated biochar/ cellulose acetate for phosphorus adsorption from aqueous solution. *The Royal Society of Chemistry*, 9: 5620-5627.
16. Anuj, K., Yuvraj, S. N., Veena, C. and Nishi, K. B. (2014). Characterization of cellulose nanocrystals produced by acid-hydrolysis from sugarcane bagasse as agro-waste. *Journal of Materials Physics and Chemistry*, 2(1): 1-8.
17. Lindh, J., Ruan, C., Stromme, M. and Mihranyan, A. (2016). Preparation of porous cellulose beads via introduction of diamine spacers. *Langmuir*, 32(22): 5600-5607.
18. Julie, C. C. S., Neena, G. and Sunil, K. N. (2016). Isolation and characterization of cellulose nanofibrils from arecanut husk fiber. *Carbohydrate Polymers,* 142: 158-166.
19. Ahmed, A. O. and Jong-Whan, R. (2016). Characterization of nanocelluloses isolated from Ushar (*Calotropis procera*) seed fiber: Effect of isolation method. *Materials Letters,* 168: 146-150.
20. Juho, S., Henrikki, L., Jouko, N. and Osmo, H. (2011). Dialdehyde cellulose microfibers generated from wood pulp by milling-induced periodate oxidation. *Carbohydrate Polymers,* 86: 260-265.
21. Chao, L., Li, B., Du, H., Lv, D., Zhang, Y. and Yu, G. (2016). Properties of nanocellulose isolated from corncob residue using sulfuric acid, formic acid, oxidative and mechanical methods. *Carbohydrate polymers,* 151:716-724.
22. Lopez-Sanchez, P., Martinez-Sanz, M., Bonilla, M. R., Wang, D., Gilbert, E. P., Stokes, J. R. and Gidley, M. J. (2017). Cellulose-pectin composite hydrogels: Intermolecular interactions and material properties depend on order of assembly. *Carbohydrate Polymers,* 162:71-81.
23. David, J. M., Christine, B., Vikram, S. R., George, P. S. and Gil, G. (2019). One-shot TEMPO-periodate oxidation of native cellulose. *Carbohydrate Polymers,* 226: 1-10.

Malaysian Journal of Analytical Sciences (MJAS)
Published by Malaysian Analytical Sciences Society

VALIDATION AND DETERMINATION OF ASCORBIC ACID IN MULTIVITAMIN TABLETS BY DIFFERENTIAL PULSE ANODIC STRIPPING VOLTAMMETRIC TECHNIQUE AT A BARE GLASSY CARBON ELECTRODE

(Validasi dan Penentuan Asid Askorbik dalam Tablet Multivitamin Menggunakan Teknik Voltammetrik Perlucutan Anodik Denyutan Pembezaan pada Elektrod Karbon Berkaca)

Nur Syamimi Zainudin*, Siti Norbaitina Shaari, Megat Ahmad Kamal Megat Hanafiah

Faculty of Applied Sciences,
Universiti Teknologi MARA Pahang Jengka Campus, 26400 Bandar Tun Abdul Razak Jengka, Pahang, Malaysia

**Corresponding author: nursyamimizainudin@uitm.edu.my*

Received: 8 August 2020; Accepted: 29 September 2020; Published: 10 December 2020

Abstract

Growth of multivitamin tablet production increases curiosity among the researchers whether ascorbic acid (AA) content is in accordance with the standards or not. The differential pulse anodic stripping voltammetry (DPASV) technique using bare glassy carbon electrode and phosphate buffer at pH 4.2 has been proposed to analyse the ascorbic acid content. The experimental voltammetric parameters were optimized to obtain a maximum response with analytical validation of the technique. The optimum instrumental conditions for electroanalytical determination of AA by the proposed DPASV technique were initial potential = 0 V, final potential = 0.7 V, accumulation time = 60 s, scan rate = 0.125 V/s, accumulation potential = 0 V and pulse amplitude = 0.150 V. The curve was linear from 5 mg L^{-1} to 300 mg L^{-1} (R^2 = 0.9999) with detection limit of 0.25 mg L^{-1}. The precisions in terms of relative standard deviation (RSD) were 1.3%, 0.5% and 0.06%. The recoveries for AA content in the two multivitamin tablets were 98% and 102%, respectively. It can be concluded that the proposed technique is precise, accurate, rugged, low cost, fast and has the potential to be an alternative method for routine analysis of AA in other pharmaceutical products in future.

Keywords: ascorbic acid, glassy carbon electrode, multivitamin, voltammetry

Abstrak

Pertambahan penghasilan multivitamin dalam bentuk tablet telah meningkatkan rasa ingin tahu para penyelidik samada kandungan asid askorbik (AA) memenuhi piawaian atau tidak. Teknik perlucutan anodik denyutan pembezaan yang menggunakan elektrod karbon berkaca tanpa pengubahsuaian dan larutan penimbal fosfat (pH 4.2) telah dicadangkan untuk menganalisa kandungan asid askorbik. Parameter-parameter eksperimen voltammetrik dioptimakan untuk mendapatkan tindakbalas maksima diikuti dengan validasi atau pengesahan teknik voltammetrik. Keadaan instrumentasi optima untuk penentuan AA dengan menggunakan teknik DPASV yang dicadangkan adalah keupayaan awal = 0 V, keupayaan akhir = 0.70 V, masa penjerapan = 60 s, kadar imbasan = 0.125 V/s, keupayaan penjerapan = 0 V dan amplitud denyut = 0.15 V. Keluk penentukuran adalah lurus daripada 5 mg L^{-1} to 300 mg L^{-1} (R^2 = 0.9999) dengan had pengesanan 0.25 mg L^{-1}. Kejituan dalam bentuk sisihan piawai relatif adalah 1.3%, 0.5% and 0.06%. Perolehan semula peratusan kandungan AA di dalam dua tablet multivitamin adalah 98% dan 102%. Kesimpulannya, teknik

yang dicadangkan adalah jitu, tepat, tahan lasak, melibatkan kos yang rendah, cepat dan berpotensi untuk menjadi satu kaedah alternatif untuk menganalisa AA dalam produk pharmaseutikal yang lain pada masa akan datang.

Kata kunci: asid askorbik, elektrod karbon berkaca, multivitamin, voltammetri

Introduction

Vitamins are one of the major nutrients that play very important roles in the body. The vitamins involved in the processes of normal metabolism, cell regulation and they are necessary for growth and development. There are thirteen vitamins that are recognized contributing in human nutrition [1]. These vitamins can be divided into fat-soluble vitamins and water-soluble vitamins. Vitamin A, D, E and K are fat-soluble vitamins. Meanwhile, ascorbic acid (AA) and B-complex are water-soluble vitamins [2]. The water-soluble vitamins dissolve easily in water and are readily excreted from the body via urine [3].

The AA in food was discovered in the twentieth century in 1907 by Holst and Frolich as a solution for scurvy. During that year, the disease had been reported to be 'ship beriberi'. In order to avoid this disease, an experiment was done on guinea pigs by feeding them with fresh apples, fresh potatoes, fresh cabbage or fresh lemon juices which is high in the AA. The guinea pigs were also fed with a simple diet like oat, barley and wheat. The results indicated that deficiency of AA caused the scurvy [4]. The AA is also known as vitamin C, L-ascorbic and 2,3-didehydro-L-threohexono-1,4-lactone as well as 3-keto-L-gulofuranolactone. It has a chemical formula of $C_6H_8O_6$ and molecular weight of 176 $gmol^{-1}$ while its chemical structural is shown in Figure 1. The AA is important for collagen production, a protein which gives structure to bones, cartilages, muscles and blood vessels [5] as well as an antioxidant and free radical scavenger [6]. The AA also helps in iron absorption and maintains capillaries, bones and teeth [7]. The main natural sources of AA are various fruits and vegetables especially kiwi, mangoes, papayas, lettuce, tomatoes, peppers, strawberries, cantaloupe and broccolis [8].

It is known that humans cannot synthesize AA. Therefore, AA must be obtained by body through diet [9]. Pharmaceutical products such as multivitamins have become one of the sources of AA to meet requirement of daily dietary intake instead of fresh fruits and vegetables [10]. Unfortunately, the AA content in pharmaceutical products tends to be lost during processing, storing and packaging since it is highly sensitive to light, heat, temperature and oxygen [11]. Hence, it is very important to have a simple, very sensitive, precise, accurate, rugged, low cost and fast method for analysing AA even at a very low-level content.

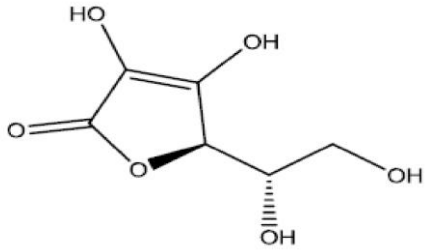


Figure 1. Chemical structure of ascorbic acid

Various analytical techniques have been applied for the AA determination. There are titrimetric method with an oxidant solution such as dichlorophenol (DCPIP) [12], potassium iodide or bromate [13], chromatographic method, particularly high performance liquid chromatography (HPLC) [11, 14, 15], spectrometric method [3, 16, 17], capillary electrophoresis method [18, 19] and fluorimetry [20]. However, HPLC methods use expensive equipment, require a long time of sample pre–treatment, use toxic organic solvent as mobile phase and various harmful reagents [21]. In titrimetric method, the difficulties are encountered with titrants and interferences often occur with coloured samples which lead to lack of specificity [6]. Meanwhile, in direct spectrophotometry, there is a matrix effect in ultraviolet (UV) region since many organic compounds in samples may exhibit UV absorbance during measurement.

Voltammetry techniques seem to have high potential for an alternative analytical method as they are very powerful and versatile tool due to their simplicity, fastness, low waste emission, low cost of chemicals and instrumentation. They have comparable sensitivity to more expensive techniques and abundance direct individual or simultaneously analysis of analyte without any or minimal sample pre-treatment or extraction [22]. These techniques are less sensitive toward the matrix effects than the other analytical techniques. Electroanalytical techniques have been applied for qualitative and quantitative analysis of a wide range of drug compounds [23].

Square-wave voltammetric technique has been used to determine AA based on its oxidation at a zeolite modified carbon paste electrode as a working electrode [24]. Cyclic and differential pulse voltammetric techniques were also used for electrochemical behaviour investigation and determination of AA at a modified carbon paste electrode with 2,7-bis (ferrocenylethynyl) fluoren-9-one [25]. Carbon nanotube paste electrode modified with 2,2-[1,2-ethanediylbis (nitriloethylidine)]-bis-hydroquinone has been used for electrochemical behaviour investigation and determination of AA using cyclic and differential pulse voltammetric techniques [26]. A multi-walled carbon nanotubes-tetradecyltrimethylammonium bromide film coated graphite electrode was used to investigate the electro-oxidation of AA by applying cyclic, differential pulse voltammetric and square-wave voltammetric techniques [27]. Simultaneous determination of AA and dopamine was carried out by differential pulse voltammetric technique at a boron doped diamond electrode [28] and gold nanoparticles film electrode [29]. The simultaneous determination of AA and acetaminophen has been conducted by differential pulse voltammetric technique at a boron doped diamond electrode using sodium sulphate as the supporting electrolyte [30].

The purpose of this study is to develop and validate a differential pulse anodic stripping voltammetric (DPASV) technique using bare glassy carbon electrode as a working electrode and phosphate buffer solution (pH 4.2) as a supporting electrolyte for quantitative analysis of AA in multivitamin tablets without prior sample preparation.

Materials and Methods

Materials

All chemicals used in this study were analytical grade reagent and all solutions were prepared in deionized water. The AA standard (MW = 176 g mol^{-1}) was obtained from Sigma Aldrich, UK. For the preparation of 1000 mg L^{-1} AA stock solution, 100 mg of the AA was dissolved in 100 mL volumetric flask. The standard working solution series were prepared by the appropriate dilution of the stock solution. All solutions were protected from light and used within 24 hours to avoid decomposition. Phosphate buffer solution (PBS) was prepared by adding and dissolving 2.70 mL of ortho phosphoric acid, 27.218 g of potassium dihydrogen phosphate, 71.630 g disodium hydrogen phosphate in the 1000 mL of volumetric flask. Sodium hydroxide with the concentration of 0.1 M was used to adjust the pH of the PBS solution to the pH 4.2.

Instrumentation

The voltammetric experiments were carried out using Autolab (Metrohm, Switzerland) that consisted of a glassy carbon electrode (GCE) as the working electrode (WE), a platinum wire as the auxiliary electrode (AE) and an Ag/AgCl (3M KCl) as the reference electrode (RE). The GCE was polished with polishing alumina on an alumina pad and then rinsed with deionized water. The Autolab was connected to a computer, installed with NOVA 1.1 for data processing. The pH meter (Hanna Instruments, UK) was employed for all pH measurements.

Voltammetric measurement: Differential pulse anodic stripping voltammetry (DPASV)

AA standard working solution was spiked into the PBS solution at pH 4.2 to give the final concentration of 10 mg L^{-1}. The initial operational instrumental parameters applied were initial potential (E_i) = 0 V, final potential (E_f) = 0.7 V, accumulation time (t_{acc}) = 10 s, scan rate (v) = 0.05 V/s, accumulation potential (E_{acc}) = 0 V and pulse amplitude = 0.075 V. These instrumental parameters for voltammetric measurements were

optimized to increase the response of the proposed DPASV technique.

An appropriate linear range with acceptable correlation coefficient (R^2), limit of detection (LOD), limit of quantification (LOQ), precision, accuracy, ruggedness and recovery of AA standard in the pharmaceutical samples were analysed in order to verify the suitability of the proposed DPASV technique for AA analysis as proposed by Miranda et al. [31]. The LOD was determined by additional lower concentration of the AA standard solution until obtaining a response that was significantly different from PBS solution at pH 4.2. The LOQ were calculated by the equations; LOD = 3 SD/m and the value of the LOQ was 3.333 times the value of the obtained LOD. The AA standard solution at the concentration of 5, 50 and 150 mg L^{-1} was applied for intra-day and inter-day precision, ruggedness and robustness with five replicates (n=5). The ruggedness of the proposed DPASV technique was investigated using the same instrument (Autolab) but had been conducted by two different analysts under the same optimum parameters. Statistical *F*-test was carried out for the ruggedness and robustness.

Collection and preservation of multivitamin tablets

Two different brands of multivitamin tablets with different labelled content of AA were obtained from a pharmacy in Jengka, Pahang. The multivitamin tablets of each brand were ground to a fine powder and dissolved in 200 mL of deionized water. Then, the samples were transferred to a covered scotch bottle to avoid degradation.

Recovery studies of AA standard in multivitamin tablets

The recovery of AA standard solution in the multivitamin tablet was determined by spiking 0.5 mL of the sample into the measuring cell containing PBS solution at pH 4.2. This study was carried out with three replicates (n = 3). Recovered concentrations of the spiked AA standard solution in the samples were calculated using the regression equation from a calibration curve from the following formula in equation 1 [32];

$$C_{sample} = \frac{C_{means\ solution} \times V_{total}}{V_{sample}} \quad (1)$$

where, $C_{means\ solution}$ is concentration in the measuring solution (mg L^{-1}), V_{total} is total volume of the measuring solution (L), V_{sample} is volume of sample in the measuring cell (L) and C_{sample} is concentration in the sample (mg L^{-1}).

Results and Discussion

DPSAV of AA

DPSAV offers a well-defined and sharp peak even at lower concentration of AA [5]. It is very important to optimize all the parameters that may influence the measurements in order to obtain the optimum response [33]. The effects of scan rate (*v*), accumulation time (t_{acc}), accumulation potential (E_{acc}) and pulse amplitude on the I_p of 10 mg L^{-1} AA standard were studied in the PBS solution at pH 4.2.

The effect of accumulation time (t_{acc})

An accumulation time (t_{acc}) is a period of time given for AA to accumulate or adsorb onto a glassy carbon electrode before being analysed further. The t_{acc} is strongly affected the peak response and contributed to the high peak in electroanalytical measurements [34]. The influence of t_{acc} on the peak response of AA in PBS solution at pH 4.2 has been studied over the range between 10 to 80 s. The I_p has increased starting from 10 s to 60 s. The t_{acc} of 60 s was considered as the optimum t_{acc} as the highest I_p has been obtained, which was 426 nA, as shown in Figure 2.

The increase of the I_p of AA with t_{acc} was contributed by the accumulation of AA at the electrode surface in large amount since longer time has been given for the accumulation to occur [35]. Besides, the higher response of measurement can be achieved with longer of t_{acc}. After the t_{acc} of 60 s, the I_p has decreased probably due to saturation of the accumulated AA at the working electrode surface [36].

The effect of scan rate (v)

The relationships between I_p of AA and various *v* such as 25, 50, 75, 100, 125 and 150 mV/s were observed

using the initial parameters. The maximum current obtained was 469 nA at E_p of 0.39978 V with *v* of 0.125 V/s in PBS solution at pH 4.2

The effect of accumulation potential (E_{acc})

Accumulation potential (E_{acc}) was the potential for AA to be accumulated at the surface of a mercury electrode, whereas an optimum E_{acc} was the most appropriate potential for the accumulation process to take place [34]. Figure 3 shows the maximum response was observed at E_{acc} of 0 mV with I_p 469 nA and E_p of 0.39978 V. It indicated that the accumulation of AA at the electrode surface effectively occurred at 0 mV.

The effect of pulse amplitude

According to De Lima et al. [37], pulse amplitude is one of the factors that affects the sensitivity of voltammetric measurements. The I_p and E_p have sharply increased from 0.075 V to 0.15 V and slowly decreased after 0.15 V, as shown in Figure 4. The pulse amplitude of 0.15 V was noted as optimum condition for analysis due the highest I_p observed which was 857 nA and E_p of 0.3598 V in PBS solution at pH 4.2.

Validation of the developed method: Linearity, limit of detection (LOD) and limit of quantification (LOQ)

The capability of the proposed DPASV technique as an analytical method for determination of AA was studied by evaluating the obtained I_p as the function of concentration under the optimized operational and instrumental parameters. The constructed calibration graph from 5 to 300 mg L^{-1} was represented by the linear equation of I_p (nA) = 109.79x – 224.01 with 0.9999 of correlation coefficient (R^2), as shown in Figure 5.The observed LOD for the standard solution was 0.25 mg L^{-1} and the LOQ was found to be 0.83 mg L^{-1}.

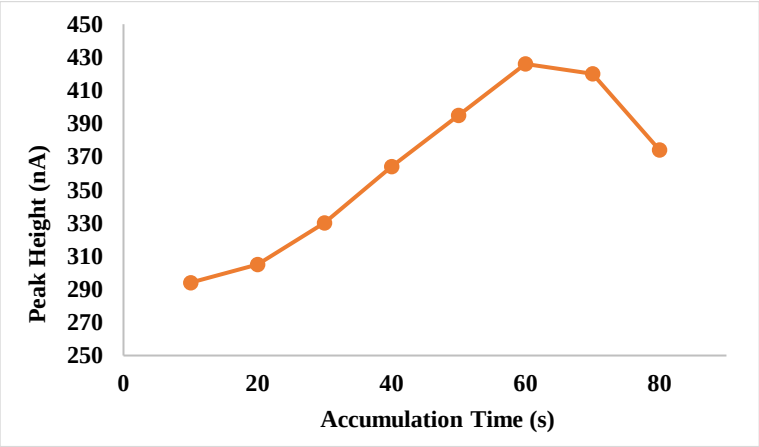


Figure 2. Plot of I_p against accumulation time (t_{acc}) of AA in phosphate buffer solution pH 4.2

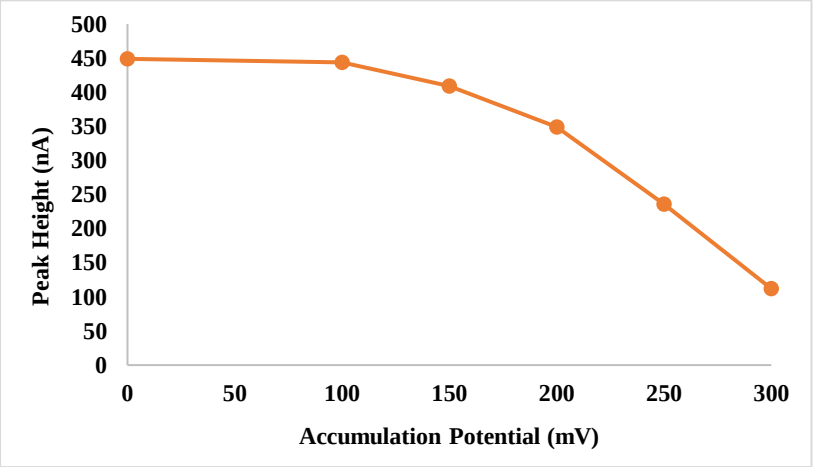


Figure 3. Plot of I_p against accumulation potential (E_{acc}) of AA in phosphate buffer solution pH 4.2

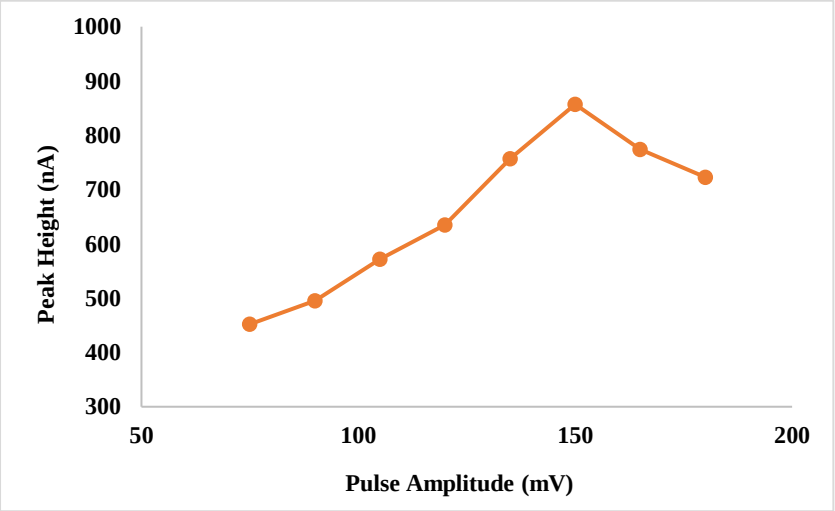


Figure 4. Plot of I_p against pulse amplitude in phosphate buffer solution pH 4.2

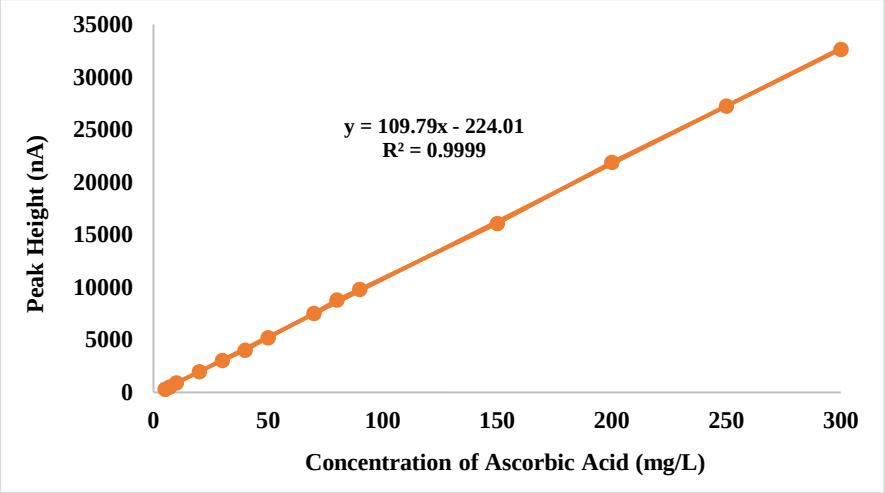


Figure 5. Linear curve of I_p against concentration of ascorbic acid in phosphate buffer solution pH 4.2. Instrument parameters were E_i = +0 V, E_f = 0.7 V, t_{acc} = 60 s, v = 0.125 V/s, E_{acc} = 0 V and pulse amplitude = 0.15 V

Precision

The precision of the proposed DPASV technique for AA analysis was determined in three replicates (n=3) at the concentrations of 5 mg L^{-1}, 50 mg L^{-1} and 150 mg L^{-1}. The RSD values obtained were 1.3%, 0.5% and 0.06% for respective concentrations. The RSD values found to be less 5% indicating that the measurements were precise and confidence [38].

Accuracy

The accuracy of the developed technique was tested by spiking three known different concentrations of AA which were 5 mg L^{-1}, 50 mg L^{-1} and 150 mg L^{-1} into a voltammetric cell containing PBS solution at pH 4.2. These spiked AA standard solutions were measured in three replicates (n=3) and the discovered amounts of the spiked solutions in the cell were calculated using the equation of I_p (nA) = 109.79x – 224.01, where x is the found concentrations of AA in the voltammetric cell. The satisfactory recoveries of 93.08 %, 98.66 % and 99.00 % were respectively achieved for the spiked concentrations of 5 mg L^{-1}, 50 mg L^{-1} and 150 mg L^{-1}.

Ruggedness

The RSD values ranged from 0.07 % to 2.93 % for the first and second analyst, respectively for the measurements of 5 mg L^{-1}, 50 mg L^{-1} and 150 mg L^{-1} AA using the same instrument [39]. From the two-tailed *F* test, there were no significant differences between the obtained variances for AA when the measurements were performed by two different analysts with the same instrument at the 5 % significance level. Hence, the results indicated that the developed technique was considered rugged.

Determination of AA in multivitamin tablets

To evaluate the application to a real sample analysis, the developed DPASV technique was used to analyse AA in multivitamin tablets. The multivitamin tablets were analysed by the developed technique under optimum parameters without any sample pre-treatment. Table 1 shows the content of AA in the multivitamin samples.

Assay results for the determination of the AA in the multivitamin tablets are shown in Table 2 by comparing the actual AA content with the labelled AA content in terms of mg/tablet [32]. The samples were analysed under the optimum instrumental parameters. The recoveries achieved for AA content in Sample A and B were 98 % and 102 %, respectively. These satisfactory recoveries indicated that the matrix did not affect the measurement of the AA in the multivitamin tablets by the proposed DPASV technique.

Table 1. Ascorbic acid content in the multivitamin tablet were analysed by the proposed DPASV technique in phosphate buffer solution at pH 4.2 (n = 3)

Sample	I_p (x 10^{-7} A) ± SD (RSD)	Concentration of Ascorbic Acid (mg/L)
A	4.40 ± 0.15 (3.40%)	490
B	8.19 ± 0.12 (1.46%)	769

Table 2. Assay results for the determination of the AA in multivitamin tablets

Sample	Labelled Content (mg/tablet)	Actual Content (mg/tablet)	Recovery (%)
A	100	98	98
B	150	153	102

Conclusion

The proposed DPASV technique had been successfully applied to determine the AA in multivitamin tablets. The present method had an advantage that a very simple sample pre-treatment was required. It was also found to be practically rapid, convenient, sensitive, accurate, precise, rugged and low in cost. Therefore, it could be an excellent alternative method for the routine determination of AA in the multivitamin tablets.

References

1. Eggersdorfer, M., Laudert, D., Letinos, U., McClymont, T., Medlock, J., Netscher, T. and Bonranth, W. (2012). One hundred years of vitamins-A success story of the natural science. *Angewandte Chemie*, 51: 12960-12990.
2. Zhang, Y., Zhou, W., Yan, J., Liu, M., Zhou, Y., Shen, X., Ma, Y., Feng, X., Yang, J. and Li, G. (2018). A review of the extraction and determination methods of thirteen essential vitamins to the human body: An update from 2010. *Molecules*, 23: 1-25.
3. Masoud, R.S., and Zahra, A. (2014). A highly sensitive kinetic spectrophotometric method for the determination of ascorbic acid in pharmaceutical samples. *Iranian Journal of Pharmaceutical Research*, 13(2): 372-382.
4. Packer, L., and Fuchs, J. (1997). Vitamin C in health and disease. CRC Press: pp. 1-525.
5. Yilmaz, S., Sadikoglu, M., Saglikoglu, G., Yagmur, S. and Askin, G. (2008). Determination of ascorbic acid in tablet dosage forms and some fruit juices by DPV. *International Journal of Electrochemical Science*. 3: 1534-1542.
6. Sona, S., Jiri, M., Jiri, S., Mojmir, B., Jindrich, K. and Tunde, J. (2015). Determination of ascorbic acid by electrochemical techniques and other methods. *International Journal of Electrochemical Science*, 10: 2421-2431.
7. Pisoschi, A. M., Pop, A., Negulescu, G. P., and Pisoschi, A. (2011). Determination of ascorbic acid content of some fruit juices and wine by voltammetry performed at Pt and carbon paste electrodes. *Molecules*, 16: 1349-1365.
8. Sadia, G., Azizuddin., Rafi, A., Kousar, Y., Fareed, A. and Iftekhar, S. (2014). Determination of ascorbic acid content of some capsicum cultivars by cyclic voltammetry performed at GCE by external

standard series calibration method. *International Journal of Electrochemical Science*, 9: 5751-5762.

9. Snezana, S. M., Danijela, A. K., Danijela, C. N. D., and Milan, N. M. (2011). Rapid and reliable HPLC method for the determination of vitamin C in pharmaceutical samples. *Tropical Journal of Pharmaceutical Research*, 10(1): 105-111.
10. Rahman, M. M., Khan, M. M. R., and Hosain, M. M. (2007). Analysis of vitamin c (ascorbic acid) contents in various fruits and vegetables by UV-spectrophotometry. *Bangladesh Journal of Scientific and Industrial Research,* 42: 417-424.
11. Gazdik, Z., Zitka, O., Petrlova, J., Adam, V., Zehnalek, J., Horna, A., Reznicek, V., Beklova, M. and Kizek, R. (2008). Determination of vitamin C (ascorbic acid) using high performance liquid chromatography coupled with electrochemical detection. *Sensors,* 8: 7097-7112.
12. Papuc, C., Pop, A., Serban, M. (2001). Metode analitice in biochimia veterinara. editura printech (Bucharest) 2001: pp. 167-169.
13. Matei, N., Magearu, V., Bieghila, S., Dobrinas, S. (2004). The determination of vitamin C from sweet cherries and cherries. *Revista de Chimie (Bucharest)*, 55: 294-296.
14. Santos, J., Mendiola, J. A., Oliveira, M. B., Ibáñez, E. and Herrero, M. (2012). Sequential determination of fat-and water-soluble vitamins in green leafy vegetables during storage. *Journal of Chromatography A*, 1261: 179-188.
15. Klimczak, I. and Gliszczy´nska-Swigło, A. (2015). Comparison of UPLC and HPLC methods for determination of vitamin C. *Food Chemistry*. 175: 100-105.
16. Mohamed, A. M. I., Mohamed, H. A., Abdel-Latif, N. M. and Mohamed, M. R. A. (2011). Spectrofluorimetric determination of some water-soluble vitamins. *Journal of AOAC International*, 94: 1758-1769.
17. Mohamed, A. M., Mohamed, H. A., Mohamed, N. A. and El-Zahery, M. R. (2011). Chemometric methods for the simultaneous determination of some water-soluble vitamins. *Journal of AOAC International*. 94: 467-481.
18. Da Silva, D. C, Visentainer, J. V., de Souza, N. E., and Oliveira, C. C. (2013). Micellar electrokinetic chromatography method for determination of the ten water-soluble vitamins in food supplements. *Food Analytical Methods*, 6: 1592-1606.
19. Aurora-Prado, M. S., Silva, C. A., Tavares, M. F. M., and Altria, K. D. (2010). Rapid determination of water-soluble and fat-soluble vitamins in commercial formulations by MEEKC. *Chromatographia*. 72: 687–694.
20. Borowski, J., Szajdek, A., Borowska, E. J., Ciska, E., and Zielinski, H. (2008). Content of selected bioactive components and antioxidant properties of broccoli (*Brassica oleracea* L.). *European Food Research and Technology*. 226: 459-465.
21. Radulescu, M. C., Bucur, B., Bucur, M. P. and Radu, G. L. (2014). Bienzymatic Biosensor for rapid detection of aspartame by flow injection analysis. *Sensors,* 14: 1028-1038.
22. Amorello, D. and Orecchio, S. (2013). Micro-determination of dithiocarbamates in pesticide formulations using voltammetry. *Microchemical Journal*, 110: 334-339.
23. Zhao, X., Tao, X., Wei, D. and Song, Q. (2006). Pharmacological activity and hydrolysis behaviour of novel ibuprofen glucopyranoside conjugates. *European Journal of Medicinal Chemistry*, 41: 1352-1358.
24. Nezamzadeh, A., Amini, M. K. and Faghihian, H. (2007). Square-wave voltammetric determination of ascorbic acid base on its electrocatalytic oxidation at zeolite-modified carbon-paste electrodes. *International Journal of Electrochemical Science*. 2: 583-594.
25. Raoof, J. B., Ojani R. and Beitollahi, H. (2007). Electrocatalytic determination of ascorbic acid at chemically modified carbon paste electrode with 2, 7-bis (ferrocenyl ethynyl) fluoren-9-one. *International Journal of Electrochemical Science*, 2: 534-548.
26. Beitollahi, H., Ardakani, M. M., Naeimi H. and Ganjipour, B. (2009). Electrochemical characterization of 2,2'–[1,2-ethanediylbis (nitrilo ethylidine)]-bis-hydroquinone-carbon nanotube paste electrode and its application to simultaneous voltammetric determination of ascorbic and uric acid. *Journal of Solid State Electrochemistry*, 13: 353-363.

27. Motahary, M., Ghoreishi, S. M., Behpour M. and Golestaneh, M. (2010). Electrochemical determination of ascorbic acid at the surface of a graphite electrode modified with a multi-walled carbon nanotubes/tetradecyltrimethylammonium bromide. *Journal of Applied Electrochemistry*, 40: 841-847.
28. Zhao, G. H., Li, M. F., Li, M. L. (2007). Differetial pulse voltammetric determination of dopamine with the coexistence of ascorbic acid on boron-doped diamond surface. *Central European Journal of Chemistry*, 5: 1114-1123.
29. Raoof, J. B., Kiani, A., Ojani, R., Valiollahi, R. and Rashid-Nadimi, S. (2010). Simultaneous voltammetric determination of ascorbic acidand dopamine at the surface of electrodes modified with self-assembled gold nanoparticle films. *Journal of Solid State Electrochemistry*, 14: 1171-1176.
30. Cofan, C., Radovan, C. and Cinghita, D. (2009). Sumultaneous anodic assessment of ascorbic acid and acetaminophen in unbuffered solutions. *Revista de Chimie*. 60: 368-372.
31. Miranda, M. P., del Rio, R., del Valle, M. A., Faundez, M. and Armijo, F. (2012). Use of fluorine-doped tin oxide electrodes for lipoic acid determination in dietary supplements. *Journal of Electroanalytical Chemistry*. 668: 1-6.
32. Barbara, Z. (2011). Voltammetric determination of vitamin C on a carbon electrode. Monograph: Electrochemistry, A Laboratory Textbook, Switzerland: pp 35-38.
33. Švorc, L., Sochr, J., Svĭtková, J., Riejav, M. and Bustin, D. (2013). Rapid and sensitive electrochemical determination of codeine in pharmaceutical formulations and human urine using a boron-doped diamond film electrode. *Electrochimica Acta*, 87: 503-510.
34. Nur Syamimi, Z., Mohamad Hadzri, Y. and Noor Zuhartini, M. M. (2016). Voltammetric determination of Reactive Black 5 in wastewater samples from the batik industry. *Malaysian Journal of Analytical Science*, 20: 1254-1268.
35. Jain, R. and Sharma, S. (2012). Glassy carbon electrode modified with multi-walled carbon nanotubes sensor for the quantification of antihistamine drug pheniramine in solubilized systems. *Journal of Pharmaceutical Analysis*, 2(1): 56-61.
36. Geremedhin, W., Amare, M. and Admassie, S. (2013). Electrochemically pretreated glassy carbon electrode for electrochemical detection of fenitrothion in tap water and human urine. *Electrochimica Acta,* 87: 749-755.
37. De Lima, F., Gozzi, F., Fiorucci, A. R., Cardoso, C. A. L., Arruda, G. J. and Ferreira, V. S. (2011). Determination of linuron in water and vegetable samples using stripping voltammetry with carbon paste electrode. *Talanta*, 83: 1763-1768.
38. Ngai, K. S, Tan, W. T, Zulkarnain, Z., Ruzniza, M. Z. and Mohammed, Z. (2013). Voltammetry detection of ascorbic acid at glassy carbon electrode modified by single-walled carbon nanotube/zinc oxide. *International Journal of Electrochemical Science*, 8: 10557-10567.
39. Jain, R. and Rather, J. A. (2011). Stripping voltammetry of tinidazole in solubilized system and biological fluids. *Colloids and Surfaces A: Physicochemical and Engineering Aspects*, 378: 27-33.

Malaysian Journal of Analytical Sciences (MJAS)
Published by Malaysian Analytical Sciences Society

PHYSICOCHEMICAL COMPOSITION OF SPENT OYSTER MUSHROOM SUBSTRATE

(Komposisi Fizikokimia bagi Sisa Substrat Cendawan Tiram)

Aina Nasuha Mortada, Mohamad Hasnul Bolhassan*, Rafeah Wahi

Faculty of Resource Science and Technology,
Universiti Malaysia Sarawak, 94300, Kota Samarahan, Sarawak, Malaysia

**Corresponding author: bmhasnul@unimas.my*

Received: 8 July 2020; Accepted: 22 September 2020; Published: 10 December 2020

Abstract

Mushroom substrate is a type of lignocellulosic material that helps promote the growth, production, and fruiting of mushrooms. The substrate contains components rich in organic matter due to the modification of the material after harvesting of mushrooms. This study analysed the physicochemical composition of spent oyster mushroom substrate (SOMS) by comparing with sterile fresh mushroom substrate (SFMS). The physicochemical analyses conducted were moisture content, ash content, pH, primary macronutrients (nitrogen, phosphorus, and potassium), secondary macronutrients (calcium and magnesium), micronutrients (iron, manganese, copper, and zinc), and carbon-to-nitrogen (C:N) ratio. The results obtained for moisture content, ash content, pH, and C:N ratio showed higher values for SOMS. The values of moisture, ash content, pH, and C:N ratio increased to 63.00%, 6.58%, 5.92, and 116.29, respectively. For the nutrients in the mushroom substrate, namely phosphorus, calcium, magnesium, iron, and copper, the values after cultivation increased to 57.14 ppm, 7366.67 ppm, 1230.83 ppm, 85.18 ppm, and 3.75 ppm, respectively. Meanwhile, the values of nitrogen, potassium, zinc, and manganese decreased to 0.38%, 706.67 ppm, 16.90 ppm, and 68.65 ppm, respectively. Sulphur content was detected in SFMS but absent in SOMS. In conclusion, mushroom cultivation changed the physicochemical composition of the mushroom substrate.

Keywords: mushroom substrate, comparison, physicochemical analysis

Abstrak

Substrat cendawan merupakan sejenis bahan yang membantu dalam menggalakkan pertumbuhan, pengeluaran dan penghasilan jana buah cendawan. Ia mengandungi komponen yang kaya dengan bahan organik hasil daripada pengubahsuaian kandungan bahan selepas penuaian cendawan. Kajian ini telah menganalisis komposisi fizikokimia sisa substrat cendawan tiram dibandingkan dengan substrat cendawan segar steril. Analisis fizikokimia seperti kelembapan, kandungan abu, pH, makronutrien primer (nitrogen, fosforus, dan kalium), makronutrien sekunder (kalsium dan magnesium), mikronutrien (besi, mangan, tembaga, dan zink), dan nisbah C:N. Keputusan yang diperolehi untuk kelembapan, kandungan abu, pH, dan nisbah C:N menunjukkan nilai yang lebih tinggi untuk sisa substrat cendawan tiram. Peratusan bagi kelembapan meningkat kepada 63.00%, kandungan abu kepada 6.58%, pH kepada 5.92, dan nisbah C:N kepada 116.29. Bagi nutrien dalam sisa substrat cendawan, iaitu fosforus, kalsium, magnesium, besi, dan tembaga, menunjukkan peningkatan selepas penanaman kepada 57.14 ppm, 7366.67 ppm, 1230.83 ppm, 85.18 ppm, dan 3.75 ppm. Bagi nitrogen, kalium, zink, dan mangan, telah menunjukkan penurunan peratusan kepada 0.38%,

706.67 ppm, 16.90 ppm, dan 68.65 ppm. Bagi substrat cendawan segar steril, kandungan sulfat telah dikesan tetapi tidak bagi sisa substrat cendawan. Proses penanaman cendawan telah merubah komposisi fizikokimia dalam substrat cendawan.

Kata kunci: substrat cendawan, perbandingan, analisis fizikokimia

Introduction

The substrate in mushroom cultivation can be defined as a type of lignocellulosic material that promotes the growth, production, and fruiting of mushrooms [1, 2]. Most of the edible species of mushrooms can utilise different types of substrate materials. In Malaysia, the substrate is prepared from rubber sawdust, rice bran, and hydrated lime in the ratio of 100 kg:10 kg:1 kg [3]. Most local farmers in Malaysia typically grow *Pleurotus* species [4] because the processing technology is relatively simple and the materials used in the production of oyster mushrooms are relatively cheap [1, 5]. Also, the species are relatively easy to grow and highly adaptable. Due to their easy preparation, low-cost production technology, and high biological efficiency (BE), the *Pleurotus* species are popular and widely cultivated worldwide, mostly in Asia, America, and Europe [6]. Compared to other mushrooms, the species have a short period of growth [7].

Pleurotus spp. is a saprophyte and it extracts nutrients from the substrate through its mycelium for obtaining essential elements for its growth, such as carbon (C), nitrogen (N), vitamins, and minerals [7]. C and N are the two key macronutrients needed by the fungi for structural and energy requirements. Phosphorus (P), potassium (K), and magnesium (Mg) are also considered as mushroom macronutrients, and trace elements, such as iron (Fe), selenium (Se), zinc (Zn), manganese (Mn), copper (Cu), and molybdenum (Mo), appear to be essential for various functions [8]. In fact, supplementation of the substrate with different materials is advised before spawning to improve the yield of mushrooms [9]. Poultry manure, rice bran, wheat bran, and peat moss have been widely used as food supplements for improved yield, biological efficiency, and growth through the supply of adequate N and slow release of nutrients [10].

Spent mushroom substrate (SMS) refer to the composted material substrate entirely used after many cycles of mushroom cultivation [3, 11]. After several cycles of mushroom cultivation, the nutrients in the substrate decrease and unsuitable to be used for new cultivation [3]. The substrates are an abundant waste product produced by the mushroom industry. For every 1 kg of mushrooms produced, approximately 5 kg of SMS is generated [12, 13]. Respective SMS types have different contents depending on various cultivated mushroom species because the substrates are made from specific ingredients and the preparation method of the substrates, and the form of cultivated mushrooms has different impacts [14]. It is known that different lignocellulose materials can be used as mushroom substrates, particularly for the production of oyster mushrooms, such as rice straw, wheat straw, and sawdust [15].

Thus, this study aims to compare the physicochemical composition of sterile fresh mushroom substrate (SFMS) and spent oyster mushroom substrate (SOMS) in terms of moisture content, ash content, pH value, primary and secondary macronutrients, micronutrients, and carbon-to-nitrogen ratio (C:N ratio) by using t-test analysis as the statistical test.

Materials and Methods

Spent oyster mushroom substrates

The SOMS was obtained from a mushroom grower located at Kampung Empila, Kota Samarahan, Sarawak, Malaysia. Forty five bags of samples were collected randomly after six cycles of harvesting. The SFMS was prepared by mixing softwood sawdust, rice bran, and lime with the ratio of 100:10:1, respectively.

Five bags of SFMS and SOMS were selected. The bags for fresh mushroom substrate were mixed and then three replicates were randomly scooped from the mixture. The same process was applied for SOMS. The substrates were left to dry for a week at room temperature and then shifted through a shifter. The substrates were kept in an airtight container for further analysis.

Physicochemical analysis

Six parameters were considered in this study for physicochemical analysis. The parameters were moisture content, ash content, pH value, primary (N, P, and K) and secondary macronutrients (Ca, Mg, and sulphur (S)), micronutrients (Zn, Fe, Mn, and Cu), and C:N ratio.

Moisture, ash, and pH test

The percentage of moisture was determined by weighing the substrate before and after drying in an oven at 105 °C [13]. The weight loss of the substrate was determined as the moisture content. The ash content was obtained using the standard AOAC method (AOAC, 2000) reported in Rasib et al. [3]. The substrate was incinerated at 550 °C in a furnace overnight. For the pH test, the procedure was based on the methods of Hoa et al. [6]. The substrate was mixed in distilled water with the ratio of 1:10 and the reading was taken by using a pH electrode meter.

Primary and secondary macronutrients and micronutrients

The total C, N, and S of the substrates were determined using a CHNS analyser (Thermo Scientific™ FlashSmart CHNS). Then, the C:N ratio was calculated based on the result of C and N obtained from the analysis.

The determination of P, K, Ca, Mg, Zn, Fe, Mn, and Cu elements was performed using Mehlich 3 (M3) extraction test [16, 17, 18]. This test used inductively coupled plasma-optical emission spectrometry (ICP-OES) (Perkin Elmer, Optima 8000 ICP) for analysis, except for P. The total P content was determined using an ultraviolet-visible (UV-Vis) spectroscopy (Agilent Cary 60 UV-Vis) at the wavelength of 882 nm.

Statistical analysis

The t-test analysis was performed using the computer software IBM SPSS Statistics version 25 to assess mean significant differences ($p \leq 0.05$) between treatments. The experiments were performed in triplicates.

Results and Discussion

The results of physicochemical properties for SFMS and SOMS are shown in Table 1. The physicochemical composition was characterised after sterilisation for SFMS and after six cycles of mushroom cultivation for SOMS. The raw materials used in SFMS and SOMS were softwood sawdust and rice bran.

SOMS showed higher moisture content that reached 63%, but moisture content dropped significantly to 56.7% for SFMS. Lopez Castro et al. [19] reported that the moisture content for SMS of oyster mushrooms was 46.9%, much lower than the data obtained for SOMS. The result may be due to the difference in the environment where the mushroom grows.

Ash is considered as part of the components for SMS. Table 1 shows the results of ash content for SFMS that reached 4.16% and increased significantly to 6.58% for SOMS. There was an increase in the amount of ash after some time. The increasing amount of ash in the SMS showed the number of extractives in SOMS after many processes involved, such as sterilisation and several cycles of mushroom cultivation [3]. According to Rasib et al. [3], the ash content for mushroom substrate was 4.345% and 5.299% for the SMS of oyster mushrooms.

From the determination of hydrogen ion concentration (pH), the substrate was acidic at an average pH of 5.85. A higher pH was recorded for SOMS (5.92), whereas for SFMS, the pH was 5.78. Based on the study of Sultana et al. [20], the optimum pH range for mycelium growth was estimated at 5.5-6.5 for SFMS. Therefore, the result for SFMS is within the optimum range for mushroom growth. For the SMS of oyster mushrooms, the optimum range was 5.1-7.4, as stated by Paredes et al. [21] and the study by Sendi et al. [22] recorded the pH value of 6.10, which was still within the range.

The results of the C content of the substrates are shown in Table 1, which reported the influence of cellulosic composition before and after mushroom cultivation on the C level. Higher C content was detected in SFMS at 45.22% before mushroom cultivation, and the C content declined significantly to 43.87% for SOMS at the end of mushroom cultivation. From the results, it showed that SOMS had lower C content than the results of the

substrate before oyster mushroom cultivation. The low C content is linked with the release of carbon dioxide (CO_2) by fungal exoenzymes during development process [23]. This phenomenon is due to the growth of mushroom mycelium during cultivation that contributed to the decomposition of cellulosic matter and released CO_2, thus leading to low C content.

The C:N ratio is very significant based on their role in the growth of mushrooms. Based on the results, SOMS achieved a higher C:N ratio (116.29%) than SFMS (102.69%). The C:N ratio increased in SOMS after six cycles of harvesting. The finding is expected due to the decrease of total C and N in SOMS because mushrooms consume C and N for growth. Also, the C:N ratio was higher than other studies due to the materials used in the substrate. For example, the substrate produced from wheat straw contained 38.50 of C:N ratio [23]. The only supplement added in the substrate was rice bran. Other substrates used other types of supplements that may differ in chemical composition. Thus, the value of C:N ratio may differ from other substrates. Furthermore, the C:N ratio of sawdust or woody tissues is 350:1 to 500:1. Thus, wood-inhabiting mushrooms, such as the *Pleurotus* species (oyster mushroom), have a unique ability to grow in such substrates, which suggests that these mushrooms can metabolise large amounts of carbohydrates, including lignin, in the presence of a very small amount of N [1].

The substrate directly affects the mineral composition as the hyphae of the fungi are in contact with the compound and withdraw essential elements [7]. The primary macronutrients for substrate, including N, P, and K, showed significant results for both SFMS and SOMS. As tabulated in Table 1, a higher N content was achieved for SFMS (0.44%) than SOMS (0.38%). The P content for SFMS was 10.73 ppm, which then increased significantly to 57.14 ppm for SOMS. The K content was 1,634.17 ppm for SFMS and decreased to 706.67 ppm for SOMS. The values of N and K decreased as mushrooms used the nutrients for growth. As for P, before cultivation, the amount of P was low because lignocellulosic materials are usually low in mineral content [7,24] and after cultivation, sawdust-based SMS contained high P content [25] and SOMS was made of sawdust-based substrate. The study from Sendi et al. [22] showed that the value of N in SMS was 0.34% compared to SOMS (0.38%), which only had a small difference. The values of P and K for SMS were 0.16% and 0.53%, respectively [22], and 0.006% of P and 0.07% of K for SOMS. The difference may be due to the raw materials used in making substrates for both studies.

The secondary macronutrients, including Ca, Mg, and S, were tested for SFMS and SOMS. SOMS showed higher Ca content (7366.67 ppm) than SFMS (3046.67 ppm). Meanwhile, the Mg content of SFMS was lower (525.83 ppm) than SOMS (1230.83 ppm). The total S was only detected in SFMS (0.16%) and for SOMS, the total S was below the detection limit based on the analysis from the CHNS analyser. According to Sendi et al. [22], the values of Ca and Mg detected for SMS were 0.51% and 0.15%, respectively. Compared to the data obtained for SOMS from this study, the values in percentage of Ca are 0.74% and 0.12% for Mg.

The micronutrients for both SFMS and SOMS, which include Zn, Mn, Fe, and Cu, were tested. The Zn content for SFMS was higher (77.50 ppm) than SOMS (16.90 ppm). For the Mn content, the value of SOMS was lower (68.65 ppm) than SFMS (97.50 ppm). The Fe content for SFMS was 20.00 ppm and then increased significantly to 85.15 ppm for SOMS. The Cu content increased significantly from SFMS (0.72 ppm) to SOMS (3.75 ppm). From the results obtained, the total Zn and Mn for SOMS decreased from SFMS, whereas for the total Fe and Cu, there are differences in the values for SOMS, which increased from SFMS. In the study by Medina et al. [26], the Fe content for SOMS was 337 mg/kg, significantly higher than the data obtained for SOMS at 85.15 ppm in this study. The Cu, Mn, and Zn contents at the values of 5.5 mg/kg, 49 mg/kg, and 20 mg/kg, respectively, are still within the range with the results in Table 1.

Table 1. Sterile fresh mushroom substrate and spent oyster mushroom substrate

Parameters	Sterile Fresh Mushroom Substrate (SFMS)	Spent Oyster Mushroom Substrate (SOMS)	LSD ($p \leq 0.05$)
pH	5.78 ± 0.03	5.92 ± 0.02	0.002
Carbon: Nitrogen Ratio	102.69 ± 4.80	116.29 ± 1.42	0.009
	---------- % ----------		
Moisture	56.70 ± 0.10	63.00 ± 0.78	0.005
Ash	4.16 ± 0.01	6.58 ± 0.02	< 0.001
Total Carbon	45.22 ± 0.26	43.87 ± 0.25	0.003
Total Nitrogen	0.44 ± 0.02	0.38 ± <0.01	0.009
Total Sulphur	0.16 ± 0.04	Null	-
	---------- ppm ----------		
Phosphorus	10.73 ± 0.74	57.14 ± 3.58	0.001
Potassium	1634.17 ± 72.86	706.67 ± 118.75	< 0.001
Calcium	3046.67 ± 178.79	7366.67 ± 580.04	< 0.001
Magnesium	525.83 ± 20.82	1230.83 ± 100.38	< 0.001
Zinc	77.50 ± 4.33	16.90 ± 0.58	0.001
Manganese	97.50 ± 4.33	68.65 ± 2.21	0.001
Iron	20.00 ± 6.61	85.18 ± 2.43	< 0.001
Copper	0.72 ± 0.03	3.75 ± 0.13	< 0.001

Conclusion

There is a significant difference between SFMS and SOMS in terms of physicochemical analysis. From the results obtained, in terms of moisture content, pH, and ash content, there are significant differences between both substrates. The data obtained showed increased moisture, pH, and ash content after mushroom cultivation. For primary macronutrients (N, P, and K), there is a significant difference between the substrates. The values of N and K decreased after six cycles of mushroom cultivation as mushrooms needed N and K for growth. For secondary macronutrients, Ca and Mg increased and are significantly different, whereas S was only detected in SOMS. Lastly, for micronutrients, the values of Fe and Cu increased, but the values of Zn and Mn decreased after mushroom cultivation. Thus, this study is valuable for future reference as the valuable nutrients in SOMS after mushroom cultivation can be used for further usage in the agricultural field and others, instead of throwing away the substrate.

Acknowledgement

The authors would like to thank the Tun Openg Chair Grants for the support through grant (F07/TOC/1739/2018), the Faculty of Resource Science and Technology for the research facilities provided and to Mr. Azis Ajim, the mushroom grower, for providing the spent oyster mushroom substrates for this study.

References

1. Miles, P. G. and Chang, S. T. (2004). Mushrooms: cultivation, nutritional value, medicinal effect, and environmental impact. CRC press.
2. Assan, N. and Mpofu, T. (2014). The influence of substrate on mushroom productivity. *Scientific Journal of Crop Science*, *3*(7): 86-91.

3. Rasib, N. A. A., Zakaria, Z., Tompang, M. F., Rahman, R. A. and Othman, H. (2015). Characterization of biochemical composition for different types of spent mushroom substrate in Malaysia. *Malaysian Journal Analytical Sciences*, 19(1): 41-45.
4. Sidik, M. A. B., Buntat, Z., Razali, M. C., Buntat, Y., Nawawi, Z., Jambak, M. I. and Smith, I. R. (2015). A new method to sterilise mushroom substrate for oyster mushroom cultivation. *International Journal of Emerging Trends Science Technology*, 4: 1-18.
5. Ficior, D., Indrea, D., Apahidean, A. S., Apahidean, M., Rodica, P. O. P., Moldovan, Z. and Paven, I. (2006). Importance of substrate disinfection on Oyster mushroom (*Pleurotus* sp.) culture. *Notulae Botanicae Horti Agrobotanici Cluj-Napoca*, 34: 48.
6. Hoa, H. T., Wang, C. L. and Wang, C. H. (2015). The effects of different substrates on the growth, yield, and nutritional composition of two oyster mushrooms (*Pleurotus ostreatus* and *Pleurotus cystidiosus*). *Mycobiology*, 43(4): 423-434.
7. Bellettini, M. B., Fiorda, F. A., Maieves, H. A., Teixeira, G. L., Ávila, S., Hornung, P. S. and Ribani, R. H. (2019). Factors affecting mushroom *Pleurotus* spp. *Saudi Journal of Biological Sciences*, 26(4): 633-646.
8. Carrasco, J., Zied, D. C., Pardo, J. E., Preston, G. M. and Pardo-Giménez, A. (2018). Supplementation in mushroom crops and its impact on yield and quality. *AMB Express*, 8(1): 146.
9. Moonmoon, M., Shelly, N. J., Khan, M. A., Uddin, M. N., Hossain, K., Tania, M. and Ahmed, S. (2011). Effects of different levels of wheat bran, rice bran and maize powder supplementation with saw dust on the production of shiitake mushroom (*Lentinus edodes* (Berk.) Singer). *Saudi Journal of Biological Sciences*, 18(4): 323-328.
10. Jafarpour, M., Jalali, A., Dehdashtizadeh, B. and Eghbalsaied, S. (2010). Evaluation of agricultural wastes and food supplements usage on growth characteristics of *Pleurotus ostreatus*. *African Journal of Agricultural Research*, 5(23): 3291-3296.
11. Fidanza, M. A., Sanford, D. L., Beyer, D. M. and Aurentz, D. J. (2010). Analysis of fresh mushroom compost. *HortTechnology*, 20(2): 449-453.
12. Medina, E., Paredes, C., Bustamante, M. A., Moral, R. and Moreno-Caselles, J. (2012). Relationships between soil physico-chemical, chemical and biological properties in a soil amended with spent mushroom substrate. *Geoderma*, 173: 152-161.
13. Ashrafi, R., Rahman, M. M., Jahiruddin, M. and Mian, M. H. (2014). Quality assessment of compost prepared from spent mushroom substrate. *Progressive Agriculture*, 25: 1-8.
14. Hui, Z., Jianhua, L., Dai Jianqing, C. M. and Yi, C. (2007). The alternative uses of spent mushroom compost. *Spore*, 2007: pp. 1-22.
15. Koshy, J. and Nambisan, P. (2012). Ethanol production from spent substrate of *Pleurotus eous*. *International Journal of Applied Biology and Pharmaceutical Technology,* 3(1): 280-286.
16. Frank, K., Beegle, D. and Denning, J. (2012). Phosphorus. In M.V. Nathan and R. Gelderman (Eds.), Recommended chemical soil test procedures for the North Central Region (2012 Revision). Missouri, USA: Missouri Agricultural Experiment Station.
17. Warncke, D. and Brown, J. R. (2012). Potassium and other basic cations. In M.V. Nathan and R. Gelderman (Eds.), Recommended chemical soil test procedures for the North Central Region (2012 Revision). Missouri, USA: Missouri Agricultural Experiment Station.
18. Zbíral, J. (2016). Determination of plant-available micronutrients by the Mehlich 3 soil extractant–a proposal of critical values. *Plant, Soil and Environment*, 62(11): 527-531.
19. Lopez Castro, R. I., Delmastro, S. and Curvetto, N. R. (2008). Spent mushroom substrate in a mix with organic soil for plant pot cultivation. *Micologia Aplicada International,* 20(1): 17-26.
20. Sultana, R., Hossain, M. I., Amin, R. and Chakraborty, R. (2018). Influence of substrate pH and watering frequency on the growth of oyster mushroom. *International Journal of Plant Biology & Research*, 6(4): 1097.

21. Paredes, C., Moral, R., Pérez-Murcia, M. D., Moreno-Caselles, J. and Pérez-Espinosa, A. (2006). Agricultural value of the spent mushroom substrate. Technology for recycling of manure and organic residues in a whole-farm perspective. Danish Institute of Agricultural Sciences, Ministry of Food, Agricultural Sciences, Tjele: pp. 301-304
22. Sendi, H., Mohamed, M. T. M., Anwar, M. P. and Saud, H. M. (2013). Spent mushroom waste as a media replacement for peat moss in Kai-Lan (*Brassica oleracea* var. Alboglabra) production. *The Scientific World Journal*, 2013: 258562.
23. Owaid, M. N., Abed, I. A. and Al-Saeedi, S. S. S. (2017). Applicable properties of the bio-fertilizer spent mushroom substrate in organic systems as a byproduct from the cultivation of *Pleurotus* spp. *Information Processing in Agriculture*, 4(1): 78-82.
24. Alananbeh, K. M., Bouqellah, N. A. and Al Kaff, N. S. (2014). Cultivation of oyster mushroom *Pleurotus ostreatus* on date-palm leaves mixed with other agro-wastes in Saudi Arabia. *Saudi journal of Biological Sciences*, 21(6): 616-625.
25. Hanafi, F. H. M., Rezania, S., Taib, S. M., Din, M. F. M., Yamauchi, M., Sakamoto, M. and Ebrahimi, S. S. (2018). Environmentally sustainable applications of agro-based spent mushroom substrate (SMS): an overview. *Journal of Material Cycles and Waste Management*, 20(3): 1383-1396.
26. Medina, E., Paredes, C., Pérez-Murcia, M. D., Bustamante, M. A. and Moral, R. (2009). Spent mushroom substrates as component of growing media for germination and growth of horticultural plants. *Bioresource Technology*, 100(18): 4227-4232.

Malaysian Journal of Analytical Sciences (MJAS)
Published by Malaysian Analytical Sciences Society

A SNAPSHOT ON THE IRON CONTENT IN MALAYSIAN CRUDE PALM OIL

(Tinjauan Mengenai Kandungan Ferum dalam Minyak Sawit Mentah Malaysia)

Farah Khuwailah Ahmad Bustamam*, Najwa Sulaiman, Yeoh Chee Beng, Nik Sasha Khatrina Khairuddin

Malaysian Palm Oil Board,
No.6, Persiaran Institusi, Bandar Baru Bangi, 43000 Kajang, Selangor, Malaysia

**Corresponding author: fkhuwailah@mpob.gov.my*

Received: 10 June 2020; Accepted: 16 October 2020; Published: 10 December 2020

Abstract

This study reported the iron content in crude palm oil (CPO) and selected secondary oils collected at the Malaysian palm oil mills through national surveys that were carried out in 2015, 2016, and 2019. Data from these surveys provided an indicative average iron content in the CPO produced by Malaysian palm oil millers. It was found that the average iron content (11.1 ppm) was higher than the result obtained from the previous national survey. To this finding, this study aimed to investigate the effect of filtration using filter paper on the potential type of iron found in CPO. Analysis of iron was conducted using an inductively coupled plasma - mass spectrometry (ICP-MS) instrument. Another quality parameter that might accelerate the iron content such as free fatty acid was also deliberated. The possible factors that might contribute to the high iron content in CPO and recommendations on the control of iron contamination were also discussed.

Keywords: iron, survey, crude palm oil, quality

Abstrak

Kajian ini melaporkan kandungan ferum dalam minyak sawit mentah (MSM) dan beberapa jenis minyak sekunder di kilang sawit Malaysia yang diperolehi daripada kaji selidik di peringkat nasional yang telah dijalankan pada tahun 2015, 2016, dan 2019. Data yang diperolehi daripada kaji selidik ini menunjukkan nilai purata kandungan ferum dalam MSM yang dihasilkan oleh pekilang di Malaysia. Nilai purata kandungan ferum (11.1 ppm) didapati lebih tinggi berbanding hasil kaji selidik yang telah dilaporkan sebelum ini. Analisis kandungan ferum telah dijalankan menggunakan instrumen spektrometri jisim - plasma gandingan aruhan (ICP-MS). Satu kajian awal telah dijalankan bagi meneroka kesan penapisan menggunakan kertas turas kepada jenis ferum yang mungkin terdapat dalam MSM. Parameter kualiti yang mungkin menjadi pemangkin kepada kandungan ferum seperti nilai asid bebas lemak dihuraikan. Faktor-faktor yang berkemungkinan menyumbang kepada kandungan ferum serta cadangan-cadangan bagi mengawal pencemaran ferum ke dalam MSM juga dibincangkan.

Kata kunci: ferum, kaji selidik, minyak sawit mentah, kualiti

Introduction

Crude palm oil (CPO) is extracted from the mesocarp of oil palm fruit under several milling processes. After refining process, refined palm oil undergoes further fractionation process producing liquid fraction namely palm olein and solid fraction namely palm stearin. Secondary oils are the oils recovered from empty palm fruit bunches by double pressing and palm fibre using solvent extraction technique. These secondary palm oils are sold as technical oil after undergoing a certain refining process for non-edible purposes.

Palm oil is widely exported as either in its crude or processed forms. In 2019, the total export of palm oil and its products were up to 27.98 million tonnes with total revenue of MYR 64.84 billion [1]. Being the second largest palm oil exporter in the world, Malaysia has set the goal to provide premium quality palm oil. Quality is an important aspect of palm oil products as well as from the trade point of view. Generally, the palm oil quality is evaluated based on parameters such as free fatty acid (FFA), deterioration of bleachability index (DOBI), and moisture and impurities (M&I). The quality requirements for palm oil trading are also based on the business-to-business contract, which the Palm Oil Refineries Association Members (PORAM) trading specifications are often referred to as the quality guidelines. Apart from that, the details on the quality of palm oil are specified in several specification documents such as Malaysian Standard, MS 814:2007, and Codex Stan CXS 210-1999 [2,3].

Quality of palm oil may deteriorate as a result of hydrolysis and oxidation reactions affected by certain factors such as excessive heat, water contamination, acidity, light, presence of oxygen, air, and pro-oxidant metals such as copper (Cu) and iron (Fe) [4]. The hydrolysis reaction resulted from the splitting of triacylglycerols (TAG) to FFA and partial glycerides will lead to an increase in the refining loss. Meanwhile, oxidation happened due to the attack of unsaturation by oxygen to form first peroxides and then secondary products by subsequent reactions, which gives a rancid smell and creates problems during the bleaching process. Quality deterioration may also occur if the oil is not handled and stored properly. In general palm oil milling practices, only the analyses of FFA, DOBI, and M&I are carried out as a tool to monitor the quality of CPO produced. Fe content is rarely measured since it is not a contractual specification despite its detrimental effect on the oil quality.

Naturally, CPO contains a small amount of Fe in the form of complexes, surrounded by proteins and phospholipids that rarely exceed 0.7 ppm [5]. The presence of Fe in CPO will exacerbate the oxidation reaction through its catalytic property that decomposes the hydroperoxides to form free radicals. High Fe content in CPO resulted in poor bleachability and oil stability [4, 6]. Fe presents in CPO is usually originated from the pick-up of machinery wear and tear, and also from fibre of the palm fruits which are contaminated with soil particles picked up during fresh fruit bunches (FFB) harvesting. A study on the CPO extracted from oil palm planted in laterite soil showed that the type of soil where the palms were planted contributed to high Fe content compared to those planted in alluvial soil [7, 8]. Fe content in palm oil is made up of two types, *i.e.* soluble and insoluble. The insoluble or particulate Fe often can be removed using a magnetic trap while soluble Fe is difficult to be removed by physical means.

In 2015, a one-year national CPO survey was conducted to gather information about the current status of palm oil quality. Based on the specifications, the overall quality performance of Malaysian CPO was satisfactory except for the high level of Fe. To this finding, further investigation is required to identify the nature of Fe in CPO during the national survey as Fe is one of the metals that is known to be pro-oxidant.

Recycling of oil residues derived from sterilizer condensate during CPO processing and empty fruit bunch liquor (EFBO) from the pressing of empty fruit bunches is a well-known practice in current CPO production [9,10] despite its negative effect on the overall quality of CPO. The recent introduction of new secondary oil namely palm pressed fibre oil (PPFO) [11, 12] has attracted our attention. The PPFO is obtained via the hexane extraction of palm pressed fibre and aimed

for the application in the production of high value phytonutrients. However, there is a concern about the possibility of re-mixing PPFO into CPO by certain irresponsible CPO traders as the CPO price is high.

Therefore, this study reported the results of Fe content obtained from the recent CPO and secondary palm oils surveys as an update for the national survey of the Malaysian palm oil industry. The type of Fe found in the CPO was investigated by measuring the Fe content before and after filtration with filter paper. The factors that may contribute to the Fe traces in CPO and the potential ways to control Fe content were also discussed.

Materials and Methods

Sampling

A total of 240 CPO samples were obtained from the production mills located at Peninsular Malaysia, Sabah, and Sarawak for the CPO survey study. Two types of secondary oils, namely PPFO and EFBO were collected from 8 producing mills in Sabah, Johor, Pahang, and Perak. For the filtration study, a total of 32 CPO samples were obtained from different production mills in Negeri Sembilan, Selangor, Johor, and Sabah. All collected samples were kept in opaque bottles (250 mL) and stored at 5 °C upon receiving prior to analysis.

Filtration of Insoluble Iron

For the filtration study, CPO samples were heated in the oven at 55 °C to ensure all samples were melted and well homogenized before the filtration process. The initial CPO sample was collected in the scintillation vial (20 mL) and labelled as "before filter". The remaining sample was filtered using filter paper Whatman No. 4, 185 mm diameter (Sigma Aldrich, Darmstadt, Germany), collected in another scintillation vial and labelled as "after filter". The purpose of filtering the CPO was to remove the filterable coarse, impurities precipitate, and probably insoluble Fe residues in the CPO. Both samples were then analysed for Fe content.

Quality analysis

FFA analysis was conducted by a titration method defined in the AOCS Official Method Ca-5a 40:2007 and expressed as a percentage of palmitic acid.

Analysis of iron content in palm oil

A homogenized CPO sample (0.5 g) was digested with concentrated nitric acid (65%) and hydrogen peroxide (30%) in a close system microwave digestion (NovaWAVE SA, SCP Science) apparatus. The digested CPO sample was diluted and analysed using inductively coupled plasma - mass spectrometry NexION 2000 ICP-MS (Perkin Elmer, California, USA).

Statistical analysis

The overall means and error bars of all data in the figures and tables were calculated from the individual mean of each state. Samples were analysed in duplicate. The statistical analysis was done using Microsoft Office Excel 2007 (Microsoft Corporation, Redmond, WA).

Results and Discussion

Overview of CPO surveys data

The average of total Fe content from 240 CPO samples obtained in the 2015 CPO survey was 11.1 ppm with a standard deviation of ± 5.1 ppm. This average Fe content was way higher as compared to the values recorded during previous national surveys in 1974, 1986, and 1997 with the average value of 3.76, 5.6, 4.89, respectively [13-15]. Figure 1 shows the distribution of average Fe content from different states in Malaysia, which exceeded the maximum acceptable level stipulated in the CODEX standard [3]. Further investigation revealed that all samples were collected from palm oil mills which have been operating for more than 10 years and some of them could be half-century old palm oil mills. High Fe content observed in the CPO from these mills may be attributed to the leaching of Fe from milling machinery, *i.e.* moving parts of milling machinery due to wear and tear suggested by Gee [8].

A previous study suggested that Fe leaching was indirectly caused by FFA content in CPO that corroded some of the Fe from the mild steel parts of machinery (*i.e.* screw press) in the mill [8]. Since the average FFA content distribution of all states in the current national survey was below 5%, hence no conclusive evidence can be drawn to support the effect of FFA on Fe content as reported.

The characteristics of secondary oils

A preliminary result of the Fe content measured in PPFO and EFBO samples are compared to CPO and shown in Table 1.

Fe content in the PPFO sample was the highest as compared to EFBO. PPFO is known to contain a high level of phosphorus and carotene, as the oil is solvent extracted from the pressed palm fibre. Another type of secondary oils, namely sterilizer condensate oil (SCO) and sludge palm oil (SPO) were reported to contain Fe up to 24.27 ppm and 9.5 ppm, respectively [16].

This clearly shows that secondary oils, *i.e.* PPFO and SCO contained higher amounts of Fe compared to CPO. Secondary oils are known to be low in quality and contain higher amounts of Fe picked up from their sources. For that reason, mixing of the secondary palm oils with freshly production CPO has caused an increase of Fe contamination during storage and transportation, forming oil at a highly oxidized state [17]. The mixing of production CPO with secondary palm oils must be totally avoided because this practice will degrade the quality of CPO produced. By not recycling these secondary palm oils into the standard CPO production helps to control the level of Fe content in CPO.

Filtration of CPO – Potential solution for particulate iron removal

The results from CPO filtration study showed that the Fe content was reduced after filtration, which proved that the particulate Fe can be removed from CPO by filtration step using Whatman No. 4 filter paper. The reduction percentage was up to 98% of the initial Fe content. There were two classes of Fe compounds found; one was soluble in CPO at temperature of 55 °C and passed through Whatman No. 4 filter paper, while the remainder was filterable Fe. The average of particulate Fe measured was 18.4 ppm with a standard deviation of 12.5 ppm, and surprisingly, the soluble Fe measured in the CPO was 5.6 ppm with a standard deviation of 3.8 ppm. This finding indicated that most Fe found in CPO was in the form of non-soluble particulates.

Over the past decades, several solutions at palm oil mills were identified for the reduction and removal of Fe in palm oil. A study on the removal of suspended impurities in CPO by centrifugation was shown to reduce the Fe content in the CPO. The Fe content measured from the residue of dried impurities samples was tremendously high (6155 ppm), indicated that most of the Fe were presented as dirt in CPO [18]. Impurities such as mineral fragments of soil and stone picked up during contact of fresh fruit bunches (FFB) or loose fruits with the ground at the plantations could be found in the oil and brought over for processing [19]. Therefore, the removal and minimization of the impurities content to a level as low as 0.05% (w/w) should be practiced reducing the Fe content in CPO. Apart from that, the installation of a magnetic trap at the end of the milling process was proven as an effective technique of removing particulate Fe from CPO [20]. However, this magnetic trap was not very effective for low level of Fe.

Instead, washing of CPO that is currently being practiced for chloride removal in order to minimize the formation of 3-MCPD esters has been a potential technique for removing a substantial amount of Fe [8]. This technique was supported by the earlier reported study on the effect of washing CPO with warm water and un-washed CPO as a control, which resulted in a 50% reduction of Fe content in washed CPO compared to unwashed [18].

In the chemical refining process, Fe can also be reduced during the settling of suspended impurities at the neutralisation stage [21]. The Fe is trapped by the installation of a magnetic trap and simultaneous removal of heavy metals with the precipitation of gum by caustic soda. At the degumming and bleaching stages, the formation of phospholipid-metal complex facilitated by the addition of calcium carbonate could remove the Fe complex associated with the phospholipid [18, 21]. This is due to the enclosure of the Fe complex into the precipitate. Besides that, the usage of non-acid activated clay with neutral and natural adsorbents during the bleaching process was found to be useful for the removal of Fe in incoming CPO [22]. Fe also can be removed by adsorption during the pre-treatment step using silica in physical refining [23].

Recommendation for controlling iron contamination in CPO

There was no significant correlation between Fe content and FFA found in this study. Regardless of the finding, the most feasible and economical way to control the quality of CPO is by regular checking on the quality of the FFB received and ensuring that only acceptable quality FFB is processed in a timely manner, preferably within 24 hours post-harvesting. This practice is not only to guarantee that the FFB is not overripe and bruised during handling, but also to minimize enzyme activity in FFB which results in high acidity of palm oil.

At the mills and refineries, important machineries that come into contact with FFB and the oil *i.e.* screw press, digesters, vacuum dryers, pumps and pipelines are recommended to be made of stainless steel materials, and with organic or epoxy coatings in tanks and pipes. This acts as a preventive measure to avoid Fe pick-up during the processes. The storage tanks should be cleaned prior to loading in order to preserve the quality of the oil, as well as to avoid any potential cross-contamination [24]. The contact between palm oil with mild steel should be minimized especially at high temperatures. Regular cleaning of palm oil processing line purifiers may also help to reduce the amount of dirt presence in oil and subsequently, the Fe content.

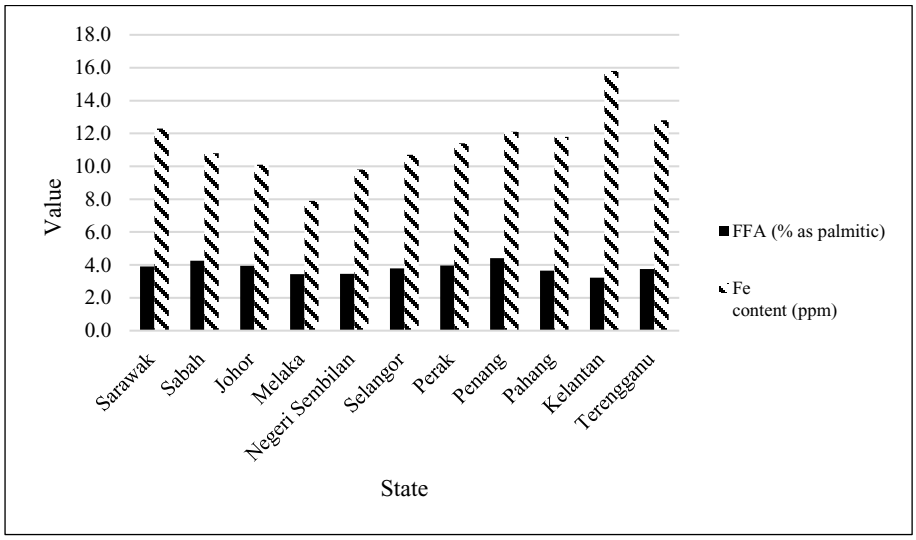


Figure 1. Average of free fatty acids and iron content in CPO from different states in Malaysia

Table 1. Iron content in CPO and secondary oils

Type of Oils	Iron Content (ppm)
PPFO	70.8 ± 44.64
EFBO (n=1)	3.9
CPO	11.1 ± 5.1

Conclusion

The increase in Fe content of CPO from the recent national survey was probably caused by particulate Fe that can be removed by filtration. This is supported by laboratory results on the findings of Fe content in CPO before and after filtration. Presently, mill and refinery already installed some devices to remove this particulate Fe. As the secondary palm oils were observed to contain high amounts of Fe, the mixing of these secondary oils into the fresh CPO should be totally avoided and prohibited. Nevertheless, preventing Fe contamination during milling, storage and transportation are crucial to safeguard the quality and safety of palm oil. High Fe content in CPO may cause a deterioration in the oil oxidative stability and subsequently affecting its keeping quality and bleachability. Further study on the effect of purifier in palm oil processing to the Fe content is necessary, in view of fact that some of the palm oil mills already omitted the usage of purifiers in their normal operation, the effect of this purifier exemption remains unknown at this point.

Acknowledgement

The authors would like to thank the Director-General of MPOB for permission to publish this article. The support and advice from the Director of Product Development and Advisory Services Division is highly acknowledged. Technical assistance from the Analytical Research Group of Product Development and Advisory Services Division is greatly appreciated.

References

1. Parveez, G. K. A., Hishamuddin, E., Loh, S. K., Ong-Abdullah, M., Salleh, K. M., Bidin, M. N. I. Z., Sundram, S., Hasan, Z. A. A. and Idris, Z. (2020). Oil palm economic performance in Malaysia and R&D progress in 2019. *Journal of Oil Palm Research*, 32(2): 159-190.
2. Department of Standard Malaysia (2007). Palm Oil - Specification (Second Revision) MS 814:2007. Malaysia: Department of Standard Malaysia.
3. Codex Standard for Named Vegetable Oils (Codex-Stan 210 - 1999). Amended 2019.
4. Salleh, M. I., Murray R. S. and Chin, C. N. (1988). Ashing technique in the determination of iron and copper in palm oil. *Journal of the American Oil Chemists' Society*, 65(11): 1767-1770.
5. Chow, M. C. and Maycock, J. H. (1990). Iron content of crude palm oil. *Palm Oil Engineering Bulletin,* 20: 4-6.
6. Ab Gapor, M. T. and Augustine, S. H. O. (1982). Some aspects of trace metals in palm oil. *Oil Palm Bulletin*, 4: 19-26.
7. Chow, M. C. (1992). An assessment of the iron and free fatty acid content of production oil from various palm oil mills. *Oil Palm Bulletin*, 24: 13-27.
8. Gee, P. T. (2018). Impacts of palm oil milling and refining on product quality – A personal view. *Malaysian Oil Science and Technology*, 27(1): 57-68.
9. Nuzul, A. I. and Menon, N. R. (2017). Mitigation for 3-MCPD esters at palm oil mills. *Palm Oil Engineering Bulletin*, 124: 11-15.
10. Alfa Laval. Recovering palm oil from empty fruit bunch (EFB) liquor - A profitable venture using Alfa Laval PANX decanter centrifuges. Access From https://www.alfalaval.com/globalassets/documents/industries/food-dairy-and-beverage/food/fat-and-oil-processing/recovering-palm-oil-from empty-fruit-bunch-liquor.pdf. Online accessed on 8 October 2020.
11. Rusnani, A. M., Abdul Wahab, M. and Choo, Y. M. (2012). Properties of residual palm pressed fibre oil. *Journal of Oil Palm Research*, 24(2): 1310-1317.
12. Ummi Kalsum, H. M. N. and Rohaya, M. H. (2019). Pressed fibre oil: quality and implications. *Palm Oil Engineering Bulletin*, 131: 16-21.
13. Jacobsberg, B. (1974). Present day palm oil quality in Malaysia - Survey of the palm oil production in 1973 - forecast of refining abilities. *Proceeding of the First Mardi Workshop on Oil Palm Technology*: pp. 71- 119.
14. Siew, W. L., Tan, Y. A. and Chong, C. L. (1989). Quality of Malaysian crude palm oil. *PORIM Report,* PO(149)89: 1-32.

15. Tan, Y. A., Kuntom, A., Siew, W. L., Yusof, M. and Chong, C. L. (2000). PORIM crude palm oil survey 97/98 quality and identity characteristics. *PORIM Technology,* 22: 1-30.
16. Prasad, K. V. S. V., George, S. and Arumugham, C. (1991). Oil characteristics and composition of palm oil process streams. *Indian Oil Palm Journal*, 1(3): 23-28.
17. George, S. and Arumughan, C. (1992). Lipid profile of process streams of palm oil mill. *Journal of the American Oil Chemists' Society*, 69(3): 283-287.
18. Chooi, S.Y. and Koh, H. F. (1981). A study of some quality aspects of crude palm oil – The stabilisation of crude palm oil at the mill. *A report of the Proceedings of the International Conference on Palm Oil Product Technology in the Eighties*: pp. 231-247.
19. Yeoh, G. H. (1976). Study of the nature and effects of iron contamination in palm oil. *Incorporated Society of Planters*: pp. 1-27.
20. Chen, Soo-Se and Berger, K. G. (1983). Current research on palm oil related to quality in Malaysia. P*roceeding of Japan Oil Chemists' Society 30th Anniversary Conference*, 1983: pp. 1-10.
21. Rakmi, A. R. (1984). Reduction of palm oil heavy metal content in the refining process. *Oil Palm Bulletin,* 9: 16-21.
22. Siew, W.L. and Cheah, K. Y. (2007). Adsorption isotherms for removal iron, phosphorus, copper and oxidation products from crude palm oil using natural and acid-activated clay. *Journal of Oil Palm Research,* 19: 356-363.
23. Sampaio, K. A., Ayala, J. V., Van Hoed, V., Monteiro, S., Ceriani, R., Verhé, R. and Meirelles, A. J. (2017). Impact of crude oil quality on the refining conditions and composition of nutraceuticals in refined palm oil. *Journal of Food Science*, 82(8): 1842-1850.
24. Chong, C. L. (1995). Handling, storage and transportation of fresh fruit bunches and palm oil products. *Palm Oil Technical Bulletin*: pp. 2-4.

Malaysian Journal of Analytical Sciences (MJAS)
Published by Malaysian Analytical Sciences Society

CHARACTERIZATION OF INCLUSION COMPLEX OF β-CYCLODEXTRIN/ISONIAZID USING SPECTROSCOPIC METHOD

(Pencirian Kompleks Kemasukan β-Siklodektrin/Isoniazid Menggunakan Kaedah Spektroskopi)

Nurul Yani Rahim* and Nurul Ain Elmira Elleas

School of Chemical Sciences,
Universiti Sains Malaysia, 11800 Gelugor, Pulau Pinang, Malaysia

**Corresponding author: nurulyanirahim@usm.my*

Received: 21 August 2020; Accepted: 29 September 2020; Published: 10 December 2020

Abstract

The inclusion behavior of isoniazid with β-cyclodextrin (β-CD) in the liquid and solid state were investigated. The absorption spectral of UV-Vis was used to determine the inclusion behavior in the liquid state. Fourier Transform Infrared (FTIR) spectrometer, Thermogravimetric Analysis (TGA), and Nuclear Magnetic Resonance (NMR) were used to investigate the inclusion behavior in the solid state. The kneading between isoniazid and β-CD was performed to produce the inclusion complex. The formation constant (K) of the inclusion complex (β-CD/isoniazid) was calculated using Benesi-Hildebrand. The results of ^{1}H NMR and NOESY indicated that β-CD formed hydrophobic interaction with isoniazid. The values of formation constant for the complex of β-CD/isoniazid at pH 4 and 9 were 17.15 and 9.86, respectively. Meanwhile, the value of formation constant for the complex at the natural condition was 25000. The stoichiometry ratio obtained for the complex of β-CD/isoniazid in acidic and basic conditions are 1:1. Meanwhile, 1:2 ratio of β-CD and isoniazid was found at natural condition.

Keywords: β-cyclodextrin, tuberculosis drug, isoniazid, formation constant, inclusion complex

Abstrak

Sifat kemasukan di antara isoniazid dengan β-siklodektrin (β-CD) dalam keadaan cecair dan pepejal telah disiasat. Spektrum penyerapapan UV-Vis telah digunakan untuk mengenal pasti sifat kemasukan dalam keadaan cecair. Spektrometer Inframerah Transformasi Fourier (FTIR), Analisis Termogravimetrik (TGA) dan Resonan Magnetik Nuklear (NMR) telah digunakan untuk menyiasat sikap kemasukan dalam keadaan pepejal. Pengulian antara isoniazid dan β-CD telah dilakukan untuk menghasilkan kompleks kemasukan. Pemalar pembentukan (K) komplek kemasukan (β-CD/isoniazid) telah kira menggunakan Benesi-Hildebrand. Keputusan ^{1}H NMR dan NOESY menunjukkan β-CD membentuk interaksi hidrofobik dengan isoniazid. Nilai pemalar pembentukan bagi kompleks β-CD/isoniazid pada pH 4 dan 9 adalah masing-masing 17.15 dan 9.86. Sementara itu, pada keadaan semula jadi nilai pemalar pembentukan kompleks ialah 25000. Nisbah stoikiometri yang diperolehi untuk kompleks β-CD/isoniazid dalam keadaan asid dan bes ialah 1:1. Sementara itu, 1:2 adalah nisbah untuk β-CD dan isoniazid pada keadaan semula jadi.

Kata kunci: β-siklodektrins, ubat anti tuberculosis, isoniazid, pemalar pembentukan, kompleks kemasukan

Introduction

Host guest systems have performed in supramolecular chemistry to introduce the broad idea of intermolecular interactions. The interaction between host and guest relies on non-covalent bonding. The common types of non-covalent interactions are hydrogen bonding, dipole-dipole, van der Waals and π-π interaction. An inclusion complex is a type of host-guest system in which one compound (the host) contains a cavity or spaces where another molecular entity (the guest) is located. Therefore, the understanding of non-covalent interactions is important in the inclusion complex formation. Towards this goal, the application of simple hosts such as cyclodextrin, crown ether and calix [n] arena is gaining attention [1-3].

Tuberculosis (TB) is a global pandemic disease caused by *Mycobacterium tuberculosis* (MTB) that has been a scourge for humanity over thousands of years [4]. According to the World Health Organization (WHO), a quarter of the global population infected by TB with had reported with 9 million cases in 2010, and the number of new cases of infected people is increasing yearly [5]. Therefore, the continuous phase for TB treatment is essential to kill the persistent or slow-growing strains of MTB [6]. Thus, the development of new drugs and strategies for eradication of TB disease and tackle the dormant MTB needs to be a concern.

Isoniazid is one of first-line drugs to treat TB initiated in 1951 [6] to stop the growth of bacteria. Isoniazid penetrated and activated the encoding catalase-peroxidase gene. The peroxidase catalase activity induced the interaction of isoniazid with toxic reactive species [7] such as oxides, hydroxyl radicals, and organic moisture to rupture the cell wall components causing the cellular integrity completely lost and lead to the death of bacterial [8].

The supramolecular cyclodextrins (CDs) are well known non-toxic cyclic oligosaccharides consist of (α-1, 4)-linked α-L-glucopyranose units with a hollow hydrophobic central cavity and a hydrophilic outer surface. This characteristic served as fundamental for various applications of CD in pharmaceuticals, foodstuffs, host-guest chemistry, textile processing, models for studying enzyme activity, molecular encapsulation, and chemical stabilization [9]. There are α-, β- and γ- denoted for six to eight α-L-glucopyranose unit in cyclodextrins. Among these types of cyclodextrins, β-cyclodextrin (β-CD) is widely used due to its structural orientation that favorable for inclusion complex formation. The toxicological profile of β-CD consists of physicochemical features that adapted for therapeutic demands [10, 11]. Previously, Razak et al. had demonstrated the experimental and theoretical study of isoniazid and β-CD complex [12, 13]. The host-guest inclusion complex of isoniazid with β-CD derivatives was explored well experimentally and theoretical [14].
In this context, the current study aimed to investigate the inclusion complex of isoniazid with β-CD. The inclusion complex was analyzed by FTIR, TGA, UV-Vis and NMR. To the best of our knowledge, in this study, there are liquid and solid-state studies about the complexation of isoniazid and β-CD. This integrated experimental method shows the host-guest mechanism between β-CD and isoniazid will benefit to the future formulation development of the drug delivery system.

Materials and Methods

Materials

β-CD (>97%) was purchased from Sigma Aldrich Company and used without further purification. Isoniazid (99%) was obtained from Across Organic and used without further purification. Methanol (LC grade), ethanol (95%) and hydrochloric acid (37%) were purchased from QRec. Sodium hydroxide (99%) and dimethyl sulfoxide (99.8%) were obtained from R&M Chemical and MagniSolv, respectively. Ultra-pure water was used to dilute the solutions.

Preparation β-CD/isoniazid complex

Kneading method was used to prepare the β-CD/isoniazid complex by grinding β-CD and isoniazid with molar ratio of 1:1 [15-18]. A few drops of ethanol were added to form homogeneous paste. The mixture was ground for 30 minutes. The sample was then kept in a desiccator.

Characterization of complex in solid state

The structural information for inclusion complexes was studied using FTIR. The absorption spectra were obtained using FTIR Perkin-Elmer 2000 system in the range from 400 to 4000 cm^{-1}. The thermal stability was studied through the Thermogravimetric Analysis (TGA) using Perkin Elmer Thermal Analysis. The analysis was done at ambient temperature from 30 to 900 °C in N_2 atmosphere to determine the weight loss profile and decomposition temperature of β-CD, isoniazid, and β-CD/isoniazid complex. The Bruker Advance spectrometer 500 MHz was used to determine ^1H NMR and NOESY of the β-CD, isoniazid, and β-CD/isoniazid complex using DMSO-d_6 as a solvent. The measurements of absorption spectra in the range of 200-400 nm were carried out using Shimadzu UV2600 spectrometer.

Characterization of complex in liquid state: Determination of formation constant and stoichiometry ratio

Firstly, the stock solutions of isoniazid (0.01mM) and β-CD (0.002 M) were prepared. Then, 2.0 mL of isoniazid (0.01 mM) and 3.2 mL of β-CD (0.002 M) solutions were pipetted into 10.0 mL of volumetric flask to produce the solution of β-CD/isoniazid. Ultra-pure water was added to the calibration mark. The absorption spectra for β-CD (0.002M), isoniazid (0.01mM) and β-CD/isoniazid were recorded using UV-Vis. The series of β-CD/isoniazid solution without pH adjustment (natural) and with pH adjustment (pH 4 and pH 9) were prepared. The natural condition was checked to be at pH 6.8 which closed to the neutral pH. Each series consist fixed concentration of isoniazid (0.01mM) and varied concentration of β-CD (0.002, 0.004, 0.005, 0.006 and 0.007 M). From the spectra, the plot of Benesi-Hildebrand was generated using Eq (1). The slope Eq (2) and coefficient of determination (r^2 near to 1) obtained from the plot was applied to determine the formation constant (K) and stoichiometry ratio of complex.

$$\frac{1}{A-A_0} = \frac{1}{(A\prime-A_0)} + \frac{1}{K(A\prime-A_0)[\beta-CD]} \quad (1)$$

$$K = \frac{1}{Slope\ (A-A_0)} \quad (2)$$

where A_0 and A attributed to the absorbance of the isoniazid and β-CD, respectively. A' is referring to the absorbance of β-CD at maximum concentration.

Results and Discussion

Characterization of inclusion complex in solid state: FT-IR

FT-IR spectroscopy was successfully provided some significant evidence about the structure of the solid state, which used to study the host-guest interaction [9]. The FT-IR spectra for β-CD, isoniazid, and complex of β-CD/isoniazid were shown in Figure 1. The FT-IR spectrum of β-CD (Figure 1(a)) was characterized by absorption bands at 3450 cm^{-1} (stretching vibration of -OH), 2936 cm^{-1} (stretching vibration of -C-H) and 1483 cm^{-1} (stretching vibration of -OH deformation). The isoniazid was characterized by the FT-IR (Figure 1(b)) with the absorption bands at 1326 cm^{-1} and 3296 cm^{-1}, which corresponds to N-H stretching vibration, 1030 cm^{-1} (C-N stretching vibration), 1617 cm^{-1} (aromatic C=C stretching vibration), and 1738 cm^{-1} (C=O stretching vibration). Upon complexation, the absorption band of the β-CD/isoniazid complex was dominated by the absorption vibrations of β-CD due to presence of seven repeated D-glucopyranose unit in the β-CD structure [12]. Hence, the recorded FT-IR spectrum of complex in Figure 1(c) was quite similar to the FT-IR spectrum of β-CD. This is due to the similar chemical bonding characteristics owned by the complex with the host molecule. Therefore, the spectrum of β-CD/isoniazid complex resulted in strong absorption vibration of polar functional groups such as C=O stretching vibration at 1738 cm^{-1} and -OH stretching vibration at 3450 cm^{-1}. The broad -OH band found in the complex is a regular phenomenon reported for β-CD inclusion complex [19]. There also absorption at 2936 cm^{-1} showing the stretching vibration of -C-H presented in β-CD/isoniazid. Meanwhile, the absorption at 1326 cm^{-1} (N-H stretching vibration) and 1030 cm^{-1} (C-N stretching vibration) in β-CD/isoniazid complex are represented the functional group from isoniazid.

Thermal analysis

The thermal stability of isoniazid, β-CD, and β-CD/isoniazid complex were investigated using TGA analysis at temperature range of 30 °C - 900 °C, as

shown in Figure 2. The TGA curve of pure isoniazid exhibited a single weight loss at 207 °C region. On the other hand, pure β-CD showed weight losses in two regions. The first weight loss at 67 °C was due to the dehydration of water, and another weight loss at 311 °C due to the decomposition of macrocycles. The TGA curve of the β-CD/isoniazid complex exhibited a weight loss at 265 °C. The TGA result showed the β-CD/isoniazid inclusion complex exhibited higher thermal stability compared to the pure isoniazid. These results confirmed the interaction between isoniazid and β-CD.

^{1} H NMR

The convincing evidence for the formation of host-guest interaction in inclusion complex was confirmed using ^{1}H NMR spectroscopy by observing the chemical shift (δ) variations [20]. The spectra and values of chemical shifts for isoniazid, β-CD, and complex of β-CD/isoniazid are shown in Figure 3 and Table 1, respectively. The changes in chemical shift for the protons of β-CD and isoniazid in their inclusion complexes were defined as induced shift (Δδ). The induced shift was gained using eq (3):

$$\Delta\delta=\delta\ (\text{complex})-\delta\ (\text{free}) \qquad (3)$$

The positive and negative signs in Table 1 were denoted as upfield and downfield, respectively. The ^{1}H NMR spectrum for β-CD (Figure 3(a)) consists six varieties of protons (H1-H6), as illustrated in Figure 4 (a). The upfield and downfield shifts were obtained for H1, H2, and H4 protons and H3, H5, and H6 protons, respectively. Besides, the ^{1}H NMR spectrum of isoniazid (Figure 3(b)) contains four varieties of protons (Ha-Hd), as illustrated in Figure 4 (b). Normally, upon complexation, the Δδ values of protons H3 and H5 of β-CD are slightly higher compared to other protons. However, the ^{1}H NMR spectrum of β-CD/isoniazid (Figure 3(c)) showed the appreciable Δδ values only for H4 and H5 protons, as listed in Table 1. The changes of chemical shift (Δδ) for H5 indicating the consequences of isoniazid penetration into the hydrophobic cavity of β-CD, due to the magnetic anisotropy effects. It can be seen the Δδ values of protons Ha and Hb of isoniazid were the highest compared to the other protons upon the formation of the inclusion complex. These large chemical shift changes suggesting that Ha and Hb protons of isoniazid are located inside cavity of β-CD. However, a small Δδ value of Hc proton suggesting that isoniazid also interacted with H4 proton of β-CD, which is located outside the cavity.

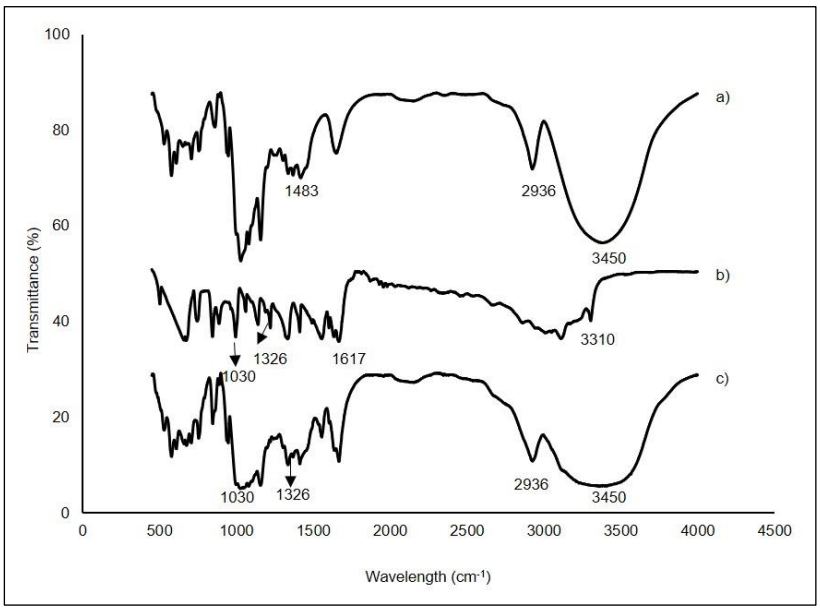


Figure 1. FTIR spectra of (a) β-CD, (b) Isoniazid and (c) β-CD/isoniazid

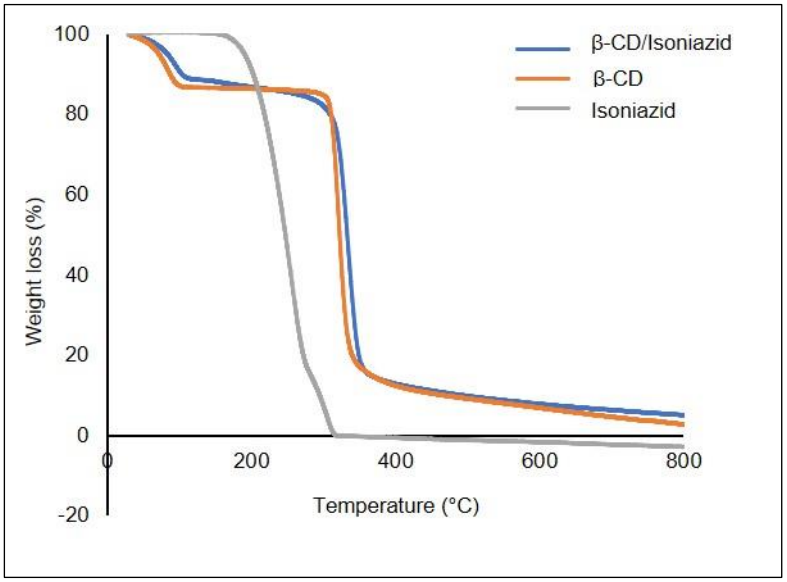


Figure 2. TGA for β-CD/isoniazid

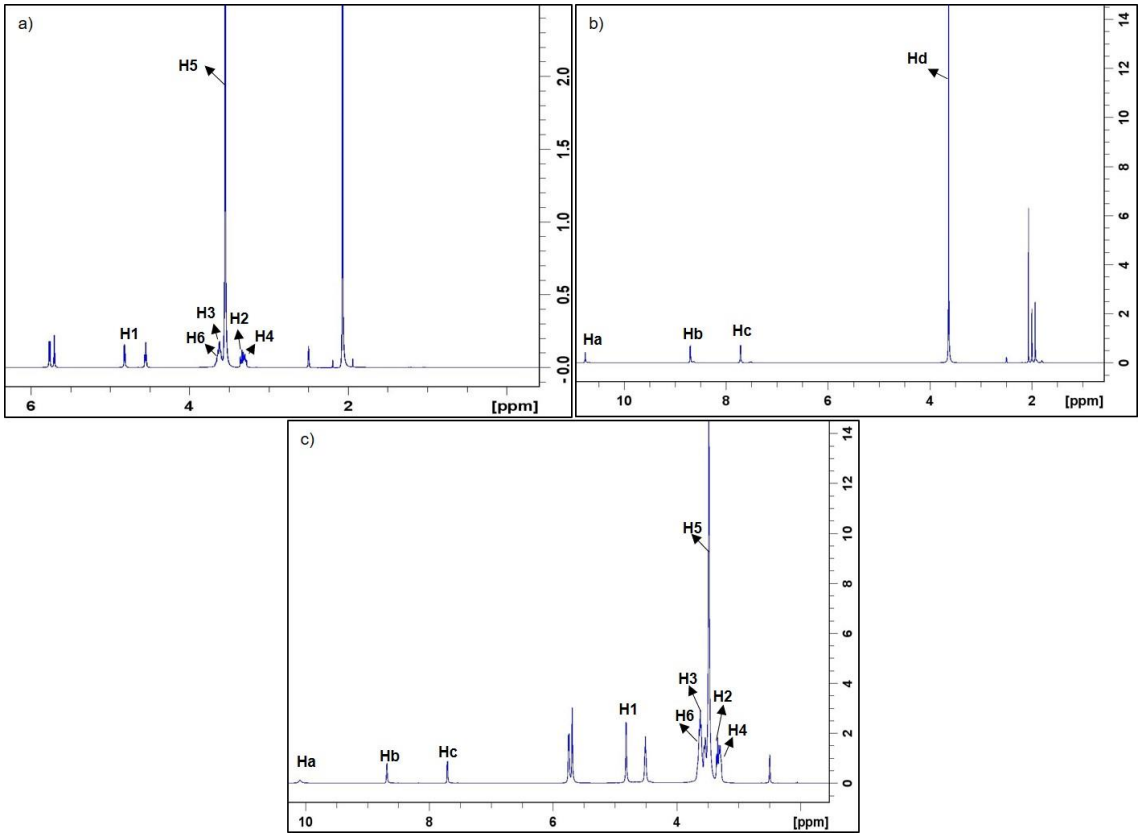


Figure 3. [1]H NMR spectra of (a) β-CD, (b) isoniazid, (c) β-CD/isoniazid

Table 1. Chemical shift corresponding to β-CD and isoniazid

Proton	β-Cyclodextrin δ	Isoniazid δ	Inclusion Complex Δ	Induced Shift Δδ
H1	4.8231	-	4.8234	+0.0003
H2	3.3585	-	3.3600	+0.0015
H3	3.6229	-	3.6220	-0.0009
H4	3.3036	-	3.3210	+0.0174
H5	3.6038	-	3.5591	**-0.0447**
H6	3.6413	-	3.6404	-0.0009
Ha	-	10.1189	10.0926	**-0.0263**
Hb	-	8.6835	8.6936	+0.0106
Hc	-	7.7079	7.7148	+0.0069
Hd	-	3.6381	-	-

*The bold values are referred to the highest induced shift for that proton

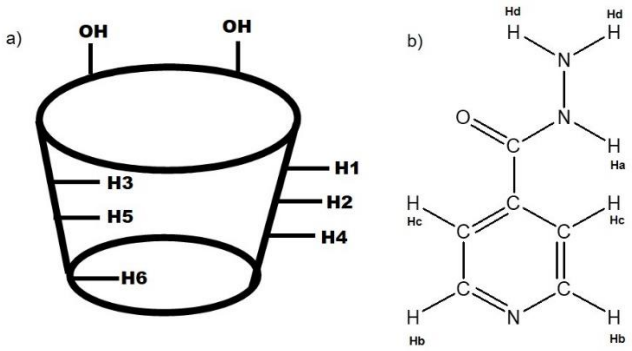


Figure 4. Structure of (a) β-CD and (b) isoniazid

NOESY NMR

The possible orientation of the isoniazid in the cavity of β-CD was obtained from ^{1}H NMR analysis. However, that obtained orientation was not definitive. The previous result was strongly supported by applying the NOESY NMR experiment to examine the configuration of isoniazid in the β-CD cavity by providing the geometry for the inclusion compound. The NOESY NMR spectra provided some significant spatial connection information between the host and guest molecules by observing intermolecular dipolar complex interactions. Figure 5 showed the contour plot of the NOESY spectrum at a section (9-10 ppm and 3-4 ppm) for the β-CD/isoniazid complex. From the figure, the cross peak was found between Ha and H3, H5 protons of isoniazid, and β-CD, respectively. By combining the information from ^{1}H NMR, a conclusion can be drawn that hydrazide moiety of isoniazid was penetrated the cavity of β-CD and forming the inclusion complex through hydrophobic interaction.

Interaction between Isoniazid and β-CD in aqueous medium: UV-Vis

The extent of interaction between the β-CD and isoniazid was measured by UV-Vis absorbance through the determination of its stoichiometric ratios and the formation constants in an aqueous medium. Figure 6 showed the absorbances of isoniazid (0.01mM), β-CD (0.003M), and the inclusion complex of β-CD/isoniazid. The absorption band of isoniazid obtained a maximum peak at 262 nm, meanwhile, β-CD showed no absorbance due to the absence of any π-electrons or non-bonding electrons [21]. Upon the addition of isoniazid with β-CD, the absorption band of β-CD/isoniazid exhibited slightly blue-shifted to a shorter wavelength at 261 nm. The absorbance of β-CD/isoniazid complex also underwent the hyperchromic effect, increasing the value of absorbance. The effect was due to the presence of hydrogen bonding and hydrophobic interaction [22] between the β-CD and isoniazid. Figure 7 showed the absorbance intensity increased by increasing the β-CD concentrations in the acidic, basic, and natural condition (neutral pH). The spectra band at maximum peak indicated an increase of intensity due to the increases of molar absorptivity of isoniazid. This finding proved that the solubility of isoniazid was enhanced with the β-CD addition. The result revealed that the drug solubility is increased with the function of β-CD concentrations. It should be mentioned that the pH changes do not significantly affect the solubility of isoniazid. According to the literature, isoniazid has at least two acid values (pKa_1= 3.53, pKa_2 = 11.40) [23]. In this regard, the molecule can be in three possible forms: acidic cation, neutral unionized species and basic anion depending on the pH values. In the range of pH-values from 5 to 9, isoniazid has an uncharged molecular form and able to enter the cavity of β-CD and forming the inclusion complex.

Benesi-Hildebrand method is commonly conducted to analyze stoichiometry and equilibrium constants of nonbonded interactions [24]. Figure 8 showed the reciprocal plots to determine the stoichiometry ratio and formation constant of the inclusion complex in the natural, acidic and basic conditions. Referring to the R^2 (close to 1) values from the reciprocal plots in Figure 8, the stoichiometry ratios for the inclusion complex formation at the natural condition was 1:2, whereas 1:1 at acidic and basic conditions were obtained. The formation constant of complex at the natural, acidic, and basic conditions are shown in Table 2. The complex of β-CD/isoniazid in the different conditions exhibited different binding intensity, thus resulting in different values of formation constant. The highest formation constant in the natural condition might be due to strong interactivity between the 1:2 ratio of β-CD and isoniazid. However, in the acidic and basic conditions, the formation constant showed insignificant values. It revealed that the pH values influenced the binding strength between β-CD and isoniazid. This is because the selectivity of inclusion is associated with certain species of isoniazid.

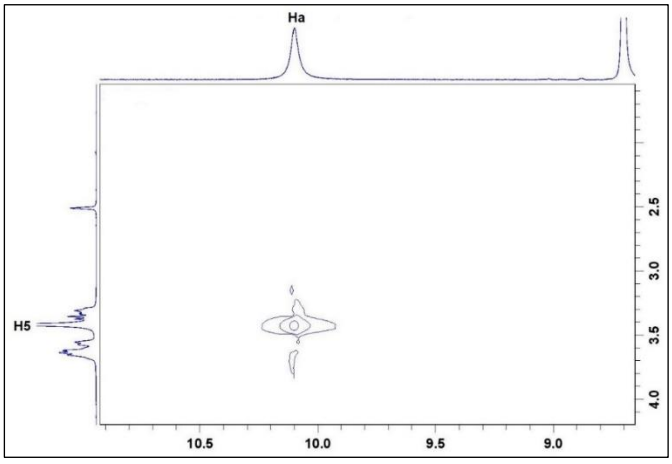


Figure 5. NOESY NMR of β-CD/isoniazid

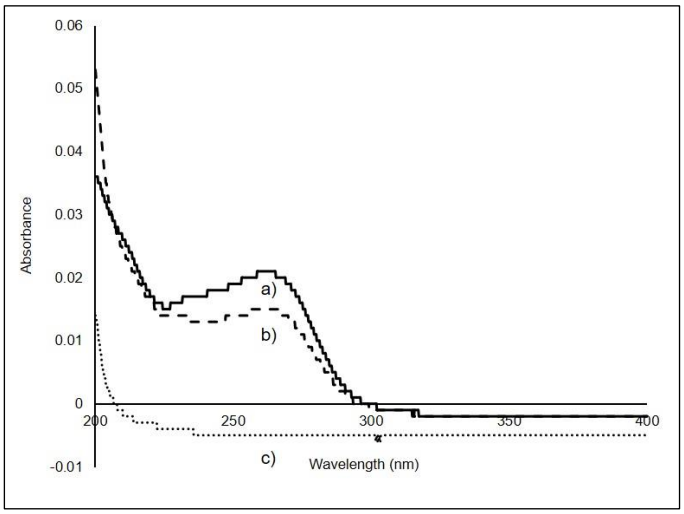


Figure 6. Absorption spectra of (a) β-CD/isoniazid complex, (b) isoniazid and (c) β-CD

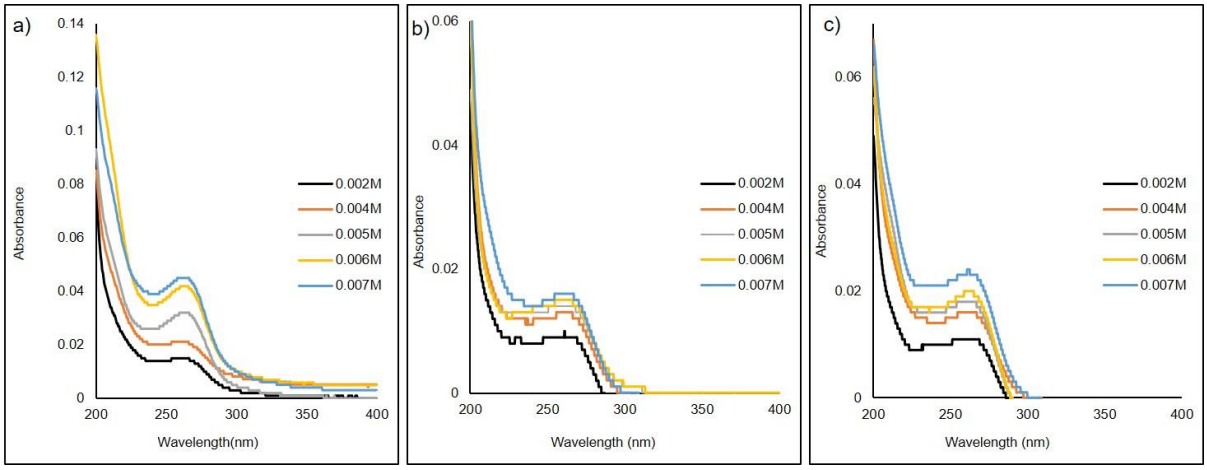


Figure 7. Absorption spectra of isoniazid with increasing concentration of β-CD for (a) pH 4, (b) pH 9 and (c) natural condition

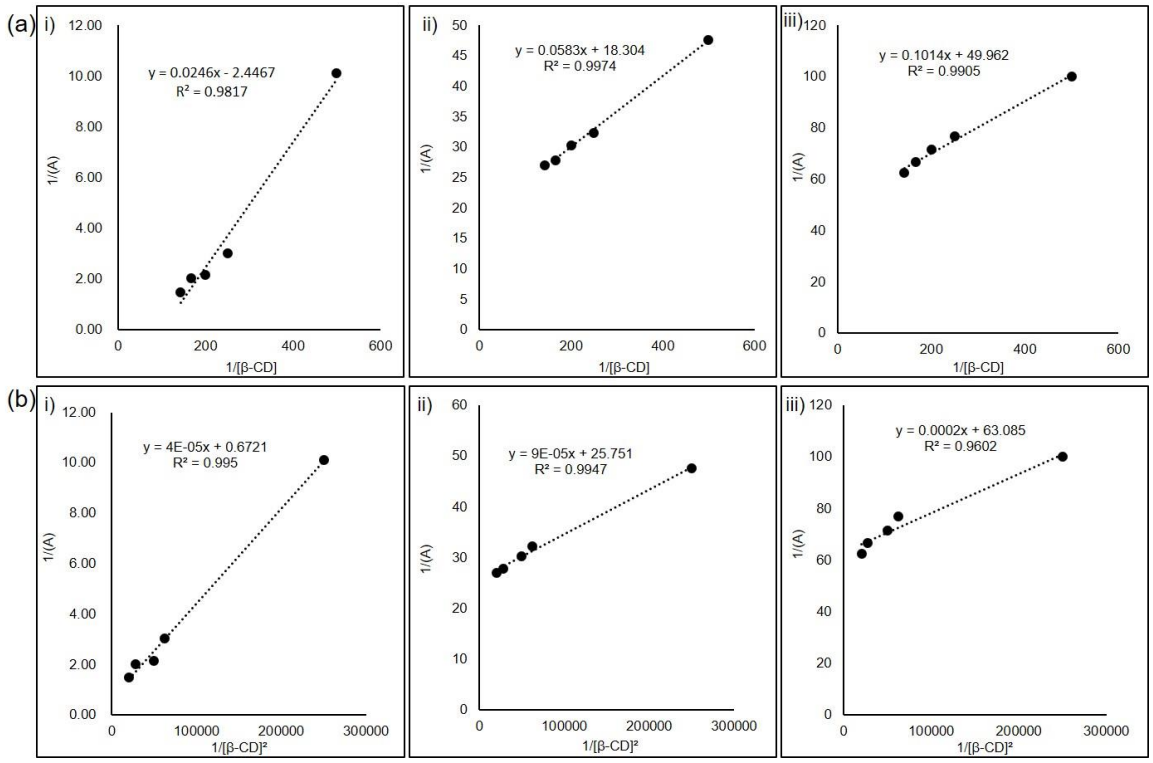


Figure 8. The reciprocal plots of (a) $\frac{1}{A}$ against $\frac{1}{[\beta-CD]}$ and (b) $\frac{1}{A}$ against $\frac{1}{[\beta-CD]^2}$ at i) natural condition, ii) pH 4 and iii) pH 9

Table 2. Formation constant (K) values for β-CD/isoniazid at various condition

pH	Formation Constant, K
Natural condition	25000
4	17.15
9	9.86

Conclusion

In the present study, we have confirmed that the isoniazid is successfully complexed with β-CD using the kneading method. The inclusion complex was verified using FT-IR, TGA, and NMR. The present result exhibited that the isoniazid was partially entrapped into the β-CD cavity. The β-CD/isoniazid complex performed with 1:1 host-guest interaction at the acidic and basic conditions with a detectable formation constant of 17.15 and 9.86, respectively. However, the β-CD/isoniazid complex performed 1:2 host-guest interaction at the natural condition with a detectable formation constant of 25000 calculated from the Benesi-Hildebrand equation. Currently, we are investigating the possibility of this complex for future applications.

Acknowledgement

The work was supported by Ministry of Higher Education for FRGS Grant (203.PKIMIA.6711641) and Universiti Sains Malaysia for the Short-Term Grant

(304/PKimia/6315106). Authors would like to thank Nur Hidayah Sazali (Universiti Sains Malaysia) for assisting analyze TGA samples.

References

1. Teixeira, M. G., de Assis, J. V., Soares, C. G., Venâncio, M. F., Lopes, J. F., Nascimento Jr, C. S., Anconi, C.P., Carvalho, G.S., Lourenço, C.S., de Almeida, M.V. and Fernandes, S. A. (2014). Theoretical and experimental study of inclusion complexes formed by isoniazid and modified β-cyclodextrins: ^{1}H NMR structural determination and antibacterial activity evaluation. *The Journal of Physical Chemistry B*, 118(1): 81-93.
2. de Assis, J. V., Teixeira, M. G., Soares, C. G., Lopes, J. F., Carvalho, G. S., Lourenço, M. C., De Almeida, M.V., de Almeida, W. B. and Fernandes, S. A. (2012). Experimental and theoretical NMR determination of isoniazid and sodium p-sulfonatocalix[n]arenes inclusion complexes. *European Journal of Pharmaceutical Sciences*, 47(3): 539-548.
3. Braegelman, A. S. and Webber, M. J. (2019). Integrating stimuli-responsive properties in host-guest supramolecular drug delivery systems. *Theranostics*, 9(11): 3017.
4. Eldehna, W. M., Fares, M., Abdel-aziz, M. M. and Abdel-aziz, H. A. (2015). Design, synthesis and antitubercular activity of certain nicotinic acid hydrazides. *Molecules,* 20(5): 8801-8806.
5. Tom, L., Nirmal, C. R., Dusthackeer, A., Magizhaveni, B. and Kurup, M. R. P. (2020). Formulation and evaluation of β-cyclodextrin-mediated inclusion complexes of isoniazid scaffolds: molecular docking and *in vitro* assessment of antitubercular properties. *New Journal of Chemistry*, 44(11): 4467-4477.
6. Gegia, M., Winters, N., Benedetti, A., Soolingen, D. Van and Menzies, D. (2016). Treatment of isoniazid-resistant tuberculosis with first-line drugs : A systematic review and meta-analysis. *The Lancet Infectious Diseases*, 3099(16): 1-12.
7. Stagg, H. R., Lipman, M. C., Mchugh, T. D. and Jenkins, H. E. (2017). Isoniazid-resistant tuberculosis: A cause for concern? *The International Journal of Tuberculosis and Lung Disease*, 21(10): 129-139.
8. Sup, Y. (2015). Challenges in the development of drugs for the treatment of tuberculosis. *Brazilian Journal of Infectious Diseases*, 17(1): 74-81.
9. Prabu, S., Samad, N. A., Ahmad, N. A., Jumbri, K., Raoov, M., Rahim, N. Y. and Mohamad, S. (2020). Studies on the supramolecular complex of a guanosine with beta-cyclodextrin and evaluation of its anti-proliferative activity. *Carbohydrate Research*, 2020: 108138.
10. Vyas, A., Saraf, S. and Saraf, S. (2008). Cyclodextrin based novel drug delivery systems. *Journal of Inclusion Phenomena and Macrocyclic Chemistry*, 62(1-2): 23-42.
11. Saokham, P., Muankaew, C., Jansook, P. and Loftsson, T. (2018). Solubility of cyclodextrins and drug/cyclodextrin complexes. *Molecules*, 23(5): 1-15.
12. Razak, S. A., Fariq, S., Syed, F., Abdullah, J. M. and Adnan, R. (2014). Characterization, phase solubility studies and molecular modeling of isoniazid and its β-cyclodextrin complexes. *Journal of Chemical and Pharmaceutical Research*, 6(11): 291-299.
13. Razak, S. A., Yacob, S. F. F. S., Abdullah, J. M. and Adnan, R. (2015). Isoniazid and β-cyclodextrin complexes: A stability study in aqueous solution. *Journal of Chemical Pharmaceutical Research*, 7(7): 346-355.
14. Teixeira, M. G., de Assis, J. V., Soares, C. G., Venâncio, M. F., Lopes, J. F., Nascimento Jr, C. S. and Fernandes, S. A. (2014). Theoretical and experimental study of inclusion complexes formed by isoniazid and modified β-cyclodextrins: 1H NMR structural determination and antibacterial activity evaluation. *The Journal of Physical Chemistry B*, 118(1): 81-93.
15. Rahim, N. Y., Tay, K. S. and Mohamad, S. (2016). β-Cyclodextrin functionalized ionic liquid as chiral stationary phase of high-performance liquid chromatography for enantioseparation of β-blockers. *Journal of Inclusion Phenomena and Macrocyclic Chemistry*, 85(3-4): 303-315.

16. Rahim, N. Y., Tay, K. S. and Mohamad, S. (2016). Chromatographic and spectroscopic studies on β -cyclodextrin functionalized ionic liquid as chiral stationary phase: Enantioseparation of flavonoids. *Chromatographia*, 79(21-22): 1445-1455.
17. Rahim, N. Y., Tay, K. S. and Mohamad, S. (2018). Chromatographic and spectroscopic studies on β-cyclodextrin functionalized ionic liquid as chiral stationary phase: Enantioseparation of NSAIDs. *Adsorption Science & Technology*, 36(1-2): 130-148.
18. Rahim, N. Y., Samad, F. H. and Rohisham, A. M. (2019). Spectroscopic studies of inclusion complex glipizide and β-cyclodextrin. *Malaysian Journal of Analytical Sciences,* 23(5): 789-798.
19. Almeida, M. V. De, Fernandes, S. A. and Almeida, W. B. De. (2013). Theoretical and experimental study of inclusion complexes formed by isoniazid and modified β-cyclodextrins: ^{1}H NMR structural determination and antibacterial activity evaluation theoretical and experimental study of inclusion complexes formed by isoniazid. *The Journal of Physical Chemistry B*, 421(12): 1-33.
20. Yang, L. J., Yang, B., Chen, W., Huang, R., Yan, S. J. and Lin, J. (2010). Host−guest system of nimbin and β-cyclodextrin or its derivatives: Preparation, characterization, inclusion mode, and solubilization. *Journal of Agricultural and Food Chemistry*, 58(15): 8545-8552.
21. Wang, X., Luo, Z. and Xiao, Z. (2014). Preparation, characterization, and thermal stability of β-cyclodextrin/soybean lecithin inclusion complex. *Carbohydrate Polymers*, 101: 1027-1032.
22. Singh, R., Bharti, N., Madan, J. and Hiremath, S. N. (2010). Characterization of cyclodextrin inclusion complexes—a review. *Journal of Pharmaceutical Science and Technology*, 2(3): 171-183.
23. Blokhina, S. V., Ol'khovich, M. V., Sharapova, A. V., Volkova, T. V. and Perlovich, G. L. (2015). Solution thermodynamics of pyrazinamide, isoniazid, and p-aminobenzoic acid in buffers and octanol. *The Journal of Chemical Thermodynamics*, 91: 396-403.
24. Çelik, S. E., Özyürek, M., Tufan, A. N., Güçlü, K. and Apak, R. (2011). Spectroscopic study and antioxidant properties of the inclusion complexes of rosmarinic acid with natural and derivative cyclodextrins. *Spectrochimica Acta Part A: Molecular and Biomolecular Spectroscopy*, 78(5): 1615-1624.

Malaysian Journal of Analytical Sciences (MJAS)
Published by Malaysian Analytical Sciences Society

PHYSICOCHEMICAL AND SENSORY PROPERTIES OF BREAD ADDED WITH CHICKEN EGGSHELL POWDER

(Fizikokimia dan Sifat Sensori Roti Ditambah dengan Serbuk Kulit Telur Ayam)

Wafiqah Zulkeflee[1], Pavalee Chompoorat[2], Raseetha Siva[1]*

[1]Faculty of Applied Sciences,
Universiti Teknologi MARA, 40450 Shah Alam, Selangor, Malaysia
[2]Faculty of Engineering and Agro-Industry,
Maejo University, Chiang Mai 50290, Thailand

**Corresponding author: raseetha@uitm.edu.my*

Received: 1 March 2020; Accepted: 23 September 2020; Published: 10 December 2020

Abstract

The purpose of this study was to determine the physicochemical properties and acceptability of bread with added chicken eggshell powder at 2%, 4% and 6%. It was found that the eggshell powder consisted ash (94.4%), fibre (50.77%) and protein (3.66%). Additionally, the eggshell powder had high calcium content, which was 27074.50 mg/100 g. The crude protein and ash content in bread increased as eggshell powder supplemented increased. The addition of eggshell powder in bread increased the calcium content present in bread significantly at 219.97 mg/100 g, 418.93 mg/100 g and 646.7 mg/100 g at 2%, 4% and 6%, respectively. Volume of bread added with eggshell powder was significantly higher compared to control. Crumb colour was observed to be increasingly yellowish while the crust appears darker with increasing level of supplementation. There was increased hardness of bread after addition of eggshell powder according to the result obtained through texture profile analysis. Sensory panelists preferred bread with 2% eggshell powder added compared to others based on overall acceptability attribute.

Keywords: bread, calcium, sensory properties, chicken eggshell

Abstrak

Tujuan kajian ini adalah untuk menentukan komposisi kimia kulit telur, sifat fizikokimia roti dan penerimaan roti yang ditambah dengan serbuk kulit telur pada 2%, 4% dan 6%. Analisis yang dilakukan pada serbuk kulit telur adalah abu, serat, protein mentah, lemak mentah dan kandungan mineral. Telah didapati bahawa kulit telur mengandungi tinggi kandungan abu iaitu sebanyak 94.40%, serat 50.77% dan diikuti oleh protein 3.66%. Serbuk telur ayam mengandungi kalsium sebanyak 27074.50 mg/100g. Bagi analisis roti, kandungan protein dan abu mentah meningkat dengan ketara seiring dengan peningkatan serbuk telur yang ditambah. Penambahan serbuk kulit telur meningkat dalam kandungan kalsium iaitu 219.97, 418.93 dan 646.7 mg/100g masing-masing pada 2%, 4% dan 6%. Bagi analisis fizikal roti, isipadu roti yang ditambah dengan kulit telur lebih tinggi berbanding dengan sampel kawalan. Warna serbuk ke arah kekuningan manakala warna kerak ke arah gelap dengan peningkatan tahap suplemen. Terdapat peningkatan terhadap kekerasan roti selepas penambahan serbuk kulit telur menurut hasil analisis profil tekstur. Panelis deria memilih roti dengan penambahan serbuk kulit telur sebanyak 2% adalah yang terbaik berbanding yang lain.

Kata kunci: roti, kalsium, sifat sensori, kulit telur ayam

Introduction

Chicken egg is considered a cheap resource that contain nutrients such as protein, fat and vitamin. The eggshell structure is composed of inner and outer shell membrane, mammillary layer, palisade layer, vertical crystal and cuticle. Weight wise the eggshell is 9-12% of the total weight of egg and majority of that is made of 94-96% calcium carbonate and other trace microelements [1]. As such, the eggshell can be a source of calcium to serve as a form of human nutrition by adding into calcium-fortified food. Additionally, it was shown that calcium carbonate ($CaCO_3$) derived from eggshell in the form of powder is easier absorbable compared to commercial $CaCO_3$ in small intestine of rat [2]. Since eggshells are not usually consumed as part of diet, which only includes egg white and yolk, the eggshells that are typically considered as waste would be an excellent source of calcium, which can be converted, and serve as a beneficial contribution to human nutrition.

Until recently, calcium deficiency in the human diet remains a common problem. Calcium is the mineral needed by human body that maintains the bone tissue. Calcium will combine with other mineral such as phosphorus to provide the structural component of bone and teeth [3]. As a probable solution to the problem, a study has shown positive feedback where an increase value of bone density to osteoporotic women was observed with a diet supplemented with eggshell powder together with vitamin D and magnesium [4]. In food application, it was suggested that the eggshell powder could be added in breads and pizzas as it was found that the powder has minimal effect on the texture while not affecting the flavour [5].

Bread is a bakery product that is made from moistened wheat flour, then undergoes kneading and baking. Bread is a popular food that widely consumed all over the world especially in the Mediterranean and Europe region [6]. Moreover, according to Malaysian Adult Nutrition Survey, the baked products consumption particularly biscuit and bread appeared in the list of top ten daily consumed although rice and noodles are the main dish to consume during breakfast, lunch and dinner in Malaysia. Due to its high consumption, incorporating eggshell powder into bread could be a good potential as a model diet in meeting calcium requirements. Hence, the objectives of this study were to determine the physicochemical properties and acceptability of bread added with eggshell powder at 2%, 4% and 6%, respectively. Analysis conducted on eggshell powder was ash, fibre, crude protein, crude fat, moisture and mineral content. Physicochemical properties needed to characterise the bread added with eggshell powder, meanwhile, acceptability test can be used to evaluate the sensory attributes of bread incorporated with eggshell powder.

Materials and Methods

Preparation of eggshell powder

Chicken eggshells used as raw materials was obtained from café at Dataran Cendikia UiTM Shah Alam. The other ingredients that was used in the bread production was obtained from Two Ply, Bakery supply store, Klang, Selangor. The chicken eggshell was washed twice and boiled using deionised water for 30 minutes. Then, the chicken eggshell was dried in cabinet drier for 24 hours at 60 °C. The dried eggshell was grounded into powder by using blender. Lastly, ground eggshell powder was passed through 120 μm sieve before use [1].

Production of bread

Bread was prepared by using previous method described by Makinde & Akinoso [6]. The ingredients together with eggshell powder in different compositions of 2%, 4% and 6% was mixed for 5 minutes in a mixer. Then, the mixture was rested for about 30 minutes in order to relieve residual stress occurred during mixing. After resting, the mixture dough was moulded into cylindrical shape to fit into an aluminium container. The prepared dough was proofed in baking pans for 40 minutes at 35 ^{o}C. The dough was then transferred into oven and baked at 180 ^{o}C for 30 minutes. Similarly, a control was prepared using the same method but without the addition of eggshell powder.

Microbial evaluation of chicken eggshell powder

Microbial evaluation was conducted according to method described by Umar et al. [7]. The eggshell powder was diluted serially. One gram of eggshell powder was weighed and placed in a test tube containing 9 mL buffered peptone water. The solution was mixed in order to make a dilution 1:10 (10^{-1}). Then 1 mL from the 1:10 was transferred to the other test tube containing 9 mL buffered peptone water to make dilution of 1:100 (10^{-2}). This procedure was repeated until a dilution 1:1000 (10^{-3}) was obtained. Thereafter, 0.1 mL from each dilution solution was inoculated onto the *Salmonella-Shigella* agar (SS agar). The inoculum was streaked on the media and incubated in inverted position at 30 ^{o}C for 72 hours. Then, the number of colonies was counted. This dilution procedure was conducted in three independent replicates.

Chemical composition

Moisture, crude protein, crude fat, ash and fibre were determined according to the standard methods described by AOAC 2000 [8].

Mineral composition

The mineral content was determined according to Kumaravel & Alagusundaram [9]. In wet digestion, 0.5 g of sample was added with 10 mL concentrated nitric acid ($HN0_3$) and the mixture was left overnight. Then, the mixture was digested on hotplate until red fumes evolve from the mixture start to ease. Next, 1 mL of hydrogen peroxide (H_2O_2) was added to the mixture and the heating was resumed. The mixture was heated until a clear solution was obtained. The mixture was then filtered and marked up to 50 ml distilled water. Multi-element standard was prepared by diluting stock standard to desired concentration, which was 0.2, 0.4, 0.6, 0.8 and 1.0 mg/L with deionized water. Minerals content of the bread and eggshell powder which are calcium (Ca), magnesium (Mg), sodium (Na), potassium (K) and Strontium (Sr) was determined by using Inductively Couple Plasma (ICP).

Specific volume of bread

Specific volume was measured by using small seeds displacement method described previously by Al-Saleh & Brennan [10]. Rapeseed was poured into a container of known volume until the bottom was covered. The loaf was placed inside the container and then seed was filled to the top. The extra rapeseeds, which equals to the loaf volume was measured in a graduated cylinder.

Colour measurement

The colour of bread was measured by using method explained by Makinde & Akinoso [6]. The crust and crumb colour were measured using chroma meter CR-400 (Konica Minolta, Japan). The sample was cut into cubes 2 x 2 x 2 cm and on the chroma meter. The colour attributes L, a and b was recorded using the Spectramagic NX software (CM-S100w).

Texture profile analysis

Texture profile analysis of the bread was conducted by using the Stable Micro System Texture Analyser (Model TA.XT2 Plus Texture Technologies Corp., Scarsdale, New York and U.S.A). The compression was performed by using a 75 mm cylindrical probe and resulting deformation curve was analysed for hardness, springiness, gumminess, cohesiveness and chewiness parameter [8].

Sensory analysis

Sensory analysis on the acceptability of bread was carried out using 30 untrained panelists. The freshly baked bread with four coded sample from different formulations was served to the panelists. The panelists were asked regarding their acceptance to the product in the terms of aroma, softness, taste, colour and overall acceptability. The score was evaluated based on nine points hedonic scale where the value of "9" indicates extremely like and "1" indicates extremely dislike [11].

Statistical analysis

The statistical analysis was determined by using the Statistical Package for the Social Sciences (SPSS, version 25) software. The data analysis was carried out using analysis of variance (ANOVA) and significant differences at (p <0.05) which was determined by Duncan's multiple range test (DMRT).

Results and Discussion

Characterisation of eggshell powder

Table 1 showed the result of chemical composition of eggshell powder. There were significant differences between all the parameters. From the results obtained, the eggshell powder contained ash (94.40%), fibre (50.77%) and protein (3.66%). The ash content from this study was similar from a previous study [12]. Meanwhile, previously, the ash content recorded in eggshell powder was 94.28% and 90.2% [1]. From Table 1, the results showed the mineral content had significant differences between each element. From all elements, calcium recorded that highest value which was 27074.50 mg/100 g. It was followed by magnesium, sodium, potassium and strontium with values of 334.57, 55.64, 33.04, 11.36 mg/100 g, respectively. The high amount of calcium was contributed by the composition of eggshell that was majorly composed of calcium carbonate at about 96% [13]. Additionally, another study reported that 3700 mg/100 g (Ca) and 500 mg/100 g (Mg) were found to be contained in eggshell powder [14]. Elemental analysis in eggshell powder is highly important as it defines which element is present in abundance that can be utilised in food application, in this research was bread particularly. This utilisation can target to minimise calcium deficiency among Malaysians, if the bread production is taken up to large scale to meet the demand for human consumption.

As for microbial analysis of eggshell powder, the bacterial count was done on SS agar. The total bacterial counts on SS agar showed negative results for the eggshell powder after boiling treatment was carried out. This finding agrees with literature [1], in that different treatments done to the eggshell powder (boiling, auto clave, microwave, oven) showed negative results on microbial growth on SS agar.

Characterisation of bread added with chicken eggshell powder

Based on the results showed in Table 2, the protein content had significant differences between all the formulations. The protein and ash content in bread significantly increased with the increased level of supplementation of eggshell powder. Both protein content (10.65%) and ash content (6.45%) were recorded the highest compared to other formulations in 6% of eggshell powder supplementation.

The mineral content in supplemented bread increased for all mineral elements measured and demonstrated significant differences between all formulations, which also meant that the amount of mineral significantly increased. The amount of calcium greatly increased at 2% supplementation compared to control, which was from 31.82 mg/100 g to 219.97 mg/100 g. This increase was consistently observed for 4% and 6% eggshell powder addition, which was to 418.93 mg/100 g and 646.71 mg/100 g, respectively. The observed increase of calcium content in this study agrees with literature [12], where a similar increase in calcium content was observed in chocolate cakes from 504.5, 816.8 and up to 1364.5 mg/100 g when supplemented with 3%, 6% and 9% eggshell. Based on the results obtained, it can be seen that the calcium content in bread was greatly influenced by high level of calcium in eggshell powder.

Then, the amount magnesium in bread increased in the range of 30.58 mg/100 g to 64.99 mg/100 g from control up to 6% supplementation of eggshell powder. Besides calcium and magnesium, sodium was high in supplemented bread where the 6% addition of eggshell powder recorded 408.21 mg/100 g compared to 126.33 mg/100 g in control formulation. For potassium content, the control bread showed 81.25 mg/100 g then increased to 108.83 mg/100 g after addition of 2% of eggshell powder. Then it increased to 110.50 mg/100 g and further to 116.77 mg/100 g in 4% and 6% supplementation, respectively. Strontium content in control also increased from 0.56 mg/100 g to 1.68 mg/100 g after 6% supplementation of eggshell powder. Similar higher levels of calcium, magnesium and potassium was also found previously in leavened bread with 1545.3%, 192.76% and 141.63%, respectively after added with 1.5% eggshell powder [15].

Specific volume showed that there were significant differences between all formulations of breads (Table 3). The specific volume of bread increased from control to 6% supplementation of eggshell powder, which ranged from 3.1 cm^3/g to 3.36 cm^3/g. The results agree with previous study that indicated the volume of cake

increased as the amount of eggshell powder added increased [12]. Naturally, the increase of loaf volume might be due to water level and high-water absorption in the dough [16]. However, protein content present in the dough could also affects water absorption where the increasing protein quality and quantity can result in high water absorption, which leads to higher loaf volume [17].

Table 3 also showed the result of breadcrumb and crust in the terms of L*, a* and b*, respectively. In terms of crumb colour, b* value was not significantly different between control and 2% supplementation of eggshell powder. However, b* values increased when 4% of eggshell powder was added compared to 2% which was from 13.05 to 15.00 then followed by 18.6 for addition of 6% eggshell powder in formulation. The increased b* values indicated the crumb was towards yellowness in colour. It agrees with previous findings [6], that the b* values was increased in crumb colour due to colour of black sesame flour. As for the crust colour, the L* values of supplemented bread with eggshell powder showed significantly lower values compared to the control. The lower L* values means that the crust is in darker colour after supplementation. The increased in darkness could be influenced by the protein content of bread and thereby affects the Maillard reaction as a result caused by the reaction between protein added and sugar. Therefore, formulation containing more protein can trigger the Maillard reaction resulting in brown colour seen on crust [18]. On the other hand, the a* values (redness) of the bread crust is higher than control formulation which was contrarily with b* values (yellowness), in that the supplemented formulation was seen to decrease from control. The surface colour depends on the physico-chemical characteristic of dough in terms of water content, pH, reducing sugar and amino acid [19]. In addition, the operating conditions during baking (temperature, humidity) could also affects the colour.

The results of texture profile analysis showed in Table 3, where the supplementation of eggshell powder significantly affects the textural properties of bread in terms of hardness, gumminess and chewiness. The hardness of bread significantly increased with increasing addition of eggshell powder in bread formulation. The hardness of bread increased from 4.58 N in control to 5.27 N, 5.42 N and 5.69 N in 2%, 4% and 6% supplementation, respectively. The increased hardness may be due to high ash content. The hardness also might be due to interaction between gluten and fibrous material [11]. The chewiness for bread supplemented with 6% eggshell powder was significantly higher compared to other formulations. Gumminess is energy needed to disintegrate a semisolid and ready to swallow while chewiness is energy needed to chew until ready to swallow [20]. Addition of natural calcium interferes with the protein-protein interaction or protein solubility thereby affecting the gumminess and chewiness [21].

Sensory evaluation of bread added with chicken eggshell powder

Table 4 indicated the summary of scores of hedonic sensory evaluations for colour, aroma, texture taste and overall acceptability. The colour of 6% supplementation had significant difference with control and 2% addition of eggshell powder. This might be due to the contrast in the yellowish colour of breadcrumb present in bread added with eggshell powder while the control demonstrated whitish in colour in which the whitish colour was more familiar to the panelists (Table 3). In the term of aroma, the bread with added eggshell powder had no significant differences with each other but was significantly different with control formulation. The higher calcium added resulted in stronger fishy smell to the product [2].

There were significant differences between all formulations in terms of texture, taste and overall acceptability. The texture of bread was significantly decreased from 2% to 4% followed by 6% of eggshell powder supplementation which was 7.20, 6.03 and 5.03, respectively. The texture maybe greatly affected by the grittiness of eggshell powder that distracted the sensation while chewing. Then, in terms of taste, the trend was similar with texture where a decrease in the mean score was observed from control up to 6% eggshell powder addition in bread formulation. As for overall acceptability, the 2% eggshell powder bread formulation had the significantly higher score (7.37)

compared to other bread formulations. This showed that the addition of eggshell powder in bread gave negative effect generally to the sensory as in agreement with study by [22], where it was stated that the addition of $CaCO_3$ should not exceed a certain level as the it will negatively affect the organoleptic properties. This was further supported in another study where 1.2% addition of chicken eggshell powder in a biscuit formulation revealed better overall acceptability in sensory evaluation among panelists [23]. Meanwhile, overall acceptability and taste attribute for leavened bread was higher when added with 1.5% chicken eggshell powder compared to other treatments such as 1.0% and 0.5% [15].

Table 1. Chemical composition of eggshell powder

Parameter (%)	**Eggshell powder (ESP)**
Ash	94.40 ± 0.03^{a}
Crude Protein	3.66 ± 0.10^{c}
Crude Fat	0.02 ± 0.10^{e}
Moisture	0.55 ± 0.02^{d}
Crude Fiber	50.77 ± 0.12^{b}
Elements (mg/100g)	**Eggshell powder (ESP)**
Ca	27074.50 ± 0.50^{a}
Mg	334.57 ± 0.62^{b}
Na	55.64 ± 0.44^{c}
K	33.04 ± 0.14^{d}
Sr	11.36 ± 0.08^{e}

*Mean values with different with different superscript letter(s) within each row differ significantly (p <0.05).

Table 2. Chemical composition of bread for all formulations

Parameter	**Eggshell powder addition (%)**			
	Control	**F1 (2%)**	**F2 (4%)**	**F3 (6%)**
Protein	9.87 ± 0.04^{d}	9.99 ± 0.08^{c}	10.39 ± 0.06^{b}	10.65 ± 0.05^{a}
Ash	1.29 ± 0.07^{d}	3.13 ± 0.01^{c}	4.65 ± 0.02^{b}	6.45 ± 0.02^{a}
Elements	**Minerals (mg/100g)**			
	Control	**F1 (2%)**	**F2 (4%)**	**F3 (6%)**
Ca	31.82 ± 0.10^{d}	219.97 ± 0.78^{c}	418.93 ± 0.50^{b}	646.7 ± 0.36^{a}
Mg	30.58 ± 0.28^{d}	40.14 ± 0.40^{c}	50.24 ± 0.50^{b}	64.99 ± 0.33^{a}
Na	126.33 ± 1.53^{d}	296.7 ± 1.74^{c}	332.77 ± 0.06^{b}	408.21 ± 0.69^{a}
K	81.25 ± 0.35^{d}	108.83 ± 0.42^{c}	110.50 ± 0.42^{b}	116.77 ± 0.12^{a}
Sr	0.56 ± 0.00^{d}	0.98 ± 0.01^{c}	1.29 ± 0.01^{b}	1.68 ± 0.02^{a}

*Mean values with different with different superscript letter(s) within each row differ significantly (p <0.05). (F1= 2% addition eggshell powder, F2 addition eggshell powder, F3= 6% addition eggshell powder).

Table 3. Physical composition of bread for all formulations

Parameter	Eggshell Powder Addition (%)			
	Control	F1 (2%)	F2 (2%)	F3 (3%)
Specific volume	3.13 ± 0.01^{d}	3.27 ± 0.01^{c}	3.39 ± 0.05^{a}	3.36 ± 0.04^{b}
L* value (crumb)	73.25 ± 0.12^{b}	73.80 ± 0.13^{a}	72.18 ± 0.03^{c}	73.12 ± 0.02^{b}
L* value (crust)	60.36 ± 0.03^{a}	53.41 ± 0.02^{c}	55.60 ± 0.15^{b}	55.35 ± 0.02^{b}
a* value (crumb)	-0.84 ± 0.01^{a}	-0.65 ± 0.00^{c}	-0.53 ± 0.01^{b}	0.62 ± 0.01^{d}
a* value (crust)	15.62 ± 0.17^{c}	17.22 ± 0.01^{a}	17.21 ± 0.06^{a}	16.11 ± 0.06^{b}
b* value (crumb)	13.12 ± 0.01^{c}	13.05 ± 0.02^{c}	15.00 ± 0.18^{b}	18.26 ± 0.01^{a}
b* value (crust)	37.32 ± 0.09^{a}	36.04 ± 0.29^{b}	35.55 ± 0.06^{c}	35.60 ± 0.02^{c}
Hardness (N)	4.58 ± 0.01^{d}	5.27 ± 0.01^{c}	5.42 ± 0.00^{b}	5.69 ± 0.00^{a}
Springiness (m)	0.92 ± 0.00^{a}	0.93 ± 0.00^{a}	0.92 ± 0.01^{a}	0.92 ± 0.00^{a}
Cohesiveness	0.83 ± 0.01^{a}	0.88 ± 0.00^{a}	0.76 ± 0.00^{b}	0.85 ± 0.04^{a}
Gumminess (N)	3.76 ± 0.00^{d}	4.74 ± 0.00^{a}	4.26 ± 0.00^{b}	4.11 ± 0.01^{c}
Chewiness (J)	3.45 ± 0.00^{c}	3.37 ± 0.01^{d}	3.58 ± 0.01^{b}	3.75 ± 0.01^{a}

*Mean values with different with different superscript letter(s) within each row differ significantly (p <0.05). (F1= 2% addition eggshell powder, F2 addition eggshell powder, F3= 6% addition eggshell powder).

Table 4. Sensory evaluation of all bread formulations

Formulation	Control	F1 (2%)	F2 (4%)	F3 (6%)
Colour	7.43±0.90^{a}	7.23±0.89^{ab}	6.70±1.21^{bc}	6.63±1.38^{c}
Aroma	7.40±1.04^{a}	7.17±1.02^{ab}	6.80±1.06^{b}	6.60±1.22^{b}
Texture	7.93±0.94^{a}	7.20±1.19^{b}	6.03±1.27^{c}	5.03±1.40^{d}
Taste	8.00±1.14^{a}	7.33±1.09^{b}	6.47±1.20^{c}	5.33±1.35^{d}
Overall acceptability	8.13±0.94^{a}	7.37±1.00^{b}	6.43±1.19^{c}	5.70±1.24^{d}

*Mean values with different with different superscript letter(s) within each row

**(F1= 2% addition eggshell powder, F2 addition eggshell powder, F3= 6% addition eggshell powder).

Conclusion

Based on results, the calcium content showed highest value present in the chicken eggshell powder, which was 27074.50 mg/100g. As for bread, the highest amount of elements recorded was calcium, which increased from 31.82 mg/100g (control) to 646.7 mg/100g (6%). In the analysis of texture profile analysis, there were significance differences between all formulations in the term of hardness, gumminess and chewiness. In terms of sensory acceptability in bread, among all the formulations, 2% of eggshell powder supplementation was considered as the best amount to be added as it could provide better nutritional values in bread while still acceptable in sensory evaluation. The findings from this study can further be explored for further fortification of calcium in bread products, which can be up-scaled to minimise the calcium deficiency problem in Malaysia.

Acknowledgement

The authors would like to thank the facilities and assistance from the lab staff at Universiti Teknologi MARA during the completion of this research. The authors have no competing conflicts of interest.

References

1. Hassan, N. M. (2015). Chicken eggshell powder as dietary calcium source in biscuits. *World Journal of Dairy & Food Science,* 10(2): 199-206.
2. Swiatkiewicz, S., Arczewska-Wosek, A., Krawczyk, J., Puchala, M. and Józefiak, D. (2015). Effects on performance and eggshell quality of particle size of calcium sources in laying hen with different Ca concentration. *Journal of Archive Animal Breed,* 58: 301-307.
3. Weaver, C. and Heany, R. P. (1999). Calcium. In J. Olson, M. Shike, & A. C. Ross, Modern nutrition in health and disease (9th Edition). Williams and Wilkins, Baltimore: pp. 141-155.
4. Shaafsma, Z., Van Doormal, J. J., Muskiet, F. A., Hofstede, G. J., Pakan, I. and van der Veer, E. (2002). Positive effects of a chicken egg shell powder-enriched vitamin-mineral supplement femoral neck bone mineral density in healthy late post menapousal dutch women. *Journal of Nutrition,* 87: 267-275.
5. Brun, L. R., Lupo, M., Delorenzi, D. A., Di Loreto, V. E. and Rigalli, A. (2013). Chicken eggshell as suitable calcium source at home. *International Journal of Food Sciences and Nutrition,* 64(6): 740-743.
6. Makinde, F. and Akinoso, R. (2014). Physical, nutritional and sensory qualities of bread samples made with wheat and black sesame (*Sesamum indicum Linn*) flours. *International Food Research Journal,* 21 (4): 1635-1640.
7. Umar, M., Muhammed, I. B., Abdul Karim, I. M., Yusuf, G., Yaya, A. A. and Leo, G. (2016). Comparative studies on the prevalence of *Salmonella* species in two homemade fermented beverages (Zobo and Kunun-Zaki) sold at Samaru, Zaria, Kaduna, Nigeria. *International Journal of Scientific and Research Publications,* 6(3): 428-435.
8. AOAC. (2000). Official methods of analysis of association of official chemists.(17th Ed).Washington D.C., USA.
9. Kumaravel, S. and Alagusundaram, K. (2014). Determination of mineral content in Indian spices by ICP-OES. *Oriental Journal of Chemistry,* 30(2): 631-636.
10. Al-Saleh, A. and Brennan, C. S. (2012). Bread wheat quality: Some physical, chemical and rheological characteristics of syrian and english bread wheat samples. *Journal of Food,* 1: 3-17.
11. Feili, R., Zaman, W., Wan Abdullah, W. N. and Yang, T. A. (2013). Physical and sensory analysis of high fiber bread. *Journal of Food Science and Technology,* 1(2): 30-36.
12. Ray, S., Barman, A. K., Roy, P. K. and Singh, B. K. (2017). Chicken eggshell powder as dietary calcium source in chocolate cakes. *The Pharma Innovation Journal,* 9(9): 1-4.
13. Hincke, M., Nys, Y., Gautron, J., Mann, K., Rodriguez-Navarro, A. B. and McKee5, M. D. (2012). The eggshell: Structure, composition and mineralization. *Journal of Bioscience,* 17: 1266-1280.
14. Rovensky, J., Stancikova, M., Masaryk, P., Sivik, K. and Istok, K. (2003). Eggshell calcium in the prevention and treatment of oesteoporosis. *International Journal of Clinical Pharmaceutical Research,* 2(3): 83-92.
15. Khan, M. R., Wahab, S., Qazi, I. M., Ayub, M., Muhammad, A., Uddin, Z., Faiq, M., Tareen, A. K., Fahad, S. and Noor, M. (2017). Effect of calcium fortification on whole wheat flour based leavened and unleavened breads by utilizing food industrial wastes. *Asian Journal of Chemistry*, 29(2): 423-430.
16. See, E., Wan Nadiah, W. A. and Noor Aziah, A. A. (2007). Physico-chemical and sensory evaluation of breads supplemented with pumpkin flour. *ASEAN Food Journal,* 14(2): 123-130.
17. Salehifar, M., Ardebili, M. S. and Azizi, M. H. (2010). Effect of wheat flour protein variations on sensory. *Journal of Food Science and Technology,* 30(3): 833-837.
18. Gomez, M., Ronda, F., Blanco, C. A., Caballero, P. A. and Apestegula, A. (2003). Effect of dietary fibre on dough rheology and bread quality. *European Food Research and Technology,* 216(1): 51-56.
19. Zanoni, B., Peri, C. and Bruno, D. (1995). Modelling of browning kinetics of bread crust during baking. *LWT – Food Science and Technology*, 28(6): 604-609.
20. Glasgow, S. and Tuoc, K. (2012). On the texture profile analysis test. Massey University: Institute of Food Nutrition and Human Health: pp. 2-3.
21. Min, B. S., Cho, M. G. and Jeong, J. Y. (2017). Eggshell and oyster shell powder as alternatives for synthetic phosphate: Effects on the quality of cooked ground pork products. *Korean Journal Food Science Animal Resources,* 37(4): 571-578.

22. Coşkun, F. and Şenoğlu, C. (2011). The effect of using different levels of calcium carbonate on the physical, chemical and sensory properties of yoghurt. *The Journal of Food,* 36(3): 129-135.

23. Welsey, J. and Renitta, R. E. (2018). Incorporation of chicken eggshell powder into biscuits. *Drug Invention Today*, 10(4): 3644-3648.

Malaysian Journal of Analytical Sciences (MJAS)
Published by Malaysian Analytical Sciences Society

DETERMINATION OF PHENANTHRENE AND FLUORANTHENE IN RICE SAMPLES BY ACTIVATED CARBON-BASED DISPERSIVE SOLID PHASE MICRO-EXTRACTION COUPLED WITH GAS CHROMATOGRAPHY-FLAME IONIZATION DETECTOR ANALYSIS

(Penentuan Phenantrena dan Fluorantena dalam Sampel Beras Menggunakan Pengekstrakan Mikro Fasa Pepejal Berserak Berasaskan Karbon Diaktifkan Bersama Analisis Pengesan Pengionan Nyalaan-Kromatografi Gas)

Nurul Nadjwa Nahrowi[1], Boon Yih Hui[2], Mohamad Shariff Shahriman[1], Noorfatimah Yahaya[2], Nur Nadhirah Mohd Zain[2], Saliza Asman[3], Md Firoz Khan[1], Kavirajaa Pandian Sambasevam[4], Vuanghao Lim[2], Muggundha Raoov[1,5]*

[1]Department of Chemistry, Faculty of Science,
Universiti Malaya, 50603 Kuala Lumpur, Malaysia
[2]Integrative Medicine Cluster, Advanced Medical & Dental Institute,
Universiti Sains Malaysia, 13200 Pulau Pinang, Malaysia
[3]Department of Physics and Chemistry, Faculty of Applied Sciences and Technology, Pagoh Education Hub,
Universiti Tun Hussein Onn Malaysia, 84000 Pagoh, Muar, Johor, Malaysia
[4]School of Chemistry and Environment, Faculty of Applied Sciences,
Universiti Teknologi MARA, Negeri Sembilan Branch, Kuala Pilah Campus, 72000 Kuala Pilah, Negeri Sembilan, Malaysia
[5]Universiti Malaya Centre for Ionic Liquids (UMCIL), Department of Chemistry, Faculty of Science,
Universiti Malaya, 50603 Kuala Lumpur, Malaysia

**Corresponding author: muggundha@um.edu.my*

Received: 12 August 2020; Accepted: 20 October 2020; Published: 10 December 2020

Abstract

A simple dispersive solid phase micro-extraction (DSPME) based on activated carbon (AC) was performed for the determination and separation of carcinogenic polycyclic aromatic hydrocarbons (PAHs), namely phenanthrene and fluoranthene, in selected white, brown and parboiled rice samples. The extraction was coupled with gas chromatography-flame ionization detector (GC-FID) for analysis. Under the optimized conditions [amount of adsorbent (5 mg), sample volume (40 mL), type (dichloromethane), and volume of desorption solvent (300 µL)], calibration curves were found to be linear for the concentration between 10 and 1000 µg kg^{-1} with coefficient of determination (R^2) from 0.9938 to 0.9955. The limit of detection (LOD) and limit of quantification (LOQ) were in the range of 0.11 - 0.15 µg kg^{-1} and 0.33 - 0.46 µg kg^{-1}, respectively. Relative standard deviation (RSD) was less than 8.02% and 5.48% for intra-day (n = 5) and inter-day (n = 5) for the present method, respectively. High pre-concentration factor (2587 - 2866) and satisfactory recoveries (90.23 - 115.63%) were also achieved. The proposed method was found to be simple, rapid and reliable for the monitoring of PAHs in rice samples.

Keywords: dispersive solid phase micro-extraction, activated carbon, polycyclic aromatic hydrocarbons, rice samples

Abstrak

Pengekstrakan mikro fasa pepejal berserak (DSPME) yang mudah berasaskan karbon diaktifkan (AC) telah dijalankan untuk penentuan dan pengasingan hidrokarbon polisiklik aromatik (PAHs) yang boleh menyebabkan barah iaitu phenantrena dan fluorantena dalam sampel beras putih, perang dan pra-rebus yang terpilih. Pengekstrakan dijalankan bersama dengan - kromatografi gas - pengesan pengionan nyalaan (GC-FID) untuk analisis. Dalam keadaan optimum [jumlah penyerapan (5 mg), jumlah isipadu sampel (40 mL) dan jenis serta jumlah isipadu pelarut penyerapan (diklorometana, 300 µL)], keluk penentukuran didapati bergerak lurus untuk kepekatan antara 10 dan 1000 µg kg^{-1} dengan pekali penentuan (R^2) daripada 0.9938 hingga 0.9955. Had pengesanan (LOD) dan had kuantifikasi (LOQ), masing-masing dalam julat 0.11 - 0.15 µg kg^{-1} dan 0.33 - 0.46 µg kg^{-1}. Berdasarkan kaedah yang sekarang, sisihan piawai relatif (RSD) menunjukkan masing-masing kurang daripada 8.02% dan 5.48% untuk hari yang sama (n=5) dan antara hari (n=5). Faktor prakepekatan tinggi (2587 - 2866) dan pemulihan yang memuaskan (90.23 - 115.63%) juga dapat dicapai. Kaedah yang dicadangkan didapati mudah, cepat dan boleh dipercayai untuk pemantauan PAH dalam sampel beras.

Kata kunci: pergekstrakan mikro fasa pepejal dispersif, karbon diaktifkan, hidrokarbon polisiklik aromatik, sampel beras

Introduction

Rice is an important food source for the world population. It is harvested seasonally and stored prior to distribution [1]. Rice plants flourish in humid environment and warm temperatures. However, rice processing operation may introduce carcinogenic compounds into the food. Recent studies found that, through the planting and manufacturing process, rice can be contaminated by carcinogenic mixtures such as polycyclic aromatic hydrocarbons (PAHs) [2-4]. PAHs are chemical compounds characterized by the presence of multiple aromatic rings in their structure with reasonably elevated desorption activation energy [5]. The bigger the molecular weight of a PAH, the more carcinogenic it will be [6]. Examples of the low molecular weight PAHs are phenanthrene and fluoranthene whereas high molecular weight PAHs include chrysene and benzo[a]pyrene.

PAHs are released from scorching coal, oil, gasoline, trash, tobacco and wood. Food processing techniques that use high temperatures, such as smoking and grilling, are common causes for the formation of PAHs in foods. PAHs are known as a cancer-causing agent that are widespread in the environment as pollutant; they mostly contaminate the soils and sediments due to anthropogenic activities [7, 8]. PAHs can accumulate at the different structures of plants, most likely in the root and husk. The accumulation usually happens in the manufacturing process of rice at the stage where the factory needs to dry the rice before removing the husk.

Although the determination of PAHs has been studied extensively in various matrices [4, 9], the need for reliable and sensitive method for the determination of PAHs in food samples is in high demand due to their potential carcinogenicity i.e. their ability to cause cancer [10]. Herein, sample preparation techniques play an important role in the development of sensitive detection method prior to instrument analysis. Previous literatures have reported numerous sample preparation techniques in determining PAHs such as liquid-liquid extraction (LLE), solid phase extraction (SPE), dispersive solid-phase extraction (DSPE) and solid phase micro-extraction (SPME). However, there are some drawbacks to these techniques which limit their performance. For example, LLE uses a large amount of organic solvent and is time-consuming to extract the analytes [11].SPE sorbents could cause low recoveries due to the sorbent bed breakthrough effect, while SPME fibres are fragile and have limited lifetime usage on organic solvents. Dispersive solid phase micro-extraction (DSPME) method, on the other hand, is a method known to be simple and use less solvent, an initiative towards green chemistry. DSPME method uses dispersive solid-phase type of adsorbents to extract and facilitate the mass transfer of analytes from samples towards adsorbents [11]. The concept of DSPME is similar to DSPE, that the difference being DSMPE only employs a small

quantity of sorbent or small volume of solvent in micro scale [12].

In this study, commercial activated carbon (AC) was chosen as an extraction material for the DSPME method because AC provides larger surface area for adsorption and can be used in small amount to extract PAHs prior to instrument detection. AC can be dispersed in solution with the help of shaker thus making it suitable to be used in DSPME. In addition, a good industrial adsorbent such as activated carbon can be used without any modification on the surface. In a previous study, an application of charcoal on soils caused the concentrations of PAHs to be decreased remarkably by using corn straw-derived biochar in old polluted soil under swamped conditions [13]. Furthermore, a small dosage of AC can adsorb high concentration of PAHs [14]. In addition, a recent study proved that AC has high affinity towards PAHs as compared to heavy metals analytes [15]. Thus, the present method (AC-DSPME-GC-FID) is deemed to be reliable and sensitive.

Materials and Methods

Material and solutions

Activated carbon (charcoal based, powdered form for analysis) was purchased from Merck (Kennilworth, NJ, USA) PAHs standards (phenanthrene and fluoranthene) were obtained from Sigma Aldrich (St. Louis, MO, USA). Acetonitrile HPLC-grade was supplied by R&M Chemicals (Essex, United Kingdom) and dichloromethane HPLC-grade by Fisher Scientific (United Kingdom). All other chemicals and reagents were analytical grade. Deionized water was produced from Milli-Q Elix Technology Inside. Acetonitrile was used to prepare standard stock solutions (1000 mg L^{-1}) and stored at -4 ℃ to avoid the degradation process.Ultrapure water was used to prepare the working standard solution to desired concentrations by dilution of the stock solutions.

Instrumentation

A mechanical shaker, Harmony Mixer Uzusio VTX-3000L was used during the extraction step to disperse the activated carbon. Agilent Technologies 7890A, Gas Chromatography equipped with –a split/splitless inlet and Flame Ionization Detector (FID) was used for the PAH quantification in this study. The carrier gas was N_2 (99.999%) with a constant flow rate of 30 mL min^{-1}. The separation was accomplished using Agilent HP5-MS (30 m × 25 mm ID × 0.25 μm film thickness, 5% phenyl-methylpolysiloxane) column. The injector and detector temperature were set at 280 ℃ with splitless mode. The GC oven was set as: 90 °C for five minutes and increased to 290 °C at 10.0 °C min^{-1} and the injection volume was 1 μL. The chromatographic data were analysed using the Chemstation software.

Samples preparation

Selected three types of rice samples were purchased from a local supermarket located in Kuala Lumpur namely white rice, brown rice and parboiled rice. The rice samples were pre-treated following the standard procedure with minor modifications [16]. In brief, the rice was ground and screened through a sieve. The rice was then dried in an oven to remove moisture before being analysed. The target analytes were spiked into 0.1 g of rice sample in a 15 mL of centrifuge tube. Thereafter, 0.6 mL of acetonitrile was added into the centrifuge tube. The rice sample was mixed under vortex for a minute before being centrifuged for three minutes at 4000 rpm. The supernatant was then collected and transferred into a 40 mL glass vial before being topped up to 15 mL of sample volume.

Dispersive solid phase micro-extraction (DSPME) procedure

An amount 15 mg of activated carbon was dispersed well in 15 mL of sample solution and mixed under vortex for three minutes to reach the equilibrium phase between the adsorbent and analytes. Then, the sample solution was transferred into 3 mL syringe that was connected to 0.45 μm nylon membrane filter. The analyte-adsorbed activated carbon was trapped in the nylon filter while the water was removed. After that, acetonitrile (1 mL) was passed through the syringe and the plunger was pressed slowly to desorb the analytes from activated carbon. The resulting desorption solution was collected into a 1.5 mL vial and 1 μL of the sample was then injected into the GC-FID system for further analysis. The graphical diagram of dispersive solid

phase micro-extraction (DSPME) procedure in full was shown in Figure 1.

Method validation

The mean and standard deviation of peak area from intra-day and inter-day were obtained and relative standard deviation (RSD) was calculated by Equation (1):

$$\text{RSD} = \frac{\text{standard deviation}}{\text{mean}} \times 100\% \quad (1)$$

Limit of detection (LOD) and limit of quantification (LOQ) were obtained by running blank solvent (dichloromethane) for ten times and peak area on the retention time same with target analytes were obtained. Then, the standard deviation for the peak areas were obtained. LOD, LOQ and pre-concentration factor (PF) were calculated by the following Equations (2), (3) and (4), respectively [7, 17]:

$$\text{LOD} = \frac{\text{standard deviation}}{\text{slope}} \times 3.3 \quad (2)$$

$$\text{LOQ} = \frac{\text{standard deviation}}{\text{slope}} \times 10 \quad (3)$$

$$\text{PF} = \frac{P_f}{P_i} \times \frac{V_f}{V_i} \quad (4)$$

The value for the slope was obtained from the matrix match calibration curve. P_f is peak area obtained from the spiked sample after extraction, while P_i is peak area obtained from the spiked solvent. V_i represents the initial sample volume and V_f is the final desorption solvent volume. The recovery studies that reflect the accuracy of the proposed DSPME method was carried out by spiking blank rice samples with three different concentration levels in triplicates (n=3). The recovery percent was calculated by using the following equation (5):

$$\text{Recovery (\%)} = \frac{C_{\text{spiked}} - C_{\text{unspiked}}}{C_o} \times 100\% \quad (5)$$

where C_{spiked} is the concentration of PAHs in the spiked sample, while C_{unspiked} is the concentration of PAHs in the unspiked sample. C_o represents the initial spiking concentration.

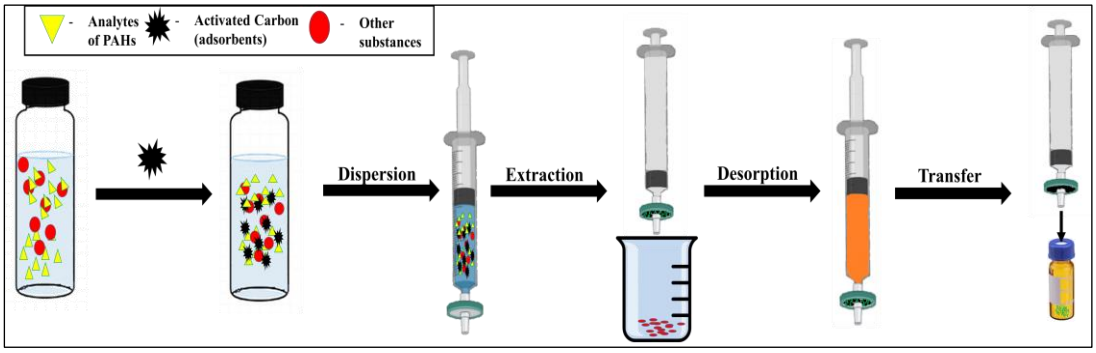


Figure 1. Graphical diagram of dispersive solid phase micro-extraction (DSPME) procedure

Results and Discussion

Optimization of AC-DSPME-GC-FID

Four important parameters that influence the extraction performance of activated carbon towards the targeted PAHs were evaluated: amount of adsorbent, sample volume, type and volume of desorption solvent. The experiment was performed in triplicate (n = 3) at spiked concentration level of 500 µg kg^{-1} for each (PAH) in blank rice samples.

Amount of adsorbent

The effect of sorbent dosage was carried out by varying the mass of activated carbon from 5 to 25 mg. As shown in Figure 2 a), the highest extraction performance was achieved at 5 mg. Lower amount (<5 mg) of adsorbent was avoided to prevent the activated carbon from sticking on the wall which will greatly affect the reproducibility of the method, and thus reduce the analytical signals. Theoretically, the higher the amount of adsorbent used, the better the extraction efficiency will be until the extraction reaches plateau. However, the increment of the sorbent amount gives negative results, probably due to larger amount of sorbents not being dispersed and separated well in the same extraction time and sample volume, which reduce the surface area that affects the efficiency of the elution process [17]. These data indicate a small amount of activated carbon is sufficient to adsorb the analytes [14] due to its high surface area and excellent adsorbing capacity [18]. Therefore, 5 mg of sorbent was selected for subsequent analysis.

Effect of sample volume

The volume of sample is one of the determining factors to obtain high enrichment factor [17]. To study this effect, the sample volume was varied from 15 to 100 mL. Based on Figure 2 b), it was observed that the higher the sample volume, the greater the extraction efficiency. This phenomenon can be explained by the fact that activated carbon achieved well dispersion in the high volume of samples, thus facilitating the mass transfer process from the water phase towards adsorbents [19]. Therefore, 40 mL of sample solutions volume was selected for further analysis due to its appropriate volume for extraction and the size of vial used in this study.

Effect of desorption solvent

Three solvents with different polarity (dichloromethane: 3.1, acetonitrile: 5.8, and methanol: 5.1) were examined for their desorption efficiency. This is an important parameter to be considered as the selection of solvent reflects the solubility of analyte (polarity of phenanthrene: 4.5, fluoranthene: 5.2) in the extracted phase [20]. Figure 2 c) depicted that dichloromethane has higher eluting capability towards PAHs followed by acetonitrile and methanol. This probably is due to different range of polarity of desorption solvent with targeted analytes. Dichloromethane, acetonitrile and methanol are non-polar, mid-polar and polar solvent respectively. [21]. Thus, dichloromethane was chosen as a desorption solvent because of its properties: it is slightly miscible with water thus good interaction with non-polar analytes and have high capability to lose the bond between analytes and adsorbents compared to other studied solvents [22].

Effect of desorption volume

The influence of desorption volume was examined in the range of 300 to 1000 µL. As seen in Figure 2 d), 300 µL shows the highest elution efficiency compared to others. This was attributable to the fact that higher concentration of targeted analytes was obtained in lower volume of desorption solvent [23]. Hence, 300 µL was selected as optimum value of the desorption solvent for the developed method.

Analytical figures of the method

A series of method validation parameters such as linearity range, precision, limit of detection (LOD), limit of quantification (LOQ) were conducted to access the performance of the developed method under optimal conditions.

Based on Table 1, the developed DSPME exhibited a dynamic linearity range between 10 and 1000 µg kg^{-1} with satisfactory coefficient of determination (R^2) ranging from 0.9955 to 0.9938 for both analytes phenanthrene (PHE) and fluoranthene (FLU). Meanwhile, the LODs were found to be at 0.11 - 0.15 µg kg^{-1}, and LOQs ranged at 0.33 - 0.46 µg kg^{-1}, indicating that at concentration as low as 0.33 µg kg^{-1}, PAHs can be accurately detected with some predefined

goals for bias and imprecision are met. The precision of the developed method was examined in spiked rice at a concentration of 100 μg kg^{-1}. The intra- and inter-day precision (n=5) were evaluated and expressed in RSDs ranging from 6.16 to 8.02% and 3.56% to 5.48%.

The pre-concentration factor (PF) was determined as the ratio of the extracted analyte concentration time's sample-to-desorb solvent volume ratio. The PF values for PHE and FLU were 2587 and 2866, respectively at 1 mg kg^{-1}. The typical GC-FID chromatogram of PAHs in blank rice samples is illustrated in Figure 3.

Real sample analysis

Three different concentrations (100 μg kg^{-1}, 300 μg kg^{-1} and 1000 μg kg^{-1}) were spiked into the blank rice samples to evaluate the sample matrix effect. The results are summarized in Table 2, in which phenanthrene had recovery values within the range of 90.41% to 115.63% while fluoranthene was within the range of 90.23% to 96.58%. The recovery values observed for these two analytes are within the acceptable range as a previous study [17]. The findings revealed that sample matrix effect was negligible in this study, signifying the clean-up and enrichment ability of the present method.

The developed method was then applied for real sample analysis to assess the safety content of PAHs in various rice samples, and the quantitative results were listed in Table 2. The results demonstrated that brown rice contained high concentration of phenanthrene that exceeded the permitted limit of PAHs in foodstuffs based on Authority of Ireland specification that the lowest limit of PAHs to be allowed in food is below 30 μg kg^{-1} for heavy molecular of PAHs [24]. Figure 4 shows the chromatograms of detected phenanthrene and fluoranthene in the tested rice samples, respectively.

Comparison study

The present method was compared with previous works on the determination of PAHs in food samples. The characteristic data and figures of merits were summarized in Table 3. Overall, the present method provides lower limits of detection and quantification. The recovery of the present method is also comparable in term of analysis parameter such as amount of dosage and extraction time. The current method also utilizes activated carbon, which is commercially available, thus a great advantage and simplifies the extraction procedure.

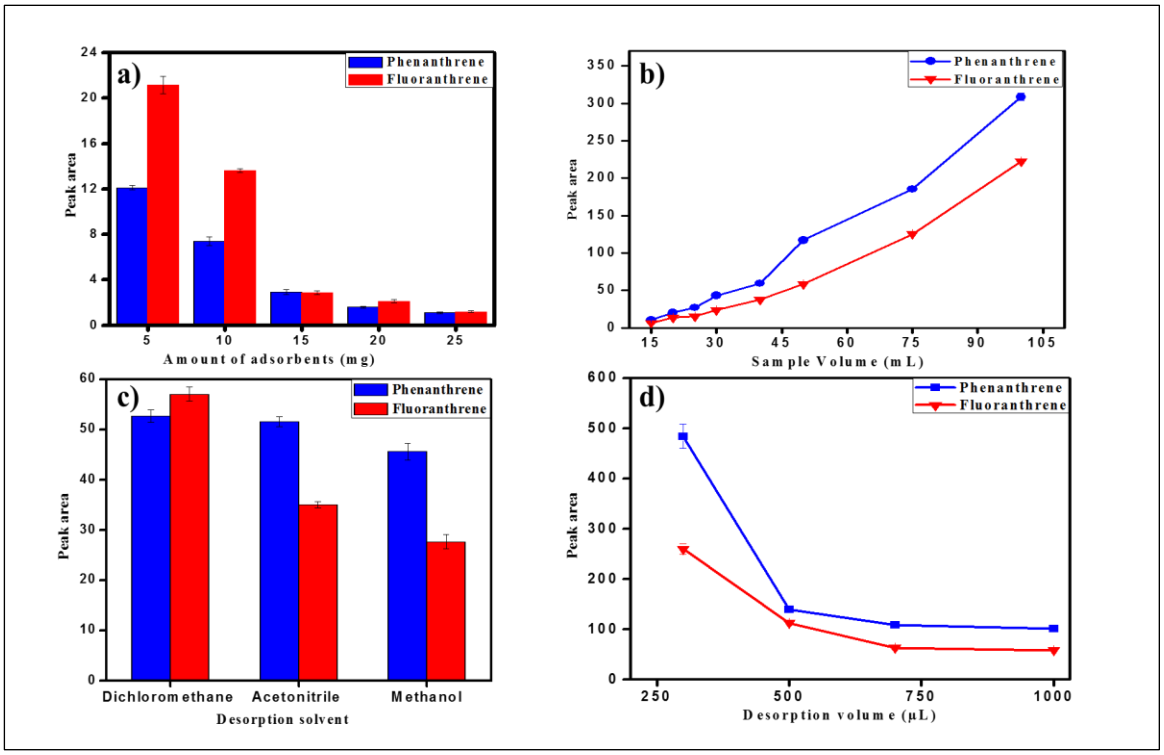


Figure 2. a) Effect of amount adsorbent on the extraction performance of PAHs (extraction conditions: 500 µg kg^{-1} of PAHs compounds, 15 mL of sample volume, 1 mL acetonitrile as desorption solvent) b) Effect of sample volume on the extraction performance of PAHs (extraction conditions: 500 µg kg^{-1} of PAHs compounds, 5 mg of amount adsorbent and 1 mL acetonitrile of desorption solvent) c) Effect of desorption solvent on the extraction performance (extraction conditions: 500 µg kg^{-1} of PAHs, 5 mg of amount adsorbent, 40 mL of sample volume and 1 mL of desorption volume) and d) Effect of desorption volume on the extraction performance (extraction conditions: 500 µg kg^{-1} of PAHs compounds, 5 mg of amount of adsorbent, 40 mL of sample volume and dichloromethane as desorption solvent)

Table 1. Analytical performance data of the proposed method

Analytes	Linear Range (µg kg^{-1})	RSD[a] (%) (n=3)	RSD[a] (%) Intra-day (n=5)	RSD[a] (%) Inter-day (n=5)	(R^2)[b]	LOD[c] (µg kg^{-1})	LOQ[d] (µg kg^{-1})	PF[e]
PHE	10-1000	1.22	6.16	5.48	0.9955	0.15	0.46	2587
FLU		4.29	8.02	3.56	0.9938	0.11	0.33	2866

[a]RSD=relative standard deviation, [b]Coefficient of determination, [c]Limit of detection, [d]Limit of quantification and [e]Pre-concentration factor at 1 mg kg^{-1}

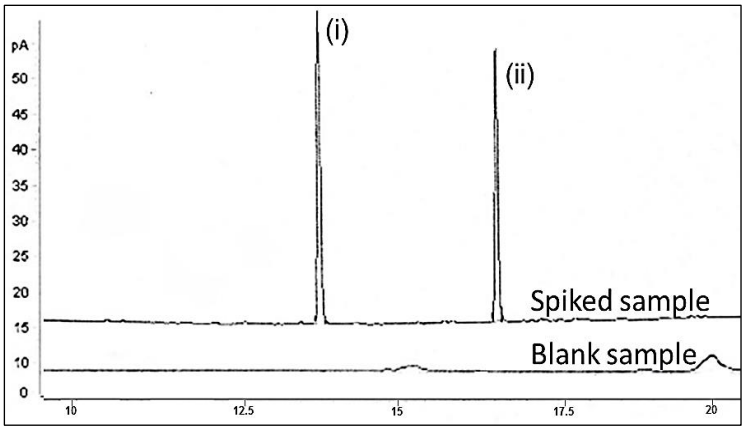


Figure 3. GC-FID chromatogram of blank sample and spiked sample with 1 mg kg^{-1} (i) Phenanthrene at retention time 12.9 minutes (ii) Fluoranthene at retention time 15.7 minutes

Table 2. The relative recoveries and concentration found in the selected rice sample of each analytes

PAHs	Spiked (µg kg^{-1})	Relative Recovery (%) ±% RSD[a] (n=3)	Concentration of Analytes Found in Real Samples (µg kg^{-1}) ± %RSD (n = 3)		
			White Rice	Brown Rice	Parboiled Rice
PHE	100	90.41(1.3)	ND[b]	171.79 ± 2.8	ND
	300	103.25(2.1)			
	1000	115.63(4.0)			
FLU	100	92.16(3.2)	13.5 ± 0.3	ND	2.41 ± 5.3
	300	96.58(2.0)			
	1000	90.23(5.4)			

[a]RSD = relative standard deviation, [b]ND = not detected

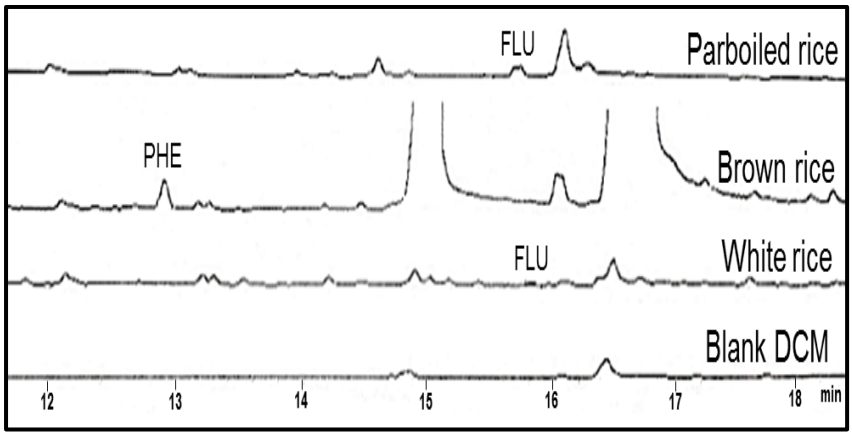


Figure 4. DSPME-GC-FID chromatogram of blank DCM solvent, white rice, brown rice and parboiled rice samples extract using the optimum extraction procedure. (i) Phenanthrene at retention time 12.9 minutes. (ii) Fluoranthene at retention time 15.7 minutes

Table 3. Comparison of the proposed method with other adsorbents for extraction of PAHs in food samples

Adsorbent	Samples	Extraction	Technique	Sample Volume (mL)	Dosage Amount (mg)	Extraction Time (min)	RSD (%)	LOD	ER (%)	Ref.
MWCNTs[a]	Water and smoked rice	SPME	GC-FID	10	20	15	0.1-4.2	0.009 - 0.013 (μg L^{-1}) 40.0 - 150.0 (μg kg^{-1})	-	[4]
-	Rice	QuEChERS	GC-MS	10	10	3	-	0.11 -0.57 (μg kg^{-1})	75.3 - 90.7	[9]
PMS[b]	Water, sugarcane juice and tea infusion	DLLME-DSPE	GC-MS	35	15	1.33	1.0-8.2	0.003 - 0.016 (μg L^{-1})	86.3-109.1	[25]
-	Meat	SPE	GC-FID	30	1	-	1.82 - 12.87	0.1 - 1.5 (μg kg^{-1})	83.69 - 94.25	[26]
Activated carbon	white rice, brown rice and parboiled rice	DSPME	GC-FID	40	5	3	1.3 - 5.4	0.11 -0.15 (μg kg^{-1})	90.23 - 115.63	Current study

[a]MWCNTs -Multiwalled carbon nanotubes , [b]PMS -Phenyl functionalized magnetic sorbent

Conclusion

In this study, the activated carbon-based DSPME coupled with GC-FID method was successfully developed as a simple, cheap, miniaturized, and reliable technique for the detection of trace levels of PAHs in rice samples. The applicability of the proposed method was tested on real rice samples and the quantitative results revealed that the target analytes were present in different samples. The study herein demonstrates the feasibility of using activated carbon coupled with this mode of microextraction technique for rice samples analysis.

Acknowledgments

The authors wish to thank the Department of Chemistry, Faculty of Science, University of Malaya for the facilities provided; and University Malaya Faculty Research Grant, for their financial supports through research vote (GPF058B-2018).

References

1. Mohanty, S. (2013) Trends in global rice consumption. *Rice Today*, 12: 44-45.
2. McGrath, T. E., Chan, W. G. and Hajaligol, M. R. (2003). Low temperature mechanism for the formation of polycyclic aromatic hydrocarbons from the pyrolysis of cellulose. *Journal of Analytical and Applied Pyrolysis.,* 66: 51-70.
3. Escarrone, A., Caldas, S., Furlong, E., Meneghetti, V., Fagundes, C., Arias, J. and Primel, E. (2014). Polycyclic aromatic hydrocarbons in rice grain dried by different processes: Evaluation of a quick, easy, cheap, effective, rugged and safe extraction method. *Food Chemistry,* 146: 597-602.

4. Matin, A. A., Biparva, P. and Gheshlaghi, M. (2014). Gas chromatographic determination of polycyclic aromatic hydrocarbons in water and smoked rice samples after solid-phase microextraction using multiwalled carbon nanotube loaded hollow fiber. *Journal Chromatography A*, 1374: 50-57.
5. Johnsen, A. R. and Karlson, U. (2005). PAH degradation capacity of soil microbial communities; does it depend on PAH exposure?. *Microbial Ecology*, 50: 488-495.
6. Eisler, R. (1987). Polycyclic aromatic hydrocarbon hazards to fish, wildlife, and invertebrates: A synoptic review. *Contaminant Hazard Reviews Report*, 11: 55.
7. Shahriman, M. S., Ramachandran, M. R., Zain, N. N. M., Mohamad, S., Manan, N. S. A. and Yaman, S. M. (2018). Polyaniline-dicationic ionic liquid coated with magnetic nanoparticles composite for magnetic solid phase extraction of polycyclic aromatic hydrocarbons in environmental samples. *Talanta*, 178: 211-221.
8. Yang, R., Zhou, R., Xie, T. and Jing, C. (2018). Historical record of anthropogenic polycyclic aromatic hydrocarbons in a lake sediment from the southern Tibetan plateau. *Environmental Geochemistry Health.*, 40: 1899-1906.
9. Bertinetti, I. A., Ferreira, C. D., Monks, J. L. F., Sanches-Filho, P. J. and Elias, M. C. (2018). Accumulation of polycyclic aromatic hydrocarbons (PAHs) in rice subjected to drying with different fuels plus temperature, industrial processes and cooking. *Journal Food Composition Analysis,* 66: 109-115.
10. Sarafraz-Yazdi, A., Ghaemi, F. and Amiri, A. (2012). Comparative study of the sol–gel based solid phase microextraction fibers in extraction of naphthalene, fluorene, anthracene and phenanthrene from saffron samples extractants. *Microchimica Acta*, 176: 317-325.
11. Tsai, W. H., Huang, T. C., Huang, J. J., Hsue, Y. H. and Chuang, H. Y. (2009). Dispersive solid-phase microextraction method for sample extraction in the analysis of four tetracyclines in water and milk samples by high-performance liquid chromatography with diode-array detection. *Journal of Chromatography. A*, 1216: 2263-2269.
12. Anastassiades, M., Lehotay, S. J., Štajnbaher, D. and Schenck, F. J. (2003). Fast and easy multiresidue method employing acetonitrile extraction/partitioning and dispersive solid-phase extraction for the determination of pesticide residues in produce. *Journal of AOAC International*, 86: 412-431.
13. Ni, N., Wang, F., Song, Y., Bian, Y., Shi, R., Yang, X., Gu, C. and Jiang, X. (2018). Mechanisms of biochar reducing the bioaccumulation of PAHs in rice from soil: Degradation stimulation vs immobilization. *Chemosphere*, 196: 288-296.
14. Gong, Z., Alef, K., Wilke, B. M. and Li, P. (2007). Activated carbon adsorption of PAHs from vegetable oil used in soil remediation. *Journal Hazardous Materials*, 143: 372-378.
15. Eeshwarasinghe, D., Loganathan, P. and Vigneswaran, S. (2019). Simultaneous removal of polycyclic aromatic hydrocarbons and heavy metals from water using granular activated carbon. *Chemosphere*, 223: 616-627.
16. Li, X., Wei, S., Sun, Y., Sun, Q., Liang, L., Zhang, B., Piao, H., Song, D. and Wang, X. (2016). Glass slides functionalized by 1-carboxyethyl-3-methylimidazolium chloride for the determination of triazine herbicides in rice using high-performance liquid chromatography. *Journal of Separation Sciences*, 39: 4585-4591.
17. Boon, Y. H., Zain, N. N. M., Mohamad, S., Osman, H. and Raoov, M. (2019). Magnetic poly (β-cyclodextrin-ionic liquid) nanocomposites for micro-solid phase extraction of selected polycyclic aromatic hydrocarbons in rice samples prior to GC-FID analysis. *Food Chemistry*, 278: 322-332.
18. Huang, X., Lu, Q., Hao, H., Wei, Q., Shi, B., Yu, J., Wang, C. and Wang, Y. (2019). Evaluation of the treatability of various odor compounds by powdered activated carbon. *Water Research*, 156: 414-424.

19. Saraji, M., Boroujeni, M. K., Bidgoli, A. A. H. (2011). Comparison of dispersive liquid–liquid microextraction and hollow fiber liquid–liquid–liquid microextraction for the determination of fentanyl, alfentanil, and sufentanil in water and biological fluids by high-performance liquid chromatography. *Analytical and Bioanalytical Chemistry*, 400: 2149.
20. Galan-Cano, F., Alcudia-Leon, M. C., Lucena, R., Cardenas, S. and Valcarcel, M. (2013). Ionic liquid coated magnetic nanoparticles for the gas chromatography/mass spectrometric determination of polycyclic aromatic hydrocarbons in waters. *Journal of Chromatography A*, 1300: 134-140.
21. Acree, Jr. W. E. (2013). IUPAC-NIST solubility data series. 98. Solubility of polycyclic aromatic hydrocarbons in pure and organic solvent mixtures revised and updated. Part 3. Neat organic solvents. *Journal of Physical and Chemical Reference Data*, 42: 013105.
22. Lehotay, S., Schenck, F. (2000). Multi-residue methods: Extraction encyclopaedia of separation science: pp. 3409-3415.
23. Zhao, G., Song, S., Wang, C., Wu, Q. and Wang, Z. (2011). Determination of triazine herbicides in environmental water samples by high-performance liquid chromatography using graphene-coated magnetic nanoparticles as adsorbent. *Analitica Chimica Acta,* 708: 155-159.
24. Food Safety Authority of Ireland (2015). Polycyclic aromatic hydrocarbons (PAHs) in food. *Food Safety Authority of Ireland*, 2: 1-10.
25. Mohd Hassan, F. W., Raoov, M., Kamaruzaman, S., Sanagi, M. M., Yoshida, N., Hirota, Y., Nishiyama, N. and Yahaya, N. (2018). Dispersive liquid–liquid microextraction combined with dispersive solid-phase extraction for gas chromatography with mass spectrometry determination of polycyclic aromatic hydrocarbons in aqueous matrices. *Journal of Separation Sciences*, 41: 3751-3763.
26. Olatunji, O. S., Fatoki, O. S., Opeolu, B. O. and Ximba, B. J. (2014). Determination of polycyclic aromatic hydrocarbons [PAHs] in processed meat products using gas chromatography flame ionization detector. *Food Chemistry*, 156: 296-300.

Malaysian Journal of Analytical Sciences (MJAS)
Published by Malaysian Analytical Sciences Society

DEVELOPMENT OF DISPERSIVE MICRO-SOLID PHASE EXTRACTION FOR THE ANALYSIS OF OFLOXACIN AND SPARFLOXACIN IN HUMAN PLASMA

(Pembangunan Pengekstrakan Fasa Pepejal-Mikro Disesarkan untuk Analisis Oflosaksin dan Sparflosaksin dalam Plasma Manusia)

Sohaib Jumaah Owaid[1], Noorfatimah Yahaya[2], Nurul Yani Rahim[1], Rania Adam Edrees Mohammad[1], Maizatul Najwa Jajuli[1], Mazidatulakmam Miskam[1]*

[1]*School of Chemical Sciences, Universiti Sains Malaysia, 11900 Minden, Pulau Pinang, Malaysia*
[2] *Integrative Medicine Cluster, Advanced Medical and Dental Institute (AMDI), Universiti Sains Malaysia, 13200 Bertam, Pulau Pinang, Malaysia*

**Corresponding author: mazidatul@usm.my*

Received: 13 August 2020; Accepted: 18 October 2020; Published: 10 December 2020

Abstract

Dispersive micro-solid phase extraction (D-µ-SPE) using C_{18} adsorbent combined with HPLV-UV was developed for the determination of ofloxacin and sparfloxacin in human plasma. Seven D-µ-SPE parameters namely type and amount of adsorbent mass, sample volume, pH of sample solution, extraction time, desorption solvent and volume were optimized. Under optimum conditions, calibration curves showed good linearity in the range of 0.5–1000 µg L^{-1} with acceptable limit of detection (LOD) of 0.73 and 1.81 µg L^{-1} and limit of quantitation (LOQ) of 2.44 and 6.03 µg L^{-1} for ofloxacin and sparfloxacin, respectively. The D-µ-SPE also demonstrated acceptable precision at the concentration of 500 dan 1000 µg L^{-1} of ofloxacin and sparfloxacin, respectively in human plasma with RSD value of ≤12.5%. A good relative recoveries was obtained between 90.1-109.5%. The developed D-µ-SPE method has proven to be a fast and simple approach which only requires low amount of extraction solvent for drug analysis.

Keywords: dispersive micro-solid phase extraction, high performance liquid chromatography, ofloxacin, sparfloxacin, human plasma

Abstrak

Pengekstrakkan fasa pepejal mikro disesarkan (D-µ-SPE) menggunakan penjerap C_{18} yang digabungkan dengan HPLC-UV telah dibangunkan untuk penentuan oflosaksin dan sparflosaksin dalam plasma manusia. Beberapa parameter D-µ-SPE seperti jenis dan jumlah jisim penjerap, isipadu sampel, pH larutan sampel, masa pengekstrakan, pelarut penyahjerap dan masa penyahjerap telah dioptimumkan. Dalam keadaan yang optimum, lengkung penentu ukuran menunjukkan lineariti yang baik dalam julat 0.5-1000 µg L^{-1} dengan had pengesanan (LOD) 0.73 dan 1.81 µg L^{-1} dan had pengukuran (LOQ) 2.44 dan 6.03 µg L^{-1} yang memuaskan masing-masing bagi ofloksaksin dan sparflosaksin. Kaedah yang dicadangkan juga menunjukkan ketepatan pada kepekatan 500 dan 1000 µg L^{-1} yang baik bagi oflosaksin dan sparflosaksin dari plasma manusia dengan RSD ≤12.5% dan pemulihan relatif yang

baik dalam julat 90.1-109.5%. Kaedah D-μ-SPE terbukti sebagai kaedah yang cepat danmudah untuk analisis ubat-ubatan kerana ia hanya memerlukan pelarut organik dalam jumlah yang kecil sewaktu analisis dijalankan.

Kata kunci: pengekstrakkan fasa pepejal mikro disesarkan, kromatografi cecair berprestasi tinggi, oflosaksin, sparflosaksin, plasma manusia

Introduction

Fluoroquinolones (FQs) are one of the most significant groups of synthetic antibiotics that possess excellent pathogenic behavior [1]. FQs are currently licensed as antibiotics under the Ministry of Health Malaysia's National Pharmaceutical Regulatory Agency (NPRA) and are listed by the WHO as important medicines for human health. Due to the increased resistance to beta-lactams and macrolides, FQs are currently used widely for the treatments of respiratory tract infections [2]. A broad-spectrum of this class of drugs demonstrated good activity against several gram-positive and gram-negative pathogenic bacteria, such as atypical respiratory pathogens [3].

Nevertheless, the concentration of FQs in human plasma are not measured in clinical practice. Considering the toxification and effectiveness of drugs, he concentration of FQs in body fluid should be tracked to change its dosage for regular use in clinical practice [4,5]. Moreover, FQs can become emerging contaminants in the environmental sample as they were partially metabolised inside the human body 20-80% were excreted out from human body in various pharmacologically active states. [6]. Therefore, appropriate analytical methods must be developed for the detection of FQs in the environmental and biological samples [7].

Several analytical techniques based on the spectrofluorimetric [6], high-performance liquid-chromatography (HPLC) with UV [8, 9], or mass spectrometry (MS) detection [10, 11] and capillary electrophoresis (CE) [12] were established for the determination of FQs. The process of sample preparation plays an important role in increasing sensitivity and reducing matrix interference, particularly when dealing with complex human plasma samples. One of the most common techniques for extraction of FQs is a solid phase extraction (SPE) by virtue of its ability to enrich analytes and eliminate matrix interferences [13-16]. However, it take a relatively long time and requires large amount of solvents during the analysis.

A recent trend in analytical chemistry is to miniaturize the separation techniques that enhance the extraction efficiency based on performance and cost consumption of the process [11]. Dispersive micro-solid phase extraction (D-μ-SPE) which is the SPE miniaturization is established to resolve the inherited disadvantages. In this extraction process, the adsorbents are applied directly to the sample solution, wherein the equilibrium can be achieved in a short time, since the surface area between the adsorbent and the aqueous solution is high [17]. D-μ-SPE offers a wide range of advantages compare to SPE due to its convenience, lower solvent use and efficiency of recovery within short time. Enhancement in the extraction efficiency can also be achieved due to the increment of contact area between adsorbent and analytes during dispersion process. It is also an economical and simple technique which can be used with different types of adsorbents [18-20].

The use of dispersed adsorbents was firstly reported by Anastassiades et al. which focused on increasing method selectivity [21]. Recently, there were only two studies of D-μ-SPE reported the determination of FQs involving ofloxacin. Amoli-Diva et al. investigated the modification of MWCNT in combination of surfactant-enhanced magnetic nanoparticles as an adsorbent for extracting FQs from plasma and urine samples [22]. With the advancement of technology, a new approach of an automated magnetic D-μ-SPE which is based on flow system using the strategy of fluidized beds. Zr-Fe-magnetic nanoparticles were used in this case as a powerful adsorbent for the determination of FQs in food samples [23].

Considering the advantages of D-μ-SPE, this study investigated the development of D-μ-SPE utilizing C_{18} adsorbent, coupled with HPLC-UV for the detection of ofloxacin and sparfloxacin. Factors that affect the extraction efficiency were evaluated and optimized. The proposed D-μ-SPE method showed an excellent performance for the detection of ofloxacin and sparfloxacin in human plasma.

Materials and Methods

Chemicals and reagents

Ofloxacin and sparfloxacin from Sigma-Aldrich (Steinheim, Germany). HPLC-grade methanol (>99.99%) and silica particles from Merck (Darmstadt, Germany). Sodium phosphate monobasic monohydrate, phosphoric acid (85%, w/w) and sodium phosphate from Sigma-Aldrich (St. Louis, MO, USA). Center for Drug Research, Universiti Sains Malaysia, Penang, Malaysia have kindly donated human plasma sample for this study. DSC-18 (C_{18} adsorbent, 50 μm particle size) from Supelco (Bellefonte, PA, USA). Ultrapure water (resistivity, 18.2 M Ω cm^{-1}) was used for the preparation of solutions in this study.

Chromatographic conditions

The chromatographic analyses were carried out using Thermo-Fisher Hypersil Gold ODS C_{18} (250 × 4.6 mm × 5 μm) at the wavelength of 254 nm. The mobile phase was prepared in the presence of methanol (MeOH) and phosphate buffer (5 mM, pH 3.0) with a ratio of 50:50, v/v. It was filtered and degassed with a 0.22 μm membrane filter (Sartorius, Germany) before use. The flow rate 1.0 mL/min and the injection volume 20 μL were used.

Preparation of stock and working solution

Stock solutions ofloxacin and sparfloxacin (20 mg L^{-1}) were prepared by dissolving both compounds in MeOH and then kept at 4°C. Working standard solutions (1000 μg L^{-1}) were prepared by diluting stock solution in 10 mL volumetric flask, then top-up to the mark before adjustment to the appropriate pH.

D-μ-SPE procedure

Approximately 1000 μg L^{-1} of the spiked ofloxacin and sparfloxacin solution was put in a 50 mL centrifuge tube that contained 20 mg of C_{18} adsorbent. The mixture was then vortexed at high speed (2400 rpm) for 1 minute to allow adsorbent to disperse in the sample. The solution was modified to pH 4 with 0.1 M HCl. Next, the adsorbent was collected on 20-25 μm filter paper (Whatman, UK) after the extraction. After that, the adsorbent was transferred to a centrifuge tube. A 200 μL of MeOH was introduced to desorb the analytes and sonicated for 5 minutes. Finally, the supernatant was filtered through 0.22 μm nylon membrane filter prior to HPLC-UV analysis.

Optimization of D-μ-SPE parameters

Seven D-μ-SPE parameters including the type and amount of adsorbent mass, sample volume, pH of sample solution, extraction time, desorption solvent and volume were studied. The optimizations were carried out using one variable at a time (OVAT) method, where an independent variable changed, while the dependent variables were kept at a constant level.

Method validation of D-μ-SPE

For D-μ-SPE, the linearity was carried out at different concentrations (0.5, 100, 250, 500, 750, 1000 μg L^{-1}). Intra-day and inter-day were evaluated at the concentration of 500 and 1000 μg L^{-1} in triplicate for the same day (n = 3) analyses. Relative recovery (%RSD) was determined as the percentage of the mean target analyte concentration detected after extraction against the concentration of spiked ofloxacin and sparfloxacin in the sample.

Sample pre-treatment for human plasma

To minimize the matrix effects prior to D-μ-SPE, 2 mL of human plasma sample was spiked prior to pH adjustment to pH 4 using 0.1 M of HCl. Then, the mixture was vortexed for 30 s to ensure complete mixing. MeOH (1 mL) was added to the blank/spiked plasma (2 mL) and the mixture was centrifuged at 4000 rpm for 10 min in order to precipitate the proteins. Then, the supernatant was collected and applied for the D-μ-SPE procedure.

Results and Discussion

Optimization of D-μ-SPE conditions: Selection of adsorbent

Selecting sorbent material is vital to the development of D-μ-SPE methods as it determines the selectivity and absorption ability of target analytes, particularly in complex matrices such as human plasma [24]. In this study, various adsorbent materials, i.e. C_{18}, -CN and -NH were investigated which can be categorized into polar adsorbent (-CN, -NH) and non-polar adsorbent (C_{18}). The retention of the analytes on the adsorbents is due to weak interactions of both compounds through the hydrogen bonding, π-π interactions and Van der Waals. Based on the result obtained, the highest extraction efficiency for ofloxacin and sparfloxacin were achieved by using C_{18} as adsorbent (Figure 1). As ofloxacin and sparfloxacin have the log *P* value of 1.86 and 2.60, respectively which can be considered as mid-polar analytes, C_{18} adsorbent provided greater adsorption as compared to -CN and -NH adsorbent. Thus, it was selected for use in the subsequent analysis.

Mass of adsorbent

To investigate the effect of C_{18} adsorbent mass on ofloxacin and sparfloxacin extraction efficiency, the mass was varied from 10–30 mg. As depicted in Figure 2, an increment of extraction efficiency was observed as the mass of C_{18} adsorbent increased. However, the reduction of extraction efficiencies was observed when more than 20 mg were used. This observation may be attributed to the agglomeration of C_{18} adsorbent, masking the sorbent active sites, thereby reduces its extraction efficiency [25]. Hence, 20 mg of C_{18} was chosen as an adsorbent in the following experiments.

Sample volume

In order to improve the partitioning between ofloxacin and sparfloxacin and C_{18} adsorbent, the effect of the sample volume on the extraction efficiency was investigated in the range of 5-20 mL. The extraction efficiency of ofloxacin and sparfloxacin improved with the increment of the sample volume to 10 mL, as shown in Figure 3. The extraction efficiency of ofloxacin and sparfloxacin sustained when the volume of sample increased more than 10 ml. Therefore, the sample with the volume of 10 mL was selected for use in the subsequent experiments.

Extraction time

The amount of analyte extracted in D-μ-SPE is based on mass transfer from the aqueous phase to the adsorbent [26]. Extraction time therefore is another significant parameter to consider. Extraction times in the range of 30-110 s were studied to evaluate the effects of extraction time on the extraction efficiency. As shown in Figure 4, extraction efficiencies improved as the extraction time increased to 60 s. The availability of abundant active regions on the adsorbent surface enabled ofloxacin and sparfloxacin to react immediately by binding to the adsorbent binding regions at the beginning of the extraction time and resulted in increased extraction efficiency with increasing extraction time [7]. There was no significant improvement on the extraction efficiency when the extraction time was prolonged. Therefore, the extraction time of 60 s was selected for the analysis.

pH of sample solution

pH has a major effect on extraction efficiency by influencing the form of the analyte by transforming the analytes into molecular forms and enhances the surface charge C_{18} adsorbent. The pH of the sample solution has a significant impact on the extraction as it specifies the ionic state of the analytes which influences the extraction process [27]. The pH of the sample solution was set within a range of 2–7 to study its effect on the extraction efficiencies. Since ofloxacin and sparfloxacin are weak base analytes with pK_a values of 5.19 to 6.42, respectively, they existed in molecular forms under acidic environment to allow the extraction to occur. Based on the results shown in Figure 5, ofloxacin and sparfloxacin were converted more in molecular forms in an acidic environment. Nonetheless, under highly acidic condition (pH 2), they could easily be degraded. At pH greater than 4, both antibiotics were in their ionizable form which restricted the extraction process. Further investigations were carried out using sample solution at pH 4.

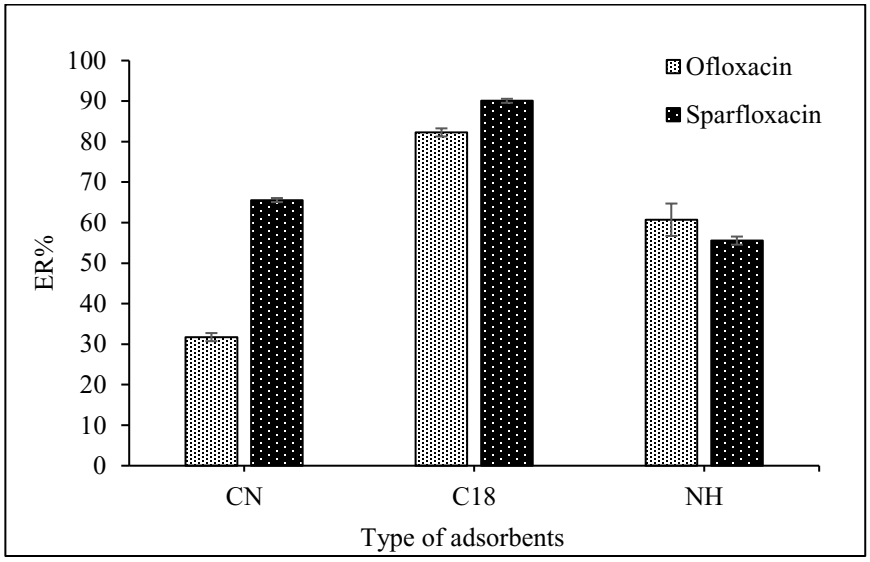


Figure 1. Effect of type of adsorbents on the extraction efficiency of ofloxacin and sparfloxacin. Extraction conditions: 1000 µg L^{-1} of ofloxacin and sparfloxacin; mass of adsorbent: 20 mg; sample volume: 10 mL at pH 4; extraction time: 60 s; desorption solvent: 200 µL of MeOH; desorption time: 5 minutes

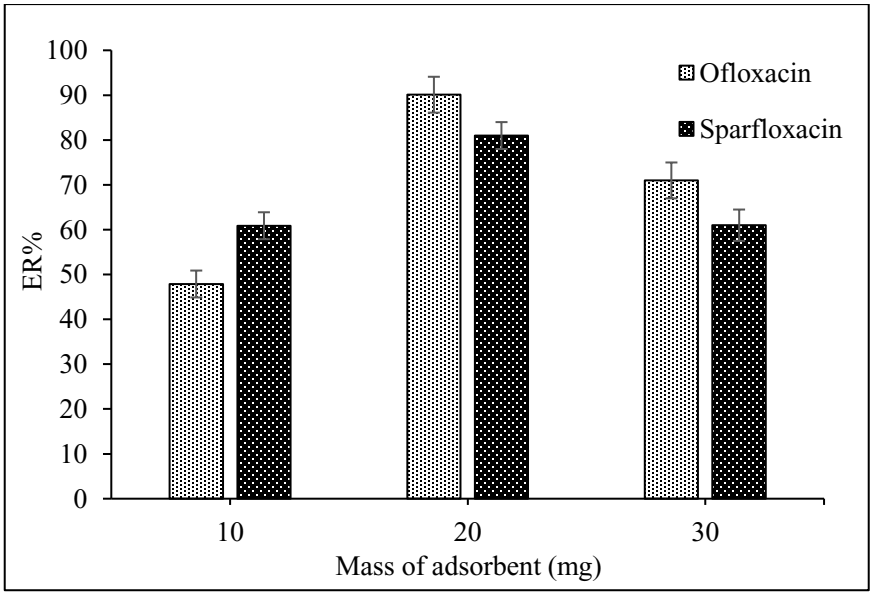


Figure 2. Effect of mass of adsorbent on the extraction efficiency of ofloxacin and sparfloxacin. Extraction conditions: 1000 µg L^{-1} of ofloxacin and sparfloxacin; type of adsorbent: C_{18} ; sample volume: 10 mL at pH 4; extraction time: 60 s; desorption solvent: 200 µL of MeOH; desorption time: 5 minutes

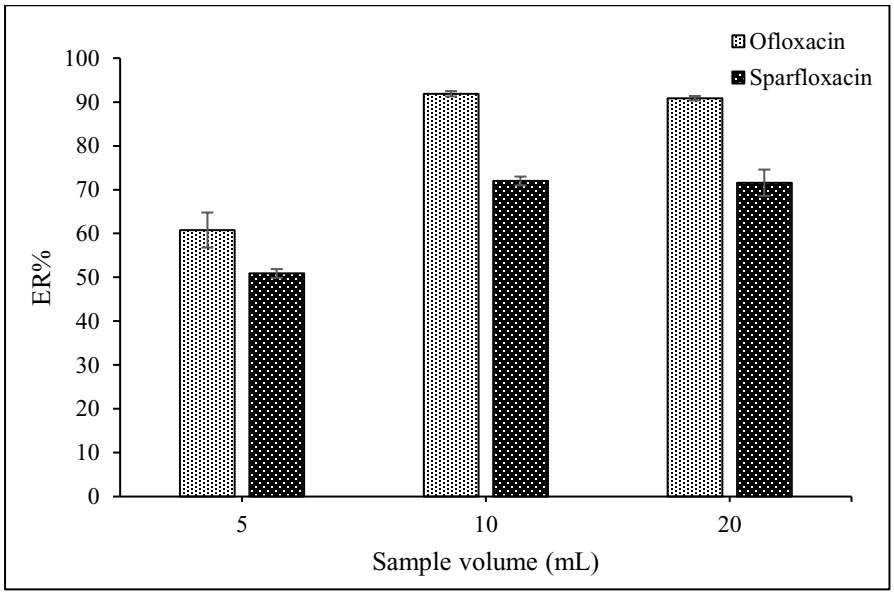


Figure 3. Effect of sample volume on the extraction efficiency of ofloxacin and sparfloxacin. Extraction conditions: 1000 µg L^{-1} of ofloxacin and sparfloxacin; adsorbent: 20 mg of C_{18}; sample solution: pH 4; extraction time: 60 s; desorption solvent: 200 µL of MeOH; desorption time: 5 minutes

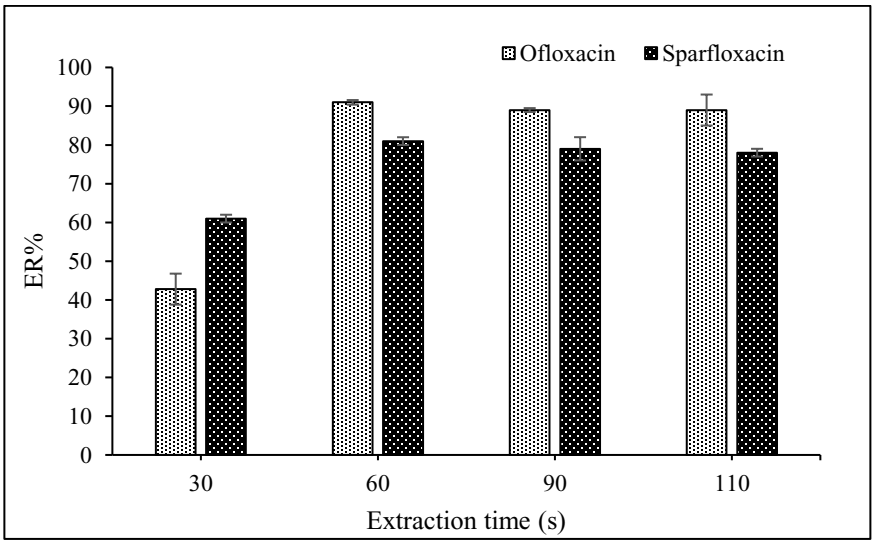


Figure 4. Effect of extraction time on the extraction efficiency of ofloxacin and sparfloxacin. Extraction conditions: 1000 µg L^{-1} of ofloxacin and sparfloxacin; adsorbent: 20 mg of C_{18}; sample solution: 10 mL at pH 4; desorption solvent: 200 µL of MeOH; desorption time: 5 minutes

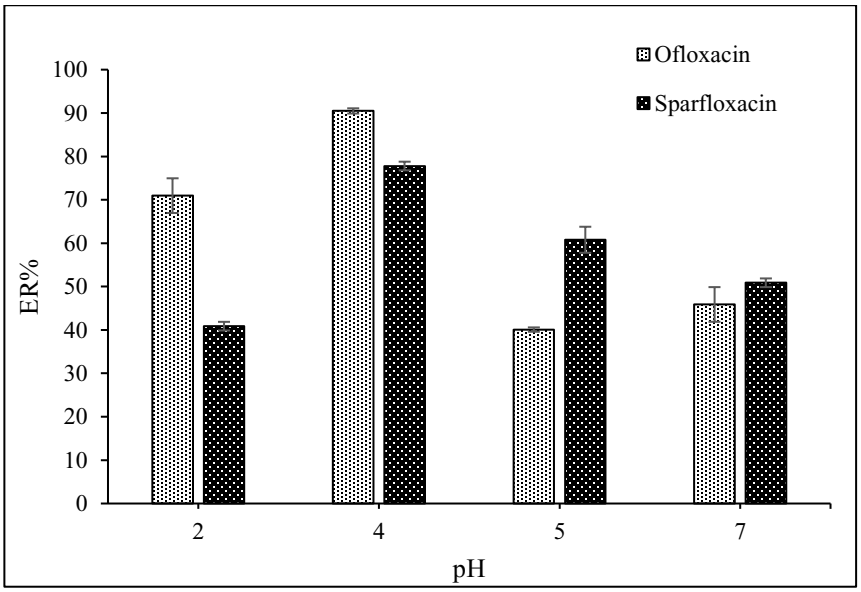


Figure 5. Effect of pH on the extraction efficiency of ofloxacin and sparfloxacin. Extraction conditions: 1000 µg L^{-1} of ofloxacin and sparfloxacin; adsorbent: 20 mg of C_{18}; sample solution: 10 mL; extraction time: 60 s; desorption solvent: 200 µL of MeOH; desorption time: 5 minutes

Desorption solvent

The selection of solvents for desorption depends on the compatibility with the HPLC-UV. This study assessed typical organic solvents, namely dichloromethane (DCM), acetonitrile (ACN) and methanol (MeOH) as desorption solvents for ofloxacin and sparfloxacin. As shown in Figure 6, MeOH showed the highest peak areas followed by ACN and DCM in most of the analytes. This result can be explained by the high solubility of ofloxacin and sparfloxacin in MeOH (both standard stock solutions were prepared in MeOH). Hence, MeOH was selected as the solvent for desorption.

Desorption time

In this analysis, several desorption times in between 3-15 minutes were analysed. At desorption time of 5 minutes, the extraction efficiency was optimum (Figure 7). There was no significant improvement was observed as the desorption time extended to 15 minutes. Therefore, desorption time of 5 minutes was chosen in the subsequent experiments.

Method validations

Analysis of human plasma

The linearity of D-µ-SPE was evaluated using five different concentrations prepared by spiking MeOH with the ofloxacin and sparfloxacin standards. The calibration curve was linear indicated by R^2 values obtained, (0.9973 for ofloxacin and 0.9907) for sparfloxacin over the studied concentration range of 0.5–000 µg L^{-1} with LOD and LOQ were 0.73 - 1.81 µg L^{-1}, respectively as shown in Table 1. Although the endogenous interferences was successfully eliminated in the pre-treatment of human plasma, the low LOD was obtained. This is primarily due to the multiple extractions in smaller quantities during the analysis.

The precisions of the analysis were measured by conducting triplicate analysis of spiked human plasma sample on the same day and on three different days at various concentrations. The proposed approach demonstrated acceptable precision based on the RSD values (Table 2). D-µ-SPE method demonstrated

significant relative recovery of ofloxacin and sparfloxacin in the range of 90.1-109.5% from human plasma samples. The recovery was acceptable with good RSD values suggesting a satisfactory extraction efficiency. Under optimum conditions, the overall extraction efficiency was evaluated by the typical chromatogram as shown in Figure 8. There was no interference in the analytes detected in the blank sample.

Comparison of D-μ-SPE with other published methods

The proposed extraction of method D-μ-SPE-HPLC-UV was compared with other published methods (Table 3). Each approach usually has its own advantages and disadvantages. SPE developed adequate sensitivity, accuracy, and recoveries due to the selective adsorbent of hydrophilic and lipophilic balance against ofloxacin and sparfloxacin [26]. A simpler process for the precipitation of proteins has recently been developed to remove drugs from human plasma. This method was fast and fulfilled the high requirements of bioanalysis for the sample yield. The detection limit was indeed not sufficient [27]. The proposed method D-μ-SPE has many benefits such as time saving, high sensitivity and flexibility, as well as applicable to human plasma. This method only used 20 mg of C_{18} adsorbent, allowing optimum interaction between analytes and adsorbent. This result in short contact time between analytes and adsorbent with greater sensitivity in comparison to other procedures. Furthermore, D-μ-SPE requires simple setup and ultrasonics instrument. Thus, the proposed method could be served as an alternative approach that is beneficial for green microextraction in biological matrices of ofloxacin and sparfloxacin.

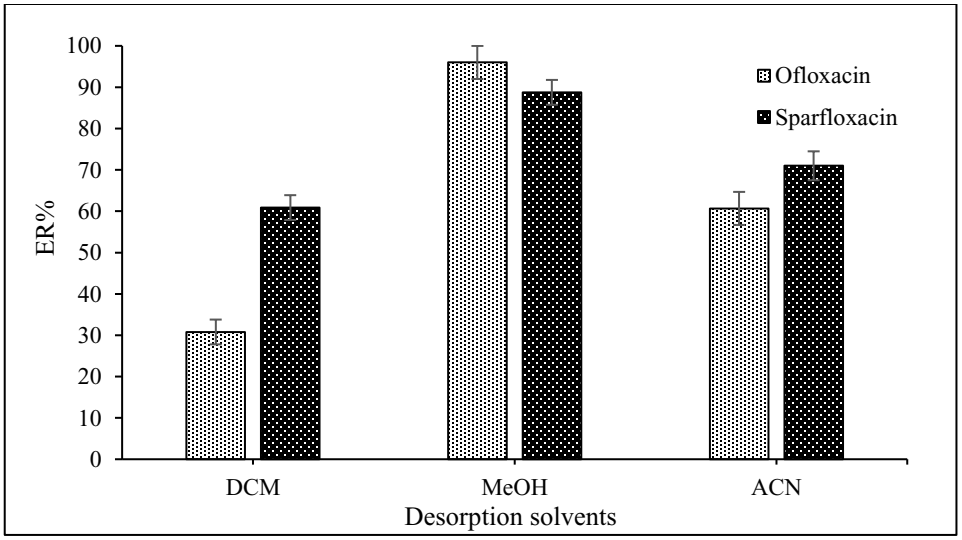


Figure 6. Effect of solvent on the extraction efficiency of ofloxacin and sparfloxacin. Extraction conditions: 1000 μg L^{-1} of ofloxacin and sparfloxacin; adsorbent: 20 mg of C_{18}; sample solution: 10 mL at pH 4; extraction time: 60 s; desorption solvent: 200 μL desorption time: 5 minutes

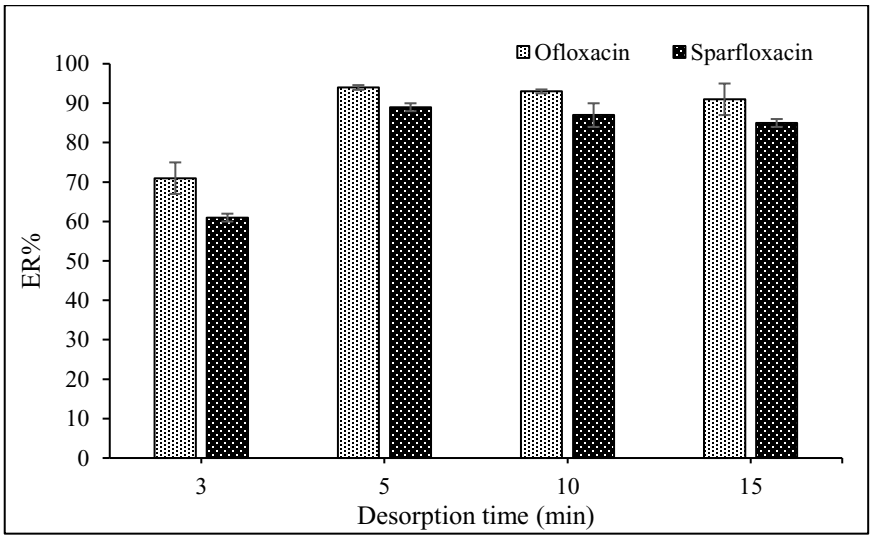


Figure 7. Effect of desorption time on the extraction efficiency of ofloxacin and sparfloxacin. Extraction conditions: 1000 µg L^{-1} of ofloxacin and sparfloxacin; adsorbent: 20 mg of C_{18}; sample solution: 10 mL at pH 4; extraction time: 60 s; desorption solvent: 200 µL of MeOH

Table 1. Validation parameters for the proposed method for ofloxacin and sparfloxacin in plasma

Matrix (Plasma) / Analytes	**Linearity Range (µg L^{-1})**	**Correlation of Determination (r^2)**	**LOD[a] (µg L^{-1})**	**LOQ[b] (µg L^{-1})**	**Precision, RSD (%, n = 3)**
Ofloxacin	0.5-1000	0.9973	0.73	2.44	5.60-9.81
Sparfloxacin	0.5-1000	0.9907	1.81	6.03	3.97-7.35

[a]Calculated from signal - to - noise =3, [b]Calculated from signal - to - noise =10

Table 2. Recoveries (%) and precisions (% RSD) of D-µ-SPE-HPLC-UV of human plasma sample

Concentration Level (µg L^{-1})	**Plasma**	
	Ofloxacin	**Sparfloxacin**
Intra-day recoveries (RSD, %, n=3)		
500	90.1± 1.9	100.1± 9.1
1000	100.6± 8.03	102.1± 5.3
Intra-day recoveries (RSD, %, n=3)		
500	98.6± 4.3	103.6± 7.1
1000	105.6± 6.32	109.5± 12.5

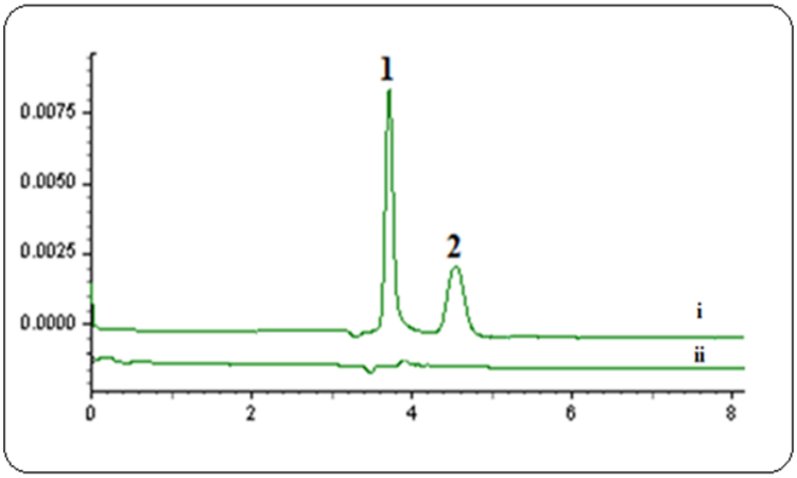


Figure 8. HPLC typical chromatogram of antibiotics drugs subjected to D-μ-SPE - HPLC-UV. i: spiked plasma (1000 μg L^{-1}); ii: unspiked human plasma under the optimized HPLC-UV conditions, Column: Thermo-Fisher Hypersil Gold ODS C_{18} (250 x 4.6 mm x 5μm); mobile phase: MeOH and phosphate buffer (5 mM, pH 3.0), (50:50) λ: 254 nm; flow rate: 1 mL min^{-1}. (1) ofloxacin and, (2) sparfloxacin

Table 3. Comparison of D-μ-SPE with other published methods for the determination of ofloxacin and sparfloxacin

Fluoroquinolone	**Matrix**	**Extraction Technique**	**Analytical Method**	**LOD (μg L^{-1})**	**Recovery (%)**	**Ref.**
Sparfloxacin	Plasma, Urine	PP	HPLC–UV	25	96.7	[28]
Gatifloxacin, Sparfloxacin and Moxifloxacin	Plasma	LLE	HPLC–UV	0.0001	80.8	[29]
Ofloxacin	Edible animal tissue	SPE	HPLC–UV	0.018	60	[30]
Ofloxacin	Plasma	LLE	HPLC–UV	15	92.9	[31]
Ofloxacin and sparfloxacin	Plasma	D-μ-SPE	HPLC–UV	0.73 and 1.81	89.5 - 102.3	Current work

SPE: Solid phase extraction, PP: Protein precipitation, LLE: Liquid -liquid extraction, D-μ-SPE: Dispersive micro-solid phase extraction

Conclusion

In this study, D-μ-SPE method coupled with HPLC-UV for the determination of ofloxacin and sparfloxacin were successfully developed and validated. It is an aqueous-based method that can be used for the direct HPLC analysis . Besides, it was found to be simple and fast approach that only used less amount of solvent for sample extraction The simplicity and sensitivity of the developed D-μ-SPE can be advantageous for the routine drugs analysis of ofloxacin and sparfloxacin in human plasma as drug monitoring system. Therefore, the dosage of drug can be monitored accurately and an appropriate dose of medicines can be given to the patients with sufficient adsorption in the body. Furthermore, the developed D-μ-SPE method might have the potential to be applied for the detection of emerging pollutants such as antibiotics in the environmental water samples.

Acknowledgement

Funding by Universiti Sains Malaysia Research Grants (Bridging: 304.PKIMIA.6316492) is highly acknowledged.

References

1. Minovski, N., Vračko, M., and Šolmajer, T. (2011). Quantitative structure-activity relationship study of antitubercular fluoroquinolones. *Molecular Diversity*, 15 (2): 417-426.
2. He, K. and Blaney, L. (2015). Systematic Optimization of an SPE with HPLC-FLD method for fluoroquinolone detection in wastewater. *Journal of Hazardous Materials,* 282:96-105.
3. Shao, H., Zhou, H., Zhang, T., Zhao, X., Jiang, Z. and Wang, Q. (2019). Preparation of molecularly imprinted hybrid monoliths for the selective detection of fluoroquinolones in infant formula powders. *Journal of Chromatography A*, 1588: 33-40.
4. Shipkova, M. and Svinarov, D. (2016). LC–MS/MS as a tool for TDM services: Where are we? *Clinical Biochemistry*, 49: 1009-1023.
5. Zeng, H. J., Yang, R., Liu, B., Lei, L. F., Li, J. J. and Qu, L. B. (2012). Simple and sensitive determination of sparfloxacin in pharmaceuticals and biological samples by immunoassay. *Journal of Pharmaceutical Analysis*, 2(3): 214-219.
6. Assadian, F. and Niazi, A. (2017). Application of response surface modeling and chemometrics methods for the determination of ofloxacin in human urine using dispersive liquid-liquid microextraction combined with spectrofluorimetry. *Journal of the Brazilian Chemical Society,* 28(12): 2291-2300.
7. Khezeli, T. and Daneshfar, A. (2017). Development of dispersive micro-solid phase extraction based on micro and nano sorbents. *Trends in Analytical Chemistry*, 89: 99-118.
8. Wu, Q., Zhao, Y., Wang, C., Sun, M., Ma, X. and Wang, Z. (2015). Mesoporous carbon reinforced hollow fiber liquid-phase microextraction for the enrichment of phenylurea herbicides followed by their determination with high performance liquid chromatography. *Analytical Methods*, 7(3): 901–908.
9. Khan, F. U., Nasir, F., Iqbal, Z., Khan, I., Shahbaz, N., Hassan, M. and Ullah, F. (2016). Simultaneous Determination of moxifloxacin and ofloxacin in physiological fluids using high performance liquid chromatography with ultraviolet detection. *Journal of Chromatography B: Analytical Technologies in the Biomedical and Life Sciences*, 1017–1018: 120-128.
10. Attimarad, M. and Alnajjar, A. (2013). A conventional HPLC-MS method for the simultaneous determination of ofloxacin and cefixime in plasma: Development and validation. *Journal of Basic and Clinical Pharmacy*, 4(2): 36.
11. Tang, Q., Yang, T., Tan, X. and Luo, J. (2009). Simultaneous determination of fluoroquinolone antibiotic residues in milk sample by solid-phase extraction - liquid chromatography-tandem mass spectrometry. *Journal of Agricultural and Food Chemistry*, 57(11): 4535-4539.
12. Tian, Z., Gao, J. J. and Qin, W. (2018). Determination of fluoroquinolones in milk by ionic liquid-mediated two-phase extraction followed by capillary electrophoresis analysis. *Madridge Journal of Analytical Sciences and Instrumentation*, 3(1): 62-67.

13. Maia, A. S., Paíga, P., Delerue-Matos, C., Castro, P. M. L. and Tiritan, M. E. (2020). Quantification of fluoroquinolones in wastewaters by liquid chromatography-tandem mass spectrometry. *Environment Pollution*, 259: 113927.
14. Rodrigues-Silva, C., Porto, R.S., dos Santos, S. G., Schneider, J. and Rath, S. (2019). Fluoroquinolones in hospital wastewater: Analytical method, occurrence, treatment with ozone and residual antimicrobial activity evaluation. *Journal of the Brazilian Chemical Society,* 30(7): 1447-1457.
15. Zheng, J., Xi, C., Wang, G., Cao, S., Tang, B., and Mu, Z. (2018). Simultaneous determination of 20 antibiotics in bovine colostrum tablet using UHPLC–MS/MS and SPE. *Chromatographia*, 81(6): 947-957.
16. Lee, H. B., Peart, E. T. and Svoboda, M. L. (2007). Determination of ofloxacin, norfloxacin, and ciprofloxacin in sewage by selective solid-phase extraction, liquid chromatography with fluorescence detection and liquid chromatography-tandem mass spectrometry. *Journal of Chromatography A*, 1139(1): 45-52.
17. Ruiz, F. J., Ripoll, L., Hidalgo, M. and Canals, A. (2019). Dispersive micro solid-phase extraction (D-μ-SPE) with graphene oxide as adsorbent for sensitive elemental analysis of aqueous samples by laser induced breakdown spectroscopy (LIBS). *Talanta*, 191: 162-170.
18. Chung, W. H., Tzing, S. H. and Ding, W. H. (2013). Dispersive micro solid-phase extraction for the rapid analysis of synthetic polycyclic musks using thermal desorption gas chromatography-mass spectrometry. *Journal of Chromatography A*, 1307: 34-40.
19. Ghorbani, M., Aghamohammadhassan, M., Ghorbani, H. and Zabihi, A. (2020). Trends in sorbent development for dispersive micro-solid phase extraction. *Microchemical Journal*, 158: 105250.
20. Jamali M. R., Firouzjah, A. and Rahnama R. (2013). Solvent-assisted dispersive solid phase extraction. *Talanta*, 116: 454-459.
21. Anastassiades, M., Lehotay, S. J., Stajnbaher, D. and Schenck, F. J. (2003). Fast and easy multiresidue method employing acetonitrile extraction/partitioning and "dispersive solid-phase extraction" for the determination of pesticide residues in produce. *Journal of AOAC International*, 86(2): 412-431.
22. Amoli-diva, M. and Pourghazi, K. (2018). $CoFe_2O_4$ nanoparticles grafted multi-walled carbon nanotubes coupled with surfactant-enhanced spectrofluorimetry for determination of ofloxacin in human plasma. *Nanochemistry Research,* 3(1): 17-23.
23. Vakh C., Alaboud, M., Lebedinets, S., Korolev, D., Postnov, V., Moskvin, L., Osmolovskaya, O. and Bulatov, A. (2018). An automated magnetic dispersive micro-solid phase extraction in a fluidized reactor for the determination of fluoroquinolones in baby food samples. *Analytica Chimica Acta,* 1001: 59-69.
24. Chisvert, A., Cardenas, S. and Lucena, R. (2019). Dispersive micro-solid phase extraction. *Trends in Analytical Chemistry*, 112: 226-233.
25. Mohd Hassan, F, W., Muggundha, R., Kamaruzaman, S., Sanagi, M, M., Yoshida, N., Hirota, Y. and Nishiyama, N. (2018). Dispersive liquid–liquid microextraction combined with dispersive solid-phase extraction for gas chromatography with mass spectrometry determination of polycyclic aromatic hydrocarbons in aqueous matrices. *Journal of Separation Science*, 41(19): 3751-3763.
26. Basheer, C., Han, G. C., Toh, M. H. and Hian, K. L. (2007). Application of porous membrane-protected micro-solid-phase extraction combined with HPLC for the analysis of acidic drugs in wastewater. *Analytical Chemistry*, 79(17): 6845-6850.
27. Roberts, J. A. (2009). Pharmacokinetic issues for antibiotics in the critically Ill patient. *Critical Care Medicine*, 37(3): 840-851.
28. Borner, K., Borner, E. and Lode, H. (1992). Determination of sparfloxacin in serum and urine by high-performance liquid chromato-graphy. *Journal of Chromatography B: Biomedical Sciences and Applications*, 579(2): 285-289.

29. Srinivas, N., Narasu, L., Shankar, B. P. and Mullangi, R. (2008). Development and validation of a HPLC method for simultaneous quantitation of gatifloxacin, sparfloxacin and moxifloxacin using levofloxacin as internal standard in human plasma: Application to a clinical pharmacokinetic study. *Biomedical Chromatography*, 22(11): 1288-1295.
30. Samanidou, V. F., Christodoulou, E. A. and Papadoyannis, I. N. (2005), Determination of fluoroquinolones in edible animal tissue samples by high performance liquid chromatography after solid phase extraction. *Journal of Separation Science*, 28(6): 555-565.
31. Garcia, M. A., Solans, C., Calvo, A., Royo, M., Hernandez, E., Rey, R. and Bregante, M. A. (2002). Analysis of ofloxacin in plasma samples by high-performance liquid chromatography. *Chromatographia*, 55(7-8): 431-434.

Malaysian Journal of Analytical Sciences (MJAS)
Published by Malaysian Analytical Sciences Society

BIO-BASED CONTENT OF OLIGOMERS DERIVED FROM PALM OIL: SAMPLE COMBUSTION AND LIQUID SCINTILLATION COUNTING TECHNIQUE

(Kandungan Berasaskan Bio dalam Oligomer daripada Minyak Sawit: Teknik Pembakaran Sampel dan Penghitungan Sintilasi Cecair)

Mohd Azmil Mohd Noor*, Tuan Noor Maznee Tuan Ismail, Razmah Ghazali

Quality and Environmental Assessment Unit, Advanced Oleochemical Technologies Division, Malaysian Palm Oil Board, No. 6, Persiaran Institusi, Bandar Baru Bangi, 43000 Kajang, Selangor, Malaysia

**Corresponding author: mohd.azmil@mpob.gov.my*

Received: 3 July 2020; Accepted: 18 September 2020; Published: 10 December 2020

Abstract

The bio-based content is defined as the ratio of weight of the bio-based carbon to the total organic carbon in the product. A radiocarbon technique, involving combustion of samples and counting of the resulting ^{14}C isotope, was applied to quantify the bio-based content of polyols derived from palm oil. The samples were combusted using a sample oxidizer and the carbon dioxide was trapped by a vapor-phase reaction with an amine, forming carbamate, which was then mixed with an appropriate scintillation cocktail. For the liquid scintillation counting, validation of the method was evaluated through recovery, while the quenching effect was corrected by constructing a quench curve. The optimized radiocarbon method was then applied to determine the ^{14}C activity (counts per minute [CPM] and disintegrations per minute [DPM]) of palm olein and the polyols derived from it. Palm olein were confirmed to have 100% bio-based content while the value for the polyols derived from them ranged from 71 to 96%, depending on the reactants used for ring-opening reaction of the epoxidized palm olein.

Keywords: palm olein polyol, renewable, radiocarbon, carbon dioxide trapping, quench

Abstract

Kandungan berasaskan bio ditakrifkan sebagai nisbah berat karbon berasaskan bio dengan jumlah karbon organik di dalam sesuatu produk. Teknik radiokarbon, yang melibatkan pembakaran sampel dan penghitungan isotop ^{14}C yang dihasilkan, telah digunakan untuk mengukur kandungan berasaskan bio dalam poliol daripada minyak sawit. Sampel dibakar menggunakan pengoksidasi sampel dan karbon dioksida diperangkap dengan amina, membentuk karbamat, yang kemudian dicampurkan dengan koktel sintilasi yang sesuai. Bagi penghitungan sintilasi cecair, ketepatan kaedah dinilai melalui pemulihan, sementara kesan pelindapkejutan dibetulkan dengan membina keluk pelindapkejutan. Kaedah radiokarbon yang dioptimumkan kemudiannya digunakan untuk menentukan aktiviti ^{14}C (hitungan per minit [CPM] dan disintegrasi per minit [DPM]) olein sawit dan poliol yang berasal daripadanya. Olein sawit disahkan mempunyai 100% kandungan berasaskan bio manakala poliol sawit berkisar antara 71 hingga 96%, bergantung kepada reaktan yang digunakan untuk tindak balas ke atas olein sawit yang teroksida.

Kata kunci: poliol olein sawit, boleh diperbaharui, radiokarbon, perangkap karbon dioksida, pelindapkejutan

Introduction

Polyurethane (PU) is extensively used in foams, composites, coatings, adhesives, sealants, and elastomers industry [1]. PU is produced by reacting polyols with isocyanates. Most of the polyols used in PU industry originate from petroleum-based source. Depleting resources of fossil energies and initiatives to reduce the emission of greenhouse gases have led to the development and use of renewable biomass resources [2]. Currently, these renewable resources, *e.g.* castor, soybean, canola and palm oils, have been successfully utilized as raw materials for polyols production [3-8]. These bio-based polyols have been subsequently incorporated in meaningful volumes in PU foam formulations [9-12].

In some countries, the bio-based content of biomass-based products need to be certified. ‘‘Biomass plastics mark’’ was authorized by Japan Bio-Plastics Association to certify biomass plastics in Japan which were made with at least 25% by weight of biomass to the total amount of the product. Certified products were then listed in the association’s positive list. Furthermore, ‘‘Biomass mark’’ was authorized by Japan Organics Recycling Association to certify biomass-based raw materials [13]. Meanwhile, the United States Department of Agriculture obliges companies in the United States that wished to join their ‘‘Bio-Preferred Voluntary Labelling Program’’ to submit the American Society of Testing and Materials (ASTM) D6866 product certification. Other certification bodies requiring ASTM D6866 bio-based content testing include Canada’s “EcoLogo” for the CCD-170 standard and Belgium’s “Vinçotte” for its OK Bio-based eco-label system.

The bio-based content is defined as the ratio of weight of the bio-based carbon in material to the total organic carbon in the product. The ASTM D6866 standard test method regulates that the bio-based content should be calculated from the percent of modern carbon. This standard regulates three measuring methods using ^{14}C concentration, *i.e.* by a liquid scintillation counter (LSC), accelerator mass spectrometry (AMS), or isotope ratio mass spectrometry.

All three methods were evaluated and it was found that the most accurate method was AMS and that the benzene synthesis and carbon absorption methods had lower accuracy [14]. The accuracy of all analysing methods, however, was acceptable. Culp et al. compared the accuracy and precision of ^{14}C between natural products and bio-based materials analysed by AMS and LSC. The results showed that accurate and precise ^{14}C measurements were achievable by both methods [15-18]. Each of the three methods has its own advantages and disadvantages. When comparing the duration and cost of analysis, the carbon absorption method is the most preferred method in the industrial application. These different methods have been used to verify bio-based additions to petrochemicals [19-22].

The method using radiocarbon technique requires the collection of carbon dioxide (CO_2) of a sample in a suitable absorbing solution. This was carried out using a sample oxidizer, in which the sample material was combusted in an oxygen-enriched atmosphere yielding water vapour and CO_2. Physical separation of ^{3}H and ^{14}C radionuclides was then achieved. The separated ^{14}C radionuclide was counted using an LSC. The counts were compared either directly or through secondary standards to the ^{14}C oxalic acid SRM 4990C with stated uncertainties. Significantly lower ^{14}C counts indicate the presence of ^{14}C-depleted carbon. Zero percent ^{14}C, when compared to the standard, signifies an entire lack of ^{14}C atoms in a material, thus indicating a petroleum-based carbon source.

The analysing method in this present study was performed using carbon absorption because of the simplicity of the process and the variation was acceptable. A radiocarbon technique, involving combustion of samples and counting of the resulting ^{14}C isotope, was applied to determine the bio-based content of vegetable oils as well as polyols derived from palm oil, fatty acid methyl ester and castor oil. After collecting CO_2 in a suitable absorbing solution, the CO_2 cocktails were submitted LSC analysis.

Materials and Methods

Chemicals and standards

Vegetable oils *i.e.* palm oil, canola oil, soybean oil, olive oil and sunflower oil were purchased from overseas supplier. Castor oil and its polyols (HCO-25, CO-25 and CO-5) were purchased from Troy Polymers Inc. USA.

Refined, bleached and deodorised palm olein was acquired from Southern Edible Oil Industries, Malaysia. Epoxidized palm olein (EPOo) and all the polyols resulting from the ring-opening with different alcohols were obtained from the Polymer and Composite group of Malaysian Palm Oil Board (MPOB) [7]. The ring-opening syntheses were conducted with different types of alcohol, *i.e.* methanol, 1,2-ethanediol, 1,2-propanediol, 1,3-propanediol, bio-based 1,3-propanediol, 1,5-pentanediol and 1,6-hexanediol; and the polyols obtained were denoted as POoP M, POoP E135, POoP PG, POoP PDO, POoP Bio PDO, POoP PTDO and POoP HDO, respectively. A commercial polyol was obtained from a local polyol producer.

Fatty acid methyl ester (FAME), containing 74.2% of $C_{18:1}$ methyl, was acquired from Carotino, Malaysia. Epoxidized FAME (E-FAME) and all the polyols resulting from the ring-opening with different alcohols were obtained from the Polymer and Composite group of MPOB [5]. The ring-opening syntheses were conducted with different types of alcohol, *i.e.* 1,3-propanediol, bio-based 1,3-propanediol, 1,4-butanediol, 1,5-pentanediol, 1,6-hexanediol and water; and the polyols obtained were denoted as PolyFAME PDO, PolyFAME Bio PDO, PolyFAME BDO, PolyFAME PTDO, PolyFAME HDO and PolyFAME H, respectively. Susterra® propanediol (DuPont, US) was used without further modification.

Amine (CarboSorb E) and scintillation cocktail (PermaFluor E+) were purchased from PerkinElmer (US). High DPM ^{14}C Spec Chec standard solution was purchased from PerkinElmer (US) with a radioactivity level of 826,000 DPM mL-1 ± 2.474 %. National Institute of Standards and Technology (NIST) standard reference material 4990C (oxalic acid) was purchased from PerkinElmer (US) with a ratio of ^{14}C massique activity of 1.2933 ± 0.0004.

Preparation of samples

All samples were homogenized before weighing. The liquid samples were weighed onto a combusto-pad, which were then placed on a combusto-cone.

Combustion of samples

Samples combustion was performed using a PerkinElmer Sample Oxidizer Model 307 (US). A portion of the sample was combusted until the absence of visible residue, which took 0.5 to 2 minutes. After the combustion, two separate samples; a sample of ^{3}H (water) and a sample of ^{14}C (CO_2) were trapped at ambient temperature in a 20 mL Teflon-coated low diffusion polyethylene vials (PerkinElmer).

The water was condensed in a cooled coil and was then washed into a vial where it was mixed with an appropriate scintillation cocktail (Monophase S). The CO_2 was trapped by a vapour-phase reaction with an amine (CarboSorb E), that formed into carbamate, which was then mixed with an appropriate scintillation cocktail (PermaFluor E+). The flow diagram of the 307 Sample Oxidizer is presented in Figure 1.

Counting of samples

After combustion, activity concentrations of ^{14}C isotopes of the samples were determined using a PerkinElmer Tri-Carb 2910TR Low Activity Liquid Scintillation Counter (Illinois, US) with an external standard (^{133}Ba) which allows the measuring of external spectral quench parameter (transformed spectral index of external standard [tSIE]). The analytical results were determined using QuantaSmart™ program.

A quench curve was constructed to determine the counting efficiency of each unknown sample. A quench standard curve is a series of standards in which the absolute radioactivity (DPM) per vial is constant and the amount of quench increases from vial to vial. A quench curve uses the relationship between counting efficiency and tSIE to correct the measured CPM to DPM. When a quench curve is made, the DPM value in each standard is known. Each standard was counted and the CPM was measured. The counting efficiency was calculated using Equation 1. At the same time, tSIE was measured for each standard. A correlation was made using the tSIE on

the X-axis and the counting efficiency on the Y-axis. A curve was fitted to the standard points.

The efficiency for each unknown sample was determined from the constructed quench curve using the measured tSIE value for each sample (Figure 2). At the same time, the CPM of the unknown sample was measured. Knowing the CPM of the unknown sample and the counting efficiency, DPM of the sample was then calculated according to Equation 2.

The DPM was compared directly to the ^{14}C oxalic acid SRM 4990c radiocarbon standard. Significantly lower DPM indicates the presence of ^{14}C-depleted carbon. Zero percent ^{14}C, when compared to the standard, signifies the entire lack of ^{14}C atoms in a material, thus, indicating a petroleum-based carbon source. The bio-based content was calculated according to Equation 3.

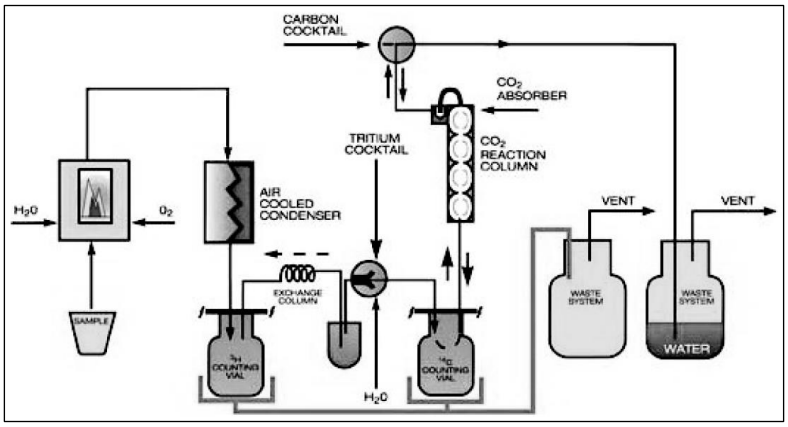


Figure 1. Flow diagram of sample preparation with the 307 Sample Oxidizer

$$Counting\ efficiency\ (\%) = \frac{Counts\ per\ minute\ (cpm)}{Disintegration\ per\ minute\ (dpm)} \times 100\% \quad (1)$$

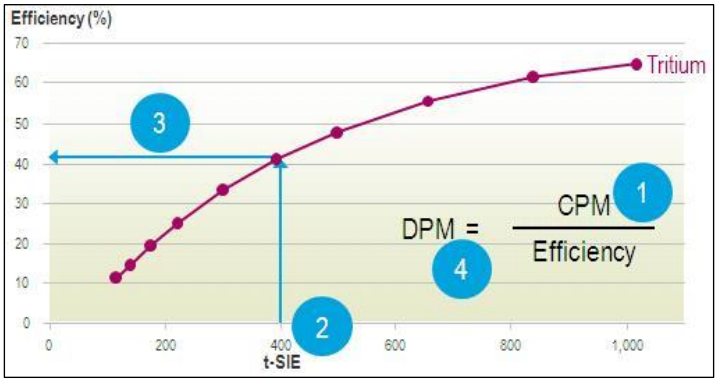


Figure 2. Usage of quench curve for determination counting efficiency and DPM

$$Disintegration\ per\ minute\ (dpm) = \frac{Counts\ per\ minute\ (cpm)}{Counting\ efficiency\ (\%)} \times 100\% \quad (2)$$

$$Bio - based\ content\ (\%) = \frac{dpm(sample)/weight(sample)}{dpm(reference)/weight(reference)} \quad (3)$$

Results and Discussion

Optimization of LSC and sample oxidizer

The minimum acceptable efficiency for ^{14}C in the range of 0-156 keV is 95% for PerkinElmer Tri-Carb 2910TR. Counting efficiency is a parameter measured as part of Instrument Performance Assessment. The performance of the LSC was assessed periodically *via* Self-Normalization and Calibration, where reference standards (^{14}C, ^{3}H and Background with known radioactivity (DPM) were counted and the counting efficiency was calculated. The counting efficiencies obtained for ^{14}C and ^{3}H were well above the minimum limit of 60% and 90%, respectively, as per the instrument's requirements specified by PerkinElmer.

The conditions of the Sample Oxidizer (amount of sample for combustion, time of combustion and amount of LSC cocktails) were investigated to find the optimum settings. The method was optimized using polyols instead of polyurethanes in order to minimize problems that may rise due to various components in polyurethanes.

Method validation

The combustion method was optimized for determination of bio-based content of palm-based polyols. Based on ICH Harmonised Tripartite Guideline Validation of Analytical Procedures: Text and Methodology Q2 (R1) (2005), this method was validated with respect to trueness (recovery and memory tests), linearity (quench curves) and precision (repeatability and interlaboratory comparison) using the optimized instrumental conditions. The quench curves, recovery and memory tests were performed with the ^{14}C Spec Chec standards.

The recovery of the method was tested by combusting a known activity of ^{14}C Spec Chec standards and those samples were compared with non-combusted samples with the same activity. The recovery (in %) was calculated using Equation 4 below.

$$Recovery\ (\%) = \frac{CPM_{combusted}}{CPM_{non-combusted}} \times 100\% \quad (4)$$

If samples with high activity were combusted, there is a possibility that some of the activities were retained in the Oxidizer and released when combusting the next samples. This is known as the memory effect, and it was investigated by combusting samples of a known activity of ^{14}C, followed by combusting an inactive standard sample after each active sample. The memory (in %) was calculated using Equation 5 below.

$$Memory\ (\%) = \frac{CPM_{inactive} - CPM_{background}}{CPM_{non-combusted}} \times 100\% \quad (5)$$

The recovery and the memory were determined in six replicates (Table 1). The average recovery was found to be 100.1 ± 1.5%, which is within the acceptable range of 85-110%. Therefore, it was decided that the method does not need correction for recovery. The memory was found to be 0.05 ± 0.03%, which is less than 0.1%. Therefore, the memory did not need to be corrected when measuring samples with normal environmental ^{14}C levels.

Construction of quench curves

The quench curve was constructed by preparing 7 calibration samples with different amounts of CarbosorbE (0, 2, 4, 6, 8, 9, 10 mL) and with the same amount of ^{14}C standard solution (82600 DPM). Each calibration sample was counted for 2 min. These samples were measured with LSC and the counting efficiency was recorded and plotted as a function of the external standard quenching parameter, tSIE (Table 2, Figure 3).

In addition to acting as CO_2 trapping agent, Carbosorb E also increases the chemical quenching effect in the scintillation cocktail. The effect of Carbosorb E amount in the scintillation cocktail was studied. Increasing the amount of Carbosorb E has reduced the CPM and thus, the counting efficiency (Table 3).

The repeatability of the method was determined by analysing four replicates of oxalic acid by the same analyst and using the same instrumentation. The resultant coefficient of variation obtained was 10.4%, which is considered as acceptable (< 15%).

Interlaboratory comparison was performed by sending two polyol samples, one commercial polyol and one of the synthesized polyols selected randomly, to an ISO 17025:2005 accredited laboratory in the US. The reported values of bio-based content were compared with the results of analyses done in MPOB on the same samples (Table 4). Cross check results with the accredited laboratory suggested that the sample oxidation method coupled with LSC is able to provide reliable results, comparable to the expensive AMS technique used by the accredited laboratory. The determination of bio-based content by AMS requires a large, expensive, and sophisticated instrument, which needs to be managed by a large research institute for its viable operation.

Table 1. Recovery and memory results for ^{14}C

Performance Parameter	Recovery (%)	Memory (%)
Sample 1	99.42	0.02
Sample 2	101.87	0.05
Sample 3	98.99	0.02
Sample 4	99.18	0.06
Sample 5	102.27	0.08
Sample 6	101.38	0.07
Average	100.09	0.05
Standard deviation	1.48	0.03

Table 2. Measured CPM and TSIE of 7 calibration samples with varying amount of Carbosorb E and with same amount of ^{14}C activity

Vial Label	Combustion Time (min)	Amount of CarboSorb E (mL)	Filter Paper (g)	Measured CPM	Injected Activity DPM	Counting Efficiency (%)	Measured tSIE
C0	0	0	0	69631	82600	84.3	794.7
C1	0.3	2	0.1	67783	82600	82.1	363.3
C2	0.3	4	0.2	71215	82600	86.2	321.3
C3	0.3	6	0.4	66132	82600	80.1	243.1
C4	0.5	8	0.6	65875	82600	79.8	197.5
C5	0.7	9	0.8	64142	82600	77.7	180.7
C6	1.0	10	1.0	60410	82600	73.1	162.7

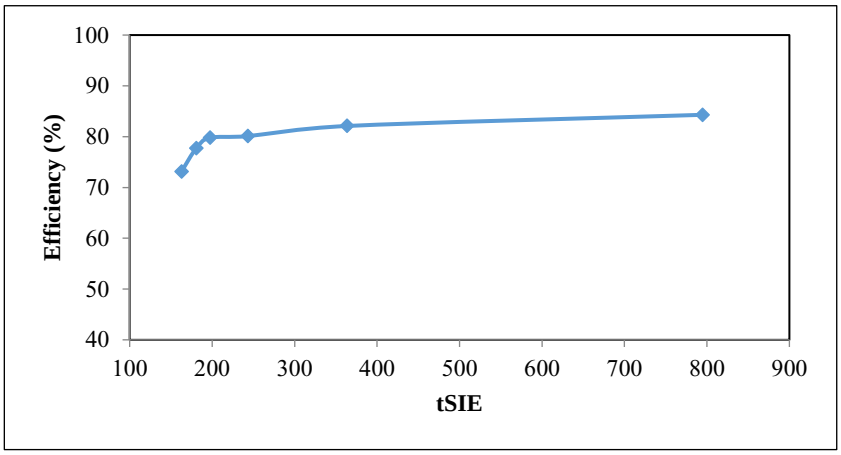


Figure 3. Quench curve for ^{14}C related to the usage of Carbosorb E

Table 3. Effect of Carbosorb E amount on CPM and counting efficiency

Carbosorb E (mL)	Measured CPM	Counting Efficiency (%)
0	69631	84.3
2	67783	82.1
4	71215	86.2
6	66132	80.1
8	65875	79.8
9	64142	77.7
10	60410	73.1

Table 4. Reported values of bio-based content by MPOB and an accredited laboratory on two polyol samples

Sample	Bio-based Content (%)	
	MPOB	Accredited Laboratory (US)
PolyFAME Bio PDO	100	98
Commercial polyol	85	89

Analyses of samples

A number of vegetable oils and polyols derived from vegetable oils were analysed to determine the bio-based content. The suitable amount (weight) of sample to be combusted was different for each sample. The weight ranged from 0.05 to 0.1 g. The amount of sample that gave counting efficiencies of 75% or higher was used to determine the bio-based content. The bio-based content was calculated according to Equation 3 and the results are tabulated in Table 5. NIST standard reference material 4990C (oxalic acid) was used as a reference.

The bio-based content of vegetable oils (palm oil, palm olein, coconut oil, canola oil, soybean oil, olive oil, sunflower oil and castor oil) was 100%. Most of the vegetable oils generally have 100% ^{14}C, which signifies an entirely modern carbon source, *i.e.* plants [13, 23]. Lower percent indicates the presence of ^{14}C-depleted carbon, which is likely to be fossil carbon source, *i.e.* petroleum.

The bio-based content of castor oil-based polyols (HCO-25, CO-25 and CO-5) ranged from 70 to 100%. HCO-25 and CO-25 have lower bio-based content, which can be due to their higher ethylene oxide degree (25 EO) compared to 5 EO for CO-5. Ethylene oxide used in the ethoxylation process is conventionally produced from fossil (petroleum) carbon source. The incorporation of ethylene oxide in the castor oil-based polyols have reduced the bio-based content.

For palm-based polyols (POoP M, POoP E135, POoP PG, POoP PDO, POoP PTDO and POoP HDO), the bio-based content ranged from 81 to 96%. The addition of reactants for ring-opening reaction of EPOo has consequently lowered the bio-based content of the resulting polyols compared to the bio-based content of EPOo and palm oil. All of the reactants, *i.e.* methanol, 1,2-ethanediol, 1,2-propanediol, 1,3-propanediol, bio-based 1,3-propanediol, 1,5-pentanediol and 1,6-hexanediol, are from fossil carbon source. Meanwhile, POoP Bio PDO had 100% bio-based content. This result is expected since the reactant (Susterra® 1,3-propanediol) used for ring-opening is also 100% bio-based.

For FAME-based polyols (PolyFAME PDO, PolyFAME BDO, PolyFAME PTDO and PolyFAME HDO), the bio-based content ranged from 71 to 74%. The addition of reactants for ring-opening reaction of E-FAME has consequently lowered the bio-based content of the resulting polyols compared to the bio-based content of E-FAME. All of the reactants are from fossil carbon source. Meanwhile, PolyFAME H had 100% bio-based content due to the addition of water, which did not contribute any carbon to the resulting polyol. PolyFAME Bio PDO had 100% bio-based content. This result is expected since the reactant (Susterra® propanediol) used for ring-opening is also 100% bio-based.

Interestingly, POoP Bio PDO and POoP PDO share the same chemical structure, yet they have significantly different bio-based content. Both polyols showed comparable glass transition temperatures, crystallinity and melt temperatures [7]. Similar findings were also observed on PolyFAME Bio PDO and PolyFAME PDO, whereby the reactants (bio-based Susterra® 1,3-propanediol and 1,3-propanediol, respectively) did not have an impact on their thermal crystallinity [5].

Overall, the presented results showed that the determination of bio-based content of products can be estimated using LSC analysis of ^{14}C cocktails with great confidence, as reported by others worldwide [17, 24-28]. It is also noteworthy to mention that this method offers reliable results at inexpensive costs which will benefit bio-based material producers in promoting the production of biomass-based products in the commercial market.

Table 5. Measured DPM, weight and calculated bio-based content of reference, vegetable oils, castor oil-based polyols, palm-based polyols and FAME-based polyols

Sample	DPM	Weight (g)	Biobased Content (%)
Reference	83	0.1099	-
Vegetable oils			
RBDPO	54	0.0547	100
RBDPOo	59	0.0501	100
Canola oil	73	0.0500	100
Soyabean oil	53	0.0519	100
Olive oil	76	0.0497	100
Sunflower oil	70	0.0802	100
Castor oil	87	0.1105	100
FAME (Methyl oleate)	59	0.0506	100
Castor oil-based polyols			
HCO-25	56	0.1052	70.5
CO-25	70	0.1048	88.4
CO-5	78	0.0849	100
EPOo	168	0.1067	100
POoP M	75	0.1099	90.4
POoP E135	69	0.1085	84.2
POoP PG	56	0.0804	92.2
POoP PDO	74	0.1082	90.6
POoP Bio PDO	86	0.1002	100
POoP PTDO	73	0.1005	96.2
POoP HDO	62	0.1010	81.3
Commercial polyol	67	0.1049	84.6
FAME-based polyols			
E-FAME	85	0.1096	100
PolyFAME H	90	0.1001	100
PolyFAME PDO	55	0.1006	72.4
PolyFAME Bio PDO	77	0.1010	100
PolyFAME BDO	58	0.1052	73.0
PolyFAME PTDO	55	0.1019	71.5
PolyFAME HDO	56	0.1005	73.8

Conclusion

A radiocarbon technique, involving combustion of samples and counting of the resulting ^{14}C isotope, was successfully developed for the determination of bio-based content of polyols derived from palm oil. The parameters of the Sample Oxidizer, *i.e.* amount of sample for combustion, time of combustion and amount of LSC cocktails, were optimized in order to provide sufficient amount of ^{14}C in the form of LSC cocktails. The cocktails were then analysed using LSC to give the ^{14}C radioactivity and subsequently, the bio-based content of the samples.

The optimized method was validated with respect to trueness (recovery and memory tests), linearity (quench curves) and precision. Recovery tests using ^{14}C standard verified the performance of Sample Oxidizer and Liquid Scintillation Counter. The quench curve for ^{14}C was constructed to take into account chemical quenching effects. A number of vegetable oils and polyols derived from the vegetable oils were analysed using the validated method to determine their bio-based content. All of the vegetable oils have 100% ^{14}C, which signifies an entirely modern carbon (biomass) source. Polyols derived from castor oil, palm oil and FAME had lower bio-based content compared to their respective oils. This is due to the addition of reactants, which are from fossil carbon source. This method, based on LSC analysis of ^{14}C cocktails, can be used as a tool to determine the bio-based content of palm-based polyols. It has been proven to be able to provide reliable results and is comparable to the more expensive AMS technique.

Acknowledgements

The authors would like to thank MPOB, especially the Director-General of MPOB and the Director of Advanced Oleochemical Technology Division of MPOB, for the support to conduct this research. We would also like to acknowledge Makmor Abd Wahab, Zamiah Hasman, Abd Halim Abd Jalal and the Polymer and Composite Research Group of MPOB for their technical assistance in completing this project.

References

1. Ionescu, M. (2005). Chemistry and technology of polyols for polyurethanes. Rapra Technology Limited, Shawbury, Shrewsbury, Shrosphire, SY4 4NR (United Kingdom).
2. Kunioka, M. (2010). Possible incorporation of petroleum-based carbons in biochemicals produced by bioprocess--biomass carbon ratio measured by accelerator mass spectrometry. *Applied Microbiology Biotechnology,* 87: 491-497.
3. Narine, S. S., Kong, X., Bouzidi, L. and Sporns, P. (2007). Physical properties of polyurethanes produced from polyols from seed oils: I. Elastomers. *Journal of the American Oil Chemists' Society,* 84: 55-63.
4. Caillol, S., Desroches, M., Boutevin, G., Loubat, C., Auvergne, R. and Boutevin, B. (2012). Synthesis of new polyester polyols from epoxidized vegetable oils and biobased acids. *European Journal of Lipid Science and Technology,* 114: 1447-1459.
5. Tuan Ismail, T. N. M., Ibrahim, N. A., Mohd Noor, M. A., Hoong, S. S., Poo Palam, K. D., Yeong, S. K., Idris, Z., Schiffman, C. M., Sendijarevic, I., Abd Malek, E., Zainuddin, N. and Sendijarevic, V. (2018). Oligomeric composition of polyols from fatty acid methyl ester: The effect of ring-opening reactants of epoxide groups. *Journal of the American Oil Chemists' Society,* 95: 509-523.
6. Mohd Noor, M. A., Sendijarevic, V., Hoong, S. S., Sendijarevic, I., Tuan Ismail, T. N. M., Hanzah, N. A., Mohd Noor, N., Poo Palam, K. D., Ghazali, R. and Abu Hassan, H. (2016). Molecular weight determination of palm olein polyols by gel permeation chromatography using polyether polyols calibration. *Journal of the American Oil Chemists' Society,* 93: 721-730.

7. Tuan Ismail, T. N. M., Ibrahim, N. A., Mohd Noor, M. A., Hoong, S. S., Poo Palam, K. D., Yeong, S. K., Idris, Z., Sendijarevic, C. M. S. I., Abd Malek, E., Zainuddin, N. and Sendijarevic, V. (2018). Oligomeric composition of palm olein-based polyols: The effect of nucleophiles. *European Journal of Lipid Science and Technology,* 120: 1700354.
8. Mohd Noor, M. A., Tuan Ismail, T. N. M., Sendijarevic, V., Schiffman, C. M., Sendijarevic, I., Ghazali, R. and Idris, Z. (2017). Molecular weight distribution of low molecular weight polyols derived from fatty acid methyl esters. *Journal of the American Oil Chemists' Society,* 94: 387-395.
9. Ain, N. H., Tuan Noor, M. T. I., Mohd Noor, M. A., Srihanum, A., Devi, K. P. P., Mohd, N. S., Mohdnoor, N., Kian, Y. S., Hassan, H. A., Campara, I., Schiffman, C. M., Pietrzyk, K., Sendijarevic, V. and Sendijarevic, I. (2016). Structure–property performance of natural palm olein polyol in the viscoelastic polyurethane foam. *Journal of Cellular Plastics,* 53: 65-81.
10. Prociak, A., Malewska, E., Kurańska, M., Bąk, S. and Budny, P. (2018). Flexible polyurethane foams synthesized with palm oil-based bio-polyols obtained with the use of different oxirane ring opener. *Industrial Crops and Products,* 115: 69-77.
11. Mohd Noor, M. A., Hanzah, N. A., Ghazali, R., Adnan, S., Poo Palam, K. D., Tuan Ismail, T. N. M. and Abu Hassan, H. (2015). Determination of volatile organic compounds in palm-based polyurethane foams using static headspace gas chromatography mass spectrometer. *Journal of Oil Palm Research,* 27: 273-281.
12. Nurul 'Ain, H., Maznee, T. I. T. N., Norhayati, M. N., Noor, M. A. M., Adnan, S., Devi, P. P. K., Norhisham, S. M., Yeong, S. K., Hazimah, A. H., Campara, I., Sendijarevic, V. and Sendijarevic, I. (2016). Natural palm olein polyol as a replacement for polyether polyols in viscoelastic polyurethane foam. *Journal of the American Oil Chemists' Society,* 93: 983-993.
13. Kunioka, M., Ninomiya, F. and Funabashi, M. (2007). Biobased contents of organic fillers and polycaprolactone composites with cellulose fillers measured by accelerator mass spectrometry based on ASTM D6866. *Journal of Polymers and the Environment,* 15: 281-287.
14. Norton, G. A. and Devlin, S. L. (2006). Determining the modern carbon content of biobased products using radiocarbon analysis. *Bioresource Technology,* 97: 2084-2090.
15. Culp, R., Noakes, J., Cherkinsky, A., Prasad, G. R. and Dvoracek, D. (2013). A decade of AMS at the University of Georgia. Nuclear instruments and methods in physics research section B: Beam interactions with materials and atoms 294: pp. 46-49.
16. Jou, R., Macario, K., Carvalho, C., Dias, R., Brum, M., Cunha, F., Ferreira, C. and Chanca, I. (2015). Biogenic fraction in the synthesis of polyethylene terephthalate. *International Journal of Mass Spectrometry,* 388: 65-68.
17. Nagakawa, Y., Yunoki, S. and Saito, M. (2014). Liquid scintillation counting of solid-state plastic pellets to distinguish bio-based polyethylene. *Polymer Testing,* 33: 13-15.
18. Norton, G. A., Hood, D. G. and Devlin, S. L. (2007). Accuracy of radioanalytical procedures used to determine the biobased content of manufactured products. *Bioresource Technology,* 98: 1052-1056.
19. Dijs, I. J., Van der Windt, E., Kaihola, L. and van der Borg, K. (2006). Quantitative determination by ^{14}C analysis of the biological component in fuels. *Radiocarbon,* 48: 315-323.
20. Edler, R. and Kaihola, L. (2010). Differentiation between fossil and biofuels by liquid scintillation beta spectrometry-direct method. *Nukleonika,* 55: 127-131.
21. Edler, R. (2008). The use of liquid scintillation counting technology for the determination of biogenic materials. *LSC*: 261-267.
22. Krištof, R. and Logar, J. K. (2013). Direct LSC method for measurements of biofuels in fuel. *Talanta,* 111: 183-188.

23. Kunioka, M., Inuzuka, Y., Ninomiya, F. and Funabashi, M. (2006). Biobased contents of biodegradable poly(ε-caprolactone) composites polymerized and directly molded using aluminium triflate from caprolactone with cellulose and inorganic filler. *Macromolecular Bioscience,* 6: 517-523.
24. Noakes, J., Culp, R., Nigam, M., Dvoracek, D. and Norton, G. (2005). A comparison of analytical methods for the certification of biobased products. *Prace Naukowe GIG. Gornictwo i Srodowisko*: pp. 19.
25. Molnar, M., Svingor, E., Nagy, S. and Svetlik, I. (2005). Refining the CO_2 absorption method for low level ^{14}C liquid scintillation counting in the ATOMKI. *ATOMKI Annual Report*: p.79.
26. Culp, R. and Noakes, J. (2009). Evaluation of bio-based content ASTM Method 6866-06A: Improvements revealed by liquid scintillation counting, accelerator mass spectrometry and stable isotopes for products containing inorganic carbon. *LSC 2008 International Conference on Advances in Liquid Scintillation Spectrometry*: pp. 269-278.
27. Tudyka, K. and Pawlyta, J. (2014). Biocomponent determination in vinegars with the help of ^{14}C measured by liquid scintillation counting. *Food Chemistry,* 145: 614-616.
28. Saito, K., Miyatake, H. and Kurihara, N. (1990). A combustion method for the simultaneous determination of ^{3}H, ^{14}C, and ^{35}S in triply labeled organic samples by liquid scintillation counting. *Analytical Biochemistry,* 190: 276-280.

Malaysian Journal of Analytical Sciences (MJAS)
Published by Malaysian Analytical Sciences Society

A USE OF AN EVERYDAY LIFE CAMERA WITH IMAGE PROCESSING AS ALTERNATIVE DETECTION FOR A FLAME PHOTOMETER

(Penggunaan Kamera Harian Dengan Pemprosesan Imej Sebagai Alternatif Pengesanan Fotometer Nyalaan)

Narong Kotchabhakdi[1,2] and Kate Grudpan[1,2]*

[1]*Department of Chemistry and Graduate programs in Chemistry, Faculty of Science*
[2]*Center of Excellence for Innovation in Analytical Science and Technology*
Chiang Mai University, Chiang Mai, 50200, Thailand

**Corresponding author: kgrudpan@gmail.com*

Received: 27 August 2020; Accepted: 26 October 2020; Published: 10 December 2020

Abstract

As alternative detector, everyday life cameras: Digital Single Lens Reflect (DSLR) and smartphone, are proposed for a Flame Atomic Emission Spectrometer (FAES) for the assays of Na, K, Ca, Ba, and Li. Image processing with Region of Interest (ROI) approach for DSLR employs imageJ while for smartphone, various available applications (Color Grab, Linear Regression, and Calculator) are used. It was found that linear correlations for calibration graphs could be obtained by a particular ratio of Red, Green, Blue (R, G, B) color intensity and concentration for each of the above metal ions in the range of 0.2-1.0 mg L^{-1}. Applications to real samples were demonstrated.

Keywords: flame photometry, digital single lens reflect camera, smartphone, image processing

Abstrak

Kamera harian: Refleksi Lensa Digital Tunggal (DLSR) dan telefon pintar, telah dicadang sebagai pengesan alternatif bagi spektrometer nyalaan pancaran atom (FAES) untuk analisis terhadap Na, K, Ca, Ba, dan Li. Pemprosesan imej dengan pendekatan Kawasan terpilih (ROI) pada imageJ DSLR manakala bagi telefon pintar, pelbagai aplikasi (Grab warna, regresi linear dan kalkulator) telah digunakan. Hasil mendapati korelasi linear diperolehi bagi graf kalibrasi berdasarkan nisbah keamatan warna merah, hijau, biru (R, G, B) dan kepekatan bagi setiap logam yang dinyatakan pada julat 0.2-1.0 mg L^{-1}. Aplikasi terhadap sampel sebenar telah berjaya dilakukan.

Kata kunci: fotometri nyalaan, kamera refleksi lensa digital tunggal, telefon pintar, pemprosesan imej

Introduction

The assays of the alkaline metal ions, including potassium, lithium, sodium, barium, and calcium, are needed applications in the fields of medicine, agriculture, industry and food [1-6]. There are some available color reagents such as: Alizarin, crown reagents, and o-Cresolphthalein Complexone, for calcium and barium determination [7,8]. Lithium,

sodium, and potassium are not usually colorimetrically assayed [9]. Due to the dominance of the spectral lines according to electronic configurations, taking advantage when excitation can be possible with low energy, the alkaline metal ions are assayed by flame photometry.

There have been some reports using a Charge Coupled Device (CCD) as a photo-sensor in a flame emission-based spectrometer [10, 11]. Using CCD, collecting video frames can be subjected to a multivariate image procedure based on Multivariate Curve Resolution – Alternating Least Squares (MCR-ALS) in connection to the Region of Interest (ROI) used to create the univariate regression model [12]. A webcam camera was also introduced as a detector for a flame photometer [13, 14]. Using recorded videos of the flame during the experiment and subsequent image treatments with an R statistics platform, flame photometry was reported for quantifying sodium in coconut water and seawater [15].

In this work, an everyday life camera (digital camera and smartphone) with image processing is proposed as a simple alternative detection system for a flame spectrometer. The developed system was demonstrated for the assays of real samples of wastewater, fish sauce, milk, fertilizer and water leaching battery for barium, sodium, calcium, potassium and lithium, respectively.

Materials and Methods

Solutions

Working solutions were prepared from the purchased standard solutions (1000 mg L^{-1}) for Atomic Absorption Spectrophotometry (AAS) (Merck, Germany) of Na, K, Ca, Ba, and Li in nitric acid (65%, Merck, Germany), and ultrapure water (Milli-Q, Merck) was used throughout the work.

Sample

Five different types of samples were selected to demonstrate in real application analysis using the proposed instrumentation and procedure. Sample of wastewater, fish sauce, milk, fertilizer and water leaching battery were model samples for Ba, Na, Ca, K and Li assays, respectively. Five different brands/sources of samples were collected. Samples of fish sauces, fertilizers and milks were prepared by acid digestion with HNO_3.

Instrumentation

The setup is illustrated in Figure 1. It consists of parts A and B. For Part A: flame compartment having burner and flame (a1), a window (a2) for conventional photometric detector (B) and another window (a3) for alternative detector (Digital Single Lens Reflect (DSLR) camera positioned at B1, or smartphone positioned at B2). In the compartment A, at a4, a white ceramic plate mounted behind the flame for reducing the background of flame serving as a screen giving a background for taking a photo by the camera detector B1or B2 and having a white future board as protective shelter ,as a box of dimension with 20 cm x 10 cm x 10 cm (a5) around the flame. For the conventional photometric detector (B), lens (b1), monochromator/grating (b2), and Photomultiplier tube (PMT) (b3) collected and measured the light. The three detectors were not in simultaneous operation but at one at a time for each.

Flame Atomic Absorption and Emission Spectrophotometer (AA-6200, Shimazu, Japan) was used and followed its Manual Instruction for operating conditions. A standard premix- burner (titanium 10 cm slot) was used. The ratios of oxidant and fuel (Air/C_2H_2) for Na, K and Li were used at 1.8: 8.0 L/min, for Ca at 2.0: 8.0 L/min, and for Ba at 3.0: 8.0 L/min, with an aspiration flow rate at 5 mL/min. The conditions of the conventional photometric detection system used for the Shimazu model AA-6200 refers to double beam (chopper mirror) operation, with a monochromator of holographic grating (1,600 lines/mm) for wavelength range: 190 to 900 nm; automated wavelength selection, having slit: 0.2 nm, or 0.7 nm manual setting, with background correction: Duterium (D_2)-Lamp method, with PMT.

DSLR camera (EOS 600D, Canon, Taiwan) (focus 22 nm, a rate of 3 images/sec and 5184 × 3456 pixels resolution) was used. Evaluation was made through ImageJ (a public image processing software (NIH, USA)). The conditions of flame photography by the DSLR camera include: 24 mm focusing distance, image resolution of 5184 x 3456 pixels, high-quality Joint

Photographic Experts Group (JPEG) Image, flash off, light control, self-timer, continuous shutting, 3shots/10 seconds, manual mode, manual exposure, aperture size (F5.6) and speed shutter 1/8. The camera was situated at 80 cm from the flame (as shown as B1 in Figure 1).

A smartphone (Samsung Galaxy Note II, Korea) with 8-megapixel camera was used in this study. Color Grab application for RGB color capture was used. For plotting of the analytical graph, a linear regression application in Android was employed. The RGB ratio and concentration values were evaluated with a Calculator application that was already available for a smartphone.

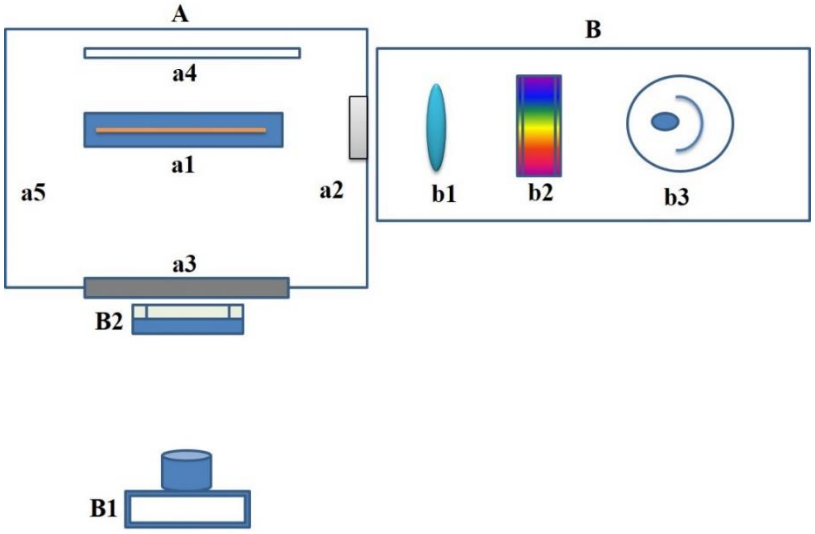


Figure 1. Top view; flame instrument set up: A) Flame compartment: Flame/Burner(a1), window for conventional photometric detector(a2), window for alternative detector (a3), screen for alternative detector (a4), protective shelter (a5), B) conventional photometric detection system: lens (b1), grating(b2), PMT(b3), B1; DSLR camera, B2; smartphone

Results and Discussion

Region of Interest (ROI) in the image processing

Region of Interest (ROI) was introduced for photographing and image processing for the flame. Image analysis requires an appropriate ROI to be representative of all images which should be acquired as high-resolution image and uncompressed file. RGB Image, as a True Color Photo Image, was stored using a 3D array M x N x 3, where M is the length and N is the width of the image in pixels. In the final dimension, each has its own color: red, green and blue.

Figure 2A illustrates the structure of the flame, which can be classified into three regions: the primary combustion zone, the interzonal region, and the secondary combustion zone. The appearance and relative size of these regions vary considerably with the oxidant-to-fuel ratio as well as with the type of oxidant and fuel. The primary combustion zone in a hydrocarbon flame exhibits blue luminescence and is seldom used for flame photometry.

Employing the DSLR camera for flame photographing with the ROI approach by capturing and recording images with storing in Tagged Image File Format (TIFF) files, the images were then pre-processed *via* ImageJ program. The criteria to select ROI are that reproducible signal with low background is obtained. This can be obtained via a histogram, as demonstrated in Figure 2B. The ROI2 would offer the lowest variation

and the intensity of the grayscale indicated low background and higher sensitivity than that of ROI1 and ROI3. Figure 2C indicates that by considering threshold, ROI2 is the least affected by the lightness distribution which affected to the variation of a signal for low concentrations range.

DSLR camera as a detector

Under the conditions, the solutions of Na^+, K^+, Ca^{2+}, Ba^{2+}, and Li^+ produce flames with the colors of yellow, violet, orange, lime green, and red, respectively, as shown in Figure 3.

Instead of using the individual R, G or B intensity value for plotting a calibration graph, the ratios of R/B, B/R, R/B, G/R and R/B are used for Na, K, Ca, Ba and Li, respectively. It was found that the relationship of the ratios of color intensities and concentrations was linear for each element, as represented in Table 1.

A smartphone as a detector

The previous DSLR camera as a detector was replaced by a smartphone as it is not only more commonly available but also offers various applications that are contained in the smartphone device itself. The applications include Color Grab, Linear Regression and Calculator, while information regarding photos taken by the DSLR camera has to be transferred to computer. Applying the previous ROI approach, using the smartphone as detector, it is arranged to focus to ROI2. R, G, B values can be obtained. This results in linear calibrations for the metal ions with a lower concentration range (Figure 4 and Table 2) (0.2-1.0 mg L^{-1} for smartphone, while 2.0 - 8.0 mg L^{-1} for DSLR camera).

The Limits of Detection (LODs) (3σ)[16] were found to be 0.13, 0.06, 0.16, 0.21, and 0.13 mg L^{-1}, while the Limit of Quantitation (LOQs) (10σ))[16] were 0.33, 0.14, 0.45, 0.55, and 0.33 mg L^{-1} for Na, K, Ca, Ba, and Li, which were comparable to that of the conventional photometer: LODs being 0.05, 0.05, 0.04, 0.15, and 0.11 mg L^{-1} , and LOQs being 0.13, 0.13, 0.15, 0.37, 0.30 mg L^{-1}, respectively. It should be noted that: (1) when using another camera brand, the conditions would be re-optimized, and (2) after every 60 minutes, 3 points calibration would be checked to ensure the experimental conditions are still valid.

Application for real samples

The camera cannot differentiate interferent species, but using the ratios of R, G, B values may overcome the color interferent to some extent. To use a camera as a detector, a sample with a specific matrix should be investigated for suitable conditions. In this work, the ions of interest in a specific matrix sample have been demonstrated, namely, Na in fish sauce, Ba in wastewater, Li in leaching battery solution, K in fertilizer, and Ca in milk. The results agreed with the conventional detector (Table 3 and Figure 5) by applying t-test where the values of $t_{observed}$ are less than $t_{critical}$ [16](see Table 3), and it indicates no observed interference in the proposed method using smartphone.

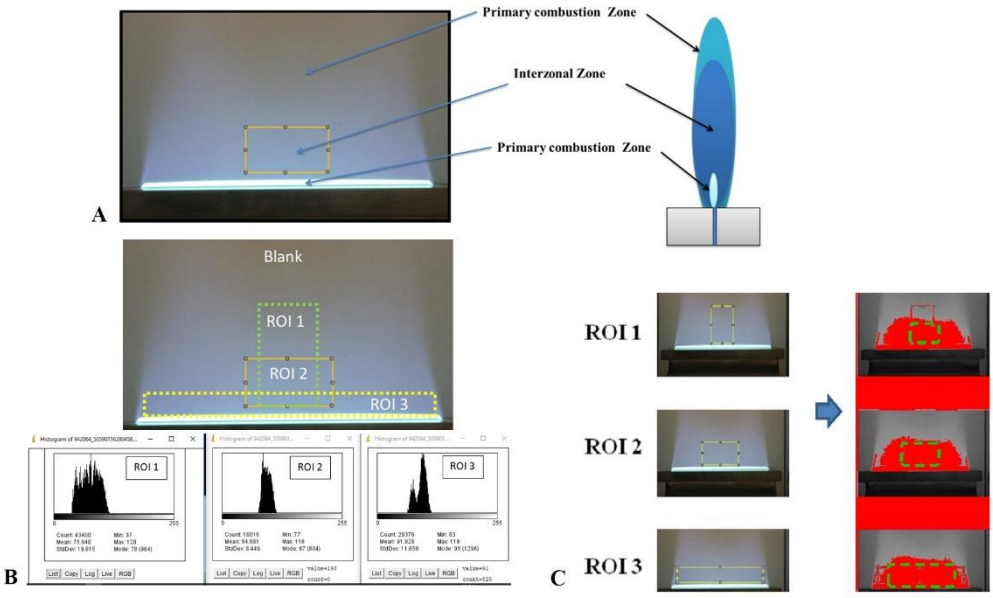


Figure 2. ROI for image processing: A; flame zones, B; the three ROIs with histogram, C; ROI with threshold

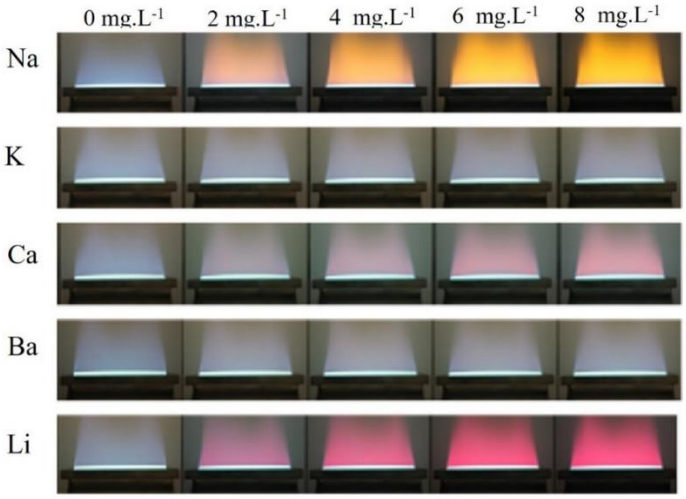


Figure 3. Illustration of photos of the flame colors due to the solutions of Na^{+}, K^{+}, $Ca^{2+,}$ $Ba^{2+,}$ and Li^{+} under the experimental conditions taken by the DSLR camera

Table 1. Calibration equations obtained by the ratio of color intensity value *vs* concentration using DSLR camera

Element (Color)	Color Intensity Ratio	Linear Equation	R^2
Na (yellow)	R/B	y = 0.38x + 0.72	0.996
K (violet)	B/R	y = 0.0046x + 1.3	0.998
Ca (orange)	R/B	y = 0.064x + 0.84	0.999
Ba (lime green)	G/R	y = 0.043x + 0.96	0.995
Li (red)	R/B	y = 0.12x + 0.91	0.998

*Concentration range: 2.0- 8.0 mg L^{-1}



Figure 4. Information of color intensity under ROI approach using Color Grab application in the smartphone

Table 2. Calibration equations obtained by the ratio of color intensity value *vs* concentration using smartphone

Element (Color)	Color Intensity Ratio	Linear Equation	R^2
Na (yellow)	R/B	y = 0.32x + 0.85	0.997
K (violet)	B/R	y = 0.11x + 0.85	0.995
Ca (orange)	R/B	y = 0.16x + 0.83	0.999
Ba (lime green)	G/R	y = 0.090x + 0.51	0.998
Li (red)	R/B	y = 0.18x + 0.88	0.996

*Concentration range: 0.2-1.0 mg L^{-1}

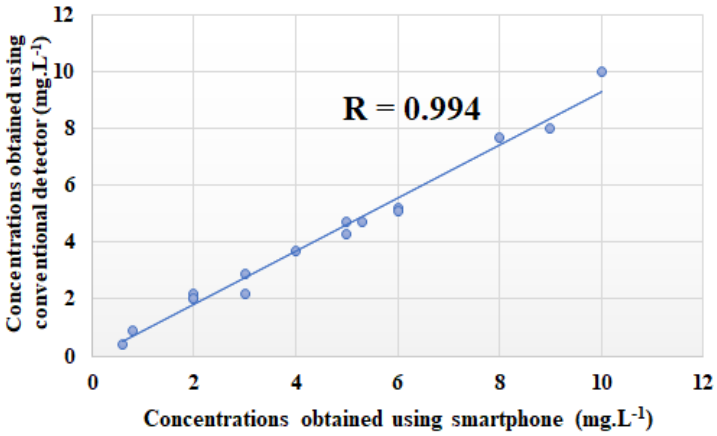


Figure 5. Correlation of the results obtained by using smartphone and conventional detector

Table 3. Determination of elements of interest in real samples using flame photometer with smartphone and conventional detectors

Element/Sample	Sample Code	Content in Solution Sample (mg L^{-1})		t value[a]	
		Smartphone	Conventional Detector	$t_{observed}$	$t_{critical}$
Na/fish sauce	FS1	5.3(±0.3)*	4.7(±0.1)*	0.59	4.30
	FS2	2.0(±0.2)**	2.0(±0.2)**		
	FS3	6.0(±0.2)*	5.2(±0.2)*		
Ba/wastewater	WT1	0.6(±0.1)	0.4(±0.1)	0.85	12.7
	WT2	0.8(±0.1)	0.9(±0.1)		
Li/water leaching battery	LBW1	2.0(±0.2)**	2.2(±0.1)**	0.35	3.15
	LBW2	2.0(±0.1)**	2.0(±0.1)**		
	LBW3	3.0(±0.2)**	2.2(±0.1)**		
	LBW4	3.0(±0.1)**	2.9(±0.1)**		
K/fertilizer	FZ1	10.0(±0.3)*	10.0(±0.1)*	0.42	12.7
	FZ2	9.0(±0.5)*	8.0(±0.5)*		
Ca/milk	MK1	8.0(±0.3)*	7.7(±0.3)*	0.38	2.78
	MK2	5.0(±0.1)*	4.7(±0.2)*		
	MK3	5.0(±0.2)*	4.3(±0.2)*		
	MK4	6.0(±0.5)*	5.1(±0.3)*		
	MK5	4.0(±0.1)*	3.7(±0.1)*		

[a]95% confidence limit, With dilution: *10-folds, **5-folds

Conclusion

The use of an everyday life camera with image processing as alternative of detection in a flame photometer has been investigated for the assays of Na, K, Ca, Ba, and Li. The cameras were DSLR and smartphone. Using a smartphone which is commonly available together with available applications offers all operations to be done within the smartphone device, including evaluation and report. Application to real samples has been demonstrated.

Acknowledgement

The TRF Distinguished Research Professor Award Grant (DPG6080002 to Kate Grudpan), Chiang Mai University (through the Center of Excellence for Innovation in Analytical Science and Technology (I-ANALY-S-T) and the Graduate School) and Lampang Rajabhat University are acknowledged. Thanks are due to Dr. Kanokwan Kiwfo for her help in manuscript preparation, and Prof. Gary Christian for editing the manuscript.

References

1. Almeida, M. I. G. S., Segundo, M. A., Lima, J. L. F. C. and Rangel, A. O. S. S. (2008). Direct introduction of slurry samples in multi-syringe flow injection analysis: Determination of potassium in plant samples. *Analytical Sciences*, 24: 601-606.
2. Rangel, A. O. S. S., and Toth, I. V. (1996). Flow injection sequential speciation of free and total potassium in fortified wines. *Analytical Sciences*, 12: 887-891.
3. Lima, J. L. F. C. A., Rangel, O. S. S. and Souto, M. R. S. (1996). Simultaneous determination of potassium and sodium in vegetables by flame emission spectrometry using a flow-injection system with two dialysis units. *Analytical Sciences*, 12: 81-85.
4. Barros, A. I., Oliveira, A. P. M., Magalhaes, R. L., and Villa, R. D. (2012). Determination of sodium and potassium in biodiesel by flame atomic emission spectrometry. *Fuel*, 93: 381-384.
5. Castanheira, I., Figueiredo, C., Andre, C., Coelho, I., Silva, A. T., Santiago, S., Fontes, T., Mota, C., and Calhau, M. A. (2009). Sampling of bread for added sodium as determined by flame photometry. *Food Chemistry,* 113: 621-628.
6. Ferreira, I. M. P. L. V. O., Lima, J. L. F. C. and Rangel, A.O. S. S. (1994). Flow injection sequential determination of chloride by potentiometry and sodium by flame emission spectrometry in instant soups. *Analytical Sciences*, 10: 801-805.
7. Wen, G. H., (2002). Spectrophotometric determination of trace amounts of calcium using the calcium complex with alizarin. *Journal of the Brazilian Chemical Society*, 13:78-81.
8. Nakashima, K., Muraki K., Nakatsuji, S. and Akiyama, S. (1989). Coloration reaction of a crowned 2,4-dinitrophenylazophenol-barium(II) complex with amines and its application to flow injection spectrophotometry. *Analyst*, 114: 501-504.
9. Wu, Y. P. and Pacey, G. E. (1984). Spectrophotometric determination of lithium ion with the chromogenic crown ether, 2",4"-dinitro-6"-trifluoromethylphenyl-4-0-aminobenzo-14-crown-4. *Analytica Chimica Acta*, 162: 285-291.
10. Nazarenko, A. Y. (2004). Educational multiwavelength atomic emission spectrometer. *Spectrocscopy. Letters*, 37(3): 235-243.
11. Bright, R. M., Momoh, P. O., Bozeman, A. D., Seney, C. S. and Sinclair, K. V. (2005). Development of a multiple-element flame emission spectrometer using CCD detection. *Journal of Chemical Education*, 82(12): 1826-1830.
12. Debus, B., Kirsanov, D., Yaroshenkoab, I., and Leginab, A., (2017). A simple design atomic emission spectrometer combined with multivariate image analysis for the determination of sodium content in urine. *Analytical Methods*, 9: 3237-3243.
13. Lyra, W. S., Santos, V. B., Dionízio, A. G. G., Martins, V. L., Almeida, L.F., Gaião, E. N. P., Dias Diniz, E. H. G., Silva, C. and Araújo, M. C. U., (2009). Digital image-based flame emission spectrometry. *Talanta*, 77: 1584-1589.

14. Lyra, W. S., Sanches, F. A. C., Cunha, F. A. S., Diniz, P. H. G. D., Lemos, S.G., Silva, E. C. and Araujo, M.C.U. (2011). Indirect determination of sodium 224 diclofenac, sodium dipyrone and calcium gluconate in injection drugs using digital image-based (webcam) flame emission. *Analytical Methods*, 3: 1975-1980.
15. Moraes, E. P., Silva, N. S. A., Morais, C. L. M., Neves, L. S. and Lima, K. M. G. J. (2014). Low-cost method for quantifying sodium in coconut water and seawater for the undergraduate analytical chemistry laboratory: Flame test, a mobile phone camera, and image processing. *Journal of Chemical Education,* 91(11): 1958-1960.
16. Christian, G. D., Dasgupta, P. K. and Schug, K. A. (2014). Analytical Chemistry. Wiley, New York: pp. 84-105.

Malaysian Journal of Analytical Sciences (MJAS)
Published by Malaysian Analytical Sciences Society

OPTIMISATION AND VALIDATION OF ULTRAHIGH PERFORMANCE LIQUID CHROMATOGRAPHY METHOD FOR QUANTIFICATION OF 25-HYDROXYVITAMIN D IN MATERNAL PLASMA

(Pengoptimuman dan Pengesahan Kaedah Kromatografi Cecair Berprestasi Ultra Tinggi untuk Kuantifikasi 25-hidroksivitamin dalam Plasma Ibu Mengandung)

Siew Siew Lee and Su Peng Loh*

Department of Nutrition,
Universiti Putra Malaysia, 43400 UPM Serdang, Selangor, Malaysia

**Corresponding author: sploh@upm.edu.my*

Received: 19 August 2020; Accepted: 25 October 2020; Published: 10 December 2020

Abstract

This study aimed to optimise and validate a simple and efficient sample preparation and extraction method for the quantification of 25-hydroxyvitamin D (25OHD) in the maternal plasma sample. Different sample preparation methods and precipitation reagent-to sample ratio used by previous studies were compared. An ultrahigh performance liquid chromatography method was developed and validated for simultaneous quantification of $25OHD_2$ and $25OHD_3$. The chromatographic separation was achieved using the COSMOCORE 2.6Cholester Column and methanol and 0.1% formic acid (79:21, %v/v) as mobile phase at a flow rate of 0.3 mL/min and diode array detection at 264 nm. The results demonstrated that a recovery of approximately 100% could be achieved by extracting samples using 1 mL of hexane, vortex for 10s and a total number of three extraction steps. The precipitation reagent-to-sample ratio of 2.8 was optimum for the quantification of $25OHD_2$ and $25OHD_3$ in a pooled maternal sample. The value obtained for validation parameters meets the criteria of the Recommendations and Acceptance Criteria for Bioanalytical Method Validation by the Food and Drug Administration. The results showed that this method could be applied for routine quantification of 25OHD, particularly in the maternal plasma sample.

Keywords: 25-hydroxyvitamin D, maternal, ultrahigh performance liquid chromatography, extraction

Abstrak

Kajian ini bertujuan mengoptimumkan dan mengesahkan kaedah penyediaan dan pengekstrakan yang mudah dan cekap untuk pengkuantitian 25-hidroksivitamin D (25OHD) di dalam sampel plasma ibu mengandung. Kaedah kromatografi cecair berprestasi ultra tinggi telah dibangunkan dan disahkan untuk pengkuantitian $25OHD_2$ and $25OHD_3$ secara serentak. Pemisahan kromatografi telah dicapai melalui turus COSMOCORE 2.6Cholester dan metanol: 0.1% asid formik (79:21, %v/v) sebagai fasa bergerak pada kadar aliran 0.3 mL/min dan pengesahan susunan diod pada 264 nm. Keputusan kajian menunjukkan bahawa kaedah pengekstrakan terbaik yang memberi kadar pemulihan yang hampir dengan 100% adalah mengekstrak sampel dengan menggunakan 1mL heksana, vorteks selama 10 s dan sejumlah 3 kali bagi langkah pengekstrakan. Kadar reagen pemendakan kepada sampel sebanyak 2.8 adalah optimum bagi pengekstrakan $25OHD_2$ dan $25OHD_3$ dalam sampel plasma ibu mengandung. Nilai yang diperolehi untuk parameter validasi adalah memenuhi kriteria cadangan dan kriteria penerimaan untuk pengesahan kaedah bioanalitikal oleh

pentadbiran makanan dan ubat-ubatan (FDA). Hasil kajian menunjukkan bahawa kaedah yang diperolehi boleh diguna untuk rutin pengkuantitian 25OHD dalam sampel plasma, terutamanya sampel plasma dari ibu mengandung.

Kata kunci: 25-hidroksivitamin D, ibu mengandung, kromatografi cecair berprestasi ultra tinggi, pengekstrakan

Introduction

It is generally agreed that 25-hydroxyvitamin D (25OHD) is the biomarker that best reflects total vitamin D exposure-from food, supplement and skin synthesis [1, 2]. There are a variety of assays available for measuring serum or plasma 25OHD. These assays can be categorized into two method types: antibody-based methods (immunoassays) and liquid-chromatography (LC)-based methods. The strengths and weaknesses of each assay have been widely discussed in previous literature [3].

The complex nature of the biological matrix makes the development of assays for the quantification of blood 25OHD challenging. In the circulation, 25OHD is tightly bound to vitamin D binding protein (VDBP) [4]. Hence, the complete dissociation of 25OHD from VDBP in the blood sample before analysis is crucial to ensure accurate quantification of total 25OHD [5]. The complete dissociation of 25OHD is concerned in the blood sample from pregnant women as pregnancy is characterized by a two- to three-fold increase in VDBP [6-8]. Previous studies have reported the inaccuracy of measuring total 25OHD via automated immunoassay in populations with different levels of VDBP [9-11]. In automated immunoassays, releasing agents, which are proprietary, were used to release 25OHD from VDBP [3]. These releasing reagents may not be as good as the organic solvent in terms of their ability to dissociate 25OHD from VDBP. The incomplete dissociation of 25OHD from the VDBP could be a source of high variability between automated immunoassays and LC-based methods [5].

The complete dissociation of 25OHD from VDBP is also important for extraction-based assays such as LC-based methods. In previously published LC-based methods, different extraction methods have been used. The differences in terms of type and volume of solvent were used for protein precipitation and extraction as well as the duration of extractions. In an investigation of the consequences of differential extraction characteristics to the quantification of 25OHD in the serum sample, Lankes et al. found that the extracted concentration of 25OHD varied with the 70% methanol-to-sample ratio and the sample-to-hexane ratio used [12]. These could be a source of interlaboratory variability and bias of 25OHD results in LC-based methods. No previous study has investigated the consequences of differential extraction methods in the blood sample from pregnant women, which has high VDBP levels. Therefore, this study aimed to optimize a simple and efficient sample preparation and extraction method for the quantification of 25OHD in maternal plasma sample. Then, this study reports a validated ultrahigh performance liquid chromatography diode array (UHPLC-DAD) detection method for the routine measurement of plasma 25OHD using the optimised method.

Materials and Methods

Reagents and chemicals

25-hydroxyvitamin D_2, 25-hydroxyvitamin D_3, Dodecanophenone (98%) and phosphate-buffered saline (PBS) tablet were purchased from Sigma-Aldrich. Bovine serum albumin (BSA) was purchased from Nacalai Tesque (Kyoto, Japan). HPLC grade methanol (MeOH) was from JT Baker (Phillipsburg, NJ, USA). HPLC grade-water, ethanol and hexane were from Fisher Scientific Ltd. (Loughborough, UK).

Instrument

UHPLC analysis was conducted on the Agilent 1290 Infinity liquid chromatography system (Agilent Technologies, Wilmington, DE, USA), which comprised of a binary pump, autosampler, and column thermostat, coupled to a Diode Array Detector (DAD). A COSMOCORE 2.6Cholester Column (2.1 mm ID × 150 mm, 2.6 µm particle size) (Nacalai Tesque, Kyoto, Japan) was used. The column was protected by using a 2.1 mm UPLC C_{18} SecurityGuard ULTRA guard cartridge (Phenomenex, Torrance, CA, USA). The

injection volume was 20 µL, and the column temperature was maintained at 50 °C. ChemStation (Agilent Technologies, Wilmington, DE, USA) was used for system control, data acquisition, and processing.

Preparation of reagents, standards, calibration solution and quality control materials

Individual calibrator stock solution of $25OHD_3$ and $25OHD_2$ was prepared at 25 µmol/L in ethanol and stored in 2 mL glass vial at -20 °C. The concentrations of each calibrator stock solution were confirmed by measuring the absorbance (AU) of each stock solution at 264 nm (UV-1800 UV-VIS Spectrophotometer, Shimadzu, Kyoto, Japan).

From the calibrator stock solutions, a combined stock solution of $25OHD_2$ and $25OHD_3$ at 5,000 nmol/L was prepared. Then, six calibrators in the range from 12.5 to 200 nmol/L were prepared by spiking the combined stock solution into 4% BSA in PBS. Each of the calibrators was prepared freshly at the beginning of each run. Working internal standard (IS), dodecanophenone was prepared at 2,000 ng/mL in 80% of methanol, which was stored in 2 mL glass vial at -20 °C.

Optimisation of chromatographic conditions

The chromatographic conditions and mobile phase composition suggested by the manufacturer (Nacalai Tesque, Kyoto, Japan) were used: isocratic elution with methanol and 0.1% formic acid (80:20, v/v) as mobile phase, run at a flow rate of 0.4 mL/min and column temperature of 50 °C. The chromatographic conditions, which include flow rate, column temperature, and mobile phase composition, were subsequently optimised to give better resolution, peak shape and retention time for the plasma sample.

Extraction procedure

Five different sample extraction methods (methods A-E) modified from previous studies [13-15] were compared at 25OHD concentration at the medium concentration (80 nmol/L). The percent recoveries of both 25OHD were calculated and presented as mean recover ± standard deviation (SD) and percent of the coefficient of variation (CV).

Optimisation of the volume of precipitation reagent

The precipitation reagent contained methanol and 0.2M of $ZnSO_4$ (70:30, v/v). The different volume of precipitation reagents (700-2,100 µL) was tested using the pooled maternal sample collected for our cross-sectional study to determine vitamin D status among pregnant women. Maternal plasma was prepared by centrifuge maternal blood at 3,500 rpm and 4 °C for 15 minutes using Kubota 2810 Centrifuge (Tokyo, Japan). Plasma from 20 respondents was pooled. The pooled maternal sample was spiked with $25OHD_2$ standard because the pooled plasma had a very low concentration of $25OHD_2$.

Sample preparation

For sample extraction, 500 µL of plasma sample or calibrator was pipetted into a 13 × 100 mm glass tube. Fifty microliters of a working IS solution was added, and the tube was vortexed for 5 s. Next, 1,400 µL of precipitation reagent was added into each tube, and the tube was allowed vortex mixing. The mixture was extracted with 1 mL of hexane by vigorous mixing using a multi-tube vortexer for 10 sand then centrifuged at 3,000 rpm for 5 minutes. The extraction process was repeated for a total of 3 extraction steps. The hexane layer (supernatant) from each tube was transferred and pooled into another 13 × 100 mm glass tubes and dried under nitrogen gas flow. The dry extract was reconstituted with 120 µL of 79 % methanol and mixed for 10 s. The samples were transferred into a sample vial with a vial insert. Twenty microliters were injected into the UHPLC system for analysis.

Method validations

The guidelines by the US Department of Health Human Services Food and Drug Administration [16] and ICH Expert Working Group [17] were used for validating this method. Three replicates of blank (4% BSA) and blank spiked with 25OHD and IS were analyzed. Chromatograms were examined for possible chromatographic interference from 25OHD.

Linearity was evaluated by constructing a six-point (concentrations) calibration curve over the range of 12.5-200 nmol/L. The peak area ratios of 25OHD relative to IS were plotted against the corresponding

concentrations. The curve was not forced through zero. The correlation coefficient (r^2), y-intercept and slope of the calibration curve were reported.

The limit of detection (LOD) and limit of quantification (LOQ) were calculated based on the calibration curve according to the following formulas of Equations 1 and 2 [15], respectively.

$$LOD = 3.3 \times (SD/m) \quad (1)$$

$$LOQ = 10 \times (SD/m) \quad (2)$$

where SD corresponds to the standard deviation of response (y-value) and m corresponds to the slope of the calibration curve.

The recovery of the sample preparation method for $25OHD_2$ and $25OHD_3$ was evaluated at three concentrations (40, 80, and 160 nmol/L for low, medium and high concentrations, respectively). These samples were prepared by spiking an appropriate volume of standard solution into 4% BSA before sample extraction (pre-spiked sample) and after sample extraction (post-spiked sample). Three replicates at each concentration were assayed. The recovery was calculated by comparing the area of the pre-spiked sample to the area of the post-extracted spiked sample (Equation 3).

$$\% \text{ Recovery} = \frac{\text{Peak area of the pre-spiked sample}}{\text{Peak area of the post-spike sample}} \times 100\% \quad (3)$$

Intra-day precision was determined by extracting and analyzing three replicates of each calibrator in the calibration curve (12.5-200 nmol/L) one run. By contrast, the inter-day precision was determined by extracting and analyzing each calibrator (12.5-200 nmol/L) in triplicates in three different days. Results were expressed as CV and percent bias for intra-and inter-day precision and accuracy, respectively. The accuracy of the method was further evaluated using the Tri-level of serum control, purchased from the UTAK Laboratories, Inc. (Valencia, CA, USA). Each level was evaluated in five replicates. Our measured values were compared with the target values provided by the manufacturer and expressed in percent.

Two levels of serum control from UTAK, Vitamin D plus Low and Vitamin D Plus Level 2 were used to evaluate post-extraction stability. After extracting the control sample, the sample was subjected to injection (0 hour) into the system for analysis. After the first injection (0 hour), sample vials were stored at -20 °C. After 18 hours, sample vials were subjected to the second injection and stored again at -20 °C. The vials were subjected for the third injection after 120 hours. The stability was calculated by comparing the peak area ratio of the sample at 18 hours (or 120 hours) with the respective peak area ratio of the sample at 0 hour.

Results and Discussion

Optimisation of chromatographic conditions

Under the chromatographic conditions suggested by the manufacturer [isocratic elution with methanol and 0.1% formic acid (80:20, v/v) as mobile phase, run at a flow rate of 0.4 mL/min and column temperature of 50 °C], $25OHD_2$ and $25OHD_3$ were separated well from each other in standard dissolved in the mobile phase and BSA but not in the pooled maternal plasma sample. Then, different ratios of methanol and 0.1% formic acid, flow rate, column temperature, and gradient elution systems were considered.

It was found that as the ratios of water in the mobile phase increased (from 20% to 21-25%), the resolution for $25OHD_2$ and $25OHD_3$ was improved, but the analytes were eluted late. Thus, the peak appeared to be broad and showed reduced sensitivity because of the reduced peak height. Given that an increase in the ratio of water could compromise the peak shape, a ratio of methanol to 0.1% formic of 79:21 (%v/v) was chosen, which produced an acceptable separation time and resolution.

The effects of flow rate and column temperature were also investigated. Different mobile phase flow rates (0.1 to 0.4 mL/min) and column temperature (40-55 °C) showed no differences in the resolution of $25OHD_2$ and $25OHD_3$ visually. As the flow rate decreased, the retention times also increased, and the peak would be broad. However, as the flow rate increased, the column backpressure also increased. Thus, a flow rate of 0.3 mL/min and a column temperature of 50 °C were used,

which produced an acceptable retention time and column backpressure.

Hence, the optimum chromatographic condition for $25OHD_2$ and $25OHD_3$ in BSA and pooled maternal sample were mobile phase composition, methanol: water of 79:21 (% v:v); column temperature, 50 °C; and flow rate, 0.3 mL/min. Under this condition, the retention times for $25OHD_3$, $25OHD_2$, and IS were 8.4, 9.2, and 16.4 minutes. The total run time was 18 minutes (Figure 1).

Optimisation of the extraction procedure

Liquid-liquid extraction (LLE) and solid-phase extraction (SPE) are two common methods used to extract 25OHD from plasma or serum. Previous studies have demonstrated that SPE was efficient in removing the interferences compounds [18-20]. However, the SPE column is expensive and required extensive optimisation. With an optimum downstream analysis, interferences compounds in the LLE sample are still can be resolute from the analyte of interest. Thus, LLE is still a preference and has been used in recent candidate reference measurement procedures (RMPs) [21, 22] and Centres for Disease Control and Prevention (CDC) refined method to access serum 25OHD.

In LLE, hexane, a non-polar solvent, is frequently used in published methods [5, 14, 15, 23, 24]. However, the volume of non-polar solvent, the total number of extraction steps and the time mixing (vortexing) varied from study to study. The volume of hexane used ranged from 1-5 mL [14, 15, 23, 24]. The total number of extraction steps is two to three times. The time of mixing ranged from 10 s to 3 minutes [13-15, 24]. Nevertheless, most studies mixed for 1 minute [13-15, 24]. These studies reported a satisfactory recovery for sample extraction, optimised an extraction method that provides good recovery, and used a minimum amount of solvent; thus, lesser time and cost spent are important.

In this study, we tested the four combinations of these extraction characteristics. The results revealed that the increase in the total number of extraction steps, from two to three times increased the recovery (Table 1). There was no significant difference in the recovery for increasing the volume of hexane used and time of mixing. The recovery of 25OHD was significantly lower when LLE was conducted twice (method A) compared to a total of three times (method B). This may indicate incomplete extraction of 25OHD from the plasma sample if the sample was extracted twice. The volume of hexane used and the time of vortex did not affect the recovery of 25OHD. The recovery of approximately 100% and satisfactory of % of CV (80-120%) can be achieved by using 1 mL of hexane, vortex for 10 s and a total number of three extraction steps. These extraction characteristics were subsequently applied to all optimisation and validation experiments.

Optimisation of the volume of precipitation reagent

In the previous published methods, precipitation reagent that was frequently used to dissociate and precipitate protein in plasma included ethanol [26, 27], acetonitrile [19, 28, 29], 70% methanol [13], methanol-2-propanol (80:20 v/v) [14, 24, 25] and zinc sulphate [30]. Before our experiment, we have tried a number of these precipitation reagents. We found that the use of methanol, ethanol or 70% methanol would make the reconstitute sample (sample before injecting into the system) very cloudy, which cannot be filtered by syringe filter nor precipitate by centrifugation. The use of acetonitrile would cause the “balling” of protein which would affect the recovery of 25OHD metabolites. We found that precipitation reagent contained methanol and 0.2M of ZnSO4 (70:30, v/v) was best for the sample (plasma).

In the absence of precipitation reagent, no $25OHD_3$ and $25OHD_2$ are detected and quantified (Table 2). This observation indicated the importance of precipitation reagent in releasing 25OHD from binding protein. Our results showed differential in precipitation reagent-to-sample-ratio affect the extracted $25OHD_2$ but not $25OHD_3$. As indicated in the values of 25OHD calculated based on the area under the peak, the use of 2,100 µL of PP reagent reduced the extracted $25OHD_2$. However, the increase in the volume of precipitation did not increase the extracted $25OHD_3$. Likewise, the differential in precipitation agent-to-sample-ratio also affects the quantification of the IS. This finding suggested the binding of IS (dodecanophenone) with

plasma protein. Overall, the results appeared that precipitation reagent-to-sample ratio of 2.8 is optimum for quantification of $25OHD_2$ and $25OHD_3$ based on peak area ratio. This finding is in agreement with the finding from Lankes et al. [12].

Method Validation

The chromatogram showed that there was no other interference at the retention time of $25OHD_2$, $25OHD_3$ and IS (Figure 2). BSA is suitable to be used as a matrix for calibrator.

The linearity of the method was evaluated in the concentration range from 12.5 to 200 nmol/L. The range was chosen based on the range of 25OHD in human plasma reported in previous studies. Table 3 shows the regression analysis of the 25OHD calibration curve. The calibration curves were linear over the concentration of 12.5-200 nmol/L with a correlation coefficient of 0.99 for both $25OHD_3$ and $25OHD_2$. The calculated LOQ and LOD for $25OHD_3$ were 11.25 nmol/L and 3.75 nmol/L, respectively. The LOQ and LOD for $25OHD_2$ were 10.25 and 3.25 nmol/L, respectively. The results were consistent with precision and accuracy results wherein the lowest concentration on the calibration curve of 12.5 nmol/L showed acceptable precision and accuracy limit, CV < 20% and accuracy ±20% of nominal concentration (Table 4).

The recovery of 25OHD was evaluated to determine the efficiency and reproducibility of the extraction method. Table 5 shows the recovery of 25OHD in a 4% BSA spiked sample. Satisfactory recovery was achieved with all mean recovery values were within ± 20% of 100%. The recovery was consistent and reproducible, which the % CV all recovery tests were <10%.

According to the FDA guidelines, acceptance criteria for precision and accuracy were CV ≤ 15%, bias = ± 15% of nominal concentrations. However, CV < 20% and bias = ± 20% for calibrator at LOQ concentration are acceptable. The Table 4 presents the inter- and intra-day precision and accuracy data. For $25OHD_3$, the intra-day CV ranged from 2.5% to 6.4% and the inter-day CV ranged from 1.8% to 10.5%. For $25OHD_2$, the intra-day CV ranged from 0.4% to 13.0%, and the inter-day CV ranged from 1.3% to 7.3%. The % of bias for both $25OHD_3$ and $25OHD_2$ was < 8% for all concentrations except for 12.5 nmol/L. The % of bias for both analytes was < 16%. The precision and accuracy of the method in this study were satisfactory. These results were consistent with the accuracy results obtained using commercial serum control (Table 6). The accuracy was approximately 91% to 99% for $25OHD_3$ and 82% to 87% for $25OHD_2$. These ranges were acceptable as they were within ± 20% of the target value provided by the manufacturer.

Table 7 shows the stability of extracted 25OHD after storing at −20°C for 18 and 120 hours. The stability ranged from 94.6% ± 1.2 % to 103.7% ± 9.4%, indicating that the extracted $25OHD_3$ and $25OHD_2$ were stable at least up to 120 hours when stored at -20 °C.

Overall, the optimised method showed satisfactory recovery, precision and accuracy. The method appeared to meet with the Recommendations and Acceptance Criteria for Bioanalytical Method Validation by the US Department of Health Human Services Food and Drug Administration [16]. The LOD and LOQ of our method are comparable with those of the published HPLC method [15, 24, 28] and with other automated immunoassays [5]. Although the LOD and LOQ of our method by our present method were higher compared with LC-MS/MS method [31, 32], this value still enable us to classify individuals with vitamin D deficiency defined as 25OHD < 25 nmol/L [1].

Strengths and limitations

Recently, a C3-epimer of $25OHD_3$ (3-epi-$25OHD_3$) has been highlighted to the confound quantification of total 25OHD [33-35]. In addition, 3-epi-$25OHD_3$ was found to contribute to approximately 6% in maternal [34, 36]. The biological significance of 3-epi-$25OHD_3$ is uncertain. The separate measurement of 3-epi-$25OHD_3$ is important to understand the biological role of the C3-epimer further. LC-MS/MS method with a specific column has been developed for separation of $25OHD_3$ from 3-epi-$25OHD_3$. However, we acknowledged our inability to separate and quantify C-3 epimers in our method as a limitation. However, this limitation does not defeat the validity of the assay.

Notably, LC-MS/MS may not be available and affordable to laboratories in developing countries. Moreover, LC-MS/MS requires highly trained operators to operate the instruments and significant instrument maintenance, which further increases the cost of the test [5]. A vitamin D assay capable of yielding accurate and reproducible results is sufficient for routine measurement of plasma 25OHD. The developed method uses low volumes of extraction solvent and time; therefore, it can be used to measure plasma 25OHD, particularly in laboratories that cannot afford to have an LC-MS/MS system. Many methods have been developed and validated previously. However, one critical aspect related to the extraction of 25OHD, particularly, in the maternal sample, which is high in VDBP was overlooked. The optimized method will be used as a reference in future studies. The effects of high VDBP will be further evaluated for an LC-based system that used MS as a detector.

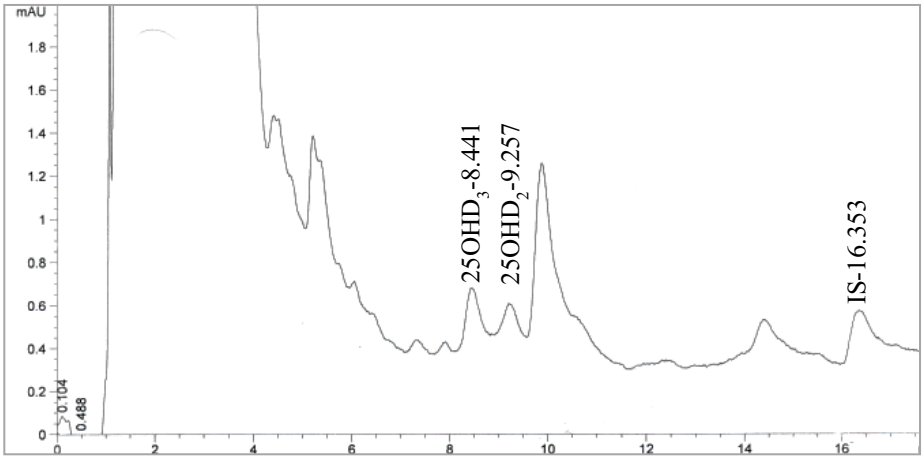


Figure 1. Representative UHPLC-chromatogram of pooled maternal sample spiked with $25OHD_2$

Table 1. Recovery of 25OHD by different extraction method

Method	Volume of Hexane (mL)	Time Vortex	Times of Extract	$25OHD_3$		$25OHD_2$	
				Recovery, %[a]	CV, %	Recovery, %[a]	CV, %
A	1	10 s	2	79.2 ± 8.6*	10.9	87.1 ± 7.8*	9.0
B	1	10s	3	99.2 ± 6.1†	6.1	100.6 ± 5.5*	5.5
C	1	3 min	3	89.2 ± 7.6*†	8.5	93.0 ± 6.6*	7.1
D	2	10s	3	100.6 ± 5.8†	5.8	99.2 ± 14.0*	14.1
E	2	3 min	3	93.6 ± 0.5†	0.53	94.4 ± 2.8*	3.0

[a] Mean followed by a different symbol within the same column indicate a significant difference (p <0.05)

Table 2. Differential in mean extracted 25OHD concentration (nmol/L) in the pooled maternal sample with different volume of precipitation reagents

Volume of Precipitation Reagent (µL)	25OHD$_3$ Concentration (nmol/L)		25OHD$_2$ Concentration (nmol/L)	
	Based on the Area[a]	Based on IS[a]	Based on the Area[a]	Based on IS[a]
0	0*	0*	0*	0*
700	31.0 ± 2.0†	45.6 ± 7.7†	20.9 ± 1.1†	36.4 ± 8.7†
1400	31.0 ± 1.0†	31.6 ± 1.9‡	20.8 ± 0.4†	23.2 ± 1.1†
2100	29.3 ± 0.6†	27.3 ± 1.5‡	17.7 ±0.6‡	17.6 ± 1.4‡

[a] Mean followed by a different symbol within the same column indicate a significant difference (p <0.05)

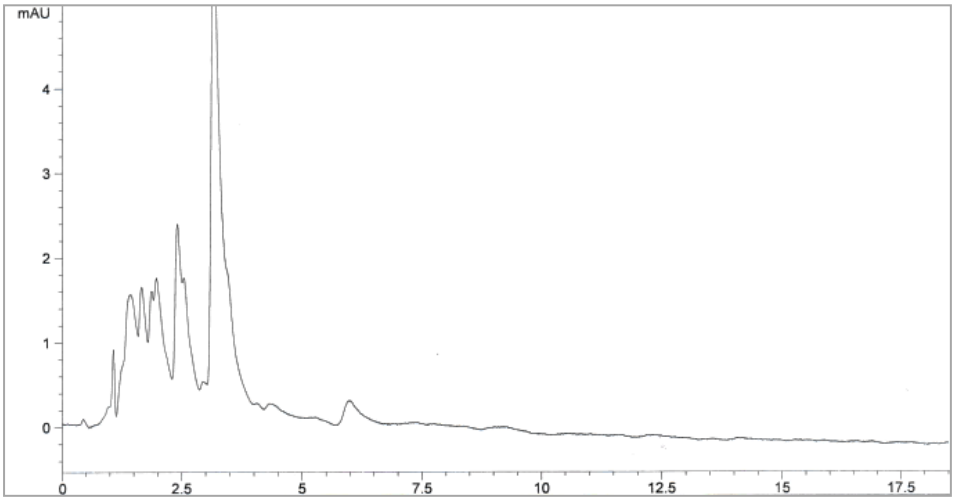


Figure 2. Representative UHPLC-chromatogram of a blank sample (4% BSA in PBS)

Table 3. Regression analysis of 25OHD calibration curve

Parameters	25OHD$_3$	25OHD$_2$
Number of concentrations per curve	6	6
Regression equation	y=0.015x + 0.027	y=0.017+ 0.053
Mean slope SD	0.015 ± 0.003	0.017 ± 0.002
Mean intercept SD	0.027 ± 0.007	0.0578 ± 0.007
Mean regression coefficient SD	0.991 ± 0.0012	0.993 ± 0.005
Limit of detection (LOD) (nmol/L)	3.75	3.25
Limit of quantification (LOQ) (nmol/L)	11.25	10.25

Table 4. Inter-intraday precision in standard

Nominal Concentrations (nmol/L)	**25OHD$_3$**				**25OHD$_2$**			
	Mean	**SD**	**CV, %**	**Bias, %**	**Mean**	**SD**	**CV, %**	**Bias, %**
Intra-day								
12.5	11.25	0.23	5.11	-9.94	13.05	0.68	13.0	4.45
25	25.10	0.64	6.35	0.40	26.93	0.57	5.28	7.7
50	46.35	0.85	4.56	-7.30	51.13	1.44	7.04	2.25
100	94.15	1.19	3.17	-5.86	93.0	0.28	0.74	-7.03
150	159.03	1.58	2.48	6.02	148.13	0.92	1.56	-1.26
200	195.95	2.07	2.64	-2.02	203.88	0.31	0.38	1.94
Inter-day								
12.5	14.40	0.61	10.54	15.26	13.63	0.35	6.5	8.96
25	25.50	0.18	1.74	1.97	26.4	0.77	7.27	5.63
50	48.35	1.10	5.68	-3.28	50.9	1.39	6.82	1.78
100	94.95	0.69	1.82	-5.06	97.23	1.47	3.79	-2.77
150	152.15	3.36	5.52	1.44	146.63	2.58	4.39	-2.24
200	200.43	1.85	2.31	0.22	203.15	1.05	1.29	1.57

Table 5. Recovery of 25OHD in 4% BSA spiked sample

Nominal Concentrations (nmol/L)	**Mean Recovery, %**	**CV, %**
25OHD$_3$		
40	85.8 ± 1.7	2.0
80	99.7 ± 5.2	5.2
160	89.1 ± 6.2	7.0
25OHD$_2$		
40	84.4 ± 2.1	2.5
80	100.2 ± 3.9	4.0
160	91.9 ± 5.9	6.4

Table 6. Validation of method with the commercial serum control at three concentration levels (n = 5)

	Target Value (nmol/L)	Measured Value (nmol/L)	Accuracy, %	CV, %
25OHD$_3$				
Level low	25	22.8 ± 1.5	90.9	5.5
Level L1	75	74.3 ± 4.0	99.0	5.2
Level L2	182.5	169.5± 4.5	92.9	2.5
25OHD$_2$				
Level low	25	21.8 ± 1.3	87.1	6.0
Level L1	75	64.0 ± 2.5	85.4	4.0
Level L2	182.5	149.5± 8.0	81.9	4.4

Table 7. Stability of 25OHD in commercial serum control

	18 hours		120 hours	
	Mean	SD	Mean	SD
25OHD$_3$				
Level low	100.4	0.7	103.5	3.2
Level L2	99.9	0.5	99.3	0.2
25OHD$_2$				
Level low	101.9	5.7	103.7	9.4
Level L2	97.8	1.5	94.6	1.2

Conclusion

In conclusion, it is important to optimise extraction and protein denaturation (or precipitation) procedure in the LC-based assay, particularly in the maternal sample, which is high in binding protein. Future studies on developing and applying methods for quantification of plasma sample, particularly maternal sample, should consider the type and volume of precipitation as well as the total number of extractions. We have developed a UHPLC-DAD method that was simple, rapid, and cost-effective. It provides good recovery and satisfactory reliability and accuracy, and is suitable to be applied to routine quantification of 25OHD, particularly in laboratories that cannot afford to have an LC-MS/MS system.

References

1. Institute of Medicine. (2011). Dietary Reference Intakes for Calcium and Vitamin D. The National Academies Press, Washington, DC: pp. 96.
2. Scientific Advisory Committee on Nutrition (2016). SACN vitamin D and Health report. https://www.gov.uk/government/publications/sacn-vitamin-d-and-health-report. [Access online 20 January 2019].
3. Wallace, A. M., Gibson, S., de la Hunty, A., Lamberg-Allardt, C. and Ashwell, M. (2010). Measurement of 25-hydroxyvitamin D in the clinical laboratory: Current procedures, performance characteristics and limitations. *Steroids*, 75(7): 477-488.

4. Bikle, D., Gee, E., Halloran, B., Kowalski, M. A., Ryzen, E. and Haddad, J. G. (1986). Assessment of the free fraction of 25-hydroxyvitamin D in serum and its regulation by albumin and the vitamin D-binding protein. *The Journal of Clinical Endocrinology & Metabolism*, 63(4): 954-959.
5. Le Goff, C., Cavalier, E., Souberbielle, J. C., Gonzalez-Antuna, A. and Delvin, E. (2015). Measurement of circulating 25-hydroxyvitamin D: A historical review. *Practical Laboratory Medicine*, 2: 1-14.
6. Bikle, D. D., Gee, E., Halloran, B. and Haddad, J. G. (1984). Free 1,25-dihydroxyvitamin D levels in serum from normal subjects, pregnant subjects, and subjects with liver disease. *The Journal of Clinical Investigation*, 74(6): 1966-1971.
7. van Hoof, H. J., de Sevaux, R. G. and van Baelen, H. (2001). Relationship between free and total 1,25-dihydroxyvitamin D in conditions of modified binding. *European Journal of Endocrinology*, 144(4): 391 – 396.
8. Jones, K. S., Assar, S., Prentice, A. and Schoenmakers, I. (2016). Vitamin D expenditure is not altered in pregnancy and lactation despite changes in vitamin D metabolite concentrations. *Scientific Reports*, 6, 26795.
9. Freeman, J., Wilson, K., Spears, R., Shalhoub, V. and Sibley, P. (2014). Influence of vitamin D binding protein on accuracy of 25-hydroxyvitamin D measurement using the ADVIA centaur Vitamin D total assay. *International Journal of Endocrinology*, 2014: 1-12.
10. Heijboer, A. C., Blankenstein, M. A., Kema, I. P. and Buijs, M. M. (2012). Accuracy of 6 routine 25-hydroxyvitamin D assays: Influence of Vitamin D binding protein concentration. *Clinical Chemistry*, 58(3): 543-548.
11. Cavalier, E., Wallace, A. M., Knox, S., Mistretta, V. I., Cormier, C. and Souberbielle, J. C. (2008). Serum vitamin D measurement may not reflect what you give to your patients. *Journal of Bone and Mineral Research*, 23(11): 1864-1865.
12. Lankes, U., Elder, P. A., Lewis, J. G. and George, P. (2015). Differential extraction of endogenous and exogenous 25-OH-vitamin D from serum makes the accurate quantification in liquid chromatography-tandem mass spectrometry assays challenging. *Annals of Clinical Biochemistry*, 52(Pt 1): 151-160.
13. Centers for Disease Control and Prevention (2010). Laboratory procedure manual; 25-hydroxyvitamin D3, 3-epi-25-hydroxyvitamin D3, 25-hydroxyvitamin D2. Access from https://wwwn.cdc.gov/Nchs/Data/Nhanes/2009-2010/LabMethods/VID_F_met_Vitamin_D.pdf. [Access 30 September 2018]
14. Turpeinen, U., Hohenthal, U. and Stenman, U. H. (2003). Determination of 25-hydroxyvitamin D in Serum by HPLC and Immunoassay. *Clinical chemistry*, 49(9): 1521 – 1524.
15. Chin, S. F., Osman, J. and Jamal, R. (2018). Simultaneous determination of 25-hydroxyvitamin D2 and 25-hydroxyvitamin D3 in human serum by ultra-performance liquid chromatography: An economical and validated method with bovine serum albumin. *Clinica Chimica Acta*, 485: 60-66.
16. US Department of Health Human Services Food and Drug Administration, Center for Drug Evaluation and Research, Center for Veterinary Medicine. (2001). Guidance for Industry: Bioanalytical method validation (Revised May 2018).
17. International Conference on Harmonization (ICH) of Technical Requirement for the Registration of Pharmaceuticals for Human Use. ICH Harmonised Tripartite Guideline: Validation of analytical procedures: text and methodology Q2 (R1).
18. Kand'ar, R. and Zakova, P. (2009). Determination of 25-hydroxyvitamin D3 in human plasma using HPLC with UV detection based on SPE sample preparation. *Journal of Separation Science*, 32(17): 2953-2957.
19. Chen, H., McCoy, L. F., Schleicher, R. L. and Pfeiffer, C. M. (2008). Measurement of 25-hydroxyvitamin D3 (25OHD3) and 25-hydroxyvitamin D2 (25OHD2) in human serum using liquid chromatography-tandem mass spectrometry and its comparison to a radioimmunoassay method. *Clinica Chimica Acta*, 391(1-2): 6-12.

20. Abu el Maaty, M. A., Hanafi, R. S., Aboul-Enein, H. Y. and Gad, M. Z. (2015). Design-of-experiment Approach for HPLC Analysis of 25-hydroxyvitamin D: A comparative assay with ELISA. *Journal of Chromatographic Science*, 53(1): 66-72.
21. Mineva, E. M., Schleicher, R. L., Chaudhary-Webb, M., Maw, K. L., Botelho, J. C., Vesper, H. W. and Pfeiffer, C. M. (2015). A candidate reference measurement procedure for quantifying serum concentrations of 25-hydroxyvitamin D(3) and 25-hydroxyvitamin D(2) using isotope-dilution liquid chromatography-tandem mass spectrometry. *Analytical and Bioanalytical Chemistry*, 407(19): 5615- 5624.
22. Stepman, H. C., Vanderroost, A., Van Uytfanghe, K. and Thienpont, L. M. (2011). Candidate reference measurement procedures for serum 25-hydroxyvitamin D3 and 25-hydroxyvitamin D2 by using isotope-dilution liquid chromatography-tandem mass spectrometry. *Clinical Chemistry*, 57(3): 441-448.
23. Hymoller, L. and Jensen, S. K. (2011). Vitamin D analysis in plasma by high performance liquid chromatography (HPLC) with C(30) reversed phase column and UV detection-easy and acetonitrile-free. *Journal of Chromatography. A*, 1218(14): 1835-1841.
24. Nurmi, T., Tuomainen, T. P., Virtanen, J., Mursu, J. and Voutilainen, S. (2013). High-performance liquid chromatography and coulometric electrode array detector in serum 25-hydroxyvitamin D(3) and 25-hydroxyvitamin d(2) analyses. *Analytical Biochemistry*, 435(1): 1-9.
25. Maunsell, Z., Wright, D. J. and Rainbow, S. J. (2005). Routine isotope-dilution liquid chromatography-tandem mass spectrometry assay for simultaneous measurement of the 25-hydroxy metabolites of vitamins D2 and D3. *Clinical Chemistry*, 51(9): 1683-1690.
26. Franke, A. A., Morrison, C. M., Custer, L. J., Li, X. and Lai, J. F. (2013). Simultaneous analysis of circulating 25-hydroxy-vitamin D3, 25-hydroxy-vitamin D2, retinol, tocopherols, carotenoids, and oxidized and reduced coenzyme Q10 by high performance liquid chromatography with photo diode-array detection using C_{18} and C_{30} columns alone or in combination. *Journal of Chromatography. A*, 1301: 1-9.
27. Hrvolová, B., Martínez-Huélamo, M., Colmán-Martínez, M., Hurtado-Barroso, S., Lamuela-Raventós, R. M. and Kalina, J. (2016). Development of an advanced HPLC-MS/MS method for the determination of carotenoids and fat-soluble vitamins in human plasma. *International Journal of Molecular Sciences*, 17(10): 1719.
28. Lensmeyer, G. L., Wiebe, D. A., Binkley, N. and Drezner, M. K. (2006). HPLC method for 25-hydroxyvitamin D measurement: Comparison with contemporary assays. *Clinical Chemistry*, 52(6): 1120 – 1126.
29. Garg, U., Munar, A., Frazee, C. nd Scott, D. (2012). A simple, rapid atmospheric pressure chemical ionization liquid chromatography tandem mass spectrometry method for the determination of 25-hydroxyvitamin D2 and D3. *Journal of Clinical Laboratory Analysis*, 26(5): 349-357.
30. Bruce, S. J., Rochat, B., Beguin, A. Pesse, B., Guessous, I., Boulat, O. and Henry, H. (2013). Analysis and quantification of vitamin D metabolites in serum by ultra-performance liquid chromatography coupled to tandem mass spectrometry and high-resolution mass spectrometry-a method comparison and validation. *Rapid Communications in Mass Spectrometry*, 27(1): 200-206.
31. Eyles, D., Anderson, C., Ko, P. Jones, A., Thomas, A., Burne, T. and McGrath, J. (2009). A sensitive LC/MS/MS assay of 25OH vitamin D3 and 25OH vitamin D2 in dried blood spots. *Clinica Chimica Acta*, 403(1-2): 145-151.
32. Zhang, S. W., Jian, W., Sullivan, S. Sankaran, B., Edom, R. W., Weng, N. and Sharkey, D. (2014). Development and validation of an LC-MS/MS based method for quantification of 25 hydroxyvitamin D2 and 25 hydroxyvitamin D3 in human serum and plasma. *Journal of Chromatography. B, Analytical Technologies in the Biomedical and Life Sciences*, 961: 62-70.

33. Karras, S. N., Kotsa, K., Angeloudi, E., Zebekakis, P. and Naughton, D. P. (2017). The Road Not So Travelled: Should Measurement of Vitamin D Epimers During Pregnancy Affect Our Clinical Decisions? *Nutrients*, 9(2): 90.
34. Aghajafari, F., Field, C. J., Rabi, D., Kaplan, B. J., Maggiore, J. A., O'Bierne, M., Hanley, D. A., Eliasziw, M., Dewey, D., Ross, S. and Apron T. (2016). Plasma 3-epi-25-hydroxycholecalciferol can alter the assessment of vitamin d status using the current reference ranges for pregnant women and their newborns. *The Journal of Nutrition*, 146(1): 70-75.
35. Yazdanpanah, M., Bailey, D., Walsh, W., Wan, B. and Adeli, K. (2013). Analytical measurement of serum 25-OH-vitamin D(3), 25-OH-vitamin D(2) and their C3-epimers by LC-MS/MS in infant and pediatric specimens. *Clinical Biochemistry*, 46(13-14): 1264-1271.
36. Kiely, M., O'Donovan, S. M., Kenny, L. C., Hourihane, J. O., Irvine, A. D. and Murray, D. M. (2017). Vitamin D metabolite concentrations in umbilical cord blood serum and associations with clinical characteristics in a large prospective mother-infant cohort in Ireland. *Journal of Steroid Biochemistry and Molecular Biology*, 167: 162-168.

Malaysian Journal of Analytical Sciences (MJAS)
Published by Malaysian Analytical Sciences Society

STABILITY AND ANTIBACTERIAL PROPERTIES OF GREEN SYNTHESIS SILVER NANOPARTICLES USING *Nephelium lappaceum* PEEL EXTRACT

(Kestabilan dan Ciri Antibakteria bagi Sintesis Hijau Nanopartikel Perak Menggunakan Ekstrak Kulit *Nephelium lappaceum*)

Nor Syazwanie Mohd Saidi[1], Hanis Mohd Yusoff[1,2]*, Irshad Ul Haq Bhat[1,2], Suganthi Appalasamy[3,4], Alia Diyana Mohamed Hassim[3], Farhanini Yusoff[1], Asnuzilawati Asari[1,2], Nurul Huda Abdul Wahab[1,2]

[1]Faculty of Science and Marine Environment, Faculty of Science and Marine Environment
[2]Advanced Nano Materials (ANoMa) Research Group, Faculty of Science and Marine Environment
Universiti Malaysia Terengganu, 21030 Kuala Nerus, Terengganu, Malaysia
[3]Institute of Food Security and sustainable Agriculture
[4]Faculty of Earth Science
Universiti Malaysia Kelantan, 17600 Jeli Campus, Kelantan, Malaysia

**Corresponding author: hanismy@umt.edu.my*

Received: 10 August 2020; Accepted: 9 October 2020; Published: 10 December 2020

Abstract

Silver nanoparticles (AgNPs) are known for its easy production with wide range of applications. The production can involve chemical, physical, biological and photochemical methods. For production of AgNPs using biological method, the synthesis normally involves plants, bacteria or other potential reducing agents that can control the size of AgNPs. In this study, *Nephelium lappaceum* or also known as rambutan peel was used as a reducing agent. *Nephelium lappaceum* extract was added to $AgNO_3$ (1 mM) solution and stirred for 1 hour. Three sets of synthesis were carried out to see the reproducibility and stability of the AgNPs. The solution obtained was analyzed by using Fourier transform-infrared spectroscopy (FTIR), UV-Vis spectrophotometer and scanning electron microscope (SEM). The stability of the obtained AgNPs was observed and compared with AgNPs synthesized by using the chemical method. FTIR spectra showed O-H, C-H, C=O and C=C stretching at 3361 cm^{-1}, 2090 cm^{-1}, 1637 cm^{-1} and 1367 cm^{-1}, respectively. The wavelength of UV-Vis obtained for the 3 sets of green synthesis is at 452 nm. The appearance of the peak around 452 nm due to the surface plasmon resonance band confirmed the formation of AgNPs. SEM images showed a mixture of spherical shapes that were agglomerated with size range of about 40 to 200 nm. The antibacterial study performed on AgNPs produced from *Nephelium lappaceum* peel extract was found to exhibited antibacterial activity on both Gram-positive and Gram-negative bacteria.

Keywords: green synthesis, reducing agent, green AgNPs, antibacterial, rambutan peel

Abstrak

Nanopartikel perak (AgNPs) dikenali dengan penghasilannya yang mudah dan aplikasi yang meluas. Kaedah penghasilan tersebut merangkumi kimia, fizikal, biologi dan fotokimia. Bagi penghasilan AgNPs menggunakan kaedah biologi, sintesis ini kebiasaannya melibatkan tumbuhan, bakteria atau agen penurunan lain yang berpotensi mengawal saiz AgNPs. Dalam kajian ini, *Nephelium lappaceum* atau dikenali juga sebagai kulit rambutan telah digunakan sebagai agen penurunan. Ekstrak *Nephelium*

lappaceum telah ditambah kepada larutan $AgNO_3$ (1 mM) dan dikacau selama 1 jam. Tiga set sintesis telah dijalankan untuk melihat kebolehterbitan dan kestabilan AgNPs. Larutan yang diperolehi telah dianalisa menggunakan spektrometer infra merah transformasi Fourier (FTIR), spektrofotometer tampak UV (UV-Vis) dan mikroskop imbasan elektron (SEM). Kestabilan larutan AgNPs yang diperolehi telah dikaji dan dibandingkan dengan AgNPs yang disintesis menggunakan teknik kimia. Spektra FTIR telah menunjukkan kewujudan regangan O-H, C-H, C=O dan C=C masing-masing adalah pada 3361 cm^{-1}, 2090 cm^{-1}, 1637 cm^{-1} dan 1367 cm^{-1}. Panjang gelombang UV-Vis bagi ketiga-tiga set adalah pada 452 nm. Kewujudan puncak sekitar 452 nm adalah disebabkan oleh jalur resonansi plasmon permukaan yang membuktikan pembentukan AgNPs. Imej SEM menunjukkan campuran bentuk sfera dan aglomerasi dengan anggaran saiz sekitar 40 hingga 200 nm. Kajian antibakteria telah dilakukan terhadap AgNPs yang dihasilkan daripada ekstrak kulit *Nephelium lappaceum* didapati menunjukkan aktiviti antibakteria pada kedua-dua bakteria Gram-positif dan Gram-negatif.

Kata kunci: sintesis hijau, agen penurun, AgNPs hijau, antibakteria, kulit rambutan

Introduction

Nanomaterials are materials that have structural compounds smaller than 1 μm in minimum of one dimension [1-2]. Metal oxide nanoparticles and metal nanoparticles are widely studied in top down approach due to various preparation methods that are considered as simple and can be modified to produce various sizes and morphologies [3-6]. Metal nanoparticles exhibit different properties compared to bulk materials even if they are made of the same atoms [2]. The physical and chemical properties of metal nanoparticles are different compared to bulk materials. Metal nanoparticles have lower melting points, higher specific surface areas, specific optical properties, mechanical strengths and specific magnetizations [7-10]. AgNPs have been widely studied and synthesized due to its wide applications in the fields of medicine, chemistry, pharmacy, industry, environment, surface modification and biology [4-11]. There are two major synthesis routes for AgNPs which are top to bottom approach and bottom up approach. Top to bottom approach involves physical methods while bottom up approach involves biological and chemical methods. The simplest and the most frequently used bulk-solution synthetic method for metal nanoparticles is by reducing the metal salts. The chemical synthetic method of AgNPs involves the ionic salt reduction in an appropriate medium with the presence of a surfactant while using different reducing agents such as sodium citrate or sodium borohydride, followed by the addition of capping agents including alkylamines and alkanethiols or any polymeric materials like gelatin and polyvinyl alcohol [7]. The function of capping agent is to stabilize the AgNPs from aggregation. The use of this capping agent and the reduction by using these chemicals can result in hazardous by-products formation which will certainly affect the use of AgNPs in biomedical fields and chemical application. Alternatively, green and cheaper methods can be used to synthesize AgNPs in order to overcome these problems [7-9].

Currently, there are green synthesis methods available involving bacteria, fungi, and plant extracts. Most of the methods involve oxidation-reduction reactions [12-15]. Green synthesis using plant extracts are the best compared to other biological methods [14]. Many plants have been used in the green synthesis of AgNPs and have the reducing agent to reduce Ag^+ to Ag^0 from silver nitrate solution [13-16]. Some examples of plant leaf extracts that have been used are from carob leaves, pine leaves, persimmon leaves, gingko leaves, and magnolia leaves [13]. The use of fruit peels was also used in the previous studies such as peel waste from pomegranates, oranges, bananas and apples [14-17]. *Nephelium lappaceum* or rambutan peel was used as the reducing agent. Phytochemical properties were determined to know the reducing compounds in rambutan peel and further applied to produce AgNPs. Many studies revolving fruit peels lack information regarding stability of AgNPs and the effect of various concentrations towards antibacterial studies. Rambutan peels are also known as waste and the full utilization of this waste could be merited in synthesizing AgNPs. This study aimed to synthesize and characterize AgNPs by using rambutan peel. The designed AgNPs were compared with AgNPs generated from a conventional chemical

method. The stability and antibacterial activity of AgNPs were carried out to determine the structural changes and their potential as antibacterial agents, respectively.

Materials and Methods

Materials and Instrumentation

Silver nitrate ($AgNO_3$) and sodium borohydride ($NaBH_4$) were purchased from Sigma Aldrich and used without further purification. Rambutan was purchased from local market in Kuala Nerus, Terengganu. Distilled water was used to prepare all the solution and Whatman No 1 filter paper was used to filter AgNPs solution.

Both green and chemically synthesized AgNPs were characterized using UV-Vis spectroscopy (UV-Vis), Fourier Transform Infrared (FTIR) and scanning electron microscope (SEM). The UV-Vis spectrophotometer model used was Shimadzu UV-1800. The wavelength used was within the range of 200-800 nm. The FTIR spectra were recorded between 4000 until 400 cm^{-1} using Perkin Elmer Spectrum 100. The sample for SEM was sonicated three times (3 minutes each) before it was mounted on a stub of metal with adhesive. Then, the sample was coated with metal gold.

Synthesis of Silver Nanoparticles (AgNPs): Preparation of rambutan peel extract

A total of 20 g of rambutan peels was washed thoroughly and finely cut into smaller pieces. The finely cut pieces were added in the Erlenmeyer flask with 200 mL of distilled water. The solution was heated at 70-80 $^{\circ}C$ for 1 hour. The extract was then filtered with Whatman No. 1 filter paper.

Phytochemical tests of rambutan peel extract

To investigate the compounds presence in the rambutan peel extract, several phytochemical tests were carried out which included alkaloid test, flavonoid test, tannin test, saponin test, steroid test, phlobatanin test, and carbohydrate test. Table 1 shows a list of methods for each test. Every test was carried out at least three times and only tests which appeared positive in two or more tests that were considered to confirm the presence of the investigated compounds in rambutan peel extract.

Green synthesis of silver nanoparticles (AgNPs)

For green synthesis, 5 mL of rambutan peel extract was added to 50 mL of $AgNO_3$ (1 mM) aqueous solution. The solution was stirred for 1 hour. Any changes in the color of the solution was observed and recorded. The temperature for the synthesis was kept at room temperature and pH 7. To study the stability of green AgNPs, three sets of synthesis were done with similar condition.

Chemical synthesis of silver nanoparticles (AgNPs)

An amount 10 mL of $AgNO_3$ (1 mM) was added dropwise for 20 drops per minute into 30 mL of sodium borohydride (2 mM). This solution was then put into an ice bath at about 4 $^{\circ}C$ and was stirred continuously [18]. The solution was centrifuged with 5000 rpm for 15 minutes and then filtered with Whatman No. 1 filter paper.

Antibacterial Study

Tests were done by the disc diffusion method. Sterile 6.0 mm diameter blank disc were used to impregnate with five different concentrations of green synthesis and chemical synthesis silver nanoparticles. The concentrations were 0.2, 0.4, 0.6, 0.8 and 1.0 mM for both syntheses. The culture of *Escherichia coli* and *Bacillus subtillis* was spread on the plates with nutrient agar uniformly using sterile hockey stick. AgNPs impregnated discs with different concentration were placed on an agar plate. Sterile distilled water was used as negative control and 10 µg Gentamicin disc (Oxoid ™, United Kingdom) was used as positive control. The plates were incubated at 37 °C for 24 hours. Triplicates were done for every concentration and different bacteria. Antibacterial activities were then measured by the clear zones of inhibition.

Table 1. Phytochemical tests methods

Tests	Methods
Alkaloid	0.5 mL of peel extract were treated with a few drops of Wagner's reagent (iodine in potassium iodide). The colour changes were observed, and a brown precipitate formed to indicates the presence of alkaloid.
Flavonoid	0.5 mL of peel extract were treated with few drops of concentrated sulphuric acid. The colour changes were observed, and a formation of orange colour indicates the presence of flavonoid.
Saponin	1 mL of peel extract was added with 2 mL of distilled water in a test tube. The solution was shaken vigorously and was observed for a stable persistent froth for 10 min.
Carbohydrate	0.5 mL of peel extract was added with few drops of iodine solution. Purple or dark blue shows the presence of carbohydrates.
Phlobatanin	0.5 mL of peel extract was boiled with 1% aqueous hydrochloric acid. Formation of red precipitate shows the presence of phlobatanin.
Steroid/Sterols	0.5 mL of peel extract were treated with few drops of acetic anhydride, boiled and cooled to room temperature. A few drops of concentrated sulphuric acid, H_2SO_4 were added to the test tube and formation of brown ring at the junction of two layers were observed. Green coloration of upper layer indicates a positive test for steroids.
Phenolic	0.5 mL of peel extract was put into test tube and 2 mL of distilled water was added followed with 2 to 3 drops of 10% iron (III) chloride solution. The presence of green or blue colour indicates the presence of phenolic compound.
Tannin	0.5 mL of each crude extract was added with distilled water followed by 1 to 2 drops of diluted ferric chloride solution. A dark green or blue-green coloration indicates the presence of tannins.

Results and Discussion

Green and chemical synthesis of AgNPs

Phytochemical tests were carried out towards the rambutan peel extract to confirm the bioactive compounds and the functional groups responsible for the reduction and the stabilization of AgNPs [20, 21]. From Table 2, the presence of alkaloid, flavonoid, saponin, phenolic and tannin in rambutan peel extract. Tests were carried out three times and labeled as A, B and C for each desired active compound to confirm the consistency of the results. Only two or more positive results were considered to confirm the presence of the investigated compounds in the rambutan peel extract. Phytochemical tests findings of flavonoid and alkaloids in this study are similar with the study by Ashok et al. [23]. The presence of phenolic compound and tannin strengthen the suggested fact that O-H group is the biomolecule responsible in the reducing and stabilizing the AgNPs produced [20].

For chemical synthesis, 1 mM of 10 mL $AgNO_3$ was added drop wise into 2 mM of 30 mL $NaBH_4$ and stirred

continuously until the color in the mixture changed from pale yellow to light brown. According to Badi'ah et al., AgNPs are formed when the colorless solution turned to pale yellow [19]. The reaction stopped when the pale-yellow change to light brown as shown in Figure 1.

AgNPs have been successfully synthesized chemically and also using the rambutan peel extract. In the green synthesis, 5 mL rambutan peel extract was added into 1 mM 50 mL silver nitrate and stirred continuously. The AgNPs were formed when light brown solution turned to dark brown which was after 10 minutes of stirring. The reaction was complete after 1 hour of stirring which the solution turned to darker brown (Figure 2). This observation is similar to the previous study by Gudikandula & Maringanti, which also mentioned that dark brownish color indicated the complete formation of AgNPs [10].

Ultraviolet-visible spectroscopy

Both chemically and green synthesized AGNPs were characterized using UV-Vis spectroscopy to confirm the formation of the particles. In Figure 3, a peak appeared at 415 nm for the AgNPs synthesized by $NaBH_4$. This peak appeared due to surface plasmon resonance which confirmed the formation of AgNPs. Surface plasmon resonance (SPR) is a common phenomenon in metal nanoparticles where electrons in the metal surface layer are excited by photons of incident light with a certain angle of incidence which then propagates parallel to the metal surface [13, 20]. As shown in Figure 4, a prominent peak also appeared at the wavelength of 452 nm with AgNPs synthesized by rambutan peel extract.

The SPR band for spherical AgNPs was normally in the range of 390-450 nm [13-24]. It has been found in a study of AgNPs synthesized using Argemone Mexican leaves as reducing agent that the SPR band was at 440 nm. They also stated that the broadening of the peak indicated that the AgNPs synthesized were polydisperse [19]. Awwad et al. stated that their AgNPs gave the highest peak at 420 nm in UV-Vis [14]. The SPR band obtained in this study which indicated the formation of AgNPs in both chemically and green synthesis method are similar with the previous studies.

In the green synthesis method, three sets of reaction with similar condition were done to check the stability of the AgNPs. The stability comparison can be seen in Table 3. The UV-Vis of the synthesized AgNPs were carried out every day until there was a shift in the wavelength of the spectra. For Set A, the color changed from light brown to dark brown after 1 hour of synthesis. After one day, the color changed to grey and the solution became cloudy. After 5 days, it could be seen that the grey color changed to brown and agglomeration of brown particles occurred. The wavelength of UV-Vis spectrum for Set A (Figure 5) also shifted after 4 days. For Set B and Set C, the color change was consistent after 1 hour and one day. But after 8 days, the solution became cloudy and agglomeration also occurred. Like Set A, the grey color also changed to brown. The wavelength of the UV-Vis spectra of both Set B (Figure 6) and Set C (Figure 7) shifted after 8 days.

To date, there is no stability study of green synthesized using rambutan peel. 7 days are considered a short-term stability and in some modified condition by considering the stabilizer agent such as citrine, stability of AgNPs could last longer [25]. These findings indicated that the AgNPs synthesized using rambutan peel extract as the reducing agent is considered having short stability. Another condition to be improved for longer stability is by modifying the pH of the solution since the phenolic functional group in the extract can act as a good reducing and stabilizing agent that can releases electrons to reduce Ag^+ to become Ag^0 under an alkaline condition instead of acidic or neutral [20].

Table 2. Phytochemical tests result towards rambutan peel extract

Tests	Set A	Set B	Set C
Alkaloid	+	+	+
Flavonoid	+	+	+
Saponin	+	+	+
Carbohydrate	-	+	+
Phlobatanin	-	-	-
Steroid/Sterols	-	-	-
Phenolic	+	+	+
Tannin	+	+	+

(+) = presence of active compounds in rambutan peel, (-) = no active compounds in rambutan peel

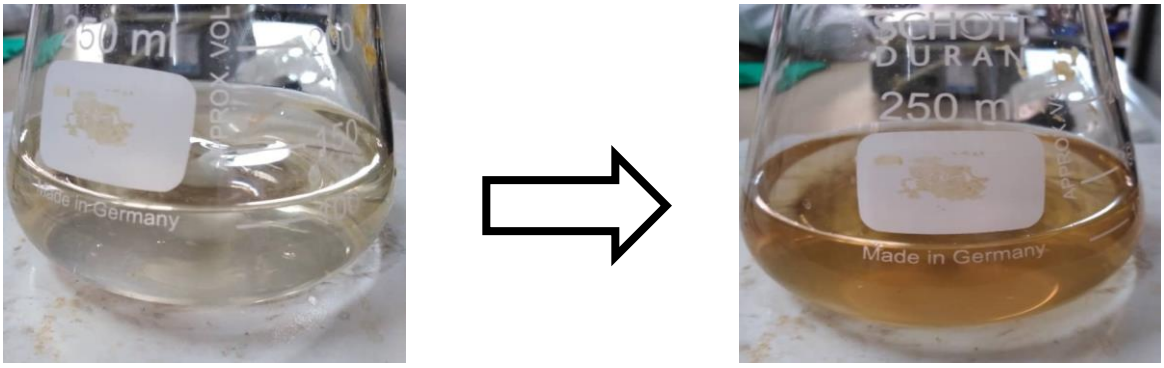


Figure 1. Colour change in chemical synthesis of AgNPs from pale-yellow to light brown

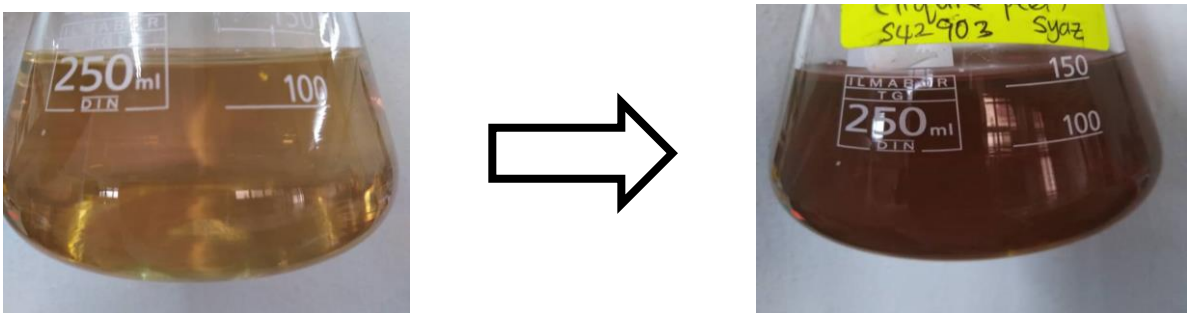


Figure 2. Color change in green synthesis of AgNPs from pale-yellow to dark brown

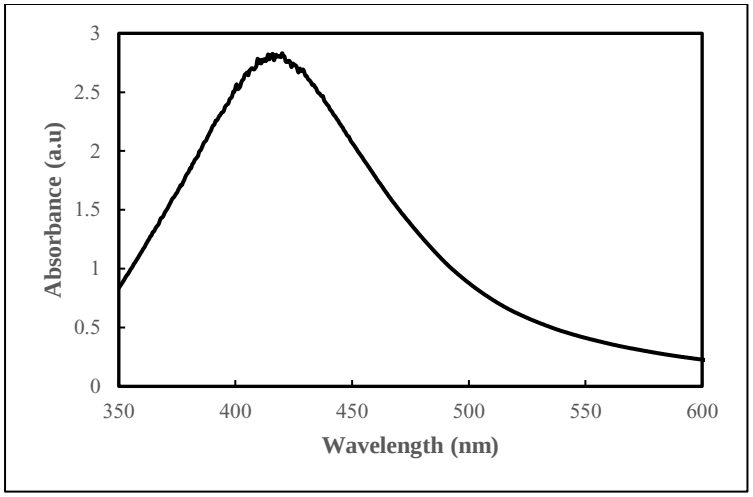


Figure 3. UV-Vis spectrum of chemically synthesized AgNPs

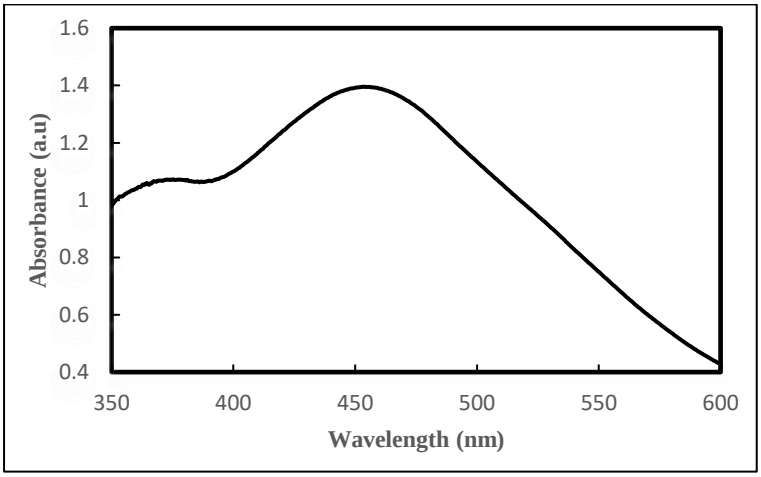


Figure 4. UV-Vis spectrum of green synthesized AgNPs

Table 3. Stability of green synthesis of AgNPs

Sets	Stability
A	5 days
B	8 days
C	8 days

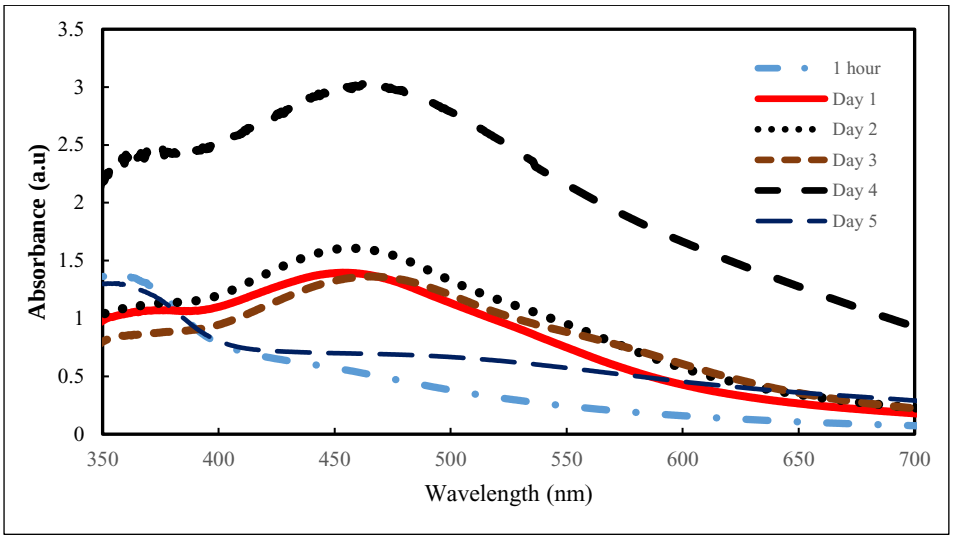


Figure 5. UV-Vis spectra of green synthesized AgNPs (Set A)

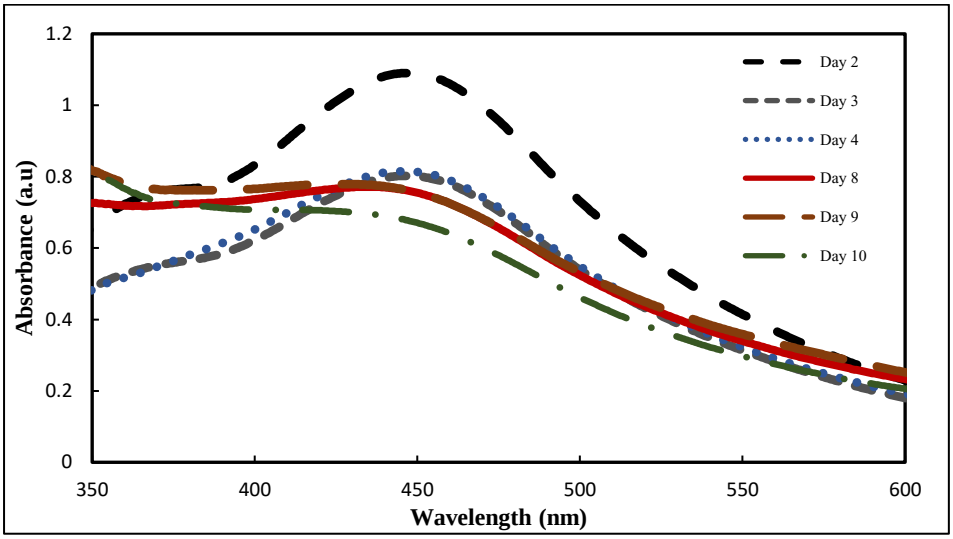


Figure 6. UV-Vis spectra of green synthesized AgNPs (Set B)

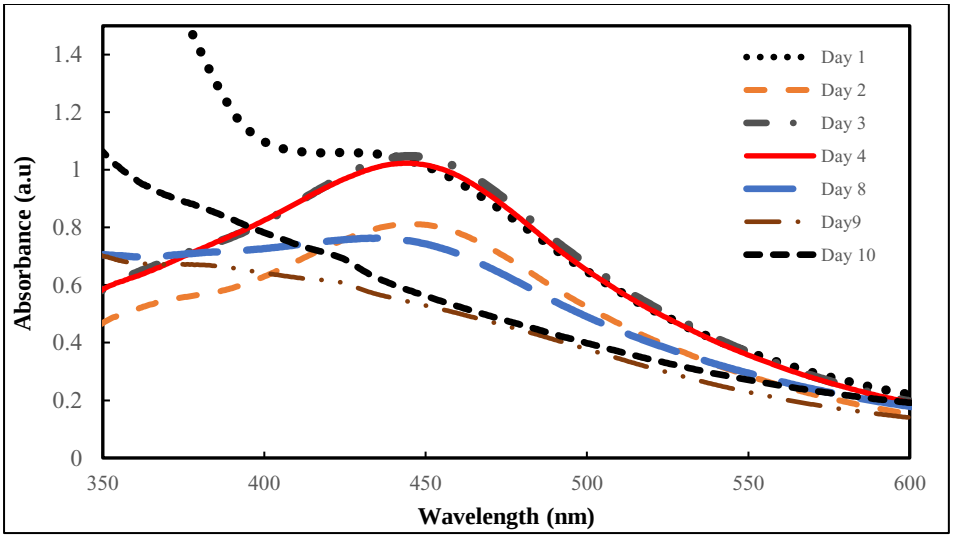


Figure 7. UV-Vis spectra of green synthesized AgNPs (Set C)

Fourier transform infrared spectroscopy

The assignment of the bands in the synthesized AgNPs from both methods are tabulated in Table 4. Figure 8 represents FTIR spectrum for green synthesized AgNPs. Strong intensity at 3361.93 cm^{-1} corresponds to the O-H stretching of the phenolic compounds in the extract [13-16, 20]. The medium intensity at 2090.84 cm^{-1} corresponds with the aliphatic C-H stretching and C-H stretching of aldehyde group [16]. The C=O stretching in the phenolic group can be found at 1637.53 cm^{-1} [13-16, 20]. The medium intensity at 1367.53 cm^{-1}shows the C=C stretching vibrations. The peak at 1242.16 cm^{-1} indicated the finger print region of C-O-C stretch [14]. The broad band at 466.77 cm^{-1} indicates the presence of Ag vibration properties in the AgNPs [13-16].

For chemical synthesis, the band and the intensity for the AgNPs were similar with green synthesis AgNPs. In green synthesis, the rambutan peel extract was used as the reducing agent due to the presence of –OH group from phenolic and –CHO from aldehyde in the extract. These groups were said to interact with Ag^{+} that was oxidized to –COOH and simultaneously Ag^{+} was reduced to Ag^{0} [7, 14, 16].

Scanning electron microscope

The AgNPs were observed under SEM to see the morphology and the size of the nanoparticles formed. The magnification used were 15000X and 30000X. Based on SEM images, the size of AgNPs produced for green synthesis ranged from 40 nm to 200 nm and seem to be correlated with previous studies [18-20]. The AgNPs seem to be in spherical shape and agglomerated (Figure 9).

Antibacterial Study

The antibacterial study was done using disk-diffusion method. Different concentrations of chemically and green synthesized nanoparticles were used in the study. Two types of bacteria namely *Escherichia coli* (gram-negative) and *Bacillus subtillis* (gram-positive) bacteria were used in this study. The result was tabulated and shown in Table 5 and Table 6 respectively.

The concentrations of AgNPs used in this study were 1.0, 0.8, 0.6, 0.4 and 0.2 mM for both synthesized AgNPs. The results show that both chemical and green synthesized AgNPs have weak and moderate activity towards bacteria. For gram-negative bacteria (Table 5), the concentration of 1.0 mM chemically synthesized AgNPs shows the highest inhibition zone at 9.0 mm in the first two trials and 10.0 mm for the third trial. There

was no inhibition show for the concentration of 0.4 mM and 0.2 mM. The green synthesized AgNPs showed inhibition towards bacteria for all concentrations used. Like chemical synthesis, the concentration of 1.0 mM green synthesized AgNPs showed the highest inhibition at 8.0 mm in the first two trials and 9.0 mm for the third trial. The concentration of 0.2 mM shows the weakest activity towards bacteria at 5.5 mm in all trials. To compare both, chemical synthesized AgNPs had more inhibition towards gram-negative bacteria, *Escherichia coli*. The inhibition zone are as shown in Figure 10. For gram-positive bacteria (Table 6), the inhibition shown by 0.8 mM chemically synthesized AgNPs is the highest and consistent at 15.0 mm in all trials while the weakest is shown by 0.2 mM AgNPs at 7.0 mm inhibition zone for the first trials and 6.5 mm for the other two trials. Unlike *Escherichia coli*, the concentration of 0.2 mM and 0.4 mM show inhibition zone towards *Bacillus subtillis*. For green synthesis AgNPs, the concentration of 0.8 mM also shows the highest inhibition zone at 10.0 mm in two trials and 9.0 mm in another. The lowest inhibition is shown by the concentration of 0.2 mM at 5.5 mm for all trials. Comparing chemically and green synthesized AgNPs, chemically synthesized still has better inhibition zone towards gram-positive bacteria, *Bacillus subtillis*. The inhibition zone is shown in Figure 11. The inhibition zones recorded in this study are comparable with previous findings where the inhibition ranges from 7 to 15 mm [24, 26, 27].

Table 4. FTIR spectra peak assignments

Peak Assignment	**Wavenumber (cm^{-1})**	
	Chemically Synthesized AgNPs	**Green Synthesized AgNPs**
O-H stretching	3346.50	3361.93
C-H stretching	2086.98	2090.84
C=O stretching	1635.64	1637.56
C=C stretching	1369.46	1367.53
C-O	1249.87	1242.16
Ag metal	466.77	439.77

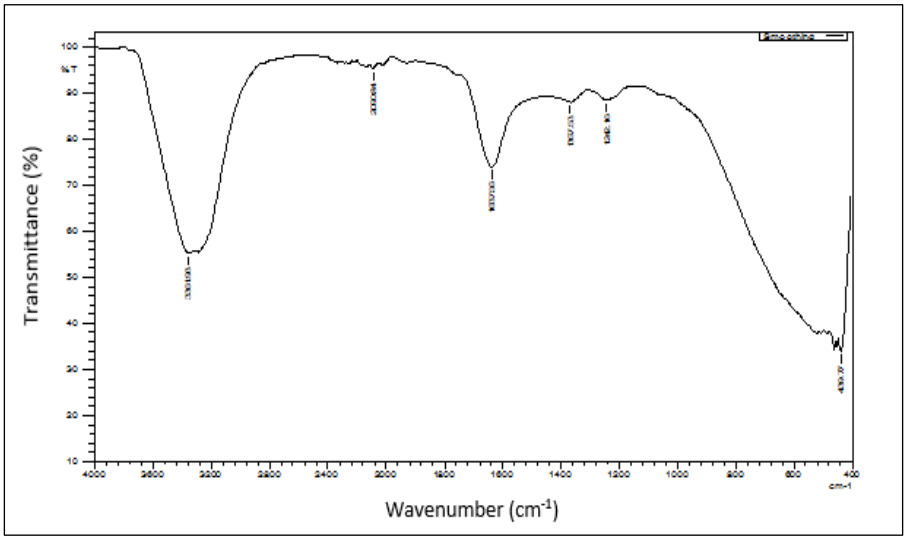


Figure 8. FTIR spectrum of green synthesized AgNPs

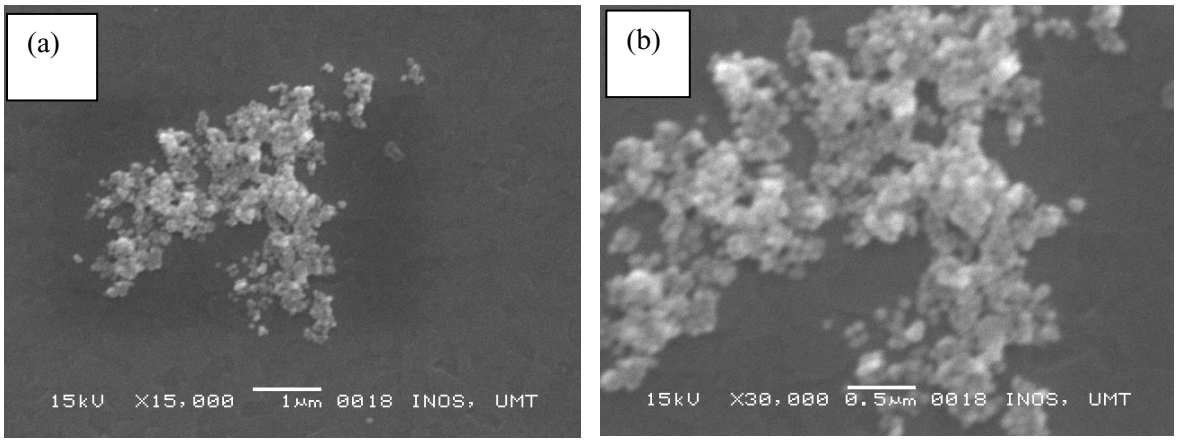


Figure 9. SEM images of green synthesis AgNPs at different magnification of (a) 15000X and (b) 30000X

Table 5. Antibacterial inhibition of green synthesis AgNPs towards *Escherichia coli*

Escherichia coli	**Chemically Synthesized AgNPs**			**Green Synthesized AgNPs**		
Concentration (mM)	**Measurement of Inhibition Zone (mm)**			**Measurement of Inhibition Zone (mm)**		
1.0	9.0	9.0	10.0	8.0	8.0	9.0
0.8	8.0	8.0	8.5	7.0	7.0	7.0
0.6	8.0	6.5	7.0	6.0	6.0	6.0
0.4	-	-	-	5.8	6.0	5.8
0.2	-	-	-	5.5	5.5	5.5
Positive control	25.0	26.0	25.0	25.0	25.0	25.0

Table 6. Antibacterial inhibition of green synthesis AgNPs towards *Bacillus subtillis*

Bacillus subtillis	**Chemically Synthesized AgNPs**			**Green Synthesized AgNPs**		
Concentration (mM)	**Measurement of Inhibition Zone (mm)**			**Measurement of Inhibition Zone (mm)**		
1.0	8.0	11.0	17.0	9.0	9.0	9.0
0.8	15.0	15.0	15.0	10.0	9.0	10.0
0.6	8.0	9.0	9.0	8.0	9.0	9.0
0.4	7.0	7.0	7.0	6.6	6.6	6.6
0.2	7.0	6.5	6.5	5.5	5.5	5.5
Positive control	25.0	25.0	25.0	25.0	25.0	25.0

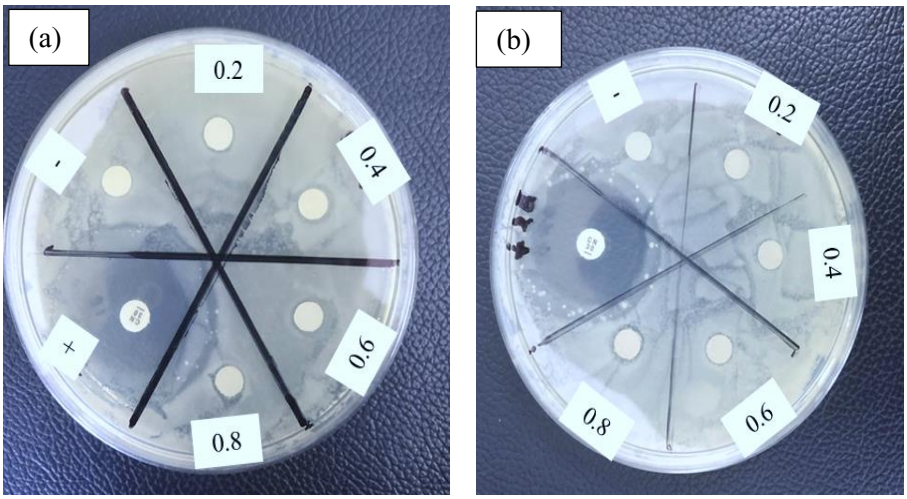


Figure 10. Inhibition zone of antibacterial study using different concentrations of (a) chemically synthesized AgNPs and (b) green synthesized AgNPs against *Escherichia coli*

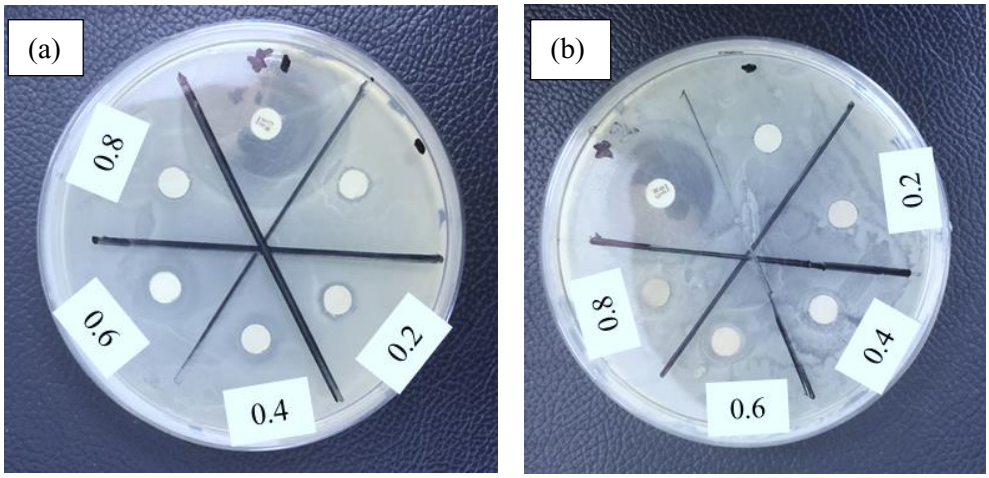


Figure 11. Inhibition zone of antibacterial study using different concentrations of (a) chemically synthesized AgNPs and (b) green synthesized AgNPs against *Bacillus subtillis*

Conclusion

In this study, AgNPs were successfully synthesized by chemical and green method. UV-Vis spectroscopy confirmed the formation of silver nanoparticles in both chemical and green synthesis by exhibiting the SPR band at 415 nm and 452 nm respectively. FTIR shows that the functional groups of -OH, C-H, C-O-C, C=C and C=O responsible in capping and stabilising of AgNPs. Green synthesized AgNPs produced are within 40 to 200 nm. The antibacterial study shows that the green synthesized AgNPs produced have moderate activity against *Escherichia coli* within the range of 5.5 to 9 mm while against *Bacillus subtillis* the inhibition zones were within 5.5 to 10 mm.

Acknowledgement

We would like to thank Universiti Malaysia Terengganu, Universiti Malaysia Kelantan and Ministry

of Higher Education (MOHE) for research grant FRGS vot number 59383 (FRGS/1/2015/SG01/UMT/02/3) for some financial support in completing this research.

References

1. Buzea, C., Pacheco, I. I. and Robbie, K. (2007). Nanomaterials and nanoparticles. *Biointerphases,* 2(4): MR17-71.
2. Solomon, S. D., Mulfinger, L., Bahadory, M., Jeyarajasingam, A. V., Rutkowsky, S. A. and Boritz, C. (2007). Synthesis and study of silver nanoparticles. *Journal of Chemical Education*, 84(2): 322-325.
3. Yusoff, H. M., Hazwani, N. U., Hassan, N. and Izwani, F. (2015). Comparison of sol gel and dehydration magnesium oxide (MgO) as a catalyst in Michael addition reaction. *International Journal of Integrated Engineering,* 7(3):43-50.
4. Yusoff, H. M., Idris, N. H., Hipul, N. F., Yusoff, N. F. M., Izham, N. Z. M. and Bhat, I. U. H. (2020). Green synthesis of zinc oxide nanoaparticles using black tea extract and its potential as anode material in sodium ion batteries. *Malaysian Journal of Chemistry,* 22(2): 43-51.
5. Mazli, S. R. A., Yusoff, H. M. and Idris N. H. (2020). Synthesis of zinc oxide nanoparticles by using aloe vera leaf extract as potential anode material in lithium ion battery. *Universiti Malaysia Terengganu Journal of Undergraduate Research,* 2(2): 1-8.
6. Yusoff, H. M., Rafit, F. A., Mohamad, F. I., Hassan, N. and Daud, A. I. (2017). The effect of calcination temperatures in the synthesis of nanocrystalline magnesium oxide via sol-gel technique. *Applied Mechanics and Materials,* 865: 36-42.
7. Lestari, P., Pratiwi I. and Juliani A. (2018). Green synthesis of silver nanoparticles using rambutan (*Nephelium lappaceum L.*) peel extract and its antibacterial activity against *Salmonella parathypi A*. *MATEC Web of Conferences*, 154: 1-4.
8. Maribel, G., Guzmán, J. D. and Stephan, G. (2009). Synthesis of silver nanoparticles by chemical reduction and their antibacterial activity. *International Journal of Chemical and Biomolecular Engineering*, 2(3): 104-111.
9. Liu, H., Wang, D., Song, Z. and Shang S. (2011). Preparation of silver nanoparticles and the application in electrochemical detection of DNA hybridization. *Cellulose,* 18**:** 67-74.
10. Gudikandula, K. and Maringanti, S., C. (2016). Synthesis of silver nanoparticles by chemical and biological methods and their antimicrobial properties. *Journal of Experimental Nanoscience,* 11(9): 714-721.
11. Yusoff, H. M., Rzeznicka, I. I., Hoshi, H., Kajimoto, S., Horimoto, N. N., Sogawa, K., & Fukumura, H. (2013). Excitation energy migration in yellow fluorescent protein (Citrine) layers adsorbed on modified gold surfaces. Applied Surface Science, 280: 776-782.
12. Zhu, X. and Gao, T. (2019). Nano-inspired biosensors for protein assay with clinical applications. Elsevier, Amsterdam: pp. 237-264.
13. Ahmed, S., Ahmad, M., Swami, B. L. and Ikram S. (2016). A review on plants extract mediated synthesis of silver nanoparticles for antimicrobial applications: A green expertise. *Journal of Advanced Research,* 7: 17-28.
14. Awwad, A. M., Salem, N. M. and Abdeen, A. O. (2013). Green synthesis of silver nanoparticles using carob leaf extract and its antibacterial activity. *International Journal of Industrial Chemistry,* 4(29): 1–6.
15. Naganathan, S. and Thirunavukkarasu, S. (2017). green way genesis of silver nanoparticles using multiple fuit peels waste and its antimicrobial, antioxidant and anti-tumor cell line studies. *2nd International Conference on Mining, Material and Metallurgical Engineering,* 191: pp. 1-7.
16. Mousa A. A., Moosa, A. A. and Allawi, M. (2015). Green synthesis of silver nanoparticles using spent tea leaves extract with atomic force microscopy. *International Journal of Current Engineering and Technology,* 5(5): 3233-3241.
17. Loo, Y. Y., Chieng, B. W., Nishibuchi, M. and Radu, S. (2012). Synthesis of silver nanoparticles by using tea leaf extract from *Camellia sinesis*. *International Journal of Nanomedicine,* 7: 4263-4267.

18. Narayanamma, A. (2016). Natural synthesis of silver nanoparticles by banana peel extract and as antibacterial agent. *IOSR Journal of Polymer and Textile Engineering,* 3(1): 17-25.
19. Badi'ah, H. I., Seedeh, F., Supriyanto, G. and Zaidan A. H. (2019). Synthesis of silver nanoparticles and the development in analysis method. *IOP Conference Series: Earth and Environmental Science,* 217: 1-8.
20. Kumar, B., Smita, K., Cymbal, L. and Angulo Y. (2020). Photosynthesis of silver nanoparticles using andean cabbage: Structural characterization and its application. *Materials Today: Proceedings,* 21: 2079-2086.
21. Singh, A., Jain, D., Upadhyay, M. K., Khandelwal, N. and Verma, H. N. (2010). Green synthesis of silver nanoparticles using agremone mexicana leaf extract and evaluation of their antimicrobial activities. *Digest Journal of Nanomaterials and Biostructures,* 5(2): 483-489.
22. Babu, S., Claville, M. O. and Ghebreyessus, K. (2015). Rapid synthesis of highly stable silver nanoparticles and its application for colourimetric sensing of cysteine. *Journal of Experimental Nanoscience,* 10(16): 1242–1255.
23. Ashok, K., Nethaji, R., Thooyavan, G. and Mullai N. K. (2015). Phytochemical profiling, antioxidant and antimicrobial activity of methanol extract in rambutan fruit (*Nephelium lappaceum*) epicarp against the human pathogens. *International Journal of Current Innovation Research*, 1(9): 201-206.
24. Reenaa, M. and Menon, A. S. (2017). Synthesis of silver nanoparticles from different citrus fruit peel extract and a comparative analysis on its antibacterial activity. *International Journal of Current Microbiology and Applied Sciences,* 6(7): 2358–2365.
25. Kavulicova, J., Mrazikova, A., Velgosova, O., Ivanova, D. and Kubovcikova, M. (2018). Stability of synthesized silver nanoparticles in citrate and mixed gelatin/citrate solution. *Acta Polytechnica,* 58(2): 104-108.
26. Peiris, M. M. K., Fernando, S. S. N., Jayaweera, P. M., Arachchi, N. D. H. and Guansekara, T. D. C. P. (2018). Comparison of antimicrobial properties of silver nanoparticles synthesized from selected bacteria. *Indian Journal Microbiology,* 58(3): 301-211.
27. Maruthai, K., Vallayyachari, K., Ravibalan, T., Phillip, A. A., Samrot, A. V. and Muthuraj, M. (2017). Antibacterial activity of the silver nanoparticles against *Escherichia coli* and *Enterobacter sp. Progress in Bioscience and Bioengineering,* 1(1): 29-35.

Malaysian Journal of Analytical Sciences (MJAS)
Published by Malaysian Analytical Sciences Society

CORROSION BEHAVIOR OF LOW-CARBON STEEL AND STAINLESS STEEL 304 UNDER TWO SOIL CONDITIONS AT PANTAI MENGABANG TELIPOT, TERENGGANU, MALAYSIA

(Kelakuan Kakisan dan Penyusutan Bahan Logam Rendah Karbon dan Keluli Tahan Karat 304 di dalam Dua Keadaan Tanih di Pantai Mengabang Telipot, Terengganu, Malaysia)

Suriani Mat Jusoh[1, 2], Wan Mohd Norsani Wan Nik[1, 3, 4], Nor Azila Azman[1], Mohammad Fakhratul Ridwan Zulkifli[1,3]*

[1]*Faculty of Ocean Engineering Technology and Informatics*
[2]*Composite Research Group (CoReG), Faculty of Ocean Engineering Technology and Informatics*
[3]*Materials and Corrosion Research Group, Faculty of Ocean Engineering Technology and Informatics*
[4]*Industrial Centre of Excellent (ICoE)*
Universiti Malaysia Terengganu, 21030 Kuala Nerus, Terengganu, Malaysia

**Corresponding author: fakhratulz@umt.edu.my*

Received: 14 June 2020; Accepted: 11 September 2020; Published: 10 December 2020

Abstract

Corrosion damage significantly affect steel structures' performance, whose control is a crucial key for design and maintenance. In this study, two different steels' corrosion behaviour, namely as low-carbon steel (LCS) and stainless steel 304 (SS 304) strip coupons, were observed in two different soils for a maximum period of 56 days. The corrosion behaviour of buried metals in different soils was characterized by weight loss (WL) measurement, potentiodynamic polarization (PP), electrochemical impedance spectroscopy (EIS), and scanning electron microscopy (SEM). The results show that the average weight loss after the observational periods of 14,28,42 and 56 days, average percentage weight loss in the LCS coupons from the sandy soil site was 0.444%, 0.831%, 2.542%, and 3.084%, respectively, representing an overall average of 6.901%. The average percentage of weight loss was 0.761%, 1.770%, 2.833%, and 5.090%, respectively, representing an overall average of 10.454% in the silt soil. Corrosion rates (CRs) for the LCS coupons from sandy soil site after 14, 28, 42, and 56 days were 0.87 mmpy, 0.80 mmpy, 1.67 mmpy and 1.54 mmpy respectively. In the silt soil, the CRs were 1.47 mmpy, 1.74 mmpy, 1.87 mmpy and 2.56 mmpy. The value of E_{corr}, shifted to more negative values with increasing soil moisture content, indicating a cathodic controlled process. Moisture content is the most influential factor in metal loss, whereas pH is relatively insignificant in underground corrosion. Also, the pits area and distribution depend on the soil conditions. The corroded area of LCS was more extensive than the SS 304, where the depth of the pitting was the same across the surface.

Keywords: corrosion, materials, materials degradation, materials selection, scanning electron microcopy

Abstrak

Kerosakan kakisan sangat mempengaruhi prestasi struktur keluli, yang kawalannya adalah aspek utama reka bentuk dan penyelenggaraan. Dalam kajian ini, kelakuan kakisan dari dua jenis keluli berbeza iaitu keluli karbon rendah (LCS) dan keluli

tahan karat 304 (SS 304) kupon jalur telah dinilai di dalam dua tanah yang berlainan untuk tempoh maksimum 56 hari. Pencirian produk kakisan telah dijalankan dengan menggunakan teknik pengurangan berat (WL), pengutuban keupayaan dinamik (PP), pengukuran spektroskopi impedans elektrokimia (EIS) dan imbasan elektron mikroskopi (SEM). Keputusan menunjukkan bahawa purata berat selepas tempoh pemerhatian 14, 28, 42 dan 56 hari, purata kehilangan berat dalam kupon LCS dari tapak tanah berpasir adalah 0.444%, 0.831%, 2.542% dan 3.084 %, mewakili purata keseluruhan sebanyak 6.901%. Di dalam tanah lumpur, purata kehilangan berat adalah 0.761%, 1.770%, 2.833% dan 5.090% mewakili purata keseluruhan 10.454%. Kadar kakisan untuk kupon LCS dari tanah berpasir selepas 14,28,42 dan 56 hari adalah 0.87 mmpy, 0.80 mmpy, 1.67 mmpy dan 1.54 mmpy, masing-masing memberikan purata komposit 1.22 mmpy. Di dalam tanah lumpur, CRs ialah 1.47 mmpy, 1.74 mmpy, 1.87 mmpy dan 2.56 mewakili purata 1.91 mmpy. Nilai E_{corr}, mengarah kepada lebih negatif dengan pertambahan kandungan kelembapan tanah menandakan proses kawalan katodik. Kandungan lembapan adalah faktor yang paling berpengaruh terhadap kehilangan logam, sedangkan pH secara relatif tidak ketara pada kakisan bawah tanah. Juga, kawasan lubang dan pengedaran juga bergantung kepada keadaan tanah. Kawasan berlubang pada logam LCS lebih besar berbanding SS 304 dan kedalaman lubang adalah sama.

Kata kunci: kakisan, bahan, penyusutan bahan, pemilihan bahan, imbasan mikroskop elektron.

Introduction

Soil corrosion problems can also be distinctive due to the difference in soil salt content, oxygen content, temperature and microbial species in various soils [1]. Soil corrosion is an essential factor that threatens the safe operation of the pipeline and is also the fundamental cause of pipeline corrosion failure [2, 3]. Observations and data derived from coupon testing have been used to determine the average rate of corrosion and the type of corrosion during the exposure interval. Corrosion rate data derived from a single exposure generally do not provide information on corrosion rate change versus time. Corrosion rate may increase, decrease, or remain constant, depending on the corrosion samples' nature and soil conditions [4]. Therefore, in this study, the corrosion behaviour and materials degradation of two metals type known as low-carbon steel and stainless steel 304 under two soil conditions were determined by different techniques such as electrochemical impedance spectroscopy (EIS), weight loss (WL) measurement and scanning electron microscopy (SEM).

Materials and Methods

Materials

Metal coupons of two metallurgies were used for this study provided by two companies (Visco Chemicals, Houston and Rohrback Cosasco Systems). They are low-carbon steel (LCS) coupons and stainless steel 304 (SS 304) coupons. Bar/strip style coupons were used in this study. The composition of LCS and SS304 are tabulated in Table 1 [5].

Sample preparation

All coupon types were cut (38 mm x 25 mm x 3mm) uniformly. The LCS and SS 304 coupon density is 7.85 g/cm^3 and 7.98 g/cm^3, respectively. There was no pre-treatment of the coupons before exposure to the soil sites and finally, the coupons were buried in a depth of 30 cm at both selected sites. Figure 1 shows both coupons after the surface preparation process.

Location

Two locations were selected to bury the test coupons (Kampung Tanjung Gelam and Kampung Gong Pak Jin). Both locations are situated nearby the beach area of Pantai Mengabang Telipot, Terengganu, Malaysia. All coupons were buried in duplicates in a depth of 30 cm at both the selected site of sandy soil and silt soil site, as depicted in Figures 2 and 3, respectively. Both selected sites randomly choose based on their properties and colour of the soil.

Weight loss and corrosion rate determination

The metal coupons were buried in the soil environments for a maximum of 56 days. For 14 days, 28 days, 42 days and 56 days, duplicate sets of the buried coupons in both sites were retrieved for analysis. On completion of every exposure experiment, the coupons were removed from the soil chamber and weight loss measurement was performed. Three coupons for each type of steels were taken out from a chamber, as depicted in Figure 4.

The buried coupon was monitored to determine the corrosion effect occurred on the coupon at the end of each observation period and to compare the effect corrosion rates in two different soil environments. Equation 1 was used to calculate the weight loss of the steel after the exposure. Total weight is the summation of initial weight (W_o) and final weight (W_f), as shown below [6].

$$\%\, Weight\ losss = \frac{W_f - W_o}{Wf} \times 100\% \quad (1)$$

The corrosion rate was calculated, assuming uniform corrosion over the entire surface of the coupons. The corrosion rate in mils per year (mmpy) was calculated from the weight loss using the formula in Equation 2 below:

$$CRs = \frac{W}{(DAT)} \times k \quad (2)$$

where: W = weight loss in gram, k = constant, D = metal density in g/cm^3, A = coupon area (cm^2) and t = time (hours).

Electrochemical impedance spectroscopy

The electrochemical impedance spectroscopy (EIS) test was performed by using Autolab PGSTAT 302N with three electrodes system. Rectangular coupons of mild steel and stainless steel were used as the working electrode. A platinum sheet was used as the auxiliary electrode and a saturated calomel electrode (SCE) was used as a reference electrode. An AC disturbance signal of 1 mV was applied on the electrode at the open circuit potential (OCP), while the measured frequency ranged from 0.01 to 105 Hz. All the electrochemical measurements were done twice at (25±1ºC). The potentiodynamic polarization curve measurement was collected at a scan rate of 5mV/s between -1.5V and +0.5V relative to the SCE.

Scanning electron microscopy

Scanning electron microscopy (SEM) was deployed to observe and analyze the morphology of the metal's surface. The experiment was conducted at the Institute of Oceanography (INOS) by using JEOL JSM-6390LA microscope model. The samples were subjected to a coating process with an ultrathin gold particle layer using JFC-1600 Auto Fine Coater (JEOL Ltd., Tokyo, Japan). The gold coated samples being electrically conductive allows for the scanning process on the sample surface at an accelerated voltage of 15 kV and a working distance of 10 mm [7]. SEM test was done after 28 days and 56 days of exposure to the soil.

Table 1. Composition of LCS and SS 304 in wt.%

Metal	C	Si	Mn	S	P	Cr	Ni	Mo	Nb	Fe
LCS	0.12	0.011	0.6	0.045	0.045	0.008	0.035	2-3	0.098	Bal
SS304	0.07	0.75	2.0	0.03	0.04	19	10	0.03	0.01	Bal

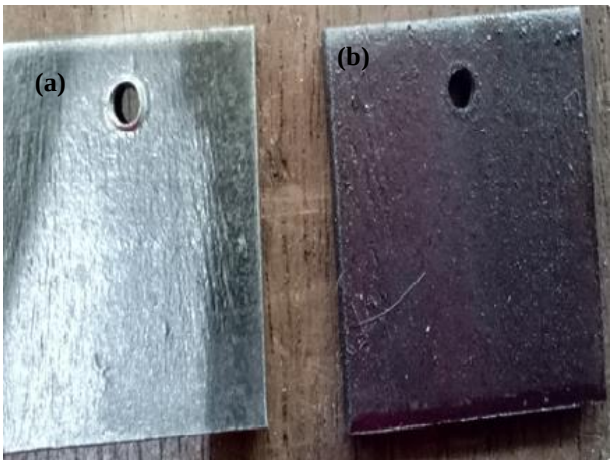


Figure 1. (a) Low carbon steel coupons and (b) Stainless steel 304 coupons



Figure 2. Sandy soil site at Kampung Tanjung Gelam, Mengabang Telipot.



Figure 3. Silt soil site at Kampung Gong Pak Jin, Mengabang Telipot

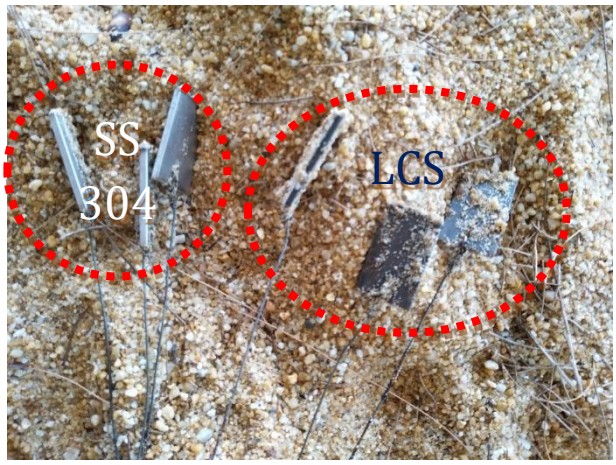


Figure 4. Three coupons for each steel taken out from a chamber.

Results and Discussion

Weight loss and corrosion rates

LCS and SS 304 coupons were buried in sandy soil and silt soil, where the condition of the two soils is different due to the moisture, pH, and temperature of the soil. Table 2 shows the value of weight loss of the studied metals, pH, temperature, and moisture content of the soils. The weight loss data was used to calculate the percentage of weight loss by using Equation 1.

The obtained weight loss data were used to determine the corrosion rates of LCS and SS304 relative to its exposure period by using Equation 2. The average corrosion rate of both coupons is tabulated in Table 3. According to the exposure period of 14, 28, 42 and 56 days, the weight loss percentage for- LCS coupons from the sandy soil site was 0.444%, 0.831%, 2.542%, and 3.084%, respectively, representing an overall average of 6.901% as depicted in Figure 5. In the silt soil site, the average percentage of weight loss was 0.761%, 1.770%, 2.833% and 5.090%, respectively, representing an overall average of 10.454%. It was found that both soil types show an increment of weight loss percentage due to the corrosion process. However, silt soil shows a higher average value of weight loss in comparison to the sandy soil.

At 14, 28, 42 and 56 days of exposure, the corrosion rates for the LCS from sandy soil were 0.87 mmpy, 0.80 mmpy, 1.67 mmpy and 1.54 mmpy, respectively, giving a total average of 1.22 mmpy. In the silt soil, the corrosion rates were 1.47 mmpy, 1.74 mmpy, 1.87 mmpy and 2.56 mmpy, respectively, representing an average of 1.91 mmpy as shown in Figure 6. As the corrosion rate's value is directly proportional to the percentage of weight loss, the trend for corrosion rate was found to be similar to the weight loss percentage trend.

In the sandy soil site, weight loss percentage for SS 304 coupons were 0.069%, 0.039%, 0.076% and 0.118% after 14.28,42 and 56 day respectively, with a total average of 0.076%, while the weight loss percentage in the silt soil were 0.035%, 0.055%, 0.118% and 0.165%, respectively, for combined average of 0.093%. Here, we see a near-similar increasing pattern as noted earlier, except for the dips on day 28 at both sites, as depicted in Figure 7. SS304 coupons show lower weight loss percentage due to its higher corrosion resistance nature as published by Anwar et al. (2017) in their study on the corrosion rate of SS304 and SS310 alloys in atmospheric, underground and seawater splash zone in the Arabian Gulf. It was determined that the corrosion rate for both SS304 and SS316 exposed under atmospheric, underground and seawater splash zone conditions is low due to higher corrosion resistance [8]. However, silt soil still gave a significant factor in weight loss percentage as it shows a higher weight loss percentage for SS304 compared with the coupons in sandy soil. Once again, moisture has become a major

factor in exhibiting this trend. A slight difference in the percentage of weight loss and the corrosion rate for LCS at 42 days could be attributed to the anodic reaction rate. The anodic dissolution was decreased due to the accumulation of corrosion products on the metal surfaces. A similar finding was also reported elsewhere [9].

Corrosion rates for the SS 304 coupons from the sandy soil site were 0.15 mmpy, 0.04 mmpy, 0.06 mmpy and 0.07 mmpy after 14, 28, 42 and 56 days, with a cumulative average of 0.08 mmpy. For the silt soil sites, corrosion rates were 0.08 mmpy, 0.06 mmpy, 0.08 mmpy and 0.09 mmpy, respectively, for a cumulative average of 0.08 mmpy in Figure 8. The corrosion rate for SS304 was found to be lower than LCS due to its better corrosion resistance. The observed pattern for SS 304 in silt soil is higher than sandy soil due to more significant moisture content in this type of soil. However, after 14 days of exposure, the percentage of weight loss and corrosion rate for SS304 were higher in the sandy soil than silt soil. This is due to the susceptibility of SS304 towards localized corrosion compared to LCS, which generally exhibits uniform corrosion [10]. Localized corrosion could be enhanced by the chloride ion concentration in which sandy soil will entrap more chloride caused by marine aerosol. The trend was found to be inversed after 14 days and remained throughout the exposure period due to the corrosion mechanism's uniformity.

The findings found that the silt soil has prominent effects on weight loss and corrosion rate. This is due to the higher value of moisture found in silt soil, which figuratively double than the sandy soil. The presence of moisture enhances the ignition of the corrosion process as moisture is a prominent factor in the corrosion process. Moisture can create a thin layer of electrolyte and tend to suppress the formation of rust on the metal surface. This is aligned with the result reported by Akkouche et al. [9], where the authors stated that soil moisture is generally considered the most influential parameter because it strongly affects the most crucial point, which is the transport of oxygen (O_2) from the atmosphere to the steel surface. O_2 was transported via convection of the gas phase, which available in partially filled pores. Silt soil has low porosity due to its smaller particles and minerals size, then O_2 permeability is higher than sandy soil. In general, soil moisture plays a vital role in controlling oxygen diffusion through soils, electrical conductivity, and ionic migration in soils as well as soil-metal interfacial characteristics, which consequently affects the corrosion process [11].

Table 2. Result of average metal loss and *in-situ* parameters

Soil type	Coupon Type	Time (day)	Weight Loss (g)	pH	Temperature (°C)	Moisture Content (%)
Sandy soil	LCS	14	0.164	7.0	32	7.5
		28	0.301	7.0	30	8.9
		42	0.939	7.0	28	3.3
		56	1.159	7.0	30	8.0
	SS 304	14	0.016	7.0	32	7.5
		28	0.024	7.0	30	8.9
		42	0.050	7.0	28	3.3
		56	0.071	7.0	30	8.0

Table 2 (cont'd). Result of average metal loss and *in-situ* parameters

Soil type	Coupon Type	Time (day)	Weight Loss (g)	pH	Temperature (°C)	Moisture Content (%)
Silt soil	LCS	14	0.276	6.1	24	17.7
		28	0.652	6.3	23	19.2
		42	1.055	6.3	25	16.9
		56	1.924	6.2	25	20.0
	SS 304	14	0.030	6.1	24	17.7
		28	0.017	6.3	23	19.2
		42	0.033	6.3	25	16.9
		56	0.051	6.2	25	20.0

Table 3. Average corrosion rates (mmpy) in coupon after 14, 28, 42 and 56 days

	Low-Carbon Steel Coupon				Stainless Steel 304 Coupon			
Days	14	28	42	56	14	28	42	56
Sandy soil	0.87	0.80	1.67	1.54	0.15	0.04	0.06	0.07
Silt soil	1.47	1.74	1.87	2.56	0.08	0.06	0.08	0.09

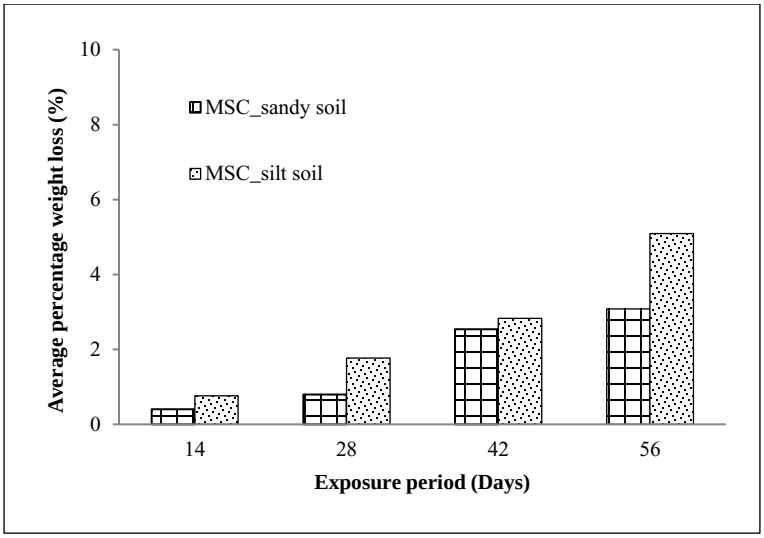


Figure 5. Average percentage weight loss in LCS coupons from sandy soil and silt soil sites

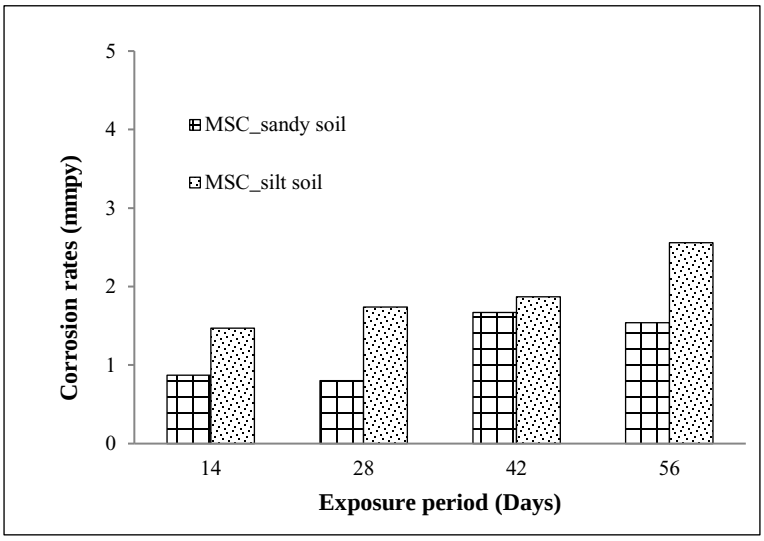


Figure 6. Corrosion rates in LCS coupons from sandy soil and silt soil sites

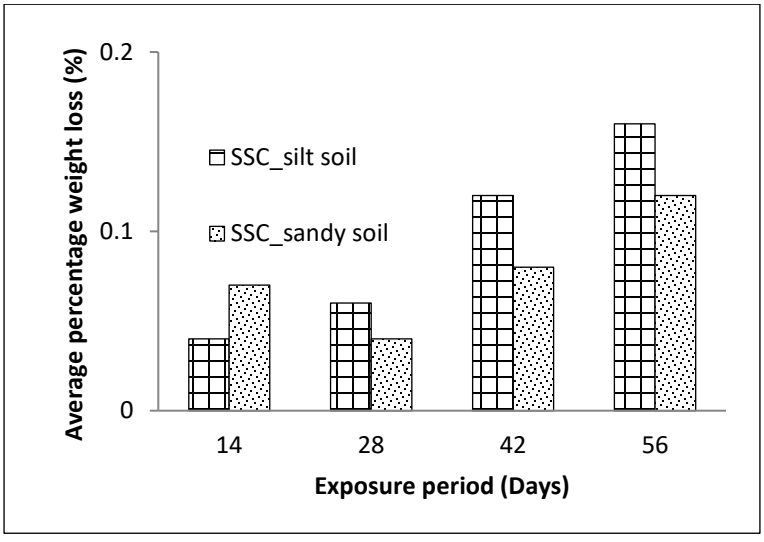


Figure 7. Percentage weight loss in SS 304 coupons from sandy soil and silt soil sites

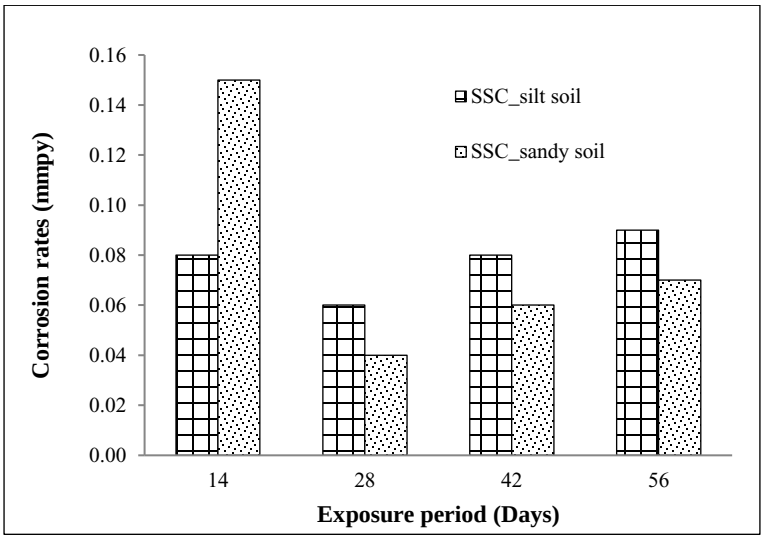


Figure 8. Corrosion rates in stainless steel 304 coupons from sandy soil and silt soil sites

Potentiodynamic polarization

The cathodic and anodic potentiodynamic polarization (PP) curves for both LCS and SS 304 in the studied soils with different conditions of the different exposure periods and at ambient temperature (30 ± 1 ◦C) for sandy soil and at ambient temperature (24 ± 1 ◦C) for silt soil. The corrosion rate can be calculated from the icorr values of LCS and SS 304 in the studied soils at different *in-situ* parameters. The PP parameters for the corrosion of both steels in the studied soils are recorded in Table 4. The value of anodic and cathodic Tafel lines (βa and βc) shows the changes of anodic and cathodic reaction for both metals in both soils. The value of βa for LCS is higher in silt soil than sandy soil due to the metals' anodic dissolution process.

Meanwhile, the value of βc for both metals in sandy soil is lower than silt soil due to the lower oxygen diffusion rate. For both sandy soil and silt soil studied, E_{corr} values were shifted to more negative values with increasing soil moisture content, indicating that the corrosion process has occurred with predominantly affected by the cathodic reaction. Similar behavior was reported elsewhere [12]. Corrosion current density (i_{Corr}) value shows a higher trend in silt soil than sandy soil. This is due to the higher ionic migration in silt soil due to the ionic conduction path provided by the moisture content in contrast to sandy soil. The corrosion rate of both metals in silt soil is also higher than sandy soil as the metals' corrosion rate is directly proportional to the i_{Corr} value.

Electrochemical impedance spectroscopy

EIS was used to investigate the effect of moisture content of the studied soils on the electrochemical behavior of LCS and SS 304 at ambient temperature. It is well known that the interpretation of EIS data largely depends on the development of equivalent circuits at the metal/electrolyte interface. The Nyquist plot for LCS and SS 304 in sandy soil and silt soil were depicted in Figure 9 - 12, respectively.

It was found that the shape of the plot represented by one semicircle due to the single time constant represented by all studied samples. A bigger semicircle is associated with better charge transfer resistance at the electrode-electrolyte interphase [13]. The value of charge transfer resistance R_{ct} in Table 5 shows that LCS and SS 304 in sandy soil have a higher value than LCS and SS 304 in silt soil. It is inferred that sandy soil provides more impedance towards corrosion activity. This is due to the

lower charge transfer process occurs at the LCS and SS 304 surface with the electrolyte.

Meanwhile, silt soil shows lower charge transfer resistance due to its nature that contained higher soil moisture, consequently facilitating the ignition of the corrosion process. The deviation from the ideal semicircle (the time constant dispersion) was also attributed to the inhomogeneities of the electrode surface [14]. However, in all studied cases, the system response in the Nyquist complex plain is an incomplete semicircle whose diameter and shape depend on the soil types and moisture content.

Scanning electron microscopy

Figure 13 - 16 depict SEM micrographs after 28 days of exposure to the sandy soils with different magnifications to see the pattern of the type that occurred on the steel surface.

Figures 13 - 20 depict SEM micrographs after 56 days of exposure to the sandy soil with different magnifications to see the pattern of the type that occurred on the steel surface.

Scanning electron microscopy (SEM) was used to observe the nature of deterioration of the test coupons. All micrographs show the surface features of the studied coupons after treatment with the cleaning solution. SEM was subjected to the surface of LCS and SS 304 after 28 days and 56 days of exposure to the sandy soil. The attachment of sediment products can be observed through SEM. The analysis of SEM confirms corrosion rates that happen to the surface of the steel coupons, and the type of corrosion that occurs on the steel surface can be observed through SEM.

SEM observed that the damage causes generally represent LCS by general corrosion, while SS304 surface damage was mainly due to the pitting corrosion. LCS surface damage is faster based on the image from the test due to the steel composition. The corroded area of LCS was found to be higher than the SS 304. The depth of the pitting that occurred was the same at all over the surface. SS 304 is resistance to corrosion compared to LCS. This argument is fixed with the result published by Wasim et al. [15] on their study reported that mild steel has more damage than the stainless steel at both sandy soil and silt soil due to the steel composition and their properties whereas mild steel is resistant to corrosion. Noor et al (2018) stated that the corrosivity of a particular soil could be related to the interaction of soil resistivity, salts in the soil, moisture content, pH, and elemental composition of the soil [16].

Table 4. Potentiodynamic polarization parameters of LCS and SS 304 in sandy soil and silt soil

Soil type	Material	Parameter				
		βc/Vdec^{-1}	βa/Vdec^{-1}	E_{Corr}/V	i_{Corr}/mA	Corr. Rate/mmpy
Sandy soil	LCS	0.79154	1.3772	-0.4929	1.64	19.061
	SS 304	1.3747	1.3304	-0.4582	0.3668	4.2625
Silt soil	LCS	0.76756	1.5054	-0.4929	1.77	20.575
	SS 304	2.073	0.46025	-0.4919	1.455	16.907

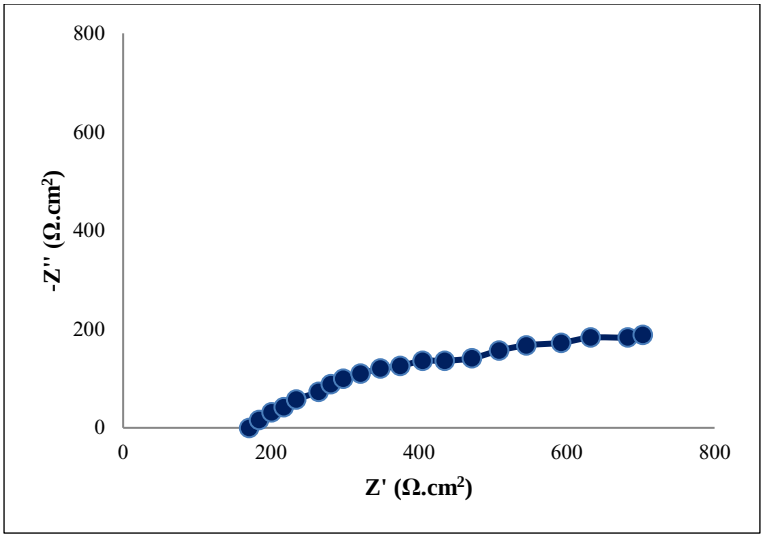


Figure 9. Nyquist plot for LCS in sandy soil

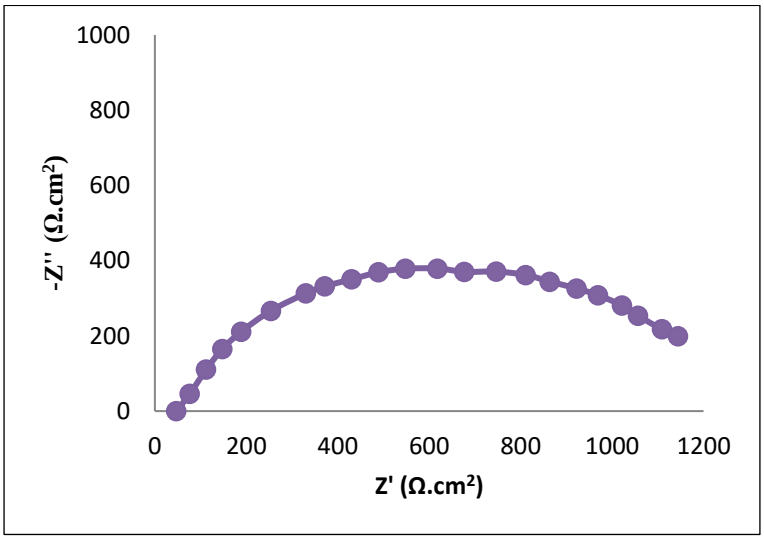


Figure 10. Nyquist plot for SS 304 in sandy soil

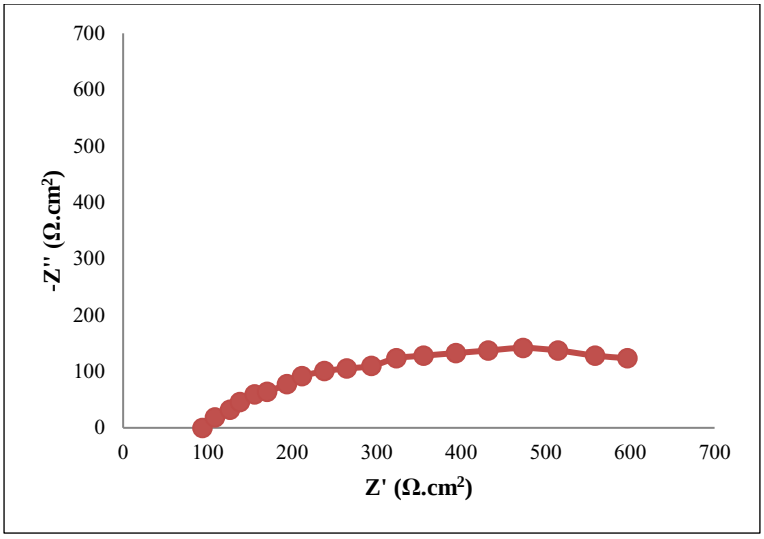


Figure 11. Nyquist plot for LCS in silt soil

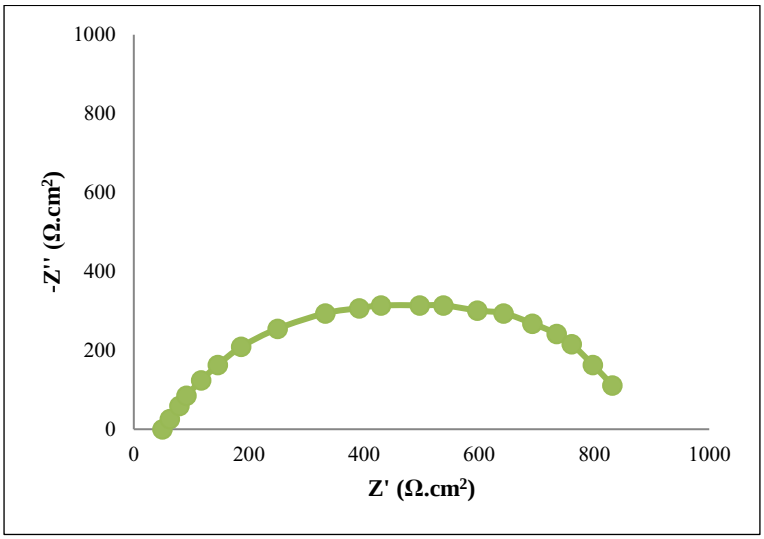


Figure 12. Nyquist plot for SS 304 in silt soil

Table 5. Solution and charge transfer resistance of LCS and SS 304 in sandy and silt soil

Soil	Material	R_s (Ω.cm²)	R_{ct} (Ω.cm²)
Sandy	LCS	170.7	801
	SS 304	46.9	1349
Silt	LCS	94.1	712
	SS 304	50.2	899

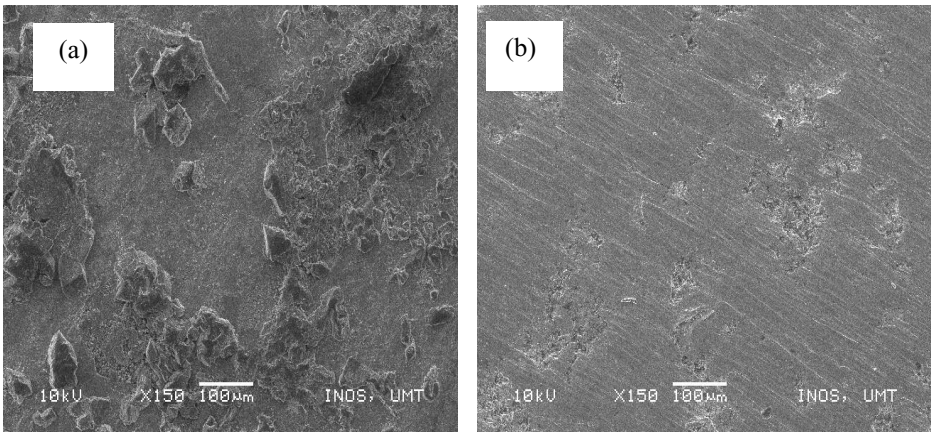


Figure 13. Surface morphology with x150 100µm magnificient of (a) LCS and (b) SS 304, respectively

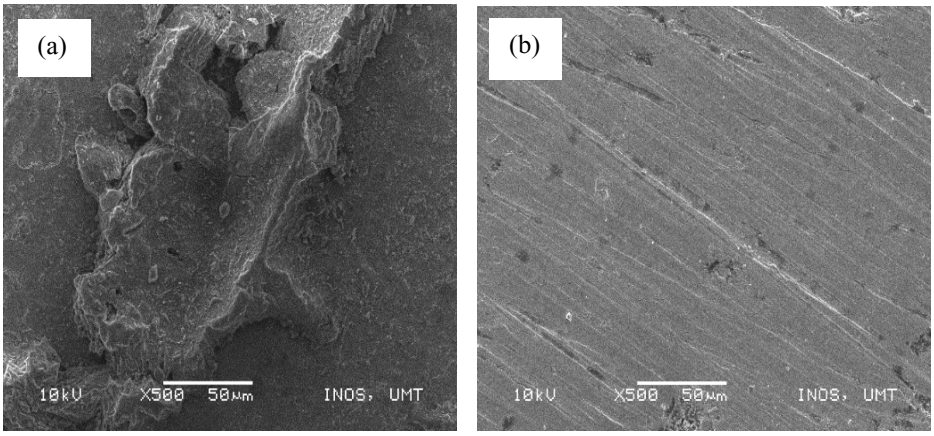


Figure 14. Surface morphology with x500 50µm magnification of (a) LCS and (b) SS 304, respectively

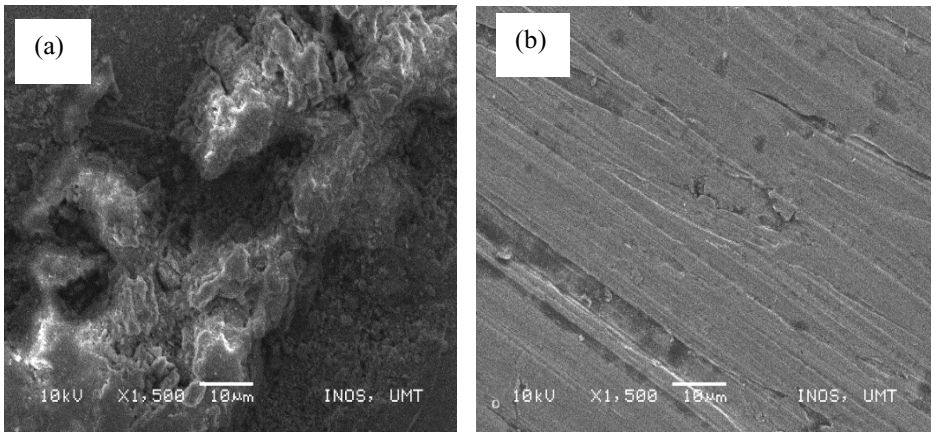


Figure 15. Surface morphology with x1,500 10µm magnification of (a) LCS and (b) SS 304, respectively

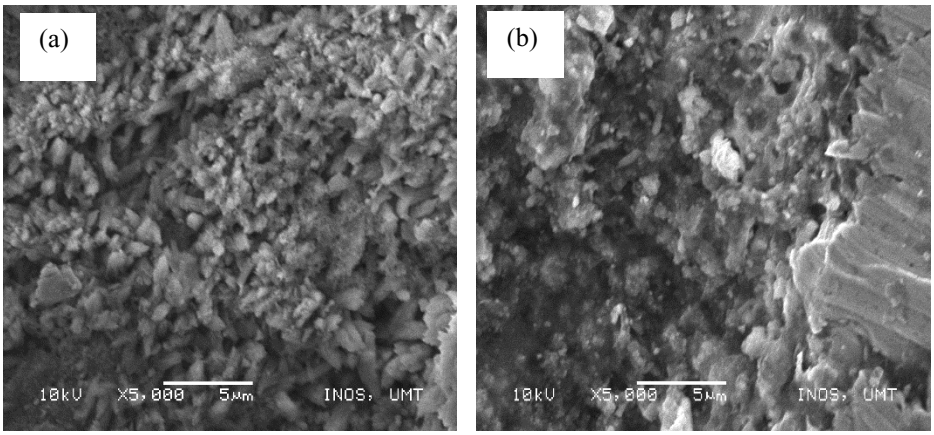


Figure 16. Surface morphology with x5,000 5µm magnification of (a) LCS and (b) SS 304, respectively

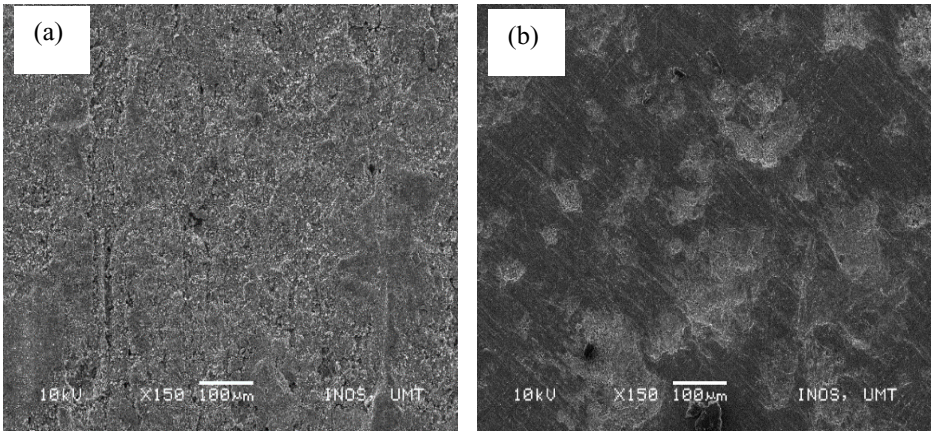


Figure 17. Surface morphology with x150 100µm magnification of (a) LCS and (b) SS 304, respectively

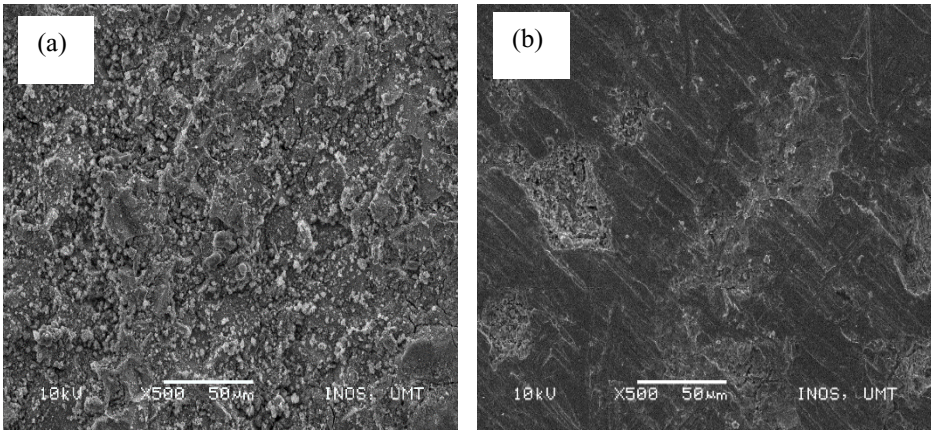


Figure 18. Surface morphology with x500 50µm magnification of (a) LCS and (b) SS 304, respectively

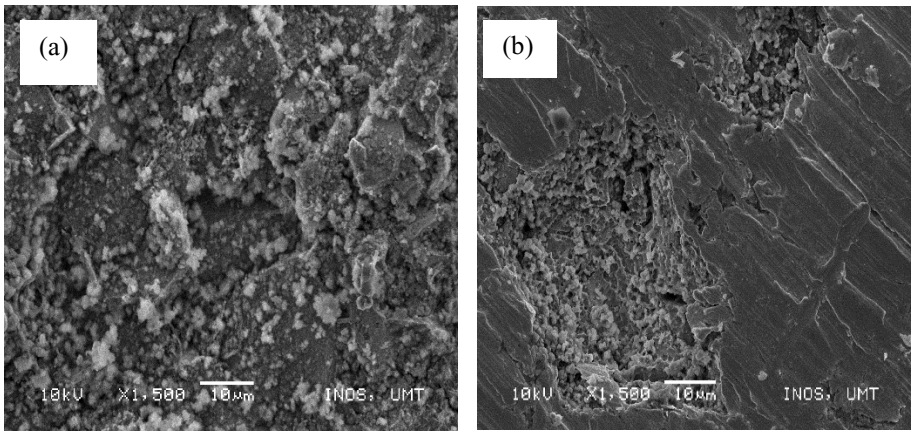


Figure 19. Surface morphology with x1,500 10µm magnificationof (a) LCS and (b) SS 304, respectively

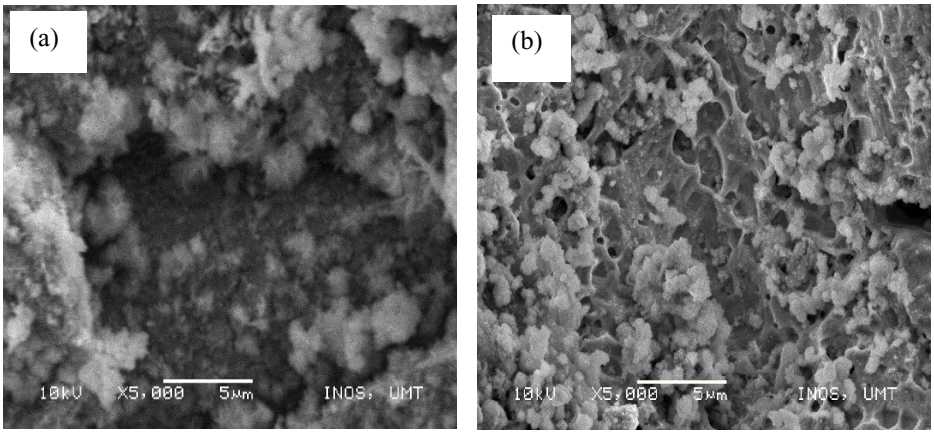


Figure 20. Surface morphology with x5,000 5µm magnification of (a) LCS and (b) SS 304, respectively

Conclusion

This study was conducted to scrutiny the corrosion behavior of LCS and SS 304 buried in two different soils, and it can be concluded that moisture content is the most influential factor on metal loss, whereas pH is relatively insignificant on underground corrosion. The electrochemical analysis shows that the value of E_{corr}, shifted to more negative values following the increment of soil moisture content, indicating that the cathodic reaction predominantly controls the corrosion process. Pitting corrosion and general corrosion occurred on both metal surfaces and both soil types. The pitting area of LCS is larger than the SS 304, and the depth of the pitting that occurred was the same across the surface. The pits area and its distribution on the metal surface also depend on the soil conditions.

Acknowledgment

The authors would like to thank all the members of CoREG (Composites Research Group) UMT, technicians, and support staff from Maritime Technology Lab, UMT, Biocomposite Lab, and INTROP and Advanced Engineering Materials and Composites Research Centre, UPM for their significant contribution and helps.

References

1. Spark, A., Cole, I., Law, D. and Ward, L. (2016). The effect of peptide-based nutrients on the corrosion of carbon steel in an agar-based system. *Corrosion Science*, 110: 174-181.
2. Yan, M., Sun, C., Xu, J. and Ke, W. (2015). Electrochemical behavior of API X80 steel in acidic soils from Southeast China. *International Journal of Electrochemical Science*, 10: 1762-1776.
3. Wu, T., Yan, M., Zeng, D., Xu, J., Sun, C., Yu, C. and Ke, W. (2015). Stress corrosion cracking of X80 steel in the presence of sulfate-reducing bacteria. *Journal of Materials Science & Technology*, 31(4): 413-422.
4. Qin, F., Jiang, C., Cui, X., Wang, Q., Wang, J., Huang, R. and Peng, P. D. (2018). Effect of soil moisture content on corrosion behavior of X70 steel. *International Journal of Electrochemical Science*, 13: 1603-1613.
5. Esfahani, M. N., Coupland, J. and Marimuthu, S. (2014). Microstructure and mechanical properties of a laser welded low carbon–stainless steel joint. *Journal of Materials Processing Technology*, 214(12): 2941-2948.
6. Mobin, M. and Aslam, R. (2018). Experimental and theoretical study on corrosion inhibition performance of environmentally benign non-ionic surfactants for mild steel in 3.5% NaCl solution. *Process Safety and Environmental Protection*, 114: 279-295.
7. Zulkifli, M. F. R., Radzi, N. M., Jusoh, S. M., Saidin, J. and Nik, W. M. N. W. (2019). Potential of cabbage extract (*Brassica oleracea*) as anti-fouling agent in alkyd undercoat for mild steel in seawater. *Malaysian Journal of Analytical Sciences*, 23(3): 451-461.
8. Anwar Ul-Hamida, Huseyin S., Abdul Qudus., Abdulrashid I. M., and Luai M. Al-Hems (2017). Corrosion study of SS304 and SS316 alloys in atmospheric, underground and seawater splash zone in the Arabian Gulf. *Corrosion Engineering, Science and Technology*, 52(2); 134-140.
9. Akkouche, R., Rémazeilles, C., Jeannin, M., Barbalat, M., Sabot, R. and Refait, P. (2016). Influence of soil moisture on the corrosion processes of carbon steel in artificial soil: Active area and differential aeration cells. *Electrochimica Acta*, 213: 698-708.
10. Faes, W., Lecompte, S., Van Bael, J., Salenbien, R., Bäßler, R., Bellemans, I. and De Paepe, M. (2019). Corrosion behaviour of different steel types in artificial geothermal fluids. *Geothermics*, 82: 182-189.
11. Azoor, R. M., Deo, R. N., Birbilis, N. and Kodikara, J. (2019). On the optimum soil moisture for underground corrosion in different soil types. *Corrosion Science*, 159: 108116.
12. Loto, R. T. and Loto, C. A. (2017). Potentiodynamic polarization behavior and pitting corrosion analysis of 2101 duplex and 301 austenitic stainless steel in sulfuric acid concentrations. *Journal of Failure Analysis and Prevention*, 17(4): 672-679.
13. Hajar, H. M., Zulkifli, F., Sabri, M. G, M., Fitriadhy, A. and Nik, W. N. W. (2017). Lawsonia inermis performance as corrosion inhibitor for mild steel in seawater. *International Journal of ChemTech Research*, 9(8): 600-608.
14. Hirschorn, B. D. (2010). Distributed time-constant impedance responses interpreted in terms of physically meaningful properties. Thesis University of Florida.
15. Wasim, M., Shoaib, S., Mubarak, N. M. and Asiri, A. M. (2018). Factors influencing corrosion of metal pipes in soils. *Environmental Chemistry Letters*, 16(3): 861-879.
16. Noor, E. A. and Al-Moubaraki, A. H. (2014). Influence of soil moisture content on the corrosion behavior of X60 steel in different soils. *Arabian Journal for Science and Engineering*, 39(7): 5421-5435.

Malaysian Journal of Analytical Sciences (MJAS)
Published by Malaysian Analytical Sciences Society

PHYTOCHEMICAL ANALYSIS AND ISOLATION OF SECONDARY METABOLITES FROM *Persea declinata*

(Analisis Fitokimia dan Pengasingan Metabolit Sekunder Daripada *Persea declinata*)

Sani Aliyu[1,2], Norazah Basar[1]*, Yakubu Rufai[1,3], Shamsul Khamis[4]

[1] *Department of Chemistry, Faculty of Science,*
Universiti Teknologi Malaysia, 81310 Johor Bahru, Johor, Malaysia
[2] *Department of Chemistry,*
Kaduna State University, P.M.B 2339, Tafawa Balewa Way, Kaduna, Nigeria
[3]*Department of Chemistry,*
Federal College of Education Okene, P.M.B 1062 Kogi State, Nigeria
[4]*School of Environment and Natural Resources Sciences, Faculty of Science and Technology,*
Universiti Kebangsaan Malaysia, 43600 UKM Bangi, Selangor, Malaysia

**Corresponding author: norazahb@utm.my*

Received: 18 July 2019; Accepted: 20 July 2020; Published: 10 December 2020

Abstract

Phytochemical analysis of *Persea declinata* leaves and stembark extracts exhibited the presence of cardiac glycosides, coumarins, reducing sugars, steroids, flavonoids, tannins, and phenolic compounds. Sesamin **(1)**, γ-sitosterol **(2),** and palmitic acid **(3)** were isolated for the first time from ethyl acetate extract of the stembark of *P. declinata* by chromatographic methods. Their structures were elucidated based on spectroscopic analysis such as infrared (IR), gas chromatography-mass spectroscopy (GC-MS), nuclear magnetic resonance (NMR), and also involved comparison with data from literatures.

Keywords: *Persea declinata*, phytochemicals, sesamin, gamma sitosterol, palmitic acid

Abstrak

Analisis fitokimia ke atas daun dan kulit batang *Persea declinata* menunjukkan kehadiran sebatian glikosida kardiak, kumarin, gula penurun, steroid, flavonoid, tanin dan sebatian fenolik. Sesamin **(1)**, γ-sitosterol **(2)**, dan asid palmitik **(3)** telah diasingkan buat pertama kali daripada ekstrak etil asetat kulit batang *P. declinata* menggunakan kaedah kromatografi. Struktur sebatian telah dicirikan berdasarkan analisis spektroskopi seperti inframerah (IR), kromatografi gas-spektroskopi jisim (GC-MS), resonans magnet nuklear (NMR) dan juga melibatkan perbandingan data dengan kajian lepas.

Kata kunci: *Persea declinata*, fitokimia, sesamin, gamma sitosterol, asid palmitik

Introduction

Diseases such as diabetes, cancer, and hypertension continue to pose a significant threat to humanity globally. The use of conventional drugs in the treatment of diseases is usually associated with side effects and is typically costly. It is, therefore, necessary to continue to search for effective, safe, and affordable medicines from natural sources. Phytochemicals contained in plant parts, including fruits and vegetables, effectively reduce the risk of cardiovascular disease, cancer, Alzheimer's disease, stroke, cataracts, and help delay ageing [1].

Persea declinata is a plant that belongs to the genus *Persea* from the Lauraceae family. Species of the genus *Persea* have been used traditionally in treating diarrhoea, hypertension, infectious diseases [2], as well as gastric analgesic and anti-inflammatory agents [3]. *P. declinata* belongs to the same genus (*Persea*) with the popularly consumed healthy plant, *Persea americana* (avocado), which is extensively studied and reported for many pharmacological activities including antidiabetic, anti-inflammatory, anti-convulsion, antibacterial, antifungal, anthelmintic [4], initiating the hypolipidemic effect [5], and as trypanocidal agent [6]. Previous studies indicate that compounds isolated from the *Persea* species (avocado) had cytotoxic, insecticidal [7, 8], and antimycobacterial activity [9]. Various phytochemicals, including flavonoids, coumarins, phenolic compounds, aliphatic acetogenins (alkanols), had been isolated from the *Persea* species [3, 7, 9, 10, 11]. A recent review showed that the Lauraceae family is generally a good source of lignans and neolignans, the most chemotaxonomic characteristics of many species of the family [12]. Previous bioactivities studies suggest that certain plant compounds, such as sesamin, were potent antioxidant agents [13] and play a role in the amelioration of oxidative stress induced by CCl_4 [14]. γ-Sitosterol had been reported for antidiabetic property [15, 16]. Palmitic acid previously isolated from *Terminalia glaucescens* root bark [17] and *Canthium parviflorum* leaves [18] and the active crude extract from which it was identified in *Kigelia pinnata* leaves exhibited a good cytotoxic effect on human colon cancer cell line (HCT-116) [19]. *P. declinata* was recently reported as having apoptotic property [20], indicating that it could be an appropriate candidate as the principal drug for many other diseases.

However, despite promising medicinal values within the *Persea* species, no single report on *P. declinata* phytochemicals is currently available in the literature. The biological and chemical characterisation of plant species has led to promising sources of biologically potent compounds [21]. Therefore, this study was carried out to evaluate the classes of phytochemicals present in the leaves and stembark of *P. declinata*, and the isolation of compounds from its stembark. To our knowledge, this is the first report on the phytochemical screening and isolation of compounds from *P. declinata*.

Materials and Methods

Chemicals and reagents

All chemicals and reagents used in this work were of analytical grade.

Plant materials

The plant samples (leaves and stembark) were collected from Gunung Jerai, Kedah, Malaysia and verified by Dr. Shamsul Khamis, Universiti Kebangsaan Malaysia. The samples were deposited at the UKMB Herbarium with a voucher No. UKMB 4350.

General experimental procedure

^{1}H and ^{13}C NMR spectra were recorded on Bruker Avance (400 MHz) spectrometer, using deuterated chloroform ($CDCl_3$) as the solvent. The IR was recorded on PerkinElmer FT-IR spectrometer, while GC-MS data were acquired using Agilent 7820A (G4350). Thin-layer chromatography (TLC) was done on 0.20 mm precoated silica gel aluminium sheets (Merk Kieselgel 60 F_{254}). TLC spots were observed under the UV light at 254 nm and 365 nm. Vanillin sulphuric acid was used as the spraying reagent.

Extraction and phytochemical screening

The leaves and stembark of *P. declinata* were air-dried and triturated to a coarse powder using a grinding machine. Each sample (50 g) was separately macerated with methanol, and another set (50 g each) were extracted using Soxhlet for comparison of yield and phytochemicals present. The extracts were concentrated

under vacuum using a rotary evaporator to obtain methanol leaves and stembark extracts from maceration and Soxhlet methods.

Phytochemical screening of the leaf and stembark extract of *P. declinata*

Preliminary phytochemical screening of leaves and stembark of *P. declinata* were done using the standard procedures of Harborne [22] and Trease and Evans [23], with slight modification as follows;

Tests for simple sugar (Fehling's test)

Approximately 1 mL of Fehling's solutions **A** and **B** were mixed and warmed for 1 minute. The mixture was added to an equal volume of the test solution. The solution was heated in a boiling water bath for 5-10 minutes. A yellow precipitate was formed, which then turned to brick red.

Test for anthraquinone glycosides (Borntrager's test)

Each test sample was mixed with 3 mL of dilute H_2SO_4, warmed, and filtered. The filtrate was cooled, and an equal volume of benzene was added to it. The solution was shaken vigorously to separate the organic layer. An equal volume of dilute ammonia solution was added to the organic layer. The inability of the ammonia layer to turn pink indicates the absence of anthraquinone glycosides.

Test for cardiac glycosides (Keller-Killiani test)

A volume of 1 mL concentrated H_2SO_4, 2 mL of glacial acetic acid, and 1 drop of $FeCl_3$ solutions were added to 5 mL of the extract. The appearance of a brown ring indicated the presence of cardiac glycosides.

Test for coumarins

The concentration of 10% NaOH was added to 2 mL of the extract. The mixture was shaken vigorously for 5 min. The appearance of yellow colouration indicated the presence of coumarins.

Test for saponins (foam test)

About 20 mL of distilled water was added to 1 mL of the extract in a measuring cylinder. The mixture was shaken well for 15 min, and no layer of foam was observed.

Tests for quinone

Concentrated H_2SO_4 was mixed with 2 mL of the extract in a test-tube and shaken vigorously for 5 min. No visible red colour was observed.

Test for steroids (Salkowski test)

About 2 mL of concentrated H_2SO_4 and 2 mL of chloroform were added to 2 mL of the extract. The solution was shaken vigorously. The chloroform layer changed to red, while the acid layer showed greenish-yellow fluorescence.

Test for alkaloids (Mayer's test)

Approximately 1 mL of dilute HCl and 1 mL of Mayer's reagent were added to 2-3 mL of filtrate, and well shaken. The formation of yellow precipitate indicated the presence of alkaloids.

Test for Flavonoids (Shinoda test)

Concentrated hydrochloric acid (HCl) was added in drops to the test solution. Magnesium turnings were put into the solution. The pink-red colour observed indicated the presence of flavonoids.

Test for tannins and phenolic compounds $FeCI_3$ solution test

A solution of 5% $FeCl_3$ was added to 2 mL of the extract. A deep blue-black colouration indicated tannins and phenolic compounds in the test sample.

Extraction and isolation procedure

Powdered stembark sample of *P. declinata* (1.5 kg) was macerated successively in increasing solvent polarity with *n*-hexane, ethyl acetate, and methanol each for 72 hours. The extracts were separately concentrated under vacuum yielding *n*-hexane, ethyl acetate, and methanol crude extracts – PDHSE, PDESE, and PDMSE. Silica gel 60 Å (Mesh size 230–400) was used for Vacum Liquid Chromatography (VLC) of the EtOAc extract, PDESE (36.44 g; extract: silica gel = 1:30) yielding 35 fractions. Fractions were pooled based on TLC profiles resulting in five sub-fractions and were labelled as A–E. Sub-fraction B (3.48 g) was further fractionated using VLC and 44 sub-fractions were obtained, which were then pooled based on the Thin-Layer Chromatography (TLC) profile and labelled as PDSE1-PDSE8. Further

purification of PDSE2 by column chromatography (CC) resulted in the isolation of sesamin (1), γ-sitosterol (2), and palmitic acid (3).

Results and Discussion

The yield of extraction of leaves and stembark of *P. declinata* using maceration and Soxhlet are shown in Table 1. Leaves extract yielded higher (13.33%) using Soxhlet compared to the maceration method (6.11%). The results of phytochemical screening of leaves and stembark maceration and Soxhlet extracts of *P. declinata* revealed the presence of reducing sugars, cardiac glycosides, coumarins, steroids, flavonoids, tannins, and alkaloids in all extracts (Table 2). Therefore, the plant under study may possess bioactive compounds with specific medicinal values.

Isolation and purification of compounds from *P. declinata* stembark

Sesamin (1)

Gravity column chromatographic separation on PDSE2 yielded compound **(1)** (5.9 mg) as white needle solid R_f = 0.52 in PE:EtOAc 4:1. The IR spectrum of **(1)** showed a band at 2881 cm^{-1} for (C-H) and an aromatic (C=C) ring stretch band at 1653 cm^{-1}. The ^1H NMR spectrum of **(1)** showed signals at δ 6.87 (2H, *d*, *J* =1.2 Hz, H-2′,2″), 6.80-6.84 (4H, m, H-5′,5″,6′,6″) representing aromatic protons. The singlet peak at δ 5.97 (4H, *s*, H-7′,7″) was assignable to methylenedioxy protons, while the signal at δ 3.05 (2H, *m*, H-1,5) was assigned to the methine protons. Other prominent chemical shifts at δ 3.89 (2H, *dd*, *J* = 3.0 and 9.0 Hz, H-2,6) and δ at 4.26 (2H, d, *J*=4.0 Hz, H-4,8β), 4.74 (2H, dt, *J*=7.0 and 9.0 Hz, H-4,8α) were assigned to methine and methylene protons, respectively. The ^{13}C spectrum showed 10 peaks representing 20 carbons in the compound being symmetrical. The peaks at chemical shifts δ 106.5, 108.1, and 119.3 were assigned to aromatic carbons at positions 2′/2″, 5′/5″, and 6′/6″ respectively. C-7′/7″ were represented by the peak at δ 101.0, while δ 135.1 was assigned to C-1′/1″. The GC-MS data shows molecular ion peak [M^+] of *m/z* 354.2 (cal. 354) corresponding to the molecular formula of compound **(1)** $C_{20}H_{18}O_6$, which has been reported previously [24]. These spectroscopic data and the data from the literature [24] confirmed compound **(1)** as sesamin.

γ- Sitosterol (2)

Continuous gravity elution of PDSE2 resulted in the isolation of compound **(2)** as a white solid (13 mg) R_f = 0.55 in PE:EtOAc 4:1. Treatment of the TLC spot with vanillin sulphuric acid reagent gave a purple colouration, indicating a terpene type of compound. The IR spectrum of **(2)** shows a broad absorption band at 3390 cm^{-1} characteristics of O-H group, while the band at 2933 cm^{-3} corresponds to sp^3 C-H stretch. The ^1H NMR of compound **(2)** shows chemical shifts at δ 0.69 (3H, *s*, H- 18), δ 1.02 (3H, *s*, H-19), (3H, *d*, *J*=6.4 Hz, H-21), δ 0.82 (3H, *d*, *J*=2.0 Hz, H-26), δ 0.84 (3H, *d*, *J*=2.0 Hz, H-27), δ 0.86 (3H, H-29) representing methyl groups in the compound. Evidence for oxymethine proton at position C-3 was indicated by the peak at δ 3.54. The signal at δ 5.37 was for the proton attached to C=C at position C-6. ^{13}C chemical shifts at δ 121 and δ 140 confirm the presence of olefinic carbons C-6 and C-5, respectively. Oxymethine carbon C-3 was represented by the signal at δ71.82. The various peaks at δ 11.85–19.80 represent the methyl groups. The GC-MS spectrum showed a molecular ion peak [M^+] at *m/z* 414.5 (calc. 414) corresponding to the molecular formula of $C_{29}H_{50}O$ [16].

Palmitic acid (3)

Compound **(3)** was also isolated from PDSE2 as a white solid (10.8 mg), R_f = 0.78 in PE:EtOAc 4:1. The IR sharp band at 3325 cm^{-1} and band at 2929 cm^{-1} correspond to O-H and C-H stretch. Evidence for the presence of a carbonyl group was seen by the appearance of C=O stretch band at 1713 cm^{-1}. The ^1H NMR of compound **(3)** indicates the presence of long-chain of multiple methylene protons at δ 1.277, while methyl protons were represented by a triplet peak at δ 0.90. Protons at C-2 were represented by the triplet signal at 2.35 (2H, *t, J*=7.2 Hz, H-2) shifted further being near to -COOH group. The ^{13}C spectrum shows peak at δ 179, which represents the carbonyl carbon (C=O) at position C-1 and the chemical shift position of

methylene carbon at position C-2 was further shifted to δ 34.03 due to de-shielding effect of the neighbouring carbonyl group. Other methylene carbons (C-4 to C-12) were represented by the intense peak and other peaks at δ 24.69-30.86. Its molecular formula $C_{16}H_{32}O_2$, was confirmed by the presence of molecular ion peak [M^+] at *m/z* 256.3 (cal. 256) in the GC-MS [17].

Spectroscopic data for isolated compounds

Sesamin (1)

IR (Neat) v_{max} cm^{-1} ($CDCl_3$): 2881.30 (C-H), 1653.15 (C=C aromatic). **^{1}H-NMR** ($CDCl_3$, 400 MHz): **δ_H** 3.05 (2H, *m*, H-1,5), 3.89 (2H, *dd*, *J* = 3.0 and 9.0 Hz, H-2,6), 4.26 (2H, d, *J*=4.0 Hz, H-4,8β), 4.74 (2H, dt, *J*=7.0 and 9.0 Hz, H-4,8α), 5.97 (4H, *s*, H-7′,7″), 6.80-6.84 (4H, m, H-5′,5″,6′,6″), 6.87 (2H, *d*, *J* =1.2 Hz, H-2′,2″). **^{13}C-NMR** ($CDCl_3$, 100 MHz): **δ_C** 135.1 (C-1'/1''), 54.3 (C-1/5), 85.7 (C-2/8), 71.7 (C-4/6), 106.5 (C-2'/2''), 147.9 (C-3'/3''), 147.1 (C-4'/4''), 108.1 (C-5'/5''), 119.3 (C-6'/6''). **GC-MS**: 65,103,149,203,239, 281, 317, 354.

γ- Sitosterol (2)

IR (Neat) v_{max} cm^{-1} ($CDCl_3$): 3390.10 (OH), 2933.58 (C-H). **^{1}H-NMR** ($CDCl_3$, 400 MHz): **δ_H** 3.50 (1H, *m,* H-3), 5.36 (1H, *t*, *J* = 2.16 Hz, H-6), 0.69 (3H, *s*, H- 18), 0.93 (3H, d, *J* = 6.4 Hz, H-21), 0.82 (3H, *d*, *J* = 2.0 Hz, H-26), 0.84 (3H, *d*, *J* = 2.0 Hz, H-27), 0.86 (3H, H-29). **^{13}C-NMR** ($CDCl_3$, 100 MHz): **δ_C** 37.26 (C-1), 32.41 (C-2), 71.82 (C-3), 42.26 (C-4), 140 (C-5), 121.71 (C-6), 31.92 (C-7), 31.63 (C-8), 50.23 (C-9), 33.72 (C-10), 21.09 (C-11), 39.79 (C-12), 42.33 (C-13), 56.08 (C-14), 26.13 (C-15), 28.24 (C-16), 56.78 (C-17), 11.85 (C-18), 19.39 (C-19), 36.51 (C-20), 19.04 (C-21), 33.97 (C-22), 26.13 (C-23), 45.86 (C-24), 29.19 (C-25), 18.25 (C-26), 19.80 (C-27), 23.09 (C-28), 12.22 (C-29). **GC-MS:** 57, 69, 81, 95, 105, 119, 133, 145, 159, 173, 187, 199, 213, 222, 231, 241, 255, 273, 283, 303, 329, 341, 354, 371, 381, 396, 414.

Palmitic acid (3)

IR (Neat) v_{max} cm^{-1} ($CDCl_3$): 3325.78 (OH), 1713.95 (C=O), 2929.34 (C-H). **^{1}H-NMR** ($CDCl_3$, 400 MHz): **δ_H** 2.35 (2H, *t, J* = 7.2 Hz, H-2), 1.61 (2H, *m*, 7.2, 7.6 Hz, H-3), 1.27 (22H, *s,* H-4 to H-13), 1.33, 0.91 (3H, *t, J* = 6.4 Hz). δ ^{13}C: 179.87, 34.03, 24.19, 29.06-30.86, 30.86, 22.68, 14.08. **^{13}C-NMR** ($CDCl_3$, 100 MHz): **δ_C** 179.87 (C-1), 34.03 (C-2), 24.19 (C-3), 29.06-30.86 (C-4-13), 30.86 (C-14), 22.68 (C-15), 14.08 (C-16). **GC-MS:** 51, 60, 73, 83, 97, 107, 115, 129, 143, 157, 171, 185, 199, 213, 227, 239, 143, 157, 171, 185, 199, 213, 227, 239, 248, 256.

Phytochemical investigation of the leaves and stembark of *P. declinata* indicated the presence of various classes of secondary metabolites, including reducing sugars, cardiac glycosides, coumarins, steroids, flavonoids, tannins, and alkaloids. The classes of compounds were known to possess medicinal values. The compounds **(1)**, **(2)**, and **(3)** belonging to lignans, sterols, and fatty acids respectively were isolated and reported for the first time from *P. declinata* and the genus *Persea* (Figure 1). Therefore, *P. declinata* containing these bioactive principles is a good candidate for further investigations of its medicinal potentials. As such, isolation and bioactivity studies of its various parts are currently on-going.

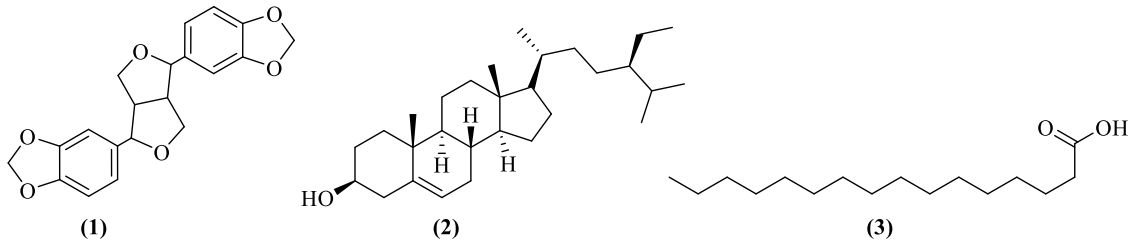
Table 1. Comparison of the yield of maceration and Soxhlet extraction methods

Sample	**Extraction method**	**Maceration**	**Soxhlet extraction**
	Sample weight (g)	50	50
Stembark	Yield (g)	3.96	3.78
	Percentage (%)	7.92	7.55
Leaf	Yield (g)	3.06	6.67
	Percentage (%)	6.11	13.33

Table 2. Summary of phytochemical screening of the leaf and stembark methanol extracts of *P. declinata*

Sample test	**Stembark**		**Leaf**	
	Maceration	**Soxhlet**	**Maceration**	**Soxhlet**
Reducing sugars	+	+	+	+
Cardiac glycosides	+	+	+	+
Coumarins	++	++	++	++
Saponins	-	-	-	-
Quinones	-	-	-	-
Steroids	+	+	+	+
Flavonoids	+	+	+	+
Phenolic compounds	++	++	++	++
Alkaloids	+	+	+	+
Anthraquinones glycosides	-	-	-	-

+ = presence, ++ = intense, - = not present



(1) **(2)** **(3)**

Figure 1. Structures of Compounds **(1)**, **(2)** and **(3)**

Conclusion

Phytochemicals found present in both the leaves and stembark of *P. declinata* include reducing sugars, cardiac glycosides, coumarins, steroids, flavonoids, tannins, and phenolic compounds. Three compounds identified as sesamin **(1)**, γ- sitosterol **(2)**, and palmitic acid **(3)** were successfully isolated and elucidated using spectroscopic techniques. It is hoped that more isolation and pharmacological tests would be undertaken in the on-going work.

Acknowledgement

We thank the Ministry of Higher Education (MOHE) for the financial support under Research University Grant (Q.J130000.2526.12H36) and the Faculty of Science, Universiti Teknologi Malaysia for providing the research facilities .

References

1. Liu, R. H. (2003). Health benefits of fruit and vegetables are from additive and synergistic combinations of phytochemicals. *American Journal of Clinical Nutrition*, 78: 3-6.
2. Adeyemi, O. O., Okpo, S. O. and Ogunti, O. O. (2002). Analgesic and anti-inflammatory effects of the aqueous extract of leaves of *Persea americana* Mill Lauraceae. *Fitoterapia*, 73(5): 375-380.
3. Alvárez, J. M., Cuca, L. E., Carrasco-Pancorbo, A., Ruiz-Muelle, A. B., Fernández, I. and Fernández-Gutiérrez, A. (2016). Phenolic constituents of leaves from *Persea caerulea* Ruiz & Pav; Mez (Lauraceae). *Biochemical Systematics and Ecology*, 67: 53-57.
4. Yasir, M., Das, S. and Kharya, M. D. (2010). The phytochemical and pharmacological profile of *Persea americana* Mill. *Pharmacognosy Reviews*, 4(7): 77-84.
5. Pahua-Ramos, M. E., Ortiz-Moreno, A., Chamorro-Cevallos, G., Hernández-Navarro, M. D., Garduño-Siciliano, L., Necoechea-Mondragón, H., and Hernández-Ortega, M. (2012) Hypolipidemic effect of avocado (*Persea americana* mill) seed in a hypercholesterolemic mouse model. *Plant Foods for Human Nutrition*, 67(1): 10-16.
6. Abe, F., Nagafuji, S., Okawa, M., Kinjo, J., Akahane, H., Ogura, T, Martinez-Alfaro, M. A. and Reyes-Chilpa, R. (2005). Trypanocidal constituents in plants 5. Evaluation of some mexican plants for their trypanocidal activity and active constituents in the seeds of *Persea americana*. *Biological & Pharmaceutical Bulletin*, 28(7): 1314-1317.
7. Oberlies, N. H., Rogers, L. L., Martin, J. M. and McLaughlin, J. L. (1998). Cytotoxic and insecticidal constituents of the unripe fruit of *Persea americana*. *Journal of Natural Products*, 61(6): 781-785.
8. Chang, C. F., Isogai, A., Kamikado, T., Murakoshi, S., Sakurai, A. and Tamura, S. (1975). Isolation and structure elucidation of growth inhibitors for silkworm larvae from avocado leaves. *Agricultural and Biological Chemistry*, 39(5): 1167-1168.
9. Lu, Y-C., Chang, H-S., Peng, C-F., Lin, C-H. and Chen, I-S. (2012). Secondary metabolites from the unripe pulp of *Persea americana* and their antimycobacterial activities. *Food Chemistry*, 135: 2904-2909
10. Gowda, D. C., Gowda, J. P. and Anjaneyalu, Y. V. (1982). Structure of an arabinoxylan from the bark of *Persea macrantha* (Lauraceae). *Carbohydrate Research*, 108(2): 261-267.
11. Lee, T. H., Tsai, Y. F., Huang, T. T., Chen, P. Y., Liang, W. L. and Lee, C. K. (2012). Heptadecanols from the leaves of *Persea americana* var. americana. *Food Chemistry*, 132(2): 921-924.
12. Li Y., Xie, S., Ying, J., Wei, W. and Gao, K. (2018). Chemical structures of lignans and neolignans isolated from lauraceae. *Molecules*, 23(12): 3164.
13. Fukuda, Y., Osawa, T., Namiki, M. and Ozaki, T. (1985). Studies on antioxidative substances in sesame seed. *Agricultural and Bilological Chemistry*, 49(2): 301-306.
14. Lv, D., Zhu, C. Q. and Liu, L. (2015). Sesamin ameliorates oxidative liver injury induced by carbon tetrachloride in rat. *International Journal of Clinical and Experimental Pathology*, 8(5): 5733-5738.
15. Balamurugan, R., Stalin, A. and Ignacimuthu, S. (2012). Molecular docking of γ -sitosterol with some targets related to diabetes. *European Journal of Medicinal Chemistry*, 47: 38-43.

16. Balamurugan, R., Duraipandiyan, V. and Ignacimuthu, S. (2011). Antidiabetic activity of γ-sitosterol isolated from *Lippia nodiflora* L. in streptozotocin induced diabetic rats. *European Journal of Pharmacology*, 667(1–3): 410-418.
17. Bulama, J. S, Dangoggo, S. M. and Mathias, S. N. (2014). Isolation and characterization of palmitic acid from ethyl acetate extract of root bark of *Terminalia glaucescens*. *Chemistry of Materials*, 6(12): 140-144.
18. Krishnan, K. R., James, F. and Mohan, A. (2016). Isolation and characterization of n-hexadecanoic acid from *Canthium parviflorum* leaves. *Journal of Chemical and Pharmaceutical Research*, 8(8): 614–617.
19. Ravi, L. and Krishnan, K. (2017). Cytotoxic potential of n-hexadecanoic acid extracted from *Kigelia pinnata* leaves. Asian Journal of Cell Biology, 12(1): 20-27.
20. Narrima, P., Paydar, M., Looi, C. Y., Wong, Y. L., Taha, H., Wong, W. F., Mohd, M. A. and Hadi A. H. (2014). *Persea declinata* (Bl.) Kosterm bark crude extract induces apoptosis in MCF-7 Cells via G0/G1 cell cycle arrest, Bcl-2/Bax/ Bcl-xl signaling pathways and ROS generation. *Evidence-Based Complementary and Alternative Medicine*, 2014: 1-14.
21. Llorent-martínez, E. J., Spínola, V. and Castilho, P. C. (2017). Phenolic profiles of Lauraceae plant species endemic to Laurisilva forest : A chemotaxonomic survey. *Industrial Crops and Products*, 107: 1-12.
22. Harborne, J. B. (1973). Phytochemical methods: A guide to modern techniques of plant analysis. Chapman and Hall Ltd, London: pp. 34-213.
23. Trease, G. E. and Evans, W. C. (2009). Trease and Evans Pharmacognosy. Elsevier, London: pp. 196-356.
24. Laggoune, S., Brouard, I., Leon, F., Calliste, C. A., Duroux, J. L., Bermejo, J., Kabouche, Z. and Kabouche, A. (2011). Lignans and an abundant flavone glycoside with free-radical scavenging activity from the roots of the endemic species *Stachys mialhesi* de Noé. *Record of Natural Products*, 5(3): 238-241.

Malaysian Journal of Analytical Sciences (MJAS)
Published by Malaysian Analytical Sciences Society

REMOVAL OF COPPER IONS FROM AQUEOUS SOLUTIONS USING POLY(VINYLBENZYL CHLORIDE)

(Penyingkiran Ion Kuprum dari Larutan Akueus Menggunakan Poli(vinilbenzil klorida))

Hamzah Gamal Abdo Allozy and Khairil Juhanni Abd Karim*

Department of Chemistry, Faculty of Science,
Universiti Teknologi Malaysia, 81310 UTM Johor Bahru, Malaysia

**Corresponding author: kjuhanni@utm.my*

Received: 18 July 2019; Accepted: 20 July 2020; Published: 10 December 2020

Abstract

Nowadays, contamination of copper (Cu(II)) has become one of the worst environmental problems. Due to its environmental resistance and persistence, the treatment of Cu(II) is crucial. Poly(vinylbenzyl chloride) (PVBC) was synthesised through reversible addition-fragmentation chain transfer (RAFT) polymerisation technique utilising monomer vinylbenzyl chloride (VBC), 4-cyanopentanoic acid dithiobenzoate (CPADB) as RAFT agent and 4,4′-Azobis (4-cyanopentanoic acid) (ACPA) as initiator. This study aims to synthesise PVBC and to test the ability of PVBC to remove Cu(II) ions from aqueous solution. In this study, PVBC was successfully synthesised when reacted for 24 h at 80 °C, and the ability of the PVBC to adsorb and remove Cu(II) ions was investigated. Important adsorption parameters such as adsorbate concentration, adsorption dosage, and contact time were studied. The maximum Cu(II) adsorption capacity (q_{max}) of PVBC was 263.15 mg/g with a copper removal rate of 95% under optimum initial concentration (160 mg/L), adsorbent dosage (14 mg), and contact time (180 min). The experimental results better fit into the Langmuir adsorption isotherm model than the Freundlich model, and the kinetics experiments were compared with the pseudo-second-order kinetic model. Polymer adsorption efficiency was above 90% after five cycles of adsorption and desorption, but the overall adsorption capability of PVBC for Cu(II) ions began to decrease after another five cycles from 80% to 54%. Given the outcomes acquired, it can be concluded that PVBC can be an efficient and potential adsorbent for the removal of Cu(II) ions from aqueous solution. The adsorption study showed that PVBC has an affinity to Cu(II) ions. The prepared PVBC is potentially useful for wastewater treatment applications.

Keywords: removal, copper(II), poly(vinylbenzyl chloride), isotherm, kinetic

Abstrak

Pada masa kini, pencemaran tembaga(II) (Cu(II)) telah menjadi salah satu masalah persekitaran yang paling teruk. Oleh kerana ketahanan persekitarannya, rawatan Cu(II) sangat penting. Poli(vinilbenzil klorida) (PVBC) disintesis melalui teknik pempolimeran pemindahan rantai penambahan-fragmentasi boleh dibalikkan (RAFT) yang menggunakan monomer vinilbenzil klorida (VBC), 4-sianopentanoik asid ditiobenzoat (CPADB) sebagai agen RAFT dan 4,4′-Azobis (asid 4-sianopentanoik) (ACPA) sebagai bahan pemula. Tujuan kajian ini adalah untuk mensintesis PVBC dan menguji kemampuan PVBC menyingkirkan ion Cu(II) dari larutan berair. Dalam kajian ini, PVBC berjaya disintesis selama 24 jam pada suhu 80 °C dan kemampuan PVBC untuk menjerap dan menyingkirkan ion Cu(II) telah dikaji. Parameter penjerapan penting seperti kepekatan adsorbat, dos penjerapan dan

masa hubungan dikaji. Kapasiti penjerapan maksimum (q_{max}) Cu(II) PVBC adalah 263.15 mg/g dengan kadar penyingkiran tembaga 95% di bawah keadaan optimum kepekatan awal (160 mg/L), dos bahan penjerap (14 mg), dan masa hubungan (180 min). Data eksperimen lebih sesuai dengan model isoterm penjerapan Langmuir daripada model Freundlich dan kajian kinetik dihubungkan dengan model kinetik pseudo-jujukan kedua. Keupayaan penjerapan polimer melebihi tahap 90% setelah lima kitaran penjerapan tetapi keupayaan penjerapan jumlah PVBC untuk ion Cu(II) mula menurun setelah lima kitaran lain iaitu dari 80% hingga 54%. Daripada hasil yang diperolehi, dapat disimpulkan bahawa PVBC dapat menjadi bahan penjerap yang efektif dan berpotensi untuk menyingkirkan ion Cu(II) dari larutan berair. Kajian penjerapan menunjukkan bahawa PVBC mempunyai pertalian dengan ion Cu(II). PVBC yang disediakan terbukti berpotensi baik untuk aplikasi dalam rawatan air sisa.

Kata kunci: penyingkiran, kuprum(II), poli(vinilbenzil klorida), isoterma, kinetic, penggunaan semula

Introduction

One of the useful monomers that enable immediate post-polymerisation functionalisation via the chloride group is 4-vinylbenzyl chloride (VBC). This monomer can readily undergo nucleophilic substitution or be used as the initiating site in the atom transfer radical polymerisation [1]. Thus, VBC has been applied as a precursor to glycopolymer stars in various systems, photo- and pH-responsive nanoparticles, combs, nanofibers, triblock copolymers, and graft star polymers [2-6]. It has also been reported that copolymerisation of VBC by reversible addition-fragmentation chain transfer (RAFT) polymerisation is a convenient technique because side reactions can be avoided (such as C-Cl bond dissociation) [7, 8].

RAFT polymerisation was discovered and documented at CSIRO by Rizzardo and co-workers [9, 10], whereby it was based on the principle of degenerative chain transfer process [11]. The selection of the right chain transfer agent is one of the factors that makes RAFT polymerisation process efficient. RAFT agents are comprised of thiocarbonylthio compounds [12]. This particular characteristic drew substantial research focus on the technique from the time it was introduced two decades ago [13]. High-molecular-weight chains (approx. 20 to 100 kg/mol) are of interest for this study because the ability to produce high-molecular-weight chains from the polymer particle surface makes it possible to increase the number of functionalised benzyl chloride groups. In addition, having a sizeable significant polymer developed from particles allows for excellent control of the particles' effective diameter by merely adjusting the polymerisation conditions to determine the polymer size. This condition could not be done in low molecular weight chains, as their relative contribution to the particle diameter is negligible.

Contamination of groundwater sources with Cu(II) ions is a severe issue in several districts, particularly in small towns and villages. Additionally, due to their high toxicity, Cu(II) ions cause serious environmental issues for humans, animals, and plants [14]. Cu(II) ions do not have biodegradable properties like organic contaminants. Moreover, it tends to accumulate in living organisms with the potential of becoming toxic and carcinogenic. Cu(II) ions are of particular concern in industrial wastewater treatment. Therefore, toxic Cu(II) ions have to be minimised in the environment to avoid catastrophic effects on living organisms, including human beings [15-18]. Therefore, the removal of Cu(II) ions is a big challenge that needs to be overcome. Several methods have been employed to remove Cu(II) ions, such as ion exchange [19], membrane filtration [20], adsorption, and electrochemical treatment technologies [21]. Adsorption is the best option due to its low operation cost, flexibility, and minimal waste generation. Furthermore, the adsorption technology eliminates different types of inorganic cations. However, the adsorption efficiency is highly dependent on the types and characteristics of the adsorbents. To achieve optimum removal efficiency, the selection of appropriate materials for removing heavy metals is paramount. The methodology used in this study is beneficial compared to the conventional methods because it requires few chemicals for the polymerisation process besides eliminating flammable and toxic solvents such as dimethylformamide (DMF) and toluene.

This research investigates polymer behavior for the removal of Cu(II) from aqueous solutions using PVBC through adsorption. This study also focuses on RAFT polymerization in the synthesis of poly(vinylbenzyl chloride) (PVBC) at a particular temperature. The polymer is then used to study the ability to remove Cu(II) ions from aqueous solution via adsorption between the polymer and the Cu(II) ions.

Materials and Methods

Synthesis of poly(vinylbenzyl chloride)

In a typical polymerisation of VBC, the VBC monomer (1 mL, 7.03 mmol), ACPA (0.0025 g, 0.0089 mmol), and RAFT agent CPADB (0.0185 g, 0.066 mmol) were placed in a 100 mL two-necked round bottom flask and stirred until dissolved. The mixture had been degassed for 40 minutes under nitrogen. The polymerisation was achieved by placing the flask in a preheated oil bath at 80 °C for 5 hours to synthesise PVBC. Then the reaction mixture was cooled to room temperature and exposed to air to stop the polymerisation. The polymer solution from the flask was precipitated by adding it dropwise to the excess cold methanol in a centrifuge tube to remove unreacted VBC monomer and other impurities. The procedure was repeated with 10, 15, 20, and 24 hours reaction mixture to find the optimum time of PVBC synthesis. The PVBC obtained via polymerisation for 24 hours at 80 °C was precipitated in a centrifuge tube. The tube was sealed with aluminium foil with a few holes to avoid contamination and was left to dry for 24 hours. In the end, a solid pink PVBC was obtained.

Analysis of Cu(II) ions

The stock solution of Cu(II) ions at a concentration of 400 ppm were prepared via dissolving $CuSO_4.5H_2O$ (249.685 g/mol) in distilled water and topped up to 1000 mL in a volumetric flask. The desired concentration of the experimental solutions was prepared by diluting the stock solution with distilled water [22].

An ultraviolet (UV) absorption spectroscopy technique was used to determine the Cu(II) concentration in the aqueous solution, and because of its simple application, elevated sensitivity and economic efficiency [23]. In particular, the 2 mL matrix Na_2EDTA (0.025 M) as chromogenic reagent was introduced to the Cu(II) ion solution (2 mL). The solution of the desired Na_2EDTA concentrations was then mixed for 5 min to ensure a sufficient complexing response. An absorption peak was identified at 268 nm [22, 24, 25].

The Cu(II) concentrations were determined based on the standard calibration curve, which was plotted using different concentrations (20–200 ppm). The solutions were prepared from the stock solution (400 ppm). The different concentrations were mixed with Na2ETDA for the development of colour and then measured using UV-1800 UV-Vis spectrophotometer from Shimadzu in a 1 cm cuvette length for determining the absorbance at λ_{max} (268 nm) [22]. A standard calibration curve was determined by plotting the graph of absorbance against concentration.

Batch model studies

In this study, the batch model experiments were performed to investigate the effect of PVBC on adsorption of Cu(II) in aqueous solution and also the effect of concentration, adsorbent dosage, and contact time on the adsorption process. The Cu(II) concentration in the remaining solution (supernatant) was calculated. The adsorption ability of Cu(II) was determined as the Cu(II) ions adsorbed per gram of PVBC (mg/g) and calculated using Equation 1:

$$q_e \text{ (mg/g)} = (C_i - C_e)\, V/m \quad (1)$$

Equation 2 was used to determine the percentage of Cu(II) adsorbed on the adsorbent.

$$\text{Cu(II) removal \%} = (C_i - C_e)/C_i \times 100 \quad (2)$$

where C_i and C_e are the initial and final concentrations of Cu(II) in ppm, while m is the mass of PVBC in g and V is the volume (L) of the solution.

Isotherm and kinetic studies

To determine adsorption isotherms at optimum conditions, 14 mg PVBC was added to a solution of 5 mL Cu(II) of various initial concentrations (20-200 ppm). Then, adsorption of Cu(II) was characterised using the isothermic model of Langmuir and Freundlich. Adsorption kinetic experiments were also performed

under optimum conditions at various contact time (30-300 minutes), and the Cu(II) adsorption was characterised using pseudo-first-order rate and pseudo-second-order rate. PVBC was isolated from the solution by filtration in all samples, and the residual concentrations of Cu(II) in the supernatant were determined.

Reusability test

Reusability of adsorbent was evaluated by repeated adsorption-desorption of copper metal ion and carried out in a batch system. Adsorbent (14 mg) was added to 50 mL of Cu(II) ions solution (160 ppm) at pH 4 in a 250 mL conical flask. The solution was stirred for 180 minutes. The adsorbent was removed from the solution and adsorbed Cu(II) ions was desorbed by stirring the adsorbent in 0.1 M HCl (10 mL), which efficiently removed the adsorbed Cu(II) ions. After thorough washing with distilled water, the adsorbent was reused for the subsequent adsorption-desorption cycle. The adsorption-desorption test of the adsorbent was repeated ten consecutive times.

Results and Discussion

Synthesis of poly(vinylbenzyl chloride)

PVBC was synthesised through reversible addition-fragmentation chain transfer (RAFT) polymerisation technique with the mole ratio of 100:1:0.1 for VBC:CPADB:ACPA at 80 °C for 5,10, 15, 20, and 24 hours, as shown in Figure 1. The PVBC synthesised was directly used for the optimisation and adsorption studies.

Effect of different Cu(II) concentration

The effect of PVBC on the adsorption process was determined using 5 mL copper sulphate pentahydrate ($CuSO_4.5H_2O$) solution of various concentrations (20-200 ppm). The experiment was conducted in different vials containing the Cu(II) solutions at different concentrations, determined at pH 4, whereby a fixed amount of PVBC was added to each vial and shaken at a specified time. The residual Cu(II) concentrations were analysed by a UV-Vis spectrophotometer. All experiments were conducted at room temperature, and the procedures were repeated in triplicates.

The effect of the initial adsorption concentration of metal ions on PVBC has a significant role in the metal ion adsorption process. Figure 2 shows that the initial concentration of Cu(II) solution adsorption on PVBC increases from 20 to 160 ppm with the removal efficiency from 63 to 87%. It was observed that at 160 ppm initial concentration percentage, removal was 87%, which was chosen as the optimum concentration of Cu(II) removal. At this point, all adsorption sites into the PVBC were saturated, as observed by the maximum interaction between the metal ions and the adsorbent binding sites at a lower concentration, resulting in a higher adsorption rate of 63% at the beginning [26]. In the case of a low initial concentration, relatively low adsorption was observed due to a reduced coefficient of diffusion and a reduced coefficient of mass transfer [27]. However, the percentage of removal efficiency decreases at higher concentrations at 180 ppm and 200 ppm. This could be due to saturated adsorption sites of the adsorbent [28]. In other words, all binding sites at a fixed dose of PVBC were already occupied. Therefore, higher Cu(II) concentrations did not lead to higher adsorption; instead, it started to decline [29].

Effect of different adsorbent dosage

Adsorption experiments were performed at ambient temperature with varying doses of PVBC, 160 rpm shaking speed, and without any changes in pH. Figure 3 shows that the adsorption efficiency of Cu(II) ions on the PVBC increased gradually from 47 to 91% along with the increase of adsorbent dose from 2 to 14 mg.

The increased adsorption dosages of PVBC increases the percentage removal of Cu(II) from 5 mL solution containing 160 ppm of Cu(II) ions, and the highest removal of Cu (II) was attained at the 14 mg of PVBC dose, which was defined as the optimum dosage of PVBC. However, no significant increase in the removal of Cu(II) ions was observed beyond the optimum dosage. The increase in the removal of adsorption with increased adsorbent dosage is consistent with the statement that all binding sites are entirely exposed to adsorption at the low adsorbent dosage, and the surface becomes saturated faster. It can be attributed to the increased adsorption surface area; thus, an increase in the number of active sites and the number of unsaturated

sites. According to the values of these parameters, Cu(II) would have greater accessibility to the PVBC surface. This would contribute to a greater extent of the adsorption process. In addition, it was also noted that when the adsorbent dose was further increased to 20 mg, Cu(II) ion adsorption efficiency on the PVBC decreased. This effect is due to the saturated adsorption sites on the adsorbent [30]. Hence, the optimum PVBC dose is 14 mg.

Effect of different contact time

A series of adsorption experiments for contact times ranging from 30 to 300 min was performed to determine the contact time required to achieve the equilibrium, and the results are shown in Figure 4.

Figure 4 shows the effect of the contact time on PVBC adsorption of Cu(II) ions at ambient temperature, along with 14 mg of adsorbent dosage, 160 ppm of initial Cu(II) ion concentration, and solution pH of 4.0. After increasing the contact time from 30 to 180 minutes, it was observed that the Cu(II) percentage removal sharply increased from 58% to 95%. By increasing the contact time within 180 min, the adsorption gradually approached equilibrium around 210 min [28, 30, 31]. It is seen that the systems attained equilibrium after 180 minutes with maximum percentage Cu(II) removal of 95%. This is attributed to the increased adsorbent time to 300 minutes, whereby the percentage of Cu(II) removal efficiency showed a slight decrease, and it was observed that the adsorption efficiency of Cu(II) ions onto the composite was almost unchanged. The initial stage of rapid adsorption makes Cu(II) ions easily contact several accessible active sites on the PVBC surface. When the contact time increased further, the active sites available gradually decreased, and the adsorption rate will be equal to the adsorption rate in the equilibrium state [32, 33]. Consequently, the trend moved towards stabilization in adsorption. According to the previous debate, we have chosen 180 min as the optimum contact time (95%).

The adsorption ability of PVBC

The quantity of Cu(II) (mg) removed per unit of PVBC (g), q_e, and Cu (II) removal percentage were obtained from Equation 1 and Equation 2. The maximum removal ability (q_{max}) using PVBC after the optimised condition was 263.15 mg of Cu(II)/ g of PVBC with 95% of removal efficiency. The comparison of the removal ability of PVBC for Cu(II) ions with different adsorbents is presented in Table 4. However, the experimental data in Table 4 could not be directly compared due to the variations in systemic experimental conditions (concentration, pH, dosage, temperature, and contact time). It can be seen that the PVBC has potential as an adsorbent to remove Cu(II) from aqueous solutions up to 95% efficiency without any modification.

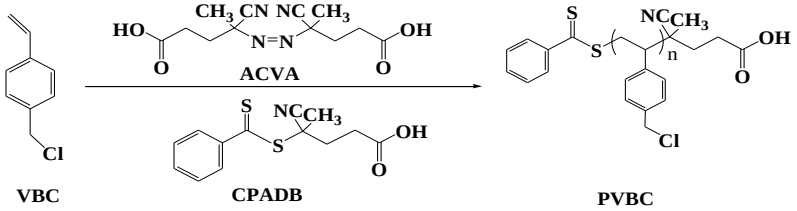


Figure 1. The RAFT polymerisation of PVBC.

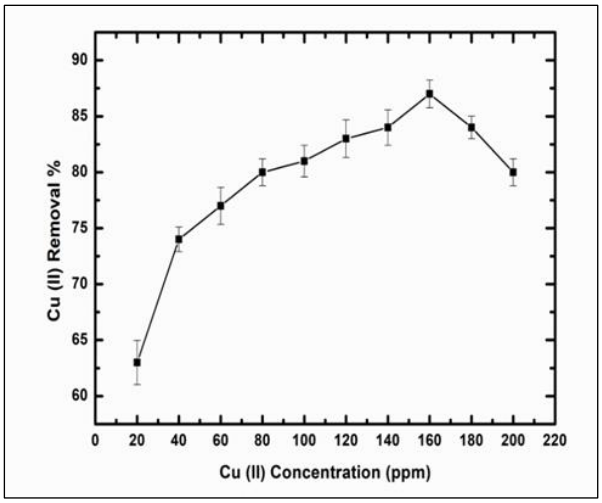


Figure 2. Removal efficiency of Cu(II) from aqueous solution using fixed amount of PVBC at different Cu(II) concentrations (ppm). Extraction conditions: 6 mg of adsorbent dose, temperature 22 °C, batch volume 5 mL, time 3 hours, and pH 4. Data are mean of three independent determinations ± standard deviation

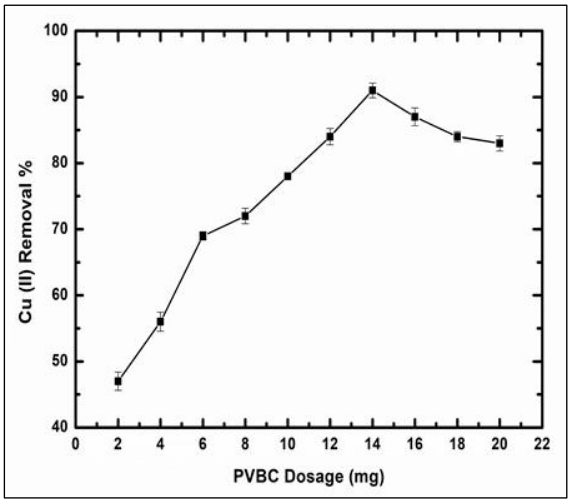


Figure 3. Removal efficiency of Cu(II) from aqueous solution using different amount of PVBC as adsorbent dosage (mg). Extraction conditions: Cu(II) concentration of 160 ppm, temperature 22 °C, batch volume 5 mL, time 3 hours, and pH 4. Data are mean of three independent determinations ± standard deviation

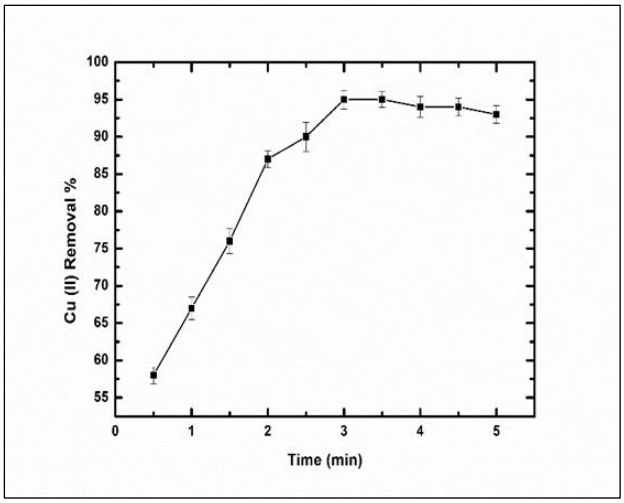


Figure 4. Removal efficiency of Cu(II) from aqueous solution at different contact time (min). Extraction conditions: 14 mg of adsorbent dose, Cu(II) concentration at 160 ppm, temperature 22 °C, batch volume 5 mL, time 3 hours, and pH 4. Data are mean of three independent determinations ± standard deviation

Adsorption kinetic study

To determine the adsorption rate of the Cu(II) ions studied at pH 4 and 22 ºC, the two most commonly used kinetic models in metal adsorption processes, namely pseudo-first-order and pseudo-second-order, were selected. The pseudo-first-order equation described in Equation 3 was used to analyse the experimental data obtained in the kinetic study [34, 35].

$$\log (qe - qt) = \log qe - K_1/2.303 * t \quad (3)$$

where K_1 (min^{-1}) is the constants rate of pseudo-first-order. The (K_1) adsorption rate constant was achieved from the slope of plotting log (qe - qt) vs. t.

The linear plots of Log (qe - qt) vs. t of the Cu(II) ions are shown in Figure 5(A). The initial high metal uptake could be due to an increase in the number of binding sites available at the initial stage because there was an increased concentration gradient between the metal ions on the adsorbent and the metal ions in solution. The results showed that the coefficients of determination for the pseudo-first-order kinetic model were lower than 0.90. Therefore, the pseudo-first-order kinetic model cannot be used to describe the adsorption rate.

Pseudo-second-order kinetic model

The pseudo-second-order kinetic model has been successfully applied using different concentrations to many kinetic adsorption systems. The constant pseudo-second-order rate and determination coefficients were calculated using Equation 4 [34, 36].

$$t/qt = 1/(K_2*(qe)2) + 1/qe * t \quad (4)$$

where K_2 (g/mg.min) is the constant rate of pseudo-second-order.

The pseudo-second-order kinetic model is valid if the plots of t/q_t vs. t give a linear relationship. The plot of t/q_t vs. time of the Cu(II) ions are shown in Figure 5(B).

The coefficients of determination for the linear plot was higher than 0.99 for Cu(II) ions. The applicability of the pseudo-second-order model indicated that chemisorption might be the rate-limiting step that governed these adsorption processes. When the experiment data fitted to the Equations 3 and Equation 4, the correlation coefficients (shown in Figure 5) indicated that the adsorption of Cu(II) on the PVBC were fitted well with Equation 4 (pseudo-second-order) rather than Equation 3 (pseudo-first-order) [33, 37].

Consequently, the mechanism of the adsorption of Cu(II) on PVBC was based on the pseudo-second-order model due to higher correlation coefficients (0.9967). The pseudo-second-order kinetic model assumes that the rate-limiting step may be chemical adsorption. In many cases, the pseudo-second-order model can be utilised to predict adsorption behaviour through the sharing of electrons between adsorbent and adsorbate. The results indicate that the adsorption perfectly correlated with the pseudo-second-order kinetic model. The pseudo-second-order rate constant (K_2) and coefficients of determination (R^2) are listed in Table 1.

Adsorption isotherm models

In this study, Langmuir and Freundlich models were used at pH 4 and 22 °C to describe the relationship between the adsorbed amount of Cu(II) ions on PVBC and its equilibrium concentration in solution. Langmuir isotherm is utilised to describe monolayer coverage utilising a kinetic method with the assumption of a single layer of adsorbed material forming a uniform surface at a constant temperature. The mathematical description of Equation 5 is [35]:

$$q_e = (q_{max}. bC_e)/(1+bC_e) \quad (5)$$

The linear form of Langmuir is described in Equation 6:

$$1/q_e = (1/q_{max}b).1/C_e + 1/q_{max} \quad (6)$$

where q_e is the concentration of Cu(II) on the adsorbent (mg/g) at equilibrium, q_{max} is the maximum achievable uptake by a system, b is the affinity between the adsorbate Cu(II) ions, and adsorbent PVBC and C_e is equilibrium solute concentrations in aqueous solution (mg/L).

The Freundlich isotherm model is not restricted to monolayer coverage, whereby a good fit of this model means there is no limit to the number of adsorbed molecules on the adsorbent (multilayer coverage). The Freundlich isotherm in Equation 7 was utilised to obtain maximum heterogeneous layer adsorption ability of the adsorbate [35].

$$q_e = K_F\, C_e^{\,(1/n)} \quad (7)$$

The linear Freundlich Equation 8 is written as [34]:

$$\text{Log } qe = \text{Log } KF + 1/n \log Ce \quad (8)$$

where K_F is the binding ability at the unit concentration (L/g) and n is the affinity between the adsorbent and adsorbate (adsorption intensity).

The Langmuir and Freundlich linearized models were fitted into the experimental data in Figure 6. The Langmuir isotherm plots of $1/q_e$ vs. $1/C_e$ for the adsorption of Cu(II) ions is shown in Figure 6(a) and the Freundlich isotherm plots of log q_e vs. log C_e for the adsorption of Cu(II) ions is shown in Figure 6(b).

Figure 7 shows a linearized Langmuir isotherm comparison of the experimental points with the expected values for Cu(II) adsorption on PVBC. It has been observed that the Langmuir isotherm equation linear expression can predict the experimental data.

The Langmuir constant, b can be expressed in terms of an equilibrium parameter known as a separation factor (R_L), based on which adsorption can be described as irreversible ($R_L = 0$), unfavourable ($R_L > 1$), favourable ($0 < R_L < 1$), and linear ($R_L = 1$) [34]. The R_L values for PVBC can be calculated from this Equation 9 [37, 38]:

$$R_L = 1/(1+bC_i) \quad (9)$$

In our study, the values of R_L were between 0.9746 and 0.7936, as shown in Table 2, indicating favourable adsorption of Cu(II) on PVBC under optimised conditions. The Langmuir constants b and q_{max} that were calculated from the slop and intercept-Y of the plotted $1/q_e$ vs $1/C_e$ is comparable to the Freundlich constants for PVBC calculated from the slop and intercept-Y of the Log q_e vs. Log C_e plot, where the slope is (1/n) whereas the intercept-Y is (log K_F), as shown in Table 3. Table 3 lists the Freundlich constants n and K_F. Freundlich parameters (K_F and n) describe whether the adsorption nature is either favourable or unfavourable. The intercept is an indicator of adsorption ability, and the slope is an indicator of adsorption intensity. If the value of n =1, the adsorption is linear, if n < 1, it implies that the adsorption process is unfavourable and if n > 1,

the adsorption is favourable. In another way, 1/n values give us whether isotherm is irreversible (1/n = 0), unfavourable (1/n > 1), or favourable (0 < 1/n < 1). The comparison of the two models indicated that both Langmuir and Freundlich models could be utilised to interpret the experimental data [39]. Based on the values of coefficients of determination (R^2) in Table 3, the Cu(II) adsorption was better explained by the Langmuir isotherm model, as it has higher R^2 values (0.9648). This result indicates that the adsorption of Cu(II) takes place on the PVBC surface at monolayer patterns. Therefore, the adsorption data in this study support the monolayer adsorption of Cu(II), which agrees with other studies [34, 35].

Reusability of the PVBC on Cu(II) solution

Reusability or recycling of adsorbent is one of the functional characteristics of adsorbents. To appraise the adsorbent's reusability, adsorption-desorption of Cu(II) were repeated ten times utilising metal ions concentration of 160 ppm and HCl (0.1 M, 10 mL) as efficient desorption solvent [29]. The adsorbent was thoroughly washed away with distilled water until the next process. It was observed that 95% of metal ions were adsorbed in the first cycle and the percentage of the following four adsorption cycles were still above 90% for Cu(II) removal: 95% in the 1st cycle; 94% in the 2nd cycle; 93% in the 3rd cycle; 92% in the 4th cycle; and 91% in the 5th cycle. The above process was repeated for five times. Figure 8 indicates that the total adsorption ability of PVBC for Cu(II) ions started to decrease from 80% to 54% for Cu(II) removal: 80% in the 6th cycle; 73% in the 7th cycle; 68% in the 8th cycle; 62% in the 9th cycle; and 54% in the 10th cycle. In these cases, reduction in adsorption efficiency has been attributed to the of PVBC weight after repeated from 14 mg to 8.6 mg, leading to a decrease in the number of adsorption sites on the adsorbent. The adsorbent indicates that the process could be repeatedly used for the removal of Cu(II), as shown in Figure 8.

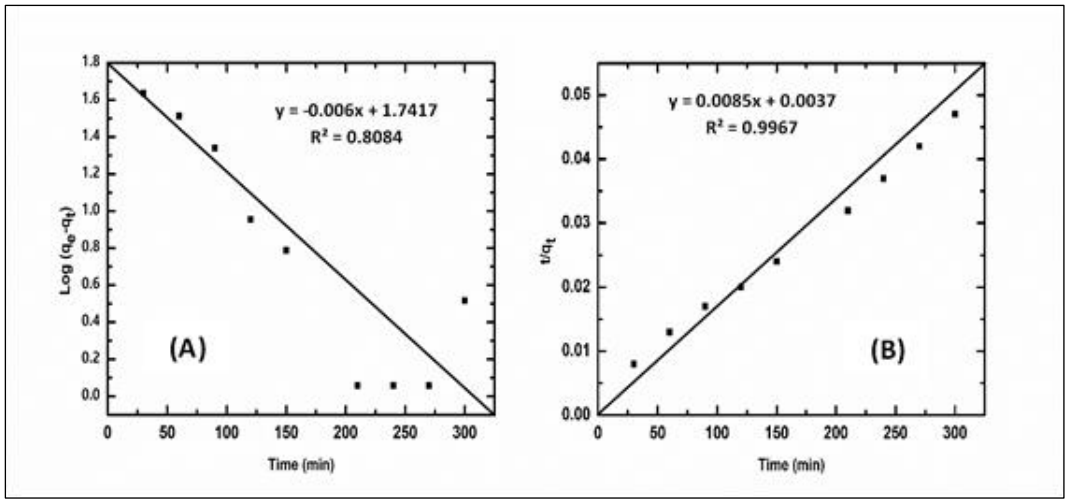


Figure 5. Adsorption Cu(II) fitting Pseudo-first-order model (A) and Pseudo-second-order model (B)

Table 1. Kinetic parameters for adsorption of Cu(II) onto PVBC

Model	Constant	Value
Pseudo-first order	q_e (mg/g)	55.17
	K_1 (min^{-1})	0.82
	R^2	0.8084
Pseudo-second order	q_e (mg/g)	117.65
	K_2(g/mg.min)	0.02
	R^2	0.9967

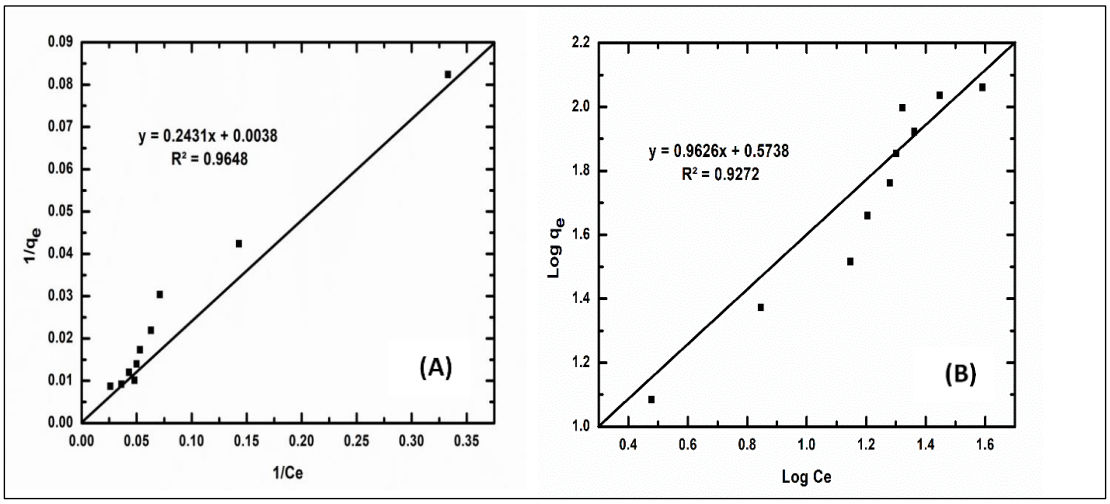


Figure 6. Adsorption Cu(II) fitting Langmuir (a) and Freundlich (b) models.

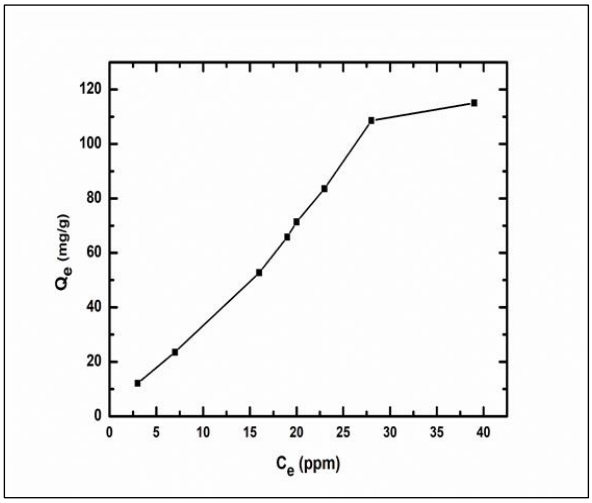


Figure 7. Adsorption isotherms of Cu(II) on PVBC: adsorbent dosage 14 mg, pH 4.0, temperature 22 °C, contact time 5 hours.

Table 2. R_L values for PVBC

Ci for Cu(II) ppm	R_L
20	0.9747
40	0.9506
60	0.9276
80	0.9058
100	0.8850
120	0.8651
140	0.8460
160	0.8278
180	0.8103
200	0.7937

Table 3. Isotherm model parameters for adsorption of Cu(II) onto PVBC

Model	Constant	Value
Langmuir	q_{max} (mg/g)	263.16
	b (L/g)	0.016
	R^2	0.9648
Freundlich	K_F (L/g)	3.75
	n	1.09
	1/n	0.96
	R^2	0.9272

Table 4. Comparison of adsorption capacities of Cu(II) ions with different adsorbents

Adsorbent	Technique	Cu(II) (mg/g)	Conc. (ppm)	pH	Reusability (% adsorption efficiency)	Ref.
PVBC-g-PSPMA2 microspheres	Adsorption process (Suspension polymerisation)	31.6	50	5	-	[40]
M10-PVBC-C beads	Adsorption process based on the use of chelating magnetic copolymer beads (Suspension polymerisation)	61.20	500	7	99.2	[41]
PVBC	Adsorption process (Bulk polymerisation)	263.15	160	4	95	This study

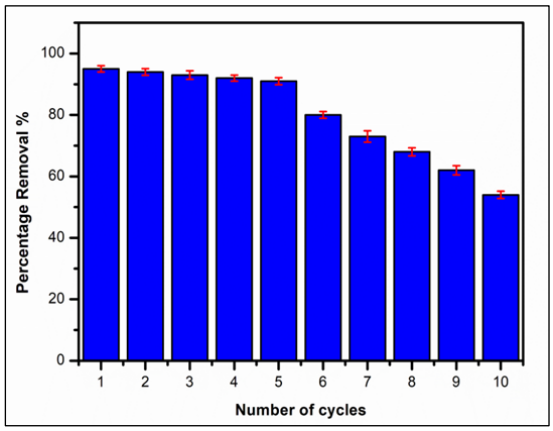


Figure 8. Adsorption-desorption cycles of the adsorbent. Extraction conditions: Cu(II) concentration, 160 ppm, adsorbent dose 14 mg, batch volume 50 mL, desorption solution, 0.1 M HCl (10 mL), contact time 180 minutes

Conclusion

In this study, we have provided a potential adsorbent for the removing Cu(II) from aqueous solutions. The advantage of using PVBC is a high adsorption capacity and environmentally friendly for the removal of Cu(II). In addition, the PVBC can be easily separated from the solution after adsorption. In the optimum points, the maximum removal of Cu(II) was 95%, and the maximum adsorption capacity obtained was 263.158 (mg/g) at 160 ppm Cu(II) concentration, 14 mg PVBC dosage, and pH 4 after 180 minutes of incubation. In addition, the adsorption data for Cu(II) adsorption had a good fit with Langmuir isotherm and pseudo-second-order kinetic model. To conclude, the results obtained confirm that PVBC was successfully prepared and can efficiently remove Cu(II) ion from aqueous solution.

Acknowledgement

The authors thank Universiti Teknologi Malaysia (UTM) and Ministry of Education Malaysia for facilitations and financial support under grant number Q.J130000.3554.06G60 to carry out this research work.

References

1. Moraes, J., Ohno, K., Gody, G., Maschmeyer, T. and Perrier, S. (2013). The synthesis of well-defined poly (vinylbenzyl chloride)-grafted nanoparticles via RAFT polymerization. *Beilstein Journal of Organic Chemistry*, 9(1): 1226-1234.
2. Bayramoglu, G., Yavuz, E., Senkal, B. F. and Arica, M. Y. (2009). Glycidyl methacrylate grafted on p (VBC) beads by SI-ATRP technique: Modified with hydrazine as a salt resistance ligand for adsorption of invertase. *Colloids and Surfaces A: Physicochemical and Engineering Aspects*, 345(1-3): 127-134.
3. Chen, Y., Chen, G. and Stenzel, M. H. (2010). Synthesis and lectin recognition of glyco star polymers prepared by "Clicking" thiocarbohydrates onto a reactive scaffold. *Macromolecules,* 43(19): 8109-8114.
4. Fu, G. D., Xu, L. Q., Yao, F., Zhang, K., Wang, X. F., Zhu, M. F. and Nie, S. Z. (2009). Smart nanofibers from combined living radical polymerization,"click chemistry", and electrospinning. *ACS Applied Materials & Interfaces,* 1(2): 239-243..
5. Quinn, J. F., Chaplin, R. P. and Davis, T. P. (2002). Facile synthesis of comb, star, and graft polymers via reversible addition–fragmentation chain transfer (RAFT) polymerization. *Journal of Polymer Science Part A: Polymer Chemistry,* 40(17): 2956-2966.

6. Strube, O. I. and Schmidt-Naake, G. (2009). Synthesis of reactive triblock copolymers via reversible addition-fragmentation chain transfer (RAFT) polymerization. *In Macromolecular Symposia*, 275(1): pp. 13-23.
7. Couture, G. and Améduri, B. (2012). Kinetics of RAFT homopolymerisation of vinylbenzyl chloride in the presence of xanthate or trithiocarbonate. *European Polymer Journal,* 48(7): 1348-1356.
8. Feng, H., Zhao, Y., Pelletier, M., Dan, Y. and Zhao, Y. (2009). Synthesis of photo-and pH-responsive composite nanoparticles using a two-step controlled radical polymerization method. *Polymer,* 50(15): 3470-3477.
9. Chiefari, J., Chong, Y. K., Ercole, F., Krstina, J., Jeffery, J., Le, T. P. and Rizzardo, E. (1998). Living free-radical polymerization by reversible addition−fragmentation chain transfer: the RAFT process. *Macromolecules,* 31(16): 5559-5562.
10. Moad, G., Rizzardo, E. and Thang, S. H. (2005). Living radical polymerization by the RAFT process. *Australian Journal of Chemistry,* 58(6): 379-410.
11. Bai, W., Zhang, L., Bai, R. and Zhang, G. (2008). A very useful redox initiator for aqueous RAFT polymerization of n-isopropylacrylamide and acrylamide at room temperature. *Macromolecular Rapid Communications,* 29(7): 562-566.
12. Moad, G. (2019). A critical survey of dithiocarbamate reversible addition-fragmentation chain transfer (RAFT) agents in radical polymerization. *Journal of Polymer Science Part A: Polymer Chemistry,* 57(3): 216-227.
13. Quinn, J. F., Davis, T. P., Barner, L. and Barner-Kowollik, C. (2007). The application of ionizing radiation in reversible addition–fragmentation chain transfer (RAFT) polymerization: Renaissance of a key synthetic and kinetic tool. *Polymer,* 48(22): 6467-6480.
14. Jachuła, J., Kołodyńska, D. and Hubicki, Z. (2011). Sorption of Cu(II) and Ni(II) ions in the presence of the methylglycinediacetic acid by microporous ion exchangers and sorbents from aqueous solutions. *Open Chemistry,* 9(1): 52-65.
15. Chuah, T. G., Jumasiah, A., Azni, I., Katayon, S. and Choong, S. T. (2005). Rice husk as a potentially low-cost biosorbent for heavy metal and dye removal: an overview. *Desalination,* 175(3): 305-316.
16. Nuhoglu, Y., Malkoc, E., Gürses, A. and Canpolat, N. (2002). The removal of Cu(II) from aqueous solutions by *Ulothrix zonata. Bioresource Technology,* 85(3), 331-333.
17. Ngah, W. W., Endud, C. S. and Mayanar, R. (2002). Removal of copper(II) ions from aqueous solution onto chitosan and cross-linked chitosan beads. *Reactive and Functional Polymers,* 50(2): 181-190.
18. Manahan, S. (2017). Environmental Chemistry. 10th edition. CRC press.
19. Lin, L. C., Li, J. K. and Juang, R. S. (2008). Removal of Cu(II) and Ni(II) from aqueous solutions using batch and fixed-bed ion exchange processes. *Desalination,* 225(1-3): 249-259.
20. Juang, R. S. and Shiau, R. C. (2000). Metal removal from aqueous solutions using chitosan-enhanced membrane filtration. *Journal of Membrane Science,* 165(2): 159-167.
21. Chen, Y., Pan, B., Li, H., Zhang, W., Lv, L. and Wu, J. (2010). Selective removal of Cu(II) ions by using cation-exchange resin-supported polyethyleneimine (PEI) nanoclusters. *Environmental Science & Technology,* 44(9): 3508-3513.
22. Xiao, S., Ma, H., Shen, M., Wang, S., Huang, Q. and Shi, X. (2011). Excellent copper (II) removal using zero-valent iron nanoparticle-immobilized hybrid electrospun polymer nanofibrous mats. *Colloids and Surfaces A: Physicochemical and Engineering Aspects,* 381(1-3): 48-54.
23. Abadi, M. D. M., Ashraf, N., Chamsaz, M. and Shemirani, F. (2012). An overview of liquid phase microextraction approaches combined with UV–Vis spectrophotometry. *Talanta,* 99: 1-12.
24. Huang, Y., Wu, D., Wang, X., Huang, W., Lawless, D. and Feng, X. (2016). Removal of heavy metals from water using polyvinylamine by polymer-enhanced ultrafiltration and flocculation. *Separation and Purification Technology,* 158: 124-136.
25. Samadi, N., Ansari, R. and Khodavirdilo, B. (2017). Removal of copper ions from aqueous solutions using polymer derivations of poly (styrene-alt-maleic anhydride). *Egyptian Journal of Petroleum,* 26(2): 375-389.
26. Singh, V., Kumari, P., Pandey, S. and Narayan, T. (2009). Removal of chromium (VI) using poly (methylacrylate) functionalized guar gum. *Bioresource Technology,* 100(6): 1977-1982.
27. Aksu, Z. and Gönen, F. (2004). Biosorption of phenol by immobilized activated sludge in a continuous packed bed: prediction of breakthrough curves. *Process Biochemistry,* 39(5): 599-613.

28. Lofrano, G., Carotenuto, M., Libralato, G., Domingos, R. F., Markus, A., Dini, L. and Chattopadhyaya, M. C. (2016). Polymer functionalized nanocomposites for metals removal from water and wastewater: an overview. *Water Research,* 92: 22-37.
29. Dou, J., Huang, Q., Huang, H., Gan, D., Chen, J., Deng, F. and Wei, Y. (2019). Mussel-inspired preparation of layered double hydroxides based polymer composites for removal of copper ions. *Journal of Colloid and Interface Science,* 533: 416-427.
30. Hosseinzadeh, H., Pashaei, S., Hosseinzadeh, S., Khodaparast, Z., Ramin, S. and Saadat, Y. (2018). Preparation of novel multi-walled carbon nanotubes nanocomposite adsorbent via RAFT technique for the adsorption of toxic copper ions. *Science of the Total Environment,* 640: 303-314.
31. Akhavan, B., Jarvis, K. and Majewski, P. (2015). Plasma polymer-functionalized silica particles for heavy metals removal. *ACS Applied Materials & Interfaces,* 7(7): 4265-4274.
32. Tan, P., Wen, J., Hu, Y. and Tan, X. (2016). Adsorption of Cu^{2+} and Cd^{2+} from aqueous solution by novel electrospun poly (vinyl alcohol)/graphene oxide nanofibers. *RSC Advances,* 6(83): 79641-79650.
33. Chávez-Guajardo, A. E., Medina-Llamas, J. C., Maqueira, L., Andrade, C. A., Alves, K. G. and de Melo, C. P. (2015). Efficient removal of Cr(VI) and Cu(II) ions from aqueous media by use of polypyrrole/maghemite and polyaniline/maghemite magnetic nanocomposites. *Chemical Engineering Journal,* 281: 826-836.
34. Li, J., Xu, Z., Wu, W., Jing, Y., Dai, H. and Fang, G. (2018). Nanocellulose/Poly (2-(dimethylamino) ethyl methacrylate) Interpenetrating polymer network hydrogels for removal of Pb(II) and Cu(II) ions. *Colloids and Surfaces A: Physicochemical and Engineering Aspects,* 538: 474-480.
35. Lin, Y., Hong, Y., Song, Q., Zhang, Z., Gao, J. and Tao, T. (2017). Highly efficient removal of copper ions from water using poly (acrylic acid)-grafted chitosan adsorbent. *Colloid and Polymer Science,* 295(4): 627-635.
36. Zhang, W., Yun, M., Yu, Z., Chen, D. and Li, X. (2019). A novel Cu(II) ion-imprinted alginate–chitosan complex adsorbent for selective separation of Cu(II) from aqueous solution. *Polymer Bulletin,* 76(4): 1861-1876.
37. Karthik, R. and Meenakshi, S. (2015). Removal of Pb(II) and Cd(II) ions from aqueous solution using polyaniline grafted chitosan. *Chemical Engineering Journal,* 263: 168-177.
38. Ong, S. T., Tay, E. H., Ha, S. T., Lee, W. N. and Keng, P. S. (2009). Equilibrium and continuous flow studies on the sorption of Congo Red using ethylenediamine modified rice hulls. *International Journal of Physical Sciences,* 4(11): 683-690.
39. Balarak, D., Mostafapour, F. K., Azarpira, H. and Joghataei, A. (2017). Langmuir, Freundlich, Temkin and Dubinin–radushkevich isotherms studies of equilibrium sorption of ampicilin unto montmorillonite nanoparticles. *Journal of Pharmaceutical Research International,* 2017: 1-9.
40. Gu, J., Yuan, S., Shu, W., Jiang, W., Tang, S., Liang, B. and Pehkonen, S. O. (2016). PVBC microspheres tethered with poly (3-sulfopropyl methacrylate) brushes for effective removal of Pb(II) ions from aqueous solution. *Colloids and Surfaces A: Physicochemical and Engineering Aspects,* 498: 218-230.
41. Lapwanit, S., Trakulsujaritchok, T. and Nongkhai, P. N. (2016). Chelating magnetic copolymer composite modified by click reaction for removal of heavy metal ions from aqueous solution. *Chemical Engineering Journal,* 289: 286-295.

Malaysian Journal of Analytical Sciences (MJAS)
Published by Malaysian Analytical Sciences Society

SYNTHESIS OF ORDERED NANOARRAYS ACTIVATED CARBON USING SBA-15 AS HARD TEMPLATE FOR ADSORPTION OF IBUPROFEN

(Sintesis Karbon Aktif Nano Berketeraturan Menggunakan SBA-15 Sebagai Templat Keras untuk Penjerapan Ibuprofen)

Maria Ulfa[1]*, Didik Prasetyoko[2], Hasliza Bahruji[3], Wega Trisunaryanti[4], Yatim Lailun Nimah[2]

[1]Chemistry Education Study Program, Faculty of Teacher Training and Education, Sebelas Maret University, Jl. Ir. Sutami 36A, Surakarta 57126, Central Java Indonesia.
[2]Department of Chemistry, Faculty of Mathematics and Natural Sciences, Institute of Technology Sepuluh Nopember, Jl Keputih, Surabaya, 61115, East Java Indonesia
[3]Centre of Advanced Material and Energy Sciences, Universiti Brunei Darussalam, Jalan Tungku Link, BE 1410, Brunei Darussalam
[4]Department of Chemistry, Faculty of Mathematics and Natural Sciences, Gadjah Mada University, Jl Sekip Utara Sleman Yogyakarta, Indonesia

**Corresponding author: ulfa.maria2015@gmail.com*

Received: 18 July 2019; Accepted: 20 July 2020; Published: 10 December 2020

Abstract

Ibuprofen is an anti-inflammatory drug primarily found as a pharmaceutical residue in water and can be removed using adsorption method. Activated carbon with nanoarrays structure was produced using SBA-15 as a hard template and further utilised as an adsorbent for ibuprofen removal. SBA-15 was synthesised using TEOS and Pluronic-F123 as a mesoporous template, followed by deposition with sucrose as a carbon precursor. Carbonisation was carried out under N_2 flow at 180 °C followed by pyrolysis at 900 °C to form carbon nanoarrays. The effect of activation using KOH solution on activated carbon nanoarrays was investigated for ibuprofen removal. Characterisation using XRD, FTIR, TEM, and N_2 adsorption-desorption revealed that the carbon adapted the highly ordered structure of SBA-15 with the diameter of nanoarrays of ~ 5 nm and surface area of ~646 m^2/g. Investigation of the adsorption of ibuprofen on activated carbon nanoarrays showed that the adsorption followed the pseudo-second-order kinetic model with the adsorption capacity of ~ 24.5 mg/g. Prolonged treatment of carbon with KOH has been shown to affect the adsorption capacity of ibuprofen due to a decrease in the surface functionality of carbon.

Keywords: activated ordered nanoarrays carbon, activated, adsorption, ibuprofen, pore

Abstrak

Ibuprofen adalah ubat anti-radang yang banyak dijumpai sebagai residu farmasi di dalam air dan dapat disingkirkan dengan kaedah penjerapan. Karbon aktif dengan struktur susunan-nano dihasilkan menggunakan SBA-15 sebagai templat keras dan selanjutnya digunakan sebagai penjerap untuk penyingkiran ibuprofen. SBA-15 disintesis menggunakan TEOS dan Pluronic-F123 sebagai templat liang-meso diikuti dengan pemendapan menggunakan sukrosa sebagai sumber karbon. Karbonisasi dilakukan di bawah aliran N_2 pada suhu 180 °C diikuti oleh pirolisis pada suhu 900 °C untuk membentuk karbon susunan-nano. Kesan pengaktifan

menggunakan larutan KOH pada susunan-nano karbon aktif dikaji dalam penyingkiran ibuprofen. Pencirian menggunakan XRD, FTIR, TEM dan N_2 penjerapan-penyerapan menunjukkan karbon menyesuaikan struktur SBA-15 yang sangat teratur dengan diameter susunan-nano ~ 5 nm dan luas permukaan ~ 646 m^2/g. Kajian penjerapan ibuprofen pada susunan-nano karbon aktif menunjukkan penjerapan diikuti model kinetik pseudo-urutan-kedua dengan kapasiti penjerapan ~ 24.5 mg/g. Rawatan karbon yang berpanjangan dengan KOH terbukti memberi kesan kapasiti penjerapan ibuprofen yang disebabkan oleh penurunan fungsi permukaan karbon.

Kata kunci: karbon aktif susunan-nano, pengaktifan, penjerapan, ibuprofen, liang

Introduction

Activated carbon is a non-toxic substance with high surface area and often utilised as an adsorbent for removal of contaminants from wastewater. Activated carbon can be synthesised using a hard carbon template with an ordered structure, high thermal stability with regulated pore size distribution [1-5]. Depending on the average diameter of the pores, porous carbon may be classified into macropore, mesopore, and micropore structures. Activated carbon typically contained micropores within the structure and its application as an adsorbent was limited to the removal of small molecule substrates [5]. Pharmaceutical residues from hospital discharge often involved bulk organic molecules such as ibuprofen. Ibuprofen is a non-steroidal anti-inflammatory drug with the molecular size of ~1.3 × 0.6 nm [6, 7]; therefore, carbon adsorbent with mesoporous structure would be beneficial to accommodate the adsorbed ibuprofen [8].

Synthesis of carbon with ordered structure and large surface area has been the main interest to enhance the adsorption capacity of carbon [9-14]. Mesoporous carbon with ordered structure was used in drug delivery systems [1], energy storage [2], catalyst [3], and as adsorbent [4]. The activation process was performed using acidic solutions such as HCl [15] and H_3PO_4 [16], and also alkaline solutions such as KOH [11] and NH_4OH [17]. The alkaline solution has a high affinity to carbon surface in comparison to acid solution due to the interaction between the OH^- and the double bond of the sp^2 carbon [16]. Activation using potassium hydroxide enhanced the surface area of carbon from 300 to 1022 m^2/g [11]. Activation of carbon by KOH also showed significant improvement in the pore volume and specific surface area of carbon, the formation of uniform pore size, and enhanced surface functional group of carbon [18]. The activation process also influenced the formation of microporous and mesoporous structures, and the use of strong base KOH eliminated the tar deposits and volatile impurities on carbon [11].

Ordered carbon nanoarrays were synthesised using reverse microemulsion, solvothermal synthesis [12], hard templating [13], and soft templating methods [18-20]. The hard-templating method employed solid silica as mould and produced carbon with controlled morphology [18]. The structure and the morphology of carbon produced from hard templating method were significantly affected by the acidity of the synthesis mixtures, the temperature and the pressure used during the synthesis, and the duration of the synthesis [19]. As activation has generally enhanced the surface functionality of carbon, the effect of activation using KOH for ibuprofen removal using carbon nanoarrays was investigated in this study. The formation of activated carbon nanoarrays was carried out using SBA-15 as a template that was synthesised and deposited with sucrose as a carbon source. Activated carbon nanoarrays were obtained following carbonisation, pyrolysis, and activation steps. Morphological and structural properties of carbon nanoarrays were characterised using transmission electron microscopy (TEM), N_2 adsorption, and Fourier-transform infrared spectroscopy (FTIR) analysis. The effect of the activation of carbon using KOH was investigated for the adsorption of ibuprofen.

Materials and Methods

Material

Materials used were absolute ethanol (Sigma Aldrich), distilled water, sucrose ≥ 99.00% (HIMEDIA Laboratories Pvt. Ltd.), triblock poly(ethylene oxide)-b-poly (propylene oxide)-b-poly (ethylene oxide)

copolymer Pluronic P123 from (Sigma), H_2SO_4 95-97% (Merck), n-hexane (Sigma Aldrich), KOH (Merck Millipore, Sigma Aldrich).

SBA-15 synthesis

Mesoporous SBA-15 was synthesised by mixing 15% of P123 with 92% ethanol and 39% water (w/w). The mixture was agitated for 2 hours in a sealed flask to avoid evaporation. Then, 4% tetraethyl orthosilicate was added to the solution containing Pluronic P123 and stirred for another 2 hours. The resulting mixture was placed in Teflon-lined autoclave and placed in at 100 °C for 24 hours. The resulting white powder was filtered, washed, and calcined at 550 °C for 5 hours.

Synthesis of carbon

The SBA-15 was mixed with sucrose solution at 4% SBA-15, 9% sucrose, 45% water, and 4% H_2SO_4 ratios and stirred for 24 hours. Carbonisation was carried out at 100 °C for 18 hours. The resulting brown powder was annealed at 160 °C for 18 hours to form black carbon. Black carbon was crushed and sieved to produce a powder with 250 mesh size. The final step involved pyrolysis of black powder under the flow of nitrogen for 5 hours at 900 °C to produce ordered nanoarrays carbon (ONC). The removal of SBA-15 on the composite carbon was carried out by HF 5%. After washing, filtering, and evaporating, carbon was activated by potassium hydroxide. The activation process was conducted by mixing ONC with KOH and stirred for 60 minutes at 29 °C. The activation times were varied at 1, 2, and 3 hours. The mixture was aged for 12 hours, washed with water, and filtered using Whatman filter paper. The resulting powder was dried in an oven at 100 °C for 24 hours. The carbon was labelled as AONC-1h, AONC-2h, and AONC-3h.

Ibuprofen adsorption

The adsorption process was carried out by mixing 100 ppm of ibuprofen with 20 mg carbon and stirred at room temperature. The aliquot was sampled every 5 min and immediately separated from carbon using a membrane filter. The adsorption was analysed using UV-Vis spectrophotometer, and the concentration was determined using the calibration curve of absorbance against the concentration of ibuprofen. The amount of absorbed ibuprofen was calculated according to the following Equation 1:

$$q_t = \frac{C_O - C_t}{W} \times V \quad (1)$$

where q_t is the amount (mg g^{-1}) of ibuprofen absorbed, C_O is the initial concentration of ibuprofen (ppm), C_t is the concentration of ibuprofen at given time (ppm), V is the volume (litres) of ibuprofen, and W is the mass (g) of activated carbon. The q_{mak} was calculated using the following Equation 2, where q_{mak} is the maximum amount of ibuprofen adsorbed.

$$\frac{Ce}{qe} = + \frac{1}{qmaks.KL} \frac{Ce}{qmaks} \quad (2)$$

Kinetics studies of ibuprofen adsorption on activated ordered nanoarrays carbon (AONC) were plotted against the pseudo-second-order model following linear regression analysis, where the pseudo-second-order equation was expressed as the following Equation 3:

$$d_q = K_2 (q_e\text{-}q_t) d_t \quad (3)$$

K_2 indicates the adsorption rate (g/mg/min), q_e represented the mass of ibuprofen adsorbed on AONC at equilibrium (mg/g), and q_t is the mass of ibuprofen adsorbed at time t (mg/g).

Characterisation

The morphology of activated carbon microspheres was characterised using scanning electron microscopy (SEM) JEOL JSM-700 at a speed of 15.0 kV voltages. The functional groups of the activated carbon were characterised using FTIR Bruker Vertex 70 at the wavelength of 500-4000 cm^{-1}. The ibuprofen adsorption was measured using UV-Vis spectroscopy (model U-2000, Hitachi, Japan) at the wavelength of 272 nm.

Results and Discussion

XRD analysis was carried out on SBA-15 and activated carbon synthesis using SBA-15 template (Figure 1). The diffraction pattern showed that the broad peak centred at 25° corresponded to the amorphous structure of SBA-15. There were no significant changes on the diffraction pattern of carbon; however, a small peak was observed

at 44°. The diffraction peaks for carbon that appeared at $2\theta = 25.5°$ corresponded to the diffraction of (002) plane and 41.7° for (100) plane [20].

Figure 2a shows the N_2 adsorption isotherm of AONC and SBA-15. The specific surface area of the carbon was analysed at ~646 m^2/g, while the SBA-15 was ~520 m^2/g. The N_2 adsorption isotherm of carbon showed similar features as SBA-15, which corresponded to the type IV isotherm adsorption associated with the presence of mesoporous structure [21]. The N_2 adsorption/desorption isotherm of carbon was divided into three stages with the first stage corresponded to the adsorption at $P/Po < 0.5$. N_2 filled the small pore of carbon and formed monolayer adsorption on the microporous surface. The volume of N_2 adsorption showed a linear increase with the pressure. The second stage involved the N_2 adsorption on the mesoporous carbon pores, as the relative pressure P/Po increased from 0.4 to 0.8. At this stage, a sharp increase in N_2 adsorption was observed due to N_2 capillary condensation in the mesopore, which was the characteristic features of the uniformed pores [22]. The sharp increase of N_2 adsorption with the relative pressure also indicated the beginning of the interconnection of pores within the structure. Two types of pores existed in the carbon, which consisted of large primary pores interconnecting with small pores known as secondary pore. The presence of small pores in carbon also recognized as pore-neck or pore-bridge [21-22]. The third stage of N_2 adsorption occurred on the microporous surface of carbon at P/P_o above 0.8 with the vertical direction features. The N_2 desorption from carbon surfaced showed a similar pattern but with hysteresis loop due to the capillary condensation. The pore distribution of carbon and SBA-15 are shown in Figure 2b. The synthesised carbon nanoarrays showed similar pore distribution as SBA-15, which are in the mesopore region. However, the pore volume showed a slight reduction. The average pore diameter of the carbon was analysed within the range of 3–6 nm.

Infrared spectra of the SBA-15 in Figure 3 shows the characteristic bands associated with the SBA-15 ribbon character at 1000-1300 cm^{-1} and 800-900 cm^{-1}, which represent the asymmetric and cyclic strain vibration of Si-O-Si [20, 21]. The wide adsorption band centred at 3600 cm^{-1} corresponded to the presence of hydrogen bonds or adsorbed water. The presence of C-H vibrational peak at 2930 cm^{-1} is also observed on SBA-15, which presumably originated from the remaining carbon from the P123 precursor. The infrared spectra of carbon also show a wide absorption peak at 3600-3100 cm^{-1} that corresponded to the presence of hydroxyl groups and adsorbed water on the surface. The broadening of the band following activation with KOH suggested the enhancement of surface hydroxyl on the carbon. The characteristics absorption band of SBA-15 at 809 cm^{-1} and 1080 cm^{-1} are absent in the carbon profile, indicating complete removal of the SBA-15 template. The absorption band appeared at 1300 cm^{-1} that corresponded with the presence of vibration strain stretch of C-H in carbon. Meanwhile, the absorption band at 1567 cm^{-1} with relatively small intensity, indicating the characteristic of sp2 carbon double bond vibration presumably from the aromatic structure in the carbon. Several vibrations bands are also observed corresponding to the presence of functional group on carbon, such as the vibration of C=O at 2347 cm^{-1} at 2072 cm^{-1} and the vibration of the CH_3 and CH_2 clusters appeared between 3000–2800 cm^{-1} [21]. KOH treatment at 1 h significantly enhanced the intensity of CH_3 and CH_2 clusters within 3000–2800 cm^{-1} region, which suggested that the treatment enhanced surface functionality of carbon. However, when the activation of carbon with KOH was extended to 2 hours and 3 hours, the C-H vibration peak at 2936 cm^{-1} disappeared, indicating the detrimental effect of prolonged treatment on the functionality of carbon.

TEM analysis shown in Figure 4 confirmed the morphology of carbon nanoarrays obtained using SBA-15 as a hard template. The micrograph of carbon shows an identical ordered nanoarray structure as SBA-15, which implied the carbon could retain the ordered structure following the removal of SBA-15 (Figure 4a, 4b, red box). Carbon micrograph also shows that the spacing between the nanoarrays is ~ 8.0 nm, while the cross-sectioned nanoarrays indicated the pore diameter of 6.3 nm (Figure 4, red circle). However, the TEM analysis of SBA-15 revealed that the spacing between the nanoarrays of SBA-15 is ~ 8.9 nm and the diameter

of the cross-sectioned of the nanoarrays is ~ 9.3 nm. The structural stability and regularity of the activated carbon nanoarrays can be identified due to the absence of TEM image defects. The regularity of the structure and microscopic features of the material in this study were observed with the TEM. The TEM carbon micrograph shows a hexagonal structure with 6 mm spaces. The regularity of carbon after activation and SBA-15 can also be seen in SAED (Selected area electron diffraction) which was obtained in TEM image by reverse space in lattice plane. TEM image of carbon also exhibits the arrangement of carbon bars when observed from the horizontal direction. TEM analysis shows that the synthesised carbon has a similar morphology to SBA-15 silica, which implies a successful replication process. In general, TEM SBA-15 and carbon nanoarray data have the same regularity as previous studies [20-21]. EDX analysis of the activated carbon following KOH treatment for 1 h (Fig. 5) indicated that the ordered nanoarrays activated carbon contained 61% of carbon with 36% oxygen. P, Mo, and K were also observed as impurities at traces level. The EDX result confirmed the removal of SBA-15 template.

Figure 6 shows the adsorption of ibuprofen on carbon following activation using KOH. The carbon was alkaline treated with KOH for 1, 2, and 3 hours prior to the ibuprofen adsorption. The adsorption isotherms showed high adsorption capacity of ibuprofen on carbon following 1 hours KOH activation. However, extending the activation period to 2 and 3 hours exhibited a reduction in the adsorption capacity of ibuprofen. For carbon produced by 1 hour of KOH treatment, the adsorption reached equilibrium within 10 minutes of the adsorption. The rate of ibuprofen adsorption is relatively fast within the first 5 minutes and continued to reach steady states at 10 minutes. Increasing the immersion time of carbon in KOH showed a detrimental effect on the adsorption of ibuprofen. The resulting carbon after 2 and 3 hours of immersion reached equilibrium at 20 minutes with the adsorption capacity of ~19 mg/g. The adsorption of ibuprofen on carbon occurred via monolayer adsorption due to the repulsion between the adsorbed ibuprofen molecules on the carbon surface with the ibuprofen in the solution, which prevented multi-layer adsorption. Understanding the mechanism of ibuprofen adsorption on carbon surface [23], it was expected that ibuprofen molecules initially adsorbed in the mesopores and experienced rapid saturation during the initial state of adsorption. Consequently, further adsorption requires ibuprofen molecules to move along the occupied sites to achieve adsorption into a deeper pore of carbon. Due to the bulky structure of ibuprofen and the repulsion with the adsorbed molecules, the rate of adsorption was significantly reduced following the initial saturation stage [24]. Infrared analysis on activated carbon indicated the disappearance of C-H surface functionality of carbon following KOH treatment at 2 and 3 hours. Meanwhile, although activation with KOH was essential to enhance surface functionality and consequently increased the adsorption, prolonged activation was proven detrimental, as it removed the required active sites for ibuprofen adsorption.

Kinetic analysis of ibuprofen adsorption on carbon was carried out using linear regression analysis pseudo-second-order kinetics model, as shown in Figure 7 [25]. The model was previously used to describe the kinetic adsorption of ibuprofen on mesoporous carbon microspheres and activated carbon [8, 23-26]. The ibuprofen adsorption kinetic data on pseudo-second-order approached the two-Semitic order model with a correlation coefficient of $R^2 = 0.999$. The ibuprofen adsorption followed the pseudo-second-order kinetic model, which suggested that ibuprofen adsorption occurred at two different carbon surface sites.

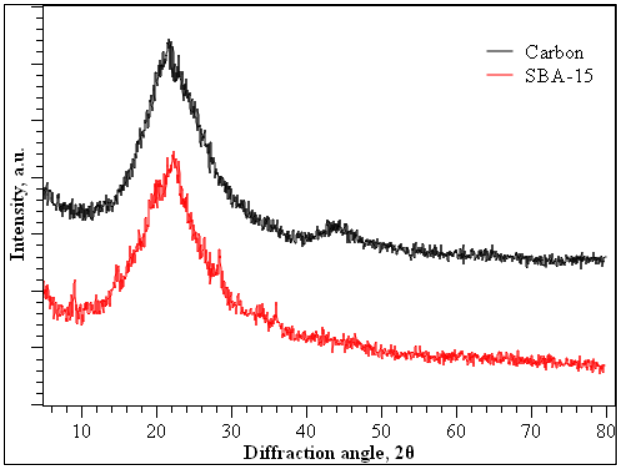


Figure 1. XRD analysis of SBA-15 and activated nanoarrays carbon

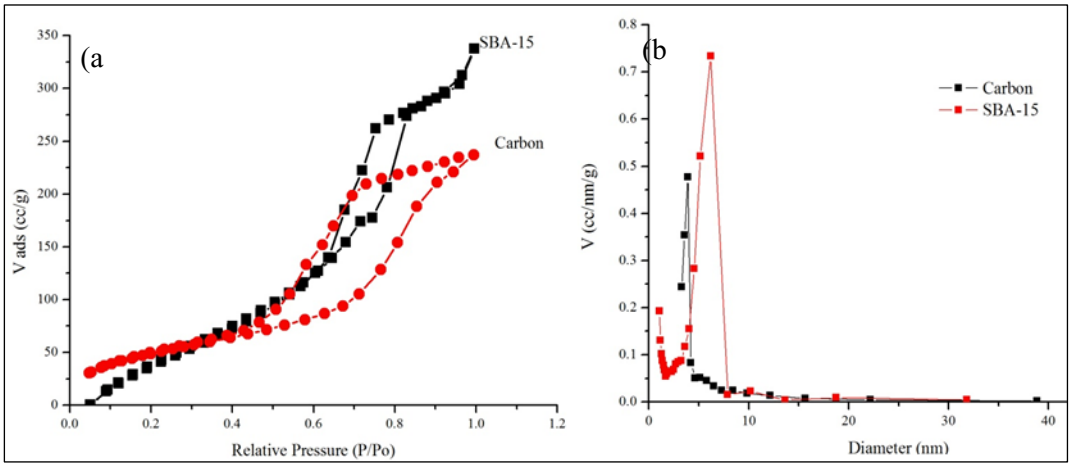


Figure 2. N_2 adsorption-desorption isotherm (a) and pore size distribution (b) of activated nanoarrays carbon (AONC-1h) and SBA-15

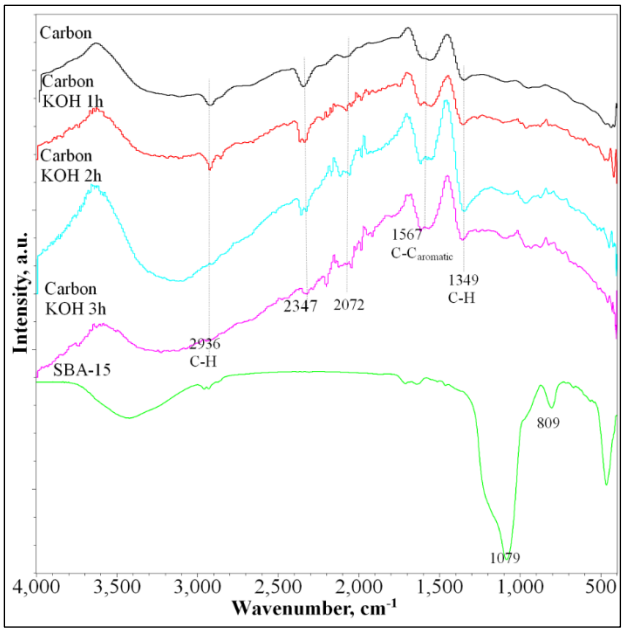


Figure 3. Infrared spectra of SBA-15 and carbon after activation with KOH

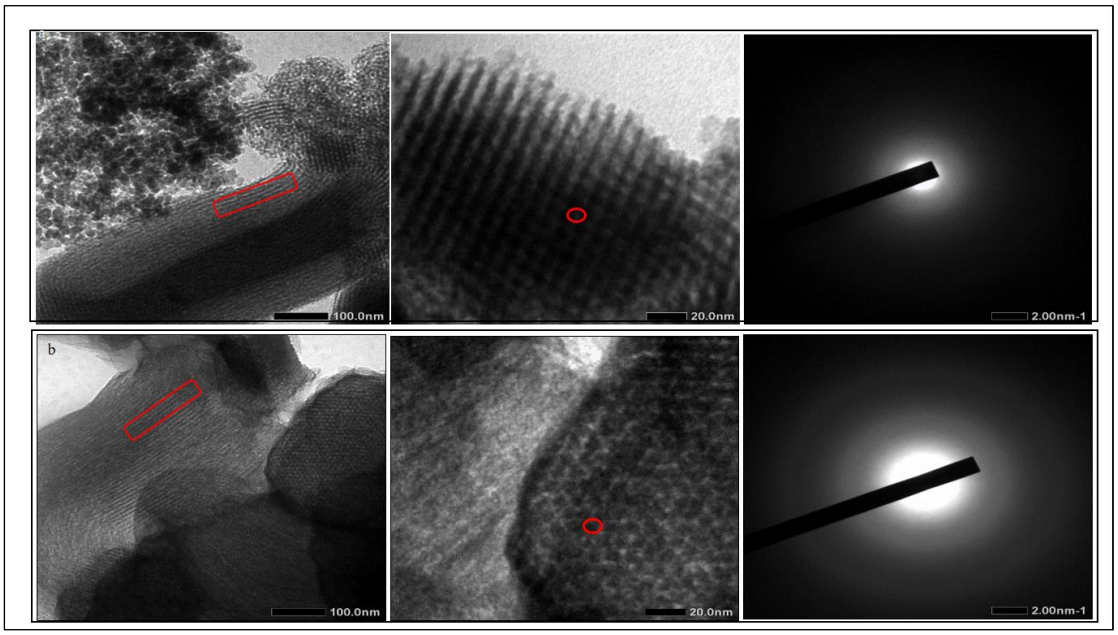
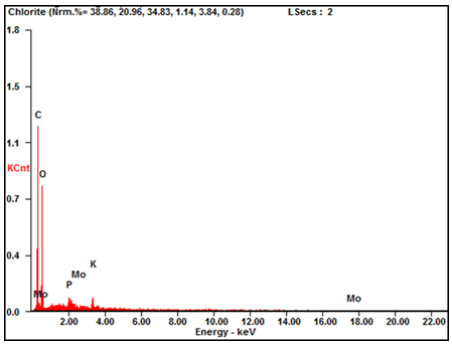


Figure 4. TEM analysis of a) SBA-15, and b) ordered nanoarrays activated carbon



Element	Wt %	At %
C	52.78	61.72
O	41.45	36.38
P	01.53	00.69
Mo	01.49	00.22
K	02.75	00.99

Figure 5. EDX analysis of ordered nanoarrays activated carbon

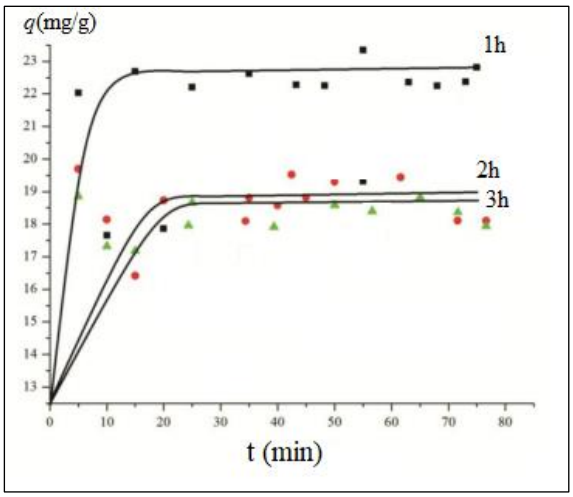


Figure 6. The adsorption of ibuprofen on carbon following activation process at 1, 2, and 3 hours

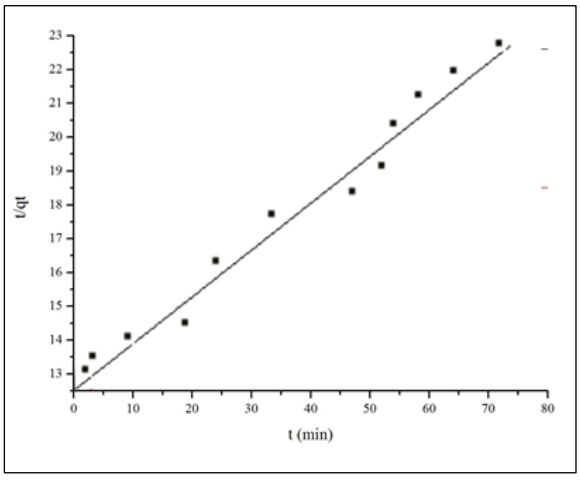


Figure 7. The pseudo-second-order linear kinetic model of ibuprofen adsorption on activated nanoarrays carbon

Conclusion

Activated ordered carbon nanoarrays (AONC) have been successfully synthesised using SBA-15 as a hard template and showed potential as an adsorbent for ibuprofen. AONC was characterised by FTIR, TEM, and nitrogen adsorption-desorption analysis that showed the replication of the SBA-15 ordered structure on the activated carbon. Adsorption studies of ibuprofen on the carbon showed the maximum adsorption capacity of ibuprofen at 24.5 mg/g with the adsorption kinetics following the pseudo-second-order kinetic model. The detrimental effect of prolonged KOH activation was observed on the decrease of ibuprofen adsorption capacity on the carbon that was due to the decrease of surface functionality, as indicated by infrared analysis.

Acknowledgments

Our research was financially supported by the Program Penelitian Kolaborasi Indonesia 2020 (Indonesia Collaboration Research Program 2020) collaborated by Sebelas Maret University (UNS), Gadjah Mada University (UGM), Sepuluh Nopember Institute of Technology (ITS), and University Brunei Darussalam (UBD).

References

1. Zhou, M. Z., Peng, S., Liao, P., Li, M. and Li, S. (2014). Design of a microencapsulated carbon nanotube-based microspheres and its application in the colon targeted drug delivery. *Drug Delivery*, 21(2): 101-109
2. Liu, M. L., Kong, C., Lu, X., Li, Y., Luo, K. and Kang, L. (2012). Close-packed mesoporous carbon polyhedrons derived from colloidal carbon microspheres for electrochemical energy storage applications. *RSC Advances*, 2(27): 10310-10315.
3. Wang., F. (2015). Simple synthesis of novel hierarchical porous carbon microspheres and their application to a rechargeable lithium-ion batteries. *Carbon NY*, 81(1): 314-321.
4. Meer, S., Kausar, A. and Iqbal, T. (2016). Synthesis of multi-walled carbon nanotube/silica nanoparticle/ polystyrene microsphere /polyaniline-based hybrids for EMI shielding application. *Fullerenes, Nanotube, and Carbon Nanostructures*, 24(8): 507-519.
5. Wang, J. and Kaskel, S. (2012). KOH activation of carbon-based materials for energy storage. *Journal of Materials Chemistry*, 22(45): 23710-23725
6. Mestre, J., Pires, J. M. F., Nogueira, Y. and Carvalho, A. P. (2007). Activated carbons for the adsorption of ibuprofen. *Carbon NY*, 45(10): 1979-1988.
7. Kumaresan, S. (2010). S+ Ibuprofen (Dexibuprofen): The superior conventional non-steroidal antiinflammatory agents for development of pharmaceuticals. I*nternational Journal of Current Pharmaceutical Research*, 2(3): 66-75.
8. Ulfa, M., Didik, P., Mahadi, A. and Hasliza, B. (2019). Size tunable mesoporous carbon microspheres using Pluronic F127 and gelatin as co-template for removal of ibuprofen. *Science of the Total Environment,* 56 (3): 24-32
9. Nieto-Márquez, A., Valverde, J. L. and Keane, M. A. (2009). Selective low temperature synthesis of carbon nanospheres via the catalytic decomposition of trichlorethylene. *Applied Catalytic Agent*, 352(2): 159-170.
10. Zhang, D. (2017). Scalable synthesis of hierarchical macropore of activated carbon-rich microspheres assembled by carbon nanoparticles for high-rate performance supercapacitors, *Journal Power Sources*, 342 (1): 363-370.
11. Lua, A. C and Yang, T. (2004). Effect of activation temperature on the textural and chemical properties of potassium hydroxide activated carbon prepared from pistachio-nut-shell. *Journal of Colloid and Interface Science,* 274 (2): 594-601.
12. Mi, Y. Z. and Liu, Y. L. (2009). A simple solvothermal route to synthesize carbon microspheres. *Xinxing Tan Cailiao/New Carbon Materials*, 24(4): 375-378.
13. Li, J., Zhong, X. Z., Yang, G. J., Lan, H. D., Tang and Liu H. Z. (2011). Simple synthesis of semi-graphitized ordered mesoporous carbons with tunable pore sizes. *Xinxing Tan Cailiao/New Carbon Materials*, 26(2): 123-129

14. Gorka, C., Fenning, K. and Jaroniec, M. (2009). Influence of temperature, carbon precursor/ copolymer ratio and acid concentration on adsorption and structural properties of mesoporous carbons prepared by soft-templating. *Colloids and Surfaces A Physicochemical and Engineering Aspects*, 352(1-3): 113-117.
15. Guo, J., Zhang, H. and Liu H. (2016). Ultra-high Rhodamine B adsorption capacities from an aqueous solution by activated carbon derived from: Phragmites australis doped with organic acid by phosphoric acid activation. *RSC Advances*, 6(47): 40818-40827.
16. Heidari, H., Younesi, A., Rashidi, A. and Ghoreyshi. A. A. (2014). Evaluation of CO_2 adsorption with eucalyptus wood-based activated carbon modified by ammonia solution through heat treatment. *Chemical Engineering Journal,* 254(3): 503-513.
17. Pflitsch, C. (2014). Chemical vapor infiltration of activated carbon with tetramethylsilane. *Carbon NY*, 79 (1): 28-35.
18. Ulfa, M., Wega, T., Iif, I. and Indriana, K. (2018). Wormhole-like mesoporous carbons from gelatine as multistep infiltration effect. *Indonesian Journal of Chemistry*, 16(3): 239-242.
19. Xie, D., Kocaefe, C., Chen, T. and Kocaefe, Y. (2016). Review of research on template methods in preparation of nanomaterials. *Journal of Nanomaterial*, 2016(23): 025-035.
20. Ma, Z., Kyotani, T., Liu, Z., Terasaki, O. and Tomita, A. (2001). Very high surface area microporous carbon with a three-dimensional nano-array structure: Synthesis and its molecular structure. *Chemistry of Materials*, 13(12): 4413-4415.
21. María E. A., Marisa, P., Magali, B., Bénédicte, L., Verónica, B. and Loreana, G. (2020). Synthesis and characterization of mesoporous SBA-15 and SBA-16 as carriers to improve albendazole dissolution rate. *Saudi Pharmaceutical Journal*, 28(1): 15-24.
22. Belmoujahid, Y. M., Bonne, Y., Scudeller, D., Schleich, Y., Grohens, B. and Lebeau, A. (2015). SBA-15 mesoporous silica as a super insulating material**.**
23. Fröhlich, A. C. R., Ocampo-Pérez, V. Diaz-Blancas, N. P. G., Salau, G. L. and Dotto. (2018). Three-dimensional mass transfer modeling of ibuprofen adsorption on activated carbon prepared by sonication. *Chemical Engineering Journal*, 341(1): 65-74.
24. Michel O., Laurence R., Sylvie G., Stéphane B., Sandrine D., Jean-Marc, L. and Laurent D. (2018). Improving the adsorption kinetics of ibuprofen on an activated carbon fabric through ultrasound irradiation: Simulation and experimental studies. *Chemical Engineering Journal*, 343(1): 163-172.
25. Syeda N. F., Ali, E. I., El-Shafey, F., Saleh Al-Busafi, Haider, A. J. and Al-Lawati. (2019). Adsorption of chlorpheniramine and ibuprofen on surface functionalized activated carbons from deionized water and spiked hospital wastewater. *Journal of Environmental Chemical Engineering*, 7(1): 28-38.
26. Hanen, G., Imadeddine, L., Laurence R., Jean-Marc, L., Nizar, B. and Laurent, D. (2020). Removal of ionic liquids and ibuprofen by adsorption on a microporous activated carbon: Kinetics, isotherms, and pore sites. *Arabian Journal of Chemistry*, 13(3): 258-270.

Malaysian Journal of Analytical Sciences (MJAS)
Published by Malaysian Analytical Sciences Society

EFFECT OF AUXIN AND METHYL JASMONATE ON TOTAL PHENOLIC CONTENT AND TOTAL FLAVONOID CONTENT IN ADVENTITIOUS ROOTS OF *Justicia gendarussa*

(Kesan Auksin dan Metil Jasmonat ke atas Jumlah Kandungan Fenolik dan Flavonoid dalam Akar Adventitius *Justicia gendarussa*)

Noor Khaleeda Arsad and Azman Abd Samad*

Department of Biosciences, Faculty of Science
Universiti Teknologi Malaysia, 81310 Johor Bahru, Johor, Malaysia

**Corresponding author: azmansamad@utm.my*

Received: 18 July 2019; Accepted: 20 July 2020; Published: 10 December 2020

Abstract

Justicia gendarussa or known as *gandarusa*, a member of the Acanthaceae family, is recognised for its medicinal properties. To date, the optimisation of total phenolic and total flavonoid contents in adventitious root biomass of *J. gendarussa* has not been reported. Therefore, in this study, the effects of auxins and methyl jasmonate (MeJa) on adventitious root biomass, total phenolic content (TPC), and total flavonoid content (TFC) of *J. gendarussa* were investigated. Adventitious root induction from leaf explant was studied when treated with different concentrations of indole butyric acid (IBA), indole acetic acid (IAA), and naphthalene acetic acid (NAA). The total phenolic content (TPC) and total flavonoid content (TFC) were recorded after 7 weeks of cultures. Results demonstrated that the maximum root biomass was obtained when treated with 2 mg/L IAA (1591.40 ± 14.14 mg). Analysis of TPC and TFC revealed that the combination of 2 mg/L IAA + 0.5 mg/L NAA had an optimum value of 0.30 ± 0.02 mg gallic acid equivalent/g dry roots and 0.24 ± 0.01 mg of (+) catechin equivalent/g dry roots, respectively. However, the addition of MeJa had reduced the root biomass, TPC, and TFC. In conclusion, a combination of IAA and NAA had a positive effect on root biomass, TPC, and TFC values.

Keywords: adventitious root, *Justicia gendarussa*, methyl jasmonate, flavonoid, phenolic

Abstrak

Justicia gendarussa atau juga dikenali sebagai gandarusa, adalah ahli keluarga Acanthaceae yang terkenal dengan ciri-ciri perubatan. Sehingga kini, pengoptimuman jumlah kandungan fenolik dan kandungan flavonoid di dalam akar adventitius masih belum dilaporkan. Oleh sebab itu, kajian ini dijalankan untuk menentukan kesan auksin dan metil jasmonat (MeJa) terhadap biojisim akar, jumlah kandungan fenolik (TPC), dan jumlah kandungan flavonoid (TFC) dalam akar adventitius *J. gendarussa*. Pengaruhan akar adventitius daripada eksplan daun yang dirawat telah dikaji dengan pelbagai kepekatan asid indol butirik (IBA), asid indol asetik (IAA), dan asid naftalena asetik (NAA). Analisa kandungan TPC dan TFC telah direkodkan selepas 7 minggu rawatan. Keputusan menunjukkan bahawa biojisim akar yang maksimum diperolehi pada rawatan 2 mg/L IAA (1591.40 ± 14.14) mg. Analisa TPC dan TFC pula menunjukkan bahawa gabungan rawatan 2 mg/L IAA + 0.5 mg/L NAA mencapai nilai optimum

TPC (0.30 ± 0.02 mg asid galik yang setara per gram akar kering) dan TFC (0.24 ± 0.01 mg (+) katekin yang setara per gram akar kering). Walau bagaimanapun, penambahan MeJa telah mengurangkan biojisim akar, TPC dan TFC. Kesimpulannya, kombinasi IAA dan NAA memberikan kesan positif kepada penambahan biojisim akar, nilai TPC dan TFC.

Kata kunci: **a**kar adventitius, *Justicia gendarussa,* metil jasmonat, flavonoid, fenolik

Introduction

Justicia gendarussa or locally known as *gandarusa* is a member of the Acanthaceae family. It is a shade-loving, quick-growing, evergreen plant and grown in moist areas [1]. It is distributed in Malaysia, China, Indonesia, India, Philippines, Sri Lanka, and Bangladesh. The *J. gendarussa* sp. has been demonstrated to exhibit bioactivities such as antioxidant, anticancer, anti-inflammatory, antibacterial, and anti-microbial activities [2]. Adventitious roots are natural, inducible, vigorously grown in supplementary medium plant growth regulators and have an excellent potential for the accumulation of valuable secondary metabolites [3]. The formation and development of adventitious roots are stimulated by wounding, hormonal application, or in response to certain stimuli from stems, leaves, and other parts of the plant [4]. *Justicia gendarussa* is found to contain lignans and naturally occurring phenolic dimers [5]. Plant phenolic is the most common and widely distributed group of flavonoids. Flavonoids play an essential role in plant pigmentation, nitrogen fixation, UV protection, and defence mechanism against predators and pathogens. Gandarusa also contains flavonoids that possess biological activities such as antioxidants and cytotoxic components [6]. Besides that, methyl jasmonate (MeJa) that acts as an elicitor, is a volatile organic compound used in the signal transduction process that regulates plant defence responses and enhances the production of various secondary metabolites. However, the effect of auxins and MeJa in root induction on TPC and TFC remains unknown. Therefore, in this study, the effects of indole acetic acid (IAA), indole butyric acid (IBA), and naphthalene acetic acid (NAA) concentrations on adventitious root biomass, total phenolic content (TPC), and total flavonoid content (TFC) from leaf explant of *J. gendarussa* were investigated. In addition, the effects of the combination of MeJa and auxins concentrations on adventitious root biomass, TPC, and TFC was also assessed.

Materials and Methods

Plant materials

The *in vitro J. gendarussa* plants were grown and maintained in the tissue culture room at the Plant Biotechnology Laboratory, Faculty of Science, Universiti Teknologi Malaysia. The young leaves (second leaves from the shoot) of four-month-old plants were used as explants.

Effect of auxins on adventitious root induction of *J. gendarussa*

For adventitious root induction, fresh leaves from four-month-old in vitro plants (0.5 cm × 0.5 cm) were placed on Murashige and Skoog (MS) [7] plates supplemented with different concentrations of IBA (1.0, 1.5, and 2.0 mg/L), IAA (1.0, 1.5, 2.0, and 2.5 mg/L), and NAA (1.0, 1.5, 2.0, and 2.5 mg/L). The steps were conducted in a strict sterile condition, and each of the plates contained five explants. Then, the cultured plates were double-sealed with parafilm and placed in the culture room for incubation, with five replicates for each treatment. All cultures were incubated at the growth conditions of 25 ± 2 °C; 16-h photoperiod, and light intensity of 17 mol m^{-2} s^{-2}. Data were collected and analysed after 49 days of culture.

Analysis of adventitious roots

Fresh adventitious roots of *J. gendarussa* were harvested and weighed. Then, the root biomass was placed in the Petri dish and dried in the oven at 40 °C for 48 hours. After that, the dried root biomass was subjected to two assays such as TPC and TFC.

Estimation of phenols and flavonoids

The ground dried root material (~ 0.5 g) was mixed with 10 mL 75% (v/v) ethanol in a 50 mL polypropylene conical tube and stirred for 15 minutes. The content was centrifuged at room temperature for 10 minutes. The filtrate was collected by filtering the supernatant under vacuum into a volumetric flask. The phenols and

flavonoids were re-extracted to a final volume of up to 12 mL.

Total estimation of TPC

TPC in adventitious root extracts was analysed spectrophotometrically using Folin-Ciocalteu reagent [8]. A volume of 100 mL methanol was mixed well with 2.5 mL sterile distilled water and 0.1 mL of Folin-Ciocalteu reagent for 6 minutes. After that, 0.15 mL 20% (w/v) sodium carbonate solution was added to the mixture. The colour changed after incubation at room temperature for 30 minutes. Finally, the absorbances were detected at 760 nm by UV-Vis spectrophotometer. The measurements were compared to the standard curve for gallic acid. The result was expressed as mg of gallic acid equivalent per gram of dry roots.

Total Estimation of TFC

The total amount of flavonoid in adventitious root extracts was analysed spectrophotometrically using aluminium chloride colourimetric method [8]. About 0.25 mL methanol was mixed with (+) catechin standard solution, 1.25 mL sterile distilled water, and 75 mL 5% sodium nitrate solution. The mixtures were mixed well and left for 6 minutes at room temperature. After that, 0.15 mL 10% (w/v) aluminium chloride solution was added to the mixture and mixed for 5 minutes. Then, 0.5 mL 1 M sodium hydroxide was added and mixed well. Next, the absorbances were detected at 510 nm using UV-Vis spectrophotometer. The measurements were compared to the standard curve for (+) catechin. The result was expressed as mg of (+) catechin equivalent per gram of dry roots.

Effect of auxins combinations on root biomass, TPC, and TFC

The leaves (0.5cm × 0.5cm) were placed on MS media containing different sets of combination concentrations of IBA+NAA and IAA+NAA ranging from 0 to 1.0 mg/L. The steps were conducted in a strict sterile condition, and each of the plates contained five explants. Then, the cultured plates were double-sealed with parafilm and placed in the culture room for incubation, with five replicates for each treatment. All cultures were incubated at growth conditions of 25 ± 2 °C, 16-h photoperiod, and light intensity of 17 mol m^{-2} s^{-2}. Data were collected and analysed after 49 days of culture. Then, TPC and TFC were measured using the same method [8].

Effect of methyl jasmonate (MeJa) on root biomass, TFC, and TFC

Adventitious root (0.1 g/L) was inoculated into MS liquid media supplemented with IAA 2.0 mg/L + NAA 0.5 mg/L and different concentrations of MeJa (50–150 µM). Adventitious roots were grown in the presence of MeJa at 30 days before subsequent phenolic and flavonoid analysis. Afterwards, root biomass was calculated. All cultures were incubated at the growth conditions of 25 ± 2 °C, 16-h photoperiod, and light intensity of 17 mol m^{-2} s^{-2}. Data were collected and analysed after 49 days of culture.

Statistical analysis

The data were analysed using SPSS for Windows software (SPSS 23.0, SPSS Inc., USA). A comparison of means for more than two treatments was conducted using analysis of variance (one-way ANOVA) with post hoc multiple comparisons, i.e., Bonferroni. The differences were considered significant if the probability is less than 0.05 (p <0.05).

Results and Discussion

Induction of Adventitious Roots by Auxin

In this experiment, the effects of IAA, IBA, and NAA on adventitious roots biomass, TPC, and TFC were studied. The adventitious roots were first observed after seven days of culture. Figure 1 shows that the amount of root biomass produced from leaf explants of *J. gendarussa* was influenced by different concentrations of auxins. For adventitious roots induction, leaf explants were cultured with different IBA concentrations (1, 1.5, and 2 mg/L), IAA (1.0, 1.5, 2.0, and 2.5 mg/L), and NAA (1.0, 1.5, 2.0, and 2.5 mg/L). Since the IBA concentration above 2 mg/L did not enhance root induction, phenols, and flavonoid content [9], it was not tested in this experiment. Leaf explants treated with 2.0 mg/L IAA produced the highest root biomass (1591.40 ± 14.14 mg) compared to 1.5 mg/L IBA (168.07 ± 18.75 mg) and 2.0 mg/L NAA (13.95 ± 1.94 mg), as shown in Figure 1.

Figure 3 shows the adventitious root induction from leaves explant treated with plant growth regulators, i.e., 1.5 mg/L IBA, 2.0 mg/L IAA, and 2.0 mg/L NAA. Besides, 2.0 mg/L IAA produced higher the root biomass than 1.5 mg/L IBA. The IAA had achieved the optimum concentration when treated with IAA at 2.0 mg/L but decreased tremendously when treated with 2.5 mg/L IAA. This indicated that the root biomass production reached maximum biomass at 2.0 mg/L IAA. Auxins such as IAA, IBA, and NAA are widely used as root stimulators that act with various phytohormones through complex crosstalk, changing their levels and actions at every level, which include biosynthesis, metabolism, transport, and signalling [10]. Different plant growth regulators participate in various steps of adventitious root formation. For example, IAA is recognised as the major plant growth regulator that promotes adventitious root formation [4] and increase adventitious root biomass up to nearly 8-fold than that of the control [11]. Besides that, IBA also promotes root induction and root biomass. IBA at 1.5 mg/L was found suitable for root induction of *Echinacea angustifolia*, *Orthosiphon prostrate,* and *Ophiorrhiza prostrate* [11], and it is widely used in clonal propagation [10]. Figures 2 and 3 show the formation of the fishbone structure and adventitious roots induced when leaf explants were treated with different types of auxin, respectively. The fishbone structure indicated the high proliferation rate of adventitious roots. Besides that, the shoot was also induced from leaf explant treated with 2.0 mg/L IAA, as shown in Figure 4.

Effect of auxins on TPC and TFC

Figure 5 shows the total phenolic content in root biomass treated with different concentrations of IBA, IAA, and NAA from leaf explants of ***J. gendarussa***. The highest TPC in root biomass was obtained when treated with 2.0 mg/L IAA (0.27 ± 0.03 mg gallic acid equivalent/g dry roots), followed by 2.0 mg/L NAA (0.12 ± 0.005 mg gallic acid equivalent/g dry roots) and 1.5 mg/L IBA (0.07 ± 0.01 mg gallic acid equivalent/g dry roots). Figure 6 reveals the total flavonoid content in root biomass treated with different concentrations of IBA, IAA, and NAA from leaf explants of *J. gendarussa*. The highest TFC in root biomass was attained when treated with 2.0 mg/L IAA (0.18 ± 0.02 mg (+) catechin equivalent/g dry roots), followed by 2.0 mg/L NAA (0.12 ± 0.012 mg (+) catechin equivalent/g dry roots) and 1.5 mg/L IBA (0.07 ± 0.004 mg (+) catechin equivalent/g dry roots). From both figures, 2.0 mg/L IAA had the highest TPC and TFC with the value of 0.27 ± 0.03 mg gallic acid equivalent/g dry roots and 0.18 ± 0.02 mg (+) catechin equivalent/g dry roots, respectively. The trends also revealed that the increment of the root biomass had a positive effect on TPC and TFC. Overall, IAA at 2.0 mg/L had optimised root biomass, TPC, and TFC. Results showed that IAA influenced adventitious root biomass, TPC, and TFC. Plant secondary metabolites began to accumulate during the stationary phase of cell growth kinetics and were successfully synthesised when the primary metabolites have an adequate amount of carbon [12]. Besides that, the phenolic and flavonoids play a role in the formation of adventitious roots, where auxin inhibits or promotes adventitious root by altering the secondary metabolites, especially phenolic content [11]. The phenolic compounds and flavonoids are affected by the presence of auxin, growth sites, and organ parts [10,12]. It suggests that the increase in root biomass is proportional to TPC and TFC. Therefore, the increment of root biomass will improve the TPC and TFC. In this study, 2.0 mg/L IAA achieved the optimum TPC and TFC values but significantly decreased when treated at 2.5 mg/L IAA. This phenomenon indicated that IAA concentration above 2.0 mg/L affected the phenolic and flavonoids content in the roots.

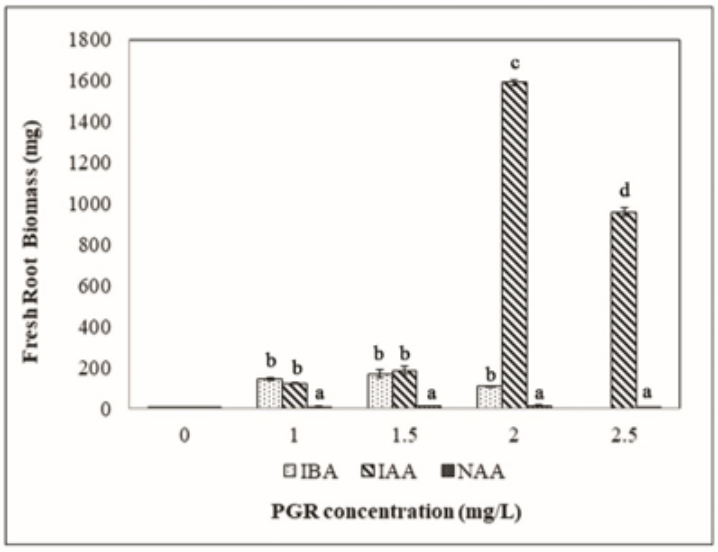


Figure 1. Root biomass produced when treated with different concentrations of IBA, IAA, and NAA from leaf explants of *J. gendarussa*



Figure 2. Fishbone structure of the adventitious root. Scale bar: 1 cm

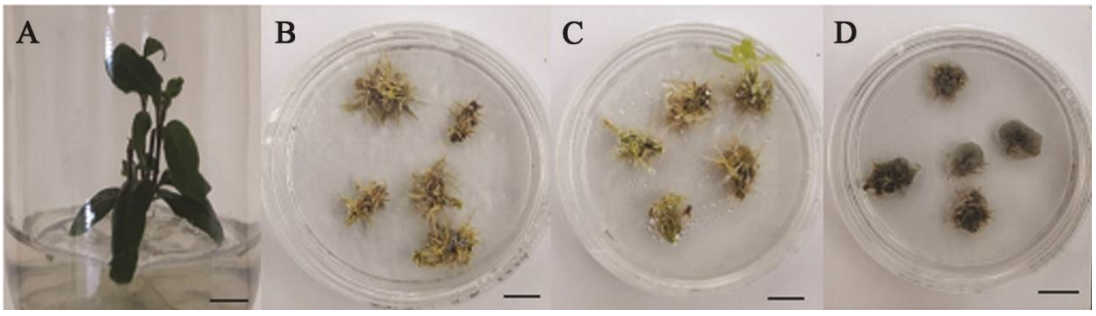


Figure 3. Adventitious root induction from leaves explant treated with auxins. (a): In vitro *J. gendarussa* plant, (b): 1.5 mg/L IBA, (c): 2.0 mg/L IAA and (d): 2.0 mg/L NAA. Scale bars: 1 cm

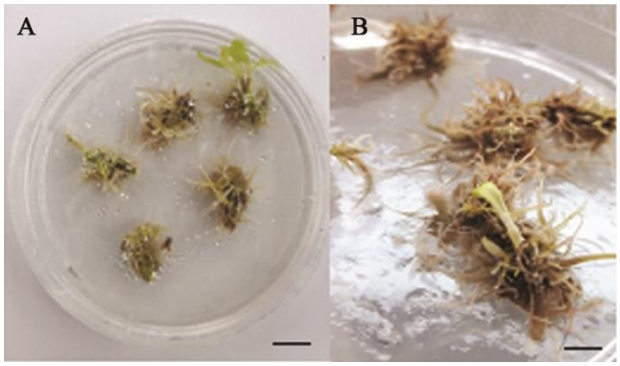


Figure 4. A: Shoot induced from leaf explant treated with 2.0 mg/L IAA. B: Close up. Scale bars: 1 cm

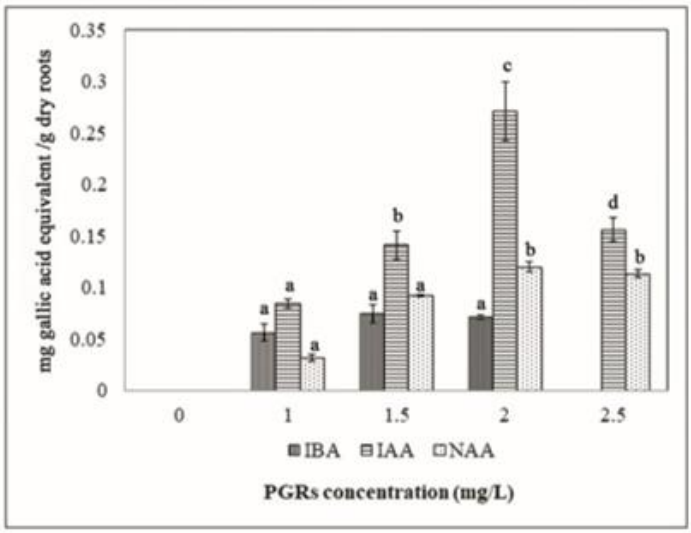


Figure 5. Total phenolic content obtained when treated with different auxin concentrations

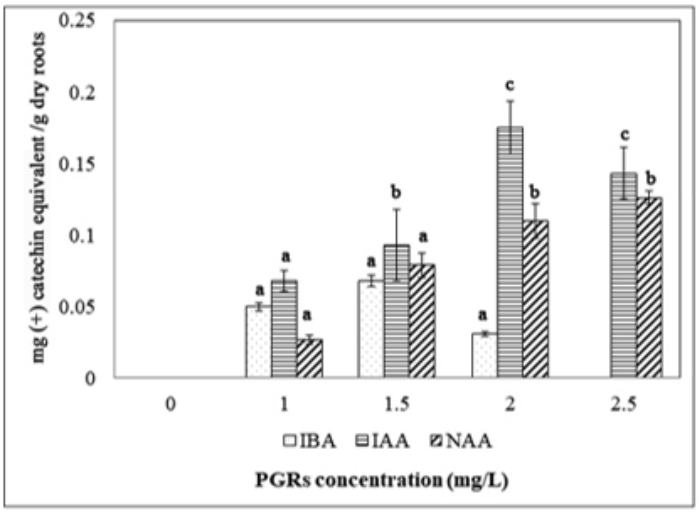


Figure 6. Total flavonoids content produced when treated with different auxin concentrations

Effect of auxin combination on root biomass, TPC, and TFC

In this experiment, the effects of the combinations of IAA, IBA, and NAA concentrations on root biomass, TPC, and TFC were studied. Adventitious roots were collected after seven weeks of culture. Figure 7 shows the amount of root biomass produced when root explants were treated with different combinations of IBA, IAA, and NAA concentrations. Total phenolic content and total flavonoid content in root biomass were also assessed, as shown in Figures 8 and 9. Two treatments, i.e., 1.5 mg/L IBA and 2.0 mg/L IAA, served as control. Results showed that the 2.0 mg/L IAA (1591.40 ± 14.14 mg) yielded the highest root biomass compared to other combinations (Figure 7). The combination of IBA 1.5 mg/L + NAA 0.1 mg/L (443.93 ± 14.68 mg) showed a significant higher root biomass than IBA 1.5 mg/L alone (168.07 ± 18.75 mg). This analysis indicated that the combination of IAA + NAA did not improve the production of root biomass. The combination of 1.5 mg/L IBA + 0.1 mg/L NAA produced optimal biomass, but the increment of NAA concentration above 0.1 mg/L reduced the production of fresh biomass. In another assessment, the combination of 2.0 mg/L IAA + NAA 0.5 mg/L showed the highest TPC (0.30 ± 0.02 mg gallic acid equivalent/g dry roots) and TFC (0.24 ± 0.01 mg (+) catechin equivalent/g dry roots) values as compared to the 2.0 mg/L IAA alone (Figures 8 and 9). This finding indicated that the combination of IAA+NAA had a positive effect on TPC and TFC but produced low root biomass. Besides, NAA has the potential to increase the amount of phenol and flavonoids in the roots [13]. It was suggested that IAA 2.0 mg/L gave the maximum root biomass and a combination of IAA 2.0 mg/L with NAA 0.5 mg/L enhanced TPC and TFC.

Effect of MeJa on root biomass, TPC, and TFC

In this experiment, the effects of combinations of auxins and MeJa on root biomass, TPC, and TFC were studied. Adventitious roots were observed after seven weeks of culture. Figure 10 shows the amount of fresh root biomass produced when treated with the combinations of auxins and MeJa. In the presence of MeJa, as for root biomass production, the combination of 2.0 mg/L IAA + 0.5 mg/L NAA + 75 µM MeJa produced the highest root biomass (470.1 ± 24.69 mg). The lowest root biomass was obtained when treated with 1.5 mg/L IBA + 0.1 mg/L NAA + 150 µM MeJa (104.95 ± 3.177 mg). However, in the absence of MeJa, 2.0 mg/L IAA alone (1591.40 ± 14.14 mg) resulted significantly higher than the addition of elicitor (490.8 ± 17.18 mg; Figures 7 and 10). This elicitor acts as an enhancer for root growth and physiological changes [11]. Besides, MeJa can trigger physiological and morphological responses and accumulation of secondary metabolites related to plant defence mechanisms [3].

Figures 11 and 12 show the TPC and TFC in root biomass treated with different combinations of auxins and MeJa concentrations. The combination of 2.0 mg/L IAA + 0.5 mg/L NAA + 100 µM MeJa recorded the highest TPC (0.27 ± 0.03 mg gallic acid equivalent/g dry roots) but no significant differences among all treatments tested. However, the combination of 2.0 mg/L IAA + 0.5 mg/L NAA had higher TPC (0.296 ± 0.02 mg gallic acid equivalent/g dry roots) and TFC (0.244 ± 0.01 mg (+) catechin equivalent/g dry roots) than the same combination with 1.0 µM MeJa. This demonstrated that the addition of MeJa elicitor reduced the production of root biomass, TPC and TFC. Elicitors could manipulate the secondary metabolites profile and improve the yield of secondary metabolites in the cultures of plant cells and organs [14]. Therefore, MeJa elicitor is not suitable to improve the yield of phenolic and flavonoid for *J. gendarussa*.

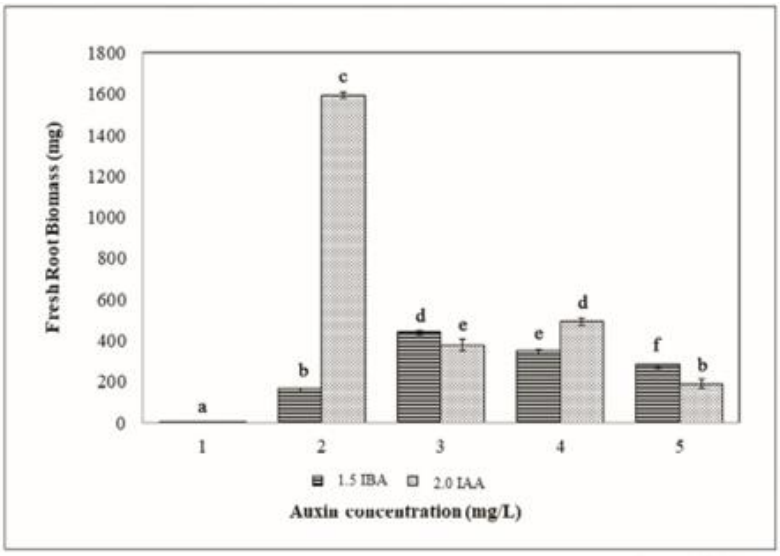


Figure 7. Amount of fresh root biomass produced after treated with different combinations of auxin concentrations. 1 = MS medium without auxin; 2 = control (1.5 IBA and 2.0 IAA); 3= 1.5 IBA + 0.1 NAA and 2.0 IAA + 0.1 NAA; 4 = 1.5 IBA + 0.5 NAA and 2.0 IAA + 0.5 NAA; 5 = 1.5 IBA + 1.0 NAA and 2.0 IAA + 1.0 NAA

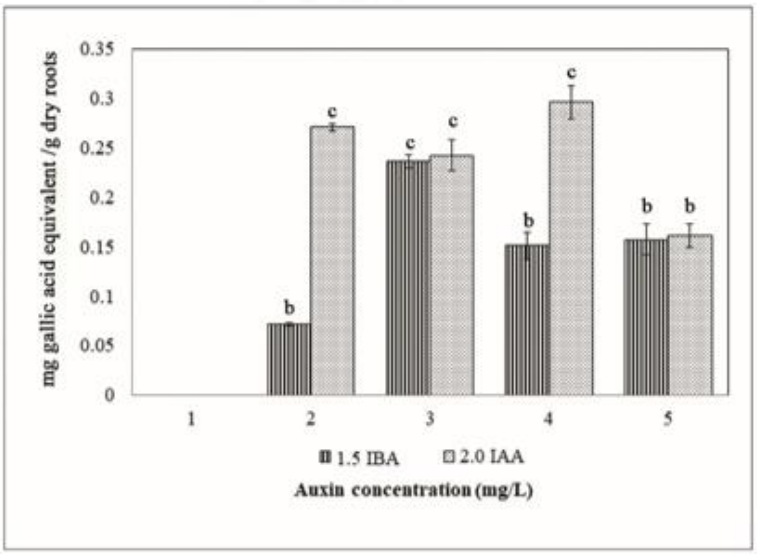


Figure 8. Total phenolic content in root biomass treated with different combinations of auxin concentrations. 1 = MS medium without auxin; 2 = control (1.5 IBA and 2.0 IAA); 3= 1.5 IBA + 0.1 NAA and 2.0 IAA + 0.1 NAA; 4 = 1.5 IBA + 0.5 NAA and 2.0 IAA + 0.5 NAA; 5 = 1.5 IBA + 1.0 NAA and 2.0 IAA + 1.0 NAA

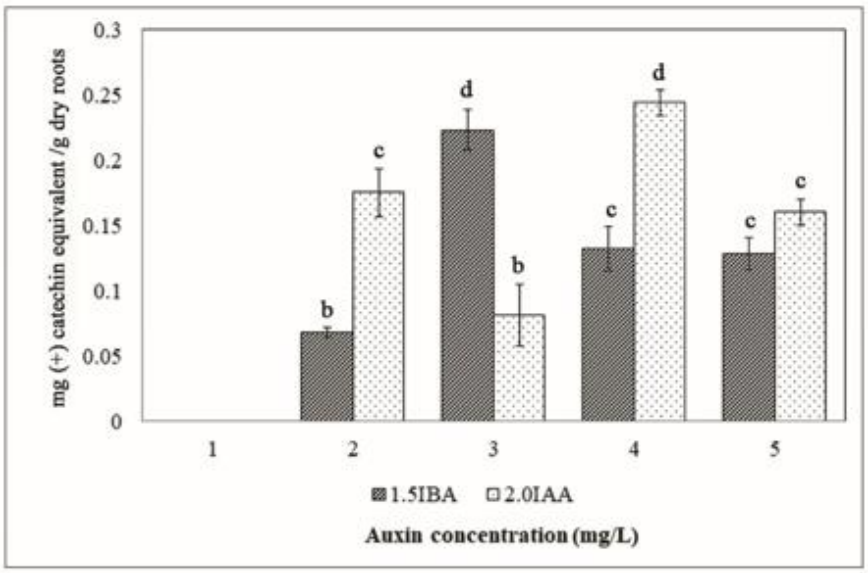


Figure 9. Total flavonoid content in root biomass treated with different combinations of auxin concentrations. 1 = MS medium without auxin; 2 = control (1.5 IBA and 2.0 IAA); 3 = 1.5 IBA + 0.1 NAA and 2.0 IAA + 0.1 NAA; 4 = 1.5 IBA + 0.5 NAA and 2.0 IAA + 0.5 NAA; 5=1.5 IBA + 1.0 NAA and 2.0 IAA + 1.0 NAA

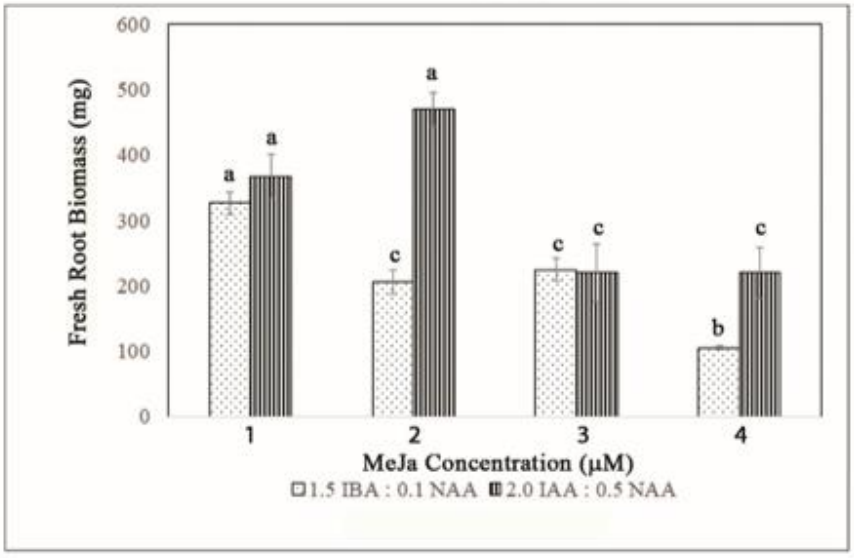


Figure 10. Fresh weight of root biomass obtained when treated with different combinations of auxin concentrations with addition of MeJa. 1 = 1.5 IBA + 0.1 NAA + 50 µM MeJa and 2.0 IAA + 0.5 NAA +50 µM MeJa ; 2 = 1.5 IBA + 0.1 NAA + 75 µM MeJa and 2.0 IAA + 0.5 NAA + 75 µM MeJa; 3 = 1.5 IBA + 0.1 NAA + 100 µM MeJa and 2.0 IAA + 0.5 NAA + 100 µM MeJa; 4= 1.5 IBA + 0.1 NAA + 150 µM MeJa and 2.0 IAA + 0.5 NAA + 150 µM MeJa

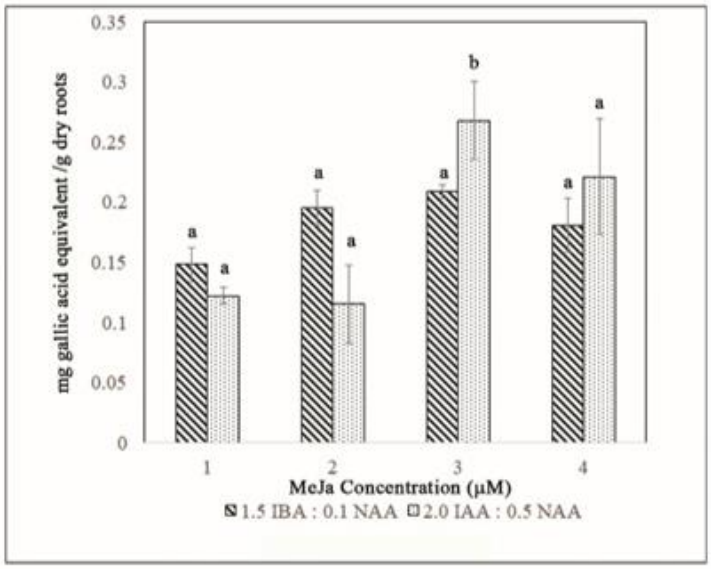


Figure 11. Total phenolic content in root biomass treated with different combinations of auxin concentrations with the addition of MeJa. 1 = 1.5 IBA + 0.1 NAA + 50 µM MeJa and 2.0 IAA + 0.5 NAA +50 µM MeJa ; 2 = 1.5 IBA + 0.1 NAA + 75 µM MeJa and 2.0 IAA + 0.5 NAA + 75 µM MeJa; 3 = 1.5 IBA + 0.1 NAA + 100 µM MeJa and 2.0 IAA + 0.5 NAA + 100 µM MeJa; 4 = 1.5 IBA + 0.1 NAA + 150 µM MeJa and 2.0 IAA + 0.5 NAA + 150 µM MeJa

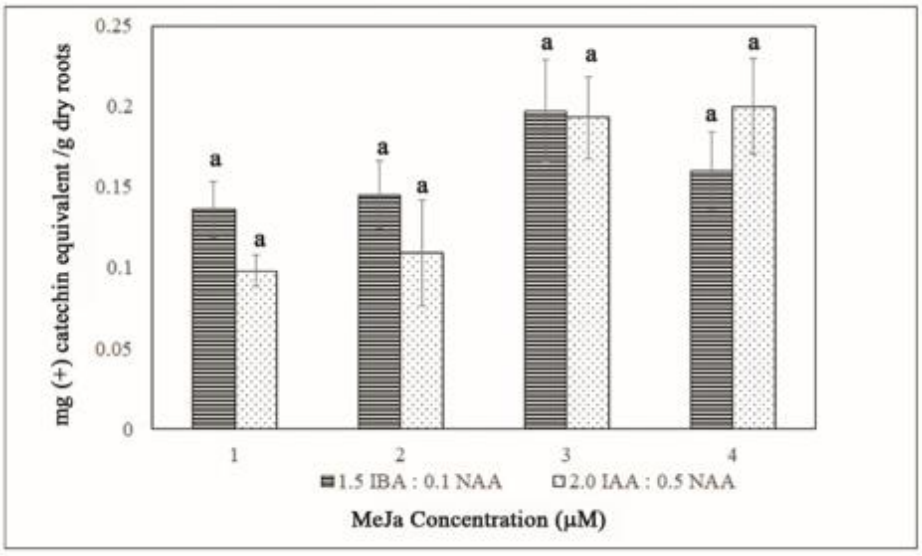


Figure 12. Total flavonoid content in root biomass treated with different combinations of auxin concentrations with addition of MeJa. 1 = 1.5 IBA + 0.1 NAA + 50 µM MeJa and 2.0 IAA + 0.5 NAA +50 µM MeJa ; 2 = 1.5 IBA + 0.1 NAA + 75 µM MeJa and 2.0 IAA + 0.5 NAA + 75 µM MeJa; 3 = 1.5 IBA + 0.1 NAA + 100 µM MeJa and 2.0 IAA + 0.5 NAA + 100 µM MeJa; 4 = 1.5 IBA + 0.1 NAA + 150 µM MeJa and 2.0 IAA + 0.5 NAA + 150 µM MeJa

Conclusion

Maximum root biomass was obtained in the treatment with IAA 2.0 mg/L. However, the combination of IAA 2.0 mg/L IAA + NAA 0.5 mg/L produced the highest TPC and TFC. As for IBA, a combination of 1.5 mg/L IBA + 0.1 mg/L NAA showed better root biomass than 1.5 mg/L IBA alone. IAA promoted root biomass production and combination IAA + NAA enhanced TPC and TFC in adventitious roots. The addition of MeJa up to 150 μM did not improve root biomass, TPC, and TFC of *J. gendarussa*.

Acknowledgment

The authors would like to thank Universiti Teknologi Malaysia (UTM; TDR Grant Vot No. 06G70), the Ministry of Education (MOE) for financial support and Plant Biotechnology Laboratory, Faculty of Science for laboratory facilities.

References

1. Uddin, R., Sinha, S., Hossain, A., Kaisar, A., Hossain, K. and Rashid, M. A. (2011). Chemical and biological investigations of *Justicia gendarussa* (Burm. F). *Dhaka University Journal of Pharmaceutical Sciences*, 10(1): 53-57.
2. Sugumaran, P., Kowsalya, N., Karthic, R. and Seshadri, S. (2013). Biomass production and antibacterial activity of *Justicia Gendarussa* : A valuable medicinal plant. *Journal of Tropical Life Science*, 3(1): 8-13.
3. Murthy, H. N., Hahn, E. J. and Paek, K. Y. (2008). Adventitious roots and secondary metabolism. *Chinese Journal of Biotechnology*, 24(5): 711-716.
4. Tesser, C., Remko, O. and Fett-neto, A. G. (2019). The role of auxin transporters and receptors in adventitious rooting of *Arabidopsis thaliana* pre-etiolated flooded seedlings. *Plant Science*, 290:110294.
5. Ratnasooriya, W. D., Deraniyagala, S. A. and Dehigaspitiya, D. C. (2007). Antinociceptive activity and toxicological study of aqueous leaf extract of *Justicia gendarussa* Burm. F. in rats. *Pharmacognosy Magazine*, 3(11): 145-155.
6. Ayob, Z., Bohari, S. P. M., Abd Samad, A. and Jamil, S. (2014) Cytotoxic activities against breast cancer cells of local *Justicia gendarussa* crude extracts. *Evidence-Based* Complementary and Alternative Medicine, 2014: 732980
7. Murashige, T. and Skoog, F. (1962). A revised medium for rapid growth and bio assays with tobacco tissue cultures. *Physiologia Plantarum*, 15(3): 473-497.
8. Lee, E. J., Park, S.Y. and Paek, K.Y. (2015). Enhancement strategies of bioactive compound production in adventitious root cultures of *Eleutherococcus koreanum Nakai* subjected to methyl jasmonate and salicylic acid elicitation through airlift bioreactors. *Plant Cell, Tissue Organ Culture*, 120: 1-10.
9. Dewir, Y. H. and Paek, K. Y. (2006). Optimization of culturing conditions for the production of biomass and phenolics from adventitious roots of *Echinacea angustifolia*. *Journal of Plant Biology*, 49(3): 193-199.
10. Wei, K., Ruan, L., Wang, L. and Cheng, H. (2019). Auxin-induced adventitious root formation in nodal cuttings of *Camellia sinensis*. *International Journal of Molecular Sciences*, 20(4817): 1-10.
11. Guan, L., Tayengwa, R., Cheng, Z. M., Peer, W. A. and Murphy, A. S. (2019). Auxin regulates adventitious root formation in tomato cuttings. *BMC Plant Biology*, 9(1): 1-16.
12. Ayob, Z., Abd Samad, A. and Bohari, S. P. M. (2013). Cytotoxicity activities in local *Justicia gendarussa* crude extracts against human cancer cell lines. *Jurnal Teknologi*, 2: 45-52.
13. Fazal, H., Abbasi, B. H. and Ahmad, N. (2014). Optimization of adventitious root culture for production of biomass and secondary metabolites in *Prunella vulgaris L*. *Applied Biochemistry and Biotechnology*, 174(6): 2086-2095.
14. Kim, Y., Hahn, E., Murthy, H. N. and Paek, K. (2004). Adventitious root growth and ginsenoside accumulation in *Panax ginseng* cultures as affected by methyl jasmonate. *Biotechnology Letters*, 26(21): 1619-1622.

Malaysian Journal of Analytical Sciences (MJAS)
Published by Malaysian Analytical Sciences Society

CELLULOSE ACETATE-TiO_2 PHOTOCATALYTIC HOLLOW FIBRE MEMBRANE FOR DEGRADATION OF METHYLENE BLUE

(Membran Fiber Berongga Fotomangkin Selulosa Asetat-TiO_2 bagi Degradasi Metilena Biru)

Siti Wafiroh*, Miriam R. Prananda, Linda Yuliana, Pratiwi Pudjiastuti, Abdulloh

Department of Chemistry, Faculty of Science and Technology,
Airlangga University, Surabaya, Indonesia

**Corresponding author: sitiwafiroh@fst.unair.ac.id*

Received: 18 July 2019; Accepted: 20 July 2020; Published: 10 December 2020

Abstract

Methylene blue (MB) used in the textile industry can cause environmental damage. Photocatalytic hollow fibre membrane (PHFM) was employed in the degradation of synthetic MB dye. This research aimed to determine the optimum concentration of TiO_2 addition on the characteristic and performance of cellulose acetate-TiO_2 PHFM for the degradation of synthetic MB dye. Hollow fibre membrane was prepared from the phase inversion method using a dope solution with the ratio of CA, formamide, and acetone of 22%:27%:51%, and TiO_2 was then added with various concentrations of 0.10%, 0.15%, 0.20%, 0.25%, and 0.30% (w/w). The results showed that the optimum concentration of TiO_2 addition to the hollow fibre membrane was 0.25% (w/w). The characterisation of PHFM involved strain, stress, Young's modulus, flux, rejection, SEM, FTIR, and efficiency degradation for MB, while the characterisation of CA-TiO_2 PHFM involved thickness, stress, strain and Young's Modulus, i.e., 0.15 mm, 5.5×10^2 kN/mm^2, 0.13, and 4.2×10^3 kN/mm^2, respectively. The flux and rejection performance of PHFM with MB feed were 25.66 L/m^2.h and 94.8%, respectively. The total efficiency of CA-TiO_2 PHFM application for MB degradation was 98.9%, and waste textile dye was 82.6%. PHFM was capable of degrading the synthetic MB.

Keywords: photocatalytic, hollow fibre membrane, cellulose acetate, TiO_2, methylene blue

Abstrak

Metilena biru (MB) yang digunakan dalam industri tekstil boleh menyebabkan kerosakan alam sekitar. Membran fiber berongga fotomangkin (PHFM) digunakan dalam pemerosotan pewarna MB sintetik. Kajian ini bertujuan untuk menentukan kepekatan optimum penambahan TiO_2 terhadap ciri dan prestasi PHFM selulosa asetat–TiO_2 untuk pemerosotan pewarna MB sintetik. Membran fiber berongga dihasilkan melalui kaedah songsangan fasa menggunakan larutan dop dengan nisbah CA, formamida, dan aseton pada 22%:27%:51%, dan TiO_2 kemudiannya ditambah pada pelbagai kepekatan sebanyak 0.10%, 0.15%, 0.20%, 0.25%, dan 0.30% (w/w). Keputusan menunjukkan kepekatan optimum penambahan TiO_2 kepada membran gentian geronggang pada 0.25% (w/w). Pencirian PHFM melibatkan terikan, tegasan, modulus Young, fluks, penyingkiran, SEM, FTIR, dan kecekapan pemerosotan MB, manakala pencirian CA-TiO_2 PHFM melibatkan ketebalan, tegasan, terikan, dan modulus Young, masing-masing pada 0.15 mm, 5.5×10^2 kN/mm^2, 0.13, and 4.2×10^3 kN/mm^2. Prestasi fluks dan penyingkiran PHFM dengan suapan MB masing-masing ialah 25.66 L/m^2.h and 94.8%. Kecekapan aplikasi CA–TiO_2 PHFM bagi pemerosotan MB ialah 98.9%, dan sisa pewarna tekstil ialah 82.6%. PHFM mampu degradasi MB sintetik.

Kata kunci: fotomangkin, membrane fiber berongga, selulosa asetat, TiO_2, metilena biru

Introduction

Dyes are one of the major pollutants in wastewater from the textile industry. The textile dyeing industry produces by-products in the form of wastewater in large quantities and contains various types of chemicals. The textile industry produces the largest amount of synthetic dye waste and produces around 50-200 mg/L dyes that could not be degraded entirely [1]. The type of dye that is widely used in the textile industry in Indonesia is methylene blue (MB) because it is a basic dye and has excellent solubility [2]. In the industry, only 5% of MB is bound, while the remaining 95% becomes waste; hence, its distribution in the aquatic environment is extensive. This phenomenon can cause disturbances in the ecosystem; e.g. it can disrupt the aesthetics of the waters and can block the penetration of sunlight into the waters. This kind of dye wastes may interfere with the photosynthesis process of aquatic plants, consequently decreasing the oxygen content in the water and eventually reduce water quality and can be fatal, especially to aquatic organisms [3, 4].

In this research, the photocatalytic method uses the concept of electron/hole pair generation in semiconductor particles because it requires the right energy (e.g., for TiO_2, λ <380 nm and similarity of band gap energy greater than 3.2 eV) [5]. The study reported the effect of plasma surfaces and triarylmethane dyes in textiles using the photocatalytic method of performance of TiO_2-chitosan [6]. Adsorption is another promising alternative method developed to treat textile synthetic dye wastes because the process is relatively simple, inexpensive, and it can work at low concentrations. This type of adsorbent has been used to reduce the concentration of aquatic dyes. MnO-activated carbon can be synthesised hydrothermally from coconut shell. This adsorption can absorb azo dyes by 99.1%. However, this process requires relatively large energy, causing the price of activated carbon to be expensive and difficult to apply in the industry [7].

Another method besides the use of photocatalytic methods and adsorption to treat textile dye waste is membrane technology, which is widely used in the industry. Various types of membranes are available, one of which is hollow fibre membranes. The geometry of this hollow fibre membrane provides greater membrane effectiveness. Excellent mechanical properties and the ease of handling during fabrication and operational processes renders hollow fibre membranes as the chosen method in the industry [8]. The manufacture of membranes is said to be optimum if the membrane has many small pores, which causes large flux values and high reproduction. Furthermore, it has high mechanical properties and low fouling. Therefore, the right combination of materials is needed. The membrane requires composites with other compounds for the production of membranes with optimum specifications [9]. One of the composites that are often used in membrane modification is the inorganic compound, TiO_2. TiO_2 is a semiconductor material that has been widely applied in the environment due to abundant resources, excellent photocatalytic performance, high refractive index, low cost, non-toxic, and high photodegradation chemical stability. TiO_2 is proven to be a promising catalyst in the management of water and air pollution [10].

Cheng et al. [11] have produced a hollow CA membrane nanofiltration to increase perm selectivity through hydrolysis reactions followed by carboxymethylation. Nanofiltration of CA hollow fibre membrane produces a flux value of about 5.2 L/m^2h, the value of NaCl rejection of 66.4%, and Na_2SO_4 rejection value of 95.4%. The modification of pure semi-permeable CA membrane yielded a flux value of 2.3 L/m^2h, NaCl rejection value of 90.8%, and Na_2SO_4 rejection value of 91.5%. In addition, the modification of CA membranes in diluted solutions of Congo red and MB increased the dye degradation rate and the value of flux in water more than twice compared to pure membranes [11]. Mozia et al. [12] reported the performance of two photocatalytic membrane reactors (PMRs), utilising ultrafiltration

(UF) - PMR1, or direct contact membrane distillation (DCMD) – PMR2, in the treatment of primary (PE) and secondary (SE) effluents of municipal wastewater treatment plant. Additionally, single UF and DCMD were also examined. TiO_2 Aeroxide® P25 (0.5–1.5 g/dm3) was applied as a photocatalyst. Photocatalysis contributed to an improved permeate flux in PMR1 compared to UF alone for 25-38% in the case of PE and 33% when SE was used [12].

Sarasidis et al. [13] have reported a laboratory pilot photocatalytic membrane reactor (PMR), employing a hybrid TiO_2/UV-A catalysis-ultrafiltration process, which was evaluated for the degradation of diclofenac (DCF), a typical micro-pollutant frequently encountered in source waters. The combination of membrane ultrafiltration with photocatalysis allows TiO_2 separation and reuse, whereas the automatic periodic membrane backwashing, combined with moderate permeate flux, effectively control membrane fouling; thus, permitting stable continuous operation with no wastewater stream [13]. Zhao et al. [14] have structured the design and observed the performance of braid-reinforced cellulose acetate (BR CA) fibre membranes that have anti-fouling properties with an average rejection value of more than 80%. The tensile strength of BR CA membranes varied from 16.0 MPa to 62.9 MPa by adjusting the braid composition [14].

Based on the description above, this research employed a membrane using CA-TiO_2 as a base material for PHFM. The CA-TiO_2 PHFM was applied for the degradation of MB. The composition of the mixture was 51% acetone, 27% formamide, and 22% CA with variations in TiO_2 concentrations of 0.10%, 0.15%, 0.20%, 0.25%, and 0.30%. The CA-TiO_2 PHFM was characterized by the determination of membrane mechanics and membrane performance. Determination of membrane mechanics was performed to specify the thickness, stress value, strain value, and Young's modulus, while the performance determination was performed to specify the value of flux and rejection. The morphological determination was performed using SEM, and the determination of functional groups by Fourier-transform infrared (FTIR). The CA-TiO_2 PHFM with mechanical properties and optimum performance was applied to the degradation of MB, waste textile dye using membrane modules for the filtration process, and photocatalytic reactors for waste textile dye degradation.

Materials and Methods

Raw materials

All materials used in this research were analytical grade chemicals and used as it is without further purification. Cellulose acetate (Mv = 50.000 g/mol), TiO_2, H_2SO_4, formamide, acetone, and phenolphthalein indicator were obtained from Merck.

Production of CA-TiO_2 PHFM

The dope solution was made with a composition of 22% CA, 51% acetone, and 27% formamide, which was slowly dissolved with acetone at room temperature in a closed Erlenmeyer flask to avoid solvent evaporation. The composition of TiO_2 solution varied in concentration; 0.10%, 0.15%, 0.20%, 0.25%, and 0.30%. Formamide was added after all CA was dissolved in acetone. The dope solution, which has been mixed, was then stirred with a magnetic stirrer at 30 °C until homogeneous. During stirring, TiO_2 was added according to the variations for several hours. The homogeneous dope solution was left overnight to eliminate air bubbles to allow the dope solutions to be moulded into hollow fibre membranes using phase inversion techniques. The hollow fibre membrane printing device was assembled first and the preparation of a coagulant tub with at 5 °C using ice just below the spinneret at 25 cm. Tube 1 was used to place a dope solution, while tube 2 is used for aquadest. The compressor is connected using a hose on tube 1. When the dope solution passes through the needle, tube valve 2 was opened. After going through the spinneret, the hollow fibre membrane formed from the dope solution enters the tub of the coagulant so that the hollow fibre membrane became solid. Then, the hollow fibre membrane was washed using water flowing to eliminate excess solvent. For the final step, the PHFM was transferred to a tube containing sodium azide solution to inhibit bacterial growth in the membrane so that it can be characterised [15]

Characterization of CA-TiO_2 PHFM

The thickness measurement was performed using micrometre screw with an accuracy of 0.01 mm. Determination of the mechanical properties of CA-TiO_2 PHFM can be carried out using tensile test, where the membrane is clamped on a tensile test tool and the puller mounted to a load unit of kN. The CA-TiO_2 PHFM was then pulled at a speed of 1 cm/min until it broke. The magnitude of the force (F) to break the membrane and the change in length (Δl) until the sample exactly broken was recorded in the monitor of the tensile tester. From these data we can determine the stress($\boldsymbol{\sigma}$) value (Equation 1), strain ($\boldsymbol{\varepsilon}$; Equation 2), and the Young's modulus (*E*; Equation 3).

$$\boldsymbol{\sigma} = \frac{\boldsymbol{F}}{\boldsymbol{A}} \quad (1)$$

$$\boldsymbol{\varepsilon} = \frac{\boldsymbol{l-lo}}{\boldsymbol{lo}} = \frac{\boldsymbol{\Delta l}}{\boldsymbol{lo}} \quad (2)$$

$$\boldsymbol{E} = \frac{\boldsymbol{\sigma}}{\boldsymbol{\varepsilon}} \quad (3)$$

The membrane performance test was determined by calculating flux value and rejection or perm selectivity value. PHFM module performance was tested using crossflow cells. Flux (J) was defined as the quantity permeated per unit of area (A) and per unit of time (t), as reported in Equation 4. The flux of water or sample passing through the membrane was determined directly by measuring flow infiltration in volume (L) per square meter per hour ($L.m^{-2}h^{-1}$) and calculated using Eq. 4. [11].

$$\boldsymbol{J} = \frac{\boldsymbol{v}}{\boldsymbol{A \times t}} \quad (4)$$

Perm selectivity or rejection value is expressed as a membrane's ability to hold or pass through a species. The coefficient of rejection can be calculated using Eq. 5.

$$R=1-Cp/Cf\times 100\% \quad (5)$$

where Cp is the concentration of permeate and Cf is the concentration of feed. Feed is MB and waste textile dye.

Application of CA-TiO_2 PHFM for MB degradation

The application is performed by comparing two methods, i.e., the filtration method using a hollow CA fibre membrane and CA-TiO_2 PHFM. Filtration using a hollow CA fibre membrane was carried out by filtering MB feed solution into the membrane. CA-TiO_2 PHFM was carried out in the same way. The resulting permeate was measured by using a UV-Vis spectrophotometer [11].

Qualitative test of CA-TiO_2 PHFM for degradation of MB

Qualitative tests of the results of MB degradation can be performed using five qualitative tests, including analysis of CO_2, NH_4^+, Cl^-, NO^-, and SO_4^{2-} with the results of the degradation of MB. The CO_2 gas test was performed using a U pipe, which allows the flow of air formed by the vacuum resulted from the degradation of MB in $Ba(OH)_2$ solution. The CO_2 formed will react with $Ba(OH)_2$ to form white sediment. The NH_4^+ ion test was performed by adding excessive NaOH to the solution resulting from the MB degradation, which was then heated. A spatula dipped in concentrated HCl was also placed in the solution. The spatula that has been dipped with concentrated HCl will form white steam on the tube wall. The SO_4^{2-} ion test was carried out with the addition of Ba^{2+} [16].

Results and Discussion

Production of CA-TiO_2 PHFM

CA hollow fibre membranes were produced using a phase inversion method, which is a process of forming polymers from a solution form into solids in a controlled manner [1]. When making a dope solution, the CA powder was dissolved with acetone using a magnetic stirrer; then, the formamide was added as an additive to form the pores of the hollow fibre membrane. An additive may be used in the production of membranes if it meets the requirements of being soluble in polymer solvents and must also be soluble in non-solvents [14]. A thick dope solution requires a push force to come out of spinneret with the compressor. The dope solution was then applied to the coagulant tub, which contains water at 5 °C. Low-temperature during moulding functions to produce asymmetrical (different pore size) membrane. The morphology of the membrane was affected by the

evaporation of solvents during the moulding process affected; therefore, an air gap of 25 cm was used. Five variations of dope solution were used in this study, with a composition of 22% CA, 51% acetone, 27% formamide, and variations in the concentration of TiO_2 additions, i.e., 0.10%, 0.15%, 0.20%, 0.25%, and 0.30%. The result of CA-TiO_2 photocatalytic membrane dope solution was in the form of a thick, white solution. PHFM that have been formed are stored in sodium azide solution to prevent bacterial membrane degradation.

Characterisation of CA-TiO_2 PHFM

The average thickness of the CA-TiO_2 PHFM was 0.13 µm. The characteristics of an excellent quality membrane are thin, transparent, and strong against pressure [15]. This will affect the permeability properties because the thicker the membrane, the further distance the bait need to take, thereby increasing the flow rate of the feed fluid, and potentially increase the occurrence of fouling due to the accumulation of feed material above the membrane surface [17].

Membranes with strong mechanical properties are characterised by high stress values, a good performance that can be seen from high flux values and significant rejection can be considered as the optimum membrane. The results of stress measurements on each variation of TiO_2 concentration are shown in Figure 1.

In each variation of TiO_2 concentration on hollow fibre membranes, the results of stress measurements decreased as the concentration of TiO_2 increasing, which lead to decreased tensile strength at the time of breaking. Deviations occur at 0.3% TiO_2 concentration because the concentration of TiO_2 in the membrane reached the maximum value at a concentration of 0.25% with the stress value of 5.5×10^2 kN/mm^2. High stress value indicates that the material has excellent strength in resisting deformation, as strong membranes are not easily broken. Increased concentration can increase stress due to the presence of more molecules from the membranes, causing the distance between molecules to become denser. The density of membrane composing molecules can reduce pore size. If the concentration of TiO_2 addition reaches the maximum limit, many TiO_2 molecules are still insoluble in the dope solution; thus, reducing the bond strength of the membrane and caused small stress value.

The strain value indicates the material's ability to increase the length before the material is broken or often called elasticity. The increasing strain values also indicate the addition of pore size when deformed by pressure. The graph of the relationship between the concentration of TiO_2 and strain is shown in Figure 2. Strain value of hollow fibre membranes tends to decrease from the concentrations of 0.1% to 0.2%. The decreasing plasticity value is due to the increasing number of particles that lead to an increasing number of intermolecular bonds [18]. At the concentration of 0.25%, the concentration increases due to the lack of homogeneous dope solution, causing the pores to be distributed less evenly, making membrane plasticity not constant [19].

Young's modulus is a comparison between stress and strain. Young's modulus is often referred to as selectivity modulus or stretch modulus. If Young's modulus value gets bigger, the strain value of the membrane gets smaller; hence, the membrane can maintain its pore size when considerable pressures are applied [20]. The graph of Young's modulus value of the CA-TiO_2 PHFM is shown in Figure 3. In general, hollow fibre membranes have a large Young's modulus value and small strain value. Conversely, if the stress value is large, Young's modulus will be higher.

In this research, the optimum concentration of TiO_2 was 0.25% with stress value of 555.88 kN/mm^2, strain value of 0.13, and Young's modulus value of 4270.50 kN/mm^2. The performance of the CA-TiO_2 PHFM was determined by the value of flux and rejection. Flux values indicate the permeate flow rate when passing through the membrane and the rejection coefficient shows the ability of the membrane to hold solute molecules [19]. Flux measurement was carried out by compacting the CA-TiO_2 PHFM in the module tested by flowing water through the membrane to obtain a constant water flux. Compaction was aimed to make the membrane pore more even, where the membrane becomes stiff, and the constant value of water flux was obtained at the given pressure [17]. The module was

then connected to the pump by applying pressure to the water flow, and water flux was measured using the volume of water collected during a specified time interval. Measurements were performed until a constant water flux was obtained and then replaced with MB solution. The flux value of the data can be identified with equation 4. The flux value of hollow fibre membranes showed the permeate flow rate to pass through the membrane by passing 100 mL of the feed solution then measuring the volume of the permeate during a specific time interval with 60-min intervals [21]. Flux value generated from the research with methylene blue feed was 25.66 L/m^2.h and rejection of 94.8%.

In the FTIR spectrum results, not many changes in the CA-TiO_2 functional group were observed compared to the standard CA (Figure 4). It is noted that the OH group in the wavenumber range of 3600–2800 cm^{-1} showed a board ribbon at 3445.78 cm^{-1}, the stretched CH group showed a little board ribbon at 2959.13 cm^{-1}, CO group in the wavenumber range of 1400–1000 cm^{-1} showed the ribbon at 1397.79 cm^{-1}, and the C=O group in the wavenumber range of 1950–1600 cm^{-1} showed two ribbons at 1631.20 cm^{-1} and 1698.94 cm^{-1}. This indicates an interaction between the C=O group and TiO_2, that is a covalent bond; therefore, two ribbons appear in the wavenumber range of 1950–1600 cm^{-1}. The absorption of TiO_2 is usually seen at wavenumbers 700–550 cm^{-1} [22]. In the research, Ti-O absorption was in wavenumber 646.80 cm^{-1}.

The purpose of morphology assessment was to know the surface structure and cross-section of the membrane obtained. The morphological results of the asymmetric cellulose acetate hollow fibre membrane at the magnification of 5000× showed membrane pores. Figure 5 shows that the hollow fibre membrane cross-section has a porous structure. The dispersion of these tightly dense membrane pores is one of the causes of the optimum strain, stress, and modulus of the optimum membrane [23, 24, 25]. The pore size of CA-TiO_2 PHFM on the outer surface was 300.5 nm, with an inner surface of 581.2 nm. Membrane surface photos show an even distribution of the pores of the CA-TiO_2 PHFM, as seen in Figure 5.

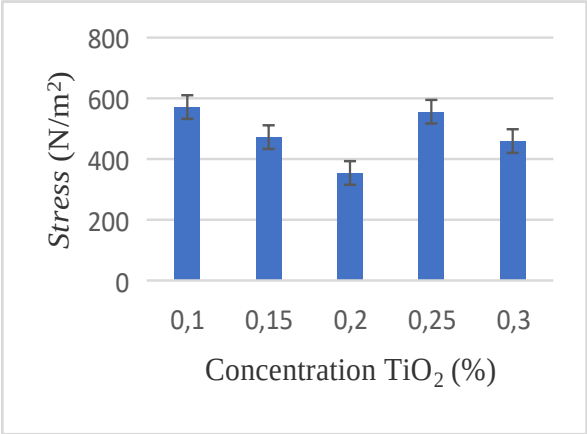


Figure 1. Graph of the relationship between stress and the concentration of TiO_2

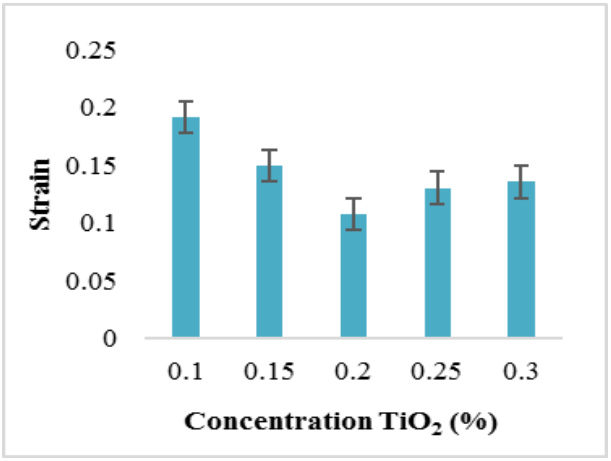


Figure 2. Graph the relationship between strain and the concentration of TiO_2

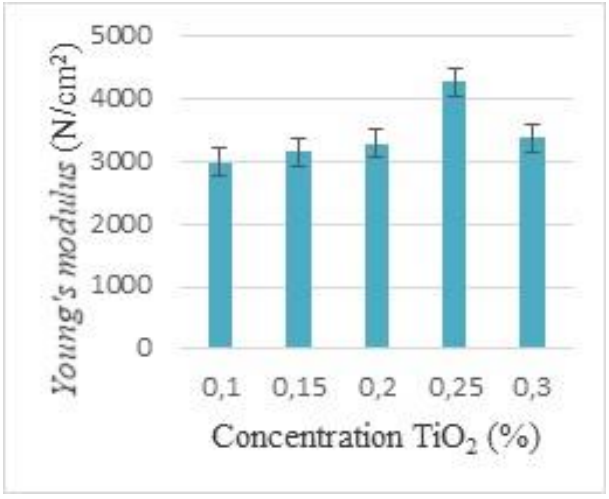


Figure 3. Graph between the concentration of TiO_2 and Young's modulus

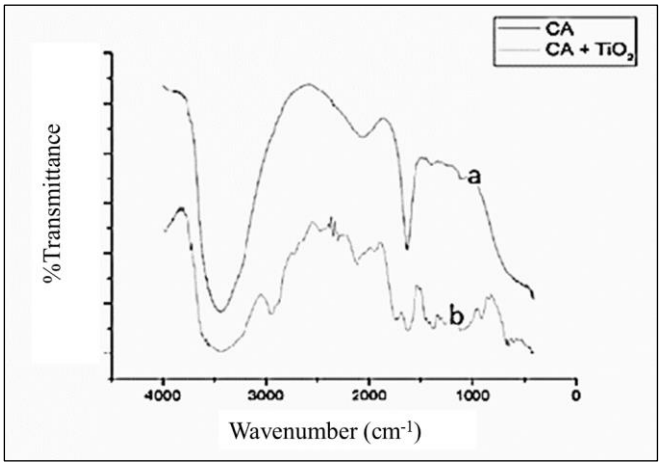


Figure 4. FTIR spectrum of (a) CA-TiO_2 PHFM, CA membrane (b)

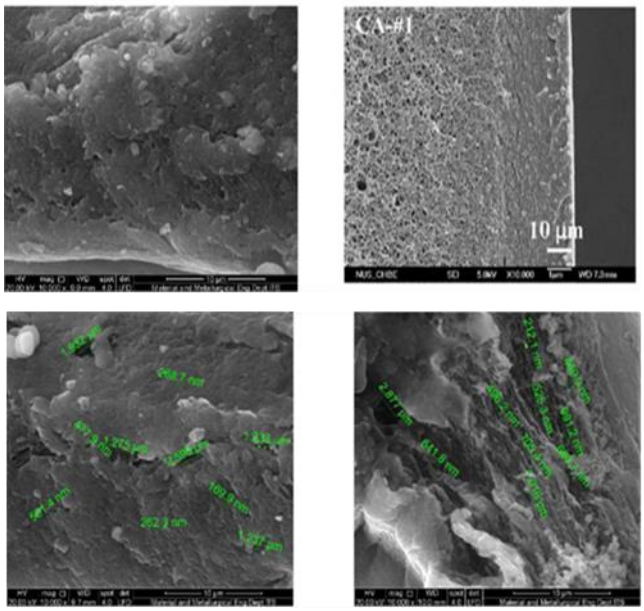


Figure 5. SEM of CA-TiO_2 PHFM

Application of CA-TiO_2 PHFM for MB Degradation

MB textile waste was taken from the textile industry in the Pakal area, Surabaya with dark brown colour due to the acidic condition of the textile waste solution. Textile waste was prepared in advance using Whatman 41 filter paper to remove large particles that were dissolved in the waste to avoid damaging the pores of the hollow fibre membrane. The initial absorbance was measured using a UV-Vis spectrophotometer with 100 times dilution as it was too concentrated, and absorbance was obtained with a concentration of 2.586 ppm. The source of energy used to start the degradation process was UV light. When UV rays provide energy to TiO_2, OH free radicals were formed to degrade the waste and MB. The photocatalytic degradation waste concentration decreased to 0.793 ppm, with a photocatalytic degradation efficiency of 82.6%. PHFM The PHFM significantly affected the use of CA and TiO_2 in the membrane on MB wastewater treatment and MB solutions, as shown in Figures 6 and 7.

CA-TiO_2 PMFC has a significant impact on the flux, rejection, and efficiency of degradation of MB and textile dye waste. Besides that, TiO_2 added to the hollow fibre membrane will also reduce membrane fouling.

Qualitative test of CA-TiO_2 PHFM for MB degradation

The qualitative test was performed based on the results of the photocatalytic degradation of MB to determine the analysis of NH^+, Cl^-, SO^{2-} ions, and CO_2 gas. The NH^{4+} ion test was completed by adding excessive NaOH in the solution resulted from degradation, which was then heated, and the spatula dipped in concentrated HCl was inserted to test for NH_4^+ compounds. The NH_4^+ test was positive because white steam was formed on the tube wall. The test to determine the existence of Cl^- ions was carried out by adding $AgNO_3$ to the degradation solution of MB, which formed white deposits of AgCl. The SO_4^{2-} ion test was carried out by adding $Ba(NO_3)_2$ to test the SO_4^{2-} compound. SO_4^{2-} tests were positive with the formation of $BaSO_4$ white deposits. CO_2 gas test was carried out using a U pipe that was flowed with the vacuumed air formed from the degradation of MB in $Ba(OH)_2$ solution. The test result was positive as $BaCO_3$ white deposits were formed. The reaction equation that occurs in each test can be written as follows [16].

$$NH_4^+ + OH^- \rightarrow NH_{3(g)} + H_2O \quad (6)$$

$$Cl^- + AgNO_3 \rightarrow AgCl_{(s)} + NO_3^- \quad (7)$$

$$SO_4^{2-} + Ba(NO_3)_2 \rightarrow BaSO_{4(s)} + 2\ NO_3 \quad (8)$$

$$Ba(OH)_{2(aq)} + CO_2 \rightarrow BaCO_{3(s)} + H_2O \quad (9)$$

The optimum CA-TiO_2 PHFM has a composition of 21.75% CA, 51% acetone, 27% formamide, and 0.25% (w/w) TiO_2 with a stress value of 5.5×10^2 kN/mm^2, strain value of 0.13, and Young's modulus value of 4.2×10^3 kN/mm^2. Performance of CA-TiO_2 PHFM with MB feed of flux and rejection were 25.66 L/m^2.h and a rejection coefficient of 94.8%. The effectiveness of the CA-TiO_2 PHFM for the degradation of MB can be seen from the efficiency of the degradation of MB, which was 98.9% and the efficiency of textile waste of 82.6%. The CA-TiO_2 PHFM can process MB textile dye waste because TiO_2 in the membrane have the photocatalytic activity and the ability of the membrane itself to be able to filter MB and waste textile dye.

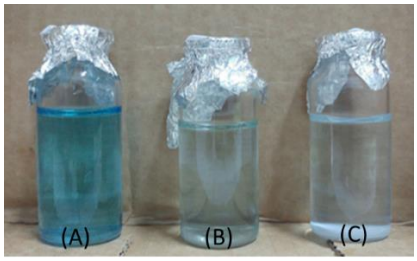


Figure 6. MB solution (a) before filtration, (b) after filtration with CA hollow fibre membrane and (c) after filtration with CA-TiO_2 PHFM

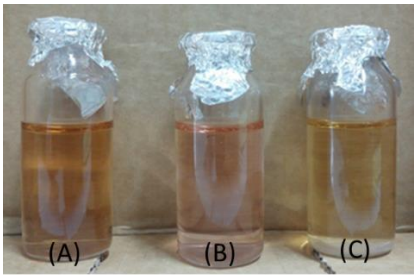


Figure 7. Waste textile dye solution (a) before filtration, (b) after filtration with CA hollow fibre membrane and (c) after filtration with CA-TiO_2 PHFM

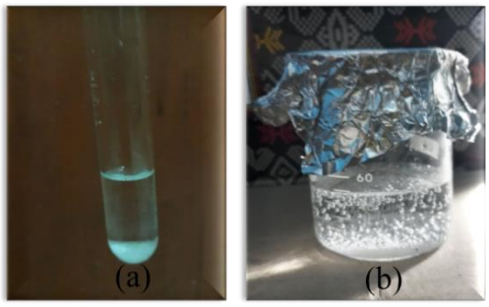


Figure 8. (a) The SO_4^{2-} ion test was carried out by adding $Ba(NO_3)_2$ produces a white precipitate $BaSO_4$ (b). The Cl^- ions was carried out by adding $AgNO_3$ formed white deposits of AgCl

Conclusion

The optimum CA-TiO_2 PHFM has a composition of 21.75% CA, 51% acetone, 27% formamide, and 0.25% (w/w) TiO_2 with a stress value of 5.5×10^2 kN/mm^2, strain value of 0.13, and Young's modulus value of 4.2×10^3 kN/mm^2. Performance of CA-TiO_2 PHFM with MB feed of flux and rejection were 25.66 L/m^2.h and a rejection coefficient of 94.8%. The effectiveness of the CA-TiO_2 PHFM for the degradation of MB can be seen from the efficiency of the degradation of MB, which was 98.9% and the efficiency of textile waste of 82.6%. The CA-TiO_2 PHFM can process MB textile dye waste because TiO_2 in the membrane have the photocatalytic activity and the ability of the membrane itself to be able to filter MB and waste textile dye.

Acknowledgement

This research was supported by the funding of the Ministry of Research and Technology, Republic of Indonesia.

References

1. Mondal, M. and De, S. (2016). Treatment of textile plant effluent by hollow fibre nanofiltration membrane and multi-component steady state modeling. *Chemical Engineering Journal,* 285: 304-318.
2. You, L., Ai, L. and Jiang. J. (2011). Removal of methylene blue from aqueous by montmorillonite/$CoFe_2O_4$ composite with magnetic separation performance. *Desalination,* 266: 72-77.
3. Chin, S., Park, E., Kim, M. and Jurng, J. (2010). Photocatalytic degradation of methylene blue with TiO_2 nanoparticles prepared by a thermal decomposition process. *Powder Technology*, 201: 171-176.
4. Dariani, R. S., Esmaeili, A., Mortezaali, A. and Dehghanpour, S. (2016). Photocatalytic reaction and degradation of methylene blue on TiO_2 nano-sized particles. *Optik,* 127:7143-7154
5. Nosaka, Y. and Zhang, Y. (2014). Mechanism of the OH radical generation in photocatalysis with TiO_2 of different crystalline types. *Journal of Physical Chemistry,* 118:10824-10832.
6. Erjavec, B., Grcic, I., Vrsaljko, D., Guyon, C. and Tatoulian, M. (2017). Influence of plasma surface pretreatment and tryarylmethane dye on the photocatalytic performance of TiO_2-chitosan coating on textile. *Progress in Organic Coatings*, 105: 277-285.
7. Rahman, Arifur, M., Amin, Ruhul, S, M., Alam and Shafiqul, A. M. (2012). Removal of methylene blue from waste water using activated carbon prepared from rice husk. *Dhaka University Journal of Science,* 60(2):185-189.
8. Jiangfeng, Y., Wang, K., Ren, M., Jefferson, Z, L. and Wang, H. (2012). Phase inversion spinning of ultrafine hollow fibre membrane through a single orifice spinneret. *Journal of Membrane Science,* 421: 8-14.
9. Jayakumar, R., Ramachandran, R., Divyarani, V. V., Chennazhi, K. P., Tamura, H. and Nair, S. V. (2011). Fabrication of chitin–chitosan/nano TiO_2-composite scaffolds for tissue engineering applications. *International Journal of Biological Macromolecules,* 48(2): 336-344.
10. Yang, X., Xiong, L., Hu, X., He, B. and Chu. G., (2012). Photocatalytic reaction and degradation of methylene blue on TiO_2 films in vacuum, an X-ray spectroscopy study. *Research Chemistry Intermediate,* 38: 67-75.
11. Cheng, Q., Yu, S., Huang, C., Liu, J., Peng, X. and Liu, M. (2013). Cellulose acetate hollow fibre nanofiltration membrane with improved perm selectivity prepared through hydrolysis followed by carboxymethylation. *Journal Membrane Science,* 434: 44-54.
12. Mozia, S., Darowna, D., Szymański, K., Grondzewska, S., Borchert, K., Wróbel, R. and Morawski, A. W. (2014). Performance of two photocatalytic membrane reactors for treatment of primary and secondary effluents. *Catalysis Today*, 236: 135-145.
13. Sarasidis, V. C., Plakas, K. V., Patsios, S. I. and Karabelas, A. J. (2014). Investigation of diclofenac degradation in a continuous photo-catalytic membrane reactor. Influence of operating parameters. *Chemical Engineering Journal,* 239: 299-311.

14. Fan, Z., Xiao, C., Liu, H., Huang, Q. and Zhao, J. (2015). Structure design and performance study on braid-reinforced cellulose acetate hollow fiber membranes. *Journal of Membrane Science*, 486: 248-256.
15. Zhang, X., Wang, D. K., Lopez, D. R. S. and da Costa, J. C. D. (2014). Fabrication of nanostructured TiO_2 hollow fibre photocatalytic membrane and application for wastewater treatment. *Journal of Chemical Engineering,* 236: 314-322.
16. Svehla, G. (2000). Textbook of macro and semimicro qualitative inorganic analysis, Wiley. New York: pp: 108-114.
17. Chen, S, C., Su, J., Fu, F, J., Mi, B. and Chung, T. S. (2013). Gypsum ($CaSO_4.2H_2O$) scaling on polybenzimidazole and cellulose acetate hollow fibre membranes under forward osmosis. *Membrane,* 4: 354-374.
18. Kopek, K, K., Ditczak S, M. and Wessling, M. (2011). Chemistry in a spinneret on the interplay of crosslink and phase inversion during spinning of novel hollow fibre membranes. *Journal of Membrane Sciences,* 18: 308-359.
19. Baker, W. R. (2012). Membrane technology and applications. 3rd edition, John Wiley & Sons, New York, pp: 265-266.
20. Dzinun, H., Othman, M. H. D., Ismail, A, F., Puteh, M, H., Rahman, M, A. and Jaafar, J. (2015). Photocatalytic degradation of nonyphenol by immobilized TiO_2 in dual layer hollow fibre membranes. *Chemical Engineering Journal,* 269: 255-261.
21. Dzinun, H., Othman, M. H. D., Ismail, A. F., Puteh, M. H., Rahman, M. A. and Jaafar, J. (2014). Morfological study of co-extruded dual-layer hollow fibre membranes incorporated with different TiO_2 loadings. *Journal of Membrane Science,* 134: 62.
22. Wessling, M., Culfaz, P. Z. and Lammertink, R. G. H. (2011). Hollow fibre ultrafiltration membranes with microstructured inner skin. *Journal Membrane Science,* 7:221-369.
23. Fan, Z. W., Xiao, C. F. and Huang, X. Y. (2015). Preparation and performance of homogeneous braid reinforced cellulose acetate hollow fibre membranes. *Cellulose,* 22: 695-707.
24. Su, J., Yang, Q., Teo, J. F. and Chung, T. S. (2010). Cellulose acetate nanofiltration hollow fibre membranes for forward osmosis processes. *Journal Membrane Science,* 355: 36-44.
25. Yao, J., Wang, J., Ren, M., Liu, J. Z. and Wang. H. (2012). Phase inversion spinning of ultrafine hollow fibre membranes through a single orifice spinneret. *Journal Membrane Science,* 421-422: 8-14.

Malaysian Journal of Analytical Sciences (MJAS)
Published by Malaysian Analytical Sciences Society

INDUCTION AND IDENTIFICATION OF BIOACTIVE COMPOUNDS FROM CALLUS EXTRACT OF *Piper betle* L. var. Nigra

(Induksi Dan Pengenalpastian Sebatian Bioaktif dari Ekstrak Kalus *Piper betle* L. var. Nigra)

Junairiah[1]*, Rizka Kusuma Rahmawati[1], Yosephine Sri Wulan Manuhara[1], Ni'matuzahroh[1], Manikya Pramudya[1], Lilis Sulistyorini[2]

[1]Department of Biology, Faculty of Science and Technology
[2]Faculty of Public Health
Universitas Airlangga, Kampus C - Mulyorejo, Surabaya 60115, Indonesia

**Corresponding author: alip.jun1@gmail.com*

Received: 18 July 2019; Accepted: 20 July 2020; Published: 10 December 2020

Abstract

Black betel (*Piper betle* L. var. Nigra) has been shown to have the potential for medicinal use. The black betel leaves contain 4.2% essential oil, alkaloids, flavonoids, saponins, tannins, eugenol, and chavicol. The application of plant tissue culture is needed to increase the production of secondary metabolites. This study aimed to investigate the impact of the combination of growth regulators (IBA, BAP, and kinetin) on the bioactive compounds of black betel callus extract. The experimental parts consisted of four treatments: I_2B_2, $I_{1.5}B_{1.5}$, $I_2K_{1.5}$, $I_1K_{1.5}$, and a control group. Callus induction time, fresh weight, dry weight, morphology, and bioactive compounds of black betel callus extract were observed. The findings showed that the combination of IBA and BAP, and IBA and kinetin influenced the growth of black betel leaves explants. The best concentration of growth regulators was the combination of 2 mg/L IBA and 2 mg/L BAP, which give the results of 9.33 days callus induction time, 650.68 mg fresh weight, and 54.22 mg dry weight. The grown callus had white to light brown colour with a compact texture. Furthermore, different treatments resulted in different bioactive compounds contained in the black betel leaves callus extract. Supplementation of I_2B_2 resulted in an extract containing 15 compounds, $I_{1.5}B_{1.5}$ supplementation yielded 8 compounds, $I_2K_{1.5}$ 12 compounds, and $I_1K_{1.5}$ 13 compounds. The bioactive compounds were predominated by methyl-β-D-Glucopyranoside (28.69%), 9,12-octadecadienoic acid (Z, Z; 15.07%), and hexadecanoic acid (11.03%).

Keywords: callus induction, bioactive compounds, *Piper betle* L. var. Nigra, IBA, BAP, kinetin

Abstrak

Sirih hitam (*Piper betle* L. var Nigra) telah terbukti berpotensi dalam kegunaan perubatan. Daun sirih hitam mengandungi 4.2% minyak pati, alkaloid, flavonoid, saponin, tanin, eugenol, dan chavikol yang penting. Penggunaan kultur tisu tumbuhan diperlukan untuk meningkatkan pengeluaran metabolit sekunder. Tujuan kajian ini adalah untuk mengkaji kesan gabungan pengawal atur tumbesaran (IBA, BAP, dan kinetin) pada sebatian bioaktif ekstrak kalus sirih hitam. Bahagian eksperimen terdiri daripada empat rawatan: I_2B_2, $I_{1.5}B_{1.5}$, $I_2K_{1.5}$, $I_1K_{1.5}$ dan kumpulan kawalan. Masa induksi kalus, berat segar, berat kering, morfologi, dan sebatian bioaktif ekstrak kalus sirih hitam telah diperhatikan. Hasil kajian menunjukkan bahawa gabungan IBA dan BAP, dan IBA dan kinetin mempengaruhi pertumbuhan eksplan daun sirih hitam. Kepekatan pengawal atur tumbesaran terbaik ialah gabungan 2 mg/L

IBA dan 2 mg/L BAP yang memberikan hasil masa induksi kalus selama 9.33 hari, berat segar 650.68 mg, dan 54.22 mg berat kering. Kalus yang tumbuh mempunyai warna putih hingga coklat muda dengan tekstur yang padat. Selanjutnya, rawatan yang berbeza menghasilkan sebatian bioaktif berbeza yang terkandung dalam ekstrak kalus daun sirih hitam. Tambahan I_2B_2 menghasilkan ekstrak yang mengandungi 15 sebatian, tambahan $I_{1.5}B_{1.5}$ menghasilkan 8 sebatian, $I_2K_{1.5}$ 12 sebatian, dan $I_1K_{1.5}$ 13 sebatian. Sebatian bioaktif didominasi oleh metil-β-D-glukopiranosida (28.69%), asid 9,12-oktadekanoic (Z, Z; 15.07%), dan asid heksadekanoik (11.03%).

Kata kunci: induksi kalus, sebatian bioaktif, *Piper betle* L. var. Nigra, IBA, BAP, kinetin

Introduction

Betel leaves are mainly used as mouth refresher and medicine for both infectious and non-infectious diseases, such as influenza, cough, asthma, bronchitis, rheumatic, conjunctivitis, constipation, wound, and others [1]. *Piper betle* L. can be used to treat various health conditions as its leaves contain 4.2% essential oil, alkaloids, flavonoids, saponins, tannins, eugenol, and chavicol [2]. The essential oil component in betel leaves is composed mostly of phenolic and terpenoid compounds [3]. Moreover, the key components of betel leaves consist of starch, sugars, diastases and essential oil composed of terpinen-4-ol, safrole, allyl pyrocatechol monoacetate, eugenol, eugenyl acetate, hydroxyl chavicol and the betle oil contains cadinene carvacrol, allyl catechol, chavicol, p-cymene, caryophyllene, chavibetol, cineole, estragol, and others [4].

The phenolic content of *P. betle* L. can protect the human body from pathogenic bacteria, either Gram-positive or -negative [1]. Betel leaves are known to contain various nutrients and enzyme substances, such as diastase and catalase, besides several types of amino acids, including lysine, histidine, and arginine [1]. In addition, the extract of betel leaves also contained fatty acids, e.g., stearate and palmitate, which exhibited antimicrobial activity against *Streptococcus mutans*. Betel leaves extract may also inhibit the growth of *Staphylococcus aureus* and *Escherichia coli* bacteria in disk-diffusion test [5].

Conventionally, secondary metabolites are obtained via direct extraction from plant organs. However, this method requires massive raw plant material, in addition to costly extraction, isolation, and purification processes [6]. Therefore, plant tissue culture can be applied as an alternative to the production of secondary metabolites. Growth regulators from the auxin group play a role in callus induction, chlorophyll formation, and morphogenesis. Low concentration of auxin will trigger adventive roots formation, whereas a high concentration of it will stimulate callus formation and suppress or inhibit morphogenesis [7]. Meanwhile, the use of cytokinin in plant tissue culture will affect cell division and differentiation of adventive shoots from callus and organ [8]. The optimum ratio of auxin and cytokinin played a significant role in plant morphogenesis. The application of exogenous plant growth substances (auxin and cytokinin) of an intermediate ratio can promote callus induction. In addition, a high ratio of auxin:cytokinin or cytokinin:auxin ratios could induce root and shoot regeneration [9].

Callus induction of *P. betle* L. can be performed by a combination of IBA and kinetin growth regulators. A study reported that the addition of 2 mg/L IBA and 1 mg/L kinetin resulted in the shortest callus induction period, i.e., 7.5 days [10]. On the other hand, a combination of 2 mg/L IBA and 1.5 mg/L kinetin resulted in the highest callus fresh weight at 177 mg and dry weight at 46.6 mg, where the grown callus had a compact texture [10]. The combination of growth regulators of 2 mg/L IBA and 2 mg/L BAP could induce *P. betle* L. callus at the shortest period of 10 days, and the response of callus formation was 100%. The same combination also resulted in the highest callus fresh weight (0.8507 grams) and dry weight (0.0769 grams). Callus morphology from this treatment was friable textured and white [11].

The combination of 2 mg/L IBA and 2 mg/L BAP growth regulators given to *Piper crocatum* Ruiz and Pav explants resulted in the shortest induction time of 28

days. Meanwhile, the combination of 1.5 mg/L IBA and 1.5 mg/L BAP produced the highest fresh weight (226 mg) and dry weight (43.2 mg). GC-MS analysis showed that the latter combination of growth regulators yielded the callus extract with 19 types of compound (19 peaks). From the 19 peaks, 2 of the highest peaks were n-hexadecanoic acid and cyloeicosane [12].

The supplementation of growth regulators 6-benzylaminopurine (BAP), 6-furfurylaminopurine (kinetin), and indole-3-butyric acid (IBA) can induce callus from several callus explants in the *Piper* genus [10,11,12]. Thus, this study was designed using the combination of growth regulators BAP, kinetin, and IBA to determine the effect of growth regulator combinations in inducing callus and to identify secondary metabolites contained in black betel (*P. betle* L. var. Nigra) leaves callus. This is a novel approach as no research has been done on black betel leaves callus culture using these growth regulators.

Materials and Methods

Materials

Young black betel leaves (*P. betle* L. var. Nigra) taken from the second or third position from the top of the plant were chose and cut into small pieces. The plants were obtained from the Bratang Flower Market, Surabaya. Chemicals used were Murashige-Skoog (MS) medium, growth regulators (BAP, IBA, and kinetin), distilled water, 20% clorox, 70% alcohol, 1 N KOH (potassium hydroxide), 5 N HCl (hydrochloric acid), and 1 N methanol.

Culture medium preparation

Plants require nutrition for their growth and development. In the laboratory setting, in vitro culture medium supplies the nutrition required by the plant cells to imitate the whole plant grown in nature [8]. The MS medium (1000 mL) was prepared to incorporate macronutrients as follows; 1650 mg NH_4NO_3, 1900 mg KNO_3, 440 mg $CaCl_2.2H_2O$, 370 mg $MgSO_4.7H_2O$, and 170 mg KH_2PO_4 dissolved one by one in 500 mL distilled water using a magnetic stirrer until the solution was homogenous. Then, 5 mL of iron stock solution, 1 mL of micronutrient stock, and 4 mL of vitamin stock solution were added, followed by 100 mg myo-inositol and 30 grams sucrose. The growth regulators were added at various levels according to treatment. The pH of the solution was recorded using pH-indicator strips (Merck) and adjusted into the optimum pH of 5.6-5.8 using 1 N KOH and/or 1 N HCl. Lastly, distilled water was topped up until 1000 mL. Approximately 8 grams of agar was added into the solution while heated to solidify the medium. The agar was mixed well until it dissolved. The liquid medium was poured into culture bottles (about ± 10 mL/bottle). The bottles were covered with aluminium foil and labelled accordingly. The bottles were then sterilised in the autoclave at 121 °C, 1.2 atm for 15 minutes. The sterile medium was left at room temperature to solidify.

Explants planting

This stage was conducted according to previous research with modifications [13]. The young black betel leaf explants were planted aseptically in the laminar airflow (LAF) cabinet. Before planted, the leaves were sterilised by soaking it in detergent water for 3 minutes while its surface was rubbed gently using hands before rinsing using tap water. The leaves were soaked again in detergent water for 2 minutes while shaken, then rinsed again. Next, they were soaked in 70% alcohol for 5 minutes and washed three times using sterile distilled water. The leaves were soaked again in a 20% clorox solution and shaken for 7-10 minutes. Lastly, the leaves were rinsed using distilled water for three times. They were then transferred to a petri dish lined with filter paper. The leaves were cut into small pieces of ± 1cm^2, before putting into medium-filled culture bottle. Each treatment used four culture bottles filled with three leave explants. The explants were incubated at room temperature (20-25 °C) with lighting from a 40-watt neon lamp positioned at 1.5-2 m above the bottle shelf.

Extraction of black betel callus

Callus grown from the leaf explants was harvested after 8 weeks of incubation and dried, according to previous research with modifications [14]. The callus was crushed into powder using mortar and pestle. The powdered callus was extracted using maceration for 24 hours using methanol. After maceration, the callus extract was filtered using a filter paper. The pulp was re-macerated using the same solvent and then re-filtered. If

the filter result was still soupy, maceration was repeated. The product was air-dried to remove the remaining solvent. The extract was then identified for secondary metabolites content using Gas Chromatography-Mass Spectrophotometry (GC-MS) method [15].

Identification of secondary metabolites of *P. betle* L. var. Nigra callus using Gas Chromatography-Mass Spectrophotometry

The result of *P. betle* L. var. Nigra callus maceration from each combination treatment was identified for secondary metabolites using GC-MS, according to previous research with modifications [15]. The methanol extract of *P. betle* L. var. Nigra callus was analysed using Agilent 190915-105 with HP-5MS column silica capillary (60 m × 200 µm × 3 µm). A volume of 1 µL sample was injected into the column. Helium was used as the carrier gas at 1 mL/minute velocity. The injector temperature was set at 280 °C, while the detector temperature was 350 °C. The oven temperature was programmed at 40 °C for 5 minutes before raised to 250 °C at the rate of 2 °C/min and then hold for 20 minutes. Compounds were identified based on mass spectrum comparison to Wiley ver. 10 mass spectrum library.

Results and Discussion

Callus induction time and percentage of callus

Comparison of mean callus induction time and percentage of callus grown from black betel leaf explants on MS medium is presented in Table 1. Black betel leaf explants responded towards the combination of IBA and BAP, also IBA and kinetin in the MS medium. The initial reactions observed were explant curving, thickening at the margin of the explant, and broadening of the leaf vein and midrib. Small white spots emerged near scars and midrib. These spots are the first feature of callus formation. Initial callus growth was marked with explant swelling, followed by white callus emergence at the margin of the explant. Table 1 shows that a 100% callus formation is found in the explants from each treatment except for the control [16]. IBA and BAP combination (0, 0.5, 1.0, 2.0, and 3.0) could induce explants to form 100% callus [17]. Similarly, the addition of 1 mg/L IBA and 1.5 mg/L kinetin induced callus in *Justicia gendarussa* leaf explants with 100% callus formation [18].

Callus fresh and dry weight

Comparison of the mean fresh and dry weight of *P. betle* L. var. Nigra callus supplemented with various combinations of IBA, BAP, and kinetin growth regulators on MS medium is presented in Table 2. The highest mean of fresh and dry weight was found from explants given 2 mg/L IBA and 2 mg/L BAP, at 650.68 mg and 54.22 mg (Table 2). Plant production is usually more accurately referred to in dry weight than fresh weight. Callus fresh weight is also affected by the environment, as well as metabolic activity and humidity [19]; thus, the dry weight is more stable compared to fresh weight. The increased dry weight of the callus is caused by rising cell activity. Inside the cell, auxin plays a role in enhancing protein synthesis, improving plasticity, and developing cell walls, while cytokinin functions in cell division and protein synthesis [6].

Morphology of black betel (*P. betle* L. var. Nigra) leaf explant callus on MS medium

Table 3 shows that *P. betle* L. var. Nigra leaf explants planted for 8 weeks on MS medium with the combination of 2 mg/L IBA and 2 mg/L IBA can form callus (Figure 1). Callus grown from this combination had a brownish white compact texture. Callus can form in response to other hormones or wounding. Transcription factors regulate wound-induced calli. Wounding upregulates the biosynthesis and signalling of cytokinin, leading to cell proliferation activation and callus formation [20]. Callus induced by injury originated from various type of cells, including vessel and cortex cells [21]. Grown callus undergoes increased cell mass and callus colour change. Indicators of growth in the explants during in vitro culture can also be seen from the colour and texture of the callus. The while explant in the control group could not form callus (Figure 2).

Table 1. Mean callus induction time and percentage of callus grown from black betel leaf explants on MS medium added with growth regulators combination of IBA and BAP, and IBA and kinetin

No.	Concentration of Growth Regulator (mg/L)			Group	Mean Induction Time (days)*	Percentage of Explants Formed Callus (%)
	IBA	BAP	Kinetin			
1.	2	2	-	I_2B_2	9.33 ± 0.47^b	100
2.	1.5	1.5	-	$I_{1.5}B_{1.5}$	13.00 ± 1.00^c	100
3.	2	-	1.5	$I_2K_{1.5}$	14.08 ± 0.83^d	100
4.	1	-	1.5	$I_1K_{1.5}$	14.75 ± 1.09^d	100
5.	-	-	-	Control	0.00 ± 0.00^a	0**

*) Mean is followed by letters, different letter indicates significant difference based on Mann-Whitney test at 5% significance level. (-) = concentration 0 mg/L. **) not formed callus

Table 2. Mean callus fresh and dry weight from black betel leaf explants on MS medium supplemented with concentration combination of IBA and BAP, and IBA and kinetin growth regulators

No.	Concentration of Growth Regulator (mg/L)			Group	Mean Fresh Weight (mg)*	Mean Dry Weight (mg)*
	IBA	BAP	Kinetin			
1.	2	2	-	I_2B_2	650.68 ± 312.07^b	54.22 ± 9.11^b
2.	1.5	1.5	-	$I_{1.5}B_{1.5}$	429.78 ± 1.00^b	48.30 ± 11.53^b
3.	2	-	1.5	$I_2K_{1.5}$	164.53 ± 49.15^c	26.14 ± 4.18^c
4.	1	-	1.5	$I_1K_{1.5}$	60.94 ± 31.56^d	10.90 ± 4.62^d
5.	-	-	-	Control	0.00 ± 0.00^a	0.00 ± 0.00^a

*) Mean is followed by letters, different letter indicates significant difference based on Games-Howell test at 5% significance level. (-) = concentration 0 mg/L.

Table 3. Description of black betel leaves callus of I_2B_2 group from 1st to 8th week

Week	Description		
	Morphology	Texture	Colour
1st	Explants margin thickened slightly, surface smooth, explants slightly levitated, explants colours remain unchanged.	-	-
2nd	Explants margin thickened, margin coloured green, midrib and vein enlarged, explants slightly curved, transparent pustules emerged in the margin.	-	Transparent
3rd	Callus emerged at explants margin, margin curved, explants surface slightly smooth, explants coloured dark green.	Friable	White

Table 3 (cont'd). Description of black betel leaves callus of I_2B_2 group from 1st to 8th week

Week	Description		
	Morphology	**Texture**	**Colour**
4th	Callus in explants margin thickened more but still not prevalent, very few calli in the underside of explants, margin became wavy, and explants curved.	Compact	Greenish white
5th	Callus thickened more in the margin of explants; callus growth was uneven.	Compact	White
6th	More callus formed in the margin and underside of explants; callus growth was uneven.	Compact	White
7th	More callus grew, explants rolled.	Compact	White
8th	More callus grew, callus colours started to be brownish.	Compact	Brownish white

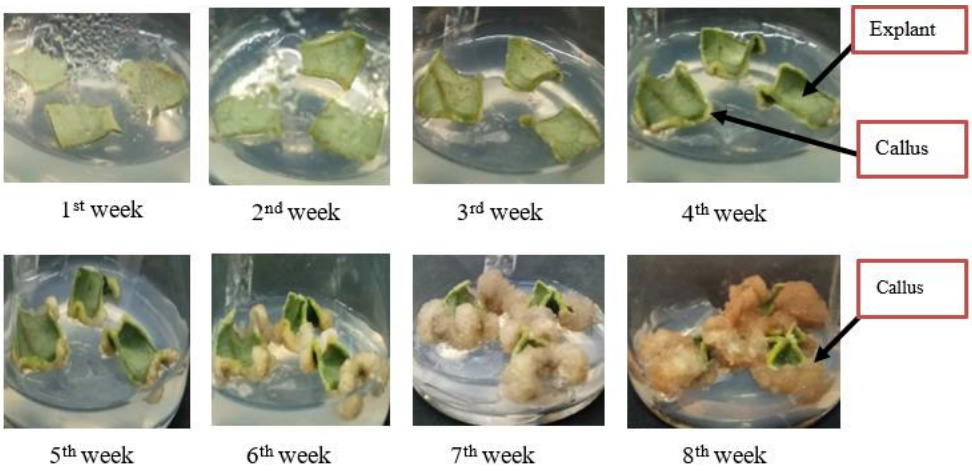


Figure 1. Callus morphology grown from black betel leaf explants from 1st to 8th week given 2 mg/L IBA and 2 mg/L BAP combination

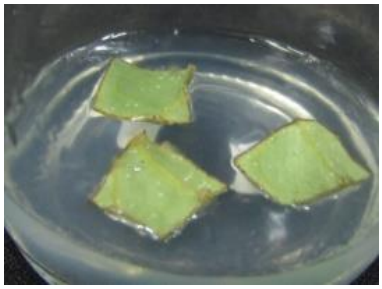


Figure 2. Explant morphology grown from black betel leaf explants without additional plant growth regulators (control group)

Secondary metabolites analysis

Compounds contained in the methanol extract of black betel callus is presented in Table 4. The positive control is the chemical content identified from the methanol extract of black betel leaves [22]. Three major secondary metabolite compounds in the 2 mg/L IBA and 2 mg/L BAP combination were 14-beta-H-pregna, n-hexadecanoic acid, and 1-docosane. Hexadecanoic acid belongs to the saturated fatty acid group. Fatty acids are the primary metabolite compounds known to possess antibacterial and antifungal properties. Fatty acids can modulate the immune response by acting directly on T cells [23]. The GC-MS analysis of the black betel callus methanol extract in combination with 1.5 mg/L IBA and 1.5 mg/L BAP showed that there were three compounds with a high percentage; methyl-β-D-glucopyranoside at 28.69%, 9,12-Octadecadienoic acid (Z, Z) at 15.07%, and hexadecanoic acid at 11.03%. Methyl-β-D-glucopyranoside belongs to the monosaccharide group. A monosaccharide is the monomer of polysaccharide and a type of primary metabolite. On the contrary, hexadecanoic acid and 5-octadecene belonged to the fatty acid group. Methyl-β-D-glucopyranoside was found in *Agrocybe aegerita* edible mushroom [24], and it was also the main compound found in *Geum montanum* L. leaves and will be accumulated throughout the lifetime of the plant. Synthesis of methyl-β-D-glucopyranoside and its derivates could reduce methanol in the cytoplasm of plant cells [25].

The main secondary metabolite present in the black betel callus methanol extract administered with 2 mg/L IBA and 1.5 mg/L kinetin combination was found to be chloroquine at 19.40%. Chloroquine is one of several malaria drug types [26]. Chloroquine is a common drug used for the treatment of *Plasmodium vivax*, which may interrupt the cycle of haemoglobin digestion process by parasite through interfering with β-hematein or inhibiting hemozoin formation [27]. Chloroquine could also inhibit plasmepsin and falcipain enzymes, which function in globin breakdown into amino acids. Hemozoin and amino acids are necessary for parasite growth; thus, inhibition of their formation will cause the parasite to die [28].

Analysis of callus extract given the combination of 1 mg/L IBA and 1.5 mg/L kinetin resulted in the production of primary metabolites, such as 9,12-Octadecadienoic acid, methyl ester, methyl-beta-D-thiopyranoside, and others. Similarly, 9,12-Octadecadienoic acid and methyl ester, which have a chemical formula of $C_{19}H_{34}O_2$, were identified from the methanol extract of *Cenchrus ciliaris* L. stem. Primary metabolite compounds identified from the GC-MS method are predominantly fatty acids, in addition to amino acids and carbohydrate polymers [29].

In the current study, the addition of IBA, BAP, and kinetin plant growth regulators (PGRs) could affect chemical formation in black betel leaf explant callus. Table 4 shows that several compounds are only formed in specific treatment. This is greatly influenced by the addition of PGRs in the MS medium. The formation of bioactive compounds and their numbers are closely related to the addition of variations in the combination of concentrations of IBA and BAP, and IBA and kinetin, which will affect endogenous hormones in explant cells that are cultured in MS medium. This current phenomenon is often studied as an essential factor in green biotechnology. PGRs play an important role in research that focuses on micropropagation of the plant [30]. One example was 14-beta-H-pregna, which can only be found in callus given the combination of 2 mg/L IBA and 2 mg/L BAP. The area percentage of 14-beta-H-pregna was found to be the highest. This indicated that 1 µL methanol extract sample of black betel callus given 2 mg/L IBA and 2 mg/L BAP contained 14-beta-H-pregna at the concentration of 15.34%. Beside 14-beta-H-pregna, another compound only found in one treatment was chloroquine. Based on GC-MS analysis, chloroquine was only produced by callus given 2 mg/L IBA and 1.5 mg/L kinetin combination. In this treatment, chloroquine was found to have the highest area percentage. This indicated that in 1 µL methanol extract sample of callus from 2 mg/L IBA and 1.5 mg/L kinetin treatment contained chloroquine at 19.4% level.

Table 4. Secondary metabolites content of black betel callus analysed based on GC-MS method

Compounds	Area (%) / Retention Time (minutes)				
	I_2B_2	$I_{1.5}B_{1.5}$	$I_2K_{1.5}$	$I_1K_{1.5}$	Positive Control
Pyridine	0.08/8.669	0.33/8.629	0.38/8.806	0.64/8.766	0.26/7.29
Methyl-pyrazine	0.03/11.404	0.18/11.455	0.38/11.478	0.75/11.633	-
Imidazole	0.04/65.282	-	-	-	0.02/21.64
Chloroquine	-	-	19.4/85.498	-	-
Piperidine	-	-	-	0.77/49.787	-
2-Picoline	-	-	-	-	0.16/6.13
Piperazine	-	-	-	-	0.01/20.23
Caryophyllene oxide	-	-	0.17/61.471	-	-
Hexacosane	1.11/110.377	-	-	-	-
Squalene	-	0.17/117.458	0.60/117.771	0.40/117.466	-
Neophytadine	0.39/72.284	-	1.69/77.418	-	-
Linuron	-	-	-	0.13/5.356	-
Dihydro-2-(3H)-thiphenone	-	-	-	0.32/10.403	-
Dihydro-2(3H)-furanone	-	-	-	0.13/16.411	-
Phytol	0.75/88.319	1.73/88.301	1.02/88.319	0.89/75.278	-
Gamma -muurolene	-	0.07/57.574	0.37/57.580	-	-
n- Hexadecanoic acid	3.26/81.990	2.47/80.033	5.83/81.887	15.62/81.801	-
Hexadecanoic acid	-	11.03/80.113	-	5.98/79.621	-
Nonadecane	0.06/78.305	-	-	-	-
Tetradecanal	0.04/86.757	-	-	-	-
Octadecanoic acid	-	-	1.06/90.894	-	-
Myrcene	-	-	-	-	0.09/7.76
Undecane	-	-	-	-	0.01/7.94
2-Dodecanone	-	-	-	-	0.01/21.02
Tetradecane	-	-	-	-	0.01/21.02
1,2-Epoxy-1 vinylcyclododecane	-	-	-	-	0.02/22.39
1-Docosane	3.58/97.548	-	-	-	-
Oxirane, 2-ethyl-2-methyl	0.03/16.262	-	-	-	-
2-Propenoic acid	-	-	0.29/97.169	0.55/97.056	-

Table 4 (cont'd). Secondary metabolites content of black betel callus analysed based on GC-MS method

Compounds	Area (%) / Retention Time (minutes)				
	I_2B_2	$I_{1.5}B_{1.5}$	$I_2K_{1.5}$	$I_1K_{1.5}$	Positive Control
Piperlonguminine	-	-	0.35/103.745	-	-
Myristcin	-	-	-	2.91/57.557	-
Ethanol	2.87/100.724	-	-	-	-
Hexadecane	1.51/109.318	-	-	-	-
Dodecanoic acid	-	0.43/60.297	-	-	-
Ethyl Alcohol	-	-	-	-	0.19/1.25
Tricosane	2.64/119.057	-	-	-	-
4-Hexenoic acid	0.23/98.641	-	-	-	-
12-Metyltricosane	0.24/102.664	-	-	-	-
14-beta-H-Pregna	15.34/129.854	-	-	-	-

Conclusion

The studied bioactive compounds of *P. betle* L. var. Nigra leaves methanol extract using GC-MS method resulted in the detection of several compounds. The compound with the highest area percentage was methylamine, at 85.08%. Methylamine is an organic compound from the amine group that was previously found to have antimicrobial bioactivity. Based on GC-MS analysis, methanol extract of black betel callus given IBA, BAP, and kinetin growth regulators combination did not contain methylamine. However, two similar compounds were identified from the methanol extract of black betel leaf, i.e., pyridine and methyl pyrazine. Both compounds belong to the alkaloid secondary metabolite group. Pyridine is essential in the manufacture of medicines and has a wide range of bioactivities, such as anti-inflammatory, analgesic, anticancer, and antimicrobe [22]. Meanwhile, methyl pyrazine can act as an anticancer medicine [31].

Acknowledgement

The authors would like to thank the Ministry of Research, Technology, and Higher Education for the funding via PTUPT (*Penelitian Terapan Unggulan Perguruan Tinggi*) research grant.

References

1. Das, S., Parida, R., Sandeep, I. S., Nayak, S. and Mohanty, S. (2016). Biotechnological intervention in betelvine (*Piper betle* L.): A review on recent advances and future prospects. *Asian Pacific Journal of Tropical Medicine*, 9(10): 938-946.
2. Khomsatun, Wahyudi, Hari R. I. W., and Gustomo Y. (2019). Effectiveness of betel leaves extract (*Piper betle*, Linn) as mosquito *Anopheles spp* repellent. *International Journal of Innovative Research in Science, Engineering and Technology*, 8(5): 5144-5152.
3. Alighiri, D., Cahyono, E., Eden, W. T., Kusuma, E. and Supardi, K. I. (2018). Study on the improvement of essential oil quality and its repellent activity of betel leaves oil (*Piper betle* L.) from Indonesia. *Oriental Journal of Chemistry,* 34 (6): 2913 - 2926.
4. Sugumaran, M., Poornima, M., Venkatraman, S., Lakshmi, M., and Srinivasansethuvani (2011). Chemical composition and antimicrobial activity of sirugamani variety of *Piper betle* Linn leaf oil. *Journal of Pharmacy Research*, 4(10): 3424-3426.

5. Hermawan, A. (2007). Pengaruh ekstrak daun sirih (*Piper betle* L.) terhadap pertumbuhan *Staphylococcus aureus* dan *Escherichia coli* dengan metode difusi disk. Thesis of Undergraduate Degree. Universitas Airlangga.
6. Utomo, B. (2015). Pengaruh kombinasi zat pengatur tumbuh *Napthalene Acetic Acid* (NAA) dan kinetin terhadap pembentukan dan kandungan metabolit sekunder kalus sirih merah (*Piper crocatum* Ruiz dan Pav.). Thesis of Undergraduate Degree. Universitas Airlangga.
7. Overvoorde, P., Fukaki, H. and Beeckman, T. (2010). Auxin control of root development. *Cold Spring Harbor Perspectives in Biology*, 2(6): a001537.
8. Saad, A. I. M. and Elshahed, A. M. (2012). Plant tissue culture media. In *Recent Advances in Plant in vitro Culture*. IntechOpen: pp. 29-40.
9. Ikeuchi, M., Sugimoto, K. and Iwase, A. (2013). Plant callus: Mechanisms of induction and repression. *The Plant Cell,* 25 (9): 3159-3173.
10. Fatin, U. (2016). Induksi kalus eksplan daun sirih hitam (*Piper betle* L.) dengan kombinasi konsentrasi zat pengatur tumbuh indol butyric acid (IBA) dan kinetin. Thesis of Undergraduate Degree. Universitas Airlangga.
11. Rachmah, A. (2016). Induksi kalus eksplan daun sirih hitam (*Piper betle* L.) dengan kombinasi konsentrsi zat pengatur tumbuh indol butyric acid (IBA) dan *6-Benzylaminopurine* (BAP). Thesis of Undergraduate Degree. Universitas Airlangga.
12. Tantri, N. A. (2015). Pengaruh variasi konsentrasi zat pengatur tumbuh *Indol Butyric Acid* (IBA) dan *Benzylaminopurine* (BAP) terhadap induksi kalus dan kandungan senyawa sirih merah (*Piper crocatum* Ruiz dan Pav.). Thesis of Undergraduate Degree. Universitas Airlangga.
13. Junairiah, J., Zuraidassanaaz, N. I., Izdihar, F. N. and Manuhara, Y. S. W. (2017). Callus induction of leaf explant *Piper betle* L. var Nigra with Combination of Plant Growth Regulators Indole-3-acetic Acid (IAA), Benzyl Amino Purine (BAP) and Kinetin. *AIP Conference Proceedings*, 1888: 020028.
14. Junairiah, J., Ni'matuzahroh, N., Zuraidassanaaz, N. I., and Sulistyorini, L. (2018). Isolation and identification of secondary metabolites of black betel (*Piper Betle* L. var. Nigra). *Jurnal Kimia Riset*, 3(2): 131-138.
15. Wahyuni, D. K., Ansori, A. N. M. and Vidiyanti, F. (2017). GC-MS Analysis of phytocomponents in methanolic extracts of leaf-derived callus of *Justicia gendarussa* Burm. f. *Bioscience Research.* 14(3): 668-677.
16. Wahyuningtyas, L., Resmiari, R. S. and Nashichuddin, A. (2014). Induksi kalus akasia (*Acacia mangium*) dengan penambahan kombinasi 2,4-D dan BAP pada media MS. https://etheses.uinmalang.ac.id/ 376/12/10620033%20Rangkuman.pdf. [Access online 26 December 2018].
17. Widyarso, M. (2010). Kajian penggunaan IBA dan BAP untuk merangsang pembentukan tunas lengkeng (*Dimocarpus longan* Lour.) varietas pingpong secara *In Vitro*. Thesis of Undergraduate Degree. Universitas Sebelas Maret.
18. Rohmatin, N. (2014). *Induksi kalus dari eksplan daun gandarusa (Justicia Gendarussa Burm. F.) dengan pemberian kombinasi zat pengatur tumbuh 2,4-D, IBA, dan kinetin***.** Thesis of Undergraduate Degree**.** Universitas Airlangga.
19. Muryanti, S., and Anggarwulan, E. (2005). Pertumbuhan dan produksi reserpin kalus pule pandak (*Rauvolia serpentine* (L.) Bentham ex. Kurz) pada pemberian metil jasmonat secara *In Vitro*. *Bioteknologi*, 2(2): 58-64.
20. Fehér, A. (2019). Callus, dedifferentiation, totipotency, somatic embryogenesis: What these terms mean in the era of molecular plant biology?. *Frontiers in Plant Science*, 10: 536.
21. Ikeuchi, M., Sugimoto, K., and Iwase, A. (2013). Plant callus: Mechanisms of induction and repression. *The Plant Cell*, 25(9): 3159-3173.
22. Junairiah, Nurhariyati, T., Ni'matuzahroh and Sulistyorini, L. (2018). GC-MS analysis of bioactive compounds in n-hexane, ethyl acetate and methanol extract of *Piper betle* L. Var. Nigra. *Bioscience Research*, 15(3): 1472-1479.

23. Aparna, V., Dileep, K. V., Mandal, P. K., Karthe, P., Sadasivan, C. and Haridas, M. (2012). Anti-inflammatory property of n-hexadecanoic acid: Structural evidence and kinetic assessment. *Chemical Biology & Drug Design*, 80 (3): 434-439.
24. Diyabalanage, T., Mulabagal, V., Mills, G., DeWitt, D. L. and Nair, M. G. (2008). Health-beneficial qualities of the edible mushroom, *Agrocybe aegerita*. *Food Chemistry*, 108(1): 97-102.
25. Aubert, S., Choler, P., Pratt, J., Douzet, R., Gout, E. and Bligniy, R. (2004). Methyl-b-D-glucopyranoside in higher plants: Accumulation and intracellular localization in *Geum montanum* L. leaves and in model systems studied by 13C nuclear magnetic resonance. *Journal of Experimantal Botany*, 55(406): 2179- 2189.
26. Isnawati, A. and Rooslamiati, I. (2013). Penetapan kadar artemisinin dalam ekstrak heksan tanaman *Artemisia annua L.* menggunakan metode densitometri. *Media Litbangkes*, 23(1): 15-22.
27. Hasugian, A. R. and Tjitra, E. (2014). Artesunat-amodiakuin dan klorokuin untuk pengobatan malaria vivaks di Puskesmas Kopeta, Maumere, Nusa Tenggara Timur, 2007. *Media Penelitian dan Pengembangan Kesehatan*, 24(4): 161 - 168.
28. Muti'ah, R. (2012). Penyakit malaria dan mekanisme obat-obat antimalaria. *Alchemy*, 2(1): 80-91.
29. Kumar, S. and Pandey, A. K. (2013). Chemistry and biological activities of flavonoids: An overview. *The Scientific World Journal*, 2013: 1-16.
30. Szopa, A., Kubica, P., Snoch, A. and Ekiert, H. (2018). High production of bioactive depsides in shoot and callus cultures of *Aronia arbutifolia* and *Aronia × prunifolia*. *Acta Physiologiae Plantarum*. 40(48): 1-11.
31. Urban, S., Hickford, S. J. H., Blunt, J. W. and Munro, M. H. G. (2000). Bioactive marine alkaloids. *Current Organic Chemistry*, 4(7): 765-807.

Malaysian Journal of Analytical Sciences (MJAS)
Published by Malaysian Analytical Sciences Society

FLAVONOIDS WITH MONOAMINE OXIDASE A AND B INHIBITORY AND ANTI-INFLAMMATORY EFFECTS FROM *Vitex grandifolia*

(Flavonoid Bersama Perencat Moniamin Oksidase A dan B dan Kesan Anti-Radang dari *Vitex grandifolia*)

Tijjani Ali*, Bello Oluwasesan Michael, Abiodun B. Ogbesejana

Department of Applied Chemistry,
Federal University Dutsin-Ma, Katsina State, Nigeria

**Corresponding author: tali@fudutsinma.edu.ng*

Received: 18 July 2019; Accepted: 20 July 2020; Published: 10 December 2020

Abstract

Vitex grandifolia is a plant that belongs to the *Lamiaceae* or *Labiatae* family. It is classified as an underutilised vegetable with little known phytochemistry. Methanol fraction of the leaves of the plant afforded the isolation of three known flavonoids: isoorientin (**1**), orientin (**2**), and isovitexin (**3**). Spectroscopic techniques, namely NMR and IR and comparison with data in the literature were used to assess the structures of the isolated compounds. The molecules isolated were tested in vitro for monoamine oxidase A (MAO-A) and monoamine oxidase B (MAO-B) human recombinant, and anti-inflammatory activities. Mostly, the isolated compounds showed selective activity towards MAO-B. Inhibition of MAO-B by isoorietin (**1**) and orietin (**2**) was 9-fold more potent (IC_{50} [µg/mL] of 11.08 and 11.04) compared to the inhibition of MAO-A (IC_{50} [µg/mL] of >100), while clorgyline and deprenyl were used as the positive standards. All flavonoids isolated from the plant displayed good activity against NF-Kb with IC_{50} (µg/mL) of 8.9, 12, and 18. The study shows a strong relationship between the structures of the flavonoids isolated with its biological activities based on the different patterns of substitution, particularly in C_2=C_3 bond and the positions of glucose in the isolates. Furthermore, the study is the first of its kind to determine the phytochemistry of the polar fraction of *V. grandifolia*, its anti-inflammatory, and neurodegenerative protective roles.

Keywords: *Vitex grandifolia,* underutilised vegetable, flavonoids, MAO-A and B, neurodegenerative

Abstrak

Vitex grandifolia ialah sejenis tumbuhan yang tergolong dalam keluarga Lamiaceae or Labiatae. Ia diklasifikasikan sebagai sayur-sayuran yang kurang digunakan dengan sedikit maklumat fitokimia. Pecahan metanol daun tumbuhan ini dapat memencilkan tiga jenis flavonoid: isoorientin (**1**), orientin (**2**), dan isovitexin (**3**). Teknik spektroskopi iaitu NMR dan IR dan perbandingan dengan data dari kajian literatur digunakan untuk menilai struktur sebatian yang dipencilkan. Molekul yang dipencilkan diuji secara *in vitro* terhadap rekombinan manusia monoamine oxidase A (MAO-A) dan monoamine oxidase B (MAO-B), dan aktiviti anti-radang. Sebatian yang dipencilkan kebanyakannya menunjukkan aktiviti memilih terhadap MAO-B. Perencatan MAO-B oleh isooretin (**1**) dan orietin (**2**) adalah 9 kali ganda lebih poten (IC_{50} [µg/mL] sebanyak 11.08 dan 11.04) berbanding perencatan terhadap MAO-A (IC_{50} [µg/mL] > 100), dengan menggunakan clorgyline dan deprenyl sebagai piawaian positif. Semua flavonoid yang dipencilkan daripada tumbuhan menunjukkan aktiviti yang baik terhadap NF-Kb with IC_{50} (µg/mL) sebanyak 8.9, 12, dan 18. Kajian ini menunjukkan hubungan yang kuat antara struktur flavonoid yang dipencilkan dengan aktiviti biologi berdasarkan

pelbagai corak penggantian, terutamanya pada ikatan C_2=C_3 bond dan kedudukan glukosa dalam pencilan tersebut. Tambahan pula, kajian ini merupakan kajian pertama seumpamanya yang menentukan fitokimia pecahan berkutub *V. grandifolia*, berserta fungsi anti-radang dan perlindungan rosotan neuro.

Kata kunci: *Vitex grandifolia,* sayur-sayuran yang kurang digunakan, flavonoids, MAO-A dan B, rosotan neuro

Introduction

Pathological and neurodegenerative pathways, Alzheimer's disease, cancer, coronary, and Parkinson diseases are the results of free-radical mediated reactions and reactive oxygen species (ROS) from the human body [1, 2]. Many epidemiological studies have shown a strong correlation in the group of people whose diet is rich in fresh fruits and leafy vegetables and a lower risk of heart disease, neurodegenerative diseases, and some particular forms of cancer [3]. Many studies are mostly dedicated to antioxidant exhibited by compounds in fruits, medicinal plants, and vegetables. Monoamine oxidase A (MAO-A) and monoamine oxidase B (MAO-B) are enzymes found in the mitochondria. These enzymes deaminate (via oxidation) monoaminergic neurotransmitters and dietary monoamines that are potentially harmful. In addition, they also regulate noradrenaline, dopamine, serotonin, and adrenaline in the brain [4-7].

Medicinal plant vegetables and other herbal products were identified to be the essential and primary basis for MAOs' inhibition, and this may validate the folkloric applications of many plants as a replacement to manage neuropsychiatric disorders, neurological problems (e.g. Parkinson's disease), and depression [8]. Secondary metabolites such as flavonoids are among the prevalent polyphenols present in medicinal plants. They are often found in many plant species and obtainable in various parts of plants, for example, in the bark, flowers, fruits, leaves, and stems [9-12]. Flavonoids were reported to show different types of biological activity, including antioxidants, enzyme inhibitors, anti-inflammatory, anticancer, antihyperglycemic, hepatoprotective activities, among others [13-16].

Nowadays, plant-based medicinal research is growing tremendously, and evidence has been gathered to demonstrate the immense potential of medicinal plants used in traditional systems [17, 18]. Many of these botanicals have been described and studied using modern scientific methods, with findings showing immense promise of medicinal plants in the field of medical-related sciences [19].

Vitex grandifolia (*V. grandifolia*) belongs to the Lamiaceae family, has edible fruits that the locals used in making the alcoholic drink. The plant bark is locally used to treat fever, bronchial complaints, diarrhoea, rickets, sore, and stomach-ache. Other uses include treatment of toothache, rheumatism, orchitis, colic, and umbilical cord infections. There was also a report by Epidi and Odili [20] on the biocidal effects of *V. grandifolia* powdered leaf against *Tribolium castaneum* Herbst in stored groundnut, *Arachis hypogaea* [20]. *V. grandifolia* is a small tree or shrub that is approximately 10–12 cm long and 5– cm width. Its trunk has 60 cm girth that bears a spreading crown and usually inhabits secondary jungle or high deciduous forest. Local names of this plant species are ooriọdan (Yoruba, Nigeria), ofonma (Egun, Republic of Benin), or ofofrin (Setangun, Republic of Benin) [21]. Surprisingly, this plant's phytochemistry was not investigated before this study. Therefore, the need to isolate compounds with biologic activity from this plant emerged. Hence, this is a report of isolation and structure elucidation of flavonoids with in vitro MAO-A and MAO-B activity (inhibition) from the leaf extract of *V. grandifolia*.

Materials and Methods

Plant sample

The whole plant of *V. grandifolia* was collected from Ilorin Metropolis, Illorin L.G.A. Kwara State, Nigeria. The collected plant was identified in the Department of Plant Biology, University of Ilorin, where voucher number was obtained after the deposition of the specimen. The leaves were air-dried, powdered, and stored in the refrigerator before further analyses.

Extraction

Following air-drying and powdering, 1.5 kg of the leaves were macerated with n-hexane (10 L) and methanol (7 L) sequentially in this order for 24 h. The extraction process was repeated three times and the extracts obtained were evaporated, under reduced pressure, to dryness.

General experiments

Reverse Phase (RP-18) with 40-63 μm mesh size silica gel and silica gel 60 was used in the column chromatography. Furthermore, Diaion HP-20 was also used for chromatographing. Pre-coated thin layer chromatography (TLC) plates coated with silica gel 60 F_{254} with the layer thickness of 0.25 mm (Merck) were used to monitor fractions obtained from the column chromatography, as a supplementary experiment. NMR spectroscopy was done on either 600 or 500 or 400 (MHz) machines (Agilent and Bruker Inc., California) for ^{1}H NMR, ^{13}C NMR, and 2D NMR experiments. Chemical shifts expression was noted in parts per million (δ) using tetramethylsilane (TMS) as the internal standard and *J* values (coupling constant values) measured in Hz. Infra-red spectroscopy was carried out using Fourier-transform infrared (FTIR; Perkin Elmer) spectrometer.

Isolation

Methanol (MeOH) extract of *V. grandifolia* was loaded onto Reverse Phase silica gel (RP-18) using Vacuum Layer Chromatography (VLC) for fractionation. Distilled water with increasing MeOH was used as eluting solvents. The eluates collected were concentrated on the rotary evaporator. TLC was used to monitor eluates. A total of 11 fractions were collected, and the first fraction (H_2O only) was picked for further fractionation because its TLC revealed spots that looked promising. This fraction was subjected to Diaion HP-20 Column for isolation. The column was eluted with water first, then with increasing concentration of MeOH and the eluates obtained were concentrated. About 12 fractions were obtained. The collected fractions were concentrated and monitored by TLC.

The eighth fraction was loaded into the column in CH_3Cl using 65:35:10 (CH_3Cl: MeOH: H_2O) as the eluting solvent, and six fractions were obtained. The third fraction produced compound (**3**; Figure 2), which was purified using CC in CH_3Cl with 65:35:10 (CH_3Cl: MeOH: H_2O) as the eluting solvent. Fractions 1 and 2 were combined based on their TLC profile and two compounds (**1** and **2**; Figure 2), were isolated from the first fraction of the repeated column after further purification with CC in CH_3Cl with 8:2:0.5 (CH_3Cl: MeOH: H_2O) as the eluting solvent. Confirmation of purity of compounds **1**, **2**, and **3** was achieved by observing a single spot each on the chromatogram.

Monoamine oxidase (MAO) assays

Isolates from *V. grandifolia* were assayed for MAO-A and MAO-B activity. Kynuramine deamination assay was chosen using 96-well plates, as reported previously [22]. The method used was adapted from previous studies [23, 24]. The isolated molecules did not display any meddling with fluorescence measurement. Clorgyline and deprenyl were used as positive controls for the experiment.

Anti-inflammatory test

The anti-inflammatory test was performed using mouse macrophages 915 (RAW264.7) from ATCC. Cell culture was carried out in phenol 916 red-free RPMI medium q with bovine calf serum (10%), penicillin G sodium (100 U/mL), and streptomycin (100 μg/mL) at 37 °C in CO_2 (5%) and humidity (95%). Subsequently, incubation of cells was done for one day (24 hours) after seeding in 96-well plates to obtain 5×10^4 cells/well. Then, compounds isolated were added to the cells after dilution in serum-free medium. LPS (5 μg/mL) was added after 30 minutes of incubation, and afterwards, the cells were again incubated for 24 hours. Determination of nitric oxide (NO) concentration was done by measuring the level of nitrite released in the supernatant using Griess reagent [25]. The percentage of nitrite production inhibition by the test flavonoids were calculated and compared with the vehicle control. Meanwhile, IC_{50} values were determined from the dose curves, and the positive control used was parthenolide [26, 27].

NF-kB activity

The NF-kB inhibition assay was carried out in human chondrosarcoma (SW1353) from ATCC. Culturing of cells was achieved in 1:1 mixture of DMEM/F12 together with FBS (10%), penicillin G sodium (100 U/mL), and streptomycin (100 µg/mL) at 37 °C in CO_2 (5%) and humidity (95%). Antibiotic and FBS-free DMEM/F12 were used to wash the cells (1.2×10^7 cells /60 mm dish) once, and then transferred into antibiotic-free DMEM/F12 (500 µL) that contained FBS (2.5%). This was followed by the addition of NF-κB luciferase plasmid construct to the cell suspension at a concentration of 50 µg/mL. Next, incubation was done for 5 minutes at room temperature. Electropermeabilisation of the cells was performed at 160 V and 70-ms pulse using cuvettes (BTX disposable) with model no. 640 and the 4-mm gap in a BTXI Electro Square Porator (T 820; San Diego, California). Subsequently, the cells were seeded into 96-well plates (1.25×10^5 cells/well density). After 24 hours, the cells were treated with different concentrations of the isolated molecules for 30 min before the addition of 70 ng/mL PMA and incubation for 8 hours. Determination of luciferase activity was done using the Luciferase Assay kit (Promega). Spectra-Max plate reader was used for the detection of light output. Luciferase activity (percentage inhibition) was calculated compared to the control vehicle, while the IC_{50} values were determined from the dose curves. The control transcription factor used was Sp-1 because it does not respond to inflammatory mediators (for example, PMA). This was done to allow easy detection of cytotoxic substances that non-specifically inhibit luciferase expression [27].

Results and Discussion

MAO-A and MAO-B assay

The isolates showed selective activity by inhibiting either MAO-A or MAO-B (Table 1). Isoorietin (1) and orietin (2) inhibited MAO-B with 9-fold potency (IC_{50} [µg/mL] of 11.08 and 11.04) compared to its inhibition against MAO-A (IC_{50} [µg/mL] of >100). Isovitexin (3), a flavonoid isolated from the wild vegetable for the first time displayed moderate selective activity against MAO-A (IC_{50} [µg/mL] of >100) compared to MAO-B (IC_{50} [µg/mL] of 21.3) just like the other two flavonoids. Meanwhile, clorgyline and deprenyl were used as positive standards.

Anti-inflammation

All isolated flavonoids displayed good activity against NF-Kb assay with IC_{50} (µg/mL) of 8.9, 12, and 18. Orientin (**2**) showed moderate activity against Sp-1 assay (IC_{50} of 23 µg/mL), while others displayed poor activity when compared with the positive standard (IC_{50} of 8 µg/mL), as shown in Table 2. Isovitexin (**3**) exhibited moderate activity against iNOS assay while others (isoorientin [**1**] and orientin [**2**]) displayed poor activity (IC_{50} of 48 and 54 µg/mL). The positive standard used in this study was parthenolide.

Isolated compounds

Compound 1 (Figure 1) is a yellow solid (21 mg) and its melting point ranges from 233–235 °C. ^{1}H NMR (400 MHz, DMSO-d6) d: 13.2 (1H, brs, 5-OH), 7.55 (1H, *dd*, *J* = 2.5, 9.0 Hz, 60-H), 7.45 (1H, *d*, *J* = 2.5 Hz,20-H), 6.85(1H, *d*, *J* = 9.0 Hz, 50-H), 6.63 (1H, s, 3-H), 4.7 (1H, *d*, *J* = 9.7 Hz, 100-H). ^{13}C NMR (100 MHz, DMSO-d6) d:163.24 (C-2), 102.68 (C-3), 182.32 (C-4), 160.74 (C-5), 108.88(C-6), 164.41 (C-7), 98.53 (C-8), 156.36 (C-9), 102.68 (C-10),122.24 (C-1′), 114.34 (C-2′), 146.22 (C-3′), 150.16 (C-4′),116.00 (C-5′), 119.71 (C-6′), 73.76 (C-1″), 70.13 (C-2″), 79.12(C-3″), 70.06 (C-4″), 82.35 (C-5″), 62.01 (C-6″). The molecular formula was taken as $C_{21}H_{20}O_{11}$ based on the combined data of ^{1}H NMR and ^{13}C NMR. Analyses of the NMR results coupled with comparison with available data in literature [28] enabled the determination of Compound 1 as isoorientin.

Compound 2 (Figure 2) is a yellow solid (15 mg) and its melting point ranges from 265–267 °C. ^{1}H NMR (600 MHz, DMSO-d6) d: 3.22–3.88 (6H, m, glucosyl-H), 4.69 (1H, *d*, *J* =9.9 Hz, H-1″), 6.25 (1H,s, H-6), 6.64 (1H, s, H-3), 6.86 (1H, *d*, *J* = 8.4 Hz, H-5′), 6.86(1H, *dd*, *J* = 2,8.4), 7.48 (1H, *d*, *J* = 2.0 Hz, H-2′), 7.54 (1H, *dd*, *J* = 2.0, 8.4 Hz, H-6′), 13.20 (1H, s, 5-OH). ^{13}C NMR (150 MHz, DMSO-d6) d:164.4 (C-2), 102.7 (C-3), 182.3 (C-4), 160.74 (C-5), 98.53(C-6), 163.24 (C-7), 104.91 (C-8), 156.86 (C-9), 104.28 (C-10), 122.24 (C-1′), 114.34 (C-2’), 146.22 (C-3’), 150.16 (C-4’),116.00 (C-5′), 119.71 (C-6′), 73.76 (C-1″), 71.13 (C-2″),

79.12(C-3″), 71.06 (C-4″), 82.35 (C-5″), 62.04 (C-6″). The molecular formula of the compound was determined to be $C_{21}H_{20}O_{11}$ from the combination of ^{1}H NMR and ^{13}C NMR data. Comparison of acquired NMR data with those in literature [29] lead to identification of compound 2 as orientin.

Compound 3 (Figure 2) is a yellow powder (19 mg) and its melting point ranges 219–221 °C. ^{1}H-NMR (600 MHz, DMSO-d6):δ_H: 13.55 (1H, brs, 5-OH), 7.93 (2H, *d*, *J* = 8.8 Hz, 3′, 5′ -H), 6.93 (2H, *d*, *J* = 8.4 Hz, 2′, 6′ - H), 6.78 (1H, s, 3-H), 6.51 (1H, s, 8-H), 4.55 (1H, *d*, *J* = 9.8 Hz, 1″ - H),3.11—4.03(6H, m, glucosyl H). ^{13}CNMR (150 MHz, DMSO-d6) δ_C: 164.36 (C-2), 104.25 (C-3), 182.81 (C-4), 161.52 (C-5), 109.75 (C-6), 164.17 (C7), 94.48 (C-8), 157.08 (C-9), 103.65 (C-10), 121.96 (C-1′), 129.34 (C-2′, 6′), 116.84 (C-3′, 5′), 162.04 (C-4′), 73.91 (C1″), 71.47 (C-2″), 79.80 (C-3″), 71.06 (C-4″), 82.46 (C-5″), 62.34 (C-6″). Based on acquired data from the results of ^{1}H NMR and ^{13}C NMR, molecular formula of the compound was determined to be $C_{21}H_{19}O_{10}$. NMR data analyses compared with information from literature [30, 31] enabled the identification of compound 3 to be the known flavonoid isovitexin.

Some structure-activity relationship (SAR) suggestions following the anti-inflammatory activity of the flavonoids obtained from *V. grandifolia* were made. They are as summarised: firstly, the presence of C_2=C_3 may confer the isolates anti-inflammatory effects [32]. It was reported that C_2=C_3 double bond could also contribute to the planarity of molecules [32]. This was discovered from the more significant anti-inflammatory effects displayed by diosmetin more than hesperetin (a compound without C_2=C_3 double bond) which resulted in a higher volume/ratio [32, 33]. Secondly, hydroxylation substitution (-OH) noticed at both C-3′ and 4′ tertiary increases the activity, especially at ring B moiety for isoorientin (**1**) and orientin (**2**). Wang et al. [32] reported the hydroxylation pattern and its importance in C-3′ hydroxylation [32, 33]. Thirdly, the position of the sugar moiety, glycosides, on ring A gives a better anti-inflammatory activity than on ring B and C [34].

Some SAR suggestions based on the inhibitory effects of the isolates against MAO-A and B were made. These are summarised as follows: (a) Hydroxyl group (-OH) substitution pattern noticed at C-3′ and C-4′ rises the inhibitory activity of MAO-A and B mostly, especially at ring B moiety of isoorientin (**1**) and orientin (**2**); but a decrease in activity was observed in isovitexin **(3)**. However, Spencer et al. [35] attested that both unsaturation degree of C_2=C_3 bond coupled with hydroxylation pattern on ring B moiety has a great significant role on the anti-neurodegenerative effects on flavonoids in general [35].

Structures of compounds **1–3** (Figure 2) were determined based on their 1D and 2D NMR, and also by comparing the acquired NMR results with the data in the literature [28, 29]. To the best of our knowledge, the isolates isoorientin (**1**), orientin (**2**), and isovitexin (**3**) were obtained from *V. grandifolia* for the first time. For instance, FTIR spectrum of compound 1 displayed absorption bands due to O-H (3376 cm^{-1}), C=O (1660 cm^{-1}), and C-C stretch in-aromatic ring at 1561and 1446, and also =C-H bend at 845 and 800 cm^{-1}. Proton NMR data of compound **1** showed that ring B protons, H-2′ and H-6′, generated a multiplet at 7.80 ppm. A doublet (J = 9 Hz) typical of H-5′ was present at 6.8 ppm. Signals at 6.75ppm (1H, s) and 6.25 ppm (1H, s) for H-8 and H-3 protons, were observed. Signal for anomeric proton due to C-glucosyl was present at 4.93 ppm (1H, d, J=7 Hz, H-1″). Overlapping sugar proton signals appeared at 3.5–4.8 ppm. The spectroscopic results compared well with information reported; hence, molecule (1) was inferred to be isoorientin [36, 37]. Assignments for compound 2 were completely achieved by combining the data from ^{1}HNMR, ^{13}CNMR, DEPTS, 2D-NMR (COSY, HSQC, and HMBC) experiments together with assignments published in the literature [37].

For example, data acquired from^{13} C NMR enabled the confirmation of the presence of –OH group at C-5′ and C-4′ in the compound. Another different moiety in the molecule was the anomeric carbon for glucopyranoside with a signal that appeared at 104.8 ppm, which indicated a glucose unit in orientin [36, 37, 38]. Therefore, based on the information obtained majorly from the NMR results and also that from supporting

literature, compound **2** was inferred to be the flavonoid known as orientin. Structure of compound **3** was established using data acquired from ^{1}HNMR, ^{13}CNMR, DEPTS, COSY, HSQC, and HMBC experiments, and by also comparing with data already reported for isovitexin structure [39]. For example, FTIR results for compound **3** indicated absorptions for OH, C=O, C=C, C-C (in-aromatic ring), and C-O at 3440 cm^{-1}, 1660 cm^{-1}, 1620 cm^{-1}, 1523 cm^{-1}, and 1017 cm^{-1} respectively. Data from ^{1}H NMR experiment for compound 3 showed signals at 6–8 ppm for flavonoid aromatic protons. There exist the resonances for the sugar moiety at 3.5-4.7 ppm. Also, the anomeric proton's signal was available at 4.88 ppm. From the mentioned spectroscopic data, which compared well with the data in the literature, compound **3** was concluded to be isovitexin.

Concoctions and extracts of medicinal plants are still the backbones of primary health care management requirements in many developing nations. According to World Health Organisation (WHO), about 80% of people over the world depends on the herbs for their day-to-day health management due to various biologic effects present in the plants [40, 41]. Therefore, it is paramount to scientifically assess the plants for possible validation of the reason for their use in age-old medicine and to acquire phytocompounds with pharmacologic effects. According to previous reports [42], most of these medicinal plants contain flavonoids, and some of these flavonoids were isolated from plants source that exhibited MAO inhibitory effects [42]. For instance, Zarmouh et al. [42] reported the selective MAO-B inhibition of some compounds from the seeds extract of *Psoraleacory lifolia*. Another study revealed that human recombinant MAO-B and MAO-A iso-enzymes were employed for the inhibition of the enzymes (MAO-B and MAO-A). The authors of that study discovered that out of the three compounds studied, only two (bavachinin and genistein) showed selective inhibition of MAO-B significantly. It was due to a significant reduction of H_2O_2 by the compounds that were produced by MAO-B compared to MAO-A [42, 43]. Monoamine oxidase inhibitors (MAOIs) differ by the MAO receptor selection; some inhibit MAO-A and MAO-B in the same manner, while others only target one type [44]. These studies corroborate with our work that some flavonoids from natural sources can selectively inhibit the MAO-B.

Table 1. IC_{50} Values of isolated compounds as MAO-A&B inhibitory agents

SN	Sample Name	MAO-A (IC_{50})	MAO-B (IC_{50})
1	Isoorientin (1)	>100	11.08
2	Orientin (2)	>100	11.04
3	Isovitexin (3)	>100	21.3
4	Clorgyline	1.6	NT
5	Deprenyl	NT	0.48

Table 2. IC_{50} Values of Isolated Compounds as Anti-inflammatory Agents

SN	Test Compounds	NF-kB	SP-1	iNOS	% cell death at 100 µg/mL
1	Isoorientin (1)	8.9	63	48	63.89
2	Orientin (2)	12	23	54	
3	Isovitexin (3)	18	41	21	
4	Parthenolide	0.9	6.5	0.18	
5	Parthenolide	0.6	8	0.15	

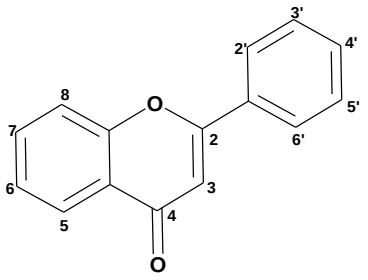


Figure 1. Nucleus of flavonoids

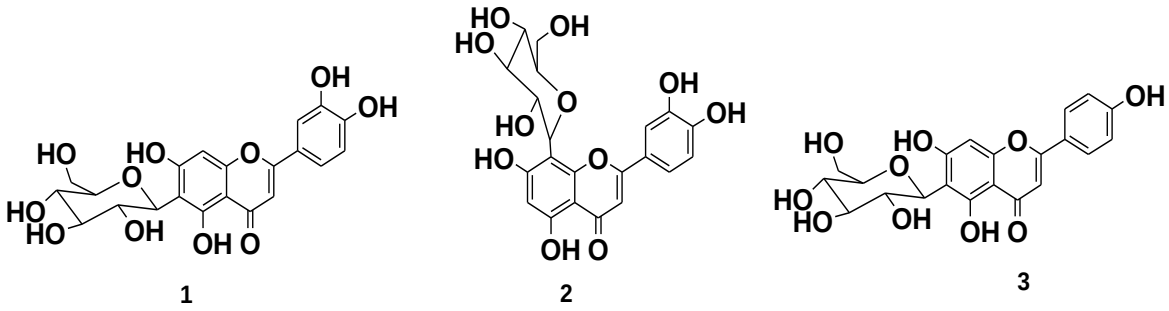


Figure 2. Isolated flavonoids from *V. grandifolia*

Conclusion

The need to assess medicinal plants for its biological properties, especially its MAO inhibitory effects, is increasing attention due to the regular use of plants as vegetable. The constituents of medicinal plants help to treat neurological disorders due to the likely association with medicines and a diet rich in dietary monoamines. The present study found that isolated flavonoids from *V. grandifolia* moderately inhibit MAO-B, and this outcome may be of significance for improved use of this wild vegetable in traditional neuropharmacological use. The use of *V. grandifolia* as vegetable is widely accepted despite being tagged as "poor man's" food. This study hopes to recognise its pivotal role as a source for the development of nutraceutical products. Prior to this work, there was no report on the inhibition of MAO-A and B by constituents of this plant with their anti-inflammatory activity.

Acknowledgement

We wish to thank Federal University Dutsin-Ma for finding us worthy of nomination for sponsorship to the National Tertiary Institution (TETFUND) sponsorship. Many thanks go TETFUND for its Sponsorship.

References

1. Ames B. N., Shigenaga, M. K. and Hagen, T. M. (1993). Oxidants, antioxidants and degenerative diseases of aging. *Proceeding National Academy Science,* 90: 7915-7922.
2. Shih, J. C., Chen, K. and Ridd, M. J. (1999). Monoamine oxidase: From genes to behaviour. *Annual Review Neuroscience*, 22:197-217.
3. Salah, N., Miller, N. J., Paganga, G., Tijburg, L., Bolwell, G. P. and Rice-Evans, C. (1995). Polyphenolic flavanols as scavengers of aqueous phase radicals and as chain breaking antioxidants. *Archives of Biochemistry and Biophysics,* 322: 339-346.
4. Yuh-Hwa, L., Wen-Chun, W., Yeh-Lin, L., Ying-Jang, L. and Wen-Chi, H. (2010). Antioxidant and amine oxidase inhibitory activities of *Hydroxyurea*. *Bioscience, Biotechnology, and Biochemistry*, 74(6):1256-1260.
5. Silverman, R. B., Ding, C.Z. and Gates, K. S. (1993). Design and meachanism of monoamine oxidase inactivators from an organic chemical perspective. In: Testa, B., Kyburz, E., Fuhrer, W., Giger, R. (Eds.), Perspectives in Medicinal Chemistry. Verlag Helvetica ChomicaActa. Basel, Weinheim, New York: pp. 73-86.
6. Kumazawa, T., Minatogawa., Matsuba, S. and Sato, J. I. (2000). An effective synthesis of isoorientin: the regioselective synthesis of a 6-C-glucosylflavone. *Carbohydrate Research*, 329: 507.
7. Abell, C.W. and Kwan, S.W. (2009). Molecular characterization of monoamine oxidase A and B. *Progress in Nucleic Acid Research and Molecular Biology,* 65:129-156.
8. Vina, J., Sastre, J., Pallardo, F. and Borras, C. (2003). Mitochondrial theory of aging: Importance to explain why females live longer than males. *Antioxidant and Redox Signalling,* 5: 549-556.
9. Bratkov V. M., Shkondrov A. M., Zdraveva P. K. and Krasteva, I. N. (2016). Flavonoids from the genus *Astragalus*: Phytochemistry and biological activity. *Pharmacognosy Review,* 10: 11-32.
10. Yadav P. and Malpathak N. (2016). Estimation of antioxidant activity and total phenol, flavonoid content among natural populations of caper (*Capparismoonii*, Wight) from Western Ghats region. *Indian Journal of Pharmaceutical Education Research*, 50: 495-501.
11. Oliveira F. G., de Lima-Saraiva S. R., Oliveira A. P., Rabêlo S. V., Rolim L. A. and Almeida, J. R. (2016). Influence of the extractive method on the recovery of phenolic compounds in different parts of *Hymenaeamartiana* Hayne. *Pharmacognosy Research*, 8:270-275.
12. El-gizawy H. A. and Hussein, M. A. (2017). Isolation, structure elucidation of ferulic and coumaric acids from *Fortunella japonica*s wingle leaves and their structure antioxidant activity relationship. *Free Radical Antioxidant*. 7: 23-30.
13. Venkatesan, A., Kathirvel, A., Prakash, S. and Sujatha, V. (2017). Antioxidant, antibacterial activities and identification of bioactive compounds from *Terminalia chebula* bark extracts. *Free Radical Antioxidant*, 7: 43-49.
14. Dutta, S. and Das, S. (2010). A study of the anti-inflammatory effect of the leaves of *Psidiumguajava* Linn. on experimental animal models. *Pharmacognosy Research,* 2: 313-317.
15. Middleton E, Jr, Kandaswami, C. and Theoharides T. C. (2000). The effects of plant flavonoids on mammalian cells: Implications for inflammation, heart disease, and cancer. *Pharmacology Review*, 52: 673-751.
16. Havsteen, B. H. (2002). The biochemistry and medical significance of the flavonoids. *Pharmacology and Therapeutics*, 96: 67-202.
17. Fiala. E. S., Reddy, B. S. and Weisburger, J. H. (1985). Naturally occurring anticarcinogenic substances in foodstuffs. *Annual Review of Nutrition*, 5:291-321.
18. Tapsell, L.C., I. Hemphill, L., Cobiac, C. S. P. and Sullivan, D. R. (2006). Health benefits of herbs and spices: The past, the present, the future. *Medical Journal Australia*, 185: S4-S24.

19. Triggiani, V., Resta, F., Guastamacchia, E., Sabba, C., Licchelli, B., Ghiyasaldin, S. and Tafaro, E. (2006). Role of antioxidants, essential fatty acids, carnitine, vitamins, phytochemicals and trace elements in the treatment of diabetes mellitus and its chronic complications. *Drug Targets,* 6: 77-93.
20. Epidi, T.T. and Odili, E.O. (2009). Biocidal activity of selected plant powders against *T. castaneum* (Herbst).in stored groundnut (*Arachishypogaea L.*). *African Journal Environment Science Technology*, 3: 1-5.
21. Burkill, H. M. (1995). The useful plants of West Tropical Africa. 2nd edition. Families J-L. Royal Botanic Gardens, 3: pp. 857.
22. Samoylenko, V., Rahman, M. M., Tekwani, B. L., Tripathi, L. M., Wang, Y. H., Khan, S. I., Khan, I. A., and Muhammad, I. (2010). *Banisteriopsiscaapi*, a unique combination of MAO inhibitory and antioxidative constituents for the activities relevant to neurodegenerative disorders and Parkinson's disease. *Journal of Ethnopharmacology*, 127: 357-369.
23. Narayan D. Chaurasiya, Mohamed A. Ibrahim, Ilias Muhammad, Larry, A. W. and Babu, L.T. (2014). Monoamine oxidase inhibitory constituents of propolis: kinetics and mechanism of inhibition of recombinant human MAO-A and MAO-B. *Molecules*, 19: 18936-18952.
24. Bankova, V., Popova, M. and Trusheva, B. (2014). Propolis volatile compounds: Chemical diversity and biological activity: A review. *Chemistry Central Journal,* 8: 28.
25. Quang, D. N., Harinantenaina, L., Nishizawa, T., Hashimoto, T., Kohchi, C., Soma, G. and Asakawa, Y. (2006). Inhibition of nitric oxide production in RAW 264.7 cells by azaphilones from Xylariaceous fungi. *Biology Pharmaceutical Bulletin*, 29: 34-37.
26. Zhao, J., Khan, S. I. and Wang, M. (2014). Octulosonic acid derivatives from Roman chamomile (*Chamaemelumnobile*) with activities against inflammation and metabolic disorder. *Journal Natural Production*, 77: 509-515.
27. Al-Taweel, A. M., El-Shafae, A. M., Perveen, S., Fawzy, G. A. and Khan, S. I. (2015). Anti-inflammatory and cytotoxic constituents of *Bauhinia retusa*. *International Journal of Pharmaceutical,* 11:372-376.
28. Li, Y., Ma, S., Yang, Y., Ye. S. and But, P. P. (2002). Antiviral activity of flavonoids and organic acid from *Trollius chinensis* Bunge. *Journal of Ethnopharmacology*, 79(3): 365-368.
29. Song, D. M. and Sun, Q. S. (2004). Chemical studies on constituents of *Trollius altaicus* CA Mey. *Medical Chemistry,*14: 233-235.
30. Ju, Y., J. N. and Sacalis, C. C. S. (1998). Bioactive flavonoids from endophyte-infected blue grass (Poaampla). *Journal of Agriculture Food Chemistry*, 46: 3785.
31. Cheng, G., Bai, Y., Zhao, Y., Tao, J., Liu, Y., Tu, G., Ma, L., Liao, N. and Xu, X. (2000). Flavonoids from *Ziziphusjujuba* Mill var. spinose. *Tetrahedron*, 56: 8915.
32. Wang, T., Li, Q. and Bi, K. (2018). Bioactive flavonoids in medicinal plants: Structure activity and biological fate. *Asian Journal of Pharmaceutical Sciences*, 13(1): 12-23.
33. Celik, H. and Kosar, M. (2012). Inhibitory effects of dietary flavonoids on purified hepatic NADH-cytochrome b5 reductase: structure-activity relationships. *Chemico-Biological Interaction,* 197(2–3): 103- 109.
34. Isoda H, Motojima H, Onaga S, Samet I, Villareal, M. O. and Han, J. (2014). Analysis of the erythroid differentiation effect of 574 flavonoid apigenin on K562 human chronic leukemia cells. *Chemico-Biological Interactions*, 575: 269-277.
35. Spencer, J. P., Vafeiadou K., Williams, R. J. and Vauzour, D. (2012). Neuroinflammation: modulation by 635 flavonoids and mechanisms of action. *Molecular Aspects of Medicine*, 33(1): 83-97.
36. Xin, Z., Jinyong, P., Guorong, F. and Yutian, W. (2015). Isolation and purification of flavonoid glycosides from *Trolliusledebouri* using high-speed counter-current chromatography by stepwise increasing the flow-rate of the mobile phase. *Journal of Chromatography A,* 1092: 216-221.

37. Sharma, K. K., Sharma, A. K., Sharma M. C. and Tanwar K. (2014). Isolation of orientin (51) and vitexin from stem bark of *parkinsoniaaculeata* (caesalpiniaceae) and their successive blending on sheep wool fiber. *International Journal of Pharmaceutical and Phytochemical Research*, 6(3): 557-561.
38. Jinfeng, Y. A., Yong, S. K. B. and Myong Jo, K. (2015). Isolation and characterization of bioactive compounds from *Lepisorus thunbergianus* (Kaulf.) *Arabian Journal of Chemistry*, 8: 407-413.
39. Peng, J., Fan, G., Hong, Z., Chai, Y. and Wu, Y. (2005). Preparative separation of isovitexin and isoorientin from *Patriniavillosa*Juss by high-speed counter-current chromatography. *Journal of Chromatography A*, 1074: 111-115.
40. Endo Y, Hayashi,H, Sato T, Maruno M, Ohta, T. and Nozoe, S. (1994). Confluentic acid and 2′-O-methylperlatolic acid, monoamine oxidase B inhibitors in a Brazilian plant, Himatanthussucuuba. *Chemical Pharmaceutical Bulletin,* 42: 1198-1201.
41. Lin R. D., Hou W. C., K.Y. Yen, and Lee, M. H. (2003). Inhibition of monoamine oxidase B (MAO-B) by Chinese herbal medicines. *Phytomedicine*, 10: 650-656.
42. Zarmouh, O. N., Mazzio, A. E., Elshami, M. F., Messaha, S. S., Eyunmi, V. K. S. and Soliman, F. A. K. (2015). Evaluation of inhibitory effects of bavachinin and bavachin on human monoamine oxidases A and B. *Evidence-Based Complementary and Alternative Medicine*, 2015: 14.
43. Lee, M., Lin, R., Shen, L., Yang, L., Yen, K. and Hou, W. (2001). Monoamine oxidase B and free radical scavenging activities of natural flavonoids in *Melastoma candidum* D. Don. *Journal Agriculture Food Chemistry*, 49(11): 5551-5555.
44. Ficarra, R., Ficarra, P., Tommasini, S., Carulli, M., Melardi, S., Di Bella, M. R., Calabro, M. L. and Casuscelli, F. (1997). Isolation and characterization of *Guierasenegalensis* J. F. Gmel. active principles. *Bollettino Chimico Farmaceutico*, 136: 454-459.

Malaysian Journal of Analytical Sciences (MJAS)
Published by Malaysian Analytical Sciences Society

ROLE OF VANADIA AND TITANIA PHASES IN THE REMOVAL OF METHYLENE BLUE BY ADSORPTION AND PHOTOCATALYTIC DEGRADATION

(Peranan Fasa Vanadia dan Titania dalam Penyingkiran Metilena Biru Melalui Penjerapan dan Degradasi Fotokatalisis)

Pei Wen Koh[1,2], Cheng Yee Leong[2], Leny Yuliati[2,3], Hadi Nur[2], Siew Ling Lee[2]*

[1]*Department of Chemistry, Faculty of Science*
[2]*Centre for Sustainable Nanomaterials, Ibnu Sina Institute for Scientific and Industrial Research*
Universiti Teknologi Malaysia, 81300 Johor Bahru, Malaysia
[3]*Ma Chung Center for Photosynthetic Pigments,*
Universitas Ma Chung, Malang 65151, Indonesia

**Corresponding author: sllee@ibnusina.utm.my*

Received: 18 July 2019; Accepted: 20 July 2020; Published: 10 December 2020

Abstract

Total removal of methylene blue (MB) over vanadia (V_2O_5) -modified titania (TiO_2) composite demonstrated that the V_2O_5 and TiO_2 phases played a vital role in the adsorption and photodegradation of MB, respectively. The 10 mol% of V_2O_5- modified TiO_2 (10V-TiO_2) showed the highest removal of MB, i.e., 26- and 2-folds better adsorption capacity than that of undoped TiO_2 and V_2O_5, respectively. The presence of surface hydroxyl, pores, and the highest amount of V^{5+} species in 10V-TiO_2 could be responsible for the high adsorption of MB. V_2O_5 induced anatase to rutile phase transformation and shifted absorption properties of TiO_2 to the visible light region. Considering the rutile phase has lower bandgap energy (3.0 eV), its presence in the sample has enhanced the photodegradation of MB. The photodegradation of MB followed pseudo-second-order reaction. The reusability test elucidated that the photodegradation performance of 10V-TiO_2 was improved by 30-folds after the second cycle, with total MB removal due to the exposure of more TiO_2 to MB.

Keywords: vanadia, titania, methylene blue, adsorption, photocatalyst, photodegradation

Abstrak

Penyingkiran metilena biru (MB) secara keseluruhan oleh komposit titania (TiO_2) yang diubahsuai dengan vanadia (V_2O_5) menunjukkan bahawa fasa V_2O_5 dan TiO_2 masing-masing memainkan peranan penting dalam penjerapan dan fotodegradasi MB. TiO_2 yang diubahsuai dengan 10 mol% V_2O_5 (10V-TiO_2) menunjukkan penyingkiran MB yang tertinggi, iaitu 26- dan 2-kali ganda kapasiti penjerapan yang lebih baik daripada TiO_2 dan V_2O_5 yang tidak didopkan. Kewujudan hidrosil di permukaan, liang, dan jumlah spesis V^{5+} tertinggi dalam 10V-TiO_2 menyumbang kepada penjerapan MB yang tinggi. V_2O_5 mendorong transformasi fasa anatase ke rutil dan sifat-sifat penyerapan TiO_2 beralih ke rantau cahaya nampak. Memandangkan fasa rutil mempunyai tenaga jurang jalur yang lebih rendah (3.0 eV), kewujudannya dalam sampel telah meningkatkan prestasi fotodegradasi MB. Fotodegradasi MB mengikuti tindak balas tertib pseudo-kedua. Ujian kebolehgunaan tersebut membuktikan bahawa prestasi

fotodegradasi 10V-TiO_2 telah ditingkatkan sebanyak 30-kali ganda selepas kitaran kedua kerana lebih banyak TiO_2 terdedah kepada MB.

Kata kunci: vanadia, titania, metilena biru, penjerapan, fotokatalis, fotodegradasi

Introduction

Soil and water contamination by dye-containing effluents are serious environmental issues. The release of these coloured compounds into the drainage system has significantly impacted human and aquatic lives due to their toxicity. Although many technologies have been developed to treat dye-containing effluent at an acceptable level before drainage, there is no single process capable of adequately treating these dye-containing wastewaters. It was suggested that a combination of different techniques would be a better solution to remove the dyes [1, 2]. Compared to the conventional biological physicochemical method, it is undeniable that adsorption is a superior method established for the removal of dye due to its simplicity in design, efficiency, and ability to treat dye in larger quantities [3]. A good adsorbent should have high selectivity and adsorption capacity for the targeted adsorbate. However, in many cases, surface modification using an expensive surfactant, chemical, or heat treatment is always applied to solve the limitations of the surface functional group of adsorbents [4]. Another shortcoming of the adsorption method is associated with the formation of secondary pollution following the adsorption process. Photocatalysis appears to be a promising green technology approach to address this problem compared to conventional treatments such as flocculation, coagulation, and adsorption, which often result in secondary pollution [5, 6]. Photocatalysis is capable of fully mineralising toxic dye to non-toxic anionic compounds. However, its usage is only applicable to trace amount of dye-containing wastewater.

Among many semiconductor photocatalysts, titanium dioxide (TiO_2) has gained considerable attention due to its high activity, high light-illumination stability, non-toxic properties, and low price [7]. However, its low surface area has limited its adsorption and photocatalytic degradation efficiency under ultraviolet (UV) light. Recently, comprehensive review and studies on the effectiveness of incorporating TiO_2 on porous adsorbents had been reported [8-10]. The catalytic performance of TiO_2 can be improved by loading TiO_2 onto various supporting adsorbents. Other drawbacks of TiO_2 photocatalyst include high recombination rate of the electron-hole, high bandgap energy, and inactivity under visible light that affected its application under sunlight. A standard method used to solve the problems above is the modification of TiO_2 via transition metal doping. Transition metal doping appears to be one of the most effective approaches to reduce the rate of electrons and holes recombination [1, 11-13]. Visible light-driven vanadia-doped titania photocatalysts in pure anatase phase have been reported [14, 15]. Their enhanced photocatalytic behaviour was attributed to the highly dispersed vanadia in the TiO_2 crystallite, which successfully reduced the bandgap energy and increased the ability to absorb visible light.

Nguyen et al. reported that 10% vanadia-doped TiO_2 (V-TiO_2) is an excellent adsorbent for decolourisation of methylene blue (MB) [16]. This material possessed anatase and a negligible percentage of brookite phases. It was claimed that the good interaction between vanadia-doped TiO_2 and the dye molecules as well as the increased oxidation states of Ti, V, and O have contributed to the excellent adsorption ability of the material, resulting in the removal of 91.6% MB after 2 hours reaction time [16]. The usage of V-TiO_2 as a photocatalyst has been widely reported. In the current study, we present new insight into the role of the respective vanadia and titania in the V-TiO_2 composite through adsorption and photocatalysis of MB. MB was selected as a model reaction because it is widely used for dyeing in many industries such as silk, paper, ink and used as cotton mordant with tannin [2].

Materials and Methods

Materials

The materials used for this study include titanium tetraisopropoxide (TTIP; 97%, Aldrich), absolute ethanol (99.98%, HmBG), acetylacetone (≥ 99%, Aldrich), and vanadyl acetylacetonate (98%, Aldrich).

Synthesis of vanadia modified titania

Vanadia-modified titania (V-TiO_2) materials were prepared through the sol-gel method. The experimental procedures were reported in previous studies [2, 17]. In a typical synthesis, titanium tetraisopropoxide (TTIP; 97%, Aldrich) was mixed with absolute ethanol (99.98%, HmBG) and acetylacetone (≥ 99%, Aldrich) according to the molar ratio of 1:100:2. The mixture was then stirred for 60 min at room temperature. Vanadia precursor was prepared separately by dissolving a pre-calculated amount of vanadyl acetylacetonate (98%, Aldrich) in acetylacetone. The two solutions were mixed and stirred for 30 minutes at room temperature, followed by evaporation at 353 K. The obtained solid material was calcined at 773 K for 5 hours. The molar ratio of vanadia in TiO_2 was varied from 1 to 10 mol%. The resulted materials were denoted as xV-TiO_2, where x represents mol% of V. Undoped TiO_2 was prepared with the same procedures without the addition of vanadyl acetylacetonate for comparison. Bulk V_2O_5 was prepared by evaporating vanadyl acetylacetonate (98%, Aldrich) in acetylacetone at 273 K, followed by calcination at 773 K for 5 hours.

Characterisation

Phase purity and crystallinity of the synthesised undoped TiO_2, vanadium oxide-modified titania, and bulk V_2O_5 samples were examined using Powder X-ray diffraction (XRD) analyser. The XRD measurements were conducted on Bruker Advance D8 X-ray diffractometer with Cu Kα radiation (λ = 0.15418 nm, 40 KV, 40 mA, scan rate 0.1˚/s). The Diffuse reflectance UV-visible (DR UV-Vis) spectra were recorded on Perkin Elmer Ultraviolet-visible Spectrometer Lambda 900 with $BaSO_4$ as reference. Bandgap energy of the samples was calculated from the extrapolation of the Tauc plot. Surface morphology of the prepared samples was investigated using Field Emission Scanning Electron Microscopy (FESEM). The samples were coated with platinum using Auto Fine Coater (JEOL JFC-1600), prior to analysis using a FESEM instrument (JSM-6701F). The surface area and pore size distribution of the samples were confirmed using Brunauer-Emmett-Teller (BET) and Barrett-Joyner-Halenda (BJH) equations from adsorption-desorption isotherms at 77 K obtained by using 3Flex Surface Characterisation Analyser (Micromeritics). Before analysis, all the samples were degassed at 573 K for 4 hours. Temperature programmed reduction (TPR) was conducted to investigate the reducible species of surface vanadia on TiO_2. Selected samples were analysed in the temperature range of 573–973 K on Micromeritics AutoChem II 2920 chemisorption analyser. Prior to measurement, the samples were pre-treated under N_2 gas flowing at 473 K for 15 minutes. Argon gas, which contained 5.1% H_2, was passed through the sample tube during measurement with the flow rate of 25 cm^3/min. Zeta potential of the samples was recorded on Malvern Zetasizer Nano ZSP.

Adsorption and photocatalytic degradation

Adsorption and photocatalytic testing were carried out on all synthesised materials. Aqueous solution of 50 mL 100 ppm MB solution and 0.1 g of the prepared material were placed in a beaker. Adsorption test was conducted prior to photocatalytic evaluation. The mixture was stirred in the dark at a constant temperature for 24 hours for the determination of adsorption capacity. Aliquots of 2 mL were withdrawn at different times within 24 hours and were put through a syringe filter. For the photocatalytic activity evaluation, the sample and MB solution were irradiated by a halogen fibre optic light illuminator (Dolan-Jenner MI 157, 150 W) as the visible light source for 24 hours, straight after the adsorption test of 24 hours. A UV cut-off filter (400 nm, Edmund Optics) was used to filter the UV light. The photocatalytic activity of the samples was assessed using UV-Vis spectrophotometer (Thermo Fisher, Genesys 10S) to measure the concentration of MB solution before and after the photodegradation. Adsorption and photocatalytic activities of undoped TiO_2 and bulk V_2O_5 were also included for comparison.

Results and Discussion

Phases formation

As evidenced by XRD analysis (Figure 1), the undoped TiO_2 was in pure anatase phase, as its XRD pattern was well-matched with that reported in JCPDS 21-1272. The anatase phase remained after doping of 1 mol% V in 1V-TiO_2, but the peak becomes slightly broader. The crystallite sizes of the samples were calculated using the Scherrer equation, and the results are shown in Table 1. The crystallite size decreased with an increasing amount of V oxide modifier, suggesting the addition V oxide inhibited the crystal growth of TiO_2. As observed, the rutile phase was detected when 2 mol% and above of V oxide was added into TiO_2, indicating the presence of an adequate amount of V has induced transformation of anatase to rutile phase. It was documented that due to the similar ionic radii of V^{4+} (0.580 Å) and V^{5+}(0.540 Å) to that of Ti^{4+} (0.605 Å) [18], making substitution of Ti by V at substitutional position possible. Therefore, it resulted in rutile phase formation [19]. The result was in good agreement with the previous study, which stated that the formation of the rutile phase upon V doping [20]. The detection of rutile phase was a good indication of successful V incorporated in the TiO_2 lattice, even though peaks assigned to V oxides were not detected in all the V-doped TiO_2 samples.

The undetectable V peaks could be attributed to a little amount of the V dopant (at low concentration of V dopant), or the dopant was highly dispersed on the TiO_2 surface. Alternatively, the undetectable vanadia peak was ascribed to amorphous nature of vanadia [21]. XRD pattern of the bulk V_2O_5 was in agreement with the reported pattern (JCPDS 01-0359), indicating it crystallised in orthorhombic structure. The current study indicated that the vanadium oxide present in the current sample was crystalline, not amorphous.

The percentage of anatase phase in the synthesized V-doped TiO_2 samples was calculated using the Spurr equation [22]:

$$A\ (\%) = 100 / (1+1.265\ I_R/I_A) \quad (1)$$

where I_R is intensity of rutile peak at $2\theta = 27.5°$ (110) and I_A is intensity of anatase peak at $2\theta = 25.5°$ (101). The percentage of rutile phase was obtained via subtraction of 100% on the calculated anatase percentage, assuming that the materials were totally crystallised.

Table 1 lists the anatase and rutile percentages in the synthesised samples. It was found that the percentage of rutile phase was independent to the amount of V dopant and remained constant in the range of 20.0% to 23.6%. The anatase to rutile transformation can be explained in terms of the valency state of the ion. Every four doping of V^{5+} in the Ti^{4+} octahedral cationic site led to one Ti^{4+} cation vacancy, which promotes the rutile phase formation. However, as the V amount increased, the accommodation of excess cation vacancy seems unfavourable in the anatase structure [23]. Hence, further addition of V oxide modifier did not promote more anatase-rutile transformation.

Optical properties

The prepared TiO_2 was a white powdered material, while the bulk V_2O_5 was an orange powder. All the V-TiO_2 samples were brownish. The colour of the V-TiO_2 samples was more intense, with the increase of the V content. A similar observation was reported previously [15]. As depicted in Figure 2, the undoped TiO_2 has absorption bands in the UV region ranged from 200-400 nm. The dominant peak found at 330 nm was identified as octahedral Ti species, while the shoulder at 230 nm was associated with tetrahedral coordinated Ti species [24]. Redshifts and new peaks of absorption within a range of 400-800 nm was observed after the modification with V oxides. In the resulting products, the extension in the absorption spectrum was demonstrated by the colour changes. The tailing of absorption curves revealed that all the V-TiO_2 materials absorbed the photon energy in the visible light region ranged 380-780 nm. The broadened peaks at 570 and 770 nm were due to V^{5+} and V^{4+}, respectively [25]. As can be seen, the intensity of the V^{5+} absorption peak increased with the increase of V content in the samples. The 10V-TiO_2 sample possessed the highest amount of V^{5+}, followed by 4V-TiO_2, 3V-TiO_2, 2V-TiO_2, and 1V-TiO_2. For bulk V_2O_5, the presence of a shoulder at 242 nm and two peaks at 380 and 480 nm were due to transitions in ligand-metal charge transfer (LMCT)

involving the charge transfer from oxygen ligands to the V^{5+} metal cation [26].

The bandgap energy of the samples was calculated from the Tauc plot. The following equation was used: $\alpha h\nu = A(h\nu - E_g)^{n/2}$, where α, h$\nu$, A, E_g are absorption coefficient, photon energy, a constant, and an optical bandgap, respectively. In this equation, n is determined by the transition type; n value is 1 and 4, for direct and indirect bandgap transitions. The value of n and E_g were first determined by plotting the graph $\ln(\alpha h\nu)$ vs. $\ln(h\nu - E_g)$, using an appropriate value of E_g. The value of n was determined from the slope of the straight line near the band edge. After that, $(\alpha h\nu)^{2/n}$ vs. hν was formed, and a tangential line was plotted along the band edge, with the tangent line *x*-intercept corresponding to the optical bandgap. The obtained results are tabulated in Table 1. The findings showed that the bandgap energy of TiO_2 (3.25 eV) dropped significantly after doping of 1 mol% V into TiO_2 (2.15 eV). The bandgap energy of TiO_2 was further decreased with increasing of V amount. It was believed that the 3d orbital of vanadia had reduced the bandgap energy of TiO_2. The lowest bandgap energy of 1.50 eV was achieved in 10V-TiO_2.

Morphology

FESEM images of undoped TiO_2 and selected V-TiO_2 samples are illustrated in Figure 3. Undoped TiO_2 (Figure 3(a)) appeared to be large blocks of coarse material. The addition of 1 mol% V dopant also displayed similar features to undoped TiO_2, but with the formation of more small particles on the large material. Also, holes are formed between the particles, as shown in Figure 3(b).

Sample 4V-TiO_2 showed more small particles agglomerated with reduced holes between the small particles on the surface of the larger particle course. The surface of 10V-TiO_2 sample was smoother and more homogeneous, with small spherical particles agglomerated on the surface of TiO_2. The current results revealed that the addition of V oxide modifier could alter the morphology of undoped TiO_2 powder to be smoother. The FESEM images of V-TiO_2 supported the XRD results whereby the addition of excess V dopants (> 2 mol%) was not favourable in the anatase structure and could have resided on the surface of TiO_2 to form V_2O_5.

Textural analysis

The nitrogen adsorption-desorption isotherms of samples are presented in Figure 4. All synthesised samples possessed type IV isotherm, which is the characteristic of a mesoporous material. From the isotherm curve, it was observed that undoped TiO_2, 1V-TiO_2, and 2V-TiO_2 have H3 hysteresis loops, indicating the samples have slit-shaped pores. As the amount of V dopant increased, the hysteresis loops changed from H3 to H2 for samples 3V-TiO_2 and 4V-TiO_2, indicating these samples have bottleneck shape pore. Meanwhile, 10V-TiO_2 has hysteresis loop of H1, denoting the pore shape was cylinder-shaped. It was observed that the closing of the hysteresis loop of samples 1 to 4 mol% V-TiO_2 was approximately at 0.45 P/P_o, while the closing loop of 10V-TiO_2 was at 0.75 P/P_o. The results suggested that former samples had smaller mesopores while the latter sample had larger mesopores. In addition, 10V-TiO_2 possessed macropores since it showed a slight increase in adsorption in 0.95–1.00 P/P_o.

The specific surface area, total pore volume, and average pore diameter of samples are tabulated in Table 2. The increasing amount of V oxide modifier increased the surface area of TiO_2 by 2-fold from 17 to 34 $m^2\ g^{-1}$. The increase of the surface area could be ascribed to the presence of V, which inhibited the crystalline growth, leading to an enlarged surface area. However, the addition of 10 mol% V reduced the surface area to 23 $m^2\ g^{-1}$. This was due to the excess modifier covering the surface of TiO_2, as demonstrated by Figure 3(d). It is evident from Figure 3(d) that the surface of 10V-TiO_2 had been covered up by the modifier compared to Figure 3(a), which depicts the TiO_2 without a modifier.

Addition of 1 to 3 mol% V has a negligible effect on the total pore volume. The increase of pore volume for 4V-TiO_2 and 10V-TiO_2 samples was in agreement with the changing of the hysteresis loop, whereby the hysteresis loop H2 of 4V-TiO_2 was larger as compared to 3V-TiO_2 sample. Meanwhile, 10V-TiO_2 has the most significant total pore volume among the samples because it

possessed macropores as evidenced by the isotherm plot.

The BJH pore size distribution is shown in Figure 5. The pore size was tuneable with the addition of V oxide modifier. The pore size distribution of samples with less than 4 mol% V became more homogenous and shifted to smaller pore size.

The current result is supported by the FESEM images where the pores between particles (textural) were reduced. The average pore diameter of 10V-TiO_2 was the largest among the samples. Figure 5 shows that 10V-TiO_2 has pores larger than 50 nm, confirming that this sample consisted of a mixture of meso and macropores, leading to the largest average pore diameter.

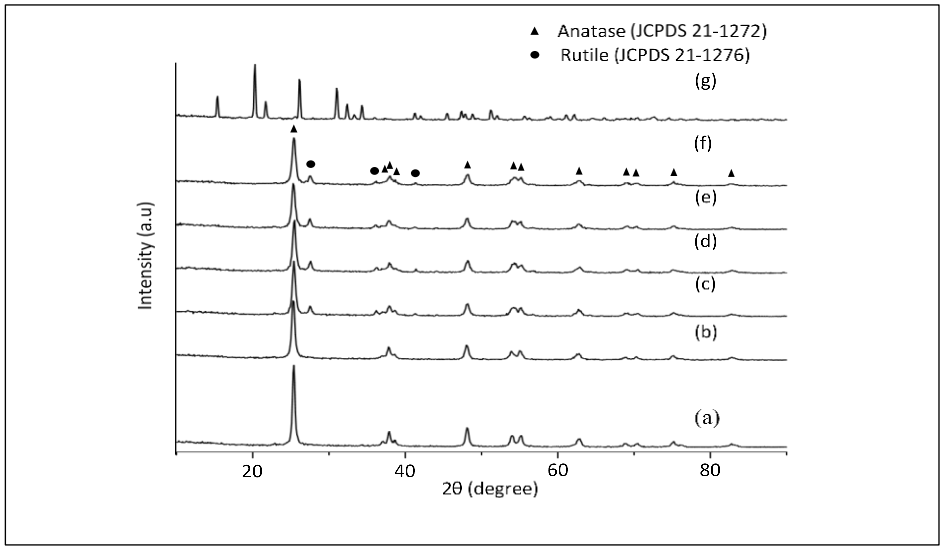


Figure 1. XRD patterns of (a) TiO_2, (b) 1V-TiO_2, (c) 2V-TiO_2, (d) 3V-TiO_2, (e) 4V-TiO_2, (f) 10V-TiO_2, and (g) V_2O_5

Table 1. Phases composition, crystallite size and bandgap energy of TiO_2, V_2O_5 and V-TiO_2 samples

Sample	Anatase (%)[a]	Rutile (%)[b]	Crystallite size (nm)	Bandgap (eV)[c]
TiO_2	100.0	n.a.	20.1	3.25
1V-TiO_2	100.0	n.a.	16.2	2.75
2V-TiO_2	80.0	20.0	16.5	2.00
3V-TiO_2	77.4	22.6	14.7	1.95
4V-TiO_2	76.4	23.6	14.8	1.80
10V-TiO_2	78.2	21.8	14.5	1.50
V_2O_5	n.a	n.a	n.a	2.30

[a] Calculated from Spurr equation, [b] Calculated from 100%- anatase phase%, [c] Calculated from extrapolation of Tauc plot and n.a. – not available

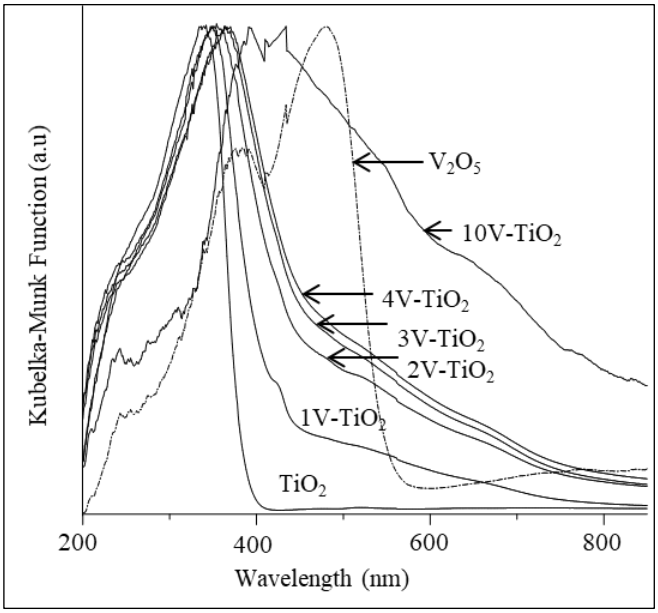


Figure 2. DR-UV-Vis spectra of TiO_2, V_2O_5, and V-doped TiO_2 samples

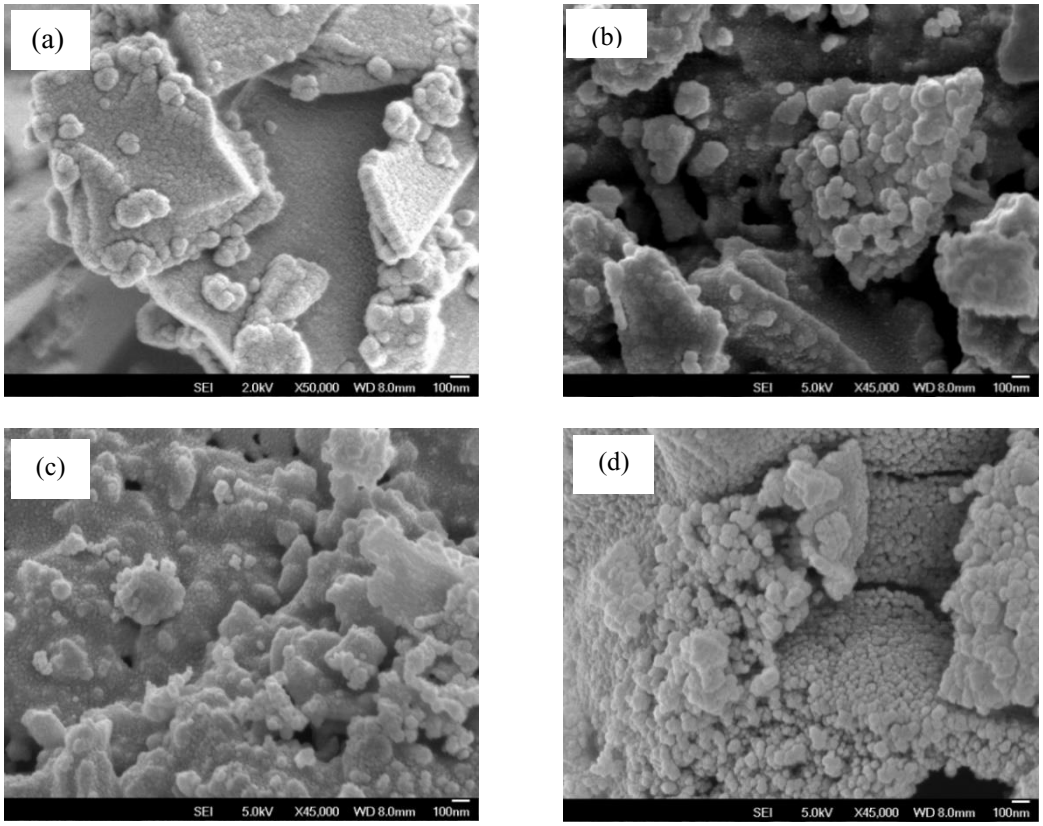


Figure 3. FESEM images of (a) TiO_2 (magnification ×50,000), (b) 1V-TiO_2 (magnification ×45,000), (c) 4V-TiO_2 (magnification ×45,000), and (d) 10V-TiO_2 (magnification ×45,000)

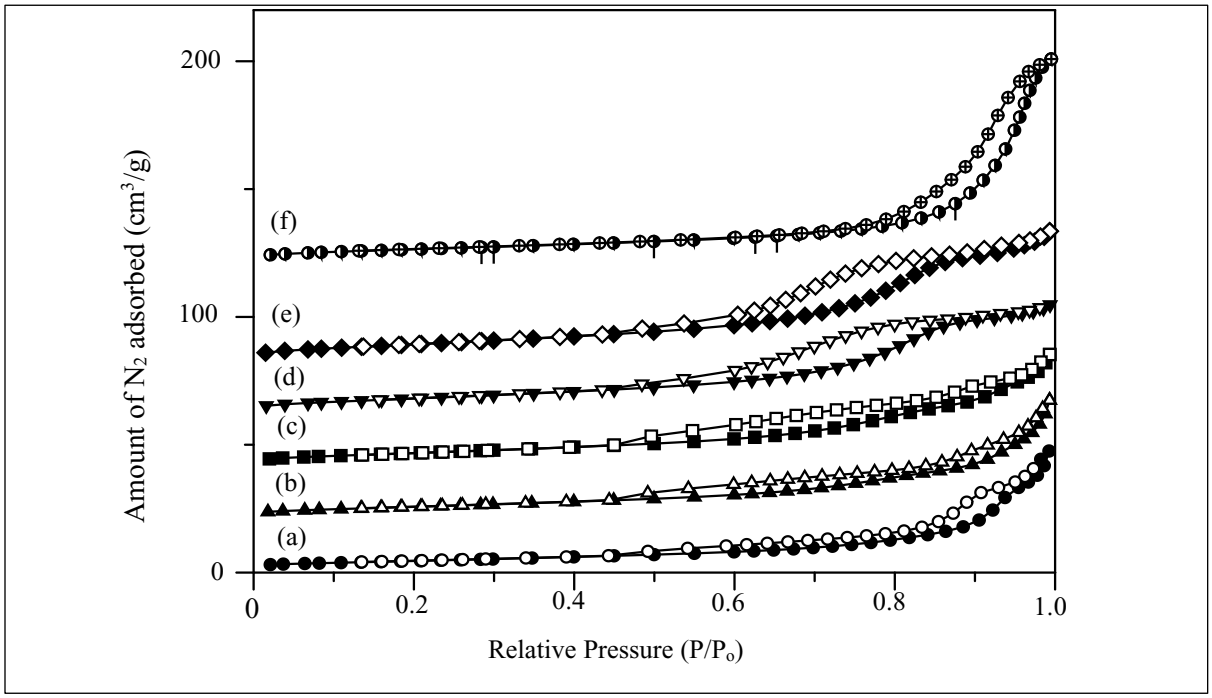


Figure 4. N_2 adsorption-desorption isotherms of (a) TiO_2, (b) 1V-TiO_2, (c) 2V-TiO_2, (d) 3V-TiO_2, (e) 4V-TiO_2, and (f) 10V-TiO_2. (Remarks: filled points are adsorption isotherms, empty points are desorption isotherms. Figures (b)–(f) are marginally moved upwards for 20, 40, 60, 80, and 120 cm^3/g, respectively for clearer presentation).

Table 2. Surface area, total pore volume and average pore diameter of TiO_2 and V-TiO_2 samples

Sample	**Surface Area ($m^2\ g^{-1}$)**	**Total Pore Volume ($cm^3\ g^{-1}$)**	**Average Pore Diameter (Å)**
TiO_2	17	0.0677	164.27
1V-TiO_2	21	0.0659	125.94
2V-TiO_2	25	0.0649	105.38
3V-TiO_2	29	0.0660	90.12
4V-TiO_2	34	0.0794	94.78
10V-TiO_2	23	0.1218	212.00

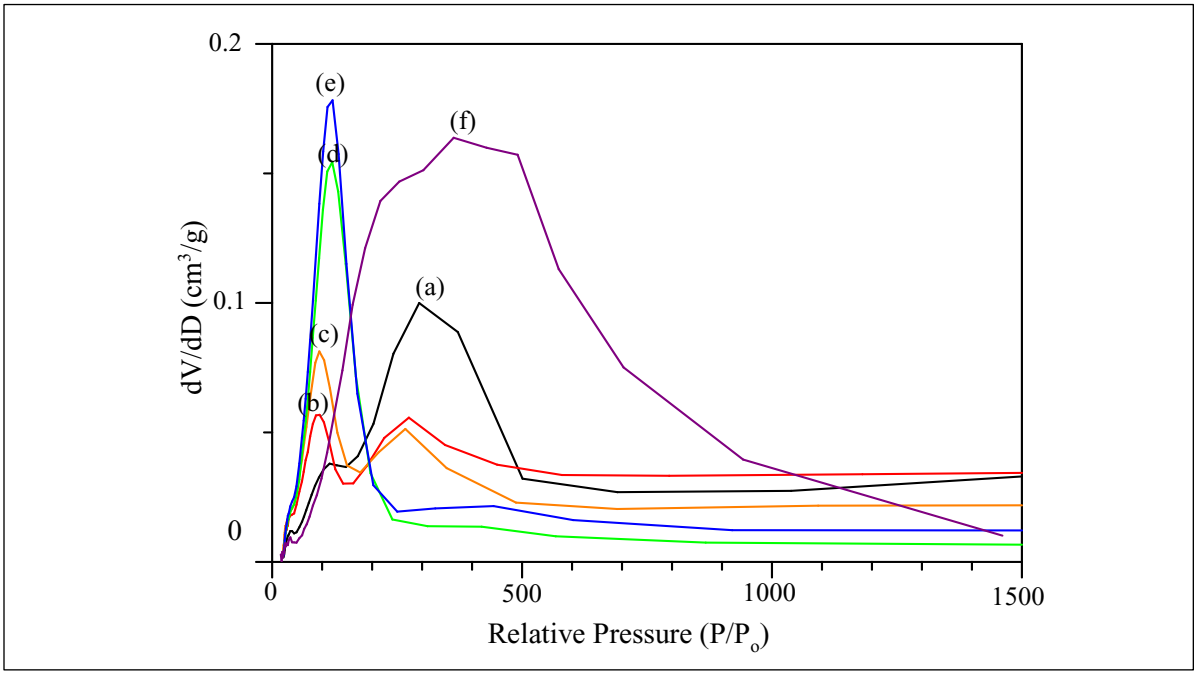


Figure 5. BJH pore size distributions of (a) TiO_2, (b) 1V-TiO_2, (c) 2V-TiO_2, (d) 3V-TiO_2, (e) 4V-TiO_2, and (f) 10V-TiO_2

Surface oxidation state analysis

Temperature program reduction (TPR) was performed on selected samples to analyse vanadium surface oxidation states in the samples. H_2-TPR spectra of V-TiO_2 samples and V_2O_5 are shown in Figure 6. The 1 mol% V gave only one reduction peak at 814.3 K, which corresponded to the reduction of V_6O_{13} to V_2O_4 [27], indicating that V^{4+} existed dominantly in 1V-TiO_2. The higher amount of V oxide modifier (4 mol%) resulted in a lower reduction peak at 647.4 K in 4V-TiO_2. This peak was associated with the reduction of V_2O_5 to V_6O_{13} [27]; hence, it was a good indication of V^{5+} species existence. The detection of this peak is always linked to the formation of the strong interaction between V species and the H_2 gas due to V-O-Ti bonds of higher reducibility. Besides, a hump at 765.1 K was also observed in 4V-TiO_2, implying the presence of trace V^{4+} species.

Similarly, 10V-TiO_2 exhibited two reduction peaks at 684.5 and 841.3 K. Figure 6 shows that the intensity of the reduction peak at 684.5 K is remarkably higher than that of 4V-TiO_2, strongly indicating the existence of more V^{5+} in 10V-TiO_2 compared to the latter sample. The maximum reduction temperature and the corresponded hydrogen consumption of each sample are tabulated in Table 3. As observed, the amount of V^{5+} in the 10V-TiO_2 was 5-fold of that in 4V-TiO_2. The bulk V_2O_5 showed only one reduction peak at 867.6 K, which corresponded to bulk vanadate. It was reported that more bulk vanadate was formed with increasing of vanadia content in vanadia-titania catalyst [27].

The contradiction could be due to different synthetic method and calcination temperature applied in the studies. The authors had synthesised vanadia-titania via the impregnation method at 673 K. Unlike the impregnation method, the sol-gel method applied in the current work was believed to enable the loading of vanadia not only on the TiO_2's surface but also in the

TiO_2 lattice. Meanwhile, the higher calcination temperature of 773 K had resulted in more interaction between vanadia and TiO_2 that facilitated the formation of more reducible V^{5+} species in the materials [28]. In the present work, the decrease of reduction temperature in V_2O_5 in the presence of TiO_2 can be explained by the structure distortion in V_2O_5 due to the extensive interaction with the TiO_2 support. A similar phenomenon was found for 12-molybdophosphoric acid supported on V_2O_5 dispersed γ-Al_2O_3 catalyst [29]. Therefore, we conclude that the presence of TiO_2 phase is essential as support for V^{5+} species formation.

Adsorption and photocatalytic performance

Adsorption and photocatalytic activity of the resulting V-TiO_2 samples were assessed over decolourisation of MB. As illustrated in Figure 7, the adsorption of MB on undoped TiO_2 is only 3% after 24 hours. Doping of 1 mol% V into TiO_2 allows 1V-TiO_2 to adsorb 9% MB after 2 hours. The increased V dopant amount of 2, 3, 4, and 10 mol% V had further enhanced the MB adsorption to 18%, 25%, 31%, and 68% after 2 hours. The adsorption of MB increased significantly by the increasing amount of V in V-TiO_2. The results demonstrated that the adsorption capacity of 10V-TiO_2 was 26-folds higher than that of undoped TiO_2. This material adsorbed 95% MB after 24 hours, confirming it was an excellent adsorbent for MB.

Zeta potential was conducted to analyse the surface charge of the samples. It was found that the increased amount of V oxide modifier to 10 mol% decreases the isoelectric point (IEP) continuously from 4.23 to 2.01 (Table 3). This could be the reason for the tremendous increase of MB adsorption, a cationic dye, up to 68% after 2 hours when TiO_2 was modified with 10 mol% V oxide. In addition, MB has a high affinity for V^{5+} [30]. This further enhanced the adsorption capacity of MB on 10V-TiO_2, which possessed the highest amount of V^{5+} among the samples. Comparatively, the adsorption ability of the bulk V_2O_5 was poorer as it adsorbed only 40% of MB after 2 hours. The lower activity of bulk V_2O_5 could be attributed to its massive structure which makes the accessibility of MB on V^{5+} more difficult. Besides, the superior adsorption capability of 10V-TiO_2 as compared to bulk V_2O_5 could be due to the existence of more surface OH^- in 10V-TiO_2 to interact with the π-electron of MB [16, 31].

The photocatalytic activity evaluation was carried out straight after the adsorption test with the samples. Figure 7 displays that the undoped TiO_2 gave an activity of 14.4% of MB photodegradation even with the utilisation of UV cut-off filter (400 nm, Edmund Optics). This can be rationalised by the photosensitisation effect [32]. Usage of MB as a model reaction in photocatalysis has been highlighted by Ohtani and co-worker [33]. The authors claimed that MB was not an acceptable pollutant for the target study, particularly when it was degraded under visible light. However, Matos et al. [34] argued that the decolourisation of MB is suitable for assessing the photocatalytic behaviour of semiconductors under steady-state conditions of the effect of photon flux upon the first-order rate constant.

Among the V-TiO_2 samples, only the 4V-TiO_2 sample has photodegraded 13.5% of MB after 24 hours under visible light irradiation. The other V-TiO_2 samples have negligible photocatalytic activity under visible light irradiation. In contrast, it had been documented that photocatalytic activity TiO_2 in dye degradation was significantly enhanced after V doping [35]. The photocatalytic improvement was always associated with the extended optical absorption of TiO_2 to the visible light, reduction in bandgap energy and the presence of anatase/rutile mixing phase. In the present study, the MB molecules were preferably adsorbed at the V site due to the high affinity of V^{5+}. The strong interaction between V^{5+} and the MB molecules was believed to hinder the diffusion of the dye molecules to the active site for photodegradation at Ti; hence, retard the photocatalytic activity of the V-doped TiO_2 samples. In 4V-TiO_2, only limited MB molecules that adsorbed at Ti site would be further photodegraded after irradiated under visible light. The schematic diagram showing roles of the vanadia and titania phases in the dye removal is illustrated in Figure 8.

Even though the photocatalytic activity of the V-TiO_2 was not comparable to its adsorption ability, the total removal of MB of V-TiO_2 significantly increased as compared to TiO_2 and V_2O_5. As mentioned, the

photocatalytic enhancement of TiO_2 was always related to the extension of optical absorption to the visible light region. By comparing the adsorption and photocatalytic testing of V-TiO_2 samples to the XRD results as represented in Figure 1 and Table 1, it can be seen that part of the anatase to rutile phase transformation induced by the doping of V into TiO_2 might have enhanced the photodegradation of MB to visible light region, attributed by the lower bandgap energy (3.0 eV) of the rutile phase as compared to the anatase phase (3.2 eV). It is suggested in this study that the vanadia and titania played a different role in the adsorption-photocatalytic activity. The vanadia responsible for the anatase to rutile phase transformation as well as the shifting of the absorption properties of TiO_2 to visible light region, and at the same time, acted as an adsorbent, while the titania acted as the photocatalyst, responsible for the photodegradation activity.

Reusability test

Since 10V-TiO_2 has the highest removal of MB, it was chosen for the reusability test. The used 10V-TiO_2 was washed with distilled water several times and dried at 333 K. The reusability test was conducted for four successive cycles under the same conditions. It was found out that the adsorption capacity of the used-10V-TiO_2 decreased significantly to 28%, 26%, and 27% for second, third, and fourth cycles, respectively. The decrease of the adsorption capacity could be attributed to the leaching problem of vanadium oxide from the material. It was believed that the loss of the vanadium oxide could have decreased the hydroxyl surface group and hence leading to less adsorption of MB [36]. It was noted that after the adsorption for the first cycle, the adsorption for the rest of the cycles was almost constant, indicating that the material has become stable. It is worth to highlight that the photocatalytic performance of 10V-TiO_2 increased to approximately 30% for the second, third, and fourth cycles (Figure 9). The improvement in photocatalytic performance could be attributed to more TiO_2 were exposed to MB, leading to a more significant degradation of MB. The study indicated that 10V-TiO_2 was a good photocatalyst for MB photodegradation after second cycles onwards.

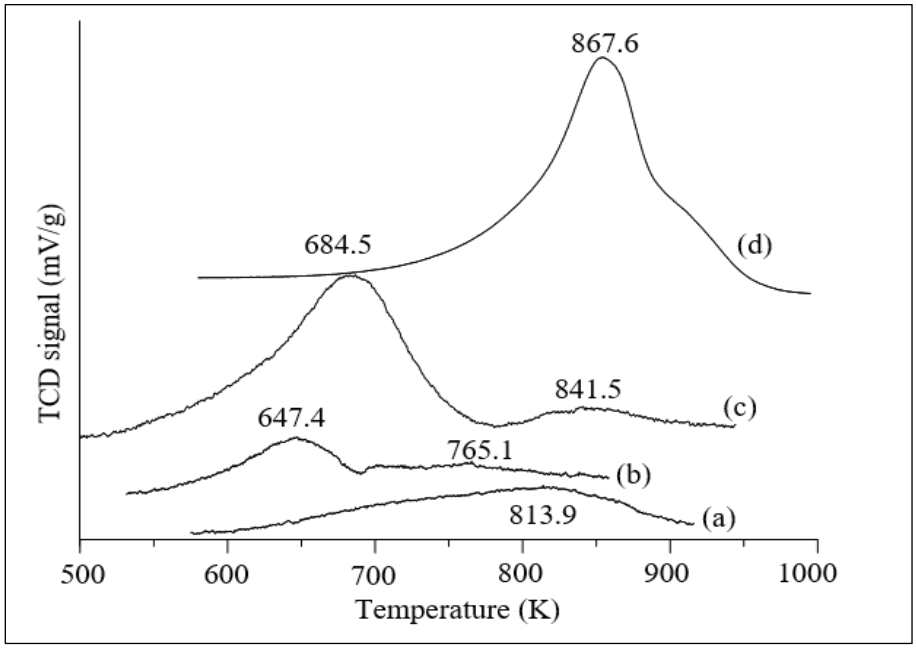


Figure 6. TPR profiles of (a)1V-TiO_2, (b) 4V-TiO_2, (c) 10V-TiO_2, (d) V_2O_5 (Intensity of V_2O_5 is multiplied with 0.1)

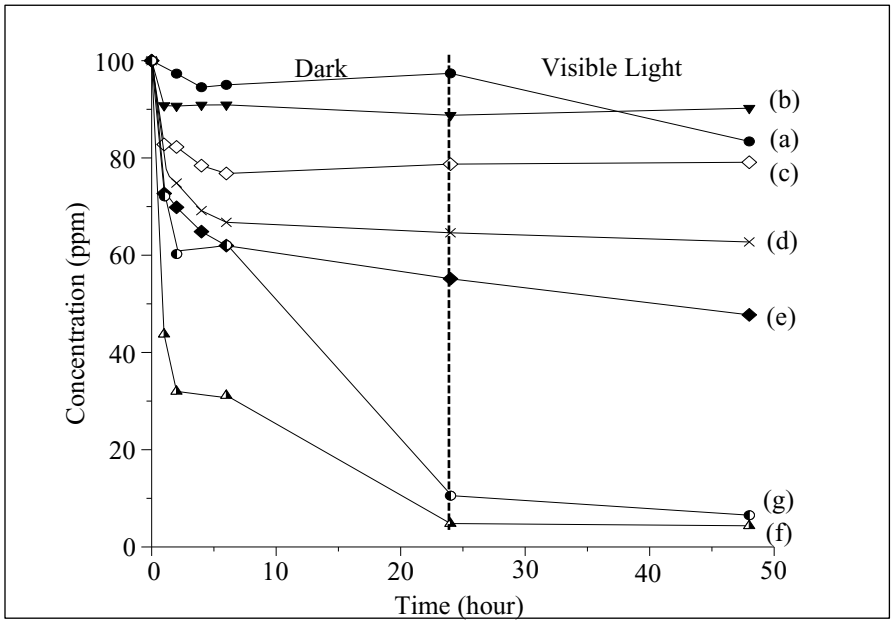


Figure 7. The adsorption and photodegradation of MB using (a) TiO_2, (b) 1V-TiO_2, (c) 2V-TiO_2, (d) 3V-TiO_2, (e) 4V-TiO_2, (f) 10V-TiO_2, (g) V_2O_5

Table 3. Isoelectric point of prepared samples and its corresponded adsorption efficiency after 2 hours

Entry	Sample	IEP/pH	Adsorption Efficiency After 2 hours /%
1	TiO_2	4.23	3
2	1V-TiO_2	4.14	9
3	2V-TiO_2	4.13	18
4	3V-TiO_2	4.12	25
5	4V-TiO_2	2.22	31
6	10V-TiO_2	2.01	68

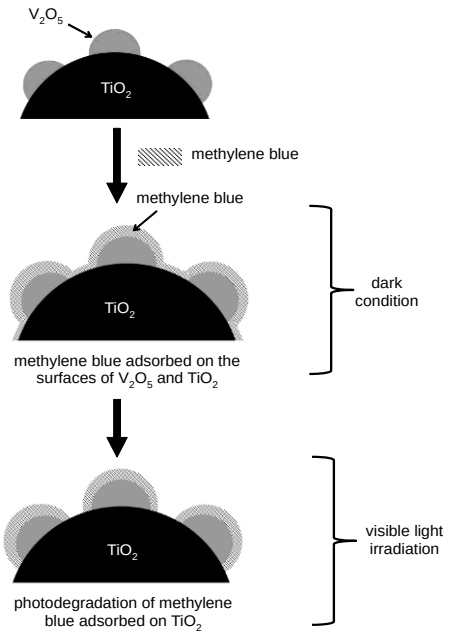


Figure 8. Schematic diagram showing the roles of vanadia and titania

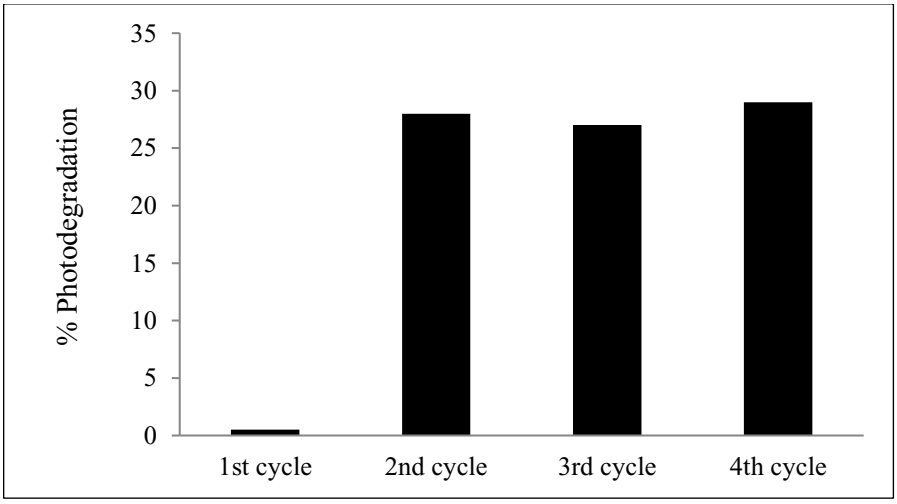


Figure 9. Reusability test of 10V-TiO_2. (Conditions: concentration of MB = 100 ppm, mass of sample used = 0.1 g)

Conclusion

A series of V modified TiO_2 was successfully synthesised *via* the sol-gel method. Roles of vanadia and titania phases in the removal of MB were examined. The results demonstrated that the presence of vanadia phase was responsible for the rutile phase generation, bandgap reduction, and wavelength extension in the V-TiO_2 samples. On the other hand, the titania phase played a crucial role as support for the formation of more V^{5+} species. In the V oxide modified TiO_2 materials, vanadia phase was an excellent adsorbent attributed to the presence of V^{5+} species is abundant, which has a high

affinity towards MB. Meanwhile, the titania phase acted as the photocatalyst in degrading MB. 10V-TiO_2 showed high photostability and reusability in photodegrading MB in second cycles and onward, attributed to more exposed of TiO_2 to MB.

Acknowledgement

Authors are grateful to financial support from Ministry of Higher Education Malaysia (MOHE) and Universiti Teknologi Malaysia through UTM Transdisciplinary Research Grant (Cost Centre No. Q.J130000.3554.07G57) and Professional Development Research University (Cost Centre No. Q.J.130000.21A2.03E61).

References

1. Koh, P. W., Yuliati, L. and Lee, S. L. (2019). Kinetics and optimization studies of photocatalytic degradation of methylene blue over Cr-doped TiO_2 using response surface methodology. *Iranian Journal of Science and Technology, Transactions A: Science,* 43(1): 95-103.
2. Koh, P. W., Hatta, M. H. M., Ong, S. T., Yuliati, L. and Lee, S. L. (2017). Photocatalytic degradation of photosensitizing and non-photosensitizing dyes over chromium doped titania photocatalysts under visible light. *Journal of Photochemistry and Photobiology A: Chemistry*, 332: 215-223.
3. Kumar, P. S., Ramalingam, S. and Sathishkumar, K. (2011). Removal of methylene blue dye from aqueous solution by activated carbon prepared from cashew nut shell as a new low-cost adsorbent. *Korean Journal of Chemical Engineering,* 28(1): 149-155.
4. Roosta, M., Ghaedi, M., Daneshfar, A., Sahraei, R. and Asghari, A. (2014). Optimization of the ultrasonic assisted removal of methylene blue by gold nanoparticles loaded on activated carbon using experimental design methodology. *Ultrasonics Sonochemistry*, 21(1): 242-252.
5. Keng, P. S., Lee, S. L., Ha, S. T., Hung, Y. T. and Ong, S. T. (2013). Cheap materials to clean heavy metal polluted waters. In Green Materials for Energy, Products and Depollution Springer, Dordrecht: pp. 335-414.
6. Leong, C.Y., Koh, P.W., Lo, Y.S., Lee, S.L. (2020). Hydrothermal synthesis of titanium dioxide nanotube with methylamine for photodegradation of Congo red. *IOP Conf. Series: Materials Science and Engineering*, 833, 012075.
7. Pirkanniemi, K. and Sillanpää, M. (2002). Heterogeneous water phase catalysis as an environmental application: a review *Chemosphere,* 48(10): 1047-1060.
8. MiarAlipour, S., Friedmann, D., Scott, J. and Amal, R. (2018). TiO_2/porous adsorbents: Recent advances and novel applications. *Journal of Hazardous Materials,* 341: 404-423.
9. Ooi, Y. K., Hussin, F., Yuliati, L. and Lee, S. L. (2019). Comparison study on molybdena-titania supported on TUD-1 and TUD-C synthesized via sol-gel templating method: Properties and catalytic performance in olefins epoxidation. *Materials Research Express,* 6(7): 074001.
10. Ooi, Y. K., Yuliati, L., Hartanto, D., Nur, H. and Lee, S. L. (2016). Mesostructured TUD-C supported molybdena doped titania as high selective oxidative catalyst for olefins epoxidation at ambient condition. *Microporous and Mesoporous Materials,* 225: 411-420.
11. Wang, N., Zhu, L. H., Li, J., and Tang, H. Q. (2007). A novel $Fe(OH)_3/TiO_2$ nanoparticles and its high photocatalytic activity. *Chinese Chemical Letters*, 18(10): 1261-1264.
12. Hamdan, H., Muhid, M. N. M., Lee, S. L., and Tan, Y. Y. (2009). Visible light enabled V and Cr doped titania-silica aerogel photocatalyst. *International Journal of Chemical Reactor Engineering*, 7(1).
13. Ooi, Y. K., Yuliati, L., and Lee, S. L. (2016). Phenol photocatalytic degradation over mesoporous TUD-1-supported chromium oxide-doped titania photocatalyst. *Chinese Journal of Catalysis*, 37(11): 1871-1881.
14. Wu, J. C. S. and Chen, C. H. (2004). A visible-light response vanadium-doped titania nanocatalyst by sol–gel method. *Journal of Photochemistry and Photobiology A: Chemistry*, 163(3): 509-515.

15. Li, H., Zhao, G., Chen, Z., Han, G. and Song, B. (2010). Low temperature synthesis of visible light-driven vanadium doped titania photocatalyst. *Journal of Colloid and Interface Science,* 344(2): 247-250.
16. Nguyen, T. B., Hwang, M. J., and Ryu, K. S. (2012). High adsorption capacity of V-doped TiO_2 for decolorization of methylene blue. *Applied Surface Science,* 258(19): 7299-7305.
17. Koh, P. W., Yuliati, L., and Lee, S. L. (2014). Effect of transition metal oxide doping (Cr, Co, V) in the photocatalytic activity of TiO_2 for congo red degradation under visible light. *Jurnal Teknologi (Sciences & Engineering)*, 69(5): 45-50.
18. Shannon, R. D. (1976). Revised effective ionic radii and systematic studies of interatomic distances in halides and chalcogenides. *Acta Crystallographica Section A: Crystal Physics, Diffraction, Theoretical and General Crystallography,* 32(5): 751-767.
19. Choi, J., Park, H. and Hoffmann, M. R. (2009). Effects of single metal-ion doping on the visible-light photoreactivity of TiO_2. *The Journal of Physical Chemistry C,* 114(2): 783-792.
20. Martin, S. T., Morrison, C. L., and Hoffmann, M. R. (1994). Photochemical mechanism of size-quantized vanadium-doped TiO_2 particles. *The Journal of Physical Chemistry,* 98(51): 13695-13704.
21. Pena, D. A., Uphade, B. S., and Smirniotis, P. G. (2004). TiO_2-supported metal oxide catalysts for low-temperature selective catalytic reduction of NO with NH_3: I. Evaluation and characterization of first row transition metals. *Journal of Catalysis,* 221(2), 421-431.
22. Spurr, R. A. and Myers, H. (1957). Quantitative analysis of anatase-rutile mixtures with an X-ray diffractometer. *Analytical Chemistry,* 29(5): 760-762.
23. Nagaveni, K., Hegde, M. S. and Madras, G. (2004). Structure and photocatalytic activity of $Ti_{1-x}M_xO_{2\pm\delta}$ (M= W, V, Ce, Zr, Fe, and Cu) synthesized by solution combustion method. *The Journal of Physical Chemistry B*, 108(52): 20204-20212.
24. Astorino, E., John, B. Peri, R. J. Willey, and Guido B. (1995). Spectroscopic characterization of silicalite-1 and titanium silicalite-1. *Journal of Catalysis,* 157(2): 482-500.
25. Bhattacharyya, K., Varma, S., Tripathi, A. K., Bharadwaj, S. R., and Tyagi, A. K. (2008). Effect of vanadia doping and its oxidation state on the photocatalytic activity of TiO_2 for gas-phase oxidation of ethene. *The Journal of Physical Chemistry C*, 112(48): 19102-19112.
26. Lewandowska, A. E., Banares, M. A., Khabibulin, D. F. and Lapina, O. B. (2009). Precursor effect on the molecular structure, reactivity, and stability of alumina-supported vanadia. *The Journal of Physical Chemistry C*, 113(48): 20648-20656.
27. Shekar, S. C., Soni, K., Bunkar, R., Sharma, M., Singh, B., Suryanarayana, M. V. S., and Vijayaraghavan, R. (2011). Vapor phase catalytic degradation of bis (2-chloroethyl) ether on supported vanadia–titania catalyst. *Applied Catalysis B: Environmental,* 103(1-2): 11-20.
28. Olthof, B., Khodakov, A., Bell, A. T. and Iglesia, E. (2000). Effects of support composition and pretreatment conditions on the structure of vanadia dispersed on SiO_2, Al_2O_3, TiO_2, ZrO_2, and HfO_2. *The Journal of Physical Chemistry B*, 104(7): 1516-1528.
29. Rao, P. S. N., Rao, K. T. V., Prasad, P. S. S. and Lingaiah, N. (2011). The role of vanadia for the selective oxidation of benzyl alcohol over heteropolymolybdate supported on alumina. *Chinese Journal of Catalysis,* 32(11-12): 1719-1726.
30. Zhao, L., Zhu, X., Feng, K., and Wang, B. (2006). Speciation analysis of inorganic vanadium (V(IV)/V (V)) by graphite furnace atomic absorption spectrometry following ion-exchange separation. *International Journal of Environmental and Analytical Chemistry*, 86(12): 931-939.
31. Dong, Y., Liu, Y., Lu, D., Zheng, F., Fang, P. and Zhang, H. (2017). Unpredictable adsorption and visible light induced decolorization of nano rutile for the treatment of crystal violet. *Solid State Sciences,* 66: 1-6.

32. Yu, L., Yuan, S., Shi, L., Zhao, Y. and Fang, J. (2010). Synthesis of Cu^{2+} doped mesoporous titania and investigation of its photocatalytic ability under visible light. *Microporous and Mesoporous Materials,* 134(1-3): 108-114.
33. Yan, X., Ohno, T., Nishijima, K., Abe, R. and Ohtani, B. (2006). Is methylene blue an appropriate substrate for a photocatalytic activity test? A study with visible-light responsive titania. *Chemical Physics Letters*, 429(4-6): 606-610.
34. Matos, J., Hofman, M. and Pietrzak, R. (2013). Synergy effect in the photocatalytic degradation of methylene blue on a suspended mixture of TiO_2 and N-containing carbons. *Carbon,* 54: 460-471.
35. Nair, R. G., Roy, J. K., Samdarshi, S. K. and Mukherjee, A. K. (2012). Mixed phase V doped titania shows high photoactivity for disinfection of *Escherichia coli* and detoxification of phenol. *Solar Energy Materials and Solar Cells,* 105: 103-108.
36. Wu, H-X, Wang, T-J, Chen, L., Jin, Y., Zhang, Y. and Dou, X-M. (2009). The roles of the surface charge and hydroxyl group on a Fe−Al−Ce adsorbent in fluoride adsorption. *Industrial & Engineering Chemistry Research*, 48(9): 4530-4534.